Bioconjugate Chemistry

Editorial

pubs.acs.org/bc

EDITORIAL: Thanks to Our Reviewers

It is a pleasure to acknowledge the contributions of the reviewers of manuscripts submitted in 2011 for publication in *Bioconjugate Chemistry*. Their unselfish service has been essential in the shaping of the 22nd volume of the journal. The scientific community is fortunate that its members are willing to share their time and specialized knowledge in this way. The reviewers are as follows:

Hinrich Abken
Seetharama A. Acharya
Samuel Achilefu
Zbigniew Adamczyk
Sita Aggarwal
Kazunari Akiyoshi
Courtney C. Aldrich
Cameron Alexander
Matthw J. Allen
Stephen Charles Alley
Joakim Andreasson
David Andreu
Kristi Anseth
Christophe Antczak
John Antos
Yasushi Arano
Steve James Archibald
Tomohiro Asai
Hiroyuki Asanuma
Shoichiro Asayama
Debra T. Auguste
Younsoo Bae
James R. Baker
Rajkumar Banerjee
Zoltan Banoczi
Ande Bao
Gillian Barratt
Philippe Barthelemy
Amit Basu
Serge L. Beaucage
Christian F.W. Becker
Annette G. Beck-Sickinger
Ambros Beer
Martin Behe
Jean-Paul Behr
Romain Bejot
Kevin D. Belfield
Dennis Benjamin
Mikhail Y. Berezin
Catherine Cecilia Berry
Santanu Bhattacharya
Gary Bignami
Claire Billotey
Ruth Birner-Gruenberger
Matthias Bochtler
Eric T. Boder
Kelly Boeneman
Otto Boerman
Alexei A. Bogdanov
Elijah Bolotin
Charles Andrew Boswell
Claudie Bourgaux
Mark Bradley
Martin W. Brechbiel
Steve Brocchini
Marcel P. Bruchez
Josh Bryson
Donald J. Buchsbaum
Peter Buchwald
Ambika Bumb
Kevin Burgess
Patrick J. Burke
Fabienne Burlina
James C. Burnett
Christopher W. Cairo
Paolo Caliceti
Peter Caravan
Carol E. Cass
David G. Castner
Vaclav Cerovsky
Chien-Hsing Ken Chang
Ravi J.V. Chari
Arabinda Chaudhuri
Xiaoyuan Chen
Xuesi Chen
Jianjun Cheng
Zhen Cheng
Sing Yian Chew
Satish K. Chitneni
Chong-Su Cho
Arvind Chopra
Shantanu Chowdhury
Peter L. Choyke
Francisco Ciruela
Michael Peter Coogan
Paul Cordopatis
Eain Cornford
Blaise Mathias Costa
Patrick Couvreur
James A. Cowan
Thomas Ashton Cropp
Gabriella Csik
Ekaterina Dadachova
Maxime Dahan
Margitta E.A. Dathe
Mark E. Davis
Thomas P. Davis
Philip E. Dawson
Rafael T.M. De Rosales
Giuseppe De Rosa
Salvatore De Rosa
Alexander Deiters
Robert Kevin Delong
Attila Demeter
Sapna K. Deo
Mahendra Deonarain
Jason E. Derouchey
Joseph M. Desimone
Scott L. Diamond
Erin B. Dickerson
Ulf Diederichsen
Chikara Dohno
Svetlana O. Doronina
Franco Dosio
Norman J. Dovichi
Cynthia Dowd
David T.F. Dryden
Gene Michael Dubowchik
Jutta Eichler
Mohamed E. H. El-Sayed
Joern Engelmann
Hans Erickson
Ramon Eritja
Clive Evans
Tarek M. Fahmy
Jun Fang
Peter Fedorocko
Conan Fee
Jean-Alain Fehrentz
Delphine Felder-Flesch
Jose M.G. Fernandez
Barbara Fingleton
Laird Forrest
Paula J. Foster
Keith R. Fox
Stefan Franzen
Peter Friedhoff
Benoit Frisch
Jinglin Fu
Hendrik Fuchs
Darin Y. Furgeson
Shiroh Futaki
Detlef Gabel
Matthias Gabriel
Hariprasad Gali
Sanjiv S. Gambhir
Munia Ganguli
Xiaohu Gao
Zoltan Gaspari
Gilles Gasser
John Gebler
Richard A. Gemeinhart
Assaf A. Gilad
Elizabeth R. Gillies
Jerry D. Glickson
Kristine Glunde
David M. Goldenberg
Michael Gozin
Duncan Graham
Anna Grandas
John Greaves
Jordan Jamieson Green
Jan Grimm
Ernest V. Groman
Hermann J. Gruber
Susanna Grundstrom
Christopher G Gulgas
Christian Hackenberger
Klaus Michael Hahn
Mark A. Haidekker
Hidde Haisma
Robert P. Hammer
Atsushi Harada
Hideyoshi Harashima
Christian G. Hartinger
Hiroto Hatakeyama
Daniel Haussinger
James G. Hecker
Jonathan Gardiner Heddle
Greg T. Hermanson
Jean Herscovici
Niko Hildebrandt
Scott Alan Hilderbrand
Patrice Hildgen
Stephan Hinderlach
Donald Hnatowich
Timothy J. Hoffman
Daniel Horak
Shi-Wen Huang
Jurgen Hubbuch
Josh Hunter
Qun Huo
Sarah Jean Hurst
Tsong-Long Hwang
Ad. P. Ijzerman
Toyoko Imae
Barbara Imperiali
Olle Inganas
Yoshihiro Ito
Bela Ivan
Hideo Iwai
Hiroo Iwata
Kenneth A. Jacobson
Kim D. Janda
N. Jayaraman
Scott Charles Jeffrey
Knud J. Jensen
Byeongmoon Jeong
Hwan-Jeong Jeong
Lei Jiang
Kai Johnsson
Arwyn T. Jones
Lee Josephson
Rudolph L. Juliano
Alois Jungbauer
Hiroyuki Kamiya
Noriho Kamiya
Keon Wook Kang
Mitsunobu Kano
Weiyuan John Kao
Julianna Kardos
Kazunori Kataoka
Yoshiki Katayama
John A. Katzenellenbogen
Hiroyoshi Kawakami
Shigeru Kawakami
Peter Kele
Gyorgy Keri
Erno Keszei
Mila Kilpelainen
Won Jong Kim
Kwangmeyung Kim
Soo-Kyung Kim
Taisun Kim
Yong Hwan Kim
Moritz Kircher
Akihiro Kishimura
Eva Kiss
Thomas H. Kissel
Yukio Kitade
J. N. Kizhakkedathu
Eiry Kobatake
Hisataka Kobayashi
Thomas Kodadek
Marcelo Javier Kogan
Jennifer J. Kohler
Makoto Komiyama
Akihiko Kondo
Lars Konermann
Kenji Kono
Roland E. Kontermann
Jindrich Kopecek
Brian A. Korgel
Yoshiyuki Koyama
Roland Kramer
Artur Krezel
Kenneth Krohn
Sergey N. Krylov
Ujendra Kumar
Hank F. Kung
Glen S. Kwon
Young Jik Kwon
Sylvain Ladame
Nobert Lange
Suzanne Lapi
Solange Lavielle
Che Law
Christopher Paul Leamon
Roger M. Leblanc
Bernard Lebleu
Sebastien Lecommandoux
Doo Sung Lee
Haeshin Lee
Hye Jin Lee
Sang-Yoon Lee
Seulki Lee

Published: January 6, 2012

ACS Publications © 2012 American Chemical Society

dx.doi.org/10.1021/bc200676c | *Bioconjugate Chem.* 2012, 23, 1–2

Table continued

Su Seong Lee
Yuan Chuan Lee
Graham J. Leggett
Benedicte Lepoittevin
Adam Lesner
Matt Levengood
Jason S. Lewis
Fuyou Li
Shyh-Dar Li
Dong Woo Lim
Chun-Cheng Lin
Lily Yun Lin
Shiyong Liu
Shuang Liu
Zhuang Liu
Guozheng Liu
Kenneth Kam-Wing Lo
Harri Lonnberg
Angelique Y. Louie
Philip S. Low
Jianzhong Lu
Wuyuan Lu
Zheng-Rong Lu
Claudio Luchinat
Krisztina Ludanyi
Philip S. Lukeman
Ying Luo
Robert Lyon
Robert H. Mach
J. Andrew Mackay
Hiroshi Maeda
Mizuo Maeda
Andras Malnasi-Csizmadia
Michael C. Marden
Wojciech T. Markiewicz
Andreas Marquardt
Koji Matsuoka
Michiya Matsusaki
William McBride
Owen J. McCarty
Michael T. McMahon
Jason D. McNeill
Thomas J. Meade
Claude F. Meares
Igor L. Medintz
Eric Meggers
Oleg Melnyk
Olivia Monika Merkel
Arben Merkoci
Damon Meyer
Gabor Mezo
Yubin Miao
Hiroyuki Michiue
Ronald Micura
Paul Scott Miller
Thomas L. Mindt

Grietje Molema
Michel Monsigny
Daniela Montesarchio
David J. Mooney
Anna Moore
Juan C. Morales
Richard Moriggl
Aaron Moss
Yohei Mukai
Willem J. M. Mulder
Leslie Muldoon
Cristina Muller
Akira Murakami
Jay L. Nadeau
Takeshi Nagasaki
Yukio Nagasaki
Natalie Winblade Nairn
Hiroyuki Nakamura
Ikuhiko Nakase
Masamichi Nakayama
Ravin Narain
Dario Neri
Ines Neundorf
Edward Neuwelt
George Richard Newkome
Nanting Ni
Julien Nicolas
Peter E. Nielsen
Christof M. Niemeyer
Takuro Niidome
Yoshihiro Nishida
Sei-Ichi Nishimoto
Tebello A. Nyokong
Andreas M. Nystrom
Rachel K. O'Reilly
Takahiro Ochiya
Manfred Ogris
Yuichi Ohya
Iwao Ojima
Nicole Okeley
Masahiro Ono
David Oupicky
Defang Ouyang
Herman S. Overkleeft
A. Yekta Ozer
Mark D. Pagel
Huaizhong Pan
Ravikiran Panakanti
Ravindra K. Pandey
Angela Pannier
Anna Maria Papini
Frederic Paques
William Pardridge
Joon Won Park
K_i Dong Park
Kinam Park

Seung Bum Park
Sung-Woo Park
Tae Gwan Park
Kathlyn A. Parker
Laszlo Patthy
Giovanni M. Pauletti
Ramasamy Paulmurugan
James C. Paulson
Gregory F. Payne
David S. Peabody
Jean-Philippe Pellois
Soledad Penades
Botond Penke
Wellington Pham
Geoff Pietersz
Rudiger Pipkorn
Hidde L. Ploegh
Franca Podo
Andrew Polson
Martin G. Pomper
Denis Pompon
Richard T. Pon
Thomas Pons
Margus Pooga
Alma Dal Pozzo
Olaf Prante
Matthew Pratt
Thomas Proft
Peter Z. Qin
Jozsef Rabai
David Rabuka
Eva Rajnavolgyi
Arunas Ramanavicius
Tariq M. Rana
Jianghong Rao
Kenneth N. Raymond
Steven L. Regen
Siegmund Reissmann
Ute Resch-Genger
Jean C. Reubi
CPM Reutelingsperger
Kevin G. Rice
Rebecca Richards-Kortum
Sjoerd Rijpkema
Luis Rivas
Kelly Lynn Robertson
John Robinson
Steve R. Roffler
Buck Edward Rogers
Michael G. Rosenblum
Sandra Jean Rosenthal
Rene Roy
Mark Roycik
Jean-Marie Ruysschaert
Maureen Ryan
Harumi Sakahara

Shinji Sakuma
Andres Salvay
Philip J. Santangelo
Helder A. Santos
Yoshihiro Sasaki
Marcus Sauer
Paul Bennett Savage
David A. Scheinberg
Cara-Lynne Schengrund
Roger Schibli
Ralf Schirrmacher
Gitta Schlosser
David W. Schmidtke
Lutz Schmitt
Rudolf J. Schneider
Mark H. Schoenfisch
Agnes Schonbrunn
David Schwartz
Frank Michael Schweizer
Frank Seela
Peter Senter
Jai Woong Seo
Norbert Sewald
Fazel Shabanpoor
Doron Shabat
Erik M. Shapiro
Jadab Sharma
Wei-Chiang Shen
Yu-Mei Shen
A. Dean Sherry
Kouichi Shiraishi
John E. Shively
Molly S. Shoichet
Subhash C. Sinha
Masahiko Sisido
A. Skerra
Rita Skoda-Foldes
Bradley D. Smith
Charles Smith
Lela Smith
Rita Song
David A. Spiegel
Thomas Comey Squier
Martina Heide Stenzel
Yasuo Suda
Millicent O.W. Sullivan
Xiankai Sun
Hsing-Wen Sung
Avadhesha Surolia
Django Sussman
Ryo Suzuki
Petr Svoboda
Musti Joginadha Swamy
Francis C. Szoka Jr.
Maryam Tabrizian
Mutsumi Takagi

Tohru Takarada
Naoya Takeda
Shinji Takeoka
Masumi Taki
Hirokazu Tamamura
Robert Tampe
C. Tamvakopoulos
Tsutomu Tanaka
John-Stephen Taylor
Jose Teixeira
Isabelle Texier
David H. Thompson
Michael D. Threadgill
Lutz F. Tietze
Nicola Tirelli
David A. Tirrell
Brian Toki
Thomas J. Tolbert
Vladimir Tolmachev
Helena Tomas
Kenneth Beamer Tomer
Andrew Tsourkas
Chuqiao Tu
Ching-Hsuan Tung
Stefano Turri
Marcellus Ubbink
Katalin Uray
Ganesan Vaidyanathan
Marcian E. Van Dort
Heather Van Epps
Johan E. Van Lier
Jean-Jacques Vasseur
Arturo Vegas
Francesco Maria Veronese
Pierre Vierling
Jarmila Vinsova
Andreas Vitalis
John D. Wade
Hans-Achim Wagenknecht
Fan Wang
Gin-Ming Wang
Jun Wang
Qian Wang
Binghe Wang
Bjorn Wangler
Paul H. Weinreb
Gregory A. Weiss
Ralph Weissleder
Michael J. Welch
Eric Wickstrom
D. Scott Wilbur
Meir Wilchek
Itamar Willner
W. David Wilson
Edward H. Wong
Bing Xu

Tetsuji Yamaoka
Hao Yan
Mingdi Yan
Xiaomei Yan
Victor C. Yang
Yi Yan Yang
Haw Yang
Kevin J. Yarema
Paul J. Yazaki
Zhaoyang Ye
Masayuki Yokoyama
Ken-Tye Yong
Samuel Zalipsky
Shubiao Zhang
Yan Zhang
Zhijun Zhang
Yan Zhao
Xue Zhi Zhao
Gang Zheng
Qi-Huang Zheng
Yujun George Zheng
Junmin Zhu
Petr Zimcik
G. Zuber
Jon A. Zubieta

Claude F. Meares, Editor-in-Chief

dx.doi.org/10.1021/bc200676c | *Bioconjugate Chem.* 2012, 23, 1–2

Bioconjugate Chemistry

Review

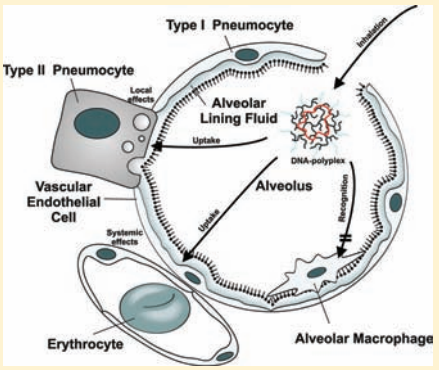
pubs.acs.org/bc

Pulmonary Gene Delivery Using Polymeric Nonviral Vectors

Olivia M. Merkel, Mengyao Zheng, Heiko Debus, and Thomas Kissel*

Department of Pharmaceutics and Biopharmacy, Philipps-Universität Marburg, Germany

ABSTRACT: Pulmonary delivery provides an easy and well tolerated means of access for the administration of biomacromolecules to the pulmonary epithelium and could therefore be an attractive approach for local and systemic therapies. A growing number of reports, which are summarized in this review, mirror the viability of pulmonary gene delivery. Special attention has been paid to the biological barriers in the lung that must be overcome for successful delivery, and which can be divided into anatomic, physical, immunologic, and metabolic barriers. In light of these barriers, successful nonviral polymer-based formulations of therapeutic genes are presented depending on the chemical nature of the polymer. In addition to polyethyleneimine-based nonviral vectors, which have been most intensively studied for pulmonary gene delivery in the past, other polymeric, dendritic, and targeted materials are also described here, including novel and biodegradable polymers. As new materials need *in vitro* or *ex vivo* testing before *in vivo* application, sophisticated models for all three approaches have been illustrated. Although pulmonary siRNA delivery enjoys popularity in clinical trials, pulmonary gene delivery has so far not been translated into clinical applications. With this review, potential hurdles are demonstrated, but novel approaches that may lead to optimized systems are described as well.



INTRODUCTION

Pulmonary delivery provides a noninvasive route for the administration of biomacromolecules like therapeutic genes, siRNA, and proteins to pulmonary epithelia.[1] It is therefore a promising approach for new treatments of genetic disorders like cystic fibrosis (CF), inherited lung diseases such as α1-antitrypsin or surfactant protein-B (SP-B) deficiency, and other widespread disorders such as asthma, chronic obstructive pulmonary disease (COPD), emphysema, or lung cancer.[2−4] The potential of pulmonary gene delivery is reflected in a large number of reports in the literature.[2−5] Due to the vast surface area and strong perfusion in the lung, pulmonary administration of small, hydrophobic drug molecules leads to rapid local and systemic effects.[6] However, the air-blood-barrier is less permeable for large, hydrophilic, and strongly negatively charged macromolecules like nucleic acids. There is evidence for a cell surface DNA-receptor,[7] but cells lack an efficient uptake mechanism for nucleic acids. Therefore, an efficient approach for cellular delivery of therapeutic nucleic acids is to formulate them into nanosized carrier systems.

For pulmonary administration and clinical application in man, gene delivery formulations have to withstand the shear forces created during nebulization. While naked DNA, viral vectors, and many lipid-based formulations often lose their biological activity, formulations with poly(ethylene imine) (PEI) are stable during the process of jet nebulization.[8−10] However, the nebulization process must also deliver the formulations to the target area within the lung. From a biopharmaceutical point of view, droplet sizes of 1−3 μm are regarded as optimal.[11] Larger droplets are lost in the oropharynx by impaction and do not result in gene expression in the lower airways.[12] Subsequently, the formulated nucleic acids need to enter their target cells and therefore have to overcome several physical obstacles. These include the mucus layer that covers the conducting airways or the liquid layer in the alveoli. The host immune system provides an additional barrier. Soluble components of the immune system like opsonins, complement factors, or antibodies[13] and cellular defense mechanisms like macrophages or dendritic cells[14] all affect delivery. Once inside the target cells, the therapeutic genes need to escape from the endosomes and be translocated into the nucleus for transcription.

BIOLOGICAL BARRIERS IN HEALTHY AND DISEASED LUNGS

The advantages of local pulmonary gene delivery include reduced systemic side effects, no interaction with serum proteins, and the possibility of reducing the dose of topically administered formulations. However, efficient gene delivery systems must first overcome anatomical, physical, immunologic, and metabolic barriers in the lung.[15,16]

Anatomic Barriers. The adult human lung is estimated to contain about 2300 km of airways, 500 million alveoli,[17] and a surface area of approximately 75−140 m^2 in a strongly branched architecture.[18,19] Therefore, for high therapeutic efficacy, gene delivery systems need to be directed to their target region within the lung and specifically taken up by their target cell populations.[20] The deposition of aerosol particles in

Received: June 7, 2011
Revised: September 23, 2011
Published: October 13, 2011

 © 2011 American Chemical Society

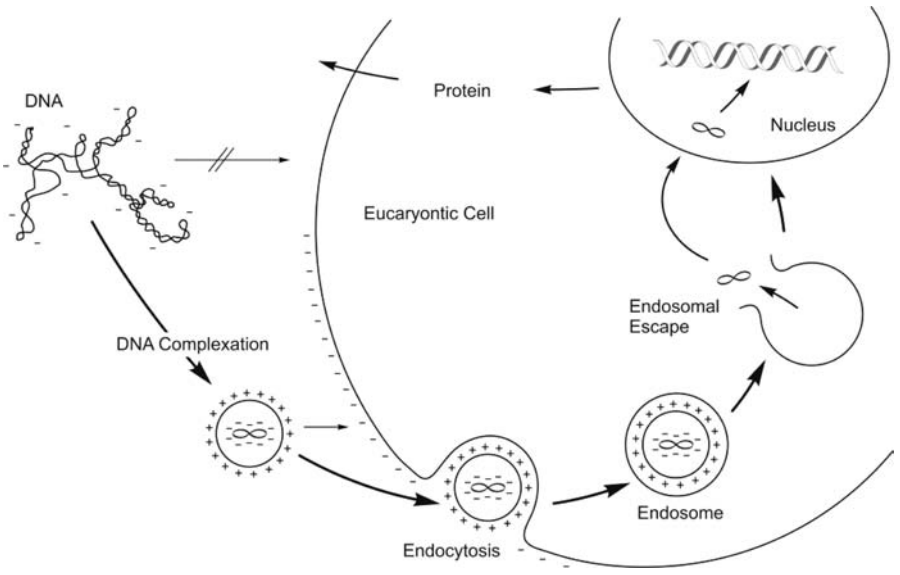


Figure 1. Since negatively charged nucleic acids are not efficiently taken up by cells, they require formulation. After adsorptive endocytosis of the gene delivery vector, therapeutic DNA needs to be released from the endosome, translocated into the nucleus where it is transcribed, and translated in the cytosol for successful transgene expression.

the lung is determined by three physical mechanisms, namely, inertial impaction, gravitational sedimentation, and Brownian diffusion.[21,22] While large particles with a mass median aerodynamic diameter (MMAD) of more than 5 μm experience impaction in the oropharynx and upper conducting airways, particles of a MMAD between 1 and 5 μm sediment into deeper airways and bronchioles. Very small particles with a MMAD of about 0.5 μm obey the principle of Brownian diffusion.[23] However, the deposition of aerosol droplets is not only affected by their size but also by their density, hygroscopicity, and shape.[12,24]

Additionally, the anatomy of the airways, which is different between rodents and humans,[6] and the breathing pattern, determine impaction, sedimentation, and diffusion of droplets in the airflow.[23] Since breath-holding maneuvers rely on the patient's compliance, this factor cannot easily be investigated in animal models. It is generally accepted that the optimal droplet size for aerosols is 1−3 μm, as particles smaller than 1 μm can possibly be exhaled without being deposited.[25] However, recent investigations showed that ultrafine particles smaller than 100 nm are effectively deposited in the alveolar region, especially in individuals suffering from asthma, and increasingly during physical exercise.[26] This size-dependent deposition can also be modeled, confirming that nanoparticles deposit more uniformly throughout the whole lung than microparticles which accumulate in bifurcations.[27] A promising approach to control the spatial deposition of aerosol particles was achieved with so-called magnetic aerosols containing superparamagnetic iron oxide particles that were directed toward a magnet in a defined manner.[28]

Physical Barriers. Among the physical barriers, respiratory secretions lining the airways and alveoli can trap polymeric particles or decrease their stability. The respiratory mucus covers the conducting airways from the nose to the bronchioles and captures foreign matter inhaled with each breath. Upon deposition in the lung, particles are wetted by mucus [29] and subsequently transported toward the esophagus by ciliated cells, which make up about 50% of the epithelium in the upper airways.[30] This so-called mucociliary clearance, mediated by the propulsive movement of about 250 cilia per ciliated cell,[31] removes particles from the lung in the proximal direction. In healthy lungs, the velocity is approximately 3.6 mm/min [32] and can be accelerated in diseased lungs.[33] The cough clearance further supports this process. While the mucus layer is 10−30 μm thick in the trachea and 2−5 μm in the bronchi of healthy individuals,[34] it is much thicker in patients suffering from CF or other respiratory diseases.[35] Mucus is excreted by goblet cells and submucosal glands in the upper respiratory tract and consists of viscoelastic, cross-linked mucins.[36] Mucins are highly glycosylated proteins that bind head-to-tail to other protein chains via disulfide bonds. The negative charge of mucins is due to N-acetylneuramic acids and sulfated hydroxyl groups of the monosaccharides present in the glycosylation pattern.[37] Additionally, mucus also contains water, electrolytes, lipids, proteoglycans, and proteins,[5] particularly albumin, proteases, antiproteases, immunoglobulins, lysozyme, and lactoferrin.[38] In contrast to nonpathologic conditions, sputum from patients with cystic fibrosis or respiratory infections additionally contains DNA and actin released from dead neutrophils, epithelial cells, and pathogens.[5] Due to their macromolecular character, DNA and actin can increase the viscosity of mucus by forming gels or interactions with mucus.[39] Comparably, symptoms of acute lung injury like incidences of edema, increased mucus production, and augmented cellular debris can further block the access of therapeutics to the target cells.[40]

Together, these barriers effectively reduce the mobility of nanoparticles upon deposition in the lung as they are captured by the biopolymer network or freely diffusing components of the mucus. This leads to aggregation of colloidal systems, especially if the latter are positively charged. Particles smaller than 100 nm can diffuse through biopolymer meshes via low-viscosity pores of about 100 nm in the mucus fiber network.[41] Interestingly, diffusion rates of nanoparticles significantly smaller than 100 nm were found not to be affected by the presence of mucus if (i) the viscosity of the pore-fill was equivalent to water and (ii) the particles did not interact with sol or gel components of the mucus.[42] The mobility of colloidal

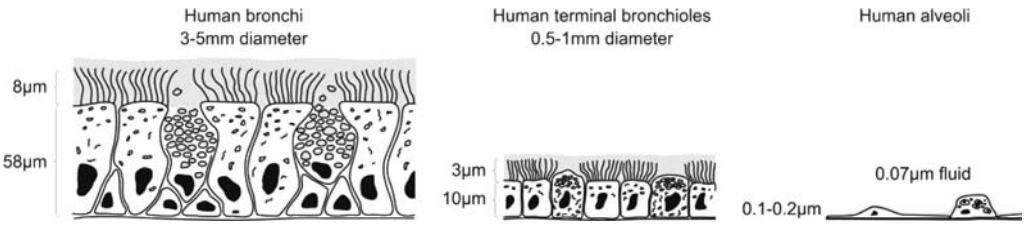


Figure 2. As the size of epithelial cells gradually decreases from the bronchi to the alveoli, the amount of ciliated cells and mucus producing cells as well as the mucus layer thickness lessen in parallel with surfactant producing cells in the alveoli instead of mucus producing cells.

drug carriers through mucus is therefore understood to be strongly size dependent with an increasing transport velocity as particles size decreases.[43−45] However, even very small polystyrene particles of 89 nm in diameter were reported to be trapped in certain regions of CF sputum,[46] which can only be explained by the presence of hydrophobic domains in the mucus.[42] As a result, not only size but also surface characteristics affect mobility in CF sputum. While negatively charged polystyrene particles bound more strongly to biopolymers than neutral nanospheres of the same material,[45] their adhesion to cervical mucus was strongly decreased by coating the surface with poly(ethylene glycol).[47]

Consequences from these observations for nonviral gene delivery systems are that these colloidal carriers may also interact with mucus compounds and may subsequently be entrapped. Since most nonviral gene delivery systems are positively charged, interaction with mucus leads to neutralization of the surface charge[48,49] and thus aggregation and inefficient cell uptake.[5] Additionally, nucleic acids can also be released from the delivery system,[50] eventually decreasing the transfection efficiency of polyplexes, lipoplexes, and adenoviral vectors.[5,49,51]

To increase the mobility in respiratory mucus, certain bacteria, viruses, and fungi produce enzymes that hydrolytically degrade mucins, thus decreasing the viscosity of mucus.[52−54] Mucolytic agents like *N*-acetyl-cysteine (NAC) or rhDNase that degrade mucins or DNA in CF sputum, respectively, have therefore also been used to increase the mobility of gene delivery systems in the lung.[43,45,55] However, when sputum from cystic fibrosis patients mounted on cultured cells was treated with mucolytic agents including *N*-acetyl-cysteine, alginase, or lysine, the transgene expression mediated by cationic liposomes or adenoviruses was not increased, whereas rhDNase treatment did have a positive effect.[51] This can be explained by the hypothesis that degradation of the biopolymer network in mucus will on one hand increase the pore size, but will also increase the viscosity of fluids inside the pores, due to an enhanced concentration of polymer released from the network.[5] Accordingly, explicit removal of mucin in a sheep trachea organ culture model increased the transfection efficiency of liposomes 25-fold.[56]

The alveolar epithelium is not covered by mucus but with a thin layer of lung surfactant excreted from type II pneumocytes as shown in Figure 2. While mucus would hamper gas exchange, phospholipids and surfactant-associated proteins in the surfactant decrease the surface tension at the air-blood-barrier and avoid the collapse of the alveoli upon exhalation.[57] While the surface activity of surfactant is mainly due to the phospholipids, surfactant proteins (SP) B and C also lower the surface tension, whereas SP-A and SP-D can opsonize foreign matter in the lung.[58] The presence of negatively charged lipids in the surfactant also inhibits the transfection efficiency of cationic lipid based nonviral gene vectors.[59] Interestingly, transgene expression mediated by carriers based on cationic polymers such as poly(ethylene imine) (PEI) and dendrimers (PAMAM) was reported to be unaffected by naturally derived and synthetic surfactant preparations *in vitro*[59,60] and *in vivo*.[61] Furthermore, the synthetic surfactant Exosurf was even reported to increase the transfection efficiency of PAMAM/pDNA complexes *in vitro*.[60] Accordingly, DNA-loaded nanoparticles prepared from biodegradable poly[vinyl-3-(diethylamino)propylcarbamate-*co*-vinyl acetate-*co*-vinyl alcohol]-graft-poly(D,L-lactide-*co*-glycolide) (DEAPA-PVA-g-PLGA) displayed enhanced transfection efficiency *in vitro* as ternary nanocomposites with bovine lung surfactant (Alveofact).[62] Additionally, it was shown that bronchial alveolar lavage fluid (BALF) proteins and glycosylated compounds adsorb more intensively to lipoplexes of Lipofectamine than to PEI-based polyplexes, resulting in a 10-fold increase of the lipoplex size.[49] Interaction with BALF decreases the surface charge of the lipoplexes only slightly, but that of polyplexes changed from positive to negative.[49]

Various shielding strategies have been applied to decrease self-aggregation of nonviral gene carriers and aggregation with extracellular components. Among these, attachment of hydrophilic, uncharged polymers like poly(ethylene glycol) (PEG)[63,64] or adsorption of negatively charged polymers like poly(propylacrylic acid) (PPAA)[65] or serum albumin[66] have been investigated to decrease the positive surface charge of gene delivery systems and thus their interactions with BALF and Alveofact.[63,67] Mucus-penetrating polystyrene particles of 100−500 nm in size, coated with a high density of low molecular weight (2 kDa) PEG were developed and show up to 1000-fold improved transport in human mucus.[47] This muco-inertness, however, interestingly decreased as the PEG-coating density decreased and the PEG chain length increased.[68]

Additionally, tight junctions between respiratory epithelial cells limit the access of gene vectors to the basolateral side.[69] In fact, several small hydrophilic drugs pass through the tight junctions.[1] Additionally, tight junctions were described to be reversibly disrupted *in vitro* in Calu-3 cells and *in vivo* in a rabbit model by polymeric excipients such as poly(acrylic acid) (PAA), leading to decreased transepithelial electrical resistance (TEER) and permeation enhancement possibly due to chelation of extracellular or tight-junctional Ca^{2+} by carboxy groups present in PAA.[70]

Immunologic Barriers. While the mucociliary escalator is the most efficient mechanism of clearance in the upper airways, nanoparticles are predominantly cleared by macrophage phagocytosis and epithelial endocytosis in the alveoli.[71] Every single alveolus is covered by 12−14 macrophages,[17] leading to an number of roughly 19 000 alveolar macrophages per microliter (1 mm^3) of BALF.[72] Due to their size of 15−22 μm, alveolar macrophages are more efficient in phagocytiz-

dx.doi.org/10.1021/bc200296q | *Bioconjugate Chem.* 2012, 23, 3−20

ing particles of 1−3 μm compared to particles of 6 μm in diameter [73] and interestingly seem to ignore nanoparticles of 260 nm and smaller sizes.[74] The latter have been reported to be translocated from the lung into the systemic circulation by caveolae-mediated endocytosis.[75,76] Endocytosis of nanoparticles into the epithelium or phagocytosis by macrophages can lead to enhanced secretion of pro-inflammatory cytokines.[77] This results in an influx of polymorphic neutrophils (PNMs),[71] generation of reactive oxygen species (ROS),[78,79] and DNA double-strand breaks.[80,81] Other immune responses that prevent the invasion of foreign material into the lung[82] are soluble components of the immune system like opsonins and complement factors. Interestingly, proteins like complement cleavage fragments C3β and C3α were found to adsorb more intensively to lipoplexes than to polyplexes.[49] Biocompatibility is also affected by size, and ultrafine particles result in enhanced cytotoxicity, allergic response, and inflammation compared to larger counterparts, due to their extensive contact surface area.[83−86] Pro-inflammatory and oxidative stress related cellular responses have been observed in cell culture models[79,87,88] and *in vivo*.[48,50,83,84] Both inflammation and oxidative stress levels additionally depend on the shape and structure of the nanoparticles. As a consequence, elongated carbon nanotubes (CNTs), which are not as easily ingested by alveolar macrophages as carbon black particles, were reported to cause interstitial granulomas in mice[89] and rats.[90]

Activation of complement and other inflammatory cascades leads to an influx of polymorphic neutrophils (PMNs) and macrophages[48,83] resulting in enhanced phagocytosis and inactivation of a large proportion of the gene delivery system.[91,92] Thereby, these immunologic barriers limit endocytosis into the epithelium and with it the extent and duration of epithelial gene expression.[15,16]

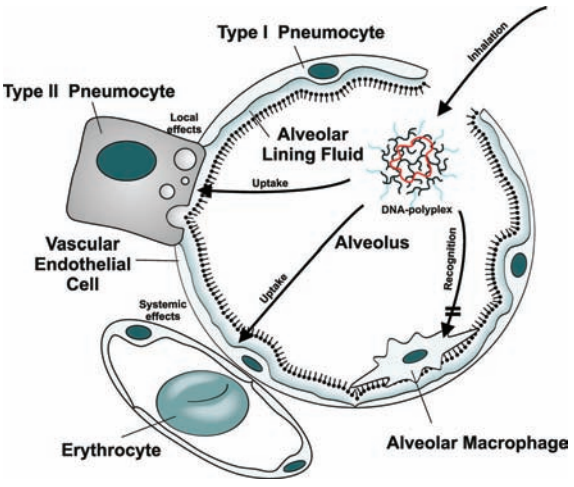


Figure 3. After entering the alveoli, gene delivery systems can possibly interact with the alveolar linage fluid or can be taken up by various cell types. Recognition by and uptake into macrophages should be avoided, for example, by adjusting the size and surface of nanoparticles. Uptake into pneumocytes could lead to local therapeutic effects, and transcytosis into the systemic circulation could lead to systemic wanted or unwanted effects.

Metabolic Barriers. Nanomaterials that are soluble in extracellular fluids or lipid membranes are rapidly absorbed through the lung epithelial membrane upon dissolution and small hydrophilic drugs can be absorbed by active transporters.[93] However, large hydrophilic substances like DNA or insoluble materials have been shown to be translocated into the systemic circulation and to other organs, depending on the region of deposition.[83] If systemic drug activity is intended, this translocation is desirable and does not constitute a barrier. However, for local effects, the translocation of gene carriers to tissues other than the epithelium decreases the active dose and potential therapeutic effects. Nanoparticles 17−20 nm in diameter and labeled with ^{192}Ir were found to be extensively translocated to the interstitium.[94] It was shown that over 24 weeks only about 20% of the inhaled dose of nanoparticles were taken up by alveolar macrophages. Interestingly, indications for nanoparticles re-entering the lung from the epithelium and interstitium to the luminal side were also observed.[94] In a different study, translocation from the lung was found to be size-dependent. Small gold particles (18 nm) remained almost completely (99.8% ID) in the lung for up to 24 h, while very small gold particles (1.4 nm) were cleared in significant amounts into the blood, liver, skin, and carcass over 24 h.[95] Additionally, other studies have shown translocation into the blood and lymph and subsequent deposition in the bone marrow, lymph nodes, spleen, and heart,[83,96] the central nervous system, and ganglia.[83,96−99] In a recent report, rapid translocation into regional lymph nodes of noncationic nanoparticles smaller than 34 nm was shown, whereas larger nanoparticles remained in the lungs. Conversely, approximately one-half of zwitterionic nanoparticles smaller than 6 nm were rapidly translocated into the systemic circulation before being cleared by the kidneys.[100] These results confirm that nanoparticle behavior after pulmonary delivery not only depends on the size but also strongly on interactions with extracellular fluids, which in turn are affected by the surface coating of colloidal systems.

Except for the presence of acid pH Proteinase I, alkaline pH Proteinase II, and a few other peptidases, the lung can be considered an organ of low enzymatic metabolism.[101] This is certainly a great advantage for pulmonary delivery of therapeutic nucleic acids.

NONVIRAL PULMONARY GENE DELIVERY SYSTEMS

According to the lessons learned from the interactions of nanoparticles with the lung, an optimal nonviral gene delivery system for pulmonary administration should not only mediate cellular delivery and intracellular release of intact DNA, but should also be nebulizable in droplets suitable for alveolar deposition, exhibit weak interaction with extracellular components, and avoid recognition by macrophages. For repeated application, the carrier system additionally needs to be biodegradable and neither cytotoxic nor immunogenic. So far, no clear correlation between the surface chemistry of synthetic nanoparticles and their mobility in mucus has been found. Muco-inert viruses could possibly be mimicked by coating nanoparticles with similarly high density of cationic and anionic surface charge groups, which however has not yet been successfully developed and would certainly exhibit immunogenicity like their natural counterparts.[42] Decreased cytotoxicity and recognition by macrophages, on the other hand, have been achieved by variations in size and surface charge as described below and summarized in Table 1.

Table 1. Overview of Studies Describing Polymers and Dendrimers as Nonviral Pulmonary Gene Delivery Vectors

delivered materials	first author and year	polymer or dendrimer	route of administration	important findings	ref
pCMV-Luc-plasmid	Rudolph, C. 2000	PEI, PAMAM	Intratracheal	Higher gene expression of PEI25k complexes compared to PAMAM dendriplexes, influence of ionic strength on size and transfection efficiency.	61
pCMV-Luc-plasmid	Rudolph, C. 2005	PEI	Aerosol	High efficiency after aerosolization, influence of osmolarity.	10
pCMV-Luc-plasmid	Dames, P. 2007	PEI	Aerosol	Influence of mouse strain on transgene expression and pDNA clearance from the lung.	174
pGL3 and peGFP-N1 plasmid	Kleemann, E. 2005	TAT-PEG-PEI	Intratracheal	TAT−PEG−PEI can improve the interaction with the cell surface in the lung.	63
pGL3 plasmid	Nguyen, J. 2008	TAT-PEG-PEI	Intratracheal	Coupling of CPPs only improved *in vivo* transfection efficiency of PEI but not that of PEG-PEI.	118
pGL3 plasmid	Kleemann, E. 2009	PEI-PEG	Intratracheal	Low molecular PEI grafted with PEG showed a better transfection efficiency in the lung than bPEI	109
pCMV-Luc and pGreenLantern-1 plasmid	Koping-Hoggard, M. 2001	Chitosan	Intratracheal	Chitosan showed equal transfection efficiency to PEI in the airway epithelium of the lung.	120
pCMV-Luc, pEGFP-F and IFN-expression pDNA	Okamoto, H. 2011	Chitosan	Intratracheal (powder)	Effective intratracheal chitosan−interferon-β gene complex powder as promising treatment of lung metastasis.	129
p53sm expression plasmid, luciferase plasmid, p53-specific luciferase plasmid	Zou, Y. 2007	PLL/protamine	Aerosol	Optimal nonviral aerosol formulation of a polylysine/protamine combination, no toxicity, higher *in vivo* transfection efficiency than PEI or cationic lipid	135
inflammatory responses of PLGA-NP	Dailey, L. A. 2006	DEAPA-PVAL-g-PLGA	Intratracheal	Inflammatory response to biodegradable nanoparticles comparable to isotonic glucose control	161
pV1J.ns-tPA DNA plasmid	Bivas-Benita, M. 2009	PLGA-PEI	Endotracheal aerosol	Pulmonary administration of PLGA−PEI nanoparticles as DNA vaccine against tuberculosis	156
pCF1CAT plasmid	Kukowska-Latallo, J. F. 2000	G9 PAMAM dendrimer	Intravascular and endobronchial	Transgene expression after local administration of dendriplexes was even lower than compared with naked DNA	168
pCMV-Luc and pCpGLuc plasmid	Uzgun, S. 2009	P(DMAEMA-*co*-OEGMA)	Intratracheal	Higher transfection efficiency of p(DMAEMA-*co*-OEGMA) in comparison to branched PEI in the lung	137

dx.doi.org/10.1021/bc200296q | *Bioconjugate Chem.* 2012, 23, 3−20

■ POLYMERIC VECTORS

Polymeric nonviral vectors have been developed for pulmonary gene transfection since the 1990s. They have been gradually considered as more potent vectors than their viral counterparts and have the additional advantage of lower toxicity and immunogenicity. Polymeric vectors also offer the possibility of industrial production following good manufacturing practice. Moreover, the gene-packaging-capacity of synthetic polymeric nonviral vectors is unlimited concerning the amount of genetic material.[102] So far, various potential polymeric nonviral vectors have been described especially for pulmonary gene delivery, including poly(ethylene imine) (PEI), poly(2-(dimethylamino)ethyl methacrylate) (pDMAEMA), the polysaccharide chitosan, the biologically occurring polyamine spermine, and the biodegradable noncationic polymer PLGA,[103] as shown in Figure 4.

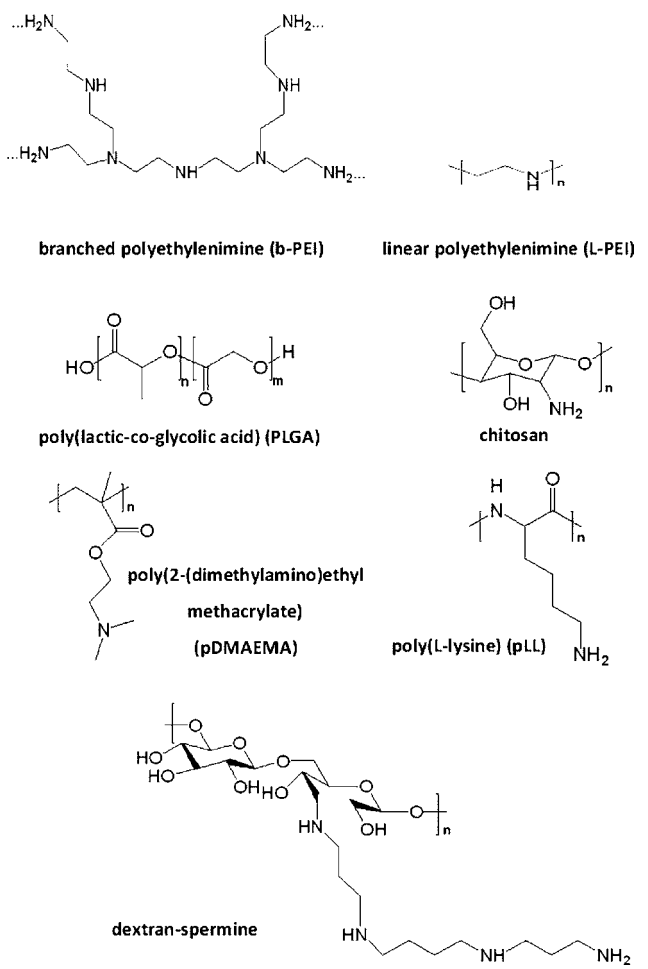


Figure 4. Polymeric vectors employed for pulmonary gene delivery.

Poly(ethylene imine) (PEI)-Based Gene Carriers. In the past decade, the cationic polymer poly(ethylene imine) (PEI) has been regarded to play the most important role in pulmonary nonviral gene delivery. In 1995, the potential of PEI as a gene delivery vector was first discussed.[104] The investigated molecular weights of PEI range from 1 kDa to 1.6 × 10^3 kDa.[105,106] Due to results from a transfection study with L929 cells, researchers found that the most suitable molecular weight of PEI for gene delivery ranges from 5 to 25 kDa. Higher molecular weight PEI can increase cytotoxicity due to cell-surface aggregation of the polymer.[107] Low molecular weight PEI is less toxic but is usually less effective as a gene delivery vector. On the one hand, due to the lower amount of positive charges within one molecule, it is difficult for small PEIs to condense the negatively charged DNA tightly. On the other hand, if the surface charge of the complexes is too low, it is almost impossible for them to induce cellular uptake through charge-mediated interactions.[108] The high cationic charge density of PEI condenses the negatively charged DNA efficiently into small complexes and protects it from nuclease degradation.[107] Moreover, PEI carries protonable amino groups, which confers the ability for PEI to change its protonation state with the pH change in the cytosol and to have a high endosomal buffering capacity, the so-called "proton-sponge" effect. This property of PEI is described to cause osmotic swelling and endosomal escape of PEI/DNA-complexes.[104] Recent research in the mouse lung indicated that polyplexes of low molecular weight PEI (5 kDa) grafted with PEG (5 kDa) exhibit higher transfection efficiency in both the bronchial and alveolar cells than high molecular weight PEI (25 kDa) grafted PEG polyplexes, which were mainly found in bronchial cells.[109]

Hyperbranched PEI and Linear PEI. PEI polymers can be classified into (hyper)branched and linear architectures. Highly branched PEI showed stronger complexation with DNA and formed smaller complexes than linear PEI.[110,111] The condensation behavior of branched PEI with DNA is less dependent on the preparation buffer conditions[110] than high molecular weight linear, which is distinctly dependent on the buffer condition. For example, complexes of linear PEI 22 kDa with DNA (1 μm) in a high ionic strength solution were larger than the complexes prepared in a low ionic strength 5% glucose solution (30−60 nm).[104,111] Interestingly, the transfection efficiency of linear PEI22 kDa/DNA complexes *in vitro* was higher than that of branched PEI800/DNA and branched PEI25 kDa/DNA complexes when complexes were prepared in a salt-containing buffer.[110] However, further *in vivo* investigations showed that linear PEI22 kDa/DNA complexes prepared in high salt condition were less active than the complexes formed in low salt condition (100-fold less). This indicates that efficient transgene expression strongly depends on the size of the DNA complexes.

PEI-g-PEG. To reduce the cytotoxicity of PEI, numerous approaches have been used, including PEG-grafted PEIs and biodegradable PEIs. Therefore, PEIs with different PEG grafting ratios were synthesized.[67,112,113] The cytotoxicity of PEI-g-PEG was greatly reduced regarding the mitochondrial metabolism in 3T3 mouse fibroblasts[114] and murine lung cell lines.[88] However, proinflammatory signaling on mRNA and protein level was interestingly increased upon PEG-grafting. Additionally, the *in vivo* gene delivery efficiency in mouse lungs was decreased with PEI-g-PEG, presumably due to reduced interaction of the PEG-coated gene vectors with the cell surface and the reduced cellular uptake.[67] To improve the interaction of PEI-g-PEG with the cell surface in the pulmonary area, PEG(3.4 kDa)-grafted PEI 25 kDa was modified with TAT, a cell-penetrating peptide derived from the HI-virus.[115] TAT-PEG-PEI exhibits better polyplex stability and DNA protection in the airways. Although TAT-PEG-PEI demonstrates low transfection efficiency *in vitro*, much higher gene expression was observed *in vivo* compared to PEI.[63] In another report, the biotinylated TAT-RGD (TR) peptide, additionally containing the arginine-glycine-aspartate (RGD) sequence, was developed

dx.doi.org/10.1021/bc200296q | *Bioconjugate Chem.* 2012, 23, 3−20

to deliver DNA into pulmonary cells.[116] The cell uptake indicated that TAT-RGD enters the cell membrane possibly by caveolae-dependent endocytosis. Interestingly, TAT-RGD showed a cooperative effect with cationic lipid based transfection reagents (such as Lipofectamine). When TAT-RGD was combined with Lipofectamine, the gene transfection in the lung cells was higher than with TAT-RGD or Lipofectamine alone.

Galactose was also investigated as a ligand to improve the binding and cell uptake of the PEG-grafted PEIs into lung cells. The polymer PEG-PEI with galactose ligands showed improved transfection efficiency in the lung of mice.[117] However, the introduction of cell-penetrating peptides to PEG-PEI did not increase the transfection efficiency as much as expected.[118] The use of low molecular weight PEI is another way to improve the cytotoxicity of PEI, but must be modified to condense DNA or RNA more strongly. Wen et al.[119] conjugated low molecular weight PEIs with polyglutamic acids by aminolysis to synthesize PEG-b-PLG-g-PEIs. Toxicity of this copolymer was reduced compared to PEI 25 kDa, and DNA condensation ability and DNA protection from nuclease degradation were also improved. Moreover, the transfection efficiencies of PEG-b-PLG-g-PEIs were greater than that of PEI 25 kDa in HeLa, HepG2, Bel 7402, and 293 cell lines. The *in vivo* gene delivery into the lung has yet to be investigated.

The highly charged surface provides PEI not only with high transfection efficiency but also with high cytotoxicity. To overcome the drawbacks of high molecular weight PEI, poly(ethylene imine)-based degradable cationic polymers may be promising cationic vectors for pulmonary gene delivery. These can, for example, be designed from cross-linked LMW PEI.

Polysaccharide-Based Gene Delivery Systems. Chitosan, which is derived by partial deacetylation of chitin from crustacean shells, is a family of linear polysaccharides consisting of D-glucosamine and *N*-acetyl-D-glucosamine. Chitosan is slowly biodegradable and can be used for delivery of genes to mucosal tissues *in vivo*.[120−122] Compared with PEI, chitosan has a lower buffer capacity and does not act as a sponge for protons or other cations in the endosomal compartment, because primary amines in chitosan have an unusually high pK_a-value of 6.5.[120] An *in vitro* study found that chitosan polyplexes were less efficient than PEI in differentiated epithelial cell lines.[120] But interestingly, in contrast to these *in vitro* findings, chitosan showed equal transfection efficiency to PEI in the airway epithelium of the lung.[120] Later, poly(ethylene glycol) (PEG) grafted trimethyl chitosan copolymers were prepared to improve solubility and biocompatibility of chitosan.[123] Additionally, these complexes mediated increased cellular uptake compared to unmodified trimethyl chitosan.[124] Another linear chitosan modified with trisaccharide branches showed 4-fold higher luciferase gene expression following lung administration in mice than unmodified linear chitosan.[125] Although chitosan has the drawback of a lower buffer capacity than PEI, it is still a potential gene delivery vector especially in the lung due to its high biocompatibility and mucoadhesive properties for mucosal surfaces. It may therefore serve as a basis for further modifications in the future.

Aerosol technology is very well developed and accepted for human use, not only for general small molecule drug delivery but also for optimal gene delivery to the lung. Since aerosol technology is clinically well established, aerosol delivery of therapeutic genetic material could have promising applications in the area of genetic diseases. Dry powder inhalation is one of the aerosol delivery techniques which is advantageous in terms of portability, lack of a propellant, and ease of handling, and improved stability of pDNA. Dry powder formulation of DNA complexes has been developed with the application of chitosan as DNA delivery vector and has been tested *in vitro* and *in vivo*.[126−128] Such DNA/chitosan dry powders can be prepared by spray-drying, lyophilization, and spray-freeze−drying. Compared with the other technologies, spray-freeze−drying (SFD) is a relatively recent and simple method for the preparation of dry powders, with the advantages of high dispersibility compared to that obtained by spray-drying and high recovery of the dry powder to save the expensive genetic material. The findings of Okamoto at al. showed enough evidence to believe that therapeutic powders of DNA complexes prepared by SFD are promising for pulmonary gene therapy.

For example, a dry plasmid DNA (pDNA) powder with chitosan was successfully prepared using a supercritical carbon dioxide technique[126,127] and spray-freeze−drying (SFD).[128] Pulmonary administration in mice with the dry plasmid DNA powder/chitosan improved stability and transfection efficiency significantly, compared with the plasmid DNA/chitosan solution.[129]

Other Polycation-Based Gene Delivery Systems. *Poly(L-lysine) (PLL).* Poly(L-lysine) (PLL) is one of the oldest polymers that have been investigated as a nonviral gene delivery vector. However, PLL has low transfection activity due to its high toxicity, especially when the molecular weight is above 25 kDa.[130] To reduce the cytotoxicity of PLL, biodegradable poly(lactic-*co*-glycolic acid) (PLGA)[131] (as discussed below), biocompatible PEG,[132,133] and even iron oxide (IONP) can be grafted to the PLL backbone.[134] Interestingly, the transgene expression mediated by IONP-PLL was much higher in lung than in other organs. An optimal nonviral gene delivery aerosol formulation of a polylysine/protamine combination was developed successfully.[135] While this polylysine/protamine combination showed 3- to 17-fold higher transfection efficiency than PEI *in vitro*, its inhalation caused only low and reversible toxicity in the lung and no systemic toxicity.

Poly(2-(dimethylamino)ethyl methacrylate) (pDMAEMA). In 1996, the polymer pDMAEMA was first described by Cherng as a water-soluble nonviral gene delivery polymer with tertiary amino side groups that condense negatively charged DNA.[136] Although pDMAEMA strongly complexes DNA, its high cytotoxicity, due to the high density of positive charges, limits the application of pDMAEMA. Instead of the so-called "PEGylation" of cationic polymers, the cytotoxicity of pDMAEMA can be reduced by modification with oligo(ethylene glycol) methyl ether methacrylates (OEGMA) during atom transfer radical polymerization (ATRP)[137] or with poly(2-hydroxyethyl methacrylate) (pHEMA) via reversible addition−fragmentation chain transfer (RAFT) polymerization.[138] Although the *in vitro* transfection efficiency of the most promising p(DMAEMA-*co*-OEGMA) copolymers in human bronchial epithelial cells was lower compared to branched PEI 25 kDa, 7-fold higher transfection efficiency could be observed for p(DMAEMA-*co*-OEGMA) in lung homogenates after *in vivo* administration in comparison to branched PEI.

Dextran−Spermine (D-SPM). PEGylated dextran−spermine was recently synthesized and successfully increased the transgene expression compared to unmodified D-SPM.[139] The

dx.doi.org/10.1021/bc200296q | *Bioconjugate Chem.* 2012, 23, 3−20

transfection efficiencies of the dextran−spermine conjugates depended on the proportion of grafted spermine. Interestingly, hydrophobization of D-spermine with oleate significantly enhanced the transfection efficiency of D-spermine because the oleate modification improved not only the stability of the polymer/DNA complexes, but also the uptake of the complexes into cells.[140] Results showed that increasing the pDNA content within the complex enhanced the complex size, with a pDNA content of 13.5 μg required for the highest gene expression in the lung. In addition, the D-spermine/pDNA weight ratio and detection time post delivery were also important parameters that affected the results of the transfection efficiency.[141]

Compared with PEI, some other cationic gene delivery vectors show no obvious advantages, such as greater transfection efficiency, due to their high cytotoxicity. Accordingly, pLL, for example, has gradually lost its importance in nonviral gene delivery. However, on the other hand, other upcoming cationic polymers have become promising gene delivery vectors of the future due to their high biocompatibility and biodegradability. One example is pDMAEMA with degradable side chains. In conclusion, all of the cationic polymers have the prerequisite of a positively charged surface for the condensation and protection of genetic materials against degradation. High cytotoxicity and aggregation of colloids due to their positive charges is the "Achilles' heel" of cationic polymer-based gene delivery systems. To improve these drawbacks, novel surface modifications, possibly after the condensation of the genetic material, may be a promising approach. Negatively charged ligand molecules could neutralize the positive charges and therefore reduce the cytotoxicity. On the other hand, the modification with targeting vectors can additionally achieve a selective uptake into target cells.

Biodegradable PLGA-Based Gene Delivery Systems. This section especially reviews the biodegradable polymers poly(lactic-*co*-glycolic acid) (PLGA) as micro- and nanoparticle formulations for pulmonary gene delivery. Owing to its biodegradability and biocompatibility, PLGA has been accepted by the U.S. Food and Drug Administration (FDA) for certain human clinical applications such as resorbable sutures, bone implants, and scaffolds in tissue engineering and has been extensively used for drug or gene material delivery. However, PLGA was not especially designed for gene delivery and shows several drawbacks such as the low encapsulation of plasmid DNA in hydrophobic PLGA micro- and nanoparticles formulations, DNA degradation during the hydrolysis of PLGA, and slow release of DNA from PLGA. To overcome the limitations of PLGA for DNA delivery, modification of the PLGA micro- or nanospheres is necessary. Nevertheless, with the help of cationic polymers, the encapsulation of plasmid DNA in PLGA can be enhanced. For example, negatively charged DNA can be precondensed with positive poly(L-lysine),[142−144] poly(ethylene imine),[145−147] chitosan,[148−150] and water-insoluble stearylamine.[151] In the case of poly(ethylene imine)-PLGA, particles of linear PEI-PLGA showed more effective DNA release than branched PEI-PLGA.[152] Enhancing the DNA release from PLGA micro- or nanospheres is a great challenge. Kusonwiriyawong et al.[151] and Tinsley-Bown et al.[153] found that using more hydrophilic PLGA not only improves the encapsulation of DNA, but also results in a faster release of DNA. Moreover, the preparation technique is an important factor for the release kinetics of DNA from PLGA. For example, DNA was released more quickly when incorporated using a water−oil emulsion/diffusion technique than when incorporated by water−oil−water emulsion.[154] Bivas-Benita et al. investigated gene delivery to pulmonary epithelium using PLGA-PEI nanoparticles.[155] Cytotoxicity of these PLGA-PEI nanoparticles depended on the PEI/DNA ratio but not the PLGA-PEI ratio. Relatively good cell viability was found for PEI/DNA ratios between 0.5 and 1. Further investigations by Bivas-Benita et al. indicated that PLGA-PEI nanoparticles can also be used successfully as pulmonary DNA vaccine delivery vector against tuberculosis.[156] Excipients such as hydroxypropylcellulose (HPC), chitosan, Carbopol, carboxymethylcellulose, hyaluronic acid, and poly(acrylic acid) are considered to be mucoadhesive agents in the airway.[157] Carbopol has been successfully used as an agent to enhance mucoadhesion in combination with other delivery systems.[158] Recent research has shown that the transfection efficiency of 0.02% Carbopol 940 (CP)-PLGA nanoparticles in A549 cells over 48 h was comparable to that of Lipofectamine 2000.[159]

Another approach to introduce cationic charges into PLGA to enable condensation of DNA is the grafting of diethylaminopropylamine polyvinyl alcohol with PLGA (DEAPA-PVAL-g-PLGA). The aim was to obtain polyesters that degrade more rapidly than PLGA and would therefore be suitable for repeated administration. Dailey et al. prepared nanoparticles for pulmonary application with this PLGA derivative[160] and studied the proinflammatory potential of this biodegradable pulmonary delivery system.[161] The results indicated that the inflammatory response of biodegradable nanoparticles based on PLGA and its DEAPA-PVAL derivative was lower than that mediated by nonbiodegradable nanoparticles such as polystyrene (PS). To further optimize the transfection efficiency of DEAPA-PVAL-g-PLGA, Nguyen et al. formed ternary nanocomposites made up of pDNA, modified PLGA, and different coating materials such as the lung surfactant, negatively charged carboxymethyl cellulose, or poloxamer. The nanocomposites were compared concerning their ability to improve the physicochemical properties, cytotoxicity, and biological activity. Coating with negatively charged carboxymethyl cellulose reduced cytotoxicity of these nanocomposites, while all other nanocomposites with positive surface charges showed a higher toxicity. Following addition of lung surfactant, the cellular uptake as well as the transfection efficiency of the nanocomposites was significantly increased.[62]

Although PLGA has some drawbacks as gene delivery vector such as the low encapsulation of plasmid DNA and relatively slow degradation rates, many biodegradable gene delivery systems are still based on PLGA. Recently, the main focus of transfection is not only on the successful delivery of the genetic material into the cells, but also on the sustained and controlled gene expression. Therefore, rationally designed polymeric vectors based on PLGA or other biodegradable polymers, which can also control the DNA release and transgene expression, will provide opportunities and challenges for pulmonary gene delivery in the future.

Several groups of nonviral polymeric gene delivery agents have been reviewed and discussed, and they all have been applied for pulmonary DNA delivery with varying degrees of success.

However, it is difficult to compare and discuss the level or efficiency of gene expression obtained by different delivery agents, different genes delivered, different promoters, and different assays used, except when the different polymeric gene delivery agents were directly compared in the same sets of experiments. In all of the polymeric DNA delivery agents,

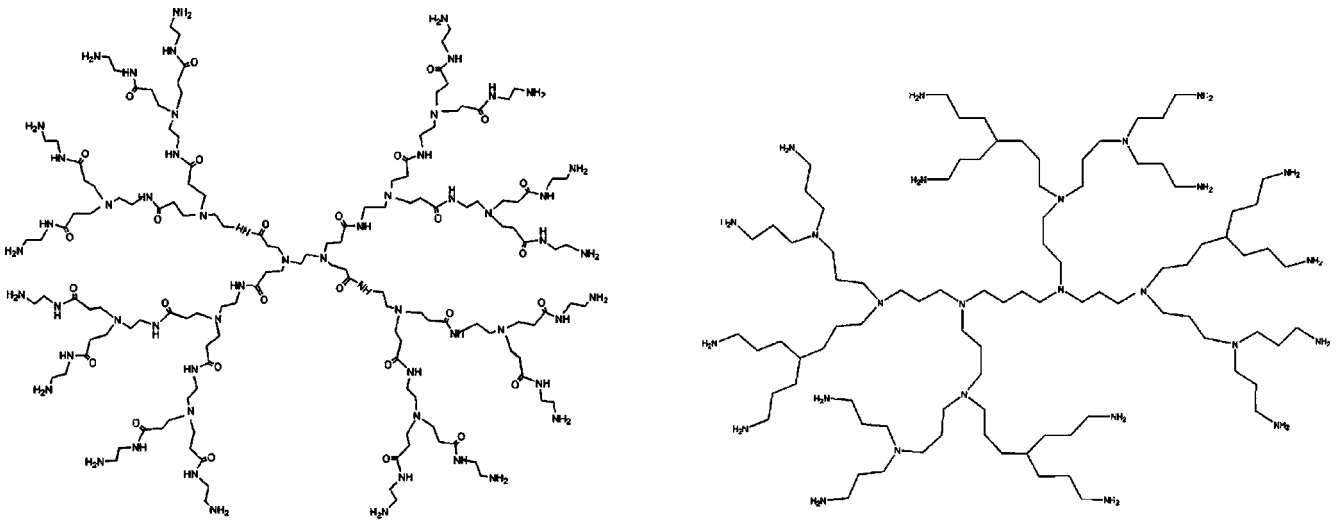


Figure 5. Chemical structures of generation 2 ethylene diamine core PAMAM and generation 3 DAB core PPI with 16 primary amines.

poly(ethylene imine) was studied most widely by various research groups and showed a very effective condensation, protection, and release of the DNA with subsequent transgene expression. In further development of polymeric DNA delivery vectors, which was based on the experience with PEI, various modifications of PEI have also been designed and applied with varying degrees of success. Polyplexes of plasmids and polymers can be prepared relatively easily, and some of the delivery systems may be nearly ready for clinical application. Recently, more and more attention has been paid to multifunctional pulmonary polymeric gene delivery vectors, which should not only be biodegradable, nontoxic, and bioresponsive. However, to also be suitable for pulmonary delivery, the delivery systems would have to be aerosolizable and would need to mediate rapid penetration of the structural lung barriers. Therefore, we believe that DNA nanocariers composed of multifunctional polymers could possibly meet these criteria and be successful in clinical trials. Addition of targeting ligands to multifunctional nanoparticles may further improve the specificity of gene transfer to airway or alveolar epithelium, which will be introduced in the following section of targeting strategies.

Dendritic Vectors. Dendrimers are globular, hyperbranched macromolecules with precise core−shell nanostructures in which every repeated sequence represents a higher generation.[162,163] Due to their hypothetical monodispersity, dendrimers are interesting carriers for small molecule drugs[164] and nucleic acids.[165] Before dendrimers were first employed for pulmonary gene delivery, the stability of DNA complexes of polyamidoamine (PAMAM) of unspecified core composition and generation was characterized in the presence of pulmonary surfactant.[59] The authors found that dendriplexes stably protected DNA from degradation by DNase I in the presence of phospholipids alone or Alveofact. Their transfection efficiency was not affected in pulmonary cell lines in the presence of the natural surfactant Alveofact and in none of the cell lines tested in the presence of the synthetic surfactant Exosurf.[59]

Interestingly, mixing of Exosurf with Starburst dendritic generation 9 PAMAM with an ethylenediamine core (G9 EDA)[166] even enhanced the dendrimer mediated luciferase expression 40-fold in primary normal human bronchial/tracheal epithelial cells (NHBE).[60] This dendrimer was synthesized via Michael addition of the nucleophilic core to methacrylate, followed by addition to a large excess of ethylene diamine.[167] It was shown that the nonionic surfactant tyloxapol, which is a component of Exosurf, acted as penetration enhancer and induced increased uptake of DNA *in vitro*.

In a study comparing the biodistribution of transgene expression as a function of administration route, DNA complexes of Starburst G9 EDA PAMAM were administered intratracheally, intranasally, and intravenously. Surprisingly, transgene expression after local administration of dendriplexes was even lower than compared with naked DNA, while the opposite was true for systemic administration. Additionally, dendriplex-mediated reporter gene expression after local administration was limited to the lung.[168] Comparably, SuperFect, a generation 4 fractured PAMAM dendrimer,[169] also generated only very low luciferase reporter gene expression in the lung,[61] although its *in vitro* efficacy was not inhibited by the presence of mucin or α1-glycoprotein.[49]

In recent years, PAMAM and diaminobutane (DAB) dendrimers were described to up- and downregulate hundreds of genes in treated cells.[170] Interestingly, generation 3 polypropylenimine diaminobutane (DAB) dendrimers with 16 protonable peripheral amines mediated high transfection efficiencies in A431 and A549 cells; however, both the dendrimer alone and the dendriplexes caused upregulation of epidermal growth factor receptor (EGFR) expression and activated its downstream Akt signaling.[171] Comparably, Starburst PAMAM was shown to induce acute lung injury *in vivo* triggered by activation of autophagic cell death by deregulation of the Akt-TSC2-mTOR signaling pathway.[172] Therefore novel, biocompatible dendritic vectors need to be developed.

A bis-(guanidinium)-tetrakis-(β-cyclodextrin) dendrimeric tetrapod was recently synthesized in two steps from a carbodiimide-β-cyclodextrin dimer in a Staudinger-Aza-Wittig tandem reaction. Two dimers were subsequently linked via nucleophilic substitution and hydrolysis of 1,2-dibromoethane. The resulting dendrimeric tetrapod achieved high gene

dx.doi.org/10.1021/bc200296q | *Bioconjugate Chem.* 2012, 23, 3−20

Table 2. Overview of Studies Describing Polymeric Nonviral Gene Delivery to the Lung Using Ligands for Active Targeting

targeting ligand	polymer	important finding	first author	year	ref
Mannuronic acid, Galacturonic acid, lactobionic acid	PEI, PEI-PEG	High gene expression with mannuronic acid-functionalized PEI in different cell lines	Weiss	2006	176
Lactose, Glucose, Mannose	PEI	Insights in the intracellular trafficking of Lactose-PEI polyplexes *in vivo*	Grosse	2008	177
Different sugars	PLL	High gene expression after pDNA delivery with lactosylated PLL in primary cystic fibrosis airway epithelial cells	Kollen	1996	178
Glucose	PEI	Efficient gene delivery after nasal application in mice	Kim	2004	8
Trisaccharide	Chitosan	Enhanced colloidal stability, uptake and gene expression with modified chitosan *in vitro* and *in vivo*	Issa	2006	125
Folate	(HPMA-stat-APMA)-b-DMAPMA	Specific knock-down in folate receptor expressing cells	York	2009	179
Lactoferrin	PEI	Specific gene expression in bronchial epithelial cells	Elfinger	2007	180
Anisamide	Protamine, lipids	Successful tumor growth inhibition after tagreted delivery of siRNA	Li	2008	181
Glucocorticoid responsive element	PEI	Increased gene expression in mouse lungs	Dames	2007	182
C105Y	PLL	Successful *in vivo* gene expression for cystic fibrosis treatment	Ziady	2002	183
Antiendothelial cell adhesion molecule-1 antibody	PEI	Transfection of mouse lung endothelial cells	Li	2000	184
Anti-Polymeric immunoglobulin receptor antibody (Fab)	PLL	Targeted DNA delivery to the respiratory endothelium of rats	Ferkol	1995	185
Clenbuterol	PEI	Increased transfection efficiency on alveolar epithelial cells	Elfinger	2009	186

transfection in primary human lung fibroblasts;[173] however, *in vivo* biocompatibility and efficacy are still to be investigated.

Targeted Vectors. As described above, PEIs can be modified with the cell penetrating peptide TAT,[63] biotinylated TAT-RGD,[116] or galactose[117] to improve their interaction with the cell surface and eventually their cellular uptake. For active targeting approaches, polyplexes are coupled with a ligand of choice that is expected to interact with a specific target on the cell surface. An overexpression of this molecule in the target cell type is necessary if high uptake is intended.

To develop successful targeted polyplexes, it is necessary to identify structures on the cell surface which could provide a selective uptake into the cell. In most cases, the target structure is an internalizing receptor on the cell surface that is targeted by its natural ligand or an antibody, but other structures on the cells might also be suitable. An approach for identifying ligands for lung targeting by phage display was described by Giordano et al.[175]

There are only a few studies describing active targeting approaches to the lung or lung cells using a polymeric nonviral vector. Of course, liposomes and viral vectors have been used for active lung targeting, but these will not be discussed in this review. This section will provide an overview on different approaches for active lung targeting using polymeric nonviral vectors. Poly(ethylene imine) (PEI) and poly(L-lysine) (PLL) are dominating this group but other polymers were used as well. The studies described are additionally outlined in Table 2.

Sugars and Sugar Derivatives. Weiss et al.[176] used uronic acids (galacturonic acid, mannuronic acid) and lactobionic acid for functionalization of PEI and PEI-PEG-copolymers. This modification was carried out in order to target specific tissues, e.g., airway epithelial cells. The conjugates prepared were characterized intensively and molecular characteristics were given. However, the authors were not able to confirm improved cell transfection in the airway epithelial cell line 16HBE14o$^-$ with lactobionic acid conjugates, which were initially intended for targeting these cells. In contrast, mannuronic acid conjugates were more successful and showed receptor-mediated cell transfection, even in the airway cells that they were not primarily intended for.

Grosse et al.[177] investigated glycosylated PEI as a potential cystic fibrosis therapy. The intracellular trafficking of lactosylated PEI *in vitro* and in mouse lungs after intranasal instillation was more efficient than for unmodified PEI.

Years before, PLL was already conjugated with gluconolactone by Kollen et al. [178] who also discussed the possibility of a cystic fibrosis treatment with these conjugates. Lactose-modified PLL/pDNA polyplexes led to high reporter gene expression in primary cystic fibrosis cells. Gene expression was further improved by the addition of chloroquine, which enhanced endosomal release.

Glucosylated PEI was used by Kim et al.[8] for the targeted treatment of lung cancer via aerosol delivery of DNA polyplexes. They examined gene regulation following delivery of a plasmid encoding a tumor suppressor gene *in vivo* and concluded that their model could be applied for noninvasive lung cancer treatment.

Chitosan was used for conjugation in a study by Issa et al.,[125] who functionalized it with a trisaccharide for targeting of cell-surface lectins. These conjugates transfected both bronchial epithelial cells and human liver hepatocytes *in vitro* and therefore did not provide cell type specificity. However, higher gene expression was shown after intratracheal administration in mice compared to unmodified chitosan.

Sugars or sugar derivatives as targeting ligands have been coupled to different polymers and have shown somewhat interesting results. Unfortunately, distinct lung specificity of these conjugates could not be shown, if not administered to the lung directly.

Receptor Ligands. Folate was likewise used as a targeting moiety for lung targeting. York et al.[179] described the synthesis of a copolymer, which consists of *N*-(2-hydroxypropyl)-methacrylamide) (HPMA), *N*-(3-aminopropyl)methacrylamide (APMA), and poly(*N*-[3-(dimethylamino)propyl]-methacrylamide) (DMAPMA). This polymer was coupled to folic acid to use the bioconjugate for polyplex formation with siRNA. These polyplexes were examined in A549 human lung cancer cells and KB cells, which are folate receptor over-expressing nasopharynx carcinoma cells. The conjugates were

dx.doi.org/10.1021/bc200296q | *Bioconjugate Chem.* 2012, 23, 3–20

shown to provide gene knockdown in KB cells by a receptor mediated pathway.

Another receptor ligand which was evaluated for targeted gene delivery to the lung is lactoferrin (Lf).

Elfinger et al.[180] detected lactoferrin receptors on bronchial epithelial cells (BEAS-2B). This finding led the authors to the preparation of conjugates of lactoferrin and PEI which were used for the complexation of pDNA. Polyplexes with Lf-PEI showed significantly higher luciferase expression after transfection of a luciferase encoding plasmid than unmodified PEI in BEAS-2B cells, but not in alveolar epithelial cells (A549). Receptor specific transfection was shown by competition with free lactoferrin which significantly reduced the luciferase expression in BEAS-2B cells.

Targeting the epidermal growth factor receptor (EGFR) was the subject of a study by Li et al.,[181] which should be mentioned here despite not using polyplexes, but self-assembled nanoparticles, for siRNA delivery. Anisamide was incorporated in these particles for treatment of tumors, especially in the lung. The treatment resulted in decreased tumor growth and exhibited synergistic effects with cisplatin.

Dames et al.[182] chose a completely different approach for targeted gene delivery to the lung. They cloned a glucocorticoid responsive element (GRE) which binds to the glucocorticoid receptor as a targeting moiety into the plasmid to be delivered and did not couple it to the surface of a polymer vector. This modified plasmid was complexed with PEI and administered to mice as aerosol. Compared to the administration of an unmodified EGFP encoding plasmid, their vector system led to a 4.7-fold higher gene expression when combined with dexamethasone treatment.

A study by Ziady et al.[183] should be mentioned in this review as well, although it described targeting to nasal epithelium and not to the lung itself, but provides evidence for the treatment of CF. The authors conjugated a ligand called C105Y targeting the serpin receptor complex to PLL. This bioconjugate was complexed with DNA encoding the human cystic fibrosis transmembrane conductance regulator (CFTR), which is involved in CF pathophysiology. In cystic fibrosis mutant mice, the chloride transport defect was partially corrected by the use of the described polyplexes.

These receptor ligand based strategies demonstrate potential for lung targeting. However, in some studies, specific uptake should have been shown by competition experiments with the unconjugated ligand. The results from the studies summarized here lead to the presumption that targeted gene delivery to these cells may be possible and provides potential for the treatment of lung diseases.

Antibodies and Fragments. An antibody-mediated targeting strategy to the pulmonary endothelium was evaluated by Li et al.[184] PEI-conjugates were prepared with an antibody against the endothelial cell adhesion molecule-1 (PECAM-1 or CD31). These conjugates were complexed with luciferase encoding pDNA, and transfection to mouse lung endothelial cells was assessed *in vitro* and after intravenous injection *in vivo*. Polyplexes with the antibody conjugates were shown to provide higher gene expression than polyplexes with PEI or with PEI coupled to an unspecific antibody.

The Fab fragments of polyclonal antibodies directed against the polymeric immunoglobulin receptor in conjugation with poly(L-lysine) were used for specific targeting of lung cells by Ferkol et al.[185] The authors evaluated biodistribution and transfection kinetics of the polyplexes with this carrier and pDNA after infusion in rats. Data on the expression of this receptor in the lung tissue are also provided and confirmed expression on serous cells of the submucosal glands. Therefore, the authors accentuate the potential of their carrier system in cystic fibrosis treatment.

Other Targeting Ligands. A completely different targeting strategy was published by Elfinger et al.[186] They did not use a protein or higher molecular weight molecule as targeting ligand, but the conventional active ingredient clenbuterol, which is a β2-receptor agonist. Because this receptor is highly expressed in lung cells, the authors assumed that this active compound would provide lung targeting. Transfection efficiency was evaluated in different bronchial and alveolar epithelial cell lines as well as after inhalation of the aerosolized formulation by mice. Furthermore, the polyplexes were characterized intensively. Plasmid DNA transfection efficiency in alveolar epithelial cells was enhanced by the clenbuterol-PEI conjugate in comparison to free PEI and also *in vivo* transfection efficiency could be increased 3-fold. The *in vitro* transfection efficiency could be inhibited by free clenbuterol, suggesting a specific uptake of the polyplexes.

In conclusion, the highest probability to successfully target the lung can be achieved by selecting an internalizing receptor that is highly expressed by the target tissue in combination with local administration by aerosol.

In Vitro and in Vivo Testing. Sophisticated in Vitro Models. Since the lung is a very complex organ in which the epithelium differentiates in layers of cells with a distinct apical and basolateral side, conventional cell culture does not accurately reflect this *in vivo* condition. Pulmonary epithelial cells are connected to each other by tight junctions and characterized by apically located cilia, which are covered underneath the mucus produced by secretory cells.[187] The Calu-3 cell line is a popular model of airway epithelium, as it develops both tight junctions and produces mucus when cultured in an air-interface culture (AIC).[187] An even better model is obtained by AIC of human primary small airway epithelial cells (HSAEC) on fibrillar collagen/fibronectin cell culture inserts. Monocytes obtained from peripheral blood mononuclear cells (PBMC) are then seeded on top and after several days of coculture differentiate into macrophages. This renders this model suitable for the investigation of the respective roles of epithelial cells and macrophages and their interplay regarding the clearance of pathogens.[188] A further development that has been used to study the interaction of the human respiratory tract with particles of 1 μm in diameter was an AIC triple coculture model using A549 epithelial cells supplemented with apical human blood monocyte−derived macrophages and basolateral dendritic cells.[189] Both coculture models could be adapted for *in vitro* investigations of cell-type specific transfection and uptake of gene delivery systems.

Ex Vivo Models. The most common *ex vivo* model is the isolated perfused lung (IPL),[190] which, however, is only viable for short periods of 2−3 h. Additionally, the absence of the tracheo-bronchial circulation renders the model kinetically unpredictive for small molecules.[6]

Another popular model uses sheep trachea tissue onto which CF sputum can additionally be mounted. In a study concerning interactions of gene carriers with extracellular components, normal sheep respiratory mucus reduced the transfection efficiency of adenoviruses or Sendai virus, but not of lipoplexes or polyplexes. However, CF sputum provides a greater hurdle for adenoviruses than for lipoplexes.[191]

In Vivo Models. Although intratracheal instillation cannot be realized for clinical administration in man, it is the most frequently applied technique in lab-scale *in vivo* research, despite the emerging lung deposition profiles often being patchy and far from physiological.[192] Since rodents are obligatory nasal breathers, intranasal administration of gene delivery vectors has successfully resulted in deposition in the lower airways.[193] However, in humans intranasal administration only leads to transgene expression in the nasal epithelia.[194] Therefore, microspray devices introduced through a bronchoscope have been developed and can improve the vector distribution throughout the lung.[195−197] For inhalation, the formulation has to withstand the shear forces during nebulization.[198] Additionally, large amounts of expensive material are lost in the aerosolization equipment, inhalation chamber, oropharynx, and in the upper airway mucosa. However, inhalation of nanoparticle aerosols is considered the optimal administration technique, as particle deposition is expected to be more uniform and closer to a physiological distribution. Accordingly, it was shown that 350 ng aerosolized pDNA formulated with PEI led to 15-fold higher transgene expression than a 140-fold higher dose of pDNA (50 μg) administered by intratracheal instillation.[10] Similar results were described for the delivery of siRNA formulated as chitosan polyplexes. Strong knockdown was observed after intratracheal aerosolization of doses as low as 260 ng siRNA[199] compared to intranasally administered chitosan complexes of 30 μg siLNA per mouse.[200] While most of the *in vivo* pulmonary gene delivery is studied in small animals such as mice and rats, a few reports can be found in the literature where swine[201] and sheep[202] served as large animal models which are clinically more relevant.

The biodistribution of gene delivery vectors is conventionally measured by quantification of transgene expression in several organs *ex vivo*.[185] Novel approaches have applied live fluorescence imaging to detect biodistribution.[203] Gamma camera imaging of radiolabeled particles has been employed for several years to detect the deposition of nanoparticles in the lung;[94,204] however, it has only recently been reported for detection of biodistribution and translocation of intratracheally administered nucleic acid delivery systems.[50] The broad opportunities for molecular imaging approaches for the measurement of biological processes in living animals have only been exploited in a few preliminary studies. This lack of study using molecular imaging reflects the need for validated biomarkers and monitoring techniques.[205] An interesting example of such a probe is Prosense-750 (Visen Medical), a near-infrared AlexaFluor 750-based probe that is activated upon cleavage by cysteine proteases, particularly cathepsin B. Prosense-750 was described to accurately visualize primary lung tumors and surrounding tissue affected by tumor progression and inflammation.[206]

Models of pathologic bronchoconstriction, human infectious diseases, emphysema, influenza, pulmonary fibrosis, cystic fibrosis, lung cancer, lung injury, and allergies have been reviewed elsewhere. Additionally, models for delivery of insulin and vaccines have been previously described.[6]

It must be noted that animal models only represent efficiency in a certain animal species and strain, and can vary substantially.[174] The anatomy of the lung of laboratory animals is different from the human anatomy; e.g., the right lung of mammals is divided in 4 lobes, whereas the left lung of mice is not divided at all.[6] Additionally, the airway branching patterns also vary between species.[207] Attention must also be paid to the reporter gene chosen for an *in vivo* study. While robust transgene expression levels were not achieved using firefly luciferase (FLuc) following transfection of AIC human airway cells or in sheep lungs *in vivo*, a novel luciferase from *Gaussia princeps* (GLuc) was shown to be a more sensitive reporter gene in preclinical models for pulmonary gene delivery.[208]

CONCLUSION

In this review, the development of nonviral pulmonary gene delivery is summarized. Because of the active interface of the airway epithelium cells with the environment, the lung has been considered a promising target organ to locally deliver genetic material. In addition to mediating high gene expression levels at low toxicity, the special requirements of a pulmonary gene delivery vector are high affinity between the vector and the pulmonary epithelial cell surface and low deposition in the conducting airways. Several recent reports have described the different toxicity levels of nondegradable polymeric gene delivery vectors.[81,88,209] Therefore, hopefully in the future greater emphasis will be placed on biodegradable and targeted nonviral vectors. With increasing attention to "toxicogenomics",[171] activation of the complement system,[209] and inflammation pathways[48] by nonviral gene delivery vectors, the future trend is expected to move toward biodegradable and more biocompatible polymers. So far, most of the pulmonary gene delivery studies have focused on preclinical investigations using *in vitro* or *in vivo* models. Clinical success not only depends on the development of more effective, biocompatible, and targeted gene delivery vectors, but also requires deeper understanding of the mechanisms of successful pulmonary gene delivery. Additionally, the development of stable formulations of therapeutic genes that can be realistically administered to man by inhalation is still a major bottleneck. In our review, the discussion is focused on nonviral pulmonary DNA delivery systems. The development of local delivery of siRNAs to the lung for the treatment of lung diseases is another rapidly developing field where clinical studies are already being undertaken.[210] It may be anticipated that this development could possibly also drive the pulmonary gene delivery sector into clinical translation. Not only the delivery system, but also the load, could be improved. Concerning the improvement and prolongation of transgene expression, especially in quiescent cells and tissues, minicircle DNA (mcDNA) may be a promising candidate and should be evaluated for pulmonary gene delivery.

AUTHOR INFORMATION

Corresponding Author

*Thomas Kissel, Philipps-Universität Marburg, Dept. Pharmaceutics and Biopharmacy, Ketzerbach 63 D-35032 Marburg, Germany. TEL: +49-6421-282 5881, FAX: +49-6421-282 7016, E-mail: Kissel@staff.uni-marburg.de.

ACKNOWLEDGMENTS

The authors thank Dr. Leigh Marsh for thoroughly editing the manuscript. MEDITRANS, an Integrated Project funded by the European Commission under the Sixth Framework (NMP4-CT-2006-026668)n, is gratefully acknowledged.

REFERENCES

(1) Patton, J. S. (1996) Mechanisms of macromolecule absorption by the lungs. *Adv. Drug Delivery Rev. 19*, 3−36.

(2) Kinsey, B. M., Densmore, C. L., and Orson, F. M. (2005) Non-viral gene delivery to the lungs. *Curr. Gene Ther. 5*, 181−94.

(3) Aneja, M. K., Geiger, J. P., Himmel, A., and Rudolph, C. (2009) Targeted gene delivery to the lung. *Expert Opin. Drug Delivery 6*, 567−83.

(4) Griesenbach, U., and Alton, E. W. F. W. (2009) Gene transfer to the lung: Lessons learned from more than 2 decades of CF gene therapy. *Adv. Drug Delivery Rev. 61*, 128−139.

(5) Sanders, N., Rudolph, C., Braeckmans, K., De Smedt, S. C., and Demeester, J. (2009) Extracellular barriers in respiratory gene therapy. *Adv. Drug Delivery Rev. 61*, 115−27.

(6) Cryan, S. A., Sivadas, N., and Garcia-Contreras, L. (2007) *In vivo* animal models for drug delivery across the lung mucosal barrier. *Adv. Drug Delivery Rev. 59*, 1133−51.

(7) Bennett, R. M., Cornell, K. A., Merritt, M. J., Bakke, A. C., Mourich, D., and Hefeneider, S. H. (1992) Idiotypic mimicry of a cell surface DNA receptor: evidence for anti-DNA antibodies being a subset of anti-anti-DNA receptor antibodies. *Clin. Exp. Immunol. 90*, 428−33.

(8) Kim, H. W., Park, I. K., Cho, C. S., Lee, K. H., Beck, G. R. Jr., Colburn, N. H., and Cho, M. H. (2004) Aerosol delivery of glucosylated polyethylenimine/phosphatase and tensin homologue deleted on chromosome 10 complex suppresses Akt downstream pathways in the lung of K-ras null mice. *Cancer Res. 64*, 7971−6.

(9) Densmore, C. L., Orson, F. M., Xu, B., Kinsey, B. M., Waldrep, J. C., Hua, P., Bhogal, B., and Knight, V. (2000) Aerosol delivery of robust polyethyleneimine-DNA complexes for gene therapy and genetic immunization. *Mol. Ther. 1*, 180−8.

(10) Rudolph, C., Schillinger, U., Ortiz, A., Plank, C., Golas, M. M., Sander, B., Stark, H., and Rosenecker, J. (2005) Aerosolized nanogram quantities of plasmid DNA mediate highly efficient gene delivery to mouse airway epithelium. *Mol. Ther. 12*, 493−501.

(11) Yang, W., Peters, J. I., and Williams, R. O. 3rd (2008) Inhaled nanoparticles--a current review. *Int. J. Pharm. 356*, 239−47.

(12) Muir, D. F. C. (1991) Particle deposition, in *The Lung: Scientific foundations* (West, R. G. C. a. J. D., Ed.) pp 1839−1843, Raven Press, Ltd., New York.

(13) Wright, J. R. (2005) Immunoregulatory functions of surfactant proteins. *Nat. Rev. Immunol. 5*, 58−68.

(14) Rothen-Rutishauser, B., Muhlfeld, C., Blank, F., Musso, C., and Gehr, P. (2007) Translocation of particles and inflammatory responses after exposure to fine particles and nanoparticles in an epithelial airway model. *Part Fibre Toxicol. 4*, 9.

(15) Look, D. C., and Brody, S. L. (1999) Engineering viral vectors to subvert the airway defense response. *Am. J. Respir. Cell Mol. Biol. 20*, 1103−6.

(16) Bromberg, J. S., Debruyne, L. A., and Qin, L. (1998) Interactions between the immune system and gene therapy vectors: bidirectional regulation of response and expression. *Adv. Immunol. 69*, 353−409.

(17) Stone, K. C., Mercer, R. R., Gehr, P., Stockstill, B., and Crapo, J. D. (1992) Allometric relationships of cell numbers and size in the mammalian lung. *Am. J. Respir. Cell Mol. Biol. 6*, 235−43.

(18) Gehr, P., Bachofen, M., and Weibel, E. R. (1978) The normal human lung: ultrastructure and morphometric estimation of diffusion capacity. *Respir. Physiol. 32*, 121−40.

(19) Groneberg, D. A., Witt, C., Wagner, U., Chung, K. F., and Fischer, A. (2003) Fundamentals of pulmonary drug delivery. *Respir. Med. 97*, 382−7.

(20) Jiang, H. L., Xu, C. X., Kim, Y. K., Arote, R., Jere, D., Lim, H. T., Cho, M. H., and Cho, C. S. (2009) The suppression of lung tumorigenesis by aerosol-delivered folate-chitosan-graft-polyethylenimine/Akt1 shRNA complexes through the Akt signaling pathway. *Biomaterials 30*, 5844−52.

(21) Courrier, H. M., Butz, N., and Vandamme, T. F. (2002) Pulmonary drug delivery systems: recent developments and prospects. *Crit. Rev. Ther. Drug Carrier Syst. 19*, 425−98.

(22) Byron, P. R. (1986) Prediction of drug residence times in regions of the human respiratory tract following aerosol inhalation. *J. Pharm. Sci. 75*, 433−8.

(23) Martonen, T. B., and Katz, I. M. (1993) Deposition patterns of aerosolized drugs within human lungs: effects of ventilatory parameters. *Pharm. Res. 10*, 871−8.

(24) Vincent, J. H., Johnston, A. M., Jones, A. D., Bolton, R. E., and Addison, J. (1985) Kinetics of deposition and clearance of inhaled mineral dusts during chronic exposure. *Br. J. Ind. Med. 42*, 707−15.

(25) Heyder, J. (2004) Deposition of inhaled particles in the human respiratory tract and consequences for regional targeting in respiratory drug delivery. *Proc. Am. Thorac. Soc. 1*, 315−20.

(26) Chalupa, D. C., Morrow, P. E., Oberdorster, G., Utell, M. J., and Frampton, M. W. (2004) Ultrafine particle deposition in subjects with asthma. *Environ. Health Perspect. 112*, 879−82.

(27) Kleinstreuer, C., Zhang, Z., and Li, Z. (2008) Modeling airflow and particle transport/deposition in pulmonary airways. *Respir. Physiol. Neurobiol. 163*, 128−38.

(28) Dames, P., Gleich, B., Flemmer, A., Hajek, K., Seidl, N., Wiekhorst, F., Eberbeck, D., Bittmann, I., Bergemann, C., Weyh, T., Trahms, L., Rosenecker, J., and Rudolph, C. (2007) Targeted delivery of magnetic aerosol droplets to the lung. *Nat. Nanotechnol. 2*, 495−9.

(29) Geiser, M., Schurch, S., and Gehr, P. (2003) Influence of surface chemistry and topography of particles on their immersion into the lung's surface-lining layer. *J. Appl. Physiol. 94*, 1793−801.

(30) Knowles, M. R., and Boucher, R. C. (2002) Mucus clearance as a primary innate defense mechanism for mammalian airways. *J. Clin. Invest. 109*, 571−7.

(31) Florea, B. I., Cassara, M. L., Junginger, H. E., and Borchard, G. (2003) Drug transport and metabolism characteristics of the human airway epithelial cell line Calu-3. *J. Controlled Release 87*, 131−8.

(32) Yeates, D. B., Aspin, N., Levison, H., Jones, M. T., and Bryan, A. C. (1975) Mucociliary tracheal transport rates in man. *J. Appl. Physiol. 39*, 487−95.

(33) Yeates, D. B., Sturgess, J. M., Kahn, S. R., Levison, H., and Aspin, N. (1976) Mucociliary transport in trachea of patients with cystic fibrosis. *Arch. Dis. Child 51*, 28−33.

(34) Widdicombe, J. G. (1997) Airway liquid: a barrier to drug diffusion? *Eur. Respir. J. 10*, 2194−7.

(35) Lopez-Vidriero, M. T., and Reid, L. (1978) Bronchial mucus in health and disease. *Br. Med. Bull. 34*, 63−74.

(36) Creeth, J. M. (1978) Constituents of mucus and their separation. *Br. Med. Bull. 34*, 17−24.

(37) Carlstedt, I., Sheehan, J. K., Corfield, A. P., and Gallagher, J. T. (1985) Mucous glycoproteins: a gel of a problem. *Essays Biochem. 20*, 40−76.

(38) Jacquot, J., Hayem, A., and Galabert, C. (1992) Functions of proteins and lipids in airway secretions. *Eur. Respir. J. 5*, 343−58.

(39) Sheils, C. A., Kas, J., Travassos, W., Allen, P. G., Janmey, P. A., Wohl, M. E., and Stossel, T. P. (1996) Actin filaments mediate DNA fiber formation in chronic inflammatory airway disease. *Am. J. Pathol. 148*, 919−27.

(40) van Heeckeren, A., Ferkol, T., and Tosi, M. (1998) Effects of bronchopulmonary inflammation induced by pseudomonas aeruginosa on adenovirus-mediated gene transfer to airway epithelial cells in mice. *Gene Ther. 5*, 345−51.

(41) Cone, R. A. (1999) Mucus, in *Mucosal Immunology* (Lamm, M. E., McGhee, J. R., Mayer, L., Mestecky, J., and Bienenstock, J., Eds.) pp 43−64, Academic Press, San Diego.

(42) Lai, S. K., Wang, Y. Y., and Hanes, J. (2009) Mucus-penetrating nanoparticles for drug and gene delivery to mucosal tissues. *Adv. Drug Delivery Rev. 61*, 158−71.

(43) Sanders, N. N., De Smedt, S. C., Van Rompaey, E., Simoens, P., De Baets, F., and Demeester, J. (2000) Cystic fibrosis sputum: a barrier to the transport of nanospheres. *Am. J. Respir. Crit. Care Med. 162*, 1905−11.

(44) Sanders, N. N., Van Rompaey, E., De Smedt, S. C., and Demeester, J. (2002) On the transport of lipoplexes through cystic fibrosis sputum. *Pharm. Res. 19*, 451−6.
(45) Dawson, M., Wirtz, D., and Hanes, J. (2003) Enhanced viscoelasticity of human cystic fibrotic sputum correlates with increasing microheterogeneity in particle transport. *J. Biol. Chem. 278*, 50393−401.
(46) Braeckmans, K., Peeters, L., Sanders, N. N., De Smedt, S. C., and Demeester, J. (2003) Three-dimensional fluorescence recovery after photobleaching with the confocal scanning laser microscope. *Biophys. J. 85*, 2240−52.
(47) Lai, S. K., O'Hanlon, D. E., Harrold, S., Man, S. T., Wang, Y. Y., Cone, R., and Hanes, J. (2007) Rapid transport of large polymeric nanoparticles in fresh undiluted human mucus. *Proc. Natl. Acad. Sci. U. S. A. 104*, 1482−7.
(48) Beyerle, A., Braun, A., Merkel, O., Koch, F., Kissel, T., and Stoeger, T. (2011) Comparative *in vivo* study of poly(ethylene imine)/siRNA complexes for pulmonary delivery in mice. *J. Controlled Release*, in press.
(49) Rosenecker, J., Naundorf, S., Gersting, S. W., Hauck, R. W., Gessner, A., Nicklaus, P., Muller, R. H., and Rudolph, C. (2003) Interaction of bronchoalveolar lavage fluid with polyplexes and lipoplexes: analysing the role of proteins and glycoproteins. *J. Gene Med. 5*, 49−60.
(50) Merkel, O. M., Beyerle, A., Librizzi, D., Pfestroff, A., Behr, T. M., Sproat, B., Barth, P. J., and Kissel, T. (2009) Nonviral siRNA delivery to the lung: investigation of PEG-PEI polyplexes and their *in vivo* performance. *Mol. Pharm. 6*, 1246−60.
(51) Stern, M., Caplen, N. J., Browning, J. E., Griesenbach, U., Sorgi, F., Huang, L., Gruenert, D. C., Marriot, C., Crystal, R. G., Geddes, D. M., and Alton, E. W. (1998) The effect of mucolytic agents on gene transfer across a CF sputum barrier *in vitro*. *Gene Ther. 5*, 91−8.
(52) Colina, A. R., Aumont, F., Deslauriers, N., Belhumeur, P., and de Repentigny, L. (1996) Evidence for degradation of gastrointestinal mucin by Candida albicans secretory aspartyl proteinase. *Infect. Immun. 64*, 4514−9.
(53) Connaris, S., and Greenwell, P. (1997) Glycosidases in mucin-dwelling protozoans. *Glycoconj. J. 14*, 879−82.
(54) Bisaillon, M., Senechal, S., Bernier, L., and Lemay, G. (1999) A glycosyl hydrolase activity of mammalian reovirus sigma1 protein can contribute to viral infection through a mucus layer. *J. Mol. Biol. 286*, 759−73.
(55) Ferrari, S., Kitson, C., Farley, R., Steel, R., Marriott, C., Parkins, D. A., Scarpa, M., Wainwright, B., Evans, M. J., Colledge, W. H., Geddes, D. M., and Alton, E. W. (2001) Mucus altering agents as adjuncts for nonviral gene transfer to airway epithelium. *Gene Ther. 8*, 1380−6.
(56) Kitson, C., Angel, B., Judd, D., Rothery, S., Severs, N. J., Dewar, A., Huang, L., Wadsworth, S. C., Cheng, S. H., Geddes, D. M., and Alton, E. W. (1999) The extra- and intracellular barriers to lipid and adenovirus-mediated pulmonary gene transfer in native sheep airway epithelium. *Gene Ther. 6*, 534−46.
(57) Goerke, J. (1998) Pulmonary surfactant: functions and molecular composition. *Biochim. Biophys. Acta 1408*, 79−89.
(58) Wattiez, R., and Falmagne, P. (2005) Proteomics of bronchoalveolar lavage fluid. *J. Chromatogr., B 815*, 169−78.
(59) Ernst, N., Ulrichskotter, S., Schmalix, W. A., Radler, J., Galneder, R., Mayer, E., Gersting, S., Plank, C., Reinhardt, D., and Rosenecker, J. (1999) Interaction of liposomal and polycationic transfection complexes with pulmonary surfactant. *J. Gene Med. 1*, 331−40.
(60) Kukowska-Latallo, J. F., Chen, C., Eichman, J., Bielinska, A. U., and Baker, J. R. Jr. (1999) Enhancement of dendrimer-mediated transfection using synthetic lung surfactant exosurf neonatal *in vitro*. *Biochem. Biophys. Res. Commun. 264*, 253−61.
(61) Rudolph, C., Lausier, J., Naundorf, S., Muller, R. H., and Rosenecker, J. (2000) *In vivo* gene delivery to the lung using polyethylenimine and fractured polyamidoamine dendrimers. *J. Gene Med. 2*, 269−78.
(62) Nguyen, J., Reul, R., Betz, T., Dayyoub, E., Schmehl, T., Gessler, T., Bakowsky, U., Seeger, W., and Kissel, T. (2009) Nanocomposites of lung surfactant and biodegradable cationic nanoparticles improve transfection efficiency to lung cells. *J. Controlled Release 140*, 47−54.
(63) Kleemann, E., Neu, M., Jekel, N., Fink, L., Schmehl, T., Gessler, T., Seeger, W., and Kissel, T. (2005) Nano-carriers for DNA delivery to the lung based upon a TAT-derived peptide covalently coupled to PEG-PEI. *J. Controlled Release 109*, 299−316.
(64) Cheng, S. H., Marshall, J., Scheule, R. K., and Smith, A. E. (1998) Cationic lipid formulations for intracellular gene delivery of cystic fibrosis transmembrane conductance regulator to airway epithelia. *Methods Enzymol. 292*, 697−717.
(65) Cheung, C. Y., Murthy, N., Stayton, P. S., and Hoffman, A. S. (2001) A pH-sensitive polymer that enhances cationic lipid-mediated gene transfer. *Bioconjugate Chem. 12*, 906−10.
(66) Carrabino, S., Di Gioia, S., Copreni, E., and Conese, M. (2005) Serum albumin enhances polyethylenimine-mediated gene delivery to human respiratory epithelial cells. *J. Gene Med. 7*, 1555−64.
(67) Rudolph, C., Schillinger, U., Plank, C., Gessner, A., Nicklaus, P., Muller, R., and Rosenecker, J. (2002) Nonviral gene delivery to the lung with copolymer-protected and transferrin-modified polyethylenimine. *Biochim. Biophys. Acta 1573*, 75−83.
(68) Wang, Y. Y., Lai, S. K., Suk, J. S., Pace, A., Cone, R., and Hanes, J. (2008) Addressing the PEG mucoadhesivity paradox to engineer nanoparticles that "slip" through the human mucus barrier. *Angew. Chem., Int. Ed. Engl. 47*, 9726−9.
(69) Walters, R. W., Grunst, T., Bergelson, J. M., Finberg, R. W., Welsh, M. J., and Zabner, J. (1999) Basolateral localization of fiber receptors limits adenovirus infection from the apical surface of airway epithelia. *J. Biol. Chem. 274*, 10219−26.
(70) Li, L., Mathias, N. R., Heran, C. L., Moench, P., Wall, D. A., and Smith, R. L. (2006) Carbopol-mediated paracellular transport enhancement in Calu-3 cell layers. *J. Pharm. Sci. 95*, 326−35.
(71) Sibille, Y., and Reynolds, H. Y. (1990) Macrophages and polymorphonuclear neutrophils in lung defense and injury. *Am. Rev. Respir. Dis. 141*, 471−501.
(72) Sutinen, S., Riska, H., Backman, R., Sutinen, S. H., and Froseth, B. (1995) Alveolar lavage fluid (ALF) of normal volunteer subjects: cytologic, immunocytochemical, and biochemical reference values. *Respir. Med. 89*, 85−92.
(73) Chono, S., Tanino, T., Seki, T., and Morimoto, K. (2006) Influence of particle size on drug delivery to rat alveolar macrophages following pulmonary administration of ciprofloxacin incorporated into liposomes. *J. Drug Targeting 14*, 557−66.
(74) Lauweryns, J. M., and Baert, J. H. (1977) Alveolar clearance and the role of the pulmonary lymphatics. *Am. Rev. Respir. Dis. 115*, 625−83.
(75) Gumbleton, M. (2001) Caveolae as potential macromolecule trafficking compartments within alveolar epithelium. *Adv. Drug Delivery Rev. 49*, 281−300.
(76) Rejman, J., Oberle, V., Zuhorn, I. S., and Hoekstra, D. (2004) Size-dependent internalization of particles via the pathways of clathrin- and caveolae-mediated endocytosis. *Biochem. J. 377*, 159−69.
(77) Muller, J., Huaux, F., Moreau, N., Misson, P., Heilier, J. F., Delos, M., Arras, M., Fonseca, A., Nagy, J. B., and Lison, D. (2005) Respiratory toxicity of multi-wall carbon nanotubes. *Toxicol. Appl. Pharmacol. 207*, 221−31.
(78) Gonzalez-Flecha, B. (2004) Oxidant mechanisms in response to ambient air particles. *Mol. Aspects Med. 25*, 169−82.
(79) Beyerle, A., Hobel, S., Czubayko, F., Schulz, H., Kissel, T., Aigner, A., and Stoeger, T. (2009) *In vitro* cytotoxic and immunomodulatory profiling of low molecular weight polyethylenimines for pulmonary application. *Toxicol. In Vitro 23*, 500−8.
(80) Vinzents, P. S., Moller, P., Sorensen, M., Knudsen, L. E., Hertel, O., Jensen, F. P., Schibye, B., and Loft, S. (2005) Personal exposure to ultrafine particles and oxidative DNA damage. *Environ. Health Perspect. 113*, 1485−90.
(81) Merkel, O. M., Beyerle, A., Beckmann, B. M., Zheng, M., Hartmann, R. K., Stoger, T., and Kissel, T. H. (2011) Polymer-related

off-target effects in non-viral siRNA delivery. *Biomaterials 32*, 2388−98.
(82) Birchall, J. (2007) Pulmonary delivery of nucleic acids. *Expert Opin. Drug Delivery 4*, 575−8.
(83) Oberdorster, G., Oberdorster, E., and Oberdorster, J. (2005) Nanotoxicology: an emerging discipline evolving from studies of ultrafine particles. *Environ. Health Perspect. 113*, 823−39.
(84) Lanone, S., and Boczkowski, J. (2006) Biomedical applications and potential health risks of nanomaterials: molecular mechanisms. *Curr. Mol. Med. 6*, 651−63.
(85) Badea, I., Wettig, S., Verrall, R., and Foldvari, M. (2007) Topical non-invasive gene delivery using gemini nanoparticles in interferon-gamma-deficient mice. *Eur. J. Pharm. Biopharm. 65*, 414−22.
(86) Warheit, D. B., Webb, T. R., Reed, K. L., Frerichs, S., and Sayes, C. M. (2007) Pulmonary toxicity study in rats with three forms of ultrafine-TiO2 particles: differential responses related to surface properties. *Toxicology 230*, 90−104.
(87) Beyerle, A., Irmler, M., Beckers, J., Kissel, T., and Stoeger, T. (2010) Toxicity pathway focused gene expression profiling of PEI-based polymers for pulmonary applications. *Mol. Pharm. 7*, 727−37.
(88) Beyerle, A., Merkel, O., Stoeger, T., and Kissel, T. (2010) PEGylation affects cytotoxicity and cell-compatibility of poly(ethylene imine) for lung application: structure-function relationships. *Toxicol. Appl. Pharmacol. 242*, 146−54.
(89) Lam, C. W., James, J. T., McCluskey, R., and Hunter, R. L. (2004) Pulmonary toxicity of single-wall carbon nanotubes in mice 7 and 90 days after intratracheal instillation. *Toxicol. Sci. 77*, 126−34.
(90) Warheit, D. B., Laurence, B. R., Reed, K. L., Roach, D. H., Reynolds, G. A., and Webb, T. R. (2004) Comparative pulmonary toxicity assessment of single-wall carbon nanotubes in rats. *Toxicol. Sci. 77*, 117−25.
(91) Worgall, S., Leopold, P. L., Wolff, G., Ferris, B., Van Roijen, N., and Crystal, R. G. (1997) Role of alveolar macrophages in rapid elimination of adenovirus vectors administered to the epithelial surface of the respiratory tract. *Hum. Gene Ther. 8*, 1675−84.
(92) McCray, P. B. Jr., Wang, G., Kline, J. N., Zabner, J., Chada, S., Jolly, D. J., Chang, S. M., and Davidson, B. L. (1997) Alveolar macrophages inhibit retrovirus-mediated gene transfer to airway epithelia. *Hum. Gene Ther. 8*, 1087−93.
(93) Patton, J. S., and Byron, P. R. (2007) Inhaling medicines: delivering drugs to the body through the lungs. *Nat. Rev. Drug Discovery 6*, 67−74.
(94) Semmler-Behnke, M., Takenaka, S., Fertsch, S., Wenk, A., Seitz, J., Mayer, P., Oberdorster, G., and Kreyling, W. G. (2007) Efficient elimination of inhaled nanoparticles from the alveolar region: evidence for interstitial uptake and subsequent reentrainment onto airways epithelium. *Environ. Health Perspect. 115*, 728−33.
(95) Semmler-Behnke, M., Kreyling, W. G., Lipka, J., Fertsch, S., Wenk, A., Takenaka, S., Schmid, G., and Brandau, W. (2008) Biodistribution of 1.4- and 18-nm gold particles in rats. *Small 4*, 2108−11.
(96) Hagens, W. I., Oomen, A. G., de Jong, W. H., Cassee, F. R., and Sips, A. J. (2007) What do we (need to) know about the kinetic properties of nanoparticles in the body? *Regul. Toxicol. Pharmacol. 49*, 217−29.
(97) Medina, C., Santos-Martinez, M. J., Radomski, A., Corrigan, O. I., and Radomski, M. W. (2007) Nanoparticles: pharmacological and toxicological significance. *Br. J. Pharmacol. 150*, 552−8.
(98) Oberdorster, G., Sharp, Z., Atudorei, V., Elder, A., Gelein, R., Kreyling, W., and Cox, C. (2004) Translocation of inhaled ultrafine particles to the brain. *Inhal. Toxicol. 16*, 437−45.
(99) Oldfors, A., and Fardeau, M. (1983) The permeability of the basal lamina at the neuromuscular junction. An ultrastructural study of rat skeletal muscle using particulate tracers. *Neuropathol. Appl. Neurobiol. 9*, 419−32.
(100) Choi, H. S., Ashitate, Y., Lee, J. H., Kim, S. H., Matsui, A., Insin, N., Bawendi, M. G., Semmler-Behnke, M., Frangioni, J. V., and Tsuda, A. (2010) Rapid translocation of nanoparticles from the lung airspaces to the body. *Nat. Biotechnol. 28*, 1300−3.
(101) Dannenberg, A. M. Jr., and Smith, E. L. (1955) Proteolytic enzymes of lung. *J. Biol. Chem. 215*, 45−54.
(102) Lollo, C. P., Banaszczyk, M. G., and Chiou, H. C. (2000) Obstacles and advances in non-viral gene delivery. *Curr. Opin. Mol. Ther. 2*, 136−42.
(103) Park, T. G., Jeong, J. H., and Kim, S. W. (2006) Current status of polymeric gene delivery systems. *Adv. Drug Delivery Rev. 58*, 467−86.
(104) Boussif, O., Lezoualc'h, F., Zanta, M. A., Mergny, M. D., Scherman, D., Demeneix, B., and Behr, J.-P. (1995) A versatile vector for gene and oligonucleotide transfer into cells in culture and *in vivo*: polyethylenimine. *Proc. Natl. Acad. Sci. U. S. A. 92*, 7297−301.
(105) Baker, A., Saltik, M., Lehrmann, H., Killisch, I., Mautner, V., Lamm, G., Christofori, G., and Cotten, M. (1997) Polyethylenimine (PEI) is a simple, inexpensive and effective reagent for condensing and linking plasmid DNA to adenovirus for gene delivery. *Gene Ther. 4*, 773−82.
(106) Meunier-Durmort, C., Grimal, H., Sachs, L. M., Demeneix, B. A., and Forest, C. (1997) Adenovirus enhancement of polyethylenimine-mediated transfer of regulated genes in differentiated cells. *Gene Ther. 4*, 808−814.
(107) Fischer, D., Bieber, T., Li, Y., Elsasser, H.-P., and Kissel, T. (1999) A novel non-viral vector for DNA delivery based on low molecular weight, branched polyethylenimine: effect of molecular weight on transfection efficiency and cytotoxicity. *Pharm. Res. 16*, 1273−1279.
(108) Godbey, W. T., Wu, K. K., and Mikos, A. G. (1999) Size matters: molecular weight affects the efficiency of poly(ethylenimine) as a gene delivery vehicle. *J. Biomed. Mater. Res. 45*, 268−75.
(109) Kleemann, E., Jekel, N., Dailey, L. A., Roesler, S., Fink, L., Weissmann, N., Schermuly, R., Gessler, T., Schmehl, T., Roberts, C. J., Seeger, W., and Kissel, T. (2009) Enhanced gene expression and reduced toxicity in mice using polyplexes of low-molecular-weight poly(ethylene imine) for pulmonary gene delivery. *J. Drug Targeting 17*, 638−51.
(110) Wightman, L., Kircheis, R., Rossler, V., Carotta, S., Ruzicka, R., Kursa, M., and Wagner, E. (2001) Different behavior of branched and linear polyethylenimine for gene delivery *in vitro* and *in vivo*. *J. Gene Med. 3*, 362−72.
(111) Goula, D., Remy, J. S., Erbacher, P., Wasowicz, M., Levi, G., Abdallah, B., and Demeneix, B. A. (1998) Size, diffusibility and transfection performance of linear PEI/DNA complexes in the mouse central nervous system. *Gene Ther. 5*, 712−717.
(112) Kichler, A., Chillon, M., Leborgne, C., Danos, O., and Frisch, B. (2002) Intranasal gene delivery with a polyethylenimine-PEG conjugate. *J. Controlled Release 81*, 379−88.
(113) Anabousi, S., Kleemann, E., Bakowsky, U., Kissel, T., Schmehl, T., Gessler, T., Seeger, W., Lehr, C.-M., and Ehrhardt, C. (2006) Effect of PEGylation on the stability of liposomes during nebulisation and in lung surfactant. *J. Nanosci. Nanotechnol. 6*, 3010−3016.
(114) Petersen, H., Merdan, T., Kunath, K., Fischer, D., and Kissel, T. (2002) Poly(ethylenimine-co-L-lactamide-co-succinamide): a biodegradable polyethylenimine derivative with an advantageous pH-dependent hydrolytic degradation for gene delivery. *Bioconjugate Chem. 13*, 812−21.
(115) Vivès, E., Brodin, P., and Lebleu, B. (1997) A Truncated HIV-1 Tat protein basic domain rapidly translocates through the plasma membrane and accumulates in the cell nucleus. *J. Biol. Chem. 272*, 16010−16017.
(116) Renigunta, A., Krasteva, G., Konig, P., Rose, F., Klepetko, W., Grimminger, F., Seeger, W., and Hanze, J. (2006) DNA transfer into human lung cells is improved with Tat-RGD peptide by caveoli-mediated endocytosis. *Bioconjugate Chem. 17*, 327−34.
(117) Chen, J., Gao, X., Hu, K., Pang, Z., Cai, J., Li, J., Wu, H., and Jiang, X. (2008) Galactose-poly(ethylene glycol)-polyethylenimine for improved lung gene transfer. *Biochem. Biophys. Res. Commun. 375*, 378−83.
(118) Nguyen, J., Xie, X., Neu, M., Dumitrascu, R., Reul, R., Sitterberg, J., Bakowsky, U., Schermuly, R., Fink, L., Schmehl, T.,

Gessler, T., Seeger, W., and Kissel, T. (2008) Effects of cell-penetrating peptides and pegylation on transfection efficiency of polyethylenimine in mouse lungs. *J. Gene Med. 10*, 1236−46.
(119) Wen, Y., Pan, S., Luo, X., Zhang, X., Zhang, W., and Feng, M. (2009) A biodegradable low molecular weight polyethylenimine derivative as low toxicity and efficient gene vector. *Bioconjugate Chem. 20*, 322−32.
(120) Koping-Hoggard, M., Tubulekas, I., Guan, H., Edwards, K., Nilsson, M., Varum, K. M., and Artursson, P. (2001) Chitosan as a nonviral gene delivery system. Structure-property relationships and characteristics compared with polyethylenimine *in vitro* and after lung administration *in vivo*. *Gene Ther. 8*, 1108−21.
(121) Lee, M., Nah, J. W., Kwon, Y., Koh, J. J., Ko, K. S., and Kim, S. W. (2001) Water-soluble and low molecular weight chitosan-based plasmid DNA delivery. *Pharm. Res. 18*, 427−31.
(122) Thanou, M., Florea, B. I., Geldof, M., Junginger, H. E., and Borchard, G. (2002) Quaternized chitosan oligomers as novel gene delivery vectors in epithelial cell lines. *Biomaterials 23*, 153−9.
(123) Mao, S., Shuai, X., Unger, F., Wittmar, M., Xie, X., and Kissel, T. (2005) Synthesis, characterization and cytotoxicity of poly(ethylene glycol)-graft-trimethyl chitosan block copolymers. *Biomaterials 26*, 6343−56.
(124) Germershaus, O., Mao, S., Sitterberg, J., Bakowsky, U., and Kissel, T. (2008) Gene delivery using chitosan, trimethyl chitosan or polyethylenglycol-graft-trimethyl chitosan block copolymers: establishment of structure-activity relationships *in vitro*. *J. Controlled Release 125*, 145−54.
(125) Issa, M. M., Koping-Hoggard, M., Tommeraas, K., Varum, K. M., Christensen, B. E., Strand, S. P., and Artursson, P. (2006) Targeted gene delivery with trisaccharide-substituted chitosan oligomers *in vitro* and after lung administration *in vivo*. *J. Controlled Release 115*, 103−12.
(126) Okamoto, H., Nishida, S., Todo, H., Sakakura, Y., Iida, K., and Danjo, K. (2003) Pulmonary gene delivery by chitosan-pDNA complex powder prepared by a supercritical carbon dioxide process. *J. Pharm. Sci. 92*, 371−80.
(127) Okamoto, H., Sakakura, Y., Shiraki, K., Oka, K., Nishida, S., Todo, H., Iida, K., and Danjo, K. (2005) Stability of chitosan-pDNA complex powder prepared by supercritical carbon dioxide process. *Int. J. Pharm. 290*, 73−81.
(128) Mohri, K., Okuda, T., Mori, A., Danjo, K., and Okamoto, H. (2010) Optimized pulmonary gene transfection in mice by spray-freeze dried powder inhalation. *J. Controlled Release 144*, 221−6.
(129) Okamoto, H., Shiraki, K., Yasuda, R., Danjo, K., and Watanabe, Y. (2011) Chitosan-interferon-beta gene complex powder for inhalation treatment of lung metastasis in mice. *J. Controlled Release 150*, 187−195.
(130) Wagner, E., Ogris, M., and Zauner, W. (1998) Polylysine-based transfection systems utilizing receptor-mediated delivery. *Adv. Drug Delivery Rev. 30*, 97−113.
(131) Jeong, J. H., and Park, T. G. (2002) Poly(L-lysine)-g-poly(D,L-lactic-co-glycolic acid) micelles for low cytotoxic biodegradable gene delivery carriers. *J. Controlled Release 82*, 159−66.
(132) Bikram, M., Ahn, C.-H., Chae, S. Y., Lee, M., Yockman, J. W., and Kim, S. W. (2004) Biodegradable poly(ethylene glycol)-co-poly(L-lysine)-g-histidine multiblock copolymers for nonviral gene delivery. *Macromolecules 37*, 1903−1916.
(133) Bikram, M., Lee, M., Chang, C. W., Janat-Amsbury, M. M., Kern, S. E., and Kim, S. W. (2005) Long-circulating DNA-complexed biodegradable multiblock copolymers for gene delivery: degradation profiles and evidence of dysopsonization. *J. Controlled Release 103*, 221−33.
(134) Xiang, J. J., Tang, J. Q., Zhu, S. G., Nie, X. M., Lu, H. B., Shen, S. R., Li, X. L., Tang, K., Zhou, M., and Li, G. Y. (2003) IONP-PLL: a novel non-viral vector for efficient gene delivery. *J. Gene Med. 5*, 803−17.
(135) Zou, Y., Tornos, C., Qiu, X., Lia, M., and Perez-Soler, R. (2007) p53 aerosol formulation with low toxicity and high efficiency for early lung cancer treatment. *Clin. Cancer Res. 13*, 4900−8.
(136) Cherng, J. Y., van de Wetering, P., Talsma, H., Crommelin, D. J., and Hennink, W. E. (1996) Effect of size and serum proteins on transfection efficiency of poly ((2-dimethylamino)ethyl methacrylate)-plasmid nanoparticles. *Pharm. Res. 13*, 1038−42.
(137) Uzgun, S., Akdemir, O., Hasenpusch, G., Maucksch, C., Golas, M. M., Sander, B., Stark, H., Imker, R., Lutz, J. F., and Rudolph, C. (2010) Characterization of tailor-made copolymers of oligo(ethylene glycol) methyl ether methacrylate and N,N-dimethylaminoethyl methacrylate as nonviral gene transfer agents: influence of macromolecular structure on gene vector particle properties and transfection efficiency. *Biomacromolecules 11*, 39−50.
(138) Samsonova, O., Pfeiffer, C., Hellmund, M., Merkel, O. M., and Kissel, T. (2011) Low molecular weight pDMAEMA-block-pHEMA block-copolymers synthesized via RAFT-Polymerization: potential non-viral gene delivery agents? *Polymers 3*, 693−718.
(139) Hosseinkhani, H., Azzam, T., Tabata, Y., and Domb, A. J. (2004) Dextran-spermine polycation: an efficient nonviral vector for *in vitro* and *in vivo* gene transfection. *Gene Ther. 11*, 194−203.
(140) Azzam, T., Eliyahu, H., Makovitzki, A., Linial, M., and Domb, A. J. (2004) Hydrophobized dextran-spermine conjugate as potential vector for *in vitro* gene transfection. *J. Controlled Release 96*, 309−323.
(141) Abdullah, S., Wendy-Yeo, W. Y., Hosseinkhani, H., Hosseinkhani, M., Masrawa, E., Ramasamy, R., Rosli, R., Rahman, S. A., and Domb, A. J. (2010) Gene transfer into the lung by nanoparticle dextran-spermine/plasmid DNA complexes. *J. Biomed. Biotechnol.*, 284840.
(142) Benoit, M. A., Ribet, C., Distexhe, J., Hermand, D., Letesson, J. J., Vandenhaute, J., and Gillard, J. (2001) Studies on the potential of microparticles entrapping pDNA-poly(aminoacids) complexes as vaccine delivery systems. *J. Drug Targeting 9*, 253−66.
(143) Capan, Y., Woo, B. H., Gebrekidan, S., Ahmed, S., and DeLuca, P. P. (1999) Preparation and characterization of poly (D,L-lactide-co-glycolide) microspheres for controlled release of poly(L-lysine) complexed plasmid DNA. *Pharm. Res. 16*, 509−13.
(144) Nie, Y., Zhang, Z. R., and Duan, Y. R. (2006) Combined use of polycationic peptide and biodegradable macromolecular polymer as a novel gene delivery system: a preliminary study. *Drug Delivery 13*, 441−6.
(145) De Rosa, G., Quaglia, F., Bochot, A., Ungaro, F., and Fattal, E. (2003) Long-term release and improved intracellular penetration of oligonucleotide-polyethylenimine complexes entrapped in biodegradable microspheres. *Biomacromolecules 4*, 529−36.
(146) Moffatt, S., and Cristiano, R. J. (2006) Uptake characteristics of NGR-coupled stealth PEI/pDNA nanoparticles loaded with PLGA-PEG-PLGA tri-block copolymer for targeted delivery to human monocyte-derived dendritic cells. *Int. J. Pharm. 321*, 143−54.
(147) Oster, C. G., Kim, N., Grode, L., Barbu-Tudoran, L., Schaper, A. K., Kaufmann, S. H., and Kissel, T. (2005) Cationic microparticles consisting of poly(lactide-co-glycolide) and polyethylenimine as carriers systems for parental DNA vaccination. *J. Controlled Release 104*, 359−77.
(148) Janes, K. A., Calvo, P., and Alonso, M. J. (2001) Polysaccharide colloidal particles as delivery systems for macromolecules. *Adv. Drug Delivery Rev. 47*, 83−97.
(149) Kumar, M. N. V. R., Mohapatra, S. S., Kong, X., Jena, P. K., Bakowsky, U., and Lehr, C. M. (2004) Cationic poly(lactide-co-glycolide) nanoparticles as efficient *in vivo* gene transfection agents. *J. Nanosci. Nanotechnol. 4*, 990−994.
(150) Nafee, N., Taetz, S., Schneider, M., Schaefer, U. F., and Lehr, C. M. (2007) Chitosan-coated PLGA nanoparticles for DNA/RNA delivery: effect of the formulation parameters on complexation and transfection of antisense oligonucleotides. *Nanomedicine 3*, 173−83.
(151) Kusonwiriyawong, C., Atuah, K., Alpar, O. H., Merkle, H. P., and Walter, E. (2004) Cationic stearylamine-containing biodegradable microparticles for DNA delivery. *J. Microencapsul. 21*, 25−36.
(152) Pai Kasturi, S., Qin, H., Thomson, K. S., El-Bereir, S., Cha, S. C., Neelapu, S., Kwak, L. W., and Roy, K. (2006) Prophylactic anti-tumor effects in a B cell lymphoma model with DNA vaccines

delivered on polyethylenimine (PEI) functionalized PLGA microparticles. *J. Controlled Release 113*, 261−70.
(153) Tinsley-Bown, A. M., Fretwell, R., Dowsett, A. B., Davis, S. L., and Farrar, G. H. (2000) Formulation of poly(D,L-lactic-co-glycolic acid) microparticles for rapid plasmid DNA delivery. *J. Controlled Release 66*, 229−41.
(154) Perez, C., Sanchez, A., Putnam, D., Ting, D., Langer, R., and Alonso, M. J. (2001) Poly(lactic acid)-poly(ethylene glycol) nanoparticles as new carriers for the delivery of plasmid DNA. *J. Controlled Release 75*, 211−24.
(155) Bivas-Benita, M., Romeijn, S., Junginger, H. E., and Borchard, G. (2004) PLGA-PEI nanoparticles for gene delivery to pulmonary epithelium. *Eur. J. Pharm. Biopharm. 58*, 1−6.
(156) Bivas-Benita, M., Lin, M. Y., Bal, S. M., van Meijgaarden, K. E., Franken, K. L., Friggen, A. H., Junginger, H. E., Borchard, G., Klein, M. R., and Ottenhoff, T. H. (2009) Pulmonary delivery of DNA encoding Mycobacterium tuberculosis latency antigen Rv1733c associated to PLGA-PEI nanoparticles enhances T cell responses in a DNA prime/protein boost vaccination regimen in mice. *Vaccine 27*, 4010−7.
(157) Alpar, H. O., Somavarapu, S., Atuah, K. N., and Bramwell, V. W. (2005) Biodegradable mucoadhesive particulates for nasal and pulmonary antigen and DNA delivery. *Adv. Drug Delivery Rev. 57*, 411−30.
(158) Kockisch, S., Rees, G. D., Young, S. A., Tsibouklis, J., and Smart, J. D. (2003) Polymeric microspheres for drug delivery to the oral cavity: an *in vitro* evaluation of mucoadhesive potential. *J. Pharm. Sci. 92*, 1614−23.
(159) Zou, W., Liu, C., Chen, Z., and Zhang, N. (2009) Studies on bioadhesive PLGA nanoparticles: A promising gene delivery system for efficient gene therapy to lung cancer. *Int. J. Pharm. 370*, 187−95.
(160) Dailey, L. A., Kleemann, E., Wittmar, M., Gessler, T., Schmehl, T., Roberts, C., Seeger, W., and Kissel, T. (2003) Surfactant-free, biodegradable nanoparticles for aerosol therapy based on the branched polyesters, DEAPA-PVAL-g-PLGA. *Pharm. Res. 20*, 2011−2020.
(161) Dailey, L. A., Jekel, N., Fink, L., Gessler, T., Schmehl, T., Wittmar, M., Kissel, T., and Seeger, W. (2006) Investigation of the proinflammatory potential of biodegradable nanoparticle drug delivery systems in the lung. *Toxicol. Appl. Pharmacol. 215*, 100−108.
(162) Boas, U., and Heegaard, P. M. (2004) Dendrimers in drug research. *Chem. Soc. Rev. 33*, 43−63.
(163) Frechet, J. M. J., and Tomalia, D. A. (2001) *Dendrimers and Other Dendritic Polymers*, John Wiley & Sons, Chichester.
(164) D'Emanuele, A., and Attwood, D. (2005) Dendrimer-drug interactions. *Adv. Drug Delivery Rev. 57*, 2147−2162.
(165) Shcharbin, D. G., Klajnert, B., and Bryszewska, M. (2009) Dendrimers in gene transfection. *Biochemistry (Mosc.) 74*, 1070−9.
(166) Kukowska-Latallo, J. F., Bielinska, A. U., Johnson, J., Spindler, R., Tomalia, D. A., and Baker, J. R. Jr. (1996) Efficient transfer of genetic material into mammalian cells using Starburst polyamidoamine dendrimers. *Proc. Natl. Acad. Sci. U. S. A. 93*, 4897−902.
(167) Tomalia, D. A., Naylor, A. M., and Goddard, W. A. (1990) Starburst dendrimers: molecular-level control of size, shape, surface chemistry, topology, and flexibility from atoms to macroscopic matter. *Angew. Chem., Int. Ed. 29*, 138−175.
(168) Kukowska-Latallo, J. F., Chen, C., Raczka, E., Qunintana, A., Rymaszewski, M., and Baker, J. R. (2000) Intravascular and endobronchial DNA delivery to murine lung tissue using a novel, nonviral vector. *Hum. Gene Ther. 11*, 1385−1395.
(169) Tang, M. X., Redemann, C. T., and Szoka, F. C. Jr. (1996) *In vitro* gene delivery by degraded polyamidoamine dendrimers. *Bioconjugate Chem. 7*, 703−14.
(170) Akhtar, S., and Benter, I. (2007) Toxicogenomics of non-viral drug delivery systems for RNAi: potential impact on siRNA-mediated gene silencing activity and specificity. *Adv. Drug Delivery Rev. 59*, 164−82.
(171) Omidi, Y., and Barar, J. (2009) Induction of human alveolar epithelial cell growth factor receptors by dendrimeric nanostructures. *Int. J. Toxicol. 28*, 113−22.
(172) Li, C., Liu, H., Sun, Y., Wang, H., Guo, F., Rao, S., Deng, J., Zhang, Y., Miao, Y., Guo, C., Meng, J., Chen, X., Li, L., Li, D., Xu, H., Wang, H., Li, B., and Jiang, C. (2009) PAMAM nanoparticles promote acute lung injury by inducing autophagic cell death through the Akt-TSC2-mTOR signaling pathway. *J. Mol. Cell Biol.*, in press.
(173) Menuel, S., Fontanay, S., Clarot, I., Duval, R. E., Diez, L., and Marsura, A. (2008) Synthesis and complexation ability of a novel bis-(guanidinium)-tetrakis-(beta-cyclodextrin) dendrimeric tetrapod as a potential gene delivery (DNA and siRNA) system. Study of cellular siRNA transfection. *Bioconjugate Chem. 19*, 2357−62.
(174) Dames, P., Ortiz, A., Schillinger, U., Lesina, E., Plank, C., Rosenecker, J., and Rudolph, C. (2007) Aerosol gene delivery to the murine lung is mouse strain dependent. *J. Mol. Med. 85*, 371−8.
(175) Giordano, R. J., Edwards, J. K., Tuder, R. M., Arap, W., and Pasqualini, R. (2009) Combinatorial ligand-directed lung targeting. *Proc. Am. Thorac. Soc. 6*, 411−415.
(176) Weiss, S. I., Sieverling, N., Niclasen, M., Maucksch, C., Thünemann, A. F., Möhwald, H., Reinhardt, D., Rosenecker, J., and Rudolph, C. (2006) Uronic acids functionalized polyethyleneimine (PEI)-polyethyleneglycol (PEG)-graft-copolymers as novel synthetic gene carriers. *Biomaterials 27*, 2302−2312.
(177) Grosse, S., Thévenot, G., Aron, Y., Duverger, E., Abdelkarim, M., Roche, A.-C., Monsigny, M., and Fajac, I. (2008) *In vivo* gene delivery in the mouse lung with lactosylated polyethylenimine, questioning the relevance of *in vitro* experiments. *J. Controlled Release 132*, 105−112.
(178) Kollen, W. J., Midoux, P., Erbacher, P., Yip, A., Roche, A. C., Monsigny, M., Glick, M. C., and Scanlin, T. F. (1996) Gluconoylated and glycosylated polylysines as vectors for gene transfer into cystic fibrosis airway epithelial cells. *Hum. Gene Ther. 7*, 1577−86.
(179) York, A. W., Zhang, Y., Holley, A. C., Guo, Y., Huang, F., and McCormick, C. L. (2009) Facile synthesis of multivalent folate-block copolymer conjugates via aqueous RAFT polymerization: targeted delivery of siRNA and subsequent gene suppression. *Biomacromolecules 10*, 936−43.
(180) Elfinger, M., Maucksch, C., and Rudolph, C. (2007) Characterization of lactoferrin as a targeting ligand for nonviral gene delivery to airway epithelial cells. *Biomaterials 28*, 3448−3455.
(181) Li, S. D., Chen, Y. C., Hackett, M. J., and Huang, L. (2008) Tumor-targeted delivery of siRNA by self-assembled nanoparticles. *Mol. Ther. 16*, 163−9.
(182) Dames, P., Laner, A., Maucksch, C., Aneja, M. K., and Rudolph, C. (2007) Targeting of the glucocorticoid hormone receptor with plasmid DNA comprising glucocorticoid response elements improves nonviral gene transfer efficiency in the lungs of mice. *J. Gene Med. 9*, 820−9.
(183) Ziady, A. G., Kelley, T. J., Milliken, E., Ferkol, T., and Davis, P. B. (2002) Functional evidence of CFTR gene transfer in nasal epithelium of cystic fibrosis mice *in vivo* following luminal application of DNA complexes targeted to the serpin-enzyme complex receptor. *Mol. Ther. 5*, 413−9.
(184) Li, S., Tan, Y., Viroonchatapan, E., Pitt, B. R., and Huang, L. (2000) Targeted gene delivery to pulmonary endothelium by anti-PECAM antibody. *Am. J. Physiol. Lung Cell Mol. Physiol. 278*, L504−11.
(185) Ferkol, T., Perales, J. C., Eckman, E., Kaetzel, C. S., Hanson, R. W., and Davis, P. B. (1995) Gene transfer into the airway epithelium of animals by targeting the polymeric immunoglobulin receptor. *J. Clin. Invest. 95*, 493−502.
(186) Elfinger, M., Geiger, J., Hasenpusch, G., Üzgün, S., Sieverling, N., Aneja, M. K., Maucksch, C., and Rudolph, C. (2009) Targeting of the [beta]2-adrenoceptor increases nonviral gene delivery to pulmonary epithelial cells *in vitro* and lungs *in vivo*. *J. Controlled Release 135*, 234−241.
(187) Mathias, N. R., Yamashita, F., and Lee, V. H. L. (1996) Respiratory epithelial cell culture models for evaluation of ion and drug transport. *Adv. Drug Delivery Rev. 22*, 215−249.
(188) Radyuk, S. N., Mericko, P. A., Popova, T. G., Grene, E., and Alibek, K. (2003) *In vitro*-generated respiratory mucosa: a new tool to

study inhalational anthrax. *Biochem. Biophys. Res. Commun. 305*, 624–32.
(189) Rothen-Rutishauser, B. M., Kiama, S. G., and Gehr, P. (2005) A three-dimensional cellular model of the human respiratory tract to study the interaction with particles. *Am. J. Respir. Cell Mol. Biol. 32*, 281–9.
(190) Beck-Broichsitter, M., Gauss, J., Packhaeuser, C. B., Lahnstein, K., Schmehl, T., Seeger, W., Kissel, T., and Gessler, T. (2009) Pulmonary drug delivery with aerosolizable nanoparticles in an ex vivo lung model. *Int. J. Pharm. 367*, 169–178.
(191) Yonemitsu, Y., Kitson, C., Ferrari, S., Farley, R., Griesenbach, U., Judd, D., Steel, R., Scheid, P., Zhu, J., Jeffery, P. K., Kato, A., Hasan, M. K., Nagai, Y., Masaki, I., Fukumura, M., Hasegawa, M., Geddes, D. M., and Alton, E. W. (2000) Efficient gene transfer to airway epithelium using recombinant Sendai virus. *Nat. Biotechnol. 18*, 970–3.
(192) Oberdorster, G. (2010) Safety assessment for nanotechnology and nanomedicine: concepts of nanotoxicology. *J. Intern. Med. 267*, 89–105.
(193) Halbert, C. L., Standaert, T. A., Wilson, C. B., and Miller, A. D. (1998) Successful readministration of adeno-associated virus vectors to the mouse lung requires transient immunosuppression during the initial exposure. *J. Virol. 72*, 9795–805.
(194) Zabner, J., Ramsey, B. W., Meeker, D. P., Aitken, M. L., Balfour, R. P., Gibson, R. L., Launspach, J., Moscicki, R. A., Richards, S. M., Standaert, T. A., et al. (1996) Repeat administration of an adenovirus vector encoding cystic fibrosis transmembrane conductance regulator to the nasal epithelium of patients with cystic fibrosis. *J. Clin. Invest. 97*, 1504–11.
(195) Schughart, K., Bischoff, R., Rasmussen, U. B., Hadji, D. A., Perraud, F., Accart, N., Boussif, O., Silvestre, N., Cordier, Y., Pavirani, A., and Kolbe, H. V. J. (1999) Solvoplex: a new type of synthetic vector for intrapulmonary gene delivery. *Hum. Gene Ther. 10*, 2891–2905.
(196) Fischer, A. C., Beck, S. E., Smith, C. I., Laube, B. L., Askin, F. B., Guggino, S. E., Adams, R. J., Flotte, T. R., and Guggino, W. B. (2003) Successful transgene expression with serial doses of aerosolized rAAV2 vectors in rhesus macaques. *Mol. Ther. 8*, 918–926.
(197) Harvey, B. G., Leopold, P. L., Hackett, N. R., Grasso, T. M., Williams, P. M., Tucker, A. L., Kaner, R. J., Ferris, B., Gonda, I., Sweeney, T. D., Ramalingam, R., Kovesdi, I., Shak, S., and Crystal, R. G. (1999) Airway epithelial CFTR mRNA expression in cystic fibrosis patients after repetitive administration of a recombinant adenovirus. *J. Clin. Invest. 104*, 1245–55.
(198) Brown, A. R., and Chowdhury, S. I. (1997) Propellant-driven aerosols of DNA plasmids for gene expression in the respiratory tract. *J. Aerosol Med. 10*, 129–146.
(199) Nielsen, E. J., Nielsen, J. M., Becker, D., Karlas, A., Prakash, H., Glud, S. Z., Merrison, J., Besenbacher, F., Meyer, T. F., Kjems, J., and Howard, K. A. (2010) Pulmonary gene silencing in transgenic EGFP mice using aerosolised chitosan/siRNA nanoparticles. *Pharm. Res. 27*, 2520–7.
(200) Glud, S. Z., Bramsen, J. B., Dagnaes-Hansen, F., Wengel, J., Howard, K. A., Nyengaard, J. R., and Kjems, J. (2009) Naked siLNA-mediated gene silencing of lung bronchoepithelium EGFP expression after intravenous administration. *Oligonucleotides 19*, 163–8.
(201) Cunningham, S., Meng, Q.-H., Klein, N., McAnulty, R. J., and Hart, S. L. (2002) Evaluation of a porcine model for pulmonary gene transfer using a novel synthetic vector. *J. Gene Med. 4*, 438–446.
(202) McLachlan, G., Baker, A., Tennant, P., Gordon, C., Vrettou, C., Renwick, L., Blundell, R., Cheng, S. H., Scheule, R. K., Davies, L., Painter, H., Coles, R. L., Lawton, A. E., Marriott, C., Gill, D. R., Hyde, S. C., Griesenbach, U., Alton, E. W. F. W., Boyd, A. C., Porteous, D. J., and Collie, D. D. S. Optimizing aerosol gene delivery and expression in the ovine lung. *Mol. Ther. 15*, 348–354.
(203) Tseng, C. L., Wu, S. Y., Wang, W. H., Peng, C. L., Lin, F. H., Lin, C. C., Young, T. H., and Shieh, M. J. (2008) Targeting efficiency and biodistribution of biotinylated-EGF-conjugated gelatin nanoparticles administered via aerosol delivery in nude mice with lung cancer. *Biomaterials 29*, 3014–22.
(204) Möller, W., Meyer, G., Scheuch, G., Kreyling, W. G., and Bennett, W. D. (2009) Left-to-right asymmetry of aerosol deposition after shallow bolus inhalation depends on lung ventilation. *J. Aerosol Med. Pulmon. Drug Delivery 22*, 333–339.
(205) Dothager, R. S., and Piwnica-Worms, D. (2009) Molecular imaging of pulmonary disease *in vivo*. *Proc. Am. Thorac. Soc. 6*, 403–410.
(206) Niedre, M. J., de Kleine, R. H., Aikawa, E., Kirsch, D. G., Weissleder, R., and Ntziachristos, V. (2008) Early photon tomography allows fluorescence detection of lung carcinomas and disease progression in mice *in vivo*. *Proc. Natl. Acad. Sci. U. S. A. 105*, 19126–31.
(207) Spektor, D. M., Hunt, P. R., Rosenthal, F., and Lippmann, M. (1985) Influence of airway and airspace sizes on particle deposition in excised donkey lungs. *Exp. Lung Res. 9*, 363–87.
(208) Griesenbach, U., Vicente, C. C., Roberts, M. J., Meng, C., Soussi, S., Xenariou, S., Tennant, P., Baker, A., Baker, E., Gordon, C., Vrettou, C., McCormick, D., Coles, R., Green, A. M., Lawton, A. E., Sumner-Jones, S. G., Cheng, S. H., Scheule, R. K., Hyde, S. C., Gill, D. R., Collie, D. D., McLachlan, G., and Alton, E. W. (2011) Secreted Gaussia luciferase as a sensitive reporter gene for *in vivo* and *ex vivo* studies of airway gene transfer. *Biomaterials 32*, 2614–24.
(209) Merkel, O. M., Urbanics, R., Bedocs, P., Rozsnyay, Z., Rosivall, L., Toth, M., Kissel, T., and Szebeni, J. (2011) *In vitro* and *in vivo* complement activation and related anaphylactic effects associated with polyethylenimine and polyethylenimine-graft-poly(ethylene glycol) block copolymers. *Biomaterials* In Press, Corrected Proof.
(210) Merkel, O. M., and Kissel, T. (2011) Nonviral pulmonary delivery of siRNA. *Acc. Chem. Res.*, accepted.

Bioconjugate Chemistry

Communication

pubs.acs.org/bc

Confocal Microscopy Imaging of NR2B-Containing NMDA Receptors Based on Fluorescent Ifenprodil-Like Conjugates

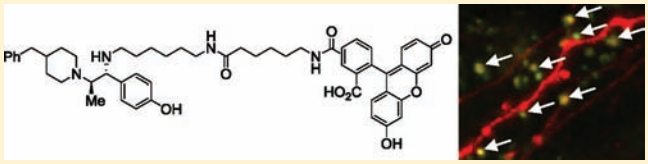
Patrice Marchand,[†,‡] Javier Becerril-Ortega,[‡] Laetitia Mony,[§] Cédric Bouteiller,[†,‡] Pierre Paoletti,[§] Olivier Nicole,[‡] Louisa Barré,[†,‡] Alain Buisson,[‡] and Cécile Perrio*[,†,‡]

[†]CEA/DSV/I2BM, GDM-TEP, [‡]CI-NAPS, CNRS UMR6232, Université de Caen - Basse Normandie, Cyceron, Boulevard Henri Becquerel, 14074 Caen Cedex, France

[§]Institut de Biologie, CNRS UMR8197, INSERM U1024, Ecole Normale Supérieure, 46 rue d'Ulm, 75005 Paris, France

Supporting Information

ABSTRACT: We describe the synthesis and pharmacological characterization of a first generation of ifenprodil conjugates **4**−**7** as fluorescent probes for the confocal microscopy imaging of the NR2B-containing NMDA receptor. The fluorescein conjugate **6** displayed a moderate affinity for NMDAR but a high selectivity for the NR2B subunit and its NTD. Fluorescence imaging of DS-red labeled cortical neurons showed an exact colocalization of the probe **6** with small protrusions along the dendrites related to a specific binding on NR2B-containing NMDARs.



The *N*-methyl-D-aspartate receptor (NMDAR) is a ligand-gated cationic channel widely expressed in the central nervous system (CNS).[1,2] The receptor plays a critical role in excitatory neurotransmission, brain development, synaptic plasticity associated with memory formation, and central sensitization during persistent pain and excitotoxicity.[3−6] Aberrant NMDAR activity is believed to be strongly related to the neuronal loss associated with neurodegenerative disorders in the human CNS that include Alzheimer's and Parkinson's diseases. The architecture of the NMDAR has been elucidated in great detail: it is a heterotetrameric complex made up of a combination of two major subunits, termed NR1 and NR2, based on the amino acid sequence identity.[7−9] Although NR1 is encoded by a single gene, the NR2 subunit exists as four subtypes encoded by four different genes (NR2A-D), each with a distinctive spatiotemporal pattern of expression. It is clear that the pharmacological and functional properties of NMDAR are highly dependent on the NR2 isoform, of which NR2A and NR2B are the most abundant. Furthermore, it has been suggested that, within an individual neuron, synaptic NMDAR subtypes can be segregated in an input-specific manner.[10] Synaptic NMDAR activation has an antiapoptotic activity, while stimulation of extrasynaptic NMDARs elicits glutamate-induced toxicity.[11] Several studies have shown that NR2B subunits, while present with NR2A subunits at many synapses, appear preferentially enriched in extrasynaptic sites and may participate in pathological processes linked to glutamatergic overstimulation. This feature rends NR2B-selective antagonists as particularly attractive therapeutic agents for neuroprotection.[12]

In order to better clarify the physiological and pathological involvement of NMDAR in neuronal fate, we aimed to develop a fluorescent ligand specific for the NR2B subunit. This fluorescent tracer might be a useful tool: for the visualization of receptors in living neurons; for the characterization of the biophysical microenvironment of the binding site; and also for dynamic studies based on fluorescence imaging.[13] As far as we know, no such tracer has been developed. Usually, fluorescent probes are obtained by creating a covalent bond between the ligand and the fluorescent moiety. Challenges often are, first, to modify the ligand (especially when it is a nonpeptidic small organic molecule with poor functionality) in order to provide an attachment point for the fluorophore; second, to perform conjugation without significantly disturbing the natural binding function. Here, we report the synthesis, the physical characterization, and the biological evaluation of a first generation of fluorescent NR2B ligands with the general formula **A**, designed on the framework of ifenprodil (Figure 1). We also show, for the first time, that it is possible to locate NR2B-containing receptor in dendrites by confocal microscopy with such a probe.

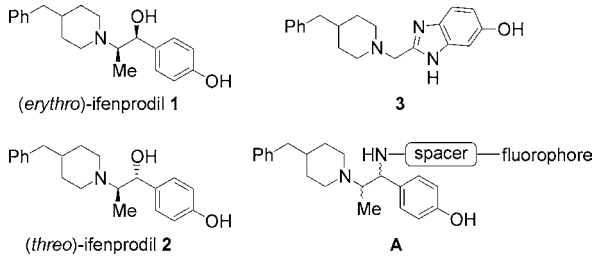
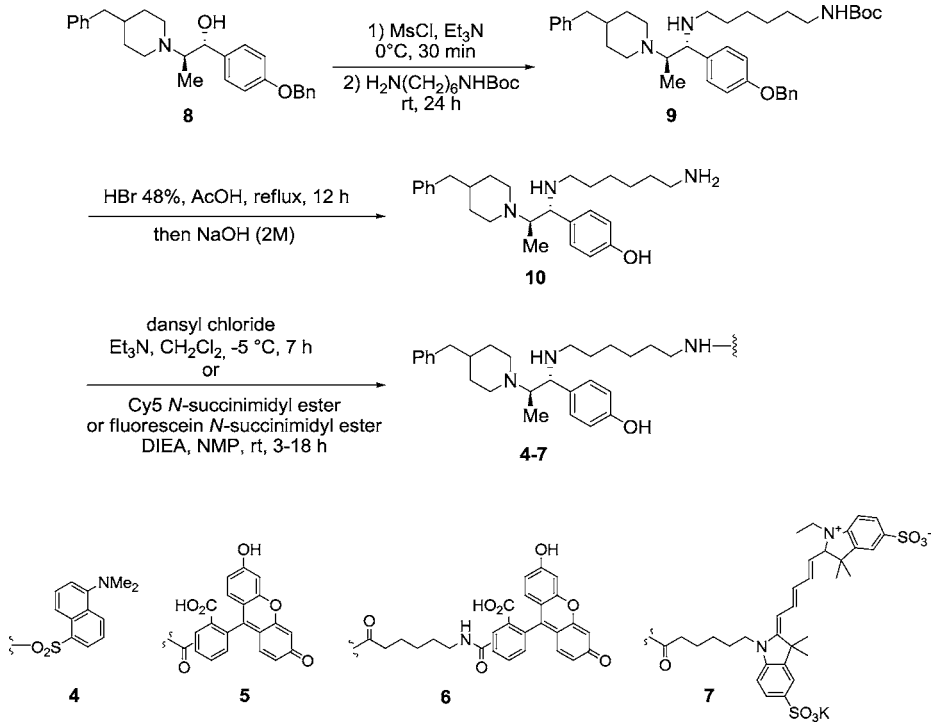


Figure 1. Selective NR1/NR2B NMDA receptor antagonists **1**−**3**, and general formula **A** of the target fluorescent probes.

Received: December 14, 2010
Revised: November 24, 2011
Published: December 9, 2011

 © 2011 American Chemical Society

Scheme 1. Synthesis of Fluorescent *N*-(Aminohexyl)ethylenediamine Conjugates 4−7



Ifenprodil is the lead compound of the major class of antagonists of NMDAR with marked selectivity for NR2B.[14−20] To date, it is the best characterized subtype-specific NMDA antagonist both *in vitro* and *in vivo*.[14,15,21−24] A major characteristic of ifenprodil at NMDARs is a high affinity, noncompetitive, and voltage-independent inhibition of receptors endowed with the NR2B subunit. Ifenprodil contains two asymmetric centers which give rise to the two diastereoisomeric forms **1** (*erythro* or *R**S*) and **2** (*threo* or *R**R*), both of which exist as a pair of enantiomers.[24] The drug substance that has become widely used as a tool to study the expression, properties, function, and distribution of NMDAR subtypes is composed entirely of the racemic (*erythro*) diastereoisomer **1**. However, the (*threo*) racemate **2** was found to be a more potent (five times) neuroprotective agent than the (*erythro*)-diastereoisomer **1** in an *in vitro* glutamate neurotoxicity test, and the (*threo*) configuration **2** also has been suggested to be important for NMDAR selectivity.[15]

Investigations of the interaction and mechanism of action of ifenprodil on NMDARs have revealed that the ifenprodil binding site coincides with the N-terminal domain (NTD) of the NR2B subunit. The potency of ifenprodil at NR2B is due to the key structural elements that incorporate a phenolic aromatic ring connected to a second phenyl ring *via* a linker containing a tertiary basic amine.[25−29] The piperidine linker provides a scaffold to hold the two aryl rings in the optimum spatial orientation in the binding site which itself contains a lipophilic pocket that accommodates the phenyl ring, as well as a hydrophobic and hydrogen bond acceptor pocket that accepts the phenol group. The basic nitrogen atom contributes to the positioning by electrostatic interaction. By mutagenesis, it has been proposed that ifenprodil binds to the central, interlobe cleft of NR2B NTD and promotes cleft closure through a hinge-bending motion (Venus flytrap mechanism).[27] The recent characterization of binding sites by experimental and computational approaches have revealed that the phenol ring of ifenprodil points toward the entrance of the cleft whereas the phenyl ring makes contact with the interlobe hinge.[28] On the basis of this pharmacophore/topological model, we assumed that the fluorescent moiety in derivatives A should not disturb the intrinsic properties of the parent ifenprodil. Hence, we selected three fluorophores, dansyl, fluorescein, and cyanine (Cy5), that possess different molecular sizes. An anchorage point for the fluorophore was provided by the secondary amine function in replacement of the benzylic hydroxyl in ifenprodil, this modification allowing the introduction of a spacer while maintaining the labile proton. Although not clearly established, the labile proton seems to be a prerequisite for selectivity based on a survey of structure−activity relationship studies.[17−21] Furthermore, it is noteworthy that ifenprodil analogues, such as the recently reported antagonist **3**, that bear a nitrogen-containing linker (i.e., an imidazole ring) instead of the hydroxypropyl moiety in ifenprodil, display an improved pharmacokinetic profile and decreased off-target activities (especially affinity for adrenergic α1 receptors and the hERG potassium channel).[30]

The synthetic route to fluorescent probes **4**−**7**, found to be representative of the class of compounds **A**, is depicted in Scheme 1. Racemic (*threo*)-*O*-benzyl ifenprodil **8**[15] was first converted into the ethylenediamine **9** according to a stereospecific mesylation/amination sequence through the use of *N*-Boc-monoprotected α,ω-hexyldiamine in a 88% yield. This transformation occurred with a complete retention of configuration as a result of a mechanism with anchimeric assistance due to the *in situ* formation of an aziridinium intermediate.[31] The configuration of compound **9** was assigned by ^{1}H NMR analysis on the basis of the chemical shifts and coupling constants for the signals of protons borne by the asymmetric centers (see the Supporting Information). Acidic double deprotection of **9** led to the phenolamine **10** with a 57% yield. Conjugation of **10** with dansyl chloride, fluorescein (with or without the spacer) or cyanine Cy5 *N*-succinimidyl ester gave the probes **4**−**7**. These compounds were purified by

dx.doi.org/10.1021/bc100571g | *Bioconjugate Chem.* 2012, 23, 21−26

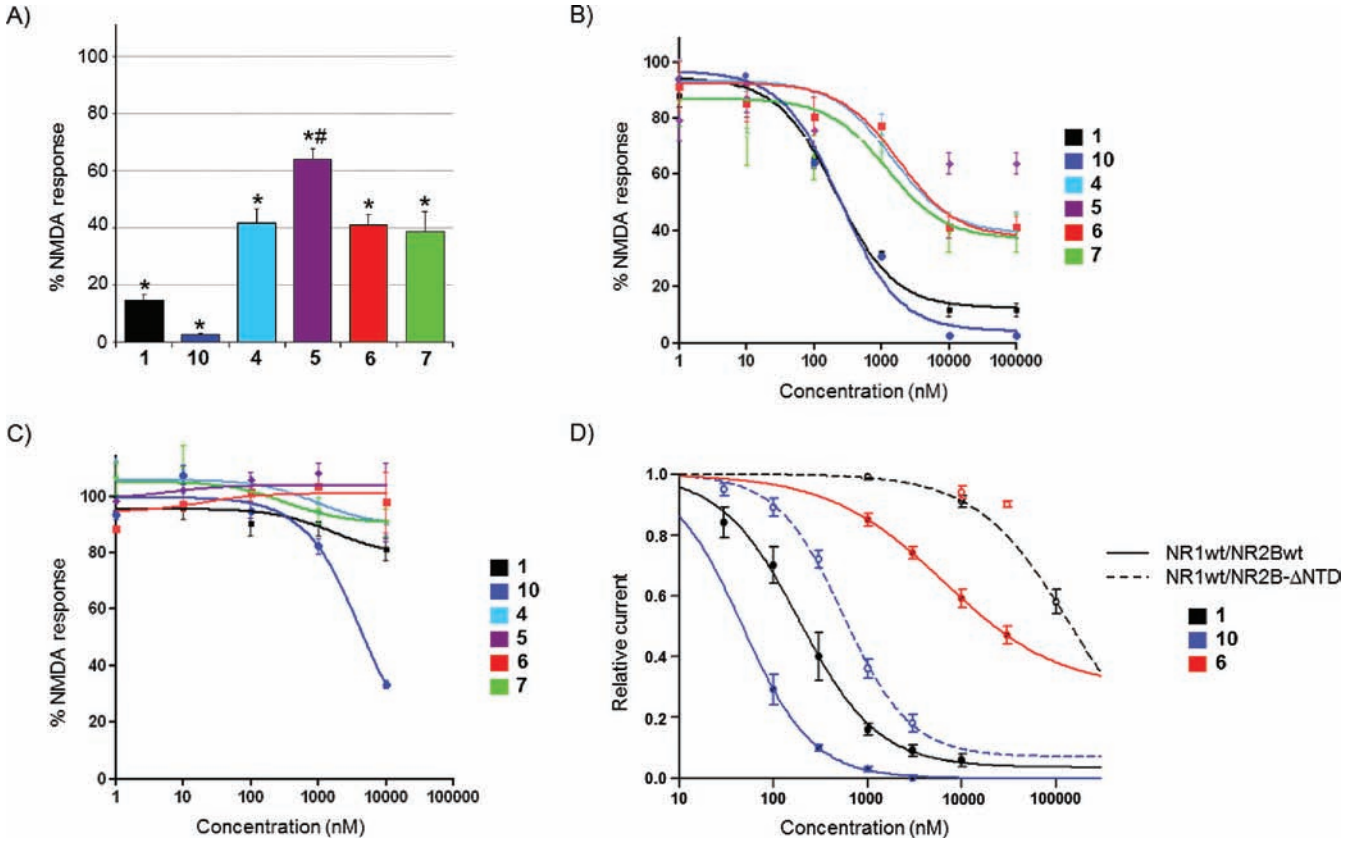


Figure 2. Evaluation of the antagonistic properties of ligands **10** and **4**–**7** compared to ifenprodil **1** by measurement of inhibition of NMDA-induced calcium influx (A, B, C) and NMDAR mediated currents (D). (A, B, C) Calcium imaging experiments performed by assessment of intracellular calcium increase after an acute stimulation with NMDA (100 μM) in the presence of glycine (10 μM) and ligand (n = 30 HEK cells transfected with NMDA receptor subunits from 3 independent culture dishes). Responses to ligand application were normalized to the mean response obtained by stimulation with NMDA (100 μM) in the presence of only glycine (10 μM) taken as the control experiment (100% value). (A) Histograms representing mean values of NMDA-induced calcium influx obtained with ligands (10 μM) evaluated toward NR1−1a/NR2B receptors. Statistical analysis (ANOVA) was performed on raw data [* indicates significantly different from NMDA alone (control); # indicates significantly different from **1** and NMDA alone]. (B) Dose−response curve for inhibition of NMDA-induced calcium influx through NR1−1a/NR2B receptors. (C) Dose−response curve for inhibition of NMDA-induced calcium influx through NR1−1a/NR2A receptors. (D) Electrophysiological experiments using two electrode voltage clamp (pH = 7.3; holding potential = −60 mV). NMDA currents were evoked by applying glutamate and glycine (100 μM each).

HPLC and characterized by mass spectrometry (see the Supporting Information). Spectroscopic properties were determined by UV and emission spectra measurements. Spectral properties were in accordance with the presence of dansyl, Cy5, or fluorescein [$\lambda_{ex}/\lambda_{em}$ of about 340/540 and 645/670 nm for ligands **4** and **7**, respectively, and of about 490/525 nm for both ligands **5** and **6**].

The target fluorescent conjugates **4**–**7** as well as the precursor **10** were evaluated as selective NR2B antagonists in a functional assay by calcium imaging (Figure 2A−C); here, we monitored intracellular calcium concentrations by videomicroscopy of HEK-293 cells transfected with the cDNA encoding either for NR1−1a and NR2B, or for NR1−1a and NR2A subunits. As NMDARs are calcium-permeable ion channels,[32] we measured calcium (Ca^{2+}) influx induced by the application of NMDA (at 100 μM for 30 s) in the presence of glycine (10 μM) and of increasing concentrations of potential antagonists. The application of NMDA induced a rapid and sustained increase in [Ca^{2+}] (determined as the 100% value), whereas the simultaneous application of NMDA and an antagonist led to a lesser increase in [Ca^{2+}]. In a first set of experiments with NR1−1a/NR2B receptor transfected cells, the compounds **4**–**7** and **10** were used at 10 μM in order to perform a rapid screening (Figure 2A). The data clearly showed that the precursor **10** potently inhibited the Ca^{2+} influx with a residual NMDA response of only 3% versus 15% for ifenprodil **1**. Although moderate, the inhibition of Ca^{2+} entry by conjugates **4**, **6**, and **7** was significant (the residual responses to NMDA were approximately 40%). Ligand **5**, in contrast, showed weak effects with a residual response to NMDA superior to 60%. The pharmacological characterization of **4**–**7** and **10** was then pursued in a second set of experiments with either NR1−1a/NR2B or NR1−1a/NR2A receptor transfected cells by establishing the dose−response curves (Figure 2B and C). The results confirmed that precursor **10** was a potent antagonist of the NR1−1a/NR2B receptor with an IC_{50} value slightly lower than that of ifenprodil **1** and that conjugates **4**, **6**, and **7** were only moderate inhibitors with IC_{50} values 4- to 6-fold higher (Table 1). Thus, the chemical modification of ifenprodil **1** into ethylenediamine **10** maintained NR2B inhibition but the introduction of the fluorophore moderately decreased ligand binding. In the case of the sterically hindered cyanine and fluorescein structures, the magnitude of this decrease was minimized by increasing the spacer length (see compounds **6** and **7** versus **5** and **4**). Finally,

dx.doi.org/10.1021/bc100571g | *Bioconjugate Chem.* 2012, 23, 21−26

Table 1. Inhibition Constants IC_{50} (μM, mean value ± sem) of Compounds 10 and 4−7 at NR1-1a/NR2B and NR1-1a/NR2A Receptor Subtypes Compared to Ifenprodil 1

	calcium imaging assay		electrophysiology	
compound	NR2B	NR2A	NR2B	NR2B-ΔNTD
1	0.275 ± 0.034	>100	0.190 ± 0.020	145 ± 2.000
10	0.244 ± 0.036	4.440 ± 0.755	0.047 ± 0.002	0.560 ± 0.090
4	1.416 ± 0.411	>100	n.d.	n.d.
5	>10	>100	n.d.	n.d.
6	1.795 ± 0.535	>100	6.400 ± 0.300	>100
7	1.203 ± 0.630	>100	n.d.	n.d.

ligands **4**, **6**, **7**, and **10** did not display any effect on NR1−1a/NR2A receptor transfected cells (except for **10** at concentration higher than 10 μM), which rend them highly selective toward the NR1−1a/NR2B receptor (Figure 2C).

A further evaluation of precursor **10** and conjugate **6** was performed in electrophysiological studies using two-electrode voltage-clamp measurements in *Xenopus laevis* oocytes that expressed recombinant NMDARs after the coinjection of cDNAs coding for wild-type (wt) NR1−1a and either wild-type NR2B or a NTD deleted NR2B subunit (Figure 2D). NMDA currents were induced by saturating concentrations of L-glutamate and glycine (100 μM each),[9,33] and the effects of ligands **10** and **6** were assessed by measuring the change in current size induced by the application of the compound during a NMDA response.[27,28] The results confirmed that ligand **10** inhibited NR1wt/NR2Bwt receptors. Inhibition by **10** was found complete (no residual current could be measured), whereas 4% of the residual current remained with ifenprodil **1** applied at saturating concentrations. Ligand **10** also displayed an inhibitory effect on NR1wt/NR2-ΔNTD receptors with an IC_{50} ~12 fold higher than that measured on the full-length receptors (Table 1). This inhibition was found to be voltage-dependent, and disappeared almost completely at depolarized potentials (data not shown). This effect probably results from an interaction of **10** with the ion channel pore as reported for polyamines such as spermine and spermidine.[34,35] This possibility could explain the low but significant inhibition of NR2A-containing receptors by compound **10** as assessed by the calcium imaging experiments (Figure 2C). The inhibition of NR2B-containing receptors by conjugate **6** was decreased when compared to precursor **10** as demonstrated by the greater IC_{50} values obtained in the current assays (Table 1). Interestingly, no inhibitory effects were detected at NR1wt/NR2-ΔNTD receptors with the conjugate **6** (Figure 2D). Thus, as shown in the calcium imaging assay, the fluorophore conjugation led to a decreased affinity though to an increased selectivity. A simple explanation might be that the interaction in the channel pore fails to occur due to the lack of a single cationic site (i.e., the terminal primary amine function) in conjugate **6** as compared to precursor ligand **10**.

Confocal microscopy imaging studies were carried out by fluorescence analysis of DS-red labeled cortical neurons incubated with conjugate **6** ($\lambda_{ex}/\lambda_{em}$ = 490/525 nm). Primary neuronal cultures (at DIV 10) were transfected with the DS-red fluorescent protein ($\lambda_{ex}/\lambda_{em}$ = 540/570 nm). Imaging experiments were performed at DIV 14 when cortical neurons expressed a subset of NMDARs similar to those observed in adults. When transfected with cDNA encoding for DS-red, neurons displayed a cytosolic expression of the fluorescent protein that allowed the visualization of the dendritic morphology (Figure 3A). After exposure to fluorescent ligand **6**, a punctate green fluorescence was demonstrable (Figure 3B). The merged image showed the yellow coloration that

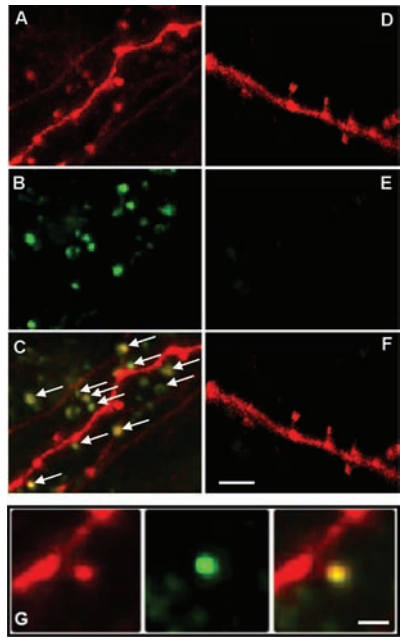


Figure 3. Confocal microscopy imaging. (A) Dendrite of Ds-red transfected cortical neurons (red, emission band 550−590 nm), (B) after 15 min exposition to 10 μM conjugate **6** (green, emission band 513−530 nm), (C) merge showing fluorescent yellow colocalization with dendritic spines (arrows). (D, E, F) Preincubation with ifenprodil **1** (15 min, 10 μM) fully blocked the probe **6** labeling. Scale bar 5 μm. (G) High magnification of a dendritic spine after 15 min exposition to 10 μM probe as in A, B, and C. Scale bar 1 μm.

characterizes the exact colocalization of red and green fluorescence, especially on small protrusions along the dendrites that could correspond to postsynaptic sites (Figure 3C). A high magnification of a spine labeled with probe **6** proved the localization of the staining on the protrusions (Figure 3G). To assess the specificity of the labeling, exposure with probe **6** was preceded by a preincubation with ifenprodil **1** (10 μM). Under these conditions, image acquisition with the same amplification setting failed to reveal any green fluorescence (Figure 3D−F). Inhibition of probe **6** staining by ifenprodil **1** strongly suggests that the fluorescent image in Figure 3B is due to a specific binding of probe **6** on NR2B-containing NMDARs.

In conclusion, we have reported here the synthesis of novel fluorescent ligands of NR2B-containing receptors on the basis of the structural framework of ifenprodil and of its original ethylenediamine analogue **10**. The derivative **10** was assayed for its ability to be recognized by the ifenprodil binding site, and to

dx.doi.org/10.1021/bc100571g | *Bioconjugate Chem.* 2012, 23, 21−26

retain NR2B selectivity. Ligand **10** was found to exhibit a potent inhibition of NR2B-containing receptors, partly through a mechanism of blockade at the channel pore. Fluorophore conjugation to ligand **10** led to fluorescent probes **4**, **6**, and **7** that displayed a moderate affinity for the NR2B subunit. Confocal microscopy imaging of DS-red labeled cortical neurons using the fluorescein conjugate **6** showed an exact colocalization of the probe with small protrusions along the dendrites which would highly support specific binding to NR2B-containing NMDARs. This unprecedented result demonstrates the proof-of-concept for NR2B-containing NMDAR imaging through the use of a selective, synthetic fluorescent ligand. The dense labeling of the dendritic spines, given the current resolution of our images, did not allow us to distinguish between an eventual synaptic and extrasynaptic localization, which will be the object of future investigations. Work is now in progress to develop novel generations of fluorescent probes with improved pharmacological profiles for further characterization, neuronal location, and biodistribution studies of NMDARs. These approaches would potentially open a wide field of applications in the pathophysiology of the central nervous system.

EXPERIMENTAL SECTION

HEK293 Cell Culture and Plasmid Transfection. CDNAs encoding the full length sequences of NR1−1a, NR2B-GFP, and NR2A-GFP were a generous gift from Dr. Stefano Vicini (Georgetown University Medical Center, Washington). Human embryonic kidney 293 cells (HEK 293) were grown in Dulbecco's medium (Invitrogen, France) supplemented with 1% L-glutamine, 1% streptomycin/penicillin/neomycin (Sigma-Aldrich), and 10% fetal bovine serum (Invitrogen). HEK cells were plated on 12 mm glass coverslips (MatTek Corporation, USA) coated with poly(D-lysine) and grown at 37 °C in a humidified atmosphere containing 5% CO_2. Twenty-four hours after plating, cells were transfected with cDNA encoding for NR1−1a/NR2A-GFP or NR2B-GFP using Transfast Reagent (Promega, France). After the transfection, HEK cells were cultured with an NMDA antagonist (D-APV at 100 μM) to prevent cell death.

Calcium Imaging. HEK 293 expressing NR1−1a/NR2B-GFP or NR1−1a/NR2A-GFP were loaded for 45 min at 37 °C with 10 μM Fura-2/AM and 0.2% pluronic acid (F-127, Invitrogen) and incubated for an additional 15 min at room temperature (rt) in HEPES and bicarbonate-buffered saline solution (HBBSS) containing (in mM) 116 NaCl; 5.4 KCl; 1.8 $CaCl_2$; 0.8 $MgSO_4$; 1.3 NaH_2PO_4; 12 HEPES; 5.5 glucose; 25 bicarbonate; and 10 μM glycine at pH 7.45. Experiments were performed at rt with continuous perfusion (at 2 mL/min) on the stage of a Nikon Eclipse inverted microscope equipped with a 100 W mercury lamp and oil immersion Nikon 40× objective with a 1.4 numerical aperture. Fura-2 (excitation: 340/380 nm, emission: 510 nm) ratio images were acquired every 2 s with a digital camera (Princeton Instruments, New Jersey, USA). Analysis was performed with the software *Metafluor 6.3* (Universal Imaging Corporation, New Jersey, USA). Measurements were carried out with amplification rates that prevented saturation of the fluorescence signal. Fluorescence ratios (340/380 nm) were converted to intracellular Ca^{2+} concentrations using the following formula:

$$[Ca^{2+}]_i = Kd[(R - R_{min})/(R_{max} - R)]F_0/F_s$$

where R is the ratio for observed 340/380 fluorescence ratio, R_{min} is a ratio for a Ca^{2+}-free solution, R_{max} is the ratio for a saturated Ca^{2+} solution, K_d = 135 nM (the dissociation constant for Fura-2), F_0 is the intensity of a Ca^{2+}-free solution at 380 nm, and F_s is the intensity of a saturated Ca^{2+} solution at 380 nm. NMDA solutions (at 100 μM) were applied for 30 s, each application was separated by a minimum of 5 min to allow the full recovery to the basal level of $[Ca^{2+}]_i$. Ifenprodil **1** (purchased from Tocris) was used in its tartaric ammonium form whereas ligand **10** was used as hydrochloride ammonium. Fluorescent tracers **4**−**7** were used as obtained after lyophilization. Ligands were prepared as 1 mL aliquots at 10 mM in water for **1**, **7**, and **10**, and in DMSO for **4**−**6**. Because the slow rate of inhibition of ifenprodil,[36] ligands **1**, **4**−**7**, and **10** were applied 60 s prior to and during NMDA application. For each experiment, ROIs (Region Of Interest) corresponding to the cell bodies were chosen. The obtained fluorescence values were plotted against time to generate graphics of the intracellular Ca^{2+} trend in response to stimulation by NMDA (100 μM) in the presence of glycine (10 μM) and to ligand administration. To calculate the percentage of inhibition induced by the compounds of interest, we measured the $[Ca^{2+}]$ signal by integrating the area under the curve (AUC) on a 2 min period after the beginning of NMDA application. Dose−response curves were analyzed on the standard slope with *GraphPad Prism 5.0*.

Electrophysiology. Recombinant NMDA receptors were expressed in *Xenopus laevis* oocytes and currents measured using the two-electrode voltage-clamp technique. Oocyte preparation, injection, and superfusion were carried out as previously reported in the literature.[28] The extracellular medium contained (in mM) 100 NaCl, 2.5 KCl, 0.3 $BaCl_2$, 5 HEPES, and 0.01 diethylenetriamine-pentaacetic acid (DTPA; to chelate trace amount of heavy metals). The pH was adjusted to 7.3. All experiments were performed at rt. Dose−response curves were analyzed by the variable Hill slope with *GraphPad Prism 5.0*.

Confocal Imaging. To analyze the binding properties of the fluorescent ligand, we performed a spatial analysis of the fluorescent signal on murine primary cortical neuron cultures (at DIV 10), transfected with Ds-Red fluorescent protein ($\lambda_{ex}/\lambda_{em}$ = 540/570 nm). Transfections were performed with the phosphate-calcium technique. Neurons were exposed to cDNA for 2 h, and returned to DMEM. Experiments were performed at DIV 14 when the primary culture of murine cortical neurons expressed a subset of NMDA receptors similar to those expressed in adults (data not shown). Neurons were exposed to the fluorescent conjugate **6** (10 μM in DMSO/HBBSS 1:9, $\lambda_{ex}/\lambda_{em}$ = 490/525 nm) for 15 min and then washed with 5 mL of HBBSS. Images were acquired with Nikon EZ-C1 software at a resolution of 1024 × 1024 pixels. Sections of 0.3 μm were acquired in a Z-stack from top to bottom of the specimen. Specific fluorescence signal yield by the probe **6** was evaluated by the intensity obtained with the same laser power and gain intensity in each set of experiments.

ASSOCIATED CONTENT

Supporting Information

Full synthetic procedures, analytical and spectral characterization data of the synthesized compounds. This material is available free of charge via the Internet at http://pubs.acs.org.

AUTHOR INFORMATION

Corresponding Author

*Phone: (33)231470281. Fax: (33)231470275. E-mail: perrio@cyceron.fr.

■ ACKNOWLEDGMENTS

We are grateful to the MESR (Ministère de l'Enseignement Supérieur et de la Recherche), CEA (Commissariat à l'Energie Atomique), CNRS (Centre National de la Recherche Scientifique), the ≪ CRUNCH ≫ Network (Pôle Universitaire Normand de Chimie Organique), the "Région Basse-Normandie", and the European Union (FEDER funding) for financial support. We also thank Dr. F. Acher for helpful discussions and Dr. Eric T. MacKenzie for his comments on the revision of this manuscript.

■ REFERENCES

(1) Brauner-Osborne, H., Egebjerg, J., Nielsen, E. O., Madsen, U., and Krogsgaard-Larsen, P. (2000) Ligands for glutamate receptors: design and therapeutic prospects. *J. Med. Chem. 43*, 2609−2645.

(2) Paoletti, P., and Neyton, J. (2007) NMDA receptor subunits: function and pharmacology. *Curr. Opin. Pharmacol. 7*, 39−47.

(3) Chazot, P. L. (2004) The NMDA receptor NR2B subunit: a valid therapeutic target for multiple CNS pathologies. *Curr. Med. Chem. 11*, 389−396.

(4) Childers, W. E. Jr., and Baudy, R. B. (2007) N-Methyl-D-aspartate antagonists and neuropathic pain: the search for relief. *J. Med. Chem. 50*, 2557−2562.

(5) Higgins, G. A., Ballard, T. M., Enderlin, M., Haman, M., and Kemp, J. A. (2005) Evidence for improved performance in cognitive tasks following selective NR2B NMDA receptor antagonist pre-treatment in the rat. *Psychopharmacology 179*, 85−98.

(6) Gogas, K. R. (2006) Glutamate-based therapeutic approaches: NR2B receptor antagonists. *Curr. Opin. Pharmacol. 6*, 68−74.

(7) Laube, B., Kuhse, J., and Betz, H. (1998) Evidence for a tetrameric structure of recombinant NMDA receptors. *J. Neurosci. 18*, 2954−2961.

(8) Loftis, J. M., and Janowsky, A. (2003) The N-methyl-D-aspartate receptor subunit NR2B: localization, functional properties, regulation, and clinical implications. *Pharmacol. Therapeutics 97*, 55−85.

(9) Paoletti, P. (2011) Molecular basis of NMDA receptor functional diversity. *Eur. J. Neurosci. 33*, 1351−1365.

(10) Cull-Candy, S. G., and Leszkiewicz, D. N. (2004) Role of distinct NMDA receptor subtypes at central synapses. *Sci. STKE 255*, re16.

(11) Hardingham, G. E., Fukunaga, Y., and Bading, H. (2002) Extrasynaptic NMDARs oppose synaptic NMDARs by triggering CREB shut-off and cell death pathways. *Nat. Neurosci. 5*, 405−414.

(12) Mony, L., Kew, J. N. C., Gunthorpe, M. J., and Paoletti, P. (2009) Allosteric modulators of NR2B-containing NMDA receptors: molecular mechanisms and therapeutic potential. *Br. J. Pharmacol. 157*, 1301−1317.

(13) McGrath, J. C., Arribas, S., and Daly, C. J. (1996) Fluorescent ligands for the study of receptors. *Trends Pharmacol. Sci. 17*, 393−399.

(14) Reynold, I. J., and Miller, R. (1989) Ifenprodil is a novel type of N-methyl-D-aspartate receptor antagonist: interaction with polyamines. *Mol. Pharmacol. 36*, 758−765.

(15) Chenard, B. L., Shalaby, I. A., Koe, B. K., Ronau, R. T., Butler, T. W., Prochniak, M. A., Schmidt, A. W., and Fox, C. B. (1991) Separation of α_1-adrenergic and N-methyl-D-aspartate antagonist activity in a series of ifenprodil compounds. *J. Med. Chem. 34*, 3085−3090.

(16) Williams, K. (2001) Ifenprodil, a novel NMDA receptor antagonist: site and mechanism of action. *Curr. Drug Targets 2*, 285−298.

(17) Borza, I., and Domany, G. (2006) NR2B selective NMDA antagonists: the evolution of the ifenprodil-type pharmacophore. *Curr. Top. Med. Chem. 6*, 687−695.

(18) Layton, M. E., Kelly, M. J. III, and Rodzinak, K. J. (2006) Recent advances in the development of NR2B subtype-selective NMDA receptor antagonists. *Curr. Top. Med. Chem. 6*, 697−709.

(19) MacCauley, J. A. (2006) Amide-containing NR2B/NMDA receptor antagonists. *Expert Opin. Ther. Patents 16*, 863−870.

(20) MacCauley, J. A. (2005) NR2B subtype-selective NMDA receptor antagonists: 2001−2004. *Expert Opin. Ther. Patents 15*, 389−407.

(21) Nikam, S. S., and Meltzer, L. T. (2002) NR2B selective NMDA receptor antagonists. *Curr. Pharm. Des. 8*, 845−855.

(22) Rosahl, T. W., Wingrove, P. B., Hunt, V., Fradley, R. L., Lawrence, J. M. K., Heavens, R. P., Treacey, P., Usala, M., Macauley, A., Bonnert, T. P., Whiting, P. J., and Wafford, K. A. (2006) A genetically modified mouse model probing the selective action of ifenprodil at the N-methyl-D-aspartate type 2B receptor. *Mol. Cell. Neurosci. 33*, 47−56.

(23) Grimwood, S., Richards, P., Murray, F., Harrison, N., Wingrove, P. B., and Hutson, P. H. (2000) Characterisation of N-methyl-D-aspartate receptor-specific [^{3}H]ifenprodil binding to recombinant human NR1a/NR2B receptors compared with native receptors in rodent brain membranes. *J. Neurochem. 75*, 2455−2463.

(24) Avenet, P., Leonardon, J., Besnard, F., Graham, D., Frost, J., Depoortere, H., Langer, S. Z., and Scatton, B. (1996) Antagonist properties of the stereoisomers of ifenprodil at NR1A/NR2A and NR1A/NR2B subtypes of the NMDA receptor expressed in Xenopus oocytes. *Eur. J. Pharmacol. 296*, 209−213.

(25) Tamiz, A. P., Whittemore, E. R., Zhou, Z.-L., Huang, J.-C., Drewe, J. A., Chen, J.-C., Cai, S.-X., Weber, E., Woodward, R. M., and Keana, J. F. W. (1998) Structure-activity relationships for a series of bis(phenylalkyl)amines: potent subtype-selective inhibitors of N-methyl-D-aspartate receptors. *J. Med. Chem. 41*, 3499−3506.

(26) Masuko, T., Kashiwagi, K., Kuno, T., Nguyen, N. D., Pahk, A. J., Fukuchi, J., Igarashi, K., and Williams, K. (1999) A regulatory domain (R1-R2) in the amino terminus of the N-methyl-D-aspartate receptor: effects of spermine, protons, and ifenprodil, and structural similarity to bacterial leucine/isoleucine/valine binding protein. *Mol. Pharmacol. 55*, 957−969.

(27) Perin-Dureau, F., Rachline, J., Neyton, J., and Paoletti, P. (2002) Mapping the binding site of the neuroprotectant ifenprodil on NMDA receptors. *J. Neurosci. 22*, 5955−5965.

(28) Mony, L., Krzaczkowski, L., Leonetti, M., Le Goff, A., Alarcon, K., Neyton, J., Bertrand, H.-O., Acher, F., and Paoletti, P. (2009) Structural basis of NR2B-selective antagonist recognition by N-methyl-D-aspartate receptors. *Mol. Pharmacol. 75*, 60−74.

(29) Ng, F.-M., Geballe, M. T., Snyder, J. P., Traynelis, S. F., and Low, C.-M. (2008) Structural insights into phenylethanolamines high-affinity binding site in NR2B from binding and molecular modeling studies. *Molecular Brain 1* (16), 1−11.

(30) MacCauley, J. A., Theberge, C. R., Romano, J. J., Billings, S. B., Anderson, K. D., Claremon, D. A., Freidinger, R. M., Bednar, R. A., Mosser, S. D., Gaul, S. L., Connolly, T. M., Condra, C. L., Xia, M., Cunningham, M. E., Bednar, B., Stump, G. L., Lynch, J. J., Macaulay, A., Wafford, K. A., Koblan, K. S., and Liverton, N. J. (2004) NR2B-Selective N-methyl-D-aspartate antagonists: synthesis and evaluation of 5-substituted benzimidazoles. *J. Med. Chem. 47*, 2089−2096.

(31) Saravanan, P., Bisai, A., Baktharaman, S., Chandrasekhar, M., and Singh, V. K. (2002) Synthesis of chiral non-racemic 1,2-diamines from O-acetyl mandelic acid: application in enantioselective deprotonation of epoxides and diethylzinc addition to aldehydes. *Tetrahedron 58*, 4693−4706.

(32) Dingledine, R., Borges, K., Bowie, D., and Traynelis, S. F. (1999) The glutamate receptor ion channels. *Pharmacol. Rev. 51*, 7−61.

(33) Yuan, H., Hansen, K. B., Vance, K. M., Ogden, K. K., and Traynelis, S. F. (2009) Control of NMDA receptor function by the NR2 subunit amino-terminal domain. *J. Neurosci. 29*, 12045−12058.

(34) For example: Rock, D. M., and MacDonald, R. L. (1992) The polyamine spermine has multiple actions on N-methyl-D-aspartate receptor single-channel currents in cultured cortical neurons. *Mol. Pharmacol. 41*, 83−88.

(35) Han, X., Tomitori, H., Mizuno, S., Higashi, K., Füll, C., Fukiwake, T., Terui, Y., Leewanich, P., Nishimura, K., Toida, T., Williams, K., Kashiwagi, K., and Igarashi, K. (2008) Binding of spermine and ifenprodil to a purified, soluble regulatory domain of the N-methyl-D-aspartate receptor. *J. Neurochem. 107*, 1566−1577.

(36) Williams, K. (1993) Ifenprodil discriminates subtypes of the N-methyl-D-aspartate receptor: selectivity and mechanisms at recombinant heteromeric receptors. *Mol. Pharmacol. 44*, 851−859.

Bioconjugate Chemistry

Communication

pubs.acs.org/bc

Template-Assisted Lateral Growth of Amyloid-β42 Fibrils Studied by Differential Labeling with Gold Nanoparticles

Muriel Arimon,[†,‡,§,¶] Fausto Sanz,[†,‡,§] Ernest Giralt,*[,∥,#] and Natàlia Carulla*[,∥]

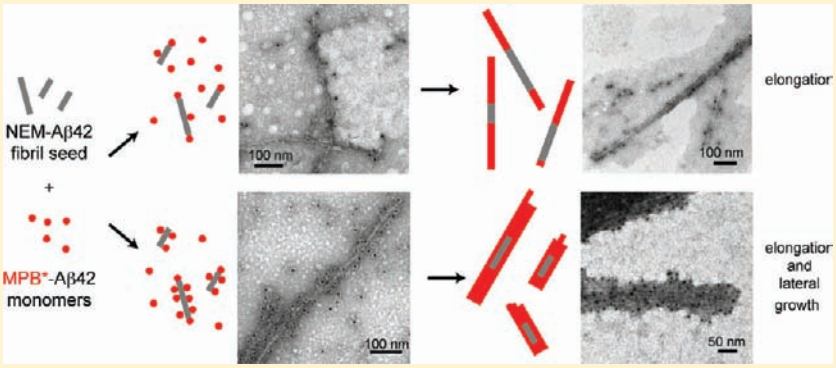
[†]Institute for Bioengineering of Catalonia (IBEC), Baldiri Reixac 15, Barcelona 08028, Spain

[‡]CIBER-BBN, Zaragoza, Spain

[§]Department of Physical Chemistry and [#]Department of Organic Chemistry, University of Barcelona (UB), Martí i Franquès 1, Barcelona 08028, Spain

[∥]Institute for Research in Biomedicine (IRB Barcelona), Baldiri Reixac 1-10, Barcelona 08028, Spain

Supporting Information



ABSTRACT: Amyloid-β protein (Aβ) aggregation into amyloid fibrils is central to the origin and development of Alzheimer's disease (AD), yet this highly complex process is poorly understood at the molecular level. Extensive studies have shown that Aβ fibril growth occurs through fibril elongation, whereby soluble molecules add to the fibril ends. Nevertheless, fibril morphology strongly depends on aggregation conditions. For example, at high ionic strength, Aβ fibrils laterally associate into bundles. To further study the mechanisms leading to fibril growth, we developed a single-fibril growth assay based on differential labeling of two Aβ42 variants with gold nanoparticles. We used this assay to study Aβ42 fibril growth under different conditions and observed that bundle formation is preceded by lateral interaction of soluble Aβ42 molecules with pre-existing fibrils. Based on this data, we propose template-assisted lateral fibril growth as an additional mechanism to elongation for Aβ42 fibril growth.

Alzheimer's disease (AD) is a neurodegenerative disease characterized by a progressive loss of cognitive abilities. One of the neuropathological hallmarks of AD is the presence of amyloid plaques in the brain of patients suffering from this disease.[1] These plaques consist primarily of the Aβ protein aggregated into amyloid fibrils. Therefore, knowing the three-dimensional structure of Aβ fibrils and understanding the mechanisms of Aβ fibril growth is crucial for understanding AD.

Regarding Aβ fibril structure, X-ray fiber diffraction data indicate that large regions of Aβ molecules within amyloid fibrils adopt a cross β-sheet structure.[2] This structure comprises β-strands that run approximately perpendicular to the fibril axis, with backbone hydrogen bonds linking the β-strands into sheets oriented essentially parallel to the fibril axis. Moreover, solid state nuclear magnetic resonance spectroscopy (SSNMR) studies on Aβ fibrils have provided residue-specific information on the regions of the Aβ protein that form β-strands, turns, and loops within the fibrils.[3,4] These studies together with evidence from other biochemical and/or biophysical measurements have provided detailed structural models of amyloid fibrils.[3−5]

Despite progress on Aβ amyloid fibril structure characterization, the molecular mechanisms of fibril growth remain poorly understood. The growth of individual fibrils[6−12] has been studied using various assays, most of which have been designed to detect molecules once they have become incorporated into the fibril. The majority of these assays have been applied to study the yeast Sup35 prion protein.[7−9] For Aβ, most work has involved the 40-residue Aβ protein (Aβ40), which is less amyloidogenic than its 42-residue analogue (Aβ42).[6,10,12] These strategies have yielded important information on the polarity and directionality of fibril growth, corroborating a growth mechanism based on elongation, that is incorporation of new soluble molecules onto fibril ends.

Fibril morphology is extremely sensitive to aggregation conditions.[13−15] For example, when aggregation occurs at high ionic strength, the resulting fibrils laterally associate into

Received: February 8, 2011
Revised: November 16, 2011
Published: November 30, 2011

ACS Publications © 2011 American Chemical Society

bundles.[13] The mechanism for fibril bundle formation is still undefined. One possibility is that fibrils form individually and subsequently coalesce into bundles. This occurs when protofibrils[16] and fibrils[13] that are formed at low ionic strength are later incubated at high ionic strength. Another possible mechanism for fibril bundle formation involves individual fibrils acting as a lateral template for soluble Aβ molecules and thereby promoting formation of new, adjacent fibrils. Since physiological conditions contain high ionic strength, understanding fibril bundle formation is biologically relevant.

In this study, we aim to elucidate the mechanism of fibril bundle formation. We developed a single-fibril growth assay based on two Aβ42 variants that are differentially immunolabeled with gold nanoparticles (NPs). Importantly, our assay differs from previously reported ones in that it does not only detect Aβ42 molecules once incorporated in the fibrils, but also detects early aggregation stages such as monomer and oligomers. Furthermore, to study the type of interactions involved in bundle formation, we performed the assay under two conditions: one leading to the formation of individual fibrils and the other to fibrillar bundles.

The single-fibril growth assay was designed to meet several requirements. First, the labeling step was to detect Aβ42 molecules at different stages of aggregation including monomer, oligomers, and fibrils. Second, fibril growth was to occur in solution, rather than on a surface, which can generate altered fibrillar species.[17] Third, the growth reaction was to be rapidly quenched to enable precise time measurements. Finally, the labeling reaction was to be performed after quenching, to avoid the label being involved in any nonspecific interactions and/or causing steric interference during fibril growth.

The two Aβ variants used in this assay are derived from the Aβ42 mutant M35L-Aβ42, in which the methionine at position 35 is replaced with leucine (SI Figure S1). M35L-Aβ42 has been described to form fibrils with indistinguishable ultrastructural morphology from those formed by wild type (wt) Aβ42. In fact, this variant has been used to establish a 3D structural model of Aβ42 fibrils.[5] This and other structural models of Aβ fibrils reveal that when Aβ molecules are incorporated into fibrils, the N-terminal residues are in a disordered conformation.[3,4] Therefore, we added an eight-residue sequence GCGGGGGG to the M35L-Aβ42 N-terminus, which provides a cysteine for subsequent labeling and serves as a spacer between the Aβ42 fibril and the label. We then exploited the reactivity of the cysteine thiol group to react the resulting peptide with either maleimide-PEG_2-biotin (MPB) or *N*-ethylmaleimide (NEM) to produce the two variants used in the assay: MPB*-Aβ42 and NEM-Aβ42, respectively (Figure 1a,b). These two variants were distinguished by their differential binding to a primary antibiotin rabbit antibody followed by a secondary antirabbit antibody conjugated to a 12 nm gold NP (Figure 1c).

To learn about the type of interactions involved in bundle formation, fibril growth was also studied under conditions where bundles would not form. Aβ42 fibril morphology is strongly dependent on buffer conditions. For example, at low pH and low ionic strength, Aβ42 aggregation leads to the formation of discrete, individual fibril structures,[13,14] whereas at neutral pH and high ionic strength to the formation of bundles of fibrils.[13] We chose to study these two fibril morphologies by running experiments under two different sets of conditions, both at room temperature and without agitation: low pH and low ionic strength, H_2O at pH 2.0 adjusted with HCl; and

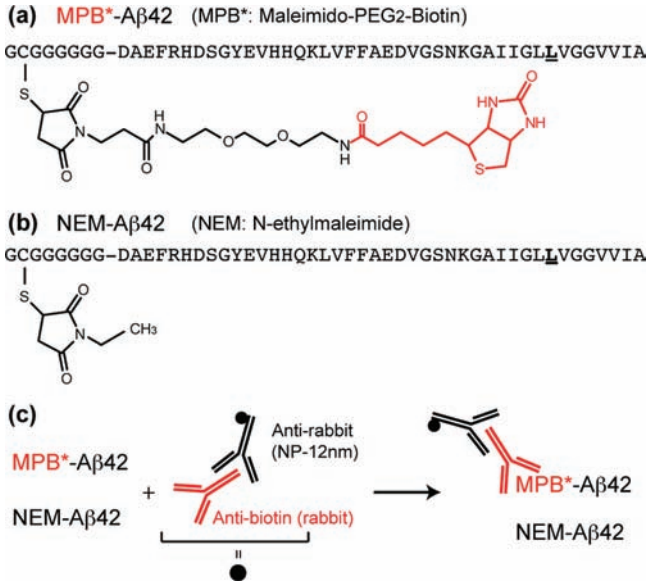


Figure 1. Amino acid sequences of the two Aβ42 variants used (a) MPB*-Aβ42 and (b) NEM-Aβ42. The chemical structures of maleimide-PEG_2-Biotin (MPB) and *N*-ethylmaleimide (NEM) molecules are shown. These moieties are attached to the Aβ42 variants through the thiol of the cysteine side-chain. The biotin moiety of MPB* is shown in red. (c) Immunogold labeling is performed with a primary antibiotin antibody followed by a secondary antibody conjugated to a 12 nm gold NP.

neutral pH and high salt concentration, 20 mM sodium phosphate, 1 mM EDTA, 0.01% NaN_3, and 150 mM NaCl at pH 6.5.

Wild-type Aβ42, MPB*-Aβ42, and NEM-Aβ42 were each incubated at low pH and low ionic strength, and the resulting fibrils were studied by transmission electron microscopy (TEM). Electron micrographs confirmed that all three proteins predominantly formed well-defined, discrete individual fibrils (SI Figure S2, and Figure 2a,c, respectively).[13,14] To confirm that MPB*-Aβ42 and NEM-Aβ42 fibrils prepared at low pH and low ionic strength conditions could be distinguished by our labeling procedure, the MPB*-Aβ42 fibrils and NEM-Aβ42 fibrils were incubated with a primary antibiotin rabbit antibody followed by a secondary antirabbit antibody conjugated to a 12 nm gold NP. After labeling, the MPB*-Aβ42 fibrils appeared covered with gold NPs (compare Figure 2a and b), whereas the NEM-Aβ42 fibrils were identical to unlabeled fibrils (compare Figure 2c and d).

Next, wt-Aβ42, MPB*-Aβ42, and NEM-Aβ42 were incubated at neutral pH and high ionic strength. As revealed by electron micrographs, all three proteins had evolved into fibrillar bundles (SI Figure S3, and Figure 3a and c, respectively). To determine the effect of N-terminal residues in MPB*-Aβ42 and NEM-Aβ42, we compared the kinetics of aggregation of the three variants using the thioflavin T binding assay (ThT) (SI Figure S4). Aβ42, NEM-Aβ42, and MPB*-Aβ42 spontaneously formed fibrils on a similar time scale. Nevertheless, the kinetics of fibril formation for NEM-Aβ42 and for MPB*-Aβ42 were slightly faster than those for Aβ42, so an impact of labels on Aβ42 aggregation cannot be entirely excluded. As with the previous experiment, we confirmed that MPB*-Aβ42 fibrils and NEM-Aβ42 fibrils could be distinguished by the immunogold labeling procedure. Again, MPB*-Aβ42 fibrils were covered with gold NPs (compare Figure 3a

dx.doi.org/10.1021/bc200077s | *Bioconjugate Chem.* 2012, 23, 27−32

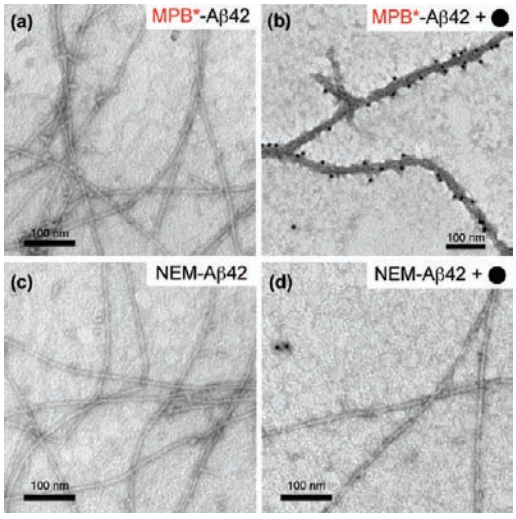


Figure 2. MPB*-Aβ42 and NEM-Aβ42 fibrils prepared at low pH and low ionic strength are equivalent except for their affinity to the immunogold label. Representative TEM images of fibrils prepared in H_2O at pH 2.0 and 37 °C for 17 days using either MPB*-Aβ42, (a) without immunogold labeling and (b) with immunogold labeling, or NEM-Aβ42 (c) without immunogold labeling and (d) with immunogold labeling.

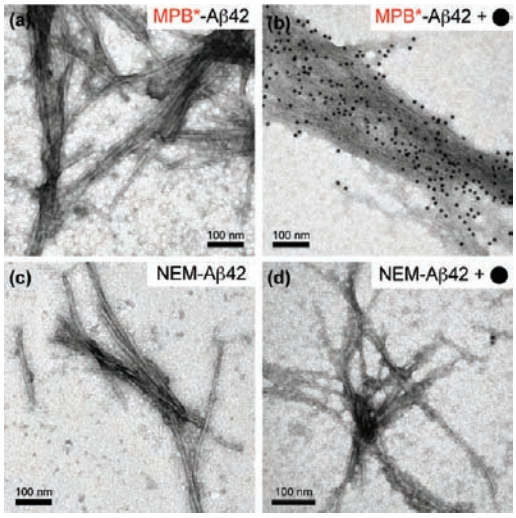


Figure 3. MPB*-Aβ42 and NEM-Aβ42 fibrils prepared at neutral pH and high ionic strength are equivalent except for their affinity to the immunogold label. Representative TEM images of fibrils prepared in 20 mM sodium phosphate, 150 mM NaCl, 1 mM EDTA, and 0.01% NaN_3 at pH 6.5 for 12 h using either MPB*-Aβ42, (a) without immunogold labeling and (b) with immunogold labeling, or NEM-Aβ42 (c) without immunogold labeling and (d) with immunogold labeling.

and b), whereas NEM-Aβ42 fibrils were not (compare Figure 3c and d).

Using the two Aβ42 variants and the immunogold labeling method, we designed an assay to monitor fibril growth (Figure 4a). Sonicated NEM-Aβ42 fibrils were used to seed polymerization of monomeric MPB*-Aβ42 in solution. The growth reaction was sampled at different time points and then rapidly quenched by depositing each sample onto the electron microscopy (EM) grid. Samples were then immunogold labeled and finally observed by TEM.

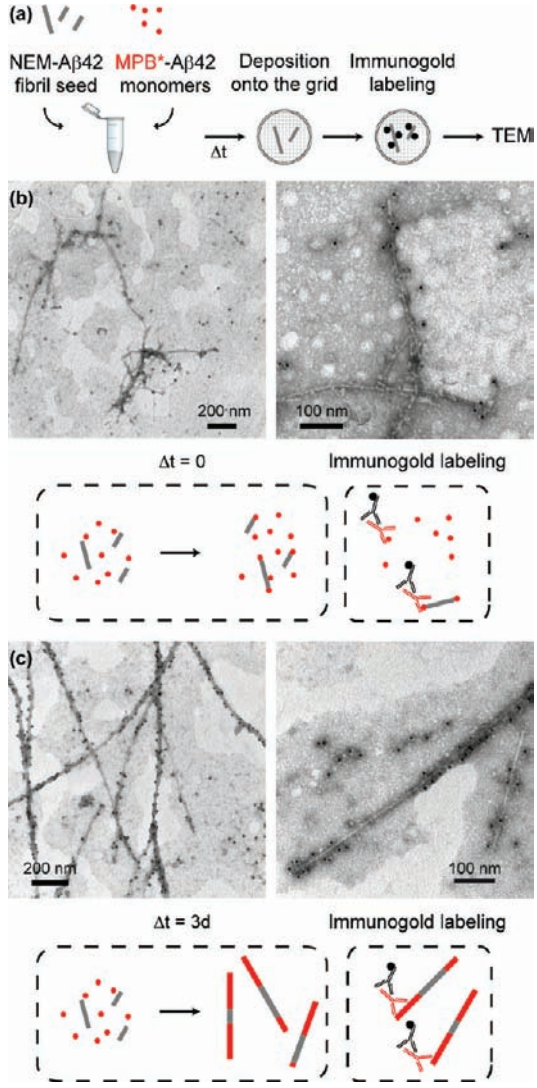


Figure 4. Aβ42 single-fibril growth assay. (a) Schematic of the assay. NEM-Aβ42 fibril seeds and MPB*-Aβ42 monomer are mixed together and incubated. The growth reaction is sampled at different times, and then quenched by deposition onto the EM grid, where the samples are immunogold labeled, and finally, visualized by TEM. Representative TEM images of immunogold labeled samples obtained at low pH and low ionic strength and graphical representations of the results obtained (b) within 1 min of mixing NEM-Aβ42 fibrils and MPB*-Aβ42 monomer, and (c) 3 days after mixing them. For the sake of clarity, some of the primary and secondary antibodies in the illustrations for (b) and (c) have been omitted.

We first ran the assay at low pH and low ionic strength. Within 1 min of mixing sonicated NEM-Aβ42 fibrils with monomeric MPB*-Aβ42, the first immunogold labeling step was performed. TEM images show MPB*-Aβ42 molecules distributed throughout the background of the grid and MPB*-Aβ42 molecules adhered to pre-existing fibrils (Figure 4b). Moreover, the density of NPs at the fibril ends was found to be higher than along the entire length of the fibril (SI Figure S5), suggesting that most of the MPB*-Aβ42 molecules had adhered to the ends of pre-existing fibrils. After incubating NEM-Aβ42 fibrils and monomeric MPB*-Aβ42 for 3 days, another round of labeling was performed, in which mixed fibrils were observed (Figure 4c). Within a single fibril, stretches of unlabeled fibrils suggestive of the initial NEM-Aβ42 fibril seeds

dx.doi.org/10.1021/bc200077s | *Bioconjugate Chem.* 2012, 23, 27–32

were observed together with stretches of fibrils completely covered with NPs suggestive of MPB*-Aβ42 molecules that had incorporated into the pre-existing NEM-Aβ42 fibrils (SI Figure S6). The fact that we observed mixed fibrils indicates that, in spite of the two different labels, the two Aβ42 variants have the same fibrilization capacity.

We then ran the assay at neutral pH and high ionic strength conditions. The first sample was also taken within 1 min of mixing sonicated NEM-Aβ42 fibrils with monomeric MPB*-Aβ42. Immunogold labeling and TEM observation showed soluble MPB*-Aβ42 molecules distributed throughout the background of the grid (Figure 5a). Surprisingly, especially after

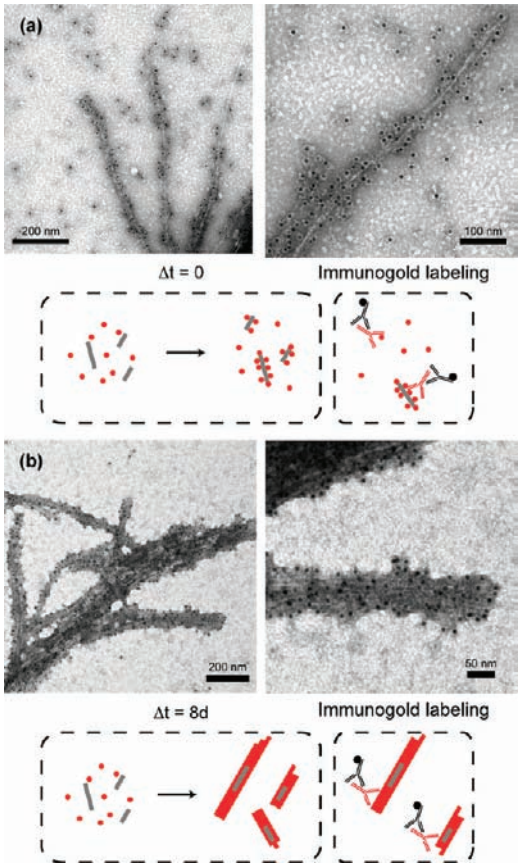


Figure 5. Representative TEM images of immunogold labeled samples obtained at neutral pH and high ionic strength and graphical representations of the results obtained (a) within 1 min of mixing NEM-Aβ42 fibrils and MPB*-Aβ42 monomer and (b) 8 days after mixing them. For the sake of clarity, some of the primary and secondary antibodies in the illustrations for (a) and (b) have been omitted.

such a short period of time, MPB*-Aβ42 molecules were found adhered to pre-existing fibrils, not only at the fibril ends but also all along the length of the fibrils (Figure 5a). Under these conditions, contrary to the results obtained at low pH and low ionic strength, where a higher density of NPs was found at the ends than throughout the length of the fibril, a lower density of NPs was found at the ends than throughout the length of the fibril (SI Figure S5). We also considered the possibility that the NPs observed were an artifact from deposition of the solution onto the flat EM grid. To test this possibility, we quantified the percentage of NPs as a function of their distance to the fibril (SI Figure S7). A higher percentage of NPs was found within 40 nm from the fibrils, while a significantly lower percentage was found further than 80 nm away (SI Figure S7a). The same quantification was performed at low pH and low ionic strength conditions (SI Figure S7b). Under these conditions, the same result was obtained. Moreover, when comparing the two conditions, there was a higher percentage of NPs within 40 nm from the fibrils at neutral pH and high ionic strength conditions (3.1%/μm^2) than at low pH and low ionic strength conditions (1.7%/μm^2) (SI Figure S7c). These results indicate that adherence of MPB*-Aβ42 molecules to pre-existing NEM-Aβ42 fibrils was not an artifact of deposition and that this interaction was more prominent at neutral pH and high ionic strength than at low pH and low ionic strength.

After incubating NEM-Aβ42 fibrils and monomeric MPB*-Aβ42 for 3 days, another round of labeling was performed. Fibrils and fibril bundles covered with NPs appeared throughout the EM grids (SI Figure S8). After this period of time, MPB*-Aβ42 may have been incorporated into NEM-Aβ42 fibrils or may have produced their own fibrils. Nevertheless, since we also observed soluble MPB*-Aβ42 molecules labeled with NPs in the background, we could not discern whether the NPs close to the fibrils derived from soluble MPB*-Aβ42 molecules adhered to the fibrils or from MPB*-Aβ42 molecules incorporated into the fibrils. After NEM-Aβ42 fibrils and monomeric MPB*-Aβ42 were incubated for 8 days, no NPs were observed in the background of the EM grids (Figure 5b). This suggests that the soluble MPB*-Aβ42 molecules which had been initially added to NEM-Aβ42 fibrils had subsequently incorporated into fibrils. The TEM images of the samples after 8 days revealed numerous fibrils, associated into bundles and totally covered with NPs (Figure 5b).

The results of the fibril growth experiment monitored at low pH and low ionic strength are most consistent with fibril growth occurring through elongation.[6−11] Evidence of this mechanism includes first that, within 1 min incubation of NEM-Aβ42 fibrils with MPB*-Aβ42 monomer, we observe a higher density of NPs at the fibril ends than along the entire length of the fibril (SI Figure S5), and second that, after 3 days of incubation, we observe mixed fibrils suggestive of a core comprising unlabeled NEM-Aβ42 fibrils further elongated by addition of MPB*-Aβ42 labeled-competent monomers (Figure 4c) (SI Figure S6).

The results obtained at neutral pH and high ionic strength suggest template-assisted lateral fibril growth, although contributions from fibril elongation or fibril fragmentation cannot be excluded. There are two observations corroborating lateral fibril growth: first, that at early time points soluble MPB*-Aβ42 molecules interact all along preformed NEM-Aβ42 fibrils; and second, that at later time points fibrils are organized within bundles. Based on these observations, we reason that fibril growth could occur by early interaction of soluble Aβ42 molecules to pre-existing fibrils, which would confer soluble, fibril-adhered Aβ42 molecules with the appropriate conformation to promote lateral fibril growth, or that interactions were driven by an increase in the effective concentration of Aβ42 molecules on fibril surfaces. Lateral interactions between soluble molecules and fibrils are also supported by results from coarse-grained simulations of an amphipathic polypeptide[20] and from an atomic force microscopy (AFM) study on insulin aggregation.[21] Nevertheless, previous reports on single-fibril growth assays have not mentioned template-assisted lateral interactions as an important growth pathway. This may be because these assays were

designed to detect molecules once incorporated into the fibril. For example, total internal reflection fluorescence (TIRF) microscopy studies use ThT as the label, but this dye only binds to fibrils.[12,17,22,23] In contrast, the single-fibril growth assay developed in this work detects both fibrillar and soluble protein.

At low pH and low ionic strength, wt Aβ42, NEM-Aβ42, and MPB*-Aβ42 each have seven positive charges, which can result in high electrostatic repulsion. In contrast, at neutral pH and high ionic strength, wt Aβ42, NEM-Aβ42, and MPB*-Aβ42 each have three net negative charges that are screened by the high salt content, which results in weaker electrostatic repulsion and a greater tendency for both intra- and intermolecular interactions. The fact that at low pH and low ionic strength we observed fibril elongation as the major growth mechanism, whereas at neutral pH and high ionic strength we observed template-assisted lateral fibril growth, suggests that the surfaces involved in these processes involve distinct hydrophobic and electrostatic interactions. This, in turn, suggests that different types of inhibitors could block each process. In conclusion, we have developed an assay that enabled us to identify lateral interactions of soluble Aβ42 molecules with mature Aβ42 fibrils as a mechanism for template-assisted lateral fibril growth. Our findings provide new insights into the molecular mechanisms of Aβ42 fibril growth and may prove valuable for the design of AD therapies that target Aβ aggregation.

■ ASSOCIATED CONTENT

Supporting Information

Materials and methods as well as figures corresponding to the sequences of the Aβ42 variants used, NP quantification, and additional TEM images. This material is available free of charge via the Internet at http://pubs.acs.org.

■ AUTHOR INFORMATION

Corresponding Author

*Ernest Giralt: Phone +34 93 4037125, fax +34 93 4037126, e-mail ernest.giralt@irbbarcelona.org. Natàlia Carulla: phone +34 93 4037123, fax +34 93 4037126, e-mail natalia.carulla@irbbarcelona.org

Present Address

[¶]MassGeneral Institute for Neurodegenerative Diseases (MIND), Massachusetts General Hospital & Harvard Medical School, Building 114, 16th Street, Charlestown, MA 02129.

■ ACKNOWLEDGMENTS

We thank an anonymous Reviewer for suggesting experiments to quantify TEM data. We thank C. López-Iglesias for technical support with TEM, immunogold labeling and critical reading of the manuscript; G. Martínez and N. Hernández for assistance with the immunogold labeling; the Mass Spectrometry Core Facility and the Protein Expression Core Facility at the IRB for technical support; and Dr. L. Ding from the Harvard NeuroDiscovery Center Optical Imaging Core, Harvard Medical School, for help with ImageJ software. M.A. acknowledges the Spanish Ministry for a predoctoral FPU fellowship. This work was supported by Program Grants from Generalitat de Catalunya 2009SGR0277 (F.S), Fundació La Caixa and Fundació La Marató de TV3 (N.C. and E.G.), MICINN-FEDER BIO2008-00799 (E.G.), and by MICINN-FEDER SAF2009-07600 (N.C.).

■ REFERENCES

(1) Selkoe, D. J. (2004) Alzheimer disease: mechanistic understanding predicts novel therapies. *Ann. Intern. Med. 140*, 627−638.

(2) Sunde, M., and Blake, C. C. (1998) From the globular to the fibrous state: protein structure and structural conversion in amyloid formation. *Q. Rev. Biophys. 31*, 1−39.

(3) Petkova, A. T., Ishii, Y., Balbach, J. J., Antzutkin, O. N., Leapman, R. D., Delaglio, F., and Tycko, R. (2002) A structural model for Alzheimer's beta-amyloid fibrils based on experimental constraints from solid state NMR. *Proc. Natl. Acad. Sci. U.S.A. 99*, 16742−16747.

(4) Paravastu, A. K., Leapman, R. D., Yau, W. M., and Tycko, R. (2008) Molecular structural basis for polymorphism in Alzheimer's beta-amyloid fibrils. *Proc. Natl. Acad. Sci. U.S.A. 105*, 18349−18354.

(5) Luhrs, T., Ritter, C., Adrian, M., Riek-Loher, D., Bohrmann, B., Dobeli, H., Schubert, D., and Riek, R. (2005) 3D structure of Alzheimer's amyloid-beta(1−42) fibrils. *Proc. Natl. Acad. Sci. U.S.A. 102*, 17342−17347.

(6) Blackley, H. K., Sanders, G. H., Davies, M. C., Roberts, C. J., Tendler, S. J., and Wilkinson, M. J. (2000) In-situ atomic force microscopy study of beta-amyloid fibrillization. *J. Mol. Biol. 298*, 833−840.

(7) Inoue, Y., Kishimoto, A., Hirao, J., Yoshida, M., and Taguchi, H. (2001) Strong growth polarity of yeast prion fiber revealed by single fiber imaging. *J. Biol. Chem. 276*, 35227−35230.

(8) Scheibel, T., Kowal, A. S., Bloom, J. D., and Lindquist, S. L. (2001) Bidirectional amyloid fiber growth for a yeast prion determinant. *Curr. Biol. 11*, 366−369.

(9) DePace, A. H., and Weissman, J. S. (2002) Origins and kinetic consequences of diversity in Sup35 yeast prion fibers. *Nat. Struct. Biol. 9*, 389−396.

(10) Ban, T., Yamaguchi, K., and Goto, Y. (2006) Direct observation of amyloid fibril growth, propagation, and adaptation. *Acc. Chem. Res. 39*, 663−670.

(11) Kellermayer, M. S., Karsai, A., Benke, M., Soos, K., and Penke, B. (2008) Stepwise dynamics of epitaxially growing single amyloid fibrils. *Proc. Natl. Acad. Sci. U.S.A. 105*, 141−144.

(12) Andersen, C. B., Yagi, H., Manno, M., Martorana, V., Ban, T., Christiansen, G., Otzen, D. E., Goto, Y., and Rischel, C. (2009) Branching in amyloid fibril growth. *Biophys. J. 96*, 1529−1536.

(13) Dahlgren, K. N., Manelli, A. M., Stine, W. B. Jr., Baker, L. K., Krafft, G. A., and LaDu, M. J. (2002) Oligomeric and fibrillar species of amyloid-beta peptides differentially affect neuronal viability. *J. Biol. Chem. 277*, 32046−32053.

(14) Kayed, R., and Glabe, C. G. (2006) Conformation-dependent anti-amyloid oligomer antibodies. *Methods Enzymol. 413*, 326−344.

(15) Petkova, A. T., Leapman, R. D., Guo, Z., Yau, W. M., Mattson, M. P., and Tycko, R. (2005) Self-propagating, molecular-level polymorphism in Alzheimer's beta-amyloid fibrils. *Science 307*, 262−265.

(16) Nichols, M. R., Moss, M. A., Reed, D. K., Lin, W. L., Mukhopadhyay, R., Hoh, J. H., and Rosenberry, T. L. (2002) Growth of beta-amyloid(1−40) protofibrils by monomer elongation and lateral association. Characterization of distinct products by light scattering and atomic force microscopy. *Biochemistry 41*, 6115−6127.

(17) Ban, T., Morigaki, K., Yagi, H., Kawasaki, T., Kobayashi, A., Yuba, S., Naiki, H., and Goto, Y. (2006) Real-time and single fibril observation of the formation of amyloid beta spherulitic structures. *J. Biol. Chem. 281*, 33677−33683.

(18) Klement, K., Wieligmann, K., Meinhardt, J., Hortschansky, P., Richter, W., and Fandrich, M. (2007) Effect of different salt ions on the propensity of aggregation and on the structure of Alzheimer's abeta(1−40) amyloid fibrils. *J. Mol. Biol. 373*, 1321−1333.

(19) Zheng, J., Ma, B., Chang, Y., and Nussinov, R. (2008) Molecular dynamics simulations of Alzheimer Abeta40 elongation and lateral association. *Front. Biosci. 13*, 3919−3930.

(20) Pellarin, R., Guarnera, E., and Caflisch, A. (2007) Pathways and intermediates of amyloid fibril formation. *J. Mol. Biol. 374*, 917−924.

(21) Jansen, R., Dzwolak, W., and Winter, R. (2005) Amyloidogenic self-assembly of insulin aggregates probed by high resolution atomic force microscopy. *Biophys. J. 88*, 1344−1353.
(22) Ban, T., Hamada, D., Hasegawa, K., Naiki, H., and Goto, Y. (2003) Direct observation of amyloid fibril growth monitored by thioflavin T fluorescence. *J. Biol. Chem. 278*, 16462−16465.
(23) Ban, T., Hoshino, M., Takahashi, S., Hamada, D., Hasegawa, K., Naiki, H., and Goto, Y. (2004) Direct observation of Aβ amyloid fibril growth and inhibition. *J. Mol. Biol. 344*, 757−767.

Bioconjugate Chemistry

Communication

pubs.acs.org/bc

Mechanistic Insights into LDL Nanoparticle-Mediated siRNA Delivery

Honglin Jin,[†,‡,§] Jonathan F. Lovell,[‡,∥] Juan Chen,[‡] Qiaoya Lin,[†,‡,§] Lili Ding,[‡] Kenneth K. Ng,[‡,∥] Rajendra K. Pandey,[⊥] Muthiah Manoharan,[⊥] Zhihong Zhang,[*,†] and Gang Zheng[*,‡,§,∥]

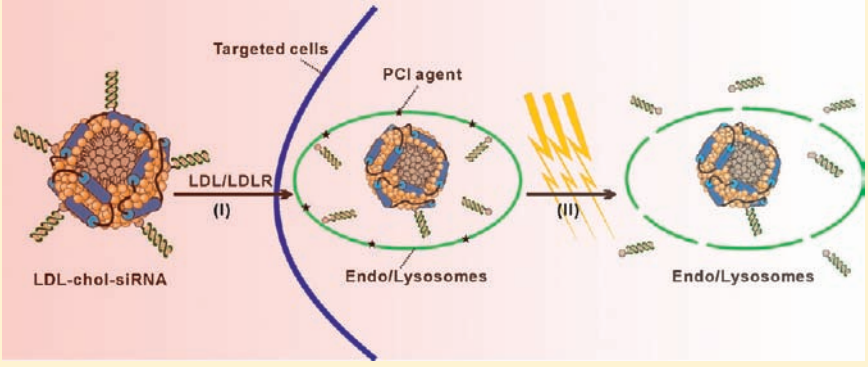
[†]Britton Chance Center for Biomedical Photonics, Wuhan National Laboratory for Optoelectronics-Huazhong University of Science and Technology, Wuhan, China

[‡]Ontario Cancer Institute and Campbell Family Cancer Research Institute, University Health Network, Toronto, Canada

[§]Department of Medical Biophysics and [∥]Institute of Biomaterials and Biomedical Engineering, University of Toronto, Toronto, Canada

[⊥]Alnylam Pharmaceuticals, Boston, Massachusetts, United States

Supporting Information



ABSTRACT: Although small interfering RNA (siRNA) can silence the expression of disease-related genes, delivery of these highly charged molecules is challenging. Delivery approaches for siRNAs are actively being pursued, and improved strategies are required for nontoxic and efficient delivery for gene knockdown. Low density lipoprotein (LDL) is a natural and endogenous nanoparticle that has a rich history as a delivery vehicle. Here, we examine purified LDL nanoparticles as carriers for siRNAs. When siRNA was covalently conjugated to cholesterol, over 25 chol-siRNA could be incorporated onto each LDL without changing nanoparticle morphology. The resulting LDL-chol-siRNA nanoparticles were selectively taken up into cells via LDL receptor mediated endocytosis, resulting in enhanced gene silencing compared to free chol-siRNA (38% gene knock down versus 0% knock down at 100 nM). However, silencing efficiency was limited by the receptor-mediated entrapment of the LDL-chol-siRNA nanoparticles in endolysosomes. Photochemical internalization demonstrated that endolysosome disruption strategies significantly enhance LDL-mediated gene silencing (78% at 100 nM).

INTRODUCTION

RNA interference (RNAi) is one of the most powerful tools for specific gene suppression and thus holds great potential for therapeutic applications, including treatment of dominant genetic disorders, autoimmune diseases, cancer, and viral infections.[1−4] Efficient and safe *in vivo* delivery of small interfering RNA therapeutics (siRNA) to target tissues is the main challenge for their clinical implementation, since highly negatively charged siRNAs cannot readily penetrate through cell membranes. Because virus-mediated nucleic acid delivery systems are hindered by potential side effects, recent developments are primarily focused on a variety of nonvirus delivery strategies including cationic lipids,[5−8] cationic liposomes,[9] cationic polymers,[10−12] peptide conjugates,[13,14] antibody conjugated polyethylenimine,[15] gold nanoparticles,[16,17] quantum dots,[18] and modified siRNAs.[19] Cationic lipids, liposomes, and polymers (such as PEI) form complexes with anionic siRNA through electrostatic interactions can enhance intracellular delivery of siRNAs. However, most cationic delivery systems have toxicity issues,[20−22] with the exception of some of the naturally derived systems, such as chitosan, which are nontoxic but are heterogeneous with large size variation.[23] The internalization mechanism of cell penetration peptides (CPPs) is still unresolved.[24] While inorganic nanoparticles, such as quantum dots and gold nanoparticles have shown siRNA delivery potential, researchers are still optimizing surface chemistries and studying their long-term toxicity.[25,26]

LDL nanoparticles are endogeneous nanocarriers possessing many advantages for drug delivery: a homogeneous size (19−25 nm) below 40 nm, biocompatibility and biodegradability,

Received: May 4, 2011
Revised: November 10, 2011
Published: December 5, 2011

 © 2011 American Chemical Society dx.doi.org/10.1021/bc200233n | *Bioconjugate Chem.* 2012, 23, 33−41

intrinsic targeting with customizable alternative targeting.[27,28] All these key features make LDL an attractive nanocarrier for siRNA delivery. Cholesterol modified siRNA (chol-siRNA) has been developed for systemic administration using a noncationic delivery system, resulting in *in vivo* gene silencing at a dose of 50 mg/kg.[19] The mechanism of delivery occurred through specific interactions between chol-siRNA and serum lipoproteins, and the resulting complexes with targeted cells. Further, when chol-siRNA was preloaded onto murine HDL (~1:1 ratio), significant enhancement of gene silencing efficiency was observed.[29] Indeed, we have recently examined HDL mimetics as candidates for siRNA delivery which use a separate internalization pathway.[30] Alternatively, the versatile apolipoprotein LDL has previously been used for the delivery of cholesterol-modified antisense oligonucleotides.[31,32] We hypothesized that stable loading and functional delivery of chol-siRNA could be achieved using LDL nanoparticles. It is known that cellular uptake of LDL nanoparticles is mediated by the LDL receptor and this pathway often leads to the entrapment of LDL and its loading drug in lysosomes,[33] and this problem might be overcome by using light-triggered endosomal disruption techniques.[34,35] Among these methods, photochemical internalization (PCI), which allows the light-induced release of endocytosed macromolecules into the cytoplasm, was chosen. The mechanism involves breakdown of endosomal/lysosomal membranes by amphipathic photosensitizers, such as disulfonated aluminum phthalocyanine ($AlPcS_{2a}$) or meso-tetraphenylporphine disulfonate ($TPPS_{2a}$).[34,36] This powerful technology has been investigated for the delivery of a variety of drugs, including siRNAs.[37−39] Recently, we demonstrated that cytosolic release of LDL loaded cargo using PCI was feasible and the efficiency was dependent on the cargo loading method.[40] Direct endolysosmal disruption by PCI resulted in efficient intracellular cytosolic release of surface-loaded cargos and partial release of protein-loaded cargo. Thus, in theory, PCI is well-suited to improve LDL-mediated siRNA delivery efficiency.

EXPERIMENTAL PROCEDURES

Materials. LDL was isolated by sequential ultracentrifugation of human plasma using previously described methods,[41] and was further purified by AKTA fast protein liquid chromatrography (FPLC) system (Amersham Biosciences) equipped with a HiLoad 16/70 Superdex 200 pg column. Human plasma was obtained from the local blood transfusion services and usage was approved by the University Health Network's research ethics board. The PCI agent $AlPcS_{2a}$ was purchased from Frontier Scientific company. All siRNAs were synthesized by Alnylam (Cambridge, MA). Cholesterol conjugated control siRNA (chol-siRNA) consisted of the following sense strand: 5′-GGAfUfCAfUfCfUfCAAGfUfCfU-fUAfCdTsdTsChol-3′ and antisense strand: 5′-GfUAAGAfCfU-fUGAGAfUGAfUfCfCdTsdT-3′. The unmodified siRNA had the same sequences but without cholesterol moiety in the sense strand. The chol-siRNA targeting apolipoprotein B (chol-si-apoB) comprised the cholesterol conjugated sense strand: 5′-GGAAUCuuAuAuuuGAUCcAAsChol-3′ and antisense strand: 5′-uuGGAUcAAAuAuAAGAuUCcscsU-3′. Dye-labeled (Cy5.5) chol-si-apoB (chol-si-Cy5.5) comprised the same sense sequence as chol-si-apoB and the Cy5.5 dye labeled antisense: 5′- Cy5.5uuGGAUcAAAuAuAAGAuUCcscsU-3′. All these sequences have been validated in a recently report.[42] Abbreviations are as follows: fC and fU, 2′-deoxy-2′-fluoro cytidine and uridine, respectively; lower case letters, 2′-O-methyl sugar modification; 's', phosphorothioate linkage.

Evaluation of siRNA Loading on LDL. LDL was mixed with control chol-siRNA at various molar ratios in PBS. After 30 min incubation, the mixture was assayed for electrophoretic mobility on a 0.8% agarose gel. The siRNA signal was visualized by UV transillumination with GelRed stain and the LDL protein signal was visualized by Coomassie blue stain.

Preparation of LDL-chol-si-apoB Nanoparticles. LDL was incubated with chol-si-apoB (4.29 nmol) at 15:1, 25:1, 30:1, 50:1 molar ratio of chol-si-apoB:LDL at room temperature for 30 min in 1 mL PBS (0.1 M NaCl, pH 7.5) The chol-si-apoB/LDL was then purified by FPLC equipped with a HiLoad 16/70 Superdex 200 pg column and eluted with Tris-buffered saline (10 mM Tris-HCl, containing 0.15 M NaCl, 1 mM EDTA, pH 7.5) at a flow rate of 1 mL/min. The chol-siRNA/LDL complex with a molar ratio of 25:1 had no free chol-si-apoB peak and had maximum siRNA loading on LDL. Thus, it was selected as the optimal formulation, and the resulting LDL-chol-si-apoB nanoparticles were further filtered through a 0.2 μm filter (Millipore) and stored at 4 °C for *in vitro* studies.

Preparation of LDL-chol-si-Cy5.5 and (Fluo-BOA)LDL-chol-si-Cy5.5. LDL-chol-si-Cy5.5 was prepared in the same way as LDL-chol-si-apoB by replacing chol-si-apoB with chol-si-Cy5.5. (Fluo-BOA)LDL-chol-si-Cy5.5 was prepared similarly by replacing LDL with (Fluo-BOA)LDL and replacing chol-si-apoB with chol-si-Cy5.5. (Fluo-BOA)LDL was prepared by a previously described procedure.[40] The resulting nanoparticles were filtered through a 0.2 μm filter and stored at 4 °C for imaging studies.

Measurement of LDL Protein Concentration. The LDL protein concentration in the LDL-chol-siRNA particles was measured using the modified Lowry protein assay (Sigma-Aldrich, St. Louis, MO).

Morphology, Size, and Surface Charge Measurement. Transmission electron microscopy (TEM) was performed using a Hitachi H-7000 transmission electron microscope (Hitachi, Inc., Japan) equipped with a digital image acquisition system to determine the morphology of an aqueous dispersion of LDL and LDL-chol-siRNA nanoparticles with 0.5% uranyl acetate as the negative stain. The volume size distribution and zeta potential of LDL and LDL-chol-siRNA were obtained using a Nanosizer (Zetasizer Nano-ZS90; Malvern Instruments, Malvern, UK).

Confocal Microscopy. HepG2 (Human hepatocellular liver carcinoma cell line) and ldlA7 (LDL receptor-deficient Chinese hamster ovary cells) cells were seeded in 8-well cover glass bottom chambers (Nunc Lab-Tek, Sigma-Aldrich) (3×10^4/well) for confocal microscopy imaging. Briefly, cells were incubated with cell culture medium containing 10% FBS and LDL-chol-si-Cy5.5 or (Fluo-BOA)LDL-chol-si-Cy5.5 at a chol-siRNA concentration of 400 nM for 3 h at 37 °C. For the inhibition study, a 20-fold excess of LDL was added. Confocal imaging was performed using Olympus FV1000 laser confocal scanning microscopy (Olympus, Tokyo, Japan) with excitation wavelengths of 488 and 633 nm, for Fluo-BOA and Cy5.5, respectively. Hoechst 33258, transferrin, and lysotracker were used for nucleus, early endosome, and lysosome organelle stains, respectively. The *ImageJ* software package was used to measure the average fluorescence intensity of cells by manual contouring cell borders.

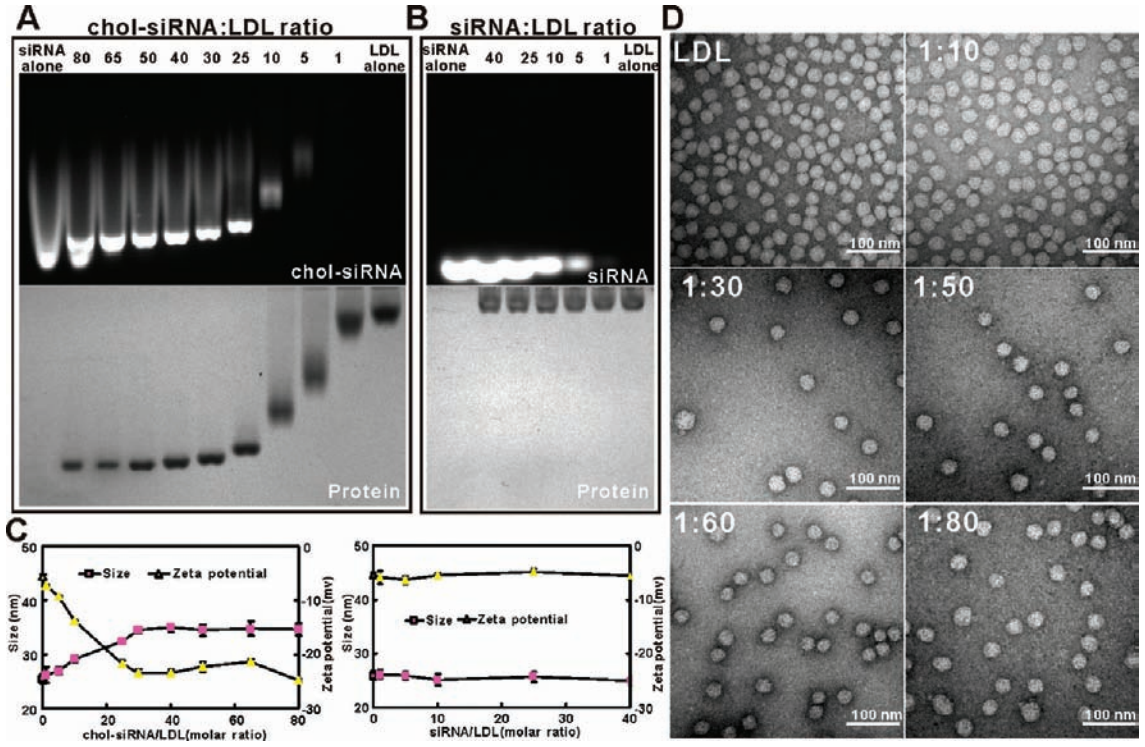


Figure 1. Optimization of payload loading of chol-siRNA onto LDL. Agarose gel electrophoresis of (A) Chol-siRNA/LDL and (B) siRNA/LDL (Top: chol-siRNA or siRNA signal visualized by UV transillumination with GelRed stain; Bottom: LDL protein signal visualized by Coomassie blue stain). (C) Size and zeta potential of chol-siRNA/LDL complex (left) and siRNA/LDL complex (right). (D) TEM imaging of chol-siRNA/LDL complex with different chol-siRNA to LDL ratios.

Cell Toxicity Study. HepG2 cells were seeded in a 96-well (1×10^4/well) plate and cultured in DMEM medium containing 10% FBS and antibiotics (denoted as complete medium) for 2 days. Experiments were started, after one quick wash with PBS buffer, by addition of 200 μL of complete medium containing various concentration of chol-si-apoB or LDL-chol-si-apoB. After 48 h incubation at 37 °C with 5% CO_2, the cells were washed twice with PBS buffer and incubated with 150 μL of complete medium with MTT tracer, 3-(4,5-dimethylthiazol-2-yl)-2,5-diphenyltetrazolium bromide (Invitrogen) at 0.5 mg/mL for 1 h. The medium was then replaced with 70% isoproponal in 0.1 M HCl solution, the plate was shaken for 20 min, and absorbance was measured at 570 nm to determine the viability relative to the untreated control.

RNAi Treatment. To investigate the apoB gene inhibition, HepG2 cells were first seeded in a 6-well (2×10^5/well) plate in complete medium and incubated for 2 days. The medium was then replaced with 500 μL of fresh complete medium containing various concentrations of chol-si-apoB or LDL-chol-si-apoB for 48 h incubation. The cells were then harvested to check apoB mRNA expression by the real-time reverse transcription polymerase chain reaction (RT-qPCR).

PCI Treatment. HepG2 cells were seeded in a 6-well (2×10^5/well) plate and cultured in complete medium for 30 h. After incubation with 10 μg/mL of $AlPcS_{2a}$ in complete medium for 18 h, cells were then washed with PBS and treated with LDL-chol-si-apoB in complete medium for 3 h. The light irradiation was performed with a 660 nm light box under various treatment durations. The cells were allowed to continue growth to total incubation time of 48 h (from the time of siRNA treatment) and harvested for further analysis.

Real Time RT-PCR. Each sample was derived from a single well of a 6-well plate. Total RNA was isolated from each well using an RNeasy Mini kit (Qiagen) and quantified by UV spectrophotometry. Complementary DNA (cDNA) was prepared from 1.5 μg of total cellular RNA using RevertAid H Minus M-MuLV Reverse Transcriptase (Fermentas, Canada) with oligo-dT18 primers according to the manufacturer's recommendations. Relative gene expression (apoB mRNA:human beta 2-microglobulin (b2m) mRNA) was determined by real time RT-PCR amplification of apoB, human b2m. Custom primers were purchased with sequence as follows: apoB, sense 5′-ACTCTACAAATCTGTTTCTCTTCCATC-3′, antisense 5′-TCCTTCCAAGCCAATCTCG-3′; Human b2m, sense 5′-TTCAGCAAGGACTGGTCTTTCTAT-3′, antisense 5′-TGCGGCATCTTCAAACCTC-3′. All the primer designs went across intron/exon boundary and the concentration used was 10 μM, with 1 μL primer mix (sense and antisense) in 25 μL q-PCR reaction solution. Q-PCR was performed using a Rotor-Gene 6000 (Corbett Research), with cycling conditions for apoB gene as follows: 1 cycle of 95 °C for 10 min; 40 cycles of 95 °C for 10 s, 60 °C for 15 s, 72 °C for 20 s; ramp from 72 to 95 °C. Inhibition of apoB mRNA was determined by comparison of the ratio between apoB and b2m mRNA for the treated groups against the untreated group.

RESULTS

To investigate the loading of siRNAs onto LDL, a control siRNA sequence was initially used. The chol-siRNA or unmodified siRNA (siRNAs lacking of cholesterol moiety) was incubated with LDL at molar ratios ranging from 0:1 to 80:1 for 30 min. Agarose gel electrophoresis of chol-siRNA/LDL showed comigration of siRNA and LDL, indicating that

dx.doi.org/10.1021/bc200233n | Bioconjugate Chem. 2012, 23, 33–41

chol-siRNA could be readily incorporated onto LDL (Figure 1A). Without cholesterol modification, siRNA did not associate with LDL (Figure 1B). Incorporation of chol-siRNA increased the particle size by up to 10 nm from 0:1 to 30:1 initial chol-siRNA:LDL ratio. Further increase of the initial chol-siRNA to LDL ratio had no impact on the nanoparticle size. An inverse correlation between zeta potential and chol-siRNA loading was also observed (Figure 1C), demonstrating the negatively charged chol-siRNA bound to LDL. No stable binding between LDL and unmodified siRNA was observed by zeta potential. These data suggest that chol-siRNA could be stably loaded on LDL with a high payload (30 of chol-siRNA per particle) and demonstrate the critical role of the cholesterol moiety for LDL association. LDL and chol-siRNA fully associated within minutes and the resultant negatively charged particles showed more migration in a gel when compared with LDL (Figure 1A). TEM images (Figure 1D) confirmed that incorporation of chol-siRNA on LDL did not change the morphology or homogeneous size distribution of the nanoparticles.

We next examined LDL-chol-siRNA that targeted the apoB gene (LDL-chol-si-apoB). As shown in Figure 2A, FPLC can separate LDL-chol-si-apoB (retention time <58 min), LDL (67 min) and unloaded free siRNAs (102 min) (Figure 2A). At the initial chol-siRNA/LDL complex ratio of 30:1 (chol-si-apoB:LDL), a free siRNA peak was present in the FPLC profiles. When adjusting the complex ratio to 25:1, negligible unloaded free chol-siRNA was present (SI Figure 1S), suggesting that the initial chol-siRNA/LDL complex ratio of 25:1 gave an optimal formulation for LDL-chol-si-apoB preparation. This optimized formulation was used for further functional and imaging studies. LDL-chol-si-apoB nanoparticles appeared monodisperse by TEM (Figure 2B) and possessed a hydrodynamic diameter of 31 nm based on dynamic light scattering, while the unmodified LDL nanoparticles had a hydrodynamic diameter of 23 nm (Figure 2C). Loading chol-si-apoB onto LDL nanoparticles dramatically changed the surface charge of the nanoparticle evidenced by the zeta potential shift from −5.3 mV of LDL to −23.9 mV of LDL-chol-si-apoB.

We next examined the specific uptake of the LDL-chol-si-apoB nanoparticles using the Cy5.5-labeled chol-si-apoB. The LDL-chol-si-Cy5.5 nanoparticles were incubated with two cell lines: HepG2 cells that have high expression of the LDL receptors and ldlA7 cells that have low expression. Confocal microscopy demonstrated that, after 3 h incubation, significant uptake of chol-si-Cy5.5 occurred within the HepG2 cells ($LDLR^+$), whereas ldlA7 ($LDLR^-$) cells displayed 10-fold less uptake (Figure 3A,B). Moreover, the delivery of chol-si-Cy5.5 was inhibited by adding a 20-fold excess of unlabeled LDL as a competitive inhibitor during the incubation. These results show that targeted siRNA delivery could be achieved using LDL.

To investigate the RNAi efficiency of LDL-chol-si-apoB, HepG2 cells were treated with various concentrations of LDL-chol-si-apoB nanoparticles or chol-si-apoB alone in the presence of complete growth medium (with 10% FBS) at 37 °C for 48 h. LDL-chol-si-apoB showed enhanced gene silencing efficiency at all the concentrations when compared with chol-si-apoB alone (Figure 4A). No concomitant cell toxicity was observed when the cells were treated with either LDL-chol-si-apoB nanoparticles or chol-si-apoB alone (Figure 4B). These data suggest that LDL is a safe nanocarrier capable of functional delivery of chol-siRNA. However, increasing LDL-chol-si-apoB concentrations only resulted in moderate decreases in apoB mRNA expression (apoB gene expression was reduced by 38%,

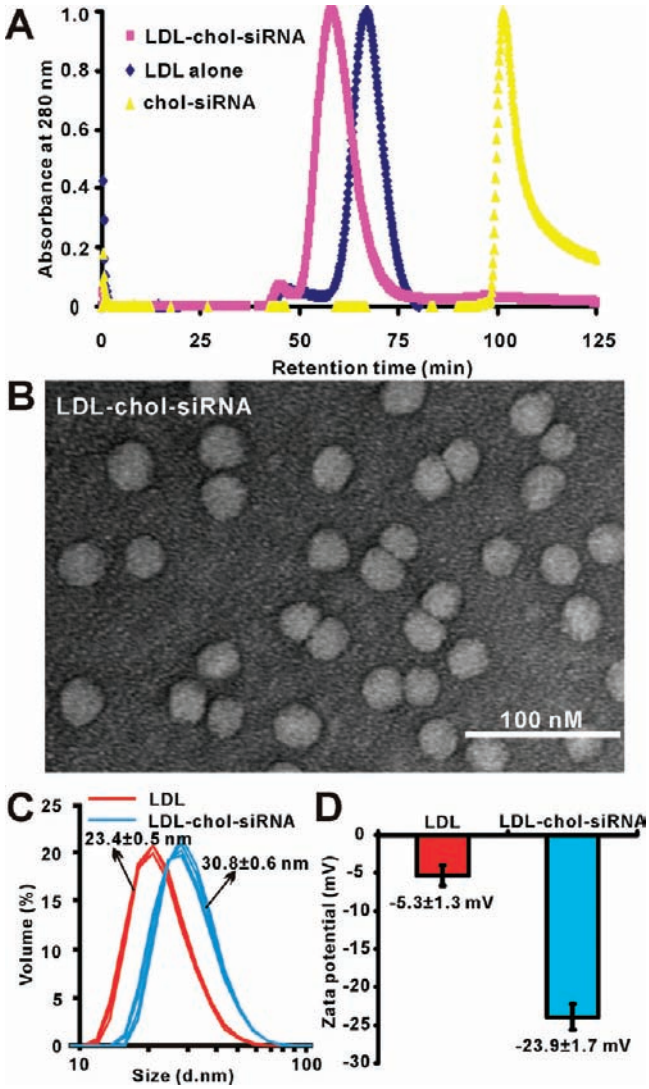


Figure 2. Characterization of LDL-chol-si-apoB. (A) FPLC profiles of LDL-chol-si-apoB (red), LDL alone (blue), and free chol-siRNA (yellow). (B) Stable morphology of LDL-chol-si-apoB nanoparticles was confirmed by TEM. (C) Dynamic light scattering size and (D) zeta potential of LDL and LDL-chol-si-apoB.

46%, and 60% with LDL-chol-si-apoB concentrations at 100, 300, and 600 nM, respectively). This limited knockdown was probably due to inefficient release of siRNAs into the cytoplasm, which limited the siRNA efficiency.

To elucidate the siRNA delivery mechanism using LDL, the intracellular behavior of the LDL-chol-si-apoB was investigated on HepG2 cells incubated with a dual dye labeled particle, (Fluo-BOA)LDL-chol-si-Cy5.5, where LDL was labeled with Fluo-BOA in the core and siRNA was labeled with Cy5.5. Confocal microscopy was used to investigate whether the chol-siRNA separated from the LDL after cellular internalization. After 3 h incubation with (Fluo-BOA)LDL-chol-si-Cy5.5, significant colocalization between Fluo-BOA and Cy5.5 signals was observed (Figure 5A), implying the nanoparticle and cargo were intact at that time. Further confocol studies showed that chol-si-Cy5.5 colocalized with transferrin (an endosomal marker, Figure 5B) and lysotracker (a lysosomal marker, Figure 5C) at the 3 h incubation time point, confirming that LDL delivered chol-siRNA into endo/lysosomes organelles of cells via receptor mediated endocytosis.

dx.doi.org/10.1021/bc200233n | *Bioconjugate Chem.* 2012, 23, 33–41

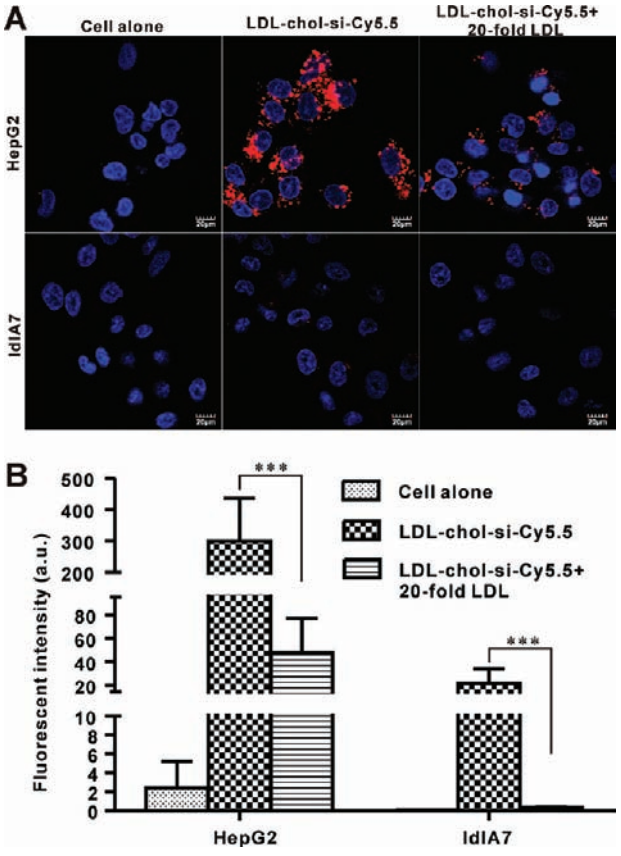


Figure 3. Targeted delivery of siRNAs via the LDL receptors using LDL-chol-siRNA. (A) Cy5.5-labeled fluorescent siRNA (chol-si-Cy5.5) was used to track the intracellular uptake of siRNAs. Confocal imaging was performed on HepG2 cells ($LDLR^+$) and ldlA7 ($LDLR^-$) cells treated with 400 nM of LDL-chol-si-Cy5.5 for 3 h. Competition uptake study was carried out by adding 20-fold excess of LDL. The nuclei were stained with Hoechst 33258 and are shown in blue staining and the internalized chol-si-Cy5.5 appears red. The scale bar is 20 μm. (B) Measurement of the average fluorescence intensity of cells from confocal images. Data was acquired from at least 20 cells from two fields of view (***$p < 0.001$).

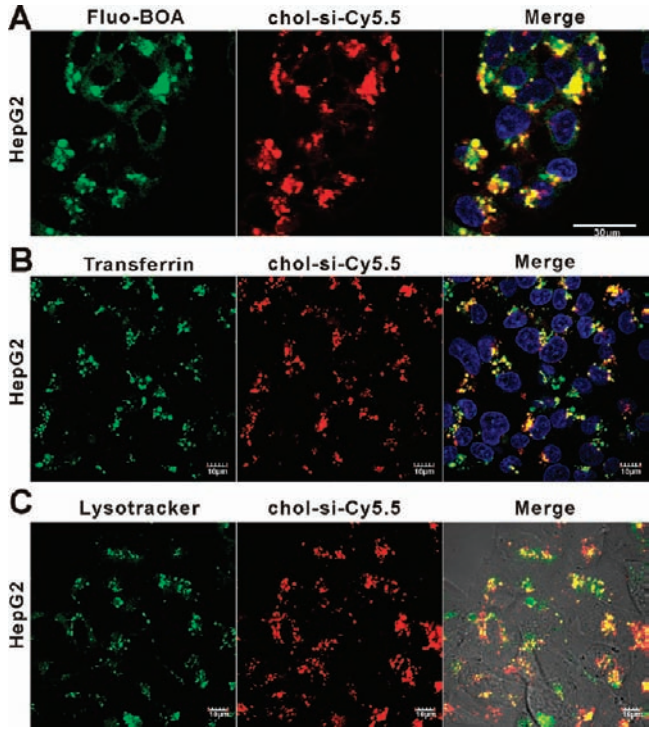


Figure 5. Investigation of cellular delivery pathway of LDL-chol-siRNA. (A) HepG2 cells were treated with (Fluo-BOA)LDL-chol-si-Cy5.5, where LDL was labeled with Fluo-BOA and siRNA was labeled with Cy5.5. The signals of Fluo-BOA (Green) and Cy5.5 (Red) colocalized at 3 h incubation. The nuclei were stained with Hoechst 33258 (blue) and the scale bar is 30 μm. (B) chol-si-Cy5.5 was found colocalized with transferrin, an early endosome maker, after 3 h incubation with HepG2 cells. The scale bar is 10 μm. (D) chol-si-Cy5.5 was also colocalized with lysotracker after 3 h incubation with HepG2 cells. The scale bar is 10 μm.

PCI is a useful technique that allows the light-induced release of endocytosed macromolecules into the cytoplasm.[34] To bypass the endolysosomal trafficking of siRNAs brought in by LDL, we combined PCI with LDL-chol-siRNA to investigate the ability to facilitate the release of chol-siRNA and enhance

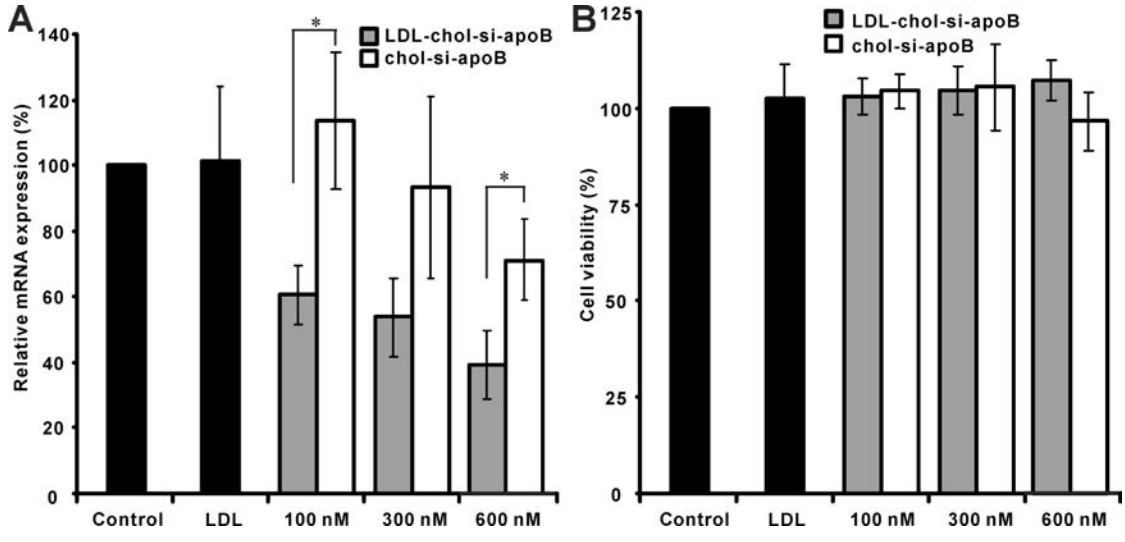


Figure 4. Evaluation of (A) gene knock-down and (B) cytotoxicity of LDL-chol-si-apoB and chol-si-apoB to HepG2 cells at various concentrations ($n = 3$, * $p < 0.05$). LDL alone and PBS buffer were used as controls. The cell visibility was determined by MTT assay ($n = 3$).

dx.doi.org/10.1021/bc200233n | *Bioconjugate Chem.* 2012, 23, 33–41

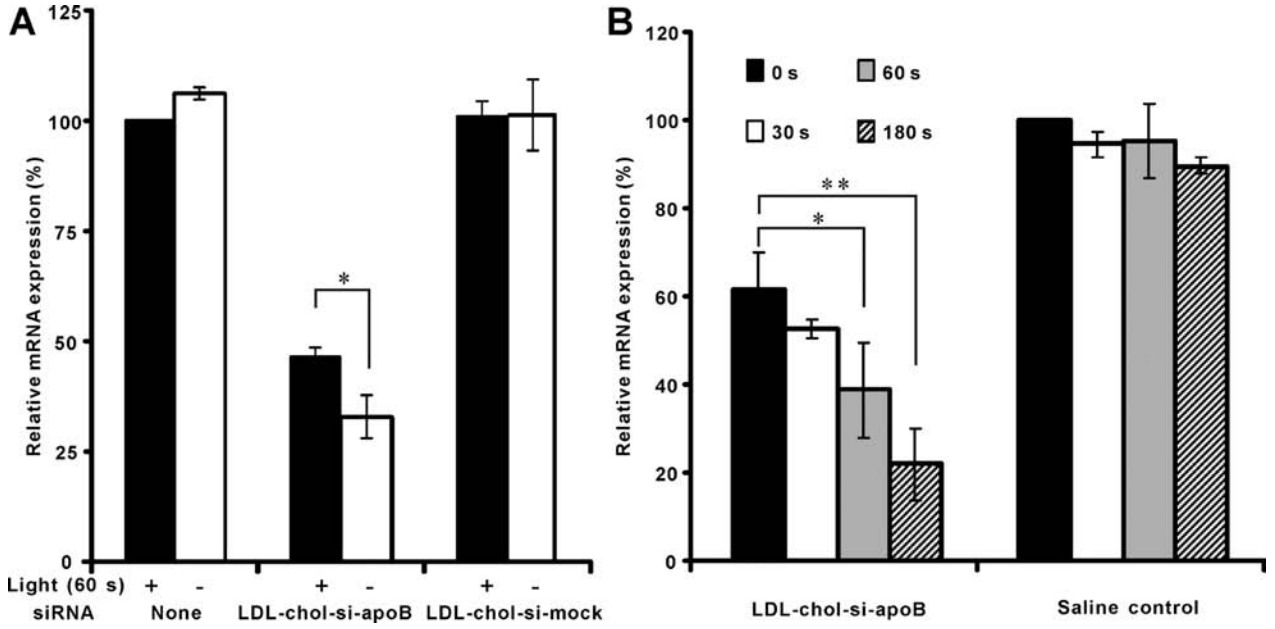


Figure 6. Improving gene silencing efficacy of LDL-chol-si-apoB using PCI. (A) Cells were incubated with or without 200 nM LDL-chol-si-apoB (based on siRNAs concentration) or LDL-chol-si-mock, and received light treatment for 60 s. (mean ± std. dev., $n = 3$, * $p < 0.05$). (B) Cells were incubated with 100 nM LDL-chol-si-apoB and received light treatment for 0, 30, 60, and 180 s. Cells incubated with saline were used as control groups. ($n = 3$, * $p < 0.05$, ** $p < 0.01$).

RNAi efficiency. To use spectrally distinct wavelengths with the PCI agent $AlPcS_{2a}$ (excitation, 675 nm; emission, 702 nm), FITC (excitation, 495 nm; emission, 525 nm) labeled chol-siRNA (chol-si-FITC) was used for the imaging of PCI release study. Although LDL delivered chol-siRNA into endo/lysosomes of cells (Figures 3 and 5), a very weak chol-si-FITC signal was observed in endo/lysosomes of cells (SI Figure S2) probably due to the fluorescence quenching of FITC at low pH condition (endo/lysosomes), which is consistent with the observation of Carraway et al.[43] Following light irradiation with PCI agent $AlPcS_{2a}$, strong signal of chol-si-FITC (green channel) escaped from endo/lysosome and spread to the cytoplasm of the cells in 5 min, demonstrating cytosolic release of siRNAs from endo/lysosomes (SI Figure S2). To examine gene knockdown, PCI light irradiation was performed using a 660 nm light box with a power density of 2.4 mW/cm^2. Since photosensitizer-induced cytotoxicity is an inherent issue with PCI, we first optimized the treatment condition by adjusting the light irradiation time. It was found that no remarkable cell death occurred after HepG2 cells incubated with $AlPcS_{2a}$ (PCI agent) for 18 h and received light irradiation up to 180 s duration (SI Figure S3). Thus, the PCI conditions of 18 h for PCI agent incubation, and less than 180 s for light irradiation were selected for gene knockdown study. Followed with the preincubation of $AlPcS_{2a}$, 3 h treatment of 200 nM LDL-chol-si-apoB, and light irradiation for 60 s, HepG2 cells were then harvested at 48 h after RNAi treatment. RT-qPCR analysis with normalization to a housekeeper gene (Figure 6A) demonstrated enhancement of apoB gene silencing by PCI, with the mRNA expression reduced from 46.3% to 32.9% ($p < 0.05$), while a mock siRNA with LDL (LDL-chol-si-mock) did not show obvious gene knockdown either with or without PCI. These results suggest that the specific gene silencing was induced by the specific sequence of siRNA and PCI is a potential option to enhance the gene silencing efficacy in the context of using LDL as a delivery vehicle. To further investigate the PCI efficacy, cells incubated with a lower concentration (100 nM) of LDL-chol-si-apoB were treated by light for 0, 30, 60, or 180 s, respectively. A clear PCI induced gene silencing was observed with the mRNA expression reducing from 62% (no light treatment) to 53%, 39%, and 22% upon light treatment of 30, 60, and 180 s, respectively. Under the longest irradiation time of 180 s, RNAi efficiency was significantly increased by 2.1-fold ($p < 0.01$). In addition, cells that were exposed to PCI but not LDL-chol-si-apoB did not show any apoB gene silencing (Figure 6B, right column).These data indicate that improved RNAi efficiency was achieved as a result of the cytosolic release of chol-siRNA through PCI.

DISCUSSION

In this study, LDL nanoparticles were used as nanocarriers for chol-siRNA. Each LDL nanoparticle could stably incorporate at least 25 molecules of chol-siRNA while maintaining structural stability. The resultant nanoparticles had a mean size of ~30 nm, which is suitable to navigate through the restricted interfibrillar openings (<40 nm) commonly present in solid tumors,[44] making them powerful carriers for the delivery of intracellular active siRNAs via systemic administration. Targeted delivery of chol-siRNA can be achieved using LDL nanoparticles because of high LDL receptor expression in a variety of cancer cells, which is believed to provide cancer cells with the necessary lipid substrates required for membrane synthesis. Although this delivery platform had superior knockdown efficiency to chol-siRNA alone, use of the LDL receptor resulted in receptor mediated endocytosis and entrapment of chol-siRNA in endolysosomal compartments. The lack of a specific cytosolic release mechanism probably limited knockdown efficiency. This was confirmed by improved knockdowns when a PCI approach was used, which released siRNAs to cytoplasm. Thus, LDL nanoparticles can be used for the cellular delivery of chol-siRNA, and PCI provides efficient

endolysosomal membrane disruption and spatiotemporal control of cytosolic release. The chol-siRNA used in the study for targeting apoB gene was used as a model proof of principle. However, the apoB gene might not be an ideal target for LDL receptor mediated delivery, since both LDL and apoB protein participate in the process of cholesterol metabolism, that may induce unexpected effects in therapeutic applications. The targeted siRNAs could be further adapted to other genes and diseases to engage in other potent mechanisms, such as the genes for induction of cancer cell apopotosis. Another challenge of using LDLR as a target for cancer theranostics is that some normal cells, such as liver hepatocytes, also express LDL receptors. PCI provides a second layer of control in the LDL delivery system for highly selective drug release. Moreover, as we reported previously,[28] the LDL delivery system is not limited to the LDL receptor. For situations where the LDLR is not highly expressed, a method for targeting LDL nanoparticles to other cancer receptors is warranted. Thus, the combination of LDL nanocarriers and PCI approach provide a useful strategy and exquisite control for therapeutic use of siRNAs. In addition, there are at least three ways for incorporating diagnostic and therapeutic agents into LDL, covalent attachment to amino acid residues of apoB-100 protein (protein modification), intercalation into the phospholipids monolayer (surface loading) and reconstitution into the lipid core of LDL (core loading).[40,45] Since the interaction between LDL and chol-siRNA is based on surface loading, the core lipid of LDL still can be replaced with other drugs for multimodality treatment or image-guided therapy, and this LDL system can be extended to other lipoprotein-based nanoparticles or lipoprotein-mimetic peptide-based delivery systems.[46−49]

■ ASSOCIATED CONTENT

Supporting Information

FPLC purification of LDL-chol-si-apoB complexes, imaging of PCI directed cytosolic release of chol-si-FITC after LDL mediated endosytosis and cytotoxicity of LDL-chol-siRNA in different experimental conditions. This material is available free of charge via the Internet at http://pubs.acs.org.

■ AUTHOR INFORMATION

Corresponding Author

*Dr Gang Zheng, Ontario Cancer Institute, TMDT 5-363, 101 College Street, Toronto, ON, M5G 1L7, Canada, E-mail: gang.zheng@uhnres.utoronto.ca. Dr Zhihong Zhang, Britton Chance Center for Biomedical Photonics, Huazhong University of Science and Technology, Wuhan 430074, China. E-mail: czyzzh@mail.hust.edu.cn.

■ ACKNOWLEDGMENTS

This study was conducted with the support by the National Basic Research Program of China (2011CB910401), the China-Canada Joint Health Research Initiative (NSFC-30911120489, CIHR CCI-102936), the Alnylam Pharmaceuticals, the Ontario Institute for Cancer Research, the Natural Sciences and Engineering Research Council of Canada, the Canadian Cancer Society, the Program for New Century Excellent Talents in University of China (NCET-08-0220 to Z.H.Z.), and the Joey and Toby Tanenbaum/Brazilian Ball Chair in Prostate Cancer Research.

■ REFERENCES

(1) Dorn, G., Patel, S., Wotherspoon, G., Hemmings-Mieszczak, M., Barclay, J., Natt, F. J., Martin, P., Bevan, S., Fox, A., Ganju, P., Wishart, W., and Hall, J. (2004) siRNA relieves chronic neuropathic pain. *Nucleic Acids Res. 32*, e49.

(2) Frank-Kamenetsky, M., Grefhorst, A., Anderson, N. N., Racie, T. S., Bramlage, B., Akinc, A., Butler, D., Charisse, K., Dorkin, R., Fan, Y., Gamba-Vitalo, C., Hadwiger, P., Jayaraman, M., John, M., Jayaprakash, K. N., Maier, M., Nechev, L., Rajeev, K. G., Read, T., Rohl, I., Soutschek, J., Tan, P., Wong, J., Wang, G., Zimmermann, T., de Fougerolles, A., Vornlocher, H. P., Langer, R., Anderson, D. G., Manoharan, M., Koteliansky, V., Horton, J. D., and Fitzgerald, K. (2008) Therapeutic RNAi targeting PCSK9 acutely lowers plasma cholesterol in rodents and LDL cholesterol in nonhuman primates. *Proc. Natl. Acad. Sci. U.S.A. 105*, 11915−11920.

(3) Lee, H., Kim, S. I., Shin, D., Yoon, Y., Choi, T. H., Cheon, G. J., and Kim, M. (2009) Hepatic siRNA delivery using recombinant human apolipoprotein A-I in mice. *Biochem. Biophys. Res. Commun. 378*, 192−196.

(4) Novina, C. D., and Sharp, P. A. (2004) The RNAi revolution. *Nature 430*, 161−164.

(5) Hassani, Z., Lemkine, G. F., Erbacher, P., Palmier, K., Alfama, G., Giovannangeli, C., Behr, J. P., and Demeneix, B. A. (2005) Lipid-mediated siRNA delivery down-regulates exogenous gene expression in the mouse brain at picomolar levels. *J. Gene. Med. 7*, 198−207.

(6) Semple, S. C., Akinc, A., Chen, J., Sandhu, A. P., Mui, B. L., Cho, C. K., Sah, D. W., Stebbing, D., Crosley, E. J., Yaworski, E., Hafez, I. M., Dorkin, J. R., Qin, J., Lam, K., Rajeev, K. G., Wong, K. F., Jeffs, L. B., Nechev, L., Eisenhardt, M. L., Jayaraman, M., Kazem, M., Maier, M. A., Srinivasulu, M., Weinstein, M. J., Chen, Q., Alvarez, R., Barros, S. A., De, S., Klimuk, S. K., Borland, T., Kosovrasti, V., Cantley, W. L., Tam, Y. K., Manoharan, M., Ciufolini, M. A., Tracy, M. A., de Fougerolles, A., MacLachlan, I., Cullis, P. R., Madden, T. D., and Hope, M. J. (2010) Rational design of cationic lipids for siRNA delivery. *Nat. Biotechnol. 28*, 172−176.

(7) Zhang, S., Zhao, B., Jiang, H., Wang, B., and Ma, B. (2007) Cationic lipids and polymers mediated vectors for delivery of siRNA. *J. Controlled Release 123*, 1−10.

(8) Zimmermann, T. S., Lee, A. C., Akinc, A., Bramlage, B., Bumcrot, D., Fedoruk, M. N., Harborth, J., Heyes, J. A., Jeffs, L. B., John, M., Judge, A. D., Lam, K., McClintock, K., Nechev, L. V., Palmer, L. R., Racie, T., Rohl, I., Seiffert, S., Shanmugam, S., Sood, V., Soutschek, J., Toudjarska, I., Wheat, A. J., Yaworski, E., Zedalis, W., Koteliansky, V., Manoharan, M., Vornlocher, H. P., and MacLachlan, I. (2006) RNAi-mediated gene silencing in non-human primates. *Nature 441*, 111−114.

(9) Yano, J., Hirabayashi, K., Nakagawa, S., Yamaguchi, T., Nogawa, M., Kashimori, I., Naito, H., Kitagawa, H., Ishiyama, K., Ohgi, T., and Irimura, T. (2004) Antitumor activity of small interfering RNA/cationic liposome complex in mouse models of cancer. *Clin. Cancer Res. 10*, 7721−7726.

(10) Beh, C. W., Seow, W. Y., Wang, Y., Zhang, Y., Ong, Z. Y., Ee, P. L., and Yang, Y. Y. (2009) Efficient delivery of Bcl-2-targeted siRNA using cationic polymer nanoparticles: downregulating mRNA expression level and sensitizing cancer cells to anticancer drug. *Biomacromolecules 10*, 41−48.

(11) Gary, D. J., Puri, N., and Won, Y. Y. (2007) Polymer-based siRNA delivery: perspectives on the fundamental and phenomenological distinctions from polymer-based DNA delivery. *J. Controlled Release 121*, 64−73.

(12) Jere, D., Arote, R., Jiang, H. L., Kim, Y. K., Cho, M. H., and Cho, C. S. (2009) Bioreducible polymers for efficient gene and siRNA delivery. *Biomed. Mater. 4*, 25020.

(13) Alam, M. R., Dixit, V., Kang, H., Li, Z. B., Chen, X., Trejo, J., Fisher, M., and Juliano, R. L. (2008) Intracellular delivery of an anionic antisense oligonucleotide via receptor-mediated endocytosis. *Nucleic Acids Res. 36*, 2764−2776.

(14) Ishihara, T., Goto, M., Kodera, K., Kanazawa, H., Murakami, Y., Mizushima, Y., and Higaki, M. (2009) Intracellular delivery of siRNA

by cell-penetrating peptides modified with cationic oligopeptides. *Drug Delivery 16*, 153−159.
(15) Chiu, S. J., Ueno, N. T., and Lee, R. J. (2004) Tumor-targeted gene delivery via anti-HER2 antibody (trastuzumab, Herceptin) conjugated polyethylenimine. *J. Controlled Release 97*, 357−369.
(16) Giljohann, D. A., Seferos, D. S., Prigodich, A. E., Patel, P. C., and Mirkin, C. A. (2009) Gene regulation with polyvalent siRNA-nanoparticle conjugates. *J. Am. Chem. Soc. 131*, 2072−2073.
(17) Lu, W., Zhang, G., Zhang, R., Flores, L. G. II, Huang, Q., Gelovani, J. G., and Li, C. (2010) Tumor site-specific silencing of NF-kappaB p65 by targeted hollow gold nanosphere-mediated photothermal transfection. *Cancer Res. 70*, 3177−3188.
(18) Qi, L., and Gao, X. (2008) Quantum dot-amphipol nanocomplex for intracellular delivery and real-time imaging of siRNA. *ACS Nano 2*, 1403−1410.
(19) Soutschek, J., Akinc, A., Bramlage, B., Charisse, K., Constien, R., Donoghue, M., Elbashir, S., Geick, A., Hadwiger, P., Harborth, J., John, M., Kesavan, V., Lavine, G., Pandey, R. K., Racie, T., Rajeev, K. G., Rohl, I., Toudjarska, I., Wang, G., Wuschko, S., Bumcrot, D., Koteliansky, V., Limmer, S., Manoharan, M., and Vornlocher, H. P. (2004) Therapeutic silencing of an endogenous gene by systemic administration of modified siRNAs. *Nature 432*, 173−178.
(20) Audouy, S. A., de Leij, L. F., Hoekstra, D., and Molema, G. (2002) In vivo characteristics of cationic liposomes as delivery vectors for gene therapy. *Pharm. Res. 19*, 1599−1605.
(21) Ma, Z., Li, J., He, F., Wilson, A., Pitt, B., and Li, S. (2005) Cationic lipids enhance siRNA-mediated interferon response in mice. *Biochem. Biophys. Res. Commun. 330*, 755−759.
(22) Rao, N. M. (2010) Cationic lipid-mediated nucleic acid delivery: beyond being cationic. *Chem. Phys. Lipids 163*, 245−252.
(23) Liu, X., Howard, K. A., Dong, M., Andersen, M. O., Rahbek, U. L., Johnsen, M. G., Hansen, O. C., Besenbacher, F., and Kjems, J. (2007) The influence of polymeric properties on chitosan/siRNA nanoparticle formulation and gene silencing. *Biomaterials 28*, 1280−1288.
(24) Patel, L. N., Zaro, J. L., and Shen, W. C. (2007) Cell penetrating peptides: intracellular pathways and pharmaceutical perspectives. *Pharm. Res. 24*, 1977−1992.
(25) Cho, W. S., Cho, M., Jeong, J., Choi, M., Cho, H. Y., Han, B. S., Kim, S. H., Kim, H. O., Lim, Y. T., Chung, B. H., and Jeong, J. (2009) Acute toxicity and pharmacokinetics of 13 nm-sized PEG-coated gold nanoparticles. *Toxicol. Appl. Pharmacol. 236*, 16−24.
(26) Geys, J., Nemmar, A., Verbeken, E., Smolders, E., Ratoi, M., Hoylaerts, M. F., Nemery, B., and Hoet, P. H. (2008) Acute toxicity and prothrombotic effects of quantum dots: impact of surface charge. *Environ. Health Perspect. 116*, 1607−1613.
(27) Cormode, D. P., Jarzyna, P. A., Mulder, W. J., and Fayad, Z. A. (2010) Modified natural nanoparticles as contrast agents for medical imaging. *Adv. Drug Delivery Rev. 62*, 329−338.
(28) Zheng, G., Chen, J., Li, H., and Glickson, J. D. (2005) Rerouting lipoprotein nanoparticles to selected alternate receptors for the targeted delivery of cancer diagnostic and therapeutic agents. *Proc. Natl. Acad. Sci. U.S.A. 102*, 17757−17762.
(29) Wolfrum, C., Shi, S., Jayaprakash, K. N., Jayaraman, M., Wang, G., Pandey, R. K., Rajeev, K. G., Nakayama, T., Charrise, K., Ndungo, E. M., Zimmermann, T., Koteliansky, V., Manoharan, M., and Stoffel, M. (2007) Mechanisms and optimization of in vivo delivery of lipophilic siRNAs. *Nat. Biotechnol. 25*, 1149−1157.
(30) Yang, M., Jin, H., Chen, J., Ding, L., Ng, K. K., Lin, Q., Lovell, J. F., Zhang, Z., and Zheng, G. (2011) Efficient Cytosolic Delivery of siRNA Using HDL-Mimicking Nanoparticles. *Small 7*, 568−573.
(31) de Smidt, P. C., Le Doan, T., de Falco, S., and van Berkel, T. J. (1991) Association of antisense oligonucleotides with lipoproteins prolongs the plasma half-life and modifies the tissue distribution. *Nucleic Acids Res. 19*, 4695−4700.
(32) Krieg, A. M., Tonkinson, J., Matson, S., Zhao, Q., Saxon, M., Zhang, L. M., Bhanja, U., Yakubov, L., and Stein, C. A. (1993) Modification of antisense phosphodiester oligodeoxynucleotides by a 5′ cholesteryl moiety increases cellular association and improves efficacy. *Proc. Natl. Acad. Sci. U.S.A. 90*, 1048−1052.
(33) Goldstein, J. L., and Brown, M. S. (1985) The LDL receptor and the regulation of cellular cholesterol metabolism. *J. Cell Sci. Suppl. 3*, 131−137.
(34) Berg, K., Folini, M., Prasmickaite, L., Selbo, P. K., Bonsted, A., Engesaeter, B. O., Zaffaroni, N., Weyergang, A., Dietze, A., Maelandsmo, G. M., Wagner, E., Norum, O. J., and Hogset, A. (2007) Photochemical internalization: a new tool for drug delivery. *Curr. Pharm. Biotechnol. 8*, 362−372.
(35) Febvay, S., Marini, D. M., Belcher, A. M., and Clapham, D. E. (2010) Targeted cytosolic delivery of cell-impermeable compounds by nanoparticle-mediated, light-triggered endosome disruption. *Nano Lett. 10*, 2211−2219.
(36) Berg, K., Selbo, P. K., Prasmickaite, L., Tjelle, T. E., Sandvig, K., Moan, J., Gaudernack, G., Fodstad, O., Kjolsrud, S., Anholt, H., Rodal, G. H., Rodal, S. K., and Hogset, A. (1999) Photochemical internalization: a novel technology for delivery of macromolecules into cytosol. *Cancer Res. 59*, 1180−1183.
(37) Varkouhi, A. K., Scholte., M, Storm., G, and Haisma., H. (2011) Endosomal escape pathways for delivery of biologicals. *J. Controlled Release 151*, 220−228.
(38) Boe., S, Saeboe-Larssen., S, and Hovig., E. (2010) Light-induced gene expression using messenger RNA molecules. *Oligonucleotides 20*, 1−6.
(39) Boe., S, Longva, A., and Hovig., E. (2007) Photochemically induced gene silencing using small interfering RNA molecules in combination with lipid carriers. *Oligonucleotides 17*, 166−173.
(40) Jin, H., Lovell, J. F., Chen, J., Ng, K., Cao, W., Ding, L., Zhang, Z., and Zheng, G. (2011) Cytosolic delivery of LDL nanoparticle cargo using photochemical internalization. *Photochem. Photobiol. Sci. 10*, 810−816.
(41) Havel, R. J., Eder, H. A., and Bragdon, J. H. (1955) The distribution and chemical composition of ultracentrifugally separated lipoproteins in human serum. *J. Clin. Invest. 34*, 1345−1353.
(42) Akinc., A, Zumbuehl., A, Goldberg., M, Leshchiner., E. S., Busini., V, Hossain., N, Bacallado., S. A., Nguyen., D. N., Fuller., J, Alvarez., R, Borodovsky., A, Borland., T, Constien., R, de Fougerolles., A, Dorkin., J. R., Narayanannair Jayaprakash, K, Jayaraman., M, John., M, Koteliansky., V, Manoharan., M, Nechev., L, Qin., J, Racie., T, Raitcheva., D, Rajeev., K. G., Sah., D. W., Soutschek., J, Toudjarska., I, Vornlocher., H. P., Zimmermann., T. S., Langer., R, and Anderson., D. G. (2008) A combinatorial library of lipid-like materials for delivery of RNAi therapeutics. *Nat. Biotechnol. 26*, 561−569.
(43) Carraway, K. L. 3rd, and Cerione, R. A. (1993) Fluorescent-labeled growth factor molecules serve as probes for receptor binding and endocytosis. *Biochemistry 32*, 12039−12045.
(44) Pluen, A., Boucher, Y., Ramanujan, S., McKee, T. D., Gohongi, T., di Tomaso, E., Brown, E. B., Izumi, Y., Campbell, R. B., Berk, D. A., and Jain, R. K. (2001) Role of tumor-host interactions in interstitial diffusion of macromolecules: cranial vs. subcutaneous tumors. *Proc. Natl. Acad. Sci. U.S.A. 98*, 4628−4633.
(45) Corbin, I. R., and Zheng, G. (2007) Mimicking nature's nanocarrier: synthetic low-density lipoprotein-like nanoparticles for cancer-drug delivery. *Nanomedicine (Lond.) 2*, 375−380.
(46) Nikanjam, M., Blakely, E. A., Bjornstad, K. A., Shu, X., Budinger, T. F., and Forte, T. M. (2007) Synthetic nano-low density lipoprotein as targeted drug delivery vehicle for glioblastoma multiforme. *Int. J. Pharm. 328*, 86−94.
(47) Zhang, Z., Cao, W., Jin, H., Lovell, J. F., Yang, M., Ding, L., Chen, J., Corbin, I., Luo, Q., and Zheng, G. (2009) Biomimetic nanocarrier for direct cytosolic drug delivery. *Angew. Chem., Int. Ed. 48*, 9171−9175.
(48) Zhang, Z., Chen, J., Ding, L., Jin, H., Lovell, J. F., Corbin, I. R., Cao, W., Lo, P. C., Yang, M., Tsao, M. S., Luo, Q., and Zheng, G. (2010) HDL-mimicking peptide-lipid nanoparticles with improved tumor targeting. *Small 6*, 430−437.

(49) Ng, K. K., Lovell, J. F., and Zheng, G. (2011) Lipoprotein-inspired nanoparticles for cancer theranostics. *Acc. Chem. Res. 44*, 1105−1113.

Bioconjugate Chemistry

Communication

pubs.acs.org/bc

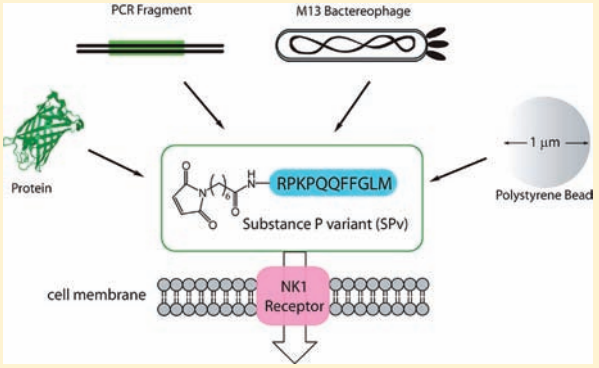
Substance P Derivatives as Versatile Tools for Specific Delivery of Various Types of Biomolecular Cargo

Shahir S. Rizk, Agnieszka Misiura, Marcin Paduch, and Anthony A. Kossiakoff*

The Department of Biochemistry and Molecular Biology, The University of Chicago, 900 East 57th Street, Chicago, Illinois, 60637, United States

Supporting Information

ABSTRACT: The use of proteins or nucleic acids as therapeutic agents has been severely hampered by their intrinsic inability to cross the cell membrane. Moreover, common techniques for driving the delivery of macromolecules lack the ability to distinguish between healthy and diseased tissue, precluding their clinical use. Recently, receptor-mediated delivery (RMD) has emerged as a technology with the potential to circumvent the obstacles associated with the delivery of drug targets by utilizing the natural endocytosis of a ligand upon binding to its receptor. Here, we describe the synthesis of variants of substance P (SP), an eleven amino acid neuropeptide ligand of the neurokinin type 1 receptor (NK1R), for the delivery of various types of cargo. The variants of SP were synthesized with an N-terminal maleimide moiety that allows conjugation to surface thiols, resulting in a nonreducible thioether. Cargos lacking an available thiol are conjugated to SP using commercially available cross-linkers. In addition to the delivery of proteins, we expand the use of SP to include nuclear delivery of DNA fragments that are actively expressed in the target cells. We also show that SP can be used to deliver whole bacteriophage particles as well as polystyrene beads up to 1 μm in diameter. The results show the ability of SP to deliver cargo of various sizes and chemical properties that retain their function within the cell. Furthermore, the overexpression of the NK1R in many tumors provides the potential for developing targeted delivery reagents that are specific toward diseased tissue.



Targeted delivery of drug molecules to diseased cells without affecting healthy tissue is of great importance for therapeutic applications. While transfection reagents are commonly used to transport nucleic acids across the cell membranes of eukaryotic cells, such reagents can be associated with a great deal of toxicity and lack cell type specificity, precluding their use for *in vivo* applications.[1−3] Recently, receptor-mediated delivery (RMD) strategies have been developed to overcome the hurdles associated with targeted drug delivery.[4−9] RMD takes advantage of the overexpression of a receptor on the surface of diseased tissue in comparison to the surrounding healthy cells. By conjugating a drug to the ligand of the overexpressed receptor, the drug is internalized along with the ligand as part of the natural endocytic pathway associated the ligand−receptor interaction. Several examples of RMD have been reported with varying degrees of success, and some have been employed for *in vivo* delivery.[10,11]

Previously, we and others developed substance P (SP), an eleven amino acid neuropeptide (Sequence: RPKPQQFFGLM-NH_2), into a robust vehicle for the delivery of synthetic antibodies (sABs)[8] and toxins.[12] SP is internalized through a high-affinity interaction with the neurokinin 1 receptor (NK1R),[13,14] a tachykinin receptor that is highly overexpressed in many tumors,[15,16] particularly in brain cancers[17,18] compared to normal human astrocytes, where its expression is undetectable.[8] SP-conjugated proteins were shown to specifically target glioblastoma cells. Importantly, we demonstrated a sufficient fraction of the introduced cargos escape the endosome to elicit and phenotype that resembles their function *in vitro*.[8]

Here, we utilize two synthetic variants of SP (SPv and SPv-NLS) for the conjugation and delivery of molecular cargo that vary in size and chemical properties. Both SPv and SPv-NLS were synthesized to contain an N-terminal maleimide moiety followed by a 6-carbon linker. SPv-NLS contains an additional nuclear localization sequence between the N-terminal melimide and the SP sequence. The maleimide of SPv and SPv-NLS can be conjugated to cysteine residues on a protein surface or a thiol-containing cross-linkers. Additionally, the nuclear localization sequence of SPv-NLS mediated the delivery of cargo to the nucleus. We present a general method for the conjugation of SP variants to highly diverse types of molecular cargo and demonstrate that conjugation to SP can be used to deliver proteins, double-stranded DNA fragments, phage particles, and polystyrene beads up to 1 μm in diameter to cells expressing

Received: September 7, 2011
Revised: December 14, 2011
Published: December 18, 2011

 © 2011 American Chemical Society

the NK1R. The high affinity of the interaction between SP and the NK1R, combined with the overexpression of the receptor in many cancers makes SP-mediated delivery a potential tool for the development of highly specific therapeutic agents.

The maleimide moiety of SPv is designed to directly react with a cysteine residue on a cargo protein to form a stable thioether. However, for many proteins, a surface cysteine residue may not always be available for conjugation. To establish a general method for attachment of SPv to proteins that have no modifiable surface cysteines, we used GFP (green fluorescent protein) as a cargo. Additionally, the fluorescence of GFP serves to directly detect uptake by mammalian cells expressing the NK1R. First, GFP was reacted with the heterobifunctional cross-linker SPDP (*N*-succinimidyl 3-(2-pyridyldithio)-propionate), which modifies surface lysine residues to produce a pyridyldithiol functional group (Figure 1A). Second, the isolated SPDP-GFP conjugate was reacted with a 50-fold excess of SPv in the presence of 1 mM TCEP (*tris*(2-carboxyethyl) phosphine). Upon reduction of the pyridyldithio-group by TCEP, the exposed thiol reacts with the maleimide of SPv to produce a stable thioether linkage between the peptide and the protein. Finally, the SPv-GFP conjugate was isolated by size-exclusion chromatography.

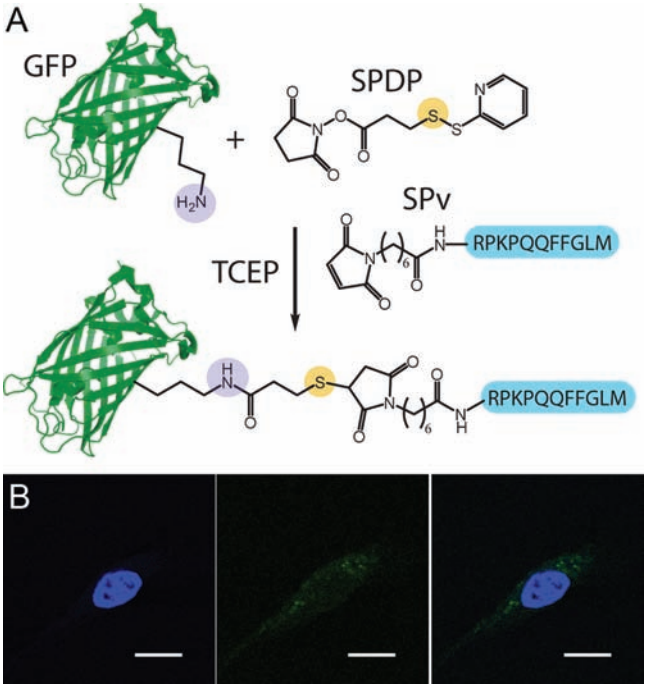


Figure 1. Delivery of GFP. (A) The cross-linker SPDP is used to modify the amine group of a lysine residue (blue) to pyridyl-dithiol. Reduction using TCEP exposes a free thiol (yellow), which reacts with the N-terminal maleimide moiety of SPv to form a thioether. (B) U87 cell treated with 20 nM GFP-SPv conjugate: nuclear stain (left), GFP fluorescence (center), merged channels (right). (Scale bar = 10 μm.)

To examine the ability of SPv to mediate the delivery of GFP, we utilized U87 glioblastoma cells, which highly express the NK1R.[17] The cells were seeded on coverslips in a 24-well plate and treated with 100 nM of the SPv-GFP conjugate for 2 h. The cells were then washed 3 times with phosphate buffered saline (PBS) to remove uninternalized conjugate and fixed with 4% *p*-formaldehyde. DAPI was used for nuclear staining followed by mounting of the coverslips on glass slides and visualization under confocal microscopy. The images show that GFP is readily internalized by U87 cells demonstrating that SPv conjugation results in uptake of the protein cargo by cells containing the NK1R (Figure 1B).

The specific delivery of genetic material to a diseased cell is a great challenge in gene therapy. To examine the ability of SP variants to deliver a gene that can be functionally expressed in mammalian cells, we designed a linear DNA fragment that includes the CMV promoter followed by the enhanced green fluorescent protein (eGFP) gene. The fragment was designed to utilize GFP expression as an indication of functional expression of the DNA molecule. The fragment was generated by PCR using oligonucleotides with incorporated modifications at the 5′ ends. The sense primer was designed with a 5′ Alexa 647 fluorescent group and the antisense primer included a 5′ amine modification. We conjugated the PCR fragment to SPv-NLS using SPDP in a two-step reaction (Figure 2A). First, the amine-reactive NHS-ester of SPDP was reacted with the amine modification of the PCR fragment, followed by size exclusion chromatography to isolate the SDPD-DNA conjugate. Second, the conjugate was mixed with a 50-fold molar excess of SPv-NLS in the presence of TCEP to allow the maleimide of SPv-

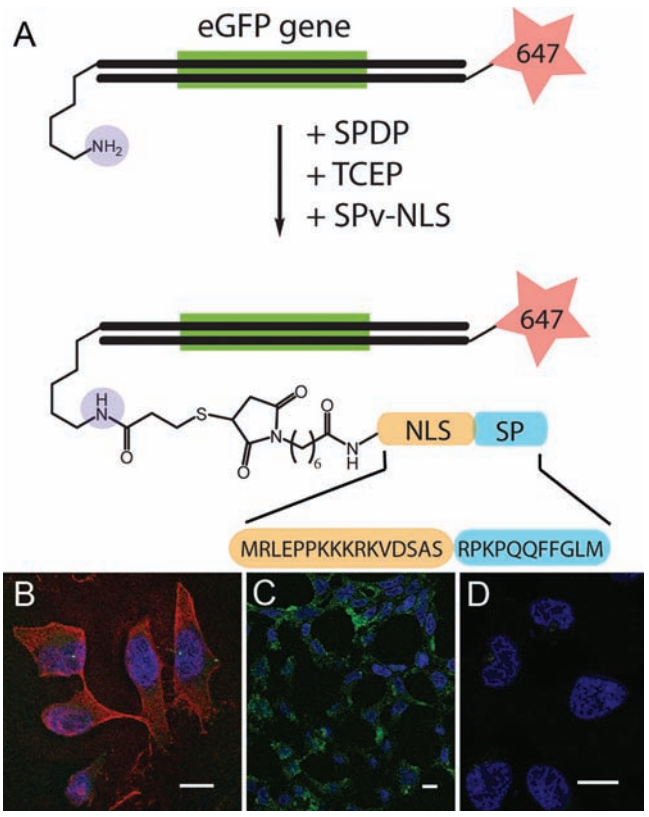


Figure 2. Delivery of functionally expressed DNA fragment. (A) A DNA fragment coding for GFP was generated by PCR with the introduction of Alexa-647 fluorophore (red) and a free amine (blue). SPDP was used to conjugate the DNA fragment to SPv-NLS, which contains an N-terminal maleimde, followed by a nuclear localization sequence (orange) and the SP sequence. (B) Hela cells transfected with the NK1R show internalization of the DNA conjugate (red) with both cytoplasmic and nuclear localization after 2 h of treatment with 200 pM DNA-SPv-NLS conjugate. (C) GFP expression (green) after 48 h of treatment. (D) Hela cells treated with DNA fragment not conjugated to SP. (Scale bar = 10 μm).

dx.doi.org/10.1021/bc200496e | *Bioconjugate Chem.* 2012, 23, 42–46

NLS to react with the pyridylodithio-group of SPDP to form a thioether linkage (Figure 2A). The final product was purified by size exclusion chromatography, and the 5′ Alexa 647 group was used to estimate the concentration of the conjugate.

To demonstrate SP-mediated delivery of an expressible gene, we utilized HeLa cells transfected with a plasmid that codes for the NK1R. The cells were treated with 200 pM of the SP-linear DNA conjugate 48 h after transfection, where expression of the NK1R was confirmed by Western blot (Supporting Information figure). After 2, 24, and 48 h incubation with the conjugate, cells were fixed and stained with DAPI and examined using confocal microscopy. The results show that cells expressing the NK1R readily internalize the linear DNA conjugate within 2 h of treatment (Figure 2B). Further, the conjugate appears to localize throughout the cytoplasm and the nucleus. GFP expression was observed after 48 h of incubation with the conjugate (Figure 2C) compared to cells treated with the PCR fragment alone (Figure 2D), indicating the ability of the conjugate to retain its activity following internalization through the SP-NK1R interaction. The results also show that a subnanomolar concentration of the SP-gene conjugate can effectively result in functional expression in the target cells.

For the potential therapeutic utilization of the delivery of genetic material, protection of the DNA molecule can serve to elongate the life of the cargo within circulation by avoiding degradation. We sought to deliver DNA molecules packaged within bacteriophage particles, a strategy that provides several advantages. First, the simple architecture of the phage coat proteins is highly stable providing protection of the encapsulated DNA molecule. Second, the self-assembly of the phage components can be used to easily package any plasmid that contains an F1 origin of replication. Third, the N-termini of the thousands of copies of the major coat protein pVIII are solvent exposed and can be used for attachment of SP variants without interfering with the DNA molecule itself. While receptor mediated delivery of phage particles has previously been reported, the efficiency of delivery and functional expression of the encoded gene has been poor.[19,20] This is because the packaged DNA is single stranded, and therefore, successful delivery of useful genetic material using phage particles requires disassembly of the phage coat upon internalization, release of the DNA cargo, and conversion of the ssDNA into dsDNA. Each of these steps can potentially form an obstacle for the delivery of transcriptionally competent DNA.

To generate phage particles packaged with peGFP-F ssDNA (Figure 3A), midlog phase XL1-Blue cells carrying the pEGFP-F plasmid were infected with KO7 helper phage and incubated overnight at 37 °C, followed by polyethylene glycol/NaCl precipitation of the phage particles. We modified the surface amines of the phage particles using a 20-fold excess of SPDP, followed by 3 phage precipitation/resuspension steps to remove excess cross-linker, and addition of 100-fold excess of SPv. The surface amines were also used to attach NHS-Cy5 for visualization of the internalized phage particles. Incubation of U87 glioblastoma cells with the SP-phage conjugate results in internalization of the phage particles as indicated by confocal microscopy (Figure 3B). After 72 h of incubation, GFP expression was observed only in cells treated with the conjugate (Figure 3C,D), indicating selective targeting of the conjugate by SP to U87 cells. While the efficiency of delivery of the phage particles is high, the efficiency of GFP expression is low. FACS analysis indicates that ∼1 in 500 cells that internalize the

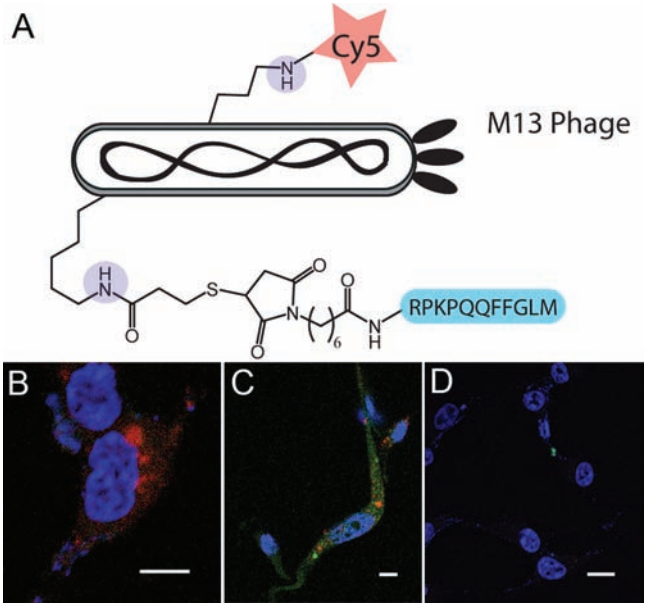


Figure 3. Delivery of bacteriophage. (A) M13 KO7 phage particles carrying ssDNA coding for GFP were conjugated to SPv via SPDP and labeled with Cy5. (B) U87 cells treated with phage-SPv conjugates showing internalization of the phage particles (red) after 2 h. (C) GFP expression (green) in U87 cells, 72 h after treatment with the phage-SPv particles. (D) U87 cells treated with Cy5 labeled phage not conjugated to SPv, 72 h following treatment. (Scale bar = 10 μm.)

conjugate are able to express GFP. While this is significantly above background green fluorescence (1 in 10 000 cells), this percentage remains low, and correlates with previously published studies where genetically modified phage particles displaying a protein ligand are used for gene delivery.[19,20]

We establish here that SP can deliver molecules of size and volume several times greater than the previously reported cargos.[8,12] To determine the size limit of the cargo that can be delivered using SP, we investigated the ability of the engineered SP variants to deliver polystyrene bead that are 1 or 6 μm in diameter. The beads, which contain an amine-derivatized surface, were conjugated to SPv using SPDP. Additionally, NHS-Cy5 was added to the reaction to fluorescently label the surface of the beads, which were then isolated from excess cross-linker, SPv, and fluorophore by centrifugation (Figure 4A). Confocal imaging of U87 cells treated with SPv conjugated to 1 μm beads shows that the beads were internalized (Figure 4B). A *z*-stack series of the cells shows that the beads lie within the cytoplasm surrounding the nucleus (Supporting Information video). The cells failed to internalize larger-sized beads conjugated to SP, providing an estimate of 1 μm for the upper limit for the size of cargo that can be delivered using SP. However, the large size of the beads produced protrusions of the cell membrane surrounding the internalized beads (Figure 4C), distorting their shape compared to untreated cells (Figure 4D). Delivery of beads, to our knowledge, has not previously been reported. This capability of SP variants can potentially be utilized to carryout optical trapping experiments to measure the forces exerted on a modified bead within live cells, provided that the beads do not interfere with the viability of the cells.

In this work, we describe the synthesis of two variants of the neuropeptide Substance P and their utilization as tools for the conjugation and receptor mediated delivery of a wide variety of

dx.doi.org/10.1021/bc200496e | *Bioconjugate Chem.* 2012, 23, 42–46

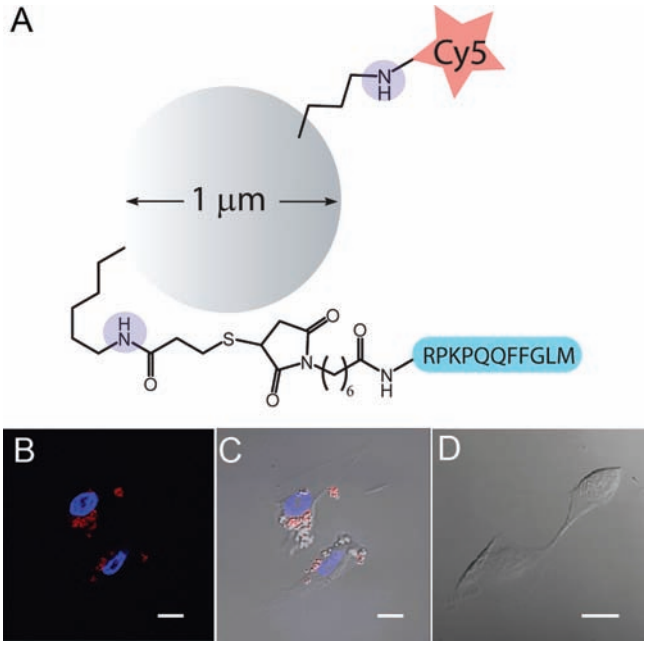


Figure 4. Delivery of polystyrene beads. (A) Amine-modified 1 μm polystyrene beads were conjugated to SPv using SPDP, and labeled with Cy5. (B) U87 cells treated with SPv-conjugated beads readily uptake the beads (red) 2 h following treatment. (C) Merged channels in B with DIC showing distortion of cell membrane upon internalization of beads. (D) Untreated cells. (Scale bar = 10 μm).

molecular cargos to mammalian cells. Both variants (SPv and SPv-NLS) contain a maleimide moiety at the N-terminus allowing conjugation to myriad molecular cargo types. Using thiol- and amine-reactive groups, all the conjugation reactions described here can be carried out efficiently under mild conditions that preserve the activity of the cargo.

Utilizing SP as a vehicle for the delivery of molecular cargo offers notable advantages over many other ligands. Unlike large proteins, the 11-amino-acid sequence of SP can be easily synthesized allowing the incorporation of a variety of chemical groups for conjugation to the cargo. Additionally, SP binds to the NK1R with high affinity (~100 pM),[21] requiring a small dose of the SP-cargo conjugate for successful delivery. Importantly, the NK1R is highly overexpressed in many tumors compared to the surrounding tissue,[15−18,22] providing a tool for specific targeting of the tumor tissue without affecting healthy cells. Further, the incorporated cargos adequately escape the endosome in most cases.

Our results demonstrate the versatility of the engineered SP variants for the delivery of various types of molecules. Cargos as large as a 1 μm bead can be readily internalized upon conjugation to SPv. In addition, we demonstrate that SP variants can transport genetic material across the cell membrane in two forms; dsDNA fragment and phage-packaged ssDNA. In both cases, the DNA was functionally expressed as indicated by green fluorescence. However, the mechanism by which the cargo is released from the endosome is still not clear and may be cargo-dependent. Even with efficient internalization, a low level of endosomal escape can contribute to the low efficiency of the function of the delivered cargo. For the case of delivering protein cargos via SP conjugation, endosomal escape appears to be relatively efficient, although it is difficult to quantify. In the cases of gene delivery described here, a small number of DNA molecules that escape the endosome can translate into a significant amount of gene expression. This may be different for the delivery of other types of cargo that require larger doses for intracellular activity. Clearly, more work must to be done to increase the efficiency of the function of the delivered cargo. Nonetheless, the utilization of SP variants for delivery of DNA can lead to the development of novel approaches to gene-based therapies.

■ ASSOCIATED CONTENT

Ⓢ Supporting Information

Detailed materials and methods, as well as one supporting figure and one supporting video are included. This material is available free of charge via the Internet at http://pubs.acs.org.

■ AUTHOR INFORMATION

Corresponding Author

*Tel: (773) 702-9257. Fax: (773) 702-0439.

■ ACKNOWLEDGMENTS

The authors thank Dr. Labno and Dr. Bindokas at the University of Chicago Microscopy core facility. This work was funded by U54GM087519. SSR was funded by NIH F32DK080619.

■ REFERENCES

(1) Dalby, B., Cates, S., Harris, A., Ohki, E. C., Tilkins, M. L., Price, P. J., and Ciccarone, V. C. (2004) Advanced transfection with Lipofectamine 2000 reagent: primary neurons, siRNA, and high-throughput applications. *Methods 33*, 95−103.

(2) Felgner, P. L., Gadek, T. R., Holm, M., Roman, R., Chan, H. W., Wenz, M., Northrop, J. P., Ringold, G. M., and Danielsen, M. (1987) Lipofection: a highly efficient, lipid-mediated DNA-transfection procedure. *Proc. Natl. Acad. Sci. U. S. A. 84*, 7413−7.

(3) Jacobsen, L. B., Calvin, S. A., Colvin, K. E., and Wright, M. (2004) FuGENE 6 Transfection Reagent: the gentle power. *Methods 33*, 104−12.

(4) Atkinson, T. J. (2008) Cystic fibrosis, vector-mediated gene therapy, and relevance of toll-like receptors: a review of problems, progress, and possibilities. *Curr. Gene Ther. 8*, 201−7.

(5) Gust, T. C., and Zenke, M. (2002) Receptor-mediated gene delivery. *Scientific World Journal 2*, 224−9.

(6) Maruyama, K., Iwasaki, F., Takizawa, T., Yanagie, H., Niidome, T., Yamada, E., Ito, T., and Koyama, Y. (2004) Novel receptor-mediated gene delivery system comprising plasmid/protamine/sugar-containing polyanion ternary complex. *Biomaterials 25*, 3267−73.

(7) Pardridge, W. M. (2007) shRNA and siRNA delivery to the brain. *Adv. Drug Delivery Rev. 59*, 141−52.

(8) Rizk, S. S., Luchniak, A., Uysal, S., Brawley, C. M., Rock, R. S., and Kossiakoff, A. A. (2009) An engineered substance P variant for receptor-mediated delivery of synthetic antibodies into tumor cells. *Proc. Natl. Acad. Sci. U. S. A. 106*, 11011−5.

(9) Tian, P., Ren, S., Ren, C., Teng, Q., Qu, S., Yao, M., and Gu, J. (1999) A novel receptor-targeted gene delivery system for cancer gene therapy. *Sci. China C: Life Sci. 42*, 216−24.

(10) Wiley, R. G., and Lappi, D. A. (2003) Targeted toxins in pain. *Adv. Drug Delivery Rev. 55*, 1043−54.

(11) Katsogiannou, M., Peng, L., Catapano, C. V., and Rocchi, P. (2011) Active-targeted nanotherapy strategies for prostate cancer. *Curr. Cancer Drug Targets 11*, 954−65.

(12) Mantyh, P. W., Rogers, S. D., Honore, P., Allen, B. J., Ghilardi, J. R., Li, J., Daughters, R. S., Lappi, D. A., Wiley, R. G., and Simone, D. A. (1997) Inhibition of hyperalgesia by ablation of lamina I spinal neurons expressing the substance P receptor. *Science 278*, 275−9.

(13) Garland, A. M., Grady, E. F., Payan, D. G., Vigna, S. R., and Bunnett, N. W. (1994) Agonist-induced internalization of the

substance P (NK1) receptor expressed in epithelial cells. *Biochem. J. 303* (Pt 1), 177−86.
(14) Wang, X., and Marvizon, J. C. (2002) Time-course of the internalization and recycling of neurokinin 1 receptors in rat dorsal horn neurons. *Brain Res. 944*, 239−47.
(15) Hennig, I. M., Laissue, J. A., Horisberger, U., and Reubi, J. C. (1995) Substance-P receptors in human primary neoplasms: tumoral and vascular localization. *Int. J. Cancer 61*, 786−92.
(16) Singh, D., Joshi, D. D., Hameed, M., Qian, J., Gascon, P., Maloof, P. B., Mosenthal, A., and Rameshwar, P. (2000) Increased expression of preprotachykinin-I and neurokinin receptors in human breast cancer cells: implications for bone marrow metastasis. *Proc. Natl. Acad. Sci. U. S. A. 97*, 388−93.
(17) Palma, C., and Maggi, C. A. (2000) The role of tachykinins via NK1 receptors in progression of human gliomas. *Life Sci. 67*, 985−1001.
(18) Lai, J. P., Douglas, S. D., Wang, Y. J., and Ho, W. Z. (2005) Real-time reverse transcription-PCR quantitation of substance P receptor (NK-1R) mRNA. *Clin. Diagn. Lab. Immunol. 12*, 537−41.
(19) Kassner, P. D., Burg, M. A., Baird, A., and Larocca, D. (1999) Genetic selection of phage engineered for receptor-mediated gene transfer to mammalian cells. *Biochem. Biophys. Res. Commun. 264*, 921−8.
(20) Chung, Y. S., Sabel, K., Kronke, M., and Klimka, A. (2008) Gene transfer of Hodgkin cell lines via multivalent anti-CD30 scFv displaying bacteriophage. *BMC Mol. Biol. 9*, 37.
(21) Gether, U., Marray, T., Schwartz, T. W., and Johansen, T. E. (1992) Stable expression of high affinity NK1 (substance P) and NK2 (neurokinin A) receptors but low affinity NK3 (neurokinin B) receptors in transfected CHO cells. *FEBS Lett. 296*, 241−4.
(22) Yamaguchi, K., Richardson, M. D., Bigner, D. D., and Kwatra, M. M. (2005) Signal transduction through substance P receptor in human glioblastoma cells: roles for Src and PKC delta. *Cancer Chemother. Pharmacol. 56*, 585−593.

Bioconjugate Chemistry

Article

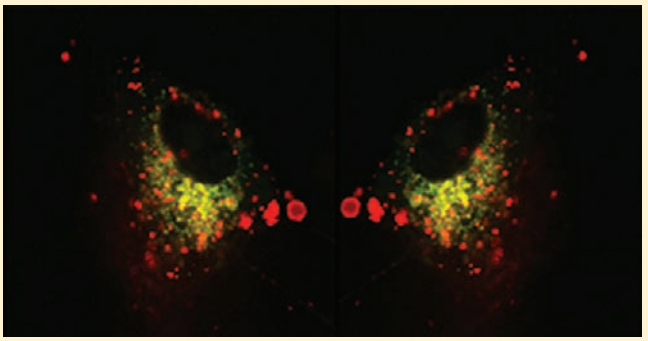
pubs.acs.org/bc

Enantiomer-Specific Bioactivities of Peptidomimetic Analogues of Mastoparan and Mitoparan: Characterization of Inverso Mastoparan as a Highly Efficient Cell Penetrating Peptide

Sarah Jones* and John Howl

Research Institute in Healthcare Science, School of Applied Sciences, University of Wolverhampton, Wulfruna Street, Wolverhampton, WV1 1LY, United Kingdom

ABSTRACT: Retro-inverso transformation has commonly been employed as a strategy both for the synthesis of proteolytically stable peptide analogues and for the detailed investigation of structure activity relationships. Herein, we adopted a similar strategy to probe the structure activity relationships of two biologically active tetradecapeptides. Analogues of the α-helical mastoparan, and the highly potent apoptogenic analogue mitoparan, were synthesized using D-amino acids assembled in both endogenous (inverso) and reverse (retro-inverso) orientations. For a more comprehensive comparison, our studies also included the retro L-enantiomer of both peptides. Contrary to expectation, comparative investigations of cytotoxicity, mast cell degranulation, and cellular penetration demonstrated that, while retro-inverso transformation abrogated the associated biological activities of these helical peptides, inverso homologues retained their bioactivities. Moreover, inverso mastoparan demonstrated the highest translocation efficacy of all analogues with much improved uptake kinetics compared to other cell penetrating peptides (CPPs) including the commonly employed inert vectors penetratin and tat. Data presented herein thus propound the utility of inverso mastoparan as a highly efficient peptide vector. Furthermore, correlation analysis of plasma membrane translocation and intracellular uptake efficacy further supports a two-compartment model of CPP import whereby the intracellular accumulation of polycationic peptides is dependent upon both the efficiency of transport into the cell and their subsequent accretion at distinct subcellular loci.



INTRODUCTION

Since the first description of mastoparan[1] (MP), a tetradecapeptide (INLKALAALAKKIL) isolated from the venom of *Vespula lewisii*, many additional analogues of this peptide, both natural and synthetic, have been reported and reviewed elsewhere.[2−4] Moreover, MP analogues have proven utility as differential secretagogues,[5] components of cell penetrating peptide vectors[2,6] and modulators of numerous cellular and pathological processes, some of which may be a downstream consequence of the receptor-independent activation of heterotrimeric G proteins (reviewed in refs 3,4). Additionally, MP and chimeric analogues including galparan[2,7] can directly modulate the activities of other membrane-bound protein targets that include Ca^{2+}-ATPases,[8] phospholipase D2,[9] and the Na^+,K^+-ATPase of rat brain frontal cortex.[7]

A major determinant of the biological activity of MP analogues is the formation of an amphiphilic helix.[10,11] Moreover, this secondary structural motif is observed when MP and related peptides are bound to either membranes[10] or the carboxyl termini of the α-subunits of heterotrimeric G proteins.[12] Based upon these and other observations (reviewed ref 4), we utilized a helical wheel projection in the design of mitoparan[13] (MitP, [Lys,[5,8]Aib[10]]MP), a peptide with enhanced amphiphilicity. MitP presents two additional lysyl side chains in the cationic face and contains α-aminoisobutyric acid (Aib), a known helix promoter,[14] substituted for Ala at position 10. More recently, a study of the crystal structure of related MP from *Polistes jadwagae*[15] has provided evidence that direct interactions between MP analogues are sufficient to promote helical formation in the absence of biological membranes.

Studies of the structure activity relationships of MP analogues identified MitP as a more potent secretagogue and cytotoxic agent.[13] Moreover, we have since determined that MitP very efficiently translocates the plasma membrane to localize with mitochondria.[16] At this locus, MitP interacts with at least one protein target, the voltage-dependent anionic channel, to initiate the release of cytochrome *c* and is clearly capable of initiating intrinsic apoptotic events in cultured cells. Thus, the effective targeting of MitP and other MP analogues to diseased cells could provide a very capable therapeutic strategy.

The MP sequence has proven value in the design of cell penetrating peptide (CPP) vectors including transportan[17] and deletion homologues such as transportan 10.[18] Our recent studies[16] have indicated that N-terminal extension of MitP with

Received: June 6, 2011
Revised: December 1, 2011
Published: December 11, 2011

ACS Publications © 2011 American Chemical Society

dx.doi.org/10.1021/bc2002924 | *Bioconjugate Chem.* 2012, 23, 47−56

targeting peptides can improve both the cell-type selectivity and potency of chimeric peptides. The *in vivo* utility of MitP and other MP analogues could, however, be compromised by combined activities of both extracellular and intracellular proteases. Moreover, the synthesis of isomeric peptides is a common approach used to both investigate structure activity relationships and to produce peptides that are more resistant to proteolytic degradation.[19,20] Thus, the objective of this study was to compare the intracellular translocation and biological properties of homologues of both MitP and MP containing mostly D-amino acids assembled in both normal (inverso) and reverse (retro-inverso) orientations.

EXPERIMENTAL PROCEDURES

Materials. *N*-(9-Fluorenylmethoxy-carbonyl)-D-Isoleucine (Fmoc-D-Ile) was purchased from Sigma-Aldrich (Poole, UK). Other Fmoc-protected amino acids for routine peptide synthesis were purchased from Novabiochem (Beeston, UK). AGTC Bioproducts Ltd. (Hessle, UK) supplied dimethylformamide and dichloromethane for solid-phase peptide synthesis. Culture medium and supplements were purchased from Sigma-Aldrich (Poole, UK), and fetal bovine serum from PAA (Yeovil, UK). Unless otherwise indicated, all other research grade chemicals were purchased from Sigma-Aldrich (Poole, UK).

Peptide Synthesis. All peptides utilized in this study were manually synthesized (0.1−0.2 mmol scale) on Rink amide methylbenzhydrylamine (MBHA) resin (Novabiochem, Beeston, UK) employing an *N*-α-Fmoc protection strategy with *O*-(6-chloro-1-hydrocibenzotriazol-1-yl)-1,1,3,3-tetramethyl-uronium hexafluorophosphate (HCTU; AGTC Bioproducts, Hessle, UK) activation. Fluorescent peptides, to be used in confocal live cell imaging and quantitative uptake analyses, were synthesized by amino-terminal acylation of CPP sequences with 6-carboxy-tetramethylrhodamine (Novabiochem, Beeston, UK) as previously described.[16] Crude peptides were purified to apparent homogeneity by semipreparative-scale high-performance liquid chromatography, and the predicted masses of all peptides used (average M + H^+) were confirmed to an accuracy of ±1 by matrix-assisted laser desorption ionization (MALDI) time-of-flight mass spectrometry operated in positive ion mode using α-cyano-4-hydroxycinnamic acid (Sigma) as a matrix.[16]

Cell Culture. The investigations described herein utilized the cell lines RBL-2H3, a widely studied mast cell model (reviewed in ref 21) and the human glioblastoma-astrocytoma line U373 MG.[22] Both lines were routinely maintained in a humidified atmosphere of 5% CO_2 at 37 °C in DMEM supplemented with L-glutamine (0.1 mg/mL) 10% (wt/vol) fetal bovine serum (FBS), penicillin (100 U/mL), and streptomycin (100 μg/mL).

Secretion Assays. β-Hexoseaminidase, secreted by peptide-stimulated RBL 2H3 cells, was assayed in samples of cell medium as previously described.[5,13] Five microliter samples were transferred into 96 well plates and incubated with *p*-nitrophenyl *N*-acetyl-β-D-glucosamide (20 μL of 1 mM in 0.1 M sodium citrate buffer, pH 4.5) for 1 h at 37 °C. Na_2CO_3/$NaHCO_3$ buffer (200 μL of 0.1 M, pH 10.5) was then added and β-hexoseaminidase activity determined by colorimetric analyses at 405 nm.

Graphical representations and EC_{50} values were calculated using GraphPad *Prism* 5 software.

Cytotoxicity Assays. Cellular viability was measured by the 3-(4,5-dimethylthazol-2-yl)-2,5-diphenyl tetrazolium bromide (MTT) conversion assay.[23] U373MG cells were cultured in 96 well plates and washed and maintained in medium without serum for 24 h prior to assay. Cells were treated with peptides for 4 h at 37 °C and further incubated with MTT (0.5 mg/mL) for 3 h at 37 °C. Medium was aspirated and the insoluble formazan product was solubilized with DMSO. MTT conversion was determined by colorimetric analysis at 540 nm. Graphical representations of changes in cell viability and LD_{50} values were calculated using GraphPad *Prism* 5 software.

Quantitative Analyses of Peptide Translocation. The method used to quantitatively assess the uptake of fluorescent peptides was based upon that previously described by Langel's group.[24] This method employed trypsin to remove cell surface-associated peptide prior to lysis. U373 MG cells were transferred to 6-well plates and grown to 80% confluence. Immediately prior to the addition of fluorescent MP and MitP analogues, cells were washed with and transferred into 1 mL of phenol red-free DMEM. Cells were incubated with fluorescent peptides at a final concentration of 5 μM for 1 h at 37 °C in a humidified atmosphere of 5% CO_2. Cells were then washed four times, detached with 300 μL of 1% (w/v) trypsin at 37 °C, collected by centrifugation and lysed in 300 μL 0.1 M NaOH for two hours on ice. 250 μL of each sample cell lysate were transferred to a black 96-well plate, and analyzed using a ThermoFischer Scientific Fluoroskan Ascent FL fluororescence spectrophotometer (λ_{Abs} 544 nm/λ_{Em} 590 nm).

Live Cell Imaging. U373MG cells were transferred to 35 mm Petri dishes with 12 mm glass bases (IWAKI, purchased from Barloworld Scientific Ltd., Stone, UK) and grown to 90% confluence (conditions as described above). Prior to the addition of fluorescent peptides and/or other materials, cells were washed with and transferred into phenol red-free DMEM. During the period of exposure to peptides, cell layers were maintained at 37 °C in a humidified atmosphere of 5% CO_2. Immediately prior to observation, cells were then washed gently (8×) and analyzed with a Carl Zeiss LSM510Meta confocal microscope.

All quantitative colocalization analyses were performed using the Carl Zeiss quantitative colocalization analysis software, incorporating an interactive scatter plot and data table linked to the images. For mitochondrial colocalization studies, cells were incubated with 200 nM Mitotracker Green FM (Molecular Probes, Invitrogen, Paisley, UK) alongside fluorescent peptides.[16] Overlap coefficients after Manders were used to quantify colocalization. Coefficients generated values between 0 and 1. A value of 0 indicated no colocalization, whereas a value of 1 indicated that all pixels were colocalized. Data were collected from an average of 9 regions of interest, between 50 and 200 μm^2 and from 3 independent experiments. For lysosomal colocalization studies, cells were incubated with either 75 nM Lysotacker Green DND-26, a generalized lysosomal stain for acid organelles, or 1 μM Lysosensor Green DND-153, a pH-dependent lysosomal stain (pK_a 7.5) that is brightly fluorescent at neutral pH (Molecular Probes, Invitrogen, Paisley, UK). Data were collected from 4 entire images and from 3 independent experiments. Colocalization (coloc) coefficients were calculated for the two different fluorophores according to the following equations: C1 = pixels channel 1 coloc/pixels channel 1 total, C2 = pixels channel 2 coloc/pixels channel 2 total and defined as relative number of colocalizing pixels in channel 1 (designated rhodamine) or 2 (designated fluorescein), respectively, as compared to the total number of pixels above threshold. Colocalization coefficients generated values from 0 to 1.0, whereby a value of 1.0 for channel 1 (designated rhodamine) and a value of 0.4 for channel 2 (designated fluorescein) would

dx.doi.org/10.1021/bc2002924 | *Bioconjugate Chem.* 2012, 23, 47−56

indicate that 100% rhodamine pixels colocalized with fluorecein pixels and 40% fluorescein pixels colocalized with rhodamine.

Lipid-PAMPA Assay. The parallel artificial membrane permeability assay (PAMPA, Millipore) was used as a non-cell-based assay to assess passive permeability of selected peptides across an artificial membrane. Using a 96-well MultiScreen Permeability plate, the assay measures the ability of compounds to diffuse from a Donor to Acceptor compartment separated by a PVDF membrane pretreated with a lipid-containing organic solvent. Briefly, 4% (w/v) L-α-phosphatidylcholine in dodecane was added at 5 μL/well to donor plates. Within 10 min, 5 μM rhodamine-labeled peptide, dissolved in PBS containing 5% DMSO (v/v), was also added at 150 μL/well to the donor plates. 300 μL PBS containing 5% DMSO was added to each well of the acceptor plates and donor plates placed directly on top. Following 6 h of incubation at room temperature, the contents of the acceptor plates were transferred to a black 96-well plate and analyzed using a ThermoFischer Scientific Fluoroskan Ascent FL fluorescence spectrophotometer (λ_{Abs} 544 nm/λ_{Em} 590 nm). Apparent permeability (cm/s) was calculated using the following eq:[25]

$$P_{app} = \frac{V_r[dC_r/dt]}{A \cdot C_d}$$

whereby V_r is the volume of the acceptor well (0.30 cm^3), dC_r is the change in concentration of the acceptor compartment, dt is the change in time (seconds), A is the area of the filter membrane corrected for porosity (0.24 cm^2), and C_d is the concentration of the donor compartment at time 0.

RESULTS

Peptide Design. Synthesized in reverse and composed of D-amino acids, retro-inverso transformation ensures that amino acid side chains are in the same orientation to that of the parent peptide while the carbonyl and amine groups that form the backbone amides are reversed. Such constructs are therefore reputed to retain biological activity owing to the preservation of their side chain orientation, while being resistant to proteolysis.[26]

Table 1. Peptide Sequences, Abbreviations, and Mass Spectrometric Analyses[a]

Peptide Abbreviation	Peptide Sequence	mW Calculated	mW Observed
Mastoparan (MP) analogues			
MP	INLKALAALAKKIL	1479.9	1480.1
*i*MP	inlkalaalakkil	1479.9	1480.8
*r*MP	LIKKALAALAKLNI	1479.9	1480.7
*ri*MP	likkalaalaklni	1479.9	1479.1
TAM-MP	TAM-INLKALAALAKKIL	1892.4	1892.9
TAM-*i*MP	TAM-inlkalaalakkil	1892.4	1892.9
TAM-*r*MP	TAM-LIKKALAALAKLNI	1892.4	1893.2
TAM-*ri*MP	TAM-likkalaalaklni	1892.4	1893.3
Mitoparan (MitP) analogues			
MitP	INLKKLAKL(Aib)KKIL	1608.1	1608.9
*i*MitP	inlkklakl(Aib)kkil	1608.1	1609.1
*r*MitP	LIKK(Aib)LKALKKLNI	1608.1	1609.1
*ri*MitP	likk(Aib)lkalkklni	1608.1	1609.6
TAM-MitP	TAM-INLKKLAKL(Aib)KKIL	2021.6	2021.4
TAM-*i*MitP	TAM-inlkklakl(Aib)kkil	2021.6	2021.2
TAM-*r*MitP	TAM-LIKK(Aib)LKALKKLNI	2021.6	2021.3
TAM-*ri*MitP	TAM-likk(Aib)lkalkklni	2021.6	2021.9

[a] L-Amino acids are denoted by capital letters and D-isomers are in lower case. Aib designates the known helix promoter α-amino-isobutyric acid. To enable both quantitative and qualitative uptake analysis, each peptide analogue was N-terminally extended with 6-carboxytetramethylrhodamine (TAMRA; TAM). The calculated masses (average M + H^+) of all peptides were confirmed to an accuracy of $\pm$1 by MALDI time of flight mass spectrometry (Kratos Kompact *Probe* operated in positive ion mode).

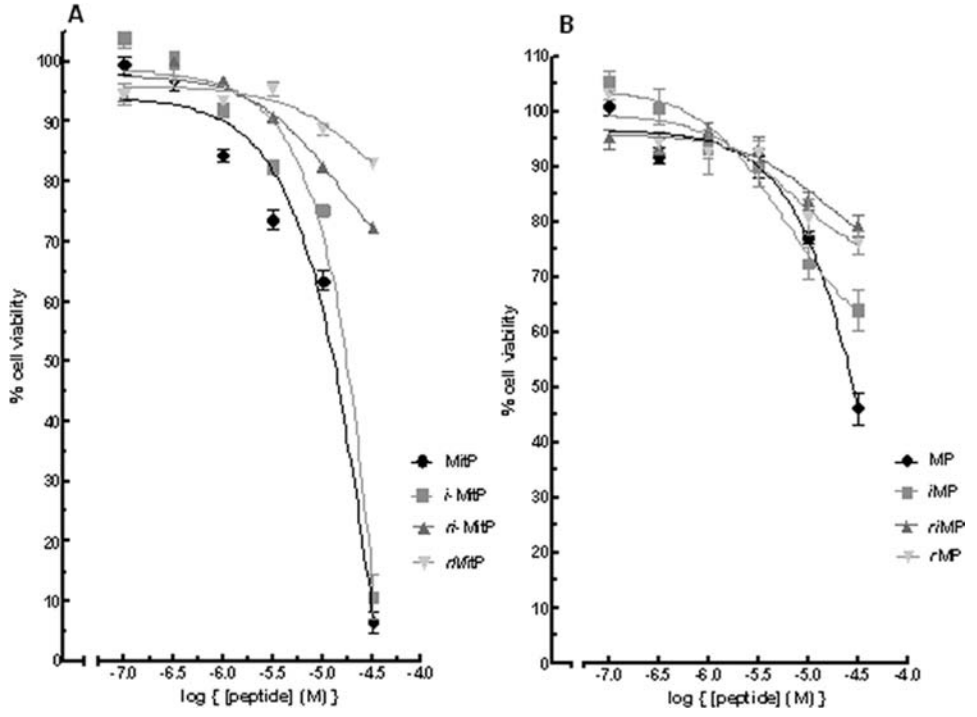


Figure 1. Comparative cytotoxicity of peptides and peptidomimetics. U373MG cells were treated with enantiomeric analogues of MitP (A) and MP (B) for 24 h at the concentrations indicated. Cell viability was measured by MTT conversion and expressed as a percentage of those cells treated with vehicle (medium) alone. Data points are mean $\pm$ SEM from 3 experiments performed in quadruplicate.

dx.doi.org/10.1021/bc2002924 | *Bioconjugate Chem.* 2012, 23, 47–56

Table 2. Biological Activities of Enantiomeric Analogues of MP and MitP[a]

Peptide	Efficacy Indices		Potencies		Translocation Efficacies
	Cytotoxicity	Secretion	Cytotoxicity (LD_{50})	Secretion (EC_{50})	
MP	1	1	28.67 μM	21.54 μM	15.82
***i*MP**	0.67	1.46	45.92 μM	13.31 μM	100.0
***r*MP**	0.44	0.25	95.46 μM	>100 μM	9.762
***ri*MP**	0.38	0.50	80.40 μM	41.56 μM	7.990
MitP	1.85	4.32	9.44 μM	7.53 μM	82.21
***i*MitP**	1.66	3.18	13.95 μM	15.30 μM	63.06
***r*MitP**	0.31	0.76	>100 μM	>100 μM	14.75
***ri*MitP**	0.52	0.68	67.15 μM	>100 μM	23.23

[a]Efficacy indices express the above basal activities of peptide analogues as a fraction of that of MP determined at a peptide concentration of 30 μM. LD_{50} values represent the concentration of peptides required to induce 50% cell death of U373MG astrocytoma. EC_{50} values represent the concentration of peptides required to induce 50% secretion of β-hexoseaminidase from RBL-2H3 cells. Translocation efficacies represent normalized data of mean intracellular fluorescence (minus background) of TAMRA-labelled peptide analogues.

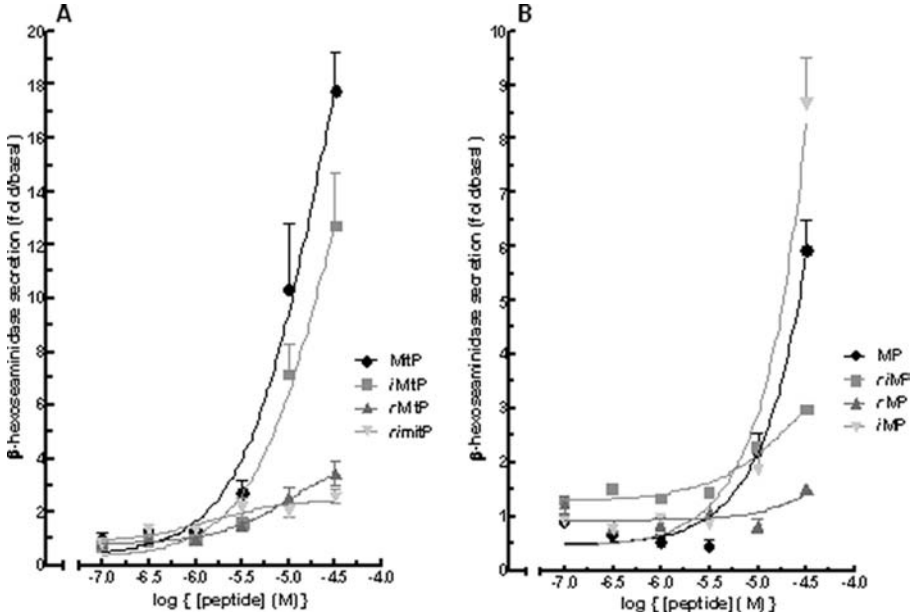


Figure 2. Comparative secretory activity of enantiomeric analogues. RBL-2H3 cells were treated with analogues of MitP (A) and MP (B) for 15 min at the concentrations indicated. Data points are mean ± SEM from 3 experiments performed in quadruplicate.

Additional peptide homologues of MitP and MP were synthesized in retro (reverse sequence), inverso (all D-amino acids) and retro-inverso (all D-amino acids in reverse sequence) orientations (Table 1).

To facilitate quantitative uptake and intracellular localization studies, N-terminal acylation of MP and MitP analogues with 6-carboxytetramethylrhodamine (TAMRA) produced highly fluorescent peptides (Table 1).

C-terminally amidated peptides were manually synthesized employing an *N*-α-Fmoc protection strategy and masses were confirmed by matrix-assisted laser desorption ionization (MALDI) time-of-flight mass spectrometry (Table 1).

Comparative Cytotoxicity of Peptides and Peptidomimetics. The highly potent MP analogue MitP translocates plasma membranes to target mitochondria and enhances mitochondria permeability with a subsequent induction of apoptotic events.[16] Thus, the cytotoxic effects of retro-inverso, retro, and inverso transformation of MitP were evaluated and MTT conversion used as a measure of cell viability. In accordance with previous reports, MitP, induced a concentration-dependent decrease in U373MG astrocytic tumor cell viability (Figure 1A) to give an LD_{50} of 9.44 μM and a cytotoxic efficacy index of 1.85 relative to MP (Table 2). Only a minor reduction in potency and efficacy, to give an LD_{50} of 13.95 μM and cytotoxic efficacy index of 1.66, was observed for the inverso analogue *i*MitP (Figure 1A, Table 2). In contrast, retro and retro-inverso transformation dramatically reduced the cytotoxic potencies of *r*MitP (LD_{50} > 100 μM) and *ri*MitP (LD_{50} = 67.15 μM). Thus, the rank order of cytotoxic potencies were MitP > *i*MitP > *ri*MitP > *r*MitP. Similarly, cytotoxicity efficacy indices followed the same rank order (Table 2).

Though MP has been reported to facilitate mitochondrial permeability transition in cell free systems,[27] in living cellular systems the cytotoxic activity of MP is more than likely induced by random membrane perturbations, particularly at higher peptide concentrations. Thus, MP dose-dependently reduced U373MG cell viability with an LD_{50} of 28.67 μM. Figure 1B and Table 2 show that inverso, retro, and retro-inverso transformation of MP reduced the cytotoxic potencies of the parent compound to give a rank order of potency of MP > *i*MP > *ri*MP > *r*MP. Cytotoxicity efficacy indices followed a similar rank order, MP > *i*MP > *r*MP > *ri*MP.

dx.doi.org/10.1021/bc2002924 | *Bioconjugate Chem.* 2012, 23, 47−56

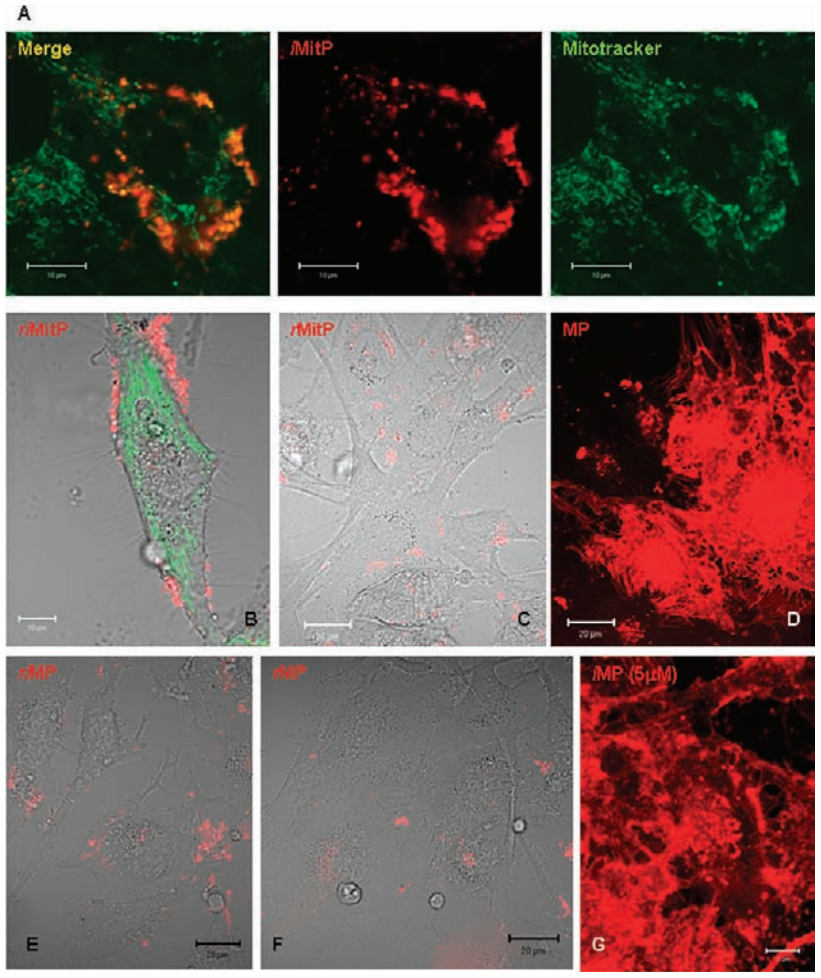


Figure 3. Differential intracellular distribution of enantiomeric MitP and MP analogues. U373MG cells were treated with 5 μM TAMRA-labeled peptides with or without 200 nM Mitotracker Green FM for 1 h and viewed by confocal live cell imaging. For MitP analogues, only the inverso analogue TAM-iMitP demonstrated cellular penetration and mitochondrial colocalization (A), whereas TAM-riMitP being restricted here to the outer plasma membrane (B) and TAM-rMitP (C) lacked efficient cell penetrant properties. For MP analogues, TAM-MP (D) appeared to predominantly localize with the plasma membrane, whereas TAM-riMP (E) and TAM-rMP (F) demonstrated minimal staining of the plasma membrane. In contrast when administered at 5 μM, TAM-iMP demonstrated both a high intensity staining of membranes and cytosolic structures (G). Confocal images for B, C, E, and F are presented here merged with images taken under transmission differential interference contrast so as to assist with visualization of subcellular distribution.

Comparative Peptide-Induced Secretion of β-Hexoseaminidase from RBL-2H3 Cells. Secretion of inflammatory mediators from mast cells is a well-defined action of MP and a component of the acute inflammatory response produced by wasp venom.[1−4] Thus, secretion of β-hexoseaminidase from the rat basophilic leukemia cell line RBL-2H3, a widely used cellular model for the study of secretory mucosal mast cells,[5,28] was used to evaluate the effects of enantiomeric transformation on MP and MitP. We have previously reported[13] that MitP demonstrates an enhanced secretory efficacy to that of MP (Table 2). Accordingly, the secretory potency of MitP was enhanced to give an EC_{50} of 7.53 μM compared to 21.54 μM for MP and a secretory efficacy of 4.32. Similar to the comparative cytotoxic observations for MitP, inverso transformation of MitP produced only minor reductions in secretory potency (15.30 μM) and efficacy (3.18), whereas *ri*MitP and *i*MitP were biologically inactive (Figure 2A, Table 2).

Inverso transformation slightly enhanced the secretory efficacy (1.46) and potency (13.31 μM) of MP, whereas retro and retro-inverso transformation reduced both secretory potency and efficacy giving a rank order of *i*MP > MP > *ri*MP > *r*MP, with *r*MP being biologically inactive (Figure 2B, Table 2).

Comparative Analysis of Qualitative and Quantitative Uptake. The mitochondriotoxic CPP MitP demonstrates an enhanced propensity for cellular penetration compared to well-characterized CPP such as penetratin.[29] Accordingly, MitP gave a translocation efficacy of 82.21 compared to that of 27.76 for penetratin (Table 2). Given that MitP translocates plasma membranes to colocalize with mitochondria,[16] other MitP analogues were evaluated for their cell penetrant ability and degree of mitochondrial colocalization using confocal live cell imaging and quantitative uptake analysis of intracellular fluorescence. Figure 3A shows that following 1 h incubation, only the inverso analogue, TAM-*i*MitP (5 μM), assumed a distinct colocalization with mitochondrial membranes of U373MG cells (overlap coefficient after Manders = 1.00 $\pm$ 0), an observed subcellular localization that is in accordance with (1) the ability of *i*MitP to induce cell death of U373MG cells with a similar potency and efficacy to that of MitP (Figure 1A, Table 2) and (2) the ability of *i*MitP to demonstrate a propensity for cellular penetration comparable to that of MitP with an efficacy index of 63.06

dx.doi.org/10.1021/bc2002924 | *Bioconjugate Chem.* 2012, 23, 47−56

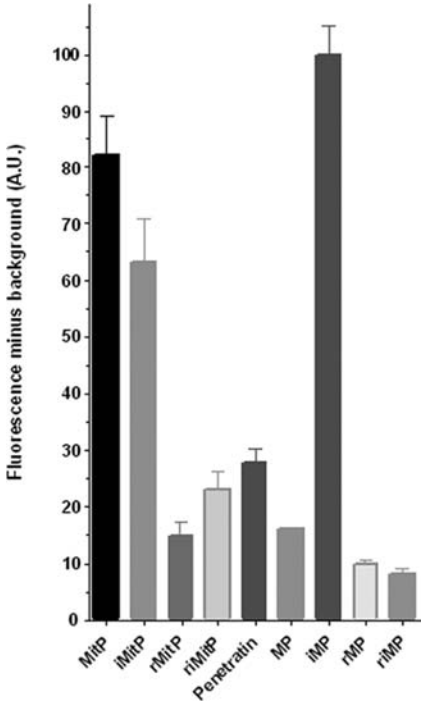


Figure 4. Comparative analysis of translocation efficacies of enantiomeric peptide analogues. U373MG cells were incubated with TAMRA-labeled peptides (5 μM) for 1 h at 37 °C. Normalized data are expressed as mean fluorescence (minus background) ± SEM from 3 experiments performed in quadruplicate.

(Figure 4, Table 2). In contrast and under identical experimental conditions, cellular penetration was minimal for *r*Mit (Figure 4, Table 2). Though quantitative uptake analysis (Figure 4, Table 2) demonstrated that *ri*MitP was moderately penetrant, with a translocation efficacy of 23.23, live confocal cell imaging analysis clearly demonstrates that TAM-*ri*MitP is largely confined and restricted to the plasma membrane (Figure 3B).

Confocal analyses further confirmed that MP and its related retro and retro-inverso analogues was poorly cell-penetrant and that TAM-MP strongly colocalized with the plasma membrane (Figure 3D). In contrast, following 1 h incubation, *i*MP demonstrated an enhanced propensity for cellular penetration, exceeding that for MitP (Figure 4, Table 2). However, at an extracellular concentration of 5 μM, TAM-*i*MP strongly labeled both the plasma membranes and intracellular organelles to a high signal intensity (Figure 3G). U373MG cells were therefore treated with a reduced peptide concentration of 1 μM TAM-*i*MP. Figure 5A clearly shows that TAM-iMP assumed an intracellular distribution, while adopting a punctuate distribution which partly colocalized with lysosomal structures. Indeed, colocalization coefficient analyses further demonstrated that 62% of intracellular TAM-*i*MP was coincident with these structures. Moreover, the CPP transportan, a chimeric analogue of MP, has been shown[30] with time to accumulate in vesicles of nonacidic pH. TAM-*i*MP was therefore tested for its ability to colocalize with pH neutral lysosomal structures. Figure 5B shows that, following 1 h, a proportion (43%) of TAM-*i*MP containing vesicles are within pH neutral lysosomes. More significantly, however, after 24 h TAM-*i*MP assumed a predominant colocalization (81%) with pH neutral lysosomes (Figure 5C).

***i*MP as a Highly Cell Penetrant Peptide.** Given that both quantitative and qualitative uptake analysis identified *i*MP as a highly penetrative sequence and biologically inactive below 3 μM, this all-D analogue was further characterized by concentration- and time-dependent intracellular uptake studies and compared to the well-characterized CPPs penetratin and tat. Figure 6A demonstrates a concentration-dependent intracellular uptake of *i*MP into U373MG cells. With an uptake efficacy of 100.00, *i*MP at a concentration of 5 μM, markedly exceeded that of both penetratin (32.71) and tat (12.24). Moreover, Figure 6B shows a time-dependent intracellular uptake of *i*MP (5 μM). Data were analyzed using GraphPad *Prism* 5 software and demonstrated that internalization of *i*MP, penetratin, and tat occurred with first-order saturable kinetics ($F = F_{max} \times t/t_{0.5} + t$). With a half-life ($t_{0.5}$) of 10.16 min and a maximum signal intensity (F_{max}) of 115.60, *i*MP demonstrated improved uptake kinetics compared to penetratin (F_{max} = 55.20, $t_{0.5}$ = 27.55) and tat (F_{max} = 17.43, $t_{0.5}$ = 10.30).

The parallel artificial membrane permeability assay (PAMPA) was used as a non-cell-based assay to assess passive permeability and direct membrane translocation of selected peptides across an artificial membrane incorporating phosphatidylcholine. *i*MP (0.1553 × 10^6 cm/s), MP (0.1165 × 10^6 cm/s), and MitP (0.0855 × 10^6 cm/s) demonstrated high apparent permeability values (P_{app}) compared to those for penetratin (0.0143 × 10^6 cm/s) and tat (0.0027 × 10^6 cm/s) (Figure 7). *ri*MP, *r*MP, *r*MitP, and *ri*MitP demonstrated no ability for passive diffusion.

Pearson correlation analysis (two-tailed, using GraphPad *Prism* 5) was used to determine whether passive permeability and translocation efficacy in living cellular systems were significantly related. Figure 8 includes P_{app}s of all peptides in this study plotted against their translocation efficacies. When analysis was restricted to analogues of MP and MitP, there was no significant relationship between passive permeability and translocation efficacy (R^2 = 0.4316, p = 0.0767). When penetratin and tat were included in the analysis, a positive correlation was observed though an R^2 value of 0.4564 indicated that only 45.64% of the variance in Y could be explained by a variation in X (p = 0.0320).

DISCUSSION

The major aim of this study was to evaluate the structure activity relationships of enantiomeric analogues of the tetradecapeptides MP and MitP. As indicated below, our findings do not support the contention that retro-inverso transformation is compatible with the bioactives of relatively short helical peptides. Moreover, we have identified *i*MP as a highly efficient CPP that could have widespread utility for the design of both inert CPP vectors and biologically active peptides.

Inverso Transformation Retains the Biological Activities of MitP and MP. To our surprise, complete retro-inverso transformation of MitP abrogated the biological activities associated with this peptide including the induction of apoptotic events and the secretion of inflammatory mediators. Similarly, retro-inverso transformation severely diminished the propensity of MitP to penetrate the plasma membrane. In contrast, the inverso analogue *i*MitP demonstrated a strong propensity for cellular penetration, a high degree of mitochondrial colocalization, while retaining the apoptogenic activity of its parent analogue. More significantly, all synthesized D-isomers of both peptides, MitP and MP, retained their associated biological activities. *i*MP like its parent homologue retained its ability, albeit at higher concentrations, to induce secretion of β-hexosaminidase and reduce cell viability, whereas the retro-inverso analogue was largely inactive. Given that *i*MitP is composed of all D-amino

dx.doi.org/10.1021/bc2002924 | *Bioconjugate Chem.* 2012, 23, 47–56

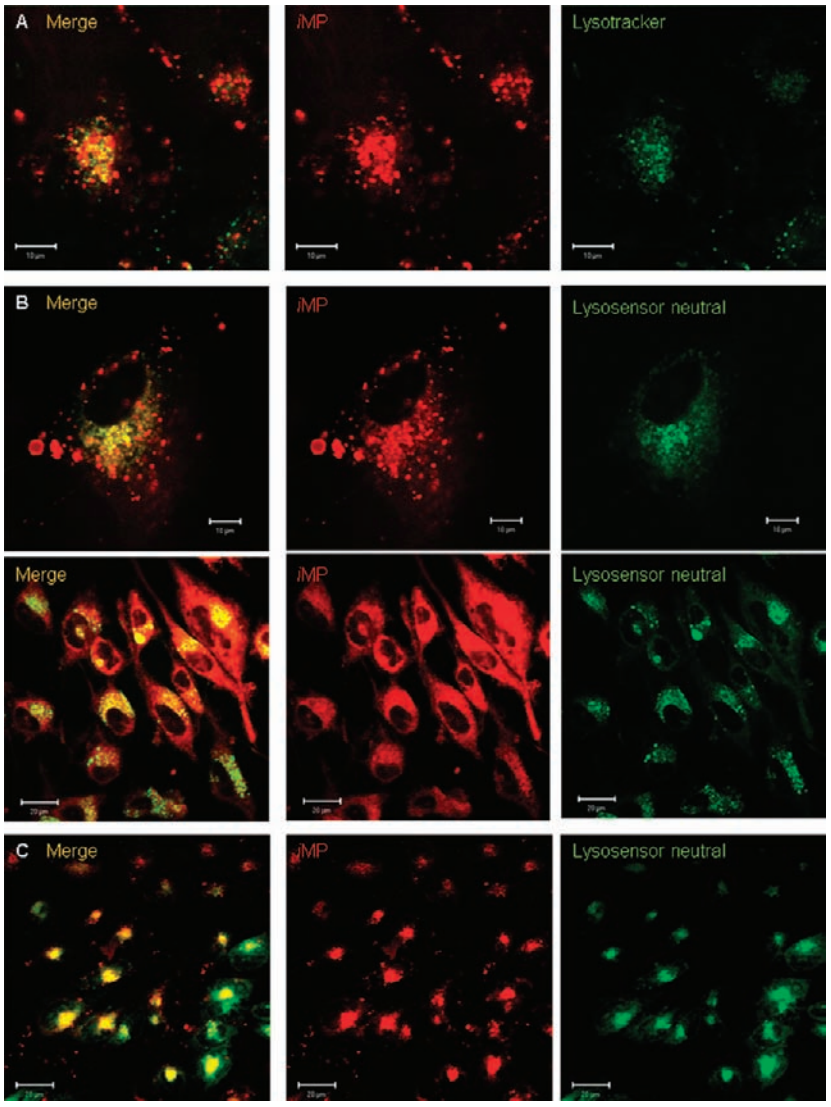


Figure 5. Accumulation of the highly cell penetrant all D-amino acid MP analogue iMP in lysosomes. U373MG cells were incubated with 1 μM TAMRA-labeled iMP, 75 nM Lysotacker Green DND-26, a generalized lysosomal stain for acid organelles, or 1 μM Lysosensor Green DND-153, a pH-dependent lysosomal stain (pK_a 7.5) specific for pH neutral lysosomal structures and visualized by live confocal cell imaging. Following 1 h incubation, TAM-iMP demonstrated a predominant lysosomal distribution (A) with some TAM-iMP containing vesicles being localized to pH neutral structures (B). Following 24 h incubation, intracellular presence of TAM-iMP was still evident with the peptide being predominantly located within pH neutral lysosomes (C).

acids, it would therefore not be presumptuous to conclude that *i*MitP is a potential protease-resistant apoptogenic peptide.

It is noteworthy that analysis of quantitative uptake data alone could be misleading when evaluating the penetrative features of MP analogues. Trypsinization merely removes membrane-bound peptide. Since MP embeds within the outer cell membrane, trypsinization alone is insufficient to remove this nonpenetrant peptide. This phenomenon is further confounded by the fact that D-amino acid containing peptides are resistant to trypsinzation. This anomaly is typified by the observation that *ri*MitP, while giving a modest uptake efficacy of 23.23, is sequestered at the plasma membrane, an observation that only live confocal cell imaging can determine.

***i*MP as a Highly Efficacious and Protease-Resistant CPP.** Of all analogues tested, *i*MP demonstrated the highest translocation efficacy, exceeding even that of MitP. Moreover, *i*MP displayed much improved uptake kinetics compared to the commonly employed CPP vectors penetratin and tat. More significantly, at a concentration of 3 μM or below, *i*MP is devoid of the biological activity of MP such as mast cell degranulation and perturbation of biological membranes. Moreover, even after 24 h of exposure and at an application dose of 3 μM *i*MP, both mitochondrial integrity and cellular viability of U373MG cells were unaffected. These data thus propound the utility of *i*MP as a potential CPP.

As previously stated, the CPP transportan is a chimeric analogue of MP and temporal analysis of its intracellular destination has shown that a significant percentage of this peptide accumulates in vesicles of nonacidic pH.[30] Data presented herein also demonstrate that, following 1 h incubation, 43% TAM-*i*MP colocalize with pH neutral lysosomes, and after 24 h incubation, TAM-*i*MP assumes a predominant colocalization (81%) with pH neutral lysosomes. As a point of conjecture, CPPs that avoid complete entrapment within acidic vesicles are of great utility. If we assume that endocytotic uptake, particularly at low concentrations of CPP, is indeed the predominant mechanism of

dx.doi.org/10.1021/bc2002924 | *Bioconjugate Chem.* 2012, 23, 47–56

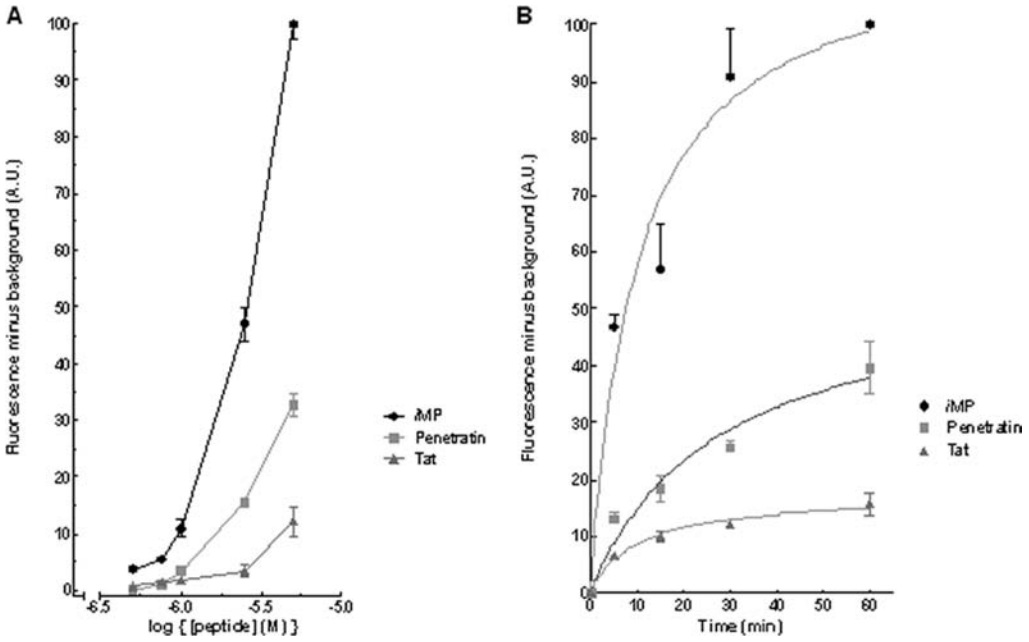


Figure 6. iMP as a highly penetrant peptide. (A) Concentration-dependent uptake of iMP as compared to the well-characterized CPP penetratin and tat. U373MG cells were treated with TAMRA-labeled peptides for 1 h at 37 °C at the concentrations indicated. (B) Temporal intracellular accumulation of iMP as compared to penetratin and tat. U373MG cells were incubated at 37 °C with TAMRA-labeled peptides (5 μM) for the times indicated. For both parts A and B, normalized data are expressed as mean fluorescence (minus background) ± SEM from 3 experiments performed in triplicate.

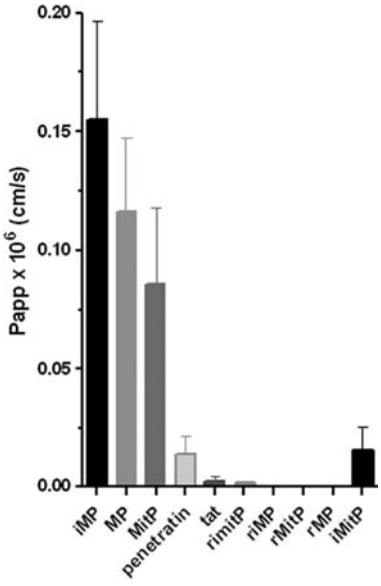


Figure 7. Apparent permeability (P_{app}) of selected peptides using the parallel artificial membrane permeability assay (PAMPA). Data points are mean ± SEM from 5 experiments performed in quintuplicate.

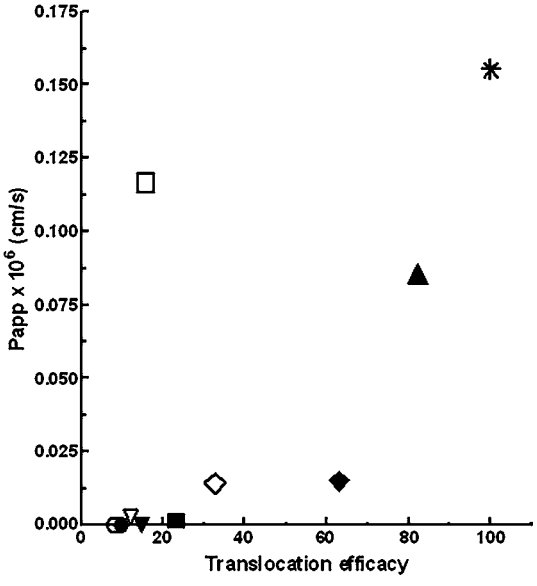


Figure 8. Correlation analysis between passive permeability and translocation efficacy. Data points are riMP (open circle), rMP (closed circle), tat (inverted open triangle), rMitP (inverted closed triangle), MP (open square), riMitP (closed square), penetratin (open diamond), iMitP (closed diamond), MitP (closed triangle), and iMP (star).

intracellular accumulation, then a pH-dependent lysosomal environment is imperative not only to the longevity of the CPP, but also to its escape and final desired destination. Such a hypothesis was proposed by Raagel et al.[30] in a study that investigated the temporal destination of 3 commonly used CPPs, poly Arg, tat, and transportan. Unlike observations with other CPPs investigated, a significant percentage of pH neutral lysosomes contained transportan. Given that acidic lysosomal compartments are detrimental to the future utility of CPP owing to inevitable proteolysis and degradation, Raagel et al.[30] proposed that peptide accumulation in pH neutral lysosomes may offer a feasible "escape route" for transportan-based CPPs. Data presented indicate that *i*MP not only escapes entrapment within acidic organelles, but being composed of all D-amino acids is also spared from proteolysis, as evidenced by its intracellular distribution 24 h after exogenous application. It is noteworthy that, in part, intracellular uptake of transportan and its deletion analogue TP10 is mediated by caveolin-dependent endocytosis,[31] an apt finding since caveolar-mediated endocytosis, entailing

dx.doi.org/10.1021/bc2002924 | *Bioconjugate Chem.* 2012, 23, 47–56

caveolae "pinch off" and the formation of nondegrative endocytic organelles, provides a nonacidic nonproteolytic means for intracellular delivery.[32−34] However, data presented herein indicate that *i*MP is still largely confined to lysosomal structures, albeit those of neutral pH. Thus, a very realistic application for this highly penetrant MP analogue could be its substitution for the MP component of TP10 in an attempt to enhance the penetrative propensity of this deletion analogue of transportan.[18] More specifically, *i*MP could be a useful component of stearylated TP10 analogues that avoid endosomal entrapment and have recently been shown to facilitate the delivery of oligonucleotides[35] and plasmids.[36]

Two-Compartment Model of CPP Accretion. The membrane mimetic PAMPA assay was used as a simple approach to initially distinguish those CPP that were capable of direct membrane translocation from those that required interaction with membrane-associated moieties such as glucoseaminoaglycans.[37] Compared to penetratin and even more so tat, MP and its analogues *i*MP and MitP demonstrated relatively high apparent permeability values (P_{app}). However, this is perhaps not so surprising owing to their adopted amphipathic α-helical structure within lipid environments.[38,39] Furthermore, confocal analyses with live cells (Figure 3D) indicated that MP adopts a predominant plasma membrane localization and is a more true depiction of its cellular destination since MP is widely reported to incorporate into plasma membranes to target heterotrimeric G proteins.[10,12]

Only a weak correlation was calculated between uptake efficacy in living cellular systems and P_{app} across an artificial membrane composed of phosphatidyl choline. These data, and a predominance of published observations, indicate that two relatively independent processes determine the accumulation of polycationic CPPs at intracellular sites. First, uptake across the plasma membrane (PM) is dependent upon direct translocation, as is mostly evident with amphipathic α-helical structures and endocytosis, as reported for nonhelical polycationic CPP such as tat, or a combination of both mechanisms. Second, the consequence of CPPs binding to intracellular targets, or accumulating within intracellular organelles, facilitates a more discrete accretion and a distinct intracellular localization. This hypothesis is no more exemplified than in the case of MP, which adopts an amphipathic α-helical structure in membrane environments. Thus, in a pure membrane mimetic environment such as the PAMPA assay, MP demonstrates a relatively large P_{app}. However, in living cells MP incorporates into the PM but subsequently binds heterotrimeric G proteins and other protein targets on the cytosolic side of the PM. This accounts for observations of MP's relatively low uptake efficacy into live cells and a final destination mostly confined to the PM as determined by confocal live cell imaging analyses.

MitP is clearly capable of direct membrane translocation owing to its relatively high P_{app}. Moreover, and unlike MP, MitP subsequently redistributes to specifically bind mitochondria.[6] Similarly and as a point of conjecture, *i*MP, demonstrating a high propensity for passive diffusion, translocates the PM to bind and colocalize within membrane-associated cholesterol-rich compartments that progress to form caveosomes of neutral pH.

This model of CPP uptake provides an interesting caveat and feasible rationale to explain why CPP-bioconjugates often adopt different uptake mechanisms from that of the CPP vector alone. For example, tat predominantly enters the cell through endocytotic mechanisms, and endosomal entrapment has proven particularly problematic for tat-mediated delivery of oligonucleotides. However, tat-mediated delivery of nuclear-targeting pro-apoptogenic peptides has demonstrated a certain degree of success[40,41] and therefore suggests that CPP-bioconjugates may facilitate differential protein targeting to that of the CPP and thus escape endosomal entrapment. Moreover, there are numerous examples of successful modulation of intracellular biology using CPP bioconjugates that have escaped endosomal confinement, which can be no more exemplified by the TP10-mediated delivery of bioactive peptide cargoes for the successful intracellular modulation of protein kinase C and p42/44 mitogen active protein kinases.[42,43] Many more examples are evident but beyond the scope of this paper.

In summary, all D-isomers of MP and MitP retain their associated biological activities, while retro-inverso transformation renders these peptides inactive. During the course of this SAR study, *i*MP demonstrated an enhanced propensity for cellular penetration and thus propounds its utility as either a novel CPP or as a component of pre-existing CPP constructs.

AUTHOR INFORMATION

Corresponding Author

*E-mail: S.Jones4@wlv.ac.uk. Tel: 01902 321130.

ABBREVIATIONS:

CPP, cell penetrating peptide; Fmoc, *N*-(9-Fluorenylmethoxycarbonyl); MALDI, matrix-assisted laser desorption ionization; MP, mastoparan; *i*MP, inverso MP; *r*MP, retro MP; *ri*MP, retro-inverso MP; MitP, mitoparan; *i*MitP, inverso MitP; *r*MitP, retro MitP; *ri*MitP, retro-inverso MitP; MTT, 3-(4,5-dimethylthazol-2-yl)-2,5-diphenyl tetrazolium bromide; PAMPA, parallel artificial membrane permeability assay; PM, plasma membrane; TAMRA (TAM), 6-carboxytetramethylrhodamine; TP10, transportan 10

REFERENCES

(1) Hirai, Y., Yasuhara, T., Yoshida, H., Nakajima, T., Fujino, M., and Kitada, C. (1979) A new mast cell degranulating peptide "mastoparan" in the venom of Vespula lewisii. *Chem. Pharm. Bull. (Tokyo) 27*, 1942−1944.

(2) Soomets, U., Hällbrink, M., Zorko, M., and Langel, Ü. (1997) From galanin and mastoparan to galparan and transportan. *Curr. Top. Pept. Prot. Res. 2*, 83−113.

(3) Jones, S., and Howl, J. (2006) Biological applications of the receptor mimetic peptide mastoparan. *Curr. Protein Pept. Sci. 7*, 501−508.

(4) Jones, S., and Howl, J. (2009) *Mastoparans. Bioactive Peptides* (Howl, J., and Jones, S., Eds.) pp 429−445, Chapter 18, CRC Press, Boca Raton.

(5) Farquhar, M., Soomets, U., Bates, R.,L., Martin, A., Langel, Ü., and Howl, J. (2002) Novel mastoparan analogs induce differential secretion from mast cells. *Chem. Biol. 9*, 63−70.

(6) Pooga, M., Hällbrink, M., Zorko, M., and Langel, Ü. (1998) Cell penetration by transportan. *FASEB J. 12*, 67−77.

(7) Langel, Ü., Pooga, M., Kairane, C., Zilmer, M., and Bartfai, T. (1996) A galanin-mastoparan chimeric peptide activates the Na^+,K^+-ATPase and reverses its inhibition by oubain. *Regul. Pept. 62*, 47−52.

(8) Longland, C. L., Mezna, M., Langel, Ü., Hällbrink, M., Soomets, U., Wheatley, M., Michelangeli, M., and Howl, J. (1988) Biochemical mechanisms of calcium mobilisation induced by mastoparan and chimeric hormone-mastoparan analogues. *Cell Calcium 24*, 27−34.

(9) Chahdi, A., Choi, W. S., Kim, Y. M., and Beaven, M. A. (2003) Mastoparan selectively activates phospholipase D2 in cell membranes. *J. Biol. Chem. 278*, 12039−12045.

(10) Higashijima, T., Burnier, J., and Ross, E. M. (1990) Regulation of G_i and G_o by mastoparan, related amphiphilic peptides and hydrophobic amines. *J. Biol. Chem. 265*, 14176−14186.
(11) Oppi, C., Wagner, T., Crisari, A., Camerini, B., and Valentini, G. P. T (1992) Attenuation of GTPase activity of recombinant $G_o\alpha$ by peptides representing sequence permutations of mastoparan. *Proc. Natl. Acad. Sci. U.S.A. 89*, 8268−8277.
(12) Sukumar, M., and Higashijima, T. (1992) G protein-bound conformation of mastopran-X, a receptor mimetic peptide. *J. Biol. Chem. 267*, 21421−21424.
(13) Jones, S., and Howl, J. (2004) Charge delocalisation and the design of novel mastoparan analogues: enhanced cytotoxicity and secretory efficacy of [Lys^5,Lys^8,Aib^{10}]MP. *Regul. Pept. 121*, 121−128.
(14) Karle, I. L. (2006) Helix-promoters, non-natural residues, retro-peptides and non-peptidic inserts. In *Peptides: Chemistry, Structure and Biology* (Kaumaya, P. T. P., and Hodges, R. S., Eds.) pp 543−545, Chapter 224, Mayflower Scientific Ltd, Kingswinford.
(15) Liu, S., Wang, F., Tang, L., Gui, W., Cao, P., Liu, X., Poon, A. W., Shaw, P. C., and Jiang, T. (2007) Crystal structure of mastoparan from Polistes jadwagae at 1.2 Å resolution. *J. Struct. Biol. 160*, 28−34.
(16) Jones, S., Martel, C., Belzacq-Casagrande, A. S., Brenner, C., and Howl, J. (2008) Mitoparan and target-selective chimeric analogues: Membrane translocation and intracellular redistribution induces mitochondrial apoptosis. *Biochim. Biophys. Acta 1783*, 849−863.
(17) Pooga, M., Hällbrink, M., Zorko, M., and Langel, Ü. (1998) Cell penetration by transportan. *FASEB J. 12*, 67−77.
(18) Soomets, U., Lindgren, M., Gallet, X., Hällbrink, M., Elmquist, A., Balaspiri, L., Zorko, M., Pooga, M., Brasseur, R., and Langel, Ü. (2000) Deletion analogues of transportan. *Biochim. Biophys. Acta 1467*, 165−176.
(19) Chorev, M., and Goodman, M. (1993) A dozen years of retro-inverso peptidomimetics. *Acc. Chem. Res. 26*, 266−273.
(20) Chorev, M., and Goodman, M. (1996) Recent developments in in retro peptides and proteins - an ongoing topochemical explanation. *Trends Biotechnol. 13*, 438−445.
(21) Passante, E., and Frankish, N. (2009) The RBL-2H3 cell line: its provenance and suitability as a model for the mast cell. *Inflamm. Res. 58*, 737−745.
(22) Pontén, J., and Macintyre, E. H. (1968) Long term culture of normal and neoplastic human glia. *Acta Pathol. Microbiol. Scand. A 74*, 465−486.
(23) Carmichael, J., DeGraff, W. G., Gazdar, A. F., Minna, J. D., and Mitchell, J. B. (1987) Evaluation of tetrazolium-based semiautomated colorimetric assay. Assessment of chemosensitivity testing. *Cancer Res. 47*, 936−942.
(24) Holm, T., Johansson, H., Lundberg, P., Pooga, M., Lindgren, M., and Langel, Ü. (2006) Studying the uptake of cell-penetrating peptides. *Nat. Protoc. 1*, 1001−1005.
(25) Seo, P. R., Teksin, Z. S., Kao, J. P. Y, and Polli, J. E. (2006) Lipid composition effect on permeability across PAMPA. *Eur. J. Pharm. Sci. 29*, 259−268.
(26) Howl, J., Prochazka, Z., Wheatley, M., and Slaninova, J. (1999) Novel strategies for the design of receptor-selective vasopressin analogues: Aib-substitution and retro-inverso transformation. *Br. J. Pharmacol. 128*, 647−652.
(27) Pfeiffer, D. R., Gudz, T. I., Novgorodov, S. A., and Erdahl, W. L. (1995) The peptide mastoparan is a potent facilitator of the mitochondrial permeability transition. *J. Biol. Chem. 270*, 4923−4932.
(28) Isersky, C., Metzger, H., and Buell, D. N. (1975) Cell cycle-associated changes in receptors for IgE during growth and differentiation of a rat basophilic leukemia cell line. *J. Exp. Med. 141*, 1147−1162.
(29) Jones, S., Holm, T., Mager, I., Langel, U., and Howl, J. (2010) Characterization of bioactive cell penetrating peptides from human cytochrome c: Protein mimicry and development of a novel apoptogenic agent. *Chem. Biol. 17*, 735−744.
(30) Raagel, H., Saalik, P., Hansen, M., Langel, U., and Pooga, M. (2009) CPP-protein constructs induce a population of non-acidic vesicles during trafficking through endo-lysosomal pathway. *J. Controlled Release 139*, 108−117.
(31) Saalik, P., Padari, K., Niinep, A., Lorents, A., Hansen, M., Jokitalo, E., Langel, U., and Pooga, M. (2009) Protein delivery with transportans is mediated by calveolae rather than flotillin-dependent pathways. *Bioconjugate Chem. 20*, 877−887.
(32) Pelkmans, L., and Helenius, A. (2002) Endocytosis via Caveolae. *Traffic 3*, 311−320.
(33) Pelkmans, L., Burli, T., Zerial, M., and Helenius, A. (2004) Caveolin-stabilized membrane domains as multifunctional transport and sorting devices in endocytic membrane traffic. *Cell 118*, 767−780.
(34) Rejman, J., Bragonzi, A., and Conese, M. (2005) Role of clathrin- and caveolae-mediated endocytosis in gene transfer mediated by lipo- and polyplexes. *Mol. Ther. 12*, 468−474.
(35) Mäe, M., El Andaloussi, S., Lundin, P., Oskolkov, N., Johansson, H. J., Guterstam, P., and Langel, U. (2009) A stearylated CPP for the delivery of splice correcting oligonucleotides using a non-covalent co-incubation strategy. *J. Controlled Release 134*, 221−227.
(36) Lehto, T., Simonson, O. E., Mäger, I., Ezzat, K., Sork, H., Copolovici, D. M., Viola, J. R., Zaghloul, E. M., Lundin, P., Moreno, P. M., Mäe, M., Oskolkov, N., Suhorutšenko, J., Smith, C. E., and El Andaloussi, S. (2011) A peptide-based vector for efficient gene transfer in vitro and in vivo. *Mol. Ther. 19*, 1457−1467.
(37) Lundin, P., Johansson, H., Guterstam, P., Holm, T., Hansen, M., Langel, U., and El Andaloussi, S. (2008) Distinct uptake routes of cell-penetrating peptide conjugates. *Bioconjugate Chem. 19*, 2535−2542.
(38) Higashijima, T., Wakamatsu, K., Takemitsu, M., Fujino, M., Nakajima, T., and Miyazawa, T. (1983) Conformational change of mastoparan from wasp venom on binding with phospholipid membrane. *FEBS Lett. 152*, 227−230.
(39) Hori, Y., Demura, M., Iwadate, M., Ulrich, A. S., Niidome, T., Aoyagi, H., and Asakura, T (2001) Interaction of mastoparan with membranes studied by ^{1}H-NMR spectroscopy in detergent micelles and by solid-state ^{2}H-NMR and ^{15}N-NMR spectroscopy in oriented lipid bilayers. *Eur. J .Biochem. 268*, 302−309.
(40) Snyder, E. L., Meade, B. R., Saenz, C. C., and Dowdy, S. F. (2004) Treatment of terminal peritoneal carcinomatosis by transducible p53-activating peptide. *PLoS Biol. 2*, 186−193.
(41) Baker, R. D., Howl, J., and Nicholl, I. D. (2007) A sychnologic cell penetrating peptide mimic of P21(WAF1/CIP1) is pro-apoptogenic. *Peptides 28*, 731−740.
(42) Howl, J., Jones, S., and Farquhar, M. (2003) Intracellular delivery of bioactive peptides to RBL-2H3 cells induces beta-hexosaminidase secretion and phospholipase D activation. *ChemBioChem 4*, 1312−1316.
(43) Jones, S., Farquhar, M., Martin, A., and Howl, J. (2005) Intracellular translocation of the decapeptide carboxyl terminal of $G_i3\alpha$ induces the dual phosphorylation of p42/p44 MAP kinases. *Biochim. Biophys. Acta 1745*, 207−214.

Bioconjugate Chemistry

Article

pubs.acs.org/bc

Bioconjugate of Lysozyme and the Antibacterial Marine Sesquiterpene Quinone Avarone and Its Derivatives

Irena Novaković,*[,†] Uroš Anđelković,[†,‡] Mario Zlatović,[§] Miroslav J. Gašić,[†,∥] and Dušan Sladić*[,§]

[†]IHTM, Center for Chemistry, University of Belgrade, Njegoševa 12, 11000 Belgrade, Serbia

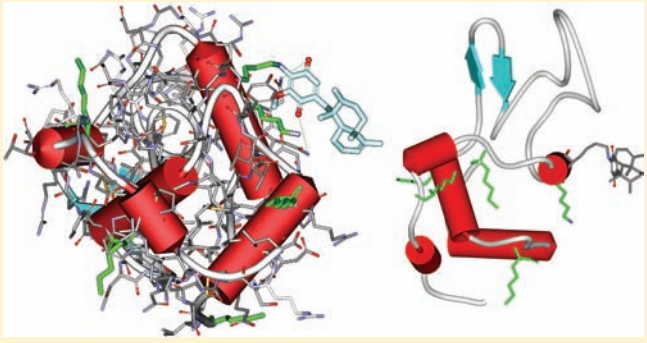
[‡]Institute of Medical Physics and Biophysics, University of Leipzig, Härtelstr. 16-18, D-04107 Leipzig, Germany

[§]Faculty of Chemistry, University of Belgrade, Studentski trg 12-16, 11000 Belgrade, Serbia

[∥]Serbian Academy of Sciences and Arts, Knez Mihailova 35, 11000 Belgrade, Serbia

Supporting Information

ABSTRACT: A conjugate of lysozyme with avarone, a bioactive sesquiterpene quinone of marine origin, and its three derivatives were synthesized. MALDI TOF mass spectral analysis and tryptic digestion showed that the only residue in lysozyme that was modified by all derivatives was lysine 97. The identity of the residue was in full correlation with the prediction obtained by molecular modeling. All bioconjugates preserved most of the enzymatic activity of lysozyme. The melting point of the conjugates was slightly increased in comparison to lysozyme, indicating a slight stabilization of structure. The antibacterial activity of all the conjugates to both Gram positive and Gram negative bacteria was stronger than the activity of either lysozyme or the quinones, the MIC values being in low micromolar range for some conjugates.



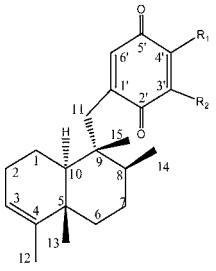
INTRODUCTION

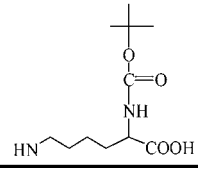
Lysozyme is a globular basic protein, present in almost all secretion body fluids and tissues of human and animal organisms.[1] It has also been isolated from some plants, bacteria, and bacteriophages.[2] Lysozyme monomer exhibits strong antibacterial activity against Gram-positive organisms.[3] This enzyme is widely used in the food industry[4] as a preservative for meat, fish, and their products, as well as for milk and dairy products and fruits and vegetables.[5] In pharmacy and medicine, it is used in the manufacture of adjuvant drugs for antibiotics in viral and bacterial infections, in treatment of leukemia and neoplastic diseases,[6] and also as a diagnostic agent, being an indicator of the occurrence and the progression of pathological changes in humans and animals.[7]

Various modifications of lysozyme caused changes in enzyme properties. Thermal modification induced formation of a dimeric form of lysozyme,[8,9] which exhibits antiviral and anti-inflammatory properties.[10] Many techiques have been used to modify enzyme surfaces and simultaneously modify enzyme properties. The most frequent is the covalent bonding of appropriate molecules to the enzyme's surface amino acids in order to improve lysozyme antibacterial activity.[11−13]

In this work, a modification of lysozyme with avarone[14] (**I**), a sesquiterpene quinone isolated from the marine sponge *Dysidea avara*,[15,16] and its derivatives (**Ia-c**) (Chart1) was performed. This quinone was selected because of its antibacterial activity, availability, and previous knowledge that it modifies predominantly lysine residues in proteins by nucleophilic addition (Scheme 1).[17,18] Such modifications are expected not to interfere much with the enzyme activity, since the mechanism of lysozyme is based on participation of carboxylic groups from aspartic and glutamic acid residues.

Chart 1. Structures of Quinones



	R_1	R_2
I	H	H
Ia	H	OCH_3
Ib	$NHCH_3$	H
Ic	H	$NHCH_3$
Id		H

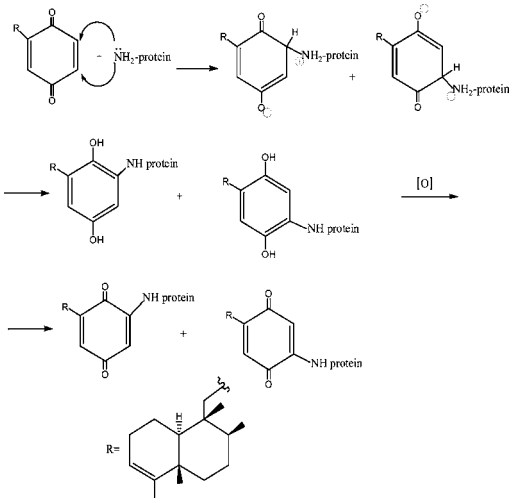
EXPERIMENTAL PROCEDURES

General Information. All reagents used were commercial products purchased from Merck and Sigma-Aldrich. Column chromatography was carried out on silica gel (0.063−0.200

Received: June 28, 2011
Revised: November 28, 2011
Published: December 9, 2011

 © 2011 American Chemical Society dx.doi.org/10.1021/bc200330m | *Bioconjugate Chem.* 2012, 23, 57−65

Scheme 1. Mechanism of Protein Amino Group Modification by Avarone



mm, Merck). Analytical thin-layer chromatography (TLC) was performed on precoated aluminum-backed plates (silica gel 60 F_{254}, Merck). ^{1}H and ^{13}C NMR spectra were recorded at 200 MHz (Oxford NMR YH) in deuterated methanol (CD_3OD). Chemical shifts are reported in parts per milion (ppm), relative to tetramethylsilane. Coupling constants are reported in hertz (Hz). Mass spectra were recorded on Mass Spectrometer 6210 Time-of-Flight LC-MS system (Agilent Technologies). $[\alpha]_D^{20}$ value was measured on Rudolph Research analytical polarimeter, Autopol IV. Elemental analysis was performed on Elementar Analysensysteme GmbH VARIO EL III CHNOS. Melting point was determined on Boetius PMHK. MALDI TOF mass spectra were recorded on Bruker Daltonics Autoflex MALDI-TOF mass spectrometer. The melting temperatures of lysozyme and its conjugates were measured using luminescence spectrometer LS 50 (Perkin-Elmer, USA). UV/vis spectra were recorded on CINTRA 40 UV/vis spectrometer.

3′-Methoxyavarone, 3′-(Methylamino)avarone, and 4′-(Methylamino)avarone. These were synthesized by previously published methods.[19,20]

*4′-((5-((tert-Butoxycarbonyl)amino)-5-carboxypentyl)-amino)avarone (**Id**).* Solutions of 80 mg avarone in 24 mL ethanol and 60 mg lysine-tBoc in 84 mL water were mixed, NH_4HCO_3 was added to a final concentration of 50 mM, and the mixture was left for 48 h at room temperature with stirring. The mixture was extracted with chloroform, and the chloroform solution was dried over anhydrous Na_2SO_4. After evaporation of chloroform, the raw product was purified by multiple column chromatography (silica gel, 0.063−0.200 mm, Merck) with toluene, chloroform, and methanol. The resulting compound was purified by preparative TLC chromatography using methanol affording 17 mg (40%) of pure product, mp 129−131 °C, $[\alpha]_D^{20} = -39$ (c 0.10; MeOH). Elemental analysis for $C_{32}H_{48}N_2O_6$ (MW = 556.7). Calcd. for C (69.04%), H (8.69%), N (5.03%). Found: C (69.01%), H (8.76%), N (4.97%). ^{1}H NMR (200 MHz, CD_3OD): δ 6.32 (s, 1H, C6′-H), 5.40 (s, 1H, C3′-H), 5.11 (bs, 1H, C3−H), 3.95 (bs, 1H, C5″-H), 3.13 (bs, 2H, C2″-H), 2.57 and 2.50 (dd, J = 6.6 Hz, 2H, C11−H), 1.51 (s, 3H, C12−H), 1.42 (s, 9H, C9″,C10″, C11″), 0.94 (d, 3H, C14−H), 0.85 (s, 3H, C15−H), 2.0−1.1 (complex signal). ^{13}C NMR (200 MHz, CD_3OD): δ_c 184.76 (C5′), 184.41 (C2′), 179.50 (C6″), 157.81 (C7″), 152.40 (C4′), 149.71 (C1′), 145.12 (C6′), 144.03 (C4), 133.25 (C3′), 121.61 (C3), 80.04 (C8″), 57.05 (C5″), 43.50 (C1″), 39.53 (C11), 38.44 (C4″), 37.46 (C8), 36.04 (C5), 33.87 (C9), 30.74 (C6), 28.79 (C9″, C10″, C11″), 28.68 (C1), 27.41 (C2), 24.27 (C2″), 23.38 (C3″), 20.49 (C7), 18.30 (C15), 18.08 (C13), 17.36 (C12), 17.17 (C14). Mass spectrum (M_w + Na) ion m/z 579. UV/vis max 225 nm ($\varepsilon = 2.53 \times 10^5$), 258 nm ($\varepsilon = 2.86 \times 10^5$), 497 nm ($\varepsilon = 5.53 \times 10^4$).

Optimization of Conditions. The reaction was studied in 20% ethanol and in 20% DMSO in the presence of 50 mM ammonium bicarbonate in normal and inert atmosphere (nitrogen). The extent of modification was evaluated by HPLC (HPLC Äkta purifier, Amersham Pharmacia Biotech). In the Waters Spherisorb C18 (RP; ODS2, 4.6 × 250 mm; 2 μm analytical column) column was injected 10 μL of the sample. The temperature of the column was 25 °C and flow rate was 200 μL/min. Eluent (A) was 0.2% formic acid/water and eluent (B) was acetonitrile. After 25 min the chromatography was stopped.

Synthesis of Conjugates. A mixture of final volume of 1.2 mL containing 960 μL aqueous solution of lysozyme (Sigma-Aldrich, from chicken egg white) and 240 μL of solution of avarone and its derivatives in 96% ethanol was made, so that the final enzyme concentration was 5 mg/mL and concentration of quinone was 2 mg/mL in 20% ethanol. Into the mixture was added NH_4HCO_3. The final concentration of the base was 50 mM. The modification reaction lasted 48 h at room temperature with constant shaking. All samples were centrifuged for 5 min at 14 000 rpm (Eppendorf Mini Spin Plus). Supernatants were purified on Sephadex G-50 column. Enzymes were eluted with distilled water. The fraction of modified enzyme (in V_0) was collected.

Purity of the Conjugates. Purity of the conjugates was checked using HPLC/MSD ESI TOF Agilent technologies system 1200 series. In the Zorbax Eclipse Plus C18 (RP; 100 × 2.1 mm; 1.8 μm) column was injected 1 μL of the sample. The temperature of the column was 40 °C and flow rate was 400 μL/min. Eluent (A) was 0.2% formic acid/water and eluent (B) was acetonitrile. After 20 min the chromatography was stopped.

SDS PAGE. SDS polyacrylamide gel was made by standard procedure[21] using Hoefer SE 600 Ruby. The running gel was 10% and stacking gel was 4%. To the gel was applied 25 μL of each sample.

Characterization of the Conjugate. Mass Spectrometry. The average molecular masses of intact and modified lysozyme were determined by Autoflex, matrix-assisted laser desorption/ionization time-of-flight mass spectrometry (MALDI-TOF MS). Samples deposited on gold-coated target were desorbed and ionized by a 337 nm nitrogen laser which operated at 3 Hz repetition rate, using an accelerating voltage of 20 kV. The matrix was sinapic acid in 30% acetonitrile with 0.1% TFA. Spectra were acquired under delayed extraction conditions and in positive-ion linear mode.

Trypsin Digestion. Protein spots were excised from Coomassie blue stained gels to perform in-gel trypsin digestion according to manufacturer's directions. The obtained proteolytic peptides of each lysozyme conjugate were separately analyzed by mass spectrometry. Trypsin for proteomics was obtained from Sigma Chemical Co. (St. Louis, MO, USA).

Enzyme Activity. Upon modification, activity of lysozyme and its conjugates was determinated in cells of *Micrococcus lysodeikticus* (Sigma-Aldrich) by standard procedure.[22] As a control, activity of lysozyme treated in the same way as during

the preparation of the conjugates, but without avarone derivatives, was determined.

Melting Temperature. Fluorescence emission spectra were recorded using luminescence spectrometer LS 50 (Perkin-Elmer, USA), equipped with a thermally controlled cell holder and a cuvette of 1 cm path length. Thermally induced unfolding of lysozyme and modified lysozymes was followed by measuring intrinsic emission fluorescence at 340 nm using excitation at 280 nm. Slit widths were set at 5 nm, for both the excitation and the emission. Measurements were performed at several temperatures between 10 and 95 °C using heating rate of 0.5 °C/min. The concentration of lysozyme and its bioconjugates was 0.04 mg/mL.

Antibacterial Activity. A microbroth dilution assay[23] was used to evaluate the antimicrobial efficacy of avarone and its derivatives, lysozyme, and its modificates against Gram-positive and Gram-negative bacteria. The Gram-positive bacteria used were as follows: *Bacillus subtilis* (ATCC 6633), *Clostridium sporogenes* (ATCC 19404), *Streptosporangium longisporum* (ATCC 25212), *Micrococcus flavus* (ATCC 10240), *Sarcina lutea* (ATCC 9341), and *Staphylococcus aureus* (ATCC 6538). The Gram-negative bacteria used were as follows: *Escherichia coli* (ATCC 25922), *Pseudomonas aeruginosa* (ATCC 9027), *Salmonella enteritidis* (ATCC 13076), and *Proteus vulgaris* (ATCC 13315). Sterile 96-well polystyrene microtiter plates with well capacities of 300 μL were used, and 100 μL of fresh Mueller Hinton broth was added to each well of the plate. One hundred microliters of the lysozyme stock solution was added to each well of the first column. Then, 100 μL of the solution was removed from the first column and mixed thoroughly with the broth in the corresponding wells of the second column six times. Subsequently, a 100 μL aliquot was removed from each well in this column and mixed with contents of the corresponding well of the next column. This doubling dilution was performed in rows across the plate except for the last row that was kept for use as control. The same procedure was repeated with stock solutions of lysozyme, treated lysozyme, and lysozyme conjugates. Ten microliters of bacterial cultures (10^8 cells per mL) were inoculated in each well of the plate. The microtiter plate was incubated at 37 °C for 24 h. After that, bacterial growth was measured. The MIC was determinated as the lowest concentration that resulted in inhibition of bacterial growth.

Theoretical Prediction. Molecular dynamics and building and geometry optimization of small molecules were performed using *Discovery Studio 2.5.5* software (DS, Accelrys Software Inc., 2009). Lysozyme structure was downloaded from Protein Data Bank (PDB, http://www.pdb.org/) in DS, carefully checked, and then the potential covalent adducts with small molecules were made using that structure. For molecular dynamics simulations, "Standard Dynamic Cascade" protocol, from *Discovery Studio 2.5.5* protocols, was used. All calculations were done on Dell Precision 690 workstation and visualized using Planar SD2620W 26 in. Widescreen Stereo/3D Monitor (Planar Systems Inc.).

■ RESULTS AND DISCUSSION

Theoretical Prediction of the Modification Site. The amino acid residue(s) most likely to be modified by avarone and its derivatives were predicted by molecular dynamics simulations. The location of the residues and possible conformational changes upon modification might greatly influence the activity of the enzyme, and if the theoretical studies predicted a significant degree of inactivation, then the reaction conditions would have to be minutely adjusted to avoid unwanted modifications.

The crystal structure of the hen egg white lysozyme chain A, PDB code 2W1X[24] was downloaded from RCSB protein database,[25] and used for molecular dynamics simulations. In previous studies, it was shown that avarone, its derivatives, and related quinones modified lysine residues in proteins by nucleophilic addition.[17,18,26] There are 6 such residues in this structure: Lys1, Lys13, Lys33, Lys96, Lys97, and Lys116. While all of them are remote enough from the active site of the enzyme, it seems that some are less available for covalent interactions than others. Lys1, for instance, is obviously involved in ion-pair formation with Glu7. Aliphatic chain of Lys33 is somewhat buried inside the hydrophobic surroundings (Phe34, Phe38, Trp123), limiting its motility and availability. Examination of rotamer libraries[27] for Lys116 showed that conformation allowing easy reaction with the quinone would have a very low probability leaving Lys96 and Lys97 as the most likely candidates for this reaction. Although both amino acids are freely accessible, Lys97 has at least two conformations with good probability that make this residue very exposed for the reactions. Also, while the amino group from Lys96 is involved in hydrogen bonding with three amide oxygens from His15−Gly16 sequence, for Lys97 only hydrogen bond with the amide oxygen of Leu75 could be easily established. Moreover, MD simulations showed that, in the case of Lys97 modification, there are possibilities for additional bonding between polar groups on the quinone moiety and the protein, without disturbance of the protein structure. MD simulations showed good root-mean-square deviation (rmsd) for the main chain of the starting structure and the resulting conformations (less than 1.000), without influence on the binding site. In conclusion, the results indicate Lys97 as the modification site, without a significant change of lysozyme conformation, although influence on solvation could not be excluded.

Optimization of the Conditions for Modification with Avarone. Selection of the medium and conditions for modification of lysozyme had to reconcile the insolubility or denaturation of the enzyme in organic solvents and the insolubility of avarone and its derivatives in water. Therefore, solvents that are miscible with water were used, limiting the concentration of the organic solvent to 20%. The nucleophilicity of the amino groups of the enzyme was enhanced by the addition of a relatively weak base, avoiding strong bases because of the enzyme stability and prevention of quinone polymerization. Ammonium bicarbonate was selected because it allows us to record mass spectra of the crude product of modification.

In order to study the effect of the atmosphere on the modification, the reaction was studied in 20% ethanol and in 20% DMSO in the presence of 50 mM ammonium bicarbonate in the normal and inert atmosphere (nitrogen). The time of the reaction was 48 h at room temperature. Although the reaction starts immediately, as evidenced by the change of color of the reaction mixture, it is completed only after 48 h. Higher temperatures could not be used due to unwanted polymerization reactions of the enzyme and of the quinones. The extent of modification was studied by HPLC. The results showed that avarone modified the enzyme in both solvents, in normal and inert atmosphere. This is an indication that the initially formed amino hydroquinone derivative could be oxidized by the still present quinone, so that amino quinone derivative was the final product. The area of the peak with the retention time of 12.09

dx.doi.org/10.1021/bc200330m | *Bioconjugate Chem.* 2012, 23, 57−65

min, corresponding to the modified lysozyme, was larger in 20% ethanol, so that it was chosen for the reaction. As expected, the hydroquinone avarol in the inert atmosphere could not modify lysozyme, irrespective of the solvent, but in the normal atmosphere it modified the enzyme in both solvents, which indicates the oxidation of the hydroquinone by oxygen and the subsequent addition reaction of the protein amino group with the obtained quinone. In conclusion, the optimum reaction conditions were as follows: lysozyme concentration 5 mg/mL, quinone concentration 2 mg/mL, 20% ethanol, 50 mM ammonium bicarbonate, room temperature, normal atmosphere, 48 h, constant stirring. The excess of quinone was used in order to ensure fast reoxidation of the amino hydroquinone intermediate in the nucleophilic addition.

Characterization of the Derivative. On SDS electrophoresis gel, untreated lysozyme had two bands: at 14 kDa for monomer and at 28 kDa for lysozyme dimer. Lysozyme modified with avarone and its derivatives also had two bands on gel (Figure 1). Bands at 14 kDa were more prominent and

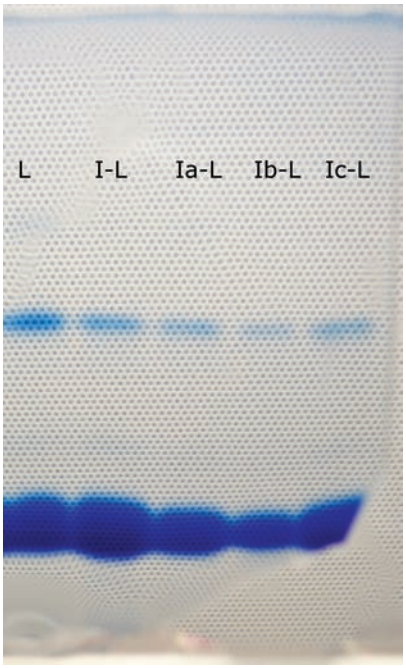


Figure 1. SDS electrophoregram.

bands at 28 kDa were weaker than bands of untreated lysozyme, indicating that the dimerization of lysozyme with avarone and its derivatives did not occur, contrary to the previous findings with β-lactoglobulin.[17,18]

Purity of the derivatives was also checked by HPLC (Figure 2). The chromatogram showed a prominent peak of the derivative at the retention time of 6.361 min (for the avarone derivative **I**-L), with a shoulder due to unmodified lysozyme at 6.325 min.

In order to determine how many quinone molecules were bound to lysozyme, mass spectra of native lysozyme and lysozyme modified by avarone (Figure 3) and its derivatives (Table 1) using MALDI TOF were recorded. Spectra of the modified lysozyme show that avarone and its derivatives were covalently attached to the monomer of lysozyme. All mass spectra had two peaks: for lysozyme monomer at 14 313 Da and for modified lysozyme at the mass of lysozyme plus mass of each compound minus 2 H atoms. The peak corresponding to the modified lysozyme is by far more abundant. It should be noted that, under the applied conditions of the quinone compound in the large excess, only one molecule of the quinone was added to one molecule of lysozyme. This result is in stark contrast to the results obtained with simpler polyhydroxylic phenols under oxidizing conditions, which accounted for addition of up to four molecules of quinoid compounds.[28]

The position of the modification site was determined by tryptic digestion of both native and modified lysozyme and analysis of fragments. After tryptic digestion of native lysozyme, tryptic peptides covering 67% of the sequence (Table 2) were obtained.

In Figure 4, MALDI TOF mass spectra of nonmodified lysozyme (Figure 4A) and lysozyme modified by avarone (Figure 4B) after tryptic digestion are shown. Spectra of modified lysozyme had additional peaks (Table 3) on mass corresponding to fragments of lysozyme which contain amino acid sequence 97−112 increased for the mass of avarone or its derivative without two H atoms. The presence of these peaks in all cases indicates that the site of attachment of avarone and its derivatives to lysozyme is lysine 97. Binding of avarone and its derivatives to lysine 97, because of the presence of their bulky groups and the loss of the positive charge, prevents tryptic digestion at the C-end of lysine 97, causing the appearance of new mass peaks with the mass for fragment 97−112, due to cleavage at Lys96, increased for the mass of each compound minus 2 H atoms. These results unambiguously indicate that lysine 97 is the site of binding of avarone and its derivatives to lysozyme. It should be mentioned that particular reactivity of Lys97 was shown in an other study[29] in which this residue was fluorescently labeled by *N*-hydroxysuccinimide esters. Namely, two residues were modified, Lys33 and Lys97, but the modification of the former was reversible and the modification of the latter was irreversible.

Lysine 97, which bound the quinone moiety, is the residue that was predicted as the probable modification site by molecular modeling. It should be emphasized that it is located on the opposite side relative to the active site of lysozyme (Figure 5). This means that the cleft is accessible for binding of the substrate, and that the activity of the enzyme should be preserved.

Enzymatic Activity. Based on the theoretical prediction, it could be expected that the activity of lysozyme would not be greatly reduced. Upon modification, activity of lysozyme was determined toward cells of *Micrococcus lysodeikticus* by standard procedure.[22] For control, lysozyme was treated in the same way as during the modification reaction, but without the addition of the quinone. The enzymatic activities of lysozyme conjugates, as well as native and treated enzyme, are shown in Table 4.

Lysozyme lost 23% of its activity after exposure to the reaction conditions. The reduction of the activity after the reaction with the quinones was less pronounced, so that 59% to 67% of the initial activity of the untreated enzyme was preserved. As expected, unsubstituted avarone (**I**) led to the lowest loss of activity, probably due to the least changes in the enzyme conformation, since addtional hydrogen bond donor/acceptor substituents are absent. The lowest activity was found for lysozyme modified with **Ib**, the only derivative in which the molecular modeling indicated an additional hydrogen bond between the methylamino group of the derivative and the backbone carbonyl of leucine 56.

dx.doi.org/10.1021/bc200330m | *Bioconjugate Chem.* 2012, 23, 57−65

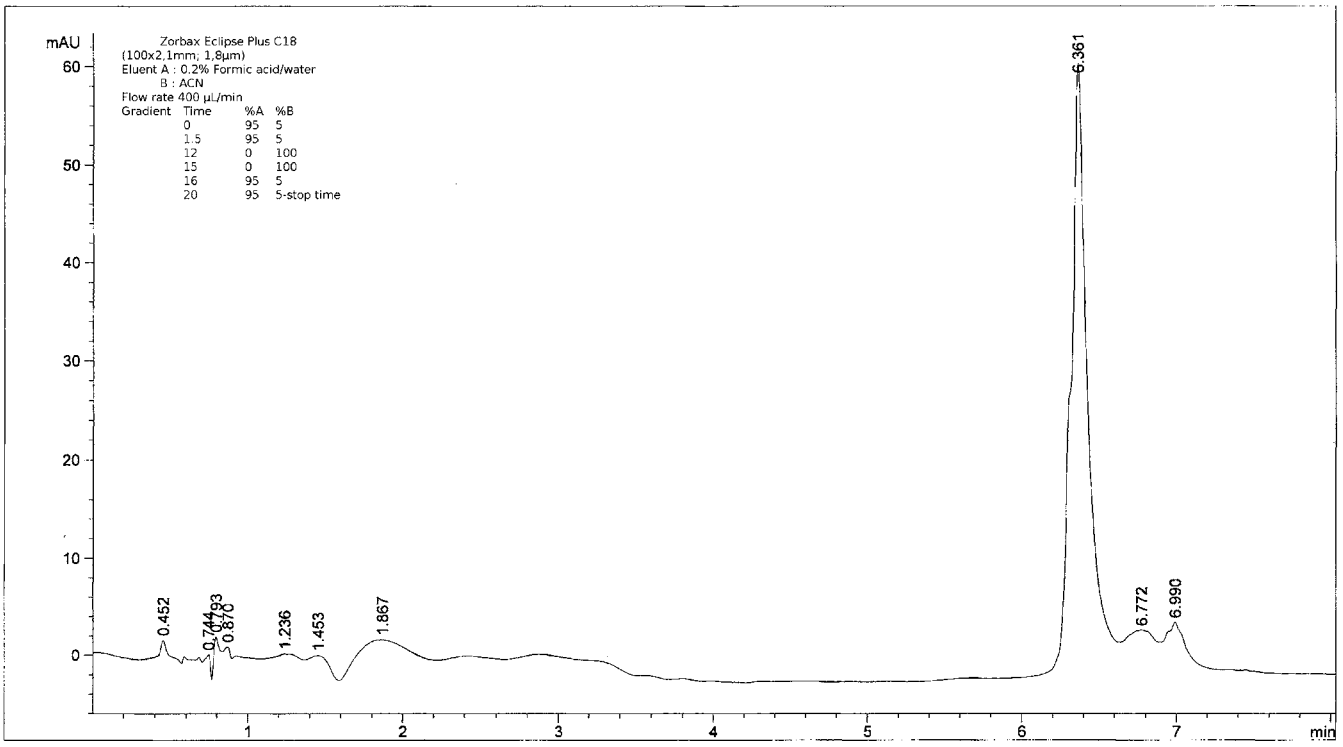


Figure 2. HPLC chromatogram of the avarone–lysozyme conjugate.

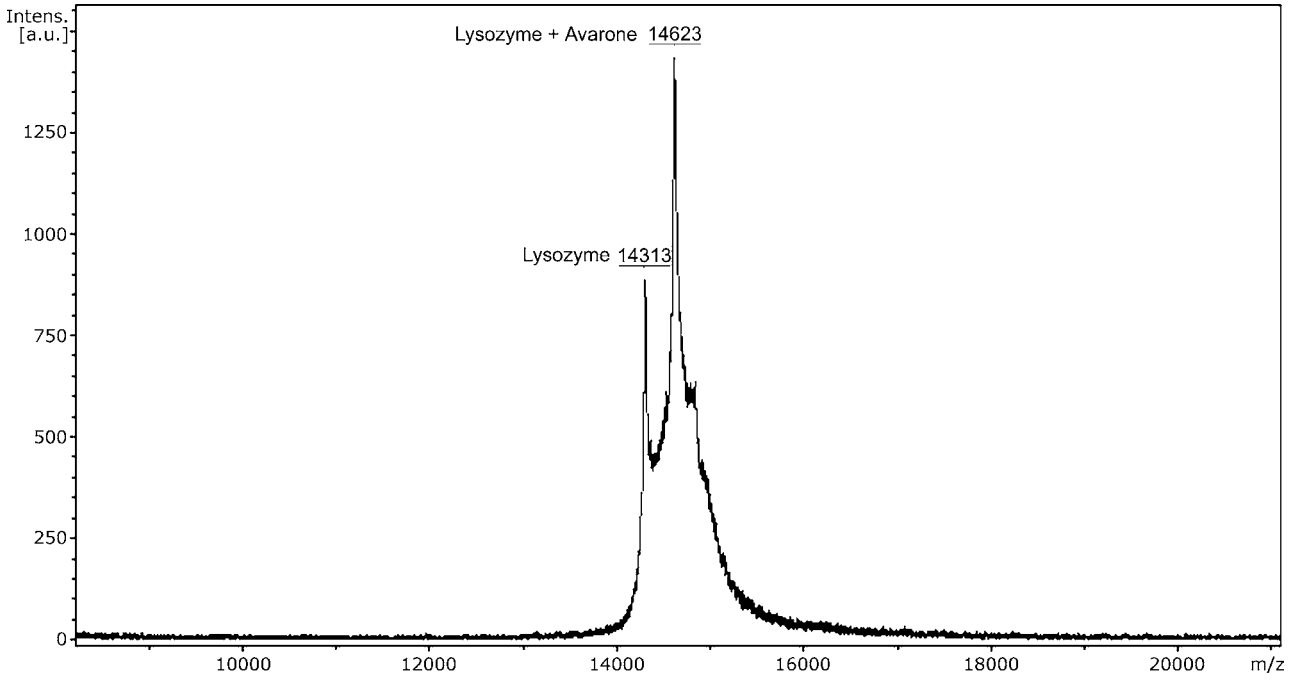


Figure 3. MALDI TOF mass spectrum of lysozyme and its conjugate with avarone.

Table 1. Second Peak on MALDI TOF Mass Spectra of Lysozyme-Conjugates with Various Derivatives of Avarone

compound		second peak (Da)
3′-Methoxyavarone	**Ia-L**	14653
4′-(Methylamino)avarone	**Ib-L**	14652
3′-(Methylamino)avarone	**Ic-L**	14652

The melting temperatures of lysozyme and the derivatives were measured by using fluorescence spectroscopy. As expected, the fluorescence intensity decreased with temperature[30] for all the derivatives. By analysis of the dependence of the wavelength maximum of the fluorescence on temperature (Figure 6), melting temperatures were found to be 72.74, 72.69, 73.01, 72.97, and 73.23 °C for lysozyme and conjugates with **I**, **Ia**, **Ib**, and **Ic**, respectively. Although the differences are not great, the general trend is that the melting point is somewhat increased in the conjugates, indicating a slight stabilization of structure in comparison to lysozyme. The slight conformational

dx.doi.org/10.1021/bc200330m | *Bioconjugate Chem.* 2012, 23, 57–65

Table 2. Peptide Fragments Obtained after Tryptic Digestion of Native Lysozyme

peptide fragment	mass (Da)
74–96	2338.7138
46–61	1754.8503
98–112	1676.8896
34–45	1429.4882
22–33	1269.4602
117–125	1046.1705

Table 3. New Peaks in the Mass Spectra of Lysozyme Conjugates with Various Derivatives of Avarone

compound		new peak mass (Da)
Avarone	**I-L**	2115.5296
3′-Methoxyavarone	**Ia-L**	2145.5496
4′-(Methylamino)avarone	**Ib-L**	2144.5696
3′-(Methylamino)avarone	**Ic-L**	2144.5696

changes resulting from additional weak stabilizing interactions might be responsible for the reduction of activity.

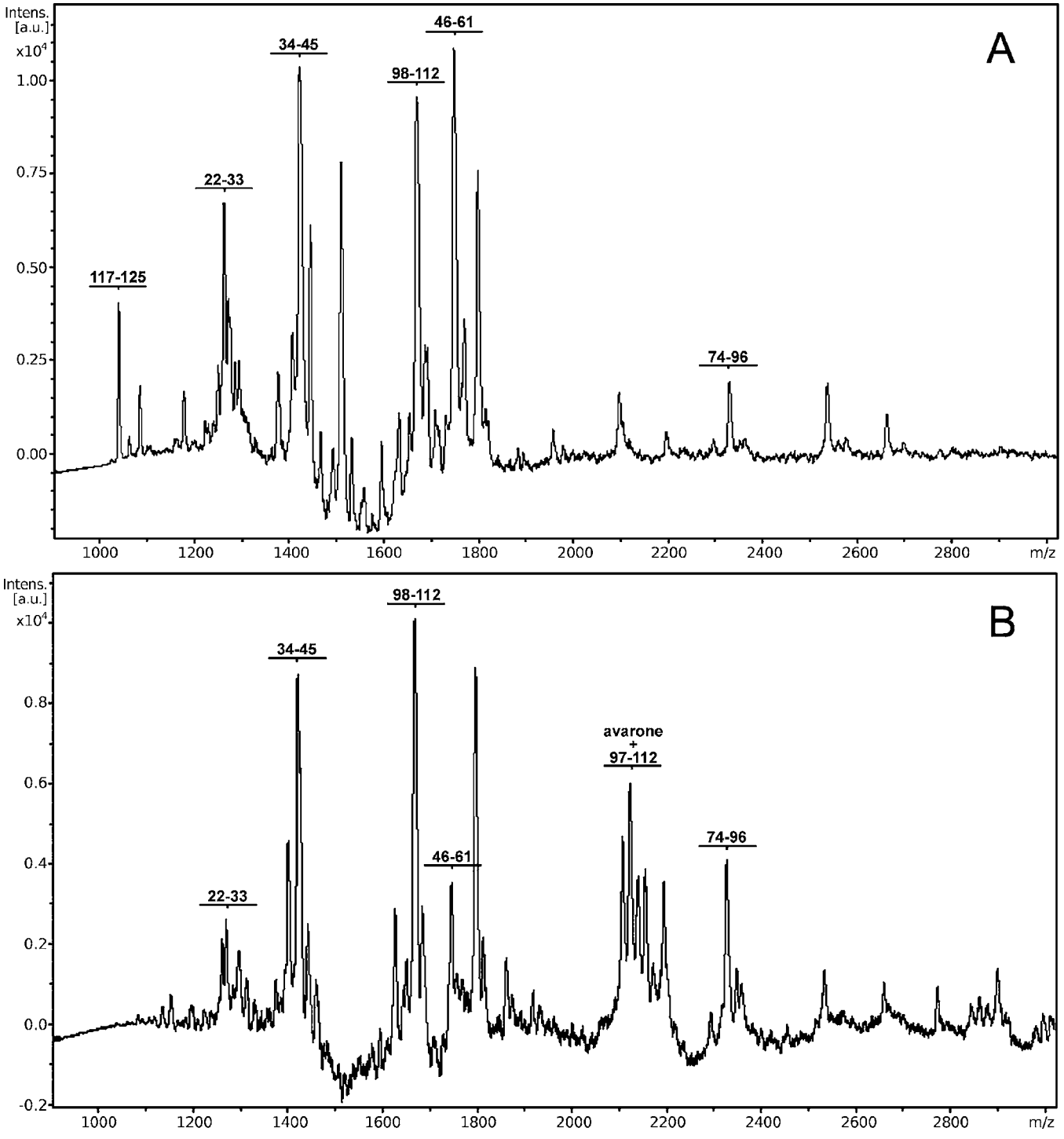


Figure 4. MALDI TOF mass spectra after tryptic digestion of nonmodified lysozyme (A) and lysozyme–avarone conjugate (B).

dx.doi.org/10.1021/bc200330m | *Bioconjugate Chem.* 2012, 23, 57–65

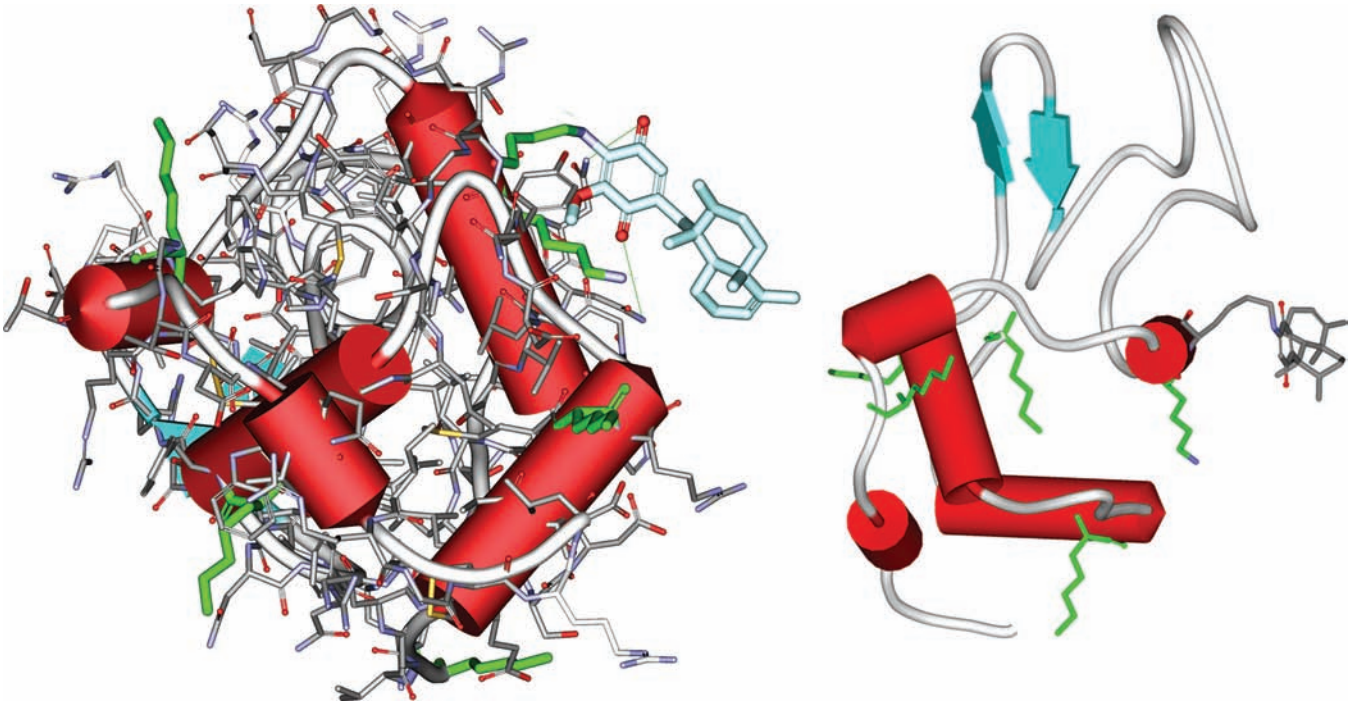


Figure 5. Images of lysozyme conjugate with avarone bound to lysine 97.

Table 4. Enzymatic Activity of Native Lysozyme and Lysozyme Conjugates after Modification

	lysozyme	treated lysozyme	I-L	Ia-L	Ib-L	Ic-L
activity (unit/mg)	43000	32977	28647	26806	25267	27787
remaining activity toward native enzyme (%)	100	77	67	62	59	65
remaining activity toward treated lysozyme (%)	-	100	87	81	77	84

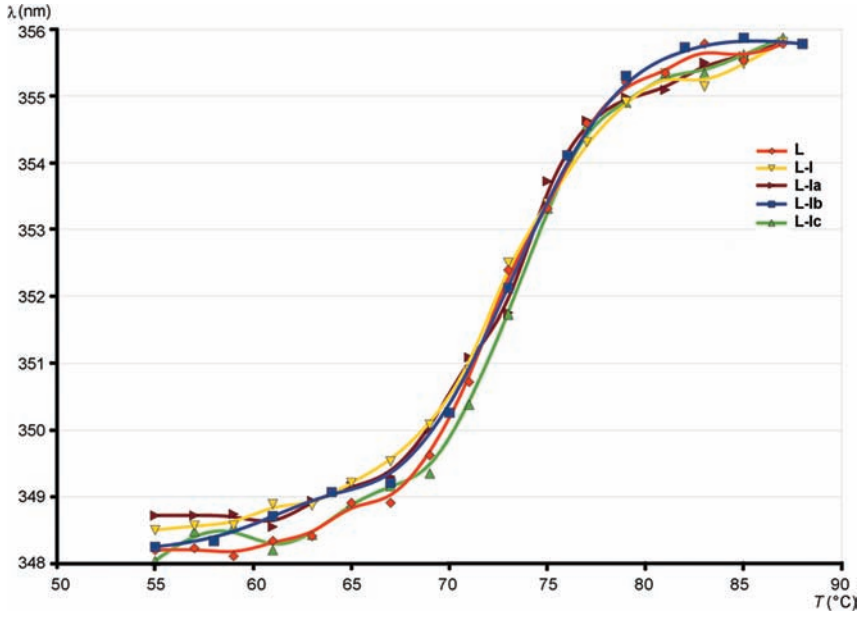


Figure 6. Change of fluorescence wavelength maximum with temperature.

Antibacterial Activity. Since lysozyme is known to show antibacterial activity against Gram-positive bacteria, the effect of quinone–lysozyme conjugates toward bacteria was investigated. Minimum inhibitory concentrations (MIC) of avarone, its derivatives, and modified lysozyme toward selected Gram-positive and Gram-negative bacteria were determined and compared to unmodified lysozyme and the standard antibiotic amikacin. The results are shown in Table 5. As shown in Table 5, avarone and 3′-methoxyavarone had an activity to Gram-positive bacteria similar to amikacin. The methylamino derivatives were weakly active or inactive. Lysozyme showed activity to all bacterial species tested, in particular, to *S. aureus*.

dx.doi.org/10.1021/bc200330m | *Bioconjugate Chem.* 2012, 23, 57–65

Table 5. Antibacterial Activity of Avarone, Its Derivatives, Lysozyme, and Its Conjugates with Various Derivatives of Avarone Towards Gram-Positive Bacteria[a]

	MIC (μM)					
Compound	*S. lutea*	*S. aureus*	*M. flavus*	*S. longisporum*	*C. sporogenes*	*B. subtilis*
I	20.03	40.06	20.03	20.03	20.03	80.13
Ia	36.55	36.55	36.55	36.55	18.27	36.55
Ib	-	-	-	-	-	-
Ic	469.21	3812.32	3812.32	3812.32	3812.32	967.74
I-L	168.23 (3.59)	5.47 (0.12)	168.23 (3.59)	168.23 (3.59)	336.46 (7.18)	168.23 (3.59)
Ia-L	95.54 (2.23)	3.07 (0.07)	191.09 (4.46)	191.09 (4.46)	191.09 (4.46)	191.09 (4.46)
Ib-L	102.38 (2.38)	1.71 (0.04)	402.68 (9.37)	204.75 (4.77)	204.75 (4.77)	204.75 (4.77)
Ic-L	95.55 (2.22)	1.54 (0.04)	395.85 (9.21)	197.92 (4.61)	197.92 (4.61)	197.92 (4.61)
Treated-L	223.57	27.94	111.79	447.15	223.57	111.79
Lysozyme	202.61	12.58	405.23	405.23	817.44	202.61
Amikacin	3.42	18.78	3.42	111.00	25.61	71.72

[a]In parentheses are the MIC of the conjugates expressed as quinone concentration.

Table 6. Antibacterial Activity of Avarone, Its Derivatives, Lysozyme, and Its Conjugates with Various Derivatives of Avarone Towards Gram-Negative Bacteria[a]

	MIC (μM)			
Compound	*E. coli*	*P. vulgaris*	*P. aeruginosa*	*S. enteritidis*
I	440.96	27.56	13.78	55.12
Ia	877.20	109.65	438.60	877.20
Ib	-	-	-	-
Ic	-	-	-	-
I-L	11.11 (0.24)	22.22 (0.47)	88.88 (1.90)	11.11 (0.24)
Ia-L	266.16 (6.21)	2.14 (0.05)	266.16 (6.21)	68.25 (1.59)
Ib-L	81.90 (1.91)	156.98 (3.65)	122.85 (2.86)	307.13 (7.15)
Ic-L	5.12 (0.12)	10.24 (0.24)	20.48 (0.48)	40.96 (0.95)
Treated-L	27.94	27.94	223.57	223.57
Lysozyme	>740.58	>740.58	188.64	370.29
Amikacin	8.54	11.95	85.38	13.66

[a]In parentheses are the MIC of the conjugates expressed as quinone concentration.

The activity of the conjugates was always similar to the activity of lysozyme or higher. The results indicate an intramolecular synergism of two components of the conjugates. Namely, the MIC values expressed as the quinone concentration were at least several times lower than MIC values of free quinones. It is particularly interesting that the conjugates with both methylamino derivatives (including the inactive 4′-derivative) showed antibacterial effects, with MIC values two to eight times lower than those of lysozyme.

The results obtained with Gram negative bacteria were even more interesting (Table 6). Lysozyme was inactive to *E. coli* and *P. vulgaris*, but showed some activity to *P. aeruginosa* and *S. enteritidis*. Avarone and 3′-methoxyavarone were active (the activity of avarone was comparable to that of amikacin) and methylamino derivatives again inactive. However, all the conjugates were active, equally or more than lysozyme (except **Ia**−L for *P. aeruginosa*), and much more than the quinones. The MIC values of **Ia**−L for *P. vulgaris* and **Ic**−L for *E. coli* (for which both components of the bioconjugate were inactive) were in low micromolar range.

The synergistic effects could be explained by different mechanisms of action, lysozyme targeting the cell wall and avarone derivatives DNA and/or proteins. Lysozyme might play the role of a vehicle that delivers the quinones to the cell. If the enzyme is attacked by bacterial hydrolytic enzymes smaller fragments containing the quinone moiety are formed, which continue to produce deleterious effects to the bacterial cell population. In order to check the effects of these hypothetical fragments, the derivative of avarone with lysine with protected α-amino group (**Id**) was synthesized and its antibacterial effects evaluated (Table 7). This derivative mimics a small modified peptide. The derivative was active to almost all bacteria, more active than methylamino derivatives of avarone. The activity was particularly strong to those bacteria that were the most susceptible to avarone−lysozyme conjugates, which means that the hypothesis that peptide fragments could retain a significant part of the activity is reasonable.

Table 7. Antibacterial Activity of 4′-((5-((*tert*-Butoxycarbonyl)amino)-5-carboxypentyl)amino)avarone (Id)

Bacteria	MIC (μM)	Amikacin
S. lutea	1124.10	3.42
S. aureus	<4.32	18.78
M. flavus	1124.10	3.42
S. longisporum	2248.20	111.00
C. sporogenes	562.05	25.61
B. subtilis	2248.20	71.72
E. coli	<4.32	8.54
P. vulgaris	2248.20	11.95
P. aeruginosa	2248.20	85.38
S. enteritidis	>8992.81	13.66

dx.doi.org/10.1021/bc200330m | *Bioconjugate Chem.* 2012, 23, 57−65

CONCLUSION

A series of conjugates of lysozyme with the derivatives of avarone were prepared. In all of them, only Lys97 added to the quinone moiety. The obtained conjugates retained most of the enzymatic activity and in many cases had an enhanced antibacterial activity compared to both the quinones and lysozyme. The intramolecular synergism might be explained by combined effects of the agents, whereby lysozyme might both target the cell wall and serve as a vehicle for delivering the quinone which acts on DNA and proteins. Further studies of the biological effects of the conjugates especially regarding the cytotoxicity and toxicity seem justified.

ASSOCIATED CONTENT

Supporting Information

Mass spectra of the conjugates before and after tryptic digestion. This material is available free of charge via the Internet at http://pubs.acs.org.

AUTHOR INFORMATION

Corresponding Author

*Irena Novaković: Telephone +381113336683; FAX +381112636061; E-mail: irenan@chem.bg.ac.rs. Dušan Sladić: Telephone +381113336679; FAX +381112636061; E-mail: dsladic@chem.bg.ac.rs.

ACKNOWLEDGMENTS

The authors are grateful to the Ministry of Education and Science of the Republic of Serbia for financial support (Project 172055). Authors wish to thank the DTPCC (Developmental Therapeutics Program Computer Center) at NCI-Frederick for using their resources for computer simulations. U.A. acknowledges a grant from Deutscher Akademischer Austausch Dienst (DAAD).

REFERENCES

(1) Calleweart, L., and Michiels, C. W. (2010) Lysozyme in the animal kingdom. *J. Biosci. 35*, 127−160.
(2) Subroto, T., Sufiati, S., and Beintema, J. J. (1999) Papaya (*Carica papaya*) lysozyme is a member of the family 19 (basic, class II) chitinases. *J. Mol. Evol. 49*, 819−821.
(3) Gao, Y. G., Zhang, S., Krentz, S., Darius, S., Power, J., and Lagarde, G. (2002) Inhibition of spoilage lactic acid bacteria by lysozyme during wine alcoholic fermentation. *Aust. J. Grape Wine Res. 8*, 76−83.
(4) Maidment, C., Dyson, A., and Beard, J. (2009) A study into measuring the antibacterial activity of lysozyme-containing foods. *Nutr. Food Sci 39*, 29−35.
(5) Cunningham, F. E., Proctor, V. A., and Goetsch, S. J. (1991) Egg-white lysozyme as a food preservative: an overview. *World Poultry Sci. J. 47*, 141−163.
(6) Proctor, V. A., and Cunningham, F. E. (1988) The chemistry of lysozyme and its use as a food preservative and a pharmaceutical. *Crit. Rev. Food Sci. Nutr. 26*, 359−395.
(7) Bratlid, D., and Moe, P. J. (1978) Serum lysozyme activity in children with acute leukemia. *Eur. J. Pediatr. 127*, 263−268.
(8) Maroufi, B., Ranjbar, B., Khajeh, K., Manesh, H. N., and Yaghoubi, H. (2008) Structural studies of hen egg-white lysozyme dimer: Comparison with monomer. *Biochim. Biophys. Acta 1784*, 1043−1049.
(9) Radziejewska, R. C., Lesnierowski, G., and Kijowski, J. (2009) Antibacterial activity of hen egg white lysozyme modified by thermochemical technique. *Eur. Food Res. Technol. 228*, 841−845.
(10) Radziejewska, R. C., Leśnierowski, G., and Kijowski, J. (2008) Properties and application of egg white lysozyme and its modified preparation − a review. *Pol. J. Food Nutr. Sci 58*, 5−10.
(11) Van der Linden, D. S., Short, D., Dittmann, A., and Yu, P. L. (2009) Synergistic effects of ovine-derived cathelicidins and other antimicrobials against *Escherichia coli* O157:H7 and *Staphylococcus aureus* 1056 MRSA. *Biotechnol. Lett. 31*, 1265−1267.
(12) Matters, D., Cooper, H. J., McDonnell, L., Iniesta, J., Heptinstall, J., Derrick, P., Walton, D., and Peterson, I. (2006) Mass spectrometry in demonstrating the site-specific nitration of hen egg white lysozyme by an improved electrochemical method. *Anal. Biochem. 356*, 171−181.
(13) Zhang, H. M., Tang, B. P., and Wang, Y. Q. (2010) The interaction of lysozyme with caffeine, theophylline and theobromine in solution. *Mol. Biol. Rep. 37*, 3127−3136.
(14) Sladić, D. M., and Gašić, M. J. (2006) Reactivity and biological activity of the marine sesquiterpene hydroquinone avarol and related compounds from sponges of the order Dictyoceratida. *Molecules 11*, 1−33.
(15) Minale, L., Riccio, R., and Sodano, G. (1974) Avarol, a novel sesquiterpenoid hydroquinone with a rearranged drimane skeleton from the sponge *Dysidea avara*. *Tetrahedron Lett. 38*, 3401−3404.
(16) De Rosa, S., Minale, L., Riccio, R., and Sodano, G. (1976) The absolute configuration of avarol, a rearranged sesquiterpenoid hydroquinone from a marine sponge. *J. Chem. Soc., Perkin Trans. 1*, 1408−1414.
(17) Novaković, I., Vujčić, Z. M., Božić, T. T., Božić, N. M., Milosavić, N. B., and Sladić, D. M. (2003) Chemical modification of β-lactoglobulin by quinones. *J. Serb. Chem. Soc. 68*, 243−248.
(18) Sladić, D. M., Novaković, I., Vujčić, Z. M., Božić, T. T., Božić, N. M., Milić, D., Šolaja, B. A., and Gašić, M. J. (2004) Protein covalent modification of biologically active quinones. *J. Serb. Chem. Soc. 69*, 901−907.
(19) Trifunović, I., Sladić, D., Dogović, N., and Gašić, M. J. (1987) Carbon-13 chemical shift assigment in substituted 1,4-cyclohexadienones. *J. Serb. Chem. Soc. 52*, 559−563.
(20) Cozzolino, R., De Giulio, A., De Rosa, S., Strazzullo, G., Gašić, M. J., Sladić, D., and Zlatović, M. (1990) Biological activities of avarol derivatives, 1. amino derivatives. *J. Nat. Prod. 53*, 699−702.
(21) Laemlli, U. K. (1970) Cleavage of structural proteins during the assembly of the head of bacteriophage T4. *Nature 227*, 680−685.
(22) Shugar, D. (1952) *Biochim. Biophys. Acta 8*, 302−309.
(23) NCCLS (National Committee for Clinical Laboratory Standards) (2000) Approval standard document M7-A5, Villanova, PA, USA.
(24) Cianci, M., Helliwell, J. R., and Suzuki, A. (2008) The interdependence of wavelength, redundancy and dose in sulfur SAD experiments. *Acta Crystallogr., Sect. D 64*, 1196−1209.
(25) http://www.rcsb.org/ .
(26) Pajić, I., Vujčić, Z., Vujčić, M., Novaković, I., Sladić, D., and Gašić, M. J. (2007) Chemical modification of the lectin of the marine coral *Gerardia savaglia* by marine quinone avarone. *J. Serb. Chem. Soc. 72*, 1271−1274.
(27) Ponder, J. W., and Richards, F. M. (1987) Tertiary templates in proteins. use of packing criteria in the enumeration of allowed sequences for different structural classes. *J. Mol. Biol. 193*, 775−791.
(28) Rawel, H. M., Kroll, J., and Rohn, S. (2001) Reactions of phenolic substances with lysozyme − physicochemical characterisation and proteolytic digestion of the derivatives. *Food Chem. 72*, 59−71.
(29) Teske, C. A., Simon, R., Niebisch, A., and Hubbuch, J. (2007) Changes in retention behavior of fluorescently labeled proteins during ion-exchange chromatography caused by different protein surface labeling positions. *Biotechnol. Bioeng. 98*, 193−200.
(30) Zielenkiewich, W., Swierzewski, R., Attanasio, F., and Rialdi, G. (2006) Thermochemical, volumetric and spectroscopic properties of lysozyme-poly(ethylene)glycol system. *J. Therm. Anal. Calorim. 83*, 587−595.

Bioconjugate Chemistry

Article

pubs.acs.org/bc

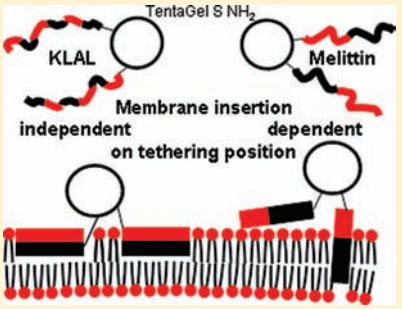
Mode of Action of Cationic Antimicrobial Peptides Defines the Tethering Position and the Efficacy of Biocidal Surfaces

Mojtaba Bagheri,[†,‡] Michael Beyermann,[†] and Margitta Dathe*[,†]

[†]Leibniz Institute of Molecular Pharmacology, Robert-Roessle-Str. 10, 13125 Berlin, Germany

[‡]Institut für Pharmazeutische Biotechnologie, Universität des Saarlandes, Universitätscampus, Gebäude C2 3, 66123 Saarbrücken, Germany

ABSTRACT: Covalent immobilization of cationic antimicrobial peptides (CAPs) at sufficient density and distance from the solid matrix has been suggested as a successful strategy for the generation of biocidal surfaces. To test the hypothesis that the mode of peptide action is decisive for the selection of an appropriate tethering position on solid surfaces, melittin (MEL), a channel-forming peptide, buforin 2 (BUF2), a peptide able to translocate bacterial membranes without permeabilization and targeting nucleic acids, and tritrpticin (TP), described to be membrane-lytic and to have intracellular targets, were C- and N-terminally immobilized on TentaGel S NH_2 resin beads as model surface. The peptide termini were modified with aminooxyacetic acid (AOA) and coupled via oxime-forming ligation. The comparison of the activities of the three peptides and their AOA-modified analogues with a KLAL model peptide which permeabilizes membranes by a so-called "carpet-like" mode provided the following results: The peptides in solution state were active against *Bacillus subtilis* and *Escherichia coli* at micromolar concentrations. MEL and TP but not BUF2-derived peptides permeabilized the inner and outer membrane of *E. coli* and enhanced the permeability of lipid bilayers at concentrations around their antimicrobial values (MICs). Immobilization reduced peptide activity to millimolar MICs. The activity reduction for KLAL was independent of the tethering position and comparably low, as reflected by a low ratio of $MIC_{tethered}/MIC_{free}$. In contrary, the pore-forming MEL was much less active when immobilized at the N-terminus compared with the C-terminally tethered peptide. C- and N-terminal TP tethering caused an identical but much pronounced activity decrease. The tethered BUF2 peptides were inactive at the tested concentrations suggesting that the peptides could not reach the intracellular targets. In conclusion, membrane active peptides seem to be most suitable for the generation of antimicrobial surfaces, but knowledge about their mode of membrane insertion and positioning is required to identify optimal tethering positions. The relationship between the mechanism of action and position of immobilization is highly relevant for the establishment of a general approach to obtain efficient biocidal solid matrices loaded with CAPs.



INTRODUCTION

Infections caused by bacterial colonization on medical devices and implants represent a serious threat to human health.[1,2] Antimicrobial coating of the materials is one strategy to prevent bacterial aggregation. Examples are bactericidal surfaces covered with antibiotics, e.g., ampicillin and penicillin.[3,4] A promising alternative which also allows circumvention of the growing emergence of bacterial resistance toward classical antibiotics[5] is the application of cationic antimicrobial peptides (CAPs). CAPs play a key role in mammalian innate immunity. The majority of the peptides act via permeabilization of the bacterial membranes.[6] Many efforts have been focused upon their development as a new class of antibiotics.[7] In addition, CAPs have been recognized as potential candidates to tackle the formation of biofilm. The inhibition of biofilm cultures of *Pseudomonas aeruginosa* or other oral pathogens by the human host defense peptide LL-37[8] or a magainin-related peptide mimetic[9] are examples of successful attempts. Because of slow enzymatic degradation,[10] conserved antimicrobial activity even at 200 °C and over a broad pH range,[11,12] and low hemolytic activity,[13,14] covalent tethering of CAPs on surfaces has gained high interest. Recent examples are magainin derivatives immobilized on resin beads and gold surfaces,[13,15] an immobilized cecropin-melittin hybrid peptide on polymer brushes,[12] cellulose membranes covered with short bactenecin analogues,[14] and nisin tethered on block copolymers.[16]

While free peptides can easily penetrate the microbial cells and cause cell death by membrane or metabolic disruptions,[6] covalent immobilization renders CAPs less flexible and peptide penetration into the bacterial cell wall is reduced.[13] The influence of physical parameters such as the length of the spacer between surface and peptide and the density of functional groups for peptide tethering upon the activity pattern have previously been studied in our group.[13] We demonstrated that tethering distinctly reduced the activity of peptides which was further decreased with reduction of the spacer length. However, peptide tethering did not change the biological activity spectrum and the membrane permeabilizing mode of action.

Received: July 12, 2011
Revised: November 28, 2011
Published: December 9, 2011

ACS Publications © 2011 American Chemical Society

dx.doi.org/10.1021/bc200367f | *Bioconjugate Chem.* 2012, 23, 66–74

We also showed that the activity of the helical amphipathic model peptide, i.e., KLAL[17] and the magainin analogue, MK5E,[18] was hardly sensitive to the chain position of linkage.[13] This is in accordance with a so-called "carpet-like" mode of membrane permeabilization where the helix axis of inserted peptides is oriented parallel to the membrane surface.[6] Others found that the activity of immobilized peptides can be position-dependent. Thus, a randomly immobilized cecropin-melittin hybrid peptide[12] and the α-helical peptide E14LKK[19] are almost inactive and should be tethered at the C- and N-termini, respectively, to be most active.

So far, systematic studies with respect to the influence of the sequence and the position of tethering on the activity pattern of peptide-covered surfaces have not been conducted. To shed light on this issue, we tethered three natural CAPs, melittin (MEL), buforin 2 (BUF2), and tritrpticin (TP), at the C-terminus and N-terminus on TentaGel S NH_2 resin beads as a model solid surface. The peptides are characterized by different modes of action. MEL acts via permeabilization of bacterial membranes.[20] Ion channels are formed by insertion of the N-terminal hydrophobic chain into the lipid matrix.[21] On the contrary, BUF2 is suggested to translocate across bacterial membranes without permeabilization and to target intracellular processes.[22] TP is active via ambiguous mechanisms such as membrane depolarization coupled to secondary intracellular targeting.[23,24]

The peptides were tethered on the resin beads using the oxime-forming ligation strategy.[13] Antimicrobial activities of the free and tethered peptides were assessed against *E. coli* (strain DH 5α) and *B. subtilis* (strain DSM 347). Inner and outer membrane permeabilizing activities against *E. coli* (strain ML-35p) and lipid bilayer permeabilization were determined to get information about the mode of action of the free peptides. The kinetics of the permeabilization of 1-palmitoyl-2-oleoyl-*sn*-glycero-3-phospho-choline/1-palmitoyl-2-oleoyl-*sn*-glycero-3-[phospho-*rac*-(1-glycerol)] (POPC/POPG) (3/1 [mol/mol]) bilayers as model of bacterial membranes was monitored to characterize C- and N-terminally immobilized sequences. The results were compared with the data derived for the free and tethered membrane-lytic KLAL model peptide[13] in order to uncover sequence requirements which impair the bioactivity with immobilization. Due to the different modes of action of CAPs, such studies are essential for the selection of peptides suitable for the generation of antibiotic surfaces.

EXPERIMENTAL PROCEDURES

Synthesis and Characterization of Free Peptides. MEL, BUF2, and TP were synthesized automatically by solid-phase peptide synthesis (SPPS) using (Fmoc)-N-protected amino acids (GL Biochem, Ltd., China) (5 equiv) and the activating reagent 2-(1*H*-benzotriazole-1-yl)-1,1,3,3-tetramethyl uronium hexafluorophosphate (IRIS Biotech, Germany) (4.9 equiv) in the presence of 10 equiv of *N*,*N*-diisopropylethylamine (Fluka, Germany) in dimethylformamide (DMF) (Fluka) as described before.[13] Syntheses were carried out on TentaGel S RAM resin (capacity: 0.26 mmol/g) (Rapp Polymere GmbH, Germany). Double coupling for 20 min was allowed. Fmoc removal proceeded with 20% piperidine in DMF for 2 × 5 min. Washes were performed with DMF.

Aminooxy acetic acid (AOA) (Fluka) was introduced before cleavage of the peptides from resin. After removal of the Fmoc protecting group, N-terminally AOA-modified sequences were prepared by adding the bifunctional AOA using hydroxybenzotriazole/*N*,*N*′-diisopropylcarbodiimide (HOBt/DIC) (IRIS Biotech/Fluka) as activating reagents.[13] For C-terminal AOA-modification, an extra lysine (K) residue with an orthogonal protecting group, Fmoc-Lys(4,4-dimethyl-2,6-dioxocyclohex-1-ylidene ethyl [Dde])−OH (Novabiochem, Germany), was introduced at the peptide's C-terminus. Following Fmoc removal, complete blocking of the N-terminal amino group of MEL, TP, or BUF2, respectively, was performed by exposure to di-*tert*-butyl dicarbonate (Boc_2O) (3 equiv in respect to the amount of free α-amino groups) in dichloromethane (CH_2Cl_2) for 1 h. After washing the resin, Dde was removed from the sequence by exposure to 2% hydrazine in DMF and, subsequently, AOA was coupled to the free ε-amino group using the HOBt/DIC activation procedure.[13]

Finally, peptides were cleaved from the resin using trifluoroacetic acid (TFA). Crude peptides were precipitated in cold diethyl ether, lyophilized, and subsequently purified by reversed-phase high-performance liquid chromatography (RP-HPLC) using a Shimadzu LC-10A system (Japan) operated at 220 nm. The compounds were further characterized by liquid chromatography/electrospray ionization time-of-flight mass spectrometry (LC/ESI-TOF MS) (Waters Corporation, U.S.A.). Analytical RP-HPLC was performed on a Jasco HPLC system (Jasco, Japan). Runs were carried out on a PolyEncap A 300 (250 × 4.0 mm) column (Bischoff Analysentechnik, Germany). The sample concentration was 1 mg/mL peptide in eluent A. The mobile phase A was 0.1% TFA in water, and B was 0.1% TFA in acetonitrile/water (4/1 v/v). The retention times (t_R) of the peptides were determined using a linear gradient of 5−95% B over 40 min at room temperature. t_R can be taken as a measure of hydrophobicity and amphipathicity of the peptides.[25]

Preparation and Characterization of Tethered Peptides. In this study, peptides were immobilized at the C-terminus and N-terminus on TentaGel S NH_2 resin beads (capacity: 0.32 mmol/g) (Rapp Polymere GmbH). The resin has a long poly(ethylene glycol) (PEG) spacer (~ 60 nm)[13] which allows the tethered peptides to span the outer wall of bacteria[26,27] and to reach the cytoplasmic membrane which is the interaction partner of membrane-lytic as well as translocating CAPs.[6] The oxime-forming ligation strategy was used for peptide coupling.[13] The list of AOA-modified analogues is given in Table 1. For the ligation reaction, 10 mg resin beads, pretreated with pyruvic acid (Fluka), were suspended in 500 μL of a peptide solution (9 mmol AOA-modified peptide dissolved in 500 μL acetate buffer (pH ≈ 4) containing 6 M guanidinium hydrochloride (Gn.HCl)). After shaking for 24 h, the solvent was removed and the beads were washed several times with DMF and CH_2Cl_2 and finally dried under high vacuum overnight.

As TentaGel S NH_2 and TentaGel S RAM (possessing a TFA cleavable linker) resin beads are similar in their chemical structure, peptide tethering was separately confirmed by immobilization on TentaGel S RAM and subsequent TFA cleavage and mass spectrometric analysis (Scheme 1, Table 2). The amount of tethered peptides was determined by measuring the absorption of the cleaved Fmoc-chromophore upon treatment of the resin-bound peptides with chloroformic acid 9-fluorenylmethyl ester (Novabiochem) according to the strategy published before.[13] The absorption was read at 301 nm (ε = 6000 M^{-1} cm^{-1}) on a Lambda 9 spectrophotometer

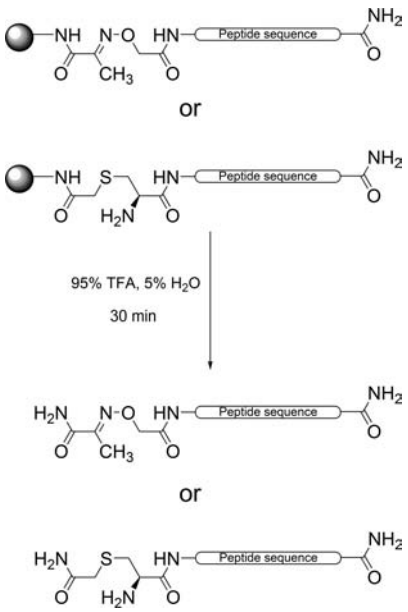
dx.doi.org/10.1021/bc200367f | *Bioconjugate Chem.* 2012, 23, 66−74

Table 1. Amino Acid Sequences, Antimicrobial Activities, Calculated and Observed Molecular Masses, and RP-HPLC t_R Values of the Free Peptides

		molecular mass [M +4H]$^{+4}$ (Da)[b]				MIC (μM)[d]	
peptide denotation	amino acid sequence[a]	calculated	observed	Q[c]	t_R (min)	*B. subtilis* (DSM 347)	*E. coli* (DH 5α)
MEL	GIGAVLKVLTTGLPALISWIKRKRQQ-NH_2	712.20	712.13	6	23.2	1.6	12.5
MEL-AOA	GIGAVLKVLTTGLPALISWIKRKRQQK(AOA)-NH_2	762.47	762.43	7	22.5	0.8	12.5
AOA-MEL	AOA-GIGAVLKVLTTGLPALISWIKRKRQQ-NH_2	730.45	730.43	6	23.4	1.6	50.0
BUF2	TRSSRAGLQFPVGRVHRLLRK-NH_2	637.62	637.81	7	12.9	25.0	6.3
BUF2-AOA	TRSSRAGLQFPVGRVHRLLRKK(AOA)-NH_2	687.89	688.10	8	12.8	25.0	25.0
AOA-BUF2	AOA-TRSSRAGLQFPVGRVHRLLRK-NH_2	655.87	655.83	7	12.9	50.0	25.0
TP	VRRFPWWWPFLRR-NH_2	476.02	476.27	5	21.1	1.6	6.3
TP-AOA	VRRFPWWWPFLRRK(AOA)-NH_2	526.30	526.26	6	18.0	1.6	6.3
AOA-TP	AOA-VRRFPWWWPFLRR-NH_2	494.27	494.48	5	17.9	0.8	12.5
KLAL[e]	KLALKLALKALKAALKLA-NH_2	469.84	470.03	6	20.6	0.8	1.6

[a]The one letter code for amino acids was used. [b]The values are monoisotopic masses in positive mode. The calculated and observed values for BUF2 reflect the masses of peptides with one TFA adduct ion. [c]Q stands for the number of positive charges. The partial charge of histidine residue has not been considered. [d]Values represent the mean of the results of three independent experiments performed in triplicate. Standard deviations were less than 5%. [e]The MIC and t_R values were taken from ref 13.

Scheme 1. Schematic Description of TFA Cleavage of TentaGel S RAM-Bound Peptides Prepared via Oxime-Forming Ligation or Thioalkylation Strategies



(Perkin-Elmer, Germany). The amount of tethered peptide per mg resin is given in Table 2.

Determination of the Minimal Inhibitory Concentration (MIC) of Free and Tethered Peptides. The MIC of free and tethered peptides against Gram-positive *B. subtilis* (strain DSM 347) and Gram-negative *E. coli* (strain DH 5α) was determined in 96-well microtiter plates and culture tubes (Sarstedt AG & Co., Germany), respectively.[13] Cells were cultivated in lysogeny broth (LB) (Sigma-Aldrich, Germany) and suspensions characterized by an optical density of 0.4 to 0.5 at 600 nm (midlog phase) were prepared. $OD_{600\ nm}$ = 1.0 for *B. subtilis* and *E. coli* corresponds to 8.8×10^7 cells/mL and 2.2×10^8 cells/mL, respectively. 150 μL of the cell suspensions were incubated with 50 μL peptide solution giving final concentrations between 100 μM and 0.05 μM in 2-fold dilution. For testing tethered peptides, an aliquot of the cell suspensions was added to culture tubes containing appropriate amounts of peptide-covered resin beads in 1 mL LB. The final number of cells per well or culture tube was 1.6×10^6 for *E. coli* and 8×10^5 for *B. subtilis*. Peptide concentrations were tested in triplicate. Culture tubes with nonmodified resin and wells without peptide were measured as controls. The test vessels were shaken (180 rpm) at 37 °C for 17 h. Then, the absorbance was read at 600 nm (Safire Microplate Reader; Tecan, Germany). MIC values were determined as the lowest peptide concentration at which no change in absorbance (no bacterial growth) was observed.

Outer and Inner Membrane Permeabilizing Activities of the Free Peptides. The outer (OM) and inner membrane (IM) permeabilizing activity of MEL, BUF2, TP, KLAL, and the AOA-modified peptides were assessed against Gram-negative *E. coli* (strain ML-35p) in 96-well microtiter plates according to the established procedure.[28] *E. coli* (strain ML-35p) expresses cytoplasmic β-galactosidase and periplasmic β-lactamase and lacks lactose permease. The nonmembrane permeabilizing nitrocefin (NCF) (Oxoid, U.K.), a substrate of β-lactamase, and *o*-nitrophenyl-β-D-galactopyranoside (ONPG) (Sigma-Aldrich), a substrate of β-galactosidase, were used to monitor peptide-induced OM and IM permeability, respectively. Cells were cultivated overnight in LB medium containing 100 g/mL ampicillin, rinsed twice, and resuspended in HEPES buffer to an $OD_{550\ nm}$ of 0.3. $OD_{550\ nm}$ = 1.0 corresponds to 3.8×10^8 cells/mL. 50 μL of this cell suspension were added to wells containing 50 μL peptide solution at concentrations close to the individual MIC values and either 50 μL of NCF stock solution (60 g/mL) or 50 μL of ONPG stock solution (300 g/mL). Wells with Polymyxin B (PMXB), a highly *E. coli* membrane permeabilizing compound,[29] at a concentration of 5 μM, and wells without peptide were used as controls. OM and IM permeabilization was monitored at λ = 500 nm and λ = 420 nm, respectively, up to about 1 h using a Safire Microplate Reader.

Bilayer Permeabilizing Activity of the Free and Tethered Peptides. To monitor the bilayer permeabilizing activity of free and tethered peptides, large unilamellar vesicles (LUV) composed of POPC/POPG (3/1 [mol/mol]) (Avanti Polar Lipids, Inc., U.S.A.) and loaded with calcein (Fluka) at self-quenching concentration (~80 mM) were prepared and characterized according to the established procedure.[13] Aliquots

dx.doi.org/10.1021/bc200367f | Bioconjugate Chem. 2012, 23, 66–74

Table 2. Density and Antimicrobial Activities of Peptides Tethered on TentaGel S NH_2, and Calculated and Observed Molecular Masses of Peptides Cleaved from TentaGel S RAM

			molecular mass $[M+4H]^{+4}$ (Da)[b]		MIC				$MIC_{tethered}/MIC_{free}$ ($\times 10^2$)	
					B. subtilis (DSM 347)		*E. coli* (DH 5α)			
peptide denotation	position of immobilization	amount of tethered peptide (μmol/mg)[a]	calculated	observed	resin (mg/mL)[c]	tethered peptides (mM)[d]	resin (mg/mL)[c]	tethered peptides (mM)[d]	*B. subtilis* (DSM 347)	*E. coli* (DH 5α)
MEL	C-terminus	0.020	779.72	779.67	3	0.06	30	0.60	0.4	0.5
	N-terminus	0.022	747.70	747.70	15	0.33	>60	>1.32	2.1	>1.1
BUF2	C-terminus	0.067	676.64	676.87	>60	>4.02	>60	>4.02	>161	>6.4
	N-terminus	0.099	673.12	673.32	ND[e]	ND	>70	>6.93	ND	>10.1
TP	C-terminus	0.147	543.55	543.77	5	0.74	20	2.94	4.6	4.7
	N-terminus	(0.147)[f]	511.52	511.75	5	(0.74)	20	(2.94)	4.6	4.7
KLAL[g]	N-terminus	0.028	509.84	510.07	5	0.14	25	0.70	1.8	4.4
	Random	0.031	509.84	509.82	5	0.15	25	0.77	1.9	4.8

[a]The amount of tethered peptides per mg resin was determined in three independent experiments. Standard deviations were less than 5%. [b]The calculated and observed values for the cleaved N-terminally tethered BUF2 reflect the masses of peptides with one TFA adduct ion. The observed mass value for randomly immobilized KLAL points to one of three peptides (with same molecular masses) cleaved after treatment with TFA. The molecular masses of the cleaved peptides were ~160 Da larger than the value for KLAL (Scheme 1). [c]The MICs of peptide-loaded resin were determined in three experiments which provided identical values. [d]The MICs of immobilized peptides were calculated on the basis of the bacterial growth inhibiting concentration of peptide-covered resin and the amount of peptides bound to resin. [e]ND − not determined. [f]Due to the absence of an Fmoc-protected amino group in the case of the N-terminally tethered TP, the amount of tethered peptide could not be determined. Thus, the MICs of N-terminally resin-bound peptide were calculated under the assumption of 0.147 μmol tethered TP per mg resin, as determined for the C-terminally bound sequence (values in parentheses). [g]The amount of tethered peptides and MIC values were taken from ref 13.

of the LUV suspension were injected into cuvettes containing either stirred solutions of KLAL, MEL, BUF2, and TP or suspensions of peptide-covered resin beads at different concentrations in buffer (10 mM Tris(hydroxymethyl) aminomethane, 154 mM NaCl, 0.1 mM EDTA, pH 7.4). The lipid concentration was 25 μM. Peptide-induced fluorescence dequenching as result of dye release from LUVs was monitored fluorimetrically (excitation at λ = 490 nm, emission at λ = 514 nm) at room temperature on a LS 50B spectrofluorimeter (Perkin-Elmer, Germany). 100% dye release was induced by addition of a 10% Triton X-100 solution. Peptide concentrations causing 50% dye release from LUVs (EC_{50}) (after 1 min) were derived from dose−response curves.

RESULTS

Characterization of MEL, BUF2, TP, and AOA-Modified Analogues. Charge, hydrophobicity, and amphipathicity represent important structural determinants of membrane-active CAPs which mediate peptide accumulation at bacterial membranes and their insertion into the lipid bilayer.[30] The investigated peptides are highly cationic with a number of positive charges (Q) between 5 in TP and 7 in BUF2 (Table 1). C-terminal K-introduction and AOA-modification enhanced the total charge by one. With $23.4 \leq t_R \geq 22.5$ min, MEL-derived peptides represent highly hydrophobic/amphipathic structures based on a charged C-terminal region and a rather hydrophobic N-terminal chain segment. C- and N-terminal AOA-modification of TP results in analogues with slightly reduced but identical hydrophobicity/amphipathicity as compared with the parent peptide. Low and identical t_R values of the BUF2 peptides reflect very low hydrophobicity and amphipathicity, independent of the position of AOA-modification. KLAL is known as a highly amphipathic helical peptide.[17]

Synthesis and Characterization of Tethered MEL, BUF2, and TP. Tethered peptides should be prepared using a chemical strategy which leads to minor modifications in the structural parameters, such as the number of positive charges, hydrophobicity, and amphipathicity.[30]

The AOA-modified MEL, BUF2, and TP were used for terminal immobilization on TentaGel S NH_2 resin beads.[13] This immobilization strategy was successful for all peptides reported here but may not work for others. For instance, the acidic buffer solution of the model KLAL peptide, which is required for the ligation reaction, showed a gel-like appearance and the reaction stopped after a few minutes. As reported elsewhere, not all peptides are soluble in buffer containing 6 M Gn.HCl.[31] To circumvent this problem, other coupling strategies such as thioalkylation can be used. Thus, KLAL-tethering on resin beads was performed using a DMF/1-propanal reaction mixture which is a good solvent for peptide solubilization.[13]

Coupling and identity of the AOA-immobilized peptides were confirmed by cleavage from TentaGel S RAM resin (Scheme 1). The molecular masses of the cleaved peptides were ~69 Da larger than the values for the AOA-modified peptides and corresponded to the theoretical data (Table 2). N-terminal tethering of all peptides was related to the loss of one cationic charge, whereas immobilization via the additional C-terminal K residue conserved the charge properties of the parent peptides.

The coupling efficiency of C- and N-terminal tethering of MEL, the most hydrophobic peptide, was almost identical and rather low with ~0.02 μmol peptide/mg resin (compare Tables 1 and 2). With ~0.15 μmol/mg, the amount of C-terminally immobilized TP was much higher. Due to the absence of Fmoc-protected amino groups, the amount of N-terminally tethered TP could not be determined. We considered the efficiency of C- and N-terminal ligation of TP to be identical for further calculations. Also, the most hydrophilic BUF2 was efficiently immobilized at the C and N-termini with about 0.07 μmol/mg (resin) and 0.1 μmol/mg resin, respectively. The data given in Table 2 for N-terminal and random tethering of KLAL had been derived before.[13]

Antimicrobial Activity of Free MEL, BUF2, and TP. The dissolved peptides showed antimicrobial activities at micromolar concentrations (Table 1). MEL peptides were highly

dx.doi.org/10.1021/bc200367f | Bioconjugate Chem. 2012, 23, 66−74

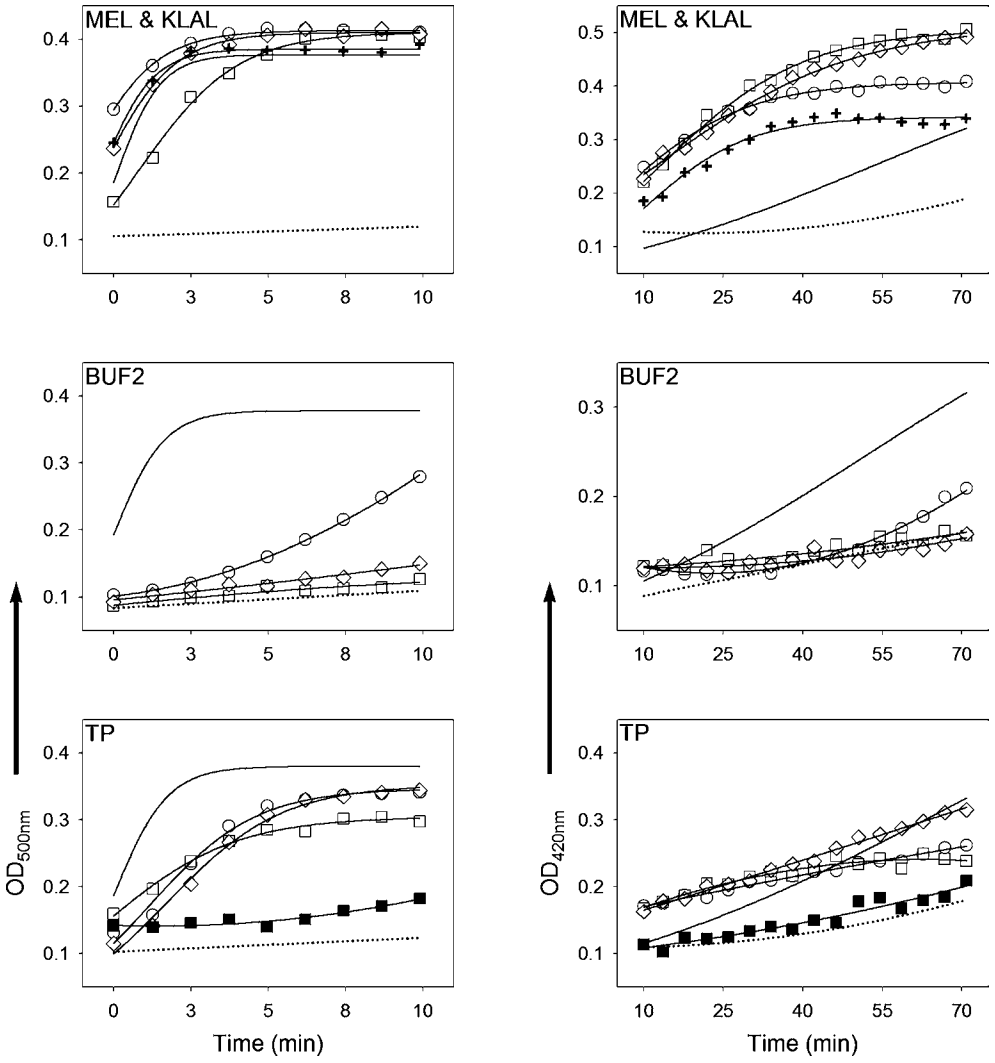


Figure 1. Kinetics of the permeabilization of the outer (left panels) and the inner (right panels) membranes of *E. coli* (strain ML-35p) induced by MEL, BUF2, TP, their AOA-modified analogues, and KLAL. Symbols represent: (+) KLAL, (○) nonmodified, (◇) C-terminally, and (□) N-terminally AOA-modified MEL, BUF, and TP. Peptide concentrations were as follows: KLAL, 3 μM; MEL peptides, 10 μM; TP and TP-AOA, 9 μM; AOA-TP, 27 μM (9 μM (represented as (■))); BUF2, 10 μM; AOA-modified BUF2, 30 μM. PMXB, 5 μM (solid line) and untreated cells (dotted line) were used as controls.

active against *B. subtilis* (0.8 μM < MICs < 1.6 μM), whereas their activity against *E. coli* was much lower. A slight variation of one dilution step in the MICs correlated with the almost identical t_R values. AOA-modification also had minor influence on the high TP activity against *B. subtilis* and *E. coli*. This is, however, different to the pronounced effect of AOA introduction upon the peptide hydrophobicity/amphipathicity (t_R). With the exception of BUF2 being more active against *E. coli* (MIC = 6.3 μM) than *B. subtilis*, the BUF2 peptides with their low t_R values were least active (25 μM < MICs < 50 μM).

Antimicrobial Activity of Tethered MEL, BUF2, and TP. Peptide immobilization led to a distinct reduction of the antimicrobial activity with MICs in the millimolar concentration range (Table 2). Tethered MEL and KLAL were most active followed by TP (see $MIC_{tethered}/MIC_{free}$ in Table 2). Higher activities of these peptides against *B. subtilis* compared with *E. coli* were in accordance with the activity profile of the soluble sequences. Whereas the activities of C- and N-terminally immobilized TP or randomly and N-terminally immobilized KLAL were almost identical, the MICs of immobilized MEL differed by 5−6 (for *B. subtilis*) and >2 (for *E. coli*) dilution steps. The low activity of the N-terminally bound MEL underscores the importance of the free N-terminus for an effective interaction with the bacterial cell membrane. The role of the tethering position for the activity of MEL is also reflected by the large difference in the $MIC_{tethered}/MIC_{free}$ ratio of C- and N-terminally immobilized peptides which was not observed for tethered TP and KLAL. BUF2 tethering provided the least active surfaces with MIC values >4 mM and >6.9 mM for C- and N-terminally bound peptides, respectively. Higher concentrations could not be investigated because of shortage in material. Comparing the increase in the MIC of the different peptides after immobilization (Table 2), it is interesting to note that this increase was most pronounced for BUF2, a peptide which is expected to translocate across the bacterial membranes to reach target sites in the cytoplasm.

Inner and Outer Membrane-Permeabilizing Activities of MEL, BUF2, and TP. To characterize the interaction of MEL, BUF2, TP, and their AOA-modified analogues with bacterial membranes, we examined their effect on the integrity of the inner and outer membrane of *E. coli* (strain ML-35p) at concentrations around their MICs and compared the results with the activity of KLAL and PMXB (Figure 1).

dx.doi.org/10.1021/bc200367f | *Bioconjugate Chem.* 2012, 23, 66−74

PMXB, KLAL, and the MEL peptides permeabilized the outer membrane of *E. coli* in a few minutes at concentrations of 3 μM, 5 μM, and 10 μM, respectively. Rapid permeabilization of the inner membrane followed. The observations confirmed the high lytic activity of the peptides.[32] TP and TP-AOA peptides permeabilized the membranes at 9 μM, a concentration at which AOA-TP was still inactive. A 3-fold higher concentration was required for AOA-TP-induced OM permeabilization (Figure 1). TP peptides also lysed the inner membrane, but the kinetics of permeabilization was slow (time period of ~1 h). The observations are in accordance with a complex mode of action. Depolarization of the bacterial cell membrane by enhancing the permeability for small ions coupled with transmembrane peptide transport have been suggested for the effect of TP.[23] BUF2 peptides showed low permeabilizing activity. Whereas BUF2 at 10 μM was slightly active upon the outer membrane, its AOA-modified analogues did not show significant permeabilizing activities even at 30 μM. The measuring values for IM permeabilization were identical to those of the nontreated cells. The antimicrobial effect (Table 1) but inability to permeabilize bacterial membranes supports early suggestions on a nonmembrane permeabilizing mode of action.[22,33,34]

Bilayer Permeabilizing Activities of Free MEL, BUF2, and TP Peptides. The bilayer-permeabilizing activities of the peptides toward negatively charged POPC/POPG (3/1 [mol/mol]) LUVs correlated well with the activity profile derived for peptide-induced bacterial membrane permeabilization (Figures 1 and 2). The activity of the peptides followed the

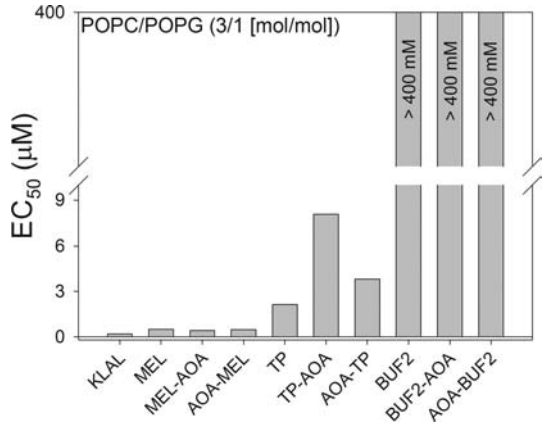


Figure 2. POPC/POPG bilayer-permeabilizing activity of MEL, BUF2, TP, KLAL, and AOA-modified analogues. The lipid concentration was 25 μM. The EC_{50} value for KLAL was derived before.[13]

order KLAL ≈ MEL > TP ≫ BUF2 (Figure 2), which is the same for the activity against *B. subtilis*, but different from the anti-*E. coli* activity profile KLAL > TP ≥ BUF2 > MEL (Table 1). These observations underscore the particular role of the *E. coli* outer wall for the peptide accessibility at the inner membrane for insertion or translocation.[35]

AOA-modification had almost no influence on the bilayer permeabilizing effect of MEL; however, it reduced the activity of TP peptides which was in accordance with the change in the activity against *E. coli*. Differences in the activity of BUF2 sequences could not be observed, as the active concentrations exceed the highest tested concentration of 400 μM.

Kinetics of Bilayer Permeabilization of Tethered MEL, BUF2, and TP Peptides. A comparison of the bilayer disturbing activity of the immobilized KLAL, MEL, TP, and BUF2 peptides confirmed the dependency of the permeabilization kinetics on peptide sequence and revealed a strong influence of the position of tethering for MEL (Figure 3). The

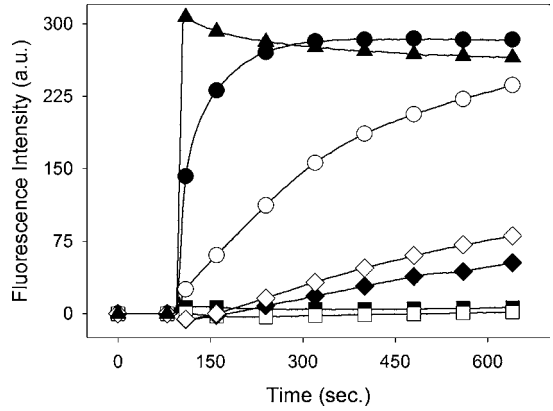


Figure 3. Kinetics of dye release from POPC/POPG (3/1 [mol/mol]) LUVs induced by tethered MEL, BUF2, TP, and KLAL. The lipid concentration was 25 μM. Peptide concentration were as follows: C-terminal tethering (black symbols), N-terminal tethering (open symbols) (●) MEL = 0.05 mM, (○) MEL = 0.06 mM; (◆) BUF2 = 0.67 mM, (◇) BUF2 = 0.99 mM; (■) TP = 0.74 mM, (□) TP = 0.74 mM; and randomly tethered (▲) KLAL = 0.05 mM.

C-terminally tethered MEL (c_P = 0.05 mM) was active as highly as the randomly tethered KLAL, whereas the N-terminally immobilized MEL showed a slow permeabilization kinetics. Such differences, also seen in the MICs (Table 2), underscore the role of the hydrophobic N-terminal chain for the MEL activity on bacterial and model membrane level. Tethered TP was inactive at about 1 mM concentration and the immobilized BUF2 showed a very slow permeabilization kinetics. As for the low loading of resin with BUF2 and the low MIC of tethered BUF2, a large amount of resin beads was required in the permeabilization experiments. Thus, the measured intensity might result from light scattering rather than dye fluorescence.

DISCUSSION

Covalent linkage of peptides via oxime-forming ligation,[13] thioalkylation,[2,12,13,36,37] disulfide exchange reaction,[16] or 1-ethyl-3-(3-dimethylaminopropyl)carbodiimide/*N*-hydroxysuccinimide activation on COOH-enriched surfaces[15,19] has been reported as a promising strategy to inhibit bacterial accumulation on surfaces. Physical parameters, such as spacer length and density of functional groups for peptide coupling,[13] and biocompatibility of the material[38] are critical for the potency of biocidal surfaces. Here, we elucidated the role of the peptide sequence and the position of immobilization upon the activity spectra of bioactive surfaces.

We tethered MEL, BUF2, and TP at the C- and N-termini on PEGylated resin beads using an oxime-forming ligation protocol.[13] The oxime chemistry is an efficient and chemoselective strategy even for immobilization of large and folded proteins.[39] The strategy was found to be most efficient for less hydrophobic/amphipathic TP and BUF2 (see Table 2 and t_R values in Table 1).

All peptides showed antimicrobial activities in the micromolar concentration range (Table 1). Permeability studies using bacteria and lipid vesicles confirmed the ability of KLAL

dx.doi.org/10.1021/bc200367f | *Bioconjugate Chem.* 2012, 23, 66–74

and MEL and the AOA-modified sequences to disturb the membrane integrity (Figures 1 and 2). Also, TPs showed a moderate permeabilizing effect, whereas BUF2 peptides were inactive in these assays.

Immobilization drastically reduced the activity of the peptides as reflected by the $MIC_{tethered}/MIC_{free}$ values (Table 2). For the KLAL model peptide, with its uniform distribution of K residues on one face of the helix surface which causes membrane permeabilization by strong accumulation at and insertion in the interface of the lipid matrix,[17] we could show that the sequence position of immobilization has only minor influence on the activity.[13] Obviously, tethering does not interfere with the localization of KLAL in the membrane and its "carpet-like" mode of action. The same was found for a tethered membrane-permeabilizing magainin 2 analogue[13] and immobilized magainin 1.[15,36]

Differently from the amphipathic KLAL helix, MEL is characterized by a sequence-based amphipathicity with basic and hydrophobic residues located mainly at the C- and N-termini, respectively. The two α-helical segments connected via a helix-breaking proline (P) localize independently upon interaction with membranes.[20] The flexible largely hydrophobic N-terminus of MEL was suggested to drive peptide insertion into lipid bilayers[21,40] and influences aggregation[41] and subsequent membrane permeabilization by formation of ion channels.[42] The highly cationic C-terminal segment strongly interacts with negatively charged head groups in the lipid bilayer surface[43] and reduces the membrane insertion and association.[44] This mode of interaction explains the pronounced reduction of the activity of N-terminally tethered MEL in comparison with the C-terminal fixation (Table 2). The activity-determining role of the N-terminal chain region of MEL is further confirmed by the following observations: The C-terminal 15-residue sequence is up to 7 times less active against bacteria than MEL.[45] Additionally, with K deletion at position 7 and K7→L exchange the lytic activity distinctly decreases,[46,47] and K7→N substitution or blocking the N-terminus with a formyl group[41] reduces the activity against Gram-negative and Gram-positive bacteria.[48]

TP is a short sequence with four arginine residues localized at the peptide termini and three tryptophans (W) flanked by P residues in the center of the sequence. Upon interaction with detergent micelles, it forms a unique amphipathic β-turn structure.[49] Membrane depolarization and translocation across the bacterial cytoplasmic membrane have been suggested as the mode of TP action.[23,24] The three W residues form a large hydrophobic domain and intercalate into membranes, while the charged termini remain exposed to the membrane surface.[24] The induction of positive curvature strain in the lipid matrix is followed by lipid displacement and pore formation.[50] Tethering at the C- and N-termini is not expected to change the TP localization in a lipid matrix. This might explain the identical activity of the terminally immobilized sequences (Table 2). The immobilized TP was active against bacteria but not able to permeabilize lipid bilayers (Figure 3). Thus, other bacterial components, such as constituents of the bacterial membrane or intracellular components, seem to be addressed.[51]

BUF2 was suggested to efficiently cross biological membranes and to bind to DNA and/or RNA[22] without inducing severe membrane permeabilization.[33,34] We confirmed that, despite remarkable antimicrobial activity, BUF2 has very low permeabilizing activity upon bacterial membranes and is not able to disrupt a negatively charged lipid bilayer (Figure 2). The massive decrease in activity after tethering (Table 2) suggests that the peptide is no longer able to interact with its target. Comparable to our findings, covalent immobilization of the lantibiotic nisin resulted in the loss of antimicrobial activity.[16] Nisin targets lipid II, a component of the bacterial cytoplasmic membrane[52] which can be reached only after migration of the free peptide across the cell membrane.[53]

CONCLUSION

In this study we showed that knowledge of the mode of peptide action can help to identify suitable sequences and appropriate sequence positions for surface tethering. Due to the limited ability of tethered CAPs to cross the bacterial cytoplasmic membrane, membrane-permeabilizing sequences such as KLAL and MEL have advantages for the preparation of antimicrobial surfaces. Moreover, the distribution of the hydrophobic and charged residues within a peptide sequence has to be taken into account. Membrane-active CAPs insert into the bacterial lipid matrix with their hydrophobic domain and disrupt the barrier function. Thus, for conserving a high antimicrobial effect, immobilization should occur at a position far away from peptide's hydrophobic domain. This was demonstrated by the higher activity of C-terminally immobilized MEL compared with the N-terminally tethered sequence. In contrast, for peptide sequences with a uniform or symmetric distribution of hydrophobic and positively charged amino acids such as KLAL and TP, the activity of the immobilized sequences is less position-dependent.

A comparison of the activities of soluble CAPs and peptides tethered at variable positions might also be helpful in getting insight into the membrane selectivity of peptides. In recent studies, colloidal gold coated cyclic CAPs containing sugar amino acids were used to identify the sites of antibiotic action.[54]

AUTHOR INFORMATION

Corresponding Author

*Phone: +49 30 94793274; Fax: +49 30 94793159, E-mail: dathe@fmp-berlin.de.

ACKNOWLEDGMENTS

The work was supported by the Investitionsbank Berlin, ProFIT Project 10134769.

REFERENCES

(1) Estrela, A. B., Heck, M. G., and Abraham, W. R. (2009) Novel approaches to control biofilm infections. *Curr. Med. Chem. 16*, 1512−1530.

(2) Gao, G., Lange, D., Hilpert, K., Kindrachuk, J., Zou, Y., Cheng, J. T., Kazemzadeh-Narbat, M., Yu, K., Wang, R., Straus, S. K., Brooks, D. E., Chew, B. H., Hancock, R. E. W., and Kizhakkedathu, J. N. (2011) The biocompatibility and biofilm resistance of implant coatings based on hydrophilic polymer brushes conjugated with antimicrobial peptides. *Biomaterials 32*, 3899−3909.

(3) Aumsuwan, N., Danyus, R. C., Heinhorst, S., and Urban, M. W. (2008) Attachment of ampicillin to expanded poly(tetrafluoroethylene): surface reactions leading to inhibition of microbial growth. *Biomacromolecules 9*, 1712−1718.

(4) Aumsuwan, N., Heinhorst, S., and Urban, M. W. (2007) The effectiveness of antibiotic activity of penicillin attached to expanded poly(tetrafluoroethylene) (ePTFE) surfaces: a quantitative assessment. *Biomacromolecules 8*, 3525−3530.

(5) Leeb, M. (2004) Antibiotics: a shot in the arm. *Nature 431*, 892−893.

(6) Brogden, K. A. (2005) Antimicrobial peptides: pore formers or metabolic inhibitors in bacteria? *Nat. Rev. Microbiol. 3*, 238−250.

(7) Yeung, A. T., Gellatly, S. L., and Hancock, R. E. W. (2011) Multifunctional cationic host defence peptides and their clinical applications. *Cell. Mol. Life Sci. 68*, 2161−2176.
(8) Overhage, J., Campisano, A., Bains, M., Torfs, E. C., Rehm, B. H., and Hancock, R. E. W. (2008) The human host defence peptide LL-37 prevents bacterial biofilm formation. *Infect. Immun. 76*, 4176−4182.
(9) Beckloff, N., Laube, D., Castro, T., Furgang, D., Park, S., Perlin, D., Clements, D., Tang, H., Scott, R. W., Tew, G. N., and Diamond, G. (2007) Activity of an antimicrobial peptide mimetic against planktonic and biofilm cultures of oral pathogens. *Antimicrob. Agents Chemother. 51*, 4125−4132.
(10) Haynie, S. L., Crum, G., and Ozen, B. O. (2000) Immobilized biocides as alternative strategy for control of microbial contamination, In *Antimicrobial/Anti-Infective Materials: Principles, Applications and Devices* (Sawan, S. P., and Manivannan, G., Eds.) pp 130−148, Chapter 6, Technomic Publishing Company, Inc., Pennsylvania, United States.
(11) Appendini, P., and Hotchkiss, J. H. (2001) Surface modification of poly(styrene) by the attachment of an antimicrobial peptide. *J. Appl. Polym. Sci. 81*, 609−616.
(12) Loose, C., O'Shaughnessy, W. S., Ferreira, L., Zumbuehl, A., Langer, R., and Stephanopoulos, G. (2007) Medical devices and coatings with non-leaching antimicrobial peptides. WO Patent 2007095393.
(13) Bagheri, M., Beyermann, M., and Dathe, M. (2009) Immobilization reduces the activity of surface-bound cationic antimicrobial peptides with no influence upon the activity spectrum. *Antimicrob. Agents Chemother. 53*, 1132−1141.
(14) Hilpert, K., Elliott, M., Jenssen, H., Kindrachuk, J., Fjell, C. D., Körner, J., Winkler, D. F, Weaver, L. L., Henklein, P., Ulrich, A. S., Chiang, S. H., Farmer, S. W., Pante, N., Volkmer, R., and Hancock, R. E. W. (2009) Screening and characterization of surface-tethered cationic peptides for antimicrobial activity. *Chem. Biol. 16*, 58−69.
(15) Humblot, V., Yala, J. F., Thebault, P., Boukerma, K., Héquet, A., Berjeaud, J. M., and Pradier, C. M. (2009) The antibacterial activity of Magainin I immobilized onto mixed thiols self-assembled monolayers. *Biomaterials 30*, 503−3512.
(16) Joshi, P. R., McGuire, J., and Neff, J. A. (2009) Synthesis and antibacterial activity of nisin-containing block copolymers. *J. Biomed. Mater. Res., Part B: Appl. Biomater. 91B*, 128−134.
(17) Dathe, M., Meyer, J., Beyermann, M., Maul, B., Hoischen, C., and Bienert, M. (2002) General aspects of peptide selectivity towards lipid bilayers and cell membranes studied by variation of the structural parameters of amphipathic helical model peptides. *Biochim. Biophys. Acta 1558*, 171−186.
(18) Dathe, M., Nikolenko, H., Meyer, J., Beyermann, M., and Bienert, M. (2001) Optimization of the antimicrobial activity of magainin peptides by modification of charge. *FEBS Lett. 501*, 146−150.
(19) Steven, M. D., and Hotchkiss, J. H. (2007) Covalent immobilization of an antimicrobial peptide on poly(ethylene) film. *J. Appl. Polym. Sci. 110*, 2665−2670.
(20) Raghuraman, H., and Chattopadhyay, A. (2007) Melittin: a membrane-active peptide with diverse functions. *Biosci. Rep. 27*, 89−223.
(21) Sitaram, N., and Nagaraj, R. (1999) Interaction of antimicrobial peptides with biological and model membranes: structural and charge requirements for activity. *Biochim. Biophys. Acta 1462*, 29−54.
(22) Park, C. B., Yi, K.-S., Matsuzaki, K., Kim, M. S., and Kim, S. C. (2000) Structure−activity analysis of buforin II, a histone H2A-derived antimicrobial peptide: The proline hinge is responsible for the cell-penetrating ability of buforin II. *Proc. Natl. Acad. Sci. U.S.A. 97*, 8245−8250.
(23) Yang, S.-T., Shin, S. Y., Hahm, K. S., and Kim, J. I. (2006) Different modes in antibiotic action of tritrpticin analogs, cathelicidin-derived Trp-rich and Pro/Arg-rich peptides. *Biochim. Biophys. Acta 1758*, 1580−1586.
(24) Salay, L. C., Procopio, J., Oliveira, E., Nakaie, C. R., and Schreier, S. (2004) Ion channel-like activity of the antimicrobial peptide tritrpticin in planar lipid bilayers. *FEBS Lett. 565*, 171−175.
(25) Krause, E., Rothemund, S., Beyermann, M., and Bienert, M. (1997) Monitoring of α-helical secondary structures in peptides by reversed-phase HPLC of replacement sets. *Anal. Chim. Acta 352*, 365−374.
(26) Matias, V. R. F., Al-Amoudi, A., Dubochet, J., and Beveridge, T. J. (2003) Cryo-transmission electron microscopy of frozen-hydrated sections of *Escherichia coli* and *Pseudomonas aeruginosa*. *J. Bacteriol. 185*, 6112−6118.
(27) Matias, V. R. F., and Beveridge, T. J. (2005) Cryo-electron microscopy reveals native polymeric cell wall structure in *Bacillus subtilis* 168 and the existence of a periplasmic space. *Mol. Microbiol. 56*, 240−251.
(28) Bagheri, M., Keller, S., and Dathe, M. (2011) Interaction of W-substituted analogs of cyclo-RRRWFW with bacterial lipopolysaccharides: the role of the aromatic cluster in antimicrobial activity. *Antimicrob. Agents Chemother. 55*, 788−797.
(29) Schindler, P. R., and Teuber, M. (1975) Action of polymyxin B on bacterial membranes: morphological changes in the cytoplasm and in the outer membrane of *Salmonella typhimurium* and *Escherichia coli* B. *Antimicrob. Agents Chemother. 8*, 95−104.
(30) Dathe, M., and Wieprecht, T. (1999) Structural features of helical antimicrobial peptides: their potential to modulate activity on model membranes and biological cells. *Biochim. Biophys. Acta 1462*, 71−87.
(31) Lateef, S. S., Gupta, S., Jayathilaka, L. P., Krishnanchettiar, S., Huang, J. S., and Lee, B. S. (2007) An improved protocol for coupling synthetic peptides to carrier proteins for antibody production using DMF to solubilize peptides. *J. Biomol. Tech. 18*, 173−176.
(32) Phadke, S. M., Lazarevic, V., Bahr, C. C., Islam, K., Stolz, D. B., Watkins, S., Tencza, S. B., Vogel, H. J., Montelaro, R. C., and Mietzner, T. A. (2002) Lentivirus lytic peptide 1 perturbs both outer and inner membranes of Serratia marcescens. *Antimicrob. Agents Chemother. 46*, 2041−2045.
(33) Kobayashi, S., Chikushi, A., Tougu, S., Imura, Y., Nishida, M., Yano, Y., and Matsuzaki, K. (2004) Membrane translocation mechanism of the antimicrobial peptide buforin 2. *Biochemistry 43*, 15610−15616.
(34) Kobayashi, S., Takeshima, K., Park, C. B., Kim, S. C., and Matsuzaki, K. (2000) Interactions of the novel antimicrobial peptide buforin 2 with lipid bilayers: proline as a translocation promoting factor. *Biochemistry 39*, 8648−8654.
(35) Hancock, R. E. W., and Chapple, D. S. (1999) Peptide antibiotics. *Antimicrob. Agents Chemother. 43*, 1317−1323.
(36) Glinel, K., Jonas, A. M., Jouenne, T., Leprince, J., Galas, L., and Huck, W. T. (2009) Antibacterial and antifouling polymer brushes incorporating antimicrobial peptide. *Bioconjugate Chem. 20*, 71−77.
(37) Gabriel, M., Nazmi, K., Veerman, E. C., Nieuw Amerongen, A. V., and Zentner, A. (2006) Preparation of LL-37-grafted titanium surfaces with bactericidal activity. *Bioconjugate Chem. 17*, 548−550.
(38) Li, P., Poon, Y. F., Li, W., Zhu, H. Y., Yeap, S. H., Cao, Y., Qi, X., Zhou, C., Lamrani, M., Beuerman, R. W., Kang, E. T., Mu, Y., Li, C. M., Chang, M. W., Leong, S. S., and Chan-Park, M. B. (2011) A polycationic antimicrobial and biocompatible hydrogel with microbe membrane suctioning ability. *Nat. Mater. 10*, 149−156.
(39) Lempens, E. H., Helms, B. A, Merkx, M., and Meijer, E. W. (2009) Efficient and chemoselective surface immobilization of proteins by using aniline-catalyzed oxime chemistry. *ChemBioChem 10*, 658−662.
(40) Klocek, G., Schulthess, T., Shai, Y., and Seelig, J. (2009) Thermodynamics of melittin binding to lipid bilayers. Aggregation and pore formation. *Biochemistry 48*, 2586−2596.
(41) Tosteson, M. T, Alvarez, O., Hubbell, W., Bieganski, R. M., Attenbach, C., Caporales, L. H., Levy, J. J., Nutt, R. F., Rosenblatt, M., and Tosteson, D. C. (1990) Primary structure of peptides and ion channels. Role of amino acid side chains in voltage gating of melittin channels. *Biophys. J. 58*, 1367−1375.
(42) Yang, L., Harroun, T. A., Weiss, T. M., Ding, L., and Huang, H. W. (2001) Barrel-stave model or toroidal model? A case study on melittin pores. *Biophys. J. 81*, 1475−1485.

(43) Hincha, D. K., and Crowe, J. H. (1996) The lytic activity of the bee venom peptide melittin is strongly reduced by the presence of negatively charged phospholipids or chloroplast galactolipids in the membranes of phosphatidylcholine large unilamellar vesicles. *Biochim. Biophys. Acta 1284*, 162−170.
(44) Monette, M., and Lafleur, M. (1995) Modulation of melittin-induced lysis by surface charge density of membranes. *Biophys. J. 68*, 187−195.
(45) Subbalakshmi, C., Nagaraj, R., and Sitaram, N. (1999) Biological activities of C-terminal 15-residue synthetic fragment of melittin: design of an analog with improved antibacterial activity. *FEBS Lett. 448*, 62−66.
(46) Blondelle, S. E., and Houghten, R. A. (1991) Hemolytic and antimicrobial activities of the twenty-four individual omission analogues of melittin. *Biochemistry 30*, 4671−4678.
(47) Blondelle, S. E., and Houghten, R. A. (1991) Probing the relationships between the structure and hemolytic activity of melittin with a complete set of leucine substitution analogs. *Pept. Res. 4*, 12−18.
(48) Oren, Z., and Shai, Y. (1997) Selective lysis of bacteria but not mammalian cells by diastereomers of melittin: structure-function study. *Biochemistry 36*, 1826−1835.
(49) Schibli, D. J., Nguyen, L. T., Kernaghan, S. D., Rekdal, Ø., and Vogel, H. J. (2006) Structure-function analysis of tritrpticin analogs: potential relationships between antimicrobial activities, model membrane interactions, and their micelle-bound NMR structures. *Biophys. J. 91*, 4413−4426.
(50) Vogel, H. J., Schibli, D. J., Jing, W., Lohmeier-Vogel, E. M., Epand, R. F., and Epand, R. M. (2002) Towards a structure-function analysis of bovine lactoferricin and related tryptophan- and arginine-containing peptides. *Biochem. Cell Biol. 80*, 49−63.
(51) Otvos, L. Jr. (2005) Antibacterial peptides and proteins with multiple cellular targets. *J. Pept. Sci. 11*, 697−706.
(52) Breukink, E., and de Kruijff, B. (2006) Lipid II as a target for antibiotics. *Nat. Rev. Drug Discovery 5*, 321−332.
(53) Wiedemann, I., Breukink, E., van Kraaij, C., Kuipers, O. P., Bierbaum, G., de Kruijff, B., and Sahl, H.-G. (2001) Specific binding of nisin to the peptidoglycan precursor lipid II combines pore formation and inhibition of cell wall biosynthesis for potent antibiotic activity. *J. Biol. Chem. 276*, 1772−1779.
(54) Pal, S., Mitra, K., Azmi, S., Ghosh, J. K., and Chakraborty, T. K. (2011) Towards the synthesis of sugar amino acid containing antimicrobial noncytotoxic CAP conjugates with gold nanoparticles and a mechanistic study of cell disruption. *Org. Biomol. Chem. 9*, 4806−4810.

Bioconjugate Chemistry

Article

pubs.acs.org/bc

Degradable Thermoresponsive Nanogels for Protein Encapsulation and Controlled Release

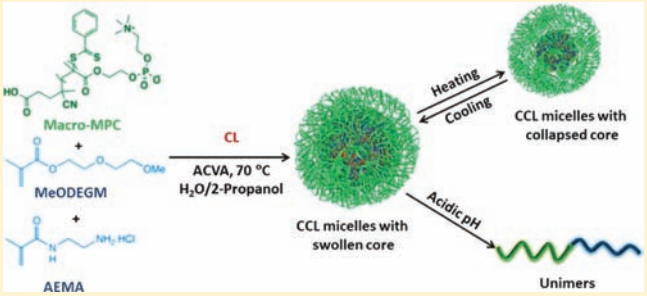
Neha Bhuchar,[†] Rajesh Sunasee,[†] Kazuhiko Ishihara,[‡] Thomas Thundat,[†] and Ravin Narain*,[†]

[†]Department of Chemical and Materials Engineering, University of Alberta, Edmonton, Alberta, T6G 2G6, Canada

[‡]Department of Materials Engineering and Department of Bioengineering, School of Engineering, The University of Tokyo, 7-3-1, Hongo, Bunkyo-ku, Tokyo 113-8656, Japan

Supporting Information

ABSTRACT: Reversible addition−fragmentation chain transfer (RAFT) polymerization technique was used for the fabrication of stable core cross-linked micelles (CCL) with thermoresponsive and degradable cores. Well-defined poly(2-methacryloyloxyethyl phosphorylcholine), poly(MPC) *macro*-RAFT agent, was first synthesized with narrow molecular weight distribution via the RAFT process. These CCL micelles (termed as nanogels) with hydrophilic poly(MPC) shell and thermoresponsive core consisting of poly(methoxydiethylene glycol methacrylate) (poly(MeODEGM) and poly(2-aminoethyl methacrylamide hydrochloride) (poly(AEMA) were then obtained in a one-pot process by RAFT polymerization in the presence of an acid degradable cross-linker. These acid degradable nanogels were efficiently synthesized with tunable sizes and low polydispersities. The encapsulation efficiencies of the nanogels with different proteins such as insulin, BSA, and β-galactosidase were studied and found to be dependent of the cross-linker concentration, size of protein, and the cationic character of the nanogels imparted by the presence of AEMA in the core. The thermoresponsive nature of the synthesized nanogels plays a vital role in protein encapsulation: the hydrophilic core and shell of the nanogels at low temperature allow easy diffusion of the proteins inside out and, with an increase in temperature, the core becomes hydrophobic and the nanogels are easily separated out with entrapped protein. The release profile of insulin from nanogels at low pH was studied and results were analyzed using bicinchoninic assay (BCA). Controlled release of protein was observed over 48 h.



INTRODUCTION

Nanogels are networks of swollen cross-linked polymers in the nanometer range. These systems are increasingly being studied for their attractive properties in drug delivery systems, biotechnology, and biomedical fields.[1−6] Nanosized particles have the advantage of enhanced permeability and retention (EPR) effect[7] owing to their small size. Apart from their small size, extra stability in aqueous medium, and high water retention, they can also be made to respond to changes in the external environment, such as temperature and pH. These so-called "smart" nanogels are increasingly being considered for drug delivery systems (DDS).[1,8] For example, change in size of pH controlled systems helps in controlled release of encapsulated drugs.[9,10] Similarly, temperature sensitive nanogels undergo a phase change from hydrophilic to hydrophobic at a transition temperature called the lower critical solution temperature (LCST). Poly(methoxydiethylene glycol methacrylate (poly(MeODEGM)) and poly(*N*-isopropylacrylamide) (poly(NIPAM)) are examples of thermoresponsive polymers. NIPAM has a LCST of 32 °C and can be easily copolymerized with other hydrophilic monomers to raise the LCST close to body temperature.[9,11] Despite the extensive biological studies, PNIPAM based materials have not yet been approved by FDA due to toxicity concerns. On the other hand, MeODEGM is widely used in medicine and pharmacology because of its excellent biocompatibility with an LCST of 24 °C.[12−14]

In order to be used as DDS, surface functionalization of nanogels with organ specific ligands can be done to target specific tissues or organs. Nanocarriers have shown very high drug loading capacity (sometimes as high as 800%, i.e., 1 mg of nanogel can load about 8.0 mg of BSA).[15] The success of using such nanocarriers relies on their ability for a controlled release of encapsulated drugs.

Nanogels have been synthesized using various approaches: physical self-assembly, covalent cross-linking of preformed polymers, and template supported nanofabrication.[16] Emulsion-free or precipitation polymerization is an easy way to produce nanomicelles where ionic surfactants are used to stabilize these nanoparticles in water. While emulsion polymerization is carried out in an aqueous medium and the core consists of the hydrophobic monomer, the inverse mini-emulsion polymerization technique is used for hydrophilic monomers like *N*-vinyl

Received: July 20, 2011
Revised: November 30, 2011
Published: December 15, 2011

ACS Publications © 2011 American Chemical Society

caprolactam.[17,18] The presence of residual surfactants with the nanogels has been a major concern of toxicity and hence is not viable for in vivo studies. Also, removal of surfactants from the nanogel is not easy. Self-assembly of amphiphilic polymers is another approach which eliminates the need for surfactants in the synthesis.

Wooley et al. synthesized triblock cross-linked micelles forming stabilized nanogels.[19−22] Multiresponsive polymeric micelles, which respond to changes in both pH and temperature, have been synthesized by Kuckling et al.[3]

Various living polymerization techniques are used for the synthesis of nanogels to maintain control over molecular weights and polydispersity of the polymer units.[7] These techniques include ring-opening polymerization, ring-opening metathesis polymerization, cyanoxyl-mediated free radical polymerization, atom transfer radical polymerization (ATRP), reversible addition−fragmentation chain transfer polymerization (RAFT), and nitroxide-mediated polymerization (NMP).[23−26] RAFT polymerization is a suitable technique and is very popular for biological applications. Micelles containing RAFT agents are easy to cross-link and thus form core cross-linked,[27−29] shell cross-linked,[30,31]or nexus between both.[32,33]

Self-assembly of the amphiphilic copolymers in water leads to the formation of micelles. However, under special conditions, like low concentration or high ionic environment, these micellar structures may not exhibit a strong amphiphilic character and hence can be unstable in aqueous solution, existing as unimers.[32,34] Cross-linking of polymers can play a significant role in imparting the required stability. This technique combines self-assembly and cross-linking and provides excellent control over the "spatial distribution of polymeric chains" in an aqueous solution.[16] Cross-linkers that degrade or hydrolyze under special conditions, for example, low pH, reductive environment, or the presence of dithiothreitol (DTT), are conducive for drug delivery, as their degradation causes the release of encapsulated macromolecules. Encapsulation of a drug prevents its fast clearance from body.[32] Responsive nanogel systems have been shown to control the activity of biopolymers and, at the same time, control the release of a therapeutic drug.[22,35,36] Previous reports have shown that nanoparticle/nanogel formation increases the stability of trapped enzymes/proteins against degradation and denaturation and modulated the release of these biomolecules at specific or targeted sites.[37−40] Protein encapsulation in nanogels, microgels, nanotubes, and nanoparticles is under intense study, and these systems have shown immense potential in drug delivery systems.[37,41−43] Protein encapsulation in hydrogel systems and controlled release of insulin, lysozome, calcitonin, and interleukin-2 has been studied intensively.[22,44−46]

The present study entails the synthesis, characterization, and application of thermoresponsive, acid degradable core cross-linked nanogels with a hydrophobic core composed of MeODEGM and AEMA cross-linked with an acid degradable cross-linker and a hydrophilic shell of poly(methacryloyloxyethyl phosphorylcholine) poly(MPC). Solubility and stability of the nanogels are attributed to the hydrophilic and zwitterionic nature of the poly(MPC) shell. The phosphorylcholine group on the methacrylate monomer resembles the polar phospholipid group present on the cell membrane. As a result, MPC based polymers show very high biocompatibility, and various copolymers of MPC are popularly used for biomedical applications.[47−49] The thermoresponsive MeODEGM core swells and shrinks with the change in temperature, which helps the entrapment of controlled encapsulation and release of therapeutic molecules. A cationic monomer, AEMA, is incorporated in the core to enhance the encapsulation of charged protein.

A range of pH domains is found in the human body. While physiological pH is 7.4, pH values in endosomes and lysosomes are 5.5−6 and 4−5, respectively. The cross-linker is acid degradable, and the release of encapsulated protein was evaluated as a function of pH. Size trends and polydispersities of various nanogels synthesized by RAFT polymerization have been analyzed. Protein encapsulation and release from such nanogels have been evaluated and compared for different cross-linker concentrations.

EXPERIMENTAL SECTION

Materials. 2-Methacryloyloxyethyl phosphorylcholine (MPC) was obtained from NOF Co (Tokyo, Japan), which was synthesized by a method reported previously.[50] 2-Hydroxyethyl methacrylate (HEMA), 2,2-dimethoxypropane, *p*-toluene sulfonic acid (pTSA), triethyl amine (TEA), and 4,4′-azobis-(cyanovaleric acid) (ACVA) were purchased from Sigma Aldrich (Canada) and were used as received. Methoxydiethylene glycol methacrylate (MeODEGM) was purchased from Sigma Aldrich (Canada) and was passed through a short pad of silica prior to use. Aminoethyl methacrylamide hydrochloride (AEMA)[51] and 4-cyanopentanoic acid dithiobenzoate (CTP)[52,53] was synthesized as described according to previous reports. 2-Propanol, HPLC grade water, acetone, hexane, and ethyl acetate were purchased from Caledon Laboratories (Canada). Micro BCA assay kit was obtained from Fisher Scientific. Gwiz *β*-galactosidase was purchased from Aldevron. Bovine serum albumin (BSA) was purchased from Promega Corporation. Insulin was obtained from Sigma Aldrich.

The chemical structures of monomers, initiator, chain transfer agent and cross-linker used in this study are depicted in Figure 1.

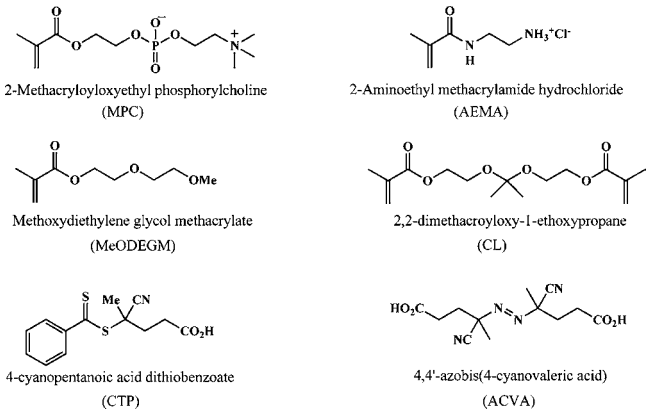


Figure 1. Chemical structures of monomers (MPC, MeODEGM and AEMA), cross-linker (CL), chain transfer agent (CTP), and initiator (ACVA).

Synthesis of 2,2-Dimethacroyloxy-1-ethoxypropane (Cross-Linker). The synthesis of the cross-linker has been recently reported by Aspinwall and co-workers.[54] However, their synthesis has been carried out under different conditions

dx.doi.org/10.1021/bc2003814 | *Bioconjugate Chem.* 2012, 23, 75−83

(refluxing in benzene for 20 h). A typical protocol for our synthesis is as follows. HEMA (2-hydroxyethyl methacrylate) (10 g, 76.8 mmol), 2,2-dimethoxypropane (4.0 g, 38.4 mmol), and *p*-TSA (66 mg, 0.34 mmol) were added to a 25 mL round-bottom flask and the mixture was stirred for 6 h at room temperature in the dark. The crude product was purified by flash column chromatography on silica gel using a mobile phase of 85:14:1 hexane/ethylacetate/TEA. Fractions containing the pure product were pooled, and the solvent was removed by rotary evaporation and dried overnight under vacuum to afford pure cross-linker as a pale yellow oil. The cross-linker was stored at 0 °C.

^{1}H NMR (400 MHz, $CDCl_3$) δ 1.39 (6H, s, $C(CH_3)_2$), 1.96 (6H, s, (6H, s, $(OCOCCH_3CH_2)_2$), 3.75 (4H, t, J = 10.1, 5.0 Hz, $C(CH_3)_2(OCH_2CH_2O)_2$), 4.30 (4H, t, J = 10.0, 5.1 Hz, $C(CH_3)_2(OCH_2CH_2O)_2$), 5.59 (2H, s, $OCOCCH_3CH_2$ − syn to methyl), 6.15 (2H, s, $OCOCCH_3CH_2$ − anti to methyl). ^{13}C NMR (100 MHz, $CDCl_3$) δ 17.9 ($OCOCCH_3CH_2$), 24.4 ($C(CH_3)_2$), 58.5 ($C(CH_3)_2(OCH_2CH_2O)_2$), 63.6 ($C(CH_3)_2(OCH_2CH_2O)_2$), 99.8 ($C(CH_3)_2$), 125.2 ($OCOCCH_3CH_2$), 135.8 ($OCOCCH_3CH_2$), 166.9 ($OCOCCH_3CH_2$). HRMS ($M+Na^+$) for $C_{15}H_{24}O_6Na$, m/z = 323.1464 observed, m/z = 323.1465 calculated.

Synthesis of Poly(MPC) MacroCTA by RAFT Polymerization. MPC macroCTA was synthesized as previously reported.[55] MPC (3 g, 10.2 mmol), CTP (2.8×10^{-2} g, 0.1 mmol), and ACVA (1.4×10^{-2} g, 0.051 mmol) were dissolved in 9 mL methanol in a 25 mL reactor. The solution was degassed by purging nitrogen for 30 min and then placed under stirring at a temperature of 60 °C for 6 h. The polymer was obtained by precipitating the mixture in acetone. Any remaining traces of monomer were removed by washing the solution in water/acetone (1:7). The precipitate was again washed with acetone for 3−4 times and the final powder was freeze−dried. The poly(MPC) macroCTA molecular weight and PDI were found to be 1.2×10^4 g/mol and 1.21, respectively, by GPC.

General Procedure for the Synthesis of poly(MPC-*b*-(MeODEGM-*st*-AEMA-*st*-CL)) Nanogel by RAFT Polymerization. The RAFT polymerizations were performed in water/2-propanol (4:1 by volume) using ACVA as initiator, Poly(MPC) as macroCTA, and 2,2-dimethacroyloxy-1-ethoxypropane as the cross-linker at 70 °C for 24 h. The molar ratio of the macroCTA and ACVA (2:1) was held constant and the molar ratio between the macroCTA and the monomers was varied in order to prepare nanogels with different chain lengths (Table 1) . A typical general procedure is as follows: Poly(MPC) macroCTA (3.9×10^{-2} g, 3.3×10^{-3} mmol), MeODEGM (0.2 g, 1.1 mmol), AEMA (4.4×10^{-2} g, 0.26 mmol), and CL (6.0×10^{-2} g, 0.19 mmol) (15 mol % with respect to total moles of MeODEGM and AEMA) were dissolved in 4 mL water and sonicated. ACVA (4.0×10^{-4} g, 1.6×10^{-3} mmol) was dissolved in 1 mL 2-propanol and added to the reaction mixture. The solution was degassed by purging with nitrogen for 30 min and the reaction was carried out at 70 °C for 24 h. Reaction was stopped by quenching in liquid nitrogen. Nanogel was centrifuged at 14 000 rpm and 40 °C. The supernatant was discarded and the precipitate was washed with distilled water 3−4 times. The final precipitate was dissolved in water and freeze−dried overnight. A white powder was recovered and stored in the refrigerator.

Protein Encapsulation. Drug loading was done using incubation method. Aqueous solutions of nanogels were prepared in 10 mg/mL concentrations. The nanogel solution was mixed with 1.5×10^2 μL solution of 1 mg/mL BSA solution and incubated for 24 h at 4 °C. The total amount of protein encapsulated was calculated after centrifuging the sample at 40 °C in Beckmann Coulter Centrifuge (Microfuge 22R) (14 000 rpm, 15 min). The solution was separated into a white precipitate and supernatant. The amount of protein encapsulated in the nanogel was measured by incubating with bicinchoninic acid (BCA assay) for 2 h at 37 °C and measuring the absorbance at 570 nm using TECAN Genios Pro microplate reader. The plate reader was precalibrated using varying concentrations of protein and data were analyzed using Boltzmann function to give the best sigmoidal fit. The feed amounts for encapsulation of insulin and β-galactosidase are 50 and 2 μg, respectively.

The amount of protein encapsulated (D) was calculated as follows:

$$D = \frac{\text{total protein} - \text{free protein}}{\text{total protein}}$$

where free protein is the protein in supernatant.

Release of Protein from Nanogels at Acidic pH. In order to study the release of encapsulated protein, the nanogel was precipitated and redispersed in a citrate buffer solution of pH 4.8 and 6.4. The solution was divided into 7 aliquots. At regular intervals, the nanogels aliquots were precipitated and total protein content in the supernatant (released protein) was determined using BCA assay.

Activity of Protein. The activity of β-galactosidase protein encapsulated in nanogel was studied by β-galactosidase assay. The nanogel was precipitated and separated from the supernatant (solution 1). The precipitate was redispersed in 100 μL sodium phosphate buffer solution (solution 2). 150 μL *O*-nitrophenyl-β-D-galactopyranoside (ONPG) (4 mg/mL) was added to 100 μL solutions 1 and 2 in the presence of 4.5 μL 100× Mg solution (0.64 μL of β-mercaptoethanol in 100 μL of 0.1 M $MgCl_2$) in a 96 well plate and was incubated for 4 h at 37 °C. The yellow color developed was detected using the TECAN Genios Pro microplate reader at 420 nm.

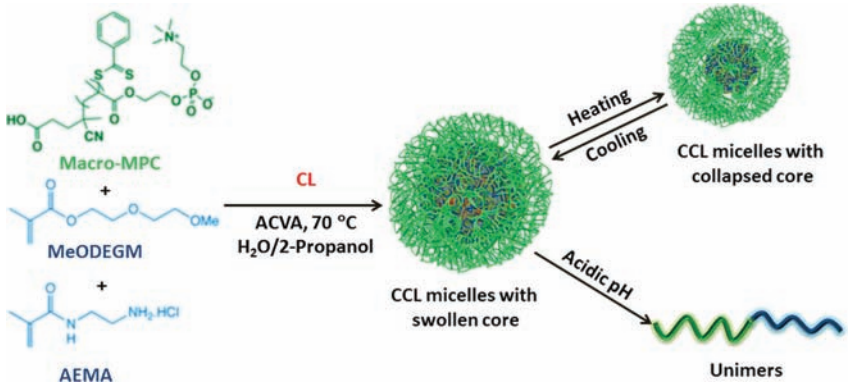
Characterizations. *Nuclear Magnetic Resonance.* ^{1}H and ^{13}C NMR spectra of the cross-linker were recorded on a

Table 1. Comparison of Hydrodynamic Diameter of MPC-*b*-(MeODEGM-*st*-AEMA-*st* CL) Nanogel with Varying Cross-Linker Concentrations and MEODEGM-AEMA Chain Length

nanogel	nanogel composition	cross-linker (mol %)	hydrodynamic diameter (nm)	polydispersity
NG1	MPC_{70}-*b*-(MeODEGM-*st*-AEMA-*st*-CL)$_{500}$	7	45	0.09
NG2	MPC_{70}-*b*-(MeODEGM-*st*-AEMA-*st*-CL)$_{300}$	10	60	0.29
NG3	MPC_{70}-*b*-(MeODEGM-*st*-AEMA-*st*-CL)$_{400}$	10	114	0.07
NG4	MPC_{43}-*b*-(MeODEGM-*st*-AEMA-*st*-CL)$_{400}$	15	140	0.09
NG5	MPC_{43}-*b*-(MeODEGM-*st*-AEMA-*st*-CL)$_{400}$	20	150	0.14
NG6	MPC_{43}-*b*-(MeODEGM-*st*-AEMA-*st*-CL)$_{400}$	25	282	0.08
NG7	MPC_{43}-*b*-(MeODEGM-*st*-AEMA-*st*-CL)$_{400}$	35	-	-

dx.doi.org/10.1021/bc2003814 | *Bioconjugate Chem.* 2012, 23, 75−83

Scheme 1. Schematic Representation of Core Cross-Linked Micelles with Thermoresponsive and Degradable Cores



Varian 400 MHz instrument. The sample was prepared using $CDCl_3$ as solvent.

MeODEGM shows thermoresponsive behavior and undergoes coil to globule transition at a lower critical solution temperature (LCST) of 24 °C. This transition was also studied at a molecular level by NMR spectroscopy in D_2O. The signal intensities of MeODEGM protons vs that of solvent protons were compared at various temperatures (below and above the LCST). To account for the chemical shift of signal intensities at elevated temperatures, 1% 4,4-dimethyl-4-silapentane-1-sulfonic acid (DSS) solution was added as a reference at 0 ppm.

Mass Spectroscopy. Mass spectroscopy was carried out in Agilent Technologies 6220 orthogonal acceleration TOF (oaTOF) (Santa Clara California, USA).

Gel Permeation Chromatography (GPC). The number average molecular weight (M_n) and polydispersity (M_w/M_n) of the macro CTA was studied using Viscotek conventional GPC connected to two Waters Ultrahydrogel linear WAT011545 columns (pore size: blend; exclusion limit = 7.0×10^6) and has a Viscotek model 250 dual detector. An acidic buffer of 0.50 M sodium acetate/0.50 M acetic acid was used as eluent. Calibration of GPC was done by six monodispersed poly(ethylene oxide) (PEO) standards ($M_p = (1.01 \times 10^3) - (1.01 \times 10^5)$ g mol^{-1}).

Dynamic Light Scattering (DLS). Size of MeODEGM nanogels was analyzed using Viscotek DLS 802 instrument, which is equipped with a He−Ne laser at a wavelength of 632 nm and a Peltier temperature controller. The aqueous nanogel solution was filtered through a 0.45 μm pore size Millipore membrane. Data were obtained at an angle of 90° within the temperature range 25−50 °C. *Omnisize* software was used to record the DLS size data. 0.5 mL aliquots were drawn at 0 min, 30 min, 1 h, 2 h, 5 h, 18 h, and 24 h of reaction time.

Transmission Electron Microscopy (TEM). Size and morphology of nanogels at room temperature were analyzed on a Philips transmission electron microscope operated at 80 kV and fitted with a CCD camera. A droplet of a properly diluted nanogel solution was placed on the TEM carbon coated copper grid and allowed to air-dry before it was stained with phosphotungstic acid (2 wt % aqueous solution) for 1 min. The sample was then allowed to dry overnight prior to observation.

RESULTS AND DISCUSSION

Nanogels (core cross-linked micelles) were successfully synthesized with a hydrophilic shell and a thermoresponsive core in a one-pot manner using the RAFT polymerization method (Scheme 1). These nanogels degraded under acidic conditions, and the rate of degradation was dependent on both pH and cross-linker concentration. The acid degradable nanogels were then used to study the encapsulation efficiency and the release profile of proteins.

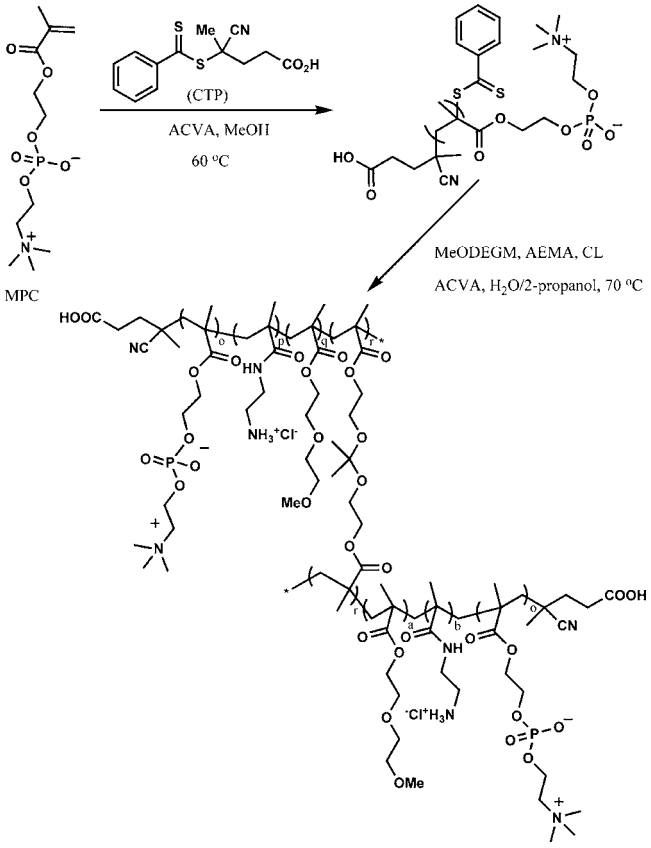
Synthesis of 2,2-Dimethacroyloxy-1-ethoxypropane (acid degradable cross-linker). The pH in the human body varies from 7.4 (physiological pH) to 5.5−6 in endosomes and 4−5 in lysosomes. Acid degradable cross-linker was synthesized for this study, to facilitate release of encapsulated proteins at low pH. Aspinwall and co-workers[54] recently reported the synthesis of the cross-linker, which involved the use of benzene as solvent under high temperature with a reaction time of 20 h. However, our synthesis proceeds under much milder conditions, namely, in the absence of organic solvent at room temperature for 6 h of reaction time. The reaction of HEMA with 2,2-dimethoxypropane in a molar ratio of 2:1 yields acid degradable cross-linker as shown in Figure S1 (Supporting Information). Excess HEMA was removed during flash column chromatography on silica gel using a small amount of triethylamine in the eluent system. The presence of triethylamine prevents the degradation of the acid sensitive cross-linker. It was observed that, if the reaction was continued for more than the specified time of 6 h, the product turned dark brown, which is possibly due to side reactions that started simultaneously. The cross-linker was stored at 0 °C to avoid these side reactions. The ^1H and ^{13}C NMR spectra of the purified cross-linker are shown in Figures S2 and S3 (Supporting Information).

Synthesis of Nanogels. Core−shell nanogels were synthesized using acid degradable cross-linker, by RAFT polymerization technique. A one-pot synthesis method developed by Pan et al.,[56] which involved the polymerization of cross-linker with the monomer to get stabilized core cross-linked micelles, was followed for synthesizing nanogels. Recently, our group has extended this powerful one-pot synthesis for the fabrication of fixed CCL micelles having primary amino groups on the outer coronas for further surface functionalization.[58] Overall, in this RAFT polymerization process, cross-linking and polymerization happened simultaneously.

The core shell nanogel comprising a temperature sensitive MeODEGM core along with a primary amine monomer AEMA, imparting an additional functionality to the core, was cross-linked by an acid degradable cross-linker (CL) and a hydrophilic shell of MPC polymer chains (Scheme 2). MPC macroCTA (M_n = 1.2 × 10^4 g/mol) was synthesized in methanol as discussed in previous protocol.[55] The conversion

dx.doi.org/10.1021/bc2003814 | *Bioconjugate Chem.* 2012, 23, 75−83

Scheme 2. RAFT Synthesis of poly(MPC-*b*-(MeODEGM-*st*-AEMA-*st*-CL)) Core Cross-Linked Micelles with Thermoresponsive and Degradable Cores



was kept low (60%) in order to prevent the formation of dead chains as a result of the termination reactions that set in toward the end of the reaction. The macroCTA was further used to copolymerize MeODEGM and AEMA in the presence of the cross-linker in water and 2-propanol using ACVA as initiator (Scheme 2). The use of ACVA as initiator is driven by two factors. First, it can be thermally decomposed and has a half-life of 10 h in aqueous solution at 69 °C, and second, it is slightly more hydrophilic than other thermally sensitive initiators like AIBN. Tao et al. observed that a hydrophobic initiator could interfere with the hydrophobic core and hence produce unstable micelles. On the contrary, ACVA, which is more hydrophilic, yields controlled and more stable nanogels.[57]

Micelle structures can easily dissociate after dilution, and in order to prevent dissociation of micelle structures of diblock copolymers, they are stabilized by cross-linking.[58] The size and stability of nanogels depend on cross-linker concentration (molar ratio with respect to the total molar monomers concentration) (expressed in percentage). For the synthesis of uniform, fixed micelles, it is necessary to have a suitable amount of cross-linker. Branched copolymers and unstable nanostructures can be formed as a result of low cross-linker concentration.[12] On the other hand, very high cross-linker concentration can result in the formation of microgel or hydrogel networks.[59] To confirm this effect, cross-linker concentration was varied from 7, 10, 15, 20, 25, and 35 mol %. The particle size and their polydispersities were determined using DLS as shown in Table 1. The evolution of hydrodynamic size of the nanogel with time was studied for varying amounts of cross-linker (Figure 2). It was observed that the nanogels attained a stable size within 5−6 h of reaction time

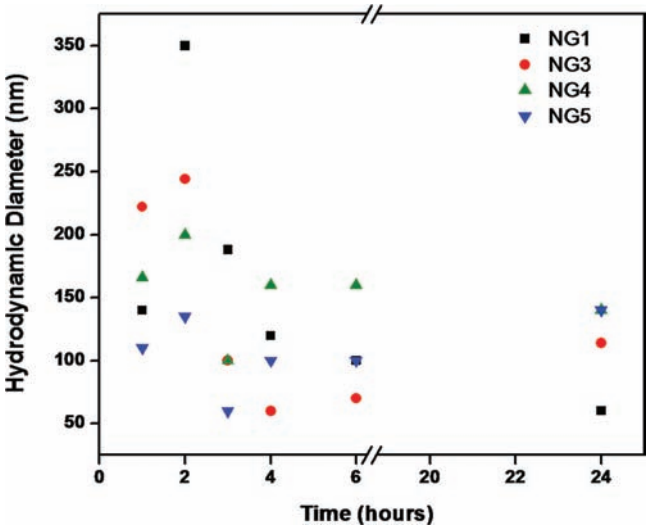


Figure 2. Evolution of hydrodynamic diameter of reaction mixture of cross-linking nanogel and variation of size with varying cross-linker (CL) concentration.

and with increasing cross-linker concentration, the hydrodynamic size also increased (Table 1).

However, for poorly degradable cross-linker concentrations (7−10 mol %), the sizes were small (45−60 nm) and increased with temperature. This may be due to the unstable micelle structures and formation of aggregates of MeODEGM polymers. On the other hand, for a high concentration of cross-linker (35 mol %), a very turbid solution was obtained. Particle precipitation was observed when the solution was left undisturbed for 10−15 min. Thus, the size of particles formed was in the micrometer range, and hence, particles were unstable in solution. Stable nanogels were obtained at an optimum cross-linker concentration of 15−20 mol % with particle sizes of 125−150 nm and low polydispersities (0.09−0.14) as determined by DLS. TEM images of these nanogels (**NG4** and **NG6**) are depicted in Figure 3 and showed that they were

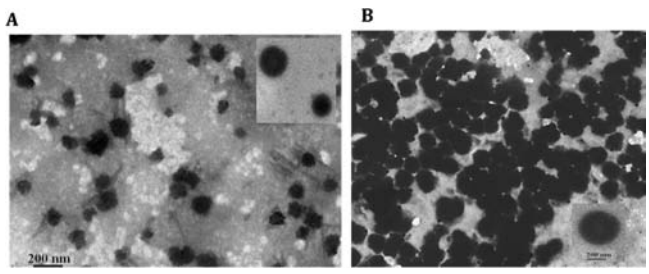


Figure 3. TEM images of nanogels showing (A) NG4 (15 mol % CL) and (B) NG6 (25 mol % CL).

spherical in shape with a smooth surface. Both **NG3** (10 mol % CL) and **NG4** (15 mol % CL) (Figure S4, Supporting Information) displayed good dispersibility; however, for **NG6** (25 mol % CL), the particles started to aggregate. More importantly, the TEM results indicated that the nanogel had a core−shell structure, which confirmed nanogel formation.

MeODEGM is a thermoresponsive polymer and experiences a phase change from being hydrophilic at low temperatures (24

dx.doi.org/10.1021/bc2003814 | *Bioconjugate Chem.* 2012, 23, 75−83

°C) to hydrophobic at high temperatures. The MeODEGM core of the micelle, therefore, collapses at high temperatures, which is indicated by a notable decrease in size above 24 °C.

Table 1 shows the variation in size of nanogels with change in MeODEGM chain length and cross-linker concentration. MeODEGM chain length has little effect on the size of nanogels, but it affects the LCST of the nanogel.

Lutz et al. observed that an increase in MeODEGM levels in the nanogel raised LCST from 24 °C to as high as 84 °C.[13,60] Temperature dependent DLS studies showed that nanoparticles shrunk from 147 nm at 15 °C to 115 nm at 50 °C (**NG4**) and 75 nm at 15 °C to 53 nm at 50 °C (**NG2**) as shown in Figure 4. The phase transition of MeODEGM from

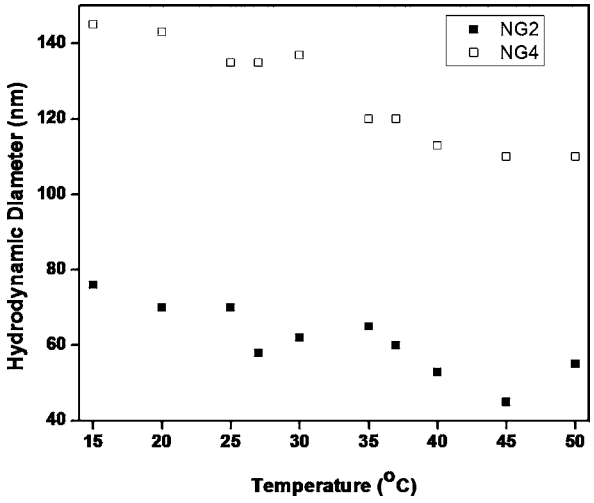


Figure 4. Decrease in mass-average hydrodynamic diameter with increase in temperature obtained for 0.5 mg/mL aqueous solution of nanogel, for varying cross-linker (CL) concentration.

hydrophilic to hydrophobic state could be seen as the solution immediately turned milky white from transparent as the temperature was raised (Figure S5, Supporting Information). The nanogels were found to be quite stable at 50 °C.

The phase transition behavior of MeODEGM core was studied using VTNMR (Variable Temperature ^{1}H NMR) as depicted in Figure S6 (Supporting Information). While disappearance of the peak for the thermoresponsive was expected at higher temperature, only a small reduction in peak intensity was observed. This shows that nanogels behave differently from homogeneous and macroscopic systems. Furthermore, Schönhoff et al. have attributed this reduction in NMR signal intensity of poly(NIPAM) to the decrease in polymer segmental mobility, which further decreases the relaxation time, T.[61] The ^{1}H NMR peak intensity of methylene group of poly(MeODEGM) at 3.4 ppm was compared with normalized solvent (D_2O) peak intensity. The reduction in polymer signal intensity above phase transition is shown in Figure 5.

The effect of pH on the nanogel was studied to find the rate of degradation of the cross-linker at low pH. The pH of distilled water is slightly acidic (pH 6.7). Nanogels in distilled water could be stored for 2−3 days without degradation. A comparative study of the rate of degradation at different pH (pH 4.5, 5.2, and 6.4) and varying cross-linker concentration (10 and 15 mol %) was carried out. As expected, the nanogels were found to be unstable and degrade under acidic conditions

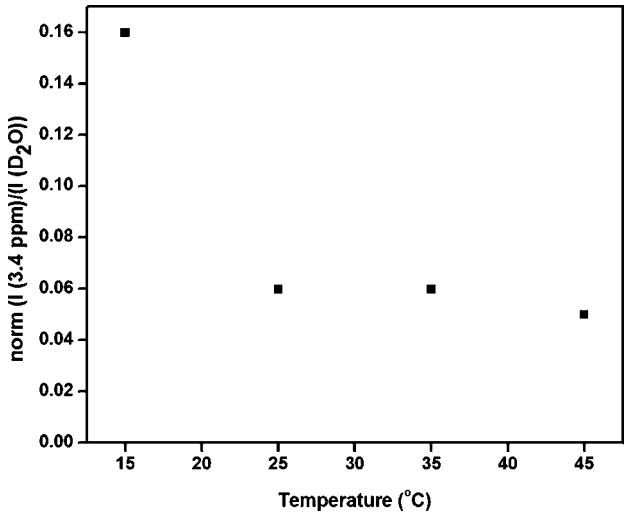


Figure 5. Normalized ratio of ^{1}H NMR signal intensity of MeODEGM protons to D_2O protons vs temperature as observed for the methylene group protons of MeODEGM at 3.4 ppm and D_2O for NG4.

(Figure 6). Also, the rate of degradation of the nanogels is more pronounced for low cross-linker concentration (10 mol %),

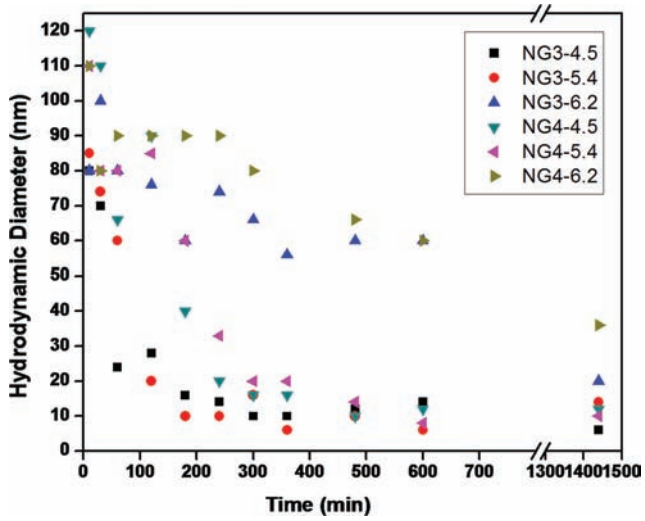


Figure 6. Degradation profile of NG3 and NG4 at pH 4.5, 5.4, and 6.2.

which degraded within 2 h at pH 4.5 and 5.2. The nanogels were found to be very stable under neutral and alkaline pH. For higher cross-linker concentrations, however, the degradation curve shifted to the right, indicating higher stability at low pH for a longer time.

Protein Encapsulation. An important application of stimuli-responsive nanogels is the encapsulation of macromolecules in their core or coronas. Cross-linking of polymers provides a stable micelle structure, which can be exploited to trap macromolecules of various sizes. However, the release of trapped drugs is only possible by the degradation of cross-linker under physiological conditions. We have used acid degradable cross-linker, which degrades at low pH, thereby releasing the encapsulated proteins.

The thermoresponsive nature of the synthesized nanogels plays a vital role for protein encapsulation, since at low temperature (4 °C), the nanogel core and shell are both

dx.doi.org/10.1021/bc2003814 | Bioconjugate Chem. 2012, 23, 75−83

hydrophilic and, as temperature increases to 37 °C, the core of the nanogels become hydrophobic and therefore the nanogels can easily be separated out of solution by simple centrifugation. Thus, the nanogels were collapsed at 37 °C to trap the protein within the core and hence the amount of entrapped protein can easily be estimated.

The protein was loaded using the incubation method. Insulin, BSA, and β-galactosidase were incubated overnight in aqueous nanogel solutions (5 mg/mL) at 4 °C. The three proteins vary largely in their sizes. Insulin is the smallest protein with size 5.81 kDa, while BSA has a molecular weight of 66.8 kDa and β-galactosidase is the largest protein of size 540 kDa. MeODEGM nanogels are hydrophobic at room temperature. The proteins were incubated at low temperature (7 °C) to ensure maximum encapsulation. The incubation method is reported to be less efficient than the encapsulation method, as per previous reports.[62] However, these nanogels showed high loading probably due to the additional functionality of the core of the nanogels (presence of protonated amino groups). The cationic nature of the core has (PAEMA-pK_a 8.8) has facilitated the encapsulation of negatively charged macromolecules. For example, BSA has a pI (isoelectric point or the point of zero charge) of 4.6 and therefore has a negative surface charge at neutral pH.

The nanogel was precipitated at 14 000 rpm and 40 °C. Before precipitating, the gels were collapsed to trap the protein within the core. The amount of entrapped protein was estimated by calculating the difference between the amount of protein added and the amount of nonencapsulated protein in the aqueous phase of precipitated protein. It was observed that two factors that dictated the amount of protein encapsulated were the cross-linker concentration and the percentage of AEMA in the core.

A comparative study of three samples is shown in Table 2. The analysis showed that 92% of insulin was encapsulated for nanogel with 15% feed cross-linker concentration and 25% feed ratio AEMA (**NG4b**). For higher cross-linker concentration, the encapsulation was reduced to 80%. A possible explanation for the strong dependence of encapsulation efficiency on the cross-linker concentration may be due to its effect on pore size of the cross-linked nanogel. A higher cross-linker concentration is expected to produce a tighter network, therefore providing a smaller pore size. Encapsulation of macromolecules is easier for a larger pore size network. While lower cross-linker concentration fails to cross-link stably, higher amounts of cross-linker decrease the pore size leading to reduced loading capacity. To study the effect of AEMA, nanogels with varying amount of cationic components were studied and compared. For the same amount of cross-linker, the AEMA component also affects the encapsulation efficiency. This may be due to the electrostatic interaction between the protein and cationic nanogel due to opposite charges of protein and MeODEGM-AEMA nanogel at neutral pH.

Table 2. Protein Encapsulation Efficiencies for Nanogels of Varying Cross-Linker Concentration and AEMA Content[a]

samples	protein	protein encapsulation (μg)	encapsulation (%)
NG4a	Insulin	46	92
	BSA	54	36
	β-Gal	-	-
NG4b	Insulin	46	92
	BSA	90	60
	β-Gal	0.7	35
NG5	Insulin	40	80
	BSA	40	27
	β-Gal	-	-

[a](A) **NG4a**: 15 mol % CL and 5% AEMA feed ratio. (B) **NG4b**: 15 mol % CL and 25% AEMA feed ratio. (C) **NG 5**: 20 mol % CL and 10% AEMA feed ratio.

Table 2 indicates that **NG4b** has the optimum cross-linker concentration (15 mol %) and AEMA concentration (5 mol %) for the encapsulation of proteins.

A careful analysis of data indicates that the size and properties of macromolecules also play an important role in determining the total encapsulation. Insulin showed highest percentage encapsulation in agreement with its smallest size and lowest molecular weight (5.81 kDa). β-Galactosidase, on the other hand, has a molecular weight of 540 kDa, and consequently the lowest encapsulation efficiency. The encapsulation efficiency decreased from 92% for insulin to 35% for β-galactosidase.

Release Profile. The release profile of nanogels was studied at varying pH. Nanogels with 15% and 20% cross-linker concentration were incubated overnight with 50 μL insulin protein (1 mg/mL). The nanogels were precipitated and the amount of protein encapsulated was determined by BCA assay. The precipitated nanogel was redispersed in buffer solutions of pH 4.8 and 6.4. Aliquots from buffer solution were taken at regular intervals and the amount of protein released was calculated. Almost 90% protein was released over a period of 48 h at pH 4.8. Thus, the release profile of insulin from MeODEGM nanogels is slow, and no burst release was observed (Figure 7).

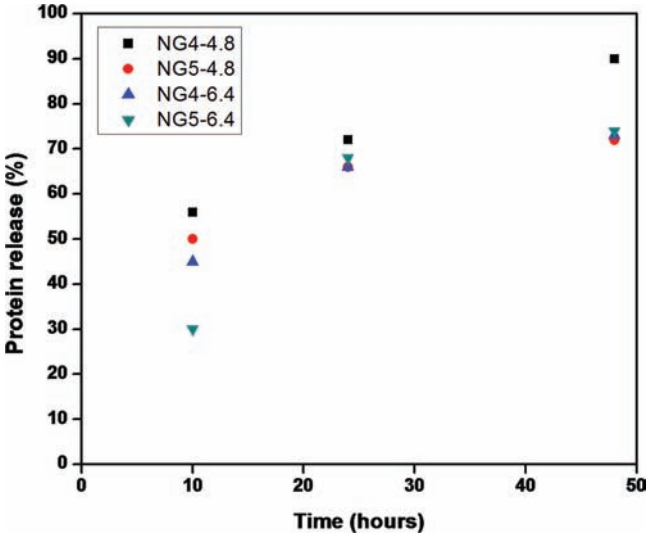


Figure 7. Cumulative release profile of insulin from NG4 and NG5 at pH 4.8 and 6.4.

To confirm the structure and activity of β-galactosidase after loading, β-galactosidase assay was conducted on the 400 μL of 5 mg/mL aqueous nanogel solution loaded with β-gal. The amount of encapsulation based on BCA assay calculation was found to be 35%. Figure S7 (Supporting Information) showed the change in color of nanogel when ONPG was hydrolyzed to *o*-nitrophenol (yellow) and galactose by β-galactosidase. The activity of protein in supernatant and nanogel was calculated to

dx.doi.org/10.1021/bc2003814 | *Bioconjugate Chem.* 2012, 23, 75–83

be 1384 mU/mg and 4642 mU/mg, respectively. It was therefore found that the protein was present mostly in its native form after encapsulation and likely retained its catalytic activity.

CONCLUSION

In summary, we have successfully synthesized novel stable thermoresponsive and acid degradable poly(MeODEGM-AEMA) core-cross-linked micelles via RAFT polymerization using poly(MPC) macro RAFT agent. Sizes of these nanogels can be tuned accordingly by varying the cross-linker concentration and MeODEGM chain length. AEMA provides cationic character to the nanogel core, which facilitates the encapsulation of oppositely charged proteins, for example, insulin, BSA, and β-galactosidase. The loading efficiency of these proteins largely depends on the pore size of nanogels, the cationic component, and the size of protein. The degradation profile of these proteins encapsulated in acid-degradable nanogels was studied at lower pH, and a controlled release profile of protein was observed. These MPC-*b*-(MeODEGM-*st*-AEMA-*st*-CL) nanogels therefore have promising applications as smart carriers for targeted drug delivery systems and controlled release.

ASSOCIATED CONTENT

Supporting Information

Synthesis of acid degradable cross-linker, HNMR and CNMR spectra of cross-linker, TEM image of **NG3**, VT-NMR study of nanogel, digital photograph of aqueous solution of nanogel on heating above and cooling below LCST, digital photograph of β-galactosidase assay conducted on aqueous solution of nanogel. This material is available free of charge via the Internet at http://pubs.acs.org.

AUTHOR INFORMATION

Corresponding Author

*E-mail: narain@ualberta.ca, Telephone: 1-780-492-1736, Fax: 1-780-492 2881.

ACKNOWLEDGMENTS

The authors acknowledge support from Natural Sciences and Engineering Research Council of Canada (NSERC) for the funding of this work.

REFERENCES

(1) Oh, J. K., Drumright, R., Siegwart, D., and Matyjaszewski, K. (2008) The development of microgels/nanogels for drug delivery applications. *Prog. Polym. Sci. 33*, 448−477.

(2) Graham, N. B., and Cameron, A. (1998) Nanogels and microgels: the new polymeric materials playground. *Pure Appl. Chem. 70*, 1271−1275.

(3) Kuckling, D., Vo, C. D., and Wohlrab, S. E. (2002) Preparation of nanogels with temperature-responsive core and pH-responsive arms by photo-cross-linking. *Langmuir 18*, 4263−4269.

(4) Koul, V., Mohamed, R., Kuckling, D., Adler, H.J. P., and Choudhary, V. (2011) Interpenetrating polymer network (IPN) nanogels based on gelatin and poly(acrylic acid) by inverse miniemulsion technique: Synthesis and characterization. *Colloids Surf., B: Biointerfaces 83*, 204−213.

(5) Kim, Y., Thapa, M., Hua, D. H., and Chang, K. O. (2011) Biodegradable nanogels for oral delivery of interferon for norovirus infection. *Antiviral Res. 89*, 165−173.

(6) Sahiner, N., Godbey, W. T., McPherson, G. L., and John, V. T. (2006) Novel nanogels as drug delivery systems for poorly soluble anticancer drugs. *Colloid Polym. Sci. 284*, 1121−1129.

(7) Fang, J., Nakamura, H., and Maeda, H. (2011) The EPR effect: Unique features of tumor blood vessels for drug delivery, factors involved, and limitations and augmentation of the effect. *Adv. Drug Delivery Rev. 63*, 136−151.

(8) Harris, J. M., and Chess, R. B. (2003) Effect of PEGylation on pharmaceuticals. *Nat. Rev. Drug Discovery 2*, 214−221.

(9) Heyden, K. V., Babooram, K., Ahmed, M., and Narain, R. (2009) Protein encapsulation and release from degradable sugar based hydrogels. *Eur. Polym. J. 45*, 1689−1697.

(10) Risbud, M. V., Hardikar, A. A., Bhat, S. V., and Bhonde, R. R. (2000) pH-sensitive freeze-dried chitosan−polyvinyl pyrrolidone hydrogels as controlled release system for antibiotic delivery. *J. Controlled Release 68*, 23−30.

(11) Prevot, M., Déjugnat, C., Möhwald, H., and Sukhorukov, G. B. (2006) Behavior of temperature-sensitive PNIPAM confined in polyelectrolyte capsules. *ChemPhysChem 7*, 2497−2502.

(12) Goh, C. C. E., and Stöver, D. H. (2002) Cross-linked poly(methacrylic acid-co-poly(ethylene oxide) methyl ether methacrylate) microspheres and microgels prepared by precipitation polymerization: A morphology study. *Macromolecules 35*, 9983−9989.

(13) Lutz, J. F., Akdemir, O., and Hoth, A. (2006) Point by point comparison of two thermosensitive polymers exhibiting a similar LCST: is the age of poly(NIPAM) over? *J. Am. Chem. Soc. 128*, 13046−13047.

(14) Hu, T., You, Y., Pan, C., and Wu, C. (2002) The coil-to-globule-to-brush transition of linear thermally sensitive poly(N-isopropylacrylamide) chains grafted on a spherical microgel. *J. Phys. Chem. B 106*, 6659−6662.

(15) Chen, Y., Zheng, X., Qian, H., Mao, Z., Ding, D., and Jiang, X. (2010) Hollow core-porous shell structure poly(acrylic acid) nanogels with a super high capacity of drug loading. *Appl. Mater. Interfaces 2*, 3532−3538.

(16) Tan, J. P. K., Tan, M. B. H., and Tam, M. (2010) Application of nanogel systems in the administration of local anesthetics. *Local Reg. Anesth. 3*, 93−100.

(17) Oh, J. K., Perineau, F., and Matyjaszewski, K. (2006) Preparation of nanoparticles of well-controlled water-soluble homopolymers and block copolymers using an inverse miniemulsion ATRP. *Macromolecules 39*, 8003−8010.

(18) Smulders, W., and Monteiro, M. J. (2004) Seeded emulsion polymerization of block copolymer core-shell nanoparticles with controlled particle size and molecular weight distribution using xanthate-based RAFT polymerization. *Macromolecules 37*, 4474−4483.

(19) Murthy, K. S., Ma, Q., Remsen, E. E., Kowalewski, T., and Wooley, K. L. (2003) Thermal shaping of shell-crosslinked (SCK) nanoparticles, facilitated by nanoconfinement of fluid-like cores. *J. Mater. Chem. 13*, 2785−2795.

(20) Arotçaréna, M., Heise, B., Ishaya, S., and Laschewsky, A. (2002) Preparation of shell cross-linked micelles by polyelectrolyte complexation. *J. Am. Chem. Soc. 124*, 3787−3793.

(21) Weaver, J. V. M, Tang, Y., Liu, S., Iddon, P. D., Grigg, R., Billingham, N. C., Armes, S. P., Hunter, R., and Rannard, S. P. (2004) Switching the inside and the outside of aggregates of water-soluble block copolymers with double thermoresponsivity. *Angew. Chem., Int. Ed. 116*, 1413−1416.

(22) Alarcon, C., de las, H., Pennadam, S., and Alexander, C. (2005) Stimuli responsive polymers for biomedical applications. *Chem. Soc. Rev. 34*, 276−285.

(23) Sciannamea, V., Jérôme, R., and Detrembleur, C. (2008) In-situ nitroxide-mediated radical polymerization (NMP) processes: their understanding and optimization. *Chem. Rev. 108*, 1104−26.

(24) Tsarevsky, N. V., and Matyjaszewski, K. (2007) Green atom transfer radical polymerization: from process design to preparation of well-defined environmentally friendly polymeric materials. *Chem. Rev. 107*, 2270−99.

(25) Moad, G., Rizzardo, E., and Thang, S. H. (2008) Toward living radical polymerization. *Acc. Chem. Res. 41*, 1133−1142.

(26) Chiefari, J., Chong, Y. K. B., Ercole, F., Krstina, J., Jeffery, J., Le, T. P. T, Mayadunne, R. T. A., Meijs, G. F., Moad, C. L., Moad, G.,

Rizzardo, E., and Thang, S. H. (1998) Living free-radical polymerization by reversible addition-fragmentation chain transfer: the RAFT process. *Macromolecules 31*, 5559−5562.
(27) Loppinet, B., Sigel, R., Larsen, A., Fytas, G., Vlassopoulos, D., and Liu, G. (2000) Structure and dynamics in dense suspensions of micellar nanocolloids. *Langmuir 16*, 6480−6484.
(28) Stewart, S., and Liu, G. (1999) Hollow nanospheres from polyisoprene-*block*-poly(2-cinnamoylethylmethacrylate)-*block*-poly(*tert*-butylacrylate). *Chem. Mater. 11*, 1048−1054.
(29) Saito, R., Ishizu, K., and Fukutomi, T. (1990) Cross-linking of the inner poly(methyl methacrylate) core of poly(methylstyrene-*b*-methyl methacrylate) micelles in selective solvent: 1. Effect of solvent selectivity. *Polymer 31*, 679−683.
(30) Butun, V., Billingham, N. C., and Armes, S. P. (1998) Synthesis of shell-cross linked micelles with tunable hydrophilic/hydrophobic cores. *J. Am. Chem. Soc. 120*, 12135−12136.
(31) Henselwood, F., and Liu, G. J. (1997) Water soluble nanospheres from poly(2-cinnamoylethyl methacrylate)-*block*-poly(acrylic acid). *Macromolecules 30*, 488−493.
(32) Zhang, L., Liu, W., Lin, L., Chen, D., and Stenzel, M. H. (2008) Degradable disulfide core-cross-linked micelles as a drug delivery system prepared from vinyl functionalized nucleosides via the RAFT process. *Biomacromolecules 9*, 3321−3331.
(33) Zhang, L., Bernard, J., Davis, T. P., Barner-Kowollik, C., and Stenzel, M. (2008) Acid-degradable core-crosslinked micelles prepared from thermosensitive glycopolymers synthesized via RAFT polymerization. *Macromol. Rapid Commun. 28*, 123−129.
(34) Hales, M., Barner-Kowollik, C., Davis, T. P., and Stenzel, M. (2004) Shell-cross-linked vesicles synthesized from block copolymers of Poly(D,L-lactide) and Poly(N-isopropyl acrylamide) as thermoresponsive nanocontainers. *Langmuir 20*, 10809−10817.
(35) Kikuchi, A., and Okano, T. (2002) Pulsatile drug release control using hydrogels. *Adv. Drug Delivery Rev. 54*, 53−77.
(36) Kim, B., Flamme, K. L., and Peppas, N. (2003) Dynamic swelling behavior of pH-sensitive anionic hydrogels used for protein delivery. *J. Appl. Polym. Sci. 89*, 1606−1613.
(37) Cai, C., Bakowsky, U., Rytting, E., Schaper, A. K., and Kissel, T. (2008) Charged nanoparticles as protein delivery systems: a feasibility study using lysozyme as model protein. *Eur. J. Pharm. Biopharm. 69*, 31−42.
(38) Soppimath, K. S., Aminabhavi, T. M., Kulkarni, A. R., and Rudzinski, W. E. (2001) Biodegradable polymeric nanoparticles as drug delivery devices. *J. Controlled Release 70*, 1−20.
(39) Panyam, J., and Labhasetwar, V. (2003) Biodegradable nanoparticles for drug and gene delivery to cells and tissue. *Adv. Drug Delivery Rev. 55*, 329−347.
(40) Smith, M. H., South, A. B., Gaulding, J. C., and Lyon, L. A. (2010) Monitoring the erosion of hydrolytically-degradable nanogels via multiangle light scattering coupled to asymmetrical flow field-flow fractionation. *Anal. Chem. 82*, 523−530.
(41) Kang, Y., Wang, Q., Liu, Y.-C., Shen, J. W., and Wu, T. (2010) Diameter selectivity of protein encapsulation in carbon nanotubes. *J. Phys. Chem. B 114*, 2869−2875.
(42) Hirakura, T., Yasugi, K., Nemoto, T., Sato, M., Shimoboji, T., Aso, Y., Morimoto, N., and Akiyoshi, K. (2010) Hybrid hyaluronan hydrogel encapsulating nanogel as a protein nanocarrier: new system for sustained delivery of protein with a chaperone-like function. *J. Controlled Release 142*, 483−489.
(43) Blanco, D., and Alonso, M. J. (1998) Protein encapsulation and release from poly(lactide-co-glycolide) microspheres: effect of the protein and polymer properties and of the co-encapsulation of surfactants. *Eur. J. Pharm. Biopharm. 45*, 285−294.
(44) Weert, M., Hof, R., Weerd, J., Heeren, R. M. A., Posthuma, G., Hennink, W. E., and Crommelin, D. J. A. (2000) Lysozyme distribution and conformation in a biodegradable polymer matrix as determined by FTIR techniques. *J. Controlled Release 68*, 31−40.
(45) Cadée, J., Groot, C. J., de., Jiskoot, W., Otter, W. den., and Hennink, W. E. (2002) Release of recombinant human interleukin-2 from dextran-based hydrogels. *J. Controlled Release 78*, 1−13.
(46) Ramkissoon-Ganorkar, C., Liu, F., Baudys, M., and Kim, S. W. (1999) Modulating insulin-release profile from pH/thermosensitive polymeric beads through polymer molecular weight. *J. Controlled Release 59*, 287−298.
(47) Kyomoto, M., Moro, T., Takatori, Y., Kawaguchi, H., Nakamura, K., and Ishihara, K. (2010) Self-initiated surface grafting with poly(2-methacryloyloxyethyl phosphorylcholine) on poly(ether-ether-ketone). *Biomaterials 31*, 1017−1024.
(48) Nakabayashi, N., and Iwasaki, Y. (2004) Copolymers of 2-methacryloyloxyethyl phosphorylcholine (MPC) as biomaterials. *Biomed. Mater. Eng. 14*, 345−354.
(49) Katakura, O., Morimoto, N., Iwasaki, Y., Akiyoshi, K., and Kasugai, S. (2005) Original article evaluation of 2-methacryloyloxyethyl phosphorylcholine (MPC) polymer-coated dressing on surgical wounds. *J. Med. Dent. Sci.*, 115−121.
(50) Ishihara, K., Ueda, T., and Nakabayashi, N. (1990) Preparation of phospholipid polymers and their properties as polymer hydrogel membranes. *Polym. J 22*, 355−360.
(51) Deng, Z., Bouchékif, H., Babooram, K., Housni, A., Choytun, N., and Narain, R. (2008) Facile synthesis of controlled-structure primary amine-based methacrylamide polymers via the reversible addition-fragmentation chain transfer process. *J. Polym. Sci., Part A: Polym. Chem. 46*, 4984−4996.
(52) Mitsukami, Y., Donovan, M. S., Lowe, A. B., and McCormick, C. L. (2001) Water-soluble polymers. 81. direct synthesis of hydrophilic styrenic-based homopolymers and block copolymers in aqueous solution via RAFT. *Macromolecules 34*, 2248−2256.
(53) Lai, J. T., Filla, D., and Shea, R. (2002) Functional polymers from novel carboxyl-terminated trithiocarbonates as highly efficient RAFT agents. *Macromolecules 35*, 6754−6756.
(54) Roberts, D. L., Ma, Y., Bowles, S. E., Janczak, C. M., Pyun, J., Saavedra, S. S., and Aspinwall, C. A. (2009) Polymer-stabilized phospholipid vesicles with a controllable, pH-dependent disassembly mechanism. *Langmuir 25*, 1908−1910.
(55) Bhuchar, N., Deng, Z., Ishihara, K., and Narain, R. (2011) Detailed study of the reversible addition−fragmentation chain transfer polymerization and co-polymerization of 2-methacryloyloxyethyl phosphorylcholine. *J. Polym. Chem. 2*, 632−639.
(56) Zheng, G., Zheng, Q., and Pan, C. (2006) One-pot synthesis of micelles with a cross-linked poly(acrylic acid) core. *Macromol. Chem. Phys. 207*, 216−223.
(57) Yan, L., and Tao, W. (2010) One-step synthesis of pegylated cationic nanogels of poly(N,N′-dimethylaminoethyl methacrylate) in aqueous solution via self-stabilizing micelles using an amphiphilic macroRAFT agent. *Polymer 51*, 2161−2167.
(58) Rapoport, N. (1999) Stabilization and activation of pluronic micelles for tumor-targeted drug delivery. *Colloids Surf., B: Biointerfaces. 16*, 93−111.
(59) Jiang, X., Liu, S., and Narain, R. (2009) Degradable thermoresponsive core cross-linked micelles: fabrication, surface functionalization, and biorecognition. *Langmuir 25*, 13344−13350.
(60) Fournier, D., Hoogenboom, R., Thijs, H. M. L., Paulus, R. M., and Schubert, U. S. (2007) Tunable pH- and temperature-sensitive copolymer libraries by Reversible Addition−Fragmentation Chain Transfer copolymerizations of methacrylates. *Macromolecules 40*, 915−920.
(61) Schönhoff, M., Larsson, A., Welzel, P. B., and Kuckling, D. (2002) Thermoreversible polymers adsorbed to colloidal silica: A ^{1}HNMR and DSC study of the phase transition in confined geometry. *J. Phys. Chem. B 106*, 7800−7808.
(62) Kabanov, A. V., and Vinogradov, S. V. (2009) Nanogels as pharmaceutical carriers: finite networks of infinite capabilities. *Angew. Chem., Int. Ed. 48*, 5418−5429.

Bioconjugate Chemistry

Article

pubs.acs.org/bc

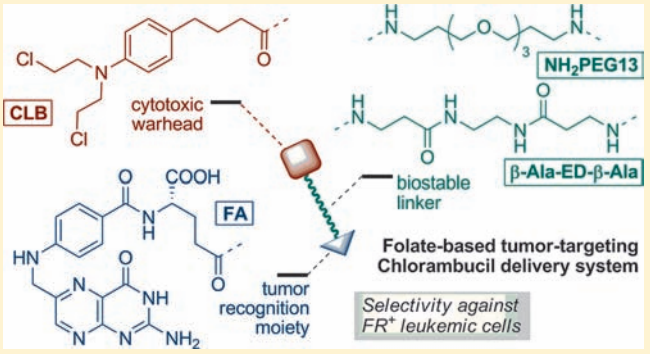
Synthesis and Evaluation of Folate-Based Chlorambucil Delivery Systems for Tumor-Targeted Chemotherapy

Annalisa Guaragna,*[,†,‡] Angela Chiaviello,[§,‡] Concetta Paolella,[†] Daniele D'Alonzo,[†] Giuseppe Palumbo,[§] and Giovanni Palumbo[†]

[†]Dipartimento di Chimica Organica e Biochimica, Università di Napoli Federico II, via Cinthia, 4 I-80126 Napoli, Italy

[§]Dipartimento di Biologia e Patologia Cellulare e Molecolare L. Califano, Università di Napoli Federico II, via S. Pansini, 5 I-80131 Napoli, Italy

ABSTRACT: The development of tumor-targeting drug delivery systems, able to selectively transport cytotoxic agents into the tumor site by exploiting subtle morphological and physiological differences between healthy and malignant cells, currently stands as one of the most attractive anticancer strategies used to overcome the selectivity problems of conventional chemotherapy. Owing to frequent overexpression of folate receptors (FRs) on the surface of malignant cells, conjugation of cytotoxic agents to folic acid (FA) via suitable linkers have demonstrated to enhance selective drug delivery to the tumor site. Herein, the chemical synthesis and biological evaluation of two novel folate-conjugates bearing the anticancer agent chlorambucil (CLB) tethered to either an aminoether (4,7,10-trioxa-1,13-tridecanediamine) or a pseudo-β-dipeptide (β-Ala-ED-β-Ala) linker is reported. The two drug delivery systems have been prepared in high overall yields (54% and 34%) through straightforward and versatile synthetic routes. Evaluation of cell specificity was examined using three leukemic cell lines, undifferentiated U937 (not overexpressing FRs, FR^-), TPA-differentiated U937 (overexpressing FRs, FR^+), and TK6 (FR^+) cells. Both conjugates exhibited high specificity only to FR^+ cells (particularly TK6), demonstrating comparable antitumor activity to CLB in its free form. These data confirm the reliability of folate-based drug delivery systems for targeted antitumor therapy; likewise, they lay the foundations for the development of other folate-conjugates with antitumor potential.



INTRODUCTION

With the exception of coronary and heart diseases, cancer remains the major cause of death in the Western world. Despite significant progress in the development of anticancer technologies (involving tumor detection, prevention, surgery, and chemotherapeutic treatments), there is still no efficient cure for patients with malignant diseases. One of the major drawbacks in anticancer chemotherapy is the lack of selectivity of cytotoxic drugs, which usually do not accurately discriminate between healthy and malignant cells, leading to systemic toxicity. To limit the onset of severe side effects, anticancer chemotherapeutics are often given at suboptimal doses, thus hampering their ability to reach tumor-destroying drug concentrations while prompting, after prolonged treatments, the development of resistance phenomena. Therefore, the construction of innovative tumor-specific drug delivery systems is urgently needed. Several approaches[1] aimed at improving selectivity of anticancer agents are currently being pursued: they are mostly based on subtle biochemical differences discriminating healthy from malignant cells. Among such approaches, those involving conjugation of the drug to tumor-specific ligands (the so-called "guided molecular missiles" or "molecular Trojan horses") have been deeply investigated over the last years.[2]

A tumor-targeting drug delivery system typically consists of a tumor recognition moiety and a cytotoxic warhead connected directly, or through a suitable linker, to form a conjugate which is inactive and sufficiently stable while in circulation; then, once selectively internalized into the cancer cell, cleavage of the conjugate restores the active cytotoxic warhead. The devised mechanism enables the conjugate to exhibit a strongly selective antitumor effect; however, to efficiently deliver the drug to the tumor site, it is important to have a detailed knowledge of the specific morphological and physiological differences distinguishing malignant from healthy tissues. Rapidly dividing cancer cells require various nutrients and vitamins to maintain their rapid growth. Therefore, those receptors involved in the uptake of the essential vitamins for cell growth are often overexpressed on the surface of malignant cells. This key finding has allowed identification of useful biomarkers either for the imaging and detection of tumor cells or for the delivery of

Received: August 12, 2011
Revised: October 31, 2011
Published: November 28, 2011

 © 2011 American Chemical Society dx.doi.org/10.1021/bc200410d | *Bioconjugate Chem.* 2012, 23, 84–96

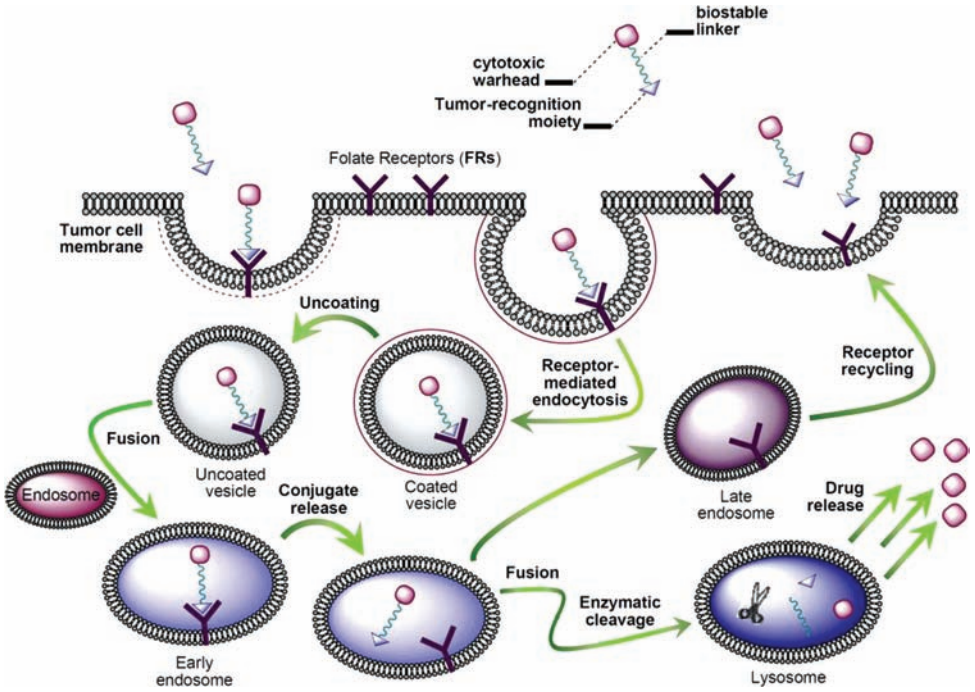
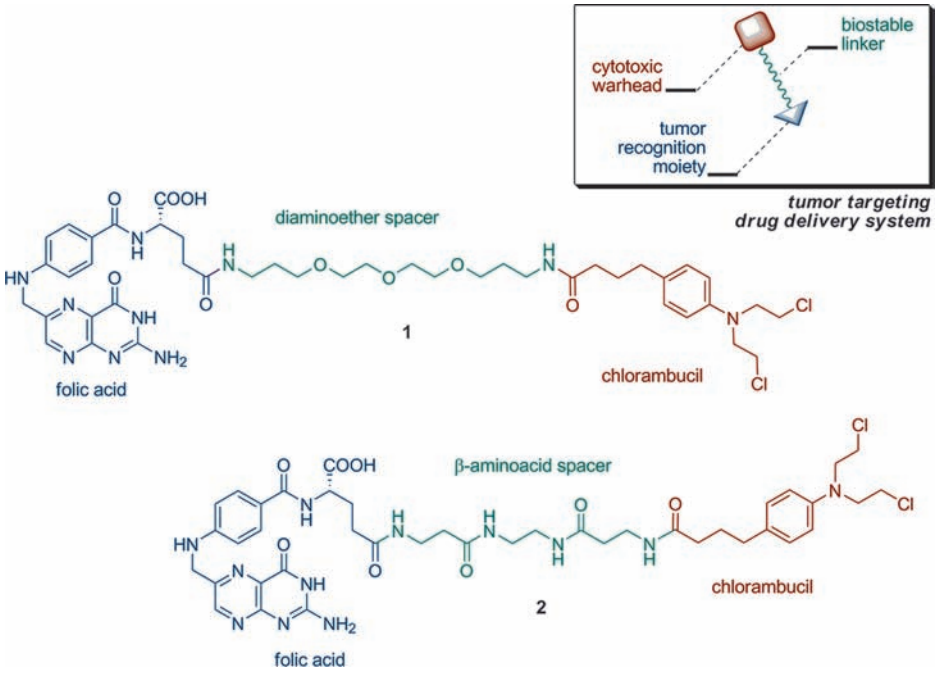


Figure 1. FR-mediated endocytosis and trafficking.

Chart 1. Tumor-Targeting Drug-Delivery Systems 1 and 2



cytotoxic agents to tumors.[3] Among such receptors, those devoted to the transport of vitamin B12,[4] biotin,[5,6] and riboflavin[7] have been quite recently introduced as methods for targeted drug delivery. On the other hand, it has long been recognized that folate receptors (FRs) are excellent biomarkers to this end.[8−10] Folic acid (FA) is the natural vitamin B9 (M_r = 441): it is required by all living cells, especially those rapidly replicating, because it is necessary for the *de novo* nucleotide biosynthesis and one-carbon metabolism. It is a stable, inexpensive, and generally poorly immunogenic chemical endowed with a remarkable affinity for FRs (K_d ∼ 0.1−1.0 nmol/L). FRs are glycosyl-phosphatidylinositol (GPI)-anchored 38 kDa membrane glycoproteins[11] which exist in three main isoforms,[12] namely, FR-α, FR-β, and FR-γ. Among them, FR-α is often up-regulated on cell surface of a wide variety of human carcinomas, including ovary, brain, kidney, breast, colon, and lung malignancies; but it is more rarely expressed on most normal cells. FR-β is expressed on activated macrophages and on the surface of malignant cells of hematopoietic origin. Since FA enters cells by receptor-mediated endocytosis (Figure 1), a striking consequence is that those FRs expressed by cancer cells can be exploited to selectively convey specific anticancer drugs.[7]

dx.doi.org/10.1021/bc200410d | *Bioconjugate Chem.* 2012, 23, 84−96

Tumor-targeting FA conjugates covalently linked via folate's γ-carboxyl moiety maintain a high affinity for the FRs, and the mechanism of cellular uptake of folate conjugates by FRs is as effective as that displayed by FA in its free form.[13] Despite their molecular complexity, folate-conjugates can still enter cells by FR-mediated endocytosis[11] and move through many organelles supplying transported materials to cell cytoplasm. The drug is then released in the endosomes/lysosomes mainly by enzymatic cleavage (owing to the acidic environment occurring in lysosomes, pH-dependent drug release has also been extensively considered).[1,8] Due to recycling of the unligated FR back to the cell surface, the uptake process can be reiterated, allowing continuous supply of folate-linked drugs into the cell (Figure 1).

Over the years, the intriguing potential of folate conjugates in targeted anticancer chemotherapy has been witnessed by the number of preclinical and clinical studies[14−17] of several drug delivery systems obtained varying both the cytotoxic warhead[18] (depending on the type of target tumor cells) and the biostable linker.[1,19] Our approach to the synthesis of folate conjugates has been focused on the construction of molecular systems bearing two novelty elements: on one hand, we have chosen the potent anticancer agent chlorambucil (CLB) as cytotoxic warhead, to evaluate its efficacy in folate-based antitumor chemotherapy. On the other hand, we have considered the introduction of β-amino acids in the spacer, to study their potential to work as biostable linkers in these drug delivery systems. Based on these aims, we conceived the synthesis and biological evaluation of the two antitumor systems **1** and **2** (Chart 1), where FA is connected through suitable linkers (aminoether and pseudo β-peptide spacers) to the cytotoxic agent CLB. While the presence of FA ensures appropriate selectivity to tumor cells to the resulting conjugates, CLB is amenable to being released at intracellular level since the amide linkage originated from the COOH terminus of CLB and the amino function of each linker should be easily cleaved by lysosomal proteases. The results reported below are evidence for how our molecular biosystems are characterized by the ability to specifically recognize, target, and kill tumor cells expressing FRs.

■ EXPERIMENTAL PROCEDURES

Materials and Methods. *Chemistry.* All moisture-sensitive reactions were performed under nitrogen atmosphere using oven-dried glassware. Solvents were dried over standard drying agents and freshly distilled prior to use. Triethylamine (TEA) and *N,N*-diisopropylethylamine (DIPEA) were redistilled from NaOH. *N,N′*-Dicyclohexylcarbodiimide (DCC) and folic acid (FA) were purchased from Sigma-Aldrich Inc. Chlorambucil (CLB), dimethyl sulfoxide (DMSO, anhydrous), and pyridine (Py, anhydrous) were used as purchased (Fluka Chemical Co.) without further purification. Reactions were monitored by TLC (precoated silica gel plate F254, Merck). Column chromatography: Merck Kieselgel 60 (70−230 mesh); flash chromatography: Merck Kieselgel 60 (230−400 mesh). Purity of all reaction intermediates and target molecules (>95%) was established by combustion analyses, which were performed by using a CHNS analyzer. Structure determination of all new compounds was carried out by NMR and MS analysis. ^{1}H and ^{13}C NMR spectra were recorded with the following instruments: Varian Gemini (200 MHz), Varian Gemini (300 MHz), Bruker DRX (400 MHz), and Varian Inova (500 MHz) spectrometers. MS spectra were recorded on a Voyager DE-PRO MALDI-TOF mass spectrometer.

Biology. *Cell Lines.* The p53-null U937 human leukemic monocyte lymphoma and the p53-positive isogenic human lymphoblast TK6 cell lines were obtained from American Type Culture Collection (Rockville, MD). Both cells lines grew in Dulbecco's Modified Eagle Medium, 2 mM L-glutamine, 100 μg/mL streptomycin, 100 units/mL penicillin, and 10% Foetal Calf Serum (FCS). All media and cell culture reagents were purchased from Life Technologies (San Giuliano Milanese, Italy).

Cell Differentiation. Differentiation of the promyelocytic cell line U937 cells into macrophages was achieved according to Sordet et al.[20] by treating cells with 20 nM 12-*O*-tetradecanoylphorbol-13-acetate (TPA) for 24 h. At the end of this time, the differentiation process was considered complete as indicated by the massive attachment of cells to the plate. TPA was obtained by Sigma Aldrich. A 100 μM stock solution was prepared in 100% DMSO.

CLB and FA-CLB Conjugates Stock Solutions. CLB was dissolved in 100% DMSO to obtain a concentrated (75 mM) stock solution. Before measurements, appropriate aliquots of this solution were diluted with Dulbecco's complete medium to the desired concentration.

Stock solutions of the same concentration (75 mM) of folate-trioxa-CLB and folate-(βAla-ED-βAla)-CLB stock solutions were (both) also obtained by dissolving the powders in 100% DMSO under continuous stirring at room temperature overnight in the dark. These concentrated solutions were stored at 4 °C wrapped in aluminum foil. Before use, appropriate amounts of each stock solution were diluted with Dulbecco's complete medium to the desired concentration.

Metabolic Activity. Metabolic activity was assayed by using the Cell Proliferation Kit II (XTT, Roche, Milan Italy). The assay is based on cleavage of the yellow tetrazolium salt XTT to form an orange formazan dye by metabolic active cells.[21] Therefore, this conversion only occurs in viable cells.

Normally 1×10^4 cells/well were seeded into 96-well plates and incubated for 24, 48, and 72 h with CLB, folate-trioxa-CLB, or folate-(βAla-ED-βAla)-CLB at established concentrations and then analyzed in triplicate.

Stability of FA-CLB Conjugates in DMSO Solutions. To assess the time-stability of CLB-folate derivatives stock solutions, we evaluated their biological effects on cell metabolic activity immediately after their preparation or after several weeks of storage. The changes in cytotoxic activity on U937 and TK6 cells of freshly prepared or stored (5 weeks) stock solutions (both 75 mM) were evaluated by comparing the residual metabolic activity of these cells (XTT assay) following 48 h treatment with scalar doses (normally 0−50 μM) of each compound. As concentrated solutions are normally more stable than the diluted ones, the check of stability and full retention of cytotoxic activity was also performed starting from 100× more diluted stock solutions (i.e., 0.75 mM in 33% DMSO). Even in this case, the assays were performed immediately after their preparation or after several weeks of storage at 4 °C (5 weeks).

Stability of FA-CLB Conjugates in Human Serum. To test the stability of FA-conjugates in human serum, we have diluted appropriate amounts of stock solutions of folate-trioxa-CLB or folate-(βAla-ED-βAla)-CLB in human serum so that the final concentrations of the drugs were in both cases 0.5 mmol/L. These CLB-containing solutions, used as drug sources, were then incubated at 37 °C for 12 h and finally used to treat

dx.doi.org/10.1021/bc200410d | *Bioconjugate Chem.* 2012, 23, 84−96

undifferentiated U937 and TK6 cells. Analysis of cell metabolic activity by XTT assay was performed 48 h later. In these experiments, CLB in free (control) or conjugated forms was 30 μM.

IC_{50} Assessment. The IC_{50} estimations of CLB and FA-conjugates were done using a point to point method according to Aloyz and co-workers,[22] except for the fact that the XTT assay was used in place of the MTT assay. IC_{50} values were derived using linear interpolation from dose response curves in which mean viability values were plotted against the drug concentrations. Straight lines between consecutive points were drawn and the IC_{50} calculated where this line crosses the value representing the 50% of residual viability. In particular, IC_{50} determinations were performed on TK6 or U937 cells incubated for 24, 48, and 72 h.

Competition Assay. In order to show that FA and FA-conjugates compete for a single class of receptors, we preincubated about 10^4 either receptor positive TPA-differentiated and TK6 cells or receptor negative cells (U937) with 1.5 mM FA. After one hour in this condition, we added to each cell line conjugates **1** and **2** and free CLB (all 30 μM). At the end of this incubation (72 h), the XTT assay was performed as indicated before.

Flow Cytometry. Undifferentiated or TPA-activated U937 cells and TK6 cells were incubated individually for 48 h with CLB or with its folate conjugated forms (30 μM). After incubation, cells were washed twice with 1 mL phosphate saline buffer pH 7.4 (PBS), and resuspended and fixed in 70% ethanol. Before analysis, fixed cells were washed, centrifuged, and resuspended in 1 mL PBS containing 1 μg RNase and 100 μg propidium iodide.[23] Samples were stored in the dark for 20 min at room temperature before final readings. The cellular orange fluorescence of propidium iodide was detected in a linear scale using a CyAn ADP Flow Cytometer (DAKOCytomation, Ely, UK) and analyzed by using *ModFit/LT* software (Verity Software, Topsham, ME). About 30 000 events (i.e., fluorescence readings, corresponding to not less than 20 000 cells) were recorded for each sample.

Electrophoresis and Western Blot Analysis. Western blot analysis was always performed on cells treated for 48 h with 30 μM CLB or CLB conjugates. Typically, total cellular protein extracts were obtained by lysing cells in 50 mM Tris (pH 7.5), 100 mM NaCl, 1% NP40, 0.1% Triton X 100, 2 mM EDTA, 10 μg/mL aprotinin, and 100 μg/mL phenylmethylsulfonyl fluoride. Protein concentration was routinely measured with the Bio-Rad protein assay. Polyacrylamide gels (10% or 15%) were prepared essentially as described by Laemmli.[24] Molecular weight standards were from New England Biolabs (Beverly, MA, USA). Proteins separated on polyacrylamide gels were blotted onto nitrocellulose filters (Hybond-C pure, Amersham Italia, Milan, Italy). Filters were washed and stained with specific primary antibodies and then with secondary antisera conjugated with horseradish peroxidase (Bio-Rad; diluted 1:2000). Filters were developed using an electro-chemiluminescent Western blotting detection reagent (Amersham Italia, Milan, Italy); profiles were acquired and grossly quantified by scanning with a Discover Pharmacia scanner equipped with a Sun Spark Classic Workstation. The anti-p53 (DO1), anti-Bax (P-19), and anti-Clusterin (N-18) were from Santa Cruz Biotechnology (Santa Cruz, CA, USA). Antitubulin (MCA77G) was from Serotec (Kidlington, UK).

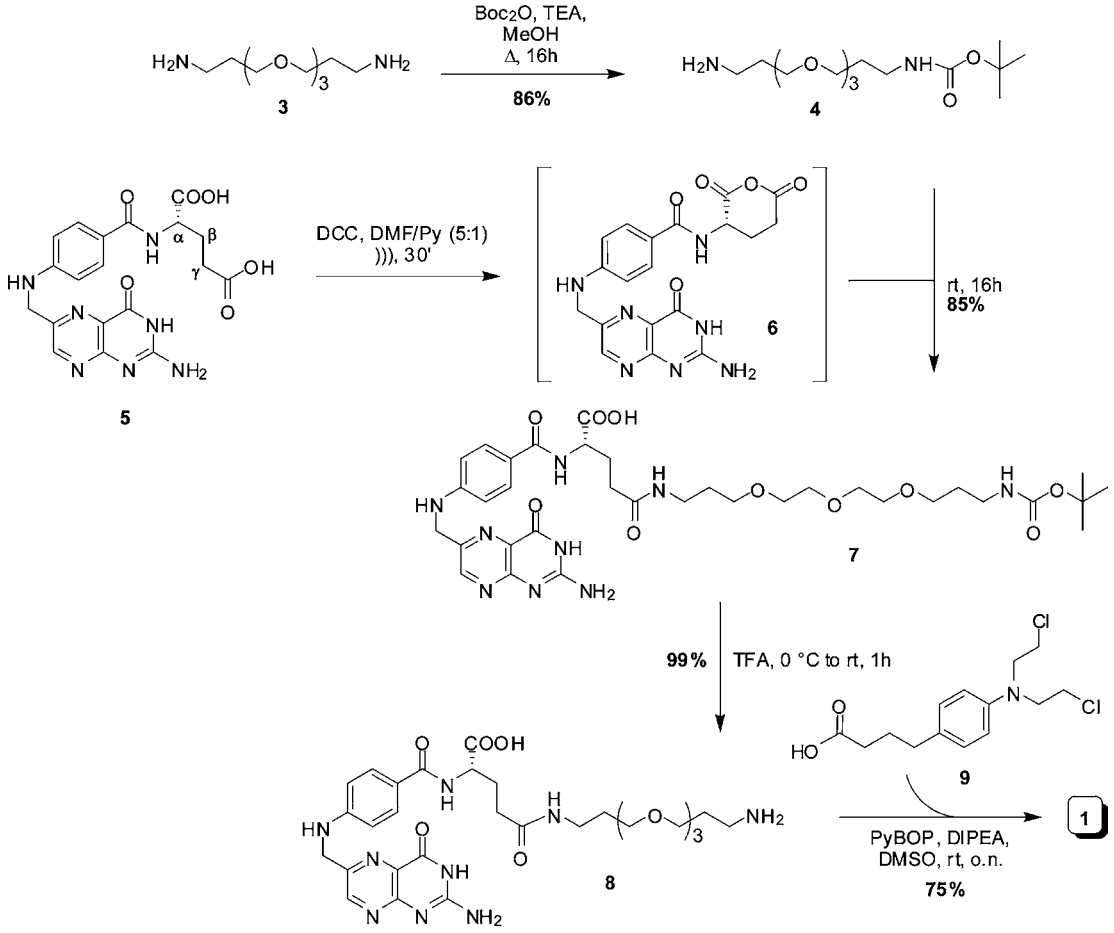
Statistical Analysis. All data are expressed as mean ± SD. Significance was assessed by the Student's *t* test for unpaired data for comparisons between two means. Statistical significance was defined as *, $p < 0.01$; **, $p < 0.001$; ***, $p < 0.0001$.

Synthetic Procedures and Characterization Data for Intermediates and Conjugates. *Compound **4**.* A stirring solution of 4,7,10-trioxa-1,13-tridecanediamine (**3**, 2.0 g, 9.1 mmol) in anhydrous CH_3OH (152.0 mL) was treated with Boc_2O (2.0 g, 9.1 mmol) and TEA (2.9 mL, 21.0 mmol). The reaction mixture was left at reflux for 16 h. The solvent was removed under reduced pressure and the resulting yellow oil was purified by silica gel chromatography ($CHCl_3$/CH_3OH/NH_4OH = 89:10:1) to give pure **4** (2.5 g, 86% yield). Oily; ^{1}H NMR (300 MHz, CD_3OD) δ: 1.44 (s, 9H), 1,73−1,78 (m, 2H), 1.90−1.96 (m, 2H), 2.03 (bs, 2H), 2.90 (t, 2H, J = 6.7 Hz), 3.12 (t, 2H, J = 6.0 Hz), 3.52 (t, 2H, J = 6.0 Hz), 3.56−3.68 (m, 10H), 5.1 (bs, 1H). ^{13}C NMR (100 MHz, $CDCl_3$) ppm: 28.2, 29.3, 32.7, 38.3, 39.3, 69.2, 69.8, 69.9, 70.2, 70.3 78.2, 156.2. MALDI-TOF MS: m/z 320.23 (calcd); 321.20 $[M+H]^+$ (found). Anal. Calcd for $C_{15}H_{32}N_2O_5$: C, 56.23; H, 10.07; N, 8.74. Found: C, 56.40; H, 10.03; N, 8.71.

*Compound **7**.* To a stirring solution of FA (**5**, 0.25 g, 0.56 mmol) in an anhydrous DMF:Py (5:1, 24 mL) solution, DCC (0.70 g, 3.4 mmol) was added in one portion. The reaction mixture was kept in an ultrasound bath in the dark for 30 min. Then, the resulting suspension was quickly filtered over a sintered funnel and the precipitate washed with a minimum amount of anhydrous DMF:Py solution. The *N*-Boc-4,7,10-trioxa-1,13-tridecanediamine (**4**) (0.18 g, 0.6 mmol) was then added to the filtrate. The resulting reaction mixture was further stirred in the dark for 16 h. Afterward, it was poured dropwise into a stirred solution of cold diethyl ether/acetone (70:30): a yellow precipitate was formed and collected on a sintered glass funnel. After washing several times with acetone and ether, the material was dried to give **7** as a yellow powder (0.35 g, 85% yield) which was used in the next step without further purification. Mp 209−210 °C; ^{1}H NMR (200 MHz, DMSO-d_6) δ: 1.34 (s, 9H), 1.49−1.65 (m, 4H), 1.80−2.05 (m, 2H), 2.12−2.34 (m, 2H), 2.86 (dd, 2H, J = 6.5, 12.4 Hz), 3.05 (bt, 2H, J = 6.1 Hz), 3.25−3.40 (m, 4H), 3.41−3.50 (m, 8H), 4.20−4.38 (m, 1H), 4.46 (bd, 2H, J = 5.4 Hz), 6.61 (bd, 2H, J = 7.6 Hz), 6.75−6.98 (m, 3H), 7.63 (bd, 2H, J = 7.6 Hz), 7.76−7.86 (m, 1H), 7.90 (bd, 1H, J = 8.4 Hz), 8.62 (bs, 1H), 11.4 (s, 1H). ^{13}C NMR (100 MHz, DMSO-d_6): ppm 29.4, 30.0, 30.4, 31.2, 36.6, 37.9, 46.7, 52.9, 68.8, 70.4, 70.5, 78.1, 111.1, 122.2, 128.7, 129.7, 149.3, 151.5, 154.5, 156.3, 156.7, 161.7, 166.9, 172.4, 174.6, 174.9. MALDI-TOF MS: m/z 743.36 (calcd); 766.20 $[M+Na]^+$, 782.20 $[M+K]^+$ (found). Anal. Calcd for $C_{34}H_{49}N_9O_{10}$: C, 54.90; H, 6.64; N, 16.95. Found: C, 55.04; H, 6.62; N, 16.89.

*Compound **8**.* TFA (1.7 mL) was added to **7** (250 mg, 0.33 mmol) at 0 °C and under magnetic stirring. The resulting mixture was stirred at room temperature for 2 h, then TFA was evaporated under vacuum and the resulting residue was dissolved in a small amount of anhydrous DMF. Pyridine was added dropwise until complete formation of a yellow precipitate, which was collected by filtration, washed with Et_2O and dried under vacuum to yield amine **8** (0.42 g, 99% yield). Yellow powder, Mp 205−207 °C; ^{1}H NMR (500 MHz, CD_3OD) δ: 1.44−1.62 (m, 2H), 1.70−1.80 (m, 2H), 1.82−2.00 (m, 2H), 2.05−2.17 (m, 2H), 2.84 (bt, 2H, J = 7.4 Hz), 2.98−3.07 (m, 2H), 3.18−3.38 (m, 2H), 3.40−3.57 (m, 10H), 4.20−4.37 (m, 1H), 4.46 (d, 2H, J = 5.8 Hz), 6.63 (d, 2H, J = 7.4 Hz), 6.80−6.98 (m, 3H), 7.65 (bd, 2H, J = 7.4 Hz), 7.85

Scheme 1. Synthesis of Conjugate 1



(bd, 1H, J = 8.0 Hz), 8.65 (s, 1H), 11.38 (bs, 1H). ^{13}C NMR (100 MHz, DMSO-d_6): ppm 27.2, 29.3, 30.6, 35.6, 36.9, 46.2, 53.8, 67.4, 68.0, 69.5, 69.6, 69.7, 111.2, 121.4, 128.3, 129.4, 148.3, 151.0, 153.3, 158.5, 160.8, 166.5, 172.1, 174.4. MALDI-TOF MS: m/z 643.31 (calcd); 666.40 $[M+Na]^+$, 682.34 $[M+K]^+$ (found). Anal. Calcd for $C_{29}H_{41}N_9O_8$: C, 54.11; H, 6.42; N, 19.58. Found: C, 54.29; H, 6.40; N, 19.50.

Compound ***1***. To a stirring solution of CLB (0.46 g, 1.5 mmol) in anhydrous DMSO (5.0 mL), DIPEA (0.26 mL, 1.5 mmol), **8** (0.32 g, 0.5 mmol) and PyBOP (0.78 g, 1.5 mmol) were sequentially added. The resulting mixture was stirred for 16 h at room temperature. Then, it was poured dropwise into a stirred solution of cold diethyl ether/acetone (70:30): a yellow precipitate was formed and collected on a sintered glass funnel. After washing several times with acetone, ether, and finally chloroform, the material was dried to give **1** as a brownish yellow solid (0.38 g, 75% yield). ^{1}H NMR (500 MHz, DMSO-d_6) δ: 1.48−1.63 (m, 4H), 1.63−1.78 (m, 2H), 1.79−1.98 (m, 2H), 2.05 (appt, 2H, J = 7.3 Hz), 2.10−2.22 (m, 2H), 2.44 (appt, 2H, J = 7.3 Hz), 3.03−3.18 (m, 2H), 3.15−3.50 (m, 14H), 3.78 (bs, 4H), 4.23−4.40 (m, 1H), 4.52 (bd, 2H, J = 4.1 Hz), 6.63−6.76 (m, 4H), 6.83−6.98 (m, 2H), 7.02 (d, 2H, J = 7.0 Hz), 7.65 (t, 1H, J = 8.0 Hz), 7.76−7.87 (m, 2H), 7.93 (bd, 1H, J = 6.6 Hz), 8.02−8.23 (m, 1H), 8.63 (s, 1H), 11.43 (bs, 1H). ^{13}C NMR (100 MHz, DMSO-d_6): ppm 27.0, 29.4, 30.6, 32.0, 33.8, 34.8, 35.6, 35.9, 40.4, 45.8, 52.2, 53.6, 58.5, 67.3, 68.0, 69.5, 69.7, 111.1, 111.9, 121.4, 127.9, 128.9, 129.5, 138.4, 144.4, 148.4, 150.7, 153.4, 155.1, 159.0, 160.9, 166.3, 171.8, 173.8, 174.0. MALDI-TOF MS: m/z 928.38 (calcd); 951.03 $[M+Na]^+$, 967.04 $[M+K]^+$ (found). Anal. Calcd for $C_{43}H_{58}Cl_2N_{10}O_9$: C, 55.54; H, 6.29; Cl, 7.63; N, 15.06. Found: C, 55.70; H, 6.27; Cl, 7.60; N, 15.00.

Compound ***12***. Conjugate **12** was obtained (82% yield) under the same conditions reported for the synthesis of compound **7** from FA and amine **11**.[25] Yellow solid, Mp 207−209 °C; ^{1}H NMR (200 MHz, DMSO-d_6) δ: 1.38 (s, 9H), 1.82−2.01 (m, 2H), 2.08−2.32 (m, 6H), 2.98−3.18 (m, 4H), 3.21−3.42 (m, 4H), 4.22−4.38 (m, 1H), 4.52 (bs, 2H), 6.62 (d, 2H, J = 7.5 Hz), 6.68−6.78 (m, 1H), 6.82−7.05 (m, 3H), 7.65 (d, 2H, J = 7.5 Hz), 7.81 (bs, 2H), 7.91−8.02 (m, 1H), 8.69 (s, 1H), 11.42 (bs, 1H). ^{13}C NMR (100 MHz, DMSO-d_6): ppm 28.3, 30.7, 31.8, 35.4, 36.0, 36.6, 39.0, 39.1, 46.0, 51.8, 77.6, 111.2, 121.4, 128.0, 129.0, 148.5, 148.7, 150.8, 153.7, 155.5, 156.6, 160.9, 166.4, 170.5, 171.7, 173.8, 174.1. MALDI-TOF MS: m/z 725.32 (calcd); 748.66 $[M+Na]^+$, 764.68 $[M+K]^+$ (found). Anal. Calcd for $C_{32}H_{43}N_{11}O_9$: C, 52.96; H, 5.97; N, 21.23. Found: C, 52.84; H, 5.96; N, 21.31.

Compound ***13***. Folate conjugate **13** was obtained (82% yield) under the same conditions reported for the preparation of compound **8**. Yellow solid, Mp 204−207 °C; ^{1}H NMR (500 MHz) (DMSO-d_6) δ: 1.79−2.15 (m, 2H), 2.18−2.30 (m, 6H), 2.99−3.32 (m, 8H), 4.38 (bs, 1H), 4.50 (bd, 2H, J = 5.0 Hz), 4.52 (bs, 2H), 6.58 (d, 2H, J = 7.3 Hz), 6.78−7.02 (m, 4H), 7.62 (d, 2H, J = 7.3 Hz), 7.78−7.98 (m, 1H), 8.02−8.08 (m, 1H), 8.65 (s, 1H), 11.40 (bs, 1H). ^{13}C NMR (100 MHz, DMSO-d_6): ppm 31.6, 32.1, 36.0, 36.8, 37.0, 38.8, 39.1, 46.5, 52.4, 111.7, 121.4, 128.0, 129.6, 148.2, 148.4, 151.8, 156.0, 157.5, 161.6, 167.1, 171.0, 172.6, 173.6, 174.0. MALDI-TOF

dx.doi.org/10.1021/bc200410d | *Bioconjugate Chem.* 2012, 23, 84−96

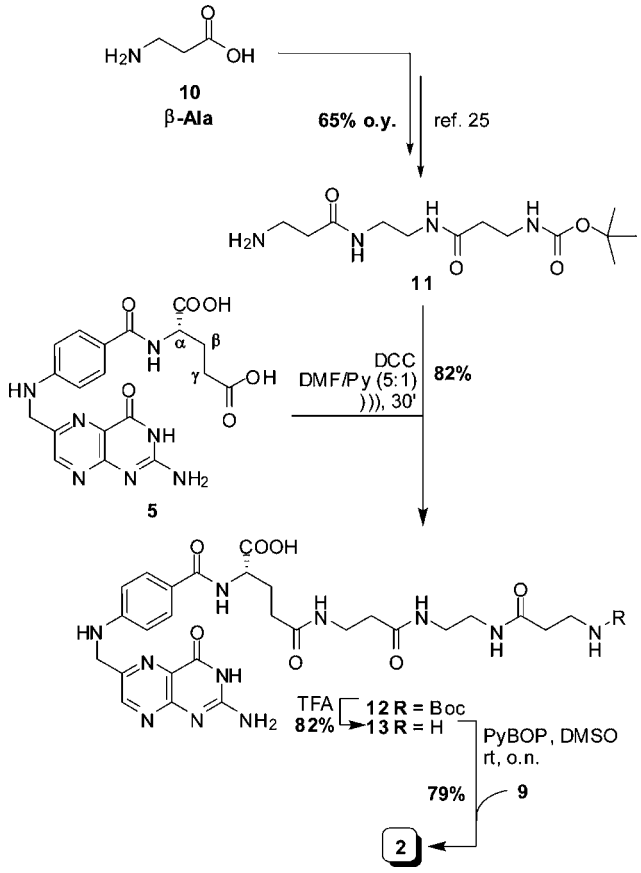
MS: *m/z* 625.45 (calcd); 648.49 $[M+Na]^+$, 664.45 $[M+K]^+$ (found). Anal. Calcd for $C_{27}H_{35}N_{11}O_7$: C, 51.83; H, 5.64; N, 24.63. Found: C, 51.96; H, 5.62; N, 24.57.

Compound 2. Folate-CLB conjugate **2** was obtained (79% yield) under the same conditions reported for the synthesis of compound **1**. Brownish purple solid, Mp 220 °C (dec.); ^1H NMR (400 MHz) (DMSO-d_6) δ: 1.65−1.69 (m, 2H), 1.79−1.98 (m, 2H), 2.03 (appt, 2H, J = 7.2 Hz), 2.14−2.26 (m, 5H), 2.30 (t, 1H, J = 6.4 Hz), 2.32−2.42 (m, 2H), 2.97−3.18 (m, 4H), 3.19−3.37 (m, 4H), 3.60 (t, 2H, J = 6.3 Hz), 3.67 (s, 2H), 4.23−4.38 (m, 1H), 4.48 (bd, 2H, J = 5.9 Hz), 6.57−6.69 (m, 4H), 6.78−7.02 (m, 4H), 7.58−7.62 (d, 2H, J = 7.3 Hz), 7.82−7.94 (m, 2H), 7.98 (t, 1H, J = 7.6 Hz), 8.10 (d, 1H, J = 7.8 Hz), 8.60 (bs, 1H), 11.41 (bs, 1H). ^{13}C NMR (100 MHz, DMSO-d_6): ppm 26.4, 30.9, 31.8, 33.5, 35.2, 35.6, 35.7, 39.0, 39.1, 40.1, 46.2, 52.6, 53.8, 111.5, 112.2, 121.7, 128.3, 129.4, 129.6, 148.9, 149.0, 151.0, 153.8, 154.1, 156.9, 161.1, 166.7, 169.9, 170.8, 172.0, 174.2. MALDI-TOF MS: *m/z* 910.34 (calcd); 933.11 $[M+Na]^+$, 949.13 $[M+K]^+$ (found). Anal. Calcd for $C_{41}H_{52}Cl_2N_{12}O_8$: C, 54.01; H, 5.75; Cl, 7.78; N, 18.43. Found: C, 54.19; H, 5.73; Cl, 7.75; N, 18.35.

RESULTS

Chemistry. Synthesis of conjugates **1** and **2** is shown in Schemes 1 and 2. We chose to attach the FA and CLB units to the distal ends of two linkers of sufficient length such that basic requirements for interaction with FRs were maintained. It must be preliminarily noted that, while choice of an aminoether linker (leading to conjugate **1**) relies on an extensively established use of polyether linkers devoted to the same purposes,[26] on the other hand preparation of a β-amino acid-based linker such as that leading to conjugate **2** beats a completely unexplored path. In this case, we conceived to replace linkers composed by natural α-amino acids, which are amenable to proteolytic degradation *in vivo*, with those containing the more stable yet biocompatible β-amino acids.[27] From a synthetic standpoint, even though preparation of **1** and **2** can be in principle carried out by a straightforward route comprising two subsequent coupling reactions between the linkers, FA and CLB, some problems regarding all FA-containing reaction intermediates must be pointed out. The main hurdle in the synthesis of FA derivatives is represented by the very poor solubility of all FA-containing products in all organic solvents (except DMSO). This made, on one hand, most reaction intermediates to be unsuitable for purification on common solid chromatographic supports. For this reason, precipitation was always preferred to purify reaction products by traces of unreacted reagents and other byproducts. On the other hand, solubility problems often resulted in low reaction rates, both in the coupling reaction of FA with various nucleophiles and in the following synthetic steps, thus leading to low yields and, after prolonged reaction times, to the formation of a complex mixture of byproducts. Therefore, accurate tuning of reaction conditions was considered to avoid contamination of reaction products by undesired compounds and thus to ensure efficient purification of desired folate conjugates. This was particularly crucial for the conjugation step with FA, since the incidental presence of any trace of unreacted FA during *in vitro* assays could hamper the subsequent binding between folate conjugates and FRs through competitive interactions.

Scheme 2. Synthesis of Conjugate 2



Synthesis of the CLB-Delivery System 1. Preparation of conjugate **1** was carried out starting from 4,7,10-trioxa-1,13-tridecanediamine (**3**), a PEG *bis*-amine (NH_2−PEG13) as the linker unit (Scheme 1). Use of this spacer offers a 2-fold advantage: (a) it is biocompatible and hydrophilic as the most commonly employed polymeric NH_2PEG linkers (NH_2PEG2000, NH_2PEG1000, etc.) and (b) it is very inexpensive if compared to other NH_2PEG linkers. *N*-Boc-monoprotection of amine **3** was achieved by treatment with Boc_2O in MeOH under refluxing conditions (86% yield). The resulting carbamate **4** was then subjected to various reaction conditions to enable conjugation to FA. After early unsatisfactory attempts using standard synthetic procedures (DCC/HOBT, DCC/NHS), amide **7** was successfully obtained by means of the activated folate anhydride **6**, in turn prepared *in situ* by treatment of **5** with dicyclohexylcarbodiimide (DCC) in a 5:1 mixture of DMF/pyridine for 30 min in an ultrasonic bath. Accordingly, once the white crystals of DCU were formed in the reaction vessel (indicating the reaction progress toward **6**), amine **4** (1 equiv) was added, smoothly leading to amide **7**. The concentrated DMF solution containing the reaction product was dropwise added to a cold mixture of acetone and diethyl ether (30:70 v/v ratio), from which desired **7** was isolated by precipitation (85% yield). *N*-Boc group removal of conjugate **7** under common reaction conditions (TFA) quantitatively released amine **8**. The latter was hence coupled with CLB (**9**): while treatment with DCC was not convenient, due to the difficulty to remove the resulting DCU from the reaction mixture, on the other hand reaction with PyBOP/DIPEA was revealed to be more effective, easily affording

dx.doi.org/10.1021/bc200410d | *Bioconjugate Chem.* 2012, 23, 84−96

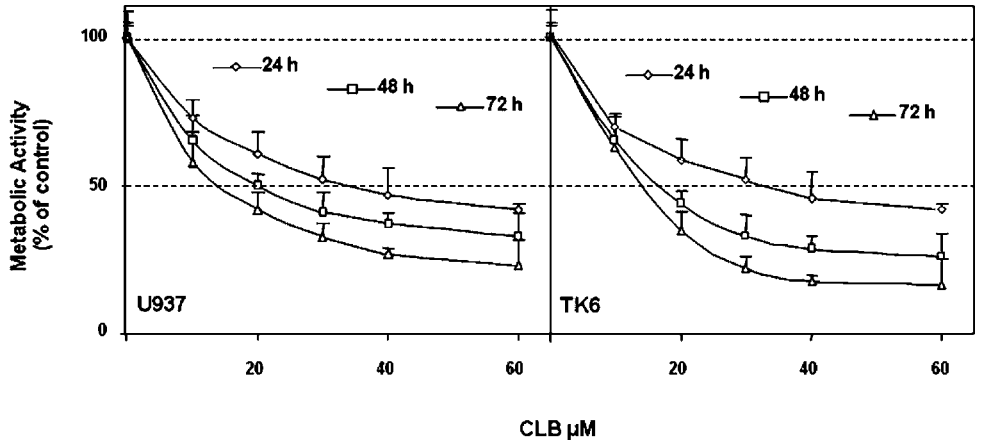


Figure 2. Metabolic activity of FR$^-$-U937 (left) and FR$^+$-TK6 cells (right) treated with increasing doses of CLB at different incubation times.

desired conjugate **1** as a brownish yellow precipitate (75% yield).

Synthesis of the CLB-Delivery System 2. Conjugate **2** was prepared by a similar synthetic route, employing a pseudo-β-dipeptide, composed by two units of β-alanine (β-Ala) bridged by an ethylenediamine (ED) moiety. The presence of ED is required to obtain two terminal amino functions in the linker. As shown in Scheme 2, *N*-Boc-β-Ala-ED-β-Ala (**11**) was obtained in satisfactory overall yield (65%) from **10** by a previously reported synthetic protocol.[25] Coupling of **11** with the *in situ* formed anhydride **6** under the above-described conditions (DCC) led to amide **12** in good yield (82%). The *N*-Boc group was then removed with TFA at 0 °C, and the obtained amine **13** was finally coupled with CLB (**9**) using PyBOP/DIPEA in anhydrous DMSO, to give conjugate **2** (as a brownish purple solid) which was isolated as described above (79% yield).

The presence in FA of two carboxyl groups, namely, α and γ, poses a problem since both can act as a joint for covalent attachment. Indeed, it has been extensively demonstrated that the FA unit of a drug delivery system linked via its γ-carboxyl group retains a strong affinity toward its receptor, whereas the corresponding α-carboxyl derivatives are not readily recognized.[8] For this reason, it was essential to establish the relative amounts of α- and γ-carboxyl-linked conjugates in compounds **1** and **2**. As confirmed by ^{1}H and COSY NMR experiments, under our conditions an almost exclusive γ-conjugation was found for both conjugates **1** and **2**, whereas the amounts of the corresponding α-regioisomers were negligible (<1%). Before biological evaluation, compounds **1** and **2** were further purified by repetitive dissolution in DMSO followed by precipitation in acetone/ether (3/7) mixtures. MALDI-TOF analysis unambiguously confirmed the expected mass values for **1** and **2**, exhibiting the characteristic isotope pattern of chlorine-containing compounds (**1**: *m/z* 951.03 ([M+Na+1]$^+$, 100%), 953.04 ([M+Na+2]$^+$, 63%), 955.16 ([M+Na+4]$^+$, 16%); **2**: *m/z* 933.11 ([M+Na+1]$^+$, 100%), 935.12 ([M+Na+2]$^+$, 51%), 937.47 ([M+Na+4]$^+$, 22%)).

Biology. *Cytotoxicity Studies with CLB.* CLB is an alkylating agent that has been mainly used in the treatment of chronic lymphocytic leukemia (CLL).[28] It has been demonstrated that CLB may induce different effects in *in vitro* systems, spanning from growth arrest to cell death.[29] In light of these observations, our initial experiments were aimed at establishing the effective CLB concentrations against the specific cell lines used in this work. To this purpose, we incubated undifferentiated U937 and TK6 cells for 48 and 72 h with CLB at concentrations ranging from 0 to 60 μM. As shown in Figure 2, metabolic activity of both cell lines was inhibited as drug concentrations and incubation times were increased. In all cases, however, changes in cell metabolic activity were less pronounced at CLB concentrations on the order of 30 μM.

Cytotoxicity Studies with CLB Conjugates 1 and 2. A first comparison between efficacy of CLB and our FA-conjugates was obtained by observing the presence/absence of statistically significant changes in metabolic activities of undifferentiated U937 and TK6 cells incubated for 24, 48, and 72 h with media containing 30 μM of CLB (to which both cell lines should presumably respond in a similar manner) or 30 μM FA-conjugates **1** and **2** (to which receptor positive cells should preferentially respond). As shown in Figure 3 (upper panel), metabolic activity of undifferentiated U937 cells treated with

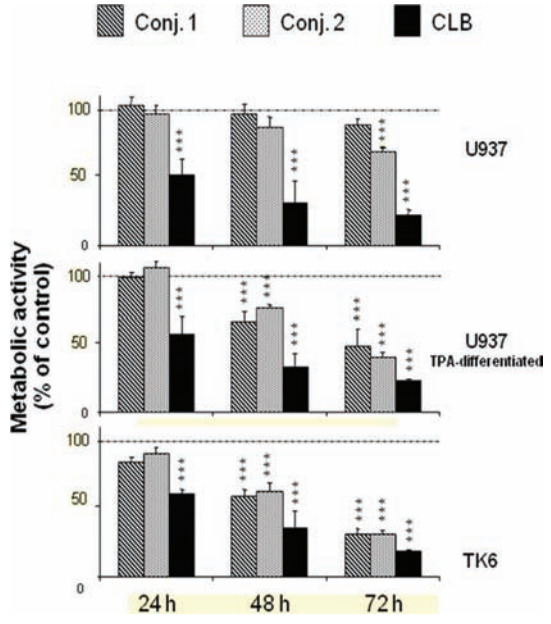


Figure 3. Effects of FA-CLB conjugates **1** and **2** on metabolic activity (XTT assay) of FR$^-$-U937 (upper panel), FR$^+$-TPA-activated U937 (middle panel), and FR$^+$-TK6 cells (lower panel). Significant differences (p < 0.0001, three asterisks) are referred to controls.

dx.doi.org/10.1021/bc200410d | *Bioconjugate Chem.* 2012, 23, 84–96

FA-CLB conjugates did not differ appreciably from the control except for long incubation times (72 h). Conversely, metabolic activity of TK6 cells, incubated in 30 μM FA-conjugates **1** or **2**, was more strongly affected as both compounds reduced cells metabolic activity to ~60 and ~30% as the incubation time was increased from 48 to 72 h, respectively (Figure 3, lower panel).

We hypothesized that a different expression level of FRs may account for such a divergent behavior. Indeed, it has been demonstrated that, while FR expression is restricted to only a few cell types,[30,31] Branda et al. reported[32] that this expression level in TK6 human lymphoblast cells is very high. At variance, while Antony reported[33] that such receptors are essentially absent in undifferentiated U937 cells, nevertheless remarkably elevated levels were demonstrated in macrophagic TPA-activated U937 cells.[34] This presence in macrophages has been largely exploited for drug targeting.[35] In line with these remarks, to finally proof that our folate conjugates **1** and **2** exerted antitumor activity by FR recognition and endocytosis, we differentiated the U937 FR^- into FR^+ activated macrophages. This was achieved by incubating the U937 with 20 nM of TPA (as outlined in the Experimental section). The U937 cells, which normally grow in suspension, when differentiated into macrophages become adherent to each other and to the surface of the culture vessel and cease to proliferate. We found that metabolic activity of TPA-activated U937 incubated with **1** and **2** (30 μM) differed significantly from that of undifferentiated U937 cells. As shown in Figure 3 (middle panel), metabolic activity of activated cells decreased significantly and progressively from 48 and 72 h. We also observed that differences in therapeutic efficacy of FA-derivatives in responsive cells were scarcely perceptible and, in any case, approached that of CLB at the longest incubation time (Figure 3).

A concluding proof of specificity of conjugates toward FA-receptor positive cells is offered by a competition experiment. In this regard, we observed that addition of FA-conjugates to responsive cells (10^4) pretreated for 1 h with a 50-fold excess (1.5 mM) of free FA prevented appreciable changes in metabolic activities even after 72 h of incubation (Figure 4). At variance, the same pretreatment gave wholly ineffective results when cells were exposed to 30 μM CLB.

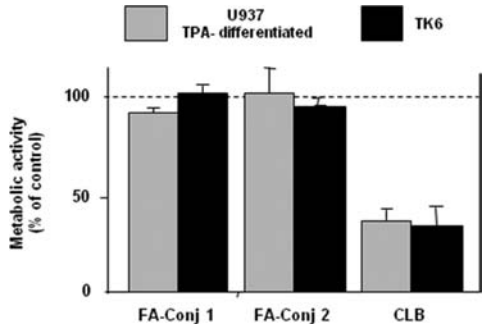


Figure 4. TK6 and TPA-differentiated U937 cells were pretreated with 1.5 mM free FA for 1 h and incubated with FA-conjugates **1** and **2**. The XTT assay was performed after 72 h of incubation.

*Stability of FA-CLB Conjugates **1** and **2** (Shelf Life and Stability in Human Serum).* The shelf life (at 4 °C) of **1** and **2** in human serum was established *in vitro* in U937 and TK6 cell lines. Activity of our FA-CLB conjugates did not change over a 5 weeks storage period (data not shown). Similarly, when conjugates **1** and **2** were incubated in fresh human serum for 12 h, their activity was preserved with negligible activity loss as determined by XTT assay. As shown in Figure 5, change in

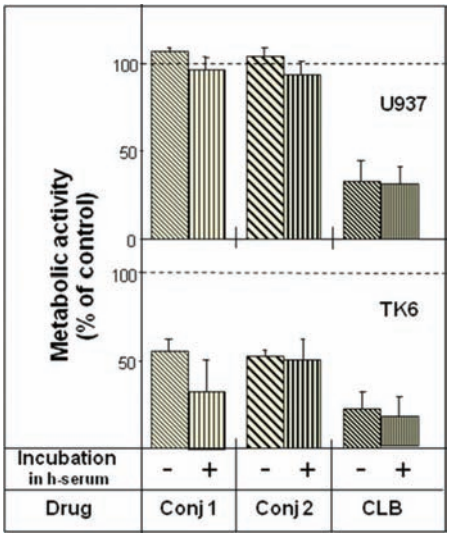


Figure 5. Stability studies of FA-CLB conjugates **1** and **2** preincubated for 12 h in fresh human serum. Details in the Methods section.

metabolic activity of both cell lines was similar to that observed by treating cells with equimolar concentrations (30 μM) of FA-CLB conjugates **1** and **2** or CLB free form. The abatement of metabolic activity of TK6 cells produced results similar to those observed in the absence of preincubation of the compounds with human serum. The U937 cells retain their unresponsiveness to both conjugates.

Molecular Studies. Although it is generally acknowledged that the bifunctional alkylating agent CLB is not cell cycle specific, it has been demonstrated that it may induce G_2/M arrest and apoptosis in several human cell lines.[29] Clarification of the molecular mechanisms of cell cycle arrest and cell death induced by different DNA-damaging chemicals, including CLB, has considerable implications for molecule-targeted cancer therapy. For this reason, it was of interest to investigate at the cellular and molecular levels how FA-CLB conjugates **1** and **2** exert their effects in undifferentiated U937 (FR^-), TPA-U937 activated (FR^+), and TK6 (FR^+) cells in comparison to their parent molecule CLB. To this purpose, we studied the cell cycle distribution and apoptosis upon sublethal treatments. We analyzed the cytofluorimetric profiles and analyzed the protein expression patterns of cells incubated for 48 h with 30 μM CLB in its free form or in conjugated forms **1** and **2**. In agreement with general literature data,[29] we confirmed in both FR^+ cell lines two major aspects: first, CLB promotes visible cell accumulation in G_2 phase and, as also suggested by the presence of a consistent sub-G1 phase, this drug induces apoptosis (Figure 6). The increase of the sub-G1 phase appears to be also associated to an appreciable up-regulation of the proapoptotic Bax and Clusterin (Figure 7). This protein has been at the core of a long-lasting debate, as conflicting data demonstrated both pro- and antiapoptotic effects. However, the controversy on Clusterin function in tumors has been clarified in that it has been demonstrated that two different *m*RNA transcripts (generated by alternative splicing) can be found in cells, one secretory and the other one coding for the nuclear

dx.doi.org/10.1021/bc200410d | *Bioconjugate Chem.* 2012, 23, 84–96

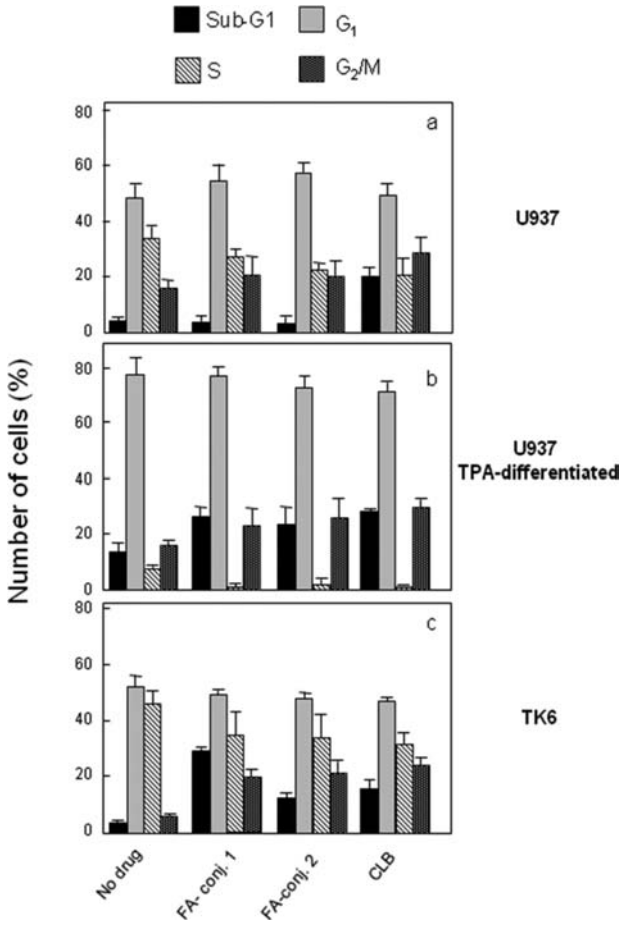


Figure 6. Cell cycle profiles for FR$^-$-U937 (panel a), differentiated FR$^+$-U937 (panel b), and FR$^+$-TK6 cells (panel c) in response to treatments (48 h) with CLB-conjugates **1**, **2** and free CLB (30 μM).

form. The activation of the latter form has proapoptotic aptitude and a regulative (negative) function in cell cycle progression.[36]

As the FR$^-$ cells (undifferentiated U937) are concerned, we found that treatment with FA-CLB conjugates did not roughly change cell cycle profile and, at variance with the effect of pure CLB, it did not determine amassing of cells in the sub-G_1 fraction. The lack of apoptosis in cells incubated for 48 h with both conjugates was also inferred by Western blot experiments, showing no changes in the expression levels of Bax and Clusterin (Figure 7, left panel, lanes 2 and 3). On the contrary, once incubated with FA-CLB conjugates (30 μM), the cell cycle profile of TK6 and TPA-differentiated U937 cells, both expressing FRs, showed a modest accumulation in G_2 phase while visibly activating apoptosis (Figure 6, panels b and c). The sub-G_1 fractions in fact amounted to $\leq$20 in TK6 cells and up to $\geq$25% of the total in TPA-treated U937 cells. The differentiation to macrophages that occurs in TPA-treated U937 cells induced synchronization in G_0/G_1 phase, and in the meanwhile, proliferation was switched off. This cytofluorimetric scenario was mirrored by Western blot experiments. Apoptosis was declared by the augmented levels of BAX and of the propapoptotic form of Clusterin (Figure 7, middle and right panels, lanes 2 and 3) in both cell lines and, as the TK6 cells are concerned, of p53 (Figure 7, right panel, lanes 2 and 3). Notably, once incubated with 30 μM free CLB, TK6 cells were characterized by a time-dependent increase in the expression level of p53. This observation agrees with literature data that point to an ongoing up-regulation of p53 protein expression to explain the onset of lymphocytic cell resistance to CLB.[37]

DISCUSSION

FA is an inexpensive, stable, and poorly immunogenic chemical endowed with high affinity for FRs, which are overexpressed in a wide amount of malignant cells. Moreover, its conjugation to cytotoxic agents via its γ-carboxyl moiety usually provide molecules able to retain the affinity for FRs. These peculiar features have been herein exploited to study the targeting properties of our FA conjugates along with the blood circulation stability features of the linkers for the selective delivery of CLB using three lymphoblastoid cell line models presenting dissimilar levels of FR expression. We therefore designed two drug delivery systems **1** and **2** as depicted in Figure 1, in which the chemical warhead, the anticancer agent CLB, is conjugated to the cell surface recognition moiety through an aminoether linker or a β-amino acid-based spacer.

One of the structural requirements necessary to ensure recognition by FR of folate conjugates is mediation of the

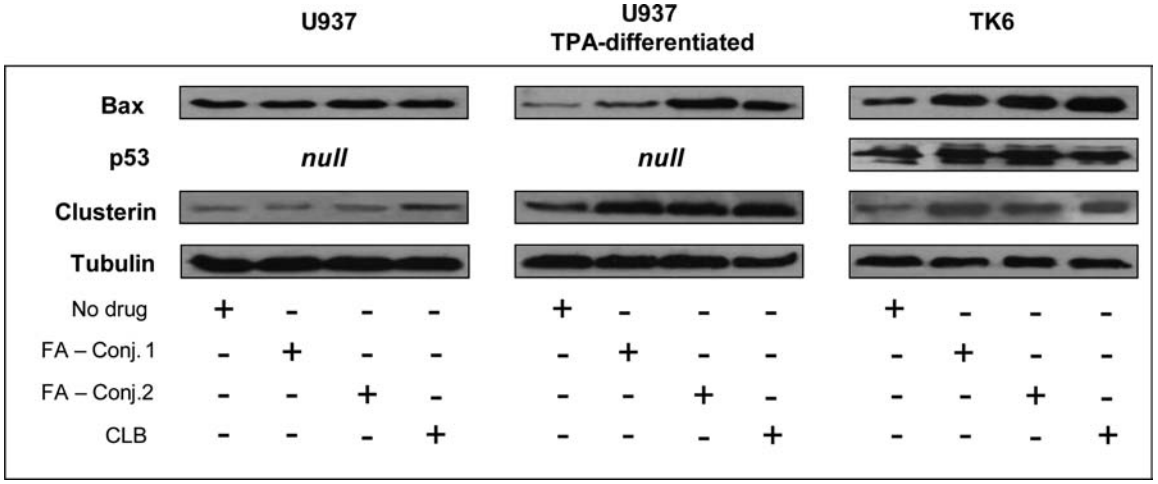


Figure 7. Protein expression in FR$^-$-U937, TPA-differentiated FR$^+$-U937, and FR$^+$-TK6 cells in response to treatments (48 h) with CLB-conjugates **1**, **2** and free CLB (30 μM).

dx.doi.org/10.1021/bc200410d | *Bioconjugate Chem.* 2012, 23, 84–96

connection of the cytotoxic warhead to FA by a suitable linker.[8] In this context, natural (e.g., albumin, chitosan, and heparin) and synthetic polymers [e.g., *N*-(2-hydroxypropyl)-methacrylamide copolymer (HPMA), polystyrene-maleic anhydride copolymer, polyethylene glycol (PEG), and poly-L-glutamic acid (PGA)] have been already proposed.[1] An ideal linker for drug delivery should be characterized by adequate biodegradability and molecular weight, which should confer favorable pharmacokinetics and pharmacodynamics properties, facilitating bioelimination from the body and hence avoiding undesired accumulation *in vivo*. Furthermore, linkers should be water-soluble, nontoxic, and nonimmunogenic; they should possess low polydispersity (to ensure acceptable homogeneity of the final conjugates) and adequate half-life in the bloodstream (to enable, at first, wide and homogeneous drug distribution and, then, prolonged accumulation into the target tumors).[38] On the basis of these requirements, two types of linkers—namely, aminoether and β-amino acid-based linkers—were chosen, owing to their hydrophilicity and medium stability. Particularly, it should be noted that, while PEG linkers and analogues (mPEG20000, NH_2PEG2000, NH_2PEG10000 and the like) have been already widely employed in targeted antitumor therapy,[39] linkers composed of β-amino acids have no precedent examples in literature. β-Amino acids are relatively rare in Nature;[40] with respect to α-amino acids to which they are structurally similar, an exception is made for an "extra" carbon atom inserted between the amino and carboxy termini. Compared to their natural counterparts, peptides composed of β-amino acids (β-peptides) exhibit a considerably stable biological profile, since they are far more resistant toward degrading and metabolizing enzymes in living organisms.[27,41] This feature does not appear to confer cytotoxic properties, as it has been demonstrated for most β-amino acids as well as for short β-peptides that, once orally administered, these molecules are indeed easily excreted.[42] On the other hand, longer-chain β-peptides have longer half-lives of clearance, even though they may require intravenous administration.[43] Given the potential hurdles in the use of α-amino acids as drug carriers, primarily due to their vulnerability *in vivo*, use of synthetically available β-amino acids[44] may effectively represent a satisfactory compromise among hydrosolubility, biocompatibility, and appropriate bloodstream half-life for a localized drug delivery effect. Herein, initial experiments aimed at testing the efficacy of β-amino acid-based linkers for targeted anticancer chemotherapy were performed using the simplest β-amino acid, β-Ala.

The selected cytotoxic warhead, CLB [*N*,*N*-bis(2-chloroethyl)-*p*-aminophenylbutyric acid, CLB, **9**] is a bifunctional alkylating chemotherapeutic agent[28] of the mustardgas type, clinically used for the treatment of chronic lymphatic leukemia, lymphomas,[45,46] and advanced ovarian and breast carcinomas. Although over the years this drug has been succeeded by fludarabine as a very effective therapeutic agent for CLL treatment,[47,48] the latest data[49−52] have suggested that CLB may be yet considered as first line treatment in selected cases. Particularly in patients aged older than 65 (who are the majority of patients with CLL), first-line treatment with fludarabine did not demonstrate better survival outcomes when compared with CLB.[49] Although in combination with immunotherapy, a re-evaluation of chlorambucil has been also reported very recently for the management and clinical treatment of mantle cell lymphoma and Indolent Non-Hodgkin Lymphoma.[50]

Like all alkylating agents, CLB toxicity stands on its oxidative stress-inducing properties that are exerted equally toward healthy and cancer tissues. However, CLB has low stability in aqueous environments and may undergo rapid metabolism,[53] although the presence of serum increases the drug's stability significantly. Even if lipophilic prodrug formulations have been already proposed to shield CLB from degradation and to deliver it directly to the tumor site,[54] to the best of our knowledge studies aimed at evaluating the efficacy of covalently linked CLB delivery systems bearing FA as the tumor recognition moiety have never been reported (the only example of evaluation of the tumor-targeting properties of a folate-CLB delivery system so far has been achieved by developing a drug carrier based on inclusion complexes between CLB and β-cyclodextrins).[55] Herein, the construction of the two FA-CLB conjugates **1** and **2** has been carried out either to explore the properties of β-amino acids-containing linkers or to investigate the potential use of CLB in tumor-targeted chemotherapy using the more traditional drug carrier NH_2PEG13.

The ability of conjugates **1** and **2** to selectively reach and have a detrimental effect on cancer cells was assessed evaluating the residual metabolic activity of cells exposed to these prodrugs by exploiting XTT assays. To prove that the observed FR-mediated cell targeting was truly selective, we compared FR^+ human lymphoblast TK6 cells with the FR^- human leukemic monocyte lymphoma U937 cells that were used as negative controls. We demonstrated that conjugates **1** and **2**, while exerting cytotoxic activities against FR^+ cells, were quite ineffective and harmless against the FR^- ones. Interestingly, increase in selectivity against FR^+ cells exhibited by the conjugates was associated to a reduced loss of cytotoxicity, as deduced by juxtaposing their cytotoxicity with that of CLB in its free form. The difference in selectivity shown by FA-conjugates in respect to free CLB could be quantitatively assessed by comparing the respective IC_{50} values. Indeed, the concentrations of CLB and FA-conjugates **1** and **2** required to produce, respectively, an IC_{50} in both cell lines after 24, 48, and 72 h of incubation are reported in Table 1.

Table 1. IC_{50} Values of Conjugates 1 and 2 *versus* CLB in U937 and TK6 Cells

		IC_{50} (μM)		
incubation (h)	cell lines	conjugate **1**	conjugate **2**	CLB
24	U937	>100	>100	32.8
	TK6	>100	>100	32.4
48	U937	68	68	19.8
	TK6	32	32	17.1
72	U937	64	62	13.6
	TK6	27	21	13.9

Another proof of a direct involvement of FRs in cell response was obtained by studying the effect of FA-conjugates **1** and **2** on TPA-activated U937 cells. Previous observations demonstrated that, upon differentiation, these cells acquired a macrophage-like phenotype, including FR expression. As expected, these cells, originally unaffected by the action of FA-CLB conjugates (except when the incubation with conjugate **2** was prolonged to 72 h) become fully responsive. Interestingly, both conjugates were manifestly selective toward FR^+ cells, since free FA (50 fold molar excess) was demonstrated to efficiently compete in the binding to the FRs, while under the same conditions, FA was ineffective in

dx.doi.org/10.1021/bc200410d | *Bioconjugate Chem.* 2012, 23, 84−96

U937 cells that do not express the receptor (Figure 4). Overall, these data highlight the selectivity of our FA-CLB conjugates in targeting FR^+ cells, as responsiveness (and unresponsiveness) of cells to conjugates **1** and **2** was strictly dependent on the FR expression on the cell membrane. Interestingly, cell cycle data of Figure 6a definitely demonstrated that FR^- cells did not significantly modify their profiles when incubated with conjugates **1** and **2**. The Sub-G_1 and G_2 fractions did not appear to be quantitatively changed except when cells were incubated with pure CLB. On the contrary, definite and meaningful alterations in the cell cycle profiles were present in prodrug-treated FR^+ cells. Indeed, treatment of these cells with both conjugates caused a significant enrichment in the number of cells staying in G_2 and Sub-G_1 phases (Figure 6b and c). The presence of the latter large fractions suggests that FR^+ cells treated for more than 24 h with the two conjugates (and both FR^+ and FR^- cells treated with unconjugated free CLB) were progressively prompted to apoptosis. This hypothesis has been definitely strengthened by Western blot experiments that enlightened significant enhancement in the expressions of the pro-apoptotic proteins BAX, Clusterin, and also p53, as the TK6 cells are concerned.

CONCLUSIONS

We have successfully reported the chemical synthesis and biological evaluation of two tumor-targeted drug delivery systems **1** and **2**, which bear an FA unit as the tumor recognition moiety and the CLB as the cytotoxic agent, the two bioactive units having been jointed by aminoether (4,7,10-trioxadecane-1,13-diamine) and pseudo-*β*-dipeptide (*β*-Ala-ED-*β*-Ala) linkers. Preparation of the two molecular systems has been devised by a straightforward and efficient route (34−54% o.y.) based on 4−7 steps starting from amines **3** and **10**. When evaluated using both FR^- (undifferentiated U937) and FR^+ (TK6 and TPA-differentiated U937) leukemic cells, both conjugates exhibited activity only against FR^+ cells (particularly TK6), exerting antitumor effects which are comparable to that displayed by CLB in its free form. Our *in vitro* results, then, show that **1** and **2** specifically bind to FR^+ cells, that this binding is significantly higher than in FR^- cells, and that the interaction is inhibited by free FA.

Given the promising results described in this paper, further research, aimed at developing other structurally related folate-based drug delivery systems, is advisible. It must be emphasized that, to the best of our knowledge, use of *β*-amino acids has never been taken into consideration to this end. For this reason, the design of other *β*-amino acid-based linkers is currently in progress, with the scope of enhancing the pharmacokinetic profiles of the corresponding conjugates, thus leading to targeted drug delivery systems endowed with improved antitumor properties.

AUTHOR INFORMATION

Corresponding Author

*Dipartimento di Chimica Organica e Biochimica, Università di Napoli Federico II, via Cinthia, 4 I-80126 Napoli, Italy. Phone/Fax: +39 081 674119; E-mail: annalisa.guaragna@unina.it.

Author Contributions

‡These authors contributed equally to this work.

ACKNOWLEDGMENTS

^1H NMR, ^{13}C NMR, and MS experiments were performed at the "Centro Interdipartimentale di Metodologie Chimico-Fisiche" (CIMCF), University of Napoli "Federico II". This work was supported by a grant to GP by MIUR, Rome, Italy (Project code E61J10000200001). The authors wish to thank Dr. L. Campanella and Dr. C. Selleri for helpful discussions on tumor-targeted chemotherapy.

ABBREVIATIONS LIST:

β-Ala, *β*-alanine; CLB, chlorambucil; CLL, chronic lymphocytic leukemia; ED, ethylenediamine; FA, folic acid; FR, folate receptor; FR^+, expressing FRs; FR^-, not expressing FRs; GPI, glycosyl-phosphatidylinositol; PEG, polyethylene glycol; TPA, 12-*O*-tetra-decanoyl-phorbol-13-acetate

REFERENCES

(1) Kratz, F., Müller, I. A., Ryppa, C., and Warnecke, A. (2008) Prodrug strategies in anticancer chemotherapy. *ChemMedChem 3*, 20−53.

(2) Allen, T. M. (2002) Ligand-targeted therapeutics in anticancer therapy. *Nat. Rev. Cancer 2*, 750−763.

(3) Russell-jones, G., Mctavish, K., Mcewan, J., Rice, J., and Nowotnik, D. (2004) Vitamin-mediated targeting as a potential mechanism to increase drug uptake by tumors. *J. Inorg. Biochem. 28*, 1625−1633.

(4) Gupta, Y., Kohli, D. V., and Jain, S. K. (2008) Vitamin B12-mediated transport: a potential tool for tumor targeting of antineoplastic drugs and imaging agents. *Crit. Rev. Ther. Drug Carrier Syst. 25*, 347−379.

(5) Ojima, I. (2008) Guided molecular missiles for tumor-targeting chemotherapy − case studies using the second-generation taxoids as warheads. *Acc. Chem. Res. 41*, 108−119.

(6) Chen, S., Zhao, X., Chen, J., Chen, J., Kuznetsova, L., Wong, S. S., and Ojima, I. (2010) Mechanism-based tumor-targeting drug delivery system. Validation of efficient vitamin receptor-mediated endocytosis and drug release. *Bioconjugate Chem. 21*, 979−987.

(7) Bareford, L. M., and Swaan, P. W. (2007) Endocytic mechanisms for targeted drug delivery. *Adv. Drug Delivery Rev. 59*, 748−758.

(8) Xia, W., and Low, P. S. (2010) Folate-targeted therapies for cancer. *J. Med. Chem. 53*, 6811−6824.

(9) Low, P. S., and Kularatne, S. A. (2009) Folate-targeted therapeutic and imaging agents for cancer. *Curr. Opin. Chem. Biol. 13*, 256−262.

(10) Low, P. S., Henne, W. A., and Doorneweerd, D. D. (2008) Discovery and development of folic-acid-based receptor targeting for imaging and therapy of cancer and inflammatory diseases. *Acc. Chem. Res. 41*, 120−129.

(11) Sabharanjak, S., and Mayor, S. (2004) Folate receptor endocytosis and trafficking. *Adv. Drug Delivery Rev. 56*, 1099−1109.

(12) Elnakat, H., and Ratnam, M. (2004) Distribution, functionality and gene regulation of folate receptor isoforms: implications in targeted therapy. *Adv. Drug Delivery Rev. 56*, 1067−1084.

(13) Wang, S., and Low, P. S. (1998) Folate-mediated targeting of antineoplastic drugs, imaging agents, and nucleic acids to cancer cells. *J. Controlled Release 53*, 39−48.

(14) Reddy, J. A., Westrick, E., Santhapuram, H. K. R., Howard, S. J., Miller, M. L., Vetzel, M., Vlahov, I., Chari, R. V. J., Goldmacher, V. S., and Leamon, C. P. (2007) Folate receptor−specific antitumor activity of EC131, a folate-maytansinoid conjugate. *Cancer Res. 67*, 6376−6382.

(15) Leamon, C. P., Reddy, J. A., Vlahov, I. R., Westrick, E., Dawson, A., Dorton, R., Vetzel, M., Santhapuram, H. K., and Wang, Y. (2007) Preclinical antitumor activity of a novel folate-targeted dual drug conjugate. *Mol. Pharmaceutics 4*, 659−667.

(16) Li, J., Sausville, E. A., Klein, P. J., Morgenstern, D., Leamon, C. P., Messmann, R. A., and LoRusso, P. (2009) Clinical

pharmacokinetics and exposure-toxicity relationship of a folate-Vinca alkaloid conjugate EC145 in cancer patients. *J. Clin. Pharmacol. 49*, 1467−1476.
(17) Leamon, C. P., Reddy, J. A., Klein, P. J., Vlahov, I. R., Dorton, R., Bloomfield, A., Nelson, M., Westrick, E., Parker, N., Bruna, K., Vetzel, M., Gehrke, M., Nicoson, J. S., Messmann, R. A., LoRusso, P. M., and Sausville, E. A. (2011) Reducing undesirable hepatic clearance of a tumor-targeted vinca alkaloid via novel saccharopeptidic modifications. *J. Pharmacol. Exp. Ther. 336*, 336−343.
(18) Vlahov, I. R., You, F., Santhapuram, H. K., Wang, Y., Vaughn, J. F., Hahn, S. J., Kleindl, P. J., Fan, M., and Leamon, C. P. (2011) Design and regioselective synthesis of a new generation of targeted therapeutics. Part 3: Folate conjugates of aminopterin hydrazide for the treatment of inflammation. *Bioorg. Med. Chem. Lett. 21*, 1202−1205.
(19) Vlahov, I. R., Santhapuram, H. K., You, F., Wang, Y., Kleindl, P. J., Hahn, S. J., Vaughn, J. F., Reno, D. S., and Leamon, C. P. (2010) Carbohydrate-based synthetic approach to control toxicity profiles of folate-drug conjugates. *J. Org. Chem. 75*, 3685−3691.
(20) Sordet, O., Rébé, C., Leroy, I., Bruey, J. M., Garrido, C., Miguet, C., Lizard, G., Plenchette, S., Corcos, L., and Solary, E. (2002) Specific involvement of caspases in the differentiation of monocytes into macrophages. *Blood 100*, 4446−4453.
(21) Sun, J., Wang, L., Waring, M. A., Wang, C., Woodman, K. K., and Sheil, A. G. (1997) Simple and reliable methods to assess hepatocyte viability in bioartificial liver support system matrices. *Artif. Organs 21*, 408−413.
(22) Aloyz, R., Grzywacz, K., Xu, Z.-Y., Loignon, M, Alaoui-Jamali, M. A., and Panasci, L (2004) Imatinib sensitizes CLL lymphocytes to chlorambucil. *Leukemia 18*, 409−414.
(23) Crescenzi, E., Chiaviello, A., Canti, G., Reddi, E., Veneziani, B. M., and Palumbo, G. (2006) Low doses of cisplatin or gemcitabine plus Photofrin/photodynamic therapy: disjointed cell cycle phase-related activity accounts for synergistic outcome in metastatic non-small cell lung cancer cells (H1299). *Mol. Cancer Ther. 5*, 776−785.
(24) Laemmli, U. K. (1971) Cleavage of structural proteins during the assembly of the head of bacteriophage T4. *Nature 227*, 680−685.
(25) Guaragna, A., Amoresano, A., Pinto, V., Monti, G., Mastrobuoni, G., Marino, G., and Palumbo, G. (2008) Synthesis and proteomic activity evaluation of a new isotope-coded affinity tagging (ICAT) reagent. *Bioconjugate Chem. 19*, 1095−1104.
(26) Dhar, S., Liu, Z., Thomale, J., Dai, H., and Lippard, S. J. (2008) Targeted single-wall carbon nanotube-mediated Pt(IV) prodrug delivery using folate as a homing device. *J. Am. Chem. Soc. 130*, 11467−11476.
(27) Seebach, D., and Gardiner, J. (2008) Beta-peptidic peptidomimetics. *Acc. Chem. Res. 41*, 1366−1375.
(28) Rajski, S. R., and Williams, R. M. (1998) DNA cross-linking agents as antitumor drugs. *Chem. Rev. 98*, 2723−2796.
(29) Amrein, L, Loignon, M., Goulet, A. C., Dunn, M., Jean-Claude, B., Aloyz, R., and Panasci, L. (2007) Chlorambucil cytotoxicity in malignant B lymphocytes is synergistically increased by 2-(morpholin-4-yl)-benzo[h]chomen-4-one (NU7026)-mediated inhibition of DNA double-strand break repair via inhibition of DNA-dependent protein kinase. *J. Pharmacol. Exp. Ther. 321*, 848−855.
(30) Sierra, E. E., and Goldman, I. D. (1999) Recent advances in the understanding of the mechanism of membrane transport of folates and antifolates. *Semin. Oncol. 26*, 11−23.
(31) Matherly, L. H., and Goldman, D. I. (2003) Membrane transport of folates. *Vitam. Horm. 66*, 403−456.
(32) Branda, R. F., O'Neill, J. P., Brooks, E. M., Trombley, L. M., and Nicklas, J. A. (2001) The effect of folate deficiency on the cytotoxic and mutagenic responses to ethyl methanesulfonate in human lymphoblastoid cell lines that differ in p53 status. *Mutat. Res. 473*, 51−71.
(33) Antony, A. C. (1996) Folate receptors. *Annu. Rev. Nutr. 16*, 501−521.
(34) Antohe, F., Radulescu., L., Puchianu, E., Kennedy, M. D., Low, P. S., and Simionescu, M. (2005) Increased uptake of folate conjugates by activated macrophages in experimental hyperlipemia. *Cell Tissue Res. 320*, 277−285.
(35) Roy, E. J., Gawlick, U., Orr, B. A., and Kranz, D. M. (2004) Folate-mediated targeting of T cells to tumors. *Adv. Drug Delivery Rev. 56*, 1219−1231.
(36) Leskov, K. S., Klokov, D. Y., Li, J., Kinsella, T. J., and Boothman, D. A. (2003) Synthesis and functional analyses of nuclear clusterin, a cell death protein. *J. Biol. Chem. 278*, 11590−11600.
(37) Johnston, J. B., Daeninck, P., Verburg, L., Lee, K., Williams, G., Israels, L. G., Mowat, M. R., and Begleiter, A. (1997) P53, MDM-2, BAX and BCL-2 and drug resistance in chronic lymphocytic leukemia. *Leuk. Lymphoma 5−6*, 435−449.
(38) Twaites, B., de las Heras Alarcón, C., and Alexander, C. (2005) Synthetic polymers as drugs and therapeutics. *J. Mater. Chem. 15*, 441−455.
(39) Duncan, R. (2006) Polymer conjugates as anticancer nanomedicines. *Nat. Rev. Cancer 6*, 688−701.
(40) Spiteller, P., Von Nussbaum, F. (2004) *b-Amino acids in nature. Highlights in Bioorganic Chemistry: Methods and Applications* (Schmuck, C., and Wennemers, H., Eds.) pp 19−91,Wiley-VCH, Weinheim.
(41) Hook, D. F., Gessier, F., Noti, C., Kast, P., and Seebach, D. (2004) Probing the proteolytic stability of b-peptides containing a-fluoro- and a-hydroxy-b-amino acids. *ChemBioChem 5*, 691−706, and references therein cited..
(42) Wiegand, H., Wirz, B., Schweitzer, A., Gross, G., Rodriguez Perez, M. I., Andres, H., Kimmerlin, T., Rueping, M., and Seebach, D. (2004) Pharmacokinetic investigation of a ^{14}C-labelled β^3/α-tetrapeptide in rats. *Chem. Biodivers. 1*, 1812−1828.
(43) Wiegand, H., Wirz, B., Schweitzer, A., Camenisch, G. P., Rodriguez Perez, M. I., Gross, G., Woessner, R., Voges, R., Arvidsson, P. I., Frackenpohl, J., and Seebach, D. (2002) The outstanding metabolic stability of a ^{14}C-labeled β-nonapeptide in rats − *in vitro* and *in vivo* pharmacokinetic studies. *Biopharm. Drug Dispos. 23*, 251−262.
(44) Guaragna, A., Pedatella, S., Pinto, V., and Palumbo, G. (2006) Synthesis of *C*-protected 2,2-dideutero b^3-amino acids. *Synthesis 23*, 4013−4016, and references therein cited..
(45) Panasci, L., Paiement, J. P., Christodoulopoulos, G., Belenkov, A., Malapetsa, A., and Aloyz, R. (2001) Chlorambucil drug resistance in chronic lymphocytic leukemia: the emerging role of DNA repair. *Clin. Cancer Res. 7*, 454−461.
(46) Reux, B., Weber, V., Galmier, M. J., Borel, M., Madesclaire, M., Madelmont, J. C., and Debiton, E. (2008) Synthesis and cytotoxic properties of new fluorodeoxyglucose-coupled chlorambucil derivatives. *Bioorg. Med. Chem. 16*, 5004−5020.
(47) Keating, M. J., Kantarjian, H., Talpaz, M., Redman, J., Koller, C., Barlogie, B., Velasquez, W., Plunkett, W., Freireich, E. J., and McCredie, K. B. (1989) Fludarabine: a new agent with major activity against chronic lymphocytic leukemia. *Blood 74*, 19−25.
(48) Keating, M. J., Kantarjian, H., O'Brien, S., Koller, C., Talpaz, M., Schachner, J., Childs, C. C., Freireich, E. J., and McCredie, K. B. (1991) Fludarabine: a new agent with marked cytoreductive activity in untreated chronic lymphocytic leukemia. *J. Clin. Oncol. 9*, 44−49.
(49) Eichhorst, B. F., Busch, R., Stilgenbauer, S., Stauch, M., Bergmann, M. A., Ritgen, M., Kranzhöfer, N., Rohrberg, R., Söling, U., Burkhard, O., Westermann, A., Goede, V., Schweighofer, C. D., Fischer, K., Fink, A.-M., Wendtner, C. M., Brittinger, G., Döhner, H., Emmerich, B., and Hallek, M., the German CLL Study Group (GCLLSG) (2009) First-line therapy with fludarabine compared with chlorambucil does not lymphocytic result in a major benefit for elderly patients with advanced chronic leukemia. *Blood 114*, 3382−3391.
(50) Dreyling, M., Polliack, A., and Tadmor, T. (2011) Chlorambucil in indolent mantle cell lymphoma-just another old drug for a new disease? *Leuk. Lymphoma 52*, 351−352.
(51) Chiappella, A., Ciochetto, C., Orsucci, L., and Vitolo, U. (2011) Update in Indolent Non-Hodgkin Lymphoma (NHL): Paradigm for Waldenström's Macroglobulinemia (WM). *Clin. Lymphoma Myeloma Leuk. 11*, 149−151.

(52) Goede, V., and Hallek, M. (2011) Optimal pharmacotherapeutic management of chronic lymphocytic leukaemia: considerations in the elderly. *Drugs Aging 28*, 163−176.
(53) Pedersen, P. J., Christensen, M. S., Ruysschaert, T., Linderoth, L., Andresen, T. L., Melander, F., Mouritsen, O. G., Madsen, R., and Clausen, M. H. (2009) Synthesis and biophysical characterization of chlorambucil anticancer ether lipid prodrugs. *J. Med. Chem. 52*, 3408−3415, and references therein cited..
(54) Bielawski, K., and Bielawska, A. (2008) Small-molecule based delivery systems for alkylating antineoplastic compounds. *ChemMedChem 3*, 536−542.
(55) Salmaso, S., Bersani, S., Semenzato, A., and Caliceti, P. (2007) New cyclodextrin bioconjugates for active tumour targeting. *J. Drug Targeting 15*, 379−390.

Bioconjugate Chemistry

Article

pubs.acs.org/bc

Design and Synthesis of High-Avidity Tetravalent Glycoclusters as Probes for *Sambucus sieboldiana* Agglutinin and Characterization of their Binding Properties

Makoto Ogata,[†,#] Megumi Yano,[‡,#] Seiichiro Umemura,[‡] Takeomi Murata,[‡] Enoch Y. Park,[†] Yuka Kobayashi,[§] Tomohiro Asai,[⊥] Naoto Oku,[⊥] Naoki Nakamura,[¶] Ichiro Matsuo,[¶] and Taichi Usui*[,†,‡]

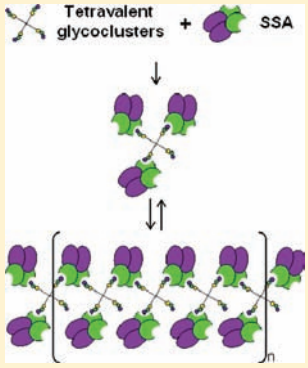
[†]Department of Bioscience, Graduate School of Science and Technology, [‡]Department of Applied Biological Chemistry, Faculty of Agriculture, Shizuoka University, 836 Ohya, Suruga ward, Shizuoka 422-8529, Japan

[§]J-Oil mills, INC, 11 Kagetoricho, Totsuka-ku, Yokohama, Kanagawa 245-0064, Japan

[⊥]Department of Medical Biochemistry, University of Shizuoka Graduate School of Pharmaceutical Sciences, 52-1 Yada, Suruga-ku, Shizuoka 422-8526, Japan

[¶]Department of Chemistry and Chemical Biology, Gunma University, 1-5-1 Tenjin-cho, Kiryu, Gunma 376-8515, Japan.

ABSTRACT: We designed and synthesized three tetravalent sialo-glycoclusters that had different separations between the terminal sialic acids and the linking carboxy groups of the ethylene glycol bis(β-aminoethyl ether)-*N*,*N*,*N*′,*N*′-tetraacetate scaffold to serve as ligands for the sialic acid-binding lectin *Sambucus sieboldiana* agglutinin (SSA). The interaction between each glycocluster and SSA was characterized by hemagglutination inhibition, quantitative precipitation, and double-diffusion assays. For the precipitation assays, the precipitin curves indicated that the ligands and SSA bound in either a 1:1 or a 1:2 ratio, i.e., stoichiometrically. The strong interactions of these sialo-glycoclusters with SSA could be ascribed to a combination of multivalency and spacer effects. We also assessed the nature of the ligand−SSA complexes by isothermal titration calorimetry and dynamic light scattering. The results of those experiments indicated that formation of intermolecular complexes occurred at less than stoichiometric ratios of ligand to SSA concentrations and that, as the concentrations of the ligands increased, larger cross-linked aggregates formed. Large aggregates that were present concurrently with visible precipitation and with a particle size centered at ∼600 to 800 nm were identified by dynamic light scattering.



INTRODUCTION

The cross-linking properties of plant and animal lectins with multivalent carbohydrates and glycoproteins are well-known.[1,2] Multivalent lectins can bind branched chain oligosaccharides,[3] glycopeptides,[3] and glycoproteins[4,5] and form cross-linked complexes. High-affinity, synthetic lectin-binding ligands are needed to characterize carbohydrate-mediated biological processes, e.g., viral and bacterial infections, cell−cell recognition, and cancer metastasis, because interactions between univalent synthetic (or naturally occurring) carbohydrates and lectins are usually weak (K_d ∼10^{-3}).[6,7] The binding affinities of lectin-binding ligands are dramatically increased if the formation of an intermolecular ligand/lectin network is possible.[8−13] The binding affinities of such ligands increase exponentially with the number of binding sites, and this phenomenon is termed the glycoside-cluster effect.[14−17] Multivalent interactions are often used by nature to control cellular processes.[18] The multivalent effect has been studied using synthetic glycoclusters,[19−22] glycodendrimers,[23−25] and glycopolymers.[26,27] Multivalency is a powerful design approach when a synthetic ligand that binds strongly to its target is desired. Because strong binding is required for interference strategies, the synthesis and evaluation of multivalent carbohydrates are important issues.

We recently designed di- and tetravalent glycosides bearing *N*-acetylglucosamine (GN), *N*,*N*′-diacetylchitobiose [$(GN)_2$], and *N*-acetyllactosamine (LN) moieties, which could precipitate wheat germ agglutinin and coral tree agglutinin.[28] Therefore, the multivalency effect can greatly enhance the binding strength of ligands even when the valency of the ligand is a relatively small number, i.e., two (divalent) or four (tetravalent). However, the design of synthetic multivalent ligands requires avoiding several potential problems. Designed multivalent ligands have often been not very soluble and poorly recognize the target lectin, because they contain only mono- or disaccharides.[8,19−22,29] Additionally, the spatial arrangement of the carbohydrates in synthetic ligands has not always been optimal for ligand binding.[8,22] From such an aspect, our strategy of molecular design is to construct an amphiphilic structure, taking into account the contribution of the asialo portion of the glycan chain, by arranging tetravalent short or long glycans, attached to a ethylene glycol bis(β-aminoethyl ether)-*N*,*N*,*N*′,*N*′-tetraacetate (EGTA) backbone. Given this background, we designed and synthesized three highly water-

Received: August 12, 2011
Revised: November 8, 2011
Published: December 15, 2011

ACS Publications © 2011 American Chemical Society

dx.doi.org/10.1021/bc200440e | *Bioconjugate Chem.* 2012, 23, 97−105

soluble tetravalent glycoclusters carrying glycans or spacers of different lengths as ligands for the sialic-acid-binding lectin *Sambucus sieboldiana* agglutinin (SSA) and assessed their binding properties. SSA, from the bark of the Japanese elderberry, specifically binds to Neu5Acα2,6Gal/GalNAc[30−32] and is a useful tool for sialylated glycoconjugate studies.[33,34] The lectin is a heterotetrameric glycoprotein containing two copies of two different subunits, one with a carbohydrate binding site and one of unknown function.[30−32]

The present paper describes herewith the design and synthesis of high-avidity tetravalent glycoclusters as probes for SSA and characterization of their binding properties. The calorimetry and light scattering experiments allowed judging of the stoichiometries and sizes of the ligand−lectin complex in the solution.

EXPERIMENTAL PROCEDURES

Materials. *N*-Acetyllactosamine (LN), 3′-sialyl-*N*-acetyllactosamine (Neu5Acα2,3LN), 6′-sialyl-*N*-acetyllactosamine (Neu5Acα2,6LN), 6′-sialyl-lactose (Neu5Acα2,6lactose), 2-(2-aminoethoxy)ethyl-β-*N*-acetyllactosamine [2-(2-aminoethoxy)-ethyl-β-LN], 2-[2-(5′-aminopentanecarboxamidoethoxy)]ethyl-β-*N*-acetyllactosaminide {2-[2-(5′-aminopentanecarboxamidoethoxy)]ethyl-β-LN}, and hexan-1,6-diyl bis-(β-*N*-acetyllactosaminide) [hexan-1,6-diyl bis-(β-LN)] were prepared as described.[35] UDP-GlcNAc, UDP-Gal, and CMP-Neu5Ac were gifts from Yamasa Corporation (Chiba, Japan). Bovine milk β1,4-galactosyltransferase (β4GalT) was purchased from Calbiochem-Novabiochem (San Diego, CA). Recombinant human β1,3-*N*-acetylglucosaminyltransferase (β3GnT) and recombinant rat α2,6-sialyltransferase (α2,6SiaT) were prepared as described.[36,37] SSA was purchased from J-OIL MILLS, Inc. (TokyoYokohama, Japan). Other chemicals were obtained from commercial sources.

Enzyme Assays. β3GnT, β4GalT, and α2,6SiaT activities were assayed as described.[35,37]

Analytical Methods. The high performance liquid chromatography (HPLC) system consisted of a Unison US-C18 column (ODS, 4.6 × 250 mm; Imtakt, Japan), a JASCO Intelligent System Liquid Chromatograph, and detection at 210 nm. Bound material was eluted in 0.05% TFA/15% or 25% methanol at 1.0 mL/min and 40 °C. The electrospray ionization (ESI) mass spectra were measured on a JMS-T100LC mass spectrometer. Matrix-assisted laser desorption/ionization time-of-flight (MALDI-TOF) mass spectra were acquired using an AutoFlex spectrometer (Bruker Daltonics, Bremen, Germany) and in the positive reflection mode with 20-kV ion acceleration and without post acceleration. The spectra were recorded with a detector voltage of 1.65 kV and were the average of at least 300 laser shots. A solution of 0.5 M 2,4,6-trihydroxyacetophenone in ethanol mixed with aqueous 0.1 M ammonium citrate dibasic (2:1 v/v) was the matrix. Each sample was dissolved in water and mixed with the matrix (1:4 v/v). Each mixture (1 μL) was spotted onto a stainless platform and allowed to crystallize at room temperature. The spectrometer was calibrated with peptide calibration standard I (Bruker Daltonics). 500 MHz ^{1}H NMR spectra and 125 MHz ^{13}C NMR spectra were recorded using a JEOL lambda-500 spectrometer. Chemical shifts were expressed in ppm relative to the methyl resonance of the external standard sodium 3-(trimethylsilyl)propionate.

Synthesis of Tetravalent Asialo-Glycoclusters. *(a). Tetravalent LN Glycocluster (1).* *N*-Ethyldiisopropylamine (0.15 mL, 0.88 mmol), HBTU (0.27 mg, 0.71 mmol), and triethylamine (0.18 mL) were added into DMSO (0.24 mL) that contained EGTA (33.8 mg, 0.08 mmol). EGTA was activated for ∼10 min. 2-(2-Aminoethoxy)ethyl-β-LN (188 mg, 0.4 mmol) dissolved in DMSO (1.0 mL) and then added to the solution of activated EGTA. The mixture was stirred at room temperature for 72 h and then loaded onto a Bio-Gel P-2 column (3.5 × 60 cm), which was developed with H_2O at a flow rate of 1.5 mL/min and a fraction size of 15 mL. Pooled fractions 45−63 were concentrated by evaporation and dissolved in 2 mL of 15% MeOH and then loaded onto an ODS column (2.0 × 50 cm). The column was developed with 15% MeOH at a flow rate of 2.0 mL/min, and a fraction size of 26 mL. An aliquot from pooled fractions 33−37 was then concentrated and lyophilized to determine the yield of compound **1** (82%, 143 mg relative to the amount EGTA). MALDI-TOF mass: *m*/*z* 2189.8 $[M+H]^+$, 2211.8 $[M+Na]^+$ (calcd for $C_{86}H_{153}N_{10}O_{54}$: 2190.0, $C_{86}H_{152}N_{10}Na_1O_{54}$: 2211.9); ^{1}H NMR ($D_2O$, 500 MHz): δ 4.58 (d, 4H, $J_{1,2}$ 8.0 Hz, H-1), 4.48 (d, 4H, $J_{1',2'}$ 8.0 Hz, H-1′), 2.83 (4H, H-b), 2.05 (s, 12H, C$\underline{H}_3$CONH-); ^{13}C NMR (D_2O, 125 MHz): δ 177.2 ($CH_3\underline{C}$ONH-), 176.5 (-NH$\underline{C}$O- of EGTA), 105.7 (C-1′), 103.8 (C-1), 81.4 (C-4), 78.2 (C-5′), 77.6 (C-5), 75.4 (C-3′), 75.3 (C-3), 73.8 (C-2′), 72.4 (C-d), 72.3 (C-β), 71.8 (C-α), 71.7 (C-γ),71.5 (C-c), 71.4 (C-4′), 63.8 (C-6′), 63.0 (C-6), 61.3 (C-a), 57.9 (C-2), 57.1 (C-b), 41.5 (C-δ), 25.1 ($\underline{C}H_3$CONH-).

(b). Tetravalent LNβ1,3LN Glycocluster (2). Compound **1** (66 mg, 0.03 mmol) and UDP-GlcNAc (117 mg, 0.18 mmol) were first dissolved in a solution that contained 10.3 mL of 50 mM Tris-HCl, pH 6.8, $MnCl_2$ (19 mg), and 0.12 mL of 1% (w/v) NaN_3, and then, 221 mU (1.6 mL) of partially purified β3GnT was added. The mixture was incubated for 220 h at 37 °C, and the reaction was terminated by boiling for 5 min. UDP-Gal (128 mg, 0.21 mmol) was dissolved into the mixture, and then 1 U (1 mL) of β4GalT was added. The mixture was incubated for 48 h at 37 °C and the reaction terminated by boiling for 5 min. The supernatant was isolated by centrifugation (8000 × *g*, 20 min) and then loaded onto an ODS column (2.0 × 50 cm) equilibrated with H_2O at flow rate of 2.7 mL/min. After washing the column with 1100 mL of H_2O, the absorbed material was eluted with 20% MeOH and a fraction size of 27 mL. The absorbance of the eluate was monitored at 210 nm. An aliquot from pooled fractions 12−18 was concentrated by evaporation and lyophilized. Compound **2** was obtained in a yield of 83% (91 mg) relative to the amount of **1**. MALDI-TOF mass: *m*/*z* 3650.7 $[M+H]^+$, 3672.6 $[M+Na]^+$, 3688.6 $[M+K]^+$ (calcd for $C_{142}H_{245}N_{14}O_{94}$: 3650.5, $C_{142}H_{244}N_{14}Na_1O_{94}$: 3672.5, $C_{142}H_{244}N_{14}K_1O_{94}$: 3688.4); ^{1}H NMR ($D_2O$, 500 MHz): δ 4.73 (d, 4H, H-1″), 4.58 (d, 4H, $J_{1,2}$ 8.0 Hz, H-1), 4.49 (d, 4H, $J_{1''',2'''}$ 8.5 Hz, H-1‴), 4.46 (d, 4H, $J_{1',2'}$ 8.5 Hz, H-1′), 4.17 (4H, H-4′), 4.01−3.94 (16H, H-6″b, H-4‴, H-6b, H-αb), 3.36 (8H, H-δ), 2.83 (4H, H-b), 2.05 (s, 24H, C$\underline{H}_3$CONH″-, C$\underline{H}_3$CONH-); ^{13}C NMR (D_2O, 125 MHz): δ 177.7 ($CH_3\underline{C}$ONH″-), 177.2 ($CH_3\underline{C}$ONH-), 176.5 (-NH$\underline{C}$O- of EGTA), 105.75 (C-1′), 105.71 (C-1‴), 105.5 (C-1″), 103.8 (C-1), 84.9 (C-3′), 81.4 (C-4), 81.1 (C-4″), 78.2 (C-5‴), 77.7 (C-5′), 77.6 (C-5), 77.4 (C-5″), 75.36 and 75.31 (C-3, C-3‴), 75.0 (C-3″), 73.8 (C-2‴), 72.8 (C-2′), 72.4 (C-d), 72.3 (C-β), 71.8 (C-α), 71.7 (C-γ),71.5 (C-c), 71.4 (C-4‴), 71.1 (C-4′), 63.8 (C-6‴, C-6′), 62.9 (C-6), 62.7 (C-6″), 61.3 (C-a), 58.0 (C-

dx.doi.org/10.1021/bc200440e | *Bioconjugate Chem.* 2012, 23, 97−105

2″), 57.8 (C-2), 57.1 (C-b), 41.5 (C-δ), 25.1 (CH$_3$CONH-), 25.0 (CH$_3$CONH″-).

*(c). Long Spacer-Linked Tetravalent LN Glycocluster (**3**).* 2-[2-(5′-Aminopentanecarboxamidoethoxy)]ethyl-β-LN (175 mg, 0.3 mmol) was coupled with EGTA (25 mg, 0.067 mmol) in a manner similar to that used to prepare **1**. Compound **3** was obtained in a total yield of 82% (144 mg) relative to the amount of EGTA. MALDI-TOF mass: *m/z* 2642.1 [M+H]$^+$, 2664.1 [M+Na]$^+$ (calcd for $C_{110}H_{197}N_{14}O_{58}$: 2642.3, $C_{110}H_{196}N_{14}Na_1O_{58}$: 2664.3); ^{1}H NMR (D$_2$O, 500 MHz): δ 4.59 (d, 4H, $J_{1,2}$ 8.0 Hz, H-1), 4.49 (d, 4H, $J_{1',2'}$ 7.5 Hz, H-1′), 4.005 (4H, H-αb), 4.004 (dd, 4H, $J_{5,6b}$ 2.5, $J_{6a,6b}$ 12.5 Hz, H-6b), 3.95 (4H, H-4′), 3.85 (dd, 4H, $J_{5,6a}$ 5.5, $J_{6a,6b}$ 12.5 Hz, H-6a), 3.56 (dd, 4H, $J_{1',2'}$ 7.5, $J_{2',3'}$ 10.0 Hz, H-2′), 3.38 (8H, H-δ), 3.24 (8H, H-ε′), 2.82 (4H, H-b), 2.27 (8H, H-α′), 2.05 (s, 12H, CH$_3$CONH-), 1.62 (8H, H-β′) 1.55 (8H, H-δ′), 1.33 (8H, H-γ′); ^{13}C NMR (D$_2$O, 125 MHz): δ 179.6 (−NHCO- of spacer), 177.2 (CH$_3$CONH-), 176.0 (-NHCO- of EGTA), 105.7 (C-1′), 103.8 (C-1), 81.4 (C-4), 78.2 (C-5′), 77.6 (C-5), 75.4 (C-3′) 75.3 (C-3), 73.8 (C-2′), 72.5 (C-d), 72.3 (C-β), 71.8 (C-α, C-γ, C-c), 71.4 (C-4′), 63.8 (C-6′), 62.9 (C-6), 61.5 (C-a), 57.9 (C-2), 57.5 (C-b), 41.8 (C-ε′), 41.7 (C-δ), 38.4 (C-α′), 31.1 (C-δ′), 28.5 (C-γ′), 27.8 (C-β′), 25.1 (CH$_3$CONH-).

Synthesis of Tetravalent Sialo-Glycoclusters. *(a). Tetravalent Neu5Acα2,6LN Glycocluster (**4**).* A mixture (1.25 mL) that contained 22 mg of **1**, 40.0 mM CMP-β-Neu5Ac, 250 mU/mL α2,6SiaT, 2.0 mM MnCl$_2$, 0.1% BSA, and 30 U/mL calf intestine alkaline phosphatase (Boehringer-Mannheim, Mannheim, Germany) in 50 mM MOPS (pH 7.4) was incubated at 37 °C for 72 h. After heating the mixture to 100 °C for 5 min and then centrifuging it at 8000 × *g* for 15 min, the supernatant was loaded onto an ODS column (1.5 × 30 cm) equilibrated with 1% MeOH. The column was developed with 1% MeOH at a flow rate of 2.5 mL/min, and a fraction size of 15 mL. An aliquot from pooled fractions 29−35 was concentrated by evaporation, dissolved in 1 mL of H$_2$O, and loaded onto a Sephadex G-25 column (2.5 × 55 cm). The column was developed with H$_2$O at a flow rate of 0.4 mL/min, and a fraction size of 4 mL. An aliquot from pooled fractions 45−51 was concentrated and lyophilized. Compound **4** was obtained in a yield of 68% (23 mg), relative to the amount of **1**. MALDI-TOF mass: *m/z* 3354.3 [M+H]$^+$, 3376.3 [M+Na]$^+$ (calcd for $C_{130}H_{221}N_{14}O_{86}$: 3354.3, $C_{130}H_{220}N_{14}Na_1O_{86}$: 3376.3); ^{1}H NMR (D$_2$O, 500 MHz): δ 4.61 (4H, H-1), 4.46 (d, 4H, $J_{1',2'}$ 8.0 Hz, H-1′), 2.85 (4H, H-b), 2.69 (dd, 4H, $J_{3''ax,3''eq}$ 12.5, $J_{3''eq,4''}$ 3.5 Hz, H-3″eq), 2.08 (s, 12H, CH$_3$CONH-), 2.05 (s, 12H, CH$_3$CONH-), 1.73 (t, 4H, $J_{3''ax,3''eq}$ 12.5, $J_{3''ax,4''}$ 12.5 Hz, H-3″ax); ^{13}C NMR (D$_2$O, 125 MHz): δ 177.7 (CH$_3$CONH″-), 177.2 (CH$_3$CONH-), 176.5 (-NHCO- of EGTA), 176.3 (HOOC″-), 106.3 (C-1′), 103.7 (C-1), 103.0 (C-2″), 83.6 (C-4), 77.3 (C-5′), 76.5 (C-5), 75.40 (C-6″), 75.37 (C-3), 75.28 (C-3′), 74.5 (C-8″), 73.6 (C-2′), 72.3 (C-β, C-d), 71.8 (C-α), 71.7 (C-γ),71.5 (C-c), 71.3 and 71.2 (C-4″, C-4′), 71.0 (C-7″), 66.2 (C-6′), 65.5 (C-9″), 63.2 (C-6), 61.4 (C-a), 57.6 (C-2, C-b), 54.8 (C-5″), 42.9 (C-3″), 41.6 (C-δ), 25.2 (CH$_3$CONH-), 24.9 (CH$_3$CONH″-).

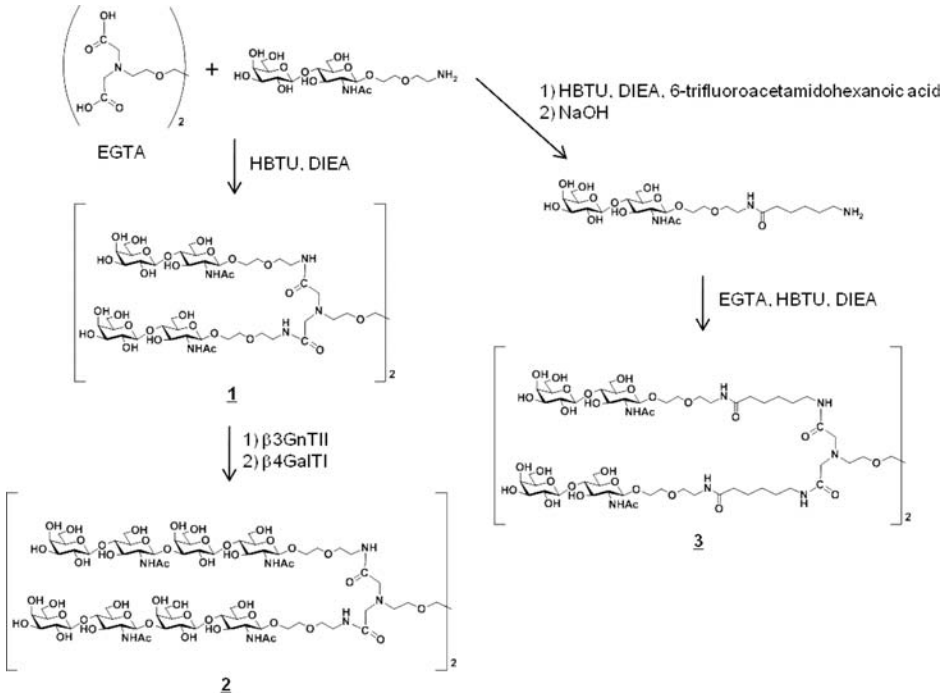
*(b). Tetravalent Neu5Acα2,6LNβ1,3LN Glycocluster (**5**).* Compound **5** was synthesized by the addition of sialic acid to **2** in a manner similar to that used to prepare **4** and was obtained in a yield of 60% (24 mg). MALDI-TOF mass: *m/z* 4814.6 [M+H]$^+$, 4836.7 [M+Na]$^+$ (calcd for $C_{186}H_{313}N_{18}O_{126}$: 4814.9, $C_{186}H_{312}N_{18}Na_1O_{126}$: 4836.9); ^{1}H NMR (D$_2$O, 500 MHz): δ 4.73 (4H, H-1″), 4.57 (d, 4H, $J_{1,2}$ 8.0 Hz, H-1), 4.48 (d, 4H, $J_{1''',2'''}$ 8.0 Hz, H-1‴), 4.47 (d, 4H, $J_{1',2'}$ 7.0 Hz, H-1′), 4.17 (4H, H-4′), 2.89 (4H, H-b), 2.69 (dd, 4H, $J_{3''''ax,3''''eq}$ 12.5, $J_{3''''eq,4''''}$ 5.0 Hz, H-3⁗eq), 2.07 (s, 12H, CH$_3$CONH⁗-), 2.05 (s, 24H, CH$_3$CONH″-, CH$_3$CONH-), 1.73 (t, 4H, $J_{3''''ax,3''''eq}$ 12.5, $J_{3''''ax,4''''}$ 12.5 Hz, H-3⁗ax); ^{13}C NMR (D$_2$O, 125 MHz): δ 177.8 (CH$_3$CONH⁗-), 177.7 (CH$_3$CONH″-), 177.2 (CH$_3$CONH-), 176.7 (-NHCO- of EGTA), 176.3 (HOOC⁗-), 106.3 (C-1‴), 105.7 (C-1′), 105.4 (C-1″), 103.9 (C-1), 103.0 (C-2⁗), 84.8 (C-3′), 83.3 (C-4″), 81.4 (C-4), 77.7 (C-5′), 77.6 (C-5), 77.1 (C-5″), 76.5 (C-5‴), 75.4 (C-6⁗), 75.3 (C-3, C-3‴), 75.1 (C-3″), 74.5 (C-8⁗), 73.6 (C-2‴), 72.8 (C-2′), 72.3 (C-β, C-d), 71.9 (C-γ), 71.8 (C-c), 71.6 (C-α), 71.3, 71.2, and 71.1 (C-4⁗, C-4‴, C-4′), 71.0 (C-7⁗), 66.2 (C-6‴), 65.5 (C-9⁗), 63.8 (C-6′), 63.0 (C-6, C-6″), 61.7 (C-a), 57.8 (C-2″, C-2), 57.5 (C-b), 54.7 (C-5⁗), 42.9 (C-3⁗), 41.8 (C-δ), 25.1 (CH$_3$CONH″-, CH$_3$CONH-), 24.9 (CH$_3$CONH⁗-).

*(c). Long Spacer-Linked Tetravalent Neu5Acα2,6LN Glycocluster (**6**).* Compound **6** was synthesized by reacting sialic acid with **3** in a manner similar to that used to prepare **4** and was obtained in a yield of 63% (24 mg). MALDI-TOF mass: *m/z* 3806.9 [M+H]$^+$, 3828.9 [M+Na]$^+$ (calcd for $C_{154}H_{265}N_{18}O_{90}$: 3806.7, $C_{154}H_{264}N_{18}Na_1O_{90}$: 3828.7); ^{1}H NMR (D$_2$O, 500 MHz): δ 4.61 (d, 4H, $J_{1,2}$ 8.0 Hz, H-1), 4.46 (d, 4H, $J_{1',2'}$ 8.0 Hz, H-1′), 3.38 (8H, H-δ), 3.26 (8H, H-ε′), 2.93 (4H, H-b), 2.68 (dd, 4H, $J_{3''ax,3''eq}$ 12.5, $J_{3''eq,4''}$ 5.0 Hz, H-3″eq), 2.27 (8H, H-α′), 2.07 (s, 12H, CH$_3$CONH″-), 2.04 (s, 12H, CH$_3$CONH-), 1.73 (t, 4H, $J_{3''ax,3''eq}$ 12.5, $J_{3''ax,4''}$ 12.5 Hz, H-3″ax), 1.61 (8H, H-β′), 1.54 (8H, H-δ′), 1.33 (8H, H-γ′); ^{13}C NMR (D$_2$O, 125 MHz): δ 179.6 (-NHCO- of spacer), 177.7 (CH$_3$CONH″-), 177.2 (CH$_3$CONH-), 176.4 (HOOC″-), 176.2 (−NHCO- of EGTA), 106.3 (C-1′), 103.7 (C-1), 103.0 (C-2″), 83.6 (C-4), 77.3 (C-5′), 76.5 (C-5), 75.4 (C-6″, C-3) 75.3 (C-3′), 74.5 (C-8″), 73.6 (C-2′), 72.3 (C-β), 72.2 (C-d), 71.9 (C-γ), 71.8 (C-α), 71.5 (C-c), 71.2 (C-4″, C-4′), 71.0 (C-7″), 66.2 (C-6′), 65.5 (C-9″), 63.2 (C-6), 62.0 (C-a), 59.4 (C-b), 57.6 (C-2), 54.8 (C-5″), 42.9 (C-3″), 42.2 (C-δ), 41.8 (C-ε′), 38.4 (C-α′), 30.8 (C-δ′), 28.4 (C-γ′), 27.8 (C-β′), 25.2 (CH$_3$CONH-), 24.9 (CH$_3$CONH″-).

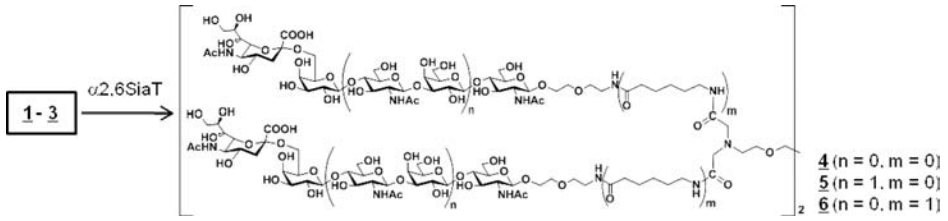
Synthesis of a Sialoglycoside that Contained Two Neu5Acα2,6LN Groups (7). A mixture (3.35 mL) that contained 25 mg of hexan-1,6-diyl bis-(β-LN), 22.0 mM CMP-β-Neu5Ac, 15 mU/mL α2,6SiaT, 2.0 mM MnCl$_2$, 0.1% BSA, and 37 U/mL alkaline phosphatase in 50 mM MOPS (pH 7.4) was incubated at 37 °C for 72 h. After heating the mixture at 100 °C for 5 min and then centrifuging it at 8000 × *g* for 15 min, the supernatant was loaded onto an ODS column (2.0 × 50 cm) equilibrated with H$_2$O. The column was developed with H$_2$O at a flow rate of 2.7 mL/min and a fraction size of 27 mL. An aliquot from pooled fractions 18−21 was concentrated by evaporation and lyophilized. Compound **7** was obtained in a yield of 58% (24 mg), relative to the initial amount of hexan-1,6-diyl bis-(β-LN). HRESIMS: *m/z* 1497.50728 [M+3Na-2H]$^+$ (calcd for $C_{56}H_{92}N_4Na_3O_{38}$, 1497.50826); ^{1}H NMR (D$_2$O, 500 MHz): δ 4.55 (d, 2H, $J_{1,2}$ 8.0 Hz, H-1), 4.45 (d, 2H, $J_{1',2'}$ 8.0 Hz, H-1′), 2.68 (dd, 2H, $J_{3''ax,3''eq}$ 12.2, $J_{3''eq,4''}$ 4.6 Hz, H-3″eq), 2.05 (s, 6H, CH$_3$CONH″-), 2.03 (s, 6H, CH$_3$CONH-), 1.71 (t, 2H, $J_{3''ax,3''eq}$ 12.2, $J_{3''ax,4''}$ 12.2 Hz, H-3″ax), 1.56 (4H, H-β), 1.30 (4H, H-γ); ^{13}C NMR (D$_2$O, 125 MHz): δ 177.8 (CH$_3$CONH″-), 177.2 (CH$_3$CONH-), 176.3 (HOOC″-), 106.3 (C-1′), 103.7 (C-1), 103.0 (C-2″), 83.5 (C-4), 77.3 (C-5′), 76.5 (C-5), 75.4 (C-6″), 75.3 (C-3), 75.2 (C-3′), 74.5 (C-8″), 73.6 (C-2′), 73.4 (C-α), 71.2 (C-4′), 71.2 (C-4″), 71.0 (C-7″), 66.1 (C-6′), 65.5 (C-9″), 63.2 (C-6), 57.7 (C-2), 54.7 (C-5″), 42.9

dx.doi.org/10.1021/bc200440e | *Bioconjugate Chem.* 2012, 23, 97−105

Scheme 1. Chemo-Enzymatic Synthesis of the Tetravalent Asialo-Glycoclusters 1, 2, and 3



Scheme 2. Enzymatic Synthesis of the Tetravalent Sialo-Glycoclusters 4, 5, and 6



(C-3″), 31.4 (C-β), 27.5 (C-γ), 25.2 ($\underline{C}H_3CONH$-), 25.1 ($\underline{C}H_3CONH$″-).

Hemagglutination Inhibition Assay. HAI assays were performed in the wells of a 96-well microtiter plate as described.[35] An SSA suspension (4 hemagglutination titers in 0.02 mL PBS) was added into the wells that each contained one of a series of 2-fold serially diluted preparations of an oligosaccharide, **7**, a tetravalent glycocluster, or the glycoprotein fetuin (concentrations were between 8000 and 0.24 μM) in phosphate-buffered saline (PBS, pH 7.4). After incubation for 60 min at 4 °C, a suspension of 4% (v/v) rabbit erythrocytes (0.04 mL) was added into each well and allowed to settle for 40 min at 4 °C. The maximum dilution that completely inhibited hemagglutination was defined as the hemagglutination inhibition titer.

Precipitation Assay. Compounds **1** and **4**−**7** (between ∼1 and 32 μM each in 50 μL PBS) were individually added into 16 μM SSA (50 μL PBS) in a microtube. After incubation for 60 min at 4 °C, each solution was centrifuged at 8000 × *g* for 15 min. The supernatants were diluted and their A_{280}s measured. The amount of soluble SSA remaining was determined with the use of a standard curve.

Double-Diffusion Assay. To prepare an agar plate, agar (3.0 g) was dissolved in 9.0 mL of 100 mM sodium phosphate (pH 7.2), 0.85% (w/v) NaCl to give a final agar concentration of 0.9%. Then, two drops of 1% sodium azide were added. The solution was poured into a glass dish (90 mm, i.d.) to form a layer ∼3 to 4 mm thick. After the agar had set, wells were made with a steel puncher. SSA [25 μM in 10 μL of 10 mM PBS (pH 7.4)] and 10 μL of a 500 μM of a test solution in 10 mM PBS (pH 7.4) were placed in the central and peripheral wells, respectively, with a syringe. The plate was incubated for 2 h at room temperature, stained with 0.5% Amido Black 10B in 7.5% acetic acid, and then washed with 7.5% acetic acid until the background cleared.

Isothermal Titration Calorimetry. SSA (2.5 μM) in 10 mM PBS (pH 7.4) was degassed and its concentration was determined using the A_{280} of the SSA solution. Compound **7** and the tetravalent sialo-glycoclusters (50 μM **7**; 25 μM **4**−**6**) were each dissolved into 10 mM PBS (pH 7.4), degassed, and loaded into a syringe. Calorimetry was performed with a VP-ITC calorimeter (Microcal Northampton, MA) at 293 K. SSA (1.4181 mL) was loaded into the sample cell. For the titrations, 8 μL of a ligand was injected every 180 s. The values for the heats of dilution obtained for 8 μL injections ligand into of 10 mM PBS (pH 7.4) into SSA solutions were subtracted from the titration data. The data were fit by nonlinear least-squares minimization. The stoichiometric constant (n), the binding constant (K_b), and the enthalpy of binding (ΔH) were determined with the use of *Origin* software. Dissociation constants ($K_d = 1/K_b$), Gibbs free energy changes of binding ($\Delta G = -RT \ln K_b$), and the entropy changes of binding ($T\Delta S = \Delta H - \Delta G$) were calculated using the values of ΔH and K_b.

dx.doi.org/10.1021/bc200440e | *Bioconjugate Chem.* 2012, 23, 97−105

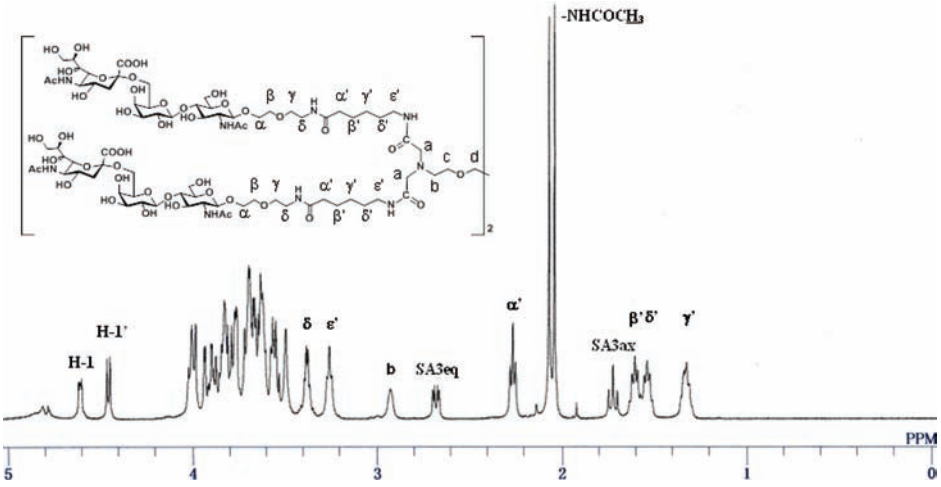


Figure 1. 500 MHz ^{1}H NMR spectrum of **6**. Solvent, D_2O; temperature, 30 °C; concentration, 30 mg/mL.

All experiments were performed with c values $10 < c < 30$ ($c = nK_b[M]_t$, where $[M]_t$ is the initial protein concentration).

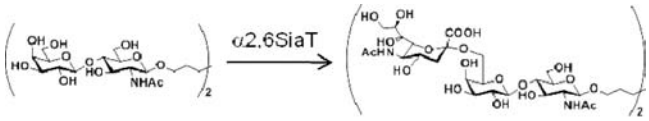
Dynamic Light Scattering (DLS). SSA (16 μM) in 10 mM PBS (pH 7.4) was filtered. Solutions containing between ~2 and 24 μM of the three tetravalent sialo-glycoclusters were prepared in 10 mM PBS (pH 7.4). Then, a ligand solution (50 μL) was added into an SSA solution (50 μL). After incubation for 60 min at 4 °C, the particle sizes of the solutes were measured by DLS at 25 °C using a Zetasizer Nano ZS (Malvern, Worcs, UK).

RESULTS

Chemo-Enzymatic Synthesis of Tetravalent Sialo-Glycoclusters. Three tetravalent sialo-glycoclusters **4**–**6** that contained different glycans and spacers and EGTA as the scaffold were designed and synthesized Schemes 1 and 2. Two LN-β-type glycosides, one with the short 2-(2-aminoethoxy)-ethyl group and one with the long 2-[2-(5′-aminopentanecarboxamidoethoxy)]ethyl group, which served as spacers, were first prepared as previously reported.[35] Both LN-β-glycosides were directly coupled to the carboxy groups of EGTA to produce the tetravalent LN glycoclusters **1** and **3** (Scheme 1). The targeted products were purified by Bio-Gel P-2 and ODS chromatographies in yields of 82% and 88%, respectively, relative to the amount of EGTA. Compound **2**, which is a tetravalent glycocluster containing tandem LNs, was enzymatically synthesized by first adding β-(1–3) GlcNAc to **1** and then β-(1–4) Gal (Scheme 1). Compound **2** was purified by ODS chromatography in a yield of 83%, relative to the amount of **1**.

Compounds **1**, **2**, and **3** were enzymatically sialylated with α2,6SiaT to form the tetravalent sialo-glycoclusters **4**, **5**, and **6**, respectively (Scheme 2). Compounds **4**, **5**, and **6** were purified by ODS and Sephadex G-25 chromatographies with yields of 68%, 60%, and 63%, respectively, relative to the amount of the acceptor. The structures of the tetravalent sialo-glycoclusters were confirmed by ^{1}H and ^{13}C NMR spectroscopies. The assigned ^{1}H NMR spectrum of **6** is shown in Figure 1. As an example of the assignments, resonances characteristic of the H-3″ methylene protons were found at δ = 2.68 ppm (dd, 4H, $J_{3''ax,3''eq}$ 12.5, $J_{3''eq,4''}$ 5.0 Hz, H-3″eq) and δ = 1.73 ppm (t, 4H, $J_{3''ax,3''eq}$ 12.5, $J_{3''ax,4''}$ 12.5 Hz, H-3″ax). In the ^{13}C NMR spectrum of **6**, the C-6′ signal was distinguished by its downfield position (δ = 66.2 ppm). These data indicated that the terminal Gal residues of **1**, **2**, and **3** had been regiospecifically sialylated with α2–6 linkages. Matrix-assisted laser desorption/ionization time-of-flight mass spectra of **4**, **5**, and **6** contained molecular ions ($[M+H]^+$) with m/z values of 3354.3, 4814.6, and 3806.9, respectively. Therefore, our chemo-enzymatic synthetic methods were easy and efficient ways to synthesis these tetravalent stereoregular sialoglycosides attached to an EGTA scaffold. Compound **7** was also prepared to use as a reference divalent ligand (Scheme 3). The divalent LN-β-glycoside precursor,

Scheme 3. Enzymatic Synthesis of the Divalent Sialoglycoside 7



7

which was easily prepared using our reported method,[38] was enzymatically sialylated by α2,6SiaT to give **7**.

The interactions of **1**–**6** with SSA were characterized by the HAI, precipitation, and double-diffusion assays, and by ITC and DLS.

HAI Assay. The interactions of the tetravalent sialo-glycoclusters and their precursors with SSA were characterized using the HAI assay to assess the effect of the sialo moiety. The results of the HAI assays indicated that a greater multivalency effect existed for **4**, **5**, and **6** than for the sialyltrisaccharides, Neu5Acα2,6-lactose/LN, and **7** (Table 1). The inhibitory activities for **4**, **5**, and **6** were between 16- and 31-fold greater than that of Neu5Acα2,6LN, and between 4- and 8-fold greater than that of **7**. Despite their relatively low molecular weights, **5** and **6** were 4-fold better inhibitors than was the naturally occurring sialoglycoprotein fetuin, which is a potent inhibitor of SSA.[39] Because SSA did not bind the asialo-derivatives, nonspecific binding of SSA by the nonsialo portions of **4**–**7** can be ruled out.

Precipitation Assay. Precipitation curves for **1** and **4**–**7** with SSA (8 μM) are shown in Figure 2. The ratio of precipitated SSA to glycoside added is the binding stoichiometry. When each tetravalent glycocluster was added to an SSA solution under the appropriate conditions, a

dx.doi.org/10.1021/bc200440e | Bioconjugate Chem. 2012, 23, 97–105

Table 1. Inhibition of SSA-Mediated Hemagglutination

inhibitors	sugar moiety	valency	IC_{50}[a] (μM)	relative ratio[b]
LN	-	1	>1000	-
Neu5Acα2,3LN	-	1	>1000	-
Neu5Acα2,6LN	-	1	46.9	1
Neu5Acα2,6lactose	-	1	93.8	0.5
7	Neu5Acα2,6LN	2	11.7	4.0
1	LN	4	>1000	-
2	$(LN)_2$	4	>1000	-
3	LN	4	>1000	-
4	Neu5Acα2,6LN	4	2.9	16.2
5	Neu5Acα2,6$(LN)_2$	4	1.5	31.2
6	Neu5Acα2,6LN	4	1.5	31.2
Fetuin	-	-	5.9	7.9

[a]Minimum concentration required to completely inhibit hemagglutination. [b]Inhibitory potency normalized to that of Neu5Acα2,6LN.

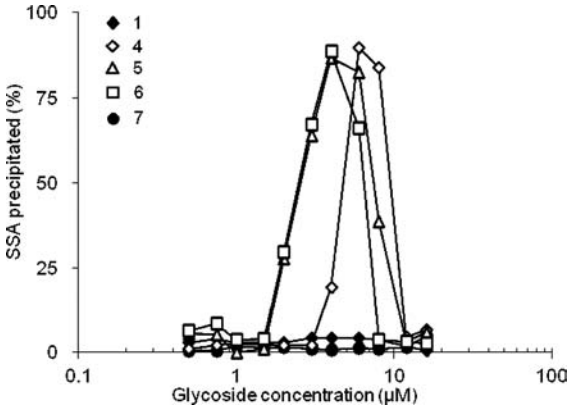


Figure 2. Precipitation curves for titration of 8 μM SSA with 0.5, 0.75, 1, 1.5, 2, 3, 4, 6, 8, 12, and 16 μM of each tetravalent sialo-glycocluster. The percentage of precipitated SSA was calculated by subtracting the amount of SSA remaining in the supernatant from the total amount of SSA.

precipitate formed within minutes. Precipitation was inhibited or reversed when Neu5Acα2,6LN was present (data not shown). The concentration of **4** at the equivalence point (the maximum in the precipitin curve) was ~6 to 8 μM, which corresponded to a 1:1 to 1:1.3 stoichiometric ratio for **4** to SSA. In contrast, the equivalence points for **5** and **6** were found at ~4 μM, which corresponded to a 1:2 stoichiometric ratio. Precipitation was not observed when **1** and **7** were used.

Double-Diffusion Assay. Figure 3 shows the double-diffusion reactions for hexan-1,6-diyl bis-(β-LN), **2**, and **4**–**7**. Precipitates can form between two lectins and glycoproteins or polysaccharides when multiple binding sites are available in both molecules.[40] Sharp precipitin bands were seen positioned between the central SSA-containing well and only the wells that contained **4**, **5**, and **6**, which was as expected. These results correlated well with those of the precipitation assay.

ITC. The titration curves for **4**, **5**, and **6** were exponential in nature. A thermogram and titration curve for the association of **6** and SSA is shown in Figure 4. The values for K_d, n, and the associated thermodynamics parameters are listed in Table 2 for **4**–**7**. Substantial differences were observed for the thermodynamic parameters of the glycoclusters, which appeared to primarily depend on their valencies. The value for K_d for **7** was 270 nM, which was greater than those for the tetravalent

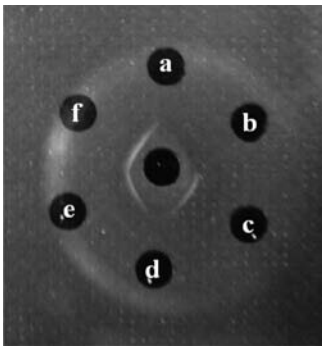


Figure 3. Double diffusion assays. An SSA solution was put into the center well, and the indicated compounds were added into the peripheral wells. (a) Hexan-1,6-diyl bis-(β-LN); (b) **7**; (c) **4**; (d) **2**; (e) **5**; (f) **6**.

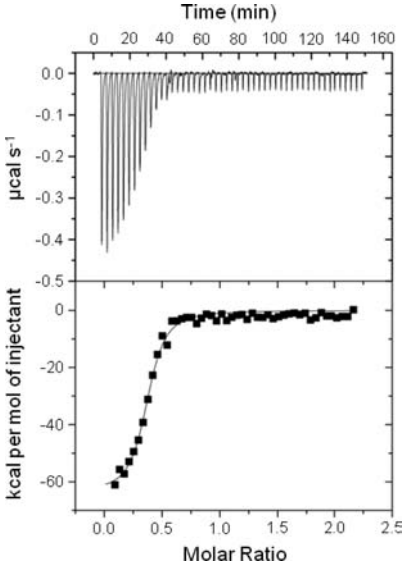


Figure 4. ITC data for the interaction of **6** and SSA. (Top) Raw titration curve. (Bottom) Integrated titration curve. The solid line is the best-fit, which used a single-site model. K_d = 47 ± 7 nM, n = 0.369 ± 0.006.

glycoclusters. Compound **4** had a 2.7-fold improvement in its affinity for SSA in comparison with **7** and its n value was 0.47, i.e., a binding ratio of 1:2 as expected for a complex that contained one molecule of **4** and two molecules of SSA. Conversely, n for **7** was 0.99, i.e., formation of a 1:1 complex between **7** and SSA, which indicated that **7** behaved as a monovalent probe with the two sialo moieties bound to the two sialo-binding sites in one SSA molecule. The enthalpic contribution of **4** was 2.3-fold more favorable than that for **7**, and its entropy change was more unfavorable as expected for a ligand of greater valency. The rigidity of tetravalent scaffold appears to be very favorable for lowering the entropy cost of binding. The K_d values for **5** and **6**, which both contain a longer glycan/spacer than does **4**, are 2- and 3-fold smaller than that for **4**. The K_d values of **5** and **6** are the smallest values measured by ITC for a ligand of SSA.[19] The values for n of 0.36 and 0.38 that were measured for **5** and **6**, respectively, might indicate that 1:3 ligand:SSA complexes were formed, although these values are somewhat greater than the expected value of 0.33 for a 1:3 complex.

dx.doi.org/10.1021/bc200440e | *Bioconjugate Chem.* 2012, 23, 97–105

Table 2. Isothermal Titration Calorimetry Measurements for Binding of 4–7 to SSA[a]

ligands	valency	n^b	ΔH (kcal mol^{-1})	$T\Delta S$ (kcal mol^{-1})	ΔG (kcal mol^{-1})	K_d (nM)	relative ratio[c]
7	2	0.99 ± 0.02	−25.6 ± 0.7	−16.8	−8.8	270 ± 30	1
4	4	0.47 ± 0.01	−57.9 ± 2.0	−48.3	−9.6	99 ± 20	2.7
5	4	0.38 ± 0.01	−57.9 ± 1.1	−47.8	−10.1	34 ± 5	7.9
6	4	0.36 ± 0.01	−63.8 ± 1.6	−53.9	−9.9	47 ± 7	5.7

[a]Conditions: 10 mM PBS, pH 7.4 at 293 K. [b]Binding stoichiometry was defined as the number of ligands bound per monomer of SSA. [c]Calculated as the ratio of the value of K_d for **7** to the value of the K_d for the ligand.

DLS Measurements. To reproduce the conditions used for the precipitation assays, 8 μM of SSA was loaded into the cell and increasing concentrations of each tetravalent glycocluster solution (1, 2, 3, 4, 6, 8, and 12 μM) were sequentially added. The DLS intensity of SSA, in the absence of a ligand, was centered at a hydrodynamic diameter of 12.1 nm (Figure 5).

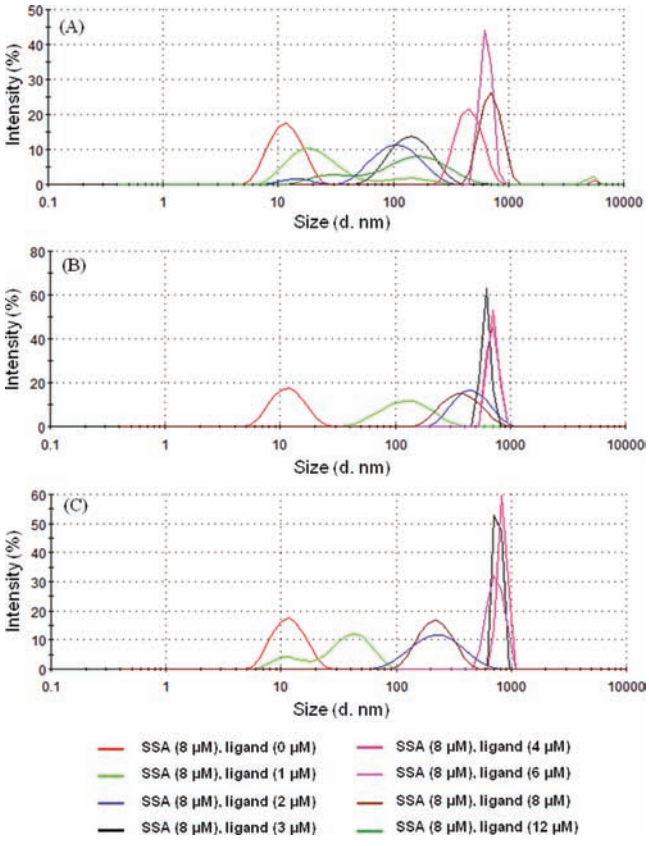


Figure 5. Dynamic light scattering measurements for the complexes formed by **4**, **5**, or **6** and SSA. SSA solutions (16 μM, 50 μL) were mixed with sequential additions of (A) 50 μL (0–24 μM) of **4**, (B) **5**, or (C) **6** in 10 mM PBS (pH 7.4). After an addition of ligand, the mixtures were each incubated for 1 h at 4 °C. Dynamic light scattering intensities were measured at 25 °C using a Zetasizer Nano ZS. The size distribution of the particles is reported relative to the scattering intensity.

For the complexes formed by SSA and **4**, **5**, and **6**, the particle sizes increased as the ligand concentrations increased. When the concentration of **4** was 1 μM, the particle size was centered at 22.5 nm (Figure 5A). This value corresponded to the sum of the hydrodynamic diameters of two SSA molecules, which most likely was a consequence of **4** having cross-linked two SSA molecules. Thus, initially an intermolecular 1:2 complex between **4** and SSA formed. As the concentration of **4** increased between 2 and 6 μM, larger aggregates were formed as the maximum intensity of the size distributions increased from 114.8 to 639.6 nm. After the 8 μM injection of **4**, the center of the size distribution was 714.0 nm, and after the 12 μM ligand injection, the size distribution center substantially decreased (Figure 5A).

Conversely, two peaks were seen after injection of 1 μM **6** with one centered at 43.0 nm, which corresponds to 3.5 SSA diameters, and one at 12.2 nm, which is the size found for SSA in the absence of ligand (Figure 5C). At concentrations of 2 and 3 μM **6**, the intensities were centered at 246.6 and 765.6 nm, respectively. At 4 μM **6**, the hydrodynamic diameter was a maximum of 843.0 nm. The hydrodynamic diameter decreased with the 6 and 8 μM injections of **6**. The behavior of the hydrodynamic diameter with respect to the concentration of injected **5** was similar (Figure 5B); however, the onset of complex formation was not clearly identified by an increase in the diameter as was observed for the complexes formed by **4** and **6**.

DISCUSSION

We recently reported a method for the synthesis of N-linked tetravalent glycosides bearing GN and GN_2 moieties and different spacer groups.[28] Using this method, we have now synthesized the spacer-O-linked tetravalent sialo-glycoclusters **4**, **5**, and **6** for use as ligands for the sialic-acid-binding lectin SSA. The sialo-glycoclusters have spacers of varying length between the nonreducing sialic acid and the EGTA scaffolding. The spacer-O-linked tetravalent α2,6-sialotrisaccharide (**4**) and the spacer-O-linked tetravalent α2,6-sialopentasaccharide (**5**) contain four single LN and tandem LN repeats, respectively, that are each attached to one of the backbone carboxy groups of EGTA. The third sialo-glycocluster, **6**, is structurally similar to **5** but incorporated a longer spacer, which was engineered by replacing an LN unit with an alkyl chain. The tetravalent glycoclusters precipitated SSA by acting as multivalent ligands, which suggested that these and other designed multivalent carbohydrate analogues would tightly bind targeted lectins and could be used as probes for studies such as virus or antibody. Our methods are easy and efficient ways to synthesize tetravalent glycoclusters with stereoregular sugars linked through carboxy groups of a scaffold.

In the present study, the contributions of the nonsialo sugars to the binding of SSA were evaluated and found to be significant. First, the HAI assay was used to assess the strength of the multivalent effect for **4**, **5**, and **6** in comparison with the divalent glycoconjugate **7**. Inhibition of hemagglutination by **5** and **6** was stronger than that by **4**. Compounds **5** and **6** exhibited strong multivalency effects, at low concentrations (IC_{50} 1.5 μM), and despite their low molecular weights, their binding strengths were a factor of 8-fold greater than that of **7**, and 4-fold greater than that of fetuin. In the precipitation assay, the equivalent points of the precipitin curves for the tetravalent

dx.doi.org/10.1021/bc200440e | Bioconjugate Chem. 2012, 23, 97–105

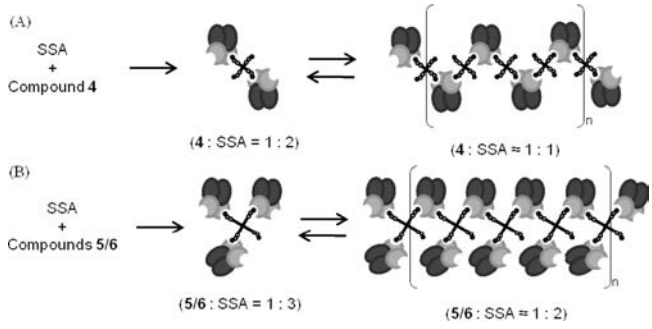
glycoclusters and SSA were almost stoichiometric, i.e., the binding of **4** to SSA was ~1:1, and **5** and **6** both bound SSA in a ~1:2 ratio (Figure 4). The binding abilities and specificities of **4**, **5**, and **6** for SSA were also confirmed by the double-diffusion assay.

According to the results of the ITC experiments, by changing the scaffold from one that could support two carbohydrate chains, i.e., that of **7**, to one that could support four carbohydrate chains, i.e., those of **4**, **5**, and **6**, a 3- to 8-fold improvement in binding was achieved. The nonsialic portions of **5** and **6** did not affect their binding strengths, as both were effective ligands. Therefore, a pentylamido group can replace an LN unit without affecting binding. The value of *n* for **4** indicated that it bound SSA in a 1:2 ratio (divalently), whereas the ratio for the binding of **5** or **6** to SSA was ~1:3 (trivalently). Therefore, none of the tetravalent glycoconjugates behaved as four-headed epitopes. The ITC studies reflected the initial formation of the glycocluster/SSA complexes. Visible precipitates were observed during the course of the titrations, which indicated that aggregation occurred. The tetravalent glycoconjugates **5** and **6** not only displayed enhanced affinity when compared to the divalent model, but they also represent the ligands with the highest affinity for SSA currently known. Cecioni and colleagues used surface plasmon resonance and ITC to demonstrate that strong interactions exist between a tetravalent calyx[4]arene glycoconjugate and a glactose-binding lectin.[21] It should be noted that ITC are not necessarily complementary to HAI and precipitation assays, since the former depend on thermodynamic equilibrations, whereas the latter depend on kinetic aggregations.

The nature(s) of the ligand/SSA complexes were also assessed using DLS.[20] The DLS experiments indicated that **4** and SSA initially formed a 1:2 intermolecular complex and that **6** formed a 1:3 complex as assessed by the increases in particle size, and these findings are in agreement with those of the ITC studies. With increasing ligand concentrations, larger cross-linked aggregates formed until aggregates of maximum sizes were obtained. For the complex between **4** and SSA, the maximum size correlated with a complex composed of one molecule of **4** and one molecule of SSA, and for the complexes composed of SSA and **5** or **6**, the particle sizes were greatest at a 1:2 ratio, which is consistent with results of the precipitation assay. The largest aggregates with a particle size centered at 600–800 nm also precipitated from solution during the DLS studies. Such large particle sizes for ligand–lectin complexes are the first to be characterized by DLS.[20,21] After the maximum sizes of the complexes had been reached, they decreased rapidly as the concentration of the ligands further increased. This indicates that the ligands act as inhibitors at the appropriate stoichiometry by the precipitation assay mentioned above. The effects of the ligands on particle size were very similar to the results of the precipitation curves. The complementarity was clearly observed between DLS and precipitation assay. Therefore, formation of ligand/SSA complexes involved cross-linking SSA molecules via the tetravalent ligands so as to form large aggregates (Scheme 4). We assume that, on average, one molecule of **4** bound two molecules of SSA and one molecule of **5** or **6** bound three molecules of SSA, associated with two different modes of binding for the ligand–lectin complexes (Scheme 4A and B).

Their results suggested that the orientations of the ligand moieties within the glycoconjugate would be glycoside compatible with the formation of cross-linked complexes, thereby enhancing binding. The cross-linking effect imparted by tetravalent ligands leads to large rate enhancements given the favorable orientation of the ligands. In conclusion, our experiments provided detailed insight into the binding processes of the tetravalent and the divalent ligands. Intermolecular complex formation is initiated at an early stage of binding. Then, the smaller complexes grow into larger ones as additional ligand and SSA molecules bind. Our results are valuable and important because they shed light on the mechanism of complex formation and because they enhance our knowledge of effective ligand–lectin interactions that can be used as input for the design of ligands directed against different lectins.

Scheme 4. Schematics of the Tetravalent Sialo-Glycoclusters/SSA Complexes Formed by (A) 4 and (B) 5 or 6 According to the Stoichiometric Ratios Determined by the ITC, the Precipitation Assay, and the DLS Measurements



AUTHOR INFORMATION

Corresponding Author

*TEL: (81) 54 238 4305, FAX: (81) 54 238 8448. E-mail address: usui@ipc.shizuoka.ac.jp.

Author Contributions

#These authors contributed equally to this work.

ACKNOWLEDGMENTS

This work was supported by a grant-in-aid for Young Scientists B (No. 22780101) from the Ministry of Education, Culture, Sports, Science, and Technology of Japan.

REFERENCES

(1) Dam, T. K., and Brewer, C. F. (2010) Multivalent lectin-carbohydrate interactions: energetics and mechanisms of binding. *Adv. Carbohydr. Chem. Biochem. 63*, 139–164.

(2) Varki, A., Cummings, R., Esko, J., Freeze, H., Hart, G., and Marth, J., Eds. (1999) *Essentials of Glycobiology*, Cold Spring Harbor Laboratory Press, Cold Spring Harbor.

(3) Bhattacharyya, L., Fant, J., Lonn, H., and Brewer, C. F. (1990) Binding and precipitating activities of *Lotus tetragonolobus* isolectins with L-fucosyl oligosaccharides. Formation of unique homogeneous cross-linked lattices observed by electron microscopy. *Biochemistry 29*, 7523–7530.

(4) Dam, T. K., Gerken, T. A., and Brewer, C. F. (2009) Thermodynamics of multivalent carbohydrate-lectin cross-linking interactions: Importance of Entropy in the bind and jump mechanism. *Biochemistry 48*, 3822–3827.

(5) Gupta, D., Kaltner, H., Dong, X., Gabius, H.-J., and Brewer, C. F. (1996) Comparative cross-linking activities of lactose-specific plant and animal lectins and a natural lactose-binding immunoglobulin G fraction from human serum with asialofetuin. *Glycobiology 6*, 843–849.

(6) Dam, T. K., Roy, R., Pagé, D., and Brewer, C. F. (2002) Thermodynamic binding parameters of individual epitopes of multivalent carbohydrates to concanavalin A as determined by "reverse" isothermal titration microcalorimetry. *Biochemistry 41*, 1359−1363.
(7) Mann, D. A., Kanai, M., Maly, D. J., and Kiessling, L. L. (1998) Probing low affinity and multivalent interactions with surface Plasmon resonance: Ligands for concanavalin A. *J. Am. Chem. Soc. 120*, 10575−10582.
(8) Chabre, Y. M., and Roy, R. (2010) Design and creativity in synthesis of multivalent neoglycoconjugates. *Adv. Carbohydr. Chem. Biochem. 63*, 165−393.
(9) Jayaraman, N. (2009) Multivalent ligand presentation as a central concept to study intricate carbohydrate-protein interactions. *Chem. Soc. Rev 38*, 3463−3483.
(10) Mammen, M., Choi, S.-K., and Whitesides, G. M. (1998) Polyvalent interactions in biological system: Implications for design and use of multivalent ligands and inhibitors. *Angew. Chem., Int. Ed. 37*, 2754−2794.
(11) Roy, R. (2003) A decade of glycodendrimer chemistry. *Trends Glycosci. Glycotechnol. 15*, 291−310.
(12) Lindhorst, T. K. (2002) Artificial multivalent sugar ligands to understand and manipulate carbohydrate-protein interactions. *Top. Curr. Chem. 218*, 201−232.
(13) Houseman, B. T., and Mrksich, M. (2002) Model systems for studying polyvalent carbohydrate binding interactions. *Top. Curr. Chem. 218*, 1−44.
(14) Lundquist, J. L., and Toone, E. J. (2002) The cluster glycoside effect. *Chem. Rev. 102*, 555−578.
(15) Chabre, Y. M., and Roy, R. (2008) Recent trends in glycodendrimer syntheses and applications. *Curr. Top. Med. Chem. 8*, 1237−1285.
(16) Chebre, Y. M., and Roy, R. (2009) in *The Sugar Code: Fundamentals of Glycosciences* (Gabius, H.-J., Ed.) pp 53−70, Wiley-VCH, Weinheim.
(17) Lee, Y. C., Townsend, R. R., Hardy, M. R., Lönngren, J., Arnarp, J., Haraldsson, M., and Lönn, H. (1983) Binding of synthetic oligosaccharides to the hepatic Gal/GalNAc lectin. *J. Biol. Chem. 258*, 199−202.
(18) Bertozzi, C. R., and Kiessling, L. L. (2001) Chemical glycobiology. *Science 291*, 2357−2364.
(19) Lindhorst, T. L., and Kieburg, C. (1996) Glycocoating of oligovalent amines: Synthesis of thiourea-bridged cluster glycosides from glycosyl lsothiocyanates. *Angew. Chem., Int. Ed. 35*, 1953−1956.
(20) Murthy, B. N., Sinha, S., Surolia, A., Indi, S. S., and Jayaraman, N. (2008) SPR and ITC determination of the kinetics and the thermodynamics of bivalent *versus* monovalent sugar ligand-lectin interactions. *Glycoconj. J. 25*, 313−321.
(21) Cecioni, S., Lalor, R., Blanchard, B., Praly, J., Imberty, A., Matthews, S. E., and Vidal, S. (2009) Achieving high affinity towards a bacterial lectin through multivalent topological isomers of calix[4]-arene glycoconjugates. *Chem.—Eur. J. 15*, 13232−13240.
(22) Marra, A., Moni, L., Pazzi, D., Corallini, A., Bridi, D., and Dondoni, A. (2008) Synthesis of sialoclusters appended to calix[4]-arene platforms *via* multiple azide-alkyne cycloaddition. New inhibitors of hemagglutination and cytopathic effect mediated by BK and influenza A viruses. *Org. Biomol. Chem. 6*, 1396−1409.
(23) Aoi, K., Itoh, K., and Okada, M. (1995) Globular carbohydrate macromolecules "Sugar Balls". 1. Synthesis of novel sugar-persubstituted poly(amino amine) dendrimers. *Macromolecules 28*, 5391−5393.
(24) Oka, H., Onaga, T., Koyama, T., Guo, C.-T., Suzuki, Y., Esumi, Y., Hatano, K., Terunuma, D., and Matsuoka, K. (2009) Syntheses and biological evaluations of carbosilane dendrimers uniformly functionalized with sialyl $\alpha(2\rightarrow3)$ lactose moieties as inhibitors for human influenza viruses. *Bioorg. Med. Chem. 17*, 5465−5475.
(25) Luczkowiak, J., Sattin, S., Sutkeviciute, I., Reina, J. J., Sánchez-Navarro, M., Thépaut, M., Martinez-Prats, L., Daghetti, A., Fieschi, F., Delgado, R., Bernardi, A., and Rojo, J. (2011) Pseudosaccharide functionalized dendrimers as potent inhibitors of DC-SIGN dependent ebola pseudotyped viral infection. *Bioconjugate Chem. 22*, 1354−1365.
(26) Xue, C., Velayudham, S., Johnson, S., Saha, R., Smith, A., Brewer, W., Murthy, P., Bagley, S. T., and Liu, H. (2009) Highly water-soluble, fluorescent, conjugated fluorine-based glycopolymers with poly(ethylene glycol)-tethered spacers for sensitive detection of *Escherichia coli*. *Chem.—Eur. J. 15*, 2289−2295.
(27) Miyachi, A., Dohi, H., Neri, P., Mori, H., Uzawa, H., Seto, Y., and Nishida, Y. (2009) Multivalent *galacto*-trehaloses: Design, synthesis, and biological evaluation under the concept of carbohydrate modules. *Biomacromolecules 10*, 1846−1853.
(28) Masaka, R., Ogata, M., Misawa, Y., Yano, M., Hashimoto, C., Murata, T., Kawagishi, H., and Usui, T. (2010) Molecular design of N-linked tetravalent glycosides bearing *N*-acetylglucosamine, *N,N′*-diacetylchitobiose and *N*-acetyllactosamine: Analysis of cross-linking activities with WGA and ECA lectins. *Bioorg. Med. Chem. 18*, 621−629.
(29) Cecioni, S., Faure, S., Darbost, U., Bonnamour, I., Parrot-Lopez, H., Roy, O., Taillefumier, C., Wimmerová, M., Praly, J.-P., Imberty, A., and Vidal, S. (2011) Selectivity among two lectins: Probing the effect of topology, multivalency and flexibility of "Clicked" multivalent glycoclusters. *Chem.—Eur. J. 17*, 2149−2159.
(30) Shibuya, N., Tazaki, K., Song, Z., Tarr, G. E., Goldstein, I. J., and Peumans, W. J. (1989) A comparative study of bark lectins from three elderberry (*Sambucus*) species. *J. Biochem. (Tokyo) 106*, 1098−1103.
(31) Kaku, H., Tanaka, Y., Tazaki, K., Minami, E., Mizuno, H., and Shibuya, N. (1996) Sialylated oligosaccharide-specific plant lectin from Japanese elderberry (*Sambucus sieboldiana*) bark tissue has a homologous structure to type II ribosome-inactivating proteins, ricin and abrin. *J. Biol. Chem. 271*, 1480−1485.
(32) Tazaki, K., and Shibuya, N. (1989) Purification and partial characterization of a lectin from the bark of Japanese elderberry (*Sambucus sieboldiana*). *Plant Cell Physiol. 30*, 899−903.
(33) Kaku, H., and Shibuya, N. (1992) Preparation of a stable subunit of Japanese elderberry (*Sambucus sieboldiana*) bark lectin and its application for the study of cell surface carbohydrates by flow cytometry. *FEBS Lett. 306*, 176−180.
(34) Kaku, H., Mori, Y., Goldstein, I. J., and Shibuya, N. (1993) Monomeric, monovalent derivative of *Maackia amurensis* leukoagglutinin. *J. Biol. Chem. 268*, 13237−13241.
(35) Ogata, M., Hidari, K. I.-P.J., Murata, T., Shimada, S., Kozaki, W., Park, E. Y., Suzuki, T., and Usui, T. (2009) Chemoenzymatic synthesis of sialoglycopolypeptides as glycomimetics to block infection by avian and human influenza virus. *Bioconjugate Chem. 20*, 538−549.
(36) Kato, T., Murata, T., Usui, T., and Park, E. Y. (2003) Improvement of GFPuv-β3GnT2 fusion protein production by suppressing protease in baculovirus expression system. *Biosci. Biotechnol. Biochem. 67*, 2388−2395.
(37) Ogata, M., Nakajima, M., Kato, T., Obara, T., Yagi, H., Kato, K., Usui, T., and Park, E. Y. (2009) Synthesis of sialoglycopolypeptide for potentially blocking influenza virus infection using a rat α2,6-sialyltransferase expressed in BmNPV bacmid-injected silkworm larvae. *BMC Biotechnol. 9* (54), 1−13.
(38) Misawa, Y., Akimoto, T., Amarume, S., Murata, T., and Usui, T. (2008) Enzymatic synthesis of spacer-linked divalent glycosides carrying *N*-acetylglucosamine and *N*-acetyllactosamine: Analysis of cross-linking activities with WGA. *J. Biochem. (Tokyo) 143*, 21−30.
(39) Green, E. D., Adelt, G., and Baenziger, J. U. (1988) The asparagines-linked oligosaccharides on bovine fetuin. *J. Biol. Chem. 263*, 18253−18268.
(40) Zeng, X., Nakaaki, Y., Murata, T., and Usui, T. (2000) Chemoenzymatic synthesis of glycopolypeptides carrying α-Neu5Ac-$(2\rightarrow3)$-β-D-Gal-$(1\rightarrow3)$-α-D-GalNAc, β-D-Gal-$(1\rightarrow3)$-α-D-GalNAc, and related compounds and analysis of their specific interactions with lectins. *Arch. Biochem. Biophys. 383*, 28−37.

Bioconjugate Chemistry

Article

pubs.acs.org/bc

Oxalic Acid Supported Si–^{18}F-Radiofluorination: One-Step Radiosynthesis of *N*-Succinimidyl 3-(Di-*tert*-butyl[^{18}F]fluorosilyl) benzoate ([^{18}F]SiFB) for Protein Labeling

Alexey P. Kostikov,*[,†] Joshua Chin,[†] Katy Orchowski,[†] Sabrina Niedermoser,[§] Miriam M. Kovacevic,[†] Antonio Aliaga,[†] Klaus Jurkschat,[‡] Bjoern Wängler,[§] Carmen Wängler,[§] Hans-Jürgen Wester,[∥] and Ralf Schirrmacher*[,†]

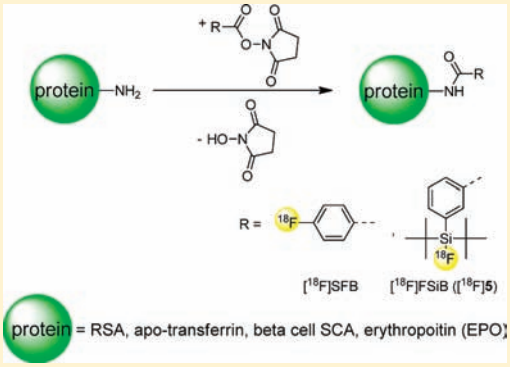
[†]McConnell Brain Imaging Centre, Montreal Neurological Institute, McGill University, Montreal, Canada;

[‡]Lehrstuhl für Anorganische Chemie II, Technische Universität Dortmund, Dortmund, Germany;

[§]Department of Nuclear Medicine, Hospital of the Ludwig-Maximilians-University, Munich, Germany,

[∥]Technical University Munich, Pharmaceutical Radiochemistry, Munich, Germany

ABSTRACT: *N*-Succinimidyl 3-(di-*tert*-butyl[^{18}F]fluorosilyl)benzoate ([^{18}F]SiFB), a novel synthon for one-step labeling of proteins, was synthesized via a simple ^{18}F–^{19}F isotopic exchange. A new labeling technique that circumvents the cleavage of the highly reactive active ester moiety under regular basic ^{18}F-labeling conditions was established. In order to synthesize high radioactivity amounts of [^{18}F]SiFB, it was crucial to partially neutralize the potassium oxalate/hydroxide that was used to elute ^{18}F$^-$ from the QMA cartridge with oxalic acid to prevent decomposition of the active ester moiety. Purification of [^{18}F]SiFB was performed by simple solid-phase extraction, which avoided time-consuming HPLC and yielded high specific activities of at least 525 Ci/mmol and radiochemical yields of 40–56%. In addition to conventional azeotropic drying of ^{18}F$^-$ in the presence of [K$^+$⊂2.2.2.]C_2O_4, a strong anion-exchange (SAX) cartridge was used to prepare anhydrous ^{18}F$^-$ for nucleophilic radio-fluorination omitting the vacuum assisted drying of ^{18}F$^-$. Using a lyophilized mixture of [K$^+$⊂2.2.2.]OH resolubilized in acetonitrile, the ^{18}F$^-$ was eluted from the SAX cartridge and used directly for the [^{18}F]SiFB synthesis. [^{18}F]SiFB was applied to the labeling of various proteins in likeness to the most commonly used labeling synthon in protein labeling, *N*-succinimidyl-4-[^{18}F]fluorobenzoate ([^{18}F]SFB). Rat serum albumin (RSA), apo-transferrin, a β-cell-specific single chain antibody, and erythropoietin were successfully labeled with [^{18}F]SiFB in good radiochemical yields between 19% and 36%. [^{18}F]SiFB- and [^{18}F]SFB-derivatized RSA were directly compared as blood pool imaging agents in healthy rats using small animal positron emission tomography. Both compounds demonstrated identical biodistributions in healthy rats, accurately visualizing the blood pool with PET.



■ INTRODUCTION

[^{18}F]Fluorine is one of the most useful radioisotopes in positron emission tomography (PET) due to its favorable decay characteristics. The relatively long half-life (110 min) allows for multistep syntheses of radiopharmaceuticals and longer PET scans, while the low positron energy (635 keV) allows for high-resolution imaging with the newest generation of PET cameras. A significant number of ^{18}F-radiotracers have been proposed and synthesized for clinical PET, but very few are widely used in nuclear medicine, with the only notable exception being 2-[^{18}F]Fluoro-2-deoxy-D-glucose ([^{18}F]FDG).[1] Harsh reaction environments, such as high temperatures and strong basic labeling conditions, are commonly required for the incorporation of anionic ^{18}F into organic molecules by means of nucleophilic substitution. These requirements limit the range of possible precursors and decrease the yield of the desired product through the formation of unwanted side products. Moreover, the formation of byproducts necessitates the use of time-consuming purification procedures. These complications become especially pronounced when labeling larger biomolecules such as peptides and proteins, where the labeling process relies on prosthetic ^{18}F-labeling agents. In this approach, a prosthetic group (labeling synthon) is synthesized in one or more steps via nucleophilic ^{18}F-fluorination and then reacted at mild conditions with the biomolecule intended for PET imaging. Numerous ^{18}F-labeled precursors have been conjugated to biomolecules by means of amidation, imidation, alkylation, and Michael addition, among others.[2−4] However, *N*-succinimidyl-4-[^{18}F]fluorobenzoate ([^{18}F]SFB), which readily acylates proteins in aqueous media, remains the standard method for protein ^{18}F-labeling since it was first

Received: September 28, 2011
Revised: December 7, 2011
Published: December 8, 2011

 © 2011 American Chemical Society

reported in 1992.[5,6] A variety of peptides and proteins have been labeled with [^{18}F]SFB, including monoclonal antibodies, albumin, transferrin, and annexin V.[7−9] Protein labeling is usually carried out in borate buffer at pH 8−9 upon incubation for 15−30 min, and the labeled protein is purified using size-exclusion chromatography. Despite the ease of the bioconjugation step, preparation of [^{18}F]SFB requires time- and labor-consuming procedures, including a three-step synthesis and HPLC purification.[10] Starting from $^{18}F^-$, the overall labeling of the peptide is carried out in four steps and two HPLC purifications, which takes over two hours to complete.

Consequently, novel methods for the fast production of ^{18}F-labeling agents of both small and larger biomolecules, ideally under mild conditions, are highly sought after. Several groups have recently started to investigate the potential of "non-conventional" silicon,[11−20] phosphorus,[21] boron,[22−24] and aluminum chelate[25−27] containing precursors for ^{18}F-labeling of organic vectors. These approaches deviate from the conventional formation of a carbon-^{18}F bond by nucleophilic substitution. We have investigated a new ^{18}F-labeling method based on the ^{18}F−^{19}F isotopic exchange at the silicon atom using no-carrier-added $^{18}F^-$ and nanomolar amounts of *para*-substituted di-*tert*-butylphenylfluorosilanes (SiFA compounds) at room temperature.[12−15] We have previously shown that ^{18}F-labeled SiFA compounds can be obtained in high radiochemical yields (RCYs) and specific activities (SAs) in a short amount of time due to the efficiency of the isotopic exchange reaction at the Si−F bond, in contrast to isotopic exchange reactions that involve a carbon−fluorine bond. Successful application of [^{18}F]SiFA-isothiocyanate ([^{18}F]SiFA−ITC) as a synthon for the labeling of proteins has been previously reported;[28] however, this compound suffers from somewhat low hydrolytic stability that limits the amount of ^{18}F incorporated into it in a one-batch synthesis or routine production. In this report, the high-yield, oxalic acid supported synthesis of *N*-succinimidyl 3-(di-*tert*-butyl[^{18}F]fluorosilyl)benzoate ([^{18}F]-SiFB), a SiFA analogue of the [^{18}F]SFB labeling synthon, via isotopic exchange and application of this synthon for the labeling of various proteins are described. Furthermore, the utilization of a novel SAX cartridge-based drying method for anhydrous basic $^{18}F^-$ in polar aprotic solvents (hereafter referred as to the Munich-method)[29] for nucleophilic fluorination has been exploited and adapted to the efficient production of [^{18}F]SiFB. A similar ^{18}F drying strategy using organic bases has recently been reported.[30]

EXPERIMENTAL SECTION

Materials and Methods. Highly enriched [^{18}O]water (>97%) was purchased from Rotem. (4-Ethoxycarbonylphenyl) trimethylammonium triflate, a precursor for the radiosynthesis of [^{18}F]SFB, as well as nonradioactive standard, were purchased from ABX (Germany). All other commercially available chemicals, such as Kryptofix 2.2.2, acetonitrile, potassium oxalate, oxalic acid, tetrapropylammonium hydroxide, and *N,N,N′,N′*-tetramethyl-*O*-(*N*-succinimidyl)uronium tetrafluoroborate, and RSA, apo-transferrin and IgG, were purchased at the highest available purity from Sigma-Aldrich. Recombinant erythropoitin (EPO) was purchased from Creative Biomart (US). The beta cell SCA was provided by Dr. S. Schneider (Innere Medizin II, Diabetologie und Endokrinologie St. Vinzenz-Hospital, Universität zu Köln). The SAX cartridges (Sep-Pak Light (46 mg) Accell Plus QMA Carbonate) were purchased from Waters (USA).

The labeling precursor *N*-succinimidyl 3-(di-*tert*-butyl-fluorosilyl)benzoate (SiFB) was synthesized as described below. Radiosynthesis of [^{18}F]SFB was performed using a Scintomics Hotbox III module, whereas labeling of SiFB was carried out manually. Radio TLCs (silicagel-60 plates) were monitored using an Instant Imager (Packard) or Mini Gita (Raytest). Analytical HPLC and labeled protein purification was performed on an Agilent Technologies 1200 system equipped with a Gabi radioactivity detector (Raytest). For [^{18}F]SFB and [^{18}F]SiFB labeled protein purifications, the following HPLC conditions were applied: Phenomenex Biosep-SEC-S4000, 0.1 M sodium phosphate buffer pH 7.2, flow 0.7 mL/min, R_t (protein) = 15 min. Animal experiments were performed using a Concorde Micro-PET camera (Siemens). The NMR experiments were carried out with Varian Mercury 300 spectrometers. The chemical shifts δ are given in ppm and referenced to the solvent peaks with the usual values calibrated against tetramethylsilane (^{1}H, ^{13}C).

Synthesis of *N*-Succinimidyl 3-(Di-*tert*-butyl-fluorosilyl)benzoate (SiFB). *(3-Bromobenzyl)oxy(tert-butyl)dimethylsilane (1).* Imidazole (4.53 g, 66.5 mmol, 2.5 equiv) and *tert*-butyl dimethylsilyl chlorid (TBSCl) (4.93 g, 32.7 mmol, 1.25 equiv) were sequentially added to a solution of 3-bromobenzyl alcohol (4.98 g, 26.6 mmol) in DMF (15 mL) at 25 °C, and the mixture was stirred at room temperature overnight. The reaction was quenched by addition of H_2O (100 mL), and the mixture was extracted with Et_2O (3 × 75 mL). The combined organic phase was washed with H_2O (50 mL), dried over Na_2SO_4, filtered, and concentrated *in vacuo*. The residue was purified by flash column chromatography on silica gel (neat hexanes) to afford **1** as a colorless liquid (7.63 g, 95%). ^{1}H NMR (300 MHz, $CDCl_3$) δ 7.48 (s, 1H), 7.37 (d, 1H, J = 7.2 Hz), 7.24 (d, 1H, J = 7.8 Hz), 7.19 (t, 1H, J = 7.5 Hz), 4.71 (s, 2H), 0.95 (s, 9H), 0.11 (s, 6H). ^{13}C NMR (300 MHz, $CDCl_3$) δ 143.8, 129.9, 129.8, 129.0, 124.4, 122.4, 64.2, 25.9, 18.4, −5.3.

Di-*tert*-butyl(3-(((*tert*-butyldimethylsilyl)oxy)methyl)-phenyl)fluorosilane (2). A solution of *tert*-butyl lithium in pentanes (1.7 M, 22.0 mL, 2.1 equiv) was added dropwise to a solution of **1** (5.36 g, 17.8 mmol) in anhydrous Et_2O (20 mL) over a period of 15 min at −78 °C. After the solution had been stirred at the same temperature for additional 15 min, a solution of di-*tert*-butyldifluorosilane (3.85 g, 21.4 mmol, 1.2 equiv) in anhydrous Et_2O (5 mL) was added dropwise over a period of 15 min at −78 °C. The reaction mixture was allowed to warm to room temperature overnight. The reaction was quenched by addition of saturated aqueous sodium chloride solution (100 mL), and the product was extracted with Et_2O (3 × 75 mL). The combined organic phase was dried over Na_2SO_4, filtered, and concentrated *in vacuo* to afford **2** as a pale-yellow liquid (7.33 g) that was carried forward without further purification.

(3-(Di-*tert*-butylfluorosilyl)phenyl)methanol (3). A concentrated aqueous hydrochloric acid solution (37 wt %, 0.5 mL) was added dropwise to a solution of crude **2** (6.77 g) in MeOH (50 mL) at 25 °C, and the mixture was stirred at room temperature overnight. After all volatiles have been removed under reduced pressure, the residue was redissolved in ether (100 mL), and the solution washed with saturated aqueous sodium bicarbonate solution (50 mL). The aqueous phase was extracted with ether (3 × 50 mL), and the combined organic phase was washed with H_2O (50 mL), dried over Na_2SO_4, filtered, and concentrated *in vacuo*. The residue was

dx.doi.org/10.1021/bc200525x | *Bioconjugate Chem.* 2012, 23, 106−114

purified by flash column chromatography on silica gel (9:1 to 7:1 hexanes/EtOAc) to afford **3** as a white solid (3.02 g, 64% over 2 steps). ^{1}H NMR (300 MHz, $CDCl_3$) δ 7.58 (s, 1H), 7.53 (d, 1H, J = 6.9 Hz), 7.44 (d, 1H, J = 7.5 Hz), 7.38 (t, 1H, J = 7.4 Hz), 4.71 (s, 2H), 1.86 (br s, 1H), 1.06 (d, 18H, $J(^1H, ^{19}F)$ = 1.2 Hz). ^{13}C NMR (300 MHz, $CDCl_3$) δ 139.9, 134.0 ($J(^{13}C, ^{19}F)$ = 53 Hz), 133.3 ($J(^{13}C, ^{19}F)$ = 17 Hz), 132.5 ($J(^{13}C, ^{19}F)$ = 17 Hz), 128.3, 127.8 ($J(^{13}C, ^{19}F)$ = 5 Hz), 65.5, 27.3 ($J(^{13}C, ^{19}F)$ = 3 Hz), 20.2 ($J(^{13}C, ^{19}F)$ = 50 Hz). ^{19}F NMR (300 MHz, $CDCl_3$) δ −188.84. HRMS (ESI, m/z): $[M+Na]^+$ calc.: 291.1551; found: 291.1545.

3-(Di-*tert*-butylfluorosilyl)benzaldehyde (4). A solution of **3** (2.50 g, 9.31 mmol) in anhydrous CH_2Cl_2 (50 mL) was added dropwise to a solution of pyridinium chlorochromate (PCC) (5.02 g, 23.3 mmol, 2.5 equiv) in anhydrous CH_2Cl_2 (250 mL) at 0 °C. The reaction mixture was stirred at 0 °C for 30 min and then allowed to warm to room temperature for 2.5 h, diluted with ether (200 mL), and filtered. The precipitate was washed with anhydrous Et_2O, and the combined organic phase was concentrated *in vacuo*. The residue was purified by flash column chromatography on silica gel (19:1 hexanes/EtOAc) to afford **4** as a yellow oil (2.28 g, 92%). ^{1}H NMR (300 MHz, $CDCl_3$) δ 10.05 (s, 1H), 8.11 (s, 1H), 7.93 (dt, 1 H, J = 7.5, 1.5 Hz), 7.87 (dt, 1H, J = 7.5, 1.2 Hz), 1.07 (d, 18H, $J(^1H, ^{19}F)$ = 1.2 Hz). ^{13}C NMR (300 MHz, $CDCl_3$) δ 192.6, 139.8 ($J(^{13}C, ^{19}F)$ = 17 Hz). 135.5 ($J(^{13}C, ^{19}F)$ = 18 Hz), 130.5, 128.3 ($J(^{13}C, ^{19}F)$ = 4 Hz), 27.2 ($J(^{13}C, ^{19}F)$ = 3 Hz), 20.2 ($J(^{13}C, ^{19}F)$ = 48 Hz). ^{19}F NMR (300 MHz, $CDCl_3$) δ −188.43. HRMS (ESI, m/z): $[M+H]^+$ calc.: 267.1575; found: 267.1571.

***N*-Succinimidyl 3-(di-*tert*-butylfluorosilyl)benzoate (5).** The *N*-succinimidyl ester was synthesized according to the procedure reported by Glaser[31] for the synthesis of [^{18}F]SFB. *N*-Hydroxysuccinimide (115 mg, 1 mmol) and **4** (53.3 mg, 0.2 mmol) were mixed in ethyl acetate (4 mL) in a 5 mL vial, and the mixture was cooled to 0 °C. Iodobenzene diacetate ($PhI(OAc)_2$) (80.5 mg, 0.25 mmol) was added in one portion, and the reaction mixture was stirred for 15 min at 0 °C and then allowed to warm to room temperature for 1 h. After dilution with hexane (4 mL), the crude product was purified by column chromatography (hexane/ether 1:1). The *N*-succinimidyl ester **5** (64 mg, 0.17 mmol, 84% yield) was obtained as an oil that solidified upon standing. ^{1}H NMR δ 8.37 (s, 1H), 8.19 (d, 1H), 7.90 (d, 1H), 7.52 (t, 1H), 2.90 (s, 4H), 1.03 (s, 18H). ^{13}C NMR δ 169.3, 162.0, 140.2 (d), 135.7, 135.3 (d), 131.6, 128.2, 124.6, 27.2, 25.7, 20.2 (d). ^{19}F NMR (300 MHz, $CDCl_3$) δ −188.42. HRMS (ESI, m/z): $[M+Na]^+$ calc.: 402.1507; found: 402.1510.

Fully Automated Synthesis of *N*-Succinimidyl-4-[^{18}F]-fluorobenzoate([^{18}F]SFB). A one-pot procedure reported by Tang et al.[10] was used for the synthesis of [^{18}F]SFB. Briefly, no-carrier-added aqueous [^{18}F]fluoride/H_2[^{18}O]O (300−450 mCi, 11.1−16.6 GBq, ~2.2 mL), generated using an IBA cyclotron (Cyclon 18/9) by the $^{18}O(p,n)^{18}F$ nuclear reaction on an enriched [^{18}O]water target, was passed through a QMA cartridge. The $^{18}F^-$ was then eluted from the QMA cartridge with a solution of Kryptofix2.2.2 (10 mg, 27 μmol) and K_2CO_3 (13.5 μmol) in CH_3CN/H_2O (96:4, 1.5 mL). The residual water was removed by coevaporation to dryness with CH_3CN using a stream of argon at 105 °C and a gentle vacuum. This step was repeated twice more with 0.5 mL CH_3CN. (4-Ethoxycarbonylphenyl) trimethylammonium triflate (5 mg, 14 μmol) dissolved in 1 mL of MeCN was added to the "dried" $[K^+\subset 2.2.2.][^{18}F]F^-$ cryptate and heated to 90 °C for 10 min. Tetrapropylammonium hydroxide (TPAH, 20 μL of 1 M aq. solution in 2 mL MeCN) was then added, and the reaction mixture was heated to 120 °C for 3 min to hydrolyze the ethyl ester. Finally, after complete evaporation of MeCN to dryness, *N,N,N′,N′*-tetramethyl-*O*-(*N*-succinimidyl)uronium tetrafluoroborate (TSTU, 12 mg, 40 μmol)dissolved in 1 mL of MeCN was added, and the reaction mixture was heated to 90 °C for 5 min. The resulting solution of crude [^{18}F]SFB was cooled by a stream of air to room temperature and diluted with 1.5 mL of HPLC eluent for direct injection onto the HPLC system (μBondapak C-18 column, MeCN/0.01 M H_3PO_4, 40:60; flow 2 mL/min; R_t = 11 min). The radioactivity peak corresponding to the [^{18}F]SFB was collected in a 50 mL round-bottom flask, and the eluent was carefully evaporated *in vacuo* under very gentle heating, as the product was volatile. The ^{18}F-labeling synthon was redissolved in borate buffer pH 9 or water to be used in the bioconjugation reaction. The radiochemical purity of [^{18}F]SFB was confirmed by radio-TLC (hexane/ethyl acetate 1:1, R_f = 0.5).

Protein Labeling with [^{18}F]SFB. An aliquot (0.5 mL) of the solution described above was added to the solution of protein (0.5 mL, 2 mg/mL, cf. Table 1) in borate buffer (pH 9),

Table 1. ^{18}F-Labeled Proteins Using [^{18}F]SiFB and [^{18}F]SFB[a]

protein	RCY (by HPLC)		RCY (isolated)	
	[^{18}F]SiFB	[^{18}F]SFB	[^{18}F]SiFB	[^{18}F]SFB
RSA (n = 3)	70 ± 9%	38 ± 3%	35 ± 8%	27 ± 3%
Apo-transferrin (n = 3)	21 ± 2%	33 ± 4%	n.i.[b]	n.i.
β-cell SCA (n = 2)[32]	18 ± 1%	14 ± 3%	n.i.	n.i.
Erythropoietin (n = 2)	63 ± 5%	27 ± 3%	19 ± 4%	19 ± 2%

[a]RCYs refer to the starting activity of the labeling synthon. [b]n.i.: not isolated.

and the mixture was incubated for 20 min at room temperature. The entire batch was then injected into an HPLC system, and the collected ^{18}F-labeled protein fraction was used in animal PET studies without further reformulation.

Small Scale Synthesis of Succinimidyl 3-(Di-*tert*-butyl[^{18}F]fluorosilyl)benzoate ([^{18}F]SiFB)([^{18}F]5) with aliquots of azeotropically dried $^{18}F^-$. [^{18}F]fluoride/H_2[^{18}O]O (370−1850 MBq, 10−50 mCi) was passed through a QMA cartridge preconditioned with 10 mL 0.5 M K_2CO_3, followed by 10 mL H_2O. The $^{18}F^-$ was then eluted from the QMA cartridge with a solution of Kryptofix2.2.2 (7.5 mg, 20 μmol) and $K_2C_2O_4$ (10 μmol) in CH_3CN/H_2O (96:4, 1 mL). The residual water was removed by coevaporation to dryness with CH_3CN using a stream of argon at 105 °C and a gentle vacuum. This step was repeated twice more with 1 mL CH_3CN. The residue containing the $[K^+\subset 2.2.2.][^{18}F]F$ cryptate was redissolved in MeCN (1 mL), and oxalic acid (0.1 M, 5 μmol) in anhydrous acetonitrile (50 μL) was added. SiFB (130 nmol, 1 μg/μL in MeCN) was added, and the reaction mixture was kept at room temperature for 5 min, diluted with distilled water (10 mL), and passed through a C-18 light cartridge (SepPak, Waters) preconditioned with 10 mL MeOH followed by 10 mL water. The cartridge was washed with 10 mL water to remove all traces of residual $[K^+\subset 2.2.2.][^{18}F]F$. The desired [^{18}F]SiFB was eluted from the cartridge with diethyl ether (3 mL) into an Eppendorf vial (5 mL), and the solvent was removed by a gentle argon stream at room temperature. Both aqueous and organic eluates were analyzed by means of radio-TLC (hexane/

dx.doi.org/10.1021/bc200525x | *Bioconjugate Chem.* 2012, 23, 106−114

ethyl acetate 1:1, R_f = 0.7) to confirm the quantitative separation of unreacted $^{18}F^-$ anion and [^{18}F]SiFB.

Synthesis of [^{18}F]SiFB ([^{18}F]5) Using the Munich Method (A: using whole ^{18}F batch; B: using ^{18}F aliquots). *Preparation of [K$^+$⊂2.2.2.]OH.* Kryptofix2.2.2 (41 mg, 110 μmol) was dissolved in aqueous potassium hydroxide (1 M, 100 μL; 100 μmol). The resulting solution was further diluted with water (~1 mL), lyophilized to dryness overnight, and dissolved in anhydrous acetonitrile (0.5 mL) immediately before use.

Retention and Elution of $^{18}F^-$ from Anion Exchange Cartridge. Bombarded water from the target ([^{18}F$^-$/[^{18}O]H_2O) was passed through a SAX cartridge (Sep-Pak Light (46 mg) Accell Plus QMA Carbonate) preconditioned with water (10 mL). The cartridge was flushed with air (20 mL), rinsed with anhydrous MeCN (5 mL) to remove traces of water, and flushed again with air (20 mL). $^{18}F^-$ was eluted with the previously described [K$^+$⊂2.2.2.]OH solution in acetonitrile (0.5 mL).

Radiolabeling A. A solution of oxalic acid in anhydrous acetonitrile (0.5 M, 150 μL, 75 μmol) was added to the eluate containing [K$^+$⊂2.2.2.][^{18}F]F$^-$ (0.5 mL, 100 μmol), followed by a solution (5×10^{-3} M) of SiFB in acetonitrile (40 μL, 200 nmol). The reaction was kept at room temperature for 30 min. Starting from 263 mCi of $^{18}F^-$, [^{18}F]SiFB (105 mCi) was synthesized in 40% isolated yield (EOS), with a specific activity of 525 Ci/mmol.

Radiolabeling B. The eluate containing [K$^+$⊂2.2.2.][^{18}F]F$^-$ (0.5 mL, 400 mCi) was aliquotized in 100 μL portions, each containing 20 μmol of KOH. A solution (0.5 M) of oxalic acid in anhydrous acetonitrile (0–40 μL, 0–20 μmol; Figure 4) was added, followed by a solution of SiFB in acetonitrile (5×10^{-3} M, 20–40 μL, 100–200 nmol), and the reaction was kept at room temperature for 5–15 min. Radiochemical yields were determined by radio-TLC (hexane/EtOAc 3:1). Three independent reaction parameters were optimized: n(KOH) = 20 μmol; $n(H_2C_2O_4)$ = 15 μmol; n(SiFB) = 100 nmol; t = 15 min; rt. Starting from 80 mCi of $^{18}F^-$, [^{18}F]SiFB (45 mCi) with a specific activity of 450 Ci/mmol (calculated lower limit) was synthesized in 56% yield (EOS).

Purification of [^{18}F]SiFB. The reaction mixture was diluted with an excess of aqueous H_3PO_4 (0.01 M, 3–5 mL) and passed through a preconditioned (10 mL MeOH, followed by 10 mL H_2O) C18 cartridge. The cartridge was washed with water (5 mL) to remove traces of K2.2.2 and unreacted $^{18}F^-$, and the desired product was eluted with diethyl ether (3 mL). The ether was removed within 5–10 min at room temperature using a stream of nitrogen. The [^{18}F]SiFB was subsequently used for protein labeling as described below. The purity of [^{18}F]SiFB was confirmed by radio-TLC and HPLC to be >98%.

Protein Labeling with [^{18}F]SiFB ([^{18}F]5). A freshly prepared solution of the protein (e.g., RSA: 3.25 mg, 50 nM) in borate buffer (1 mL, pH 9) was added to an Eppendorf vial containing dried [^{18}F]SiFB. The mixture was incubated for 30 min at room temperature. The entire batch was then injected into an HPLC system, and the collected protein was used directly for animal PET studies (Phenomenex Biosep-SEC-S4000, 0.1 M sodium phosphate buffer pH 7.2, flow 0.7 mL/min, R_t (protein) = 15 min, k'(proteins) = 3).

Small Animal PET Studies. Rats for small animal PET studies were housed in a 12 h light/dark cycle at 21 °C with access to food and water *ad libitum*, treatment was according to the Guide to the Care and Use of Experimental Animals (Ed2) of the Canadian Council on Animal Care. The MicroPET imaging protocol was approved by the Animal Care Committee of McGill University (Montreal, Canada). Respiration rate, heart rate, and body temperature were monitored throughout the scan (Biopac systems MP150, Goleta, CA, USA).

PET images of [^{18}F]SiFB-RSA (11.7 MBq, 0.31 mCi) and [^{18}F]SFB-RSA (11.25 MBq, 0.3 mCi) were obtained from male Sprague–Dawley rats. Maximum intensity projections were obtained after the injection of [^{18}F]SiFB- and [^{18}F]SFB-RSA into a healthy rat. Data were acquired 5 s post tracer administration over 3600 s with the Concorde MicroPET R4 small animal tomograph. All images were reconstructed using the filtered back projection after applying normalized scatter correction for attenuation and radioactive decay. The PET images were analyzed using *ASIPRO* software (Concorde Microsystems) with 3D regions of interest (RIO) drawn around areas of increased tracer accumulation. The time–activity curves (TAC) were obtained from ROIs in heart (LV), artery, liver, kidney, and bone. Uptake of [^{18}F]SiFB-RSA and [^{18}F]SFB-RSA in the tissues were expressed as standard uptake value (%SUV) calculated as average tissue concentration (MBq/cc) divided by the ratio of injected dose (MBq) over subject mass multiplied by 100%.

RESULTS AND DISCUSSION

Design and Radioactive Labeling of [^{18}F]SiFB. Non-site-specific acylation with [^{18}F]SFB remains the most widely used method of ^{18}F protein labeling (Figure 1). The radiochemical

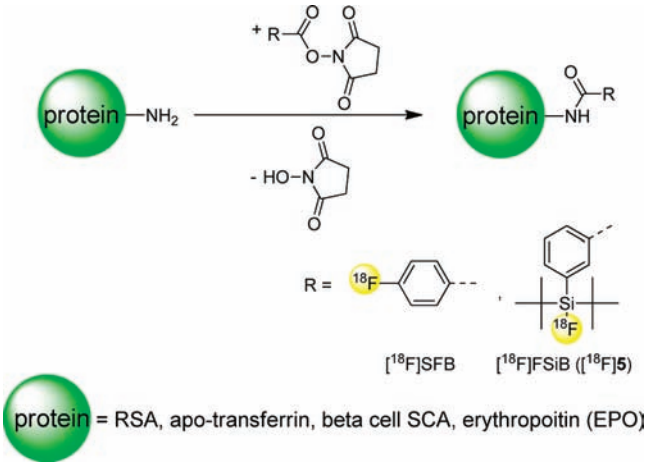


Figure 1. Radioactive labeling of various proteins using [^{18}F]SiFB ([^{18}F]**5**) and the most commonly applied synthon in protein labeling

synthesis of this prosthetic group has been improved over the years. Recently, a relatively simple one-pot procedure was reported by Tang et al.;[10] however, this procedure required a three-step synthesis and a final HPLC purification in order to obtain highly pure [^{18}F]SFB. The goal of the present study was to develop a novel ^{18}F protein labeling prosthetic group based on SiFA group radiochemistry, which could be (1) synthesized in one simple step (e.g., ^{19}F for ^{18}F isotopic exchange), (2) purified using fast, solid-phase extraction technique, and (3) used like [^{18}F]SFB for protein labeling. Since the labeling and conjugation reactions should be each one-step reactions, we investigated the direct isotopic ^{19}F-for-^{18}F exchange reaction on SiFB (**5**). This SiFA labeling precursor consists of a highly reactive group, e.g., the succinimidyl ester for the conjugation

dx.doi.org/10.1021/bc200525x | *Bioconjugate Chem.* 2012, 23, 106–114

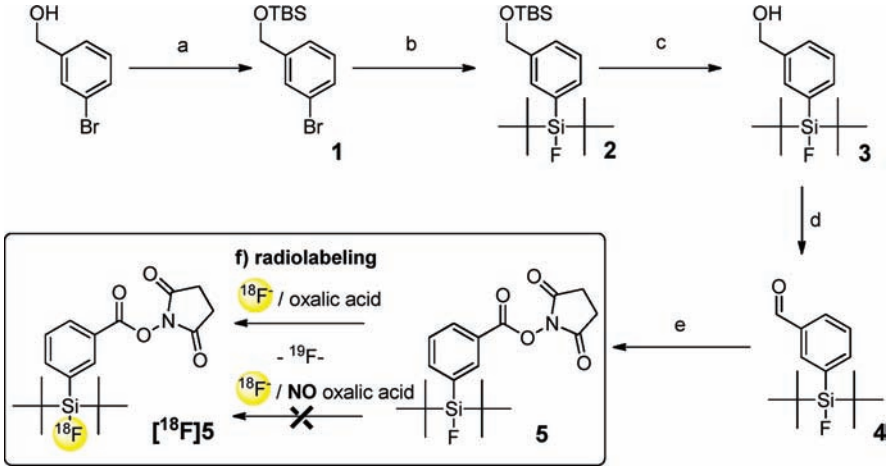


Figure 2. Synthetic scheme for SiFB (**5**) and its ^{18}F-fluorination: (a) TBSCl/imidazole, DMF, rt; 95%; (b) *t*-BuLi/$(t\text{-Bu})_2SiF_2$, ether, −78 °C → rt; (c) HCl, MeOH, rt; 64% over 2 steps; (d) PCC, DCM, −0 °C → rt; 92%; (e) NHS/PhI$(OAc)_2$, EtOAc, 0 °C → rt; 84%; (f) $^{18}F^-/K_2C_2O_4$/K2.2.2/$H_2C_2O_4$, MeCN, rt (*note*: no product formation without oxalic acid).

to a protein and a di-*tert*-butylfluorosilyl group for highly efficient isotope exchange (Figure 2). Although in conventional ^{18}F radiochemistry, like the [^{18}F]SFB synthesis, a succinimidyl ester moiety results in the formation of the corresponding acid [^{18}F]fluorides that hydrolyze upon analyses, we assumed that the SiFA approach might be able to overcome this limitation. Most recently, Olberg et al. reported the elegant one-step synthesis of 6-[^{18}F]fluoronicotinic acid 2,3,5,6-terafluorophenyl ester ([^{18}F]F-Py-TFP), another new prosthetic group for protein labeling.[33] The tetrafluorophenyl ester moiety of this reported labeling synthon survived the basic reaction conditions for ^{18}F-labeling at 40 °C.

The [^{18}F]SFB synthon contains ^{18}F in the *para*-position to the succinimidyl group because the aromatic nucleophilic ^{18}F fluorination of the precursor (4-ethoxycarbonylphenyl) trimethylammonium triflate is facilitated by an electron-withdrawing ester group in the *para*-position. However, for highly reactive SiFA compounds, the relative orientation of the SiFA group to the other substituents in the molecule does not play a significant role in the isotope exchange reaction, making an activated aromatic system unnecessary. On the contrary, preliminary hydrolysis studies gave reason to expect a faster hydrolysis rate for *para*-substituted SiFA compounds compared to *meta*-substituted ones. For this reason, we designed N-[^{18}F]succinimidyl 3-(di-*tert*-butylfluorosilyl)benzoate ([^{18}F]SiFB) as a novel prosthetic molecule for protein labeling, bearing the SiFA building block in *meta*-position to the active ester moiety (Figure 2). Of primary concern was the inability to label SiFB in one step without hydrolyzing the *N*-succinimidyl ester under typical basic labeling conditions (Figure 2f).

Optimization of the Reaction Conditions for the Synthesis of [^{18}F]SiFB and Its Purification. The base used for the azeotropic drying of $^{18}F^-$appeared to have a crucial influence on ^{18}F-incorporation yields into SiFA compounds. Utilizing potassium carbonate as a base in this particular ^{18}F-fluorination led to a side product that did not correspond to the desired [^{18}F]SiFB. Thus, a milder base, potassium oxalate, was used in all of the subsequent isotope exchange reactions leading to [^{18}F]SiFB. However, even with this very mild base, the concentration of the $[K^+\subset 2.2.2.]_2C_2O_4$ had to be kept at the very low level (1 mg/mL or 2.7 μmol/mL, approximately 10-times more dilute than for conventional S_N2 fluorination reactions) to avoid formation of the aforementioned byproduct. Under these conditions, the reaction mixture had to be cooled down to a minimum of 0 °C to prevent fast hydrolysis of the initially formed [^{18}F]SiFB under nucleophilic fluorination conditions. This short shelf-life in even slightly basic solution necessitated the immediate use of [^{18}F]SiFB for protein labeling. Furthermore, utilizing a full batch of azeotropically dried $^{18}F^-$ did not give a high radioactivity amount of [^{18}F]SiFB.

The labeling procedure was substantially improved by addition of oxalic acid to the basic labeling cocktail before the isotope exchange reaction was initiated. Oxalic acid was selected over inorganic acids for two reasons: First, it contains the same anion as potassium oxalate, which is already present in the reaction mixture, thus limiting the possibility of anion-induced side reactions; and second, oxalic acid is soluble in anhydrous acetonitrile and therefore could be added to the $[K^+\subset 2.2.2.][^{18}F]F$ cryptate complex after azeotropic drying. The dependence of the incorporation yield of ^{18}F into SiFB on the ratio of $K_2C_2O_4$ used for $^{18}F^-$ elution from QMA to $H_2C_2O_4$ was thoroughly investigated (Figure 3). The addition of an excess of $H_2C_2O_4$ led to a decrease in RCY, which was probably due to a formation of H^{18}F, which is not as reactive as nucleophilic $^{18}F^-$. The optimal molar ratio for obtaining highest

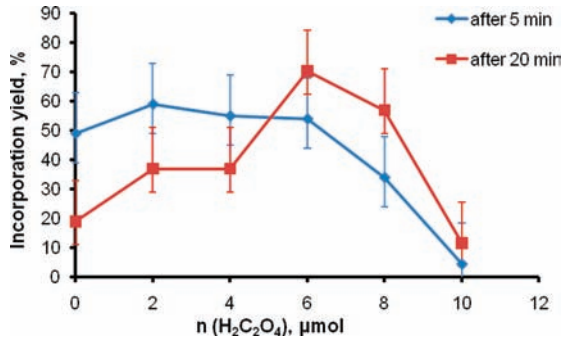


Figure 3. Using azeotropic $^{18}F^-$ drying ($[K^+\subset 2.2.2.]_2C_2O_4^{2-}$): Dependence of incorporation yield of $^{18}F^-$ into SiFB (**5**) (50 μg, 130 nmol) by isotopic exchange on the amount of added oxalic acid (range: 0–10 μmol), keeping a constant $K_2C_2O_4$ amount (10 μmol) after 5 and 20 min reaction time (n = 10 for each point, errors are expressed as SEM).

dx.doi.org/10.1021/bc200525x | *Bioconjugate Chem.* 2012, 23, 106–114

RCYs with a full batch of azeotropically dried $^{18}F^-$ was found to be $\nu([K^+\subset 2.2.2.]_2C_2O_4^{2-}):\nu(H_2C_2O_4)$ = 2:1. These conditions provided the stability of the *N*-succinimidyl ester group over time up to 30 min without compromising incorporation yields of the isotope exchange.

Addition of the optimum amount of $H_2C_2O_4$ was a rather delicate task due to unpredictable surface adsorption effects of the $[K^+\subset 2.2.2.]_2C_2O_4^{2-}$cryptate on the walls of the azeotropic drying receptacle (Wheaton vial).

To control the true amount of basic oxalate in the labeling solution, the most recently described cartridge-based procedure, developed by Wester et al. (Munich-Method),[29] was employed to obtain anhydrous $^{18}F^-$ in polar aprotic solvents without azeotropic drying. In this procedure, lyophilized $[K^+\subset 2.2.2.]OH$ cryptate, resolubilized in dry acetonitrile, is used to elute $^{18}F^-$ from the SAX cartridges of different sizes in acetonitril.

Here, a solution of $[K^+\subset 2.2.2.]OH$ cryptate formed by lyophilization of 110 μmol K2.2.2 and 100 μmol KOH and redissolved in 0.5 mL of anhydrous acetonitrile was used to elute the retained $^{18}F^-$ from the SAX cartridge. When the labeling reaction was carried out using a 100 μL aliquot of the 0.5 mL full batch solution of $[K^+\subset 2.2.2.]^{18}F$ (containing 100 μmol potassium hydroxide or potassium carbonate, respectively), 15 μmol of oxalic acid had to be added to the 20 μmol of KOH in order to get the required incorporation yields (Figure 4). This is consistent with a 2:1 ratio of oxalate to

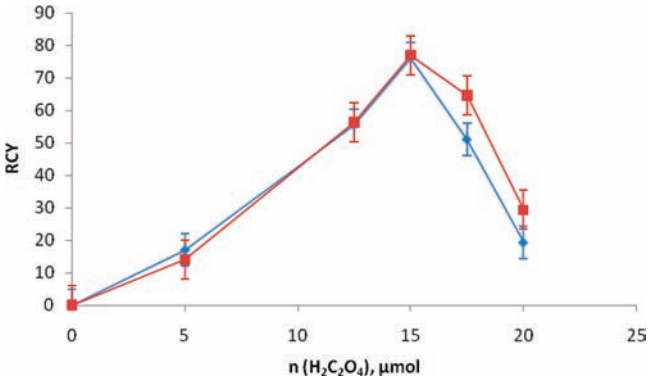


Figure 4. Using the Munich method for $^{18}F^-$ drying: Radiochemical incorporation yields of ^{18}F into $[^{18}F]$SiFB versus amount of oxalic acid after 5 (red line) and 10 (blue line) minutes reaction time ([Kryptofix]OH = 20 μmol, *n*(SiFB) = 100 nmol, *n* = 10 for each point, errors are expressed as SEM).

oxalic acid. Any deviation from this ratio led to a significant decrease of RCYs. The Munich method reduced the overall synthesis time by 20 min and significantly decreased the technical complexity for preparing anhydrous $^{18}F^-$, for which no heating, vacuum, or gas flow was needed. The amount of the SiFA-compound **5** also had to be optimized in order to obtain the maximal specific activity of $[^{18}F]$**5** without lowering its radiochemical yield. The acceptable incorporation yield of 50−70% was achieved using as little as 38 μg (100 nmol) of the precursor. Figure 5 summarizes the different compounds and methods used in this investigation.

The synthesis time for $[^{18}F]$SiFB varied between 20 and 50 min depending on the method used to obtain anhydrous $^{18}F^-$ (either azeotropic drying or the Munich cartridge method) and whether the full $^{18}F^-$ batch or a smaller $^{18}F^-$ aliquot was used (Figure 5). The preparation time for anhydrous $^{18}F^-$ was reduced to 5 min when the Munich method was used. This was four times faster than conventional azeotropic drying and only required a single anion exchange cartridge. When a full batch of $^{18}F^-$ containing 100 μmol of KOH in 0.5 mL acetonitrile was used, the isotopic exchange reaction took 30 min to obtain incorporation yields of $^{18}F^-$ of 50−70%. This was a result of the larger reaction volume. Smaller aliquots of 100 μL from the 0.5 mL stock solution required a reaction time of only 5−10 min to ensure sufficient $^{18}F^-$ incorporation. In one experiment, a starting activity of 400 mCi $[K^+\subset 2.2.2.]^{18}F$ in 0.5 mL of acetonitrile was used. From this stock solution, a 100 μL aliquot containing 80 mCi yielded 45 mCi of $[^{18}F]$SiFB after 20 min.

Next, optimized conditions for the purification of $[^{18}F]$**5** were developed. A main advantage of $[^{18}F]$SiFA compounds is their relatively simple purification without use of HPLC. Due to the aforesaid optimized mild reaction conditions, no radioactive side-products other than unreacted $^{18}F^-$ were observed. As a result of their very different lipophilicities, the separation of $[^{18}F]$**5** from $^{18}F^-$ was achieved by simple solid-phase cartridge extraction. The crude reaction mixture was diluted with aqueous H_3PO_4 (0.01 M, 1:10 v/v) and passed through a C18 cartridge. $[^{18}F]$**5** was quantitatively retained on the solid-phase material, whereas the $^{18}F^-$ and Kryptofix2.2.2 fraction were discarded. It is possible to easily elute $[^{18}F]$**5** from the cartridge using common organic solvents, such as MeOH, MeCN, THF, or ether. Since the organic solvent had to be completely removed without overheating the *N*-succinimidyl ester in order for a successful subsequent bioconjugation reaction to occur, volatile diethyl ether was chosen as an eluent. The radiochemical purity (RCP) of $[^{18}F]$**5** was usually >99%, as determined by radio-TLC. In direct comparison with the $[^{18}F]$SFB synthesis, no HPLC purification was needed, and the total preparation time for $[^{18}F]$**5** could be reduced to 55 min if a 100 μL $^{18}F^-$ aliquot is used (Figure 5A,D). Besides saving valuable synthesis time, the technical effort to obtain $[^{18}F]$**5** as a labeling synthon for proteins is marginal. Even laboratories with limited equipment would be able to obtain ^{18}F-labeled proteins by minimizing the synthetic effort.

Bioconjugation of $[^{18}F]$SiFB with Proteins. Bioconjugation of $[^{18}F]$SFB to proteins is usually carried out in aqueous borate buffers at pH 8−9 in the absence of organic solvents. The rate of *N*-acylation under these conditions is considered comparable to or better than that of ester hydrolysis and typically yields 30−50% within 15−30 min. These same conditions were applied for coupling of $[^{18}F]$SiFB with proteins, as it follows the same functional group chemistry. In a previous publication,[34] we reported an average half-life of SiFA compounds of 2 h at pH 10. Therefore, the extent of hydrolysis at pH 9 within 30 min was not expected to be very significant and within acceptable limits.

After 20−30 min reaction time, the purification of the labeled protein was carried out on HPLC, using a size-exclusion column and sodium phosphate buffer as an eluent. Since neither organic solvents nor potassium salts were used in the HPLC solvent, the eluate (pH 7.4) was suitable for animal injection. As expected, three competing pathways during the $[^{18}F]$**5** protein labeling were observed: (i) bioconjugation of $[^{18}F]$**5** to the protein; (ii) hydrolysis of the *N*-succinimidyl ester; and (iii) hydrolysis of di-*tert*-butyl$[^{18}F]$fluorosilyl group yielding anionic $^{18}F^-$. The predominant pathway appeared to be the bioconjugation of $[^{18}F]$**5** to the protein. Typically, four major peaks were observed on the chromatogram: (i) labeled protein (up to 80%); (ii) unreacted $[^{18}F]$SiFB (~10%); (iii) unknown by-product (~5%, most likely 3-di-*tert*-butyl$[^{18}F]$fluorosilylbenzoic

dx.doi.org/10.1021/bc200525x | *Bioconjugate Chem.* 2012, 23, 106−114

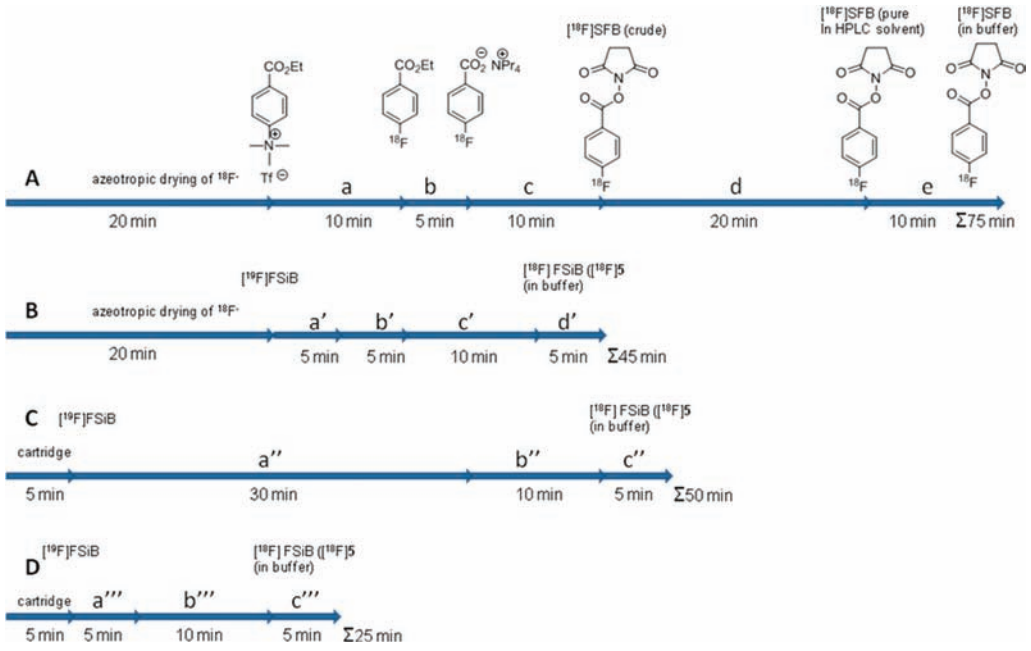


Figure 5. Synthetic time line of stepwise syntheses of [^{18}F]SFB and [^{18}F]SiFB. (A) *[^{18}F]SFB synthesis*: (a) reaction of (4-ethoxycarbonylphenyl) trimethylammonium triflate with ^{18}F; (b) hydrolysis of ethyl ester with TPAH; (c) evaporation of solvent and coupling with TSTU; (d) HPLC purification; (e) evaporation of solvent and reformulation. (B) *[^{18}F]SiFB synthesis using an ^{18}F$^-$ aliquot obtained by azeotropic drying of ^{18}F$^-$*: (a′) K2.2.2/$K_2C_2O_4$/^{18}F$^-$ cooled to rt; (b′) addition of oxalic acid and reaction of **5** with ^{18}F$^-$; (c′) cartridge purification of [^{18}F]**5**; (d′) evaporation of ether and reformulation in buffer. (C) *[^{18}F]SiFB synthesis using a full batch of ^{18}F$^-$obtained by the Munich method*: (a″) addition of oxalic acid reaction of **5** with ^{18}F$^-$ (0.5 mL); (b″) cartridge purification of [^{18}F]**5**; (c″) evaporation of ether and reformulation in buffer. [^{18}F]SiFB (D) *[^{18}F]SiFB synthesis using an aliquot of ^{18}F$^-$ batch in 0.5 mL acetonitrile obtained by the Munich method*: (a‴) addition of oxalic acid reaction of **5** with aliquot of ^{18}F$^-$ (0.1 mL); (b‴) cartridge purification of [^{18}F]**5**; (c‴) evaporation of ether and reformulation in buffer.

acid); and (iv) ^{18}F$^-$ (∼ 5%). In a typical experiment starting from 7.5 mCi [^{18}F]**5**, 1.7 mCi of labeled RSA in 1.5 mL of phosphate buffer was collected, and the resulting solution was used for animal experiments without further reformulation. The results of protein labeling with [^{18}F]SiFB ([^{18}F]**5**) and [^{18}F]SFB are summarized in Table 1. Only labeled RSA and erythropoietin were purified via HPLC and prepared as injectable solutions. The overall preparative RCYs in these two cases were comparable. The obvious discrepancy between the RCYs determined via HPLC and the de facto isolated RCYs in the case of [^{18}F]SiFB might be explainable by a higher absorption of unreacted [^{18}F]SiFB (and/or hydrolysis products) on the column material in comparison to the less lipophilic [^{18}F]SFB. The absorption might take place at the very beginning of the column preventing a later detection via UV and radioactivity detection.

[^{18}F]SiFB to Protein Ratio. In order to preserve the biological activity of the protein, the ratio of the labeling synthon to the molecule to be labeled should not exceed two to three.[35,36] Proteins, especially antibodies, lose their biological integrity when there are higher amounts of derivatization sites. In this study, the initial labeling procedure required 100 nmol of SiFB as a starting material, whereas the amount of labeled RSA (1 mg, MW ≈ 65 kDa) was 15.4 nmol. Therefore, the resulting ratio of 6.5:1 was not ideal. In attempts to reduce the ratio, the amount of nonradioactive SiFB was decreased and the mass of RSA remained constant. However, this led to significantly reduced incorporation yields of ^{18}F into the SiFA molecule. In the next attempt, the amount of protein was increased to 50 nmol (3.25 mg), while the concentration of SiFB remained at 100 nmol, thus reaching a 2:1 ratio. This approach proved to be more successful, as the desired ratio was achieved without compromising the yield of the labeled bioconjugate, and a full batch of [^{18}F]SiFB could be used. Regarding the other proteins employed for labeling, the following molar amounts were used for the labeling with [^{18}F]SiFB: transferrin (1 mg, 12.5 nmol), EPO (1 mg, 50 nmol), and a β-cell SCA (1 mg, 32 nmol). The amount of [^{18}F]SiFB (from a stock solution containing 100 nmol SiFB) used for labeling was adjusted in order to not exceed the targeted SiFB:protein ratio of 2:1. In order to permit a direct comparison between the labeling efficiency of [^{18}F]SiFB and [^{18}F]SFB, the molar amounts of protein were kept the same for both labeling synthons.

Animal Experiments. Blood pool imaging in planar or single photon emission computer tomography is capable of determining left and right ventricular volumes and ejection fractions in both humans and animals. It has been shown that radiolabeled serum albumins are excellent tracers for small animal PET blood pool studies. In this experiment, rat serum albumin was labeled with either [^{18}F]SFB or [^{18}F]SiFB according to the above-described procedures. The labeled compounds were then injected into healthy rats (n = 3 for each labeled RSA), and the biodistribution was studied for 60 min from the time of injection. Images revealed that the blood pool in the heart could be well delineated. Tracer accumulation was clearly observed in large arteries, the liver, and the left ventricle of the heart. Furthermore, the right ventricle and atria were also noticeable. No significant bone uptake was observed, proving the stability of the labeled protein *in vivo* toward defluorination (Figure 6).

The time activity curves depicting the radioactivity amount in different organs (heart, liver, and kidney), the main artery, and bone, indicated that there were no major differences in

dx.doi.org/10.1021/bc200525x | *Bioconjugate Chem.* 2012, 23, 106–114

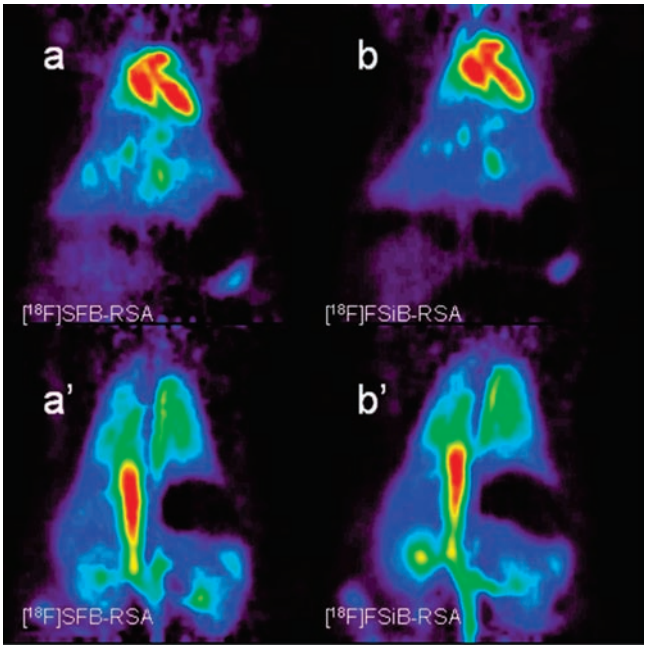


Figure 6. Biodistribution of labeled RSA in rat [(a + a'): [^{18}F]SFB-RSA; (b + b'): [^{18}F]SiFB-RSA; coronal plane sum images t = 5–60 min].

distributions between SFB and SiFB labeled RSA (Figure 7). The time activity curves corroborated that both labeled RSAs

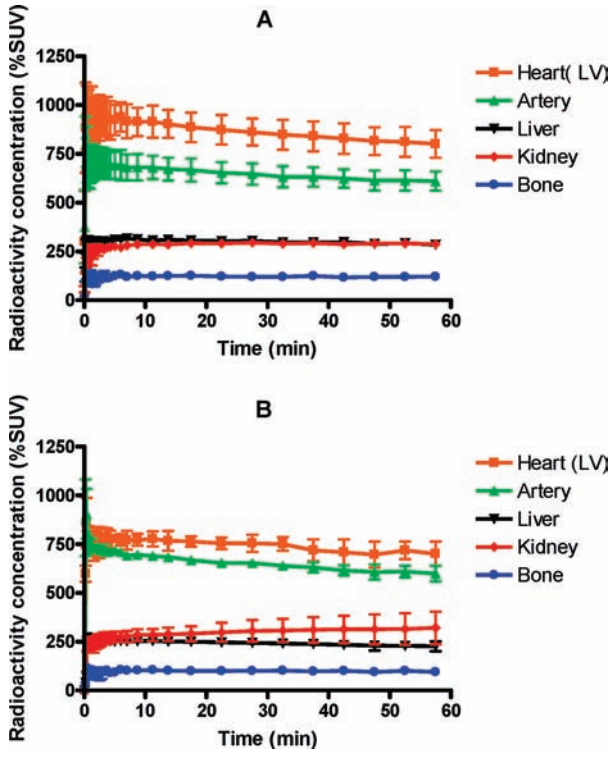


Figure 7. Time–activity curves for small bone, vessel, spleen, aorta, and liver extracted from *in vivo* PET scan for up to 60 min post injection of [^{18}F]SiB-RSA (A) and [^{18}F]SFB-RSA (B). Each point represents the mean of three independent animal experiments and errors are expressed as SEM (number of animals: n = 3).

displayed the characteristics of a blood pool imaging agent, particularly the very low level of bone uptake that signifies unbound [^{18}F]F$^-$.

CONCLUSIONS

A novel prosthetic group for non-site-specific protein labeling was designed and synthesized in one step by simple ^{19}F–^{18}F isotopic exchange. Addition of oxalic acid was crucial to prevent decomposition of the active ester moiety. Pure (>99%) [^{18}F]SiFB was obtained in up to 56% yield (EOS, non-decay-corrected) within 20–55 min depending on the synthetic method employed. The technical effort to obtain [^{18}F]SiFB is incomparably smaller than for [^{18}F]SFB. The resulting [^{18}F]SiFB was used for labeling of various proteins, such as RSA in RCYs comparable to those obtained with [^{18}F]SFB. RSA labeled with [^{18}F]SiFB showed the same biodistribution as [^{18}F]SFB-labeled RSA in healthy rats, accurately depicting blood flow using small animal PET. The number of introduced labeling sites to the protein using [^{18}F]SiFB is uncritical, guaranteeing an uncompromised biological integrity of the given protein. This conclusively demonstrates the applicability of [^{18}F]SiFB as a novel labeling synthon for protein labeling. [^{18}F]SiFB has the potential to become a valuable, easily accessible alternative to [^{18}F]SFB as a result of its easy preparation and similar reactivity toward protein labeling.

AUTHOR INFORMATION

Corresponding Author

*Alexey Kostikov: Tel: 514 398 8527, alexey.kostikov@mcgill.ca. Ralf Schirrmacher: Tel: 514 398 1857, Fax: 514 398 1392, ralf.schirrmacher@mcgill.ca.

ACKNOWLEDGMENTS

The authors wish to acknowledge financial support from the following agencies: Bayern-Quebec-Allianz to S.N.; DFG grant no. WA 2132/3-1 to B.W.; Canada Foundation for Innovation Project#: 203639 to R.S.; Canadian Institutes of Health Research (CIHR), Operating Grant #97970 to R.S.

REFERENCES

(1) Hamacher, K., Coenen, H. H., and Stöcklin, G. (1986) Efficient stereospecific synthesis of no-carrier-added 2-[^{18}F]-fluoro-2-deoxy-D-glucose using aminopolyether supported nucleophilic substitution. *J. Nucl. Med. 27*, 235–238.

(2) Cai, L., Lu, S., and Pike, V. W. (2008) Chemistry with [^{18}F]fluoride ion. *Eur. J. Org. Chem.*, 2853–2873.

(3) Wester, H. J., and Schottelius, M. (2007) The Driving Force in Molecular Imaging, In *PET Chemistry* (Schubiger, P. A., Lehmann, L., and Friebe, M., Eds.) pp79–111, Chapter 4, Springer-Verlag, Berlin.

(4) Smith, G. E., Sladen, H. L., Biagini, C. G., and Blower, P. J. (2011) Inorganic approaches for radiolabelling biomolecules with fluorine-18 for imaging with positron emission tomography. *Dalton Trans. 40*, 6196–6205.

(5) Vaidyanathan, G., and Zalutsky, M. R. (1992) Labeling proteins with fluorine-18 using N-succinimidyl 4-[^{18}F]fluorobenzoate. *Nucl. Med. Biol. 19*, 275–281.

(6) Vaidyanathan, G., and Zalutsky, M. R. (1994) Improved synthesis of N-succinimidyl 4-[^{18}F]fluorobenzoate and its application to the labeling of a monoclonal antibody fragment. *Bioconjugate Chem. 5*, 352–356.

(7) Wester, H. J., Hamacher, K., and Stöcklin, G. (1996) A comparative study of n.c.a. fluorine-18 labeling of proteins via acylation and photochemical conjugation. *Nucl. Med. Biol. 23*, 365–372.

(8) Toretsky, J., Levenson, A., Weinberg, I. N., Tait, J. F., Üren, A., and Mease, R. C. (2004) Preparation of F-18 labeled annexin V: a potential PET radiopharmaceutical for imaging cell death. *Nucl. Med. Biol. 31*, 747–752.

(9) Wüst, F., Hultsch, C., Bergmann, R., Johanssen, B., and Henle, T. (2003) Radiolabelling of isopeptide N$^{\epsilon}$-(γ-glutamyl)-L-lysine by

conjugation with N-succinimidyl-4-[^{18}F]fluorobenzoate. *Appl. Radiat. Isot. 59*, 43−48.
(10) Tang, G., Tang, X., and Wang, X. (2010) A facile automated synthesis of N-succinimidyl 4-[^{18}F]fluorobenzoate ([^{18}F]SFB) for ^{18}F-labeled cell-penetrating peptide as PET tracer. *J. Labelled Compd. Radiopharm. 53*, 543−547.
(11) Rosenthal, M. S., Bosch, A. L., Nickles, R. J., and Gatley, S. J. (1985) Synthesis and some characteristics of no-carrier added [^{18}F]fluorotrimethylsilane. *Int. J. Appl. Radiat. Isot. 36*, 318−319.
(12) Schirrmacher, R., Bradtmöller, G., Schirrmacher, E., Thews, O., Tillmanns, J., Siessmeier, T., Buchholz, H. G., Bartenstein, P., Wängler, B., Niemeyer, C. M., and Jurkschat, K. (2006) ^{18}F-labelling of peptides by means of an organosilicon-based fluoride acceptor. *Angew. Chem., Int. Ed. 45*, 6047−6050.
(13) Schirrmacher, E., Wängler, B., Cypryk, M., Bradtmöller, G., Schäfer, M., Eisenhut, M., Jurkschat, K., and Schirrmacher, R. (2007) Synthesis of p-(tBu_2[^{18}F]FSi)C_6H_4C(O)H) with high specific activity by isotopic exchange: a convenient labeling synthon for the ^{18}F-labeling of N-aminooxy derivatized peptides. *Bioconjugate Chem 18*, 2085−2089.
(14) Wängler, B., Quandt, G., Iovkova, L., Schirrmacher, E., Wängler, C., Boening, G., Hacker, M., Schmoeckel, M., Jurkschat, K., Bartenstein, P., and Schirrmacher, R. (2009) Kit-like ^{18}F-labeling of proteins: synthesis of 4-(di-tert-butyl[^{18}F]fluorosilyl)benzenethiol (Si[^{18}F]FA-SH) labeled rat serum albumin for blood pool imaging with PET. *Bioconjugate Chem. 20*, 317−321.
(15) Iovkova, L., Wängler, B., Schirrmacher, E., Schirrmacher, R., Quandt, G., Boening, G., Schürmann, M., and Jurkschat, K. (2009) para-Functionalized aryl-di-tert-butylfluorosilanes as potential labeling synthons for ^{18}F-radiopharmaceuticals. *Chem.—Eur. J. 15*, 2140−2147.
(16) Tietze, L. F., and Schmuck, K. (2011) SiFA azide: A new building block for PET imaging using click chemistry. *Synlett*, 1697−1700.
(17) Hohne, A., Yu, L., Mu, L., Reiher, M., Voigtmann, U., Klar, U., Graham, K., Schubiger, P. A., and Ametamey, S. M. (2009) Organo-fluorosilanes as model compounds for ^{18}F-labeled silicon-based PET tracers and their hydrolytic stability: experimental data and theoretical calculations. *Chem.—Eur. J. 15*, 3736−3743.
(18) Mu, L., Hohne, A., Schubiger, P. A., Ametamey, S. M., Graham, K., Cyr, J. E., Dinkelborg, L., Stellfeld, T., Srinivasan, A., Voigtmann, U., and Klar, U. (2008) Silicon based building blocks for one-step 18F-radiolabeling of peptides for PET imaging. *Angew. Chem., Int. Ed. 47*, 4922−4925.
(19) Hohne, A., Mu, L., Honer, M., Schubiger, P. A., Ametamey, S. M., Graham, K., Stellfeld, T., Borkowski, S., Berndorff, D., Klar, U., Voigtmann, U., Cyr, J. E., Friebe, M., Dinkelborg, L., and Srinivasan, A. (2008) Synthesis, ^{18}F-labeling, and in vitro and in vivo studies of bombesin peptides modified with silicon-based building blocks. *Bioconjugate Chem. 19*, 1871−1879.
(20) Schulz, J., Vimont, D., Bordenave, T., James, D., Escudier, J.-M., Allard, M., Szlosek-Pinaud, M., and Fouquet, E. (2011) Silicon-based chemistry: An original and efficient one-step approach to [^{18}F]-nucleosides and [^{18}F]-oligonucleotides for PET imaging. *Chem.—Eur. J. 17*, 3096−3100.
(21) Studenov, A. R., Adam, M. J., Wilson, J. S., and Ruth, T. J. (2005) New radiolabelling chemistry: synthesis of phosphorus-[^{18}F] fluorine compounds. *J. Labelled Compd. Radiopharm 48*, 497−500.
(22) Ting, R., Adam, M. J., Ruth, T. J., and Perrin, D. M. (2005) Arylfluoroborates and alkylfluorosilicates as potential PET imaging agents: high-yielding aqueous bimolecular ^{18}F-labeling. *J. Am. Chem. Soc. 127*, 13094−13095.
(23) Ting, R., Harwig, C., auf dem Keller, U., McCormick, S., Austin, P., Overall, C. M., Adam, M. J., Ruth, T. J., and Perrin, D. M. (2008) Toward [^{18}F]-labeled aryltrifluoroborate radiotracers: in vivo positron emission tomography imaging of stable arylfluoroborate clearance in mice. *J. Am. Chem. Soc. 130*, 12045−12055.
(24) auf dem Keller, U., Bellac, C. L., Li, Y., Lou, Y., Lange, P. F., Ting, R., Harwig, C., Kappelhoff, R., Dedhar, S., Adam, M. J., Ruth, T. J., Bénard, F., Perrin, D. M., and Overall, C. M. (2010) Novel matrix metalloproteinase inhibitor [^{18}F]marimastat-arylfluoroborate as a probe for in vivo positron emission tomography imaging cancer. *Cancer Res. 70*, 7562−7569.
(25) McBride, W. J., Sharkey, R. M., Karacay, H., D'Souza, C. A., Rossi, E. A., Laverman, P., Chang, C.-S., Boerman, O. C., and Goldenberg, D. M. (2009) A novel method of ^{18}F radiolabeling for PET. *J. Nucl. Med. 50*, 991−998.
(26) Laverman, P., McBride, W. J., Sharkey, R. M., Eek, A., Joosten, L., Oyen, W. J. G., Goldberg, D. M., and Boerman, O. (2010) A novel facile method of labeling octreotide with ^{18}F-fluorine. *J. Nucl. Med. 51*, 454−460.
(27) McBride, W. J., D'Souza, C. A., Sharkey, R. M., Karacay, H., Rossi, E. A., Chang, C.-S., and Goldenberg, D. M. (2010) Improved ^{18}F labeling of peptides with a fluoride-aluminium-chelate complex. *Bioconjugate Chem 21*, 1331−1340.
(28) Rosa-Neto, P., Wängler, B., Iovkova, L., Boening, G., Reader, A., Jurkschat, K., and Schirrmacher, E. (2009) [^{18}F]SiFA-isothiocyanate: a highly new efficient radioactive labeling agent for lysine-containing peptides. *ChemBioChem 10*, 1321−1324.
(29) Wessmann, S., Henriksen, G., Wester, H. J. (2011) Cryptate mediated nucleophilic ^{18}F-fluorination without azeotropic drying. *J. Nucl. Med. 52* (Supplement): 76 (abstract) , Wessmann, S., Henriksen, G., Wester, H. J. (2011) Cryptate mediated nucleophilic ^{18}F-fluorination without azeotropic drying. *Nuklearmedizin 50* [Online Early Access]
(30) Lemaire, C. F., Aerts, J. J., Voccia, S., Libert, L. C., Mercier, F., Goblet, D., Plenevaux, A. R., and Luxen, A. J. (2010) Fast production of highly reactive no-carrier-added [^{18}F]fluoride for labeling of radiopharmaceuticals. *Angew. Chem., Int. Ed. 49*, 3161−3164.
(31) Glaser, M., Árstad, E., Luthra, S. K., and Robins, E. G. (2009) Two-step radiosynthesis of [^{18}F]N-succinimidyl-4-fluorobenzoate ([^{18}F]SFB). *J. Labelled Compd. Radiopharm. 52*, 327−330.
(32) Ueberberg, S., Meier, J. J., Wängler, C., Schechinger, W., Dietrich, J. W., Tannapfel, A., Schmitz, I., Schirrmacher, R., Koeller, M., Klein, H. H., and Schneider, S. (2009) Generation of novel single-chain antibodies by phage-display technology to direct imaging agents highly selective to pancreatic β- or α-cells in vivo. *Diabetes 58*, 2324−2334.
(33) Olberg, D. E., Arukwe, J. M., Grace, D., Hjelstuen, O. K., Solbakken, M., Kindberg, G. M., and Cuthbertson, A. (2010) One step radiosynthesis of 6-[^{18}F]fluoronicotinic acid 2,3,5,6-tetrafluorophenyl ester ([^{18}F]F-Py-TFP): A new prosthetic group for efficient labeling of biomolecules with fluorine-18. *J. Med. Chem. 53*, 1732−1740.
(34) Kostikov, A. P., Iovkova, L., Chin, J., Schirrmacher, E., Wängler, B., Wängler, C., Jurkschat, K., Cosa, G., and Schirrmacher, R. (2011) A novel lead compound for the development of hydrophilic SiFA-based prosthetic groups for ^{18}F-labeling. *J. Fluor. Chem. 132*, 27−34.
(35) Nikula, T. K., Bocchia, M., Curcio, M. J., Sgouros, G., Ma, Y., Finn, R. D., and Scheinberg, D. A. (1995) Impact of high tyrosine fraction in complementary determining regions: measured and predicted effects of radioiodination on IgG immunoreactivity. *Mol. Immunol. 32*, 865−872.
(36) Wängler, C., Moldenhauer, G., Eisenhut, M., Haberkorn, U., and Mier, W. (2008) Antibody-dendrimer conjugates: the number, not the size of the dendrimers, determines the immunoreactivity. *Bioconjugate Chem. 19*, 813−820.

Bioconjugate Chemistry

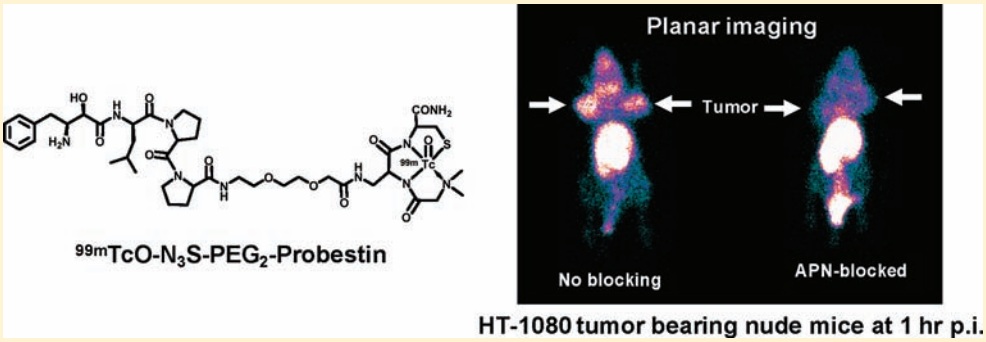
Article

pubs.acs.org/bc

Synthesis and Evaluation of Novel Tc-99m Labeled Probestin Conjugates for Imaging APN/CD13 Expression In Vivo

Gopal Pathuri,[†] Andria F. Hedrick,[†] Bryan C. Disch,[†] John T. Doan,[§] Michael A. Ihnat,[†,‡] Vibhudutta Awasthi,[†] and Hariprasad Gali*[,†,‡]

[†]Department of Pharmaceutical Sciences, College of Pharmacy, [§]Department of Radiological Sciences, Division of Nuclear Medicine, College of Medicine, and [‡]Experimental Therapeutics Program, Peggy and Charles Stephenson Oklahoma Cancer Center, The University of Oklahoma Health Sciences Center, Oklahoma City, Oklahoma 73117, United States



ABSTRACT: The enzyme aminopeptidase N (APN, also known as CD13) is known to play an important role in tumor proliferation, attachment, angiogenesis, and tumor invasion. In this study, we hypothesized that a radiolabeled high affinity APN inhibitor could be potentially useful for imaging APN expression in vivo. Here, we report synthesis, radiolabeling, and biological evaluation of new probestin conjugates containing a tripeptide, *N,N*-dimethylglycyl-L-lysinyl-L-cysteinylamide (N_3S), chelator. New probestin conjugates were synthesized by solid-phase peptide synthesis method, purified by reversed-phase HPLC, and characterized by electrospray mass spectrometry. The conjugates were complexed with Re(V) and ^{99m}Tc(V) by transmetalation using corresponding Re(V) or ^{99m}Tc(V) gluconate synthon. The mass spectral analyses of ReO-N_3S-Probestin conjugates were consistent with the formation of neutral Re(V)O−N_3S complexes. Initial biological activity of ReO-N_3S-Probestin conjugates determined by performing an *in vitro* APN enzyme assay using intact HT-1080 cells demonstrated higher inhibition of APN enzyme activity than bestatin. *In vivo* biodistribution and whole body planar imaging studies of ^{99m}TcO-N_3S-PEG$_2$-Probestin performed in nude mice xenografted with human fibrosarcoma tumors derived from HT-1080 cells demonstrated a tumor uptake value of 2.88 ± 0.64%ID/g with tumor-to-blood and tumor-to-muscle ratios of 4.8 and 5.3, respectively, at 1 h postinjection (p.i.). Tumors were clearly visible in whole body planar image obtained at 1 h p.i., but not when the APN was competitively blocked with a coinjection of excess nonradioactive ReO-N_3S-PEG$_2$-Probestin conjugate. These results demonstrate the feasibility of using high affinity APN inhibitor conjugates as targeting vectors for *in vivo* targeting of APN.

INTRODUCTION

Aminopeptidase N (APN, EC 3.4.11.2) is a zinc-dependent membrane-bound exopeptidase that catalyzes the removal of N-terminal amino acids from peptides.[1,2] It is expressed by many tissues, particularly the brush border membrane of the small intestine, the proximal renal tubules, synaptic membranes in the central nervous system, and monocytes and granulocytes.[1−5] Look et al. reported that human myeloid plasma membrane glycoprotein CD13 is identical to APN.[1] High levels of APN/CD13 expression have been detected in various solid tumors.[4,6−10] APN/CD13 is shown to play an active role in degradation and invasion of extracellular matrix by metastatic tumor cells.[11,12] Pasqualini et al. have shown that APN/CD13 is specifically expressed on the endothelium of tumor angiogenic, but not normal, vasculature.[13] APN inhibitors, such as inhibitory antibodies and bestatin (ubenimex), suppressed angiogenesis and tumor growth.[13] Bhagwat et al. have shown that endogenous APN/CD13 levels in primary cells and cell lines are up-regulated in response to hypoxia, angiogenic growth factors, and signals regulating capillary tube formation during angiogenesis.[14] APN inhibitors interfered with tube formation but not proliferation of primary vascular endothelial cells, suggesting that APN/CD13 functions in the control of endothelial cell morphogenesis.[14] The association of APN/CD13 with the growth of different human cancers suggested it as a suitable target for anticancer therapy. Thus, several new diagnostic and therapeutic constructs directed toward APN/CD13 have been developed.[13,15−27] These

Received: October 7, 2011
Revised: December 8, 2011
Published: December 11, 2011

 © 2011 American Chemical Society

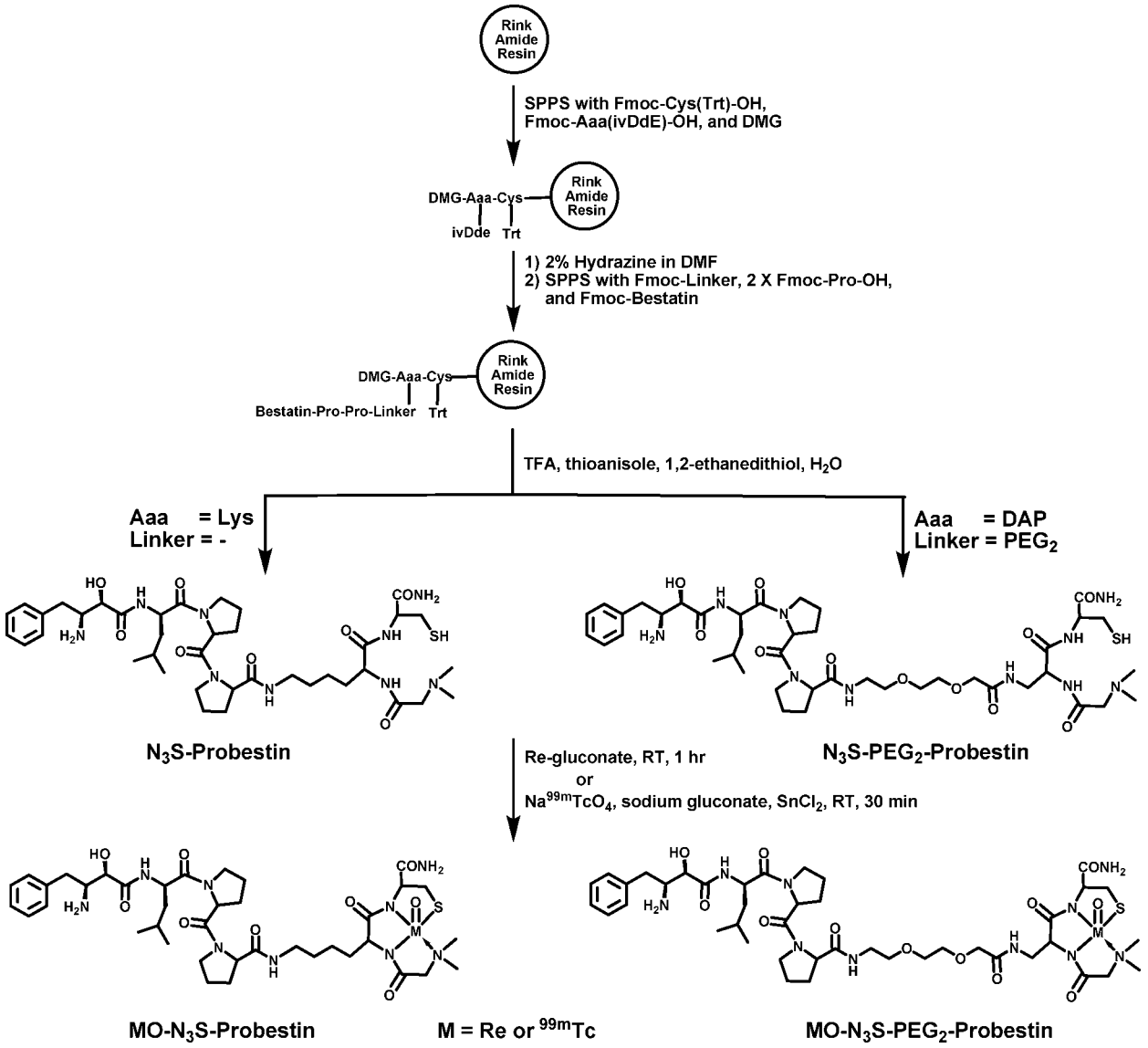


Figure 1. Synthesis and complexation of N_3S-Probestin conjugates with $[Re/^{99m}Tc(V)O]^{3+}$-core.

constructs utilized a cyclic CNGRC peptide known to bind APN/CD13.[13]

Recent studies have shown that asparagine-glycine-arginine (NGR) motif can rapidly convert to isoaspartate-glycine-arginine (*iso*DGR) by asparagine deamidation, generating $\alpha_v\beta_3$ ligands capable of affecting endothelial cell functions and tumor growth.[28−32] Biochemical, NMR structure analysis, and $\alpha_v\beta_3$ docking studies showed that *iso*DGR, but not NGR and DGR, can fit into the RGD-binding pocket of $\alpha_v\beta_3$ integrin, not only recapitulating the canonical RGD/$\alpha_v\beta_3$ contacts, but also establishing additional polar interactions.[28,30] However, it is unclear whether cyclic CNGRC peptide based constructs reported so far were binding APN/CD13 or $\alpha_v\beta_3$ integrin under tested in vivo conditions. Our recent in vivo blocking studies using a ^{99m}Tc-labeled cyclic C*iso*DGRC conjugate demonstrated selective binding to the tumors and other tissues expressing $\alpha_v\beta_3$-integrin.[33] Furthermore, cyclic CNGRC peptide is shown to have moderate binding affinity to APN as evidenced by enzyme inhibition studies.[34]

We hypothesized that a radiolabeled high affinity APN inhibitor could be potentially useful for imaging APN expression in vivo. We designed and evaluated two novel probestin conjugates to examine our hypothesis. Probestin is a high affinity inhibitor of APN.[35] Here, we report synthesis, radiolabeling, and biological evaluation of the new probestin conjugates containing a tripeptide, *N,N*-dimethylglycyl-L-lysinyl-L-cysteinylamide (N_3S), chelator.

MATERIALS AND METHODS

General. All chemicals obtained commercially were used without further purification. Bestatin was obtained from Acros Organics (Geel, Belgium). Fmoc-bestatin was synthesized as previously reported.[36] Rink amide MBHA resin (100−200 mesh, 0.3−0.8 mmol/g) and Fmoc-LYS(ivDde)-OH were obtained from EMD Chemicals Inc. (Gibbstown, NJ). Fmoc-8-amino-3,6-dioxaoctanoic acid (PEG_2) was obtained from Peptides International Inc. (Louisville, KY). Fmoc-DAP-(ivDde)-OH was obtained from Bachem Americas, Inc. (Torrance, CA). Other Fmoc-protected amino acids and coupling agents were obtained from Advanced ChemTech (Louisville, KY). Chemicals used for peptide cleavage were obtained from Sigma-Aldrich (St. Louis, MO). BDH brand

dx.doi.org/10.1021/bc200546b | *Bioconjugate Chem.* 2012, 23, 115−124

ACS grade solvents were obtained from VWR International, LLC (Radnor, PA). $Na^{99m}TcO_4$ was obtained from the University of Oklahoma Nuclear Pharmacy. Human fibrosarcoma HT-1080 cells were obtained from American Type Culture Collection (Manassas, VA). The cells were cultured in ATCC-formulated Eagle's Minimum Essential Medium supplemented with 10% fetal calf serum (Invitrogen Corporation, Carlsbad, CA) and 1% Pen Strep (Invitrogen Corporation, Carlsbad, CA) containing 10 000 units of penicillin and 10 000 μg of streptomycin per mL. Cells were grown routinely in a monolayer culture at 37 °C in a 5% CO_2 humidified air atmosphere. Eight-week-old female athymic nude NU/J mice (Homozygous for *Foxn1*^{nu}) were purchased from the Jackson Laboratory (Bar Harbor, ME). Electrospray mass spectral analysis was performed by the University of Oklahoma Health Sciences Center (OUHSC) Molecular Biology-Proteomics Facility. The small animal SPECT imaging was conducted in the OU College of Pharmacy Research Imaging Facility using a two-detector NanoSPECT In Vivo Preclinical Imager (Bioscan, Inc., Washington, DC, USA). All animal studies were conducted in accordance with the protocols approved by the OUHSC institutional animal care and use committee.

Reversed-phase HPLC analyses of N_3S-Probestin conjugates and their Re(V)/^{99m}Tc(V) complexes were performed on a Beckman System Gold HPLC equipped with a Beckman model 126 pump, 166 absorption detector, and a Bioscan model B-FC-300 radioactivity detector. HPLC solvents consisted of water containing 0.1% trifluoroacetic acid (solvent A) and acetonitrile containing 0.1% trifluoroacetic acid (solvent B). A Sonoma C_{18} (ES Industries, 10 μm, 100 Å, 4.6 × 250 mm) column was used with a flow rate of 1.5 mL/min. The HPLC gradient system began with an initial solvent composition of 95% A and 5% B for 2 min followed by a linear gradient to 50% A and 50% B in 15 min, after which the column was reequilibrated. The absorption detector was set at 254 nm.

Solid-Phase Peptide Synthesis (SPPS). SPPS was performed manually using conventional Fmoc chemistry. Standard side chain protecting groups were utilized and the peptide was assembled on Rink amide resin (0.05 mmol) using HBTU-mediated coupling as shown in Figure 1. Amino acid coupling was achieved by treating the resin with Fmoc-protected amino acid (3.3 equiv) in DMF (500 μL), HBTU (3.3 equiv) in DMF (500 μL), HOBt (3.3 equiv) in DMF (250 μL), and DIPEA (6.6 equiv) in DMF (250 μL) for 60 min at room temperature followed by five washes with DMF (1 mL). The Fmoc deprotection was achieved by treating the resin with 20% piperidine in DMF (2 mL) for 1 × 10 min and 1 × 20 min at room temperature followed by five washes with DMF (1 mL). Orthogonally protected Lys, Fmoc-Lys(ivDde)-OH, or Fmoc-DAP(ivDde)-OH was used to obtain the tripeptide chelator sequence (DMG-Lys-Cys or DMG-DAP-Cys). The ivDde group was selectively deprotected by treating the resin with 2% hydrazine in DMF (2 mL) for 1 × 10 min and 1 × 20 min at room temperature followed by five washes with DMF (1 mL). Finally, the resin was washed five times with DMF (1 mL) followed by dichloromethane (1 mL), and dried for 30 min by nitrogen purging. The peptide was cleaved from the resin and the side chains were deprotected by treating the resin with a cocktail (1 mL) containing trifluoroacetic acid, water, ethanedithiol, and thioanisol in a ratio of 90:2.5:2.5:5 for 2 h at room temperature. The crude peptide was isolated by precipitation in ice cold methyl-*t*-butyl ether, purified by HPLC, and dried on a rotary evaporator under vacuum. After drying, the peptide was dissolved in 0.1 M ascorbic acid (2 mg/mL) and aliquots of 50 μL were dispensed into 1.5 mL microcentrifuge tubes and dried using SpeedVac centrifugation. The tubes containing N_3S-Probestin conjugate (~100 μg) and ascorbic acid (~880 μg) were stored at −20 °C and used for radiolabeling with Tc-99m. The N_3S-Probestin conjugates were characterized by electrospray mass spectrometry.

Re(V) Complexation. Re complexation of N_3S-Probestin conjugates was achieved by transmetalation from Re(V)-gluconate prepared as previously described.[37] Briefly, a stock solution of Re(V)-gluconate was freshly prepared by mixing a nitrogen-purged (5 min) solution of $SnCl_2$ (32 mg) in 0.1 M HCl (200 μL) with a nitrogen-purged (10 min) solution of ammonium perrhenate (45.5 mg) in 0.5 M sodium gluconate (2.5 mL) and incubated at RT for over 1 h until the solution is turned to deep blue color. For complexation, an aliquot of Re(V)-gluconate stock solution (100 μL) and 0.5 M sodium gluconate (400 μL) were added to N_3S-Probestin conjugate (5 mg), vortexed for 30 s, and incubated at RT for 1 h. The ReO-N_3S-Probestin conjugate was then purified by HPLC and analyzed by electrospray mass spectrometry. The ReO-N_3S-Probestin conjugates were obtained in >85% yield after HPLC purification.

Tc-99m Labeling. The N_3S-Probestin was labeled with ^{99m}Tc by transmetalation from ^{99m}Tc(V)-gluconate.[38] Briefly, a stannous gluconate stock solution was prepared by mixing $SnCl_2$ (2 mg) in nitrogen-purged (10 min) 0.5 M sodium gluconate (1 mL). A diluted stock solution was prepared by mixing the previous stock solution (20 μL) with nitrogen-purged (10 min) 0.5 M sodium gluconate (400 μL). For labeling, an aliquot of water (100 μL), an aliquot of the diluted stannous gluconate stock solution (20 μL), and an isotonic saline solution of $^{99m}TcO_4^-$ (500 μL, ~370 MBq) were added to a 1.5 mL microcentrifuge tube containing N_3S-Probestin (100 μg). The tube was vortexed for 30 s and incubated at RT for 30 min. The ^{99m}TcO-N_3S-Probestin was purified by HPLC. The pure fraction was collected into 0.2 M sodium phosphate at pH 8 (200 μL). The HPLC collected fraction was concentrated to ~200 μL by purging with nitrogen at 75 °C. The ^{99m}TcO-N_3S-Probestin conjugates were obtained in 50–60% radiochemical yield with >98% radiochemical purity after HPLC purification. The specific activity of the final product was not determined since the unlabeled N_3S-Probestin conjugate was efficiently separated from the product by HPLC. The ^{99m}TcO-N_3S-Probestin conjugates were characterized by comparing their HPLC retention time with corresponding Re(V) conjugates.

APN Enzyme Activity. Cell surface APN activity of intact cells was measured by a spectrophotometric assay as previously described using alanine *p*-nitroanilide (Ala-*p*NA) as a substrate for APN.[39] Assays were performed with intact confluent cell monolayers, grown in 96 well plates by plating about 5 × 10^4 cells/well. Cells were allowed to grow for 24 h followed by washing three times with PBS50. Cells were incubated with increasing concentrations (top dose of 1 mM) of bestatin or ReO-N_3S-Probestin conjugate in PBS50 (100 μL) and 2 mM Ala-*p*NA in PBS50 (100 μL) at RT for 30 min. The amount of *p*-nitroaniline formed was measured spectrophotometrically at 405 nm by ELx800 Absorbance Microplate Reader (BioTek Instruments, Inc., Winooski, VT). Assays were run in triplicate, and cell-free and substrate-free blanks were run in parallel. EC_{50} values were calculated using *GraphPad Prism 5* using nonlinear

regression (sigmoidal dose−response relation variable slope) analysis (GraphPad Software, La Jolla, CA).

HT-1080 Tumor-Bearing Nude Mice. The mice were housed five animals per cage in sterile micro isolator cages in a temperature- and humidity-controlled room with a 12 h light/12 h dark schedule. The animals were fed autoclaved rodent chow (Ralston Purina Company, St. Louis, MO) and water ad libitum. Animals were housed for an acclimation period of one week prior to inoculation of tumor cells. The mice were anesthetized with 2% isoflurane (Baxter Healthcare Corp., Deerfield, IL) in oxygen at 2 L/min through a nonrebreathing anesthesia vaporizer.

Human fibrosarcoma xenografts were induced by subcutaneous injection of approximately 6.6×10^6 HT-1080 cells in a suspension of 50 μL sterile normal saline per injection site bilaterally into the subscapular region of mice. Two to three weeks after inoculation of the tumor cells, when the tumors reached 0.5−1 cm in diameter, the mice were recruited for biodistribution and SPECT imaging studies.

Biodistribution Studies. Four HT-1080 tumor-bearing nude mice (22−24 g) were anesthetized with 2% isoflurane in oxygen at 2 L/min and injected with a dose of ^{99m}TcO-N_3S-PEG$_2$-Probestin (1.28 MBq) in 50 μL 0.2 M PBS (pH 8) through the tail vein. The mice were euthanized and tissues/organs were excised at 1 h postinjection (p.i.). The tissues/organs were washed with normal saline, dried by blotting on a tissue paper, and transferred to preweighed tubes. The tubes were weighed and radioactivity associated with each tissue was recorded on a Packard Cobra II automated gamma counter. Undiluted standard dose (8 μL) was counted along with the samples. All the data were corrected for ^{99m}Tc-decay. The percent injected dose (%ID) and percent injected dose per gram of tissue (%ID/g) for each tissue/organ was calculated. The total blood and muscle were estimated as 5.7% and 40% of the total body weight, respectively. The weight of stomach and intestines included their contents.

Planar Imaging. HT-1080 tumor-bearing nude mice were anesthetized using 2% isoflurane in oxygen at 2 L/min, in a polypropylene induction chamber. When fully anesthetized, a dose of ^{99m}TcO-N_3S-PEG$_2$-Probestin (18.5 MBq) in 60 μL 0.2 M PBS (pH 8) was injected through the tail vein. For the blocking experiment, a dose of ^{99m}TcO-N_3S-PEG$_2$-Probestin (24 MBq) in 70 μL 0.2 M PBS (pH 8) along with 1 mg of ReO-N_3S-PEG$_2$-Probestin was injected. The mice were sacrificed at 1 h p.i. and imaged in prone position using a parallel-hole collimator of the NanoSPECT camera. Static planar images with a frame size of 512 × 512 were acquired for 10 min. Planar images were visualized using *InVivoScope* (Bioscan, Washington, DC) software package.

SPECT Imaging. HT-1080 tumor-bearing nude mice were anesthetized using 2% isoflurane in oxygen at 2 L/min, in a polypropylene induction chamber. When fully anesthetized, a dose of ^{99m}TcO-N_3S-PEG$_2$-Probestin (25.2 MBq) in 70 μL 0.2 M PBS (pH 8) was injected through the tail vein. One mouse was sacrificed at 30 min and the other at 3 h p.i. The mouse was placed on the mouse bed of the NanoSPECT camera and the SPECT imaging data were acquired in a helical scanning mode with 20 projections with an acquisition time of 60 s per projection. Raw SPECT data were reconstructed using *HiSPECT* (Bioscan, Washington, DC) software package. Reconstructed SPECT data were visualized using *InVivoScope* (Bioscan, Washington, DC) software package.

RESULTS AND DISCUSSION

It is now widely accepted that angiogenesis is the rate-limiting step for the growth of solid tumors.[40−43] Anti-angiogenesis therapy is currently being investigated around the world using recombinant antiangiogenic proteins, monoclonal antibodies, and various drugs.[44] These anti-angiogenesis therapies have led to an increased interest in imaging as a means of monitoring therapeutic effect.[45,46] Tumor angiogenesis imaging is intensively studied by targeting molecular markers of angiogenesis such as receptors, enzymes, integrins, or extracellular matrix proteins. One of the most promising targets in this respect is integrin $\alpha_v\beta_3$, which has been successfully studied in patients and healthy volunteers by single photon emission computed tomography (SPECT) and positron emission tomography (PET) using Tc-99m and F-18 labeled RGD peptide conjugates.[47−50]

APN/CD13 is another potential target that could be exploited for imaging tumor angiogenesis. However, currently there is no targeting vector available for imaging APN/CD13 expression by using nuclear imaging techniques. We are exploring the possibility of using radiolabeled high affinity APN inhibitor conjugates as vectors to target APN/CD13 in vivo. We synthesized two probestin conjugates containing a N_3S chelator to enable Tc-99m labeling. We attached the chelator at C-terminus of the probestin since N-terminus is involved in binding with the enzyme, which preferentially releases amino acids from the N-terminal end of small peptides.[2] The N_3S-Probestin conjugates were manually synthesized by SPPS method employing traditional fmoc chemistry and HBTU activation of carboxyl groups on the reactant with the N-terminal amino group on the growing peptide anchored *via* the C-terminus to the resin (Figure 1). We used orthogonally protected Lys or DAP (Fmoc-Lys-(ivDde)-OH or Fmoc-DAP(ivDde)-OH) as they allow us to build the tripeptide chelator sequence on the N-terminus of probestin. The 4-carbon side chain of the Lys residue acted as a spacer between the probestin and the chelator in N_3S-Probestin, whereas 8-amino-3,6-dioxaoctanoic acid (AEEA) acted as a linker between the probestin and the chelator in N_3S-PEG$_2$-Probestin. The ivDde group was selectively deprotected using 2% hydrazine in DMF. The N_3S-Probestin conjugates were obtained in an overall yield of 10−15% with >98% purity after HPLC purification. Mass spectral analyses were consistent with the molecular weights calculated for each conjugate (Table 1).

Table 1. HPLC and Mass Spectrometry Data

Peptide	HPLC Retention Time (min:sec)	Mass	
		Calcd	Obsd
N_3S-Probestin	13:00	817.5	818.4
ReO-N_3S-Probestin	14:14 (minor) 14:35	1017.4	1018.3
^{99m}TcO-N_3S-Probestin	14:54	-	-
N_3S-PEG$_2$-Probestin	11:50	920.5	921.5
ReO-N_3S-PEG$_2$-Probestin	13:37	1120.4	1121.4
^{99m}TcO-N_3S-PEG$_2$-Probestin	13:39	-	-

Tc-99m is a preferred radionuclide for SPECT due to its favorable nuclear properties (γ = 140.5 KeV, 89.1% abundance,

dx.doi.org/10.1021/bc200546b | *Bioconjugate Chem.* 2012, 23, 115−124

half-life 6.02 h), lower cost, well-established radiochemistry, and availability.[51−53] Tetradentate tripeptide chelators of the N_3S type are frequently employed in the development of receptor-avid peptide based T-99m radiopharmaceuticals. For example, clinically used Acutect (Tc-99m Apcitide) and Neotect (Tc-99m Depreotide) radiopharmaceuticals (currently discontinued) were based on peptide targeting vectors linked to a tripeptide N_3S chelator.[54,55] However, most tetradentate chelators containing a chiral carbon or an *N*-alkylated moiety produce diastereomers when a $[M(V)O]^{3+}$ (M = Tc, Re) core is bound to the donor groups in a square pyramidal coordination geometry as pendant groups are disposed in either *syn* or *anti* position relative to the M═O bond.[56−61] In our case, the tripeptide chelator sequence, DMG-Aaa-Cys (Aaa = Lys or DAP), is expected to form a neutral M(V)O−N_3S (M = ^{99m}Tc, Re) complex with the loss of three protons of the donor groups (the amide proton of Lys or DAP and the amide and thiol protons of Cys), while the tertiary amine of DMG is expected to coordinate to the $[M(V)O]^{3+}$ core through its lone pair of electrons and form a coordinate bond with the metal.

Cold Recomplexation was achieved by reacting N_3S-Probestin with an excess of Re(V)-gluconate synthon. Re conjugate was expected to present as two peaks on the HPLC chromatogram due to the formation of *syn* and *anti* conformations of Lys or DAP side chain with respect to the M═O bond. However, HPLC analysis of the reaction mixture revealed a broad peak indicative of formation of the diastereomers appearing as a merged single peak under our HPLC conditions (Figure 2). Mass spectral analyses of the Re conjugates were consistent with the formation of neutral Re(V)O−N_3S complexes (Table 1). ReO-N_3S-Probestin conjugates were obtained in 50−75% yield after HPLC purification.

Radiolabeling of N_3S-Probestin conjugates with Tc-99m was performed by transmetalation using ^{99m}Tc(V) gluconate synthon as previously described (Figure 1).[38] The HPLC retention times of ^{99m}Tc(V)-labeled probestin conjugates were matched to the corresponding cold Re(V) conjugates, which confirmed the formation of the radiolabeled product. The HPLC chromatograms in Figure 2 show the elution profiles of the N_3S-PEG_2-Probestin conjugate and its Re(V) and ^{99m}Tc(V) complexes. The figure also shows that both the Re- and Tc-99m conjugates were eluted at 14.3 min. The ^{99m}TcO-N_3S-PEG_2-Probestin conjugate eluted ∼1 min after the unlabeled N_3S-PEG_2-Probestin conjugate under our HPLC conditions enabling the collection of high specific activity, essentially carrier-free ^{99m}TcO-N_3S-PEG_2-Probestin. The radiochemical purity of the HPLC-purified product was found to be >98%.

Initial biological activity of ReO-N_3S-Probestin conjugates was determined by performing an in vitro APN enzyme assay using intact HT-1080 cells and Ala-*p*NA as APN substrate with EC_{50} values determined using nonlinear regression analysis. The results of the experiments (Figure 3) demonstrated higher inhibition of APN enzyme activity by ReO-N_3S-Probestin conjugates when compared to bestatin, a known slow-binding competitive inhibitor of APN.[62] The EC_{50} values were determined to be 979.2, 39.6, and 23.6 μM for bestatin, ReO-N_3S-Probestin, and ReO-N_3S-PEG_2-Probestin, respectively. Results obtained from these in vitro APN enzyme activity assay confirms that the attachment of a chelator at C-terminus of probestin does not affect its ability to bind the enzymatic active site of APN.

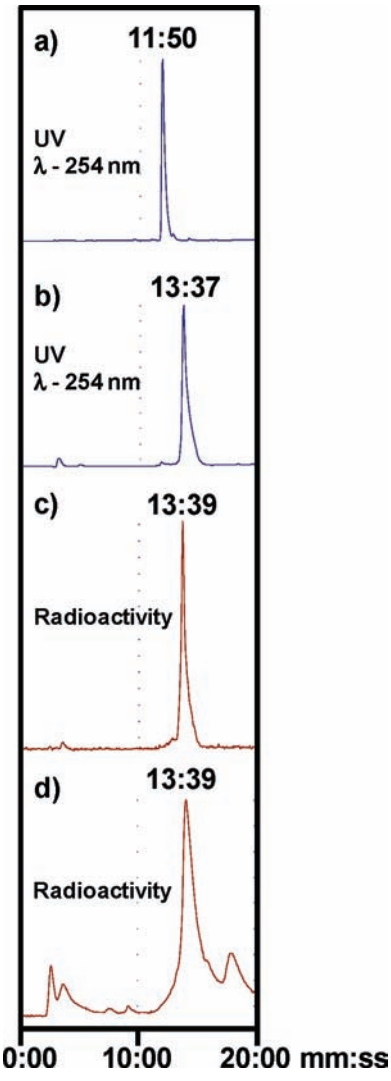


Figure 2. Radio-HPLC chromatograms of (a) N_3S-PEG_2-Probestin, (b) ReO-N_3S-PEG_2-Probestin, (c) ^{99m}TcO-N_3S-PEG_2-Probestin, and (d) mouse urine collected at 10 min p.i. of ^{99m}TcO-N_3S-PEG_2-Probestin.

In vivo biodistribution studies of ^{99m}TcO-N_3S-PEG_2-Probestin were performed in nude mice xenografted in their midflanks with human fibrosarcoma tumors derived from HT-1080 cells. The selection of ^{99m}TcO-N_3S-PEG_2-Probestin for in vivo evaluation was based on two reasons: (1) it demonstrated slightly better EC_{50} value than ^{99m}TcO-N_3S-Probestin, and (2) it was relatively more hydrophilic than ^{99m}TcO-N_3S-Probestin (HPLC retention times differ by >1 min, Table 1). In general, increasing hydrophilic character of a small peptide conjugate increases its clearance via renal−urinary pathway, which is preferable for the rapid clearance of background signals in images. Results obtained at 1 h p.i. are summarized in Table 2. A tumor uptake value of 2.88 ± 0.64%ID/g and a low residual radioactivity of 0.60 ± 0.33%ID/g in blood yielded tumor-to-blood and tumor-to-muscle ratios of approximately 4.8 and 5.3, respectively. These results indicate fast clearance of ^{99m}TcO-N_3S-PEG_2-Probestin from the bloodstream. High uptake values in kidney, liver, and intestine of 48.0 ± 3.4%ID/g, 12.0 ± 0.8% ID/g, and 4.8 ± 0.3%ID/g, respectively, indicate that ^{99m}TcO-N_3S-PEG_2-Probestin is eliminated from the body via renal and hepatobiliary clearance pathways. However, it is unclear from

dx.doi.org/10.1021/bc200546b | *Bioconjugate Chem.* 2012, 23, 115−124

	Bestatin	ReO-N_3S-Probestin	ReO-N_3S-PEG_2-Probestin
Hill Slope	-0.41	-0.38	-0.46
EC_{50} (μM)	979.2	41.4	23.6

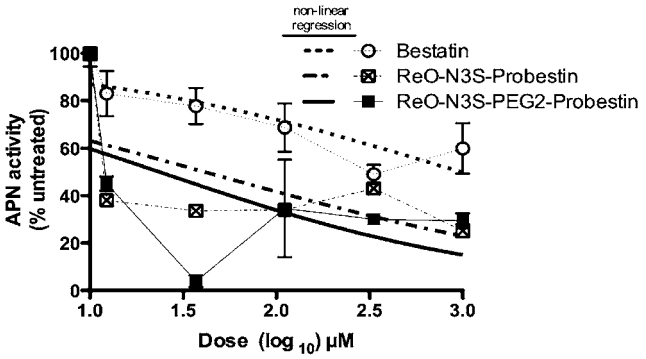


Figure 3. Enzyme activity of APN present on HT-1080 cells in the presence of increasing concentrations of bestatin or ReO-N_3S-Probestin conjugates. The enzyme activity was estimated by measuring the absorbance at 405 nm of *p*-nitroaniline formed by the hydrolysis of L-alanine-*p*-nitroanilide (substrate) at room temperature in 30 min. EC_{50} values were calculated by nonlinear regression (dose−response, variable slope) analysis using *GraphPad Prism*.

Table 2. Biodistribution of ^{99m}TcO-N_3S-PEG_2-Probestin in HT-1080 Tumor Bearing Nude Mice at 1 h p.i.[a]

Tissue	%ID/g of tissue	%ID/organ
Blood	0.60 ± 0.33	0.74 ± 0.41
Heart	1.18 ± 0.22	0.12 ± 0.02
Lung	0.91 ± 0.53	0.15 ± 0.02
Liver	12.0 ± 0.8	12.6 ± 1.1
Spleen	2.40 ± 0.45	0.28 ± 0.07
Stomach	1.28 ± 0.59	0.54 ± 0.19
Intestine	4.78 ± 0.33	10.8 ± 1.4
Kidney	48.0 ± 3.4	15.7 ± 2.2
Muscle	0.54 ± 0.25	4.69 ± 2.14
Tumor	2.88 ± 0.64	3.63 ± 2.29
Tumor/Blood	4.8	-
Tumor/Muscle	5.3	-

[a]Values are expressed as the mean ± SD; n = 4.

these results that the radioactivity uptake is due to normal metabolism of ^{99m}TcO-N_3S-PEG_2-Probestin or specific uptake by tissue-associated APN expression. It is known that APN is highly expressed on the renal proximal tubules, brush border membranes of the small intestine, and liver.[4,63]

Planar images of HT-1080 tumor-bearing nude mice injected with ^{99m}TcO-N_3S-PEG_2-Probestin alone or along with a large excess of ReO-N_3S-PEG_2-Probestin to block APN active sites obtained at 1 h p.i. are shown in Figure 4 and Figure 5a. The 1 h p.i. whole body planar image of the unblocked mouse demonstrates increased uptake in the tumor sites, thymus, kidneys, liver, and intestine in descending level of intensity relative to the background soft tissues (Figure 4). The 1 h p.i. whole body planar image of the APN-blocked mouse reveals no significant radiotracer uptake in the tumor sites, thymus, or kidneys (Figure 4). There is relatively increased radioactivity in the liver and intestine in the APN-blocked mouse compared to the unblocked mouse (Figure 5a). The negligible uptake of radioactivity in the tumor sites, thymus, and kidneys suggests adequate blockade of the APN in those tissue/organs, and the radioactivity uptake seen in the unblocked mouse is APN-specific. The relatively increased radioactivity in the liver and intestine is consistent with the increased radioactivity excretion via the hepatobiliary and GI tract in APN-blocked mouse. Secondary to the increased excretory activity in the hepatobiliary and GI tract, the APN blockade in the liver and intestinal lining is likely masked.

Early and delayed SPECT images of HT-1080 tumor-bearing mice injected with ^{99m}TcO-N_3S-PEG_2-Probestin (Figure 5b and c, respectively) were obtained at 30 min p.i. (early) and at 3 h p.i. (delayed). The early SPECT images, MIP and transverse views (Figure 5b), reveal intense radioactivity in the kidneys with significantly less radioactivity in the intestine. Intense radioactivity was also noted in the urinary bladder as radioactive urine is excreted from the kidneys into the urinary bladder. Delayed SPECT images, MIP and transverse views (Figure 5c), demonstrate background radioactivity in the kidneys with intensity level similar to that of blood radioactivity seen in the aorta. Unlike the observation made in the early SPECT images, the delayed SPECT images show intense radioactivity in the intestine compared to the radioactivity in the kidneys, which is essentially at background/blood level. Decreased radioactivity in the kidneys and tumor sites on delayed SPECT images relative to early SPECT images is suggestive of reversible binding of ^{99m}TcO-N_3S-PEG_2-Probestin to APN. Reversible binding is taken as binding of ^{99m}TcO-N_3S-PEG_2-Probestin to APN for a short time period (<3 h) and then detaching from APN as an intact molecule without any internalization. Although the reversible binding of ^{99m}TcO-N_3S-PEG_2-Probestin to APN may not be desirable for delayed imaging, it may be very useful for early phase imaging studies especially when used with short-lived radionuclides. Radioactivity seen in the urinary bladder on both SPECT MIP images (Figure 5b and c) demonstrates the presence of urinary excretion in addition to GI tract excretion of radioactivity, which confirms the results obtained from the biodistribution studies.

The HPLC analysis of urine samples collected during the imaging studies from HT-1080 tumor-bearing nude mice injected with ^{99m}TcO-N_3S-PEG_2-Probestin showed that the radiotracer is excreted intact (Figure 2). This result further suggests reversible binding of ^{99m}TcO-N_3S-PEG_2-Probestin to APN and that this agent is eliminated via glomerular filtration when released from APN sites in kidneys as it is a low-molecular-weight hydrophilic and neutral compound.

The ^{99m}TcO-N_3S-PEG_2-Probestin evaluated in this study is a first-generation conjugate. Further improvements in the structure of the conjugate may improve its tumor uptake and make it an attractive candidate for imaging APN expression in vivo. One strategy that has been successfully applied to improve tumor uptake of the radiolabeled cyclic RGD peptide conjugates is to have multiple RGD units in the conjugate.[64,65] Apparently, a multimeric preparation significantly enhances the binding affinity of the receptor−ligand interaction through the polyvalency effect.[64,66] Together with the choice of appropriate linker for desired pharmacokinetics, it may be possible to exploit multimerization approach for enhanced tumor uptake of the probestin motif via APN-targeting.

Due to high abdominal uptake, as seen with ^{99m}TcO-N_3S-PEG_2-Probestin, the potential application of APN-targeted radiotracers could be envisaged for imaging primary tumors that are outside of the abdomen. Particularly, when SPECT/CT is employed for anatomic localization, the separation of physiologic activity in the abdominal organs versus tumor activity could be possible. Thus, APN-targeted radiotracers may

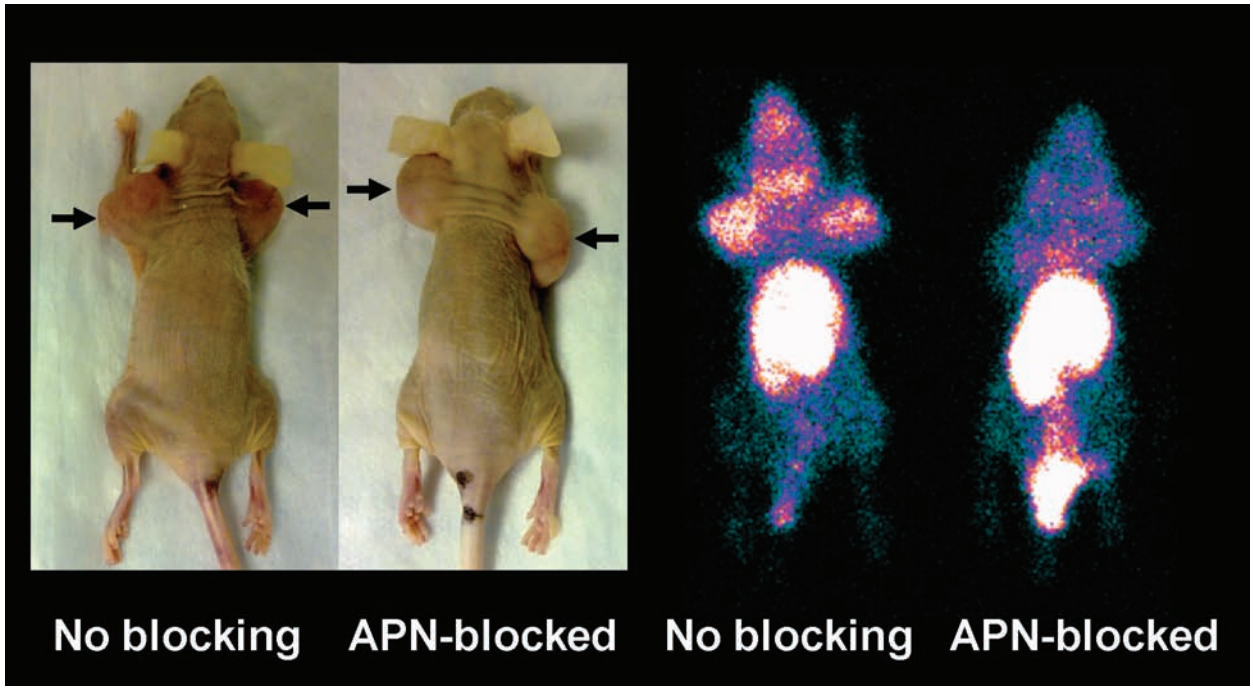


Figure 4. Photograph of the HT-1080 tumor-bearing nude mice used for imaging with ^{99m}TcO-N_3S-PEG_2-Probestin (arrows indicate tumor) and whole body planar images of the same mice at 1 h p.i. ReO-N_3S-PEG_2-Probestin (1 mg) was coinjected intravenously along with the ^{99m}TcO-N_3S-PEG_2-Probestin for blocking APN specific uptake of the radioactivity. Planar images were acquired in prone position.

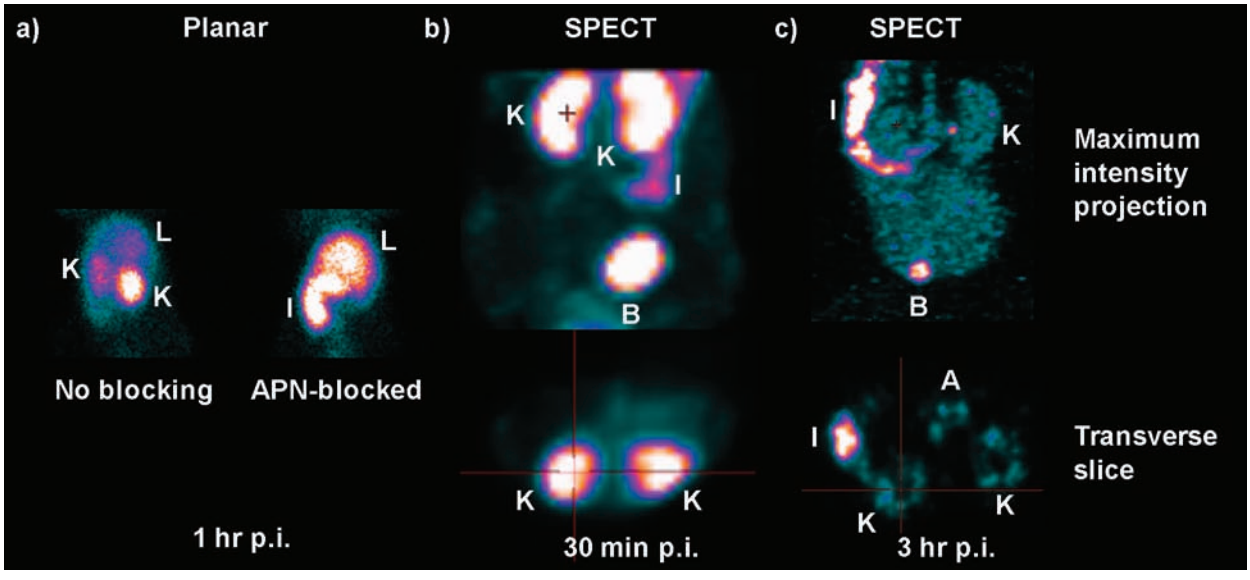


Figure 5. (a) Abdomen planar images of the HT-1080 tumor-bearing nude mice injected with ^{99m}TcO-N_3S-PEG_2-Probestin at 1 h p.i. ReO-N_3S-PEG_2-Probestin (1 mg) was coinjected intravenously along with the ^{99m}TcO-N_3S-PEG_2-Probestin for blocking APN specific uptake of the radioactivity. Planar images were acquired in prone position. (b) Early and (c) delayed abdomen SPECT images of a HT-1080 tumor-bearing nude mouse injected with ^{99m}TcO-N_3S-PEG_2-Probestin. Labels: K, kidney; L, Liver; I, Intestine; B, Bladder.

find potential application for imaging breast and lung tumor angiogenesis.

■ CONCLUSIONS

We have successfully synthesized and evaluated the first generation ^{99m}Tc-labeled probestin conjugates. The in vitro APN enzymatic studies performed in human fibrosarcoma HT-1080 cells showed that ReO-N_3S-Probestin conjugates are more effective inhibitors than bestatin. The in vivo biodistribution and imaging studies of ^{99m}TcO-N_3S-PEG_2-Probestin in nude mice xenografted with HT-1080 human fibrosarcoma tumors showed high radioactivity uptake in tumors coupled with rapid elimination of the radioactivity from the bloodstream via the renal and the hepatobiliary clearance pathways. The image findings collectively demonstrate the radiotracer uptake is APN-specific and suggests reversible binding of ^{99m}TcO-N_3S-PEG_2-Probestin to APN active sites, particularly in the kidneys. The results of these studies demonstrate the feasibility of using probestin as a vector for targeting APN in vivo and provide a foundation for the development of novel APN-targeted

dx.doi.org/10.1021/bc200546b | *Bioconjugate Chem.* 2012, 23, 115–124

radiotracers with a potential application in imaging tumor angiogenesis.

AUTHOR INFORMATION

Corresponding Author

*The University of Oklahoma College of Pharmacy, 1110 N. Stonewall Avenue, Room 301, Oklahoma City, OK 73117, USA. E-mail: hgali@ouhsc.edu. Phone: (405) 271-6593 Ext 47877. FAX: (405) 271-7505.

ACKNOWLEDGMENTS

This work was funded by the American Cancer Society IRG Seed Grant C5052202 and the OU College of Pharmacy Startup Grant. We acknowledge funding from the NIH grant S10RR025652 for the NanoSPECT system. We acknowledge the OU Nuclear Pharmacy for providing Tc-99m. We gratefully acknowledge the assistance of Dr. Vivek Yadav during tumor cell inoculation and Mr. Kaustav Sahoo for operating the NanoSPECT system.

REFERENCES

(1) Look, A. T., Ashmun, R. A., Shapiro, L. H., and Peiper, S. C. (1989) Human myeloid plasma membrane glycoprotein CD13 (gp150) is identical to aminopeptidase N. *J. Clin. Invest. 83*, 1299−307.

(2) Sjostrom, H., Noren, O., and Olsen, J. (2000) Structure and function of aminopeptidase N. *Adv. Exp. Med. Biol. 477*, 25−34.

(3) Shipp, M., and Look, A. (1993) Hematopoietic differentiation antigens that are membrane-associated enzymes: cutting is the key! *Blood 82*, 1052−1070.

(4) Dixon, J., Kaklamanis, L., Turley, H., Hickson, I. D., Leek, R. D., Harris, A. L., and Gatter, K. C. (1994) Expression of aminopeptidase-n (CD 13) in normal tissues and malignant neoplasms of epithelial and lymphoid origin. *J. Clin. Pathol. 47*, 43−47.

(5) Kenny, A. J., and Maroux, S. (1982) Topology of microvillar membrance hydrolases of kidney and intestine. *Physiol. Rev. 62*, 91−128.

(6) Tokuhara, T., Hattori, N., Ishida, H., Hirai, T., Higashiyama, M., Kodama, K., and Miyake, M. (2006) Clinical significance of aminopeptidase N in non-small cell lung cancer. *Clin. Cancer Res. 12*, 3971−8.

(7) Hashida, H., Takabayashi, A., Kanai, M., Adachi, M., Kondo, K., Kohno, N., Yamaoka, Y., and Miyake, M. (2002) Aminopeptidase N is involved in cell motility and angiogenesis: its clinical significance in human colon cancer. *Gastroenterology 122*, 376−86.

(8) Ishii, K., Usui, S., Sugimura, Y., Yoshida, S., Hioki, T., Tatematsu, M., Yamamoto, H., and Hirano, K. (2001) Aminopeptidase N regulated by zinc in human prostate participates in tumor cell invasion. *Int. J. Cancer 92*, 49−54.

(9) Wickström, M., Larsson, R., Nygren, P., and Gullbo, J. (2011) Aminopeptidase N (CD13) as a target for cancer chemotherapy. *Cancer Sci. 102*, 501−508.

(10) Menrad, A., Speicher, D., Wacker, J., and Herlyn, M. (1993) Biochemical and functional characterization of aminopeptidase N expressed by human melanoma cells. *Cancer Res. 53*, 1450−1455.

(11) Saiki, I., Yoneda, J., Azuma, I., Fujii, H., Abe, F., Nakajima, M., and Tsuruo, T. (1993) Role of aminopeptidase N (CD13) in tumor-cell invasion and extracellular matrix degradation. *Int. J. Cancer 54*, 137−143.

(12) Fujii, H., Nakajima, M., Saiki, I., Yoneda, J., Azuma, I., and Tsuruo, T. (1995) Human melanoma invasion and metastasis enhancement by high expression of aminopeptidase N/CD13. *Clin. Exp. Metastasis 13*, 337−344.

(13) Pasqualini, R., Koivunen, E., Kain, R., Lahdenranta, J., Sakamoto, M., Stryhn, A., Ashmun, R. A., Shapiro, L. H., Arap, W., and Ruoslahti, E. (2000) Aminopeptidase N is a receptor for tumor-homing peptides and a target for inhibiting angiogenesis. *Cancer Res. 60*, 722−7.

(14) Bhagwat, S. V., Lahdenranta, J., Giordano, R., Arap, W., Pasqualini, R., and Shapiro, L. H. (2001) CD13/APN is activated by angiogenic signals and is essential for capillary tube formation. *Blood 97*, 652−659.

(15) Zhang, Z., Hatta, H., Ito, T., and Nishimoto, S. (2005) Synthesis and photochemical properties of photoactivated antitumor prodrugs releasing 5-fluorouracil. *Org. Biomol. Chem. 3*, 592−6.

(16) Ndinguri, M. W., Solipuram, R., Gambrell, R. P., Aggarwal, S., and Hammer, R. P. (2009) Peptide targeting of platinum anti-cancer drugs. *Bioconjugate Chem. 20*, 1869−1878.

(17) van Laarhoven, H. W., Gambarota, G., Heerschap, A., Lok, J., Verhagen, I., Corti, A., Toma, S., Gallo Stampino, C., van der Kogel, A., and Punt, C. J. (2006) Effects of the tumor vasculature targeting agent NGR-TNF on the tumor microenvironment in murine lymphomas. *Invest. New Drugs 24*, 27−36.

(18) Zhang, Z., Harada, H., Tanabe, K., Hatta, H., Hiraoka, M., and Nishimoto, S. (2005) Aminopeptidase N/CD13 targeting fluorescent probes: synthesis and application to tumor cell imaging. *Peptides 26*, 2182−7.

(19) Moffatt, S., Wiehle, S., and Cristiano, R. J. (2005) Tumor-specific gene delivery mediated by a novel peptide-polyethylenimine-DNA polyplex targeting aminopeptidase N/CD13. *Hum. Gene Ther. 16*, 57−67.

(20) van Hensbergen, Y., Broxterman, H. J., Elderkamp, Y. W., Lankelma, J., Beers, J. C., Heijn, M., Boven, E., Hoekman, K., and Pinedo, H. M. (2002) A doxorubicin-CNGRC-peptide conjugate with prodrug properties. *Biochem. Pharmacol. 63*, 897−908.

(21) Curnis, F., Sacchi, A., Borgna, L., Magni, F., Gasparri, A., and Corti, A. (2000) Enhancement of tumor necrosis factor alpha antitumor immunotherapeutic properties by targeted delivery to aminopeptidase N (CD13). *Nat. Biotechnol. 18*, 1185−90.

(22) Arap, W., Pasqualini, R., and Ruoslahti, E. (1998) Cancer treatment by targeted drug delivery to tumor vasculature in a mouse model. *Science 279*, 377−80.

(23) Zhang, Z., Hatta, H., Tanabe, K., and Nishimoto, S. (2005) A new class of 5-fluoro-2′-deoxyuridine prodrugs conjugated with a tumor-homing cyclic peptide CNGRC by ester linkers: synthesis, reactivity, and tumor-cell-selective cytotoxicity. *Pharm. Res. 22*, 381−9.

(24) von Wallbrunn, A., Waldeck, J., Holtke, C., Zuhlsdorf, M., Mesters, R., Heindel, W., Schafers, M., and Bremer, C. (2008) In vivo optical imaging of CD13/APN-expression in tumor xenografts. *J. Biomed. Opt. 13*, 011007.

(25) Oostendorp, M., Douma, K., Hackeng, T. M., Dirksen, A., Post, M. J., van Zandvoort, M. A. M. J., and Backes, W. H. (2008) Quantitative molecular magnetic resonance imaging of tumor angiogenesis using cNGR-labeled paramagnetic quantum dots. *Cancer Res. 68*, 7676−7683.

(26) Ellerby, H. M., Bredesen, D. E., Fujimura, S., and John, V. (2008) Hunter-killer peptide (HKP) for targeted therapy. *J. Med. Chem. 51*, 5887−5892.

(27) Gregorc, V., Zucali, P. A., Santoro, A., Ceresoli, G. L., Citterio, G., De Pas, T. M., Zilembo, N., De Vincenzo, F., Simonelli, M., Rossoni, G., Spreafico, A., Grazia Vigano, M., Fontana, F., De Braud, F. G., Bajetta, E., Caligaris-Cappio, F., Bruzzi, P., Lambiase, A., and Bordignon, C. (2010) Phase II study of asparagine-glycine-arginine-human tumor necrosis factor {alpha}, a selective vascular targeting agent, in previously treated patients with malignant pleural mesothelioma. *J. Clin. Oncol. 28*, 2604−2611.

(28) Curnis, F., Longhi, R., Crippa, L., Cattaneo, A., Dondossola, E., Bachi, A., and Corti, A. (2006) Spontaneous formation of L-isoaspartate and gain of function in fibronectin. *J. Biol. Chem. 281*, 36466−36476.

(29) Curnis, F., Sacchi, A., Gasparri, A., Longhi, R., Bachi, A., Doglioni, C., Bordignon, C., Traversari, C., Rizzardi, G.-P., and Corti, A. (2008) Isoaspartate-glycine-arginine: a new tumor vasculature-targeting motif. *Cancer Res. 68*, 7073−7082.

(30) Spitaleri, A., Mari, S., Curnis, F., Traversari, C., Longhi, R., Bordignon, C., Corti, A., Rizzardi, G.-P., and Musco, G. (2008)

Structural basis for the interaction of isoDGR with the RGD-binding site of {alpha}v{beta}3 integrin. *J. Biol. Chem. 283*, 19757−19768.
(31) Curnis, F., Cattaneo, A., Longhi, R., Sacchi, A., Gasparri, A. M., Pastorino, F., Di Matteo, P., Traversari, C., Bachi, A., Ponzoni, M., Rizzardi, G.-P., and Corti, A. (2010) Critical role of flanking residues in NGR-to-isoDGR transition and CD13/Integrin receptor switching. *J. Biol. Chem. 285*, 9114−9123.
(32) Corti, A., Curnis, F., Arap, W., and Pasqualini, R. (2008) The neovasculature homing motif NGR: more than meets the eye. *Blood 112*, 2628−2635.
(33) Pathuri, G., Sahoo, K., Awasthi, V., and Gali, H. (2010) Synthesis and in vivo evaluation of Tc-99m-labeled cyclic CisoDGRC peptide conjugates for targeting [alpha]v[beta]3 integrin expression. *Bioorg. Med. Chem. Lett. 20*, 5969−5972.
(34) Plesniak, L. A., Salzameda, B., Hinderberger, H., Regan, E., Kahn, J., Mills, S. A., Teriete, P., Yao, Y., Jennings, P., Marassi, F., and Adams, J. A. (2010) Structure and activity of CPNGRC: a modified CD13/APN peptidic homing motif. *Chem. Biol. Drug Des. 75*, 551−562.
(35) Aoyagi, T., Yoshida, S., Nakamura, Y., Shigihara, Y., Hamada, M., and Takeuchi, T. (1990) Probestin, a new inhibitor of aminopeptidase M, produced by Streptomyces azureus MH663−2F6. I. Taxonomy, production, isolation, physico-chemical properties and biological activities. *J. Antibiot. (Tokyo) 43*, 143−8.
(36) Itoh, Y., Ishikawa, M., Naito, M., and Hashimoto, Y. (2010) Protein knockdown using methyl bestatin−ligand hybrid molecules: design and synthesis of inducers of ubiquitination-mediated degradation of cellular retinoic acid-binding proteins. *J. Am. Chem. Soc. 132*, 5820−5826.
(37) Noll, B., Kniess, T., Friebe, M., Spies, H., and Johannsen, B. (1996) Rhenium(V) gluconate, a suitable precursor for the preparation of rhenium(V) complexes. *Isotopes in Environmental and Health Studies 32*, 21−29.
(38) Smith, C. J., Gali, H., Sieckman, G. L., Higginbotham, C., Volkert, W. A., and Hoffman, T. J. (2003) Radiochemical investigations of (99m)Tc-N(3)S-X-BBN[7−14]NH(2): an in vitro/in vivo structure-activity relationship study where X = 0-, 3-, 5-, 8-, and 11-carbon tethering moieties. *Bioconjugate Chem. 14*, 93−102.
(39) Ashmun, R., and Look, A. (1990) Metalloprotease activity of CD13/aminopeptidase N on the surface of human myeloid cells. *Blood 75*, 462−469.
(40) Folkman, J. (1995) Angiogenesis in cancer, vascular, rheumatoid and other disease. *Nat. Med. 1*, 27−31.
(41) Hanahan, D., and Folkman, J. (1996) Patterns and emerging mechanisms of the angiogenic switch during tumorigenesis. *Cell 86*, 353−64.
(42) Plate, K. H., Breier, G., and Risau, W. (1994) Molecular mechanisms of developmental and tumor angiogenesis. *Brain Pathol. 4*, 207−18.
(43) Folkman, J. (1971) Tumor angiogenesis: therapeutic implications. *N. Engl. J. Med. 285*, 1182−6.
(44) Folkman, J. (2007) Angiogenesis: an organizing principle for drug discovery? *Nat. Rev. Drug Discovery 6*, 273−286.
(45) Beer, A. J., Wester, H.-J., and Schwaiger, M. (2010) *Molecular Imaging of Angiogenesis*, 105−115.
(46) Hsu, A. R., and Chen, X. (2008) Advances in anatomic, functional, and molecular imaging of angiogenesis. *J. Nucl. Med. 49*, 511−514.
(47) Kenny, L. M., Coombes, R. C., Oulie, I., Contractor, K. B., Miller, M., Spinks, T. J., McParland, B., Cohen, P. S., Hui, A.-M., Palmieri, C., Osman, S., Glaser, M., Turton, D., Al-Nahhas, A., and Aboagye, E. O. (2008) Phase I trial of the positron-emitting Arg-Gly-Asp (RGD) peptide radioligand 18F-AH111585 in breast cancer patients. *J. Nucl. Med. 49*, 879−886.
(48) Bach-Gansmo, T., Danielsson, R., Saracco, A., Wilczek, B., Bogsrud, T. V., Fangberget, A., Tangerud, A., and Tobin, D. (2006) Integrin receptor imaging of breast cancer: a proof-of-concept study to evaluate 99mTc-NC100692. *J. Nucl. Med. 47*, 1434−9.
(49) Beer, A. J., Niemeyer, M., Carlsen, J., Sarbia, M., Nahrig, J., Watzlowik, P., Wester, H.-J., Harbeck, N., and Schwaiger, M. (2008) Patterns of {alpha}v{beta}3 expression in primary and metastatic human breast cancer as shown by 18F-Galacto-RGD PET. *J. Nucl. Med. 49*, 255−259.
(50) Mittra, E. S., Goris, M. L., Iagaru, A. H., Kardan, A., Burton, L., Berganos, R., Chang, E., Liu, S., Shen, B., Chin, F. T., Chen, X., and Gambhir, S. S. (2011) Pilot pharmacokinetic and dosimetric studies of (18)F-FPPRGD2: a PET radiopharmaceutical agent for imaging alpha(v)beta(3) integrin levels. *Radiology 260*, 182−91.
(51) Arano, Y. (2002) Recent advances in Tc-99m radiopharmaceuticals. *Ann. Nucl. Med. 16*, 79−93.
(52) Jurisson, S. S., and Lydon, J. D. (1999) Potential technetium small molecule radiopharmaceuticals. *Chem. Rev. 99*, 2205−2218.
(53) Bartholoma, M. D., Louie, A. S., Valliant, J. F., and Zubieta, J. (2010) Technetium and gallium derived radiopharmaceuticals: comparing and contrasting the chemistry of two important radiometals for the molecular imaging era. *Chem. Rev. 110*, 2903−2920.
(54) Francesconi, L. C., Zheng, Y., Bartis, J., Blumenstein, M., Costello, C., and De Rosch, M. A. (2004) Preparation and characterization of [99TcO] apcitide: a technetium labeled peptide. *Inorg. Chem. 43*, 2867−2875.
(55) Cyr, J. E., Pearson, D. A., Nelson, C. A., Lyons, B. A., Zheng, Y., Bartis, J., He, J., Cantorias, M. V., Howell, R. C., and Francesconi, L. C. (2007) Isolation, characterization, and biological evaluation of syn and anti diastereomers of [99mTc]technetium depreotide: a somatostatin receptor binding tumor imaging agent. *J. Med. Chem. 50*, 4295−4303.
(56) Cantorias, M. V., Howell, R. C., Todaro, L., Cyr, J. E., Berndorff, D., Rogers, R. D., and Francesconi, L. C. (2007) MO tripeptide diastereomers (M = 99/99mTc, Re): models to identify the structure of 99mTc peptide targeted radiopharmaceuticals. *Inorg. Chem. 46*, 7326−7340.
(57) Wong, E., Fauconnier, T., Bennett, S., Valliant, J., Nguyen, T., Lau, F., Lu, L. F. L., Pollak, A., Bell, R. A., and Thornback, J. R. (1997) Rhenium(V) and technetium(V) oxo complexes of an N2N'S peptidic chelator: evidence of interconversion between the syn and anti conformations. *Inorg. Chem. 36*, 5799−5808.
(58) Francesconi, L. C., Graczyk, G., Wehrli, S., Shaikh, S. N., McClinton, D., Liu, S., Zubieta, J., and Kung, H. F. (1993) Synthesis and characterization of neutral MVO (M = technetium, rhenium) amine-thiol complexes containing a pendant phenylpiperidine group. *Inorg. Chem. 32*, 3114−3124.
(59) Lever, S. Z., Baidoo, K. E., and Mahmood, A. (1990) Structure proof of syn/anti isomerism in N-alkylated diaminedithiol (DADT) complexes of technetium. *Inorg. Chim. Acta 176*, 183−184.
(60) Valliant, J. F., Riddoch, R. W., Hughes, D. W., Roe, D. G., Fauconnier, T. K., and Thornback, J. R. (2001) The solid phase synthesis and NMR spectroscopy of a 99Tc chelate-bombesin derived peptide conjugate. *Inorg. Chim. Acta 325*, 155−163.
(61) Wong, E., Bennett, S., Lawrence, B., Fauconnier, T., Lu, L. F. L., Bell, R. A., Thornback, J. R., and Eshima, D. (2001) Tuftsin receptor-binding peptide labeled with technetium: chemistry and preliminary in vitro receptor-binding study. *Inorg. Chem. 40*, 5695−5700.
(62) Bauvois, B., and Dauzonne, D. (2006) Aminopeptidase-N/CD13 (EC 3.4.11.2) inhibitors: chemistry, biological evaluations, and therapeutic prospects. *Med. Res. Rev. 26*, 88−130.
(63) Stange, T., Kettmann, U., and Holzhausen, H. J. (1996) Immunoelectron microscopic single and double labelling of amino-peptidase N (CD 13) and dipeptidyl peptidase IV (CD 26). *Acta Histochem. 98*, 323−31.
(64) Li, Z.-b., Cai, W., Cao, Q., Chen, K., Wu, Z., He, L., and Chen, X. (2007) 64Cu-labeled tetrameric and octameric RGD peptides for small-animal PET of tumor {alpha}v{beta}3 integrin expression. *J. Nucl. Med. 48*, 1162−1171.
(65) Liu, S. (2009) Radiolabeled cyclic RGD peptides as integrin $\alpha v\beta 3$-targeted radiotracers: maximizing binding affinity via bivalency. *Bioconjugate Chem. 20*, 2199−2213.
(66) Mammen, M., Choi, S. K., and Whitesides, G. M. (1998) Polyvalent interactions in biological systems: Implications for design

and use of multivalent ligands and inhibitors. *Angew. Chem., Int. Ed. 37*, 2755−2794.

Bioconjugate Chemistry

Article

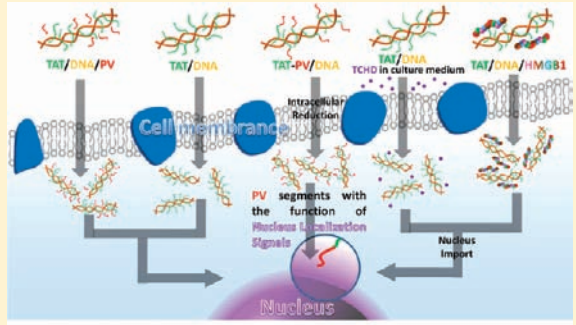
pubs.acs.org/bc

Enhanced Nuclear Import and Transfection Efficiency of TAT Peptide-Based Gene Delivery Systems Modified by Additional Nuclear Localization Signals

Wen-Jie Yi, Juan Yang, Cao Li, Hui-Yuan Wang, Chen-Wei Liu, Li Tao, Si-Xue Cheng, Ren-Xi Zhuo, and Xian-Zheng Zhang*

Key Laboratory of Biomedical Polymers of Ministry of Education & Department of Chemistry, Wuhan University, Wuhan 430072, P. R. China

ABSTRACT: Cellular uptake and nuclear localization are two major barriers in gene delivery. In order to evaluate whether additional nuclear localization signals (NLSs) can improve gene transfection efficiency, we introduced different kinds of NLSs to TAT-based gene delivery systems to form three kinds of complexes, including TAT-PV/DNA, TAT/DNA/PV, and TAT/DNA/HMGB1. The DNA binding ability of different vectors was evaluated by agarose gel electrophoresis. The *in vitro* transfections mediated by different complexes under different conditions were carried out. The cells treated by different complexes were observed by confocal microscopy. The MTT assay showed that all complexes did not exhibit apparent cytotoxicity in both HeLa and Cos7 cell lines even at high N/P ratios. The luciferase reporter gene expression mediated by TAT-PV/DNA complexes exhibited about 200-fold enhancement as compared with TAT/DNA complexes. Confocal study showed that, except TAT/DNA/PV, all other complexes exhibited enhanced nuclear accumulation and cellular uptake in both HeLa and Cos7 cell lines. These results indicated that the introduction of nuclear localization signals could enhance the transfection efficacy of TAT-based peptides, implying that the TAT peptide-based vectors demonstrated here have promising potential in gene delivery.



TAT peptide-based gene delivery systems

INTRODUCTION

Gene therapy has attracted a great deal of attention for the treatment for both acquired and inherited diseases since the first clinical trial in 1990.[1,2] The success of gene therapy is mainly dependent on the gene delivery vectors since naked nucleic acids are easily degraded either *in vitro* or *in vivo*.

Generally, the gene delivery vectors can be divided into two types, viral gene vectors and nonviral ones.[3,4] Although viruses are capable of delivering nucleic acids into cells effectively, safety problems such as endogenous virus recombination, oncogenic effects and unexpected immune response do limit their applications.[5] After several medical accidents caused by viral vectors,[6−8] nonviral vectors such as cationic liposomes[9] and polymers[10] have gained much attention as attractive alternatives due to their safety, multifunction, low cost, and easy preparation.

Cellular internalization of therapeutic agents is a critical issue in gene delivery because the plasma membranes are nearly impermeable barriers. To across these barriers, cell-penetrating peptides (CPPs) have been developed as delivery agents for various therapeutic agents.[11,12] A typical example of CPPs is HIV-1 TAT, the first found and most widely used CPP, which is derived from the transcriptional activator protein encoded by human immunodeficiency virus type 1 (HIV-1).[13] One main characteristic of TAT protein is the ability to cross the plasma membrane of neighboring cells.[14] The minimal sequence used as transduction domain of TAT is the amino acid residues of 48 to 57 (Gly-Arg-Lys-Lys-Arg-Arg-Gln-Arg-Arg-Arg);[15−17] after being covalently or noncovalently linked to cargo molecules, TAT peptide can mediate efficient intracellular delivery.

As nuclear transport is a major barrier in gene delivery, several attempts to target DNA to nucleus have been reported, including the use of electrostatic binding of DNA to cationic nuclear localization signal (NLS) -containing peptides or proteins.[18,19] One of the most frequently used NLS peptide sequences is PKKKRKV, presented in the Simian Virus 40 large T antigen. It was reported that a combination of the NLS peptide to vectors could improve the nuclear import of plasmid DNA, and thereby benefit the transfection efficiency.[20−22] HMGB1 is a nuclear protein which has been used to carry DNA to pass through the nuclear pore complexes.[23−26] TCHD is an amphiphilic molecule which has been studied to enhance the nuclear uptake by nonselective gating of nuclear pores.[27]

To improve nuclear accumulation, as well as cellular uptake, the combination of nuclear localization signals and cell-penetrating peptides has attracted much research interest.[28,29] Recently, we constructed a new gene vector made up of cell-penetrating peptide R_8 with N-terminal stearylated nuclear

Received: October 9, 2011
Revised: December 9, 2011
Published: December 11, 2011

 © 2011 American Chemical Society dx.doi.org/10.1021/bc2005472 | *Bioconjugate Chem.* 2012, 23, 125−134

localization signal.[30] As for TAT peptide, some literatures reported that TAT peptide possessed the ability of nuclear localization.[31] However, other literature certified that TAT was localized primarily in the cytosol of cells, with very limited nuclear accumulation.[32] To improve the transfection efficacy of TAT, in this study, we introduced different kinds of nuclear localization signals, including NLS sequence PKKKRKV, nuclear protein high mobility group box protein 1 (HMGB1) to the TAT-based gene vector. In addition, trans-cyclohexane-1,2-diol (TCHD) was also used in the DMEM medium to improve the nuclear accumulation of the TAT peptide.

EXPERIMENTAL PROCEDURES

Materials. 2-Chlorotrityl chloride resin (100−200 mesh, loading: 1.26 mmol/g), N-fluorenyl-9-methoxycarbonyl (FMOC) protected L-amino acids (FMOC-Gly-OH, FMOC-Arg(Pbf)-OH, FMOC-Lys(Boc)-OH, FMOC-Gln(Trt)-OH, FMOC-Pro-OH, FMOC-Val-OH), *o*-benzotriazol-*N*,*N*,*N*′,*N*′-tetramethyluronium hexafluorophosphate (HBTU) were purchased from GL Biochem Ltd. and used as received. Diisopropylethylamine (DiEA) was acquired from GL Biochem Ltd. and distilled prior to use. *N*-Hydroxybenzotriazole (HOBt), piperidine, trifluoroacetic acid (TFA), and phenol were purchased from Shanghai Reagent Chemical Co. and used directly. *N*,*N*-Dimethylformamide (DMF) and dichloromethane (DCM) were obtained from Shanghai Reagent Chemical Co. and distilled before use. Ethanedithiol (EDT), triisopropylsilane (TIS), thioanisole, and polyethylenimine (branched PEI, M_w 25 kDa) were obtained from ACROS and used as received.

QIAfilter plasmid purification Giga Kit was purchased from Qiagen. GelRed was purchased from Biotium. Fetal bovine serum (FBS), Dulbecco's Modified Eagle's Medium (DMEM), penicillin−streptomycin, 0.25% Trypsin-EDTA solution A, 3-(4,5-dimethylthiazol-2-yl)-2,5-diphenyltetrazolium bromide (MTT), and Dulbecco's phosphate buffered saline (PBS) were obtained from Invitrogen. Dimethyl sulfoxide (DMSO), high mobility group box 1 (HMGB1), and trans-cyclohexane-1,2-diol (TCHD) were obtained from Sigma-Aldrich. Molecular probes (YOYO-1 and Hoechst 33258) were purchased from Invitrogen. The Micro BCA protein assay kit was acquired from Pierce. All other reagents were analytically pure and used directly.

Synthesis of Peptides and Preparation of Different Complexes. GRKKRRQRRR-NH_2 (TAT), PKKKRKV-NH_2 (PV), and GRKKRRQRRRPKKKRKV-NH_2 (TAT-PV) were synthesized manually using standard solid-phase synthesis method based on Fmoc (1-(9*H*-fluoren-9-yl)-methoxycarbonyl)/*tert*-butyl chemistry.[33,34] The molecular weights of peptides were detected by electrode spray ionization mass spectrometry (ESI-MS).

Both TAT/DNA and TAT-PV/DNA binary complexes were prepared as follows. The peptide was dissolved in 150 mM NaCl buffer with a certain concentration and stored at −20 °C until use. The peptide/DNA complexes were prepared by mixing particular volume of peptide solution with 5 μL DNA solution (200 ng/μL in 40 mM Tris−HCl buffer solution) with different N/P ratios. Then, 150 mM NaCl solution was added into the complexes to a total volume of 100 μL and vortexed for 10 s. The system was incubated at 37 °C for 30 min to form stable complexes.

TAT/DNA/PV ternary complexes were prepared as follows. 5 μL DNA solution (200 ng/μL in 40 mM Tris−HCl buffer solution) was mixed with TAT solution at a particular N/P ratio (N/P = 20). Then, NaCl solution was added to a total volume of 50 μL. After incubation at 37 °C for 15 min, PV solution with certain volume was added to the solution containing TAT/DNA complexes. Then, NaCl solution was added to a total volume of 100 μL, and incubated at 37 °C for 15 min.

TAT/DNA/HMGB1 ternary complexes were prepared as follows. 5 μL DNA solution (200 ng/μL in 40 mM Tris−HCl buffer solution) was mixed with TAT solution at a particular N/P ratio (N/P = 20). After incubation at 37 °C for 15 min, HMGB1 solution with a particular concentration was then added to the TAT/DNA complex-containing solution due to a certain HMGB1/DNA weight ratio (w/w = 2) and incubated at 37 °C for 15 min.

Agarose Gel Electrophoresis. The stabilities of all complexes with different compositions were evaluated by agarose gel electrophoresis assay. In brief, for TAT/DNA and TAT-PV/DNA binary complexes, 0.5 μL DNA (200 ng/μL in 40 mM Tris−HCl buffer solution) was mixed with the vector solutions at different N/P ratios. Then, 150 mM NaCl solution was added to a total volume of 8 μL and the complexes were incubated at 37 °C for 30 min. For TAT/DNA/PV ternary complexes, 0.5 μL DNA (200 ng/μL) was mixed with TAT solution at a particular N/P ratio (N/P = 20) and incubated at 37 °C for 15 min. Then, different volumes of PV solution were added to the solution containing TAT/DNA complexes. Then, NaCl solution was added to a total volume of 8 μL, and the system incubated at 37 °C for another 15 min. After complexes were electrophoresed on the 0.7% (w/v) agarose gel containing GelRed with TAE running buffer at 80 V for 60 min, a Vilber Lourmat UV-transiluminator was used for the visualization of DNA. Naked DNA was used as control.

Particle Size and Zeta Potential Measurements. The particle size and zeta potential of all complexes were measured by a Nano-ZEN3600 zetasizer (Malvern Instruments) at room temperature. All complexes with different compositions were prepared as mentioned above, and deionized water was added to a total volume of 1 mL for dilution.

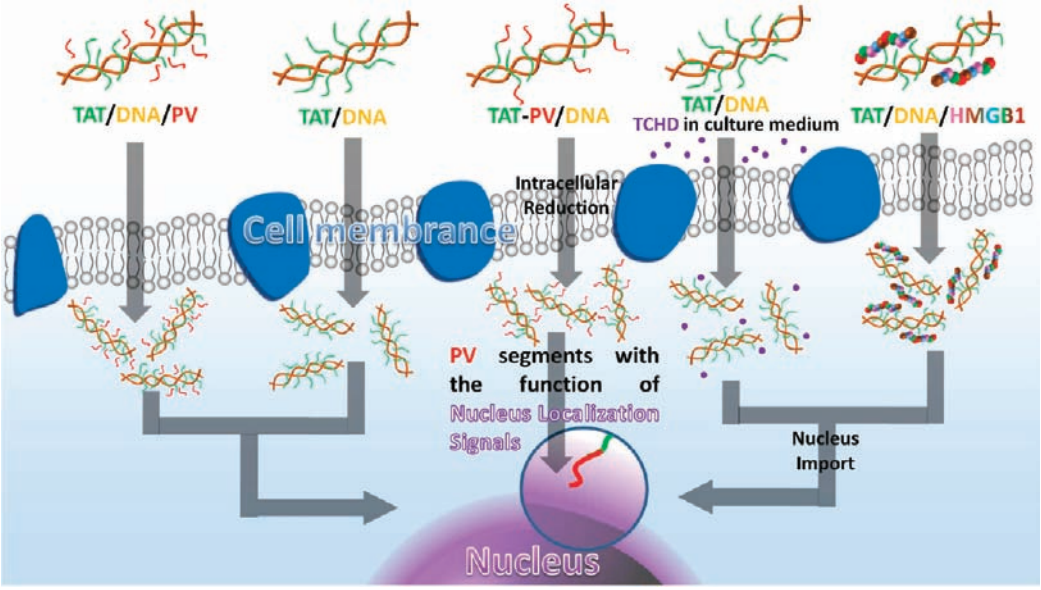
Cell Culture and Amplifications of Plasmid DNA. Human cervix carcinoma (HeLa) cells and African green monkey kidney (Cos7) cells were acquired from China Center for Typical Culture Collection (Wuhan, China) and were incubated in DMEM medium containing 10% FBS and 1% antibiotics at 37 °C in humidified atmosphere with 5% CO_2.

pGL-3 plasmid was used as a reporter gene. pGL-3 plasmid was first transformed in *Escherichia coli* JM 109 and then was amplified in terrific broth media at 37 °C overnight. After that, an EndoFree QiAFilter Plasmid Giga Kit was used for purification of the plasmid. The purified plasmid DNA was dissolved in TE buffer solution and stored at −20 °C before use.

***In Vitro* Cytotoxicity Assay.** The cytotoxicity assay *in vitro* was examined in HeLa and Cos7 cells by MTT assay. Cells were seeded in 96-well plates at a density of 6×10^3 cells/well in 200 μL DMEM medium containing 10% FBS. After 24 h of incubation, the medium was replaced with 200 μL serum-free DMEM. And then for TAT/DNA, TAT-PV/DNA, TAT/DNA/PV, and TAT/DNA/HMGB1 complexes, the vector/DNA complex-containing solutions (20 μL containing 0.2 μg DNA) with different compositions were added into each well, and cultured at 37 °C for 4 h. For transfection mediated by addition of TCHD in DMEM medium, the TAT/DNA

dx.doi.org/10.1021/bc2005472 | *Bioconjugate Chem.* 2012, 23, 125−134

Scheme 1. Gene Delivery Mediated by Different TAT Peptide-Based Gene Vectors, Including TAT/DNA, TAT-PV/DNA, TAT/DNA/PV, TAT/DNA/HMGB1, and TAT/DNA with TCHD in DMEM Medium



complex-containing solutions (20 μL containing 0.2 μg DNA) at N/P ratio of 20 were added into each well. After transfection for 4 h, the medium was removed and serum-free DMEM medium with TCHD was added and cultured for another 1 h. Thereafter, 20 μL of MTT (5 mg/mL) solution was added into each well and further incubated for 4 h. Then, the medium was removed and 200 μL DMSO was added to dissolve the formazan crystals. The absorption was evaluated at 570 nm using a microplate reader (BIO-RAD, Model 550, USA). The cell viability was calculated according to the equation: Cell viability = $[OD_{570}(\text{treated}) - OD_{570}(\text{background})/OD_{570}(\text{untreated}) - OD_{570}(\text{background})] \times 100\%$.

***In Vitro* Transfection.** The transfecion efficiencies of all complexes including TAT-PV/DNA, TAT/DNA/PV, and TAT/DNA/HMGB1 in the absence of TCHD and TAT/DNA with the presence of TCHD were evaluated in HeLa and Cos7 cell lines. TAT/DNA complexes were used as control.

Cells were seeded in 24-well plates at a density of 6×10^4 cells/well and cultured in 1 mL DMEM medium containing 10% FBS at 37 °C. After incubation for 24 h, the medium was replaced by 1 mL serum-free DMEM containing complexes with different compositions and incubated for 4 h. For transfection in the presence of TCHD, after cultured for 4 h, the medium was replaced and serum-free DMEM with different contents of TCHD was added into each well and cultured for another 1 h. Thereafter, the medium was replaced by fresh DMEM containing 10% FBS and incubated for another 44 h.

In order to assess the luciferase expression of plasmid DNA, the medium was removed and 200 μL phosphate buffered saline (PBS, 0.1 M, pH 7.4) was added into each well to wash out the medium remained. Then, cells were lysed with 200 μL reporter lysis buffer each well. The luciferase activity was assessed with chemiluminometer (Lumat LB9507, EG&G Berthold, Germany). The total protein was measured with a BCA protein assay kit. Luciferase activity was determined as RLU/mg protein.

Cellular Uptake Study. The cellular uptake study was measured by a confocal laser scanning microscope. Cells were seeded into 6-well plates at a density of 1×10^5 per well and cultured with 2 mL DMEM containing 10% FBS at 37 °C for 1 day. Green molecular probe YOYO-1 and blue molecular probe Hoechst 33258 were used to tag pGL-3 and stain nucleus, respectively. One microgram plasmid was mixed with 2.5 μL YOYO-1 solution (10 μM/L) and incubated at 37 °C for 30 min before addition of vectors. After 30 min of incubation, the complexes were added into each well and cultured for 4 h. Then, the complexes were removed and the cells were washed with serum-free DMEM 3 times and PBS 3 times. After that, the nucleus were stained with 20 μL (2 μg/μL) Hoechst 33258. After incubation for further 15 min, the cells were washed again with serum-free DMEM and PBS, and then 1 mL fresh DMEM containing 10% FBS was added. The fluorescence was observed by a confocal laser scanning microscope (Confocal-Si, Nikon, Japan).

Table 1. Sequences and Molecular Weights of Peptides

	Peptide Sequence	$[M+nH]^{n+}$	Molecular Weight
TAT	GRKKRRQRRR-NH_2	466.6 (n = 3)	1396.7
PV	PKKKRKV-NH_2	442.6 (n = 2)	883.1
TAT-PV	GRKKRRQRRRPKKKRKV-NH_2	566.6 (n = 4)	2261.8

RESULTS AND DISCUSSION

Synthesis of Peptides. In this study, different nuclear localization signals, including PKKKRKV sequence and HMGB1 were introduced to the TAT-based gene vector to form different vector/DNA complexes (Scheme 1). All peptides including GRKKRRQRRR-NH_2 (TAT), PKKKRKV-NH_2 (PV), and GRKKRRQRRRPKKKRKV-NH_2 (TAT-PV) were synthesized manually using standard FMOC solid-phase synthesis technique. The molecular weight of peptides was determined by $[M+nH]^{n+}$ founded in ESI-MS. As shown in Table 1, the molecular weights of TAT, PV, and TAT-PV detected in ESI-MS were 466.6 $[M+3H]^{3+}$, 442.6 $[M+2H]^{2+}$, and 566.6 $[M+4H]^{4+}$, respectively, which coincided with their theoretical molecular weights.

dx.doi.org/10.1021/bc2005472 | *Bioconjugate Chem.* 2012, 23, 125–134

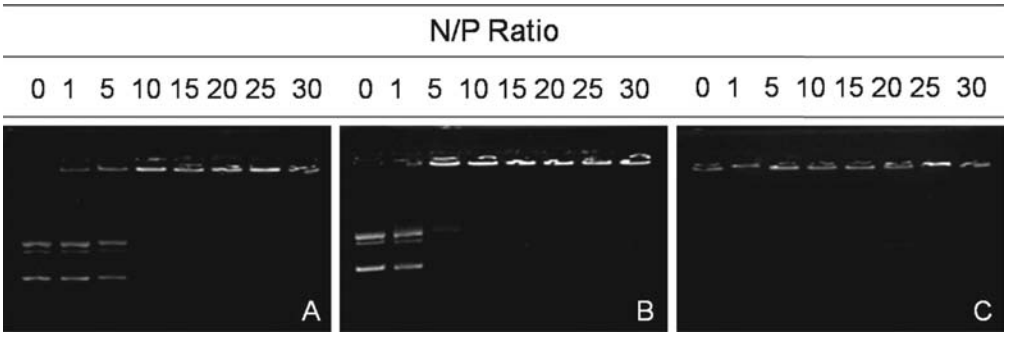


Figure 1. Agorose gel electrophoresis retardation assay of (A) TAT/DNA at N/P ratios from 0 to 30; (B) TAT-PV/DNA at N/P ratios from 0 to 30; and (C) TAT/DNA/PV, to form the ternary complexes, DNA was packed with TAT first, following by the addition of PV peptide at the indicated N/P ratio of 0 to 30. The N/P ratio between TAT and DNA was 20 for all groups, and the final N/P ratios listed as TAT/DNA/NLS were 20/1/0 to 20/1/30.

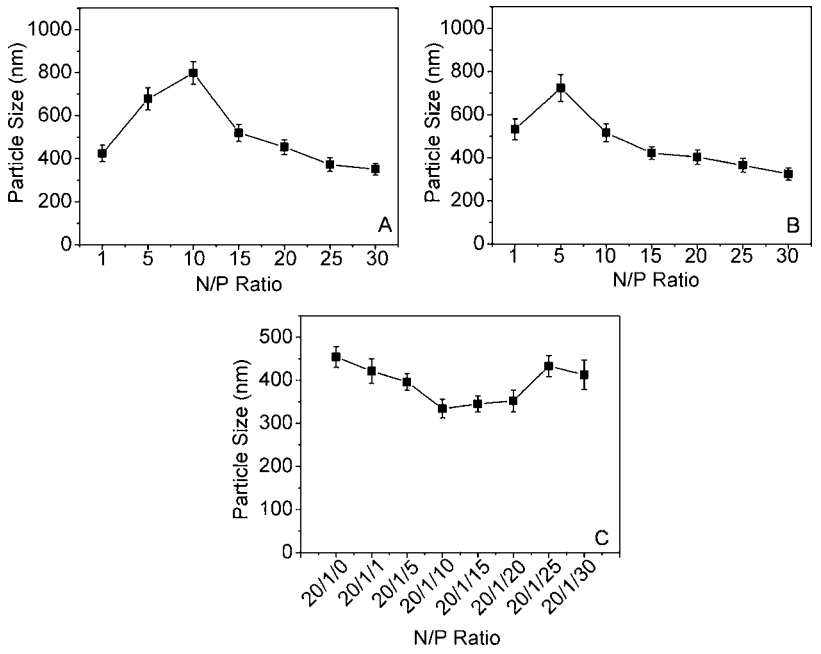


Figure 2. Particle size of (A) TAT/DNA at N/P ratios ranging from 1 to 30; (B) TAT-PV/DNA at N/P ratios ranging from 1 to 30; and (C) TAT/DNA/PV at N/P ratios ranging from 20/1/0 to 20/1/30. Data are shown as mean ± SD (n = 3).

DNA Binding Ability of Different Complexes. DNA binding ability is generally considered to be a prerequisite for gene delivery system.[35] In this study, the binding and condensing abilities of the vector/DNA complexes with different N/P ratios were evaluated by gel retardation assay. As shown in Figure 1A,B, the TAT and TAT-PV peptides were able to condense DNA at N/P ratio higher than 10 and 5, respectively, which showed that both TAT and TAT-PV peptides possessed strong DNA condensing abilities. We also evaluated the DNA condensing ability of TAT/DNA/PV complexes. As shown in Figure 1C, no significant difference was observed by addition of PV peptide into TAT/DNA complexes even at a high N/P ratio of 30. This further indicated that TAT peptide was effective in binding and condensing DNA and the binding ability was not susceptible to PV peptide.

The particle size and zeta potential can reveal the DNA binding ability of vectors and influence the intracellular uptake and subsequent gene transfection efficiency. The particle sizes of different complexes were measured in 150 mM NaCl solution in order to simulate the physiological conditions. As shown in Figure 2A, the average size of the TAT/DNA complexes increased from about 400 to 800 nm before the N/P ratio reached 10. The particle size of complexes was large when N/P ratios were 5 and 10 due to their slightly negative or neutral zeta potentials, which suggested that complexes might aggregate at neutral conditions. When the N/P ratio was higher than 15, the particle size descended gradually, and the average size of the complexes was less than 400 nm, indicating the formation of compact complexes. For TAT-PV/DNA complexes, as presented in Figure 2B, the size changed in a similar trend. In detail, the size of TAT-PV/DNA ascended with the increasing N/P ratio when the ratio was lower than 5. When the N/P ratio was higher than 5, the particle size descended to a minimum of 325 nm at the N/P ratio of 30. As for the TAT/DNA/PV complexes, as shown in Figure 2C, the average size descended with the increasing N/P ratio of PV/DNA, which demonstrated that the addition of positively charged PV could benefit the DNA condensing ability of the complexes. However, the effect of the addition of PV peptide on the complex size is limited and the complexes exhibited mean size between 350 and 450 nm.

dx.doi.org/10.1021/bc2005472 | *Bioconjugate Chem.* 2012, 23, 125–134

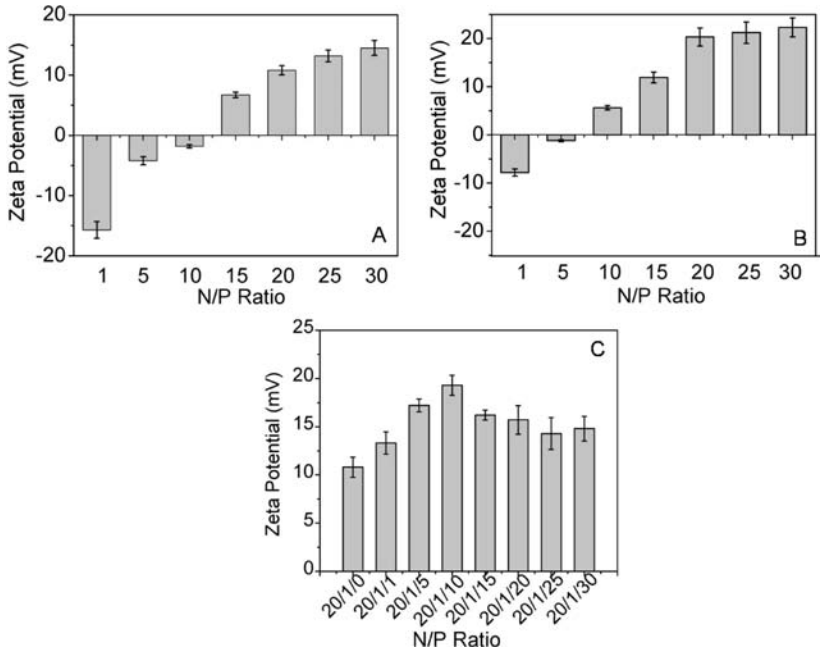


Figure 3. Zeta potential of (A) TAT/DNA at N/P ratios ranging from 1 to 30; (B) TAT-PV/DNA at N/P ratios ranging from 1 to 30; and (C) TAT/DNA/PV at N/P ratios ranging from 20/1/0 to 20/1/30. Data are shown as mean ± SD (n = 3).

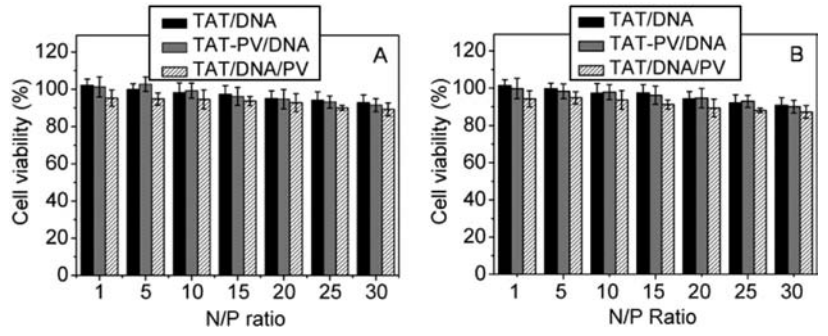


Figure 4. Cell viabilities of TAT/DNA at N/P ratio from 1 to 30, TAT-PV/DNA at N/P ratio from 1 to 30, and TAT/DNA/PV complexes at ratio from 20/1/1 to 20/1/30 TAT/DNA N/P ratio was 20/1 for all groups) in (A) HeLa cells and (B) Cos7 cells. Data are shown as mean ± SD (n = 3).

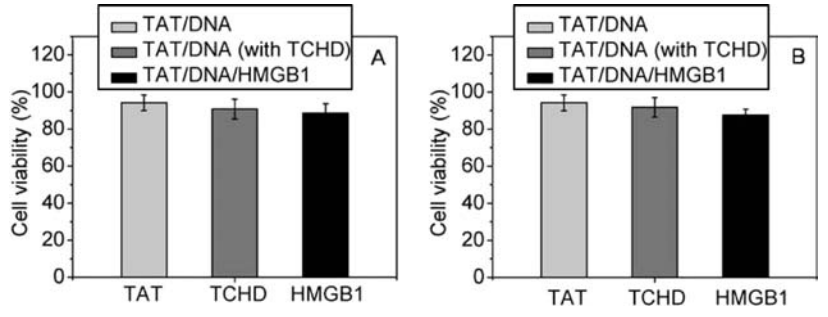


Figure 5. Cell viabilities of TAT/DNA at N/P ratio of 20, TAT/DNA/HMGB1 at N/P ratio of 20 (HMGB1/DNA weight ratio was 2), and TAT/DNA at N/P ratio of 20 (with 1.5% w/v TCHD in DMEM medium) in (A) HeLa cells and (B) Cos7 cells. Data are shown as mean ± SD (n = 3).

The positive charge of vectors is crucial for the complexes to enter cells due to the negatively charged cell membrane.[3] As shown in Figure 3, the zeta potential of TAT/DNA and TAT-PV/DNA binary complexes and TAT/DNA/PV ternary complexes displayed a similar increasing trend with the increase in N/P ratio. Positive potentials were observed when the N/P ratio was higher than 15 for TAT/DNA and higher than 10 for TAT-PV/DNA. For TAT-PV/DNA, the maximum potential was 22.3 mV at N/P ratio of 30, while the maximum potential of TAT/DNA was 14.5 mV at the same N/P ratio. As for TAT/DNA/PV ternary complexes, the potential remained positive and increased with the increase of PV amount due to the slight positive charge of PV peptide.

***In Vitro* Cytotoxicity.** The biocompatibility of gene vectors is of importance for the success of gene therapy.[36] To evaluate the cytotoxicity of vectors, MTT assay was conducted in both

dx.doi.org/10.1021/bc2005472 | *Bioconjugate Chem.* 2012, 23, 125–134

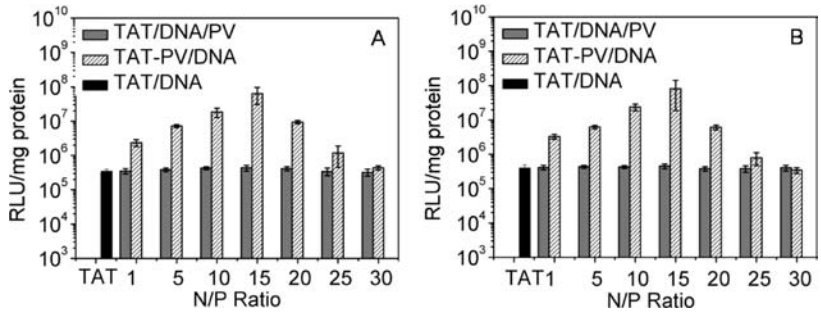


Figure 6. Luciferase expression mediated by TAT/DNA at N/P ratio of 20, TAT-PV/DNA at N/P ratios from 1 to 30, and TAT/DNA/PV complexes at ratio from 20/1/1 to 20/1/30 (the N/P ratio between TAT and DNA was 20 for all groups) in (A) HeLa cells and (B) Cos7 cells. Data are shown as mean ± SD (n = 3).

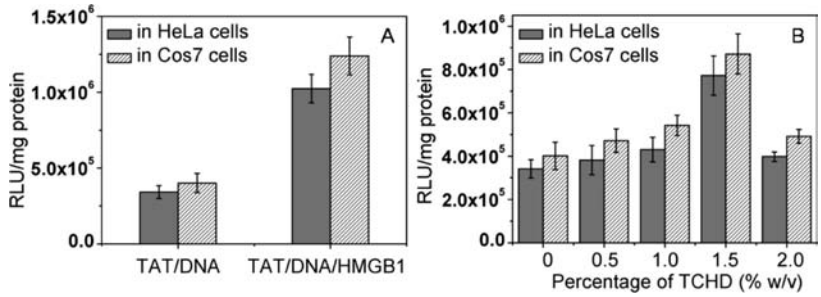


Figure 7. Luciferase expression mediated by (A) TAT/DNA/HMGB1 at N/P ratio of 20 (HMGB1/DNA weight ratio was 2) and (B) TAT/DNA at N/P ratio of 20 (with different amounts of TCHD in DMEM medium). Data are shown as mean ± SD (n = 3).

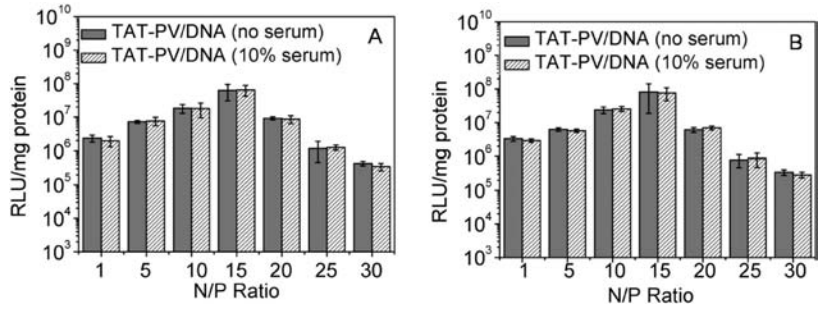


Figure 8. Luciferase expression mediated by TAT-PV/DNA complexes at N/P ratios from 1 to 30 with or without serum: (A) in HeLa cells, and (B) in Cos7 cells. Data are shown as mean ± SD (n = 3).

HeLa and Cos7 cell lines. As shown in Figure 4, no significant cell toxicity was observed in both cell lines for TAT/DNA, TAT-PV/DNA, and TAT/DNA/PV complexes. Moreover, we found that the cytotoxicity of different complexes primarily depended on the N/P ratio of vector/DNA. With an increase in N/P ratio, the cell viability slightly decreases. Nevertheless, all complexes exhibited very low cytotoxicities with cell viabilities higher than 90%.

We also evaluated the cell toxicity of TAT/DNA/HMGB1 complexes and TAT/DNA complexes with the presence of 1.5% w/v TCHD in DMEM medium. According to the results in Figure 5, for both cell lines, the cytotoxicity values of TAT/DNA (with 1.5% w/v TCHD in DMEM medium) and TAT/DNA/HMGB1 complexes were slight higher than that of TAT/DNA complexes alone, which was due to the additional toxicity of TCHD and HMGB1. Nevertheless, both complexes showed more than 85% cell viability.

***In Vitro* Transfection.** In order to observe the influence of additional nuclear localization signals on the TAT/DNA complexes, the transfection efficiencies of different complexes were assessed in different cell lines. As shown in Figure 6, TAT-PV/DNA complexes exhibited significantly improved transfection efficiency. In detail, the gene expression of TAT-PV/DNA increased with the increasing N/P ratio from 1 to 15, but further increase in N/P ratio did not result in the improvement in transfection. At N/P ratio of 15, the complexes showed the highest luciferase expression in both cell lines (HeLa: 6.29 × 10^7 RLU/mg Protein; Cos7: 8.12 × 10^7 RLU/mg Protein), which exhibited about 200-fold enhancement as compared with TAT/DNA complexes (HeLa: 3.41 × 10^5 RLU/mg Protein; Cos7: 4.01 × 10^5 RLU/mg Protein). One reason for enhanced gene efficiency was the addition of cationic PV, which increases the positive charge density of the complexes. Another reason was the addition of PV peptide causing a decrease in particle size of TAT/DNA complexes to some extent. As we know, an appropriate particle size is a prerequisite for gene transfection. Small particles may exhibit higher transfection efficiencies compared with larger ones, as small particles are able to penetrate throughout the submucosal layers while the larger particles are predominantly localized in the epithelial lining.[37]

dx.doi.org/10.1021/bc2005472 | *Bioconjugate Chem.* 2012, 23, 125–134

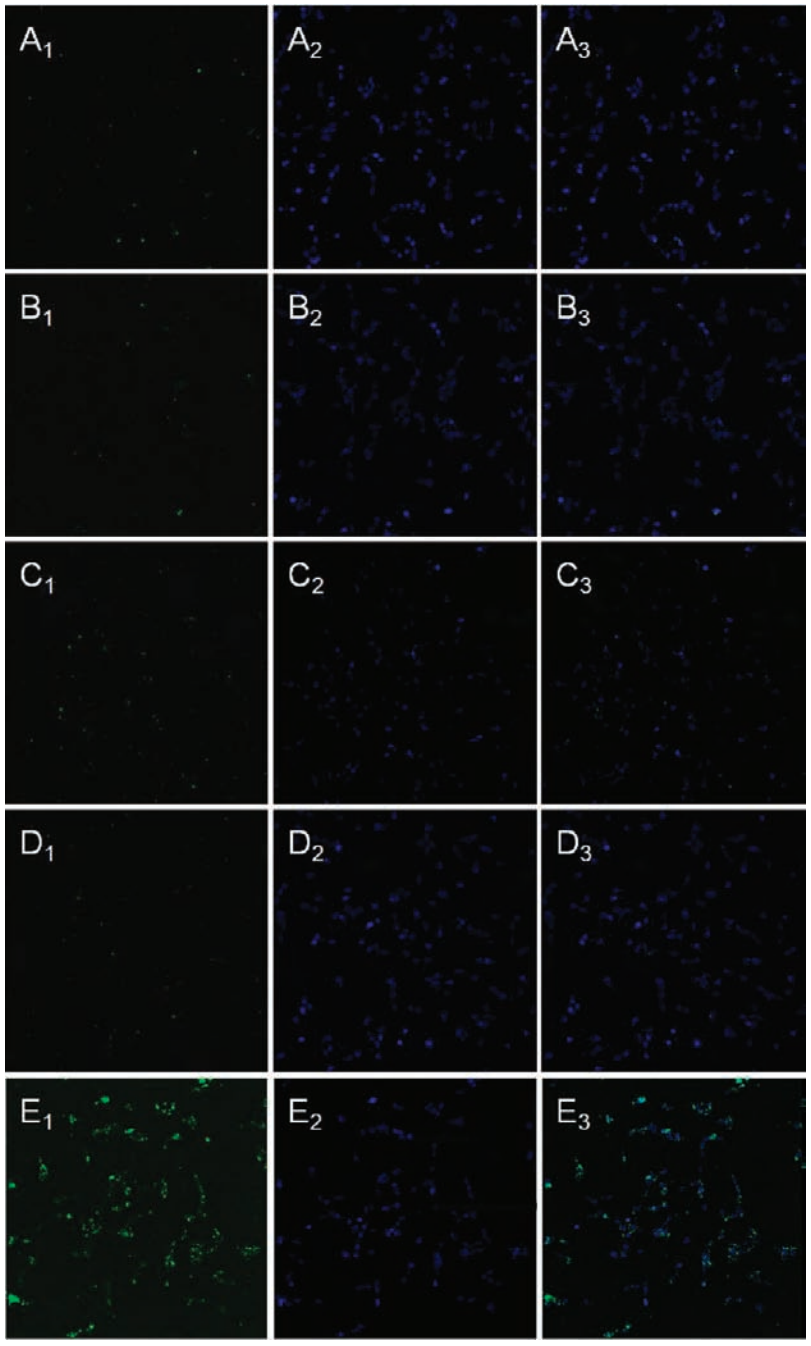


Figure 9. Confocal microscopy images of intracellular trafficking in HeLa cells: (A) TAT/DNA at N/P ratio of 20; (B) TAT/DNA/PV at ratio of 20/1/10; (C) TAT/DNA at N/P ratio of 20 (with 1.5% w/v TCHD in DMEM medium); (D) TAT/DNA/HMGB1 at N/P ratio of 20 (HMGB1/DNA weight ratio was 2); and (E) TAT-PV/DNA at N/P ratio of 15.

However, larger particles have slightly higher DNA release than small ones,[38] so a medium-sized complex may be important in gene delivery. Furthermore, the introduction of NLS sequence could also benefit the gene transfection. As we know, nuclear transport of vector/DNA complexes is one major barrier in nonviral gene delivery systems. Nuclear pore complexes (NPCs) are large proteinaceous assemblies spanning the nuclear envelope, functioning as mediators of a two-way alternative between the nucleoplasmic and cytoplasmic compartments.[39] Generally, macromolecules such as DNA and proteins have difficulty passing through the NPCs due to their large size, and the most possible way for DNA complexes to enter the nucleus is through nuclear envelope fracture during mitosis.[40] So, introduction of NLS sequence may provide a large benefit for nuclear import and subsequent transfection of TAT/DNA complexes. However, introduction of PV sequence to the gene delivery system through electrostatic complexation did not show obvious enhancement in gene expression. This is due to the fact that TAT/DNA/PV ternary complexes were unstable and the contribution of noncovalent bound NLS peptide is limited for the enhancement of gene expression.

We also introduced HMGB1 and TCHD to the gene delivery systems. As shown in Figure 7, for TAT/DNA/HMGB1 complexes with HMGB1/DNA weight ratio of 2,[30] the luciferase expression increased by about 3-fold in HeLa cells and Cos7 cells (HeLa: 1.02×10^6 RLU/mg Protein; Cos7: 1.24

dx.doi.org/10.1021/bc2005472 | *Bioconjugate Chem.* 2012, 23, 125−134

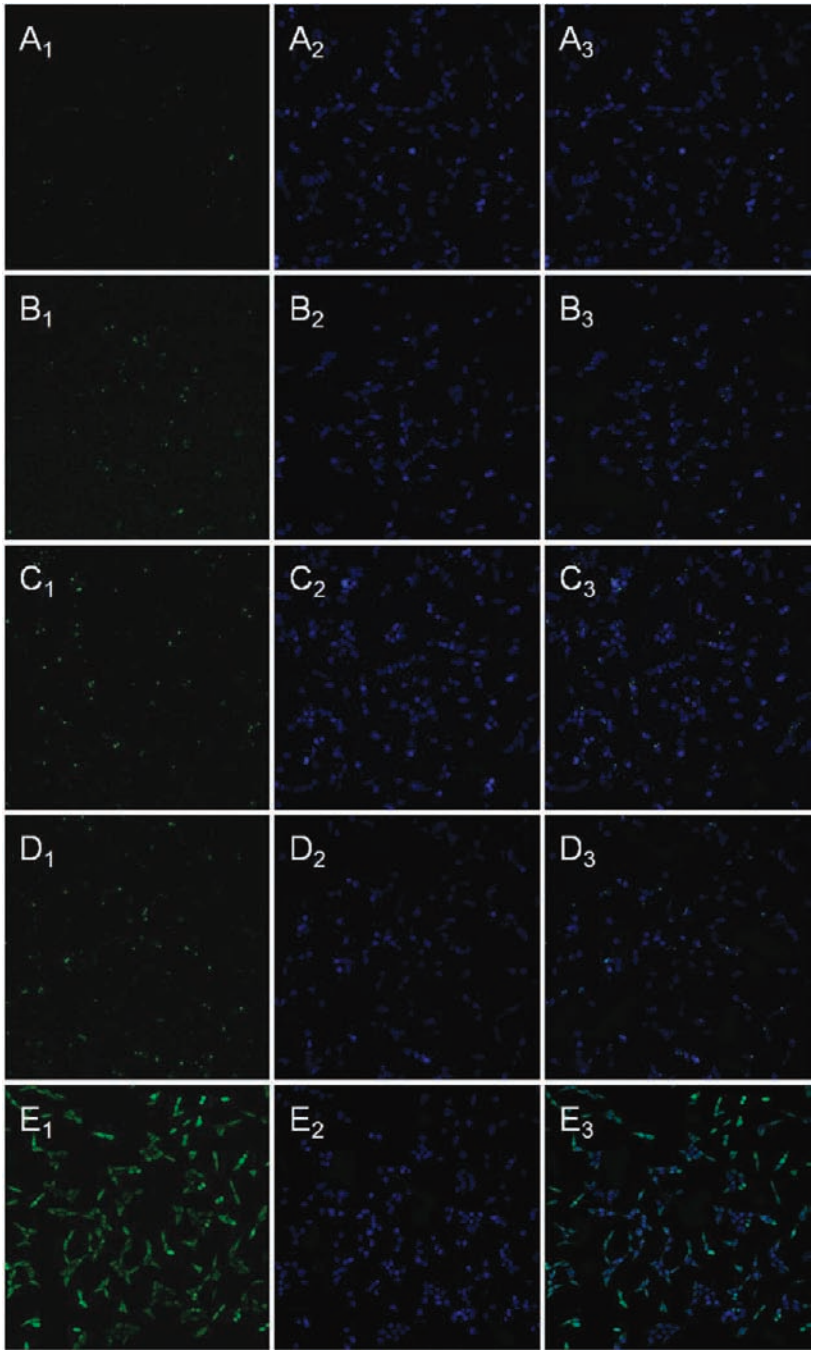


Figure 10. Confocal microscopy images of intracellular trafficking in Cos7 cells. (A) TAT/DNA at N/P ratio of 20; (B) TAT/DNA/PV at ratio of 20/1/10; (C) TAT/DNA at N/P ratio of 20 (with 1.5% w/v TCHD in DMEM medium); (D) TAT/DNA/HMGB1 at N/P ratio of 20 (HMGB1/DNA weight ratio was 2); and (E) TAT-PV/DNA at N/P ratio of 15.

$\times 10^6$ RLU/mg Protein). For TAT/DNA complexes with 1.5% w/v TCHD in DMEM medium, the luciferase expression increased by more than 2-fold in both cell lines (HeLa: 7.72×10^5 RLU/mg Protein; Cos7: 8.71×10^5 RLU/mg Protein). Those results indicated the presence of both HMGB1 and TCHD could increase nuclear transport and thus increase the luciferase expression mediated by the complexes.

To assess the effect of serum, we also evaluated transfections of TAT-PV/DNA complexes in both cell lines in the presence of 10% serum. As shown in Figure 8, no significant decrease was detected in both HeLa and Cos7 cells. For example, in HeLa cells, at N/P ratio of 10, the luciferase expression of TAT-PV/DNA in 10% serum was 1.63×10^7 RLU/mg protein, which is comparable to that without serum (1.86×10^7 RLU/mg protein), which indicated that the TAT-PV vector possessed stability in serum and had potential application *in vivo*.

Cellular Uptake Study of Vector/DNA Complexes by Confocal Laser Scanning Microscopy. In order to investigate the effects of the nuclear localization signals on the complexes in nuclear accumulation and cellular internalization, the HeLa cells and Cos7 cells treated by different complexes were observed by a confocal laser scanning

dx.doi.org/10.1021/bc2005472 | *Bioconjugate Chem.* 2012, 23, 125–134

microscope. Molecular probes YOYO-1 and Hoechst 33258 were used to tag DNA and nucleus.

As shown in Figure 9, after coincubating with TAT/DNA complexes with N/P ratio of 20 for 4 h, only a few green fluorescence dots could be observed in the cytoplasm and almost no green fluoroescence dots were detected in the nucleus of HeLa cells. The results were in accordance with our transfection results above, indicating the limited capacity of TAT peptide in nuclear target. As for TAT/DNA/HMGB1 with N/P of 20 and HMGB1/DNA weight ratio of 2 and TAT/DNA complexes with 1.5% w/v TCHD in DMEM medium, the increase in the number of green fluoroescence dots detected in the cytoplasm is limited.

For HeLa cells treated with TAT-PV/DNA with N/P ratio of 15, apparent increase of green fluorescence dots in the cytoplasm could be detected, and quite a few green fluorescence dots were observed in the nucleus of the cells, which indicated that the covalently bound NLS peptide contributed a lot to the cellular uptake and nuclear accumulation of TAT-based gene delivery systems. However, TAT/DNA/PV complexes did not show obvious enhancement in cellular uptake and nuclear accumulation as compared with TAT/DNA complexes. The possible reason is that the ternary complexes formed by electrostatic complexation were not stable enough and may be degraded in cytoplasm.

Cellular uptake and nuclear accumulation in Cos7 cells were also detected. As shown in Figure 10, consistent with results in HeLa cells, similar trends were observed in Cos7 cells, i.e., TAT-PV/DNA complexes exhibited the highest cellular uptake and nuclear accumulation.

CONCLUSIONS

In this study, we introduced different kinds of nuclear localization signals to TAT-based gene delivery systems to form three kinds of complexes, including TAT-PV/DNA, TAT/DNA/PV, and TAT/DNA/HMGB1. *Trans*-cyclohexane-1,2-diol (TCHD) was also added in DMEM medium to improve the transfection efficiency of TAT/DNA complexes. We found that, except TAT/DNA/PV, the presence of nuclear localization signals in all other complexes benefited nuclear accumulation and resulted in enhanced cellular uptake of plasmid DNA in both HeLa and Cos7 cell lines. Moreover, the luciferase reporter gene expression mediated by TAT-PV/DNA complexes exhibited about 200-fold enhancement as compared with TAT/DNA complexes. These results indicated that additional nuclear localization signals could improve the nuclear transport and cellular uptake of TAT-based gene delivery systems. The modification strategy in this study could effectively improve the gene transfection ability of peptide-based nonviral gene vectors.

AUTHOR INFORMATION

Corresponding Author

*Tel.: + 86 27 6875 5993; fax: + 86 27 6875 4509. E-mail address: xz-zhang@whu.edu.cn (X.Z. Zhang).

ACKNOWLEDGMENTS

This work was financially supported by the Ministry of Science and Technology of China (2011CB606202), National Natural Science Foundation of China (20974083), and the Fundamental Research Funds for the Central Universities.

REFERENCES

(1) Verma, I. M., and Somina, N. (1997) Gene therapy- promises, problems and prospects. *Nature 389*, 239−42.
(2) Zhang, S., Zhao, Y., Zhao, B., and Wang, B. (2010) Hybrids of nonviral vectors for gene delivery. *Bioconjugate Chem. 21*, 1003−9.
(3) Luo, D., and Saltzman, W. M. (2010) Synthetic DNA delivery systems. *Nat. Biotechnol. 18*, 33−7.
(4) Kay, M. A., Glorioso, J. C., and Naldini, L. (2001) Viral vectors for gene therapy: the art of turning infectious agents into vehicles of the therapeutics. *Nat. Med. 7*, 33−40.
(5) Niidome, T., and Huang, L. (2002) Gene therapy progress and prospects: nonviral vectors. *Gene Ther. 9*, 1647−52.
(6) Marshall, E. (1999) Gene therapy death prompts review of adenovirus vector. *Science 286*, 2244−5.
(7) SoRelle, R. (2000) Human gene therapy: science under fire. *Circulation 101*, 9023−4.
(8) Ostrove, J. M. (1994) Safety testing programs for gene therapy viral vectors. *Cancer Gene Ther. 1*, 123−31.
(9) Li, S., and Huang, L. (2000) Nonviral gene therapy: promises and challenges. *Gene Ther. 7*, 31−4.
(10) Merdan, T., Kopecek, J., and Kissel, T. (2002) Prospects for cationic polymers in gene and oligonucleotide therapy against cancer. *Adv. Drug Rev. 54*, 715−58.
(11) Foged, C., and Nielsen, H. M. (2008) Cell-penetrating peptides for drug delivery across membrane barriers. *Expert Opin. Drug Delivery 5*, 105−17.
(12) Joliot, A., and Prochiantz, A. (2004) Transduction peptides: from technology to physiology. *Nat. Cell Biol. 6*, 189−96.
(13) Kaplan, I. M., Wadia, J. S., and Dowdy, S. F. (2005) TAT peptide transduction domain enters cells by macropinocytosis. *J. Controlled Release 102*, 247−53.
(14) Frankel, A. D., and Pabo, C. O. (1988) Cellular uptake of the tat protein from human immunodeficiency virus. *Cell 55*, 1189−93.
(15) Josephson., L., Tung, C. H., Moore, A., and Weissleder, R. (1999) High-efficiency intracellular magnetic labeling with novel superparamagnetic-Tat conjugates. *Bioconjugate Chem. 10*, 186−91.
(16) Rudolph, C., Plank, C., Lausier, J., Schillinger, U., Muller, R. H., and Rosenecker, J. (2003) Oligomers of the arginine-rich motif of the HIV-1 TAT protein are capable of transferring plasmid DNA into cells. *J. Biol. Chem. 278*, 11411−8.
(17) Soundara Manickam, D., Bisht, H. S., Wan, L., Mao, G., and Oupicky, D. (2005) Influence of TAT-peptide polymerization on properties and transfection activity of TAT/DNA polyplexes. *J. Controlled Release 102*, 293−306.
(18) Trabulo, S., Mano, M., Faneca, H., Cardoso, A. L., Duarte, S., Henriques, A., Paiva, A., Gomes, P., Simões, S., and de Lima, M. C. P. (2008) S4(13)-PV cell penetrating peptide and cationic liposomes act synergistically to mediate intracellular delivery of plasmid DNA. *J. Gene Med. 10*, 1210−22.
(19) Bremner, K. H., Seymour, L. W., Logan, A., and Read, M. L. (2004) Factors influencing the ability of nuclear localization sequence peptides to enhance nonviral gene delivery. *Bioconjugate Chem. 15*, 152−61.
(20) Zanta, M. A., Belguise-Valladier, P., and Behr, J. P. (1999) Gene delivery: a single nuclear localization signal peptide is sufficient to carry DNA to the cell nucleus. *Proc. Natl. Acad. Sci. U. S. A. 96*, 91−6.
(21) Lungwitz, U., Breunig, M., Blunk, T., and Göpferich, A. (2005) Polyethylenimine-based non-viral gene delivery systems. *Eur. J. Pharm. Biopharm. 60*, 247−66.
(22) Keller, M., Harbottle, R. P., Perouzel, E., Colin, M., Shah, I., Rahim, A., Vaysse, L., Bergau, A., Moritz, S., Brahimi-Horn, C., Coutelle, C., and Miller, A. D. (2003) Nuclear localization sequence templated nonviral gene delivery vectors: investigation of intracellular trafficking events of LMD and LD vectors systems. *ChemBioChem 4*, 286−98.
(23) Youn, J. H., and Shin, J. S. (2006) Nucleocytoplasmic shuttling of HMGB1 is regulated by phosphorylation that redirects it toward secretion. *J. Immunol. 177*, 7889−97.

(24) Zhang, Q., Li, F., Zhuo, R. X., Zhang, X. Z., and Cheng, S. X. (2011) Self-assembled complexes with dual-targeting properties for gene delivery. *J. Mater. Chem. 21*, 4636−43.
(25) Kim, K., Han, J. S., Kim, H. A., and Lee, M. (2008) Expression, purification and characterization of TAT-high mobility group box-1A peptide as a carrier for nucleic acids. *Biotechnol. Lett. 30*, 1331−7.
(26) Shen, Y., Peng, H., Pan, S., Feng, M., Wen, Y., Deng, J., Luo, X., and Wu, C. (2010) Interaction of DNA/nuclear protein/polycation and the terplexes for gene delivery. *Nanotechnology 21*, 045102.
(27) Ribbeck, K., and Gorlich, D. (2002) The permeability barrier of nuclear pore complexes appears to operate via hydrophobic exclusion. *EMBO. J. 21*, 2664−71.
(28) Trabulo, S., Mano, M., Faneca, H., Cardoso, A. L., Duarte, S., Henriques, A., Paiva, A., Gomes, P., Simões, S., and de Lima, M. C. P. (2008) S4(13)-PV cell penetrating peptide and cationic liposomes act synergistically to mediate intracellular delivery of plasmid DNA. *J. Gene Med. 10*, 1210−22.
(29) Bremner, K. H., Seymour, L. W., Logan, A., and Read, M. L. (2004) Factors influencing the ability of nuclear localization sequence peptides to enhance nonviral gene delivery. *Bioconjugate Chem. 15*, 152−61.
(30) Wang, H. Y., Chen, J. X., Sun, Y. X., Deng, J. Z., Li, C., Zhang, X. Z., and Zhuo, R. X. (2011) *J. Controlled Release 152*, 26−33.
(31) Zorko, M., and Langel, U. (2005) Cell-penetrating peptides: mechanism and kinetics of cargo delivery. *Adv. Drug Rev. 57*, 529−45.
(32) Zaro, J. L., Vekich, J. E., Tran, T., and Shen, W. C. (2009) Nuclear localization of cell-penetrating peptides is dependent on endocytosis rather than cytosolic delivery in CHO cells. *Mol. Pharmaceutics 6*, 337−44.
(33) Fields, G. B., and Noble, R. L. (1990) Solid phase peptide synthesis utilizing 9-fluorenylmethoxycarbonyl amino acids. *Int. J. Pept. Res. 35*, 161−214.
(34) Chen, C. S., Ji, T. J., Xu, X. D., Zhang, X. Z., and Zhuo, R. X. (2010) Nanofibers self-assembled from structural complementary borono-decapeptides. Macromol. Rapid Commun. *Macromol. Rapid Commun. 31*, 1903−8.
(35) Wender, P. A., Mitchell, D. J., Pattabiraman, K., Pellkey, E. T., Steinman, L., and Rothbard, J. B. (2000) The design, synthesis, and evaluation of molecules that enable or enhance cellular uptake: peptoid molecular tranporters. *Proc. Natl. Acad. Sci. U.S.A. 97*, 13003−8.
(36) Zeng, X., Sun, Y. X., Zhang, X. Z., and Zhuo, R. X. (2009) Biotinylated disulfide containing PEI/avidin bioconjugate shows specific enhanced transfection efficiency in HepG2 cells. *Org. Biomol. Chem. 7*, 4201−10.
(37) Gan, Q., Wang, T., Cochrane, C., and McCarron, P. (2005) Modulation of surface charge, Particle size and morphological properties of chitosan-TPP nanoparticles intended for gene delivery. *Colloids Surf., B: Biointerfaces 44*, 65−73.
(38) Prabha, S., Zhou, W. Z., Panyam, J., and Labhasetwar, V. (2002) Size-dependency of nanoparticle-mediated gene transfection: studies with fractionated nanoparticles. *Int. J. Pharm. 244*, 105−15.
(39) Lim, R. Y., and Fahrenkrog, B. (2006) The nuclear pore complex up close. *Curr. Opin. Cell Biol. 18*, 342−7.
(40) Rout, M. P., Aitchison, J. D., Suprato, A., Hjertaas, K., Zhao, Y., and Chait, B. T. (2000) The yesdt nuclear pore complex: composition, architecture, and transport mechanism. *J. Cell. Biol. 148*, 635−51.

Bioconjugate Chemistry

Article

pubs.acs.org/bc

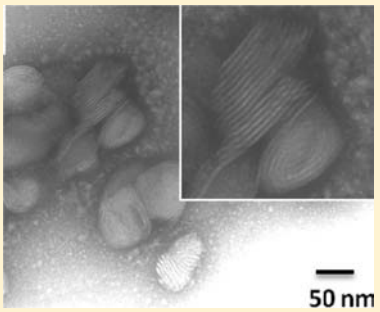
Combinatorial Library of Lipidoids for In Vitro DNA Delivery

Shuo Sun,[†] Ming Wang,[‡] Sarah A. Knupp,[‡] Yadira Soto-Feliciano,[§] Xiao Hu,[‡] David L. Kaplan,[‡] Robert Langer,[§] Daniel G. Anderson,[§] and Qiaobing Xu*[,†,‡]

[†]Department of Chemical and Biological Engineering, [‡]Department of Biomedical Engineering, Tufts University, 4 Colby Street, Medford, Massachusetts 02155, United States

[§]Department of Chemical Engineering, Division of Health Science and Technology, David H. Koch Institute for Integrative Cancer Research, Massachusetts Institute of Technology, 77 Massachusetts Avenue, Cambridge, Massachusetts 02139, United States

ABSTRACT: A combinatorial library of lipidoids was constructed and studied for *in vitro* gene delivery. The library of lipidoids was synthesized by reacting commercially available amines with lipophilic acrylates, acrylamides, or epoxides. Lipidoids derived from amine **86** (*N*,*N*-bis(2-hydroxyethyl)ethylene diamine) and amine **87** (*N*-(3-aminopropyl)-diethaneamine) showed high efficiency in DNA delivery, some with a higher transfection efficiency than Lipofectamine 2000, a commonly used commercial gold standard for *in vitro* gene delivery. The structure−activity relationship between the lipidoids was further studied with respect to small variations in chemical structures and the resulting efficiency in DNA delivery *in vitro*. Since these lipidoids are easy to synthesize and do not require a colipid for efficient DNA delivery, they could offer an inexpensive but effective alternative to other commonly used commercial gene delivery carriers.



INTRODUCTION

Recently, a combinatorial library of lipid-like materials termed "lipidoids" was developed, and their utility as carriers for the delivery of siRNA and antisense oligonucleotides was described.[1−5] These lipidoids were prepared by reacting commercially available amines with lipophilic acrylates, acrylamides, or epoxide. The lipidoids have several advantages as a potential new class of nucleic acid delivery reagents: (i) the chemistry used to synthesize lipidoids is simple and economical, (ii) a library of structural diversity was already developed, (iii) a correlation between structure and function of delivery systems could be constructed from the large data sets accumulated from screening the library of lipidoids.

Utilizing lipidoids for DNA delivery, however, has not been previously reported. Lipidoids are structurally similar to many reported cationic lipids widely used for nonviral delivery of DNA.[6−9] In this paper, we evaluated the potential of lipidoids to facilitate DNA delivery *in vitro*. We demonstrated the capability of lipidoids synthesized from hydroxyl terminated diamines to deliver DNA efficiently into HeLa cells. We also studied structure−activity relationships of the lipidoids with regard to facilitating DNA delivery by designing a series of lipidoids with the same head and tail groups and differing linkers. We found that the lipidoids synthesized through amine and acrylamide addition reactions resulted in the most efficient DNA delivery compared to other lipidoids in the library. However, lipidoids synthesized with an ester linker were not stable and degraded completely in an hour via hydrolysis, hence losing the ability to facilitate DNA delivery.

RESULTS AND DISCUSSION

Lipidoids were prepared by heating commercially available amines with lipophilic acrylamides, acrylates, or epoxides without solvent or catalysts, according to our previously reported methods.[2,4] The simplicity of these reactions allowed us to build a structurally diverse library of lipidoids by varying the types of amines, and the lengths and types (acrylamide/acrylate/epoxide) of tails.[2,4] The resulting crude products were directly used for *in vitro* delivery of DNA.

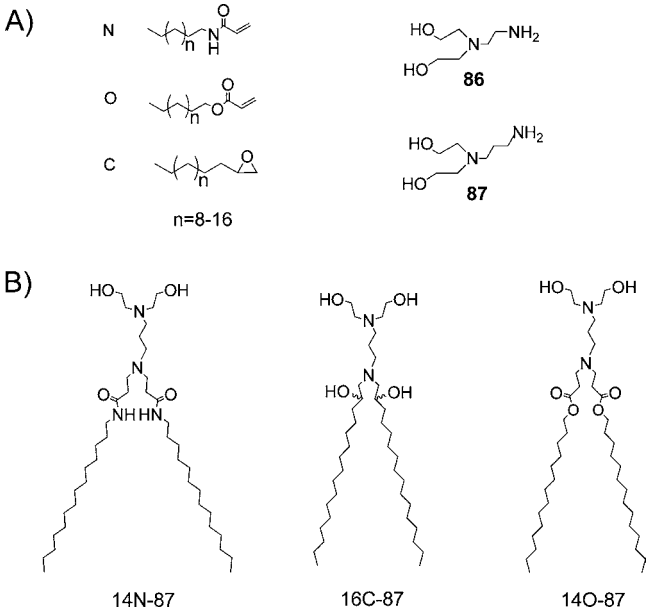
In order to facilitate high-throughput library screening, plasmid DNA encoding β-galactosidase (β-gal) was employed as the reporter gene. The β-gal enzymatic assay was carried out to measure the level of β-gal expression. HeLa cells, in their exponential growth phase, were seeded at 10 000 cells per well into 96-well plates to ∼80% confluency the day before transfection. The library of crude lipidoids was initially screened by delivering lipidoid/DNA complex to the HeLa cells in 96-well plates. The screening results showed that most lipidoids were not effective in facilitating DNA delivery, with transfection efficiencies lower than the leading transfection reagent, Lipofectamine 2000 (data not shown). However, we observed the crude lipidoids derived from amine **86** (*N*,*N*-bis(2-hydroxyethyl)ethylene diamine) and amine **87** (*N*-(3-aminopropyl)diethaneamine) (Scheme 1A) generally showed relatively high efficiency in DNA delivery, sometimes equal to or higher than Lipofectamine. This observation led us to synthesize a refined library of purified lipidoids from the reaction of amines (**86** and **87**) and different types and lengths

Received: October 25, 2011
Revised: December 6, 2011
Published: December 9, 2011

ACS Publications © 2011 American Chemical Society

dx.doi.org/10.1021/bc200572w | *Bioconjugate Chem.* 2012, 23, 135−140

Scheme 1. Combinatorial Synthesis of Lipidoids for DNA Delivery[a]



[a](A) Alkyl-acrylamide, alkyl-acrylate, alkyl-epoxide, and amine molecules used for the library synthesis. (B) Chemical structures of the selected lipidoids with high DNA delivery efficiency. Lipidoids are named as follows: (carbon numbers of tail) (acrylate, acrylamide, or epoxide)-(amine number).

of tails (acrylamide, acrylate, and epoxide), shown in Scheme 1A.

The lipidoids with different tail lengths were purified from the crude reaction mixtures by column chromatography and tested for their ability to deliver β-gal DNA to HeLa cells. The screening results showed that most of the pure lipidoids in the refined library supported DNA delivery into the HeLa cell with expression of β-gal (Figure 1); however, the efficiency varied

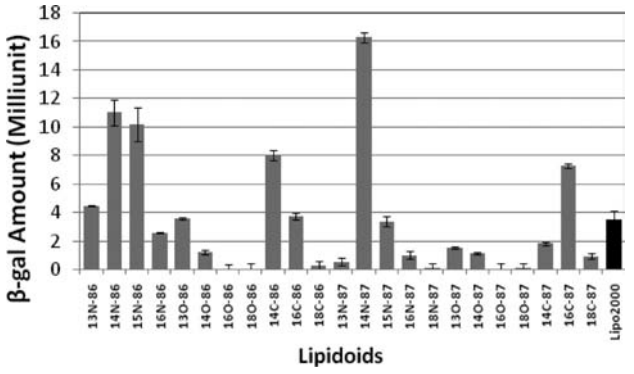


Figure 1. Initial *in vitro* screening of lipidoids for DNA delivery. Lipidoids were screened by delivering plasmid DNA encoding β-gal into HeLa cells. Relative β-gal expression level was determined by assaying the enzyme activity according to reported methods.

depending on the lipidoid structure. Lipidoids derived from amine **86** and **87** with two medium-length tails (e.g., C14 or C15 for acrylamide and acrylate, respectively, and C14 or C16 for epoxide) displayed high transfection efficiencies, in some cases higher than Lipofectamine 2000. We observed that the linkers between tail and head groups of the lipidoids affect the efficiency in facilitating DNA delivery. The lipidoids with amide linkers displayed substantially higher delivery efficiency than those with ester and hydroxyl groups. The delivery efficiency also varied with the amine molecules utilized for lipidoids synthesis; for example, the acrylamide and epoxide conjugated with amine **87** (14N-87 and 16C-87) delivered DNA more efficiently than those conjugated with amine **86** (14N-86 and 16C-86), while for the lipidoids synthesized from acrylate, the reverse results were observed (Figure 1).

To further investigate the structure–activity relationship of these lipidoids for DNA delivery, we selected lipidoids prepared from the reaction of amine **87** with acrylamide (14N-87), epoxide (16C-87), and acrylate (14O-87) (Scheme 1B), which displayed high delivery efficiency. DNA was then complexed with these lipidoids (immediately dissolved in sodium acetate buffer (50 mM, pH = 5.5) before use) in different weight ratios for delivery. The results showed the lipidoid to DNA ratios (w/w) affected the delivery efficiency and the resulting β-gal activity. These lipidoids have a M_w around 680 Da and two positive charges; a single base pair of DNA has a M_w around 660 Da and two negative charges. The weight/weight (w/w) ratio of the lipidoid/DNA has a similar value to the molar ratio and positive/negative (P/N) charge ratio. For all lipidoids selected, β-gal enzyme activity was detectable at the lipidoid/DNA ratio of 1:1 (Figure 2). The delivery efficiency was

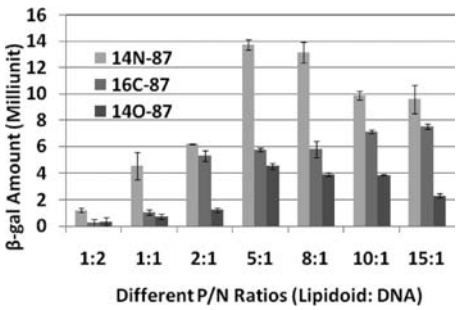


Figure 2. Relationship of positive to negative charge (P/N) ratios of lipidoids/DNA and DNA delivery efficiency. Lipidoids 14C-87, 16C-97, and 14O-87 were selected according to initial screening results. The efficiency was monitored as the β-gal expression level.

enhanced by an increasing ratio. For 14N-87 and 14O-87, the transfection efficiency increased to the highest level at a lipidoid/DNA ratio of 5:1 and slowly declined by further increasing the ratio. Lipidoid 16C-87, on the other hand, enhanced its transfection efficiency until the lipidoid/DNA ratio increased to 15:1. At the dose level used in these experiments, no obvious cytotoxicity was observed from the delivery reagents used. Under the same conditions, the 14N-87 showed higher tranfection efficiency compared with 14O-87 and 16C-87.

It is known that the transfection efficiency of a given lipid-DNA complex depends on its structure and physicochemical properties.[10] We used negative-staining transmission electron microscopy (TEM) to study the size and morphology of the lipidoid-DNA complexes and to illustrate a structure–function correlation of lipidoids with biological activity. The 14N-87 was able to efficiently self-assemble with DNA through electrostatic interactions and form condensed multilamellar structure nanocomplexes (~100 nm) with DNA intercalated between the lipid bilayers (Figure 3). In contrast, 14O-87 and 16C-87 tended to form loose "spaghetti and meatball-like structures".[10]

dx.doi.org/10.1021/bc200572w | *Bioconjugate Chem.* 2012, 23, 135–140

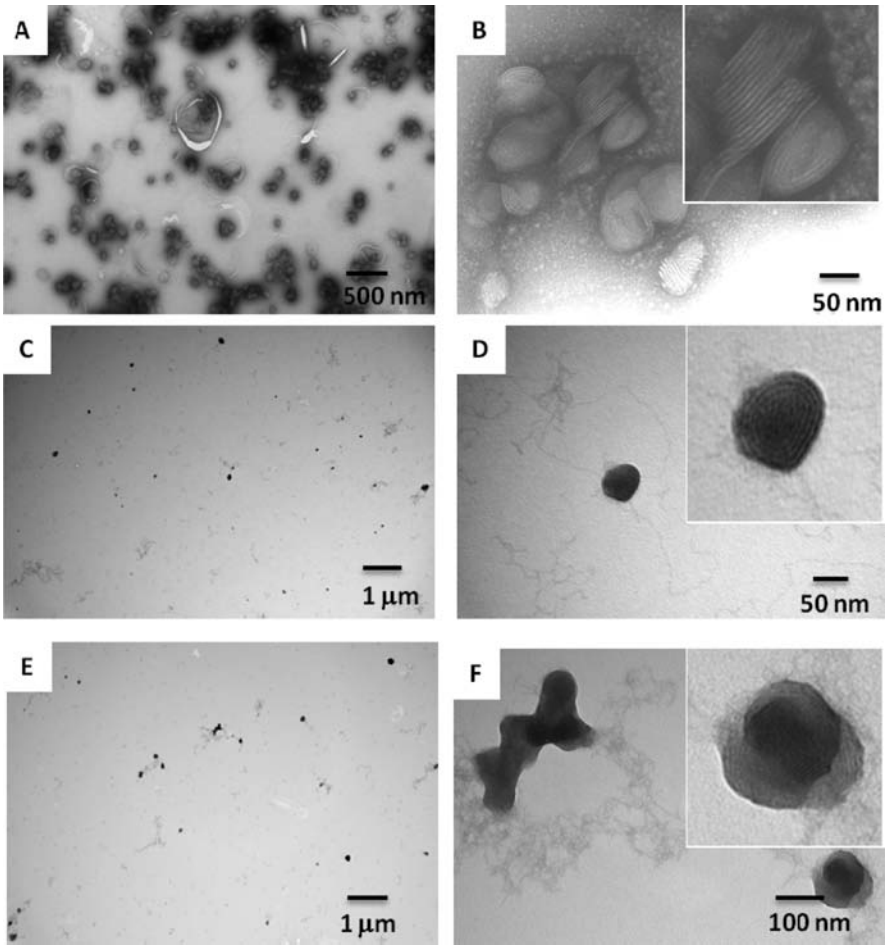


Figure 3. Negative staining TEM images of lipidoids/DNA (w/w = 5:1) nanoparticles. A and B: 14N-87/DNA complex; C and D: 16C-87/DNA complexes; E and F: 14O-87/DNA complexes.

The higher transfection efficiency of DNA delivery by 14N-87 may be attributed to its higher efficiency in nanoparticle formation compared with 14O-87 and 16C-87.

We next determined the efficiency of DNA encapsulation by different lipidoids at different P/N ratio using PicoGreen assay (Figure 4). At a low P/N ratio (<5), the DNA encapsulation

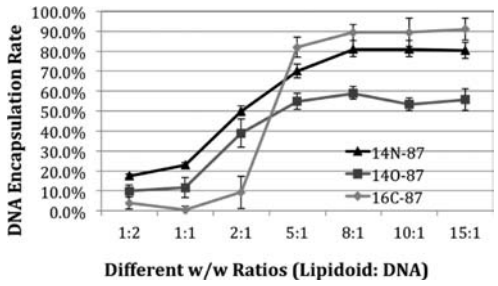


Figure 4. Picogreen assay of the lipidoids (14N-87, 16C-87, and 14O-87)/β-gal encoding DNA complexes in different ratios.

percentage was low for all three lipidoids, which led to the observed low transfection efficiency (Figure 3). All three lipidoids showed increased DNA encapsulation with an increase of the P/N ratio. 14N-87 and 16C-87 had a maxium percentage of encapsulation of 80−90%, while 14O-87 reached 60%, which may explain why DNA delivery by 14N-87 and 16C-87 was more efficient than by 14O-87. Although lipidoids 14N-87 and 16C-87 displayed similar binding abilities with DNA in ratios above 5:1, 14N-87 was generally more efficient in mediating DNA delivery than 16C-87. This was probably due to 16C-87 and DNA forming a large amount of flocculent nanostructures, while 14N-87 and DNA formed condensed individual multilamellar nanoparticles (Figure 3).

We noticed that 14O-87 lost its capability in DNA delivery when the as-prepared solution was stored for a certain period of time (>2 h), a phenomenon not observed with the other two lipidoids, 14N-87 and16C-87. No successful DNA delivery was observed using the stored 14O-87 compared with the freshly prepared sample (Figure 5). We observed that the stored 14O-87 and DNA are not able to assemble to form nanoparticles. We hypothesize that the loss of ability to mediate DNA delivery is ascribed to the hydrolysis of the ester linker in 14O-87. This was confirmed by FTIR analysis of fresh and stored 14O-87 solutions (Figure 6). The peak at 1720 cm^{-1} assigned to the ester bond in 14O-87 weakened after 1 h in a sodium acetate solution and a new peak at 1680 cm^{-1} appeared. It has been observed that the rapid degradation of amine-containing polyesters is attributed to the intramolecular nucleophilc assistance by the pendant amine groups.[11−13] In the case of 14O-87, we speculate that the rapid hydrolysis attributed to the nucleophilic attack of the free hydroxyl group of the molecule itself or nearby molecules.[14]

dx.doi.org/10.1021/bc200572w | *Bioconjugate Chem.* 2012, 23, 135−140

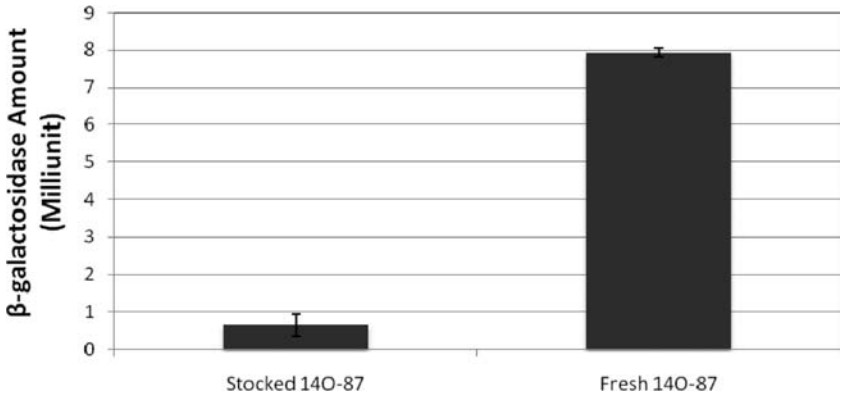


Figure 5. Different β-gal expression level delivered by fresh and stocked 14O-87/DNA complex. The delivery efficiency was converted from the β-gal activity assay. Lipidoid/DNA with a ratio of 5:1 was used in the experiment.

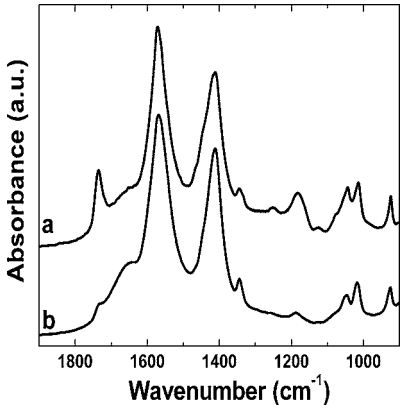


Figure 6. Normalized FT-IR spectra of fresh 14O-87 (a) and stocked (b) solution. 14O-87 was dissolved in sodium acetate buffer solution (50 mM, pH = 5.5).

CONCLUSIONS

We report the evaluation of a library of lipidoids for *in vitro* DNA delivery through a facile combinatorial approach. The mild reactions between amines and acrylamides, acrylates, or epoxides enabled the construction of a library to screen for efficient gene delivery carriers. The initial screening for DNA delivery indicated that lipidoids formed through amine and acrylamide addition reactions generated higher delivery efficiencies than acrylate- and epoxide-derived counterparts. The rapid hydrolysis of lipidoids with ester linkages decreased efficiency in DNA delivery. The structure−activity relationships demonstrated provide insight for designing new lipidoids for gene delivery. These lipidoids are easy to synthesize and do not require a colipid for efficient DNA delivery. We believe these systems could offer an inexpensive and effective alternative to other commonly used commercial gene delivery agents.

EXPERIMENTAL SECTION

Synthesis of Lipidoids. Lipidoid library synthesis was performed and characterized as previously described.[2,4] Amines and 1-aminoalkanes were purchased from Sigma-Aldrich (St. Louis, MO) and TCI America (Portland, OR). Acrylamides were synthesized by the dropwise addition of acryloyl chloride to a solution of the appropriate 1-aminoalkane in dichloromethane in an ice-bath under an inert atmosphere. Lipidoids were synthesized by conjugation addition of amines to acrylamides, acrylates, or epoxides. These reactions were performed in 5 mL Teflon-lined glass screw-top vials. For lipioids prepared from acrylamides, the number of equivalents of acrylamide was equal to maximum number of conjugate additions possible for each amine (2 for primary amines). The reactions were performed on a 200 mg scale (of amine). The mixture was stirred at 90 °C for 7 days. After cooling, the lipid mixtures were used without purification unless otherwise specified. Representative library members were characterized by thin layer chromatography, IR, NMR, and mass spectroscopy.[2,4]

In Vitro DNA Transfection. HeLa cells were obtained from ATCC (Manassas, VA) and cultured in phenol red-free DMEM supplemented with 10% fetal bovine serum and 100 units/mL of penicillin/streptomycin at 37 °C and 5% CO_2. All cell culture reagents were purchased from Invitrogen Corporation (Carlsbad, CA) unless otherwise noted. pCMV β-gal DNA was also purchase from Elim Biopharmaceuticals, Inc. (Hayward, CA). To facilitate screening throughput, lipidoid-DNA complexes were formed by simple mixing of lipidoid-DNA solutions in 50 mM sodium acetate buffer solution pH 5.5 in microtiter plates. For transfection in 96-well plates, HeLa cells were seeded (10 000 cells per well) into each well of an opaque white 96-well plate and allowed to attach overnight. Cells were transfected with 200 ng of DNA (per well) complexed with lipidoids at fixed lipidoid/DNA weight ratio of 5:1. The lipidoids were added to the DNA solutions, and then incubated for 10 min at room temperature to allow for complex formation. The lipidoid/DNA solution was immediately added to cells in each well. After transfection, cells were incubated for 24 h at 37 °C and 5% CO_2 before analyzing for β-gal protein expression. Control experiments were also performed with Lipofectamine 2000 (Invitrogen, Carlsbad, CA), as described by the vendor. Transfection was performed in quadruplicate.

***β*-gal Activity of Cell Culture.** β-gal activity assay is described by the developed protocol[15] with slight modification. Briefly, after the transfection over 24 h, all growth medium in the 96-well plate was removed by vacuum aspiration. 100 μL PBS was added into each well to wash the cell for 5 min (×2) on ice. 50 μL Triton (Sigma-Aldrich, St. Louis, MO) solution (0.5% in PBS) was added into each well right after removal of PB. The plate was then left on the ice for 10 min. 50 μL of *o*-nitrophenyl-β-D-galactoside (ONPG) (Sigma-Aldrich, St. Louis, MO) solution (4 mg/mL in z-buffer)[15] was added into each well by multichannel pipet. The plate was incubated for 15 min

at 37 °C. The concentration of β-gal was determined by measuring the absorbance at 409 nm.

DNA Binding Assay. PicoGreen assay was performed as previously described.[16] Briefly, in 96-well plate, 50 μL/well of lipidoid solutions at 1 mg/mL in NaOAc buffer was added to 50 μL/well of DNA (60 μg/mL in NaOAc buffer). The solutions were mixed vigorously and allowed to sit undisturbed for 5 min to allow for lipidoid-DNA complex formation. Then, 100 μL/well of PicoGreen working solution (Invitrogen,Carlsbad, CA) was added. PicoGreen working solution was prepared by diluting 52.8 μL of the purchased stock into 9.9 mL NaOAc buffer. After 5 min, 30 μL/well of lipidoid-DNA-PicoGreen solution was added to 200 μL/well of DMEM media in a black 96-well polystyrene plate. The plate fluorescence was then measured on a SpectraMax M2Multi-Mode Microplate Reader (Molecular Devices, Inc. California, USA) at excitation of 485 nm and emission of 535 nm. The relative fluorescence (*RF*) was calculated by the following relationship:

$$RF = (F_{\text{sample}} - F_{\text{blank}})/(F_{\text{DNA}} - F_{\text{blank}})$$

where F_{sample} is the fluorescence of the lipidoid-DNA-PicoGreen sample, F_{blank} is the fluorescence of a sample with lipidoid or DNA (only PicoGreen), and F_{DNA} is the fluorescence of a sample with DNA-PicoGreen without lipidoid. The DNA encapsulation is $1 - RF$.

Transmission Electron Microscopy (TEM). Lipidoid/DNA complexes were prepared with the same protocols as *in vitro* experiments (5:1 weight ratio of total lipidoid to DNA). Droplets of the sample (5 μL) were applied to hydrophilized carbon-covered copper grids (300 meshes) for 30 min. The sample was subsequently rinsed with contrasting material (1% uranyl acetate at pH 4.5). The remaining stain solution was removed with a filter paper and air-dried. TEM microstructure was determined using a Tecnai FEG TEM (FEI Tecnai 12 Spirit Biotwin, FEI Company, Hillsboro, OR) operating at 80 kV.

Fourier Transform Infrared Spectroscopy (FTIR). The structural characteristics were observed using FTIR as previously reported by Hu et al.[17,18] Lipidoid/DNA nanoparticles were prepared as described in TEM section. Before the measurement, the lipidoid/DNA solution was dropped onto the detector stage, blowing with the air gun at room temperature until all the solvent evaporated. Normalization of the curve was established through the protocol described in Hu's paper.[17,18]

AUTHOR INFORMATION

Corresponding Author

*E-mail Address: qiaobing.xu@tufts.edu.

ACKNOWLEDGMENTS

This research was supported by Tufts University. D. G. A. and R. L. acknowledge the grants from NIH under NIH R01-EB000233 and RO1-CA132091. Q. X. also acknowledges Tufts FRAC award. We want to thank Nicki Watson at Whitehead Institute, MIT, for the help on TEM imaging.

REFERENCES

(1) Akinc, A., Goldberg, M., Qin, J., Dorkin, J. R., Gamba-Vitalo, C., Maier, M., Jayaprakash, K. N., Jayaraman, M., Rajeev, K. G., Manoharan, M., Koteliansky, V., Rohl, I., Leshchiner, E. S., Langer, R., and Anderson, D. G. (2009) Development of lipidoid−siRNA formulations for systemic delivery to the liver. *Mol. Ther. 17* (5), 872−879.

(2) Akinc, A., Zumbuehl, A., Goldberg, M., Leshchiner, E. S., Busini, V., Hossain, N., Bacallado, S. A., Nguyen, D. N., Fuller, J., Alvarez, R., Borodovsky, A., Borland, T., Constien, R., de Fougerolles, A., Dorkin, J. R., Jayaprakash, K. N., Jayaraman, M., John, M., Koteliansky, V., Manoharan, M., Nechev, L., Qin, J., Racie, T., Raitcheva, D., Rajeev, K. G., Sah, D. W. Y., Soutschek, J., Toudjarska, I., Vornlocher, H. P., Zimmermann, T. S., Langer, R., and Anderson, D. G. (2008) A combinatorial library of lipid-like materials for delivery of RNAi therapeutics. *Nat. Biotechnol. 26*, 561−569.

(3) Cho, S. W., Hartle, L., Son, S. M., Yang, F., Goldberg, M., Xu, Q., Langer, R., and Anderson, D. G. (2008) Delivery of small interfering RNA for inhibition of endothelial cell apoptosis by hypoxia and serum deprivation. *Biochem. Biophys. Res. Commun. 376* (1), 158−163.

(4) Love, K. T., Mahon, K. P., Levins, C. G., Whitehead, K. A., Querbes, W., Dorkin, J. R., Qin, J., Cantley, W., Qin, L. L., Racie, T., Frank-Kamenetsky, M., Yip, K. N., Alvarez, R., Sah, D. W. Y., de Fougerolles, A., Fitzgerald, K., Koteliansky, V., Akinc, A., Langer, R., and Anderson, D. G. (2010) Lipid-like materials for low-dose, in vivo gene silencing. *Proc. Natl. Acad. Sci. U. S. A. 107* (5), 1864−1869.

(5) Whitehead, K. A., Sahay, G., Li, G. Z., Love, K. T., Alabi, C. A., Ma, M., Zurenko, C., Querbes, W., Langer, R. S., and Anderson, D. G. (2010) Synergistic silencing: combinations of lipid-like materials for efficacious siRNA delivery. *Mol. Ther. 19* (9), 1688−1694.

(6) Wheeler, C. J., Felgner, P. L., Tsai, Y. J., Marshall, J., Sukhu, L., Doh, S. G., Hartikka, J., Nietupski, J., Manthorpe, M., Nichols, M., Plewe, M., Liang, X., Norman, J., Smith, A., and Cheng, S. H. (1996) A novel cationic lipid greatly enhances plasmid DNA delivery and expression in mouse lung. *Proc. Natl. Acad. Sci. U. S. A. 93* (21), 11454−11459.

(7) Byk, G., Dubertret, C., Escriou, V., Frederic, M., Jaslin, G., Rangara, R., Pitard, B., Crouzet, J., Wils, P., Schwartz, B., and Scherman, D. (1998) Synthesis, activity, and structure−activity relationship studies of novel cationic lipids for DNA transfer. *J. Med. Chem. 41* (2), 224−235.

(8) Felgner, J. H., Kumar, R., Sridhar, C. N., Wheeler, C. J., Tsai, Y. J., Border, R., Ramsey, P., Martin, M., and Felgner, P. L. (1994) Enhanced gene delivery and mechanism studies with a novel series of cationic lipid formulations. *J. Biol. Chem. 269*, 2550−2561.

(9) Felgner, P. L., Gadek, T. R., Holm, M., Roman, R., Chan, H. W., Wenz, M., Northrop, J. P., Ringold, G. M., and Danielsen, M. (1987) Lipofection: a highly efficient, lipid-mediated DNA-transfection procedure. *Proc. Natl. Acad. Sci. U. S. A. 84* (21), 7413−7417.

(10) Chesnoy, S., and Huang, L. (2000) Structure and function of lipid-DNA complexes for gene delivery. *Annu. Rev. Biophys. Biomol. Struct. 29*, 27−47.

(11) Lim, Y., Choi, Y. H., and Park, J. (1999) A self-destroying polycationic polymer: biodegradable poly(4-hydroxy-l-proline ester). *J. Am. Chem. Soc. 121* (24), 5633−5639.

(12) Lim, Y., Kim, C., Kim, K., Kim, S. W., and Park, J. (2000) Development of a safe gene delivery system using biodegradable polymer, poly[α-(4-aminobutyl)-l-glycolic acid]. *J. Am. Chem. Soc. 122* (27), 6524−6525.

(13) Lynn, D. M., and Langer, R. (2000) Degradable poly(β-amino esters): synthesis, characterization, and self-assembly with plasmid DNA. *J. Am. Chem. Soc. 122* (44), 10761−10768.

(14) Capon, B., McDowell, T. S., and Raftery, W. V. (1973) Hydroxy-group participation in ester hydrolysis. *J. Chem. Soc., Perkin Trans. 2*, 1118−1125.

(15) Miller, J. H. (1972) *Experiments in Molecular Genetics*, pp 352−355, Cold Spring Harbor, New York.

(16) Green, J. J., Zugates, G. T., Tedford, N. C., Huang, Y. H., Griffith, L. G., Lauffenburger, D. A., Sawicki, J. A., Langer, R., and Anderson, D. G. (2007) Combinatorial modification of degradable polymers enables transfection of human cells comparable to adenovirus. *Adv. Mater. 19* (19), 2836−2842.

(17) Hu, X., Kaplan, D., and Cebe, P. (2006) Determining beta-sheet crystallinity in fibrous proteins by thermal analysis and infrared spectroscopy. *Macromolecules 39* (18), 6161−6170.
(18) Hu, X., Kaplan, D., and Cebe, P. (2008) Dynamic protein−water relationships during β-sheet formation. *Macromolecules 41* (11), 3939−3948.

Bioconjugate Chemistry

Technical Note

pubs.acs.org/bc

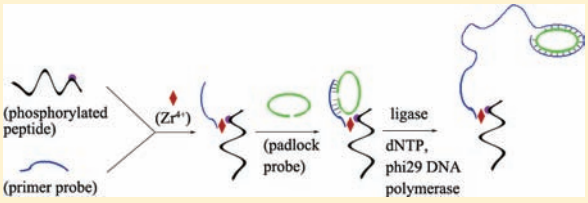
Electrochemical Strategy for Sensing Protein Phosphorylation

Peng Miao,[†,‡] Limin Ning,[‡] Xiaoxi Li,[‡] Pengfei Li,[†] and Genxi Li*[,†,‡]

[†]Laboratory of Biosensing Technology, School of Life Sciences, Shanghai University, Shanghai 200444, P.R. China

[‡]Department of Biochemistry and National Key Laboratory of Pharmaceutical Biotechnology, Nanjing University, Nanjing 210093, P.R. China

ABSTRACT: We herein report a novel electrochemical method in this paper to monitor protein phosphorylation and to assay protein kinase activity based on Zr^{4+} mediated signal transition and rolling circle amplification (RCA). First, substrate peptide immobilized on a gold electrode can be phosphorylated by protein kinase A. Then, Zr^{4+} links phosphorylated peptide and DNA primer probe by interacting with the phosphate groups. After the introduction of the padlock probe and phi29 DNA polymerase, RCA is achieved on the surface of the electrode. As the RCA product, a very long DNA strand, may absorb a large number of electrochemical speices, $[Ru(NH_3)_6]^{3+}$, via the electrostatic interaction, localizing them onto the electrode surface, initiated by protein kinase A, a sensitive electrochemical method to assay the enzyme activity is proposed. The detection limit of the method is as low as 0.5 unit/mL, which might promise this method as a good candidate for monitoring phosphorylation in the future.



INTRODUCTION

Protein kinase-catalyzed phosphorylation is an important biological process in metabolism and plays vital regulatory roles in cell communication. The abnormal regulations of protein kinase may lead to various diseases including cancer, diabetes, and some neurodegenerative diseases.[1,2] Therefore, the identification of protein kinase activity as well as its inhibition is not only an important research topic of basic biology, but also a promising approach to early diagnosis and drug discovery.[3−6] Many methods have been proposed for the detection of protein kinase-catalyzed phosphorylation with various techniques, including electrochemical,[7−11] optical,[12−14] and fluorescent approaches.[15−17] Also, nanoparticles such as Au, TiO_2, and Ag nanoparticles are exploited for the detection of phosphorylation.[18,19]

Considering the increased interest in the study of phosphorylation, we present a novel electrochemical method in this paper for assay of protein kinase activity based on Zr^{4+} mediated signal transition and rolling circle amplification (RCA), a simple enzymatic process that generates very long single-stranded DNA under isothermal conditions.[20−27] Compared with other signal amplification methods such as polymerase chain reaction and nanoparticle mediated signal amplification, RCA have many advantages: (1) the reaction can be carried out at a constant temperature, so neither a thermally stable DNA polymerase nor sophisticated instrumentation is required; (2) high specificity can be achieved over DNA single base mismatch; (3) the created long DNA chains can meet the requirement of in situ amplification; (4) the experiment is carried out in pure biological system without the influence of nonbiological materials like nanoparticles. In this strategy, substrate peptide is first modified on a gold electrode. After phosphorylation by PKA, the phosphorylated peptide is linked to the DNA primer probe for RCA by Zr^{4+}.[28] Consequently, RCA can be achieved on the surface of the electrode with the help of template probe and phi29 DNA polymerase. After the binding of the electrochemical speices, $[Ru(NH_3)_6]^{3+}$ on the RCA products,[29,30] sensitive electrochemical response can be obtained for the detection of phosphorylation and the assay of the protein kinase activity with cascade signal amplification. The detection limit of this method is 0.5 unit/mL, which is similar to that of a recently reported fluorescent method[16] and the lowest one using an electrochemical assay.[7] Moreover, the linear detection range of this method is improved to be 5 to 500 unit/mL, which is rather wide.

EXPERIMENTAL PROCEDURES

Materials and Chemicals. Substrate peptide LRRASLGGGGC and control peptide WKGEWTGRRGC were synthesized by Shanghai Ketai Biotechnology Co., Ltd. Oligonucleotides named as primer probe (5′-AAAAAAAAAAAAAAAAACCCTATAAATACCCTAAC-3′) and padlock probe (5′-TTATAGGGTTAGGGTTAGGGT-TAGGGTAT-3′) were synthesized and purified by Shanghai Invitrogen Biotechnology Co., Ltd. Both of them were designed to contain 5′-phosphoryl ends. Fetal calf serum was purchased from NanJing SunShine Biotechnology Co., Ltd. Phi29 DNA polymerase was obtained from New England Biolabs Ltd. cAMP-dependent protein kinase (PKA), T4 DNA ligase, H−89, ethylenediaminetetraacetic acid (EDTA), mercaptohexanol (MCH), hexaammineruthenium(III) chloride ($[Ru(NH_3)_6]^{3+}$), tris(2-carboxyethyl)phosphine hydrochloride (TCEP), dNTP, ATP, cAMP, and $ZrOCl_2$ were purchased from Sigma. All other chemicals were of analytical grade and used as received. Water

Received: September 21, 2011
Revised: December 1, 2011
Published: December 11, 2011

ACS Publications © 2011 American Chemical Society

dx.doi.org/10.1021/bc200523p | *Bioconjugate Chem.* 2012, 23, 141−145

purified with a Milli-Q purification system (Barnstead) was used to prepare Tris-HCl buffer solution (pH 7.5, TBS) and all the other solutions.

Preparation of Substrate Peptide Modified Electrode. A gold electrode (3 mm diameter) was first soaked in piranha solution (98% H_2SO_4/30% H_2O_2 = 3:1) for 5 min (*Caution: Piranha solution dangerously attacks organic matter!*) and then rinsed with water. Then, the electrode was polished carefully to a mirror-like surface with P3000 silicon carbide paper and 1 μm, 0.3 μm, and 0.05 μm alumina slurry, respectively. After that, it was sonicated for 5 min in ethanol, and then in water. The pretreated electrode was further soaked in nitric acid (50%) for 30 min, followed by being electrochemically cleaned with 0.5 M H_2SO_4 to remove any remaining impurities. After being dried with nitrogen, the electrode was incubated with peptide solution (0.2 mM, 20 mM HEPES, containing 10 mM TCEP, pH 6.0) for 12 h at room temperature, followed by a 0.5 h treatment with 0.1 mM MCH. Finally, the electrode was washed first with TBS containing 0.5% Tween to block the adsorption of free enzymes and nonspecific proteins, and then with blank TBS and pure water, respectively.

Phosphorylation on the Electrode. PKA stock solution was diluted to a series of concentrations with 10 mM HEPES (pH 6.5) containing 200 μM ATP, 600 μM cAMP, 5 mM TCEP, and 10 mM $MgCl_2$. Then, the substrate peptide-modified electrode was immersed in the above solutions for 30 min at 37 °C, followed by an electrode washing procedure.

For the control experiment, the control peptide instead of the substrate peptide was modified on the electrode before the phosphorylation.

For the inhibition experiments, different amount of H-89 was dissolved in the PKA reaction solution to check the inhibition of H-89 to PKA during this study.

Linkage of Peptide with Primer Probe Mediated by Zr^{4+} and the Execution of RCA. The peptide modified electrode which had been pretreated by PKA was first immersed in a Zr^{4+} solution (0.2 mM, TBS) at room temperature for 1 h, so that Zr^{4+} could bind to the phosphorylation site of the peptide by electrostatic interaction. Based on the same mechanism, primer probes were further bound with Zr^{4+} by incubating the modified electrode in 1 μM primer probe at room temperature for 1 h. Consequently, the peptide and the primer probe were linked mediated by Zr^{4+}.

For hybridization of primer probe and padlock probe, the above electrode was incubated with 0.1 mL phosphate buffered saline (pH 7.4) containing 1 μM padlock probe for 0.5 h at 37 °C. In this process, the linear padlock probe transforms into circle template after hybridization with primer probe. The nick was linked by T4 DNA ligase (6 unit/mL) prepared in 50 mM TBS containing 10 mM $MgCl_2$, 10 mM DTT, and 1 mM ATP at 37 °C, the duration of which was about 1 h.

The achievement of RCA also required phi29 DNA polymerase (50 unit/mL), which was prepared in 50 mM TBS containing 10 mM $MgCl_2$, 10 mM $(NH_4)_2SO_4$, 4 mM DTT, and 0.2 mg/mL BSA. dNTP was also added in the reaction solution with the concentration of 0.5 mM. After 1 h RCA reaction at 37 °C, phi29 DNA polymerase was inactivated by heating the reaction solution at 95 °C for 5 min.

Electrochemical Measurements. Electrochemical impedance spectroscopy (EIS), cyclic voltammetry (CV), and chronocoulometry (CC) were performed on an electrochemical analyzer (CHI660B, CH Instruments) by using three-electrode system consisting of the modified gold electrode as the working electrode, a saturated calomel reference electrode (SCE), and a platinum auxiliary electrode. The test solution for EIS was 1 M KNO_3 containing 5 mM $Fe(CN)_6^{3-/4-}$ and the experiments were performed upon application of the biasing potential 0.259 V, applying 5 mV amplitude in the frequency range of 0.1 Hz to 100 kHz. For CV and CC experiments, the test solution was 10 mM TBS containing 50 μM $[Ru(NH_3)_6]^{3+}$. The scan rate was 100 mV/s for CV, and the pulse period was 250 ms for CC.

RESULTS AND DISCUSSION

The strategy in this work to monitor phosphorylation by electrochemical technique coupled with cascade signal amplification has been illustrated in Figure 1. First, the gold

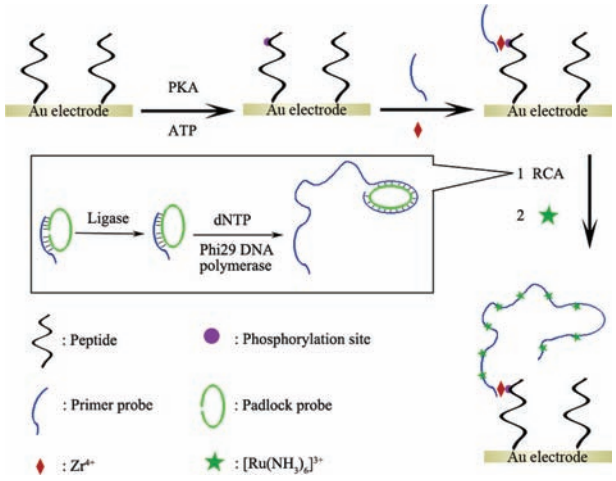


Figure 1. Schematic illustration of the strategy for monitoring the activity of protein kinase.

electrode is modified with the substrate peptide through its cysteine end. After the phosphorylation of the peptide by PKA as the model kinase in this work to phosphorylate the serine in the substrate peptide, Zr^{4+} is attached to the phosphorylation sites due to the steady interaction between Zr^{4+} and the phosphate groups. Then, primer probe with 5′-phosphoryl end will also interact with Zr^{4+} with the same mechanism; thus, the peptide and the primer probe are linked by Zr^{4+}. After that, the linear padlock probe, designed to match primer probe in a head to tail fashion, hybridizes with the primer probe, followed by ligation with T4 DNA ligase. Consequently, the formed circular padlock probe, coupled with primer probe and phi29 DNA polymerase, can then generate a long DNA strand based on the RCA reaction. Therefore, since $[Ru(NH_3)_6]^{3+}$, the electrochemical species, may bind to the anionic phosphate of the DNA strands, cascade electrochemical signals are obtained, and sensitive electrochemical methods for the detection of phosphorylation and for the assay of PKA activity can be proposed.

Electrochemistry at the Gold Electrodes. Nyquist plot of impedance of the electrode has been obtained after each treatment of the gold electrode. In the impedance spectra, the linear part at lower frequencies corresponds to diffusion and the semicircle portion at higher frequencies relates to the interfacial charge transfer resistance. In Figure 2, the bare electrode contains no semicircle portion, and after the immobilization of substrate peptide, a semicircle can be observed indicating the increased interfacial charge transfer resistance. After phosphor-

dx.doi.org/10.1021/bc200523p | *Bioconjugate Chem.* 2012, 23, 141–145

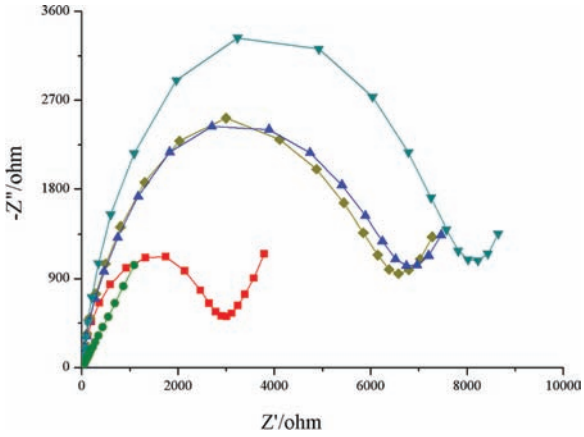


Figure 2. Nyquist plot of impedance of the electrode obtained after each treatment, from bottom to top: the bare gold electrode; the immobilization of substrate peptide; phosphorylation on the peptide by 50 unit/mL PKA; the capture of primer probe by Zr^{4+}; the execution of RCA.

ylation on the peptide, the negatively charged phosphorylation sites electrostatically repel the redox species, $Fe(CN)_6^{3-/4-}$. Moreover, the latter primers captured and long DNA strands generated are also negatively charged, which can further inhibit interfacial charge transfer. So, following the experiment process, the semicircle diameter becomes larger and larger (Figure 2).

We have also employed CV to characterize the electrochemistry of the modified electrode with the electrochemical species $[Ru(NH_3)_6]^{3+}$ which may bind to the long DNA chains (RCA product) on the electrode surface. Figure 3 shows that

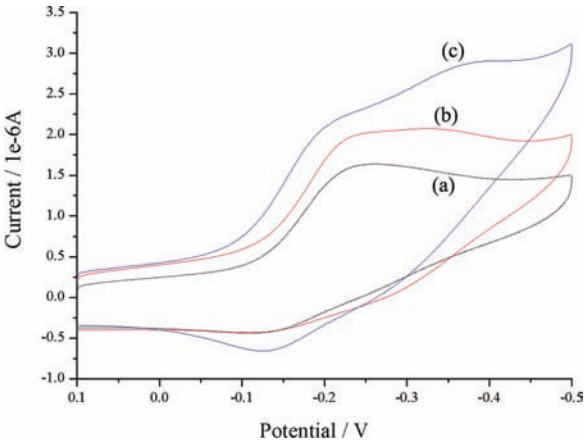


Figure 3. Cyclic voltammograms obtained at substrate peptide modified electrode, pretreated by (a) 0 unit/mL, (b) 20 unit/mL, and (c) 400 unit/mL PKA. Scan rate: 100 mV/s.

two pairs of peaks can be obtained. While $[Ru(NH_3)_6]^{3+}$ diffused to MCH contributes to the peak pair at −0.2 V, $[Ru(NH_3)_6]^{3+}$ electrostatically bound to the phosphate backbone of DNA contributes to the peak pair at −0.35 V. Moreover, the peak currents at −0.35 V increases with the concentration of PKA, indicating more RCA reaction occurs with more PKA-catalyzed phosphorylation; thus, a new approach to monitor phosphoylation may be developed.

Quantitative Detection of PKA by Chronocoulometry. CC technique can provide an accurate approach to measure the redox charges of $[Ru(NH_3)_6]^{3+}$ confined at the electrode surface. As shown in Figure 4, the redox charges of $[Ru(NH_3)_6]^{3+}$ increase with PKA and reach the saturation

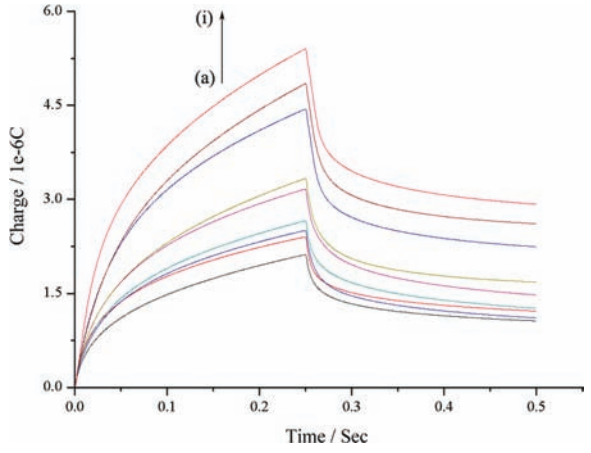


Figure 4. Chronocoulometry curves for the modified electrode. The peptide on the electrode was phosphorylated by (a–i) 0, 5, 20, 50, 200, 250, 400, 450, and 500 unit/mL PKA.

condition when the PKA concentration is higher than 500 unit/mL. Anson plots can then be obtained by plotting charge versus $t^{1/2}$. The linear part of the Anson plot can be extrapolated back to time zero to obtain the intercept for the plot, which can then be used to determine the concentration of PKA (Figure 5). The

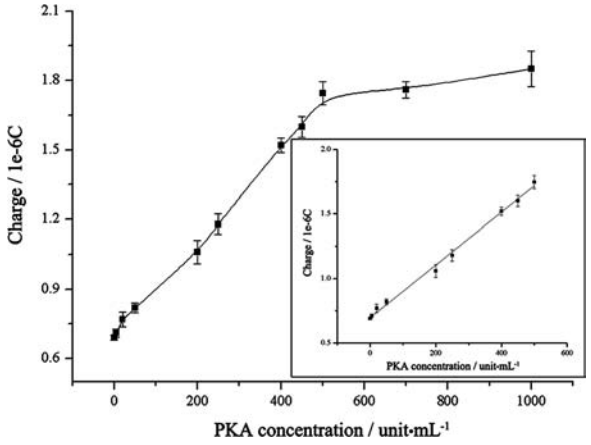


Figure 5. Calibration curve corresponding to the increased redox charge of $[Ru(NH_3)_6]^{3+}$ for variable concentration of PKA from 0 to 1000 unit/mL. Error bars represent standard deviations of measurements (n = 3). The inset shows a linear relationship between the charge and the concentration of PKA from 5 to 500 unit/mL.

results shown in the inset of Figure 5 have revealed a good linear relationship between the charge and the concentration of PKA. The linear fitting equation is $y = 0.69657 + 0.00204x$, where y is the charge, $\times 10^{-6}$ C; x is the concentration of PKA; n = 3; r = 0.9967. The linear range is 5 to 500 unit/mL. The detection limit is calculated to be 0.5 unit/mL (S/N = 3), which is rather low, compared with some previous reports.

In the control experiment, no obvious increase of the electrochemical signal can be observed, and in the inhibition experiments, with the increase of H−89, the redox charge of $[Ru(NH_3)_6]^{3+}$ decreases significantly, demonstrating the specificity of this method and the potential to monitor the inhibition of phosphorylation in the future (Figure 6).

dx.doi.org/10.1021/bc200523p | *Bioconjugate Chem.* 2012, 23, 141–145

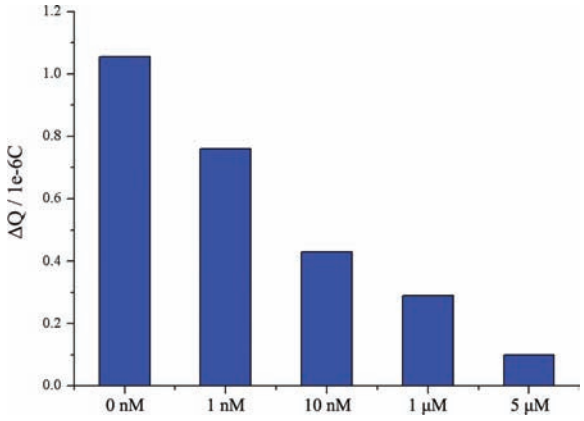


Figure 6. Calculated chronocoulometric results of the assays to detect 500 unit/mL PKA with different amount of H-89 as the inhibitor.

PKA Assay in Biological Fluids. To further demonstrate the application of the proposed method in biological fluids, a certain amount of PKA is added into fetal calf serum and the concentration of PKA in the serum is then measured with our proposed method. Table 1 shows that the relative errors of two different concentration detections are all within 10%, which promises that this method is utilizable for the detection of PKA in biological fluids such as serum.

Table 1. Detection of PKA with the Samples Prepared with Serum

Samples	PKA added in the serum (unit/mL)	Results of detection with the proposed method (unit/mL)	Relative error (%)
1	20	21.21	6.05
2	50	45.79	8.42

CONCLUSIONS

In conclusion, we have proposed an electrochemical method to monitor phosphorylation and to assay the activity of PKA. Due to the linkage by Zr^{4+} between the phosphorylated peptide and DNA probe, and the signal amplification by RCA reaction, highly sensitive detection of PKA can be achieved. This work may not only offer new prospects for monitoring phosphorylation and protein kinase activities, but also propose a new aspect of the application of RCA for protein studies.

AUTHOR INFORMATION

Corresponding Author

*Tel.: +86 25 83593596. Fax: +86 25 83592510. E-mail: genxili@nju.edu.cn (G. Li).

ACKNOWLEDGMENTS

This work is supported by the National Science Fund for Distinguished Young Scholars (Grant No. 20925520), and the Leading Academic Discipline Project of Shanghai Municipal Education Commission (J50108).

REFERENCES

(1) Manning, G., Whyte, D. B., Martinez, R., Hunter, T., and Sudarsanam, S. (2002) The protein kinase complement of the human genome. *Science 298*, 1912−1934.

(2) Sebolt-Leopold, J. S., and English, J. M. (2006) Mechanisms of drug inhibition of signalling molecules. *Nature 441*, 457−462.

(3) Cohen, P. (2002) Protein kinases - the major drug targets of the twenty-first century? *Nat. Rev. Drug Discovery 1*, 309−315.

(4) Himmel, S., Wolff, S., Becker, S., Lee, D., and Griesinger, C. (2010) Detection and identification of protein-phosphorylation sites in histidines through HNP correlation patterns. *Angew. Chem., Int. Ed. 49*, 8971−8974.

(5) Montminy, M. (1997) Transcriptional regulation by cyclic AMP. *Annu. Rev. Biochem. 66*, 807−822.

(6) Domanski, D., Murphy, L. C., and Borchers, C. H. (2000) Assay development for the determination of phosphorylation stoichiometry using multiple reaction monitoring methods with and without phosphatase treatment: application to breast cancer signaling pathways. *Anal. Chem. 82*, 5610−5620.

(7) Xu, X. H., Nie, Z., Chen, J. H., Fu, Y. C., Li, W., Shen, Q. P., and Yao, S. Z. (2009) A DNA-based electrochemical strategy for label-free monitoring the activity and inhibition of protein kinase. *Chem. Commun.*, 6946−6948.

(8) Song, H. F., Kerman, K., and Kraatz, H. B. (2008) Electrochemical detection of kinase-catalyzed phosphorylation using ferrocene-conjugated ATP. *Chem. Commun.*, 502−504.

(9) Wieckowska, A., Li, D., Gill, R., and Willner, I. (2008) Following protein kinase acivity by electrochemical means and contact angle measurements. *Chem. Commun.*, 2376−2378.

(10) Wang, J., Shen, M., Cao, Y., and Li, G. X. (2010) Switchable "On-Off" electrochemical technique for detection of phosphorylation. *Biosens. Bioelectron. 26*, 638−642.

(11) Freeman, R., Gill, R., and Willner, I. (2007) Following a protein kinase activity using a field-effect transistor device. *Chem. Commun.*, 3450−3452.

(12) Allen, J. J., Li, M. Q., Brinkworth, C. S., Paulson, J. L., Wang, D., Hubner, A., Chou, W. H., Davis, R. J., Burlingame, A. L., Messing, R. O., Katayama, C. D., Hedrick, S. M., and Shokat, K. M. (2007) A semisynthetic epitope for kinase substrates. *Nat. Methods 4*, 511−516.

(13) Green, K. D., and Pflum, M. K. H. (2007) Kinase-catalyzed biotinylation for phosphoprotein detection. *J. Am. Chem. Soc. 129*, 10−11.

(14) Wang, Z. X., Levy, R., Fernig, D. G., and Brust, M. (2006) Kinase-catalyzed modification of gold nanoparticles: A new approach to colorimetric kinase activity screening. *J. Am. Chem. Soc. 128*, 2214−2215.

(15) Sahoo, H., Hennig, A., Florea, M., Roth, D., Enderle, T., and Nau, W. M. (2007) Single-label kinase and phosphatase assays for tyrosine phosphorylation using nanosecond time-resolved fluorescence detection. *J. Am. Chem. Soc. 129*, 15927−15934.

(16) Xu, X. H., Liu, X., Nie, Z., Pan, Y. L., Guo, M. L., and Yao, S. Z. (2011) Label-free fluorescent detection of protein kinase activity based on the aggregation behavior of unmodified quantum dots. *Anal. Chem. 83*, 52−59.

(17) Freeman, R., Finder, T., Gill, R., and Willner, I. (2010) Probing protein kinase (CK2) and alkaline phosphatase with CdSe/ZnS quantum dots. *Nano Lett. 10*, 2192−2196.

(18) Ji, J., Yang, H., Liu, Y., Chen, H., Kong, J., and Liu, B. (2009) TiO2-assisted silver enhanced biosensor for kinase activity profiling. *Chem. Commun.*, 1508−1510.

(19) Kerman, K., and Kraatz, H. B. (2009) Electrochemical detection of protein tyrosine kinase-catalysed phosphorylation using gold nanoparticles. *Biosens. Bioelectron. 24*, 1484−1489.

(20) Fujii, R., Kitaoka, M., and Hayashi, K. (2006) Error-prone rolling circle amplification: the simplest random mutagenesis protocol. *Nat. Protoc. 1*, 2493−2497.

(21) Cheng, Y. Q., Zhang, X., Li, Z. P., Jiao, X. X., Wang, Y. C., and Zhang, Y. L. (2009) Highly sensitive determination of microRNA using target-primed and branched rolling-circle amplification. *Angew. Chem., Int. Ed. 48*, 3268−3272.

(22) Hu, J. A., and Zhang, C. Y. (2010) Sensitive detection of nucleic acids with rolling circle amplification and surface-enhanced raman scattering spectroscopy. *Anal. Chem. 82*, 8991−8997.

(23) Murakami, T., Sumaoka, J., and Komiyama, M. (2009) Sensitive isothermal detection of nucleic-acid sequence by primer generation-rolling circle amplification. *Nucleic Acids Res. 37*, e19.
(24) Reiss, E., Holzel, R., and Bier, F. F. (2009) Synthesis and stretching of rolling circle amplification products in a flow-through system. *Small 5*, 2316−2322.
(25) Wilner, O. I., Shimron, S., Weizmann, Y., Wang, Z. G., and Willner, I. (2009) Self-assembly of enzymes on DNA scaffolds: en route to biocatalytic cascades and the synthesis of metallic nanowires. *Nano Lett. 9*, 2040−2043.
(26) Yan, J. A., Song, S. P., Li, B., Zhang, Q. Z., Huang, Q., Zhang, H., and Fan, C. H. (2010) An on-nanoparticle rolling-circle amplification platform for ultrasensitive protein detection in biological fluids. *Small 6*, 2520−2525.
(27) Zhou, Y. T., Huang, Q., Gao, J. M., Lu, J. X., Shen, X. Z., and Fan, C. H. (2010) A dumbbell probe-mediated rolling circle amplification strategy for highly sensitive microRNA detection. *Nucleic Acids Res. 38*, e156.
(28) Monot, J., Petit, M., Lane, S. M., Guisle, I., Leger, J., Tellier, C., Talham, D. R., and Bujoli, B. (2008) Towards zirconium phosphonate-based microarrays for probing DNA-protein interactions: Critical influence of the location of the probe anchoring groups. *J. Am. Chem. Soc. 130*, 6243−6251.
(29) Lao, R. J., Song, S. P., Wu, H. P., Wang, L. H., Zhang, Z. Z., He, L., and Fan, C. H. (2005) Electrochemical interrogation of DNA monolayers on gold surfaces. *Anal. Chem. 77*, 6475−6480.
(30) Steel, A. B., Herne, T. M., and Tarlov, M. J. (1998) Electrochemical quantitation of DNA immobilized on gold. *Anal. Chem. 70*, 4670−4677.

Bioconjugate Chemistry

Review

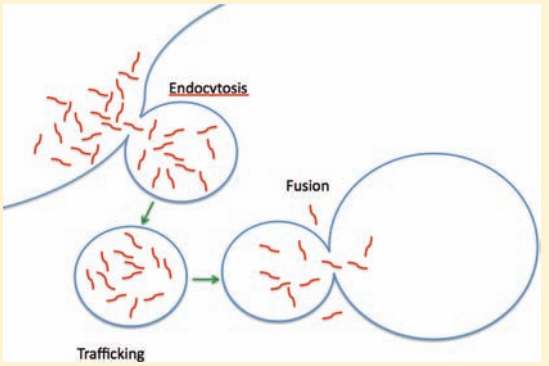
pubs.acs.org/bc

Cellular Uptake and Intracellular Trafficking of Antisense and siRNA Oligonucleotides

Rudolph L. Juliano,* Xin Ming, and Osamu Nakagawa

Division of Molecular Pharmaceutics, UNC Eshelman School of Pharmacy, University of North Carolina, Chapel Hill, North Carolina 27599, United States

ABSTRACT: Significant progress is being made concerning the development of oligonucleotides as therapeutic agents. Studies with antisense, siRNA, and other forms of oligonucleotides have shown promise in cellular and animal models and in some clinical studies. Nonetheless, our understanding of how oligonucleotides function in cells and tissues is really quite limited. One major issue concerns the modes of uptake and intracellular trafficking of oligonucleotides, whether as "free" molecules or linked to various delivery moieties such as nanoparticles or targeting ligands. In this review, we examine the recent literature on oligonucleotide internalization and subcellular trafficking in the context of current insights into the basic machinery for endocytosis and intracellular vesicular traffic.



INTRODUCTION

The concept of using oligonucleotides as therapeutic agents emerged more than three decades ago when antisense molecules were first described.[1] More recently, enthusiasm for this approach was rekindled by the discovery of RNA interference[2] and the ability to activate this process using exogenous short double-stranded RNAs (siRNAs).[3] The potential of oligonucleotide-based therapeutics has been further reinforced by new discoveries concerning the complex roles of noncoding RNAs in regulating many facets of genome function.[4] Currently, multiple approaches are available for employing oligonucleotides to influence the extent and pattern of gene expression. This includes using conventional antisense or siRNA molecules to selectively degrade mRNA,[5,6] antagomirs to block the actions of miRNAs,[7] splice shifting oligonucleotides to alter gene expression patterns,[8] decoys to block transcription factors,[9] CpG rich oligonucleotides to stimulate the immune system,[10] and triplex oligonucleotides for targeted mutagenesis.[11] Each of these approaches has benefited immensely from recent progress in oligonucleotide chemistry that has resulted in the creation of stable and potent molecules.[12−14] However, despite many research advances and the initiation of multiple clinical trials,[5,15] the evolution of oligonucleotides as therapeutic agents has been hindered by the fact that delivery of these large, usually highly charged, molecules to their intracellular sites of action is a very challenging task.[16,17] In this article, we review current information concerning the uptake of oligonucleotides and their intracellular trafficking. We consider the fate of "free" oligonucleotides, of conjugates with various targeting ligands, and of oligonucleotides associated with nanoparticle carriers. The emphasis will be on events at the cellular and subcellular level rather than on whole animal pharmacokinetics and biodistribution, although some informative *in vivo* studies will be discussed. A theme that will pervade this article is the enormous complexity of the processes that govern intracellular traffic of internalized molecules and that thus influence the therapeutic potential of exogenously administered oligonucleotides.

1. OVERVIEW OF ENDOCYTOTIC AND TRAFFICKING PATHWAYS

Although it is commonly accepted that antisense and siRNA oligonucleotides usually enter cells via endocytosis, this broad statement masks the complexities inherent in multiple pathways of internalization and subsequent intracellular trafficking. Here, we will describe some of these events and discuss the implications for oligonucleotide pharmacology. We will also emphasize the intricate and highly selective protein machinery that underlies all aspects of endocytosis and trafficking.

a. Pathways of Endocytosis and the Associated Protein Machinery. Over the past few years, it has become clear that there exist multiple pathways of endocytosis in addition to the archetypal clathrin-coated pit pathway.[18−20] A diagram depicting some of these pathways is shown in Figure 1. In classical clathrin-mediated endocytosis, cell surface receptors and their associated ligands interact with adapter proteins including AP-2 and with a host of accessory factors that cluster the receptors into specialized membrane areas subtended by a

Received: July 14, 2011
Revised: October 6, 2011
Published: October 13, 2011

 © 2011 American Chemical Society

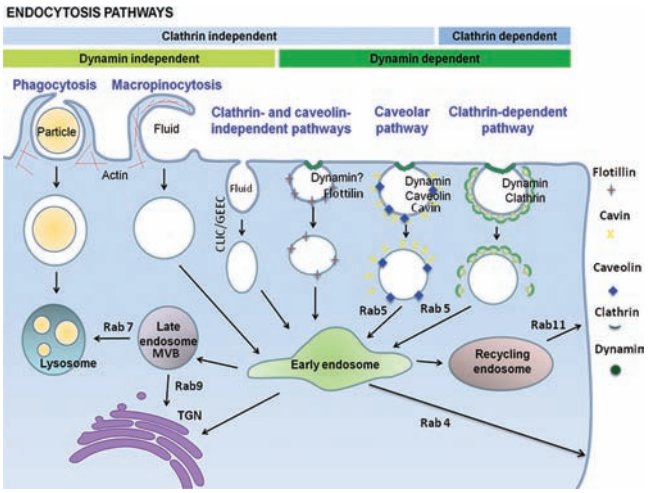


Figure 1. Pathways of endocytosis and trafficking. Several of the major internalization pathways discussed in the text are illustrated. Phagocytosis takes places only in specialized cells such as macrophages and granulocytes, while the other pathways are found in many cell types. A few of the key proteins involved in some of the pathways are indicated; however, many other proteins that play a role are not depicted. Some aspects of the intracellular vesicular trafficking between various endomembrane compartments are also illustrated. Specific Rab GTPases play key roles controlling the flow of shuttle vesicles between individual compartments.

network of clathrin triskelions. The clathrin network, as well as specialized BAR domain proteins such as SNX9 and amphiphysin that sense and promote membrane curvature, contribute to invagination; this is followed by pinching off of a clathrin-coated vesicle through the agency of the dynamin GTPase.[21] The coated endosome quickly uncoats under the influence of a set of proteins including auxilin and hsc70, and now, the uncoated vesicle is ready to begin its intracellular journey. Many important receptors and ligands are internalized via the clathrin pathway including LDL, transferrin, and many activated G protein coupled receptors.[20,22]

The caveolar pathway has also evoked a great deal of interest.[23] Many cells display small invaginations that are rich in cholesterol and sphingolipids and that contain caveolin1, a 21 kD protein that inserts a hydrophobic hairpin into the membrane while both N- and C-termini are cytosolic. Additionally, the cavins are coat proteins that help stabilize caveolar structures. There is some controversy as to whether caveolae generate independent intracellular vesicles or whether they remain as tubular structures linked to the plasma membrane; however, substantial evidence suggests that caveolae generate vesicles that can contribute to intracellular membrane traffic. In general, caveolar structures are smaller (<100 nm) than other forms of endocytotic vesicles, which may reach several hundred nanometers in diameter. Cholera toxin (CTxB), SV40 virus, and GPI-linked membrane proteins are among the entities that are preferentially internalized via caveolae (however, some of these moieties are also internalized by other pathways). It seems likely that dynamin is involved in the disjunction of caveolae, but the evidence is not as clear as for the clathrin-mediated pathway. Many proteins in addition to caveolin have been observed to be associated with caveolae; in particular, these structures are rich in molecules involved in signal transduction.[24−26]

Recently, a number of clathrin- and caveolin-independent pathways have been delineated to various degrees. These pathways are often defined either in terms of the morphologies of the vesicles they generate or in terms of the cargo that is preferentially internalized. For example, the flotillins are membrane-inserted proteins that may be involved in ordering lipid domains and subsequent endocytosis similarly to caveolin. Both CTxB and GPI-linked proteins have been associated with flotillin-rich membrane microdomains. Interestingly, some reports suggest that dynamin is not needed for internalization of cargo via flotillin-containing vesicles.[27] Thus, the flotillin pathway represents one example of a clathrin and caveolin independent internalization mechanism.

Another key internalization mechanism is the CLIC/GEEC pathway that seems to be particularly important for fluid-phase endocytosis.[20] The acronym is for clathrin and dynamin independent carriers (CLIC)/GPI-AP enriched early endosomal compartments (GEEC). This pathway gives rise to high-volume tubular endosomes that are rich in GPI-proteins (including the folate receptor FRα) and that typically contain fluid-phase markers such as dextrans. As the name implies, dynamin is not necessary for the pinching off of these vesicles. Instead, membrane scission may be mediated by GRAF1, a BAR domain containing GTPase activating protein.[28]

Additional clathrin and caveolin independent pathways exist.[20,28] This includes a pathway involved in the internalization of a form of the IL2-Receptor, certain potassium channels, and the FCεR1 immunoglobulin receptor. This pathway involves dynamin-mediated disjunction of vesicles from the plasma membrane; as well, this pathway seems to be regulated by protein kinases of the PAK family. Another pathway that generates both vesicular and tubular structures has been implicated in the internalization of MHC class I histocompatibility proteins; a role for dynamin has not yet been found for this pathway.

Macropinocytosis describes a process by which cell protrusions pinch off large volumes of extracellular fluid and is thus an important aspect of fluid-phase endocytosis.[29] It is also involved in the internalization of clustered, activated receptor tyrosine kinases. Generation of these relatively large structures involves the actinomyosin contractile machinery and is thus associated with typical regulators of such processes including the Rac GTPase and PAK family kinases, but probably not dynamin. Other large volume internalization mechanisms such as phagocytosis and entosis come into play in specialized cells or unusual circumstances, but these are unlikely to play much of a role in the processing of oligonucleotides in the majority of cell types.[20] The actin cytoskeleton plays an important role in most of the endocytotic processes described above; however, not all internalizations require actin. Thus, certain arenaviruses enter cells by a pathway that is independent of clathrin, caveolin, dynamin, and actin.[30] Interestingly, we recently found that phosphorothioate antisense oligonucleotides seem to enter cells by this pathway as well.[31]

In summary, we know of multiple pathways for endocytosis with more probably remaining to be discovered. This provides daunting complexity but also exciting opportunities for oligonucleotide pharmacology. Thus, by targeting antisense or siRNA to specific cell surface receptors it is possible to influence the initial route of internalization. As we will discuss below, this may have important implications for further

processing and for the ultimate biological effect of the oligonucleotide.

b. Trafficking Downstream of Initial Internalization—Rabs, Tethers, and Snares. Whether presented in unmodified form, as a chemical conjugate, or associated with a nanocarrier, an oligonucleotide entering a cell in an endosome encounters a complex maze of intracellular pathways that can lead to many destinations and that is regulated by intricate protein machinery.[32] Key subcellular membrane bound compartments include early and recycling endosomes, late endosomes/multivesicular bodies, lysosomes, the Golgi apparatus, and the endoplasmic reticulum (see Figure 1). Trafficking is not a random process, but rather it is a carefully orchestrated ballet that allows the cell to transport endogenous and exogenous materials to the most appropriate place. Many pathogens have learned to exploit these events; for example, certain viruses as well as many bacterial toxins engage the so-called retrograde transport process[33] and are thus delivered to the trans-Golgi compartment from which they seem to have ready access to the cytosol. Ultimately, this is the goal of oligonucleotide delivery as well, to leave membrane bound compartments and access the cytosol and nucleus. It seems increasingly clear that appropriate manipulation of endocytotic and trafficking pathways can help attain this goal. For example, inhibition of intracellular protein kinase A activity with small molecule drugs can prevent trafficking into the late endosomal/lysosomal compartments in cellular delivery of nucleic acids via polyplexes and lipoplexes, thus improving the transfection efficiency.[34]

We only partially understand how endocytotic cargos are delivered to particular subcellular compartments. Many of the internalization pathways described above converge at the stage of early endosomes. This raises the question of how receptors, ligands, and cargo that have been internalized by different initial endocytotic mechanisms traffic to different subcellular destinations. Recent evidence suggests that membrane domains originating from different internalization pathways maintain their identity within early endosomes, thus setting the stage for specific sorting and trafficking to distinct downstream destinations.[28]

The past few years have seen enormous progress in understanding the molecular mechanisms of intracellular trafficking. All membrane traffic proceeds by the same basic steps: (a) a coated vesicle is pinched off from a larger donor membrane compartment; (b) the vesicle uncoats allowing the display of tethering and fusion proteins; (c) the vesicle is carried to its destination along "tracks" provided by actin- or tubulin-based cytoskeletal structures; (d) the vesicle recognizes its target membrane compartment using tethering proteins and then utilizes SNARE proteins to complete the fusion process and deliver membrane and contents to the target compartment.[32] A simplified diagram of this process is shown in Figure 2. There are numerous variations of the overall theme and still some uncertainty about the exact sequence of events, but the overall picture is quite clear.

For a more detailed discussion of intracellular trafficking mechanisms, it is necessary to introduce the Rab proteins. The Rabs comprise a large (>60) family of GTPases that serve as molecular switches to regulate multiple aspects of intracellular vesicular traffic.[35,36] In their active GTP-loaded form, Rabs bind to and modulate the function of downstream effector proteins. In their inactive GDP-loaded form, they associate with Rab-GDI (Rab GDP Dissociation Inhibitor) proteins that both

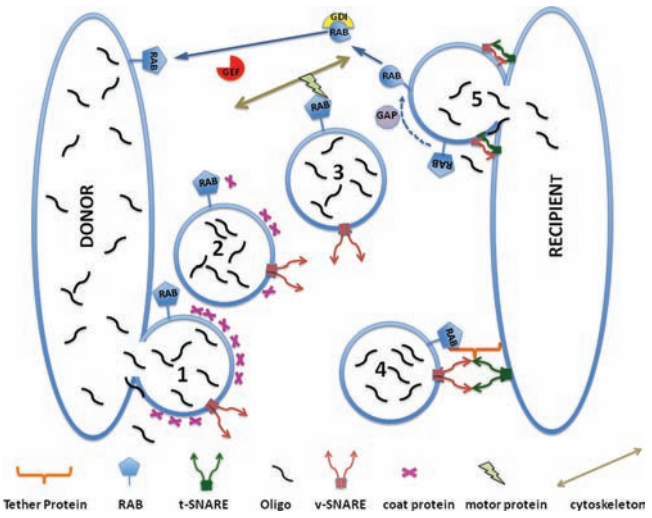


Figure 2. Proposed mechanism of vesicular trafficking of oligonucleotides. Oligonucleotides are initially accumulated in an endomembrane compartment (the DONOR compartment, for example, early endosomes) and are then trafficked by means of shuttle vesicles to various other endomembrane compartments (the RECIPIENT compartment, for example, the trans-Golgi). The first step (1) involves disjunction ("pinching off") of a shuttle vesicle under the influence of a coat protein as well as other accessory proteins. At this stage, there are nonbilayer regions at the junction between the membranes of the DONOR compartment and the shuttle vesicle. This provides an opportunity for some oligonucleotide to escape to the cytosol. Step 2 involves uncoating of the coated vesicle; Rab proteins can contribute to this step. Step 3 comprises movement of the shuttle vesicle toward its destination along cytoskeletal tracks. Motor proteins such as various myosins (for the actin system) or dyneins or kinesins (for the microtubular system) propel the vesicle. Rab proteins are involved in forming the appropriate linkages to the cytoskeleton. Step 4 entails recognition of the RECIPIENT ("target") compartment by the shuttle vesicle. Tether proteins work with Rab proteins to provide interaction specificity while v-SNARE proteins in the vesicle membrane interact with t-SNARE proteins in the RECIPIENT compartment membrane to provide firm bridging, as well as contributing to specificity. In step 5, the SNARE proteins undergo major conformational changes, and with the assistance of accessory proteins, trigger fusion of the shuttle vesicle membrane with the membrane of the RECIPIENT compartment. At this stage, nonbilayer regions exist at the junction between shuttle and RECIPIENT membranes, potentially allowing escape of oligonucleotide.

stabilize the inactive form and serve as chaperones to regulate the balance between cytosolic and membrane-bound Rab. As with other small GTPases, the equilibrium between active and inactive forms is regulated by Rab-specific GEFs (guanine nucleotide exchange factors) and GAPs (GTPase activating proteins).

Rabs serve many different roles in regulating intracellular trafficking including vesicle uncoating, vesicle movement along cytoskeletal tracks, and the ultimate fusion events. For example, Rab5 regulates the uncoating of clathrin-coated vesicles during classical receptor mediated endocytosis, while Rab 27A links melanosomes to the myosin Va motor protein via a Rab-binding adaptor protein. Rabs also associate with tethering proteins, a good example being the association of Rab1 with Golgin-type tethers. Because of their high specificity, Rab proteins serve as excellent markers of individual membrane trafficking pathways. Thus, Rab5 is associated with the movement of clathrin-coated vesicles to the early endosome,

dx.doi.org/10.1021/bc200377d | Bioconjugate Chem. 2012, 23, 147–157

Rab 4 with the early endosome and recycling to the plasma membrane, Rab7 with late endosomes/lysosomes, Rab9 with late endosome to Golgi traffic, and Rab11 with a slowly recycling perinuclear endomembrane compartment (see Figure 1). However, a complex aspect of Rab function concerns the formation of "Rab domains" within particular endosomes. Thus, studies using low levels of expressed green fluorescent protein-Rab chimeras, have shown that different Rab proteins localized on the same organelle can occupy distinct membrane microdomains.[35] This segregation of Rabs may play a role in the endosomal sorting processes discussed above.[28]

As mentioned above, the initial event in intracellular trafficking is the pinching off of a coated vesicle from a donor membrane. The formation of clathrin-coated vesicles (CCVs) at the plasma membrane is a good example, but other types of coats exist such as the COPI and COPII coats of the Golgi and ER. Disjunction of the coated vesicle is accomplished by dynamin in the case of CCVs, but by other mechanisms as well. For example, budding off of vesicles from late endosomes to the trans-Golgi is accomplished by the retromer complex with its BAR-domain containing SNX proteins.[37]

Tethering proteins impart selectivity to vesicle traffic by supporting preferential interactions between the vesicle and its ultimate target membrane compartment. There are two broad classes of tethering molecules: the coiled-coil tethers such as the Golgins and the multisubunit tethers.[38] Tethers are thought to bridge membranes and promote fusion by binding to both Rab proteins and to SNARES. There is some uncertainty about when and how tethering proteins associate with trafficking vesicles, particularly whether tethers interact with vesicle coat proteins or if tethering takes place after uncoating.[32,35]

The ultimate transfer of both the membrane material and the contents of the shuttle vesicle to the recipient compartment is accomplished via a fusion process mediated by SNAREs (soluble *N*-methylmaleimide sensitive factor attachment protein receptors).[39] After recognition is accomplished by tethering proteins, SNARES on the vesicle (v-SNARES) interact with SNARES on the target membrane (t-SNARES) to form a four-helix bundle that undergoes conformational change to induce membrane fusion. There is considerable specificity in this process since only specific cognate pairs of v- and t-SNARES will sustain fusion. Resegregation of the v-SNARES and t-SNARES is mediated by the ATP-dependent NSF/SNAP protein complex.

c. Escape from Endosomes during Intracellular Trafficking. The complex machinery described above is designed to move endogenous molecules to specific membrane destinations within the cell. Although it is quite efficient and selective, nonetheless there is some opportunity for molecules to escape from endomembrane compartments to the cytosol. Intracellular trafficking involves a highly dynamic flux of membrane vesicles that engage in a multitude of fusion and disjunction events. In recent years, fusion mechanisms in both natural membranes and artificial lipid membranes have been studied in great detail.[40,41] While this literature is largely beyond the scope of this review, there are a few key points to be noted. First, fusion involves localized stress on the fusion partners including the formation of nonbilayer lipid domains.[40,42] Second, there is good evidence that nonbilayer regions of membranes can be much leakier than bilayer regions.[43,44] Third, many enveloped viruses fuse with cells via specialized membrane interacting proteins that, while differing in sequence, act in a manner similar to cellular SNARE proteins; the influenza virus fusion protein is a good example.[45] In many cases, these proteins can also induce increases in membrane permeability.[46] Therefore, there is an intrinsic relationship between the fusion events inherent in intracellular trafficking and transient leakage of vesicular contents (see Figure 2). Thus, the innate activity of oligonucleotides taken up by cells is likely due to a modest amount of continuous leakage from endomembrane compartments that spontaneously occurs during intracellular trafficking, while much of the current technology for enhancing oligonucleotide effects is aimed at increasing the extent of endosomal release, as discussed below.

d. Nuclear Entry. Antisense oligonucleotides encounter their pharmacological targets in the nucleus, but nuclear entry may not be the rate-limiting step for oligonucleotide pharmacology. Studies have shown that oligonucleotides, particularly those with phosphorothioate backbones, are able to continuously shuttle between the nucleus and the cytoplasm. This is an active process mediated by nuclear pore structures; however, it does not require classical nuclear localization signals. For conventional phosphodiester oligonucleotides, both passive diffusion and active transport have been described as nuclear entry mechanisms.[47,48]

2. UPTAKE AND TRAFFICKING OF "FREE" OLIGONUCLEOTIDES

There has been considerable work done trying to understand the cellular uptake, trafficking, and tissue distribution of oligonucleotides themselves, absent any specific targeting or carrier mechanisms. Some of the earlier literature has been covered elsewhere,[49] and more recent reviews have updated information on the pharmacokinetics and biodistribution of antisense and siRNA.[5,50] While uncharged oligonucleotides such as morpholino and peptide nucleic acid derivatives, as well as most forms of siRNA, are rapidly excreted via the kidney, phosphorothioate (PS) oligonucleotides display substantial binding to plasma proteins and cells and are thus retained in the body for longer periods. Preferential *in vivo* uptake by certain cell types, particularly kidney proximal tubule cells and liver Kupffer cells, has been noted both for PS antisense compounds and for siRNA.[51,52] Recent publications have provided new insights into the uptake and trafficking of "free" or "naked" oligonucleotides. Thus, a study using phosphorothioate antisense oligonucleotides in a transformed liver cell line and in murine livers has suggested the coexistence of productive and nonproductive routes of uptake.[53] The nonproductive pathway seems to involve trafficking to lysosomes, while the pathway that results in RNase H dependent antisense effects involves trafficking that eventually leads to interaction with cellular pre-mRNA. A somewhat confusing observation is that the productive pathway is not blocked by siRNA targeting clathrin but is blocked by siRNA targeting AP2M1 an adapter protein in the clathrin endocytotic pathway. In any case, this study provides one of the most detailed accounts to date of the subcellular fate of free oligonucleotides in cells and tissues. Other interesting studies, both in cell culture and in mouse models, have involved the so-called "gymnotic" uptake of antisense oligonucleotides modified with LNA (locked nucleic acid) moieties.[54,55] In contrast with the previously mentioned study, which used nanomolar concentration of PS oligonucleotides, the antisense effects of "naked" LNA usually required micromolar concentrations. Subcellular distribution studies surprisingly suggested

that the deoxy LNA compounds became associated with P-bodies that are usually thought to be sites of siRNA action.[54]

There have been many attempts to identify endogenous receptors for antisense or siRNA molecules; however, much of this literature is problematic and no direct evidence for their involvement in oligonucleotide trafficking has been provided. Integrins of the beta2 subclass,[56] as well as scavenger receptors,[51] have been suggested as candidates, but this is controversial.[57] A putative oligonucleotide transporter has also been described,[58,59] but there has not been a great deal of confirmatory work on this finding by other groups. Another interesting candidate is the mammalian homologue of the double-stranded RNA (dsRNA) transport protein SID-1 found in *Caenorhabditis elegans*.[60] SID-1 clearly plays a key role in the spread of RNA interference from cell to cell in some invertebrates. However, initial reports of a role for SID-1 in uptake of siRNA by mammalian cells[61−63] have not been followed by more advanced mechanistic studies. An interesting variant on oligonucleotide delivery involves the stimulation of siRNA uptake by phosphorothioate oligonucleotides;[64] the phenomenon seems clear, although the underlying mechanism is still not fully resolved.

The most convincing examples of cellular receptors for oligonucleotides involve the toll-like receptor (TLR) family.[65,66] As a simplistic summary, TLR9 binds DNA having CpG motifs, TLRs7/8 bind single-stranded RNA, while TLR3 binds double-stranded RNA. Although these TLRs are usually found within endosomes rather than at the cell surface, in some cases they seem to be able to assist in the accumulation of oligonucleotides by cells. For example, as discussed in more detail below, a CpG oligonucleotide was able to substantially enhance the cell uptake and effect of a conjugated siRNA.[67]

In summary, at this point there is only a limited amount of information about the mechanisms involved in cell uptake and subcellular trafficking of "free" oligonucleotides, with many contradictions needing to be resolved. This seems an important topic to address, since most of the clinical studies with antisense or siRNA to date have used "free" compounds.

3. UPTAKE AND TRAFFICKING OF CONJUGATES AND COMPLEXES OF OLIGONUCLEOTIDES WITH CELL PENETRATING PEPTIDES

Over the past decade, there has been substantial interest in using so-called "cell penetrating peptides" (CPPs) for the delivery of oligonucleotides. CPPs (sometimes called "protein transduction domains") are peptides, usually rich in cationic residues, that purportedly have the ability to cross membranes and in doing so convey attached cargoes into the cytosol. The TAT and Antennepedia peptides are the archetypal forms, but a large variety of new CPPs have been described more recently.[68−70] Originally, it was thought that the CPPs could directly translocate across the plasma membrane (and some recent publications still support this view[71,72]). However, most reports suggest that cationic CPPs bind initially to negatively charged proteoglycans at the cell surface, are internalized into endosomes, and may then escape from those structures. Studies have linked the entry pathway of TAT or its conjugates to clathrin-mediated endocytosis,[73] macropinocytosis,[74] or calveolar endocytosis[75] in various cell types and experimental circumstances. In any case, it is clear that the nature of the attached cargo plays a major role in CPP uptake mechanisms and in the effectiveness of cytosolic delivery.[76,77] In general, as might be anticipated, smaller cargos are delivered more effectively; for example, TAT-containing proteins are mostly trapped in cytoplasmic vesicles after cellular uptake, while the TAT−peptide conjugates distribute throughout the cell.[76]

There have been numerous studies of both chemical conjugates and noncovalent complexes of antisense and siRNA with CPPs. Work on the chemical conjugates has been the subject of recent reviews.[78,79] In general, conjugates of CPPs with charged oligonucleotides have not proven to be very promising, while conjugates with uncharged oligonucleotides such as morpholinos or peptide nucleic acids (PNAs) have displayed more activity. This may be of particular interest in the context of splice-shifting oligonucleotides (SSOs) that can be used to correct or modify RNA splicing processes.[8] Recent work with conjugates of novel CPPs to PNA[80] or morpholino[81] SSOs has shown good splice-correction results in cell culture and promising therapeutic performance in mouse models of Duchenne muscular dystrophy.[82,83] Another interesting approach has been to make CPP−oligonucleotide conjugates that also contain a lipid moiety;[84] this seems to lead to enhanced endosomal escape and thus greater efficacy of the conjugated PNA SSO.

Despite some early studies to the contrary, chemical conjugation of classic antisense or siRNA oligonucleotides to CPPs has been problematic. For this reason, a number of laboratories have turned to noncovalent complexation of CPPs with anionic oligonucleotides to form various nanoparticles. This strategy has been the subject of recent reviews.[85,86] The complexation of cationic CPPs with oligonucleotides results in the formation of nanoscale particles.[87−89] These entities can be very effective in delivering oligonucleotides; for example, siRNA complexed with a CPP modified with a lysosomotropic chloroquine analogue provided strong "knockdown" in a number of difficult to transfect cell lines.[90] SSOs complexed with PepFect 14, a new stearylated CPP, induced higher splicing correction than the commercially available lipid-based vector Lipofectamine 2000, and the CPP/SSO complexes could be incorporated into solid dispersions so that the stability was improved significantly.[89] CPP/oligonucleotide complexes have also been tested *in vivo*.[87,90] However, there are some obvious concerns about systemic administration of such nanoparticles in terms of rapid clearance by the reticuloendothelial system, limited biodistribution, and toxicity.[17] Perhaps the proponents of CPP/oligonucleotide complexes can adapt approaches from other nanoparticle technologies, such as use of PEG to improve biodistribution characteristics.

There has been only limited investigation of basic uptake and trafficking mechanisms of CPP oligonucleotide conjugates or complexes. One type of CPP/siRNA complex has received extensive biophysical analysis leading to the suggestion that these complexes can enter cells by nonendocytotic means;[85] however, physical analysis may offer only limited insights into cellular mechanisms. Other studies of these complexes using pharmacological inhibitors also suggested non-endocytotic uptake pathways.[91] In contrast, a recent study using complexes of novel CPPs with 2′-*O*-methyphosphorothioate splice switching oligonucleotides presents a very different picture, with the initial uptake occurring mainly by clathrin-mediated endocytosis as discerned by using pharmacological inhibitors of uptake pathways.[92] The effectiveness of the splice correction was not dependent on total uptake but rather on increased release of the SSO from endosomes. There have been some relatively recent mechanistic studies of chemical conjugates of CPPs with SSOs [80] also suggesting cell entry via clathrin-mediated

endocytosis. Unfortunately, most of the studies of complexes or conjugates of CPPs with oligonucleotides have relied on use of rather nonspecific pharmacological inhibitors to evaluate uptake mechanisms. While this is a useful first step, such studies should be followed up by further analysis using molecular means to alter uptake and trafficking pathways, and by more detailed studies of colocalization with known markers of intracellular membrane compartments.

4. UPTAKE AND TRAFFICKING OF RECEPTOR TARGETED LIGAND-OLIGONUCLEOTIDE CONJUGATES

In addition to the CPP−oligonucleotide conjugates described above, there has been substantial work involving other covalent modifications of antisense and siRNA to enhance their biological properties, as summarized in several recent reviews.[93−96] Much of this has focused on conjugation with cholesterol or other lipophilic moieties to increase oligonucleotide lifetime in the circulation and to promote uptake via lipoprotein receptors in the liver and elsewhere.[7,63,97] By contrast, there is a relative paucity of reports concerning the synthesis of monomolecular conjugates of oligonucleotides with ligands designed to target specific cell surface receptors. A few early studies on this topic involved folate-conjugated antisense oligonucleotides that associated with the FRα receptor,[98] *N*-acetyl galactosamine conjugates that targeted the hepatic asialoglyoprotein receptor,[99] and conjugates of siRNA with insulin-like growth factor 1 for targeting its cognate receptor.[100]

More recently, there has been a substantial increase in work on receptor targeting of oligonucleotides. This includes our own reports on RGD peptide conjugates of splice switching antisense oligonucleotides that can be delivered to melanoma cells via the $\alpha v\beta 3$ integrin,[31,101] as well as bombesin conjugates that are targeted to prostate cancer cells via the BB2 receptor, a member of the G protein-coupled receptor (GPCR) superfamily.[102] We have also targeted oligonucleotides to tumor cells using anisamide, a high-affinity small molecule ligand for the σ receptor.[103] Another interesting approach is the delivery of siRNA by targeting TLRs.[67] Thus, an unmethylated CpG oligonucleotide known to bind to TLR9 was chemically conjugated to a siRNA. This resulted in enhanced uptake by dendritic cells, macrophages, and B-cells, all known to express TLR9, as well as "knockdown" of endogenous and reporter genes. *In vivo* use of a CpG siRNA targeting the immunosuppressive regulator Stat3 resulted in enhanced antitumor immune responses. Another very promising approach to receptor-specific delivery of oligonucleotides involves use of nucleic acid aptamers.[104] A pioneering report described the characterization of chimeric oligonucleotides comprising an aptamer that bound with high affinity to the PMSA receptor in prostate cancer cells and siRNAs that affected key survival genes such as *Plk1* and *Bcl2*.[105] These conjugates were taken up selectively by cells that expressed PSMA receptor, were effective at "knockdown" of the target messages in cell culture, and displayed antitumor activity when locally administered. More recently, a chemically optimized version of a PMSA aptamer-Plk1siRNA chimera displayed antitumor activity against PMSA expressing tumors when given by systemic administration.[106] In another impressive study, similar aptamer-siRNA chimeras inhibited tumor growth *in vivo* using siRNAs directed against *Upf2* and *Smg1*, two genes involved in nonsense mediate mRNA decay and thus in immune regulation of tumors.[107] Other important examples of aptamer-siRNAchimeras are also beginning to emerge.[108] These various studies have validated the concept that monomeric ligand−oligonucleotide conjugates can produce significant pharmacological effects both in cell culture and in animals, in the absence of any transfection agents. A recent review has provided an extensive overview of receptor targeting of oligonucleotides.[109]

Recent work on receptor-targeted oligonucleotide conjugates has also provided an important new insight for the problem of effective delivery of antisense and siRNA molecules. The essence is that the initial route of uptake (and subsequent trafficking) plays an important role in determining the pharmacological effectiveness of the oligonucleotide. Thus, in our studies comparing effects of "free" or receptor-targeted SSOs, we consistently noted that the targeted conjugates were more effective in attaining splice correction, even when the targeted and free oligonucleotide were accumulated to the same level in cells.[31,101,102] Studies with the CpG siRNA conjugate revealed that the presence of TLR9 was critical for attaining effective "knockdown" even though cells lacking the TLR could still take up the conjugate.[67] This also suggests a receptor-specific aspect to intracellular trafficking and biological outcome. These observations also harmonize with recent cell culture and *in vivo* studies of free phosphorothioate oligonucleotides that suggest the coexistence of productive and nonproductive routes of internalization.[53,110] These various observations support the concept that it may be possible to optimize the effectiveness of an antisense or siRNA molecule by controlling its pathway of uptake and intracellular trafficking, without resorting to harsh cationic lipid or cationic polymer transfection agents.

Consequently, investigators interested in the design of new receptor-targeted oligonucleotide conjugates should consider several basic issues. First, and most obvious, the ligand must display high affinity for the receptor, preferably in the low nanomolar range. Second, in order to achieve cell-type specific delivery there must be differential expression of the receptor in the cell of interest as compared to other cell types. An initial estimate of relative receptor expression in various tissues or between tumors and normal tissue can be gleaned from contemporary gene expression databases, at least at the mRNA level (for example, http://www.ebi.ac.uk/gxa/). Third, in order to deliver sufficient quantities of oligonucleotide, the receptor of interest must be relatively abundant. The abundance of various receptors can range from a few copies per cell up to hundreds of thousands of copies. However, there are relatively few compact sources for this type of information at the protein level, and thus, the literature must be searched for values for specific receptors. Fourth, the receptor of interest must cycle efficiently between the plasma membrane and endosomes. There is information in the literature on the propensity of various families of receptors to be internalized and recycle. For example, different members of the integrin family can be internalized via caveolae or via coated pits and be recycled via Rab4- or Rab11-dependent trafficking processes.[111] Agonist binding can stimulate the internalization of GPCRs via clathrin-coated vesicles and their ultimate recycling to the plasma membrane or sorting to multivesicular bodies for degradation in lysosomes.[112] Receptor tyrosine kinases of the EGF-R family also respond to agonist binding by internalization via the clathrin pathway followed by trafficking to multivesicular bodies and lysosomes.[113] Another important consideration is the point

at which the receptor-targeted oligonucleotide ceases to parallel the intracellular trafficking of the receptor itself and enters separate pathways. It is not yet clear which pathway of internalization and trafficking will be optimal for oligonucleotide delivery, but it is clear that trafficking pathways must be taken into account. Thus, the design of novel targeted oligonucleotide conjugates should start with a clear picture of the underlying receptor biology in order to have a reasonable chance of success.

5. UPTAKE AND TRAFFICKING OF OLIGONUCLEOTIDES ASSOCIATED WITH NANOCARRIERS

The most popular approach to enhancing delivery of antisense, siRNA, or other types of oligonucleotides is to incorporate the nucleic acid into some form of nanoparticle, with the intent of overcoming biological barriers and increasing both cell uptake and escape from membrane compartments.[16,17,114,115] Lipid-based carriers have proven to be very efficacious for the delivery of siRNA to the liver,[116] while a variety of polymeric nanoparticles[117] and other types of nanocarriers[118] have also been developed for siRNA delivery. Functional delivery of siRNA to tumors has been challenging, but recently targeted lipid-based nanoparticles have displayed substantial activity in this context.[119] Nonetheless, there remain concerns about possible toxicities associated with the cationic polymers or lipids most commonly used to form nanocarriers for oligonucleotide delivery.[120,121] Since there is such a vast literature on use of nanoparticles as oligonucleotide delivery agents, we will focus our discussion on a relatively few reports that have mechanistically addressed issues of cellular uptake and trafficking.

a. Uptake and Trafficking of Nontargeted Oligonucleotide Nanocarriers. A very interesting report has challenged the conventional view that cationic lipid carriers functionally deliver siRNA via endocytosis followed by escape from endosomes.[122] This group found that, while much of the lipid and siRNA did enter cells by some form of endocytosis, it was only a minor component of the cell-associated siRNA that contributed to "knockdown" function and that this component probably came from fusion between the siRNA lipoplexes and the plasma membrane. This study is notable for going beyond simplistic use of chemical inhibitors and employing molecular reagents such as dominant negative versions of dynamin and caveolin to probe uptake pathways. Another interesting recent study followed the uptake and trafficking of siRNA associated with perfluorocarbon nanoparticles,[123] finding that delivery was via formation of cell−nanoparticle hemifusion complexes followed by lipid raft mediated internalization. This study made good use of the strategy of colocalization with markers that are known to be internalized via particular pathways. A recent investigation from our laboratory compared the uptake and trafficking pathways of splice switching antisense oligonucleotides as delivered via cationic lipids or via PEI, a cationic polymer.[124] Several strategies including pharmacological inhibitors, colocalization with known markers of internalization, as well as use of molecular reagents were employed in this study. Interestingly, in agreement with the study on siRNA delivery discussed above, functional delivery of antisense associated with lipoplexes was apparently due to fusion at the plasma membrane, while delivery via polyplexes took place through an unconventional form of endocytosis. Thus, even with widely utilized transfection agents there seems to be a diversity of delivery mechanisms that need to be better understood.

b. Uptake and Trafficking of Targeted Oligonucleotide Nanocarriers. Over the past few years, several very interesting forms of targeted nanoparticles have been developed for purposes of siRNA delivery, and some very impressive functional results have been attained. For a review of some of the early literature, see refs 79,125. However, there is a dearth of information about the mechanistic aspects of the interplay of these particles with cells. For example, some very high profile publications have described a strategy where a chimeric polypeptide is formed between a targeting moiety and a cationic polyarginine sequence; the cationic sequence is used to complex siRNA, while the targeting moiety provides receptor selective delivery. Thus, a chimera including a rabies virus peptide that binds an acetylcholine receptor was used to target siRNA to neuronal cells and demonstrated therapeutic effects in a mouse model of viral encephalitis.[126] In another study, a single chain antibody to the T cell protein CD7 was used as the targeting moiety and a siRNA cocktail to CCR5 and to viral genes was used to inhibit HIV infection.[127] This same general approach has also been used to modulate inflammatory conditions and the growth of other viruses.[128,129] However, these various studies provide no information on the mechanism of cellular uptake and subsequent trafficking of these interesting chimeric complexes. A somewhat similar strategy involved complexation of siRNA to chimeric fusion proteins that included a single chain antibody as the targeting moiety and a segment of protamine to bind the nucleic acid. This strategy has been used in models of HIV and leukocyte activation.[130,131] However, despite very interesting functional data, once again there is little information on the mechanism of delivery. Another interesting approach involves preparation of a complex polymer that includes covalently attached siRNA, PEG, and a *N*-acetylgalactosamine targeting ligand for interaction with the liver asialoglycoprotein receptor.[132] Similarly, lactosylated PEG−siRNA conjugates formed into polyplexes have been used to target hepatic carcinoma models.[133] However, no substantial information on trafficking is available concerning these hepatic targeting approaches. Lipid nanoparticles incorporating anisamide, a small molecule ligand for the σ receptor, have shown promising effects in several animal tumor models,[134,135] but only limited information is available concerning uptake and trafficking. One type of targeted siRNA nanoparticle has already been tested in the clinic in patients with solid tumors.[136] The formulation comprises siRNA against ribonucleotide reductase, a cationic cyclodextrin-containing polymer, poly(ethylene glycol), and human transferrin as a targeting ligand. While some work has been done concerning the cellular uptake[137] and overall biodistribution and tumor uptake of these materials,[138] there are few details concerning their intracellular trafficking. Thus, for targeted nanoparticles containing oligonucleotides there is a dearth of information concerning the mechanistic details of the uptake and trafficking processes. Studies of this type could help to make the future development of these materials more efficient.

CONCLUSIONS

The thrust to develop antisense, siRNA, and other types of oligonucleotides as therapeutic agents has, to some degree, outstripped our fundamental knowledge of how these molecules behave in cells and in the body. While extensive information exists regarding the overall pharmacokinetics and

tissue distribution of both classic antisense and siRNA, we lack an equivalent depth of knowledge about behavior at the cellular and intracellular level. This deficit applies both to oligonucleotides administered in "free" or "naked" form and to these molecules when incorporated into nanocarriers or conjugated to targeting ligands. Recent work has provided some interesting and possibly surprising observations concerning the uptake and intracellular trafficking of oligonucleotides. Thus, conventional phosphorothioate antisense molecules, which have been studied for years, turn out to have an unusual uptake mechanism that involves both a productive and a less productive path to nuclear sites of action. Work from our laboratory and from others has shown that the pharmacological effectiveness of an antisense or siRNA can strongly depend on its route of uptake and trafficking. In particular, certain receptor-mediated processes seem to support productive delivery. As the oligonucleotide therapeutics field matures, and particularly as investigators seek to enhance specificity through targeted delivery, it will be important to employ basic cell biological principles in the design of delivery approaches. This includes identification of target receptors that are abundant, are differentially expressed, and are strongly linked to endocytotic pathways. Further insights into the intracellular trafficking of oligonucleotides will also facilitate the design of effective delivery systems.

AUTHOR INFORMATION

Corresponding Author

*E-mail: arjay@med.unc.edu.

ACKNOWLEDGMENTS

This work was supported by NIH grant RO1 CA151964 to R.L.J.

REFERENCES

(1) Zamecnik, P. C., and Stephenson, M. L. (1978) Inhibition of Rous sarcoma virus replication and cell transformation by a specific oligodeoxynucleotide. *Proc. Natl. Acad. Sci. U. S. A. 75*, 280−4.

(2) Mello, C. C., and Conte, D. Jr. (2004) Revealing the world of RNA interference. *Nature 431*, 338−42.

(3) Elbashir, S. M., Harborth, J., Lendeckel, W., Yalcin, A., Weber, K., and Tuschl, T. (2001) Duplexes of 21-nucleotide RNAs mediate RNA interference in cultured mammalian cells. *Nature 411*, 494−8.

(4) Moazed, D. (2009) Small RNAs in transcriptional gene silencing and genome defence. *Nature 457*, 413−20.

(5) Bennett, C. F., and Swayze, E. E. (2010) RNA targeting therapeutics: molecular mechanisms of antisense oligonucleotides as a therapeutic platform. *Annu. Rev. Pharmacol. Toxicol. 50*, 259−93.

(6) Castanotto, D., and Rossi, J. J. (2009) The promises and pitfalls of RNA-interference-based therapeutics. *Nature 457*, 426−33.

(7) Krutzfeldt, J., Rajewsky, N., Braich, R., Rajeev, K. G., Tuschl, T., Manoharan, M., and Stoffel, M. (2005) Silencing of microRNAs in vivo with 'antagomirs'. *Nature 438*, 685−9.

(8) Sazani, P., and Kole, R. (2003) Therapeutic potential of antisense oligonucleotides as modulators of alternative splicing. *J. Clin. Invest. 112*, 481−6.

(9) Soldati, C., Bithell, A., Conforti, P., Cattaneo, E., and Buckley, N. J. (2011) Rescue of gene expression by modified REST decoy oligonucleotides in a cellular model of Huntington's disease. *J. Neurochem. 116*, 415−25.

(10) Vollmer, J., and Krieg, A. M. (2009) Immunotherapeutic applications of CpG oligodeoxynucleotide TLR9 agonists. *Adv. Drug Delivery Rev. 61*, 195−204.

(11) Chin, J. Y., and Glazer, P. M. (2009) Repair of DNA lesions associated with triplex-forming oligonucleotides. *Mol. Carcinog. 48*, 389−99.

(12) Deleavey, G. F., Watts, J. K., and Damha, M. J. (2009) Chemical modification of siRNA. *Current Protocols in Nucleic Acid Chemistry*, Chapter 16, Unit 16 3.

(13) Corey, D. R. (2007) RNA learns from antisense. *Nat. Chem. Biol. 3*, 8−11.

(14) Kurreck, J. (2009) RNA interference: from basic research to therapeutic applications. *Angew. Chem. 48*, 1378−98.

(15) Vaishnaw, A. K., Gollob, J., Gamba-Vitalo, C., Hutabarat, R., Sah, D., Meyers, R., de Fougerolles, T., and Maraganore, J. (2010) A status report on RNAi therapeutics. *Silence 1*, 14.

(16) Whitehead, K. A., Langer, R., and Anderson, D. G. (2009) Knocking down barriers: advances in siRNA delivery. *Nat. Rev. Drug Discovery 8*, 129−38.

(17) Juliano, R., Bauman, J., Kang, H., and Ming, X. (2009) Biological barriers to therapy with antisense and siRNA oligonucleotides. *Mol. Pharm. 6*, 686−95.

(18) Mayor, S., and Pagano, R. E. (2007) Pathways of clathrin-independent endocytosis. *Nat. Rev. Mol. Cell Biol. 8*, 603−12.

(19) Kirkham, M., and Parton, R. G. (2005) Clathrin-independent endocytosis: new insights into caveolae and non-caveolar lipid raft carriers. *Biochim. Biophys. Acta 1746*, 349−63.

(20) Doherty, G. J., and McMahon, H. T. (2009) Mechanisms of endocytosis. *Annu. Rev. Biochem. 78*, 857−902.

(21) Mettlen, M., Pucadyil, T., Ramachandran, R., and Schmid, S. L. (2009) Dissecting dynamin's role in clathrin-mediated endocytosis. *Biochem. Soc. Trans. 37*, 1022−6.

(22) Wolfe, B. L., and Trejo, J. (2007) Clathrin-dependent mechanisms of G protein-coupled receptor endocytosis. *Traffic 8*, 462−70.

(23) Lajoie, P., and Nabi, I. R. (2010) Lipid rafts, caveolae, and their endocytosis. *Int. Rev. Cell Mol. Biol. 282*, 135−63.

(24) Sorkin, A., and von Zastrow, M. (2009) Endocytosis and signalling: intertwining molecular networks. *Nat. Rev. Mol. Cell Biol. 10*, 609−22.

(25) Lingwood, D., and Simons, K. (2010) Lipid rafts as a membrane-organizing principle. *Science 327*, 46−50.

(26) Chidlow, J. H. Jr., and Sessa, W. C. (2010) Caveolae, caveolins, and cavins: complex control of cellular signalling and inflammation. *Cardiovasc. Res. 86*, 219−25.

(27) Glebov, O. O., Bright, N. A., and Nichols, B. J. (2006) Flotillin-1 defines a clathrin-independent endocytic pathway in mammalian cells. *Nat. Cell Biol. 8*, 46−54.

(28) Howes, M. T., Mayor, S., and Parton, R. G. (2010) Molecules, mechanisms, and cellular roles of clathrin-independent endocytosis. *Curr. Opin. Cell Biol. 22*, 519−27.

(29) Kerr, M. C., and Teasdale, R. D. (2009) Defining macropinocytosis. *Traffic 10*, 364−71.

(30) Kunz, S. (2009) Receptor binding and cell entry of Old World arenaviruses reveal novel aspects of virus-host interaction. *Virology 387*, 245−9.

(31) Alam, M. R., Ming, X., Dixit, V., Fisher, M., Chen, X., and Juliano, R. L. (2010) The biological effect of an antisense oligonucleotide depends on its route of endocytosis and trafficking. *Oligonucleotides 20*, 103−9.

(32) Angers, C. G., and Merz, A. J. (2011) New links between vesicle coats and Rab-mediated vesicle targeting. *Semin. Cell Dev. Biol. 22*, 18−26.

(33) Johannes, L., and Popoff, V. (2008) Tracing the retrograde route in protein trafficking. *Cell 135*, 1175−87.

(34) Rehman, Z. U., Hoekstra, D., and Zuhorn, I. S. (2011) Protein kinase A inhibition modulates the intracellular routing of gene delivery vehicles in HeLa cells, leading to productive transfection. *J. Controlled Release* DOI:10.1016/j.jconrel.2011.07.015.

(35) Stenmark, H. (2009) Rab GTPases as coordinators of vesicle traffic. *Nat. Rev. Mol. Cell Biol. 10*, 513−25.

(36) Hutagalung, A. H., and Novick, P. J. (2011) Role of Rab GTPases in membrane traffic and cell physiology. *Physiol. Rev. 91*, 119−49.

(37) Bonifacino, J. S., and Hurley, J. H. (2008) Retromer. *Curr. Opin. Cell Biol. 20*, 427−36.
(38) Brocker, C., Engelbrecht-Vandre, S., and Ungermann, C. (2010) Multisubunit tethering complexes and their role in membrane fusion. *Curr. Biol. 20*, R943−52.
(39) Malsam, J., Kreye, S., and Sollner, T. H. (2008) Membrane fusion: SNAREs and regulation. *Cell. Mol. Life Sci. 65*, 2814−32.
(40) Blumenthal, R., Clague, M. J., Durell, S. R., and Epand, R. M. (2003) Membrane fusion. *Chem. Rev. 103*, 53−69.
(41) Wickner, W., and Schekman, R. (2008) Membrane fusion. *Nat. Struct. Mol. Biol. 15*, 658−64.
(42) Weinreb, G., and Lentz, B. R. (2007) Analysis of membrane fusion as a two-state sequential process: evaluation of the stalk model. *Biophys. J. 92*, 4012−29.
(43) Allen, T. M., Hong, K., and Papahadjopoulos, D. (1990) Membrane contact, fusion, and hexagonal (HII) transitions in phosphatidylethanolamine liposomes. *Biochemistry 29*, 2976−85.
(44) Ortiz, A., Killian, J. A., Verkleij, A. J., and Wilschut, J. (1999) Membrane fusion and the lamellar-to-inverted-hexagonal phase transition in cardiolipin vesicle systems induced by divalent cations. *Biophys. J. 77*, 2003−14.
(45) Martens, S., and McMahon, H. T. (2008) Mechanisms of membrane fusion: disparate players and common principles. *Nat. Rev. Mol. Cell Biol. 9*, 543−56.
(46) Frolov, V. A., Dunina-Barkovskaya, A. Y., Samsonov, A. V., and Zimmerberg, J. (2003) Membrane permeability changes at early stages of influenza hemagglutinin-mediated fusion. *Biophys. J. 85*, 1725−33.
(47) Lorenz, P., Misteli, T., Baker, B. F., Bennett, C. F., and Spector, D. L. (2000) Nucleocytoplasmic shuttling: a novel in vivo property of antisense phosphorothioate oligodeoxynucleotides. *Nucleic Acids Res. 28*, 582−92.
(48) Hartig, R., Shoeman, R. L., Janetzko, A., Grub, S., and Traub, P. (1998) Active nuclear import of single-stranded oligonucleotides and their complexes with non-karyophilic macromolecules. *Biol. Cell 90*, 407−26.
(49) Juliano, R. L., Alahari, S., Yoo, H., Kole, R., and Cho, M. (1999) Antisense pharmacodynamics: critical issues in the transport and delivery of antisense oligonucleotides. *Pharm. Res. 16*, 494−502.
(50) Geary, R. S. (2009) Antisense oligonucleotide pharmacokinetics and metabolism. *Expert Opin. Drug Metab. Toxicol. 5*, 381−91.
(51) Butler, M., Stecker, K., and Bennett, C. F. (1997) Cellular distribution of phosphorothioate oligodeoxynucleotides in normal rodent tissues. *Lab. Invest. 77*, 379−88.
(52) Molitoris, B. A., Dagher, P. C., Sandoval, R. M., Campos, S. B., Ashush, H., Fridman, E., Brafman, A., Faerman, A., Atkinson, S. J., Thompson, J. D., Kalinski, H., Skaliter, R., Erlich, S., and Feinstein, E. (2009) siRNA targeted to p53 attenuates ischemic and cisplatin-induced acute kidney injury. *J. Am. Soc. Nephrol. 20*, 1754−64.
(53) Koller, E., Vincent, T. M., Chappell, A., De, S., Manoharan, M., and Bennett, C. F. (2011) Mechanisms of single-stranded phosphorothioate modified antisense oligonucleotide accumulation in hepatocytes. *Nucleic Acids Res. 39*, 4795−807.
(54) Stein, C. A., Hansen, J. B., Lai, J., Wu, S., Voskresenskiy, A., Hog, A., Worm, J., Hedtjarn, M., Souleimanian, N., Miller, P., Soifer, H. S., Castanotto, D., Benimetskaya, L., Orum, H., and Koch, T. (2010) Efficient gene silencing by delivery of locked nucleic acid antisense oligonucleotides, unassisted by transfection reagents. *Nucleic Acids Res. 38*, e3.
(55) Zhang, Y., Qu, Z., Kim, S., Shi, V., Liao, B., Kraft, P., Bandaru, R., Wu, Y., Greenberger, L. M., and Horak, I. D. (2011) Down-modulation of cancer targets using locked nucleic acid (LNA)-based antisense oligonucleotides without transfection. *Gene Ther. 18*, 326−33.
(56) Benimetskaya, L., Loike, J. D., Khaled, Z., Loike, G., Silverstein, S. C., Cao, L., el Khoury, J., Cai, T. Q., and Stein, C. A. (1997) Mac-1 (CD11b/CD18) is an oligodeoxynucleotide-binding protein. *Nat. Med. 3*, 414−20.
(57) Butler, M., Crooke, R. M., Graham, M. J., Lemonidis, K. M., Lougheed, M., Murray, S. F., Witchell, D., Steinbrecher, U., and Bennett, C. F. (2000) Phosphorothioate oligodeoxynucleotides distribute similarly in class A scavenger receptor knockout and wild-type mice. *J. Pharmacol. Exp. Ther. 292*, 489−96.
(58) Hanss, B., Leal-Pinto, E., Bruggeman, L. A., Copeland, T. D., and Klotman, P. E. (1998) Identification and characterization of a cell membrane nucleic acid channel. *Proc. Natl. Acad. Sci. U. S. A. 95*, 1921−6.
(59) Hanss, B., Leal-Pinto, E., Teixeira, A., Christian, R. E., Shabanowitz, J., Hunt, D. F., and Klotman, P. E. (2002) Cytosolic malate dehydrogenase confers selectivity of the nucleic acid-conducting channel. *Proc. Natl. Acad. Sci. U. S. A. 99*, 1707−12.
(60) Winston, W. M., Sutherlin, M., Wright, A. J., Feinberg, E. H., and Hunter, C. P. (2007) Caenorhabditis elegans SID-2 is required for environmental RNA interference. *Proc. Natl. Acad. Sci. U. S. A. 104*, 10565−70.
(61) Duxbury, M. S., Ashley, S. W., and Whang, E. E. (2005) RNA interference: a mammalian SID-1 homologue enhances siRNA uptake and gene silencing efficacy in human cells. *Biochem. Biophys. Res. Commun. 331*, 459−63.
(62) Tsang, S. Y., Moore, J. C., Huizen, R. V., Chan, C. W., and Li, R. A. (2007) Ectopic expression of systemic RNA interference defective protein in embryonic stem cells. *Biochem. Biophys. Res. Commun. 357*, 480−6.
(63) Wolfrum, C., Shi, S., Jayaprakash, K. N., Jayaraman, M., Wang, G., Pandey, R. K., Rajeev, K. G., Nakayama, T., Charrise, K., Ndungo, E. M., Zimmermann, T., Koteliansky, V., Manoharan, M., and Stoffel, M. (2007) Mechanisms and optimization of in vivo delivery of lipophilic siRNAs. *Nat. Biotechnol. 25*, 1149−57.
(64) Overhoff, M., and Sczakiel, G. (2005) Phosphorothioate-stimulated uptake of short interfering RNA by human cells. *EMBO Rep. 6*, 1176−81.
(65) Robbins, M., Judge, A., and MacLachlan, I. (2009) siRNA and innate immunity. *Oligonucleotides 19*, 89−102.
(66) Kawai, T., and Akira, S. (2011) Toll-like receptors and their crosstalk with other innate receptors in infection and immunity. *Immunity 34*, 637−50.
(67) Kortylewski, M., Swiderski, P., Herrmann, A., Wang, L., Kowolik, C., Kujawski, M., Lee, H., Scuto, A., Liu, Y., Yang, C., Deng, J., Soifer, H. S., Raubitschek, A., Forman, S., Rossi, J. J., Pardoll, D. M., Jove, R., and Yu, H. (2009) In vivo delivery of siRNA to immune cells by conjugation to a TLR9 agonist enhances antitumor immune responses. *Nat. Biotechnol. 27*, 925−32.
(68) Juliano, R. L., Alam, R., Dixit, V., and Kang, H. M. (2009) Cell-targeting and cell-penetrating peptides for delivery of therapeutic and imaging agents. *Wiley Interdiscip. Rev. Nanomed. Nanobiotechnol. 1*, 324−35.
(69) Johnson, R. M., Harrison, S. D., and Maclean, D. (2011) Therapeutic applications of cell-penetrating peptides. *Methods Mol. Biol. 683*, 535−51.
(70) Lindgren, M., and Langel, U. (2011) Classes and prediction of cell-penetrating peptides. *Methods Mol. Biol. 683*, 3−19.
(71) Ter-Avetisyan, G., Tunnemann, G., Nowak, D., Nitschke, M., Herrmann, A., Drab, M., and Cardoso, M. C. (2009) Cell entry of arginine-rich peptides is independent of endocytosis. *J. Biol. Chem. 284*, 3370−8.
(72) Saalik, P., Niinep, A., Pae, J., Hansen, M., Lubenets, D., Langel, U., and Pooga, M. (2011) Penetration without cells: Membrane translocation of cell-penetrating peptides in the model giant plasma membrane vesicles. *J. Controlled Release 153*, 117−25.
(73) Richard, J. P., Melikov, K., Brooks, H., Prevot, P., Lebleu, B., and Chernomordik, L. V. (2005) Cellular uptake of unconjugated TAT peptide involves clathrin-dependent endocytosis and heparan sulfate receptors. *J. Biol. Chem. 280*, 15300−6.
(74) Wadia, J. S., Stan, R. V., and Dowdy, S. F. (2004) Transducible TAT-HA fusogenic peptide enhances escape of TAT-fusion proteins after lipid raft macropinocytosis. *Nat. Med. 10*, 310−5.
(75) Fittipaldi, A., Ferrari, A., Zoppe, M., Arcangeli, C., Pellegrini, V., Beltram, F., and Giacca, M. (2003) Cell membrane lipid rafts mediate

caveolar endocytosis of HIV-1 Tat fusion proteins. *J. Biol. Chem. 278*, 34141−9.
(76) Tunnemann, G., Martin, R. M., Haupt, S., Patsch, C., Edenhofer, F., and Cardoso, M. C. (2006) Cargo-dependent mode of uptake and bioavailability of TAT-containing proteins and peptides in living cells. *FASEB J. 20*, 1775−84.
(77) El-Andaloussi, S., Jarver, P., Johansson, H. J., and Langel, U. (2007) Cargo-dependent cytotoxicity and delivery efficacy of cell-penetrating peptides: a comparative study. *Biochem. J. 407*, 285−92.
(78) Lebleu, B., Moulton, H. M., Abes, R., Ivanova, G. D., Abes, S., Stein, D. A., Iversen, P. L., Arzumanov, A. A., and Gait, M. J. (2008) Cell penetrating peptide conjugates of steric block oligonucleotides. *Adv. Drug Delivery Rev. 60*, 517−29.
(79) Juliano, R., Alam, M. R., Dixit, V., and Kang, H. (2008) Mechanisms and strategies for effective delivery of antisense and siRNA oligonucleotides. *Nucleic Acids Res. 36*, 4158−71.
(80) Ivanova, G. D., Arzumanov, A., Abes, R., Yin, H., Wood, M. J., Lebleu, B., and Gait, M. J. (2008) Improved cell-penetrating peptide-PNA conjugates for splicing redirection in HeLa cells and exon skipping in mdx mouse muscle. *Nucleic Acids Res. 36*, 6418−28.
(81) Abes, R., Moulton, H. M., Clair, P., Yang, S. T., Abes, S., Melikov, K., Prevot, P., Youngblood, D. S., Iversen, P. L., Chernomordik, L. V., and Lebleu, B. (2008) Delivery of steric block morpholino oligomers by (R-X-R)4 peptides: structure-activity studies. *Nucleic Acids Res. 36*, 6343−54.
(82) Yin, H., Saleh, A. F., Betts, C., Camelliti, P., Seow, Y., Ashraf, S., Arzumanov, A., Hammond, S., Merritt, T., Gait, M. J., and Wood, M. J. (2011) Pip5 transduction peptides direct high efficiency oligonucleotide-mediated dystrophin exon skipping in heart and phenotypic correction in mdx mice. *Mol. Ther. 19*, 1295−303.
(83) Goyenvalle, A., Babbs, A., Powell, D., Kole, R., Fletcher, S., Wilton, S. D., and Davies, K. E. (2010) Prevention of dystrophic pathology in severely affected dystrophin/utrophin-deficient mice by morpholino-oligomer-mediated exon-skipping. *Mol. Ther. 18*, 198−205.
(84) Koppelhus, U., Shiraishi, T., Zachar, V., Pankratova, S., and Nielsen, P. E. (2008) Improved cellular activity of antisense peptide nucleic acids by conjugation to a cationic peptide-lipid (CatLip) domain. *Bioconjugate Chem. 19*, 1526−34.
(85) Deshayes, S., Morris, M., Heitz, F., and Divita, G. (2008) Delivery of proteins and nucleic acids using a non-covalent peptide-based strategy. *Adv. Drug Delivery Rev. 60*, 537−47.
(86) Endoh, T., and Ohtsuki, T. (2009) Cellular siRNA delivery using cell-penetrating peptides modified for endosomal escape. *Adv. Drug Delivery Rev. 61*, 704−9.
(87) Crombez, L., Morris, M. C., Dufort, S., Aldrian-Herrada, G., Nguyen, Q., Mc Master, G., Coll, J. L., Heitz, F., and Divita, G. (2009) Targeting cyclin B1 through peptide-based delivery of siRNA prevents tumour growth. *Nucleic Acids Res. 37*, 4559−69.
(88) Lundberg, P., El-Andaloussi, S., Sutlu, T., Johansson, H., and Langel, U. (2007) Delivery of short interfering RNA using endosomolytic cell-penetrating peptides. *FASEB J. 21*, 2664−71.
(89) Ezzat, K., El Andaloussi, S., Zaghloul, E. M., Lehto, T., Lindberg, S., Moreno, P. M., Viola, J. R., Magdy, T., Abdo, R., Guterstam, P., Sillard, R., Hammond, S. M., Wood, M. J., Arzumanov, A. A., Gait, M. J., Smith, C. I., Hallbrink, M., and Langel, U. (2011) PepFect 14, a novel cell-penetrating peptide for oligonucleotide delivery in solution and as solid formulation. *Nucleic Acids Res. 39*, 5284−98.
(90) Andaloussi, S. E., Lehto, T., Mager, I., Rosenthal-Aizman, K., Oprea, I. I., Simonson, O. E., Sork, H., Ezzat, K., Copolovici, D. M., Kurrikoff, K., Viola, J. R., Zaghloul, E. M., Sillard, R., Johansson, H. J., Said Hassane, F., Guterstam, P., Suhorutsenko, J., Moreno, P. M., Oskolkov, N., Halldin, J., Tedebark, U., Metspalu, A., Lebleu, B., Lehtio, J., Smith, C. I., and Langel, U. (2011) Design of a peptide-based vector, PepFect6, for efficient delivery of siRNA in cell culture and systemically in vivo. *Nucleic Acids Res. 39*, 3972−87.
(91) Crombez, L., Aldrian-Herrada, G., Konate, K., Nguyen, Q. N., McMaster, G. K., Brasseur, R., Heitz, F., and Divita, G. (2009) A new potent secondary amphipathic cell-penetrating peptide for siRNA delivery into mammalian cells. *Mol. Ther. 17*, 95−103.
(92) Said Hassane, F., Abes, R., El Andaloussi, S., Lehto, T., Sillard, R., Langel, U., and Lebleu, B. (2011) Insights into the cellular trafficking of splice redirecting oligonucleotides complexed with chemically modified cell-penetrating peptides. *J. Controlled Release 153*, 163−72.
(93) Marlin, F., Simon, P., Saison-Behmoaras, T., and Giovannangeli, C. (2010) Delivery of oligonucleotides and analogues: the oligonucleotide conjugate-based approach. *ChemBioChem 11*, 1493−500.
(94) Corey, D. R. (2007) Chemical modification: the key to clinical application of RNA interference? *J. Clin. Invest. 117*, 3615−22.
(95) Singh, Y., Murat, P., and Defrancq, E. (2010) Recent developments in oligonucleotide conjugation. *Chem. Soc. Rev. 39*, 2054−70.
(96) Watts, J. K., Deleavey, G. F., and Damha, M. J. (2008) Chemically modified siRNA: tools and applications. *Drug Discovery Today 13*, 842−55.
(97) Uno, Y., Piao, W., Miyata, K., Nishina, K., Mizusawa, H., and Yokota, T. (2011) High-density lipoprotein facilitates in vivo delivery of alpha-tocopherol-conjugated short-interfering RNA to the brain. *Hum. Gene Ther. 22*, 711−9.
(98) Li, S., Deshmukh, H. M., and Huang, L. (1998) Folate-mediated targeting of antisense oligodeoxynucleotides to ovarian cancer cells. *Pharm. Res. 15*, 1540−5.
(99) Biessen, E. A., Sliedregt-Bol, K., PA, T. H., Prince, P., Van der Bilt, E., Valentijn, A. R., Meeuwenoord, N. J., Princen, H., Bijsterbosch, M. K., Van der Marel, G. A., Van Boom, J. H., and Van Berkel, T. J. (2002) Design of a targeted peptide nucleic acid prodrug to inhibit hepatic human microsomal triglyceride transfer protein expression in hepatocytes. *Bioconjugate Chem. 13*, 295−302.
(100) Cesarone, G., Edupuganti, O. P., Chen, C. P., and Wickstrom, E. (2007) Insulin receptor substrate 1 knockdown in human MCF7 ER+ breast cancer cells by nuclease-resistant IRS1 siRNA conjugated to a disulfide-bridged D-peptide analogue of insulin-like growth factor 1. *Bioconjugate Chem. 18*, 1831−40.
(101) Alam, M. R., Dixit, V., Kang, H., Li, Z. B., Chen, X., Trejo, J., Fisher, M., and Juliano, R. L. (2008) Intracellular delivery of an anionic antisense oligonucleotide via receptor-mediated endocytosis. *Nucleic Acids Res. 36*, 2764−76.
(102) Ming, X., Alam, M. R., Fisher, M., Yan, Y., Chen, X., and Juliano, R. L. (2010) Intracellular delivery of an antisense oligonucleotide via endocytosis of a G protein-coupled receptor. *Nucleic Acids Res. 38*, 6567−76.
(103) Nakagawa, O., Ming, X., Huang, L., and Juliano, R. L. (2010) Targeted intracellular delivery of antisense oligonucleotides via conjugation with small-molecule ligands. *J. Am. Chem. Soc. 132*, 8848−9.
(104) Thiel, K. W., and Giangrande, P. H. (2009) Therapeutic applications of DNA and RNA aptamers. *Oligonucleotides 19*, 209−22.
(105) McNamara, J. O. 2nd, Andrechek, E. R., Wang, Y., Viles, K. D., Rempel, R. E., Gilboa, E., Sullenger, B. A., and Giangrande, P. H. (2006) Cell type-specific delivery of siRNAs with aptamer-siRNA chimeras. *Nat. Biotechnol. 24*, 1005−15.
(106) Dassie, J. P., Liu, X. Y., Thomas, G. S., Whitaker, R. M., Thiel, K. W., Stockdale, K. R., Meyerholz, D. K., McCaffrey, A. P., McNamara, J. O. 2nd, and Giangrande, P. H. (2009) Systemic administration of optimized aptamer-siRNA chimeras promotes regression of PSMA-expressing tumors. *Nat. Biotechnol. 27*, 839−49.
(107) Pastor, F., Kolonias, D., Giangrande, P. H., and Gilboa, E. (2010) Induction of tumour immunity by targeted inhibition of nonsense-mediated mRNA decay. *Nature 465*, 227−30.
(108) Wheeler, L. A., Trifonova, R., Vrbanac, V., Basar, E., McKernan, S., Xu, Z., Seung, E., Deruaz, M., Dudek, T., Einarsson, J. I., Yang, L., Allen, T. M., Luster, A. D., Tager, A. M., Dykxhoorn, D. M., and Lieberman, J. (2011) Inhibition of HIV transmission in human cervicovaginal explants and humanized mice using CD4 aptamer-siRNA chimeras. *J. Clin. Invest. 121*, 2401−12.

(109) Ming, X. (2011) Cellular delivery of siRNA and antisense oligonucleotides via receptor-mediated endocytosis. *Expert Opin. Drug Delivery 8*, 435−49.
(110) Geary, R. S., Wancewicz, E., Matson, J., Pearce, M., Siwkowski, A., Swayze, E., and Bennett, F. (2009) Effect of dose and plasma concentration on liver uptake and pharmacologic activity of a 2′-methoxyethyl modified chimeric antisense oligonucleotide targeting PTEN. *Biochem. Pharmacol. 78*, 284−91.
(111) Caswell, P. T., Vadrevu, S., and Norman, J. C. (2009) Integrins: masters and slaves of endocytic transport. *Nat. Rev. Mol. Cell Biol. 10*, 843−53.
(112) Hanyaloglu, A. C., and von Zastrow, M. (2008) Regulation of GPCRs by endocytic membrane trafficking and its potential implications. *Annu. Rev. Pharmacol. Toxicol. 48*, 537−68.
(113) Sorkin, A., and Goh, L. K. (2009) Endocytosis and intracellular trafficking of ErbBs. *Exp. Cell Res. 315*, 683−96.
(114) Akhtar, S., and Benter, I. F. (2007) Nonviral delivery of synthetic siRNAs in vivo. *J. Clin. Invest. 117*, 3623−32.
(115) Tamura, A., and Nagasaki, Y. (2010) Smart siRNA delivery systems based on polymeric nanoassemblies and nanoparticles. *Nanomedicine (Lond.) 5*, 1089−102.
(116) Love, K. T., Mahon, K. P., Levins, C. G., Whitehead, K. A., Querbes, W., Dorkin, J. R., Qin, J., Cantley, W., Qin, L. L., Racie, T., Frank-Kamenetsky, M., Yip, K. N., Alvarez, R., Sah, D. W., de Fougerolles, A., Fitzgerald, K., Koteliansky, V., Akinc, A., Langer, R., and Anderson, D. G. (2010) Lipid-like materials for low-dose, in vivo gene silencing. *Proc. Natl. Acad. Sci. U. S. A. 107*, 1864−9.
(117) Kabanov, A. V., and Vinogradov, S. V. (2009) Nanogels as pharmaceutical carriers: finite networks of infinite capabilities. *Angew. Chem., Int. Ed. Engl. 48*, 5418−29.
(118) Petros, R. A., and DeSimone, J. M. (2010) Strategies in the design of nanoparticles for therapeutic applications. *Nat. Rev. Drug Discovery 9*, 615−27.
(119) Tseng, Y. C., Mozumdar, S., and Huang, L. (2009) Lipid-based systemic delivery of siRNA. *Adv. Drug Delivery Rev. 61*, 721−31.
(120) Lv, H., Zhang, S., Wang, B., Cui, S., and Yan, J. (2006) Toxicity of cationic lipids and cationic polymers in gene delivery. *J. Controlled Release 114*, 100−9.
(121) Akhtar, S. (2010) Cationic nanosystems for the delivery of small interfering ribonucleic acid therapeutics: a focus on toxicogenomics. *Expert Opin. Drug Metab. Toxicol. 6*, 1347−62.
(122) Lu, J. J., Langer, R., and Chen, J. (2009) A novel mechanism is involved in cationic lipid-mediated functional siRNA delivery. *Mol. Pharm. 6*, 763−71.
(123) Kaneda, M. M., Sasaki, Y., Lanza, G. M., Milbrandt, J., and Wickline, S. A. (2010) Mechanisms of nucleotide trafficking during siRNA delivery to endothelial cells using perfluorocarbon nanoemulsions. *Biomaterials 31*, 3079−86.
(124) Ming, X., Sato, K., and Juliano, R. L. (2011) Unconventional internalization mechanisms underlying functional delivery of antisense oligonucleotides via cationic lipoplexes and polyplexes. *J. Controlled Release 153*, 83−92.
(125) Pirollo, K. F., and Chang, E. H. (2008) Targeted delivery of small interfering RNA: approaching effective cancer therapies. *Cancer Res. 68*, 1247−50.
(126) Kumar, P., Wu, H., McBride, J. L., Jung, K. E., Kim, M. H., Davidson, B. L., Lee, S. K., Shankar, P., and Manjunath, N. (2007) Transvascular delivery of small interfering RNA to the central nervous system. *Nature 448*, 39−43.
(127) Kumar, P., Ban, H. S., Kim, S. S., Wu, H., Pearson, T., Greiner, D. L., Laouar, A., Yao, J., Haridas, V., Habiro, K., Yang, Y. G., Jeong, J. H., Lee, K. Y., Kim, Y. H., Kim, S. W., Peipp, M., Fey, G. H., Manjunath, N., Shultz, L. D., Lee, S. K., and Shankar, P. (2008) T cell-specific siRNA delivery suppresses HIV-1 infection in humanized mice. *Cell 134*, 577−86.
(128) Kim, S. S., Ye, C., Kumar, P., Chiu, I., Subramanya, S., Wu, H., Shankar, P., and Manjunath, N. (2010) Targeted delivery of siRNA to macrophages for anti-inflammatory treatment. *Mol. Ther. 18*, 993−1001.
(129) Subramanya, S., Kim, S. S., Abraham, S., Yao, J., Kumar, M., Kumar, P., Haridas, V., Lee, S. K., Shultz, L. D., Greiner, D., N, M., and Shankar, P. (2010) Targeted delivery of small interfering RNA to human dendritic cells to suppress dengue virus infection and associated proinflammatory cytokine production. *J. Virol. 84*, 2490−501.
(130) Song, E., Zhu, P., Lee, S. K., Chowdhury, D., Kussman, S., Dykxhoorn, D. M., Feng, Y., Palliser, D., Weiner, D. B., Shankar, P., Marasco, W. A., and Lieberman, J. (2005) Antibody mediated in vivo delivery of small interfering RNAs via cell-surface receptors. *Nat. Biotechnol. 23*, 709−17.
(131) Peer, D., Zhu, P., Carman, C. V., Lieberman, J., and Shimaoka, M. (2007) Selective gene silencing in activated leukocytes by targeting siRNAs to the integrin lymphocyte function-associated antigen-1. *Proc. Natl. Acad. Sci. U. S. A. 104*, 4095−100.
(132) Rozema, D. B., Lewis, D. L., Wakefield, D. H., Wong, S. C., Klein, J. J., Roesch, P. L., Bertin, S. L., Reppen, T. W., Chu, Q., Blokhin, A. V., Hagstrom, J. E., and Wolff, J. A. (2007) Dynamic PolyConjugates for targeted in vivo delivery of siRNA to hepatocytes. *Proc. Natl. Acad. Sci. U. S. A. 104*, 12982−7.
(133) Oishi, M., Nagasaki, Y., Nishiyama, N., Itaka, K., Takagi, M., Shimamoto, A., Furuichi, Y., and Kataoka, K. (2007) Enhanced growth inhibition of hepatic multicellular tumor spheroids by lactosylated poly(ethylene glycol)-siRNA conjugate formulated in PEGylated polyplexes. *ChemMedChem 2*, 1290−7.
(134) Chen, Y., Bathula, S. R., Yang, Q., and Huang, L. (2010) Targeted nanoparticles deliver siRNA to melanoma. *J. Invest. Dermatol. 130*, 2790−8.
(135) Li, J., Chen, Y. C., Tseng, Y. C., Mozumdar, S., and Huang, L. (2010) Biodegradable calcium phosphate nanoparticle with lipid coating for systemic siRNA delivery. *J. Controlled Release 142*, 416−21.
(136) Davis, M. E., Zuckerman, J. E., Choi, C. H., Seligson, D., Tolcher, A., Alabi, C. A., Yen, Y., Heidel, J. D., and Ribas, A. (2010) Evidence of RNAi in humans from systemically administered siRNA via targeted nanoparticles. *Nature 464*, 1067−70.
(137) Bartlett, D. W., and Davis, M. E. (2007) Physicochemical and biological characterization of targeted, nucleic acid-containing nanoparticles. *Bioconjugate Chem. 18*, 456−68.
(138) Bartlett, D. W., Su, H., Hildebrandt, I. J., Weber, W. A., and Davis, M. E. (2007) Impact of tumor-specific targeting on the biodistribution and efficacy of siRNA nanoparticles measured by multimodality in vivo imaging. *Proc. Natl. Acad. Sci. U. S. A. 104*, 15549−54.

Bioconjugate Chemistry

Communication

pubs.acs.org/bc

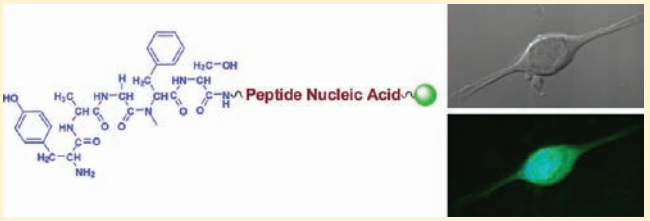
Fluorescent Peptide–PNA Chimeras for Imaging Monoamine Oxidase A mRNA in Neuronal Cells

Dalip Sethi,[†] Chang-Po Chen,[†] Rui-Yan Jing,[†] Mathew L. Thakur,[‡,§] and Eric Wickstrom*[,†,§]

[†]Departments of Biochemistry & Molecular Biology, [‡]Radiology, and [§]Kimmel Cancer Center, Thomas Jefferson University, Philadelphia, Pennsylvania 19107, United States

Supporting Information

ABSTRACT: Monoamine oxidases (MAO) catalyze the oxidative deamination of many biogenic amines and are integral proteins found in the mitochondrial outer membrane. Changes in MAO-A levels are associated with depression, trait aggression, and addiction. Here we report the synthesis, characterization, and *in vitro* evaluation of novel fluorescent peptide–peptide nucleic acid (PNA) chimeras for *MAOA* mRNA imaging in live neuronal cells. The probes were designed to include *MAOA*-specific PNA dodecamers, separated by an N-terminal spacer to a μ-opioid receptor targeting peptide (DAMGO), with a spacer and a fluorophore on the C-terminus. The probe was successfully delivered into human SH-SY5Y neuroblastoma cells through μ-opioid receptor-mediated endocytosis. The K_d by flow cytometry was 11.6 ± 0.8 nM. Uptake studies by fluorescence microscopy showed ~5-fold higher signal in human SH-SY5Y neuroblastoma cells than in negative control CHO-K1 cells that lack μ-opioid receptors. Moreover, a peptide-mismatch control sequence showed no significant uptake in SH-SY5Y cells. Such mRNA imaging agents with near-infrared fluorophores might enable real time imaging and quantitation of neuronal mRNAs in live animal models.



Monoamine oxidases (MAO) catalyze the oxidative deamination of many biogenic amines. MAO are expressed in various neuronal and non-neuronal cells in the central nervous system (CNS) and peripheral organs.[1] In the CNS, MAO carries out metabolic inactivation of released monoamine transmitters, but also creates cytotoxic free radicals throughout aging and neurodegenerative diseases. MAO exists in two isoforms, MAO-A and MAO-B, which differ by their substrate specificity and more for inhibitor selectivity. MAO-A preferentially deaminates serotonin, dopamine, and norepinephrine in catecholaminergic neurons in the human brain, in particular, adrenergic and noradrenergic neurons. On the other hand, MAO-B preferentially degrades exogenous bioamines ingested in the diet such as phenylethylamine and benzylamine. The catalytic activity of MAO-A, located in the mitochondria of presynaptic terminals in monoamine-releasing neurons, has a critical role in regulating the release and degradation of monoamines throughout the brain.[2,3]

Differential expression of the *MAOA* gene, called by some the "warrior gene", has been linked to numerous CNS disorders, particularly aggression,[4−6] antisocial behavior, attention deficit hyperactivity disorder,[7,8] anxiety,[9] anorexia nervosa,[10,11] bipolar disorder,[12−14] drug abuse,[15,16] and Alzheimer's disease.[17] Elevated MAO-A levels in affect modulating regions are believed to exert an important monoamine-lowering process during key depressive episodes of major depressive disorder. In postpartum depression, MAO-A levels and affinity increase sharply due to a decline (100- to 1000-fold) in estrogen levels, which creates a high risk for depressive episodes.[18]

On the other hand, genetic deletion of *MAOA* produces aggressive phenotypes across species. Studies have found links between *MAOA* gene products and violent behavior. Lower MAO-A activity in cortical and subcortical brain regions results in higher self-reported trait aggression.[19] MAO-A also plays a critical role in alcohol[20,21] and cocaine addiction.[22] A recent study showed up-regulated MAO-A expression in alcoholic individuals, using whole genome sequencing of mRNA transcripts (RNA-Seq).[21] In another study, *MAOA*-L (low repeat allele) carrier males with cocaine use disorders (CUD) revealed greater gray matter volume (GMV) reduction in the brain as compared to their healthy counterparts.[22] Over the last two decades, positron emission tomography (PET) has been used extensively for measuring MAO-A enzyme activity in different tissues.[3] ^{11}C-clorgyline is one of the example of compounds used for such studies.[23] However, no such method is available for noninvasive measurement of *MAOA* mRNA expression.

The objective of the present study was to develop an *MAOA* mRNA imaging agent composed of a complementary peptide nucleic acid (PNA) labeled with a fluorescent dye for imaging, and attached to a peptide moiety for receptor-mediated intracellular delivery. PNA, an oligonucleotide analogue where the sugar-phophodiester backbone is replaced with a peptide-like aminoethylglycine backbone, has great potential for biomedical applications.[24,25] Owing to their achiral, uncharged, flexible

Received: August 21, 2011
Revised: December 26, 2011
Published: January 13, 2012

ACS Publications © 2012 American Chemical Society

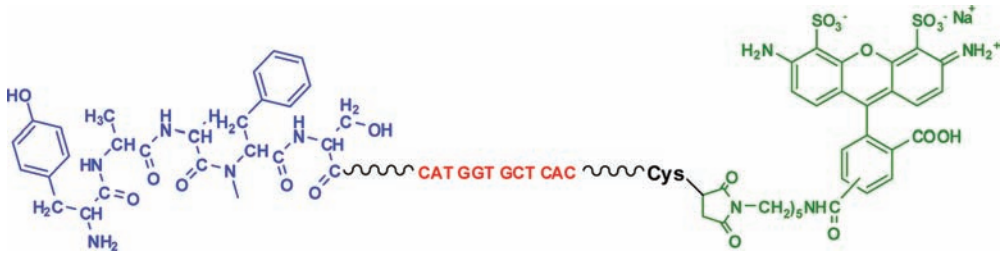


Figure 1. *ChemDraw* representation of WT4879. Targeting peptide (blue) is linked to PNA (red) at N-terminus and to AlexaFluor488 (green) at C-terminus via thiol-maleimide linkage.

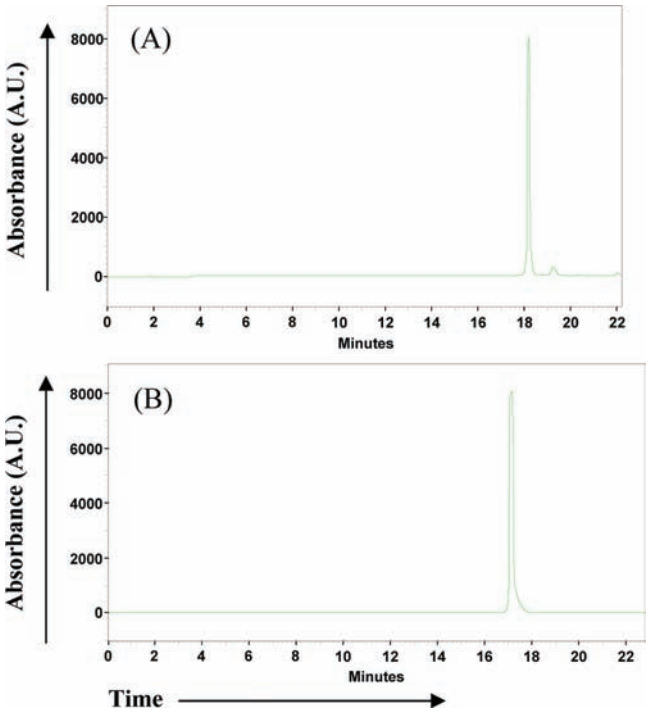


Figure 2. HPLC profiles of (A) Tyr-D-Ala-Gly-N-MePhe-Ser-AEEA-CAT GGT GCT CAC-AEEA-Cys-AlexaFluor488, WT4879 [DAMGO-MAOA-AlexaFluor488, m/z 4878.78 (calculated), 4879.20 (observed)]; and (B) Ala-D-Ala-Gly-N-MePhe-Ser-AEEA-CAT GGT GCT CAC-AEEA-Cys-AlexaFluor488, WT4786 [peptide-mismatch-MAOA-AlexaFluor488, m/z 4786.78 (calculated), 4786.08 (observed)] on a 10 × 250 mm Alltima C_{18} column, eluted at 2.5 mL/min with a 30 min gradient from 5% to 60% CH_3CN in aqueous 0.1% CF_3CO_2H, at 50 °C, monitored at 488 nm.

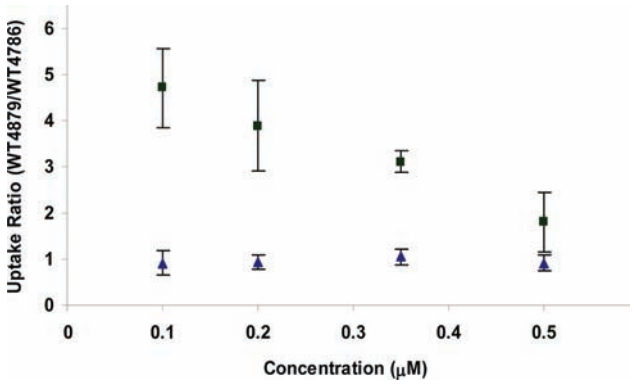


Figure 3. Specificity of uptake in SH-SY5Y (■) and CHO-K (▲) cells of WT4879 (μ-opioid receptor-specific agent) vs WT4786 (peptide mismatch agent) over a ramp of concentrations measured by flow cytometry. Ratios of specific to nonspecific uptake, after background correction, were calculated and plotted against concentration (μM), averaged over three replicate experiments.

backbone, PNAs hybridize with mRNA more strongly than normal RNA or DNA with mRNA. They are resistant to enzymatic degradation and are stable over a wide range of pH. However, due to its uncharged nature, naked PNA is poorly taken up by mammalian cells.[26]

As a result, incorporation of a receptor-targeting peptide is an efficient way to deliver PNA imaging agents into targeted cells.[25] To specifically target our probes to neuronal cells, we extended a modified DAMGO μ-opioid targeting peptide, Tyr-D-Ala-Gly-NMePhe-Ser, from the N-terminus of PNA. DAMGO is an enkephalin analogue that binds tightly to μ-opioid receptors on neuronal cells and induces internalization.[27] The phenolic hydroxyl (−OH) group of the N-terminal Tyr residue with a free cationic α-amino ($-NH_3^+$) group, similar to the tyramine moiety of morphine, and an aromatic amino acid separated by one or two residues, are the core requirements for the binding of opioid peptides.[28] The replacement of the glycinol moiety with L-serine maintains receptor affinity (K_i value 0.56 ± 0.006 nM for DAMGO with glycinol, 0.68 ± 0.02 nM for DAMGO with L-serine).[29]

Here we report the synthesis, characterization, and *in vitro* evaluation of peptide-PNA-fluorophore chimeras for *MAOA* mRNA imaging. A receptor-specific agent, Tyr-D-Ala-Gly-N-MePhe-Ser-AEEA-CAT GGT GCT CAC-AEEA-Cys-AlexaFluor488 (WT4879) (Figure 1), and a peptide mismatch control, Ala-D-Ala-Gly-N-MePhe-Ser-AEEA-CAT GGT GCT CAC-AEEA-Cys-AlexaFluor488 (WT4786) were synthesized by Fmoc-based solid phase coupling (Supporting Information, Scheme S1). The chimeras were purified using reverse phase-high performance liquid chromatography (RP-HPLC) using C_{18} columns (Figure 2) and characterized by mass spectrometry. AlexaFluor488-maleimide (Invitrogen, Carlsbad CA) was coupled to the C-terminal cysteine thiol in aqueous buffer under standard conditions. The human neuroblastoma cell line SH-SY5Y (ATCC), which expresses both μ-opioid receptor and *MAOA* mRNA,[30,31] was used for *in vitro* studies of agent uptake. SH-SY5Y cells were maintained in a 1:1 (v/v) DMEM:F12 medium supplemented with 10% fetal bovine serum (FBS). Chinese hamster ovarian cells, CHO-K1 (ATCC), were used as a negative control. CHO-K1 cells were maintained in Ham's F12 medium containing 10% FBS. Cells were incubated at 37 °C under 5% CO_2 in a humidified chamber.

In order to determine the K_d for WT4879, a competition binding assay was performed. In brief, 4 × 10^4 SH-SY5Y cells/tube were incubated with a ramp of concentrations (0, 4, 8 16, 32, 64, and 128 nM) of WT4879 (with and without 20× free DAMGO peptide, Set I and II) for 1 h at 4 °C in the dark. After incubation, cells were washed twice with cold 1×

dx.doi.org/10.1021/bc2004507 | *Bioconjugate Chem.* 2012, 23, 158−163

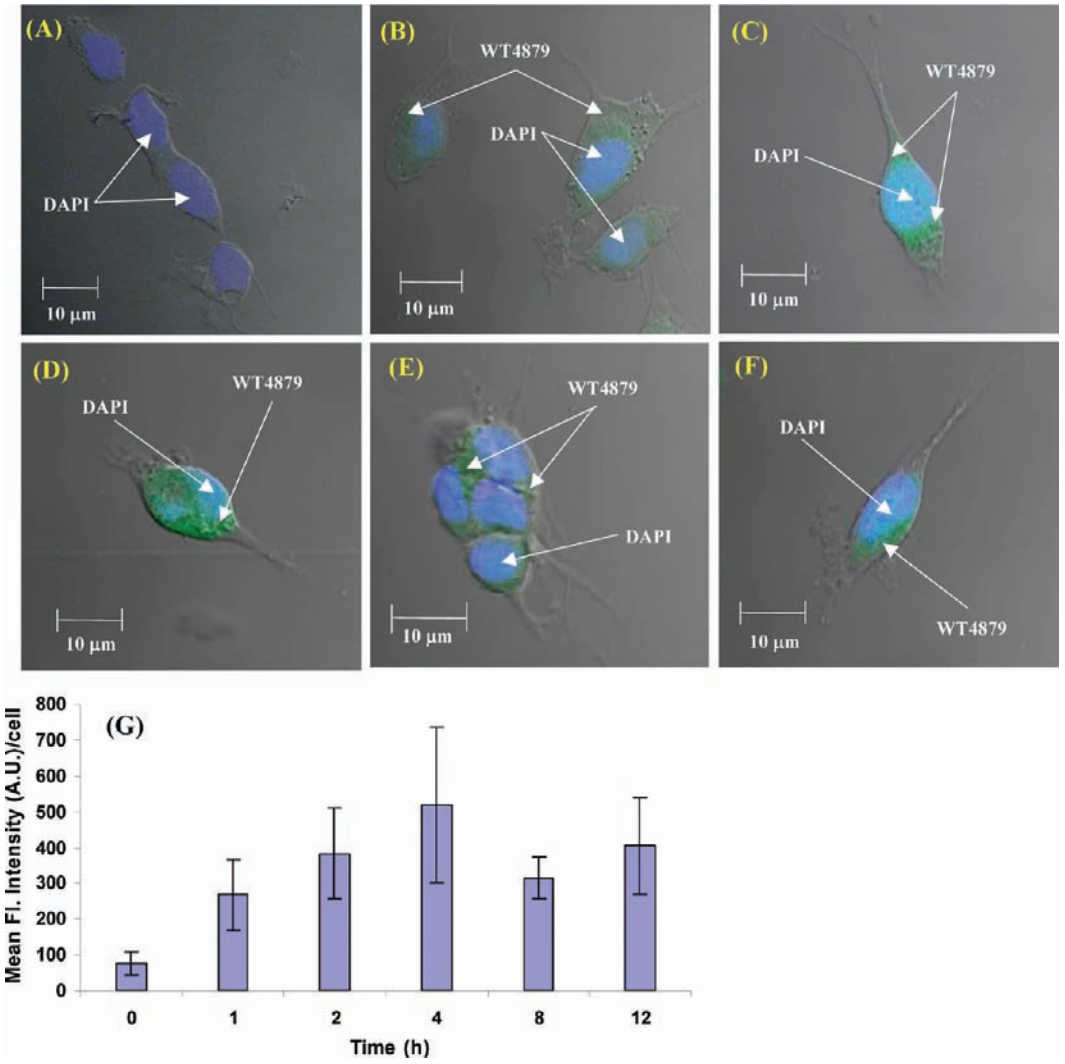


Figure 4. Confocal fluorescent images of WT4879 uptake in SH-SH5Y cells: (A) Control, (B) After 1 h, (C) 2 h, (D) 4 h, (E) 8 h, (F) 12 h, and (G) histogram showing mean fluorescence intensity (arbitrary units, A.U.) per cell measured at different times, averaged over three regions of interest.

calcium−magnesium-free phosphate buffered saline, CMF-PBS-5, containing 5% FBS, to remove the unbound probe. Subsequently, cells were fixed with CMF-PBS-5 + 1% paraformaldehyde for 10 min at 25 °C in the dark, washed twice with CMF-PBS-5, resuspended in 300 μL of CMF-PBS-5, and analyzed on a FACS Calibur flow cytometer (BD Biosciences, San Jose, CA). In each case, the fluorescence intensities of 5000 vital cells were acquired. Vital cells were gated based on sideward and forward scatter. To calculate specific uptake, both nonspecific uptake with 20× free DAMGO and background were subtracted from total uptake. The K_d was found to be 11.6 ± 0.8 nM.

To evaluate the specificity of uptake, a ramp of concentrations (0.1, 0.2, 0.35, and 0.5 μM) of WT4879 (receptor-specific agent) and WT4786 (peptide mismatch agent) were prepared in 1:1 (v/v) DMEM:F12 medium. 2 ×10^5 SH-SY5Y cells/well were cultured in 6-well plates to ∼70% confluence and the cells were incubated with imaging agent solutions for 6 h at 37 °C under 5% CO_2 in a humidified incubator. After incubation, cells were washed with cold CMF-PBS-5 (3 mL) and detached using 0.05% trypsin. The cells were washed and fixed as described above and finally resuspended in 300 μL of CMF-PBS-5 for flow cytometry. 25 000 vital cells were screened for each sample. A ratio of specific over nonspecific uptake was calculated and plotted against concentration (μM) (Figure 3). The results revealed that specificity of uptake follows an inverse relationship to the concentration of the probe. At 0.1 μM, WT4879 probe showed ∼5-fold higher uptake than WT4786, indicating high uptake specificity. A similar experiment was performed using the CHO-K1 negative control cell line in Ham's F12 medium. The specificity ratio for WT4879 was found to be 1 ± 0.3 at all the concentrations, implying no specific uptake in cells lacking the μ-opioid receptor.

The results of the above experiments were used to evaluate the time course of agent uptake. Briefly, 6.5 × 10^4 SH-SY5Y cells were seeded in each well of a poly(D-lysine) coated 4-well microslide (BD Biosciences) one day before the experiment. Cells were incubated with 0.1 μM WT4879 for increasing times (0, 0.25, 0.5, 1, 2, 4, 8, and 12 h) at 37 °C in a humidified chamber with 5% CO_2. After the incubation, cells were washed twice with CMF-PBS-5 and fixed using 4% paraformaldehyde in CMF-PBS-5 for 15 min. Prolong Gold Antifade (Invitrogen) with DAPI was used as mounting media for microslides. The slides were visualized using a LSM 510 Meta confocal microscope (Zeiss, New York NY) using the 488 nm line of an argon

dx.doi.org/10.1021/bc2004507 | *Bioconjugate Chem.* 2012, 23, 158−163

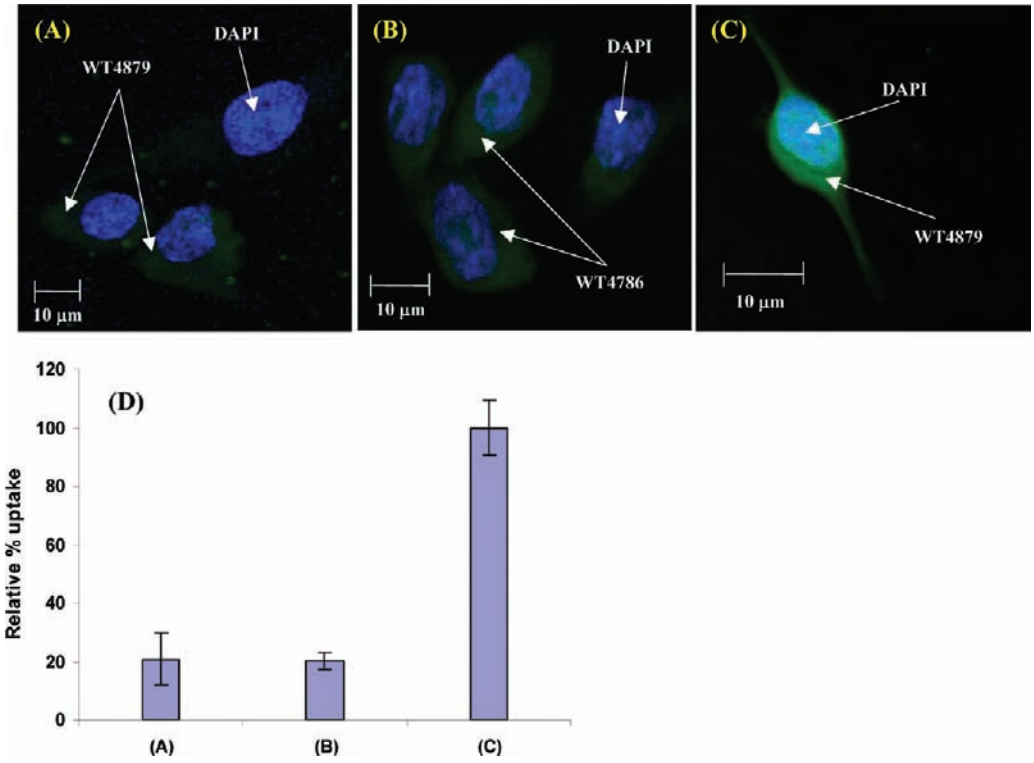


Figure 5. Confocal fluorescent images of (A) WT4879 uptake in CHO-K1 cells, (B) WT4786 uptake in SH-SH5Y cells, (C) WT4879 uptake in SH-SY5Y cells after 4 h of incubation at 37 °C with 0.1 μM agent in respective growth media, and (D) histogram showing the relative percent of uptake for 3 fields on each slide.

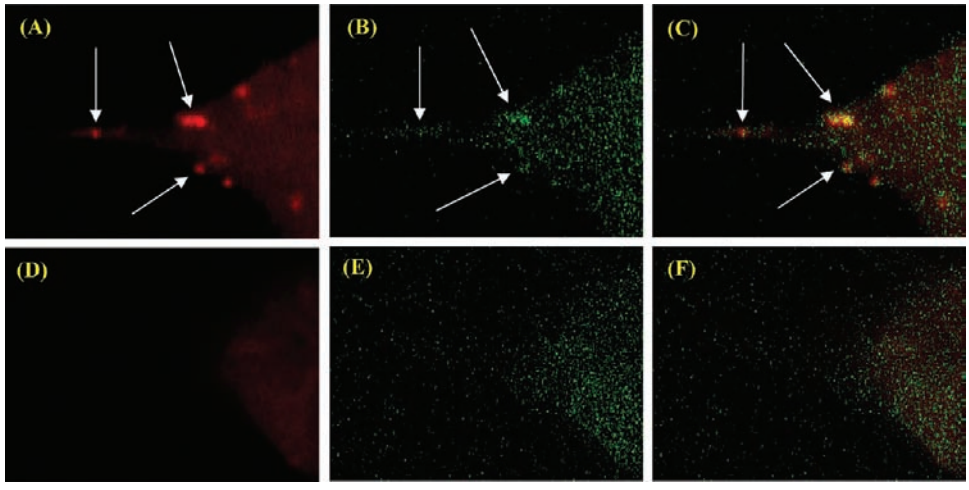


Figure 6. Confocal fluorescent images of live SH-SY5Y cells showing the (A) localization of RFP-labeled Rab5, (B) WT4879 in endosomes, (C) colocalization of RFP labeled Rab5 and WT4879, (D) RFP-labeled Rab5, (E) WT4879 distribution in cells after an additional 1 h incubation at 37 °C, and (F) merged image of (D) and (E).

ion laser with a BP 505−550 nm band-pass filter. DAPI was visualized using a 405 nm diode laser. Following image acquisition, images were quantified with *ImageJ* software (http://rsbweb.nih.gov/ij). No significant uptake was observed at 0.25 and 0.5 h (data not shown). WT4879 was taken up strongly after 1 h and found to be uniformly distributed in the cytoplasm (Figure 4). The uptake intensity increased with time up to 4 h, leveling off thereafter.

In order to study the specificity for receptor-targeted delivery, a comparative uptake study was performed using CHO-K1 (1.5×10^4 cells/well) and SH-SY5Y (6.5×10^4 cells/well) by the same protocol, as described above. Cells were incubated for 4 h at 37 °C with 0.1 μM WT4879 and WT4786 in respective growth media. Three fields were quantitated on each slide. The results revealed that negative control CHO-K1 cells took up ~21% as much receptor-specific WT4879 agent as did SH-SY5Y cells (Figure 5A,C). In SH-SY5Y cells, the peptide mismatch WT4786 agent showed ~20% uptake relative to the specific WT4879 (Figure 5B,C), consistent with the receptor-specific uptake observed by flow cytometry. In a structural control experiment, an agent with a fluorophore on the N-terminus, and DAMGO on the C-terminus, showed similarly

dx.doi.org/10.1021/bc2004507 | *Bioconjugate Chem.* 2012, 23, 158−163

low uptake by SH-SY5Y cells (data not shown), consistent with the requirement for a free N-terminal cationic amine on DAMGO.[28]

Following the specificity study, a live cell study was performed to evaluate the uptake mechanism of WT4879 in SH-SY5Y cells. Briefly, 2×10^5 cells/dish were seeded in 35 mm dishes (μ-dishes, ibidi GmbH, Germany) and transfected with CellLight BacMam reagent (Invitrogen), according to the manufacturer's protocol (Invitrogen), to label early endosomes with RFP-labeled Rab5 protein. After the expression of RFP-labeled Rab5 protein, cells were incubated for 1 h at 37 °C with 0.1 μM WT4879 in phenol red-free growth medium. The dishes were washed with phenol red-free medium (3×2 mL) and visualized using a heated stage on the LSM 510 Meta confocal microscope. The cells showed colocalization of WT4879 with Rab5 in early endosomes (Figure 6A,B,C). The same section of each dish was scanned after additional 1 h incubation at 37 °C. The endosomes disappeared and WT4879 was found to be uniformly distributed in the cytoplasm (Figure 6D,E,F). The control cells expressed RFP-labeled Rab5 but did not showed any green fluorescence. The intensities of RFP for labeled Rab5 and AlexaFluor 488 for WT4879 were measured along the *x*-axis using *Amira 5* software, which showed >95% overlap (Supporting Information, Figure S1). These results imply receptor-specific uptake of WT4879 into early endosomes, followed by cytosolic dispersal of cargo.

The toxicity of WT4879 on SH-SY5Y cells was measured with a Vybrant MTT Cell Proliferation Assay Kit (Invitrogen). Briefly, cells were seeded in 96-well microtiter plates (2×10^4 cells/well) and cultivated overnight in phenol red-free DMEM:F12 medium (Invitrogen). Subsequently, SH-SY5Y cells were incubated with three concentrations (0.1, 0.5, and 1 μM) of WT4879 for 12 h at 37 °C. Cells were then incubated with MTT dye at a concentration of 1 mg/mL for 4 h. The formazan product was solubilized with Me_2SO (50 μL). Cell viability was determined by measuring the absorbance of each sample at 540 nm using a microplate reader. The cells exposed to increasing concentrations of WT4879 survived just as well as control cells (Supporting Information, Figure S2). No cellular toxicity was observed at any concentration tested, suggesting the biocompatibility of the synthesized probes.

In conclusion, a new *MAOA* mRNA imaging agent, coupled to a receptor-targeting peptide for specific intracellular delivery, was designed and synthesized. Initial *in vitro* studies demonstrated that WT4879 was specifically delivered to SH-SY5Y cells, which express μ-opioid receptors and *MAOA* mRNA, with high efficiency. The receptor-specific probe (WT4879) showed ~5 times higher uptake than the nonspecific probe (WT4786), in SH-SY5Y cells, using flow cytometry and confocal microscopy. The control cell-line (CHO-K1) showed minimal nonspecific uptake of WT4879. Moreover, an MTT assay of WT4879 revealed high compatibility with SH-SY5Y cells. Such mRNA imaging agents, with near-infrared fluorophores, might enable real time imaging and quantitation of neuronal mRNAs in live animal models.

■ ASSOCIATED CONTENT

Supporting Information

Additional data on synthesis and experimental results with *MAOA* probes. This material is available free of charge via the Internet at http://pubs.acs.org.

■ AUTHOR INFORMATION

Corresponding Author

*Phone: 215.955.4578, Fax: 215.955.4580. E-mail: eric@tesla.jci.tju.edu.

■ ACKNOWLEDGMENTS

We thank Dr. Andrew Quong for mass spectrometry. This work was supported by NIH grant DA027746 to E.W. M.L.T. and E.W. hold shares in GeneSeen LLC, which might ultimately benefit from the results of this investigation, but did not support the work.

■ ABBREVIATIONS:

AEEA, aminoethoxyethoxyacetyl, DAPI, 4′,6-diamidino-2-phenylindole; MAO, monoamine oxidase; MTT, 3-(4,5-dimethylthiazol-2-yl)-2,5-diphenyltetrazolium bromide; PBS, phosphate buffered saline; PNA, peptide nucleic acid

■ REFERENCES

(1) Rendu, F., Peoc'h, K., Berlin, I., Thomas, D., and Launay, J.-M. (2011) Smoking related diseases: the central role of monoamine oxidase. *Int. J. Environ. Res. Public Health 8*, 136−147.

(2) Bolasco, A., Carradori, S., and Fioravanti, R. (2010) Focusing on new monoamine oxidase inhibitors. *Expert Opin. Ther. Pat. 20*, 909−39.

(3) Fowler, J. S., Logan, J., Volkow, N. D., and Wang, G. J. (2005) Translational neuroimaging: positron emission tomography studies of monoamine oxidase. *Mol. Imaging Biol. 7*, 377−87.

(4) Brunner, H. G., Nelen, M., Breakefield, X. O., Ropers, H. H., and van Oost, B. A. (1993) Abnormal behavior associated with a point mutation in the structural gene for monoamine oxidase A. *Science 262*, 578−80.

(5) Manuck, S. B., Flory, J. D., Ferrell, R. E., Mann, J. J., and Muldoon, M. F. (2000) A regulatory polymorphism of the monoamine oxidase-A gene may be associated with variability in aggression, impulsivity, and central nervous system serotonergic responsivity. *Psychiatry Res. 95*, 9−23.

(6) Newman, T. K., Syagailo, Y. V., Barr, C. S., Wendland, J. R., Champoux, M., Graessle, M., Suomi, S. J., Higley, J. D., and Lesch, K. P. (2005) Monoamine oxidase A gene promoter variation and rearing experience influences aggressive behavior in rhesus monkeys. *Biol. Psychiatry 57*, 167−72.

(7) Jiang, S., Xin, R., Lin, S., Qian, Y., Tang, G., Wang, D., and Wu, X. (2001) Linkage studies between attention-deficit hyperactivity disorder and the monoamine oxidase genes. *Am. J. Med. Genet. 105*, 783−8.

(8) Lawson, D. C., Turic, D., Langley, K., Pay, H. M., Govan, C. F., Norton, N., Hamshere, M. L., Owen, M. J., O'Donovan, M. C., and Thapar, A. (2003) Association analysis of monoamine oxidase A and attention deficit hyperactivity disorder. *Am. J. Med. Genet. B Neuropsychiatr. Genet. 116B*, 84−9.

(9) Tadic, A., Rujescu, D., Szegedi, A., Giegling, I., Singer, P., Moller, H. J., and Dahmen, N. (2003) Association of a MAOA gene variant with generalized anxiety disorder, but not with panic disorder or major depression. *Am. J. Med. Genet. B Neuropsychiatr. Genet. 117B*, 1−6.

(10) Urwin, R. E., Bennetts, B. H., Wilcken, B., Lampropoulos, B., Beumont, P. J., Russell, J. D., Tanner, S. L., and Nunn, K. P. (2003) Gene-gene interaction between the monoamine oxidase A gene and solute carrier family 6 (neurotransmitter transporter, noradrenalin) member 2 gene in anorexia nervosa (restrictive subtype). *Eur. J. Hum. Genet. 11*, 945−50.

(11) Urwin, R. E., and Nunn, K. P. (2005) Epistatic interaction between the monoamine oxidase A and serotonin transporter genes in anorexia nervosa. *Eur. J. Hum. Genet. 13*, 370−5.

(12) Gutierrez, B., Arias, B., Gasto, C., Catalan, R., Papiol, S., Pintor, L., and Fananas, L. (2004) Association analysis between a functional

polymorphism in the monoamine oxidase A gene promoter and severe mood disorders. *Psychiatr. Genet. 14*, 203−8.
(13) Preisig, M., Bellivier, F., Fenton, B. T., Baud, P., Berney, A., Courtet, P., Hardy, P., Golaz, J., Leboyer, M., Mallet, J., Matthey, M. L., Mouthon, D., Neidhart, E., Nosten-Bertrand, M., Stadelmann-Dubuis, E., Guimon, J., Ferrero, F., Buresi, C., and Malafosse, A. (2000) Association between bipolar disorder and monoamine oxidase A gene polymorphisms: results of a multicenter study. *Am. J. Psychiatry 157*, 948−55.
(14) Rubinsztein, D. C., Leggo, J., Goodburn, S., Walsh, C., Jain, S., and Paykel, E. S. (1996) Genetic association between monoamine oxidase A microsatellite and RFLP alleles and bipolar affective disorder: analysis and meta-analysis. *Hum. Mol. Genet. 5*, 779−82.
(15) Huang, Y. Y., Cate, S. P., Battistuzzi, C., Oquendo, M. A., Brent, D., and Mann, J. J. (2004) An association between a functional polymorphism in the monoamine oxidase a gene promoter, impulsive traits and early abuse experiences. *Neuropsychopharmacology 29*, 1498−505.
(16) Vanyukov, M. M., Maher, B. S., Devlin, B., Tarter, R. E., Kirillova, G. P., Yu, L. M., and Ferrell, R. E. (2004) Haplotypes of the monoamine oxidase genes and the risk for substance use disorders. *Am. J. Med. Genet. B Neuropsychiatr. Genet. 125B*, 120−5.
(17) Takehashi, M., Tanaka, S., Masliah, E., and Ueda, K. (2002) Association of monoamine oxidase A gene polymorphism with Alzheimer's disease and Lewy body variant. *Neurosci. Lett. 327*, 79−82.
(18) Sacher, J., Wilson, A. A., Houle, S., Rusjan, P., Hassan, S., Bloomfield, P. M., Stewart, D. E., and Meyer, J. H. (2010) Elevated brain monoamine oxidase A binding in the early postpartum period. *Arch. Gen. Psychiatry 67*, 468−74.
(19) Alia-Klein, N., Goldstein, R. Z., Kriplani, A., Logan, J., Tomasi, D., Williams, B., Telang, F., Shumay, E., Biegon, A., Craig, I. W., Henn, F., Wang, G. J., Volkow, N. D., and Fowler, J. S. (2008) Brain monoamine oxidase A activity predicts trait aggression. *J. Neurosci. 28*, 5099−104.
(20) Mokrovic, G., Matosic, A., Hranilovic, D., Stefulj, J., Novokmet, M., Oreskovic, D., Balija, M., Marusic, S., and Cicin-Sain, L. (2008) Alcohol dependence and polymorphisms of serotonin-related genes: association studies. *Coll. Antropol. 32* (Suppl 1), 127−31.
(21) Zhou, Z., Yuan, Q., Mash, D. C., and Goldman, D. (2011) Substance-specific and shared transcription and epigenetic changes in the human hippocampus chronically exposed to cocaine and alcohol. *Proc. Natl. Acad. Sci. U. S. A. 108*, 6626−31.
(22) Alia-Klein, N., Parvaz, M. A., Woicik, P. A., Konova, A. B., Maloney, T., Shumay, E., Wang, R., Telang, F., Biegon, A., Wang, G. J., Fowler, J. S., Tomasi, D., Volkow, N. D., and Goldstein, R. Z. (2011) Gene x disease interaction on orbitofrontal gray matter in cocaine addiction. *Arch. Gen. Psychiatry 68*, 283−94.
(23) Fowler, J. S., MacGregor, R. R., Wolf, A. P., Arnett, C. D., Dewey, S. L., Schlyer, D., Christman, D., Logan, J., Smith, M., Sachs, H., et al. (1987) Mapping human brain monoamine oxidase A and B with 11C-labeled suicide inactivators and PET. *Science 235*, 481−5.
(24) Nielsen, P. E. (2010) Peptide nucleic acids (PNA) in chemical biology and drug discovery. *Chem. Biodivers. 7*, 786−804.
(25) Ray, A., and Norden, B. (2000) Peptide nucleic acid (PNA): its medical and biotechnical applications and promise for the future. *FASEB J. 14*, 1041−60.
(26) Gray, G. D., Basu, S., and Wickstrom, E. (1997) Transformed and immortalized cellular uptake of oligodeoxynucleoside phosphorothioates, 3′-alkylamino oligodeoxynucleotides, 2′-O-methyl oligoribonucleotides, oligodeoxynucleoside methylphosphonates, and peptide nucleic acids. *Biochem. Pharmacol. 53*, 1465−1476.
(27) Wang, Y., Van Bockstaele, E. J., and Liu-Chen, L. Y. (2008) In vivo trafficking of endogenous opioid receptors. *Life Sci. 83*, 693−9.
(28) Borics, A., and Toth, G. (2010) Structural comparison of mu-opioid receptor selective peptides confirmed four parameters of bioactivity. *J. Mol. Graph. Model. 28*, 495−505.
(29) Lowery, J. J., Yeomans, L., Keyari, C. M., Davis, P., Porreca, F., Knapp, B. I., Bidlack, J. M., Bilsky, E. J., and Polt, R. (2007) Glycosylation improves the central effects of DAMGO. *Chem. Biol. Drug Des. 69*, 41−7.
(30) Muller, T., Przuntek, H., Rieks, M., and Mackowiak, A. (2008) Selegiline reduces cisplatin-induced neuronal death in neuroblastoma cells. *Neurol. Res. 30*, 417−9.
(31) Toll, L. (1990) Mu-opioid receptor binding in intact SH-SY5Y neuroblastoma cells. *Eur. J. Pharmacol. 176*, 213−7.

Bioconjugate Chemistry

Article

pubs.acs.org/bc

Amino-Modified and Lipid-Conjugated Dicer-Substrate siRNA Enhances RNAi Efficacy

Takanori Kubo,*[,†] Yoshifumi Takei,[‡] Keichiro Mihara,[§] Kazuyoshi Yanagihara,[†] and Toshio Seyama[†]

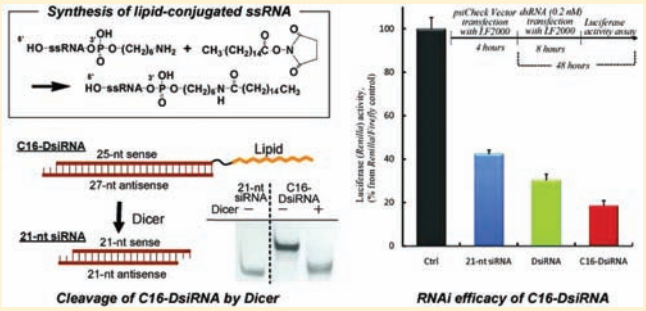
[†]Laboratory of Molecular Cell Biology, Department of Life Science, Yasuda Women's University Faculty of Pharmacy, Hiroshima, Japan

[‡]Department of Biochemistry, Nagoya University Graduate School of Medicine, Nagoya, Japan

[§]Department of Hematology and Oncology, Research Institute for Radiation Biology and Medicine, Hiroshima University, Hiroshima, Japan

Supporting Information

ABSTRACT: The development of Dicer-substrate small interfering RNAs (DsiRNAs) has been pursued in recent years because these molecules exhibit a much more potent gene-silencing effect than 21-nucleotide (nt) siRNAs. In the present study, we designed eight different types of amino-modified DsiRNAs and a palmitic acid-conjugated DsiRNA expected to result in improved biological properties of siRNAs, including their stability against nuclease degradation, membrane permeability, and RNAi efficacy. The DsiRNAs were modified with an amine at the 5′- and/or 3′-end of the sense and/or antisense strand. Dicer enzyme cleaved most of the amino-modified DsiRNAs to lead to the release of 21-nt siRNA; some of them, however, were not or partly cleaved. All amino-modified DsiRNAs exhibited strong resistance against nuclease degradations. Among the amino-modified DsiRNAs, the DsiRNA modified with an amine restricted at the 3′-end of the sense strand showed the most enhanced gene-silencing effect and maintained its potent gene suppression after one week of cell transfection against *Renilla* luciferase activity. For further improvement, palmitic acid was conjugated to DsiRNA at the 3′-end of the sense strand (C16-DsiRNA) to facilitate the membrane permeability and potent gene-silencing activity. The C16-DsiRNA showed enhanced membrane permeability to HeLa cells. The C16-DsiRNA exhibited extremely high inhibition of *Renilla* luciferase activity.



INTRODUCTION

RNA interference (RNAi) technology, discovered by Fire et al. using long double-stranded RNA (dsRNA),[1] has potent gene silencing in a sequence specific manner, and has attracted much attention for applications to biosciences and medicines.[2−5] In the cytoplasm of mammalian cells, long dsRNAs are cleaved to small dsRNAs [called small interfering RNAs (siRNAs) consisting of 21-nucleotides (nt), having a phosphate at the 5′-end and a 2-nt overhang at the 3′-end] by Dicer.[6,7] The 21-nt siRNA is bound to a protein complex called an RNA-induced silencing complex (RISC).[8] The RISC cleaves the target mRNA at a sequence-specific position, guided by the antisense strand of the siRNA. The 21-nt siRNA has advantages over the long dsRNA in that the 21-nt siRNA can be easily prepared by chemical synthesis, easily handled during biological assays, and avoids interferon activation of the RNAi. Although chemically synthesized 21-nt siRNAs showed potent RNAi effects, they still have the problems of poor membrane permeability and nuclease resistance which limit their applicability to therapeutic use.[9,10]

A variety of chemically modified siRNAs have been developed, mostly with the goal of improving their resistance against nuclease degradation.[11−20] Modifications at 2′-OH of the nucleotide of 21-nt siRNAs, such as 2′-O-methyl, 2′-fluoro, and locked nucleic acid (LNA), demonstrated a high nuclease stability.[11−13] In addition, in order to increase the nuclease resistance of the siRNA, the phosphate backbone in siRNA was replaced with a phosphorothioate or boranophosphate backbone.[14−16] A series of nucleobase-modified siRNA duplexes were reported to exhibit enhanced thermodynamic stability and gene-silencing activity.[17−20] Direct conjugation of bioactive molecules, including polymers,[21,22] peptides,[23−25] and lipids,[26−29] to siRNAs has been reported to improve the biological properties of siRNAs *in vitro* and *in vivo*. Among these conjugations, the covalent conjugation of cholesterol, bile acids, and long-chain fatty acids to siRNAs at the 3′-end of the sense strand were shown to mediate siRNA uptake in cells.[26,27] These lipid-conjugated siRNAs interacted with lipoprotein particles, lipoprotein receptors, and transmembrane proteins, and they influenced the uptake behaviors of the siRNA.[27] Although the

Received: June 24, 2011
Revised: December 6, 2011
Published: January 12, 2012

 © 2012 American Chemical Society dx.doi.org/10.1021/bc200333w | *Bioconjugate Chem.* 2012, 23, 164−173

chemical modifications and direct conjugations to the siRNAs, as described above, could solve some of the problems of RNAi, such as nuclease stability or cell permeability, most of them weaken the gene-silencing efficacy.

The structurally accurate designed siRNAs showed enhanced gene-silencing efficacy and nuclease resistance compared with a normally designed 21-nt siRNA to the same target gene. Blunt-ended 27-nt dsRNAs, which are cleaved by Dicer to lead to the release of 21-nt siRNAs, exhibited a several-fold higher gene-silencing effect than 21-nt siRNAs.[30,31] Dicer-substrate siRNA (DsiRNA), which is an asymmetric duplex RNA composed of a 25-nt sense strand with a blunt-end at the 3′-end and a 27-nt antisense stand with a 2-nt overhang at the 3′-end (25D/27-nt), could be directly cleaved by Dicer, leading to the release of a single primary 21-nt siRNA product, and exhibited a potent gene-silencing effect.[32−34] The asymmetric terminal structures of siRNA, which were composed of a 19-nt sense strand and 21-nt antisense strand with unilateral 2-nt 3′-overhangs on the antisense strand, and strand asymmetry siRNAs and shRNAs having a mismatch near the 5′-end of the antisense strand, exhibited enhanced RNAi activity with a reduced off-target effect.[35−38] Although these structurally accurate designed siRNAs exhibited enhanced RNAi potency, they still have problems of poor membrane permeability and low resistance against nuclease degradation.

In the present study, we designed eight different types of amino-modified DsiRNAs and palmitic acid conjugated DsiRNA (C16-DsiRNA) to improve the biological properties of DsiRNA, including their stability against nuclease degradation, membrane permeability, and RNAi efficacy. All DsiRNA modifications and conjugations were with respect to Dicer cleavage, stability in serum, cellular uptake, and RNAi efficacies. We showed that the C16-DsiRNA revealed the best potential for development into a new generation of RNAi molecules.

EXPERIMENTAL PROCEDURES

Design and Synthesis of 21-nt siRNA, DsiRNA, and Amino-Modified DsiRNAs. 21-nt siRNA and 25D/27-nt DsiRNA were designed to target the *Renilla* luciferase gene (Figure 1A). The 21-nt and 27-nt single-stranded RNAs (ssRNAs; antisense and sense strand), and 23-nt ssRNA plus 2-nt DNA at 3′-end (sense strand), including amino-modifications at the 5′-end or 3′-end, were purchased from Integrated DNA Technologies Inc. (IDT, Coralville, IA). The molecular weights of all ssRNAs were confirmed by MALDI-TOF mass spectrometry (Ultraflex; Bruker Daltonics, Bremen, Germany) using saturated solutions of 2,4,6-trihydroxyacetophenone (Sigma-Aldrich, St. Louis, MO) in 50 mg/mL diammonium hydrogen citrate in 50% acetonitrile as a matrix.[39] All MALDI-TOF mass spectrometry measurements were carried out in linear-negative mode. The concentrations of all ssRNAs were calculated using their absorbance at 260 nm as detected spectrophotometrically (V-670 spectrophotometer; Jasco, Tokyo, Japan). The sense and antisense strands of RNAs were annealed in buffer [50 mM Tris-HCl (pH 7.5), 100 mM NaCl] to prepare dsRNAs following the manufacturer's instructions. Briefly, each ssRNA was diluted using sterile RNase-free water to a final concentration of 50 μM, and then 20 μL of each ssRNA (sense and antisense) solution was combined with 10 μL of annealing buffer (5×). The solutions were incubated for 1 min at 90 °C and cooled slowly afterward to room temperature (the final concentration of the siRNA was 20 μM (20 pmol/μL)). The dsRNA formation was confirmed by 20% polyacrylamide gel electrophoresis (PAGE; 30 mA, 70 min) and visualized by silver staining (DNA Silver Stain Kit; GE Healthcare, Piscataway, NJ).

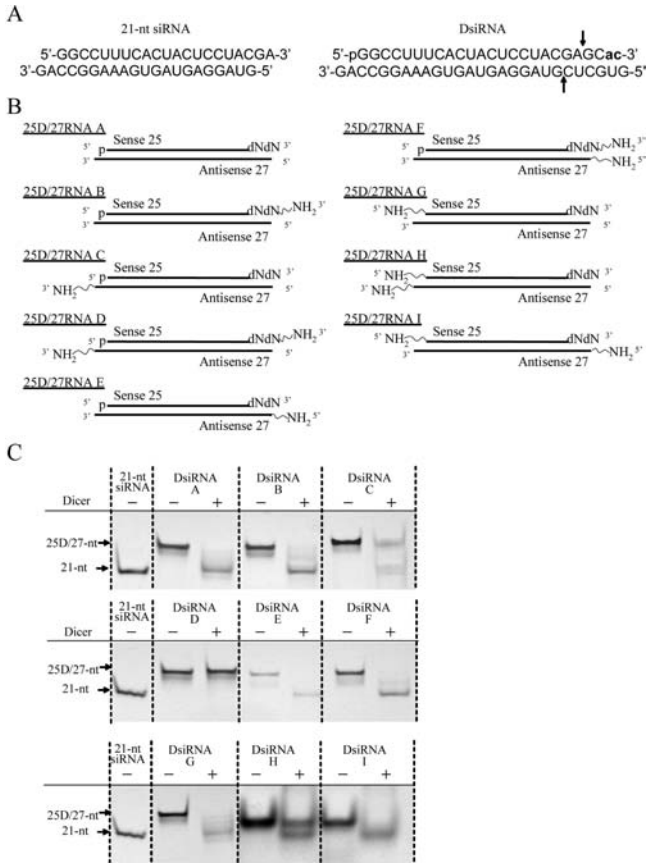


Figure 1. Design and structure of amino-modified DsiRNAs, and Dicer cleavage. (A) Sequence of 21-nt siRNA and DsiRNA molecule targeted to Renilla luciferase gene. Ribonucleotides are upper-case, and deoxyribonucleotides are bold lower-case. The letter 'p' represents 5′-phosphate. Arrows are the expected Dicer cleavage sites. (B) Structures of unmodified (DsiRNA A) and amino-modified DsiRNAs (DsiRNA B−I). Eight different types of amino-modified DsiRNAs were designed. (C) Dicer-substrate of amino-modified DsiRNAs. The amino-modified DsiRNAs were reacted with Dicer for 12 h at 37 °C. The reaction products were electrophoresed on 20% PAGE and visualized by silver staining.

Synthesis of Palmitic Acid-Conjugated DsiRNA. Amino-modified ssRNA at the 3′-end (4 nmol in 20 μL water) was reacted with 40 nmol palmitic acid *N*-hydroxysuccinimide ester (Sigma-Aldrich) dissolved in 10 μL *N,N*-dimethylformamide (DMF; Sigma-Aldrich) containing 0.7 μL *N,N*-diisopropylethylamine (DIEA; Sigma-Aldrich) in a 100 μL isopropanol/water (1:1) mixture, for 12 h at room temperature. The ssRNA with palmitic acid conjugation at the 3′-end (C16-ssRNA) was purified by reversed-phase HPLC (RP-HPLC) using an ODS column (4.6 × 150 mm, 5 μm) under a linear gradient from 7% to 70% acetonitrile over 40 min in 20 mM triethylammonium acetate (TEAA) (pH 7.0). The molecular weight of the conjugate was confirmed by MALDI-TOF mass spectrometry (Ultraflex; Bruker Daltonics) as predicted under the same conditions above (calculated mass: 8320.3, found mass: 8319.2). The yield of the conjugate was spectrophotometrically calculated on the basis of absorbance at 260 nm wavelength.

dx.doi.org/10.1021/bc200333w | *Bioconjugate Chem.* 2012, 23, 164−173

To prepare the C16-DsiRNA, antisense 27-nt ssRNA, which was complementary to the mRNA strands of the *Renilla* luciferase gene and was synthesized independently, was annealed with the C16-ssRNAs described above in an annealing buffer according to the manufacturer's protocol. The quality of the C16-DsiRNA was confirmed by PAGE with a 20% gel.

***in Vitro* Cleavage of DsiRNAs by the Recombinant Dicer.** DsiRNAs, including amino-modifications and C16-conjugation (20 pmol), were mixed with 1 U of recombinant Dicer (Gene Therapy Systems Inc., San Diego, CA) in 10 μL of 20 mM Tris-HCl (pH 8.0) containing 150 mM NaCl and 2.5 mM $MgCl_2$. The mixtures were incubated at 37 °C for 12 h and the reaction was stopped by adding 2 μL of the stop-solution (Gene Therapy Systems Inc.). The reaction products were detected and analyzed by PAGE (20% gel), silver staining, and LAS4000 imaging system (Fujifilm, Tokyo, Japan).

Stability against Nuclease Degradation in Cell-Culture Medium. Ten microliters of DsiRNAs, including amino-modifications and C16-conjugation (200 pmol), were added to 90 μL of Dulbecco's modified Eagle's medium (DMEM; Wako, Osaka, Japan) containing 10% heat-inactivated FBS (Invitrogen, La Jolla, CA). The samples were incubated for different time intervals (0, 0.5, 1, 2, 4, 6, 8, 12, 24, and 48 h) at 37 °C. Aliquots (10 μL) were taken from each sample. The samples were frozen in liquid nitrogen to stop the nuclease reaction and were kept at −20 °C. The RNA products of nuclease degradation were detected and analyzed as described the above section.

Cell Cultures and Transfections. HeLa cells were cultured in DMEM (Wako) supplemented with 10% heat-inactivated FBS (Invitrogen), 100 U/mL penicillin (Wako), and 100 μg/mL streptomycin (Wako). To evaluate the RNAi potency of DsiRNAs, including amino-modifications and C16-conjugation, after short-term (48 h) and long-term (96 and 168 h) targeting the *Renilla* luciferase gene in either the presence or absence of Lipofectamine 2000 (LF2000; Invitrogen), we used psiCHECK-2 vector (Promega, Madison, WI) as a reporter gene, which contains both the *Firefly* and *Renilla* luciferase genes, in HeLa cells. *Renilla* luciferase activity was used to estimate the RNAi efficacy. The second reporter, *Firefly* luciferase, was used as a control.

To evaluate the short-term RNAi activity of DsiRNAs, HeLa cells were seeded at 5×10^4 cells/mL in 100 μL medium in each well of a 96-well multiplate and cultured in a 100% humidified atmosphere (5% CO_2, 37 °C). Twelve hours later, 0.02 μg of psiCHECK-2 vector was first incubated with 0.2 μL of LF2000 in 10 μL of Opti-MEM (Invitrogen) for 30 min according to the manufacturer's protocol, and then 10 μL of the mixture was added to each well of a 96-well multiplate containing the cells in 90 μL fresh culture medium without antibiotics. To investigate RNAi in the presence of LF2000, the DsiRNAs at different concentrations (10, 5, 2, 1, 0.5, and 0.2 nM) were preincubated with LF2000 as described for the psiCHECK-2 vector. Four hours after the vectors were transfected, 10 μL of the preincubated mixtures of DsiRNAs with LF2000 were added to each well containing 90 μL of fresh culture medium. After another 8 h of incubation, the culture medium was replaced with 100 μL fresh medium and the cells were cultured for 48 h to assess RNAi. To investigate the RNAi effect in the absence of LF2000, first the psiCHECK-2 vector was transfected using LF2000 by the same procedure as described above, and then the cells were washed three times with culture medium after 4 h of vector transfection. The DsiRNAs at different concentrations (200, 100, 50, and 25 nM) without any transfection reagents were added to the cells and incubated for 48 h.

To evaluate the long-term RNAi activity of DsiRNAs, HeLa cells were seeded at 1×10^4 cells/mL in 100 μL medium in each well of a 96-well multiplate and cultured under the same conditions as described above. Twelve hours later, 5 pmol of the DsiRNAs preincubated with 0.2 μL LF2000 were added to each well of a 96-well multiplate. Eight hours after the DsiRNAs were transfected, the culture medium was replaced with 100 μL fresh medium and the cells were cultured for 48, 96, and 168 h to assess RNAi. Forty-eight hours before RNAi analysis, the psiCHECK-2 vector was transfected using LF2000 by the same procedure as described above, and then the cells were washed three times with culture medium after 4 h of transfection.

Gene Silencing of *Renilla* Luciferase. The efficacy of RNAi against *Renilla* luciferase was evaluated by the Dual-Glo Luciferase Assay System (Promega), which is designed to analyze both *Renilla* and *Firefly* luciferase activities. To detect *Firefly* luciferase activity as an intraplasmid control, 50 μL of Dual-Glo luciferase reagent-1 (beetle luciferin) was added to each well of a 96-well multiplate containing 100 μL culture medium including DsiRNA samples. The plates were incubated in the dark for 10 min at room temperature. Luminescence emitted from the *Firefly* luciferase catalytic reaction was measured for 1 s for each well on a microplate reader (Wallac 1420 ARVO MX; Perkin-Elmer, Waltham, MA). To measure the *Renilla* luciferase activity and to quench the luminescence from the *Firefly* luciferase catalytic reaction, 50 μL of Dual-Glo Stop and Glo reagent-2 (containing coelenterazine) were added to each well. The luminescence arising from the *Renilla* luciferase catalytic reaction was measured in the same way as described above for *Firefly* luciferase activity, and normalized by the luminescence of *Firefly* luciferase activity in each well of the 96-well multiplates. The RNAi of DsiRNA, including amino-modifications and C16-conjugation, toward the *Renilla* luciferase was assessed as a percentage of the control (DsiRNA nontreated) sample.

Intracellular Delivery of DsiRNAs. To prepare fluorescence (FAM)-labeled DsiRNA, antisense ssRNA was labeled with 5′-fluorescein phosphoramidite (6-FAM; Glen Research, Sterling, VA) at the 5′-end. The FAM-labeled antisense 27-nt ssRNA, which was prepared for *Renilla* luciferase, was annealed with palmitic acid-conjugated (3′-end) and unconjugated sense 23-nt ssRNA plus 2-nt DNA at the 3′-end, respectively, in an annealing buffer as in the protocols described above.

To deliver the prepared DsiRNAs intracellularly, 200 pmol of DsiRNAs, including C16-conjugation labeled with FAM, were incubated with 2 μL LF2000 in 100 μL Opti-MEM diluted twice for 30 min at room temperature. Then, 100 μL of the mixture was added to 900 μL of culture medium supplemented with 10% heat-inactivated FBS (Invitrogen), 100 U/mL penicillin (Wako), and 100 μg/mL streptomycin (Wako) of HeLa cells (5×10^4 cells) and incubated for 6 h in the dark under a humidified atmosphere (5% CO_2, 37 °C). The cells were washed several times with fresh medium, and an intracellularly incorporated amount of DsiRNAs labeled with FAM in cells were examined under a fluorescent confocal microscope (IX70; Olympus, Tokyo, Japan).

Another approach was used to investigate the intracellular delivery of DsiRNA, including C16-conjugation labeled with FAM, by flow cytometry. The forward- and side-scatter parameters were adjusted to accommodate the inclusions of

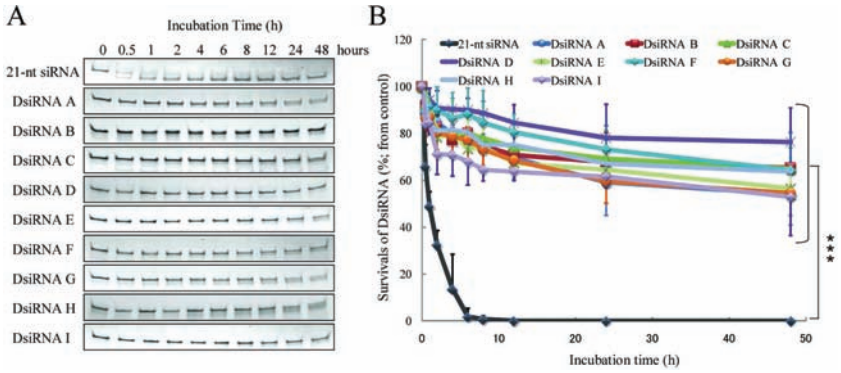


Figure 2. Stability of amino-modified DsiRNAs against nuclease degradation. Samples (21-nt siRNA and DsiRNA A-I) were incubated in culture medium containing 10% FBS at 37 °C for 0, 0.5, 1, 2, 4, 6, 8, 12, 24, or 48 h, and aliquots were analyzed on 20% PAGE. (A) Representative PAGE patterns of 21-nt siRNA and DsiRNAs, including amino-modifications, after treated with culture medium. (B) Survivals of 21-nt siRNA and DsiRNAs, including amino modifications, in culture medium. The mean and SD values from three independent experiments. ***, $P < 0.001$ at 48 h of incubation time.

each of the dissociated cell lines with the aid of FAM as a marker. Five thousand cells were analyzed and no cell was excluded from the analysis. Data were collected and analyzed using Epics XL and XL System II software (Beckman Coulter, Fullerton, CA).

Effects of Unaltered Serum on the Function of C16-DsiRNA. The stability, RNAi efficacy, and membrane permeability of DsiRNA, including C16-conjugation, were investigated in the presence of unaltered serum (serum without heat-inactivation). The stabilities of these siRNAs in unaltered FBS were studied as described above. Finally, the RNAi efficacies and membrane permeabilities of the siRNAs in the presence of unaltered FBS were investigated using HeLa cells as described above.

■ RESULTS AND DISCUSSION

The Dicer Substrate of Amino-Modified DsiRNAs. We synthesized eight different types of DsiRNAs modified with amines at the terminal of the sense and/or antisense strand targeting the *Renilla* luciferase gene (Figure 1B: DsiRNA B–I). We investigated whether the amino-modified DsiRNAs were cleaved by Dicer leading to release of the 21-nt siRNAs (Figure 1C). Nonmodified DsiRNA (DsiRNA A) was cleaved to the 21-nt siRNA by Dicer. The DsiRNAs modified with amines at the 3′- or 5′-end of the sense and/or 5′-end of the antisense strand (DsiRNA B, E, F, G, and I) were substrates of Dicer leading to release of the 21-nt siRNA. In contrast, the DsiRNAs modified with amines at least at the 3′-end of the antisense strand (DsiRNA C and H) were partly cleaved. A DsiRNA modified with amines at the 3′-end of both the sense and antisense strands (DsiRNA D) was not cleaved. These results can help to elucidate how Dicer approaches the DsiRNA. It was realized from the results for DsiRNA D and I that the 3′-end site of the DsiRNA was essential for approaching to Dicer, because the DsiRNA I was cleaved to the 21-nt siRNA, whereas the DsiRNA D was not converted to any product after reaction with Dicer. Kim et al. also reported that the presence of the 3′-end modification in long dsRNA blocked the Dicer processing.[30] In addition, despite the finding that DsiRNA B was almost completely cleaved, the DsiRNA C was partly cleaved to produce the 21-nt siRNA under the same reaction conditions. Thus, the entrance of Dicer to the DsiRNA was, in part, obstructed by the amino-group at the 3′-end of the antisense strand on the DsiRNA. In other words, the Dicer approaching to the DsiRNA from 3′-overhang (2-nt) of the antisense strand might play a role in attaching the modifications at the 3′-blunt-end of the sense strand in the DsiRNA. Other reports have also described that the 2-nt 3′-overhang structure is important for recognition of the PAZ domain, which is one of the essential domain of Dicer, and consequently Dicer measures from the 3′-end of the dsRNA to be cut by its RNaseIII domain leading to release of 21-nt siRNA.[40−43]

Stability of Amino-Modified DsiRNAs in Serum. All amino-modified DsiRNAs showed strong stability in the cell-culture medium containing 10% FBS, whereas the 21-nt siRNA was immediately degraded (Figure 2). Among them, the DsiRNAs with the 3′-end amino-modifications (DsiRNA B, C, and D) exhibited appreciably strong resistance against nuclease degradation in comparison with not only DsiRNA A, but also DsiRNAs modified with amine at 5′-end. The amino-modifications at the 3′-end might protect the DsiRNA against 3′-exonuclease degradation. The degradation of siRNAs in cell-culture medium supplemented with FBS could be explained by the primary 3′-exonuclease and RNase A activities in serum. It is widely accepted that the hydrolysis of single-stranded oligonucleotides in plasma occurs exclusively by 3′- to 5′-exonuclease,[44] while the hydrolysis of dsRNA in serum occurs by RNase A.[39] We previously described the hypothetical mechanism of the 21-nt siRNA degradation in serum confirmed by MALDI-TOF mass and PAGE analysis.[45] The 2-nt overhangs of the 21-nt siRNA rapidly degraded to release a 19-nt dsRNA catalyzed by 3′-exonuclease, and then the 19-nt dsRNA was gradually degraded in a reaction catalyzed by RNase A. Thus, the acquisition of the exonuclease resistance is linked to the protection of the 3′-end in the siRNA. The other factors of the stability of dsRNAs are length and sequence. We previously demonstrated that the blunt-ended dsRNAs manifested a higher stability in comparison with the 21-nt siRNA.[46−48] Therefore, our amino-modified DsiRNAs, especially those with 3′-end modifications, appeared to have strong stability against nuclease degradation.

RNAi Efficacy of Amino-Modified DsiRNAs. The RNAi efficacies of 21-nt siRNA, DsiRNA A, and amino-modified DsiRNAs were evaluated using a luciferase gene reporter assay in the presence of LF2000 (Figure 3). Although the *Renilla* luciferase activity was reduced to two-thirds of the control value (nontreated cells) by the RNAi of 21-nt siRNA, the effect of gene-silencing using the DsiRNA A was intensified to a much

dx.doi.org/10.1021/bc200333w | *Bioconjugate Chem.* 2012, 23, 164–173

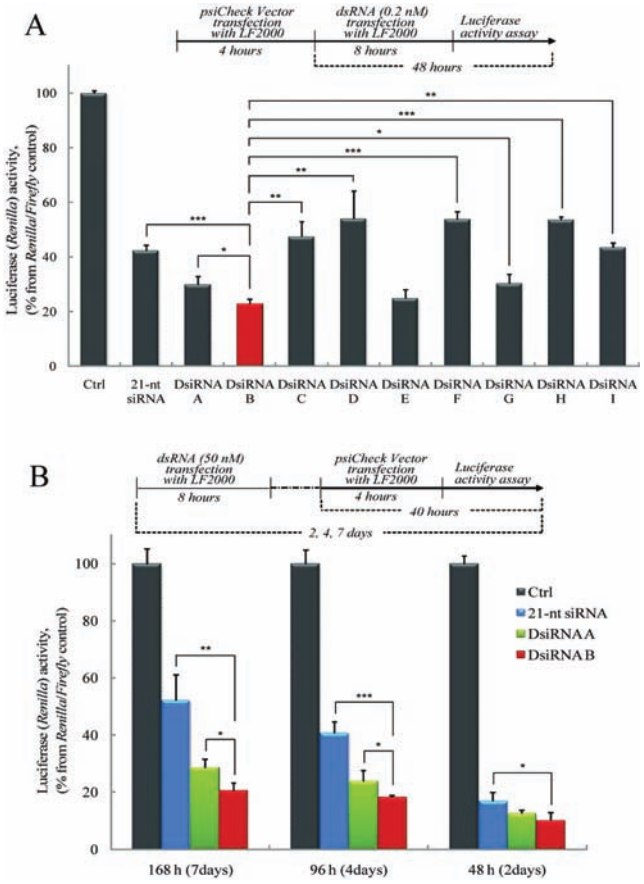


Figure 3. Short-term (A) and long-term (B) RNAi activity of amino-modified DsiRNAs. (A) RNAi against *Renilla* luciferase activity in HeLa cells after 48 h of incubation with amino-modified DsiRNAs. psiCHECKTM-2 vector was transfected into HeLa cells by LF2000. Four hours after the vector transfection, amino-modified DsiRNA (0.2 nM) was transfected into the same cells by LF2000. The *Renilla* luciferase activity was measured 48 h after the vector transfection. The mean and SD values are from three independent experiments. *, $P < 0.05$; **, $P < 0.01$; and ***, $P < 0.001$ (*t* test). (B) RNAi against *Renilla* luciferase activity in HeLa cells after one-week incubation with amino-modified DsiRNA. Amino-modified DsiRNA (50 nM) was transfected into HeLa cells by LF2000. After 8 h, the medium was changed and the cells were cultured within 2, 4, and 7 days in a humidified atmosphere (5% CO_2, 37 °C). psiCHECKTM-2 vector was transfected into the same cell by LF2000, and the *Renilla* luciferase activity was detected 48 h after the vector transfection. The mean and SD values are from three independent experiments. *, $P < 0.05$; **, $P < 0.01$; and ***, $P < 0.001$ (*t* test).

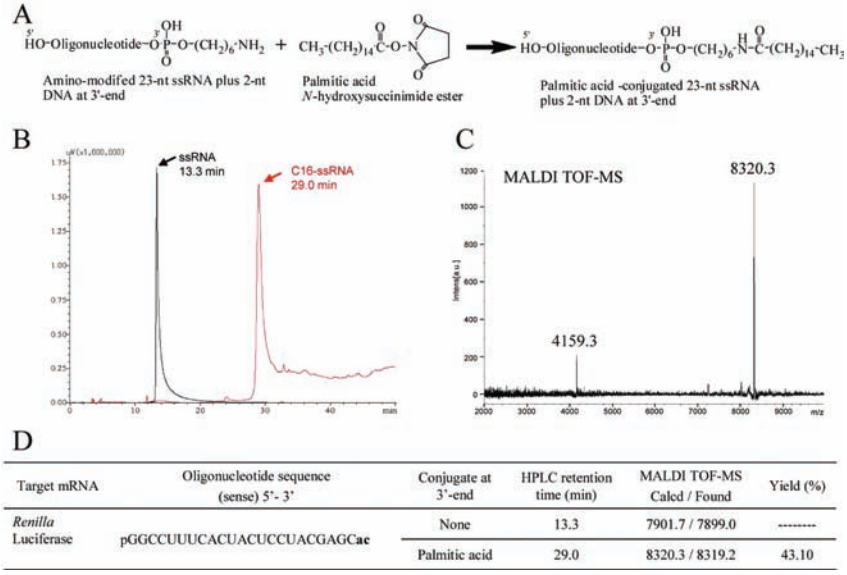
greater extent (by less than 10%) than the 21-nt siRNA value at a concentration of 0.2 nM after incubation for 48 h (Figure 3A). Almost all amino-modified DsiRNAs manifested strong RNAi efficacy at the same concentrations, but exhibited different RNAi potencies. The strongest gene-silencing effect was exhibited in DsiRNA B, which suppressed the Renilla luciferase activity of cells by about 80%. A slightly increased inhibitory effect was found in the DsiRNA E and DsiRNA G, but the other amino-modified DsiRNAs showed a decrease in RNAi potency compared with DsiRNA A. This suggested that the potent gene-silencing activity of DsiRNA B was attributable to its ability to serve as a substrate of Dicer (Figure 1B) and its strong resistance against nuclease degradation (Figure 2). On the other hand, DsiRNA D exhibited the weakest gene-silencing efficacy of all amino-modified DsiRNAs. The results suggest that the RNAi potency was appreciably dependent on the behavior of Dicer-cleavage, even though the amino-modified DsiRNAs had a high level of stability in culture medium containing 10% FBS. The DsiRNA C and DsiRNA H also showed a weak gene-silencing efficacy.

We performed an analysis of the long-term RNAi activity against *Renilla* luciferase gene using the 21-nt siRNA, DsiRNA A, and DsiRNA B, which were analyzed after 48, 96, and 168 h of cell transfection at a concentration of 50 nM (Figure 3B). All samples exhibited a high-level gene-silencing effect, inhibiting *Renilla* luciferase activity by about 80−90%, after 48 h of cell transfection. However, a significant difference in the gene-silencing efficacy between 21-nt siRNA and DsiRNAs after 96 h cell transfection was verified. The 21-nt siRNA decreased the gene-silencing effect, which suppressed the *Renilla* luciferase activity of cells by about 60%; in contrast, the DsiRNA A and DsiDNA B still exhibited a high level gene-silencing effect that was almost the same as the RNAi activity after 48 h. After 168 h of transfection, although both DsiRNA A and DsiRNA B showed a slight decrease in inhibitory effect, they still maintained potent RNAi activity. In particular, the *Renilla* luciferase activity was reduced to one-fifth of the control value by the RNAi of the DsiRNA B that was almost the same as the RNAi activity after 48 h. In contrast, the 21-nt siRNA showed a remarkable loss of gene suppression after one week of cell transfection at the same concentration. Another report showed that the chemical modification pattern of DsiRNAs using 2′-*O*-methyl or 2′-fluoro had high stability in serum and a long-lived gene-silencing effect, but it showed a reduction in RNAi activity compared with nonmodified DsiRNA.[46] Our results suggested that the amino-modified DsiRNAs at the 3′-end of sense strand had several advantages over the chemically modified DsiRNAs: (i) strong gene-silencing was exhibited; (ii) many kinds of functional molecules are acceptable for conjugation; (iii) synthesis can be performed at low cost. Therefore, we proposed that the modifications and conjugations to the DsiRNA ought to be confined to the 3′-end of the sense strand.

Synthesis and Biological Properties of Lipid-Conjugated DsiRNA. High RNAi potency of lipid-conjugated siRNA molecules such as cholesterol and fatty acid has been reported both *in vitro* and *in vivo*.[26−29] However, in the literature,[26−29] the direct conjugation of lipids to the siRNAs has been limited by the conjugating position to the siRNA, mostly to the 3′-end using lipophile-bearing solid supports[27] or to the 5′-end using phosphoramidite derivatives,[28] which involves complicated synthesis. We previously reported a simple and efficient synthesis, and demonstrated the potent RNAi efficacy of lipid-conjugated 21-nt siRNAs.[50] However, lipid-conjugated 21-nt siRNAs may, in part, obstruct certain functions of RISC.

We developed the C16-DsiRNAs to overcome the problems of siRNAs. Because we previously demonstrated that C16 was most influenced by cellular uptake and the inhibitory effect of direct conjugation of 21-nt siRNA to functional molecules,[50] conjugation of C16 to DsiRNA was restricted to the 3′-end of the sense strand. The C16-DsiRNA was expected to have a high membrane permeability and to be cleaved by Dicer to the 21-nt siRNA, leading to release of the C16.

To prepare the ssRNA (sense strand) conjugated with C16 at the 3′-end (C16-ssRNA), amino-modified ssRNA at the 3′-end was condensed with palmitic acid *N*-hydroxysuccinimide ester in solution (Figure 4A). The crude C16-ssRNA was purified by RP-HPLC, and the molecular weight of C16-ssRNA



Target mRNA	Oligonucleotide sequence (sense) 5'- 3'	Conjugate at 3'-end	HPLC retention time (min)	MALDI TOF-MS Caled / Found	Yield (%)
Renilla Luciferase	pGGCCUUUCACUACUCCUACGAGC**ae**	None	13.3	7901.7 / 7899.0	--------
		Palmitic acid	29.0	8320.3 / 8319.2	43.10

Figure 4. Synthesis and characterization of C16-DsiRNA. (A) Simple synthesis of C16-ssRNA for C16-DsiRNA. (B) HPLC profiles of ssRNA and C16-ssRNA. HPLC was performed using an ODS column (4.6 × 150 mm, 5 μm) under a linear gradient condition of acetonitrile while shifting the concentrations from 7% to 70% for 40 min in 20 mM TEAA (pH 7.0). (C) Molecular-weight confirmation by MALDI-TOF mass spectrometry. MALDI-TOF mass was carried out in linear-negative mode using a saturated solution of 2,4,6-trihydroxyacetophenone in 50 mg/mL diammonium hydrogen citrate in 50% acetonitrile as a matrix. (D) Sequence and summarized character data of C16-ssRNA.

was confirmed by MALDI-TOF mass spectrometry. The RP-HPLC retention time of C16-ssRNA was found to be slower than that of nonconjugated ssRNA under the purified condition (Figure 4B). The precise molecular weight of C16-ssRNA was determined by MALDI-TOF mass analysis (Figure 4C).

The C16-ssRNA was annealed with the antisense 27-nt ssRNA, which was complementary to mRNA strands of the target *Renilla* luciferase, and was synthesized independently in order to make C16-DsiRNA (Figure 5A). The C16-DsiRNA was the substrate of Dicer cleaved to 21-nt siRNA, leading to release of the C16 (Figure 5B). Thus, we demonstrated that Dicer recognized and cleaved the C16-DsiRNA even though the C16 was covalently bound to the 3′-end of the sense strand. It is predicted that the C16-DsiRNA does not obstruct certain functions of RISC linked to potent RNAi activity.

The nuclease stability of C16-DsiRNA in culture medium containing 10% heat-inactivated FBS was evaluated using PAGE analysis (Figure 5C1). The C16-DsiRNA exhibited higher resistance compared with not only 21-nt siRNA but also DsiRNA A (Figure 5C2). It was suggested that the pronounced nuclease resistance of C16-DsiRNA was conferred by properties of lipid-molecules. Another report also described that the lipid-siRNAs showed much greater survival compared to nonmodified siRNAs interacting with lipoprotein particles.[27] The stability of C16-DsiRNA in culture medium containing 10% unaltered FBS was also investigated. All of the samples (21-nt siRNA, DsiRNA A, and C16-DsiRNA) in unaltered FBS were degraded faster than those in heat-inactivated FBS (see Figure S1 in the Supporting Information). The 21-nt siRNA showed an especially fast disappearance. In contrast, C16-DsiRNA survived after 48 h of incubation. On the other hand, DsiRNA A was almost degraded after 48 h.

RNAi Efficacy of Lipid-Conjugated DsiRNA. The RNAi efficacy of C16-DsiRNA was compared with that of 21-nt siRNA and DsiRNA A targeted to the *Renilla* luciferase in HeLa cells cultured in DMEM containing heat-inactivated FBS in either the presence or absence of LF2000. In the presence of LF2000, *Renilla* luciferase gene expression was dose-dependently suppressed in all samples (21-nt siRNA, DsiRNA A, and C16-DsiRNA) with high potency (Figure 6A). It is noteworthy that the RNAi efficacy of C16-DsiRNA was superior to that of 21-nt siRNA and DsiRNA A at below 1 nM concentrations.

For development of siRNA-based gene-silencing therapy for clinical applications, establishment of sufficient delivery of the molecules to the target cells is one of the important challenges. Various types of delivering regents for siRNAs, such as lipid-like delivery materials,[51] peptide-mediated carriers,[52,53] protein-mediated carriers,[54] and polyethylenimine (PEI)-based carriers,[55] have been developed, but most of them were cytotoxic to the cells and were limited in terms of their *in vivo* application. A naked siRNA is most safe and convenient, but it cannot penetrate the cell membrane, and is rapidly degraded by nuclease. In fact, many papers have reported that naked siRNA exhibited no gene-silencing effect at a high concentration.[22,23,56,57] Our data showed that the naked siRNA did not inhibit *Renilla* luciferase activity at any concentration even at concentrations as high as 200 nM in the absence of transfection reagent (Figure 6B). On the other hand, the cells treated with C16-DsiRNA showed a reduction in *Renilla* luciferase activity in a dose-dependent manner. Thus, the data suggested that C16-DsiRNA was able to efficiently interact with the cellular membrane and penetrate cells affected by C16. The C16-DsiRNA developed herein can be used for clinical application without cytotoxic transfection reagents.

We investigated the RNAi efficacy of C16-DsiRNA and its effects on unaltered FBS using a *Renilla* luciferase reporter assay in HeLa cells. All of the samples (21-nt siRNA, DsiRNA A, and C16-DsiRNA) in the presence of unaltered serum exhibited decreased RNAi efficacy, compared with the values in heat-inactivated serum (see Figure S2 in the Supporting Information). However, even in the unaltered serum, C16-DsiRNA exhibited strong and remarkably high RNAi potency, compared with those of 21-nt siRNA and DsiRNA A, irrespective of the presence of LF2000. These results could

dx.doi.org/10.1021/bc200333w | *Bioconjugate Chem.* 2012, 23, 164–173

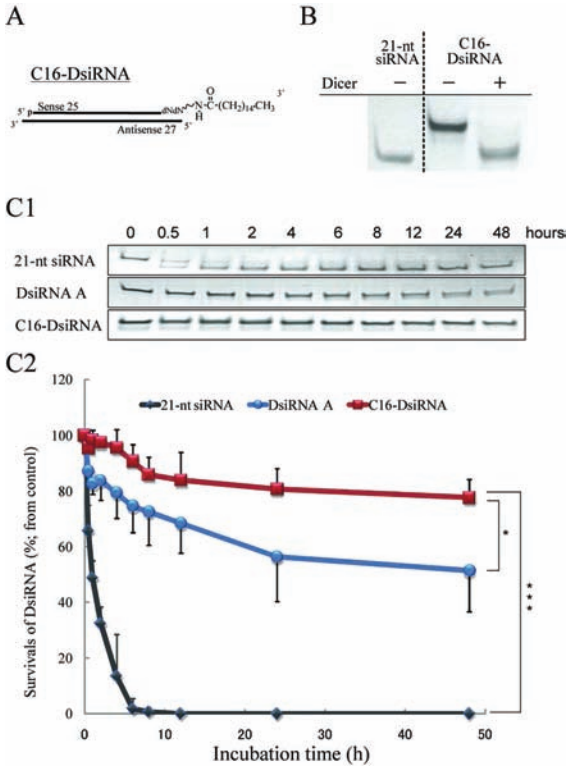


Figure 5. Structure, Dicer cleavage, and serum stability of C16-DsiRNA. (A) Structure of C16-DsiRNA. The C16 was covalently attached to DsiRNA at the 3′-sense end. (B) Dicer-substrate C16-DsiRNA. The C16-DsiRNA was reacted with Dicer for 12 h at 37 °C. The reaction products were electrophoresed on 20% PAGE and visualized by silver staining. (C) Stability of C16-DsiRNA against nuclease degradation. Samples (21-nt siRNA, DsiRNA A, and C16-DsiRNA) were incubated in culture medium containing 10% FBS at 37 °C for 0, 0.5, 1, 2, 4, 6, 8, 12, 24, or 48 h, and aliquots were analyzed on 20% PAGE. Representative PAGE patterns (C1) and survivals (C2) of 21-nt siRNA, DsiRNA A, and C16-DsiRNA after incubation with culture medium were shown. The mean and SD values are from three independent experiments. *, $P < 0.05$; and ***, $P < 0.001$ (t test) at 48 h of incubation time.

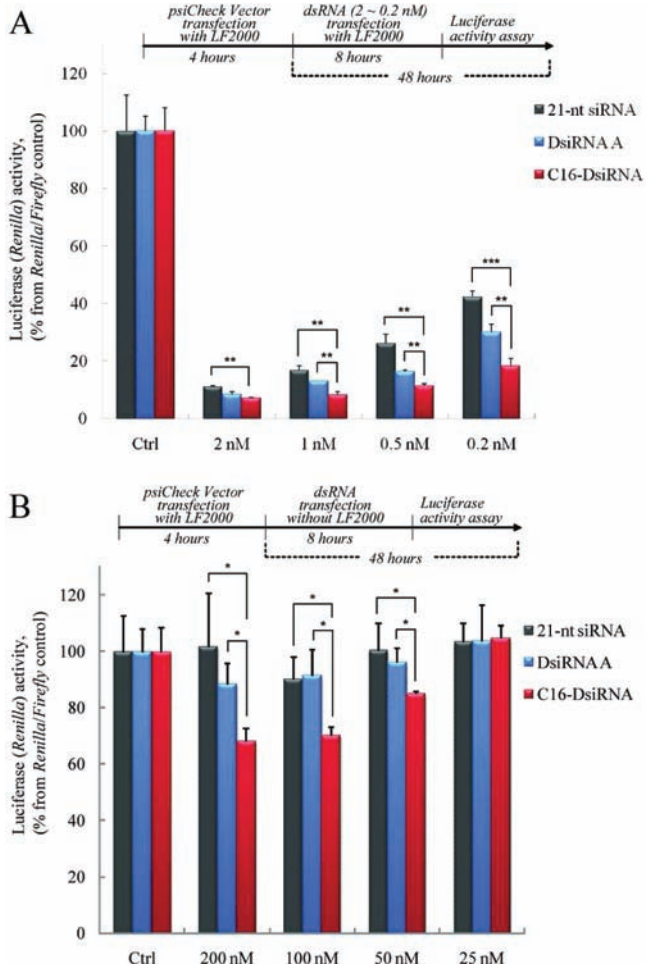


Figure 6. Gene-silencing efficacy of C16-DsiRNA targeted to *Renilla* luciferase in HeLa cells in either the presence (A) or absence (B) of LF2000. The controls were given only PBS (-). The luminescence of *Renilla* luciferase activity was normalized by the luminescence of *Firefly* luciferase activity. The mean and SD values are from three independent experiments. *, $P < 0.05$; **, $P < 0.01$; and ***, $P < 0.001$ (t test).

open a new avenue for the application of C16-DsiRNA in *in vivo* treatments.

Intracellular Delivery of C16-DsiRNA. The membrane permeability of DsiRNA A and C16-DsiRNA were investigated in HeLa cells cultured in DMEM containing heat-inactivated FBS in the presence of LF2000 using confocal microscopy and FACS analysis (Figure 7). The confocal microscopy images of the cells treated with the DsiRNAs are shown in Figure 7A. No fluorescence signals were detected in control cells (nontreated), whereas the cells treated with DsiRNAs labeled with FAM exhibited bright fluorescence. Among them, the cell treated with the C16-DsiRNA labeled with FAM showed an extremely high fluorescence intensity. The results of FACS analysis showed similar results as the microscope observations. In Figure 7B, the logarithm of the fluorescence intensity is shown on the horizontal axis, and the number of cells is shown on the longitudinal axis. The area of the histogram is separated into four parts (a–d) along with the fluorescence intensity. The histogram of the cells treated with C16-DsiRNA labeled with FAM exhibited a higher fluorescence intensity region (c and d) than the histogram of the cells treated with DsiRNA A. In contrast, the low fluorescence intensity area (a and b) was

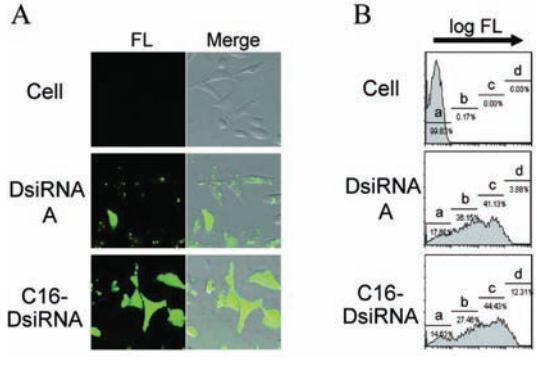


Figure 7. Confocal microscopic images (A) and FACS analysis (B) of HeLa cells treated with DsiRNA A and C16-DsiRNA labeled with FAM, in the presence of LF2000. FL, fluorescent image; Merge, merged image of FL and Trans. In the FACS analysis, the logarithm of the fluorescence intensity is shown on the horizontal axis, and the number of cells is shown on the longitudinal axis. The area of the histogram is separated into four parts (a–d) along with the fluorescence intensity.

dx.doi.org/10.1021/bc200333w | *Bioconjugate Chem.* 2012, 23, 164–173

decreased in the cells treated with C16-DsiRNA in comparison with the cells treated with DsiRNA A. Accordingly, the C16-DsiRNA showed enhanced cell membrane permeability in culture cells, as predicted by the properties of palmitic acid.

The membrane permeabilities of DsiRNA A and C16-DsiRNA in unaltered FBS were also evaluated. The fluorescence intensity of the cells treated with the DsiRNA A and C16-DsiRNA in the presence of unaltered FBS was decreased, compared with that in heat-inactivated FBS via confocal microscopy and FACS analysis (see Figure S3 in the Supporting Information). It seemed from the results of nuclease stability (Figure 5C2 and Figure S1) that the numbers of DsiRNA molecules, including C16-conjugates, in the cells in the presence of unaltered FBS were less than those in the cells in the presence of heat-inactivated FBS. Therefore, in the confocal microscopy images, the surviving DsiRNAs, including C16-conjugates, in unaltered FBS appeared to be almost all in the cytoplasm, whereas the surviving DsiRNAs, including C16-conjugates, in heat-inactivated FBS in both the nucleus and cytoplasm. Despite this, the cells treated with C16-DsiRNA revealed brighter fluorescence, compared with the cells treated with DsiRNA A. The FACS analysis also showed similar results. These results suggested the potential feasibility of C16-DsiRNA for therapeutic use.

CONCLUSION

We designed eight different types of amino-modified DsiRNAs to improve nuclease stability, membrane permeability, and RNAi potency. Almost all of the amino-modified DsiRNAs were cleaved by Dicer leading to release of the 21-nt siRNA, but some of them (DsiRNA C, D, and H) were partly or hardly cleaved by Dicer. We confirmed that the 5′-end of the antisense strand including the 2-nt overhang of DsiRNA is essential for the first contact of Dicer to the DsiRNA. Here, we focused on the properties of DsiRNA B, which was completely cleaved by Dicer, leading to release of 21-nt siRNA, and exhibited excellent RNAi potency with longevity of gene suppression. Thus, the DsiRNA B was superior to the other amino-modified DsiRNA as an RNAi molecule. In addition, the DsiRNA B can be directly conjugated with many kinds of functional molecules through the amine at the 3′-end of the sense strand.

For further improvement, we developed C16-DsiRNA. The C16 was conjugated to the 3′-end of the sense strand of DsiRNA. The C16-DsiRNA is cleaved by Dicer cleaved to 21-nt siRNA, leading to release of lipid, and can avoid the reduction of RNAi potency induced by lipids. The C16-DsiRNA exhibited efficient gene-silencing activity in HeLa cells cultured in DMEM containing either heat-inactivated FBS or unaltered FBS in the presence or absence of LF2000. In particular, finding a remarkable gene-silencing effect by C16-DsiRNA in the absence of any transfection reagent was notable, since it suggested that C16-DsiRNA might be applicable to various biotechnologies, including *in vivo* applications. Moreover, the C16-DsiRNA had excellent cell membrane permeability.

Our newly developed C16-DsiRNA was found to be an appropriate set of next-generation RNAi molecules to facilitate the intracellular delivery of siRNA, to enhance RNAi potency, and potentially to achieve gene silencing *in vivo*.

ASSOCIATED CONTENT

Supporting Information

Figures S1−S3. This material is available free of charge via the Internet at http://pubs.acs.org.

AUTHOR INFORMATION

Corresponding Author

*Tel.: +81-82-878-9473; Fax: +81-82-878-9540; E-mail: kubo-t@yasuda-u.ac.jp.

REFERENCES

(1) Fire, A., Xu, S., Montgomery, M. K., Kostas, S. A., Driver, S. E., and Mello, C. C. (1998) Potent and specific genetic interference by double-stranded RNA in Caenorhabditis elegans. *Nature 391*, 806−811.

(2) John, M., Constien, R., Akinc, A., Goldberg, M., Moon, Y. A., Spranger, M., Hadwiger, P., Soutschek, J., Vornlocher, H. P., Manoharan, M., Stoffel, M., Langer, R., Anderson, D. G., Horton, J. D., Koteliansky, V., and Bumcrot, D. (2007) Effective RNAi-mediated gene silencing without interruption of the endogenous microRNA pathway. *Nature 449*, 745−747.

(3) Karagiannis, T. C., and El-Osta, A. (2005) RNA interference and potential therapeutic applications of short interfering RNAs. *Cancer Gene Ther. 12*, 787−795.

(4) Pan, X., Thompson, R., Meng, X., Wu, D., and Xu, L. (2011) Tumor-targeted RNA-interference: functional non-viral nanovectors. *Am. J. Cancer Res 1*, 25−42.

(5) Geisbert, T. W., Lee, A. C., Robbins, M., Geisbert, J. B., Honko, A. N., Sood, V., Johnson, J. C., Jong, S., Tavakoli, I., Judge, A., Hensley, L. E., and MacLachlan, I. (2010) Postexposure protection of non-human primates against a lethal Ebola virus challenge with RNA interference: a proof-of-concept study. *The Lancet 375*, 1896−1905.

(6) Myers, J. W., Jones, J. T., Meyer, T., and Ferrell, J. E. (2003) Recombinant Dicer efficiently converts large dsRNAs into siRNAs suitable for gene silencing. *Nat. Biotechnol. 21*, 324−328.

(7) Macrae, I. J., Zhou, K., Li, F., Repic, A., Brooks, A. N., Cande, W. Z., Adams, P. D., and Doudna, J. A. (2006) Structural basis for double-stranded RNA processing by Dicer. *Science 311*, 195−198.

(8) Silhavy, D., Molnar, A., Lucioli, A., Szittya, G., Hornyik, C., Tavazza, M., and Burgyan, J. (2002) A viral protein suppresses RNA silencing and binds silencing-generated, 21- to 25-nucleotide double-stranded RNAs. *EMBO J. 21*, 3070−3080.

(9) Schütze, N. (2004) siRNA technology. *Mol. Cell. Endocrinol. 213*, 115−119.

(10) Leung, R. K., and Whittaker, P. A. (2005) RNA interference: from gene silencing to gene-specific therapeutics. *Pharmacol. Ther. 107*, 222−239.

(11) Amarzguioui, M., Holen, T., Babaie, E., and Prydz, H. (2003) Tolerance for mutations and chemical modifications in a siRNA. *Nucleic Acids Res. 31*, 589−595.

(12) Braasch, D. A., Jensen, S., Liu, T., Kaur, K., Arar, K., White, M. A., and Corey, D. R. (2003) RNA interference in mammalian cells by chemically-modified RNA. *Biochemistry 42*, 7967−7975.

(13) Sipa, K., Sochacka, E., Kazmierczak-Baranska, J., Maszewska, M., Janicka, M., Nowak, G., and Nawrot, B. (2007) Effect of base modifications on structure, thermodynamic stability, and gene silencing activity of short interfering RNA. *RNA 13*, 1301−1316.

(14) Choung, S., Kim, Y. J., Kim, S., Park, H. O., and Choi, Y. C. (2006) Chemical modification of siRNAs to improve serum stability without loss of efficacy. *Biochem. Biophys. Res. Commun. 342*, 919−927.

(15) Grunweller, A., Wyszko, E., Bieber, B., Jahnel, R., Erdmann, V. A., and Kurreck, J. A. (2003) Comparison of different antisense strategies in mammalian cells using locked nucleic acids, 2′-O-methyl RNA, phosphorothioates and small interfering RNA. *Nucleic Acids Res. 12*, 3185−3193.

(16) Hall, A. H., Wan, J., Spesock, A., Sergueeva, Z., Shaw, B. R., and Alexander, K. A. (2006) High potency silencing by single-stranded boranophosphate siRNA. *Nucleic Acids Res. 34*, 2773−2781.
(17) Chiu, Y. L., and Rana, T. M. (2003) siRNA function in RNAi: A chemical modification analysis. *RNA 9*, 1034−1048.
(18) Corey, D. R. (2007) Chemical modification: the key to clinical application of RNA interference? *J. Clin. Invest. 117*, 3615−3622.
(19) Behlke, M. A. (2008) Chemical modification of siRNAs for *in vivo* use. *Oligonucleotides 18*, 305−319.
(20) Snøve, O. Jr., and Rossi, J. J. (2006) Chemical modifications rescue off-target effects of RNAi. *ACS Chem. Biol. 1*, 274−276.
(21) Jung, S., Lee, S. H., Mok, H., Chung, H. J., and Park, T. G. (2010) Gene silencing efficiency of siRNA-PEG conjugates: Effect of PEGylation site and PEG molecular weight. *J. Controlled Release 144*, 306−313.
(22) Oishi, M., Nagasaki, Y., Itaka, K., Nishiyama, N., and Kataoka, K. (2005) Lactosylated poly(ethylene glycol)-siRNA conjugate through acid-labile beta-thiopropionate linkage to construct pH-sensitive polyion complex micelles achieving enhanced gene silencing in hepatoma cells. *J. Am. Chem. Soc. 127*, 1624−1625.
(23) Moschos, S. A., Jones, S. W., Perry, M. N., Williams, A. E., Erjefalt, J. S., Turner, J. J., Barnes, P. J., Sproat, B. S., Gait, M. J., and Lindsay, M. A. (2007) Lung delivery studies using siRNA conjugated to TAT(48−60) and Penetratin reveal peptide induced reduction in gene expression and induction of innate immunity. *Bioconjugate Chem 18*, 1450−1459.
(24) Turner, J. J., Jones, S., Fabani, M. M., Ivanova, G., Arzumanov, A. A., and Gait, M. J. (2007) RNA targeting with peptide conjugates of oligonucleotides, siRNA and PNA. *Blood Cells Mol. Dis. 38*, 1−7.
(25) Detzer, A., Overhoff, M., Wunsche, W., Rompf, M., Turner, J. J., Ivanova, G. D., Gait, M. J., and Sczakiel, G. (2009) Increased RNAi is related to intracellular release of siRNA via a covalently attached signal peptide. *RNA 15*, 627−636.
(26) Soutschek, J., Akinc, A., Bramlage, B., Charisse, K., Constien, R., Donoghue, M., Elbashir, S., Geick, A., Hadwiger, P., Harborth, J., John, M., Kesavan, V., Lavine, G., Pandey, P. K., Racie, T., Rajeev, K. G., Röhl, I., Toudjarska, I., Wang, G., Wuschko, S., Bumcrot, D., Koteliansky, V., Limmer, S., Manoharan, M., and Vornlocher, H. P. (2004) Therapeutic silencing of an endogenous gene by systemic administration of modified siRNAs. *Nature 432*, 173−178.
(27) Wolfrum, C., Shi, S., Jayaprakash, K. N., Jayaraman, M., Wang, G., Pandey, R. K., Rajeev, K. G., Nakayama, T., Charrise, K., Ndungo, E. M., Zimmermann, T., Koteliansky, V., Manoharan, M., and Stoffel, M. (2007) Mechanisms and optimization of *in vivo* delivery of lipophilic siRNAs. *Nat. Biotechnol. 25*, 1149−1157.
(28) Nishina, K., Unno, T., Uno, Y., Kubodera, T., Kanouchi, T., Mizusawa, H., and Yokota, T. (2008) Efficient *in vivo* delivery of siRNA to the liver by conjugation of alpha-tocopherol. *Mol. Ther. 16*, 734−740.
(29) Wong, N., Liu, Z., and Dai, H. (2005) Functionalization of carbon nanotubes via cleavable disulfide bonds for efficient intracellular delivery of siRNA and potent gene silencing. *J. Am. Chem. Soc. 127*, 12492−12493.
(30) Kim, D. H., Behlke, M. A., Rose, S. D., Chang, M. S., Choi, S., and Rossi, J. J. (2005) Synthetic dsRNA Dicer substrates enhance RNAi potency and efficacy. *Nat. Biotechnol. 23*, 222−226.
(31) Marques, J. T., Devosse, T., Wang, D., Zamanian-Daryoush, M., Serbinowski, P., Hartmann, R., Fujita, T., Behlke, M. A., and Williams, B. R. (2006) A structural basis for discriminating between self and nonself double-stranded RNAs in mammalian cells. *Nat. Biotechnol. 24*, 559−565.
(32) Rose, S. D., Kim, D. H., Amarzguioui, M., Heidel, J. D., Collingwood, M. A., Davis, M. E., Rossi, J. J., and Behlke, M. A. (2005) Functional polarity is introduced by Dicer processing of short substrate RNAs. *Nucleic Acids Res. 33*, 4140−4156.
(33) Amarzguioui, M., Lundberg, P., Cantin, E., Hagstrom, J., Behlke, M. A., and Rossi, J. J. (2006) Rational design and *in vitro* and *in vivo* delivery of Dicer substrate siRNA. *Nat. Protoc. 1*, 508−517.
(34) Amarzguioui, M., Rossi, J. J., and Kim, D. (2005) Approaches for chemically synthesized siRNA and vector-mediated RNAi. *FEBS Lett. 579*, 5974−5981.
(35) Sano, M., Sierant, M., Miyagishi, M., Nakanishi, M., Takagi, Y., and Sutou, S. (2008) Effect of asymmetric terminal structures of short RNA duplexes on the RNA interference activity and strand selection. *Nucleic Acids Res. 36*, 5812−5821.
(36) Sun, X., Rogoff, H. A., and Li, C. J. (2008) Asymmetric RNA duplexes mediate RNA interference in mammalian cells. *Nat. Biotechnol. 26*, 1379−1382.
(37) Chu, C. Y., and Rana, T. M. (2008) Potent RNAi by short RNA triggers. *RNA 14*, 1714−1719.
(38) Ding, H., Liao, G., Wang, H., and Zhou, Y. (2007) Asymmetrically designed siRNAs and shRNAs enhance the strand specificity and efficacy in RNAi. *J. RNAi Gene Silencing 4*, 269−280.
(39) Turner, J. J., Jones, S. W., Moschos, S. A., Lindsay, M. A., and Gait, M. J. (2007) MALDI-TOF mass spectral analysis of siRNA degradation in serum confirms an RNase A-like activity. *Mol. Biosyst. 3*, 43−50.
(40) MacRae, I. J., Zhou, K., and Doudna, J. A. (2007) Structural determinants of RNA recognition and cleavage by Dicer. *Nat. Struct. Mol. Biol. 14*, 934−940.
(41) Vermeulen, A., Behlen, L., Reynolds, A., Wolfson, A., Marshall, W. S., Karpilow, J., and Khvorova, A. (2005) The contributions of dsRNA structure to Dicer specificity and efficiency. *RNA 11*, 674−682.
(42) Ameres, S. L., Martinez, J., and Schroeder, R. (2007) Molecular basis for target RNA recognition and cleavage by human RISC. *Cell 130*, 101−112.
(43) Salomon, W., Bulock, K., Lapierre, J., Pavco, P., Woolf, T., and Kamens, J. (2010) Modified dsRNAs that are not processed by Dicer maintain potency and are incorporated into the RISC. *Nucleic Acids Res. 38*, 3771−3779.
(44) Eder, P. S., DeVine, R. J., Dagle, J. M., and Walder, J. A. (1991) Substrate specificity and kinetics of degradation of antisense oligonucleotides by a 3′ exonuclease in plasma. *Antisense Res. Dev. 1*, 141−151.
(45) Kubo, T., Zhelev, Z., Ohba, H., and Bakalova, R. (2008) Chemically modified symmetric and asymmetric duplex RNAs: an enhanced stability to nuclease degradation and gene silencing effect. *Biochem. Biophys. Res. Commun. 365*, 54−61.
(46) Kubo, T., Zhelev, Z., Ohba, H., and Bakalova, R. (2007) Modified 27-nt dsRNAs with dramatically enhanced stability in serum and long-term RNAi activity. *Oligonucleotides 17*, 445−464.
(47) Kubo, T., Zhelev, Z., Bakalova, R., and Ohba, H. (2007) Enhancement of gene silencing potency and nuclease stability by chemically modified duplex RNA. *Nucleic Acids Symp. Ser. 51*, 407−408.
(48) Kubo, T., Zhelev, Z., Bakalova, R., and Ohba, H. (2008) Highly efficient gene suppression by chemically modified 27 nucleotide double-stranded RNAs. *Jpn. J. Appl. Phys. 47*, 1346−1350.
(49) Collingwood, M. A., Rose, S. D., Huang, L., Hillier, C., Amarzguioui, M., Wiiger, M. T., Soifer, H. S., Rossi, J. J., and Behlke, M. A. (2008) Chemical modification patterns compatible with high potency dicer-substrate small interfering RNAs. *Oligonucleotides 18*, 187−200.
(50) Kubo, T., Ohba, H., Toyobuku, H., and Hayashi, H. (2009) Lipid-modified double-stranded RNA having potent RNA interference effect, PCT Int. Appl. WO/2009/054551.
(51) Akinc, A., Zumbuehl, A., Goldberg, M., Leshchiner, E. S., Busini, V., Hossain, N., Bacallado, S. A., Nguyen, D. N., Fuller, J., Alvarez, R., Borodovsky, A., Borland, T., Constien, R., Fougerolles, A., Dorkin, J. R., Jayaprakash, K. N., Jayaraman, M., John, M., Koteliansky, V., Manoharan, M., Nechev, L., Qin, J., Racie, T., Raitcheva, D., Rajeev, K. G., Sah, D. WY., Soutschek, J., Toudjarska, I., Vornlocher, H. P., Zimmermann, T. S., Langer, R., and Anderson, D. G. (2008) A combinatorial library of lipid-like materials for delivery of RNAi therapeutics. *Nat. Biotechnol. 26*, 561−569.

(52) Kitamatsu, M., Kubo, T., Matsuzaki, R., Endoh, T., Ohtsuki, T., and Sisido, M. (2009) Carrier PNA for shRNA delivery into cells. *Bioorg. Med. Chem. Lett. 19*, 3410−3413.
(53) Laufer, S. D., and Restle, T. (2008) Peptide-mediated cellular delivery of oligonucleotide-based therapeutics *in vitro*: quantitative evaluation of overall efficacy employing easy to handle reporter systems. *Curr. Pharm. Des. 14*, 3637−3655.
(54) Eguchi, A., Meade, B. R., Chang, Y. C., Fredrickson, C. T., Willert, K., Puri, N., and Dowdy, S. F. (2009) Efficient siRNA delivery into primary cells by a peptide transduction domain-dsRNA binding domain fusion protein. *Nat. Biotechnol. 27*, 567−571.
(55) Shim, M. S., and Kwon, Y. J. (2009) Acid-responsive linear polyethylenimine for efficient, specific, and biocompatible siRNA delivery. *Bioconjugate Chem. 20*, 488−499.
(56) Alshamsan, A., Haddadi, A., Incani, V., Samuel, J., Lavasanifar, A., and Uludağ, H. (2009) Formulation and delivery of siRNA by oleic acid and stearic acid modified polyethylenimine. *Mol. Pharm. 6*, 121−133.
(57) Yezhelyev, M. V., Qi, L., O'Regan, R. M., Nie, S., and Gao, X. (2008) Proton-sponge coated quantum dots for siRNA delivery and intracellular imaging. *J. Am. Chem. Soc. 130*, 9006−9012.

Bioconjugate Chemistry

Article

pubs.acs.org/bc

SiRNA Delivery Systems Based on Neutral Cross-Linked Dendrimers

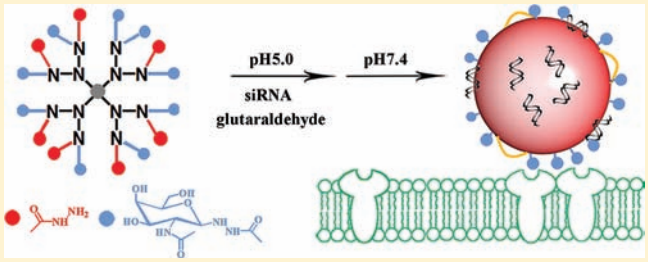
Jie Liu,[†] Jihan Zhou,[‡] and Ying Luo*[,†]

[†]Department of Biomedical Engineering, College of Engineering, Peking University, Room 206, Fangzheng Building, 298 Chengfu Road, Haidian District, Beijing, China 100871

[‡]Beijing National Laboratory for Molecular Sciences and the Key Laboratory of Polymer Chemistry and Physics of Ministry of Education, College of Chemistry and Molecular Engineering, Peking University, Beijing, China, 100871

Supporting Information

ABSTRACT: A neutral cross-linked dendritic system is described for use of delivering small interfering RNA (siRNA) for targeted gene silencing. By replacing the terminal amines with hydrazide groups and N-acetylgalactosamine (GalNAc) ligands, cationic polyamidoamine (PAMAM) dendrimers were transformed into neutral glycosylated carriers for siRNA delivery. Mainly owing to the pH sensitivity and the proton-absorption capability of the tertiary amines within the interior branches, these PAMAM derivatives showing neutrality under physiological conditions (pH 7.4) formed complexes with siRNA through electrostatic interactions at pH 5. Cross-linking procedures via reactions with glutaraldehyde were established, and cytocompatible cross-linked systems loaded with siRNA obtained, with the particulate properties variable with the cross-linking condition and the GalNAc level in the dendritic carrier. *In vitro* cellular uptake and RNAi experiments showed that the cross-linked dendritic systems with an appropriate level of GalNAc composition effectively interacted with HepG2 cells and inhibited the expression of a luciferase reporter gene. Neutral cross-linked dendritic systems provide a new paradigm for designing siRNA delivery systems with biocompatibility and targeting capability.



INTRODUCTION

RNA interference (RNAi) is a fundamental cellular pathway through which the post-transcriptional gene expression is down-regulated via small RNA molecules. As an effective exogenous RNAi inducer, chemically synthesized small interfering RNA (siRNA), with 21−23 nucleotides in length, has not only provided powerful tools in cell culture for fundamental research,[1] but also ushered in opportunities for new clinical therapeutics with great potential.[2−7] However, as siRNA is susceptible to degradation by RNase and by itself can hardly cross the cell membrane due to its polyanionic nature and relatively large molecular weight, successful translation of siRNAs into clinical products is contingent on safe and efficient delivery systems. Numerous materials and methods have been investigated to create siRNA-containing nanoparticles, with a few promising examples advancing to nonhuman primate preclinical and further clinical studies in recent years.[8−12] As illustrated by these studies regarding the design criteria for siRNA delivery systems, minimizing the toxicity and side effects of delivery materials (e.g., immunogenicity), and in the meantime ensuring the stability and transfection efficiency of siRNA-loaded systems are the most critical problems remaining to be addressed for optimal *in vivo* results; investigating strategies that can provide an integral solution is therefore of great importance.

As in the development of delivery systems for DNA-based therapy, investigations on nonviral siRNA delivery have mainly centered on cationic carrier materials, typically prepared from polymers, lipids, and peptides which can electrostatically complex with siRNA under physiological aqueous conditions.[13] The ease and convenience have allowed the development of formulations and processing methods aiming at controlling the various properties of delivery systems with respect to particle size, stability, toxicity, and targeting capability. However, it is notable that the cationic materials as the carrier for nucleic acids may bear inherent disadvantages attributable to their positively charged components. First, the cytotoxicity of materials is often associated with cations such as the protonated primary amines, which have been found to cause membrane damage, apoptosis pathway activation, and medium depletion.[14−17] Second, the electrostatic forces could be unstable in binding materials and siRNA together, which could cause dissociation or deformation of polyelectrolyte complexes. For example, it was reported that the particles made from siRNA and a cationic polypropyleneimine dendrimer exhibited apparent alterations in size after 48 h in PBS buffer;[18] environmental factors such as ionic strength and shear stress may also change the structure and property of polyelectrolyte delivery systems.[19−22] Third, the release of siRNA from polyelectrolyte complexes is an uncontrollable process, since no specific conditions or signals can be defined for breaking the electrostatic interaction.

Received: August 8, 2011
Revised: December 6, 2011
Published: January 31, 2012

 © 2012 American Chemical Society dx.doi.org/10.1021/bc200433s | *Bioconjugate Chem.* 2012, 23, 174−183

In this study, we intend to devise a neutral cross-linked system which can provide stability, safety, and controllability for siRNA delivery, so as to overcome some of the limitations inherent to cationic polymers or lipids. Toward this goal, we focus on transforming a cationic dendritic polymer material—polyamidoamine (PAMAM) which has been used for gene delivery—into neutral targeted carriers for siRNA. In particular, G4.0 PAMAMs with the surface primary amines substituted by neutral cross-linkable hydrazide groups and carbohydrate-targeting ligands, *N*-acetyl-galactosamine (GalNAc), were investigated. These glycosylated dendritic materials, which are neutral at physiological conditions, can become protonated when pH is lowered, owing to the pH sensitivity and the proton-adsorption capability of the interior tertiary amine within the PAMAM scaffolds.[23] This property allows the neutral dendritic materials to form complexes with siRNA at pH 5, which can be cross-linked via the reaction with glutaraldehyde for the preparation of a new type of stable siRNA delivery system.

Based on the cross-linking methodology, we investigated variables affecting the properties of the cross-linked dendritic delivery systems. Formulations that could most effectively induce RNAi in HepG2 cells were studied and discussed. In summary, cross-linked delivery systems based on neutral dendritic materials may offer advantages over conventional delivery systems and hold promise for development of new nucleic acid-based therapeutics.

MATERIALS AND METHODS

Materials. Water was distilled and deionized at 18 MΩ resistance (Gelante Pure Water, Shijiazhuang, China). Generation 4.0 and 5.0 PAMAMs, methyl acrylate, GalNAc, adipic acid dihydrazide (ADH), and diethyl pyrocarbonate (DEPC) were purchased from Sigma-Aldrich (Milwaukee, WI) and hydrazine hydrate from Alfa Aesar (Ward Hill, MA). GeneFinder nucleic acid stain was obtained from Bio-V (Xiamen, China). NHS-fluorescein and BCA protein assay kit were purchased from Pierce (Rockford, IL). Firefly luciferase reporter vector pGL4.51[*luc2*/CMV/Neo], Glo Lysis Buffer, Bright-Glo luciferase assay kits, and CellTiter 96 AQueous One Solution Cell Proliferation Assay (MTS) systems were from Promega (Madison, WI). Cell culture reagents and Lipofectamine 2000 were obtained from Invitrogen (Carlsbad, CA) unless otherwise specified. SiRNAs against firefly luciferase with or without Cy3 labeling and the scrambled control siRNA were synthesized by RiboBio (Guangzhou, China). The siRNA sequences for luciferase were 5′-UGAAGAGCCUGAUCAAAUA dTdT-3′ (sense) and 3′-dTdT ACUUCUCGGACUAGUUUAU-5′ (antisense), and the scrambled siRNA sequences were 5′-UUCUCCGAACGUGUCACGU dTdT (sense) and 3′-dTdT AAGAGGCUUGCACAGUGCA-5′ (antisense). Suppliers of other chemicals, biological reagents, and equipment are specified below.

Synthesis of PAMAM-Hydrazide (PAMAM-HYD) and GalNAc Modified PAMAM-HYD (GPH). PAMAM-HYD and GPH dendrimers were synthesized via a protocol established in our laboratory.[24] To synthesize PAMAM-HYD bearing hydrazide terminal groups, G4.5 PAMAM was first prepared starting from commercially obtained G4.0 PAMAM.[25] Briefly, a 50 mg/mL G4.0 PAMAM solution was reacted with methyl acrylate in 10-fold molar excess of the primary amines on the PAMAM surface at 37 °C for 48 h. The solvent and the unreacted methyl acrylate were removed at 65 °C by rotary evaporation. The resulting G4.5 PAMAM was dried under vacuum and stored at 4 °C. To introduce hydrazide groups to the dendrimer surface, hydrazine hydrate in 10-fold molar excess of the methyl esters of PAMAM was added to a G4.5 PAMAM solution (5 mg/mL in ethanol). The reaction was run under reflux at 55 °C for 24 h, before the ethanol was removed by rotary evaporation. The crude product was purified by extensive dialysis against deionized water using a cellulose membrane (10 kDa MWCO, Union Carbide, NY). The final product was lyophilized and stored at −20 °C for future use.

To conjugate GalNAc ligands, 10 mg/mL PAMAM-HYD in PBS at pH 5.0, was reacted with GalNAc of 0.5, 1, or 1.5 mol equiv of the hydrazide groups. The reaction was kept at 50 °C for 24 h, before the GPH products were purified through extensive dialysis against deionized water using the 10 kDa MWCO cellulose membrane and dried via lyophilization. The GalNAc modification level in each product was analyzed by ^{1}H NMR.

Complexation of siRNA with Dendritic Materials and Preparation of Cross-Linked Delivery Systems. 10× siRNA stock solutions were prepared at 20 μM in DEPC treated water. To study the siRNA−dendrimer complex, siRNA in PBS (2 μM) was added with an equal volume of a dendrimer solution with a prescribed concentration between 1.3 μM and 6.6 μM. The complexation experiments were investigated under both acidic and physiological neutral conditions, with the pH value set at 5.0 and 7.4, respectively.

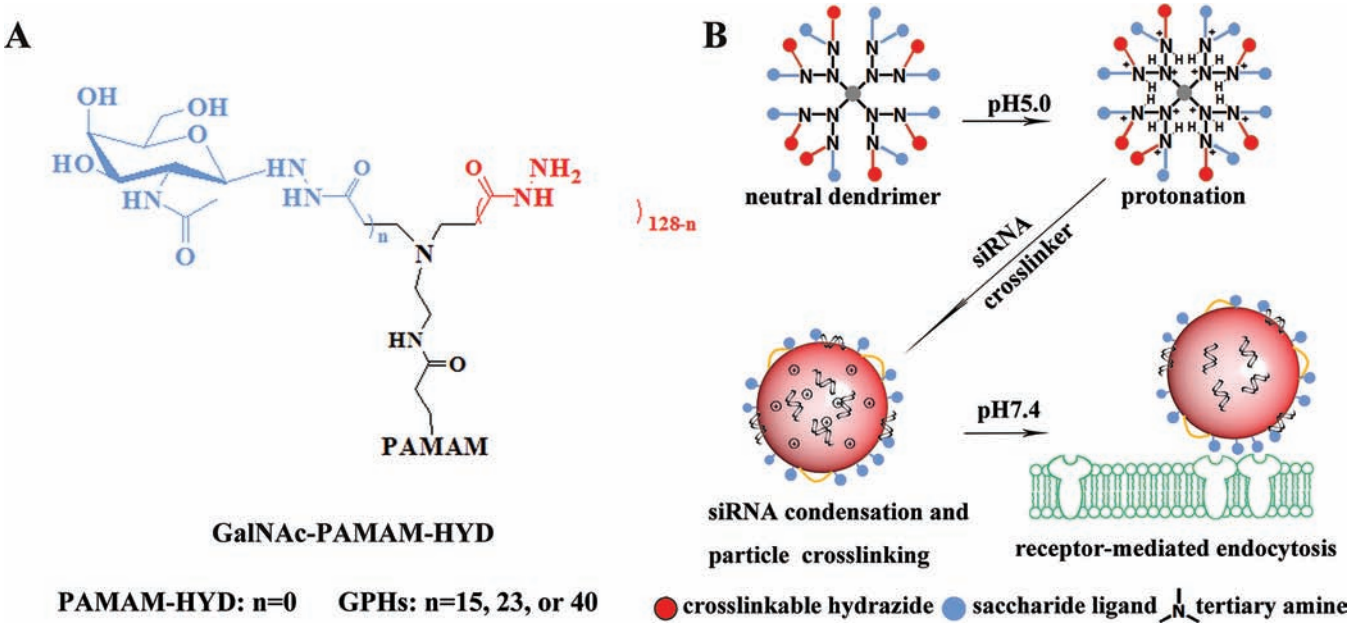
To prepare cross-linked systems, siRNA (2 μM), the selected dendrimer material (3.3 μM) and glutaraldehyde were separately dissolved in PBS at pH 5.0 and mixed at 1:1:1 volume ratio. Typically, glutaraldehyde and siRNA were first mixed well before the third part containing dendrimers was added. The glutaraldehyde concentration was specified below in each experiment. After the ternary blends were incubated at 37 °C for 1 h, an excessive amount of ADH was added to terminate the cross-linking reaction. The pH was adjusted to 7 using a 0.2 M NaOH solution, and cross-linked dendritic systems containing siRNA were dialyzed against PBS at pH 7.4 for 2 h using Slide-A-Lyzer MINI Dialysis Devices (3500 MWCO, Pierce, Rockford, IL). The resulting products were used directly for characterization and cellular studies.

Gel Retardation Analysis. To evaluate whether siRNA can form complexes with the dendritic carrier material or be trapped in the cross-linked system, gel retardation experiments were performed to visually analyze the unbound siRNA in solution. The ternary systems comprising siRNA, dendrimer, and glutaraldehyde were loaded in 3.5% agarose gel in a pH 8.5 TBE buffer, and imaged by a Tanon-1600 Gel Documentation System (Tanon, Shanghai, China). To prepare cross-linked systems, siRNA, PAMAM-HYD, and glutaraldehyde were mixed at equal volumes and cross-linked at pH 5.0 as described above; the glutaraldehyde concentration was varied from 0.17 mM to 83 mM. To understand the effect of pH conditions, the siRNA, PAMAM-HYD and glutaraldehyde (1.7 mM to 8.3 mM) solutions were also prepared and mixed at pH 7.4, and then electrophoresed in the agarose gel.

To study the ability of GPH cross-linked systems to trap siRNA, siRNA, dendrimer, and glutaraldehyde (25 mM) were mixed and cross-linked under acidic conditions as described above. The samples were then electrophoresed; naked siRNA and the siRNA-PAMAM-HYD mixture without glutaraldehyde were control systems for comparison.

dx.doi.org/10.1021/bc200433s | *Bioconjugate Chem.* 2012, 23, 174−183

Scheme 1[a]



[a](A) The structure of GalNAc and hydrazide decorated PAMAM dendrimer; (B) schematic process of preparing cross-linked dendritic systems for siRNA delivery.

Fluorescent Dye Exclusion Assay. To quantitatively determine the unbound siRNA in binary mixtures of siRNA and dendrimer materials, a nucleic acid stain, GeneFinder, was used. Briefly, GeneFinder was added to the siRNA solution (2 μM) at 1:50 volume ratio, and the siRNA was then blended with a dendrimer solution as described above. The fluorescence signals (excitation: 488 nm; emission: 522 nm) resulting from GeneFinder intercalating with siRNA were measured by a SpectraMax M2 microplate reader (Molecular Devices, CA). To study the siRNA loading efficiency in cross-linked systems, a 2 μM siRNA solution was used to prepare cross-linked system with PAMAM-HYD or GPH materials as described above. After pH adjustment, 20 μL of each sample was diluted with 80 μL PBS (pH 7.4), before the GeneFinder solution was added to the sample solutions at 1:100 volume ratio and the fluorescence signals measured.

Zeta-Potential and Particle Size Analysis. To characterize the zeta-potentials of un-cross-linked siRNA–dendrimer complexes and cross-linked systems, samples were prepared as described in the section, Complexation of siRNA with Dendritic Materials and Preparation of Cross-linked Delivery Systems. To prepare PAMAM-HYD cross-linked system, the concentration of glutaraldehyde was varied from 0.83 to 833 mM. For GPH cross-linked systems, the glutaraldehyde concentration was fixed at 8.3 mM. To perform zeta-potential measurements, all final mixed or cross-linked systems were diluted 10 times using deionized water and analyzed through electrophoretic light scattering experiments by a ZetaPALS (Brookhaven Instruments, NY).

To determine the size of siRNA-loaded systems, samples were analyzed through dynamic light scattering (DLS) experiments at an angle of 90° by the ZetaPALS instrument. DLS experiments were also conducted in Dr. Dehai Liang's Laboratory at the College of Chemistry and Molecular Engineering of Peking University, using a commercialized spectrometer (Brookhaven Inc., Holtsville, NY) equipped with a BI-200SM Goniometer and a BI-TurboCo Digital Correlator. A solid-state laser (100 mW, 532 nm, Changchun, China) polarized at the vertical direction was used as the light source and the scattering angles were from 30° to 120°. By using a Laplace inversion program, CONTIN, the normalized distribution function of the characteristic line width which could be further converted into the hydrodynamic radius R_h distribution was obtained (Supporting Information S1).

Cellular Studies of Dendritic Materials and Cross-Linked siRNA Delivery Systems. To conduct cellular studies, HepG2 cells were seeded in 96-well plates at a density of 1.5×10^4 cells per well and allowed to attach to surface and grow for 24 h before being used for further experiments. SiRNA-loaded cross-linked systems made from PAMAM-HYD or GPH dendrimers were prepared by siRNA (2 μM), dendrimer (3.3 μM), and glutaraldehyde (25 mM) solutions as described above. The cross-linked systems were diluted in the DMEM medium to appropriate concentrations for cellular experiments.

Cytotoxicity Assay. Dendritic material solutions of a series of concentrations or cross-linked delivery systems were prepared in DMEM containing 10% FBS. The samples of dendrimer materials and cross-linked delivery systems were then incubated with HepG2 cells cultured with 10% serum for 24 and 48 h, respectively. To analyze cytotoxicity, the cell culture supernatants were replaced by 100 μL of fresh DMEM medium and 20 μL of MTS reagent. After incubation at 37 °C with 5% CO_2 for 1 h, the light absorbance at 490 nm of each well was recorded by the SpectraMax M2 microplate reader.

RNAi Experiments. HepG2 cells were transfected with firefly luciferase reporter vector pGL4.51 using Lipofectamine 2000 following the manufacturer's guide. After 24 h, siRNA (2 μM) against the firefly luciferase gene or with scrambled sequences was loaded in cross-linked systems, and reconstituted at 1:10 volume ratio in DMEM supplemented with 10% FBS. 200 μL of the solutions with approximate 10 pmol siRNA were

dx.doi.org/10.1021/bc200433s | Bioconjugate Chem. 2012, 23, 174–183

dispensed into each well containing HepG2 cells expressing firefly luciferase. After incubation for 48 h, the medium was removed, and the cells were treated with Glo Lysis Buffer for 20 min. The luciferase protein expression was measured by a Bright-Glo luciferase assay system. To normalize the gene silencing efficiency, the total protein was measured via a BCA protein assay kit.

Fluorescence Microscopy of Cellular Uptake of Dendritic Materials and Cross-Linked Delivery Systems. For microscopic cellular uptake studies, dendritic materials were labeled with a fluorescein dye. Specifically, NHS-fluorescein (0.1 mg/mL) and dendrimer (2 mg/mL) solutions were mixed at 2:1 molar ratio, with DPBS made up volume to 50 μL and reacted for 3 h at 37 °C. The labeled dendrimer solutions were diluted in DMEM to a concentration of 1.6 μM, and 100 μL of sample solutions were added to HepG2 cells. After 24 h incubation, the medium was removed, and the cells were washed with DPBS for three times. Fluorescence images were captured by an IX71 fluorescence microscope (Olympus, Japan), and cellular uptake of materials were compared. To investigate siRNA delivery, cross-linked systems containing Cy3-labeled siRNA were prepared and diluted in DMEM with siRNA concentration at 50 nM. Samples were incubated with HepG2 cells for 12 h before imaging studies.

Data Analysis and Statistics. Quantitative results were presented as means ± standard error of measurements (S.E.M.). Statistical comparisons were performed by one-way analysis of variance (ANOVA) followed by the Newman-Keuls tests to compare selected data pairs using *SigmaStat* 3.5. The level of significance was denoted by * and **, with P values set at <0.05 and <0.01, respectively.

RESULTS

Synthesis of Neutral PAMAM-Based Delivery Materials. In this study, we aim to investigate neutral delivery systems that can encapsulate siRNA in cross-linked dendrimer materials. G4.0 PAMAM dendrimers originally bearing 64 amine groups on the surface were expanded for half generation; the resulting G4.5 products, theoretically containing 128 methyl ester branches, were further substituted with hydrazides and GalNAc monosaccharide ligands. GalNAc is, in particular, selected here to target the asialoglycoprotein receptors of hepatocytes for facilitating endocytosis-mediated delivery. Scheme 1A illustrates the chemical structures of PAMAM-HYD and GPHs, and in Scheme 1B, a general route for assembling cross-linked siRNA-containing particles using these materials is shown. Different from the original PAMAM, the dendrimers synthesized here are noncharged and neutral at physiological conditions, as both hydrazide[26−29] and tertiary amine groups[30−32] have a pK_a lower than 7. However, PAMAM-HYD and GPHs do maintain the proton-absorption capabilities because of the internal preserved tertiary amines of the PAMAM scaffolds. This property makes PAMAM-HYD and GPHs become positively charged to bind to siRNA under acidic conditions, resulting in complexes that are cross-linkable to produce siRNA-containing particles.

By controlling the feed ratio of GalNAc to PAMAM-HYD during the conjugation reaction, dendritic conjugates with different levels of monosaccharide modification were obtained as demonstrated by the NMR analysis (SI Figure S2). Three products with the average percentages of GalNAc modification at 11.8%, 18.4%, and 31.5% were used in this study, and they are abbreviated as GPH-15, GPH-23, and GPH-40, respectively, with the number suffixed to GPH indicating the average number of GalNAc ligands per PAMAM-HYD scaffold.

Complexation of siRNA with PAMAM-HYD and GPHs at Acidic and Neutral Conditions. To understand the complexation between siRNA and modified PAMAM dendrimers, a GeneFinder exclusion assay was performed to quantitatively analyze how dendrimer materials could competitively bind with siRNA in the presence of a nucleic acid stain. As shown in Figure 1A, neither PAMAM-HYD nor GPHs at pH 7.4 exhibited any ability to condense siRNA when the dendrimer/siRNA molar ratio (D/S ratio) was varied from 0.5 to 3.5. In contrast, when the pH was lowered to 5.0, the amount of siRNA bound to the nucleic acid stain was shown to gradually decrease with the increasing amounts of the dendrimer components, and approximately 90% of the siRNA in solution was complexed with PAMAM-HYD or GPHs when the D/S ratio was raised to 3.5. It is noted that the level of condensed siRNA showed no significant differences among the different types of dendrimers, indicating that the complexation process is independent of the GalNAc modification level in the dendrimer carrier.

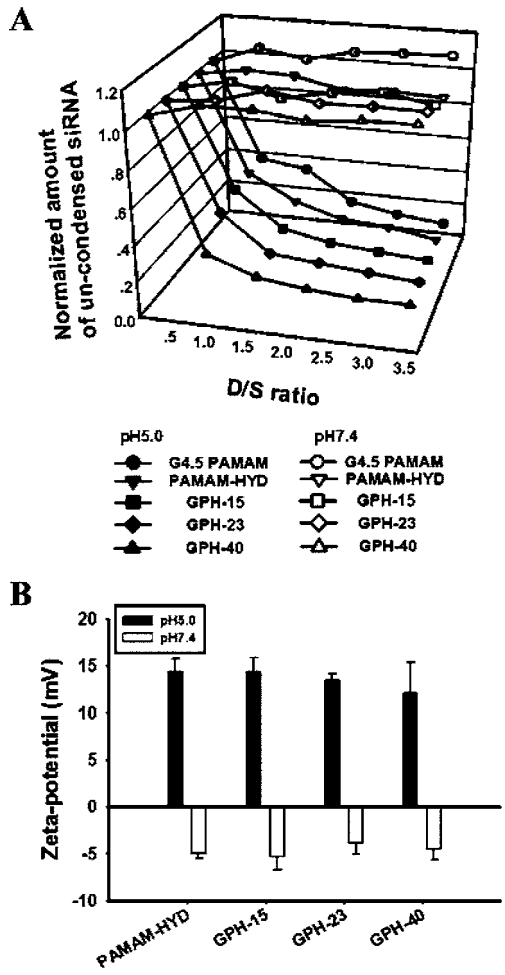


Figure 1. Complexation of siRNA with PAMAM-HYD and GPH dendrimers at pH 5.0 and pH 7.4: (A) normalized amounts of uncondensed siRNA with the dendrimer/siRNA molar ratio (D/S ratio) varied from 0.5 to 3.5 and (B) zeta-potentials of siRNA–dendrimer mixtures with the D/S ratio fixed at 1.7 (n = 3).

dx.doi.org/10.1021/bc200433s | *Bioconjugate Chem.* 2012, 23, 174−183

To confirm the pH sensitivity of PAMAM-HYD and GPHs, zeta-potential measurements were performed. It is noted that the siRNA–dendrimer mixtures did possess positive potentials at pH 5.0, ranging from 12 to 15 mV (Figure 1B). In contrast, all dendrimer–siRNA binary systems had slightly negative potentials when blended at pH 7.4.

Preparation of siRNA-Loaded Cross-Linked Dendritic Systems. To prepare cross-linked siRNA delivery systems, glutaraldehyde was introduced into siRNA-PAMAM-HYD mixtures at pH 5.0 to react with the hydrazide groups on the dendrimer surface. It is speculated that, in the ternary acidic blends, the siRNA and dendritic materials would electrostatically assemble to form complexes, which were simultaneously cross-linked by glutaraldehyde. The cross-linking reaction was terminated by raising pH to neutral conditions and adding excessive ADH to block the unreacted glutaraldehyde residue.

Electrophresis experiments were performed to study whether siRNA could be trapped in the ternary complexes and the movement of RNA retarded in the agarose gel. With a fixed D/S molar ratio at 1.7, the cross-linker concentration was varied from 0.17 mM to 83 mM. It was found that the siRNA bands gradually became fainter until they were invisible with the glutaraldehyde concentration approximately reaching 8.3 mM (Figure 2A). The disappearance of the siRNA band indicates

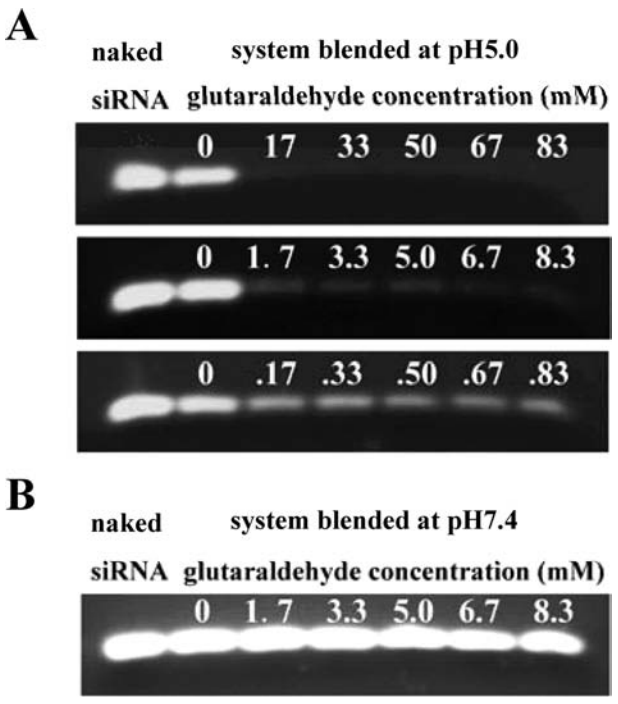


Figure 2. (A) Retardation of siRNA in gel electrophoresis (in pH 8.5 TBE buffer) after cross-linking the PAMAM-HYD-siRNA complexes at pH 5.0 with varied glutaraldehyde concentrations (0–83 mM). (B) siRNA remained unbound in the ternary system blended at pH 7.4 (glutaraldehyde concentration: 0–8.3 mM).

successful entrapment of siRNA in the cross-linked dendritic systems (Figure 2A). In the ternary systems blended and cross-linked under pH 7.4, however, the siRNA remained basically unbound and was electrophoresed as the naked siRNA with bright bands observed for all glutaraldehyde concentrations (Figure 2B).

Further studies were carried out to confirm whether GalNAc-modified dendritic materials can be used to prepare siRNA-loaded systems in a similar way. Cross-linked systems using GPH materials were prepared and electrophoresed. Compared to the siRNA bands in the first two lanes resulting from the naked siRNA and the un-cross-linked siRNA-PAMAM-HYD mixture, only faint siRNA bands were observed for GPH cross-linked systems (Figure 3A), with the band intensity seemingly

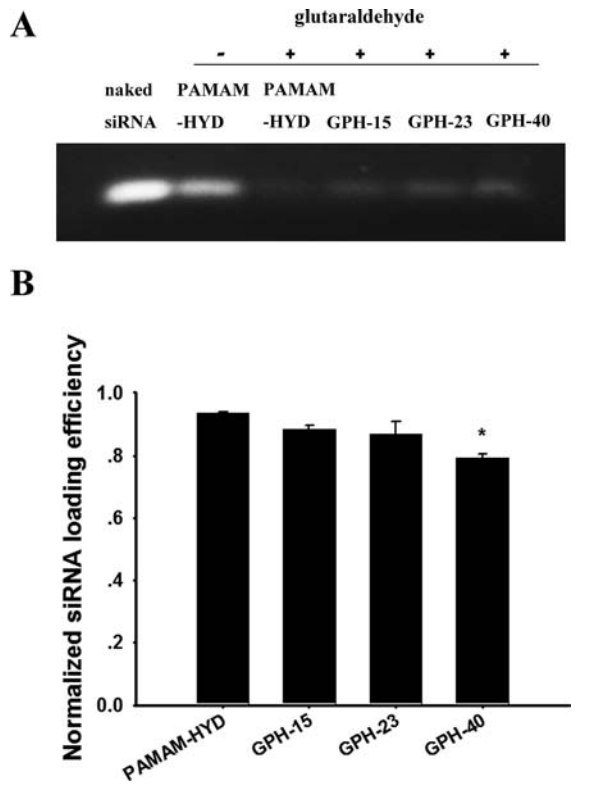


Figure 3. (A) Retardation of siRNA in gel electrophoresis (in pH 8.5 TBE buffer) by different cross-linked systems; (B) quantitative measurements of siRNA loading efficiency in different cross-linked systems (n = 3).

increasing with the GalNAc modification level. When quantitatively studied, the average loading efficiency of PAMAM-HYD and GPHs falls in the range of 79–94% (Figure 3B). It is shown that, at a fixed ratio of siRNA, dendrimer, and cross-linker, the siRNA loading efficiency in the cross-linked systems indeed exhibited a decreasing trend with the increasing GalNAc modification, which is probably related to the reduced number and density of hydrazide groups on the surface of GPH materials.

Particle Size and Zeta-Potential Characterization. Dynamic light scattering experiments were performed to characterize the particle size of different cross-linked dendritic systems, and to discover its correlation with the cross-linker concentration and the surface characteristics of the dendrimer carrier. As shown in Figure 4A, both nano- and microscale particles were obtained for cross-linked PAMAM-HYD systems; the average particle size exhibited a biphasic pattern with the cross-linker concentration, showing a peak around 4.5 μm and deceasing to about 230 nm at the high end of the glutaraldehyde concentration. When PAMAM-HYD and GPH systems were compared by fixing the molar ratio of dendrimer, siRNA, and glutaraldehyde, it is noted that the particle size was reduced with the increasing glycosylation level in the dendrimer

dx.doi.org/10.1021/bc200433s | Bioconjugate Chem. 2012, 23, 174–183

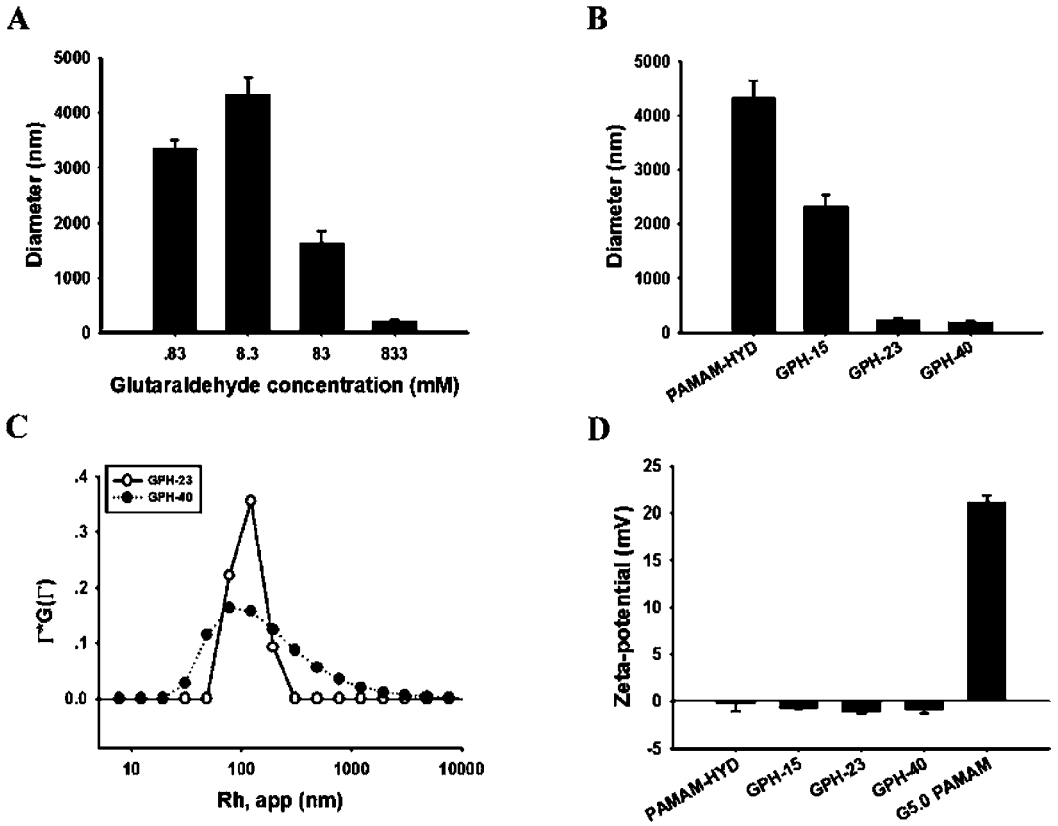


Figure 4. (A) Particle sizes of PAMAM-HYD systems cross-linked with varied glutaraldehyde concentrations; (B) particle sizes of cross-linked systems prepared using different types of dendrimers; (C) hydrodynamic radius R_h distribution of GPH-23 and GPH-40 systems measured at scattering angle of 90°; (D) comparison of zeta-potentials of cross-linked dendritic systems with siRNA-PAMAM complexes (n = 4).

(Figure 4B), with cross-linked GPH-23 and GPH-40 systems reaching about 200 nm in diameter in solution (Figure 4C).

As to the surface potentials, the siRNA delivery systems made from PAMAM-HYD and GPHs are neutral or slightly negatively charged within −3 mV at pH 7.4, revealing a significant contrast with the siRNA system formulated with cationic G5.0 PAMAM (Figure 4D). Cross-linked dendritic delivery systems can therefore be regarded as neutral vehicles under physiological conditions.

Cytotoxicity and Transfection Efficiency. To assess the delivery capabilities of cross-linked dendritic systems, the biocompatibility of neutral dendrimers and G5.0 PAMAM was first compared via MTS cytotoxicity assay. As shown in Figure 5A, PAMAM-HYD had minimal effects on HepG2 proliferation within the concentration range tested. In comparison, significant cytotoxicity was observed for G5.0 PAMAM when its concentration was above 10 nmol/mL. The cytotoxicity of G5.0 PAMAM was found to be more severe on primary cells when different dendrimer materials were tested on human umbilical cord endothelial cells (SI Figure S3), while neutral PAMAM-HYD again demonstrated cytocompatibility (Figure S3). After formulating the delivery materials with siRNA for transfection experiments, all delivery systems maintained the cell viability above 95% (Figure 5B).

For transfection experiments, HepG2 cells cultured with 10% FBS were treated with 50 nM siRNA specifically against the firefly luciferase; the results normalized over total protein measurements are presented (Figure 5C). Among all experimental groups, the cells treated by GPH-15, GPH-23, and Lipofectamine 2000 delivery systems showed lowered luciferase expression. In particular, the GPH-23 system obtained the most significant silencing effect, even compared to Lipofectamine 2000, by reaching approximately 60% knockdown efficiency. The inhibition of luciferase expression does not linearly increase with the GalNAc ligand modification level, as no significant silencing effects were observed for the GPH-40 system.

When the siRNA with scrambled sequences was formulated in cross-linked systems and delivered to cells, it is found that no significant gene silencing effects were induced (Figure 5D). The results indicate that the down-regulation of the luciferase expression as observed in Figure 5C could be mostly attributed to the sequence-specific RNA interference.

To further understand the siRNA delivery mechanisms, the cellular uptake of dendritic materials and siRNA-loaded cross-linked systems were examined via fluorescence microscopy. As shown in Figure 6A, almost no fluorescence was captured for the HepG2 cells treated with PAMAM-HYD; in contrast, fluorescent HepG2 cells were observable for GPH materials, with GPH-23 and GPH-40 visually showing stronger fluorescence signals compared to GPH-15. As to the cellular uptake of the siRNA loaded in different cross-linked delivery systems, only a few residual particles were observed in HepG2 cell samples treated with PAMAM-HYD systems; the siRNA carried by GPHs seemed able to distribute in the cytoplasm of HepG2 cells. It is noted that the system with a moderate glycosylation level, GPH-23, allowed the highest siRNA level in cells visually (Figure 6B), a result that was consistent with the transfection study.

dx.doi.org/10.1021/bc200433s | Bioconjugate Chem. 2012, 23, 174−183

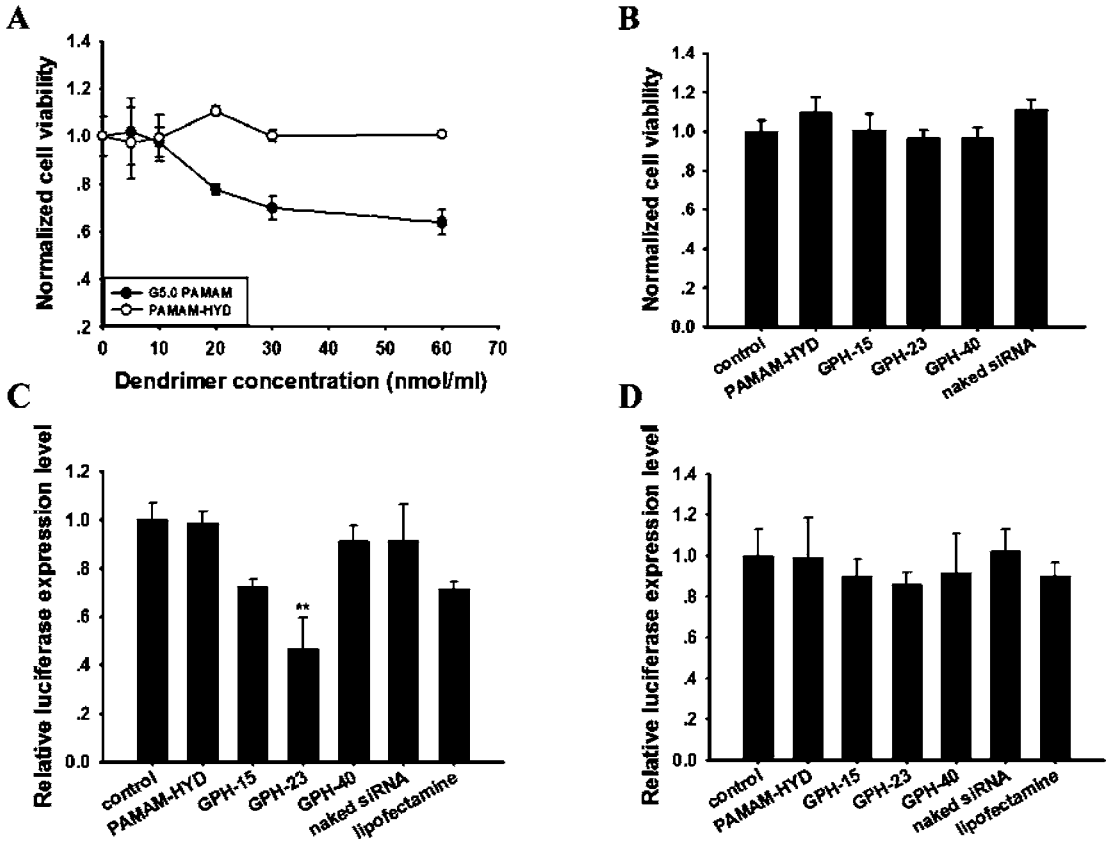


Figure 5. (A) Cytotoxicity measurements of neutral PAMAM-HYD and G5.0 PAMAM. (B) Cytotoxicity measurements of siRNA-loaded delivery systems. (C) Luciferase expression in HepG2 cells after transfection by 50 nM luciferase siRNA for 48 h with 10% FBS (n = 4). (D) Luciferase expression in HepG2 cells after transfection by 50 nM siRNA with scrambled sequences for 48 h with 10% FBS (n = 4).

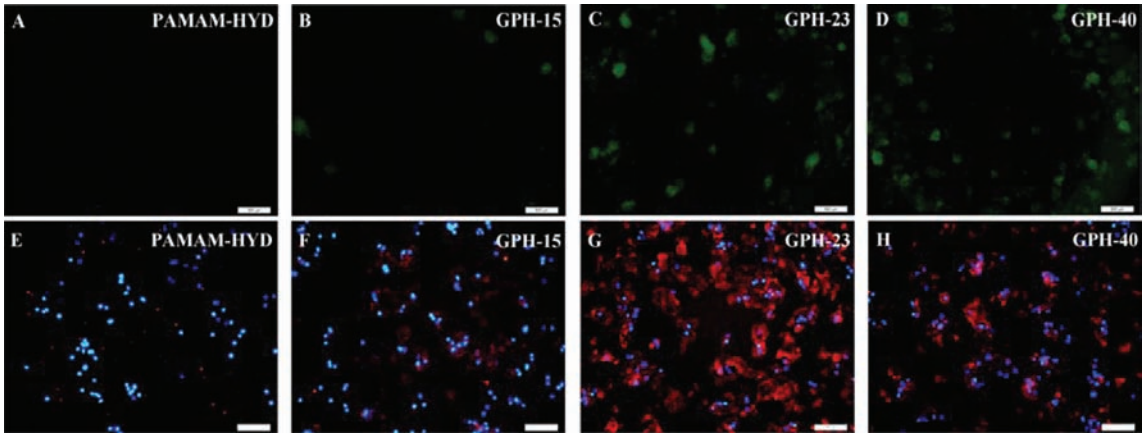


Figure 6. Cellular uptake studies of different neutral dendritic materials (A–D) and siRNA encapsulated in different cross-linked delivery systems (E–H). Dendrimers (A–D) and siRNA (E–H) were labeled with fluorescein (green) and Cy3 (red), respectively; nuclei in E–H were stained by DAPI (blue).

DISCUSSION

Although using cationic materials remains the main approach to prepare delivery systems for nucleic acid-based therapeutics, safety issues often raise concern about their *in vivo* applications. For example, cationic dendrimers have been reported to exhibit cytotoxicity, hemolytic/hematological toxicity and *in vivo* toxicity,[15] which could be caused by the cationic amines on the dendrimer surface. A blockade of surface positive charges through acetylation of primary amine groups has been attempted previously to reduce the toxicity of PAMAM.[33] However, the method could not completely eliminate the negative effects of cations without compromising the siRNA binding and delivery capabilities of the original PAMAM. Neutral cross-linked systems described in this study therefore can potentially provide a new approach for developing gene delivery systems that support safe and effective delivery of nucleic acid-based therapeutics *in vitro* and *in vivo*.

Cross-linked systems have been previously developed for increasing the stability of nucleic acid complexes with cationic carriers.[18,20,21,34–38] What differs in this study is that the preparation of cross-linked delivery systems was undertaken

under acidic conditions when the neutral dendrimers turned "cationic". PAMAM-HYD and GPHs have two possible sites for protonation—the internal tertiary amine and terminal hydrazide. As reported in the literature, the pK_a of the tertiary amine within the interior branches of PAMAM dendrimers is between 6 and 7,[30−32] while that of carboxylic hydrazide groups is as low as 3.6.[28] It is then reasonable to assume that most surface hydrazide groups of PAMAM-HYD or GPHs remained unprotonated at pH 5, and the complexation of siRNA occurred predominantly through the internal charged tertiary amine groups of the dendrimer materials. This speculation is consistent with the results in Figure 1, in which comparison of PAMAM-HYD and GPHs at all D/S ratios shows no differences in terms of siRNA binding efficiency. Previous studies on neutralized PAMAM materials also provide the evidence that dendrimers are capable of forming complexes with nucleic acids or anionic drugs through the cationic groups in interior branches.[23,39,40]

In the ternary blends of dendrimer, siRNA, and glutaraldehyde, PAMAM-HYD or GPHs would simultaneously bind with siRNA and react with glutaraldehyde. In this dynamic system, cross-linking would occur within the siRNA−dendrimer complexes. In addition, the initially cross-linked particulates could further bond with each other as long as hydrazide groups were available, and the secondary interparticulate cross-linking may explain why the average size of the PAMAM-HYD system initially increased with the glutaraldehyde concentration (Figure 4A). However, when the amount of glutaraldehyde reaches a certain threshold capable of saturating the surface hydrazide groups, interparticulate cross-linking could be prohibited, allowing the formation of smaller particles. It is interesting to note that the size of cross-linked systems can be modulated by carbohydrate modification. Decorating the dendrimer surface with GalNAc likely increased the surface hydrophilicity and blocked the accessibility of surface hydrazide groups, thereby reducing the extent of interparticulate cross-linking.

Cross-linked systems made of glycosylated dendrimers are multifunctional in nature. Besides providing biocompatibility, stability, and control over particle size, the glycosylated systems developed in this study can offer mechanisms that support cell targeting and intracellular release of siRNA. The biological properties of noncharged systems are tunable via surface modification with ligands or other bioactive moieties for favorable cell−material interaction. The fluorescence microscopy studies (Figure 6) indicate that the GalNAc played a key role in mediating the cellular uptake of cross-linked dendritic systems, although other factors such as particle size should be taken into consideration in interpreting the RNAi results. Another feature of the PAMAM-based cross-linked systems is the preservation of the interior structure of dendrimer materials, which contains tertiary amines capable of triggering escape of the endocytosed substance through the "proton sponge" mechanism.

When using cationic materials to complex with nucleic acids, it is known that the electrostatic force may restrict the gene cargoes from leaving the delivery system into the cytoplasm, as it was reported that overly condensed particles are not an optimal choice for gene delivery.[41−45] In contrast, the release of siRNA from the cross-linked systems developed here can principally occur upon the breakage of the hydrazone cross-linking bonds in acidic endosomal environment. To explore future applications of cross-linked systems, other types of labile chemical bonds, such as disulfide or peptide bonds, may potentially be incorporated to allow the cytoplasmic release of siRNA through a defined mechanism.

CONCLUSIONS

PAMAM-HYD and GPH dendritic materials have the ability to complex with siRNA under acidic conditions and give rise to a new type of neutral dendritic systems after being cross-linked. The delivery systems offer a wide range of tunable properties, and RNAi can be effectively induced by optimizing the particle size and dendrimer surface properties. The concept of neutral cross-linked systems warrants further study for designing biocompatible nonviral gene delivery systems for *in vivo* applications.

ASSOCIATED CONTENT

Supporting Information

Detailed DLS calculation (S1), NMR spectra of GPH materials (Figure S2), cytotoxicity of PAMAM-HYD and G5.0 PAMAM on HUVECs (Figure S3). This material is available free of charge via the Internet at http://pubs.acs.org.

AUTHOR INFORMATION

Corresponding Author

*Tel +86 (10) 8252-9288; Fax +86 (10) 8252-9288; e-mail ying.luo@pku.edu.cn.

ACKNOWLEDGMENTS

The research was supported by the Beijing Natural Science Foundation (Project# 7102088), National High-Tech R&D Program of China (Project# 2009AA03Z314), and the Georgia Tech-Emory-PKU Seed Grant. We thank Bing Lv for his information on the biocompatibility of dendrimer materials and Fang Wang and Xiaopeng Liu for their technical assistance. The authors are grateful to Dr. Dehai Liang for providing kind help with the light scattering experiments.

REFERENCES

(1) Elbashir, S. M., Harborth, J., Weber, K., and Tuschl, T. (2002) Analysis of gene function in somatic mammalian cells using small interfering RNAs. *Methods 26*, 199−213.

(2) Oh, Y. K., and Park, T. G. (2009) siRNA delivery systems for cancer treatment. *Adv. Drug Delivery Rev. 61*, 850−862.

(3) Takahashi, Y., Nishikawa, M., and Takakura, Y. (2009) Nonviral vector-mediated RNA interference: its gene silencing characteristics and important factors to achieve RNAi-based gene therapy. *Adv. Drug Delivery Rev. 61*, 760−766.

(4) Bennett, C. F., and Swayze, E. E. (2010) RNA targeting therapeutics: molecular mechanisms of antisense oligonucleotides as a therapeutic platform. *Annu. Rev. Pharmacol. Toxicol. 50*, 259−293.

(5) Pecot, C. V., Calin, G. A., Coleman, R. L., Lopez-Berestein, G., and Sood, A. K. (2011) RNA interference in the clinic: challenges and future directions. *Nat. Rev. Cancer 11*, 59−67.

(6) Whitehead, K. A., Langer, R., and Anderson, D. G. (2009) Knocking down barriers: advances in siRNA delivery. *Nat. Rev. Drug Discovery 8*, 129−138.

(7) Tokatlian, T., and Segura, T. (2010) siRNA applications in nanomedicine. *Wiley Interdiscip. Rev. Nanomed. Nanobiotechnol. 2*, 305−315.

(8) Davis, M. E. (2009) The first targeted delivery of siRNA in humans via a self-assembling, cyclodextrin polymer-based nanoparticle: from concept to clinic. *Mol. Pharm. 6*, 659−668.

(9) Davis, M. E., Zuckerman, J. E., Choi, C. H. J., Seligson, D., Tolcher, A., Alabi, C. A., Yen, Y., Heidel, J. D., and Ribas, A. (2010)

Evidence of RNAi in humans from systemically administered siRNA via targeted nanoparticles. *Nature 464*, 1067−1070.
(10) Zimmermann, T. S., Lee, A. C., Akinc, A., Bramlage, B., Bumcrot, D., Fedoruk, M. N., Harborth, J., Heyes, J. A., Jeffs, L. B., John, M., Judge, A. D., Lam, K., McClintock, K., Nechev, L. V., Palmer, L. R., Racie, T., Rohl, I., Seiffert, S., Shanmugam, S., Sood, V., Soutschek, J., Toudjarska, I., Wheat, A. J., Yaworski, E., Zedalis, W., Koteliansky, V., Manoharan, M., Vornlocher, H. P., and MacLachlan, I. (2006) RNAi-mediated gene silencing in non-human primates. *Nature 441*, 111−114.
(11) Akinc, A., Zumbuehl, A., Goldberg, M., Leshchiner, E. S., Busini, V., Hossain, N., Bacallado, S. A., Nguyen, D. N., Fuller, J., Alvarez, R., Borodovsky, A., Borland, T., Constien, R., de Fougerolles, A., Dorkin, J. R., Jayaprakash, K. N., Jayaraman, M., John, M., Koteliansky, V., Manoharan, M., Nechev, L., Qin, J., Racie, T., Raitcheva, D., Rajeev, K. G., Sah, D. W. Y., Soutschek, J., Toudjarska, I., Vornlocher, H. P., Zimmermann, T. S., Langer, R., and Anderson, D. G. (2008) A combinatorial library of lipid-like materials for delivery of RNAi therapeutics. *Nat. Biotechnol. 26*, 561−569.
(12) Love, K. T., Mahon, K. P., Levins, C. G., Whitehead, K. A., Querbes, W., Dorkin, J. R., Qin, J., Cantley, W., Qin, L. L., Racie, T., Frank-Kamenetsky, M., Yip, K. N., Alvarez, R., Sah, D. W., de Fougerolles, A., Fitzgerald, K., Koteliansky, V., Akinc, A., Langer, R., and Anderson, D. G. (2010) Lipid-like materials for low-dose, in vivo gene silencing. *Proc. Natl. Acad. Sci. U. S. A. 107*, 1864−1869.
(13) Zhang, S. B., Zhao, B., Jiang, H. M., Wang, B., and Ma, B. C. (2007) Cationic lipids and polymers mediated vectors for delivery of siRNA. *J. Controlled Release 123*, 1−10.
(14) Hunter, A. C. (2006) Molecular hurdles in polyfectin design and mechanistic background to polycation induced cytotoxicity. *Adv. Drug Delivery Rev. 58*, 1523−1531.
(15) Jain, K., Kesharwani, P., Gupta, U., and Jain, N. K. (2010) Dendrimer toxicity: let's meet the challenge. *Int. J. Pharm. 394*, 122−142.
(16) Stasko, N. A., Johnson, C. B., Schoenfisch, M. H., Johnson, T. A., and Holmuhamedov, E. L. (2007) Cytotoxicity of polypropylenimine dendrimer conjugates on cultured endothelial cells. *Biomacromolecules 8*, 3853−3859.
(17) Mukherjee, S. P., Davoren, M., and Byrne, H. J. (2010) In vitro mammalian cytotoxicological study of PAMAM dendrimers - towards quantitative structure activity relationships. *Toxicol. In Vitro 24*, 169−177.
(18) Taratula, O., Garbuzenko, O. B., Kirkpatrick, P., Pandya, I., Savla, R., Pozharov, V. P., He, H. X., and Minko, T. (2009) Surface-engineered targeted PPI dendrimer for efficient intracellular and intratumoral siRNA delivery. *J. Controlled Release 140*, 284−293.
(19) Adami, R. C., Collard, W. T., Gupta, S. A., Kwok, K. Y., Bonadio, J., and Rice, K. G. (1998) Stability of peptide-condensed plasmid DNA formulations. *J. Pharm. Sci. 87*, 678−683.
(20) Adami, R. C., and Rice, K. G. (1999) Metabolic stability of glutaraldehyde cross-linked peptide DNA condensates. *J. Pharm. Sci. 88*, 739−746.
(21) McKenzie, D. L., Smiley, E., Kwok, K. Y., and Rice, K. G. (2000) Low molecular weight disulfide cross-linking peptides as nonviral gene delivery carriers. *Bioconjugate Chem. 11*, 901−909.
(22) Zezin, A. B., and Kabanov, V. A. (1982) A new class of complex water-soluble polyelectrolytes. *Russ. Chem. Rev. 51*, 833−855.
(23) Yang, K., Weng, L. A., Cheng, Y. Y., Zhang, H. F., Zhang, J. H., Wu, Q. L., and Xu, T. W. (2011) Host-guest chemistry of dendrimer-drug complexes. 6. Fully acetylated dendrimers as biocompatible drug vehicles using dexamethasone 21-phosphate as a model drug. *J. Phys. Chem. B 115*, 2185−2195.
(24) Liu, X., Liu, J., and Luo, Y. (2012) Facile glycosylation of dendrimers for elicitation of specific cell-material Interactions. *Polym. Chem. 3*, 310−313.
(25) Tomalia, D. A., Huang, B., Swanson, D. R., Brothers, H. M., and Klimash, J. W. (2003) Structure control within poly(amidoamine) dendrimers: size, shape and regio-chemical mimicry of globular proteins. *Tetrahedron 59*, 3799−3813.
(26) Alfaro, J. F., Gillies, L. A., Sun, H. G., Dai, S. J., Zang, T. Z., Klaene, J. J., Kim, B. J., Lowenson, J. D., Clarke, S. G., Karger, B. L., and Zhou, Z. S. (2008) Chemo-enzymatic detection of protein isoaspartate using protein Isoaspartate methyltransferase and hydrazine trapping. *Anal. Chem. 80*, 3882−3889.
(27) Raddatz, S., Mueller-Ibeler, J., Kluge, J., Wass, L., Burdinski, G., Havens, J. R., Onofrey, T. J., Wang, D., and Schweitzer, M. (2002) Hydrazide oligonucleotides: new chemical modification for chip array attachment and conjugation. *Nucleic Acids Res. 30*, 4793−4802.
(28) Radushev, A. V., Chekanova, L. G., Gusev, V. Y., and Sazonova, E. A. (2000) Determination of hydrazides and 1,2-diacylhydrazines of aliphatic carboxylic acids by conductometric titration. *J. Anal. Chem. 55*, 445−448.
(29) Schluep, T., and Cooney, C. L. (1998) Purification of plasmids by triplex affinity interaction. *Nucleic Acids Res. 26*, 4524−4528.
(30) Cakara, D., Kleimann, J., and Borkovec, M. (2003) Microscopic protonation equilibria of poly(amidoamine) dendrimers from macroscopic titrations. *Macromolecules 36*, 4201−4207.
(31) Diallo, M. S., Christie, S., Swaminathan, P., Balogh, L., Shi, X., Um, W., Papelis, C., Goddard, W. A. 3rd, and Johnson, J. H. Jr. (2004) Dendritic chelating agents. 1. Cu(II) binding to ethylene diamine core poly(amidoamine) dendrimers in aqueous solutions. *Langmuir 20*, 2640−2651.
(32) Niu, Y. H., Sun, L., and Crooks, R. A. (2003) Determination of the intrinsic proton binding constants for poly(amidoamine) dendrimers via potentiometric pH titration. *Macromolecules 36*, 5725−5731.
(33) Waite, C. L., Sparks, S. M., Uhrich, K. E., and Roth, C. M. (2009) Acetylation of PAMAM dendrimers for cellular delivery of siRNA. *BMC Biotechnol. 9*, 38−47.
(34) Kakizawa, Y., Harada, A., and Kataoka, K. (2001) Glutathione-sensitive stabilization of block copolymer micelles composed of antisense DNA and thiolated poly(ethylene glycol)-block-poly(L-lysine): a potential carrier for systemic delivery of antisense DNA. *Biomacromolecules 2*, 491−497.
(35) Oupicky, D., Carlisle, R. C., and Seymour, L. W. (2001) Triggered intracellular activation of disulfide crosslinked polyelectrolyte gene delivery complexes with extended systemic circulation in vivo. *Gene Ther. 8*, 713−724.
(36) McKenzie, D. L., Kwok, K. Y., and Rice, K. G. (2000) A potent new class of reductively activated peptide gene delivery agents. *J. Biol. Chem. 275*, 9970−9977.
(37) Yang, Y. H., Park, Y., Man, S. H., Liu, Y. H., and Rice, K. G. (2001) Cross-linked low molecular weight glycopeptide-mediated gene delivery: relationship between DNA metabolic stability and the level of transient gene expression in vivo. *J. Pharm. Sci. 90*, 2010−2022.
(38) Miyata, K., Kakizawa, Y., Nishiyama, N., Harada, A., Yamasaki, Y., Koyama, H., and Kataoka, K. (2004) Block catiomer polyplexes with regulated densities of charge and disulfide cross-linking directed to enhance gene expression. *J. Am. Chem. Soc. 126*, 2355−2361.
(39) Patil, M. L., Zhang, M., Taratula, O., Garbuzenko, O. B., He, H., and Minko, T. (2009) Internally cationic polyamidoamine PAMAM-OH dendrimers for siRNA delivery: effect of the degree of quaternization and cancer targeting. *Biomacromolecules 10*, 258−266.
(40) Lee, J. H., Lim, Y. B., Choi, J. S., Lee, Y., Kim, T. I., Kim, H. J., Yoon, J. K., Kim, K., and Park, J. S. (2003) Polyplexes assembled with internally quaternized PAMAM-OH dendrimer and plasmid DNA have a neutral surface and gene delivery potency. *Bioconjugate Chem. 14*, 1214−1221.
(41) Redlich, O. (1946) The dissociation of strong electrolytes. *Chem. Rev. 39*, 333−356.
(42) Dong, C. L., Wen, G. L., Ai, J. Z., Shu, J. S., Nan, C., Gang, G., Jing, Y. Z., and Kang, D. Y. (2006) Pre-deliver chitosanase to cells: a novel strategy to improve gene expression by endocellular degradation-induced vector unpacking. *Int. J. Pharm. 314*, 63−71.
(43) Zhou, L. Z., Gan, L., Li, H. B., and Yang, X. L. (2007) Studies on the interactions between DNA and PAMAM with fluorescent probe [Ru(phen)(2)dppZ]2(+). *J. Pharm. Biomed. Anal. 43*, 330−334.

(44) Godbey, W. T., Wu, K. K., and Mikos, A. G. (1999) Tracking the intracellular path of poly(ethylenimine)/DNA complexes for gene delivery. *Proc. Natl. Acad. Sci. U.S.A. 96*, 5177−5181.
(45) Liu, X. H., Yang, J. W., Miller, A. D., Nack, E. A., and Lynn, D. M. (2005) Charge-shifting cationic polymers that promote self-assembly and self-disassembly with DNA. *Macromolecules 38*, 7907−7914.

Bioconjugate Chemistry

Article

pubs.acs.org/bc

Fibronectin Binding to the *Treponema pallidum* Adhesin Protein Fragment rTp0483 on Functionalized Self-Assembled Monolayers

Matthew T. Dickerson,[†] Morgan B. Abney,[†] Caroline E. Cameron,[‡] Marc Knecht,[§] Leonidas G. Bachas,[§] and Kimberly W. Anderson*[,†]

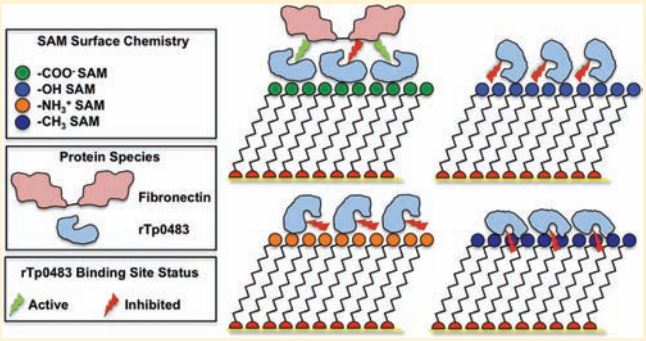
[†]Department of Chemical and Materials Engineering, University of Kentucky, Lexington, Kentucky 40506-0054, United States

[‡]Department of Biochemistry and Microbiology, University of Victoria, Victoria, British Columbia V8P 5C2, Canada

[§]Department of Chemistry, University of Miami, Miami, Florida 33124-4620, United States

Supporting Information

ABSTRACT: Past work has shown that *Treponema pallidum*, the causative agent of syphilis, binds host fibronectin (FN). FN and other host proteins are believed to bind to rare outer membrane proteins (OMPs) of *T. pallidum*, and it is postulated that this interaction may facilitate cell attachment and mask antigenic targets on the surface. This research seeks to prepare a surface capable of mimicking the FN binding ability of *T. pallidum* in order to investigate the impact of FN binding with adsorbed Tp0483 on the host response to the surface. By understanding this interaction, it may be possible to develop more effective treatments for infection and possibly mimic the stealth properties of the bacteria. Functionalized self-assembled monolayers (SAMs) on gold were used to investigate rTp0483 and FN adsorption. Using a quartz crystal microbalance (QCM), rTp0483 adsorption and subsequent FN adsorption onto rTp0483 were determined to be higher on negatively charged carboxylate-terminated self-assembled monolayers ($-COO^-$ SAMs) compared to the other surfaces analyzed. Kinetic analysis of rTp0483 adsorption using surface plasmon resonance (SPR) supported this finding. Kinetic analysis of FN adsorption using SPR revealed a multistep event, where the concentration of immobilized rTp0483 plays a role in FN binding. An examination of relative QCM dissipation energy compared to the shift in frequency showed a correlation between the physical properties of adsorbed rTp0483 and SAM surface chemistry. In addition, AFM images of rTp0483 on selected SAMs illustrated a preference of rTp0483 to bind as aggregates. Adsorption on $-COO^-$ SAMs was more uniform across the surface, which may help further explain why FN bound more strongly. rTp0483 antibody studies suggested the involvement of amino acids 274–289 and 316–333 in binding between rTp0483 to FN, while a peptide blocking study only showed inhibition of binding with amino acids 316–333. Finally, surface adsorbed rTp0483 with FN bound significantly less anti-RGD and gelatin compared to FN adsorbed directly to $-COO^-$ SAMs, indicating that one or both binding regions may play a role in binding between rTp0483 and FN.



INTRODUCTION

Syphilis is a chronic, multistage disease caused by the spirochete bacterium *Treponema pallidum*. The scarcity of antigenic targets on the surface of the bacterium is thought to play a role in the ability of *T. pallidum* to evade the immune response and establish a chronic infection.[1−9] *T. pallidum* elicits an acute immune response during the primary stage of the disease, after which the disease enters a latent phase that is characterized by periodic reoccurrence of disease symptoms. The primary factor responsible for the capacity of *T. pallidum* to establish prolonged periods of latency is believed to be the unique composition of the *T. pallidum* outer membrane. The surface of *T. pallidum* lacks lipopolysaccharide, which is a potent modulator of inflammation, and displays a dearth of surface proteins.[5,10] The initial immune response is likely due to recognition of one or more antigenic outer membrane proteins (OMPs) on the bacterium, but it remains unclear why a portion of the bacteria are able to persist within the host and produce a secondary infection at a later time.[1,4,6−9]

Studies have shown that *T. pallidum* binds to a number of extracellular matrix (ECM) components, including fibronectin (FN), as a method of adherence and infiltration through the host.[1−3,11−13] FN is a common protein found in the blood as well as in the ECM. A number of proteins of the integrin family as well as a number of other biologically important molecules, such as fibrin, collagen, and heparin, are known to interact with FN.[14] One possible explanation for the propensity of *T. pallidum* to circumvent the detrimental effects of antibodies and

Received: August 10, 2011
Revised: December 15, 2011
Published: December 18, 2011

 © 2011 American Chemical Society dx.doi.org/10.1021/bc200436x | *Bioconjugate Chem.* 2012, 23, 184−195

immune effector cells is that host proteins, such as fibronectin, become bound to exposed antigenic targets and render them inaccessible to host defense mechanisms. In a study by Cameron et al., two putative outer membrane proteins of *T. pallidum* capable of binding FN, identified as Tp0483 and Tp0155, were expressed as recombinant protein fragments.[3] The C-terminal fragment of Tp0483 employed in the study was shown to retain the expected FN binding capacity. In addition, work by Brinkman et al. identified a third putative membrane protein (Tp0136) that demonstrated similar affinity for the ECM components FN and laminin.[1] While Tp0483, Tp0155, and Tp0136 all bound insoluble ECM FN, only Tp0483 showed an affinity for soluble FN.[3] Binding of ECM FN can be reasonably assumed to be for the purpose of host attachment and tissue infiltration; however, the pathogenic advantage conferred by soluble FN binding to the bacterium remains unclear. Here, it is postulated that soluble FN is bound for the purpose of obscuring exposed antigenic targets from detection. This property is referred to as antigenic disguise.

This work seeks to better characterize the hypothesized interaction between Tp0483 and FN as well as prepare a surface capable of mimicking the FN binding properties of *T. pallidum*. Such a coating could possibly mimic the antigenic disguise properties of whole *T. pallidum* and lead to a reduction in adverse reactions to synthetic materials in the body. Tp0483 was selected because of its ability to bind soluble FN. The recombinant C-terminal portion of Tp0483 (rTp0483) expressed by Cameron et al. was examined to determine its ability to bind soluble FN on a range of surface chemistries in an attempt to mimic the interaction between FN and natural Tp0483 found on the surface of *T. pallidum*.[3] Physical adsorption of rTp0483 on self-assembled monolayers (SAMs) and subsequent FN adsorption to rTp0483 were investigated using quartz crystal microbalance (QCM) and surface plasmon resonance spectroscopy (SPR) approaches. Atomic force microscopy (AFM) was used to analyze further the binding of rTp0483 to each of the functionalized SAM surfaces. Two regions of the Tp0483 protein sequence contained within the expressed rTp0483 fragment were identified as probable FN binding sites, following which peptides and antibodies matching these regions were produced to test their involvement in FN binding. Numerous studies have suggested that the RGD cell-binding sequence located in the 10th type III domain of FN plays a significant role in *T. pallidum* adhesion.[12,15−17] In addition, a number of other binding domains exist on FN, including binding sites specific for heparin and collagen/gelatin.[14] Previous studies have revealed that the binding of certain species of bacteria is modulated by these heparin or collagen/gelatin-binding domains of FN.[18,19] In order to elucidate a more complete profile of rTp0483 FN binding, anti-RGD, heparin, and gelatin binding were studied to determine their involvement in the binding of FN on surfaces coated with rTp0483 compared to unmodified $-COO^-$ SAMs.

EXPERIMENTAL PROCEDURES

Proteins and Antibodies. Human plasma fibronectin (FN) and all other chemicals not specifically mentioned were purchased from Sigma Aldrich (St. Louis, MO). An antibody against the RGD (Arginine-Glycine-Aspartate) cell-binding site of FN was purchased from Chemicon International (Temecula, TN) and later from Abcam (Cambridge, MA). The protein fragment rTp0483 was expressed and purified on the basis of the procedure used by Cameron et al.[20] BL21 (DE3)pLysS cells from Invitrogen (Carlsbad, CA) were transformed with a pRSETc plasmid containing the rTp0483 gene with a 6xHis tag. Protein expression was induced during log-phase growth with 0.5 mM isopropyl β-D-thiogalactopyranoside for 3 h at 30 °C, and the cells were recovered by centrifugation at 4000 rpm for 15 min and then lysed with a series of sonication cycles. The pellet was resuspended and sonicated in binding buffer (20 mM Tris, 5 mM imidazole, 0.5 M NaCl, pH 7.9) with 0.1% NP-40 and 1% (v/v) EDTA free, Halt protease inhibitor cocktail (HPIC) from Thermo Scientific (Rockford, IL). The lysed cell contents were recovered by centrifugation at 13,000 rpm for 15 min. The pellet was resuspended in binding buffer with 1% (v/v) HPIC, sonicated, and recovered by centrifugation two additional times. Insoluble rTp0483 in the pellet was recovered by suspension in binding buffer with 6 M urea, after which the suspension was applied to a Ni-NTA superflow column from Qiagen (Hilden, Germany). The column was washed with binding buffer also with 6 M urea and 20 mM imidazole. Bound rTp0483 was recovered with elution buffer (20 mM Tris, 0.5 M NaCl, 1 M imidazole, pH 7.9). A process for protein renaturation was adapted from Zhang et al.[21] Zwittergent 3-12 was added to the protein to a final concentration of 0.5% (w/v), and the sample was dialyzed consecutively with renaturation buffer 1 (100 mM Tris, 200 mM NaCl, 10 mM EDTA, pH 8.0) and renaturation buffer 2 (50 mM Tris, 200 mM NaCl, 0.5 mM EDTA). The presence of rTp0483 was confirmed with SDS-PAGE and Western Blot (see Supporting Information).

Aves Laboratories (Tigard, OR) identified two probable FN binding peptide sequences on rTp0483 using Hopp-Woods and Kyte-Doolittle (hydrophilicity), Emini (surface probability), Karplus-Shulz (chain flexibility), and Jameson-Wolf (a combination of attributes) methods. Peptides corresponding to residues 274−289 (D1, QMHSDSKQVDVKLDGN) and 316−333 (D2, QRKEDDSMYSYVTGTMKY) of the complete Tp0483 sequence were prepared along with monoclonal antibodies (anti-Tp0483#1 IgY, chicken # 5507−5508, against residues 274−289; anti-Tp0483#2 IgY, chicken # 5509−5510, against residues 316−333) by Aves Laboratories. Two other peptides (A3, AYSSGAPPMPPF; P1, HSSYWYAFNNKT) were provided for use as negative controls.

Self-Assembled Monolayers (SAMs). SAMs were assembled on gold QCM and SPR surfaces by incubation overnight in selected 1 mM alkanethiol solutions; 11-mercaptoundecanoic acid was purchased from Sigma Aldrich (St. Louis, MO); 11-hydroxy-1-undecanethiol, 1-dodecanethiol, and 11- amino-1-undecanethiol hydrochloride were purchased from Asemblon (Redmond, WA). Gold QCM surfaces were purchased from Biolin Scientific (Linthicum, MD), and gold SPR surfaces were purchased from Biacore AB (Uppsala, Sweden). Monolayers were characterized using contact angle analysis and X-ray photoelectron spectroscopy (XPS), and they were compared to literature values.[22−28] Contact angle studies were completed on a Future Digital Scientific Contact Angle Goniometer (Long Island, NY). XPS data were gathered using Mg from a twin anode XR3E2 X-ray source and the CLAM4MCD analyzer from Thermo VG Scientific (Waltham, MA). Prior to protein adsorption studies, the gold surfaces containing SAMs were removed from their alkanethiol solution and washed for 15 s in ACS grade ethanol followed by deionized (using a Millipore Milli-Q deionizer) water. The surfaces were dried with ultrapure nitrogen gas just before analysis. After use, surfaces were regenerated by either 5 min

dx.doi.org/10.1021/bc200436x | Bioconjugate Chem. 2012, 23, 184−195

immersion in a 5:1:1 mixture of deionized water, ammonium hydroxide, and hydrogen peroxide at 75 °C followed by 10 min exposure to UV/ozone or a 20 min exposure to O_2 plasma at a flow rate of 1 standard ft^3/h (SCFH) and a pressure of 700 mTorr in a PDC-002 (230 V) plasma cleaner with Plasmaflo unit from Harrick Plasma (Ithaca, NY) followed by immersion in ACS grade ethanol for at least 14 h.

rTp0483 and FN Adsorption and Kinetic Modeling. A Q-Sense E4 quartz crystal microbalance (QCM) from Biolin Scientific (Linthicum, MD) was used for both rTp0483 and FN adsorption studies. SAMs were prepared as previously described. Dulbecco's phosphate buffered saline (DPBS, 137 mM NaCl, 2.7 mM KCl, 8 mM Na_2HPO_4, 1.5 mM KH_2PO_4, pH 7.4) was employed as a running buffer in the QCM and used to dilute all proteins to the desired concentration for analysis. Changes in signal as a result of protein adsorption were measured as a frequency change (Δf) in hertz (Hz). Changes in dissipation energy (D) were also tracked. Dissipation energy is the sum of all energy lost from the system during a single oscillation divided by the total energy in the system. This parameter is related to the physical properties of an adsorbed layer. Factors such as hydration and layer fluidity can lead to increases in the dissipation energy of a sample, and based on this, it is possible to compare the binding states of proteins on different surfaces. A simple Sauerbrey equation was employed to estimate the surface mass density of adsorbed protein.[29,30]

$$\Gamma = -\frac{C}{n}\Delta f \tag{1}$$

Here Γ is the surface mass density (pg/mm^2), n is the QCM overtone (n = 1, 3, 5, 7, 9), and C is a constant for a quartz crystal of a specified resonant frequency. Overtone refers to the oscillation frequency of the QCM crystal relative to its fundamental frequency. In this case, the fundamental frequency of the crystal was 5 MHz and C = 177 $pg/Hz{\cdot}mm^2$. So, for example, the third overtone corresponds to three times the fundamental frequency or 15 MHz. In order to employ this expression, the adsorbed layer was assumed to be homogeneous and rigid with a no slip condition between the gold layer and adsorbed protein.[29,30] To fulfill these conditions, a dissipation energy of less than 10^{-5} is required.[30] Moreover, when the dissipation energy is low, it can be assumed that the deviation between overtones is negligible. For this study, data corresponding to the ninth overtone were used.

To investigate protein adsorption, 20 μg rTp0483/mL was introduced into the system for 2 min at 50 μL/min. Two mg of BSA/mL was then introduced for 2 min at 50 μL/min to block the surface not covered by rTp0483 and, hence, prevent nonspecific binding of FN. Finally, 100 μg FN/mL was introduced into the QCM for 2 min at 50 μL/min. Prior to and after the introduction of each protein, surfaces were equilibrated with DPBS at a flow rate of 50 μL/min until the QCM signal stabilized.

A surface plasmon resonance (SPR) spectrometer (Biacore X from Biacore AB (Uppsala, Sweden)) was used for all kinetic studies. SAMs were prepared as previously described. DPBS was employed as a running buffer and was used to dilute all proteins to the desired concentrations. Any change in SPR signal was measured in response units (RUs), where a change of 1 RU was equivalent to a change of 1 pg/mm^2 of protein on the surface.[31]

To investigate the kinetics of rTp0483 binding, 100 μL of rTp0483 was injected at concentrations of 5, 10, and 20 μg rTp0483/mL at 50 μL/min. The corresponding adsorption sensorgrams were analyzed using Biacore BIAevaluation software v3.0.2 to model kinetic parameters.

For FN kinetic analysis, 100 μL of rTp0483 was injected at 5 and 20 μg rTp0483/mL at 50 μL/min. A volume of 100 μL of 2 mg BSA/mL was injected to block the surface not covered by rTp0483 at 50 μL/min. Finally, 100 μL of FN was injected at concentrations of 10, 20, and 40 μg FN/mL at 50 μL/min. These lower FN concentrations were used in order to limit the potential of mass transport effects. The corresponding adsorption sensorgrams were analyzed using Biacore BIAevaluation software v3.0.2 in order to model kinetic parameters. As with the QCM studies, each surface was equilibrated with DPBS at a flow rate of 50 μL/min until the SPR signal stabilized prior to and after each protein injection.

To determine the effect of surface chemistry on rTp0483 binding and subsequently FN binding to rTp0483 on the selected SAMs, the kinetics of rTp0483 and FN adsorption were modeled using the Biacore BIAevaluation software v3.0.2 package. Adsorption was compared on the selected SAMs representing negatively charged, positively charged, hydrophilic, and hydrophobic surface chemistries. rTp0483 and FN were adsorbed onto SAM surfaces under the conditions detailed above, and both binding and dissociation kinetics were obtained in order to determine binding affinity. The strength of protein binding was represented by an affinity constant (K_A) for each surface, where K_A was calculated by dividing the rate of protein binding by the rate of protein dissociation. Direct rTp0483 binding to each surface was modeled as a simple 1:1 Langmuir binding event. For comparison, a model including mass transport effects was also generated. FN binding to adsorbed rTp0483 on $-COO^-$ functionalized SAMs was also modeled on the basis of 1:1 Langmuir binding with and without mass transport limitations; however, neither model adequately represented the adsorption event. FN is a dimeric protein, so each FN molecule has the potential to bind two molecules of rTp0483. A bivalent model was used in order to represent this aspect of FN. A bivalent model with mass transport limitations was also analyzed (data not shown); however, the fit was poor, indicating that for FN adsorption onto rTp0483 there were no mass transport limitations.

1:1 Langmuir Binding. The binding kinetics for 1:1 Langmuir binding are represented in eq 2, and the related rate equations are summarized in eqs 3 and 4. A is rTp0483 or FN, B is a binding site on the surface, and AB is a protein A bound to site B on the surface. The bulk concentration of A was assumed to be constant; thus, the rate equations were written with respect to the change in the number of occupied sites on the surface.

$$A + B \leftrightarrow AB \tag{2}$$

$$\frac{\partial[B]}{\partial t} = -(k_a[A][B] - k_d[AB]) \tag{3}$$

$$\frac{\partial[AB]}{\partial t} = k_a[A][B] - k_d[AB] \tag{4}$$

The injected concentration was known for each test, and the number of occupied sites was assumed to be zero initially ($[AB]_0 = 0$). The maximum binding capacity (R_{max}) was determined empirically for each surface and assumed to be

dx.doi.org/10.1021/bc200436x | Bioconjugate Chem. 2012, 23, 184–195

equal to the number of sites B initially ($[B]_0 = R_{max}$). Adsorption sensorgrams at the aforementioned concentrations were generated. The binding and dissociation kinetics were determined using BIAevaluation software v3.0.2 and used to calculate K_A.

1:1 Langmuir Binding with Mass Transport Limitations. In this model, the prior 1:1 model was modified to account for limitations in the transfer of A from bulk solution to the surface. Equations 5 and 6 illustrate the modified process. The impact on binding kinetics was accounted for through the inclusion of an additional term as shown in eq 7. This term includes a mass transfer coefficient (k_t) along with a term for the bulk concentration of A in solution ($[A]_s$), which was taken to be a constant value. The remaining rate equations are shown in eqs 8 and 9.

$$A_s \Leftrightarrow A \tag{5}$$

$$A + B \Leftrightarrow AB \tag{6}$$

$$\frac{\partial[A]}{\partial t} = k_t([A]_s - [A]) - (k_a[A][B] - k_d[AB]) \tag{7}$$

$$\frac{\partial[B]}{\partial t} = -(k_a[A][B] - k_d[AB]) \tag{8}$$

$$\frac{\partial[AB]}{\partial t} = k_a[A][B] - k_d[AB] \tag{9}$$

As previously discussed, the injected concentration was known, all sites were assumed to be empty initially ($[AB]_0 = 0$), and the total number of sites was determined empirically for each surface that was analyzed ($[B]_0 = R_{max}$). Additionally, the concentration of A was assumed to be zero initially ($[A]_0 = 0$). BIAevaluation software v3.0.2 was used to determine the binding and dissociation kinetics based on adsorption sensorgrams and then used to calculate K_A.

Bivalent Analyte. A bivalent analyte adsorption model represents a system where an analyte (A) binds to a ligand (B) as described above; however, once AB is formed, it further reacts with a second ligand B, resulting in the complex AB_2. In this case, A was FN and B was adsorbed rTp0483. As in the case of 1:1 Langmuir binding, the concentration of A was assumed to be constant, and the equations were solved with respect to sites on the surface occupied by either AB or AB_2. These reactions are represented below in eqs 10 and 11 and the corresponding rate equations are shown in eqs 12−14.

$$A + B \Leftrightarrow AB \tag{10}$$

$$AB + B \Leftrightarrow AB_2 \tag{11}$$

$$\frac{\partial[B]}{\partial t} = -(k_{a1}[A][B] - k_{d1}[AB]) - (k_{a2}[AB][B] - k_{d2}[AB_2]) \tag{12}$$

$$\frac{\partial[AB]}{\partial t} = (k_{a1}[A][B] - k_{d1}[AB]) - (k_{a2}[AB][B] - k_{d2}[AB_2]) \tag{13}$$

$$\frac{\partial[AB_2]}{\partial t} = k_{a2}[AB][B] - k_{d2}[AB_2] \tag{14}$$

The same assumptions were made for this model as detailed above. In addition, the initial concentration of AB_2 was assumed to be zero ($[AB_2]_0 = 0$). BIAevaluation software v3.0.2 was used to determine the binding and dissociation kinetics for both reactions based on adsorption sensorgrams and then used to calculate K_{A1} and K_{A2}.

rTp0483 Monolayer Dissipation Energy Analysis. The Q-Sense E4 was employed for the analysis of rTp0483 monolayer dissipation energy. SAMs were prepared as previously described. For dissipation energy studies, 100 μg rTp0483/mL was injected into the QCM for 2 min at 50 μL/min. The higher concentration of rTp0483 was used in this study to produce a more complete protein monolayer. Prior to and after protein binding, each surface was equilibrated with DPBS at a flow rate of 50 μL/min until the SPR signal stabilized. The change in dissipation energy for each surface was divided by the frequency change in order to calculate the dissipation energy as a function of protein surface mass density.

AFM Imaging of rTp0483 on SAMs. A Molecular Imaging PicoSPM from Agilent Technologies (Tempe, AZ) using Tap300 Intermittent Contact Tips from Budget Tips (Sofia, Bulgaria) was used to provide images of rTp0483 adsorption on each of the SAMs. Data analysis was completed using PicoScan Software (Agilent Technologies) and Gwyddion Software 2.5 (General Public License, development supported by the Czech Metrology Institute, Brno, Czech Republic). Freshly prepared SAMs were incubated in a solution of 10 μg rTp0483/mL for 15 min at room temperature. Surfaces were rinsed with Milli-Q water, dried with ultrapure nitrogen gas, and imaged immediately.

rTp0483 Binding Domain Analysis. The Biacore X SPR spectrometer was used for all anti-rTp0483 antibody and rTp0483 peptide studies. SAMs were prepared as previously described. The selected rTp0483 antibodies were prepared at a concentration of 200 μg antibody/mL. Initially, 100 μL of 20 μg rTp0483/mL was injected and adsorbed onto a surface at 50 μL/min. After stabilization, 100 μL of 2 mg BSA/mL was injected to block the surface not covered by rTp0483 at 50 μL/min. To test the effect of FN on antibody binding, 100 μL of 100 μg FN/mL was injected at 50 μL/min and, once the SPR signal was stable, 100 μL of anti-Tp0483#1 or anti-Tp0483#2 was injected at 50 μL/min. Nonspecific antibody binding on the BSA blocked portion of the surface was analyzed by injecting 100 μL of 2 mg BSA/mL at 50 μL/min followed by 100 μL of anti-Tp0483#1 or anti-Tp0483#2 at 50 μL/min. Prior to protein binding, each surface was equilibrated with DPBS at a flow rate of 50 μL/min until the SPR signal stabilized.

To determine the effect of rTp0483 antibodies on FN binding, rTp0483 was injected, followed by BSA, as detailed previously. This was followed by 100 μL of anti-Tp0483#1 or anti-Tp0483#2 at 50 μL/min. Once the SPR signal was stable, 100 μL of 100 μg FN/mL was injected at 50 μL/min.

Because the analogous rTp0483 antibodies bound to rTp0483 only on negatively charged SAMs, only $-COO^-$ terminated SAMs were examined in these studies. Samples containing a 20:1 molar ratio of a specific rTp0483 peptide or a nonspecific control peptide and FN were prepared. First, 100 μL of 20 μg rTp0483/mL was injected and adsorbed to each surface at 50 μL/min. After stabilization, 100 μL of 2 mg BSA/mL was injected to block the surface not covered by rTp0483 at 50 μL/min. After the SPR signal stabilized, 100 μL of one of the 20:1 peptide/FN solutions was injected at 50 μL/min.

dx.doi.org/10.1021/bc200436x | Bioconjugate Chem. 2012, 23, 184−195

Alternately, after rTp0483 had been adsorbed and blocked with BSA, 100 μL of 100 μg FN/mL was injected for comparison at 50 μL/min. Prior to and after protein binding, each surface was equilibrated with DPBS at a flow rate of 50 μL/min until the SPR signal stabilized. Binding inhibition was determined using eq 15:

$$\%\text{FN binding} = 100 \frac{\text{FN + peptide on rTp0483}\left(\frac{\text{pg}}{\text{mm}^2}\right)}{\text{FN on rTp0483}\left(\frac{\text{pg}}{\text{mm}^2}\right)} \quad (15)$$

FN Binding Domain Analysis. The Biacore X SPR spectrometer was used for all FN binding domain studies. SAMs were prepared as previously described. Because FN bound preferentially to rTp0483 adsorbed on negatively charged surfaces, only $-COO^-$ terminated SAMs were analyzed in these tests. First, 100 μL of 100 μg rTp0483/mL was injected and adsorbed onto a $-COO^-$ terminated SAM at 50 μL/min. After the SPR signal stabilized, 100 μL of 100 μg FN/mL was injected at 50 μL/min. The signal was again allowed to stabilize, and then 50 μL of 2 mg heparin/mL was injected at 50 μL/min. Alternately, 100 μL of 100 μg FN/mL was injected and adsorbed onto a $-COO^-$ terminated SAM without rTp0483 at 50 μL/min followed by 50 μL of 2 mg/mL heparin at 50 μL/min. This process was repeated for anti-RGD (20 μg/mL) and type A gelatin (1 mg/mL). Prior to and after protein binding, each surface was equilibrated with DPBS at a flow rate of 50 μL/min until the SPR signal stabilized.

As the RGD peptide sequence had previously been implicated in the adhesion of *T. pallidum* to FN, the interaction via this site was further characterized. The Biacore X was used to analyze the involvement of the RGD peptide sequence in the binding of FN to surface-adsorbed rTp0483 on $-COO^-$ functionalized SAMs. SAMs were prepared as previously described. A volume of 100 μL of 20 μg rTp0483/mL was injected over the course of 2 min at 50 μL/min. Then, 100 μL of 2 mg BSA/mL was injected to block the surface not covered by rTp0483 at 50 μL/min. After signal stabilization, 50 μL of FN blocked with 20 μg/mL or 50 μg/mL was injected to evaluate adsorption onto rTp0483 over a 1 min period at 50 μL/min. This lower FN concentration was employed in order to minimize the volume of RGD antibody required for testing. Alternately, 50 μL of 10 μg FN/mL was injected alone onto adsorbed rTp0483 at 50 μL/min. Nonspecific antibody adsorption was also measured by injecting 50 μL of anti-RGD alone at 20 μg/mL and 50 μg/mL at 50 μL/min. Prior to and after protein binding, each surface was equilibrated with DPBS at a flow rate of 50 μL/min until the SPR signal stabilized. The mass of adsorbed anti-RGD+FN complex was adjusted to account for the added mass of the bound antibodies. Because FN is dimeric, it was assumed that each FN bound two molecules of anti-RGD. This added mass was accounted for multiplying the observed SPR response by a correction factor as shown in eqs 16 and 17.

$$\text{correction factor} = \frac{\text{FN } M_W}{\text{FN + antibody } M_W} = \frac{440,000 \text{ Da}}{440,000 \text{ Da} + (2 \times 150,000 \text{ Da})} = 0.595 \quad (16)$$

$$\text{fibronectin concentration} = \text{observed concentration} \times 0.595 \quad (17)$$

RESULTS

Self-Assembled Monolayers. Functionalized SAMs displaying $-COO^-$, $-OH$, $-NH_3^+$, and $-CH_3$ groups were prepared as previously described. Contact angle and XPS data (see Supporting Information) were determined and compared with literature values.[22−28] The contact angles corresponded well with literature values, and XPS data relating surface composition indicated SAM formation.

rTp0483 and FN Adsorption and Kinetic Modeling. Adsorption results for rTp0483 onto functionalized SAMs are shown in Figure 1A. Results for $-COO^-$ SAMs indicated an

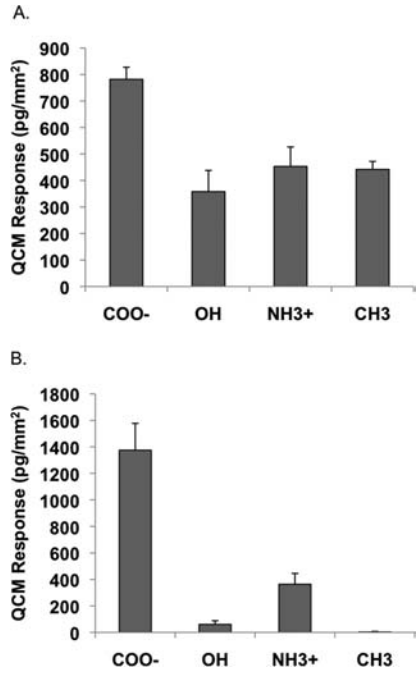


Figure 1. (A) Average rTp0483 binding on SAMs determined by QCM and (B) average FN binding to adsorbed rTp0483 on SAMs determined by QCM. ANOVA indicates higher rTp0483 and FN binding on $-COO^-$ SAMs ($p < 0.05$). Data is reported as a mean ($n = 3$) for all sample groups, with error bars representing standard error.

average surface mass density of 782 ± 46 pg/mm^2 while $-OH$, $-NH_3^+$, and $-CH_3$ SAMs were 358 ± 80 pg/mm^2, 453 ± 73 pg/mm^2, and 442 ± 30 pg/mm^2, respectively. ANOVA indicated that adsorption on the $-COO^-$ SAMs was significantly greater than that on the other three surfaces ($p < 0.05$) and that all of the other surfaces were indistinguishable.

The adsorption of FN onto rTp0483 on functionalized SAMs is shown in Figure 1B. As previously mentioned, the portion of each surface not covered by rTp0483 was blocked

dx.doi.org/10.1021/bc200436x | *Bioconjugate Chem.* 2012, 23, 184−195

with BSA; hence, any FN adsorption observed is onto rTp0483. Minimal binding of FN was observed to rTp0483 on the −OH (60 ± 28 pg/mm^2), $-NH_3^+$ (363 ± 82 pg/mm^2), and $-CH_3$ (3.5 ± 3.5 pg/mm^2) surfaces; however, the $-COO^-$ SAMs demonstrated significantly higher binding (1380 ± 200 pg/mm^2, $p < 0.05$) than the other three surfaces, which were not significantly different from one another. Because there was significantly more FN binding to rTp0483 adsorbed to $-COO^-$ functionalized SAMs, it was the only surface employed for further study of FN binding to adsorbed rTp0483.

rTp0483 was injected into the Biacore X SPR and adsorbed onto functionalized SAMs over a range of concentrations as previously described, and the adsorption sensorgrams were used to model the kinetics of rTp0483 adsorption. Adsorption data was fit to a 1:1 Langmuir model as well as a 1:1 Langmuir model with mass transfer limitations. The χ^2 parameter (mean square of signal noise) was used as a gauge of how well each binding model corresponded to experimental results. The lower the χ^2 value, the more closely a model correlated to the experimental data. In general, χ^2 should be of the same magnitude as the noise inherent in a fit to be considered acceptable.[32] The best fit was chosen on the basis of the lowest χ^2 value and, after being chosen, the χ^2 value was compared to the range of noise in the model versus the experimental data. A 1:1 Langmuir binding model with mass transfer limitations produced the best fit for rTp0483 adsorption. χ^2 values ranged from 2.5 to 4.7 RU, while noise deviated from 0 RU up to 10 RU compared to experimental data. Model rTp0483 adsorption and experimental results for each of the selected functionalized SAMs are shown in Figure 2, and the corresponding values for K_A are included in Table 1. The K_A for rTp0483 adsorption to functionalized SAMs was found to be (13.10 ± 0.19) × 10^7 1/M for $-COO^-$ SAMs, (7.23 ± 0.21) × 10^7 1/M for −OH SAMs, (5.12 ± 0.25) × 10^7 1/M for $-NH_3^+$ SAMs, and (4.93 ± 0.08) × 10^7 1/M for $-CH_3$ SAMs. ANOVA analysis indicated significant differences between these values ($p < 0.05$), except for $-NH_3^+$ and $-CH_3$ SAMs, whose values were the same.

Using the Biacore X SPR, rTp0483 was injected and adsorbed onto $-COO^-$ SAMs followed by BSA in order to block any uncoated area against nonspecific adsorption. This was followed by the injection and adsorption of FN at a range of concentrations detailed previously. The resulting adsorption sensorgrams were employed to model the kinetics of FN adsorption onto rTp0483. A bivalent analyte model was found to fit best the adsorption behavior of FN onto rTp0483 immobilized on $-COO^-$ SAMs. χ^2 values for the bivalent analyte model were 4.0 RU and 4.8 RU for the concentrations of rTp0483 studied, while noise deviated from 0 RU up to 15 RU compared to experimental data. The experimental results of FN adsorption onto rTp0483 immobilized on $-COO^-$ surfaces along with the model fit are shown in Figure 3. The corresponding values for K_{A1} and K_{A2} are included in Table 2. The K_{A1} was found to be slightly higher with 5 μg rTp0483/mL adsorbed to the surface ((1.53 ± 0.13) × 10^9 1/M) compared to the value with 20 μg rTp0483/mL adsorbed to the surface ((1.03 ± 0.08) × 10^9 1/M). However, the K_{A2} for FN adsorption to rTp0483 was higher when 20 μg rTp0483/mL was adsorbed to the surface ((4.03 ± 0.47) × 10^{-2} 1/RU) compared to the value when 5 μg rTp0483/mL was adsorbed ((2.25 ± 0.21) × 10^{-2} 1/RU). The second reaction was expressed as a function of surface mass density rather than concentration because it is purely a surface reaction. The

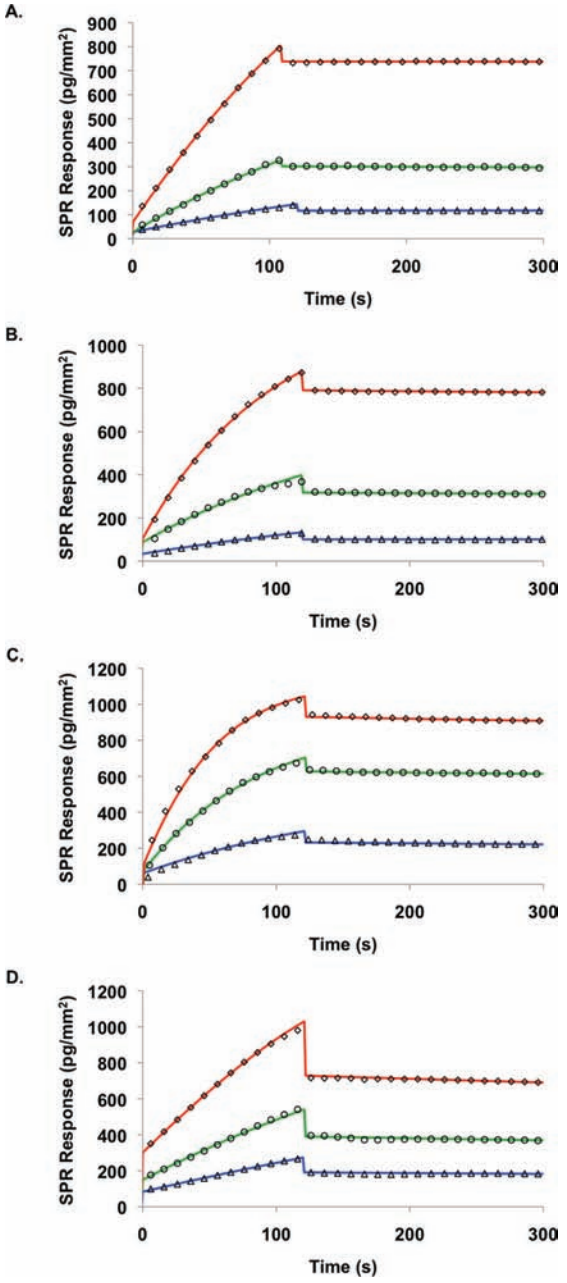


Figure 2. 1:1 Langmuir binding with mass transport limitations for rTp0483 adsorption onto SAMs at 5 (Δ), 10 (○), and 20 (◇) μg rTp0483/mL with surfaces functionalized with (A) $-COO^-$, (B) −OH, (C) $-CH_3$, and (D) $-NH_3^+$. Solid lines are predicted fits based on 1:1 Langmuir binding with mass transport limitations for 5 (blue line), 10 (green line), and 20 (red line) μg rTp0483/mL.

Table 1. Kinetic Constants for 1:1 Langmuir Binding with Mass Transport Limitations for rTp0483 Binding on Functionalized SAMs[c]

SAM type	K_A (1/M)[a]	χ^2 (RU)[b]
$-COO^-$	(13.10 ± 0.19) × 10^7	2.5
−OH	(7.23 ± 0.21) × 10^7	2.4
$-CH_3$	(4.93 ± 0.08) × 10^7	3.7
$-NH_3^+$	(5.12 ± 0.25) × 10^7	4.7

[a] K_A, affinity constant. [b] χ^2, goodness of fit. [c] K_A was significantly different between surfaces ($p < 0.05$) except for $-CH_3$ and NH_3^+, which were the same ($n = 3$).

dx.doi.org/10.1021/bc200436x | Bioconjugate Chem. 2012, 23, 184–195

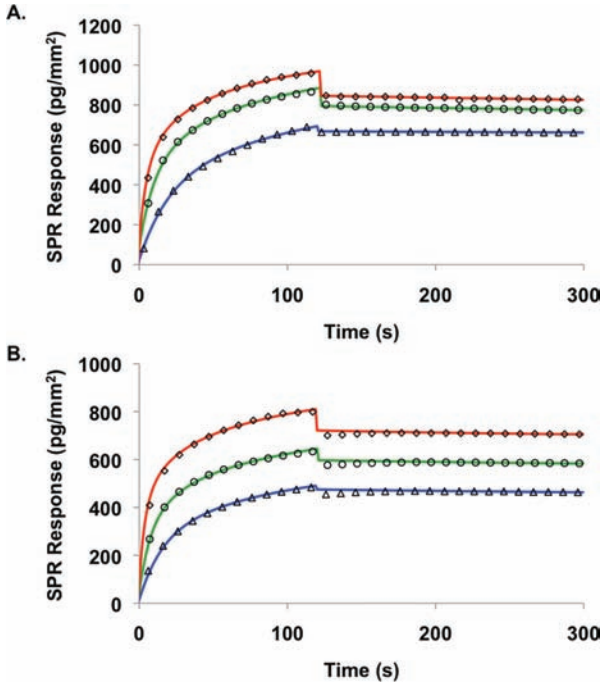


Figure 3. Bivalent FN binding to adsorbed rTp0483 on $-COO^-$ SAMs at 10 (Δ), 20 (○), and 40 (◇) μg FN/mL with (A) 5 μg rTp0483/mL and (B) 20 μg rTp0483/mL rTp0483 adsorbed. Solid lines are predicted fits based on a bivalent analyte model for 10 (blue line), 20 (green line), and 40 (red line) μg FN/mL.

Table 2. Kinetic Constants for Bivalent FN Binding to rTp0483 on $-COO^-$ SAMs[c]

rTp0483 (μg/mL)	K_{A1} (1/M)[a]	K_{A2} (1/RU)[b]	χ^2 (RU)
5	$(1.53 \pm 0.13) \times 10^9$	$(2.25 \pm 0.21) \times 10^2$	4.8
20	$(1.03 \pm 0.08) \times 10^9$	$(4.03 \pm 0.47) \times 10^2$	4.0

[a] K_{A1}, affinity constant for reaction 1. [b] K_{A2}, affinity constant for reaction 2. [c] K_{A1} and K_{A2} were significantly different between 5 and 20 μg/mL adsorbed rTp0483 ($p < 0.05$) ($n = 3$).

dissociation constants (K_{D1}) were calculated by taking the inverse of the first K_A value at each concentration; for 5 μg rTp0483/mL, the K_{D1} was 0.65 ± 0.05 nM, and for 20 μg rTp0483/mL, the K_{D1} was 0.97 ± 0.07 nM, both of which indicate very strong interactions between rTp0483 and FN.

Adsorbed rTp0483 Dissipation Energy Analysis. The changes in dissipation energy divided by the frequency shift for adsorbed rTp0483 are shown in Figure 4. SAM terminal groups were found to have a measurable effect on the relative dissipation energy. Adsorption of rTp0483 on −OH SAMs produced the largest value ($(0.220 \pm 0.013) \times 10^{-6}$ Hz^{1-}) while adsorption of rTp0483 on $-CH_3$ SAMs produced the lowest value ($(0.105 \pm 0.011) \times 10^{-6}$ Hz^{1-}). The values for $-COO^-$ ($(0.1432 \pm 0.0085) \times 10^{-6}$ Hz^{1-}) and $-NH_3^+$ ($(0.1675 \pm 0.0035) \times 10^{-6}$ Hz^{1-}) were located between the two. ANOVA analysis indicated that the ratio of dissipation energy to frequency change for −OH SAMs was higher than those of the other three groups ($p < 0.05$), that the value for $-CH_3$ SAMs was lower than those of the other three groups ($p < 0.05$), and that the values for $-COO^-$ and $-NH_3^+$ SAMs were statistically equivalent.

AFM Imaging of Tp0483 on SAMs. AFM was employed to investigate the surface arrangement of rTp0483 on

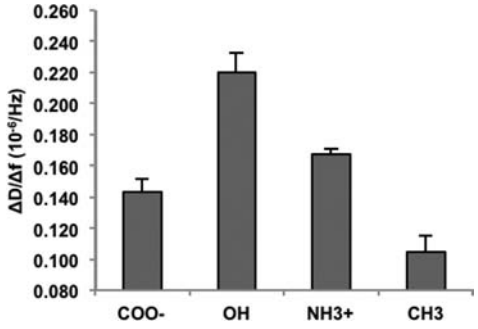


Figure 4. Ratio of QCM dissipation energy change (ΔD) to frequency shift (Δf) for rTp0483 adsorption at 100 μg rTp0483/mL on functionalized SAMs. ANOVA indicates a difference between the groups, with −OH being the highest, $-CH_3$ being the lowest, and $-COO^-$ and $-NH_3^+$ being statistically indistinguishable. Data are reported as a mean ($n = 3$) for all sample groups, with error bars representing standard error.

functionalized SAMs. Figure 5 shows representative AFM images of rTp0483 binding on each of the functionalized SAM layers and compares them to an unfunctionalized gold surface and to a model SAM ($-CH_3$). On the basis of its molecular weight, the average area occupied by a rTp0483 molecule would be expected to be considerably less than the area occupied by the observed protein aggregates. Aggregation was less pronounced on the $-COO^-$ SAM, where the protein was more evenly spread across the entire area. Also, the size of rTp0483 aggregates appeared larger on the $-NH_3^+$ SAM than on the other three.

rTp0483 Binding Site Analysis. SPR was used to probe two potential FN binding sites located on rTp0483. Polyclonal antibodies were raised against two amino acid sequences of rTp0483, which were predicted to be surface-exposed and used to determine if they play a role in FN binding to rTp0483. Antibody binding onto rTp0483 adsorbed on $-CH_3$, −OH, and $-NH_3^+$ SAMs was indistinguishable from binding to the respective SAMs in the absence of protein, indicating that the targets were inaccessible when bound on these surfaces (results not shown). When considering the $-COO^-$ SAM, significantly more of both antibodies bound to the adsorbed rTp0483 than directly to the unmodified surface ($p < 0.05$).

Figure 6A shows that, when adsorbed onto rTp0483, FN significantly decreased the binding of both antibodies ($p < 0.05$). The binding of anti-Tp0483#1 decreased from 540 ± 28 pg/mm² to 341 ± 19 pg/mm², and anti-Tp0483#2 decreased from 465 ± 49 pg/mm² to 204 ± 16 pg/mm².

Figure 6B shows that when adsorbed rTp0483 on the $-COO^-$ surface was blocked with anti-Tp0483#1 or anti-Tp0483#2, FN adsorption was significantly reduced ($p < 0.05$). FN originally bound to rTp0483 at 846 ± 40 pg/mm², which decreased to 373 ± 71 pg/mm² in the presence of anti-Tp0483#1 and to 270 ± 73 pg/mm² in the presence of anti-Tp0483#2.

Figure 6C shows the results of blocking of FN, with the peptide sequences corresponding to the selected antibodies. Binding of FN blocked with D1 was indistinguishable from FN alone (92% ± 10%). D2 was shown to have a measurable effect on FN binding, reducing FN binding to 88.0% ± 4.5% of FN alone ($p < 0.05$). No inhibition of FN binding was observed for either negative control (A3, 101.9% ± 7.7%; P1, 110% ± 12%).

FN Binding Domain Analysis. Figure 7 shows a comparison of binding of selected molecules to adsorbed FN

dx.doi.org/10.1021/bc200436x | Bioconjugate Chem. 2012, 23, 184–195

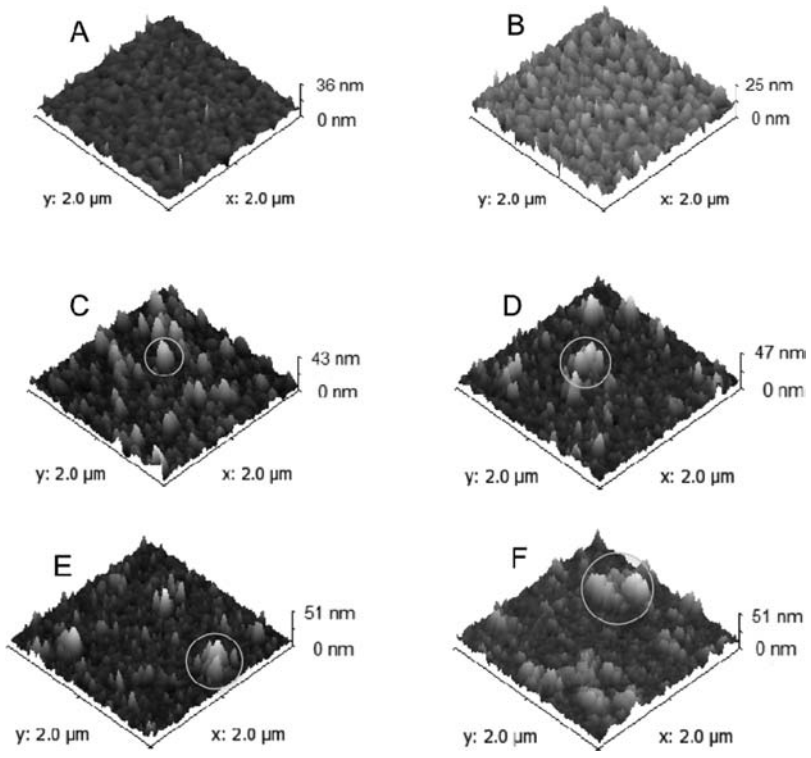


Figure 5. AFM comparison of gold, a model $-CH_3$ SAM, and 10 μg rTp0483/mL coated SAMs. (A) Unmodified gold surface; (B) model SAM ($-CH_3$); (C) rTp0483 on $-COO^-$ SAM; (D) rTp0483 on $-CH_3$ SAM; (E) rTp0483 on $-OH$ SAM; and (F) rTp0483 on $-NH_3^+$ SAM. Representative areas with aggregated proteins are noted.

or rTp0483+FN on $-COO^-$ SAMs. The difference in heparin binding was not statistically significant on FN (61.3 ± 7.0 pg/mm^2) and rTp0483+FN (25 ± 13 pg/mm^2). Binding of anti-RGD antibody on FN (540 ± 72 pg/mm^2) was significantly higher than that on rTp0483+FN (267 ± 46 pg/mm^2) ($p < 0.05$). Binding of gelatin on FN (940 ± 120 pg/mm^2) was significantly greater than that on rTp0483+FN (211 ± 12 pg/mm^2) ($p < 0.05$).

Figure 8 shows the binding of FN that had been preincubated with anti-RGD and alone to rTp0483 on $-COO^-$ SAMs. The surface mass density bound was 91 ± 25 and 47 ± 33 pg/mm^2 for FN with 20 μg/mL and 50 μg/mL anti-RGD, respectively. The amount of FN alone that bound was 282 ± 15 pg/mm^2. ANOVA indicated that when blocked with anti-RGD at either ratio, FN binding was significantly reduced ($p < 0.05$), suggesting the involvement of the RGD peptide sequence in rTp0483 binding. The same test indicated that the difference in binding between the two blocking concentrations was negligible.

DISCUSSION

This work sets out to investigate the interactions between the recombinant protein fragment rTp0483 and human plasma FN on functionalized SAMs displaying a variety of surface chemistries with the goal of further understanding the interactions in order to mimic the FN binding capacity of *T. pallidum*. The long-term goal is to reproduce the ability of *T. pallidum* to interact with host proteins such as FN with potential applications in biomaterial development or disease treatment. With this goal in mind, functionalized SAMs were selected because of their versatility in biocompatibility characterization and the attractiveness of their uniform surface chemistry, stability, and ease of synthesis. Such surfaces are widely employed to analyze important factors in biocompatibility such as plasma protein binding, platelet binding and activation, and various complement and coagulation activation processes.[33−37] For this reason, physical protein adsorption onto functionalized SAMs was employed to probe the binding of FN and rTp0483.

QCM analysis indicated that all selected functionalized SAMs bound equal quantities of rTp0483, with the exception of $-COO^-$, which bound significantly more than the other groups, as seen in Figure 1A. Likewise, Figure 1B shows that adsorbed rTp0483 on $-COO^-$ SAMs bound significantly more FN than the others under the selected conditions. The rTp0483 kinetic data shown in Table 1 indicated the affinity of rTp0483 for $-COO^-$ SAMs was significantly higher than those of the other functionalized surfaces. Interestingly, under the conditions employed in the adsorption studies, rTp0483 binding on $-OH$, $-NH_3^+$, and $-CH_3$ SAMs was similar; however, a kinetic analysis revealed that the K_A was slightly higher on $-OH$ SAMs than the other two.

The apparent similarity in SPR rTp0483 binding data was primarily due to mass transport effects. When mass transport plays a significant role in an adsorption event, the process is broken down into two steps. First, the analyte moves from bulk solution to the surface, and second, the analyte binds to the surface. When mass transport is slower than binding, adsorption is limited by how quickly analyte is transported to the surface, which is the case for rTp0483 adsorption measured by SPR. The rate of mass transport can be increased above the rate of adsorption, or the rate of adsorption can be decreased below the rate of mass transport to reduce or eliminate these effects. Decreasing analyte concentration or increasing the number of surface binding sites can accomplish this goal. The sensor area of a QCM substrate is substantially larger than the

dx.doi.org/10.1021/bc200436x | *Bioconjugate Chem.* 2012, 23, 184−195

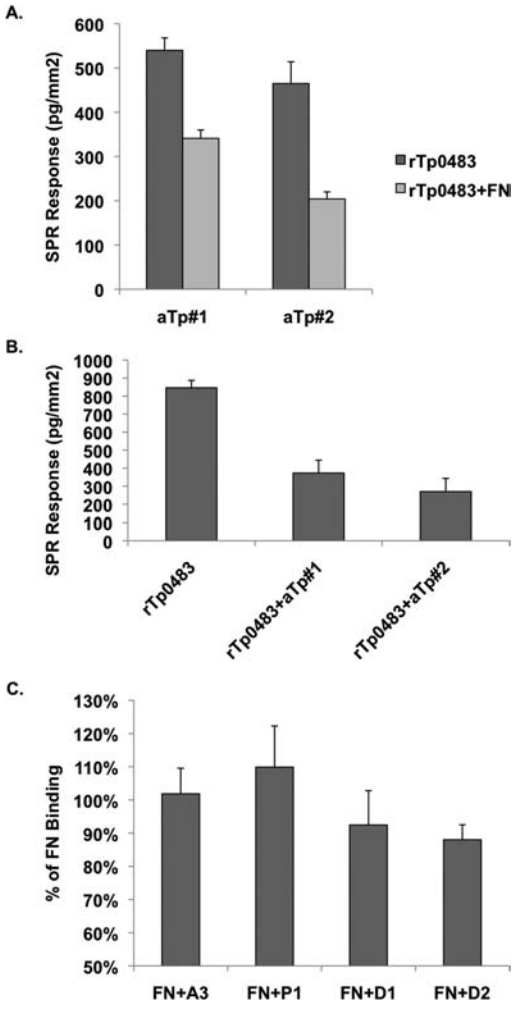


Figure 6. rTp0483 binding site studies. (A) anti-rTp0483 antibody binding on surfaces with adsorbed rTp0483 or rTp0483+FN; (B) FN binding on surfaces with adsorbed rTp0483 with and without antibodies; (C) FN binding when blocked with peptide sequences compared to FN alone on surfaces with adsorbed rTp0483. Binding of FN to rTp0483 reduced the binding of aTp#1 and aTp#2 ($p < 0.05$). Data represent mean ($n = 2$), with error bars representing standard error. Binding of FN onto rTp0483 and aTp#1 or aTp#2 was lower than binding of FN on rTp0483 alone ($p < 0.05$). Data represent mean ($n = 2$), with error bars representing standard error. Peptide D2 reduced FN binding ($p < 0.05$). Data represent mean ($n = 6$), with error bars representing standard error.

sensor area of an SPR substrate (154 mm^2 and 1.2 mm^2, respectively), thus, by moving from SPR to QCM analysis, the number of rTp0483 binding sites was greatly increased while rTp0483 concentration, injection volume, and flow rate remained unchanged. Increase in the rate of mass transport for QCM testing as a result of additional binding sites eliminated mass transport effects and allowed for a more accurate representation of binding kinetics. These results suggest that $-COO^-$ functionalized SAMs provide the best conditions for rTp0483 binding, which is likely due to the high isoelectric point (pI) of the protein. The pI of rTp0483 is 9.3, and since all studies were conducted at a physiological pH (7.4), the protein would possess a net positive charge. This in turn should lead rTp0483 to interact most strongly with the negatively charged SAM via electrostatic interactions.

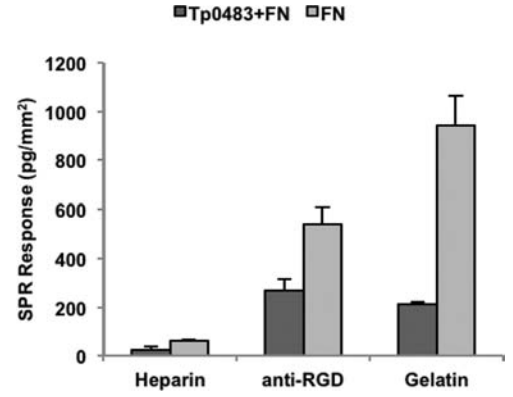


Figure 7. Binding of heparin, anti-RGD antibody, and gelatin to FN or rTp0483+FN on $-COO^-$ SAMs. Binding to Tp0483+FN was determined to be significantly less than that to FN for anti-RGD and gelatin ($p < 0.05$). Data represent mean ($n = 3$), with error bars representing standard error.

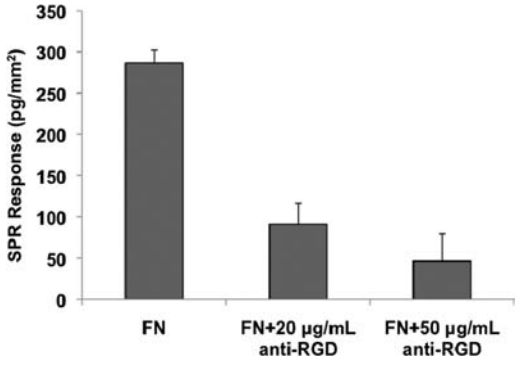


Figure 8. Comparison of the binding of FN to rTp0483 versus the binding of FN when blocked with 20 or 50 μg/mL anti-RGD. Significant inhibition was observed at a concentration of 20 μg/mL anti-RGD ($p < 0.05$). No statistical difference was noted between 20 μg/mL and 50 μg/mL anti-RGD. Data are reported as a mean, with error bars representing standard error ($n = 10$ for FN, $n = 5$ for 20 μg/mL anti-RGD, and $n = 5$ for 50 μg/mL anti-RGD).

This idea can also be seen in the dissipation energy data shown in Figure 4. Dissipation energy is a measure of the total energy lost per cycle during QCM operation.[29,30] The amount of energy lost is related to the physical properties of the material adsorbed on the quartz sensing crystal. A soft, fluid layer deforms while oscillating, which leads to high dissipation energy while a rigid, closely packed layer does not deform and as a result has low dissipation energy. rTp0483 adsorption on $-CH_3$ SAMs resulted in the lowest energy configuration, while adsorption on $-OH$ SAMs resulted in the highest energy configuration. This indicates that on a hydrophobic surface rTp0483 forms a more tightly packed layer with low fluidity, and on a hydrophilic surface rTp0483 forms a much more deformable, fluid layer. The dissipation energy for rTp0483 on $-COO^-$ and $-NH_3^+$ SAMs was similar; however, there was a clear difference in both rTp0483 and FN adsorption. This difference can be explained as a combination of hydrophobic and charge effects. The observed trend is that the dissipation energy of rTp0483 is inversely proportional to hydrophobicity. By this logic, it would follow that rTp0483 adsorption on $-COO^-$ SAMs would result in a dissipation energy value close to that of an $-OH$ SAM and slightly higher than that of an $-NH_3^+$ SAM, which in turn should be higher than that of a

dx.doi.org/10.1021/bc200436x | Bioconjugate Chem. 2012, 23, 184–195

$-CH_3$ SAM. This, however, does not take into consideration the ionic properties of $-COO^-$ and $-NH_3^+$ SAMs. rTp0483 possesses a net positive charge under experimental conditions, so it would be expected to bind more tightly to a negatively charged, hydrophilic surface than to a hydrophilic surface with no charge. By the same reasoning, binding to a positively charged surface would be looser than to an uncharged surface with similar hydrophobicity. It is also possible that this charge interaction contributes to the raised FN binding capacity of rTp0483 adsorbed onto $-COO^-$ SAMs. The observation that FN binds preferably to $-COO^-$ SAMs suggests that an interaction between the protein and the negative surface plays a role in FN binding. Specific areas of rTp0483 would be attracted to each of the functionalized SAM chemistries on the basis of charge as well as hydrophobicity. It is possible that the binding orientation of rTp0483 differs on the basis of surface chemistry and that the FN binding site is only displayed when it is bound to $-COO^-$ SAMs. Another possibility is that the FN binding site of rTp0483 is normally concealed within a fold of the protein, and when rTp0483 encounters a $-COO^-$ SAM, a change in conformation occurs, thereby exposing the binding site and allowing FN to bind.

FN binding with rTp0483 adsorbed on $-COO^-$ SAMs was analyzed at two rTp0483 concentrations in order to gain more information about the mechanism of binding. Initial analysis at 20 μg rTp0483/mL suggested a bivalent analyte mechanism as stated above. Since FN is a dimeric protein with two nearly identical units, each should be able to bind rTp0483; thus, a bivalent analyte mechanism is reasonable. Assuming this convention, one unit of a FN molecule encounters and binds rTp0483 on the surface, followed by the second unit binding to an additional rTp0483 protein to complete the AB_2-type complex. Following this study, it was of interest to determine whether with decreasing rTp0483 surface mass density there existed a point where the distance between proteins became too great for adsorbed FN to reach the second rTp0483 required for AB_2 formation. For this purpose, the concentration of rTp0483 was reduced to 5 μg rTp0483/mL and FN adsorption was evaluated. Interestingly, the K_{A1} for FN adsorption was higher for 5 μg rTp0483/mL, while K_{A2} was higher for 20 μg rTp0483/mL. FN (440 kDa) is significantly larger than rTp0483 (22 kDa), so complete coverage of the surface by rTp0483 is not necessary and, according to these results, may actually lead to a lower surface mass density of FN. rTp0483 and FN adsorption studies along with AFM analysis suggest that protein aggregation on the surface may play a role. The most significant FN binding correlated to rTp0483 adsorbed on $-COO^-$ SAMs, which also displayed the smallest and most evenly distributed aggregate formation. As the rTp0483 concentration increases, the size of the protein aggregates would also likely increase. It is possible that as the aggregate size increases, the affinity for FN of proteins within the aggregate becomes limited due to steric hindrance. This agrees with the minimal FN binding to rTp0483 adsorbed on the other SAM surfaces, which displayed larger rTp0483 aggregates when compared to $-COO^-$ SAMs. Thus, at the lower concentration of 5 μg rTp0483/mL, aggregates would be smaller, and likewise, K_{A1} for FN would be greater. Conversely, at a concentration of 20 μg rTp0483/mL, the size of rTp0483 aggregates would increase to limit the binding of a portion of rTp0483 proteins, leading to a smaller K_{A1}. The spacing of aggregates on each surface can help account for differences in K_{A2}. Once it has bound to rTp0483, FN would be stationary, and as a consequence, the chance of interacting with a second rTp0483 is limited to the range of motion of the unbound FN unit. While the initial affinity of FN for rTp0483 was less at 20 μg rTp0483/mL than at 5 μg rTp0483/mL, for the secondary binding event, the distance between aggregates becomes important. At 20 μg rTp0483/mL, the distance between aggregates is likely less than that at 5 μg rTp0483/mL, and accordingly, the chance that a bound FN is able to reach a second rTp0483 increases.

Unfortunately, the crystal structure of rTp0483 has not been elucidated; however, an estimation of its size can be made. The partial specific volume (υ) of a large number of globular proteins was determined experimentally to fall within a tight range from 0.70 to 0.75 cm^3/g.[38] Using this value as a starting point, an estimate of protein volume was made on the basis of the rTp0483 molecular weight using eq 18. Here υ was assumed to fall in the middle of the range (0.73 cm^3/g), M_W (g/mol) was the molecular weight of rTp0483, and N_A was Avogadro's number (6.02×10^{23} molecules/mol).

$$\frac{\upsilon \times 10^{24}\ \frac{A^3}{cm^3} \times M_W}{N_A} \times 0.001\ \frac{nm^3}{A^3} = (1.21 \times 10^{-3}) M_W\ \frac{m^3}{molecule} \quad (18)$$

The molecular weight of rTp0483 is 22 kDa, and the estimated volume is 27 nm^3. If surface adsorbed rTp0483 molecules are approximated as spheres, the average surface area occupied by a single rTp0483 molecule can be estimated. On the basis of this approximation, the surface area occupied by an rTp0483 molecule is 11.3 nm^2.

The shape of rTp0483 likely varies from surface to surface on the basis of dissipation energy data; however, this is not as apparent in Figure 5 because the surfaces were dried prior to imaging, which may have impacted protein shape. However, on the basis of Figure 5, it is apparent that for all surfaces the elevated areas have an area greater than 11.3 nm^2, which supports the theory that rTp0483 binds in aggregate form rather than as single proteins. The size of these protein islands was found to vary with surface chemistry. On $-NH_3^+$ SAMs, protein islands were larger compared to the other surfaces. For $-OH$ and $-CH_3$ surfaces, rTp0483 islands were smaller than for $-NH_3^+$, while the distance between each island was similar. Adsorbed rTp0483 aggregates were the smallest on $-COO^-$ SAMs and were spread evenly across the entire surface. The size of the rTp0483 aggregates can be correlated to FN binding capacity. The $-COO^-$ SAMs displayed the least aggregation and the most uniform binding of rTp0483 across the surface. Because rTp0483 molecules are more spread out, it is probable that a greater number are able to take on an ideal binding configuration. As aggregates form, nearby rTp0483 may become restricted and, thus, access to potential binding sites could be inhibited.

Two peptide sequences of rTp0483 were identified as probable binding sites, and antibodies toward each were produced. The data show that anti-Tp0483#1 and anti-Tp0483#2 were able to inhibit FN binding to rTp0483 ($p < 0.05$). When FN was added to rTp0483 prior to the antibodies, there was also a significant drop in antibody binding ($p < 0.05$). Additionally, the two antibodies only bound to rTp0483 when immobilized on $-COO^-$ SAMs, which supports the idea that the targeted sites are obscured on all SAMs except for $-COO^-$.

dx.doi.org/10.1021/bc200436x | Bioconjugate Chem. 2012, 23, 184–195

Peptides matching the proposed FN binding sites on rTp0483 were synthesized and used to block FN. Peptides were evaluated because their small size eliminates the possibility of steric effects, which could result from blocking with the larger antibodies. Only D2 resulted in a significant decrease in FN binding ($p < 0.05$). On the basis of this study, it appears that D1 did not play a direct role in FN−rTp0483 binding. It is probable that D2 plays some role; however, the observed reduction is not large enough to account for the entire binding event. The fact that significant inhibition was observed for both antibodies while little inhibition was seen for the specific peptides may indicate that the active FN binding sites of rTp0483 are located near the expressed sequences but do not coincide perfectly with them. Further characterization of the tertiary structure of Tp0483 is required to reach a conclusion.

FN domain studies were conducted to determine the regions of FN that are involved in rTp0483 binding. This was done on the basis of changes in binding to FN when it was bound to rTp0483 compared to on unmodified $-COO^-$ SAMs. In a native environment, the RGD binding site of FN enables the protein to bind to cells and cellular components throughout the body, thereby modulating cell processes such as attachment, migration, growth, and differentiation.[14] It is also thought to play some role in the binding of FN by *T. pallidum,* which helps the bacteria to infiltrate the body via interactions with cells and the ECM.[1−3,11−13] Further, it has been theorized that the adhesion of various host proteins, including FN, to the outer surface of *T. pallidum* partially contributes to the bacterium's ability to remain in the body for long periods of time between outbreaks. When FN was bound to rTp0483 adsorbed on $-COO^-$ SAMs, a 50% reduction in anti-RGD binding was observed compared to when FN was adsorbed on unmodified $-COO^-$ SAMs. To investigate further the involvement of the RGD site, an antibody specific to the cell-binding domain of FN was used to block the RGD peptide sequence in an effort to determine whether this site plays a role in rTp0483 binding. This study demonstrated a significant decrease in FN binding when blocked with 20 μg/mL anti-RGD, which agrees with previous reports that indicated a measurable inhibition of *T. pallidum* binding to FN when it was incubated with anti-RGD.[12,15−17]

The heparin-binding domains of FN were also examined, as they have been implicated previously as potential bacterial targets on FN.[19] Results did not show strong heparin binding on either of the prepared protein coatings. One possible explanation lies in the location of the major heparin-binding sites. The stronger heparin II site is very close to the central cell-binding domain (CCBD); thus, if there is an interaction in this region, it is reasonable to expect low binding on Tp0483+FN due to steric effects.[14] Low binding on FN can be accounted for on the basis of electrostatic interactions. Heparin is strongly negative, and conversely, its binding site is strongly positive. When FN was adsorbed onto $-COO^-$ SAMs, the positively charged binding site could have been attracted to the negatively charged surface, resulting in minimal binding. The balance of heparin binding can be accounted for by the weaker heparin I site; since it is located farther away from the cell-binding domain, it would remain unaffected by the binding of rTp0483 and FN.

Lastly, gelatin binding was examined. Gelatin is a denatured form of collagen; therefore, the gelatin-binding domain also serves as a binding domain for collagen. Like the CCBD and heparin-binding domains, certain species of bacteria have been shown to interact with FN through this domain.[18] Studies revealed an 80% reduction in gelatin binding when FN was bound to rTp0483 adsorbed on $-COO^-$ SAMs compared to FN bound to unmodified $-COO^-$ SAMs. This outcome suggests that the gelatin/collagen-binding domain of FN may play a role in rTp0483 binding.

CONCLUSIONS

Binding of *T. pallidum* recombinant protein fragment rTp0483 was shown to be greatest on negatively charged $-COO^-$ SAMs, while FN only bound in significant quantities to rTp0483 adsorbed on these surfaces. Kinetic analysis of rTp0483 adsorption revealed that the strength of the bond between the protein and each surface was dependent on the surface chemistry. Also, kinetic analysis of FN binding on adsorbed rTp0483 demonstrated that the surface mass density of rTp0483 affects the strength of FN binding. Decreasing the concentration of adsorbed rTp0483 from 20 to 5 μg/mL increased K_{A1} and decreased K_{A2} for FN binding. A blocking study toward the RGD sequence of FN demonstrated an involvement in rTp0483 binding, and through the use of antibodies and peptides, rTp0483 amino acids 316−333 were observed to play a role in FN binding. A QCM study examining the dissipation energy to frequency shift ratio of rTp0483 adsorption to functionalized SAMs suggested different binding configurations based on surface chemistry, while AFM analysis illustrated that rTp0483 binds as protein aggregates rather than single proteins. FN binding domain studies reinforced the importance of the RGD sequence and pointed toward the association of the collagen/gelatin-binding domain in rTp0483 binding. Through the development of an rTp0483 surface coating capable of binding FN with high affinity, it will be possible to analyze the effect of rTp0483 on various aspects of the host response with and without FN in a manner resembling that of natural Tp0483 on the surface of *T. pallidum*. In the future this may lead to a better understanding of *T. pallidum* as well as potential applications in development of materials with antigenic disguise properties.

ASSOCIATED CONTENT

Supporting Information

Figures noted in the text. This material is available free of charge via the Internet at http://pubs.acs.org.

AUTHOR INFORMATION

Corresponding Author

*Telephone: + 1 859 257 4815. Fax: 859 323 1929. E-mail address: kanderson@engr.uky.edu.

ACKNOWLEDGMENTS

We would like to thank Dr. Tonglei Li for the use of his contact angle goniometer, Jeffrey Lenihan for his protein purification contributions, and the Institute of Advanced Materials and Renewable Energy at the University of Louisville for the use of its XPS facility. This work was supported by an NSF Integrative Graduate Education and Research Traineeship (IGERT) program on Engineered Bioactive Interfaces and Devices at the University of Kentucky (DGE-0653710), by NASA (KWA and MBA), and by the Public Health Service grant AI-51334 (CEC) from the National Institutes of Health.

REFERENCES

(1) Brinkman, M. B., McGill, M. A., Pettersson, J., Rogers, A., Matejkova, P., Smajs, D., Weinstock, G. M., Norris, S. J., and Palzkill, T. (2008) A novel Treponema pallidum antigen, Tp0136, is an outer membrane protein that binds human fibronectin. *Infect. Immunol. 76*, 1848−1857.

(2) Cameron, C. E. (2003) Identification of a *Treponema pallidum* laminin-binding protein. *Infect. Immunol. 71*, 2525−2533.

(3) Cameron, C. E., Brown, E. L., Kuroiwa, J. M. Y., Schnapp, L. M., and Brouwer, N. L. (2004) *Treponema pallidum* fibronectin-binding proteins. *J. Bacteriol. 186*, 7019−7022.

(4) Cox, D. L., Luthra, A., Dunham-Ems, S., Desrosiers, D. C., Salazar, J. C., Caimano, M. J., and Radolf, J. D. (2010) Surface immunolabeling and consensus computational framework to identify candidate rare outer membrane proteins of *Treponema pallidum*. *Infect. Immunol. 78*, 5178−5194.

(5) Desrosiers, D. C., Anard, A., Luthra, A., Dunham-Ems, S. M., LeDoyt, M., Cummings, M. A. D., Eshghi, A., Cameron, C. E., Cruz, A. R., Salazar, J. C., Caimano, M. J., and Radolf, J. D. (2011) Tp0326, a Treponema pallidum β-barrel assembly machinery A (BamA) orthologue and rare outer membrane protein. *Mol. Microbiol. 80*, 1496−1515.

(6) Liu, S. Q., Wang, S. P., Wu, Y. M., Zhao, F. J., Zeng, T. B., J., Z. Y., Zhang, Q. G., and Gao, D. M. (2010) Production of proinflammatory cytokines in the human THP-1 monocyte cell line following induction by Tp0751, a recombinant protein of *Treponema pallidum*. *Sci. China: Life Sci. 53*, 229−233.

(7) Radolf, J. D. (1994) Role of outer membrane architecture in immune evasion by *Treponema pallidum* and *Borrelia burgdorferi*. *Trends Microbiol. 2*, 307−311.

(8) Salazar, J. C., Hazlett, K. R. O., and Radolf, J. D. (2002) The immune response to infection with *Treponema pallidum*, the stealth pathogen. *Microbes Infect. 4*, 1133−1140.

(9) Tomson, F. L., Conley, P. G., Norgard, M. V., and Hagman, K. E. (2007) Assessment of cell-surface exposure and vaccinogenic potentials of *Treponema pallidum* candidate outer membrane proteins. *Microbes Infect. 9*, 1267−1275.

(10) Anderson, K. V. (2000) Toll signalling pathways in the innate immune response. *Curr. Opin. Immunol. 12*, 13−19.

(11) Fitzgerald, T. J., and Repesh, L. A. (1985) Interaction of fibronectin with *Treponema pallidum*. *Genitourin. Med. 61*, 147−155.

(12) Lee, J. H., Choi, H. J., Jung, J., Lee, M. G., Lee, J. B., and Lee, K. H. (2003) Receptors for *Treponema pallidum* attachment to the surface and matrix proteins of cultured human dermal microvascular endothelial cells. *Yonsei Med. J. 44*, 371−378.

(13) Peterson, K. M., Baseman, J. B., and Alderete, J. F. (1983) *Treponema pallidum* receptor binding proteins interact with fibronectin. *J. Exp. Med. 157*, 1958−1970.

(14) Pankov, R., and Yamada, K. M. (2002) Fibronectin at a glance. *J. Cell Sci. 115*, 3861−3863.

(15) Ouaissi, M. A. (1988) Role of the RGD sequence in parasite adhesion to host cells. *Parasitol. Today 4*, 169−173.

(16) Thomas, D. D., Baseman, J. B., and Alderete, J. F. (1985) Fibronectin mediates Treponema pallidum cytadherence through recognition of fibronectin cell-binding domain. *J. Exp. Med. 161*, 514−525.

(17) Thomas, D. D., Baseman, J. B., and Alderete, J. F. (1985) Fibronectin tetrapeptide is target for syphilis spirochete cytoadherence. *J. Exp. Med. 162*, 1715−1719.

(18) Atkin, K. E., Brentnall, A. S., Harris, G., Bingham, R. J., Erat, M. C., Millard, C. J., Schwarz-Linek, U., Staunton, D., Vakonakis, I., Campbell, I. D., and Potts, J. R. (2010) The streptococcal binding site in the gelatin-binding domain of fibronectin is consistent with a non-linear arrangement of modules. *J. Biol. Chem. 285*, 36977−36983.

(19) van der Flier, M., Chhun, N., Wizemann, T. M., Min, J., McCarthy, J. B., and Tuomanen, E. I. (1995) Adherence of *Streptococcus pneumoniae* to immobilized fibronectin. *Infect. Immun. 63*, 4317−4322.

(20) Cameron, C. E., Lukehart, S. A., Castro, C., Molini, B., Godornes, C., and Van Voorhis, W. C. (2000) Opsonic potential, protective capacity, and sequence conservation of the Treponema pallidum subspecies pallidum Tp92. *J. Infect. Dis. 181*, 1401−1413.

(21) Zhang, H. H., Blanco, D. R., Exner, M. M., Shang, E. S., Champion, C. I., Phillips, M. L., Miller, J. N., and Lovett, M. A. (1999) Renaturation of recombinant *Treponema pallidum* rare outer membrane protein 1 into a trimeric, hydrophobic, and porin-active conformation. *J. Bacteriol. 181*, 7168−7175.

(22) Chung, Y. C., Chiu, Y. H., Wu., Y. W., and Tao, Y. T. (2005) Self-assembled biomimetic monolayers using phospholipid-containing disulfides. *Biomaterials 26*, 2313−2324.

(23) Keselowsky, B. G., Collard, D. M., and Garcia, A. J. (2003) Surface chemistry modulates fibronectin conformation and directs integrin binding and specificity to control cell adhesion. *J. Biomed. Mater. Res., Part A 66A*, 247−259.

(24) Ling, J. C., and Chuang, W. H. (2000) Synthesis, surface characterization, and platelet reactivity evaluation for the self-assembled monolayer of alkanethiol with sulfonic acid functionality. *J. Biomed. Mater. Res. 51*, 413−423.

(25) Michael, K. E., Vernekar, V. N., Keslowsky, B. G., Meredith, J. C., Latour, R. A., and Garcia, A. J. (2003) Adsorption-induced conformational changes in fibronectin due to interactions with well-defined surface chemistries. *Langmuir 19*, 8033−8040.

(26) Nuzzo, R. G., Dubois, L. H., and Allara, D. L. (1990) Fundamental studies of microscopic wetting on organic surfaces. 1. Formation and structural characerization of self-consistent series of polyfunctional organic monolayers. *J. Am. Chem. Soc. 112*, 558−569.

(27) Sperling, C., Schweiss, R. B., Streller, U., and Werner, C. (2005) *In vitro* hemocompatibility of self-assembled monolayers displaying various functional groups. *Biomaterials 26*, 6547−6557.

(28) Tanahashi, M., and Matsuda, T. (1997) Surface functional group dependence on apatite formation on self-assembled monolayers in a simulated body fluid. *J. Biomed. Mater. Res. 34*, 305−315.

(29) Dixon, M. C. (2008) Quartz crystal microbalance with dissipation monitoring: Enabling real-time characterization of biological materials and their interactions. *J. Biomol. Tech. 19*, 151−158.

(30) Hemmersam, A. G., Rechendorff, K., Foss, M., Sutherland, D. S., and Besenbacher, F. (2008) Fibronectin adsorption on gold, Ti-, and Ta-oxide investigated by QCM-D and RSA modelling. *J. Colloid Interface Sci. 320*, 110−116.

(31) Stenberg, E., Persson, B. R. H., and Urbaniczky, C. (1991) Quantitative determination of surface concentration of protein with surface plasmon resonance by using radiolabeled proteins. *Colloids Interface Sci. 143*, 513−526.

(32) Biacore AB. (1997) *BIAevaluation 3.0 Software Handbook*; Uppsala, Sweden.

(33) Benesch, J., Svedhem, S., Svensson, S. C. T., Valiokas, R., Liedberg, B., and Tengvall, P. (2001) Protein adsorption to oligo(ethylene glycol) self-assembled monolayers: Experiments with fibrinogen, heparinized plasma, and serum. *J. Biomater. Sci., Polym. Ed. 12*, 581−597.

(34) Fischer, M., Sperling, C., and Werner, C. (2010) Synergistic effect of hydrophobic and anionic surface groups triggers blood coagulation *in vitro*. *J. Mater. Sci.: Mater. Med. 21*, 931−937.

(35) Lestelius, M., Liedberg, B., and Tengvall, P. (1997) *In vitro* plasma protein adsorption on w-functionalized alkanethiolate self-assembled monolayers. *Langmuir 13*, 5900−5908.

(36) Rodrigues, S. N., Goncalves, I. C., Martins, M. C. L., Barbosa, M. A., and Ratner, B. D. (2006) Fibrinogen adsorption, platelet adhesion and activation on mixed hydroxyl-/methyl-terminated self-assembled monolayers. *Biomaterials 27*, 5357−5367.

(37) Sperling, C., Fischer, M., Maitz, M. F., and Werner, C. (2009) Blood coagulation on biomaterials requires the combination of distinct activation processes. *Biomaterials 30*, 4447−4456.

(38) Harpaz, Y., Gerstein, M., and Chothia, C. (1994) Volume changes on protein folding. *Structure 15*, 641−649.

Bioconjugate Chemistry

Article

pubs.acs.org/bc

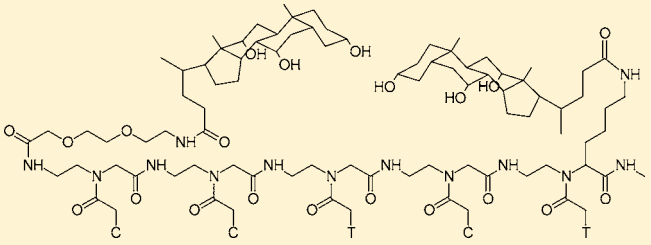
Nanomolar Cellular Antisense Activity of Peptide Nucleic Acid (PNA) Cholic Acid ("Umbrella") and Cholesterol Conjugates Delivered by Cationic Lipids

Takehiko Shiraishi[#] and Peter E. Nielsen*[,#,‡]

[#]Department of Cellular and Molecular Medicine and [‡]Department of Molecular Drug Research, Faculty of Health and Medical Sciences, University of Copenhagen, The Panum Institute, Blegdamsvej 3c, 2200 Copenhagen N, Denmark

Supporting Information

ABSTRACT: Limited cellular uptake and low bioavailability of peptide nucleic acids (PNAs) have restricted widespread use of PNAs as antisense/antigene agents for cells in culture and not least for *in vivo* applications. We now report the synthesis and cellular antisense activity in cultured HeLa pLuc705 cells of cholesterol and cholic acid ("umbrella") derivatives of splice correction antisense PNA oligomers. While the conjugates alone were practically inactive up to 1 μM, their activity was dramatically improved when delivered by a cationic lipid transfection agent (LipofectAMINE2000). In particular, PNAs, conjugated to cholesterol through an ester hemisuccinate linker or to cholic acid, exhibited low nanomolar activity (EC_{50} ~ 25 nM). Excellent sequence specificity was retained, as mismatch PNA conjugates did not show any significant antisense activity. Furthermore, we show that increasing the transfection volume improved transfection efficiency, suggesting that accumulation (condensation) of the PNA/lipid complex on the cellular surface is part of the uptake mechanism. These results provide a novel, simple method for very efficient cellular delivery of PNA oligomers, especially using PNA−cholic acid conjugates which, in contrast to PNA−cholesterol conjugates, exhibit sufficient water solubility. The results also question the generality of using cholic acid "umbrella" derivatives as a delivery modality for antisense oligomers.



INTRODUCTION

It is generally accepted that the full potential of antisense and RNA interference agents is still unleashed due to suboptimal delivery technologies resulting in poor bioavailability at the intracellular nucleic acid target.[1] This is also the case concerning peptide nucleic acids (PNAs),[2] despite the recent progress exploiting cell penetrating peptides[3] and polyethylene imine conjugates.[4]

However, these methods typically result in only micromolar activity even when boosting the activity with endosomolytic agents, such as chloroquine[5,6] or photodynamic dyes,[7] whereas almost 1000-fold higher activity can be achieved via delivery of analogous anionic PNA−peptidephosphonate conjugates by cationic liposomes (Lipofectamine2000), constituting the most effective PNA delivery system at present.[8]

The ideal molecules for cellular uptake are overall hydrophilic but exhibit transient lipophilicity, i.e., they can exist in equilibrium between an overall hydrophilic and an overall lipophilic state. For small molecules, this is often achieved by amine protonation equilibrium, and for larger molecules, including oligonucleotides the amphipatic properties of cholic acid has been exploited in order to create "umbrella" molecules, in which the hydrophilic surface of the cholic acid ligands is facing the solvent in an aqueous environment, whereas the hydrophobic surface is facing the lipids when traversing the cellular membrane.[9,10] In an attempt to exploit this approach, we have synthesized cholic acid umbrella derivatives of active antisense PNAs. Furthermore, inspired by the progress in the oligonucleotide siRNA field using cholesterol conjugates,[11−14] we also synthesized PNAs conjugated to a cholesterol moiety via two different linkers. The cellular activity of the PNA conjugates was determined by using the well established HeLa pLuc 705 cell culture assay,[15] in which nuclear antisense activity via targeting a cryptic splice site of the engineered luciferase gene is sensitively measured. Unexpectedly, we find that the umbrella cholic acid PNA conjugates were practically inactive up to 1 μM. However, their activity was very dramatically improved when delivered by a cationic lipid transfection agent (LipofectAMINE2000). In particular, PNAs, conjugated to cholesterol through an ester hemisuccinate linker or to cholic acid, exhibited low nanomolar antisense activity (EC_{50} ~ 25 nM). These results provide a novel, simple method for very efficient cellular delivery of PNA oligomers, especially using PNA−cholic acid conjugates which, in contrast to PNA−cholesterol conjugates, exhibit sufficient water solubility.

Received: August 23, 2011
Revised: January 12, 2012
Published: January 13, 2012

 © 2012 American Chemical Society dx.doi.org/10.1021/bc200460t | *Bioconjugate Chem.* 2012, 23, 196−202

Table 1. PNA Oligomers

no.	name	sequence[a]	mass[e]	purity (%)
2389	Naked PNA	H-CCTCTTACCTCAGTTACA-NH_2	4766 (4765)	95
2964	Cholate-PNA	Cholic acid-CCTCTTACCTCAGTTACA-NH_2	5156 (5158)	98
3086	$(Cholate)_2$-PNA	Cholic acid-Lys(Cholic acid)-CCTCTTACCTCAGTTACA-NH_2	5675 (5674)	98
3087	$(Cholate)_3$-PNA	Cholic acid-[Lys(Cholic acid)]$_2$-CCTCTTACCTCAGTTACA-NH_2	6190 (6192)	95
3088	$(Cholate)_4$-PNA	Cholic acid-[Lys(Cholic acid)]$_3$-CCTCTTACCTCAGTTACA-NH_2	6709 (6710)	90
2974	Cholate-PNA$(Cholate)_3$	Cholic acid-eg1[b]-CCTCT$_{Lys(Chol)}$[c]TACCT$_{Lys(Chol)}$CA GTT$_{Lys(Chol)}$ACA-NH_2	6341 (6337)	95
2977	Chol-hs-PNA	Cholesteryl hemisuccinate-CCTCTTACCTCAGTTACA-NH_2	5234 (5234)	98
2978	Chol-cbm-PNA	Cholesteryl carbamate-CCTCTTACCTCAGTTACA-NH_2	5177 (5178)	98
3587	Chol-hs-PNA-MM[d]	Cholesteryl hemisuccinate-CCTCT**G**ACCTCA**T**TTACA-NH_2	5241 (5235)	98
3588	Cholate-PNA-MM	Cholic acid-CCTCT**G**ACCTCA**T**TTACA-NH_2	5153 (5157)	95

[a]The sequences of the PNAs are written from N-terminal to C-terminal end. Cholic acid and Cholesterol derivatives were conjugated to N-terminal of the PNA (or Lys) and the ε-amino group of a lysine residue. [b]eg1, ethylene glycol linker (8-amino-3,6-dioxaoctanoic acid). [c]Cholic acid was conjugated to the ε-amino group of the lysine backbone thymine residue (T_{Lys}).[17] [d]MM, mismatch PNA sequence (the two mismatches are indicated in bold). [e]Found (Calculated).

MATERIALS AND METHODS

PNA Synthesis. The sequences of the PNAs are listed in Table 1. PNA synthesis was carried out by the *tBoc* method as reported previously.[16] Cholic acid and cholesterol conjugates were obtained by solution HBTU coupling of the corresponding carboxylic acid derivatives to PNA at the N-terminal and/or the ε-amino group of lysine residues in the PNA backbone: 3 mg HBTU dissolved in 50 μL DMF was mixed with 5 mg cholic acid (or cholestrylhemisuccintate) dissolved in 200 μL DMSO and to this mixture was added 10 μL DIEA. After 30 min incubation at RT, 2 mg PNA2389 dissolved in 200 μL DMSO was added and the reaction is allowed to proceed overnight. The cholesterol carbamate conjugate was synthesized by reacting 1.2 mg PNA2389 dissolved in 50 μL DMSO in solution with 2.8 mg cholesteryl chloroformate dissolved in 50 μL DMSO and adding 6 μL DIEA in 100 μL DMF. The mixture was incubated at RT overnight. The resulting PNA conjugates were HPLC purified and characterized by MALDI-TOF mass spectrometry (see Supporting Information). The PNAs were lyophilized and stored at 4 °C until use. The PNAs containing thymines with lysine modified backbone were synthesized as previously described.[17]

Cell Culture. HeLa pLuc705 cells[15] were purchased from GENE TOOLS (USA). Cells were grown in RPMI1640 medium (Sigma) supplemented with 10% fetal bovine serum (FBS, Sigma), 1% glutamax (Gibco), 100 U/mL penicillin, and 100 μg/mL streptomycin (Gibco) at 37 °C in humidified air with 5% CO_2. The cells were seeded on the plate 16−24 h before treatment at a cell density of 1.2×10^4 cells/well or 7.2×10^4 cells/well for 96 well plates and 24 well plates, respectively.

PNA Transfection. For the unaided delivery, the cells (replated in the plate the day before transfection) were incubated in OPTI-MEM (Invitrogen) containing PNA for 4 h. Then, the cells were incubated further for 20 h after supplementing an equal volume of growth medium containing 20% FBS and subjected to further analysis. For cationic lipid mediated transfection, the cells were incubated with the PNA/lipid complex in RPMI (10% FBS, 1% glutamax) for 24 h and subjected to further analysis. The PNA−lipid complex was formed by incubating 30 μL of PNA solution (in water) with 30 μL of diluted LipofectAMINE2000 (LFA2000, Invitrogen) in OPTI-MEM for 10 min at room temperature. The resulting lipoplex solution was mixed with 0.24 mL of RPMI1640 (10% FBS, 1% glutamax) and used for transfection. For DNA-assisted PNA transfection, PNA/DNA heteroduplexes were formed as published previously[8] using PNA2389 and cDNA (5′-AATATGTAACTGAGGTA-3′).

Luciferase Assay. Luciferase activity of the cells was measured by using the Bright-Glo Luciferase assay system (Promega) according to the manufacturer's instructions. Luminescent readings from 96 well plate formats were background subtracted and presented as relative light units (RLU/well). For the 24 well plate format, the cells were lyzed with Passive Lysis buffer (Promega) and subjected to the luciferase assay. Luminescent readings from the 24-well format were background-subtracted and normalized by protein concentrations, and are presented as RLU/mg protein. Protein concentrations were determined by the BCA protein assay (Pierce) according to the manufacturer's instruction.

Cytotoxicity Test. The cells in 96 well plates were transfected and assayed for viability by using the CellTiter 96 Aqueous Non-Radioactive Cell Proliferation Assay (MTS-assay, Promega) according to the manufacturer's instructions. Alternatively, cell lysates in passive lysis buffer (from the luciferase assay) were analyzed for ATP content by using the CellTiter-Glo Luminescent cell viability assay (Promega) according to the manufacturer's instructions. The values are presented as relative cellular viability (the value from non-PNA-treated cells was set as 100%).

RT-PCR. Total RNA was extracted from cell lysates in passive lysis buffer using the RNeasy Mini kit (Qiagen) according to the manufacturer's instruction. Four nanograms of total RNA was used for each RT-PCR reaction (20 μL/reaction) by using the OneStep RT-PCR kit (Qiagen). Primers for the RT-PCR were as follows: 5′-TTGATATGTG-GATTTCGAGTCGTC-3′ (forward primer) and 5′-TGTCAATCAGAGTGC-TTTTGGCG-3′ (reverse primer). The RT-PCR program was as follows: [(55 °C, 35 min) × 1 cycle, (95 °C, 15 min) × 1 cycle, (94 °C, 0.5 min; 55 °C, 0.5 min; 72 °C, 0.5 min) × 26−28 cycles]. RT-PCR DNA products were analyzed on a 2% agarose gel with 1× TBE buffer and visualized by ethidium bromide staining. Gel images were captured by *ImageMaster* (Pharmacia Biotech) and analyzed by *UN-SCAN-IT* software (Silk Scientific Corporation).

RESULTS

A series of cholic acid PNA conjugates were synthesized based on a PNA sequence that in a variety of delivery contexts has shown excellent splice correction antisense activity[4−8] in the

dx.doi.org/10.1021/bc200460t | *Bioconjugate Chem.* 2012, 23, 196−202

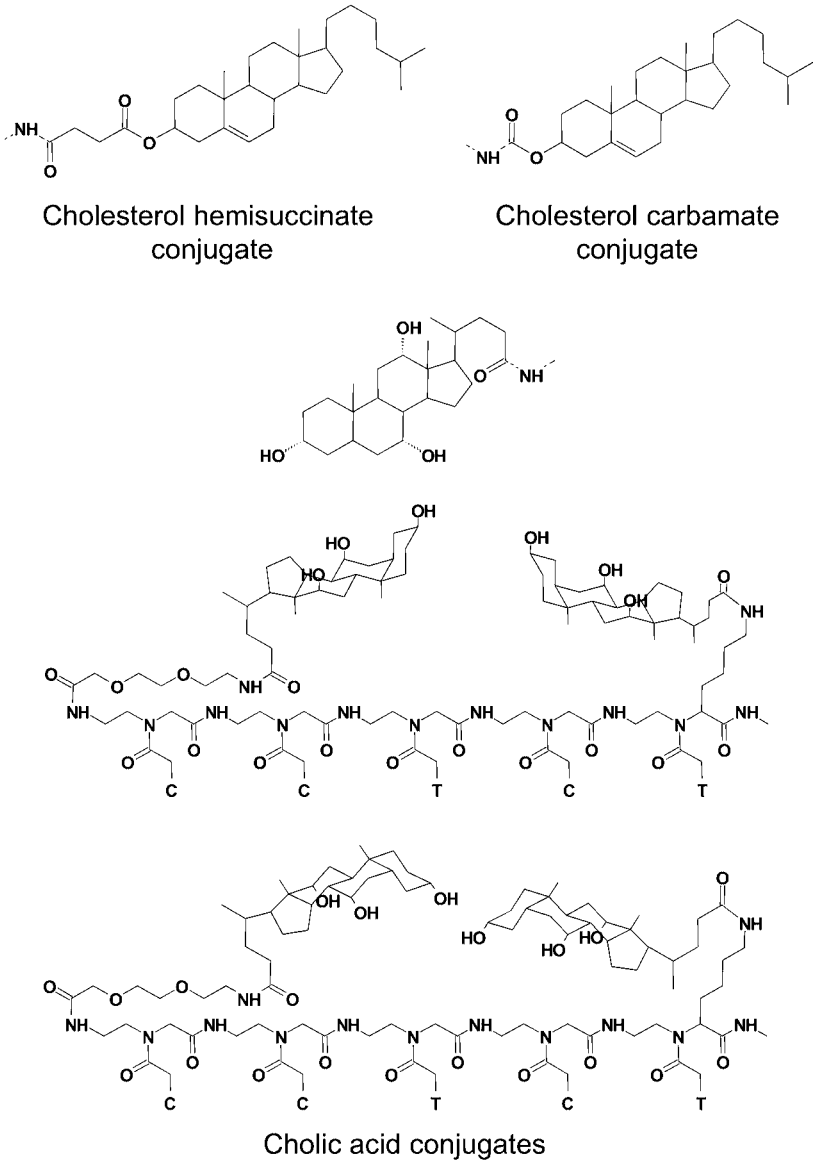


Figure 1. Chemical structures of the lipophilic conjugates used in this study. Cholic acid was conjugated to the N-terminal amine and to the ε-amino groups of PNA backbone lysines (at T-residues), and both "lipo-face in" or "lipo-face out" conformations are shown.

pLuc705 HeLa cell culture assay.[15] PNA−cholate conjugates containing one to four cholate moieties attached to the amino end of the PNA via a lysine scaffold or four cholate moieties attached along the PNA oligomer via lysine modifications in the PNA backbone (Table 1, Figure 1). Furthermore, PNA cholesterol conjugates via a hemisuccinate or a carbamate linkage at the amino terminal of the PNA were synthesized (Table 1, Figure 1). None of the PNAs showed any significant antisense activity without cationic lipids (unaided delivery) even at the highest concentration tested (1 μM) (Figure 2a), and they did not show any cellular toxicity either (Figure 3a). This very low antisense activity and by inference poor cellular uptake of the cholic acid conjugates is unexpected in view of previous reports in other systems[9,10] (see Discussion). In contrast to the unaided delivery, these PNA conjugates showed excellent antisense activity upon cationic lipid-mediated transfection (Figure 2b). This is in full analogy to our previous findings with PNA conjugated to lipophilic, polyheteroaromatic ligands,[19] but the present conjugates exhibit more than 10-fold higher efficiency. It is noteworthy that increasing the number of cholate ligands at the N-terminal had little or no effect on the activity, and the monocholate-PNA (PNA2964)) showed similar activity to the PNA with four cholate modifications distributed along the PNA (PNA2974) (having one cholic acid at the N-terminal and three cholic acids attached to in the PNA backbone). In addition, the tri- and tetra-cholate PNA conjugates showed increased cell toxicity upon lipofection (Figure 3b). Interestingly, the two simplest PNA conjugates containing a single cholic acid (PNA3588) or a cholesterol with a hemisuccinate linker (PNA3587) showed the highest antisense activity exhibiting EC_{50} ~ 25 nM, which was confirmed by directly measuring the relative amount of corrected luciferase mRNA by an RT-PCR assay (Figure 4). Finally, the antisense activity obtained with the cholate−PNA and cholesterol−PNA conjugates is several-fold higher than that obtained by PNA delivery via a cDNA carrier[18] (Figure 4). In order to ascertain that the observed effects are indeed caused by a bona fide antisense mechanism, we tested double mismatched (nucleobase interchange) PNA oligomers of the

dx.doi.org/10.1021/bc200460t | *Bioconjugate Chem.* 2012, 23, 196−202

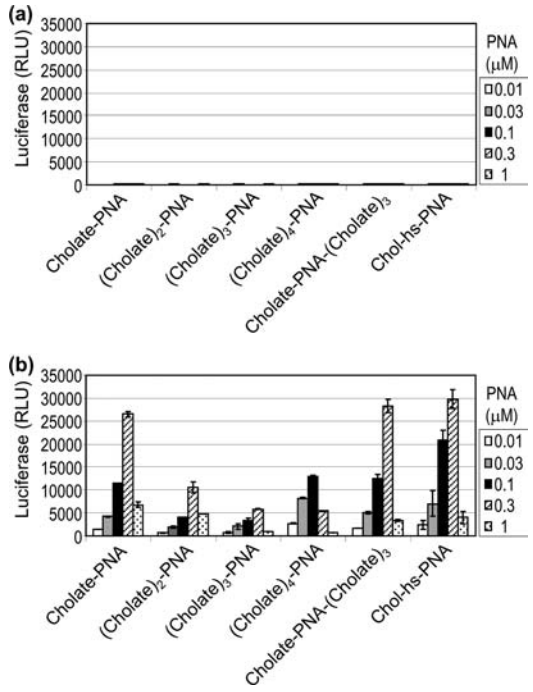


Figure 2. Cellular uptake of the PNAs conjugated with different ligands (cholesterol or a different number of cholic acids) for the transfection. HeLa pLuc705 cells were treated with the conjugates in the absence (a) or with the aid (b) of cationic lipids Lipofect-AMINE2000 for 24 h and subjected to the luciferase assay. The values represent the mean ± SD of three experiments.

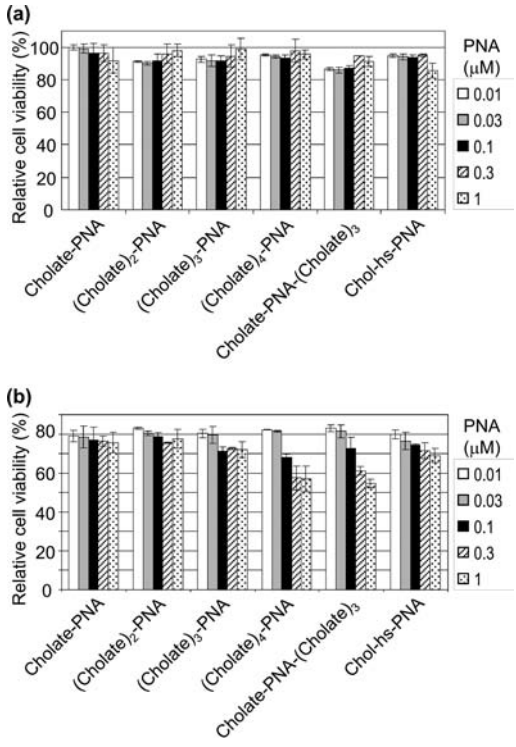


Figure 3. Comparison of the cellular viability of the cells treated with PNAs conjugated with different ligands (cholesterol or a different number of cholic acids). HeLa pLuc705 cells were treated with the conjugates in the absence (a) or with the aid (b) of cationic lipids LipofectAMINE2000 for 24 h and subjected to the cellular viability test using MTS-assay (Promega). The values were normalized to the value of nontreated samples and represented as mean ± SD of three experiments.

cholate and cholesterol hemisuccinate PNAs, and these showed practically no luciferase activating effect (Figure 5).

Finally, we also tested a cholesterol derivative conjugated through a carbamate linker instead of the hemisuccinate linker, and this showed significantly lower activity (aprrox. 4-fold; Supporting Information Figure 1). Whether this difference is due to the stability of the linker (the ester of the hemisuccinate is susceptible to esterase cleavage) remains to be seen.

Cellular delivery via cationic lipid carriers involves the formation of lipoplexes in the form of liposomes, aggregates, or nanoparticles with positive zeta potential which have affinity for the negatively charged cell surface. Thus, the lipoplexes could up-concentrate on the cells, and thus, dose−response dependence relations would correlate with the amount of lipoplexes (in a proportionally larger volume) rather than with concentration *per se*. In order to address this issue, we tested the effect of different volumes of the transfection solution in a 10-fold range at different PNA concentrations (3−300 nM by varying the amount of the PNA while using a fixed concentration of cationic lipids) (Figure 6). As only the volume is changed and the PNAs have no charge, the lipoplex concentration and structure are expected to be virtually unchanged in these experiments. The results clearly showed that PNA antisense activity increased in a PNA dose-dependent manner for all transfection volumes (Figure 6a), but also showed that increased volume (hence increasing the total amount of PNA lipoplex/well) resulted in higher antisense activity with an almost linear relationship up to 4 relative volumes (the leveling off could be due to surface saturation), while an increase of toxicity with increasing volume was only significant at the highest PNA concentration (300 nM). These results indicate that a large fraction of the PNA lipoplexes accumulated onto the cell membrane surface (analogous observations have been reported for PNA−CPP conjugates[20]). Thus, with cationic transfection reagents the efficacy of the reagent will be a relative measure dependent on the specific transfection conditions. Nonetheless, the present method appears far superior to using, e.g., cell penetrating peptides for delivery of PNA oligomers to eukaryotic cells in culture, for which in the same pLuc705 HeLa cell system under comparable conditions more than 10-fold higher PNA-CPP concentrations ($EC_{50} \sim 1\ \mu M$) are required to yield similar antisense effects.[5,7,21−23]

■ DISCUSSION AND CONCLUSIONS

The present results show that PNA oligomers conjugated to a cholic acid or cholesterol moiety and complexed with cationic lipids are very potent antisense agents in HeLa cells in culture, thereby implying that this method efficiently delivers PNA to (the nucleus of) eukaryotic cells. Notably (and disappointingly), we also find that PNA-cholic acid "umbrella" conjugates did not show any significant antisense effect in the very sensitive pLucHeLa system without lipoplexation. PNAs are charge neutral molecules and thus would be expected to constitute much less challenging cargos than, for instance, polyanionic oligonucleotides for which significantly improved penetration of synthetic phopholipid bilayers has been reported using cholic acid umbrella conjugates.[24] The pLucHeLa system directly reports biological (nuclear) effects, and we therefore consider this a much more reliable assay in terms of predicting

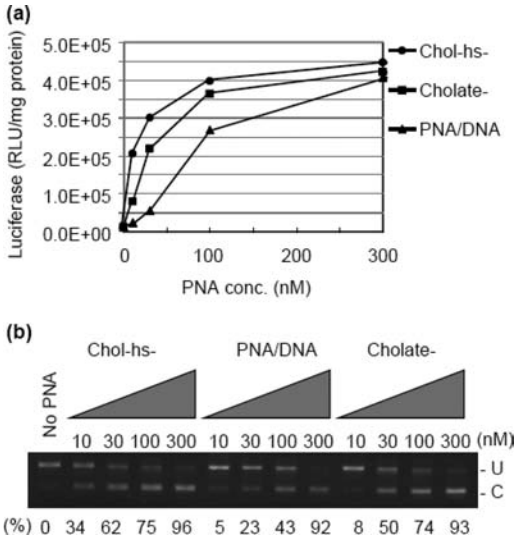


Figure 4. Comparison of the antisense activity of two PNA conjugates (PNA2977 (Chol-hs-) and PNA2964 (Cholate-)) and that of unmodified PNA delivered as PNA/DNA heteroduplex by lipofection. PNA conjugates and PNA/DNA heteroduplex were complexed with LipofectAMINE2000 and delivered to the HeLa pLuc 705 cells for 24 h. After transfection, the cells were subjected to the further analysis: (a) Luciferase activity. The values were normalized to protein concentration and represented as mean of two experiments. (b) RT-PCR analysis of the mis-splicing correction of luciferase pre-mRNA by PNA. U: fragments without correction (268 bp). C: Fragments with mis-splicing correction (142 bp). The numbers under the figure indicate the relative amount (%) of the corrected form to the sum of corrected form and uncorrected form.

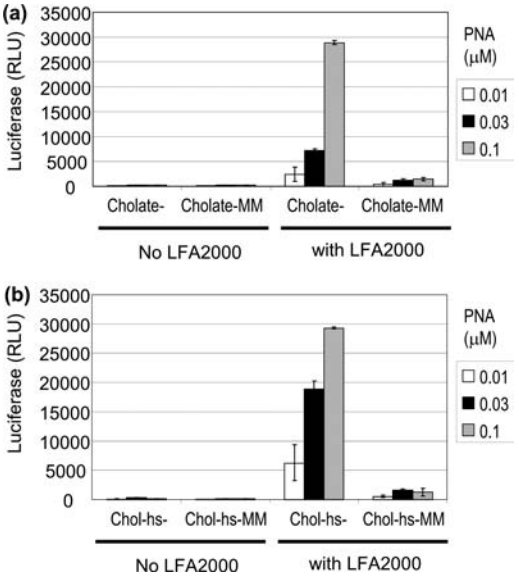


Figure 5. Comparison of two antisense PNA conjugates (PNA2977 (Chol-hs-) and PNA2964 (Cholate-)) with mismatch PNAs (PNA3587 (Chol-hs-MM) and PNA3588 (Cholate-MM)). HeLa pLuc705 cells were treated with the conjugates with the aid (a) or in the absence (b) of cationic lipids LipofectAMINE2000 for 24 h. After transfection, the cells were subjected to the luciferase analysis.

effective cellular delivery than solely relying on fluorescence techniques and synthetic lipid vesicles. Mechanistically, the umbrella effect of cholic acid should shield hydrophilic cargos through interactions with the hydrophilic face of the cholic acid,

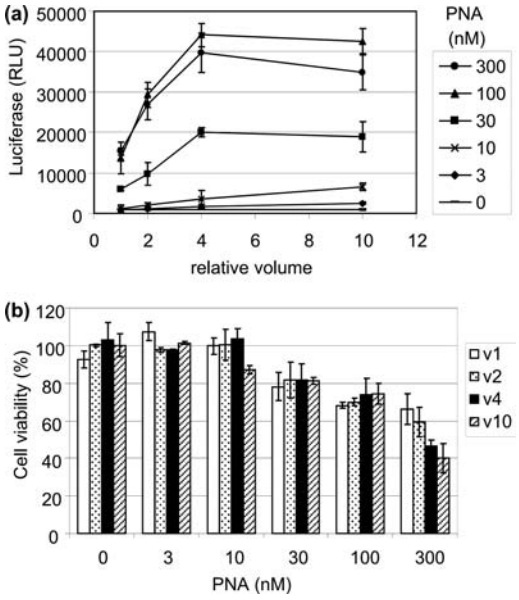


Figure 6. Effect of transfection volume for the transfection of PNA cholesterol hemisuccinate conjugate (PNA2977). The PNA conjugate (at the concentrations indicated) was complexed with fixed concentration of LipofectAMINE2000 and then mixed with growth medium for transfection. Different volumes of the growth medium containing PNA/LFA2000 complex (0.25 mL/well for a relative volume 1) was added to the HeLa pLuc 705 cells in a 24 well plate and incubated for 24 h. After transfection, the cells were subjected to the further analysis. The values represent the mean ± SD of three experiments. (a) Luciferase analysis. (b) Cellular viability measured using CellTiter-Glo Luminescent cell viability assay (Promega). The values were normalized to the value of non-PNA-treated sample of relative volume 2 (v2).

thus presenting the hydrophobic face of the cholic acid to the environment (see Figure 1), and thereby giving the conjugate a hydrophobic surface that should allow membrane penetration by diffusion. While this principle seems effective for small molecule cargoes,[10] examples of cellular target effects of umbrella oligonucleotides are still lacking. However, it is more challenging both structurally and kinetically to cover a larger linear oligomer like an oligonucleotide or a PNA sufficiently with cholic acid moieties to make this conjugate migrate through the robust cellular membrane lipid bilayer. In the present study, we designed two tetra-cholate PNAs with one cholate per 4.5 nucleobases and having the cholates either concentrated at the "head" of the PNA (PNA3088) or evenly distributed along the PNA chain (PNA2974). Clearly, neither of these showed significant biological antisense activity, indicating poor intracellular bioavailability and thus membrane penetration. Of course, these specific umbrella conjugates have not been optimized, and further studies are clearly warranted, but the total lack of cellular activity of these PNAs do raise questions concerning the general utility of umbrella type compounds for cellular (and *in vivo*) delivery of antisense agents, or at least show that major chemical optimization will be required for obtaining high efficacy.

It has previously been found that conjugation of lipophilic, polyaromatic ligands to antisense PNA oligomers very significantly enhances cationic lipid mediated cellular delivery.[19] However, the present cholesterol and cholic acid conjugates show 10-fold higher activity. Although they are still around 10-fold less active than the most active PNA–peptidephosphonate

dx.doi.org/10.1021/bc200460t | *Bioconjugate Chem.* 2012, 23, 196–202

conjugates,[8] because of easy chemical accessibility and charge neutrality they could well be the conjugates of choice for cell culture studies and for future *in vivo* drug discovery approaches, and maybe could also be used in combination with novel peptide delivery strategies such as Pepfect[26] and CADY[27] technologies. In particular, we favor the cholic acid conjugates, as these do not have the solubility challenges posed by cholesterol conjugates. The high efficiency of the cholic acid conjugates may seem somewhat surprising because cholic acid is significantly less hydrophobic than cholesterol and therefore could be expected to form less stable lipoplexes. On the other hand, the lower hydrophobicity could facilitate dissociation from the lipids once inside the cell and provide better intracellular bioavailability. The structure of the lipoplexes is not known at present. However, because the PNAs are charge neutral, in contrast to oligonucleotides they do not affect the overall charge of the lipoplexes, and they cannot engage in charge dependent aggregation and nanoparticle formation. Therefore, most likely the cholate−PNA lipoplexes have liposome rather than nanoparticle character, but further studies are warranted to elucidate the detailed mechanism of the delivery.

Clearly, the present approach should also be useful more generally for delivery of other charge neutral antisense (and antigene) agents including, for example, morpholino oligomers (PMOs), and possibly also for therapeutic peptides. Finally, cholesterol and cholic acid PNA conjugates may be of particular interest for liver specific therapy *in vivo* as indicated by the successful liver targeting of cholesterol[12,13,24] or cholic acid[28]conjugates.

■ ASSOCIATED CONTENT

Supporting Information

Additional figure and spectra as described. This material is available free of charge via the Internet at http://pubs.acs.org.

■ AUTHOR INFORMATION

Corresponding Author

*Tel: +45 35 32 77 62. Fax: +45 35 32 60 42. E-mail: ptrn@sund.ku.dk.

Notes

The authors declare no competing financial interest.

■ ACKNOWLEDGMENTS

This work was supported by the Lundbeck Foundation. The expert technical assistance of Ms. Jolanta Ludvigsen for PNA synthesis and characterization is gratefully acknowledged.

■ REFERENCES

(1) De Rosa, G., and La Rotonda, M. I. (2009) Nano and microtechnologies for the delivery of oligonucleotides with gene silencing properties. *Molecules 14*, 2801−23.

(2) Shiraishi, T., and Nielsen, P. E. (2009) Cellular Biovailability of Peptide Nucleic Acids (PNAs) Conjugated to Cell Penetrating Peptides. In *Delivery Technologies for Biopharmaceuticals, Peptides, Proteins, Nucleic Acids and Vaccines* (Jørgensen, L., and Mørck Nielsen, H., Eds.) pp 305−338, Wiley, Chichester, UK.

(3) Mae, M., Andaloussi, S. E., Lehto, T., and Langel, U. (2009) Chemically modified cell-penetrating peptides for the delivery of nucleic acids. *Expert Opin. Drug Delivery 6*, 1195−205.

(4) Berthold, P. R., Shiraishi, T., and Nielsen, P. E. (2010) Cellular delivery and antisense effects of peptide nucleic acid conjugated to polyethyleneimine via disulfide linkers. *Bioconjugate Chem. 21*, 1933−8.

(5) Shiraishi, T., Pankratova, S., and Nielsen, P. E. (2005) Calcium ions effectively enhance the effect of antisense peptide nucleic acids conjugated to cationic tat and oligoarginine peptides. *Chem. Biol. 12*, 923−9.

(6) Abes, S., Williams, D., Prevot, P., Thierry, A., Gait, M. J., and Lebleu, B. (2006) Endosome trapping limits the efficiency of splicing correction by PNA-oligolysine conjugates. *J. Controlled Release 110*, 595−604.

(7) Shiraishi, T., and Nielsen, P. E. (2006) Photochemically enhanced cellular delivery of cell penetrating peptide-PNA conjugates. *FEBS Lett. 580*, 1451−6.

(8) Shiraishi, T., Hamzavi, R., and Nielsen, P. E. (2008) Subnanomolar antisense activity of phosphonate-peptide nucleic acid (PNA) conjugates delivered by cationic lipids to HeLa cells. *Nucleic Acids Res. 36*, 4424−32.

(9) Janout, V., Staina, I. V., Bandyopadhyay, P., and Regen, S. L. (2001) Evidence for an umbrella mechanism of bilayer transport. *J. Am. Chem. Soc. 123*, 9926−7.

(10) Ge, D., Wu, D., Wang, Z., Shi, W., Wu, T., Zhang, A., Hong, S., Wang, J., Zhang, Y., and Ren, L. (2009) Cellular uptake mechanism of molecular umbrella. *Bioconjugate Chem. 20*, 2311−6.

(11) Bijsterbosch, M. K., Rump, E. T., De Vrueh, R. L., Dorland, R., van Veghel, R., Tivel, K. L., Biessen, E. A., van Berkel, T. J., and Manoharan, M. (2000) Modulation of plasma protein binding and in vivo liver cell uptake of phosphorothioate oligodeoxynucleotides by cholesterol conjugation. *Nucleic Acids Res. 28*, 2717−25.

(12) Joshi, R., Mishra, R., Pohmann, R., and Engelmann, J. (2010) MR contrast agent composed of cholesterol and peptide nucleic acids: design, synthesis and cellular uptake. *Bioorg. Med. Chem. Lett. 20*, 2238−41.

(13) Bijsterbosch, M. K., Manoharan, M., Dorland, R., Van Veghel, R., Biessen, E. A., and Van Berkel, T. J. (2002) bis-Cholesteryl-conjugated phosphorothioate oligodeoxynucleotides are highly selectively taken up by the liver. *J. Pharmacol. Exp. Ther. 302*, 619−26.

(14) Soutschek, J, Akinc, A, Bramlage, B, Charisse, K, Constien, R, Donoghue, M, Elbashir, S, Geick, A, Hadwiger, P, Harborth, J, John, M, Kesavan, V, Lavine, G, Pandey, R. K., Racie, T, Rajeev, K. G., Röhl, I, Toudjarska, I, Wang, G, Wuschko, S, Bumcrot, D, Koteliansky, V, Limmer, S, Manoharan, M, and Vornlocher, H. P. (2004) Therapeutic silencing of an endogenous gene by systemic administration of modified siRNAs. *Nature 432*, 173−8.

(15) Kang, S. H., Cho, M. J., and Kole, R. (1998) Up-regulation of luciferase gene expression with antisense oligonucleotides: implications and applications in functional assay development. *Biochemistry 37*, 6235−9.

(16) Christensen, L., Fitzpatrick, R., Gildea, B., Petersen, K. H., Hansen, H. F., Koch, T., Egholm, M., Buchardt, O., Nielsen, P. E., Coull, J., and Berg, R. H. (1995) Solid-phase synthesis of peptide nucleic acids. *J. Pept. Sci. 1*, 175−83.

(17) Haaima, G., Lohse, A., Buchardt, O., and Nielsen, P. E. (1996) Peptide nucleic acids (PNAs) containing thymine monomers derived from chiral amino acids: hybridization and solubility properties of D-Lysine PNA. *Angew. Chem. 35*, 1939−1941.

(18) Doyle, D. F., Braasch, D. A., Simmons, C. G., Janowski, B. A., and Corey, D. R. (2001) Inhibition of gene expression inside cells by peptide nucleic acids: effect of mRNA target sequence, mismatched bases, and PNA length. *Biochemistry 40*, 53−64.

(19) Shiraishi, T., Bendifallah, N., and Nielsen, P. E. (2006) Cellular delivery of polyheteroaromate-peptide nucleic acid conjugates mediated by cationic lipids. *Bioconjugate Chem. 17*, 189−94.

(20) Hallbrink, M., Oehlke, J., Papsdorf, G., and Bienert, M. (2004) Uptake of cell-penetrating peptides is dependent on peptide-to-cell ratio rather than on peptide concentration. *Biochim. Biophys. Acta 1667*, 222−8.

(21) Shiraishi, T., and Nielsen, P. E. (2006) Enhanced delivery of cell-penetrating peptide-peptide nucleic acid conjugates by endosomal disruption. *Nat. Protoc. 1*, 633−6.

(22) Bendifallah, N., Rasmussen, F. W., Zachar, V., Ebbesen, P., Nielsen, P. E., and Koppelhus, U. (2006) Evaluation of cell-penetrating peptides (CPPs) as vehicles for intracellular delivery of antisense peptide nucleic acid (PNA). *Bioconjugate Chem. 17*, 750−758.
(23) Koppelhus, U., Shiraishi, T., Zachar, V., Pankratova, S., and Nielsen, P. E. (2008) Improved cellular activity of antisense peptide nucleic acids by conjugation to a cationic peptide-lipid (CatLip) domain. *Bioconjugate Chem. 19*, 1526−1534.
(24) Janout, V., Jing, B., and Regen, S. L. (2005) Molecular umbrella-assisted transport of an oligonucleotide across cholesterol-rich phospholipid bilayers. *J. Am. Chem. Soc. 127*, 15862−70.
(25) Cline, L. L., Janout, V, Fisher, M, Juliano, R. L., and Regen, S. L. (2011) A molecular umbrella approach to the intracellular delivery of small interfering RNA. *Bioconjugate Chem. 22*, 2210−6.
(26) Ezzat, K., El Andaloussi, S., Zaghloul, E. M., Lehto, T., Lindberg, S., Moreno, P. M., Viola, J. R., Magdy, T., Abdo, R., Guterstam, P., Sillard, R., Hammond, S. M., Wood, M. J., Arzumanov, A. A., Gait, M. J., Smith, C. I., Hallbrink, M., and Langel, U. (2011) PepFect 14, a novel cell-penetrating peptide for oligonucleotide delivery in solution and as solid formulation. *Nucleic Acids Res. 39*, 5284−98.
(27) Crombez, L., and Divita, G. (2011) A non-covalent peptide-based strategy for siRNA delivery. *Methods Mol. Biol. 683*, 349−60.
(28) Betebenner, D. A., Carney, P. L., Zimmer, A. M., Kazikiewicz, J. M., Brücher, E, Sherry, A. D., and Johnson, D. K. (1991) Hepatobiliary delivery of polyaminopolycarboxylate chelates: synthesis and characterization of a cholic acid conjugate of EDTA and biodistribution and imaging studies with its indium-111 chelate. *Bioconjugate Chem. 2*, 117−23.

Bioconjugate Chemistry

Article

pubs.acs.org/bc

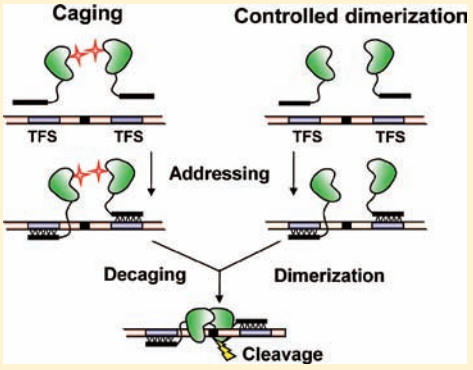
Catalytic Activity Control of Restriction Endonuclease—Triplex Forming Oligonucleotide Conjugates

Arunas Silanskas, Mindaugas Zaremba, Giedrius Sasnauskas, and Virginijus Siksnys*

Institute of Biotechnology, Vilnius University, Graiciuno 8, LT-02241 Vilnius, Lithuania

Supporting Information

ABSTRACT: Targeting of individual genes in complex genomes requires endonucleases of extremely high specificity. To direct cleavage at the unique site(s) in the genome, both naturally occurring and artificial enzymes have been developed. These include homing endonucleases, zinc-finger nucleases, transcription activator-like effector nucleases, and restriction or chemical nucleases coupled to a triple-helix forming oligonucleotide (TFO). The desired cleavage has been demonstrated both *in vivo* and *in vitro* for several model systems. However, to limit cleavage strictly to unique sites and avoid undesired reactions, endonucleases with controlled activity are highly desirable. In this study we present a proof-of-concept demonstration of two strategies to generate restriction endonuclease−TFO conjugates with controllable activity. First, we combined the restriction endonuclease caging and TFO coupling procedures to produce a caged MunI−TFO conjugate, which can be activated by UV-light upon formation of a triple helix. Second, we coupled TFO to a subunit interface mutant of restriction endonuclease Bse634I which shows no activity due to impaired dimerization but is assembled into an active dimer when two Bse634I monomers are brought into close proximity by triple helix formation at the targeted site. Our results push the restriction endonuclease−TFO conjugate technology one step closer to potential *in vivo* applications.



INTRODUCTION

Homologous recombination is one of the most promising strategies for genome editing in various types of eukaryotic cells. To achieve replacement of the deficient gene through homologous recombination, the correct gene sequence should be supplied *in trans*. Alternatively, homologous recombination can also be used for gene inactivation, insertion, and deletion.[1,2] The major limitation of this approach is extremely low frequency ($\sim 10^{-6}$) of natural recombination between an exogenous DNA and the homologous chromosomal target. Remarkably, the frequency can be greatly increased (up to $\sim 10^{-1}$) by introducing a recombinogenic double-strand break at or near the targeted gene.[3] Therefore, site-specific nucleases capable of cleavage at unique sites in eukaryotic genome hold great potential for genetic studies, biotechnology, and gene therapy.

Currently, several classes of natural and artificial nucleases are available for highly specific DNA cleavage.[4] Homing endonucleases, which recognize long DNA sequences (up to 30 base pairs, Figure 1A), have been applied to gene editing in numerous experimental designs and cell types.[5−7] The protein−DNA interface of these enzymes can be engineered to create novel endonucleases with tailored specificities, thereby expanding the list of available gene targets, yet preserving the tight coupling of cleavage activity to DNA recognition inherent to native enzymes.[4]

Artificial nucleases, dubbed zinc-finger nucleases (ZFN), have been also developed for the purpose of gene targeting. They are created by fusing zinc-finger motifs, which serve a DNA recognition module, to the nonspecific DNA cleavage domain of the FokI restriction endonuclease.[8−11] As each zinc-finger is specific for a DNA base triplet, tethering multiple zinc-finger motifs in a series allows for specific targeting of a wide variety of extended DNA sequences. The activity control of ZFNs is achieved due to weak dimerization of the FokI cleavage domain. Being unable to dimerize in free solution, two FokI cleavage domains form a catalytically competent dimer only when are brought into close proximity and in correct orientation by the zinc-finger domain binding to the adjacent DNA sites (Figure 1B). DNA cleavage is typically performed using a pair of ZFNs that heterodimerize at the target site. To reduce off-target cleavage caused by formation of catalytically competent homodimers, FokI cleavage domain variants with impaired homodimerization and improved heterodimerization capability were produced.[3,11] Alternatively, a photoswitchable variant of zinc-finger nuclease has been engineered to decrease off-target cleavage activity.[12] A similar design strategy to ZFNs was recently used to create novel chimeric nucleases consisting of the FokI catalytic domain fused to the truncated transcription activator-like effector (TALE) domains (Figure 1C)[13−15] or a cleavage deficient variant of I-SceI homing endonuclease.[16]

Received: September 2, 2011
Revised: December 15, 2011
Published: January 12, 2012

 © 2012 American Chemical Society dx.doi.org/10.1021/bc200480m | *Bioconjugate Chem.* 2012, 23, 203−211

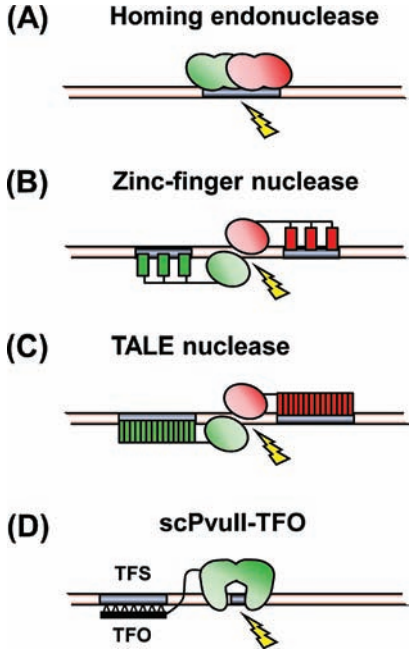


Figure 1. Endonucleases for genome engineering. Naturally occurring homing endonucleases (A), zinc-finger nucleases consisting of the nonspecific FokI DNA cleavage domain fused to zinc-finger DNA binding modules (B), and TALE nucleases comprising the FokI cleavage domain fused to an array of TALE repeat domains (C) were successfully used to increase the efficiency of homologous recombination for gene correction by cleaving the eukaryotic genome at specific sites. (D) The restriction endonuclease PvuII − triplex forming oligonucleotide (TFO) conjugate recognizes a bipartite DNA sequence consisting of the triplex forming sequence (TFS) and the restriction endonuclease site.

The third group of site-specific genome cleavage reagents is based on the fusion of triplex forming oligonucleotides to various DNA damaging compounds.[17−19] Typically, a polypurine tract in target DNA duplex is specifically recognized by a triplex forming oligonucleotide (TFO) that binds in the major groove to the purine strand in parallel (polypyrimidine TFO) or antiparallel (polypurine TFO) orientation via Hoogsteen hydrogen bonds.[20] Because the sequence specificity of such interaction can be designed *a priori*, it eliminates the screening step usually required for the development of homing endonucleases or zinc-finger domains with tailored specificities. To decrease potential toxicity of the chemical nucleases, TFO-restriction enzyme conjugates have been developed by fusing TFO with a type II restriction endonuclease (REase). Given the wide choice of available type II REases, this approach provides combinatorial flexibility in addressing bipartite recognition sequences consisting of the REase target site next to a longer triplex forming site (TFS).

The proof-of-concept demonstration of REase-TFO conjugate was presented by Eisenschmidt and colleagues.[21] A single-chain variant of PvuII REase (scPvuII) was fused to TFO to produce a conjugate that cuts a specific DNA site *in vitro*. Since the kinetics of triple helix formation is much slower than DNA binding and cleavage by PvuII, the "addressed" cleavage reaction was performed in two stages. First, the scPvuII−TFO conjugate was preincubated with substrate DNA under conditions that prevent DNA binding and cleavage by PvuII (buffer devoid of Mg^{2+} ions) to allow formation DNA triplexes. This step ensures that the REase module is guided to the target sequence via the TFO−TFS interaction rather than by its inherent DNA binding ability. In the second step, DNA cleavage is triggered by addition of Mg^{2+} ions. The requirement for the preincubation step in the absence of Mg^{2+} limits the application of the scPvuII−TFO conjugate to *in vitro* DNA manipulations, as Mg^{2+} ions, normally present in cellular milieu, would trigger DNA cleavage by the PvuII REase before the TFO-TFS interaction has occurred. For *in vivo* purposes, it would be desirable to generate REase−TFO conjugates with switchable endonuclease activity such that it could be activated only after stable DNA triplex has been formed. In this study, we present proof-of-concept demonstrations of two alternative strategies for generation of controllable REase−TFO conjugates that may open new avenues for developing REase−TFO conjugates for *in vivo* experiments.

EXPERIMENTAL PROCEDURES

Plasmids. The plasmid pUHE25−2-MunI-H6G4C encoding the MunI variant with the C-terminal His-tag (His-tagged MunI) was derived from the pUHE25−2-MunIR plasmid[22] by inserting a DNA fragment encoding the GGSHHHHHHGGGGC amino acid sequence immediately downstream of the C-terminal amino acid of native MunI. The DNA fragment encoding the His-tag was derived by PCR using the pRIZ′-scPvuII-H6G4C plasmid[21] as a template. The plasmid pBse634IR-H6G4C encoding the Bse634I mutant R226A+C10S+C186S with the C-terminal His-tag mentioned above (His-tagged Bse634I) was generated using the pBse634IR3.7 plasmid[23] as a template using PCR-based site-directed mutagenesis. Plasmid DNA substrates used in activity measurements are derivatives of the 5.5 kbp plasmid pECFP provided by K. Eisenschmidt.[21] Prior to reactions the plasmid containing an "addressed" MunI site was precleaved with VspI and NsbI, and the plasmid containing an "addressed" Bse634I was linearized with VspI.

Protein Expression and Purification. His-tagged MunI was expressed in *E. coli* ER2267 cells containing compatible plasmids pUHE25−2-MunI-H6G4C (Ap^r) and pMunIM6.2 (Tc^r, Cm^r). The cells were grown in LB medium containing 50 mg/L ampicillin and 30 mg/L chloramphenicol at 37 °C to late log phase, induced with 0.2 mM IPTG for 4 h, and harvested by centrifugation. His-tagged Bse634I was expressed in *E. coli* ER2267 cells containing plasmids pBse634IR-H6G4C (Ap^r) and p*Hpa*IIM (Cm^r).[23] Cells were grown in LB medium containing 50 mg/L ampicillin and 30 mg/L chloramphenicol at 37 °C overnight. Both proteins were purified on 1 mL Ni^{2+} HisTrap HP and 1 mL HiTrap Heparin HP columns (GE Healthcare). The fractions containing His-tagged MunI or Bse634I proteins were pooled, dialyzed against the respective storage buffers [10 mM Tris-HCl (pH 7.4 at 25 °C), 100 mM KCl, 1 mM EDTA, 1 mM DTT, 50% (v/v) glycerol for MunI, 10 mM potassium phosphate, (pH 7.4 at 25 °C), 100 mM KCl, 0.1 mM EDTA, 50% (v/v) glycerol for Bse634I] and stored at −20 °C. The enzymes were >95% homogeneous as shown by SDS-PAGE and Coomassie Blue analysis. The protein concentrations were determined spectrophotometrically at 280 nm using the extinction coefficient of 45 720 M^{-1} cm^{-1} for MunI and 35 410 $M^{-1}cm^{-1}$ for Bse634I monomers.

Oligonucleotides. The triplex forming oligonucleotide (TFO) containing unmodified heterocyclic bases and a 5′-C_{12} linker with a terminal amino group 5′-NH_2-$(CH_2)_{12}$-CTCTCTCTCTTTTTT-3′ used to generate the caged MunI-TFO cross-link was purchased from Metabion (Mar-

dx.doi.org/10.1021/bc200480m | *Bioconjugate Chem.* 2012, 23, 203−211

tinsried, Germany). TFOs 5′-NH_2-$(CH_2)_{12}$-MPMPMPMPMPPPPPP-3′ (TFO1) and 5′-NH_2-$(CH_2)_{12}$-PMPPMPPMPPPMPPP-3′ (TFO2) containing modified heterocyclic bases M (5-methyl-2′-deoxycytidine) and P (5-[1-propynyl]-2′-deoxyuridine) used for coupling with His-tagged Bse634I were purchased from Eurogentec (Liege, Belgium).

Generation and Purification of REase-TFO Cross-Links. His-tagged MunI was loaded on the 1 mL HiTrap Heparin HP column and washed with Buffer A [10 mM sodium phosphate (pH 7.4 at 25 °C), 100 mM NaCl, no reducing agent]. Next, copper phenantroline solution (0.2 mM $CuSO_4$ and 0.8 mM phenantroline in Buffer A) was loaded on the column to stimulate formation of intersubunit disulfide bonds between the C-terminal Cys residues. After 10 min incubation, copper phenantroline was washed from the column with 100 mM EDTA in Buffer A and protein was eluted using 0.1−1.0 M NaCl gradient. The resultant protein was partially denatured with 1 M guanidinium chloride (GdmCl) and the exposed dimerization interface cysteines (Cys123) were modified by caging with 2-nitrobenzyl bromide (NBB) as described previously.[24] The reaction mixture was dialyzed against Buffer A supplemented with 50 mM DTT and the resultant monomeric caged MunI was separated from the uncaged homodimer on the Heparin HP column using a gradient of 10 mM sodium phosphate (pH 6.0 at 25 °C), 0.1−1.0 M NaCl, and 0.2 mM tris(2-carboxyethyl)phosphine (TCEP). Finally, the regenerated thiol groups of caged MunI were used for coupling with TFO according to the method described by Eisenschmidt et al.[21] His-tagged Bse634I was used for the TFO1 and TFO2 coupling reactions directly after dialysis against 10 mM sodium phosphate (pH 7.0 at 25 °C), 100 mM NaCl, and 0.2 mM TCEP. The resultant caged MunI−TFO and Bse634I−TFO cross-links were purified on a MonoQ 5/50 GL column (GE Healthcare) using 20 mM Tris-HCl (pH 7.0 at 25 °C) and a linear gradient of 0.1−1.0 M NaCl. Unreacted proteins eluted in the flowthrough, whereas REase−TFO conjugates and excess of unreacted TFO eluted as separate peaks. Fractions containing MunI−TFO and Bse634I−TFO conjugates were dialyzed against the MunI and Bse634I storage buffers mentioned above and stored at −20 °C. Conjugate concentrations were determined by densitometric analysis of SDS-PAGE gels containing samples of REase−TFO conjugates along with known amounts of His-tagged proteins.

DNA Cleavage Activity. DNA cleavage activity of caged MunI−TFO conjugate was tested on an equimolar mixture of the "addressed" DNA substrate (1880 bp DNA fragment containing a single MunI site separated by 9 bp from two symmetrically positioned triplex forming sequences 5′-GAGA-GAGAGAAAAAA-3′) and the "nonaddressed" substrate (3675 bp DNA fragment containing a single MunI site and no TFS). 100 nM samples of both DNA fragments were preincubated overnight with 400 nM of caged MunI−TFO at 4 °C in 80 mM Tris-phosphate (pH 6.1 at 25 °C), 1.0 M NaCl, and 4 mM Mg^{2+}. To activate the MunI−TFO conjugate, the reaction mixture was supplemented with 20 mM of DTT, placed into a quartz cuvette, and irradiated with 330 nm UV light for 1 h at 4 °C. A Fluoromax-3 (Horiba Jobin Yvon, Stanmore, UK) spectrofluorimeter equipped with a Xe lamp was used as the UV source. DNA cleavage was initiated by 10-fold dilution with the reaction buffer [80 mM Tris-phosphate (pH 7.1 at 25 °C), 4 mM Mg^{2+}] and incubated at 20 °C. Samples were collected at given time intervals, quenched with loading dye solution [50 mM EDTA (pH 8.0 at 25 °C), 0.1% SDS, 50% (v/v) glycerol, 0.01% bromphenol blue], and analyzed by agarose electrophoresis.

DNA cleavage activity of the Bse634I−TFO cross-link was studied on a linearized 5.5 kbp plasmid bearing seven Bse634I recognition sites, one of which (the "addressed" site) is separated by 9 bp from the triplex forming sequences 5′-TTTTTTCTCTCTCTC-3′ (TFS1) and 5′-AGAAGAAGAAA-GAAA-3′ (TFS2). To analyze "addressed" cleavage, 50 nM linear DNA was incubated with equimolar mixture of Bse634I−TFO1 and Bse634I−TFO2 conjugates (total concentration 200 nM monomer) at 37 °C in 80 mM Tris-phosphate (pH 6.1 at 37 °C), 2 mM spermine, 2 mM $MgCl_2$, and 10 mM DTT. The reactions were quenched and analyzed as described above.

RESULTS

Strategy. We propose two strategies to control the activity of the REase−TFO conjugates: (i) a caging strategy to introduce inactivating modifications that could be removed by an external signal (preferably by light) after formation of a stable triple helix (Figure 2, "caging"); (ii) a controlled oligomerization strategy to trigger dimerization of the catalytically inactive REase monomers brought into close proximity by triple helix formation at the target site (Figure 2, "controlled dimerization").

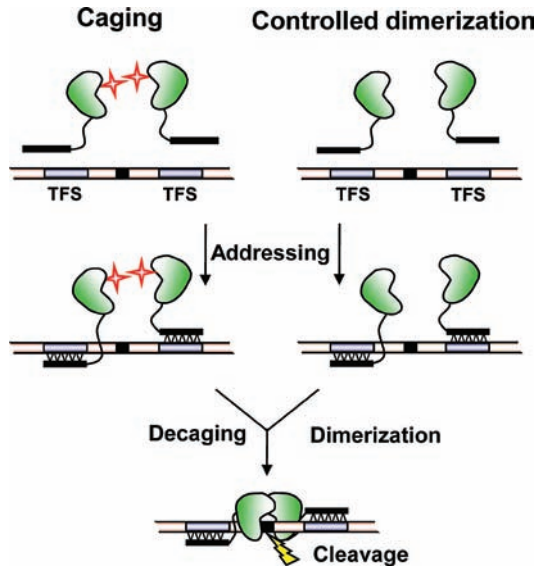


Figure 2. Experimental strategy for generation of restriction enzyme−TFO conjugates with the adjustable activity. The active restriction endonuclease homodimer can be inactivated either by caging (left panel, "caging") or by mutations at the dimerization interface (right panel, "controlled dimerization"). After triple helix is formed, the activity of caged restriction endonuclease would be restored upon decaging, while the enzyme with attenuated dimerization interface should form an active dimer due to increased local protein concentration.

Caging strategy. A simple and highly efficient procedure was recently developed to cage cysteine residues at the dimer interface of MunI REase. Attachment of the bulky nitrobenzyl moiety precluded dimerization of MunI resulting in a complete loss of catalytic activity. However, upon removal of the nitrobenzyl group by irradiation with UV light, up to 50% of the initial MunI activity is restored.[24] To generate a photoswitchable MunI−TFO conjugate, we attached a

photocaged MunI variant to the triple helix forming oligodeoxynucleotide.

Controlled Oligomerization. The "addressed" DNA cleavage by a photoswitchable REase still requires a preincubation step to ensure formation of stable DNA triplexes that would guide all caged enzyme to the "addressed" site (Figure 2, "caging"). Otherwise, a free enzyme left in the reaction mixture upon decaging will become engaged in the nonaddressed cleavage reactions directed solely by the REase specificity. This limitation can be overcome by the controlled oligomerization approach which makes use of the observation that subunit interactions of some orthodox REases can be attenuated by mutations.[25,26] For example, the R226A mutation at the dimerization/tetramerization interface of restriction endonuclease Bse634I converts the native tetramer into inactive monomers[26] which are still able to form a functional dimer at increased protein concentrations. Fusion of the two REase monomers to different TFOs should bring inactive monomers into close proximity at the Bse634I recognition site and promote the assembly of the catalytically active dimer. In contrast to the FokI fusions, which employ a nonspecific nuclease domain as a cleavage module, a monomer of orthodox REase, which bears both catalytic and sequence recognition elements, is used for the fusion with TFO. The attenuated dimerization should completely prevent cleavage of nonaddressed DNA sites at low enzyme concentrations, but cleavage of "addressed" sites would be turned on when two TFO-coupled monomers are guided to the "addressed" REase site by TFO–TFS interactions (Figure 2, "controlled dimerization").

Engineering an Addressable and Photoswitchable REase–TFO Conjugate. To generate an addressable and photoswitchable REase–TFO conjugate, we selected MunI as a model system. MunI is well characterized in terms of both structure[27] and function.[28,29] It is a homodimeric protein that recognizes the palindromic DNA sequence 5′-C/AATTG-3′ and uses two symmetrically positioned active sites to cut both DNA strands in a Mg^{2+}-dependent reaction ('/' marks the cleavage position).

A native MunI dimer contains two cysteine residues (one per monomer) at position 123. These cysteines are buried at the dimerization interface and therefore are not available for TFO coupling. Instead, they are an excellent target for caging with a bulky photoremovable compound. Disruption of MunI dimer in the presence of 1 M GdmCl followed by attachment of the nitrobenzyl (NB) moiety to Cys123 resulted in an inactive MunI monomer that could be reactivated by UV light.[24] Coupling of TFO to MunI by standard thiol chemistry would require an extra solvent accessible cysteine residue located distantly from the DNA binding cleft. To this end we engineered a hexahistidine tag followed by four glycines and a cysteine[21] at the C-terminus of native MunI.

To selectively modify the subunit interface cysteine with the photoremovable compound and the C-terminal cysteine with a triplex forming oligonucleotide, we took advantage of different accessibility of these cysteine residues (Figure 3). First, a sample of His-tagged MunI was incubated with copper phenantroline (see Experimental Procedures for details). This resulted in efficient formation (the yield close to 95% according to SDS-PAGE analysis, Figure S1A, Supporting Information) of intersubunit disulfide bonds. Very low yield of cross-linked species (<5%, data not shown) in the case of native MunI lacking the C-terminal His_6Gly_4Cys sequence suggests that the

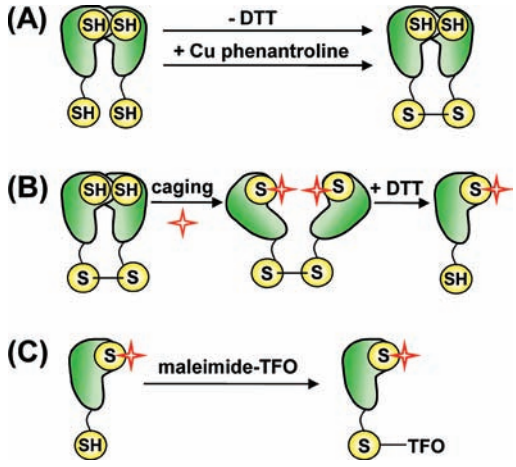


Figure 3. Generation of the caged MunI–TFO conjugate. In the first step, the C-terminal cysteines were protected from thiol-reactive reagents by forming intersubunit disulfide bonds (A). Next, the MunI dimerization interface residues Cys123 where modified by caging with 2-nitrobenzylbromide. After cleavage of intersubunit disulfide bond with DTT, a monomeric caged MunI with a free C-terminal cysteine was obtained (B) that was used for coupling with a triplex forming oligonucleotide via a maleimide group (C).

disulfide bonds were formed almost exclusively between the C-terminal cysteines. This conclusion is also consistent with the available MunI structural data. Indeed, the length of the highly flexible C-terminal His_6Gly_4C sequences should be sufficient to allow direct contacts between the terminal cysteines of different MunI subunits. Conversely, the dimerization interface cysteines are completely buried within the hydrophobic core of the protein and therefore are protected from disulfide bond formation.[24,27]

To modify the dimerization interface cysteines with the photoremovable 2-nitrobenzyl (NB) group, we followed the previously developed procedure.[24] The Cys123 residues were exposed to the solvent by partial denaturation of MunI in 1 M GdmCl solution and covalently modified with 2-nitrobenzyl bromide (Figure 3B). During this step the C-terminal cysteines were protected from NBB modification due to disulfide bond formation. Subsequent dialysis against buffer containing DTT removed the GdmCl with the caging reagent and restored the C-terminal cysteines. Ensuing chromatography on heparin sepharose in the pH 6.0 buffer enabled separation of the caged monomeric MunI bearing a single His tag from the unreacted dimer (see Experimental Procedures section for details). The yield of the caging reaction was close to 100% as judged from the ratio of monomeric and dimeric forms of MunI eluting from the Heparin sepharose column (Figure S1B, Supporting Information). Finally, the purified caged MunI was coupled to TFO by following the procedure described by Eisenschmidt et al.[21] Briefly, the TFO was first coupled with the bifunctional cross-linker GMBS (*N*-[γ-maleimidobutyryloxy]succinimide ester) via amide bond formation between the 5′-terminal C_{12}-amino group of the TFO and the succinimide group of GMBS, and then the TFO–GMBS adduct was coupled with the C-terminal cysteine of MunI via the maleimide group of GMBS to give the desired caged MunI–TFO product (Figure 3C and Figure S1C, Supporting Information). MunI–TFO conjugate was separated from unreacted MunI and TFO by ion exchange chromatography (Figure S1D, Supporting Information). In agreement with complete inactivation of MunI by caging,[24] the

caged MunI–TFO conjugate was catalytically inactive (data not shown).

DNA Cleavage by the MunI–TFO Conjugate. The MunI–TFO conjugate differs from the scPvuII–TFO adduct used in the pioneering study of Eisenschmidt and colleagues[21] in the stoichiometry of the DNA–conjugate interaction. A single scPvuII–TFO molecule, containing two catalytic centers, is able to recognize and cleave the bipartite "addressed" DNA site consisting of the PvuII site and an adjacent triplex forming site. A caged MunI–TFO monomer contains only a single active site; therefore, two enzyme–TFO conjugates must be guided to a single site in order to form an active homodimer capable of double-stranded DNA cleavage. This would require a tripartite recognition sequence consisting of the MunI recognition site embedded between two symmetrically positioned triplex forming sequences that match the twofold symmetry of the decaged homodimeric MunI–TFO conjugate.

Activity and specificity of the TFO-coupled MunI was tested on the equimolar mixture of 1880 and 3675 bp DNA fragments. The 1880 bp fragment contained the tripartite "addressed" site consisting of two triplex forming sequences positioned 9 bp downstream and upstream of the MunI recognition site (Figure 4A). The 3675 bp fragment contained a MunI recognition site without the adjacent triplex forming sequences. Control experiments confirmed equal susceptibility of MunI sites in both fragments to native MunI (Figure 4B, lane K). Incubation of the 1880 and 3675 bp fragments with the caged MunI–TFO conjugate in a buffer compatible with triple helix formation, irradiation of the reaction mixture with UV light and further dilution in the reaction buffer (see Experimental Procedures section for details) resulted in hydrolysis of the "addressed" MunI site in the 1880 bp fragment; no cleavage of the 3675 bp fragment could be detected even after prolonged incubation (Figure 4B). Assuming that ~30% of the addressed site was cleaved in less than 60 min, and no cleavage of the nonaddressed substrate was detected after 3 h, the cleavage rates of the "addressed" and the "nonaddressed" substrates must differ at least 100-fold (the estimate is based on the lower detection limit of band intensity analysis of ethidium bromide stained gels, 10 ng or ~1% of total DNA in a gel lane). In conclusion, we have successfully combined MunI caging with TFO coupling to generate a highly specific and photoswitchable DNA cleavage tool.

Engineering an Addressable Restriction Endonuclease with an Attenuated Dimerization Interface. To generate an addressable REase with an attenuated dimerization interface, we have chosen Bse634I REase as a model system. Wt Bse634I is a stable homotetrameric protein specific for the degenerate DNA sequence 5′-R/CCGGY-3′ (where R stands for A/G and Y for T/C) and cuts DNA after the first nucleotide (cleavage position indicated by "/"). Four subunits of the wt enzyme assemble into a dimer of two primary dimers positioned back-to-back to each other with DNA binding clefts facing into opposite directions. Two DNA sites are required for optimal Bse634I activity with only residual activity level observed on a single recognition site.[30] It was demonstrated that alanine replacement of the R226 residue located at the dimer–dimer interface converts Bse634I into a monomer.[26] DNA binding studies revealed that the R226A mutant preserved the ability to dimerize on cognate DNA forming a specific protein–DNA complex, albeit only at high enzyme concentrations.[26] Dimerization of Bse634I R226A on DNA is also supported by the nonlinear dependence of DNA cleavage

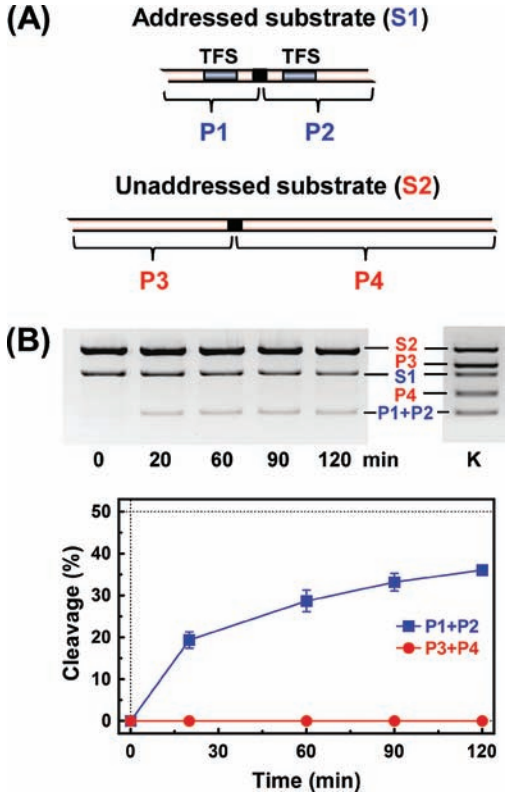


Figure 4. Addressed DNA cleavage by the caged MunI–TFO conjugate. (A) DNA substrates. The 1880 bp "addressed" substrate containing a MunI recognition site 5′-CAATTG-3′ embedded between two triplex forming sequences (TFSs), and the 3675 bp "unaddressed" substrate containing a MunI site without the adjacent TFS, were used in competition. (B) DNA cleavage. The equimolar mixture of "addressed" and "unaddressed" substrates was preincubated with caged MunI–TFO at 4 °C to allow triplex formation in a buffer containing 4 mM $MgCl_2$ and 1 M NaCl. After irradiation by UV light and dilution the cleavage kinetics was determined. Only the "addressed" substrate is cleaved at an appreciable rate (P1+P2 products). The gel lane K contains the mixture of "addressed" and "unaddressed" substrates cleaved with His-tagged MunI lacking a TFO. The data points are presented as mean values from 3 independent experiments ± 1 standard deviation.

activity on enzyme concentration: contrary to the wt enzyme that rapidly hydrolyzes DNA even at low concentrations (Figure S2A, Supporting Information), the mutant is almost inactive at 200 nM concentration (the DNA nicking rate is ~0.1 h^{-1}, no double-strand cleavage detectable after 8 h incubation), but regains detectable activity at 500 nM, and full catalytic activity at 5000 nM concentration (the rate of ds DNA cleavage ~4 min^{-1}). Moreover, distinctly from wt Bse634I, the R226A mutant is fully active on DNA substrates with a single recognition site (Figure S2B–D, Supporting Information).

Wt Bse634I monomer contains two Cys residues at positions 10 and 186. In order to limit TFO coupling to the Bse634I R226A mutant at a single position, we replaced the native Bse634I cysteines by Ser (mutations C10S and C186S) and engineered the His_6Gly_4Cys sequence containing a unique cysteine at the C-terminus of the protein. The resulting His-tagged variant of Bse634I R226A+C10S+C186S mutant (His-tagged Bse634I) displayed the same nonlinear dependence of enzymatic activity on the protein concentration as the untagged Bse634I R226A. The Bse634I–TFO conjugates were prepared

dx.doi.org/10.1021/bc200480m | Bioconjugate Chem. 2012, 23, 203–211

using two 15 nt triplex forming oligonucleotides (TFO1 and TFO2) containing 5-methyl-2′-deoxycytidine (for deoxycytidine) and 5-[1-propynyl]-2-deoxyuridine (for thymidine) modifications that increase DNA triplex stability at near-neutral pH. Similarly to MunI, the TFOs were coupled to the C-terminal cysteine of His-tagged Bse634I via the bifunctional cross-linker GMBS. Ion exchange chromatography enabled separation of the Bse634I–TFO conjugates from the unreacted protein and triplex forming oligonucleotides (see Figure S3, Supporting Information, and Experimental Procedures section for details).

Activity and Specificity of the Bse634I–TFO Conjugates. First, we compared the activity of the His-tagged Bse634I and the Bse634I–TFO conjugates on a supercoiled plasmid substrate pUCAT1[30] bearing a single Bse634I recognition site with no adjacent triplex forming sequences. TFO conjugation to the C-terminus of Bse634I reduced the DNA nicking rate approximately 20-fold (to ~0.005 h^{-1} with 200 nM of Bse634I–TFO conjugate, Figure S4, Supporting Information). Presumably, the repulsion between the negatively charged TFO and the DNA duplex or between two TFOs impedes association of Bse634I monomers with the recognition site.

To assess the ability of Bse634I–TFO conjugates to specifically recognize and hydrolyze the addressed DNA sites, we employed a 5.5 kbp linear DNA fragment containing 7 Bse634I recognition sites. One of these sites was flanked by two different 15 bp pyrimidine tracts (Figure 5A) that form triple helixes with TFO1 and TFO2 (see Experimental Procedures section for sequence details). A control experiment with 2 μM of His-tagged Bse634I confirmed that the enzyme without the attached TFO has no preference for the "addressed" site (Figure S5, Supporting Information).

Incubation of the substrate with equimolar mixture of Bse634I–TFO1 and Bse634I–TFO2 conjugates (total conjugate concentration 200 nM) in a reaction buffer that is compatible with both DNA triplex formation and DNA hydrolysis resulted in relatively slow appearance of the 3257 and 2298 bp DNA fragments that correspond to cleavage of the addressed Bse634I site (Figure 5B). Approximately 25% of the substrate was cleaved during 8 h incubation time without any detectable nonaddressed cleavage products (Figure 5F). Assuming that the 5.5 kbp substrate contains a 6-fold excess of nonaddressed Bse634I sites over the addressed site, and taking into account the detection limit of the ethidium bromide stained DNA bands (~10 ng or ~1% of total DNA in an agarose gel lane), the cleavage rates of the "addressed" and the "nonaddressed" Bse634I sites must differ at least 100-fold.

To verify that both TFO1–TFS1 and TFO2–TFS2 interactions are required for the "addressed" cleavage reaction, we performed control experiments using (i) the His-tagged Bse634I lacking a conjugated TFO; (ii) only the Bse634I–TFO1 conjugate, and (iii) only the Bse634I–TFO2 conjugate. Experiments with His-tagged Bse634I lacking a conjugated TFO yielded no double-strand breaks during 8 h incubation (Figure 5C), confirming that TFO–TFS interactions are obligatory for the assembly of Bse634I monomers on DNA. Individual Bse634I–TFO cross-links generated detectable amounts of the addressed cleavage products (Figure 5D,E), but cleavage extent was 2.5-fold (Bse634I–TFO1) and 3-fold (Bse634I–TFO2) lower than in the experiment with the equimolar mixture of both Bse634I–TFO1 and Bse634I–TFO2 conjugates. This suggests that under our reaction

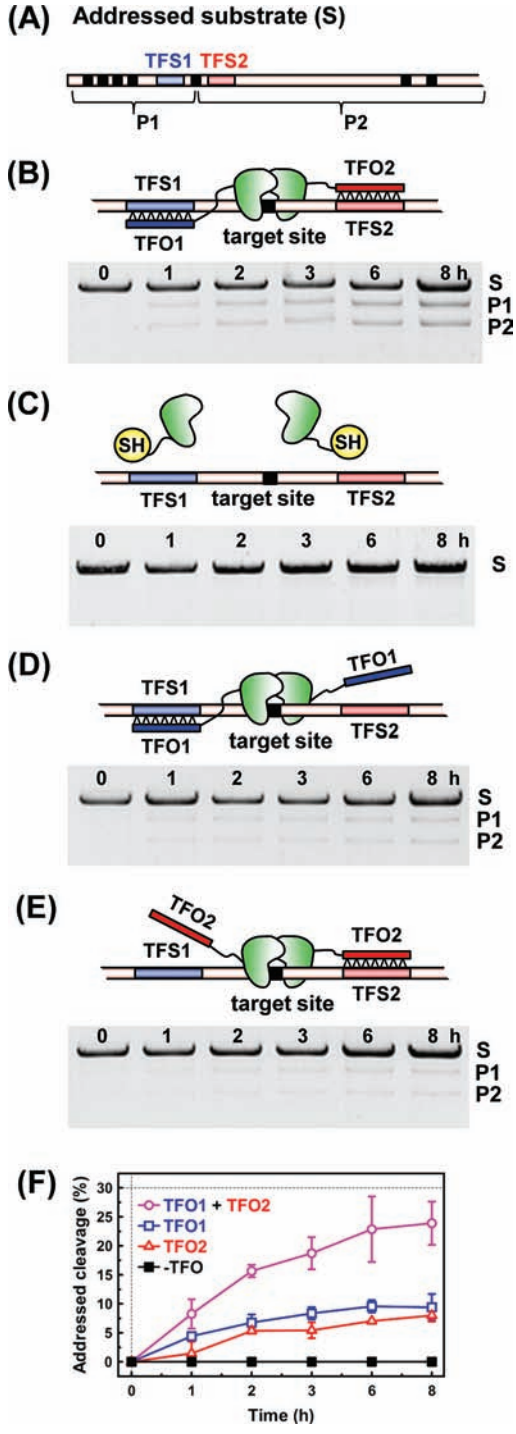


Figure 5. Addressed DNA cleavage by the Bse634I-TFO conjugates. The 5.5 kbp linear DNA substrate, containing one "addressed" Bse634I site [having triplex forming sequences TFS1 (blue box) and TFS2 (red box) 9 bp away from the Bse634I site 5′-ACCGGT-3′] and six "unaddressed" sites (A) was incubated with equimolar mixture of Bse634I–TFO1 and Bse634I–TFO2 conjugates at 37 °C (B). Only the "addressed" cleavage products (the 2298 bp and 3257 bp fragments P1 and P2) are formed during 1–8 h incubation. Control experiments were performed with His-tagged Bse634I lacking a TFO (C) and individual Bse634I–TFO1 or Bse634I–TFO2 conjugates (D,E). The extent of DNA cleavage in different experiments is summarized in panel F. The data points are presented as mean values from 3 (TFO1+TFO2) or 2 (TFO1, TFO2) independent experiments ± 1 standard deviation.

dx.doi.org/10.1021/bc200480m | *Bioconjugate Chem.* 2012, 23, 203–211

conditions (200 nM Bse634I–TFO conjugate) the catalytically competent Bse634I dimers assemble on the "addressed" site by two pathways. In the optimal scenario, both Bse634I monomers are guided to the "addressed" site by the TFO–TFS interactions, resulting in the highest extent of DNA cleavage. In a less favorable scenario, a single Bse634I monomer guided to the addressed site by triplex formation captures the second Bse634I monomer from free solution.

DISCUSSION

In the present study, we provide proof-of-concept demonstrations of two alternative strategies to control the DNA cleavage activity of restriction endonuclease–TFO conjugates. In the first approach we successfully combined the restriction endonuclease photocaging and TFO-coupling to generate a photoswitchable MunI–TFO conjugate (Figure 2, "caging"). The caged MunI–TFO conjugate has two important advantages in comparison to the scPvuII–TFO conjugate described in the study by Eisenschmidt and colleagues.[21] First, the preincubation of caged REase–TFO conjugate with target DNA can be performed in any buffer that is compatible with triple helix formation. In particular, the reaction buffer may contain Mg^{2+} ions present in cellular milieu that would otherwise induce DNA binding and cleavage of unaddressed sites by the restriction endonuclease module of the REase–TFO conjugate. Second, it employs the native homodimeric form of an orthodox restriction endonuclease MunI rather than an artificial single chain (sc) variant. Sc variants may be advantageous in addressing bipartite sites consisting of one TFS adjacent to the restriction endonuclease site. However, the sc variant is currently available only for PvuII, and may be difficult to create for other homodimeric restriction enzymes due to structural limitations. Instead, we show here that REase–TFO conjugates based on the homodimeric REase can be used to address tripartite sequences consisting of the restriction endonuclease site surrounded by two triplex forming sequences. Given the wide choice of structurally characterized homodimeric restriction endonucleases, TFO-coupling combined with photocaging of essential functional regions of homodimeric REases (e.g., dimerization interface or DNA binding surface[24]) has the potential of becoming a general approach to targeted DNA cleavage. Indeed, unnatural amino acids with photoremovable compounds (6-nitroveratryloxycarbonyl, azophenylalanine and 4′-carboxyphenylazophenylalanine), were incorporated by *in vitro* translation at the dimer interface of *Bam*HI to generate photoswitchable restriction enzyme.[31−33] Moreover, chemical modification of the scPvuII variant by the photosensitive azobenzene derivative which reversibly isomerizes between *cis* and *trans* forms under the influence of light, resulted in the photoswitchable derivative of the scPvuII.[34]

The alternative strategy presented here makes use of attenuated dimerization of the monomeric mutant of restriction endonuclease Bse634I (Figure 2, "controlled dimerization"). In general, it resembles the artificial zinc-finger and TALE nuclease strategy (Figure 1B–C): in all cases two nuclease monomers dimerize and cut DNA only when are brought into close proximity by the site-specific interactions of the DNA binding modules, the only difference being the identity of the nuclease (site-specific REase vs nonspecific DNA cleavage domain) and DNA binding module (triplex forming oligonucleotides vs an array of zinc-finger or TALE repeat domains).

Triggering of DNA cleavage activity by Bse634I upon triple helix formation should enable addressed DNA cleavage without a separate preincubation step given the reaction buffer is compatible with triplex formation and DNA cleavage. We met these requirements by using TFOs with methyl-2′-deoxycytidine and 5-[1-propynyl]-2-deoxyuridine modifications that stabilize triplex formation at near-neutral pH and the reaction buffer supplemented with Mg^{2+} (see Experimental Procedures for details). Indeed, the equimolar mixture of monomeric Bse634I-TFO1 and Bse634I-TFO2 conjugates cuts the "addressed" DNA site and shows no cleavage at the nonaddressed Bse634I sites (Figure 5). Currently, this experimental approach is limited by the availability of restriction endonucleases with attenuated dimerization interface. In fact, the R226A mutant of Bse634I is the only biochemically characterized REase that meets the practical requirements, such as high stability and solubility of the monomeric form and the ability to dimerize on cognate DNA at high concentrations. The nonspecific catalytic domain of FokI, currently used in the zinc-finger nuclease technology, might also be coupled to TFO. However, in this case the specificity of the FokI(nuclease)–TFO conjugate will be determined solely by the TFO–TFS interaction that might be insufficient for highly specific DNA cleavage. It would be interesting to see whether the monomeric Bse634I mutant could substitute for the FokI cleavage domain in the artificial zinc-finger or TALE endonucleases, as the extra specificity of the restriction endonuclease module might reduce off-target cleavage.

The ultimate goal of REase–TFO conjugates is cleavage of unique genomic DNA sites *in vivo*. This would require effective means to deliver the conjugate into the cell nucleus, chemical stabilization of TFOs to prevent degradation by cellular nucleases, stabilization of the TFO–TFS interaction to ensure formation of triple helixes under cellular milieu conditions, and means to control the nonaddressed DNA cleavage. The MunI–TFO and Bse634I–TFO conjugates presented here are the first step toward *in vivo* applications. However, a number of limitations have to be overcome: (i) UV irradiation reactivates the MunI–TFO conjugate permanently; upon prolonged incubation this may lead to accumulation of free MunI dimers in solution that would cleave nonaddressed DNA sites; (ii) formation of stable triplexes by the unmodified oligonucleotide (caged MunI–TFO conjugate) and even oligonucleotides containing 5-methyl-2′-deoxycytidine and 5-[1-propynyl]-2-deoxyuridine modifications (Bse634I–TFO conjugates) requires stabilizing factors such as high salt or spermine that are incompatible with cellular environment; (iii) the long tripartite sequences recognized by the MunI–TFO homodimer or by the combination of two Bse634I–TFO conjugates (the REase site surrounded by two long polypurine tracts) may be too rare in the genomic regions of interest; (iv) the Bse634I monomer guided to the recognition site by TFO–TFS interaction may capture the second Bse634I monomer from solution; this may decrease the specificity of Bse634I–TFO conjugates due to cleavage of additional Bse634I sites containing only a single adjacent TFS. However, all the above limitations could be addressed using recent advancements in protein engineering and triplex forming oligonucleotide technology. For example, the permanent activation problem could be solved by using azobenzene-modified restriction endonuclease derivatives that can be reversibly switched on and off by light. Such reversible control over a 16-fold activity range was recently demonstrated

for scPvuII.[34] Triplex formation under native-like conditions would require longer TFOs with extra stabilizing modifications or coupling of chemically modified peptide nucleic acids.[35−38] This would concomitantly decrease the concentrations of conjugates required for addressed cleavage. Moreover, the development of oligonucleotides which allow specific recognition of mixed purine/pyrimidine sequences by triple helix formation[39−41] might expand the list of potential REase−TFO recognition sites in the target DNA. Finally, the dimerization interface of Bse634I endonuclease could be redesigned to prevent homodimerization and capture of the second subunit from solution as demonstrated for the FokI cleavage domain.[3,11] Despite the limitations for the *in vivo* applications, the MunI−TFO and Bse634I−TFO conjugates presented here represent useful tools for highly specific DNA cleavage *in vitro* and an advance in the development of REase−TFO conjugates as tools for genome editing.

■ ASSOCIATED CONTENT

Supporting Information

Generation of the MunI−TFO and Bse634I−TFO conjugates, catalytic activity of wt Bse634I and the monomeric mutant R226A, catalytic activity of His-tagged Bse634I and Bse634I−TFO conjugates on the supercoiled pUCAT1 DNA, DNA cleavage by the His-tagged Bse634I and the Bse634I−TFO conjugate. This material is available free of charge via the Internet at http://pubs.acs.org.

■ AUTHOR INFORMATION

Corresponding Author

*Tel: +370-5-2602108; Fax: +370-5-2602116; E-mail: siksnys@ibt.lt.

■ ACKNOWLEDGMENTS

We thank Prof. A. Pingoud and Dr. W. Wende for helpful discussions. We also acknowledge Dr. K. Eisenschmidt for plasmids and help with the cross-linking experiments. This work has been supported by the European Union Grant FP6-2006-15509-NEST.

■ REFERENCES

(1) Smithies, O., Gregg, R. G., Boggs, S. S., Koralewski, M. A., and Kucherlapati, R. S. (1985) Insertion of DNA sequences into the human chromosomal beta-globin locus by homologous recombination. *Nature 317*, 230−4.

(2) Mombaerts, P., Clarke, A. R., Hooper, M. L., and Tonegawa, S. (1991) Creation of a large genomic deletion at the T-cell antigen receptor beta-subunit locus in mouse embryonic stem cells by gene targeting. *Proc. Natl. Acad. Sci. U. S. A. 88*, 3084−7.

(3) Szczepek, M., Brondani, V., Buchel, J., Serrano, L., Segal, D. J., and Cathomen, T. (2007) Structure-based redesign of the dimerization interface reduces the toxicity of zinc-finger nucleases. *Nat. Biotechnol. 25*, 786−93.

(4) Silva, G., Poirot, L., Galetto, R., Smith, J., Montoya, G., Duchateau, P., and Paques, F. (2011) Meganucleases and other tools for targeted genome engineering: perspectives and challenges for gene therapy. *Curr. Gene Ther. 11*, 11−27.

(5) Arnould, S., Chames, P., Perez, C., Lacroix, E., Duclert, A., Epinat, J. C., Stricher, F., Petit, A. S., Patin, A., Guillier, S., Rolland, S., Prieto, J., Blanco, F. J., Bravo, J., Montoya, G., Serrano, L., Duchateau, P., and Paques, F. (2006) Engineering of large numbers of highly specific homing endonucleases that induce recombination on novel DNA targets. *J. Mol. Biol. 355*, 443−58.

(6) Paques, F., and Duchateau, P. (2007) Meganucleases and DNA double-strand break-induced recombination: perspectives for gene therapy. *Curr. Gene Ther. 7*, 49−66.

(7) Grizot, S., Epinat, J. C., Thomas, S., Duclert, A., Rolland, S., Paques, F., and Duchateau, P. (2010) Generation of redesigned homing endonucleases comprising DNA-binding domains derived from two different scaffolds. *Nucleic Acids Res. 38*, 2006−18.

(8) Kim, Y. G., Cha, J., and Chandrasegaran, S. (1996) Hybrid restriction enzymes: zinc finger fusions to Fok I cleavage domain. *Proc. Natl. Acad. Sci. U. S. A. 93*, 1156−60.

(9) Bibikova, M., Golic, M., Golic, K. G., and Carroll, D. (2002) Targeted chromosomal cleavage and mutagenesis in Drosophila using zinc-finger nucleases. *Genetics 161*, 1169−75.

(10) Beumer, K., Bhattacharyya, G., Bibikova, M., Trautman, J. K., and Carroll, D. (2006) Efficient gene targeting in Drosophila with zinc-finger nucleases. *Genetics 172*, 2391−403.

(11) Miller, J. C., Holmes, M. C., Wang, J., Guschin, D. Y., Lee, Y. L., Rupniewski, I., Beausejour, C. M., Waite, A. J., Wang, N. S., Kim, K. A., Gregory, P. D., Pabo, C. O., and Rebar, E. J. (2007) An improved zinc-finger nuclease architecture for highly specific genome editing. *Nat. Biotechnol. 25*, 778−85.

(12) Chou, C., and Deiters, A. (2011) Light-activated gene editing with a photocaged zinc-finger nuclease. *Angew. Chem., Int. Ed. Engl.*, DOI: 10.1002/anie.201101157.

(13) Christian, M., Cermak, T., Doyle, E. L., Schmidt, C., Zhang, F., Hummel, A., Bogdanove, A. J., and Voytas, D. F. (2010) Targeting DNA double-strand breaks with TAL effector nucleases. *Genetics 186*, 757−61.

(14) Li, T., Huang, S., Zhao, X., Wright, D. A., Carpenter, S., Spalding, M. H., Weeks, D. P., and Yang, B. (2011) Modularly assembled designer TAL effector nucleases for targeted gene knockout and gene replacement in eukaryotes. *Nucleic Acids Res.*,.

(15) Wood, A. J., Lo, T. W., Zeitler, B., Pickle, C. S., Ralston, E. J., Lee, A. H., Amora, R., Miller, J. C., Leung, E., Meng, X., Zhang, L., Rebar, E. J., Gregory, P. D., Urnov, F. D., and Meyer, B. J. (2011) Targeted genome editing across species using ZFNs and TALENs. *Science 333*, 307.

(16) Lippow, S. M., Aha, P. M., Parker, M. H., Blake, W. J., Baynes, B. M., and Lipovsek, D. (2009) Creation of a type IIS restriction endonuclease with a long recognition sequence. *Nucleic Acids Res. 37*, 3061−73.

(17) Arimondo, P. B., Thomas, C. J., Oussedik, K., Baldeyrou, B., Mahieu, C., Halby, L., Guianvarc'h, D., Lansiaux, A., Hecht, S. M., Bailly, C., and Giovannangeli, C. (2006) Exploring the cellular activity of camptothecin-triple-helix-forming oligonucleotide conjugates. *Mol. Cell. Biol. 26*, 324−33.

(18) Majumdar, A., Muniandy, P. A., Liu, J., Liu, J. L., Liu, S. T., Cuenoud, B., and Seidman, M. M. (2008) Targeted gene knock in and sequence modulation mediated by a psoralen-linked triplex-forming oligonucleotide. *J. Biol. Chem. 283*, 11244−52.

(19) Simon, P., Cannata, F., Perrouault, L., Halby, L., Concordet, J. P., Boutorine, A., Ryabinin, V., Sinyakov, A., and Giovannangeli, C. (2008) Sequence-specific DNA cleavage mediated by bipyridine polyamide conjugates. *Nucleic Acids Res. 36*, 3531−8.

(20) Frank-Kamenetskii, M. D., and Mirkin, S. M. (1995) Triplex DNA structures. *Annu. Rev. Biochem. 64*, 65−95.

(21) Eisenschmidt, K., Lanio, T., Simoncsits, A., Jeltsch, A., Pingoud, V., Wende, W., and Pingoud, A. (2005) Developing a programmed restriction endonuclease for highly specific DNA cleavage. *Nucleic Acids Res. 33*, 7039−47.

(22) Siksnys, V., Zareckaja, N., Vaisvila, R., Timinskas, A., Stakenas, P., Butkus, V., and Janulaitis, A. (1994) CAATTG-specific restriction-modification munI genes from Mycoplasma: sequence similarities between R.MunI and R.EcoRI. *Gene 142*, 1−8.

(23) Grazulis, S., Deibert, M., Rimseliene, R., Skirgaila, R., Sasnauskas, G., Lagunavicius, A., Repin, V., Urbanke, C., Huber, R., and Siksnys, V. (2002) Crystal structure of the Bse634I restriction endonuclease: comparison of two enzymes recognizing the same DNA sequence. *Nucleic Acids Res. 30*, 876−85.

(24) Silanskas, A., Foss, M., Wende, W., Urbanke, C., Lagunavicius, A., Pingoud, A., and Siksnys, V. (2011) Photocaged variants of the MunI and PvuII restriction enzymes. *Biochemistry 50*, 2800−7.
(25) Fritsche, P., and Alves, J. (2004) A monomeric mutant of restriction endonuclease EcoRI nicks DNA without sequence specificity. *Biol. Chem. 385*, 975−85.
(26) Zaremba, M., Sasnauskas, G., Urbanke, C., and Siksnys, V. (2006) Allosteric communication network in the tetrameric restriction endonuclease Bse634I. *J. Mol. Biol. 363*, 800−12.
(27) Deibert, M., Grazulis, S., Janulaitis, A., Siksnys, V., and Huber, R. (1999) Crystal structure of MunI restriction endonuclease in complex with cognate DNA at 1.7 A resolution. *Embo J. 18*, 5805−16.
(28) Lagunavicius, A., Grazulis, S., Balciunaite, E., Vainius, D., and Siksnys, V. (1997) DNA binding specificity of MunI restriction endonuclease is controlled by pH and calcium ions: involvement of active site carboxylate residues. *Biochemistry 36*, 11093−9.
(29) Sasnauskas, G., Jeltsch, A., Pingoud, A., and Siksnys, V. (1999) Plasmid DNA cleavage by MunI restriction enzyme: single-turnover and steady-state kinetic analysis. *Biochemistry 38*, 4028−36.
(30) Zaremba, M., Sasnauskas, G., Urbanke, C., and Siksnys, V. (2005) Conversion of the tetrameric restriction endonuclease Bse634I into a dimer: oligomeric structure-stability-function correlations. *J. Mol. Biol. 348*, 459−78.
(31) Endo, M., Nakayama, K., and Majima, T. (2004) Design and synthesis of photochemically controllable restriction endonuclease BamHI by manipulating the salt-bridge network in the dimer interface. *J. Org. Chem. 69*, 4292−8.
(32) Nakayama, K., Endo, M., and Majima, T. (2004) Photochemical regulation of the activity of an endonuclease BamHI using an azobenzene moiety incorporated site-selectively into the dimer interface. *Chem. Commun. (Camb.)*, 2386−7.
(33) Nakayama, K., Endo, M., and Majima, T. (2005) A hydrophilic azobenzene-bearing amino acid for photochemical control of a restriction enzyme BamHI. *Bioconjugate Chem. 16*, 1360−6.
(34) Schierling, B., Noel, A. J., Wende, W., Hien le, T., Volkov, E., Kubareva, E., Oretskaya, T., Kokkinidis, M., Rompp, A., Spengler, B., and Pingoud, A. (2010) Controlling the enzymatic activity of a restriction enzyme by light. *Proc. Natl. Acad. Sci. U.S.A. 107*, 1361−6.
(35) Keppler, M. D., James, P. L., Neidle, S., Brown, T., and Fox, K. R. (2003) DNA sequence specificity of triplex-binding ligands. *Eur. J. Biochem. 270*, 4982−92.
(36) Osborne, S. D., Powers, V. E., Rusling, D. A., Lack, O., Fox, K. R., and Brown, T. (2004) Selectivity and affinity of triplex-forming oligonucleotides containing 2′-aminoethoxy-5-(3-aminoprop-1-ynyl)-uridine for recognizing AT base pairs in duplex DNA. *Nucleic Acids Res. 32*, 4439−47.
(37) Gerrard, S. R., Edrees, M. M., Bouamaied, I., Fox, K. R., and Brown, T. (2010) CG base pair recognition within DNA triple helices by modified N-methylpyrrolo-dC nucleosides. *Org. Biomol. Chem. 8*, 5087−96.
(38) Hansen, M. E., Bentin, T., and Nielsen, P. E. (2009) High-affinity triplex targeting of double stranded DNA using chemically modified peptide nucleic acid oligomers. *Nucleic Acids Res. 37*, 4498−507.
(39) Gowers, D. M., Bijapur, J., Brown, T., and Fox, K. R. (1999) DNA triple helix formation at target sites containing several pyrimidine interruptions: stabilization by protonated cytosine or 5-(1-propargylamino)dU. *Biochemistry 38*, 13747−58.
(40) Rusling, D. A., Powers, V. E., Ranasinghe, R. T., Wang, Y., Osborne, S. D., Brown, T., and Fox, K. R. (2005) Four base recognition by triplex-forming oligonucleotides at physiological pH. *Nucleic Acids Res. 33*, 3025−32.
(41) Wang, Y., Rusling, D. A., Powers, V. E., Lack, O., Osborne, S. D., Fox, K. R., and Brown, T. (2005) Stable recognition of TA interruptions by triplex forming oligonucleotides containing a novel nucleoside. *Biochemistry 44*, 5884−92.

Bioconjugate Chemistry

Article

pubs.acs.org/bc

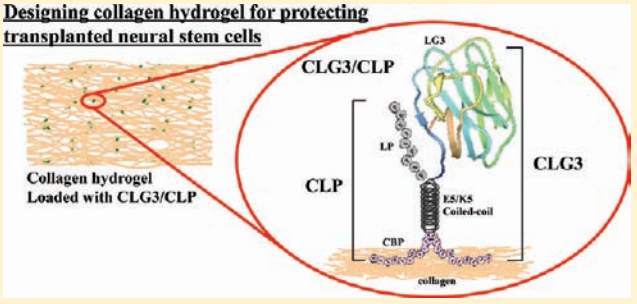
Improvement of Neural Stem Cell Survival in Collagen Hydrogels by Incorporating Laminin-Derived Cell Adhesive Polypeptides

Tadashi Nakaji-Hirabayashi,[†] Koichi Kato,[‡] and Hiroo Iwata*

Institute for Frontier Medical Sciences, Kyoto University, 53 Kawahara-cho, Shogoin, Sakyo-ku, Kyoto 606-8507, Japan

Supporting Information

ABSTRACT: Cell transplantation is a potential methodology for the treatment of Parkinson's disease. However, the therapeutic effect is limited by poor viability of transplanted cells. To overcome this problem, we hypothesized that a dual step approach, whereby providing an adhesive substrate for transplanted cells and, at the same time, by preventing the infiltration of activated microglia into the site of transplantation promotes the cell survival. To establish above conditions, attempts were made to prepare 3-D matrices using collagen hydrogels that incorporated integrin-binding polypeptides derived from laminin-1. Tandem combinations of laminin globular domains as well as a single globular domain 3 were prepared using recombinant DNA technology as a fusion with hexahistidine and bound to metal chelated surfaces to screen for the adhesion and proliferation of neural stem cells (NSCs). In addition, a small peptide derived from laminin γ1 chain was prepared and heterodimerized with the globular domain-containing chimeric proteins to evaluate for the enhancement of integrin-mediated cell adhesion. As a result, a heterodimer consisting of the globular domain 3 of the laminin α1 chain and the peptide from the laminin γ1 chain was selected as the best candidate among the polypeptides studied here for the incorporation into a collagen hydrogel. It was shown that the survival of NSCs was indeed promoted in the collagen hydrogel incorporating the heterodimer compared to the pure collagen hydrogel.



INTRODUCTION

Cell transplantation has been regarded as a potential treatment for Parkinson's disease.[1] To date animal studies have been carried out using cell sources such as embryonic stem cells,[2] induced-pluripotent stem cells,[3] and embryonic neural stem cells (NSCs).[4] These studies have reported encouraging results. However, various problems still remain to be addressed before clinical applications of this treatment.

One of the most critical problems is poor viability of transplanted cells, which limits the efficacy of cell transplantation.[5,6] For instance, Piccini et al. reported that most of the cells infused into the striatum of an animal Parkinson's model died at an early stage after transplantation.[6] The following two mechanisms may be involved in the poor survival of transplanted cells: One is apoptotic cell death caused by disruption of cell−cell and cell−substrate interactions,[7,8] and the other is cell damage caused by acute inflammatory responses.[9,10]

To overcome this problem, we hypothesized that a dual step approach would be beneficial, whereby providing an adhesive substrate for transplanted cells and, at the same time, by preventing infiltration of activated microglia into the site of transplantation would promote the cell survival. To establish the above conditions, we have utilized biodegradable hydrogels in which integrin-binding peptides are incorporated. The hydrogel is expected to serve as a physical barrier against invading inflammatory microglia that would impair transplanted cells by phagocytosis, while the peptides bind to integrins to transduce adhesion signaling in order to prevent apoptotic cell death.

According to the previous studies,[11−15] we first considered designing laminin-based hydrogels to provide cell adhesive substrates. Although similar approaches such as incorporating cell adhesive polypeptides were also adopted by others, using the native form of laminin is not practical because of the difficulty in controlling the amount of immobilized protein and maintaining its activity due to the large size (a heterotrimer of approximately 90 kDa) and poor stability. Therefore, in our previous study,[16,17] a hydrogel such as type I collagen or keratin was modified with a peptide derived from the G3 domain of a laminin α3 chain. The G3 domain of laminin α3 chain was reported to have an affinity for $\alpha_3\beta_1$ integrin.[18] Our results showed that a population containing NSCs survived longer periods in the modified collagen hydrogel than in the pure collagen hydrogel.

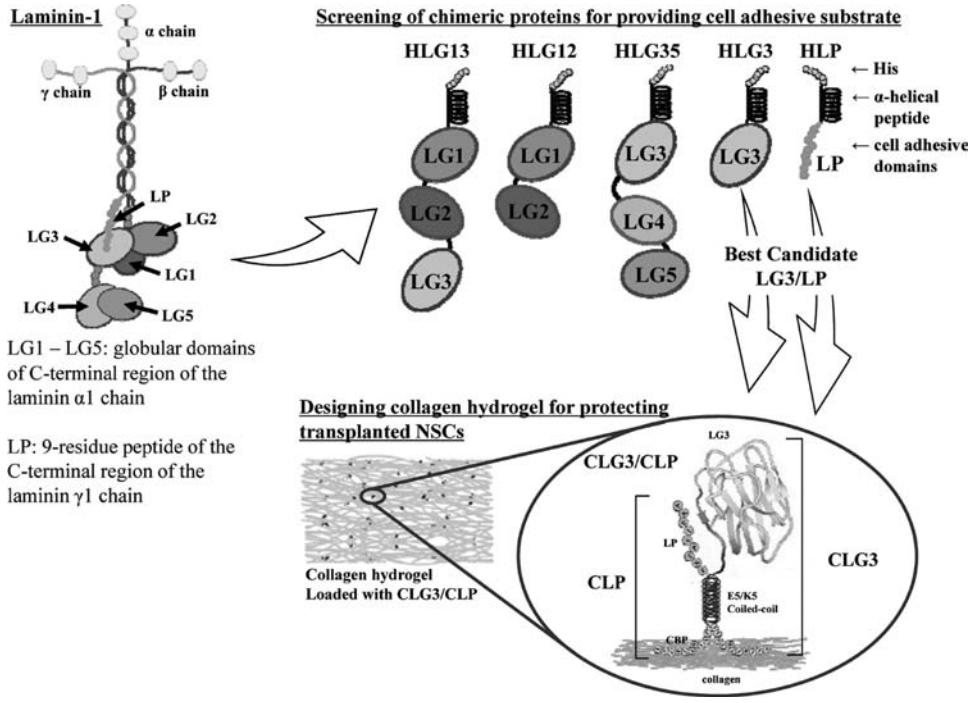
In an attempt to seek more effective ligands than the laminin α3 chain-derived ligand, the present study was undertaken to explore the effect of other domains derived from laminin. In this study, tandem combinations of globular domains derived from laminin α1 chain as well as a single G3 domain (these

Received: September 2, 2011
Revised: December 17, 2011
Published: January 10, 2012

ACS Publications © 2012 American Chemical Society

dx.doi.org/10.1021/bc200481v | Bioconjugate Chem. 2012, 23, 212−221

Scheme 1. Schematic Illustration of Our Strategy in the Present Work[a]



[a]We focused on the cell adhesive domains of laminin-1 for designing hydrogels to protect NSCs. Chimeric proteins containing laminin-derived cell adhesive polypeptides, HLGs and HLP, were prepared and screened for the best candidate to promote cell adhesion. Consequently the complex containing LG3 and LP was selected as the best candidate. Then, LG3/LP complex containing collagen binding peptide (CLG3/CLP) was prepared to construct a collagen hydrogel in which adhesion signals are transduced into NSCs through interactions of their integrins with CLG3/CLP.

proteins are referred to as LGs hereafter) were prepared using recombinant DNA technology as a fusion with a peptide for immobilizing to materials (Scheme 1).

■ EXPERIMENTAL PROCEDURES

Expression Constructs. *Hexahistidine-Tagged LGs (HLGs).* A laminin α1 chain contains five globular domains (G1 to G5) at the C-terminal region. We amplified DNAs encoding one or some of the globular domains by polymerase chain reaction (PCR) using a human brain cDNA library as a template. These DNAs encoded G1 and G2 (LG12), G1 to G3 (LG13), G3 to G5 (LG35), and G3 alone (LG3). In addition, DNA encoding an α-helical peptide (E5; $[KELASVE]_5$) was separately amplified by PCR using pET22-EGF-E5 plasmid[19] as a template. Primers used for these PCR were designed to perform subsequent overlap extension and to obtain chimeric DNAs encoding E5 and one of the LGs. The sequences of all primers are shown in Table S1a (Supporting Information). A forward primer for E5 contained an Nde I site (this site contained the start codon) and a sequence encoding hexahistidine (His). A reverse primer for E5 and forward primers for LGs contained 20-nucleotide sequences that overlap each other. Reverse primers for LGs contained a stop codon and a Xho I site. PCR was carried out under the following cycling conditions: For E5, 35 cycles of denaturation for 30 s at 96 °C, annealing for 30 s at 58 °C, and extension for 30 s at 72 °C; For LGs, 35 cycles of denaturation for 30 s at 96 °C, annealing for 30 s at 56 °C, and extension for 2 min at 72 °C. The overlapping fragments thus obtained were denatured, annealed to generate heteroduplexes, and extended to obtain full-length chimeric DNAs. For this fill-in reaction, the following cycling conditions were employed: 7 cycles of denaturation for 1 min at 96 °C and annealing/extension for 4 min at 61 °C. Then, products obtained by the fill-in reaction were used to amplify chimeric DNAs by priming with outer primers (forward primer for E5 and reverse primer for LGs) under the following cycling conditions: 35 cycles of denaturation for 30 s at 96 °C, annealing for 30 s at 56 °C, and extension for 2 min at 72 °C. The amplified DNAs were digested with Nde I and Xho I and then unidirectionally ligated to pET-22b (Novagen, Darmstadt, Germany) previously linearized by Nde I and Xho I. The plasmids were cloned in *Escherichia coli* (*E. coli*) strain DH5α to obtain expression constructs (pET22-HX, X = LG12, LG13, LG35, or LG3). The correctness of the inserts was verified by sequencing.

Histidine-Tagged LP (HLP). A plasmid was constructed for the expression of a fusion protein that contained (in the order from N- to C-terminus) enhanced green fluorescent protein (EGFP), thrombin-cleavage site (TCS), hexahistidine (His), α-helical peptide (K5, $[EKLASVK]_5$),[19] and LP (FNTPSIEKP). DNA encoding EGFP was amplified using pEGFP-C1 (Clontech Laboratories, Inc., Mountain View, CA) as a template. The primers used were designed to introduce an Nde I site at the 5′ end of the product, and TCS and BamH I sites at the 3′ end (Table S1b, Supporting Information). PCR was carried out under the following cycling conditions: 35 cycles of denaturation for 30 s at 96 °C, annealing for 30 s at 56 °C, and extension for 1 min at 72 °C. Then, the DNA fragment was inserted to the Nde I–BamH I site of pET-22b(+) to obtain pET22-EGFP. Separately, DNA encoding K5 was amplified using pET22-EGF-K5[19] as a template. A forward primer contained a BamH I site and a sequence encoding His. A reverse primer contained a sequence encoding LP, a stop codon, and a Xho I site (Table S1c, Supporting Information).

dx.doi.org/10.1021/bc200481v | *Bioconjugate Chem.* 2012, 23, 212–221

PCR was carried out under the following cycling conditions: 35 cycles of denaturation for 30 s at 96 °C, annealing for 30 s at 58 °C, and extension for 30 s at 72 °C. The DNA fragment thus obtained was inserted to the BamH I−Xho I site of pET22-EGFP to obtain pET22-EGFP-HLP. The correctness of the inserts was verified by sequencing.

Collagen Binding LG3 and LP (CLG3 and CLP). Plasmids for the expression of LG3 and LP fused with CBP (SYIRIADTNIT)[20] were constructed in a similar fashion to the case of His-tagged LGs and LP described above, but forward primers containing a sequence encoding His-TCS-CBP were used in the PCR for the amplification of E5- and K5-genes (Table S1d, Supporting Information). DNA encoding CBP-E5-LG3 and CBP-K5-LP was amplified using pET22-HLG3 and pET22-EGFP-HLP as a template, respectively. This allowed us to obtain CBP-E5-LG3 and CBP-K5-LP after removal of His by digestion of TCS with thrombin. The plasmids constructed here are referred to as pET22-CBP-LG3 and pET22-EGFP-CBP-LP.

Expression, Purification, and Refolding of Proteins. *E. coli* strain BL21-codon plus (Stratagene, La Jolla, CA) was transformed with pET22-HLGs, pET22-EGFP-HLP, pET22-CBP-LG3, or pET22-EGFP-CBP-LP, and grown using Overnight Express Autoinduction System (Novagen).

HLG13, HLG12, HLG35, HLG3, and CLG3 expressed as inclusion bodies were extracted with 20 mM phosphate buffer containing 8 M urea, 20 mM imidazole, and 10 mM 2-mercaptoethanol, and purified by Ni-chelate chromatography using an ÄKTA Prime system (GE Healthcare Bio-Science Corp., Piscataway, NJ) equipped with a His Trap HP column (GE Healthcare). These proteins were refolded by stepwise dialysis against a series of buffer solutions (compositions are shown in Table S2, Supporting Information). After refolding, His was removed from His-TCS-CBP-LG3 using a Thrombin Cleavage Capture kit (Novagen) to obtain CBP-LG3.

HLP and CLP fused with EGFP were obtained in the soluble form. These proteins were loaded to His Trap HP columns. To these columns, 10 units/mL thrombin solution in 20 mM tris(hydroxymethyl)aminomethane (Tris)-HCl, 150 mM NaCl, and 2.5 mM $CaCl_2$ (pH 8.0) were injected to allow for digestion of the TCS at 37 °C for 16 h. Then, EGFP cleaved was eluted with 20 mM sodium phosphate buffer (pH 7.4) containing 20 mM imidazole and 0.2% Tween 20. Subsequently, HLP and CLP left in the columns were eluted with 20 mM sodium phosphate buffer (pH 7.4) containing 500 mM imidazole. Finally, the solutions containing HLP and CLP were dialyzed against phosphate buffered saline (PBS) using dialyzer (MWCO 3.5 kDa).

The purity and the molecular size of the proteins were analyzed by sodium dodecylsulfate-polyacrylamide gel electrophoresis (SDS-PAGE) under reduced conditions.

Circular Dichroism Spectroscopy. Stock solutions of HLG3 and HLP were diluted with 5 mM Tris-HCl buffer (pH 8.0) to a mean residual concentration of 0.87 mM (HLG3) and 0.89 mM (HLP). Similarly, a solution containing both HLG3 and HLP (HLG3/HLP) was prepared by mixing 10.6 μM HLG3 with 10.6 μM HLP. Circular dichroism (CD) spectra were recorded for these solutions with a JASCO J-805 spectropolarimeter (JASCO International Co. Ltd., Tokyo, Japan) using a 0.1 cm path length cell at 20 °C with an accumulation of 8 scans.

To assess heterodimerization, the CD spectrum of the mixture of HLG3 and HLP was compared with the synthetic curve obtained from the individual spectra of HLG3 and HLP. The synthetic curve was obtained using the following equation:

$$[\theta](\lambda)_{syn} = \frac{N_{HLG3}[\theta](\lambda)_{HLG3} + N_{HLP}[\theta](\lambda)_{HLP}}{N_{HLG3} + N_{HLP}} \quad (1)$$

where $[\theta](\lambda)_{syn}$ is the molar ellipticity of a synthetic curve at a wavelength of λ. $[\theta](\lambda)_{HLG3}$ and $[\theta](\lambda)_{HLP}$ are the molar ellipticity of HLG3 and HLP, respectively, at a wavelength of λ. N_{HLG3} and N_{HLP} are the number of amino acid residues contained in HLG3 and HLP, respectively.

Immobilization of His-Tagged Chimeric Proteins onto Glass Surface. As previously reported,[19,21−24] HLGs and HLP were anchored to the Ni^{2+}-bound surface of a glass plate. In brief, the self-assembled monolayer of 11-mercapto-1-undecanoic acid (COOH-SAM) was formed on a gold-evaporated glass surface. The terminal carboxylic acid was activated by 1-ethyl-3-(3-dimethylaminopropyl)carbodiimide and *N*-hydroxysuccinimide and then coupled with *N*-(5-amino-1-carboxypentyl) iminodiacetic acid to introduce triacetic acid onto the surface. The surface was then exposed to $NiSO_4$ solution to chelate Ni(II) ions followed by exposure to the solutions of HLGs or HLP (3 μM) to coordinate these proteins to the fixed Ni(II) ions. To examine the effects of HLG/HLP dimers, an equal volume of each protein solution (each 35 μM) was mixed and diluted to the final concentration of each 3 μM just before coordination.

The amount of immobilized proteins was determined using a microBCA protein assay kit (Pierce Biotechnology, Inc., Rockford, IL). A silicon frame having a square window (inner area: 3.96 cm^2) was placed on the surface with immobilized chimeric protein. The microBCA reaction mixture (325 μL) was pipetted within the window, and the temperature was kept at 37 °C for 2 h to allow for coloring reaction. The absorbance at 570 nm was measured for the resultant solution using a microplate reader (model 680, Bio-Rad Laboratories, Inc., Hercules, CA). The amount of immobilized chimeric protein was determined using bovine serum albumin as a standard.

Immobilization of CLG3/CLP onto Collagen-Coated Substrates. Types I and III atelocollagen solution (0.1 mg/mL, Nippon Meat Packers, Inc., Osaka, Japan, referred to as just collagen hereafter) in HCl solution (pH 2−3) was added to a tissue culture polystyrene dish and incubated for 1 h to adsorb collagen onto the dish. The dish was then washed with 0.01 M HCl solution to remove unbound collagen. Subsequently, PBS was added to the dish and incubated for 2 h at 37 °C to allow for the regeneration of collagen fibrils. Then, the collagen-coated dish was exposed to PBS with or without CLG3 and CLP (each 3 μM). After 2 h incubation, the dish was extensively washed with PBS to remove weakly bound CLG3 and CLP. As a negative control, a collagen-coated dish was exposed to a mixture of CBP-deficient HLG3 and HLP (each 3 μM).

Cell Isolation and Culture. The striatum was isolated from fetuses (E16) of Fischer344 rats according to the guidelines of the Animal Welfare Committee of the institute, and dissociated into single cells by treating with 0.05% trypsin solution containing 0.53 mM ethylenediamine-*N*,*N*,*N*′,*N*′-tetraacetic acid (EDTA). The single cells obtained were suspended in a base medium [DMEM/F12 (1:1) (Invitrogen, Carlsbad, CA) containing 3 mM glutaMAX (Invitrogen), 5 μg/mL heparin,

100 unit/mL penicillin, and 100 μg/mL streptomycin] supplemented with 2% B27 (Invitrogen), 20 ng/mL basic fibroblast growth factor, and 20 ng/mL epidermal growth factor (EGF), and cultured for 4−5 days to form neurospheres. Then, neurospheres were dissociated into single cells by treating with 0.05% trypsin solution containing 0.53 mM EDTA and seeded to the EGF-anchored substrates[23] at a density of 2.9×10^4 cells/cm^2. The cells were cultured for 7 days in the base medium containing 2% B27 at 37 °C under 5% CO_2. According to the result of immunostaining, more than 95% of the cells expressed nestin, a marker for neural stem cells (NSCs). This population is referred to as NSCs in this paper.

Cell Adhesion and Proliferation Assays. NSCs were harvested from the EGF-anchored substrate by treating with 0.05% trypsin-EDTA solution for 2 min, and suspended in the base medium containing 2% B27 and 20 ng/mL EGF. The cells were plated to the glass substrate with immobilized HLGs and HLP at a density of 3×10^4 cells/cm^2. Then, the cells were incubated for 1−7 days at 37 °C under 5% CO_2 atmosphere. Finally, cells were washed gently with the base medium to remove weakly adhering cells, and observed with a phase-contrast optical microscope (IX71, Olympus Optical CO., Ltd., Tokyo, Japan).

To quantify cell number, cells grown on the substrates were fixed with 4% paraformaldehyde solution, and cell nuclei were stained with Hoechst33258 (Dojindo Laboratories, Kumamoto, Japan). Stained nuclei were counted on the area of 656×870 μm^2 under a fluorescent microscope. On the other hand, fixed cells were first permeabilized with 0.5% Triton X-100 solution, and cytosolic F-actin was stained with Alexa Fluor 594 phalloidin (Invitrogen). The area occupied by cells was determined on the fluorescent image of stained cells using *Image J* (National Institutes of Health, Bethesda, MD), and was normalized in respect to total cell numbers.

To investigate integrin-mediated cell adhesion, NSCs were suspended in the base medium containing 2% B27, 20 ng/mL EGF with or without 5 μg/mL antibody to α_6 or β_1 integrin (both from Santa Cruz Biotechnology, Inc., Santa Cruz, CA) and seeded to the surface with immobilized HLG3 or HLG3/HLP. As positive and negative controls, laminin-1 (Invitrogen) and bovine serum albumin (Sigma-Aldrich Corp., St. Louis, MO), respectively, were adsorbed to the surface of COOH-SAM. After 1 d culture, cells were fixed, permeabilized, and stained with Hoechst as described above. Stained nuclei were observed with the fluorescent microscope and counted on ten different sites on a single sample. The data are shown here as the mean ± standard deviation for five independent samples.

Amount of CLG3/CLP Remaining in Collagen Hydrogel. Collagen solution was neutralized by mixing with buffer solution (50 mM NaOH, 260 mM $NaHCO_3$, and 200 mM HEPES), 5-fold concentrated base medium, and chimeric protein solution (CLG3 and CLP) on ice at a volume ratio of 9:2:4:5. The final concentration of collagen in the mixture was 4.5 mg/mL, and that of chimeric proteins was 3 μM for both CLG3 and CLP. This mixture (1 mL) was added into each well of a 12-well nontreated tissue culture polystyrene plate and incubated for 1.5 h at 37 °C to allow for gelation. Then, the base medium (2.5 mL) was added over the gel and kept at 37 °C. The medium was exchanged every 12 h. A piece of collagen hydrogel (ca. 150 mg) was collected at 1, 3, 5, and 7 days of incubation. The samples were dissolved in an equal volume (ca. 150 μL) of Laemmli sample buffer (Bio-Rad Laboratories) containing 5% β-mercaptoethanol, heated at 95 °C for 10 min, and electrophoresed in 12.5% polyacrylamide gel. Proteins migrated in the gel were stained with Coomassie brilliant blue. The band intensity of CLG3 was determined using *Image J* software (National Institutes of Health, Bethesda, MD), and the amount of CLG3 remaining in a hydrogel was determined using a standard curve obtained with CLG3 solutions of known concentrations.

Cell Culture in Collagen Hydrogel. NSCs were cultured in two different manners: sandwich and 3-D cultures.

Sandwich Culture. Four hundred and fifty microliters of 10 mg/mL collagen solution was mixed with 100 μL buffer solution containing 50 mM NaOH, 260 mM $NaHCO_3$, and 200 mM HEPES and 200 μL of 5-fold concentrated base medium supplemented with 10% B27. To this collagen solution, a mixed solution of CLG3/CLP was added to the final concentration of 3 μM for each protein. An aliquot of the mixture (500 μL) was added into each well of a 12-well nontreated tissue culture polystyrene plate, and incubated at 37 °C for 1 h to allow for the formation of hydrogels with a thickness of approximately 250 μm. NSCs harvested from the EGF-anchored substrate were suspended in 1 mL of base medium containing 2% B27, and seeded onto the previously formed hydrogel at 5×10^4 cells/cm^2 (1×10^5 cells/mL). Cells were incubated for 2−3 h to adhere on the hydrogel. After washing with base medium to remove weakly adhering cells, 500 μL of the mixed solution (the same solution as for the basement hydrogel) was added to the cell layer to establish sandwich culture. Finally, base medium containing 2% B27 and 20 ng/mL EGF was mounted on the collagen hydrogel, and cells were further cultured for 1−7 days in an incubator at 37 °C under 5% CO_2 atmosphere.

3-D Culture. Collagen solution of the same condition described above was prepared on ice and then mixed with NSCs (1×10^5 cells/mL). The hydrogel/cell mixtures were added to each well of a 12-well nontreated tissue culture polystyrene plate. After 1 h incubation at 37 °C, the base medium (1 mL) containing 2% B27 and 20 ng/mL EGF was mounted on the hydrogels. Cells were further cultured for 7 days.

Assay for Living Cells. The live/dead assay for cells cultured in a hydrogel was performed as previously reported.[25] In brief, cells cultured for 1−7 days in a hydrogel with or without incorporated chimeric proteins were exposed to the base medium containing 2 μg/mL 3′,6′-di(*O*-acetyl)-4′5′-bis[*N*,*N*-bis(carboxymethyl)aminomethyl]fluorescein tetraacetoxymethyl ester (calcein-AM, Dojindo Laboratories) and 4 μg/mL propidium iodide (PI, BD Pharmingen) for 30 min in collagen hydrogel and then washed with PBS containing 0.05 mM $MgCl_2$ and 0.9 mM $CaCl_2$. In this procedure, calcein-AM penetrates into the cytosol of living cells and fluorescently stains them green, while PI fluorescently stains the nucleus of dead cells in red. The microphotographs of cells stained in green and red were recorded using a fluorescent microscope. To quantify total and living cells, hydrogels were immersed in a solution containing 1% collagenase for 1 h at 37 °C to completely dissolve hydrogel. Then trypsin-EDTA solution was added to concentration of 0.05% into collagenase-treated sample and incubated for 15 min at 37 °C to release stained cells. The cells were collected by centrifugation and suspended in 100 μL PBS. Cells stained in green (living cell) were counted on a hemocytometer under a fluorescent microscope, while total cell numbers were determined by staining nuclei with Hoechst. The number of living and dead cells was normalized

by total cell number. The data are presented here as the mean ± standard deviation for seven independent samples.

RESULTS

Synthesis and Surface Immobilization of Chimeric Proteins. Figure 1A shows the domain structure of chimeric

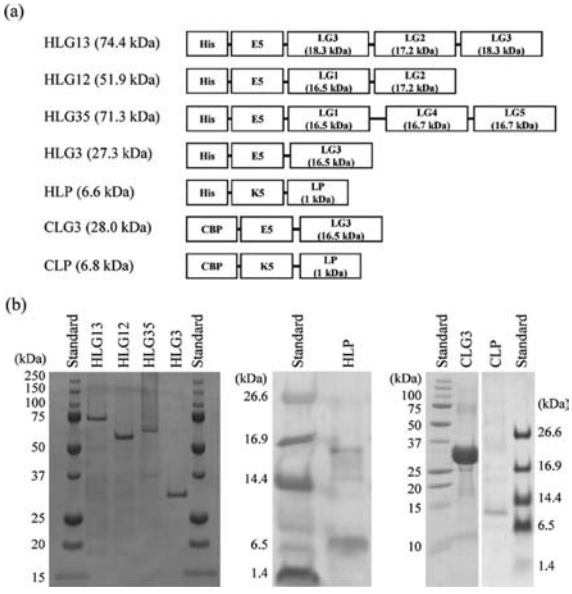


Figure 1. Chimeric proteins synthesized in this study. (a) Domain structures and nomenclatures of the chimeric proteins. His: hexahistidine. E5 and K5: α-helical oligopeptides. LG1−LG5: laminin α1 chain G1−G5 domains. LP: laminin γ1 chain C-terminal peptide. CBP: collagen binding peptide. Numbers in parentheses are molecular weights (kDa) predicted from the amino acid sequence. (b) Results of SDS-PAGE analyses for the chimeric proteins. Lane identification is shown above the images. Standard: molecular weight standard.

proteins synthesized in this study. As shown in Figure 1B, all of the chimeric proteins were obtained and separated as single bands in SDS-PAGE. The molecular weights estimated from the mobility of protein bands are in near agreement with those estimated from their amino acid sequences.

The His-tagged chimeric proteins were immobilized alone or in combination with one of the HLGs with HLP (alone, HLGs; combination, HLGs/HLP) onto the Ni^{2+}-bound surface. Table 1 shows the result of microBCA assays for the surface density of immobilized proteins. As can be seen, all of the proteins were successfully immobilized. However, their surface densities were different depending on the type of proteins. This variation is primarily due to the difference in the molecular weight of these proteins (Figure S1, Supporting Information).

Screening of Chimeric Proteins. NSCs were dissociated into single cells and plated to substrates with various chimeric proteins. Surfaces with adsorbed albumin and laminin were used as negative and positive controls, respectively. Figure 2 shows the phase contrast micrographs of cells cultured for 3 days. To determine cell density, nuclei were stained with Hoechst and cells were counted on fluorescent micrographs (Figure S2, Supporting Information). Moreover, cell spreading was assessed from total areas occupied by phalloidin-stained cells (Figure S2, Supporting Information). The quantitative results are shown in Figure 3. It can be seen that cell adhesion and spreading are noticeable on the substrates with

Table 1. Surface Density of Immobilized Proteins Determined by Micro BCA Assays

immobilized protein	surface density (μg/cm^2)[a]
HLG13	1.02 ± 0.11
HLG13 + HLP	1.11 ± 0.32
HLG12	0.95 ± 0.16
HLG12 + HLP	0.89 ± 0.13
HLG35	0.99 ± 0.09
HLG35 + HLP	1.01 ± 0.36
HLG3	0.70 ± 0.13
HLG3 + HLP	0.61 ± 0.11
HLP	0.27 ± 0.11
Albumin[b]	1.02 ± 0.17
Laminin[b]	0.71 ± 0.09

[a]Expressed as mean ± standard deviation (n = 3). [b]Physically adsorbed to the COOH SAM from PBS containing 100 μg/mL albumin or laminin.

immobilized G3 domain-containing proteins including HLG13, HLG35, and HLG3, as well as the substrate with adsorbed laminin. In contrast, cell adhesion and spreading are less obvious on the surfaces with immobilized HLG12 or HLP as well as the substrate with adsorbed albumin. When HLP was coimmobilized with HLG3 or HLG35 (HLG3/HLP or HLG35/HLP), cell adhesion and spreading were significantly enhanced. These results indicate that HLP has an additional effect, though this peptide alone does not promote cell adhesion and extension. On the other hand, combining HLP with HLG13 (HLG13/HLP) exhibited minor effects. In HLG13, the G1 and G2 domains lie between the E5 polypeptide and the G3 domain. We speculate that these two domains hinder the proximal association of G3 with LP.

The combination of HLP with HLG3 (HLG3/HLP) gave rise to the highest number of adhering cells and the highest level of cell spreading among the HLG−HLP combinations studied, reaching the performance of the laminin-adsorbed surface. Accordingly, we focused on the HLG3/HLP combination in the succeeding study.

Substrate with Immobilized HLG3/HLP. To gain insight into the structure of HLG3 and HLP, CD spectra were recorded for their single solutions and mixture. As shown in Figure 4a, HLG3 (Figure 4a, solid line) in a single solution gave a spectrum that indicated the presence of β-sheet, turn, and random structures. The presence of these structures is consistent with the secondary structure contained in this domain determined by X-ray crystallography.[26,27] In addition, our previous study[20] revealed that the E5 polypeptide dissolved alone in solution had random structure. The spectrum for HLP (Figure 4a, dotted line) in a single solution represents α-helical structure with a negative Cotton effect at a wavelength of 208 and 222 nm, most likely due to the fact that K5 alone forms α-helical structure in solution, being similar to the case with dimerization of E5 and K5 polypeptides both fused with epidermal growth factor.[20] The CD spectrum for the mixture of HLG3 and HLP (Figure 4b, solid line) exhibited a profile similar to synthetic spectra (Figure 4b, dotted line) obtained from spectra for HLG3 (Figure 4a, solid line) and HLP (Figure 4a, dotted line) using eq 1, but the negative Cotton effects at 208 and 222 nm were obviously enhanced by combining HLG3 with HLP. This result suggests the formation of a coiled-coil between K5 and E5 and thus a HLG3−HLP heterodimer as we expected.

dx.doi.org/10.1021/bc200481v | Bioconjugate Chem. 2012, 23, 212−221

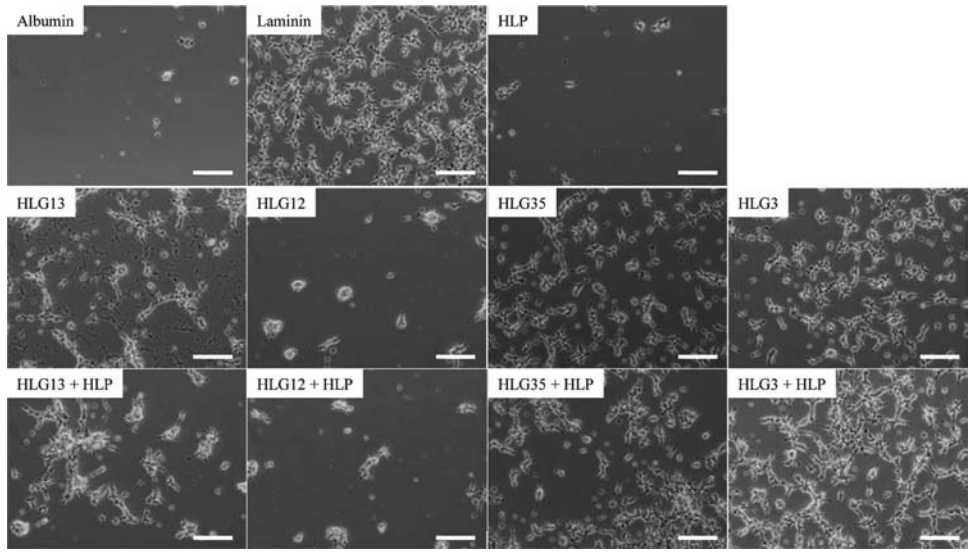


Figure 2. Phase contrast micrographs of cells cultured for 3 d on the surface with various chimeric and control proteins. Proteins immobilized or adsorbed to the surface are indicated on each micrograph. Scale bar: 100 μm.

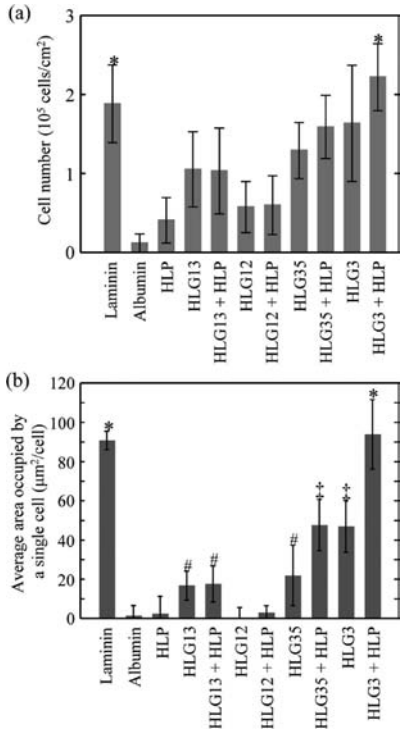


Figure 3. Screening of chimeric proteins: (a) the number and (b) the area occupied by cells on the surfaces with various chimeric proteins. The data are expressed as the mean ± standard deviation (n = 5). Symbols *, ‡, and # in (a) and (b) represent statistical significance (Tukey's HSD test, $p < 0.05$): * The substrate with laminin or HLG3/HLP was compared with all other substrates. ‡ The substrate with HLG3 or HLG35/HLP was compared with the substrate with albumin, HLP, HLG13, HLG13/HLP, HLG12, HLG12/HLP, or HLG35. # The substrate with HLG13, HLG13/HLP, or HLG35 was compared with the substrate with albumin, HLP, HLG12, or HLG12/HLP.

As shown in Figure 5, cell adhesion to the surface with HLG3 and HLP was totally inhibited by adding anti-α_6 or anti-β_1 integrin antibody to the medium. The addition of a mixture of HLG3 and HLP to the medium also inhibited cell adhesion. These results suggested that cell adhesion to the surface with immobilized HLG3/HLP was mediated exclusively by binding of surface-bound HLG3/HLP with integrin $\alpha_6\beta_1$ complex. On the surface with adsorbed laminin, the addition of these antibodies as well as HLG3/HLP partially impaired cell adhesion. Although $\alpha_6\beta_1$ integrin complex is considered to be a major target of the G3 domain of the laminin α1 chain[28,29] (The α1 chain is a component of laminin-1), an interaction with other integrins such as $\alpha_3\beta_1$ and $\alpha_7\beta_1$ complexes[30] might be involved in cell adhesion to the laminin-adsorbed surface.

Chimeric proteins, CLG3 and CLP, were further designed to display LG3 and LP on collagen using the decorin-derived CBP as an adaptor. Collagen was first adsorbed to the surface of a glass substrate. This was followed by the formation of the heterodimer of CLG3 and CLP (CLG3/CLP) by mixing of CLG3 solution and CLP solution at the same concentration and was immobilized on the collagen. The surface density of immobilized CLG3/CLP was determined by the microBCA assay in which collagen-adsorbed surface was used as background. As shown in Table 2, the CLG3/CLP was bound to the collage-adsorbed surface at a density of 0.33 μg/cm^2.

As shown in Figure 6, a large number of cells adhered and extended on the glass surface coated with collagen and subsequently exposed to a mixed solution of CLG3 and CLP (CLG3/CLP). On the contrary, few cells adhered to the surface that was coated with collagen and exposed to a solution of CBP-deficient HLG3 and HLP (HLG3/HLP), to a level similar to the collagen coated surface with no chimeric protein. These results demonstrate that CLG3/CLP are capable of binding to collagen to promote adhesion of NSCs likely through interactions with $\alpha_6\beta_1$ integrin.

Incorporation of CLG3/CLP into Collagen Hydrogel. A collagen solution was neutralized and immediately mixed with a solution of CLG3 and CLP (CLG3/CLP). The mixture was then kept for more 30 min at 37 °C to allow for gelation. To verify incorporation of these proteins, the hydrogel formed was immersed in a culture medium at 37 °C and the amount of remaining chimeric proteins was determined from the intensity of a CLG3 band separated by SDS-PAGE and visualized with Coomassie brilliant blue. As shown in Figure 7, approximately

dx.doi.org/10.1021/bc200481v | Bioconjugate Chem. 2012, 23, 212–221

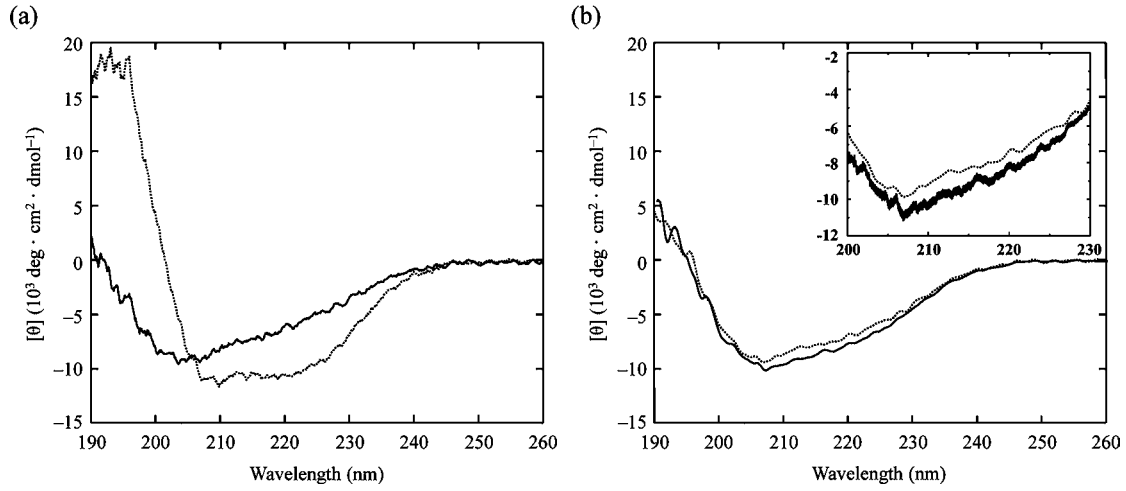


Figure 4. CD spectra of HLG3 (a, solid line), HLP (a, dotted line), and equimolar mixture of HLG3 and HLP (b, solid line). The dotted line in b represents the synthetic curve obtained from spectra of HLG3 and HLP (see Experimental Procedures for details). An inset in b represents magnified spectra for the wavelength of 200−230 nm, in which the molar ellipticity for the mixture of HLG3 and HLP is plotted as the mean ± standard deviation for 3 experiments. Note that the negative Cotton effect due to α-helical structure is significantly enhanced by combining HLG3 with HLP.

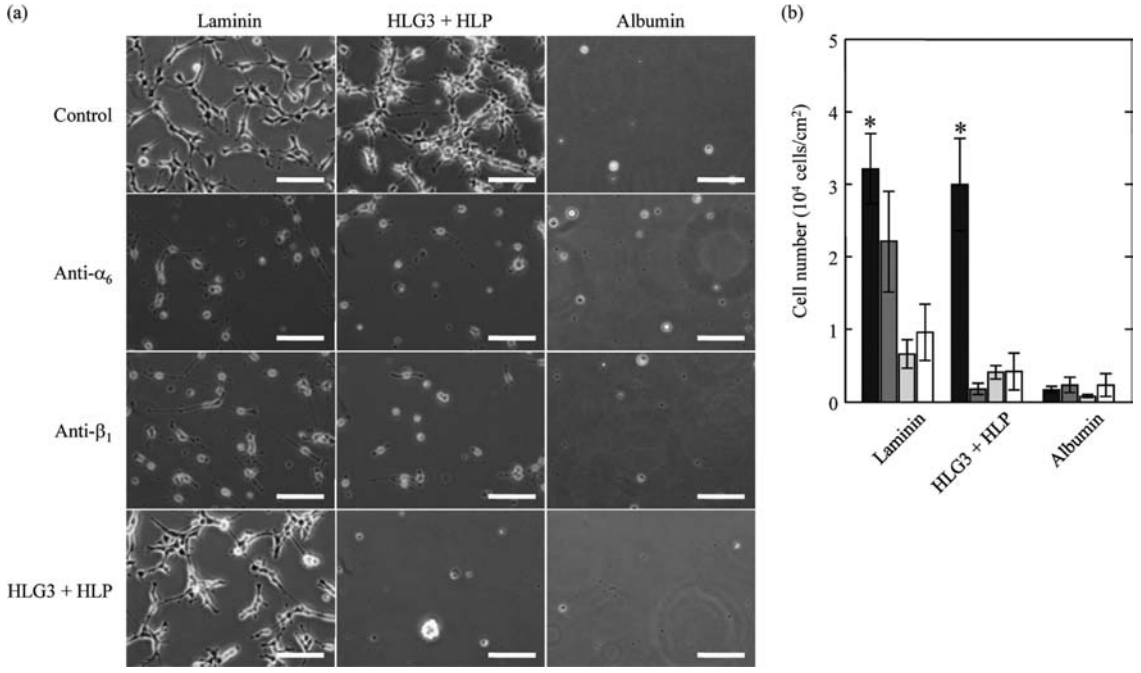


Figure 5. (a) Phase contrast micrographs of cells cultured for 1 d on the surface with adsorbed laminin, immobilized HLG3 and HLP, and adsorbed albumin. Anti-α_6 integrin antibody (2.5 μg/mL), anti-β_1 integrin antibody (2.5 μg/mL), or the mixture of HLG3 and HLP (3.6 μg/mL) was added to a medium. Scale bar: 100 μm. (b) The number of cells adhered to the surface with laminin, HLG3 + HLP, or albumin. A medium was added with (dark gray) HLG3 + HLP, (light gray) anti-α_6 integrin antibody, (white) anti-β_1 integrin antibody, or (black) no inhibitor (control). The data are expressed as the mean ± standard deviation (n = 3). The asterisk indicates the statistical significance compared to the condition of medium added with inhibitors (Tukey's HSD test, $p < 0.05$).

Table 2. Surface Density of Adsorbed Collagen and Immobilized CLG3/CLP Determined by MicroBCA Assays

protein	surface density (μg/cm^2)[a]
Collagen	3.29
Collagen + CLG3/CLP	3.62
CLG3/CLP[b]	0.33

[a]Average of two experimental results. [b]The density of CLG3/CLP was determined as a difference between surface densities for collagen and collagen+CLG3/CLP.

50% of chimeric proteins were released from the hydrogel during initial 24 h, probably due to bursting of unbound CLG3/CLP present in excess. However, after this initial period, release of the proteins was negligible up to the seventh day. In contrast, CBP-deficient HLG3 and HLP (HLG3/HLP) were totally released from collagen hydrogels during the initial 3 days. These results suggest that CLG3/CLP is stably incorporated in the hydrogel through the CBP−collagen interaction.

dx.doi.org/10.1021/bc200481v | *Bioconjugate Chem.* 2012, 23, 212−221

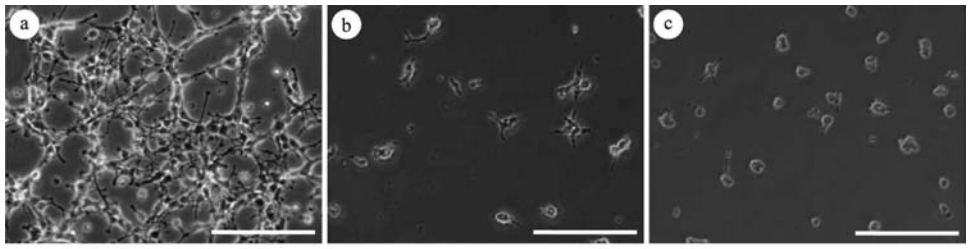


Figure 6. Phase contrast micrographs of cells cultured for 4 d on the collagen-coated surfaces exposed to (a) CLG3/CLP or (b) HLG3/HLP and on (c) pristine collagen-coated surface. Scale bar: 100 μm.

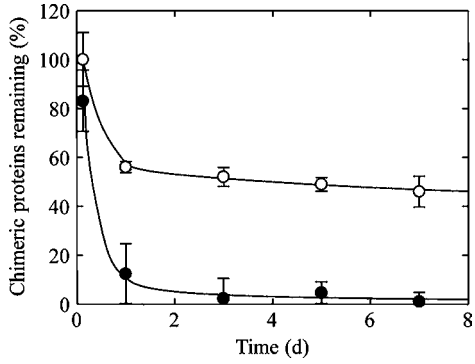


Figure 7. Amount of CLG3/CLP (open circle) and HLG3/HLP (closed circle) remaining in a collagen hydrogels during incubation in a culture medium. The polypeptides remaining in the hydrogels were analyzed by SDS-PAGE.

Viability of NSCs in Collagen Hydrogel. Figure 8a shows the micrograph of NSCs cultured for 7 d in a collagen hydrogel that incorporated CLG3 and CLP (CLG3/CLP). The micrograph for the hydrogel without cell-adhesive chimeric protein is shown in Figure 8b. The phase contrast images are not clear because cells extended in 3D spaces even in the sandwich culture. As can be seen, the number of cells was much larger in the hydrogel with chimeric proteins than in the control hydrogel. The incorporation of CLG3/CLP also promoted cell viability, as evidenced by the abundance of living cells in the collagen hydrogel with CLG3/CLP (Figure 8c,d). Living cell number was determined and shown in Figure 8e. In the hydrogel with CLG3/CLP, living cell number increased 7-fold during 7 days. In the pure collagen hydrogel, a living cell density was almost constant during 7 days. This is presumably a consequence of the fact that part of the cells died in this period while the rest of the cells proliferated.

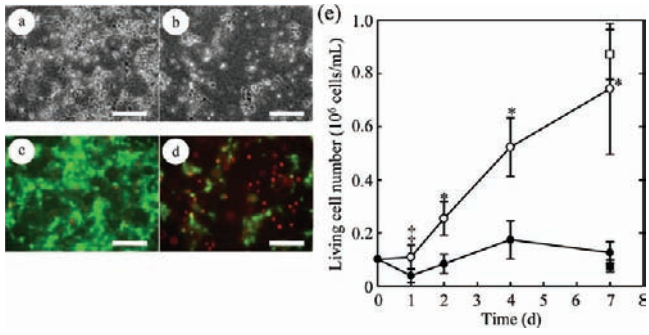


Figure 8. Phase contrast and fluorescent micrographs of cells cultured for 7 d in collagen hydrogel (a,c) with or (b,d) without incorporated CLG3/CLP. (c,d) Living cells were stained with calcein-AM (green), whereas dead cells were stained with PI (red). Scale bar: 100 μm. (e) The number of living cells after culture in the sandwich gel system (open circle) with or (closed circle) without CLG3/CLP. Open and closed square symbols represent living cell numbers determined after 7 day culture in 3-D environment. The data are expressed as the mean ± standard deviation (sandwich culture, n = 7; 3-D culture, n = 3). The asterisk indicates statistical significance compared to hydrogel without CLG3/CLP (Tukey's HSD test, * $p < 0.01$, ‡ $p < 0.05$).

For comparison, the results from 3-D cell culture are also plotted in Figure 8e. As can be seen, living cell numbers in 3-D culture are similar to those in sandwich culture.

DISCUSSION

From our previous study,[16] we considered that integrins could be activated more effectively by integrin-interacting polypeptide domains with 3-D conformation than the small peptide; a further study was undertaken to investigate the effect of the whole G3 domain on cell survival by incorporating this polypeptide into a keratin-based hydrogel.[17] Although our previous studies[16,17] demonstrated that incorporation of the G3 domain into hydrogel promoted cell survival, there was some room for improvement in the hydrogel design. It might indicate that the effect of signal transduction through $\alpha_3\beta_1$ integrin is not sufficient for improving survival of NSCs and neuronal cells, and therefore more effective ligands will possibly improve the effectiveness of the hydrogel system.

In this study, a special attention was paid to the G3 domain of the laminin α1 chain, because this domain binds to $\alpha_6\beta_1$ integrin complex abundantly expressed on NSCs.[18,30] In addition, we examined the effect of coincorporating the 9-residue peptide of the C-terminal region of the laminin γ1 chain (LP), because this peptide was proved to modulate integrin ligation by the globular domains of a laminin α1 chain.[31]

Although the effect of G3 domain was focused on here, we were not aware of involvement of other domains in cell adhesion. Therefore, we synthesized several tandem combinations of globular domains that contained the G3 domain. Other tandem combinations without the G3 domain were also prepared as controls. First, histidine-tagged LGs (HLGs) and LP (HLP) were prepared. The HLGs, HLP, and their combinations (HLGs/HLP) were screened by a 2-D cell adhesion assay for selection of the best candidate for incorporation into a collagen hydrogel. That was followed by preparation of the LG3 and LP fused with a collagen binding peptide derived from decorin[20] (these are abbreviated as CLG3 and CLP, respectively) (Scheme 1). The mixture of CLG3 and CLP (CLG3/CLP) was used for 3D cell culture assays in collagen hydrogels. In order to examine exclusively the effect of these cell adhesive proteins on cell survival, we used here an *in vitro* culture system in which interference from inflammatory reactions could be avoided. The effect of the hydrogel system

dx.doi.org/10.1021/bc200481v | *Bioconjugate Chem.* 2012, 23, 212–221

on the prevention of microglial infiltration may be studied by an *in vitro* microglia migration assay[32] or a transplantation study into the animal brain. The result of an *in vivo* study will be reported elsewhere.

It is considered that globular domains of a laminin α chain are involved in the interactions of laminin with integrins.[18] Concerning the interactions of laminin-1 with $\alpha_6\beta_1$ integrin, many studies have shown that the G3 domain of the α chain plays an essential role among the globular domains.[28,29] This is in accordance with our results that the G3 domain containing proteins (HLG13, HLG35, and HLG3) promoted cell adhesion and proliferation. It was further observed that HLG3 was more effective than HLG13 and HLG35. This result suggests that globular domains, G1, G2, G4, and G5, rather hinder the function of G3 domain in the chimeric proteins at surface.

According to Ido et al.,[31] the binding of the G3 domain of the laminin α5 chain to $\alpha_6\beta_1$ integrin is modulated by LP. This also applies to the laminin α3 G3 domain to $\alpha_3\beta_1$ integrin. These findings inspired us to combine LGs with LP. As demonstrated in the present study, adhesion of NSCs was indeed promoted by coimmobilizing HLG3 or HLG35 with HLP (HLG3/HLP or HLG35/HLP), despite that we employed the globular domains of the laminin α1 chain instead of α3 chain. It is interesting to note that, in the case of HLG13, coimmobilization of HLP is ineffective for promoting cell adhesion, even though HLG13 contains the G3 domain. This result emphasizes that the proximity between the G3 domain and LP has an effect on the integrin binding activity of HLG/HLP heterodimers. In HLG13, G1 and G2 domains are inserted between the G3 domain and the E5 peptide. These two intermittent domains may hamper the modulation of the G3 domain by LP.

This study demonstrates that chimeric proteins containing G3 domain derived from a laminin α1 chain, especially HLG3, enhance the adhesion of NSCs when presented on the substrates. This effect is more prominent when the chimeric protein is displayed in the form of a heterodimer with HLP. The complex of HLG3 with HLP provides a substrate on which NSCs adhere to a similar level with a laminin-coated surface. The promotion of cell adhesion is also the case when the cognate proteins (CLG3 and CLP) are incorporated into a collagen hydrogel through the specific interaction with CBP. Consequently, we succeeded in construction of collagen-based hydrogels that facilitate improving the viability of NSCs entrapped in the hydrogel.

Based on the consideration that cell death in the course of transplantation into the brain is primarily caused by tentative destruction of cell−cell and/or cell−matrix interactions, attempts were made here to promote integrin ligation by their ligands and hence to prevent apoptotic cell death. Another background is that laminin-1 provides an excellent substrate for NSCs to adhere to when coated on a substrate, which suggests that NSCs express integrins specific for laminin-1, most likely $\alpha_6\beta_1$ integrin complex.[30] It appears that the ligation of this integrin serves to prevent apoptotic cell death by activating the intracellular signaling pathway of mitogen-activated protein kinase (MAPK) and Akt.[33] These two aspects just described led us to suppose that, when polypeptides capable of binding to $\alpha_6\beta_1$ integrin are incorporated into hydrogel, NSCs can survive longer periods within the hydrogel.

As shown in Figure 6, the CLG3/CLP complex stably binds to collagen. This is owing to the CBP derived from decorin. It was reported that decorin binds to the triple helical region near the C terminus of type I collagen[34] at a dissociation constant of 6 nM[19] and that the binding site of decorin was mapped to the SYIRIADTNIT in the leucine-rich repeat 6.[20] The synthetic peptide SYIRIADTNIT inhibits the decorin−collagen interaction at an inhibition constant of 4 μM.[20] In our protein design, CBP was fused to both LG3 and LP. Therefore, it can be considered that the complex of CLG3 and CLP firmly binds to collagen through divalent collagen−CBP interactions. However, it appears that the binding of CBP to collagen does not affect the formation of an E5-K5 heterodimer. This is because a stronger association can be expected between E5 and K5. Actually, Tripet et al.[35] reported an association constant of the order of 10^8 to 10^{10} M^{-1} for coiled-coils made from peptides with similar sequences to E5 and K5.

Accordingly, we could construct the hydrogel that promotes the survival of NSCs using CLG3/CLP as well as collagen as a main component. The microenvironment within the hydrogel displays laminin-derived ligands for cell surface integrins. It appears that the hydrogel mimics in part the function of the basement membrane. There are several advantages with this construct from the practical point of view: Collagen has been clinically used as wound dressing, hemostatic agents, and so forth, and the recombinant proteins CLG3 and CLP are prepared under animal-free conditions. These aspects warrant the safety of the hydrogel as an implant for clinical use. In addition, the mixture of collagen, CLG3, CLP, and cells are injectable into tissues with a syringe to form *in situ* a composite hydrogel. In practice, *in vivo* study is currently underway to evaluate the effectiveness of the hydrogel system for promoting the survival of transplanted cells.

■ CONCLUSIONS

It was shown that the number of living NSCs was significantly higher in a collagen hydrogel with incorporated CLG3/CLP than the control hydrogel with no chimeric proteins. It may be concluded that the collagen hydrogel containing CLG3/CLP is of potential as a vehicle for transplanting NSCs.

■ ASSOCIATED CONTENT

Ⓢ Supporting Information

Additional tables and graphics. This material is available free of charge via the Internet at http://pubs.acs.org.

■ AUTHOR INFORMATION

Corresponding Author

*E-mail: iwata@frontier.kyoto-u.ac.jp, Tel: +81-75-751-4119, Fax: +81-75-751-4646.

Present Addresses

[†]Frontier Research Core for Life Sciences, University of Toyama, 3190, Gofuku, Toyama 930−8555, Japan

[‡]Graduate School of Biomedical Sciences, Hiroshima University, 1−2−3 Kasumi, Minami-ku, Hiroshima 734−8553, Japan

■ ACKNOWLEDGMENTS

This study was supported by the Grant-in-Aid for Scientific Research (No. 22300164, 22700468) from the Ministry of Education, Culture, Sports, Science and Technology, Japan.

■ REFERENCES

(1) Goldman, S. (2005) Stem and progenitor cell-based therapy of the human central nervous system. *Nat. Biotechnol. 23*, 862−871.

(2) Takagi, Y., Takahashi, J., Saiki, H., Morizane, A., Hayashi, T., Kishi, Y., Fukuda, H., Okamoto, Y., Koyanagi, M., Ideguchi, M., Hayashi, H., Imazato, T., Kawasaki, H., Suemori, H., Omachi, S., Iida, H., Itoh, N., Nakatsuji, N., Sasai, Y., and Hashimoto, N. (2005) Dopaminergic neurons generated from monkey embryonic stem cells function in a Parkinson primate model. *J. Clin. Invest. 115*, 102−109.
(3) Tsuji, O., Miura, K., Okada, Y., Fujiyoshi, K., Mukaino, M., Nagoshi, N., Kitamura, K., Kumagai, G., Nishino, M., Tomisato, S., Higashi, H., Nagai, T., Katoh, H., Kohda, K., Matsuzaki, Y., Yuzaki, M., Ikeda, E., Toyama, Y., Nakamura, M., Yamanaka, S., and Okano, H. (2010) Therapeutic potential of appropriately evaluated safe-induced pluripotent stem cells for spinal cord injury. *Proc. Natl. Acad. Sci. U.S.A. 107*, 12704−12709.
(4) Okano, H. (2002) Stem cell biology of the central nervous system. *J. Neurosci. Res. 69*, 698−707.
(5) Armstrong, R. J., and Svendsen, C. N. (2000) Neural stem cells: from cell biology to cell replacement. *Cell Transplant 9*, 139−152.
(6) Piccini, P., Pavese, N., Hagell, P., Reimer, J., Björklund, A., Oertel, W. H., Quinn, N. P., Brooks, D. J., and Lindvall, O. (2005) Factors affecting the clinical outcome after neural transplantation in Parkinson's disease. *Brain 128*, 2977−2986.
(7) Marchionini, D. M., Collier, T. J., Camargo, M., McGuire, S., Pitzer, M., and Sortwell, C. E. (2003) Interference with anoikis-induced cell death of dopamine neurons: implications for augmenting embryonic graft survival in a rat model of Parkinson's disease. *J. Comp. Neurol. 464*, 172−179.
(8) Imitola, J., Comabella, M., Chandraker, A. K., Dangond, F., Sayegh, M. H., Synder, E. Y., and Khoury, S. J. (2004) Neural stem/progenitor cells express costimulatory molecules that are differentially regulated by inflammatory and apoptotic stimuli. *Am. J. Pathol. 164*, 1615−1625.
(9) Tambur, A. R. (2004) Transplantation immunology and the central nervous system. *Neurol. Res. 26*, 243−255.
(10) Kim, D. E., Tsuji, K., Kim, Y. R., Mueller, F. J., Eom, H. S., Snyder, E. Y., Lo, E. H., Weissleder, R., and Schellingerhout, D. (2006) Neural stem cell transplant survival in brains of mice: assessing the effect of immunity and ischemia by using real-time bioluminescent imaging. *Radiology 241*, 822−830.
(11) Nakamura, M., Yamaguchi, K., Mie, M., Nakamura, M., Akita, K., and Kobatake, E. (2009) Promotion of angiogenesis by an artificial extracellular matrix protein containing the laminin-1-derived IKVAV sequence. *Bioconjugate Chem 20*, 1759−1764.
(12) Rizzi, S. C., Ehrbar, M., Halstenberg, S., Raeber, G. P., Hagenmüller, H., Muller, R., Weber, F. E., and Hubbell, J. A. (2006) Recombinant protein-co-PEG networks as cell-adhesive and proteolytically degradable hydrogel matrixes. Part II: Biofunctional characteristics. *Biomacromolecules 7*, 3019−3029.
(13) Hou, S., Xu, Q., Tian, W., Cui, F., Cai, Q., Ma, J., and Lee, I. S. (2005) The repair of brain lesion by implantation of hyaluronic acid hydrogels modified with laminin. *J. Neurosci. Meth. 148*, 60−70.
(14) Bryan, N., Rhodes, N. P., and Hunt, J. A. (2009) Derivation and performance of an entirely autologous injectable hydrogel delivery system for cell-based therapies. *Biomaterials 30*, 180−188.
(15) Bjugstad, K. B., Redmond, D. E., Lampe, K. J., Kern, D. S., Sladek, J. R., and Mahoney, M. J. (2008) Biocompatibility of PEG-based hydrogels in primate brain. *Cell Transplant. 17*, 409−415.
(16) Hiraoka, M., Kato, K., Nakaji-Hirabayashi, T., and Iwata, H. (2009) Enhanced survival of neural cells embedded in hydrogels composed of collagen and laminin-derived cell adhesive peptide. *Bioconjugate Chem. 20*, 976−983.
(17) Nakaji-Hirabayashi, T., Kato, K., and Iwata, H. (2008) Self-assembled chimeric protein for the construction of biodegradable hydrogels capable of interaction with integrins expressed on neural stem/progenitor cells. *Biomacromolecules 9*, 1411−1416.
(18) Belkin, A. M., and Stepp, M. A. (2000) Integrins as receptors for laminins. *Microsci. Res. Tech. 51*, 280−301.
(19) Kalamajski, S., Aspberg, A., and Oldberg, A. (2007) The decorin sequence SYIRIADTNIT binds collagen type I. *J. Biol. Chem. 282*, 16062−16067.
(20) Nakaji-Hirabayashi, T., Kato, K., and Iwata, H. (2009) Surface-anchoring of spontaneously dimerized epidermal growth factor for highly selective expansion of neural stem cells. *Biomaterials 20*, 102−109.
(21) Nakaji-Hirabayashi, T., Kato, K., Arima, Y., and Iwata, H. (2007) Oriented immobilization of epidermal growth factor onto culture substrates for the selective expansion of neural stem cells. *Biomaterials 28*, 3517−3529.
(22) Nakaji-Hirabayashi, T., Kato, K., and Iwata, H. (2008) Essential role of structural integrity and firm attachment of surface-anchored epidermal growth factor in adherent culture of neural stem cells. *Biomaterials 29*, 4403−4408.
(23) Konagaya, S., Kato, K., Nakaji-Hirabayashi, T., and Iwata, H. (2011) Design of culture substrates for large-scale expansion of neural stem cells. *Biomaterials 32*, 992−1001.
(24) Nakaji-Hirabayashi, T., Kato, K., Arima, Y., and Iwata, H. (2008) Multifunctional chimeric proteins for the sequential regulation of neural stem cell differentiation. *Bioconjugate. Chem. 19*, 516−524.
(25) Nakaji-Hirabayashi, T., Kato, K., and Iwata, H. (2009) Hyaluronic acid hydrogel loaded with genetically-engineered brain-derived neurotrophic factor as a neural cell carrier. *Biomaterials 30*, 4581−4589.
(26) Carafoli, F., Clout, N. J., and Hohenester, E. (2009) Crystal structure of the LG1−3 region of the laminin alpha2 chain. *J. Biol. Chem. 284*, 22786−22792.
(27) Timpl, R., Tisi, D., Talts, J. F., Andac, Z., Sasaki, T., and Hohenester, E. (2000) Structure and function of laminin LG modules. *Matrix Biol. 19*, 309−317.
(28) Bello-Deocampo, D., Kleinman, H. K., Deocampo, N. D., and Webber, M. M. (2001) Laminin-1 and $\alpha 6\beta 1$ integrin regulate acinar morphogenesis of normal and malignant human prostate epithelial cells. *Prostate 46*, 142−153.
(29) Ferletta, M., Kikkawa, Y., Yu, H., Talts, J. F., Durbeej, M., Sonnenberg, A., Timpl, R., Campbell, K. P., Ekblom, P., and Genersch, E. (2003) Opposing roles of integrin $\alpha 6A\beta 1$ and dystroglycan in laminin-mediated extracellular signal-regulated kinase activation. *Mol. Biol. Cell 14*, 2088−2103.
(30) Lathia, J. D., Patton, B., Eckley, D. M., Magnus, T., Mughal, M. R., Sasaki, T., Caldwell, M. A., Rao, M. S., Mattson, M. P., and Ffrench-Constant, C. (2007) Patterns of laminins and integrins in the embryonic ventricular zone of the CNS. *J. Comp. Neurol. 505*, 630−643.
(31) Ido, H., Nakamura, A., Kobayashi, R., Ito, S., Li, S. L., Futaki, S., and Sekiguchi, K. (2007) The requirement of the glutamic acid residue at the third position from the carboxyl termini of the laminin gamma chains in integrin binding by laminins. *J. Biol. Chem. 282*, 11144−11154.
(32) Marella, M., and Chabry, J. (2004) Neurons and astrocytes respond to prion infection by inducing microglia recruitment. *J. Neurosci. 24* (23), 620−627.
(33) Gu, J. G., Nada, S., Okada, M., and Sekiguchi, K. (2003) Csk regulates integrin-mediated signals: involvement of differential activation of ERK and Akt. *Biochem. Biophys. Res. Commun. 303*, 973−977.
(34) Keene, D. R., San Antonio, J. D., Mayne, R., McQuillan, D. J., Sarris, G., Santoro, S., and Iozzo, R. V. (2000) Decorin binds near the C terminus of type I collagen. *J. Biol. Chem. 275*, 21801−21804.
(35) Tripet, B., Wagschal, K., Lavigne, P., Mant, C. T., and Hodge, R. S. (2000) Effect of side-chain characteristics on stability and oligomerization state of a *de novo*-designed model coiled-coil: 20 Amino acid substitutions in position "d". *J. Mol. Biol. 300*, 377−402.

Bioconjugate Chemistry

Article

pubs.acs.org/bc

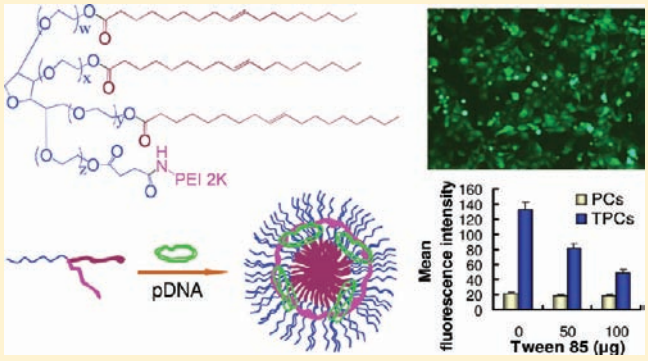
Low Molecular Weight Polyethylenimine-*graft*-Tween 85 for Effective Gene Delivery: Synthesis and *in Vitro* Characteristics

Jisheng Xiao,[†] Xiaopin Duan,[†,‡] Qi Yin,[†] Lingli Chen,[†] Zhiwen Zhang,[†] and Yaping Li*[,†]

[†]Center of Pharmaceutics, Shanghai Institute of Materia Medica, Chinese Academy of Sciences, Shanghai 201203, China

[‡]School of Pharmacy, Shenyang Pharmaceutical University, Shenyang 110016, China

ABSTRACT: The development of safe and efficient gene delivery systems is still a challenge for successful gene therapy. In this work, low molecular weight polyethylenimine (PEI 2K) was modified by Tween 85, which bears three oleate chains. Tween 85 modified PEI 2K (TP) could condense DNA efficiently, and TP/DNA complexes (TPCs) showed high resistance to salt-induced aggregation and enzymatic degradation. In addition, TP did not show the obvious cytotoxicity. The introduction of Tween 85 led to a significant increase in the cellular uptake of complexes with higher transfection efficiency, which was strongly inhibited by the addition of free Tween 85 in MCF-7/ADR cells, but not in MCF-7 cells. These results indicated that TP could be a potentially safe and effective copolymer for gene delivery, and TPCs could be taken up mainly by Tween 85-mediated endocytosis in MCF-7/ADR cells.



INTRODUCTION

Gene therapy is thought to be a potential approach to treating genetic disorders such as severe combined immunodeficiency, cystic fibrosis, and Parkinson's disease, and as an alternative method to traditional chemotherapy for cancer.[1] However, successful gene therapy highly depends on effective and safe delivery vectors. In the past decade, nonviral vectors have attracted more and more attention because they are safer, simpler to handle, and less expensive than viral vectors.[2] Among nonviral vectors, cationic lipids and cationic polymers have shown low cytotoxicity and high transfection efficiency with excellent potential for gene delivery.[3−5] One of the most promising cationic polymers for gene delivery is polyethylenimine (PEI), which is available in linear or branched form with the molecular weight from about 0.4 to 800 kDa, and higher molecular weight PEI (e.g., 25 kDa) leads to higher transfection efficiency with higher cytotoxicity. Recently, low molecular weight PEI (LPEI, e.g., 2 kDa) has attracted more interest because of its low cytotoxicity,[6−8] but LPEI is not very effective for DNA delivery, in particular, because the complexes formed between DNA and LPEI by electrostatic interaction were unstable and precipitated out of the buffer solution or dissociated and aggregated in physiological environments because of the overall positive charge of the complexes.[2,9−11]

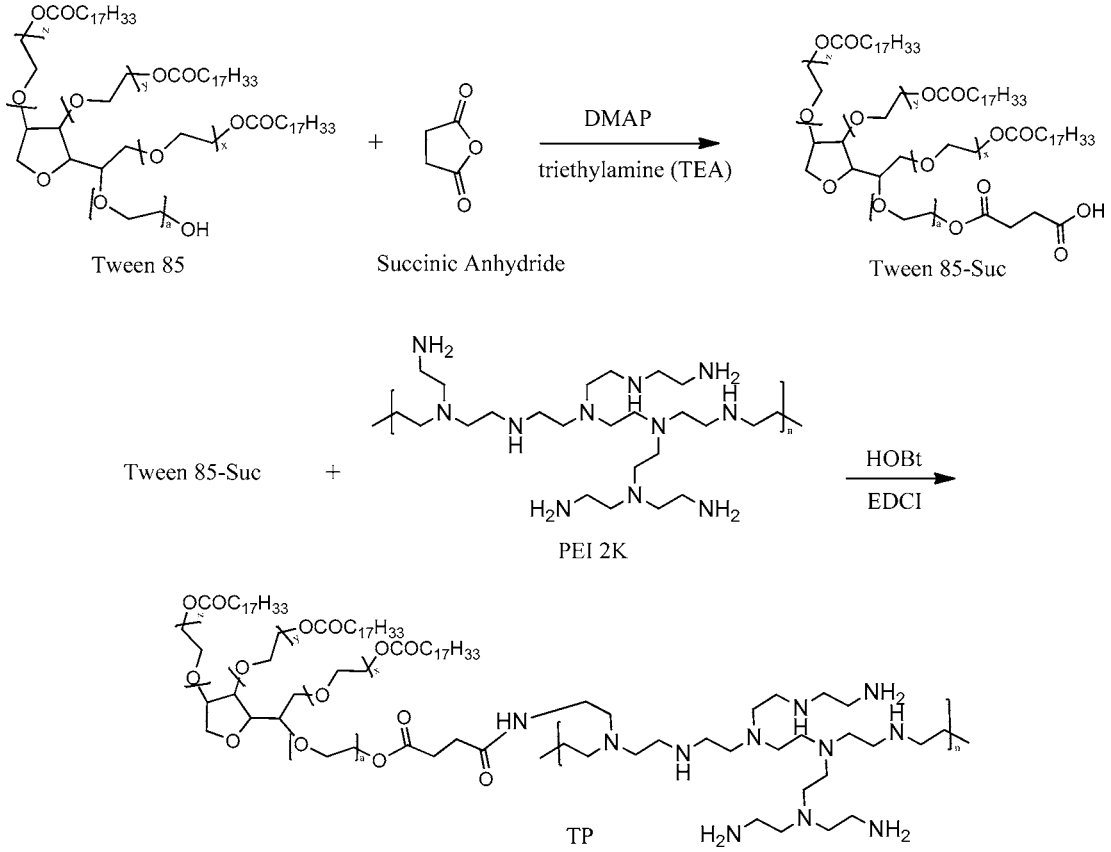
In order to improve transfection efficiency and stability of LPEI/DNA complexes, many efforts have been made; for example, the conjugates of LPEI were synthesized by amide- and ester-bearing linkers or disulfide bond-bearing linkers to increase molecular weight,[12−15] thereby improving the ability of LPEI to condense DNA, but this method would induce high charge density, which was related to cytotoxicity and the aggregation of complexes in physiologic environment. In addition, lipid-substitution of PEI 2K could increase DNA delivery to cells. Nevertheless, lipid substitution could increase the toxicity of the polymers *in vitro* and reduce the ability of the polymers to complex DNA.[8] Copolymers of LPEI with other polymers were also synthesized, such as PEG-b-PLL-g-LPEI and (Dex-HMDI)-g-PEIs to render the vector biodegradability.[16,17] However, the conjugation decreased the number of primary amines in PEI, and led to steric hindrance, which could impair the binding capability of the polymer to DNA, as well as the stability of complex. In addition, it also was investigated to improve the stability and prolong their circulation time by PEGylation covering the polyplex surface.[18−22] Recently, it was reported that the presence of the lipid layer provided a charge shielding of the otherwise positive PEI/DNA core.[2] The endogenous lipids such as oleic acid and stearic acid were suggested to allow for physical encapsulation of siRNA, which could contribute to the superior condensing and protective effect when compared with parent PEI.[23] These progresses highlighted the importance of PEG and lipid components in cationic polymers for efficient gene delivery.

In this work, a new copolymer was synthesized by Tween 85 conjugating to PEI 2K via the succinic anhydride linker, and the physicochemical characteristics of TPCs, such as condensation ability, stability against salt-induced aggregation and protection

Received: September 13, 2011
Revised: November 9, 2011
Published: December 15, 2011

 © 2011 American Chemical Society dx.doi.org/10.1021/bc200504v | *Bioconjugate Chem.* 2012, 23, 222−231

Scheme 1. Synthesis of Branched Low-Molecular-Weight PEI-*graft*-Tween 85



against DNase I were determined. *In vitro* cytotoxicity, transfection efficiency, cellular uptake, and intracellular distribution of TPCs in MCF-7 and MCF-7/ADR cell lines were investigated. The experimental results indicated that TP could be a potentially safe and effective copolymer for gene delivery.

EXPERIMENTAL PROCEDURES

Materials. Branched PEI 2K and PEI 25K, ethidium bromide, and 3-(4,5-dimethylthiazol-2-yl)-2,5-diphenyltetrazolium bromide (MTT) were obtained from Sigma (St. Louis, MO). Plasmid EGFP-N1 was purchased from Clontech (Palo Alto, CA, USA). The plasmid DNA was amplified in DH5α strain of *E. coli* and purified by EndFree Plasmid Mega Kit (Qiagen GmbH, Hilden, Germany). YOYO-1, Hoechst 33342, and Lyso Trancker Red Kit were purchased from Molecular Probes (Eugene, OR). All the other reagents were of analytical grade.

The cell lines MCF-7/ADR and MCF-7 were obtained from the American Type Culture Collection (ATCC, Manassas, VA) and cultured in DMEM containing 10% fetal bovine serum (FBS), 100 Unit/mL penicillin G sodium, and 100 μg/mL streptomycin sulfate (complete DMEM medium). Cells were maintained at 37 °C in a humidified and 5% CO_2 incubator.

Synthesis and Characterizations of TP. TP was synthesized via a two-step reaction as shown in Scheme 1. Carboxyl-terminated Tween 85 (Tween 85-Suc) was prepared using succinic anhydride ring-opening reaction in the presence of 4-dimethylamiopryidine (DMAP) and trimethylamine (TEA).[24] Briefly, Tween 85 (10 g, 5.44 mmol) and succinic anhydride (702 mg, 7.07 mmol) were dissolved in anhydrous tetrahydrofuran (THF). After DMAP (858 mg, 7.07 mmol) and TEA (710 mg, 7.07 mmol) were added, the mixture was stirred for 2 days at 25 °C. Then, the reaction mixture was concentrated by rotary evaporation, and the residue was dialyzed using cellulose dialysis membranes (MWCO: 2000, Spectrum Co.) against THF for 2 days. THF was removed by the evaporation with reduced pressure, and Tween 85-Suc was analyzed by ^{1}H NMR.

Tween 85-Suc was conjugated to PEI 2K using a condensation reaction between carboxyl group and amino group. Briefly, Tween 85-Suc (305.4 mg, 0.15 mmol), [1-ethyl-3-(dimethylamino)propyl] carbodiimide hydrochloride (EDCI) (37.4 mg, 0.195 mmol), and N-hydroxybenzotriazole (HOBt) (26.4 mg, 0.195 mmol) were added into anhydrous ethanol. After the mixture changed clear, PEI 2K (100 mg, 0.05 mmol) solubilized in 2.0 mL of ethanol was added. The reaction was performed at room temperature under stirring for 12 h. Then, the solution was dialyzed against 95% ethanol using a membrane (MWCO: 3500, Spectrum Co.) for 2 days, and the dialysis medium was refreshed every 12 h. TP was obtained after the concentration of the polymer solution and dried under vacuum. The structure of product was confirmed by ^{1}H NMR recorded on Varian Mercury Plus-400 NMR spectrometer (Varian, USA) operated at 400 MHz. The molecular weight and distribution were determined by gel permeation chromatograph (GPC).

Preparation and Characteristics of TPCs. To prepare TPCs with the required N/P ratio, 100 μL of pEGFP (0.2 mg/mL) was added to 100 μL of TP solution prediluted with sterile distilled water to different concentrations under vortexing for 30 s (XW-80A Vortex mixer, Shanghai). The complexes were

dx.doi.org/10.1021/bc200504v | *Bioconjugate Chem.* 2012, 23, 222–231

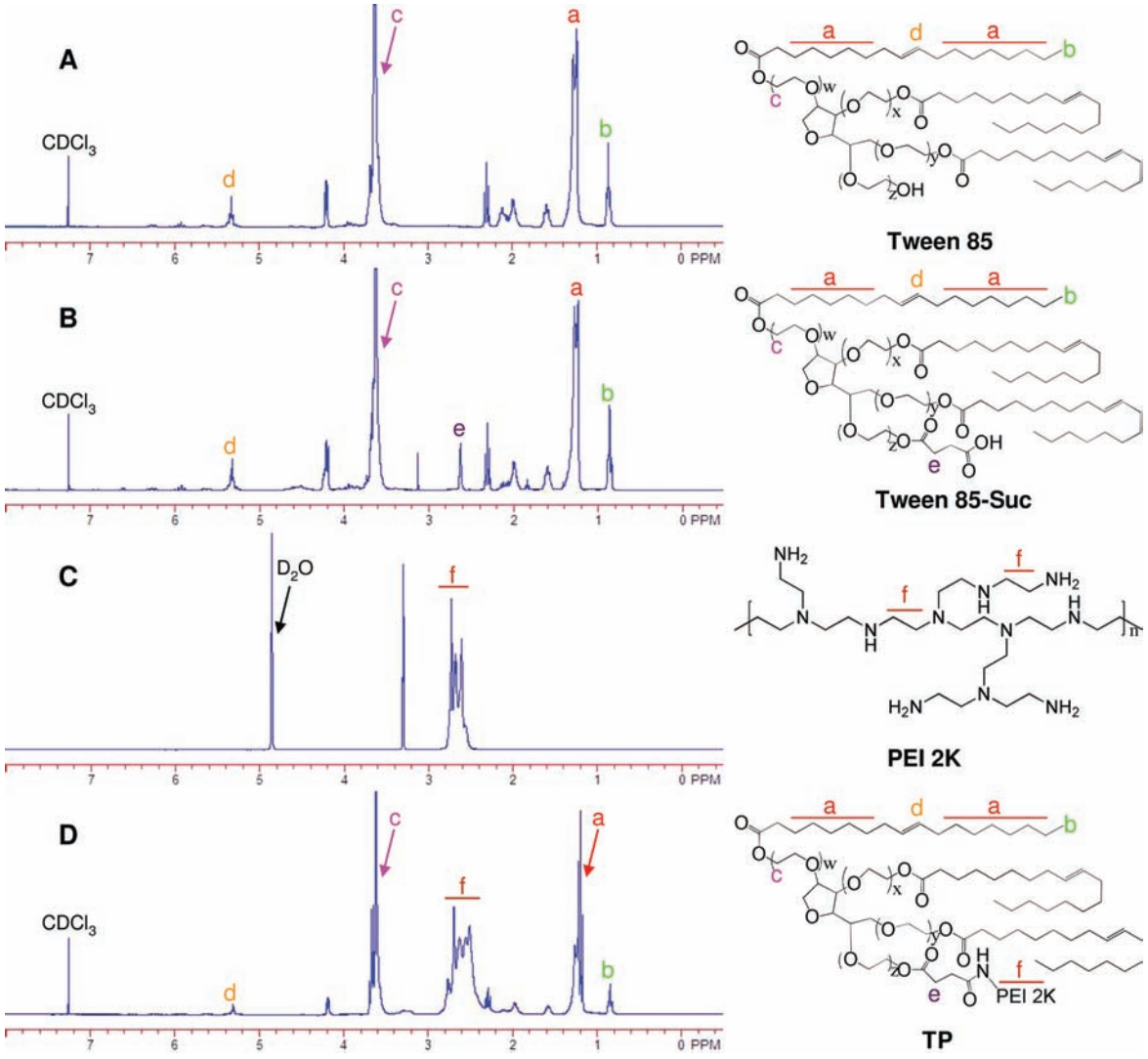


Figure 1. [1]H NMR spectra of Tween 85 (A), Tween 85-Suc (B), PEI 2K (C), and TP (D). TP was synthesized with a feeding molar ratio of Tween 85 to PEI 2K of 3:1.

allowed to stand at room temperature for 30 min. As a control, the unmodified PEI 2K/pEGFP complexes (UPCs) were also prepared by the same process as described for TPCs above. To confirm the formation of the complexes, the different N/P ratios of TPCs and UPCs were loaded onto a 0.8% (w/v) agarose gel in Tris-acetate-EDTA buffer and electrophoresed at 90 V for 25 min. The DNA migration pattern stained with ethidium bromide (0.2 μg/mL) was revealed under UV irradiation.

The particle size and zeta potential of TPCs and UPCs were assessed by laser light scattering using a Nicomp 380/ZLS zeta potential analyzer (Particle Sizing System, USA). Zeta potential was measured by a dilution of 1:10 in distilled water at 25 °C with a scattering angle of 15° and the electric field strength of 10 V/cm.

Stability against Salt-Induced Aggregation and DNase I. The stability of TPCs against the salt-induced aggregation was measured by monitoring the particle size of TPCs (hydrodynamic diameter). NaCl solution (0.3 M) was added to the suspension of TPCs up to a final concentration (0.15 M) while measuring the size at the predetermined time points. As control, UPCs were also treated by the same process as described for TPCs above.

To evaluate whether pEGFP was protected by TP, TPCs were incubated with DNase I at the ratio of 10 units/μg of pEGFP, and the absorbance of pEGFP at 260 nm was determined every 10 min for 1 h. The values were plotted in a curve (relative absorbance vs time). UPCs prepared at the same N/P ratio and naked pEGFP were used as control.

Cytotoxicity Assay. MTT assay was performed to assess the cytotoxicity of TP. Briefly, MCF-7/ADR and MCF-7 cells were seeded in 96 well plates at a density of 5×10^3 cells per well with 200 μL complete media and cultured for 24 h. The different concentrations of TP, PEI 25K, PEI 2K, and Tween 85 were prepared in sterile distilled water, respectively. After the medium was replaced with fresh medium, 20 μL of the solution was added to each well and incubated for a further 48 h. Then, 20 μL of MTT solution (5 mg/mL) was added to each well. After incubation at 37 °C for an additional 4 h, the medium was removed, and 150 μL DMSO was added to dissolve the MTT formazan crystals. The plates were mildly shaken for 10 min before the absorbance at 570 nm was recorded using a microplate reader (Bio-RAD, model 550) and

dx.doi.org/10.1021/bc200504v | *Bioconjugate Chem.* 2012, 23, 222–231

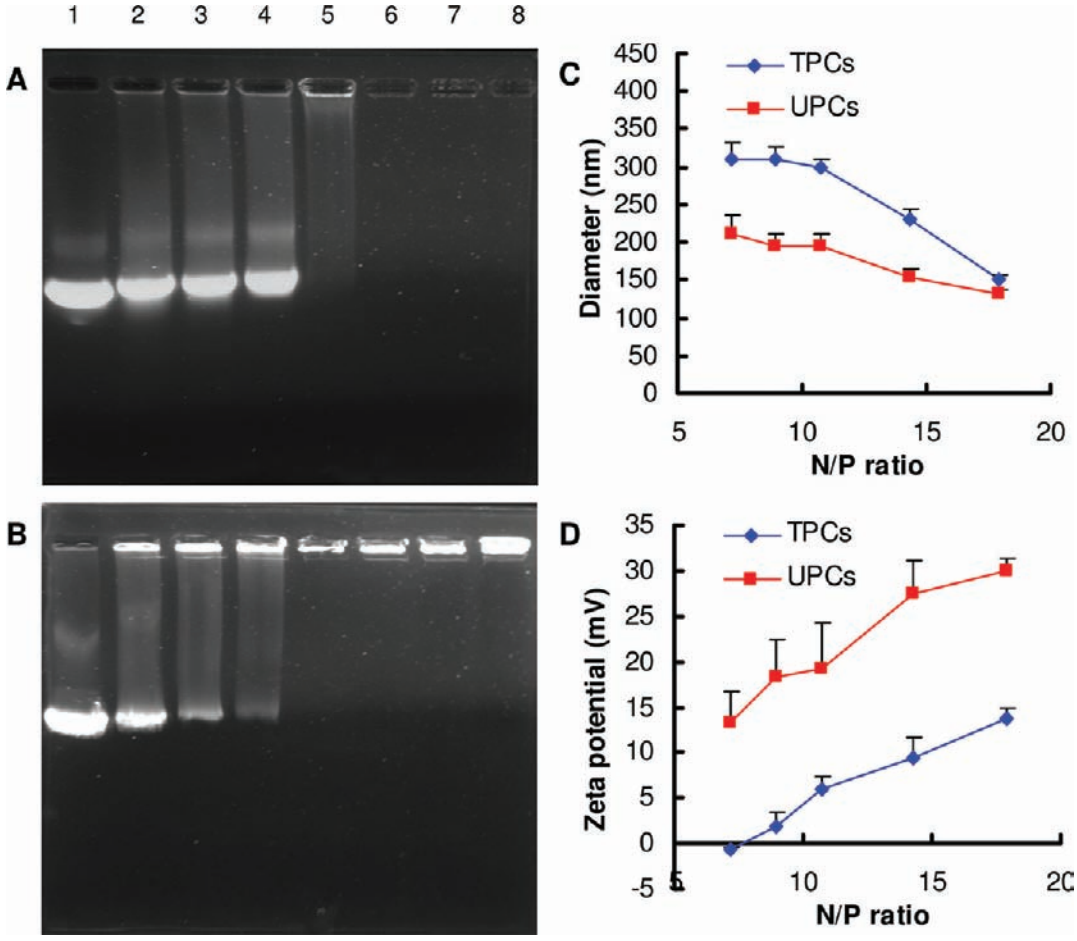


Figure 2. Physicochemical characterization of TPCs: Agarose gel electrophoresis of UPCs (A) and TPCs (B). Lane 1, naked pEGFP; lanes 2−8, complexes prepared at N/P ratios of 0.1, 0.3, 0.5, 1, 2, 4, and 6, respectively. Particle size (C) and zeta potential (D) of UPCs (red) and TPCs (blue) at various N/P ratios.

blanked with DMSO solution. The results were expressed as the percentage relative to that from control experiments. Each experiment was done in triplicate.

***In Vitro* Transfection.** MCF-7/ADR and MCF-7 cells were seeded in 24-well culture plates at a density of 3×10^4 cells/well in 500 μL complete medium and incubated for 24 h. Then, the medium was replaced with fresh medium containing TPCs with 3 μg/well of DNA at the N/P ratio of 8, and cells were incubated at 37 °C in 5% CO_2 for 3 h, After that, the medium containing complexes was replaced, and cells were further incubated for 48 h. The EGFP expressing cells were visualized using fluorescence inversion microscope system (Olympus, Japan) and quantified by a fluorescence activated cell sorter (FACSCalibur, Becton Dickinson, USA). PEI 25K/DNA complexes (PCs) at N/P ratio of 10 were used as positive control. In order to know the effect of Tween 85 on the transfection of TPCs, the inhibition experiment was performed as described above except for the addition of free Tween 85 when the complexes were incubated with the cells.

Cellular Uptake. MCF-7/ADR and MCF-7 cells were seeded in 24-well plates at a density of 1×10^5 cells/well and incubated with 500 μL complete medium for 24 h. pEGFP was fluorescently labeled with YOYO-1 at the ratio of 1 nM dye molecule/μg pEGFP, and incubated for 30 min at room temperature in the dark. TPCs with N/P ratios of 8 were added to the cells at equivalent YOYO-1-labeled pEGFP per well and incubated with cells for 2 h. PCs at N/P ratio of 10 were used as control. Then, the cells were washed twice with PBS and collected. The cellular uptake of complexes was investigated by flow cytometric analysis. To investigate the impact of Tween 85 on the cellular uptake of complexes, TPCs were added to the cells together with free Tween 85. PCs with the same concentration of free Tween 85 were used as control.

Intracellular Localization. MCF-7/ADR and MCF-7 cells were seeded on 10 mm^2 glass coverslips placed in 24-well plates and incubated for 24 h. pEGFP was fluorescently labeled with YOYO-1 as described above. TPCs at N/P ratio of 8 were added to the cells with 3 μg DNA/well and incubated for 1.5 h. The lysosome and nuclei were stained with Lyso Tracker Red and Hoechst 33342 for 30 min, respectively. Then, the cells were washed twice with PBS, and fixed with 4% paraformaldehyde immediately. Intracellular localization was visualized using confocal microscopy (FluoView FV1000, Olympus). The influence of Tween 85 on the intracellular distribution of complexes was investigated by adding different concentrations of free Tween 85 when complexes were incubated with cells.

Statistical Analysis. Statistical analysis was performed using a Student's t test. The differences were considered significant for $p < 0.05$ and $p < 0.01$ indicative of a very significant difference.

dx.doi.org/10.1021/bc200504v | *Bioconjugate Chem.* 2012, 23, 222−231

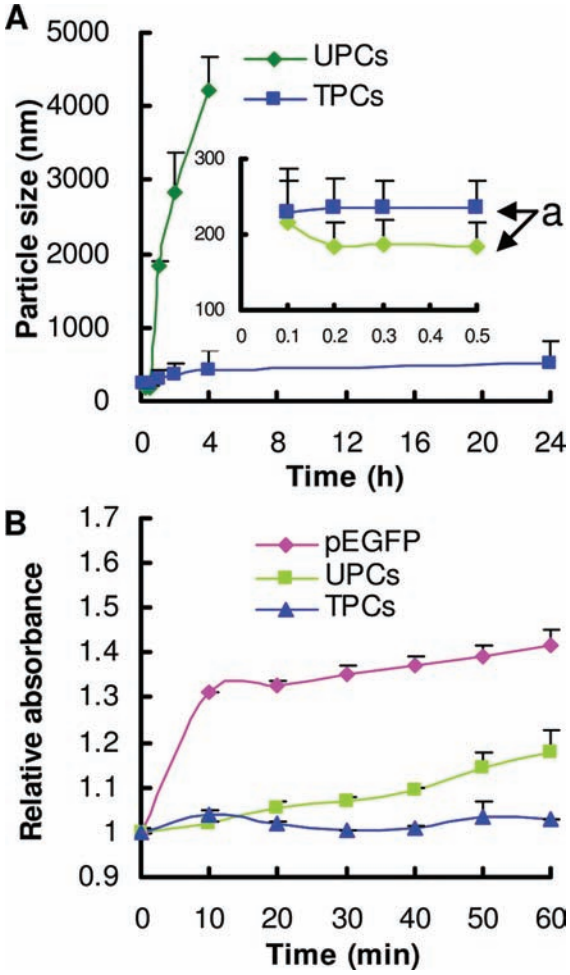


Figure 3. Stability against salt-induced aggregation and DNase I degradation. (A) Colloidal stability of TPCs against salt-induced aggregation. The particle size of TPCs showed a little increase, while UPCs aggregated immediately after adding salt (a: 0.3 M NaCl was added). (B) Resistance of TPCs against DNase I degradation, UPCs, and naked pEGFP were used as control.

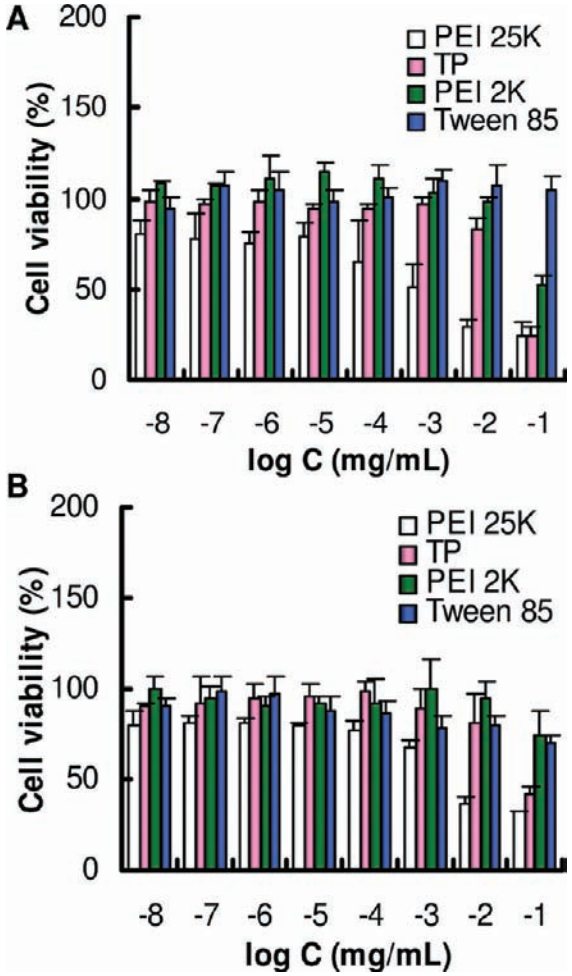


Figure 4. Cell viability determined by MTT for TP, PEI 25K PEI 2K, and Tween 85 at various concentrations against MCF-7/ADR cells (A) and MCF-7 cells (B).

RESULTS AND DISCUSSION

Synthesis and Characterizations of TP. Tween 85 contains an average of 20 units of ethylene oxide and three oleate chains, which were reported to be able to encapsulate siRNA because of their flexibility.[23] We speculated that the conjugation of Tween 85 and PEI could improve DNA delivery through the combination of the favorable properties of poloxyethylene and lipid component. The conjugation of Tween 85 with branched PEI through the amide linkage was shown in scheme 1. The hydroxy groups of Tween 85 were activated with succinic anhydride at the ratio of 1:1.3 (mol/mol) and conjugated with amine groups of PEI 2K. The molar ratio of Tween 85-Suc to PEI 2K was 3:1. The structures of Tween 85-Suc and TP were confirmed by ^{1}H NMR (Figure 1). After the succinic anhydride reaction, a new peak appeared at 2.6 ppm (Figure 1B), which could be assigned to $-CH_2CH_2-$ of succinic acid. Compared with ^{1}H NMR of Tween 85-Suc (Figure 1B), that of TP conjugate (Figure 1D) had a PEI peak at 2.4−3.0 ppm, and the peaks at 0.9 ppm and 1.1−1.4 ppm could be attributed to $-CH_3$ and $-CH_2-$ of oleate of Tween 85, respectively. The peak at 3.5−3.7 ppm in Figure 1D could result from $-OCH_2CH_2O-$ of Tween 85. These results confirmed the successful linkage between Tween 85 and PEI 2K. The graft ratio, the number of Tween 85 chains conjugated to per PEI molecule, was determined by the ratio of the peak area corresponding to the methyl group in Tween 85 block to that of the methylene in PEI. The experimental result showed that the graft ratio of TP was about 3, which indicated that about three Tween 85 molecules were grafted onto one PEI molecule. According to the graft ratio, the molecular weight (MW) of TP was about 8105 Da, which was also confirmed by GPC (8617 Da). In addition, the GPC of TP showed only one peak, and the elution volume was smaller than that of Tween 85 and PEI, which also demonstrated that the copolymer TP was synthesized successfully.

Physicochemical Characteristics of TPCs. To assess the ability of polymers to condense pEGFP, gel retardation assay was performed (Figure 2A,B). The N/P ratio of polymers/pEGFP at which the electrophoretic mobility of pEGFP was completely retarded was 2 for PEI 2K and 1 for TP, respectively, which demonstrated that TP was able to condense pEGFP at lower N/P ratios compared with PEI 2K. The superior condensing effect of TP over PEI 2K could attribute to Tween 85, which contains oxyethylene spacers and three oleate chains. It was reported that the oxyethylene spacers might be folded in a way that facilitated the interaction with DNA,

dx.doi.org/10.1021/bc200504v | Bioconjugate Chem. 2012, 23, 222−231

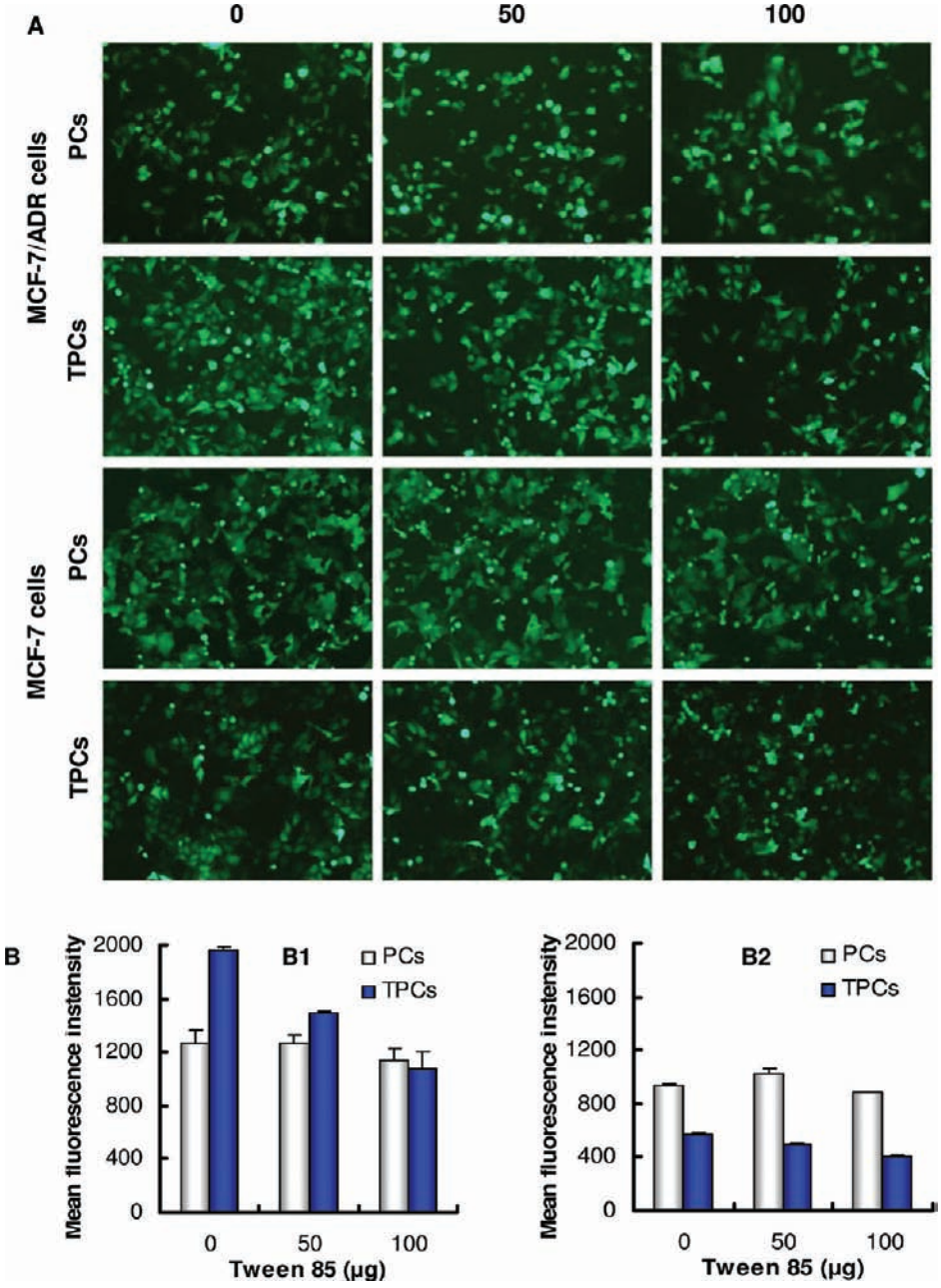


Figure 5. (A) Fluorescent images of MCF-7/ADR cells and MCF-7 cells incubated with TPCs and PCs in media which contain various contents of free Tween 85. (B) Quantitative analysis of the transfection efficiency of TPCs and PCs in the absence or presence of different contents of free Tween 85 in MCF-7/ADR cells (B1) and MCF-7 cells (B2).

thereby binding DNA more efficiently,[25] and oleate chains also could enhance condensation capability of PEI.[23]

The particle size and zeta potential of TPCs and UPCs were shown in Figure 2C,D. The mean particle size of TPCs decreased from 311.1 to 152.1 nm with the N/P ratio increasing, and that of UPCs decreased from 211.7 to 131.7 nm. Zeta potential of TPCs increased from −0.56 to +13.72 mV with N/P ratios rising from 7 to 19, while UPCs showed a higher positive surface charge, which increased from 13.36 to 30.07 mV with the same change of N/P ratios. The results showed that the conjugation of Tween 85 to LPEI decreased the surface charge of complexes, which could be attributed to the fact that the primary nitrogens of PEI were partially acetylated by reaction with Tween 85-Suc to form secondary amides, and resulted in a decrease of the average protonation constant of the polymer.[26] In addition, Tween 85 in TP could cover the surface of TPCs thereby partly shielding the positive charge.

Resistance of Salt-Induced Aggregation and Enzymatic Digestion. Traditional PEI/DNA polyplexes tend to aggregate rapidly under physiologically high salt condition.[10] To know the stabilizing effect of TPCs against the salt-induced aggregation, 0.3 M NaCl solution was added to the suspension of complexes to a final concentration of 0.15 M, the particle size of TPCs was monitored before and after adding NaCl solution. As expected, UPCs aggregated immediately after NaCl solution was added, and the hydrodynamic diameter of UPCs increased continuously and precipitated at 16 h. However, TPCs remained stable without significant aggregation within 24 h (Figure 3A). The strong resistance of TPCs against the salt-

dx.doi.org/10.1021/bc200504v | *Bioconjugate Chem.* 2012, 23, 222−231

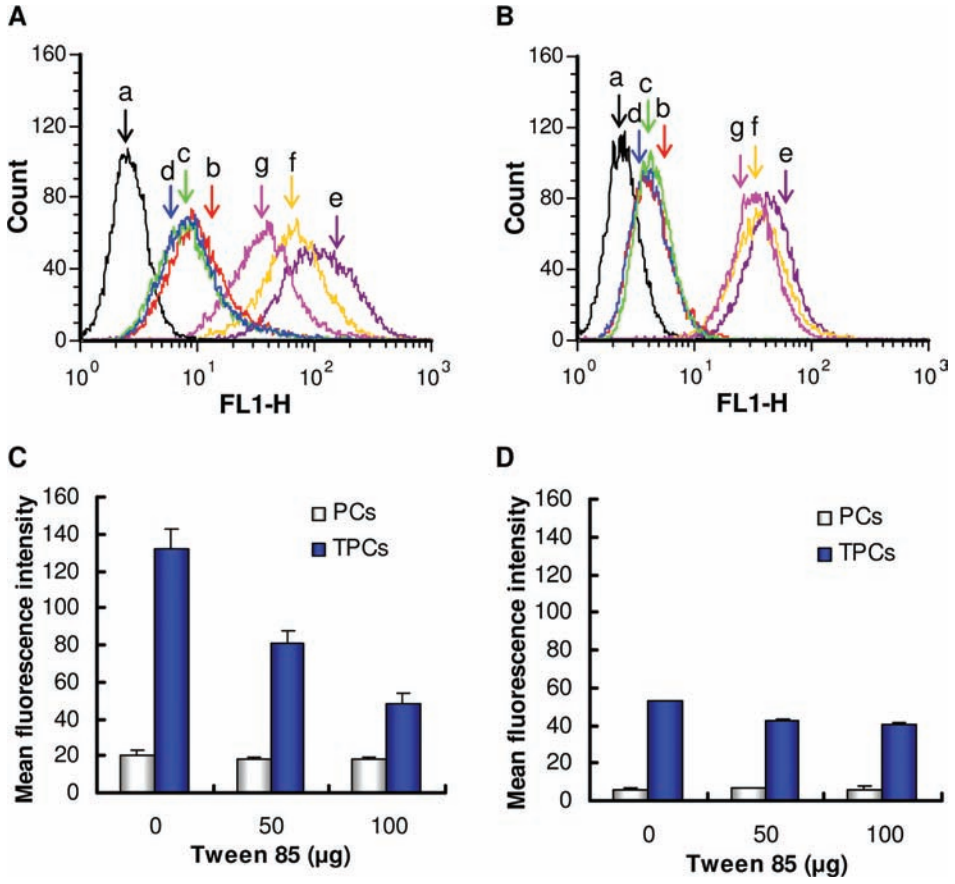


Figure 6. Flow cytometry pictures of control cells (a, black), and cells treated with PCs (b, red), PCs with 50 μg Tween 85 (c, green), PCs with 100 μg Tween 85 (d, blue), TPCs (e, violet), TPCs with 50 μg Tween 85 (f, gold), TPCs with 100 μg Tween 85 (g, pink) in MCF-7/ADR (A) and MCF-7 cells (B). Quantitative analysis of cellular uptake of TPCs and PCs in the absence or presence of different contents of free Tween 85 in MCF-7/ADR cells (C) and MCF-7 cells (D).

induced aggregation showed the superiority of TP in gene delivery. It was reported that the high salt concentration in physiological conditions was one of the mechanisms responsible for the poor *in vivo* stability of PEI/DNA polyplexes.[27] These polyplexes were formed by strong electrostatic interaction between PEI and DNA, and colloidally stabilized by electrostatic repulsion among the particles. Under the physiological conditions, however, an increased salt concentration triggered the aggregation of polyplex particles as a result of screening of the electrostatic repulsion forces between the polyplex particles along with concurrent dissociation of the polyplex particles due to screening of attractive electrostatic interaction between polycations and polyanionic DNA.[28] In addition, TP not only provided the steric stabilization by polyoxyethylene portions, whose analogues, PEG, were reported to decrease the sensitivity of the polyplexes of PEG-grafted PEI/DNA to the salt-induced aggregation,[2] but also contributed to the good stability in high salt condition by shielding the positive charge of the polyplex core with the sorbitan trioleate. Additionally, TP could condense pEGFP more efficiently due to the oleate chains in Tween 85. The access of salt was blocked by Tween 85 barrier from the outer environment to the PEI/pEGFP cores, which provided the protection against the salt-induced aggregation.

The protective effect of TP was determined by loading pEGFP against enzymatic degradation (Figure 3B). Naked pEGFP and UPCs were used as control. The native pEGFP was degraded immediately after adding DNase I; the absorbance increased up to about 40% within 1 h. The pEGFP in UPCs showed a lower degradation than naked pEGFP with 20% increase in the absorbance after adding DNase I. However, pEGFP in TPCs remained intact without significant degradation occurring for 1 h, which indicated that pEGFP was well protected from nuclease degradation.

***In Vitro* Cytotoxicity.** Figure 4 showed the viability of MCF-7/ADR and MCF-7 cells after incubating for 48 h with TP, PEI 25K, PEI 2K, or Tween 85 at different concentrations by the MTT assay. The cytotoxicity of TP was neglible as that of PEI 2K and Tween 85, but PEI 25K caused severe cytotoxicity with the concentration increasing up to 0.1 mg/mL. Compared with PEI 25K, the improved cytocompatibility of TP could be due to the lower MW of PEI, which has less cytotoxicity, and the introduction of Tween 85, which could partly shield the high positive charge density of PEI.[2,5]

***In Vitro* Transfection.** The fluorescent images of MCF-7/ADR and MCF-7 cells transfected with TPCs and PCs were shown in Figure 5A, MCF-7/ADR cells incubated with TPCs showed higher green fluorescence in cytoplasm than PCs, while MCF-7 cells treated with TPCs demonstrated a little lower fluorescence than that incubated with PCs, which also was further confirmed by flow cytometry. As shown in Figure 5B, the transfection efficiency of TPCs was about 1.5 times that of PCs in MCF-7/ADR cells and about 70% that of PCs in MCF-7 cells. The mean fluorescence intensity of cells transfected with UPCs was also determined; however, only a very little fluorescence was detected (data not shown). When the

dx.doi.org/10.1021/bc200504v | *Bioconjugate Chem.* 2012, 23, 222–231

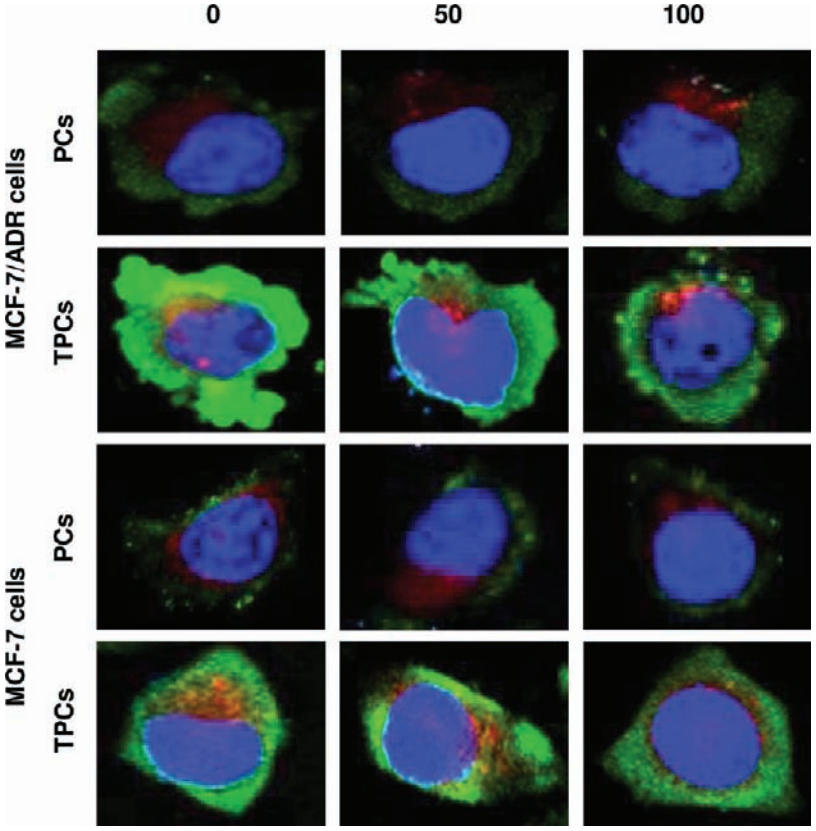


Figure 7. Confocal microscopic images of MCF-7/ADR cells and MCF-7 cells after treatment with TPCs and PCs in the absence or presence of different free Tween 85 contents. Nuclei (blue), lysosomes (red), and pDNA (green) were stained with Hoechst, lysotracker Red, and YOYO-1, respectively.

concentration of free Tween 85 reached 100 μg/well, the fluorescence intensity of TPCs decreased significantly up to about 50% of the original in MCF-7/ADR cells. On the contrary, the transfection efficiency of TPCs decreased slightly in MCF-7 cells, and even if free Tween 85 increased to 100 μg/well, the transfection efficiency of TPCs remained close to that of TPCs without free Tween 85. As to PCs, no obvious changes were observed in both cell lines when free Tween 85 was added. The improved transfection efficiency of TPCs in both cell lines could result from the fact that TP condensed DNA more effectively with the modification by Tween 85, which could lead to the formation of more stable complexes. Furthermore, it was reported that MCF-7/ADR cells showed a higher expression of the low-density lipoprotein receptor (LDLR) than MCF-7 cells,[29] and the polysorbates (Tween 80) on the surface of nanoparticles could anchor LDLR, mimic low-density lipoprotein particles to interact with LDLR, and result in increasing uptake.[30] Tween 85 also could have a similar role of enhancing the uptake of complexes, resulting in increasing the transfection efficiency. The result of inhibition experimentation from free Tween 85 indirectly confirmed that the improvement in the transfection efficiency of TPCs might be attributed to Tween 85-mediated endocytosis. In addition, it was reported that a series of cationic lipids containing an oxyethylene spacer between the cationic ammonium head groups and lipid components showed high transfection efficacy when mixed with naturally occurring helper lipid (DOPE).[25,31−33] However, TP could easily form complexes with DNA, and show high cytocompatibility. In addition, TPCs were pretty stable in the presence of NaCl (0.15 M) and DNase I. In particular, TP could significantly improve transfection efficiency without the help of other lipids or polymers.

***In Vitro* Cellular Uptake.** The cellular uptake of TPCs was performed using YOYO-1 labeled pEGFP on both cells (Figure 6). The results showed that the uptake of TPCs in both cell lines was more efficient than PCs, and more TPCs were taken up by MCF-7/ADR cells than MCF-7 cells. The uptake of TPCs by MCF-7/ADR cells was reduced with free Tween 85 increasing. By contrast, for MCF-7 cells, the uptake of TPCs did not show significant change when Tween 85 was added, and the uptake of PCs was not obviously affected by Tween 85 in both cell lines. It was suggested that Tween 80 showed the fusogenic property that could enhance the fluidity of the cell membrane.[34] The differences of uptake of TPCs in both cell lines could be attributed to the different expression of LDLR because the targeted binding interaction between surplus free Tween 85 molecules and the receptors on the cell surface would prevent the binding between Tween 85 in TPCs and the receptors, thereby reducing the endocytosis of TPCs in MCF-7/ADR cells. The improvement of the transfection efficiency of TPCs was much lower than the cellular uptake, which could be due to the poor lysosome escape ability resulting from the poor buffer capacity of TP compared with PEI 25K (data not shown). Although TPCs could be taken up more efficiently, part of them was trapped in the lysosome, and could not reach the nuclear region of the cells.

Intracellular Location. The confocal microscopic images of MCF-7/ADR cells and MCF-7 cells after incubation with TPCs and PCs showed that all the complexes were localized in the cytoplasm after internalization (Figure 7). TPCs led to

dx.doi.org/10.1021/bc200504v | *Bioconjugate Chem.* 2012, 23, 222−231

more intense green fluorescence than PCs in both cells. In addition, the treatment with TPCs resulted in a distinct increase of fluorescence intensity in MCF-7/ADR cells than in MCF-7 cells, which indicated that TPCs were more readily diffused into MCF-7/ADR cells. Furthermore, more endocytosed TPCs were colocated with lysosomes than PCs, which demonstrated that the increase with different degrees in the uptake and transfection efficiency was due to the poor lysosome escape ability. The fluorescence intensity of YOYO-1-labeled pEGFP from the MCF-7/ADR cells decreased drastically when the content of free Tween 85 increased from 0 to 100 μg, while the effect of free Tween 85 on the intracellular distribution of TPCs in MCF-7 cells was neglible, and the fluorescence intensity from both cell lines treated with PCs in the presence of free Tween 85 was apparently not altered. The results also confirmed the deduction that TPCs could be taken up mainly by Tween 85-mediated endocytosis in MCF-7/ADR cells, but not in MCF-7 cells.

CONCLUSION

The new copolymer, TP, was synthesized to enhance the transfection efficiency of PEI 2K and retain the low toxicity. TP showed strong DNA binding capacity and high protection of DNA against nuclease degradation. The uptake and transfection efficiency of TPCs were significantly enhanced by Tween 85 modification in both MCF-7 and MCF-7/ADR cells, and were strongly inhibited by the addition of Tween 85 in MCF-7/ADR cells, but not in MCF-7 cells, which indicated that Tween 85 could target MCF-7/ADR cells through LDLR. These results suggested that TP could be a promising safe and effective gene delivery carrier, especially in the cells that express high LDLR, such as HT29-dx cells, A549-dx cells, HepG2 cells, and so on.[29] Next, we will further investigate the detailed uptake mechanism and improve the lysosome escape capability.

AUTHOR INFORMATION

Corresponding Author

*501 Haike Road, Shanghai 201203, China. Phone: +86-21-20231979. Fax: +86-21-20231979. E-mail: ypli@mail.shcnc.ac.cn.

ACKNOWLEDGMENTS

The National Basic Research Program of China (2010CB934000 and 2012CB932500), the National Natural Science Foundation of China (30925041, 81102388), and Shanghai Elitist Program (11XD1406200) are gratefully acknowledged for financial support.

REFERENCES

(1) Mintzer, M. A., and Simanek, E. E. (2009) Nonviral vectors for gene delivery. *Chem. Rev. 109*, 259−302.

(2) Ko, Y. T., Kale, A., Hartner, W. C., Papahadjopoulos-Sternberg, B., and Torchilin, V. P. (2009) Self-assembling micelle-like nanoparticles based on phospholipids-polyethyleneimine conjugates for systemic gene delivery. *J. Controlled Release 133*, 132−138.

(3) Bhattacharyaw, S., and Bajajza, A. (2009) Advances in gene delivery through molecular design of cationic lipids. *Chem. Commun.*, 4632−4656.

(4) Tiera, M. J., Shi, Q., Winnik, F. M., and Fernandes, J. C. (2011) Polycation-based gene therapy: current knowledge and new perspectives. *Curr. Gene Ther. 11*, 288−306.

(5) Mustapa, M. F. M., Grosse, S. M., Kudsiova, L., Elbs, M., Raiber, E.-A., Wong, J. B., Brain, A. P. R., Armer, H. E. J., Warley, A., Keppler, M., Ng, T., Lawrence, M. J., Hart, S. L., Hailes, H. C., and Tabor, A. B. (2009) Stabilized integrin-targeting ternary LPD (lipopolyplex) vectors for gene delivery designed to disassemble within the target cell. *Bioconjugate Chem. 20*, 518−532.

(6) Wen, Y., Pan, S., Luo, X., Zhang, X., Zhang, W., and Feng, M. (2009) A biodegradable low molecular weight polyethylenimine derivative as low toxicity and efficient gene vector. *Bioconjugate Chem. 20*, 322−332.

(7) Bajaj, A., Kondaiah, P., and Bhattacharya, S. (2008) Synthesis and gene transfection efficacies of PEI-cholesterol-based lipopolymers. *Bioconjugate Chem. 19*, 1640−1651.

(8) Neamnark, A., Suwantong, O., Bahadur K. C., R., Supaphol, P., and Uludag, H. (2009) Aliphatic lipid substitution on 2 kDa polyethylenimine improves plasmid delivery and transgene expression. *Mol. Pharmaceutics 6*, 1798−1815.

(9) Nguyen, H. K., Lemieux, P., Vinogradov, S. V., Gebhart, C. L., Guerin, N., Paradis, G., Bronich, T. K., Alkov, V. Y., and Kabanov, A. V. (2000) Evaluation of polyether-polyethyleneimine graft copolymers as gene transfer agents. *Gene Ther. 7*, 126−138.

(10) Zintchenko, A., Philipp, A., Dehshahri, A., and Wagner, E. (2008) simple modifications of branched PEI lead to highly efficient siRNA carriers with low toxicity. *Bioconjugate Chem. 19*, 1448−1455.

(11) Neu, M., Fischer, D., and Kissel, T. J. (2005) Recent advances in rational gene transfer vector design based on poly(ethylene imine) and its derivatives. *Gene. Med. 7*, 992−1009.

(12) Thomas, M., Ge, Q., Lu, J. J., Chen, J. Z., and Klibanov, A. M. (2005) Cross-linked small polyethylenimines: while still nontoxic, deliver DNA efficiently to mammalian cells in vitro and in vivo. *Pharm. Res. 22*, 373−380.

(13) Xu, P. S., Quick, G. K., and Yeo, Y. (2009) Gene delivery through the use of a hyaluronate-associated intracellularly degradable crosslinked polyethyleneimine. *Biomaterials 30*, 5834−5843.

(14) Liu, J., Jiang, X. L., Xu, L., Wang, X. M., Hennink, W. E., and Zhuo, R. X. (2010) Novel reduction-responsive cross-linked polyethylenimine derivatives by click chemistry for nonviral gene delivery. *Bioconjugate Chem. 21*, 1827−1835.

(15) Peng, Q., Hu, C., Cheng, J., Zhong, Z., and Zhuo, R. (2009) Influence of disulfide density and molecular weight on disulfide cross-linked polyethylenimine as gene vectors. *Bioconjugate Chem. 20*, 340−346.

(16) Dai, J., Zou, S., Pei, Y., Cheng, D., Ai, H., and Shuai, X. (2011) Polyethylenimine-grafted copolymer of Poly(L-lysine) and Poly(ethylene glycol) for gene delivery. *Biomaterials 32*, 1694−1705.

(17) Sun, Y., Xiao, W., Cheng, S., Zhang, X., and Zhuo, R. (2008) Synthesis of (Dex-HMDI)-g-PEIs as effective and low cytotoxic nonviral gene vectors. *J. Controlled Release 128*, 171−178.

(18) Lungwitz, U., Breunig, M., Liebl, R., Blunk, T., and Goepferich, A. (2008) Methoxy poly(ethylene glycol) − Low molecular weight linear polyethylenimine-derived copolymers enable polyplex shielding. *Eur J. Pharm. Biopharm. 69*, 134−148.

(19) Neu, M., Germershaus, O., Behe, M., and Kissel, T. (2007) Bioreversibly crosslinked polyplexes of PEI and high molecular weight PEG show extended circulation times in vivo. *J. Controlled Release 124*, 69−80.

(20) Jiang, H., Kwon, J., Kim, E., Kim, Y., Arote, R., Jere, D., Jeong, H., Jang, M., Nah, J., Xu, C., Park, I., Cho, M., and Cho, C. (2008) Galactosylated poly(ethylene glycol)-chitosan-graft-polyethylenimine as a gene carrier for hepatocyte-targeting. *J. Controlled Release 131*, 150−157.

(21) Cheng, H., Zhu, J., Zeng, X., Jing, Y., Zhang, X., and Zhuo, R. (2009) Targeted gene delivery mediated by folate-polyethylenimine-block-poly(ethylene glycol) with receptor selectivity. *Bioconjugate Chem. 20*, 481−487.

(22) Noh, S. M., Park, M. O., Shim, G., Han, S. E., Lee, H. Y., Huh, J. H., Kim, M. S., Choi, J. J., Kim, K., Kwon, I. C., Kim, J. S., Baek, K. H., and Oh, Y. K. (2010) Pegylated poly-L-arginine derivatives of chitosan for effective delivery of siRNA. *J. Controlled Release 69*, 134−148.

(23) Alshamsan, A., Haddadi, A., Incani, V., Samuel, J., Lavasanifar, A., and Uludag, H. (2009) Formulation and delivery of siRNA by oleic

acid and stearic acid modified polyethylenimine. *Mol. Pharmaceutics 6*, 121−133.
(24) Wang, C., and Hsiue, G. (2005) Polymer-DNA hybrid nanoparticles based on folate-polyethylenimine-block-poly(L-lactide). *Bioconjugate Chem. 16*, 391−396.
(25) Bajaj, A., Paul, B., Kondaiah, P., and Bhattacharya, S. (2008) Structure-activity investigation on the gene transfection properties of cardiolipin mimicking gemini lipid analogues. *Bioconjugate Chem. 19*, 1283−1300.
(26) Forrest, M. L., Meister, G. E., Koerber, J. T., and Pack, D. W. (2004) Partial acetylation of polyethylenimine enhances in vitro gene delivery. *Pharm. Res. 21*, 365−371.
(27) Akinc, A., Thomas, M., Klibanov, A. M., and Langer, R. (2005) Exploring polyethylenimine mediated DNA transfection and the proton sponge hypothesis. *J. Gene. Med. 7*, 657−663.
(28) Reschel, T., Konak, C., Oupicky, D., Seymour, L. W., and Ulbrich, K. (2002) Physical properties and in vitro transfection efficiency of gene delivery vectors based on complexes of DNA with synthetic polycations. *J. Controlled Release 81*, 201−217.
(29) Kopecka, J., Campia, I., Olivero, P., Pescarmona, G., Ghigo, D., Bosia, A., and Riganti, C. (2011) LDL-masked liposomal-doxorubicin reverses drug resistance in human cancer cells. *J. Controlled Release 149*, 196−205.
(30) Sun, W., Xie, C., Wang, H., and Hu, Y. (2004) Specific role of polysorbate 80 coating on the targeting of nanoparticles to the brain. *Biomaterials 25*, 3065−3071.
(31) Dileep, P. V., Antony, A., and Bhattacharya, S. (2001) Incorporation of oxyethylene units between hydrocarbon chain and pseudoglyceryl backbone in cationic lipid potentiates gene transfection e¤ciency in the presence of serum. *FEBS Lett. 509*, 327−331.
(32) Bhattacharya, S., and Dileep, P. V. (2004) Cationic oxyethylene lipids. synthesis, aggregation, and transfection properties. *Bioconjugate Chem. 15*, 508−519.
(33) Bajaj, A., Kondaiah, P., and Bhattacharya, S. (2007) Synthesis and gene transfer activities of novel serum compatible cholesterol-based gemini lipids possessing oxyethylene-type spacers. *Bioconjugate Chem. 18*, 1537−1546.
(34) Liu, F., Yang, J., Huang, L., and Liu, D. (1996) New cationic lipid formulations for gene transfer. *Pharm. Res. 13*, 1856−1860.

Bioconjugate Chemistry

Article

pubs.acs.org/bc

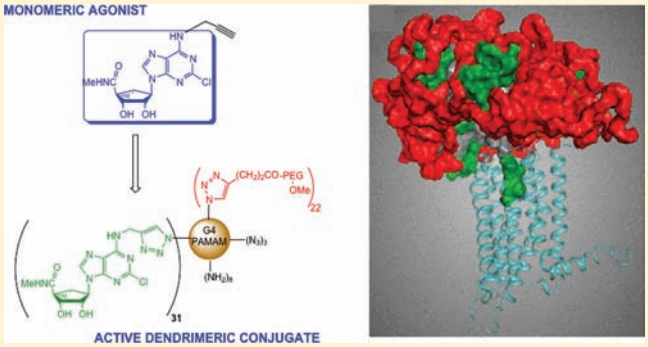
Click Modification in the N^6 Region of A_3 Adenosine Receptor-Selective Carbocyclic Nucleosides for Dendrimeric Tethering that Preserves Pharmacophore Recognition

Dilip K. Tosh, Khai Phan, Francesca Deflorian, Qiang Wei, Lena S. Yoo, Zhan-Guo Gao, and Kenneth A. Jacobson*

Molecular Recognition Section, Laboratory of Bioorganic Chemistry, National Institute of Diabetes and Digestive and Kidney Diseases, National Institutes of Health, Bethesda, Maryland 20892, United States

Supporting Information

ABSTRACT: Adenosine derivatives were modified with alkynyl groups on N^6 substituents for linkage to carriers using Cu(I)-catalyzed click chemistry. Two parallel series, both containing a rigid North-methanocarba (bicyclo[3.1.0]hexane) ring system in place of ribose, behaved as A_3 adenosine receptor (AR) agonists: (5′-methyluronamides) or partial agonists (4′-truncated). Terminal alkynyl groups on a chain at the 3 position of a N^6-benzyl group or simply through a N^6-propargyl group were coupled to azido derivatives, which included both small molecules and G4 (fourth-generation) multivalent poly(amidoamine) (PAMAM) dendrimers, to form 1,2,3-triazolyl linkers. The small molecular triazoles probed the tolerance in A_3AR binding of distal, sterically bulky groups such as 1-adamantyl. Terminal 4-fluoro-3-nitrophenyl groups anticipated nucleophilic substitution for chain extension and ^{18}F radiolabeling. N^6-(4-Fluoro-3-nitrophenyl)-triazolylmethyl derivative **32** displayed a K_i of 9.1 nM at A_3AR with ~1000-fold subtype selectivity. Multivalent conjugates additionally containing click-linked water-solubilizing polyethylene glycol groups potently activated A_3AR in the 5′-methyluronamide, but not 4′ truncated series. N^6-Benzyl nucleoside conjugate **43** (apparent K_i 24 nM) maintained binding affinity of the monomer better than a N^6-triazolylmethyl derivative. Thus, the N^6 region of 5′-methyluronamide derivatives, as modeled in receptor docking, is suitable for functionalization and tethering by click chemistry to achieve high A_3AR agonist affinity and enhanced selectivity.



INTRODUCTION

Selective ligands of the A_3 adenosine receptor (AR), a G protein-coupled receptor (GPCR), have antiinflammatory, anticancer, antiischemic, and myeloprotective activities.[1,2] A_3AR agonists are already in clinical trials for liver cancer, rheumatoid arthritis, psoriasis, and dry eye disease, with additional envisioned applications for bowel inflammation, ischemia, and other autoimmune inflammatory disorders.[3−7] The feasibility of using A_3AR antagonists for the treatment of glaucoma has been demonstrated in animal models.[8−10]

Poly(amidoamine) (PAMAM) dendrimers may serve as biocompatible carriers for various GPCR drugs, for example, multivalent nucleoside conjugates for activation of ARs that do not require drug cleavage.[11−13] Such GPCR ligand−dendrimer (GLiDe) conjugates are sufficiently large to bridge multiple binding sites present in GPCR dimers and other higher-order receptor aggregates and have already demonstrated enhanced pharmacological properties in comparison to the monomeric ligands.[14−18]

Monomeric nucleoside derivatives that bind selectively to the A_3AR have demonstrated a range of efficacies, from antagonist to full agonist,[19] and detailed structure activity relationship (SAR) studies have already been conducted. A prototypical A_3AR agonist, e.g., ribose 5′-*N*-methyluronamide Cl-IB-MECA **1**, is highly receptor subtype-selective and has entered clinical trials for liver cancer.[3] The 4′-thio modification, present in the potent agonist **2**, was found to be well-tolerated in receptor binding.[20] Later generation carbocyclic nucleosides containing a North (N)-methanocarba (bicyclo[3.1.0]hexane) ring system in place of the ribose tetrahydrofuryl moiety have led to A_3AR agonists of high affinity and selectivity. These agonists include the antiischemic nucleoside MRS3558 **3** and its 3-iodo analogue **4**, in which the rigid, fused bicyclic system maintains a receptor-preferred conformation.[21] A parallel approach to selective binding to the A_3AR is based on truncation of the 5′-uronamide group in ribonucleosides, 4′-thionucleosides, and carbocyclics, as in **5**−**8**. The effect of truncation is to reduce efficacy in activation of the receptor, while not precluding

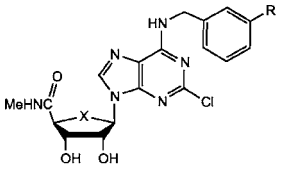
Received: September 23, 2011
Revised: November 30, 2011
Published: December 17, 2011

ACS Publications This article not subject to U.S. Copyright. Published 2011 by the American Chemical Society

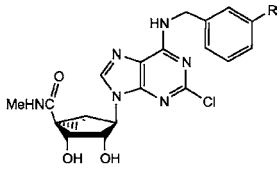
dx.doi.org/10.1021/bc200526c | *Bioconjugate Chem.* 2012, 23, 232−247

selectivity of binding to the A_3AR. Thus, truncated oxo **5** and thio **6** nucleosides are antagonists of the A_3AR, and truncated 3-halo substituted **7** and **8** are partial agonists.[22−24] Compound **6** lowered intraocular pressure in a mouse model of glaucoma,[9] an action characteristic of A_3AR antagonists, and compounds **7** and **8** were radiolabeled with ^{76}Br and ^{125}I, respectively, for use as radioligand probes of the A_3AR in vitro and in vivo.[25] These agonists, antagonists, and partial agonists all contained a 3-substituted benzyl group at the N^6 position, which enhanced A_3AR selectivity (Chart 1).

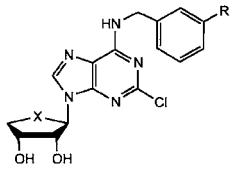
Chart 1. Representative Nucleosides That Bind to the A_3AR with High Affinity and Selectivity[a]



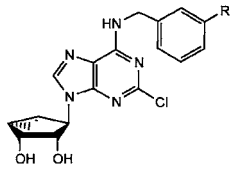
1 X = O, R = I Cl-IB-MECA, *1.4*
2 X = S, R = I LJ568, *0.38*



3 R = Cl MRS3558, *0.29*
4 R = I MRS1898, *1.51*



5 X = O, R = Br *13.0*
6 X = S, R = I LJ1251, *4.16*



7 R = Br MRS5147, *0.73*
8 R = I MRS5127, *1.44*

[a]Binding K_i values in nM at the human homologue given.

This study applies to multivalent GLiDe conjugates the SAR developed for monomeric nucleosides as receptor agonists. The linking step involved click chemistry, which encompasses various principles of reactivity and has been used extensively for orthogonal coupling of small molecules to polymers.[26,27] In particular, Cu(I)-catalyzed [3 + 2] cycloaddition reactions that combine azido and acetylene moieties to form triazole rings are a convenient and efficient means of linking two molecules.[28] Recently, we incorporated dialkynyl groups on an extended adenine C2 substituent of AR agonists for tethering to PAMAM dendrimers by Cu(I)-catalyzed click chemistry.[29] In the present series, we have applied this chemistry as a functionalization approach around the N^6 region of adenosine and its family of A_3AR agonists. As with the C2-conjugated series, the proximal alkyne is designed to promote receptor recognition, and the distal alkyne may serve as a site for coupling to macromolecular carriers while maintaining receptor recognition. Thus, we have used click chemistry to identify another region on the nucleoside for covalent attachment that is distal from the pharmacophore and does not interfere with binding/activation. This region of the nucleosides is predicted by modeling to extend into the extracellular portion of the A_3AR.[23,30]

EXPERIMENTAL PROCEDURES

Chemistry. *General Methods.* All reagents and solvents (regular and anhydrous) were of analytical grade and obtained from commercial suppliers and used without further purification. Reactions were conducted under an atmosphere of nitrogen whenever anhydrous solvents were used. All reactions were monitored by thin-layer chromatography (TLC) using silica gel coated plates with a fluorescence indicator which were visualized: (a) under UV light, (b) by dipping in a mixture of anisaldehyde (2.5 mL)/conc. H_2SO_4 (5 mL)/methanol (425 mL), or (c) by dipping the plate in a solution of ninhydrin (0.3 g in 100 mL EtOH, containing AcOH, 1.3 mL) followed by heating. Silica gel column chromatography was performed with silica gel (SiO_2, 200−400 mesh, 60 Å) using moderate air pressure. Evaporation of solvents was carried out under reduced pressure at a temperature below 50 °C. After column chromatography, appropriate fractions were pooled, evaporated, and dried at high vacuum for at least 12 h to give the desired products in high purity. ^{1}H NMR ascertained sample purity and spectra were recorded with a Bruker 400 MHz NMR spectrometer. Chemical shifts are reported in parts per million (ppm) relative to tetramethylsilane or using deuterated solvent as the internal standard (δH: $CDCl_3$ 7.26 ppm). For ^{19}F NMR spectra, CF_3CO_2H was set as 0 ppm. ESI−high resolution mass spectroscopic (HRMS) measurements were performed on a proteomics optimized Q-TOF-2 (Micromass-Waters) using external calibration with polyalanine. Observed mass accuracies are those expected on the basis of known performance of the instrument as well as the trends in masses of standard compounds observed at intervals during the series of measurements. Reported masses are observed masses uncorrected for this time-dependent drift in mass accuracy.

*(1S,2R,3S,4R,5S)-4-[2-Chloro-6-{3-(1,6-heptadiynyl)}-9H-purin-9-yl]-2,3-dihydroxybicyclo[3.1.0]hexane-1-carboxylic Acid N-Methylamide (**9**).* To a solution of compound **4** (50 mg, 0.09 mmol) in anhydrous DMF (2 mL), $PdCl_2(PPh_3)_2$ (12.6 mg, 0.01 mmol), CuI (1.7 mg, 0.008 mmol), 1,6-heptadiyne (0.1 mL, 0.9 mmol), and then triethylamine (0.12 mL, 0.89 mmol) were added and stirred overnight at room temperature. Solvent was evaporated under vacuum, and the residue was purified on flash silica gel column chromatography (CH_2Cl_2:MeOH = 60:1) to give compound **9** (38 mg, 81%) as syrup. ^{1}H NMR ($CDCl_3$, 400 MHz) δ 7.8 (s, 1H), 7.42 (s, 1H), 7.24−7.30 (m, 3H), 5.03 (d, J = 6.0 Hz, 1H), 4.84 (s, 1H), 4.79 (br s, 1H), 4.13 (d, J = 6.4 Hz, 1H), 2.94 (s, 3H), 2.55 (t, J = 7.2 Hz, 2H), 2.36−2.41 (m, 2H), 2.18−2.22 (m, 1H), 2.00 (t, J = 2.8 Hz, 1H), 1.68 (t, J = 9.2 Hz, 1H), 1.85−1.79 (m, 2H), 1.37−1.41 (m, 1H). HRMS calculated for $C_{27}H_{28}ClN_6O_3$ (M + H)$^+$: 519.1911; found 519.1930.

*(1S,2R,3S,4R,5S)-4-[2-Chloro-6-{3-(1,7-octadiynyl)}-9H-purin-9-yl]-2,3-dihydroxybicyclo[3.1.0]hexane-1-carboxylic Acid N-Methylamide (**10**).* Compound **10** (85%) was synthesized from compound **4** and 1,7-octadiyne following the same procedure as for compound **2**. ^{1}H NMR (CD_3OD, 400 MHz) δ 8.04 (s, 1H), 7.40 (s, 1H), 7.26−7.34 (m, 3H), 5.08 (d, J = 6.8 Hz, 1H), 4.81 (s, 1H), 4.73 (br s, 2H), 4.60 (br s, 2H), 4.01 (d, J = 6.4 Hz, 1H), 2.87 (s, 3H), 2.43 (t, J = 6.8 Hz, 2H), 2.21−2.26 (m, 2H), 2.05−2.08 (m, 1H), 1.68−1.71 (m, 1H), 1.38−1.40 (m, 1H). HRMS calculated for $C_{28}H_{30}ClN_6O_3$ (M + H)$^+$: 533.2068; found 533.2070.

*(1S,2R,3S,4R,5S)-4-[2-Chloro-6-{3-(1,8-nonadiynyl)}-9H-purin-9-yl]-2,3-dihydroxybicyclo[3.1.0]hexane-1-carboxylic Acid N-Methylamide (**11**).* Compound **11** (79%) was synthesized from compound **4** and 1,8-nonadiyne following the same procedure as for compound **2**. ^{1}H NMR ($CDCl_3$, 400 MHz) δ 7.92 (s, 1H), 7.43 (s, 1H), 7.25−7.32 (m, 3H), 5.10 (d, J = 6.6 Hz, 1H), 4.85 (s, 1H), 4.78 (br s, 2H), 4.15 (d, J = 6.3 Hz, 1H), 2.93 (s, 3H), 2.42 (t, J = 6.0 Hz, 2H), 2.22−2.23

dx.doi.org/10.1021/bc200526c | *Bioconjugate Chem.* 2012, 23, 232−247

(m, 2H), 1.97 (t, J = 2.8 Hz, 1H), 1.71−1.78 (m, 2H), 1.58−1.61 (m, 6H), 1.48−1.52 (m, 1H). HRMS calculated for $C_{29}H_{32}ClN_6O_3$ $(M + H)^+$: 547.2224; found 547.2239.

*(1S,2R,3S,4R,5S)-4-(2-Chloro-6-(3-(5-(1-(4-fluoro-3-nitrophenyl)-1H-1,2,3-triazol-4-yl)pent-1-ynyl)benzylamino)-9H-purin-9-yl)-2,3-dihydroxybicyclo[3.1.0]hexane-1-carboxylic Acid-N-methylamide (**12**).* 4-Fluoro-3-nitro-phenylazide (9.3 mg, 0.051 mmol) and TBTA[31] (1 mg, 0.001 mmol) were added to a solution of compound **9** (19 mg, 0.036 mmol) in *t*-butanol (0.6 mL)/CH_2Cl_2 (0.6 mL)/water (0.6 mL) at room temperature. Freshly prepared 1 M solution of sodium ascorbate (36.6 μL) followed by 7.5% solution of copper sulfate (60.7 μL, 0.018 mmol) was also added into the reaction mixture and stirred at room temperature overnight. Solvent was evaporated, and the residue was purified on flash silica gel column chromatography (CH_2Cl_2:MeOH = 40:1) to give compound **12** (23 mg, 90%) as a syrup. ^{1}H NMR (CD_3OD, 400 MHz) δ 8.53−8.62 (m, 1H), 8.49 (s, 1H), 8.22−8.19 (m, 1H), 8.04 (s, 1H), 7.60−7.67 (m, 2H), 7.39−23 (m, 3H), 5.05 (d, J = 5.6 Hz, 1H), 4.81 (s, 1H), 4.71 (br s, 2H), 4.00 (d, J = 6.8 Hz, 1H), 2.98 (t, J = 7.6 Hz, 2H), 2.86 (s, 3H), 2.53 (t, J = 6.8 Hz, 2H), 2.02−2.08 (m, 3H), 1.82 (t, J = 4.8 Hz, 1H), 1.36−1.39 (m, 1H). HRMS calculated for $C_{33}H_{31}ClFN_8O_3$ $(M + H)^+$: 701.2151; found 701.2175.

*(1S,2R,3S,4R,5S)-4-(2-Chloro-6-(3-(6-(1-(4-fluoro-3-nitrophenyl)-1H-1,2,3-triazol-4-yl)hex-1-ynyl)benzylamino)-9H-purin-9-yl)-2,3-dihydroxybicyclo[3.1.0]hexane-1-carboxylic Acid-N-methylamide (**13**).* Compound **13** (94%) was synthesized from compound **10** following the same procedure as for compound **12**. ^{1}H NMR (CD_3OD, 400 MHz) δ 8.65−8.58 (m, 1H), 8.45 (s, 1H), 8.23−8.19 (m, 1H), 8.03 (s, 1H), 7.65 (t, J = 8.8 Hz, 1H), 7.41 (s, 1H), 7.33−7.25 (m, 2H), 5.07 (d, J = 6.8 Hz, 1H), 4.80 (s, 1H), 4.72 (br s, 2H), 4.00 (d, J = 6.8 Hz, 1H), 2.87 (s, 3H), 2.51 (t, J = 6.8 Hz, 2H), 2.07−2.04 (m, 1H), 1.97−1.91 (m, 2H), 1.82 (t, J = 5.2 Hz, 2H), 1.74−1.69 (m, 2H), 1.39−1.35 (m, 1H). HRMS calculated for $C_{34}H_{33}ClFN_{10}O_5$ $(M + H)^+$: 715.2308; found 715.2302.

*(1S,2R,3S,4R,5S)-4-(2-Chloro-6-(3-(7-(1-(4-fluoro-3-nitrophenyl)-1H-1,2,3-triazol-4-yl)hept-1-ynyl)benzylamino)-9H-purin-9-yl)-2,3-dihydroxybicyclo[3.1.0]hexane-1-carboxylic Acid-N-methylamide (**14**).* Compound **14** (96%) was synthesized from compound **11** following the same procedure as for compound **12**. ^{1}H NMR (CD_3OD, 400 MHz) δ 8.55−8.59 (m, 1H), 8.41 (s, 1H), 8.16−8.12 (m, 1H), 8.03 (s, 1H), 7.60 (t, J = 9.2 Hz, 1H), 7.36 (s, 1H), 7.30−7.20 (m, 2H), 5.08 (d, J = 6.4 Hz, 1H), 4.80 (s, 1H), 4.69 (br s, 2H), 4.01 (d, J = 6.4 Hz, 1H), 2.87−2.82 (m, 5H), 2.44 (t, J = 6.4 Hz, 2H), 2.08−2.05 (m, 1H), 1.84−1.81 (m, 3H), 1.68−1.58 (m, 4H), 1.39−1.38 (m, 1H). HRMS calculated for $C_{35}H_{35}ClFN_{10}O_5$ $(M + H)^+$: 729.2464; found 729.2463.

*(1S,2R,3S,4R,5S)-4-(2-Chloro-6-(3-(6-(1-(adamantyl)-1H-1,2,3-triazol-4-yl)hex-1-ynyl)benzylamino)-9H-purin-9-yl)-2,3-dihydroxybicyclo[3.1.0]hexane-1-carboxylic Acid-N-methylamide (**15**).* Compound **15** (93%) was synthesized from compound **10** following the same procedure as for compound **12**. ^{1}H NMR (CD_3OD, 400 MHz) δ 8.04 (s, 1H), 7.40 (s, 1H), 7.35−7.26 (m, 3H), 5.09 (d, J = 6.8 Hz, 1H), 4.82 (s, 1H), 4.73 (s, 2H), 4.02 (d, J = 6.8 Hz, 1H), 2.87 (s, 1H), 2.44 (t, J = 6.8 Hz, 2H), 2.26−2.21 (m, 3H), 2.17 (m, 8H), 2.08−2.05 (m, 1H), 1.82 (t, J = 4.8 Hz, 1H), 1.70−1.69 (m, 10H), 1.39−1.36 (m, 1H), 0.94−0.88 (m, 1H). HRMS calculated for $C_{38}H_{45}ClN_9O_3$ $(M + H)^+$: 710.3257; found 710.3248.

*(1S,2R,3S,4R,5S)-4-(2-Chloro-6-(3-(5-(1-(4-fluoro-3-aminophenyl)-1H-1,2,3-triazol-4-yl)pent-1-ynyl)benzylamino)-9H-purin-9-yl)-2,3-dihydroxybicyclo[3.1.0]hexane-1-carboxylic Acid-N-methylamide (**16**).* Zinc dust (3 mg, 0.045 mmol) was added to a solution of compound **12** (5 mg, 0.007 mmol) in acetonitrile (0.5 mL)/acetic acid (0.5 mL) at 0 °C. After addition, the reaction mixture was brought to room temperature and stirred for 2 h under the same conditions. The reaction mixture was filtered on a Celite bed, and the filtrate was evaporated under vacuum. The residue was purified on flash silica gel column chromatography (CH_2Cl_2:MeOH = 20:1) to give compound **16** (3 mg, 62%). ^{1}H NMR (CD_3OD, 400 MHz) δ 8.65−8.58 (m, 1H).

*(1S,2R,3S,4R,5S)-4-(2-Chloro-6-(3-(7-(1-(4-fluoro-3-aminophenyl)-1H-1,2,3-triazol-4-yl)hept-1-ynyl)benzylamino)-9H-purin-9-yl)-2,3-dihydroxybicyclo[3.1.0]hexane-1-carboxylic Acid-N-methylamide (**17**).* Compound **17** (64%) was synthesized from compound **14** following the same procedure as for compound **16**. ^{1}H NMR (CD_3OD, 400 MHz) δ 8.12 (s, 1H), 8.03 (s, 1H), 7.38 (s, 1H), 7.32−7.21 (m, 4H), 7.06−7.02 (m, 1H), 6.90−6.86 (m, 1H), 5.08 (d, J = 7.2 Hz, 1H), 4.80 (s, 1H), 4.70 (br s, 2H), 4.01 (d, J = 6.4 Hz, 1H), 2.87 (s, 3H), 2.80 (t, J = 7.2 Hz, 2H), 2.44 (t, J = 6,8 Hz, 2H), 2.02−2.09 (m, 1H), 1.83−1.78 (m, 2H), 1.68−1.54 (m, 5H), 0.89−0.93 (m, 1H). HRMS calculated for $C_{40}H_{37}ClFN_8O$ $(M + H)^+$: 699.2763; found 699.2745.

*(1R,2R,3S,4R,5S)-4-(2-Chloro-6-(3-(hepta-1,6-diynyl)-benzylamino)-9H-purin-9-yl) 2,3-O-isopropylidine-bicyclo-[3.1.0]hexane (**19**).* $PdCl_2(PPh_3)_2$ (29.7 mg, 0.04 mmol), CuI (8.0 mg, 0.04 mmol), and 1,6-heptadiyne (0.24 mL, 2.11 mmol) followed by triethylamine (60 μL, 0.41 mmol) were added to a solution of compound **18** (114 mg, 0.211 mmol) in anhydrous DMF (2 mL), and the reaction mixture was stirred overnight at room temperature. Solvent was evaporated under vacuum, and the residue was purified on flash silica gel column chromatography (hexane:ethyl acetate = 2:1) to give compound **19** (83 mg, 78%) as foamy syrup. ^{1}H NMR ($CDCl_3$, 400 MHz) δ 7.72 (s, 1H), 7.42 (s, 1H), 7.28−7.42 (m, 3H), 6.31 (br s, 1H), 5.35 (t, J = 6.0 Hz, 1H), 4.98 (s, 1H), 4.81 (br s, 2H), 4.65 (d, J = 7.6 Hz, 1H), 2.55 (t, J = 7.2 Hz, 2H), 2.38 (dd, J_1 = 2.8 Hz, J_2 = 3.2 Hz, 2H), 2.08−2.14 (m, 1H), 1.99 (t, J = 2.8 Hz, 1H), 1.82−1.85 (m, 2H), 1.64−1.67 (m, 2H), 1.56 (s, 3H), 1.26 (s, 3H), 0.93−1.00 (m, 1H). HRMS calculated for $C_{28}H_{29}ClN_5O_2$ $(M + H)^+$: 502.2032; found 502.2029.

*(1R,2R,3S,4R,5S)-4-(2-Chloro-6-(3-(nona-1,8-diynyl)-benzylamino)-9H-purin-9-yl) 2,3-O-isopropylidene-bicyclo-[3.1.0]hexane (**21**).* Compound **21** (80%) was synthesized from compound **18** and 1,8-nonadiyne following the same procedure as for compound **19**. ^{1}H NMR ($CDCl_3$, 400 MHz) δ 7.71 (s, 1H), 7.42 (s, 1H), 7.27−7.34 (m, 3H), 6.33(br s, 1H), 5.35 (t, J = 6.4 Hz, 1H), 4.98 (s, 1H), 4.80 (br s, 2H), 4.64 (d, J = 7.2 Hz, 1H), 2.41 (t, J = 3.6 Hz, 2H), 2.28−2.21 (m, 3H), 2.14−2.08 (m, 1H), 1.97−1.96 (t, J = 2.8 Hz, 1H), 1.54−1.68 (m, 10H), 1.26 (s, 3H), 0.88−0.99 (m, 1H). HRMS calculated for $C_{30}H_{33}ClN_5O_2$ $(M + H)^+$: 530.2323; found 530.2315.

*(1R,2R,3S,4R,5S)-4-(2-Chloro-6-(3-(hepta-1,6-diynyl)-benzylamino)-9H-purin-9-yl) bicyclo[3.1.0]hexane-2,3-diol (**22**).* A solution of compound **19** (92 mg, 0.18 mmol) in CH_2Cl_2 (4 mL) and trifluoromethane sulfonic acid:water (2:1, 3 mL) was stirred at room temperature overnight. Solvent was evaporated, and the residue was purified on flash silica gel chromatography (CH_2Cl_2:MeOH = 70:1) to give compound

22 (77 mg, 92%) as a syrup. ^{1}H NMR ($CDCl_3$, 400 MHz) δ 7.80 (s, 1H), 7.42 (s, 1H), 7.29−7.35 (m, 3H), 6.41 (br s, 1H), 4.87 (s, 1H), 4.81 (br s, 2H), 4.02 (d, J = 6.4 Hz, 1H), 4.00 (s, 1H), 2.69 (d, J = 6.3 Hz, 1H), 2.56 (t, J = 6.8 Hz, 2H), 2.36−2.41 (m, 2H), 2.03−2.08 (m, 1H), 2.00 (t, J = 2.8 Hz, 1H), 1.85−1.82 (m, 2H), 1.68−1.64 (m, 1H), 1.26−1.30 (m, 2H), 0.90−0.80 (m, 1H). HRMS calculated for $C_{25}H_{25}ClN_5O_2$ (M + H)$^+$: 462.1697; found 462.1696.

*(1R,2R,3S,4R,5S)-4-(2-Chloro-6-(3-(octa-1,7-diynyl)-benzylamino)-9H-purin-9-yl) bicyclo[3.1.0]hexane-2,3-diol (**23**).* $PdCl_2(PPh_3)_2$ (5.7 mg, 0.008 mmol), CuI (1.0 mg, 0.005 mmol), and 1,7-octadiyne (27 μL, 0.2 mmol) followed by triethylamine (57 μL, 0.4 mmol) were added to a solution of compound **18** (20.4 mg, 0.04 mmol) in anhydrous DMF (1.2 mL) and the reaction mixture was stirred overnight at room temperature. Solvent was evaporated under vacuum, and the residue was roughly purified on flash silica gel column chromatography and the obtained product was dissolved in CH_2Cl_2 (3 mL) and 2 mL of trifluoromethane sulfonic acid−water (2:1) were added into it and stirred at room temperature overnight. Solvent was evaporated, and the residue was purified on flash silica gel chromatography (CH_2Cl_2:MeOH = 60:1) to give compound **23** (12.6 mg, 70%) as a syrup. ^{1}H NMR ($CDCl_3$, 400 MHz) δ 7.80 (s, 1H), 7.42 (s, 1H), 7.35−7.29 (m, 3H), 6.43 (br s, 1H), 4.88 (s, 1H), 4.80 (br s, 2H), 4.03 (d, J = 7.2 Hz, 1H), 3.97 (s, 1H), 2.64 (m, 1H), 2.45 (t, J = 6.4 Hz, 2H), 2.29−2.26 (m, 3H), 2.08−2.06 (m, 1H), 1.98 (t, J = 2.4 Hz, 1H), 1.71−1.66 (m, 3H), 1.28−1.31 (m, 1H), 0.86−0.82 (m, 1H). HRMS calculated for $C_{26}H_{27}ClN_5O_2$ (M + H)$^+$: 476.1853; found 476.1869.

*(1R,2R,3S,4R,5S)-4-(2-Chloro-6-(3-(nona-1,8-diynyl)-benzylamino)-9H-purin-9-yl) bicyclo[3.1.0]hexane-2,3-diol (**24**).* Compound **24** (89%) was synthesized from compound **21** following the same procedure as for compound **22**. ^{1}H NMR (CD_3OD, 400 MHz) δ 8.15 (s, 1H), 7.40 (s, 1H), 7.26−7.33 (m, 3H), 4.80 (s, 1H), 4.74−4.69 (m, 1H), 4.60 (br s, 2H), 3.92 (d, J = 6.4 Hz, 1H), 2.41 (t, J = 6.4 Hz, 2H), 2.18−2.19 (m, 3H), 2.01−1.96 (m, 1H), 1.70−1.65 (m, 1H), 1.59−1.50 (m, 6H), 1.34−1.30 (m, 1H), 0.80−0.74 (m, 1H). HRMS calculated for $C_{27}H_{29}ClN_5O_2$ (M + H)$^+$: 490.2010; found 490.2000.

*(1R,2R,3S,4R,5S)-4-(2-Chloro-6-(3-(5-(1-(4-fluoro-3-nitro-phenyl)-1H-1,2,3-triazol-4-yl)pent-1-ynyl)benzylamino)-9H-purin-9-yl)-bicyclo[3.1.0]hexane-2,3-diol (**25**).* 4-Fluoro-3-nitro-phenylazide (7.5 mg, 0.041 mmol) and TBTA (1 mg, 0.001 mmol) were added to a solution of compound **22** (13.5 mg, 0.029 mmol) in CH_2Cl_2/t-butanol (0.6 mL)/water (0.6 mL) at room temperature. Freshly prepared 1 M solution of sodium ascorbate (29.2 μL) followed by 7.5% solution of copper sulfate (48 μL, 0.015 mmol) was also added into the reaction mixture stirred at room temperature overnight. Solvent was evaporated, and the residue was purified on flash silica gel column chromatography (CH_2Cl_2:MeOH = 45:1) to give compound **25** (17 mg, 91%) as a syrup. ^{1}H NMR (CD_3OD, 400 MHz) δ 861−8.59 (m, 1H), 8.49 (s, 1H), 8.23−8.19 (m, 1H), 8.14 (s, 1H), 7.65 (t, J = 9.2 Hz, 1H), 7.39 (s, 1H), 7.33−7.24 (m, 3H), 4.79 (s, 1H), 4.72−4.70 (m, 3H), 3.90 (d, J = 6.4 Hz, 1H), 2.99 (t, J = 7.6 Hz, 2H), 2.53 (t, J = 6.8 Hz, 2H), 2.08−1.96 (m, 3H), 1.69−1.65 (m, 1H), 1.33−1.30 (m, 1H), 0.79−0.75 (m, 1H). HRMS calculated for $C_{31}H_{28}ClFN_9O_4$ (M + H)$^+$: 644.1937; found 644.1962.

*(1R,2R,3S,4R,5S)-4-(2-Chloro-6-(3-(6-(1-(4-fluoro-3-nitro-phenyl)-1H-1,2,3-triazol-4-yl)hex-1-ynyl)benzylamino)-9H-purin-9-yl)-bicyclo[3.1.0]hexane-2,3-diol (**26**).* Compound **26** (95%) was synthesized from compound **23** following the same procedure as for compound **25**. ^{1}H NMR ($CDCl_3$, 400 MHz) δ 8.44−8.39 (m, 1H), 8.07−8.11 (m, 1H), 7.83 (s, 1H), 7.77 (s, 1H), 7.51−7.43 (m, 2H), 7.33−7.26 (m, 3H), 6.58 (br s, 1H), 4.87 (s, 1H), 4.79 (br s, 2H), 4.15 (s, 1H), 4.02 (d, J = 6.8 Hz, 1H), 2.89 (t, J = 7.6 Hz, 2H), 2.49 (t, J = 6.8 Hz, 2H), 2.08−2.04 (m, 1H), 1.96−1.90 (m, 2H), 1.76−1.64 (m, 3H), 1.31−1.28 (m, 1H), 0.79−0.85 (m, 1H). HRMS calculated for $C_{32}H_{30}ClFN_9O_4$ (M + H)$^+$: 658.2093; found 658.2124.

*(1R,2R,3S,4R,5S)-4-(2-Chloro-6-(3-(7-(1-(4-fluoro-3-nitro-phenyl)-1H-1,2,3-triazol-4-yl)hept-1-ynyl)benzylamino)-9H-purin-9-yl)bicyclo[3.1.0]hexane-2,3-diol (**27**).* Compound **27** (91%) was synthesized from compound **24** following the same procedure as for compound **25**. ^{1}H NMR (CD_3OD, 400 MHz) δ 8.56−8.54 (m, 1H), 8.40 (s, 1H), 8.13−8.18 (m, 2H), 7.60 (t, J = 8.8 Hz, 1H), 7.37 (s, 1H), 7.30 (d, J = 6.8 Hz, 1H), 7.24−7.21 (m, 2H), 4.79 (s, 1H), 4.72−4.69 (m, 3H), 3.90 (d, J = 6.4 Hz, 1H), 2.84 (t, J = 7.2 Hz, 2H), 2.45 (t, J = 6.8 Hz, 2H), 2.01−1.95 (m, 1H), 1.86−1.79 (m, 2H), 1.68−1.58 (m, 5H), 1.33−1.30 (m, 1H), 0.82−0.72 (m, 1H). HRMS calculated for $C_{33}H_{32}ClFN_9O_4$ (M + H)$^+$: 672.2250; found 672.2245.

*(1S,2R,3S,4R,5S)-Ethyl-4-(2-chloro-6-(prop-2-ynylamino)-9H-purin-9-yl)-2,3-O-isopropylidine-bicyclo[3.1.0]hexane-1-carboxylate (**29**).* Propargylamine (0.5 mL, 7.5 mmol) and triethylamine (2.1 mL, 15 mmol) were added to a solution of compound **28** (620 mg, 0.14 mmol) in anhydrous methanol (10 mL) and stirred overnight at room temperature. Solvent was evaporated, and the residue was purified on flash silica gel column chromatography (hexane:ethyl acetate = 1:1) to give compound **29** (511 mg, 79%) as a syrup. ^{1}H NMR ($CDCl_3$, 400 MHz) δ 7.73 (s, 1H), 6.20 (br s, 1H), 5.89 (d, J = 7.0 Hz, 1H), 4.88 (s, 1H), 4.74 (d, J = 7.1 Hz, 1H), 4.47 (br s, 2H), 4.32−4.28 (m, 2H), 4.27−4.13 (m, 1H), 2.32 (s, 1H), 2.24−2.20 (m, 1H), 1.76−1.72 (m, 1H), 1.68 (s, 3H), 1.57−1.53 (m, 4H), 1.36 (t, J = 7.2 Hz, 3H), 1.30−1.25 (m, 1H). HRMS calculated for $C_{20}H_{23}ClN_5O_4$ (M + H)$^+$: 432.1367; found 432.1362.

*(1S,2R,3S,4R,5S)-4-(2-Chloro-6-(prop-2-ynylamino)-9H-purin-9-yl)-2,3-O-isopropylidine-N-methyl bicyclo[3.1.0]-hexane-1-carboxamide (**30**).* Methylamine (40% solution, 3 mL) was added to a solution of compound **29** (244 mg, 0.56 mmol) in methanol (9 mL) and stirred for 2 d at room temperature. Solvent was evaporated under vacuum, and the residue was purified on flash silica gel column chromatography (CH_2Cl_2:MeOH = 70:1) to give compound **30** (148 mg, 63%) as a syrup. ^{1}H NMR (CD_3OD, 400 MHz) δ 8.08 (s, 1H), 5.75 (d, J = 7.2 Hz, 1H), 4.97 (s, 1H), 4.84 (d, J = 6.8 Hz, 1H), 4.35 (br s, 2H), 2.86 (s, 3H), 2.63 (t, J = 2.4 Hz, 1H), 2.15−2.11 (m, 1H), 1.57−1.54 (m, 4H), 1.40 (t, J = 5.2 Hz, 1H), 1.29 (s, 3H). HRMS calculated for $C_{19}H_{21}ClN_6O_3$ (M + H)$^+$: 416.1364; found 416.1374.

*(1S,2R,3S,4R,5S)-4-(2-Chloro-6-(prop-2-ynylamino)-9H-purin-9-yl)-2,3-dihydroxy-N-methylbicyclo[3.1.0]hexane-1-carboxamide (**31**).* 10% Trifluoroacetic acid (3 mL) was added to a solution of compound **30** (70 mg, 0.167 mmol) in methanol (4 mL) and heated at 70 °C overnight. Solvent was evaporated under vacuum, and the residue was purified on flash silica gel column chromatography (CH_2Cl_2:MeOH = 40:1) to give compound **31** (55 mg, 87%) as a syrup. ^{1}H NMR (CD_3OD, 400 MHz) δ 8.06 (s, 1H), 5.09 (d, J = 5.6 Hz, 1H), 4.8 (s, 1H), 4.36 (br s, 2H), 4.01 (d, J = 6.4 Hz, 1H), 2.88 (s, 3H), 2.63 (t, J = 2.4 Hz, 1H), 2.08−2.04 (m, 1H), 1.82 (t, J =

4.8 Hz, 1H), 1.40−1.37 (m, 1H). HRMS calculated for $C_{16}H_{18}ClN_6O_3$ $(M + H)^+$: 377.1129; found 377.1124.

*(1S,2R,3S,4R,5S)-4-(2-Chloro-6-((1-(4-fluoro-3-nitrophenyl)-1H-1,2,3-triazol-4-yl)methylamino)-9H-purin-9-yl)-2,3-dihydroxy-N-methylbicyclo[3.1.0]hexane-1-carboxamide (**32**).* 4-Fluoro-3-nitro-phenylazide (9.7 mg, 0.053 mmol) and TBTA (1 mg, 0.001 mmol) were added to a solution of compound **31** (14.4 mg, 0.038 mmol) in *t*-butanol (0.8 mL)/water (0.8 mL) at room temperature. Freshly prepared 1 M solution of sodium ascorbate (38.2 μL) followed by 7.5% solution of copper sulfate (63 μL, 0.019 mmol) was also added into the reaction mixture stirred at room temperature overnight. Solvent was evaporated, and the residue was purified on flash silica gel column chromatography (CH_2Cl_2:MeOH = 30:1) to give compound **32** (19 mg, 92%) as a syrup. ^{1}H NMR (CD_3OD, 400 MHz) δ 8.62−8.61 (m, 2H), 8.27−8.24 (m, 1H), 8.06 (s, 1H), 7.69−7.64 (m, 1H), 5.08 (d, *J* = 6.8 Hz, 1H), 4.94 (br s, 2H), 4.81 (s, 1H), 4.01 (d, *J* = 6.0 Hz, 1H), 2.87 (s, 3H), 2.07−2.04 (m,1H), 1.82 (t, *J* = 4.8 Hz, 1H), 1.39−1.37 (m, 1H). HRMS calculated for $C_{22}H_{21}ClFN_{10}O_5$ $(M + H)^+$: 559.1369; found 559.1346.

*(1S,2R,3S,4R,5S)-4-(2-Chloro-6-((1-(4-fluoro-3-amino)-1H-1,2,3-triazol-4-yl) methylamino)-9H-purin-9-yl)-2,3-dihydroxy-N-methylbicyclo[3.1.0]hexane-1-carboxamide (**33**).* Compound **33** (73%) was synthesized from compound **32** following the same procedure as for compound **16**. ^{1}H NMR (CD_3OD, 400 MHz) d 8.32 (s, 1H), 8.06 (s, 1H), 7.27−7.25 (m, 1H), 7.13−7.08 (m, 1H), 6.99−6.95 (m, 1H), 5.08 (d, *J* = 7.2 Hz, 1H), 4.82 (s, 2H), 4.00 (d, *J* = 6.8 Hz, 1H), 2.87 (s, 3H), 2.07−2.04 (m,1H), 1.82 (t, *J* = 4.8 Hz, 1H), 1.40−1.38 (m, 1H). HRMS calculated for $C_{22}H_{23}ClFN_{10}O_3$ $(M + H)^+$: 529.1627; found 529.1616.

*(1S,2R,3S,4R,5S)-4-(2-Chloro-6-((1-(4-(3-fluoropropylcarbamoyl)phenyl)-1H-1,2,3-triazol-4-yl)-methylamino)-9H-purin-9-yl)-2,3-dihydroxy-N-methylbicyclo[3.1.0] hexane-1-carboxamide (**34**).* Compound **34** (89%) was synthesized from compound **31** following the same procedure as for compound **32**. ^{1}H NMR (CD_3OD, 400 MHz) δ 8.56 (s, 1H), 8.06 (s, 1H), 8.02 (d, *J* = 8.8 Hz, 2H), 7.96 (d, *J* = 8.8 Hz, 2H), 5.08 (d, *J* = 6.8 Hz, 2H), 4.95 (br s, 2H), 4.82 (s, 1H), 4.61 (t, *J* = 5.6 Hz, 1H), 4.51 (t, *J* = 5.6 Hz, 1H), 4.00 (d, *J* = 6.8 Hz, 1H), 3.54 (t, *J* = 6.8 Hz, 2H), 2.87 (s, 3H), 2.08−1.96 (m, 3H), 1.82 (t, *J* = 4.8 Hz, 1H), 1.40−1.36 (m, 1H). HRMS calculated for $C_{26}H_{29}ClFN_{10}O_4$ $(M + H)^+$: 599.2046; found 599.2030.

*(1S,2R,3S,4R,5S)-4-(2-Chloro-6-((1-(adamantyl)-1H-1,2,3-triazol-4-yl)methylamino)-9H-purin-9-yl)-2,3-dihydroxy-N-methylbicyclo[3.1.0]hexane-1-carboxamide (**35**).* Compound **35** (95%) was synthesized from compound **31** following the same procedure as for compound **32**. ^{1}H NMR (CD_3OD, 400 MHz) δ 8.04 (s, 1H), 8.03 (s, 1H), 5.08 (d, *J* = 6.8 Hz, 1H), 4.82 (s, 2H), 4.01 (d, *J* = 6.4 Hz, 1H), 2.87 (s, 3H), 2.25 (s, 9H), 2.07−2.04 (m, 1H), 1.84−1.81 (m, 7H), 1.40−1.36 (m, 1H). HRMS calculated for $C_{26}H_{33}ClN_9O_3$ $(M + H)^+$: 554.2395; found 554.2383.

*(1R,2R,3S,4R,5S)-4-(2-Chloro-6-(prop-2-ynylamino)-9H-purin-9-yl) 2,3-O-isopropylidene-bicyclo[3.1.0]hexane (**37**).* Propargylamine (47 μL, 0.7 mmol) and triethylamine (0.28 mL, 1.9 mmol) were added to a solution of compound **36** (50 mg, 0.14 mmol) in anhydrous methanol (2 mL) and stirred overnight at room temperature. Solvent was evaporated, and the residue was purified on flash silica gel column chromatography (hexane:ethyl acetate = 1:1) to give compound **37** (45 mg, 85%) as a syrup. ^{1}H NMR (CD_3OD, 300 MHz) δ 7.80 (s, 1H), 6.25 (br s, 1H), 5.34 (t, *J* = 5.7 Hz, 1H), 4.98 (s, 1H), 4.64 (d, *J* = 7.2 Hz, 1H), 4.48 (s, 2H), 2.03−2.12 (m, 1H), 1.78 (s, 1H), 1.62−1.67 (m, 1H), 1.54 (s, 3H), 1.25 (s, 3H), 0.88−0.98 (m, 2H). HRMS calculated for $C_{17}H_{19}ClN_5O_2$ $(M + H)^+$: 360.1227; found 360.1218.

*(1R,2R,3S,4R,5S)-4-(2-Chloro-6-(prop-2-ynylamino)-9H-purin-9-yl) bicyclo[3.1.0]hexane-2,3-diol (**38**).* A solution of compound **37** (40 mg, 0.11 mmol) in methanol (3 mL) and 10% trifluoromethane sulfonic acid−water (3 mL) was heated at 70 °C overnight. Solvent was evaporated, and the residue was purified on flash silica gel chromatography (CH_2Cl_2:MeOH = 50:1) to give compound **38** (33 mg, 93%) as a syrup. ^{1}H NMR (CD_3OD, 300 MHz) δ 8.15 (s, 1H), 4.79 (s, 1H), 4.70 (t, *J* = 6.0 Hz, 1H), 4.36 (s, 2H), 3.89 (d, *J* = 6.6 Hz, 1H), 2.62 (s, 1H), 1.95−2.01 (m, 1H), 1.62 −1.68 (m, 1H), 1.28−1.32 (m, 1H), 0.72−0.79 (m, 1H). HRMS calculated for $C_{14}H_{15}ClN_5O_2$ $(M + H)^+$: 320.0914; found 320.0898.

*(1R,2R,3S,4R,5S)-4-(2-Chloro-6-((1-(4-fluoro-3-nitrophenyl)-1H-1,2,3-triazol-4-yl)methylamino)-9H-purin-9-yl)bicyclo-[3.1.0]hexane-2,3-diol (**39**).* 4-Fluoro-3-nitro-phenylazide (9.88 mg, 0.054 mmol) and TBTA (1 mg, 0.001 mmol) were added to a solution of compound **38** (12.4 mg, 0.038 mmol) in *t*-butanol (0.6 mL)/water (0.6 mL) at room temperature. A freshly prepared 1 M solution of sodium ascorbate (38.7 μL) followed by 7.5% solution of copper sulfate (51.6 μL, 0.015 mmol) were also added to the reaction mixture, which was then stirred at room temperature overnight. Solvent was evaporated, and the residue was purified on flash silica gel column chromatography (CH_2Cl_2:MeOH = 30:1) to give compound **39** (18 mg, 96%) as a syrup. ^{1}H NMR (CD_3OD, 300 MHz) δ 8.60−8.64 (m, 2H), 8.22−8.27 (m, 1H), 8.15 (s, 1H), 7.62−7.68 (m, 1H), 4.79 (s, 1H), 4.70 (t, *J* = 5.1 Hz, 1H), 4.37 (s, 2H), 3.88 (d, *J* = 6.6 Hz, 1H), 2.62 (t, *J* = 2.4 Hz, 1H), 1.95−1.99 (m, 1H), 1.62−1.68 (m, 1H), 1.26−1.32 (m, 1H), 0.72−0.79 (m, 1H). HRMS calculated for $C_{20}H_{18}ClFN_9O_4$ $(M + H)^+$: 502.1154; found 502.1150.

*(1R,2R,3S,4R,5S)-4-(2-Chloro-6-(1-adamantyl-1H-1,2,3-triazol-4-yl)methylamino)-9H-purin-9-yl)bicyclo[3.1.0]hexane-2,3-diol (**40**).* Compound **40** (92%) was prepared from compound **38** following the same method for compound **37**. ^{1}H NMR (CD_3OD, 300 MHz) δ 8.13 (s, 1H), 8.02 (s, 1H), 4.81−4.84 (m, 2H), 4.79 (s, 1H), 4.70 (t, *J* = 6.0 Hz, 1H), 3.89 (d, *J* = 6.0 Hz, 1H), 2.24 (s, 10H), 1.95−1.97 (m, 1H), 1.82 (s, 6H), 1.63−1.66 (m, 1H), 1.28−1.32 (m, 1H), 0.73−0.77 (m, 1H). HRMS calculated for $C_{24}H_{30}ClN_8O_2$ $(M + H)^+$: 497.2180; found 497.2164.

Dendrimer Conjugates. Synthetic procedures for each of three dendrimer conjugates are provided below. After reaction in DMSO as specified, each conjugate was separated from small molecular weight impurities by extensive dialysis for 2 d and then lyophilized. We utilized Spectra/Por dialysis tubing, MWCO 3500, diameter 11.5 mm (Spectrum Laboratories, Rancho Dominguez, CA, USA). Typically, 10−15 mg of dendrimer from the reaction mixture was to a volume of 5−7 mL with DMSO, transferred to the tubing, and placed in stirring water in a 1.5 L beaker. The water was changed every 2 h, 5× daily, for 3 d. Then, after lyophilization each dendrimer conjugate was redissolved in DMSO (∼1 mL per 2 mg) and treated with an equal volume of aqueous sodium−EDTA solution (0.5 M) to remove the residual copper by complexation. The mixture was stirred overnight at room temperature followed by extensive dialysis for 2 d as before and lyophilization to give the desired dendrimer conjugate.

For multiple steps of ultrafiltration and biological assays, dilute solutions (1 μM) of the dendrimer conjugates were prepared in 50 mM Tris-HCl (pH 7.5) and 10 mM $MgCl_2$ buffer. Wash buffer solutions whose concentrations of Tris-HCl, $MgCl_2$, and DMSO match those of the solutions of dendrimer conjugates were also prepared for rinsing the centrifugal filters prior to ultrafiltration. Centrifugal filters (Milipore Ltd., Amicon Ultra-0.5, 10 000 MW Cutoff) were rinsed with 400 μL of wash buffer for 5 min at 14 000 × *g*, after which the filters were placed into new microcentrifuge tubes.

Ultrafiltration of the solutions of dendrimer conjugates was then performed by adding 400 μL of each solution to a filter, spinning the filters for 15 min at 14 000 × *g*, transferring the filtrate to a microcentrifuge tube for analysis in a radioligand binding assay and resuspending the material remaining in each filter in 400 μL of buffer. This process was repeated 8 times to ensure the complete removal of contaminants. After the eighth spin, the remaining material was collected by inverting the filters, placing them into new microcentrifuge tubes, and spinning the filters for 2 min at 1000 × *g*. Once collected, the remaining material for each dendrimer sample (approximately 20 μL) was resuspended in 400 μL of 50 mM Tris-HCl (pH 7.5) and 10 mM $MgCl_2$ buffer. Finally, each of the fractions collected during the rinse and ultrafiltration steps and the resuspended material retained by the filter were tested in a radioligand binding assay using A_3 expressing CHO cell derived membranes to determine binding activity. This confirmed that no small molecular impurities remained following multiple ultrafiltration steps.

*G4 PAMAM, Conjugated with Compound **9** and PEG (**43**).* Freshly prepared aqueous sodium ascorbate (1 M, 22 μL) was added to a mixture of PEG-azide dendrimer **42** (15 mg, 0.25 μmol, prepared as described[32]) and compound **9** (5.7 mg, 10.98 μmol) in a mixture of DMSO (0.7 mL) and water (0.7 mL), followed by addition of 7.5% aqueous cupric sulfate (146 μL, 43.93 μmol). The reaction mixture was stirred at room temperature overnight, and the product was purified by dialysis and EDTA treatment, as described above. The mixture was lyophilized to give compound **41** (14 mg, 72%) as a colorless foamy solid. ^{1}H NMR (DMSO, 400 MHz) δ 8.88 (s), 8.10 (s), 7.82 (s), 7.56 (s), 7.37 (s), 7.29 (br s), 5.42 (s), 4.93 (s), 4.82 (m), 4.66 (m), 4.35 (s), 4.13 (s), 3.32 (s), 3.10 (br s), 2.87 (br s), 2.33 (s), 2.17 (br s), 1.73 (br s), 1.60 (br s), 1.29 (br s). ESI-MS: calcd. 77 501; found 77 512.

*G4 PAMAM, Conjugated with Compound **23** (**45**).* Freshly prepared aqueous sodium ascorbate (1 M, 90 μL) was added to a mixture of azido dendrimer **44** (5.6 mg, 0.35 μmol, prepared as described[29]) and compound **23** (10.7 mg, 22.4 μmol) in a mixture of DMSO (0.6 mL) and water (0.6 mL), followed by addition of 7.5% aqueous cupric sulfate (150 μL, 44.8 μmol). The reaction mixture was stirred at room temperature overnight, and the product was purified purified by dialysis and EDTA treatment, as described above. The mixture was lyophilized to give compound **45** (12.9 mg, 79%) as a white foamy solid. ^{1}H NMR (DMSO, 400 MHz) δ 8.86 (s), 8.24 (s), 7.25−7.36 (m), 5.13 (d, J = 4.4 Hz), 4.63 (br s), 4.54 (d, J = 7.2 Hz), 3.79 (br s), 2.76 (s), 2.67 (s), 2.43 (t, J = 6.4 Hz), 2.33 (br s), 2.21 (br s), 1.81 (br s), 1.59 (br s), 1.51 (br s), 1.23 (s), 1.11 (d, J = 3.6 Hz), 0.62 (br s). ESI-MS: calcd. 46 343; found 46 024.

*G4 PAMAM, Conjugated with Compound **31** and PEG (**46**).* Compound **46** (63%) was prepared from compound **31** following the same method as for compound **43**. ^{1}H NMR (CD_3OD, 400 MHz) δ 8.56 (br s, 1H), 8.10−7.94 (br m), 7.56 (br s), 5.42 (br s), 4.94 (s), 4.67 (br m), 4.35 (br s), 4.12 (br s), 3.50 (br s), 3.2 (s), 2.8 (br s), 2.31 (br s), 1.82 (br s), 1.59 (br s), 1.29 (br s). ESI-MS: calcd. 71 511; found 71 413.

Pharmacology. *Cell Culture and Membrane Preparation.* Chinese hamster ovary (CHO) cells stably expressing either the recombinant hA_1 or hA_3AR and human embryonic kidney (HEK) 293 cells stably expressing the human (h) $A_{2A}AR$ were cultured in DMEM and F12 (1:1), supplemented with 10% fetal bovine serum, 100 units/mL penicillin, 100 μg/mL streptomycin, and 2 μmol/mL glutamine. In addition, we added 800 μg/mL Geneticin to the $hA_{2A}AR$ media and 500 μg/mL Hygromycin B to the hA_1AR, $hA_{2B}AR$, and hA_3AR media. After harvesting the cells, we centrifuged them at 250 × *g* for 5 min at 4 °C. The pellet was resuspended in 50 mM Tris-HCl buffer (pH 7.5), containing 10 mM $MgCl_2$. The suspension was homogenized with an electric homogenizer for 10 s and was then recentrifuged at 20 000 × *g* for 30 min at 4 °C. The resultant pellet was homogenized again, resuspended in the buffer mentioned above in the presence of 3 U/mL adenosine deaminase, finally pipetted into 1 mL vials, and this crude membrane preparation was stored at −80 °C until binding experiments were conducted. The concentration of protein was determined using a BCA Protein Assay Kit from Pierce Biotechnology (Rockford, IL).[33]

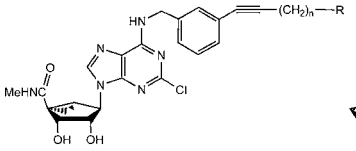
Radioligand Binding Studies. Radioligand binding assays at A_1, A_{2A}, and A_3ARs were performed according to the procedures described previously.[34−36] Each tube in the binding assay contained 100 μL of a crude membrane preparation in suspension (20 μg of protein), 50 μL of a stock solution of agonist radioligand, and 50 μL of increasing concentrations of the test ligands in Tris-HCl buffer (50 mM, pH 7.5) containing 10 mM $MgCl_2$. Nonspecific binding was determined using a final concentration of 10 μM 5′-*N*-ethylcarboxamidoadenosine (NECA), a nonspecific agonist, diluted with the buffer.

The mixtures were incubated at 25 °C for 60 min. Binding reactions were terminated by filtration through Whatman GF/B filters under a reduced pressure using a MT-24 cell harvester (Brandell, Gaithersburg, MD). Filters were washed three times with 5 mL of 50 mM ice-cold Tris-HCl buffer (pH 7.5). The radioactive agonists [^{3}H]R-N^6-(phenylisopropyl)adenosine (*R*-PIA) **47** and [^{3}H]2-[*p*-(2-carboxyethyl)phenyl-ethylamino]-5′-*N*-ethylcarboxamidoadenosine (CGS21680) **48** were used for the A_1 and $A_{2A}AR$ assays, respectively, while [^{125}I]N^6-(4-amino-3-iodobenzyl)adenosine-5′-*N*-methyluronamide (I-AB-MECA) **49** was used for the A_3AR assay. Filters for A_1 and $A_{2A}AR$ binding were placed in scintillation vials containing 5 mL of Hydrofluor scintillation buffer and counted using a PerkinElmer Tricarb 2810TR Liquid Scintillation Analyzer. Filters for A_3AR binding were counted using a PerkinElmer Cobra II γ-counter.

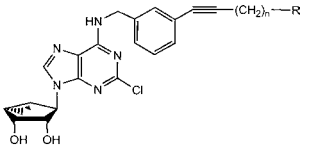
Cyclic AMP Accumulation Assay. Intracellular cyclic AMP levels were measured with a competitive protein binding method.[37] CHO cells that expressed the recombinant hA_3AR were harvested by trypsinization. After centrifugation and resuspending in medium, cells were planted in 24-well plates in 1.0 mL medium. After 24 h, the medium was removed and cells were washed three times with 1 mL DMEM, containing 50 mM HEPES, pH 7.4. Cells were then treated with the agonist NECA (10 μM) and/or test compound (1 or 10 μM) in the presence of rolipram (10 μM) and adenosine deaminase (3 units/mL). After 30 min, forskolin (10 μM) was added to the medium, and incubation was continued for an additional 15

dx.doi.org/10.1021/bc200526c | *Bioconjugate Chem.* 2012, 23, 232−247

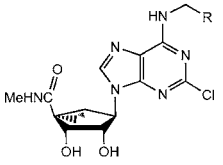
Table 1. Potency of a series of (N)-methanocarba adenosine derivatives at three subtypes of human ARs



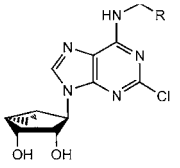
9–17, 43



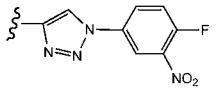
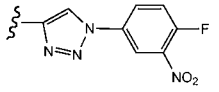
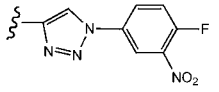
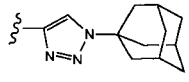
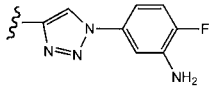
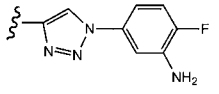
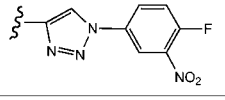
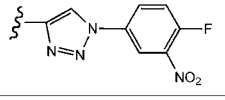
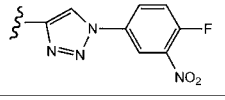
23, 25–27, 45

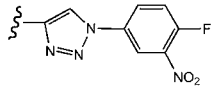
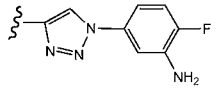
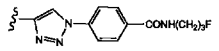
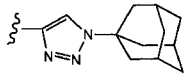
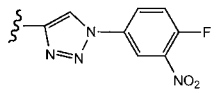
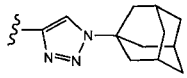


31–35, 46



38–40

0	n =	R =	AR Affinity K_i, nM or *(% inhibition)*[a]		
			A_1	A_{2A}	A_3
4[b,c]	-		136 ± 22	784 ± 97	1.5 ± 0.2
8[b,c]	-		3040 ± 610	1080 ± 310	1.44 ± 0.60
9	3	-C≡CH	104 ± 24	4950 ± 960	8.1 ± 3.1
10	4	-C≡CH	1490 ± 230	*(19.7 ± 2.4%)*	113 ± 24
11	5	-C≡CH	*(47.7 ± 6.1%)*	*(7.0 ± 4.3%)*	87.2 ± 49
12	3		37.4 ± 12.0	1960 ± 50	3.2 ± 1.1
13	4		2420 ± 230	*(28.6 ± 5.7%)*	71.7 ± 54
14	5		1290 ± 290	*(25.2 ± 12.6%)*	30.1 ± 13
15	4		1720 ± 240	*(17.0 ± 8.7%)*	21.8 ± 5.3
16	3		640 ± 140	2730 ± 380	14.3 ± 2.3
17	5		3780 ± 280	550 ± 90	47.6 ± 11.3
23	4	-C≡CH	*(48.5 ± 5.1%)*	*(44.1 ± 5.4%)*	2500 ± 640
25	3		*(11.0 ± 9.4%)*	*(16.7 ± 10.7%)*	897 ± 20
26	4		*(24.3 ± 3.0%)*	*(8.2 ± 4.6%)*	933 ± 720
27	5		*(29.5 ± 8.4%)*	*(18.0 ± 9.7%)*	521 ± 250

0	n =	R =	AR Affinity K_i, nM or *(% inhibition)*[a]		
			A_1	A_{2A}	A_3
31	-	-C≡CH	400 ± 70	*(23.0 ± 1.6%)*	1.5 ± 0.2
32	-		*(38.0 ± 14.8%)*	*(19.3 ± 10.1%)*	9.1 ± 1.9
33	-		1670 ± 230	*(17.1 ± 2.0%)*	22.6 ± 7.0
34	-		1380 ± 300	1840 ± 140	36.7 ± 4.1
35	-		*(38.4 ± 0.5%)*	*(4.9 ± 3.6%)*	38.1 ± 14.4
38	-	-C≡CH	5870 ± 830	*(28.3 ± 2.8%)*	302 ± 26
39	-		*(44.7 ± 16%)*	*(19.2 ± 3.9%)*	390 ± 170
40	-		*(38.6 ± 5.0%)*	*(22.5 ± 7.3%)*	2190 ± 160
41[d]	-	Dendrimer precursor	*(22 ± 18%)*[f]	*(29.7 ± 4.0%)*[f]	*(70.2 ± 3.7%)*[f]
43[e]	3	N^6-Benzyl dendrimer conjugate, 5′-$CONHCH_3$	*(11±3%)*[f]	*(0%)*[f]	24 ± 6
45[e]	4	N^6-Benzyl dendrimer conjugate, 4′-truncated	*(4±2%)*[f]	*(0%)*[f]	*(42%)*[f]
46[e]	-	N^6-Triazolylmethyl dendrimer conjugate, 5′-$CONHCH_3$	*(8±8%)*[f]	*(0%)*[f]	55 ± 8

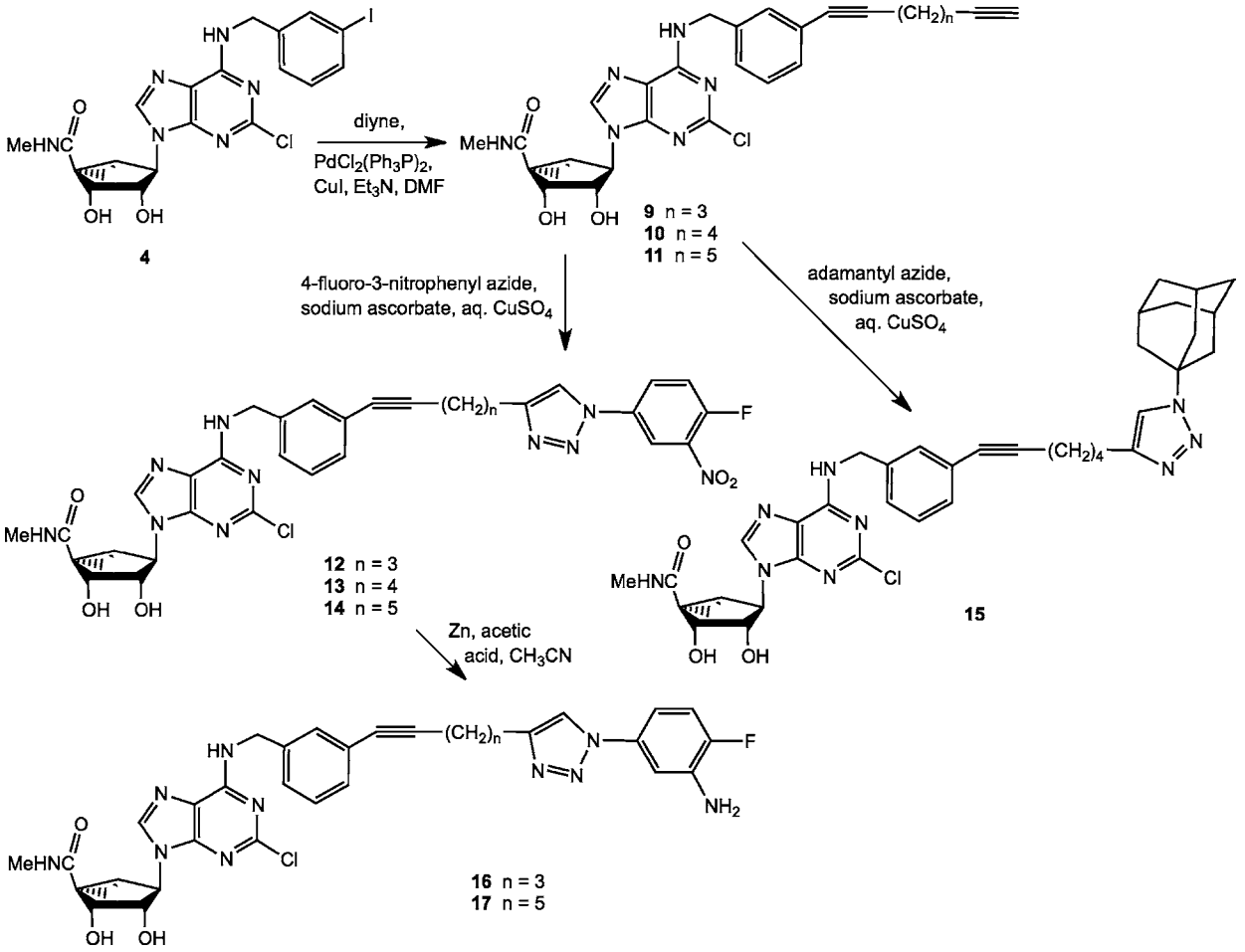
[a]All experiments were done on CHO or HEK293 (A_{2A} only) cells stably expressing one of three subtypes of hARs. The binding affinity for A_1, A_{2A}, and A_3ARs was expressed as K_i values (n = 3−5) and was determined by using agonist radioligands ([^{3}H]R-PIA, **47**; [^{3}H]CGS21680, **48**; or [^{125}I]I-AB-MECA, **49**; respectively), unless noted. A percent in parentheses refers to inhibition of radioligand binding at 10 μM, unless noted. $K_{i\ app}$ values

dx.doi.org/10.1021/bc200526c | *Bioconjugate Chem.* 2012, 23, 232–247

Table 1. continued

are provided for the dendrimer derivatives **43** and **46**. [b]Values from Tchilibon et al.[21] and Tosh et al.[23] [c]**4**, MRS1898; **8**, MRS5127; **16**, MRS5362; **32**, MRS5415; **33**, MRS5519; **43**, MRS5351; **46**, MRS5439. [d]Control dendrimer structures given in Scheme 5; binding data for **41** as reported.[32] [e]Nucleoside dendrimer conjugate structures given in Scheme 5. [f]Percent inhibition of radioligand binding at 1 μM.

Scheme 1. Synthesis of 5′-*N*-Methyluronamide (N)-Methanocarba Adenosine Derivatives Linked through a N^6-Benzyl Group as Model Compounds



min. The reaction was terminated by removing the supernatant, and cells were lysed upon the addition of 200 μL of 0.1 M ice-cold HCl. The cell lysate was resuspended and stored at −20 °C. For determination of cyclic AMP production, a cyclic AMP kit (Sigma, St. Louis, MO) was used.

Data Analysis. Binding and functional parameters were calculated using *Prism 5.0* software (GraphPAD, San Diego, CA, USA). IC_{50} values obtained from competition curves were converted to K_i values using the Cheng-Prusoff equation.[38] Data were expressed as mean ± standard error. The concentrations of the dendrimer-ligand complexes are measured by the concentration of the dendrimer, not the ligand. Therefore, binding K_i values of the dendrimer derivative are expressed as $K_{i\ app}$ values.

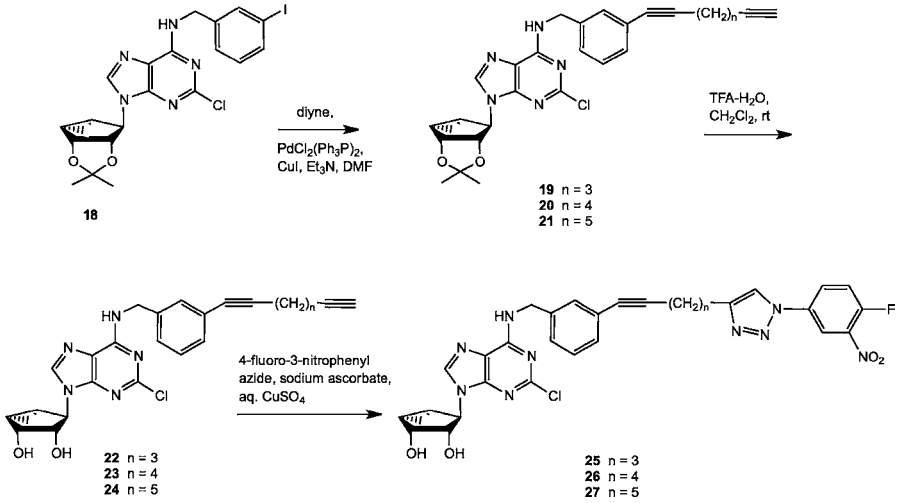
Molecular Modeling. *Homology Model and Ligand Construction.* Detailed modeling procedures and a Scheme (S2) are in the Supporting Information. Briefly, the sequence of the human A_3AR was mapped onto the crystal structure of the A_{2A}AR (minus the T4-lysozyme insertion) in complex with the agonist UK-432097[39] (PDB ID 3QAK)[40] as a structural template for the homology modeling of the A_3AR. The UK-A_{2A}AR X-ray structure[39] shows four disulfide bridges present in the EL region of this receptor, but only one is relevant to the A_3AR, i.e., a bond between Cys77 (TM3) and Cys166 (EL2) that is conserved among family A GPCRs. The conformational differences in the EL region between A_{2A}AR with its four disulfides and A_3AR with a single disulfide and their effects on ligand recognition are the subject of ongoing studies. The top-ranked A_3AR model built using the Homology Model tool of *Molecular Operating Environment*[53] was used for the docking of nucleosides.

The structure of conjugate **46** was imported as a mol file into MOE, where it was subjected to energy minimization using the CHARMM27 forcefield and subjected to 230 ns of Molecular Dynamics (MD) simulations in a solvated system using Desmond[54] as implemented in the software from Schrödinger (Cambridge, MA). The final configuration of the dendrimer−PEG conjugate **46** from the simulation in water was then used for the building of the complex A_3AR-dendrimer conjugate.

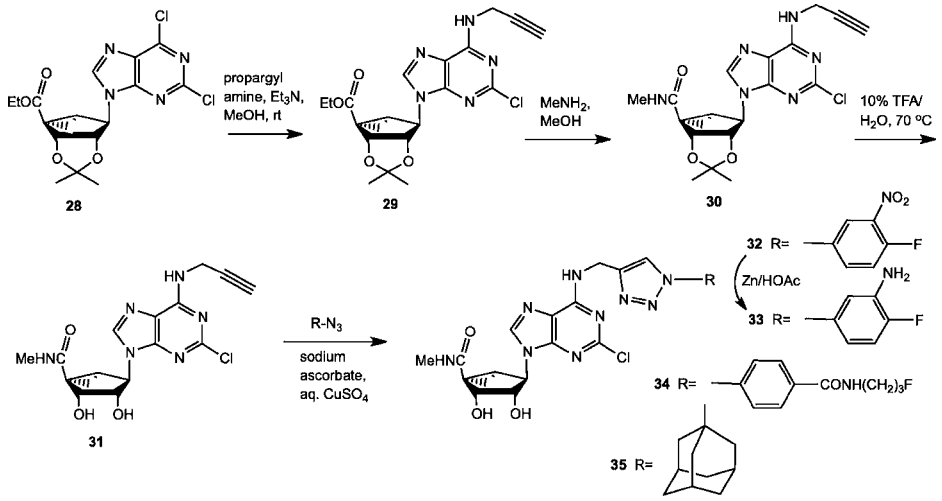
Molecular Docking. A portion of **46** containing the N^6-triazolylmethyl (N)-methanocarba nucleoside moiety and part of the dendrimer chain (Figure S1) was minimized with the

dx.doi.org/10.1021/bc200526c | *Bioconjugate Chem.* 2012, 23, 232−247

Scheme 2. Synthesis of 4′-Truncated (N)-Methanocarba Adenosine Derivatives Linked through a N^6-Benzyl Group as Model Compounds



Scheme 3. Synthesis of 5′-*N*-Methyluronamide (N)-Methanocarba Adenosine Derivatives Linked through a N^6-Triazolylmethyl Group as Model Compounds



Polak-Ribiere conjugate gradient (PRCG) minimization and used as starting point for the docking study. The flexible docking of the ligand in the A_3AR model was performed by means of *Glide* and *MacroModel* in the software from Schrödinger, LLC. The molecular docking of the compound was performed in a rigid binding site of the A_3AR model with *Glide* using the SP (standard precision) procedure. The best-ranked complex receptor−ligand was subjected to conformational analysis by means of MCMM for further structural optimization and energy minimization. During the conformational search, full flexibility was granted to the ligands and the residues within a radius of 4 Å from the ligand.

*Complex of A_3AR with Dendrimer Conjugate **46**.* Randomly, one of the N^6-triazolylmethyl nucleoside moieties of **46** was replaced with the docked conformation of the ligand in the A_3AR binding site. The dendrimer conjugate **46** with a docked nucleoside terminal inside the A_3AR binding site was then subjected to minimization in MOE with MMFF94 forcefield to a root-mean-square gradient of 0.001.

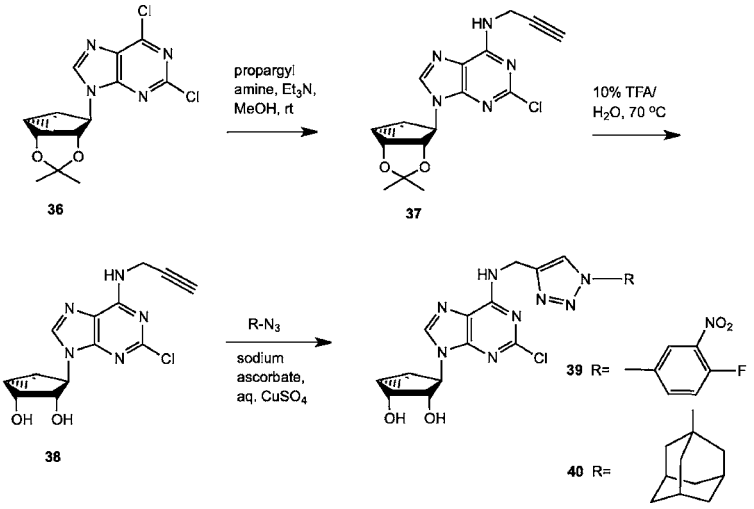
RESULTS

Chemical approaches to couple ring-constrained nucleoside monomers by click chemistry through their N^6 position to PAMAM dendrimers were explored. The effects of these structural changes on receptor recognition were examined in radioligand binding assays and functional assays of cyclic AMP. Furthermore, the binding of a representative dendrimer conjugate was visualized and specific amino acid interaction predicted with molecular modeling using an A_3AR homology model based on the recently reported X-ray structures of an agonist-bound A_{2A}AR.[39]

Chemical Synthesis. We prepared various (N)-methanocarba adenosine derivatives (Table 1) to act as selective ligands of the A_3AR. Both small molecular model compounds (**9**−**17**, **22**−**40**) and PAMAM dendrimeric precursors and nucleoside conjugates (**41**−**46**) were included. There were two variations of the (N)-methanocarba ring system: either bearing a 5′-*N*-methyluronamide or unsubstituted, i.e., "truncated", at the 4′ position. Prior to coupling the nucleosides to dendrimer carriers, we explored the SAR of alkyne-functionalized chains on the N^6 substituent and the resultant click products, i.e.,

dx.doi.org/10.1021/bc200526c | *Bioconjugate Chem.* 2012, 23, 232−247

Scheme 4. Synthesis of 4′-Truncated (N)-Methanocarba Adenosine Derivatives Linked through a N^6-Triazolylmethyl Group as Model Compounds



1,2,3-triazoles. The modification of the N^6-substituent was accomplished either through the extension of a dialkynyl chain at the 3-position of a N^6-benzyl group with subsequent Cu(I)-catalyzed click reaction of the terminal alkyne[41] as shown in Schemes 1 and 2 or by formation of an aromatic ring (i.e., 1,2,3-triazole) at a N^6-methylene carbon (Schemes 3 and 4). The triazole was formed in the latter case from a N^6-propargyl group combined with an azido derivative using click chemistry. The rationale for these two N^6 variations were incorporation of either a 3-substituted N^6-benzyl group, which is known to enhance A_3AR selectivity, or a N^6-triazolylmethyl group, with the expectation that this newly formed 5-membered aromatic ring would serve the same role in A_3AR recognition as the six-membered N^6-benzyl ring. An arylmethyl group at the N^6 position generally favors high affinity binding to the A_3AR with selectivity that is species-independent.

The dialkynyl chains at the 3-position of N^6-benzyl moieties in **9**−**11** and **19**−**21** were introduced by a Sonogashira reaction[42] at the 3-iodo position of a N^6-benzyl ring. In the case of the 5′-*N*-methylcarboxamides, the 2′ and 3′ hydroxyl groups were unprotected during this step, i.e., reaction of derivative **4** to yield intermediates **9**−**11**. However, for the truncated series, Sonogashira reactions were performed on isopropylidene-protected derivative **18** to provide intermediates **19**−**21**. Compounds **19** and **21** were isolated as pure products, but **20** was subjected to the next synthetic step without isolation. The isopropylidene groups were then removed to yield dialkyne intermediates **22**−**24**.

Then, a dialkyne that was introduced at the 3-position of a N^6-benzyl group in 5′-methyluronamide derivatives **9**−**11** or in the truncated nucleoside series, i.e., derivatives **22**−**24**, could be subjected for further reaction with azido groups, which generally occurred exclusively at the distal alkyne. Alternately, a N^6-propargyl group in **31** and **38** could react with an azido derivative, such as the commercially available 4-fluoro-3-nitrophenylazide. These arylfluoride derivatives provided an additional means of chain derivatization by nucleophilic substitution.

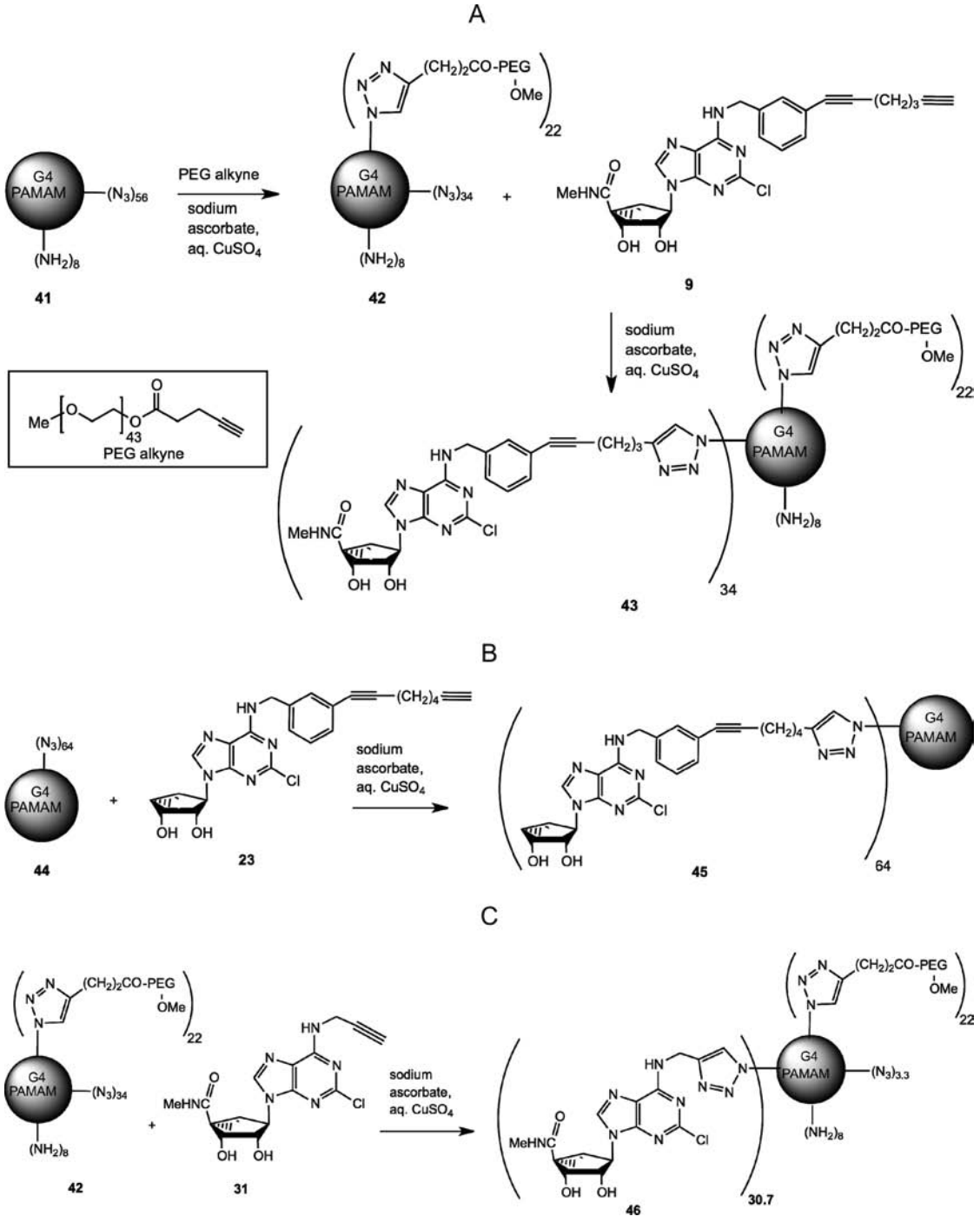
Routes to the dendrimer conjugates involved similar click chemistry. In the case of dendrimer precursor **41**, most (56 out of 64) of the peripheral amino groups of the precursor PAMAM dendrimers were first substituted with azido groups (Scheme 5A).[32] Alternately, the dendrimer precursor **44** was fully substituted with azido groups (Scheme 5B), formed using a previously reported procedure.[29,43] Then, some of the azido groups on the dendrimer **41** were reacted with alkyne-derivatized PEG chains for water solubility to form **42**. These azido-modified dendrimers **42** and **44** were then cross-linked by click chemistry[28] with terminal alkynyl groups at the N^6 position of (N)-methanocarba nucleoside derivatives. Thus, a dialkyne introduced at the 3-position of a N^6-benzyl group in 5′-methyluronamide derivative **9** (i.e., based on full A_3AR agonists) or in the truncated nucleoside series **23** (i.e., based on partial A_3AR agonists) could be subjected for further reaction with azido groups on the dendrimer. Alternately, a N^6-propargyl group on adenosine derivative **31** could react with the azido-derivatized dendrimer **42** (Scheme 5C). The substitution of the resulting conjugates **43**, **45**, and **46** was determined by mass spectroscopy, indicating an average of 34, 64, and 30.7 nucleoside moieties, respectively, present out of the 64 possible sites on each G4 dendrimer. Approximately 3.3 azido groups per molecule of **46** remained unreacted.

Quantification of Pharmacological Activity. We initially tested the nucleoside derivatives in binding assays at three hAR subtypes; we used standard nucleoside radioligands **47**−**49** and membrane preparations from CHO cells (A_1 and A_3) or HEK293 cells (A_{2A}) stably expressing a hAR subtype (Table 1).[34−36,44,45] We used the previously reported agonist molecular probes of the A_3AR (**4** and **8**) for comparison in the biological assays.[23] We included the parent dendrimers **41**, which contained both azido and amino groups, and the fully azido-substituted **44** as controls; they were inactive or weakly active in inhibiting AR binding.

The small molecular ligands indicated a dependence of the AR affinity on the chain length. For example, in diyne series **9**−**11**, the affinity tended to decrease upon homologation from 3 to 5 methylenes. Compound **9** displayed a K_i of 8.1 nM at the A_3AR, and its click product **12** with 4-fluoro-3-nitro-phenylazide was also the most potent in that homologous series. Reduction of the nitroaryl group to the corresponding amine as in **16** and **17** slightly reduced A_3AR affinity. However, the 4′-truncated dialkyne **23** was weak in AR binding, and the click products **25**−**27** were only slightly more potent. In that homologous series of 1-(4-fluoro-3-nitro-phenyl)-triazole de-

dx.doi.org/10.1021/bc200526c | *Bioconjugate Chem.* 2012, 23, 232−247

Scheme 5. Synthesis of Dendrimeric Conjugates of Strategically Functionalized Nucleoside Derivatives[a]



[a]The derivatives contain (N)-methanocarba adenosine derivatives linked through a N^6-benzyl (A,B) or N^6-triazolylmethyl (C) group. A 5′-*N*-methyluronamide (A,C) or 4′-truncated nucleoside (B) is present. Average structures are shown.

rivatives missing a 5′-uronamide, the binding affinity at the A_3AR was independent of chain length. Therefore, the 5′-methyluronamide moiety appears to stabilize a binding mode of the nucleoside such that it interacts with the extracellular regions of the ARs in a more structure-sensitive manner.

The N^6-propargyl intermediate **31** in the 5′-methyluronamide series was potent in binding to the A_3AR (K_i 1.5 nM) and 270-fold selective in comparison to the A_1AR. The click product **32**, a 1-(4-fluoro-3-nitrophenyl)-triazole, bound to the A_3AR with a K_i of 9.1 nM and over 100-fold selectivity, and the corresponding 3-amino derivative **33** was slightly weaker. A large 1-adamantyl group on the triazole ring of **35** was also tolerated with respect to A_3AR binding. The corresponding 4′-truncated series **38**−**40** did not achieve high AR affinity; thus, the 5′-methyluronamide was an important recognition element for the small molecules.

Two of the multivalent dendrimer derivatives, **43** and **46**, obtained through click conjugation of the corresponding 5′-methyluronamide alkynyl nucleoside precursors, retained potent binding activity at the A_3AR and displayed enhanced

dx.doi.org/10.1021/bc200526c | *Bioconjugate Chem.* 2012, 23, 232−247

selectivity over the monomer precursors. Water-solubilizing PEG chains, also incorporated by click linkage, did not prevent receptor binding. The binding assays were performed on conjugate preparations subjected to 8 sequential cycles of ultrafiltration to ensure that no small molecular weight contaminants were present. The N^6-benzyl derivative **43** had a $K_{i\ app}$ value of 24 nM in binding to the A_3AR, which is 3-fold less potent than the alkynyl precursor **9**, and the affinity at A_1 and A_{2A}ARs was greatly decreased. The multivalent N^6-triazolylmethyl derivative **46** was also potent in binding to the A_3AR ($K_{i\ app}$ 55 nM) and selective in comparison to the A_1AR, but it was 37-fold less potent at the A_3AR than the propargyl precursor **31**. However, the multivalent 4′-truncated N^6-benzyl dendrimer **45** was nearly inactive in binding at the A_3AR, consistent with the weak affinity of the alkyne precursor **23**.

We tested the small molecular derivatives and nucleoside conjugates in a functional assay at the A_3AR consisting of inhibition of forskolin-stimulated cyclic AMP production in A_3AR-expressing CHO cells (Table 2). These GLiDe conjugates displayed A_3AR agonist properties with varying degrees of maximal inhibition of cyclic AMP production at 1 or 10 μM The concentration selected was generally in >100-fold excess of the K_i value for each 5′-methyluronamide nucleoside, to approximate the maximal effect. The relative efficacy was compared to that of NECA (10 μM), taken as a reference standard. The small molecular 5′-methyluronamide derivatives **9**, **13**, **15**, **17**, and **31**−**35** displayed ≥80% of the maximal effect of NECA, indicated nearly full agonism. Other 5′-uronamide derivatives reached only intermediate efficacy despite a high affinity in A_3AR binding, e.g., terminal alkyne intermediates **10** and **11** and aryl fluorides **14** and **16**. 4′-Truncated small molecules **23**, **25**−**27**, and **38**−**40** displayed low efficacy (≤27% of the maximal effect) at the A_3AR, consistent with their roughly micromolar K_i values and with the tendency of truncation to reduce A_3AR efficacy. Consistent with the binding results, only dendrimer conjugates of 5′-methyluronamide derivatives, **43** and **46**, displayed considerable activity in the functional assay. Both were full A_3AR agonists at 1 μM.

Table 2. Maximal Efficacy of (N)-Methanocarba Adenosine Derivatives in a Functional Assay at the hA$_3$AR Consisting of Inhibition of Cyclic AMP Accumulation

compound	% inhibition[a,b]
Cl-IB-MECA[b]	97
NECA[b]	100
4	100[c]
8	44 ± 6[c]
9	80.0 ± 6.4
10	57.3 ± 10.6
11	57.8 ± 21.2
12	92.0 ± 7.6
13	101 ± 8
14	64.1 ± 11.5
15	79.8 ± 4.4
16	66.7 ± 5.6
17	96.6 ± 14.3
23	7.8 ± 1.4
25	6.6 ± 2.6
26	9.9 ± 2.1
27	20.1 ± 5.2
31	103 ± 8
32	107 ± 5
33	88.3 ± 4.3
34	81.5 ± 4.8
35	106 ± 5
38	14.3 ± 0.7
39	6.4 ± 2.8
40	27.1 ± 4.3
43[b]	86.8 ± 3.2
45[b]	4.0 ± 2.4
46[b]	91.3 ± 3.4

[a]The efficacy at the hA$_3$AR was determined by inhibition of forskolin-stimulated cyclic AMP production in AR-transfected CHO cells, as described in the text. Percent inhibition is shown, in comparison to the maximal effect of a full agonist NECA at 10 μM. Data are expressed as mean ± standard error (n = 3−5). [b]Concentrations used were Cl-IB-MECA and NECA at 10 μM and dendrimer derivatives **43**, **45**, and **46** at 1.0 μM, and all other compounds were determined at 10 μM. ND, not determined. [c]Values from Tosh et al.[23] **4**, MRS1898; **8**, MRS5127.

Molecular Modeling. With X-ray crystallographic structures of agonist-bound forms of the hA$_{2A}$AR now known,[39,46] it is possible to extend the modeling analysis of agonist binding by homology to other AR subtypes. In the X-ray crystal structure (PDB ID: 3QAK)[39] of the A_{2A}AR bound to agonist UK-432097 (complex designated here: UK-A$_{2A}$AR), large N^6 and C2 substituents project toward the opening of the nucleoside binding cleft, consistent with the biological activity of dendrimer-linked conjugates.

A homology model of the human A_3AR was built using UK-A$_{2A}$AR as template, which was chosen among the available agonist-bound A_{2A}AR crystal structures[39,46] because it was found to be suitable for the modeling of the binding pocket embedding other N^6-substituted agonists. In fact, in the UK-A$_{2A}$AR crystal structure the conformation of the third extracellular loop (EL3), connecting TM6 and TM7, is open allowing the accommodation of the bulky N^6 substituent of the agonist UK-432097. In the adenosine-bound or NECA-bound structures,[46] instead, EL3 appears closer to EL2 with an H-bond interaction between His264(EL3) and Glu169(EL2). The agonist-bound model of A_3AR was built with the Homology Modeling module of MOE and utilized for the initial ligand docking.

We chose for receptor docking the conjugate **46**, containing a triazole ring in place of the usual phenyl ring of the typical N^6-benzyl derivatives, rather than the more potent conjugate **43**. Because the receptor binding of N^6-benzyl derivatives has been modeled in previous studies,[19,21,23,30] we wanted to probe the similarity between the two aromatic rings in their docked conformations. Initially, a fragment of **46**, i.e., a chain-extended version of a N^6-triazolylmethyl derivative (related to the 5′-methyluronamide (N)-methanocarba nucleoside series **32**−**35**) was drawn (designated compound **47**, Figure S1). After this theoretical agonist-containing terminal portion of the PAMAM conjugate was docked to the A_3AR model binding site with *Glide*, and the best scored docking pose was further optimized by means of a Monte Carlo Multiple Minima (MCMM) conformational search of the ligand and the residues in the binding site, in order to take into account the flexibility of the receptor residues.

Separately, the model of the entire PEGylated dendrimer conjugate **46** was built and optimized by means of MD. To take into account the remainder of the PAMAM moiety of the dendrimer conjugate **46** in the receptor docking model, the extended N^6-triazolylmethyl chain of the docked nucleoside

ligand **47** was fused to a portion of the preoptimized conjugate **46**. In other words, after the MD simulation of **46**, one of the nucleoside terminals of this dendrimer conjugate was randomly chosen and replaced by the ligand previously docked in the binding site of the A_3AR model. The model of the docked dendrimer conjugate **46** in complex with A_3AR was then subjected to further minimization in order to release possible overlays and steric clashes between the dendrimer and the receptor.

The docking pose of the functionalized nucleoside in the binding site of A_3AR model was stabilized by several H-bond and van der Waals (vdW) interactions with the residues in the binding cavity, as shown in Figure 1A. In particular, the adenine ring of the molecule was anchored to Asn250(6.55) (the number in parentheses refer to the Ballesteros-Weinstein numbering system[47]) by H-bond interactions with the N^6 amino group and the *N*7 of the nucleoside. Moreover, the aromatic adenine ring of the ligand was stabilized by a $\pi-\pi$ stacking interaction with the aromatic ring of Phe168(EL2) and favorable vdW interactions with the hydrophobic residues Leu246(6.51) and Ile268(7.39). The ribose moiety of the N^6-triazolylmethyl nucleoside derivative was found deeper in the binding pocket, locked by H-bond interactions of the 2′- and 3′-OH groups with His272(7.43) and Ser271(7.42), respectively. The carbonyl group of the 5′-*N*-ethylcarboxamido moiety was H-bonded to Thr93(3.36). Other favorable vdW interactions were found between the ribose moiety and hydrophobic residues, i.e., Trp243(6.48), Leu90(3.32), Leu91(3.33), Ile98(3.40), and Ile186(5.47). The long N^6 chain of the agonist was oriented toward the extracellular solvent, exiting the binding pocket among TM5, TM6, TM7, EL3, and EL2. In particular, the triazole moiety of the N^6 chain was located in close proximity to Gln167(EL2), Leu264(7.35), Ile249(6.54), Met174(5.35), Ile253(6.58), and Val169(EL2), similar to the docked position of the N^6-benzyl ring of known A_3AR agonists (not shown).

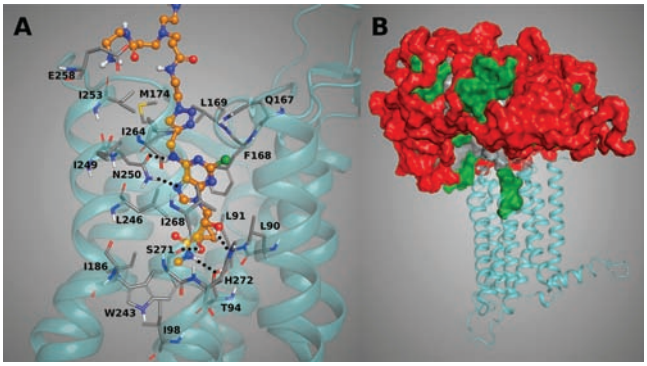


Figure 1. (A) Docking pose of (N)-methanocarba adenosine derivative **47** (structure in Figure S1), which is a fragment of conjugate **46**, in the binding site of the A_3AR model based on homology to the agonist-bound A_{2A}AR crystal structure.[39] The nucleoside moiety of the ligand is anchored in the binding site by key H-bond interactions (highlighted with dotted lines) with the residues Thr94 (TM3), Asn250 (TM6), and Ser271 and His272 (TM7). The ligand, in ball-and-stick representation, is depicted with carbon atoms colored in orange. The receptor residues are shown in stick model with carbons in gray. (B) A molecular model of the complex A_3AR-dendrimer conjugate **46**. The receptor is represented as a cartoon colored in light blue. The dendrimer conjugate **46** is represented by a molecular surface, with the PEG chains colored in red, the ligand moieties in green, and the PAMAM moiety in gray. The likely glycosylation of the receptor in EL2 is not included in the model. Graphic images were made with *PYMOL* v 0.99, Delano Scientific LLC, CA, USA.

The molecular model of the A_3AR-dendrimer conjugate complex showed how the hydrophilic PEG chains surrounded the dimethylamide moiety of the hydrophobic dendrimer (Figure 1B), possibly favoring the solubility of the conjugate. Nevertheless, the ligand moieties attached to the dendrimer were still exposed to the solvent.

DISCUSSION

We previously demonstrated that coupling of strategically functionalized A_3AR agonists to PAMAM dendrimers by click chemistry through functionalized chains attached at the adenine C2 position achieved higher affinities than coupling by amide formation.[29] The present study focused exclusively on coupling through the N^6 position of methanocarba nucleoside ligands using several different approaches to linkage by click chemistry. The small molecules were selected for probing the effects of sterically bulky groups at the end of a functionalized chain. Within the four separate structural series examined here, a terminal adamantyl group generally served as a suitable high affinity replacement for a substituted phenyl ring in the small model compounds, i.e., in compounds **15** and **35**. However, the same substitution in truncated nucleoside **40**, containing a shorter tether from the adenine exocyclic amine, did not preserve binding affinity. The results indicated that the N^6 position of functionalized nucleosides, like the C2 position, is also viable for the click conjugation to macromolecular carriers.

The two chemical linking strategies used here were (1) reaction of a dialkyne moiety introduced at the N^6 position (similar to the linker chemistry used at the C2 position) and (2) formation of a triazolylmethylene moiety, intended to promote A_3AR selectivity, by the click reaction of a N^6-propargyl group. One objective of this study was to determine if a N^6-triazolylmethyl group formed by Cu(I)-catalyzed click chemistry could substitute for a N^6-benzyl group in the receptor binding site. In the triazolylmethyl products, high A_3AR affinity and selectivity was maintained in the 5′-methyluronamide series, but not in the 4′-truncated series. In the case of linking through a N^6-benzyl group, only the 5′-methyluronamide derivatives (Schemes 1 and 5A) maintained high AR affinity consistently, while the 4′-truncated derivatives were only weakly active both in the form of chain-extended small molecules and as a multivalent conjugate (Scheme 5B). Thus, truncated monomer **23** was not a suitable intermediate for dendrimeric conjugation to achieve high A_3AR affinity.

The results were found to be consistent with the recently elucidated X-ray structure of the A_{2A} receptor with a N^6 substituted adenosine derivative bound. In a docking model, the nucleoside moiety of the dendrimer conjugate **46** was found to be located deep in the binding pocket anchored by strong H-bond and hydrophobic interactions with the receptor residues, while the long chain at the N^6 position of the nucleoside is oriented toward the extracellular part of the receptor exiting to the solvent among the extracellular terminals of TM5, TM6, and TM7, between EL3 and EL2. The long PEG chains are embedding the ligand-functionalized dendrimer moiety exposing the hydrophilic monomers to the solvent and coating the PAMAM dendrimer chains. Nevertheless, the nucleoside terminals of the dendrimer conjugate are still exposed to the solvent and clearly accessible for the binding to the receptor.

A_3AR homodimers have been proposed to exist at the cell surface.[48] Whether this GLiDe conjugate participates in multivalent interaction with higher order receptor aggregates is unknown.

In addition to therapeutic applications,[49] dendrimer-based drug conjugates have been applied to biological imaging modalities, such as luminescent, fluorescent, magnetic resonance, and radioactive.[50,51] Given the high A_3AR affinity observed in the small molecular series, there is now a possibility of introducing radioisotopes to produce new radioligands for receptor characterization in vitro and in vivo. Prosthetic groups for targeting, therapeutic applications or diagnostic purposes, such as fluorescent reporter groups, might be introduced. Several fluorinated analogues and other small molecular analogues bound to the A_3AR with high affinity and raised the possibility of their use as radioligands. This suggested the application of these structures for incorporation of the positron emitter ^{18}F for in vivo imaging of the A_3AR.[25,52] The fluorine in aryl amino analogues **16** and **17** would be stable toward nucleophilic displacement, while the 4-fluoro group of the corresponding nitro analogues could be readily substituted. Therefore, a radioisotope (^{18}F) could potentially be introduced by nucleophilic fluoride attack at the nitro stage, e.g., with **12** as substrate, followed by reduction to the more stable amine. The most potent of the compounds in this series was 3-amino-4-fluoro derivative **16** with a K_i value of 14.3 nM at the A_3AR, while 3-amino-4-fluoro derivative **33** was less potent in binding.

In conclusion, we have extended the SAR of small monomeric adenosine agonists derivatized at the N^6 position to the multivalent state. We have explored a new linking strategy to achieve the high A_3AR agonist affinity and selectivity in two PEGylated GLiDe conjugates of A_3AR-binding nucleosides from chemical, pharmacological, and structural perspectives. The structural features of the pharmacophore, the chemical nature of the linking and terminal groups of the dendrimer all modulate the biological properties of a multivalent conjugate. The success of this approach was demonstrated for G4 PAMAM dendrimers as carriers, and the application of the same triazole linkage to other dendrimer carriers, with different degrees of loading or in combination with other terminal groups, remains to be investigated.

New GLiDe conjugates of 5′-methyluronamide derivatives presented here are highly potent and selective at the A_3AR and are suitable for examination in models of autoimmune inflammatory diseases, ischemia, cancer, and other diseases subject to amelioration by A_3AR agonists. Specific combinations of receptor ligands on the same dendrimer carrier might achieve synergistic effects and prove useful for disease treatment. The in vivo properties of the two active conjugates introduced in this study could now be explored.

■ ASSOCIATED CONTENT

Ⓢ Supporting Information

^{1}H NMR and mass spectra of representative compounds and modeling procedures. This material is available free of charge via the Internet at http://pubs.acs.org.

■ AUTHOR INFORMATION

Corresponding Author

*E-mail: kajacobs@helix.nih.gov. Molecular Recognition Section, Bldg. 8A, Rm. B1A-19, NIH, NIDDK, LBC, Bethesda, MD 20892-0810. Tel.: 301-496-9024, Fax: 301-480-8422.

■ ACKNOWLEDGMENTS

We thank Dr. John Lloyd and Dr. Noel Whittaker (NIDDK) for the mass spectral determinations and Angela Kecskés for technical assistance. This research was supported by the Intramural Research Program of the NIH, NIDDK.

■ ABBREVIATIONS:

AR, adenosine receptor; DMSO, dimethylsulfoxide; EDC, *N*-ethyl-*N*′-dimethylaminopropylcarbodiimide; cyclic AMP, adenosine 3′,5′-cyclic phosphate; CGS21680, 2-[*p*-(2-carboxyethyl)phenyl-ethylamino]-5′-*N*-ethylcarboxamidoadenosine; CHO, Chinese hamster ovary; Cl-IB-MECA, 2-chloro-N^6-(3-iodobenzyl)-5′-*N*-methylcarboxamidoadenosine; DMEM, Dulbecco's modified Eagle's medium; GPCR, G protein-coupled receptor; HEK, human embryonic kidney; HRMS, high resolution mass spectroscopy; NECA, 5′-*N*-ethylcarboxamidoadenosine; NMR, nuclear magnetic resonance; DIPEA, diisopropylethylamine; DMF, *N*,*N*-dimethylformamide; HEPES, 4-(2-hydroxyethyl)-1-piperazineethanesulfonic acid; MCMM, Monte Carlo Multiple Minima; PAMAM, polyamidoamine; PEG, polyethylene glycol; PET, positron emission tomography; R-PIA, (R)-N^6-(phenylisopropyl)adenosine; TBTA, tris[(1-benzyl-1*H*-1,2,3-triazol-4-yl)methyl] amine; TEA, triethylamine; TLC, thin layer chromatography; UK-432097, 6-(2,2-diphenylethylamino)-9-((2*R*,3*R*,4*S*,5*S*)-5-(ethylcarbamoyl)-3,4-dihydroxytetrahydrofuran-2-yl)-*N*-(2-(3-(1-(pyridin-2-yl)piperidin-4-yl)-ureido)ethyl)-9*H*-purine-2-carboxamide

■ REFERENCES

(1) Fredholm, B. B., IJzerman, A. P., Jacobson, K. A., Linden, J., and Müller, C. (2011) Nomenclature and classification of adenosine receptors – An update. *Pharmacol. Rev. 63*, 1–34.

(2) Gessi, S., Merighi, S., Varani, K., and Borea, P. A. (2011) Adenosine receptors in health and disease. *Adv. Pharmacol. 61*, 41–75.

(3) Fishman, P., Jacobson, K. A., Ochaion, A., Cohen, S., and Bar-Yehuda, S. (2007) The anti-cancer effect of A_3 adenosine receptor agonists: A novel, targeted therapy. *Immun. Endoc. Metab. Agents Med. Chem. 7*, 298–303.

(4) Silverman, M. H., Strand, V., Markovits, D., Nahir, M., Reitblat, T., Molad, Y., Rosner, I., Rozenbaum, M., Mader, R., Adawi, M., Caspi, D., Tishler, M., Langevitz, P., Rubinow, A., Friedman, J., Green, L., Tanay, A., Ochaion, A., Cohen, S., Kerns, W. D., Cohn, I., Fishman-Furman, S., Farbstein, M., Yehuda, S. B., and Fishman, P. (2008) Clinical evidence for utilization of the A_3 adenosine receptor as a target to treat rheumatoid arthritis: Data from a phase II clinical trial. *J. Rheumatol. 35*, 41–48.

(5) Zheng, J., Wang, R., Zambraski, E., Wu, D., Jacobson, K. A., and Liang, B. T. (2007) A novel protective action of adenosine A_3 receptors: Attenuation of skeletal muscle ischemia and reperfusion injury. *Am. J. Physiol. Heart Circ. Physiol. 293*, 3685–3691.

(6) Ge, Z. D, Peart, J. N., Kreckler, L. M., Wan, T. C., Jacobson, M. A., Gross, G. J., and Auchampach, J. A. (2006) Cl-IB-MECA [2-chloro-N^6-(3-iodobenzyl)adenosine-5′-N-methylcarboxamide] reduces ischemia/reperfusion injury in mice by activating the A_3 adenosine receptor. *J. Pharmacol. Exp. Ther. 319*, 1200–1210.

(7) Barczyk, K., Ehrchen, J., Tenbrock, K., Ahlmann, M., Kneidl, J., Viemann, D., and Roth., J. (2010) Glucocorticoids promote survival of anti-inflammatory macrophages via stimulation of adenosine receptor A_3. *Blood 116*, 446–455.

(8) Avila, M. Y., Stone, R. A, and Civan, M. M. (2002) Knockout of A_3 adenosine receptors reduces mouse intraocular pressure. *Invest. Ophthalmol. Vis. Sci. 43*, 3021–3026.

(9) Wang, Z., Do, C. W., Avila, M. Y., Peterson-Yatorno, K., Stone, R. A., Gao, Z. G., Joshi, B. V., Besada, P., Jeong, L. S., Jacobson, K. A., and

Civan, M. M. (2010) Nucleoside-derived antagonists to A_3 adenosine receptors lower mouse intraocular pressure and act across species. *Exp. Eye Res. 90*, 146−154.
(10) Okamura, T., Kurogi, Y., Nishikawa, H., Hashimoto, K., Fujiwara, H., and Nagao, Y. (2002) 1,2,4-Triazolo[5,1-*i*]purine derivatives as highly potent and selective human adenosine A_3 receptor ligands. *J. Med. Chem. 45*, 3703−3708.
(11) Menjoge, A. R., Kannan, R. M., and Domalia, D. A. (2010) Dendrimer-based drug and imaging conjugates: design considerations for nanomedical applications. *Drug Disc. Today 15*, 171−185.
(12) Kim, Y., Hechler, B., Klutz, A., Gachet, C., and Jacobson, K. A. (2008) Toward multivalent signaling across G protein-coupled receptors from poly(amidoamine) dendrimers. *Bioconjugate Chem. 19*, 406−411.
(13) Villaraza, A. J., Bumb, A., and Brechbiel, M. W. (2010) Macromolecules, dendrimers, and nanomaterials in magnetic resonance imaging: the interplay between size, function, and pharmacokinetics. *Chem. Rev. 110*, 2921−2959.
(14) Ivanov, A. A., and Jacobson, K. A. (2008) Molecular modeling of a PAMAM-CGS21680 dendrimer bound to an A_{2A} adenosine receptor homodimer. *Bioorg. Med. Chem. Lett. 18*, 4312−4315.
(15) Maurice, P., Kamal, M., and Jockers, R. (2011) Asymmetry of GPCR oligomers supports their functional relevance. *Trends Pharmacol. Sci. 32*, 514−520.
(16) Jacobson, K. A. (2010) GPCR ligand-dendrimer (GLiDe) conjugates: future smart drugs? *Trends Pharmacol. Sci. 31*, 575−579.
(17) Fuxe, K., Marcellino, D., Borroto-Escuela, D. O., Frankowska, M., Ferraro, L., Guidolin, D., Ciruela, F., and Agnati, L. F. (2010) The changing world of G protein-coupled receptors: from monomers to dimers and receptor mosaics with allosteric receptor-receptor interactions. *J. Recept. Signal. Transduct. Res. 30*, 272−283.
(18) Ferré, S., Baler, R., Bouvier, M., Caron, M. G., Devi, L. A., Durroux, T., Fuxe, K, George, S. R., Javitch, J. A., Lohse, M. J., Mackie, K., Milligan, G., Pfleger, K. D., Pin, J. P., Volkow, N. D., Waldhoer, M., Woods, A. S., and Franco, R. (2009) Building a new conceptual framework for receptor heteromers. *Nat. Chem. Biol. 5*, 131−134.
(19) Gao, Z. G., Kim, S. K., Biadatti, T., Chen, W., Lee, K., Barak, D., Kim, S. G., Johnson, C. R., and Jacobson, K. A. (2002) Structural determinants of A_3 adenosine receptor activation: Nucleoside ligands at the agonist/antagonist boundary. *J. Med. Chem. 45*, 4471−4484.
(20) Jeong, L. S., Jin, D. Z., Kim, H. O., Shin, D. H., Moon, H. R., Gunaga, P., Chun, M. W., Kim, Y. C., Melman, N., Gao, Z. G., and Jacobson, K. A. (2003) N^6-Substituted D-4′-thioadenosine-5′-methyluronamides: Potent and selective agonists at the human A_3 adenosine receptor. *J. Med. Chem. 46*, 3775−3777.
(21) Tchilibon, S., Joshi, B. V., Kim, S. K., Duong, H. T., Gao, Z. G., and Jacobson, K. A. (2005) N)-Methanocarba 2,N^6-disubstituted adenine nucleosides as highly potent and selective A_3 adenosine receptor agonists. *J. Med. Chem. 48*, 1745−1758.
(22) Lee, H. W., Kim, H. O., Choi, W. J., Choi, S., Lee, J. H., Park, S. G., Yoo, L., Jacobson, K. A., and Jeong, L. S. (2010) Design, synthesis, and binding of homologated truncated 4′-thioadenosine derivatives at the human A_3 adenosine receptors. *Bioorg. Med. Chem. 20*, 7015−7021.
(23) Tosh, D. K., Chinn, M., Ivanov, A. A., Klutz, A. M., Gao, Z. G., and Jacobson, K. A. (2009) Functionalized congeners of A_3 adenosine receptor-selective nucleosides containing a bicyclo[3.1.0]hexane ring system. *J. Med. Chem. 52*, 7580−7592.
(24) Auchampach, J. A., Gizewski, E., Wan, T. C., de Castro, S., Brown, G. G., and Jacobson, K. A. (2010) Synthesis and pharmacological characterization of [^{125}I]MRS5127, a high affinity, selective agonist radioligand for the A_3 adenosine receptor. *Biochem. Pharmacol. 79*, 967−973.
(25) Kiesewetter, D. O., Lang, L., Ma, Y., Bhattacharjee, A. K., Gao, Z. G., Joshi, B. V., Melman, A., de Castro, S., and Jacobson, K. A. (2009) Synthesis and characterization of [^{76}Br]-labeled high affinity A_3 adenosine receptor ligands for positron emission tomography. *Nucl. Med. Biol. 36*, 3−10.
(26) van Dijk, M., Rijkers, D. T. S., Liskamp, R. M. J., van Nostrum, C. F., and Hennink, W. E. (2009) Synthesis and applications of biomedical and pharmaceutical polymers via click chemistry methodologies. *Bioconjugate Chem. 20*, 2001−2016.
(27) Iha, R. K., Wooley, K. L., Nyström, A. M., Burke, D. J., Kade, M. J., and Hawker, C. J. (2009) Applications of orthogonal "click" chemistries in the synthesis of functional soft materials. *Chem. Rev. 109*, 5620−5686.
(28) Best, M. D. (2009) Click chemistry and bioorthogonal reactions: Unprecedented selectivity in the labeling of biological molecules. *Biochemistry 48*, 6571−6584.
(29) Tosh, D. K., Yoo, L. S., Chinn, M., Hong, K., Kilbey, S. M., Barrett, M. O., Fricks, I. P., Harden, T. K., Gao, Z. G., and Jacobson, K. A. (2010) Polyamidoamine (PAMAM) dendrimer conjugates of "clickable" agonists of the A_3 adenosine receptor and coactivation of the $P2Y_{14}$ receptor by a tethered nucleotide. *Bioconjugate Chem. 21*, 372−384.
(30) Gao, Z. G., Duong, H. T., Sonina, T., Lim, S. K., Van Rompaey, P., Van Calenbergh, S., Mamedova, L., Kim, H. O., Kim, M. J., Kim, A. Y., Liang, B. T., Jeong, L. S., and Jacobson, K. A. (2006) Orthogonal activation of the reengineered A_3 adenosine receptor (neoceptor) using tailored nucleoside agonists. *J. Med. Chem. 49*, 2689−2702.
(31) Chan, T. R., Hilgraf, R., Sharpless, K. B., and Fokin, V. V. (2004) Polytriazoles as copper(I)-stabilizing ligands in catalysis. *Org. Lett. 6*, 2853−2855.
(32) Kecskés, A., Tosh, D. K., Wei, Q., Gao, Z. G., and Jacobson, K. A. (2011) GPCR ligand dendrimer (GLiDe) conjugates: Adenosine receptor interactions of a series of multivalent xanthine antagonists. *Bioconjugate Chem. 22*, 1115−1127.
(33) Bradford, M. M. (1976) A rapid and sensitive method for the quantitation of microgram quantities of protein utilizing the principle of protein-dye binding. *Anal. Biochem. 72*, 248−254.
(34) Schwabe, U., and Trost, T. (1980) Characterization of adenosine receptors in rat brain by (-)[^{3}H]N^6-phenylisopropyladenosine. *Naunyn Schmiedebergs Archives Pharmacology 313*, 179−187.
(35) Jarvis, M. F., Schutz, R., Hutchison, A. J., Do, E., Sills, M. A., and Williams, M. (1989) [^{3}H]CGS 21680, an A_2 selective adenosine receptor agonist directly labels A_2 receptors in rat brain tissue. *J. Pharmacol. Exp. Ther. 251*, 888−893.
(36) Olah, M. E., Gallo-Rodriguez, C., Jacobson, K. A., and Stiles, G. L. (1994) ^{125}I-4-Aminobenzyl-5′-N-methylcarboxamidoadenosine, a high affinity radioligand for the rat A_3 adenosine receptor. *Mol. Pharmacol. 45*, 978−982.
(37) Nordstedt, C., and Fredholm, B. B. (1990) A modification of a protein-binding method for rapid quantification of cAMP in cell-culture supernatants and body fluid. *Anal. Biochem. 189*, 231−234.
(38) Cheng, Y. C., and Prusoff, H. R. (1973) Relationship between the inhibition constant (K1) and the concentration of inhibitor which causes 50% inhibition (I50) of an enzymatic reaction. *Biochem. Pharmacol. 22*, 3099−3108.
(39) Xu, F., Wu, H., Katritch, V., Han, G. W., Jacobson, K. A., Gao, Z. G., Cherezov, V., and Stevens, R. C. (2011) Structure of an agonist-bound human A_{2A} adenosine receptor. *Science 332*, 322−327.
(40) Berman, H. M., Westbrook, J., Feng, Z., Gilliland, G., Bhat, T. N., Weissig, H., Shindyalov, I. N., and Bourne, P. E. (2000) The Protein Data Bank. *Nucleic Acids Res. 28*, 235−242.
(41) Tosh, D. K., Chinn, M., Yoo, L., Kang, D. W., Luecke, H., Gao, Z. G., and Jacobson, K. A. (2010) 2-Dialkynyl derivatives of (N)-methanocarba nucleosides: "Clickable" A_3 adenosine receptor-selective agonists. *Bioorg. Med. Chem. 18*, 508−517.
(42) Chincshilla, R., and Nájera, C. (2007) The Sonogashira reaction: A booming methodology in synthetic organic chemistry. *Chem. Rev. 107*, 874−922.
(43) Goddard-Borger, E. D., and Stick, R. V. (2007) An efficient, inexpensive, and shelf-stable diazotransfer reagent: Imidazole-1-sulfonyl azide hydrochloride. *Org. Lett. 9*, 3797−3800.
(44) Englert, M., Quitterer, U., and Klotz, K. N. (2002) Effector coupling of stably transfected human A_3 adenosine receptors in CHO cells. *Biochem. Pharmacol. 64*, 61−65.
(45) Jacobson, K. A., Park, K. S., Jiang, J. -l., Kim, Y. C., Olah, M. E., Stiles, G. L., and Ji, X. d. (1997) Pharmacological characterization of

novel A_3 adenosine receptor-selective antagonists. *Neuropharmacology 36*, 1157−1165.
(46) Lebon, G., Warne, T., Edwards, P. C., Bennett, K., Langmead, C. J., Leslie, A. G. W., and Tate, C. G. (2011) Agonist-bound adenosine A_{2A} receptor structures reveal common features of GPCR activation. *Nature 474*, 521−525.
(47) Ballesteros, J., and Weinstein, H. (1995) Integrated methods for the construction of three-dimensional models of structure-function relations in G protein-coupled receptors. *Methods Neurosci. 25*, 366−428.
(48) May, L. T., Bridge, L. J., Stoddart, L. A., Briddon, S. J., and Hill, S. J. (2011) Allosteric interactions across native adenosine-A_3 receptor homodimers: quantification using single-cell ligand-binding kinetics. *FASEB J. 25*, 3465−3476.
(49) Mullen, D. G., McNerny, D. Q., Desai, A., Cheng, X. M., Dimaggio, S. C., Kotlyar, A., Zhong, Y., Qin, S., Kelly, C. V., Thomas, T. P., Majoros, I., Orr, B. G., Baker, J. R., and Banaszak Holl, M. M. (2011) Design, synthesis, and biological functionality of a dendrimer-based modular drug delivery platform. *Bioconjugate Chem. 22*, 679−689.
(50) Alcala, M. A., Kwan, S. Y., Shade, C. M., Lang, M., Uh, H., Wang, M., Weber, S. G., Bartlett, D. L., Petoud, S., and Lee, Y. J. (2011) Luminescence targeting and imaging using a nanoscale generation 3 dendrimer in an in vivo colorectal metastatic rat model. *Nanomed. Nanotechnol. Biol. Med. 7*, 249−258.
(51) Kojima, C., Turkbey, B., Ogawa, M., Bernardo, M., Regino, C. A. S., Bryant, L. H., Choyke, P. L., Kono, K., and Kobayashi, H. (2011) Dendrimer-based MRI contrast agents: the effects of PEGylation on relaxivity and pharmacokinetics. *Nanomed. Nanotechnol. Biol. Med. 7*, 1001−1008.
(52) Haeusler, D., Nics, L., Mien, L. K., Ungersboeck, J., Lanzenberger, R. R., Karem, S., Sindelar, K. M., Viernstein, H., Wagner, K. H., Dudczak, R., Kletter, K., Wadsak, W., and Mitterhauser, M. (2010) [^{18}F]FE@SUPPY and [^{18}F]FE@SUPPY:2 - metabolic considerations. *Nucl. Med. Biol. 37*, 421−426.
(53) *Molecular Operating Environment* (MOE), 2010.10; Chemical Computing Group Inc., 1010 Sherbooke St. West, Suite #910, Montreal, QC, Canada, H3A 2R7, 2010.
(54) *Glide*, version 5.7; *MacroModel*, version 9.9; *Maestro*, version 9.2; *Desmond*, version 3.0; Schrödinger, LLC: New York, NY, 2010.

Bioconjugate Chemistry

Article

pubs.acs.org/bc

Site-Specific PEGylation at Histidine Tags

Yuehua Cong,[†,○] Estera Pawlisz,[†,○] Penny Bryant,[†] Sibu Balan,[†,○] Emmanuelle Laurine,[†] Rita Tommasi,[†] Ruchi Singh,[†] Sitara Dubey,[†] Karolina Peciak,[†] Matthew Bird,[†] Amrita Sivasankar,[†] Julia Swierkosz,[†] Maurizio Muroni,[†,§] Sibylle Heidelberger,[§] Monika Farys,[†] Farzad Khayrzad,[†] Jeff Edwards,[†] George Badescu,[†] Ian Hodgson,[‡] Charles Heise,[‡] Satyanarayana Somavarapu,[§] John Liddell,[‡] Keith Powell,[†] Mire Zloh,[§] Ji-won Choi,*[,†] Antony Godwin,*[,†] and Steve Brocchini*[,†,§]

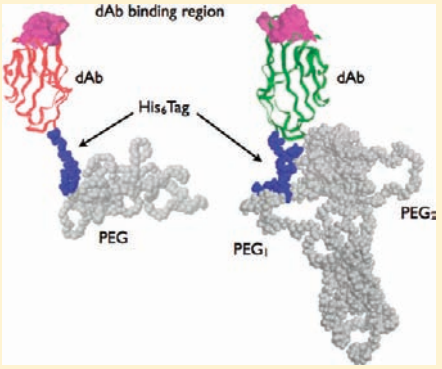
[†]PolyTherics Ltd, The London Bioscience Innovation Centre, 2 Royal College Street, London NW1 0NH, United Kingdom

[‡]Fujifilm Diosynth Biotechnologies, Belasis Avenue, Billingham TS23 1LH, United Kingdom

[§]UCL School of Pharmacy, University College London, 29-39 Brunswick Square, London WC1N 1AX, United Kingdom

S *Supporting Information*

ABSTRACT: The efficacy of protein-based medicines can be compromised by their rapid clearance from the blood circulatory system. Achieving optimal pharmacokinetics is a key requirement for the successful development of safe protein-based medicines. Protein PEGylation is a clinically proven strategy to increase the circulation half-life of protein-based medicines. One limitation of PEGylation is that there are few strategies that achieve site-specific conjugation of PEG to the protein. Here, we describe the covalent conjugation of PEG site-specifically to a polyhistidine tag (His-tag) on a protein. His-tag site-specific PEGylation was achieved with a domain antibody (dAb) that had a 6-histidine His-tag on the C-terminus (dAb-His_6) and interferon α-2a (IFN) that had an 8-histidine His-tag on the N-terminus (His_8-IFN). The site of PEGylation at the His-tag for both dAb-His_6-PEG and PEG-His_8-IFN was confirmed by digestion, chromatographic, and mass-spectral studies. A methionine was also inserted directly after the N-terminal His-tag in IFN to give His_8Met-IFN. Cyanogen bromide digestion studies of PEG-His_8Met-IFN were also consistent with PEGylation at the His-tag. By using increased stoichiometries of the PEGylation reagent, it was possible to conjugate two separate PEG molecules to the His-tag of both the dAb and IFN proteins. Stability studies followed by *in vitro* evaluation confirmed that these PEGylated proteins retained their biological activity. *In vivo* PK studies showed that all of the His-tag PEGylated samples displayed extended circulation half-lives. Together, our results indicate that site-specific, covalent PEG conjugation at a His-tag can be achieved and biological activity maintained with therapeutically relevant proteins.



INTRODUCTION

During the last 30 years, therapeutic protein and peptide-based pharmaceuticals have become a broad group of medicines that are used to treat many medical indications. With the general exception of monoclonal antibodies, the efficacy of therapeutic proteins and peptides is often compromised because of rapid clearance. The imposition of frequent dosing due to rapid clearance can pose an increased safety risk due to potential immunogenicity and an increased incidence of side effects.

Much effort has been spent to solve the fundamental limitation of suboptimal pharmacokinetics in the development and use of protein-based medicines. Three general approaches are followed to prolong the circulation half-life of proteins: (i) increase the overall size of the protein molecule in circulation while decreasing proteolytic and aggregation pathways (e.g., PEGylation,[1−8] glycoengineering[9−12]), (ii) exploit recycling mechanisms (e.g., protein fusion to Fc or albumin for endocytic recycling; or bispecific motifs to allow binding to a circulating blood protein such as albumin[13−22]), and (iii) utilize release systems to prolong dosing into the bloodstream (e.g., colloids, pumps).

Of these strategies, protein PEGylation has been clinically proven to be a general approach,[1] and in some cases, the PEGylated protein has become a first line treatment.[23,24] Much clinical experience has shown that PEGylated proteins are safe and there are at least 10 registered PEGylated medicines in the clinic. PEG is often conjugated to various residues on different amino acids of the same protein yielding positional isomers.[25−27] Considering the PEGylated proteins in development,[3] site-specific PEGylation strategies are increasingly dominating the development of mono-PEGylated proteins, which tend to be used for cell surface receptor targets.

The site of PEGylation can impact biological and pharmacodynamic (PD)/pharmacokinetic (PK) properties of

Received: September 26, 2011
Revised: January 15, 2012
Published: January 16, 2012

 © 2012 American Chemical Society dx.doi.org/10.1021/bc200530x | *Bioconjugate Chem.* 2012, 23, 248−263

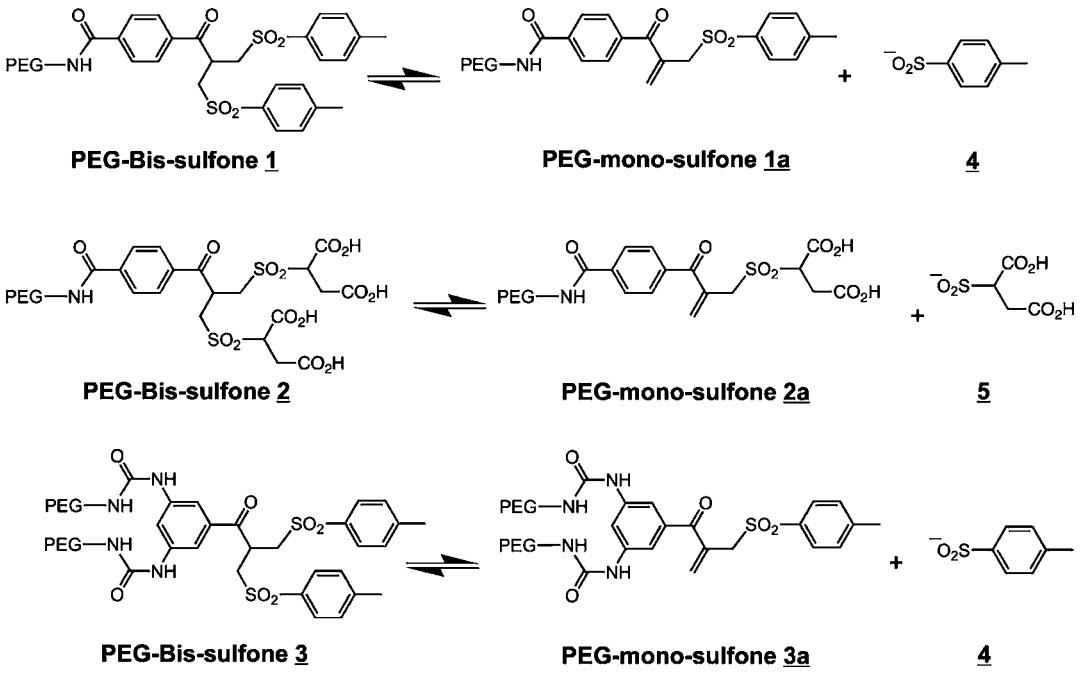
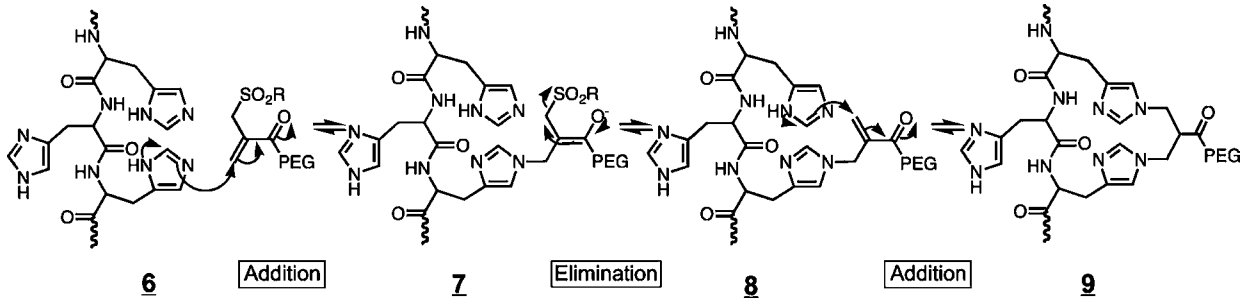


Figure 1. PEG-*bis*-sulfones **1**−**3** followed by elimination of sulfinate anion to give the corresponding PEG-*mono*-sulfones **1a**−**3a**.

Scheme 1. Possible Mechanism for Site-Specific PEGylation at a His-Tag by *Bis*-Alkylation with PEG-*Mono*-Sulfones 1a−3a



the protein.[25,28] PEGylation can decrease the measured protein binding,[25] probably due to reduced on-rates caused by steric shielding effects,[29] and often decreased activity is observed for the PEGylated protein compared to the un-PEGylated protein. Preclinical development could be accelerated if site-specific PEGylation was easier to accomplish, because in some cases, it appears that when PEG is conjugated to the same site on a protein, *in vitro* activity can be broadly maintained as PEG size is changed.[30] However, there is still much to be learned about how *in vitro* biological properties for PEGylated proteins correlate to what is observed *in vivo*.[31,32] The possibility exists that, if higher potency can be achieved while the protein displays extended circulation times, then lower doses or less frequent dosing schedules may be possible, either of which may be important as a means to minimize side effects over a given course of treatment.

PEGylation does not cause a protein to display varied biological functions;[33−35] however, each PEG positional isomer will inevitably display different relative biological activities.[26,27,36−39] It is becoming increasingly clear that the clinical use of protein-based medicines is complex. Clearly, there are consequences from the processes used in the manufacture of proteins as well as the inherent complexity of protein structure. Unwanted side effects such as an increased susceptibility to infections or malignancies may develop long after treatment has started or even after treatment has stopped.[40] Post-approval safety-related regulatory actions have been issued for about 23% of these medicines in the U.S. and European Union.[41] This regulatory vigilance led to the withdrawal of efalizumab in 2009 and gemtuzumab ozogamicin in 2010. The presence of heterogeneous mixtures may contribute to long-term safety related issues of protein-based medicines.[42] To minimize the formation of positional isomers for future PEGylated products, there is a need for robust strategies that are economically viable to conjugate PEG site-specifically to a protein.

Of the many strategies that have been described to conjugate PEG site-specifically to a protein, few have been scaled and developed clinically.[43] We now describe how PEG-*bis*-sulfone **1**[30,44] along with two new PEG-*bis*-sulfones **2** and **3** (Figure 1) can site-specifically PEGylate a polyhistidine-tag (His-tag) on a protein (Scheme 1). These reagents **1**−**3** are capable of undergoing site-specific conjugation by *bis*-alkylation after elimination of 1 equiv of sulfinic acid to give the latently cross-conjugated PEG-*mono*-sulfones **1a**−**3a** (Figure 1). Previously, we described how PEG-*bis*-sulfone **1** could be used to undergo *bis*-alkylation with two thiols derived from the two sulfurs in a disulfide bond in a protein.[30,44]

Inclusion of a His-tag is useful for purification during early studies of a protein and can also increase expression yields[45] and aid refolding.[46] A His-tag will not usually compromise the

dx.doi.org/10.1021/bc200530x | *Bioconjugate Chem.* 2012, 23, 248−263

function of the protein;[47] however, care must be exercised with the location and size of the His-tag.[48] While His-tagged proteins are being used in the clinic,[49−52] their more widespread therapeutic use may have been hampered by (i) the lack of a defined function for the His-tag post purification and (ii) anxiety that there will be an increased propensity of a secondary antibody response to the tag. PEGylation at a His-tag will remove the first of these concerns and is expected to address the second concern.

Development of a generic approach for the site-specific PEGylation of a protein at a His-tag may provide the opportunity to develop more effective PEGylated proteins by ensuring that both half-life and biological activity can be optimized, since His-tags can often be fused at either the protein C- or N-terminus. Either or both termini in many therapeutic proteins are generally accessible for conjugation and are not generally directly involved with binding. PEGylation at the His-tag may generally result in high retained activity while extending half-life.

We describe the His-tag-specific PEGylation of two proteins: (i) a domain antibody (dAb)[53] that binds tumor necrosis factor alpha (TNFα) and has a 6-histidine His-tag on the C-terminus (dAb-His_6) and (ii) interferon α-2a (IFN) that has a 8-histidine His-tag on the N-terminus (His_8-IFN). The dAb was selected because it exemplifies short half-life antibody fragments and alternative scaffolds, several of which are in clinical development.[54] For many indications, these novel proteins require an increased circulation half-life to become clinically viable. IFN was selected because its PEGylated variants have been widely studied. For dAb-His_6, PEGylation was conducted with PEG-*bis*-sulfone **1** to conjugate 1 and 2 molecules of PEG to the His_6-tag. For His_8-IFN, PEGylation was additionally conducted with the new PEG-*bis*-sulfones **2** and **3**.

EXPERIMENTAL SECTION

Materials. Sequencing-grade modified trypsin was purchased from Promega. Anti-PEG Rabbit Monoclonal antibody was obtained from Epitomics, anti-His-tag Monoclonal antibody was purchased from Clontech. HiTrap SP FF, HiTrap SP HP, HisPrep FF, HiTrap Desalting, MacroCap SP, PD-10 Desalting, and Resource S columns were all purchased from GE Healthcare. MacroTrap peptide column (C8) was purchased from MICHROM Bioresources Inc. SDS-PAGE was conducted with XCell Surelock Mini-Cell (Invitrogen), NuPAGE 4−12% Bis-Tris gels, and MOPS or MES running buffer, all from Invitrogen. Vivaspin 20 centrifugal concentrators with 10 000 MWCO (polyethersulfone) membrane were purchased from Generon. Novex Sharp protein markers (Invitrogen) were used as molecular weight standards. The gels were stained with InstantBlue (Expedeon) for proteins and barium iodide for PEG and PEGylated proteins. PEGylated conjugates were purified using an ÄKTAprime system (GE Healthcare). A Jasco HPLC instrument running *EZChrom* software was used for further analysis of purified PEGylated products.

Methods. *Preparation of His-Tag-Specific PEGylated dAb-His_6.* A representative preparation is described using 20 kDa PEG-*bis*-sulfone reagent **1**. To a solution of dAb-His_6 (1.25 mg/mL, 0.8 mL) in 50 mM sodium phosphate, 150 mM sodium chloride and 10 mM EDTA, pH 6.7, was added 1.5 mol equiv of PEG-*bis*-sulfone reagent **1** in 5 mM sodium phosphate, 15 mM sodium chloride, and 1 mM EDTA, pH 8 (20 mg/mL PEG reagent, 0.12 mL). The PEG-*bis*-sulfone reagent **1** had incubated in the buffer for 3 h at ambient temperature prior to its addition to the dAb-His_6 solution. The reaction solution was incubated at ambient temperature for a further 3 h. Purification was performed using either a HiTrap SP HP 5 mL or Resource S 1 mL column depending on the scale of purification. The reaction mixture was first buffer exchanged into a loading buffer (20 mM sodium acetate, pH 4.5). A total of 10 column volumes of loading buffer were then used to wash the column to remove residual PEG. A gradient elution from 0% to 100% elution buffer (20 mM sodium acetate, 0.7 M sodium chloride, pH 4.5) was carried out, typically over 30 min at 1 mL/min flow rate for 1 mL column, to separate the PEGylated proteins. Eluates were fractionated and analyzed by SDS-PAGE. The same procedure was followed with a larger excess of the PEG-*bis*-sulfone reagent **1** (2.4 equiv) to prepare dAb-His_6-$(PEG)_2$.

Preparation of PEG-His_8-IFN and $(PEG)_2$-His_8-IFN. PEGylation studies were conducted using PEG molecular weights ranging from 10 to 40 kDa. Depending on the PEG and reaction type, varying protein to PEG molar ratios were used (0.5−6 mol equiv of PEG reagent). During optimization of the PEGylation process, reactions were performed at temperatures ranging from 4 to 25 °C and the reaction time ranged from 2 to 17 h. Reactions that were conducted on a scale necessary to isolate larger amounts of material for PK studies were conducted overnight at 20 °C. The PEG-*bis*-sulfone reagents **1**−**3** were generally preincubated as described above to generate the corresponding PEG-*mono*-sulfones *in situ* before adding to the protein solution. Immediately after PEGylation, each reaction mixture was buffer-exchanged using either a PD-10 or HiPrep 26/10 column to the buffer compatible with ion exchange chromatography. The choice of column was obtained after scouting experiments. At the end of each purification step, the fractions were analyzed by SDS-PAGE to confirm the separation of the PEGylated product from unreacted PEG and protein.

A representative preparation of PEG-His_8-IFN is described using 20 kDa PEG-*bis*-sulfone reagent **1**: To a solution of His_8-IFN (1.37 mg/mL, 0.7 mL) in sodium acetate buffer, pH 5.3, containing 35 μM hydroquinone, was added 2.0 mol equiv of PEG-*bis*-sulfone reagent **1** (0.096 mL, 20 mg/mL) in 50 mM sodium phosphate, pH 7.4. The *bis*-sulfone reagent **1** was preincubated in the buffer for 8 h at at 37 °C prior to its addition to the His_8-IFN solution. The reaction solution was incubated for 17 h at 20 °C. The reaction mixture was then treated with sodium triacetoxyborohydride (25 mM final concentration and added as a solid) and further incubated for 1 h at 4 °C. Purification was performed using a HiTrap SP HP 5 mL cation exchange column, followed by polishing purification step using a Superdex 200 pep grade size exclusion column. The PEGylation reaction mixture was first buffer-exchanged into loading buffer (50 mM sodium acetate buffer, pH 4.0) using a PD-10 column. A total of 10 column volumes of loading buffer were then used to wash the column to remove residual PEG. A gradient elution from 0% to 100% elution buffer (50 mM sodium acetate, 1.0 M sodium chloride, pH 4.0) was carried out, typically over 30 min at 1 mL/min flow rate, to separate the PEGylated proteins. Eluates were fractionated and analyzed by SDS-PAGE. Fractions containing mono-PEGylated product were pooled and concentrated to 2 mL using a Vivaspin concentrator (10 000 MWCO, 3000 *g*, 4 °C). The solution was then purified with a Superdex 200 pep grade column at a flow rate of 1 mL/min and 50 mM sodium phosphate buffer, 150 mM NaCl, pH 7.5, as a mobile phase.

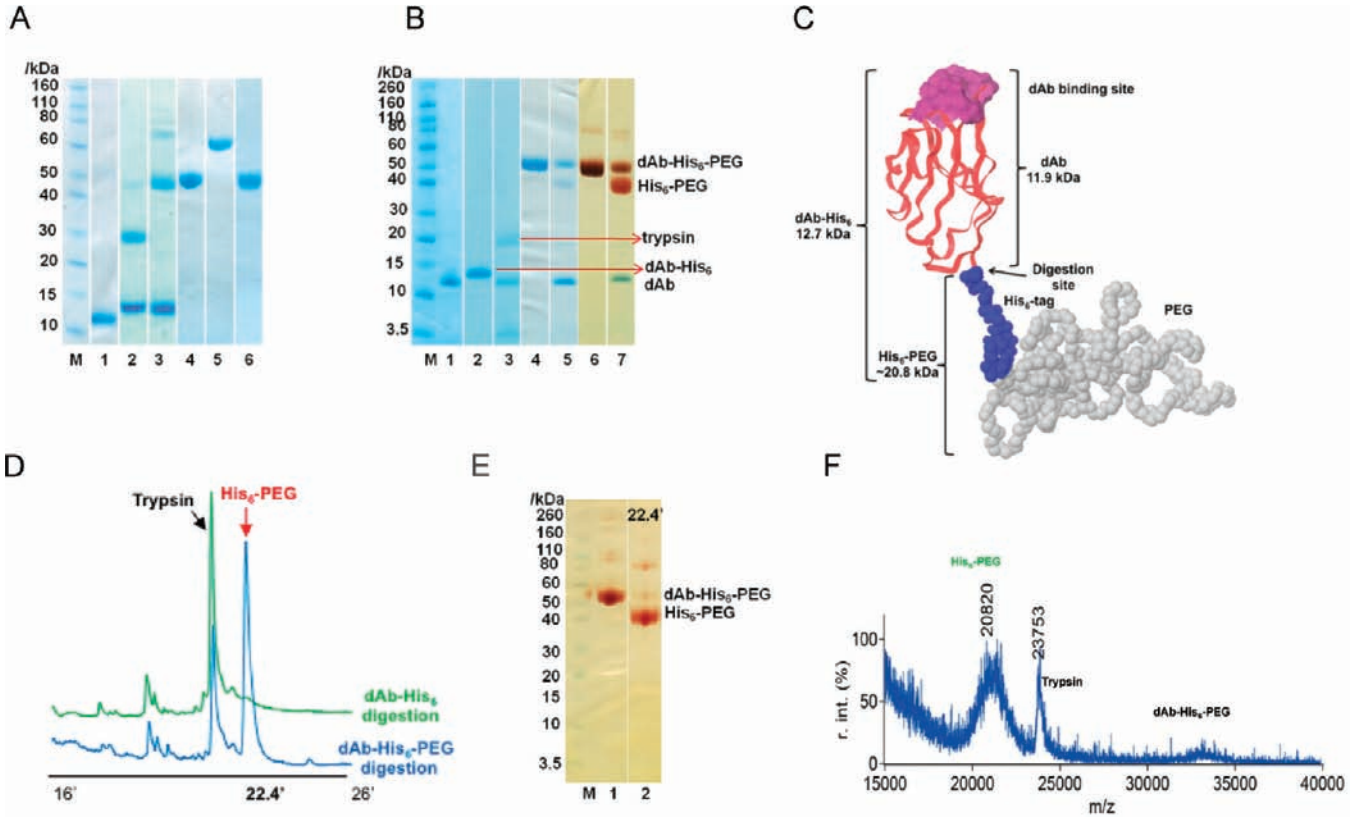


Figure 2. (A) Representative SDS-PAGE gels (colloidal blue) for the PEGylation of dAb-His_6 with 10 kDa and 20 kDa PEG-*bis*-sulfone **1**: Lane M, protein standards; Lane 1, control reaction of dAb and 20 kDa PEG-*bis*-sulfone **1** (2 equiv); Lane 2, 10 kDa PEGylation reaction of dAb-His_6; Lane 3, 20 kDa PEGylation reaction of dAb-His_6; Lane 4, purified dAb-His_6-PEG (20 kDa PEG); Lane 5, purified dAb-His_6-$(PEG)_2$ (2 × 20 kDa PEG); and Lane 6, purified dAb-His_2-PEG (20 kDa PEG). (B) Tryptic digestion of dAb-His_6-PEG (20 kDa PEG), representative SDS-PAGE gels (colloidal blue, lanes 1−5; Colloidal blue-barium iodide lanes 6−7): Lane M, protein standards; Lane 1, dAb; Lane 2, dAb-His_6; Lane 3, trypsin digest mixture of dAb-His_6; Lane 4, purified dAb-His_6-PEG; Lane 5, trypsin digest mixture of dAb-His_6-PEG; Lane 6, purified dAb-His_6-PEG; and Lane 7, trypsin digest mixture of dAb-His_6-PEG. (C) Representative structure of dAb-His_6-PEG showing the digestion site adjacent to the His_6-tag and fragment molecular weights. (D) RP-HPLC chromatogram of the tryptic digest mixtures of dAb-His_6 and dAb-His_6-PEG (20 kDa). (E) SDS-PAGE of the RP-HPLC fraction containing the PEGylated peptide fragment (colloidal blue-barium iodide): Lane M, protein standards; Lane 1, purified dAb-His_6-PEG; Lane 2 RP-HPLC fraction collected at 22.4 min. (F) MALDI-TOF mass spectrum of the fraction collected at 22.4 min with peaks labeled from dAb-His_6-PEG (~33.1 kDa), trypsin (23.7 kDa), and His_6-PEG (~20.8 kDa).

For preparation of $(PEG)_2$-His_8-IFN, 2.5 mol equiv of PEG-*bis*-sulfone reagent **1** was added to the protein solution, using the same reaction conditions as described for PEG-His_8-IFN. The purification conditions were optimized so that the di-PEGylated conjugate could be separated from unconjugated PEG, mono-PEGylated and unreacted His_8-IFN using ion exchange chromatography only. Purification was performed using a MacroCap SP 5 mL cation exchange column with 100 mM sodium acetate buffer, pH 4.0, as the loading buffer. A step elution (0%, 27%, 38%, 60%, 100%) was carried out using 100 mM sodium acetate, 1.0 M sodium chloride, pH 4.0, as an elution buffer, typically over 60 min at 2 mL/min flow rate, to separate the PEGylated proteins. Eluates were fractionated and analyzed by SDS-PAGE. Fractions containing di-PEGylated product were pooled and repurified on the Macrocap SP 5 mL cation exchange column using the same method to enhance the purity of $(PEG)_2$-His_8-IFN.

Tryptic Peptide Digestion and MALDI-TOF-MS Analysis. Sequence grade modified trypsin was reconstituted (0.2 mg/mL) in 50 mM acetic acid. Trypsin solution (60 μL) was then added to solutions of dAb-His_6 and PEGylated dAb-His_6 samples (0.26 mg/mL, 1 mL) in 25 mM ammonium acetate, and the digestion reactions were incubated at 37 °C for up to 30 h. For PEGylated His_8-IFN products, trypsin was reconstituted (0.2 mg/mL) in 50 mM ammonium bicarbonate, pH 8.5. Typically, 23.4 μL of trypsin solution was added to 100 μL of a 1 mg/mL protein solution in 50 mM ammonium bicarbonate, pH 8.5, and the digestion reactions were incubated at 37 °C for 8 h. Cyanogen bromide (CNBr) digestion was performed on reduced and denaturated samples (10 mM DTT in 6 M Gu.HCl, 20 mM Tris pH 8.0). Prior to digestion, hydrochloric acid was added to the sample (final concentration 0.5 M), then solid CNBr reagent was added (final concentration of 1 M, protein final concentration of 0.1 mg/mL, 0.1 mL). Digestion was carried out overnight at room temperature in the dark and terminated by buffer exchange using a MacroTrap (C8) column. Digest mixtures were fractionated by RP-HPLC performed on a VariTide RPC column (VARIAN, 5 μm, 100 Å, Column dimensions: 250 × 4.6 mm). Fractions were collected, lyophilized, and then analyzed by MALDI-TOF-MS, SDS-PAGE, Western blot, and dot blot performed with anti-His-tag and anti-PEG antibodies.

The masses of the mono-PEGylated and di-PEGylated species and recovered protein were confirmed by MALDI-TOF mass spectrometry using a Voyager DE-PRO MALDI-TOF (Applied Biosystems). The instrument was calibrated

dx.doi.org/10.1021/bc200530x | *Bioconjugate Chem.* 2012, 23, 248−263

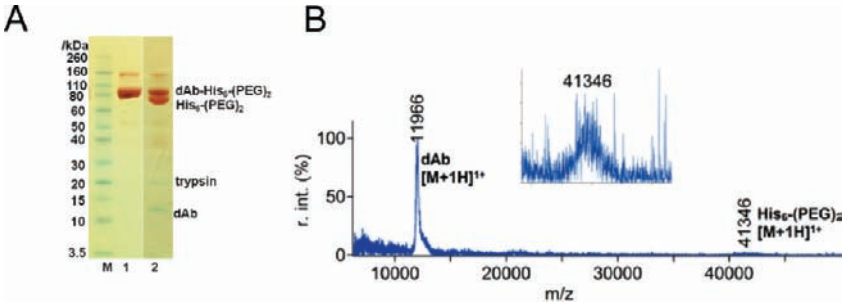


Figure 3. (A) SDS-PAGE (colloidal blue-barium iodide) of the tryptic digestion mixture of dAb-His_6-$(PEG)_2$ (2 × 20 kDa PEG). Lane M, protein standards; Lane 1, purified dAb-His_6-$(PEG)_2$; Lane 2, trypsin digest mixture of dAb-His_6-$(PEG)_2$. (B) MALDI-TOF mass spectrum of the fraction obtained at 23 min from the digestion of dAb-His_6-$(PEG)_2$ (2 × 20 kDa PEG) showing His_6-$(PEG)_2$ (2 × 20 kDa PEG) at ~41.3 kDa, also present in this fraction was dAb (11.9 kDa).

with the BSA calibration standard kit from AB Sciex. Positive linear mode was used for high molecular mass measurements and reflectron mode was used for low molecular mass measurements. Sinapinic acid (10 mg/mL in acetonitrile/water + 0.1% TFA 50:50 (v/v)) or α-cyano-4-hydroxycinnamic acid (10 mg/mL in acetonitrile/water + 0.1% TFA 50:50 (v/v)) was used as the matrix. Samples were prepared by serial dilution with a matrix solution and allowed to dry before induction into the mass spectrometer. The data were processed using *Data Explorer* software (AB Sciex) and *mMass* software.[55]

Stability Studies. A solution of dAb-His_6-PEG (0.15 mg/mL) in 50 mM sodium phosphate buffer containing 150 mM sodium chloride, pH 7.4, was aliquoted into 7 different tubes and incubated at 37 °C for up to 7 days. The pH stability of the dAb-His_6-PEG was investigated by adding either HCl (1.0 M) or NaOH (1.0 M) to the PEG-protein stock solution to a final concentration of 0.15 mg/mL and following by incubation at (i) ambient temperature and (ii) 37 °C for up to 55 min. Sample integrity, before and after incubation, was determined by SDS-PAGE. Longer-term stability was also evaluated by SDS-PAGE analysis of samples before and after storing at 4 °C for 2 months. For samples of dAb-His_6-PEG used in the PK study, accelerated stability studies were also performed in 10 mM ammonium bicarbonate at 50 °C (1 h) and 90 °C (10 min) with or without the addition of 10 mM DTT.

PEG-His_8-IFN was incubated in 50 mM sodium phosphate buffer, 150 mM NaCl pH 7.5 at 4 °C, room temperature or 37 °C. To each tested sample was added 1 mM sodium azide to prevent bacterial growth and protease inhibitor cocktail (dilution 1:500) to inhibit proteolytic digestion. For samples used in the pharmacokinetic studies, accelerated stability studies were also performed in 10 mM ammonium bicarbonate at 50 °C (1 h) and 90 °C (10 min) with or without the addition of 10 mM DTT.

■ RESULTS

Site-Specific PEGylation of a C-Terminal His_6 Domain Antibody (dAb-His_6). PEG-*bis*-sulfone **1** (10 and 20 kDa PEG molecular weight) was preincubated to allow the formation of the corresponding PEG-*mono*-sulfone **1a** before addition (1.5 mol equiv) to a solution of the dAb-His_6 to give a mono-PEGylated domain antibody (dAb-His_6-PEG) product (Figure 2A, lanes 2 and 3). Addition of the PEG-*bis*-sulfone **1** (20 kDa) to a dAb variant without the His_6-tag under the same conditions did not result in any PEGylation of the dAb (Figure 2A, lane 1).

Using dAb-His_6, the PEGylation conditions were optimized with the 20 kDa PEG-*bis*-sulfone **1**. The mono-PEGylated product (dAb-His_6-PEG) was the major product (40−50%), with a di-PEGylated dAb product (dAb-His_6-$(PEG)_2$) also being formed (10−15%). A trace amount of a tri-PEGylated product could also be observed by SDS-PAGE. The optimal concentration for PEGylation of the dAb-His_6 was in the range of 1−2.5 mg/mL. The PEGylation reaction was reproducible and was conducted at scales of up to 30 mg dAb-His_6. Increasing the stoichiometry of the PEG-*bis*-sulfone **1** (20 kDa) to 2.4 equiv allowed the formation of a greater amount of the di-PEGylated dAb (dAb-His_6-$(PEG)_2$). Using optimized conditions with PEG-*bis*-sulfone **1** (20 kDa), purification of both dAb-His_6-PEG and dAb-His_6-$(PEG)_2$ was achieved by ion exchange chromatography (Figure 2A, lanes 4 and 5, respectively). When an IMAC column was used, the PEGylated species displayed decreased binding affinities compared to the starting dAb-His_6. IMAC binding decreased with increased PEGylation. Hence, dAb-His_6-$(PEG)_2$ eluted first, followed by dAb-His_6-PEG, and then unreacted dAb-His_6 was sequentially eluted from the IMAC column with increasing imidazole concentration.

A dAb with a C-terminal 2-histidine tag (dAb-His_2) was also prepared (Supporting Information (SI) Figure S1-D). The dAb-His_2 was found to undergo reaction with 1 equiv of PEG-*bis*-sulfone **1** (20 kDa) in conditions where no conjugation was observed for the dAb without a His-tag. The PEGylated product, dAb-His_2-PEG, was purified (Figure 2A, lane 6). Additional His-tag motifs were considered by examining the PEGylation of C-terminal His-tag variants of chemerin-9, which corresponds to the C terminus of processed chemerin (149-YFPGQFAFS-157).[56] Chemerin-9 peptides with C-terminal His-tags of 2, 4, and 6 histidines were allowed to react with PEG-*bis*-sulfone **1** (SI Figure S2-A). In each case, PEGylation was observed by RP-HPLC. No PEGylation was observed for the non-His-tag version of chemerin-9. A variant of chemerin-9 with a HGHGHG tag was also observed to undergo PEGylation (SI Figure S2-B).

The mass, as recorded by MALDI-TOF-MS of the purified dAb-His_6-PEG (20 kDa PEG) was 32.7 kDa (SI Figure S1-E). The PEGylation product from the reaction of 20 kDa PEG-*bis*-sulfone **1** and dAb-His_6 was subjected to trypsin digestion (Figure 2B, lanes 4−7). There is a cleavage site (lysine-arginine) adjacent to the His-tag (SI Figure S1-A, Figure 2C). It was found in multiple (>12) experiments that this cleavage site was digested more quickly than the other cleavage sites within the dAb (Figure 2B, lane 3). Digestion of dAb-His_6-PEG (20

dx.doi.org/10.1021/bc200530x | *Bioconjugate Chem.* 2012, 23, 248−263

kDa) followed by SDS-PAGE analysis produced a band that is consistent for the dAb fragment and a band consistent for His_6-PEG that was slightly below that of the dAb-His_6-PEG (Figure 2B, lanes 5 and 7). MALDI-TOF-MS analysis of the digestion mixture (SI Figure S1-F) was consistent with the SDS-PAGE analysis. Masses of fragments obtained by digestion were observed that were consistent with the non-His-tag dAb (11.9 Da) and the expected mass of 20.8 kDa for His_6-PEG (0.8 for His_6 tag + ~20 kDa for PEG) (SI Figure S1-F).

Further analysis of the trypsin digestion mixture by RP-HPLC (Figure 2D) showed a new fraction in the digestion mixture at 22.4 min for the 20 kDa dAb-His_6-PEG compared to the digestion mixture of dAb-His_6. This fraction contained the PEG conjugated fragment (Figure 2E, lane 2). MALDI-TOF-MS analysis of this fraction (Figure 2F) indicated that its mass was approximately 20.8 kDa, which is the expected mass for His_6-PEG. The difference in mass between dAb-His_6-PEG and His_6-PEG is 11.9 kDa, which is the expected mass of the dAb fragment without the His_6 fragment. A mass for the free dAb (11.9 kDa) was also observed in the digestion mixture (SI Figure S1-F). The observed (theoretical) masses of the starting dAb-His_6 and dAb are 12755 (12756.2) and 11996 (11933.3) Da, respectively (SI Figures S1-C and S1-B, respectively).

The purified di-PEGylated product, dAb-His_6-$(PEG)_2$ (2 × 20 kDa PEG) displayed a mass as recorded by MALDI-TOF-MS of ~55.4 kDa (SI Figure S1-G) and appeared to undergo digestion more slowly than the mono-PEGylated dAb-His_6. Again, a single PEGylated band was seen by SDS-PAGE after digestion (Figure 3A, lane 2) and it appeared to be about 12 kDa less than the band observed for the undigested dAb-His_6-$(PEG)_2$ (Figure 3A, lane 1). A new peak in the RP-HPLC (SI Figure S1-H) was observed at 23 min from the digestion mixture of dAb-His_6-$(PEG)_2$ and the mass of this peak as determined by MALDI-TOF-MS was ~41.3 kDa (Figure 3B). Tryptic digestion and SDS-PAGE analysis of dAb-His_2-PEG (20 kDa) was also consistent with PEGylation having occurred at the His-tag (SI Figure S1-I).

Prior to biological evaluation, the PEGylated dAb was examined for its stability (SI Figure S3-A). There was no evidence of dePEGylation by SDS-PAGE analysis when dAb-His_6-PEG (20 kDa PEG) was stored at a concentration of 0.15 mg/mL in PBS solution at pH 7.4 for 60 d at 4 °C. Storage at 37 °C in the same solution for 5 d also did not appear to cause the loss of PEG from the dAb. Since the PEG-*bis*-sulfone **1** undergoes *bis*-alkylation by a sequence of conjugate addition and elimination reactions, stability was also evaluated at pH 2 and at pH 13. When dAb-His_6-PEG was stored as a solution at a concentration of 0.15 mg/mL at 37 °C for up to 55 min at both of these pH values, the conjugate was stable.

The PEGylated dAb appeared to maintain the same relative conformational structure as determined by circular dichrosim (CD) (SI Figure S3-B). The thermal denaturation profiles of dAb-His_6, dAb-His_6-PEG, and dAb-His_6-$(PEG)_2$ were also conducted using CD (SI Figure S3-C). Attaching 1 or 2 PEG molecules did not alter the secondary structure of dAb-His_6 or cause thermal instability. Further corroboration that the conformational structure of the dAb-His_6 was maintained after PEGylation was obtained by molecular dynamics simulation studies (SI Figure S3-D). These computational modeling experiments suggested that when two PEGs are conjugated to the His-tag they may both extend independently from the protein, but from the same relative site on the protein without effecting protein conformation.

The dAb and its PEGylated products were evaluated for their ability to inhibit TNFα-mediated cytotoxicity in a L929 cell-based assay (Figure 4A, SI Figure S4). The activity of the dAb-

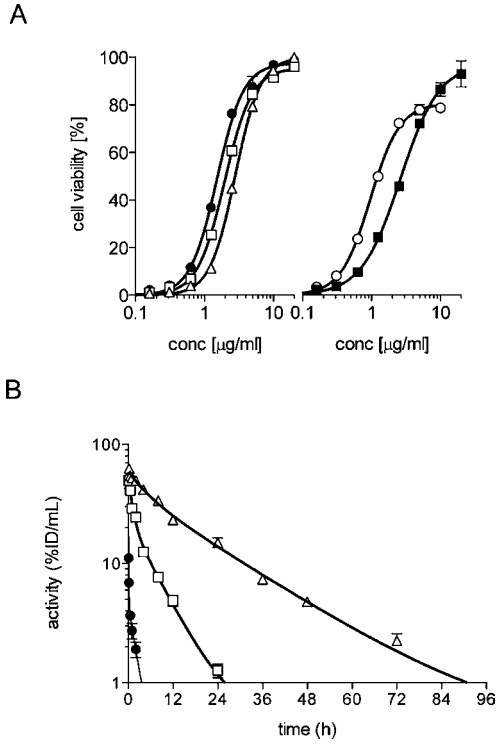


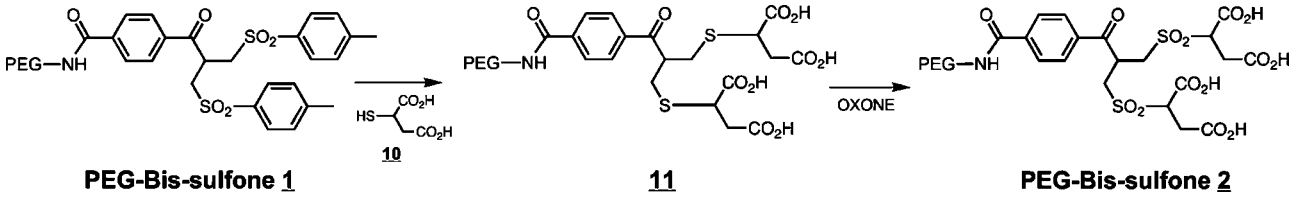
Figure 4. (A) *In vitro* activity of dAb-His_6 in L929 cytotoxicity assay. dAb-His_6 (closed circle), dAb-His_6-PEG (20 kDa PEG; open square) and dAb-His_6-$(PEG)_2$ (2 × 20 kDa PEG; open triangle), and dAb-His_2 (open circle) and dAb-His_2-PEG (20 kDa PEG; closed square). (B) Pharmacokinetic profile of iodinated dAb-His_6 and PEGylated dAb-His_6 in mice. dAb-His_6 (closed circle), dAb-His_6-PEG (20 kDa PEG; open square), and dAb-His_6-$(PEG)_2$ (2 × 20 kDa PEG; open triangle).

His_6 was not significantly different (1 way ANOVA with Bonferroni's multiple comparison test) with the nontagged dAb (2.4 ± 1.0 μg/mL (n = 10) and 3.1 ± 0.6 μg/mL (n = 4), respectively). Following PEGylation, the mono-PEGylated product, dAb-His_6-PEG (20 kDa PEG), retained more than 90% of its activity with an ED_{50} value of 2.6 ± 0.3 μg/mL (n = 16). The di-PEGylated product, dAb-His_6-$(PEG)_2$ (2 × 20 kDa PEG), was also active with an ED_{50} value of 4.8 ± 0.6 μg/mL (n = 5). The mono-PEGylated product, dAb-His_6-PEG (10 kDa PEG), also appeared to retained most of its activity (ED_{50} = 1.0 μg/mL, n = 1). Similarly for dAb-His_2, the *in vitro* activity for both dAb-His_2 and dAb-His_2-PEG (20 kDa PEG) displayed similar ED_{50} values (2.7 ± 1.6 μg/mL (n = 3) and 2.7 μg/mL (n = 1), respectively). These results indicate a high retention of activity *in vitro* remained after PEGylation at the C-terminal His-tag on the dAb.

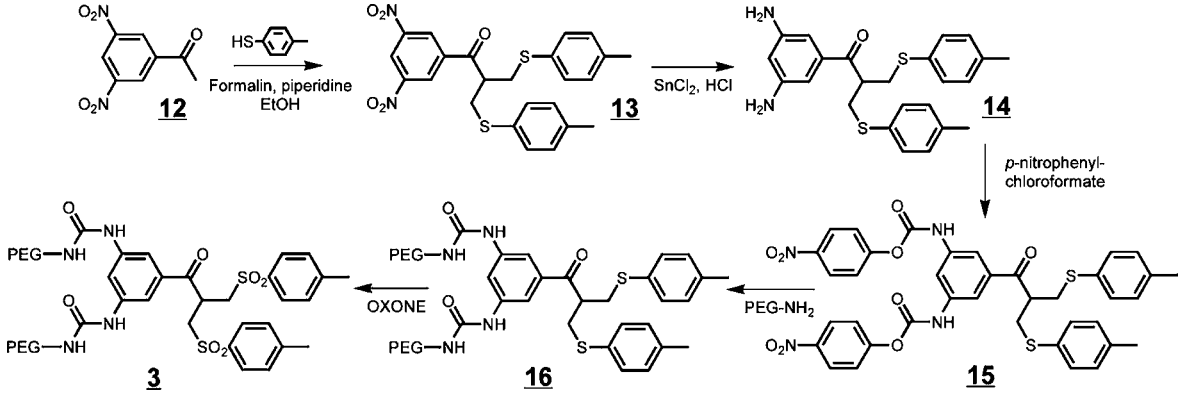
Blood circulation half-lives of I^{125} radiolabeled dAb-His_6, dAb-His_6-PEG (20 kDa PEG) and dAb-His_6-$(PEG)_2$ (2 × 20 kDa PEG) were estimated following their administration to mice and determination of radioactivity levels in plasma (Figure 4B). The non-PEGylated dAb-His_6 had a half-life of approximately 5 min. With one 20 kDa PEG conjugated to His_6, the half-life was extended to 4.8 h, and with two 20 kDa PEG molecules attached, it was extended further to 18 h. The AUC for non-PEGylated dAb-His_6 was 14.4 %ID.h/mL, which

dx.doi.org/10.1021/bc200530x | *Bioconjugate Chem.* 2012, 23, 248–263

Scheme 2. Preparation of PEG-*bis*-Sulfone 2 from PEG-*bis*-Sulfone 1



Scheme 3. Synthetic Route Followed for the Preparation of PEG-*bis*-Sulfone 3



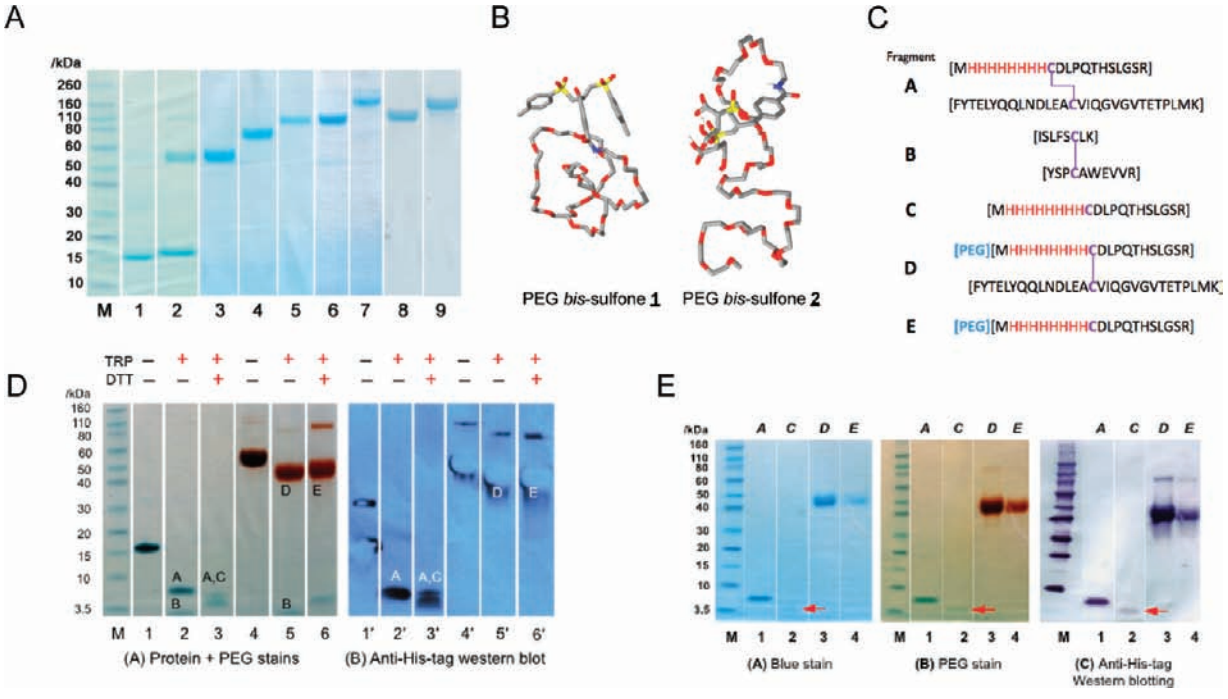


Figure 5. (A) Representative SDS-PAGE (colloidal blue) for the PEGylation of His_8-IFN with PEG-*bis*-sulfones **2** and **3**. Lane M, protein standards; Lane 1, control reaction of 20 kDa PEG-*bis*-sulfone **2** (1.5 equiv) and IFN; Lane 2, reaction mixture of 20 kDa PEG-*bis*-sulfone **2** (1.5 equiv) and His_8-IFN; Lane 3, purified PEG-His_8-IFN (20 kDa PEG); Lane 4, purified PEG-His_8-IFN (30 kDa PEG); Lane 5, purified PEG-His_8-IFN (40 kDa PEG); Lane 6, purified $(PEG)_2$-His_8-IFN (2 × 20 kDa PEG); and Lane 7, purified $(PEG)_2$-His_8-IFN (2 × 30 kDa PEG). Lanes 8 and 9 show the *b*-PEG-His_8-IFN derived from PEG-*bis*-sulfone **3**. Lane 8, purified *b*-PEG-His_8-IFN (40 kDa PEG) and Lane 9, *b*-PEG-His_8-IFN (60 kDa PEG). (B) Computationally calculated (AMMP molecular mechanics) lowest energy conformations of PEG-*bis*-sulfones **1** and **2** to illustrate the change in conformation of PEG (22 repeat units) with the two different leaving groups used in these reagents. (C) Table of expected relevant peptide fragments from both His_8-IFN (fragments A–C) and PEG-His_8-IFN (fragments D and E) after tryptic digestion. (D) Comparative tryptic digestions of native His_8-IFN (lanes 1–3) and PEG-His_8-IFN (20 kDa PEG) (lanes 4–6); Lane M, protein standards; Lane 1, His_8-IFN; Lane 2, tryptic digestion of His_8-IFN; Lane 3, DTT treatment of His_8-IFN followed by tryptic digestion; Lane 4, PEG-His_8-IFN; Lane 5, tryptic digestion of PEG-His_8-IFN; and Lane 6, DTT treatment of PEG-His_8-IFN followed by tryptic digestion. Lanes 1′ to 6′ correspond to anti-His-tag Western blots of lanes 1 to 6. (E) SDS-PAGE (colloidal blue, barium iodide, Western blot) of the RP-HPLC fractions for the tryptic digestion fragments obtained for His_8-IFN (A, C, lanes 1–2) and PEG-His_8-IFN (20 kDa PEG) (D, E, lanes 3–4). Arrow indicates the presence of a faint band corresponding to fragment C.

dx.doi.org/10.1021/bc200530x | *Bioconjugate Chem.* 2012, 23, 248–263

was increased by 13-fold (188 %ID.h/mL) and 64-fold (919 % ID.h/mL) following the addition of one or two 20 kDa PEG molecules, respectively.

Site-Specific PEGylation of an N-Terminal His_8 Interferon α-2a (His_8-IFN). PEG-*bis*-sulfone **1** underwent reaction with His_8-IFN as it did with dAb-His_6 (SI Figure S5-A). Control reactions under the conjugation conditions with non-histidine-tagged IFN indicated that IFN did not undergo PEGylation with PEG-*bis*-sulfone **1** unless a His_8-tag was present in the protein (SI Figure S5-A, lane 1). To examine different reagent variants, PEG-*bis*-sulfones **2** and **3** were prepared (Figure 1). PEG-*bis*-sulfone reagent **2** was prepared directly from reagent **1** (Scheme 2) to examine the effects of the sulfinic acid leaving group (e.g., **4** vs **5**). Reagent **3** was prepared (Scheme 3) to conjugate two PEG chains through the conjugation of one molecule of the reagent to the protein.

PEG-*bis*-sulfone **2** (20 kDa PEG) was preincubated to allow the partial formation of the corresponding PEG-*mono*-sulfone **2a** before 1.5 mol equiv was added to a solution of His_8-IFN to give the mono-PEGylated product (PEG-His_8-IFN) (Figure 5A, lane 2). Several PEG-His_8-IFN variants including di-PEGylated products (i.e., $(PEG)_2$-His_8-IFN) derived from the conjugation of two molecules of PEG-*mono*-sulfone **2a** were produced and purified (Figure 5A, lanes 3−7). As with PEG-*bis*-sulfone **1**, control reactions with non-His-tagged IFN indicated that IFN did not undergo PEGylation with PEG-*bis*-sulfone **2** in the conditions used for conjugation unless a His_8-tag was present in the protein (Figure 5A, lane 1). During purification and as with dAb-His_6-PEG, differential binding was observed between PEGylated and unPEGylated His_8-IFN species when metal affinity columns were used.

Generation of the PEG-*mono*-sulfones (Figure 1) can be tailored by reaction conditions (e.g., pH, concentration)[44] so that PEGylation can be optimized for a given protein. The structure of the leaving sulfinic acid moiety (**4** or **5**) was found to influence the rate of PEGylation. The PEG-*bis*-sulfone **2** appeared to be less reactive during conjugation than the PEG-*bis*-sulfone **1**. For example, during optimization for the PEGylation of His_8-IFN, a larger equivalence of PEG-*bis*-sulfone **2** (6 equiv) was required than was used for the PEG-*bis*-sulfone **1** (2−3 equiv) to prepare the di-PEGylated product $(PEG)_2$-His_8-IFN. Once the PEGylation reaction is complete, both the PEG-*bis*-sulfones **1** and **2** generate the same three-carbon linkage and conjugate (e.g., structure **9**, Scheme 1).

Reduction of the reactivity of PEG-*bis*-sulfone **2** was initially thought to be due to the sulfinic acid **5** being a weaker leaving group compared to sulfinic acid **4**. Semiempirical calculations, carried out using MOPAC 2009 and PM6 methods, indicated that there was little difference in the charges and bond orders of sulfinic acids **4** and **5**. However, conformational searches did suggest that there is a greater association of the PEG polymer with the succinic acid moieties of the PEG-*bis*-sulfone **2** compared to the PEG polymer with the tolyl leaving groups in the PEG-*bis*-sulfone **1** (Figure 5B). These increased interactions of PEG could contribute to reducing the reactivity of the PEG-*bis*-sulfone **2** or its *mono*-sulfone analogue by a relative reduction of the steric accessibility of the reacting moiety with the protein.

The PEG-*bis*-sulfone **3** was also incubated to generate the corresponding *mono*-sulfone **3a**, which then underwent reaction with His_8-IFN to give the "branched" product, *b*-PEG-His_8-IFN (Figure 5A, lanes 8 and 9). PEG-*bis*-sulfone **3** reagents were prepared with either a total of 40 kDa or 60 kDa PEG bound to the conjugating linker (i.e., two 20 kDa or two 30 kDa PEG chains bound to each linker moiety, respectively). The PEG-*bis*-sulfone **3** also displayed a lower apparent relative reactivity compared to the PEG-*bis*-sulfone **1**. Modulation of the PEGylation reactivity by simple changes in the structure of the PEG-*bis*-sulfone reagents **1**−**3** and the conditions used to generate the corresponding PEG-*mono*-sulfone provide a unique means to optimize site-specific PEGylation with a wide range of His-tag variant proteins.

Conducting tryptic digestion of His_8-IFN without prior treatment with dithiothreitol (DTT) results in the formation of two disulfide-containing peptide fragments, A and B (Figure 5C; SI Figure S5-B). In native IFN, there are two disulfides: one at the N-terminus between Cys1 and Cys98 and the other between Cys29 and Cys138. Fragments A and B are higher in molecular weight than the other tryptic fragments in IFN due to the presence of the disulfides. Fragment A has the N-terminal disulfide and in His_8-IFN also includes the His-tag. Fragment D is analogous to fragment A but with PEG conjugated to the His_8-tag. Fragment D would be expected for PEG-His_8-IFN when digested without prior DTT treatment. If DTT treatment occurs either before or after tryptic digestion, then fragment E is expected for PEG-His_8-IFN.

Both His_8-IFN and PEG-His_8-IFN (derived from PEG-*bis*-sulfone **2**, 20 kDa PEG) were subjected to trypsin digestion with and without prior reduction with DTT (Figure 5D). Tryptic digestion of His_8-IFN is shown in lanes 1−3 and for PEG-His_8-IFN is shown in lanes 4−6 (Figure 5D). Lanes 1−6 are dyed with both colloidal blue to detect protein and barium iodide to detect PEG. The corresponding Western blots for lanes 1−6 are shown in lanes 1′−6′ (Figure 5D). Two bands were observed in lane 2 for the digestion of His_8-IFN without prior DTT treatment. The migration of the higher molecular weight band is consistent with this band being the disulfide-containing fragment A. The lower band is consistent with the other disulfide-containing fragment B along with other fragments. Only the higher molecular weight fragment in lane 2 was detected in the corresponding anti-His-tag Western blot (Figure 5D, lane 2′) indicating that this band was indeed fragment A.

The band for fragment A disappeared when the digestion of His_8-IFN was preceded by DTT treatment (Figure 5D, lane 3). Depending on the extent of tryptic digestion and disulfide reduction, fragment A is expected to yield at least two separate fragments, with at least one fragment containing the His-tag. This fragment is labeled as fragment C (Figure 5C). There are multiple lysine-arginine cleavage sites for trypsin in His_8-IFN (SI Figure S5−B), so a His_8-tag fragment C (Figure 5D, lane 3) could also be composed of incomplete or mis-cleaved fragments along with a trace amount of fragment A as was observed in the anti-His-tag Western blot (Figure 5D, lanes 3 and 3′).

Tryptic digestion of PEG-His_8-IFN (20 kDa PEG) without any DTT treatment (Figure 5D, lane 5) gave one band for a PEG peptide fragment. Western blot analysis using an anti-His-tag antibody indicated that this PEG protein band also possessed the His-tag. This band is labeled fragment D (Figure 5C), which is analogous to fragment A that was observed from the tryptic digestion of the unPEGylated protein, His_8-IFN. Fragment A is not present in lane 5 as it was in lane 2, which suggests that the His-tag containing fragment was PEGylated. The other band in lane 5 (Figure 5D), which is analogous to

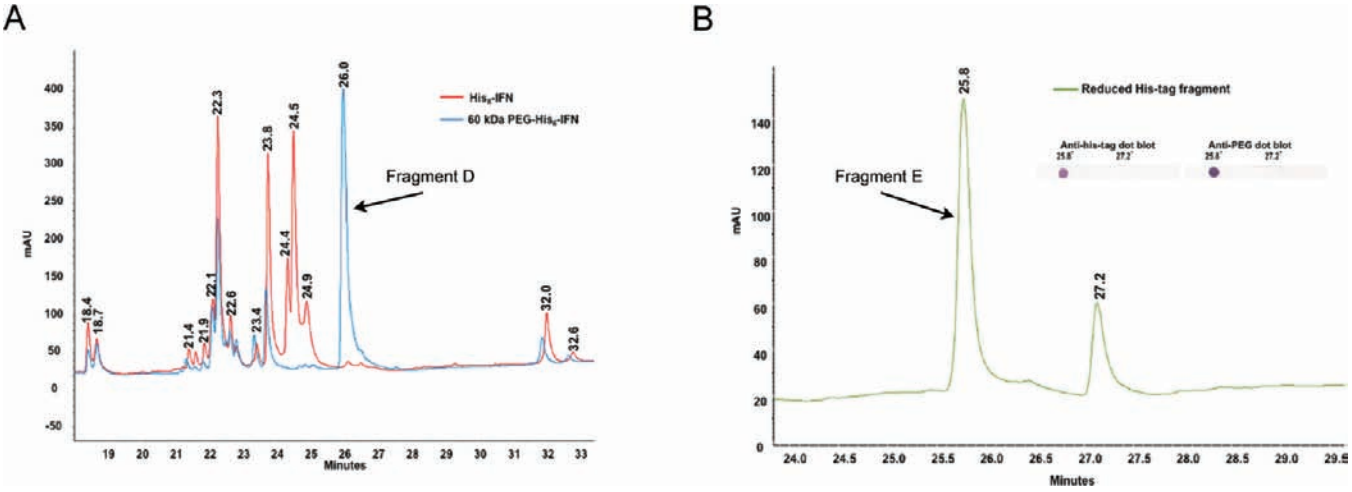


Figure 6. (A) Superposition of the RP-HPLC chromatograms after tryptic digestion of His_8-IFN and *b*-PEG-His_8-IFN (60 kDa PEG) and (B) DTT treatment of the PEG fraction (25.8 min) of *b*-PEG-His_8-IFN followed by anti-PEG and anti-His-tag dot blot indicating the presence of both PEG and the His-tag.

the second band (fragment B) in lane 2, is not PEGylated and therefore appears to be fragment B.

Treatment of PEG-His_8-IFN (20 kDa PEG) with DTT followed by tryptic digestion gave the bands shown in lanes 6 and 6′ (Figure 5D). The PEGylated peptide fragment in lane 6 was the only band detected in the corresponding anti-His-tag Western blot in lane 6′ and this fragment was labeled peptide fragment E (Figure 5D), which is thought to be derived from the disulfide-containing His_8-tag fragment D.

RP-HPLC was used to separate the digestion mixtures of His_8-IFN and PEG-His_8-IFN (20 kDa PEG, derived from PEG-*bis*-sulfone **2**) that were obtained with and without prior treatment with DTT (SI Figures S5 C–F). SDS-PAGE and Western blot analyses of the separated fractions indicated that PEG was conjugated only to the His_8-tagged fragments D and E (Figure 5E). MALDI-TOF spectra were consistent for the expected masses for fragments D (5.8 kDa for the peptide fragment + ~20 kDa for PEG) and E (2.5 kDa for the peptide fragment + ~20 kDa for PEG) (SI Figure S5 G,H).

Several variants of PEGylated His_8-IFN derived from the PEG-*bis*-sulfones (**1**–**3**) of different molecular weights were subjected to analogous tryptic digestion studies (SI Figures S6 A–E). All these digestion studies consistently showed that PEGylation occurred on the His-tag fragment as determined by SDS-PAGE and anti-His-tag Western blots. No nonspecific PEGylation occurred when there was a His-tag present in the protein. Further confirmation of this was obtained by analyzing the RP-HPLC fractions after tryptic digestion by dot blot analysis using both anti-PEG and anti-His-tag antibodies. Trpytic digestion of *b*-PEG-His_8-IFN (60 kDa PEG) without prior treatment with DTT was followed by RP-HPLC (Figure 6A). This allowed isolation of fragment D (listed in Figure 5C), which after treatment with DTT gave two fragments (Figure 6B). One fragment was detected by both anti-PEG and anti-His-tag antibodies in a dot blot analysis (Figure 6B) and corresponded to fragment E (listed in Figure 5C).

To further evaluate methodologies to avoid potential ambiguity due to incomplete tryptic digestion or the possibility that conjugation had occurred at another site in the His-tag containing fragment, His_8Met-IFN was cloned and produced in *E. coli*. A methionine was inserted directly after the N-terminal His-tag as a specific site for cyanogen bromide (CNBr) digestion. The His_8Met-IFN was PEGylated using PEG-*bis*-sulfone **1** (10 kDa PEG). Both the His_8Met-IFN and PEG-His_8Met-IFN were subjected to CNBr digestion and the digest mixtures were separated by RP-HPLC (Figure 7A). The fraction at 46.2 min was detected by both anti-His-tag and anti-PEG antibodies in a dot blot analysis (Figure 7B). MALDI-TOF-MS analysis of this fraction (Figure 7C) displayed a mass of approximately 11.3 kDa, which is consistent with the conjugation of 10 kDa PEG to a His_8 fragment (1.2 kDa).

It was thought that, compared to PEG-*bis*-sulfones **1** and **2**, the two urethanes in PEG *bis*-sulfone **3** would result in lower electron withdrawing character in the PEG reagent ketone needed for conjugate addition to covalently link the PEG to the protein. The PEG–IFN conjugates were thus treated with sodium triacetoxyborohydride to reduce the reagent ketone after conjugation to prevent any possibility of dePEGylation by an elimination reaction. A control reaction with His_8-IFN indicated that the observed ED_{50} of His_8-IFN in the *in vitro* EMCV-A549 antiviral assay was 10.5 ± 1.1 pg/mL (n = 2) after treatment with the hydride reagent. This was comparable to the observed ED_{50} (9.6 ± 1.4 pg/mL (n = 2)) for His_8-IFN when it was stored in the same conditions without the hydride reagent. Prior to biological evaluation, both mono- and di-PEGylated His_8-IFN were evaluated for their stability in a wide range of conditions including higher temperature (up to 90 °C) and in the presence of DTT to ensure that there was no dePEGylation (SI Figure S7 A–E). No evidence of free protein was observed by SDS-PAGE.

The His_8-IFN and its PEGylated variants were then evaluated for their *in vitro* EMCV-A549 antiviral activity (Figure 8A). His_8-IFN which was used for all the PEGylation reactions displayed an ED_{50} of 7 pg/mL, which was comparable to that reported for interferon α-2a in terms of specific activity.[57] All the mono-PEGylated His_8-IFN products derived from both PEG-*bis*-sulfones **1** and **3** displayed an ED_{50} in the range of 50–300 pg/mL. Conjugating two separate 20 kDa PEGs onto the His_8 resulted in ED_{50} values within the range of 370–720 pg/mL. Similarly, *b*-PEG-His_8-IFN products displayed ED_{50} values in the range of 230–680 pg/mL. Blood circulation half-lives following subcutaneous injection were estimated in both mice and rats from the IFN activity in serum determined using the EMCV-A549 antiviral assay. The half-lives increased with

dx.doi.org/10.1021/bc200530x | *Bioconjugate Chem.* 2012, 23, 248–263

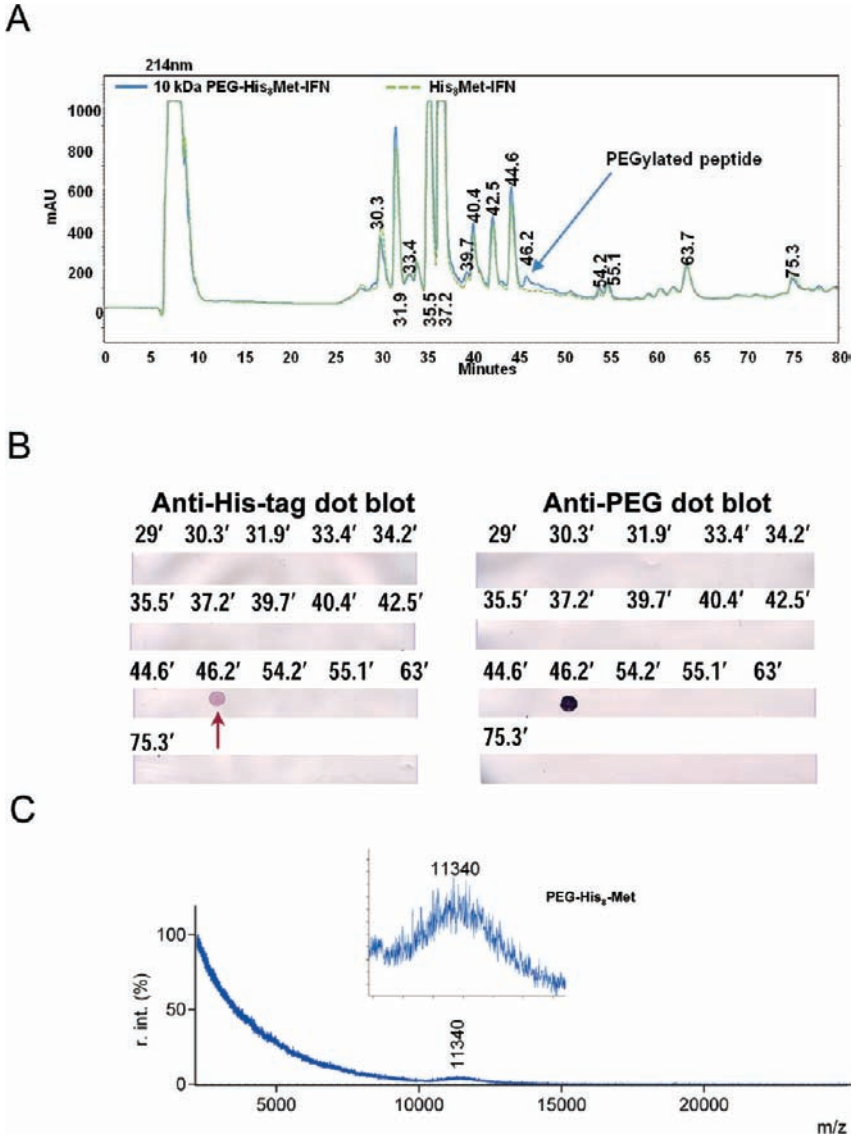


Figure 7. (A) CNBr digestion of His_8Met-IFN and PEG-His_8Met-IFN (10 kDa PEG), RP-HPLC chromatograms of digested His_8Met-IFN (dotted line) and PEG-His_8Met-IFN (10 kDa PEG) (continuous line); (B) dot blot analysis of each fraction with anti-His-tag and anti-PEG antibodies; and (C) MALDI-TOF mass spectrum analysis of the fraction (46.2 min) showing the mass of the PEG-His_8Met fragment (10 kDa PEG) (~11.3 kDa).

increasing PEG molecular weight and the relative amount of PEG (Table 1, Figure 8B), with those products conjugated with two PEGs or with a *b*-PEG showing the longest $t_{1/2}$ (30−49.6 h) compared to the native His_8-IFN (1 h).

DISCUSSION

Targeting a His-tag for stable, covalent conjugation using the PEG-*bis*-sulfones **1**−**3** does not rely on metal chelation. Metal chelation has previously been used to label and to conjugate moieties to a His-tag (for example, ref 58), often for purification purposes.[59] Some proteins do have clusters of histidines at their surface,[60] but most do not. Histidines generally have a lower pK_a than other nucleophilic residues in a protein, i.e., lysine and arginine, and so are generally more reactive at lower pH. Only the histidines within a polyhistidine sequence appear to display enhanced reactivity with the PEG-*bis*-sulfone reagents **1**−**3**. Isolated histidine residues in the protein mainchain are less reactive toward the PEG-*bis*-sulfone reagents, and so we consider a His-tag a good reactive moiety for conjugation with our reagents.

The PEG-*bis*-sulfones are thought to undergo *bis*-alkylation[30,44] by a sequence of addition−elimination reactions as drawn in Scheme 1. The PEGylations were conducted in reaction conditions that are thought to lead to the formation of the thermodynamically favored conjugate. DePEGylation was generally not observed to have occurred, and the dAb-His_6-PEG products appeared to be stable in a range of conditions (SI Figure S3-A). The same was also generally true for the PEGylated His_8-IFN products. Analogous to reductive amination, it is possible to avoid any risk of dePEGylation by reduction of the ketone derived from the PEG reagent with a hydride reagent (e.g., sodium triacetoxyborohydride) after PEGylation. To explore hydride reduction of our reagents post-PEGylation, we elected to treat the PEGylated His_8-IFN products that were made. These PEGylated conjugates were stable to the loss of PEG (SI Figure S7 A−E), even in what are considered to be harsh conditions. By using our PEG-*bis*-sulfone reagents **1**−**3**, the resulting PEGylated protein can, in principle, also be easily labeled with a tritiated reducing agent for use in preclinical PK studies.

dx.doi.org/10.1021/bc200530x | *Bioconjugate Chem.* 2012, 23, 248−263

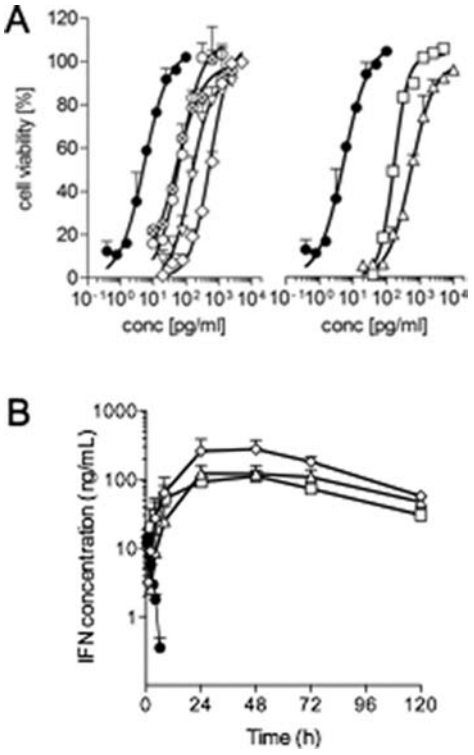


Figure 8. (A) *In vitro* activity of PEG-His_8-IFN (A549 cytotoxicity): (Left) His_8-IFN α-2a (closed circle), PEG-His_8-IFN α-2a (20 kDa PEG; open circle), PEG-His_8-IFN α-2a (30 kDa PEG; crossed circle), PEG-His_8-IFN α-2a (40 kDa PEG; open reverse triangle), and $(PEG)_2$-His_8-IFN α-2a (2 × 20 kDa PEG; open rhombus). (Right) His_8-IFN α-2a (closed circle), *b*-PEG-His_8-IFN (40 kDa PEG; open square) and *b*-PEG-His_8-IFN (60 kDa PEG; open triangle). (B) Pharmacokinetic profile of PEG-His_8-IFN in rats; His_8-IFN α-2a (closed circle), *b*-PEG-His_8-IFN (40 kDa PEG; open square), $(PEG)_2$-His_8-IFN (2 × 20 kDa PEG; open rhombus), *b*-PEG-His_8-IFN (60 kDa PEG; open triangle).

Table 1. Pharmacokinetic Data of PEGylated Analogues of His_8-IFN in Rats and Mice

parameter	unit	His_8-IFN	PEG-His_8-IFN (20 kDa PEG)	$(PEG)_2$-His_8-IFN (2 × 20 kDa PEG)	*b*-PEG-His_8-IFN[b] (40 kDa PEG)	*b*-PEG-His_8-IFN[b] (60 kDa PEG)
rat						
dose	μg/kg	67	nd	68	68	68
T_{max}	h	0.5	nd	24	24	48
C_{max}	ng/mL	14.5	nd	286	119	144
k	1/h	0.7115	nd	0.0231	0.0216	0.0140
$t_{1/2}$	h	1.0	nd	30.0	32.1	49.6
AUC_t	ng.h/mL	29.1	nd	23700	10200	13600
AUC	ng.h/mL	29.3	nd	24200	10400	14800
mouse						
dose	μg/kg	100	100	100	100	100
$t_{1/2}$	h	1.2[a]	13.3[a]	25.4	34.1	49.3

[a]Conducted in a preliminary PK study separate from the other three samples. [b]Derived from PEG-*bis*-sulfone **3**.

The PEG-*bis*-sulfone reagents **1**−**3** undergo elimination of a sulfinic acid (either **4** or **5**) to give the corresponding PEG-*mono*-sulfones **1a**−**3a**. It is the PEG-*mono*-sulfone, which then is thought to undergo PEGylation with the protein. The rate of generation of the PEG-*mono*-sulfone can be tailored by reaction conditions (e.g., pH, concentration)[44] so that PEGylation can be optimized for any given protein. Our computational modeling experiments comparing PEG-*bis*-sulfones **1** and **2** and their observed reactivity suggest that the structure of the leaving sulfinic acid groups may also interact with PEG to influence conjugation rates. This provides another means to tailor the PEGylation reagent to the structure of a given protein. To our knowledge, these simple means to modulate reactivity while maintaining specificity are not possible for any other type of PEGylation reagent. Additionally, the structure of the leaving group can be used in unique ways, potentially to aid conjugation. For example, the acidic moieties of PEG-*bis*-sulfone **2** can be used to bind this reagent to an anion exchange column. In this case, the PEG reagent could be bound to a column and then made to undergo reaction without the product being required to bind to the column.

Once reaction is complete, the PEG-*bis*-sulfones all generate the same three-carbon linkage that is conjugated to the protein. PEG-*bis*-sulfones **1** and **2** generate the same conjugate, while PEG-*bis*-sulfone **3** generates a conjugate that is derived from two PEG chains linked to the reacting moiety. This is often referred to in the literature as a "branched" PEGylation reagent. Extension of protein half-life is often a function of PEG size and the biochemical attributes of the protein, e.g., recycling mechanisms and susceptibility to proteolytic degradation. In the case of nonendogenous proteins, simple conjugation of PEG will cause extended half-life primarily due to the increased size of the PEG. The "branched" PEG reagents are often described as giving conjugates that have more extended circulation half-lives than conjugates derived from the corresponding linear PEG reagent.[61−65] Since PEGylation using the PEG-*bis*-sulfone reagents is selective for a His-tag and since more than one PEG molecule can be conjugated to the His-tag, there may be the possibility to further modify the circulation half-life for a given molar mass of PEG.

During optimization of the PEGylation reaction of His_8-IFN it was observed by SDS-PAGE that PEG-*bis*-sulfone **1** could occasionally undergo a small observable amount of PEGylation with non-His-tag interferon α-2a (IFN) depending on the pH or the reactant concentrations that were used. There was, however, no indication from any of the digestion or MALDI studies that nonspecific reactions occurred when there was a His-tag present in the protein. Histidine is less reactive as a nucleophile than a free thiol, so a longer incubation time was required to maximize the PEGylation yields than is necessary when the PEG-*bis*-sulfone **1** is used in reaction with thiols. Conducting control reactions with the non-His-tagged version of a protein in conditions optimal for His-tag PEGylation may therefore be problematic. In many reactions, a slight excess of the PEG reagent is used, and at appropriate conditions and in the absence of free thiol, reaction appears to be most favored at the His-tag rather than at other nucleophilic residues along the protein backbone.

Digestion studies of the PEGylated dAb-His_6 and His_8-IFN products (Figures 2,3, 5−7; SI Figures S1, S5, and S6) were all consistent with PEGylation occurring at the His-tag. The most available and labile digestion cleavage point in the dAb-His_6 was adjacent to the His-tag, which after partial digestion left essentially the intact dAb without the His_6-tag (Figures 2−3). Although the His-tag could be detected in the starting dAb-His_6 in Western blot experiments, it could not be detected after

digestion of either the starting dAb-His_6 or its PEGylated products. For His_8-IFN, the cleavage point is at least 12 amino acids away from the His-tag. The relative size of the His-tag fragment in His_8-IFN compared to dAb-His_6 may have facilitated Western blot detection of the His-tag in IFN after digestion. Interestingly, in the CNBr digestion experiments the cleavage point is adjacent to the His-tag, and in this case, it was still possible to observe the His-tag fragment by anti-His-tag Western blot. The length of the 8-histidine tag in both His_8-IFN and His_8-Met-IFN may therefore have aided these Western blot detection experiments.

The clinical use of proteins that have a His-tag appears to be safe.[49,51,52,66] Most therapeutic proteins do elicit some type of an immunogenic response in a proportion of patients in which they are used.[41,42,67] As far as we can discern from the literature, no immunogenic response due specifically to a His-tag on a therapeutic protein has been reported in humans. It is known that the steric shielding provided by PEG acts to reduce the immunogenicity of a therapeutic protein.[1,68] PEGylation at a His-tag would be expected to reduce any potential immunogenic response that could be directed at a His-tag in a protein. A strategy to further reduce the likelihood of any potential His-tag derived immunogenicity may be to simply reduce the size of the His-tag that is PEGylated. Our data do indicate that it is possible to shorten or modify a His-tag for site-specific PEGylation.

Many different chemical and biological strategies are being examined for the site-specific conjugation of polymers and other molecules to proteins (for example, refs 69−72). Efforts to conjugate PEG site-specifically to a protein have been the focus of various strategies including the incorporation of non-native amino acids[73−79] and free unpaired cysteines.[80−83] Incorporation of non-native amino acids probably requires that cellular biochemical pathways be robustly modified[75,84] to ensure that the efficiency of protein production is not compromised by reversion to the wild-type phenotype.

Incorporation of a single cysteine is best exploited for site-specific PEGylation of therapeutic proteins that do not have any disulfides. For example, a protein scaffold derived from a fibronectin type III domain which does not have a disulfide in its structure has been engineered to have a free cysteine for PEGylation and is currently in clinical trials.[85,86] Thiol conjugation is efficient and site-specific as long as the reagent that is used is stable during and after conjugation. Many of the maleimide-based reagents are known to be hydrolytically labile,[87] which can result in contamination by acidic byproducts. These reagents also undergo exchange reactions *in vivo*.

In addition to monocysteine-specific conjugation, other amino acids[88−91] (e.g., arginine, glutamic acid) and glycosyl moieties[92−95] have also been described as targets for conjugation. PEGylation of either the C-[96] or N-terminus[97−104] of proteins has also been described. Of these, reductive amination at the N-terminus appears to have been investigated more.[100−102,105−108] Reductive amination is often considered to be a site-specific method for PEGylation.[102,105,106,109] Imine formation is the first step in reductive amination with water as the byproduct. While reaction conditions have been described that indicate that reductive amination can lead to broadly site-specific PEGylation[105] and can be used to produce a clinical product,[101,105,109] exploiting a slight difference in the pK_a of a *single* N-terminal amino acid to achieve high yielding and homogeneous imine formation in an aqueous medium is not generally efficient in terms of reagent stoichiometry or site specificity.[106,107] One advantage of the His-tag as a functional unit is that it appears to offer a more efficient moiety for conjugation than is generally observed for a single amino group at the amino terminus of a protein.

As a chemical process, protein PEGylation is often thought of as simple to implement. Considering some of the reagents that are used to produce currently marketed therapeutic products, the perception that PEGylation is straightforward can be misplaced. While reductive amination is a sensitive reaction that often requires a very narrow set of conditions to be useful, it is generally inefficient due to the need for imine formation. Another example involves PEGylation with active ester reagents (e.g., *N*-hydroxysuccinimide esters), which tend to be hydrolytically labile and not selective. Optimization and scalability of PEGylation with these reagents often requires considerable effort and tedious purification processes to obtain a reproducible and robust process that is scalable. This is true even with maleimide reagents due to their propensity for hydrolysis to acidic byproducts and to undergo exchange with other thiol reactive molecules *in vivo*.

His-tagged proteins can often be purified effectively using immobilized metal affinity chromatography (IMAC). The scalability of IMAC for commercial production has been described where its limitations have been solved[47,110] and clinical grade proteins can be produced.[50,51] While PEGylation at a histidine tag allows the protein to be purified by IMAC, the use of IMAC is not a requirement. Ion exchange chromatography was often found to be adequate for our purposes, since the amount of PEG-*bis*-sulfone reagent that was generally required was only a slight excess. There may be advantages for considering IMAC. One example would be if PEGylation is conducted during early development of a new protein where a lysate mixture may contain some His-tag variant of the protein(s) of interest.

The needs we are addressing are to develop a robust and easy to implement site-specific PEGylation methodology. Many new proteins are not endogenous, so engineering a tag for PEGylation may be appropriate for their development. We believe this will allow for more cost-effective medicines that in some cases will be more efficacious. As our data show, His-tag conjugation at either terminus of a protein may be a general strategy to achieve relatively high activity without the need to try to place a conjugation site within the protein main chain. Different classes of proteins (e.g., α-helical barrel proteins, antibodies) and peptides have emerged as structural motifs for therapeutic applications. In many therapeutic proteins, one or both termini are not involved with the binding associated with the biological activity of the protein. Often the termini of a protein can be much more flexible than other regions of the protein. Terminal His-tag PEGylation of both dAb-His_6 and His_8-IFN resulted in good retention of activity in vitro.

In conclusion, we describe a general strategy for the covalent, site-specific PEGylation at a His-tag in therapeutically relevant proteins. Site-specific PEGylation using PEG-*bis*-sulfones **1**−**3** at a His-tag has general utility. Excluding conjugation to cysteine thiols, PEGylation to a His-tag may be the next most efficient method available for site-specific conjugation of PEG to native amino acids in proteins.

■ ASSOCIATED CONTENT

Ⓢ Supporting Information

Additional experimental procedures used in this study are described for (1) the preparation of the PEG-*bis*-sulfones **1**−**3**

dx.doi.org/10.1021/bc200530x | *Bioconjugate Chem.* 2012, 23, 248−263

and proteins, (2) PEGylation of chemerin, (3) determination of protein concentration, *in vitro* activity and circulation half-lives, and (3) computational modeling of dAb-His_6-PEG and PEG-*bis*-sulfones **1**−**2**. Additional data include the following: *For dAb-His_6*: (i) MALDI-TOF spectra of starting dAb variants and peptide fragments obtained after proteolytic digestion; (ii) SDS-PAGE analysis of the stability of dAb-His_6-PEG; (iii) CD and denaturation profiles of dAb-His_6-PEG; (iv) comparative ribbon representations of the protein domain for dAb and dAb-His_6-PEG; (v) images depicting the visual assessment used to determine TNF-α mediated cytopathic activity; and (vi) comparative HPLCs of different His-tag motifs of chemerin. *For His_8-IFN:* (i) comparative SDS-PAGE gels showing the mobilities of His_8-IFN conjugated to PEG-*bis*-sulfone **1** of different molecular weights; (ii) RP-HPLC chromatograms of trypsin digested His_8-IFN and PEG-His_8-IFN (20 kDa PEG) derived from PEG-*bis*-sulfone **2** and digestion data for several other PEG-His_8-INF conjugates; (iii) SDS-PAGE gels from stability studies of several PEG-His_8-INF conjugates. This material is available free of charge via the Internet at http://pubs.acs.org.

AUTHOR INFORMATION

Corresponding Author

*Ji-won Choi: ji-won.choi@polytherics.co.uk. Antony Godwin: antony.godwin@polytherics.co.uk. Steve Brocchini: steve.brocchini@pharmacy.ac.uk

Author Contributions

°Equal contribution for first authorship.

Notes

The authors declare the following competing financial interest(s): S.B. is a full-time academic employee of the UCL School of Pharmacy. As a co-founder of PolyTheris Ltd he has equity in the company, but receives no financial compensation. He is a non-paid director and acts as a non-paid CSO. M.M. is also a full time employee of the UCL School of Pharmacy. His position is funded as a postdoctoral researcher by the UK government (Knowledge Transfer Partnership, 67%) and PolyTherics (33%).

ACKNOWLEDGMENTS

Some of the work was partially funded by the UK Technology Strategy Board to Avecia (now Fujifilm Diosynth Biotechnologies) for dAb preparation and to PolyTherics Ltd. for dAb PEGylation. Funding from the UK Knowledge Transfer Partnership (KTP) has been provided for M.M. PolyTherics Ltd. financially supported the remaining work. Funding for S.B. is also gratefully acknowledged from the EPSRC through the EPSRC Centre for Innovative Manufacturing in Emergent Macromolecular Therapeutics. Financial support from the industry and user partners supporting the Centre programme is also acknowledged.

REFERENCES

(1) Bailon, P., and Won, C. (2009) PEG-modified biopharmaceuticals. *Expert Opin. Drug Delivery 6* (1), 1−16.

(2) Jevsevar, S., Kunstelj, M. I., and Porekar, V. G. (2010) PEGylation of therapeutic proteins. *Biotechnol. J. 5* (1), 113−128.

(3) Kang, J., Deluca, P., and Lee, K. (2009) Emerging PEGylated drugs. *Expert Opin. Emerg. Drugs 14* (2), 363−380.

(4) Fishburn, C. (2008) The pharmacology of PEGylation: Balancing PD with PK to generate novel therapeutics. *J. Pharm. Sci. 97* (10), 4167−4183.

(5) Hamidi, M., Rafiei, P., and Azadi, A. (2008) Designing PEGylated therapeutic molecules: advantages in ADMET properties. *Expert Opin. Drug Dis. 3* (11), 1293−1307.

(6) Veronese, F. (2001) Peptide and protein PEGylation a review of problems and solutions. *Biomaterials 22* (5), 405−417.

(7) Pisal, D. S., Kosloski, M. P., and Balu-Iyer, S. V. (2010) Delivery of therapeutic proteins. *J. Pharm. Sci. 99* (6), 2557−2575.

(8) Payne, R. W., Murphy, B. M., and Manning, M. C. (2010) Product development issues for PEGylated proteins. *Pharmaceutical Dev. Technol.*, 1−18.

(9) Marshall, S., Lazar, G., Chirino, A., and Desjarlais, J. (2003) Rational design and engineering of therapeutic proteins. *Drug Discovery Today 8* (5), 212−221.

(10) Elliott, S., Lorenzini, T., Asher, S., Aoki, K., Brankow, D., Buck, L., Busse, L., Chang, D., Fuller, J., and Grant, J. (2003) Enhancement of therapeutic protein in vivo activities through glycoengineering. *Nat. Biotechnol. 21* (4), 414−421.

(11) Sola, R. J., and Grievenow, K. (2010) Glycosylation of therapeutic proteins an effective strategy to optimize efficacy. *Biodrugs 24* (1), 9−21.

(12) Li, H., and D'anjou, M. (2009) Pharmacological significance of glycosylation in therapeutic proteins. *Curr. Opin. Biotechnol. 20* (6), 678−684.

(13) Andersen, J., and Sandlie, I. (2009) The versatile MHC class I-related FcRn protects IgG and albumin from degradation: Implications for development of new diagnostics and therapeutics. *Drug Metabol. Pharmacokinetics 24* (4), 318−332.

(14) Kim, H., Robinson, S., and Csaky, K. (2009) FcRn receptor-mediated pharmacokinetics of therapeutic IgG in the eye. *Mol. Vis. 15*, 2803−2812.

(15) Otagiri, M., and Chuang, V. (2009) Pharmaceutically important pre-and posttranslational modifications on human serum albumin. *Biol. Pharm. Bull. 32* (4), 527−534.

(16) Stork, R., Campigna, E., Robert, B., Muller, D., and Kontermann, R. E. (2009) Biodistribution of a bispecific single-chain diabody and its half-life extended derivatives. *J. Biol. Chem. 284* (38), 25612−25619.

(17) Tuan Giam Chuang, V., Kragh-Hansen, U., and Otagiri, M. (2002) Pharmaceutical strategies utilizing recombinant human serum albumin. *Pharm. Res. 19* (5), 569−577.

(18) Dennis, M., Zhang, M., Meng, Y., Kadkhodayan, M., Kirchhofer, D., Combs, D., and Damico, L. (2002) Albumin binding as a general strategy for improving the pharmacokinetics of proteins. *J. Biol. Chem. 277* (38), 35035−35043.

(19) Sung, C., Nardelli, B., Lafleur, D., Blatter, E., Corcoran, M., Olsen, H., Birse, C., Pickeral, O., Zhang, J., and Shah, D. (2003) An IFN-β-albumin fusion protein that displays improved pharmacokinetic and pharmacodynamic properties in nonhuman primates. *J. Interferon Cytokine Res. 23* (1), 25−36.

(20) Halpern, W., Riccobene, T., Agostini, H., Baker, K., Stolow, D., Gu, M., Hirsch, J., Mahoney, A., Carrell, J., and Boyd, E. (2002) Albugranin TM, a recombinant human granulocyte colony stimulating factor (G-CSF) genetically fused to recombinant human albumin induces prolonged myelopoietic rffects in mice and monkeys. *Pharm. Res. 19* (11), 1720−1729.

(21) Subramanian, G. M., Fiscella, M., Lamousé-Smith, A., Zeuzem, S., and Mchutchison, J. G. (2007) Albinterferon α-2b: a genetic fusion protein for the treatment of chronic hepatitis C. *Nat. Biotechnol. 25* (12), 1411−1419.

(22) Trussel, S., Dumelin, C., Frey, K., Villa, A., Buller, F., and Neri, D. (2009) New strategy for the extension of the serum half-life of antibody fragments. *Bioconjugate Chem. 20*, 2286−2292.

(23) Foster, G. R. (2010) Pegylated interferons for the treatment of chronic hepatitis C: pharmacological and clinical differences between Peginterferon α-2a and Peginterferon α-2b. *Drugs 70* (2), 147−165.

(24) Yang, B. (2006) Integration of pharmacokinetics and pharmcodynamics into the drug development of Pegfilgrastim, a PEGylated Protein, in *Pharmacokinetics and Pharmacodynamics of*

Biotech Drugs (Meibohm, B., Ed.) pp 373−393, Wiley-VCH, Weinheim.
(25) Grace, M., Lee, S., Bradshaw, S., Chapman, J., Spond, J., Cox, S., Delorenzo, M., Brassard, D., Wylie, D., Cannon-Carlson, S., Ccullen, Indelicato, S., Voloch, M., and Bordens, R. (2005) Site of pegylation and polyethylene glycol molecule size attenuate interferon-α antiviral and antiproliferative activities through the JAK/STAT signaling pathway. *J. Biol. Chem. 280* (8), 6327−6336.
(26) Foser, S., Schacher, A., Weyer, K., Brugger, D., Dietel, E., Marti, S., and Schreitmullerc, T. (2003) Isolation, structural characterization, and antiviral activity of positional isomers of monopegylated interferon ⟨-2a (PEGASYS). *Protein Expression Purif. 30*, 78−87.
(27) Pettit, D., Bonnert, T., Eisenman, J., Srinivasan, S., Paxton, R., Beers, C., Lynch, D., Miller, B., Yost, J., and Grabstein, K. (1997) Structure-function studies of interleukin-15 using site-specific mutagenesis, poly(ethylene glycol) conjugation, and homology modeling. *J. Biol. Chem. 272* (4), 2312.
(28) Dhalluin, C., Ross, A., Huber, W., Gerber, P., Brugger, D., Gsell, B., and Senn, H. (2005) Structural, kinetic, and thermodynamic analysis of the binding of the 40 kDa PEG-interferon-alpha 2a and its individual positional isomers to the extracellular domain of the receptor IFNAR2. *Bioconjugate Chem. 16*, 518−527.
(29) Kubetzko, S., Sarkar, C., and Pluckthun, A. (2005) Protein PEGylation decreases observed target association rates via a dual blocking mechanism. *Mol. Pharmacol. 68*, 1439−1454.
(30) Shaunak, S., Godwin, A., Choi, J., Balan, S., Pedone, E., Vijayarangam, D., Heidelberger, S., Teo, I., Zloh, M., and Brocchini, S. (2006) Site-specific PEGylation of native disulfide bonds in therapeutic proteins. *Nat. Chem. Biol.*, 312−313.
(31) Caliceti, P., and Veronese, F. (2003) Pharmacokinetic and biodistribution properties of poly (ethylene glycol)−protein conjugates. *Adv. Drug Delivery Rev. 55* (10), 1261−1277.
(32) Hamidi, M., Azadi, A., and Rafiei, P. (2006) Pharmacokinetic consequences of Pegylation. *Drug Delivery 13* (6), 399−409.
(33) Gonnelli, M., and Strambini, G. B. (2009) No effect of covalently linked poly (ethylene glycol) chains on protein internal dynamics. *Biochim. Biophpys. Acta* No. 1794, 569−576.
(34) Rodríguez-Martínez, J., Solá, R., Castillo, B., Cintrón-Colón, H., Rivera-Rivera, I., Barletta, G., and Griebenow, K. (2008) Stabilization of α-chymotrypsin upon PEGylation correlates with reduced structural dynamics. *Biotechnol. Bioeng. 101* (6), 1142−1149.
(35) Lu, Y., Harding, S. E., Turner, A., Smith, B., and Athwal, D. S. (2008) Effect of PEGylation on the solution conformation of antibody fragments. *J. Pharm. Sci. 97* (6), 2062−2079.
(36) Youngster, S., Wang, Y. S., Grace, M., Bausch, J., Bordens, R., and Wyss, D. F. (2002) Structure, biology, and therapeutic implications of pegylated interferon alpha-2b. *Curr. Pharm. Des. 8* (24), 2139−2157.
(37) Wang, Y., Youngster, S., Bausch, J., Zhang, R., Mcnemar, C., and Wyss, D. (2000) Identification of the major positional isomer of pegylated interferon alpha-2b. *Biochemistry 39*, 10634−10640.
(38) Wang, Y., Youngster, S., Grace, M., Bausch, J., and Wyss, D. (2002) Structural and biological characterization of pegylated recombinant interferon alpha-2b and its therapeutic implications. *Adv. Drug Delivery Rev. 54*, 547−570.
(39) Dhalluin, C., Ross, A., Leuthold, L., Foser, S., Gsell, B., Muller, F., and Senn, H. (2005) Structural and biophysical characterization of the 40 kDa PEG-interferon-a2a and its individual positional isomers. *Bioconjugate Chem. 16*, 504−517.
(40) Mancini, S., Amorotti, E., Vecchio, S., Ponz De Leon, M., and Roncucci, L. (2010) Infliximab-related hepatitis: discussion of a case and review of the literature. *Intern. Emerg. Med. 5* (3), 193−200.
(41) Giezen, T., Mantel-Teeuwisse, A., Straus, S., Schellekens, H., Leufkens, H., and Egberts, A. (2008) Safety-related regulatory actions for biologicals approved in the United States and the European Union. *J. Am. Med. Assoc. 300* (16), 1887−1896.
(42) Singh, S. K. (2011) Impact of product-related factors on immunogenicity of biotherapeutics. *J. Pharm. Sci. 100* (2), 354−387.
(43) Smolen, J., Landewe, R. B., Mease, P., Brzezicki, J., Mason, D., Luijtens, K., Van Vollenhoven, R. F., Kavanaugh, A., Schiff, M., Burmester, G. R., Strand, V., Vencovsky, J., and Van Der Heijde, D. (2009) Efficacy and safety of certolizumab pegol plus methotrexate in active rheumatoid arthritis: the RAPID 2 study. A randomised controlled trial. *Ann. Rheum. Dis. 68* (6), 797−804.
(44) Balan, S., Choi, J., Godwin, A., Teo, I., Laborde, C., Heidelberger, S., Zloh, M., Shaunak, S., and Brocchini, S. (2007) Site-specific PEGylation of protein disulfide bonds using a three-carbon bridge. *Bioconjugate Chem. 18* (1), 61−76.
(45) Woestenenk, E., Hammarström, M., Van Den Berg, S., Härd, T., and Berglund, H. (2004) His tag effect on solubility of human proteins produced in Escherichia coli: a comparison between four expression vectors. *J. Struct. Funct. Genomics 5* (3), 217−229.
(46) Li, M., and Huang, D. (2007) On-column refolding purification and characterization of recombinant human interferon-λ1 produced in Escherichia coli. *Protein Expression Purif. 53* (1), 119−123.
(47) Gaberc-Porekar, V., and Menart, V. (2005) Potential for using histidine tags in purification of proteins at large scale. *Chem. Eng. Technol. 28* (11), 1306−1314.
(48) Arnau, J., Lauritzen, C., Petersen, G., and Pedersen, J. (2006) Current strategies for the use of affinity tags and tag removal for the purification of recombinant proteins. *Protein Expression Purif. 48* (1), 1−13.
(49) Mayer, A., Francis, R. J., Sharma, S. K., Tolner, B., Springer, C. J., Martin, J., Boxer, G. M., Bell, J., Green, A. J., Hartley, J. A., Cruickshank, C., Wren, J., Chester, K. A., and Begent, R. H. J. (2006) A Phase I study of single administration of antibody-directed enzyme prodrug therapy with the recombinant anti-carcinoembryonic antigen antibody-enzyme fusion protein MFECP1 and a bis-iodo phenol mustard prodrug. *Clin. Cancer Res. 12* (21), 6509−6516.
(50) Tolner, B., Smith, L., Hillyer, T., Bhatia, J., Beckett, P., Robson, L., Sharma, S., Griffin, N., Vervecken, W., and Contreras, R. (2007) From laboratory to Phase I/II cancer trials with recombinant biotherapeutics. *Eur. J. Cancer 43* (17), 2515−2522.
(51) Murphy, R., Green, S., Ritter, G., Cohen, L., Ryan, D., Woods, W., Rubira, M., Cebon, J., Davis, I., Sjolander, A., Kypridis, A., Kalnins, H., Mcnamara, M., Moloney, M., Ackland, J., Cartwright, G., Rood, J., Dumsday, G., Healey, K., Maher, D., Maraskovsky, E., Chen, Y., Hoffman, E., Old, L., and Scott, A. (2005) Recombinant NY-ESO-1 cancer antigen: production and purification under cGMP conditions. *Prep. Biochem. Biotechnol. 35* (2), 119−134.
(52) Kaslow, D., and Shiloach, J. (1994) Production, purification and immunogenicity of a malaria transmission-blocking vaccine candidate: TBV25H expressed in yeast and purified using nickel-NTA agarose. *Nat. Biotechnol. 12* (5), 494−499.
(53) Ward, E. S., Güssow, D., Griffiths, A. D., Jones, P. T., and Winter, G. (1989) Binding activities of a repertoire of single immunoglobulin variable domains secreted from Escherichia coli. *Nature 341* (6242), 544−546.
(54) Gebauer, M., and Skerra, A. (2009) Engineered protein scaffolds as next-generation antibody therapeutics. *Curr. Opin. Chem. Biol. 13* (3), 245−255.
(55) Strohalm, M., Kavan, D., Novak, P., Volný, M., and Havlicek, V. (2010) mMass3: A cross-platform software environment for precise analysis of mass spectrometric data. *Anal. Chem. 82* (11), 4648−4651.
(56) Wittamer, V. (2003) The C-terminal nonapeptide of mature chemerin activates the chemerin receptor with low nanomolar potency. *J. Biol. Chem. 279* (11), 9956−9962.
(57) *European Pharmacopeia.* (2008) p 1110.
(58) Lata, S., and Piehler, J. (2005) Stable and functional immobilization of histidine-tagged proteins via multivalent chelator headgroups on a molecular poly (ethylene glycol) brush. *Anal. Chem. 77* (4), 1096−1105.
(59) Zaveckas, M., Žvirblienė, A., Žvirblis, G., Chmieliauskaitė, V., Bumelis, V., and Pesliakas, H. (2007) Effect of surface histidine mutations and their number on the partitioning and refolding of recombinant human granulocyte-colony stimulating factor (Cys17Ser)

in aqueous two-phase systems containing chelated metal ions. *J. Chromatogr., B 852* (1−2), 409−419.
(60) Bolanos-Garcia, V., and Davies, O. (2006) Structural analysis and classification of native proteins from E. coli commonly co-purified by immobilised metal affinity chromatography. *Biochim. Biophys. Acta 1760* (9), 1304−1313.
(61) Kusterle, M., Jevševar, S., and Porekar, V. G. (2008) Size of Pegylated Protein Conjugates Studied by Various Methods. *Acta. Chem. Slov. 55*, 594−601.
(62) Fee, C. (2007) Size comparison between proteins PEGylated with branched and linear poly (ethylene glycol) molecules. *Biotechnol. Bioeng. 98* (4), 725−731.
(63) Veronese, F. M., Caliceti, P., and Schiavon, O. (1997) Branched and linear poly(ethylene glycol): Influence of the polymer structure on enzymological, pharmacokinetic, and immunological properties of protein conjugates. *J. Bioact. Compat. Polym. 12*, 196−207.
(64) Monfardini, C., Schiavon, O., Caliceti, P., Morpurgo, M., Harris, J. M., and Veronese, F. M. (1995) A branched monomethoxypoly (ethylene glycol) for protein modification. *Bioconjugate Chem. 6* (1), 62−69.
(65) Fee, C. J., and Van Alstine, J. M. (2004) Prediction of the viscosity radius and the size exclusion chromatography behavior of PEGylated proteins. *Bioconjugate Chem. 15* (6), 1304−1313.
(66) Li, X., Shang, B., Wang, D., Zhang, S., Wu, S., and Y, A. (2011) Endostar, a modified recombinant human endostatin, exhibits synergistic effects with dexamethasone on angiogenesis and hepatoma growth. *Cancer Lett. 301*, 212−220.
(67) Schellekens, H. (2002) Immunogenicity of therapeutic proteins: clinical implications and future prospects. *Clinical Therapeutics 24* (11), 1720−1740.
(68) Veronese, F., Monfardini, C., and Caliceti, P. (1996) Improvement of pharmacokinetic, immunological and stability properties of asparaginase by conjugation to linear and branched monomethoxy poly(ethylene glycol). *J. Controlled Release 40*, 199−209.
(69) Carrico, I. S. (2008) Chemoselective modification of proteins: hitting the target. *Chem. Soc. Rev. 37* (7), 1423−1431.
(70) Broyer, R. M., Grover, G. N., and Maynard, H. D. (2011) Emerging synthetic approaches for protein−polymer conjugations. *Chem. Commun. 47*, 2212−2226.
(71) Ban, H., Gavrilyuk, J., and Barbas III, C. F. (2010) Tyrosine bioconjugation through aqueous ene-type reactions: A click-like reaction for tyrosine. *J. Am. Chem. Soc. 132* (5), 1523−1525.
(72) Minamihata, K., Goto, M., and Kamiya, N. (2011) Site-specific protein cross-linking by peroxidase-catalyzed activation of a tyrosine-containing peptide tag. *Bioconjugate Chem. 22*, 74−81.
(73) Johnson, J. A., Lu, Y. Y., Van Deventer, J. A., and Tirrell, D. A. (2010) Residue-specific incorporation of non-canonical amino acids into proteins: recent developments and applications. *Curr. Opin. Chem. Biol. 14*, 774−780.
(74) Liu, C. C., and Schultz, P. G. (2010) Adding new chemistries to the genetic code. *Annu. Rev. Biochem. 79*, 413−444.
(75) Voloshchuk, N., and Montclare, J. K. (2009) Incorporation of unnatural amino acids for synthetic biology. *Mol. BioSyst. 6* (1), 65−80.
(76) Connor, R. E., and Tirrell, D. A. (2007) Non-canonical amino acids in protein polymer design. *Polym. Rev. 47* (1), 9−28.
(77) Wang, A., Winblade Nairn, N., Johnson, R. S., Tirrell, D. A., and Grabstein, K. (2008) Processing of N-terminal unnatural amino acids in recombinant human interferon-β inEscherichia coli. *ChemBioChem. 9* (2), 324−330.
(78) Liao, J. (2007) Protein and cellular engineering with unnatural amino acids. *Biotechnol. Prog. 23* (1), 28−31.
(79) Van Hest, J. (2007) Biosynthetic-synthetic polymer conjugates. *Polym. Rev. 47* (1), 63−92.
(80) Yang, K., Basu, A., Wang, M., Chintala, R., Hsieh, M., Liu, S., Hua, J., Zhang, Z., Zhou, J., Li, M., Phyu, H., Petti, G., Mendez, M., Janjua, H., Peng, P., Longley, C., Borowski, V., Mehlig, M., and Filpula, D. (2003) Tailoring structure-function and pharmacokinetic properties of single-chain Fv proteins by site-specific PEGylation. *Protein Eng. 16* (10), 761−770.
(81) Rosendahl, M., Doherty, D., Smith, S., Carlson, S., Chlipala, E., and Cox, G. (2005) A long-acting, highly potent interferon ⟨-2 conjugate created using site-specific PEGylation. *Bioconjugate Chem. 16*, 200−207.
(82) Mei, B., Pan, C., Jiang, H., Tjandra, H., Strauss, J., Chen, Y., Liu, T., Zhang, X., Severs, J., Newgren, J., Chen, J., Gu, J., Subramanyam, B., Fournel, M. A., Pierce, G. F., and Murphy, J. E. (2010) Rational design of a fully active, long-acting PEGylated factor VIII for hemophilia A treatment. *Blood. 116* (2), 270−279.
(83) Doherty, D. H., Rosendahl, M. S., Smith, D. J., Hughes, J. M., Chlipala, E. A., and Cox, G. N. (2005) Site-specific PEGylation of engineered cysteine analogues of recombinant human granulocyte-macrophage colony-stimulating factor. *Bioconjugate Chem. 16* (5), 1291−1298.
(84) Filipovska, A., and Rackham, O. (2008) Building a parallel metabolism within the cell. *ACS Chem. Biol. 3* (1), 51−63.
(85) Bloom, L., and Calabro, V. (2009) FN3: a new protein scaffold reaches the clinic. *Drug Discovery Today 14*, 949−955.
(86) Lipovsek, D. (2011) Adnectins: engineered target-binding protein therapeutics. *Protein Eng. 24* (1−2), 3−9.
(87) Alley, S., Benjamin, D., Jeffrey, S., Okeley, N., Meyer, D., Sanderson, R., and Senter, P. (2008) Contribution of linker stability to the activities of anticancer immunoconjugates. *Bioconjugate Chem. 19*, 759−765.
(88) Gauthier, M. A., and Klok, H. A. (2011) Arginine-specific modification of proteins with poly(ethylene glycol). *Biomacromolecules 12*, 482−493.
(89) Sato, H. (2002) Enzymatic procedure for site-specific pegylation of proteins. *Adv. Drug Delivery Rev. 54*, 487−504.
(90) Maullu, C., Raimondo, D., Caboi, F., Giorgetti, A., Sergi, M., Valentini, M., Tonon, G., and Tramontano, A. (2009) Site-directed enzymatic PEGylation of the human granulocyte colony-stimulating factor. *FEBS J. 276* (22), 6741−6750.
(91) Rabuka, D. (2010) Chemoenzymatic methods for site-specific protein modification. *Curr. Opin. Chem. Biol. 14*, 790−796.
(92) Defrees, S., Wang, Z. G., Xing, R., Scott, A. E., Wang, J., Zopf, D., Gouty, D. L., Sjoberg, E. R., Panneerselvam, K., Brinkman-Van Der Linden, E., Bayer, R. J., Tarp, M., and Clausen, H. (2006) GlycoPEGylation of recombinant therapeutic proteins produced in Escherichia coli. *Glycobiology 16* (9), 833−843.
(93) Plesner, B., Westh, P., and Nielsen, A. (2011) Biophysical characterisation of GlycoPEGylated recombinant human factor VIIa. *Int. J. Pharm. 406*, 62−68.
(94) Stennicke, H. R., Østergaard, H., Bayer, R. J., Kalo, M. S., Kinealy, K., Holm, P. K., Sørensen, B. B., Zopf, D., and Bjørn, S. E. (2008) Generation and biochemical characterization of glycoPEGylated factor VIIa derivatives. *Tierärztliche Praxis Großtiere 36* (3), 163−169.
(95) Henderson, G. E., Isett, K. D., and Gerngross, T. U. (2011) Site-specific modification of recombinant proteins: A novel platform for modifying glycoproteins expressed in E. coli. *Bioconjugate Chem. 22* (5), 903−912.
(96) Gault, V. A., Kerr, B. D., Irwin, N., and Flatt, P. R. (2008) C-terminal mini-PEGylation of glucose-dependent insulinotropic polypeptide exhibits metabolic stability and improved glucose homeostasis in dietary-induced diabetes. *Biochem. Pharmacol. 75* (12), 2325−2333.
(97) Rajan, R. S., Li, T., Aras, M., Sloey, C., Sutherland, W., Arai, H., Briddell, R., Kinstler, O., Lueras, A. M. K., and Zhang, Y. (2006) Modulation of protein aggregation by polyethylene glycol conjugation: GCSF as a case study. *Protein Sci. 15* (5), 1063−1075.
(98) Basu, A., Yang, K., Wang, M., Liu, S., Chintala, R., Palm, T., Zhao, H., Peng, P., Wu, D., and Zhang, Z. (2006) Structure-function engineering of interferon-β-1b for improving stability, solubility, potency, immunogenicity, and pharmacokinetic properties by site-selective mono-PEGylation. *Bioconjugate Chem. 17* (3), 618−630.

(99) Gaertner, H. F., and Offord, R. E. (1996) Site-specific attachment of functionalized poly (ethylene glycol) to the amino terminus of proteins. *Bioconjugate Chem. 7* (1), 38−44.
(100) Na, D. H., Lee, K. C., and Deluca, P. P. (2005) PEGylation of Octreotide: II. Effect of N-terminal mono-PEGylation on biological activity and pharmacokinetics. *Pharm. Res. 22* (5), 743−749.
(101) Nie, Y., Zhang, X., Wang, X., and Chen, J. (2006) Preparation and stability of N-terminal mono-PEGylated recombinant human endostatin. *Bioconjugate Chem. 17* (4), 995−999.
(102) Lee, H., Jang, I. H., Ryu, S. H., and Park, T. G. (2003) N-terminal site-specific mono-PEGylation of epidermal growth factor. *Pharm. Res. 20* (5), 818−825.
(103) Gilmore, J. M., Scheck, R. A., Esser-Kahn, A. P., Joshi, N. S., and Francis, M. B. (2006) N-Terminal protein modification through a biomimetic transamination reaction. *Angew. Chem., Int. Ed. 45* (32), 5307−5311.
(104) Lee, B., Kwon, J., Kim, H., and Yamamoto, S. (2007) Solid-phase PEGylation of recombinant interferon α-2a for site-specific modification: process performance, characterization, and *in vitro* bioactivity. *Bioconjugate Chem. 18* (6), 1728−1734.
(105) Kinstler, O., Molineux, G., Treuheit, M., Ladd, D., and Gegg, C. (2002) Mono-N-terminal poly(ethylene glycol)-protein conjugates. *Adv. Drug Delivery Rev. 54* (4), 477−485.
(106) Wang, J., Hu, T., Liu, Y., Zhang, G., Ma, G., and Su, Z. (2011) Kinetic and stoichiometric analysis of the modification process for N-terminal PEGylation of staphylokinase. *Anal. Biochem. 412* (1), 114−116.
(107) Cindric, M., Cepo, T., Galic, N., Bukvic-Krajacic, M., Tomczyk, N., Vissers, J. P. C, Bindila, L., and Peter-Katalinic, J. (2007) Structural characterization of PEGylated rHu-GCSF and location of PEG attachment sites. *J Pharmaceut. Biomed. 44* (2), 388−395.
(108) Zhai, Y., Zhao, Y., Lei, J., Su, Z., and Ma, G. (2009) Enhanced circulation half-life of site-specific PEGylated rh-GCSF: Optimization of PEG molecular weight. *J. Biotechnol. 14*, 259−266.
(109) Tong, Y., Zhong, K., Tian, H., Gao, X., Xu, X., Yin, X., and Yao, W. (2010) Characterization of a mono PEG20000-Endostar. *Int. J. Biol. Macromol. 46* (3), 331−336.
(110) Block, H., Kubicek, J., Labahn, J., Roth, U., and Schäfer, F. (2008) Production and comprehensive quality control of recombinant human Interleukin-1β: A case study for a process development strategy. *Protein Expression Purif. 57*, 244−254.

Bioconjugate Chemistry

Article

pubs.acs.org/bc

S-Nitrosated Human Serum Albumin Dimer is not only a Novel Anti-Tumor Drug but also a Potentiator for Anti-Tumor Drugs with Augmented EPR Effects

Yu Ishima,[†,‡] Di Chen,[†] Jun Fang,[§,#] Hiroshi Maeda,[#] Ai Minomo,[†] Ulrich Kragh-Hansen,[¶] Toshiya Kai,[†,∥] Toru Maruyama,[†,‡] and Masaki Otagiri*[,†,§,#]

[†]Department of Biopharmaceutics, Graduate School of Pharmaceutical Sciences, and [‡]Center for Clinical Pharmaceutical Science, Kumamoto University, 5-1 Oe-honmachi, Kumamoto 862-0973, Japan

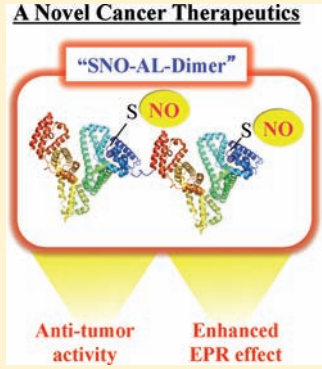
[§]Faculty of Pharmaceutical Sciences and [#]Drug Delivery System Research Institute, Sojo University, 4-22-1 Ikeda, Kumamoto 860-0082, Japan

[¶]Department of Medical Biochemistry, University of Aarhus, DK-8000 Aarhus C, Denmark

[∥]Tohoku Nipro Pharmaceutical Corporation, 428 Okanouchi, Kagamiishimachi, Iwasegun, Fukushima 969-0401, Japan

Supporting Information

ABSTRACT: Macromolecules have been developed as carriers of low-molecular-weight drugs in drug delivery systems (DDS) to improve their pharmacokinetic profile or to promote their uptake in tumor tissue via enhanced permeability and retention (EPR) effects. In the present study, recombinant human serum albumin dimer (AL-Dimer), which was designed by linking two human serum albumin (HSA) molecules with the amino acid linker $(GGGGS)_2$, significantly accumulated in tumor tissue even more than HSA Monomer (AL-Monomer) and appearing to have good retention in circulating blood in murine colon 26 (C26) tumor-bearing mice. Moreover, we developed *S*-nitrosated AL-Dimer (SNO-AL-Dimer) as a novel DDS compound containing AL-Dimer as a carrier, and nitric oxide (NO) as (i) an anticancer therapeutic drug/cell death inducer and (ii) an enhancer of the EPR effect. We observed that SNO-AL-Dimer treatment induced apoptosis of C26 tumor cells *in vitro*, depending on the concentration of NO. In *in vivo* experiments, SNO-AL-Dimer was found to specifically deliver large amounts of cytotoxic NO into tumor tissue but not into normal organs in C26 tumor-bearing mice as compared with control (untreated tumor-bearing mice) and SNO-AL-Monomer-treated mice. Intriguingly, *S*-nitrosation improved the uptake of AL-Dimer in tumor tissue through augmenting the EPR effect. These data suggest that SNO-AL-Dimer behaves not only as an anticancer therapeutic drug, but also as a potentiator of the EPR effect. Therefore, SNO-AL-Dimer would be a very appealing carrier for utilization of the EPR effect in future development of cancer therapeutics.



INTRODUCTION

Lack of efficiency in delivering therapeutic agents to a target tumor region leading to severe toxic side effects is most often a barrier to the clinical application of novel therapeutic anticancer drugs in cancer therapy. To limit the side effects of cancer chemotherapy, drug delivery systems (DDS) are being developed with specific targeting for cancers and increased retention in tumor tissues,[1−3] and/or to enhance the stability and half-life of low-molecular-weight drugs such as nitric oxide (NO) in the circulation.[4] Previous reports have shown that macromolecules such as human serum albumin (HSA) and synthetic polymers seem to be useful as carriers of low-molecular-weight drugs in DDS systems to improve the pharmacokinetic profile of the drugs or to promote the uptake of drugs in tumor tissue via enhanced permeability and retention (EPR) effects.[5−7] These findings have inspired research toward the development of DDS with specific targeting potential for tumor tissues in cancer therapy.

NO has been reported to cause DNA damage and direct cell death at high concentrations.[8,9] Therefore, it has been realized that NO has potential for cancer therapy, and it is emerging as an antioncogenic agent which, in contrast to conventional therapeutic agents,[10,11] is able to overcome the often-seen tumor cell resistance to treatment. Although there are several NO donors, such as *S*-nitrosoglutathione (GSNO) and NO-donating nonsteroidal anti-inflammatory drugs (NO-NSAIDs), which were shown to induce apoptosis of tumor cells *in vitro*,[12,13] their clinical use is limited by some problems, such as toxicity at high concentrations due to lack of specificity for tumor cells or side effects occurring during long-term application.[14−16] As a consequence, binding of NO to a

Received: September 29, 2011
Revised: November 23, 2011
Published: January 7, 2012

ACS Publications © 2012 American Chemical Society

dx.doi.org/10.1021/bc2005363 | *Bioconjugate Chem.* 2012, 23, 264−271

potential carrier to form a stable NO-releasing DDS is proposed as an approach that would overcome these problems.

Recombinant human serum albumin dimer (AL-Dimer), in which the C-terminus of one HSA molecule was linked to the N-terminus of another HSA molecule by the amino acid linker $(GGGGS)_2$, was designed and successfully produced by the yeast *Pichia pastoris*. It has been reported that AL-Dimer has a longer circulation time than the monomeric form of HSA (AL-Momomer).[17] Because of that finding, we presumed that AL-Dimer would be a good candidate to improve the pharmacokinetic profile of a low-molecular-weight drug such as NO which otherwise has a very short plasma half-life *in vivo*. Moreover, AL-Dimer is expected to have an enhanced accumulation in solid tumor via the EPR mechanism[18,19] due to its large molecular weight (130 kDa). Therefore, it is possible that AL-Dimer could be of great clinical use as a new DDS material with a superior plasma retention property (e.g, prolonged plasma half-life) as well as with increased tumor specific accumulation.

In this study, we developed a novel DDS system of NO, a potential anticancer therapeutic, using AL-Dimer as a carrier, namely, *S*-nitrosated AL-Dimer (SNO-AL-Dimer), and examined its physicochemical properties. Then, the biodistribution and anticancer ability of SNO-AL-Dimer was evaluated both *in vitro* in murine colon 26 (C26) tumor cells and *in vivo* in C26 tumor-bearing mice. In addition, we also investigated whether SNO-AL-Dimer enhanced the EPR effect by delivering NO.

EXPERIMENTAL PROCEDURES

Chemicals. AL-Monomer and AL-Dimer were synthesized using the yeast *Pichia pastoris* (*P. pastoris*) (strain GS115).[17] AL-Monomer and AL-Dimer were defatted by means of a charcoal treatment as described by Chen.[20] Sephadex G-25 (φ 1.6 × 2.5 cm) was from GE Healthcare (Kyoto, Japan). *S*-Nitrosoglutathione (GSNO) was purchased from Dojindo Laboratories (Kumamoto, Japan). 1,4-Dithiothreitol (DTT) was from Sigma-Aldrich (St. Louis, MO). Isoamyl nitrite (IAN) was bought from Wako Chemicals (Osaka, Japan). Diethylenetriaminepentaacetic acid (DTPA) and EDTA were purchased from Nacalai Tesque (Kyoto, Japan). $^{111}InCl_3$ was a gift from Nihon Medi-Physics Co., Ltd. (Hyogo, Japan).

Cells and Animals. C26 cells were cultured in RPMI-1640 containing 10% fetal bovine serum (San kou junyaku, Co., Ltd., Japan), 100 units/mL penicillin, and 100 μg/mL streptomycin, incubated in a humidified (37 °C, 5% CO_2 and 95% air) incubator, grown in 75 cm^2 flask (Falcon BD), and passaged when 75% confluency was reached. Male BALB/cAnNCrlCrlj mice (5 weeks old, 17−22 g) were purchased from Charles River Laboratories, Japan. A C26 solid tumor model was established by subcutaneously implanting of 1×10^6 C26 cells into the back of the mice.

Synthesis of SNO-HSAs. SNO-HSAs were prepared according to a previous report.[21] In brief, the HSA forms (20 mg/mL) were incubated with 3 mM DTT for 5 min at 37 °C. Afterward, the DTT was removed quickly by Sephadex G-25 gel filtration and eluted with 0.1 M potassium phosphate buffer (pH 7.4) containing 0.5 mM DTPA. DTT-treated HSAs (20 mg/mL) were incubated with 3 mM isoamyl nitrite (IAN) for 60 min protected from light at 37 °C. SNO-HSAs were purified by Sephadex G-25 gel filtration, eluted with phosphate buffered saline (PBS) (pH 7.4). These samples were stored at −80 °C until used in the experiments.

Physicochemical Characterization of HSAs. *CD Spectra.* Circular dichrosim (CD) spectra of AL-Monomer and AL-Dimer were measured using J-720-type spectropolarimeter (JASCO, Tokyo, Japan). For the calculation of mean residue ellipticity [θ], the molecular weight was considered as 66.5 kDa for AL-Monomer and 130 kDa for AL-Dimer.[17]

Capillary Zone Electrophoresis. The P/ACE MDQ system (Beckman Instruments, Fullerton, CA, USA) in conjunction with a photodiode array detector was employed to determine the net charge of AL-Dimer compared with AL-Monomer. Capillaries with total capillary length of 60 cm (50 cm to the detector) were used. New capillaries were initialized by flushing with water (5 min), 0.1 M NaOH (5 min), water (5 min), and run buffer (5 min) before use. Between analyses the capillary was rinsed with 0.1 M NaOH (3 min), water (3 min), and run buffer (3 min). Injection was performed at a pressure of 0.5 psi for 5 s, and detection was performed at a wavelength of 214 nm.

SDS-PAGE. The purity of AL-Monomer and AL-Dimer was examined by 8% reduced sodium dodecyl sulfate polyacrylamide gel electrophoresis (SDS-PAGE). Gross conformational changes induced by *S*-nitrosation of AL-Monomer and AL-Dimer were assessed by means of nonreducing SDS-PAGE (8%) at 4 °C in the dark. The bands were stained by using Coomassie Brilliant Blue (CBB).

Anti-Oxidant Activity of HSAs. For 1,1′-diphenyl-2-picrylhydrazyl (DPPH) radicals, the radical scavenging activity of the HSAs (0.67 mg/mL; AL-Monomer 10 μM; AL-Dimer 5 μM) was determined from the decrease in the absorbance of DPPH radicals at 517 nm due to their scavenging of an unpaired electron of the stable DPPH radical in a mixture of 10 mL ethanol, 10 mL of 50 mM 2-(*N*-morpholino)ethanesulfonic acid (Mes) buffer (pH 5.5), and 5 mL of 0.5 mM DPPH in ethanol.[22] For $O_2^{\bullet-}$, the xanthine/xanthine oxidase (X/XO) system was used to generate $O_2^{\bullet-}$ to measure the superoxide-scavenging activity of the HSAs. Briefly, 1 mL of solution contained 100 μg/mL X, 0.01 U/mL XO, 250 μM DTPA, and 500 μM luminol in the absence or presence of 0.67 ng/mL of HSAs (AL-Monomer 10 nM; AL-Dimer 5 nM). The chemiluminescence (CL) response was continuously recorded for 4 min at room temperature using Mini Lumat LB 9506 luminometer (EG&G Berthold, Germany). CL was obtained from the slope of the counts versus the time graph. To evaluate the NO scavenging activity of the HSAs, we measured the amount of the *S*-nitroso moiety of HSAs after incubation with NO by means of HPLC coupled with a flow reactor assay, as previously reported.[23] Briefly, 10 mg/mL HSAs (AL-Monomer 150 μM; AL-Dimer 75 μM) was incubated with 5 mM NOC7 for 10 min in PBS at 25 °C in the dark. To stop the reaction, 1.5 mM *N*-ethylmaleimide was added to these reaction solutions; the resulting solutions were kept at −80 °C until analysis.

Determination of SNO-Moiety and Stability of SNO-HSAs. The amounts of the SNO-moiety of the SNO-HSAs were quantified by HPLC coupled with a flow reactor system, as previously reported.[23] The stability of the SNO-moiety on storage was examined as follows. SNO-HSAs were dissolved in PBS with 0.5 mM DTPA (pH 7.4) and protected from light at 4 or 25 °C. At appropriate times after the start of incubation, aliquots of the SNO-HSA solutions were taken, and the SNO-moieties were determined by HPLC as mentioned above.

Pharmacokinetic Experiments. The HSAs and SNO-HSAs were labeled with ^{111}In by using DTPA anhydride as a

dx.doi.org/10.1021/bc2005363 | *Bioconjugate Chem.* 2012, 23, 264−271

bifunctional chelating agent.[24,25] The pharmacokinetics and body distribution of HSAs and SNO-HSAs were carried out in a C26 solid tumor model. In brief, ^{111}In-labeled protein was dissolved in saline, and the concentration of ^{111}In-labeled protein was adjusted by addition of nonradiolabeled protein to the solution. The ^{111}In-labeled protein solution was administrated intravenously via the tail vein at a dose of 1 mg/kg. At scheduled times after the intravenous injection, the mice were sacrificed, and blood was collected from the inferior vena cava. Tumor tissue was collected for tumor distribution. The radioactivity of each sample was counted using a well-type NaI scintillation counter ARC-2000 (Aloka, Tokyo, Japan).

Cell Death Induced by the HSAs. For detection of C26 cell death induced by the HSAs with and without *S*-nitrosation, the cells were seeded in flat-bottomed 96-well plates (1×10^4 cells per well). After culturing for 21 h, the media were refreshed and HSAs with different NO concentrations were added into the plates. After further 24 h, cell death was evaluated by the lactate dehydrogenase (LDH) assay from Wako Pure Chemical (Osaka, Japan). The percentage of dead cells was determined using the following formula: $(T - L)/(H - L) \times 100$, where T is the absorbance at 490 nm of supernatants of HSA-treated cells, using 630 nm as a reference, L is the absorbance of supernatants of control untreated cells, and H is the absorbance corresponding to the maximal (100%) LDH release of Triton-lysed cells.

In Vivo Measurement of NOx. C26 tumor-bearing mice were produced with the method mentioned above. 100 μL SNO-AL-Dimer, SNO-AL-Monomer, or GSNO were administrated intravenously via the tail vein at dose of 1.3 μmol NO/kg. At 6 h after the intravenous injection, the mice were sacrificed, and blood was collected from inferior vena cava, followed by collection of tumors as well as normal tissues, i.e., liver and kidney. The collected blood was centrifuged, and 100 μL of plasma was used for this study. The tumor and normal tissues were homogenized by use of BioMashaer. NO*x* (NO_2^- + NO_3^-) level was measured by the HPLC flow-reactor system, and NO*x*, the oxidative metabolites of NO, were quantified by the Griess reaction.

Effect of SNO-HSAs on Solid Tumor Vascular Permeability. C26 tumors obtained from at least six mice per group at 10 days after tumor cell inoculation were used for the *in vivo* vascular permeability experiments, as previously reported.[26] SNO-AL-Monomer and SNO-AL-Dimer were administered i.v. via the tail vein at doses of 1.3 μmol NO/kg. To assess vascular permeability in solid tumors, Evans blue dye that binds to serum albumin quickly *in vivo* to behave as a macromolecule was injected i.v. at a dose of 10 mg/kg into the tumor-bearing mice at 6 h after administration of the SNO-HSAs. At 24 h after the Evans blue dye injection, the dye in the solid tumor was extracted with formamide and quantified by UV absorption at 620 nm, as described previously.[5]

Statistical Analysis. The statistical significance of collected data was evaluated using the ANOVA analysis followed by Newman-Keuls method for more than 2 means. Differences between the groups were evaluated by Student's *t* test. $P < 0.05$ was regarded as statistically significant.

RESULTS AND DISCUSSION

Physicochemical and Structural Properties of AL-Dimer Compared with AL-Monomer. Physicochemical properties of macromolecular carriers including molecular weight and electric charge influence their biological properties, such as plasma half-life, tumor accumulation, and tumor cell uptake which are important factors for tumor targeted carriers.[27] Therefore, we examined the physicochemical and structural properties of AL-Dimer. First, SDS-PAGE was used to evaluate the molecular weight and purity of AL-Dimer generated by the *P. pastoris* system. From Figure 1A, it is seen

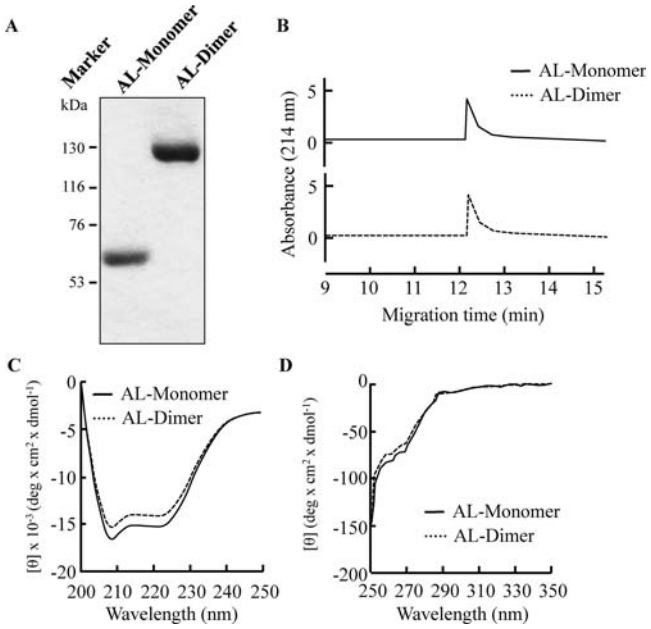


Figure 1. (A) Reduced SDS-PAGE (8%) of AL-Monomer and AL-Dimer visualized by CBB staining. (B) Capillary zone electrophoresis examination of AL-Monomer and AL-Dimer (both at a concentration of 10 mg/mL) in PBS (pH 7.4) solution. Far-UV (C) and near-UV (D) CD spectra of AL-Monomer and AL-Dimer in PBS (pH 7.4) solution at 25 °C.

that under reducing conditions AL-Dimer shows as a single band with a molecular mass of 130 kDa, which is approximately twice the molecular weight of AL-Monomer. This finding indicates a successful generation of pure AL-Dimer. The net charge of HSA was not modified by dimerization, because capillary zone electrophoresis shows that the net charge related to the amount of protein is the same for AL-Dimer and AL-Monomer (Figure 1B). The conformational structure of the two albumin forms were evaluated by CD spectra. As shown in Figure 1C and D, AL-Dimer has CD spectra which are only slightly different from those of AL-Monomer. These results suggest that AL-Dimer has a conformational structure similar to that of AL-Monomer. Furthermore, we checked the effect of AL-Dimerization on the accessibility of ^{34}Cys using DTNB, and as seen from Table 1, dimerization of HSA did not affect the accessibility of ^{34}Cys. Finally, we studied the scavenging activity of the two albumin forms against three different ROS, namely, DPPH, $O_2^{\bullet}$, and NO (Table 1). In all three examples, AL-Dimer has a significantly higher scavenging activity than AL-Monomer, suggesting small but facilitating changes in the microenvironment of other antioxidative amino acid residues in AL-Dimer than ^{34}Cys (Figure 1C and D).

Physicochemical Properties of SNO-AL-Dimer Compared with SNO-AL-Monomer. Nonreducing SDS-PAGE was used to confirm the purity of SNO-AL-Dimer after *S*-nitrosation reaction (Supporting Information Figure 1). It revealed only a single band for SNO-AL-Dimer with the same

dx.doi.org/10.1021/bc2005363 | *Bioconjugate Chem.* 2012, 23, 264–271

Table 1. Physicochemical Characterization of AL-Monomer and AL-Dimer

	Number of free Cysteine (mol SH/mol protein)	SH accessibility to DTNB[a] (A_5/A_{60}/mol SH)	radical scavenging activities (%)		
			DPPH	$O_2^{\bullet-}$	NO
AL-Monomer	1	0.73 ± 0.08[b]	36 ± 6.4	30 ± 9.4	26 ± 8.4
AL-Dimer	2	0.68 ± 0.13	47 ± 4.4*	45 ± 8.6*	37 ± 6.6*

[a]The accessibility was evaluated as A_5/A_{60}, where A_5 and A_{60} is the sample absorbance at 405 nm after 5 and 60 min (maximal absorbency), respectively, of incubation with DTNB. [b]Results are expressed as means ± SD (n = 3–9). *P < 0.05, as compared with AL-Monomer.

Table 2. Physicochemical Characterization of SNO-AL-Monomer and SNO-AL-Dimer

	SNO moiety (mol SNO/mol protein)	half-lives ($T_{1/2}$) in PBS at 4 °C (day)	half-lives ($T_{1/2}$) in PBS at 25 °C (day)	decomposition products
SNO-AL-Monomer	0.52 ± 0.20[a]	25.4 ± 12.2	21.3 ± 7.4	AL-Monomer
SNO-AL-Dimer	1.48 ± 0.25*	46.8 ± 15.1*	39.0 ± 11.9*	AL-Dimer

[a]Results are expressed as means ± SD (n = 3–6). *P < 0.05, as compared with AL-Monomer.

molecular mass of AL-Dimer, which indicated that *S*-nitrosation did not cause dimerization of AL-Dimer via disulfide bond formation, or fragmentation or gross conformational changes of AL-Dimer. The analysis also showed no gross conformational changes in the case of *S*-nitrosation of AL-Monomer. From Table 2 it is seen that the present approach is efficient in *S*-nitrosation of the AL-Dimer, because the preparation contains on average 1.48 mol of NO per mol of protein.

We determined the stability of the two SNO-preparations in phosphate buffer protected from light. At 4 °C the apparent half-life of the SNO-moiety of SNO-AL-Dimer is about 47 days, which is significantly longer than that of the SNO-AL-Monomer (i.e., 25 days) (Table 2). Also at 25 °C, the half-lives were long, i.e., 39 and 21 days for SNO-AL-Dimer and SNO-AL-Monomer, respectively. This result provided evidence that the SNO-HSAs are fairly stable compounds in neutral buffer even at room temperature.

Accumulation of AL-Dimer in Tumor Tissue Compared with AL-Monomer. The adverse side effects of anticancer drugs, resulting from lack of specificity in conventional therapies, usually limit the increase of dose intensity which is required to eradicate the cancerous growth.[28−30] One of the developing strategies for the enhancement of tumor specific delivery of the therapeutics is albumin-based drug delivery technology.[1,31] Albumin has emerged as a drug carrier in the past 10 years for drug targeting and for improving the pharmacokinetic profile of various therapeutic drugs.[31−33] Examples are the antitumor therapeutic drug doxorubicin−albumin conjugate,[34] and the use of cationized albumin as drug carrier for blood-brain barrier transport.[35,36] In order to clarify whether intravenously injected AL-Dimer accumulate in solid tumor tissue, we performed a biodistribution analysis of AL-Dimer given to C26 tumor-bearing mice. As shown in Figure 2A, it was observed that at 24 h after injection the accumulation of AL-Dimer in the tumor tissue was 1.8 times higher than that of AL-Monomer. Moreover, AL-Dimer showed a much higher level of blood retention compared with that of AL-Monomer (Figure 2B). These findings are consistent with a previous study showing that proteins with molecular weights ranging from 12 to 150 kDa correlated with the rate of tumor uptake, and that long circulation times lead to enhanced tumor uptakes of the protein.[34] Thus, AL-Dimer seems to be a good candidate as a drug carrier, because in addition to a prolonged blood retention it has a good accumulation in tumor tissue.

Thus, the physicochemical characterization showed that AL-Dimer has a conformational structure and net charge which in principle are similar to those of AL-Monomer. Furthermore, the pharmacokinetics and biodistribution studies very importantly showed that AL-Dimer has superior blood retention properties and tumor targeting potential. Therefore, based on

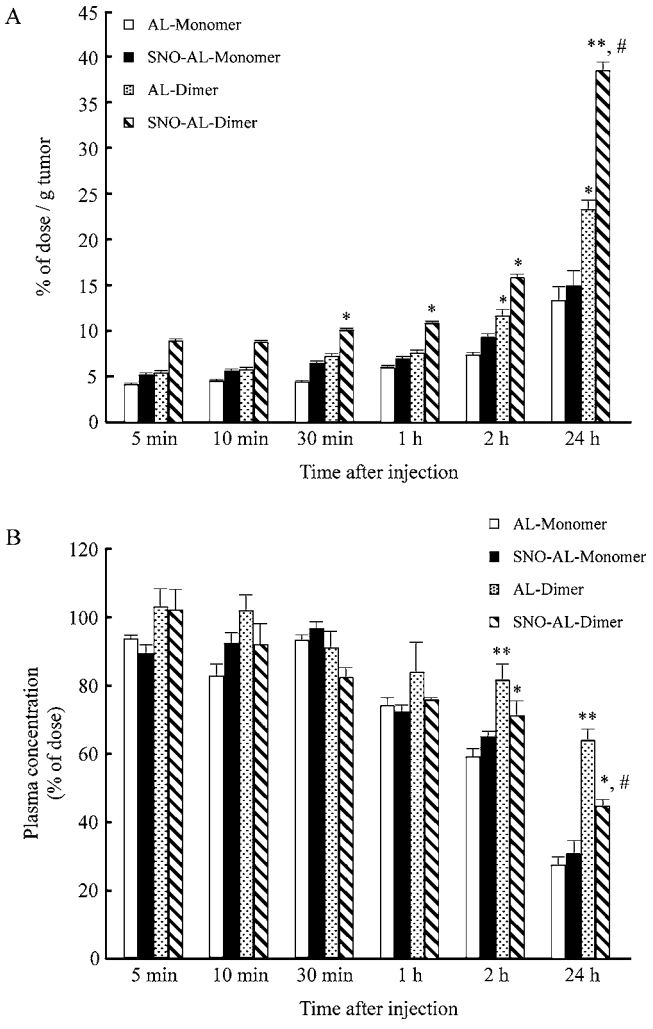


Figure 2. Tumor accumulation (A) and blood retention (B) of ^{111}In-labeled AL-Monomer and AL-Dimer with and without *S*-nitrosation after intravenous administration to C26 tumorbearing mice at a dose of 1 mg/kg. Results are means ± SD (n = 4). * P < 0.05, ** P < 0.01 compared with AL-Monomer or SNO-AL-Monomer, # P < 0.05 compared with AL-Dimer.

dx.doi.org/10.1021/bc2005363 | *Bioconjugate Chem.* 2012, 23, 264−271

these findings, we found that exploiting recombinant AL-Dimer as a drug carrier would have several advantages over HSA: (a) the use of commercial and possibly pathogenic albumin is avoided; (b) AL-Dimer is expected to be effective in binding albumin-binding drugs, among other things because it has two molecules of ^{34}Cys. (c) AL-Dimer could enhance the stability of therapeutic drugs both *in vitro* and *in vivo* and improve their blood retention and tumor accumulation *in vivo*. These potential advantages stimulated our attempt to utilize AL-Dimer as a carrier of antitumor therapeutic drugs and thereby to develop a new drug delivery system for cancer therapy. We chose to use NO as the potential anticancer agent and developed SNO-AL-Dimer to confirm the potential of AL-Dimer as a carrier in anticancer DDS. First, for evaluating whether *S*-nitrosation of AL-Dimer changes its pharmacokinetic parameters, we performed a biodistribution analysis of SNO-AL-Dimer in C26 tumor-bearing mice. Promisingly, the results showed that the accumulation of SNO-AL-Dimer in tumor tissue was 2.6 and 1.6 times higher than that of SNO-AL-Monomer and AL-Dimer, respectively, suggesting that *S*-nitrosation of AL-Dimer further enhanced its EPR effect, probably via NO release from SNO-AL-Dimer.

C26 Tumor Cell Death Induced by SNO-AL-Dimer Compared with SNO-AL-Monomer. C26 tumor cells were used for investigating the cytotoxicity of different albumin preparations, and cell death was assayed by the quantification of extracelluar LDH release. As shown in Figure 3A, both AL-Dimer and AL-Monomer have a small cytotoxic effect, i.e., only about 10% of the cells were dead after 24 h of exposure to 20 mg protein/mL. By contrast, SNO-AL-Dimer or SNO-AL-Monomer treatment resulted in a much more pronounced LDH release from the cells and in a NO-dose dependent manner, i.e., 70% or more of the cells died in the presence of 80 μM of SNO (Figure 3B). This result is in agreement with a previous study which reports that NO donors such as sodium nitroprusside (SNP) caused cell death depending on the NO concentration.[12] Importantly, the present findings clearly proved that NO, but not AL-Dimer, is the tumor cell death inducer, thus suggesting that AL-Dimer is a suitable carrier for anticancer drugs such as NO. Accordingly, we considered that SNO-AL-Dimer may become a new NO donor with superior pharmacological (cytotoxic) effect. Further, because of the significantly improved *in vivo* pharmacokinetics of SNO-AL-Dimer as described above, it is reasonable to expect that SNO-AL-Dimer would show a much improved antitumor effect, as well as a substantial reduction of the toxicity profile compared with traditional NO donors which are known to cause adverse side effects at high concentrations during long-term treatment.[14,15] The data obtained so far led us to perform the following *in vivo* experiments.

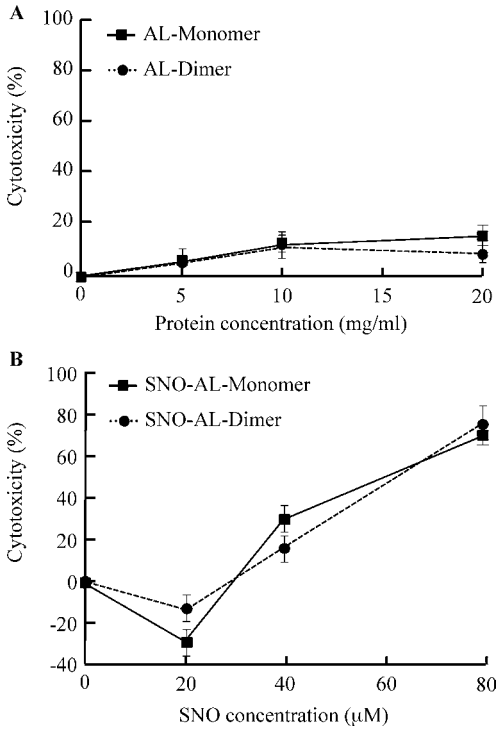


Figure 3. Cytotoxity of AL-Dimer and AL-Monomer without (A) and with (B) *S*-nitrosation. C26 cells were cultured at a density of 1×10^4 cells/well for 21 h in RPMI1640 supplemented with 10% FBS. After that period of time the medium was refreshed with AL-Dimer, AL-Monomer, SNO-AL-Dimer, or SNO-AL-Monomer for 24 h, and cell death was assessed by measurement of extracellular LDH activity. In (B), the protein concentrations were approximately 2–9 mg/mL. Results are means ± SD (n = 3–5).

NO Delivery by SNO-AL-Dimer for Tumor Targeting. To evaluate whether AL-Dimer successfully delivers NO to tumor tissue *in vivo*, a C26 solid tumor model was utilized, and the delivery of NO into tumor tissue by SNO-AL-Dimer was determined by quantification of NO*x* level in the tumor and compared with those of SNO-AL-Monomer and the commercially available NO donor GSNO. From Figure 4A it can be seen that intravenous treatment with SNO-AL-Dimer, but not with SNO-AL-Monomer or GSNO, caused a significant increase in the tumor level of NO*x*. By contrast, none of the

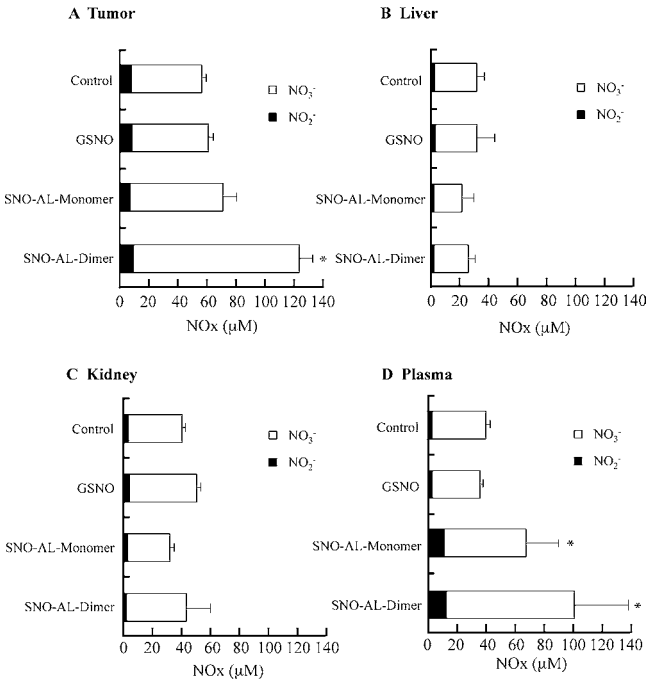


Figure 4. NO*x* levels in tumor tissue (A), liver (B), kidney (C), and plasma (D) at 6 h after administration of GSNO, SNO-AL-Monomer, or SNO-AL-Dimer (40 nmol NO/mouse) were determined by the HPLC flow-reactor system. Controls were mice which had not been treated with a NO-containing compound. Results are means ± SD (n = 3–11). * $P < 0.05$ compared with control.

dx.doi.org/10.1021/bc2005363 | *Bioconjugate Chem.* 2012, 23, 264–271

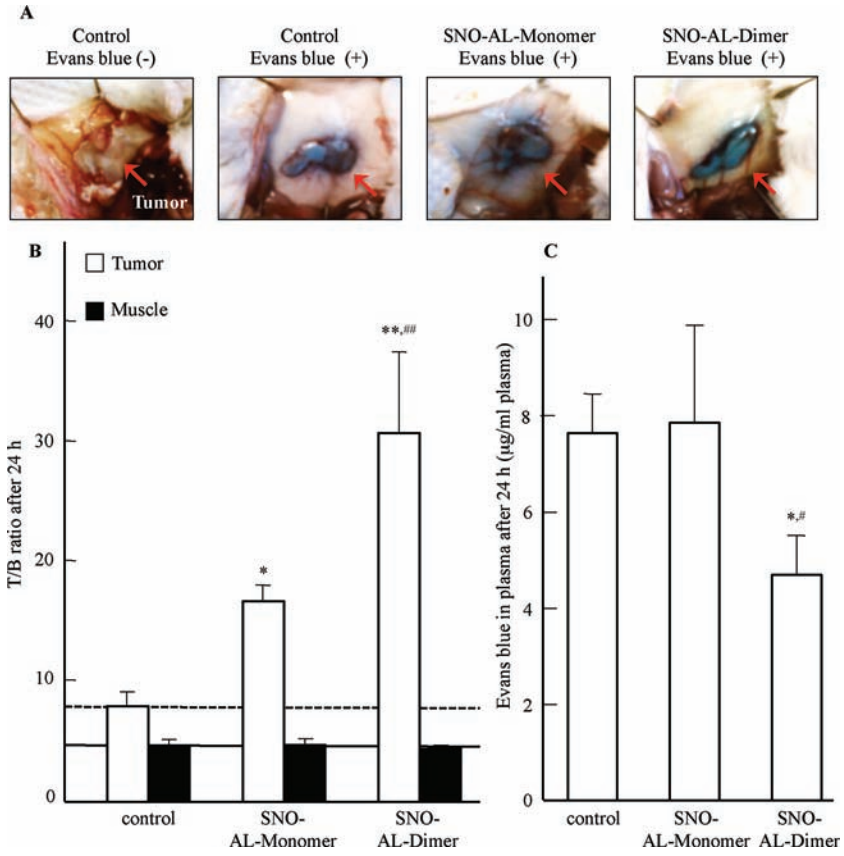


Figure 5. Extravasation of Evans blue induced by SNO-AL-Monomer and SNO-AL-Dimer. 1 $\times 10^6$ C26 cells were subcutaneously inoculated into the dorsal skin. The mice were kept for 10 days until the tumor had reached a certain volume. (A) After 10 days, saline (controls), SNO-AL-Monomer (40 nmol NO/mouse) or SNO-AL-Dimer (40 nmol NO/mouse) was injected intravenously. Six hours after administration of the different solutes, Evans blue dye was injected i.v. at a dose of 10 mg/kg into three of the four groups of the tumor-bearing mice. Twenty-four hours later, the mice were assessed. (B) Tissue−blood ratio at 24 h after intravenous injection of Evans blue dye in the C26 tumor-bearing mice. (C) Plasma concentrations of Evans blue in the mice at 24 h after i.v. injection. Results are means ± SD (n = 6−8). * $P < 0.05$, ** $P < 0.01$ compared with control, $^{\#}$ $P < 0.05$, $^{\#\#}$ $P < 0.01$ compared with SNO-AL-Monomer.

preparations induced increased NO*x* levels in other organs such as liver (Figure 4B) or kidney (Figure 4C). Finally, especially SNO-AL-Dimer has a high level of blood retention (Figure 4D). These results showed that SNO-AL-Dimer is more efficient for tumor delivery of NO than a traditional NO donor such as GSNO. The findings also showed that SNO-AL-Dimer caused a much higher concentration of NO*x* in the tumor than SNO-AL-Monomer which has been proven as a novel anticancer drug. This may be due to the possibility that SNO−^{34}Cys is relatively stable and effective in providing a steady-state NO level *in vivo* compared with other sites binding to NO.[21]

EPR Effect was Enhanced by NO Released from SNO-AL-Dimer. To evaluate whether SNO-AL-Dimer enhances the EPR effect by delivering NO, the extravasation of Evans blue in the tumor tissue after treatment with SNO-AL-Dimer was determined, compared with SNO-AL-Monomer, using the C26 tumor-bearing mice as *in vivo* model (Figure 5A). Figure 2 shows that the accumulation of SNO-AL-Dimer in tumor tissue is 2.6 times higher than that of SNO-AL-Monomer, suggesting that S-nitrosation of AL-Dimer further enhanced its EPR effect. This enhanced effect on EPR is a most important finding in our study, and we used the Evans blue method to confirm it. Evans blue dye binds to albumin noncovalently *in vivo* after i.v. injection, and the albumin−dye complex (molecular mass of ca. 70 kDa) is extravasated in the tumor tissue due to the EPR effect. Thus, extravasation of Evans blue dye is considered to be a marker for the EPR effect of macromolecules in solid tumor.[26] Figure 5B shows that the extravasation of Evans blue dye in tumor tissue, but not in normal tissue (i.e., muscle), was significantly increased by intravenous treatment of both SNO-AL-Dimer and SNO-AL-Monomer. However, SNO-AL-Dimer induced more extravasation of Evans blue than SNO-AL-Monomer, suggesting that SNO-AL-Dimer enhances EPR effect in a much more pronounced manner, probably due to the significantly increased tumor delivery of NO from SNO-AL-Dimer as described above. In accordance with that proposal, Figure 5C shows that the plasma concentration of Evans blue after 24 h of injection is much lower in the presence of SNO-AL-Dimer than in the presence of SNO-AL-Monomer.

It has been reported by Yasuda[10] and Seki et al.[37] that the EPR effect can also be enhanced by, i.e., applying nitroglycerin (NG) ointment on the skin of tumor-bearing animals. Therefore, we compared the potential of SNO-AL-Dimer and NG on augmentation of the EPR effect. As the result, both the NO*x* level in tumor tissue (Supporting Information Figure 2) and the extravasation of Evans blue (Supporting Information Figure 3) are 2-fold higher in the animals given SNO-AL-Dimer than in the animals treated with NG. In light of these results, we propose that SNO-AL-Dimer possesses a powerful EPR effect. To elaborate this idea further, it is necessary to investigate the effect of SNO-AL-Dimer on the tumor

dx.doi.org/10.1021/bc2005363 | *Bioconjugate Chem.* 2012, 23, 264−271

accumulation and antitumor activity of other anticancer drugs such as Doxil or Abraxane. Our drug delivery system is also open for linking SNO-AL-Dimer to human antitumor protein toxins such as human RNase, tBID (truncated BH3-interacting domain death agonist), granzyme B, and AIF (apoptosis-inducing factor). The facile production and broad applicability make our drug delivery system a viable vehicle for anticancer drugs.

Conclusion. Our study had three major findings. First, SNO-AL-Dimer can accumulate in tumor tissue (Figure 2). Second, SNO-AL-Dimer delivers NO selectively to tumor tissue, resulting in cytotoxicity to the tumor cells (Figure 3 and Figure 4). Third, SNO-AL-Dimer behaves as a powerful enhancer of the EPR effect via NO release in the tumor (Figure 5). These findings lead to the idea that SNO-AL-Dimer possesses the clinical possibility for being not only an anticancer drug, but also a valuable tumor targeting delivery system due to enhancement of the EPR effect. In addition, we thus believe that using SNO-AL-Dimer as a carrier of anticancer drugs might be expected to improve the therapeutic potential due to the superior blood retention properties and tumor specific accumulation.

■ ASSOCIATED CONTENT

Supporting Information

Additional experimental methods and figures as described in the text. This material is available free of charge via the Internet at http://pubs.acs.org.

■ AUTHOR INFORMATION

Corresponding Author

*Tel.: +81-96-371-4150; Fax: +81-96-362-7690; E-mail: otagirim@ph.sojo-u.ac.jp.

■ ACKNOWLEDGMENTS

This research was supported by Grant-in-Aid for Scientific Research from Japan Society for the Promotion of Science (JSPS) (KAKENHI 18390051 and 22790162). This work was in part supported by grants from the Uehara Memorial Fund. Thanks are also due to members of the Gene Technology Center in Kumamoto University for their important contributions to the experiments.

■ REFERENCES

(1) Kerr, D. J., and Los, G. (1993) Pharmacokinetic principles of locoregional chemotherapy. *Cancer Surv. 17*, 105−22.

(2) Reddy, L. H. (2005) Drug delivery to tumours: recent strategies. *J. Pharm. Pharmacol. 57*, 1231−42.

(3) Moses, M. A., Brem, H., and Langer, R. (2003) Advancing the field of drug delivery: taking aim at cancer. *Cancer Cell 4*, 337−41.

(4) Katayama, N., Nakajou, K., Komori, H., Uchida, K., Yokoe, J., Yasui, N., Yamamoto, H., Kai, T., Sato, M., Nakagawa, T., Takeya, M., Maruyama, T., and Otagiri, M. (2008) Design and evaluation of *S*-nitrosolated human serum albumin as novel anticancer drug. *J. Pharmacol. Exp. Ther. 325*, 69−76.

(5) Matsumura, Y., and Maeda, H. (1986) A new concept for macromolecular therapeutics in cancer chemotherapy: mechanism of tumoritropic accumulation of proteins and the antitumor agent smancs. *Cancer Res. 46*, 6387−92.

(6) Maeda, H., and Matsumura, Y. (1989) Tumoritropic and lymphotropic principles of macromolecular drugs. *Crit. Rev. Ther. Drug Carrier Syst. 6*, 193−210.

(7) Maeda, H., Seymour, L. W., and Miyamoto, Y. (1992) Conjugates of anticancer agents and polymers: advantages of macromolecular therapeutics in vivo. *Bioconjugate Chem. 3*, 351−62.

(8) Kiziltepe, T., Hideshima, T., Ishitsuka, K., Ocio, E. M., Raje, N., and Catley, L. (2007) JS-K, a GST-activated nitric oxide generator, induces DNA double-strand breaks, activates DNA damage response pathways, and induces apoptosis in vitro and in vivo in human multiple myeloma cells. *Blood 110*, 709−18.

(9) Ishima, Y., Yoshida, F., Kragh-Hansen, U., Watanabe, K., Katayama, N., Nakajou, K., Akaike, T., Kai, T., Maruyama, T., and Otagiri, M. (2011) Cellular uptake mechanisms and responses to NO transferred from mono- and poly-S-nitrosated human serum albumin. *Free Radic. Res. 45*, 1196−206.

(10) Yasuda, H. (2008) Solid tumor physiology and hypoxia-induced chemo/radio-resistence: Novel stragegy for cancer therapy: Nitric oxide donor as a therapeutic enhancer. *Nitric Oxide 19*, 205−16.

(11) Yasuda, H., Yamaya, M., Kubo, H., and Sasaki, H. (2006) Randomized phase II trial comparing nitroglycerin plus vinorelbine and cisplatin with vinorelbine and cisplatin alone in previously untreated stage IIIB/IV non-small cell lung cancer. *J. Clin. Oncol. 24*, 688−94.

(12) Messmer, U. K., Reimer, D. M., and Brune, B. (1996) Nitric oxide-induced apoptosis: p53-dependent and p53-indeoendent signaling pathways. *Biochem. J. 319*, 299−305.

(13) Ulrich, C. M., Bigler, J., and Potter, J. D. (2006) Non-steroidal anti-inflammatory drugs for cancer prevention: promise, perils and pharmacogenetics. *Nat. Rev. Cancer 6*, 130−40.

(14) Hryniuk, W. A., Figueredo, A., and Goodyear, M. (1987) Applications of dose intensity to problems in chemotherapy of breast and colorectal cancer. *Semin. Oncol. 11*, 3−11.

(15) Hogg, N. (2000) Biological chemistry and clinical potential of S-nitrosothiols. *Free Radic. Biol. Med. 28*, 1478−86.

(16) Wallace, J. L., Del., and Soldato, P. (2003) The therapeutic potential of NO-NSAIDs. *Fundam. Clin. Pharmacol. 17*, 11−20.

(17) Matsushita, S., Chuang, V. T., Kanazawa, M., Tanase, S., Kawai, K., Maruyama, T., Suenaga, A., and Otagiri, M. (2006) Recombinant human serum albumin dimer has high blood circulation activity and low vascular permeability in comparison with native human serum albumin. *Pharm. Res. 23*, 882−91.

(18) Maeda, H., Wu, J., Sawa, T., Matsumura, Y., and Hori, K. (2000) Tumor vascular permeability and the EPR effect in macromolecular therapeutics: a review. *J. Controlled Release 65*, 271−84.

(19) Tanaka, T., Shiramoto, S., Miyashita, M., Fujishima, Y., and Kaneo, Y. (2004) Tumor targeting based on the effect of enhanced permeability and retention and the mechanism of receptor-mediated endocytosis. *Int. J. Pharm. 227*, 39−61.

(20) Chen, R. F. (1967) Removal of fatty acids from serum albumin by charcoal treatment. *J. Biol. Chem. 242*, 173−81.

(21) Ishima, Y., Sawa, T., Kragh-Hansen, U., Miyamoto, Y., Matsushita, S., Akaike, T., and Otagiri, M. (2007) *S*-nitrosylation of human variant albumin Liprizzi (R410C) confers potent antibacterial and cytoprotective properties. *J. Pharmacol. Exp. Ther. 320*, 969−77.

(22) Sassa, H., Takaishi, Y., and Terada, H. (1990) The triterpene celastrol as a very potent inhibitor of lipid peroxidation in mitochondria. *Biochem. Biophys. Res. Commun. 172*, 890−7.

(23) Akaike, T. (2000) Mechanisms of biological *S*-nitrosation and its measurement. *Free Radic. Res. 33*, 461−9.

(24) Yamasaki, Y., Sumimoto, K., Nishikawa, M., Yamashita, F., Yamaoka, K., Hashida, M., and Takakura, Y. (2002) Pharmacokinetic analysis of in vivo disposition of succinylated proteins targeted to liver nonparenchymal cells via scavenger receptors: importance of molecular size and negative charge density for in vivo recognition by receptors. *J. Pharmacol. Exp. Ther. 301*, 467−77.

(25) Peters, T., Jr. (1996) *All about Albumin: Biochemistry, Genetics, and Medical Applications*, Academic Press, San Diego.

(26) Wu, J., Akaike, T., and Maeda, H. (1998) Modulation of enhanced vascular permeability in tumors by a bradykinin antagonist, a cyclooxygenase inhibitor, and a nitric oxide scavenger. *Cancer Res. 58*, 159−65.

(27) Dreher, M., Liu, W., Michelich, C. R., Dewhirst, M. W., Yuan, F., and Chilkoti, A. (2006) Tumor vascular permeability, Accumulation, and penetration of macromolecular drug carriers. *J. Natl. Cancer Inst. 98*, 335−44.
(28) Jain, R. K. (2001) Delivery of molecular and cellular medicine to solid tumors. *Adv. Drug Delivery Rev. 46*, 149−68.
(29) Sehouli, J., Stengel, D., Oskay, G., Camara, O., Hindenburg, H. J., Klare, P., Blohmer, J., Heinrich, G., Elling, D., Ledwon, P., Lichtenegger, W., and NOGGO study group (2002) A phase II study of topotecan plus gemcitabine in the treatment of patients with relapsed ovarian cancer after failure of first-line chemotherapy. *Ann. Oncol. 13*, 1749−55.
(30) Allen, T. M., and Cullis, P. R. (2004) Drug delivery systems: entering the mainstream. *Science 303*, 1818−22.
(31) Wosikowski, K., Biedermann, E., and Rattel, B. (2003) In vitro and in vivo antitumor activity of methotrexate conjugated to human serum albumin in human cancer cells. *Clin. Cancer Res. 9*, 1917−26.
(32) Burger, A. M., Hartung, G., Stehle, G., Sinn, H., and Fiebig, H. H. (2001) Pre-clinical evaluation of a methotrexate-albumin conjugate (MTX-HSA) in human tumor xenografts in vivo. *Int. J. Cancer 92*, 718−24.
(33) Dennis, M. S., Zhang, M., Meng, Y. G., Kadkhodayan, M., Kirchhofer, D., Combs, D., and Damico, L. A. (2002) Albumin binding as a general strategy for improving the pharmacokinetics of proteins. *J. Biol. Chem. 38*, 35035−43.
(34) Felix, K. (2008) Albumin as a drug carrier: Design of prodrugs, drug conjugates and nanoparticles. *J. Controlled Release 132*, 171−83.
(35) Bickel, U., Yoshikawa, T., and Pardridge, W. M. (2001) Delivery of peptides and proteinsthrough the blood-brain barrier. *Adv. Drug Delivery Rev. 46*, 247−79.
(36) Lu, W., Sun, Q., Wan, J., She, Z., and Jiang, X. G. (2006) Cationic albumin-conjugated pegylated nanoparticles allow gene delivery into brain tumors via intravenous administration. *Cancer Res. 66*, 11878−87.
(37) Seki, T., Fang, J., and Maeda, H. (2009) Enhanced delivery of macromolecular antitumor drugs to tumors by nitroglycerin application. *Cancer Sci. 100*, 2426−30.

Bioconjugate Chemistry

Article

pubs.acs.org/bc

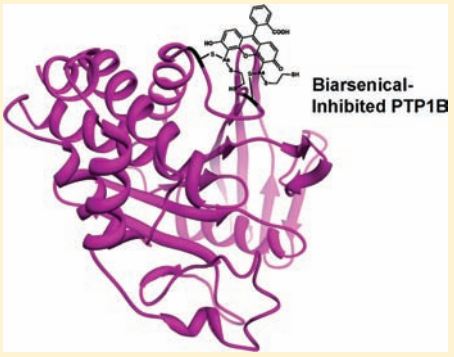
Specific Inhibition of Sensitized Protein Tyrosine Phosphatase 1B (PTP1B) with a Biarsenical Probe

Oliver B. Davis and Anthony C. Bishop*

Amherst College, Department of Chemistry, Amherst, Massachusetts 01002, United States

Supporting Information

ABSTRACT: Protein tyrosine phosphatase 1B (PTP1B) is a key regulator of the insulin-receptor and leptin-receptor signaling pathways, and it has therefore emerged as a critical antitype-II-diabetes and antiobesity drug target. Toward the goal of generating a covalent modulator of PTP1B activity that can be used for investigating its roles in cell signaling and disease progression, we report that the biarsenical probe FlAsH-EDT_2 can be used to inhibit PTP1B variants that contain cysteine point mutations in a key catalytic loop of the enzyme. The site-specific cysteine mutations have little effect on the catalytic activity of the enzyme in the absence of FlAsH-EDT_2. Upon addition of FlAsH-EDT_2, however, the activity of the engineered PTP1B is strongly inhibited, as assayed with either small-molecule or phosphorylated-peptide PTP substrates. We show that the cysteine-rich PTP1B variants can be targeted with the biarsenical probe in either whole-cell lysates or intact cells. Together, our data provide an example of a biarsenical probe controlling the activity of a protein that does not contain the canonical tetra-cysteine biarsenical-labeling sequence CCXXCC. The targeting of "incomplete" cysteine-rich motifs could provide a general means for controlling protein activity by targeting biarsenical compounds to catalytically important loops in conserved protein domains.



INTRODUCTION

Biarsenical probes are small molecules, based on the prototype 4′,5′-bis(1,3,2-dithioarsolan-2-yl)fluorescein (FlAsH-EDT_2, Figure 1A), that specifically tag the tetra-cysteine peptide motif CCXXCC through the formation of covalent arsenic−sulfur bonds.[1−3] Introduction of a tetra-cysteine motif into any target protein therefore allows for the rapid and specific formation of a covalent protein/small-molecule conjugate for the protein of interest. Although the first biarsenical tags were developed as cell-permeable protein-visualization tools (the FlAsH/tetra-cysteine conjugate is much more fluorescent than the bis-ethanedithiol adduct FlAsH-EDT_2),[1] subsequent work has demonstrated that biarsenical probes are highly versatile biochemical and biophysical tools:[3] Biarsenicals can be used to monitor protein folding, conformation, denaturation, and aggregation;[4−7] as receptors for light-induced protein inactivation;[8] and even as direct modulators of protein activity.[9−11]

Our lab has been particularly interested in the latter application of biarsenical chemistry: we have shown that FlAsH-EDT_2 can be used to either inhibit[11−13] or upregulate[14] the activity of engineered protein tyrosine phosphatases (PTPs). With regard to PTP inhibition, we have demonstrated that insertion of an optimized tetra-cysteine motif (CCPGCC) in the conserved WPD loop of the catalytic domain of a target PTP is sufficient for "sensitizing" the resulting mutant (PTP-CCPGCC) to inhibition by FlAsH.[11] In other words, the PTP-CCPGCC/FlAsH conjugate has much lower PTP activity than the PTP-CCPGCC enzyme in the absence of FlAsH. FlAsH-EDT_2 has no significant effect on any naturally occurring PTP assayed to date;[12] therefore, FlAsH sensitization provides a systematic means for specifically inhibiting a single PTP with a covalently attached small-molecule probe, even in the presence of many homologous enzymes. A key advantage of using protein engineering for targeting PTPs is that successful sensitization approaches may be applicable to many PTPs: the position of the sensitizing CCPGCC insertion is readily identifiable from primary sequence alignments. In principle, then, off-target PTPs can become targets (in separate experiments, targeting different PTP activities) simply by introduction of biarsenical sensitivity into subsequent PTPs that one wishes to study.[12] It is likely that targeting of sensitized PTPs will be readily applicable to the systematic delineation of PTP function in whole-cell signaling experiments, as introduction of a gene encoding a sensitized PTP into a cell potentially generates a system in which only a single PTP can be inhibited by a biarsenical ligand.

For some PTP targets, however, a significant limitation of the peptide-insertion approach to sensitization lies in the radical nature of the CCPGCC insertion. For example, the insertion mutant deriving from protein tyrosine phosphatase 1b (PTP1B-CCPGCC) demonstrates drastically reduced activity even in the absence of FlAsH-EDT_2: PTP1B-CCPGCC has a 50-fold reduction in the value of k_{cat}, as compared with the naturally occurring PTP1B.[12] It is unclear whether this loss of activity

Received: October 20, 2011
Revised: January 11, 2012
Published: January 22, 2012

ACS Publications © 2012 American Chemical Society

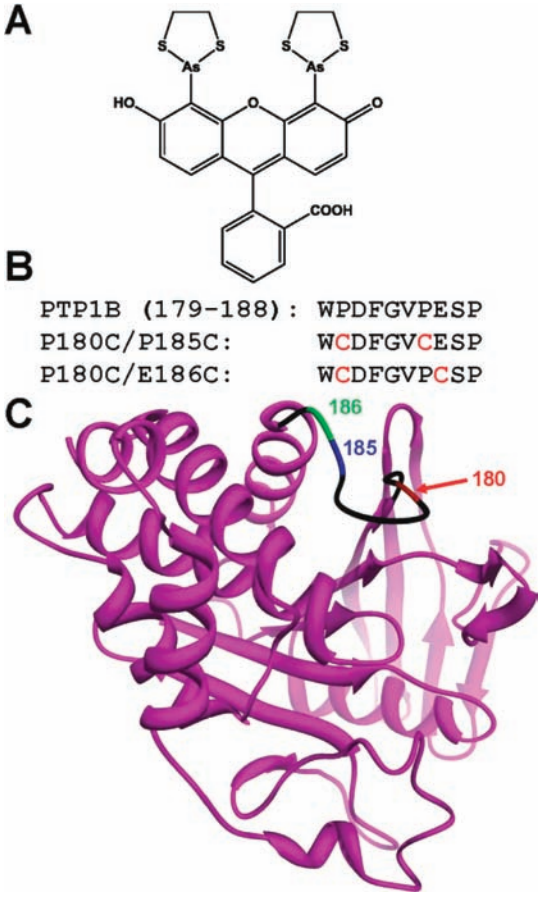


Figure 1. Design of biarsenical-sensitized mutants of PTP1B. (A) Chemical structure of FlAsH-EDT$_2$. (B) Sequence alignment of the WPD loops (residues 179−188) of wild-type PTP1B, P180C/P185 PTP1B, and P180C/E186C PTP1B. The positions of the site-directed cysteine mutations are highlighted in red. (C) Placement of sensitizing cysteine mutations within the three-dimensional structure of PTP1B. PTP1B is shown as a ribbon, with its WPD loop in the "open" conformation (PDB: 2HNQ).[29] The WPD loop is shown in black, with the exception of the positions of the sensitizing mutations introduced in the present study: 180 (red), 185, (blue), and 186 (green).

results from an inherent deficiency in the catalytic activity in folded PTP1B-CCPGCC protein or a destabilization of the PTP-domain fold that leads to a partially unfolded protein. Regardless, this insertion-induced loss of activity limits the prospects of using PTP1B-CCPGCC as a ligand-sensitive protein target in mammalian cellular studies, as a critical criterion for the biological usefulness of such approaches is that the engineered target can "silently" replace the function of the wild-type.[15−17] PTP1B-CCPGCC is thus predicted to be a poor candidate for use in signaling studies; one would predict that it would not reconstitute the function of wild-type PTP1B in the absence of FlAsH-EDT$_2$ due to its intrinsically low activity and/or stability.

The failure to identify a highly active biarsenical-sensitive variant of PTP1B through CCPGCC insertion is particularly vexing because of the biological importance of this phosphatase target. PTP1B it is arguably the most important classical PTP in the biological and pharmaceutical literature due to its key role as a signaling regulator of the insulin- and leptin-response pathways.[18−22] Despite intensive PTP1B-inhibitor-discovery efforts, most known PTP1B inhibitory compounds suffer from a lack of target specificity (other classical PTP catalytic domains share a significant degree of sequence and structural homology with PTP1B) and poor bioavailability (at physiological pH, most of the known PTP1B-binding pharmacophores contain negatively charged pTyr mimetics that lower an inhibitor's cellular permeability). Therefore, chemical tools that are capable of specifically inhibiting PTP1B with high target specificity in a cellular context are still needed.

Here, we report that introduction of a minimized biarsenical-binding motif can be used to identify a highly active and biarsenical-sensitive variant of PTP1B. Using a cysteine-rich motif developed on a homologous PTP, we show that two cysteine mutations in a conserved loop of the PTP domain are sufficient to sensitize PTP1B to inhibition by a biarsenical probe *in vitro*. We also demonstrate that the activity of the resulting biarsenical-sensitized PTP mutant can be successfully targeted in the contexts of whole-cell lysates and intact bacterial cells.

EXPERIMENTAL PROCEDURES

General. FlAsH-EDT$_2$ was synthesized as described[1,2,11] and dissolved in DMSO. All PTP assays were performed in triplicate; error bars and " ± " values represent the standard deviations of at least three independent experiments.

Cloning and Mutagenesis of a PTP1B-Expression Vector. A plasmid for the expression of PTP1B was generated by cloning the gene encoding PTP1B from the plasmid pGEX-KG-PTP1B[23] (Zhong-Yin Zhang, Indiana University) into pET-21b. (See Supporting Information for all primer sequences.) A PTP1B-encoding PCR product and pET-21b were doubly digested with *Eco*RI and *Sal*I, gel purified, and ligated using T4 DNA ligase, yielding pOBD002, which encodes PTP1B with a C-terminal six-histidine tag (PTP1B-His$_6$). Mutations to the PTP1B gene were introduced using the Quikchange site-directed mutagenesis kit (Stratagene) according to the manufacturer's instructions. Desired mutations were confirmed by sequencing (Cornell Biotechnology Resource Center).

Expression and Purification of Wild-Type and Mutant PTP1B Enzymes. BL21(DE3)-codonPLUS-RIL *E. coli* (Stratagene) containing the appropriate PTP1B-encoding plasmid were grown overnight at 37 °C in LB. Cultures were diluted, grown to midlog phase (OD$_{600}$ = 0.5), induced with 0.2 mM isopropyl-1-thio-β-D-galactopyranoside (IPTG), and shaken at 23 °C for 14 h. The cells were harvested by centrifugation, resuspended in binding buffer (50 mM Tris pH 7.8, 500 mM NaCl, 5 mM imidazole), and lysed by French Press at ∼2000 psi. Lysates were clarified by centrifugation, and enzyme purifications were carried out using SwellGel Nickel Chelated Discs (Pierce) according to the manufacturer's instructions. The protein solutions obtained were exchanged into storage buffer (50 mM 3,3-dimethylglutarate pH 7.0, 1 mM EDTA, 1 mM DTT), concentrated, flash-frozen in liquid nitrogen, and stored at −80 °C. Bradford assays and SDS-PAGE were used to estimate enzyme concentrations.

Phosphatase Activity and Inhibition Assays with *p*NPP. PTP1B assays using *para*-nitrophenyl phosphate (*p*NPP) as substrate were carried out in a total volume of 200 μL, containing PTP buffer (50 mM 3,3-dimethyl glutarate, 50 mM NaCl, 1 mM EDTA, pH 7.0), enzyme (diluted to 20−75 nM in PTP buffer; final DTT concentration: ≤ 2 μM), and *p*NPP (0.625−10 mM). PTP reactions were quenched by the addition of 40 μL of 5 M NaOH, and the absorbances (405

nm) of 200 μL of the resulting solutions were measured on a VersaMax plate reader (Molecular Devices). Kinetic constants were determined by fitting the data to the Michaelis−Menten equation using *SigmaPlot 11.0*. For FlAsH-inhibition experiments, PTP1B samples (100 nM) were incubated with FlAsH-EDT_2 concentrations ranging from 62.5 nM to 2 μM, or with DMSO only, for two hours at room temperature. The PTP activities of the solutions were then measured by assaying them with *p*NPP as described above at a *p*NPP concentration equal to the previously determined K_M of the enzyme.

Phosphatase Activity and Inhibition Assays with Phosphopeptide. PTP1B assays using phosphopeptide as substrate were carried out in a total volume of 140 μL, containing peptide buffer (50 mM 3,3-dimethyl glutarate, 125 mM NaCl, 1 mM EDTA, pH 7.0), enzyme (diluted to 25−125 nM; final DTT concentration: ≤ 2 μM), and phosphopeptide substrate (100 μM, DADEpYLIPQQG, Calbiochem). Reactions were initiated by the addition of the phosphopeptide after preincubation of the enzyme with FlAsH-EDT_2 (5 × PTP1B concentration). The change in absorbance at 282 nm was measured over time and kinetic constants were determined by fitting the data to the integrated Michaelis−Menten as described previously.[24]

Fluorescence. Solutions containing wild-type or mutant PTP1B (1 μM) and FlAsH-EDT_2 (25 nM) in PTP buffer were incubated at room temperature for two hours. Fluorescence values (excitation: 510 nm, emission: 540 nm, cutoff: 530 nm) of the solutions were measured on a Molecular Devices SpectraMax M5 fluorimeter.

Sensitized PTP1B Inhibition in Cell Lysates and Intact Cells. Lysates: PTP activity of the total lysate from cells expressing the PTP of interest was measured using *p*NPP (see above). To prepare lysates, 50 mL aliquots of BL21(DE3)-CodonPlus *E. coli* cells expressing the PTP of interest were removed from larger cultures (see above), pelleted, and stored at −80 °C. The pellets were then resuspended in PTP buffer, lysed by French Press, and clarified by centrifugation. Lysates were incubated with FlAsH-EDT_2 (concentrations ranging 0.1−10 μM) or DMSO for 2 h at room temperature and assayed with *p*NPP.

Intact bacteria: PTP1B overexpression was carried out in 50 mL cultures essentially as described above, except that cultures were induced with IPTG for 5 h, after which the cultures were centrifuged for 15 min at 4500 rpm. Media was removed and the cell pellets were washed with 20 mL of extracellular buffer[25] (ECB: 135 mM NaCl, 5 mM KCl, 10 mM HEPES, 2 mM $MgCl_2$, 2 mM $CaCl_2$, pH 7.4). The resuspended cells were then split into two 10 mL portions and centrifuged for 10 min at 4500 rpm. The supernatant was removed and the cell pellets were resuspended in 5 mL of ECB containing 5 μM FlAsH-EDT_2 or DMSO vehicle and incubated for 4 h at room temperature with gentle agitation. The cells were then washed 3 times, as before, with 10 mL ECB. After the third wash, the cell pellets were resuspended in 5 mL of PTP buffer, lysed by French Press, and clarified by centrifugation. The PTP activities of the lysates (5 μL) were assayed using *p*NPP as substrate as described above.

RESULTS AND DISCUSSION

Design Strategy. In an attempt to generate biarsenical-sensitized mutants of PTP1B that retain wild-type-like activity and stability in the absence of FlAsH-EDT_2, we introduced cysteine point mutations in the enzyme's WPD loop (Figure 1B, C).[26] The WPD loop is a highly conserved motif of the PTP fold that can alternate between "open" and "closed" conformations.[27] The dynamics of the open/closed transition is of key importance for PTP activity, as the WPD loop contains a critical aspartic-acid residue (the "D" of WPD) that can only perform its general acid/base functions when the loop is in the closed form.[28] We have shown previously that, when FlAsH is specifically targeted to an engineered WPD loop, the binding of the small molecule to the WPD loop can alter the kinetics of the open/closed transition and either inhibit[11] or activate[14] the target PTP's activity.

Based on homology to a previously sensitized PTP,[13,26] we selected three positions in PTP1B's WPD loop as potential sensitization sites (Figure 1B, C): proline 180 (P180), proline 185 (P185), and glutamate 186 (E186).[29] Mutations at these positions could potentially confer affinity for biarsenical small molecules to PTP1B's WPD loop without affecting the overall length of the loop or the chemical structure of residues that have previously been shown to be important for PTP1B's enzyme activity and/or substrate recognition.[28,30,31] Hypothesizing that we would need, at the minimum, two properly spaced cysteine residues to confer a specific interaction with biarsenicals (one thiol to react with each arsenic atom), we generated two potentially biarsenical-sensitized double mutants P180C/P185C and P180C/E186C PTP1B. Six-histidine tagged constructs of both double mutants expressed well from *E. coli* (∼ 20 mg/L of culture) and were readily purified using immobilized metal affinity chromatography. In contrast to the instability and temperature sensitivity that we have observed with the PTP1B-CCPGCC insertion mutant (unpublished observations), the point mutants P180C/P185C and P180C/E186C PTP1B demonstrated no qualitative differences, with respect to wild-type PTP1B or each other, in their benchtop stabilities or resistance to freeze/thaw cycles.

Activities of Biarsenical-Sensitized PTP1B Mutants. To investigate the effects of the cysteine mutations on the inherent activities of P180C/P185C and P180C/E186C PTP1B, we measured the kinetic constants of these enzymes with the general PTP substrate *para*-nitrophenyl phosphate (*p*NPP) and compared the values with those derived from the wild-type enzyme (Table 1). Encouragingly, the results indicated that the minimized FlAsH-sensitization strategy could be used to produce a PTP1B mutant that exhibits kinetic characteristics similar in nature to wild-type PTP1B, namely, P180C/E186C PTP1B. The 180/186 double mutant exhibits a catalytic rate constant (k_{cat}) that differs from that of wild-type PTP1B by less than a factor of 2 and a catalytic efficiency (k_{cat}/K_M) that is 25% higher than the wild-type value. In contrast, P180C/P185C PTP1B exhibits a substantially greater defect in catalytic rate constant (7.5-fold lower than that of wild-type), and as a result this mutant was not investigated further.

Table 1. Kinetic Constants for Wild-Type PTP1B, P180C/P185C PTP1B, and P180C/E186C PTP1B with *p*NPP as Substrate

enzyme	k_{cat} (s^{-1})	K_M (mM)	k_{cat}/K_M (mM^{-1} s^{-1})
wild-type PTP1B	13.36 ± 2.87	2.29 ± 0.21	5.82 ± 1.13
P180C/P185C PTP1B	1.77 ± 0.26	2.03 ± 0.25	0.87 ± 0.14
P180C/E186C PTP1B	7.12 ± 0.34	0.98 ± 0.09	7.34 ± 1.08

dx.doi.org/10.1021/bc200562y | *Bioconjugate Chem.* 2012, 23, 272−278

To ensure that P180C/E186C PTP1B retains activity with more physiologically relevant substrates than the small-molecule substrate *p*NPP, we investigated the mutant's ability to dephosphorylate the phosphopeptide DADEpYLIPQQG, corresponding to an autophosphorylation site on the epidermal growth factor receptor (EGFR).[32] As observed with the *p*NPP assay, P180C/E186C PTP1B dephosphorylates DADEpY-LIPQQG with catalytic rate constants similar to those of wild-type PTP1B (Table 2). P180C/E186C PTP1B exhibits a

Table 2. Kinetic Constants for Wild-Type PTP1B and P180C/E186C PTP1B with the Phosphopeptide DADEpYLIPQQG as Substrate

enzyme	k_{cat} (s^{-1})	K_M (μM)	k_{cat}/K_M (μM^{-1} s^{-1})
wild-type PTP1B	15.72 ± 1.67	6.47 ± 2.54	2.75 ± 1.26
P180C/E186C PTP1B	8.28 ± 0.84	11.92 ± 4.46	0.74 ± 0.20

k_{cat} that is less than 2-fold reduced from that of the wild-type, almost precisely paralleling the result with *p*NPP (Table 1). Moreover, the Michaelis constant (K_M) values of wild-type PTP1B and P180C/E186C PTP1B agree within their associated error of measurement.

Biarsenical Sensitivity of P180C/E186C PTP1B. After finding that P180C/E186C PTP1B exhibited wild-type-like PTP activity, we set out to determine whether its minimized FlAsH-binding motif was sufficient to confer novel FlAsH sensitivity. To do so, we preincubated wild-type and P180C/E186C PTP1B with a range of FlAsH-EDT_2 concentrations (or DMSO vehicle) and measured the activities of the resulting enzymes (Figure 2A). We observed, consistent with earlier findings on other wild-type phosphatases, that the activity of wild-type PTP1B was unaffected by FlAsH-EDT_2 up to a concentration of 2 μM. By contrast, the P180C/E186C PTP1B was strongly inhibited by FlAsH-EDT_2 in a dose-dependent manner. Under the conditions of the assay (100 nM enzyme), the observed 50% inhibition concentration (IC_{50}) was approximately 130 nM, with maximal inhibition achieved at approximately 1 μM. (Under conditions of such potent, essentially stoichiometric, inhibition, measured IC_{50} values are highly dependent on the enzyme concentration used, and, therefore, of little fundamental significance. For example, at 100 nM enzyme, it is theoretically impossible that an inhibitor which binds enzyme in a 1:1 manner could demonstrate a 50% inhibition value of less than 50 nM, half the enzyme concentration.) Collectively, the data in Figure 2A show that, indeed, the P180C/E186C double mutation is sufficient to confer strong FlAsH sensitivity into PTP1B.

Because of the lack of fundamental thermodynamic meaning in FlAsH-EDT_2's IC_{50} value described above, we attempted to achieve a quantitative measurement of the strength of the protein/small-molecule interaction using a more sensitive readout of FlAsH's binding affinity. FlAsH's fluorescence intensity increases upon binding to a tetra-cysteine motif;[1] therefore, fluorescence is a potentially useful tool for determining the strength with which FlAsH binds to target proteins. Indeed, fluorescence has been used by our lab[33] and others[34] to characterize the strength of protein/biarsenical interactions, and we sought to use this property to measure the binding constant of FlAsH to P180C/E186C PTP1B. We measured the fluorescence of FlAsH-EDT_2-treated wild-type PTP1B (negative control), P180C/E186C PTP1B, and, as a

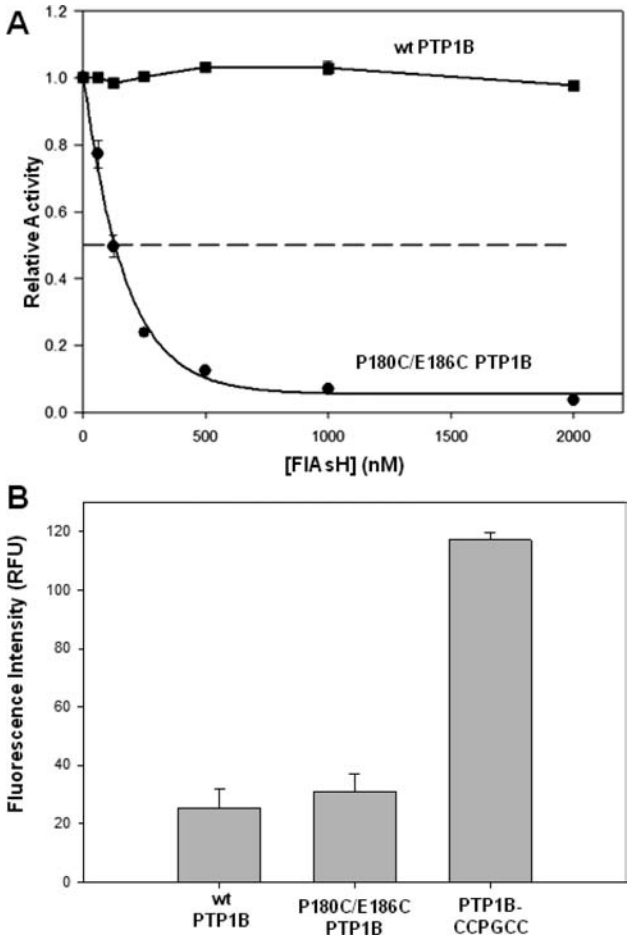


Figure 2. FlAsH sensitivity of P180C/E186C PTP1B. (A) Wild-type (squares) or P180C/E186C PTP1B (circles) was incubated at the indicated FlAsH-EDT_2 concentrations and assayed for activity using *p*NPP as substrate. All activities were normalized to a DMSO-only control for the corresponding enzyme. (B) Fluorescence of FlAsH in the presence of wild-type (wt) PTP1B, P180C/E186C PTP1B, and PTP1B-CCPGCC. The indicated PTP variants (1 μM) were incubated with FlAsH-EDT_2 (25 nM), and the FlAsH fluorescence of the resulting solutions was measured (excitation: 510 nm, emission: 540 nm).

positive control for FlAsH fluorescence, a PTP1B mutant that contains a complete tetra-cysteine motif, PTP1B-CCPGCC (Figure 2B).[12] As expected, FlAsH's fluorescence intensity increases significantly upon incubation with PTP1B-CCPGCC. However, we found that the fluorescence of FlAsH in the presence of P180C/E186C PTP1B is not substantially different from that of FlAsH incubated in the presence of wild-type PTP1B. As a result, fluorescence could not be used to estimate a binding constant for the interaction between FlAsH and P180C/E186C PTP1B. Nevertheless, when considered in conjunction with the findings presented in Figure 2A, the data in Figure 2B suggest that FlAsH's utility in controlling protein activity can be completely decoupled from its more established role in protein visualization, and that the two applications have different target-sequence requirements. P180C/E186C PTP1B provides a second example of our earlier observation that a PTP's activity can be controlled by a biarsenical with exquisite potency and specificity, even if that PTP does not induce the signature increase in biarsenical fluorescence.[14]

dx.doi.org/10.1021/bc200562y | *Bioconjugate Chem.* 2012, 23, 272–278

Due to the lack of a direct physical readout of FlAsH's binding to P180C/E186C PTP1B, we wished to confirm its inhibitory specificity, observed previously with *p*NPP, in an assay with a different PTP substrate. We therefore investigated the ability of FlAsH-EDT_2 to inhibit the dephosphorylation of DADEpYLIPQQG; this phosphopeptide represents a substrate that is more physiologically relevant than *p*NPP, and an alternate assay could provide assurance that the observed FlAsH inhibition is not an artifact of the colorimetric *p*NPP assay. We found that, indeed, P180C/E186C PTP1B's biarsenical sensitivity is substrate independent. Upon preincubation with a 5-fold molar excess of FlAsH-EDT_2, the inhibition of P180C/E186C PTP1B is essentially complete, as well as completely specific to the mutant (Figure 3). These data are consistent with the results with *p*NPP (Figure 2A), and taken together, the two *in vitro* experiments establish that biarsenical targeting of P180C/E186C PTP1B meets the necessary preconditions that would be required for its use in a complex cellular environment: FlAsH-induced P180C/E186C PTP1B inhibition is potent, specific, and substrate-independent.

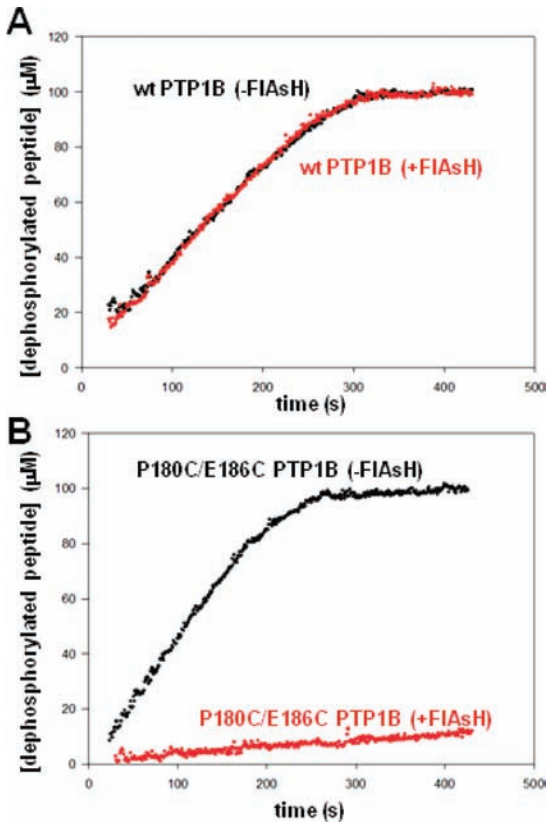


Figure 3. Target-specific inhibition of P180C/E186C PTP1B using the phosphopeptide DADEpYLIPQQG as substrate. The activities of wild-type PTP1B (A, 25 nM) and P180C/E186C PTP1B (B, 62.5 nM) were measured in the absence (black) or presence (red) of a 5-fold molar excess of FlAsH-EDT_2. Time-dependent phosphopeptide dephosphorylation was monitored by the increase in absorbance at 282 nm as described previously.[24].

Targeting of P180C/E186C PTP1B in Cell Lysates and Intact Cells. We next investigated whether or not P180C/E186C PTP1B could be targeted by FlAsH in the context of a complex mixture of cellular components. (All of the experiments illustrated in Figures 2 and 3 were performed using purified enzymes.) It has previously been established that naturally occurring proteins that are capable of binding FlAsH do exist,[35,36] and it is quite possible that these proteins (as well others that remain to be identified) could compete with P180C/E186C PTP1B for FlAsH binding and thereby interfere with the compound's specificity and potency. To determine whether P180C/E186C PTP1B's sensitivity to FlAsH persists in a complex proteomic mixture, we prepared crude lysates of *E. coli* cell cultures that express either wild-type or P180C/E186C PTP1B and assayed the PTP activities of the lysates after incubation in the presence or absence of FlAsH-EDT_2. (Since bacterial genomes do not encode PTPs, total PTP activity in crude lysates from *E. coli* strains that overexpress exogenous PTPs can be used for a direct readout of specific-PTP activity.) The data in Figure 4 show that FlAsH binding is strong and specific for P180C/E186C PTP1B, even when inhibition occurs in a complex mixture of cellular components. The PTP activity of the lysate containing P180C/E186C PTP1B dropped in a dose-dependent manner, with an apparent IC_{50} value of approximately 1.75 μM, while the PTP activity of the wild-type PTP1B containing lysate remained unaffected at all FlAsH-EDT_2 concentrations tested.

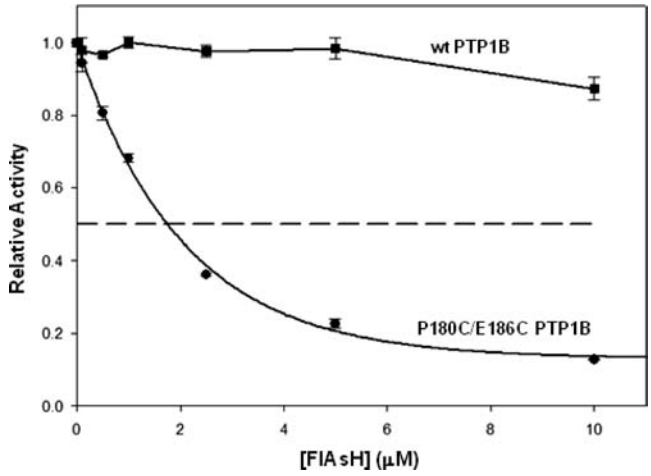


Figure 4. Target-specific inhibition of P180C/E186C PTP1B in a complex proteomic mixture. Crude cell lysates derived from *E. coli* that expressed either wild-type PTP1B (squares) or P180C/E186C PTP1B (circles) were incubated at the indicated FlAsH-EDT_2 concentrations and assayed for activity using *p*NPP as a substrate.

To further investigate FlAsH's ability to target P180C/E186C PTP1B, we asked whether it could do so in intact *E. coli* cells. However, the literature precedents concerning the biarsenical cell permeability (or lack thereof) with *E. coli* are somewhat mixed.[3] Some authors report that bacterial cell walls are refractory to biarsenicals,[37] whereas some have presented fluorescence data derived from the use of biarsenicals in living *E. coli* cells.[36] (Perhaps these apparent conflicts arise from differing definitions of "permeable". Cellular compound concentrations that are sufficient for labeling at the lower limit of fluorescence detection may differ from those needed for full labeling of a target protein.) Our previous investigations have shown that a cycle of freeze–thaw is necessary to "get" FlAsH-EDT_2 into cells.[33] Nevertheless, we were intrigued by a recent report of strong *in vivo* FlAsH labeling in *E. coli* using small amounts of divalent cations in the buffer (2 mM $MgCl_2$, 2 mM $CaCl_2$),[25] and we utilized these conditions for incubations of wild-type and P180C/E186C PTP1B-expressing cells with

FlAsH-EDT$_2$. After copiously rinsing away excess FlAsH-EDT$_2$, we lysed the cells and assayed the resulting preparations for PTP activity. We found that the PTP activity derived from wild-type-PTP1B-expressing cells was indistinguishable between DMSO-treated and FlAsH-EDT$_2$-treated samples (Figure 5).

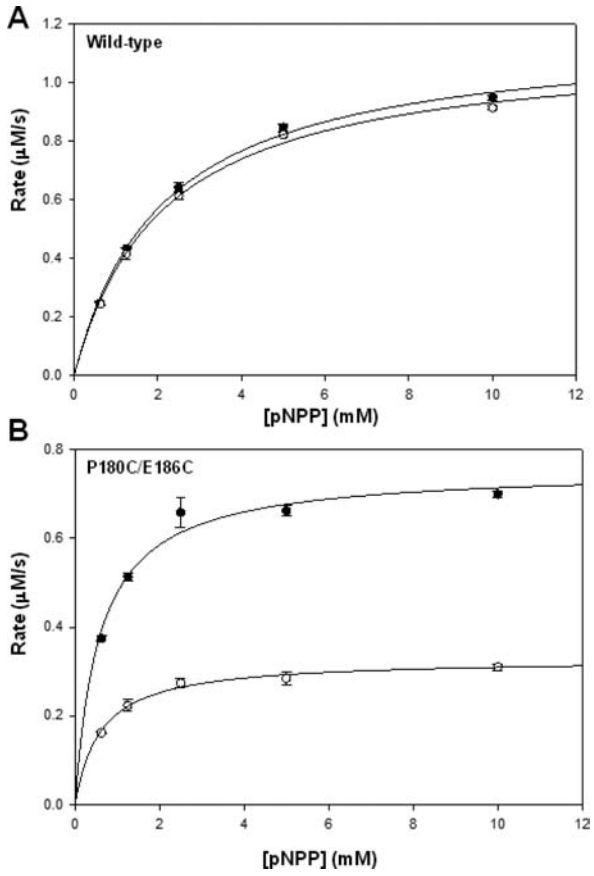


Figure 5. Target-specific inhibition of P180C/E186C PTP1B in living cells. *E. coli* cells expressing either wild-type (A) or P180C/E186C PTP1B (B) were incubated in the absence (filled circles) or presence of FlAsH-EDT$_2$ (5 μM, open circles). The cells were pelleted, washed three times, and subsequently lysed. The PTP activity of the lysates was assayed using *p*NPP at the indicated concentrations.

Importantly, PTP activity in the lysates from P180C/E186C PTP1B-expressing *E. coli* was inhibited in the FlAsH-EDT$_2$-treated samples, as compared to the vehicle-treated samples. The degree of inhibition roughly corresponded to an approximately 50% reduction in maximum velocity (V_{max}) and was consistent over a range of substrate concentrations investigated (Figure 5).

The reasons for the modest level of inhibition even after prolonged (4 h) incubation in the presence of FlAsH-EDT$_2$ are not clear. Most likely, given the previously noted complexities associated with biarsenical cell permeability in bacteria, FlAsH-EDT$_2$ is entering the cells only at concentrations much lower than the concentration in the buffer (5 μM). Thus, it is unwise to ascribe physical or quantitative significance to the "IC$_{50}$" observed in the cellular experiments. Nevertheless, since the two cell populations used in these experiments (wild-type- vs P180C/E186C-PTP1B expressing) differ only by the identity of two amino acid side chains in a single protein, the observed differences in inhibition must unambiguously derive from FlAsH binding to its target sequence in the WPD loop of the engineered PTP. These results represent the first demonstration that FlAsH can be used to target PTP1B for inhibition in intact cells for future PTP1B targeting in eukaryotic cells.

More generally, our observation that FlAsH can inhibit a target protein that contains as few as two properly spaced cysteine residues without producing a notable change in fluorescence does present a potentially troubling implication: it suggests that FlAsH may bind to a substantial number of as-yet-unidentified, naturally occurring proteins, and that these hypothetical FlAsH-binding proteins would not be detectable by fluorescence (the standard technique for identifying protein/FlAsH interactions). With regard to using FlAsH-EDT$_2$ to study PTP1B-mediated signaling, however, the key observation is that FlAsH-EDT$_2$ does not inhibit wild-type PTP1B or any wild-type PTP assayed to date.[11−13] Although FlAsH-EDT$_2$ (like any small molecule) may have multiple potential binding partners in the cell, for the purposes of controlling PTP activity, our experiments suggest that the compound can possess exquisite selectivity for the engineered PTP1B target over all wild-type PTPs. Since the mammalian-cell permeability of biarsenical reagents is well established,[37] it is likely that the biarsenical targeting of P180C/E186C PTP1B can be used to delineate the precise functions of PTP1B in mammalian cell culture.

CONCLUSION

PTP1B is a wide-ranging signaling molecule, with particularly important roles in the insulin-receptor and leptin-receptor signaling pathways. Small molecules that can inhibit cellular PTP1B activity are thus important tools in chemical biology, yet cell-permeable compounds that can target PTP1B with high selectivity over all other PTPs are not known. We have shown that site-directed mutagenesis can be used to generate a double mutant variant of PTP1B, P180C/E186C-PTP1B, that is sensitive to inhibition by the biarsenical probe FlAsH-EDT$_2$. Upon addition of FlAsH-EDT$_2$, the activity of P180C/E186C-PTP1B is strongly inhibited, even under experimental conditions in which FlAsH and enzyme are present at almost equal concentrations. Importantly, P180C/E186C-PTP1B demonstrates near wild-type activity levels in the absence of FlAsH-EDT$_2$, and FlAsH-EDT$_2$ has no significant effect on PTP activity of wild-type PTP1B. We have also shown that FlAsH can target-specifically inhibit P180C/E186C PTP1B in the context of whole-cell lysates and intact cells. Collectively, our results provide a small-molecule tool that can be used to inhibit PTP1B in complex proteomic mixtures with exquisite selectivity.

ASSOCIATED CONTENT

Supporting Information

Sequences of all primers used for cloning and mutagenesis. This material is available free of charge via the Internet at http://pubs.acs.org.

AUTHOR INFORMATION

Corresponding Author

*Tel.: 413-542-8316; Fax: 413-542-2735; E-mail: acbishop@amherst.edu.

Notes

The authors declare no competing financial interest.

■ ACKNOWLEDGMENTS

This research was supported by the National Institutes of Health (2 R15 GM071388-02) and Amherst College.

■ REFERENCES

(1) Griffin, B. A., Adams, S. R., and Tsien, R. Y. (1998) Specific covalent labeling of recombinant protein molecules inside live cells. *Science 281*, 269−272.

(2) Adams, S. R., Campbell, R. E., Gross, L. A., Martin, B. R., Walkup, G. K., Yao, Y., Llopis, J., and Tsien, R. Y. (2002) New biarsenical ligands and tetracysteine motifs for protein labeling in vitro and in vivo: synthesis and biological applications. *J. Am. Chem. Soc. 124*, 6063−6076.

(3) Pomorski, A., and Krezel, A. (2011) Exploration of biarsenical chemistry-Challenges in protein research. *ChemBioChem 12*, 1152−1167.

(4) Ignatova, Z., and Gierasch, L. M. (2004) Monitoring protein stability and aggregation in vivo by real-time fluorescent labeling. *Proc. Natl. Acad. Sci. U.S.A. 101*, 523−528.

(5) Roberti, M. J., Bertoncini, C. W., Klement, R., Jares-Erijman, E. A., and Jovin, T. M. (2007) Fluorescence imaging of amyloid formation in living cells by a functional, tetracysteine-tagged alpha-synuclein. *Nat. Methods 4*, 345−351.

(6) Hu, Y., Su, B. H., Kim, C. S., Hernandez, M., Rostagno, A., Ghiso, J., and Kim, J. R. (2010) A strategy for designing a peptide probe for detection of beta-amyloid oligomers. *ChemBioChem 11*, 2409−2418.

(7) Scheck, R. A., and Schepartz, A. (2011) Surveying protein structure and function using bis-arsenical small molecules. *Acc. Chem. Res. 44*, 654−665.

(8) Marek, K. W., and Davis, G. W. (2002) Transgenically encoded protein photoinactivation (FIAsH-FALI): Acute inactivation of synaptotagmin I. *Neuron 36*, 805−813.

(9) Erster, O., Eisenstein, M., and Liscovitch, M. (2007) Ligand interaction scan: a general method for engineering ligand-sensitive protein alleles. *Nat. Methods 4*, 393−395.

(10) Xia, X., Wang, G., Peng, Y., Tu, M. G., Jen, J., and Fang, H. (2005) The endogenous CXXC motif governs the cadmium sensitivity of the renal Na+/glucose co-transporter. *J. Am. Soc. Nephrol. 16*, 1257−1265.

(11) Zhang, X. Y., and Bishop, A. C. (2007) Site-specific incorporation of allosteric-inhibition sites in a protein tyrosine phosphatase. *J. Am. Chem. Soc. 129*, 3812−3813.

(12) Zhang, X. Y., Chen, V. L., Rosen, M. S., Blair, E. R., Lone, A. M., and Bishop, A. C. (2008) Allele-specific inhibition of divergent protein tyrosine phosphatases with a single small molecule. *Bioorg. Med. Chem. 16*, 8090−8097.

(13) Zhang, X.-Y., and Bishop, A. C. (2008) Engineered inhibitor sensitivity in the WPD loop of a protein tyrosine phosphatase. *Biochemistry 47*, 4491−4500.

(14) Chen, V. L., and Bishop, A. C. (2010) Chemical rescue of protein tyrosine phosphatase activity. *Chem. Commun. 46*, 637−639.

(15) Bishop, A. C., Buzko, O., and Shokat, K. M. (2001) Magic bullets for protein kinases. *Trends Cell Biol. 11*, 167−172.

(16) Bishop, A. C., Zhang, X. Y., and Lone, A. M. (2007) Generation of inhibitor-sensitive protein tyrosine phosphatases via active-site mutations. *Methods 42*, 278−288.

(17) Bishop, A. C., Ubersax, J. A., Petsch, D. T., Matheos, D. P., Gray, N. S., Blethrow, J., Shimizu, E., Tsien, J. Z., Schultz, P. G., Rose, M. D., Wood, J. L., Morgan, D. O., and Shokat, K. M. (2000) A chemical switch for inhibitor-sensitive alleles of any protein kinase. *Nature 407*, 395−401.

(18) Zhang, S., and Zhang, Z. Y. (2007) PTP1B as a drug target: recent developments in PTP1B inhibitor discovery. *Drug Discov. Today 12*, 373−381.

(19) Jiang, Z. X., and Zhang, Z. Y. (2008) Targeting PTPs with small molecule inhibitors in cancer treatment. *Cancer Metastasis Rev. 27*, 263−272.

(20) Barr, A. J. (2010) Protein tyrosine phosphatases as drug targets: strategies and challenges of inhibitor development. *Future Med. Chem. 2*, 1563−1576.

(21) Blaskovich, M. A. (2009) Drug discovery and protein tyrosine phosphatases. *Curr. Med. Chem. 16*, 2095−2176.

(22) Yip, S. C., Saha, S., and Chernoff, J. (2010) PTP1B: a double agent in metabolism and oncogenesis. *Trends Biochem. Sci. 35*, 442−449.

(23) Shen, K., Keng, Y. F., Wu, L., Guo, X. L., Lawrence, D. S., and Zhang, Z. Y. (2001) Acquisition of a specific and potent PTP1B inhibitor from a novel combinatorial library and screening procedure. *J. Biol. Chem. 276*, 47311−47319.

(24) Zhang, Z. Y., Maclean, D., Thieme-Sefler, A. M., Roeske, R. W., and Dixon, J. E. (1993) A continuous spectrophotometric and fluorimetric assay for protein tyrosine phosphatase using phosphotyrosine-containing peptides. *Anal. Biochem. 211*, 7−15.

(25) Yang, H., He, J., Hu, F., Zheng, C., and Yu, Z. (2010) Detection of Escherichia coli enoyl-ACP reductase using biarsenical-tetracysteine motif. *Bioconjugate Chem. 21*, 1341−1348.

(26) Andersen, J. N., Mortensen, O. H., Peters, G. H., Drake, P. G., Iversen, L. F., Olsen, O. H., Jansen, P. G., Andersen, H. S., Tonks, N. K., and Moller, N. P. (2001) Structural and evolutionary relationships among protein tyrosine phosphatase domains. *Mol. Cell. Biol. 21*, 7117−7136.

(27) Barr, A. J., Ugochukwu, E., Lee, W. H., King, O. N. F., Filippakopoulos, P., Alfano, I., Savitsky, P., Burgess-Brown, N. A., Muller, S., and Knapp, S. (2009) Large-scale structural analysis of the classical human protein tyrosine phosphatome. *Cell 136*, 352−363.

(28) Zhang, Z. Y. (2003) Chemical and mechanistic approaches to the study of protein tyrosine phosphatases. *Acc. Chem. Res. 36*, 385−392.

(29) Barford, D., Flint, A. J., and Tonks, N. K. (1994) Crystal structure of human protein tyrosine phosphatase 1B. *Science 263*, 1397−1404.

(30) Wang, W. Q., Sun, J. P., and Zhang, Z. Y. (2003) An overview of the protein tyrosine phosphatase superfamily. *Curr. Top. Med. Chem. 3*, 739−748.

(31) Zhang, Z. Y., Wang, Y., and Dixon, J. E. (1994) Dissecting the catalytic mechanism of protein-tyrosine phosphatases. *Proc. Natl. Acad. Sci. U.S.A. 91*, 1624−1627.

(32) Zhang, Z. Y., Thieme-Sefler, A. M., Maclean, D., McNamara, D. J., Dobrusin, E. M., Sawyer, T. K., and Dixon, J. E. (1993) Substrate specificity of the protein tyrosine phosphatases. *Proc. Natl. Acad. Sci. U.S.A. 90*, 4446−4450.

(33) Walton, Z. E., and Bishop, A. C. (2010) Target-specific control of lymphoid-specific protein tyrosine phosphatase (Lyp) activity. *Bioorg. Med. Chem. 18*, 4884−4891.

(34) Luedtke, N. W., Dexter, R. J., Fried, D. B., and Schepartz, A. (2007) Surveying polypeptide and protein domain conformation and association with FlAsH and ReAsH. *Nat. Chem. Biol. 3*, 779−784.

(35) Stroffekova, K., Proenza, C., and Beam, K. G. (2001) The protein-labeling reagent FLASH-EDT2 binds not only to CCXXCC motifs but also non-specifically to endogenous cysteine-rich proteins. *Pflugers Arch. 442*, 859−866.

(36) Wang, T., Yan, P., Squier, T. C., and Mayer, M. U. (2007) Prospecting the proteome: identification of naturally occurring binding motifs for biarsenical probes. *ChemBioChem 8*, 1937−1940.

(37) Griffin, B. A., Adams, S. R., Jones, J., and Tsien, R. Y. (2000) Fluorescent labeling of recombinant proteins in living cells with FlAsH. *Methods Enzymol. 327*, 565−578.

Bioconjugate Chemistry

Article

pubs.acs.org/bc

Facile Double-Functionalization of Designed Ankyrin Repeat Proteins using Click and Thiol Chemistries

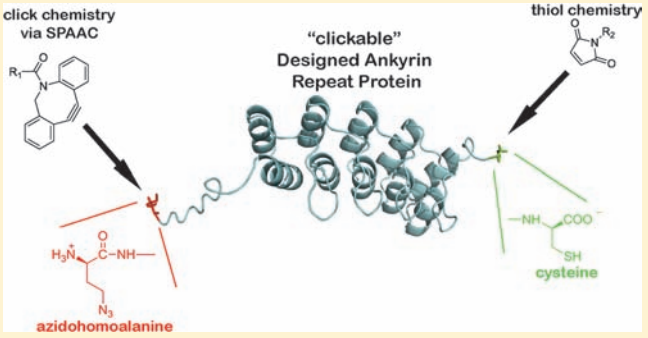
Manuel Simon,[§,†] Uwe Zangemeister-Wittke,[§,†] and Andreas Plückthun*[,§]

[§]Department of Biochemistry, Winterthurerstrasse 190, University of Zurich, CH-8057 Zurich, Switzerland

[†]Institute of Pharmacology, Friedbühlstrasse 49, University of Bern, CH-3010 Bern, Switzerland

Supporting Information

ABSTRACT: Click chemistry is a powerful technology for the functionalization of therapeutic proteins with effector moieties, because of its potential for bio-orthogonal, regio-selective, and high-yielding conjugation under mild conditions. Designed Ankyrin Repeat Proteins (DARPins), a novel class of highly stable binding proteins, are particularly well suited for the introduction of clickable methionine surrogates such as azidohomoalanine (Aha) or homopropargylglycine (Hpg), since the DARPin scaffold can be made methionine-free by an M34L mutation in the N-cap which fully maintains the biophysical properties of the protein. A single N-terminal azidohomoalanine, replacing the initiator Met, is incorporated in high yield, and allows preparation of "clickable" DARPins at about 30 mg per liter *E. coli* culture, fully retaining stability, specificity, and affinity. For a second modification, we introduced a cysteine at the C-terminus. Such DARPins could be conveniently site-specifically linked to two moieties, polyethylene glycol (PEG) to the N-terminus and the fluorophore Alexa488 to the C-terminus. We present a DARPin selected against the epithelial cell adhesion molecule (EpCAM) with excellent properties for tumor targeting as an example. We used these doubly modified molecules to measure binding kinetics on tumor cells and found that PEGylation has no effect on dissociation rate, but slightly decreases the association rate and the maximal number of cell-bound DARPins, fully consistent with our previous model of PEG action obtained *in vitro*. Our data demonstrate the benefit of click chemistry for site-specific modification of binding proteins like DARPins to conveniently add several functional moieties simultaneously for various biomedical applications.



INTRODUCTION

Over the past decade, the highly efficient and selective Cu(I)-dependent azido-alkyne cycloaddition (CuAAC), often denoted by the term "click chemistry", has been introduced to biological molecules.[1] The bio-orthogonal nature of the reaction renders click chemistry ideal for the assembly of bioconjugates in a regio-selective manner, as it allows several simultaneous modifications, avoiding unwanted side products.[2,3]

The covalent conjugation of polyethylene glycol (PEG) to a biomolecule is a clinically validated strategy for the functional modulation of biopharmaceuticals and therefore one of the most relevant covalent modifications of therapeutic proteins.[4,5] For site-specific PEGylation, coupling at Cys is most widely used. Although in principle PEGylation of proteins using CuAAC is straightforward,[6] the biomedical application of these products is limited since an azide or alkyne needs to be introduced into the protein. Furthermore, the instability of Cu(I) makes it challenging to scale up the reaction and maintain high yields. Moreover, CuAAC often requires highly insoluble ligands as chelating additives and Cu(I) is itself potentially cytotoxic and must thus be carefully removed, as it binds to the protein.

Recently, Cu-free click chemistry has been introduced to allow the conjugation of PEG moieties by coupling substituted cyclooctynes and azides without the need for a heavy metal catalyst and additives.[7,8] This strain-promoted azido-alkyne cycloaddition (SPAAC) offers efficient conjugation of azide-labeled proteins under mild conditions. It is thus well-suited for site-specific modification of proteins, particularly of enzymes and binding molecules engineered for therapeutic and diagnostic purposes.[9]

Designed Ankyrin Repeat Proteins (DARPins) have been introduced recently as a class of designed alternative scaffold proteins with features superior over monoclonal antibodies and recombinant antibody fragments.[10] Besides showing high expression yield in *E. coli*, DARPins are very stable, have favorable biophysical properties and carry no cysteine and no essential methionine.[11] Moreover, DARPins of very high affinity can be generated using well-established selection techniques, such as ribosome display and phage display, as previously shown for many different examples.[10] We previously described, among other applications, the successful generation and preclinical testing of DARPins selected for high stability, affinity, and

Received: November 6, 2011
Revised: December 13, 2011
Published: December 22, 2011

 © 2011 American Chemical Society dx.doi.org/10.1021/bc200591x | *Bioconjugate Chem.* 2012, 23, 279–286

tumor targeting directed against the human epidermal growth factor receptor (EGFR),[12] against Her2[13,14] and the Epithelial Cell Adhesion Molecule (EpCAM).[15,16]

DARPins contain no conserved methionine in the randomized repeats, and the only Met present in the original design, besides the initiator codon, is in the N-capping repeat (pos. 34), and can be easily exchanged to leucine. This substitution is suggested by the fact that all following repeats in DARPins have a leucine at the corresponding position. Thus, the resulting protein retains its high solubility, stability, and binding affinity (see below) after the mutation M34L. Some DARPins, such as, e.g., the EpCAM-specific binder Ec1,[16] had already mutated Met34 through the random mutagenesis in ribosome display. Additionally, DARPins are usually expressed with an N-terminal $MRGSH_6$ tag, from which the methionine is not cleaved,[17] and this is also true when an amino acid analogue is introduced.[18] Conversely, if the second amino acid is small, the amino acid analogue will be cleaved off, allowing the introduction of a unique Aha or Hpg at a position elsewhere in the chain.

The click chemistry can be carried out in either orientation, since both the non-natural Met analogues azidohomoalanine (Aha) and homopropargylglycine (Hpg) can be efficiently introduced, simply by exchanging the growth medium shortly before induction and by using a methionine-auxotrophic *E. coli* strain. The resulting "clickable" DARPins can be expressed in high amounts and are capable of bio-orthogonal coupling to "clickable" substrates containing the corresponding azides or alkynes for Cu(I)-dependent coupling or substituted cyclooctynes for Cu(I)-independent click chemistry, respectively.

We demonstrate the utility of this bio-orthogonal coupling by simultaneously derivatizing DARPins with PEG and with a fluorescent dye. Since DARPins are devoid of cysteines, we can introduce a single C-terminal cysteine into Aha-modified clickable DARPins for maleimide coupling of a second tag, in this case a fluorophore. PEGylation has been widely used to extend the serum persistence of proteins.[4,5,13] However, PEGylation can also lead to a decrease in the functional affinity of the molecule to which it is applied, even when the PEG attachment site is most distal to the antigen binding regions.[19] To extend our previous studies, where this phenomenon has been investigated with *in vitro* binding kinetics and mathematical modeling, we now used association and dissociation kinetics determined directly on cells[13,20] by FACS analyses and thus requiring an additional fluorescent label, which must be attached identically in the PEGylated and non-PEGylated molecule.

Here, we present a clickable DARPin recognizing the tumor-associated antigen EpCAM and describe its convenient mono-PEGylation using Cu-free click chemistry at the N-terminus in combination with C-terminal tagging with a fluorescent dye using maleimide coupling. We exploit these doubly modified molecules by showing that PEG has an effect on the on-rate of DARPin binding to cells, but not its off-rate, and also decreases the maximal number of targeting proteins that can be bound to the cell, compared to the non-PEGylated control. This convenient site-specific double tagging may further expand the engineering space of DARPins for biomedical applications.

EXPERIMENTAL PROCEDURES

Materials. If not otherwise stated, all chemicals were obtained from Sigma-Aldrich (Buchs, Switzerland). *E. coli* strain B834 (DE3) (F^- *ompT gal* $hsdS_B$ (r_B^- m_B^-) *met dcm lon* (*lacI, lacUV5-T7 gene 1, ind1, sam7, nin5*)) was from EMD Chemicals, Inc. (U.S.A.) and *E. coli* strain XL1 blue (*recA1 endA1 gyrA96 thi-1 hsdR17 supE44 relA1 lac* [F′ proAB $lacI^qZ\Delta M15$ Tn10 (Tet^r)]) was purchased from Stratagene (Agilent Technologies, Inc., Santa Clara, CA, U.S.A.). *N*-(3-Aminopropionyl)-5,6-dihydro-11,12-didehydrodibenzo-[b,f]azocine (amino-*aza*-dibenzo-cyclooctyne, DBCO-NH_2) and DBCO-$PEG_{20\ kDa}$ were a kind gift of Click Chemistry Tools (Scottsdale, Arizona, U.S.A.).

Site-Directed Mutagenesis of DARPins Containing Internal Methionine Codons. A single point mutation was introduced into the nonbinding control DARPin N3C[21] to generate the mutation M34L, leading to a gene product devoid of internal methionines. The plasmid pQE30ss-N3C was amplified using the primers 5′-ATCCTGCTGGCTAACGGTGCTGACGTT-3′ and 5′-TAGCCAGCAGGATACGAACTT CGTCGT-3′ followed by a *Dpn*I digest for 2 h. The mutated vector was transformed into chemocompetent *E. coli* XL1 blue cells and single colonies were used to inoculate overnight cultures. After sequencing, a positive clone was subcloned into the expression vector pQIq (a $lacI^q$ encoding variant of pQE30 (Qiagen, Hilden, Germany) with a double stop codon) using *Bam*HI and *Hin*dIII.

Tumor Cell Culture. The EpCAM-positive MCF7 breast carcinoma cell line was obtained from ATCC (American Type Culture Collection, LGC Standards S.à.r.l., Molsheim Cedex, France) and grown in a mixture of Dulbecco modified Eagle's medium (DMEM) (50% v/v) and Ham F12 medium (50% v/v) (Sigma, Buchs, Switzerland) supplemented with 10% fetal calf serum (Amimed, Bioconcept, Allschwil, Switzerland), 100 units/mL of penicillin and 100 μg/mL of streptomycin (Sigma). The cells were incubated at 37 °C in a humidified atmosphere (containing 5% CO_2) and were tested mycoplasma-negative.

Expression and Purification of Clickable DARPins. *E. coli* B834 (DE3) was freshly transformed with the plasmid pQIq encoding anti-EpCAM DARPin Ec1[16] or the off-target control DARPin N3C. The latter is a full-consensus DARPin[21] without any specificity for EpCAM or any other cell-binding activity. A single colony was used to inoculate an overnight culture of 2 × YT medium supplemented with 100 μg/mL ampicillin and 1% glucose. On the next day, 1 L of 2 × YT medium supplemented with 50 μg/mL ampicillin and 1% glucose was inoculated at an optical density at 600 nm (OD_{600}) of 0.1 and grown in a shake flask at 37 °C until an OD_{600} of 1.0−1.2 was reached. The culture was subsequently centrifuged (5000 × *g*, 15 min, 4 °C) and washed thoroughly by resuspending the pellet in ice−cold 0.9% NaCl solution. The washing step was repeated 2 times on ice and the residual pellet transferred into M9 minimal medium (SelenoMethionine Medium Base (Molecular Dimensions LTD, Newmarket, United Kingdom) supplemented with a nutrient mix containing 19 amino acids (Molecular Dimensions Ltd., New Market, Suffolk, U.K.), 50 mg/L ampicillin and 40 mg/L L-azidohomoalanine (Aha) (Bapeks, Riga, Latvia) or L-homopropargylglycine (Hpg) (Chiralix B.V., Nijmegen, Netherlands). The cultures were shaken for 15 min at 30 °C and then induced with 1 mM IPTG. After expression for 4 h, cultures were pelleted by centrifugation (20 min, 5000 × *g*, 4 °C), the pellet was washed with 0.9% NaCl and stored overnight at −80 °C.

After thawing, the bacterial cultures were lysed 3−4 times using a French press (Aminco) at 1200 psi and the DARPin was purified by IMAC.[11] The protein was eluted with PBS_E (1 × PBS, 300 mM imidazole, pH 7.4), dialyzed overnight against 1 × PBS pH 7.4, analyzed by 15% SDS PAGE, and stored at 4 °C.

N-Terminal Sequencing. Incorporation of the non-natural amino acid Aha was verified using N-terminal protein sequencing. A volume of 2 μL DARPin (ca. 5 μg) was diluted

in 100 μL 0.1% TFA and loaded on a Prosorb Sample Preparation Cartridge (ABI). The membrane was washed twice with 0.1% TFA. Edman degradation was performed using a PROCISE cLC492 system to determine N-terminal amino acid residues.

Amino Acid Hydrolysis. The amino acid composition of clickable DARPin was quantified by amino acid hydrolysis using the AccQ Tag Ultra kit (Waters GmbH, Eschborn, Germany). The protein (22.6 μg in 10 μL PBS) was dried followed by a vapor phase hydrolysis in 6 M HCl for 24 h at 110 °C under argon. The dried sample was dissolved in 50 μL borate buffer before 10 μL of the sample were derivatized according to the manufacturer's recommendations. A UPLC system (Waters) was used to separate the amino acids, including norvaline as an internal standard and transferrin as a reference protein.

ELISA. The binding of Aha-Ec1 and Met-Ec1 was compared using an ELISA as previously described.[16]

Synthesis of DBCO-PEG$_{20\ kDa}$. Five milligrams (1 equiv, 13.45 mM) DBCO-NH$_2$ (Click Chemistry Tools, Macon, GA, U.S.A.) was dissolved in 1 mL dichloromethane and 400 mg (1.5 equiv, 20 mM) NHS-mPEG$_{20\ kDa}$ (JenKem Technology Inc., U.S.A.) was added in 3 mL dichloromethane. This solvent was used to decrease viscosity. The reaction was stirred overnight at room temperature under N_2 atmosphere, and an aliquot was analyzed using thin layer chromatography (TLC) and ninhydrin staining. Finally, the reaction was quenched with a 1000-fold molar excess of ethylene diamine (4 h, at RT), followed by evaporation of the organic solvent under vacuum (Rotavapor, Büchi, Flawil, Switzerland). The resulting modified PEG polymer was redissolved in ddH_2O and lyophilized to complete dryness for 48 h in a freeze−dryer (Brouwer, Rotkreuz, Switzerland). During the course of this study, purified DBCO-PEG$_{20\ kDa}$ became commercially available (Click Chemistry Tools) and was also used for PEGylation of clickable DARPins.

Cu-Free Click PEGylation of DARPins. The clickable DARPin Aha-Ec1 was reacted with a 2-fold molar excess of DBCO-PEG$_{20\ kDa}$ at 4 °C and aliquots were taken over time, snap frozen, and stored at −20 °C. The time-dependent reaction was analyzed by 15% SDS PAGE and Coomassie staining.

Dual-Tagging of DARPins by Conjugation with Alexa488 and DBCO-PEG$_{20\ kDa}$. For dual-tagging, the clickable DARPin Aha-Ec1 containing a C-terminal cysteine was expressed, purified, dialyzed, and stored frozen as described above. The DARPin (12 mg/mL in PBS) was thawed on ice and reduced for 30 min at 37 °C with 50 mM Tris(2-carboxyethyl)-phosphine hydrochloride (TCEP, Pierce, Thermo Fisher Scientific, Lausanne, Switzerland) followed by desalting on a PD-10 column (GE Healthcare Europe GmbH, Switzerland), equilibrated with freshly degassed and N_2-flushed PBS pH 7.2. The concentrations of the desalted DARPins were determined at 280 nM (Nanodrop 1000, Thermo Scientific, Switzerland) (usually around 300 μM) and a 2-fold molar excess of Alexa Fluor 488 C5 maleimide (Invitrogen, Life Technologies Europe BV, Zug, Switzerland) was added in typically 100 μL DMF. The dye was coupled for 1.5 h at 37 °C and quenched with a 10-fold molar excess of DTT. The conjugate was further purified by anion exchange chromatography with a MonoQ GL 5/50 column connected to an Äkta Explorer FPLC device (GE Healthcare Europe GmbH, Glattbrugg, Switzerland). The protein was diluted in buffer A (50 mM Hepes, 20 mM NaCl, pH 8.5), loaded on the MonoQ column and eluted with a gradient of buffer B (50 mM Hepes, 1 M NaCl, pH 8.5). The fractions containing labeled DARPin were pooled and concentrated (Amicon Ultra-4 Centrifugal Filter Unit, MWCO 3 kDa, Millipore, U.S.A.) according to the manufacturer's protocol.

An aliquot of the Alexa-labeled DARPin (typically around 300 μM) was mixed with a 2-fold molar excess of DBCO-PEG$_{20\ kDa}$ (Click Chemistry Tools) from a 5 mM stock in PBS and vortexed. The click reaction was performed at 4 °C for 72 h in PBS pH 7.2 without agitation, and PEGylated DARPin was separated from free DBCO-PEG$_{20\ kDa}$ and non-PEGylated DARPin using anion exchange chromatography (MonoQ GL 5/50) sequentially equilibrated with buffers A and B via a step gradient. The PEG$_{20\ kDa}$-DARPin-Alexa488 conjugate was further concentrated using an Amicon centrifugal filter unit (MWCO 3 kDa, Millipore, U.S.A.) before the quality was assessed by 15% SDS PAGE in combination with a fluorimeter (LAS 3000, Fujifilm Europe GmbH, Düsseldorf, Germany) followed by Coomassie staining. The protein concentration was quantified using the Pierce 660 nm protein assay kit (Pierce) and unlabeled Ec1 to generate a standard curve as reference. Dual tagged DARPins were stored in the dark at −80 °C until use.

Analytical Gel Filtration. Unconjugated and PEG-conjugated DARPins were evaluated by analytical gel filtration with a Superdex 200 PC3.2/30 column in combination with an Äkta Micro FPLC (GE Healthcare Europe GmbH, Switzerland). Degassed and sterile filtered PBS pH 7.2 was used as running buffer. A standard containing β-amylase, BSA, and cytochrome *c* was used to determine the apparent molecular weights ($M_{w,app}$) of the DARPin.

Preparation of Cells for Affinity Measurement. Affinity measurements with DARPins on cells were performed using a Partec CyFlow Space flow cytometer (Partec GmbH, Görlitz, Germany). MCF7 cells were grown as described above to a confluency of 70%. The cells were washed twice with PBS and detached with trypsin-EDTA, followed by resuspension in PBS-BA (1 × PBS, 1% BSA, 0.2% NaN_3). Cells were quantified with a CASY cell counter (Roche Diagnostics GmbH, Germany) and incubated for 30 min at 37 °C in this azide-containing buffer to inhibit further receptor internalization.

Determination of Dissociation Rates from Cells. After centrifugation (300 × *g*, 3 min, RT), 0.75 × 10^6 cells/mL were resuspended in PBS-BA containing 100 nM Ec1-Alexa488, PEG$_{20\ kDa}$-Ec1-Alexa488, or the nonbinding controls N3C-Alexa488 or PEG$_{20\ kDa}$-N3C-Alexa488, which were used to assess nonspecific background binding on cells. Cells were incubated for 1.5 h at 4 °C on a rocker to allow complete saturation with the binder. A typical off-rate experiment was started by centrifugation of cells (300 × *g*, 3 min, RT) followed by removal of the supernatant and resuspension of the pellet in PBS-BA supplemented with 1 μM unlabeled Ec1 as competitor to prevent rebinding. Untreated cells were used to determine background autofluorescence. The median fluorescence intensities (MFI) of the time points (corrected for any sample preparation time) were determined using the *FlowJo* software (v 7.6.4, Treestar Inc., U.S.A.). The data was plotted using *Prism* (v 5.04, GraphPad Software Inc., U.S.A.) and all curves were fitted using a monoexponential decay function.

Determination of Association Rates on Cells. A final concentration of 67.5 nM, 22.5 nM, 7.5 nM, and 2.5 nM of Ec1-Alexa488 and PEG20$_{kDa}$-Ec1-Alexa488 was prepared in 6 mL PBS-BA at room temperature. The association measurement was started by addition of 2.1 × 10^6 MCF7 cells in 1 mL PBS-BA (final concentration 3 × 10^5 cells/mL, total volume 7 mL for each construct and concentration). N3C-Alexa488 and PEG$_{20\ kDa}$-N3C-Alexa488 were used as controls to assess

dx.doi.org/10.1021/bc200591x | *Bioconjugate Chem.* 2012, 23, 279−286

nonspecific background binding on cells. The MFI of the data points were determined as described above and fitted to a mono-exponential function of time using the *Prism* software. The corresponding k_{off} measured in the dissociation experiment on cells for each binder was used as a constraint to calculate k_{on}.

RESULTS

Expression and Purification of Clickable DARPin Ec1c. To obtain a unique label at the N-terminus of the DARPin, we introduced the non-natural amino acid azidohomoalanine (Aha), a methionine mimic, to allow modification by bio-orthogonal click chemistry. We used the methionine-auxotroph *E. coli* strain B834 (DE3) and exchanged the medium to M9 minimal medium supplemented with Aha to allow quantitative incorporation of Aha at amino acid position one. Since the second amino acid is Arg, the initiator Met is not cleaved.[17,18] Freshly transformed cells were first grown in 2 × YT medium to obtain fast growth rates and high cell densities, followed by washing to deplete extracellular methionine from the expression cultures. After inoculation into M9 minimal medium, residual intracellular methionine pools were additionally decreased by a delayed induction of the cultures with IPTG. Expression of DARPin was shown to continue in a time-dependent manner as monitored by SDS PAGE (SI Figure S1). After IMAC purification, a yield of 30 mg of protein per liter culture in shake flasks was determined (SI Figure S2).

Analysis of Clickable DARPin. The IMAC-purified clickable DARPin was analyzed by N-terminal Edman sequencing in comparison to unmodified DARPin Ec1 (SI Figure S3). In the latter, methionine gave a specific peak with a retention time of 17.5 min, whereas this peak was decreased to background levels in the chromatogram of clickable DARPin. For these proteins, Edman degradation revealed a new peak for the first N-terminal amino acid with a retention time of approximately 16 min, which can be assigned to the non-natural amino acid Aha. The N-terminal sequence was Aha-Arg-Gly-Ser, with a minor fraction starting with the sequence Arg-Gly-Ser, indicating that the N-terminal Aha was cleaved off. The proteins were completely devoid of methionine. Conventionally expressed DARPin showed the amino acid sequence Met-Arg-Gly-Ser (with a minor fraction starting with Arg-Gly-Ser) without the appearance of a peak at 16 min, which was seen with the protein prepared from *E. coli* grown in the presence of Aha.

The single introduction of Aha into the DARPin and the absence of methionines was further confirmed by amino acid analysis after total hydrolysis (SI Table S1). A complete absence of methionine in the Aha-containing DARPins was determined, whereas one methionine, the initiator codon, was present in conventionally expressed DARPin Ec1, as expected from the amino acid sequence. Both Aha- and Met-containing DARPins were further compared by ELISA. Binding to EpCAM was fully retained after the introduction of the non-natural amino acid at position 1 (SI Figure S4).

In addition, we expressed Hpg-containing DARPins using the medium exchange method. Both Hpg-DARPins and Aha-DARPins were reactive under CuAAC conditions using Cu(I) as catalyst, and could thus be coupled to each other, forming a covalent dimer (SI Figure S5), while suitable controls showed no dimer formation.

Synthesis of DBCO-PEG$_{20\ kDa}$. DBCO-PEG$_{20\ kDa}$ was prepared from DBCO-NH$_2$ and NHS-mPEG. The resulting polymer was devoid of free amino groups, as analyzed by TLC and ninhydrin staining, demonstrating that DBCO-NH$_2$ had quantitatively reacted with the excess of NHS-mPEG overnight (Figure 1). After quenching with ethylene diamine and lyophilization, the generated DBCO-PEG$_{20\ kDa}$ was used for Cu-free PEGylation of "clickable" DARPin.

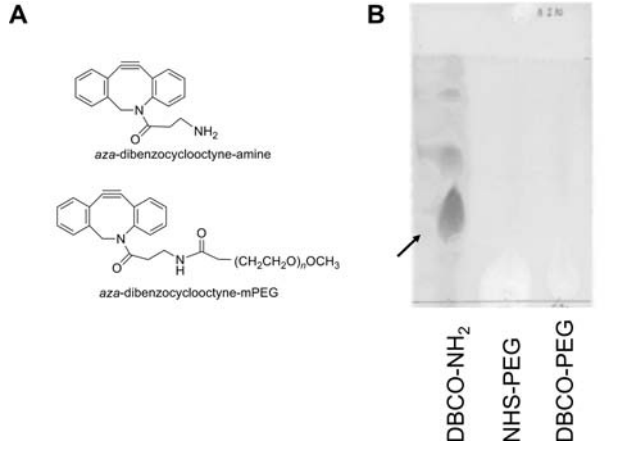


Figure 1. (A) Chemical structure of DBCO-NH$_2$ and DBCO-PEG. (B) Analysis of DBCO-PEG using thin layer chromatography and ninhydrin staining.

Bio-Orthogonal Coupling of Clickable DARPins Using Cu-Free Click Chemistry. The DBCO-PEG$_{20\ kDa}$ was coupled to "clickable" DARPins resulting in PEGylation exclusively at the N-terminus. A 2-fold molar excess of DBCO-PEG$_{20\ kDa}$ was found to be a good compromise to maximize reactivity and minimize viscosity of the reaction mixture, and was thus used for further reactions (SI Figure S6). "Clickable" DARPins reacted with DBCO-PEG$_{20\ kDa}$ in several buffers and pH values tested almost to completion over 48 h at 4 °C (data not shown) without agitation. PEGylation with DBCO-PEG$_{20\ kDa}$ led to a distinct mono-PEGylated product, monitored as a shift to a single band by SDS PAGE in a time-dependent manner (Figure 2).

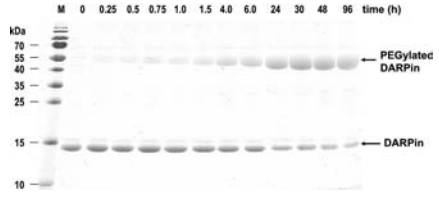


Figure 2. PEGylation of 100 μM Aha-Ec1 using a 2-fold molar excess of DBCO-PEG$_{20\ kDa}$ as a function of time at 4 °C. The conversion to PEGylated DARPin was analyzed by 15% SDS PAGE.

Preparation of Ec1-Alexa488 and PEG$_{20\ kDa}$-Ec1-Alexa488 for Affinity Measurements. N-terminally "clickable" DARPins, which also carried a single C-terminal cysteine-tag (Gly-Gly-Cys), were expressed using the medium exchange method described above for incorporation of Aha to allow site-specific PEGylation via click chemistry, and Alexa488-labeling on the same molecule via thiol chemistry (Figure 3). First, the IMAC-purified clickable DARPin was completely reduced, since disulfide bridged dimers form during the production. To prevent

dx.doi.org/10.1021/bc200591x | *Bioconjugate Chem.* 2012, 23, 279–286

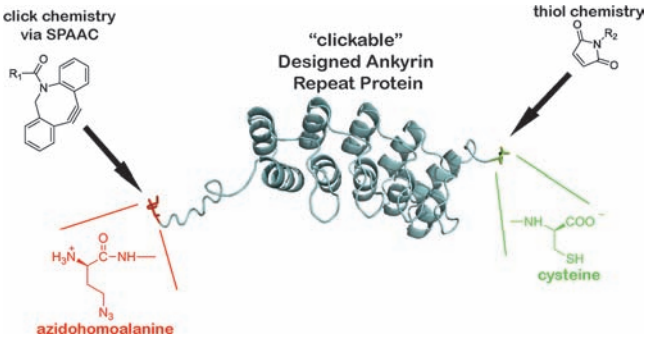


Figure 3. Schematic illustration of the EpCAM-targeting "clickable" DARPin Ec1. The protein can be labeled N-terminally via click chemistry and C-terminally via thiol chemistry using different conjugates.

interference of a high excess of TCEP with the coupling reaction, the samples were desalted prior to the addition of Alexa dye in degassed PBS. Ec1-Alexa488 was subsequently purified using anion exchange chromatography to separate the product from free dye and unlabeled DARPin. As shown in SI Figure S7A, the labeled protein eluted at higher salt concentration than the unlabeled one as a consequence of the increased negative charge of Ec1-Alexa488.

In a second step, one-half of the resulting Ec1-Alexa488 was N-terminally PEGylated using DBCO-$PEG_{20\,kDa}$, leading to a mono-PEGylated product. The Cu-free click-PEGylation was run for 72 h at 4 °C allowing high conversion of the DARPin to the PEGylated form. The reaction mixture was purified by anion exchange chromatography (SI Figure S7B) as described elsewhere,[22] concentrated and analyzed by 15% SDS PAGE. All constructs were obtained at high purity with the expected band for the mono-PEGylated DARPins Ec1 and N3C (Figure 4).

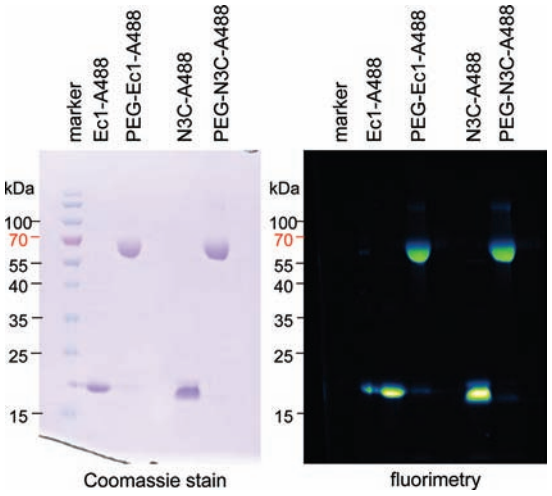


Figure 4. SDS PAGE analysis of non-PEGylated and PEGylated Alexa488-labeled DARPins Ec1 and N3C used for affinity measurements on cells. The proteins were analyzed by Coomassie stain (left) and fluorimetry to detect Alexa488 (right).

Analytical Gel Filtration. Ec1-Alexa488 and $PEG_{20\,kDa}$-Ec1-Alexa488 were analyzed by gel filtration in order to determine the increase in hydrodynamic radius caused by mono-PEGylation at the N-terminus (SI Figure S8). Non-PEGylated Ec1-Alexa488 eluted with a retention volume of 1.81 mL ($M_{w,app}$ = 17.4 kDa). PEGylation of Ec1-Alexa488 lead to an increase in its hydrodynamic radius with a retention volume of 1.31 mL ($M_{w,app}$ = 250 kDa). It is well-known[23] that the hydrodynamic radius of a PEGylated protein is much larger than its nominal M_w of 19 + 20 = 39 kDa.

Binding Kinetics: Determination of the Dissociation and Association Rates on Cells. $PEG_{20\,kDa}$-Ec1-Alexa488 and Ec1-Alexa488 were used as fluorescent probes to determine the dissociation rates from MCF7 breast carcinoma cells. For both binders, nearly identical k_{off} values were determined (Ec1-Alexa488: 2.35 × 10^{-5} s^{-1}; $PEG_{20\,kDa}$-Ec1-Alexa488: 1.96 × 10^{-5} s^{-1}). However, the maximum MFI differed for both constructs, with PEGylated DARPins reaching a maximal intensity of only 65% of the original signal of the non-PEGylated DARPins (Figure 5).

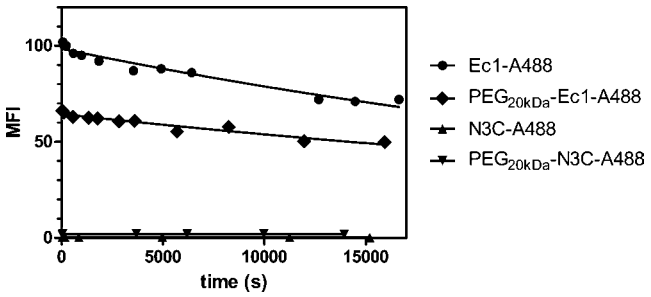


Figure 5. Determination of dissociation rates of PEGylated and non-PEGylated Ec1 from MCF7 cells.

The association rates of PEGylated and non-PEGylated DARPins were also assessed by flow cytometry and monitored over time using four different concentrations of DARPins (Figure 6). Non-PEGylated Ec1-Alexa488 associated with a k_{on}

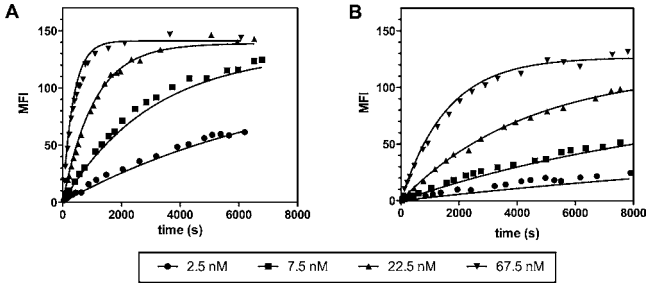


Figure 6. Determination of the association rate of Ec1-Alexa488 (A) and $PEG_{20\,kDa}$-Ec1-Alexa488 (B) on MCF7 cells.

of 4.0 × 10^4 M^{-1} s^{-1}. In contrast, conjugation of a single $PEG_{20\,kDa}$ polymer at the N-terminus led to a decrease in association rates with a k_{on} of 8.9 × 10^3 M^{-1} s^{-1}. The off-target control DARPins N3C-Alexa488 and $PEG_{20\,kDa}$-N3C-Alexa488 showed only minor background binding on MCF7 cells.

The overall K_D of Ec1-Alexa488 on the tumor cells was thus determined from k_{off}/k_{on} as 578 pM. Mono-PEGylation of Ec1-Alexa488 resulted in a decreased affinity with a K_D of 2.18 nM (Table 1).

DISCUSSION

There is growing interest in using alternative scaffolds as binding proteins for biomedical applications as they show distinct advantages over monoclonal antibodies and recombinant antibody fragments, particularly with respect to options for rational engineering, provided the proteins are very robust.[24] As an

dx.doi.org/10.1021/bc200591x | Bioconjugate Chem. 2012, 23, 279–286

Table 1. Results from Affinity Measurements on MCF7 Cells Using Flow Cytometry

	k_{on} (M^{-1} s^{-1})	k_{off} (s^{-1})	K_D (M)	fold change (over Ec1)
Ec1-Alexa488	4×10^4	2.3×10^{-5}	5.8×10^{-10}	-
$PEG_{20\ kDa}$-Ec1-Alexa488	8.9×10^3	2.0×10^{-5}	2.2×10^{-9}	3.8

example, DARPins can be conveniently engineered to well expressing, stable high-affinity binders in mono- and multispecific formats and fusion proteins, and they can be used for tumor targeting either as pure binding proteins to inhibit growth factor receptor signaling, or as bioconjugates equipped with various effector functions.[10]

Performance and Analysis of the Click Chemistry with DARPins. Site-directed coupling of two or more different moieties to one and the same binding protein would increase its modularity and functional spectrum for biomedical applications. For example, a DARPin might be conjugated to a drug to deliver antitumor activity, and it could be further equipped with a PEG moiety at a distinct site to modify its pharmacokinetic properties.[4] DARPins have no natural cysteines, and thus single Cys residues can be easily engineered into suitable positions to enable site-specific conjugation with various effector moieties, typically by using maleimide chemistry, to couple chelators for radiolabeling, liposomes, PEG, or cytotoxic anticancer agents.[25]

However, the problem comes with introducing the second conjugate. If two cysteines were used, difficult separations of positional isomers need to be established. If lysines are used, heterogeneity is almost unavoidable.[26] If the N-terminal amino group is used, which is privileged because of greater reactivity than lysines,[6,20,27] reaction conditions and separation must be optimized to avoid reaction with lysines as a side reaction and/or large amounts of nonreacted protein.

Here, we report that orthogonal click chemistry together with site-specific maleimide linkage is fully compatible with engineering different effector functions into one binding protein to obtain a heterobifunctional bioconjugate. We demonstrate this with an EpCAM-specific DARPin (Ec1) as an example of a binding protein selected for tumor targeting.[16] First, maleimide-Alexa488 was coupled to a C-terminal cysteine and purified using anion exchange chromatography, before in a second step the fluorescent DARPin was PEGylated with the polymer DBCO-$PEG_{20\ kDa}$ using Cu-free click chemistry. The so-modified Ec1 DARPin was fully functional and used in this study to determine the effect of PEGylation on binding to EpCAM on tumor cells without the shortcomings of conventional unspecific labeling techniques.[1,26]

The copper(I)-catalyzed azide−alkyne [3 + 2] cycloaddition (CuAAC) reaction was described as a pioneering platform for the synthesis of orthogonal conjugates and could prove useful for site-specific modification of therapeutic proteins as shown for superoxide dismutase[6] or antibody fragments.[28] However, even in well purified preparations, contamination by potentially cytotoxic copper, reducing agents, and poorly soluble Cu(I)-stabilizing chelating ligands, required to catalyze the triazole formation, limits biomedical applications and may interfere with the protein's activity.[29] Recently, reagents for strain-promoted azido-alkyne cycloaddition (SPAAC) became available that have enabled site-specific coupling under mild conditions without the shortcomings of CuAAC mentioned above.[30] The click reactions between substituted cyclooctynes and azides have now repeatedly been described as a good alternative for efficient and specific protein labeling *in vitro*[7] and *in vivo*.[8,31] Furthermore, numerous linker constructs have become available promoting fast conversion reactions in aqueous solution. One of these compounds, *aza*-dibenzocyclooctyne (abbreviated either as DIBAC or DBCO), offers favorable properties for click conjugation. Recently, a DBCO-$mPEG_{2\ kDa}$ moiety was generated for PEGylation of Aha-CalB, an azido-containing lipase, using Cu(I)-free click chemistry without loss of enzymatic activity. Unfortunately, the study unveiled increased stoichiometries of PEG attached to the protein, which occurred in a time-dependent manner. In this case, the presence of five ATG codons in the CalB gene resulted in the metabolic introduction of five Aha's into the enzyme during expression, responsible for the limited control over PEGylation stoichiometries and attachment sites.[9,32] Thus, a protein with multiple methionine codons would not provide an ideal basis to selective site-specific labeling.

DARPins have no methionine in the internal repeats, and the one in the original N-cap design (M34) can be replaced by a leucine—a residue found at the corresponding position in the internal repeats—to give a fully equivalent molecule. In general, the occurrence of methionines in the randomized positions of DARPins is very low, an excellent prerequisite for the introduction of clickable methionine surrogates at well-defined positions and quantities for practically all members of the library. The choice of the second amino acid after the initiator codon determines whether the first amino acid is cleaved off or not.[17,18] If Aha is to be introduced at another position, a small amino acid has to be chosen for position 2.

With other proteins, such as antibody fragments, this N-terminal labeling strategy is more challenging due to their high content of internal methionines[28] and the additional complication with the cleavable signal sequence needed for transport to the periplasm, or, in its absence, the necessity of refolding.

Here, we expressed "clickable" DARPins using a medium exchange method for the introduction of Aha specifically at the N-terminus. Despite the use of minimal medium, up to 30 mg/L soluble protein was obtained from *E. coli* cultures after IMAC purification. Since DARPins in general can be expressed in high amounts, this property inherent to DARPins seems to be maintained even in the presence of the unnatural amino acid.[11,16] The "clickable" DARPins did not show any difference from conventionally expressed DARPins as analyzed on SDS PAGE, or on gel filtration or ELISA (SI Figures S2, S4, S8). Approximately 85% of the DARPin reacted with PEG, and we assume that the remaining 15% had lost the N-terminal Aha due to processing of the primary amino acid, presumably by *E. coli* methionine amino-peptidase,[18] as detected by N-terminal sequencing. The click reaction itself is thus essentially complete.

In summary, the click chemistry leads to very clean products and convenient regiospecific labeling, and in conjunction with maleimide−thiol chemistry, to a facile and versatile double labeling procedure suitable for scale-up.

Analysis of Binding Kinetics of PEGylated DARPins on Cells with Doubly Labeled DARPins. Being able to introduce PEG at the N-terminus of a DARPin at a single functional azide together with Alexa488 at a C-terminal cysteine permitted us to measure association and dissociation kinetics on tumor cells. PEGylated and non-PEGylated DARPins showed similar dissociation rates, which we previously also reported for PEGylated Her2-binding antibody fragments using surface plasmon resonance measurements.[19] On the other hand, comparison of the absolute levels of bound PEGylated and non-PEGylated

dx.doi.org/10.1021/bc200591x | *Bioconjugate Chem.* 2012, 23, 279−286

DARPins unveiled a difference, suggesting that the number of receptors accessible to the PEGylated DARPin was reduced due to steric hindrance by the PEG tails of already surface-bound DARPins, resulting in dynamic blocking effects.[19] Once the DARPin binds to its target, the conjugated PEG probably shields neighboring epitopes on the cells, resulting in *inter*molecular inhibition, without affecting the dissociation rate constant k_{off}.

Determination of the association rate constant k_{on} of PEGylated DARPins on cells by using FACS identified a clear difference between non-PEGylated and mono-PEGylated binders, with the PEGylated DARPins associating with a 3.8-fold slower rate, probably due to the *intra*molecular shielding effects by the large hydration shell provided by the PEG moiety.[5] Since the off-rate is unchanged and the on-rate is reduced, the resulting affinity of the PEGylated DARPin Ec1 on EpCAM-positive cells was reduced 3.8-fold, compared to the non-PEGylated counterpart (2.18 nM vs 578 pM, respectively).

Previously, studies of the effect of PEG on the on-rate and off-rate of binding proteins were limited to label-free methods such as surface plasmon resonance.[19] However, being now able to produce binding molecules that can simultaneously be conjugated via thiol and click chemistries allowed us to study these and other phenomena directly on cells in detail.

Our finding on cells are fully consistent with those previously found *in vitro*.[19] Without the double labeling, only the equilibrium binding on cells could previously be measured, showing a 5-fold reduced binding affinity after PEGylation, which is again fully consistent with our current findings. The fact that these effects are observed for DARPins and for antibody scFv fragments also emphasizes that they are generic and determined by the properties of PEG, and much less by the properties of the protein. Briefly, in all these cases the PEG was attached at a position most distal from the target binding site and PEG did not statically prevent binding in any way. Also, the population of molecules was fully functional, i.e., all binding molecules (DARPins and scFv) could be bound to the target when target was in excess.[19] Furthermore, the binding site was not distorted, since the off-rate was identical within experimental error.

Our data are consistent with the previous notion that PEGylation has two intrinsic effects: First, it transiently and dynamically blocks the binding site, decreasing the number of binders which can associate at any one time, thereby decreasing the observed on-rate. This is not an effect of diffusion, as the off-rate is not influenced, as detailed previously.[19] Since ultimately all molecules can bind, this inhibition is transient, and is only seen in the association kinetics. We have termed this *"intra*molecular blocking".

The second effect comes into play after binding to a surface, previously the surface on a BIACORE chip,[19] in the present work a cell surface. The PEG moiety prevents binding to epitopes on neighboring molecules, thereby decreasing the total amount of available binding epitopes. This effect also influences the observed kinetics at intermediate times.[19] We have termed this *"inter*molecular blocking".

We have thus shown for the first time directly that these effects are also operational on cells. We hypothesize that, by the nature of these effects, this will be observed for any PEGylated protein, and thus a small decrease of on-rate—and consequently of affinity—is intrinsic to the derivatization with a hydrophilic tail, while the effect on the saturation level of binding will depend on the receptor density of the cell.

CONCLUSIONS

In summary, the compatibility of the DARPin format with click chemistry and site-specific maleimide coupling together with an expanding amount of commercially available moieties for bioconjugation holds promise for tailor-made functionalization of these binding proteins. Potential fields of biomedical application include tumor targeting with therapeutic and diagnostic payloads, such as "click-ready" nanoparticles,[33] virus-like particles,[34] dendrimers,[35] radioisotopes,[36] or fluorophores,[37] but also applications in making diagnostic devices, where specifically derivatized DARPins may have to be coupled in a site-directed manner to a surface.

ASSOCIATED CONTENT

Supporting Information

One supplementary table, and 8 supplementary figures document purification and analysis of the bioconjugates. This material is available free of charge via the Internet at http://pubs.acs.org.

AUTHOR INFORMATION

Corresponding Author

*E-mail: plueckthun@bioc.uzh.ch. Tel.: +41-44-635-5570. Fax: +41-44-635-5712.

ACKNOWLEDGMENTS

We thank Nikolas Stefan and Dr. Jörg Ziegler for their help and scientific discussion, Christian Reichen and Marc-Simon Schwer for the model of the structure Aha-Ec1c, Dr. Peter Hunziker for N-terminal sequencing and amino acid analysis at the Functional Genomics Center Zurich (FGCZ), and Dr. Andrei Polukhtin for scientific discussion and provision of DBCO-$PEG_{20\ kDa}$. Funding was obtained from Swiss Cancer League KFS 02448-08-2009 and Schweizerischer Nationalfonds 310030_119859 to UZW and 3100A0-113720 to AP.

REFERENCES

(1) Finn, M. G., and Fokin, V. V. (2010) Click chemistry: function follows form. *Chem. Soc. Rev. 39*, 1231−1232.

(2) Nwe, K., and Brechbiel, M. W. (2009) Growing applications of "click chemistry" for bioconjugation in contemporary biomedical research. *Cancer Biother. Radiopharm. 24*, 289−302.

(3) Lutz, J.-F., and Zarafshani, Z. (2008) Efficient construction of therapeutics, bioconjugates, biomaterials and bioactive surfaces using azide-alkyne "click" chemistry. *Adv. Drug Delivery Rev. 60*, 958−970.

(4) Veronese, F. M., and Pasut, G. (2005) PEGylation, successful approach to drug delivery. *Drug Discovery Today 10*, 1451−1458.

(5) Caliceti, P., and Veronese, F. (2003) Pharmacokinetic and biodistribution properties of poly(ethylene glycol)-protein conjugates. *Adv. Drug Delivery Rev. 55*, 1261−1277.

(6) Deiters, A., Cropp, T. A., Summerer, D., Mukherji, M., and Schultz, P. G. (2004) Site-specific PEGylation of proteins containing unnatural amino acids. *Bioorg. Med. Chem. 14*, 5743−5745.

(7) Sletten, E. M., and Bertozzi, C. R. (2008) A hydrophilic azacyclooctyne for Cu-free click chemistry. *Org. Lett. 10*, 3097−3099.

(8) Baskin, J. M., Prescher, J. A., Laughlin, S. T., Agard, N. J., Chang, P. V., Miller, I. A., Lo, A., Codelli, J. A., and Bertozzi, C. R. (2007) Copper-free click chemistry for dynamic in vivo imaging. *Proc. Natl. Acad. Sci. U.S.A. 104*, 16793−16797.

(9) Debets, M. F., van Berkel, S. S., Schoffelen, S., Rutjes, F. P. J. T., van Hest, J. C. M., and van Delft, F. L. (2010) Aza-dibenzocyclooctynes for fast and efficient enzyme PEGylation via copper-free (3 + 2) cycloaddition. *Chem. Commun. 46*, 97−99.

(10) Boersma, Y. L., and Plückthun, A. (2011) DARPins and other repeat protein scaffolds: advances in engineering and applications. *Curr. Opin. Biotechnol. 22*, 849−857.
(11) Binz, H. K., Stumpp, M. T., Forrer, P., Amstutz, P., and Plückthun, A. (2003) Designing Repeat Proteins: Well-expressed, soluble and stable proteins from combinatorial libraries of consensus ankyrin repeat proteins. *J. Mol. Biol. 332*, 489−503.
(12) Steiner, D., Forrer, P., and Plückthun, A. (2008) Efficient selection of DARPins with sub-nanomolar affinities using SRP phage display. *J. Mol. Biol. 382*, 1211−1227.
(13) Zahnd, C., Kawe, M., Stumpp, M. T., de Pasquale, C., Tamaskovic, R., Nagy-Davidescu, G., Dreier, B., Schibli, R., Binz, H. K., Waibel, R., and Plückthun, A. (2010) Efficient tumor targeting with high-affinity designed ankyrin repeat proteins: effects of affinity and molecular size. *Cancer Res. 70*, 1595−1605.
(14) Zahnd, C., Pecorari, F., Straumann, N., Wyler, E., and Plückthun, A. (2006) Selection and characterization of Her2-binding Designed Ankyrin Repeat Proteins. *J. Biol. Chem. 281*, 35167−35175.
(15) Martin-Killias, P., Stefan, N., Rothschild, S., Plückthun, A., and Zangemeister-Wittke, U. (2011) A novel fusion toxin derived from an EpCAM-specific designed ankyrin repeat protein has potent antitumor activity. *Clin. Cancer Res. 17*, 100−110.
(16) Stefan, N., Martin-Killias, P., Wyss-Stoeckle, S., Honegger, A., Zangemeister-Wittke, U., and Plückthun, A. (2011) DARPins recognizing the tumor-associated antigen EpCAM selected by phage and ribosome display and engineered for multivalency. *J. Mol. Biol. 413*, 826−843.
(17) Hirel, P., Schmitter, J., Dessen, P., Fayat, G., and Blanquet, S. (1989) Extent of N-terminal methionine excision from Escherichia coli proteins is governed by the side-chain length of the penultimate amino acid. *Proc. Natl. Acad. Sci. U.S.A. 86*, 8247−8251.
(18) Wang, A., Winblade Nairn, N., Johnson, R. S., Tirrell, D. A., and Grabstein, K. (2008) Processing of N-terminal unnatural amino acids in recombinant human interferon-beta in Escherichia coli. *ChemBioChem 9*, 324−330.
(19) Kubetzko, S., Sarkar, C. A., and Plückthun, A. (2005) Protein PEGylation decreases observed target association rates via a dual blocking mechanism. *Mol. Pharmacol. 68*, 1439−1454.
(20) Tamaskovic, R., Simon, M., Stefan, N., Schwill, M., and Plückthun, A. (2012) Designed Ankyrin Repeat Proteins (DARPins): From research to therapy. *Methods Enzymol 503*, 101−134.
(21) Wetzel, S. K., Settanni, G., Kenig, M., Binz, H. K., and Plückthun, A. (2008) Folding and unfolding mechanism of highly stable full-consensus ankyrin repeat proteins. *J. Mol. Biol. 376*, 241−257.
(22) Seely, J. E., and Richey, C. W. (2001) Use of ion-exchange chromatography and hydrophobic interaction chromatography in the preparation and recovery of polyethylene glycol-linked proteins. *J. Chromatogr. 908*, 235−241.
(23) Yang, K., Basu, A., Wang, M., Chintala, R., Hsieh, M. C., Liu, S., Hua, J., Zhang, Z., Zhou, J., Li, M., Phyu, H., Petti, G., Mendez, M., Janjua, H., Peng, P., Longley, C., Borowski, V., Mehlig, M., and Filpula, D. (2003) Tailoring structure-function and pharmacokinetic properties of single-chain Fv proteins by site-specific PEGylation. *Protein Eng. Des. Sel. 16*, 761−770.
(24) Binz, H. K., Amstutz, P., and Plückthun, A. (2005) Engineering novel binding proteins from nonimmunoglobulin domains. *Nat. Biotechnol. 23*, 1257−1268.
(25) Stumpp, M. T., Binz, H. K., and Amstutz, P. (2008) DARPins: A new generation of protein therapeutics. *Drug Discovery Today 13*, 695−701.
(26) Hermanson, G. T. (2008) *Bioconjugate Techniques*, 2nd ed. Academic Press, London.
(27) Kinstler, O., Molineux, G., Treuheit, M., Ladd, D., and Gegg, C. (2002) Mono-N-terminal poly(ethylene glycol)-protein conjugates. *Adv. Drug Delivery Rev. 54*, 477−485.
(28) Selvakumar, E., Rameshkumar, N., Lee, S.-G., Lee, S.-J., and Park, H.-S. (2010) In vivo production of functional single-chain Fv fragment with an N-terminal-specific bio-orthogonal reactive group. *ChemBioChem 11*, 498−501.
(29) Bundy, B. C., and Swartz, J. R. (2010) Site-specific incorporation of p-propargyloxyphenylalanine in a cell-free environment for direct protein-protein click conjugation. *Bioconjugate Chem. 21*, 255−263.
(30) Jewett, J. C., and Bertozzi, C. R. (2010) Cu-free click cycloaddition reactions in chemical biology. *Chem. Soc. Rev. 39*, 1272−1279.
(31) Laughlin, S. T., and Bertozzi, C. R. (2009) In vivo imaging of Caenorhabditis elegans glycans. *ACS Chem. Biol. 4*, 1068−1072.
(32) Schoffelen, S., Lambermon, M. H. L., Eldijk, M. B. V., and Hest, J. C. M. V. (2008) Site-specific modification of Candida antarctica Lipase B via residue-specific incorporation of a non-canonical amino acid. *Bioconjugate Chem. 19*, 1127−1131.
(33) de Graaf, A. J., Kooijman, M., Hennink, W. E., and Mastrobattista, E. (2009) Nonnatural amino acids for site-specific protein conjugation. *Bioconjugate Chem. 20*, 1281−1295.
(34) Patel, K. G., and Swartz, J. R. (2011) Surface functionalization of virus-like particles by direct conjugation using azide−alkyne click chemistry. *Bioconjugate Chem. 22*, 376−387.
(35) Ledin, P. A., Friscourt, F., Guo, J., and Boons, G.-J. (2011) Convergent assembly and surface modification of multifunctional dendrimers by three consecutive click reactions. *Chem.—Eur. J. 17*, 839−846.
(36) Bouvet, V., and Wuest, M. (2011) Copper-free click chemistry with the short-lived positron emitter fluorine-18. *Org. Biomol. Chem. 9*, 7393−7399.
(37) Qi, J., Han, M.-S., Chang, Y.-C., and Tung, C.-H. (2011) Developing visible fluorogenic "click-on" dyes for cellular imaging. *Bioconjugate Chem. 22*, 1758−1762.

Bioconjugate Chemistry

Technical Note

pubs.acs.org/bc

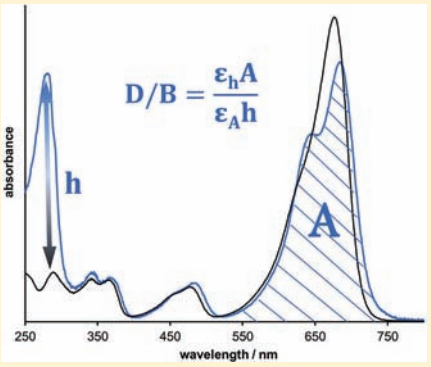
Determination of the Labeling Density of Fluorophore–Biomolecule Conjugates with Absorption Spectroscopy

Markus Grabolle,[†] Robert Brehm,[†] Jutta Pauli,[†] Franziska M Dees,[‡] Ingrid Hilger,[‡] and Ute Resch-Genger*[,†]

[†]BAM Federal Institute for Materials Research and Testing, Division Biophotonic, Richard-Willstaetter-Str. 11, D-12489 Berlin, Germany

[‡]Institut für Diagnostische und Interventionelle Radiologie des Klinikums der Friedrich-Schiller-Universität Jena (IDIR), Forschungszentrum Lobeda, Erlanger Allee 101, D-07747 Jena, Germany

ABSTRACT: Dye–biomolecule conjugation is frequently accompanied by considerable spectral changes of the dye's absorption spectrum that limit the use of the common photometrical method for the determination of labeling densities. Here, we describe an improvement of this method using the integral absorbance of the dye instead of its absorbance at the long wavelength maximum to determine the concentration of the biomolecule-coupled dye. This approach is illustrated for three different cyanine dyes conjugated to the antibody IgG.



INTRODUCTION

One of the most important issues in the life sciences is the sensitive, selective, fast, and reliable detection of analytes such as physiological and disease-related biomarkers or potentially hazardous species at low concentrations, often in parallel (multiplexed assays) and in high-throughput screening assays or even *in vivo* in animal models for cancer research.[1−4] The use of highly sensitive and simple fluorescence techniques for target recognition and quantification typically requires labeling of biomolecules such as antibodies, antibody fragments, proteins or peptides with fluorescent reporters. In addition, fluorophore-labeled (secondary) antibodies are also common tools, e.g., for immunohistochemistry, flow cytometry, and fluorescence microscopy.[5,6] One key parameter to bright and comparable dye–biomolecule conjugates presents the (average) number of dye molecules attached to a biomolecule (labeling density).[7−9] Knowledge of the labeling density is relevant, e.g., for the evaluation and optimization of labeling procedures and, due to the use of such dye–biomolecule conjugates as analytical and detection tools, also for the accuracy and reproducibility of the accordingly obtained results as well as for the comparison of label performance.[6,10−13]

Dye-to-biomolecule (D/B) ratios are typically determined photometrically as recommended in the literature[8,14] and by many manufacturers of dyes and labeling kits due to the simplicity and cost efficiency of this approach and the widespread availability of spectrometers and microplate readers measuring absorption spectra. The concentrations of the dye c_D and the biomolecule c_B are obtained from the absorbance at the dye's long wavelength absorption maximum A_D and the absorbance at the absorption maximum of the biomolecule A_{UV} (280 nm for proteins; 260 nm for DNA and RNA) and the D/B is calculated according to eq 1.

$$D/B = \frac{c_D}{c_B} = \frac{\varepsilon_{B,UV} \cdot A_D}{\varepsilon_D \cdot (A_{UV} - f \cdot A_D)} \quad (1)$$

Here, ε_D and $\varepsilon_{B,UV}$ are the molar absorption coefficients of the dye and the biomolecule at its respective absorption maximum. The factor f that accounts for the absorbance of the fluorophore at the biomolecule's absorption maximum equals the ratio of the dye absorbance at this wavelength to its absorbance at the long wavelength absorption maximum of the dye.

This approach, referred to here as *maximum method*, assumes that the absorption spectrum of the dye–biomolecule conjugate is a linear combination of the absorption spectra of the nonconjugated dye and the biomolecule. Hence, accurate results are only obtained in the absence of conjugation-induced changes of the label's and the biomolecule's absorption spectrum.[8] However, in many cases, binding-induced alterations in the absorption spectrum of the dye occur due to (i) changes in the fluorophore's microenvironment (solvent polarity, specific dye–biomolecule interactions) and (ii) dye–dye interactions.[11,15−18] The occurrence and size of these changes that are most pronounced for dye aggregation depend on chromophore class, dye substitution pattern,[8,10,15,16,19] and

Received: June 29, 2011
Revised: December 19, 2011
Published: December 31, 2011

ACS Publications © 2011 American Chemical Society

the distance between the biomolecule-bound dyes.[11,12,20−23] In the case of such alterations, use of eq 1 can introduce significant errors in the determination of dye-to-biomolecule ratios.

Here, we describe a simple modification of the common photometric method which can account for significant binding-induced changes in the dye's absorption spectrum due to the use of the integral absorbance of the dye's long wavelength absorption band (referred to here as *integral method*). Although this integral method has been previously used infrequently,[12,24] up to now, no explicit description of this procedure has been given. In addition, this procedure is detailed here for three representative fluorescent labels and the antibody immunoglobuline G (IgG) and the labeling densities obtained with the conventional maximum method and the integral method are compared.

EXPERIMENTAL SECTION

DY-676, DY-678, and DY-682 were provided by Dyomics GmbH (Jena, Germany). Polyclonal IgG from rabbit serum for the preparation of the IgG conjugates was purchased from Sigma-Aldrich Chemie GmbH (Steinheim, Germany). All solvents used were of spectroscopic grade and purchased from Sigma Aldrich. Phosphate buffered saline solution (PBS, pH 7.4) was obtained from GIBCO Life Sciences (Paisley, Scotland). IgG conjugates of DY-676, DY-678, and DY-682 were obtained by reacting IgG with the amine-reactive *N*-hydroxysuccinimidyl (NHS) esters of the dyes (statistical labeling) in DMF in accordance with the manufacturer's protocol using identical reaction conditions for all the chromophores (e.g., solvent, pH, temperature, reaction time). Dye NHS ester-to-IgG ratios of 3:1, 6:1, and 24:1 (starting materials) were always used to vary the labeling density. The resulting IgG conjugates were purified chromatographically (column filled with Sephadex G-25 Medium; GE-Healthcare Amersham, Freiburg, Germany). SDS (sodium dodecyl sulfate) was purchased from Sigma Aldrich. All spectra were recorded on a CARY 5000 spectrometer (Varian Inc., Palo Alto, USA) using 1 cm quartz cells for the IgG conjugated dyes and quartz cells with optical pathlengths varying from 0.01 to 1 cm for the aggregation studies of the free dyes. The molar absorption coefficients of the dyes in PBS were determined to be 1.15×10^5, 1.30×10^5, and 1.10×10^5 M^{-1} cm^{-1} for DY-676, DY-678, and DY-682 using dye concentrations where dye dimerization can be neglected. For IgG, a molar absorption coefficient of 2.10×10^5 M^{-1} cm^{-1} at 280 nm was employed (information from the manufacturer).

RESULTS AND DISCUSSION

Integral Method. The integral method relies on the assumption that the integral absorption coefficient ε_F (see eq 2) associated with the long wavelength absorption band remains approximately constant upon binding to the biomolecule (see next section).

$$\varepsilon_F = \int_{\Delta\nu} \varepsilon(\nu)\, d\nu \approx \text{const} \tag{2}$$

Here, ν is the wavenumber or frequency. Hence, instead of using the absorbance at the absorption maximum A_D to determine the dye concentration c according to eq 3 (l is the optical path length)

$$A_D = c \cdot l \cdot \varepsilon_D \tag{3}$$

we employ the integral absorbance F (eq 4).

$$F = c \cdot l \cdot \int_{\Delta\nu} \varepsilon(\nu)\, d\nu = \int_{\Delta\nu} A(\nu)\, d\nu \tag{4}$$

The dye-to-biomolecule ratio D/B can then be calculated using eq 5.

$$D/B = \frac{\varepsilon_{B,UV} \cdot F}{\varepsilon_F \cdot (A_{UV} - x \cdot F)} \tag{5}$$

The integral absorption coefficient of the dye ε_F which substitutes ε_D in eq 1 is obtained from eq 6

$$\varepsilon_F = \varepsilon_D \frac{F}{A_D} \tag{6}$$

The factor x in eq 5 (substituting f in eq 1) that accounts for the absorbance of the dye at the wavelength of the biomolecule's absorption maximum, is obtained from the absorption spectrum of the free dye by determining the ratio of the absorbance at this wavelength $A_{D,UV}$ to the integral absorbance F of the dye's long wavelength band (see eq 7).

$$x = \frac{\varepsilon_{D,UV}}{\varepsilon_F} = \frac{A_{D,UV}}{F} \tag{7}$$

The integration required for the calculation of F (eq 4) has to be performed on a wavenumber (or frequency) scale. As the spectra provided by most spectrometers are given on a wavelength scale, this requires transformation of the measured spectra to a wavenumber scale prior to integration. Alternatively, the integration can be performed on a wavelength scale after division of the absorbance at wavelength λ, $A(\lambda)$, by λ^2 (eq 8).

$$F = \int_{\Delta\lambda} \frac{A(\lambda)}{\lambda^2}\, d\lambda \tag{8}$$

Numerically, the integration is performed as a summation over the complete wavelength region covered by the dye's long wavelength absorption band (eq 9).

$$F = \sum_i \frac{A(\lambda_i)}{\lambda_i^2}(\lambda_{i+1} - \lambda_i) \tag{9}$$

The index i indicates the data point number i of the spectrum. For long wavelength absorbing dyes and spectral changes comparable in size to those shown here (see, e.g., Figure 2), division by λ^2 can be omitted as detailed below, if an accordingly introduced systematic error in F of maximal 3% is acceptable. Then, eqs 10 and 11 can be employed.

$$F \approx \int_{\Delta\lambda} A(\lambda)\, d\lambda \tag{10}$$

$$F \approx \sum_i A(\lambda_i) \cdot (\lambda_{i+1} - \lambda_i) \tag{11}$$

In any case, the calculation of F has to be performed consistently using either eqs 8 and 9 or eqs 10 and 11 because of the different numerical values obtained with both methods. The term $(\lambda_{i+1} - \lambda_i)$ in eqs 9 and 11 that accounts for the spacing of the data points on the wavelength axis (step size) can be omitted if the step size is identical for all spectra used for the determination of the labeling density.

Integral Absorption Coefficient: Dye–Dye and Biomolecule–Dye Interaction. The integral method relies on the assumption that irrespectively of alterations in the shape of the absorption spectrum, the integral absorption coefficient of the dye's long wavelength absorption band does not change upon attachment to the biomolecule. This is not necessarily the case. The most pronounced alterations of the absorption spectrum upon bioconjugation are attributed to dye–dye interactions on the biomolecule, i.e., the formation of aggregates. Despite of these alterations in the shape of the spectrum, the integral absorption coefficient is expected to remain constant. This follows from exciton theory which describes dye–dye interactions as an interaction between the transition dipole moments of the individual chromophores.[25,26] For biomolecule-bound dyes, aggregation should be limited to the formation of dimers or small aggregates consisting of only few dye molecules.[8,15,18,19,23,27–30] In this case, the intensity of the absorption is only spectrally redistributed and the integral absorption coefficient should remain constant (conservation of oscillator strength). Deviations in oscillator strength have been only reported for large aggregates consisting of a high number of dye molecules (hyper- or hypochromism)[31,32] the formation of which seems rather unlikely for typical D/B ratios employed in bioconjugation.

Other possible sources of changes in absorption present interactions between the dye and the biomolecule. A change in (local) refractive index at the protein surface sensed by the dye affects the integral absorption coefficient, with the relative change of this coefficient equaling the relative change of the refractive index.[33,34] Variations of the refractive index can also influence the dye's transition dipole moment. As estimated from absorption measurement in different solvents, such effects can lead to deviations in the integral absorbance of about 10–20% for π–π^* transitions, the type of optical transition corresponding to the long wavelength absorption band of common labels.[35,36] Also, it cannot be precluded that charged groups at the biomolecule as well as aromatic moieties of amino acids or nucleotides interact with the dye resulting in a different integral absorption. As the actual microenvironment of an individual dye is generally not known, it is difficult to quantify the size of these effects. Nevertheless, this uncertainty does not diminish the advantage of the integral method because the maximum method is equally subject to such changes in the integral absorption.

Application Example: Labeling Density of Fluorophore–IgG Conjugates. To exemplify the use of the integral method and compare its results with the labeling densities obtained with the conventional maximum method, we determined the D/B ratios of three model bioconjugates consisting of the antibody IgG covalently labeled with various amounts of the cyanine dyes DY-676, DY-678, and DY-682, often used, e.g., as fluorescent reporters for molecular imaging applications. Figure 1 shows the normalized absorption spectra of the IgG-bound dyes for different labeling densities together with the spectra of the free dyes in PBS. With increasing dye-to-biomolecule ratio, the absorption band of IgG at 280 nm decreases relative to the absorption band of the dye located at about 660 nm. For all dyes, IgG conjugation results in a small red shift of the absorption band of the chromophore, denoting a change in the polarity of the dye's microenvironment, and to an enhanced absorption blue-shifted from the chromophore's main absorption band, superimposed on the vibronic shoulder of the free dye's absorption band. This new absorption band,

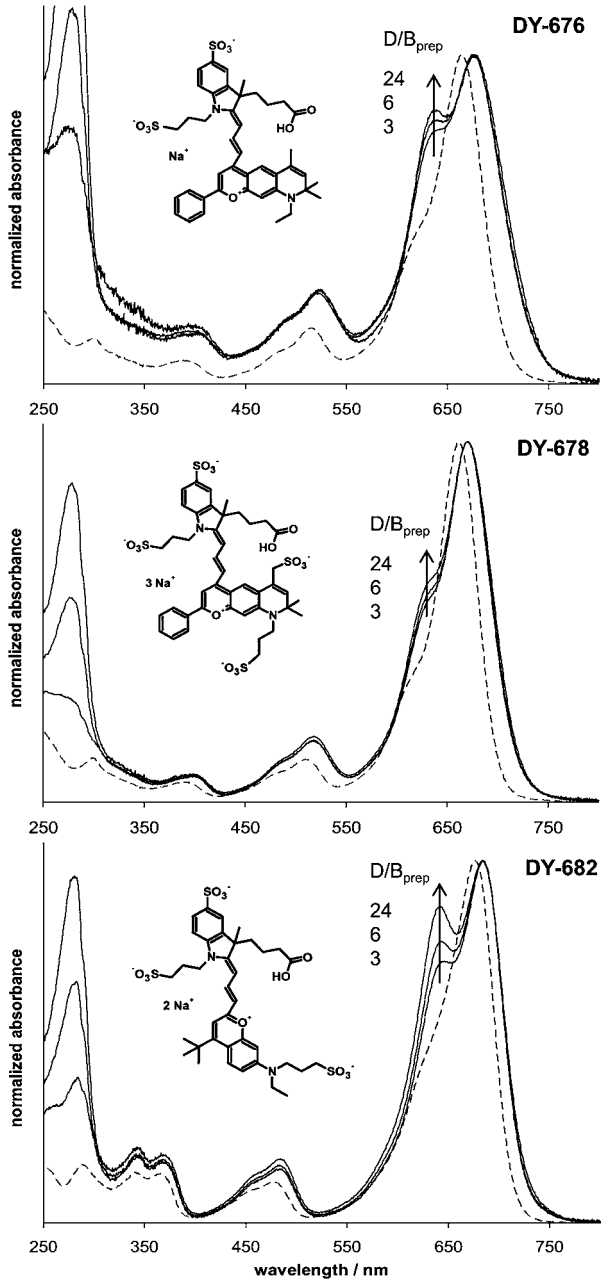


Figure 1. Normalized absorption spectra of IgG conjugated DY-676, DY-678, and DY-682 differing in dye-to-biomolecule (D/B) ratio (solid lines) and the normalized absorption spectra of the non-conjugated dyes (dashed line) in PBS. The insets show the chemical structures of the dyes.

the intensity of which increases with advancing D/B ratios, is indicative of the formation of H-type dimers of the protein-bound dyes.[11,15,16]

Dimer formation was verified by the measurement of concentration-dependent absorption spectra of the free dyes (Figure 2), leading to similar spectral changes of the long wavelength absorption band as shown in Figure 1. The isosbestic points found for all dyes (Figure 2) emphasize the sole existence of two spectroscopically distinguishable species that are assigned to monomeric and dimeric dye molecules. A similar behavior has been reported for many analytically and bioanalytically relevant chromophores such as fluorescein, rhodamine, cyanine, and BODIPY dyes.[11,15,16]

dx.doi.org/10.1021/bc2003428 | Bioconjugate Chem. 2012, 23, 287–292

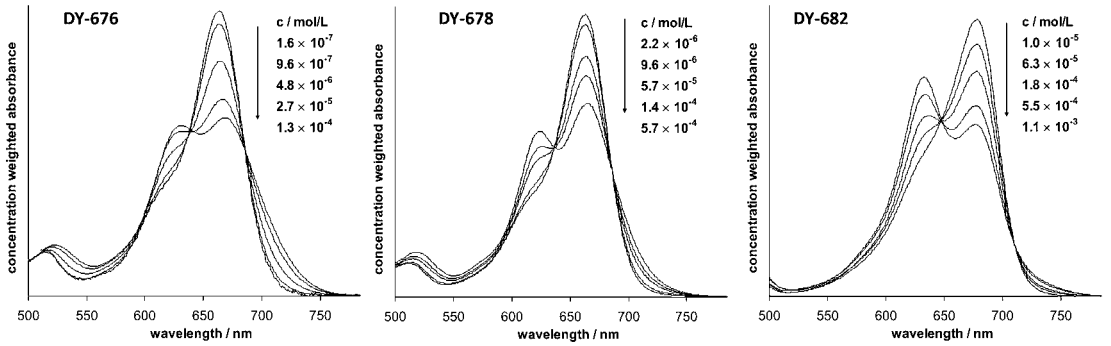


Figure 2. Aggregation-induced changes of the absorption spectra of DY-676, DY-678, and DY-682. Shown are the concentration-weighted absorbances for different dye concentration in PBS.

Subsequently, we used the maximum and the integral method for the calculation of the labeling densities of our bioconjugates from the spectra shown in Figure 1. For the integral method, integration was performed on a wavelength scale using eq 9. The lower integration limit was the local minimum of each spectrum located at 530−570 nm on the short wavelength side of the main absorption band. The upper limit was 800 nm for all spectra, thus integrating over the complete $S_0 \rightarrow S_1$ transition. The choice of the short wavelength integration boundary can introduce a small uncertainty as the spectral overlap between the $S_0 \rightarrow S_1$ transition and transitions to higher electronic states are not taken into account. A more accurate procedure considering this spectral overlap would require decomposition of each absorption spectrum into individual absorption bands.

The D/B values obtained with both methods are summarized in Table 1. Figure 3 illustrates the differences between the D/B ratios calculated with both methods in dependence of the D/B ratio employed in the preparation mixtures. For all samples studied, the integral method yields significantly higher D/B values, with the size of the deviation between both methods being moderately dye-specific. For all dyes, the difference increases with labeling density. For DY-676, we observed a deviation of a factor of 1.9 for the highest labeling density when comparing both methods. In the case of less aggregating DY-678 and DY-682, this factor was on the order of 1.7. These results demonstrate the significant systematic deviations that can be introduced into photometrically determined D/B values by the use of the intensity of the dye's main absorption band and eq 1. The differences in the D/B values obtained with both methods depend solely on the size of the binding-induced changes in the shape of the dye's absorption spectrum. Independent of the type of dye employed, the spectral position of its absorption band, and the origin of these binding-induced changes, similar alterations in the spectral shape result in similar deviations between the integral and the maximum method. The D/B ratios calculated here always present average values due to the chosen bioconjugation chemistry that allows only for statistical labeling.

Table 1. D/B Ratios of the IgG Conjugates of DY-676, DY-678, and DY-682 Obtained with the Maximum Method (eq 1) and the Integral Method (eq 5)

dye	D/B in preparation mixture	maximum method $(D/B)_{max}$	integral method $(D/B)_{int}$	$(D/B)_{int}/(D/B)_{max}$
DY-676	3	1.04	1.75	1.68
	6	1.61	2.83	1.76
	24	2.68	5.07	1.90
DY-678	3	2.45	3.25	1.33
	6	3.97	5.61	1.41
	24	9.81	16.3	1.66
DY-682	3	1.81	2.46	1.36
	6	2.77	4.04	1.46
	24	5.35	9.34	1.75

Protein Unfolding. To verify the higher D/B values obtained with the integral method, we measured the absorption spectra of the previously studied IgG conjugates in the presence of the protein-unfolding agent SDS.[8,16,37,38] The absorption spectra of IgG conjugates of DY-676 and DY-682, differing in the chemical structure and in dye hydrophilicity, before and after addition of 5% SDS are exemplarily shown in Figure 4. In the presence of SDS, the enhanced absorption shoulder at the short wavelength side of the dye's main absorption band, indicative of the presence of H-type dimers, decreases whereas the absorption of the main peak increases in intensity, thus indicating more or less complete deaggregation of the IgG-bound dye (see Figure 2). For these deaggregated systems, nearly identical D/B ratios are obtained with the maximum method and the integral method (see Table 2) with the D/B ratios resulting from the latter method being unaffected by SDS addition. The slightly lower D/B values of the SDS-treated conjugates calculated with the maximum method can be attributed to a very small fraction of remaining aggregates.

Integral Absorbance on a Wavelength Scale. In order to estimate the systematic error of the integral method introduced by integration on a wavelength scale without division by λ^2 (see eqs 10 and 11), we compared the integral absorbances obtained with eqs 9 and 11 for the absorption spectra of DY-682 at concentrations of 1.0×10^{-5} and 1.1×10^{-3} M that show the most pronounced spectral deviations. Division by λ^2 (eq 9) yields identical values of the integrals for both spectra, whereas without division by λ^2 (eq 11), both integrals differ by 2.8%. Hence, for bioconjugation-induced spectral changes similar in size or less pronounced than the changes described here (Figure 2), integration without division by λ^2 can be thus used as a good approximation.

CONCLUSION AND OUTLOOK

With the replacement of the dye absorbance at the long wavelength maximum by the integral absorbance of the long wavelength absorption band, we describe a simple improvement of the common photometrical method for the

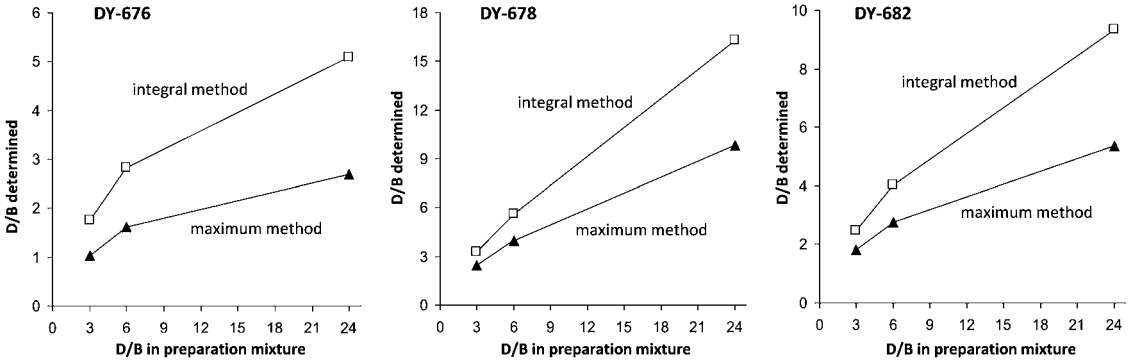


Figure 3. D/B ratios of the IgG conjugates of DY-676, DY-678, and DY-682 calculated with the maximum method (eq 1) and the integral method (eq 5) dependent on the D/B ratio employed in the preparation mixtures.

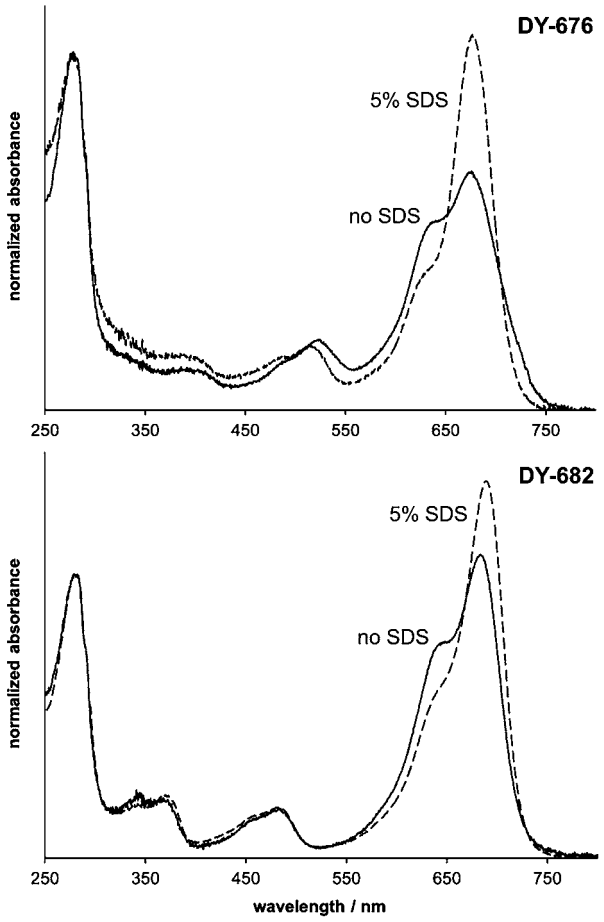


Figure 4. Effect of the protein-unfolding agent SDS on the absorption spectra of the IgG conjugates of DY-676 and DY-682; absorption spectra before (solid lines) and after (dashed lines) treatment of the bioconjugates (D/B ratio in the preparation mixtures of 3:1) with 5% SDS. The spectra are normalized at the absorption maximum of the protein.

determination of labeling densities of dye–biomolecule conjugates that show significant changes in the dye absorption spectrum compared to the nonconjugated dye. Using this integral method, we obtain 30–90% higher labeling densities for the studied cyanine dyes coupled to IgG than with the common maximum method. The integral method is valid for all types of biomolecules and bioconjugates, independent of the fluorescent reporter used, the spectral position of the dye's absorption band and the origin of changes in the spectral shape of the dye's absorption band. Its application is expected, e.g., to improve the overall comparability of literature data on fluorophore–biomolecule conjugates, thereby providing the basis for a more reliable evaluation of label performance. Compared to other procedures suggested for the characterization of such conjugates that are based on the use of agents like SDS or formamide,[8,16,37,38] the integral method is more simple and less time-consuming and the dye-labeled proteins are not denatured, maintaining their biological function.

Table 2. D/B Ratios of the IgG Conjugates of DY-676 and DY-682 before and after Addition of 5% SDS as Protein-Unfolding Agent Calculated with the Maximum Method (eq 1) and the Integral Method (eq 5) and the Ratios of the D/B Values Obtained with Both Methods[a]

dye	solvent	maximum method $(D/B)_{max}$	integral method $(D/B)_{int}$	$(D/B)_{int}/(D/B)_{max}$
DY-676	no SDS	1.19	2.12	1.78
	5% SDS	1.96	2.02	1.03
DY-682	no SDS	1.86	2.54	1.37
	5% SDS	2.43	2.58	1.06

[a]The dye-to-protein ratio in the reaction mixture for the synthesis of the IgG conjugates was always 3:1.

AUTHOR INFORMATION

Corresponding Author

*Phone: ++49 30 8104 1134, fax: ++49 30 8104 1157, e-mail: ute.resch@bam.de.

ACKNOWLEDGMENTS

We are grateful to DYOMICS GmbH (Jena, Germany) for the generous supply of DY-676, DY-678, and DY-682.

REFERENCES

(1) Weissleder, R., and Pittet, M. J. (2008) Imaging in the era of molecular oncology. *Nature 452*, 580.

(2) Wu, J., Fu, Z. F., Yan, F., and Ju, H. X. (2007) Biomedical and clinical applications of immunoassays and immunosensors for tumor markers. *Trends Anal. Chem. 26*, 679.

(3) Master, S. R., Bierl, C., and Kricka, L. J. (2006) Diagnostic challenges for multiplexed protein microarrays. *Drug Discovery Today (DDT) 11*, 1007.

(4) Borisov, S. M., and Wolfbeis, O. S. (2008) Optical biosensors. *Chem. Rev. 108*, 423.

(5) Andreeff, M., and Pinkel, D. (1999) *Introduction to Fluorescence In Situ Hybridization: Principals and Clinical Applications*, Wiley-Liss, New York.
(6) Resch-Genger, U. (2008) *Standardization and Quality Assurance in Fluorescence Measurements II Bioanalytical and Biomedical Applications*, 1st ed., Springer-Verlag, Berlin.
(7) Waggoner, A. (1995) Covalent labeling of proteins and nucleic-acids with fluorophores. *Methods Enzymol. 246*, 362.
(8) Mujumdar, R. B., Ernst, L. A., Mujumdar, S. R., Lewis, C. J., and Waggoner, A. S. (1993) Cyanine dye labeling reagents - sulfoindocyanine succinimidyl esters. *Bioconjugate Chem. 4*, 105.
(9) Wells, A. F., Miller, C. E., and Nadel, M. K. (1966) Rapid fluorescein and protein assay method for fluorescent-antibody conjugates. *Appl. Microbiol. 14*, 271.
(10) Resch-Genger, U., Grabolle, M., Cavaliere-Jaricot, S., Nitschke, R., and Nann, T. (2008) Quantum dots versus organic dyes as fluorescent labels. *Nat. Methods 5*, 763.
(11) Gruber, H. J., Hahn, C. D., Kada, G., Riener, C. K., Harms, G. S., Ahrer, W., Dax, T. G., and Knaus, H. G. (2000) Anomalous fluorescence enhancement of Cy3 and Cy3.5 versus anomalous fluorescence loss of Cy5 and Cy7 upon covalent linking to IgG and noncovalent binding to avidin. *Bioconjugate Chem. 11*, 696.
(12) Luchowski, R., Matveeva, E. G., Gryczynski, I., Terpetschnig, E. A., Patsenker, L., Laczko, G., Borejdo, J., and Gryczynski, Z. (2008) Single molecule studies of multiple-fluorophore labeled antibodies. Effect of homo-FRET on the number of photons available before photobleaching. *Curr. Pharmaceut. Biotechnol. 9*, 411.
(13) Berlier, J. E., Rothe, A., Buller, G., Bradford, J., Gray, D. R., Filanoski, B. J., Telford, W. G., Yue, S., Liu, J., Cheung, C.-Y., Chang, W., Hirsch, J. D., Beechem, J. M., and Haughland, R. P. (2003) Quantitative comparison of long-wavelength Alexa Fluo dyes to Cy dyes: fluorescence of the dyes and their bioconjugates. *J. Histochem. Cytochem. 51*, 1699.
(14) Haughland, R. P. (1995) *Coupling of monoclonal antibodies with fluorophores*, Vol *45*, Humana Press, Totowa, NJ, .
(15) Pauli, J., Vag, T., Haag, R., Spieles, M., Wenzel, M., Kaiser, W. A., Resch-Genger, U., and Hilger, I. (2009) An in vitro characterization study of new near infrared dyes for molecular imaging. *Eur. J. Med. Chem. 44*, 3496.
(16) Mujumdar, R. B., Ernst, L. A., Mujumdar, S. R., and Waggoner, A. S. (1989) Cyanine dye labeling reagents containing isothiocyanate groups. *Cytometry 10*, 11.
(17) Ogawa, M., Kosaka, N., Choyke, P. L., and Kobayashi, H. (2009) H-type dimer formation of fluorophores: a mechanism for activatable, in vivo optical molecular imaging. *ACS Chem. Biol. 4*, 535.
(18) Packard, B. Z., Komoriya, A., Toptygin, D. D., and Brand, L. (1997) Structural characteristics of fluorophores that form intra-molecular H-type dimers in a protease substrate. *J. Phys. Chem. B 101*, 5070.
(19) Luschtinetz, F., Dosche, C., and Kumke, M. U. (2009) Influence of streptavidin on the absorption and fluorescence properties of cyanine dyes. *Bioconjugate Chem. 20*, 576.
(20) Toutchkine, A., Nalbant, P., and Hahn, K. M. (2002) Facile synthesis of thiol-reactive Cy3 and Cy5 derivatives with enhanced water solubility. *Bioconjugate Chem. 13*, 387.
(21) Johansson, M. K., and Cook, R. M. (2003) Intramolecular dimers: A new design strategy for fluorescence-quenched probes. *Chem.—Eur. J. 9*, 3466.
(22) Burke, M., O'Sullivan, P. J., Ponomarev, G. V., Yashunsky, D. V., and Papkovsky, D. B. (2007) Analysis of close proximity quenching of phosphorescent metalloporphyrin labels in oligonucleotide structures. *Anal. Chim. Acta 585*, 139.
(23) Schobel, U., Egelhaaf, H.-J., Brecht, A., Oelkrug, D., and Gauglitz, G. (1999) New donor-acceptor pair for fluorescent immunoassays by energy transfer. *Bioconjugate Chem. 10*, 1107.
(24) Matveeva, E. G., Terpetschnig, E. A., Stevens, M., Patsenker, L., Kolosova, O. S., Gryczynski, Z., and Gryczynski, I. (2009) Near-infrared squaraine dyes for fluorescence enhanced surface assay. *Dyes Pigm. 80*, 41.
(25) Davydov, A. S. (1971) *Theory of Molecular Excitons*, Plenum Press, New York.
(26) Kasha, M., Rawls, H. R., and El-Bayoumi, M. A. (1965) The exciton model in molecular spectroscopy. *Pure Appl. Chem. 11*, 371.
(27) Packard, B. Z., Komoriya, A., Nanda, V., and Brand, L. (1998) Intramolecular excitonic dimers in protease substrates: Modification of the backbone moiety to probe the H-dimer structure. *J. Phys. Chem. B 102*, 1820.
(28) Buschmann, V., Weston, K. D., and Sauer, M. (2003) Spectroscopic study and evaluation of red-absorbing fluorescent dyes. *Bioconjugate Chem. 14*, 195.
(29) Eisfeld, A., and Briggs, J. S. (2006) The J- and H-bands of organic dye aggregates. *Chem. Phys. 324*, 376.
(30) Pauli, J., Grabolle, M., Brehm, R., Spieles, M., Hamann, F. M., Wenzel, M., Hilger, I., and Resch-Genger, U. (2011) Suitable labels for molecular imaging - influence of dye structure and hydrophilicity on the spectroscopic properties of IgG conjugates. *Bioconjugate Chem. 22*, 1298.
(31) Rhodes, W. (1961) Hypochromism and other spectral properties of helical polynucleotides. *J. Am. Chem. Soc. 83*, 3609.
(32) Vekshin, N. L. (2002) *Photonics of Biopolymers*, Springer, Berlin.
(33) Valeur, B. (2001) *Molecular Fluorescence*, Wiley-VCH, Weinheim.
(34) Birks, J. B. (1970) *Photophysics of Aromatic Molecules*, Wiley-Interscience, London.
(35) Knox, R. S. (2003) Dipole and oscillator strengths of chromophores in solution. *Photochem. Photobiol. 77*, 492.
(36) Myers, A. B., and Birge, R. R. (1980) The effect of solvent environment on molecular electronic oscillator-strengths. *J. Chem. Phys. 73*, 5314.
(37) Southwick, P. L., Ernst, L. A., Tauriello, E. W., Parker, S. R., Mujumdar, R. B., Mujumdar, S. R., Clever, H. A., and Waggoner, A. S. (1990) Cyanine dye labeling reagents - carboxymethylindocyanine succinimidyl esters. *Cytometry 11*, 418.
(38) Reddington, M. V. (2007) Synthesis and properties of phosphonic acid containing cyanine and squaraine dyes for use as fluorescent labels. *Bioconjugate Chem. 18*, 2178.

Bioconjugate Chemistry

Technical Note

pubs.acs.org/bc

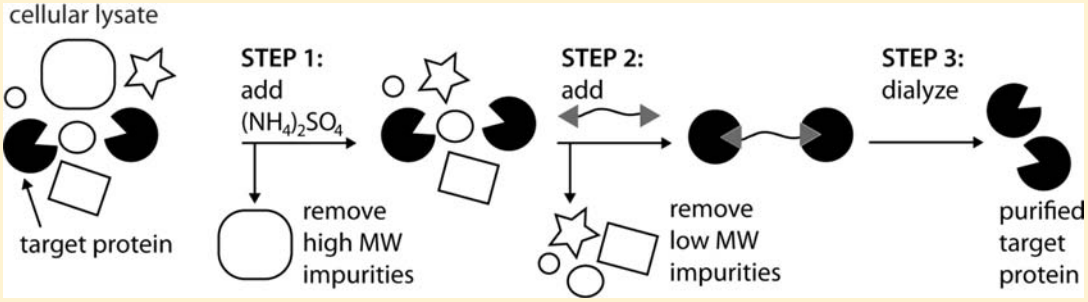
Selective Precipitation and Purification of Monovalent Proteins Using Oligovalent Ligands and Ammonium Sulfate

Katherine A. Mirica,[†] Matthew R. Lockett,[†] Phillip W. Snyder,[†] Nathan D. Shapiro,[†] Eric T. Mack,[†] Sarah Nam,[†] and George M. Whitesides*[,†,‡]

[†]Department of Chemistry and Chemical Biology, Harvard University, 12 Oxford Street, Cambridge, Massachusetts 02138, United States

[‡]Wyss Institute for Biologically Inspired Engineering, Harvard University, 60 Oxford Street, Cambridge, Massachusetts 02138, United States

Supporting Information



ABSTRACT: This paper describes a method for the selective precipitation and purification of a monovalent protein (carbonic anhydrase is used as a demonstration) from cellular lysate using ammonium sulfate and oligovalent ligands. The oligovalent ligands induce the formation of protein−ligand aggregates, and at an appropriate concentration of dissolved ammonium sulfate, these complexes precipitate. The purification involves three steps: (i) the removal of high-molecular-weight impurities through the addition of ammonium sulfate to the crude cell lysate; (ii) the introduction of an oligovalent ligand and the selective precipitation of the target protein−ligand aggregates from solution; and (iii) the removal of the oligovalent ligand from the precipitate by dialysis to release the target protein. The increase of mass and volume of the proteins upon aggregate formation reduces their solubility, and results in the selective precipitation of these aggregates. We recovered human carbonic anhydrase, from crude cellular lysate, in 82% yield and 95% purity with a trivalent benzene sulfonamide ligand. This method provides a chromatography-free strategy of purifying monovalent proteins—for which appropriate oligovalent ligands can be synthesized—and combines the selectivity of affinity-based purification with the convenience of salt-induced precipitation.

INTRODUCTION

The solubility of a protein in an aqueous solution depends on the complex interaction of four parameters: (i) its physical properties (shape, flexibility, molecular weight, and isoelectric point), (ii) the distribution of the hydrophobic, hydrophilic, and charged groups on its surface, (iii) the temperature and pH of the solution, and (iv) the composition and concentration of various cosolutes.[1] Current theory suggests the relative importance of each of these parameters in determining the solubility of a protein. While the theory is unable to predict protein solubility in an experimental context,[2] the purification of proteins by precipitation is often a very convenient procedure, despite the fact that it remains a largely empirical process.[3,4]

This paper describes a method for the precipitation of (and thus, the purification of) monomeric proteins, selectively, with a combination of oligovalent ligands and ammonium sulfate. The interaction of multiple ligands—where a ligand is defined as a small molecule that specifically binds to a protein or receptor of interest—attached to a single entity with multiple receptors on another entity is common in biology and, especially, immunology: a multivalent interaction. We define an oligovalent ligand, in the context of this work, as a single organic molecular scaffold containing less than ten ligands, of the same chemical structure, that target a single protein receptor.

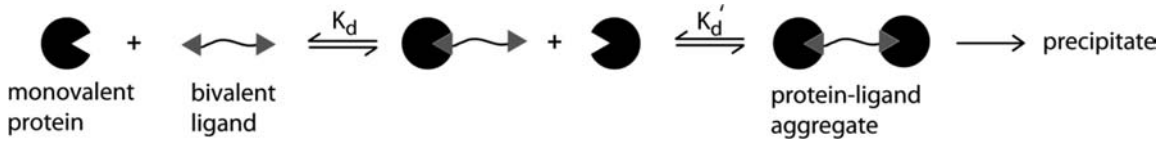
The formation of a protein−ligand aggregate (i.e., multiple proteins interacting with a single oligovalent ligand) increases the molecular mass and volume of the protein of interest and decreases the solubility of the aggregate; this increase allows the aggregate to be removed from solution as a precipitate (Scheme 1). Modulating the solubility of a given protein—by introducing oligovalent ligands that form protein−ligand aggregates of known stoichiometries—provides a strategy for

Received: July 19, 2011
Revised: December 16, 2011
Published: December 22, 2011

ACS Publications © 2011 American Chemical Society

dx.doi.org/10.1021/bc200390q | *Bioconjugate Chem.* 2012, 23, 293−299

Scheme 1. Selective Precipitation of Proteins with Oligovalent Ligands[a]



[a]The dissociation constant (K_d) dictates the formation and stability of a bivalent protein−ligand aggregate, in which a bivalent ligand of known binding affinity is introduced into a solution containing the protein. The K_d of the monovalent and bivalent complex is assumed to be the same in this system. The increase in mass (and volume) of the aggregates, in solution, results in the decreased solubility of the protein(s), and promotes precipitation.

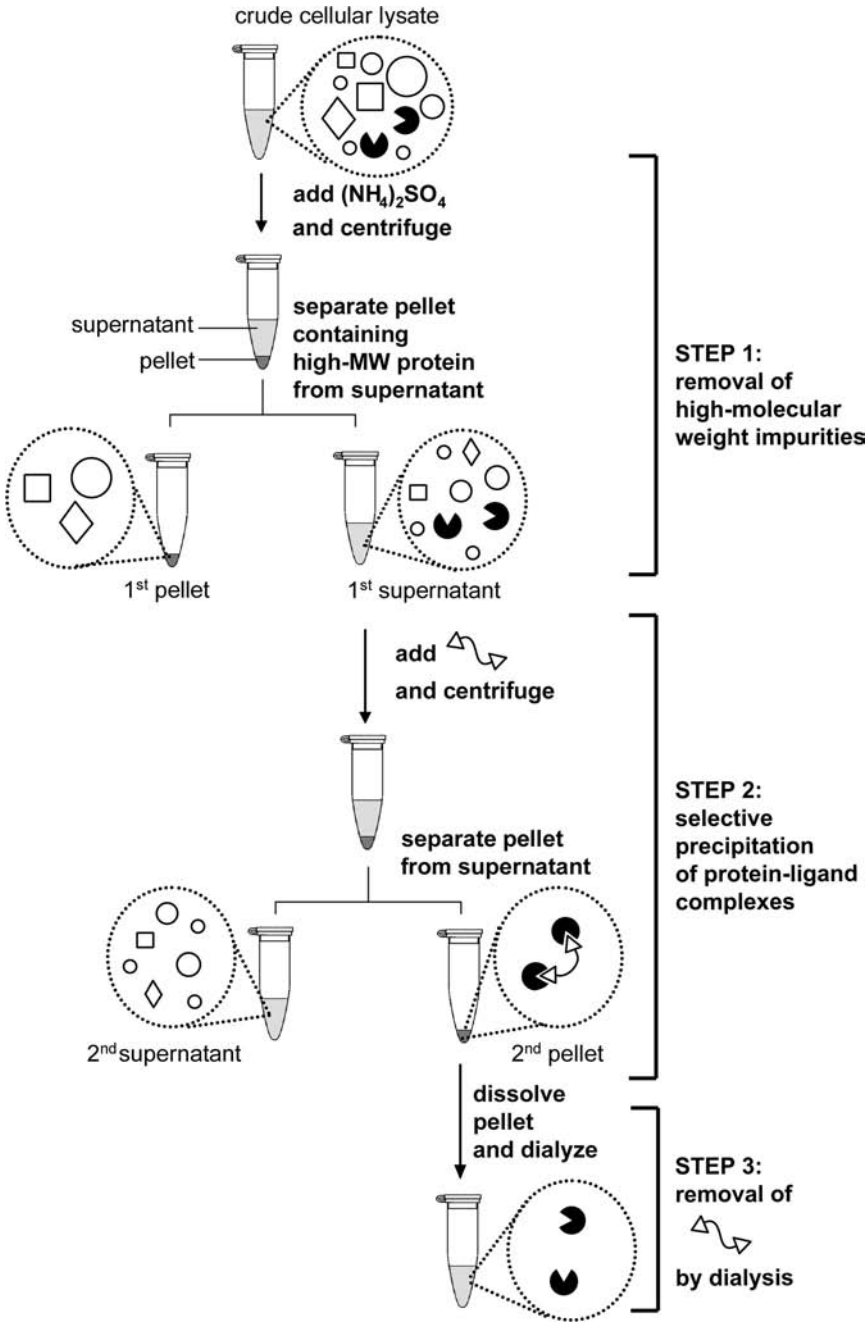


Figure 1. General strategy for purifying proteins using oligovalent ligands. The ligands induce aggregation of monovalent proteins and reduce their solubility in aqueous solutions containing dissolved ammonium sulfate.

purifying proteins, for which appropriate ligands are available or can be synthesized without the need of chromatographic methods.

The salt-induced precipitation of proteins is a simple, rapid, and inexpensive method of purification.[3−5] Many proteins have similar solubility in aqueous solutions of a salt, however, and

dx.doi.org/10.1021/bc200390q | *Bioconjugate Chem.* 2012, 23, 293−299

precipitate simultaneously; salt-induced precipitation of proteins is, for this reason, generally the first step in a series of steps of purification. The lack of selective and simple protein purification methods has led to the development of chromatographic techniques (e.g., ion exchange, size-exclusion, and affinity).[3−5] Affinity chromatography is a selective method for purifying proteins when a tight-binding (K_d < 100 μM) ligand for the protein is known; affinity chromatography, however, (i) is time-consuming, (ii) requires large volumes of eluent to remove the protein from the solid support (thus diluting the sample), (iii) requires pumps and fraction collectors (as well as supporting auxiliary equipment), and (iv) is limited in throughput. An ideal method of purification would have the selectivity of affinity chromatography, but the speed, low cost, and throughput of salt-induced precipitation.

We and others have developed several methods that aim to combine the convenience of salt-induced precipitation with the selectivity of affinity chromatography. Bilgiçer et al. used a combination of bivalent ligands and ammonium sulfate (AMS) precipitation to purify antibodies from ascites fluid with yields of >80% and with >95% purity.[6]

Another method of purification—based on altering the solubility of proteins—is "affinity precipitation",[5,7−9] which relies on multivalent ligands to modify the solubility of proteins, but does not involve the addition of AMS. Affinity precipitation was developed initially for the selective precipitation of multimeric proteins with bivalent ligands; the ligands cause precipitation by inducing the formation of an insoluble, cross-linked, macromolecular network of the protein complex.[7] This strategy was utilized to purify monomeric proteins with polymeric scaffolds that contain both an affinity ligand and another functional group that controls the solubility of the polymer.[8,9] The solubility of the polymeric ligand can be regulated, typically, by changes in pH, temperature, or ionic strength of the medium.[10] This method has three limitations: (i) the ligands immobilized on a polymeric scaffold tend to bind less strongly than their monovalent analogues; (ii) the resolubilization of the protein in the presence of the polymer is slow; and (iii) the cross-linked aggregates of proteins and polymers can trap impurities during precipitation.

Selective Isolation of Protein by Combining Oligovalent Aggregation with Ammonium Sulfate (AMS) Precipitation. This paper describes a method that combines the selectivity of affinity-based methods with the convenience of AMS precipitation. We use nonpolymeric, oligovalent ligands (with molecular weights <5000 Da) to induce the aggregation of monomeric proteins—containing a single ligand binding site—by selectively binding the protein to the oligovalent small molecules. The formation of a higher-molecular-weight aggregate, at a concentration of ammonium sulfate that is just below that required to precipitate the monomeric protein, selectively converts the targeted protein from a soluble monomer to an insoluble aggregate.

The procedure has three steps (Figure 1): (i) impurities that are higher in molecular weight than the target protein are removed by precipitation with AMS (the concentration of AMS is such that the protein of interest does not precipitate); (ii) the target protein is caused to aggregate and precipitate by adding an oligovalent ligand; the precipitate is isolated and redissolved in solution by the addition of buffer that does not contain AMS; (iii) the ligand is removed by dialysis.

This technique of purifying proteins has five useful characteristics: i) it is selective; ii) it can be adapted easily to improve the efficiency of existing processes that rely on salt-induced precipitation; iii) it is rapid; iv) it should scale easily to large volumes (>1 L); and v) it both purifies and concentrates the target protein. This method also has limitations: i) it requires both a small-molecule ligand that binds tightly (K_d < 100 μM) to the target protein, and a practical synthetic route to prepare the oligovalent ligand; ii) it requires separating the protein from the ligand after precipitation. In general, i) is the most constraining of these limitations.

EXPERIMENTAL DESIGN AND RATIONALE

Choice of Protein−Ligand System. We chose carbonic anhydrase (CA, E.C. 4.2.1.1) as our model system, as the binding of benzene sulfonamides to CA is conserved, has been extensively studied, and is well characterized with X-ray crystallography. There are numerous benzene sulfonamides that are available commercially, with a range of binding affinities, that are attached easily to oligovalent scaffolds.[11,12] We have reviewed the relevant characteristics of CA as a model system for biophysical studies in great depth,[11] and have extensive experience studying the interaction of benzene sulfonamide ligands with CA.

In this study, we precipitated bovine carbonic anhydrase II (BCA), selectively, from buffered solutions with oligovalent benzene sulfonamide ligands (monovalent to trivalent). We used pure BCA as a model system to examine the relationships between the relevant experimental parameters (e.g., dissociation constants (K_d) of the ligand, the stoichiometry of the aggregate, and the concentration of AMS). We also purified human carbonic anhydrase II (HCA), selectively, from crude *E. coli* lysate with a trivalent benzene sulfonamide ligand.

Choice of Salt. We precipitated aggregates of CA and an oligovalent benzene sulfonamide ligand in the presence of AMS. This salt is commonly used in preparative protein purification[3−5] as it is commercially available in high purity (>99.9%) and low cost (<$0.01 per gram), is soluble in water at concentrations up to 4 M, possesses a low enthalpy of dissolution, and is nonbuffering and nondenaturing.

Oligovalent Ligand Scaffolds. We linked the benzene sulfonamide molecules with units of oligoethylene glycol (OEG) because of their flexibility and relative inertness. We synthesized the oligovalent ligands (Figure 2) from commercially available starting materials, by linking the nucleophilic amine of the OEG scaffold with the *N*-hydroxysuccinimide (NHS)-activated 4-carboxybenzenesulfonamide (unless otherwise noted) using standard condensation chemistries.[13] We also synthesized a monovalent control (Figure 2) to show that the presence of the oligoethylene glycol tail does not inhibit protein−ligand binding and, in turn, interfere with protein precipitation. The Supporting Information outlines the details of the synthetic procedures used to make each benzene sulfonamide ligand, as well as their corresponding ^{1}H NMR and mass spectra.

RESULTS AND DISCUSSION

Characterization of the Binding of the Oligovalent Ligands to CA. We measured the monovalent dissociation constant (K_d) of each of the benzene sulfonamide scaffolds from BCA with a fluorescence-based competition assay.[14−16] To determine K_d, we used a model that assumed independent and equivalent binding of each benzene sulfonamide to BCA. This model yielded the following monovalent dissociation

dx.doi.org/10.1021/bc200390q | *Bioconjugate Chem.* 2012, 23, 293−299

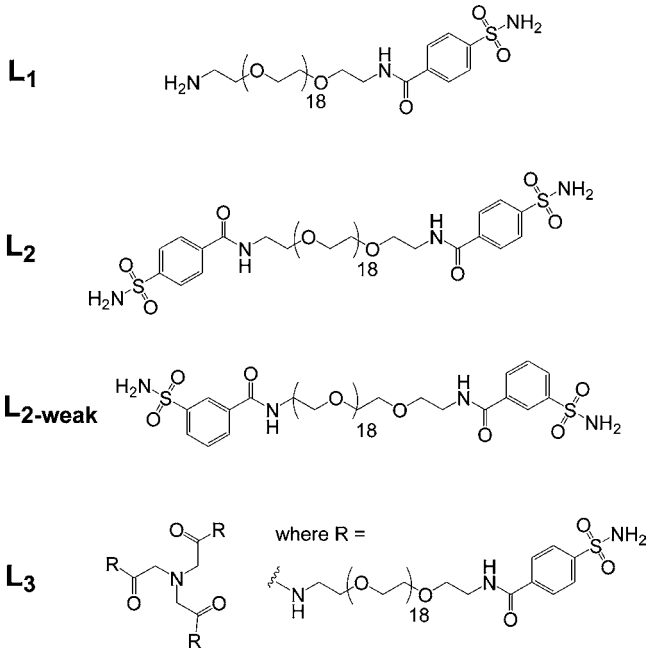


Figure 2. Structures of the ligands used for the selective precipitation of CA from aqueous solutions of ammonium sulfate.

constants for the benzene sulfonamides within these ligands, from BCA: K_d (monovalent, L_1) = 0.5 ± 0.1 μM, K_d (bivalent, L_2) = 0.4 ± 0.1 μM, K_d (trivalent, L_3) = 0.6 ± 0.6 μM.

Effect of Oligovalent Ligands on the Solubility of Proteins in Aqueous Solutions of AMS. We precipitated BCA—in a buffered solution containing ammonium sulfate, ranging 1.5–3.6 M—in the presence of no ligand, L_1, L_2, and L_3 (Figure 3). In these experiments, we combined BCA, AMS, and

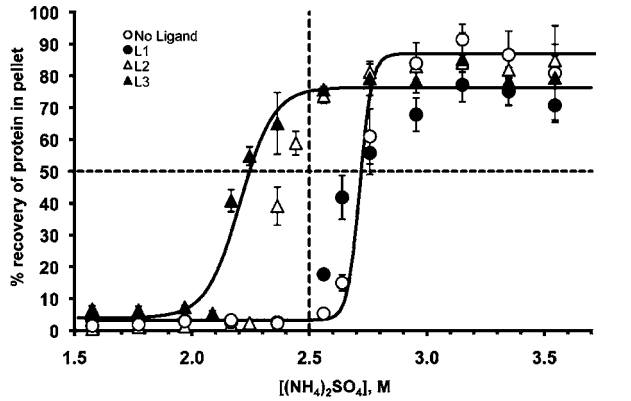


Figure 3. Precipitation of BCA from AMS in Tris-Gly buffer (pH = 7.5, 4 °C) in the presence of L_1, L_2, L_3, and no ligand. The concentration of each component is as follows: $[BCA]_0$ = 15 μM, $[L_1]_0$ = 90 μM, $[L_2]_0$ = 45 μM, and $[L_3]_0$ = 30 μM. The ratio of ligand to protein was optimized empirically to maximize the yield of precipitate. The error bars represent the deviation from three independent measurements; for clarity, we have only included the best fits (solid lines) for the experiments with no added ligand, and with L_3. The horizontal dashed line represents the point at which 50% of the BCA was precipitated from solution and the vertical dashed line corresponds to 2.5 M AMS.

the ligand in 20 mM NaH_2PO_4 buffer, pH = 7.5 (see Supporting Information for details of this experiment), vortexed this mixture for ~10 s to promote rapid mixing, gently agitated the mixture using a rocker-type shaker for 4 h at 4 °C to allow sufficient time for precipitation to occur,[17] and then centrifuged the mixture to separate the precipitate from the supernatant. We resuspended the pellet in 20 mM NaH_2PO_4 buffer (pH = 7.5) and determined the concentration of protein in the pellet with UV–vis absorption measurements. Figure 3 reports the fraction of protein recovered in the pellet in relation to the total amount of protein.

Figure 3 illustrates the ligand-dependent solubility of BCA in AMS; the solubility of BCA decreases as the size of the putative oligovalent aggregate increases for a given concentration of AMS. The horizontal dashed line in Figure 3 corresponds to the concentration of AMS required to precipitate 50% of the BCA present in solution. The vertical dashed line shows that no BCA precipitates in the absence of ligand at a concentration of 2.5 M, whereas over 70% of the BCA precipitates in the presence of the bi- and trivalent ligand. Together, these results serve as a basis for the expected selectivity, and thus selective precipitation, for a protein in a complex mixture.

Experimental Parameters for Protein Precipitation. The choice of experimental parameters—the type of buffer, the pH of the AMS solution, the length of OEG linker, the K_d of the ligand, and the concentration of protein in solution—may all affect the efficiency of protein precipitation with oligovalent ligands from a solution of AMS.

Linker Length. The distance between binding sites, in an oligovalent ligand, must sufficiently separate the proteins of interest to enable the oligovalent aggregate to form. We estimated—based on X-ray crystallographic structural information of CA—that a bivalent ligand must separate the two binding sites of CA by a total distance of 3 nm, and hypothesized that combinations of ligands and linkers that fall short of this 3 nm requirement would fail to promote the precipitation of CA from an AMS solution. We synthesized several analogues of the L_2 ligand (Figure 2) with linkers of various oligoethylene glycol (OEG) units: OEG 1, OEG 2, OEG 10, and OEG 19. We found that L_2 connected by OEG 19 (~5.5 nm between each ligand) was the most efficient at reducing the solubility of BCA in AMS, and that analogues having shorter linkers of OEG were less effective, and less reproducible.[18]

Protein Concentration and K_d. We examined the relationship between the K_d of the ligand and the concentration of protein. We expected that the ligand would determine the solubility of the protein if the protein–ligand aggregate were thermodynamically stable (e.g., had low values of K_d and K_d'), as the formation of a precipitate drives the equilibrium toward the formation of the bivalent aggregate (Scheme 1). We previously proposed an analytical model to predict the concentration of bivalent ligand needed to form the maximum amount of the protein–ligand complex in a solution containing the monomeric, monovalent protein.[19] Equation 1 describes the optimum concentration of bivalent ligand needed to maximize the formation of a protein–ligand complex[19] between L_2 (K_d = 0.4 ± 0.1 μM) and 20 μM of BCA:

$$[L_2]_{0,max} = \frac{K_d(L_2)}{2} + \frac{[BCA]_0}{2} = 10.2\ \mu M \quad (1)$$

We designed two experiments to compare the concentration of L_2 needed (as determined experimentally) with the values predicted by eq 1: (i) we examined aggregate precipitation at several concentrations of BCA (2–20 μM) with a fixed

dx.doi.org/10.1021/bc200390q | Bioconjugate Chem. 2012, 23, 293–299

concentration (40 μM) of L_2; (ii) we synthesized a chemical analogue of L_2 ($L_{2\text{-weak}}$, Figure 2) with a reduced K_d: $K_d(L_2)$ = 0.4 ± 0.1 μM vs $K_d(L_{2\text{-weak}})$ = 10.8 ± 0.7 μM.

The precipitation of BCA with L_2 was most effective for the highest concentration of BCA (20 μM): 4 equiv of L_2 per mole of BCA. This concentration of ligand exceeds the value predicted by eq 1 by a factor of 4. We attribute the disparity in the observed and predicted optimum concentrations of L_2 to differences in the experimental conditions and the conditions assumed in the model.[19] Equation 1 applies to binding processes under equilibrium conditions where the individual binding partners and their binding complexes are dispersed uniformly in solution. The system we present here is not under equilibrium conditions, and thus we do not expect this equilibrium model to predict the exact concentration of ligand needed, as (i) the binding occurs in a highly concentrated AMS solution that promotes the aggregation and precipitation of the protein−ligand complexes from solution; (ii) the kinetic process of precipitation alters the concentration of protein, ligand, and their complex in solution during the course of the experiment. We see this model, however, as a means of predicting a starting point for semiempirical experimental optimization.

$L_{2\text{-weak}}$ was less effective than L_2 (Figure 2) at promoting the precipitation of 20 μM BCA from a solution of AMS. Less than 20% of the BCA (20 μM) precipitated in the presence of a large excess of $L_{2\text{-weak}}$ ligand (e.g., 200 μM, 20 equivalents of ligands per mole of BCA), a result that agrees, qualitatively, with eq 1: the lower the value of K_d for a ligand, the lower the concentration of ligand needed to aggregate and precipitate the protein.

Solution pH and Buffer Conditions. We examined the effect of the buffer composition and pH on protein precipitation. We anticipated that neither would influence precipitation; the excess of AMS dominates the ionic strength of the aqueous solutions used for precipitation. We confirmed this hypothesis experimentally, and conclude that both the type of salt used to buffer the AMS solution and the pH of solution (6.0−7.5) has negligible effects on the efficiency of this precipitation process.[20]

Selective Precipitation of CA from Cellular Lysate. We selectively precipitated human CA (HCA) from a complex mixture of other proteins (i.e., crude lysate) with a trivalent ligand. First, we added a known amount of HCA to *E. coli* lysate (1 mg/10 mL, 3.4 μM); this experiment allowed us to quantify the efficiency of the precipitation process. In a separate experiment, we purified HCA from crude *E. coli* lysate in which the protein was overexpressed.[11,21] The selective precipitation of overexpressed protein from cellular lysate provides a means of purifying protein produced on a small scale without the need for chromatography.

To determine the optimal salt concentration required to precipitate the majority of the proteins in the lysate while retaining HCA in the supernatant, we incubated *E. coli* lysate—containing a known amount of HCA—in different concentrations of AMS (1.6−3.2 M, final concentration in 1.0 mL samples). We resuspended the precipitate in an equal volume of phosphate buffered saline (1× PBS), determined the amount of protein contained in the supernatant and in the precipitate with SDS-PAGE, and quantified the total protein concentration for each supernatant and precipitate sample with a standard Bradford assay.[22] The majority of the proteins from the cellular lysate samples were precipitated (62% of the total proteins, as determined with a standard Bradford assay) in 2.4 M AMS, while greater than 70% of the HCA was retained in solution at that concentration of AMS, as estimated by SDS PAGE.

To determine the optimum ligand concentration needed to precipitate a known amount of HCA in cellular lysate (100 μg of HCA total; 3.4 μM), we added known amounts of trivalent ligand (0, 5, 12.5, and 25 μM) to a 1.0 mL suspension of *E. coli* supernatant in 2.4 M AMS, and rocked the mixture at 4 °C for 4 h.[17] The precipitate contained a small amount of unwanted proteins, which we removed by washing and recentrifuging the pellet: the pellet was resuspended in 100 μL of 2.4 M AMS, centrifuged, and the supernatant removed. The pellet, precipitated with the trivalent ligand, contained 82 ± 2% of the HCA (n = 7 measurements) in the cellular lysate, and was >95% pure, as judged by gel electrophoresis. A fraction of the total HCA, 11 ± 4% (n = 7 measurements) was precipitated in the absence of ligand.

We also precipitated a sample of overexpressed HCA from crude *E. coli* lysate.[11,21] Figure 4 summarizes the results of a representative precipitation experiment, as analyzed with SDS PAGE, in which 50 μM of the trivalent ligand was added to 1.0 mL of *E. coli* crude lysate, the sample was incubated at 4 °C for four hours, and the protein−ligand aggregate precipitated. In this case, addition of trivalent ligand precipitated HCA that was ~90% pure, and a single wash of the precipitated protein provided HCA that was >95% pure as determined via Bradford assay.

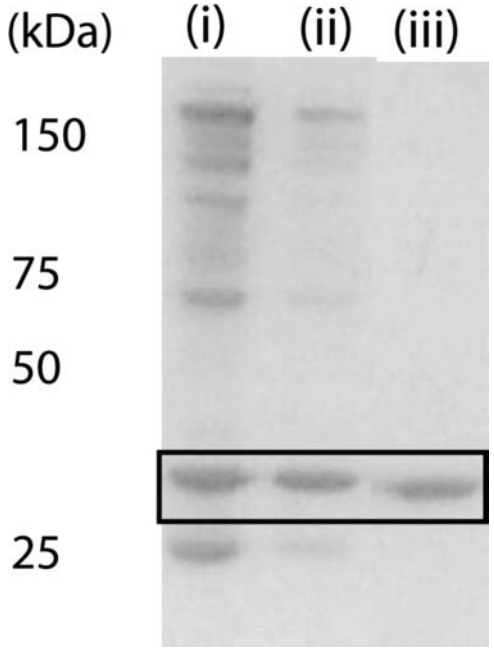


Figure 4. Precipitation of HCA with AMS and L_3 from a cellular lysate. Images of SDS PAGE lanes showing (i) the total number of proteins remaining in 2.4 M AMS after centrifugation, (ii) the total number of proteins precipitated after the addition of 50 μM L_3 ligand, (iii) the remaining HCA after the pellet of precipitated protein obtained from (ii) was washed with 1× PBS solution. The black box marks the bands corresponding to HCA.

Formation of an Oligomeric Aggregate between HCA and an Oligovalent Ligand Is Necessary for Selective Precipitation. We performed an experiment analogous to that presented in Figure 3 and precipitated a known amount of

dx.doi.org/10.1021/bc200390q | *Bioconjugate Chem.* 2012, 23, 293−299

HCA (100 μg; 3.4 μM)—in the presence of L_1, L_2, and L_3—from 2.5 mL of crude *E. coli* lysate. Each reaction contained an equivalent amount of benzene sulfonamide groups available for binding to HCA (i.e., 75 μM L_1, 37.5 μM L_2, and 25 μM L_3). A control experiment was also performed in which HCA was precipitated in the absence of ligand. We washed the precipitated pellets containing aggregates of protein and ligand to remove nonspecifically bound proteins and then analyzed the precipitates qualitatively with SDS PAGE, and quantitatively with a Bradford assay: $L_1 \sim 15 \pm 6\%$, $L_2 = 55 \pm 3\%$, $L_3 = 82 \pm 2\%$ of the total HCA contained in each lysate sample. These data are consistent with those obtained for the BCA samples (Figure 3); the amount of protein recovered increased with the size of the protein–ligand aggregate.

A small number of unwanted proteins were present in both the bi- and trivalent ligand precipitates, but were successfully removed by a single washing step. The total protein content of each pellet was determined directly after precipitation, after a single washing step, and after four washing steps. The trivalent pellet was ~90% pure HCA after precipitation, before any of the wash steps. The amount of HCA present in the pellet was not statistically different after one and four washes; only a single band was present in the SDS PAGE.

The monovalent ligand precipitated 25 ± 4% of the total protein contained in the *E. coli* lysate, while 11 ± 4% of the protein was precipitated in the absence of ligand. L_1 should not induce the precipitation of HCA from solution, as the mass and volume of the protein–ligand aggregate has not changed significantly. The majority of the precipitated proteins for L_1, and for experiments containing no added ligand were not HCA, as determined with SDS PAGE. We repeatedly washed the L_1 precipitate several times with 1× PBS to remove the nonspecifically adsorbed proteins; the pellet contained ~15 ± 6% of the HCA after four washes. This value is a relative estimate, as bands from protein impurities were still evident in the SDS PAGE.

Considerations for the Design of an Oligovalent Ligand. The design of the oligovalent ligand determines its compatibility with the strategy—the selective precipitation and purification with an oligovalent ligand, via the formation of an aggregate of the protein and the ligand—presented here. The ligand also determines the efficiency of the formation of the stable protein–ligand aggregate that precipitates in the presence of AMS. There are three important parameters that must be considered before designing and synthesizing the oligovalent ligand: (i) the K_d of the ligand, (ii) the number of ligands attached to a central scaffold (i.e., the valency of the ligand), and (iii) the length of the linker that connects the individual ligands.

The K_d of the ligand—the measure of the strength of the protein–ligand association—determines the concentration of ligand needed to precipitate an aggregate composed of the monovalent protein and the ligand from the AMS solution. An increase in the K_d of the bivalent ligand resulted in a reduced amount of BCA precipitating from a 2.36 M AMS solution: 60% of the BCA in solution precipitated in the presence of 40 μM of the L_2 ligand (K_d = 0.4 μM), while 20% of the BCA in solution precipitated in the presence of 200 μM of $L_{2\text{-weak}}$ (K_d = 10 μM).

The amount of precipitated protein increases with the valency of the oligovalent ligand; the number of ligands present corresponds to an increased mass and volume of the protein–ligand aggregate. The trend observed for mono-, bi-, and trivalent ligands is a decrease in the solubility of the aggregate with an increase in valency of the ligand. The synthesis of oligovalent ligands with higher valency should further decrease the solubility of the protein–ligand aggregate, thereby, in principle, increasing the amount of precipitated protein.

Lengthening the linker that connects the individual benzene sulfonamide molecules to the oligovalent ligand increased the efficiency of BCA precipitation. For our purification strategy to be successful, the length of the linker must be long enough to span the distance between the binding sites of two protein molecules without enthalpic penalty from steric interactions between atoms of the proteins. This distance, of course, will depend on the structure and size of the protein of interest.

■ CONCLUSIONS

This paper describes the combination of oligovalent ligands and AMS for the selective precipitation and purification of a model protein, carbonic anhydrase, from cellular lysate. An optimized procedure produced HCA in 82% yield, and approximately 95% purity.

This method combines the ease and speed of salt-induced precipitation with the selectivity of affinity chromatography and offers a rapid and selective approach to purifying monomeric proteins that have known ligands. This method has five useful characteristics for protein purification: (i) it is rapid (formation of precipitate occurs within minutes); (ii) it is selective for a target protein, and ensures that the purified protein contains an intact active site; (iii) it is mild and nondenaturing (AMS promotes folding of proteins and protects proteins from degradation by proteases); (iv) it concentrates the protein during purification; (v) it should scale easily to large volumes. This method has also two limitations: (i) it requires a ligand (with a sufficiently low K_d, < 100 μM) that binds to the protein; (ii) it involves the separation of the ligand from the protein after purification.

We believe this method may be particularly attractive for (i) improving the efficiency of existing purification processes that rely on salt-induced precipitation; (ii) streamlining purification schemes that involve a series of chromatographic and nonchromatographic steps; (iii) replacing affinity chromatography to reduce the cost, time, and volume of eluent in purification. This method provides a simple means that can be applied to the routine purification of proteins of interest, at natively and overexpressed concentrations, from cellular lysate.

■ ASSOCIATED CONTENT

Supporting Information

General methods; detailed synthetic procedures and ^{1}H NMR and mass spectra; additional figures (Figures S1 − S8). This material is available free of charge via Internet at http://pubs.acs.org.

■ AUTHOR INFORMATION

Corresponding Author

*E-mail: gwhitesides@gmwgroup.harvard.edu.

■ ACKNOWLEDGMENTS

This work was partially supported by NIH award GM030367 and the Wyss Institute of Biologically Inspired Engineering. N.D.S. thanks the NIH for a postdoctoral fellowship. K.A.M. thanks Başar Bilgiçer for helpful discussions and assistance with synthesizing L_3, Scott T. Phillips for helpful discussions and

help synthesizing L_2, and Demetri T. Moustakas for his help with Figure S5.

REFERENCES

(1) Arakawa, T., and Timasheff, S. N. (1985) Theory of protein solubility. *Methods Enzymol. 114*, 49−77.
(2) Chiew, Y. C., Kuehner, D., Blanch, H. W., and Prausnitz, J. M. (1995) Molecular thermodynamics for salt-induced protein precipitation. *AIChE J. 41*, 2150−2159.
(3) Hatti-Kaul, R., and Mattiasson, B. (2003) *Isolation and purification of proteins*, Marcel Dekker, New York.
(4) Wheelwright, S. M. (1991) *Protein purification: design and scale up of downstream processing*, Hanser Publishers; Distributed in the U.S.A. and in Canada by Oxford University Press, New York.
(5) Scopes, R. K. (1994) *Protein purification: principles and practice*, Springer-Verlag, New York.
(6) Bilgicer, B., Thomas, S. W., Shaw, B. F., Kaufman, G. K., Krishnamurthy, V. M., Estroff, L. A., Yang, J., and Whitesides, G. M. (2009) A non-chromatographic method for the purification of a bivalently active monoclonal IgG antibody from biological fluids. *J. Am. Chem. Soc. 131*, 9361−9367.
(7) Flygare, S., Griffin, T., Larsson, P. O., and Mosbach, K. (1983) Affinity precipitation of dehydrogenases. *Anal. Biochem. 133*, 409−416.
(8) Gupta, M. N., Kaul, R., Guoqiang, D., Dissing, U., and Mattiasson, B. (1996) Affinity precipitation of proteins. *J. Mol. Recognit. 9*, 356−359.
(9) Hilbrig, F., and Freitag, R. (2003) Protein purification by affinity precipitation. *J. Chromatogr., B: Anal. Technol. Biomed. Life Sci. 790*, 79−90.
(10) Mammen, M., Choi, S. K., and Whitesides, G. M. (1998) Polyvalent interactions in biological systems: implications for design and use of multivalent ligands and inhibitors. *Angew. Chem., Int. Ed. 37*, 2754−2794.
(11) Krishnamurthy, V. M., Kaufman, G. K., Urbach, A. R., Gitlin, I., Gudiksen, K. L., Weibel, D. B., and Whitesides, G. M. (2008) Carbonic anhydrase as a model for biophysical and physical-organic studies of proteins and protein-ligand binding. *Chem. Rev. 108*, 946−1051.
(12) Mack, E. T., Snyder, P. W., Perez-Castillejos, R., and Whitesides, G. M. (2011) Using covalent dimers of human carbonic anhydrase ii to model bivalency in immunoglobulins. *J. Am. Chem. Soc. 133*, 11701−11715.
(13) Jain, A., Huang, S. G., and Whitesides, G. M. (1994) Lack of effect of the length of oligoglycine-derived and oligo(ethylene-glycol)-derived para-substituents on the affinity of benzenesulfonamides for carbonic-anhydrase-II in solution. *J. Am. Chem. Soc. 116*, 5057−5062.
(14) Krishnamurthy, V. M., Semetey, V., Bracher, P. J., Shen, N., and Whitesides, G. M. (2007) Dependence of effective molarity on linker length for an intramolecular protein-ligand system. *J. Am. Chem. Soc. 129*, 1312−1320.
(15) Wang, Z.-X. (1995) An exact mathematical expression for describing competitive binding of two different ligands to a protein molecule. *FEBS Lett. 360*, 111−114.
(16) The experimental details of the fluorescence-based competition assay can be found in the Supporting Information section.
(17) We found, experimentally, that the yield of the precipitation reaction did not change significantly after a 4 h incubation period, at 4 °C.
(18) Figure S4 of the Supporting Information contains the experimental results comparing the number of the oligoethylene units in linker and its effectiveness at precipitating BCA from solution.
(19) Mack, E. T., Perez-Castillejos, R., Suo, Z., and Whitesides, G. M. (2008) Exact analysis of ligand-induced dimerization of monomeric receptors. *Anal. Chem. 80*, 5550−5555.
(20) Figures S2 and S3 of the Supporting Information contain the experimental results comparing the effectiveness of different buffer (S2) and pH (S3) conditions at precipitating BCA from solution.
(21) Nair, S. K., Calderone, T. L., Christianson, D. W., and Fierke, C. A. (1991) Altering the mouth of the hydrophobic pocket. structure and kinetics of human carbonic anhydrase II mutants at residue Val-121. *J. Biol. Chem. 266*, 17320−17325.
(22) Figure S7 contains the total concentration of protein contained in each precipitate and supernatant sample, as determined with a standard Bradford assay. The values reported in S7 are from $n = 10$ samples. Figure S8 contains a representative SDS PAGE image of the total protein content for each precipitate and supernatant sample.

Bioconjugate Chemistry

Technical Note

pubs.acs.org/bc

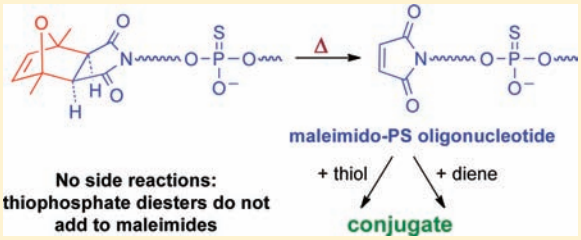
Conjugation Reactions Involving Maleimides and Phosphorothioate Oligonucleotides

Albert Sánchez, Enrique Pedroso, and Anna Grandas*

Departament de Química Orgànica and IBUB, Facultat de Química, Universitat de Barcelona, Martí i Franquès 1-11, 08028 Barcelona, Spain

Supporting Information

ABSTRACT: Phosphorothioate diester oligonucleotides proved to be fully compatible with maleimides in the context of two different conjugation reactions: (a) reaction of 5′diene-[phosphorothioate oligonucleotides] with maleimido-containing compounds to afford the Diels–Alder cycloadduct; (b) conjugation of 5′maleimido-[phosphorothioate oligonucleotides] with thiol-containing compounds. No evidence of reaction between phosphorothioate diesters and maleimides was found in any of these processes. Importantly, in the preparation of 5′maleimido-[phosphorothioate oligonucleotides] from [protected maleimido]-[phosphorothioate oligonucleotides], which requires the maleimide to be deprotected by retro-Diels–Alder reaction (heating for 3–4 h in toluene at 90 °C), no addition of phosphorothioate diester to the maleimide was found either. Finally, maleimide-[phosphorothioate monoester] conjugation was also explored for comparison purposes.



INTRODUCTION

Replacement of one of the nonbridging phosphate oxygens with sulfur was among the first modifications of the oligonucleotide backbone shown to down-regulate gene expression,[1] and of the nucleic acid drugs approved so far (Vitravene and Macugen) one has internucleoside phosphorothioate linkages.

Phosphorothioate-modified oligonucleotides (PS-ONs) have increased stability to nucleases and direct RNase H-mediated degradation of RNA in hybrid duplexes. Thiophosphate internucleoside linkages are more lipophilic than the natural phosphate diesters, but they do not significantly improve cell uptake. Hence, special formulations or covalent attachment to other molecules (that is, derivatization as conjugates) are often required to facilitate transport across cell membranes.

Sulfur nucleophilicity was previously utilized for the preparation of oligonucleotide conjugates.[2] Thiols were reacted with electrophiles such as bromo- or iodoacetyl groups, with maleimide Michael acceptors, and with other thiols to form disulfides. Thiophosphates were also used as nucleophiles in some of these reactions, but literature information as to their compatibility with other functional groups is somehow contradictory. It has been said, probably stating a fairly general feeling, that thiol–maleimide conjugation is not compatible with PS-ONs.[3] However, data not supporting this feeling have also been made available.

Phosphorothioate diesters have been described to react with activated disulfides such as the Ellman reagent,[4] most likely forming mixed thiol-thiophosphate disulfides.[5] Yet, phosphorothioate diesters have also been reported not to react with pyridyldisulfide groups.[6] In fact, there are various reports on the synthesis of disulfide-linked conjugates of phosphorothioated oligonucleotides,[7−9] showing that disulfides between two thiols can be formed in the presence of and with no interference from phosphorothioate groups.

Thiophosphates, either mono- or diesters, are known to react with bromo- or iodoacetyl groups,[10,11] and this was reported to be the preferred reaction when PS-ONs and bifunctional linkers containing maleimide and haloacetyl groups were mixed.[12]

Phosphorothioate monoesters and the ω-thiophosphate of nucleoside di- and triphosphates react with maleimides,[13−17] giving the corresponding Michael-type adduct. The Michael addition has been described as being more difficult in the case of thiophosphate diesters, especially in comparison with the thiol–maleimide reaction, but taking place to a non-negligible extent. In this respect, it is worth noting that the thiol–maleimide Michael-type addition has been described to occur when maleimido-[PS-ONs] react with thiol-containing compounds, as well as when thiol-derivatized PS-ONs react with maleimide-containing compounds.[18−20]

Interest in modified oligonucleotides and conjugates continues to increase, because of applications in the biopharmaceutical and nanotechnological fields (gene silencing studies, use of oligonucleotides to suppress immune responses, immobilization of oligonucleotides for the preparation of microarrays and biosensors, etc.).[21−26] Introduction of phosphorothioate linkages is a common, useful modification of oligonucleotide chains, so it is important to assess under what circumstances PS-ONs can be reliably used.

In this work, we wish to describe how reaction between diene-derivatized PS-ONs and maleimides gives the Diels–Alder

Received: November 8, 2011
Revised: December 21, 2011
Published: January 13, 2012

ACS Publications © 2012 American Chemical Society

dx.doi.org/10.1021/bc200598g | Bioconjugate Chem. 2012, 23, 300–307

cycloadduct, showing that phosphorothioate diesters do not interfere with this reaction. We also applied the methodology that allows maleimido-oligonucleotides to be on-resin assembled[27] to the synthesis of maleimide-[PS-ONs], which proved that in the heating process required to obtain maleimido-[PS-ONs] from [protected-maleimido]-[PS-ONs] there is no addition of the thiophosphate diester to the maleimide. Furthermore, and as expected, reaction between these maleimido-[PS-ONs] and thiol-containing compounds provided the target conjugates. Finally, maleimide-[phosphorothioate monoester] conjugation was also explored for comparison purposes.

MATERIALS AND METHODS

Nucleoside phosphoramidites, DMT-O−CH_2CH_2−SO_2−CH_2CH_2−O-P(OCNE)N^{i}Pr$_2$ and CPG supports were from either Link Technologies or Glen Research Corporation. Oligonucleotide chains were elongated in a 3400 ABI automatic synthesizer at the 1 μmol scale, using standard phosphite triester approach synthesis cycles and the phosphoramidite derivatives of dA^{Pac}, dC^{Ac}, dG^{iPrPac}, and dT (Pac = phenoxyacetyl, iPrPac = (4-isopropyl-phenoxy)acetyl). Sulfurization of phosphite triesters was carried out with the Beaucage reagent.[28]

Maleimido-biotin derivative **4a** was from Thermo Scientific (*EZ*-Link Maleimide-PEG$_2$-Biotin). D-(+) Biotin *N*-hydroxysuccinimide ester (biotin-OSu) was from Berry & Associates. Diene-phosphoramidite (see Scheme 1) was synthesized as described by Hill et al.[29] Syntheses of [protected maleimido]-phosphoramidite (see Scheme 2) and H-Cys-Lys-Glu-Thr-Ala-Ala-Ala-Lys-Phe-Glu-Arg-Gln-His-Met-Asp-Ser-Ser-Thr-Ser-Ala-Ala-OH (Cys-peptide, **8b**) are described in reference 27. Preparation of maleimido-Lys-Glu-Thr-Ala-Ala-Ala-Lys-Phe-Glu-Arg-Gln-His-Met-Asp-Ser-Ser-Thr-Ser-Ala-Ala-OH (Mal-peptide, **4b**) is described in reference 30.

TLC was carried out on silica gel plates 60 F_{254} from Merck.

Reversed-phase HPLC analysis and purification was performed using analytical and semipreparative Waters systems. Unless otherwise indicated, a Kromasil C18 column (10 μm, 100 Å, 250 × 4.0 mm) from Akzo Nobel, solvent A: 0.05 M triethylammonium acetate, solvent B: H_2O/acetonitrile (1:1, v/v), flow: 1 mL/min, detection wavelength: 254 nm, linear gradients from 10% to 80% of B in 30 min were used in analytical HPLC. Semipreparative conditions: Jupiter C18 column (10 μm, 300 Å, 250 × 10.0 mm) from Phenomenex, solvent A: 0.1 M triethylammonium acetate, solvent B: H_2O/acetonitrile (1:1, v/v), flow: 3 mL/min, detection wavelength: 260 nm, linear gradient from 10% to 80% of B in 30 min.

MALDI-TOF mass spectra were recorded on a 4800 *Plus* ABSciex instrument. Typical analysis conditions were as follows: 1:1 (v/v) 2,4,6-trihydroxyacetophenone/ammonium citrate (THAP/CA) in the negative mode (3-hydroxypicolinic acid, HPA, was used instead of THAP in some cases); 2,5-dihydroxybenzoic acid +0.1% trifluoroacetic acid in the positive mode; unless otherwise indicated, spectra were recorded in the negative mode and reflector was used. ESI mass spectra were obtained using an LC/MSD-TOF Agilent Technologies spectrometer.

Diene-[Phosphorothioate Oligonucleotides] (3). Resin-linked phosphorothioate oligonucleotides **2** were assembled using standard procedures (phosphite triester approach), and the same chemistry was used to incorporate the diene moiety at the 5′ end.[31] A 0.05 M solution of the Beaucage reagent in anhydrous acetonitrile was used for the sulfurization step. To optimize the coupling yield, diene-phosphoramidite was incorporated using a double 5 min coupling. Deprotection and cleavage was carried out by reaction with conc aqueous ammonia at room temperature (4 h). Pure diene-oligonucleotides **3** were obtained after purification by HPLC (SI Figure S3).

Diene-$^{5'}$[PS-dT$_{10}$] (**3a**): t_R = 16.4 min; MALDI-TOF MS: m/z 3297.7 [M-H]$^-$, M calcd. 3298.7.

Diene-$^{5'}$[PS-dTCTCCCAGCGTGCGCCAT] (**3b**): t_R = 14.7 min; MALDI-TOF MS (linear): m/z 5850.4 [M-H]$^-$, M calcd. 5856.5.

Synthesis of Conjugates (5) by Diels−Alder Cycloaddition. Maleimido-containing compounds can be quantified by measuring the absorbance at 299 nm (in water, ε_{299}= 551.46 M^{-1} cm^{-1}).

Maleimido-containing compound **4** (2 equiv) was added to diene-[PS-ON] **3** (2 OD$_{260}$), and the mixture was heated in a metal block for 15 h at 37 °C (concentration of **3** in the conjugation reaction mixture: 50 μM; solvent: water). The reactions with **4a** did not go to completion (as shown by HPLC analysis: Figure 2c, d), so an additional amount of **4a** was added (10 equiv) and the reaction pursued overnight. Pure conjugates **5** were obtained after purification by HPLC. Their identity was confirmed by MALDI-TOF MS.

Biotin-$^{5'}$[PS-dT$_{10}$]: t_R = 15.6 min; MALDI-TOF MS: m/z 3822.6 [M-H]$^-$, M calcd. 3823.5.

Biotin-$^{5'}$[PS-dTCTCCCAGCGTGCGCCAT]: t_R = 14.4 min; MALDI-TOF MS (linear): m/z 6375.7 [M-H]$^-$, M calcd. 6381.8.

Peptide-$^{5'}$[PS-dT$_{10}$]: t_R = 14.4 min; m/z 5613.4 [M-H]$^-$, M calcd. 5614.4.

Peptide-$^{5'}$[PS-dTCTCCCAGCGTGCGCCAT]: t_R = 13.2 min; MALDI-TOF MS (linear): m/z 8166.2 [M-H]$^-$, M calcd. 8172.6.

[Protected Maleimido]-[Phosphorothioate-Oligonucleotides] (6). Resin-linked phosphorothioate oligonucleotides **2** were assembled using standard procedures (phosphite triester approach), and the same chemistry was used to incorporate the protected maleimide moiety at the 5′ end. A 0.05 M solution of the Beaucage reagent in anhydrous acetonitrile was used for the sulfurization step. To optimize the coupling yield, [protected maleimido]-phosphoramidite was incorporated using a double 5 min coupling. Deprotection and cleavage were carried out by reaction with conc aqueous ammonia at room temperature (4 h). Pure [protected maleimido]-oligonucleotides **6** were obtained after purification by HPLC (Figure S5). As stated before,[27] peaks with m/z ratios corresponding to both [protected maleimido]-[PS-ON] and maleimido-[PS-ON] were observed upon recording MALDI-TOF MS spectra. Analysis using softer ionization techniques (ESI, data not shown) confirmed that the target [protected maleimido]-[PS-ON] had been obtained.

[Protected maleimido]-$^{5'}$[PS-dT$_{10}$] (**6a**): t_R = 13.9 min; MALDI-TOF MS: m/z 3436.5 [M-H]$^-$, M calcd. 3437.3.

[Protected maleimido]-$^{5'}$[PS-dTCTCCCAGCGTGCGCCAT] (**6b**): t_R = 14.0 min; MALDI-TOF MS (HPA/CA): m/z 5994.6 [M-H]$^-$, M calcd. 5995.6.

Maleimido-Oligonucleotides (7). The maleimide moiety of [protected maleimido]-oligonucleotides **6** was deprotected by heating in toluene: A solution of **6** was introduced in a vial and evaporated to dryness under vacuum. The resulting residue was dried by coevaporation with toluene (3×), and toluene was added (the amount that would be required to obtain a 25 μM solution were the oligonucleotide soluble in toluene). This mixture was heated in a metal heating block for 3 h, after which

dx.doi.org/10.1021/bc200598g | *Bioconjugate Chem.* 2012, 23, 300−307

time toluene was removed under reduced pressure. The resulting crude was dissolved in water and analyzed by HPLC (Figure 3). Maleimido-[PS-ONs] **7** were used in conjugation reactions immediately after deprotection.

Maleimido-$^{5'}$[PS-dT_{10}] (**7a**): t_R = 12.5 min; MALDI-TOF MS: m/z 3340.5 $[M-H]^-$, M calcd. 3341.3.

Maleimido-$^{5'}$[PS-dTCTCCCAGCGTGCGCCAT] (**7b**): t_R = 13.0 min; MALDI-TOF MS (linear, HPA/CA): m/z 5894.5 $[M-H]^-$, M calcd. 5899.5.

Synthesis of Conjugates (9) by Thiol Addition to Maleimides. Quantification of free thiols in thiol-containing compounds was carried out using the Ellman test.[32]

The conjugation reaction was carried out at room temperature in the following conditions: 0.5 M triethylammonium acetate, pH = 7.8; concentration of **7** in the conjugation reaction mixture: 25 μM; 1:10 maleimido-[PS-ON]/thiol molar ratio; reaction time: 15 h. The required amounts of each of the reagents were mixed, the mixture was diluted with the conjugation buffer, and the pH adjusted to 7.8. Conjugation crudes were analyzed by HPLC (Figure 4), which showed that the conjugation yield was virtually quantitative. Pure conjugates **9** (identity assessed by MALDI-TOF MS) were obtained after purification by HPLC.

Biotin-$^{5'}$[PS-dT_{10}]: t_R = 15.2 min; MALDI-TOF MS: m/z 3643.5 $[M-H]^-$, M calcd. 3644.4.

Biotin-$^{5'}$[PS-dTCTCCCAGCGTGCGCCAT]: t_R = 13.8 min; MALDI-TOF MS: m/z 6201.8 $[M-H]^-$, M calcd. 6202.6.

Peptide-$^{5'}$[PS-dT_{10}]: t_R = 14.0 min; MALDI-TOF MS (HPA/CA): m/z 5608.6 $[M-H]^-$, M calcd. 5609.3.

Peptide-$^{5'}$[PS-dTCTCCCAGCGTGCGCCAT]: t_R = 12.9 min; MALDI-TOF MS (linear, HPA/CA): m/z 8163.1 $[M-H]^-$, M calcd. 8167.5.

5′-Thiophosphate-dT_{10} (10). The oligonucleotide chain was assembled using the standard phosphite triester methodology, which was also used to thiophosphorylate the 5′ end (incorporation of DMT-O−CH_2CH_2−SO_2−CH_2CH_2−O-P-(OCNE)N^iPr_2 was followed by sulfurization using the Beaucage reagent). DMT-O−CH_2CH_2−SO_2−CH_2CH_2−O-P(S)-(OCNE)-$^{5'}$*O*-[protected dT_{10}]-resin was treated with conc aqueous ammonia (500 μL) overnight at 60 °C, and the resulting crude was analyzed by HPLC (Figure S6a) and MALDI-TOF MS. Purification by semipreparative HPLC did not provide pure **10** (Figure S6b), but the mixture of **10** and dephosphorylated dT_{10} that was used in the conjugation reactions.

P(S)(O^-)(O^-)-$^{5'}$$dT_{10}$ (**10**): t_R = 20.5 min; MALDI-TOF MS: m/z 3073.6 $[M-H]^-$, M calcd. 3074.5.

dT_{10}: t_R = 21.8 min; MALDI-TOF MS: m/z 2977.7 $[M-H]^-$, M calcd. 2978.5.

Synthesis of Conjugates (11) by Addition of the Thiophosphate Monoester to the Maleimide. P(S)(O^-)-(O^-)-dT_{10} (**10**, 0.2 OD_{260}, plus the dT_{10} impurity) was dissolved in 0.5 M triethylammonium acetate buffer, pH = 7.8). Ten equivalents (with respect to compound **10**, 75% in the mixture as shown by HPLC; Figure S6b) of maleimido-derivative **4** (the required amount of a 3.86 mM aqueous solution of maleimido-biotin **4a**, or of a 2.76 mM aqueous solution of maleimido-peptide **4b**) was added, as well as buffer so that the final volume was 200 μL (concentration of **10** in the conjugation reaction mixture: 25 μM). The resulting mixture was stirred overnight at room temperature under an Ar atmosphere. The crudes were analyzed by HPLC (gradient from 10% to 40% of B in 30 min; Figure S6c,d), the different peaks were collected and mass spectrometric analysis allowed the target conjugate (**11**) to be identified. Pure conjugates **11** were isolated after HPLC purification. Conjugation yields: P(S)(O^-)(O^-)-dT_{10} (**10**) + HS-biotin (**8b**) 63%, P(S)(O^-)(O^-)-dT_{10} (**10**) + maleimido-peptide (**4b**) 43%.

Biotin-dT_{10}: t_R = 20.9 min; MALDI-TOF MS: m/z 3598.6 $[M-H]^-$, M calcd. 3599.7

Peptide-dT_{10}: t_R = 20.5 min; MALDI-TOF MS: m/z 5389.5 $[M-H]^-$, M calcd. 5390.5.

RESULTS AND DISCUSSION

The first experiments we performed aimed to confirm, in a model system, that maleimides and phosphorothioate diesters are compatible, in other words, that they do not react with each other. These experiments were similar to those previously described in the literature,[15] and consisted of mixing model compound dT-PS-dT (**1**, Figure 1) with *N*-methylmaleimide and analyzing the reaction mixture.

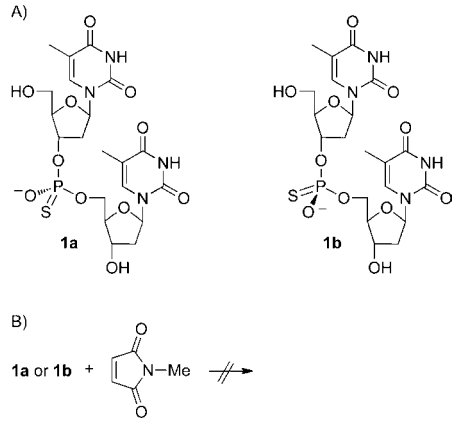


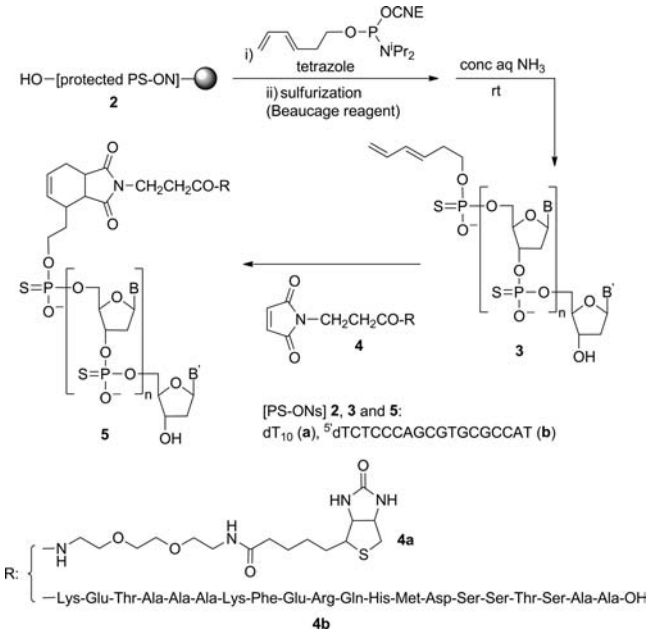
Figure 1. (A) Structures of the two dT-PS-dT diastereomers (**1a** and **1b**). (B) Neither of these compounds reacted with *N*-methylmaleimide.

Dinucleotide **1** was assembled by standard solid-phase synthesis, the phosphite triester sulfurized by reaction with the Beaucage reagent, and permanent protecting groups removed by reaction with conc aqueous ammonia. HPLC analysis of the crude showed the presence of two main peaks, both having the mass of the target dinucleotide, which were collected separately (Figure S1). Access to each of the two phosphorothioate diastereomers, **1a** and **1b** (Figure 1), offered the possibility of assessing whether they might react differently.

Mixtures of either thiophosphate isomer and *N*-methylmaleimide (1:10 and 1:100 molar ratios) were left to react overnight at room temperature, under conditions similar to those that we had used in thiol−maleimide conjugations.[27] Subsequent HPLC (Figure S2) and mass spectrometric analyses showed the presence of only **1a** or **1b** in the corresponding crudes. In other words, no adduct resulting from Michael addition of the thiophosphate to the double bond of the maleimide ring was found, which indicated that no intermolecular maleimide−thiophosphate reaction had taken place. This is in contrast with a literature report stating that phosphorothioate diesters can add to the maleimide double bond,[15] in which the reaction between *N*-(1-pyrene)-maleimide and 100-fold excess of either dT-PS-dT or β-mercaptoethanol was monitored by fluorescence spectroscopy. The authors found the extent of the reaction of the maleimide with the thiophosphate diester to be about 25% of that with the thiol, which is usually quantitative. Certainly their reaction and especially their analysis conditions were different from ours, but

dx.doi.org/10.1021/bc200598g | *Bioconjugate Chem.* 2012, 23, 300−307

Scheme 1. Conjugation of Diene-Derivatized PS-ONs with Maleimido-Derivatized Compounds Making Use of the Diels-Alder Cycloaddition



we should have been able to detect formation of the Michael adduct had the reaction between **1** and *N*-methylmaleimide taken place even to a lower extent.

As previously stated, different experiments have pointed to thiols being much more reactive than phosphorothioate diesters in Michael-type reactions in which the electrophilic species is a maleimide. Yet, it has not been proven that the Diels−Alder reaction between dienes and maleimides is also compatible with thiophosphate diesters.

Two diene-derivatized PS-ONs (**3**, Scheme 1) were prepared following described procedures,[31] with the only difference that all phosphite triesters were sulfurized instead of oxidized (Figure S3). The synthesis of maleimido−peptide **4b** has previously been reported.[30] Cycloadditions were carried out overnight, in water, at 37 °C. HPLC analysis of the crudes (Figure 2) showed that reactions of diene−oligonucleotides **3** with 2 equiv of maleimido−peptide **4b** had nearly gone to completion (98−99% yields), whereas in the same conditions the yield of the cycloadditions involving **3** and maleimido−biotin (**4a**) ranged between 31% and 34%. Very good to excellent conjugation yields (91−99%) were obtained using a higher excess of maleimido−biotin **4a** (Figure 2e, f). This result is in agreement with previous findings in the group, which indicated that the Diels−Alder cycloaddition between

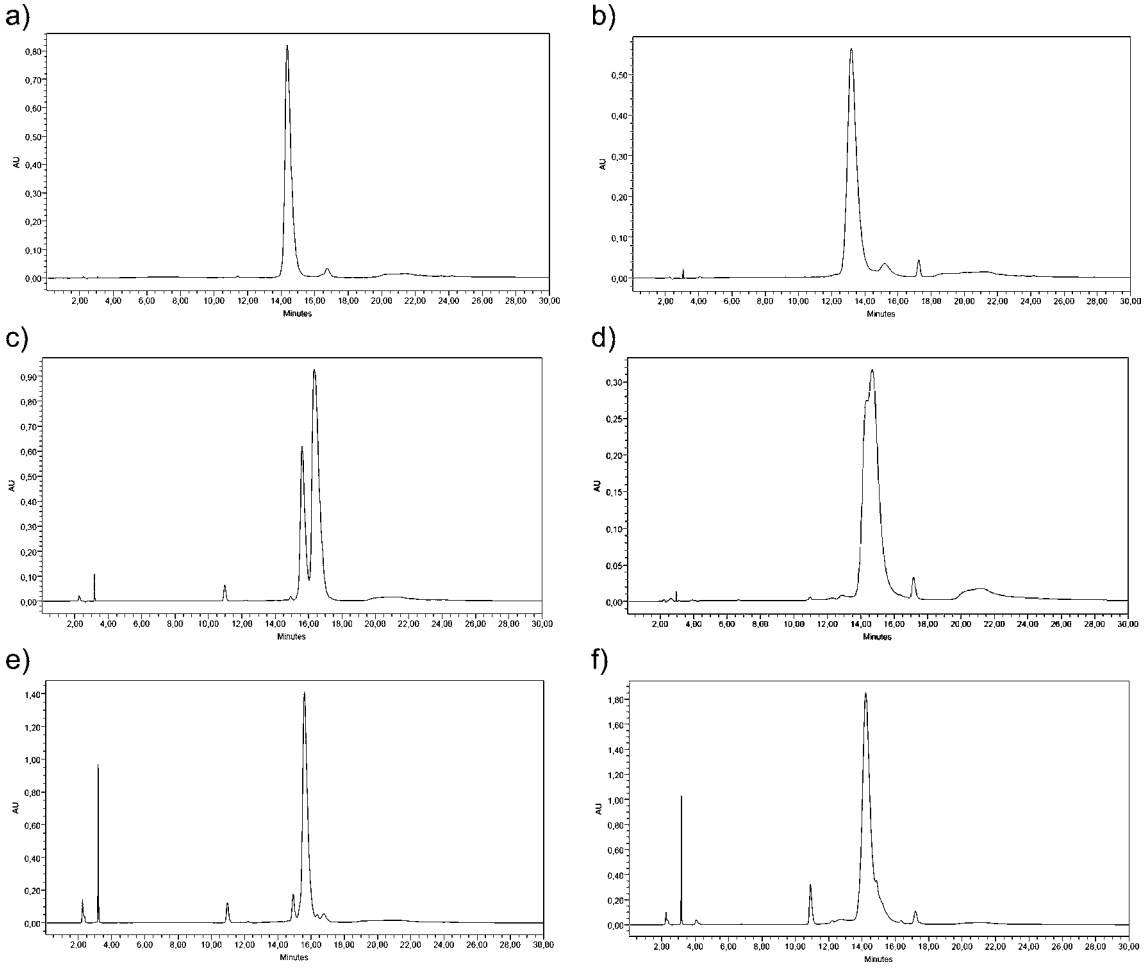
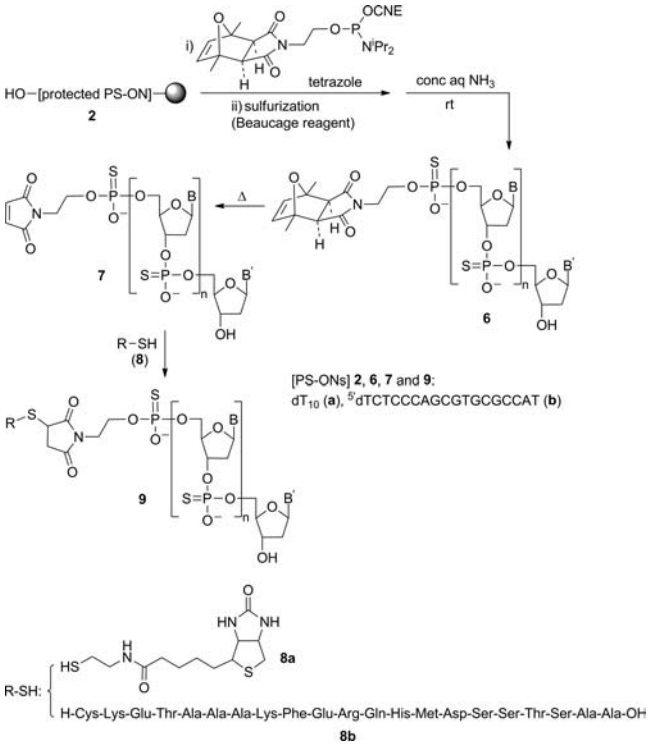


Figure 2. HPLC profiles of the Diels−Alder conjugation crudes. (a) Diene-$^{5'}$[PS-dT_{10}] (**3a**) + maleimido-peptide (**4b**), 1:2 molar ratio; (b) diene-$^{5'}$[PS-dTCTCCCAGCGTGCGCCAT] (**3b**) + maleimido-peptide (**4b**), 1:2 molar ratio; (c) diene-$^{5'}$[PS-dT_{10}] (**3a**) + maleimido-biotin (**4a**), 1:2 molar ratio; (d) diene-$^{5'}$[PS-dTCTCCCAGCGTGCGCCAT] (**3b**) + maleimido-biotin (**4a**), 1:2 molar ratio; (e) 5′-diene-[PS-dT_{10}] (**3a**) + maleimido-biotin (**4a**), 1:12 molar ratio; (f) diene-$^{5'}$[PS-dTCTCCCAGCGTGCGCCAT] (**3b**) + maleimido-biotin (**4a**), 1:12 molar ratio.

dx.doi.org/10.1021/bc200598g | *Bioconjugate Chem.* 2012, 23, 300−307

Scheme 2. Preparation of Maleimido-Derivatized [PS-ONs] (7), and Conjugation with Thiols (Michael-Type Reaction)



diene−oligonucleotides and maleimido−peptides or carbohydrates is much faster than with compounds less polar or having low affinity for the oligonucleotide chain.[33]

As shown in Figure 2, HPLC profiles of the reaction crudes were very clean. A single main peak was found in all cases, which suggests formation of a single conjugation compound. This was confirmed by the fact that only the one-to-one conjugate (in other words, the molecule incorporating one oligonucleotide and either one peptide chain or one biotin label) was detected by mass spectrometric analysis of the crude. Should any of the phosphorothioate internucleoside linkages have reacted with the maleimide ring, mixtures of one-to-one conjugates with different retention times could have been obtained, in addition to conjugates with higher masses formed either by various intermolecular Michael reactions or by Michael reactions in addition to the cycloaddition. Since none of these was detected, we definitely conclude that the conjugates have the structure shown in Scheme 1 (**5**), that is, the compounds resulting from the Diels−Alder cycloaddition.

The subsequent, more demanding experiments, aimed to evaluate whether thiophosphate diesters and a maleimide moiety can be introduced in the same oligonucleotide chain by stepwise solid-phase synthesis (Scheme 2). We have recently described that maleimido-oligonucleotides can be on-resin assembled making use of a maleimide protecting group that remains stable to ammonia,[27] namely, the *exo* isomer of the adduct resulting from reaction of maleimide with 2,5-dimethylfuran. Fully protected maleimido-oligonucleotides can be synthesized using standard solid-phase methodology, and subsequent reaction with conc aqueous ammonia removes permanent protecting groups on the oligonucleotide chain and provides [protected maleimido]-oligonucleotides. Then, a retro-Diels−Alder reaction allows the maleimide moiety to be deprotected and affords the target maleimido-oligonucleotides. Therefore, use of this methodology for the preparation of maleimido-[PS-ONs] requires phosphorothioates to not react with the maleimide during the heating process that deprotects it.

Before undertaking the solid-phase synthesis of maleimido-oligonucleotides, mixtures of either diastereomer of dT-PS-dT (**1a** or **1b**) and *N*-methylmaleimide were submitted to the retro-Diels−Alder conditions that remove the 2,5-dimethylfuran maleimide protecting group from the maleimide.[27] Both HPLC (Figure S4) and MALDI-TOF MS analysis of the crudes showed the dinucleotide to remain unaltered, indicating that in these retro−Diels−Alder conditions maleimides do not react with phosphorothioates.

For the synthesis of derivative **8a** (Scheme S1), the *N*-hydroxysuccinimido ester of biotin was reacted with cysteamine.[34] Peptide **8b** was obtained as previously described.[27]

Fully protected maleimido-[PS-ONs] were assembled on CPG, using a [protected-maleimido]-phosphoramidite synthon in the last synthesis cycle (Scheme 2) and the Beaucage reagent for the sulfurization of all phosphite triesters. Treatment with conc aqueous ammonia at room temperature deprotected the oligonucleotide chain, and, after purification, [protected maleimido]-[PS-ONs] **6** (Figure S5) were suspended in toluene and heated for 3 h at 90 °C. HPLC analysis (Figure 3) showed the homogeneity of crude maleimido-[PS-ONs] **7** to be similar to that of maleimido-ONs.[27] Notably, mass spectrometric analysis of the crudes confirmed formation of the target maleimido-oligonucleotides (**7**), and thus the compatibility between maleimides and phosphorothioate internucleoside linkages under retro−Diels−Alder deprotection conditions. Additional evidence for a reactive maleimide moiety in oligonucleotides **7** was obtained upon conjugation of maleimido-[PS-ONs] **7** with thiols (**8**), which yielded fairly homogeneous crudes (Figure 4) in which the main peaks were the expected one-to-one conjugates

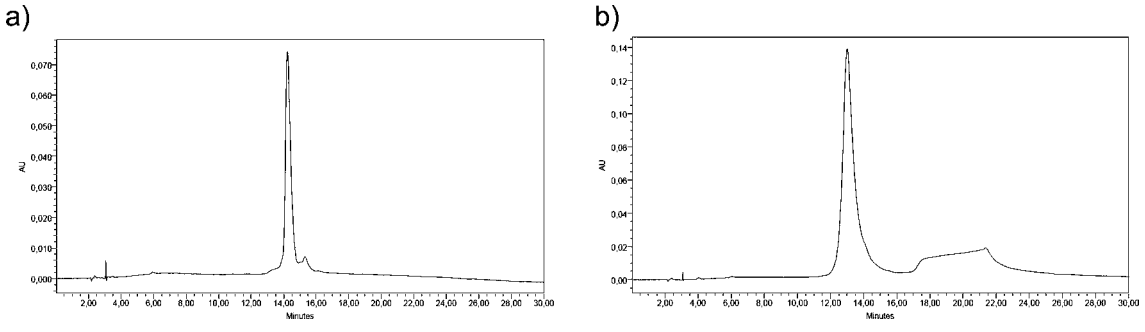


Figure 3. Crude maleimido-oligonucleotides (**7**) after heating in toluene (3 h, 90 °C). (a) Maleimido-5′[PS-dT_{10}] (**7a**); (b) maleimido-5′[PS-dTCTCCCAGCGTGCGCCAT] (**7b**).

dx.doi.org/10.1021/bc200598g | *Bioconjugate Chem.* 2012, 23, 300−307

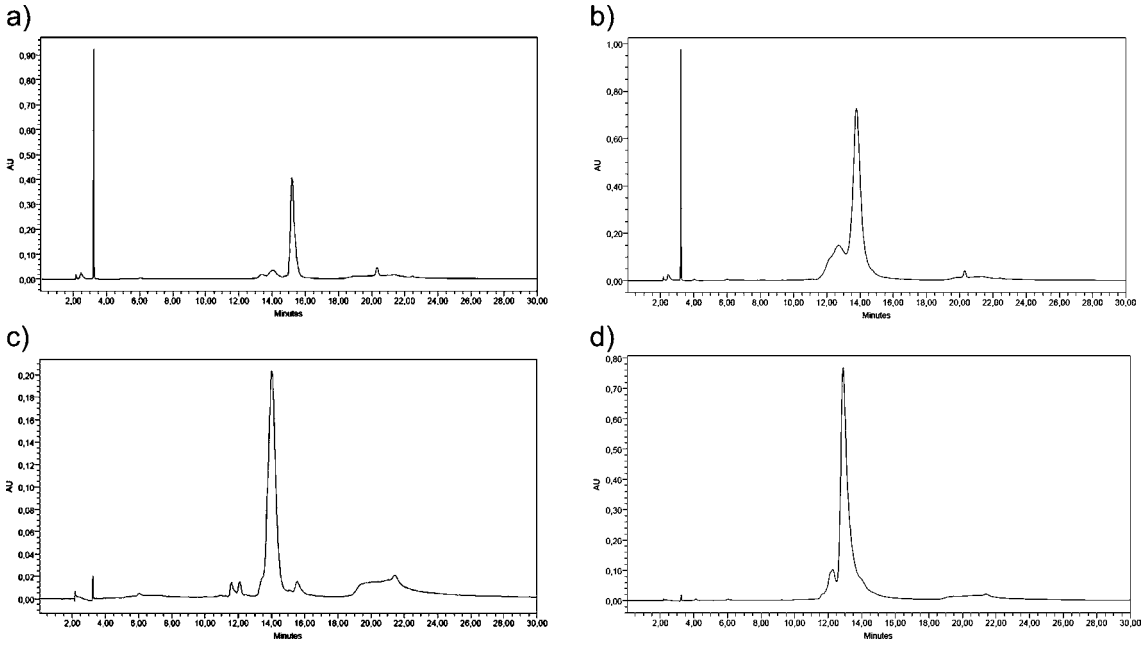
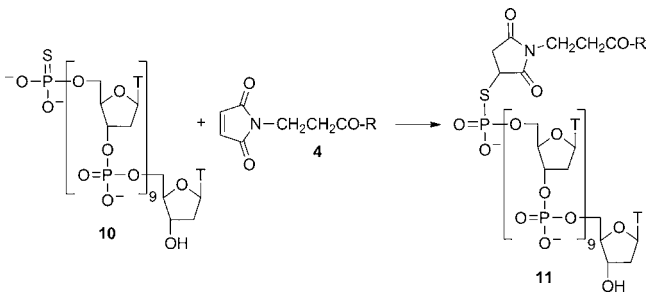


Figure 4. HPLC profiles of the thiol−maleimide conjugation crudes. (a) Maleimido-$^{5'}$[PS-dT$_{10}$] (**7a**) + HS-biotin (**8a**); (b) maleimido-$^{5'}$[PS-dT-CTCCCAGCGTGCGCCAT] (**7b**) + HS-biotin (**8a**); (c) maleimido-$^{5'}$[PS-dT$_{10}$] (**7a**) + Cys-peptide (**8b**); (d) maleimido-$^{5'}$[PS-dTCTCCCA-GCGTGCGCCAT] (**7b**) + Cys-peptide (**8b**).

(**9**, with one oligonucleotide chain and either **8a** or **8b**), as confirmed by MALDI-TOF MS. As already discussed (synthesis of conjugates **5**, see above), the possibility that conjugates **9** had the structure of mixed disulfides rather than Michael adducts can be ruled out.

Finally, with the aim to compare conjugations involving maleimides and terminal phosphorothioate monoesters (Scheme 3) with Diels−Alder cycloadditions and maleimide−

Scheme 3. Conjugation by Reaction between 5′-Phosphorothioate-[dT$_{10}$] (10) and Maleimido-Compounds 4 (Structures Shown in Scheme 1)



thiol Michael reactions, oligonucleotide 5′-thiophosphate-dT$_{10}$ (**10**) was synthesized, and reacted with **4a** and **4b**.

Oligonucleotide **10** was assembled by coupling the 5′-phosphorylating reagent DMT-O−CH_2CH_2−SO_2−CH_2CH_2−O-P(OCNE)N^{i}Pr$_2$ to resin-linked dT$_{10}$, sulfurization, and deprotection with ammonia. **10** was found to undergo dephosphorylation quite easily (Figure S6a,b).[35] However, since dT$_{10}$ does not interfere with the conjugation reaction, a mixture of **10** and dT$_{10}$ was used in the conjugation with maleimido-compounds **4**. HPLC analysis of the crudes showed that conjugation yields were lower than those of the other conjugation methodologies (Figure S6c,d). Both Diels−Alder and Michael-type conjugation reactions between suitably derivatized PS-ONs and an excess (2−10 equiv) of the other reagent (maleimide or thiol, respectively) had gone to completion after overnight reaction, while unreacted **10** was still found to be present in the conjugation crude after overnight reaction with 10 equiv of **4**. In any case, the target conjugates (**11**) were obtained, isolated, and characterized, confirming that 5′-thiophosphate oligonucleotides do react with maleimides while phosphorothioate diesters do not.

CONCLUSIONS

In summary, phosphorothioate diesters do not react with maleimides in conditions that are suitable for the preparation of conjugates, or at least not to an extent detectable by the analysis techniques used in this study (HPLC and MALDI-TOF MS). Diene-derivatized PS-ONs successfully underwent Diels−Alder cycloadditions with maleimido-containing compounds, and reaction between maleimido-[PS-ONs] and thiol-containing compounds also provided the target conjugates.

An important point is that maleimido-[PS-ONs] can be synthesized using solid-phase methodologies, by incorporation of a [protected maleimido]-phosphoramidite building block to resin-linked PS-ONs. The [protected maleimido]-[PS-ONs] obtained after treatment with ammonia can be heated to remove the maleimide protecting group, and no maleimide-phosphorothioate diester reaction was observed even in these relatively harsh conditions. The maleimido-[PS-ONs] thus obtained were of the same purity as maleimido-[phosphodiester-containing oligonucleotides].

Altogether, these results provide additional, strong support to the compatibility between thiophosphate diesters of PS-ONs and maleimides, and disagree with previous claims suggesting the contrary. They confirm that the most reactive sulfur nucleophile is the one that preferably gives the conjugate addition, and that phosphorothioate diesters do not interfere with the thiol-maleimide addition.

dx.doi.org/10.1021/bc200598g | *Bioconjugate Chem.* 2012, 23, 300−307

Finally, [thiophosphate monoester]-maleimide conjugation was also examined. On one hand, it was found that 5′-thiophosphate-dT_{10} underwent dephosphorylation, which resulted in considerable loss of reagent. On the other, the yield of the conjugation reactions was lower than that of the other methods. Briefly, in our hands either Diels–Alder or maleimide–thiol conjugations gave better results than reaction between maleimides and oligonucleotides with a 5′-thiophosphate monoester.

■ ASSOCIATED CONTENT

Supporting Information

Synthesis and characterization of compounds **1** and **8a**, HPLC traces of compounds **3**, **6**, **10** and **11**, and preliminary experiments to assess thiophosphate-maleimide reactivity. This material is available free of charge via the Internet at http://pubs.acs.org.

■ AUTHOR INFORMATION

Corresponding Author

*Phone: + 34934021263. Fax: + 34933397878. E-mail: anna.grandas@ub.edu.

■ ACKNOWLEDGMENTS

This work was supported by funds from the Ministerio de Ciencia e Innovación (grant CTQ2010-21567-C02-01, and the project RNAREG, grant CSD2009-00080, funded under the programme CONSOLIDER INGENIO 2010), and the Generalitat de Catalunya (2009SGR-208). A. S. was a recipient fellow of the Generalitat de Catalunya.

■ REFERENCES

(1) Matsukura, M., Shinozuka, K., Zon, G., Mitsuya, H., Reitz, M., Cohen, J. S., and Broder, S. (1987) Phosphorothioate analogs of oligodeoxynucleotides: inhibitors of replication and cytopathic effects of human immunodeficiency virus. *Proc. Natl. Acad. Sci. U.S.A. 84*, 7706–7710.

(2) Goodchild, J. (1990) Conjugates of oligonucleotides and modified oligonucleotides: A review of their synthesis and properties. *Bioconjugate Chem. 1*, 165–187.

(3) Diala, I., Osada, A., Maruoka, S., Imanisi, T., Murao, S., Ato, T., Ohba, H., and Fujii, M. (2007) Synthesis of phosphorothioate oligonucleotide-peptide conjugates by solid phase fragment condensation. *Bioorg. Med. Chem. Lett. 17*, 6575–6578.

(4) Goody, R. S., and Eckstein, F. (1971) Thiophosphate analogs of nucleoside di- and triphosphates. *J. Am. Chem. Soc. 93*, 6252–6257.

(5) Wettstein, P. J., Borson, N. D., Park, J. G., McNallan, K. T., and Reed, A. M. (2005) Cysteine-tailed class I-binding peptides bind to CpG adjuvant and enhance primary CTL responses. *J. Immunol. 205*, 3681–3689.

(6) Antopolsky, M., Azhayeva, E., Tengvall, U., Auriola, S., Jääskeläinen, I, Rönkkö, S., Honkakoski, P., Urtti, A., Lönnberg, H., and Azhayev, A. (1999) Peptide-oligonucleotide phosphorothioate conjugates with membrane translocation and nuclear localization properties. *Bioconjugate Chem. 10*, 598–606.

(7) Bongartz, J. P., Aubertin, A.-M., Milhaud, P. G., and Lebleu, B. (1994) Improved biological activity of antisense oligonucleotides conjugated to a fusogenic peptide. *Nucleic Acids Res. 22*, 4681–4688.

(8) Stetsenko, D. A., Arzumanov, A. A., Korshun, V. A., and Gait, M. J. (2000) Peptide conjugates of oligonucleotides as enhanced antisense agents. *Mol. Biol. 34*, 852–859.

(9) Gait, M. J. (2003) Peptide-mediated cellular delivery of antisense oligonucleotides and their analogues. *Cell. Mol. Life Sci. 60*, 844–853.

(10) Fidanza, J. A., and McLaughlin, L. W. (1989) Introduction of reporter groups at specific sites in DNA containing phosphorothioate diesters. *J. Am. Chem. Soc. 111*, 9117–9119.

(11) Gryaznov, S. M., and Letsinger, R. L. (1993) Chemical ligation of oligonucleotides in the presence and absence of a template. *J. Am. Chem. Soc. 115*, 3808–3809.

(12) Lee, J. H., Wong, N. Y., Tan, L. H., Wang, Z., and Lu, Y. (2010) Controlled alignment of multiple proteins and nanoparticles with nanometer resolution via backbone-modified phosphorothioate DNA and bifunctional linkers. *J. Am. Chem. Soc. 132*, 8906–8908.

(13) Lee, P., and Colman, R. F. (2005) Adenosine 2′-monophosphate, 5′-*O*-[*S*-(4-succinimidylbenzophenone)-thiophosphate]: a new photoaffinity label for the coenzyme site of porcine NADP-specific isocitrate dehydrogenase. *Bioconjugate Chem. 16*, 650–659.

(14) Karim, A. S., and Weltman, J. K. (1993) Formation of protein conjugates of phosphorothioate nucleoside diphosphate beta-S. *Nucleic Acids Res. 21*, 5281–5282.

(15) Karim, A. S., Johansson, C. S., and Weltman, J. K. (1995) Maleimide-mediated protein conjugates of a nucleoside triphosphate gamma-S and an internucleotide phosphorothioate diester. *Nucleic Acids Res. 23*, 2037–2040.

(16) Ahn, D.-R., Han, K.-C., Kwon, H. S., and Yang, E. G. (2007) ATP-conjugated peptide inhibitors for calmodulin-dependent protein kinase II. *Bioorg. Med. Chem. Lett. 17*, 147–151.

(17) Kaneda, M., Masuda, S., Tomohiro, T., and Hatanaka, Y. (2007) A simple and efficient photoaffinity method for proteomics of GTP-binding proteins. *ChemBioChem 8*, 595–598.

(18) Kim, S. H., Jeong, J. H., Mok, H., Lee, S. H., Kim, S. W., and Park, T. G. (2007) Folate receptor targeted delivery of polyelectrolyte complex micelles prepared from ODN-PEG-folate conjugate and cationic lipids. *Biotechnol. Prog. 23*, 232–237.

(19) Alam, M. R., Dixit, V., Kang, H., Li, Z.-B., Chen, X., Trejo, J., Fisher, M., and Juliano, R. L. (2008) Intracellular delivery of an anionic antisense oligonucleotide via receptor-mediated endocytosis. *Nucleic Acids Res. 36*, 2764–2776.

(20) Rabe, K. S., and Niemeyer, C. M. (2011) Selective covalent conjugation of phosphorothioate DNA oligonucleotides with streptavidin. *Molecules 16*, 6916–6926.

(21) Hussain, S., Plückthun, A., Allen, T. M., and Zangemeister-Wittke, U. (2006) Chemosensitization of carcinoma cells using epithelial cell adhesion molecule-targeter liposomal antisense against bcl-2/bcl-xL. *Mol. Cancer Ther. 5*, 3170–3180.

(22) Sassolas, A., Leca-Bouvier, B. D., and Blum, L. J. (2008) DNA biosensors and microarrays. *Chem. Rev. 108*, 109–139.

(23) Williams, B. A. R., Diehnelt, C. W., Belcher, P., Greving, M., Woodbury, N. W., Johnston, S. A., and Chaput, J. C. (2009) Creating protein affinity reagents by combining peptide ligands on synthetic DNA scaffolds. *J. Am. Chem. Soc. 131*, 17233–17241.

(24) Putta, M. R., Zhu, F.-G., Wang, D.-Q., Bhagat, L., Dai, M., Kandimalla, E. R., and Agrawal, S. (2010) Peptide conjugation at the 5′-end of oligodeoxynucleotides abrogates Toll-like receptor 9-mediated immune stimulatory activity. *Bioconjugate Chem. 21*, 39–45.

(25) Niemeyer, C. M. (2010) Semisynthetic DNA-protein conjugates for biosensing and nanofabrication. *Angew. Chem., Int. Ed. 49*, 1200–1216.

(26) Yanai, H., Chiba, S., Ban, T., Nakaima, Y., Onoe, T., Honda, K., Ohdan, H., and Taniguchi, T. (2011) Suppression of immune responses by nonimmunogenic oligodeoxynucleotides with high affinity for high-mobility group box proteins (HMGBs). *Proc. Natl. Acad. Sci. U.S.A. 108*, 11542–11547.

(27) Sánchez, A., Pedroso, E., and Grandas, A. (2011) Maleimide-dimethylfuran *exo* adducts: Effective maleimide protection in the synthesis of oligonucleotide conjugates. *Org. Lett. 13*, 4364–4367.

(28) Iyer, R. P., Egan, W., Regan, J. B., and Beaucage, S. L. (1990) 3*H*-1,2-benzodithiole-3-one 1,1-dioxide as an improved sulfurizing reagent in the solid-phase synthesis of oligodeoxyribonucleoside phosphorothioates. *J. Am. Chem. Soc. 112*, 1253–1254.

(29) Hill, K. W., Taunton-Rigby, J., Carter, J. D., Kropp, E., Vagle, K., Pieken, W., McGee, D. P., Husar, G. M., Leuck, M., Anziano, D. J., and

Sebesta, D. P. (2001) Diels-Alder bioconjugation of diene-modified oligonucleotides. *J. Org. Chem. 66*, 5352−5358.
(30) Pulido, D., López-Alonso, J. P., Marchán, V., González, C., Grandas, A., and Laurents, D. V. (2008) Preparation of ribonuclease S domain-swapped dimers conjugated with DNA and PNA: Modulating the activity of ribonucleases. *Bioconjugate Chem. 19*, 263−270.
(31) Marchán, V., Ortega, S., Pulido, D., Pedroso, E., and Grandas, A. (2006) Diels-Alder cycloadditions in water for the straightforward preparation of peptide-oligonucleotide conjugates. *Nucleic Acids Res. 34*, e24.
(32) Ellman, G. L (1959) Tissue sulfhydryl groups. *Arch. Biochem. Biophys. 82*, 70−77.
(33) Ortega, S., Marchán, V., and Grandas, A. unpublished results.
(34) Lo Conte, M., Pacifico, S., Chambery, A., Marra, A., and Dondoni, A. (2010) Photoinduced addition of glycosyl thiols to alkynyl peptides: use of free-radical thiol−yne coupling for post-translational double-glycosylation of peptides. *J. Org. Chem. 75*, 4644−4647.
(35) Ashley, G. W., and Kushlan, D. M. (1991) Chemical synthesis of oligodeoxynucleotide dumbbells. *Biochemistry 30*, 2927−2933.

■ NOTE ADDED AFTER ASAP PUBLICATION

This paper was published on the Web on Jan 13, 2012, with errors in the first paragraph. The corrected version was reposted on Feb 15, 2012.

Bioconjugate Chemistry

Correction

pubs.acs.org/bc

Correction to Comparison Study of [^{18}F]FAl-NOTA-PRGD2, [^{18}F]FPPRGD2, and [^{68}Ga]Ga-NOTA-PRGD2 for PET Imaging of U87MG Tumors in Mice

Lixin Lang, Weihua Li, Ning Guo, Ying Ma, Lei Zhu, Dale O. Kiesewetter, Baozhong Shen, Gang Niu, and Xiaoyuan Chen*

Bioconjugate Chemistry **2011**, *22* (12), 2415−2422. DOI: 10.1021/bc200197h

The authors regret an error throughout the manuscript where "[^{18}F]FPPRDG2" should read "[^{18}F]FPPRGD2".

Published: January 12, 2012

ACS Publications © 2012 American Chemical Society

Bioconjugate Chemistry

Review

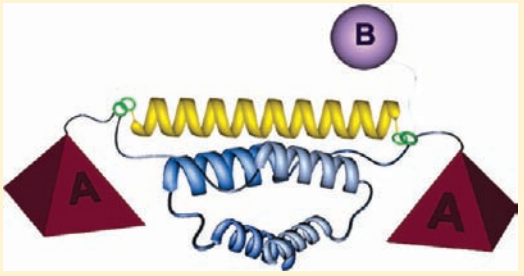
pubs.acs.org/bc

The Dock-and-Lock Method Combines Recombinant Engineering with Site-Specific Covalent Conjugation To Generate Multifunctional Structures

Edmund A. Rossi,*[,†] David M. Goldenberg,[‡] and Chien-Hsing Chang[†,§]

[†]IBC Pharmaceuticals, Inc.; [‡]Garden State Cancer Center, Center for Molecular Medicine and Immunology; and [§]Immunomedics, Inc.; each in Morris Plains, New Jersey, United States

ABSTRACT: Advances in recombinant protein technology have facilitated the production of increasingly complex fusion proteins with multivalent, multifunctional designs for use in various *in vitro* and *in vivo* applications. In addition, traditional chemical conjugation remains a primary choice for linking proteins with polyethylene glycol (PEG), biotin, fluorescent markers, drugs, and others. More recently, site-specific conjugation of two or more interactive modules has emerged as a valid approach to expand the existing repertoires produced by either recombinant engineering or chemical conjugation alone, thus advancing the range of potential applications. Five such methods, each involving a specific binding event, are highlighted in this review, with a particular focus on the Dock-and-Lock (DNL) method, which exploits the natural interaction between the dimerization and docking domain (DDD) of cAMP-dependent protein kinase (PKA) and the anchoring domain (AD) of A-kinase anchoring proteins (AKAP). The various enablements of DNL to date include trivalent, tetravalent, pentavalent, and hexavalent antibodies of monospecificity or bispecificity; immnocytokines comprising multiple copies of interferon-alpha (IFNα); and site-specific PEGylation. These achievements attest to the power of the DNL platform technology to develop novel therapeutic and diagnostic agents from both proteins and nonproteins for unmet medical needs.



The continuing development of new technologies for both rational and combinatorial protein engineering has increased the variety and magnitude of potential molecules that may be designed and produced for biotechnological and biomedical applications. An essential factor for these accomplishments is that many natural proteins have their functional properties located in discrete domains, which can be manipulated as molecular modules and exploited as building blocks for devising artificial structures with multiple functions. Molecular modules derived from the binding domains of antibodies or nonantibodies, or those based on protein display scaffolds, currently have received the most attention, as described in several reviews.[1−5] Molecular modules that confer effector functions of proteins, for example, the Fc of an IgG or the catalytic domain of an enzyme, also constitute an important class of components in the architecture of designer proteins.[6,7] In addition, peptide motifs with the innate ability to self-associate are often built into fusion proteins to facilitate the formation of dimeric, trimeric, or multimeric products composed of the same or different polypeptides.[8−12] Examples of self-associating peptides that have been utilized successfully for this purpose include Fos/Jun, the C-terminal multimerization domain of the tumor suppressor protein p53, a streptavidin subdomain, the trimerization domain of collagen XVIII, and triplet-forming collagen-like peptides.[13−16] Fusion of TNFα, which exists naturally as a trimer, to the C-terminus of a scFv antibody resulted in a homotrimeric structure with retained binding ability of the scFv as well as TNFα activity.[17,18] Indeed, the power of recombinant technology has facilitated the creation of diverse, multivalent, multifunctional fusion proteins. Nevertheless, we have recognized that innovative fusion proteins created by recombinant engineering may be built into more complex structures to gain additional attributes that are highly desirable, yet not technically attainable, in the individual engineered construct. To date, such goals are commonly achieved, with varied success, by judicious application of conjugation chemistries. Well-known examples include pegylated cytokines to increase serum half-lives,[19] biotinylated proteins to enable immobilization into microarrays,[19,20] and intein-mediated assembly of protein−DNA chimeras to quantify specific molecules to which the protein binds.[21]

A number of methods exploiting the specific interaction between a receptor protein and its cognate small molecule ligand have been developed for the selective labeling of fusion proteins with small molecules, such as fluorescent dyes, and/or immobilization of fusion proteins. For this group of technologies, fusion proteins are recombinantly tagged with small molecule-binding receptor proteins, which include the Halo-Tag,[22] SNAP-Tag,[23] TC-Tag,[24] dihydrofolate reductase,[25] and FKBP-Tag.[26] The purified tagged proteins can be labeled, either *in vitro* or *in vivo*,[23−26] with a fluorescent dye coupled to

Received: September 8, 2011
Revised: November 14, 2011
Published: December 14, 2011

 © 2011 American Chemical Society dx.doi.org/10.1021/bc2004999 | *Bioconjugate Chem.* 2012, 23, 309−323

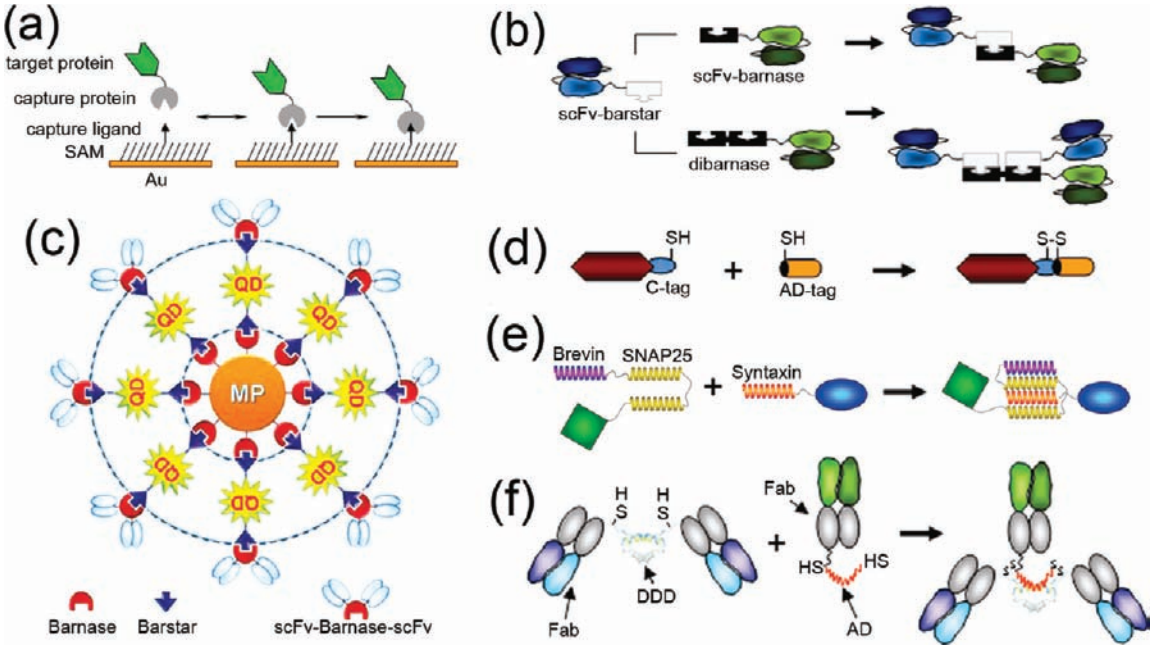


Figure 1. Representative examples of linking interactive modules into covalent or quasi-covalent structures. (a) Self-assembled monolayer (SAM) projecting the capture ligand (phosphonate) is tethered on a gold surface. A capture protein (cutinase) fused to the protein of interest specifically binds to the capture ligand, which leads to covalent immobilization of the protein of interest without altering its activity or orientation (adapted from *Proc Natl. Acad. Sci. U.S.A. 99*, 5048−5052). (b) Multimeric complexes can be assembled by linking one module containing barstar to another module containing barnase. Bispecific binding constructs composed of two or more scFvs are generated using this approach (adapted from *Nat. Biotechnol. 21*, 1486−1492). (c) Multifunctional nanoparticles comprising a barnase-magnetic particle (MP), barstar-quantum dots (QD), and di-scFv-barnase. Adapted from *Proc. Natl. Acad. Sci. U.S.A. 104*, 14753−14758. (d) A docking tag derived from the first 15 amino acids of human RNase I is fused to a targeting protein to enable the attachment of a payload module that contains the S-protein of human RNase I as an adapter. The use of an optimized pair (C-tag and Ad-C) for this system further allows the formation of a disulfide-stabilized adduct (adapted from *Bioconjug. Chem. 17*, 912−919.). (e) The α helices of synaptobrevin (brevin), SNAP25, and syntaxin form a tetrahelical bundle known as the SNARE complex. A tag comprising the two α helices of SNAP25 plus the α helix of synaptobrevin is fused to the protein represented by the green diamond. The α helix of syntaxin is fused to the protein represented by a blue oval. (f) The α helices (DDD and AD) involved in the natural binding interaction of PKA and AKAPs are utilized to dock two types of modules (shown as fusion proteins of Fab) that are further locked by disulfide linkages (adapted from *Proc. Natl. Acad. Sci. U.S.A. 103*, 6841−6846).

the synthetic small molecule ligand, which binds tightly and specifically to the tag. Alternatively, the tagged protein can be immobilized on a matrix, which is coupled with the ligand.[27,28] While these methods are highly effective for site-specific coupling of small molecules to recombinant proteins, they are less appealing for the construction of complex, multifunctional proteins, because the requisite chemical conjugation of the small molecule ligand to a protein may be nonsite-specific and may interfere with biological activity.

The most popular binary affinity system utilizes the uniquely strong biotin−streptavidin interaction. However, attachment of either biotin or streptavidin (normally tetrameric) to a target protein traditionally requires chemical conjugation, which is typically not site-specific. Recombinant methods have been developed for site-specific fusion of both streptavidin and biotin. Recombinant fusion of streptavidin to a precursor protein results in the formation of a tetrameric module, which may be advantageous or disadvantageous, depending on the intended application. Site-specific biotinylation can be accomplished by recombinant fusion of a biotin acceptor peptide to a precursor protein followed by enzymatic biotinylation with a biotin ligase.[29] Biotinylation can even be accomplished *in vivo* when a biotin acceptor peptide-fused protein is expressed in a biotin ligase-tansfectant host production cell.[30] Because the streptavidin−biotin system is well established with countless original articles as well as reviews,[31,32] it will not be included in this review.

Relatively new to the bioconjugate field are promising strategies for tethering two or more molecular modules of distinct functions into covalent or quasi-covalent assemblies following a binding event. We present here an overview of five such strategies (Figure 1), each employing a different mode of attraction to assemble the interactive constituents, with an option for covalent stabilization of the resulting structures via directed ligation. We will provide a proof-of-concept example to elucidate each strategy, and then we will focus on the Dock-N-Lock (DNL) platform technology,[33] which has the potential for making an unlimited number of bioactive molecules with multivalency, multifunctionality, and defined composition. We highlight the advantages of DNL, describe potential alternatives for DNL, and outline the challenges and prospects presented by DNL.

■ ENZYME/INHIBITOR MODULES BASED ON CUTINASE AND PHOSPHONATE

The introduction of protein microarrays has underscored a need for methods that can selectively, rapidly, efficiently, and irreversibly immobilize proteins in a defined orientation to preserve their folded conformation and function.[34] This has been accomplished using some of the receptor−small molecule systems, such as the SNAP-tag, discussed above.[27] Another

immobilization strategy that has been successfully applied to achieve these goals involves active site-directed capture of surface-attached suicide substrate by an enzyme-tagged protein, with subsequent reaction to secure a covalent link (Figure 1a).[35] In essence, a protein of choice is fused to *Fusarium solani pisi* cutinase, a 22-kDa serine esterase that forms a site-specific adduct with phosphonates, to serve as the bait agent.[36,37] Self-assembled monolayers of alkanethiolates with terminal 4-nitrophenyl phosphates are tethered to gold-coated glass to present the capture ligand. The binding of cutinase to phosphonate leads to the displacement of *p*-nitrophenol by the catalytic serine, resulting in covalent immobilization of the protein onto the monolayer surface. Antibody chips thus prepared exhibit desirable characteristics that include a single orientation of the immobilized antibody with a controlled density, as well as high affinity and selectivity for the target antigens.[38]

This system has been applied to specifically and covalently label membrane proteins of live cells with quantum dots.[39] Cutinase was recombinantly embedded in the extracellular domain of lymphocyte function-associated antigen-1 (LFA-1), and *p*-nitrophenyl phosphonate (pNPP)-conjugated quantum dots were covalently coupled to cutinase-LFA-1 on the surface of live transfectant cells. The dynamic redistribution of LFA-1 during locomotion of BAF cells, which were transfected with cutinase-LFA-1, was imaged using pNPP-Alexa488 on glass slides coated with ICAM-1 (for adhesion) and SDF-1 (for chemokinesis).

ENZYME/INHIBITOR MODULES BASED ON BARNASE AND BARSTAR

The barnase−barstar module provides an interesting approach for engineering multivalent, multifunctional protein complexes that takes advantage of a tight association ($K_D \sim 10^{-14}$ M) of the ribonuclease barnase with the barstar inhibitor.[40] Fusion proteins tagged with one barnase (or two in series) or barstar were generated separately, purified, and subsequently combined to form quasi-covalent heterodimers or heterotrimers (Figure 1b). Since the initial report of the production, refolding, and purification of barnase and barstar fusion proteins in *E. coli*, expressions of scFv-barnase in mammalian HEK 293T cells,[41] and scFv-barstar in tobacco plants,[42] also have been described.

Recently, the barnase−barstar system has been utilized to generate trifunctional superstructures comprising magnetic iron oxide particles, fluorescent nanoparticles, and multiple scFv antibody fragments (Figure 1c).[43] As core modules, magnetic particles of different sizes and chemical compositions were conjugated with multiple barnase groups. Two types of fluorescent quantum dots were chemically coupled with multiple barstar groups and used to decorate the magnetic particle−barnase core. A third layer of a dimeric anti-Her2/neu scFv-barnase module was added to the superstructure. The nanoparticles bound to and fluorescently labeled Her2/neu+ ovarian carcinoma cells (SCOV-3) and concentrated them in areas with a strong magnetic field gradient, demonstrating the designed trifunctionality.

Although this system can be useful for the modular assembly of binary and more complexes, two significant drawbacks may hamper its practical application. First, the toxicity of barnase to the host cell requires the coexpression of barstar with barnase fusion proteins, thus entailing denaturation and chromatography under denaturing conditions for barstar removal and subsequent refolding. Second, utilization of barnase (110 amino acids) and barstar (89 amino acids) as a heterodimerization pair adds significant protein mass (~22 kDa), which, combined with their bacterial origin, will likely render the complexes immunogenic.

ADAPTER/DOCKING-TAG MODULES BASED ON MUTATED FRAGMENTS OF RNASE I

The development of the adapter/docking-tag system based on the high affinity interaction between the two fragments of human pancreatic ribonuclease (RNase I) enables site-specific conjugation of a payload with a targeting protein.[44] In this approach, a peptide derived from the first 15 amino acids of RNase I is fused to a targeting protein to serve as a docking tag for an adapter that comprises the S-protein of RNase I (residues 21−127) derivatized with a diagnostic or therapeutic agent (Figure 1d). The optimized method uses a docking tag, named C-tag, containing a cysteine in position 4 (R4C mutant), and an adapter, named Ad-C, containing a cysteine in position 118 (V118C mutant), to facilitate the formation of a C4−C118 disulfide bond upon association of C-tag and Ad-C.[45] A further modification of Ad-C involves the introduction of an additional cysteine in position 88 (N88C) to allow site-specific ligation of an effector. The source of Ad-C is a chimera (BH-RNase) consisting of the N-terminal 29 amino acids of bovine ribonuclease A fused to 30−127 amino acids of RNase I, which can be selectively cleaved with the bacteria protease subtilisin at the A20-S21 bond to release the S-protein.[46]

This technology has been adapted for covalent coupling of targeting fusion proteins containing the C-tag to liposomes decorated with Ad-C.[47] Proof-of-principle was demonstrated using vascular endothelial growth factor fused with a C-terminal C-tag and a fragment of anthrax lethal factor fused with a N-terminal C-tag. Both proteins retained functional activity when coupled to drug-loaded Ad-C-liposomes.

SNARE MODULES

A modular method for making binary complexes via site-specific combination of recombinant fusion protein modules, which is based on a tetrahelical bundle known as the SNARE (soluble *N*-ethylmaleimide-sensitive factor attachment protein receptor) complex, has been reported recently.[48] The neuronal SNARE system is based on the natural interaction of three proteins, syntaxin, synaptobrevin, and SNAP25, which contribute two, two, and one α-helices, respectively, to form a very tight tetrahelical bundle commonly known as the SNARE complex.[49] Although the interaction is not covalent, the SNARE complex is remarkably stable and resistant to harsh treatments, including urea and sodium dodecyl sulfate.[50]

In one embodiment of this method, recombinant modules are made as fusion proteins with a precursor protein fused with either SNAP25 (206 amino acids) or synaptobrevin (60 amino acids) tags. The modules are then stapled together using a synthetic syntaxin peptide (50 amino acids). Proof-of-principle was established using a modular assembly of botulinum neurotoxin type A from its subunits.[51] Fusing the receptor-binding domain with the synaptobrevin SNARE motif allowed delivery of the active part of botulinum neurotoxin, which was tagged with SNAP25, into neurons, where it was able to cleave its intraneuronal molecular target and to inhibit release of neurotransmitters. To increase the utility of the system, incorporation of biotin into the synthetic syntaxin peptide

dx.doi.org/10.1021/bc2004999 | *Bioconjugate Chem.* 2012, 23, 309−323

allowed the receptor binding portion of the toxin to be used to deliver streptavidin-coated quantum dots into neurons.

As an alternative, the three-part system was adapted to a binary system where two of the three components were combined into a single tag (Figure 1e).[48] In one variation, SNAP25 and synaptobrevin were fused with glutathione S-transferase (GST), which showed highly stable binding to syntaxin-coupled beads or to a syntaxin-coupled Biacore sensor chip. In another variation, a combination of synaptobrevin and syntaxin, is used as a single tag, referred to as Nano-Lock (NL), which binds to a SNAP25-tagged module. Proof-of-principle was demonstrated using gold nanoparticles, where GST-SNAP25 was immobilized on gold nanoparticles derivatized with NL. Similarly, GST-NL specifically coupled to nanoparticles was derivatized with SNAP25.

DNL TECHNOLOGY

The basis of the DNL method is the exploitation of the specific protein−protein interactions occurring in nature between the regulatory (R) subunits of cAMP-dependent protein kinase PKA and the anchor domain (AD) of A-kinase anchor proteins (AKAPs).[52,53] Two types of R subunits (RI and RII) are found in PKA, and each has α and β isoforms. The R subunits have been isolated only as stable dimers, with the dimerization domain shown to consist of the first 44 amino-terminal residues.[54] The AD of AKAPs for PKA is an amphipathic helix of 14−18 residues,[55] which binds only to dimeric R subunits. For human RIIα, the AD binds to a hydrophobic surface formed by the 23 amino-terminal residues.[56] Thus, the dimerization domain and AKAP binding domain of human RIIα are both located within the same N-terminal 44 amino acid sequence[54,57] and are referred to as the dimerization and docking domain (DDD).

For the DNL method, AD and DDD peptide sequences, which are modified with cysteine residues for covalent "locking" via disulfide bridges, are fused to a precursor protein (or other entity) to make DNL-modules, which are produced and stored independently (Figure 2a and c). The DDD-derivatized proteins (DDD-modules) spontaneously form stable homodimers; therefore, DDD-modules always comprise two copies of the precursor protein (Figure 2b). Upon design, any DDD-module can be paired with any AD-module to generate a wide variety of stable conjugates comprising two and one copies of the DDD-module and AD-module precursors, respectively (Figure 2d).

In our first study,[33] we showed the DDD of human RIIα (designated DDD1) and the AD derived from AKAP-*IS*,[58] a synthetic peptide optimized for RII-selective binding with a reported K_D of 4×10^{-10} M (designated AD1), to be an excellent pair of linker peptides for docking two entities into a noncovalent complex, which could be further locked into a stably tethered structure through the introduction of cysteine residues into both the DDD and AD at strategic positions to facilitate the formation of disulfide bonds. The cysteine-modified versions of AD1 and DDD1, designated AD2 (**C**GQIEYLAKQIVDNAIQQAG**C**) and DDD2 (**C**GHIQIPPGLTELLQGYTVEVLRQQPPDLVEFAVEYFTRLREARA), respectively, are the preferred peptide linker pairing of the DNL method.

Besides the unique feature that a DDD-derivatized precursor is always presented in two copies, additional advantages of the DNL method that together distinguish it from other site-specific conjugation methods[19−21,35,40,45] are summarized as follows.

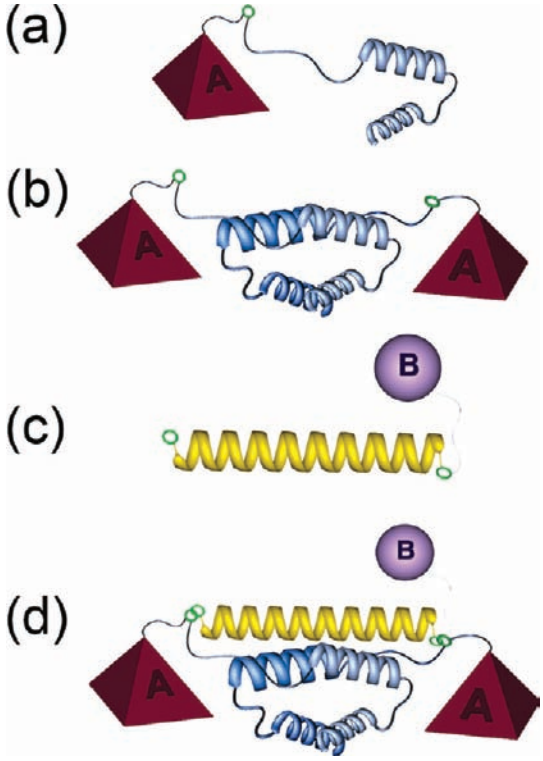


Figure 2. Basic features of the DNL method. (a) DDD-module of precursor *A*. (b) DDD-mediated dimer of precursor *A*. (c) AD-module of precursor *B*. (d) Stably tethered DNL conjugate comprising two copies of precursor *A* and one of precursor *B*. Green rings indicate SH groups of the engineered cysteine residues of DDD (blue helix) and AD (yellow helix). The "locking" disulfide bonds are depicted as interlocking green rings.

The completely modular nature of DNL allows the rapid and facile creation of a large number of potentially useful conjugates. Each DDD- or AD-containing entity serves as a module, and any DDD-module can be paired with any AD-module. Such modules can be produced independently, stored separately, and combined on demand. There is essentially no limit on the types of precursors that can be converted into a DDD- or AD-module, so long as the resulting modules do not interfere with the dimerization of DDD or the binding of DDD to AD. Many DNL conjugates can be made combinatorially from a relatively small number of each type of module. For example, 400 different conjugates could be made from a pool of 20 AD- and 20 DDD-modules.

DNL is versatile. Modules can be made recombinantly or synthetically. Recombinant modules, which may be produced in mammalian, microbial, or other expression systems, may include fusions of antibodies or antibody fragments, cytokines, enzymes, carrier proteins (e.g., human serum albumin and human transferrin), or a variety of natural or artificial nonantibody binding or scaffold proteins.[1,2,4,5] Furthermore, DDD or AD can be coupled to the amino-terminal or carboxyl terminal end or even positioned internally within the fusion protein, preferably with a spacer containing an appropriate length and composition of amino acid residues, provided that the binding activity of the DDD or AD and the desired activity of the polypeptide fusion partners are not compromised. Two

dx.doi.org/10.1021/bc2004999 | *Bioconjugate Chem.* 2012, 23, 309−323

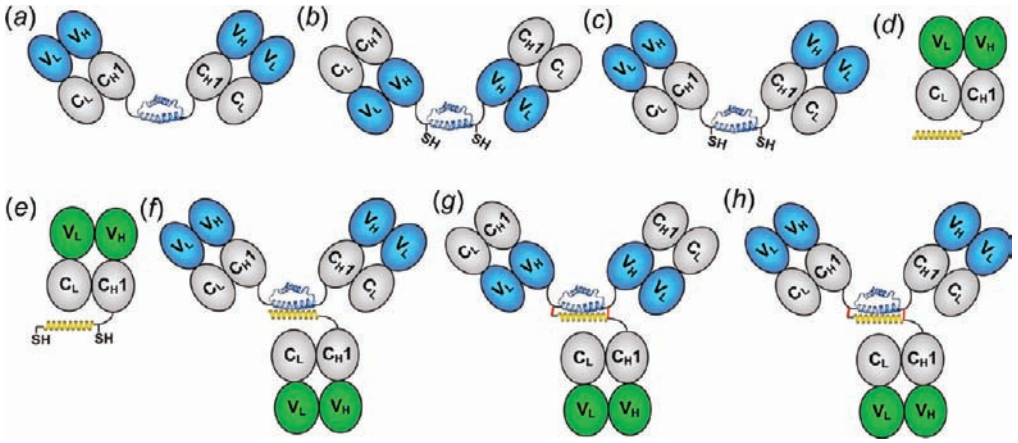


Figure 3. Fab-based DNL-modules and TFs. (a) C_H1-DDD1-Fab, a Fab-DDD-module without "locking" cysteine residues in the DDD, which is fused to the carboxyl-terminal end of the Fd chain. (b) *N*-DDD2-Fab, a Fab-DDD-module with added cysteine residues in the DDD, which is fused to the amino-terminal end of the Fd chain. (c) C_H1-DDD2-Fab, a Fab-DDD-module with cysteine residues in the DDD, which is fused to the carboxyl-terminal end of the Fd chain. (d) C_H1-AD1-Fab, a Fab-AD-module without "locking" cysteine residues in the AD, which is fused to the carboxyl-terminal end of the Fd chain. (e) C_H1-AD2-Fab, a Fab-AD-module with cysteine residues in the AD, which is fused to the carboxyl-terminal end of the Fd chain. (f) Binary, noncovalent complex of C_H1-DDD1-Fab-hMN-14 and C_H1-AD1-Fab-h679. (g) TF1, a covalent complex of N-DDD2-Fab-hMN-14 and C_H1-AD2-Fab-h679. (h) TF2, a covalent complex of C_H1-DDD2-Fab-hMN-14 and C_H1-AD2-Fab-h679. Variable (V, blue or green) and constant (C, gray) domains of the heavy (H) and light (L) chains are represented as ovals. The DDD and AD peptides are shown as blue and yellow helices, respectively, with the locations indicated for the reactive sulfhydryl groups (SH) of the engineered cysteine residues in AD2 and DDD2, and the disulfide bridges (red line) that they form in TF1 and TF2. Adapted from *Proc. Natl. Acad. Sci. U.S.A. 103*, 6841−6846.

or more AD peptides can be incorporated into AD modules to create a scaffold for attachment of multiple DDD modules.

Modules can also be made synthetically, to comprise peptides, polyethylene glycol (PEG), dendrimers, nucleic acids, chelators with or without radioactive or nonradioactive metals, drugs, dyes, oligosaccharides, natural or synthetic polymeric substances, nanoparticles, fluorescent molecules, or quantum dots, depending on the intended applications.[59]

DNL manufacturing is easy. The DNL method is basically a one-pot preparation and requires three simple steps to recover the product from the starting materials: (i) combine DDD- and AD-modules in stoichiometric amounts; (ii) add redox agents to facilitate the self-assembly of the DNL-conjugate; and (iii) purify by an appropriate affinity chromatography process. The DNL-modules can be purified and stored prior to their use in a DNL conjugation. However, purification of the modules is not necessary. DNL conjugation can be accomplished in mixtures of cell lysates and/or culture supernatant fluids containing the DNL-modules, with subsequent isolation of the DNL-conjugate by affinity chromatography. A single-step affinity purification process with commonly used affinity media, such as Protein A or immobilized metal, typically results in >95% purity of the DNL conjugate, which is sufficient for most preclinical applications. However, for manufacturing of clinical material, further processing steps, such as additional affinity chromatography, ion exchange chromatography, low pH treatment, and ultrafiltration, are required to ensure adequate removal of viral and other contaminants.

The site-specific conjugation associated with DNL results in quantitative yields of a homogeneous product with a defined composition. The high-affinity binding between the DDD- and AD-modules results in nearly 100% conversion of each into the desired DNL product. The DNL method results in a preparation of defined and homogeneous molecular size and composition, for which the full activity of each module is usually preserved. Further, DNL conjugates are highly stable *in vitro* and *in vivo*. Various DNL conjugates were completely stable in serum and whole blood for more than 7 days at 37 °C.[60−63]

A potential disadvantage of DNL comes from a commercial standpoint. Although the modular nature of DNL is clearly an advantage for constructing many fusion proteins from a much smaller number of modules, and also allows the assembly of complex structures that would not be possible with conventional recombinant engineering, two (or possibly more) modules need to be synthesized in order to make a single product. Obviously, this results in increased production costs due to the establishment of two host cell lines and bioreactor production of each module. However, this concern is mitigated by current advances in manufacturing capabilities, which allow bioreactor production of some recombinant proteins at the scale of several grams per liter.

Another potential technical complication, which we have yet to suffer from, is the potential for irreversible inactivation of precursor molecules during the mild redox conditions during DNL conjugation. The cysteine residues involved in DNL docking are exposed and readily reduced under mild conditions. Internal disulfides, which might be present in a precursor, are less affected under these conditions, and even if reduced, they are likely to re-form upon reoxidation. However, it is possible that some precursors might denature or aggregate during the redox reaction.

■ DNL MODULES AND CONJUGATES

Fab-Based Modules and Tri-Fabs. In our first study,[33] the DNL method was applied to generate bispecific trivalent complexes comprising three Fab fragments by combining DDD-modules constructed from the Fab of hMN-14, a humanized monoclonal antibody (mAb) with specificity for the A3B3 domains of human carcinoembryonic antigen (CEACAM5),[64] with AD-modules constructed from the Fab of h679, a humanized mAb with specificity for the hapten histamine-succinyl-glycine (HSG).[65]

dx.doi.org/10.1021/bc2004999 | *Bioconjugate Chem.* 2012, 23, 309−323

Three Fab-DDD-modules and two Fab-AD2-modules were used to generate three different Tri-Fabs (TFs), each comprising two hMN-14 Fabs and one h679 Fab. Fab-based modules are purified by affinity chromatography using Protein L or KappaSelect affinity media. C_H1-DDD1-Fab-hMN-14 (Figure 3a) and C_H1-AD1-Fab-h679 (Figure 3d) are Fab-DDD- and Fab-AD-modules of the respective parent mAbs, fused at the carboxyl-terminal end of the F_d chain (C-terminal end of C_H1 domain) to DDD1 and AD1, respectively. Upon mixing of the two modules, the formation of a binary complex (Figure 3f) was readily demonstrated by SE-HPLC with the K_D determined by equilibrium gel filtration analysis[66] to be about 8 nM, which is presumably too weak of an affinity for *in vivo* applications. DDD1 was converted to DDD2 by incorporation of a cysteine residue at the amino-terminal end of the DDD peptide. Thus, the naturally dimeric DDD2-modules have two reactive cysteine residues. Two additional modules were generated for the hMN-14 Fab, *N*-DDD2-Fab-hMN-14 (Figure 3b) and C_H1-DDD2-Fab-hMN-14 (Figure 3c), where the DDD2 peptide was fused to the amino- or carboxyl-terminal end of the F_d chain, respectively. A cysteine residue was added to each end of AD1 to create AD2, which was included in the C_H1-AD2-Fab-h679 module (Figure 3e). Two stably tethered trivalent bispecific structures, referred to as TF1 (Figure 3g) for the conjugate of *N*-DDD2-Fab-hMN-14 and C_H1-AD2-Fab-h679 and TF2 (Figure 3h) for the conjugate of C_H1-DDD2-Fab-hMN-14 and C_H1-AD2-Fab-h679, were produced in nearly quantitative yields and characterized extensively. TF1 and TF2 were isolated by affinity chromatography using the h679-binding hapten HSG, and they were each resolved by SE-HPLC as a single peak of the expected molecular size (~150 kDa). BIAcore demonstrated bispecific binding, which was confirmed by competition ELISA to be equivalent to hMN-14 IgG and h679 Fab, reflecting the retention of valency and binding affinity. Furthermore, TF1 and TF2 were stable for at least 7 days at 37 °C in human or mouse serum. The superiority of TF2 as a pretargeting agent for diagnostic imaging has been demonstrated in numerous animal studies.[67−70] Recent clinical results have confirmed that TF2 is effective for pretargeted radioimmune detection in patients with CEA-CAM5+ tumors (Figure 4a).

Since the generation of TF1 and TF2, the modular DNL method has allowed the rapid development of over 20 different trivalent bispecific Fab-based complexes, referred to as the TF series, by combinatorial pairing of monomeric Fab-AD2 and dimeric Fab-DDD2 modules.[71−81] Several of the TFs have exhibited excellent performance in pretargeting applications (Figure 4b). The technology platform has also been expanded to generate a variety of conjugates, including multivalent, multifunctional antibodies and immunocytokines, which are highlighted below.

IgG-AD2-Modules. After establishing proof of principle with the TF series using Fab-based DDD2- and AD2-modules, we next developed AD2-modules for IgG, which allowed the synthesis of a variety of complex, IgG-based DNL conjugates. C_H3-AD2-IgG modules were produced recombinantly by appending, in frame, the coding sequence for AD2, preceded by a flexible peptide linker, to the 3′ end of the coding sequence of the C_H3 domain of IgG (Figure 5a). This method allowed the simple conversion of any existing IgG-expression plasmid vector into one for IgG-AD2 expression. Because IgG naturally forms a heterotetramer comprising two heavy and two light chains, IgG-AD2-modules possess two AD2 peptides, having

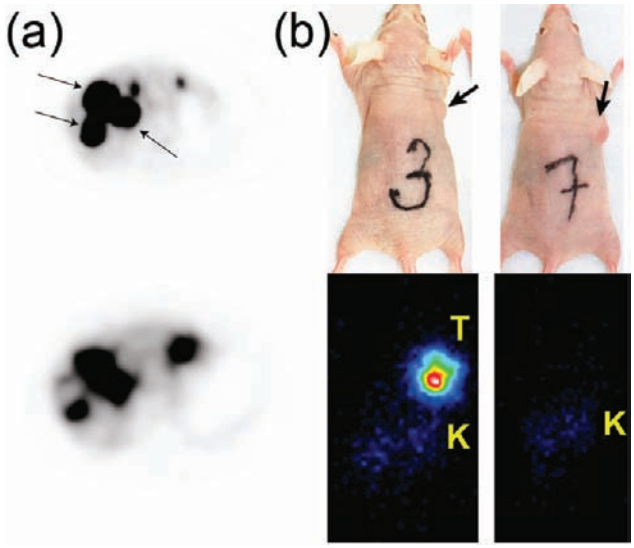


Figure 4. (a) Transverse cross sections of an ^{18}F-FDG-PET (top) and corresponding pretargeted immunoSPET image (bottom) of a patient with liver metastases of a colon carcinoma. The immunoSPECT image was taken 4 h after injection of an ^{111}In-labeled hapten-peptide (100 ug,185 MBq), that was given 24 h after TF2 (75 mg). Arrows in the ^{18}F-FDG image show the regions of tumor uptake that are also seen in the immunoSPECT image. (b) Pretargeted imaging of pancreatic xenografts with TF10. Nude mice bearing CaPan-1 human pancreatic cancer xenograft in their upper right flank (top; arrows). Tumors were ~0.5 cm in the longest diameter. The bottom panels show planar whole-body images of mice given ^{111}In-labeled hapten-peptide alone (bottom right) or pretargeted 16 h prior with TF10, a bispecific Tri-Fab directed against a pancreatic mucin and to the hapten HSG (bottom left). T, tumor; K, kidneys.

one on the carboxyl-terminal end of each heavy chain (Figure 5b). The IgG-AD2-modules are purified in a manner similar to that used for IgG, using Protein A affinity chromatography. Each AD2 binds a dimeric X-DDD2 module, resulting in defined DNL structures comprising an IgG fused at its carboxyl terminus to four X groups, where X denotes an entity that could be a protein, peptide, polymer, drug, or other molecule (Figure 5c).

Hexavalent Antibodies. IgG-AD2-modules were first used to construct hexavalent antibodies (HexAbs), which were produced by combination of IgG-AD2 with the same Fab-DDD2 modules used in the TF series (Figure 3c), highlighting the advantage of the modular nature of DNL (Figure 5d). Initially, monospecific HexAbs were produced using IgG-AD2- and Fab-DDD2-modules derived from the same parental mAb. As an example, a HexAb was made for the humanized anti-CD20 mAb, veltuzumab (aka hA20),[82] where C_H3-AD2-IgG-hA20 was combined with C_H1-DDD2-Fab-hA20.[61] The DNL conjugation resulted in a homogeneous preparation of a conjugate comprising an Fc and six functional anti-CD20 Fabs, which each retain the binding affinity of veltuzumab. The construct, originally named Hex-hA20, has been redesignated 20-(20)-(20), using a standardized naming system where the first code indicates the IgG-AD2-module and the codes in parentheses indicate dimeric Fab-DDD2-modules. Compared to veltuzumab, 20-(20)-(20) exhibited 3-fold higher binding avidity by ELISA, and a 3-fold slower off-rate from live NHL cells by flow cytometry, which demonstrated that all six binding arms can bind CD20 on cells (Figure 6). *In vitro*, 20-(20)-(20) inhibited proliferation of NHL cells at subnanomolar

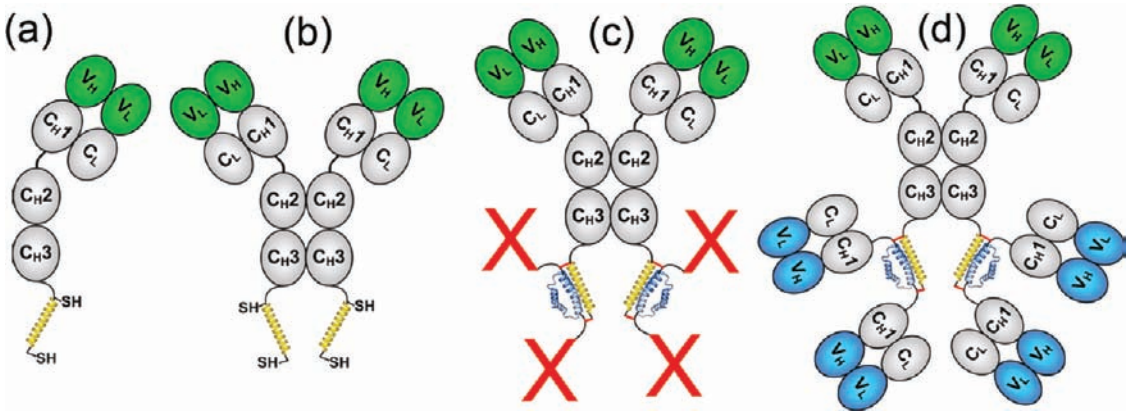


Figure 5. IgG-AD2 modules. (a) Recombinant fusion of an AD2 peptide (yellow helix) to the carboxyl-terminal end of the heavy chain C_H3 domain of an IgG. (b) IgG-AD2 module equipped with two AD2 peptides. (c) DNL conjugate of an IgG-AD2 with two dimeric X-DDD2 modules. (d) bsHexAb comprising an IgG and two stabilized Fab dimers. Variable (V, green) and constant (C, gray) domains of the heavy (H) and light (L) chains of the IgG-AD2 and Fab-DDD2 are represented as ovals. Yellow helix, AD2; Blue helices, DDD2; SH, sulfhydryl groups of the engineered cysteine residues in AD2; red line, "locking" disulfide bridges.

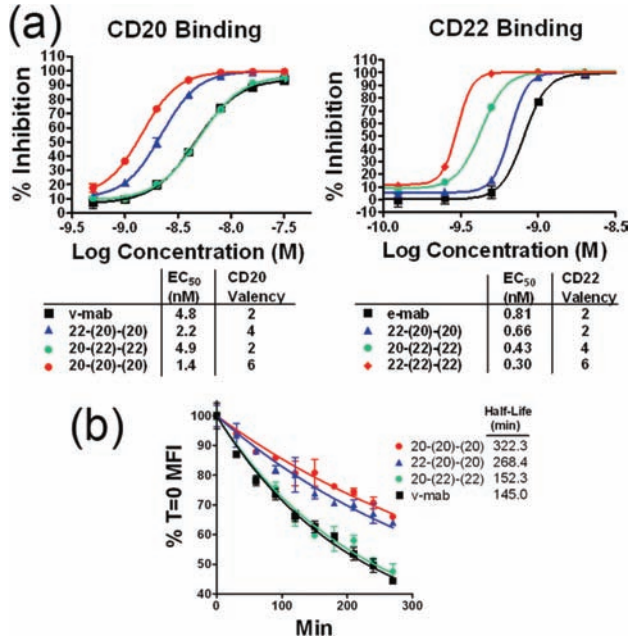


Figure 6. Binding properties of hexavalent antibodies. (a) Competition ELISA showing relative binding avidity of veltuzumab, 22-(20)-(20) (bivalent anti-CD22, tetravalent anti-CD20), 20-(22)-(22) (bivalent anti-CD20, tetravalent anti-CD22), 22-(22)-(22) (hexavalent anti-CD22), and 20-(20)-(20) (hexavalent anti-CD20) for binding to WR2, the anti-Id antibody to veltuzumab (left) and to WN, and the anti-Id antibody to epratuzumab (right). (b) Analysis of dissociation rates from live Raji. Cells were saturated with PE-mAbs, and the fluorescence intensity was measured over time by flow cytometry. % maximal binding (MFI $T = 0$) was calculated by dividing MFI $T = x$ into MFI $T = 0$ and plotted vs time. Adapted from *Blood 113*, 6161–6171.

concentrations without the need for an additional cross-linking antibody. For 20-(20)-(20), some of the Fc-associated effector functions, including antibody-dependent cellular cytotoxicity (ADCC), are retained, while others, such as complement-dependent cytotoxicity (CDC), may be compromised. Even though 20-(20)-(20) is a nearly 2.5-fold larger molecule than veltuzumab, the circulating serum half-life is shorter for the former, suggesting that its interaction with the neonatal Fc receptor (FcRn) is altered. Indeed, we have recently observed diminished FcRn binding of 20-(20)-(20) and other similarly designed HexAbs by surface plasmon resonance (BIAcore). Alternative formats of HexAbs, designed to maintain all Fc function including CDC and FcRn binding, are under development. Although 20-(20)-(20) has reduced circulating half-life and CDC, it still demonstrated antitumor efficacy, which was comparable to the case of veltuzumab at equivalent doses, in tumor-bearing mice.

We have produced numerous bispecific hexavalent antibodies (bsHexAbs) by combining an IgG-AD2 module with a Fab-DDD2 module derived from a different parental mAb (Figure 5d). The first bsHexAbs produced were derived from the humanized anti-CD22 mAb, epratuzumab (aka hLL2),[83] and veltuzumab.[62] Combination of C_H3-AD2-IgG-hA20 with C_H1-DDD2-Fab-hLL2 produced 20-(22)-(22), which comprises veltuzumab with four Fabs of epratuzumab. A bsHexAb of the opposite configuration, 22-(20)-(20), which has four Fabs of veltuzumab fused to epratuzumab, was generated from C_H3-AD2-IgG-hLL2 and C_H1-DDD2-Fab-hA20. Characterization of the bsHexAbs demonstrated that the DNL conjugation resulted in highly purified covalent structures of the expected size and composition. Both 22-(20)-(20) and 20-(22)-(22) retain the binding properties of their parental Fab/IgGs, with all six Fabs apparently capable of binding simultaneously (Figure 6). The bsHexAbs exhibited biological activities that were not observed using a mixture of the parental mAbs. Treatment of cells with the bsHexAbs, but not veltuzumab plus epratuzumab, resulted in translocation of both CD22 and CD20 into lipid rafts, induction of apoptosis and growth inhibition without second-antibody cross-linking, and homotypic adhesion. The bsHexAbs induced significant increases in the levels of phosphorylated p38 and PTEN, and also notable differences in signaling events from those incurred by cross-linking veltuzumab or rituximab with a secondary antibody.[84] Thus, the greatly enhanced direct toxicity of these bsHexAbs correlates with their ability to alter the basal expression of various intracellular proteins involved in regulating cell growth, survival, and apoptosis, with the net outcome leading to cell death. Indeed, the bsHexAbs killed lymphoma cells *in vitro* much more potently than the parental mAb mixture (Figure 7a).

dx.doi.org/10.1021/bc2004999 | *Bioconjugate Chem.* 2012, 23, 309–323

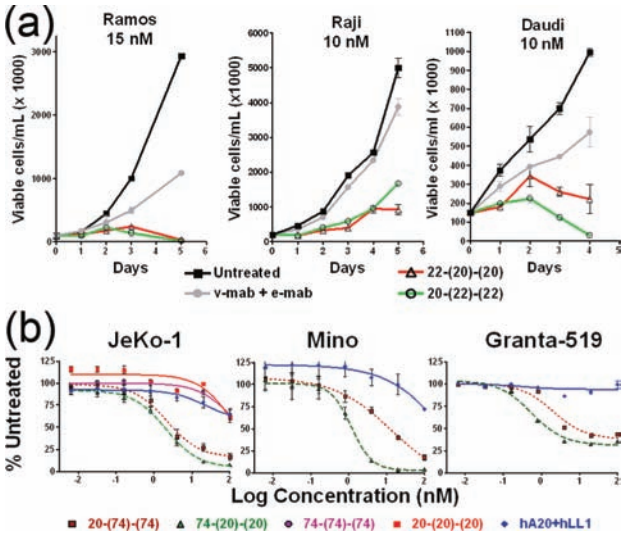


Figure 7. *In-vitro* antiproliferation with hexavalent antibodies. (a) Indicated NHL cells were seeded in T-flasks at 100k cells/mL and treated with 22-20-20, 20-22-22, or a combination of veltuzumab and epratuzumab at indicated concentrations. Viable cell densities (VCD) were determined daily by flow cytometry using Guava Viacount. On day 3, cultures were split 1:2 to maintain logarithmic growth over the course of the assay. The data are plotted as the VCD corresponding to the undiluted culture. Adapted from *Blood 113*, 6161−6171. (b) *In-vitro* cytotoxicity of mantle cell lymphoma cell lines with hexavalent antibodies. Indicated MCL cells were treated for four days with increasing concentrations of the indicated hexavalent antibodies or a combination of veltuzumab (hA20) and milatuzumab (hLL1). The relative viable cell densities were measured with MTS. The % of the signal obtained from untreated cells was plotted vs the log of the nanomolar concentration. Error bars, SD.

As observed previously for the monospecific HexAbs, both bsHexAbs exhibited ADCC, but not CDC (*in vitro*), and had shorter circulating half-lives than the parent mAbs. Intriguingly, 22-(20)-(20) and 20-(22)-(22) killed human lymphoma cells in preference to normal B cells in whole human blood (*ex vivo*), whereas the parental veltuzumab depleted malignant and normal B cells about equally. *In-vivo* studies with NHL xenografts revealed that 20-(22)-(22), despite having a shorter serum half-life, had antitumor efficacy comparable to that of veltuzumab. The 22-(20)-(20) was less potent than 20-(22)-(22) but more effective than epratuzumab and control bsAbs.

We recently reported the potent activity of anti-CD20/CD74 bsHexAbs against various B-cell lymphomas including mantle cell lymphoma (MCL), which is an aggressive subtype, generally having a poor prognosis with no established standard of care (Gupta et al. *Blood*, in press). The same Fab-DDD and IgG-AD modules of veltuzumab were combined with IgG-AD2 and Fab-DDD2 modules, respectively, of milatuzumab (an antagonistic anti-CD74 humanized mAb) to generate the bsHexAbs 74-(20)-(20) and 20-(74)-(74).

Similar to the anti-CD20/CD22 bsHexAbs, 74-(20)-(20) and 20-(74)-(74) inhibited growth of NHL cell lines without the need for additional cross-linking. They inhibited Burkitt lymphoma lines with a similar potency to the CD20/CD22 bispecifics. Of note, 74-(20)-(20) and 20-(74)-(74) effectively inhibited MCL lines, including JeKo-1, Granta-519, and Mino, which were relatively resistant to 20-(22)-(22) and 22-(20)-(20) and unnaffected by combinations of the parental antibodies, veltuzumab and milatuzumab (Figure 7b). A variety of events were observed at the molecular and organelle levels, which together culminated in cell death, following bsAb-induced juxtaposition of CD74 and CD20, but not treatment with the combined parental mAbs. Potentially important signaling events noted were a sustained phosphorylation of ERK and JNK MAP kinases, inhibition of Akt, and a reduction of p65 NF-κB nuclear translocation. Additionally, the antiapoptotic protein Bcl-xL was downregulated. The bsHex-Abs induced a strong homotypic adhesion associated with reorganization of the actin cytoskeleton, an increase in lysosomal volumes coupled with membrane permeability and leakage of cathepsins and other lysosomal contents into the cytosol, a decrease in mitochondrial membrane potential, and increased levels of reactive oxygen species. The bsHexAbs induced a nonclassical apoptosis, which was caspase-independent and not associated with autophagy (Gupta et al., *Blood*, in press).

More Antibody-Based-Modules and Multivalent Antibodies. We have produced many bispecific TF and HexAb DNL conjugates that are of 1 × 2 and 2 × 4 Fab formats, respectively. In addition, we have produced trispecific HexAbs (2 × 2 × 2) by combining two different Fab-DDD2-modules with an IgG-AD2-module of a third specificity (unpublished results). A wide variety of alternative formats of multispecific antibodies is attainable with the introduction of new types of DNL modules. For example, we have produced a Fab-based module with tandem AD2 peptides fused to the carboxyl-terminal end of the F_d (Figure 8a). Combination with a Fab-DDD2 module resulted in a 1 × 4 bispecific conjugate comprising five Fabs, without an F_c (Figure 8b), demonstrating that multiple AD2s can be incorporated into a single module (unpublished data). Application of this concept to an IgG module (IgG-AD2-AD2) would allow the creation of a multispecific IgG having a total of 10 Fabs, via combination with existing Fab-DDD2 modules. AD2- and DDD2-modules could be generated for other types of antibody-based proteins/fragments, including scFv, diabody, minibody, dual variable domain IgG, etc., providing for a myriad of possible multispecific antibody formats. As a final example, we have generated a bispecific dual variable domain IgG-AD2 module (Figure 8c), which was combined with a Fab-DDD2 module to generate a 2 × 2 × 4 trispecific octavalent antibody (Figure 8d, unpublished data).

Nonantibody-Based DNL Modules. DNL is not restricted to antibody-based constructs, as recombinant DDD2 or AD2 modules can be constructed for almost any protein. We have applied the DNL method to various cytokines, including interferon-alpha (IFNα), erythropoietin, and granulocyte colony-stimulating factor (G-CSF), to generate various immunocytokines (Figure 9).[59,63,85] The cytokine-modules were produced in either *E. coli* or mammalian cell culture, with AD2 or DDD2 fused at their amino- or carboxyl-terminal ends. We have utilized a DDD2-module of human protamine, which, when paired with an IgG-AD2 module, can be used for targeted cellular delivery of nucleic acids, such as siRNA. As an example of a module of a precursor that is both an enzyme and a toxin, a DDD2-module of ranpirnase (Rap, a cytotoxic ribonuclease from *Rana pipiens*) has been combined with various IgG-AD2 modules for targeted delivery of the toxin to tumor cells. In addition to recombinant protein modules, nonprotein DNL-modules can be assembled using synthetic AD2 peptides coupled to a variety of synthetic precursor molecules.[59]

dx.doi.org/10.1021/bc2004999 | *Bioconjugate Chem.* 2012, 23, 309−323

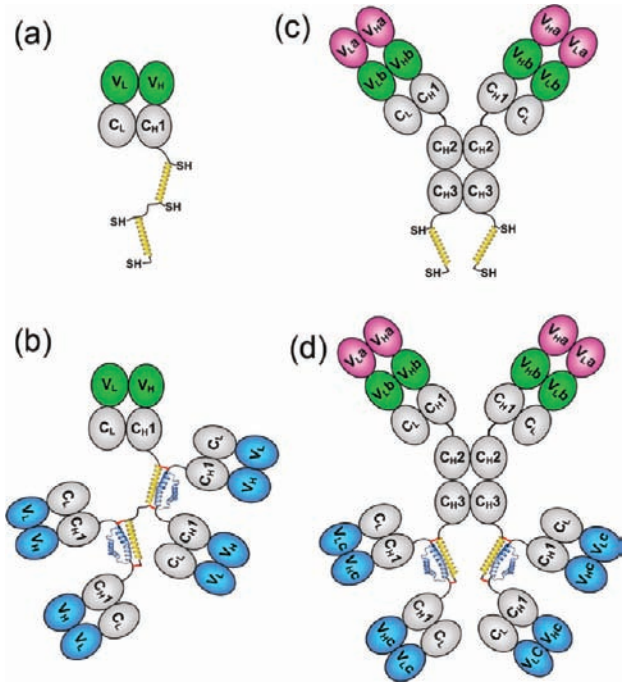


Figure 8. Additional antibody-based DNL modules for multivalent antibodies. (a) C_H1-$(AD2)_2$-Fab, a Fab module comprising tandem AD2 helices separated by a short peptide linker. (b) Bispecific antibody comprising five Fabs produced with C_H1-$(AD2)_2$-Fab and C_H1-DDD2-Fab modules. (c) C_H3-AD2-DVD-IgG, a dual variable domain IgG-AD2 module, with binding specificities "a" and "b", and possessing two AD2 peptides. (d) A trispecific octavalent antibody comprising a dual variable domain IgG, having binding specificities "a" and "b", and two stabilized Fab dimers of binding specificity "c". Variable (V, pink, green, or blue) and constant (C, gray) domains of the heavy (H) and light (L) chains are represented as ovals. The DDD2 and AD2 peptides are shown as blue and yellow helices, respectively, with the locations indicated for the reactive sulfhydryl groups (SH) and disulfide bridges (red line).

IFNα2b-DDD2. Our most utilized cytokine module, IFNα2b-DDD2, which is produced with a recombinant myeloma cell culture, has a carboxyl-terminal DDD appended to IFNα2b (Figure 9a). We have combined IFNα2b-DDD2 with various IgG-AD2-modules to create a panel of IgG-IFNα for targeted delivery of IFNα to various malignancies.

The prototype, 20-2b-2b (aka 20-2b), which is a conjugate of IFNα2b-DDD2 and C_H3-AD2-IgG-hA20, comprises veltuzumab and four copies of IFNα2b (Figure 9c).[63] All of the IgG-IFNα made by DNL, including 20-2b-2b, retain the binding specificity and affinity of their targeting mAb, and they also exhibit IFNα specific activity approaching that of recombinant IFNα2b (Table 1).[63,85] Cytokine fusion proteins made by traditional recombinant engineering or chemical conjugation often suffer extensive loss of biological activity. For example, where 20-2b-2b has similar activity to rIFNα2b, traditional recombinant anti-CD20-IFNα fusion proteins showed a 300-fold reduction in IFNα activity.[86] We believe that high-level activity of the DNL constructs is maintained due to the site-specific conjugation, which is spatially removed from the functional domain.

Compared to veltuzumab, 20-2b-2b shows enhanced ADCC but lacks CDC (*in vitro*), consistent with other constructs comprising C_H3-AD2-IgG-hA20. It inhibits *in vitro* proliferation of lymphoma cells and depletes them from whole human blood more potently than a combination of veltuzumab and IFNα. Comparative pharmacokinetic (Pk) analysis in mice demonstrated a longer circulating serum half-life for 20-2b-2b (23.4 h) compared to the commercial PEGylated IFNα drugs peginterferonalfa-2a (14.9 h) or peginterferonalfa-2b (9.3 h). Due to high specific activity, extended Pk, and tumor targeting, 20-2b-2b demonstrated superior therapeutic efficacy compared to PEGASYS, veltuzumab, or nontargeting IgG-IFNα in human lymphoma xenograft models, even though mouse immune cells respond poorly to human IFNα2b (Figure 10a). Targeting IFNα with an anti-CD20 mAb makes the immunocytokine more potent than either agent alone or in combination.

On the basis of encouraging preclinical results, 20-2b-2b, the prototype IgG-IFNα, is now under development for CD20-targeted immunotherapy of NHL. CD20 is a preferred target for this disease because it is expressed at high levels on the cell surface of many B-cell lymphomas, and its expression on normal cells is essentially limited to B cells. The potential benefits of therapy with 20-2b-2b are likely limited to non-Hodgkin lymphoma (NHL) and possibly chronic lymphocytic leukemia (CLL) patients. Using the combination of the IFNα2b-DDD2 module with C_H3-AD2-IgG-hL243, we have recently developed an IgG-IFNα named C2-2b-2b, which has tetrameric IFNα2b fused to an anti-HLA-DR mAb (hL243).[87] HLA-DR is an attractive target because it is expressed on the cell surface of many hematopoietic malignancies.[88] The broad range and high-level expression of HLA-DR makes C2-2b-2b attractive for use in the therapy of diverse malignancies. *In vitro*, C2-2b-2b inhibited 20 cell lines, including B-cell lymphoma (Burkitt, mantle cell, and follicular), leukemia (hairy cell, AML, ALL, and CLL), and myeloma. In most cases, this immunocytokine was more effective than CD20-targeted mAb-IFNα or a mixture comprising the parental mAb and IFNα. The responsiveness of each hematopoietic tumor cell line correlated with HLA-DR expression/density and sensitivity to IFNα and hL243. C2-2b-2b induced more potent and longer-lasting IFNα signaling compared to nontargeted IFNα. *In vivo*, C2-2b-2b demonstrated superior efficacy compared to nontargeting mAb-IFNα, peginterferonalfa-2a, or a combination of hL243 and IFNα using human lymphoma and myeloma xenografts (Figure 10b and c).[87]

The modular nature of DNL enabled the production of the first bispecific immunocytokine, 20-C2-2b, which comprises two copies of IFN-α2b and a stabilized $F(ab)_2$ of hL243 (humanized anti-HLA-DR) site-specifically linked to veltuzumab (Figure 9d).[85] This was achieved by combining C_H3-AD2-IgG-hA20 (Figure 5b) with two DDD-modules, IFNα2b-DDD2 (Figure 9a) and C_H1-DDD2-Fab-hL243 (Figure 3c). Due to the random association of either DDD-module with the two AD2 groups, two side-products, 20-(C2)-(C2) and 20-2b-2b, are formed in addition to 20-C2-2b, which was purified from the mixture by a multistep affinity chromatography process.

Following reduction of 20-C2-2b, its five component polypeptides were identified by LC-MS (Table 2). We determined that ~15% of the polypeptides comprising the IFNα2b-DDD2 module are O-glycosylated, with the observed mass indicating an O-linked glycan having the structure NeuGc-NeuGc-Gal-GalNAc, which was also predicted (<1 ppm) for 20-2b-2b. LC-MS identified both veltuzumab and hL243 kappa chains as well as hL243-Fd-DDD2 as a single, unmodified species, with observed masses matching the calculated ones (<35 ppm). Two major glycoforms of

dx.doi.org/10.1021/bc2004999 | *Bioconjugate Chem.* 2012, 23, 309–323

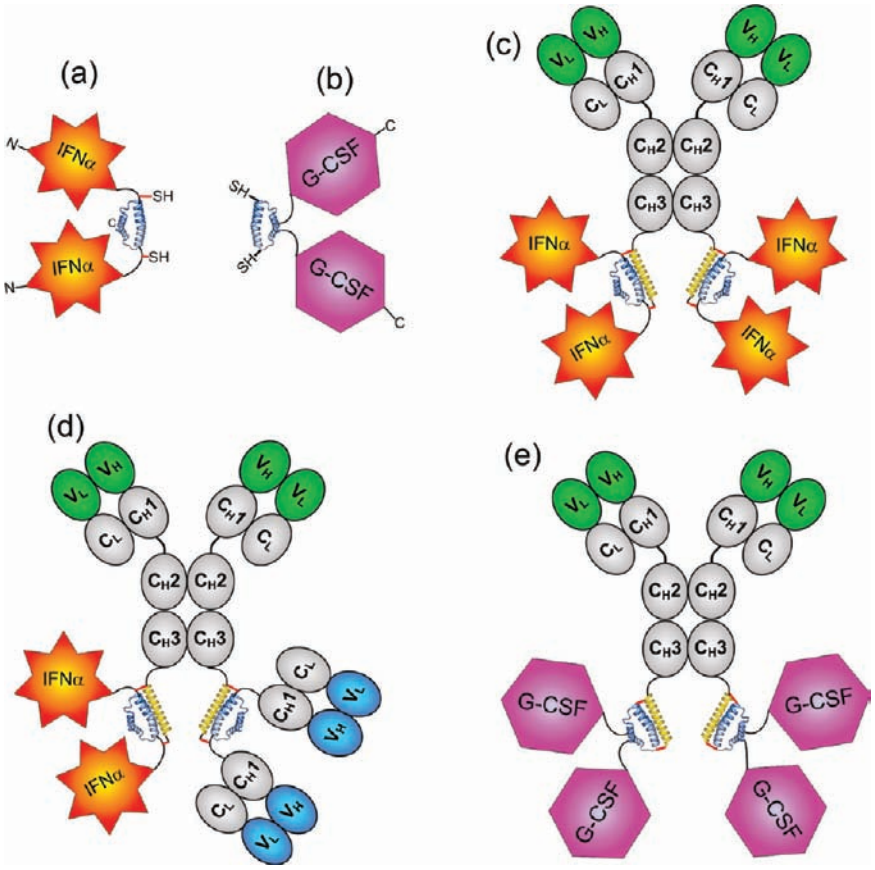


Figure 9. Cytokine modules and immunocytokines. (a) IFNα-DDD2, a dimeric module comprising DDD2 fused to the carboxyl-terminal end of IFNα. (b) DDD2-G-CSF, a dimeric module comprising DDD2 fused to the amino-terminal end of G-CSF. (c) IgG-2b-2b (e.g., 20-2b-2b), an immunocytokine comprising an IgG and four IFNα groups. (d) IgG-$(Fab)_2$-2b (e.g., 20-C2-2b), a bispecific immunocytokine comprising an IgG, a stabilized Fab dimer, and two IFNα groups. (e) IgG-G-CSF-G-CSF, an immunocytokine comprising an IgG and four G-CSF groups.

Table 1. IFNα Specific Activity in IU/pmol[a]

	antibody target	IFNα/ molecule	lot 1	lot 2	lot 3
20-2b-2b	CD20	4	5322 (±405)	4146 (±661)	4481 (±393)
C2-2b-2b	HLA-DR	4	5426 (±84)	3880 (±438)	3928 (±428)
734-2b-2b	In-DTPA	4	5671 (±297)	3906 (±684)	3764 (±619)
14-2b-2b	CEACAM5	4	5895 (±663)	4468 (±138)	
20(L)-2b-2b	CD20	4	4146 (±661)		
1R-2b-2b	IGF-1R	4	3919 (±488)		
E1−2b-2b	Trop2	4	6318 (±101)		
22-2b-2b	CD22	4	5983 (±294)		
20-C2-2b	CD20 and HLA-DR	2	2455 (±174)		
PEGASYS[b]	none	1	68 (±6)	32 (±8)	
PEG-Intron[b]	none	1	1872 (±438)	1347 (±125)	
362-2b[b]	none	2	2940 (±52)		
413-2b[b]	none	2	816 (±52)		
457-2b[b]	none	2	1474 (±171)		

[a]Specific activities, reported as IU/pmol (± standard deviation), were measured with the iLite Human Interferon Alpha Cell-Based Assay Kit (PBL Interferon Source, Piscataway, NJ). Data combined from three experiments. [b]PEGylated.

veltuzumab heavy chain-AD2 were identified as having masses of 53,714.73 (70%) and 53,877.33 (30%), indicating G0F and G1F N-glycans, respectively, which are typically associated with IgG. The analysis also confirmed that the amino terminus of the heavy chain-AD2 is modified to pyroglutamate, as predicted for polypeptides having an amino terminal glutamine.

The predicted biochemical and biological properties of 20-C2-2b were confirmed experimentally. It bound bispecifically to CD20+/HLA-DR+ cells. With two IFNα2b groups, 20-C2-2b exhibited half of the level of IFNα specific activity, compared to IgG-IFNα with four IFNα (e.g., 20-2b-2b; Table 1). The bispecific IgG-IFNα potently inhibited lymphoma and myeloma cell lines, and in some cases, more effectively than 20-2b-2b or C2-2b-2b (Figure 11).

Nonprotein DNL Modules. DNL is not restricted to conjugation of protein-based modules. As an example, we have

dx.doi.org/10.1021/bc2004999 | *Bioconjugate Chem.* 2012, 23, 309−323

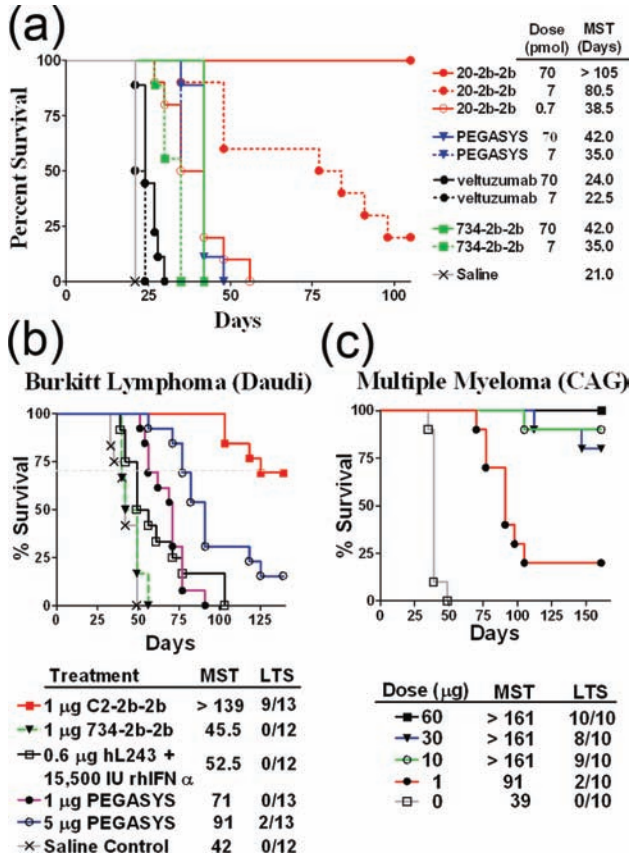


Figure 10. (a) Survival curves showing the therapeutic efficacy of 20-2 b-2b (a) and C2-2b-2b (b and c) in established disseminated Daudi Burkitt lymphoma (a and b) and CAG multiple myeloma (c) xenograft models. Female C.B. Seventeen SCID mice were administered cells intravenously on day 0. Groups of mice were given a single subcutaneous dose on day 7. Survival curves were analyzed using Prism software. MST, median survival time. (a) Efficacy of 20-2b-2b compared to veltuzumab and IFNα. Treatments consisted of 20-2b-2b (red), nontargeting IgG-IFNα 734-2b-2b (green), veltuzumab (black), PEGASYS (blue), or saline (gray). Adapted from *Blood 114*, 3864−3871. (b) Efficacy of C2-2b-2b compared to hL243 and IFNα. Treatments consisted of C2-2b-2b (red ■, 1 μg, 4 pmol, 15,500 IU), 734-2b-2b (green ▼, 1 μg, 4 pmol, 15,500 IU), 0.6 μg (4 pmol) hL243 IgG_1, + 15,500 IU rIFNα2b (black □) or PEGASYS [1 μg, 16 pmol (purple ●) and 5 μg, 80 pmol (blue ○)]. (c) Dose-escalation. Mice were treated with C2-2b-2b at 1 μg (red ●), 10 μg (blue ○), 30 μg (green ▼), or 60 μg (black ■). Adapted from *Blood 118*, 1877−1884.

Table 2. LC/MS Analysis of Reduced 20-C2-2b[a]

polypeptide	M_{obs}	M_{calc}	Δ (ppm)	Δ (mDa)	modifications
IFNα2b-DDD2	26074.90	26074.94	−1.5	−40	
	27055.16	27055.56	−14.8	−400	NeuGc-NeuGc-Gal-GalNAc- (+979.852)
hA20 Kappa	23205.21	23205.99	−33.6	−780	
hL243 Kappa	23376.54	23376.23	12.4	290	
hL243-Fd-DDD2	29510.62	29511.45	−28.1	−830	pQ (−18)
hA20-HC-AD2	53714.73	53715.50	−14.3	−770	pQ (−18); G0F (+1445.36)
	53877.33	53877.64	−5.8	−310	pQ (−18); G1F (+1607.50)

[a] M_{calc}, calculated mass including indicated modifications; M_{obs}, observed LC/MS mass; Δ (ppm), difference between M_{calc} and M_{obs} in parts per million; Δ (mDa), difference between M_{calc} and M_{obs} in millidaltons; pQ, pyroglutamate from amino terminal glutamine; G0F and G1F, N-linked glycans.

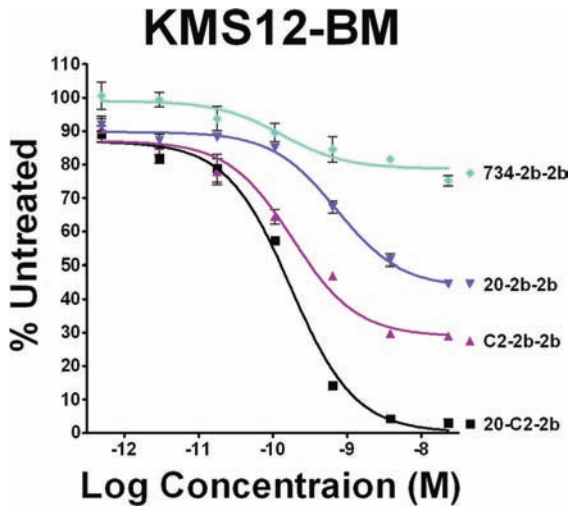


Figure 11. *In-vitro* cytotoxicity of a CD20+ multiple myeloma cell line with IgG-IFNα immunocytokines. KMS12-BM multiple myeloma cells were treated for four days with increasing concentrations of the indicated immunocytokines. The relative viable cell densities were measured with MTS. The % of the signal obtained from untreated cells was plotted vs the log of the molar concentration. Error bars, SD. Adapted from *Cancer Res. 70*, 7600−7609.

developed a novel DNL-based PEGylation technology using synthetic PEG-AD2 modules.[59] The 21 amino acid residue AD2 peptide was synthesized using Fmoc technology on EDANS resin, which resulted in the coupling of an EDANS fluorescent tag to the peptide (Figure 12a). The sequence of the peptide, IMP360, is CGQIEYLAKQIVDNAIQQAGC(SS-tbu)-EDANS. The two linear PEG-AD2 modules were prepared by coupling IMP360 to mPEG-OPTE of 20-kDa or 30-kDa, resulting in IMP362 or IMP413, respectively (Figure 12b). A third PEG-AD2 module, IMP457, was generated with a 40-kDa branched PEG (Figure 12c). The sulfhydryl group of the N-terminal cysteine of IMP360 displaces pyridine-2-thiol from mPEG-OPTE and forms a thioester bond to mPEG. A subsequent reaction of the adjacent amino group with the carbonyl group of the thioester leads to the formation of a more stable amide bond and the regeneration of the sulfhydryl group. The PEG-AD2 modules (IMP362, IMP413, and IMP457) can be conjugated with any DDD-module, resulting in a site-specific PEGylation.

Proof of principle was established using the IFNα2b-DDD2 module.[59] The dimeric IFNα2b-DDD2 was conjugated to IMP362, IMP413, and IMP457, resulting in PEGylated DNL conjugates α2b-362, α2b-413, and α2b-457, respectively (Figure 12d and e). SDS-PAGE and MALDI-TOF mass spectrometry demonstrated that α2b-362, α2b-413, and α2b-457 were generated as designed and substantially pure. Traditional, nonsite-specific PEGylation results in a heterogeneous mixture of isomers of mono-PEGylated product contaminated with the unPEGylated and multiply PEGylated precursor protein, which must be removed. Further, the mono-PEGylated isomers have varying specific activities, which are often substantially reduced, particularly with larger PEG

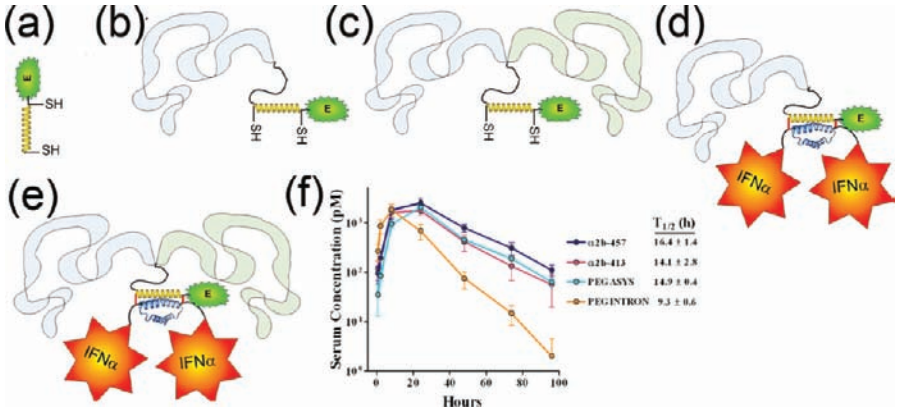


Figure 12. Site-specific PEGylation using DNL. (a) The 21 amino acid residue AD2 peptide IMP360 synthesized using Fmoc technology on EDANS resin. (b) Unbranched synthetic PEG-AD2 module (e.g., IMP362 or IMP413). (c) Branched synthetic PEG-AD2 module (e.g., IMP457). (d) 362-2b or 413-2b, monoPEGylated dimeric IFNα with an unbranched PEG of 20 kDa or 30 kDa, respectively. (e) 457-2b, monoPEGylated dimeric IFNα with a 40 kDa branched PEG. Ribbons, PEG; green starburst, EDANS (E) fluorescent tag. (f) Blood clearance of IMP-457, IMP-413, PEGASYS, and PEGINTRON following a single subcutaneous injection in male Swiss-Webster mice. Adapted from *Bioconjug. Chem. 20*, 1899–1907.

species. The site-specific DNL conjugation results in a homogeneous preparation of mono-PEGylated product that retains high specific activity, even with larger PEG species (Table 1). For example, α2b-457 has 20-fold higher specific activity compared to peginterferonalfa-2a (PEGASYS), even though both use a branched 40-kDa PEG. The pharmacokinetics of the various PEGylated IFNα conjugates directly correlates with the size of the PEG (Figure 12f). Of the three DNL conjugates, α2b-457 (40 kDa PEG) had the longest circulating half-life.[59] Each of the DNL conjugates exhibited potent *in vitro* antiviral activity, as well as *in vivo* efficacy in the Daudi Burkitt lymphoma xenograft model.

In addition to various PEGs, a variety of effector molecules, including peptides, nucleic acids, drugs, toxins, chelators, dyes, fluorescent molecules and radionuclides, can be coupled to a synthetic AD2 peptide, such as IMP360. An array of synthetic AD2-modules can be coupled with various protein-DDD2-modules to create defined and stable protein/nonprotein conjugates, which have added function and retain the biological activity of the parental protein.

Variations on DNL. Several potential variations on the DNL method as described above are possible. In addition to the DDD sequence of human RIIα, other DDD sequences may be selected from human RIα, human RIβ, or human RIIβ. The DDD sequence of choice can be matched with a highly interactive AD sequence, which can be deduced from the literature[89] or determined experimentally.

Alternative Linker Modules. The X-type four-helix bundle dimerization motif that is a structural characteristic of the DDD[54,55] is found in other classes of proteins. For example, over 300 proteins that are involved in either signal transduction or transcriptional activation contain a module of 65–70 amino acids termed the sterile α motif (SAM) domain, which has a variation of the X-type four-helix bundle present on its dimerization interface. Such proteins include the S100 proteins (for example, S100B and calcyclin), and the hepatocyte nuclear factor (HNF) family of transcriptional factors (for example, HNF-1α and HNF-1β). In the case of S100B, this X-type four-helix bundle enables the binding of each dimer to two p53 peptides derived from the *C*-terminal regulatory domain (residues 367–388) with micromolar affinity.[90] Similarly, the *N*-terminal dimerization domain of HNF-1α (HNF-p1) was shown to associate with a dimer of DCoH (dimerization cofactor for HNF-1) via a dimer of HNF-p1.[91] These naturally occurring systems may also be adapted as linker modules using the DNL approach. However, S100 proteins have biological activities such as tumorigenesis, thus rendering them less desirable as alternative sources for the DDD.

Alternative Covalent Stabilization. In addition to the use of disulfide linkages for preventing the dissociation of the assembled components, other methods for enhancing the overall stability of the tethered structure may be employed. For example, various cross-linking agents or methods that are commercially available or used in research may be selected. A potentially useful agent is glutaraldehyde, which has been widely used for probing the structures of noncovalently associated multimeric proteins by cross-linking the constituting subunits to form stable conjugates. Also of interest are two chemical methods involving oxidative cross-linking of protein subunits. One is a proximity labeling technique that employs either hexahistidine-tagged[92] or *N*-terminal glycine-glycine-histidine-tagged proteins.[93] These tags bind Ni^{2+} tightly and, when oxidized with a peracid, a Ni^{3+} species is produced to mediate a variety of oxidative reactions, including protein–protein cross-linking. Another technique, termed PICUP for photoinduced cross-linking of unmodified proteins, uses $[Ru(II)(bipy)_3]^{2+}$, ammonium persulfate, and visible light to induce protein–protein cross-linking.[94] A general concern, however, is that these approaches would be less specific and efficient than the DDD2/AD2 coupling systems.

Future Perspectives. Clinical evaluations have begun or are planned for several of the DNL-based fusion proteins described in this paper. TF2 is currently under phase I clinical investigation for imaging and therapy of colorectal and lung cancers (Clinicaltrial.gov #s NCT01273402, NCT01221675, NCT00860860, NCT00895323). Additional TFs are being manufactured for clinical use in pretargeted imaging and therapy of pancreatic (TF10) and prostate (TF12) cancers.[78] The immunocytokine, 20-2b-2b, is under development for CD20-targeted immunotherapy of lymphoma, and C2-2b-2b is under consideration as a therapeutic agent for a variety of hematopoietic cancers. Preliminary results suggest that some of the bsHexAbs, including 74-(20)-(20) and others, might be effective agents for the treatment of certain autoimmune

dx.doi.org/10.1021/bc2004999 | *Bioconjugate Chem.* 2012, 23, 309–323

diseases. Several additional multifunctional antibodies and immunocytokines have shown promise, but they are at earlier stages of development.

It has been six years since the invention of the DNL method, and it is still evolving. We continue to produce new classes of DNL-modules, and with the introduction of each new module, the repertoire of potentially useful DNL conjugates increases exponentially. Thus far, much of our effort has focused on the creation of agents for cancer therapy via multivalent/multifunctional antibodies and antibody-targeted delivery of radionuclides, cytokines, or toxins. The indications and modalities for which the DNL method can be applied expand with the increasing library of DNL-modules and conjugates. These also raise the potential applications to diseases other than cancer.

AUTHOR INFORMATION

Corresponding Author

*Address: Immunomedics, Inc., 300 American Rd, Morris Plains, NJ 07950. E-mail: Erossi@immunomedics.com. Phone: 973-605-8200. Fax: 973-605-1340.

Notes

All authors are employees or hold stock in Immunomedics, Inc. and/or IBC Pharmaceuticals, Inc.

ABBREVIATIONS

AD, anchor domain; ADCC, antibody-dependent cellular cytotoxicity; AKAP, A-kinase anchor protein; CDC, complement-dependent cytotoxicity; DDD, dimerization and docking domain; DNL, dock-and-lock; FcRn, neonatal Fc receptor; GST, glutathione S-transferase; HexAb, hexavalent antibody; HSG, histamine-succinyl glycine; IFNα, interferon-alpha; IgG-IFNα, immunocytokine comprising an IgG and IFNα; LFA-1, lymphocyte function-associated antigen-1; MCL, mantle cell lymphoma; mAb, monoclonal antibody; NL, Nano-Lock; PEG, polyethylene glycol; Pk, pharmacokinetics; PKA, A-kinase; pNPP, *p*-nitrophenyl phosphonate; SNARE, soluble *N*-ethylmaleimide-sensitive factor attachment protein receptor; TF, tri-Fab

REFERENCES

(1) Binz, H. K., Amstutz, P., and Pluckthun, A. (2005) Engineering novel binding proteins from nonimmunoglobulin domains. *Nat. Biotechnol. 23*, 1257−1268.

(2) Binz, H. K., and Pluckthun, A. (2005) Engineered proteins as specific binding reagents. *Curr. Opin. Biotechnol. 16*, 459−469.

(3) Cuesta, A. M., Sainz-Pastor, N., Bonet, J., Oliva, B., and varez-Vallina, L. (2010) Multivalent antibodies: when design surpasses evolution. *Trends Biotechnol. 28*, 355−362.

(4) Hey, T., Fiedler, E., Rudolph, R., and Fiedler, M. (2005) Artificial, non-antibody binding proteins for pharmaceutical and industrial applications. *Trends Biotechnol. 23*, 514−522.

(5) Hosse, R. J., Rothe, A., and Power, B. E. (2006) A new generation of protein display scaffolds for molecular recognition. *Protein Sci. 15*, 14−27.

(6) Lo, K. M., Sudo, Y., Chen, J., Li, Y., Lan, Y., Kong, S. M., Chen, L., An, Q., and Gillies, S. D. (1998) High level expression and secretion of Fc-X fusion proteins in mammalian cells. *Protein Eng. 11*, 495−500.

(7) Pastan, I. (2003) Immunotoxins containing Pseudomonas exotoxin A: a short history. *Cancer Immunol. Immunother. 52*, 338−341.

(8) Kishore, U., Strong, P., Perdikoulis, M. V., and Reid, K. B. (2001) A recombinant homotrimer, composed of the alpha helical neck region of human surfactant protein D and C1q B chain globular domain, is an inhibitor of the classical complement pathway. *J. Immunol. 166*, 559−565.

(9) Kostelny, S. A., Cole, M. S., and Tso, J. Y. (1992) Formation of a bispecific antibody by the use of leucine zippers. *J. Immunol. 148*, 1547−1553.

(10) Pack, P., Muller, K., Zahn, R., and Pluckthun, A. (1995) Tetravalent miniantibodies with high avidity assembling in Escherichia coli. *J. Mol. Biol. 246*, 28−34.

(11) Terskikh, A. V., Le Doussal, J. M., Crameri, R., Fisch, I., Mach, J. P., and Kajava, A. V. (1997) "Peptabody": a new type of high avidity binding protein. *Proc. Natl. Acad. Sci. U. S. A 94*, 1663−1668.

(12) Willuda, J., Kubetzko, S., Waibel, R., Schubiger, P. A., Zangemeister-Wittke, U., and Pluckthun, A. (2001) Tumor targeting of mono-, di-, and tetravalent anti-p185(HER-2) miniantibodies multimerized by self-associating peptides. *J. Biol. Chem. 276*, 14385−14392.

(13) Cuesta, A. M., Sanchez-Martin, D., Sanz, L., Bonet, J., Compte, M., Kremer, L., Blanco, F. J., Oliva, B., and varez-Vallina, L. (2009) In vivo tumor targeting and imaging with engineered trivalent antibody fragments containing collagen-derived sequences. *PLoS One 4*, e5381.

(14) Deyev, S. M., and Lebedenko, E. N. (2008) Multivalency: the hallmark of antibodies used for optimization of tumor targeting by design. *Bioessays 30*, 904−918.

(15) Fan, C. Y., Huang, C. C., Chiu, W. C., Lai, C. C., Liou, G. G., Li, H. C., and Chou, M. Y. (2008) Production of multivalent protein binders using a self-trimerizing collagen-like peptide scaffold. *FASEB J. 22*, 3795−3804.

(16) Pack, P., and Pluckthun, A. (1992) Miniantibodies: use of amphipathic helices to produce functional, flexibly linked dimeric FV fragments with high avidity in Escherichia coli. *Biochemistry 31*, 1579−1584.

(17) Borsi, L., Balza, E., Carnemolla, B., Sassi, F., Castellani, P., Berndt, A., Kosmehl, H., Biro, A., Siri, A., Orecchia, P., Grassi, J., Neri, D., and Zardi, L. (2003) Selective targeted delivery of TNFalpha to tumor blood vessels. *Blood 102*, 4384−4392.

(18) Halin, C., Gafner, V., Villani, M. E., Borsi, L., Berndt, A., Kosmehl, H., Zardi, L., and Neri, D. (2003) Synergistic therapeutic effects of a tumor targeting antibody fragment, fused to interleukin 12 and to tumor necrosis factor alpha. *Cancer Res. 63*, 3202−3210.

(19) Pepinsky, R. B., LePage, D. J., Gill, A., Chakraborty, A., Vaidyanathan, S., Green, M., Baker, D. P., Whalley, E., Hochman, P. S., and Martin, P. (2001) Improved pharmacokinetic properties of a polyethylene glycol-modified form of interferon-beta-1a with preserved in vitro bioactivity. *J. Pharmacol. Exp. Ther. 297*, 1059−1066.

(20) Tan, L. P., Lue, R. Y., Chen, G. Y., and Yao, S. Q. (2004) Improving the intein-mediated, site-specific protein biotinylation strategies both in vitro and in vivo. *Bioorg. Med. Chem. Lett. 14*, 6067−6070.

(21) Burbulis, I., Yamaguchi, K., Gordon, A., Carlson, R., and Brent, R. (2005) Using protein-DNA chimeras to detect and count small numbers of molecules. *Nat. Methods 2*, 31−37.

(22) Los, G. V., and Wood, K. (2007) The HaloTag: a novel technology for cell imaging and protein analysis. *Methods Mol. Biol. 356*, 195−208.

(23) Keppler, A., Gendreizig, S., Gronemeyer, T., Pick, H., Vogel, H., and Johnsson, K. (2003) A general method for the covalent labeling of fusion proteins with small molecules in vivo. *Nat. Biotechnol. 21*, 86−89.

(24) Griffin, B. A., Adams, S. R., and Tsien, R. Y. (1998) Specific covalent labeling of recombinant protein molecules inside live cells. *Science 281*, 269−272.

(25) Miller, L. W., Cai, Y., Sheetz, M. P., and Cornish, V. W. (2005) In vivo protein labeling with trimethoprim conjugates: a flexible chemical tag. *Nat. Methods 2*, 255−257.

(26) Robers, M., Pinson, P., Leong, L., Batchelor, R. H., Gee, K. R., and Machleidt, T. (2009) Fluorescent labeling of proteins in living cells using the FKBP12 (F36V) tag. *Cytometry A 75*, 207−224.

(27) Engin, S., Trouillet, V., Franz, C. M., Welle, A., Bruns, M., and Wedlich, D. (2010) Benzylguanine thiol self-assembled monolayers for

the immobilization of SNAP-tag proteins on microcontact-printed surface structures. *Langmuir 26*, 6097−6101.
(28) Recker, T., Haamann, D., Schmitt, A., Kuster, A., Klee, D., Barth, S., and Muller-Newen, G. (2011) Directed covalent immobilization of fluorescently labeled cytokines. *Bioconjugate Chem. 22*, 1210−1220.
(29) Saviranta, P., Haavisto, T., Rappu, P., Karp, M., and Lovgren, T. (1998) In vitro enzymatic biotinylation of recombinant fab fragments through a peptide acceptor tail. *Bioconjugate Chem. 9*, 725−735.
(30) Duffy, S., Tsao, K. L., and Waugh, D. S. (1998) Site-specific, enzymatic biotinylation of recombinant proteins in Spodoptera frugiperda cells using biotin acceptor peptides. *Anal. Biochem. 262*, 122−128.
(31) Airenne, K. J., Marjomaki, V. S., and Kulomaa, M. S. (1999) Recombinant avidin and avidin-fusion proteins. *Biomol. Eng. 16*, 87−92.
(32) Laitinen, O. H., Nordlund, H. R., Hytonen, V. P., and Kulomaa, M. S. (2007) Brave new (strept)avidins in biotechnology. *Trends Biotechnol. 25*, 269−277.
(33) Rossi, E. A., Goldenberg, D. M., Cardillo, T. M., McBride, W. J., Sharkey, R. M., and Chang, C. H. (2006) Stably tethered multifunctional structures of defined composition made by the dock and lock method for use in cancer targeting. *Proc. Natl. Acad. Sci. U. S. A 103*, 6841−6846.
(34) MacBeath, G., and Schreiber, S. L. (2000) Printing proteins as microarrays for high-throughput function determination. *Science 289*, 1760−1763.
(35) Hodneland, C. D., Lee, Y. S., Min, D. H., and Mrksich, M. (2002) Selective immobilization of proteins to self-assembled monolayers presenting active site-directed capture ligands. *Proc. Natl. Acad. Sci. U. S. A 99*, 5048−5052.
(36) Mannesse, M. L., Boots, J. W., Dijkman, R., Slotboom, A. J., van der Hijden, H. T., Egmond, M. R., Verheij, H. M., and de Haas, G. H. (1995) Phosphonate analogues of triacylglycerols are potent inhibitors of lipase. *Biochim. Biophys. Acta 1259*, 56−64.
(37) Martinez, C., de Geus, P., Lauwereys, M., Matthyssens, G., and Cambillau, C. (1992) Fusarium solani cutinase is a lipolytic enzyme with a catalytic serine accessible to solvent. *Nature 356*, 615−618.
(38) Kwon, Y., Han, Z., Karatan, E., Mrksich, M., and Kay, B. K. (2004) Antibody arrays prepared by cutinase-mediated immobilization on self-assembled monolayers. *Anal. Chem. 76*, 5713−5720.
(39) Bonasio, R., Carman, C. V., Kim, E., Sage, P. T., Love, K. R., Mempel, T. R., Springer, T. A., and von Andrian, U. H. (2007) Specific and covalent labeling of a membrane protein with organic fluorochromes and quantum dots. *Proc. Natl. Acad. Sci. U. S. A 104*, 14753−14758.
(40) Deyev, S. M., Waibel, R., Lebedenko, E. N., Schubiger, A. P., and Pluckthun, A. (2003) Design of multivalent complexes using the barnase*barstar module. *Nat. Biotechnol. 21*, 1486−1492.
(41) Glinka, E. M., Edelweiss, E. F., Sapozhnikov, A. M., and Deyev, S. M. (2006) A new vector for controllable expression of an anti-HER2/neu mini-antibody-barnase fusion protein in HEK 293T cells. *Gene 366*, 97−103.
(42) Semenyuk, E. G., Stremovskiy, O. A., Edelweiss, E. F., Shirshikova, O. V., Balandin, T. G., Buryanov, Y. I., and Deyev, S. M. (2007) Expression of single-chain antibody-barstar fusion in plants. *Biochimie 89*, 31−38.
(43) Nikitin, M. P., Zdobnova, T. A., Lukash, S. V., Stremovskiy, O. A., and Deyev, S. M. (2010) Protein-assisted self-assembly of multifunctional nanoparticles. *Proc. Natl. Acad. Sci. U. S. A 107*, 5827−5832.
(44) Backer, M. V., Gaynutdinov, T. I., Patel, V., Jehning, B. T., Myshkin, E., and Backer, J. M. (2004) Adapter protein for site-specific conjugation of payloads for targeted drug delivery. *Bioconjugate Chem. 15*, 1021−1029.
(45) Backer, M. V., Patel, V., Jehning, B. T., and Backer, J. M. (2006) Self-assembled "dock and lock" system for linking payloads to targeting proteins. *Bioconjugate Chem. 17*, 912−919.
(46) Gaynutdinov, T. I., Myshkin, E., Backer, J. M., and Backer, M. V. (2003) Chimeric ribonuclease as a source of human adapter protein for targeted drug delivery. *Protein Eng. 16*, 771−775.
(47) Backer, M. V., and Backer, J. M. (2010) A "dock and lock" approach to preparation of targeted liposomes. *Methods Mol. Biol. 605*, 257−266.
(48) Ferrari, E., Darios, F., Zhang, F., Niranjan, D., Bailes, J., Soloviev, M., and Davletov, B. (2010) Binary polypeptide system for permanent and oriented protein immobilization. *J. Nanobiotechnol. 8*, 9.
(49) Sutton, R. B., Fasshauer, D., Jahn, R., and Brunger, A. T. (1998) Crystal structure of a SNARE complex involved in synaptic exocytosis at 2.4 A resolution. *Nature 395*, 347−353.
(50) Hu, K., Carroll, J., Fedorovich, S., Rickman, C., Sukhodub, A., and Davletov, B. (2002) Vesicular restriction of synaptobrevin suggests a role for calcium in membrane fusion. *Nature 415*, 646−650.
(51) Darios, F., Niranjan, D., Ferrari, E., Zhang, F., Soloviev, M., Rummel, A., Bigalke, H., Suckling, J., Ushkaryov, Y., Naumenko, N., Shakirzyanova, A., Giniatullin, R., Maywood, E., Hastings, M., Binz, T., and Davletov, B. (2010) SNARE tagging allows stepwise assembly of a multimodular medicinal toxin. *Proc. Natl. Acad. Sci. U. S. A 107*, 18197−18201.
(52) Baillie, G. S., Scott, J. D., and Houslay, M. D. (2005) Compartmentalisation of phosphodiesterases and protein kinase A: opposites attract. *FEBS Lett. 579*, 3264−3270.
(53) Wong, W., and Scott, J. D. (2004) AKAP signalling complexes: focal points in space and time. *Nat. Rev. Mol. Cell Biol. 5*, 959−970.
(54) Newlon, M. G., Roy, M., Morikis, D., Hausken, Z. E., Coghlan, V., Scott, J. D., and Jennings, P. A. (1999) The molecular basis for protein kinase A anchoring revealed by solution NMR. *Nat. Struct. Biol. 6*, 222−227.
(55) Carr, D. W., Stofko-Hahn, R. E., Fraser, I. D., Bishop, S. M., Acott, T. S., Brennan, R. G., and Scott, J. D. (1991) Interaction of the regulatory subunit (RII) of cAMP-dependent protein kinase with RII-anchoring proteins occurs through an amphipathic helix binding motif. *J. Biol. Chem. 266*, 14188−14192.
(56) Colledge, M., and Scott, J. D. (1999) AKAPs: from structure to function. *Trends Cell Biol. 9*, 216−221.
(57) Newlon, M. G., Roy, M., Morikis, D., Carr, D. W., Westphal, R., Scott, J. D., and Jennings, P. A. (2001) A novel mechanism of PKA anchoring revealed by solution structures of anchoring complexes. *EMBO J. 20*, 1651−1662.
(58) Alto, N. M., Soderling, S. H., Hoshi, N., Langeberg, L. K., Fayos, R., Jennings, P. A., and Scott, J. D. (2003) Bioinformatic design of A-kinase anchoring protein-in silico: a potent and selective peptide antagonist of type II protein kinase A anchoring. *Proc. Natl. Acad. Sci. U. S. A 100*, 4445−4450.
(59) Chang, C. H., Rossi, E. A., Cardillo, T. M., Nordstrom, D. L., McBride, W. J., and Goldenberg, D. M. (2009) A new method to produce monoPEGylated dimeric cytokines shown with human interferon-alpha2b. *Bioconjugate Chem. 20*, 1899−1907.
(60) Rossi, E. A., Goldenberg, D. M., Cardillo, T. M., McBride, W. J., Sharkey, R. M., and Chang, C. H. (2006) Stably tethered multifunctional structures of defined composition made by the dock and lock method for use in cancer targeting. *Proc. Natl. Acad. Sci. U. S. A 103*, 6841−6846.
(61) Rossi, E. A., Goldenberg, D. M., Cardillo, T. M., Stein, R., Wang, Y., and Chang, C. H. (2008) Novel designs of multivalent anti-CD20 humanized antibodies as improved lymphoma therapeutics. *Cancer Res. 68*, 8384−8392.
(62) Rossi, E. A., Goldenberg, D. M., Cardillo, T. M., Stein, R., and Chang, C. H. (2009) Hexavalent bispecific antibodies represent a new class of anticancer therapeutics: 1. Properties of anti-CD20/CD22 antibodies in lymphoma. *Blood 113*, 6161−6171.
(63) Rossi, E. A., Goldenberg, D. M., Cardillo, T. M., Stein, R., and Chang, C. H. (2009) CD20-targeted tetrameric interferon-alpha, a novel and potent immunocytokine for the therapy of B-cell lymphomas. *Blood 114*, 3864−3871.
(64) Blumenthal, R. D., Hansen, H. J., and Goldenberg, D. M. (2005) Inhibition of adhesion, invasion, and metastasis by antibodies targeting

CEACAM6 (NCA-90) and CEACAM5 (carcinoembryonic antigen). *Cancer Res. 65*, 8809−8817.
(65) Rossi, E. A., Sharkey, R. M., McBride, W., Karacay, H., Zeng, L., Hansen, H. J., Goldenberg, D. M., and Chang, C. H. (2003) Development of new multivalent-bispecific agents for pretargeting tumor localization and therapy. *Clin. Cancer Res. 9*, 3886S−3896S.
(66) Gegner, J. A., and Dahlquist, F. W. (1991) Signal transduction in bacteria: CheW forms a reversible complex with the protein kinase CheA. *Proc. Natl. Acad. Sci. U. S. A 88*, 750−754.
(67) Schoffelen, R., van der Graaf, W. T., Franssen, G., Sharkey, R. M., Goldenberg, D. M., McBride, W. J., Rossi, E. A., Eek, A., Oyen, W. J., and Boerman, O. C. (2010) Pretargeted ^{177}Lu radioimmunotherapy of carcinoembryonic antigen-expressing human colonic tumors in mice. *J. Nucl. Med. 51*, 1780−1787.
(68) Sharkey, R. M., Rossi, E. A., McBride, W. J., Chang, C. H., and Goldenberg, D. M. (2010) Recombinant bispecific monoclonal antibodies prepared by the dock-and-lock strategy for pretargeted radioimmunotherapy. *Semin. Nucl. Med. 40*, 190−203.
(69) McBride, W. J., Sharkey, R. M., Karacay, H., D'Souza, C. A., Rossi, E. A., Laverman, P., Chang, C. H., Boerman, O. C., and Goldenberg, D. M. (2009) A novel method of ^{18}F radiolabeling for PET. *J. Nucl. Med. 50*, 991−998.
(70) Sharkey, R. M., Karacay, H., Vallabhajosula, S., McBride, W. J., Rossi, E. A., Chang, C. H., Goldsmith, S. J., and Goldenberg, D. M. (2008) Metastatic human colonic carcinoma: molecular imaging with pretargeted SPECT and PET in a mouse model. *Radiology 246*, 497−507.
(71) Karacay, H., Sharkey, R. M., McBride, W. J., Rossi, E. A., Chang, C. H., and Goldenberg, D. M. (2011) Optimization of hapten-peptide labeling for pretargeted immunoPET of bispecific antibody using generator-produced ^{68}Ga. *J. Nucl. Med. 52*, 555−559.
(72) Schoffelen, R., Sharkey, R. M., Goldenberg, D. M., Franssen, G., McBride, W. J., Rossi, E. A., Chang, C. H., Laverman, P., Disselhorst, J. A., Eek, A., van der Graaf, W. T., Oyen, W. J., and Boerman, O. C. (2010) Pretargeted immuno-positron emission tomography imaging of carcinoembryonic antigen-expressing tumors with a bispecific antibody and a 68Ga- and 18F-labeled hapten peptide in mice with human tumor xenografts. *Mol. Cancer Ther. 9*, 1019−1027.
(73) Sharkey, R. M., Rossi, E. A., McBride, W. J., Chang, C. H., and Goldenberg, D. M. (2010) Recombinant bispecific monoclonal antibodies prepared by the dock-and-lock strategy for pretargeted radioimmunotherapy. *Semin. Nucl. Med. 40*, 190−203.
(74) Sharkey, R. M., Rossi, E. A., Chang, C. H., and Goldenberg, D. M. (2010) Improved cancer therapy and molecular imaging with multivalent, multispecific antibodies. *Cancer Biother. Radiopharm. 25*, 1−12.
(75) Karacay, H., Sharkey, R. M., Gold, D. V., Ragland, D. R., McBride, W. J., Rossi, E. A., Chang, C. H., and Goldenberg, D. M. (2009) Pretargeted radioimmunotherapy of pancreatic cancer xenografts: TF10-90Y-IMP-288 alone and combined with gemcitabine. *J. Nucl. Med. 50*, 2008−2016.
(76) Sharkey, R. M., Karacay, H., Johnson, C. R., Litwin, S., Rossi, E. A., McBride, W. J., Chang, C. H., and Goldenberg, D. M. (2009) Pretargeted versus directly targeted radioimmunotherapy combined with anti-CD20 antibody consolidation therapy of non-Hodgkin lymphoma. *J. Nucl. Med. 50*, 444−453.
(77) Sharkey, R. M., Karacay, H., Litwin, S., Rossi, E. A., McBride, W. J., Chang, C. H., and Goldenberg, D. M. (2008) Improved therapeutic results by pretargeted radioimmunotherapy of non-Hodgkin's lymphoma with a new recombinant, trivalent, anti-CD20, bispecific antibody. *Cancer Res. 68*, 5282−5290.
(78) Gold, D. V., Goldenberg, D. M., Karacay, H., Rossi, E. A., Chang, C. H., Cardillo, T. M., McBride, W. J., and Sharkey, R. M. (2008) A novel bispecific, trivalent antibody construct for targeting pancreatic carcinoma. *Cancer Res. 68*, 4819−4826.
(79) Sharkey, R. M., Karacay, H., Vallabhajosula, S., McBride, W. J., Rossi, E. A., Chang, C. H., Goldsmith, S. J., and Goldenberg, D. M. (2008) Metastatic human colonic carcinoma: molecular imaging with pretargeted SPECT and PET in a mouse model. *Radiology 246*, 497−507.
(80) Goldenberg, D. M., Rossi, E. A., Sharkey, R. M., McBride, W. J., and Chang, C. H. (2008) Multifunctional antibodies by the Dock-and-Lock method for improved cancer imaging and therapy by pretargeting. *J. Nucl. Med. 49*, 158−163.
(81) Sharkey, R. M., Karacay, H., McBride, W. J., Rossi, E. A., Chang, C. H., and Goldenberg, D. M. (2007) Bispecific antibody pretargeting of radionuclides for immuno single-photon emission computed tomography and immuno positron emission tomography molecular imaging: an update. *Clin. Cancer Res. 13*, 5577s−5585s.
(82) Stein, R., Qu, Z., Chen, S., Rosario, A., Shi, V., Hayes, M., Horak, I. D., Hansen, H. J., and Goldenberg, D. M. (2004) Characterization of a new humanized anti-CD20 monoclonal antibody, IMMU-106, and Its use in combination with the humanized anti-CD22 antibody, epratuzumab, for the therapy of non-Hodgkin's lymphoma. *Clin. Cancer Res. 10*, 2868−2878.
(83) Carnahan, J., Stein, R., Qu, Z., Hess, K., Cesano, A., Hansen, H. J., and Goldenberg, D. M. (2007) Epratuzumab, a CD22-targeting recombinant humanized antibody with a different mode of action from rituximab. *Mol. Immunol. 44*, 1331−1341.
(84) Gupta, P., Goldenberg, D. M., Rossi, E. A., and Chang, C. H. (2010) Multiple signaling pathways induced by hexavalent, monospecific, anti-CD20 and hexavalent, bispecific, anti-CD20/CD22 humanized antibodies correlate with enhanced toxicity to B-cell lymphomas and leukemias. *Blood 116*, 3258−3267.
(85) Rossi, E. A., Rossi, D. L., Stein, R., Goldenberg, D. M., and Chang, C. H. (2010) A bispecific antibody-IFNalpha2b immunocytokine targeting CD20 and HLA-DR is highly toxic to human lymphoma and multiple myeloma cells. *Cancer Res. 70*, 7600−7609.
(86) Xuan, C., Steward, K. K., Timmerman, J. M., and Morrison, S. L. (2010) Targeted delivery of interferon-alpha via fusion to anti-CD20 results in potent antitumor activity against B-cell lymphoma. *Blood 115*, 2864−2871.
(87) Rossi, E. A., Rossi, D. L., Cardillo, T. M., Stein, R., Goldenberg, D. M., and Chang, C. H. (2011) Preclinical studies on targeted delivery of multiple IFN{alpha}2b to HLA-DR in diverse hematologic cancers. *Blood 118*, 1877−1884.
(88) Stein, R., Gupta, P., Chen, X., Cardillo, T. M., Furman, R. R., Chen, S., Chang, C. H., and Goldenberg, D. M. (2010) Therapy of B-cell malignancies by anti-HLA-DR humanized monoclonal antibody, IMMU-114, is mediated through hyper-activation of ERK and JNK MAP kinase signaling pathways. *Blood 115*, 5180−5190.
(89) Burns-Hamuro, L. L., Ma, Y., Kammerer, S., Reineke, U., Self, C., Cook, C., Olson, G. L., Cantor, C. R., Braun, A., and Taylor, S. S. (2003) Designing isoform-specific peptide disruptors of protein kinase A localization. *Proc. Natl. Acad. Sci. U. S. A 100*, 4072−4077.
(90) Rustandi, R. R., Drohat, A. C., Baldisseri, D. M., Wilder, P. T., and Weber, D. J. (1998) The Ca(2+)-dependent interaction of S100B(beta beta) with a peptide derived from p53. *Biochemistry 37*, 1951−1960.
(91) Rose, R. B., Bayle, J. H., Endrizzi, J. A., Cronk, J. D., Crabtree, G. R., and Alber, T. (2000) Structural basis of dimerization, coactivator recognition and MODY3 mutations in HNF-1alpha. *Nat. Struct. Biol. 7*, 744−748.
(92) Fancy, D. A., Melcher, K., Johnston, S. A., and Kodadek, T. (1996) New chemistry for the study of multiprotein complexes: the six-histidine tag as a receptor for a protein crosslinking reagent. *Chem. Biol. 3*, 551−559.
(93) Brown, K. C., Yu, Z., Burlingame, A. L., and Craik, C. S. (1998) Determining protein-protein interactions by oxidative cross-linking of a glycine-glycine-histidine fusion protein. *Biochemistry 37*, 4397−4406.
(94) Fancy, D. A., and Kodadek, T. (1999) Chemistry for the analysis of protein-protein interactions: rapid and efficient cross-linking triggered by long wavelength light. *Proc. Natl. Acad. Sci. U. S. A 96*, 6020−6024.

Bioconjugate Chemistry

Communication

pubs.acs.org/bc

2-Nitroimidazole-Tricarbocyanine Conjugate as a Near-Infrared Fluorescent Probe for *in Vivo* Imaging of Tumor Hypoxia

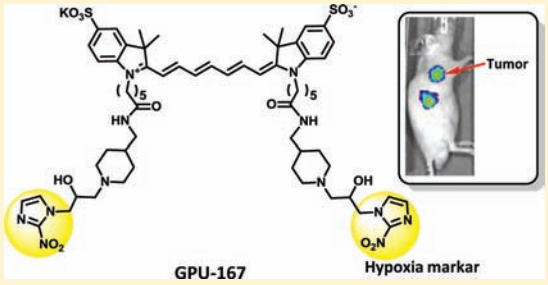
Kensuke Okuda,[†] Yasuyuki Okabe,[†] Tetsuya Kadonosono,[‡] Takahiro Ueno,[†] Bahaa G. M. Youssif,[†] Shinae Kizaka-Kondoh,[‡] and Hideko Nagasawa*,[†]

[†]Laboratory of Pharmaceutical and Medicinal Chemistry, Gifu Pharmaceutical University, Gifu 501-1196, Japan

[‡]Department of Biomolecular Engineering, Graduate School of Bioscience and Biotechnology, Tokyo Institute of Technology, Yokohama 226-8501, Japan

Supporting Information

ABSTRACT: We developed a novel near-infrared (NIR) fluorescent probe, GPU-167, for *in vivo* imaging of tumor hypoxia. GPU-167 comprises a tricarbocyanine dye as an NIR fluorophore and two 2-nitroimidazole moieties as exogenous hypoxia markers that undergo bioreductive activation and then selective entrapment in hypoxic cells. After treatment with GPU-167, tumor cells contained significantly higher levels of fluorescence in hypoxia than in normoxia. *In vivo* fluorescence imaging specifically detected GPU-167 in tumors 24 h after administration. *Ex vivo* analysis revealed that fluorescence showed a strong correlation with hypoxia inducible factor (HIF)-1 active hypoxic regions. These data suggest that GPU-167 is a promising *in vivo* optical imaging probe for tumor hypoxia.



The microenvironments of solid tumors are characterized by low pO_2 and pH, which are considerably below physiological levels and completely different from those of normal tissues.[1] The hypoxic status of various solid tumors has been considered to be an indicator of adverse prognosis because of tumor progression toward a more malignant phenotype with increased metastatic potential and resistance to treatment.[2] Tumor hypoxia should be measured to assess the aggressiveness of the tumor and predict the outcome of therapy. Therefore, over the past decade, various methods have been employed to assess the level of oxygenation in solid tumors, including invasive and noninvasive techniques using various modalities, such as positron emission tomography (PET), single-photon emission computed tomography (SPECT), and magnetic resonance imaging (MRI). Various exogenous and endogenous markers for hypoxia are also currently available and have been studied in relation to each other for the evaluation of tumor microenvironments.[3,4]

Recently, more studies have been conducted using noninvasive optical imaging because it is safer and easier to perform than nuclear imaging.[5] Several small molecule fluorescent probes have been developed for hypoxia.[6−10] They rely on the change in fluorescence properties after selective biological reduction in tumor hypoxic regions. However, these fluorescent probes have some drawbacks. The greatest drawback is that they rely on chromophores with maximum absorption/fluorescence peaks in the ultraviolet/visible region of the spectra. Because of insufficient tissue penetration into the region of interest and absorption by endogenous biomolecules (e.g., hemoglobin), most excitation (Ex)/emission (Em) light could not be utilized for detection, causing inadequate *in vivo* imaging. Autofluorescence refers to the intrinsic fluorescence of the tissue caused by excitation by optical radiation, and it can hamper *in vivo* imaging because of poor signal-to-noise ratios. To overcome these drawbacks and improve noninvasive *in vivo* fluorescent imaging, the use of light in the near-infrared (NIR) region (700−900 nm) is a promising alternative. Light scattering and autofluorescence are decreased and tissue penetration is increased in NIR, thereby leading us to attempt to develop an NIR probe that provides a high signal-to-background ratio *in vivo*. The optical imaging is currently mechanistically limited to use in superficial tumors because of the minimal tissue penetration (<1−2 cm depth) even by NIR wavelength light. However, NIR fluorescence cancer imaging is a growing field for preclinical and clinical applications due to its advantages such as high spatial resolution, portability, and real-time display.[11] Actually, NIR fluorescence probes are being applied to endoscopy and surgical guidance in humans despite its limited penetration depth. Accordingly, NIR fluorescence imaging could be one of the powerful tools for future seamless transition between research and clinical cancer imaging technology.

Recently, a hypoxia probe with Ex/Em wavelengths of 650/670 nm, which are in the visible-NIR transition region, was developed by Nagano et al.[12] This was the first report of *in vivo* fluorescence imaging for acute ischemia hypoxia. *In vivo*

Received: August 28, 2011
Revised: February 2, 2012
Published: February 16, 2012

ACS Publications © 2012 American Chemical Society

dx.doi.org/10.1021/bc2004704 | *Bioconjugate Chem.* 2012, 23, 324−329

imaging of tumors transplanted from the skin surface of mice has also been achieved with Ex/Em wavelengths of 605/645 nm using a novel indium complex as a hypoxia-sensing phosphorescence probe.[13] Here we report the development of a hypoxia NIR fluorescent probe, GPU-167, with longer Ex/Em wavelengths of 753/778 nm than those used in previous studies, and the evaluation of GPU-167 for the *in vivo* imaging of tumor hypoxia using mouse xenograft models.

In the development of imaging probes for tumor hypoxia, nitroimidazoles have received particular attention as exogenous markers because of their unique behavior in hypoxic environments owing to their high electron affinity.[4,14] The specificity of nitroimidazole imaging would depend on oxygen concentration as well as nitroreductase levels in the tumor cells. Nitroaromatics are selectively reduced by nitroreductase enzymes under hypoxic conditions to form reactive products that can irreversibly bind to cellular nucleophiles (Figure 1). Currently,

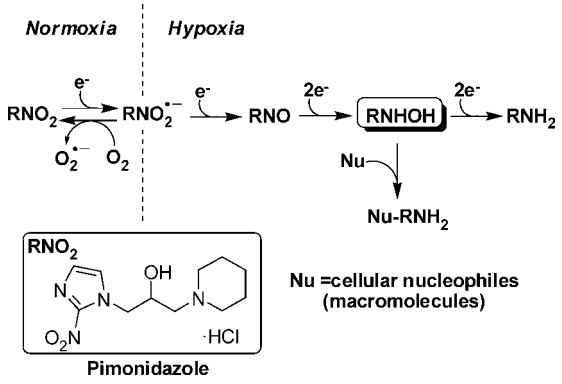


Figure 1. Proposed mechanism for hypoxia selective covalent binding reaction of hydroxylamine intermediates provided by bioreductive metabolism in hypoxia with cellular nucleophiles.

Pimonidazole (Pimo) is believed to be the standard exogenous hypoxic marker for immunohistochemical assessment of hypoxia in solid tumors. The binding of nitroimidazole hypoxia markers such as Pimo to cellular macromolecules has been shown to increase considerably below an oxygen concentration of 10 mmHg and is believed to indicate chronic hypoxia.[15] Recently, a 2-nitroimidazole-indocyanine green (ICG) conjugate was reported to persist in the tumors for a significantly longer period than ICG as shown by NIR-fluorescence tomography,[16,17] suggesting a possible application of the hypoxia selectivity of 2-nitroimidazole for *in vivo* fluorescence imaging. Although the author confirmed existence of hypoxia in tumor using anti-Pimo antibody stain after sacrifice, it was difficult to correlate the NIR fluorescence image with the Pimo staining.[17] Therefore, we designed GPU-167, a novel functionalized tricarbocyanine NIR fluorescence dye conjugated with a Pimo moiety for noninvasive detection of hypoxia in tumors and evaluated the potency and function of GPU-167 as an *in vivo* hypoxia marker by comparison to bioluminescent imaging of hypoxia inducible factor (HIF)-1 expression using a mouse xenograft model of SUIT-2/HRE-Luc cells.[18]

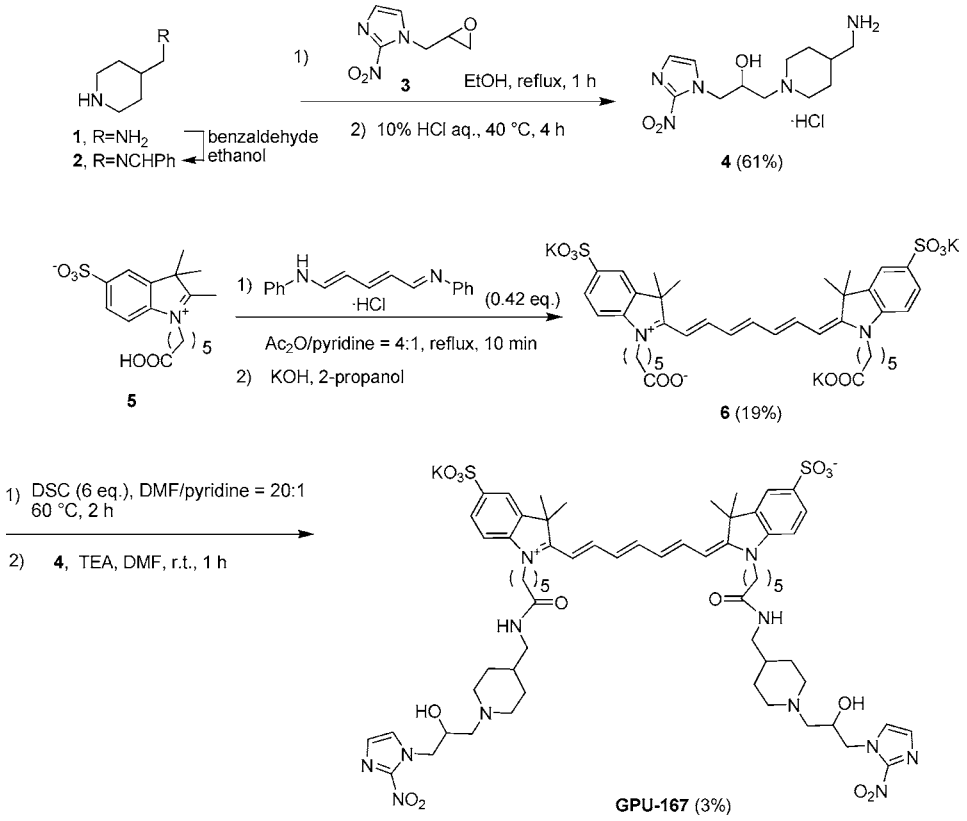
GPU-167 is composed of tricarbocyanine dye as a NIR fluorophore and two Pimo moieties as hypoxia markers with an alkyl linker to combine the two Pimo moieties with the tricarbocyanine dye and synthesized as shown in Scheme 1. Because of the synthetic convenience saving extra synthetic steps, we designed symmetric cyanine dye which contained dual Pimo moiety. The process of synthesis was as follows. First, 4-aminomethylpiperidine (**1**) was converted to Schiff base *N*-benzylidene-1-(piperidin-4-yl)methanamine (**2**),[19] then coupled to 2-nitro-1-(2-oxiranylmethyl)-1*H*-imidazole (**3**)[20,21] to yield 1-[4-(aminomethyl)piperidin-1-yl]-3-(2-nitro-1*H*-imidazol-1-yl)propan-2-ol hydrochloride (**4**) in 61% yield (3 steps), which was a derivative of Pimo with a functional amino group to be covalently modified. Tricarbocyanine dye **6**, which possesses bis alkyl linker moieties with carboxyl groups, was prepared from 1-(ε-carboxypentyl)-2,3,3-trimethyl-3*H*-indolenium-5-sulfonate (**5**) as previously reported.[22] After activation of the carboxylic groups by disuccinimidyl carbonate, reaction with compound **4** yielded the final target molecule GPU-167. It was purified by C18 reversed-phase flash chromatography. Purity and identity were determined by LCMS-IT to yield a single peak and a high-resolution mass spectrum with m/z 1299.5897 for $C_{63}H_{87}N_{12}O_{14}S_2$ ([M-K +2H]$^+$) (see Supporting Information). The evaluation of photophysical properties of GPU-167 was revealed to show narrow absorption and emission bands between the absorption and emission peaks at 753 and 778 nm respectively, which are typical wavelengths of the tricarobocyanine dye and in the NIR region of the spectrum (Figure 2). Its large extinction coefficient (4.8×10^4 M^{-1} cm^{-1} at 753 nm), high quantum yield (0.18), and sufficient water solubility showed that GPU-167 had adequate optical properties to be used as a fluorescent probe for *in vivo* imaging.

First, to evaluate the specific binding of GPU-167 to hypoxic cells, an *in vitro* fluorescence assay was performed with SUIT-2/HRE-Luc pancreatic cancer cells, which stably carry plasmid p5HRE-luciferase and express firefly luciferase under the influence of a HIF-1-dependent promoter.[18] The cells were preincubated under normoxic (21% O_2) or hypoxic (0.1% O_2) conditions for 4 h, followed by incubation with 0.2−20 μM of GPU-167 for 30 min. After the cells were washed, they were further incubated in fresh medium for 1 h under aerobic conditions to release unbound probe. The fluorescence intensity of the cell suspension was measured in a radioimmunoprecipitation assay (RIPA) buffer with excitation at 740 nm and emission at 780 nm. As shown in Figure 3, treatment with GPU-167 at concentrations of 5 and 20 μM resulted in the detection of significantly higher levels of fluorescence in the cells cultured under hypoxia than those in cells cultured under normoxia. These results indicated that GPU-167 might bind to intracellular substances irreversibly and be selectively retained in hypoxic cells for more than 48 h. However, fluorescence intensity under normoxia was also rather high because the probe may cause nonspecific noncovalent binding to cell components and/or persisting as an unbound form in cells due to its electronic and lipophilic features.

Next, *in vivo* imaging of hypoxic cells in tumor-bearing mice inoculated with SUIT-2/HRE-Luc cells was attempted.[23] The SUIT-2/HRE-Luc cells stably carry 5HRE-luciferase,[18] a luciferase reporter gene under the control of the HIF-1-dependent promoter, and thus HIF-1-activity in xenografts can be monitored by bioluminescence imaging. All of fluorescence images were acquired with IVIS imaging system using a 710 ± 15 nm the excitation filter and an 800 ± 10 nm emission filter. When GPU-167 was injected at a dose of 10 nmol into mice carrying subcutaneous xenografts of SUIT-2/HRE-Luc cells via the tail vein, fluorescence signals were detected throughout the body of the mice within 30 min and gradually became weaker (Figure 4A). Signals of GPU-167 in tumors were detected as

dx.doi.org/10.1021/bc2004704 | *Bioconjugate Chem.* 2012, 23, 324−329

Scheme 1. Synthesis of Hypoxia Probe, GPU-167



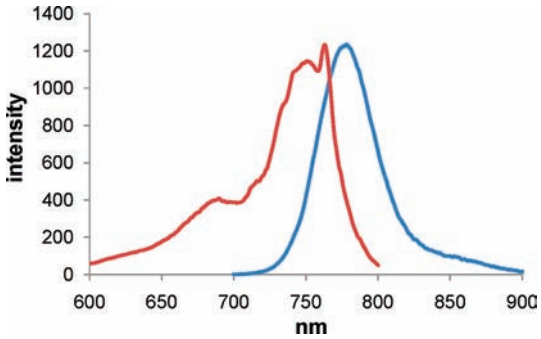


Figure 2. Excitation (magenta) and emission spectra (blue) of GPU-167 in MeOH.

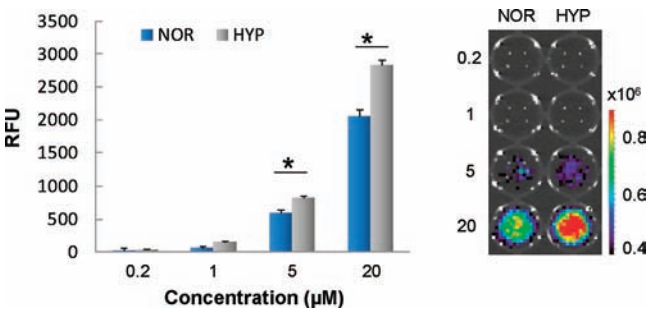


Figure 3. Specific binding of GPU-167 to hypoxic cells *in vitro*. The SUIT-2/HRE-Luc cells (2×10^5 cells) cultured under normoxic (NOR) or hypoxic (HYP) conditions were treated with GPU-167 and analyzed by measurement of fluorescent intensity with an Ex/Em wavelength of 740 nm/780 nm ($^*P < 0.05$, $n = 3$). Representative fluorescence images are also shown in right.

soon as 3 h after injection (Figure 4A). Most of the GPU-167 was rapidly cleared from the mice within 3 h (Figure 4B), and tumor-specific images were obtained 24 h after GPU-167 administration, resulting in the highest T/B ratio (Figure 4C). In addition to the clear accumulation of GPU-167 in the tumors, fluorescence signal was also detected in the abdominal region (Figure 4A). Then, to determine whether GPU-167 accumulation actually correlated with hypoxic conditions within the tumors, a bioluminescent signal emitted from HIF-1-active hypoxic cells in SUIT-2/HRE-Luc xenografts 24 h after administration of GPU-167 was also examined (Figure 4A, right panel). A positive correlation was observed between the fluorescent and luminescent images of the tumor, suggesting that the fluorescence owing to GPU-167 in the tumor was related to hypoxic conditions.

For a more detailed examination, we performed *ex vivo* imaging. Although the comparison of fluorescence by GPU-167 with immunohistochemical staining by anti-Pimo antibody of a tissue section might be helpful for clarifying their spatial relationship, such a double stain analysis needs cumbersome and difficult experiments. On the other hand, the SUIT-2/HRE-Luc xenograft is superior for detection hypoxic tumor cells *in vivo* and *ex vivo* directly. High fluorescence intensity for GPU-167 was detected in the liver, and a moderate intensity was detected in the tumors, kidney, and stomach (Figure 5A,B). In the SUIT-2/HRE-Luc tumor cells, HIF-1α expression was undetectable under normoxic and severe hypoxic ($pO_2 < 10$ mmHg) conditions but significantly increased under relatively mild hypoxic conditions.[18] Therefore, bioluminescence signals from the SUIT-2/HRE-Luc xenografts indicated that the HIF-1-active cells were located in relatively mild hypoxic regions, which proportionally exist adjacent to severe hypoxic regions.[24]

dx.doi.org/10.1021/bc2004704 | *Bioconjugate Chem.* 2012, 23, 324–329

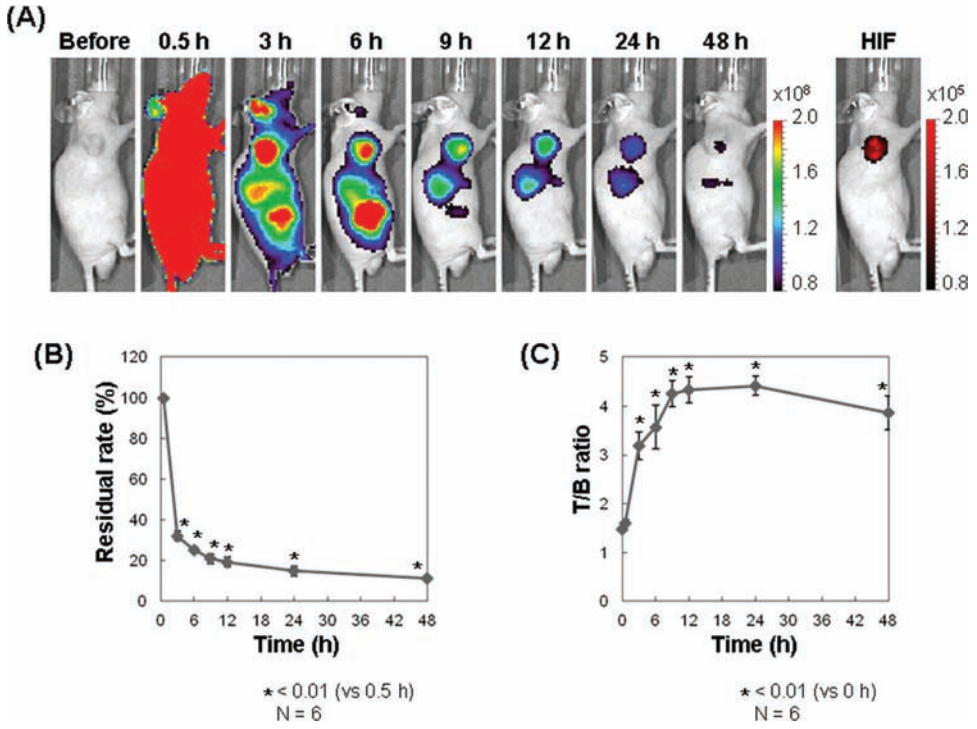


Figure 4. (A) *In vivo* optical imaging of subcutaneous cancers with GPU-167. Representative *in vivo* image after 10 nmol of GPU-167 administration. Nude mice carrying SUIT-2/HRE-Luc xenografts in both forefeet were imaged at the indicated time after GPU-167 injection. The right panel (HIF) shows bioluminescence image of HIF-1-active hypoxic tumor at 24 h. (B) Time-dependent clearance of GPU-167 from whole mouse. Fluorescence intensities of the muscle of the hind foot were measured at the indicated time after administration of GPU-167 and decrease in the intensity was represented by the relative value (Fluorescence intensity at 0.5 h after GPU-167 administration = 100%). (C) Specific accumulation of GPU-167 to subcutaneous xenografts. The relative fluorescence intensity of the tumor to the muscle (T/B ratio) was shown. Fluorescence intensities of the SUIT-2/HRE-Luc xenografts and the muscle of the hind foot were measured at the indicated time after GPU-167 administration. Three mice and six tumors were used for each point on each curve.

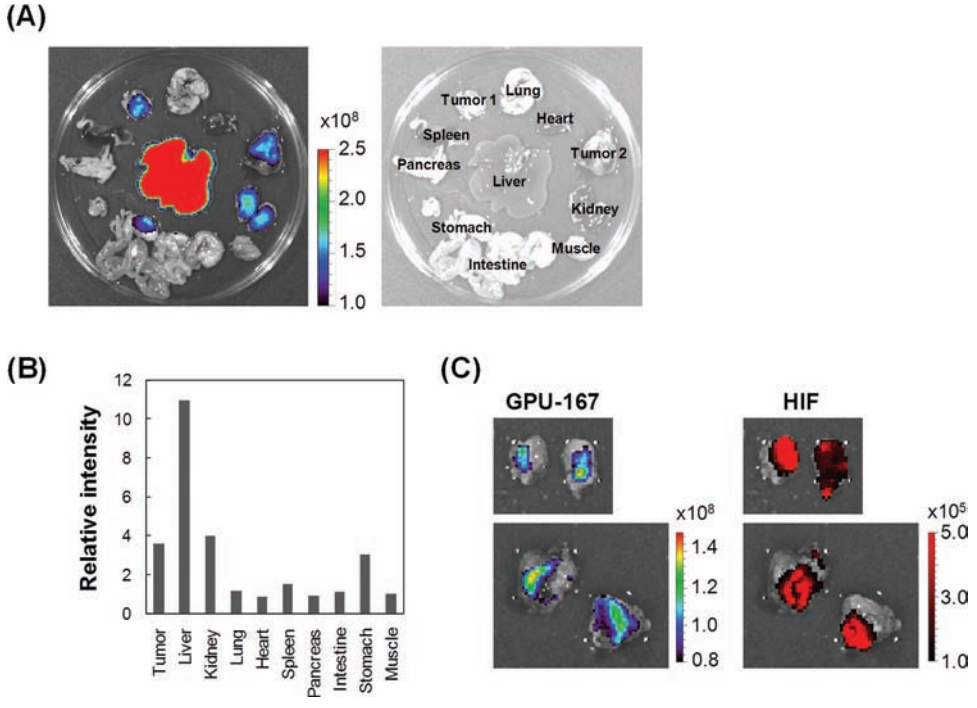


Figure 5. (A) *Ex vivo* fluorescence imaging of organs of tumor bearing mouse. The mouse shown in Figure 4A was analyzed by *ex vivo* imaging. Fluorescence image at 48 h after GPU-167 administration was shown. (B) Fluorescence intensity/organ size values were shown as relative intensity (the value of muscle = 1). (C) *Ex vivo* optical imaging of excised subcutaneous tumors. *Ex vivo* fluorescence (GPU-167) and bioluminescence (HIF) images of excised subcutaneous tumors shown in (A) were analyzed.

dx.doi.org/10.1021/bc2004704 | *Bioconjugate Chem.* 2012, 23, 324–329

Nitroimidazole such as Pimonidazole compounds are detected at absolute oxygen concentrations below 10 mmHg, suggesting that nitroimidazole probes are specific markers for severe hypoxia. Although these hypoxia markers depend on different mechanisms, their relationship and comparison have been well-researched in various solid tumors.[4] Our immunohistochemical analysis also revealed that the cells with HIF-1α expression and the ones with Pimonidazole-binding were adjacent to each other in SUIT-2/HRE-Luc xenografts.[18] *Ex vivo* imaging of tumors at 48 h after GPU-167 injection revealed that most fluorescence images of GPU-167 were proportional and similar to the bioluminescent images (Figure 5C). These observations suggest that GPU-167 efficiently would detect hypoxic regions *in vivo*. Assessment of such severe hypoxic fractions in tumors, which are regarded not only as adverse prognostic factors but also as indicators of the necessity for tumor-specific treatment, would provide diagnostic and therapeutic advantages for cancer treatment.[25]

Important criteria for effective fluorescence imaging probes include suitable pharmacological properties such as aqueous solubility, low nonspecific binding, rapid clearance of the free dye, and low toxicity that include appropriate photophysical properties such as excitation and emission maxima in the NIR region between 700−900 nm, high quantum yield, and chemical and optical stability. With regard to pharmacological properties of GPU-167, its aqueous solubility was sufficiently high and its hydrophobicity was higher than that of ICG based on its larger hydrophobicity index (Rm), which was 1.62 versus 0.84 for ICG, both determined using a reversed-phase thin layer chromatographic system (mobile phase: 20% 5 mM sodium phosphate buffer (pH 7.4)/80% MeOH). ICG was selectively distributed to the liver and then excreted rather rapidly into the bile, because it was tightly bound to serum proteins[26] and rapidly washed out from tumors in merely less than 3 h.[17] On the other hand, GPU-167 was retained for a relatively longer period (more than 48 h) in the body even though it maintained a good T/B ratio (>2.5). Furthermore, the considerably high liver distribution of GPU-167 disturbed its selective imaging of tumors. Thus, to improve pharmacokinetic properties of GPU-167, further studies of structure−property relationship of NIR probes are required, controlling the number of negatively charged groups (e.g., sulfonates),[27] positively charged groups (e.g., amines), and hydrophobic alkyl groups.

In conclusion, an efficient NIR fluorescent probe, GPU-167, comprising 2-nitroimidazole and tricarbocyanine dye, was developed for *in vivo* imaging of tumor hypoxia. It was trapped in tumor cells cultured under hypoxic condition significantly more than normoxic condition. We also demonstrated that tumors were clearly visualized by NIR fluorescence with significant T/B ratio 24 h after GPU-167 administration to living mice in a mouse xenograft model. We are currently making a structural modification of the hypoxia-selective NIR probe having improved pharmacological properties.

■ ASSOCIATED CONTENT

Supporting Information

Synthesis, purification, and characterization of organic compounds; optical properties; *in vitro* and *in vivo* evaluation. This material is available free of charge via the Internet at http://pubs.acs.org.

■ AUTHOR INFORMATION

Corresponding Author

*Telephone and FAX: +81-58-230-8112; E-mail: hnagasawa@gifu-pu.ac.jp.

Notes

The authors declare no competing financial interest.

■ ACKNOWLEDGMENTS

This research was supported in part by a Grant from The Saijiro Endo Memorial Foundation for Science & Technology (to K.O.), a Grant-in-Aid for Young Scientists (B) (22790042 to K.O.), a Grant-in-Aid for Scientific Research on Priority Areas (20011009 to H.N.) from the Japan Society for the Promotion of Science, and a Grant-in-Aid for Scientific Research on Innovative Areas "Integrative Research on Cancer Microenvironment Network" (22112009 to S.K.K.) from the Ministry of Education, Culture, Sports, Science, and Technology of Japan. We also thank Ms. Hiroko Osamura and Ms. Emi Inaba for their technical assistance.

■ REFERENCES

(1) Vaupel, P. (2004) Tumor microenvironmental physiology and its implications for radiation oncology. *Semin. Radiat. Oncol. 14*, 198−206.
(2) Wilson, W. R., and Hay, M. P. (2011) Targeting hypoxia in cancer therapy. *Nat. Rev. Cancer 11*, 393−410.
(3) Sun, X., Niu, G., Chan, N., Shen, B., and Chen, X. (2011) Tumor hypoxia imaging. *Mol. Imaging Biol. 13*, 399−410.
(4) Kizaka-Kondoh, S., and Konse-Nagasawa, H. (2009) Significance of nitroimidazole compounds and hypoxia-inducible factor-1 for imaging tumor hypoxia. *Cancer Sci. 100*, 1366−73.
(5) Keereweer, S., Kerrebijn, J., van Driel, P., Xie, B., Kaijzel, E., Snoeks, T., Que, I., Hutteman, M., van der Vorst, J., Mieog, J., Vahrmeijer, A., van de Velde, C., Baatenburg de Jong, R., and Löwik, C. (2011) Optical Image-guided Surgery—Where Do We Stand? *Mol. Imaging Biol. 13*, 199−207.
(6) Tanabe, K., Hirata, N., Harada, H., Hiraoka, M., and Nishimoto, S. (2008) Emission under hypoxia: one-electron reduction and fluorescence characteristics of an indolequinone-coumarin conjugate. *ChemBioChem 9*, 426−32.
(7) Zhu, W., Dai, M., Xu, Y., and Qian, X. (2008) Novel nitroheterocyclic hypoxic markers for solid tumor: synthesis and biological evaluation. *Bioorg. Med. Chem. 16*, 3255−60.
(8) Nakata, E., Yukimachi, Y., Kariyazono, H., Im, S., Abe, C., Uto, Y., Maezawa, H., Hashimoto, T., Okamoto, Y., and Hori, H. (2009) Design of a bioreductively-activated fluorescent pH probe for tumor hypoxia imaging. *Bioorg. Med. Chem. 17*, 6952−8.
(9) Komatsu, H., Harada, H., Tanabe, K., Hiraoka, M., and Nishimoto, S. (2010) Indolequinone-rhodol conjugate as a fluorescent probe for hypoxic cells: enzymatic activation and fluorescence properties. *MedChemComm 1*, 50−53.
(10) Cui, L., Zhong, Y., Zhu, W., Xu, Y., Du, Q., Wang, X., Qian, X., and Xiao, Y. (2011) A New Prodrug-Derived Ratiometric Fluorescent Probe for Hypoxia: High Selectivity of Nitroreductase and Imaging in Tumor Cell. *Org. Lett. 13*, 928−931.
(11) Kosaka, N., Ogawa, M., Choyke, P. L., and Kobayashi, H. (2009) Clinical implications of near-infrared fluorescence imaging in cancer. *Future Oncol. 5*, 1501−11.
(12) Kiyose, K., Hanaoka, K., Oushiki, D., Nakamura, T., Kajimura, M., Suematsu, M., Nishimatsu, H., Yamane, T., Terai, T., Hirata, Y., and Nagano, T. (2010) Hypoxia-Sensitive Fluorescent Probes for in Vivo Real-Time Fluorescence Imaging of Acute Ischemia. *J. Am. Chem. Soc. 132*, 15846−15848.
(13) Zhang, S., Hosaka, M., Yoshihara, T., Negishi, K., Iida, Y., Tobita, S., and Takeuchi, T. (2010) Phosphorescent light-emitting iridium complexes serve as a hypoxia-sensing probe for tumor imaging in living animals. *Cancer Res. 70*, 4490−8.

(14) Chitneni, S. K., Palmer, G. M., Zalutsky, M. R., and Dewhirst, M. W. (2011) Molecular imaging of hypoxia. *J. Nucl. Med. 52*, 165−8.
(15) Raleigh, J. A., Chou, S. C., Arteel, G. E., and Horsman, M. R. (1999) Comparisons among Pimonidazole binding, oxygen electrode measurements, and radiation response in C3H mouse tumors. *Radiat. Res. 151*, 580−9.
(16) Pavlik, C., Biswal, N. C., Gaenzler, F. C., Morton, M. D., Kuhn, L. T., Claffey, K. P., Zhu, Q., and Smith, M. B. (2011) Synthesis and fluorescent characteristics of imidazole-indocyanine green conjugates. *Dyes Pigm. 89*, 9−15.
(17) Biswal, N. C., Pavlik, C., Smith, M. B., Aguirre, A., Xu, Y., Zanganeh, S., Kuhn, L. T., Claffey, K. P., and Zhu, Q. (2011) Imaging tumor hypoxia by near-infrared fluorescence tomography. *J. Biomed. Opt. 16*, 066009.
(18) Kizaka-Kondoh, S., Itasaka, S., Zeng, L., Tanaka, S., Zhao, T., Takahashi, Y., Shibuya, K., Hirota, K., Semenza, G. L., and Hiraoka, M. (2009) Selective Killing of Hypoxia-Inducible Factor-1−Active Cells Improves Survival in a Mouse Model of Invasive and Metastatic Pancreatic Cancer. *Clin. Cancer Res. 15*, 3433−3441.
(19) Diouf, O., Depreux, P., Chavatte, P., and Poupaert, J. H. (2000) Synthesis and preliminary pharmacological results on new naphthalene derivatives as 5-HT4 receptor ligands. *Eur. J. Med. Chem. 35*, 699−706.
(20) Sercel, A. D., Beylin, V. G., Marlatt, M. E., Leja, B., Showalter, H. D. H., and Michel, A. (2006) Synthesis of the Enantiomers of the Dual Function 2-Nitroimidazole Radiation Sensitizer RB 6145. *J. Heterocycl. Chem. 43*, 1597−1604.
(21) Webb, P., and Threadgill, M. D. (1990) Labelled compounds of interest as antitumour agents. Part II (1). Synthesis of 2H and 3H isotopomers of RSU 1069 and Ro 03−8799 (Pimonidazole). *J. Labelled Compd. Radiopharm. 28*, 257−264.
(22) Mujumdar, R. B., Ernst, L. A., Mujumdar, S. R., Lewis, C. J., and Waggoner, A. S. (1993) Cyanine dye labeling reagents: sulfoindocyanine succinimidyl esters. *Bioconjugate Chem. 4*, 105−111.
(23) Kuchimaru, T., Kadonosono, T., Tanaka, S., Ushiki, T., Hiraoka, M., and Kizaka-Kondoh, S. (2010) In vivo imaging of HIF-active tumors by an oxygen-dependent degradation protein probe with an interchangeable labeling system. *PLoS One 5*, e15736.
(24) Sobhanifar, S., Aquino-Parsons, C., Stanbridge, E. J., and Olive, P. (2005) Reduced expression of hypoxia-inducible factor-1alpha in perinecrotic regions of solid tumors. *Cancer Res. 65*, 7259−66.
(25) Bache, M., Kappler, M., Said, H. M., Staab, A., and Vordermark, D. (2008) Detection and specific targeting of hypoxic regions within solid tumors: current preclinical and clinical strategies. *Curr. Med. Chem. 15*, 322−38.
(26) Baker, K. J. (1966) Binding of sulfobromophthalein sodium and indocyanine green by plasma alpha-1 lipoproteins. *Proc. Soc. Exp. Biol. Med. 122*, 957−963.
(27) Hamann, F. M., Brehm, R., Pauli, J., Grabolle, M., Frank, W., Kaiser, W. A., Fischer, D., Resch-Genger, U., and Hilger, I. (2011) Controlled modulation of serum protein binding and biodistribution of asymmetric cyanine dyes by variation of the number of sulfonate groups. *Mol. Imaging 10*, 258−69.

Bioconjugate Chemistry

Communication

pubs.acs.org/bc

New Macrobicyclic Chelator for the Development of Ultrastable ^{64}Cu-Radiolabeled Bioconjugate

Darpan N. Pandya,[†] Ajit V. Dale,[†] Jung Young Kim,[‡] Hochun Lee,[§] Yeong Su Ha,[†] Gwang Il An,[‡] and Jeongsoo Yoo*[,†]

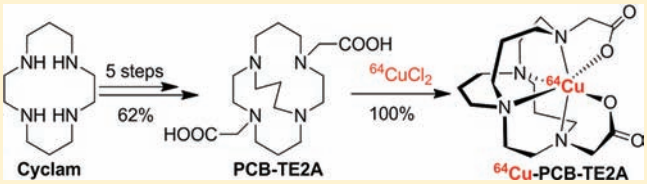
[†]Department of Molecular Medicine, Kyungpook National University, Daegu 700-422, South Korea

[‡]Molecular Imaging Research Center, Korea Institute of Radiological and Medical Sciences, Seoul 139-706, South Korea

[§]Department of Energy Systems Engineering, Daegu Gyeongbuk Institute of Science & Technology, Daegu, 711-873, South Korea

Supporting Information

ABSTRACT: Ethylene cross-bridged cyclam with two acetate pendant arms, ECB-TE2A, is known to form the most kinetically stable ^{64}Cu complexes. However, its usefulness as a bifunctional chelator is limited because of its harsh radiolabeling conditions. Herein, we report new cross-bridged cyclam chelator for the development of ultrastable ^{64}Cu-radiolabeled bioconjugates. Propylene cross-bridged TE2A (PCB-TE2A) was successfully synthesized in an efficient way. The Cu(II) complex of PCB-TE2A exhibited much higher kinetic stability than ECB-TE2A in acid decomplexation studies, and also showed high resistance to reduction-mediated demetalation. Furthermore, the quantitative radiolabeling of PCB-TE2A with ^{64}Cu was achieved under milder conditions compared to ECB-TE2A. Biodistribution studies strongly indicate that the ^{64}Cu complexes of PCB-TE2A cleared out rapidly from the body with minimum decomplexation.



Bifunctional chelators (BFCs), which form stable complexes with metal ions, are an essential component for the successful development of metal-based imaging and therapeutic agents.[1,2] This is especially the case in the field of nuclear imaging and radioimmunotherapy, where significant advances have been made during the past few decades.[3,4] Among the various available radiometal ions, radioactive copper ions (^{60}Cu, ^{61}Cu, ^{62}Cu, ^{64}Cu, ^{67}Cu) have received a great deal of interest because of their attractive decay characteristics and half-life for medical imaging as well as therapy.[5,6] Many ^{64}Cu-radiolabeled bioconjugates have been developed employing several existing BFCs, and some of them are currently in the clinical trial stage.[7−9]

So far, tetraazamacrocycles, such as DOTA[10−13] and TETA,[14−17] have commonly been chosen as a BFC for chelating ^{64}Cu ions, but several previous studies demonstrated that ^{64}Cu-DOTA and ^{64}Cu-TETA complexes are not stable under physiological conditions, but they release some free copper ions within several hours.[18−21] These released ^{64}Cu ions increase the background noise in positron emission tomography (PET) imaging and also increase the amount of unnecessary radiation exposure in nontargeted organs. In order to address this stability issue, many acyclic and macrocyclic BFCs have been synthesized and tested, but ethylene cross-bridged cyclam with two acetate pendant arms, ECB-TE2A, was found to form the most kinetically stable Cu(II) complexes.[7−9]

ECB-TE2A was first introduced in 2000 by Weisman et al.[22] and various derivatives have since been synthesized,[23−29] but it still produces the most kinetically stable Cu(II) complexes known.[23,25,26] In particular, its cyclen counterpart, ECB-DO2A, exhibited much lower kinetic stability than ECB-TE2A when complexed with ^{64}Cu.[20] Thanks to the high in vivo kinetic stability of ^{64}Cu labeled ECB-TE2A complexes, the ^{64}Cu radiotracers derived from ECB-TE2A showed much lower background noise and faster body clearance compared to their counterparts using other BFCs.[30−34] However, its usefulness as a BFC is limited because of two major drawbacks. First, its synthesis is not easy: a total of 6 steps involving a total reaction time of 35 days leading to 45% overall yield from cyclam.[22] Another big obstacle is its harsh ^{64}Cu labeling conditions. Even though its ^{64}Cu complexes show very high stability after radiolabeling, ECB-TE2A can be radiolabeled with ^{64}Cu only at elevated temperatures of at least 75 °C, at which most heat-sensitive biomolecules are degraded.[20,35]

In an attempt to develop new BFCs, we designed a new class of cross-bridged macrocyclics using ECB-TE2A as a starting point. Even though several ECB-TE2A derivatives having different macrocyclic backbones and *N*-substituents were reported previously,[23−29] no cyclam derivative based on modification of the ethylene-bridge has been previously reported. Here, we increased the length of the cross-bridge from ethylene to propylene in the hope of achieving easier fit of the Cu(II) ion into the chelator, but tighter retention after complexation.

Propylene cross-bridged TE2A (PCB-TE2A) was successfully synthesized in five steps starting from cyclam using a *trans*-alkylation/cross-bridge reaction/deprotection strategy. The regioselective *trans*-disubstitution of the *tert*-butyl acetate groups on the nonadjacent *N*-atoms of cyclam was achieved

Received: October 1, 2011
Revised: February 8, 2012
Published: February 14, 2012

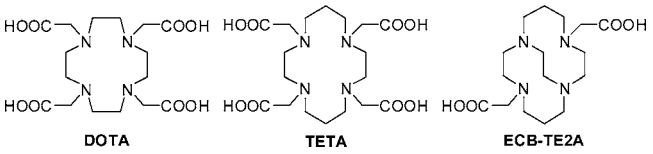
 © 2012 American Chemical Society dx.doi.org/10.1021/bc200539t | *Bioconjugate Chem.* 2012, 23, 330−335

in quantitative yield via the bisaminal protection of four *N*-atoms followed by the alkylation of 4 equiv *tert*-butyl bromoacetate groups.[21] Due to its ionic character, compound **3** was insoluble in CH_3CN and, therefore, was isolated quantitatively by simple filtration. There was no indication of the formation of *cis*-disubstituted byproducts in ^{13}C NMR spectrum during the course of the reaction.[36] The selective cleavage of the bisaminal bonds of compound **3** was carried out simply by basic hydrolysis using 3 M NaOH to afford the *trans*-disubstituted cyclam **4** in quantitative yield. The key step, the propylene cross-bridging reaction, had to be optimized. To the best of our knowledge, only one propylene cross-bridged tetraazamacrocylic compound, PCB-cyclen, has been reported by Springborg in 1995, and recently, Wong et al. reported another derivative PCB-DO2A.[37,38] The Cu complex of PCB-DO2A shows higher in vitro stability than Cu-ECB-TE2A. However, its usefulness as a potential chelator for Cu ions is limited because of its harsh radiolabeling conditions and poor in vivo stability. A mixture of the disubstituted cyclam **4** and 1,3-propanediol di-*p*-tosylate was refluxed in dried toluene in the presence of K_2CO_3. By changing the solvent from acetonitrile, in a previous report, to toluene and increasing the reaction temperature, the reaction time was reduced dramatically from six to two days. The tosylate counteranion was removed by treatment with 20% NaOH, and the crude product was column purified to yield the salt-free form of compound **5** in 70% yield. The deprotection of the *tert*-butyl ester groups of the intermediate **5** was carried out by acidic hydrolysis using 6 M HCl to give the final product, PCB-TE2A, in the form of the hydrochloric salt. By designing an efficient synthetic route, all of the intermediates and products except for compound **5** were isolated in quantitative yield without tedious column purification. The total reaction time was less than 5 days and the overall yield from cyclam reached 62%, which is superior compared to the reaction time of 35 days and overall yield of 45% in the synthesis of ECB-TE2A. All of the spectroscopic data of PCB-TE2A exactly matched the expected values (see the Supporting Information).

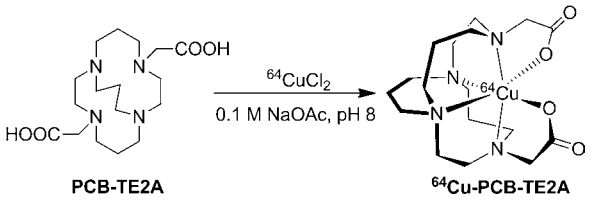
The reflux reaction of PCB-TE2A with $Cu(ClO_4)_2 \cdot 6H_2O$ in the presence of NaOH in methanol afforded the expected Cu-PCB-TE2A complexes in 81% yield. The Cu(II) complex of ECB-TE2A was also prepared according to the previously reported procedure[22] for use in direct comparison studies. Then, in order to evaluate the kinetic stability of the two Cu(II) complexes, which is known to be a more critical factor for the stability of Cu complexes under physiological conditions than their thermodynamic stability,[8,39] acidic decomplexation and cyclic voltammetry experiments were carried out.[25,40]

Acidic decomplexation studies, although conducted at conditions markedly different from physiological conditions, are known to provide a good indication of in vivo stability of metal complexes.[7,25] The complex, Cu-PCB-TE2A showed exceptionally high stability under highly acidic conditions. Even though the half-life of the Cu-TETA complex in 5 M HCl at 90 °C is only 4.7 min,[21] the Cu-PCB-TE2A sample did not show any absorption change in a UV spectrophotometer under the same conditions. Therefore, we carried out the same studies under more harsh conditions, viz., in 12 M HCl at 90 °C, and the

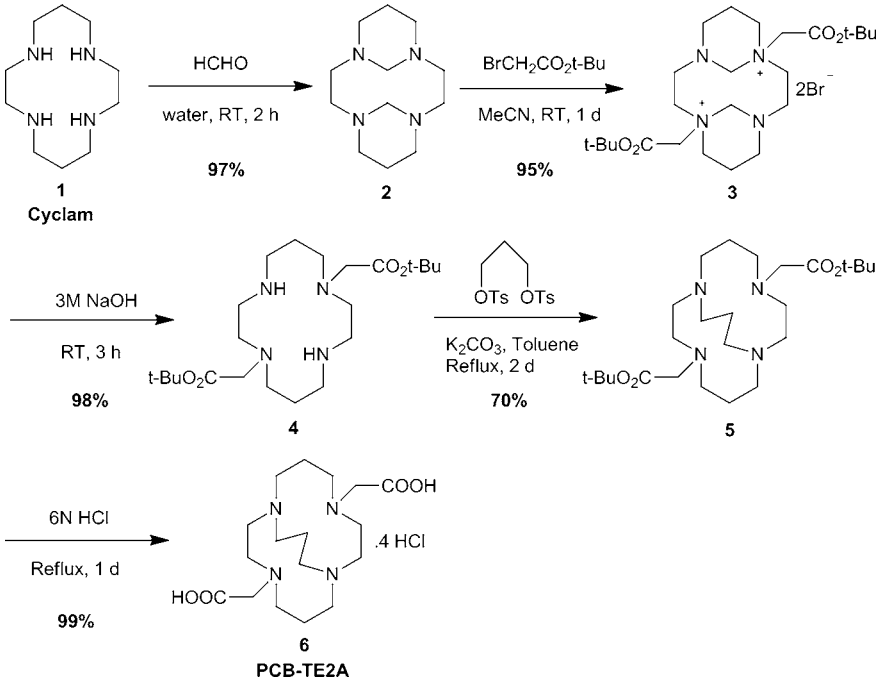
Scheme 1. Some Commonly Used Bifunctional Chelators



Scheme 3. Radiolabeling of PCB-TE2A with ^{64}Cu



Scheme 2. Synthesis of Propylene Cross-Bridged TE2A (PCB-TE2A)



dx.doi.org/10.1021/bc200539t | *Bioconjugate Chem.* 2012, 23, 330–335

degradation pattern was monitored using an HPLC system (Figure 1a,b). Surprisingly, Cu-PCB-TE2A did not show any sign of degradation for up to seven days (Figure 1a). In contrast, more than 75% of Cu-ECB-TE2A was decomposed after 3 h and less than 3% of intact Cu-ECB-TE2A complex remained at 8 h post-heating in 12 M HCl (Figure 1b). The faster decomposition rate of Cu-ECB-TE2A could also be simply monitored by the color change of its solution from light blue to greenish yellow after 1 h of incubation under the same conditions, while the light blue color of the Cu-PCB-TE2A solution remained exactly the same even after seven days (see the Supporting Information, Figure S2).

One important decomplexation mechanism of Cu(II) macrocyclic complexes is the reduction of Cu(II) ions to Cu(I) followed by the demetalation of the free copper ions from the chelators.[8,25,40] By measuring the reduction/oxidation behavior of the Cu(II) complexes using cyclic voltammetry, their resistance to in vivo demetalation by reduction could be anticipated. In our experiments, the two complexes, Cu-PCB-TE2A and Cu-ECB-TE2A, showed very different cyclic voltammograms in 0.2 M phosphate buffer at pH 7 (Figure 1c,d). Cu-PCB-TE2A yielded quasi-reversible reduction/oxidation peaks ($E_{1/2}$ = −0.80 V, ΔE = 80 mV) in addition to a negligible oxidation peak of free Cu(I) ions to Cu(II) at −0.06 V (vs Ag/AgCl), which implies that the Cu-PCB-TE2A holds Cu(I) ion in the coordination geometry and the demetalation is quite suppressed upon the reduction of Cu(II)-PCB-TE2A to Cu(I)-PCB-TE2A. In contrast, Cu-ECB-TE2A showed an irreversible reduction peak at −1.07 V without any oxidation peak responsible for reoxidation of intact Cu(I)-ECB-TE2A. Instead, the significant oxidation current was observed at −0.04 V, which is obviously due to the oxidation of free Cu(I) to Cu(II). These direct comparison studies clearly reveal that Cu-PCB-TE2A is much more resistant to the demetalation upon the reduction than Cu-ECB-TE2A, although Cu-PCB-TE2A is more subject to the reduction by a factor of 230 mV than Cu-ECB-TE2A. Previously, Cu-ECB-TE2A was also reported to show quasi-reversible behavior in 0.1 M sodium acetate solution adjusted to pH 7.[40] However, we observed significant pH rise in this buffer solution after the voltammetric measurement, and decided to use more reliable 0.2 M phosphate buffer which maintains pH 7 throughout the whole measurement.

The extremely high in vitro stability of Cu-PCB-TE2A encouraged us to further examine the ^{64}Cu-radiolabeling and in vivo stability of the complexes. Although the Cu-PCB-TE2A complexes were prepared using the strong base NaOH at reflux condition in good yield, the radiolabeling of PCB-TE2A with ^{64}Cu should be carried out under milder conditions because the targeting biomolecules conjugated to this BFC could be degraded under these harsh complexation conditions.[6] First, we tested the reported sophisticated but time-consuming labeling methods used for the ^{64}Cu radiolabeling of ECB-TE2A: 30 min preincubation of chelator using Cs_2CO_3 in EtOH at 75 °C followed by centrifugation, and then another 30 min incubation with ^{64}Cu at 75 °C.[20] Both the PCB-TE2A and ECB-TE2A chelators were radiolabeled with ^{64}Cu in quantitative yield (Figure 2). Then, we tried simple 0.1 M sodium acetate buffer adjusted to pH 8 as a labeling medium. Unexpectedly, PCB-TE2A was radiolabeled with ^{64}Cu in 89% yield at 70 °C within 10 min, and the labeling yield reached 100% after 1 h (Figure 3). However, when ECB-TE2A was used, the same labeling conditions yielded at least two radiolabeled peaks in addition to the free copper peak in radio-TLC (silica, MeOH/10% NH_4OAc = 1/1), but actually several byproduct peaks in the radio-HPLC analysis (Xbridge C18, 4.6 × 150 mm). The labeling yield of Cu-ECB-TE2A was measured to be only 45% after 1 h of incubation under the same conditions (Figure 3). In the following radiolabeling studies at lower temperatures, PCB-TE2A consistently showed better ^{64}Cu-labeling capacity in the sodium acetate buffer than ECB-TE2A. One hour incubation of PCB-TE2A with ^{64}Cu at 50 °C yielded ^{64}Cu-PCB-TE2A in 89% yield, and the labeling yield reached 58% after 90 min of incubation, even at 40 °C. In contrast, the labeling yield was only 25% at 40 °C after 90 min incubation of ECB-TE2A with ^{64}Cu (Figure 3).

As expected from its extremely high in vitro kinetic stability, ^{64}Cu-PCB-TE2A did not show any sign of decomplexation for up to 24 h in the serum stability test performed at 37 °C. The in vivo behavior and body clearance pattern of ^{64}Cu-PCB-TE2A was compared with those of ^{64}Cu-ECB-TE2A in the biodistribution studies in Sprague−Dawley rats (Figure 4). Both complexes showed rapid clearance from the body.

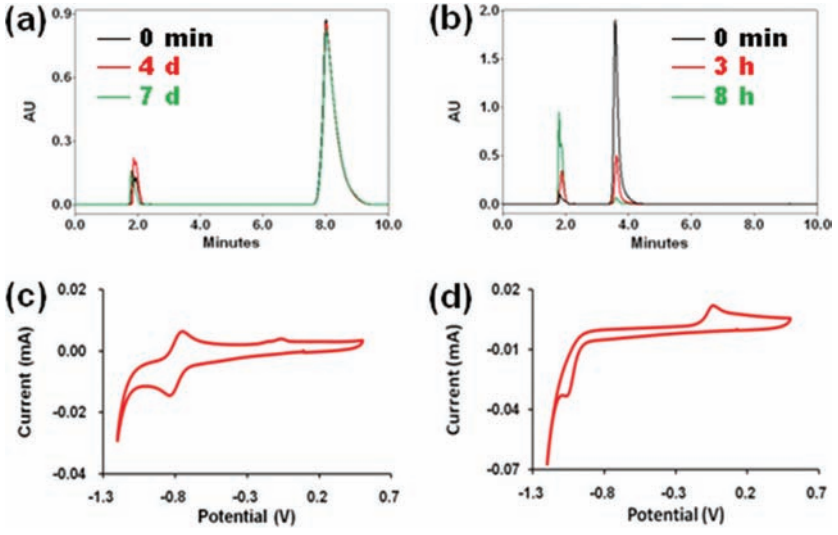


Figure 1. Time-dependent UV-HPLC chromatograms of Cu-PCB-TE2A (a) and Cu-ECB-TE2A (b) during acidic decomplexation in 12 M HCl at 90 °C. Cyclic voltammograms (scan rate 100 mV/s, 0.2 M phosphate buffer, pH 7) of Cu-PCB-TE2A (c) and Cu-ECB-TE2A (d).

dx.doi.org/10.1021/bc200539t | *Bioconjugate Chem.* 2012, 23, 330−335

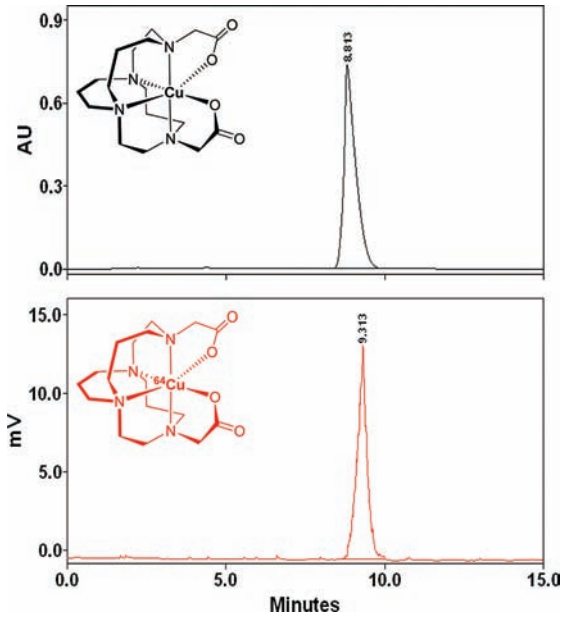


Figure 2. UV-HPLC chromatogram of nonradioactive Cu-PCB-TE2A complexes (top) and radio-HPLC chromatogram of ^{64}Cu-PCB-TE2A (bottom).

The percent injected dose per organ (%ID/organ) in all of the collected organs was lower than 1%, except in the liver, at 4 h postinjection. Whereas ^{64}Cu-PCB-TE2A showed more than double liver uptake than ^{64}Cu-ECB-TE2A (3.20 ± 0.28 vs 1.56 ± 0.32%ID/organ) at 30 min postinjection but cleared out gradually from the liver (1.22 ± 0.20%ID/organ at 4 h), a comparable uptake pattern was observed in the kidneys (1.86 ± 0.36 vs 1.57 ± 0.13%ID/organ at 30 min), which could be attributed to the greater lipophilicity of the propylene cross-bridge compared to the ethylene cross-bridge. The partition coefficient experiment (octanol/water) confirmed greater lipophilicity of ^{64}Cu-PCB-TE2A to ^{64}Cu-ECB-TE2A. The log *P* value of ^{64}Cu-PCB-TE2A was measured to be higher than that of ^{64}Cu-ECB-TE2A (−2.84 ± 0.03 vs −3.08 ± 0.04).

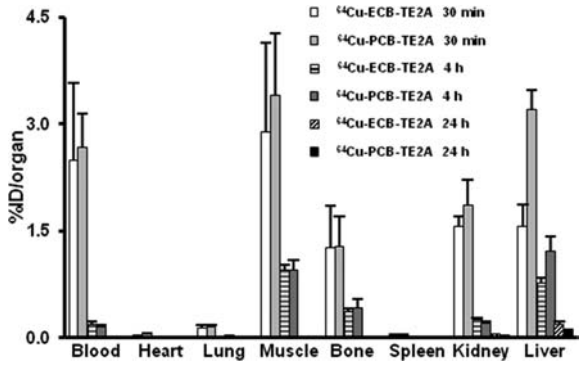


Figure 4. Biodistribution data of ^{64}Cu-radiolabeled PCB-TE2A and ECB-TE2A at 30 min, 4 h, and 24 h (n = 5).

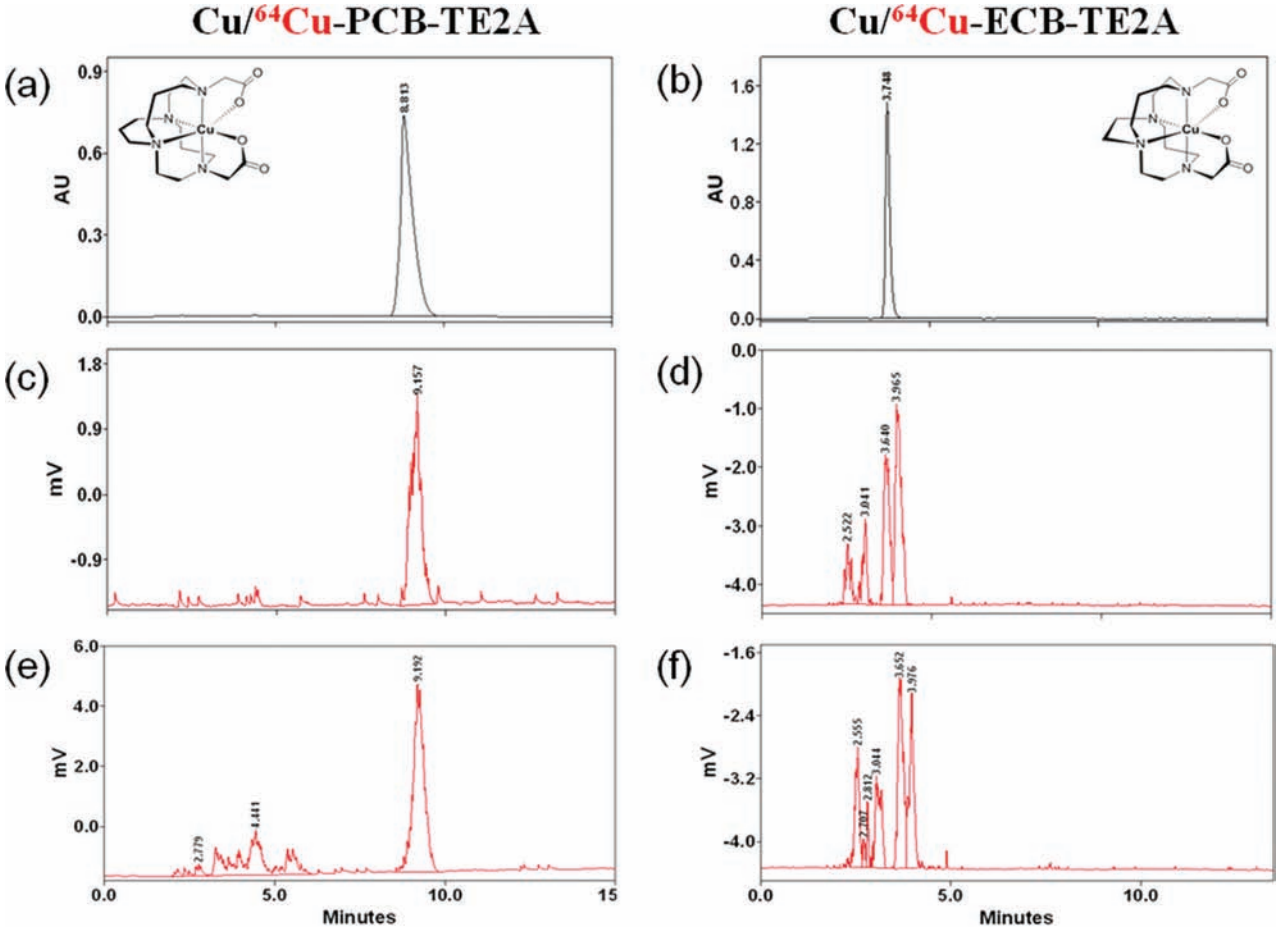


Figure 3. UV-HPLC chromatogram (280 nm) of nonradioactive Cu-PCB-TE2A (a) and Cu-ECB-TE2A complex (b); radio-HPLC chromatogram of ^{64}Cu-PCB-TE2A (c) and ^{64}Cu-ECB-TE2A (d) at 70 °C (1 h incubation) and radio-HPLC chromatogram of ^{64}Cu-PCB-TE2A (e) and ^{64}Cu-ECB-TE2A (f) at 40 °C (90 min incubation).

dx.doi.org/10.1021/bc200539t | *Bioconjugate Chem.* 2012, 23, 330−335

Except for liver, the Cu(II) complexes of PCB-TE2A and ECB-TE2A showed very similar %ID/organ values in all of the organs. At the 24 h time point, the counted activities in all of the organs, except for the liver and kidneys, were at the background level. The liver uptake of ^{64}Cu-PCB-TE2A was decreased dramatically to only 0.12 ± 0.01%ID/organ, which is even lower than the value of 0.18 ± 0.04%ID/organ for ^{64}Cu-ECB-TE2A. The kidneys also showed lower remaining activity in the case of ^{64}Cu-PCB-TE2A compared to ^{64}Cu-ECB-TE2A (0.038 ± 0.005 vs 0.055 ± 0.005%ID/organ). These biodistribution data imply that ^{64}Cu-ECB-TE2A cleared out at least as fast as ^{64}Cu-PCB-TE2A with minimum transchelation of free copper ions from the chelators to biomolecules.[18,41]

The PCB-TE2A can be used as a bifunctional chelator by its direct conjugation with peptide or antibody just as ECB-TE2A was conjugated with various biomolecules.[26,30,42] Even though the direct conjugation of PCB-TE2A with biomolecules using one acetate pendent arm would work well, more versatile conjugation strategy could be achieved by straightforward pendant arm modification.[43]

In conclusion, we describe a straightforward means of synthesizing propylene cross-bridged TE2A. The Cu(II) complex of PCB-TE2A exhibited extremely robust stability in the acidic decomplexation studies and also showed high resistance to demetalation in the cyclic voltammograms. In contrast to the ethylene cross-bridged TE2A, PCB-TE2A was radiolabeled with ^{64}Cu in simple sodium acetate buffer in good yield even at low temperatures. Our biodistribution data strongly implies that the decomplexation of ^{64}Cu-PCB-TE2A is minimized under physiological conditions and that the intact ^{64}Cu-PCB-TE2A is cleared from the body at least as fast as ^{64}Cu-ECB-TE2A. The above results demonstrate that PCB-TE2A has greater potential as a BFC than ECB-TE2A. We hope that many radioactive copper-based diagnostic and therapeutic bioconjugates would be prepared employing PCB-TE2A as a BFC and utilized in biomedical studies as well as clinics. Ultrahigh stability nature of Cu-PCB-TE2A would encourage the synthesis of various metal complexes utilizing the related chelators, which could find further application in catalyst and material sciences.

■ ASSOCIATED CONTENT

Ⓢ Supporting Information

Syntheses and spectroscopic data of compounds **4**, **5**, and **6**, acid decomplexation studies, electrochemical studies, radiolabeling studies of PCB-TE2A and ECB-TE2A, table of biodistribution data. This material is available free of charge via the Internet at http://pubs.acs.org.

■ AUTHOR INFORMATION

Corresponding Author

*Fax: +82-53-426-4944. Tel: +82-53-420-4947. E-mail: yooj@knu.ac.kr.

Notes

The authors declare no competing financial interest.

■ ACKNOWLEDGMENTS

This work was supported by the Nuclear R&D (grant code: 20090081817, 20110030161) and BAERI (grant code: 20090078235) Programs of NRF, funded by MEST, and the Brain Korea 21 Project in 2011. The CV studies were supported partially by MEST & DGIST (11-BD-0405) for Prof. Hochun Lee. The Korea Basic Science Institute (Daegu) is acknowledged for the NMR and HR-Mass measurements.

■ REFERENCES

(1) Liu, S. (2008) Bifunctional coupling agents for radiolabeling of biomolecules and target-specific delivery of metallic radionuclides. *Adv. Drug Delivery Rev. 60*, 1347−1370.

(2) Wadas, T. J., Wong, E. H., Weisman, G. R., and Anderson, C. J. (2010) Coordinating Radiometals of Copper, Gallium, Indium, Yttrium, and Zirconium for PET and SPECT Imaging of Disease. *Chem. Rev. 110*, 2858−2902.

(3) Nayak, T. K., and Brechbiel, M. W. (2009) Radioimmunoimaging with Longer-Lived Positron-Emitting Radionuclides: Potentials and Challenges. *Bioconjugate Chem. 20*, 825−841.

(4) Holland, J. P., Williamson, M. J., and Lewis, J. S. (2010) Unconventional nuclides for radiopharmaceuticals. *Mol. Imaging 9*, 1−20.

(5) Williams, H. A., Robinson, S., Julyan, P., Zweit, J., and Hastings, D. (2005) A comparison of PET imaging characteristics of various copper radioisotopes. *Eur. J. Nucl. Med. Mol. Imaging 32*, 1473−1480.

(6) Smith, S. V. (2007) Molecular imaging with copper-64 in the drug discovery and development arena. *Expert Opin. Drug Discovery 2*, 659−672.

(7) Wadas, T. J., Wong, E. H., Weisman, G. R., and Anderson, C. J. (2007) Copper chelation chemistry and its role in copper radiopharmaceuticals. *Curr. Pharm. Des. 13*, 3−16.

(8) Shokeen, M., and Anderson, C. J. (2009) Molecular Imaging of Cancer with Copper-64 Radiopharmaceuticals and Positron Emission Tomography (PET). *Acc. Chem. Res. 42*, 832−841.

(9) Anderson, C. J., and Ferdani, R. (2009) Copper-64 Radiopharmaceuticals for PET Imaging of Cancer: Advances in Preclinical and Clinical Research. *Cancer Biother. Radiopharm. 24*, 379−393.

(10) Backer, M. V., Levashova, Z., Patel, V., Jehning, B. T., Claffey, K., Blankenberg, F. G., and Backer, J. M. (2007) Molecular imaging of VEGF receptors in angiogenic vasculature with single-chain VEGF-based probes. *Nat. Med. 13*, 504−509.

(11) Xiong, C., Huang, M., Zhang, R., Song, S., Lu, W., Flores, L. 2nd, Gelovani, J., and Li, C. (2011) In Vivo Small-Animal PET/CT of EphB4 Receptors Using ^{64}Cu-Labeled Peptide. *J. Nucl. Med. 52*, 241−248.

(12) Olafsen, T., Betting, D., Kenanova, V. E., Salazar, F. B., Clarke, P., Said, J., Raubistchek, A. A., Timmerman, J. M., and Wu, A. M. (2009) Recombinant anti-CD20 antibody fragments for small-animal PET imaging of B-cell lymphomas. *J. Nucl. Med. 50*, 1500−1508.

(13) Vavere, A. L., Biddlecombe, G. B., Spees, W. M., Garbow, J. R., Wijesinghe, D., Andreev, O. A., Engelman, D. M., Reshetnyak, Y. K., and Lewis, J. S. (2009) A Novel Technology for the Imaging of Acidic Prostate Tumors by Positron Emission Tomography. *Cancer Res. 69*, 4510−4516.

(14) Anderson, C. J., Jones, L. A., Bass, L. A., Sherman, E. L. C., McCarthy, D. W., Cutler, P. D., Lanahan, M. V., Cristel, M. E., Lewis, J. S., and Schwarz, S. W. (1998) Radiotherapy, toxicity and dosimetry of copper-64-TETA-octreotide in tumor-bearing rats. *J. Nucl. Med. 39*, 1944−1951.

(15) Lewis, M. R., Boswell, C. A., Laforest, R., Buettner, T. L., Ye, D., Connett, J. M., and Anderson, C. J. (2001) Conjugation of monoclonal antibodies with TETA using activated esters: Biological comparison of ^{64}Cu-TETA-1A3 with ^{64}Cu-BAT-2IT-1A3. *Cancer Biother. Radiopharm. 16*, 483−494.

(16) Anderson, C. J., Dehdashti, F., Cutler, P. D., Schwarz, S. W., Laforest, R., Bass, L. A., Lewis, J. S., and McCarthy, D. W. (2001) ^{64}Cu-TETA-octreotide as a PET imaging agent for patients with neuroendocrine tumors. *J. Nucl. Med. 42*, 213−221.

(17) Liu, D., Overbey, D., Watkinson, L. D., Smith, C. J., Daibes-Figueroa, S., Hoffman, T. J., Forte, L. R., Volkert, W. A., and Giblin, M. F. (2010) Comparative Evaluation of Three ^{64}Cu-Labeled E. coli Heat-Stable Enterotoxin Analogues for PET Imaging of Colorectal Cancer. *Bioconjugate Chem. 21*, 1171−1176.

(18) Jones-Wilson, T. M., Deal, K. A., Anderson, C. J., McCarthy, D. W., Kovacs, Z., Motekaitis, R. J., Sherry, A. D., Martell, A. E., and Welch, M. J. (1998) The in vivo behavior of copper-64-labeled azamacrocyclic complexes. *Nucl. Med. Biol. 25*, 523−530.
(19) Bass, L. A., Wang, M., Welch, M. J., and Anderson, C. J. (2000) In Vivo Transchelation of Copper-64 from TETA-Octreotide to Superoxide Dismutase in Rat Liver. *Bioconjugate Chem. 11*, 527−532.
(20) Boswell, C. A., Sun, X., Niu, W., Weisman, G. R., Wong, E. H., Rheingold, A. L., and Anderson, C. J. (2004) Comparative in Vivo Stability of Copper-64-Labeled Cross-Bridged and Conventional Tetraazamacrocyclic Complexes. *J. Med. Chem. 47*, 1465−1474.
(21) Pandya, D. N., Kim, J. Y., Park, J. C., Lee, H., Phapale, P. B., Kwak, W., Choi, T. H., Cheon, G. J., Yoon, Y.-R., and Yoo, J. (2010) Revival of TE2A; a better chelate for Cu(II) ions than TETA? *Chem. Commun. 46*, 3517−3519.
(22) Wong, E. H., Weisman, G. R., Hill, D. C., Reed, D. P., Rogers, M. E., Condon, J. S., Fagan, M. A., Calabrese, J. C., Lam, K.-C., Guzei, I. A., and Rheingold, A. L. (2000) Synthesis and Characterization of Cross-Bridged Cyclams and Pendant-Armed Derivatives and Structural Studies of Their Copper(II) Complexes. *J. Am. Chem. Soc. 122*, 10561−10572.
(23) Sun, X., Wuest, M., Weisman, G. R., Wong, E. H., Reed, D. P., Boswell, C. A., Motekaitis, R., Martell, A. E., Welch, M. J., and Anderson, C. J. (2002) Radiolabeling and in vivo behavior of copper-64-labeled cross-bridged cyclam ligands. *J. Med. Chem. 45*, 469−477.
(24) Lewis, E. A., Boyle, R. W., and Archibald, S. J. (2004) Ultrastable complexes for in vivo use: a bifunctional chelator incorporating a cross-bridged macrocycle. *Chem. Commun.*, 2212−2213.
(25) Heroux, K. J., Woodin, K. S., Tranchemontagne, D. J., Widger, P. C. B., Southwick, E., Wong, E. H., Weisman, G. R., Tomellini, S. A., Wadas, T. J., Anderson, C. J., Kassel, S., Golen, J. A., and Rheingold, A. L. (2007) The long and short of it: the influence of N-carboxyethyl versus N-carboxymethyl pendant arms on in vitro and in vivo behavior of copper complexes of cross-bridged tetraamine macrocycles. *Dalton Trans.*, 2150−2162.
(26) Sprague, J. E., Peng, Y., Fiamengo, A. L., Woodin, K. S., Southwick, E. A., Weisman, G. R., Wong, E. H., Golen, J. A., Rheingold, A. L., and Anderson, C. J. (2007) Synthesis, Characterization and In Vivo Studies of Cu(II)-64-Labeled Cross-Bridged Tetraazamacrocycle-amide Complexes as Models of Peptide Conjugate Imaging Agents. *J. Med. Chem. 50*, 2527−2535.
(27) Boswell, C. A., Regino, C. A. S., Baidoo, K. E., Wong, K. J., Bumb, A., Xu, H., Milenic, D. E., Kelley, J. A., Lai, C. C., and Brechbiel, M. W. (2008) Synthesis of a Cross-Bridged Cyclam Derivative for Peptide Conjugation and ^{64}Cu Radiolabeling. *Bioconjugate Chem. 19*, 1476−1484.
(28) Liu, W., Hao, G., Long, M. A., Anthony, T., Hsieh, J.-T., and Sun, X. (2009) Imparting Multivalency to a Bifunctional Chelator: A Scaffold Design for Targeted PET Imaging Probes. *Angew. Chem., Int. Ed. 48*, 7346−7349.
(29) Stigers, D. J., Ferdani, R., Weisman, G. R., Wong Edward, H., Anderson, C. J., Golen, J. A., Moore, C., and Rheingold, A. L. (2010) A new phosphonate pendant-armed cross-bridged tetraamine chelator accelerates copper(II) binding for radiopharmaceutical applications. *Dalton Trans. 39*, 1699−1701.
(30) Sprague, J. E., Peng, Y., Sun, X., Weisman, G. R., Wong, E. H., Achilefu, S., and Anderson, C. J. (2004) Preparation and biological evaluation of copper-64-labeled Tyr3-octreotate using a cross-bridged macrocyclic chelator. *Clin. Cancer Res. 10*, 8674−8682.
(31) Wei, L., Ye, Y., Wadas, T. J., Lewis, J. S., Welch, M. J., Achilefu, S., and Anderson, C. J. (2009) ^{64}Cu-Labeled CB-TE2A and diamsar-conjugated RGD peptide analogs for targeting angiogenesis: comparison of their biological activity. *Nucl. Med. Biol. 36*, 277−285.
(32) Hausner, S. H., Kukis, D. L., Gagnon, M. K. J., Stanecki, C. E., Ferdani, R., Marshall, J. F., Anderson, C. J., and Sutcliffe, J. L. (2009) Evaluation of [^{64}Cu]Cu-DOTA and [^{64}Cu]Cu-CB-TE2A chelates for targeted positron emission tomography with an alpha vbeta 6-specific peptide. *Mol. Imaging 8*, 111−121.
(33) Hoffman, T. J., and Smith, C. J. (2009) True radiotracers: Cu-64 targeting vectors based upon bombesin peptide. *Nucl. Med. Biol. 36*, 579−585.
(34) Garrison, J. C., Rold, T. L., Sieckman, G. L., Figueroa, S. D., Volkert, W. A., Jurisson, S. S., and Hoffman, T. J. (2007) In vivo evaluation and small-animal PET/CT of a prostate cancer mouse model using ^{64}Cu bombesin analogs: side-by-side comparison of the CB-TE2A and DOTA chelation systems. *J. Nucl. Med. 48*, 1327−1337.
(35) Wadas, T. J., and Anderson, C. J. (2006) Radiolabeling of TETA- and CB-TE2A-conjugated peptides with copper-64. *Nat. Protoc. 1*, 3062−3068.
(36) Yoo, J., Reichert, D. E., and Welch, M. J. (2003) Regioselective N-substitution of cyclen with two different alkyl groups: synthesis of all possible isomers. *Chem. Commun.*, 766−767.
(37) Springborg, J., Kofod, P., Olsen, C. E., Toftlund, H., and Soetofte, I. (1995) Synthesis and crystal structure of a small bicyclic tetraaza proton sponge, 1,4,7,10-tetraazabicyclo[5.5.3]pentadecane dibromide perchlorate. *Acta Chem. Scand. 49*, 547−554.
(38) Odendaal, A. Y., Fiamengo, A. L., Ferdani, R., Wadas, T. J., Hill, D. C., Peng, Y., Heroux, K. J., Golen, J. A., Rheingold, A. L., Anderson, C. J., Weisman, G. R., and Wong, E. H. (2011) Isomeric Trimethylene and Ethylene Pendant-armed Cross-bridged Tetraazamacrocycles and in Vitro/in Vivo Comparisions of their Copper(II) Complexes. *Inorg. Chem. 50*, 3078−3086.
(39) Anderson, C. J., Wadas, T. J., Wong, E. H., and Weisman, G. R. (2008) Cross-bridged macrocyclic chelators for stable complexation of copper radionuclides for PET imaging. *Q. J. Nucl. Med. Mol. Imaging 52*, 185−192.
(40) Woodin, K. S., Heroux, K. J., Boswell, C. A., Wong, E. H., Weisman, G. R., Niu, W., Tomellini, S. A., Anderson, C. J., Zakharov, L. N., and Rheingold, A. L. (2005) Kinetic inertness and electrochemical behavior of copper(II) tetraazamacrocyclic complexes: Possible implications for in vivo stability. *Eur. J. Inorg. Chem.*, 4829−4833.
(41) Yoo, J., Reichert David, E., and Welch Michael, J. (2004) Comparative in vivo behavior studies of cyclen-based copper-64 complexes: regioselective synthesis, X-ray structure, radiochemistry, log P, and biodistribution. *J. Med. Chem. 47*, 6625−6637.
(42) Wadas, T. J., Eiblmaier, M., Zheleznyak, A., Sherman, C. D., Ferdani, R., Liang, K., Achilefu, S., and Anderson, C. J. (2008) Preparation and biological evaluation of ^{64}Cu-CB-TE2A-sst2-ANT, a somatostatin antagonist for PET imaging of somatostatin receptor-positive tumors. *J. Nucl. Med. 49*, 1819−1827.
(43) Silversides, J. D., Smith, R., and Archibald, S. J. (2011) Challenges in chelating positron emitting copper isotopes: tailored synthesis of unsymmetric chelators to form ultra stable complexes. *Dalton Trans. 40*, 6289−6297.

Bioconjugate Chemistry

Communication

pubs.acs.org/bc

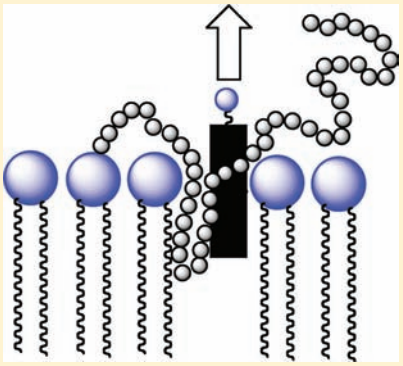
Stimulated Release of Cholesterol from Liposomal Membranes by a PEGylated Phospholipid

Vaclav Janout, Trevor A. Daly, Lauren L. Cline, Leah J. Kulp, and Steven L. Regen*

[†]Department of Chemistry, Lehigh University, Bethlehem, Pennsylvania 18015, United States

Supporting Information

ABSTRACT: PEGylated phospholipids are commonly used to increase the blood-circulation time of liposomes by providing a steric barrier around them. This paper documents a fundamentally new property of these lipids—an ability to stimulate the release of cholesterol from phospholipid membranes. Evidence for such stimulation has been obtained by measuring the transport of dehydroergosterol (DHE), a fluorescent simulant of cholesterol, from donor liposomes made from 1-palmitoyl-2-oleoyl-*sn*-glycero-3-phosphocholine (POPC), 1,2-distearoyl-*sn*-glycero-3-phosphoethanolamine-*N*-[methoxy(polyethylene glycol)-2000 (DSPE-PEG$_{2000}$), and DHE to acceptor liposomes made from POPC, 1-palmitoyl-2-oleoyl-*sn*-glycero-3-phosphoglycerol (POPG), and cholesterol. The potential of PEGylated lipids to serve as novel cholesterol-lowering agents is briefly discussed.



Phospholipids that contain poly(ethylene glycol) in their headgroup are known to increase the blood-circulation times of liposomes.[1−3] One such phospholipid, DSPE-PEG$_{2000}$, is a key component in a liposomal formulation (i.e., Doxil) that is currently used to treat advanced ovarian cancer, myeloma, and AIDS-related Kaposi sarcoma (Figure 1). The main role that these "PEGylated" lipids are thought to play is to create a steric barrier that helps liposomes evade the host defense system.[1,4] In this paper, we demonstrate an entirely new property of PEGylated phospholipids—an ability to stimulate the release of cholesterol from phospholipid membranes.

Recent molecular dynamics simulations and Langmuir monolayer measurements have led to the hypothesis that PEGylated phospholipids may insert their polyether moiety into fluid-phase phospholipid bilayers.[5] If this were to occur, hydrophobic interactions between neighboring lipids are expected to be reduced and the membrane then converted into a more loosely packed state. As a consequence, if cholesterol were also present in the membrane, its ability to escape from the bilayer should be enhanced.[6−9]

Before carrying out transport experiments to test for a stimulated release of cholesterol by a PEGylated lipid, we sought to determine whether polyether penetration into phospholipid membranes could be detected using the phase-sensitive probe, Laurdan. As discussed elsewhere, generalized polarization (GP) values for Laurdan reflect the polarity and tightness within phospholipid membranes. Specifically, lower GP values reflect looser membranes having a more polar microenvironment.[10] Here, GP = $(I_{440} - I_{490})/(I_{440} + I_{490})$, where I_{440} and I_{490} represent the emission intensities at these indicated wavelengths (λ_{ex} = 350 nm). With this aim in mind, we investigated model membranes made from 1,2-dipalmitoyl-*sn*-glycero-3-phosphocholine (DPPC) above and below its gel to liquid-crystalline phase transition temperature (T_m = 41 °C) in the presence of 4 mol % DPPE-PEG$_{2000}$ [i.e., 1,2-dipalmitoyl-sn-glycero-3-phosphoethanolamine-N-[methoxy(polyethylene glycol)-2000]. For comparison, similar measurements were made using analogous membranes in which DPPE-PEG$_{2000}$ was replaced with 1,2-dipalmitoyl-*sn*-glycero-3-phosphoglycerol (DPPG), having the same T_m value.

As shown in Figure 2, a modest lowering of the GP values for Laurdan is evident for those liposomes that contain DPPE-PEG$_{2000}$ relative to ones bearing DPPG, but only above 41 °C where the membrane is in the fluid phase. To confirm this lowering, three completely independent measurements were made using three different liposome preparations having the same compositions, in the presence and in the absence of DPPE-PEG$_{2000}$ in the fluid phase (52.7 °C). Thus, when DPPE-PEG$_{2000}$ was present, the GP value was −0.267 ± 0.003. When DPPE-PEG$_{2000}$ was replaced with DPPG, the GP value was −0.222 ± 0.004. When the same liposomes were measured in the gel phase (28.3 °C), the presence of DPPE-PEG$_{2000}$ led to a GP value of 0.485 ± 0.003, which was slightly higher than the DPPG-containing liposomes (i.e., 0.472 ± 0.002) at that temperature. These results are consistent with the hypothesis that gel-phase membranes exclude PEG from their hydrocarbon interior and that penetration can occur in the liquid-crystalline phase along with some loosening of the assembly.[5] It should be noted that poly(ethylene glycol)s are known to become more hydrophobic with increasing temperatures.[11] Such changes may contribute to the polyether's ability to penetrate lipid bilayers.

Received: December 17, 2011
Revised: February 14, 2012
Published: February 29, 2012

ACS Publications © 2012 American Chemical Society

dx.doi.org/10.1021/bc200669e | *Bioconjugate Chem.* 2012, 23, 336−339

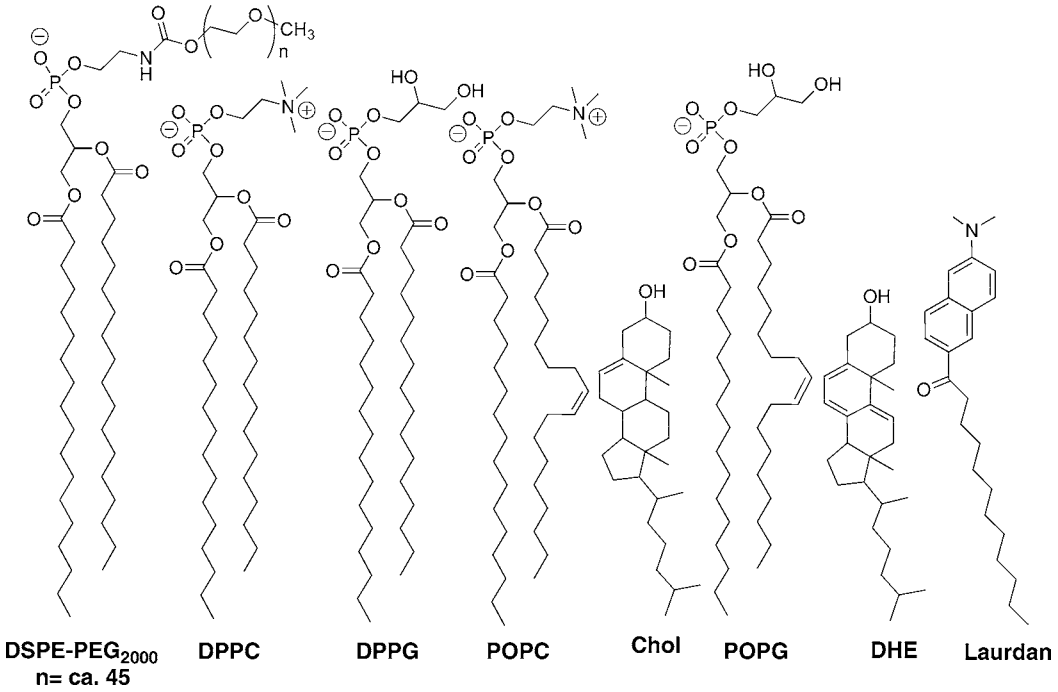


Figure 1. Molecular structures of the lipids used in this work.

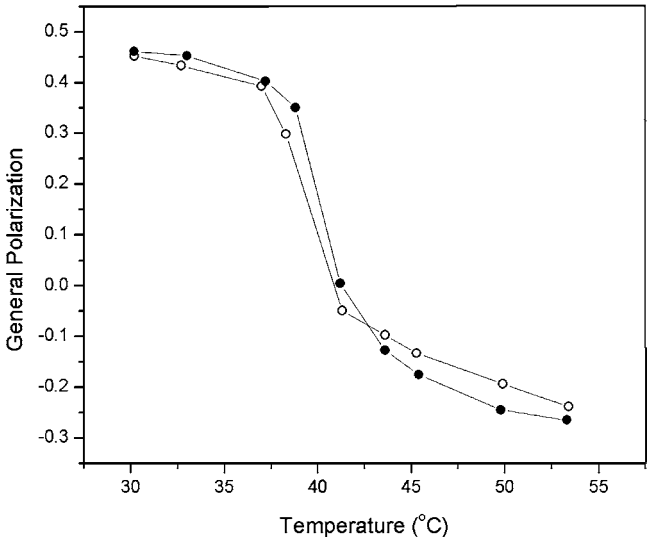


Figure 2. Plot of general polarization versus temperature for liposomes made from (○) DPPC/DPPG/Laurdan, 95.5/4/0.5 (mol/mol/mol), and (●) DPPC/DPPE-PEG$_{2000}$/Laurdan, 95.5/4/0.5 (mol/mol/mol).

For sterol transport experiments, we investigated the action of the popular PEGylated lipid, DSPE-PEG$_{2000}$, on the release of dehydroergosterol (DHE) from donor liposomes made from POPC. Since DHE is very similar to cholesterol, in terms of its molecular structure and its transport properties, and because it is fluorescent, DHE has become widely used as a simulant for mechanistic studies.[12−18]

In an initial series of measurements, donor liposomes (prepared by extrusion through 200 nm nuclepore membranes) were made from POPC/DSPE-PEG$_{2000}$/DHE (76/4/20, mol/mol/mol). Acceptor liposomes were then assembled in multilamellar form (i.e., MLVs) from POPC/DSPE-PEG$_{2000}$/Chol (76/4/20, mol/mol/mol). Incubation of donor liposomes with a 10-fold excess of acceptor liposomes at 37 °C, followed by pelleting to remove the latter (14 000 × *g*, 8−20 min), allows one to monitor intermembrane transport of DHE by following the decrease in the fluorescence intensity of the

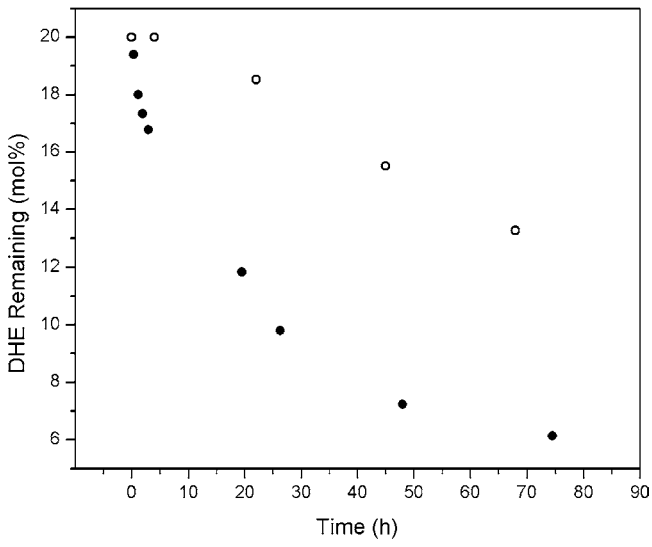


Figure 3. Plot of percentage of DHE remaining as a function of time in donor liposomes made from (●) POPC/DSPE-PEG$_{2000}$/DHE (76/4/20, mol/mol/mol), upon incubation with with acceptor liposomes made from POPC/DSPE-PEG$_{2000}$/Chol (76/4/20, mol/mol/mol), and donor liposomes made from (○) POPC/POPG/DHE (76/4/20, mol/mol/mol) that were incubated with acceptor liposomes made from POPC/POPG/Chol (76/4/20, mol/mol/mol) at 37 °C.

residual dispersion (Figure 3). That the donor liposomes remain fully dispersed (>98%) and the MLVs are fully removed (>99%) under such conditions was confirmed by fluorescence measurements and by phosphorus analysis, respectively. Thus, phosphorus analysis, made after an extended transport of DHE (ca. 70%) in the presence of 4 mol % DSPE-PEG$_{2000}$,

dx.doi.org/10.1021/bc200669e | *Bioconjugate Chem.* 2012, 23, 336−339

confirmed that the donor liposomes remained fully dispersed after centrifugation (Supporting Information). Analogous transport experiments were then carried out in which DSPE-PEG_{2000} was replaced by POPG. Such replacement produces the same net charge on the membrane surface without increasing its compactness. In this case, a significantly slower rate of transport was observed.

To determine the sensitivity of this stimulated release with respect to the concentration of DSPE-PEG_{2000} that is present in the membrane, we measured initial rates of release using donor liposomes bearing 0.0, 0.4, 2.0, and 4.0 mol % of the PEGylated lipid. Thus, transport experiments were carried out using donor liposomes made from POPC/POPG/DSPE-PEG_{2000}/DHE (76/4/0/20), (76/3.6/0.4/20), (76/2/2/20), and (76/0/4/20), respectively. Because the kinetics of sterol release is complex and the extent of transport is variable, as previously reported, only the initial rates of release have been used for this comparison.[19] To ensure that differences in transport rates were due to differences in the concentration of the PEGylated lipid present and not due to heterogeneity among the MLVs, a common batch of acceptor liposomes was used for these transport experiments, which was made from POPC/POPG/Chol (76/4/20). The initial rates of release from liposomes containing 0, 0.4, 2.0, and 4.0 mol % of DSPE-PEG_{2000} were <0.1, 0.1, 0.67, and 1.72 mol %/h, respectively (Figure 4).

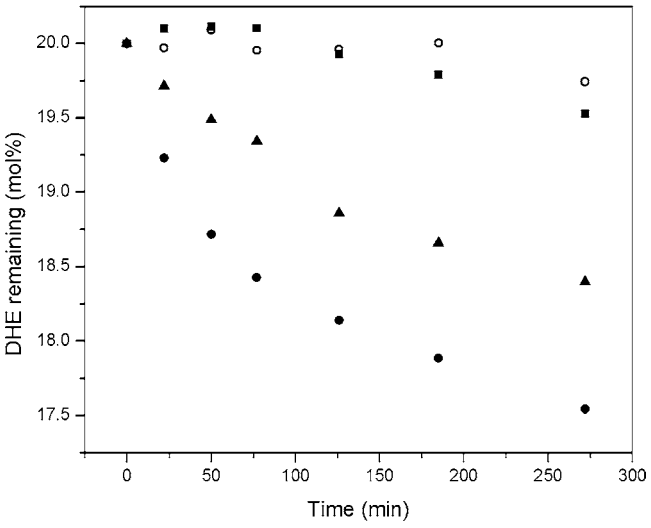


Figure 4. Plot of percentage of DHE remaining in the donor liposomes as a function of time using donor liposomes made from POPC/POPG/DSPE-PEG_{2000}/DHE having the following mole percentages: (●) 76/0/4/20, (▲) 76/2/2/20, (■) 76/3.6/0.4/20, and (○) 76/4/0/20, and acceptor liposomes made from POPC/POPG/Chol (76/4/20). Each data point represents the average of two independent experiments where the deviation lies within the symbols given.

These results clearly show that this PEGylated phospholipid does, indeed, stimulate the release of DHE from donor liposomes.

The precise mechanism that underlies this stimulated release remains to be established. Although we presently favor a model in which there is partial penetration of the polyether moiety into the lipid bilayer, and a loosening of the membrane, we cannot rule out other possible mechanisms. For example, one can also envision that a poly(ethylene glycol) molecule that becomes anchored to the surface of a membrane may produce a "partially hydrophobic escape route" for the release of sterol into the aqueous phase.

The ability of PEGylated phospholipids to stimulate the release of cholesterol from phospholipid membranes reported herein suggests that compounds of this type could lead to new classes of cholesterol-lowering agents. In particular, one can imagine that PEGylated lipids that become bound to the enterocyte/intestinal lumen interface could stimulate the release of cholesterol directly into the intestinal lumen. Such stimulation, in combination with fecal elimination, could then result in a net lowering of cholesterol levels in peripheral tissues.

Efforts aimed at exploiting the stimulated release of cholesterol by PEGylated lipids and at creating suitable means of delivery to enterocytes, with a view toward establishing new classes of cholesterol-lowering agents, are continuing in our laboratories.

■ ASSOCIATED CONTENT

Supporting Information

Experimental procedures. This material is available free of charge via the Internet at http://pubs.acs.org.

■ AUTHOR INFORMATION

Corresponding Author

*E-mail: slr0@lehigh.edu.

Notes

The authors declare no competing financial interest.

■ ACKNOWLEDGMENTS

We are grateful to Lehigh University for financial support of this research.

■ REFERENCES

(1) Stanton, M. G., and Colletti, S. L. (2010) Medicinal chemistry of siRNA delivery. *J. Med. Chem. 53*, 7887−7901.

(2) Lasic, D. D., and Needham, D. (1995) Stealth liposomes: a prototypical biomaterial. *Chem. Rev. 95*, 2601−2628.

(3) Gabizon, A. A., Shmeeda, H., and Zalipsky, S. (2006) Pros and cons of the liposome platform in cancer drug targeting. *J. Liposome Res. 16*, 175−183.

(4) Hristova, K., Kenworthy, A., and McIntosh, T. J. (1995) Effect of bilayer composition on the phase behavior of liposomal suspensions containing poly(ethylene glycol)-lipids. *Macromolecules 28*, 7693−7699.

(5) Stepniewski, M., Pasenkiewicz-Gierula, M., Rog, T., Danne, R., Orlowski, A., Karttunen, M., Urtti, A., Yliperttula, M., Vuorimaa, E., and Bunker, A. (2011) Study of PEGylated lipid layers as a model for PEGylated liposome surfaces: molecular dynamics simulation and Langmuir monolayer studies. *Langmuir 27*, 7788−7798.

(6) McLean, L. R., and Phillips, M. C. (1981) Mechanism of cholesterol and phosphatidylcholine exchange or transfer between unilamellar vesicles. *Biochemistry 20*, 2893−2900.

(7) McLean, L. R., and Phillips, M. C. (1984) Cholesterol transfer from small and large unilamellar vesicles. *Biochim. Biophys. Acta 776*, 21−26.

(8) Steck, T. L., and Lange, Y. (2010) Cell cholesterol homeostasis: mediation by active cholesterol. *Trends Cell Biol. 20*, 680−687.

(9) Lange, Y., and Steck, T. L. (2008) Cholesterol homeostasis and the escape tendency (activity) of plasma membrane cholesterol. *Prog. Lipid Res. 47*, 319−332.

(10) Parassi, T., DiStefano, M., Loiero, M., Ravagnan, G., and Gratton, E. (1994) Influence of cholesterol on phospholipid bilayers phase domains as detected by Laurdan fluorescence. *Biophys. J. 66*, 120−132.

(11) Israelachvili, J. (1997) The different faces of poly(ethylene glycol). *Proc. Natl. Acad. Sci. U.S.A. 94*, 8378−8379.
(12) Nemecz, G., Fontaine, R. N., and Schroeder, F. (1988) A fluorescence and radiolabel study of sterol exchange between membranes. *Biochim. Biophys. Acta 943*, 511−521.
(13) Schroeder, F., Barenholz, Y., Gratton, E., and Thompson, T. E. (1987) A fluorescence study of dehydroergosterol in phosphatidylcholine bilayer vesicles. *Biochemistry 26*, 2441−2448.
(14) Mukheerjee, S., Zha, X., Tabas, I., and Maxfield, F. R. (1998) Cholesterol distribution in living cells: fluorescence imaging using dehydroergosterol as a fluorescent cholesterol analogue. *Biophys. J. 75*, 1915−1925.
(15) John, K., and Kubelt, J. (2002) Rapid transbilayer movement of the fluorescent sterol dehydroergosterol in lipid membranes. *Biophys. J. 83*, 1525−1534.
(16) Hao, M, Lin, S. X., Karylowski, O. J., Wustner, D., McGraw, T. E., and Maxfield, F R. (2002) Vesicular and non-vesicular sterol transport in living cells. The endocytic recycling compartment is a major sterol storage organelle. *J. Biol. Chem. 277*, 609−617.
(17) Estronca, L. M. B.B., Moreno, M. J., and Vaz, W. L.C. (2007) Kinetics and thermodynamics of the association of dehydroergosterol with lipid bilayer membranes. *Biophys. J. 93*, 4244−4253.
(18) Garvik, O., Benedikston, P., Simonsen, A. C., Ipsen, J. H., and Wustner, D. (2009) The fluorescent cholesterol analog dehydroergosterol induces liquid-ordered domains in model membranes. *Chem. Phys. Lipids 159*, 114−118.
(19) Mady, M. M. (2006) Cholesterol exchange between phospholipid vesicles. *Romanian J. Biophys. 16*, 21−29.

Bioconjugate Chemistry

Article

pubs.acs.org/bc

Gold Nanoparticles Capped by a GC-Containing Peptide Functionalized with an RGD Motif for Integrin Targeting

Giorgio Scarì,[‡] Francesca Porta,*[,†] Umberto Fascio,[▽] Svetlana Avvakumova,[†] Vladimiro Dal Santo,[#] Mariarosaria De Simone,[⊥] Michele Saviano,[∥] Marilisa Leone,[§] Annarita Del Gatto,[§] Carlo Pedone,[⊥] and Laura Zaccaro[§]

[†]Dipartimento di Chimica Inorganica Metallorganica Analitica "Lamberto Malatesta", University of Milan and CNR−Istituto di Scienze e Tecnologie Molecolari, Via Venezian 21, Milan 20133, Italy

[‡]Dipartimento di Biologia, CIMA Center, University of Milan, Via Golgi 19, Milan 20133, Italy

[§]Istituto di Biostrutture e Bioimmagini-CNR, Via Mezzocannone, 16, Naples 80134, Italy

[∥]Istituto di Crystallografia-CNR, Via Amendola 122/O, Bari 70126, Italy

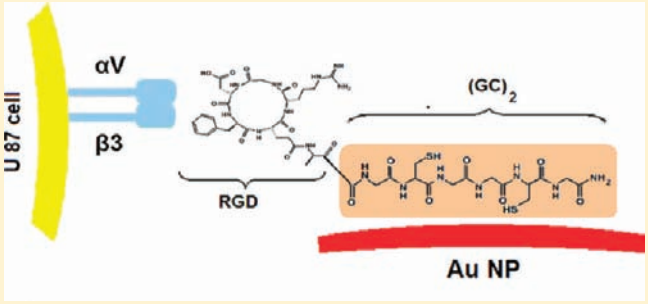
[⊥]Dipartimento delle Scienze Biologiche, Università di Napoli "Federico II", Via Mezzocannone, 16, Naples 80134, Italy

[#]Istituto di Scienze e Tecnologie Molecolari-CNR, Via C. Golgi 19, Milan 20133, Italy

[▽]C.I.M.A. Interdepartmental Centre of Advanced Microscopy, University of Milan, Via Golgi 19, Milan 20133, Italy

Supporting Information

ABSTRACT: Gold nanoparticles were obtained by reduction of a tetrachloroaurate aqueous solution in the presence of a RGD-$(GC)_2$ peptide as stabilizer. As comparison, the behavior of the $(GC)_2$ peptide has been studied. The $(GC)_2$ and RGD-$(GC)_2$ peptides were prepared ad hoc by Fmoc synthesis. The colloidal systems have been characterized by UV−visible, TGA, ATR-FTIR, mono and bidimensional NMR techniques, confocal and transmission (TEM) microscopy, ζ-potential, and light scattering measurements. The efficient cellular uptake of Au-RGD-$(GC)_2$ and Au-$(GC)_2$ stabilized gold nanoparticles into U87 cells (human glioblastoma cells) were investigated by confocal microscopy and compared with the behavior of $(GC)_2$ capped gold nanoparticles. A quantitative determination of the nanoparticles taken up has been carried out by measuring the pixel brightness of the images, a measure that highlighted the importance of the RGD termination of the peptide. Insight in the cellular uptake mechanism was investigated by TEM microscopy. Various important evidences indicated the selective uptake of RGD-$(GC)_2$ gold nanoparticles into the nucleus.



INTRODUCTION

In the past years gold nanoparticles (AuNPs) have been extensively investigated for biomedical applications due to their unique optical properties, excellent stability, and biocompatibility, relatively easy preparation, and surface modifications.[1−4]

One of the main challenges in the nanotechnology field is the development of safe and effective systems for tumor targeting and selective therapy. Currently, the main limit of the anticancer agents is the nonspecific action on the healthy cells, limiting the dosages that can be applied and leading to serious side effects. In this context, AuNPs play a pivotal role in providing new types of delivery systems to permit the entry of one or multiple drugs into the primary tumor, as well as at the site of metastasis and its microenvironment by a passive (Enhanced Permeability and Retention, EPR) or active mechanism.[5] AuNPs can be indeed used to deliver an anticancer drug or a radionuclide to tumor sites; also, they can be employed in tumor photothermal therapy because of their plasmon resonance properties.[6] In both cases, the targeted drug approach (active mechanism) can be achieved by the exploitation of specific molecular markers, such as receptors, that are overexpressed in cancerous tissues. The functionalization of nanoparticle surface with targeting ligands, able to recognize these markers, allows receptor-mediated endocytosis and nanoparticle internalization, thus, improving therapeutic efficacy for cancer drugs.[7] The range of molecules that can be used as targeting agents is greatly expanded since many ligands (antibody, peptides, carbohydrates, etc.) can be linked to NPs to create higher affinity to tumor biomarkers. Among them, the peptides represent the best candidates[8] since they have a number of distinct advantages over proteins and antibodies, such as small size, simple preparation by chemical and biological methods, possibility to be functionalized and

Received: March 23, 2011
Revised: February 29, 2012
Published: February 29, 2012

 © 2012 American Chemical Society

conjugated, low toxicity, low immunogenicity, and high affinity and specificity for the receptors.

Peptides can be used not only as ligands for targeting biomarkers but also as multidentate agents to stabilize gold nanoparticles. Recently, we have reported new peptide sequences displaying thiol (GC) or amine groups (GK) as capping agents.[9,10] A special feature of these peptides is that they do not lead to particle aggregation by cross-linking.

It is well-known that RGD containing peptides can specifically bind the integrin $\alpha_v\beta_3$ receptor, generally recognized to be a tumor and angiogenesis marker,[11] and RGD-conjugated nanoparticles have been successfully employed for tumor imaging and photo thermal therapy.[12,13]

In the present article, the design and the synthesis of a chimeric peptide (thereafter named RGD-$(GC)_2$), displaying motifs for both targeting and capping functions, are described. RGD-$(GC)_2$ encompasses an RGD cyclic motif, chosen as a targeting ligand for $\alpha_v\beta_3$ integrin and a $(GC)_2$ linear part to stabilize the AuNPs. AuNPs stabilized by RGD-$(GC)_2$ and $(GC)_2$ (for comparison) peptides were prepared and fully characterized by UV−visible, ATR-FTIR, and NMR spectroscopies, confocal and TEM microscopy, and ζ-potential and light scattering measurements. The cellular uptake of Au-RGD-$(GC)_2$ and Au-$(GC)_2$ nanoparticles into U87 glioblastoma cells was investigated, and a correlation between uptake and brightness of the images collected by confocal microscopy was attempted. Moreover, TEM experiments concerning the presence of Au-RGD-$(GC)_2$ and Au-$(GC)_2$ nanoparticles in U87 cells were performed in order to understand if the receptor-mediated entrance could be favored. Then, the fate of nanoparticles inside the cell was observed, and surprisingly, it was discovered that the RGD-peptide behaves as a nucleus penetrating molecule.

EXPERIMENTAL PROCEDURES

Chemicals. Sodium tetrachloroaurate dihydrate (99% w/w), sodium borohydride (98.5% w/w), phenylsilane, and tetra(triphenylphosphine)palladium were purchased from Sigma-Aldrich. Polypropylene reaction vessels and sintered polyethylene frits were supplied by Alltech Italia. NovaSyn TGR resin, coupling reagents, and all amino acids were from Novabiochem. *N*,*N*-Diisopropylethylamine (DIPEA) was purchased from Romil and piperidine from Biosolve. mQ water was used as solvent in all colloidal experiments. Peptide and gold aqueous stock solutions were filtered through 0.45 μm Millipore syringe filters before the use.

Peptide Synthesis. The chimeric cyclopeptide RGD-$(GC)_2$ and the linear peptide $(GC)_2$ (Figure 1) were manually synthesized using the Fmoc (fluorenylmethyloxycarbonyl) solid-phase strategy (0.1 mmol). The syntheses were carried out on NovaSyn TGR resin (loading 0.28 mmmol/g resin), using all standard amino acids except for Fmoc-Glu-OAll. The amino acids in 10-fold excess were preactivated with 2-(1*H*-benzotriazole-1-yl)-1,1,3,3-tetramethyluronium hexafluorophosphate (HBTU) (9.8 equiv)/1-hydroxybenzotriazole (HOBT) (9.8 equiv)/DIPEA (10 equiv) in DMF for 5 min and then added to the resin in the presence of DIPEA (10 equiv) in DMF.

The Cys residues were coupled in 5-fold excess with HBTU (5 equiv)/2,4,6-trimethylpyridine (5 equiv) in DMF/DCM (1:1 v/v) for 90 min without preactivation to prevent racemization.[14]

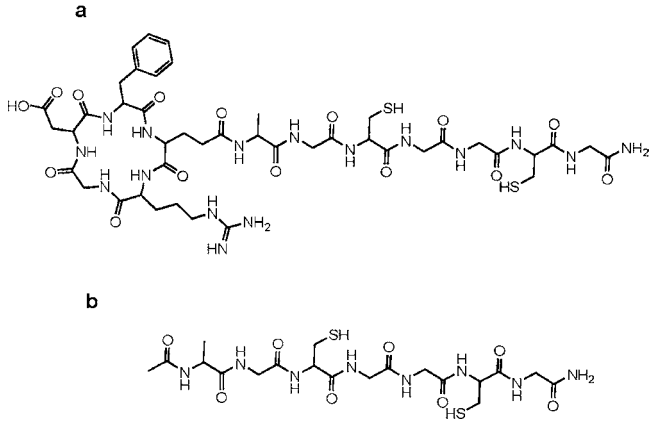


Figure 1. Peptide sequences of (a) RGD-$(GC)_2$ and (b) $(GC)_2$.

The Fmoc deprotection step was performed with 30% piperidine in DMF for 10 min. Before the final Fmoc deprotection of the Arg^1 in RGD-$(GC)_2$, a selective deprotection of the Glu residue from the allyl group was carried out by treatment of the peptidyl resins with $PhSiH_3$ (24 equiv)/$Pd(PPh_3)_4$ (0.25 equiv) in DCM twice for 30 min. The cyclization reaction was carried out on the resin with benzotriazole-1-yl-oxytripyrrolidinophosphonium hexafluorophosphate (PyBop) (1.5equiv)/HOBt (1.5equiv)/DIPEA (2 equiv) in DMF for 3 h and monitored by the Kaiser test.

The peptides were cleaved off the resin by treatment with a mixture of trifluoroacetic acid/water/ethandithiol/triisopropylsilane (94:2.5:2.5:1 v/v/v/v) for 3 h at room temperature. The resins were filtered, and the crude peptides were precipitated with diethyl ether, dissolved in a H_2O/CH_3CN solution, and lyophilized.

The products were purified by preparative RP-HPLC on a Shimadzu system equipped with a UV−visible detector SPD10A using a Phenomenex Jupiter Proteo column (21.2 × 250 mm; 4 μm; 90 Å) and a linear gradient of H_2O (0.1% TFA)/CH_3CN (0.1% TFA) from 5 to 70% of CH_3CN (0.1% TFA) in 30 min at flow rate of 20 mL/min. The collected fractions containing the peptides were lyophilized. The identity and purity of the compounds were assessed by an ESI-LC-MS ThermoFinnigan instrument equipped with a diode array detector combined with an electrospray ion source and ion trap mass analyzer on a Phenomenex C_{18} column (250 × 2 mm; 4 μm; 90 Å) at a flow rate of 200 μL/min (Figure 1, Supporting Information).

Preparation of Au-RGD-$(GC)_2$ Nanoparticles (10.2 nm). To 60 mL of mQ water, a $NaAuClB_4$ aqueous solution (0.06 mmol, 5.07×10^{-2} M) was added. Under vigorous stirring, the aqueous solutions of RGD-$(GC)_2$ peptide (3×10^{-5} mmol, 3.95×10^{-3} M) and $NaBH_4$ (0.12 mmol, 0.112 M) were added. A red sol was immediately formed and left under stirring for further 120 min. Then, the particles were purified by dialysis for 48 h, by using Spectra/Por 6 dialysis tubing, 2K MWCO. The dialyzed sol was analyzed by HPLC to verify the absence of free peptide, by using the conditions reported in Peptide Synthesis.

Preparation of Au-$(GC)_2$ Nanoparticles (13.9 nm). To 40 mL of mQ water, the aqueous solutions of $NaAuCl_4$ (0.03 mmol, 3.41×10^{-2} M) and $(GC)_2$ peptide (2.1×10^{-4} mmol, 7.96×10^{-4} M) were added under vigorous stirring. After 5 min, a $NaBH_4$ aqueous solution (0.06 mmol, 0.1 M) was quickly added, obtaining a cherry red sol that was left under

dx.doi.org/10.1021/bc200143d | *Bioconjugate Chem.* 2012, 23, 340−349

stirring for further 120 min. The AuNPs were purified by dialysis for 48 h by using Spectra/Por CE dialysis tubing, 500−1000 MWCO. The dialyzed sol was analyzed by HPLC, to verify the absence of free peptide, by using the conditions reported in Peptide Synthesis.

UV−visible, ATR-FTIR, and NMR Spectroscopic Studies. UV−visible spectra were recorded on a JASCO V530 spectrometer using 1 cm path length quartz cuvettes and a solution obtained by diluting three times the original sols with mQ water. ATR-FTIR analysis was performed on a Biorad FTS-40 spectrometer equipped with a Specac Golden Gate ATR platform with a diamond crystal. The spectra of free peptides were recorded in the solid state, while the Au capped nanoparticles were analyzed throughout the formation of a colloidal thin film structured on the ATR crystal surface. NMR samples were prepared dissolving 2 mg of RGD-$(GC)_2$ and $(GC)_2$ peptides or 0.5 mg of the lyophilized nanopowders of Au-RGD-$(GC)_2$ and Au-$(GC)_2$ nanoparticles in 650 μL of a H_2O/D_2O (90:10) mixture. Before NMR analysis, a part of the lyophilized brown material was suspended in mQ H_2O and sonicated for 10 min. Only when a red sol (usually darker than the original one) was obtained after sonication and a visible spectrum confirmed a slightly changed plasmon peak, the NMR analysis was carried out.

NMR spectra were collected at 25 °C on a Varian UNITY INOVA 600 MHz spectrometer equipped with a cold probe. Proton resonances of RGD-$(GC)_2$ and $(GC)_2$ peptides were assigned using a standard protocol[15] based on the comparison of 2D [1H, 1H] TOCSY[16] (mixing time: 70 ms) and 2D [^{1}H, ^{1}H] ROESY[17] (mixing times: 150 and 200 ms) experiments. 2D experiments for resonance assignments were generally recorded with 16 scans, 128−256 FIDs in t_1, 1024 or 2048 data points in t_2.

NMR spectra (1D proton and 2D [^{1}H, ^{1}H] TOCSY (mixing time: 70 ms) of a dispersion of Au-RGD-$(GC)_2$ and Au-$(GC)_2$ nanoparticles were recorded with 1024 scans for 1D and 256 scans for 2D experiments, respectively. Water signal was suppressed by means of either the WATERGATE PFG[18] or the DPFGSE (Double Pulsed Field Gradient Selective Echo) techniques.[19] Proton resonances were referenced to the water signal at 4.75 ppm. Spectra were processed with the Varian software VNMRJ 1.1D and analyzed with NEASY as implemented in CARA (http://www.nmr.ch/).

Cell Culture. The U87 cells (human glioblastoma cell line) (see http://www.ihop-net.org/UniPub/iHOP/gs/157442.html, for the adhesion molecule expressed) were cultivated in Dulbecco MEM, supplemented with 10% heat-inactivated fetal calf serum, 1% (v/v) antibiotic mixture (Sigma), and 2 × 10^{-3} M L-glutamine. At confluence, the cells were split on sterile coverslips in 3 mL of the above-described medium.

Transmission Electron Microscopy Studies on AuNPs. TEM micrographs of the colloidal solutions were obtained using an EFTEM Leo 912 AB instrument at an accelerating voltage of 100 kV. Carbon-supported copper grids were used to support the colloidal sols. The samples were prepared by evaporating a drop of gold sol onto carbon-coated copper grids. The histograms of the particle size distribution and the average particle diameter were obtained by measuring about 150 particles by using Measure IT Olympus Software.

Confocal and Transmission Electron Microscopy Studies on Cell Culture. Cells were incubated with 100 μL of Au-RGD-$(GC)_2$ and Au-$(GC)_2$ nanoparticles in 3 mL of the medium for 5, 30, and 60 min (for each sol). Confocal microscopy studies on the cells were performed by a Leica TCS-NT instrument using reflected-light optics at a magnification of 63× (1.53 NA Plan-Apochromat). The samples were illuminated with a 488 nm Argon/Krypton laser, using an intensity of AOTF filter by 10%. A neutral filter RT 30/70 was used as the beam splitter and placed at a 45° angle in the path of beam. Quantitative analyses were carried out measuring the brightness of the images of the samples, containing Au-RGD-$(GC)_2$ and Au-$(GC)_2$ nanoparticles inside U87 cells. By using Leica Confocal Software, similar cellular areas, containing Au-RGD-$(GC)_2$ and Au-$(GC)_2$ nanoparticles (about 780 μm^2), were examined. The pixels, concerning the brightness of the two cellular systems of similar area, were measured and compared.

In TEM studies, the cells were fixed in a 2% glutaraldehyde solution buffered with 0.1 M sodium cacodylate, at pH 7.2 for 15 min, successively washed with 3 portions of a 0.2 M sodium cacodylate buffer solution at pH 7.2, and postfixed for 10 min with a solution containing 1% (v/v) OsO4 solution buffered with 0.1 M sodium cacodylate at pH 7.4. Finally, the cells were washed three times with the 0.2 M sodium cacodylate buffer solution and dehydrated in an ascending ethanol series.[20] Propylene oxide was used as solvent. The cells were infiltrated for 2 h in a 1:1 mixture of Epon-Araldite and propylene oxide, and then the mixture was removed and replaced with 100% Epon-Araldite-resin. The specimens were polymerized for 24 h at 60 °C. The resin embedded specimens were thinly sectioned (30 nm) by ultramicrotome (Ultracut Reichert), and then mounted on a 300 mesh copper grid. The specimens were observed using an EFTEM LEO 912AB transmission electron microscope operating at 100 kV. Digital images were obtained by a CCD Camera System and Leo Image software.

Dynamic Light Scattering and ζ-Potential Measurements. Dynamic Light Scattering (DLS) measurements were performed at 90° with a 90 Plus Particle Size Analyzer from Brookhaven Instrument Corporation (Holtsville, NY) working at 15 mW of a solid-state laser (λ = 661 nm). Measurements were carried out at 25 °C in aqueous media. The ζ-potential was determined with the same instrument equipped with an AQ-809 electrode, and data were processed by ZetaPlus Software. The ζ-potential was automatically calculated from electrophoretic mobility based on the Smoluchowski theory. For measurements, Au-$(GC)_2$ and Au-RGD-$(GC)_2$ NPs were diluted with mQ water in order to obtain a concentration of Au NPs close to 0.01 mg/mL. The samples were sonicated for several minutes to avoid the formation of large aggregates and filtered through a 0.45 μm cellulose acetate membrane.

ICP Analysis. Au contents were determined by ICP-OES (ICAP 6300, Thermo Fisher Scientific) and an external calibration methodology, after digestion of the samples. The Au-RGD-$(GC)_2$ NPs and Au $(GC)_2$ NPs dispersed over TiO_2 samples have been microwave digested in a mixture of 2 mL of HCl (36% by vol) and 1 mL of HNO_3 (68% by vol), diluted with Milli-Q water. Finally, the support residues have been eliminated by filtration.

TGA Analysis. TGA analyses were performed on Perkin-Elmer 7 HT thermobalance. Au-$(GC)_2$ and Au-RGD-$(GC)_2$ NPs were prepared scaling up the amounts of reagents in order to obtain 10^{-3} mmol of peptides in the resulting sols. The sols were lyophilized and subsequently washed several times with mQ water (5 mL each) and centrifuged at 2000 rpm for 5 min. The resulting dark brown powders were used for TGA measurements. The analyses were performed as follows: the

samples were maintained at 120 °C, under isothermic conditions, for 1 h to remove any residual water and then ramped at 5 °C/min to 900 °C.

RESULTS AND DISCUSSION

The interaction of biocompatible AuNPs with cellular targets is of great interest in biology and medicine for developing new drug delivery systems and setting up various biotechnological applications.[21−27] In particular, AuNPs have been capped with cell penetrating peptides to improve internalization[28−30] or to target the nucleus,[29−33] pointing out that a proper functionalization with peptides can produce high selective systems. However, it was reported that some peptide sequences can act as stabilizers of the colloidal solutions.[34,35] In this article, we report on the preparation of two systems of AuNPs capped by the peptides named RGD-$(GC)_2$ and $(GC)_2$ (Figure 1). The RGD-$(GC)_2$ peptide is a chimeric molecule of 12 amino acids that contains two parts, encompassing a RGD-sequence and a $(GC)_2$-motif for integrin targeting and nanoparticle capping, respectively. The portion containing RGD sequence was derived from the c(RGDfK) peptide, an $\alpha_v\beta_3$ antagonist, where the lysine residue was replaced by glutamic acid to allow the conjugation to the $(GC)_2$-motif by its γ-carboxylic group. The $(GC)_2$ portion contains a sequence of glycines and cysteines similar to the previously reported capping agent GC15[10] containing cysteine residues needed for the binding to the gold surface. The two cysteines of $(GC)_2$ portion (either in RGD-$(CG)_2$ or in $(GC)_2$ peptides) supply two thiol groups that can establish covalent bonds to the gold surface[9,10] and protect the particles by steric stabilization. A disposal of $(CG)_2$ portion of the peptides parallel to the gold particle surface is suggested (presumably multilayers of peptides lay over the particle).[9,10] The peptides were synthesized in solid phase and purified by RP-HPLC giving the pure products with high yield (21% and 95% for RGD-$(GC)_2$ and $(GC)_2$, respectively) (Figure 1, Supporting Information).

AuNPs were prepared by borohydride reduction of sodium tetrachloroaurate in the presence of the RGD-$(GC)_2$ or $(GC)_2$ peptides. Afterward, the U87 glioblastoma cell line, overexpressing $\alpha_v\beta_3$ integrin receptor, was chosen for *in vitro* cellular uptake assay with the aim of demonstrating an enhancement of the Au-RGD-$(GC)_2$ nanoparticle entrance compared to Au-$(GC)_2$ one, lacking the integrin recognizing RGD-sequence.

Au-RGD-$(GC)_2$ and Au-$(GC)_2$ sols show the characteristic plasmon absorption bands in the UV−visible spectra (Figure 2, Supporting Information) (λ_{max} (Au-RGD-$(GC)_2$) = 529 nm; λ_{max} (Au-$(GC)_2$) = 514 nm) in agreement with the average mean diameters of the particles obtained by TEM (*d* Au-RGD-$(GC)_2$ = 10.20 nm; *d* Au-$(GC)_2$ = 13.90 nm) (Figure 2A and B). However, the hydrodynamic diameter of nanoparticles obtained by light scattering experiments highlights the presence of nanoparticle aggregates, being close to 46 and 45 nm for Au-$(GC)_2$ and Au-RGD-$(GC)_2$, respectively (Figures 3 and 4, Supporting Information). The superficial charges of both NPs, obtained by ζ-potential measurements, resulted in −27.27 mV and −40.59 mV for Au-RGD-$(GC)_2$ and Au-$(GC)_2$, respectively, confirming good colloidal stability. Although Au-$(GC)_2$ NPs show a more negative charge value compared to Au-RGD-$(GC)_2$, the former can specifically absorb proteins from the culture medium on their surface assuming a charge close to the Au-RGD-$(GC)_2$ one, as reported previously.[36] Consequently, the higher uptake to U87 cells of Au-RGD-$(GC)_2$ respect to Au-$(GC)_2$ is mainly mediated by $\alpha_v\beta_3$

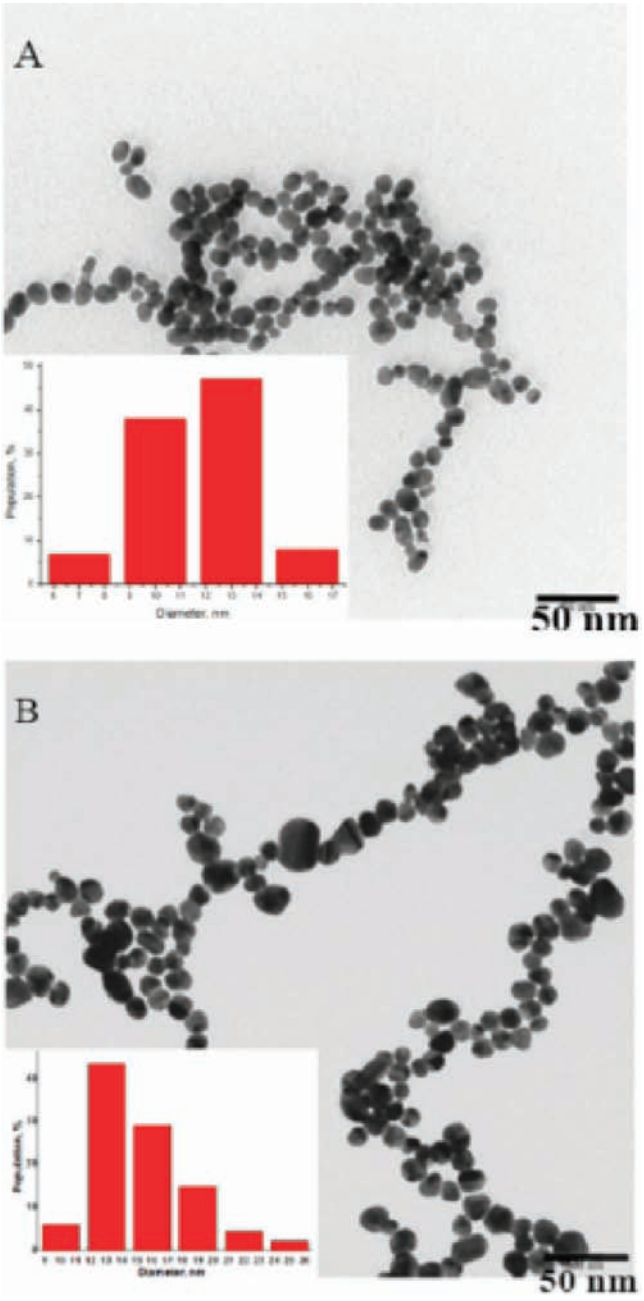


Figure 2. (A) TEM micrograph and histogram of Au-RGD-$(GC)_2$ nanoparticles. Mean diameter = 10.2 nm. (B) TEM micrograph and histogram of Au-$(GC)_2$ nanoparticles. Mean diameter = 13.9 nm.

receptor-based endocytosis due to the presence of an RGD motif on Au-RGD-$(GC)_2$ NPs. The higher Z-potential value of Au-$(GC)_2$ with respect to the Au-RGD-$(GC)_2$ one can be due to various factors such as the different surface concentrations of the two ligands (*vide infra*), eventual different ionic dissociations or zwitterionic forms of the peptides, different conformations of Au-$(GC)_2$ and Au-RGD-$(GC)_2$ systems, different interactions of the two organic chains with water, and, most importantly, different ionic strengths of the solutions (due to some residual electrolyte (NaCl) still being present after the washings).[37]

The number of gold nanoparticles was calculated by using UV−vis spectroscopy data. Huo Q. et al. have found that the nanoparticle extinction coefficient is independent of the

dx.doi.org/10.1021/bc200143d | *Bioconjugate Chem.* 2012, 23, 340−349

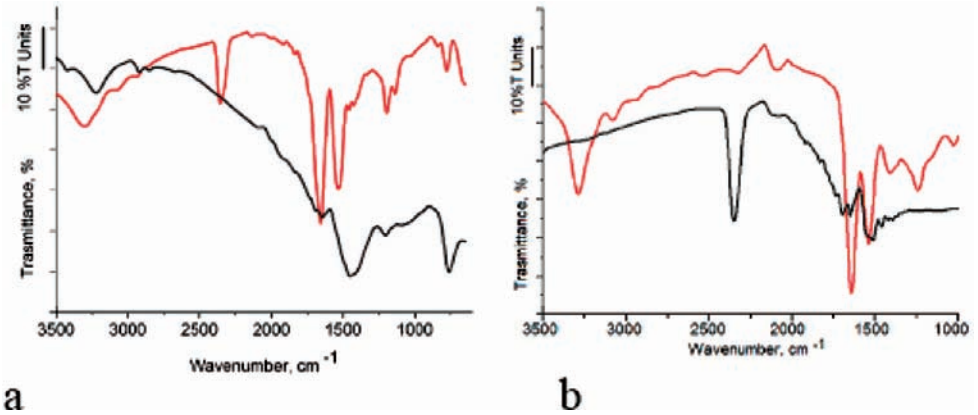


Figure 3. (a) Comparison of ATR-FTIR spectra of free RGD-$(GC)_2$ peptide (red line) and Au-RGD-$(GC)_2$ nanoparticles (black line). (b) Comparison of the ATR-FTIR spectra of free $(GC)_2$ peptide (red line) and Au-$(GC)_2$ nanoparticles (black line).

capping ligands and the sol medium; it depends only on the nanoparticle core diameter (see Supporting Information).[38] Thus, correlating the values of mean diameter of gold core and plasmon resonance absorbance, we calculated the quantity of gold nanoparticles in both colloidal solutions that resulted around 5×10^{12} Au-RGD-$(GC)_2$ and 8×10^{11} Au-$(GC)_2$ NPs. The total gold amount, determined by ICP analysis of 1% (w/w) Au loaded Au-RGD-$(GC)_2/TiO_2$ and Au-$(GC)_2/TiO_2$ samples, was respectively, 0.97 and 0.94 mg, in perfect agreement with the theoretical values.

The number of peptide molecules bound to each nanoparticle was determined by using TGA analyses (see the Experimental Procedures section and Supporting Information for details). TGA proved to be a useful technique for our hybrid inorganic−organic nanostructures allowing us to quantify accurately the organic coating, surrounding the gold nanoparticle, even if its amount was very low. The thermograms of both systems showed a first weight loss between room temperature and 120 °C due to the evaporation of residual and physisorbed water, which can be neglected for our calculations (Figures 5 and 6 in Supporting Information). Then, weight losses of 1.609% and 1.058% were recorded for lyophilized Au-RGD-$(GC)_2$ and Au-$(GC)_2$, respectively, in the 120−450 °C heating range. Since AuNPs were thoroughly washed from peptide excess, the weight losses can be entirely assigned to the combustion of the peptide ligand capping gold particles. Such weight loss is fully consistent with the one observed in thermograms performed on the pure free peptides (data not shown). Following the method described by De Palma and co-workers,[39] we calculated the number of peptide molecules residing on each gold nanoparticle. Each gold nanoparticle is surrounded by about 94 RGD-$(GC)_2$ molecules, while Au-$(GC)_2$ NPs have about 298 $(GC)_2$ molecules residing on their surface.

Structural investigations of gold ligand shell were performed by the ATR-FTIR technique in the solid state and NMR spectroscopy. A comparison between the ATR-FTIR spectra of the free RGD-$(GC)_2$ peptide and Au-RGD-$(GC)_2$ nanoparticles is shown in Figure 3a, while the comparison of the spectra of the free $(GC)_2$ peptide and Au-$(GC)_2$ nanoparticles is illustrated in Figure 3b. Pure $(GC)_2$ and RGD-$(GC)_2$ peptides (red lines in Figure 3b and a) show similar FTIR spectra; the main differences are in the amide I and II regions where $(GC)_2$ shows two peaks located at 1644 and 1540 cm^{-1}, whereas RGD-$(GC)_2$ peaks fall at 1655 and 1534 cm^{-1}. In the N−H stretching region, $(GC)_2$ has a sharper band located at 3292 cm^{-1}, whereas RGD-$(GC)_2$ shows a broader two component band with one component at 3301 and a shoulder at 3205 cm^{-1}. S−H bond stretching vibration falls around 2550 cm^{-1} for free cysteine; unfortunately, such a vibration was not clearly revealed in any of the recorded FTIR spectra. In pure $(GC)_2$ peptide, a broad feeble band located at 2547 cm^{-1} appears, but in the literature, a feeble but sharp band of the S−H bond vibration is usually reported.[40] Upon interaction with the gold surface, the whole spectrum of $(GC)_2$ is strongly affected (black line in Figure 3b): amide I and II bands undergo significant splitting, and the band located at 1644 cm^{-1} in the free peptide now shows a main component at 1652 cm^{-1} plus a shoulder at 1620 cm^{-1}. In addition, two bands at 1698 and 1687 cm^{-1} appear; the band at 1540 cm^{-1} is split into three components at 1555, 1544, and 1513 cm^{-1}. The N−H stretching band, which in the free peptide is located around at 3264 cm^{-1}, is almost absent when $(GC)_2$ interacts with gold, probably forbidden by the surface selection rule. This result agrees with a flat and parallel disposition of $(GC)_2$ over gold surface.

The FTIR spectrum of the RGD-$(GC)_2$ peptide interacting with AuNPs also shows some changes (black line, Figure 3a): the amide I band shows two feeble components at 1686 and 1646 cm^{-1}, and amide II shows a broad band centered at 1455 cm^{-1}. The N−H stretching band is also affected: in the free peptide, there is a strong absorption at 3301 cm^{-1} with 3195 and 3065 cm^{-1} less intense components, whereas only a strong band at 3221 cm^{-1} is evident upon interaction. These data suggest that both CO and NH groups of the amide bonds are affected by the interaction of the peptides with the gold surface and that the backbone conformation and the hydrogen bonding pattern of the conjugated peptides undergo significant changes.

We implemented FTIR results with NMR spectroscopy to further validate the binding of the $(GC)_2$ and RGD-$(CG)_2$ peptides to the gold surface and to identify key organic residues involved in this interaction. In the first stage of the NMR analysis, we determined proton resonance assignments for the $(GC)_2$ and RGD-$(GC)_2$ peptides in their free forms. Because of the fast tumbling of these small peptides, no NOE contacts could be observed in 2D [^{1}H, ^{1}H] NOESY experiments;[41] thus, we recorded 2D [^{1}H, ^{1}H] ROESY spectra.[17] By comparing 2D [^{1}H, ^{1}H] TOCSY and 2D [^{1}H, ^{1}H] ROESY, we could identify all of the different spin-systems and also sequentially assign them (Figure 7, Supporting Information). In particular, the

presence of strong sequential ROE contacts of the type H_{Ni}-$H_{\alpha i-1}$ allowed us to clearly connect all the residues. Then, we investigated by NMR spectroscopy the binding to the nanoparticles of the $(GC)_2$ peptide lacking the integrin binding motif. The strong interaction between this peptide and AuNPs is evident from inspection of 1D proton spectra (Figure 8, Supporting Information), where a large broadening of all the NMR signals can be observed upon binding to the nanoparticles. Cysteine residues are highly influenced by the interaction, and their β-CH_2 proton signal either moves or totally disappears with respect to the corresponding peak in the spectrum of the free $(GC)_2$ peptide (Figure 8, Supporting Information). Similarly, we compared the 1D proton and 2D [^{1}H, ^{1}H] TOCSY spectra of the RGD-$(GC)_2$ peptide with those of the Au-RGD-$(GC)_2$ nanoparticles (Figures 4 and 5).

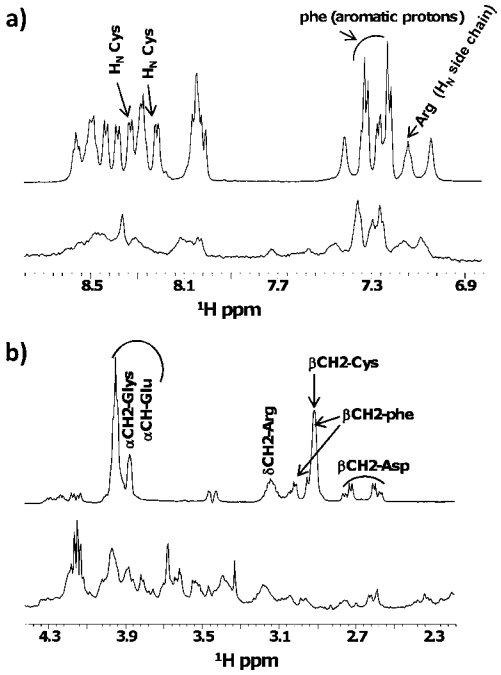


Figure 4. Comparison of 1D proton spectra of the RGD-$(GC)_2$ peptide (upper panels) and Au-RGD-$(GC)_2$ nanoparticles (lower panels). An expansion of the H_N and aromatic protons region is reported in panel a, while signals from side-chain protons are shown in panel b.

As can be seen in Figure 4, the interaction of the peptide with the large hydrophobic gold surface causes a severe enlargement of all the NMR lines. Line broadening is, in fact, widespread in the 1D proton spectrum in the HN and aromatic region (Figure 4a) as well as in the side-chain region (Figure 4b). It is worth noting that the peak around 2.9 ppm, corresponding to the β-CH_2 groups of the cysteines in the free peptide, (Figure 4b upper panel) vanishes when the peptide binds to the nanoparticles (Figure 4b, lower panel). This feature has been previously observed for resonances belonging to the protons that are located rather close to the gold surface.[9] Changes can be better seen in 2D [^{1}H, ^{1}H] TOCSY experiments (Figure 5). The large broadening of the resonances causes the loss of many peaks and highly reduces the quality of the 2D spectrum. The use of a cold-probe allowed us to partially overcome this problem. In fact, spin systems for Ala, Arg, Asp, and Glu can be easily recognized in the spectrum of the Au-RGD-$(GC)_2$ nanoparticles (Figure 5, right panel). Correlations between

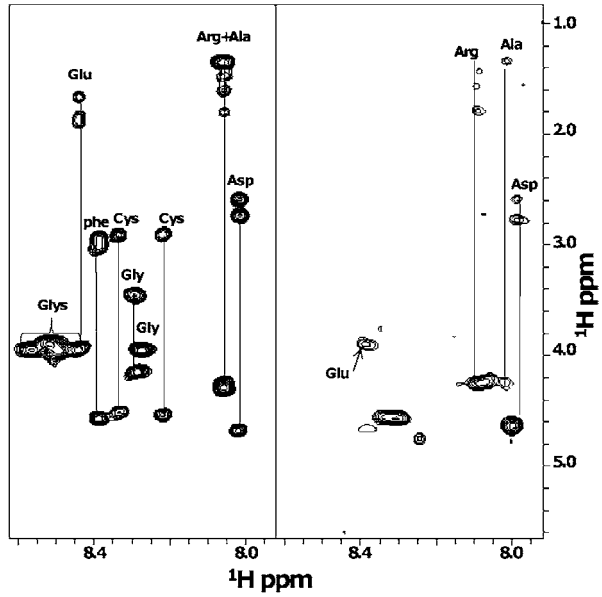


Figure 5. Comparison of 2D [^{1}H, ^{1}H] TOCSY spectra of the RGD-$(GC)_2$ peptide (left) and Au-RGD-$(GC)_2$ nanoparticles (right). The H_N-aliphatic protons correlation region is reported and spin system assignments indicated.

HN and side-chain protons disappear for the two Cys residues. Line broadening is accompanied by small chemical shifts changes that are mainly affecting the backbone HN group of the Arg (8.05 ppm in the apo-form and 8.16 ppm in the bound-form) as well as the β-CH_2 protons of the Asp (2.75−2.61 ppm in the apo-form and 2.82−2.64 ppm in the bound-form), thus indicating that only a small structural rearrangement takes place in the peptide-cyclic portion.

From the perusal of spectroscopic ATR-FTIR and NMR data, some common conclusions can be drawn, and a hypothesis about $(GC)_2$ and RGD-$(GC)_2$ interactions with gold nanoparticles can be proposed. Both the techniques indicate a strong interaction of the $(GC)_2$ moiety with the gold surface via the sulfur atom of cysteine residues, which results in a strong perturbation of (i) CO and NH groups (as shown by FTIR data) and (ii) absence of the Cys β-CH_2 proton signal (due to the proximity to the Au surface, as shown by NMR data). On the contrary, the rigid RGD ring seems to be almost unaffected upon interaction with gold: from NMR spectra, only a minor structural rearrangement of the peptide-cyclic portion can be detected. In the FTIR spectra, the different band patterns of amide I and amide II between Au-RGD-$(GC)_2$ and Au-$(GC)_2$ (Figure 3a and b) can be assigned to the NH and CO contributes to the RGD moiety (the amide I band can be forbidden by the surface selection rule causing its low intensity).

Summing up, the interaction between $(GC)_2$ or RGD-$(GC)_2$ and AuNPs mainly consists of the formation of S−Au bonds between the cysteine thiol residues of $(CG)_2$ and gold surface atoms, leaving the RGD moiety almost unaffected and free for the interaction with receptor.

The U87 cells, which express the appropriate receptor for RGD-motif,[42] were incubated with Au-RGD-$(GC)_2$ and Au-$(GC)_2$ systems for comparison. The cellular uptake of both systems was studied after 5 and 30 min of incubation by confocal microscopy using the reflected-light method. In particular, Figure 6 shows the Au content after 30 min and

dx.doi.org/10.1021/bc200143d | *Bioconjugate Chem.* 2012, 23, 340−349

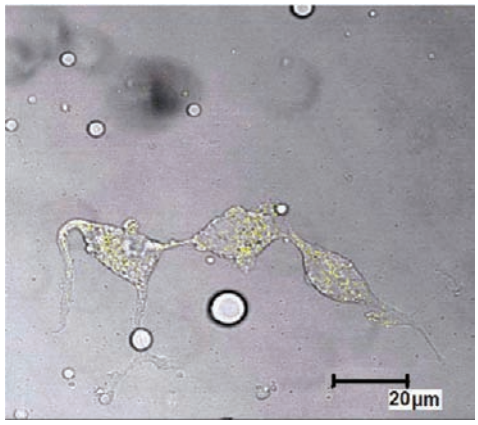


Figure 6. Confocal microscopy reflected-light image of Au-RGD-$(GC)_2$ nanoparticles taken up by U87 cancer cells, after 30 min. The AuNPs are colored yellow for clarity. A large amount of AuNPs are located inside the cells.

highlights a high concentration of Au-RGD-$(GC)_2$ nanoparticles taken up in comparison with a very poor concentration obtained when the $(GC)_2$ peptide was used as the stabilizer after 30 min (Figure 7). Indeed, further details of

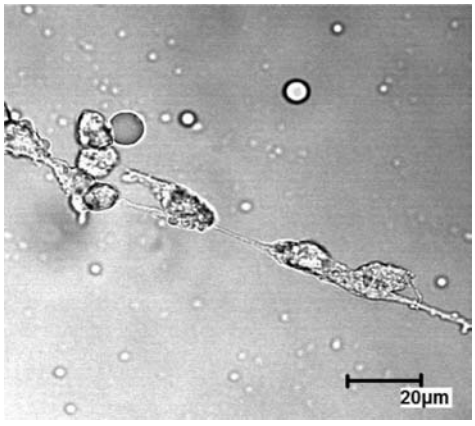


Figure 7. Confocal microscopy reflected-light image of Au-$(GC)_2$ nanoparticles taken up by U87 cancer cells, after 30 min. The AuNPs are colored yellow for clarity. Most of the AuNPs are located outside the cells.

the systems can be derived by the images of the gold incubated cells (collected in reflection, transmission, and overlaid modalities, reported in Figures 9 and 10 in Supporting Information).

In order to determine the amounts of Au-RGD-$(GC)_2$ and Au-$(GC)_2$ nanoparticles taken up by the cells, quantitative determinations were carried out, measuring the pixel brightness of the images obtained by confocal microscopy containing capped AuNPs. By using Leica Confocal Software, similar cellular areas (780 μm^2), containing Au-RGD-$(GC)_2$ and Au-$(GC)_2$ nanoparticles, respectively, both incubated for 5 and 30 min, were examined. The pixels related to the brightness of the two cellular areas were compared and reported in Table 1. The results indicate that the system based on AuNPs functionalized with theRGD motif promotes cellular uptake (0.87 pixels after 5 min and 133 pixels after 30 min of incubation). In contrast, Au-$(GC)_2$ nanoparticles did not enter into the cells after the same period of time. This behavior is reasonably due to an

Table 1. Comparison of Au-RGD-$(GC)_2$ and Au-$(GC)_2$ Nanoparticles Taken Up by U87 Glioblastoma Cells[a]

peptide	pixel brightness (5 min)	pixel brightness (30 min)
RGD-$(GC)_2$	0.87	13.3
$(GC)_2$	0.07	0

[a]The brightness (pxl) of similar areas (780 μm^2) measured by the images collected by confocal microscopy of Au-RGD-$(GC)_2$ and Au-$(GC)_2$ nanoparticles was calculated by the Leica Confocal Software.

entrance mechanism by the recognition between the integrin receptor expressed on the U87 cells and the RGD sequence in the peptide.

The cellular uptake mechanism was further investigated by TEM microscopy. Both Au-RGD-$(GC)_2$ and Au-$(GC)_2$ systems were investigated. The behavior of Au-$(GC)_2$ nanoparticles is shown in Figure 8, in which we can observe that even after 1 h, the AuNPs are outside the cells and located near the cellular membrane.

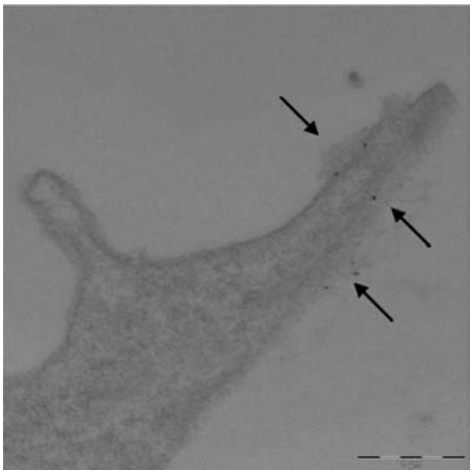


Figure 8. TEM micrograph of Au-$(GC)_2$ nanoparticles after 1 h of incubation into U87 cancer cells. The AuNPs are located outside the cellular membrane (black arrows). Bar = 1 μm.

On the contrary, the Au-RGD-$(GC)_2$ nanoparticles were easily taken up by U87 cells, and after 1 h (Figure 9A), we found some of them enclosed in the endosome (Figure 9B); thus, we relate these results with the mechanism of internalization by $\alpha_v\beta_3$ receptors recognition.[43] However, after 1 h, we observed also a lot of free Au-RGD-$(GC)_2$ nanoparticles in the cell cytoplasm, some others close to the nucleus (Figure 9C and D), and a relevant number of them in the nuclear membrane complex (Figure 9F and G). These findings let us conclude that there is a fast cellular traffic not yet well understood. In recent times, some articles have appeared in the literature highlighting the cellular uptake mechanisms and the different pathways of nanoparticles inside the cells.[44−46]

Moreover, in our experiment, the observations of gold particles in the nucleolus (Figure 9D) and the presence of AuNPs located across nuclear cisternae (Figure 9F) let us believe that the endosomial escape mechanism could be operative also in this case, as observed with TAT oligopeptides.[45]

The presence of many Au-RGD-$(GC)_2$ nanoparticles in the nucleus was confirmed by confocal microscopy as well (Figure 10). In the overlaid image, corresponding to the treatment time

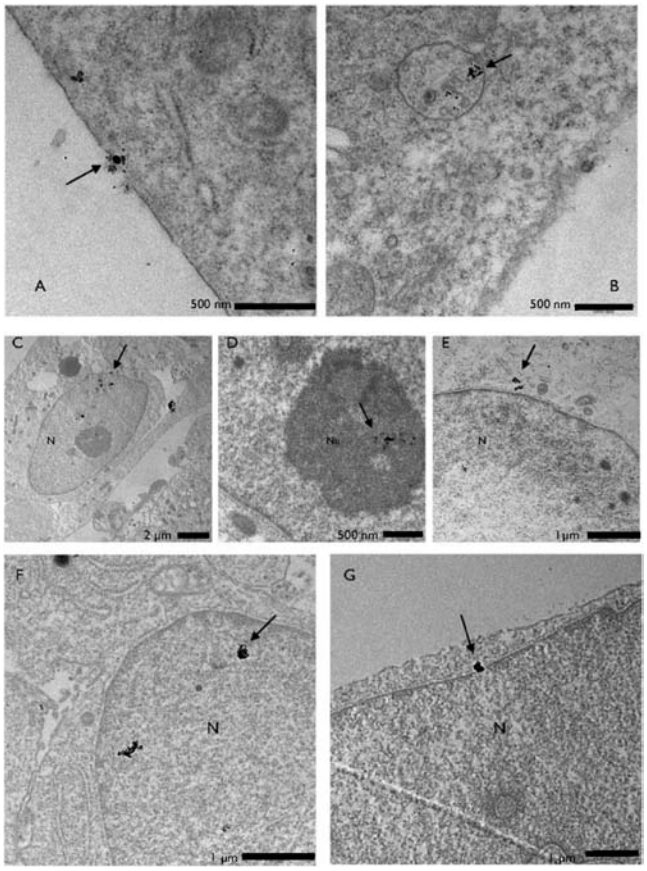


Figure 9. TEM micrographs of Au-RGD-$(GC)_2$ nanoparticles taken up by U87 cancer cells: (A) AuNPs adhere to plasma membrane (arrow); (B) AuNPs internalized in one endosome; AuNPs close (C) and inside (E,G) the nucleus and nucleolus (D) (arrows). Moreover, we detected a relevant amount of Au-RGD-$(GC)_2$ nanoparticles crossing the nuclear pore complex (F).

of 45 min (Figure 10, panel C), we can observe a large amount of Au-RGD-$(GC)_2$ nanoparticles inside the cells, confirming TEM results and the nucleus penetrating ability of the RGD-$(GC)_2$ peptide.

However, further studies are needed to explain the appearance of Au-RGD-$(GC)_2$ nanoparticles in the cytosol and the intracellular fate of nanoparticles, as the ability to direct nanoparticles toward the nucleus is a topic of great interest in this field.

CONCLUSIONS

Biocompatible and stable AuNPs can be prepared by using as stabilizer an RGD-$(GC)_2$ molecule, a peptide designed and synthesized ad hoc. It contains an RGD-sequence and a $(GC)_2$-motif, important both for coordination to the gold surface and integrin targeting. We compared their behavior with Au-$(GC)_2$ nanoparticles lacking the RGD moiety. Both AuNP systems showed the characteristics (plasmon resonance peaks and size distribution) foreseen for their composition in agreement with previous results.[9,10] The Au-RGD-$(GC)_2$ and Au-$(GC)_2$ sols contain 5×10^{12} and 8×10^{11} gold nanoparticles, respectively (ICP measurements), and a ligand/particle ratio equal to 92 and 298, respectively (TGA analyses). The superficial charges, obtained by ζ-potential measurements, confirmed a good colloidal stability of both NPs. Accurate ATR-FTIR and mono- and bidimensional NMR studies allowed us to be confident of

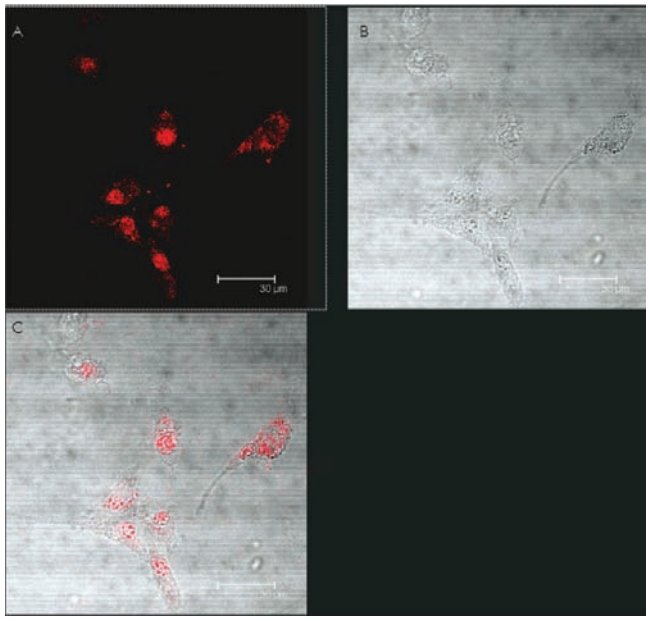


Figure 10. Confocal microscopy reflected-light image of Au-RGD-$(GC)_2$ nanoparticles taken up by U87 cancer cells, after 45 min. The AuNPs are colored red for clarity. Most of the AuNPs are located inside the nucleus as evidenced by the A image collected in the reflection mode.

the coordination of the studied peptides to the gold surface throughout the thiol groups. In particular, the obtained NMR data clearly indicate that the AGCGGCG tail of RGD-functionalized peptide is responsible for binding to the AuNPs. The changes that can be observed in the NMR spectra are indicative of a strong interaction in which cysteine residues play a crucial role.

The uptake of the peptide capped AuNPs by U87 glioblastoma cells gave interesting results and allowed us to discriminate the entrance of Au-RGD-$(GC)_2$ nanoparticles with respect to the Au-$(GC)_2$ ones, owing to RGD targeting. In particular, measuring the pixel brightness of the images obtained by confocal microscopy, we can affirm that only Au-RGD-$(GC)_2$ nanoparticles are accumulated in the cells and that their entrance pathway most likely drives them into the endosome. However, further phenomena must occur inside the cell as we observed free AuNPs in the cytosol, in the nucleus, and nucleolus (Figure 9).

Thus, we must conclude that further studies are needed to optimize particle delivery, combining the cellular uptake and intracellular targeting.

ASSOCIATED CONTENT

Supporting Information

RP-HPLC chromatograms and corresponding mass spectra of $(GC)_2$ and RGD-$(GC)_2$; electronic spectra of the sols; 2D [^{1}H, ^{1}H] TOCSY and 2D [^{1}H, ^{1}H] ROESY spectra of the free peptides and peptide-capped AuNPs; 1D proton spectra of the peptides and capped AuNPs; confocal microscopy images of particles taken up in U87 cells; calculation of AuNP number and Au quantification by ICP analyses; and HPLC analyses of peptides in the mother liquors of both sols. This material is available free of charge via the Internet at http://pubs.acs.org.

dx.doi.org/10.1021/bc200143d | *Bioconjugate Chem.* 2012, 23, 340–349

AUTHOR INFORMATION

Corresponding Author

*Department of Chimica Inorganica Metallorganica Analitica L. Malatesta, University of Milano, Milano, Italy. Phone: 0039 02 50314361. E-mail: Francesca.Porta@unimi.it.

Notes

The authors declare no competing financial interest.

ACKNOWLEDGMENTS

Financial support from the Fondazione CARIPLO, PON n. 1078 MUIR and PRIN 2008 n. F5A3AF_001 MIUR are gratefully acknowledged. We thank Dr. Maura Francolini of Pharmacology, Chemotherapy and Medical Toxicology, Department of Milan, Italy for providing U87 cells, Dr. G. Perretta and Mr. L. De Luca from IBB-CNR of Naples for technical assistance, and Dr. Paolo Verderio for Z-potential measurements.

REFERENCES

(1) Smith, A. M., and Nie, S. M. (2010) Semiconductor nanocrystals: structure, properties, and bandgap engineering. *Acc. Chem. Res. 43*, 190−200.

(2) Eustis, S., and El-Sayed, M. A. (2006) Why gold nanoparticles are more precious than pretty gold: noble metal surface plasmon resonance and its enhancement of the radiative and nonradiative properties of nanocrystals of different shapes. *Chem. Soc. Rev. 35*, 209−217.

(3) Lu, A. H., Salabas, E. L., and Schuth, F. (2007) Magnetic nanoparticles: synthesis, protection, functionalization, and application. *Angew. Chem., Int. Ed. 46*, 1222−1244.

(4) Cai, W. B., and Chen, X. Y. (2007) Nanoplatforms for targeted molecular imaging in living subjects. *Small 3*, 1840−1854.

(5) Iyer, A. K., Khaled, G., Fang, J., and Maeda, H. (2006) Exploiting the enhanced permeability and retention effect for tumor targeting. *Drug Discovery Today 11*, 812−818.

(6) Cai, W., Gao, T., Hong, H., and Sun, J. (2008) Applications of gold nanoparticles in cancer nanotechnology. *Nanotechnol., Sci. Appl. 1*, 17−32.

(7) Patra, C. R., Bhattacharya, R., Mukhopadhyay, D., and Mukherjee, P. (2008) Application of Gold Nanoparticles for Targeted Therapy in Cancer. *J. Biomed. Nanotechnol. 4*, 99−132.

(8) Pangburn, T. O., Petersen, M. A., Waybrant, B., Adil, M. M., and Kokkoli, E. (2009) Peptide and aptamer-functionalized nanovectors for targeted delivery of therapeutics. *J. Biomech. Eng. 131*, 074005−1−074005−20.

(9) Krpetic, Z., Nativo, P., Porta, F., and Brust, M. (2009) A multidentate peptide for stabilization and facile bioconjugation of gold nanoparticles. *Bioconjugate Chem. 20*, 619−624.

(10) Porta, F., Speranza, G., Krpetić, Ž., Dal Santo, V., Francescato, P., and Scarì, G. (2007) Gold nanoparticles capped by peptides. *Mater. Sci. Eng., B 140*, 187−194.

(11) Cai, W., and Chen, X. (2006) Multimodality imaging of integrin $\alpha_v\beta_3$ expression. *Anticancer Agents Med. Chem. 6*, 407−28.

(12) Li, Z., Huang, P., Zhang, X., Lin, J., Yang, S., Liu, B., Gao, F., Xi, P., Ren, Q., and Cui, D. (2010) RGD-conjugated dendrimer-modified gold nanorods for in vivo tumor targeting and photothermal therapy. *Mol. Pharmaceutics 7*, 94−104.

(13) De la Fuente, J. M., Berry, C. C., Riehle, M. O., and Curtis, A. S. (2006) Nanoparticle targeting at cells. *Langmuir 22*, 3286−3293.

(14) Han, Y., Albericio, F., and Barany, G. (1997) Occurrence and minimization of cysteine racemization during stepwise solid-phase peptide synthesis. *J. Org. Chem. 62*, 4307−4312.

(15) Wuthrich, K. (1986) *NMR of Proteins and Nucleic Acids*, John Wiley & Sons: New York.

(16) Griesinger, C., Otting, G., Wüthrich, K., and Ernst., R. R. (1988) Clean TOCSY for proton spin system identification in macromolecules. *J. Am. Chem. Soc. 110*, 7870−7872.

(17) Bax, A., and Davis, D. G. (1985) Practical aspects of two-dimensional transverse NOE spectroscopy. *J. Magn. Reson. 63*, 207−213.

(18) Piotto, M., Saudek, V., and Sklenár, V. (1992) Gradient-tailored excitation for single-quantum NMR spectroscopy of aqueous solutions. *J. Biomol. NMR 2*, 661−665.

(19) Dalvit, C. (1998) Efficient multiple-solvent suppression for the study of the interaction of organic solvents with biomolecules. *J. Biomol. NMR 11*, 437−444.

(20) Mühlfeld, C., Rothen-Rutishauser, B., Vanhecke, D., Blank, F., Gehr, P., and Ochs, M. (2007) Visualization and quantitative analysis of nanoparticles in the respiratory tract by transmission electron microscopy. Interactions of nanoparticles with pulmonary structures and cellular responses. *Part. Fibre Toxicol 4*, 11.

(21) De, M., Ghosh, P. S., and Rotello, V. M. (2008) Applications of nanoparticles in biology. *Adv. Mater. 20*, 4225−4241.

(22) Rosi, N. L., and Mirkin, C. A. (2005) Nanostructures in biodiagnostics. *Chem. Rev. 105*, 1547−1562.

(23) Alivisatos, P. (2004) The use of nanocrystals in biological detection. *Nat. Biotechnol. 22*, 47−52.

(24) Boisselier, E., and Astruc, D. (2009) Gold nanoparticles in nanomedicine: preparations, imaging, diagnostics, therapies and toxicity. *Chem. Soc. Rev. 38*, 1759−1782.

(25) Murphy, C. J., Gole, A. M., Stone, J. W., Sisco, P. N., Alkilany, A. M., Goldsmith, E. C., and Baxter, S. C. (2008) Gold nanoparticles in biology: beyond toxicity to cellular imaging. *Acc. Chem. Res. 41*, 1721−1730.

(26) Sperling, R. A., Rivera, G. P., Zhang, F., Zanella, M., and Parak, W. J. (2008) Biological applications of gold nanoparticles. *Chem. Soc. Rev. 37*, 1896−1908.

(27) Chen, P. C., Mwakwari, S. C., and Oyelere, A. K. (2008) Gold nanoparticles: from nanomedicine to nanosensing. *Nanotechnol., Sci. Appl. 1*, 45−66.

(28) Ryan, J. A., Overton, K. W., Speight, M. E., Oldenburg, C. N., Loo, L., Robarge, W., Franzen, S., and Feldheim, D. L. (2007) Cellular uptake of gold nanoparticles passivated with BSA-SV40 large T antigen conjugates. *Anal. Chem. 79*, 9150−9159.

(29) Liu, Y., Shipton, M. K., Ryan, J., Kaufman, E. D., Franzen, S., and Feldheim, D. L. (2007) Synthesis, stability, and cellular internalization of gold nanoparticles containing mixed peptide-poly (ethylene glycol) monolayers. *Anal. Chem. 79*, 2221−2229.

(30) Sun, L., Liu, D., and Wang, Z. (2008) Functional gold nanoparticle-peptide complexes as cell-targeting agents. *Langmuir 24*, 10293−10297.

(31) Oyelere, A. K., Chen, P. C., Huang, X., El-Sayed, I. H., and El-Sayed, M. A. (2007) Peptide-conjugated gold nanorods for nuclear targeting. *Bioconjugate Chem. 18*, 1490−1497.

(32) Tkachenko, A. G., Xie, H., Liu, Y., Coleman, D., Ryan, J., Glomm, W. R., Shipton, M. K., Franzen, S., and Feldheim, D. L. (2004) Cellular trajectories of peptide-modified gold particle complexes: comparison of nuclear localization signals and peptide transduction domains. *Bioconjugate Chem. 15*, 482−490.

(33) Tkachenko, A. G., Xie, H., Coleman, D., Glomm, W., Ryan, J., Anderson, M. F., Franzen, S., and Feldheim, D. L. (2003) Multifunctional gold nanoparticle-peptide complexes for nuclear targeting. *J. Am. Chem. Soc. 125*, 4700−4701.

(34) Olmedo, I., Araya, E., Sanz, F., Medina, E., Arbiol, J., Toledo, P., Alvarez-Lueje, A., Giralt, E., and Kogan, M. J. (2008) How changes in the sequence of the peptide CLPFFD-NH_2 can modify the conjugation and stability of gold nanoparticles and their affinity for β-amyloid fibrils. *Bioconjugate Chem. 19*, 1154−1163.

(35) Levy, R., Thanh, N. T. K., Doty, R. C., Hussain, I., Nichols, R. J., Schiffrin, D. J., Brust, M., and Fernig, D. G. (2004) Rational and combinatorial design of peptide capping ligands for gold nanoparticles. *J. Am. Chem. Soc. 126*, 10076−10084.

(36) Zhang, Y., Yang, M., Portney, N. G., Cui, D., Budak, G., Ozbay, E., Ozkan, M., and Ozkan, C. S. (2008) *Biomed. Microdevices 10*, 321−328.
(37) Hunter, R. J. (1989) Foundations of colloid science. *Oxford Science Pub. NY 2*, 739−745.
(38) Liu, X., Atwater, M., Wang, J., and Huo, Q. (2007) Extinction coefficient of gold nanoparticles with different sizes and different capping ligands. *Colloids Surf., B 58*, 3−7.
(39) De Palma, R., Peeters, S., Van Bael, M. J., Van den Rul, H., Bonroy, K., Laureyn, W., Mullens, J., Borghs, G., and Maes, G. (2007) Silane ligand exchange to make hydrophobic superparamagnetic nanoparticles water-dispersible. *Chem. Mater. 19*, 1821−1831.
(40) Aryal, S., Remant, B. K. C., Dharmaraj, N., Bhattarai, N., Kim, C. H. H., and Kim, Y. (2006) *Spectrochim. Acta, Part A 63*, 160−163.
(41) Kumar, A., Ernst, R. R., and Wuthrich, K. (1980) A two-dimensional nuclear Overhauser enhancement (2D NOE) experiment for the elucidation of complete proton-proton cross-relaxation networks in biological macromolecules. *Biochem. Biophys. Res. Commun. 95*, 1−6.
(42) Ong, H. T., Trejo, T. R., Pham, L. D., Oberg, A. L., Russell, S. J., and Kah, W. P. (2009) Intravascularly Administered RGD-displaying measles viruses bind to and infect neovessel endothelial cells in vivo. *Mol. Ther. 17*, 1012−1021.
(43) Juliano, R. L., Alam, R., Dixit, V., and Kang, H. M. (2009) Cell-targeting and cell-penetrating peptides for delivery of therapeutic and imaging agents. *Wiley Interdiscip. Rev.: Nanomed. Nanobiotechnol. 1*, 324−335.
(44) Brandenberger, C., Mühlfeld, C., Ali, Z., Lenz, A. G., Schmid, O., Parak, W. J., Gehr, P., and Rothen-Rutishauser, B. (2010) Quantitative evaluation of cellular uptake and trafficking of plain and polyethylene glycol-coated gold nanoparticles. *Small 6*, 1669−1678.
(45) Chou, L. Y., Ming, K., and Chan, W. C. (2011) Strategies for the intracellular delivery of nanoparticles. *Chem. Soc. Rev. 40*, 233−45.
(46) Nativo, P., Prior, I. A., and Brust, M. (2008) Uptake and intracellular fate of surface-modified gold nanoparticles. *ACS Nano 2*, 1639−1644.

■ NOTE ADDED IN PROOF

After the submission of the present article, a paper related to the argument herein discussed, titled Cyclic RGD Functionalized Gold Nanoparticles for Tumor Targeting, by D. Arosio, L. Manzoni, E. M. V. Araldi, and C. Scolastico, was published in *Bioconjugate Chemistry* (2011) *22* (4), 664−672, doi 10.1021/bc100448r.

Bioconjugate Chemistry

Article

pubs.acs.org/bc

Novel Cyanine Dyes with Vinylsulfone Group for Labeling Biomolecules

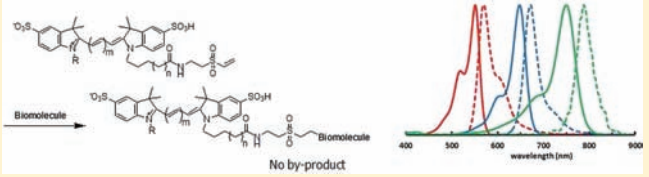
Jin Woo Park,[†,‡] YoungSoo Kim,[†] Kee-Jung Lee,[‡,*] and Dong Jin Kim*[,†]

[†]Center for Neuro-Medicine, Brain Science Institute, Korea Institute of Science and Technology, L2317, 39-1 Hawolgok-dong, Sungbuk-ku, Seoul, Korea 136-791

[‡]Department of Chemical Engineering, Hanyang University, 17 Haengdang-dong, Seongdong-gu, Seoul, Korea 133-791

Supporting Information

ABSTRACT: Novel vinylsulfone cyanine dyes (em. 550−850 nm) were designed and synthesized for fluorescent labeling of biomolecules via 1,2-addition reaction in aqueous conditions. Due to the virtue of chemical structures of both fluorophore and reactive group, these dyes could be significantly stable and reactive in various aqueous/organic conditions. A wide variety of pH, temperature, buffer concentration, and protein were tested for the optimal labeling condition.



INTRODUCTION

Optical imaging based on fluorescence probes is one of the most famous and widely used tools in life sciences due to the power of visualization.[1−3] Fluorescence probes enable researchers to detect particular components of complex biomolecular assemblies with their exquisite sensitivity and selectivity.[4−7] Labeled target molecules are then analyzed via imaging instruments such as confocal microscopes, fluorescence scanners, microarray readers, flow cytometers, capillary electrophoresis apparatus, DNA sequencers, and microfluidic devices.[8]

Among the various fluorescent dyes, cyanine compounds have been used in a wide range of chemical, biological, and artistic applications, from recording media to genomic/proteomic microarrays.[9] Cyanine is a family of dyes containing polymethine group linking two heterocyclic rings containing nitrogen.[9,10] CyDye Fluors (GE Healthcare UK Limited, U.K.) are well-known cyanine dyes for their water solubility, stability, sharp fluorescence band, high sensitivity, and ease of modification of reaction site.[11,12] These molecules have reactive groups on either one or both heterocyclic rings so that they can be chemically conjugated to either nucleic acids or protein molecules.[11−13] The most popular forms among these series of dyes are amine-reactive cyanine dyes such as *N*-hydroxysuccinimidyl (NHS) esters, which are widely used in the conjugation to proteins, peptides, ligands, synthetic oligonucleotides, and other biomolecules.[14]

However, NHS ester is unstable and has a short lifetime in aqueous solution, and *N*-hydroxysuccinimide is released as a byproduct along with the labeled molecules via nucleophilic substitution.[14−16] In order to eliminate this undesired by-product, we searched for various functional groups that have been used for dyeing animal fibers, comprising proteins. Among various reactive groups such as NHS ester, isothiocyanine, monochlorotriazine, dichlorotriazine, methylsulfonyl pyrimidine, dichloroquinoxaline, chlropyrimidine, and vinylsulfone, it was found that the azo dyes containing vinylsulfone (VS) group[17−21] have been utilized in dyeing natural fabrics such as wool and cellulose in various temperatures since the 1960s.[22] Moreover, the dyeing process of VS dye is run in an aqueous solution,[17,24,25] and even at a medium temperature 35 °C.[17,22−24] Also, 1,2-addition as its dyeing mechanism does not allow any byproduct (Scheme 1).[16,23]

Herein we report the synthesis and evaluations of novel VS cyanine dyes having various emission wavelengths with improved stability.

EXPERIMENTAL PROCEDURES

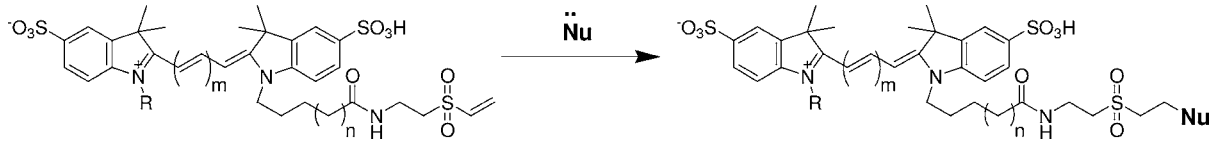
Apparatus and Reagents. All chemicals and organic solvents were purchased from Sigma-Aldrich Co. and Tokyo Chemical Industry (TCI, Japan). CyDye Fluors dyes were purchased from GE Healthcare UK Ltd., bovine serum albumin protein from TCI. Molecular weight size marker was bought from GE Healthcare UK Ltd. and Takara Bio Inc. (Japan).

For the normal phase flash chromatography, kiesel gel 60 (230−400 mesh, Merck, Germany) was used. Silica gel 60 RP-18 F254S (0.25 mm, glass type, Merck) was used in reverse thin layer chromatography (TLC), and reverse column chromatography was carried out in an apparatus for medium pressure liquid chromatography system (MPLC, Buchi, Switzerland) equipped with a Lichroprep RP-18 reverse phase column (40−63 μm, Merck) and a Fraction Collector R-660. High performance liquid chromatography (HPLC) analysis was carried out using Bondapak C18 10 μm 125A (Waters Corp., MA) and Gemini 5u C6-Phenyl 110A (Phenomenex, Inc., CA) with 1100 series (Agilent Technologies, CA). FT-NMR spectra data were obtained with Avance 300 and Avance 400 (Bruker,

Received: May 4, 2011
Revised: January 16, 2012
Published: January 16, 2012

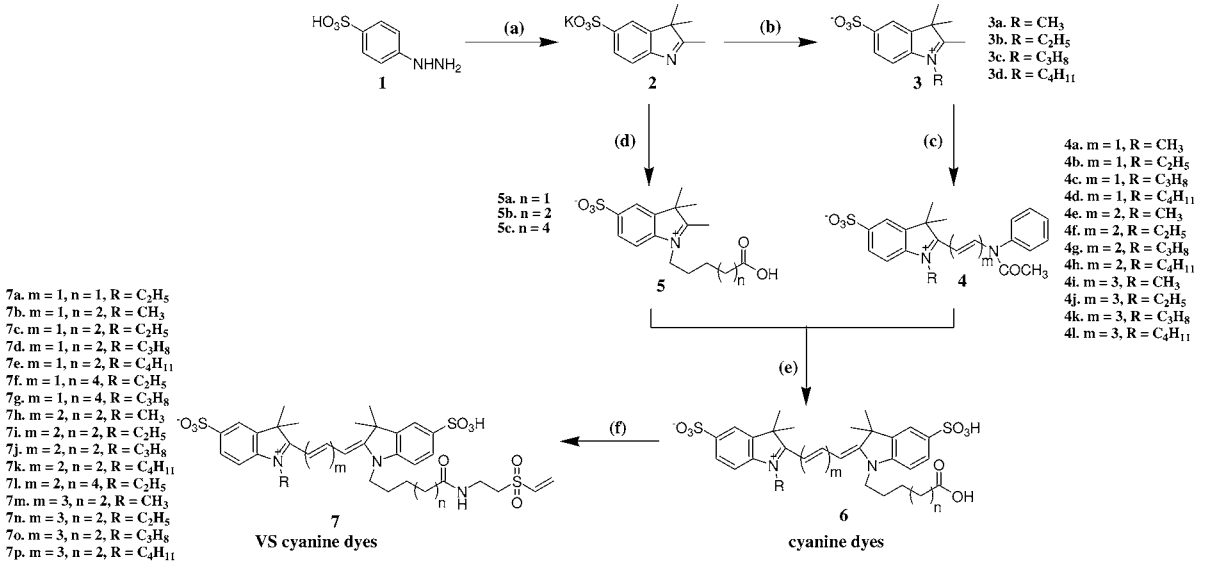
 © 2012 American Chemical Society dx.doi.org/10.1021/bc200232d | *Bioconjugate Chem.* 2012, 23, 350−362

Scheme 1. Dyeing Mechanism for VS Cyanine Dye with the Nucleophiles[a]



[a] m = 1, 2, 3; n = 1, 2, 4; R: methyl, ethyl, propyl, butyl; Nu: nucleophiles.

Scheme 2. Synthetic Scheme for VS Cyanine Dyes



(a) 3-methyl-2-butanone, AcOH, reflux; KOH, MeOH/PrOH, RT
(b) iodomethane (**3a**), iodoethane (**3b**),iodopropane (**3c**), iodobutane (**3d**), reflux
(c) N,N'-diphenylformamidine, AcOH, reflux (**4a-d**), malonaldehyde dianil hydrochloride, Ac_2O/AcOH, reflux (**4e-4h**), glutaconaldehyde dianil hydrochloride, Ac_2O, 100°C (**4i-l**)
(d) 5-bromovaleric acid (**5a**), 6-bromohexanoic acid (**5b**), 8-bromooctanoic acid (**5c**), 1,2-dichlorobenzene, reflux
(e) Ac_2O/Py, 110°C (**6a-g**), Py, 110°C (**6h-k**), Py, 40°C (**6m-p**)
(f) DSC, Py, DMF; 2-(2-chloroethylsulfonyl)ethylamine hydrochloride (*36*), Hünig's base, DMF

Germany) and molecular mass was measured by LC/MS 1200 L Quadrupole (Varian, CA) and Voyager MALDI-TOF DE. The absorption spectra and wavelength data were measured by Lambda 45 UV/vis spectrophotometer (Perkin-Elmer, MA) and fluorescent spectra and wavelength data were obtained from LS-55 fluorescence spectrophotometer (Perkin-Elmer, MA).

The apparatus for gel electrophoresis was PowerPac Basic Power Supply (Catalog No. 164−5050, BIO-RAD Laboratories, Inc., CA) coupled to an SE 260 mini-vertical gel electrophoresis unit (Amersham Biosciences, Sweden). PAGEr Gold Precast Gels (Polyacrylamide gels for protein electrophoresis, 10−20% Tris-Glycine gels, Catalog No. 59506, Lonza, ME) were used for this appratus. Geliance 600 (Perkin-Elmer, MA) was used to observe the labeled biomolecules and measure fluorescence intensity. Light sources used herein were Geliance Blue Epi (Catalog No. L7110027). The measurement was carried out using Geliance Blue Light Filter (550−600 nm) as filters.

General Synthesis. Synthesis of cyanine dyes with carboxylic acid was followed from the literature.[10−12,23−31]

*3H-Indole-2,3,3-trimethyl-5-sulfonic Acid, Potassium Salt (**2**).* A stirred solution of *p*-hydrazinobenzenesulfonic acid (**1**) (10.0 g, 53.0 mmol) in acetic acid (30 mL) was treated with 3-methyl-2-butanone (17 mL, 160.0 mmol) at 25 °C. The reaction mixture was heated to reflux for 4 h, cooled down to 25 °C, filtered through a paper filter. The residue was washed with ethyl acetate and dried under reduced pressure to provide the sulfonic acid as a pink powder (11.3 g, 89%), which was used in the next step without further purification. A solution of crude sulfonic acid (5.1 g, 21.2 mmol) in methanol (35 mL) was added dropwise to a stirred solution of potassium hydroxide (1.4 g, 25.4 mmol) in propanol (35 mL). The resulting mixture was stirred at 25 °C for 24 h and filtered through a paper filter. The residue was dried under reduced pressure to provide the crude **2** (5.4 g, 90%). To obtain spectroscopic data, a small portion of crude **2** was purified with reverse phase chromatography (RP-C18, 15% acetonitrile−water). R_f = 0.68 (RP-C18, 20% acetonitrile−water); ^{1}H NMR (300 MHz, D_2O): δ 7.60 (s, 1H), 7.58 (d, 1H, J = 8.3 Hz), 7.32 (d, 1H, J = 7.9 Hz), 2.08 (s, 3H), 1.06 (s, 6H).

*3H-Indolium, 1-Methyl-2,3,3-trimethyl-5-sulfonate (**3a**).* A slurry of crude **2** (18.0 g, 64.8 mmol) in iodomethane (70 mL, 1.0 mol) under N_2 was heated to reflux for 24 h and cooled down to 25 °C. The liquid phase was decanted, and the residue was washed with acetone (3 × 50 mL), filtered with a paper filter, and dried under reduced pressure at 40 °C to afford the crude **3a** as a pink solid (13.5 g, 82%). To obtain spectroscopic data, small portion of crude **3a** was purified with reverse phase chromatography (RP-C18, 15% acetonitrile−water). R_f = 0.13 (RP-C18, 20% acetonitrile−water); ^{1}H NMR (400 MHz, DMSO-d_6): δ 7.38−7.34 (m, 2H), 6.58−6.56 (m, 1H), 3.88 (s,

dx.doi.org/10.1021/bc200232d | *Bioconjugate Chem.* 2012, 23, 350−362

2H), 2.49 (s, 3H), 1.26 (s, 6H); LC/MS *m/z* 253.04 ($C_{12}H_{15}NO_3S^+$ requires 253.08).

*3H-Indolium, 1-Ethyl-2,3,3-trimethyl-5-sulfonate (**3b**).* Compound **3b** was prepared from compound **2** (20.0 g, 72.1 mmol) and iodoethane (110 mL, 1.4 mol) by the procedure utilized for compound **3a** (18.4 g, 95%). R_f = 0.18 (RP-C18, 20% acetonitrile−water); ^{1}H NMR (400 MHz, D_2O): δ 7.99 (s, 1H), 7.88 (d, 1H, J = 8.2 Hz), 7.80 (d, 1H, J = 8.4 Hz), 4.43 (m, 2H), 1.52−1.40 (m, 12H); LC/MS *m/z* 268.16 ($C_{13}H_{18}NO_3S^+$ requires 268.10).

*3H-Indolium, 1-Propyl-2,3,3-trimethyl-5-sulfonate (**3c**).* Compound **3c** was prepared from compound **2** (20.0 g, 72.1 mmol) and iodopropane (107 mL, 1.1 mol) by the procedure utilized for compound **3a** (19.8 g, 98%). R_f = 0.45 (RP-C18, 20% acetonitrile−water); ^{1}H NMR (400 MHz, MeOD-d_4): δ 8.15 (s, 1H), 8.02 (s, 2H), 4.55 (t, 2H, J = 7.5 Hz), 2.04 (q, 2H, J = 7.5 Hz), 1.68 (s, 6H), 1.09 (t, 3H, J = 7.2 Hz); LC/MS *m/z* 282.30 ($C_{14}H_{20}NO_3S^+$ requires 282.12).

*3H-Indolium, 1-Butyl-2,3,3-trimethyl-5-sulfonate (**3d**).* Compound **3d** was prepared from compound **2** (18.0 g, 64.8 mmol) and iodobutane (37 mL, 0.2 mol) by the procedure utilized for compound **3a** (5.7 g, 96%). R_f = 0.58 (RP-C18, 20% acetonitrile−water); ^{1}H NMR (400 MHz, DMSO-d_6): δ 8.01 (s, 1H), 7.89 (d, 1H, J = 8.9 Hz), 7.80 (d, 1H, J = 8.9 Hz), 4.47−4.40 (m, 2H), 1.94−1.89 (m, 2H), 1.52 (s, 6H), 1.45−1.39 (m, 2H), 0.99−0.89 (br m, 3H); LC/MS *m/z* 296.04 ($C_{15}H_{22}NO_3S^+$ requires 296.13).

*3H-Indolium, 1-(4-Carboxybutyl)-2,3,3-trimethyl-5-sulfonate (**5a**).* A slurry of the crude **2** (11.0 g, 39.7 mmol) in 1,2-dichlorobenzene (15 mL) under N_2 was treated with 5-bromovaleric acid (9.1 g, 50 mmol). The reaction mixture was heated to reflux for 12 h, cooled down to 25 °C, and liquid phase was decanted. The residue was treated with 2-propanol (50 mL), and the resulting mixture was filtered through a paper filter. The residue was dried under reduced pressure to afford the crude **5a** as a pink solid (10.2 g, 64%). To obtain spectroscopic data, small portion of crude **5a** was purified with reverse phase chromatography (RP-C18, 15% acetonitrile−water). R_f = 0.13 (RP-C18, 20% acetonitrile−water); ^{1}H NMR (400 MHz, DMSO-d_6): δ 7.37−7.34 (m, 2H), 6.56 (t, 1H, J = 8.0 Hz), 3.90 (d, 2H, J = 12.4 Hz), 2.25 (t, 2H), 1.66−1.22 (br m, 13H).

*3H-Indolium, 1-(5-Carboxypentyl)-2,3,3-trimethyl-5-sulfonate (**5b**).* Compound **5b** was prepared from compound **2** (2.8 g, 10.0 mmol) and 6-bromohexanoic acid (2.3 g, 12.0 mmol) by the procedure utilized for compound **5a** (2.7 g, 75%). R_f = 0.08 (RP-C18, 20% acetonitrile−water); ^{1}H NMR (400 MHz, D_2O): δ 8.00 (s, 1H), 7.90 (d, 1H, J = 8.8 Hz), 7.77 (d, 1H, J = 8.4 Hz), 4.37 (t, 2H, J = 7.4 Hz), 2.25 (t, 2H, J = 7.0 Hz), 1.85 (m, 2H), 1.57−1.26 (br m, 13H); LC/MS *m/z* 354.18 ($C_{17}H_{24}NO_5S^+$ requires 354.14).

*3H-Indolium, 1-(7-Carboxyheptyl)-2,3,3-trimethyl-5-sulfonate (**5c**).* Compound **5c** was prepared from compound **2** (1.7 g, 6.0 mmol) and 8-bromooctanoic acid (1.3 g, 6.0 mmol) by the procedure utilized for compound **5a** (1.9 g, 81%). R_f = 0.20 (RP-C18, 20% acetonitrile−water); ^{1}H NMR (400 MHz, DMSO-d_6): δ 7.36−7.32 (m, 2H), 6.53 (t, 1H, J = 8.0 Hz), 3.87 (d, 2H, J = 7.4 Hz), 2.08 (t, 2H), 1.51−1.42 (m, 19H); LC/MS *m/z* 381.12 ($C_{19}H_{27}NO_5S^+$ requires 381.16).

*3H-Indolium, 2-[3-[1-(4-Carboxybutyl)-1,3-dihydro-3,3-dimethyl-5-sulfo-2H-indol-2-ylidene]-1-propen-1-yl]-1-ethyl-3,3-dimethyl-5-sulfonate (**6a**).* A slurry of crude **3b** (3.4 g, 12.5 mmol) and *N,N′*-diphenylformamidine (2.8 g, 14.1 mmol) in acetic acid (15 mL) under N_2 was heated to reflux for 4 h, cooled down to 25 °C, and agitated a heterogeneous mixture by addition of ethyl acetate (20 mL). The resulting mixture was filtered through a paper filter, and the residue was dried under reduced pressure to provide the crude **4b** (4.6 g, 96%). A stirred solution of the crude **4b** (4.2 g, 10.0 mmol) in pyridine (20 mL) and acetic anhydride (20 mL) under N_2 was treated with the crude **5a** (3.4 g, 10.0 mmol) at 25 °C. Reaction mixture was heated to 110 °C for 4 h, cooled down to 25 °C, and agitated a heterogeneous mixture by addition of ethyl acetate (80 mL). Resulting mixture was filtered through a paper filter, and the residue was dried under reduced pressure and purified with flash chromatography (Lichroprep RP-18, 15% acetonitrile−water) to afford **6a** as a red powder (1.47 g, 24%). R_f = 0.71 (RP-C18, 30% acetonitrile−water); ^{1}H NMR (300 MHz, DMSO-d_6): δ 8.35 (t, 1H, J = 13.5 Hz), 7.79 (s, 2H), 7.68 (d, 2H, J = 8.22 Hz), 7.41 (m, 2H), 6.57 (q, 2H, J = 5.0 Hz), 4.18−4.11 (m, 4H), 2.05 (t, 2H), 1.69−0.83 (br m, 19H); LC/MS *m/z* 615.28 ($C_{30}H_{35}N_2O_8S_2^-$ requires 615.18).

*3H-Indolium, 2-[3-[1-(5-Carboxypentyl)-1,3-dihydro-3,3-dimethyl-5-sulfo-2H-indol-2-ylidene]-1-propen-1-yl]-1-methyl-3,3-dimethyl-5-sulfonate (**6b**).* Compound **6b** was prepared from compound **3a** (1.4 g, 5.6 mmol) and compound **5b** (2.0 g, 5.6 mmol) by the procedure utilized for compound **6a** (0.94 g, 27%). R_f = 0.80 (RP-C18, 30% acetonitrile−water); ^{1}H NMR (300 MHz, D_2O): δ 7.95 (m, 1H), 7.84−7.62 (m, 4H), 7.46 (d, 2H, J = 7.8 Hz), 6.51 (d, 2H, J = 8.2 Hz), 4.41 (t, 2H, J = 8.0 Hz), 3.56 (s, 3H), 1.90 (m, 2H), 1.70−1.24 (br m, 18H); MALDI-TOF M/S *m/z* 617.53 ($C_{30}H_{37}N_2O_8S_2^+$ requires 617.2).

*3H-Indolium, 2-[3-[1-(5-Carboxypentyl)-1,3-dihydro-3,3-dimethyl-5-sulfo-2H-indol-2-ylidene]-1-propen-1-yl]-1-ethyl-3,3-dimethyl-5-sulfonate (**6c**).* Compound **6c** was prepared from compound **3b** (0.64 g, 2.4 mmol) and compound **5b** (0.86 g, 2.4 mmol) by the procedure utilized for compound **6a** (0.37 g, 24%). R_f = 0.70 (RP-C18, 30% acetonitrile−water); ^{1}H NMR (300 MHz, D_2O): δ 8.38 (t, 1H, J = 13.5 Hz), 7.78 (s, 2H), 7.73 (t, 2H, J = 7.4 Hz), 7.23 (q, 2H, J = 7.9 Hz), 6.24 (q, 2H, J = 4.7 Hz), 3.97 (m, 4H), 2.23 (t, 2H, J = 7.2 Hz), 1.73−1.20 (br m, 21H); LC/MS *m/z* 631.31 ($C_{31}H_{39}N_2O_8S_2^+$ requires 631.21).

*3H-Indolium, 2-[3-[1-(5-Carboxypentyl)-1,3-dihydro-3,3-dimethyl-5-sulfo-2H-indol-2-ylidene]-1-propen-1-yl]-1-propyl-3,3-dimethyl-5-sulfonate (**6d**).* Compound **6d** was prepared from compound **3c** (6.5 g, 23 mmol) and compound **5b** (8.1 g, 23 mmol) by the procedure utilized for compound **6a** (3.1 g, 21%). R_f = 0.49 (RP-C18, 30% acetonitrile−water); ^{1}H NMR (300 MHz, DMSO-d_6): δ 8.34 (t, 1H, J = 13.2 Hz), 7.78 (s, 2H), 7.65 (d, 2H, J = 8.0 Hz), 7.39 (m, 2H), 6.56 (q, 2H, J = 13.4 Hz), 4.10 (m, 4H), 1.88 (t, 2H, J = 6.8 Hz), 1.77−1.38 (br m, 21H), 0.96 (t, 3H, J = 7.2 Hz); LC/MS *m/z* 643.29 ($C_{32}H_{39}N_2O_8S_2^-$ requires 643.22).

*3H-Indolium, 2-[3-[1-(5-Carboxypentyl)-1,3-dihydro-3,3-dimethyl-5-sulfo-2H-indol-2-ylidene]-1-propen-1-yl]-1-butyl-3,3-dimethyl-5-sulfonate (**6e**).* Compound **6e** was prepared from compound **3d** (2.1 g, 7.1 mmol) and compound **5b** (2.5 g, 7.1 mmol) by the procedure utilized for compound **6a** (1.09 g, 23%). R_f = 0.61 (RP-C18, 30% acetonitrile−water); ^{1}H NMR (400 MHz, DMSO-d_6): δ 8.34 (t, 1H, J = 13.4 Hz), 7.86 (s, 2H), 7.79 (d, 2H, J = 7.7 Hz), 7.38 (d, 2H, J = 6.1 Hz), 6.56 (q, 2H, J = 13.6 Hz), 4.11 (m, 4H), 1.92 (t, 2H, J = 6.9 Hz), 1.76−1.22 (br m, 25H), 0.92 (t, 3H, J = 7.2 Hz); LC/MS *m/z* 657.28 ($C_{33}H_{41}N_2O_8S_2^-$ requires 657.23).

*3H-Indolium, 2-[3-[1-(7-Carboxyheptyl)-1,3-dihydro-3,3-dimethyl-5-sulfo-2H-indol-2-ylidene]-1-propen-1-yl]-1-ethyl-3,3-dimethyl-5-sulfonate (**6f**).* Compound **6f** was prepared from compound **3b** (0.72 g, 2.27 mmol) and compound **5c** (0.93 g, 2.27 mmol) by the procedure utilized for compound **6a** (0.31 g, 25%). R_f = 0.6 (RP-C18, 25% acetonitrile−water); ^{1}H NMR (400 MHz, DMSO-d_6): δ 8.35 (t, 1H), 7.80 (s, 2H), 7.68−7.66 (m, 2H), 7.40−7.38 (m, 2H), 6.32−6.29 (m, 2H), 4.20−4.10 (m, 4H), 1.98 (t, 2H), 1.80−1.05 (br m, 25H); LC/MS m/z 656.9 ($C_{33}H_{41}N_2O_8S_2^-$ requires 657.23).

*3H-Indolium, 2-[3-[1-(7-Carboxyheptyl)-1,3-dihydro-3,3-dimethyl-5-sulfo-2H-indol-2-ylidene]-1-propen-1-yl]-1-propyl-3,3-dimethyl-5-sulfonate (**6g**).* Compound **6g** was prepared from compound **3c** (2.8 g, 10.0 mmol) and compound **5c** (3.8 g, 10.0 mmol) by the procedure utilized for compound **6a** (2.09 g, 31%). R_f = 0.52 (RP-C18, 25% acetonitrile−water); ^{1}H NMR (400 MHz, DMSO-d_6): δ 8.35 (t, 1H), 7.79 (s, 2H), 7.66 (d, 2H), 7.43−7.37 (m, 2H), 6.60−6.45 (m, 2H), 4.15−4.07 (m, 4H), 1.97 (t, 2H), 1.80−1.20 (br m, 24H), 0.96 (t, 3H); LC/MS m/z 671.04 ($C_{34}H_{43}N_2O_8S_2^-$ requires 671.25).

*3H-Indolium, 2-[5-[1-(5-Carboxypentyl)-1,3-dihydro-3,3-dimethyl-5-sulfo-2H-indol-2-ylidene]-1,3-pentadien-1-yl]-1-methyl-3,3-dimethyl-5-sulfonate (**6h**).* A stirred mixture of crude **3a** (2.9 g, 11.5 mmol) and malonaldehyde dianil hydrochloride (3.7 g, 13.9 mmol) in a mixture of acetic acid (60 mL) and acetic anhydride (60 mL) under N_2 was heated to reflux for 4 h, cooled down to 25 °C, and agitated a heterogeneous mixture by addition of ethyl acetate (120 mL). The resulting mixture was filtered through a paper filter, and the residue was dried under reduced pressure to provide the crude **4e** (4.7 g, 96%). A stirred solution of the crude **4e** (4.1 g, 9.6 mmol) in pyridine (100 mL) under N_2 was treated with crude **5b** (3.4 g, 9.6 mmol) at 25 °C. Reaction mixture was stirred at 60 °C for 4 h, cooled down to 25 °C, and agitated a heterogeneous mixture by addition of ethyl acetate (100 mL). Resulting mixture was filtered through a paper filter, and the residue was dried under reduced pressure and purified with flash chromatography (Lichroprep RP-18, 25% acetonitrile−water) to afford **6h** as a blue powder (1.35 g, 22%). R_f = 0.63 (RP-C18, 30% acetonitrile−water); ^{1}H NMR (300 MHz, DMSO-d_6): δ 7.91 (t, 2H, J = 13.7 Hz), 7.74−7.69 (m, 4H), 7.24 (t, 2H, J = 8.4 Hz), 6.45 (t, 1H, J = 12.5 Hz), 6.16−6.11 (m, 2H), 3.98 (t, 2H, J = 5.9 Hz), 3.49 (s, 3H), 2.11 (t, 2H, J = 7.0 Hz), 1.73−1.34 (br m, 18H); LC/MS m/z 641.27 ($C_{32}H_{37}N_2O_8S_2^-$ requires 641.2).

*3H-Indolium, 2-[5-[1-(5-Carboxypentyl)-1,3-dihydro-3,3-dimethyl-5-sulfo-2H-indol-2-ylidene]-1,3-pentadien-1-yl]-1-ethyl-3,3-dimethyl-5-sulfonate (**6i**).* Compound **6i** was prepared from compound **3b** (3.9 g, 14.6 mmol) and compound **5b** (5.1 g, 14.6 mmol) by the procedure utilized for compound **6h** (2.1 g, 22%). R_f = 0.58 (RP-C18, 30% acetonitrile−water); ^{1}H NMR (400 MHz, DMSO-d_6): δ 8.34 (t, 2H, J = 13.2 Hz), 7.80 (s, 2H), 7.63 (d, 2H, J = 8.1 Hz), 7.30 (q, 2H, J = 2.8 Hz), 6.58 (t, 1H, J = 12.2 Hz), 6.30 (q, 2H, J = 8.6 Hz), 4.13−4.06 (m, 4H), 1.98 (t, 2H, J = 6.8 Hz), 1.72−1.18 (br m, 21H); LC/MS m/z 655.24 ($C_{33}H_{39}N_2O_8S_2^-$ requires 655.22).

*3H-Indolium, 2-[5-[1-(5-Carboxypentyl)-1,3-dihydro-3,3-dimethyl-5-sulfo-2H-indol-2-ylidene]-1,3-pentadien-1-yl]-1-propyl-3,3-dimethyl-5-sulfonate (**6j**).* Compound **6j** was prepared from compound **3c** (5.5 g, 19.7 mmol) and compound **5b** (6.9 g, 19.7 mmol) by the procedure utilized for compound **6h** (2.2 g, 16%). R_f = 0.49 (RP-C18, 30% acetonitrile−water); ^{1}H NMR (400 MHz, DMSO-d_6): δ 8.34 (t, 2H, J = 12.8 Hz), 7.79 (s, 2H), 7.61 (d, 2H, J = 7.8 Hz), 7.31 (t, 2H, J = 9.2 Hz), 6.59 (t, 1H, J = 12.1 Hz), 6.30 (q, 2H, J = 3.5 Hz), 4.05 (m, 4H), 1.97 (t, 2H, J = 6.9 Hz), 1.72−1.22 (br m, 21H), 0.92 (t, 3H, J = 7.2 Hz); LC/MS m/z 669.30 ($C_{34}H_{41}N_2O_8S_2^-$ requires 669.23).

*3H-Indolium, 2-[5-[1-(5-Carboxypentyl)-1,3-dihydro-3,3-dimethyl-5-sulfo-2H-indol-2-ylidene]-1,3-pentadien-1-yl]-1-butyl-3,3-dimethyl-5-sulfonate (**6k**).* Compound **6k** was prepared from compound **3d** (2.1 g, 7.1 mmol) and compound **5b** (2.5 g, 7.1 mmol) by the procedure utilized for compound **6h** (1.2 g, 24%). R_f = 0.42 (RP-C18, 30% acetonitrile−water); ^{1}H NMR (400 MHz, DMSO-d_6): δ 8.34 (t, 2H, J = 12.0 Hz), 7.80 (s, 2H), 7.62 (d, 2H, J = 7.2 Hz), 7.32 (m, 2H), 6.59 (t, 1H, J = 11.5 Hz), 6.31 (m, 2H), 4.08 (m, 4H), 2.04 (t, 2H), 1.77−1.21 (br m, 25H), 0.90−0.79 (m, 3H); LC/MS m/z 683.33 ($C_{35}H_{43}N_2O_8S_2^-$ requires 683.25).

*3H-Indolium, 2-[5-[1-(7-Carboxyheptyl)-1,3-dihydro-3,3-dimethyl-5-sulfo-2H-indol-2-ylidene]-1,3-pentadien-1-yl]-1-ethyl-3,3-dimethyl-5-sulfonate (**6l**).* Compound **6l** was prepared from compound **3b** (1.6 g, 6.0 mmol) and compound **5c** (2.3 g, 6.0 mmol) by the procedure utilized for compound **6h** (0.90 g, 22%). R_f = 0.48 (RP-C18, 30% acetonitrile−water); ^{1}H NMR (400 MHz, DMSO-d_6): δ 8.29 (t, 2H, J = 13.6 Hz), 7.75 (s, 2H), 7.58 (d, 2H, J = 8.4 Hz), 7.26 (d, 2H, J = 8.4 Hz), 6.55 (t, 1H, J = 12.2 Hz), 6.30−6.23 (m, 2H), 4.07−4.03 (m, 4H), 1.86 (t, 2H), 1.70−1.10 (br m, 25H); LC/MS m/z 682.9 ($C_{35}H_{43}N_2O_8S_2^-$ requires 683.25).

*3H-Indolium, 2-[7-[1-(5-Carboxypentyl)-1,3-dihydro-3,3-dimethyl-5-sulfo-2H-indol-2-ylidene]-1,3,5-heptatrien-1-yl]-1-methyl-3,3-dimethyl-5-sulfonate (**6m**).* A stirred mixture of crude **3a** (3.2 g, 12.5 mmol) and glutaconaldehyde dianil hydrochloride (4.3 g, 15.0 mmol) in anhydrous acetic acid (15 mL) under N_2 was heated to 100 °C for 1 h, cooled down to 25 °C, and agitated to a heterogeneous mixture by addition of ethyl acetate (15 mL). The resulting mixture was filtered through a paper filter, and the residue was dried under reduced pressure to provide the crude **4i** (4.3 g, 76%). A stirred solution of the crude **4i** (7.9 g, 12.5 mmol) in pyridine (80 mL) under N_2 was treated with the crude **5b** (4.4 g, 12.5 mmol) at 25 °C. The reaction mixture was heated to 40 °C for 1 h, cooled down to 25 °C, and agitated to a heterogeneous mixture by addition of ethyl acetate (85 mL). Resulting mixture was filtered through a paper filter, and the residue was dried under reduced pressure and purified with flash chromatography (Lichroprep RP-18, 30% acetonitrile−water) to afford **6m** as a green powder (1.33 g, 16%). R_f = 0.43 (RP-C18, 30% acetonitrile−water); ^{1}H NMR (300 MHz, DMSO-d_6): δ 7.80−7.62 (m, 5H), 7.33 (t, 2H, J = 13.2 Hz), 7.17 (t, 2H, J = 7.3 Hz), 6.34 (t, 2H, J = 12.2 Hz), 6.06 (q, 2H, J = 5.2 Hz), 3.92 (m, 2H), 3.44 (s, 3H), 2.10 (t, 2H, J = 7.4 Hz), 1.90−1.20 (br m, 18H); LC/MS m/z 667.33 ($C_{34}H_{39}N_2O_8S_2^-$ requires 667.22).

*3H-Indolium, 2-[7-[1-(5-Carboxypentyl)-1,3-dihydro-3,3-dimethyl-5-sulfo-2H-indol-2-ylidene]-1,3,5-heptatrien-1-yl]-1-ethyl-3,3-dimethyl-5-sulfonate (**6n**).* Compound **6n** was prepared from compound **3b** (4.7 g, 17.5 mmol) and compound **5b** (5.94 g, 17.5 mmol) by the procedure utilized for compound **6m** (2.7 g, 23%). R_f = 0.38 (RP-C18, 30% acetonitrile−water); ^{1}H NMR (400 MHz, DMSO-d_6): δ 7.87 (t, 2H, J = 12.8 Hz), 7.72 (m, 3H), 7.50 (d, 2H, J = 11.9 Hz), 7.28 (d, 2H, J = 8.2 Hz), 6.58−6.49 (m, 2H), 6.36 (d, 2H, J = 13.7 Hz), 4.10−4.03 (m, 4H), 1.98 (t, 2H), 1.70−1.22 (br m, 21H); LC/MS m/z 681.28 ($C_{35}H_{41}N_2O_8S_2^-$ requires 681.23).

dx.doi.org/10.1021/bc200232d | *Bioconjugate Chem.* 2012, 23, 350−362

*3H-Indolium, 2-[7-[1-(5-Carboxypentyl)-1,3-dihydro-3,3-dimethyl-5-sulfo-2H-indol-2-ylidene]-1,3,5-heptatrien-1-yl]-1-propyl-3,3-dimethyl-5-sulfonate (**6o**).* Compound **6o** was prepared from compound **3c** (5.3 g, 18.7 mmol) and compound **5b** (6.6 g, 18.7 mmol) by the procedure utilized for compound **6m** (2.60 g, 20%). R_f = 0.37 (RP-C18, 30% acetonitrile−water); ^{1}H NMR (300 MHz, DMSO-d_6): δ 7.92−7.73 (m, 5H), 7.62 (d, 2H, J = 8.1 Hz), 7.30 (t, 2H, J = 7.6 Hz), 6.50 (t, 2H), 6.38 (q, 2H, J = 4.0 Hz), 4.04 (m, 4H), 2.01 (t, 2H, J = 6.9 Hz), 1.75−1.23 (br m, 21H), 0.94 (t, 3H, J = 7.3 Hz); LC/MS m/z 695.29 ($C_{36}H_{43}N_2O_8S_2^-$ requires 695.25).

*3H-Indolium, 2-[7-[1-(5-Carboxypentyl)-1,3-dihydro-3,3-dimethyl-5-sulfo-2H-indol-2-ylidene]-1,3,5-heptatrien-1-yl]-1-butyl-3,3-dimethyl-5-sulfonate (**6p**).* Compound **6p** was prepared from compound **3d** (2.1 g, 7.1 mmol) and compound **5b** (2.5 g, 7.1 mmol) by the procedure utilized for compound **6m** (1.26 g, 25%). R_f = 0.35 (RP-C18, 30% acetonitrile−water); ^{1}H NMR (400 MHz, DMSO-d_6): δ 7.79−7.73 (m, 5H), 7.61 (d, 2H, J = 6.8 Hz), 7.29 (q, 2H, J = 3.5 Hz), 6.56 (t, 2H, J = 12.1 Hz), 6.36 (d, 2H, J = 13.6 Hz), 4.04 (m, 4H), 2.01 (t, 2H), 1.50−1.33 (br m, 25H), 0.90 (t, 3H, J = 7.1 Hz); LC/MS m/z 709.34 ($C_{37}H_{45}N_2O_8S_2^-$ requires 709.26).

General Synthesis of Cyanine Dyes with Vinylsulfone. A stirred solution of **6a−p** (0.174 mmol) in DMF (22 mL) under N_2 was heated to 55 °C and treated with a solution of disuccinimdyl carbonate (DSC, 135.0 mg, 0.527 mmol) in a mixture of pyridine (0.11 mL) and DMF (2.5 mL). Resulting mixture was stirred at 55 °C for 1 h, cooled down to 25 °C, and agitated a heterogeneous mixture by the addition of ethyl acetate (30 mL). Resulting mixture was filtered through a paper filter, and the residue was washed with ethyl acetate and diethyl ether, dried under reduced pressure, and redissolved in DMF (20 mL). The solution was treated with *N,N*-diisopropylethylamine (0.30 mL) and a solution of 2-(2-chloroethylsulfonyl)-ethylamine hydrochloride (36 mg, 0.18 mmol)[32] in DMF (1 mL). The reaction mixture was stirred at 25 °C for 24 h under N_2 and quenched with distilled water (20 mL). The aqueous phase was washed with dichloromethane (3 × 50 mL) and concentrated under reduced pressure. Flash chromatography provided (RP-C18, 15% acetonitrile−water) VS cyanine dye, **7a−p**.

*3H-Indolium, 2-[3-[1-[5-[(2-(Vinylsulfonyl)ethyl)amino]-5-oxopentyl]-1,3-dihydro-3,3-dimethyl-5-sulfo-2H-indol-2-ylidene]-1-propen-1-yl]-1-ethyl-3,3-dimethyl-5-sulfonate (**7a**).* Red powder (93.6 mg, 75.8%); R_f = 0.70 (RP-C18, 30% acetonitrile−water); ^{1}H NMR (400 MHz, DMSO-d_6): δ 8.34 (t, 1H, J = 13.7 Hz), 8.07 (m, 1H), 7.80 (s, 2H), 7.67 (d, 2H, J = 7.6 Hz), 7.39 (q, 2H, J = 3.9 Hz), 6.94 (q, 1H, J = 10.1 Hz), 6.51 (d, 2H, J = 13.3 Hz), 6.21 (m, 2H), 4.08 (m, 4H), 3.21 (t, 2H, J = 6.7 Hz), 2.04 (t, 2H, J = 6.8 Hz), 1.68−1.23 (br m, 20H); LC/MS m/z 734.07 ($C_{34}H_{44}N_3O_9S_3^+$ requires 734.22).

*3H-Indolium, 2-[3-[1-[6-[(2-(Vinylsulfonyl)ethyl)amino]-6-oxohexyl]-1,3-dihydro-3,3-dimethyl-5-sulfo-2H-indol-2-ylidene]-1-propen-1-yl]-1-methyl-3,3-dimethyl-5-sulfonate (**7b**).* Red powder (107.9 mg, 84%); R_f = 0.71 (RP-C18, 30% acetonitrile−water); ^{1}H NMR (300 MHz, DMSO-d_6): δ 8.31 (t, 1H), 8.06 (t, 1H, J = 5.8 Hz), 7.64 (s, 2H), 7.65 (m, 2H), 7.38 (q, 2H, J = 4.3 Hz), 6.97 (q, 1H, J = 9.9 Hz), 6.46 (q, 2H, J = 5.2 Hz), 6.23 (m, 2H), 4.08 (m, 4H), 3.64 (s, 3H), 3.21 (t, 2H, J = 6.7 Hz), 2.04 (t, 2H, J = 6.8 Hz), 1.68−1.23 (br m, 20H); LC/MS m/z 732.47 ($C_{34}H_{42}N_3O_9S_3^-$ requires 732.21).

*3H-Indolium, 2-[3-[1-[6-[(2-(Vinylsulfonyl)ethyl)amino]-6-oxohexyl]-1,3-dihydro-3,3-dimethyl-5-sulfo-2H-indol-2-ylidene]-1-propen-1-yl]-1-ethyl-3,3-dimethyl-5-sulfonate (**7c**).* Red powder (106.4 mg, 82%); R_f = 0.65 (RP-C18, 30% acetonitrile−water); ^{1}H NMR (400 MHz, DMSO-d_6): δ 8.32 (t, 1H, J = 13.4 Hz), 8.02 (t, 1H, J = 4.9 Hz), 7.80 (s, 2H), 7.67 (m, 2H), 7.39 (q, 2H, J = 3.0 Hz), 6.96 (q, 1H, J = 9.9 Hz), 6.53 (q, 2H, J = 4.3 Hz), 6.23 (m, 2H), 4.17−4.09 (m, 4H), 3.21 (m, 2H), 2.04 (t, 2H, J = 6.9 Hz), 1.69−1.28 (br m, 23H); LC/MS m/z 746.27 ($C_{35}H_{44}N_3O_9S_3^-$ requires 746.22).

*3H-Indolium, 2-[3-[1-[6-[(2-(Vinylsulfonyl)ethyl)amino]-6-oxohexyl]-1,3-dihydro-3,3-dimethyl-5-sulfo-2H-indol-2-ylidene]-1-propen-1-yl]-1-propyl-3,3-dimethyl-5-sulfonate (**7d**).* Red powder (114.6 mg, 84%); R_f = 0.55 (RP-C18, 30% acetonitrile−water); ^{1}H NMR (400 MHz, DMSO-d_6): δ 8.35 (t, 1H, J = 13.4 Hz), 7.99 (m, 1H), 7.79 (s, 2H), 7.66 (d, 2H, J = 7.8 Hz), 7.39 (q, 2H, J = 8.6 Hz), 6.96 (q, 1H, J = 9.9 Hz), 6.51 (t, 2H, J = 9.2 Hz), 6.23 (m, 2H), 4.09 (m, 4H), 3.21 (m, 2H), 2.05 (m, 2H), 1.76−1.24 (br m, 23H), 0.96 (t, 3H, J = 6.9 Hz); LC/MS m/z 760.30 ($C_{36}H_{46}N_3O_9S_3^-$ requires 760.24).

*3H-Indolium, 2-[3-[1-[6-[(2-(Vinylsulfonyl)ethyl)amino]-6-oxohexyl]-1,3-dihydro-3,3-dimethyl-5-sulfo-2H-indol-2-ylidene]-1-propen-1-yl]-1-butyl-3,3-dimethyl-5-sulfonate (**7e**).* Red powder (108.7 mg, 81.9%); R_f = 0.60 (RP-C18, 30% acetonitrile−water); ^{1}H NMR (400 MHz, DMSO-d_6): δ 8.36 (t, 1H), 8.02 (t, 1H), 7.81 (s, 2H), 7.68 (d, 2H), 7.40 (d, 2H), 6.97 (d, 1H), 6.53 (d, 2H), 6.23 (m, 2H), 4.12 (m, 4H), 3.22 (t, 2H), 2.05 (t, 2H), 1.75−1.18 (br m, 27H), 0.93 (t, 3H); LC/MS m/z 774.53 ($C_{37}H_{48}N_3O_9S_3^-$ requires 774.26).

*3H-Indolium, 2-[3-[1-[8-[(2-(Vinylsulfonyl)ethyl)amino]-8-oxooctyl]-1,3-dihydro-3,3-dimethyl-5-sulfo-2H-indol-2-ylidene]-1-propen-1-yl]-1-ethyl-3,3-dimethyl-5-sulfonate (**7f**).* Red powder (71.1 mg, 53%); R_f = 0.55 (RP-C18, 30% acetonitrile−water); ^{1}H NMR (400 MHz, DMSO-d_6): δ 8.35 (t, 1H), 7.96 (t, 1H), 7.79 (s, 2H), 7.69−7.65 (m, 2H), 7.40−7.38 (m, 2H), 6.99−6.93 (m, 1H), 6.51 (d, 2H), 6.25−6.21 (m, 1H), 4.17−4.10 (m, 4H), 3.62−3.55 (m, 2H), 3.20−3.09 (m, 2H), 2.01 (t, 2H), 1.70−1.10 (br m, 25H); LC/MS m/z 774.00 ($C_{37}H_{48}N_3O_9S_3^-$ requires 774.26).

*3H-Indolium, 2-[3-[1-[8-[(2-(Vinylsulfonyl)ethyl)amino]-8-oxooctyl]-1,3-dihydro-3,3-dimethyl-5-sulfo-2H-indol-2-ylidene]-1-propen-1-yl]-1-propyl-3,3-dimethyl-5-sulfonate (**7g**).* Red powder (63.2 mg, 46%); R_f = 0.45 (RP-C18, 30% acetonitrile−water); ^{1}H NMR (300 MHz, DMSO-d_6): δ 8.35 (t, 1H), 7.96 (t, 1H), 7.80 (s, 2H), 7.66 (d, 2H), 6.99−6.93 (m, 2H), 6.54−6.49 (m, 2H), 6.25−6.20 (m, 2H), 4.15−4.05 (m, 4H), 3.65−3.57 (m, 2H), 3.26−3,20 (m, 2H), 2.01 (t, 2H), 1.80−1.17 (br m, 24H), 0.97 (t, 3H); LC/MS m/z 788.27 ($C_{38}H_{50}N_3O_9S_3^-$ requires 788.27).

*3H-Indolium, 2-[5-[1-[6-[(2-(Vinylsulfonyl)ethyl)amino]-6-oxohexyl]-1,3-dihydro-3,3-dimethyl-5-sulfo-2H-indol-2-ylidene]-1,3-pentadien-1-yl]-1-methyl-3,3-dimethyl-5-sulfonate (**7h**).* Blue powder (107.9 mg, 81%); R_f = 0.63 (RP-C18, 30% acetonitrile−water); ^{1}H NMR (400 MHz, DMSO-d_6): δ 8.34 (t, 2H, J = 13.5 Hz), 8.00−7.94 (m, 3H), 7.79 (s, 2H), 7.61 (t, 2H, J = 8.0 Hz), 7.30 (q, 2H, J = 3.0 Hz), 6.97 (q, 1H, J = 10.5 Hz), 6.57 (t, 1H, J = 12.2 Hz), 6.31−6.21 (m, 4H), 4.06 (m, 2H), 3.58 (s, 3H), 3.21 (t, 2H, J = 6.6 Hz), 2.02 (t, 2H, J = 7.0 Hz), 1.67−1.24 (br m, 20H); LC/MS m/z 758.47 ($C_{36}H_{44}N_3O_9S_3^-$ requires 758.22).

*3H-Indolium, 2-[5-[1-[6-[(2-(Vinylsulfonyl)ethyl)amino]-6-oxohexyl]-1,3-dihydro-3,3-dimethyl-5-sulfo-2H-indol-2-ylidene]-1,3-pentadien-1-yl]-1-ethyl-3,3-dimethyl-5-sulfonate (**7i**).* Blue powder (107.3 mg, 79%); R_f = 0.58 (RP-C18, 30% acetonitrile−water); ^{1}H NMR (300 MHz, DMSO-d_6): δ 8.35

(t, 2H, J = 13.0 Hz), 8.00 (t, 1H, J = 5.2 Hz), 7.81 (s, 2H), 7.62 (d, 2H, J = 10.3 Hz), 7.31 (d, 2H, J = 7.5 Hz), 6.98 (q, 1H, J = 9.9 Hz), 6.62 (t, 1H, J = 12.3 Hz), 6.32−6.21 (m, 4H), 4.13−4.07 (m, 4H), 3.25 (m, 2H), 2.03 (t, 2H, J = 7.1 Hz), 1.68−1.23 (br m, 23H); LC/MS m/z 774.29 ($C_{37}H_{48}N_3O_9S_3^+$ requires 774.25).

*3H-Indolium, 2-[5-[1-[6-[(2-(Vinylsulfonyl)ethyl)amino]-6-oxohexyl]-1,3-dihydro-3,3-dimethyl-5-sulfo-2H-indol-2-ylidene]-1,3-pentadien-1-yl]-1-propyl-3,3-dimethyl-5-sulfonate (**7j**).* Blue powder (124.9 mg, 88%); R_f = 0.55 (RP-C18, 30% acetonitrile−water); ^{1}H NMR (300 MHz, DMSO-d_6): δ 8.34 (t, 2H, J = 12.6 Hz), 7.97 (t, 1H), 7.80 (s, 2H), 7.62 (d, 2H, J = 7.8 Hz), 7.31 (t, 2H), 6.95 (q, 1H, J = 9.8 Hz), 6.58 (t, 1H, J = 11.9 Hz), 6.33−6.21 (m, 4H), 4.06 (m, 4H), 3.21 (t, 2H, J = 6.8 Hz), 2.03 (t, 2H, J = 6.9 Hz), 1.74−1.24 (br m, 23H), 0.93 (t, 3H, J = 7.2 Hz); LC/MS m/z 786.34 ($C_{38}H_{48}N_3O_9S_3^-$ requires 786.26).

*3H-Indolium, 2-[5-[1-[6-[(2-(Vinylsulfonyl)ethyl)amino]-6-oxohexyl]-1,3-dihydro-3,3-dimethyl-5-sulfo-2H-indol-2-ylidene]-1,3-pentadien-1-yl]-1-butyl-3,3-dimethyl-5-sulfonate (**7k**).* Blue powder (107.3 mg, 77%); R_f = 0.51 (RP-C18, 30% acetonitrile−water); ^{1}H NMR (400 MHz, DMSO-d_6): δ 8.35 (t, 2H, J = 12.4 Hz), 8.00 (t, 1H), 7.80 (s, 2H), 7.61 (d, 2H, J = 8.3 Hz), 7.30 (q, 2H, J = 4.2 Hz), 6.96 (m, 1H), 6.58 (t, 1H), 6.31−6.21 (m, 4H), 4.07 (m, 4H), 3.22 (t, 2H, J = 6.6 Hz), 2.03 (t, 2H, J = 7.0 Hz), 1.53−1.22 (br m, 27H), 0.91 (t, 3H, J = 7.2 Hz); LC/MS m/z 800.36 ($C_{39}H_{50}N_3O_9S_3^-$ requires 800.27).

*3H-Indolium, 2-[5-[1-[8-[(2-(Vinylsulfonyl)ethyl)amino]-8-oxooctyl]-1,3-dihydro-3,3-dimethyl-5-sulfo-2H-indol-2-ylidene]-1,3-pentadien-1-yl]-1-ethyl-3,3-dimethyl-5-sulfonate (**7l**).* Blue powder (56.9 mg, 41%); R_f = 0.40 (RP-C18, 30% acetonitrile−water); ^{1}H NMR (400 MHz, DMSO-d_6): δ 8.35 (t, 2H), 7.96 (t, 1H), 7.80 (s, 2H), 7.80−7.61 (m, 2H), 7.31 (d, 2H), 6.70−6.93 (m, 1H), 6.57 (t, 1H), 6.32−6.21 (m, 3H), 4.13−4.08 (m, 4H), 3.62−3.58 (m, 2H), 3.28−3.20 (m, 2H), 2.01 (t, 2H), 1.65−1.18 (br m, 25H); LC/MS m/z 800.00 ($C_{39}H_{50}N_3O_9S_3^-$ requires 800.27).

*3H-Indolium, 2-[7-[1-[6-[(2-(Vinylsulfonyl)ethyl)amino]-6-oxohexyl]-1,3-dihydro-3,3-dimethyl-5-sulfo-2H-indol-2-ylidene]-1,3,5-heptatrien-1-yl]-1-methyl-3,3-dimethyl-5-sulfonate (**7m**).* Green powder (117.7 mg, 84%); R_f = 0.57 (RP-C18, 30% acetonitrile−water); ^{1}H NMR (400 MHz, DMSO-d_6): δ 8.00 (m, 1H), 7.88−7.86 (m, 2H), 7.73 (m, 3H), 7.61 (t, 2H, J = 6.6 Hz), 7.28 (q, 2H, J = 8.1 Hz), 7.10−6.90 (m, 1H), 6.53−6.49 (m, 2H), 6.34−6.22 (m, 4H), 4.02 (m, 2H), 3.57 (s, 3H), 3.22 (t, 2H), 2.03 (t, 2H), 1.74−1.22 (br m, 20H); LC/MS m/z 784.47 ($C_{38}H_{46}N_3O_9S_3^-$ requires 784.24).

*3H-Indolium, 2-[7-[1-[6-[(2-(Vinylsulfonyl)ethyl)amino]-6-oxohexyl]-1,3-dihydro-3,3-dimethyl-5-sulfo-2H-indol-2-ylidene]-1,3,5-heptatrien-1-yl]-1-ethyl-3,3-dimethyl-5-sulfonate (**7n**).* Green powder (103.8 mg, 73%); R_f = 0.50 (RP-C18, 30% acetonitrile−water); ^{1}H NMR (400 MHz, DMSO-d_6): δ 8.03 (t, 1H), 7.88−7.60 (m, 7H), 7.29 (q, 2H, J = 3.2 Hz), 6.97 (m, 1H), 6.54 (m, 2H), 6.39−6.22 (m, 4H), 4.10−4.03 (m, 4H), 3.23 (m, 2H), 2.03 (t, 2H, J = 7.0 Hz), 1.62−1.12 (br m, 23H); LC/MS m/z 800.32 ($C_{39}H_{50}N_3O_9S_3^+$, calcd 800.27).

*3H-Indolium, 2-[7-[1-[6-[(2-(Vinylsulfonyl)ethyl)amino]-6-oxohexyl]-1,3-dihydro-3,3-dimethyl-5-sulfo-2H-indol-2-ylidene]-1,3,5-heptatrien-1-yl]-1-propyl-3,3-dimethyl-5-sulfonate (**7o**).* Green powder (102.9 mg, 70%); R_f = 0.48 (RP-C18, 30% acetonitrile−water); ^{1}H NMR (400 MHz, DMSO-d_6): δ 7.98 (m, 1H), 7.87 (t, 2H, J = 10.6 Hz), 7.73 (m, 3H), 7.61 (d, 2H, J = 8.1 Hz), 7.29 (q, 2H, J = 8.4 Hz), 6.96 (q, 1H, J = 10.1 Hz), 6.54 (t, 2H, J = 12.1 Hz), 6.36 (t, 2H, J = 14.1 Hz), 6.23 (m, 2H), 4.03 (m, 4H), 3.22 (m, 2H), 2.03 (t, 2H, J = 7.2 Hz), 1.74−1.22 (br m, 23H), 0.93 (t, 3H, J = 7.2 Hz); LC/MS m/z 812.35 ($C_{40}H_{50}N_3O_9S_3^-$ requires 812.27).

*3H-Indolium, 2-[7-[1-[6-[(2-(Vinylsulfonyl)ethyl)amino]-6-oxohexyl]-1,3-dihydro-3,3-dimethyl-5-sulfo-2H-indol-2-ylidene]-1,3,5-heptatrien-1-yl]-1-butyl-3,3-dimethyl-5-sulfonate (**7p**).* Green powder (99.6 mg, 69%); R_f = 0.44 (RP-C18, 30% acetonitrile−water); ^{1}H NMR (400 MHz, DMSO-d_6): δ 8.02−7.72 (m, 6H), 7.63 (d, 2H), 7.28 (m, 2H), 6.98 (d, 1H), 6.55 (t, 2H), 6.36 (d, 2H), 6.28−6.22 (m, 2H), 4.05 (m, 4H), 3.23 (m, 2H), 2.02 (t, 2H), 1.70−1.21 (br m, 23H), 0.92 (t, 3H); LC/MS m/z 826.80 ($C_{41}H_{52}N_3O_9S_3^-$ requires 826.29).

Measurement of Optical Properties. The synthesized **7a**−**7p** dye compounds were dissolved in distilled water at 1 mg/100 uL, and then were diluted to 0.01 mM, 0.005 mM, and 0.0025 mM for measurement of absorbance and fluorescence spectrum with UV/vis spectrophotometer and fluorescence spectrophotometer. Beer−Lambert equation was used to determine the molar extinction coefficient of each compound at the maximum absorbable wavelength, and statistical measurements were done to ensure that all values are valid. The maximum absorbable wavelength was set at 0.0025 mM and 25 °C, and the fluorescence spectrum and the maximum fluorescence wavelength were measured.

Reactivity Test. *Dependence of Spacer.* Stock solutions were prepared by dissolving bovine serum albumin (BSA, 10 mg/mL) in 0.1 M sodium phosphate buffer (pH 9.5) and **7a**, **7c**, **7f**, **7g**, **7i**, **7l**, and **7n** (10 mg/mL) in distilled water. Each dye solution (**7a** (11.0 μL), **7c** (11.2 μL), **7f** (11.6 μL), **7g** (11.9 μL), **7i** (11.7 μL), **7l** (12.1 μL), and **7n** (12.1 μL)) was reacted with the BSA solution (1 mL) in equivalent at 25 °C for 6 h. The labeling reactions were then monitored every 1 h via HPLC at 550, 650, and 750 nm (Gemini C6-Phenyl Column, 15−25% acetonitrile−water, 1.5 mL/min).

Dependence of pH. Stock solutions (10 mg/mL) were prepared by dissolving BSA in 0.1 M sodium phosphate buffers (pH 8.5, 9, and 9.5), PBS, and distilled water and **7g**, **7l**, and **7n** (10 mg/mL) in distilled water. Each protein solution (1 mL) was reacted with each dye solution (**7g** (11.9 μL), **7l** (12.1 μL), and **7n** (12.1 μL)) in equivalent at 25 °C for 6 h. The labeling reactions were then monitored every 1 h via HPLC at 550, 650, and 750 nm (Gemini C6-Phenyl Column, 15−25% acetonitrile−water, 1.5 mL/min).

Dependence of Temperature. Stock solutions (10 mg/mL) were prepared by dissolving BSA in 0.1 M sodium phosphate buffer (pH 9.5) and **7g**, **7l**, and **7n** (10 mg/mL) in distilled water. The protein solution (1 mL) was reacted with each dye solution (**7g** (11.9 μL), **7l** (12.1 μL), and **7n** (12.1 μL)) in equivalent at 25 and 36.5 °C for 4 h. The labeling reactions were then monitored every 1 h via HPLC at 550, 650, and 750 nm (Gemini C6-Phenyl Column, 15−25% acetonitrile−water, 1.5 mL/min).

Dependence of Buffer Concentration. Stock solutions (10 mg/mL) were prepared by dissolving BSA in pH 9.5 sodium phosphate buffers (0.5 M, 0.1 M, 0.01 M, and 0.001 M) and **7g**, **7l**, and **7n** (10 mg/mL) in distilled water. Each protein solution (1 mL) was reacted with each dye solution (**7g** (11.9 μL), **7l** (12.1 μL), and **7n** (12.1 μL)) in equivalent at 25 °C for 3 h. The labeling reactions were then monitored every 0.5 h via HPLC at 550, 650, and 750 nm (Gemini C6-Phenyl Column, 15−25% acetonitrile−water, 1.5 mL/min).

Stability Test. *Water Stability.* Stock solutions of **7g**, **7l**, and **7n** (10 mg/mL in distilled water, 10 μL) were diluted with distilled water (1 mL), and the changes in the absorption intensities were then monitored for 24 h via HPLC at 550, 650, and 750 nm (Bondapak C18 10 μm 125A, 15−25% acetonitrile−water, 1.0 mL/min).

pH Stability. Stock solutions of **7g**, **7l**, and **7n** (10 mg/mL in distilled water, 5 μL) were added to 0.1 M sodium phosphate buffer (100 μL) in pH 5, 7.5, and 10 and the changes in absorption intensities were then monitored for 24 h via HPLC at 550, 650, and 750 nm (Bondapak C18 10 μm 125A, 15−25% acetonitrile−water, 1.0 mL/min).

Dye Conjugation Test. For the first test, stock solutions (2 mg/mL) were prepared by dissolving BSA in 0.1 M sodium phosphate buffers (pH 9.5) and **7g**, **7l**, and **7n** (10 mg/mL) in distilled water. Each protein solution (1 mL) was reacted with each dye solution (**7g** (11.9 μL), **7l** (12.1 μL), and **7n** (12.1 μL)) in equivalent at 25 °C for 4 h. Each resulting mixture was filtered using disposable PD-10 desalting column (GE Healthcare UK Ltd.) and VIVASPIN 500 (5 kDa, Sartorius Stedim Biotech GmbH, Germany). Labeled proteins were diluted in distilled water, and then absorption intensity values (A_{280}, A_{dye}) at each maximum absorption wavelength BSA (280 nm), **7g** (280 nm, 549 nm), **7l** (280 nm, 647 nm), and **7n** (280 nm, 749 nm)) were measured using UV/vis spectrophotometer. Dye/protein ratio (D/P) was calculated using the equation ($D/P = (A_{dye}E_{prot})/((A_{280} - A_{D.C.}A_{dye})E_{dye})$).[12] The extinction coefficient of dye (E_{dye}) or BSA (E_{prot}) was calculated using Beer−Lambert equation. The denominator factor for dye absorption at 280 nm ($A_{D.C.}$) was obtained by dividing absorption intensity value at 280 nm by absorption intensity value at maximum absorption wavelength.

For the second test, the above BSA solution was mixed with each dye solution at a molar ratio of 1:7 at 25 °C for 4 h. The labeling reactions were then monitored for a period of 1 h, 2 h, and 4 h via HPLC at 550, 650, and 750 nm (Bondapak C18 10 μm 125A, 15−25% acetonitrile−water, 1.0 mL/min).

Labeling Test. Dye stock solutions (10 mg/mL) were prepared by dissolving Cy3-NHS in DMF and **7g** in distilled water. Protein molecular weight markers (Broad, Code No.3452 available from Takara Bio Inc.), including myosin (200 kDa), β-galactosidase (116 kDa), phosphorylase B (97.2 kDa), serum albumin (66.4 kDa), ovalbumin (44.3 kDa), carbonic anhydrase (29 kDa), trypsin inhibitor (20.1 kDa), lysozyme (14.3 kDa), aprotinin (6.5 kDa), EDTA, NaCl, glycerol, and tris buffer solution, were respectively filtered using VIVASPIN 500 (5 kDa, Sartorius Stedim Biotech GmbH, Germany). Those filtered proteins (1 μL) were placed in each of 10 e-tubes and diluted with 0.1 M sodium phosphate buffer solution (pH 9.5, 18 μL). The stock solutions of Cy3-NHS (0.25 μL, 0.125 μL, 0.0625 μL, 0.025 and 0.0025 μL) and **7g** (0.25 μL, 0.125 μL, 0.0625 μL, 0.025, and 0.0025 μL) were added to each of protein solution in ten e-tubes, and solvents (DMF or distilled water) were appropriately added to adjust the reaction volume (20 μL). The mixtures were vigorously mixed using a vortex shaker and each e-tube was incubated in a heating block at 25 °C for 4 h. SDS-PAGE gel electrophoresis (125 V, 2 h) was employed to separate labeled proteins, and then the fluorescent imaging was observed via Geliance 600.

RESULTS

Synthesis. *p*-Hydrazinobenzenesulfonic acid (**1**) was reacted with 3-methyl-2-butanone via Fisher Indole synthesis protocol, and then treated with potassium hydroxide to provide 2,3,3-trimethyl-3*H*-indole-5-sulfonic acid, potassium salt (**2**) in Scheme 2. The indole compound **2** was converted to its *N*-alkylated compound **3** with corresponding alkylating agents. The Methyl group on C-2 in **3** was condensed with acetanilidovinyl moiety in the presence of acetic anhydride to produce compound **4**. In order to induce the VS reactive group, the indole intermediate **5** that has a fixed length of carbon linkers (spacer) with carboxylic acid group is a prerequisite. Accordingly, the intermediate **5** having five, six, or eight carbons was synthesized in 1,2-dichlorobenzene under refluxing condition.

The asymmetrical cyanine dye **6** was prepared by reacting with intermediates **4** and **5** in the presence of pyridine.[12,25,26] Finally, the carboxylic group of **6** was activated to ester by using DSC and pyridine, which was subsequently reacted with VS intermediate, 2-(2′-chloroethylsulfonyl)ethylamine hydrochloride,[32] under the polar condition of Hünig's base and DMF to afford the desired VS cyanine dye **7**. Especially, during column purification process, alcoholic solvents such as methanol must be excluded, since they can react with activated VS group by nucleophilic attack.

Optical Properties. Optical data of the synthesized VS cyanine dyes are shown in Table 1. Absorption and emission wavelengths of cyanine dyes depend on the number of double bonds between two indole compounds, and thus, our synthesized VS cyanine dyes were classified into 3 groups (**7a**−**7g**, **7h**−**7l**, and **7m**−**7p**). It is shown that variations in the length of the spacer between the fluorophores and VS (*n*) or the alkyl groups on indoles (R) have relatively little effect on the wavelength of VS cyanine dyes. Among them, the highest extinction coefficient was observed with **7g** (*m* = 1), **7l** (*m* = 2), and **7n** (*m* = 3). In Figure 1, absorbance and fluorescence wavelength spectra are marked with matched maximum absorbance, absorbance at maximum fluorescence wavelength, and fluorescence intensity. All spectra showed approximately 20 nm of Stokes shift.

Table 1. Optical Data of VS Cyanine Dyes (Absorption Maximum Wavelength (λ_{abs}), Extinction Coefficient (ε_{max}), and Emission Maximum Wavelength (λ_{em}))

dye no.	*m*	*n*	R	λ_{Abs} (nm)	ε_{max} (×10 L/molcm)	λ_{em} (nm)
7a	1	1	CH_2CH_3	549	0.87	567
7b	1	2	CH_3	549	0.75	565
7c	1	2	CH_2CH_3	549	1.03	566
7d	1	2	$CH_2CH_2CH_3$	549	1.12	568
7e	1	2	$CH_2CH_2CH_2CH_3$	550	1.33	567
7f	1	4	CH_2CH_3	549	1.07	568
7g	**1**	**4**	**$CH_2CH_2CH_3$**	**549**	**1.46**	**570**
7h	2	2	CH_3	646	1.70	670
7i	2	2	CH_2CH_3	647	1.41	668
7j	2	2	$CH_2CH_2CH_3$	648	1.84	672
7k	2	2	$CH_2CH_2CH_2CH_3$	647	2.45	670
7l	**2**	**4**	**CH_2CH_3**	**647**	**2.72**	**671**
7m	3	2	CH_3	746	1.12	779
7n	**3**	**2**	**CH_2CH_3**	**746**	**2.25**	**782**
7o	3	2	$CH_2CH_2CH_3$	749	1.86	780
7p	3	2	$CH_2CH_2CH_2CH_3$	749	1.20	779

Reactivity. Various spacers, pH, temperature, and buffer concentration were applied to evaluate reactivity of VS cyanine

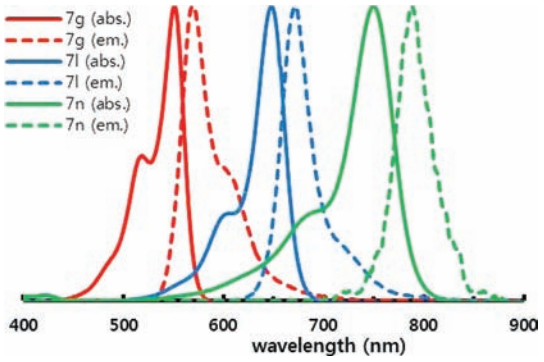


Figure 1. Absorption and emission spectra of **7g**, **7l**, and **7n** in distilled water.

dyes with biomolecules, and BSA was chosen as a target protein.[33,34] All tests were analyzed by measuring the relative amounts of conjugated and free dyes via HPLC. Through our various reactivity tests, the conjugation reaction condition of VS dyes was optimized when BSA was dissolved in pH 9.5, 0.5 M sodium phosphate buffer at 36.5 °C for 1 h.

Dependence of Spacer. To test the variability of reaction time depending on the length of the spacer where the VS group is incorporated, a cyanine dye with equal wavelength was chosen for comparison. Each dye and BSA were used at the same molar concentration, and HPLC analysis was done at every hour for 6 h. Although the BSA and dye have the same molar equivalent weight, it was difficult to measure how many dye molecules were conjugated to the BSA molecule, because it is possible for big BSA molecules to conjugate to multiple dye molecules. Therefore, dye consumption ratio was calculated by using HPLC analysis data of the dye preconjugation and postconjugation. Here, we observed the trend of dye consumption to see how the length of the spacer affected the reaction time.

For the spacer-dependent reactivity test, dyes with the highest extinction coefficients (**7g**, **7l**, and **7n**) and those with ethyl groups as R on indole (**7a**, **7c**, **7f**, and **7i**) were selected. As a result, dyes with longer spacers were observed to have faster binding affinity to BSA (Figure 2). Among **7a**, **7c**, **7f**, and **7g**, with the same absorption wavelength at ~550 nm (m = 1), **7g** showed the highest labeling rate. In the case of **7i** and **7l**, with ~650 nm (m = 2), **7l** with an eight-carbon spacer showed much stronger labeling performance than **7i**. **7n** with 750 nm of the absorption wavelength (m = 3) reached the saturation point within one hour, which was faster than any other dyes compared here. Compounds with the longest spacers exhibited faster conjugation rate compared to other spacers. Considering that BSA (66 430 Da) is at least 80 times larger in size than VS dyes, flexibility endowed by long spacers may provide better accessibility to the target molecule for those compounds.

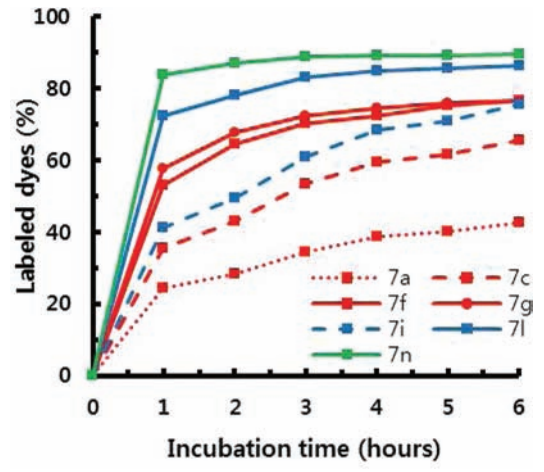


Figure 2. Spacer-dependent reactivity of VS cyanine dyes. **7a**, **7c**, **7f**, **7g**, **7i**, **7l**, and **7n** were mixed with BSA in equivalent at 25 °C for 6 h. Labeling reactions were then monitored every 1 h via HPLC. Dyes with longer spacer (n = 2 or 4) showed faster conjugation with BSA.

Dependence of pH. To establish a proper conjugation method of these novel VS cyanine dyes, the previously chosen **7g**, **7l**, and **7n** dyes were used to optimize the reaction time and yield with various pHs. Water was used as the solvent for VS dyes. pH was kept basic, as most commercially available NHS ester dyes are recommended to be used at pH 9.0. Because most commercially available proteins are sold as diluted in PBS, sodium phosphate buffer at pH 9.5, 9.0, and 8.5; PBS; and distilled water were used as solvents. The yields were recorded for comparison every hour for 6 h. The result showed that labeling rates of tested dyes increased in proportion to the pH of labeling solutions (Figure 3). This tendency agreed with the specific characteristics of reactions with the VS group.[16,22,23,35] In the case of **7l** and **7n**, binding reaction was saturated within 2 h at pH 9.5.

Dependence of Temperature. This experiment lies in determining the effects of temperature variation, as this is an important factor for conjugation. Depending on manufacturers of proteins and antibodies, products in solid form are to be kept at between 2 °C and room temperature, and −20 °C for buffer diluted ones. Most references indicated room temperature as their optimal conjugation temperature, without any cases above the body temperature. The reactions between BSA and VS reactive dyes are known to take place at 25 °C and pH 9.5.[12] We tried to determine the point where reaction time could be shortened while avoiding high temperature. We postulated the body temperature (~36.5 °C) as the limit. As done in previous experiments, molar equivalent amounts of BSA and dye were used to measure the reaction time of dye consumption rate.

The labeling rates of VS cyanine dyes were expected to increase in proportion to the temperature. Protein labeling at the body temperature becomes saturated within 1 h, while at 25 °C relatively slower binding was observed (Figure 4). It is evident that reaction speed usually increases with temperature. However, it was quite remarkable that the reaction continued at high pH 9.5 and at 25 °C. In the case of compound **7g**, the reaction process was about 20% slower than that at 25 °C at the 1 h point, but in general, the other three compounds reached the maximum yield after 2 h. The reaction certainly became faster with temperature. However, considering the stability and safety of the conjugation target (protein, antibody, etc), we concluded that room temperature (25 °C) would be more appropriate.

Dependence of Buffer Concentration. This experiment was to find the optimal molar concentration of sodium phosphate buffer, because it would have minimal effect on the stability of the dye while achieving a high conjugation yield. The previously optimized reaction temperature of 25 °C was used, and sodium phosphate buffer was made in-house. As seen in previous results, compound **7n** showed the fastest reaction time, followed by compounds **7l** and **7g**. However, in this experiment, the reactions for all three compounds could be

dx.doi.org/10.1021/bc200232d | *Bioconjugate Chem.* 2012, 23, 350−362

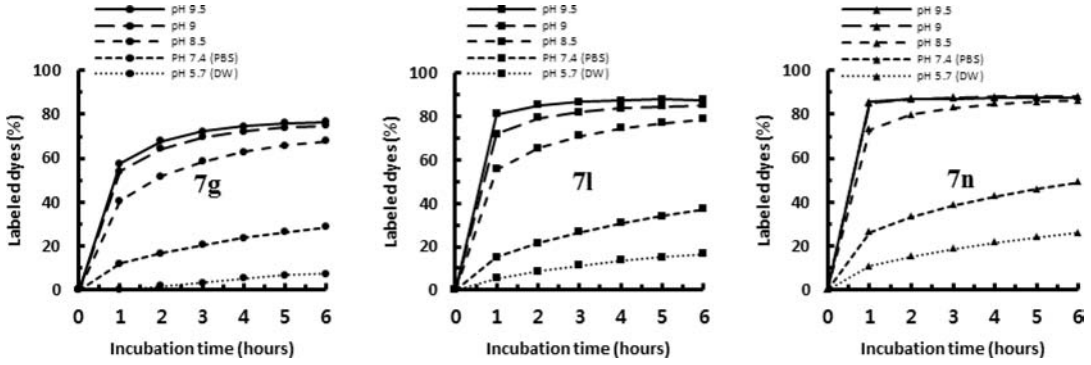


Figure 3. pH-dependent reactivity of VS cyanine dyes. **7g** (λ_{abs} 550 nm, left), **7l** (λ_{abs} 650 nm, middle), and **7n** (λ_{abs} 750 nm, right) were mixed with BSA in equivalent at 25 °C for 6 h in various pH solutions. Labeling reactions were then monitored every 1 h via HPLC. Dyes showed the fastest conjugation with BSA in pH 9.5 solution.

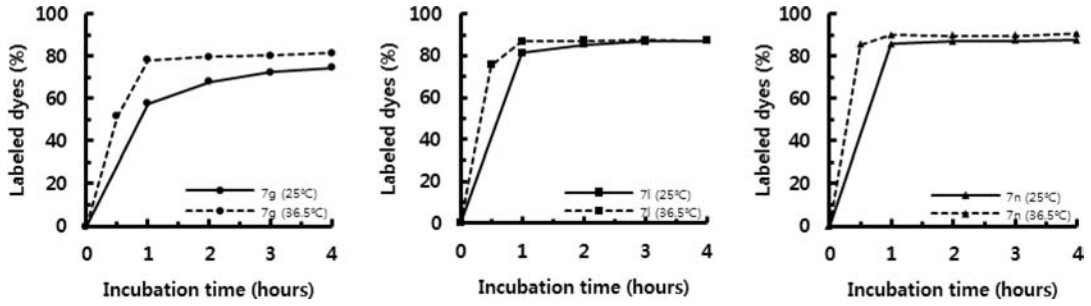


Figure 4. Temperature-dependent reactivity of VS cyanine dyes. **7g** (λ_{abs} 550 nm, left), **7l** (λ_{abs} 650 nm, middle), and **7n** (λ_{abs} 750 nm, right) were mixed with BSA in equivalent at 25 °C for 6 h at room temperature (25 °C) and the body temperature (36.5 °C). Labeling reactions were then monitored every 1 h via HPLC. Dyes showed the fastest conjugation with BSA at 36.5 °C.

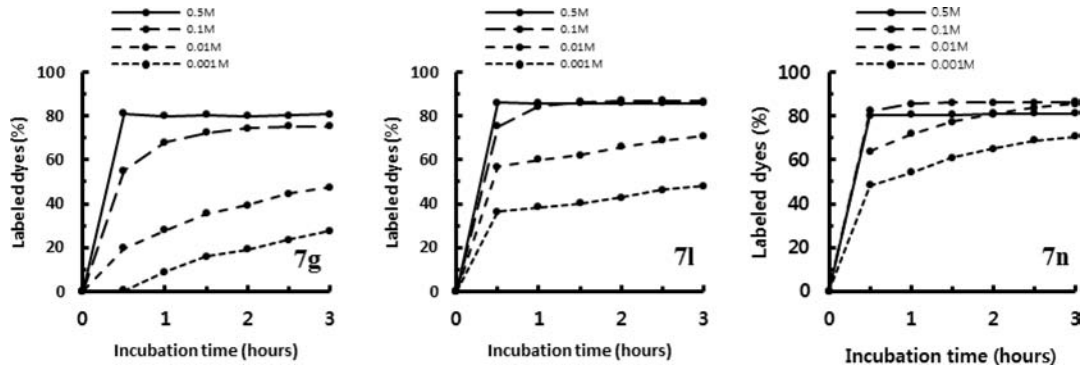


Figure 5. Buffer concentration-dependent reactivity of VS cyanine dyes. **7g** (λ_{abs} 550 nm, left), **7l** (λ_{abs} 650 nm, middle), and **7n** (λ_{abs} 750 nm, right) were mixed with BSA in various concentrations of sodium phosphate buffer in pH 9.5 (0.5 M, 0.1 M, 0.01 M, and 0.001 M). Labeling reactions were then monitored every 1 h via HPLC. Dyes showed the fastest conjugation with BSA in a 0.5 M solution.

finished 30 min earlier with 0.5 M sodium phosphate buffer (Figure 5). Protein labeling in 0.5 M buffer becomes saturated within 30 min showing relatively slower binding in lower concentration buffer. The high concentration buffer might be promoted due to hydrolysis reaction of the VS group; however, unexpectedly high salt concentration of the buffer solution accelerated the labeling reaction.[16,23]

Stability. *Water Stability.* In this study, all VS cyanine dyes were dissolved in water. It is common to keep the dye stock solution at −20 °C; however, we tested the stability of the VS dyes at room temperature (25 °C) for their stability in water. HPLC results showed that VS cyanine dyes were highly stable in water by displaying no change at 25 °C for 1 day (Figure 6). Accordingly, the fluorescent dyes with VS reactive groups can be safely stored not only at −20 °C, which is the general temperature for storing the dye stock solution, but also at room temperature. In addition, those dyes can be safely stored and used even in water instead of organic solvent such as DMSO or DMF, which provides advantages of avoiding organic solvents in biological assays using fluorescence dyes. Therefore, it can be expected that the dilution factor is controlled easily and the dye is easily retrieved with the use of a freeze−dryer.

pH Stability. This experiment was to confirm the stability of the dyes in three conditions: acidic, neutral, and basic conditions. Sodium phosphate buffers of pH 5.0, 7.5, and 10.0 were used, and the experimental method was similar to that of the water stability test. Through HPLC analysis, change in peak level and appearance of new peaks were observed. The HPLC data collected with the dye dissolved in water were used as the standard. All three compounds were the most stable in

dx.doi.org/10.1021/bc200232d | *Bioconjugate Chem.* 2012, 23, 350−362

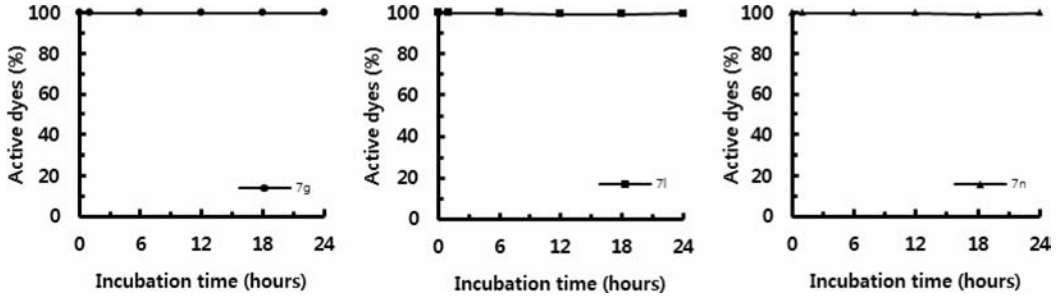


Figure 6. Water stability of VS cyanine dyes. **7g** (λ_{abs} 550 nm, left), **7l** (λ_{abs} 650 nm, middle), and **7n** (λ_{abs} 750 nm, right) were dissolved in water for 24 h. Dye solutions were then monitored every 1 h via HPLC. Dyes showed no changes in water during the test.

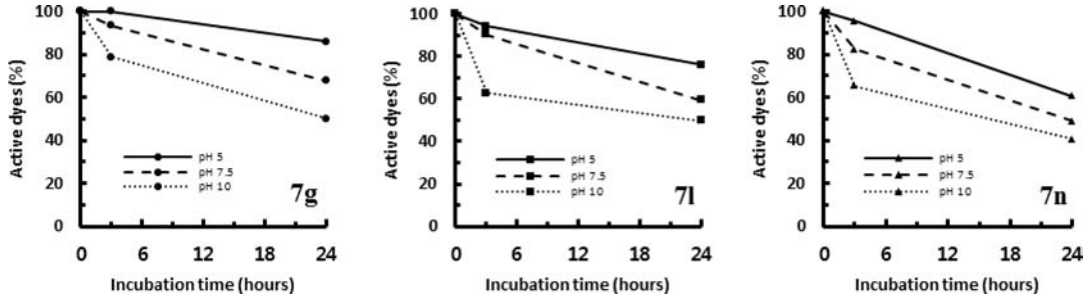


Figure 7. pH stability of VS cyanine dyes. **7g** (λ_{abs} 550 nm, left), **7l** (λ_{abs} 650 nm, middle), and **7n** (λ_{abs} 750 nm, right) were dissolved in 0.1 M sodium phosphate buffers (pH 5, 7.5, and 9.5). Dye solutions were then monitored every 1 h via HPLC. Dyes showed high stability in various pH conditions.

acidic condition, and especially, compound **7g** was the most stable compound in all three conditions as well as pHs. During the first 1 h period, **7l** and **7n** showed similar decrease. However, after 24 h, **7n** showed approximately 10% less unconsumed dye than **7l** in all pH conditions. Even in pH 10, the remaining ratio of active VS dyes for **7n** was more than 60% after 3 h, and more than 50% of dyes remained in the active state after 24 h (Figure 7). Therefore, VS cyanine dyes are expected to be used when either long-term reaction or labeling the biomolecules is needed, because they are stable even under the severe basic conditions. With this result taken into consideration, VS cyanine dyes are expected to show a good labeling yield in the reaction in an aqueous solution.

Dye Conjugation Test. Labeling proteins usually requires large amount of dyes. To determine how many dyes are conjugated to each protein, an equation called D/P ratio is being widely used. D/P ratio utilizes the maximum absorbance wavelength. Here, a correction factor is included in the denominator to normalize the molar extinction coefficient and main absorbance wavelength values of protein, and this correction factor can be obtained with a UV spectrophotometer. The molar extinction coefficient used in this experiment for BSA was 42 665 M^{-1} cm^{-1} at 280 nm, similar to literature. For each BSA molecule, the numbers of dye molecules conjugated to **7g**, **7l**, and **7n** were approximately 0.657, 0.594, and 0.901, respectively. In the buffer concentration experiment mentioned previously, **7g**, **7l**, and **7n** showed 70%, 80%, and 83% dye consumption rate, respectively. These numbers were different from the D/P ratio numbers by approximately 5% to 10%. When a UV/vis spectrophotometer was used, the concentration of the protein was about 1/5 lower at 2 mg/mL, and absorbance was measured only with water. However, when HPLC was used, besides the difference in concentrations, two solvents were used as mobile phases for separation. This may be the culprit of the difference in calculated values.

Based on the previous results, HPLC was considered reliable in measuring the strength of conjugation. Thus, we used this method to observe the change in strength of conjugation as the amount of dye increased. The amount of dye was approximately seven times the molar equivalent to the protein. Initial absorbance level of each dye at the maximum absorbance wavelength, and absorbance level at every hour were measured to find out the D/P ratio based on the dye consumption amount. At the first 1 h spot, most samples were found to have 1 or 2 as the calculated values (Figure 8). However, **7g** did not show any increase in D/P ratio even after incubation hours, while **7l** and **7n** were shown to conjugate to three or four dye molecules conjugated after 4 h. These results suggest that VS dyes can continuously be reacted over time. It is predicted that more dye would be consumed over time; however, **7g** seemed to have a threshold of a saturation point.

Labeling Test. To test affinity of synthesized dyes to various proteins, **7g** was selected to stain nine different proteins and compared with commercially available Cy3-NHS dye. To get rid of ingredients (glycerol, EDTA, NaCl, etc.), molecular weight cutoff filters were used, and were diluted with pH 9.5 sodium phosphate buffer. Cy3-NHS dye was dissolved in DMF, and compound **7g** in water. The molecular weights of Cy3-NHS and **7g** are 765.95 and 790.02, respectively; thus, 0.25 μL of Cy3-NHS and **7g** contained 0.00326 μmol and 0.00321 μmol, respectively. After SDS-PAGE, significant amount of unreacted dye could be found at the bottom of the gel. Small amount of unreacted dye was present even with just 0.025 μL of dyes. In the literature, as well as the manufacturer's protocol for labeling of Cy3-NHS, it was recommended that up to 20 times the molar equivalent of dye and protein be used. At least up to land C of the gel, we determined that the comparison

dx.doi.org/10.1021/bc200232d | *Bioconjugate Chem.* 2012, 23, 350–362

study was feasible since it seemed that the amount of dye used was more than necessary.

As a result (Figure 9), the labeling intensity of both dyes increased in proportion to the usage of dyes. Cy3-NHS tended

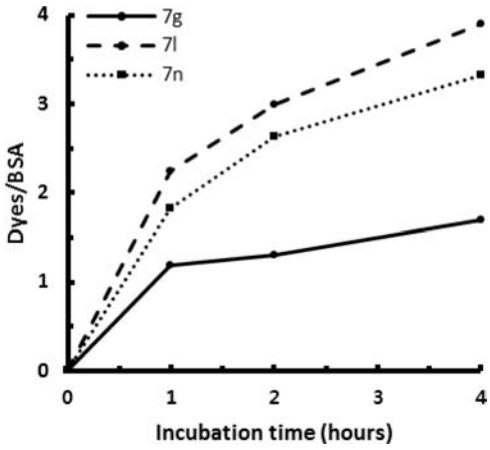


Figure 8. The number of dyes that conjugated to BSA. Labeling solutions were monitored for 4 h via HPLC.

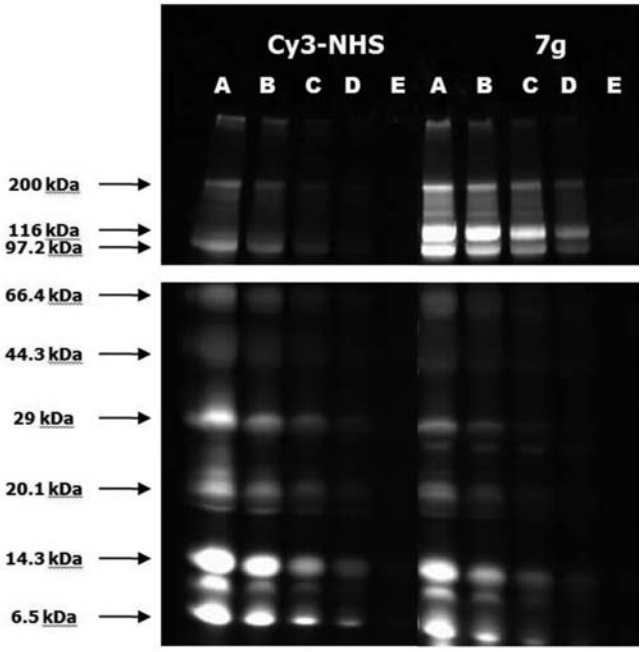


Figure 9. Comparison of labeling intensity using various proteins. Each protein (1 μL) was diluted with pH 9.5, 0.1 M sodium phosphate buffer (18 μL). Stock solutions of Cy3-NHS (A, 0.25 μL; B, 0.125 μL; C, 0.0625 μL; D, 0.025 μL; and E, 0.0025 μL) and **7g** (A, 0.25 μL; B, 0.125 μL; C, 0.0625 μL; D, 0.025 μL; and E, 0.0025 μL) were added to the protein solutions. The mixed protein solutions were incubated at 25 °C for 4 h. Fluorescent molecular weight markers (Takara Bio Inc., Japan) were used.

to stain low molecular weight proteins (less than 29 kDa), and **7g** stained high molecular weight proteins (more than 97.2 kDa). Because VS cyanine dye has greater long-term stability and reactivity in basic condition than NHS-type dyes, VS cyanine dyes were more evenly labeled with whole proteins.

DISCUSSION

Labeling protein, antibody, or peptide with NHS ester fluorescent dyes can be quite burdensome, as these dyes are unstable at high temperature or high pH, and hydrolyze in aqueous solutions. The main objective of this research was to develop stable fluorescent dyes to facilitate the labeling of dyes. Among various intermediates reacting with nucleophiles, intermediates with the VS group are known to be very stable in aqueous solution, high pH, and high temperature. Keeping these advantages in mind, we utilized VS groups in place of NHS ester groups of cyanine-based fluorophores, since they are widely used in biochemistry research. Our biggest concerns in constructing a cyanine-based dye were its hydrophobicity and the length of the spacer between the VS group and the main body, as those factors have significant impact on reacting with biological materials.

Following the references, cyanine dyes with NHS ester were synthesized. A VS intermediate, 2-(2′-chloroethylsulfonyl)-ethylamine hydrochloride, was introduced as a nucleophile in the presence of *N,N*-diisopropylethylamine at 25 °C. We were able to obtain cyanine dyes with VS groups with this method. These dyes were divided into 550, 650, and 750 nm excitation wavelength ranges, and their emission wavelengths were 570, 671, and 782 nm, respectively. In the functionality standpoint, the fluorescence intensity of these dyes is the most important factor. The general consensus is that the intensity is directly proportional to the molar extinction coefficient of the dyes. According to references,[12] the molar extinction coefficients of cyanine dyes at the three wavelengths mentioned above range from 150 000 to 250 000. As seen in Table 1, the VS in cyanine dyes exhibited molar extinction coefficients within that range. To achieve the highest fluorescence intensity, we selected **7g**, **7l**, and **7n** showing 550, 650, and 750 nm, respectively, since they had the highest molar extinction coefficient. The difference in the length of the spacer, and the introduction of methyl, ethyl, propyl, and butyl group for controlling hydrophobicity, did not have any notable impact on the molar extinction coefficients, and we have selected compounds with the highest values. The results suggest that absorbance and fluorescence spectra of the three cyanine-based VS dyes are similar to those of cyanine-based NHS ester dyes reported in the reference.[12] We also confirmed that red shift of emission, by 100 nm, occurs depending on the length of the polymethine group.

To ensure labeling efficiency, we aimed to determine whether there is any effect from the difference in the length of the spacer. For the 550 nm range, **7a**, **7c**, **7f**, and **7g** having five, six, eight, and eight carbon atoms in the spacer, respectively, were chosen. **7g** was included for its highest extinction coefficient in the 550 nm wavelength, as well as for its future use as a standard compound. Compound **7g**, having 8 carbon atoms, exhibited the fastest labeling time, and had the least amount of unreacted dye after 6 h. Given enough reaction time, dyes at other wavelengths should give approximately 85% labeling efficiency. Both **7f** and **7g** showed 85% labeling efficiency. However, **7g** was found to be quicker in labeling after just 1 h, since its labeling efficiency was about 5% higher than that of **7f**. Regarding compounds **7i** and **7l**, both of which are in the 650 nm wavelength range, compound **7l** with two more carbon atoms was more efficient in labeling than **7i** when compared at 1 and 6 h. No additional compound was added, since **7n** already exhibited 90% efficiency. This result suggests

that the length of the spacer affects the overall flexibility of the structure of the dyes.

According to established labeling protocols and references on dye labeling, the determinant factors for labeling efficiency were pH, solvent, and temperature. Organic solvents such as DMF or DMSO were not used in this study, since the majority of proteins and antibodies in the market are either in solid form or diluted in aqueous solution. **7g**, **7l**, and **7n** compounds as well were water-soluble. Moreover, DMF and DMSO are toxic and can become cumbersome during compound analysis.

Reactivity tests showed that dye conjugation is accelerated in basic pH conditions and in body temperature (36.5 °C), where amine groups of targeted proteins can easily react with vinylsulfone. Additionally, 0.1 M or higher phosphate buffer positively affected dye labeling. For further experimentation, reaction conditions of pH 9.5, 25 °C, 0.1 M phosphate buffer were chosen for optimized dye conjugation, considering that common biological experiments prefer 25 °C where there is less than 20% labeling efficacy difference from body temperature, and 0.5 M phosphate buffer tends to have a salting out effect which led decrease in conjugation rate of **7n**.

Also, to determine the stability of the dye in aqueous solutions, the dye was dissolved in water and underwent HPLC analysis in order to monitor hydrolysis of the VS group. Results indicated that **7g**, **7l**, and **7n** showed no change at 25 °C for at least one day. We predicted that, as long as the pH is not extremely high, the reactivity of dye would not drastically change, in spite of minor changes in the stability of cyanine chromophore (Figure 7). The overall data of **7g**, **7l**, and **7n** suggested that compound **7g** exhibited the slowest reaction time but with the best stability, and **7n** exhibited the fastest reaction time and was proven to be unstable with the change in reaction conditions. Reaction time and stability can be easily changed depending on the chemical structure of the dyes. Therefore, more intensive research on the relationship of various cyanine compounds with their reaction time and stability is necessary to improve reactivity and stability.

When labeling protein, antibody, or peptide with fluorescent dyes, excessive amounts of dye are usually used due to limited labeling conditions including intricate structure of biologics, temperature, solvent, time, and so forth. For more accurate quantification of dye labeling, the D/P ratio equation is being widely used, with unique equations for different wavelengths. This equation can also be used to determine how many dyes should be used for proteins with different sizes. Experimental results suggested that 0.7−0.8 molecule of dye is conjugated to a protein molecule when molar equivalents of both dye and protein were reacted together and when the D/P ratio equation was incorporated for **7g**, **7l**, and **7n**, only with less than 10% error (Table 2). When an excessive amount of dye by 7× molar equivalent was used, a higher number of molecules of each dye was conjugated to a protein molecule with **7l** being the most conjugated. However, we cannot jump to the conclusion that this result would be reproducible with other kinds of protein. There are various factors to be considered in protein such as size, structure, affinity to dye, the number and location of amine groups in the protein molecule, and so forth.

For the study on labeling feature of VS cyanine dyes to proteins, compound **7g** was compared with GE Healthcare's Cy3-NHS dye. The reaction of Cy3-NHS was carried out under the manufacturer's suggested conditions, whereas compound **7g** was done in its optimal condition stated above. Considering the variability in structures and characteristics of proteins, a marker protein (protein ladder for SDS-PAGE) containing nine different proteins was used. This marker was not labeled with dyes, thus enables us to directly compare how Cy3-NHS and **7g** conjugate to the proteins. The conjugation efficiency varied depending on the protein size. When the two dyes were compared, compound **7g** was conjugated better with higher molecular weight proteins such as myosin, β-galactosidase, and phosphorylase B. Cy3-NHS showed higher intensity with small molecular weight proteins such as trypsin inhibitor, lysozome, and aprotinin. We determined that compound **7g** performed better with high molecular weight proteins. On the other hand, Cy3-NHS performed better with low molecular weight proteins because of the shorter reaction time.

Table 2. Number of Conjugated VS Cyanine Dyes (Absorption Intensity Values (A_{280}, A_{dye}) at Each Maximum Absorption Wavelength (BSA (280 nm), 7g (280 nm, 549 nm), 7l (280 nm, 647 nm), and 7n (280 nm, 749 nm)), BSA Extinction Coefficient (E_{prot}), BSA Extinction Coefficient (E_{dye}), Denominator Factor for Dye Absorption at 280 nm ($A_{D.C.}$), and Dye/Protein Ratio (D/P = $(A_{dye}E_{prot})/(A_{280} - A_{D.C.}A_{dye})E_{dye})$)

dye no. (conjuated BSA)	$A_{D.C.}$	E_{dye} ($\times 10^5$ L/mol cm)	E_{prot}/E_{dye}	A_{280}	A_{dye}	D/P
7g	0.067	1.46	0.292	0.204	0.398	0.657
7l	0.023	2.72	0.157	0.132	0.461	0.594
7n	0.03	2.25	0.19	0.147	0.610	0.901

■ ASSOCIATED CONTENT

Ⓢ Supporting Information

Reactivity test of VS cyanine dye with benzyl amine; dye conjugation study via MALDI-TOF M/S; multiple band analysis using SDS-PAGE. This material is available free of charge via the Internet at http://pubs.acs.org.

■ AUTHOR INFORMATION

Corresponding Author

*Kee-Jung Lee: Tel +82-2-2220-0528, Fax +82-2-2298-4101, E-mail: leekj@hanyang.ac.kr. Dong Jin Kim: Tel +82-2-958-5142, Fax +82-2-958-5189, E-mail: djk2991@kist.re.kr.

Notes

The authors declare no competing financial interest.

■ ACKNOWLEDGMENTS

This work was supported by the project No. 10033024 from the Advanced Technology Center (ATC) Support Program of Ministry of Knowledge Economy (Republic of Korea). We thank Kinam Park, Ph.D. (Professor of Pharmaceutics, Purdue University) for support in dye conjugation ratio measurements, Sang Yeul Lee, Ph.D. (Sogang University), and Namho Kim (BioActs Co. Ltd.). The three novel cyanine compounds (**7g**, **7l**, and **7n**) are available by BioActs Co. Ltd (Code No. PWA1119, PWA1215, and PWA1308).

■ REFERENCES

(1) Qin, C., Zhu, S., and Tian, J. (2010) New optical molecular imaging systems. *Curr. Pharm. Biotechnol. 11*, 620−7.

(2) Chen, Y., He, Z., Cao, S., Sang, J., Pi, J., and Hu, Y. (2008) The application of in vivo optical imaging technologies with bioluminescence and fluorescence on the research of stem cell. *Shengwu Jishu Tongxun 19*, 280−282.

(3) Glunde, K., and Li, C. (2008) Optical imaging probes and techniques for cancer imaging. *Recent Advances of Bioconjugation Chemistry in Molecular Imaging*, 243−260.
(4) Shah, K. (2005) Current advances in molecular imaging of gene and cell therapy for cancer. *Cancer Biol. Ther. 4*, 518−523.
(5) Hilderbrand, S. A., and Weissleder, R. (2010) Near-infrared fluorescence: application to in vivo molecular imaging. *Curr. Opin. Chem. Biol. 14*, 71−79.
(6) Petrovsky, A., Schellenberger, E., Josephson, L., Weissleder, R., and Bogdanov, A. (2003) Near-infrared fluorescent imaging of tumor apoptosis. *Cancer Res. 63*, 1936−1942.
(7) Lee, S., Xie, J., and Chen, X. Y. (2010) Peptide-Based Probes for Targeted Molecular Imaging. *Biochemistry 49*, 1364−1376.
(8) Lee, S., Park, K., Kim, K., Choi, K., and Kwon, I. C. (2008) Activatable imaging probes with amplified fluorescent signals. *Chem. Commun. (Camb.)*, 4250−60.
(9) Mishra, A., Behera, R. K., Behera, P. K., Mishra, B. K., and Behera, G. B. (2000) Cyanines during the 1990s: A Review. *Chem. Rev. 100*, 1973−2012.
(10) Hannah, K. C., and Armitage, B. A. (2004) DNA-templated assembly of helical cyanine dye aggregates: A supramolecular chain polymerization. *Acc. Chem. Res. 37*, 845−853.
(11) Mujumdar, R. B., Ernst, L. A., Mujumdar, S. R., and Waggoner, A. S. (1989) Cyanine dye labeling reagents containing isothiocyanate groups. *Cytometry 10*, 11−9.
(12) Mujumdar, R. B., Ernst, L. A., Mujumdar, S. R., Lewis, C. J., and Waggoner, A. S. (1993) Cyanine dye labeling reagents: sulfoindocyanine succinimidyl esters. *Bioconjugate Chem. 4*, 105−11.
(13) Hilal, H., and Taylor, J. A. (2008) Cyanine dyes for the detection of double stranded DNA. *J. Biochem. Biophys. Methods 70*, 1104−1108.
(14) Cline, G. W., and Hanna, S. B. (1988) Kinetics and Mechanisms of the Aminolysis of N-Hydroxysuccinimide Esters in Aqueous Buffers. *J. Org. Chem. 53*, 3583−3586.
(15) Wilchek, M., and T., M. (1987) Limitations of N-Hydroxysuccinimide Esters in Affinity Chromatography and Protein Immobilization. *Biochemistry 26*, 2155−2161.
(16) Lewis, D. M. (1992) *Wool dyeing*, Society of Dyers and Colourists, Bradford.
(17) Anderton, K. (1994) Water-soluble reactive dyes and their use, Eur. Patent Application 578357.
(18) Tzikas, A., and Aeschlimann, P. (1991) Fiber-reactive dyes containing a substituted carbamoylphenylamino or -naphthylamino reactive moiety, U.S. Patent 5,023,325.
(19) Tzikas, A. (1988) Bifunctional reactive triazine group-containing dyes, Eur. Patent Application 297044.
(20) Tzikas, A., and Burdeska, K. (1989) Pyrimidinyl group-containing yellow reactive azo dyes which can be used at low temperatures, Eur. Patent Application 298041.
(21) Seiler, H. (1983) Reactive dyes, Eur. Patent Application 70,806.
(22) Heyna, J. (1963) Reactive dyes containing vinylsulfonyl groups. *Angew. Chem. 2*, 20.
(23) Venkataraman, K. (1974) *The chemistry of synthetic dyes*, Vol. *6*, Academic Press, New York.
(24) Yamamoto, K., and Nakazaki, M. (1975) Direct Synthesis of Indole by the Fischer Indole Synthesis. *J. Org. Chem. 41*, 1877.
(25) Oswald, B., Patsenker, L., Duschl, J., Szmacinski, H., Wolfbeis, O. S., and Terpetschnig, E. (1999) Synthesis, spectral properties, and detection limits of reactive squaraine dyes, a new class of diode laser compatible fluorescent protein labels. *Bioconjugate Chem. 10*, 925−31.
(26) Mader, O., Reiner, K., Egelhaaf, H. J., Fischer, R., and Brock, R. (2004) Structure property analysis of pentamethine indocyanine dyes: identification of a new dye for life science applications. *Bioconjugate Chem. 15*, 70−8.
(27) Korbel, G. A., Lalic, G., and Shair, M. D. (2001) Reaction microarrays: a method for rapidly determining the enantiomeric excess of thousands of samples. *J. Am. Chem. Soc. 123*, 361−2.
(28) Jung, M. E., and Kim, W. J. (2006) Practical syntheses of dyes for difference gel electrophoresis. *Bioorg. Med. Chem. 14*, 92−7.
(29) Illy, H., and Funderburk, L. (1968) Fischer Indole Synthesis. Direction of Cyclization of Ieopropylmethyl Ketone Phenylhydrazone. *J. Org. Chem. 33*, 4283−4285.
(30) Hilderbrand, S. A., and Weissleder, R. (2007) Optimized pH-responsive cyanine fluorochromes for detection of acidic environments. *Chem. Commun. (Camb.)*, 2747−9.
(31) Ernst, L. A., Gupta, R. K., Mujumdar, R. B., and Waggoner, A. S. (1989) Cyanine dye labeling reagents for sulfhydryl groups. *Cytometry 10*, 3−10.
(32) Kim, D. C., Kim, D. J., Park, S. U., and Park, U. S. (2001) Method for preparation of 2-(2-chloroethylsulfonyl)ethylamine HCl salt, Republic of Korea Patent 2001098033.
(33) Smith, G. P. (2006) Kinetics of amine modification of proteins. *Bioconjugate Chem. 17*, 501−6.
(34) Yam, R., Nachliel, E., and Gutman, M. (1988) Time-Resolved Proton-Protein Interaction. Methodology and Kinetic Analysis. *J. Am. Chem. Soc. 110*, 2636−2640.
(35) Von der Eltz, H. U. (1973) Vinyl sulfone dyes. From conception to success. *Colourage Annual*, 63−83.

Bioconjugate Chemistry

Article

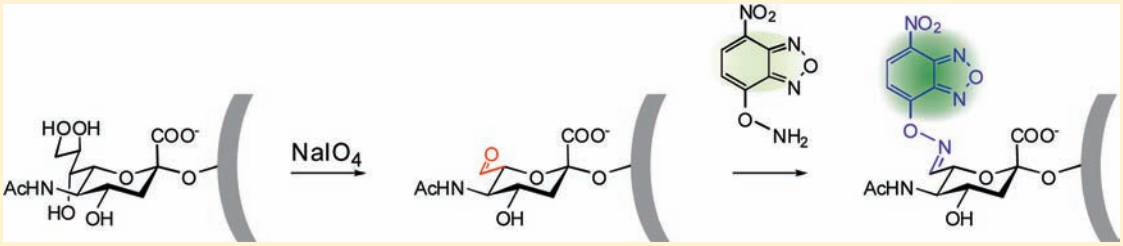
pubs.acs.org/bc

Detection of Cellular Sialic Acid Content Using Nitrobenzoxadiazole Carbonyl-Reactive Chromophores

Jessie A. Key, Caishun Li, and Christopher W. Cairo*

Alberta Glycomics Centre, Department of Chemistry, University of Alberta, Edmonton, Alberta T6G 2G2, Canada

Supporting Information



ABSTRACT: The selective ligation of hydrazine and amino-oxy compounds with carbonyls has gained popularity as a detection strategy with the recognition of aniline catalysis as a way to accelerate the labeling reaction in water. Aldehydes are a convenient functional group choice since there are few native aldehydes found at the cell surface. Aldehydes can be selectively introduced into sialic acid containing glycoproteins by treatment with dilute sodium periodate. Thus, the combination of periodate oxidation with aniline-catalyzed ligation (PAL) has become a viable method for detection of glycoconjugates on live cells. Herein we examine two fluorescent nitrobenzoxadiazole dyes for labeling of glycoproteins and cell surface glycoconjugates. We introduce a novel 4-aminooxy-7-nitro-benz-[2,1,3-*d*]-oxadiazole (NBDAO) (**5**) fluorophore, and offer a comparison to commercial dyes including the known 4-hydrazino-7-nitro-benz-[2,1,3-*d*]-oxadiazole (NBDH) (**2**) and Bodipy FL hydrazide. We confirm specificity for sialic acid moieties and that both dyes are suitable for in vitro and in vivo labeling studies using PAL and fluorescence spectroscopy. The dyes examined here are attractive labeling agents for microscopy, as they can be excited by a 488 nm laser line and can be made in a few synthetic steps. These carbonyl-reactive chromophores provide a one step alternative to avidin−biotin labeling strategies and simplify the detection of sialic acid in cells and glycoproteins.

INTRODUCTION

Sensitive detection of biomolecules by derivatization with fluorescent dyes is a critical technique used in histology, cell biology, and biochemistry.[1−3] Specific detection of conjugates relies on chemoselective ligation of functional groups found on the biomolecule and the label.[4] As a result, strategies to introduce reactive functional groups into biomolecules have been developed. Typical strategies include the metabolic incorporation of synthetic labels and chemical modification of native biomolecules.[4,5] A well-known strategy for labeling of glycoproteins is the use of sodium periodate to oxidize the glycerol side-chain of sialic acid to an aldehyde.[6] While this method is more commonly used in vitro, it has recently been extended to the labeling of glycans in live cells.[7,8] Live cell labeling requires mild conditions and near-quantitative reactions, which has been achieved by performing the oxidation reaction at low temperature, and accelerating the conjugation reaction with an aniline catalyst.[8] This method of periodate oxidation and aniline-catalyzed ligation (PAL) can then be used to label glycoconjugates for microscopy.

Sialic acids are a class of carbohydrates which have important biological functions in embryogenesis, development, and immune response.[9−11] Methods of detecting sialylation include metabolic labeling, lectins, and chemical modification.[12] Metabolic labeling allows the introduction of unique functional groups that provide sensitive detection;[13] however, this strategy can suffer from incomplete label incorporation. Lectins can be large proteins which may suffer from relatively low affinities. Importantly, many lectins or antibodies can perturb cells by cross-linking receptors—limiting their application in live cells.[14,15] Selective chemical modification of sialic acids using PAL presents an attractive alternative.[8] However, previous reports of PAL on cells have relied upon biotin-amino-oxy conjugates which were then detected by fluorescently labeled streptavidin. This two-step method required the use of a 60 kDa tetrameric protein for labeling a single carbohydrate residue (ca. 300 Da).[7,16] Such a bulky label could mask other epitopes on the same cell or macromolecule, and may have reduced labeling capacity due to molecular crowding.

Small molecule fluorophores which contain either hydrazine or amino-oxy functional groups can be applied to bioorthogonal and PAL labeling strategies.[17−19] 7-Nitro-benz-[2,1,3-*d*]-oxadiazoles (NBDs) are a class of small, synthetically accessible, and environmentally sensitive fluorophores which can be easily modified for use with PAL. In general, NBDs possess relatively high fluorescence quantum yields (0.3 for primary amine

Received: May 31, 2011
Revised: January 17, 2012
Published: January 30, 2012

 © 2012 American Chemical Society dx.doi.org/10.1021/bc200276k | *Bioconjugate Chem.* 2012, 23, 363−371

derivatives of NBDCl)[2] and long excitation and emission wavelengths when compared to fluorophores of similar size, such as coumarins.[20] Interestingly, the attachment of a hydrazine functional group to these dyes results in fluorogenic derivatives which allow direct detection of carbonyl derivatives upon formation of the corresponding hydrazone. Reported fluorogenic and fluorescent hydrazino-NBD derivatives include 7-hydrazino-4-nitrobenzo-2-oxa-1,3,-diazole (NBDH),[21] 4-(*N*,*N*-dimethylaminosulfonyl)-7-hydrazino-benz-2,1,3-oxadiazole (DBDH),[22] 4,4-aminosulfonyl-7-hydrazino-2,1,3-benzoxadiazole (ABDH),[22] 4-(*N*,*N*-dimethylaminosulfonyl)-7-*N*-methylhydrazino-benz-2,1,3-oxadiazole (MDBDH),[23] 4-[2-(*N*,*N*-dimethylamino)ethylaminosulfonyl]-7-*N*-methylhydrazino-benz-2,1,3-oxadiazole (DAABD-MHz),[24] and *N*-methyl-4-hydrazino-7-nitrobenzofurazan (MNBDH).[25] Several of these derivatives are commercially available and have found application in biological assays,[26] as well as the detection of trace carbonyls in air samples such as automobile exhaust.[23]

We considered that small molecule labels compatible with PAL should be of interest for fluorescence microscopy and quantitation of glycoconjugates. To take advantage of the PAL strategy, the fluorophore should contain a nucleophilic group that will react with an aldehyde rapidly in water. Although hydrazines have been explored for this purpose, we chose to investigate an amino-oxy-containing fluorophore.[8] Herein we describe the synthesis of a novel amino-oxy fluorophore, NBDAO (**5**), which has improved sensitivity over existing dyes for selective labeling of sialic acid glycoconjugates on live cells. We contrast the properties of NBDAO to a known carbonyl reactive fluorophore, NBDH (**2**).[21] We first observed labeling of cells with a fluorescence microplate reader. Additionally, NBDAO was used to label a glycoprotein in conjunction with PAL, followed by fluorescence detection in SDS-PAGE. Finally, we compared the performance of NBDAO to commercially available hydrazine dyes NBDH and Bodipy FL hydrazide in fluorescence microscopy and flow cytometry assays. We conclude that these dyes can be used as an effective one-step live-cell labeling strategy for glycoconjugates, and that NBDAO provides the best level of sensitivity among the dyes tested.

METHODS

General Experimental Methods. Reagents were purchased from commercial sources such as Sigma-Aldrich (Oakville, Ont) and used without additional purification. Proton (^{1}H) and carbon (^{13}C) NMR spectra were obtained on Varian 300, 400, 500, or 700 MHz instruments at room temperature as noted. Deuterated solvents were obtained from Cambridge Isotope Laboratories (Andover, MA). Mass spectrometry was performed using an MS50G positive electron impact instrument from Kratos Analytical (Manchester, UK) and a Mariner Biospectrometry positive ion electrospray instrument from Applied Biosystems (Foster City, CA).

Spectroscopy. Absorbance spectra for all compounds were collected at room temperature with a Hewlett-Packard (Palo Alto, CA) model 8453 diode array UV−visible spectrophotometer or Varian (Walnut Creek, CA) Cary 50 spectrophotometer. Fluorescence spectra for all compounds were collected at room temperature with a Photon Technology International model MP1 steady-state fluorimeter. Absorbance and fluorescence measurements were taken using NSG Precision Cells ES quartz cuvettes (190−2000 nm; Farmingdale, NY).

Synthesis of Dyes and Model Conjugates. *4-Hydrazinyl-7-nitrobenz-[2,1,3-d]-oxadiazole (**2**, **NBDH**).* 4-Chloro-7-nitrobenz-[2,1,3-*d*]-oxadiazole (**1**) (100 mg, 0.5 mmol, 1 equiv) was dissolved in chloroform (50 mL). A 1% hydrazine solution (0.77 mL hydrazine in 50 mL methanol) was then added to the solution and allowed to stir at room temperature for 1 h. A yellow-brown precipitate was formed and isolated without further purification (104 mg, quant.) ^{1}H NMR (400 MHz, D_2O): δ 7.04 (d, 1H, ^3J = 10.5 Hz), 6.37 (d, 1H, ^3J = 10.5 Hz); ^{13}C NMR (100 MHz, D_2O): δ 147.6, 145.4, 131.4, 121.9, 120.8, 115.1; IR (microscope): ν = 3378, 3278, 3191, 3051, 2984, 2692, 1618, 1542, 1500, 1465, 1213, 1019, 982, 873, 794 cm^{-1}. ES-HRMS calculated for $C_5H_5N_5O_3Na$: 218.0285, observed: 218.0284.

*4-(2-Benzylidenehydrazinyl)-7-nitrobenz-[2,1,3-d]-oxadiazole (**3**).* 4-Hydrazinyl-7-nitrobenz-[2,1,3-*d*]-oxadiazole (**2**) (25 mg, 0.13 mmol, 1 equiv) was dissolved in methanol (10 mL). Benzaldehyde (0.13 mL, 1.3 mmol, 10 equiv) was added, turning the reaction mixture a red color. The product gradually formed as a dark red-black precipitate and was isolated by vacuum filtration. Additional product was isolated from the supernatant after flash column chromatography (EtOAc/hexanes). The precipitate and column fractions were combined (27 mg, 74%). ^{1}H NMR (400 MHz, $(CD_3)_2CO$): 8.62 (d, 1H, ^3J = 8.8 Hz), 8.59 (s, 1H), 7.92−7.79 (m, 2H), 7.56−7.39 (m, 3H), 7.31 (d, 1H, ^3J = 8.8 Hz); ^{13}C NMR (100 MHz, $(CD_3)_2CO$): δ 149.9, 145.2, 144.1, 141.0, 137.0, 134.9, 131.6, 129.8, 128.4, 126.0, 102.7; IR (microscope): ν = 3486, 3307, 3219, 3144, 3060, 2955, 1603, 1581, 1515, 1446, 1406, 1295, 1117, 997 cm^{-1}. ES-HRMS calculated for $C_{13}H_{10}N_5O_3$: 284.0778, observed: 284.0778. R_f = 0.23 (1:3 EtOAc/hexanes).

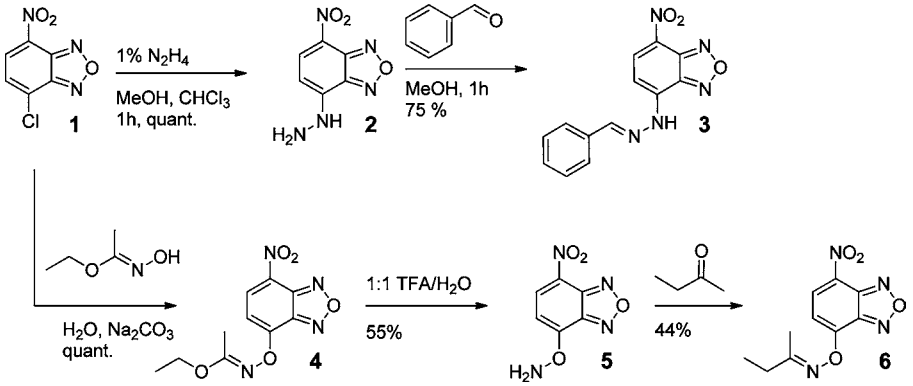
*Ethyl N-7-nitrobenz-[2,1,3-d]-oxadiazol-4-yloxyacetimidate (**4**).* Ethyl *N*-hydroxyacetimidate (35 mg, 0.34 mmol, 3 equiv) was dissolved in H_2O (2 mL). Sodium carbonate (100 mg, 0.94 mmol, 7.5 equiv) was added and the reaction mixture was allowed to stir for 10 min. 4-Chloro-7-nitrobenz-[2,1,3-*d*]-oxadiazole (**1**) (25 mg, 0.125 mmol, 1 equiv) was then added and allowed to stir at room temperature for approximately 15 min. The resulting brown-yellow precipitate was isolated by vacuum filtration without further purification (35 mg, quant.). ^{1}H NMR (300 MHz, $CDCl_3$): δ 8.54 (d, 1H, ^3J = 8.4 Hz), 7.25 (d, 1H, ^3J = 8.4 Hz), 4.27 (q, 2H, ^3J = 6.9 Hz), 2.32 (s, 3H), 1.42 (t, 3H, ^3J = 6.9 Hz); ^{13}C NMR (100 MHz, $CDCl_3$): δ 170.2, 154.3, 144.2, 143.9, 134.6, 129.7, 106.2, 64.4, 15.3, 14.5. IR (microscope): ν = 3133, 3090, 2999, 2988, 1933, 1713, 1645, 1623, 1537, 1451, 1379, 1164, 997, 854 cm^{-1}. ES-HRMS calculated for $C_{10}H_{10}N_4O_5Na$: 289.0543, observed: 289.0541. R_f = 0.69 (1:3 EtOAc/hexanes).

*O-(7-Nitrobenzo-[2,1,3-d]-oxadiazol-4-yl)hydroxylamine (**5**, **NBDAO**).* Ethyl *N*-7-nitrobenz-[2,1,3-*d*]-oxadiazol-4-yloxyacetimidate (**4**) (250 mg, 0.94 mmol, 1 equiv) was dissolved in 1:1 TFA/water (25 mL) and allowed to stir at room temperature for 2 h. The TFA was removed in vacuo, and the resulting aqueous solution was concentrated by lyophilization. The product was isolated by flash column chromatography with a dichloromethane mobile phase (94 mg, 55%). ^{1}H NMR (700 MHz, $CDCl_3$): δ 8.56 (d, 1H, ^3J = 8.4 Hz), 7.40 (d, 1H, ^3J = 8.4 Hz), 6.51 (s, 2H). ^{13}C NMR (175 MHz, $CDCl_3$): δ 156.0, 143.9, 143.5, 134.0, 130.1, 105.7; IR (microscope): ν = 3325, 3255, 3167, 3104, 2918, 2851, 1641, 1588, 1537, 1328, 1083, 997, 729 cm^{-1}. ES-HRMS calculated for $C_6H_4N_4O_4Na$: 219.0125, observed: 219.0127. R_f = 0.25 (1:3 EtOAc/hexanes).

*Butan-2-one O-7-nitrobenzo-[2,1,3-d]-oxadiazol-4-yl oxime (**6**).* *O*-(7-Nitrobenz-[2,1,3-*d*]-oxadiazol-4-yl)-hydroxylamine (**5**) (27 mg, 0.14 mmol, 1 equiv) was dissolved

dx.doi.org/10.1021/bc200276k | *Bioconjugate Chem.* 2012, 23, 363−371

Scheme 1. Synthesis of NBDH (2) and NBDAO (5) Carbonyl Reactive Chromophores and Model Hydrazone and Oxime Ligation Products (3 and 6)



in methylethylketone (MEK) (0.08 mL, 0.83 mmol, 6 equiv). The reaction was allowed to run at room temperature for 2 h. Excess MEK was removed in vacuo and the remaining residue was purified as an inseparable mixture of *E*/*Z* isomers (1.36:1) using flash column chromatography (EtOAc/hexanes) (15 mg, 44%). ^{1}H NMR (400 MHz, $CDCl_3$): δ 8.56 (d, 1H, ^3J = 9.3 Hz), 7.35 (d, 1H, ^3J = 9.6 Hz), 2.73 (q, 0.90H, ^3J = 7.8 Hz), 2.48 (q, 1.29H, ^3J = 7.5 Hz), 2.25 (s, 1.88H), 2.14 (s, 1.38H), 1.26 (m, 5.23H); ^{13}C NMR (125 MHz, $CDCl_3$): δ 169.7, 168.8, 153.98, 153.92, 144.0, 143.8, 134.4, 129.8, 106.6, 29.8, 24.0, 19.3, 15.5, 10.4; IR (microscope): ν = 3113, 3092, 2987, 2987, 2919, 2849, 1633, 1533, 1453, 1369, 1327, 887, 854, 733 cm^{-1}. ES-HRMS calculated for $C_{10}H_{11}N_4O_4$: 251.0775, observed: 251.0778. R_f = 0.67 (1:1 EtOAc/hexanes).

Reaction Kinetics. Dye solutions of NBDH (6.88×10^{-5} M) or NBDAO (2.50×10^{-5} M) were prepared in 1 mL aliquots with or without aniline (4.38×10^{-4} M) in buffer (0.1 M sodium acetate, pH 4.7; or 0.1 M HEPES, pH 7.4). An aliquot of MEK (10 μL, 1.11×10^{-4} M) was added and the fluorescence emission of the reaction was monitored for 1500 s (ex. 480 nm; em. 540 nm).

Glycoprotein Labeling. Fetal calf serum fetuin (1 mg/mL, 0.5 mL aliquots) was treated with 1 mL aliquots of neuraminidase from *Clostriduim perfringens* (*C. Welchii*) (0.1 mg/mL) in sodium acetate buffer (0.1 M, pH 5.4) for 0.5 h at 37 °C. Sodium acetate buffer was removed by ultrafiltration (Millipore, Billerica, MA) for 15 min at 1600 g, followed by a water wash (1 mL). Oxidation was performed by treatment with sodium periodate (300 μL, 0.1 M) for 30 min at 4 °C. Excess periodate was removed by ultrafiltration for 15 min at 1600 *g*, followed by a water wash (1 mL). Aliquots of the protein (20 or 10 μL) were then treated with a labeling solution (20 μL) consisting of NBDAO (1.25×10^{-5} M) and aniline (4.38×10^{-4} M) in sodium acetate buffer (0.1 M, pH 4.7) for 0.5−1 h at 4 °C. Labeled proteins were resolved by SDS PAGE (stacking 4%, resolving 12%). The resulting gels were imaged using a FujiFilm Fluorescent Image Analyzer FLA-5000 (Fujifilm medical systems USA Inc., Stamford, CT) with 473 nm excitation and a low band-pass filter. Coomassie staining was used to detect molecular weight standards.

Microplate Assay. HeLa cells were grown in Dulbecco's modified Eagle medium (DMEM) with 10% fetal bovine serum (FBS) at 37 °C under 5% CO_2 to approximately 80% confluency. Cells were trypsinized, and then added to 96 well plates (~2000 cells/well) (tissue culture treated; Corning, Corning, NY). The plate was then incubated for 96 h at 37 °C in a humidified incubator. The growth media was removed and the plates were washed with Dulbecco's phosphate buffered saline (DPBS). Wells were then treated with sodium periodate (80 μL, 1 mM) or DPBS buffer control (80 μL) for 30 min at 4 °C. The solution was removed by inversion, and the plates were washed with DPBS (2 × 100 μL). Control and sample wells were treated with dye for 1 h at 4 °C (NBDH, 2.50×10^{-5} M; NBDAO, 2.5×10^{-5} M; or Bodipy-FL hydrazide, 2.50×10^{-5} M). Dye solutions were prepared in 1 mL aliquots with or without aniline (4.38×10^{-4} M) in DPBS (pH 7.4) or 0.1 M sodium acetate buffer (pH 4.7) as indicated. Fluorescence measurements were taken on a Molecular Devices M2e plate reader (Sunnyvale, CA).

Fluorescence Microscopy. HeLa cells were added to a 6-well plate (~10 000 cells/well) containing treated coverglass (1% (m/v) BSA in TBS), and grown to approximately 60% confluence. The growth media was removed and the wells were washed with DPBS. Sample wells received sodium periodate in DPBS (1 mL, 1 mM) treatment; control wells received DPBS (2 mL); samples were then incubated for 30 min at 4 °C. Cells can optionally be fixed at this point by washing with sodium acetate buffer (0.1 M, pH 4.7; 2 × 2 mL), incubation for 10 min in a 1:1 solution of sodium acetate buffer and methanol, and incubation for 10 min in methanol. Fixing solution is then removed, and the samples are washed with sodium acetate buffer (2 × 2 mL). The double negative control was treated with buffer solution, while control and experimental wells were then treated with dye for 0.5 to 1 h at 4 °C (NBDH, 2.50×10^{-5} M; NBDAO, 2.50×10^{-5} M; or Bodipy-FL hydrazide, 2.50×10^{-5} M). Dye solutions were prepared in 1 mL aliquots with aniline (4.38×10^{-4} M) in sodium acetate buffer (0.1 M, pH 4.7). Each treatment was observed in triplicate. Cells were washed with buffer after staining, and then visualized using a Nikon Eclipse Ti inverted fluorescence microscope with 60× objective (NA 1.49). Images were acquired with a Photometrics QuantEM 512SC camera.

Flow Cytometry. Jurkat cells were grown in RPMI 1640 media (Invitrogen, Carlsbad, CA) with 10% fetal bovine serum (FBS) at 37 °C under 5% CO_2 to approximately 1×10^6 cells/mL. The growth media was removed and the cells were washed with DPBS. Control cell aliquots were incubated in DPBS for 1 h at 37 °C. Sialidase-treated cell aliquots were incubated at 37 °C in the presence of *Clostridium perfringens* neuraminidase (0.4 mg/mL; Sigma-Aldrich, St. Louis, MO). Cells were pelleted by centrifugation (2000 *g* × 4 min) and washed with DPBS. Oxidation-treated aliquots received sodium periodate in

dx.doi.org/10.1021/bc200276k | *Bioconjugate Chem.* 2012, 23, 363−371

Table 1. Photophysical Properties of NBDH, NBDAO, Hydrazone, and Oxime Conjugates

compound	solvent	λ max$_{abs}$[a] [nm]	λ max$_{em}$ [nm]	Φ_F (R6G)[b]	ε[c] absorption coefficient [cm^{-1} M^{-1}]	brightness
NBDH (**2**)	aq. pH 7.4	271, 374, 494	na	na	na	na
	aq. pH 5.4	271, 372, 496	552	0.001	14800	10
	aq. pH 4.7	377	na	na	2950	na
	CH_3CN	280, 405, 425	531, 548	0.003	56700	170
	EtOH	334, 470	537	0.280	110500	31547
hydrazone (**3**)	aq. pH 7.4	360, 444	na	na	67900	34
	aq. pH 5.4	356, 440, 495	552	0.006	52100	320
	aq. pH 4.7	379, 506	598	0.004	630	2.5
	CH_3CN	306, 323, 492	555	0.026	98000	2501
	EtOH	307, 327, 493	555	0.038	25600	977
NBDAO (**5**)	aq. pH 4.7	291, 381, 470	552	0.006	8000	46
	CH_3CN	279, 376, 466	541	0.133	14000	1863
	EtOH	275, 376, 472	540	0.054	10200	548
oxime (**6**)	aq. pH 4.7	390, 465	566	0.003	16700	42
	CH_3CN	264, 380, 470	538	0.138	15600	2150
	EtOH	270, 378, 467	545	0.160	7900	1263

[a]Absorbance maxima are listed with the peak used for fluorescence excitation underlined. [b]Fluorescence quantum yield (Φ_F) standard was rhodamine 6G in ethanol measured with excitation at 485 nm. [c]Molar absorption coefficient, ε, measured at 485 nm.

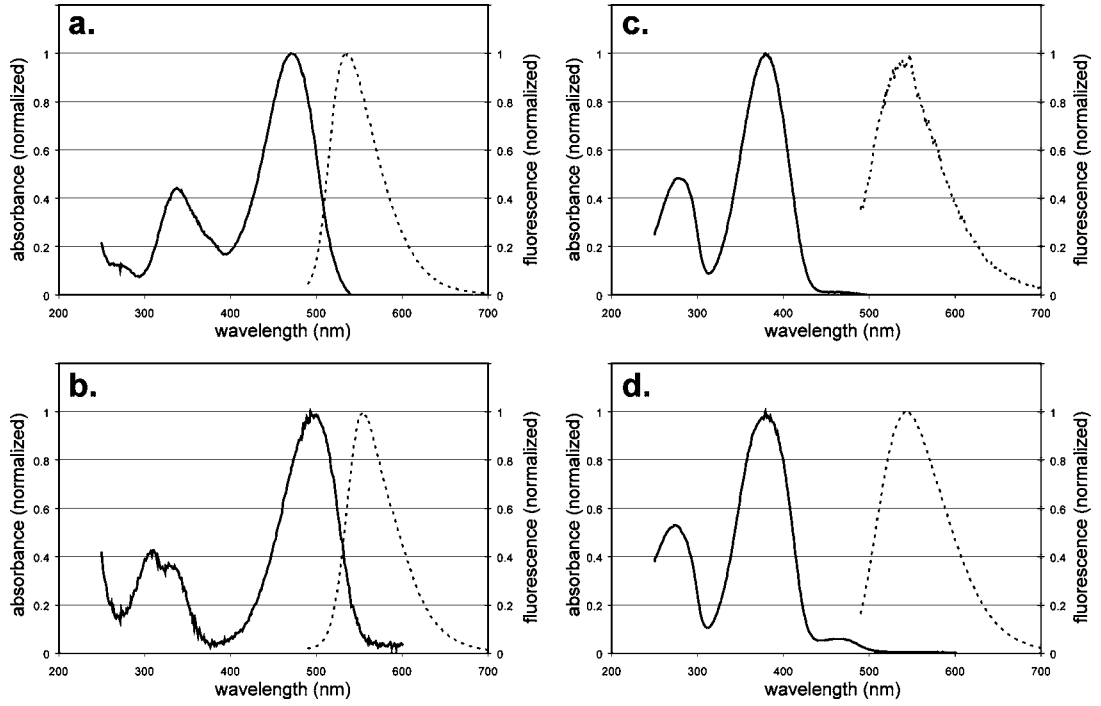


Figure 1. Absorbance and emission spectra in ethanol (excitation 475 nm) of (a) NBDH (**2**), (b) hydrazone (**3**), (c) NBDAO (**5**), and (d) oxime (**6**).

DPBS (1 mL, 1 mM); nonoxidized aliquots received DPBS (1 mL). Samples were then incubated for 30−45 min at 4 °C. Cells were again pelleted by centrifugation (2000 $g \times 4$ min) and washed three times with DPBS. Unlabeled control aliquots were treated with buffer solution, while a set of nonoxidized and oxidized aliquots were treated with dye (100 μL) for 1−1.5 h at 4 °C (NBDAO, 2.50×10^{-5} M; Bodipy-FL hydrazide 2.50×10^{-5} M (Invitrogen, Carlsbad, CA); NBDH 2.50×10^{-5} M). Dye solutions were prepared in 1 mL aliquots with aniline (4.38×10^{-4} M) in sodium acetate buffer (0.1 M, pH 4.7). Cells were pelleted by centrifugation (2000 $g \times 4$ min) and washed three times with DPBS before flow cytometry. Flow cytometry was performed on an Accuri C6 cytometer (Ann Arbor, MI) with 488 nm excitation and 533 nm detection. Each treatment was observed in triplicate runs with 10 000 events.

RESULTS AND DISCUSSION

Fluorophore Synthesis. NBDH (**2**) was synthesized from commercially available 7-nitro-4-chlorobenz-2,1,3-oxadiazole (NBDCl) (**1**) in chloroform by reaction with 1% hydrazine as described by Gubitz et al.[21] Alternatively, the NBDH·NH_2NH_2 salt may be prepared from 7-nitro-4-fluorobenz-2,1,3-oxadiazole using the method of Uzu and colleagues.[22] A hydrazone derivative, **3**, was then generated in good yield by conjugation with benzaldehyde in methanol at room temperature (Scheme 1). NBDAO (**5**) was synthesized by an initial S_NAr of NBDCl (**1**) with ethyl *N*-hydroxyaceti-

dx.doi.org/10.1021/bc200276k | *Bioconjugate Chem.* 2012, 23, 363−371

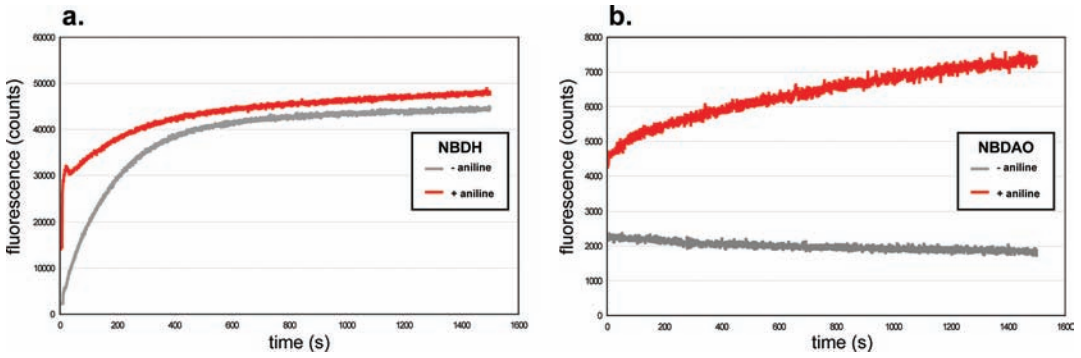


Figure 2. Reaction kinetics of (a) NBDH (**2**) and (b) NBDAO (**5**) with MEK at pH 4.7. The rates of both reactions are enhanced by the presence of aniline in the reaction mixture. The excitation wavelength was 485 nm, and emission was monitored at 540 nm for 1500 s.

midate under basic conditions, to generate the ethyl acetohydroxamate intermediate (**4**).[27] The acetimidate functions as a protected amino-oxy group, and reported deprotection protocols for aryl substrates involve the use of strong acids, such as perchloric acid and hydrofluoric acid.[27,28] We found that the amino-oxy functional group could be unveiled in moderate yield by hydrolysis with aqueous trifluoroacetic acid. Care must be taken at the deprotection step to avoid alkaline workup conditions. In our hands, basic solutions lead to decomposition of the amino-oxy compound, presumably to the corresponding phenolate.[29] Additionally, we found that care should be taken to remove any trace amounts of ketone or aldehyde contaminants (such as acetone) to avoid the rapid formation of the oxime. A representative oxime derivative (**6**) was generated by reaction with neat MEK at room temperature.

Fluorophore Characterization. The NBD dyes (**2** and **5**) and corresponding hydrazone (**3**) and oxime (**6**) conjugates were characterized to determine their absorbance spectra, fluorescence emission, molar absorption coefficients, and fluorescence quantum yields (Φ_F) (Table 1). Quantum yield was determined using a Rhodamine 6G standard in ethanol. Similar to other NBD derivatives, the photophysical properties of these compounds were found to be environmentally sensitive.[3,30] Consistent with previous reports, we confirmed conversion of **2** to **3** was fluorogenic with an 8.5-fold increase in Φ_F and a 15-fold increase in brightness in acetonitrile. Additionally, we observed that NBDH derivatization was fluorogenic in water, particularly at low pH. For example, at pH 5.4 the hydrazone (**3**) has a 9.2-fold increase in Φ_F and 32-fold increase in brightness relative to the starting hydrazine (**2**). However, NBDH and its hydrazone derivative shows less fluorescence in water relative to ethanol and acetonitrile solutions.

The derivatization of NBDAO (**5**) to an oxime (**6**) leads to an increase in the absorption coefficient of the dye; however, there is only a slight shift in the emission wavelength (Figure 1). Both NBDAO and its oxime conjugate (**6**) show a remarkably increased Stokes shift relative to NBDH, which should result in improved sensitivity. Both NBDAO and the oxime derivative have reduced environmental sensitivity when compared to compounds **2** and **3**, respectively, though both dyes (**5** and **6**) exhibited a smaller range of brightness among water, ethanol, and acetonitrile as compared to the hydrazine and hydrazone derivatives (**2** and **3**). The conversion of NBDAO to the oxime appeared to be fluorogenic in certain solvent environments (ethanol), but was relatively static in others. However, we note that several of these values are close to the lower limit of detection, and therefore may not be accurate enough to make this determination. We observed that NBDAO (**5**) underwent degradation to the corresponding phenolate in the presence of alkaline water,[29] which could complicate its use in assays which require high pH. In labeling experiments, we found that this degradation product could be easily removed by performing a wash step after dye treatment.

Reaction Kinetics. The mechanism of oxime or hydrazone formation by NBDAO and NBDH is expected to be accelerated in the presence of aniline, which acts as a nucleophilic catalyst in acidic media.[31,32] Differences in the fluorescent properties of these dyes and their conjugates could be used as a method to observe the rate of the reaction directly. To confirm the role of aniline in these reactions, we observed the kinetics of ligation for NBDH (**2**) or NBDAO (**5**) with MEK in the presence or absence of aniline using a time-based fluorescence assay (Figure 2). As expected, we found that aniline did increase the rate of reaction for both dyes at pH 4.7. In the case of NBDH, the rate acceleration was limited to the early phase of the reaction (<400 s). In the case of the NBDAO dye, the rate acceleration was more substantial, with limited formation of the oxime in the absence of aniline. These findings suggest that NBDAO may be a more selective labeling agent than NBDH when used with aniline catalysis. At pH 7.4, we found that aniline did not increase the rate of reaction for either dye.

Glycoprotein Labeling. To explore the utility of NBDAO for the detection of glycoconjugates, we tested the ability of the dyes to specifically label a known glycoprotein in SDS PAGE. Fetal calf serum fetuin is a commonly used, commercially available sialoprotein.[33,34] Detection of fetuin was performed by treatment with periodate followed by labeling with NBDAO in the presence of aniline (Figure 3). Labeling of a band (~64 kDa) corresponding to the protein was visible by fluorescence imaging. To demonstrate the specificity of this methodology for sialic acid, controls were performed using fetuin which was pretreated with neuraminidase (NEU). As expected, the dye only labeled the glycoprotein when sialic acid was present, and only after periodate treatment—confirming that the labeling chemistry was specific for sialylated protein. We observed only minor residual staining in control samples; and factors that may contribute to background staining could include nonspecific binding[35] and naturally occurring protein oxidation.[36]

Live Cell Labeling. We tested the ability of NBDH (**2**) and NBDAO (**5**) to detect glycans on live cells using PAL. We tested HeLa cells cultured in a microplate which were exposed to periodate, washed, and then treated with one of the

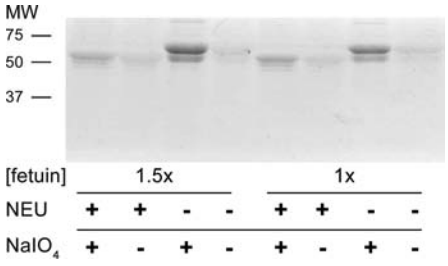


Figure 3. Fluorescent detection of glycoproteins in gel. Labeling of fetal calf serum fetuin by PAL was performed with NBDAO (**5**). Control lanes used protein which was treated with neuraminidase (NEU), and protein not treated with periodate as indicated. Molecular weights are given in kDa.

carbonyl-reactive dyes. Control wells lacked the periodate oxidation step, but were otherwise identical. After labeling, the fluorescence of treated cells was compared to that of the control wells. We found that the mean fluorescence after PAL with both dyes resulted in specific labeling when performed at acidic pH. The NBDH dye gave an increase of 1.3-fold at pH 4.7, and the Bodipy FL hydrazide 3.0-fold, while NBDAO gave a larger increase of 4.3-fold (Figure 4). Labeling by hydrazine

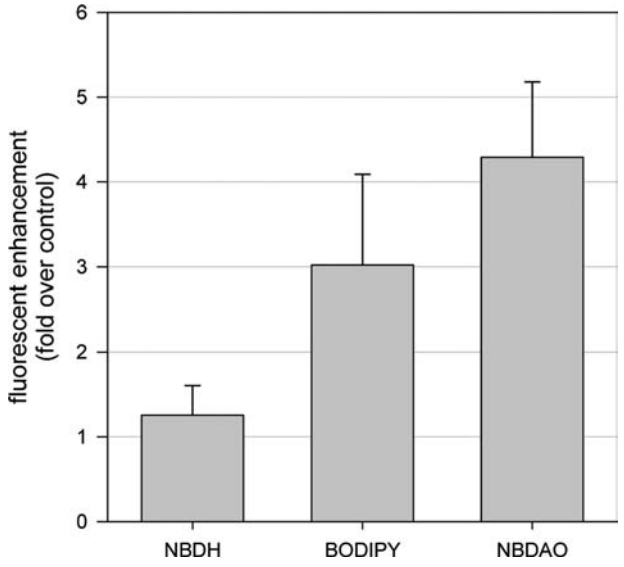


Figure 4. Fluorescence enhancement, expressed as fold enhancement over negative control of 96 well plates after PAL treatment with NBDH (**2**), Bodipy FL hydrazide, or NBDAO (**5**) at pH 4.7. Each point represents at least 8 wells of a representative experiment; error is shown as the standard deviation. All dyes were used at 2.50×10^{-5} M, excitation was at 485 nm, and emission was observed at 538 nm.

and aminooxy dyes were similar to control when the labeling was performed at pH 7.4 (data not shown).

Fluorescence Microscopy. In order to explore the utility of these dyes for imaging applications, we tested their ability to label glycoconjugates in fixed and live cells. HeLa cells were treated with periodate, followed by a solution of dye containing aniline. Both the oxidation and labeling steps were performed at low temperature based on the protocol of Zeng et al.[8] Cells were then imaged using fluorescence microscopy and DIC (Figure 5). To determine the background staining, we included controls that were treated with no periodate and no dye (--), no periodate and dye (-+), and periodate and dye (++). We employed conditions for staining of live and fixed cells for all

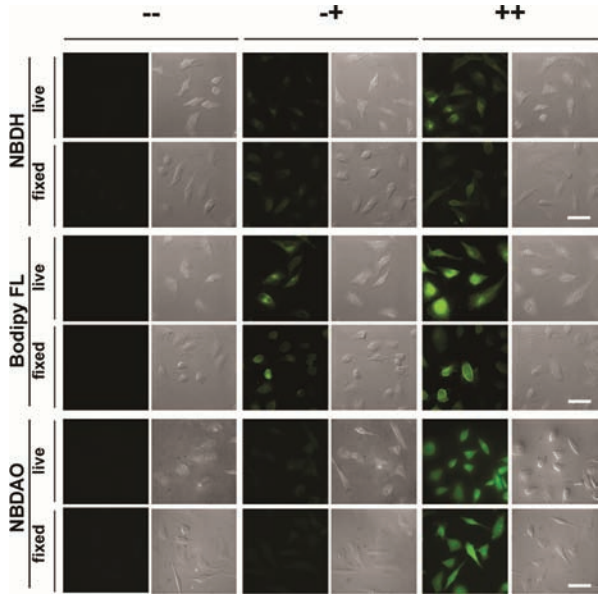


Figure 5. Fluorescence and brightfield images of HeLa cells labeled with NBDH, Bodipy, and NBDAO at pH 4.7. For each dye, cells were observed after one of the following treatments: no periodate and no dye (--); no periodate and dye (-+); and periodate with dye (++). Fluorescence images (488 nm ex/515 nm em) are shown on the left, and DIC images of the same field are shown on the right. Scale bars represent 50 μm. Dye labeling is shown for live and fixed cells (see Materials and Methods).

treatments. We evaluated labeling conditions at pH 4.7, 5.4, 6.1, and 7.4. In our hands, pH 4.7 gave the best results for dye labeling. Fluorescence images of NBDH-treated cells showed staining which was dependent on the use of both periodate and dye. The Bodipy FL hydrazide dye showed higher background than NBDH in samples not treated with periodate (-+), and provided intense labeling of cells after periodate treatement (++). The NBDAO dye provided both low background in samples not treated with periodate (-+), and bright staining of cells treated with periodate (++). Additional controls performed with compound **6** typically showed only background staining (data not shown). Based on these results, we concluded that NBDAO was more suited to fluorescence imaging, and presents a significant improvement over NBDH and Bodipy FL hydrazide. We also note that PAL labeling protocols which exploit small-molecule fluorophores should require fewer steps than affinity-based reagents.[8] The data in Figure 5 suggest that staining by all three dyes in live cells is not restricted to the cell membrane. These results may indicate that periodate oxidation and the dyes used here can penetrate to intracellular compartments. Previous reports have observed labeling of intracellular compartments by NBD-based dyes[37,38] and protein conjugates.[39]

Flow Cytometry. To determine the applicability of small molecule dyes for quantitation of cellular sialic acid content, we examined labeling of Jurkat cells by flow cytometry (Figure 6). Cells were treated with periodate, followed by a solution of dye containing aniline. As with the experiments described above, the oxidation and labeling step was performed at low temperature. To compare the background staining, we included samples that were treated without periodate or dye (--), periodate and no dye (+-), no periodate and dye (-+), and both periodate and dye (++). We tested NBDAO in the assay, and compared it to NBDH and Bodipy FL hydrazide. The NBDAO

dx.doi.org/10.1021/bc200276k | Bioconjugate Chem. 2012, 23, 363–371

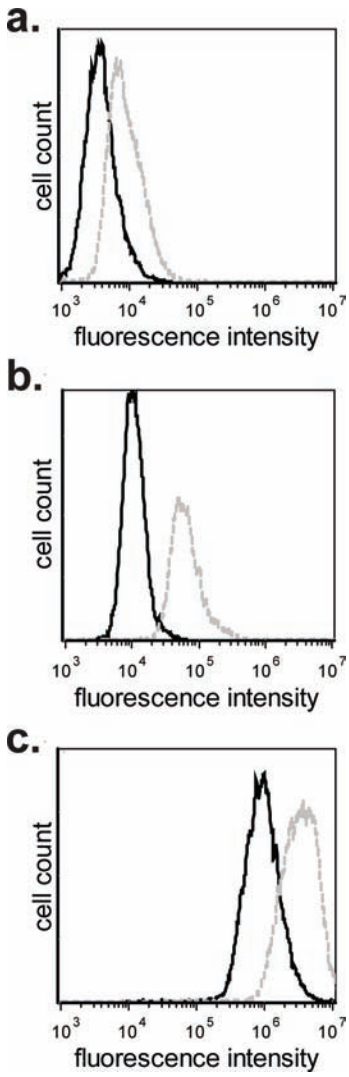


Figure 6. Representative flow cytometry histograms of the relative fluorescence of Jurkat cells treated with a solution containing only the fluorophore (-+, solid black line), or the fluorophore after PAL-treatment of the cells (++, dashed gray line). Dyes shown are (a) NBDH, (b) NBDAO, and (c) Bodipy FL hydrazide.

and NBDH-treated cells showed minor nonspecific background staining (-+) which increased the mean fluorescence intensity (MFI) of cells by approximately 4.5- and 3.0-fold over untreated controls, respectively (see Supporting Information). In contrast, the Bodipy FL hydrazide dye gave a larger increase in background staining (approximately 500-fold). This result likely indicates that the Bodipy fluorophore is more hydrophobic, leading to integration of the dye into the cell membrane. To determine the fidelity of sialic acid detection for each dye, we compared cells which were dye treated (-+) to those which were PAL and fluorophore treated (++). In the case of the NBDAO dye, cells showed an almost 7-fold increase in fluorescence after staining. This was the largest increase we observed, as both commercial dyes (NBDH and Bodipy FL hydrazide) gave only 2−3-fold increases over background. Based on these data we concluded that NBDAO gave the best combination of low background and high signal-to-noise for sialic acid detection. Jurkat cells that were treated with bacterial neuraminidase for one hour, followed by PAL and NBDAO, showed reduced MFI (78 ± 8%) compared to untreated cells, suggesting that this method may be useful to monitor enzymatic changes to sialoproteins in vitro.

Detection strategies for sialic acid on cells and glycoproteins currently include the use of lectins, metabolic labels, or bioconjugation of dyes. In this study, we have examined the utility of small molecule dyes that contain either hydrazine or amino-oxy functional groups to label sialic acid based on the PAL conditions of Zeng et al.[8] In previous studies, labeling of sialic acid by PAL employed a biotin−streptavidin complex; however, here we have explored the utility of small molecule dyes for direct detection of sialoforms using fluorescence. We tested two commercially available dyes, and compared them to the NBDAO dye reported here. Our synthesis of NBDAO (**5**) was carried out in two steps: an S_NAr to form the ethyl acetohydroxamate intermediate (**4**), followed by acidic deprotection.[27] The synthesis of NBDH (**2**) was performed using the method established by Gubitz et al.,[21] and this dye is also commercially available. The kinetics of the reactions between NBDH or NBDAO with MEK were evaluated using a time-based fluorescence assay. Increased reaction rates were observed for both NBDH and NBDAO in the presence of aniline for both reagents at low pH. Comparison of the spectroscopic properties of the dyes and their conjugates initially suggested that the fluorogenic NBDH would have improved signal-to-noise over NBDAO. However, we found that NBDAO was superior to NBDH in the plate assay and microscopy experiments. Importantly, both the NBDH and Bodipy FL hydrazide dyes had poor sensitivity when compared to NBDAO in flow cytometry experiments. These observations may be due to the increased Stokes shift of compound **5** and its oxime conjugates, or the increased stability of the oxime linkage formed between NBDAO and the aldehyde.[40]

■ SUMMARY

We report the synthesis and application of the carbonyl reactive fluorophore, NBDAO, for the selective labeling of sialic acid using PAL. We compared the labeling of NBDAO to two commercially available carbonyl reactive dyes, NBDH and Bodipy FL hydrazide. We found that NBDH and NBDAO dyes can be used to follow the kinetics of hydrazone or oxime formation when combined with an aldehyde substrate. Importantly, when used in conjunction with aniline catalysis these dyes are ideal for labeling of glycoproteins, detection of the sialic acid content of whole cells, and as small-molecule fluorophore stains of glycans on live cells.[41] We demonstrated that these dyes can be used as a simple procedure for sialic acid labeling when combined with periodate oxidation as a method for modifying sialic acids in cells.[8,41] As well, we have shown these dyes can be used as a method for quantitative detection of sialic acid content by flow cytometry. The NBDAO dye showed significant staining of sialic acid over background (6.7-fold), which was superior to the commercially available fluorophores NBDH (2.0-fold) and Bodipy FL hydrazide (2.9-fold). We expect this methodology will prove useful for a variety of applications in glycobiology, particularly in the study of changes to sialic acid content and subcellular location in live cells. These dyes may also prove useful in other carbonyl ligation strategies.[42−45]

■ ASSOCIATED CONTENT

Supporting Information

Absorption and emission spectra of compounds **2**, **3**, **5**, and **6** in water, acetonitrile, and ethanol and flow cytometry histograms.

dx.doi.org/10.1021/bc200276k | *Bioconjugate Chem.* 2012, 23, 363−371

This material is available free of charge via the Internet at http://pubs.acs.org.

AUTHOR INFORMATION

Corresponding Author

*Tel.: 780 492 0377; fax: 780 492 8231; e-mail: ccairo@ualberta.ca.

Notes

The authors declare no competing financial interest.

ACKNOWLEDGMENTS

This work was supported by Natural Sciences and Engineering Research Council of Canada (NSERC) and the Alberta Glycomics Centre (AGC). We would like to thank the Canadian Foundation for Innovation for infrastructure support. The authors would like to thank the University of Alberta Spectral Services laboratory, and M. R. Richards and N. A. Romaniuk (UofA) for helpful discussions.

REFERENCES

(1) Cairo, C. W., Key, J. A., and Sadek, C. M. (2010) Fluorescent small-molecule probes of biochemistry at the plasma membrane. *Curr. Opin. Chem. Biol. 14*, 57−63.

(2) Lavis, L. D., and Raines, R. T. (2008) Bright ideas for chemical biology. *ACS Chem. Biol. 3*, 142−55.

(3) Demchenko, A. P., Mely, Y., Duportail, G., and Klymchenko, A. S. (2009) Monitoring Biophysical Properties of Lipid Membranes by Environment-Sensitive Fluorescent Probes. *Biophys. J. 96*, 3461−3470.

(4) Tiefenbrunn, T. K., and Dawson, P. E. (2010) Chemoselective Ligation Techniques: Modern Applications of Time-Honored Chemistry. *Biopolymers 94*, 95−106.

(5) Sletten, E. M., and Bertozzi, C. R. (2009) Bioorthogonal Chemistry: Fishing for Selectivity in a Sea of Functionality. *Angew. Chem., Int. Ed. 48*, 6974−6998.

(6) Van lenten, L., and Ashwell, G. (1971) Studies on chemical and enzymatic modification of glycoproteins - general method for tritiation of sialic acid-containing glycoproteins. *J. Biol. Chem. 246*, 1889−1894.

(7) De Bank, P. A., Kellam, B., Kendall, D. A., and Shakesheff, K. M. (2003) Surface engineering of living myoblasts via selective periodate oxidation. *Biotechnol. Bioeng. 81*, 800−808.

(8) Zeng, Y., Ramya, T. N. C., Dirksen, A., Dawson, P. E., and Paulson, J. C. (2009) High-efficiency labeling of sialylated glycoproteins on living cells. *Nat. Methods 6*, 207−209.

(9) Varki, N. M., and Varki, A. (2007) Diversity in cell surface sialic acid presentations: implications for biology and disease. *Lab. Invest. 87*, 851−857.

(10) Du, J., Meledeo, M. A., Wang, Z. Y., Khanna, H. S., Paruchuri, V. D. P., and Yarema, K. J. (2009) Metabolic glycoengineering: Sialic acid and beyond. *Glycobiology 19*, 1382−1401.

(11) Bi, S., and Baum, L. G. (2009) Sialic acids in T cell development and function. *Biochim. Biophys. Acta 1790*, 1599−1610.

(12) Chen, X., and Varki, A. (2010) Advances in the Biology and Chemistry of Sialic Acids. *ACS Chem. Biol. 5*, 163−176.

(13) Dube, D. H., and Bertozzi, C. R. (2003) Metabolic oligosaccharide engineering as a tool for glycobiology. *Curr. Opin. Chem. Biol. 7*, 616−625.

(14) Anderson, J., and Melchers, F. (1976) Lymphocyte stimulation by concanavalin A, in *Concanavalin A as a Tool* (Bittiger, H., and Schnebli, H. P., Eds.) pp 505−522, John Wiley & Sons, New York.

(15) Hernandez, J. D., and Baum, L. G. (2002) Ah, sweet mystery of death! Galectins and control of cell fate. *Glycobiology 12*, 127R−136R.

(16) Diamandis, E. P., and Christopoulos, T. K. (1991) The biotin-(strept)avidin system: principles and applications in biotechnology. *Clin. Chem. 37*, 625−36.

(17) Rayo, J., Amara, N., Krief, P., and Meijler, M. M. (2011) Live Cell Labeling of Native Intracellular Bacterial Receptors Using Aniline-Catalyzed Oxime Ligation. *J. Am. Chem. Soc. 133*, 7469−7475.

(18) Dilek, O., and Bane, S. (2011) Synthesis and Spectroscopic Characterization of Fluorescent Boron Dipyrromethene-Derived Hydrazones. *J. Fluoresc. 21*, 347−354.

(19) Dilek, Ö., and Bane, S. L. (2008) Synthesis of boron dipyrromethene fluorescent probes for bioorthogonal labeling. *Tetrahedron Lett. 49*, 1413−1416.

(20) Key, J. A., Koh, S., Timerghazin, Q. K., Brown, A., and Cairo, C. W. (2009) Photophysical characterization of triazole-substituted coumarin fluorophores. *Dyes Pigm. 82*, 196−203.

(21) Gubitz, G., Wintersteiger, R., and Frei, R. W. (1984) Fluorogenic labeling of carbonyl compounds with 7-hydrazino-4-nitrobenzo-2-oxa-1,3,-diazole (NBD-H). *J. Liq. Chromatogr. 7*, 839−854.

(22) Uzu, S., Kanda, S., Imai, K., Nakashima, K., and Akiyama, S. (1990) Fluorogenic Reagents - 4-Aminosulphonyl-7-Hydrazino-2,1,3-Benzoxadiazole, 4-(*N*,*N*-Dimethylaminosulphonyl)-7-Hydrazino-2,1,3-Benzoxadiazole and 4-Hydrazino-7-Nitro-2,1,3-Benzoxadiazole Hydrazine for Aldehydes and Ketones. *Analyst 115*, 1477−1482.

(23) Jachmann, N., and Karst, U. (2001) Synthesis and application of 4-(N,N-dimethylaminosulfonyl)-7-N-methylhydrazino-2,1,3-benzoxadiazole (MDBDH) as a new derivatizing agent for aldehydes. *Fresenius J. Anal. Chem. 369*, 47−53.

(24) Santa, T., Al-Dirbashi, O. Y., Ichibangase, T., Rashed, M. S., Fukushima, T., and Imai, K. (2008) Synthesis of 4-[2-(*N*,*N*-dimethylamino)ethylaminosulfonyl]-7-N-methylhydrazino-2,1,3-benzoxadiazole (DAABD-MHz) as a derivatization reagent for aldehydes in liquid chromatography/electrospray ionization-tandem mass spectrometry. *Biomed. Chromatogr. 22*, 115−8.

(25) Buldt, A., and Karst, U. (1999) *N*-methyl-4-hydrazino-7-nitrobenzofurazan as a new reagent for air monitoring of aldehydes and ketones. *Anal. Chem. 71*, 1893−1898.

(26) Raindlová, V., Pohl, R., Scaronanda, M., and Hocek, M. (2010) Direct Polymerase Synthesis of Reactive Aldehyde-Functionalized DNA and Its Conjugation and Staining with Hydrazines. *Angew. Chem., Int. Ed. 49*, 1064−1066.

(27) Miyazawa, E., Sakamoto, T., and Kikugawa, Y. (1997) Preparation of ring-substituted phenoxylamine derivatives. *Org. Prep. Proced. Int. 29*, 594−600.

(28) Carpino, L. A. (1960) O-acylhydroxylamines 0.2. o-mesitylenesulfonyl-hydroxylamine, o-para-toluenesulfonyl-hydroxylamine and o-mesitylhydroxylamine. *J. Am. Chem. Soc. 82*, 3133−3135.

(29) Salahuddin, S., Renaudet, O., and Reymond, J. L. (2004) Aldehyde detection by chromogenic/fluorogenic oxime bond fragmentation. *Org. Biomol. Chem. 2*, 1471−5.

(30) Key, J. A., and Cairo, C. W. (2011) Identification of fluorogenic and quenched benzoxadiazole reactive chromophores. *Dyes Pigm. 88*, 95−102.

(31) Dirksen, A., Hackeng, T. M., and Dawson, P. E. (2006) Nucleophilic catalysis of oxime ligation. *Angew. Chem., Int. Ed. Engl. 45*, 7581−4.

(32) Cordes, E. H., and Jencks, W. P. (1963) The Mechanism of Hydrolysis of Schiff Bases Derived from Aliphatic Amines. *J. Am. Chem. Soc. 85*, 2843−2848.

(33) Dziegielewska, K. M., Brown, W. M., Casey, S. J., Christie, D. L., Foreman, R. C., Hill, R. M., and Saunders, N. R. (1990) The complete cDNA and amino acid sequence of bovine fetuin - its homology with alpha 2HS glycoprotein and relation to other members of the cystatin superfamily. *J. Biol. Chem. 265*, 4354−4357.

(34) Yang, Y., and Orlando, R. (1996) Identifying the glycosylation sites and site-specific carbohydrate heterogeneity of glycoproteins by matrix-assisted laser desorption/ionization mass spectrometry. *Rapid Commun. Mass Spectrom. 10*, 932−936.

(35) Matsushita, Y., Takahashi, M., and Moriguchi, I. (1986) Binding of fluorescent 7-amino-4-nitrobenzoxadiazole derivatives to bovine serum albumin. *Chem. Pharm. Bull. 34*, 333−9.

(36) Ahn, B., Rhee, S. G., and Stadtman, E. R. (1987) Use of fluorescein hydrazide and fluorescein thiosemicarbazide reagents for the fluorometric determination of protein carbonyl groups and for the detection of oxidized protein on polyacrylamide gels. *Anal. Biochem. 161*, 245−57.
(37) Xie, Z., Wang, K., Zhang, C., Yang, Z., Chen, Y., Guo, Z., Lu, G.-Y., and He, W. (2011) A fluorometric/colorimetric dual-channel Hg2+ sensor derived from a 4-amino-7-nitro-benzoxadiazole (ANBD) fluorophore. *New J. Chem. 35*, 607−613.
(38) Xu, Z., Kim, G.-H., Han, S. J., Jou, M. J., Lee, C., Shin, I., and Yoon, J. (2009) An NBD-based colorimetric and fluorescent chemosensor for Zn2+ and its use for detection of intracellular zinc ions. *Tetrahedron 65*, 2307−2312.
(39) Barak, L. S., Yocum, R. R., and Webb, W. W. (1981) In vivo staining of cytoskeletal actin by autointernalization of nontoxic concentrations of nitrobenzoxadiazole-phallacidin. *J. Cell Biol. 89*, 368−372.
(40) Kalia, J., and Raines, R. T. (2008) Hydrolytic stability of hydrazones and oximes. *Angew. Chem., Int. Ed. 47*, 7523−7526.
(41) Kohler, J. J. (2009) Aniline: a catalyst for sialic acid detection. *ChemBioChem 10*, 2147−2150.
(42) Chen, I., Howarth, M., Lin, W., and Ting, A. Y. (2005) Site-specific labeling of cell surface proteins with biophysical probes using biotin ligase. *Nat. Methods 2*, 99−104.
(43) Brustad, E. M., Lemke, E. A., Schultz, P. G., and Deniz, A. A. (2008) A General and Efficient Method for the Site-Specific Dual-Labeling of Proteins for Single Molecule Fluorescence Resonance Energy Transfer. *J. Am. Chem. Soc. 130*, 17664−17665.
(44) Whitman, C. M., Yang, F., and Kohler, J. J. (2011) Modified GM3 gangliosides produced by metabolic oligosaccharide engineering. *Bioorg. Med. Chem. Lett. 21*, 5006−5010.
(45) Rannes, J. B., Ioannou, A., Willies, S. C., Grogan, G., Behrens, C., Flitsch, S. L., and Turner, N. J. (2011) Glycoprotein Labeling Using Engineered Variants of Galactose Oxidase Obtained by Directed Evolution. *J. Am. Chem. Soc. 133*, 8436−8439.

Bioconjugate Chemistry

Article

pubs.acs.org/bc

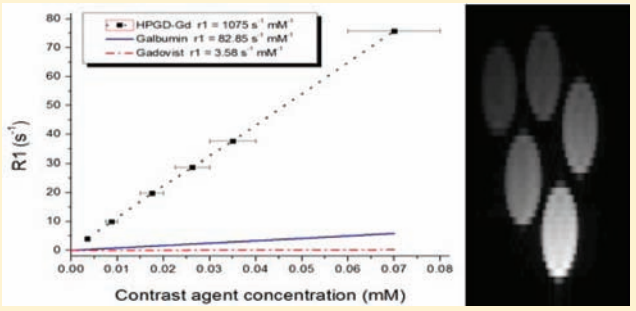
Hyperbranched Polyglycerols as Trimodal Imaging Agents: Design, Biocompatibility, and Tumor Uptake

Katayoun Saatchi,[†] Peter Soema,[†] Nikolaus Gelder,[†] Ripen Misri,[†] Kelly McPhee,[‡] Jennifer H.E. Baker,[‡] Stefan A. Reinsberg,[‡] Donald E. Brooks,[§] and Urs O. Häfeli*[,†]

[†]Faculty of Pharmaceutical Sciences, [‡]Department of Physics, and [§]Centre for Blood Research, University of British Columbia, Vancouver, British Columbia, Canada

Supporting Information

ABSTRACT: Combining various imaging modalities often leads to complementary information and synergistic advantages. A trimodal long-circulating imaging agent tagged with radioactive, magnetic resonance, and fluorescence markers is able to combine the high sensitivity of SPECT with the high resolution of MRI over hours and days. The fluorescence marker helps to confirm the *in vivo* imaging information at the microscopic level, in the context of the tumor microenvironment. To make a trimodal long-circulating probe, high-molecular-weight hyperbranched polyglycerols (HPG) were modified with a suitable ligand for ^{111}In radiolabeling and Gd coordination, and additionally tagged with a fluorescent dye. The resulting radiopharmaceutical and contrast agent was nontoxic and hemocompatible. Measured radioactively, its total tumor uptake increased from 2.6% at 24 h to 7.3% at 72 h, which is twice the increase expected due to tumor growth in this time period. Both *in vivo* MRI and subsequent histological analyses of the same tumors confirmed maximum HPG accumulation at 3 days post injection. Furthermore, Gd-derivatized HPG has an excellent contrast enhancement on T1-weighted MRI at 10× lower molar concentrations than commercially available Galbumin. HPG derivatized with gadolinium, radioactivity, and fluorescence are thus long-circulating macromolecules with great potential for imaging of healthy and leaky blood vessels using overlapping multimodal approaches and for the passive targeting of tumors.



INTRODUCTION

Over the past few decades, imaging has become a vital tool for cancer research, clinical diagnosis, and treatment. Various imaging techniques such as MRI (magnetic resonance imaging), SPECT (single photon emission computed tomography), PET (positron emission tomography), and others have grown tremendously and are widely applied in medicine.[1] These techniques are useful for locating tumors and investigating various biological processes. They each possess different characteristics regarding spatial resolution, depth penetration, tissue contrast, time needed for imaging, and cost. To overcome specific limitations, it is becoming increasingly common to combine several imaging modalities. Multimodality imaging allows for the visualization of pharmacokinetics, and helps to elucidate complicated mechanisms of drug uptake and/or action, and processes that influence tumor behavior. As a result of multimodal imaging, there is an increasing need for multimodal contrast agents.

This report summarizes our findings on the use of a macromolecule as a suitable platform for multimodal imaging. Our focus on a macromolecular agent is partly motivated by a long-standing problem in the MR imaging of tumor vasculature: uptake of low-molecular-weight agents currently used in dynamic contrast-enhanced imaging always yields data that can be interpreted as a combination of both tumor perfusion and extravasation. This is the result of the typically leaky vasculature located in tumors, such that low molecular weight agents expected to remain intravascular in other tissues actually leak out of the tumor vasculature and can accumulate in the extravascular space.[2,3] A higher molecular weight contrast agent that could be expected to remain intravascular even within leaky tumor vasculature would yield data that could be interpreted more specifically to represent the physiological parameters of permeability and perfusion.

Hyperbranched polyglycerols are recently described globular macromolecules with narrow size distribution.[4,5] Kainthan et al. then developed in 2006 a one-pot synthesis method that extended the 30 kDa molecule narrow size distribution to larger than 100 kDa molecules.[6] HPG have radii of 5−10 nm, are highly water-soluble, are easily made by a one-step synthesis, unlike the otherwise similar dendrimers,[7] are somewhat asymmetrical, and are highly biocompatible.[8−11] Their biocompatibility is similar to that of poly(ethylene glycol) (PEG)[12] or polysaccharides. HPG, however, is thermally and

Received: June 1, 2011
Revised: January 30, 2012
Published: February 6, 2012

 © 2012 American Chemical Society dx.doi.org/10.1021/bc200280g | *Bioconjugate Chem.* 2012, 23, 372−381

oxidatively more stable than the linear PEG, and produces less viscous solutions at analogous molecular weights due to its globular structure. HPGs are thus useful over larger concentration ranges and behave more like proteins than PEG.[9] Already tested applications of HPGs are as human serum substitute,[13] as drug delivery vehicles for the treatment of bladder cancer,[14,15] and as a protectant of cell surfaces.[16,17]

Many macromolecules have been modified for use in imaging and tumor targeting. We were interested in investigating HPG as a potential new tracer and smart nanoprobe for the characterization of vessel leakiness and perfusion with multimodal imaging techniques. For this purpose, HPG was modified with radioactive, MRI contrast enhancing, and fluorescent tags, and thus became a bioprobe for detection with SPECT, MRI, and fluorescent imaging. Having multiple probes on the same carrier molecule is preferred and obviates the need to administer two or more compounds with somewhat different pharmacokinetics. *In vivo* MR imaging of the Gd-labeled HPG can yield physiologically relevant data regarding vascular function, while SPECT allows to quantitatively asses the agent's biodistribution over time. The microregional location of the agent within the tumor microenvironment, including for how long the agent remains intravascular, can be determined at the microscopic level using the fluorescent tags imaged using fluorescence microscopy. Together, these data can provide specific insight regarding the physiological function of tumor blood vessels.

To prepare the radioactive and magnetic compound, the chelator 1,4,7,10-tetraazacyclododecane-1,4,7,10-tetraacetic acid (DOTA) was used to prepare the radioactive and paramagnetic probes as it coordinates both In^{3+} and Gd^{3+} metal ions with good stability. HPG was also modified with a fluorescent dye which made it possible to observe the distribution of HPG at the end of the experiment *ex vivo* using fluorescence microscopy. The gamma emitting isotope ^{111}In ($t_{1/2}$ = 67 h; γ = 172, and 245 keV) has ideal characteristics for extended investigation of slowly clearing compounds and is commonly used for SPECT imaging. For MR imaging, however, Gd complexes are commonly used as contrast agents. The R1 relaxation rate of water in tissue is increased with Gd, and the presence of Gd can thus be qualitatively and quantitatively assessed *in vivo*.

The trimodal HPG described here was used for biodistribution analyses by radiation and MR imaging, as well as for more exact fluorescent tumor tissue distribution studies with histological methods. The multifunctional nature of the HPG nanoprobe allows for more complete investigation of observed effects at different time points and resolutions. Syntheses and characterization of the trimodal HPG, as well as metal coordination/radiolabeling, biodistribution, and MR and fluorescent tumor imaging studies are reported herein.

■ MATERIALS AND METHODS

All chemicals were purchased from Sigma/Aldrich. $^{111}InCl_3$ was purchased from MDS Nordion (Ottawa, ON, Canada). Alexa Fluor 647 and fluorescamine were purchased from Invitrogen (Carlsbad, CA, USA), while *p*-NH_2-Bn-DOTA came from Macrocyclics (Houston, TX, USA). ^1H NMR spectra were recorded on a Bruker AV-300 or AV-400 at 300.13 or 400.13 MHz. Inductive coupled plasma (ICP) analyses were obtained from Exova (Surrey, BC, Canada). Molecular weights and polydispersities of polyglycerol samples were determined by gel permeation chromatography (GPC) on a Waters 2690 separation module fitted with a DAWN EOS multiangle laser light scattering (MALLS) detector from Wyatt Technology Corp.[6] Sephadex G-25 M columns (i.e., PD10; contains 0.15% Kathon CG as preservative) were from GE Healthcare (Piscataway, NJ, USA). Instant thin layer chromatography (ITLC) was performed on green TEC-Control strips (Cat# 150−771; Biodex, Shirley, NY, USA) using a 33.3% mixture of saline, HCl (0.1 M), and Na_2EDTA (0.1 M) as the mobile phase. Dialysis tubing was from SPECTRUM laboratories (Rancho Dominguez, CA, USA) with MWCO of 1000. The radioactive TLCs were made visible using a phosphor imager (Cyclone with 12.5 × 25 cm^2 phosphor screen, Perkin-Elmer, Waltham, MA, USA) and analyzed using *OptiQuant* software. Ultracel-YM100 microconcentrators with a 100 kDa MWCO were from Millipore Corporation (Billerica, MA, USA). Fresh blood was obtained from healthy volunteers immediately before the hemocompatibility studies. Results are the average of at least triplicate repetitions.

HPG. The high-molecular-weight polyglycerol (HPG) was synthesized in Brook's laboratories with a narrow polydispersity of PDI = 1.01 by ring-opening multibranching polymerization of glycidol using dioxane as the reaction medium, according to a published procedure.[6] ^1H NMR (D_2O): δ 3.3−3.9 (br, m, $[-CH_2-CHCH_2-OH\text{-}O]n$), GPC: M_n 509 kDa. For spectra, see Supporting Information (SI).

Ligand Modified HPG (HPGD). HPG was dissolved (353 mg, 0.76 μmol) in 5 mL of water. A solution of H_5IO_6 (24.4 mg, 107 μmol) in 1 mL water was added dropwise with stirring. After 1 h the solution was dialyzed against 2.5 L water overnight, and water was changed once. *p*-NH_2-Bn-DOTA (46 mg, 63 μmol) was dissolved in 5 mL water, added to the reaction mixture in a round-bottom flask, and stirred for 1 h. Ethanolamine (90 μL, 10% solution, 1.5 mmol) was added and stirred for another 1 h. $NaBH_3CN$ (excess, 18 mg, 286 μmol) was dissolved in 100 μL water and added (pH ∼ 5), followed by acetic acid to decrease the pH to 3. The solution was stirred overnight, dialyzed for 3 days against water with daily water changes, and then lyophilized. ^1H NMR (D_2O): δ 2.2−3.8 (*b*, overlapping multiplets, HPG $[-CH_2-CHCH_2-OH\text{-}O]_n$, DOTA N-$CH_2CH_2$-N and N-$CH_2$-COOH), 7.0 (d, DOTA CH_2-C_6H_5). GPC: M_n 583 kDa, PDI = 1.07. For spectra, see SI.

HPGD-NH_2. In a 50 mL round-bottom flask, HPG (247 mg, 0.5 μmol) was dissolved in 10 mL of water and 5 mL H_5IO_6 solution (101 mg, 442 μmol) added dropwise with stirring. After 1 h, the solution was dialyzed against water for 2 days and water was changed 3 times. *p*-NH_2-Bn-DOTA (112.5 mg, 155 μmol) was dissolved in 5 mL water and added to the reaction mixture after transferring back to the flask and stirred for 1 h. *N*-Boc-ethylenediamine (24 mg, 150 μmol) was dissolved in 500 μL of ethanol and added. After 1 h, ethanolamine (400 μL, 10% (V/V) solution, 660 μmol) was added and stirred for another 1 h. $NaBH_3CN$ (50 mg, 794 μmol) was dissolved in 1 mL of water, added to the reaction mixture (pH ∼ 6), and pH adjusted to 5 with acetic acid and then stirred overnight. The reaction mixture was dialyzed for 4 days against water with daily fresh water and finally lyophilized to collect 207 mg of HPGD-NHBoc. For deprotection, 86 mg of HPGD-NHBoc was dissolved in HCl (1.25 M in MeOH) and stirred at 1000 rpm for 5 days. The solution was diluted with water (50%) and dialyzed for 3 days against 2.5 L of water (water changed twice daily). A fluffy white solid (HPGD-NH_2) was collected after lyophilization (81 mg). Quantification of NH_2 was by using a ninhydrin assay according to published literature using

dx.doi.org/10.1021/bc200280g | *Bioconjugate Chem.* 2012, 23, 372−381

ethanolamine as standard; each sample was measured in triplicate.[18,19] The standard plot of absorbance versus concentration of different dilutions for ethanolamine was then used to calculate the concentration of amine functionality on the HPGD-NH_2 to be 2680 nmol NH_2 per mg HPGD.

Fluorescent HPGD (HPGDF). For quick examination of the free amine groups, 30 μL of HPGD-NH_2 solution (1.7 mg/100 μL 0.2% NaCl solution) was added to 50 μL of fluorescamine (3 mg/mL in dry acetone) in triplicate.[20] The fluorescence of each sample was read in a plate reader upon excitation at 390 nm and emission at 470 nm (57803 ± 382 RFU vs 812 ± 14 RFU for the background). The background was corrected against a mixture of fluorescamine solution and 0.2% NaCl. For *in vivo* experiments, a more stable fluorescent HPG was prepared. HPGD-NH_2 (75 mg) was dissolved in 2 mL borate buffer 0.1 M and 400 μL of the succinimidyl ester of Alexa647 in DMSO (1 mg/mL) was added and shaken overnight in the dark at 500 rpm on an Eppendorf thermomixer at 22 °C. The blue solution was purified and washed three times in a microconcentrator, and collected in 200 μL of saline. The fluorescence emission of HPGDF was checked at 668 nm. The fluorescence was 500 times relative to background.

Gd Coordination. To a solution of HPGD (or HPGDF) was added $GdCl_3 \cdot 6H_2O$ (1.14 mg per 5 mg of HPGD), and it was heated at 70 °C for 30 min in a thermomixer at 1000 rpm. After cooling to room temperature, the excess Gd was removed either by dialysis or by using a microconcentrator. ICP: [Gd]/mg HPG found 20.2 μg (calculated 21.72 μg). The fluorescence of HPGDF-Gd after metal coordination (5400 RFU vs 7 for background) was very similar to the starting HPGDF.

^{111}In-HPGD. To a solution of HPGD (0.5 mg/5 μL water) was added $^{111}InCl_3$ (5 μL, 8.40 MBq) and the volume made up to 500 μL with NH_4OAc (0.15 M). After 30 min shaking at 70 °C, the solution was cooled to room temperature. A 250 μL aliquot was placed on a PD10 column and eluted with 30 × 500 μL aliquots of saline. The activity of each fraction was measured in a gamma-counter. Fractions from 2 to 5 mL were combined and contained the ^{111}In-HPG, while the fraction between 6 and 8 mL contained the so-called "free" activity. The peak between instant thin layer chromatography was also used on the original mixture, the images developed using a phosphor imager first, and then the ITLCs were cut and the two parts were counted in the gamma-counter. Labeling efficiency was >95%.

^{111}In-HPGDF. To prepare a fluorescent radiolabeled product, the above procedure was performed with HPGDF instead of HPGD with similar labeling results (>95%).

EDTA Challenge. To determine the binding stability of the metals to the HPG derivative, Na_2EDTA (750 μL, 0.1 M) was added to the remaining solution of ^{111}InHPGD (250 μL, 4.07 MBq) and the solution heated at 37 °C while shaking. At 1 and 24 h post mixing, 250 μL samples of this solution were eluted on a PD 10 column.

Transferrin Challenge. A HPGD solution (1 mg/10 μL H_2O) in 490 μL of NH_4OAc (0.15 M) with $^{111}InCl_3$ (5 μL, 9.88 MBq) was shaken at 1000 rpm on a thermomixer for 30 min at 99 °C. Apotransferrin solution in PBS (2.5 mg/mL; 500 μL) was added to 250 μL of this solution. The solution was shaken on a mixer at 1000 rpm at 37 °C. At 1 and 24 h, 370 μL of the solution was separated in a microconcentrator and the activity measured for both the supernatant and the ^{111}In-HPGD.

Cell Viability Assay (MTT Assay). A quantitative analysis of cell viability was performed with HPG and HPGD in human vascular endothelial cells (HUVECs) using 3-(4,5-dimethylthiazol-2-yl)-2,5-diphenyltetrazolium bromide assay (MTT assay).[21] The cells (100 μL, 5000 cells/mL) were plated into 96-well plates and incubated at 37 °C and 5% CO_2 for 2 days. HPGD and HPG at concentrations 10, 2, 1, 0.5, and 0.1 mg/mL were added in 100 μL of medium (EBM-2 Basal Medium, Lonza) to the wells and incubated for 24 h. MTT stock solution (5 mg/mL; 20 μL) was added to each well, incubated for 3 h, the supernatant gently removed, and 150 μL DMSO added to every well. The plate was shaken at 1000 rpm and at 37 °C for 1 h and the optical density measured at 540 nm on a Multiscan Ascent plate reader.

RBC Aggregation Test. Red blood cell (RBC) aggregation was tested by incubating whole blood with HPGD, Gd-HPGD, and HPG. HPGs (10 μL, 10 mg/mL) were added to 40 μL citrate anticoagulated whole blood and incubated at 37 °C for 30 min. The RBC were then isolated by spinning down the blood for 30 s. Plasma (4 μL) was resuspended and diluted such that single RBC or aggregations were visible under the bright field light microscope (Zeiss Axioskop 2plus). A drop was placed on a wet-mounted slide and images were taken with a mounted black and white CCD camera (Qimaging Retiga 1300).

Clinical Coagulation Assays. Prothrombin time (PT) and activated partial thromboplastin time (APTT) were measured to evaluate the influence of the HPG solutions on extrinsic and common coagulation pathway of blood (ST4 Diagnostica Stago device). A polymer solution (1 mg/mL) was prepared in platelet poor plasma (PPP) and 3× 100 μL of it heated to 37 °C; Innovin (200 μL, for the PT assay) or actin and calcium chloride (100 μL each, for the APTT assay) were incubated with PPP and the time to fibrin clot formation recorded. The PPP was produced by spinning down whole blood at 1500 *g* for the maximum time of 15 min and the plasma was separated from the RBC. Each measurements contained 3 samples of polymer/PPP and one plasma control. The experiment was repeated 3 times.

Thrombelastograph (TEG). The platelet function and mechanical clot stability was analyzed in a thrombelastograph (TEG) hemostasis system 5000 (Hemoscope Corp, Niles, IL, USA). The TEG measures the physical properties of the clot in an oscillating cylindrical cup holding the blood sample, at an angle of 4°45′. Each of the rotational cycles lasted 10 s and the properties were measured by a stationary pin. Fresh citrated blood (360 μL) was mixed with 40 μL of the polymer test solutions (1 mg/mL) and $CaCl_2$ (20 μL, 0.2 M) added in the thrombelastograph and the resulting curves analyzed by TEG's proprietary software.

Complement Activation. The complement activation pathway of the body upon exposure to the polymers was investigated using the Quidel C3a enzyme immunoassay kit.[22] For this purpose, samples (1 mg/mL) and controls were diluted 1:100 with sample buffer and added to a 96 microassay plate coated with C3a antibody coated strips. After 60 min of incubation at room temperature, 100 μL of C3a conjugate was added into each well. After 60 min the substrate was added and incubated for another 15 min. The reaction was then stopped and read at 450 and 650 nm on a plate reader.

Platelet Activation. Platelet activation, which is the tethering of platelets occurring on sites of vascular injuries, was investigated by measuring the CD62 expression level in the blood by marking it with CD62 mouse human antibodies.[23] Fresh donated citrate anticoagulated blood was centrifuged at

800 *g* (900 rpm) for 30 s to separate the RBCs from the plasma without spinning down the platelets to get Platelet Rich Plasma (PRP). PRP (150 μL) was then incubated at 37 °C with 15 μL of the polymer solutions to obtain a final concentration of 1 mg/mL. Aliquots were withdrawn after 10, 30, and 60 min; 5 μL was added to 45 μL of PBS and 5 μL of CD62 mouse human antibodies and analyzed in the flow cytometer. As a positive control, 45 μL of PBS was mixed with 5 μL of PRP, 5 μL of CD62 mouse human antibodies (Immunotech, Marseille France), and 5 μL of Gly-Pro-Arg-Pro (GPRP). To prove that platelets were present in the PRP, CD42 antibodies were added instead of CD62.

Radioactive Biodistribution Studies. To assess the organ uptake of HPG radiolabeled with a gamma emitter, a biodistribution study was performed at the animal resource center of the BC Cancer Research Centre (BCCRC) in accordance with an approved animal protocol. The female C57Bl/6 mice aged 6–8 weeks (Jackson Laboratory, Bar Harbor, ME, USA) were injected subcutaneously with 3×10^5 LL/2 (Lewis Lung) tumor cells (CRL-1642, American Type Culture Collection (ATCC), Manassas, VA, USA) in 50 μL of media (DMEM supplemented with 4 mM L-glutamine, 4.5 g/L glucose, and 10% fetal bovine serum) into the flanks of the animals. Once the tumors reached a size of about 6 mm in diameter, 0.5 mg of ^{111}In-HPG (74 kBq) in 200 μL of sterile phosphate buffered saline pH 7.4 was injected intravenously into the tail vein of 2 groups of 5 animals each. Groups were sacrificed at 24 and 72 h and organs were removed, weighed, and their activity determined using a Packard Cobra II auto gamma counter with settings for ^{111}In (energy window 140–280 keV). Results were corrected for blood content according to the method by Bally et al. and then expressed as the percentage of the injected dose per gram of tissue (%ID/g).[24]

***In Vivo* Imaging and Histological Tumor Microdistribution Studies.** To assess the feasibility of HPGDF as an MR contrast agent, the R1 relaxation rate of HPGDF was measured in a buffer solution at concentrations between 2 and 40 mg/mL at room temperature.

To assess tumor uptake and retention of HPGDF, an MRI study and subsequent histological analysis were performed. Experiments followed a protocol approved by the UBC Committee on animal care. Mice were anaesthetized with isoflurane throughout imaging and maintained at 37 °C body temperature. Six female NOD/SCID mice (bred and maintained in-house in accordance with the Canadian Council of Animal Care guidelines) with HT29 human colorectal carcinoma (ATCC) xenografts were randomly assigned to three groups. All mice were injected with a dose of 300 or 600 mg/kg of HPGDF via the tail vein. Groups 1 and 2 received intravenous HPGDF injections while MR imaging was performed on a 7 T Bruker Biospec 70/30 using a combination of volume (*Tx*)/surface (*Rx*) coils. *T*1 measurement and *T*1-weighted images were obtained. The first group was euthanized at 60 min post injection without waking from anesthesia. The second group was reimaged 3, 6, and up to 14 days post injection, and euthanized following the final imaging. Animals in the third group received HPGDF via intravenous injection and were euthanized 2 min following injection, without obtaining MR images. All tumors were excised immediately following euthanasia, and were frozen for subsequent cryosectioning.

For histological analysis, 10 μm cryosections from the same central region of each tumor as imaged with MRI were obtained and imaged for native fluorescence (625 nm) using a robotic microscope and camera to obtain tiled images of whole tumor sections. Images for individual tumors were cropped to tumor tissue boundaries, with artifacts and nonviable tissue removed using *ImageJ* software.[25] Whole tumor section fluorescence was measured as a reflection of contrast agent accumulation in tumor tissue, and was normalized by subtracting native tissue fluorescence background levels of tumors without HPGDF. Differences in fluorescence due to different doses were corrected for by assuming a linear relationship between dose and fluorescence.

MR Methods. The concentration-dependent ability of HPGDF to increase the relaxation rates of the surrounding water protons can be described by

$$\Delta R1 = r1[\mathrm{HPGDF}] \quad (1)$$

where $r1$ is the relaxivity, $\Delta R1$ is the change in relaxation rate measured for the HPGDF solution compared to the solvent alone. Relaxation times were measured for each sample by a nonimaging inversion recovery experiment and converted to relaxation rates ($R1 = 1/T1$).[26]

The MRI protocol consisted of axial RARE *T*1-weighted images for morphological reference and orientation, a variable flip angle experiment to obtain RF field maps (FLASH TR/TE = 400/2.75; FA = 125°, 180°, 215°; slice = 1 mm),[27] and a variable flip angle experiment to obtain *T*1 (FLASH, TR/TE = 100/2.77; FA = 10°, 20°, 50°, 60°; slice = 1 mm), and a *T*1-weighted image (RARE TR/TE = 1300/7.5; FA = 180°; slice = 1 mm). Following these images, the contrast agent was injected, and approximately 40 min post-injection, the variable flip angle experiment and RARE *T*1-weighted imaging were repeated. Imaging on days following the agent injection consisted of the same imaging protocol, but without contrast injection, and the associated repeated *T*1 and RARE images. There was no contrast injection or repeat imaging on those days.

MRI postprocessing was performed using NIH-*ImageJ*,[28] and *Matlab* v 7.8 (The MathWorks Inc., Natick, MA, U.S.A.). Regions of interest with axial morphological images depicting a central tumor area were drawn with *ImageJ* and transferred to variable-flip-angle FLASH images. *T*1 maps were calculated from the variable flip angle experiment. Reported *R*1 values are averages calculated from a slice selected in the central region of each tumor.

RESULTS AND DISCUSSION

Multimodality imaging can be highly valuable in elucidating complicated mechanisms of drug uptake and/or action. This report summarizes our findings on the use of our multimodal HPG as a suitable platform for combined imaging using SPECT, MRI, and fluorescence microscopy. These probes can be used individually or in combination with each other if/when required. Ultimately, the overlapping application of HPG using these modalities will provide physiologically specific information regarding biodistribution, tumor vascular function, and response to treatment in preclinical investigations. HPG was synthesized and modified with a ligand suitable to bind ^{111}In for SPECT and Gd for MR imaging. HPG was also simultaneously tagged with an Alexa dye as a fluorescent probe for fluorescence imaging, resulting in a multimodal probe.

The commercially available bifunctional chelator, DOTA, that was chosen for use here, has a high binding stability for trivalent metals,[29] reaching a p*M* of 23.9 for In^{3+} and a p*M* of 24 for Gd^{3+}.[30] Due to the rigid ring structure, its metal

dx.doi.org/10.1021/bc200280g | *Bioconjugate Chem.* 2012, 23, 372–381

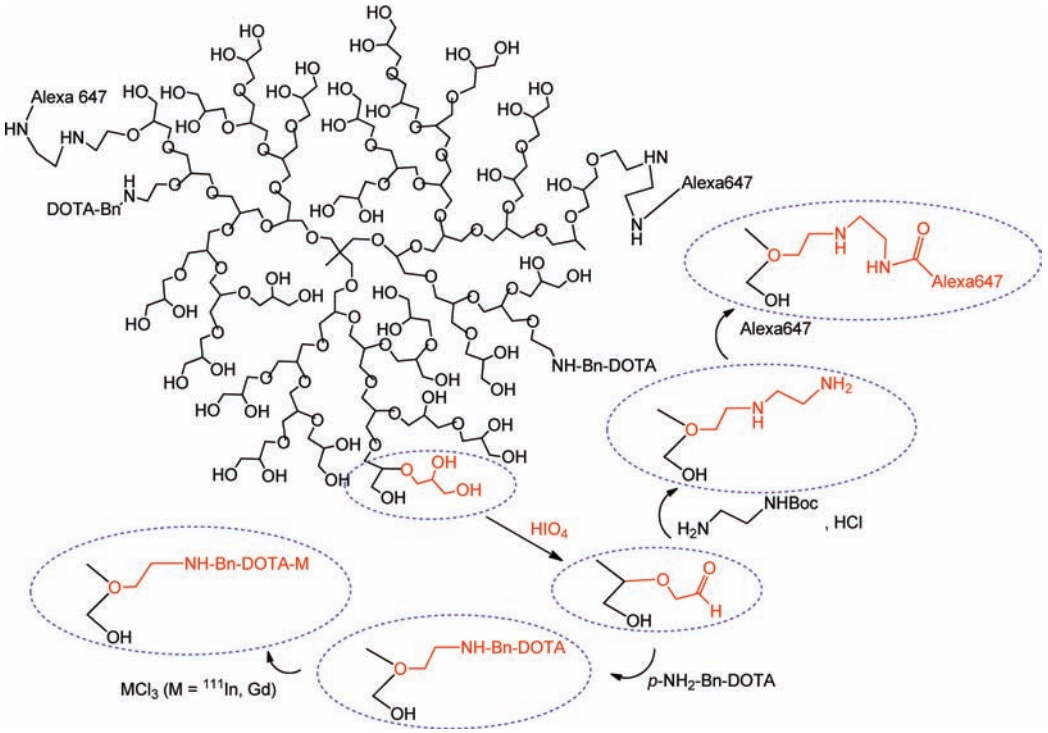


Figure 1. Synthetic scheme of HPG derivatization.

complexes tend to be kinetically inert to dissociation and are also highly thermodynamically stable.[31] Since DOTA binds In^{3+} as well as Gd^{3+}, and shows high reported *in vivo* stability for both metal complexes, we chose DOTA for HPG modification in our studies. The fact that the formation of DOTA metal complexes is kinetically slow[32] was not a problem for our application, since heating does not degrade HPG.

The synthetic scheme for HPGD, HPGDF, and Gd/In-HPGDF is shown in Figure 1. Hydroxyl functionalities on HPG were oxidized to aldehyde and then coupled to *p*-NH_2-Bn-DOTA by reductive amination. To attach the flourescent probe similar chemistry was carried to attach a linker arm (*N*-Boc-en) first. After Boc deprotection, the free amine was reacted with the activated fluorescent dye (succinimidyl ester of Alexa 647) to bind the fluorescent probe. The side product of the first reaction (i.e., formaldehyde) was removed by extensive dialysis. The product was then characterized by ^{1}H NMR and GPC indicative of a successful modification. Since there are no other aromatic protons in the structure but the ones of the benzyl backbone of DOTA, the appearance of the signal in the ^{1}H NMR spectrum of HPGD was a confirmation of ligand modification. Also, the ^{1}H NMR spectrum was used to calculate the number of DOTA groups attached (38 or 300 DOTAs per HPG) based on the integration ratio of the aromatic and aliphatic protons and the calculated total number of protons per HPGD molecule. Metal coordination was confirmed first using various concentrations of nonradioactive gadolinium. Measured by ICP, a [Gd^{3+}] concentration of 20.2 μg per mg of HPG was found (calculated 21.72 μg) when excess Gd was added so that all DOTA groups were coordinated. Theoretically, both metal ions can be coordinated consecutively (partial coordination of DOTAs with Gd^{3+} first and then radiolabeling with $^{111}In^{3+}$ to coordinate the remaining DOTAs) if a SPECT/MR imaging is to be undertaken simultaneously. This was not attempted in this work.

Radiolabeling of HPGD with ^{111}In was performed with different concentrations as well (0.03 to 1 mCi/mg HPGD) as different temperatures (70−100 °C) for 30 min with excellent labeling efficiencies exceeding 95%. Figure 2 shows a typical

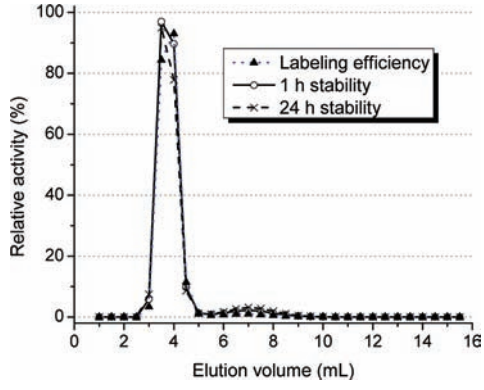


Figure 2. PD10 size exclusion trace of ^{111}In-HPGD directly after labeling (labeling efficiency) and after a stability challenge with EDTA 0.1 M at 1 and 24 h (stability), pointing to almost complete binding (peak at 4.0 mL) and very low instability (peak at 7.0 mL).

PD10 size exclusion profile of the radiolabeled HPGD. Almost all activity elutes in the first radioactive fraction around 4 mL, while only traces of activity are visible at 7.5 mL where In-EDTA would elute.

The stability of ^{111}In-HPGD for *in vivo* use was predicted by a challenge test with the competitive ligand ethylenediaminetetraacetic acid (EDTA). EDTA was chosen due to its log *K* of 25.3 for In, while In-DOTA has a log *K* of 23.9 and the physiologically present metal scavenger, transferrin, a log *K* of 18.30.[33] The EDTA challenge resulted in 94.9% and 92.7% of ^{111}In being HPGD bound after 1 and 24 h of incubation

dx.doi.org/10.1021/bc200280g | *Bioconjugate Chem.* 2012, 23, 372−381

(Figure 2), while the transferrin challenge resulted in 95.7% and 94.9% stability after 1 and 24 h.

To tag HPG with a fluorescent dye, a linker arm was attached with primary amine end groups (Figure 1). The use of a succinimidyl ester of Alexa dye was a simple way of coupling it to the amine groups on the HPG.

Toxicity of In-HPGD. Biocompatibility is extremely important for any pharmaceutical. To confirm the nontoxicity of our derivatives, we performed cell viability and hemocompatibility assays.

Cell Viability. After intravenous injection, the first cells that HPG come in contact with are the lining of the blood vessels and therefore the human vascular endothelial cells (HUVECs). To test for any potential cytotoxic effects of HPG and HPGD, we investigated HUVEC viability in an MTT assay (Figure 3).

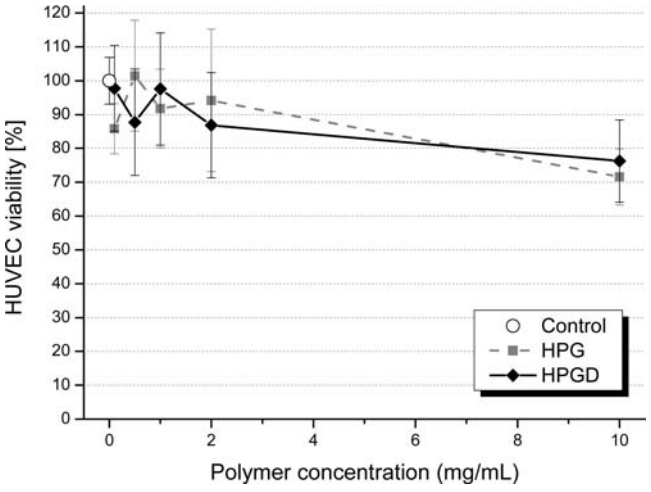


Figure 3. Cell viability of HUVECs after 24 h incubation with HPG and HPGD.

There was only a slight, nonstatistically significant cell viability loss at the highest polymer concentration of 10 mg/mL (p = 0.485 and p = 0.138, respectively). HPGD behaves thus almost identically to HPG, despite the additional free carboxyl and nitrogen groups on HPGD, and is considered to be biocompatible.

RBC Aggregation. Erythrocytes are a large group of cells in the human body which are in direct contact with any molecule injected into the bloodstream. They can aggregate naturally with molecules like fibrin as natural protection from injuries. Macromolecules such as antibodies and high-molecular-weight dextrans can also trigger this aggregation.[9−22] The HPGD were tested by incubating the whole blood for 30 min with an added concentration of 10 mg/mL. No aggregation or cell shape change of RBC occurred as seen in Figure 4. Infrequent stacking, known as rouleaux, occurred because of the stop of motion, but could be disassembled easily by resuspension. The RBC shape thus was not changed indicating that the cells retain their functionality.[34]

Clinical Coagulation Assays. The effect of the HPG derivatives at concentrations of 1 mg/mL on the common extrinsic (PT) and intrinsic (APTT) coagulation pathway was tested. All results were within normal ranges (30.4−31.1 s for APTT; 9.7−10.1 s for PT) and very close to the saline control (32.7 s for APTT (normal 30−45 s);[35] 10.1 s for PT (normal 10−13 s)[35]). The derivatized HPG molecules thus do not

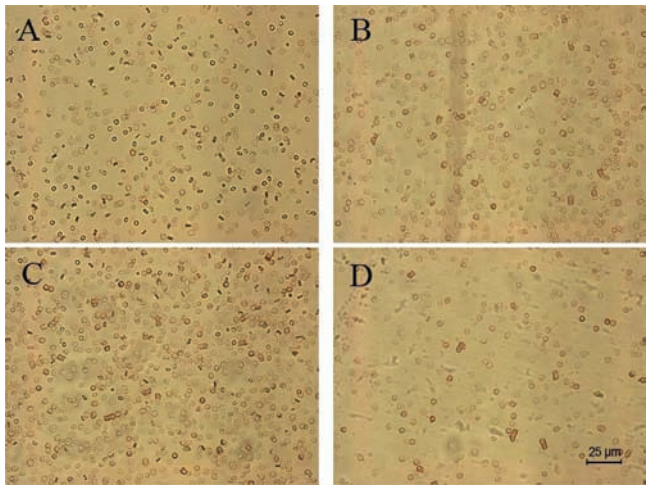


Figure 4. Microscopy pictures of red blood cells in the RBC aggregation assay. (A) HPG, (B) HPGD-Gd, (C) Control, (D) HPGD.

influence the fibrin clot formation and seem to be biocompatible.

Mechanical Blood Clot Properties. An additional blood biocompatibility test with a thrombolastograph (TEG) looked at other factors that influence the mechanical strength of the formed blood clot. The results in Figure 5 show a much broader variance than the other blood compatibility tests, but are certainly within normal values when compared to calibration data obtained from U.S. hospitals (thrombelastograph manual). The larger variances are due to the long duration of the test and the fact that fresh donor blood is required for each test, which made the use of different donors with individual clotting kinetics necessary.

Complement Activation. The nonspecific immune response expressed by complement activation was also investigated. This cascade of reactions involves C3 and a fragment C3a which act as diffusible signals for inflammatory response leading to cell lysis, clumping, phagocytosis, and chemotaxis.[22] Measuring the concentration of C3a at two different time points and using inulin as a positive and EDTA as a negative control, both HPG and HPGD were shown to produce similar concentrations of C3a (Figure 6). No complement activation thus occurs with the chelating molecules present on the HPG surface.

Platelet Activation. The effect of HPG and derivatives on blood platelets was investigated by incubation with plasma followed by detection of the CD62 level, which is increased upon platelet activation.[23] Both derivatized and nonderivatized HPG slightly activated platelets to similar levels, as shown in Table 1. The values, however, showed fibrinogen binding levels below 10%, which is similar to that caused by saline[9] and is still within the normal range, and could have been triggered by stress from shaking or pipetting.

Biodistribution. ^{111}In-HPGD is a long circulating blood pool agent with a biological half-life of 32.6 h. This result, however, is not very exact, as only two data points (59.6% of total injected activity in blood pool 24 h after injection, and 27.8% after 72 h) were available for the calculation. The rest of the activity was mainly found in organs of the reticuloendothelial system, the liver, and the spleen (Figure 7).

Tumor uptake was very similar to activity uptake in the reticulo-endothelial system, and the tumor to blood ratio increased in parallel from an earlier 0.295 to 0.891 at the later

dx.doi.org/10.1021/bc200280g | Bioconjugate Chem. 2012, 23, 372−381

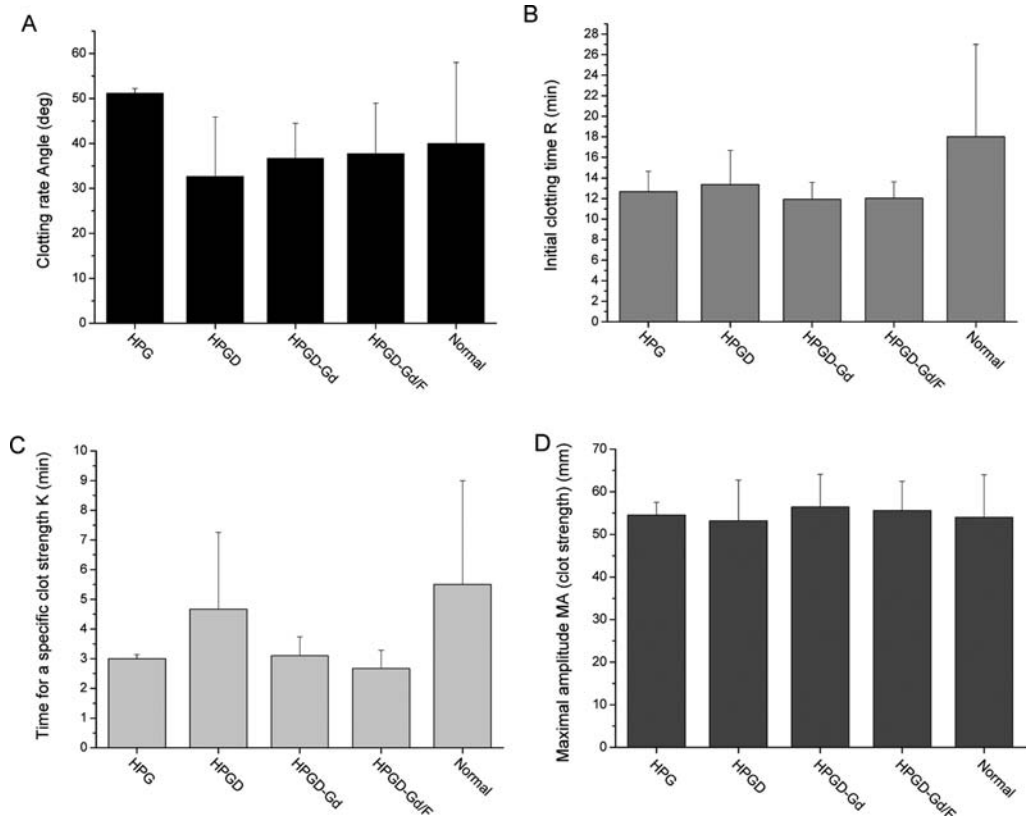


Figure 5. Diverse blood clotting parameters measured in whole blood with added HPG, HPGD, HPGD-Gd, and HPGD-Gd/F (1 mg/mL) using a Thrombelastograph (samples run in triplicates ± S.D.). The Normal value is the published U.S. calibration value from a pool of blood donors.

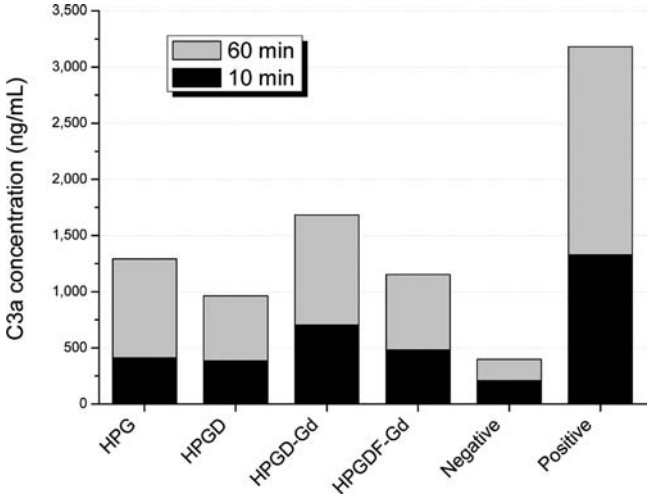


Figure 6. Complement activation in plasma after incubation with different HPGs for 1 h.

time point (Figure 7). In absolute activity uptake into the tumors, the increase from 2.5% of total injected activity in the tumor at 24 h to 6.0% of activity in the tumor at 72 h was 2.4-fold, while the tumors grew in this time only by 1.7-fold, from a volume of 0.22 ± 0.06 mL to 0.38 ± 0.02 mL. Extravasation from leaky tumor vasculature and consequent accumulation in the tumor, also known as the enhanced permeation and retention (EPR) effect,[36] might be responsible for this increase. To take advantage of the EPR effect, long-circulating nanocarriers are needed that are not quickly removed from the vasculature by the reticulo-endothelial system (i.e., by phagocytosis or excretion). Our HPG derivative described here is clearly such a long-circulating macromolecule.

Table 1. Platelet Activation Caused by HPGD and Derivatives (1 mg/mL) in Whole Blood Measured by the CD62 Expression Level in Percentage of Measured Platelets[a]

compound	10 min	30 min	60 min
Positive control	97.0 ± 0.3%	96.5 ± 0.1%	95.4 ± 0.6%
Negative control	0.0%	0.0%	0.0%
Platelet measurement	99.8 ± 0.1%	99.8 ± 0.1%	99.8 ± 0.1%
HPG	5.9 ± 0.7%	11.0 ± 1.1%	6.9 ± 0.9%
HPGD	6.8 ± 0.5%	12.3 ± 0.4%	8.3 ± 0.9%
HPGD-Gd	5.9 ± 0.2%	10.6 ± 0.3%	6.6 ± 0.2%
HPGDF-Gd	6.6 ± 0.1%	11.0 ± 0.9%	7.9 ± 0.9%

[a]Experiments were done in triplicate ± S.D.

MR Imaging and Fluorescent Histology Analysis. The HPGD-Gd relaxivity was measured to be 1075 mM^{-1} s^{-1} (Figure 8). The relaxivity of HPGD-Gd was found to be significantly higher than that of the commercially available Galbumin ($r1$ = 82.85 mM^{-1} s^{-1}), and conventional commercially available agents (e.g., Bayer Healthcare's Gadovist, $r1$ = 3.58 mM^{-1} s^{-1}) (Figure 8). The inset in Figure 8 is a $T1$-weighted image of 5 vials, each containing a different concentration of HPGD-Gd visually demonstrating the signal contrast achievable in MRI. Assuming similar capacity to facilitate proton relaxation in the free as well as HPGD-Gd, one can estimate a coordination of 200−300 Gd-DOTA molecules per HPG macromolecule. Further, since less HPG may be administered for a similar $T1$ effect, dosage of HPGDF-Gd administered was not limited by viscosity. The 0.33 mM stock

dx.doi.org/10.1021/bc200280g | Bioconjugate Chem. 2012, 23, 372−381

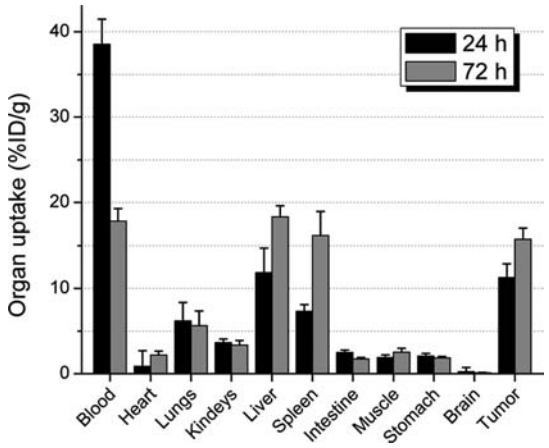


Figure 7. Biodistribution of ^{111}In-HPGD 24 and 72 h after tail vein injection. The percent injected dose per gram of tissue is given ± SD (n = 5).

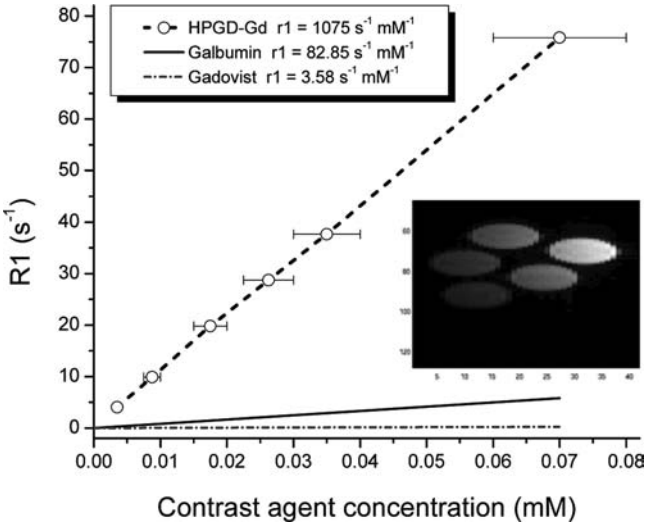


Figure 8. Relaxation rate, $R1$, for HPGD-Gd increases much faster with molar concentration in comparison to galbumin and low-molecular-weight contrast agent Gadovist. Correspondingly, relaxivity, $r1$, is orders of magnitude higher for HPGD-Gd. The graph inset shows a $T1$-weighted MR image of 5 vials with different concentrations of HPGD-Gd, demonstrating image contrast achieved by varying concentrations of the agent.

solution of Galbumin is rather "oily" and cannot easily be more concentrated before injection.

Both $R1$ relaxation rate measurements from *in vivo* MRI and subsequent histological analyses of the same tumors show accumulation of HPGDF-Gd to reach a maximum, followed by a slow decrease. Relaxation rate $R1$ measurements of tumors receiving HPGDF show a maximum at 3 days post-injection (Figure 9). Compare this to the expected fast peaking and washout using the low-molecular-weight agent Gadovist (black bars) in the same figure. Fluorescence measurements show a maximum between 60 min and 6 days post-injection. The group-averaged fluorescence from histological sections is plotted over a bar graph of relaxation rate $R1 = 1/T1$ from MRI data at different time points in Figure 9.

MRI results show heterogeneous signal enhancement following injection of HPGDF-Gd. Figure 10 shows $T1$-weighted RARE MRI images of a tumor (c) prior to and (d) 40

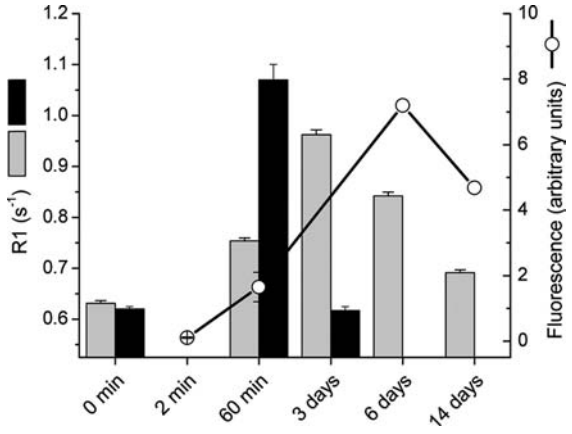


Figure 9. *In vivo* tumor MR $R1$ relaxation rate measurements for HPGDF (gray bars) and Gadovist (black bars) are compared to the overlaid corresponding HPGDF fluorescence values (white circles) obtained from histological tumor sections.

min post-injection of HPGDF-Gd, while (a) shows the corresponding histological HPGDF-Gd fluorescence image of the same tumor at 60 min post-injection. The heterogeneous distribution of HPGDF-Gd observed in the MR and histological images is the likely result of variable perfusion, extravasation, and retention known to exist in solid tumors (for a comprehensive review, see Dreher et al.[37]). These findings warrant further study and will be examined in greater detail in a future publication in combination with other biomarkers of the heterogeneous tumor microenvironment.

■ CONCLUSIONS

We developed a novel trimodal imaging agent suitable for combined SPECT, MR, and optical imaging. The tested high-molecular-weight HPG was biocompatible, highly soluble, with a long-circulating plasma half-life, and could be labeled with ^{111}In with excellent labeling efficiency and good stability, yielding quantitative biodistribution data. Gd coordination to HPG resulted in an MRI contrast agent with 10-fold enhanced relaxivity relative to that of other macromolecular agents such as the commercially available Galbumin. In *in vivo* experiments, HPG was found to have greater effect on average tumor $T1$ than Galbumin. Our biodistribution study and MRI $T1$ relaxation measurements demonstrated an increased uptake of HPGs by the tumors over time. Additionally, *ex vivo* fluorescence microscopy of tumors following MRI supported these findings. A heterogeneous distribution of HPGDF-Gd was observed in the MR and histological images, likely due to variable perfusion, extravasation, and retention. This provides additional rationale regarding the importance of distinguishing the physiological parameters of perfusion and permeability measured using MRI and histological methods, which can demonstrate considerable inter- and intratumor heterogeneity. These data could prove valuable for evaluating tumor vascular response to treatment by antiangiogenic or vascular targeting strategies, as well as for interpreting naïve tumor vascular characteristics and consequently effective treatment options. All three imaging modalities combined and overlapped are especially useful in preclinical investigations to yield highly specific and quantitative data regarding tumor vascular function *in vivo*.

dx.doi.org/10.1021/bc200280g | *Bioconjugate Chem.* 2012, 23, 372–381

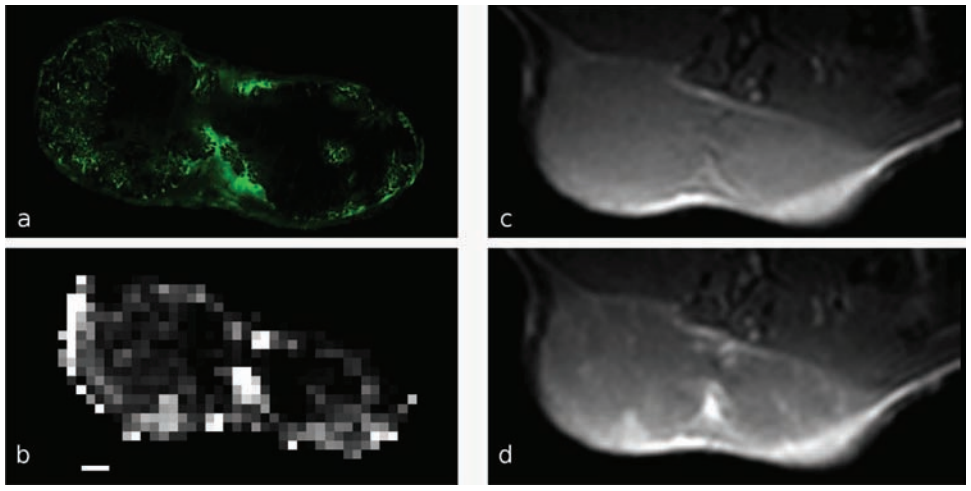


Figure 10. (a) Image of HPGDF-Gd fluorescence of a tumor cryosection. (b) HPGDF-Gd concentration from calibrated change in *R*1 relaxation rate (range from 0 to 1 s^{-1}) of the same slice and orientation *in vivo*. Corresponding *T*1-weighted RARE MR images are shown (c) prior to and (d) 40 min post-injection of 600 mg/kg of HPGDF-Gd. Scale bar indicates 1 mm.

■ ASSOCIATED CONTENT

Supporting Information

Additional ^{1}H NMR spectra and GPC data of the polymers. This material is available free of charge via the Internet at http://pubs.acs.org.

■ AUTHOR INFORMATION

Corresponding Author

*E-mail: urs.hafeli@ubc.ca; Tel. (604) 822-7133; Fax (604) 822-3035.

Notes

The authors declare no competing financial interest.

■ ACKNOWLEDGMENTS

We thank Dr. Dawn Waterhouse for providing us with animals for the ^{111}In biodistribution study. This research was partly funded by a research/operating grant "Alternative radiopharmaceuticals for medical imaging" to UH from both the Canadian Institutes of Health Research (CIHR) and the Natural Sciences and Engineering Research Council of Canada (NSERC). The Canadian Cancer Society and the Canadian Breast Cancer Foundation (JHEB) also supported this study.

■ REFERENCES

(1) Condeelis, J., and Weissleder, R. (2010) In vivo imaging in cancer. *Cold Spring Harbor Perspectives in Biology 2*, a003848.

(2) O'Connor, J. P., Jackson, A., Parker, G. J., and Jayson, G. C. (2007) DCE-MRI biomarkers in the clinical evaluation of antiangiogenic and vascular disrupting agents. *Br. J. Cancer 96*, 189−95.

(3) Tofts, P. S., Brix, G., Buckley, D. L., et al. (1999) Estimating kinetic parameters from dynamic contrast-enhanced T(1)-weighted MRI of a diffusable tracer: standardized quantities and symbols. *J. Magn. Reson. Imaging 10*, 223−32.

(4) Sunder, A., Hanselmann, R., Mulhaupt, R., and Frey, H. (1999) Controlled synthesis of hyperbranched polyglycerols by ring-opening multibranching polymerization. *Macromolecules 32*, 4240−4246.

(5) Frey, H., and Haag, R. (2002) Dendritic polyglycerol: a new versatile biocompatible-material. *J. Biotechnol. 90*, 257−67.

(6) Kainthan, R. K., Muliawan, E. B., Hatzikiriakos, S. G., and Brooks, D. E. (2006) Synthesis, characterization, and viscoelastic properties of high molecular weight hyperbranched polyglycerols. *Macromolecules 39*, 7708−7717.

(7) Cheng, Y., Zhao, L., Li, Y., and Xu, T. (2011) Design of biocompatible dendrimers for cancer diagnosis and therapy: current status and future perspectives. *Chem. Soc. Rev. 40*, 2673−703.

(8) Kainthan, R. K., and Brooks, D. E. (2007) In vivo biological evaluation of high molecular weight hyperbranched polyglycerols. *Biomaterials 28*, 4779−87.

(9) Kainthan, R. K., Hester, S. R., Levin, E., Devine, D. V., and Brooks, D. E. (2007) In vitro biological evaluation of high molecular weight hyperbranched polyglycerols. *Biomaterials 28*, 4581−90.

(10) Kainthan, R. K., Gnanamani, M., Ganguli, M., et al. (2006) Blood compatibility of novel water soluble hyperbranched polyglycerol-based multivalent cationic polymers and their interaction with DNA. *Biomaterials 27*, 5377−90.

(11) Kainthan, R. K., Janzen, J., Levin, E., Devine, D. V., and Brooks, D. E. (2006) Biocompatibility testing of branched and linear polyglycidol. *Biomacromolecules 7*, 703−9.

(12) Hoffman, A. S. (1998) A commentary on the advantages and limitations of synthetic polymer-biomolecule conjugates, in*Biorelated polymers and gels* (Okano, T., Ed.) pp 231−248, Academic Press, Boston.

(13) Kainthan, R. K., Janzen, J., Kizhakkedathu, J. N., Devine, D. V., and Brooks, D. E. (2008) Hydrophobically derivatized hyperbranched polyglycerol as a human serum albumin substitute. *Biomaterials 29*, 1693−1704.

(14) Kainthan, R. K., and Brooks, D. E. (2008) Unimolecular micelles based on hydrophobically derivatized hyperbranched polyglycerols: biodistribution studies. *Bioconjugate Chem. 19*, 2231−8.

(15) Kainthan, R. K., Mugabe, C., Burt, H. M., and Brooks, D. E. (2008) Unimolecular micelles based on hydrophobically derivatized hyperbranched polyglycerols: ligand binding properties. *Biomacromolecules 9*, 886−895.

(16) Rossi, N. A. A., Constantinescu, I., Brooks, D. E., Scott, M. D., and Kizhakkedathu, J. N. (2010) Enhanced cell surface polymer grafting in concentrated and nonreactive aqueous polymer solutions. *J. Am. Chem. Soc. 132*, 3423−3430.

(17) Rossi, N. A., Constantinescu, I., Kainthan, R. K., Brooks, D. E., Scott, M. D., and Kizhakkedathu, J. N. (2010) Red blood cell membrane grafting of multi-functional hyperbranched polyglycerols. *Biomaterials 31*, 4167−78.

(18) Moore, S., and Stein, W. H. (1948) Photometric ninhydrin method for use in the chromatography of amino acids. *J. Biol. Chem. 176*, 367−88.

(19) Moore, S., and Stein, W. H. (1954) A modified ninhydrin reagent for the photometric determination of amino acids and related compounds. *J. Biol. Chem. 211*, 907−13.

(20) Lorenzen, A., and Kennedy, S. W. (1993) A fluorescence-based protein assay for use with a microplate reader. *Anal. Biochem. 214*, 346−8.
(21) Pieters, R., Huismans, D. R., Leyva, A., and Veerman, A. J. P. (1989) Comparison of the rapid automated MTT-assay with a dye exclusion assay for chemosensitivity testing in childhood leukaemia. *Br. J. Cancer 59*, 217−220.
(22) Alberts, B., Johnson, A., Lewis, J., Raff, M., Roberts, K., and Walter, P. (2008) Renewal by multipotent stem cells: Blood cell formation, *Mol. Biol. Cell*, 5th ed., pp 1450−1462, Garland Science, New York.
(23) Patrono, C., and Davi, G. (2008) Platelet activation and atherothrombosis - Reply. *N. Engl. J. Med. 358*, 1638−1639.
(24) Bally, M. B., Mayer, L. D., Hope, M. J., and Nayar, R. (1993) Pharmacodynamics of liposomal drug carriers: Methodological considerations, in *Liposome Technology*, 2nd ed., (Gregoriadis, G., Ed.) pp 27−41, Vol *III*, CRC Press, Boca Raton.
(25) Collins, T. J. (2007) ImageJ for microscopy. *Biotechniques 43*, 25−30.
(26) Haacke, E. M., Brown, R. W., Thompson, M. R., Venkatesan, R. (1999) Magnetic Resonance Imaging: Physical Principles and Sequence Design, Wiley-Liss, New York.
(27) Dowell, N. G., and Tofts, P. S. (2007) Fast, accurate, and precise mapping of the RF field in vivo using the 180 degrees signal null. *Magn. Reson. Med. 58*, 622−30.
(28) Abramoff, M. D., Magelhaes, P. J., and Ram, S. J. (2004) Image Processing with ImageJ. *Biophoton. Int. 7*, 36−42.
(29) Liu, Y., Liu, G., and Hnatowich, D. J. (2010) A brief review of chelators for radiolabeling oligomers. *Materials 3*, 3204−3217.
(30) Martell, A. E., Motekaitis, R. J., Clarke, E. T., Delgado, R., Sun, Y., and Ma, R. (1996) Stability constants of metal complexes of macrocyclic ligands with pendant donor groups. *Supramol. Chem. 6*, 353−363.
(31) De Leon-Rodriguez, L. M., and Kovacs, Z. (2008) The synthesis and chelation chemistry of DOTA-peptide conjugates. *Bioconjugate Chem. 19*, 391−402.
(32) Liu, S. (2004) The role of coordination chemistry in the development of target-specific radiopharmaceuticals. *Chem. Soc. Rev. 33*, 445−61.
(33) Reichert, D. E., Lewis, J., and Anderson, C. J. (1999) Metal complexes as diagnostic tools. *Coord. Chem. Rev. 184*, 3−66.
(34) Kobuchi, Y., Ito, T., and Ogiwara, A. (1988) A model for rouleaux pattern formation of red blood cells. *J. Theor. Biol. 130*, 129−145.
(35) Porter, R. S., Kaplan, J. L., and Homeier, B. P., Eds. (2011) Common Medical Tests: Blood Tests, in *The Merck Manuals Online Medical Library*, Merck & Co., Whitehouse Station, NJ, USA.
(36) Maeda, H. (2010) Tumor-selective delivery of macromolecular drugs via the EPR effect: background and future prospects. *Bioconjugate Chem. 21*, 797−802.
(37) Dreher, M. R., Liu, W., Michelich, C. R., Dewhirst, M. W., Yuan, F., and Chilkoti, A. (2006) Tumor vascular permeability, accumulation, and penetration of macromolecular drug carriers. *J. Natl. Cancer Inst. 98*, 335−44.

Bioconjugate Chemistry

Article

pubs.acs.org/bc

G-Quadruplex-Forming Oligonucleotide Conjugated to Magnetic Nanoparticles: Synthesis, Characterization, and Enzymatic Stability Assays

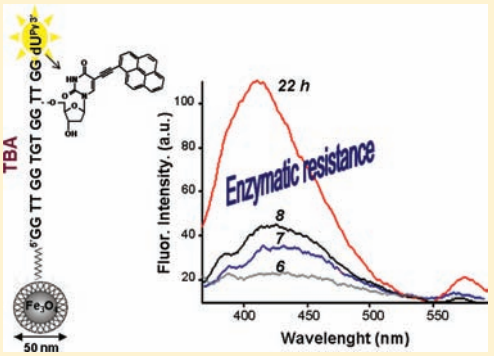
Domenica Musumeci,*[,†,‡] Giorgia Oliviero,[†] Giovanni N. Roviello,[‡] Enrico M. Bucci,[‡] and Gennaro Piccialli[†]

[†]Dipartimento di Chimica delle Sostanze Naturali, Università di Napoli "Federico II", Via D. Montesano 49, 80131 Napoli, Italy

[‡]Istituto di Biostrutture e Bioimmagini − CNR, via Mezzocannone 16, I-80134 Napoli, Italy

Supporting Information

ABSTRACT: In the present work, we report the conjugation of superparamagnetic nanoparticles to a fluorescently labeled oligodeoxyribonucleotide (ODN) able to fold into stable unimolecular guanine quadruple helix under proper ion conditions by means of its thrombin-binding aptamer (TBA) sequence. The novel modified ODN, which contained a fluorescent dU^{Py} unit at 3′-end and a 12-amino-dodecyl spacer (C_{12}−NH_2) at 5′ terminus, was characterized by ESI-MS and optical spectroscopy (UV, CD, fluorescence), and analyzed by RP-HPLC chromatography and electrophoresis. From CD and fluorescence experiments, we verified that dU^{Py} and C_{12}−NH_2 incorporation does not interfere with the conformational stability of the G-quadruplex. Subsequently, the conjugation of the pyrene-labeled ODN with the magnetite particles was performed, and the ODN-conjugated nanoparticles were studied through optical spectroscopy (UV, CD, fluorescence) and by enzymatic and chemical assays. We found that the nanoparticles enhanced the stability of the TBA ODN to enzymatic degradation. Finally, we evaluated the amount of the TBA-conjugated nanoparticles immobilized on a magnetic separator in view of the potential use of the nanosystem for the magnetic capture of thrombin from complex mixtures.



INTRODUCTION

Due to their promising properties, nanoscaled iron oxide particles covalently linked to drugs, proteins, enzymes, antibodies, or nucleic acids have been widely investigated for their great potential in biomedical applications[1−4] such as magnetic bioseparation,[5,6] drug delivery,[7−10] MRI,[11−14] magnetofection[7,15−21] and cancer treatment by hyperthermia.[22−25] Generally, most of these applications require that these nanoparticles have high magnetization values and sizes smaller than 100 nm, with an overall narrow particle size distribution suitable to ensuring uniform physical and chemical properties. In this regard, iron oxide nanoparticles with magnetic core diameter <100 nm exhibit superparamagnetic phenomena, with each particle acting as a single magnetic domain and not retaining any residual magnetism upon removal of the magnetic field.[26] In addition, biomedical applications require a suitable coating of the magnetic particles, which has to be biocompatible, providing colloidal stability and allowing the nanoparticle transport and interaction with biological tissues.[1,2,4,26] Polysaccharides such as dextran have been used for this purpose due to their biocompatibility, low toxicity, and versatility for nanoparticle suspension in cell culture media. Dextran enhances blood circulation time and stabilizes the colloidal solution. Homogeneous suspensions of magnetic nanoparticles with proper surface coating into a suitable solvent are called ferrofluids. This type of suspension can interact with an external magnetic field and be positioned to a specific area. For example, magnetic nanoparticles conjugated to anti-inflammatory drugs could be delivered to the exact area of inflammation reducing drug dosages and potential side effects to healthy tissues, and increasing the rapidity of action. Particles ranging from about 10 to 100 nm are optimal for intravenous injection and are characterized by prolonged blood circulation times. The particles in this size range are small enough to evade reticuloendothelial system (RES) of the body as well as penetrate the very small capillaries within the body tissues and, therefore, may offer the most effective distribution in certain tissues.

In the present work, we report the conjugation of 50 nm superparamagnetic nanoparticles to a fluorescently labeled G-rich oligodeoxyribonucleotide (ODN), able to fold into quadruple helix under proper ion conditions. The selected particles have a single-domain magnetite core (Fe_3O_4) of 20 nm diameter, thus possessing a superparamagnetic magnetization, and a carboxymethyl dextran-biocompatible coating of 15 nm thickness. A pyrene fluorescent group was attached to

Received: June 12, 2011
Revised: December 6, 2011
Published: January 12, 2012

 © 2012 American Chemical Society dx.doi.org/10.1021/bc200305t | *Bioconjugate Chem.* 2012, 23, 382−391

the 3′-end of the ODN in order to follow the ODN fate when anchored to the nanoparticles.[27,28] As ODN, we selected the thrombin-binding aptamer (TBA) sequence, which exists as unstructured in buffers like TRIS, but folds into a stable unimolecular guanine quadruple helix in the presence of ions such as K^+ and of the thrombin protein, recognized with nanomolar affinity.[29−33] Thus, this is clearly the reason for a wide number of scientific studies on the TBA sequence[34−42] in view of its possible use as a highly potent inhibitor of thrombin clotting activity[43−46] or as a probe for detection of K^+ concentrations in living organisms.[47,48] However, to the best of our knowledge, this is the first report in the literature on the conjugation of this particular sequence to magnetite nanoparticles. The potential in biomedical applications of this conjugate, as magnetic biosensor or therapeutic agent, can be understood considering the combination of the attractive properties of both the TBA sequence and the magnetic nanoparticles. Indeed, since each nanoparticle carries more than one ODN, this system could be very useful to obtain high local concentrations of both the aptamer and the magnetic nanoparticles, especially when high doses of the therapeutic are needed to accumulate at the target site.

The novel TBA−nanoparticle conjugate was studied through optical spectroscopy (UV, CD, fluorescence), and its resistance to enzymatic degradation was evaluated in 76% murine plasma.

Furthermore, we evaluated the amount of the TBA-conjugated nanoparticles immobilized on a steel matrix-filled column placed in a strong permanent magnet estimating in this way the potential capture capacity of thrombin by this nanosystem, in view of its use for the magnetic capture of thrombin from complex mixtures.

EXPERIMENTAL SECTION

Materials, Apparatus, and General Methods. CPG Universal Support 500 (49 μmol/g loading), 5′-dimethoxytrityl-*N*-acyl-2′-deoxyribonucleoside, 3′-[(2-cyanoethyl)-(*N*,*N*-diisopropyl)]-phosphoramidites (dN-CE Phosphoramidites), 5′-dimethoxytrityl-5-(pyren-1-yl-ethynyl)-2′-deoxyUridine, 3′-[(2-cyanoethyl)-(*N*,*N*-diisopropyl)]-phosphoramidite (Pyrene-dU-CE Phosphoramidite), 12-(4-monomethoxytritylamino)-dodecyl-1-[(2-cyanoethyl)-(*N*,*N*-diisopropyl)]-phosphoramidite (5′-Amino-Modifier C12), and standard DNA-synthesis reagents (Amidite diluent, Activator solution, Cap A, Cap B, Acetonitrile wash B, Oxidizer) were purchased from Primm (Milan, Italy). Acetonitrile external wash (wash A) was from Biosolve (<10 ppm water). The ferrofluid fluidMAG-CMX was purchased from Chemicell GmbH (Berlin, Germany) and consisted of an aqueous dispersion (25 mg/mL, 1.3×10^{13} particles per mg) of 50-nm-diameter magnetite nanoparticles (80%, w/w; single-domain 20 nm diameter magnetite core; 40 kDa dextran coating of 15 nm thickness) with a COOH surface. All other reagents and solvents were from Sigma-Aldrich (EDC, NHS, MES-buffer, CH_3CN for HPLC, Acrylamide/Bis Acrylamide 19:1 - 40%, TRIS, Boric acid, EDTA, TEMED, APS, Glycerol, Bromophenol blue-Xylenecyanol solid mixture [gel tracking dyes], KCl, $MgCl_2$, $CaCl_2$, Urea, Formamide, Ethidium bromide). DNase I from bovine pancreas (1 mg/mL) was kindly provided by Dr. Sonia Di Gaetano, IBB-CNR, Napoli (Italy).

DNA solid phase synthesis was performed on an ABI Expedite 8909 oligosynthesizer. HPLC chromatographic analyses and purifications were performed using a Jasco PU-2089 Plus gradient pump, equipped with the Jasco UV-2075 Plus UV/vis detector.

Desalting of purified oligomers was performed on NAP-25 columns (GE Healthcare). Samples were lyophilized in a Alpha 1−4 LD Freeze-Dryer (Martin Christ) for 16 h.

UV measurements were obtained on a JASCO V-550 UV/vis spectrophotometer equipped with a Peltier block by using 1 cm quartz cells of both 0.5 and 3 mL internal volume (Hellma).

Oligomer quantification was achieved measuring the absorbance (λ = 260 nm) at 80 °C, using the molar extinction coefficients calculated for the unstacked oligonucleotides. The molar extinction coefficients used for the calculations were as follows: A, 15.06; T, 8.56; G, 12.18; C, 7.10; U, 9.66 m^{-1} M^{-1}.[49] Annealing of all the duplexes was performed by dissolving equimolar amounts of the two complementary strands in Milli-Q water, heating the solution at 85 °C (5 min) and then allowing to slowly cool to room temperature.

LC/ESI-MS analyses were performed on a MSQ mass spectrometer (ThermoElectron, Milan, Italy) equipped with an ESI source operating at 3 kV needle voltage (T = 320 °C), and with a complete Surveyor HPLC system, comprising a MS pump, an autosampler, and a PDA detector. Elution was performed on a Phenomenex Jupiter C18 300 Å (5 μm, 4.6 × 150 mm) column, monitoring at 260 nm, by building up a gradient starting with H_2O (0.03% TFA) and applying increasing amounts of CH_3CN (0.03% TFA), with a flow rate of 0.8 mL/min.

All CD spectra were collected on a Jasco J715 spectropolarimeter equipped with a Peltier element for temperature control, using a Teflon stoppered 1 cm quartz cuvette of 3 mL internal volume (Hellma), and a tandem cell (2 × 4.375 mm, Suprasil quartz, Hellma). CD parameters were the following: spectral window 200−320 nm, data pitch 1 nm, bandwidth 2 nm, response 4 s, scanning speed 50 nm/min, 3 accumulations. The CD binding studies in the tandem cell were obtained by recording the "sum" spectrum (buffered solution of **1** or **2** in one chamber and buffered solution of **3** in the other) and the "complex" spectrum (after mixing of the two solutions) at 15 °C.

UV melting curves were recorded by following the absorbance changes at a determined wavelength as the temperature was increased (melting parameters: heating rate 0.5 °C/min, monitoring wavelength 295[50] or 260 nm, bandwidth 2 nm, response 16 s). T_m values were calculated as the maxima of the plots of the first derivative of the Absorbance versus temperature (error values, ±0.5 °C).

Fluorescence spectra were obtained on a Varian Cary Eclipse fluorimeter (Varian, Oxford, UK). We registered emission fluorescence spectra exciting at 335 nm (unless otherwise specified) and maintaining the excitation and emission slits at 5 nm.

Electrophoretic analysis was performed on a Scie-Plas mini-gel unit (Standard TV100, twin-plate 10 × 10 cm^2) equipped with a APELEX PS 503/500 V Power Supply (Eppendorf srl, Italy). Gels were exposed to UV light (254 nm) after ethidium bromide staining and photographed by digital camera (Nikon Coolpix S5).

ODN Synthesis, Purification, and Characterization. The ODN sequences were the following: NH_2-C_{12}-G G T T G G T G T G G T T G G - d U ^{Py} − O H (**1**), GGTTGGTGTGGTTGG (**2**), and CCAACCACACCAACC (**3**). DNA solid phase synthesis was performed on a CPG Universal Support (35 mg, 1.4 μmol) using 1 μmol scale

standard protocol, with the DMT-OFF option for oligomers **2** and **3**, and the DMT-ON one for the pyrene-labeled oligomer **1**. Coupling efficiency during the automated synthesis was estimated spectrophotometrically by the DMT cation released during the detritylation steps. Double coupling and 6 min coupling time were employed for the Pyrene-dU-CE and 5′-amino-modifier C12 phosphoramidites.

The oligos were deprotected and cleaved from the solid support with 1.5 mL 30% ammonium hydroxide: for 16 h at 55 °C for oligomer **2** and **3**, and for 1 h at room temperature followed by 17 h at 40 °C for oligomer **1**. After evaporation of the solvent, the resulting crude mixtures of **1**−**3** were chromatographed on C18 analytical column (Thermo Hypersil-100, 4.6 × 250 mm, 5 μm) using a linear gradient of CH_3CN in 0.1 M TEAB solution (flow rate 1 mL min^{-1}). UV detection was achieved at 260 nm. **1**: 8% (2 min) to 40% CH_3CN in 0.1 M TEAB over 30 min, t_R = 16.3 min (23.2% CH_3CN). **2**: 8% to 20% CH_3CN in 0.1 M TEAB over 25 min, t_R = 13.4 min (14.4% CH_3CN). **3**: 8% (2 min) to 28% CH_3CN in 0.1 M TEAB over 26 min, t_R = 13.1 min (16.5% CH_3CN).

Purified oligonucleotides **1**−**3** were lyophilized, and then ODN **1** was treated with 2 mL acetic acid/water (80:20) at room temperature for 2 h in order to remove the MMT group, followed by evaporation of the solvents under vacuum. Subsequently, all the oligomers were dissolved in 2.5 mL H_2O and desalted using prepacked NAP-25 columns. Desalted oligos were lyophilized, dissolved in a known amount of Milli-Q water and quantified by UV measurements. The epsilon values used for the quantification of the oligos are as follows: **1** (G_9T_6U) ε_{260} = 170.64 m^{-1} M^{-1}; **2** (G_9T_6) ε_{260} = 160.98 m^{-1} M^{-1}; **3** (C_9A_6) ε_{260} = 154.26 m^{-1} M^{-1}. UV quantification of the oligos provided the following values: **1** = 252 nmol (18% yield); **2** = 448 nmol (32% yield); **3** = 490 nmol (35% yield).

For LC/ESI-MS characterization, the ODN **1**−**3** stock solutions (200 μM) were diluted to 20 μM in an aqueous solution of 1% CH_3COOH, and 50 μL aliquots of each sample were injected into the LC/MS system by the autosampler and acquired in positive ion mode. ESI-MS data were the following: **1** = m/z 1374.3 (found), 1376.9 (expected for $[M+4H]^{4+}$), 1100.6 (found), 1101.7 (expected for $[M+5H]^{5+}$); **2** = m/z 1577.0 (found), 1576.4 (expected for $[M+3H]^{3+}$), 1181.1 (found), 1182.5 (expected for $[M+4H]^{4+}$), 944.9 (found), 946.2 (expected for $[M+5H]^{5+}$); **3** = m/z 1105.2 (found), 1106.0 (expected for $[M+4H]^{4+}$), 882.9 (found), 885.0 (expected for $[M+5H]^{5+}$).

Conjugation to Nanoparticles. An aqueous suspension of fluidMAG-CMX (40 mg in 1.6 mL) was dialyzed two times (for 15 and 7 h) against MES buffer (0.5 M, pH = 6.3) in a 5 mL Float-A-Lyzer G2 column (Spectrumlab.com) with a molecular weight cutoff of 100 kDa. Subsequently, a 0.52 M solution (0.4 mL) of EDC (40 mg) and a 100 μM solution (1 mL) of ODN **1**, both in 0.5 M MES buffer, were added to the nanoparticle suspension, and the reaction mixture was gently stirred at room temperature. After 15 h the crude was dialyzed against water to remove residual EDC and ODN molecules, and then against 20 mM TRIS HCl (pH 7.4) to cap the eventual unreacted carboxylate groups on the nanoparticles by the aminomethane derivative.

Enzymatic Assay with DNase. To 500 μL of the conjugated fluidMAG suspension (8 mg/mL) in 20 mM TRIS HCl (pH 7.4), 50 μL of 200 mM TRIS and 10 μL bovine pancreatic DNase I (1 mg/mL) were added, and the mixture was allowed to gently stir at room temperature. After 1 h, 28 μL $MgCl_2$ (600 mM) and 14.7 μL $CaCl_2$ (200 mM) were added, obtaining a final volume of 602.7 μL and the following final concentrations: 6.6 mg/mL nanoparticles, 33 mM TRIS, 0.0166 mg/mL DNase, 28 mM $MgCl_2$, 4.9 mM $CaCl_2$. After 20 h, the reaction mixture was dialyzed against water 3 times. The dialyzed fractions were concentrated, lyophilized, dissolved in 1 mL Milli-Q water, and loaded on a equilibrated Sep-pack C18 column (Millipore). Elution: 2.6 mL water (fraction 1), 3 mL 4:6 H_2O/CH_3CN (fraction 2), 3.4 mL CH_3CN (fraction 3). Emission fluorescence spectra were performed on the 3 eluted fractions (λ_{ex} = 340 nm; excitation slits = 5 nm, PNT Detector Voltage = 800 V): only fraction 2 showed fluorescence signal. The same experiment was conducted on the unconjugated fluidMAG suspension.

Acidic Treatment of the Nanoconjugate. In order to further confirm the presence of the fluorescent ODN on the nanoparticle surface, we treated 500 μL of the conjugated fluidMAG suspension (8 mg/mL) with 0.4 M HCl (500 μL) at 65 °C for 15 h. The reaction crude was divided in two aliquots. One aliquot was dialyzed against water, and the dialyzed fractions were concentrated under vacuum and analyzed via fluorescence spectroscopy. On the other aliquot, DCM/water extraction of the reaction mixture was performed: the aqueous and organic phases were dried, dissolved in a small volume (450 μL) of water and CH_3CN, respectively, and analyzed by UV. The chemical assay was also performed on the same amount of nanoparticles from the fluidMAG stock solution which was subsequently analyzed as described before.

Enzymatic Stability Assays. 60 μL oligonucleotide sequence **1** (30.6 μM) in H_2O was added to a plastic vial containing 190 μL 100% murine plasma, and the mixture was incubated at 37 °C (final conc.: 7.2 μM ODN, 76% plasma). 13.5 μL samples, withdrawn from the reaction mixture at different times (0, 10, 20, 30, 40, 60, 120, 180, 240, 300, 360 min), were added to 10 μL electrophoretic loading buffer (TBE 1×, 50% glycerol, 40% formamide, 0.2% gel tracking dyes) in eppendorf tubes, and the mixtures were kept for 3 min at 90 °C and frozen until further analysis. Samples (10 μL), preheated at 90 °C for 1 min, were loaded on a 15% denaturing polyacrylamide gel containing 7 M urea, and the gel was run on the electrophoretic system for 1 h at 95 V in TBE 1×/7 M urea running buffer.

600 μL of the conjugated nanoparticles (8 mg/mL) in 20 mM TRIS HCl, pH 7.4, were added to 1.9 mL 100% murine plasma in a plastic falcon tube, and the mixture was incubated at 37 °C (final conc.: 1.9 mg/mL nanoparticles, 76% plasma). After gentle stirring of the falcon for 20 s, 150 μL samples were withdrawn from the degradation mixture at various times (0, 20, 40 min; 1, 2, 3, 4, 5, 6, 7, 8, 22, 24, 26 h). Each sample was diluted to 1 mL and dialyzed against water. The dialyzed fractions were concentrated to 450 μL and analyzed by fluorescence spectroscopy.

Magnetic Separation of the TBA^{Py}-Conjugated Nanoparticles. The TBA-nanoparticle conjugate solution (11.7 μL, 8.00 mg/mL) was diluted 85.5-fold to 1 mL (0.0936 mg/mL iron content) and loaded on a spherical steel matrix column (LD-MACS, Miltenyi Biotec), pre-equilibrated with 3 × 2 mL H_2O, placed in the MidiMACS Magnetic Separator (Miltenyi Biotec). Elution by gravity on the magnetic separator: 5 × 2 mL H_2O, fractions 1−5 (2 mL each). Elution out of the magnetic separator by using the plunger: 3 × 2 mL H_2O, fractions 6−8 (2 mL each). Fractions 1−3 (6 mL in total) and fractions 6−7

dx.doi.org/10.1021/bc200305t | Bioconjugate Chem. 2012, 23, 382−391

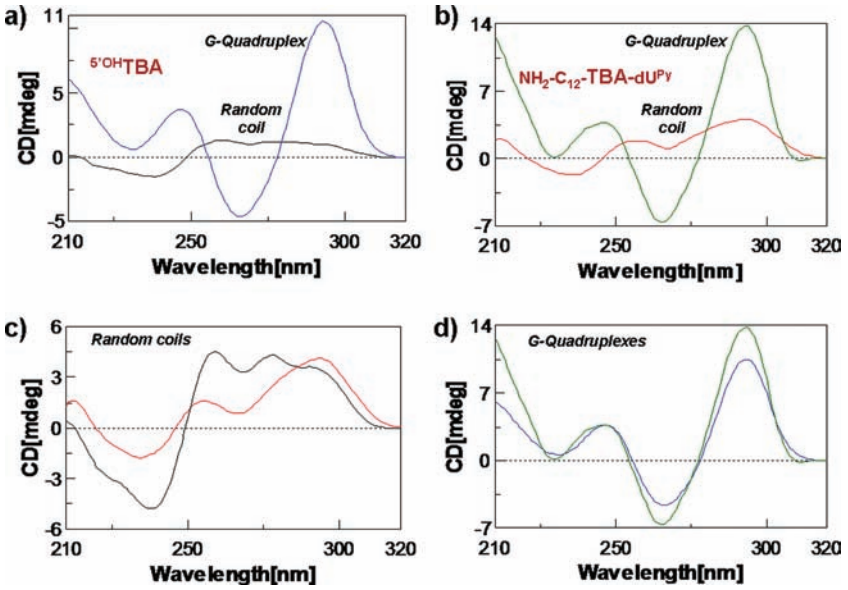


Figure 1. Overlapped CD spectra of (a) 2 μM $^{5'OH}$TBA, in 20 mM TRIS (black line) and in 20 mM TRIS/150 mM KCl (blue line); (b) 2 μM NH_2-C_{12}-TBA-dU^{Py}, in 20 mM TRIS (red line) and in 20 mM TRIS/150 mM KCl (green line); (c) $^{5'OH}$TBA (black) and NH_2-C_{12}-TBA-dU^{Py} (red), 2 μM in 20 mM TRIS; (d) $^{5'OH}$TBA (blue) and NH_2-C_{12}-TBA-dU^{Py} (green), 2 μM in 20 mM TRIS/150 mM KCl.

(4 mL in total) were separately unified and analyzed by UV spectroscopy.

RESULTS AND DISCUSSION

Design, Synthesis, and Characterization of the NH_2–C_{12}-TBA-dU^{Py} Oligomer and Description of Some Magnetic Nanoparticle Properties. We designed and synthesized a fluorescently labeled ODN conjugated to magnetic particles. The magnetic nanoparticles selected by us consisted of a 80% (w/w) single-domain magnetite core 20 nm in diameter with a 40 KDa dextran coating of 15 nm thickness bearing methylene carboxylic groups. In particular, the ferrofluid fluidMAG-CMX used by us consisted of an aqueous dispersion of magnetic iron oxide nanoparticles (25 mg/mL) with hydrodynamic diameter of 50 nm and, thus, with superparamagnetic properties. Approximately, there were 1.3 $\times$ 10^{13} particles per mg of the solid component.

The ODN sequence selected by us was GG TT GG TGT GG TT GG, which is the thrombin-binding aptamer (TBA) sequence, and the fluorescent group chosen was the pyrene.

Initially, UV spectra of the ferrofluid at various dilutions, starting from 100 to 3200-fold, was performed covering a wavelength range from 220 to 700 nm (Supporting Information, Figure S1).

From these experiments we concluded that to observe an absorbance below 1 (or between 1 and 2), in the 220–400 nm range, where the ODN and pyrene group contribute, the fluidMAG dispersion should be diluted 1600-fold (magenta line, Figure S1) (or 800-fold, red line) corresponding to a 0.0156 mg/mL (or 0.0312 mg/mL) iron concentration. At these dilutions, considering the binding capacity of the particles with the ODN-pyrene molecules, there would be an ODN-Py concentration of about 4 nM (or 8 nM). Thus, considering the molar absorption coefficients (ε), the high UV absorption of iron over the whole range of visible light greatly predominates over the ODN-pyrene UV contribution which would probably not be appreciable by the UV spectrophotometer.

In this respect, we intended to monitor the ODN anchored to the nanoparticles through the pyrene fluorescence. The pyrene group not only provides fluorescence spectra which result very sensitively to its concentration, and thus to the ODN concentration, but is also a very sensitive fluorescent probe for conformational changes of the oligomer to which is attached.[27,28] Iron oxides do not exhibit any fluorescence signal, as we verified by performing several fluorimetry experiments. We registered emission fluorescence spectra of fluidMAG from 400 to 600 nm at various dilutions (800, 1600, 3200, 6400-fold) exciting at different wavelengths (340, 350, 360, 370, 380 nm), taking into consideration the fluorescence properties of the pyrene group: no fluorescence was detected.

Furthermore, iron oxides are not expected to interfere with the pyrene fluorescence. Indeed, in a recent work on the synthesis of magnetite nanoparticles with polymeric shell including pyrene groups, it was demonstrated that fluorescent spectra of pyrene-polymeric shell particles in the presence or absence of the magnetic core were almost identical.[51]

Hence, we proceeded with the synthesis of the pyrene-labeled ODN, constituted by a 5-(pyren-1-yl-ethynyl)-2′-deoxyUridine (dU^{Py}) at the 3′ end, the TBA sequence (GG TT GG TGT GG TT GG) and a 12-amino-dodecyl spacer (5′-Amino-Modifier C12) at the 5′ terminus, useful for the conjugation to the nanoparticles. The modified ODN was synthesized on solid phase at 1 μmol scale by phosphoramidite chemistry using an automatic synthesizer. After cleavage/deprotection, the oligo was purified by reverse phase HPLC on a C18 analytical column (Supporting Information, Figure S2), and the MMT group was removed by mild acidic treatment of the purified ODN.

The amino-free ODN (NH_2-C_{12}-TBA-dU^{Py}, **1**) was desalted by gel filtration, and characterized by ESI-MS and optical spectroscopy (UV, CD, fluorescence), and analyzed by RP-HPLC chromatography and electrophoresis. UV spectrum, shown in Figure S3 (Supporting Information), revealed the characteristic absorptions of both the TBA sequence, with the double-hump band between 230 and 300 nm, and the pyrene

dx.doi.org/10.1021/bc200305t | Bioconjugate Chem. 2012, 23, 382–391

group, with the characteristic UV contribution in the range 320−450 nm (inset of Figure S3). Absorbance measurements at 260 nm, considering the molar extinction coefficient of the ODN afforded a 18% yield of the purified oligomer.

Electrophoretic mobility of the new NH_2-C_{12}-TBA-dU^{Py} molecule was evaluated on a denaturing polyacrylamide gel (15%) and compared with that of the $^{5'OH}$TBA, synthesized as control: as evidenced by the band position in Figure S4 (Supporting Information), in these conditions, the two ODNs have almost the same mobility, differing only for the color of the bands revealed by UV light (254 nm) after ethidium bromide staining.

Circular dichroism properties of the ODN containing the dU^{Py} and C_{12}−NH_2 modifications were investigated and compared with that of the natural $^{5'OH}$TBA (**2**, Figure 1a,b). We also detected and compared the conformational change from unstructured to G-quadruplex of both ODNs after adding KCl (Figure 1c,d). From these CD data we verified that the incorporation of dU^{Py} and C_{12}−NH_2 does not interfere with the formation of the G-quadruplex.

Then, we studied the conformational change of NH_2-C_{12}-TBA-dU^{Py} from unstructured to G-quadruplex also by fluorescence. Hyperchromic and bathochromic shifts were observed, as reported in Figure 2. The random coil structure

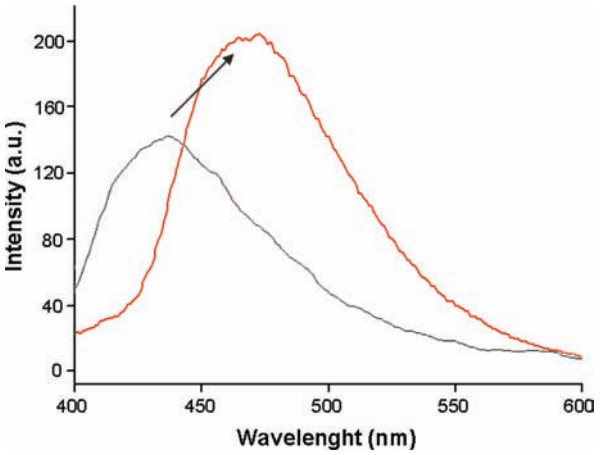


Figure 2. Overlapped fluorescence spectra of 0.4 μM NH_2-C_{12}-TBA-dU^{Py} in 20 mM TRIS (black line) and in 20 mM TRIS/150 mM KCl (red line).

showed an emission band at λ_{max} = 430 nm (black line), which shifted to 475 nm on transition to the G-quadruplex structure after adding KCl (red line).

Finally, we verified the binding of the modified TBA ODN **1** to its complementary sequence (CCAACCACACCAACC, **3**) and compared the stability of the resulting duplex with that of the nonmodified one. CD experiments performed in a tandem cell evidenced the formation of a complex between **1** and **3** (Figure 3a) which is certainly a duplex structure, also considering the similarity of the *mix* CD spectrum of the **1**−**3** complex with that of the duplex formed between the natural TBA **2** and the complementary strand **3** (Figure 3b,c). The **1**−**3** duplex is formed also by mixing preformed TBA quadruplex **1** (in 150 mM KCl) with complementary strand **3** (Figure 3d), in analogy to the behavior of the natural TBA **2** (data not shown).[52]

Melting temperatures (T_m) of the modified quadruplex **1** (in 150 mM KCl) and the **1**/**3** duplex, obtained by UV measurements (T_m = 52.5 and 57.4, respectively), were almost identical to the natural counterparts, quadruplex **2** and duplex **2**/**3** (T_m = 47.3 and 54.8, respectively, Figure 4), denoting that the two modifications (dU^{py} and C_{12}-linker) do not interfere with the stability of the TBA-forming structures, but rather stabilize the resulting structures, probably thanks to the dU^{py}-duplex or dU^{py}-quadruplex interaction (stacking effect).[53]

Conjugation of the NH_2-C_{12}-TBA-dU^{Py} Oligomer with the Magnetic Nanoparticles. After the chemical−physical characterization of the NH_2-C_{12}-TBA-dU^{Py} ODN, we performed its conjugation with the magnetic nanoparticles. The covalent coupling between the ODN amino groups and the COOH on the nanoparticles was achieved by carbodiimide activation method using EDC (25 °C, 15 h). Unbound ODN and EDC derivatives were removed from the conjugate suspension by a series of dialyses against water. By selecting the proper membrane pore cutoff of the dialysis column (100 KDa), unconjugated ODN, EDC excess, and EDC derivatives passed outside the membrane, whereas iron nanoparticles remained inside. Dialyzed fractions were checked by UV measurements until no further UV signal was detected on the concentrated fraction.

UV spectrum of the conjugation mixture, in comparison with the starting fluidMAG, is shown in Figure 5. As expected, no substantial difference in the spectra between conjugated and unconjugated nanoparticles was revealed.

Subsequently, both the FluidMAG stock solution and the ODN-conjugated nanoparticles were subjected to thermal analysis, following the UV absorbance value at 260 and 650 nm upon increasing the temperature from 15 to 70 °C. In the overall temperature range, no change in the A_{260} and A_{650} was detected, and the UV spectra of both the samples, recorded after each thermal experiment, were superimposable on that obtained before the analysis, at the same temperature (15 °C). Thus, these results suggest that both the FluidMAG stock solution and the ODN-conjugated nanoparticles are stable to temperature growth up to 70 °C, since the optical properties of both samples are not affected by changes in temperature.

Furthermore, no CD signal of the ODN−nanoparticle conjugate solution was detected (indeed spectra resulted perturbed by the high potential), even at various dilutions (40, 100, 400, 800-fold), and even by adding KCl (150 mM) at each diluted sample in order to allow the formation of the G-quadruplex on the nanoparticle, which, possessing a higher CD signal, would have been able to increase the CD sensitivity.

Unexpectedly, also fluorescence spectra of the ODN−nanoparticle conjugate did not reveal any signal. In particular, perturbed signals were detected even at different dilutions of the conjugated mixture from 100- to 1660-fold, and exciting at different wavelengths (340, 350, 360, 370, 380 nm). Thus, our data apparently disagree with a previous report in which the magnetite core of nanoparticles with the pyrene-containing polymeric coating did not perturb the pyrene fluorescence.[51] This apparent discordance can be explained on the basis of the different pyrene/magnetite ratio which was much higher in the cited work than in our case.

Subsequently, we verified the presence of the fluorescent ODN on the nanoparticle by treating a known amount of the conjugated fluidMAG with bovine pancreatic deoxyribonuclease I (DNase I) in proper conditions. DNase I is a DNA-specific endonuclease able to hydrolyze the phosphodiester linkages of double-stranded or single-stranded DNA to a mixture of oligo- and mononucleotides. Since the ODN was

dx.doi.org/10.1021/bc200305t | *Bioconjugate Chem.* 2012, 23, 382−391

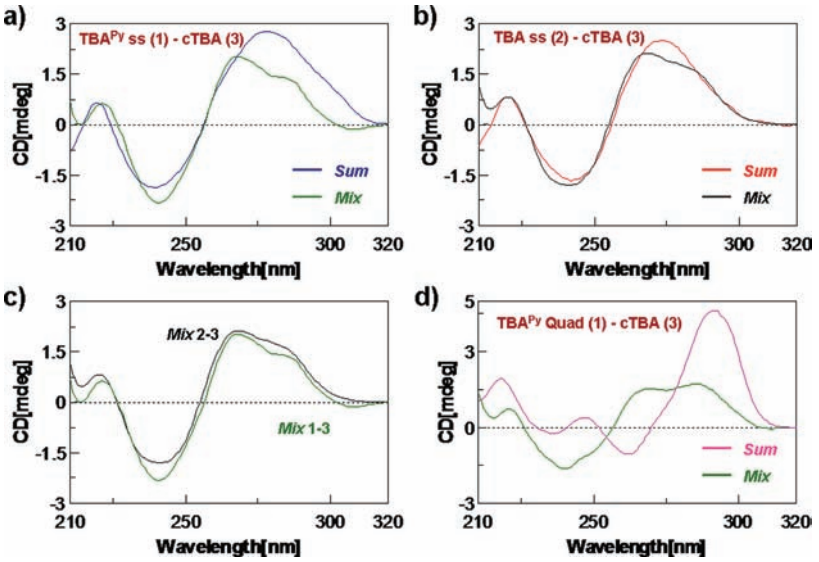


Figure 3. (a) Overlapped *sum* and *mix* spectra of ODNs **1** and **3**, 2 μM each strand, 20 mM TRIS, tandem cell. (b) Overlapped *sum* and *mix* spectra of ODNs **2** and **3**, 2 μM each strand, 20 mM TRIS, tandem cell. (c) Comparison of the CD spectra of the **1**−**3** and **2**−**3** complexes. (d) Quadruplex-Duplex competition experiment in tandem cell: *sum* (magenta) and *mix* (green) spectra of TBA quadruplex **1** and cTBA **3**, 2 μM each strand in 20 mM TRIS/150 mM KCl.

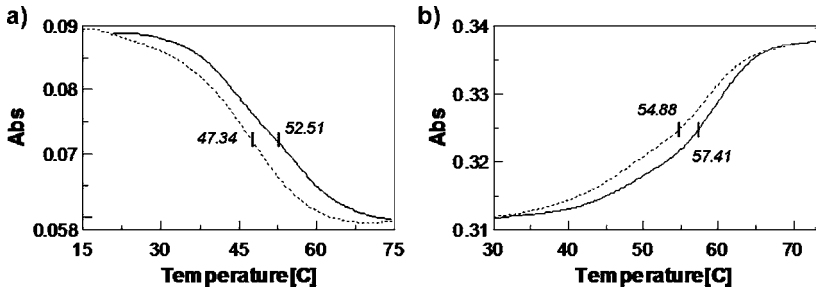


Figure 4. Overlapped melting curves of (a) 2 μM NH_2-C_{12}-TBA-dU^{Py} (**1**, straight line) and 2 μM $^{5'OH}$TBA (**2**, dashed line) in 20 mM TRIS and 150 mM KCl, at 295 nm, (b) 1 μM **1**−**3** duplex (straight line) and 1 μM **2**−**3** duplex (dashed line) in 20 mM TRIS and 150 mM KCl, at 260 nm.

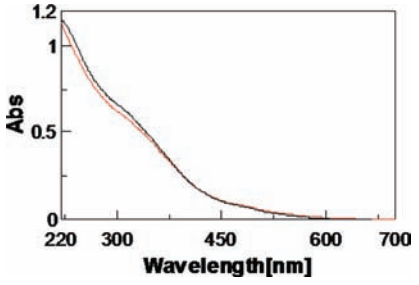


Figure 5. UV spectra of the conjugated nanoparticle (red line) and starting fluidMAG (black line) solutions, at 1:800 and 1:1600 dilutions, respectively.

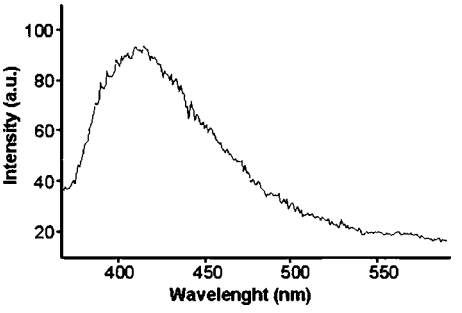


Figure 6. Fluorescence spectrum of the dialyzed fractions after DNase treatment of the conjugated fluidMAG.

linked to the nanoparticles through its 5′-end, whereas the pyrene fluorophore was positioned at the 3′-terminus, far from the steric hindrance of the nanoparticle, we expected to find ODN fragments also containing the fluorophore after DNase degradation. Actually, after dialysis of the DNase reaction mixture, we found a clear fluorescent signal in the concentrated dialyzed fractions (Figure 6), which was absent in the case of the dialyzed fraction from the fluidMAG stock solution treated with DNase in the same conditions used for the conjugated fluidMAG. From this experiment we were also able to determine the approximate number of ODN molecules per particle, as described in the Supporting Information (Figure S5).

In order to further confirm the presence of the fluorescent ODN on the nanoparticle surface, we treated another known amount of conjugated fluidMAG with 0.4 M HCl at 65 °C for 15 h. In these conditions, we expected depurination and probably loss of the pyrene group to occur. The reaction crude was divided into two aliquots. One was subjected to dialysis against water: we found fluorescent signal in the concentrated dialyzed fractions (Figure 7a), which was absent in the case of the dialyzed fraction from the fluidMAG stock solution treated

dx.doi.org/10.1021/bc200305t | *Bioconjugate Chem.* 2012, 23, 382−391

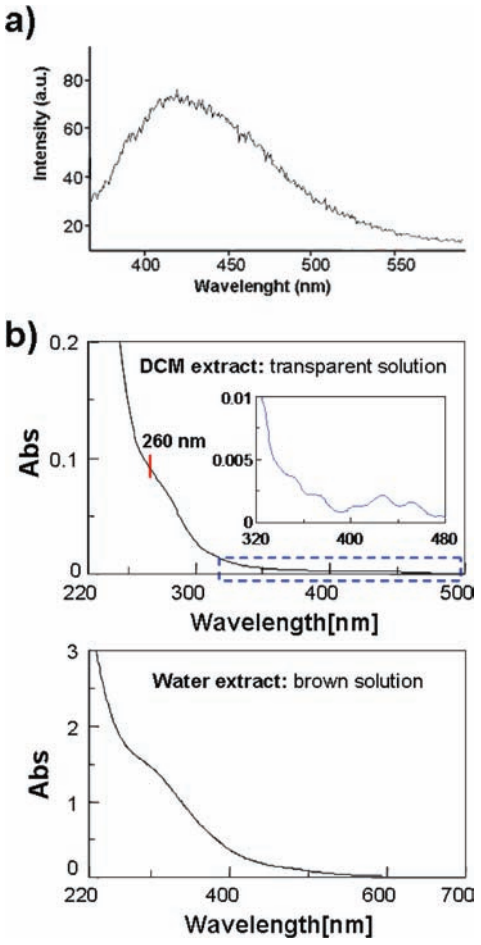


Figure 7. (a) Fluorescence spectrum of the dialyzed fraction after HCl treatment of the conjugated fluidMAG; (b) UV spectra of the DCM and water extracts after HCl treatment of the conjugated fluidMAG. The inset shows enlargements of the 320−480 nm region of the spectrum.

with HCl in the same conditions as the conjugated one. On the other aliquot DCM/water extraction of the reaction mixture was performed: the aqueous and organic phases were dried, dissolved in a small volume of water and CH_3CN, respectively, and analyzed by UV. The aqueous phase revealed the usual strong iron absorption, while the organic one showed bands of both nucleotidic and pyrene nature, shifted at higher wavelengths in CH_3CN and characterized by low intensity due to the small amount of starting nanoparticle mixture (Figure 7b). No significant UV absorbance was detected in the organic phase relative to the HCl treatment of the fluidMAG stock solution, performed as a control.

The resistance to enzymatic degradation of the TBA^{Py}-conjugated nanoparticles was explored and compared with that of the free TBA^{Py}. We expected a protection of the ODN from enzymatic degradation thanks to the presence of the nanoparticles, in analogy to recent works.[54,55] Thus, unconjugated TBA ODN **1** (7.2 μM) was incubated, as a control, in 76% murine plasma at 37 °C, and its degradation was monitored by electrophoretic analysis of several aliquots, withdrawn from the reaction mixture at different times (0, 10, 20, 30, 40, 60, 120, 180, 240, 300, 360 min; Figure 8a). In these conditions the ODN exhibited an half-life of about 30 min. The same experiment was carried out by incubating the conjugated nanoparticles (1.9 mg/mL) in 76% murine plasma. The analysis of the samples, withdrawn from the degradation mixture of the conjugate at various times (0, 20, 40 min; 1, 2, 3, 4, 5, 6, 7, 8, 22, 24, 26 h) was performed by dialyzing the samples against water and recording the fluorescence spectra of the dialyzed and concentrated fractions. Fluorescence instead of electrophoresis analysis was performed on the nanoconjugate degradation mixture in order to increase the sensitivity of the method: indeed the dialysis, carried out on every sample withdrawn with the aim of separate the iron components from the oligonucleotide samples, required the analysis of large volumes. No degradation products was detected within 5 h. The first fluorescence signal was revealed for the sample collected at 6 h (gray line), while the last one was for the 22 h sample (red line, Figure 8b).

Magnetic Separation of the TBA^{Py}-Conjugated Nanoparticles. In view of the potential use of the TBA-conjugated nanoparticles for the capture of thrombin from a complex mixture we characterized with respect to our conjugate solution, the LD-MACS column (Miltenyi Biotec), associated with the MidiMACS Separator and generally used for the magnetic cell separation. When a MACS column, composed of a spherical steel matrix, is placed in a MACS Separator, consisting of a strong permanent magnet, a high gradient magnetic field is induced within the column, and a certain amount of magnetically labeled cells can be efficiently retained.

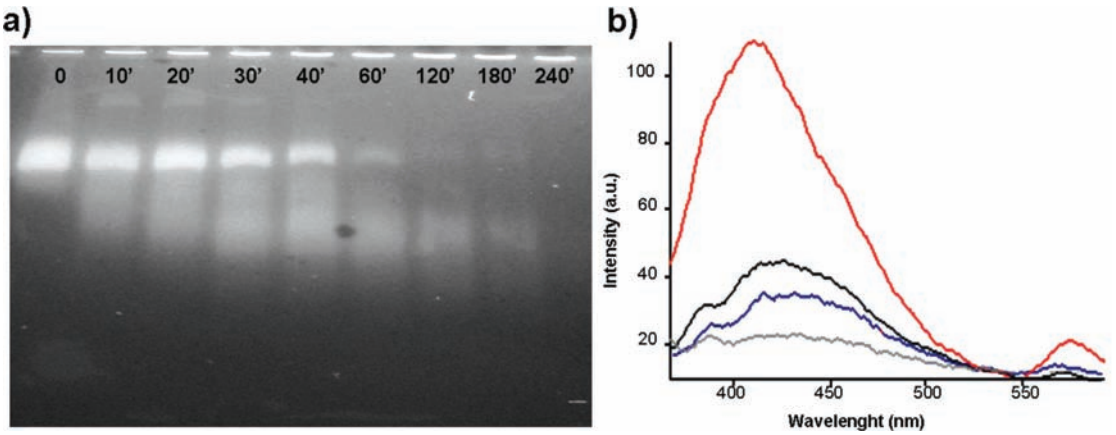


Figure 8. (a) Gel electrophoresis image of TBA^{Py} degradation in plasma; (b) fluorescence spectra of the dialyzed fractions derived from the degradation of the TBA^{Py}-conjugated nanoparticles in plasma withdrawn at 6 (gray), 7 (blue), 8 (black), and 22 h (red).

dx.doi.org/10.1021/bc200305t | *Bioconjugate Chem.* 2012, 23, 382−391

The TBA−nanoparticle conjugate solution was diluted 85.5-fold (0.0936 mg/mL iron content) to 1 mL and UV spectrum was recorded (black line, Figure 9). This sample was then loaded on the LD-MACS column, placed in the Magnetic Separator, and 5 × 2 mL H_2O washings were applied. Some brown solution was collected in the fractions 1−3 (2 mL each), while fractions 4 and 5 contained clear water solutions. Then, the column was removed from the magnetic field and the retained nanoparticles were flushed out with 3 × 2 mL in three separated fractions (6−8) by using the plunger. The first two fractions (6 and 7) contained magnetite nanoparticles, while the third one was a clear solution. Subsequently, fractions 1−3 (unretained nanoparticles, 6 mL in total) and fractions 6−7 (retained nanoparticles, 4 mL in total) were separately unified, and UV spectra were recorded. In Figure 9, we report the UV spectra of the retained (blue line) and unretained (red line) nanoparticles, normalized with respect to the dilution of the loaded sample.

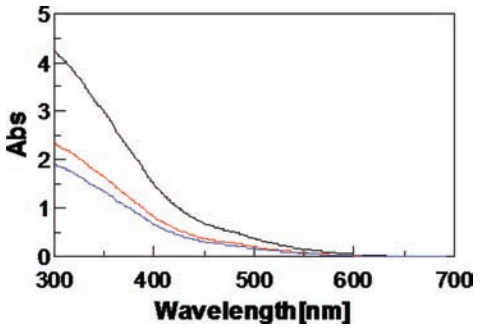


Figure 9. Overlapped UV spectra of the conjugate TBA-magnetic nanoparticles solution. Black line: 0.0936 mg/mL nanoparticle before loading on LD-MACS column; red line: not-retained nanoparticles (spectrum normalized with respect to the dilution of the loaded sample); blue line: retained nanoparticles (spectrum normalized with respect to the dilution of the loaded sample).

From the UV analysis of the spectra reported in Figure 9, it was deduced that (1) the amount of the magnetite nanoparticles loaded in the MACS column was 0.0936 mg, corresponding to 1.22×10^{12} particles, (2) the amount of the unretained particles was 0.0514 mg (6.69×10^{11} particles), (3) the amount of the retained particles was 0.0421 mg (5.47×10^{11} particles). Considering that there are approximately 10 TBA oligomers per particle (Supporting Information, Figure S5), the number of TBA molecules retained on the column was about 5.5×10^{12} (~10 pmol). Thus, the magnetic separation of our TBA−nanoparticle conjugate, immobilized on the LD-MACS column, could permit at maximum the capture, from a complex mixture, of about 10 pmol thrombin each time. The captured protein could then be easily released from the TBA immobilized on the column, for example, by adding the TBA complementary sequence (CC AA CC ACA CC AA CC), as reported in a recent literature report.[56]

CONCLUSIONS

In this paper we reported the conjugation of superparamagnetic nanoparticles to an oligodeoxyribonucleotide (ODN), able to fold into stable unimolecular guanine quadruple helix under proper ion conditions thanks to its nucleobase sequence (TBA sequence). The high potential in biomedical applications of this conjugate, as magnetic nanosensor or therapeutic agent, can be understood considering the combination of the attractive properties of both the TBA sequence and the magnetic nanoparticles. A pyrene fluorescent group, by means of a dU^{Py} unit, was attached to the ODN 3′-end before the conjugation to nanoparticles, in order to follow the ODN fate when anchored to the nanoparticle, whereas a 12-amino-dodecyl spacer (5′-Amino-Modifier C12) was incorporated at the 5′-end, in order to allow the coupling of the amino group on the ODN with the COOH groups on the nanoparticles. The novel pyrene-labeled ODN was characterized by ESI-MS and optical spectroscopy (UV, CD, fluorescence), and analyzed by RP-HPLC chromatography and electrophoresis. Then, we performed the conjugation of the pyrene-labeled ODN with the magnetite nanoparticles, optimizing the workup protocol, which took advantage of repeated dialyses against water. Subsequently, we studied the ODN-conjugated magnetic fluid through optical spectroscopy (UV, CD, fluorescence). None of these techniques, directly performed on the conjugate, revealed the presence of the ODN. As expected, the UV and CD optical properties of the ODN were obscured by the high magnetite absorption over the whole range of visible light. Unexpectedly, the fluorescence measurements on the ODN−nanoparticle conjugate also did not reveal any signal, in contrast with a previous report in which the magnetite core of nanoparticles with a pyrene-contained polymeric coating did not perturb the pyrene fluorescence. This discordance could be explained by considering the different pyrene/magnetite ratio, which was very high in the cited work, whereas it was approximately 10 in our case. However, we demonstrated indirectly the presence of the fluorescent ODN on the nanoparticles by enzymatic (DNase) and chemical (HCl) assays.

Furthermore, we investigated the enzymatic degradation stability of the ODN−nanoparticle conjugate in 76% murine plasma. No degradation products were detected within 5 h, while unconjugated TBA were completely digested after 3 h (half-life of about 30 min). We found that TBA oligomers were still present on the nanoparticles until 8 h, and no more degradation products were detected after 22 h. Thus, as we expected, the nanoparticles enhanced the stability of ODN to enzymatic degradation.

Finally, in view of the potential use of the ODN-conjugated nanoparticles for the capture of a target protein from a complex mixture, we evaluated the amount of TBA-magnetite nanoparticles retained on a Magnetic Separator based on a steel matrix-filled column placed in a strong permanent magnet. From UV analysis, we were able to estimate the maximum capture capacity of our system relative to its target, in this case the thrombin protein.

ASSOCIATED CONTENT

Supporting Information

UV spectra of the magnetic nanoparticle solution. Synthetic conditions and purification of the modified ODN **1**. UV spectrum of the pyrene-labeled ODN **1**. Electrophoretic analysis of natural and modified TBA ODN. Determination of the nanoparticle loading by fluorescence measurements. This material is available free of charge via the Internet at http://pubs.acs.org.

AUTHOR INFORMATION

Corresponding Author

*E-mail: domymusu@alice.it; Fax: +39-(0)81-678552.

■ ACKNOWLEDGMENTS

We acknowledge the University of Naples "Federico II" for the financial support under the PRIN 2007 Project. We are also grateful to Giuseppe Perretta for his invaluable technical assistance.

■ ABBREVIATIONS:

APS, ammonium persulfate; CD, circular dichroism; CPG, controlled-pore glass; DCM, dichloromethane; DMT, dimethoxytrityl; DNase, deoxyribonuclease; EDC, ethyl-3-(3-dimethylaminopropyl)carbodiimide; EDTA, ethylenediaminetetraacetic acid disodium salt dehydrate; MES, 2-(*N*-morpholino)ethanesulfonic acid; MMT, monomethoxytrityl; MRI, magnetic resonance imaging; NHS, *N*-hydroxysuccinimide; RP-HPLC, reverse phase-HPLC; TBE, Tris-Borate-EDTA; TEAB, triethylammonium bicarbonate; TEMED, *N*,*N*,*N*′,*N*′-tetramethylethylenediamine; TRIS, Tris-(hydroxymethyl)aminomethane

■ REFERENCES

(1) Gupta, A. K., and Gupta, M. (2005) Synthesis and surface engineering of iron oxide nanoparticles for biomedical applications. *Biomaterials 26*, 3995−4021.

(2) Laurent, S., Forge, D., Port, M., Roch, A., Robic, C., Vander Elst, L., and Muller, R. N. (2008) Magnetic iron oxide nanoparticles: synthesis, stabilization, vectorization, physicochemical characterizations, and biological applications. *Chem. Rev. 108*, 2064−2110.

(3) Gao, J., Gu, H., and Xu, B. (2009) Multifunctional magnetic nanoparticles: design, synthesis, and biomedical applications. *Acc. Chem. Res. 42*, 1097−1107.

(4) Mahmoudi, M., Stroeve, P., Milani, A. S., Arbab, A. S. (2011) *Superparamagnetic Iron Oxide Nanoparticles: Synthesis, Surface Engineering, Cytotoxicity and Biomedical Applications*, Nova Science Pub Inc.

(5) Yang, H. H., Zhang, S. Q., Chen, X. L., Zhuang, Z. X., Xu, J. G., and Wang, X. R. (2004) Magnetite-containing spherical silica nanoparticles for biocatalysis and bioseparations. *Anal. Chem. 76*, 1316−21.

(6) Berensmeier, S. (2006) Magnetic particles for the separation and purification of nucleic acids. *Appl. Microbiol. Biotechnol. 73*, 495−504.

(7) Takeda, S., Terazono, B., Mishima, F., Nakagami, H., Nishijima, S., and Kaneda, Y. (2006) Novel drug delivery system by surface modified magnetic nanoparticles. *J. Nanosci. Nanotechnol. 6*, 3269−76.

(8) Arruebo, M., Fernandez-Pacheco, R., Ibarra, M. R., and Santamaria, J. (2007) Magnetic nanoparticles for drug delivery. *Nano Today 2* (3), 22−32.

(9) Hanessian, S., Grzyb, J. A., Cengelli, F., and Juillerat-Jeanneret, L. (2008) Synthesis of chemically functionalized superparamagnetic nanoparticles as delivery vectors for chemotherapeutic drugs. *Bioorg. Med. Chem. 16*, 2921−31.

(10) Williams, P. S., Carpino, F., and Zborowski, M. (2009) Magnetic nanoparticle drug carriers and their study by quadrupole magnetic field-flow fractionation. *Mol. Pharmaceutics 6*, 1290−306.

(11) Thorek, D. L., Chen, A. K., Czupryna, J., and Tsourkas, A. (2006) Superparamagnetic iron oxide nanoparticle probes for molecular imaging. *Ann. Biomed. Eng. 34*, 23−38.

(12) Duguet, E., Vasseur, S., Mornet, S., and Devoisselle, J. M. (2006) Magnetic nanoparticles and their applications in medicine. *Nanomedicine 1* (2), 157−68.

(13) Peng, X. H., Qian, X., Mao, H., Wang, A. Y., Chen, Z. G., Nie, S., and Shin, D. M. (2008) Targeted magnetic iron oxide nanoparticles for tumor imaging and therapy. *Int. J. Nanomedicine 3*, 311−21.

(14) Laurent, S., Boutry, S., Mahieu, I., Vander Elst, L., and Muller, R. N. (2009) Iron oxide based MR contrast agents: from chemistry to cell labeling. *Curr. Med. Chem. 16* (35), 4712−4727.

(15) Plank, C., Schillinger, U., Scherer, F., Bergemann, C., Remy, J. S., Kroetz, F., Anton, M., Lausier, J., and Rosenecker, J. (2003) The magnetofection method: using magnetic force to enhance gene delivery. *J. Biol. Chem. 384*, 737−747.

(16) Schillinger, U., Brill, T., Rudolph, C., Huth, S., Gersting, S., Krötz, F., Hirschberger, J., Bergemann, C., and Plank, C. (2005) Advances in magnetofection-magnetically guided nucleic acid delivery. *J. Magn. Magn. Mater. 293*, 501−508.

(17) Kamau, S. W., Hassa, P. O., Steitz, B., Petri-Fink, A., Hofmann, H., Hofmann-Amtenbrink, M., von Rechenberg, B., and Hottiger, M. O. (2006) Enhancement of the efficiency of non-viral gene delivery by application of pulsed magnetic field. *Nucl. Acid Res. 34* (5), e40.

(18) Chorny, M., Polyak, B., Alferiev, I. S., Walsh, K., Friedman, G., and Levy, R. J. (2007) Magnetically driven plasmid DNA delivery with biodegradable polymeric nanoparticles. *FASEB J. 21*, 2510−2519.

(19) Yang, S. Y., Sun, J. S., Liu, C. H., Tsuang, Y. H., Chen, L. T., Hong, C. Y., Yang, H. C., and Horng, H. E. (2008) Ex vivo magnetofection with magnetic nanoparticles: a novel platform for nonviral tissue engineering. *Artif. Organs 32*, 195−204.

(20) McBain, S. C., Griesenbach, U., Xenariou, S., Keramane, A., Batich, C. D., Alton, E. W. F. W., and Dobson, J. (2008) Magnetic nanoparticles as gene delivery agents: enhanced transfection in the presence of oscillating magnet arrays. *Nanotechnology 19*, 405102.

(21) Pino, P., Munoz-Javier, A., Vlaskou, D., Rivera Gil, P., Plank, C., and Parak, W. J. (2010) Gene silencing mediated by magnetic liposphere tagged with small interfering RNA. *Nano Lett. 10*, 3914−3921.

(22) Gupta, A. K., Naregalkar, R. R., Vaidya, V. D., and Gupta, M. (2007) Recent advances on surface engineering of magnetic iron oxide nanoparticles and their biomedical applications. *Nanomedicine 2*, 23−39.

(23) Kettering, M., Winter, J., Zeisberger, M., Bremer-Streck, S., Oehring, H., Bergemann, C., Alexiou, C., Hergt, R., Halbhuber, K. J., Kaiser, W. A., and Hilger, I. (2007) Magnetic nanoparticles as bimodal tools in magnetically induced labelling and magnetic heating of tumour cells: an in vitro study. *Nanotechnology 18*, 1−9.

(24) Xu, C., and Sun, S. (2009) Superparamagnetic nanoparticles as targeted probes for diagnostic and therapeutic applications. *Dalton Trans. 29*, 5583−5591.

(25) Chen, B., Wu, W., and Wang, X. (2011) Magnetic iron oxide nanoparticles for tumor-targeted therapy. *Curr. Cancer Drug Targets 11*, 184−9.

(26) Lu, A. H., Salabas, E. L., and Schüth, F. (2007) Magnetic nanoparticles: synthesis, protection, functionalization, and application. *Angew. Chem., Int. Ed. Engl. 46*, 1222−44.

(27) Seo, Y. J., Lee, I. J., Yi, J. W., and Kim, B. H. (2007) Probing the stable G-quadruplex transition using quencher-free end-stacking ethynyl pyrene-adenosine. *Chem. Commun.*, 2817−2819.

(28) Seo, Y. J., Lee, I. J., and Kim, B. H. (2008) Detection of structure-switching in G-quadruplexes using end-stacking ability. *Bioorg. Med. Chem. Lett. 18*, 3910−3913.

(29) Bock, L. C., Griffin, L. C., Latham, J. A., Vermaas, E. H., and Toole, J. J. (1992) Selection of sinlge-stranded DNA molecules that bind and inhibit human thrombin. *Nature 355*, 564−566.

(30) Macaya, R. F., Schultze, P., Smith, F. W., Roe, J. A., and Feigon, J. (1993) Thrombin-binding DNA aptamer forms a unimolecular quadruplex structure in solution. *Proc. Natl. Acad. Sci. U.S.A. 90*, 3745−3749.

(31) Wang, K. Y., McCurdy, S., Shea, R. G., Swaminathan, S., and Bolton, P. H. (1993) A DNA aptamer which binds to and inhibits thrombin exhibits a new structural motif for DNA. *Biochemistry 32*, 1899−1904.

(32) Padmanabhan, K., Padmanabhan, K. P., Ferrara, J. D., Sadler, J. E., and Tulinsky, A. (1993) The structure of alpha-thrombin inhibited by a 15-mer single-stranded DNA aptamer. *J. Biol. Chem. 268*, 17651−17654.

(33) Schultze, P., Macaya, R. F., and Feigon, J. (1994) Three-dimensional solution structure of the thrombin-binding DNA aptamer d(GGTTGGTGTGGTTGG). *J. Mol. Biol. 235*, 1532−1547.

(34) Wang, K. Y., Krawczyk, S. H., Bischofberger, N., Swaminathan, S., and Bolton, P. H. (1993) The tertiary structure of a DNA aptamer

which binds to and inhibits thrombin determines activity. *Biochemistry 32*, 11285−11292.
(35) Smirnov, I., and Shafer, R. H. (2000) Effect of loop sequence and size on DNA aptamer stability. *Biochemistry 39*, 1462−1468.
(36) Sacca, B., Lacroix, L., and Mergny, J.-L. (2005) The effect of chemical modifications on the thermal stability of different G-quadruplex-forming oligonucleotides. *Nucleic Acids Res. 33*, 1182−1192.
(37) Tang, C.-F., and Shafer, R. H. (2006) Engineering the quadruplex fold: nucleoside conformation determines both folding topology and molecularity in guanine quadruplexes. *J. Am. Chem. Soc. 128*, 5966−5973.
(38) Martino, L., Virno, A., Randazzo, A., Virgilio, A., Esposito, V., Giancola, C., Bucci, M., Cirino, G., and Mayol, L. (2006) A new modified thrombin binding aptamer containing a 5′-5′ inversion of polarity site. *Nucleic Acids Res. 34*, 6653−6662.
(39) Virno, A., Randazzo, A., Giancola, C., Bucci, M., Cirino, G., and Mayol, L. (2007) A novel thrombin binding aptamer containing a G-LNA residue. *Bioorg. Med. Chem. 15*, 5710−5718.
(40) Pagano, B., Martino, L., Randazzo, A., and Giancola, C. (2008) Stability and binding properties of a modified thrombin binding aptamer. *Biophys. J. 94*, 562−569.
(41) Nallagatla, S. R., Heuberger, B., Haque, A., and Switzer, C. (2009) Combinatorial synthesis of thrombin-binding aptamers containing iso-guanine. *J. Comb. Chem. 11*, 364−369.
(42) Russo Krauss, I., Merlino, A., Giancola, C., Randazzo, A., Mazzarella, L., and Sica, F. (2011) Thrombin-aptamer recognition: a revealed ambiguity. *Nucleic Acids Res. 39*, 7858−67.
(43) Coppolla, T., Varra, M., Oliviero, G., Galeone, A., D'Isa, G., Mayol, L., Morelli, E., Bucci, M. R., Vallecco, V., Cirino, G., and Borbone, N. (2008) Synthesis, structural studies and biological properties of new TBA analogues containing acyclic nucleotide. *Bioorg. Med. Chem. 16*, 8244−8253.
(44) Raviv, S. M., Horvath, A., Aradi, J., Bagoly, Z., Fazakas, F., Batta, Z., Muszbek, L., and Harsfalvi, J. (2008) 4-Thio-deoxyuridylate-modified thrombin aptamer and its inhibitory effect on fibrin clot formation, platelet aggregation and thrombus growth on subendothelial matrix. *J. Thromb. Homeost. 6*, 1764−1771.
(45) Bonifacio, L., Church, F., and Jarstfer, M. (2008) Effect of locked-nucleic acid on a biologically active G-quadruplex. A structure-activity relationship of the thrombin aptamer. *Int. J. Mol. Sci. 9*, 422−433.
(46) Pasternak, A., Hernandez, F. J., Rasmussen, L. M., Vester, B., and Wengel, J. (2011) Improved thrombin binding aptamer by incorporation of a single unlocked nucleic acid monomer. *Nucleic Acids Res. 39*, 1155−64.
(47) Nagatoishi, S., Nojima, T., Juskowiak, B., and Takenaka, S. (2005) A Pyrene-labeled Gquadruplexoligonucleotide as a fluorescent probe for potassium ion detection in biological applications. *Angew. Chem., Int. Ed. 44*, 5067−5070.
(48) Nagatoishi, S., Nojima, T., Galezowska, E., Juskowiak, B., and Takenaka, S. (2006) G quadruplex-based FRET probes with the thrombin-binding aptamer (TBA) sequence designed for the efficient fluorometric detection of the potassium Ion. *ChemBioChem 7*, 1730−1737.
(49) Cavaluzzi, J. M., and Borer, P. N. (2004) Revised UV extinction coefficients for nucleoside-5′-monophosphates and unpaired DNA and RNA. *Nucleic Acids Res. 32* (1), e13 DOI: 10.1093/nar/gnh015.
(50) Mergny, J. L., Phan, A. T., and Lacroix, L. (1998) Following G-quartet formation by UV-spectroscopy. *FEBS Lett. 435*, 74−78.
(51) Nagao, D., Yokoyama, M., Yamauchi, N., Matsumoto, H., Kobayashi, Y., and Konno, M. (2008) Synthesis of highly monodisperse particles composed of a magnetic core and fluorescent shell. *Langmuir 24*, 9804−9808.
(52) Kankia, B. I. (2004) Optical absorption assay for strand-exchange reactions in unlabeled nucleic acids. *Nucleic Acids Res. 32* (19), e154.
(53) Seo, Y. J., and Kim, B. H. (2006) Probing the B-to-Z-DNA duplex transition using terminally stacking ethynyl pyrene-modified adenosine and uridine bases. *Chem. Commun.*, 150−152.
(54) Seferos, D. S., Prigodich, A. E., Giljohann, D. A., Patel, P. C., and Mirkin, C. A. (2009) Polyvalent DNA nanoparticle conjugates stabilize nucleic acids. *Nano Lett. 9*, 308−311.
(55) Milano, G., Musumeci, D., Gaglione, M., and Messere, A. (2010) An alternative strategy to synthesize PNA and DNA magnetic conjugates forming nanoparticle assembly based on PNA/DNA duplexes. *Mol. BioSyst. 6*, 553−61.
(56) Song, G., Chen, M., Chen, C., Wang, C., Hu, D., Ren, J., and Qu, X. (2010) Design of proton-fueled tweezers for controlled, multi-function DNA-based molecular device. *Biochimie 92*, 121−127.

Bioconjugate Chemistry

Article

pubs.acs.org/bc

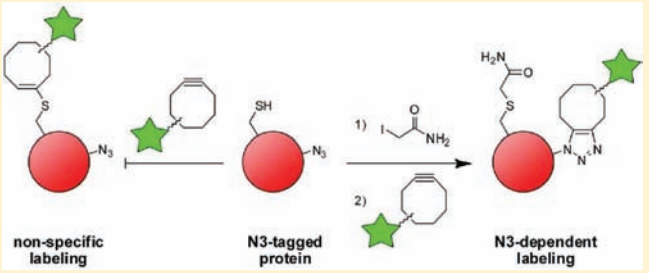
Preventing Thiol-Yne Addition Improves the Specificity of Strain-Promoted Azide–Alkyne Cycloaddition

Remon van Geel,[†] Ger J. M. Pruijn,[†] Floris L. van Delft,[‡] and Wilbert C. Boelens*[,†]

[†]Biomolecular Chemistry and [‡]Synthetic Organic Chemistry, Nijmegen Center for Molecular Life Sciences, Institute for Molecules and Materials and Netherlands Proteomics Centre, Radboud University Nijmegen, The Netherlands

Supporting Information

ABSTRACT: The 1,3-dipolar cycloaddition of azides with ring-strained alkynes is one of the few bioorthogonal reactions suitable for specific biomolecule labeling in complex biological systems. Nevertheless, azide-independent labeling of proteins by strained alkynes can occur to a varying extent, thereby limiting the sensitivity of assays based on strain-promoted azide–alkyne cycloaddition (SPAAC). In this study, a subset of three cyclooctynes, dibenzocyclooctyne (DIBO), azadibenzocyclooctyne (DIBAC), and bicyclo[6.1.0]nonyne (BCN), was used to evaluate the azide-independent labeling of proteins in vitro. For all three cyclooctynes, we show that thiol-yne addition with reduced peptidylcysteines is responsible for most of the azide-independent polypeptide labeling. The identity of the reaction product was confirmed by LC-MS and NMR analysis. Moreover, we show that undesired thiol-yne reactions can be prevented by alkylating peptidylcysteine thiols with iodoacetamide (IAM). Since IAM is compatible with SPAAC, a more specific azide-dependent labeling is achieved by preincubating proteins containing reduced cysteines with IAM.



INTRODUCTION

Click chemistry refers to a set of chemical reactions that proceed rapidly in a highly specific and efficient manner, even within a complex chemical environment.[1] Thanks to these unique properties, click chemistry has become increasingly popular in diverse research areas, including polymer science, combinatorial drug development, and the labeling and imaging of biomolecules in biological systems.[2] The latter includes labeling of newly synthesized or modified biomolecules such as proteins, DNA, or RNA.[3,4] These applications require bioorthogonality, meaning that the reaction occurs efficiently under physiological conditions while its components are inert to biological functionalities.

One of the most well-known click chemistry reactions is the 1,3-dipolar cycloaddition of azides with alkynes to form triazoles, which is also known as the azide–alkyne Huisgen cycloaddition (Figure 1A).[5,6] The reaction with a terminal alkyne proceeds with tremendous rate enhancement upon addition of substoichiometric amounts of copper(I), known as the copper(I)-catalyzed azide–alkyne cycloaddition (CuAAC) or click reaction. CuAAC is characterized by efficient and specific conversion in aqueous solutions under mild conditions[7,8] and has found numerous applications including the labeling of various biomolecules.[9] The use of a highly reactive strained cyclooctyne allows efficient and specific labeling under physiological conditions without the toxic copper(I) catalyst, enabling labeling of biomolecules in vivo.[10,11] The strain-promoted azide–alkyne cycloaddition (SPAAC) has been applied for studying protein–protein interactions,[12] determining DNA modifications[13] and biological processes such as protein synthesis[14] and lipidation of cell surface proteins.[15] Furthermore, it has been used to detect biomolecules, such as glycoconjugates, in living cells[16] and even in living animals such as zebrafish[17] and mice.[18]

The SPAAC is considered one of the very few bioorthogonal reactions suitable for labeling of biomolecules in vivo. However, it has been noted that strained alkynes can bind to a varying extent to biological functionalities in an azide-independent manner, thereby limiting the sensitivity of assays based on this reaction.[10,14] To improve the understanding of this reaction, we investigated the azide-independent labeling for a panel of three strained cyclooctynes, dibenzocyclooctyne (DIBO), azadibenzocyclooctyne (DIBAC), and bicyclo[6.1.0]nonyne (BCN), all applicable for SPAAC (Figure 1B). DIBO is characterized by aromatic rings that provide excellent reaction kinetics in SPAAC, presumably due to additional ring strain and conjugation with the alkyne. DIBO was initially applied successfully for labeling of cell-surface glycoconjugates in living cells,[19] but also appeared more generally applicable.[13,20] DIBAC was designed to reduce the hydrophobicity of DIBO, which might compromise its bioavailability, while retaining the excellent reaction kinetics. This was done by introducing a nitrogen atom in the strained ring system and thereby interrupting the hydrophobic surface area. Conveniently, DIBAC proved to be

Received: July 11, 2011
Revised: February 28, 2012
Published: February 28, 2012

ACS Publications © 2012 American Chemical Society

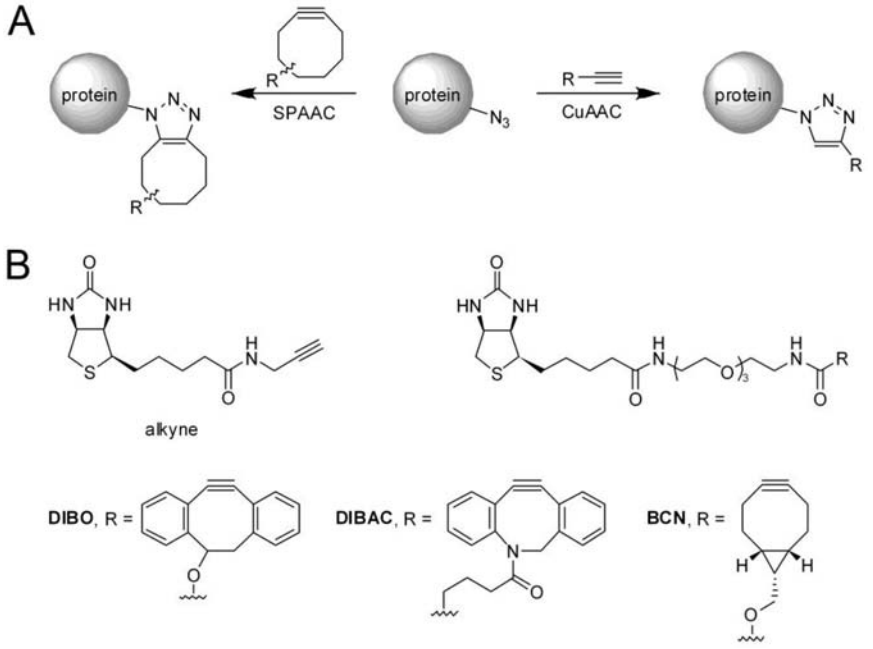


Figure 1. Azide–alkyne cycloadditions and structures of alkynes used in this study. (A) Copper(I)-catalyzed (CuAAC) or strain-promoted azide–alkyne cycloaddition (SPAAC). (B) Biotinylated terminal and ring-strained alkynes.

slightly more reactive than DIBO when applied for the PEGylation of azido-containing protein CalB.[20] Bicyclo[6.1.0]-nonyne (BCN) is even less lipophilic due to the absence of the aromatic rings. The fused cyclopropane moiety strongly enhances the reactivity of plain cyclooctyne, resulting in comparable reaction kinetics as observed for DIBAC. Its relatively straightforward and scalable synthetic route makes this strained alkyne readily accessible. BCN was applied successfully for labeling of azido-containing virus capsid proteins and for labeling of cell-surface glycoconjugates in living cells.[21]

Here, we report that azide-independent protein labeling by strained cyclooctynes mainly occurs via thiol-yne addition at reduced peptidylcysteine residues. We show that blocking of the free thiol groups with the alkylating agent iodoacetamide (IAM) increases the specificity of SPAAC significantly without affecting the efficiency of the azide–alkyne cycloaddition itself. The latter is demonstrated using a SPAAC-based chemical reporter strategy[4,10] to detect proteins post-translationally modified by transglutaminase 2 (TG2).

■ EXPERIMENTAL PROCEDURES

Reagents and solvents were used as commercially provided, unless stated otherwise. Bovine serum albumin was purchased from Sigma. ^{1}H NMR spectra were recorded on a Varian Inova 400. ^{1}H NMR chemical shifts (δ) are reported in ppm and coupling constants (J) are reported in hertz (Hz). ESI-MS analyses were performed using a Thermo Scientific Advantage LCQ linear-ion trap (LRMS). For LC-MS analysis, the system was equipped with a Reprosil 100 C18, 3 μm, 150 mm × 3 mm analytical column (Screening Devices) and a MeCN/water gradient containing 0.1% formic acid was applied (5–95%, 5–30 min). Thin layer chromatography (TLC) was carried out on Merck precoated silica gel 60 F-254 plates and the retardation factor (R_F) is reported where applicable. Column chromatography was performed using Merck silica gel 60 (0.015–0.040 mm). 5-Azidopentylamine hydrochloride, the biotinylated terminal alkyne,[22] and the strained cyclooctynes DIBO,[19] DIBAC,[20] and BCN[21] were synthesized as previously described. Expression and purification of recombinant rat HspB6 was performed as previously described.[23]

Transglutaminase-Catalyzed Cross-Linking of HspB6. Reactions were performed in a volume of 50 μL containing 25 μM HspB6, 250 μM acyl acceptor substrate, 5 μg guinea pig transglutaminase 2 (TG2, Sigma-Aldrich), 50 mM Tris-HCl, pH 7.5, 150 mM NaCl, 20% glycerol, and 5 mM $CaCl_2$. Either 5-azidopentylamine or 5-(biotinamido)pentylamine (Invitrogen) was used as acyl acceptor substrate. Reactions were incubated for 2 h at 37 °C.

Cell Culture and Preparation of Lysates. HeLa cells were cultured in Dulbecco's modified Eagle's medium (Invitrogen) and supplemented with 10% Fetal Bovine Serum Gold (PAA Laboratories). Cells were harvested using trypsin (Sigma-Aldrich). Cells were washed twice with phosphate-buffered saline (PBS) and resuspended in ice-cold lysis buffer (25 mM Tris-HCl, pH 7.5, 150 mM NaCl, 1% NP40, Complete EDTA-Free Protease Inhibitor Cocktail (Roche)). Lysates were incubated on ice for 15 min, sonicated at 0 °C, and centrifuged at 15 700 × g for 10 min at 4 °C. Protein concentrations of the supernatants were determined using the Pierce BCA Protein assay (Thermo Scientific). Lysates were either used directly for labeling with biotinylated alkynes or stored at −20 °C.

Labeling with Biotinylated Alkynes. The labeling reaction was performed in a PBS solution with a final volume of 15 μL containing 100 μM of the appropriate alkyne and either 10 μg cell lysate proteins or 1 μg HspB6 cross-linked with 5-azidopentylamine. For Cu(I)-dependent cycloadditions, 1.5 μL 10× freshly prepared working solution was added, containing 10 mM $CuSO_4$, 10 mM sodium ascorbate, and 10 mM Tris((1-((*O*-ethyl)carboxymethyl)-(1,2,3-triazole-4-yl))-methylamine (triazole ligand). The reaction mixtures were incubated at 4 °C for 1 h, after which 4× sample buffer (8% SDS, 20% β-mercaptoethanol, 40% glycerol, 0.12% bromophenol

dx.doi.org/10.1021/bc200365k | *Bioconjugate Chem.* 2012, 23, 392–398

blue, and 1 M Tris-HCl, pH 6.8; for the nonreducing condition β-mercaptoethanol was omitted) was added, and reaction products were analyzed by SDS-PAGE and Western blotting as described below.

SDS-PAGE and Western Blot Analysis. Sodium dodecyl sulfate polyacrylamide gelelectrophoresis (SDS-PAGE) was performed according to standard procedures unless stated otherwise. Protein staining was performed according to standard protocols using Coomassie Brilliant Blue G 250 (Serva). Proteins were transferred to nitrocellulose membranes (GE Healthcare) by electroblotting. The membranes were incubated with primary antibodies (rabbit polyclonal anti-HspB6, mouse monoclonal anti-γ-tubulin (GTU-88, Abcam)) or with NeutrAvidin Dylight 800 (Pierce Biotechnology), which was used to detect biotinylated proteins. Bound antibodies were detected by incubation with IRDye 680CW-conjugated polyclonal goat antimouse or goat antirabbit antibodies (Li-Cor) and visualized using an Odyssey Infrared Imaging System (Li-Cor).

RESULTS AND DISCUSSION

Reactivity of Alkynes toward Cellular Proteins. The reactivity of the strained alkynes DIBO, DIBAC, and BCN and a terminal alkyne toward cellular proteins was evaluated by incubating the biotinylated alkynes with a HeLa cell lysate. The terminal alkyne was incubated together with 1 mM $CuSO_4$, 1 mM sodium ascorbate, and 1 mM triazole ligand to mimic conditions required for CuAAC. Labeling was analyzed by SDS-PAGE followed by Western blotting and detection of biotinylated polypeptides with labeled NeutrAvidin (Figure 2).

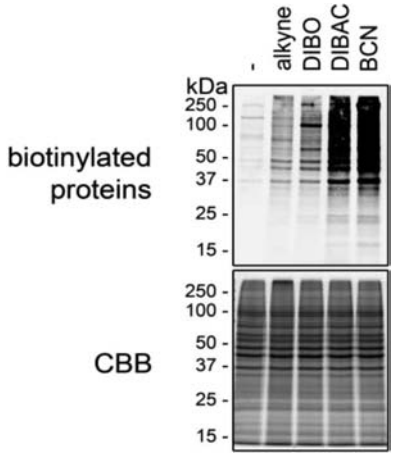


Figure 2. Reactivity of biotinylated alkynes with proteins in HeLa cell lysates. HeLa cell lysates were incubated for 1 h without (-) or with a terminal alkyne or the strain-promoted alkynes DIBO, DIBAC, or BCN, all conjugated to biotin. Protein biotinylation was monitored by Western blotting using labeled NeutrAvidin (upper panel), whereas total protein patterns were visualized by Coomassie Brilliant Blue (CBB) staining (lower panel).

Conjugation to cellular proteins was observed for all alkynes. The labeling pattern resembled the total protein pattern, indicating that the reactivity is largely directed against proteins in general, although some polypeptides appeared to be preferentially labeled. All cyclooctynes showed higher reactivities than observed for the terminal alkyne, suggesting that additional instability introduced by the ring-strain and/or the increased hydrophobicity enhances the efficiency by which they react with proteins. BCN and DIBAC resulted in more intense signals than DIBO, which fits with the previously reported observation showing a higher azide-independent cell-surface labeling for BCN than for DIBO.[21]

Effect of IAM on the Reactivity of Alkynes toward Cellular Proteins. A likely candidate responsible for the azide-independent labeling of cellular proteins is the thiol group of reduced cysteines. In polymer chemistry, the thiol-yne addition is often used as a radical reaction, which needs to be enhanced by light or a photoinitiator.[24] However, spontaneous addition of cyclooctynes to thiols may occur under certain conditions.[14,25] To investigate if alkynes can indeed react with peptidylcysteine side chains, thiol groups were blocked with iodoacetamide (IAM) (Figure 3A).[26] HeLa cell lysates were

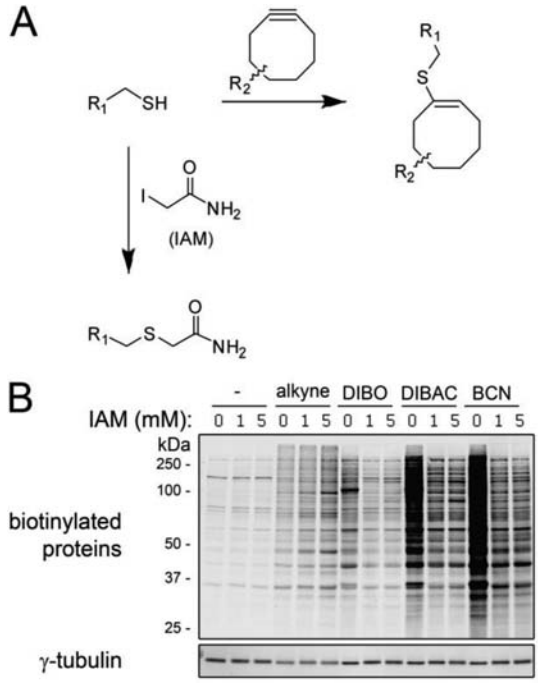


Figure 3. Reactivity of alkynes with HeLa cell proteins containing alkylated thiols. (A) Putative reaction of a thiol with a cyclooctyne and reaction of a thiol with iodoacetamide (IAM). (B) HeLa cell lysates were preincubated without or with 1 and 5 mM IAM and subsequently incubated with the biotinylated alkynes as indicated. Protein biotinylation was monitored by Western blotting using labeled NeutrAvidin (upper panel). As a loading control, γ-tubulin was detected by immunoblotting using a monoclonal antibody (lower panel).

preincubated with 1 or 5 mM IAM for 30 min at room temperature and subsequently incubated with the biotinylated alkynes. After separation by SDS-PAGE, the proteins were analyzed by Western blotting for biotin conjugation using labeled NeutrAvidin. As a loading control, γ-tubulin was visualized (Figure 3B). Preincubation with IAM reduced the amount of proteins labeled by the cyclooctynes on average by 70−80%, indicating that they are indeed mainly reactive with the free thiol group of peptidylcysteines. IAM treatment did not completely abolish labeling of proteins, which may be due to either incomplete alkylation of reduced cysteines or reactivity of the cyclooctynes toward other functionalities in the proteins. Since protein biotinylation is not further repressed by increasing concentrations of IAM, the latter explanation

dx.doi.org/10.1021/bc200365k | Bioconjugate Chem. 2012, 23, 392−398

seems more plausible. After the IAM treatment, DIBAC and BCN still gave the most profound labeling, suggesting that the more activated cyclooctynes are not only more reactive toward thiols, but also toward other functionalities in proteins. IAM treatment does not decrease labeling of proteins by the terminal alkyne, suggesting that only strained alkynes are reactive toward peptidylcysteines.

Reactivity of Cyclooctynes toward Thiols. To confirm that thiols are the main reactive functionalities in proteins, we used heat shock protein 20 (HspB6) as a model. HspB6 contains one cysteine, and in purified recombinant HspB6, which assembles into an oligomeric complex, this cysteine residue forms an intermolecular disulfide bridge with the cysteine of a neighboring subunit.[27] The reactivity of the alkynes toward oxidized, reduced, and alkylated HspB6 was determined to establish the contribution of the peptidylcysteine to biotin conjugation. Reduced HspB6 was obtained by incubating 1 mg/mL (56 μM) purified recombinant (oxidized) HspB6 with 1 mM dithiothreitol (DTT) for 30 min followed by dialysis to remove the remaining DTT. Alkylated HspB6 was obtained by incubating the reduced HspB6 with 1 or 5 mM of IAM for 30 min. The resulting preparations of HspB6 were incubated with the alkynes, separated by nonreducing SDS-PAGE, and analyzed by Western blotting to detect both total levels of HspB6 isoforms and their biotinylation (Figure 4A). All cyclooctynes appeared to be reactive with the reduced HspB6, but not or to a much lesser extent with the oxidized or alkylated HspB6. For the terminal alkyne, no labeling could be detected, regardless of the state of HspB6. These data substantiate the reactivity of the strained cyclooctynes with thiols in proteins. Labeled monomeric HspB6 migrated slightly slower than the nonlabeled monomer, which is most likely due to the mass increase resulting from biotin−cyclooctyne conjugation. The appearance of a single sharp band for the labeled HspB6 monomer is consistent with the presence of a single cysteine in this protein. Furthermore, all cyclooctynes, but DIBAC and BCN in particular, showed a weak labeling of oxidized and alkylated HspB6 (Figure 4A), indicating that labeling can occur via other functionalities, although free peptidylcysteines are clearly preferred. This result fits with the observation that the labeling of the lysate proteins was not completely abolished by preincubation with IAM (Figure 3).

Cyclooctynes have a hydrophobic nature which may contribute to nonspecific interactions with proteins. Such interactions may favor reactivity toward peptidylcysteines over nonpeptidyl thiols. To investigate this possibility, reduced HspB6 was incubated with the cyclooctynes for 1 h at 4 °C in either the absence or the presence of increasing concentrations of β-mercaptoethanol (BME), DTT, glutathione (GSH), or bovine serum albumin (BSA), which contains one free thiol (peptidylcysteine). Due to gel loading limitations, the highest concentration used for BSA (0.1 mM) was 100-fold lower than that for the small thiol-containing molecules. The results of the Western blot analysis (Figure 4B) showed that 250- and 2500-fold excesses of BME, DTT, and GSH compared to the peptidyl thiol of HspB6 reduced the labeling of HspB6. At 25-fold excess, weak competition could be observed for BSA as well as for BME, DTT, and GSH, showing that the peptidylcysteine in BSA competes as well as a nonpeptidyl thiol, indicating that cyclooctynes do not have a preference for peptidyl thiols.

Effect of Thiol-Yne Addition on the Selectivity of SPAAC. To show that the reaction of cyclooctynes with azides

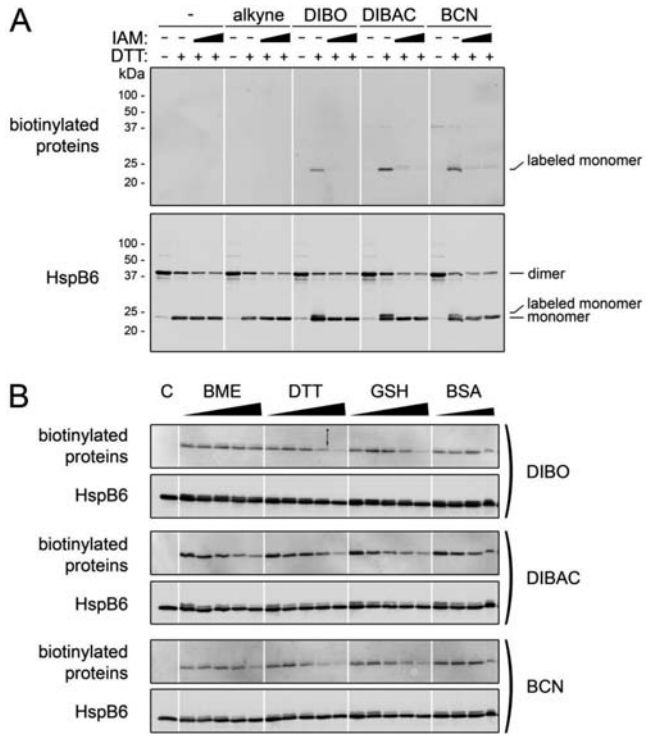


Figure 4. Reactivity of cyclooctynes toward thiols. (A) Oxidized (- DTT), reduced (+ DTT), and alkylated (1 and 5 mM IAM) HspB6 were incubated with the biotinylated terminal and ring-strained alkynes, separated by nonreducing SDS-PAGE, and analyzed by Western blotting using either labeled NeutrAvidin (upper panel) or antibodies to HspB6 (lower panel). The positions of the isoforms of HspB6 are indicated on the right. (B) Reduced HspB6 (4 μM) was incubated with the biotinylated cyclooctynes DIBO, DIBAC, and BCN (0.1 mM) in the presence of different concentrations of thiol-containing compounds. The thiol concentrations used for β-mercaptoethanol (BME), dithiothreitol (DTT), and glutathione (GSH) were 0, 0.01, 0.1, 1, and 10 mM and for bovine serum albumin (BSA) 0, 0.001, 0.01, and 0.1 mM. Reduced HspB6 was included as a control (C). Polypeptides were separated by SDS-PAGE and analyzed by Western blotting using either labeled NeutrAvidin or antibodies to HspB6.

is much more efficient than with thiol groups, competition experiments were performed between benzyl azide and L-glutathione with BCN and DIBAC and analyzed by NMR (Supporting Information Figures S1 and S2). After a complete reaction, only SPAAC products could be detected and no thiol-yne products. Also, DIBO has been shown to be highly reactive toward azides but not toward thiols.[19] However, these results cannot be extrapolated to the labeling of azido-functionalized proteins, not only because the ratios between azides, thiols, and cyclooctynes are different, but also because detection of cyclooctyne labeling by Western blotting is much more sensitive than by NMR.

To test whether the cyclooctynes also specifically undergo SPAAC when incubated with an azido- and thiol-containing protein, HspB6 was functionalized with an azide using transglutaminase 2 (TG2).[22] TG2 catalyzes the formation of isodipeptide bonds between the ε-amino group of peptidyllysine or small primary amine substrates and the γ-carboxamide group of peptidylglutamine.[28] This cross-linking activity is generally monitored with labeled acyl acceptor substrates, such as 5-(biotinamido)pentylamine (BPA), which can be covalently attached to a subset of acyl donor substrate proteins by TG2.

dx.doi.org/10.1021/bc200365k | Bioconjugate Chem. 2012, 23, 392−398

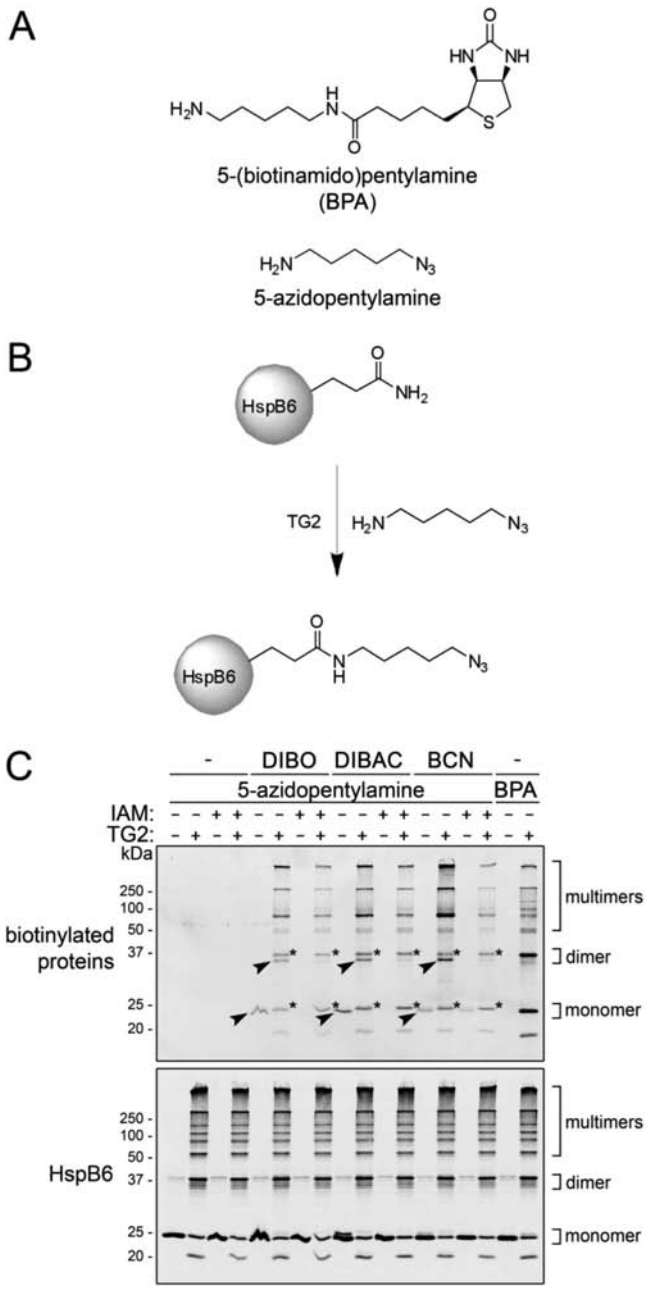


Figure 5. Effect of IAM on SPAAC-based detection of transglutaminase-catalyzed labeling of HspB6. (A) Structures of the biotinylated and azido-functionalized transglutaminase acyl acceptor substrates. (B) Introduction of an azide handle in HspB6 with the TG2 catalyzed acyl-transfer reaction and 5-azidopentylamine. (C) 5-Azidopentylamine was cross-linked to reduced HspB6 by TG2 and subsequently incubated with or without 1 mM IAM for 30 min, followed by incubations with biotinylated DIBO, DIBAC, or BCN. Incubations without alkyne and/or TG2 were used as negative controls. The biotinylated TG2 substrate BPA was used as positive control for TG2 activity. HspB6 isoforms were separated by SDS-PAGE and analyzed by Western blotting using either labeled NeutrAvidin (upper panel) or antibodies to HspB6 (lower panel). The monomeric and dimeric HspB6 azide-independent and azide-dependent reaction products are indicated by arrowheads and asterisks, respectively.

Here, the azido-functionalized pentylamine (Figure 5A) was used as a TG2 acyl acceptor substrate to label recombinant HspB6, which is an excellent acyl donor substrate (Figure 5B).[23,29] Reduced HspB6 was incubated with either 5-azidopentylamine or the directly biotinylated substrate BPA in the presence or absence of active TG2. Reactions with 5-azidopentylamine were incubated with or without IAM (1 mM) for 30 min at room temperature and subsequently biotinylated via SPAAC using DIBO, DIBAC, or BCN. Reaction products were separated by SDS-PAGE and analyzed by Western blotting for biotinylated proteins and HspB6 (Figure 5C). TG2-catalyzed intermolecular cross-linking leads to the formation of di- and multimeric isoforms of HspB6.[23,29] When the enzymatic reaction was performed in the presence of BPA, TG2-dependent labeling of the different forms of HspB6 was observed. When the enzymatic reaction was performed in the presence of 5-azidopentylamine followed by incubation with the biotinylated cyclooctynes, a comparable biotinylated polypeptide pattern was obtained. This indicates that the TG2-dependent introduction of an azide handle in HspB6 and the subsequent cyclooctyne-mediated biotinylation proceeds efficiently. However, additional bands (Figure 5C, indicated by arrowheads) were observed at the monomer and dimer positions, the appearance of which was repressed by preincubation with IAM. More slowly migrating TG2 reaction products, representing HspB6 multimers, also became less intense, suggesting that these products were labeled in both azide-dependent and azide-independent manners. The ratio between azide-dependent and azide-independent labeling could not be improved by reducing incubation time and/or lowering the cyclooctyne concentration (data not shown). These results show that, although the cyclooctynes are much more reactive toward azides, their selectivity may be limited in proteins containing free thiols. However, it should be noted that free thiols are relatively uncommon in proteins exposed to nonreducing conditions, such as extracellular proteins. Importantly, IAM treatment did not reduce the intensity of the bands of the monomer and dimer products that were solely labeled via the incorporated 5-azidopentylamine (Figure 5C, indicated by asterisks). Hence, IAM treatment improves the specificity of SPAAC and thereby results in a higher signal-to-noise ratio.

Identification of the Thiol-Cyclooctyne Conjugate. To identify the reaction product of the thiol-yne addition, we used biotinylated BCN and GSH, thereby assuming that a vinyl sulfide would be formed by direct addition of the thiol to the alkyne triple bond (Figure 6A). The two compounds were incubated either separately or as a mixture for 72 h at 4 °C and subsequently analyzed by LC-MS. When incubating BCN and GSH together, a product was generated as indicated by the altered chromatographic elution profile (Figure 6B). The product shows an m/z of 902.6 in the positive mode (Figure 6C), which corresponds to the mass (M+H) of the predicted compound for thiol-yne addition (Figure 6A). Furthermore, beside the single adduct, a double adduct also formed by a tandem thiol-yne/thiol-ene reaction could be observed by MS analysis when incubating nonlabeled BCN with cysteine methyl ester (SI Figure S3).

Thiol-yne addition was further examined by ^{1}H NMR analysis of the purified reaction product formed by the incubation of nonlabeled BCN with cysteine in D_2O. The NMR spectrum was consistent with the direct addition of the thiol to the alkyne leading to the corresponding vinyl sulfide (SI Figure S4). Additionally, a partial protonation was observed (approximately 13%) instead of deuteration of the double bond of the resulting vinyl sulfide. This suggests a radical-based mechanism: a purely nucleophilic mechanism involving attack of thiolate anion onto the triple bond of the alkyne would generate an intermediate vinyl sulfide anion,

dx.doi.org/10.1021/bc200365k | Bioconjugate Chem. 2012, 23, 392–398

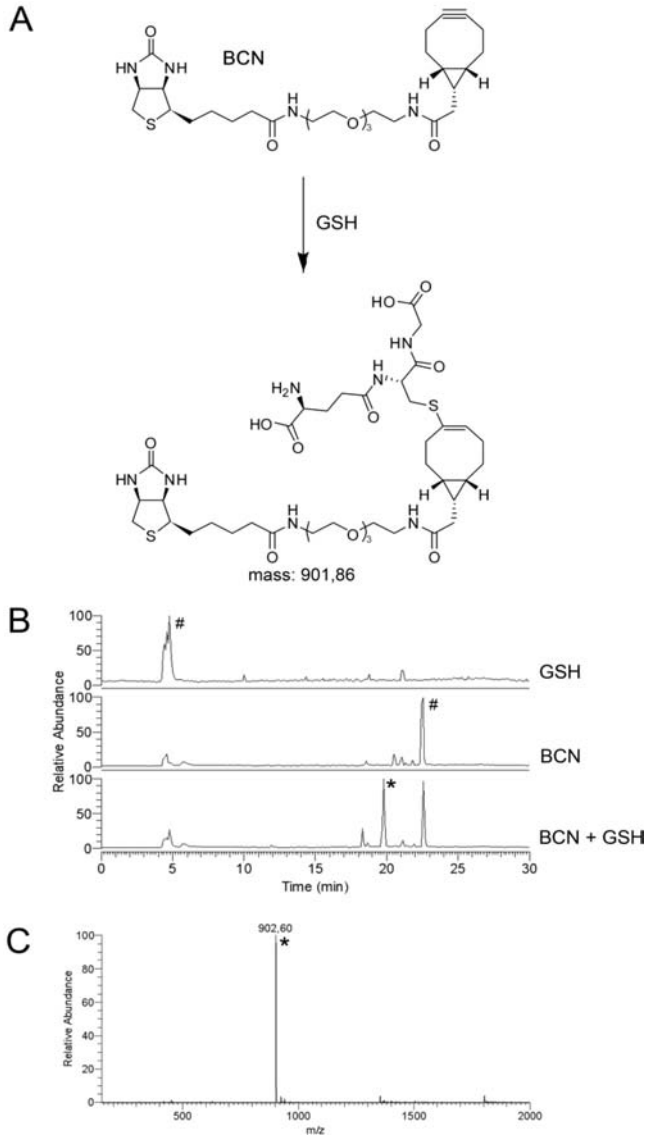


Figure 6. Analysis of the reaction product of BCN and glutathione (GSH). (A) The putative reaction of BCN with GSH. (B) 1 mM BCN and 1 mM GSH were incubated separately or together for 72 h at 4 °C and analyzed by electrospray LC-MS. Ion chromatograms (positive mode) show the elution profiles of the starting materials (#) and the reaction products (the main product is marked with an asterisk). (C) Mass spectrum (positive mode) at the retention time of the main reaction product (*).

expected to instantaneously abstract deuterium from D_2O. In contrast, a radical-based mechanism would involve an intermediate vinyl sulfide radical that is likely to abstract (to some extent at least) a hydrogen radical from a (nondeuterated) thiol. Moreover, a radical-based mechanism, facilitated by reactive oxygen species, has also been suggested previously for the spontaneous addition of thiols to alkynes.[25] However, no detectable reduction of the azide-independent labeling of cellular proteins by DIBO, DIBAC, or BCN was observed when adding up to 5 mM of sodium ascorbate (data not shown). The latter suggests that the reaction mechanism might be dependent on the experimental conditions that are used.

Our results clearly demonstrate that cyclooctynes are susceptible to thiol-yne addition with peptidylcysteines. These conjugation reactions are responsible for the majority of the undesired azide-independent labeling when performing SPAAC with a cell lysate. Although other investigators report differently,[30] we observed a strong IAM-dependent repression of thiol-yne addition, and as a consequence a significantly enhanced specificity of labeling via SPAAC. While being compatible with SPAAC itself, IAM treatment is therefore favored when labeling azido-modified proteins in a cell lysate, for example, with fluorescent or biotin tags for visualization or with biotin or epitope tags for purification.

When cyclooctynes are applied in living cells or animals, preincubation with IAM is undesired, since this reagent will interfere with biological processes. However, in the case of in vivo labeling of extracellular proteins with a membrane-impermeable cyclooctyne the background problem will be limited, because most extracellular peptidylcysteines are in the oxidized state and thus do not react. Nevertheless, when injected into mice, cyclooctynes have been reported to react in an azide-independent manner with serum albumin, which contains in contrast to BSA two reduced cysteines.[18] Due to the very high abundance of albumin, the nonspecific binding may severely reduce the availability of the cyclooctyne at the sites where the azide functionalities are present and in this way may indirectly affect the efficiency of azide detection.

Alternatively, variants of cyclooctynes may be designed that are less prone to thiol-yne addition and thereby may display more selective labeling. The cyclooctynes investigated here indeed show considerable variation in their reactivity toward thiols, thus giving space for improvements. Also, a variation in reactivity toward thiol was shown for the cell-permeable difluorinated cyclooctyne and the less reactive mono- or nonfluorinated variants.[14] While more reactive cyclooctynes are usually favored for their superior azide-dependent labeling, their possible reactivity toward thiols should be taken into consideration when highly specific labeling is required.

■ CONCLUSIONS

Cysteine thiols are the major reactive functionalities responsible for azide-independent labeling of proteins with cyclooctynes. Our data indicate that thiols in general are susceptible to thiol-yne addition, since no clear preference for specific peptidylcysteines was observed. Alkylation of peptidylcysteines with IAM results in a strong reduction of the azide-independent labeling of proteins by cyclooctynes. Since IAM is compatible with SPAAC, preincubation with this reagent is recommended to achieve a more specific azide-dependent labeling.

■ ASSOCIATED CONTENT

Ⓢ Supporting Information

^{1}H NMR spectra of competition experiments between benzyl azide and GSH with either BCN or DIBAC. ^{1}H NMR spectra of DIBAC incubated with excess GSH. MS spectra of the reaction mixture of BCN with cysteine methyl ester and ^{1}H NMR and MS spectra of the purified mono thiol-yne adduct of BCN and cysteine. This material is available free of charge via the Internet at http://pubs.acs.org.

■ AUTHOR INFORMATION

Corresponding Author

*Phone: +31 24 3616753. Fax: +31 24 3540525. E-mail: w.boelens@ncmls.ru.nl.

Notes

The authors declare no competing financial interest.

■ ACKNOWLEDGMENTS

Jan Dommerholt is kindly acknowledged for the ^{1}H NMR analyses and Dennis Löwik and Marjoke Debets for their help with the synthesis of the transglutaminase substrates. Part of this work was financially supported by The Netherlands Proteomics Centre, a program embedded in The Netherlands Genomics Initiative.

■ REFERENCES

(1) Kolb, H. C., Finn, M. G., and Sharpless, K. B. (2001) Click chemistry: diverse chemical function from a few good reactions. *Angew. Chem., Int. Ed. 40*, 2004−2021.

(2) Moses, J. E., and Moorhouse, A. D. (2007) The growing applications of click chemistry. *Chem. Soc. Rev. 36*, 1249−1262.

(3) Best, M. D. (2009) Click chemistry and bioorthogonal reactions: unprecedented selectivity in the labeling of biological molecules. *Biochemistry 48*, 6571−6584.

(4) Sletten, E. M., and Bertozzi, C. R. (2009) Bioorthogonal chemistry: fishing for selectivity in a sea of functionality. *Angew. Chem., Int. Ed. 48*, 6974−6998.

(5) Huisgen, R. (1963) Kinetik und mechanismus 1.3-dipolarer cycloadditionen. *Angew. Chem., Int. Ed. 75*, 742−754.

(6) Huisgen, R. (1963) 1.3-dipolare cycloadditionen: ruckschau und ausblick. *Angew. Chem., Int. Ed. 75*, 604−637.

(7) Rostovtsev, V. V., Green, L. G., Fokin, V. V., and Sharpless, K. B. (2002) A stepwise Huisgen cycloaddition process: copper(I)-catalyzed regioselective "ligation" of azides and terminal alkynes. *Angew. Chem., Int. Ed. 41*, 2596−2599.

(8) Tørnoe, C. W., Christensen, C., and Meldal, M. (2002) Peptidotriazoles on solid phase: [1,2,3]-triazoles by regiospecific copper(I)-catalyzed 1,3-dipolar cycloadditions of terminal alkynes to azides. *J. Org. Chem. 67*, 3057−3064.

(9) Meldal, M., and Tørnoe, C. W. (2008) Cu-catalyzed azide-alkyne cycloaddition. *Chem. Rev. 108*, 2952−3015.

(10) Baskin, J. M., and Bertozzi, C. R. (2007) Bioorthogonal click chemistry: covalent labeling in living systems. *QSAR Comb. Sci. 26*, 1211−1219.

(11) Lutz, J. F. (2008) Copper-free azide-alkyne cycloadditions: new insights and perspectives. *Angew. Chem., Int. Ed. 47*, 2182−2184.

(12) Hur, G. H., Meier, J. L., Baskin, J., Codelli, J. A., Bertozzi, C. R., Marahiel, M. A., and Burkart, M. D. (2009) Crosslinking studies of protein-protein interactions in nonribosomal peptide biosynthesis. *Chem. Biol. 16*, 372−381.

(13) Song, C. X., Szulwach, K. E., Fu, Y., Dai, Q., Yi, C. Q., Li, X. K., Li, Y. J., Chen, C. H., Zhang, W., Jian, X., Wang, J., Zhang, L., Looney, T. J., Zhang, B. C., Godley, L. A., Hicks, L. M., Lahn, B. T., Jin, P., and He, C. A. (2011) Selective chemical labeling reveals the genome-wide distribution of 5-hydroxymethylcytosine. *Nat. Biotechnol. 29*, 68−75.

(14) Beatty, K. E., Fisk, J. D., Smart, B. P., Lu, Y. Y., Szychowski, J., Hangauer, M. J., Baskin, J. M., Bertozzi, C. R., and Tirrell, D. A. (2010) Live-cell imaging of cellular proteins by a strain-promoted azide-alkyne cycloaddition. *ChemBioChem 11*, 2092−2095.

(15) Neef, A. B., and Schultz, C. (2009) Selective fluorescence labeling of lipids in living cells. *Angew. Chem., Int. Ed. 48*, 1498−1500.

(16) Agard, N. J., Prescher, J. A., and Bertozzi, C. R. (2004) A strain-promoted [3 + 2] azide-alkyne cycloaddition for covalent modification of blomolecules in living systems. *J. Am. Chem. Soc. 126*, 15046−15047.

(17) Laughlin, S. T., Baskin, J. M., Amacher, S. L., and Bertozzi, C. R. (2008) In vivo imaging of membrane-associated glycans in developing zebrafish. *Science 320*, 664−667.

(18) Chang, P. V., Prescher, J. A., Sletten, E. M., Baskin, J. M., Miller, I. A., Agard, N. J., Lo, A., and Bertozzi, C. R. (2010) Copper-free click chemistry in living animals. *Proc. Natl. Acad. Sci. U.S.A. 107*, 1821−1826.

(19) Ning, X. H., Guo, J., Wolfert, M. A., and Boons, G. J. (2008) Visualizing metabolically labeled glycoconjugates of living cells by copper-free and fast huisgen cycloadditions. *Angew. Chem., Int. Ed. 47*, 2253−2255.

(20) Debets, M. F., van Berkel, S. S., Schoffelen, S., Rutjes, F., van Hest, J. C. M., and van Delft, F. L. (2010) Aza-dibenzocyclooctynes for fast and efficient enzyme PEGylation via copper-free (3 + 2) cycloaddition. *Chem. Commun. 46*, 97−99.

(21) Dommerholt, J., Schmidt, S., Temming, R., Hendriks, L. J. A., Rutjes, F., van Hest, J. C. M., Lefeber, D. J., Friedl, P., and van Delft, F. L. (2010) Readily accessible bicyclononynes for bioorthogonal labeling and three-dimensional imaging of living cells. *Angew. Chem., Int. Ed. 49*, 9422−9425.

(22) van Geel, R., Debets, M. F., Lowik, D. W., Pruijn, G. J., and Boelens, W. C. (2011) Detection of transglutaminase activity using click chemistry. *Amino Acids*, DOI: 10.1007/s00726-011-1198-2.

(23) Boros, S., Kamps, B., Wunderink, L., de Bruijn, W., de Jong, W. W., and Boelens, W. C. (2004) Transglutaminase catalyzes differential crosslinking of small heat shock proteins and amyloid-beta. *FEBS Lett. 576*, 57−62.

(24) Hoogenboom, R. (2010) Thiol-yne chemistry: a powerful tool for creating highly functional materials. *Angew. Chem., Int. Ed. 49*, 3415−3417.

(25) Fairbanks, B. D., Sims, E. A., Anseth, K. S., and Bowman, C. N. (2010) Reaction rates and mechanisms for radical, photoinitated addition of thiols to alkynes, and implications for thiol-yne photopolymerizations and click reactions. *Macromolecules 43*, 4113−4119.

(26) Ying, J., Clavreul, N., Sethuraman, M., Adachi, T., and Cohen, R. A. (2007) Thiol oxidation in signaling and response to stress: detection and quantification of physiological and pathophysiological thiol modifications. *Free Radical Biol. Med. 43*, 1099−1108.

(27) Kappe, G., Franck, E., Verschuure, P., Boelens, W. C., Leunissen, J. A. M., and de Jong, W. W. (2003) The human genome encodes 10 alpha-Crystallin-related small heat shock proteins: HspB1−10. *Cell Stress Chaperon. 8*, 53−61.

(28) Fesus, L., and Piacentini, M. (2002) Transglutaminase 2: an enigmatic enzyme with diverse functions. *Trends Biochem. Sci. 27*, 534−539.

(29) Boros, S., Ahrman, E., Wunderink, L., Kamps, B., de Jong, W. W., Boelens, W. C., and Emanuelsson, C. S. (2006) Site-specific trans-amidation and deamidation of the small heat-shock protein Hsp20 by tissue transglutaminase. *Proteins Struct. Funct. Bioinf. 62*, 1044−1052.

(30) Stockmann, H., Neves, A. A., Stairs, S., Ireland-Zecchini, H., Brindle, K. M., and Leeper, F. J. (2011) Development and evaluation of new cyclooctynes for cell surface glycan imaging in cancer cells. *Chem. Sci. 2*, 932−936.

Bioconjugate Chemistry

Article

pubs.acs.org/bc

Synthesis and In Vivo Evaluation of the Biodistribution of a ^{18}F-Labeled Conjugate Gold-Nanoparticle-Peptide with Potential Biomedical Application

Simon Guerrero,[†,□] José Raul Herance,[‡,□] Santiago Rojas,[‡] Juan F. Mena,[†] Juan Domingo Gispert,[‡] Gerardo A. Acosta,[§,∥] Fernando Albericio,*[,§,∥,⊥] and Marcelo J. Kogan*[,†,#]

[†]Departamento de Química Farmacológica y Toxicológica, Facultad de Ciencias Químicas y Farmacéuticas, Universidad de Chile, Sergio Livingstone 1007, Independencia, Santiago, Chile

[‡]Institut d'Alta Tecnologia/CRC Centre d'Imatge Molecular - Parc de Recerca Biomedica de Barcelona, C/Dr, Aiguader 88, 08003, Barcelona, Spain

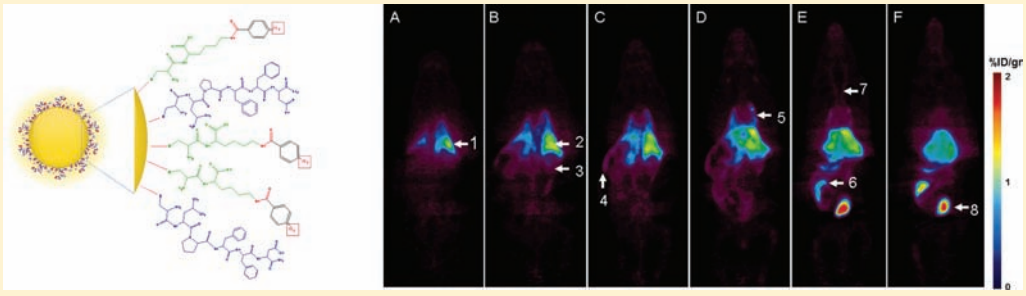
[§]Institute for Research in Biomedicine, Barcelona Science Park, Baldiri Reixac 10, E-08028, Barcelona, Spain

[∥]CIBER-BBN, Networking Centre on Bioengineering, Biomaterials and Nanomedicine, Barcelona Science Park, Baldiri Reixac 10, E-08028, Barcelona, Spain

[⊥]Department of Organic Chemistry, University of Barcelona, Martí i Franquès 1, 08028, Barcelona, Spain

[#]Centro para la Investigación Interdisciplinaria Avanzada en Ciencias de los Materiales (CIMAT), Santiago, Chile

S *Supporting Information*



ABSTRACT: Gold nanoparticles (AuNPs) have been extensively used in biological applications because of their biocompatibility, size, and ease of characterization, as well as an extensive knowledge of their surface chemistry. These features make AuNPs readily exploitable for biomedical applications, including drug delivery and novel diagnostic and therapeutic approaches. In a previous work, we studied *ex vivo* distribution of the conjugate C(AuNP)-LPFFD for its potential uses in the treatment of Alzheimer's disease. In this study, we covalently labeled the conjugate with [^{18}F]-fluorobenzoate to study the *in vivo* distribution of the AuNP by positron emission tomography (PET). After intravenous administration in rat, the highest concentration of the radiolabeled conjugate was found in the bladder and urine with a lower proportion in the intestine, demonstrating progressive accumulation compatible with biliary excretion of the conjugate. The conjugate also accumulated in the liver and spleen. PET imaging allowed us to study the *in vivo* biodistribution of the AuNPs in a noninvasive and sensitive way using a reduced number of animals. Our results show that AuNPs can be covalently and radioactively labeled for PET biodistribution studies.

■ INTRODUCTION

Gold nanoparticles (AuNPs) have been extensively used in biological applications because of their biocompatibility, size, and ease of characterization, as well as an extensive knowledge of their surface chemistry. These features make AuNPs readily exploitable for biomedical applications,[1] including drug delivery and novel diagnostic and therapeutic approaches.[2−4] These particles have been used in cancer therapy as molecular surgery tools for the destruction of cancer cells and for the selective killing of bacteria that cause a variety of cutaneous infections.[5]

In a previous study, we demonstrated the ability of targeted spherical AuNPs conjugated to the amphipathic peptide CLPFFD to remove the toxic β-amyloid aggregates involved in Alzheimer's disease and their remote removal by locally applied irradiation with weak microwaves.[6,7] Recently, we showed in a biodistribution study that 12-nm-diameter C(AuNP)LPFFD conjugates increase the penetration of these particles into the rat brain.[8] However, an important drawback is that these experiments were performed *ex vivo* and that they are not fully representative of *ante mortem* conditions. To study the

Received: July 16, 2011
Revised: January 19, 2012
Published: January 30, 2012

ACS Publications © 2012 American Chemical Society

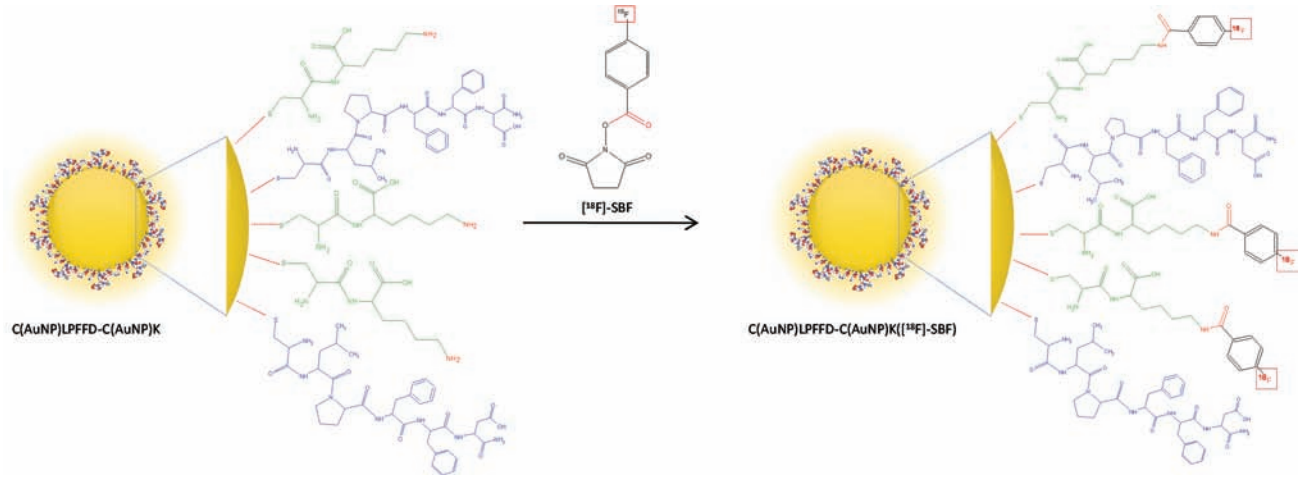


Figure 1. Chemical structures of the peptides attached to the nanoparticle and of the ^{18}F-SFB probe. The CK and CLPFFD peptides are represented in green and blue, respectively. The exposed amino group of the CK peptide and the carbonyl group of the [^{18}F]-SFB probe are shown in red (left). After reaction with the probe, the labeled conjugate C(AuNP)LPFFD-C(AuNP)K([^{18}F]-SFB) is formed (right).

in vivo biodistribution of the AuNPs, we employed positron emission tomography (PET). PET is a highly sensitive, noninvasive isotopic imaging tool that allows the determination of quantitative pharmacokinetics by imaging the uptake of the candidate nanoparticles (NPs). In addition to conventional *ex vivo* biodistribution techniques, PET studies can also provide a reliable biodistribution profile for nanomaterials.[9] One drawback of the traditional use of radiometal-chelator complexes for biodistribution studies is that the radiometal can detach from the surface of the NPs either by a leaching process or through *in vivo* displacement from complexes as a result of transchelation in the presence of high plasma protein concentrations. As a result, the *in vivo* data may fail to reflect the true pharmacokinetics and biodistribution of the NPs.[10,11] However, there are stable complexes of ^{64}Cu[12] and ^{68}Ga[13] that can be used for *in vivo* applications. In this work we covalently bound the label *N*-succinimidyl-4-[^{18}F]-fluorobenzoate ([^{18}F]-SFB) to the C(AuNP)LPFFD conjugate. ^{18}F has been used to label a variety of nanoparticles, including magnetic-upconversion nanophosphors,[14] quantum dots,[15] and lipid-shelled microbubbles,[16] and recently in our group diamond nanoparticles were labeled with [^{18}F]-SFB.[17] To the best of our knowledge, this study represents the first time that AuNPs have been labeled with the radioisotope ^{18}F for PET imaging.

We used the probe [^{18}F]-SFB, which reacts with primary and secondary amino groups[17,18] to label the conjugate. In the C(AuNP)LPFFD conjugate, the α-amino group of the Cys residue (C) is hidden because of its adsorption onto the gold surface[19,20] and is thus unavailable for interaction with the probe. The C residue contains a thiol group that is chemisorbed easily to the gold surface. To provide an available amino group for the reaction with [^{18}F]-SFB and to take advantage of the possibility of NPs multifunctionalization, the AuNPs were functionalized with two peptides, CLPFFD and CK, to obtain the conjugate C(AuNP)LPFFD−C(AuNP)K (Figure 1). The introduction of the dipeptide CK into the NP provided an additional amino functionality through the K side chain, which can react with the radioactive [^{18}F]-SFB moiety. After the synthesis of the probe, the biodistribution of the radiolabeled conjugate C(AuNP)LPFFD-C(AuNP)K([^{18}F]-SFB) (Figure 1) was studied by PET.

EXPERIMENTAL PROCEDURES

Synthesis of Peptides CK and CLPFFD. The peptides were synthesized manually on H-Rink Amide ChemMatrix resin (100 mg, 0.68 mmol/g) and chlorotrityl resin (100 mg, 1 mmol/g) using a Fmoc/tBu strategy for CLPFFD and CK, respectively, in polypropylene syringes, each fitted with a polyethylene porous disk. Solvents and soluble reagents were removed by suction. CLPFFD and CK are amide and carboxy C-terminal, respectively. Washings between deprotection, couplings, and subsequent deprotection steps were carried out with DMF and DCM using around 10 mL solvent per gram of resin each time. The Fmoc group was removed by treatment with a mixture of piperidine−DMF (1:4 v/v) (2 × 10 min). After Fmoc removal, coupling reactions were carried out with Fmoc-amino acids (4 equiv), HOAt (4 equiv), and DIC (4 equiv) in DMF for 1.5 h. The Kaiser colorimetric test assay[21] was used for the detection of solid-phase primary amines, while the De Clercq[22] test was used for secondary amines bound to solid phase.

When necessary, recouplings were done with PyBOP (4 equiv), HOAt (4 equiv), and DIEA (12 equiv) for 1.5 h. For the deprotection of side chain groups and concomitant cleavage of the peptides from the support, the resin was washed with DCM (3 × 1 min), dried, and treated with a TFA-H_2O-TIS (95:2.5:2.5) cocktail for 1 h. TFA was then removed by evaporation with a N_2 stream and peptides were precipitated with cold anhydrous *tert*-butyl methyl ether (TBME), dissolved in H_2O-MeCN (1:1) and freeze−dried. The crude peptides were purified using a semipreparative RP-HPLC [Waters 2487 Dual λ Absorbance Detector (Waters, MA, USA) equipped with a Waters 2700 Sample Manager, a Waters 600 controller, a Waters Fraction Collector, a Symmetry column (C18, 5 μm, 30 × 100 mm), and Millenium software with a flow rate of 10 mL/min in a gradient of 0−20% B for 5 min, 20−40% B for 35 min, 40−100% B]. Peptides were desalted using a NAP10 Sephadex G25 column. The column was equilibrated with 10 mL of H_2O and the peptide was then loaded (10 mg/mL) and eluted with H_2O. One mL fractions were collected and analyzed by RP-HPLC. Fractions containing the peptide were lyophilized.

Peptides were characterized by MALDI-TOF mass spectrometry [Voyager-DE RP MALDI-TOF, PE Biosystems with a N_2 laser of 337 nm], by HPLC-MS [Waters Alliance 2695

equipped with 2998 photodiode array detector, ESI-MS micromass ZQ, Sunfire C18 column (2.1 mm × 100 mm, 3.5 μm, Waters) and *Masslynx* software; flow rate = 0.3 mL/minute; gradient = 0−100% B in 8 min (A = 0.1% formic acid in H_2O, and B = 0.07% formic acid in MeCN)], by high resolution mass spectra were recorded on a LTQ-FT Ultra (Thermo Scientific) and by analysis of amino acids [Waters 600 equipped with a Delta 600 pump, 2487 UV detector, 717 automatic injector, Waters AccQ-tag amino acids analysis column Nova-pak C18 (3.9 × 150 mm, 4 μm, Waters), and *Masslynx* software].

Synthesis of AuNPs. Citrate-coated AuNPs (12 ± 0.5 nm) were prepared by citrate reduction of $HAuCl_4$. An aqueous solution of $HAuCl_4$ (100 mL, 1 mM) was refluxed for 5−10 min, and a warm (50−60 °C) aqueous solution of sodium citrate (10 mL, 38.8 mM) was added quickly. Reflux was continued for another 30 min until a deep red solution appeared. The solution was filtered through a 0.45 μm Millipore syringe filter to remove any precipitate, pH was adjusted to 7.4 by adding dilute NaOH solution, and the final colloid solution was stored at 4 °C. AuNP were observed by transmission electronic microscopy (TEM) using a JEOL JEM-1010 microscope. The specimen was prepared by dropping AuNPs on Formvar carbon-coated copper microgrids and letting them dry. UV−vis absorption spectra were recorded at room temperature with a Unicam UV−vis spectrophotometer (UV3).

Obtention of C(AuNP)LPFFD-C(AuNP)K. The AuNP−peptide conjugates were prepared by mixing a colloidal gold solution with peptide solutions containing CLPFFD and CK in various proportions to obtain functionalized gold surfaces. 1 mL aliquots of the peptide solutions were added to 20 ml of AuNPs Solutions to reach the different proportions of CK/CLPFFD: 4 mM/1 mM, 2 mM/1 mM, 1 mM/1 mM, and 1 mM/2 mM. The most stable C(AuNP)LPFFD-C(AuNP)K conjugates were obtained by mixing a 5.2 nM AuNP solution with a mixture of CK/CLPFFD (4 mM/1 mM). The conjugation was performed in the presence of excess peptide to ensure full conversion of the AuNPs.

The conjugates were purified first through a 450 nm filter and then by 3 days of dialysis in a Spectra/Por MWCO 6−8000 membrane against 1.2 mM sodium citrate (6 buffer changes) to eliminate excess peptide. UV−vis absorption spectra were recorded at room temperature with a Unicam UV−vis spectrophotometer (UV3). To confirm the absence of nonconjugated peptide, 3 mL of the conjugated solution was centrifuged at 13500 rpm for 30 min to provide AuNP−peptide sediments. The supernatant was then evaporated to dryness, and an amino acid analysis was carried out.

Determination of AuNP Concentration and Estimation of the Number of Peptide Molecules Per Nanoparticle. The peptide load of the AuNPs was calculated by dividing the amount of peptide grafted [obtained by amino acid analysis (AAA) of the pellet] by the amount of AuNPs in solution, estimated according to Liu et al.[23] by considering the number of gold atoms per nanoparticle according to the size determined by TEM and the concentration of gold in the solution obtained by inductively coupled plasma mass spectrometry (ICP-MS).

The ICP-MS determinations were carried out in triplicate. The ICP multielement standard was obtained from high purity standards (QCS-26). The samples were digested in a Milestone MLS-1200 Mega plus EM-45 microwave oven using USEPA Method IO-3.1. To summarize, this method consisted of the extraction of the elements using a nitric acid−hydrogen peroxide (10:1) solution. After the digestion process, the gold concentration was directly determined by ICP-MS (Agilent, ICP-MS 7500 cx with collision chamber).

The average number of gold atoms per nanoparticle could be calculated from the TEM analysis. Using the *ImageJ* software, the average core diameters of the particles (D, nm) were measured. Assuming a spherical shape and a uniform fcc structure, the average number of gold atoms (N) for each type of nanosphere was calculated by eq 1, where ρ is the density for fcc gold (19.3 g/cm^3) and M represents the atomic weight of gold (197 g/mol):

$$N = \pi\rho D^3/6M = 30.89602\, D^2 \quad (1)$$

The concentration of AuNPs solution was 5.2 ± 0.2 nM.

To determine the peptide concentration, an amino acid analysis was performed on the pellet obtained following the centrifugation of the conjugates at 13500 rpm (16200 × g) for 30 min, conditions that result in the sedimentation of the NPs. The number of peptide molecules per AuNP was obtained by dividing the number of peptide molecules per milliliter of solution by the number of particles per milliliter of solution. This ratio was obtained in triplicate in three independent repetitions of the synthesis and conjugation procedure. There were 122 ± 5 and 75 ± 5 molecules of CK and CLPFFD per nanoparticle, respectively.

Preparation of [^{18}F]-SFB. The synthesis was performed in assembled Eckert & Ziegler modules following the methodology described by Mäding et al.[24] with minor changes. Briefly, [^{18}F] was produced by the bombardment of [^{18}O]-H_2O with high-energy protons (18 MeV) in an 18/9 IBA cyclotron. The radioisotope [^{18}F] was sent to the automatic module where it was contained in a QMA cartridge. Then, [^{18}F] was extracted into the reactor by passing a mixture of 2 mg of K_2CO_3 and 1.8 mg of Kryptofix 222 in 0.8 mL of a 1:1 mixture of H_2O/CH_3CN through the QMA cartridge. The reactor was heated at 100 °C, and He flow and vacuum were applied for 5 min to dry the [^{18}F]. To ensure that the drying process went to completion, an extra 1 mL of anhydrous CH_3CN was added to dry the mixture, as described above, with an extra 5 min of vacuum applied.

Next, a solution of 5 mg of 4-(*tert*-butoxycarbonylmethyl)-phenyl trimethylammonium trifluoromethanesulfonate in 1 mL of anhydrous CH_3CN was added to the dried [^{18}F]. The mixture was stirred for 10 min at 90 °C, and 0.5 mL of 1 M HCl was then added to the solution. The reaction mixture was heated at 100 °C for 5 min. After cooling to 25 °C, the reaction mixture was diluted with 9 mL of water and passed through a C18 HELA cartridge for solid extraction. Subsequently, 3 mL of CH_3CN was passed through the cartridge, and the solution was sent to a second reactor. This eluate was treated with 20 mL of 25% methanolic Me_4NOH in 500 mL of CH_3CN. The reaction mixture was then dried at 90 °C by passing a continuous He flow and applying vacuum. The drying process was completed by the addition of another 3 mL of anhydrous CH_3CN. Then, a solution of 15 mg of *N,N,N′,N′*-tetramethyl-*O*-(*N*-succinimidyl)uronium tetrafluoroborate in 500 mL of anhydrous CH_3CN was added, and the mixture was heated at 90 °C for 2 min. The mixture was cooled to 25 °C and diluted with 5% aqueous acetic acid. The crude product was purified with semipreparative HPLC using a Teknokroma Mediterranean Sea-18 (25 cm × 1 cm, 5 mm) column in isocratic mode with a

dx.doi.org/10.1021/bc200362a | *Bioconjugate Chem.* 2012, 23, 399−408

mobile phase composed of a 42.5:57.5 ratio of CH_3CN/ammonium formiate (3.15 g/1 L H_2O, pH = 5) at 5 mL/min. The purification was monitored by isotopic and UV−vis (254 nm) detectors. The desired fraction (9−11 min) was collected in 20 mL of 0.9% saline solution. This solution was passed through a C18 cartridge, rinsed with 20 mL of water, and extracted with 3 mL of anhydrous acetone. One aliquot was submitted for quality control, and the remaining solution was dried with gaseous N_2. The quality control was performed by HPLC using a Teknokroma Mediterranean Sea-18 (25 mm × 0.46 cm, 5 mm) column in gradient mode with a flow rate of 2 mL/min and CH_3CN/ammonium formate (3.15 g/1 L H_2O, pH = 5) as a mobile phase, starting at a 10:90 ratio and reaching 40:60 in 10 min. The eluent was monitored by isotopic and UV−vis (254 nm) detectors. The desired compound, [^{18}F]-SFB, eluted at 10.3 min. Under these reaction conditions, we achieved a 37% yield (decay corrected) of [^{18}F]-SFB that had purity >99% and 110 ± 15 GBq/μmol of specific activity.

Preparation of C(AuNP)LPFFD-C(AuNP)K([^{18}F]-SFB). Two mL of a 5.2 nM solution of C(AuNP)LPFFD-C(AuNP)K was centrifuged at 4200 rpm (1980 × *g*) for 15 min. The supernatant was then removed, and a mixture containing 20 μL of DMSO and 80 μL of 1.2 mM of sodium citrate (pH = 10) was added to the solid. The resulting red solution was added to 4.44 ± 1.11 GBq of the solid residue of [^{18}F]-SFB. The mixture was stirred at 50 °C for 1 h. After this incubation, 900 μL of 1.2 mM of sodium citrate solution (pH = 10) was added to the red mixture and centrifuged at 4200 rpm (1980 × *g*) for 15 min. The solid was washed 3 times, and the radioactivity of the liquid was monitored each time with an activimeter. Following the final wash, the washing solution contained no radioactivity. Finally, the solid was dissolved in a mixture of 2 mL of 1.2 mM of sodium citrate (pH = 10) and 50 μL of Tween-80, maintaining the characteristic red color. The labeling yield of AuNPs was 0.8 ± 0.3%. There were 27 ^{18}F atoms per nanoparticle. The radiolabeling yield was decay-corrected and calculated from the initial pure [^{18}F]-SFB content added to the reaction.

Zeta Potential. The zeta potential (ZetaSizer 3000, Malvern Instruments, UK) measurements of the nanoparticles were performed five times in solution. Because the zeta potential measurements were performed in an aqueous solution, the Smoluchowski approximation was used to calculate the zeta potential from the measured electrophoretic mobility. The measurements were conducted with a disposable polycarbonate capillary cell (DTS 1061, Malvern) under precise temperature control (25 °C). The concentration of C(AuNP)-LPFFD-C(AuNP)K(SFB) was 5.2 nM, the solution of the nanoparticles was 1.2 mM citrate (pH = 7.4). The concentration of C(AuNP)LPFFD-C(AuNP)K was 5.2 nM, and the solution was citrate at pH = 7.4 .

Dynamic Light Scattering (DLS). A Malvern ZetaSizer Nano ZS instrument (Malvern Instruments, UK) operating at a wavelength of 633 nm and a fixed scattering angle of 173° was used to measure the NP sizes. An aliquot of 1 mL of each solution was placed in a cell for the DLS analyses. The measurements were conducted with a disposable polycarbonate capillary cell (DTS 1061, Malvern) under precise temperature control (25 °C). The concentration of C(AuNP)LPFFD-C(AuNP)K was 5.2 nM, and the media was sodium citrate (pH = 7.4). The concentration of C(AuNP)LPFFD-C(AuNP)K-(SFB) was 5.2 nM the media was sodium citrate (pH = 7.4). In addition we carried out DLS measurements of both conjugates at different concentrations using citrate 1.2 mM pH 7.4 and PBS as dissolvent, respectively.

Stability of the Conjugate in PBS. A 500 μL aliquot of the conjugate solution (5.2 nM) was mixed with 500 μL of PBS, and the resulting mixture was incubated at room temperature (25 °C) and at 37 °C for 7 days. UV−vis absorption spectra were recorded at room temperature with a Unicam UV−vis spectrophotometer (UV3).

Stability of C(AuNP)LPFFD-C(AuNP)K(SBF) in Plasma. To determine the plasma stability of the conjugate, 1 mL aliquots of the conjugate (5.2 nM) were centrifuged at 13200 rpm (16200 × *g*) for 15 min, and the resulting pellets were resuspended in plasma and incubated at 37 °C. The samples were centrifuged at 13200 rpm (16200 × *g*) and resuspended in citrate pH = 7.4. The UV−visible spectra, DLS analyses, and zeta potential measurements were obtained after 1, 2, 4, and 24 h.

Stability of C(AuNP)LPFFD-C(AuNP)K([^{18}F]-SBF) in Plasma. The pellet obtained after preparing and washing (3×) the labeled conjugate C(AuNP)LPFFD-C(AuNP)K-([^{18}F]-SBF) (10 ± 4 μCi) was resuspended in 1 mL of plasma and incubated at 37 °C. Aliquots of 150 μL were removed at different time periods up to three hours and centrifuged at 16200 × *g* during 10 min. The radioactivity was determined in the supernatants and pellets. The proportion of radioactivity in the supernatants was determined by dividing the radioactivity in the supernatant by the total radioactivity of the sample (supernatant + pellet).

Animals. Adult male Sprague−Dawley rats weighing 571 ± 112 g (mean ± standard deviation; Charles River, Spain; n = 3) were used in this study. The animal studies were conducted in compliance with the Spanish legislation on the Protection of Animals Used for Experimental and Other Scientific Purposes and in accordance with the Directives of the European Union.

PET Image Acquisition. The animals were anesthetized with isoflurane vaporized in O_2 and received an intravenous bolus injection of 3.1 ± 2.7 kBq (mean ± standard deviation) of ^{18}F-radiolabeled nanoparticles. Immediately after injection, the animals were placed in an animal-dedicated camera (microPET R4; Concorde, Siemens, Knoxville, TN, USA) for dynamic whole body image acquisition. Whole body data were acquired for 120 min. During all of the acquisition procedures, the anesthesia was maintained with a facial mask and a concentration of 2.5% of isoflurane vaporized in O_2.

Image Analysis. To obtain dynamic whole body images (frames = 18), the PET data were corrected for detector nonuniformity, random coincidences, and radionuclide decay, but not for photon scatter or attenuation. The images were then reconstructed into a matrix size of 128 × 128 × 63 and a voxel size of 0.85 × 0.85 × 1.21 mm^3 with a filtered backprojection algorithm (FBP). After reconstruction, volumes of interest (VOI) were manually drawn in the different organs, and the time−activity curves were calculated. One of the VOIs was placed in the heart region to obtain a representative measurement of the concentration of radioactivity in blood. The concentration of radioactivity obtained at the end of the acquisition was used to calculate the percentage of the injected dose for each gram of tissue based on the PET data. Mean activity curves for the three animals were also calculated for each organ.

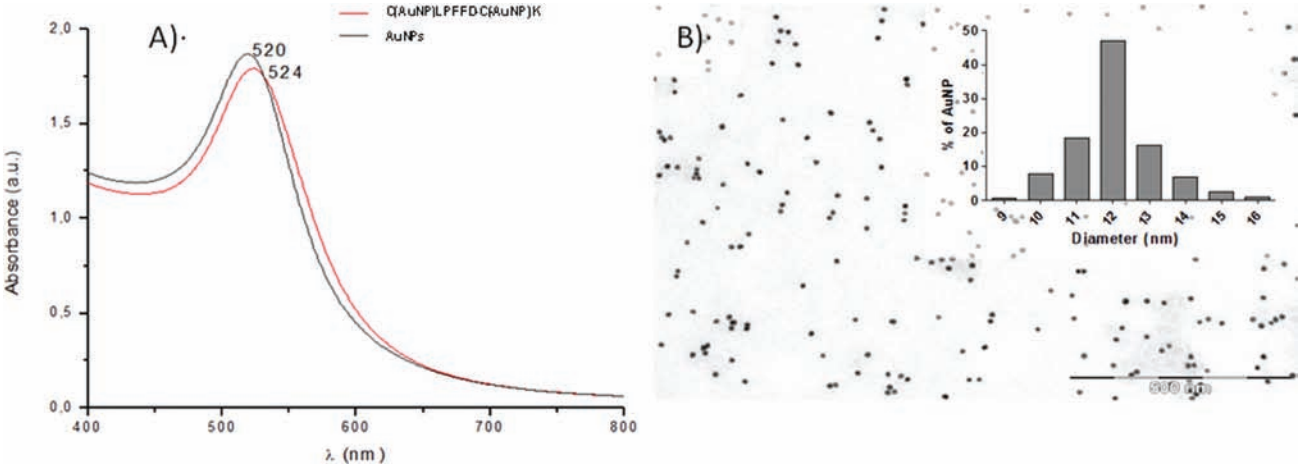


Figure 2. (A) UV−vis spectra of AuNPs and C(AuNP)LPFFD-C(AuNP)K . (B) TEM micrograph of C(AuNP)LPFFD-C(AuNP)K. The inset shows the size distribution. The bar represents 500 nm.

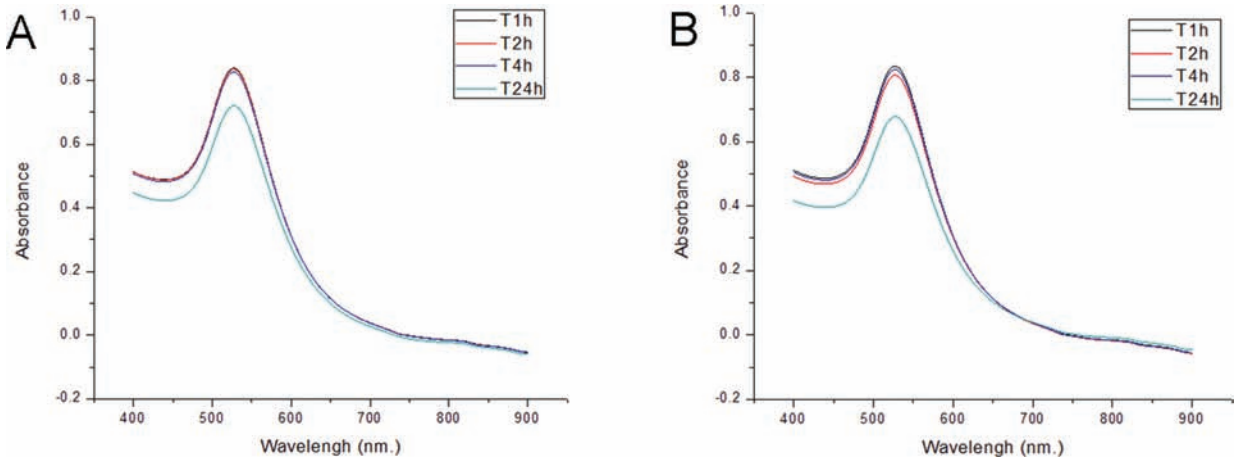


Figure 3. UV−vis spectra of the conjugate C(AuNP)LPFFD-C(AuNP)K(SFB) in PBS after incubation for different periods of time at 25 °C (A) and at 37 °C (B).

RESULTS AND DISCUSSION

Synthesis and Characterization of C(AuNP)LPFFD-C(AuNP)K(SFB). AuNPs with a diameter of 12 nm were obtained using the sodium citrate reduction method.[25] The AuNP−peptide conjugates were prepared by mixing the AuNPs solution with a solution of CK and CLPFFD. The most stable C(AuNP)LPFFD-C(AuNP)K conjugate was obtained by mixing a 5.2 nM AuNPs solution with a mixture of CK/CLPFFD (4 mM/1 mM). We performed the conjugation using different proportions of the peptides (see Experimental Procedures section) and studied the stability of the resulting conjugates by determining the UV−vis spectra, DLS, and zeta potential properties over time. In the case of the conjugates prepared from the 4 mM/1 mM solution, the plasmon band remained centered at the same position with respect to time, as did the hydrodynamic diameters (Supporting Information Figure S3). In contrast, a shift to higher wavelengths or a band broadening was observed in the UV−vis spectra of the conjugates prepared by using different CK/CLPFFD ratios (for 2/1; 1/2), and an increase in the hydrodynamic diameter was observed for all of the conjugates (2/1, 1/2, 1/1). On the other hand, the zeta potential values observed for the conjugate prepared from 4 mM/1 mM solution not significant variations were appreciated.

The peptides were synthesized by solid phase synthesis following a Fmoc/tBu protocol and were characterized by HPLC and mass spectrometry (Supporting Information, Figures S1, S2 and Table S1). The conjugates were exhaustively characterized by various techniques [UV−vis, transmission electron microscopy (TEM), X-ray photoelectron spectroscopy (XPS), dynamic light scattering (DLS), and zeta potential; see Supporting Information]. The UV−vis spectra showed a defined plasmon resonance peak at 520 nm (Figure 2), which was attributed to the presence of AuNPs with a diameter of approximately 12 nm. After conjugation with CK and CLPFFD, the wavelength of maximum absorption shifted to longer wavelengths with respect to AuNPs (524 and 520 nm, respectively) as a result of the capping of the AuNP surfaces with the peptide molecules. The TEM images showed particles (12 ± 0.5 nm) with regular shapes and a narrow size distribution (Figure 2).

Further characterization of C(AuNP)LPFFD-C(AuNP)K by XPS was performed. The peaks expected from the S 2p, S 2s, and Au 4f core levels were detected. High-resolution data were also recorded in the S 2p, S 2s, and Au 4f spectral regions. The S 2p signal consisted of a broad band with a maximum at 162.2 eV that corresponds to the chemisorption of sulfur grafted onto gold (Supporting Information, Figure S4).

dx.doi.org/10.1021/bc200362a | *Bioconjugate Chem.* 2012, 23, 399−408

The peptide load of AuNP was calculated by dividing the amount of peptide grafted [obtained by the amino acid analysis (AAA) of the pellet] by the amount of AuNPs in solution determined by ICP-MS and considering the diameters obtained by TEM according with Liu et al.[23] For each nanoparticle, there were 122 and 75 molecules of CK and CLPFFD present, respectively.

To incorporate *N*-succinimidyl-4-fluorobenzoate (SFB) into the conjugates, the NPs were centrifuged and resuspended in a 1:4 DMSO:1.2 mM sodium citrate mixture (pH = 10) that had been mixed with SFB to render the conjugate C(AuNP)-LPFFD-C(AuNP)K(SFB) by a reaction between SFB and the primary ε-amino group of the lysine residue of the CK peptide anchored to the AuNPs (Figure 1). According to the DLS and zeta potential measurements, the NPs had a hydrodynamic diameter of 23 nm (PI:0.3) and −43± mV, respectively. DLS measurements were carried out by using a 633 nm laser which could complicate the dynamic light scattering measurements due to the absorbance of the particles.[26] In order to discard effects given by the concentration of the samples, we carried out the measurements at different concentrations of nanoparticles, and no appreciable changes in the intensities and sizes of the nanoparticles were observed (Supporting Information, Figure S5).

Prior to any *in vivo* examination of C(AuNP)LPFFD-C(AuNP)K(SFB), *in vitro* stability studies were carried out in PBS at 25 and 37 °C (Figure 3). The conjugate was incubated with PBS, and UV−vis spectra were obtained. In Figure 3, one can see that the plasmon peak remains unchanged, allowing us to conclude that the colloids were stable at the two tested temperatures in PBS.

We also studied the stability of these nanoparticles in plasma, a condition that more faithfully reproduces the *in vivo* environment. By UV−vis, we observed a shift in the plasmon band from 527 nm (for the conjugate before incubation with plasma as can be seen in Figure 3) to 531 nm, which could be attributed to the capping of the nanoparticles with proteins to form the protein corona (Supporting Information, Figure S6), in accord with Olmedo et al.[19] In addition, we carried out DLS experiments in which we observed the presence of different populations of different sizes. In samples incubated for 1 h, two different populations of particles were observed where one is centered at 45 nm and the other at 500 nm, which could be attributed to a capping with proteins and/or to aggregation process. After 2 h, there was an increase in the sizes of the nanoparticles which could be attributed to aggregation processes. On the other hand, we carried out zeta potential measurements observing that there were no dramatic variations on the corresponding values with the incubation time (Supporting Information, Figure S6).

For the biodistribution studies, the C(AuNP)LPFFD-C(AuNP)K(SFB) conjugate was capped with Tween-80 to increase its stability under physiological conditions. After the injection of the nanoparticles into the plasma, the aforementioned capping occurs, and dilution could cause the desorption of Tween and consequent aggregation. To test the conjugate under conditions resembling this physiological scenario, we used UV−vis to study the stability of the conjugate capped with Tween and incubated with plasma after dialysis against PBS for 48 h (Supporting Information Figure S7). The UV−vis spectra of the conjugates were taken at different times, and it was observed that no modifications of the spectra occurred within the first 24 h. A small diminution of the intensity band was observed at 48 h without an observable broadening. From these results, we can infer that the depletion of the Tween detergent by the filtration and the dilution during dialysis did not induce a significant aggregation.

The labeled conjugate was obtained by reaction with [^{18}F]-SFB. This reaction had a labeling efficiency of about 1% as determined by radioactivity counting. The labeled NPs in PBS solution were stable for at least 5 h (according to UV−vis spectra, data not shown).

To probe the stability of the labeled conjugate C(AuNP)-LPFFD-C(AuNP)K([^{18}F]-SFB), we carried out stability studies at 37 °C. We incubated the C(AuNP)LPFFD-C(AuNP)K-([^{18}F]-SFB) conjugate in plasma at 37 °C, and samples from the incubation mixture were taken at different times for 3 h and were then centrifuged. The centrifugation procedure used was sufficient to separate the [^{18}F]-AuNPs from the radioactive degradation products. Therefore, the amount of radioactivity in the supernatant is proportional to the degree of degradation of the radiolabeled nanoparticles. The supernatants and pellets were counted in a well counter, and the percentage of radioactivity in the supernatant is shown in Supporting Information (Figure S8). Radioactivity was observed in both fractions supernatant and pellet. The presence of radioactivity in the supernatants could be attributed to free metabolites or to the presence of [^{18}F]-AuNPs nanoparticles that did not sediment after centrifugation. As was mentioned previously, nanoparticles in plasma are in a different aggregation state. Notably, it is necessary to consider for *in vivo* experiments that from the beginning of the incubation there is a free labeled species that could be filtered by the kidney and consequently excreted by a renal mechanism. Remarkably, it is important to mention that the radioactivity content in plasma was constant with time, which was not compatible with the detachment of the radiolabel from the AuNPs after incubation. Rather, a time-dependent increase in the radioactivity of the supernatant would be expected as a consequence of the detachment of the radiolabel, which does not occur in this case.

In Vivo Distribution of C(AuNP)LPFFD-C(AuNP)K([^{18}F]-SFB). The biodistribution of the newly synthesized conjugate was monitored by PET imaging at various time points following intravenous injection into rats. Figure 4 shows PET images of

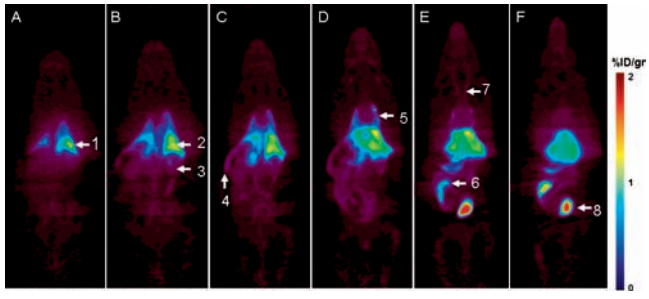


Figure 4. Representative image of a 120 min PET scan after an intravenously injection of a 5.2 nM solution of C(AuNP)LPFFD−C(AuNP)K([^{18}F]-SBF) in rats. Coronal sections of the animal from dorsal (A) to ventral (F). Organs that presented elevated uptake of the radiolabeled compound are clearly seen. Liver appears in all the images, arrows 1 and 2. Lungs can be visualized in images A−E (5). Kidneys and spleen can be visualized in images B and C, arrows 3 and 4. Bladder and intestines are clearly visible in images E and F, arrows 8 and 6. Interestingly, supraortic vessels can be appreciated in image E, arrow 7.

dx.doi.org/10.1021/bc200362a | *Bioconjugate Chem.* 2012, 23, 399−408

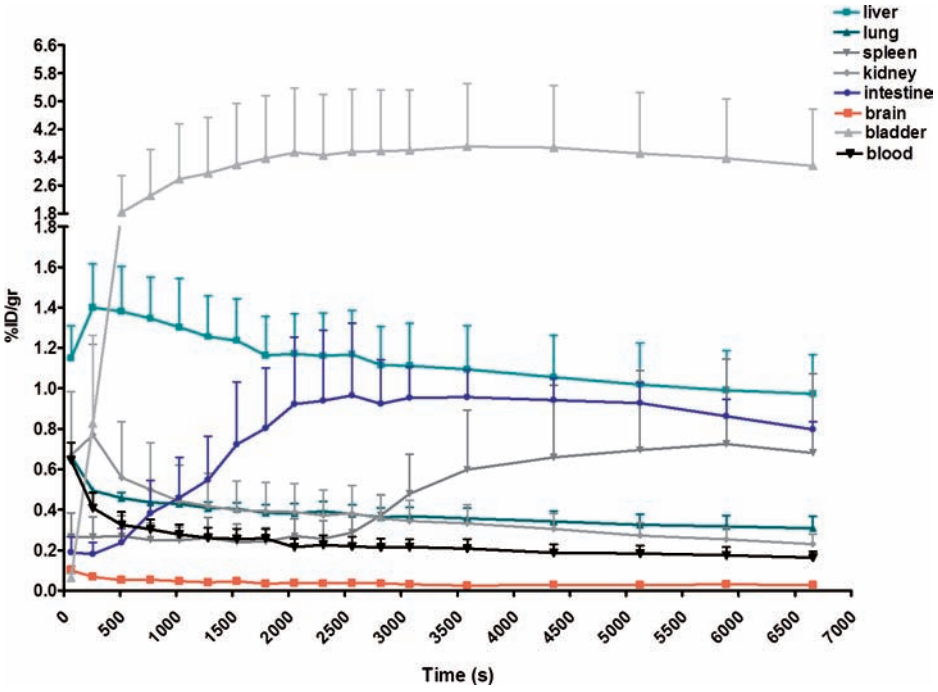


Figure 5. Mean time−activity curves of the levels of radioactivity in the different organs obtained from the PET images. The bars represent the standard deviation. The radioactivity accumulated in the bladder and intestine, reflecting the dual excretory mechanisms of the nanoparticle.

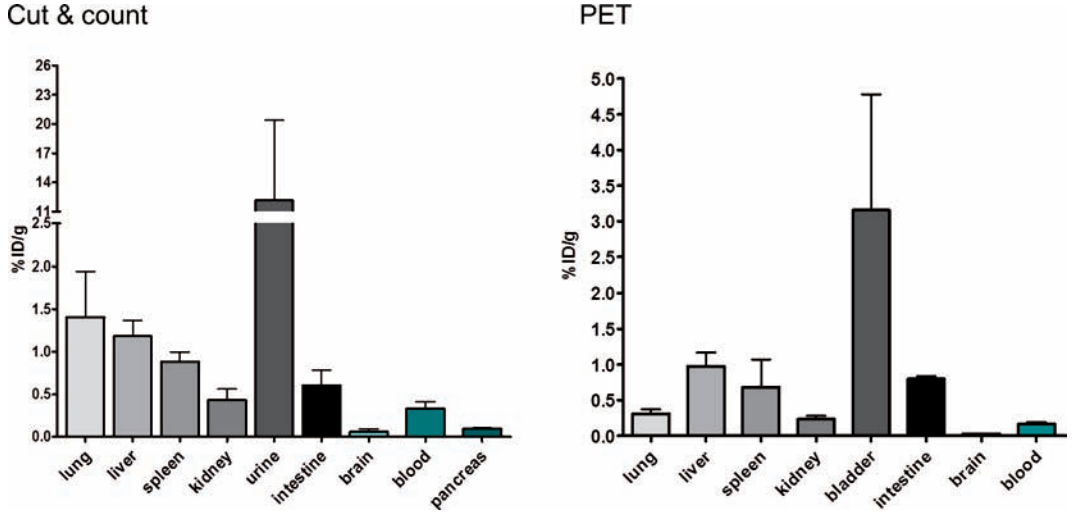


Figure 6. Graphs showing the %ID/gr in each tissue calculated from the cut and count study or the PET scans.

the labeled AuNPs, demonstrating that elevated concentrations of radioactivity could be observed in the kidneys, liver, bladder, and intestine 120 min after injection. The spleen was clearly visible in the images of all the animals, indicating considerable trapping of the NPs by the reticuloendothelial system (RES), a finding that is consistent with our previous *ex vivo* results in rats.[8] Moreover, the lungs showed high levels of radioactivity, thereby suggesting the trapping of the conjugate in the vascular bed of this organ which could be attributed to the presence of species of high size (approximately 500 nm). The great vessels were visible in the images, which could indicate the binding of the labeled compound to the vascular endothelium. Alternatively, these images could represent the blood volume of the vessels produced by the nanoparticles that remained in the blood until the end of the experiment. The supraortic vessels were visible in the images, indicating the binding of the labeled compound to the vascular endothelium. Other tissues, including the brain, displayed low levels of radioactivity, which could be related to the rapid washout of the conjugate from the blood (see Figure 4).

The time−activity curves obtained from the PET images showed that the highest concentration of the compound was present in the bladder, indicative of the urinary excretion of the NPs (Figure 5). The intestine also progressively accumulated radioactivity, which is compatible with the biliary excretion of the conjugate. A time−activity curve of radioactivity in the spleen showed that the accumulation of the conjugate was high at the beginning of the scan and increased only slightly with time, a pattern compatible with the phagocytosis of the circulating NPs by the RES components of this organ. The concentration of radioactivity in the blood decreased quickly during the first minutes of the study in parallel with an increase

dx.doi.org/10.1021/bc200362a | *Bioconjugate Chem.* 2012, 23, 399−408

in the urine, reflecting the rapid urinary excretion of part of the injected dose. After this initial rapid decline, the radioactivity in blood decreased slowly, similar to the liver, lung, and kidney. Finally, the brain contained a very low level of radioactivity. This level decreased with time, which possibly reflects the clearance of the compound from the vascular compartment.

The results calculated from the PET images showed similar values of the percentage of injected dose for each gram of tissue (%ID/gr) as the cut and count study (Figure 6). The calculation of %ID/gr from the cut and count results revealed that the urine contained the highest concentration of the radiolabeled compound. The presence of radioactivity in urine could be attributed to the filtration and excretion of nanoparticles or radioactive metabolites produced by the exchange of radioactive peptide molecules attached to the surface by thiolated molecules (i.e., peptides or proteins) present in the blood. To determine whether the measured radioactivity corresponded to the conjugate or to ^{18}F-labeled metabolites, we injected two animals with the labeled nanoparticles and collected their urine 1 h after injection. The urine samples were centrifuged under the same conditions described previously for the plasma stability experiment with the labeled conjugate. The results showed that the level of radioactivity in the supernatant was less than 0.02% of the total radioactivity in the urine (Supporting Information, Table S2). The fact that the total radioactivity observed in urine remained in the pellet after centrifugation could indicate that the signal observed in the urinary system in the microPET study corresponded to C(AuNP)LPFFD-C(AuNP)K([^{18}F]-SBF). However, renal excretion of free metabolites cannot be excluded due to the possible presence of them in the *in vivo* conditions, as was observed in the *in vitro* stability assay in plasma.

The lungs, liver, and spleen were the organs with the next highest levels of radioactivity, followed by the intestine, kidneys, and blood. The pancreas and brain, however, accumulated very low concentrations of radiolabeled nanoparticles. The results are in agreement with the %ID/gr observed in Figure 5. Only the results obtained from the bladder were clearly different from the results obtained in the urine count. However, this difference is only in the absolute magnitude of %ID/gr, not in its relationship with the values from the other tissues. In fact, the bladder also had the highest concentration of radioactivity in the PET quantification. The other tissues showed a similar pattern of radioactivity concentration and %ID/gr values as in the cut and count study. The differences observed in lung and blood was not significant and could be related to the low number of animals included in the study and the accuracy in the VOI delineation. We performed a statistical analysis of the data comparing the cut and count and PET results for the lung using Student's *t* test and the nonparametric Mann–Whitney test. In fact, because of the low resolution of the microPET systems, the signal from the liver could slightly increase the signal detected in the lung. This phenomenon is known as the partial volume effect. The influence of the partial volume effect on the results could potentially be reduced with a more precise delineation of the VOIs in the lungs, or by using a respiratory gating, or by avoiding the quantification of the inferior segments of these organs that are in the proximity of the liver. At the level of the heart, a VOI was delineated as a measurement of circulating blood, but this VOI also included the myocardium, contributing to the reduction in the %ID/gr observed in the PET study with respect to the cut and count study.

In summary, the conjugate C(AuNP)LPFFD-C(AuNP)K was covalently labeled with the probe [^{18}F]-SFB, producing a stable conjugate that allowed us to perform AuNPs biodistribution studies with PET imaging. The highest concentration of the radiolabeled conjugate was found in the bladder and urine and in a lower proportion in intestine, which showed progressive accumulation that was compatible with the biliary excretion of the conjugate. The AuNPs were removed by renal clearance; however, this process is efficient for NPs with a diameter below 5.5 nm. Under this size, NPs such as quantum dots can easily enter the urine by glomerular filtration or tubular secretion.[27] However, the renal clearance of larger NPs, including diamond nanoparticles and carbon nanotubes (CNTs), is also possible.[13,28] In addition to its metabolic function, the liver is also a major excretion route for larger NPs.[29,30] The excretion occurs across hepatocytes through the biliary production pathway. Hepatocytes have been shown to have phagocytic ability, although they are not as effective as Kupffer cells in capturing nanoparticles. Furumoto et al.[31] have found that polystyrene nanoparticles are taken up by both Kupffer cells and hepatocytes after intravenous administration.

The conjugate accumulated in liver and spleen, as was observed *ex vivo* in rats by our group[8] and by other authors for AuNPs of similar sizes.[32−36] This behavior can be attributed to the conjugate's negative superficial charge, which favors the interaction with the RES. When the NPs are administered, a variety of plasma proteins bind to their surfaces. The conjugates can then be recognized by the macrophage cell surface and internalized, leading to a significant loss of NPs from circulation. Some of the serum proteins that bind and cap the NPs are opsonins. These proteins may be recognized and captured by macrophages, thereby contributing to a major loss of the administered dose as a result of retention by the RES and the consequent accumulation in the liver and spleen.[8]

PET imaging allowed us to study the *in vivo* biodistribution of the AuNPs in a noninvasive and sensitive way using a reduced number of animals. Our results show that AuNPs can be covalently and radioactively labeled for PET biodistribution studies.

■ ASSOCIATED CONTENT

Supporting Information

Peptides HPLC and mass spectrometry, global yield of synthesis, X-ray photoelectron spectroscopy, obtention of conjugates with different proportions of peptides, stability of conjugates in plasma, radioactivity in urine. This material is available free of charge via the Internet at http://pubs.acs.org.

■ AUTHOR INFORMATION

Corresponding Author

*E-mail: mkogan@ciq.uchile.cl; albericio@irbbarcelona.org.

Author Contributions

□These authors contributed equally to the work.

Notes

The authors declare no competing financial interest.

■ ACKNOWLEDGMENTS

The authors would like to acknowledge Elisenda Coll of Serveis Cientificotècnics (Universitat de Barcelona) for assistance in transmission electronic microscopy. This work was supported

by AECID, FONDECYT 1090143, MECESUP-UCH-0811, ACT-95, CICYT (CTQ2009-07758), the Instituto de Salud Carlos III (CB06_01_0074), the Generalitat de Catalunya (2009SGR 1024), the Institute for Research in Biomedicine, and the Barcelona Science Park, the CDTI under the CENIT Programme (AMIT Project) and the Spanish Ministry of Science and Innovation.

REFERENCES

(1) Bhattacharya, R., Mukherjee, P., Xiong, Z., Atala, A., Soker, S., and Mukhopadhyay, D. (2004) Gold Nanoparticles Inhibit VEGF165-Induced Proliferation of HUVEC Cells. *Nano Lett. 4*, 2479−2481.

(2) Kogan, M. J., Olmedo, I., Hosta, L., Guerrero, A. R., Javier Cruz, L., and Albericio, F. (2007) Peptides and Metallic Nanoparticles for Biomedical Applications. *Nanomedicine 2* (3), 287−306.

(3) Hosta, L., Olmedo, I., Arbiol, J., Cruz, L. J., Kogan, M. J., and Albericio, F. (2010) Multifunctionalized Gold Nanoparticles with Peptides Targeted to Gastrin-Releasing Peptide Receptor of a Tumor Cell Line. *Bioconjugate Chem. 21* (6), 1070−1078.

(4) Hosta, L., Pla-Roca, M., Arbiol, J., Lopez-Iglesias, C., Samitier, J., Cruz, L. J., Kogan, M. J., and Albericio, F. (2009) Conjugation of Kahalalide F with Gold Nanoparticles to Enhance in Vitro Antitumoral Activity. *Bioconjugate Chem. 20* (1), 138−146.

(5) Zharov, V. P., Mercer, K. E., Galitovskaya, E. N., and Smeltzer, M. S. (2006) Photothermal Nanotherapeutics and Nanodiagnostics for Selective Killing of Bacteria Targeted with Gold Nanoparticles. *Biophys. J. 90*, 619−627.

(6) Kogan, M. J., Bastus, N. G., Amigo, R., Grillo-Bosch, D., Araya, E., Turiel, A., Labarta, A., Giralt, E., and Puntes, V. F. (2006) Nanoparticle-mediated local and remote manipulation of protein aggregation. *Nano Lett. 6* (1), 110−115.

(7) Araya, E., Olmedo, I., Bastus, N. G., Guerrero, S., Puntes, V. F., Giralt, E., and Kogan, M. J. (2008) Nanoparticles and Microwave Irradiation Inhibit Beta-Amyloid Amyloidogenesis. *Nanoscale Res. Lett. 3*, 435−443.

(8) Guerrero, S., Araya, E., Fiedler, J. L., Arias, J. I., Adura, C., Albericio, F., Giralt, E., Arias, J. L., Fernández, M. S., and Kogan, M. J. (2010) Improving the Brain Delivery of Gold Nanoparticles by Conjugation with an Amphipathic Peptide. *Nanomedicine 5*, 897−913.

(9) Reiner, T., Keliher, E. J., Earley, S., Marinelli, B., and Weissleder, R. (2011) Synthesis and In Vivo Imaging of a ^{18}F-Labeled PARP1 Inhibitor Using a Chemically Orthogonal Scavenger-Assisted High-Performance Method. *Angew. Chem., Int. Ed. 50*, 1922−1925.

(10) Xiea, H., Wang, Z. J., Bao, A., Goins, B., and Phillips, W. T. (2010) In Vivo PET Imaging and Biodistribution of Radiolabeled Gold Nanoshells in Rats with Tumor Xenografts. *Int. J. Pharm. 395*, 324−330.

(11) Zhou, M., Zhang, R., Huang, M., Lu, W., Song, S. H., Melancon, M. P, Tian, M., Liang, D., and Li, C. (2010) A Chelator-Free Multifunctional [^{64}Cu]CuS Nanoparticle Platform for Simultaneous Micro-PET/CT Imaging and Photothermal Ablation Therapy. *J. Am. Chem. Soc. 132* (34), 15351−15358.

(12) Yang, X. Q., Hong, H., Grailer, J. J., Rowland, I. J., Javadi, A., Hurley, S. A., Xiao, Y. L., Yang, Y. A., Zhang, Y., Nickles, R., Cai, W. B., Steeber, D. A., and Gong, S. Q. (2011) cRGD-functionalized, DOX-conjugated, and (64)Cu-labeled superparamagnetic iron oxide nanoparticles for targeted anticancer drug delivery and PET/MR imaging. *Biomaterials 32* (17), 4151−4160.

(13) Ambrosinia, V., Campana, D., Tomassetti, P., Grassetto, G., Rubello, D., and Fantia, S. (2011) PET/CT with (68)Gallium-DOTA-peptides in NET: An overview. *Eur. J. Radiol. 80* (2), E116−E119.

(14) Liu, Q., Sun, Y., Li, Ch., Zhou, J, Li, Ch., Yang, T., Zhang, X., Yi, T., Wu, D., and Li, F. (2011) ^{18}F-Labeled Magnetic-Upconversion Nanophosphors via Rare-Earth Cation-Assisted Ligand Assembly. *ACS Nano 5* (4), 3146−3157.

(15) Patt, M., Schildan, A., Habermann, B., Mishchenko, O., Patt, J. T., and Sabri, O. (2010) (18)F- and (11)C-labelling of quantum dots with n.c.a. [(18)F]fluoroethyltosylate and [(11)C] methyliodide: a feasibility study. *J. Radioanal. Nucl. Chem. 283* (2), 487−494.

(16) Tartis, M. S., Kruse, D. E., Zheng, H, Zhang, H, Kheirolomoom, A, Marik, J, and Ferrara, K. W. (2008) Dynamic microPET imaging of ultrasound contrast agents and lipid delivery. *J. Controlled Release 131* (3), 160−166.

(17) Rojas, S., Gispert, J. D., Martin, R., Abad, S., Menchón, C., Pareto, D., Víctor, V. M., Alvaro, M., Garcia, H., and Herance, J. R. (2011) Biodistribution of Amino-Functionalized Diamond Nanoparticles. In Vivo Studies Based on 18F Radionuclide Emission. *ACS Nano 5* (7), 5552−5559.

(18) Okarvi, S. M. (2001) Recent Progress In Fluorine-18 Labelled Peptide Radiopharmaceuticals. *Eur. J. Nucl. Med. 28*, 929−938.

(19) Olmedo, I., Araya, E., Sanz, F., Medina, E., Arbiol, J., Toledo, P., Alvarez-Lueje, A., Giralt, E., and Kogan, M. J. (2008) How Changes in the Sequence of the Peptide CLPFFD-NH_2 can Modify the Conjugation and Stability of Gold Nanoparticles and their Affinity for β-Amyloid Fibrils. *Bioconjugate Chem. 19*, 1154−1163.

(20) Guerrero, A. R., Caballero, L., Adeva, A., Melo, F., and Kogan, M. J. (2010) Exploring the Surface Charge on Peptide−Gold Nanoparticle Conjugates by Force Spectroscopy. *Langmuir 26* (14), 12026−12032.

(21) Kaiser, E., Colescott, R. L., Bossinger, C. D., and Cook, P. I. (1970) Color test for detection of free terminal amino groups in the solid-phase synthesis of peptides. *Anal. Biochem. 34* (2), 595−598.

(22) Madder, A., Farcy, N., Hosten, N. G. C., De Muynck, H., De Clercq, P. J., Barry, J., and Davis, A. P. A. (1999) Novel Sensitive Colorimetric Assay for Visual Detection of Solid-Phase Bound Amines. *Eur. J. Org. Chem. 11*, 2787−2791.

(23) Liu, X., Atwater, M., Wang, J., and Huo, Q. (2007) Extinction coefficient of gold nanoparticles with different sizes and different capping ligands. *Colloids Surf., B 58*, 3−7.

(24) Mading, P., Fuchtner, F., and Wuest, F. (2005) Module-assisted synthesis of the bifunctional labelling agent N-succinimidyl 4-[(18)F]fluorobenzoate. *Appl. Radiat. Isot. 66*, 329−332.

(25) Turkevich, J., Stevenson, P. C., and Hillier, J. (1951) A Study of the Nucleation and Growth Processes in the Synthesis of Colloidal Gold. *Discuss. Faraday Soc. 11*, 55−75.

(26) Hackley, A., and Clogston, J. D. (2011) Measuring the Hydrodynamic Size of Nanoparticles in Aqueous Media Using Batch-Mode Dynamic Light Scattering, Vol *697*, *Characterization of Nanoparticles Intended for Drug Delivery, Methods in Molecular Biology* (McNeil, S., Ed.) pp 32−52, Chapter 2, Human Press, UK.

(27) Choi, H. S., Liu, W., Misra, P., Tanaka, E., Zimmer, J. P., Ipe, B. I., Bawendi, M. G., and Frangioni, J. V. (2007) Renal Clearance Of Quantum Dots. *Nat. Biotechnol. 25*, 1165−1170.

(28) Lacerda, L., Soundararajan, A., Singh, R., Pastorin, G., Al-Jamal, K. T., Turton, J., Frederik, P., Herrero, M. A., Li, S., Bao, A., Emfietzoglou, D., Mather, S., Phillips, W. T., Prato, M., Bianco, A., Goins, B., and Kostarelos, K. (2008) Dynamic Imaging of Functionalized Multi-Walled Carbon Nanotube Systemic Circulation and Urinary Excretion. *Adv. Mater. 20* (2), 225−230.

(29) Yamago, S., Tokuyama, H., Nakamura, E., Kikuchi, K., Kananishi, S., Sueki, K., Nakahara, H., Enomoto, S., and Ambe, F. (1995) In vivo Biological Behavior of Water-Miscible Fullerenes. ^{14}C-Labeling, Absorption, Distribution, Excretion and Acute Toxicity. *Chem. Biol. 2*, 385−389.

(30) Cho, M. J., Cho, W. S., Choi, M., Kim, S. J., Han, B. S., Kim, S. H., Kim, H. O., Sheen, Y. Y., and Jeong, J. Y. (2009) The Impact of Size on Tissue Distribution and Elimination by Single Intravenous Injection of Silica Nanoparticles. *Toxicol. Lett. 189*, 177−183.

(31) Furumoto, K., Ogawara, K., Yoshida, M., Takakura, Y., Hashida, M., Higaki, K., and Kimura, T. (2001) Biliary Excretion of Polystyrene Microspheres Depends on the Type of Receptor-Mediated Uptake in Rat Liver. *Biochim. Biophys. Acta 1526*, 221−226.

(32) Lasagna-Reeves, C., Gonzalez-Romero, D., Barria, M., Olmedo, I., Clos, A., Ramanujam, V. M. S., Urayama, A., Vergara, L., Kogan, M. J., and Soto, C. (2010) *BBRC 393*, 649−655.

(33) Hillyer, J. F., and Albrecht, R. M. (2001) Gastrointestinal Persorption and Tissue Distribution of Differently Sized Colloidal Gold Nanoparticles. *J. Pharm. Sci. 90*, 1927−1936.
(34) Semmler-Behnke, M., Kreyling, W. G., Lipka, J., Fertsch, S., Wenk, A., Takenaka, S., Schmid, G., and Brandau, W. (2008) Biodistribution of 1.4- and 18-nm Gold Particles in Rats. *Small 4*, 2108−2111.
(35) De Jong, W. H., Hagens, W. I., Krystek, P., Burger, M. C., Sips, A. J., and Geertsma, R. E. (2008) Particle Size Dependent Organ Distribution of Gold Nanoparticles after Intravenous Administration. *Biomaterials 29*, 1912−1919.
(36) Sonavane, G., Tomoda, K., and Makino, K. (2008) Biodistribution of Colloidal Gold Nanoparticles after Intravenous Administration: Efect of Particle Size. *Colloids Surf., B 66*, 274−280.

Bioconjugate Chemistry

Article

pubs.acs.org/bc

Reagents for Astatination of Biomolecules. 6. An Intact Antibody Conjugated with a Maleimido-*closo*-Decaborate(2-) Reagent via Sulfhydryl Groups Had Considerably Higher Kidney Concentrations than the Same Antibody Conjugated with an Isothiocyanato-*closo*-Decaborate(2-) Reagent via Lysine Amines

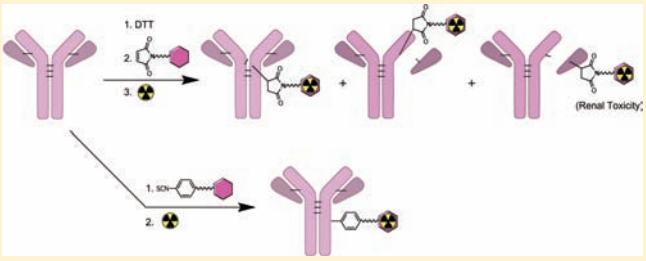
D. Scott Wilbur,*[,†] Ming-Kuan Chyan,[†] Hirohisa Nakamae,[§] Yun Chen,[§] Donald K. Hamlin,[†] Erlinda B. Santos,[§] Brian T. Kornblit,[§] and Brenda M. Sandmaier[‡,§]

[†]Departments of Radiation Oncology and [‡]Medicine, University of Washington, Seattle, Washington, United States

[§]Clinical Research, Fred Hutchinson Cancer Research Center, Seattle, Washington, United States

Supporting Information

ABSTRACT: We are investigating the use of an ^{211}At-labeled anti-CD45 monoclonal antibody (mAb) as a replacement of total body irradiation in conditioning regimens designed to decrease the toxicity of hematopoietic cell transplantation (HCT). As part of that investigation, dose-escalation studies were conducted in dogs using ^{211}At-labeled anticanine CD45 mAb, CA12.10C12, conjugated with a maleimido-*closo*-decaborate(2-) derivative, **4**. Unacceptable renal toxicity was noted in the dogs receiving doses in the 0.27−0.62 mCi/kg range. This result was not anticipated, as no toxicity had been noted in prior biodistribution and toxicity studies conducted in mice. Studies were conducted to understand the cause of the renal toxicity and to find a way to circumvent it. A dog biodistribution study was conducted with ^{123}I-labeled CA12.10C12 that had been conjugated with **4**. The biodistribution data showed that 10-fold higher kidney concentrations were obtained with the maleimido-conjugate than had been obtained in a previous biodistribution study with ^{123}I-labeled CA12.10C12 conjugated with an amine-reactive phenylisothiocyanato-CHX-A″ derivative. The difference in kidney concentrations observed in dogs for the two conjugation approaches led to an investigation of the reagents. SE-HPLC analyses showed that the purity of the CA12.10C12 conjugated via reduced disulfides was lower than that obtained with amine-reactive conjugation reagents, and nonreducing SDS-PAGE analyses indicated protein fragments were present in the disulfide reduced conjugate. Although we had previously prepared *closo*-decaborate(2-) derivatives with amine-reactive functional groups (e.g., **6** and **8**), a new, easily synthesized, amine-reactive (phenylisothiocyanate) derivative, **10**, was prepared for use in the current studies. A biodistribution was conducted with coadministered ^{125}I- and ^{211}At-labeled CA12.10C10 conjugated with **10**. In that study, lower kidney concentrations were obtained for both radionuclides than had been obtained in the earlier study of the same antibody conjugated with **4** after reduction of disulfide bonds.



INTRODUCTION

We are investigating the use of monoclonal antibody (mAb)-targeted α-emitting radionuclides as a replacement for the total body irradiation (TBI) to decrease the toxicity of hematopoietic cell transplantation (HCT) conditioning regimens.[1] In our prior studies, we found that stable engraftment could be obtained in a dog model when either an anti-CD45 or anti-TCR$\alpha\beta$ mAb labeled with the α-emitting radionuclide bismuth-213 (^{213}Bi) was used to replace TBI in the conditioning regimen.[2,3] While successful, the translation of the ^{213}Bi-labeled mAbs to clinical studies was not practical due to the high cost[28] and low availability of the parent radionuclide actinium-225. Therefore, we are presently evaluating the use of another α-emitting radionuclide, astatine-211 (^{211}At) in the place of the ^{213}Bi in the conditioning regimen. Importantly, ^{211}At is readily available at our institution, and at a cost[28] that will allow translation to a clinical study.

As part of the transition from ^{213}Bi to ^{211}At, studies were conducted in mice to determine the best method to use for labeling mAbs with ^{211}At, and to compare the efficacy of ^{211}At-labeled anti-CD45 mAb to the same mAb labeled with ^{213}Bi. Due to concern about the in vivo stability of ^{211}At-labeled mAbs,[4] biodistributions of ^{211}At-labeled anti-CD45 mAbs, 30F11, obtained from two ^{211}At-labeling approaches were conducted. Those labeling approaches (A and B) are depicted in Figure 1. In the studies, the often used mAb-labeling

Received: July 23, 2011
Revised: January 23, 2012
Published: February 1, 2012

ACS Publications © 2012 American Chemical Society

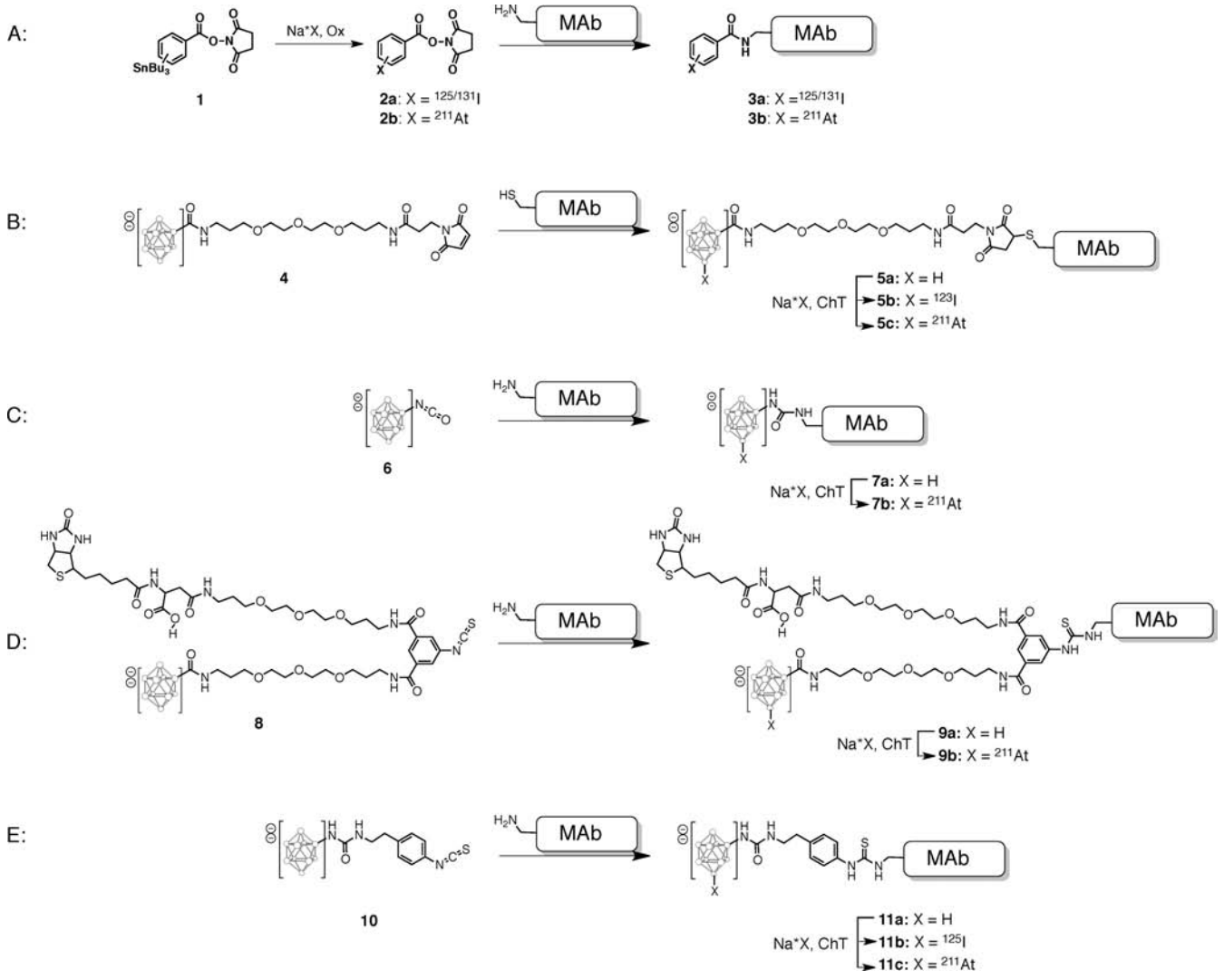


Figure 1. Approaches to conjugation and radiolabeling mAbs with ^{211}At. Approach A is a "two-step" labeling approach where a succinimidyl stannylbenzoate ester **1** is initially labeled, then the resultant ^{211}At-labeled succinimidyl benzoate [^{211}At]**2b** is conjugated with lysine amines on a mAb. Approach B is direct labeling approach where sulfhydryl groups produced by reduction of disulfides on a mAb are conjugated with a maleimido-*closo*-decaborate(2-) reagent **4**, followed by ^{211}At-labeling of the mAb-B10 conjugate to give [^{211}At]**5c**. C, D, and E are direct labeling approaches where lysine amines on a mAb are conjugated with an isocyanato- or isothiocyanatophenyl-*closo*-decaborate(2-) reagent (**6**, **8**, or **10**), followed by ^{211}At-labeling of the mAb-B10 conjugate to give [^{211}At]**7b**, [^{211}At]**9b**, or [^{211}At]**11c**.

approach, employing a N-succinimidyl ester of *meta*-trialkylstannylbenzoic acid **1** to prepare N-succinimidyl *meta*-[^{211}At]-astatobenzoate **2**, was compared with conjugation of a maleimido-*closo*-decaborate(2-) derivative **4**, which had been previously shown to be stable to in vivo deastatination.[5] The comparison studies demonstrated that ^{211}At-labeled maleimido-*closo*-decaborate(2-) mAb conjugate, [^{211}At]**5c** had a higher in vivo stability than the ^{211}At-labeled benzoate mAb conjugate [^{211}At]**3b**. Importantly, conjugation of **4** to the mAb allowed direct labeling of the conjugate **5a**, which made the labeling procedure much simpler and provided higher radiochemical yields than the 2-step labeling procedure used to prepare [^{211}At]**3b**. Subsequently, studies were conducted in mice to compare the hematopoietic cell-killing efficacy of [^{213}Bi]30F11 with [^{211}At]30F11, labeled after conjugation with **4**. Those studies demonstrated that the ^{211}At-labeled mAb was equal or superior to the ^{213}Bi-labeled mAb in depleting hematopoietic cells.[6] From the data obtained, it was estimated that 50 μCi of [^{211}At]30F11 would provide a higher dose to the target cells in the spleen (294 Gy) than 500 μCi [^{213}Bi]30F11 (117 Gy) when delivered on 10 μg mAb, while the radiation dose to the other tissues was similar for the two radiolabeled mAb doses.

Encouraged by the results obtained in mice, a dose-escalation study of ^{211}At-labeled anticanine CD45 mAb was conducted using [^{211}At]CA12.10C12, [^{211}At]**5c**, labeled after conjugation with **4**. The dose-escalation study was stopped when blood samples showed that renal function was impaired in some of the dogs. This toxicity was unanticipated, as no toxicity had been previously observed in the ^{211}At-labeled anti-CD45 mAb mouse studies. While the cause of the kidney toxicity was unknown, it was suspected that the toxicity might be caused by the nature of the mAb conjugate. To determine if that suspicion was correct, HPLC, IEF, and SDS-PAGE analyses were run on the mAb conjugates **5a**, **7a**, **9a**, and **11a**, prepared by conjugation of **4** after reduction of disulfides or by conjugation of the amine-reactive reagents, **6**, **8**, and **10** with mAb lysine amines. The amine-reactive *closo*-decaborate(2-) conjugation reagents, **6** and **8** had been previously reported, while a

dx.doi.org/10.1021/bc200401b | *Bioconjugate Chem.* 2012, 23, 409–420

synthesis of **10** was carried out. Additionally, biodistributions of radiolabeled mAb-conjugates [^{123}I]**5a** and [^{125}I]**11b**/[^{211}At]**11c** were conducted in dogs to compare concentrations of the radionuclides in blood and tissues at time of necropsy. The results of the investigation of mAb-*closo*-decaborate(2-) conjugates and the synthesis of the new amine-reactive *closo*-decaborate(2-) reagent, **10**, used for conjugation are described herein.

EXPERIMENTAL PROCEDURES

Reagents. Chemicals purchased from commercial sources were analytical grade or better and were used without further purification. Decaborane ($B_{10}H_{14}$) was obtained from Alfa Aesar (Ward Hill, MA). 4-(2-Aminoethyl)aniline, **13**, DL-dithiothreitol (DTT), chloramine-T (ChT), and phosphate buffered saline (PBS) were obtained from Sigma-Aldrich (Sigma, St. Louis, MO). Solvents for HPLC analysis were obtained as HPLC grade and were filtered (0.2 μm) prior to use. Sephadex G-25 desalting columns (PD-10 and NAP-10; GE Healthcare) and Vivaspin 6 centrifugation filters (30 kDa molecular weight cutoff (MWCO); GE Healthcare) were obtained from Fisher Scientific (Houston, TX).

Radioactive Materials. All radioactive materials were handled according to approved protocols at the University of Washington and Fred Hutchinson Cancer Research Center. Standard methods for safely handling radioactive samples were employed.[7] Na[^{123}I]I was purchased from Nordion (Vancouver, BC) as a radiochemical in 0.1 N NaOH. Na[^{125}I]I was purchased from PerkinElmer Life Sciences (Billerica, MA) as high concentration/high specific activity radioiodide in 0.1 N NaOH. ^{211}At was produced by irradiation of a thin layer (0.007 in.; 0.18 mm) of bismuth metal (99.999%, Aldrich) with 29.0 MeV α-particles on a Scanditronix MC-50 cyclotron using the conditions previously described.[8] The ^{211}At was isolated from the bismuth target material using a "wet chemistry" isolation procedure (described below). All handling and processing of the irradiated target was done in a glovebox (Innovative Technologies, Inc., radioisotope glovebox) which was vented through a charcoal filter on the glovebox exhaust and subsequently through a second charcoal-filtered Plexiglas enclosure (12 × 16 × 21 in.^{3}; Biodex 112−038) within a radiochemical fume hood.

All radiohalogenation reactions were conducted in a charcoal-filtered Plexiglas enclosure (radioiodine fume hood, 20 × 24 × 36 in.^{3}, Biodex Medical Systems Inc., Shirley, NY) housed within a radiochemical fume hood. The radiohalogenation reactions were conducted in vials capped with Teflon-coated septa, and were vented through a 10 mL charcoal filled syringe. Additions of reagents to, or removal of materials from, the radiohalogenation vessel were conducted by passing a syringe needle through the septa.

Measurement of ^{123}I, ^{125}I, and ^{211}At were conducted on a Capintec CRC-15R Radioisotope Calibrator using the preprogrammed ^{123}I button and calibration numbers 319 and 44 for ^{125}I and ^{211}At, respectively (designated by Capintec Technical Services). Tissue samples were counted in a Packard Cobra II gamma counter (PerkinElmer Life and Analytical Services, Wellesley, MA). The tissue samples containing ^{211}At and ^{125}I were counted within 24 h of necropsy to obtain both ^{211}At and ^{125}I counts, and were recounted after 3−5 days (0.1% or less ^{211}At remaining) to obtain ^{125}I counts. Radioactivity counts were imported into an *Excel* spreadsheet (Microsoft Corp., Redmond, WA) where calculations were made. The ^{211}At counts were obtained by subtracting ^{125}I counts from total counts. Individual tissue counts for ^{211}At were corrected for decay from the time of counting the first standard (at the beginning of the tissue counting process).

Isolation of Na[^{211}At]At. ^{211}At was isolated from the irradiated bismuth target by a "wet chemistry" approach, as follows: An irradiated aluminum-backed bismuth target containing 18−22 mCi[29] of ^{211}At was placed flat (with Bi down) in a 1 L polypropylene dissolution chamber, and 10 mL of concentrated HNO_3 was added. This dissolution process was allowed to continue for 10 min at room temperature. The HNO_3 solution was removed from the chamber using a pipet and was placed in a 50 mL round-bottom flask. An additional 5 mL of conc. HNO_3 was added to the dissolution chamber containing the irradiated target (as a rinse). The HNO_3 solution was removed and placed in the round-bottom flask with the other HNO_3 solution. The flask containing HNO_3 solution was connected to a distillation apparatus. A hot plate (preheated) at 305 °C was used to distill the HNO_3 leaving a white residue (~20 min) in the flask. After cooling, 8 mL of 8 M HCl was added to the flask with stirring to dissolve the white residue. The resultant clear solution was removed and placed in a 20 mL scintillation vial. The flask was rinsed with additional 2 mL aliquot of 8 M HCl, and that was added to the scintillation vial. An 8 mL quantity of freshly distilled diisopropylether (DIPE), pre-equilibrated with 8 M HCl[30], was added to the scintillation vial and that mixture was stirred at room temperature for 10 min. The 8 M HCl was removed by pipet to waste, and an additional 5 mL of 8 M HCl was added and stirred for 5 min. The 8 M HCl was removed to waste. This rinse was repeated 3 more times to minimize the amount of bismuth remaining in the DIPE.[31] To the DIPE was added 1.2 mL of 4 M NaOH to make the solution basic. The basic solution was brought to near neutral pH (6.5−7.5) with 4 N HCl and 0.5 N HCl.[32] The final volume of the ^{211}At solution was 1.5−2 mL with 12−15 mCi.[33]. The Na[^{211}At]At vial was tightly sealed, placed in sealed (Ziploc) plastic bag, and then transferred from the glovebox to the Biodex radiolabeling enclosure within a radiochemical fume hood.

Monoclonal Antibodies. The anticanine CD45 mAb, CA12.10C12, an IgG1 isotype mAb,[9] was used for targeting hematopoietic cells in the dog model.[2,10] For flow cytometry, mAbs against canine CD45 (CA12.10C12, IgG1), CD4 (CA13.1.E4, IgG1), CD8 (CA9.JD3, IgG2a)[11] were used. The mAb 31A (IgG1) directed at the mouse Thy-1 receptor served as an irrelevant isotype-matched control, because it did not cross-react with canine cells.[12] All mAbs were produced and purified at the Biologics Production Facilities of the Fred Hutchinson Cancer Research Center (Seattle, WA).

Spectral Analyses. ^{1}H NMR and ^{11}B NMR spectra of compounds **10** and **14** were obtained on a Bruker AV 500 (500 MHz) instrument. Proton chemical shifts are expressed as ppm using tetramethylsilane as an internal standard (δ = 0.0 ppm). Boron chemical shifts used $BF_3.OEt_2$ as an external standard. High-resolution mass spectral (HRMS) data were obtained on a Bruker APEX III 47e Fourier Transform Mass Spectrometer using electrospray ionization. For analysis, the samples were dissolved in MeOH and were introduced by an integral syringe infusion pump (Cole Parmer Series 74900).

Chromatography. Synthetic reactions were monitored by HPLC. Analytical samples were assessed on a system that contained a Hewlett-Packard quaternary 1050 gradient pump, a variable wavelength UV detector (254 nm), and an Alltech

ELSD 2000 evaporative light-scattering detector (Deerfield, IL). Analyses of HPLC data were conducted using Hewlett-Packard HPLC *ChemStation* software. Reversed-phase HPLC chromatography was carried out on an Alltech Altima C-18 column (5 μm, 250 × 4.5 mm) using a gradient solvent system at a flow rate of 1 mL/min. A gradient of MeOH and 0.05 M Et_3NHOAc was used. Starting with 20% MeOH, the initial solvent mixture was increased to 100% MeOH over the next 15 min, then held at 100% MeOH for 5 min. Retention times (t_R) obtained under these conditions are provided in the Experimental Procedures.

Preparative chromatography was conducted on nonradioactive compounds. Purification was accomplished using a Biotage SP Flash Purification System (Charlottesville, VA) on a reversed-phase C18 Flash 25+M or 40+M column, eluting with a mixture of MeOH and 0.05 M triethylammonium acetate (Et_3NHOAc) in water. A gradient was used which started with 100% Et_3NHOAc and was increased over 20 min to 100% MeOH. Fractions containing the desired product were combined and evaporated to dryness under vacuum on a rotary evaporator.

Halogen-Reactive *closo*-Decaborate(2-) Conjugation Molecules. The sulfhydryl-reactive maleimido-*closo*-decaborate(2-) derivative, **4**, and amine-reactive biotin-containing, isothiocyanatophenyl-*closo*-decaborate(2-) derivative **8** were obtained as previously described.[5]

$[Et_3NH]_2B_{10}H_9$-NCO, 6. This compound was synthesized using the method described by Hawthorne et al.[13] Briefly, oxalyl chloride (0.838 mL, 9.76 mmol) was added dropwise to a solution of $[Et_3NH]_2B_{10}H_{10}$, **12** (3.0 g, 9.30 mmol)[14] and anhydrous CH_3CN (80 mL) at 0 °C. The resultant solution was stirred at 0 °C for 0.5 h. After the ice-bath was removed the solution was stirred for another 0.5 h. To that solution was added solid NaN_3 (1.27 g, 19.53 mmol), and the solution was stirred at room temperature for 24 h. The mixture was filtered, and then the volume of the filtrate was reduced to ~40 mL by rotary evaporator under vacuum. Et_2O (200 mL) was added slowly to the solution with stirring, and the mixture was stirred at ice-bath temperature for 2 h. The solvents were decanted, and the light-brown product was dried under vacuum overnight to yield 2.66 g (79%) of **6** as tacky light brown solid. HPLC: t_R = 4.4 min.

$[Et_3NH]_2B_{10}H_9$-NHCONH-CH_2CH_2-Ph-NH_2, 14. A solution of **6** (0.50 g, 1.375 mmol), 4-(2-aminoethyl)aniline, **13** (0.187 g, 1.375 mmol), Et_3N (0.288 mL, 2.063 mmol), and anhydrous dimethylformamide (4 mL) was stirred and heated by microwave (Biotage Initiator; Biotage, LLC, Charlotte, N.C.) at 150 °C for 5 min. To the reaction mixture was added 5 mL H_2O, and then the crude product solution was purified via Biotage Flash Chromatography (C18 FLASH 25+M column) via a gradient elution. The isolated fractions containing product were evaporated on a rotary evaporator under vacuum to yield 0.38 g (55%) of **14** as a light-yellow tacky solid. ^1H NMR [includes Et_3NH](CD_3CN, 500 MHz): δ 0.18−0.95 (m, 9H), 1.22 (t, J = 7.2 Hz, 18H), 2.66 (t, J = 7.3 Hz, 2H), 3.10 (q, J = 7.2 Hz, 12H), 3.26 (m, 2H), 6.60 (d, J = 8.5 Hz, 2H), 7.03 (d, J = 8.5 Hz, 2H), 7.14 (s, 1H). ^{11}B NMR (CD_3CN, 160.4 MHz): δ 0.25 (1B), −4.67 (1B), −14.64 (1B), −23.89 (2B), −24.36 (2B), −26.57 (1B), −27.28 (1B), −29.87 (1B). HRMS (ES^-) $C_9H_{22}B_{10}N_3O$ $(M+H)^-$ calcd: 298.2699. Found: 298.2692. HPLC: t_R = 6.5 min.

$[Et_3NH]_2$ $B_{10}H_9$-NHCONH-CH_2CH_2-Ph-NCS, 10. Solid thiocarbonyldiimidazole (0.086 g, 0.48 mmol) and **14** (0.20 g, 0.40 mmol) were dissolved in anhydrous CH_3CN (10 mL). The resultant solution was stirred at room temperature for 1 h. To the reaction solution 10% EtOAc/hexanes (100 mL) was slowly added with stirring, and the mixture was allowed to stir at room temperature for 1 h. The solvents were decanted, the residue was washed with 10% EtOAc/hexanes (20 mL), dried under vacuum for overnight to yield 0.21 g (97%) of **10** as a tacky light-yellow solid. ^1H NMR [includes Et_3NH](CD_3CN, 500 MHz): δ-0.15−0.98 (m, 9H), 1.23 (t, J = 7.3 Hz, 18H), 2.83 (t, J = 7.0 Hz, 2H), 3.12 (q, J = 7.3 Hz, 12H), 3.38 (m, 2H), 7.21 (d, J = 8.6 Hz, 2H), 7.35 (d, J = 8.6 Hz, 2H). ^{11}B NMR (CD_3CN, 160.4 MHz): δ 0.45 (1B), −4.61 (1B), −14.67 (1B), −23.73 (2B), −24.22 (2B), −26.54 (1B), −27.25 (1B), −29.71 (1B). HRMS (ES^-) $C_{10}H_{18}B_{10}N_3OS$ $(M-H)^-$ calcd: 338.2107. Found: 338.2100. HPLC: t_R = 12.9 min.

CA12.10C12 Sulfhydryl Conjugation of 4. To a 1.5 mL solution of 6.1 mg/mL CA12.10C12 in PBS was added 200 μL of 100 mM dithiothreitol. After 1 h of gentle mixing at room temperature, the reduced protein was eluted over a PD-10 column with PBS (pH 6.5 containing 1 mM EDTA). The protein-containing fractions were pooled to give 6 mL of eluate at a concentration of 1.4 mg/mL (UV 280 nm). To that solution was added 39 μL (10 equiv) of a 10 mg/mL solution of **4** in DMSO. The reaction solution was gently mixed for 30 min at room temperature before quenching with 1.8 mg of sodium tetrathionate. The protein was concentrated in a Vivaspin 30K MWCO concentrator and washed 5× with 10 mL each of PBS pH 7.2, concentrating between each wash. The isolated CA12.10C12-**4** was obtained in 2.0 mL solution at a concentration of 3.9 mg/mL (85% protein recovery).

CA12.10C12 Lysine Conjugation of 6. To a 250 μL solution of 1.0 mg/mL CA12.10C12 in PBS was added 250 μL of 100 mM sodium bicarbonate, pH 9.0. To that solution was added 10 equiv (1.8 μL) of a 3.2 mg/mL solution of **6** in DMSO. The mixture was tumbled gently overnight at room temperature. The reaction mixture was then placed on a size-exclusion column (PD-10) and was eluted with PBS. The protein-containing fractions were pooled and concentrated to give 150 μL of 1.0 mg/mL (62% protein recovery) solution of the mAb conjugate. A second conjugation reaction, in which the quantities and conditions employed were the same except 20 equivalents (13.6 μL) of a 3.2 mg/mL solution of **6** in DMSO was added, resulted in 120 μL of 1.1 mg/mL (54% protein recovery) solution of the mAb conjugate.

CA12.10C12 Lysine Conjugation of 8. To a 200 μL solution of 5.4 mg/mL CA12.10C12 in PBS was added 200 μL of 100 mM HEPES buffer, pH 8.5. To that solution was added 5 equiv (5.3 μL) of an 8.3 mg/mL solution of **8** in DMSO. The mixture was tumbled gently overnight at room temperature. The reaction mixture was then placed on a size-exclusion column (PD-10) and was eluted with PBS. The protein-containing fractions were pooled and concentrated to give 135 μL of 5.2 mg/mL (70% protein recovery) solution of the mAb conjugate. A second conjugation reaction, in which the quantities and conditions employed were the same except 10 equiv (10.5 μL) of a 3.2 mg/mL solution of **8** in DMSO was added, resulted in 170 μL of 4.5 mg/mL (77% protein recovery) solution of the mAb conjugate. HABA analysis[7] indicated that there were 0.5 and 1.2 biotins per antibody, respectively, for the isolated mAb conjugated with **8**. [Note: running the conjugation in sodium bicarbonate pH 9.0 produced similar results.]

CA12.10C12 Lysine Conjugation of 10. *Analytical Scale.* To 180 μL of CA12.10C12 at 5.5 mg/mL in PBS was added 180 μL HEPES buffer (100 mM with 150 mM NaCl, pH 8.6) followed by 5, 10, or 20 equiv (18, 36, or 72 μg) of **10** at 7 mg/mL in dimethyl sulfoxide. The reactions were run overnight at room temperature with gentle tumbling. In the morning, each reaction mixture was eluted over a separate size-exclusion (PD-10) column using PBS as eluant. The protein containing fractions were combined and concentrated in Vivaspin 6 centrifugal filters (30 kDa MWCO) to yield 700−880 μg of each of the three conjugates.

Preparative Scale. To 1.0 mL of CA12.10C12 at 9.68 mg/mL in PBS was added 1.0 mL HEPES buffer (100 mM with 150 mM NaCl, pH 8.6) followed by 10 equiv (0.350 mg) of **10** at 7 mg/mL in DMSO (50 μL). The reaction was run overnight at room temperature with gentle tumbling. In the morning, the reaction was split into two fractions and was eluted over two size-exclusion (PD-10) columns using PBS as eluant. The protein containing fractions were combined and concentrated in a Vivaspin 6 centrifugal filter (30 kDa MWCO) to yield 8.9 mg of conjugate at 3.5 mg/mL (92%).

mAb Conjugate Characterization. mAb conjugates were evaluated by size-exclusion (SE)-HPLC. Nonradioactive mAb conjugates were also evaluated on IEF gels to determine changes in charge (isoelectric point, pI) as described below. Additionally, nonradioactive mAb conjugates were characterized by nonreducing and reducing SDS-PAGE analyses to determine molecular weights of conjugates and whether the interchain disulfide bonds were intact in those conjugates (nonreducing). Cell binding was evaluated for the mAb conjugate **11a** by flow cytometry. A brief description of the methods and equipment used in these assays is provided below.

Isoelectric Focusing. IEF analyses were conducted on a Novex PowerEase 500 instrument with the XCell II chamber using Invitrogen (Novex) precast gels, pH 3−10 or pH 3−7 (1.0 mm thick × 12 wells), running under the standard IEF program. The protein was stained with GelCode Blue Stain (Pierce). IEF standards were from Serva Electrophoresis GmbH: pH 10.7, cytochrome C; 9.5, ribonuclease A; 8.3, 8.0, 7.8, lectin; 7.4, 6.9, myoglobin; 6.0, carbonic anhydrase; 5.3, 5.2, γ-lactoglobulin; 4.5, trypsin inhibitor; 4.2, glucose oxidase; 3.5, amyloglucosidase.

SDS-PAGE. Reducing and nonreducing SDS-PAGE analyses were conducted as instructed for use with the Invitrogen (Carlsbad, CA) Novex Tris-Glycine Gels in the XCell SureLock Mini-Cell apparatus. Briefly, the test samples were denatured in aqueous Tris-Glycine SDS Sample Buffer, with or without NuPAGE reducing agent by heating at 85 °C for 2 min. The samples and SeeBlue Plus2 prestained standards were loaded on the gel. The electrophoresis was run at 125 V for ∼90 min. After that time, the sample proteins were visualized by gentle rocking in a GelCode Blue Stain Reagent solution. Following staining the gel was placed in a rack to air-dry, then it was scanned for digital archiving. Molecular weight (kDa) standards for Tris-Glycine Gels are: myosin, 250; phophorylase, 148; BSA, 98; glutamic dehydrogenase, 64; alcohol dehydrogenase, 50; carbonic anhydrase, 36; lysozyme, 16 and aprotinin, 6.

Flow Cytometry. Flow cytometry was used to evaluate the antigen binding of CA12.10C12 after the conjugation reaction using 5, 10, or 20 equiv of reagent **10**. Two hundred thousand normal dog peripheral blood mononuclear cells (PBMC) in 50 μL of 15% horse serum (HS)-1× PBS were incubated with 50 μg/mL of the CA12.10C12 or one of the three **11a** conjugates on ice for 20 min. After washing, cells were resuspended in 50 μL of 15% HS-PBS and were added 10 μg/mL of the secondary antibody, goat antimouse fluorescein isothiocyanate (FITC)-labeled $F(ab')_2$ (Biosource, Camarillo, CA), and incubated on ice for 20 min. To test the blocking ability of the antibody, 10 μg/mL FITC-conjugated CA12.10C12 was added to cells incubated with CA12.10C12 or the **11a** conjugates. After incubation, cells were washed once with 2% HS-PBS, then once with 1× PBS and resuspended in 200 μL of 1% paraformaldehyde. Cells were analyzed on a FACScan Flow cytometer (Becton Dickinson, San Jose, CA).

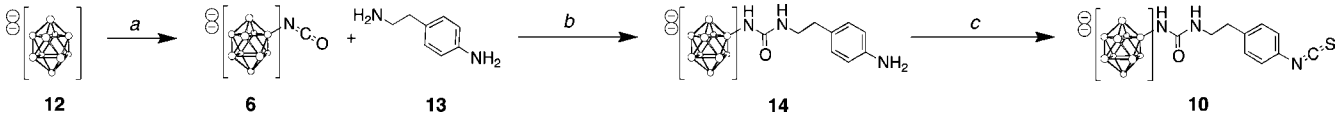
Radioiodination to Prepare [^{123}I]5b. To 640 μL of a 3.9 mg/mL solution of CA12.10C12 sulfhydryl conjugate **5a** in PBS was added 300 μL of sodium phosphate (0.5 M, pH 7.2) followed by 82 μL of Na[^{123}I]I (3.92 mCi in 0.1 N NaOH). To that solution was added 85 μL of a 1 mg/mL solution of chloramine-T in H_2O. After 2 min at room temperature the reaction was quenched with 85 μL of a 1 mg/mL solution of sodium metabisulfite in H_2O. The reaction mixture was then eluted over a Sephadex G-25 size-exclusion column (PD-10) using PBS as the eluant. The protein fractions were combined to yield 2.76 mCi (73% radiochemical yield). The purified [^{123}I]**5b** was diluted with a calculated amount of **5a** to prepare an injectate that contained 5.15 mg of labeled [^{123}I]**5b** in 3.7 mL PBS.

Radioiodination to Prepare [^{125}I]11b. To 286 μL of a 3.5 mg/mL solution of CA12.10C12 lysine conjugate **11a** in PBS was added 50 μL of sodium phosphate (0.5 M, pH 7.2) followed by 3 μL of Na[^{125}I]I (1.42 mCi in 0.1 N NaOH). To that solution was added 3.5 μL of a 10 mg/mL solution of chloramine-T in H_2O. After 1 min at room temperature the reaction was quenched with 3.5 μL of a 10 mg/mL solution of sodium metabisulfite in H_2O. The reaction mixture was then eluted over a Sephadex G-25 size-exclusion column (PD-10) using PBS as the eluant. Protein fractions were combined to yield 0.55 mCi (39% radiochemical yield) on 850 μg of [^{125}I]**11b**. The [^{125}I]**11b** was mixed with [^{211}At]**11c** for injection as described below.

Astatination to Prepare [^{211}At]11c. To 571 μL of a 3.5 mg/mL solution of CA12.10C12 lysine conjugate **11a** in PBS was added 300 μL of sodium phosphate (0.5 M, pH 7.2) followed by 500 μL of Na[^{211}At]At (11 mCi at pH 7). To the resultant solution was added 14 μL of a 10 mg/mL solution of chloramine-T in H_2O. After 2 min at room temperature, the reaction was quenched with 14 μL of a 10 mg/mL solution of sodium metabisulfite in H_2O. The reaction mixture was then eluted over a Sephadex G-25 size-exclusion column (PD-10) using PBS as the eluant. Protein fractions were combined to yield 6.58 mCi (62% radiochemical yield) on 1.7 mg of [^{211}At]**11c**. The [^{211}At]**11c** was combined with [^{125}I]**11b** and a calculated quantity of **11a** to prepare an injectate that contained a total of 5.08 mg of **11a/b/c** in 5.4 mL PBS.

Dogs. Dogs were selected from litters of beagles and mini-mongrel−beagle crossbreeds raised at the Fred Hutchinson Cancer Research Center (Seattle, WA) or purchased from other commercial kennels in the United States. The dogs were quarantined for 1 month and judged to be disease-free before study. They were immunized against distemper, leptospirosis, hepatitis, papilloma virus, and parvovirus. The experimental protocol for the biodistributions and dose-escalation studies were approved by the Institutional Animal Care and Use Committee of the Fred Hutchinson Cancer Research Center. The study was performed in accordance with the principles

Scheme 1. Reactions Used to Obtain Isothiocyanatophenyl-*closo*-decaborate(2-) Derivative 10 for Conjugations with mAb-Lysine Amines[a]



[a](a) $(COCl)_2$, 0, 30 min, NaN_3, rt, 24 h, 79%; (b) Et_3N, anh. DMF, 150 °C (microwave), 5 min, 55%; (c) TCDI, CH_3CN, rt, 1 h, 97%.

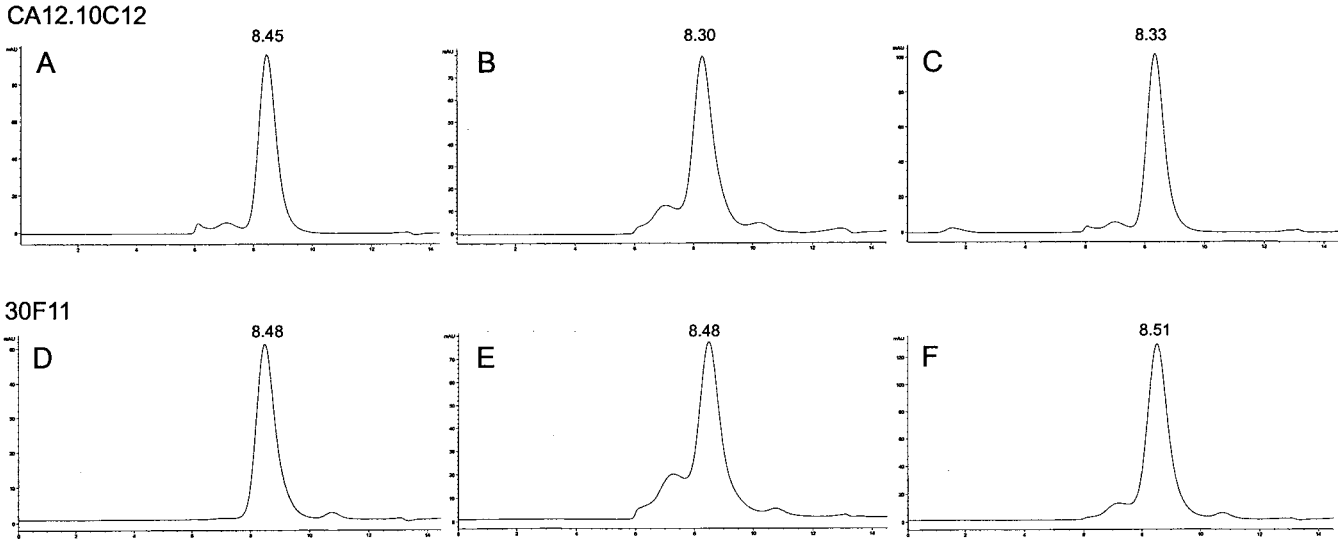


Figure 2. SE-HPLC chromatograms of unmodified and conjugated anti-CD45 mAbs CA12.10C12 and 30F11. Unmodified mAbs are shown in panels A and D; mAbs modified by disulfide reduction and conjugation with **4** are shown in panels B and E; CA12.10C12 modified by conjugation of **10** is shown in panel C, and 30F11 modified by conjugation of **10** is shown in panel F. *X*-axis shows elution time in minutes. Elution times are shown above the major peak in each chromatogram. Shorter elution times obtained in panels B and C are presumably due to differences in injections not in elution properties.

outlined in the *2004 Lippincott Williams & Wilkins Guide for the Care and Use of Laboratory Animals* (Institute of Laboratory Animal Resources). The kennels are certified by the American Association for Accreditation of Laboratory Animal Care.

Dose Escalation. Five dogs (H034, G530, G982, H117, and H115)[34] were treated with escalating quantities of ^{211}At-labeled on 0.5 mg/kg of modified CA12.10C12, [^{211}At]**5c**, conjugated via sulfhydryl groups produced by disulfide reduction. An initial injection of 10% of the total mAb (0.05 mg/kg) was given as a predose to diminish nonspecific uptake in liver.[15] The remaining 0.45 mg/kg of mAb was injected with the radiolabel at 1−1.5 h post the predose injection. Peripheral blood samples were obtained daily until hematological recovery was noted, and continued biweekly until the end of the study. Hepatic and renal functions were assessed weekly in the first month, then biweekly to monthly until the end of the study.

Biodistribution Studies. Two biodistribution studies were conducted. In the first biodistribution study, a 10.8 kg dog (G996)[34] was first injected with 0.05 mg/kg **5a** followed 1 h later by injection of a solution containing 2.56 mCi [^{123}I]**5b** (0.45 mg/kg CA12.10C12). In the second biodistribution a 11.3 kg dog (H137) was first injected with 0.57 mg (0.05 mg/kg) of **11a** followed 1 h later by injection of a solution containing a mixture of 0.55 mCi [^{125}I]**11b** and 6.33 mCi [^{211}At]**11c** on a total of 0.45 mg/kg of CA12.10C12. In each study, blood samples were taken at 5 min, 15 min, 30 min, 1 h, 2 h, 3 h, 4 h, and 21 or 24 h post injection to obtain blood clearance data. The dog injected with [^{123}I]**5b** was euthanized at 24 h post injection and the dog injected with [^{125}I]**11b**/[^{211}At]**11c** was euthanized at 21 h post injection. Necropsies were performed to evaluate the concentrations of radioactivity in blood and selected tissues. Triplicate samples of tissues were excised, blotted free of blood, weighed, and counted. Calculation of percent injected dose (%ID) and percent injected dose per gram (%ID/g) for the collected tissues was accomplished using injection standards for ^{123}I, ^{125}I or ^{211}At counts. The full data set obtained in each biodistribution study is provided as Tables S1 & S2 in the Supporting Information.

RESULTS

Syntheses of *closo*-Decaborate(2-) Conjugates. The sulfhydryl-reactive protein conjugation reagent **4** and the lysine amine-reactive protein conjugation reagents **6** and **8** were obtained as previously described.[5] The amine-reactive reagent **10** was prepared in three synthetic steps from the readily accessible triethyl ammonium salt of decahydro-*closo*-decaborate(2-), **12**, as shown in Scheme 1. Reaction of **12** with oxalyl chloride at 0 °C for 30 min, followed by reaction with NaN_3 at room temperature for 24 h as previously described by Shelly et al.[13] provided the isocyanate-derivatized *closo*-decaborate(2-) **6** in 79% yield. Reactivity of the isocyanate functionality in **6** with amine nucleophiles is low, presumably due to the electron donation from the dianionic *closo*-decaborate(2-) moiety. Therefore, reaction with aminoethylaniline **13** was conducted in dimethylformamide at 150 °C for 5 min using a microwave reactor. After purification, a 55% yield of the adduct **14** was obtained. Conversion of the aniline **14** to the protein-reactive phenylisothiocyanate derivative **10** was

dx.doi.org/10.1021/bc200401b | *Bioconjugate Chem.* 2012, 23, 409−420

accomplished in nearly quantitative yield using thiocarbonyldiimidazole (TCDI) in CH_3CN at room temperature for 1 h.

mAb Conjugates. In this study, conjugations of CA12.10C12 were conducted with the sulfhydryl-reactive reagent **4** and amine-reactive reagents **6**, **8**, and **10** as depicted in Figure 1. Conjugation of maleimido-*closo*-decaborate(2-) **4** with dithiothreitol-reduced disulfides on CA12.10C12 at pH 6.5 was rapid, being complete within 30 min at room temperature as previously described.[4] After size-exclusion chromatography (PD-10) purification, an 85% recovery of **5a** was obtained. Conjugation of the lysine amines on CA12.10C12 with **6** or **8** at pH 8.5 (50 mM $NaHCO_3$) was considerably slower, taking up to 16 h at room temperature for completion. Similarly, conjugation of CA12.10C12 with **10** at room temperature in HEPES buffer at pH 8.6 was allowed to react overnight to obtain 72–92% protein recovery after purification by size-exclusion chromatography.

Conjugates of CA12.10C12 (**5a**, **7a**, **9a**, and **11a**) were characterized by size-exclusion (SE) HPLC, SDS-PAGE, IEF electrophoresis, and flow cytometry. A comparison of SE-HPLC chromatograms for conjugations of the anti-CD45 mAbs CA12.10C12 and 30F11 are shown in Figure 2. The HPLC chromatograms show that reduction with dithiothreitol and subsequent conjugation with the maleimido-*closo*-decaborate(2-) reagent **4** with either mAb produces some higher molecular weight species, but appears to produce only a small amount of lower molecular weight species. In contrast, conjugations of the mAbs with the isothiocyanate derivative **8** or **10** under basic conditions show only very minor changes in the chromatograms from the observed for the unmodified mAb.

Based on previous studies, most conjugation reactions were conducted using 10 equiv of the protein-reactive molecule for each equivalent of the mAb. Evaluation of the mAb conjugate obtained from this ratio of reagents by IEF often showed a significant change in the pI, indicating that all of the mAb molecules had at least one pendant group (e.g., Figure 2, ref 4; Figure 3, ref 5). However, since conjugation reagent **10** had not previously been used, conjugation reactions of CA12.10C12 with **10** were conducted using three molar quantities (5, 10, and 20 equiv) to determine the best ratio of reagents. An IEF gel (Figure 3) shows how the pI (and thus number of conjugates) varies with the number of equivalents offered. While the actual number of conjugates is not readily obtained, the shift of bands from unmodified CA12.10C12 (pI 6.1–6.5) is made increasingly more acidic as more equivalents of **10** are added to the conjugation reaction mixture; 5 equiv (pI ~5.4–6.4), 10 equiv (pI ~5.2–6.3), and 20 equiv (pI ~5.1–6.1).

Analysis of samples on nonreducing SDS-PAGE provided evidence of the presence of protein species having molecular weights significantly different from the unmodified mAb. Figure 4 shows the migration of denatured proteins on reducing and nonreducing SDS-PAGE gels for CA12.10C12 conjugates formed by reaction with maleimide **4** (**5a**), isocyanate **6** (**7a**), isothiocyanate **8** (**9a**), or isothiocyanate **10** (**11a**). It is readily apparent that the disulfide reduction followed by conjugating with maleimide-containing reagent **4** results in having several smaller protein species present (lane marked **5a**). In contrast, mAb conjugations with amine-reactive reagent **10**, under basic conditions, do not produce protein fragments, as shown in Figure 4, right panel.

The effect on binding with normal dog PBMC expressing the CD45 antigen brought about by conjugation of CA12.10C12 with 5, 10, and 20 equiv of **10** was assessed by flow cytometry.

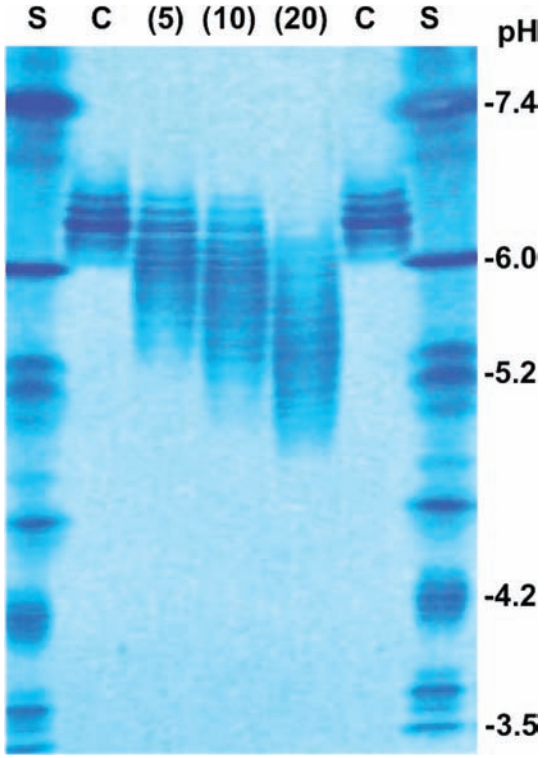


Figure 3. Digitized isoelectric focusing gel (pH 3–7) showing protein bands of CA12.10C12 after reaction with 5, 10, and 20 equiv of reagent **10**. The column markers correspond to the following: S = molecular weight standards; C = unmodified CA12.10C12; and (5), (10), and (20) indicate the number of equivalents of **10** reacted with CA12.10C12 to form the conjugate **11a**.

Binding histograms from the FACS analysis of those conjugates are shown in Figure 5. The histograms indicated that there was a minimal effect on dog peripheral blood mononuclear cell (PBMC) binding after conjugation of **10** with CA12.10C12 (upper panel), and that an effective blocking of FITC-labeled CA12.10C12 and the CA12.10C12 conjugates, **11a**, could be obtained in the presence of excess CA12.10C12 (lower panel). However, when considering which of the reactions (5, 10, or 20 equiv offered) to use in future studies, the fact that the binding histogram for conjugate **11a** prepared from 20 equiv of **10** is broader than the other histograms (left panel), and does not overlie the other histograms in the competition assay, was concerning. Conjugate **11a**, obtained from reaction of CA12.10C12 with 10 equiv of **10**, was chosen as the best candidate for future studies, as we had previously observed that higher radiolabeling yields could be obtained when an mAb conjugate had a higher number of pendant *closo*-decaborate(2-) moieties attached.

Radiohalogenation of CA12.10C12 Conjugates, 5a and 11a. Direct radioiodination of the CA12.10C12 conjugate **5a** with Na[^{123}I]I was accomplished in 2 min at room temperature using chloramine-T as the oxidant to provide [^{123}I]**5b** in 73% radiochemical yield after purification. Under similar radioiodination conditions, reaction of CA12.10C12 conjugate **11a** with Na[^{125}I]I gave a 39% purified radiochemical yield of [^{125}I]**11b**, while labeling with Na[^{211}At]At provided a 62% radiochemical yield of [^{211}At]**11c**.

Dose Escalation Studies. Five dogs were administered a dose of 0.07 mCi/kg (H034), 0.12 mCi/kg (G530), 0.27 mCi/kg (G982), 0.57 mCi/kg (H117), or 0.62 mCi/kg (H115)[34] of

dx.doi.org/10.1021/bc200401b | *Bioconjugate Chem.* 2012, 23, 409–420

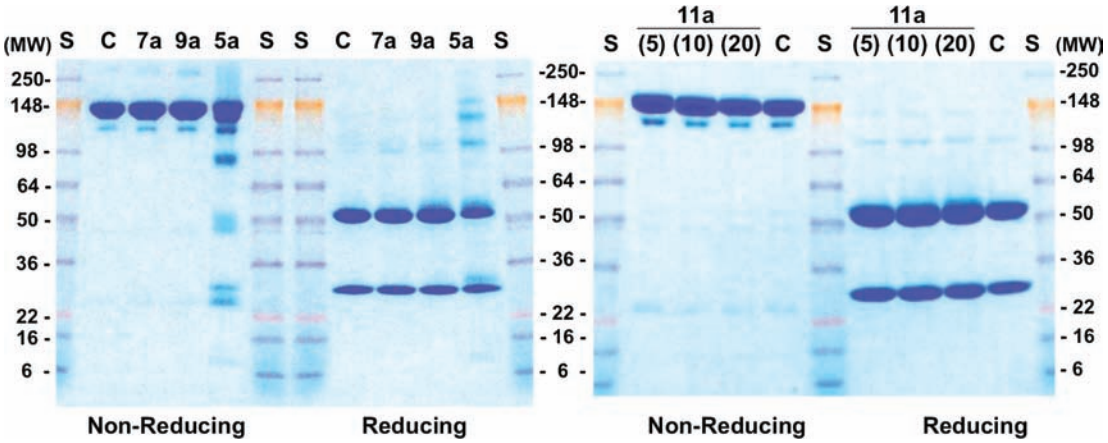


Figure 4. SDS-PAGE gels showing molecular weights of conjugates under reducing and nonreducing conditions. In the left panel gel, the column markers correspond to the following: S = molecular weight standards; C = unmodified CA12.10C12; **5a**, CA12.10C12 conjugated with **4**; **7a**, CA12.10C12 conjugated with **6**; **9a**, CA12.10C12 conjugated with **8**. In the right panel gel, CA12.10C12 was conjugated with varying quantities of **10**. The column markers correspond to the following: S = molecular weight standards; C = unmodified CA12.10C12; and (5), (10), and (20) indicate the number of equivalents of **10** reacted with CA12.10C12 to form conjugate **11a**.

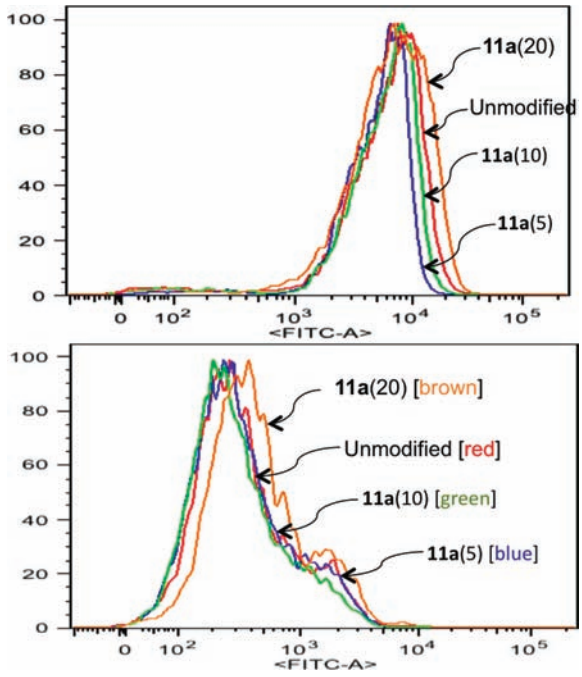


Figure 5. Cell-binding histograms from flow cytometry (FACS) showing unmodified anticanine CD45 mAb, CA12.10C12 (red lines) and conjugates of CA12.10C12 prepared by reaction with 5 (blue line), 10 (green line), or 20 (brown line) equiv of conjugation reagent **10** with normal dog peripheral blood mononuclear cells (PBMC). [Top Panel] Binding of unmodified CA12.10C12 and **11a** conjugates with PBMC. [Bottom Panel] Blocked binding of FITC-conjugated CA12.10C12 and **11a** conjugates to PBMC in the presence of an excess of CA12.10C12.

the sulfhydryl-conjugate [^{211}At]**5c**. The two dogs receiving the lowest doses (0.07 and 0.12 mCi/kg) did not show any toxicity, and survived >33 weeks. The three dogs given higher doses (0.27–0.62 mCi/kg) had significantly elevated blood urea nitrogen (BUN) and creatinine concentrations indicating reduced kidney function. The BUN and creatinine concentrations for the 5 dogs in the study are plotted in Figure 6. The three dogs given higher doses were euthanized in poor condition due to renal failure between 10 and 27 weeks post administration of the [^{211}At]**5c**.

Blood Clearance and Biodistribution Studies. Two biodistribution studies were conducted in dogs to provide tissue concentration and blood clearance data. In the initial study, 2.56 mCi of ^{123}I-labeled CA12.10C12 conjugated with **4**, i.e., [^{123}I]**5b**, was injected into a dog. Blood samples were obtained at 5 min, 15 min, 30 min, 1 h, 2 h, 3 h, 4 h, and 24 h (at time of necropsy). Serial images were obtained on a gamma camera (data not shown) and the dog was euthanized at 24 h post injection. Triplicate samples (most tissues) of 30 tissues, bone marrow biopsy and marrow "squeeze" were taken during necropsy. In the subsequent study, 0.55 mCi ^{125}I-labeled CA12.10C12 conjugated with **10**, [^{125}I]**11b**, was mixed with 6.33 mCi ^{211}At-labeled CA12.10C12 conjugated with **10**, [^{211}At]**11c**, and that mixture was injected.[35] No imaging was done, but the same blood and tissue samples were taken during necropsy (21 h) as in the initial study. Comparison of the blood clearance (graphs in Figure 7 and data in Figure 1S - Supporting Information) indicated that [^{125}I]**11b** and [^{211}At]**11c** cleared more slowly than [^{123}I]**5b**, perhaps due to localization in kidneys. However, the primary purpose of the second biodistribution was to determine if the tissue concentrations (particularly kidney) were changed in the amine-conjugated mAb relative to that seen in the thiol-conjugated mAb. Bar graphs showing the concentrations of radioactivity in a selected set of tissues are shown in Figure 7. Also included (left panel, black bars) are data from a prior study. In that study, CA12.10C12 was conjugated with the DTPA derivative CHX-A″ for subsequent chelation of ^{213}Bi. It is apparent from the plotted data that the labeled mAbs targeted CD45-expressing cells to a similar extent (i.e., spleen concentrations), and that the kidney concentrations were much lower in the radiolabeled mAbs in which the labeling pendant groups were conjugated through a lysine amine. The complete biodistribution data are available in Supporting Information (Table S1).

■ DISCUSSION

The method used to attach the short-lived ($t_{1/2}$ = 7.21 h) α-emitting radionuclide ^{211}At to proteins can dramatically alter

dx.doi.org/10.1021/bc200401b | *Bioconjugate Chem.* 2012, 23, 409–420

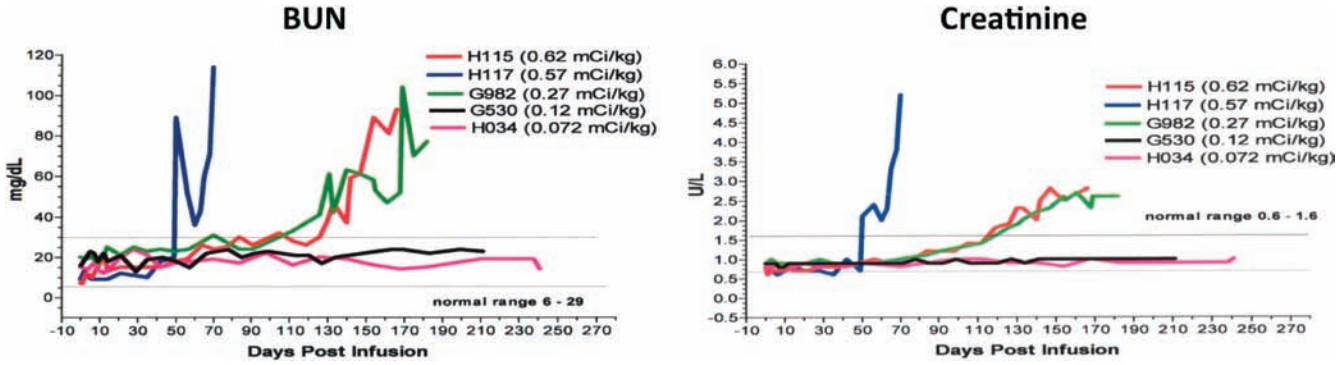


Figure 6. Graphs of renal function as assessed by blood urea nitrogen (BUN) and serum creatinine in 5 dogs administered [^{211}At]**5c** on a dose-escalation protocol. Quantity of [^{211}At]**5c** administered to each dog is shown in the legends. Gray lines in graphs indicate the range of BUN and creatinine found in dogs with normal renal function.

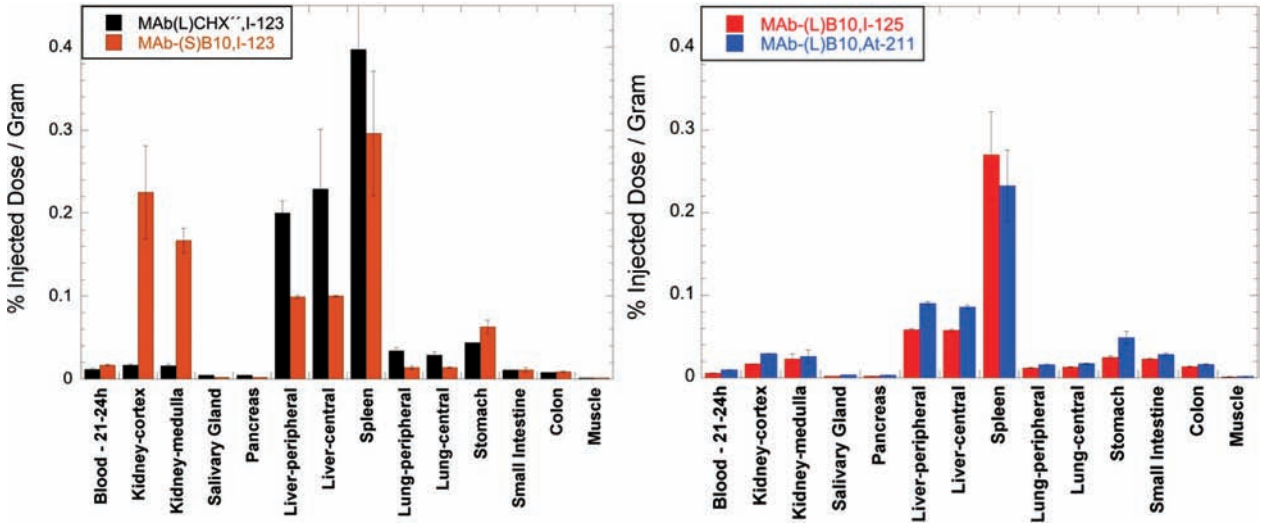


Figure 7. Concentrations of [^{123}I]**5b** (left panel; brown bars) and [^{125}I]**11b**/[^{211}At]**11c** (right panel; red and blue bars, respt.) in selected tissues of two dogs at 24 h post injection and 21 h post injection, respectively. [Left Bar Graph] Data plotted were obtained from two separate biodistribution studies. Error bars show ± standard deviation in 3 samples taken from different locations in the listed tissue. Black bars represent the tissue concentrations at 22 h post injection of CA12.10C12 conjugated with the chelate CHX-A″ and radiolabeled with ^{123}I. Data plotted as black bars were taken from Sandmaier et al.[2] Brown bars represent the tissue concentration in a dog (G996) at 24 h post injection of CA12.10C12 conjugated with **4** and radiolabeled with ^{123}I, [^{123}I]**5c**. [Right Bar Graph] Data were obtained from coadministered radiolabeled mAb in a single dog (H137) at 21 h post injection. Red bars represent tissue concentrations of CA12.10C12 conjugated with **10** and labeled with ^{125}I, [^{125}I]**11b**. Blue bars represent tissue concentrations of CA12.10C12 conjugated with **10** and labeled with ^{211}At, [^{211}At]**11c**. Full data set of tissue concentrations obtained in the dogs is provided in Supporting Information as Table S1.

the outcome of therapy studies. The labeling method is particularly important with ^{211}At, as in vivo stability can be problematic.[16] Indeed, rapidly metabolized ^{211}At-labeled compounds, such as peptides and small molecules release free [^{211}At]astatide in vivo.[17,18] We have investigated boron cage molecules to circumvent the instability, and have found that high in vivo stability of ^{211}At-labeled compounds can be obtained using *closo*-decaborate(2-) pendant groups.[5,17−19] Intact mAbs, which are slowly metabolized, are used to target ^{211}At to hematopoietic cells in the conditioning regimens for HCT. The fact that the mAbs are slowly metabolized raised the question of whether a *closo*-decaborate(2-) conjugate was required in the studies. Therefore, our first study was a comparison of the often used ^{211}At-labeling reagent, N-succinimidyl *meta*-[^{211}At]astatobenzoate, [^{211}At]**2b**[20,21] with a maleimido-*closo*-decaborate(2-) derivative, **4**, that had been prepared for conjugation with sulfhydryl groups on Fab′[5] and engineered mAb fragments containing a cysteine residue.[22] That study demonstrated that higher in vivo stability was obtained, but more importantly, ^{211}At-labeling yields were much higher and the labeling process was much simpler when using the *closo*-decaborate(2-) mAb conjugate, **5a**, than obtained in the two-step conjugation procedure required for use of [^{211}At]**2b**.[4] In a subsequent study in mice directly comparing ^{211}At-labeled anti-CD45 mAb (30F11 conjugated with **4**) and ^{213}Bi-labeled anti-CD45 mAb (30F11 conjugated with CHX-A″-DTPA), it was noted that tissue distributions and therapeutic outcomes were similar. However, ^{211}At-labeled 30F11 showed a more favorable therapeutic profile with less hepatic toxicity and somewhat superior myelosuppressive properties.[6] Based on the encouraging results from the studies in mice, we began dose-escalation studies of [^{211}At]**5c** in the dog model.

Dose-escalation of the ^{211}At-labeled CA12.10C12 conjugated with **4** through reduced disulfide bonds, i.e., [^{211}At]**5c**, resulted in unexpected renal toxicity, as indicated by high BUN and

creatinine concentrations in blood (Figure 6). The knowledge that radiolabeled protein fragments can be sequestered in kidneys[23] prompted us to evaluate whether the reduction of disulfides followed by conjugation resulted in protein fragments that localized to kidney. A biodistribution of [^{123}I]**5b** in a dog (Figure 7, left panel) supported that theory, as the kidney concentration was 10x higher than that obtained with ^{123}I-labeled CA12.10C12 conjugated through lysine amines to the DTPA-CHX-A″ chelate. This large difference in kidney concentration was noted even though both labeled mAb conjugates appear to target CD45-expressing cells in the spleen to about the same extent. It is believed that reduction with low concentrations of dithiothreitol (DTT) or tris(2-carboxyethyl)-phosphine (TCEP) can selectively cleave hinge-region disulfides for site-specific conjugations[24,25] That was our belief when conjugating **4** to CA12.10C12, but there is evidence that the reduction is not that selective.[26] This is an important distinction as the hinge-region contains more than one disulfide, making it possible to conjugate there and have other disulfides remain or reform resulting in no fragments being formed. However, if the conjugation occurs on a reduced disulfide that is between the light and heavy chains, conjugation of one sulfhydryl results in an inability to reform the disulfide bond between the light and heavy chains. If a radiolabeled noncovalently bonded light chain were to dissociate from the intact mAb, its small molecular size might cause it to be localized in kidney. Such a process could explain the higher kidney concentrations (cortex, 0.225, %ID/g; medulla, 0.167% ID/g) observed for [^{123}I]**5b**, versus those observed (cortex, 0.017%ID/g; medulla, 0.016%ID/g) when CA12.10C12 was conjugated with a DTPA derivative and labeled with ^{123}I.[2] Figure 7 (left panel) shows that comparison in a bar graph.

With the belief that the renal toxicity could be caused by the process of conjugating the maleimide reagent, conjugates of two amine-reactive *closo*-decaborate(2-)-containing reagents, **6** and **8**,[5] with CA12.10C12 were prepared for comparison with **5a** and unmodified CA12.10C12. Evaluation of the conjugates by nonreducing SDS-PAGE analysis (Figure 4, left panel) clearly showed that there were protein fragments present after disulfide reduction and conjugation of **4**, whereas there were none if lysine amines were conjugated. From this data it was apparent that conjugations with lysine amines were more favorable, so a choice of reagent was required. The isocyanato-*closo*-decaborate(2-) reagent **6** has low reactivity and the biotin-containing phenylisothiocyanate reagent **8** is more complex and synthetically more difficult to obtain than desired. Thus, a new amine-reactive conjugation reagent, **10**, which is easily synthesized (Scheme 1), was prepared. Conjugation of 5, 10, and 20 equiv of **10** with CA12.10C12 provided increased loading of reagent (Figure 3), but had minimal effect on the antigen binding of the conjugate (Figure 5). Comparison of the SE-HPLC chromatograms of CA12.10C12 conjugated with **4** or **10** to that of unmodified CA12.10C12 showed that amine conjugation with **10** has little effect on the protein (Figure 2). Evaluation of samples from earlier studies by SE-HPLC showed (Figure 2) the rat antimouse CD45 mAb, 30F11 conjugated with the same two reagents had similar chromatographic profiles.

A second biodistribution was conducted in the dog model to confirm our belief that conjugation of an amine-reactive reagent would alleviate the kidney localization problem. In that study, the CA12.10 conjugate, **11a**, was labeled with ^{125}I and ^{211}At. The dual label experiment was carried out to ascertain if the two radionuclides had the same in vivo distribution. The concentrations in the kidneys of [^{125}I]**11b** (cortex, 0.017%ID/g; medulla, 0.023%ID/g) and [^{211}At]**11c** (cortex, 0.029%ID/g; medulla, 0.026%ID/g) were low (Figure 7, right graph) compared to that observed for the ^{123}I-labeled CA12.10C12 conjugated with maleimide reagent **4** (Figure 7, left graph, green bars). Interestingly, the concentration of radioactivity in the liver for [^{125}I/^{211}At]-labeled CA12.10C12 was about the same as the sulfhydryl conjugate, but lower than the DTPA-CHX-A″ conjugate. The favorable biodistribution results led to resumption of dose-escalation studies using the ^{211}At-labeled CA12.10C12 conjugate, [^{211}At]**11c**. The results of that investigation will be described elsewhere,[27] but no kidney toxicity was seen at the same dose levels that were problematic with the reduced disulfide conjugation and labeling approach.

CONCLUSION

This investigation has demonstrated the importance of the method of conjugation when developing mAb-targeted α-emitting radiopharmaceuticals. The studies proved that conjugation of lysine amines with an amine-reactive *closo*-decaborate(2-) reagent, **10**, rather than using a method of conjugation that employs reduction of disulfide bonds on the mAb provides a more specific delivery of the ^{211}At to the targeted CD45-expressing cells. Based on the high cytotoxicity of the α-emission from ^{211}At, it is likely that even a small quantity of ^{211}At-labeled mAb fragment localizing to kidneys can cause damage. The new ^{211}At-reactive protein conjugation reagent, **10**, is simple to use and has provided high labeling yields (up to 92%) for direct labeling of the mAb conjugate. These results make this labeling approach particularly attractive for our continuing studies in the dog model and for future clinical studies.

ASSOCIATED CONTENT

Supporting Information

A table (Table S1) containing biodistribution data from CA12.10C12 conjugates [^{123}I]**5b** and [^{125}I]**11b**/[^{211}At]**11c** and a graph (Figure S1) plotting the blood clearance of [^{123}I]**5b** and [^{125}I]**11b**/[^{211}At]**11c** are provided. This material is available free of charge via the Internet at http://pubs.acs.org.

AUTHOR INFORMATION

Corresponding Author

*D. Scott Wilbur, Ph.D., Department of Radiation Oncology, University of Washington, Box 355016, 616 N.E. Northlake Place, Seattle, WA 98105. Phone: 206-616-9246. E-mail: dswilbur@u.washington.edu.

Notes

The authors declare no competing financial interest.

ACKNOWLEDGMENTS

We appreciate the funding provided by NIH (CA118940 and CA113431) for these studies.

ABBREVIATIONS:

ChT, chloramine-T; cpm, counts per minute; DTPA-CHX-A″; DIPE, diisopropylether; DMSO, dimethyl sulfoxide; DTPA, derivative with cyclohexane in backbone; DTT, dithiothreitol; FITC, fluorescein isothiocyanate; HCT, hematopoietic cell transplantation; IEF, isoelectric focusing; mAb, monoclonal antibody; MWCO, molecular weight cutoff; PBS, phosphate

buffered saline; %ID/g, percent injected dose/gram; pI, isoelectric point; rt, room temperature; SDS-PAGE, sodium dodecyl sulfate polyacrylamide gel electrophoresis; SE-HPLC, size-exclusion HPLC; TBI, total body irradiation; TCDI, 1,1′-thiocarbonyldiimidazole; TFA, trifluoroacetic acid

REFERENCES

(1) Bethge, W. A., Wilbur, D. S., and Sandmaier, B. M. (2006) Radioimmunotherapy as non-myeloablative conditioning for allogeneic marrow transplantation. *Leukemia & Lymphoma 47*, 1205−14.

(2) Sandmaier, B. M., Bethge, W. A., Wilbur, D. S., Hamlin, D. K., Santos, E. B., Brechbiel, M. W., Fisher, D. R., and Storb, R. (2002) Bismuth-213-labeled anti-CD45 radioimmunoconjugate to condition dogs for nonmyeloablative allogeneic marrow grafts. *Blood 100*, 318−26.

(3) Bethge, W. A., Wilbur, D. S., Storb, R., Hamlin, D. K., Santos, E. B., Brechbiel, M. W., Fisher, D. R., and Sandmaier, B. M. (2003) Selective T-cell ablation with bismuth-213-labeled anti-TCR$\alpha\beta$ as nonmyeloablative conditioning for allogeneic canine marrow transplantation. *Blood 101*, 5068−75.

(4) Wilbur, D. S., Thakar, M. S., Hamlin, D. K., Santos, E. B., Chyan, M. K., Nakamae, H., Pagel, J. M., Press, O. W., and Sandmaier, B. M. (2009) Reagents for Astatination of Biomolecules. 4. Comparison of Maleimido-*closo*-Decaborate(2-) and *meta*-[^{211}At]Astatobenzoate Conjugates for Labeling anti-CD45 Antibodies with [^{211}At]Astatine. *Bioconjugate Chem. 20*, 1983−1991.

(5) Wilbur, D. S., Chyan, M. K., Hamlin, D. K., Vessella, R. L., Wedge, T. J., and Hawthorne, M. F. (2007) Reagents for Astatination of Biomolecules. 2. Conjugation of Anionic Boron Cage Pendant Groups to a Protein Provides a Method for Direct Labeling that is Stable to in Vivo Deastatination. *Bioconjugate Chem. 18*, 1226−40.

(6) Nakamae, H., Wilbur, D. S., Hamlin, D. K., Thakar, M. S., Santos, E. B., Fisher, D. R., Kenoyer, A. L., Pagel, J. M., Press, O. W., Storb, R., and Sandmaier, B. M. (2009) Biodistributions, myelosuppression, and toxicities in mice treated with an anti-CD45 antibody labeled with the alpha-emitting radionuclides bismuth-213 or astatine-211. *Cancer Res. 69*, 2408−15.

(7) Wilbur, D. S., Hamlin, D. K., Vessella, R. L., Stray, J. E., Buhler, K. R., Stayton, P. S., Klumb, L. A., Pathare, P. M., and Weerawarna, S. A. (1996) Antibody fragments in tumor pretargeting. Evaluation of biotinylated Fab′ colocalization with recombinant streptavidin and avidin. *Bioconjugate Chem. 7*, 689−702.

(8) Wilbur, D. S., Vessella, R. L., Stray, J. E., Goffe, D. K., Blouke, K. A., and Atcher, R. W. (1993) Preparation and evaluation of *para*-[^{211}At]astatobenzoyl labeled anti-renal cell carcinoma antibody A6H F(ab′)$_2$. In vivo distribution comparison with *para*-[^{125}I]iodobenzoyl labeled A6H F(ab′)$_2$. *Nucl. Med. Biol. 20*, 917−27.

(9) Caniatti, M., Roccabianca, P., Scanziani, E., Paltrinieri, S., and Moore, P. F. (1996) Canine lymphoma: immunocytochemical analysis of fine-needle aspiration biopsy. *Veterinary Pathology 33*, 204−12.

(10) Bethge, W. A., Wilbur, D. S., Storb, R., Hamlin, D. K., Santos, E. B., Brechbiel, M. W., and Sandmaier, B. M. (2004) Radioimmunotherapy with Bismuth-213 as Conditioning for Nonmyeloablative Allogeneic Hematopoietic Cell Transplantation in Dogs: A Dose Deescalation Study. *Transplantation 78*, 352−359.

(11) Moore, P. F., Rossitto, P. V., Danilenko, D. M., Wielenga, J. J., Raff, R. F., and Severns, E. (1992) Monoclonal antibodies specific for canine CD4 and CD8 define functional T-lymphocyte subsets and high-density expression of CD4 by canine neutrophils. *Tissue Antigens 40*, 75−85.

(12) Denkers, E. Y., Badger, C. C., Ledbetter, J. A., and Bernstein, I. D. (1985) Influence of antibody isotype on passive serotherapy of lymphoma. *J. Immunol. 135*, 2183−6.

(13) Shelly, K., Knobler, C. B., and Hawthorne, M. F. (1992) Synthesis of Monosubstituted Derivatives of *closo*-Decahydrodecaborate(2-). X-ray Crystal Structures of [*closo*-2-$B_{10}H_9CO]^-$ and [*closo*-2-$B_{10}H_9NCO]^{2-}$. *Inorg. Chem. 31*, 2889−2892.

(14) Hawthorne, M. F., and Pilling, R. L. (1967) 5. Bis-(Triethylammonium) Decahydrodecaborate (2-). *Inorg. Synth. 9*, 16−19.

(15) Bianco, J. A., Sandmaier, B., Brown, P. A., Badger, C., Bernstein, I., Eary, J., Durack, L., Schuening, F., Storb, R., and Appelbaum, F. (1989) Specific Marrow Localization of an ^{131}I-labeled Anti-myeloid Antibody in Normal Dogs: Effects of a "Cold" Antibody Pretreatment Dose on Marrow Localization. *Exp. Hematol. 17*, 929−934.

(16) Wilbur, D. S. (2008) [^{211}At]Astatine-Labeled Compound Stability: Issues with Released [^{211}At]Astatide and Development of Labeling Reagents to Increase Stability. *Curr. Radiopharm. 1*, 144−176.

(17) Wilbur, D. S., Chyan, M. K., Hamlin, D. K., Kegley, B. B., Risler, R., Pathare, P. M., Quinn, J., Vessella, R. L., Foulon, C., Zalutsky, M., Wedge, T. J., and Hawthorne, M. F. (2004) Reagents for astatination of biomolecules: comparison of the in vivo distribution and stability of some radioiodinated/astatinated benzamidyl- and *nido*-carboranyl compounds. *Bioconjugate Chem. 15*, 203−23.

(18) Wilbur, D. S., Hamlin, D. K., Chyan, M. K., Kegley, B. B., Quinn, J., and Vessella, R. L. (2004) Biotin reagents in antibody pretargeting. 6. Synthesis and in vivo evaluation of astatinated and radioiodinated aryl- and *nido*-carboranyl-biotin derivatives. *Bioconjugate Chem. 15*, 601−16.

(19) Wilbur, D. S., Chyan, M. K., Hamlin, D. K., and Perry, M. A. (2009) Reagents for Astatination of Biomolecules. 3. Comparison of *closo*-Decaborate(2-) and *closo*-Dodecaborate(2-) Moieties as Reactive Groups for Labeling with Astatine-211. *Bioconjugate Chem. 20*, 591−602.

(20) Zalutsky, M. R., and Narula, A. S. (1988) Astatination of Proteins using an N-Succinimidyl Tri-*n*-Butylstannyl Benzoate Intermediate. *Appl. Radiat. Isot. 39*, 227−232.

(21) Zalutsky, M. R., Garg, P. K., Friedman, H. S., and Bigner, D. D. (1989) Labeling monoclonal antibodies and F(ab′)$_2$ fragments with the alpha-particle-emitting nuclide astatine-211: preservation of immunoreactivity and in vivo localizing capacity. *Proc. Natl. Acad. Sci. U.S.A. 86*, 7149−53.

(22) Steffen, A. C., Almqvist, Y., Chyan, M. K., Lundqvist, H., Tolmachev, V., Wilbur, D. S., and Carlsson, J. (2007) Biodistribution of ^{211}At labeled HER-2 binding affibody molecules in mice. *Oncol. Rep. 17*, 1141−7.

(23) Akizawa, H., Uehara, T., and Arano, Y. (2008) Renal uptake and metabolism of radiopharmaceuticals derived from peptides and proteins. *Adv. Drug Delivery Rev. 60*, 1319−28.

(24) Hermentin, P., Doenges, R., Franssen, U., Bieva, C., Vander Brugghen, F. J., Stryckmans, P., Friesen, H. J., Optaczy, B., Schneider, S., Ax, W., et al. (1990) Hinge-thiol coupling of monoclonal antibody to silanized iron oxide particles and evaluation of magnetic cell depletion. *Bioconjugate Chem. 1*, 411−8.

(25) del Rosario, R. B., Wahl, R. L., Brocchini, S. J., Lawton, R. G., and Smith, R. H. (1990) Sulfhydryl Site-Specific Cross-Linking and Labeling of Monoclonal Antibodies by a Fluorescent Equilibrium Transfer Alkylation Cross-Link Reagent. *Bioconjugate Chem. 1*, 51−59.

(26) Sun, M. M., Beam, K. S., Cerveny, C. G., Hamblett, K. J., Blackmore, R. S., Torgov, M. Y., Handley, F. G., Ihle, N. C., Senter, P. D., and Alley, S. C. (2005) Reduction-alkylation strategies for the modification of specific monoclonal antibody disulfides. *Bioconjugate Chem. 16*, 1282−90.

(27) Chen, Y., Kornblit, B., Hamlin, D. K., Sale, G. E., Santos, E. B., Wilbur, D. S., Storer, B. E., Storb, R., and Sandmaier, B. M. (2012) Durable Donor Engraftment after Radioimmunotherapy Using Alpha-Emitter Astatine-211-Labeled Anti-CD45 Antibody for Conditioning in Allogeneic Hematopoietic Cell Transplantation. *Blood*,in press.

(28) The cost of radionuclide in an early clinical study using ^{213}Bi-labeled anti-CD45 for conditioning in hematopoietic cell transplantation was estimated at $225,000. That amount is based on injection of 2 mCi/kg with an average 70 kg patient (probably higher) making the total injected 140 mCi/70 kg patient. Due to decay during labeling and QC (^{213}Bi half-life 45.6 min) one can expect a 50% yield at best, so one would have to start with a minimum of 280 mCi ^{213}Bi. That amount of ^{213}Bi activity could be obtained from a 150 mCi ^{225}Ac

generator if two injections were made (more injections would be problematic). At present the cost of ^{225}Ac is $1500/mCi so that generator would cost $225,000. In contrast, the longer half-life of ^{211}At makes it possible to treat with 0.2 mCi/kg. Therefore, a 70 kg patient might require 14 mCi of ^{211}At-labeled anti-CD45 for haploidentical transplantation. Currently the (internal) cost for cyclotron time is ~$600/hour and about 60 mCi could be obtained in a 3 h irradiation. With the current isolation procedure, 60%, or 36 mCi, could be isolated from the irradiated target. With labeling yields and QC time, one can estimate that at least 50% of the activity could be isolated as ^{211}At-labeled anti-CD45 mAb, providing at least 18 mCi for patient treatment. The estimated cost of ^{211}At might be $1800 for cyclotron time + $1200 for target, personnel and other costs, resulting in a total of ~$3000 for ^{211}At used in the treatment of a patient.

(29) Measurement of ^{211}At activity in the target must be considered an approximation due to attenuation and geometry.

(30) Pre-equilibration of the DIPE with 8 M HCl, and also pre-equilibration of 8 M HCl with DIPE, appears to provide better control of the amounts of reagents added and removed during the wet chemistry processing.

(31) Analysis of the amount of bismuth remaining in the 8 M HCl provided data that indicates 4 washes are required to minimize it.

(32) The neutralization process was begun with 4 N HCl to minimize the solution volume, but 0.5 N HCl was used when the pH was lower than 11 so that the targeted pH was not passed (i.e., becoming too acidic).

(33) In 48 ^{211}At-isolation experiments using this wet chemistry approach, radiochemical yields of 82.0% ± 18.1% (decay corrected; or 61.1% ± 14.3% actual) were obtained from targets containing 20.5 ± 2.2 mCi.

(34) Numbers in parentheses are those used to identify the dog.

(35) It should be noted that an amount of ~10-fold ^{211}At as ^{125}I was injected to obtain similar number of counts for each radionuclide at 21 h post injection due to the short half-life of ^{211}At. After 21 h approximately 13% of ^{211}At remains.

Bioconjugate Chemistry

Article

pubs.acs.org/bc

Synthesis of Tunable and Multifunctional Ni-Doped Near-Infrared QDs for Cancer Cell Targeting and Cellular Sorting

Narendra Singh,[†,⊥] Shobhit Charan,[†,‡,§,⊥] Kumar Sanjiv,[∥] Shih-Hsin Huang,[†] Yu-Chu Hsiao,[†] Chiung-Wen Kuo,[†] Fan-Ching Chien,[†] Te-Chang Lee,[∥] and Peilin Chen*[,†]

[†]Research Center for Applied Sciences, Academia Sinica, Taipei 115, Taiwan

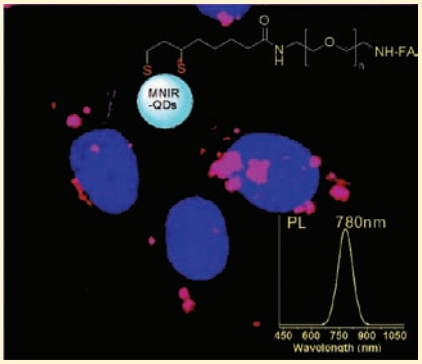
[‡]Department of Chemistry, National Taiwan University, Taipei 106, Taiwan

[§]Taiwan International Graduate Program, Nanoscience and Technology Program, Academia Sinica, Taipei 115, Taiwan

[∥]TIGP Molecular Medicine Program, Institute of Biomedical Sciences, Academia Sinica, Taipei- 115, Taiwan

Supporting Information

ABSTRACT: Here, we report the facile preparation of tunable magnetic Ni-doped near-infrared (NIR) quantum dots (MNIR-QDs) as an efficient probe for targeting, imaging, and cellular sorting applications. We synthesized the MNIR-QDs via a hot colloidal synthesis approach to yield monodisperse and tunable QDs. These hydrophobic QDs were structurally and compositionally characterized and further functionalized with amino-PEG and carboxyl-PEG to improve their biocompatibility. Since QDs are known to be toxic due to the presence of cadmium, we have evaluated the *in vitro* and *in vivo* toxicity of our surface-functionalized MNIR-QDs. Our results revealed that surface-functionalized MNIR-QDs did not exhibit significant toxicity at the concentrations used in the experiments and are therefore suitable for biological applications. For further *in vitro* applications, we covalently linked folic acid to the surface of amino-PEG-coated MNIR-QDs through NHS chemistry to target the folate receptors largely present in the HeLa cells to demonstrate the specific targeting and magnetic behavior of these MNIR-QDs. Improved specificity has been observed with treatment of HeLa cells with the folic acid-linked amino PEG-coated MNIR QDs (FA-PEG-MNIR-QDs) compared to the one without folic acid. Since the synthesized probe has magnetic property, we have also successfully demonstrated sorting between the cells which have taken up the probe with the use of a magnet. Our findings strongly suggest that these functionalized MNIR-QDs can be a potential probe for targeting, cellular sorting, and bioimaging applications.



INTRODUCTION

Conventional optical imaging probes such as fluorescent organic dyes and fluorescent proteins are already widely employed for cellular targeting and imaging applications.[1] However, photodegradation or photobleaching limits their application in long-term tracking experiments. Therefore, an optical imaging probe that is robust and less susceptible to photobleaching is highly desired. Semiconductor nanocrystals (NCs) or quantum dots (QDs) can satisfy these properties. In comparison to organic fluorophores, QDs are highly resistant to photobleaching, exhibit narrow spectral bandwidth, and are size-tunable, so as to be excitable using only a single wavelength. Therefore, it is easier to excite QDs for luminescence than it is to excite traditional fluorescent molecules that require a specific excitation wavelength, resulting in their broad applications for *in vitro* and *in vivo* applications.

Recently, colloidal core−shell QDs with surface bioconjugation have attracted tremendous attention due to their unique optical properties.[2−7]These core/shell QDs of II−VI semiconductors are classified into three categories:[8] (i) type-I QDs (e.g., CdSe/ZnS[9−12]), (ii) reverse type-I QDs (e.g., CdS/HgS,[13] CdS/CdSe,[14] and ZnSe/CdSe[15]), and (iii) type-II QDs (e.g., CdSe/ZnTe,[16] CdTe/ZnSe,[17] and alloyed $CdTe_xSe_{1-x}$/CdS QDs).[18] Typically, these QDs with cadmium cores are coated with a shell of higher energy band gap material (i.e., CdS or ZnS) to enhance the quantum yield (QY) and to protect them from oxidation. Additionally, the shell thickness also enables the emission wavelengths to be shifted toward the near-infrared region in the case of reverse type-I and type-II QDs. The latest advancement in QD research led to the development of water-soluble NIR-emitting QDs due to minimal auto fluorescence generated by water, hemoglobin, or amino acids in that region,[19] with simultaneous fluorescent and magnetic properties.[20−23] This combination of optical and magnetic properties will enable simultaneous biolabeling/imaging and magnet-assisted cellular sorting applications. The remarkable properties obtained by magnetic doping enable fluorescent QDs to exhibit superparamagnetic,[24] paramagnetic,[25,26] or ferromagnetic properties[22,27] in one system, i.e., as a multifunctional probe for biomedical application.[25] However, most of these reports are based on

Received: August 10, 2011
Revised: January 5, 2012
Published: February 6, 2012

ACS Publications © 2012 American Chemical Society

QDs-magnetic nanoparticle hybrids or nanocomposites (QDs-iron oxides), and there are very few reports with doped magnetic impurity especially in NIR-emitting QDs for biological applications.[25,26] This can possibly be due to synthetic challenges, toxicity, aggregation, and loss of optical properties when exposed to the biological environment. Therefore, magnetic QDs possessing improved QY and long-term colloidal stability with biocompatible surface functionalization are highly desired for biological applications.

Herein, nickel-doped quantum dots are explored as an alternative ferromagnetic material for specific targeting, cellular sorting, and bioimaging applications. We have synthesized monodisperse Ni-doped CdTeSe/CdS QDs (MNIR-QDs) via modified one-pot synthesis[28] with improved quantum yield and ferromagnetic properties. To our knowledge, there are no reports yet for nickel doping inside NIR-emitting QDs. Because of toxicity concerns associated with QDs, we then systematically modified the surface of these MNIR-QDs with amino-PEG and carboxyl-PEG to provide colloidal stability and biocompatibility followed by *in vitro* and *in vivo* toxicity assessment. The toxicity assessment showed no significant toxicity of these surface functionalized MNIR-QDs, thus reflecting functionalized MNIR-QDs as a safe material for biological applications. Furthermore, covalently linking the amino-PEG-MNIR-QDs with folic acid (FA) imparted specific targeting in HeLa cells followed by a magnet-assisted cellular sorting application, thereby indicating their multifunctional capability. Hence, our results demonstrated that the functionalized MNIR-QDs can be considered as a promising probe for simultaneous specific targeting, imaging, and cellular sorting applications.

EXPERIMENTAL SECTION

Materials. Cadmium oxide (CdO), selenium (Se) powder, tellurium (Te) powder, sulfur (S) powder, nickel(II) acetylacetonate [$Ni(acac)_2$], trioctylphosphine (TOP), trioctylphosphine oxide (TOPO, 99%), stearic acid (St), folic acid (FA), *N*-hydroxidesuccinimide (NHS), thiotic acid (TA), polyethylene glycol (PEG), molecular weight 400, and solvents were purchased from Sigma Aldrich. PEG derivatives of DHLA-PEG_{400}-NH_2 (amino-PEG) and DHLA-PEG_{400}-$NHCOCH_2COOH$ (carboxyl-PEG) were prepared by reported protocols. The dihydrolipoic acid (DHLA) terminal end of the compound was obtained after the reduction of thiotic acid.[29,30] The structure of these compounds is available in the Supporting Information (Figure S1).

Instrumentation. Transmission electron microscopy (TEM)/EDAX samples were performed on a JEOL JEM-2100F that was operated at 200 kev. Powder X-ray diffraction (XRD) measurements were performed using a Philips X'Pert-Pro diffractometer with Cu−K_α radiation with a wavelength of λ = 1.540 Å. X-ray photoelectron spectra (XPS) were recorded with a PHI 5000 Versa Probe (Chigaski, Japan) XPS system. Dynamic light scattering (DLS) and zeta potential were performed at room temperature by using a 35 mW diode laser on a Brookhaven 90Plus Particle Size Analyzer. FT-IR spectra were recorded as attenuated total reflectance (ATR) on a Perkin-Elmer Spectrum between 400 and 4000 cm^{-1}. The magnetic properties of MNIR-QDs were measured using a superconducting quantum interference device (SQUID) magnetometer with a maximum field of 20000 Oe. UV−visible absorption and photoluminescence spectra were measured with a Molecular Devices Spectra Max M_2^e spectrophotometer, a USB 2000 miniature Fiber Optics spectrometer USB2E7502, and an Agilent 8453 spectrophotometer. For both absorption and photoluminescence spectra measurements, a glass cuvette with a 3-mm and 10-mm light path length was used, and the spectra were recorded from 400 to 1100 nm. The excitation wavelength of 488 nm was used for the emission spectra of MNIR-QDs. The quantum yield of MNIR-QDs was determined by comparison to rhodamine 101 dye by applying the reported formula $QY_{Qds} = QY_{dye} \times (absorbance_{dye}/absorbance_{QDs}) \times$ (peak area QDs/peak area dye) $\times (\eta_{QDs}\ solvent)^2/(\eta_{Dye}\ solvent)$.[29] The cellular images were obtained by laser scanning microscope (Leica, SP5).

Synthesis of MNIR-QDs. Briefly, a mixture of molar solutions (1M) of Se and Te in the ratio of 75:25 was prepared and stored at room temperature under argon gas. Separately, cadmium oxide (0.514 g, 4 mmol) and stearic acid (4 g) were poured in a three-neck flask and heated to 150 °C for 10 min to form colorless solution of cadmium stearate and cooled to RT. Later on, nickel acetylacetonate (0.256 g, 1 mmol) and TOPO (8 g) were added, and the mixture was heated at ∼300 °C for 1 h under argon gas. To this hot reaction mixture, 1 mL (1M) of the TOP:Se:Te was injected under vigorous stirring, and the reaction mixture temperature was decreased and maintained at 230 °C for 5−10 min for particle growth. Then, 1 mL (1M) of oleylamine-sulfur solution was slowly injected at 230 °C into the reaction mixture solution. After the addition, the temperature was decreased to 200 °C, and stirring was continued for an hour to complete the reaction. After 1 h of stirring, the reaction mixture was cooled to RT, and 5 mL of toluene was added to protect the solidification of TOPO at RT. Finally, quantum dots were precipitated by the addition of methanol, centrifuged at 7000 rpm, and redispersed in hexane. This experimental condition is purely applied to achieve a reproducible 780 nm wavelength. Experimental temperature conditions may vary from 5 to 15 °C to achieve different emission wavelengths.

Before utilizing these quantum dots for surface functionalization, the hexane dispersion of QDs were purified via a syringe filter of 0.45 μm pore diameter for complete removal of unreacted precursor. This purification cycle was repeated twice, and the hexane solution of purified QDs was stored at RT under argon atmosphere.

Surface Functionalization of MNIR-QDs with Amino-PEG and Carboxyl-PEG. The surface functionalization of MNIR-QDs was achieved by drying the hexane solutions of MNIR-QDs (1 mL, ∼4 mg) through an N_2 stream in a 2 mL glass vial. To the dried product, 20 μL of amino-PEG and 50 μL of ethanol were added, and the reaction mixture was stirred overnight at 60−70 °C under argon atmosphere. After overnight stirring, a homogeneous solution was obtained, which was further precipitated by adding the solvent mixture of hexane/ethanol/chloroform in the ratio of 5:1:0.5, followed by centrifugation at 5000 rpm for 5 min. The resulting pellet was washed with the solvent mixture for 2−3 times, dried under a N_2 stream, and redispersed in distilled water. Finally, the aqueous QDs solution was filtered through a 200-nm filter and stored at 4 °C.

A similar procedure was applied for carboxyl-PEG functionalization over MNIR-QDs. The surface functionalized carboxyl-PEG-MNIR-QDs were redispersed in 1 M NaOH solution, which was filtered through 200-nm filter. For biological applications, both amino and carboxyl-PEG-MNIR-QDs were dispersed in PBS, pH 7.4

Preparation of FA-PEG-MNIR-QDs for Specific Targeting. To decorate the MNIR-QDs with specific targeting functionality, we conjugated the folic acid to target the folate

receptor overexpressed inside HeLa cells. Initially, folic acid (220 mg) and *N*-hydroxysuccinimide (115 mg, NHS) were dissolved in DMSO (5 mL) and cooled to 20 °C followed by stirring for 5 min. After which, a solution of DCC (206 mg dissolved in 5 mL of DMSO) was slowly added and stirred overnight at room temperature, centrifuged at 14000 rpm, and filtered through a syringe filter with 200-nm pore diameter to obtain a highly reactive intermediate, i.e., FA-NHS. This intermediate can subsequently react with amino groups present in the amino-PEG-MNIR-QDs to form FA-PEG-MNIR-QDs. To achieve this, an aqueous solution of QDs was added to this FA-NHS solution at a ratio of 1:10 and stirred for 4 h at RT. After 4 h of stirring, the QDs were precipitated by adding water and centrifuged for 5 min at 7000 rpm. The QDs that were conjugated with FA settled down as pellets were purified with DI water and redispersed in PBS, pH 7.4

Cytotoxicity Evaluation. The human cervical epithelioid carcinoma (HeLa) cell line was ordered from Biosource Collection and Research Center (BCRC, Hsinchu, Taiwan). Cells were maintained in Dulbecco's Modified Eagle's Medium (DMEM) (GIBCO, Invitrogen, Carlsbad, CA) supplemented with 10% fetal bovine serum (FBS) (Hyclone, Logan, UT) and 1% penicillin−streptomycin−ampicillin antibiotic mixture (Hyclone) in a 37 °C, 5% CO_2 incubator (Thermo Forma). Cells were plated at a seeding density of 1×10^5 cells per well onto a 96 well plates for 18 h to allow the cells to attach for MTT assay measurements. Cells were treated with various concentrations ranging from 0.1 nM to 100 nM of amino-PEG-MNIR-QDs, carboxyl-PEG-MNIR-QDs, and FA-PEG-MNIR-QDs for 4 h. Control experiments were carried out with cells treated with an equivalent volume of medium without quantum dots. Cell viability was measured by MTT assay kit (Sigma) by following the manufacturer's protocol. Typically, a PBS solution containing 10 μL of 5 mg/mL of 3-[4,5-dimethylthiazol-2-yl]-2,5-diphenyltetrazoliumbromide (MTT) solution was added to each well and incubated for an additional 4 h. After mixing, 90 μL of MTT solubilization solution was added to each well. The stain was aspirated, and purple colored crystals were dissolved with acidic isopropyl alcohol. The optical density (OD) of the solvent was measured at 570 nm using a microplate reader (Molecular devices Spectra Max M_2^e spectrophotometer). All experiments were carried out three times.

Cellular Separation and Confocal Imaging of MNIR-QDs. Typically, cells (~1×10^5 cells) were grown on a 35-mm cell culture dish containing a glass coverslip of 24 mm in diameter (Fisher Scientific). After overnight incubation at 37 °C, the medium was removed, and cells were washed three times with PBS. The amino-PEG-MNIR-QDs or FA-PEG-MNIR-QDs were added to the cells with a concentration of 20 nM and incubated for 4 h. Later on, these cells were detached from the surface by the addition of trypsin and suspended in fresh medium and transferred to a 1.5 mL microtube. Cellular sorting was performed by placing a 1.5 mL microtube on the side wall of a magnet (1.2 T) for 10 min. After the sorting, the supernatant with unsorted cells was pipetted out and plated onto a culture disk, the magnet was then removed, and the sorted cells collected as a pellet on the side wall of the microtube was resuspended in medium and plated onto a culture disk. These (sorted and unsorted) cells were incubated for 6 h for reattachment on the surface of a glass coverslip. The fluorescent images for cellular sorting were obtained using a Leica confocal microscope SP5 with a 40× objective lens with excitation and emission wavelengths of 488 nm and 780 nm, respectively. For visualizing the location of surface-modified MNIR-QDs, the cells were incubated with 4 nM of quantum dots at 37 °C, fixed with 3.7% formaldehyde solution, and stained with DAPI at room temperature, followed by washing with PBS, and studied under confocal microscope using a 63× objective.

***In Vivo* Toxicity Evaluation of Functionalized MNIR-QDs in BALB/C Mice.** Hematological and biochemical blood parameters and the histopathology of the liver, kidney, lung, and spleen in mice treated with QDs were examined at the Pathology Core of Institute of Biomedical Sciences, Academia Sinica, and Taiwan Mouse Clinic. The typical procedure is as follows: mice were injected intravenously with 100 μL of MNIR-QDs with 100, 400, and 800 pmol concentration. After 15 days of administration, mice were sacrificed, and blood and other organs were collected for analysis. Hematological data were analyzed with an Abbott Cell-Dyn 3700 machine, and biochemical data were analyzed with a Fuji Dri-Chem Clinical Chemistry Analyzer FDC 3500. Use of the mouse model for toxicity was approved by and followed the guidelines of the Academia Sinica Institutional Animal Care and Utilization Committee. Male 6-week-old BALB/c mice were obtained from a breeding stock of Institute of Biomedical Sciences (IBMS), Academia Sinica, Taipei, Taiwan. The animals were housed in a specific pathogen-free environment under controlled conditions of light and humidity and were given sterilized food and water ad libitum.

Biodistribution. From the ICP-MS analysis, the 800 pmol MNIR-QDs represent 22.41 μg of Cd and 22.95 μg of Cd in amino and carboxyl modified MNIR QDs. An intravenous tail vein injection with an injection dose was given to the animal model. The typical procedure is as follows: mice were injected intravenously with 100 μL of MNIR-QDs with the mentioned concentration, and 15 days after administration, mice were sacrificed, and the major organs were collected for analysis. Saline solution was used as the control. Microwave-assisted digestion was adopted for 90 min to dissolve Cd ions out of the organs using aqua regia. Later, 0.1 mL of treated solution was diluted to 50 mL in a volumetric flask. The signal of dissolved Cd ion solution was measured by ICP-MS, and the concentration was calculated using the calibration method. ICP-MS (inductively coupled plasma mass spectrometer) (Thermo-II) was used with direct nebulization in normal mode using optimized conditions consisting of an Xs skimmer cone with a platinum sampler cone. The extraction voltage was typically −573 V, the Rf power was 1,250 W, focus voltage was 17.5 V, and the nebulizer gas flow rate was 0.91 L/min. Dwell times were 10 ms for ^{111}Cd, and 100 sweeps were required per replicate and 10 replicates per samples.

■ RESULTS AND DISCUSSION

Characterization of MNIR-QDs. The MNIR-QDs were synthesized via the modified one-pot method as reported elsewhere.[25] The as prepared MNIR-QDs in Figure 1a show the tunable photoluminescence spectra from 750 to 820 nm, which can be obtained by a precise controlled temperature protocol. Such tunable characteristics in magnetic impurity doped NIR-QDs are reported for the first time. In addition, the quantum yield (QY) of the MNIR-QDs was found to be ~20% when compared to that of rhodamine 101 dye and is higher compared to reported synthetic methods showing 10%[31] and 15%[25] with a similar synthetic strategy.

dx.doi.org/10.1021/bc200435e | *Bioconjugate Chem.* 2012, 23, 421−430

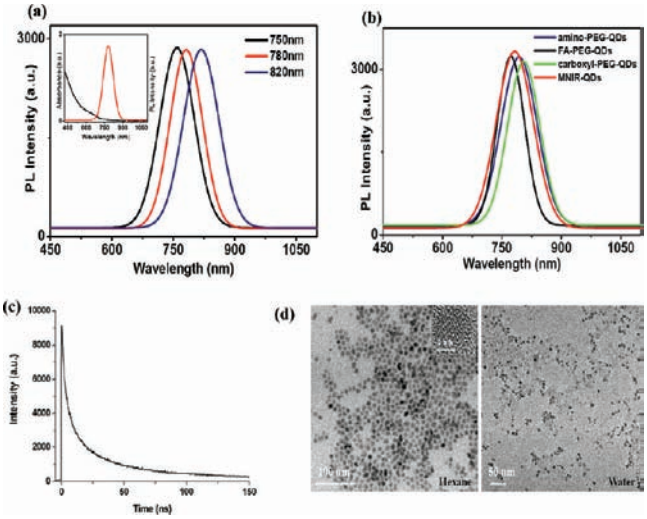


Figure 1. (a) Tunable photoluminescence spectra of MNIR-QDs. Excitation wavelength: 488 nm. Inset: UV−visible absorption spectra and emission spectra of 780 nm MNIR-QDs. (b) PL spectra of MNIR-QDs of emission wavelength 780 nm before and after surface functionalization. The spectra shows the red shift in the emission wavelength of amino-PEG-MNIR-QDs and carboxyl-PEG-MNIR-QDs while FA-PEG-MNIR-QDs blue-shifted compared to nonmodified QDs. (c) Fluorescence lifetime spectrum of MNIR-QDs. The excitation wavelength was 467 nm. The lifetime was calculated to be 70.6 ns. (d) TEM images of MNIR-QDs dispersed in hexane (left) and water (right).

In this experiment, we chose QDs with an emission wavelength of 780 nm for further studies. Surface modification with amino-PEG, carboxyl-PEG, and folic acid modified MNIR-QDs showed (Figure 1b) slight changes in the fluorescence spectra, but no changes in the fluorescence intensity was observed even after a few weeks of storage at 4 °C. This indicates that the synthesized and PEG-modified MNIR-QDs have improved optical properties and colloidal stability in contrast with lysine,[25] thiol,[18] or polymeric-ligand[32] coated NIR-QDs. This improvement can be due to the stability of -PEG at neutral or low pH conditions. Furthermore, PEG modification helps to reduce the toxicity and can be conjugated with biomolecules for *in vitro* and *in vivo* targeting applications.[32]

To further investigate the fluorescence properties of MNIR-QDs, we performed the time-resolved photoluminescence measurements as shown in Figure 1c. The normalized decay curve was well-fitted by a single exponential curve. From the fitting results, the lifetime was calculated to be 70.6 ns (Figure 1c), which is two or three times larger than that of the type-I core/shell QDs (e.g., CdSe/ZnS). Moreover, the lifetime of type-II QDs (CdTe/CdSe) is about ∼57 ns, as reported by Kim et al.[16] It was suggested that the longer decay lifetime may be due to the spatial separation of charges in the type-II core/shell structure. The lifetime of NIR core/shell QDs, including CdTe,[33] CdTe/CdS,[34] and CdTe/CdSe,[35] was reported to be in the range of 10−30 ns. It was explained that the lifetime increased with increasing inorganic shell (CdS or CdSe) over core QDs, where the contribution of the nonradiative process to exciton decay is significantly reduced after shell growth. However, a much longer lifetime (70−80 ns) was reported for CdSeTe/CdS[36] and Mn-doped CdSeTe/CdS QDs.[28] In the Ni doped CdTeSe/CdS QDs reported here, we assume that the structure of MNIR-QDs is similar to that of CdTe/CdSe, where CdTe is the core, and CdSe is the shell over CdTe. In a recent study, it was reported by Baily et al. that the nucleation rate of CdTe was faster than that of CdSe.[31] It was also assumed that the magnetic Ni was embedded in the matrix of CdTeSe, which was further over coated with CdS for oxidation protection.

High resolution TEM (HRTEM) micrograph indicates that the particle size was in the range of 6−8 nm with monodisperse distribution (Figure 1d). Furthermore, selected area electron diffractions (SAED) (Supporting Information, Figure S2) confirmed that most of the synthesized MNIR-QDs were polycrystalline, displaying a wurtzite structure. Additionally, crystal structure of the synthesized MNIR-QDs was also examined by X-ray diffraction (XRD) analysis. In Figure 2a, the XRD pattern (a, b, and d) is the calculated standard XRD database of Joint Committee on Powder Diffraction Standards (JCPDS) used for the comparison with the experimental XRD pattern (c). The calculated spectra are different due to the different crystal structures of CdTe, CdTeSe, and CdSe, which were used to compare the XRD pattern of our synthesized QDs. For example, the CdTeSe XRD pattern contained the mixed XRD pattern of CdTe and CdSe; therefore, we compared our CdTeSe based quantum dots with all the possible XRD patterns to reveals their correct crystal structure.The diffraction peaks appeared between the wurtzite diffraction pattern of bulk CdTe (JCPDS number 82-0474), CdSe (JCPDS number 77-2307) and CdS where the broad Bragg scattering peaks can be attributed to the 002, 110, and 201 lattice planes of the hexagonal pattern of CdTeSe nanocrystal shown in Figure 2a, which are consistent with the bulk CdTeSe (JCPDS number 41-1325) wurtzite structure.

The Bragg peaks were found to be broad due to poor crystallinity and their amorphous nature. In addition, no separate peaks of CdSe, CdS, or traces of nickel nanoparticles were observed, thereby indicating that nickel was perfectly embedded or doped inside the matrix of MNIR-QDs.[28,36] X-ray photoelectron spectroscopy (XPS) measurements were performed to investigate the presence of elements in MNIR-QDs. The full scan survey spectra (Supporting Information, Figure S3a) were obtained using 171-eV pass energy. To measure the exact surface energy of each element, the high resolution spectra were also recorded (Supporting Information, Figure S3b). The Ni($2p_{3/2}$) spectra split into two lines at ∼856 eV and ∼861 eV, as shown in Figure 2b. The peak at 856 eV is the main peak, and the other is the satellite peak which matched well with the reported values.[37] Additionally, due to better penetration depth of 1 μm than XPS,[28] elemental analysis by EDAX was also performed and indicated the presence of all composition elements, Cd, Te, Se, S, and Ni (Supporting Information, Figure S4). The stoichiometry ratio of the elements for Cd/Te/Se/S/Ni was measured to be 1:0.15:0.35:0.68:0.015.

For biological applications, hydrodynamic diameter and colloidal stability in aqueous media are of utmost importance. Therefore, dynamic light scattering analysis of functionalized MNIR-QDs indicated the hydrodynamic diameter of 13.5, 18.4, and 28.4 nm for amino-PEG, carboxyl-PEG, and folic acid capped MNIR-QDs, respectively (Supporting Information, Figure S5). In addition, the zeta potential of +21.5 mV, −28 mV, and −15.4 mV was measured for amino, carboxyl, and FA-coated MNIR-QDs, respectively, indicating good colloidal stability in aqueous medium due to the presence of PEG coating (i.e., to protect against aggregation in aqueous medium).[29]

dx.doi.org/10.1021/bc200435e | *Bioconjugate Chem.* 2012, 23, 421−430

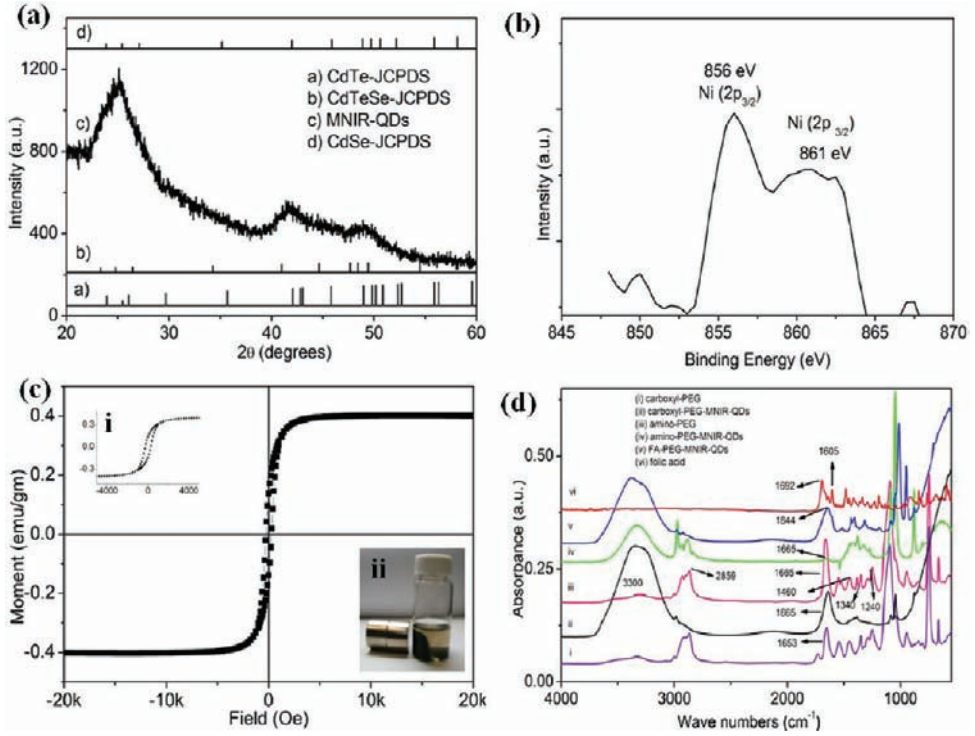
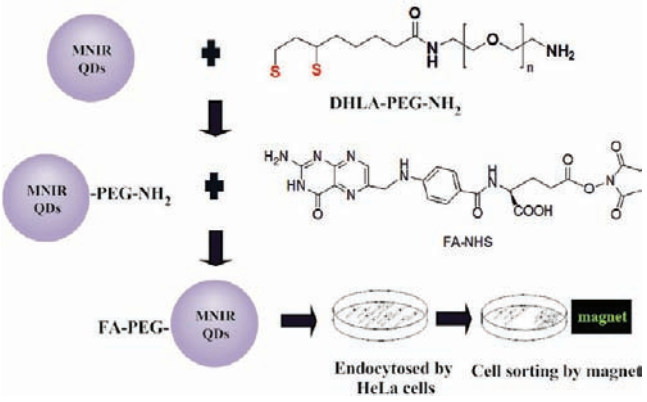


Figure 2. (a) X-ray diffraction spectrum of MNIR-QDs against standard QDs. [The XRD pattern (a, b, and d) are the calculated standard XRD database of Joint Committee on Powder Diffraction Standards (JCPDS) used for the comparison with the experimental XRD pattern (c)]. (b) High resolution XPS of the Ni($2p_{3/2}$) peak. (c) Magnetization (M) versus magnetic field (H) at RT. (i) The inset showing the open hysteresis in the low field region and (ii) photographs showing magnetic separation of MNIR-QDs in hexane solution. (d) IR spectra of surface-modified MNIR-QDs.

Since, the nickel doping provides ferromagnetic characteristics to MNIR-QDs for cellular sorting applications, superconducting quantum interference device (SQUID) measurement was employed for magnetic characterization as shown in Figure 2c. The presence of Ni in QDs yielded the hysteresis curves, confirming the characteristic nature of ferromagnetic material at room temperature (RT). The coercivity (Hc) of MNIR-QDs was measured and found to be 300 Oe at RT. Figure 2c, ii, shows magnetic separation of the prepared MNIR-QDs after an applied external magnetic field. A dark brown precipitate was collected on the side wall of the sample tube near the magnet, leaving the solution clear and transparent, and thereby indicating magnetic attraction due to its ferromagnetic nature. This property could allow MNIR-QDs to be employed or used for cellular sorting applications.

Surface Modification of MNIR-QDs for Targeting and Imaging. For biological applications, it is very important to engineer the MNIR-QDs such that they are soluble in water and biocompatible. In this experiment, the surface of the hydrophobic QDs were decorated with amino-PEG and carboxyl-PEG by a reported method[29] to render them with water-soluble and biocompatible property. To prove their biocompatibility, *in vitro* and *in vivo* toxicity assessments were performed. Subsequently, for specific targeting, the amino-PEG-MNIR-QDs were further covalently conjugated with folic acid via NHS coupling (Scheme 1) and referred to as FA-PEG-MNIR-QDs to target the folate receptors present over the cell membrane. To further confirm the successful conjugation of folic acid, the emission spectra of FA-conjugated MNIR-QDs were examined at an excitation wavelength of 380 nm, where the emission peak of folic acid was observed at 450 nm and that of the QDs at 765 nm (Supporting Information, Figure S6).

Scheme 1. Schematic Diagram for Surface Modification of MNIR-QDs



IR spectroscopy was used for the identification of the functional groups present over the surface of QDs after surface modification with carboxyl-PEG, amino-PEG, and FA. Figure 2d showed the absorption bands at 2859 cm^{-1}, 1460 cm^{-1}, 1340 cm^{-1} that correspond to C−H vibrations, bands centered at 1090 cm^{-1} and 1240 cm^{-1} originated from the C−O−C bonds of PEG, and the 3300 cm^{-1} and 1665 cm^{-1} were ascribed to νN−H of amine and amide bands, respectively, for all the surface-modified MNIR-QDs. However, FA-PEG-MNIR-QDs showed slightly shifted amide peaks (~1644 cm^{-1}) toward lower wave numbers which merged with the other folic acid peaks of amino-PEG. Additionally, no peaks were observed for TOPO (Supporting Information, Figure S7) in the surface-modified MNIR-QDs suggesting the successful coating of carboxyl-PEG, amino-PEG and FA over the surface of MNIR-QDs.

dx.doi.org/10.1021/bc200435e | *Bioconjugate Chem.* 2012, 23, 421−430

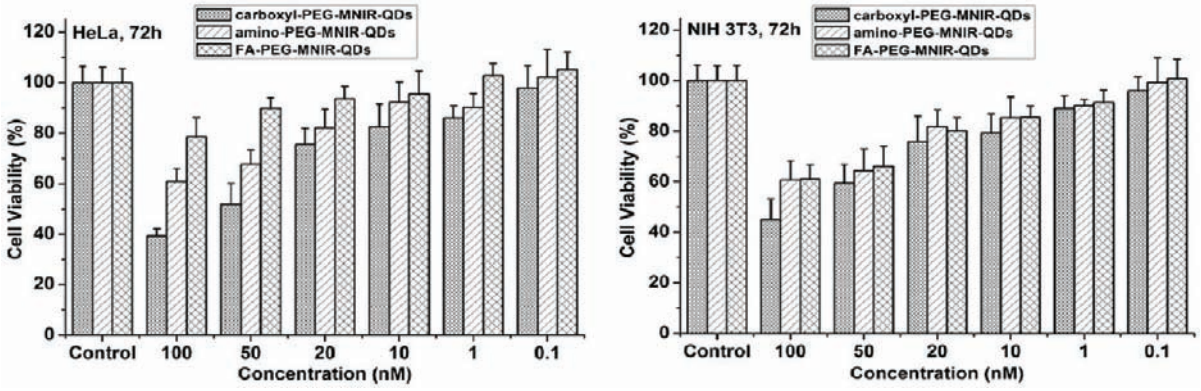


Figure 3. Cell viability assay (MTT assay) of HeLa and NIH 3T3 cells treated with different concentrations of carboxyl-PEG-MNIR-QDs, amino-PEG-MNIR-QDs, and FA-PEG-MNIR-QDs. The highest toxicity was monitored at the concentration of 100 nM of carboxyl-PEG-MNIR-QDs, amino-PEG- MNIR-QDs, and FA-PEG-MNIR-QDs after 72 h of incubation.

***In Vitro* Cytotoxicity.** The toxicity issue of cadmium-based QDs for biological applications have been reported by several groups.[38,39] The presence of cadmium ions was found to be the major reason for the measured cytotoxicity. To overcome the toxicity of QDs, a layer of inorganic material was used to coat the core QDs, which protected the core cadmium from oxidation and photobleaching. It has been shown that no significant toxicity was observed for the well-coated core/shell QDs when used in both *in vitro* and *in vivo* experiments.[40] Therefore, it is necessary to check the cytotoxicity of the functionalized MNIR-QDs before they can be used for subsequent biological applications. In this experiment, we treated HeLa cells with different concentrations of amino-PEG-MNIR-QDs, carboxyl-PEG-MNIR-QDs, and FA-PEG-MNIR-QDs for different time points and assessed cell viability by the MTT assay. Figure 3 shows the results of the cytotoxicity measurements in HeLa cells and NIH 3T3 cells after 72 h of incubation with surface-modified MNIR-QDs. It can be seen that the highest toxicity was at a concentration of 100 nM, and ~40%, ~61%, and ~80% of HeLa cells and ~45%, ~61%, and ~61% for NIH 3T3 cells were found to be viable after 72 h of incubation with carboxyl-PEG-MNIR-QDs, amino-PEG-MNIR-QDs, and FA-PEG-MNIR-QDs, respectively. At lower concentrations, no significant cytotoxicity was observed for carboxyl-PEG-MNIR-QDs, amino-PEG-MNIR-QDs, and FA-PEG-MNIR-QDs. The cytotoxicity data at different points, i.e., 1 h, 4 h, 24 h, and 48 h are available in Supporting Information (Figure S8). Moreover, similar cell viability was observed for FA and amino PEG-MNIR-QDs in NIH 3T3 due to the lack of overexpression of folate receptors; therefore, the rate of cellular uptake for both will be the same. Additionally, Figure 4 showed the cell viability of HeLa cells treated with 20 nM FA-PEG-MNIR-QDs and amino-PEG-MNIR-QDs at different time points. The same concentration was further used for targeting and cellular sorting applications.

Targeting and Cellular Sorting Applications. There are three distinct functions of the synthesized surface functionalized MNIR-QDs: robust NIR emission, specific targeting, and ferromagnetic property for magnet-assisted cellular sorting applications. To test the ferromagnetic property of the MNIR-QDs, a 20 nM solution of FA-PEG-MNIR-QDs was incubated with HeLa cells for 4 h and then was separated by a strong magnet (Table 1). Shown in Figure 5a is the confocal image of the HeLa cells separated by a magnetic field, where about 87% of HeLa cells were found to exhibit NIR emission. The confocal

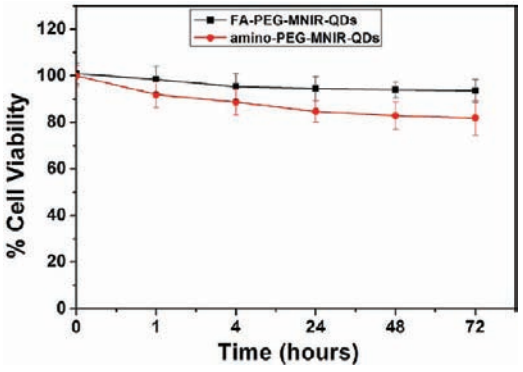


Figure 4. Cell viability of HeLa cells treated with 20 nM FA-PEG-MNIR-QDs and amino-PEG-MNIR-QDs at different time points.

image of the remaining HeLa cells is shown in Figure 5b. It was found that most of the HeLa cells that incorporated FA-PEG-MNIR-QDs can be separated by a magnetic field, indicating a potential application for cellular sorting by the MNIR-QDs. It is known that there are folate receptors present over the surface of the HeLa cells, which can bind specifically to the folic acid. Therefore, when the HeLa cells were incubated with FA-PEG-MNIR-QDs, they bind to the overexpressed receptor over the outer cell plasma membrane as evident by the confocal image in Figure 5c. In addition, the cellular sorting of HeLa cells was also performed with amino-PEG-MNIR-QDs under conditions similar to those of folic acid conjugated MNIR-QDs. Figure 5d clearly indicates the significantly less cellular sorting of 15% with some nonspecific binding of amino-PEG-QDs in contrast with FA-PEG-MNIR QDs, thus, demonstrating the specificity and selectivity of FA-PEG-MNIR-QDs.

Furthermore, to examine the uptake efficiency, we used NIH 3T3 cells as a negative control. Typically, 3T3 cells were also exposed with the same concentration of FA-PEG-MNIR-QDs as that used for HeLa cells (4 nM QDs incubated for 4 h) and examined the uptake efficiency of QDs by using the Leica confocal microscope. We observed that the uptake of QDs in NIH 3T3 cells (Supporting Information, Figure S9) is significantly less in contrast with that of HeLa cells (Figure 5c and f), possibly due to the absence of the overexpression of folic acid receptor in NIH 3T3 cells. Thus, these observations indicated the selective targeting potential of our synthesized QD based probe.

dx.doi.org/10.1021/bc200435e | *Bioconjugate Chem.* 2012, 23, 421–430

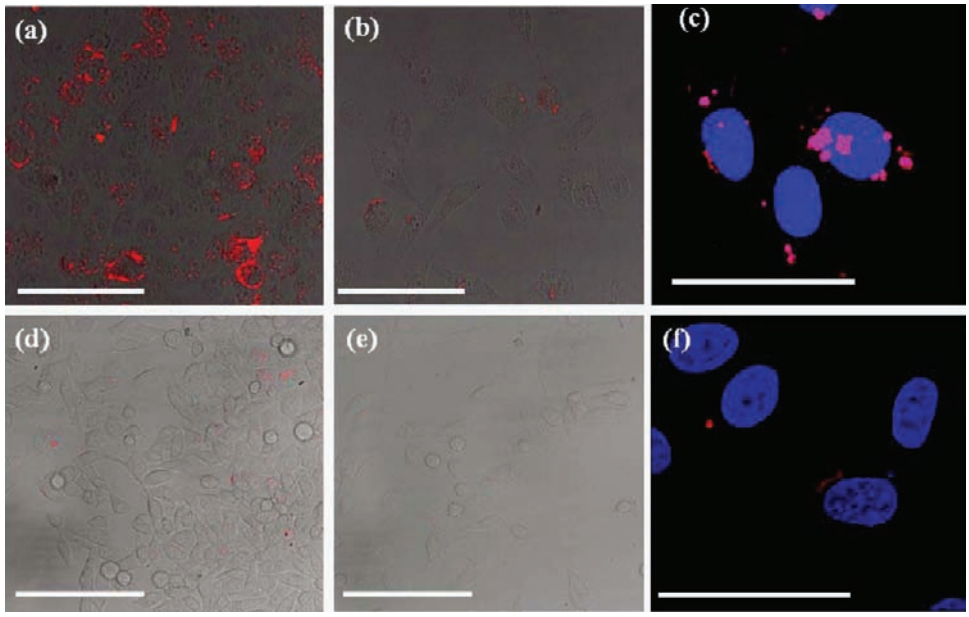


Figure 5. Confocal microscopy images of HeLa cells after incubation with amino-PEG-MNIR-QDs or FA-PEG-MNIR-QDs for 4 h for specific targeting and cellular sorting with a laser excitation wavelength of 488 nm; fluorescence merged images of HeLa cells. (a) Live sorted cells labeled with FA-PEG-MNIR-QDs. (b) Live unsorted cells labeled with FA-PEG-MNIR-QDs. (c) fixed cells labeled with FA-PEG-MNIR-QDs. (d) Live Sorted cells labeled with amino-PEG-MNIR-QDs. (e) Live unsorted cells labeled with amino-PEG-MNIR-QDs. (f) Fixed cells labeled with amino-PEG- MNIR-QDs. (Concentration used for cellular sorting in panels a, b, d,and e = 20 nM and for targeting panels c and f = 4 nM.) (Red. QDs; blue, nucleus. Bar: 100 μm (a, b, d, and e) and 50 μm (c and f).

Table 1. Experimental Conditions for Cellular Sorting of MNIR-QDs in HeLa Cells

MNIR-QDs	cell numbers	QDs concn	incubation time	sorted HeLa cells	unsorted HeLa cells	magnet strength	applied time
FA-PEG-MNIR-QDs	10^5	20 nM	4 h	87%	13%	1.2 T	10 min
amino-PEG-MNIR-QDs	10^5	20 nM	4 h	15%	85%	1.2 T	10 min

***In Vivo* Toxicity Measurement.** *In vitro* cytotoxicity measurements may not reflect the same response when exposed to an *in vivo* environment. Therefore, *in vivo* toxicity measurements are highly desired. In this experiment, we conducted short-term *in vivo* toxicity assessment of functionalized MNIR-QDs. Both amino-PEG-MNIR-QDs and carboxyl-PEG-MNIR-QDs were injected with 100 μL of MNIR-QDs with 100, 400, and 800 pmol concentration to BALB/c mice model via tail vein injection. After 15 days, mice were sacrificed, and blood and major organs were harvested for hematological and clinical biochemistry studies.

Histological Analysis. Aside from blood parameters, histological assessment of major organs was conducted in a BALB/c mice model treated with MNIR-QDs. The organs (kidney, heart, spleen, lung, and liver) were harvested at 15 days after treatment. On histopathological examination of the liver, lung, heart, and spleen, no sign of any toxicity was observed for mice treated with amino-PEG-MNIR-QDs and carboxyl-PEG-MNIR-QDs. However, amino-PEG-MNIR-QDs treated mice showed tubule dilation and vacuolar degeneration in some areas of the kidney. Dilatation of tubules and vacuolar degeneration are reversible changes that are associated with heavy metal excretion through the kidney. In carboxyl-PEG functionalized MNIR-QD treated mice, a few focal necrotic tubular degenerations in the kidney as well as focal infiltration of neutrophils in liver were observed. On the basis of the enzyme profile and histopathological examination, we concluded that the toxicity was very low in either modified MNIR-QD treated mice in the concentration used for the experiment (Supporting Information, Figure S10)

Hematological and Clinical Biochemistry Analysis. Toxicity of QDs in mice has been reported previously[28,36] where the toxicity of QDs depended on the metals used in the formulation of QDs. Basically, the MNIR-QDs contain Cd, Te, Se, S, and Ni, which are metabolized by the liver and finally excreted out by the kidney. Reports have suggested that degradation of QD surface coatings or core material may induce changes in the hematological indicators such as RBC count due to Cd toxicity.[41] In the present study, mice treated with amino-PEG/carboxyl-PEG functionalized MNIR-QDs at various concentrations (100, 400, and 800 pmol) showed no significant difference in white blood cell (WBC) count in comparison to the control group. However, little toxic effect on the bone marrow was observed, which was indicated by a slight reduction in red blood cell (RBC) count and hemoglobin (Hgb) concentration for amino-PEG-MNIR-QDs (Table 2). The rest of the blood parameters of the MNIR-QD treated mice are shown in Tables S1 and S2 (Supporting Information) which are quite similar to those of the control group.

We further analyzed a few major blood enzyme concentrations such as AST (aspartate aminotransferase), ALT (alanine transaminase), CRE (creatinine), BUN (blood urine nitrogen), and GLU (glucose) in Tables 3 and 4 for amino and carboxyl-PEG-MNIR-QDs. The results indicated that the AST and ALT levels were increased with increased dose levels. However, all the measured factors were within normal range, and no significant difference was observed in renal function

Table 2. Blood Profile in BALB/c Mice Treated with Functionalized MNIR-QDs Collected after 15 Days of Treatment[a]

blood parameter	normal range	control	100 pmol	400 pmol	800 pmol
Amino-PEG-MNIR-QDs					
WBC count (10^9/L)	5.0−13.7	4.73 ± 1.51	4.26 ± 2.71	4.97 ± 0.34	9.21 ± 0.51
RBC count (10^{12}/L)	7.9−10.1	9.73 ± 0.49	10.13 ± 1.17	10.17 ± 0.46	10.43 ± 0.17
Hgb value (g/dL)	10.2−16.6	14.52 ± 0.82	11.2375 ± 1.8	10.23 ± 1.59	10.46 ± 0.12
Carboxyl-PEG-MNIR-QDs					
WBC count (10^9/L)	5.0−13.7	4.73 ± 1.51	4.45 ± 0.22	6.29 ± 0.22	7.77 ± 0.52
RBC count (10^{12}/L)	7.9−10.1	9.73 ± 0.49	10.243 ± 0.19	10.4 ± 0.21	9.73 ± 0.59
Hgb value (g/dL)	10.2−16.6	14.52 ± 0.82	15.575 ± 0.19	14.8 ± 0.66	14.14 ± 1.49

[a]Data are the averages of those from four mice.

Table 3. Biochemical Profiles of Plasma in Mice Treated with Amino-PEG-MNIR-QDs[a]

enzymes	normal range	control	100 pmol	400 pmol	800 pmol
ALT (U/L)	17−77	33.9 ± 4.9	42.75 ± 10.63	48.3 ± 3.86	49.6 ± 2.62
AST (U/L)	54−298	53.37 ± 7.2	51.5 ± 14.53	54.3 ± 11.4	63.7 ± 4.49
CRE (mg/dL)	0.20−0.90	0.35 ± 0.11	0.35 ± 0.05	0.46 ± 0.04	0.53 ± 0.04
BUN (mg/dL)	9.0−33	23.8 ± 1.2	23.75 ± 3.05	24.6 ± 0.9	28.4 ± 2.77
GLU (mg/dL)	140−263	143.6 ± 5.3	143.25 ± 20.81	145 ± 13.6	144 ± 9.93

[a]Various biochemical enzyme parameters were measured in the blood of BALB/c mice 15 days after the treatment. Data are the averages of those from four mice.

Table 4. Biochemical Profiles of Plasma in Mice Treated with Carboxyl-PEG-MNIR-QDs[a]

enzymes	normal range	control	100 pmol	400 pmol	800 pmol
ALT (U/L)	17−77	33.9 ± 4.9	39.5 ± 9.93	43.33 ± 5.92	58.3 ± 6.01
AST (U/L)	54−298	53.37 ± 7.2	56.25 ± 1.78	65.33 ± 5.31	78.6 ± 16.35
CRE (mg/dL)	0.20−0.90	0.35 ± 0.11	0.35 ± 0.05	0.37 ± 0.64	0.40 ± 0.147
BUN (mg/dL)	9.0−33	23.8 ± 1.2	24.175 ± 2.69	24.13 ± 2.63	31.3 ± 2.73
GLU (mg/dL)	140−263	143. 6. ± 5.3	146.25 ± 2.38	149 ± 6.53	154.3 ± 8.17

[a]Various biochemical enzyme parameters were measured in the blood of BALB/c mice 15 days after the treatment. Data are the averages of those from four mice.

parameters such as blood urea nitrogen and creatine levels. These results suggested that there was no significant toxicity of the surface-modified MNIR-QDs.

In addition, to obtain the precise amount of quantum dots in various organs, we used ICP-MS to detect the Cd-concentration in tissues after 15 days of administration. Figure 6 indicates that after

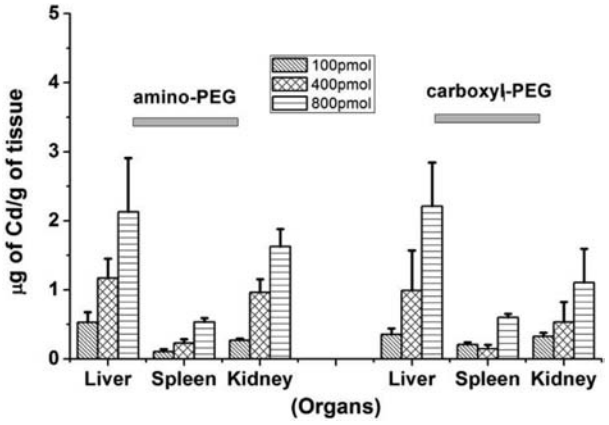


Figure 6. Biodistribution of QDs after 15 days of intravenous injection of amino-PEG-MNIR-QDs and carboxyl-PEG-MNIR-QDs.

15 days of injection, the quantum dots mostly accumulate in the liver, spleen, and kidney for amine and carboxyl modified quantum dots. Additionally, no traceable amounts of cadmium were detected in other organs, possibly due to low-dose injection and excretion of quantum dots in 15 days.[42,43] The accumulation in the kidney can possibly be due to the renal clearance from the body after the degradation of quantum dots by digestive chemicals present in phagocytic cells.[44] One study revealed that 3 μg Cd g^{-1} in the kidney is insufficient to cause toxicity;[41] hence, the our results can also be considered to be nontoxic at the concentration used in our experiments.

CONCLUSIONS

In summary, we demonstrated the facile preparation of Ni-doped MNIR-QDs with a tunable emission wavelength in the near-infrared region. Surface modification with PEG-based amino and carboxyl termination groups provided them better colloidal stability with negligible loss in optical properties when exposed to biological fluids. In addition, covalent linkage with folic acid imparted specificity followed by magnet-assisted cellular sorting applications. Nonetheless, *in vitro* and short-term *in vivo* toxicity evaluation showed no significant toxicity in the concentration used in our experiment. Hence, by obtaining these results we expect that our Ni-doped NIR-based QDs may find possible utility in specific targeting, imaging, and cellular sorting applications.

ASSOCIATED CONTENT

Supporting Information

Additional figures and tables as described in the text. This material is available free of charge via the Internet at http://pubs.acs.org.

AUTHOR INFORMATION

Corresponding Author

*Research Center for Applied Sciences, Academia Sinica, 128, Section 2, Academia Road, Nankang, Taipei 115, Taiwan. Phone: +886-2-27898000. Fax: +886-2-27896680. E-mail: peilin@gate.sinica.edu.tw.

Author Contributions

⊥These authors contributed equally to this work.

ACKNOWLEDGMENTS

This research was supported, in part, by the National Science Council, Taiwan, under contract NSC 100-2113-M-001-027-MY3 and the Academia Sinica Research Project on Nano Science and Technology.

REFERENCES

(1) Medintz, I. L., Uyeda, H. T., Goldman, E. R., and Mattoussi, H. (2005) Quantum dot bioconjugates for imaging, labelling and sensing. *Nat. Mater. 4*, 435−446.

(2) Colvin, V. L., Schlamp, M. C., and Alivisatos, A. P. (1994) Light-emitting diodes made from cadmium selenide nanocrystals and a semiconducting polymer. *Nature 370*, 354−357.

(3) Tessler, N., Medvedev, V., Kazes, M., Kan, S., and Banin, U. (2002) Efficient near-infrared polymer nanocrystal light-emitting diodes. *Science 295*, 1506−1508.

(4) Coe, S., Woo, W.-K., Bawendi, M., and Bulovic, V. (2002) Electroluminescence from single monolayers of nanocrystals in molecular organic devices. *Nature 420*, 800−803.

(5) Bruchez, M., Moronne, M., Gin, P., Weiss, S., and Alivisatos, A. P. (1998) Semiconductor nanocrystals as fluorescent biological labels. *Science 281*, 2013−2016.

(6) Chan, W. C. W., and Nie, S. (1998) Quantum dot bioconjugates for ultrasensitive nonisotopic detection. *Science 281*, 2016−2018.

(7) Mattoussi, H., Mauro, J. M., Goldman, E. R., Anderson, G. P., Sundar, V. C., Mikulec, F. V., and Bawendi, M. G. (2000) Self-assembly of CdSe:ZnS quantum dot bioconjugates using an engineered recombinant protein. *J. Am. Chem. Soc. 122*, 12142−12150.

(8) He, X., Wang, K., and Cheng, Z. (2010) In vivo near-infrared fluorescence imaging of cancer with nanoparticle-based probes. *Wiley Interdiscip. Rev.: Nanomed. Nanobiotechnol. 2*, 349−366.

(9) Peng, Z. A., and Peng, X. (2000) Formation of high-quality CdTe, CdSe, and CdS nanocrystals using CdO as precursor. *J. Am. Chem. Soc. 123*, 183−184.

(10) Murray, C. B., Norris, D. J., and Bawendi, M. G. (1993) Synthesis and characterization of nearly monodisperse CdE (E = sulfur, selenium, tellurium) semiconductor nanocrystallites. *J. Am. Chem. Soc. 115*, 8706−8715.

(11) Hines, M. A., and Guyot-Sionnest, P. (1996) Synthesis and characterization of strongly luminescing ZnS-capped CdSe nanocrystals. *J. Phys. Chem. 100*, 468−471.

(12) Dabbousi, B. O., Rodriguez-Viejo, J., Mikulec, F. V., Heine, J. R., Mattoussi, H., Ober, R., Jensen, K. F., and Bawendi, M. G. (1997) (CdSe)ZnS core-shell quantum dots:synthesis and characterization of a size series of highly luminescent nanocrystallites. *J. Phys. Chem. B 101*, 9463−9475.

(13) Mews, A., Eychmueller, A., Giersig, M., Schooss, D., and Weller, H. (1994) Preparation, characterization, and photophysics of the quantum dot quantum well system cadmium sulfide/mercury sulfide/cadmium sulfide. *J. Phys. Chem. 98*, 934−941.

(14) Battaglia, D., Li, J. J., Wang, Y., and Peng, X. (2003) Colloidal two-dimensional systems: CdSe quantum shells and wells. *Angew. Chem., Int. Ed. 42*, 5035−5039.

(15) Zhong, X., Xie, R., Zhang, Y., Basche, T., and Knoll, W. (2005) High-quality violet- to red-emitting ZnSe/CdSe core/shell nanocrystals. *Chem. Mater. 17*, 4038−4042.

(16) Kim, S., Fisher, B., Eisler, H.-J., and Bawendi, M. (2003) Type-II quantum dots: CdTe/CdSe(core/shell) and CdSe/ZnTe(core/shell) heterostructures. *J. Am. Chem. Soc. 125*, 11466−11467.

(17) Smith, A. M., Mohs, A. M., and Nie, S. (2009) Tuning the optical and electronic properties of colloidal nanocrystals by lattice strain. *Nat. Nano 4*, 56−63.

(18) Jiang, W., Singhal, A., Zheng, J., Wang, C., and Chan, W. C. W. (2006) Optimizing the synthesis of red- to near-IR-emitting CdS-capped CdTexSe1-x alloyed quantum dots for biomedical imaging. *Chem. Mater. 18*, 4845−4854.

(19) Aswathy, R., Yoshida, Y., Maekawa, T., and Kumar, D. (2010) Near-infrared quantum dots for deep tissue imaging. *Anal. Bioanal. Chem. 397*, 1417−1435.

(20) Adarsh Sandhu, H. H. a. M. A. (2010) Synthesis and applications of magnetic nanoparticles for biorecognition and point of care medical diagnostics. *Nanotechnology 21*, 442001.

(21) Di Corato, R., Bigall, N. C., Ragusa, A., Dorfs, D., Genovese, A., Marotta, R., Manna, L., and Pellegrino, T. (2011) Multifunctional nanobeads based on quantum dots and magnetic nanoparticles: synthesis and cancer cell targeting and sorting. *ACS Nano 5*, 1109−1121.

(22) Sun, P., Zhang, H., Liu, C., Fang, J., Wang, M., Chen, J., Zhang, J., Mao, C., and Xu, S. (2009) Preparation and characterization of Fe3O4/CdTe magnetic/fluorescent nanocomposites and their applications in immuno-labeling and fluorescent imaging of cancer cells. *Langmuir 26*, 1278−1284.

(23) Tan, Y. F., Chandrasekharan, P., Maity, D., Yong, C. X., Chuang, K.-H., Zhao, Y., Wang, S., Ding, J., and Feng, S.-S. (2011) Multimodal tumor imaging by iron oxides and quantum dots formulated in poly (lactic acid)-d-alpha-tocopheryl polyethylene glycol 1000 succinate nanoparticles. *Biomaterials 32*, 2969−2978.

(24) Wang, D., He, J., Rosenzweig, N., and Rosenzweig, Z. (2004) Superparamagnetic Fe_2O_3 beads−CdSe/ZnS quantum dots core−shell nanocomposite particles for cell separation. *Nano Lett. 4*, 409−413.

(25) Ken-Tye, Y. (2009) Mn-doped near-infrared quantum dots as multimodal targeted probes for pancreatic cancer imaging. *Nanotechnology 20*, 015102.

(26) Sahoo, Y., Poddar, P., Srikanth, H., Lucey, D. W., and Prasad, P. N. (2005) Chemically fabricated magnetic quantum dots of InP:Mn. *J. Phys. Chem. B 109*, 15221−15225.

(27) Selvan, S. T., Patra, P. K., Ang, C. Y., and Ying, J. Y. (2007) Synthesis of silica-coated semiconductor and magnetic quantum dots and their use in the imaging of live cells. *Angew. Chem. Int. Ed. 119*, 2500−2504.

(28) Yong, K.-T. (2009) Mn-doped near-infrared quantum dots as multimodal targeted probes for pancreatic cancer imaging. *Nanotechnology 20*, 015102.

(29) Liu, W., Howarth, M., Greytak, A. B., Zheng, Y., Nocera, D. G., Ting, A. Y., and Bawendi, M. G. (2008) Compact biocompatible quantum dots functionalized for cellular imaging. *J. Am. Chem. Soc. 130*, 1274−1284.

(30) Susumu, K., Uyeda, H. T., Medintz, I. L., and Mattoussi, H. (2007) Design of biotin-functionalized luminescent quantum dots. *J. Biomed. Biotechnol. 2007*, 1−7.

(31) Bailey, R. E., and Nie, S. (2003) Alloyed semiconductor quantum dots: tuning the optical properties without changing the particle size. *J. Am. Chem. Soc. 125*, 7100−7106.

(32) Rui, H., Yong, K.-T., Roy, I., Ding, H., Law, W.-C., Cai, H., Zhang, X., Vathy, L. A., Bergey, E. J., and Prasad., P. N. (2010) Functionalized near-infrared quantum dots for in vivo tumor vasculature imaging. *Nanotechnology 21*, 145105.

(33) Wuister, S. F., van Driel, F., and Meijerink, A. (2003) Luminescence and growth of CdTe quantum dots and clusters. *Phys. Chem. Chem. Phys. 5*, 1253−1258.

(34) Wang, J., Long, Y., Zhang, Y., Zhong, X., and Zhu, L. (2009) Preparation of highly luminescent CdTe/CdS core/shell quantum dots. *ChemPhysChem 10*, 680−685.

(35) Chin, P. T. K., de Mello Donegá, C., van Bavel, S. S., Meskers, S. C. J., Sommerdijk, N. A. J. M., and Janssen, R. A. J. (2007) Highly

luminescent CdTe/CdSe colloidal heteronanocrystals with temperature-dependent emission color. *J. Am. Chem. Soc. 129*, 14880−14886.
(36) Yong, K.-T., Roy, I., Ding, H., Bergey, E. J., and Prasad, P. N. (2009) Biocompatible near-infrared quantum dots as ultrasensitive probes for long-term in vivo imaging applications. *Small 5*, 1997−2004.
(37) Naghash, A. R., Etsell, T. H., and Xu, S. (2006) XRD and XPS study of Cu−Ni interactions on reduced copper−nickel−aluminum oxide solid solution catalysts. *Chem. Mater. 18*, 2480−2488.
(38) Alivisatos, P. (2004) The use of nanocrystals in biological detection. *Nat. Biotechnol. 22*, 47−52.
(39) Ron, H. (2006) A toxicologic review of quantum dots: toxicity depends on physicochemical and environmental factors. *Environ. Health Perspect. 114*, 165−172.
(40) Ryman-Rasmussen, J. P., Riviere, J. E., and Monteiro-Riviere, N. A. (2006) Surface coatings determine cytotoxicity and irritation potential of quantum dot nanoparticles in epidermal keratinocytes. *J. Invest. Dermatol. 127*, 143−153.
(41) Hauck, T. S., Anderson, R. E., Fischer, H. C., Newbigging, S., and Chan, W. C. W. (2010) In vivo quantum-dot toxicity assessment. *Small 6*, 138−144.
(42) Jorina Geys, A. N., Verbeken, E., Smolders, E., Ratoi, M., Hoylaerts, M. F., Nemery, B., and Hoet., P. H. M. (2008) Acute toxicity and prothrombotic effects of quantum dots: impact of surface charge. *Environ Health Perspect 116*, 1607−1613.
(43) Kim, S., Lim, Y. T., Soltesz, E. G., De Grand, A. M., Lee, J., Nakayama, A., Parker, J. A., Mihaljevic, T., Laurence, R. G., Dor, D. M., Cohn, L. H., Bawendi, M. G., and Frangioni, J. V. (2004) Near-infrared fluorescent type II quantum dots for sentinel lymph node mapping. *Nat. Biotechnol. 22*, 93−97.
(44) Soo Choi, H., Liu, W., Misra, P., Tanaka, E., Zimmer, J. P., Itty Ipe, B., Bawendi, M. G., and Frangioni, J. V. (2007) Renal clearance of quantum dots. *Nat. Biotechnol. 25*, 1165−1170.

Bioconjugate Chemistry

Article

pubs.acs.org/bc

Synthesis of [^{18}F]-Labeled (6-Fluorohexyl)triphenylphosphonium Cation as a Potential Agent for Myocardial Imaging using Positron Emission Tomography

Dong-Yeon Kim,[†,‡] Hee-Jung Kim,[†] Kook-Hyun Yu,*[,†] and Jung-Joon Min*[,‡,§]

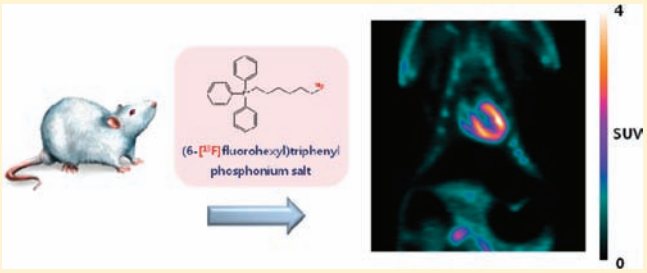
[†]Department of Chemistry, Dongguk University-seoul, Seoul, Korea

[‡]Department of Nuclear Medicine, Chonnam National University Hwasun Hospital, Hwasun, Korea

[§]Laboratory of In Vivo Molecular Imaging, Department of Nuclear Medicine, Chonnam National University Medical School, Gwangju, Korea

Supporting Information

ABSTRACT: Lipophilic cations such as phosphonium salts penetrate the hydrophobic barriers of the plasma and mitochondrial membranes and accumulate in mitochondria in response to the negative inner-transmembrane potentials. Thus, as newly developed noninvasive imaging agents, [^{18}F]-labeled phosphonium salts may serve as molecular "voltage sensor" probes to investigate the role of mitochondria, particularly in myocardial disease. The present study reports the radiosynthesis of (6-fluorohexyl)triphenylphosphonium salt (**3**) as a potential agent for myocardial imaging by using positron emission tomography (PET). The reference compound of (6-[^{18}F]fluorohexyl)triphenylphosphonium salt ([^{18}**F**]**3**) was synthesized with 74% yield via three-step nucleophilic substitution reactions. The reference compound was radiolabeled via two-step nucleophilic substitution reactions of no-carrier-added [^{18}F]fluoride with the precursor hexane-1,6-diyl bis(4-methylbenzenesulfonate) in the presence of Kryptofix 2.2.2 and K_2CO_3. The radiolabeled compound was synthesized with 15−20% yield. The radiochemical purity was >98% by analytical HPLC, and the specific activity was >6.10−6.47 TBq/μmol. The cellular uptake assay showed preferential uptake of [^{18}**F**]**3** in cardiomyocytes. The results of biodistribution and micro-PET imaging studies of [^{18}**F**]**3** in mice and rats showed preferential accumulation in the myocardium. The results suggest that this compound would be a promising candidate for myocardial imaging.



INTRODUCTION

Nuclear medicine imaging by single-photon emission tomography (SPECT) using [^{99m}Tc]-sestamibi, [^{99m}Tc]-tetrofosmin, or ^{201}thallium has been validated extensively. SPECT is a widely used tool for the assessment of myocardial infarction (MI) size[1,2] for the risk stratification of patients. It also is an attractive surrogate end point instead of mortality for determining the efficacy of therapeutic strategies in clinical trials.[1] However, the technical limitations of SPECT imaging, such as low spatial resolution and the assessment of only relative tracer inhomogeneities resulting from soft tissue attenuation or scatter, may compromise the delineation of small infarcts and the diagnostic accuracy of SPECT.[2]

Positron emission tomography (PET) has several technical advantages over SPECT, such as higher spatial resolution. Owing to accurate attenuation correction, PET can provide quantitative measures of myocardial tracer uptake.[3] However, the short half-life of currently used PET tracers for myocardial imaging, including [^{13}N]-ammonia, ^{82}rubidium, and [^{15}O]-water, limit the widespread clinical use of PET due to the need for a nearby cyclotron or generator. Because of their longer half-life, [^{18}F]-labeled tracers would avoid this limitation and facilitate clinical protocols.

To address this need, we developed a [^{18}F]-labeled phosphonium cation.[4] Similar to SPECT tracers such as [^{99m}Tc]-sestamibi and [^{99m}Tc]-tetrofosmin, phosphonium cations accumulate in cardiomyocytes to a higher degree than in normal cells.[5] This phenomenon is attributed to the highest density and higher electrochemical membrane potential of the mitochondria in cardiomyocytes.[5−7] Loss of the mitochondrial membrane potential is an early event in cell death caused by myocardial ischemia.[8] Cumulative evidence suggests that mitochondria-controlled apoptosis underlies cell loss in heart failure.[9] Previous publications have reported that [^{18}F]-labeled phosphonium cations such as [^{18}F]-fluorobenzyl triphenylphosphonium ([^{18}F]-FBnTP) are metabolically stable and demonstrate excellent characteristics as cardiac imaging agents in healthy and coronary artery disease models.[5,7,10]

Received: August 15, 2011
Revised: January 12, 2012
Published: January 22, 2012

 © 2012 American Chemical Society dx.doi.org/10.1021/bc2004439 | *Bioconjugate Chem.* 2012, 23, 431−437

Herein, we report the synthesis and characterization of a novel [^{18}F]-labeled phosphonium cation, (6-[^{18}F]fluorohexyl)-triphenylphosphonium salt ([^{18}F]**3**) (Figure 1). Biological studies, such as a cellular uptake assay, biodistribution studies, and micro-PET imaging, were performed to test and optimize the kinetics for radiolabeled phosphonium cation.

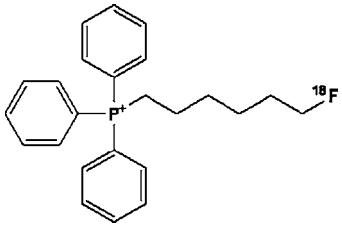


Figure 1. Schematic structure of (6-[^{18}F]fluorohexyl)-triphenylphosphonium salt ([^{18}F]**3**).

EXPERIMENTAL PROCEDURES

General. All commercial reagents and solvents were purchased from Sigma-Aldrich or Merck, were of analytical grade, and were used without further purification. [^{3}H]-tetraphenylphosphonium ([^{3}H]-TPP) was purchased from Moravek Biochemicals, Inc. The ^{1}H and ^{13}C NMR spectra were recorded on a JEOL ECA-500 FT-NMR spectrometer (Advanced Radiation Technology Institute, Korea Atomic Energy Research Institute). All chemical shifts were reported on the ppm scale with tetramethylsilane as an internal standard. Mass spectra were recorded on a JEOL JMS-AX505WA spectrometer. Compounds were measured by electrospray ionization (ESI) and fast atom bombardment (FAB) methods at the National Center for Interuniversity Research Facilities (NCIRF). Gravity column chromatography was performed on Merck silica gel 60 (70−230 mesh ASTM). Thin layer chromatography (TLC) was performed on Merck silica gel 60 F_{254} glass plates and was visualized by UV light. Purification was achieved by HPLC, with a SP930D pump, UV730D UV detector (Young-Lin Inc., Korea), and FC-3200 high energy gamma detector (Bioscan, USA) to measure the radioactive flow. The UV detection wavelength was 254 nm for all experiments. Both semipreparative (Phenomenex Luna, C18, 10 mm × 250 mm) and analytical (Waters Atlantis C18, 4.6 mm × 250 mm) reverse-phase HPLC columns were used. A CRC-712MH radioisotope calibrator (Capintec Instruments, USA) was used for radioactivity measurements. [^{18}F] analysis was performed with a 1480 WIZARD 3 gamma counter (Perkin-Elmer, USA), and [^{3}H] was measured with an LS 6500 liquid scintillation counter (Beckman, USA). Normal rats were imaged and analyzed by micro-PET (Inveon, Siemens). No-carrier-added (n.c.a) [^{18}F]fluoride was produced on a PETtrace cyclotron (16.4 MeV, General Electric Company, USA) by irradiation of a [^{18}O]H_2O water target.

Synthesis of Hexane-1,6-diyl Bis(4-methylbenzenesulfonate) (1). Compound **1** was prepared by the modification of a previously reported method.[11] Hexane-1,6-diol (1.77 g, 15.0 mmol) in 30.0 mL of anhydrous pyridine was added to 4-methylbenzene-1-sulfonyl chloride (8.58 g, 45.0 mmol) at 0 °C. The mixture was stirred at room temperature for 3 h, quenched with 3.0 mL of water, and stirred for a further 30 min. Methylene chloride and 1.0 M HCl were added to the reaction mixture, and the pyridine was extracted from the organic phase. The organic phase was washed twice with water and brine, dried over sodium sulfate, and filtered. After evaporation of the solvent, the solution was purified by column chromatography (methylene chloride:*n*-hexane:acetone = 48:50:2) and recrystallized from methylene chloride:*n*-hexane to yield 5.12 g (80%) of compound **1**. mp 77−79 °C; ^{1}H NMR (500 MHz, $CDCl_3$) δ 1.25−1.27 (m, 4H), 1.57−1.60 (m, 4H), 2.45 (s, 6H), 3.97 (t, J = 6.3 Hz, 4H), 7.34 (d, J = 8.4 Hz, 4H), 7.77 (d, J = 8.4 Hz, 4H); ^{13}C NMR (125 MHz, $CDCl_3$) δ 21.60, 21.75, 28.26, 70.08, 127.96, 130.00, 133.01, 144.96; HRMS (ESI) m/z calculated for $C_{20}H_{26}O_6S_2Na$ $[M+Na]^+$ 449.1064; found 449.1068.

Synthesis of 6-Fluorohexyl 4-Methylbenzenesulfonate (2). Anhydrous acetonitrile (3.0 mL) was added to tetrabutylammonium fluoride trihydrate (TBAF, 1.43 g, 4.54 mmol). The mixture was evaporated under reduced pressure to remove the water. This procedure was repeated twice. Compound **1** (1.94 g, 4.54 mmol) in 10.0 mL of anhydrous acetonitrile was added to the reaction flask. The mixture was stirred for 4 h at 85 °C in a closed tube. The solvent was evaporated under reduced pressure. Column chromatography (methylene chloride:*n*-hexane:acetone = 49:50:1) provided 0.60 g (48% yield) of compound **2** as a yellow oil. ^{1}H NMR (500 MHz, $CDCl_3$) δ 1.34−1.35 (m, 4H), 1.58−1.65 (m, 4H), 2.44 (s, 3H), 4.02 (t, J = 6.3 Hz, 2H), 4.39 (dt, J = 47.3, 6.0 Hz, 2H), 7.34 (d, J = 8.0 Hz, 2H), 7.78 (d, J = 7.5 Hz, 2H); ^{13}C NMR (125 MHz, $CDCl_3$) δ 21.73, 24.74, 28.82, 30.16, 70.49, 83.95, 127.98, 129.92, 133.21, 144.81; MS (FAB) m/z 275 $[M+H]^+$, 173 (100); HRMS (FAB) m/z calculated for $C_{13}H_{20}FO_3S$ $[M+H]^+$ 275.1117; found 275.1120.

Synthesis of (6-Fluorohexyl)triphenylphosphonium Salt (3). Compound **3** was prepared by the modification of a previously reported method.[12] Triphenylphosphine (1.0 g, 3.81 mmol) dissolved in 10.0 mL anhydrous acetonitrile was added to compound **2** (1.05 g, 3.81 mmol). The solution was refluxed for 19 h. The solvent was evaporated under reduced pressure. Column chromatography (methylene chloride:methanol:ethyl acetate = 8:1:1) provided 1.03 g (74%) of compound **3** as a powder. Retention factor (R_f): 0.45−0.50 (methylene chloride:methanol = 9:2); mp 220−223 °C; ^{1}H NMR (500 MHz, $CDCl_3$) δ 1.31−1.36 (m, 2H), 1.50−1.61 (m, 6H), 2.28 (s, 3H), 3.56−3.61 (m, 2H), 4.33 (dt, J = 47.2, 6.1 Hz, 2H), 7.04 (d, J = 7.8 Hz, 2H), 7.63−7.79 (m, 17H); ^{13}C NMR (125 MHz, $CDCl_3$) δ 21.60, 22.01, 22.56, 24.75, 29.90, 84.03, 118.08, 118.75, 126.22, 128.32, 130.55, 133.61, 135.03. 138.50, 144.67; MS (FAB) m/z 365 $[M]^+$, 365 (100); HRMS (FAB) m/z calculated for $C_{24}H_{27}FP$ $[M]^+$ 365.1834; found 365.1834.

Radiolabeling of (6-Fluorohexyl)-triphenylphosphonium Salt ([^{18}F]3). [^{18}F]Fluoride was produced by an ^{18}O(p, n)^{18}F reaction on a PETtrace cyclotron. The activity was extracted from $H_2{}^{18}O$ by an anion exchanger and was eluted by aqueous potassium carbonate (25.0 mmol) into the reaction vessel. The radioactive solution was dried together with 4.0 mg of Kryptofix 2.2.2 in 1.0 mL of acetonitrile under nitrogen at 100 °C. The solution was evaporated at 100 °C by bubbling nitrogen gas. The residue was dried by azeotropic distillation with acetonitrile (1 mL, 3 times). Then, 4.0 mg of compound **1** dissolved in 1.0 mL of anhydrous acetonitrile were added. The mixture was heated for 5 min at 90 °C in the closed state. Radio-TLC showed a >80% yield of compound [^{18}F]**2**. The solution was passed through a small silica Sep-Pak cartridge. Six milligrams of triphenylphosphine dissolved in 1.0 mL of toluene were added to the reaction

dx.doi.org/10.1021/bc2004439 | *Bioconjugate Chem.* 2012, 23, 431−437

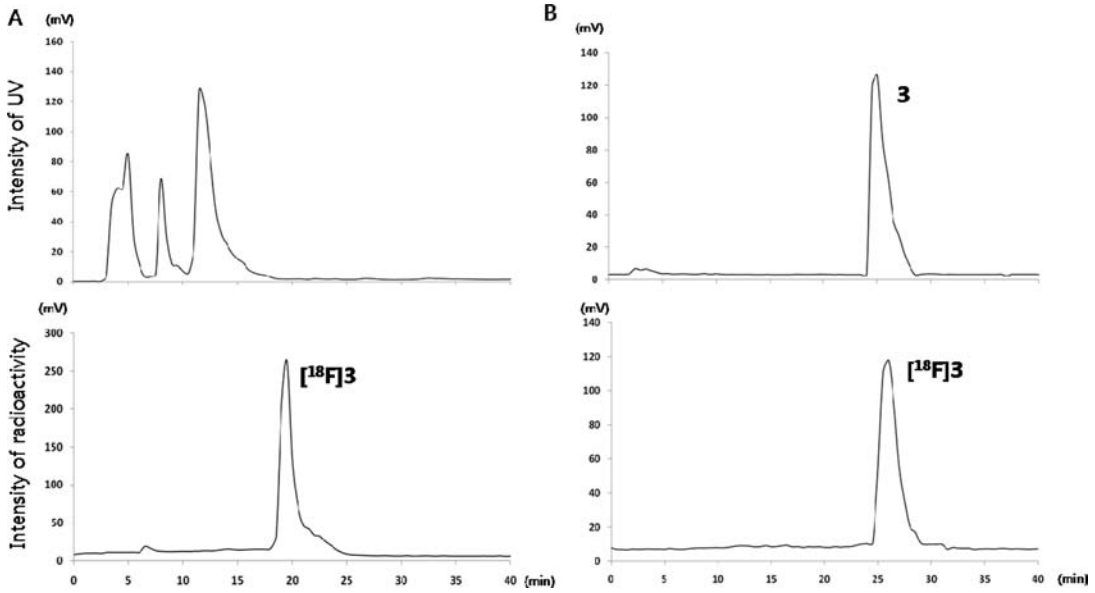


Figure 2. (A) Purification of [^{18}F]**3** on semipreparative HPLC. The reaction mixture was injected on a C18 column and was eluted with acetonitrile: phosphate-buffered saline = 50:50 at a flow rate of 3.0 mL/min. UV impurities were not observed. (B) Analytical HPLC chromatogram of [^{18}F]**3** coinjected with the nonradioactive compound **3**.

vessel, and the solution was heated to 220 °C for 3 min with no separation step (Scheme 2).

The solution was cooled and injected into a semipreparative HPLC column system for purification (mobile phase, acetonitrile:phosphate-buffered saline = 50:50; flow rate, 3 mL/min; 254 nm; t_R: 19.5 min) (Figure 2A). For identification of the radioproduct, the collected HPLC fraction was coinjected with cold compound **3**. [^{18}F]**3** was dried, made isotonic with sodium chloride, and passed through a 0.20 μm membrane filter into a sterile multidose vial for in vitro and in vivo experiments. The total reaction time of [^{18}F]**3** was within 60 min, and the overall decay-corrected radiochemical yield was approximately 15−20%. Radiochemical purity was >98% by the analytical HPLC system (with the same isocratic as used for the semipreparative HPLC system). The specific activity was >6.10−6.47 TBq/μmol (Figure 2B).

In Vitro Stability Study. For the labeling stability test, [^{18}F]**3** (0.37 MBq/100 μL) was incubated with human serum (1.0 mL) in a 37 °C water bath for 4 h and then was analyzed by chromatography on ITLC-sg strips developed with methylene chloride:methanol = 9:2. After they were developed, the chromatographic strips were scanned on an automatic TLC scanner, and TLC was performed at various time points. All experiments were performed in triplicate.

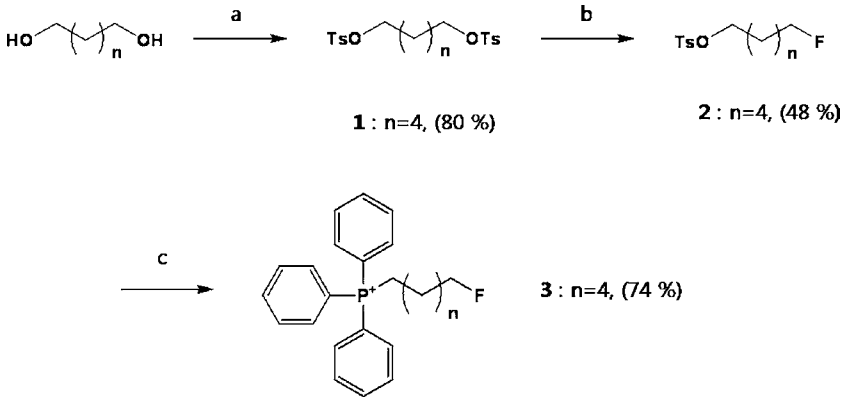
Partition Coefficient. After the complete removal of volatiles of [^{18}F]**3**, the residue was dissolved in a mixture of 3 mL of saline and 3 mL of *n*-octanol in a round-bottom flask. The mixture was vigorously stirred for 20 min at room temperature and then was transferred to a 15 mL Falcon conical tube. The tube was centrifuged at 3000 rpm for 5 min. Samples in triplets from *n*-octanol and aqueous layers were obtained and were counted on a gamma counter. The log *P* value was reported as an average of the data obtained in three independent measurements.[13]

Cell Lines, Culture Conditions, and Cell Uptake Studies. [^{18}F]**3** accumulation was measured in cell culture with rat embryonic cardiomyoblast (H9c2) and mouse normal fibroblast (NIH/3T3) cell lines. All cells were grown in Deficient DMEM (Dulbecco's modified Eagle medium) High Glucose (containing 5.3 mmol/L KCl and 110.34 mmol/L NaCl; Life Technologies) plus 5% fetal bovine serum (FBS), 1% penicillin-streptomycin, and 1% L-glutamine. Cells were incubated at 37 °C for 0.5, 1, or 2 h with radioactive culture medium and [^{18}F]**3** (0.74 MBq/200 μL). The radioactive medium was removed, and the radioactivity was measured. The wells were washed three times with cold phosphate-buffered saline. The cells were harvested, and the cell-associated radioactivity was determined. The mitochondrial membrane potential-dependent cellular uptake of [^{18}F]**3** was further assessed with H9c2 cells treated with carbonyl cyanide *m*-chlorophenylhydrazone (CCCP), which is a protonphore that selectively abolishes the mitochondrial membrane potential.[14] The compound was dissolved in dimethyl sulfoxide and diluted to the desired concentration with low K^+ HEPES buffer. The final concentration of dimethyl sulfoxide was <0.1%. CCCP solution (0.50 μM) was added to 5.0×10^4 cells at 30 min before the start of the experiment. After incubation with [^{18}F]**3**, radioactivity was determined by a gamma counter.[15] The mitochondrial membrane potentials of both cell lines were assessed by a cell uptake study with [^{3}H]-TPP (37 kBq/200 μL). The [^{3}H]-TPP uptake assay is a standard method for measuring mitochondrial membrane potential in vitro.[7] After incubation with [^{3}H]-TPP, radioactivity was determined with a liquid scintillation counter. Triplicate samples were obtained for all uptake studies. Data are expressed as the accumulation ratio (%) ± SD calculated by dividing the radioactivity in the pellet by the total radioactivity (supernatant + pellet).

Murine Biodistribution Studies. To confirm the activity of [^{18}F]**3** in vivo, biodistribution studies were performed with a murine model. Biodistribution in different organs was assessed in BALB/c mice (18−20 g, Orient, Kyunggido, Korea) at 10, 30, 60, and 120 min after i.v. injection of 7.4 MBq radiotracer. Blood, heart, lung, liver, spleen, stomach, intestine, kidney, pancreas, bone, and muscle were sampled from mice, and the radioactivity of each organ was measured with a gamma counter. Radioactivity determinations were normalized by the

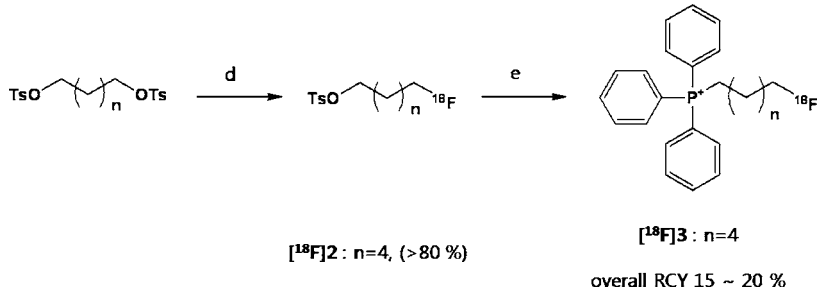
dx.doi.org/10.1021/bc2004439 | *Bioconjugate Chem.* 2012, 23, 431−437

Scheme 1. Synthesis of (6-Fluorohexyl)triphenylphosphonium Salt[a]



[a]Reagents and conditions: (a) 4-methylbenzene-1-sulfonyl chloride, pyridine, room temp, 3 h; (b) tetra butyl ammonium fluoride, acetonitrile, 85 °C, 4 h; (c) triphenylphosphine, acetonitrile, reflux, 19 h.

Scheme 2. Radiosynthesis of (6-Fluorohexyl)triphenylphosphonium Salt[a]



[a]Reagents and conditions: (d) [^{18}F]KF, Kryptofix 2.2.2, acetonitrile, 90 °C, 5 min; (e) triphenylphosphine, toluene, 220 °C, 3 min.

weight of the tissue and the amount of radioactivity injected to obtain the % ID/g.

Micro-PET Imaging Studies. Normal rats were imaged with micro-PET at 0.5 and 1.0 h after i.v. injection of 37 MBq of [^{18}F]**3**. Eight-week-old male Sprague–Dawley rats (250–260 g, Orient, Kyunggido, Korea) were used for this study. Animal care, all experiments, and euthanasia were performed in accordance with protocols approved by the Chonnam National University Animal Research Committee and the Guide for the Care and Use of Laboratory Animals published by the National Institutes of Health (NIH publication 85–23, revised 1985). Rats were anesthetized by ketamine hydrochloride (100 mg/kg) and xylazine hydrochloride (2.5 mg/kg).

RESULTS AND DISCUSSION

Synthesis and Radiochemistry. The total synthesis of compounds **3** and [^{18}F]**3** is shown in Schemes 1 and 2. The reference compound was synthesized *via* three-step procedures and was analyzed by ^{1}H, ^{13}C NMR, and FAB high-resolution mass spectroscopy to confirm the identity.

For synthesis of the reference compound, compound **1** was first prepared by commercially available hexane-1,6-diol reacted with an excess of 4-methylbenzene-1-sulfonyl chloride in pyridine. Compound **1** was synthesized with an 80% yield and was treated thereafter with TBAF in acetonitrile, to generate the fluoro compound **2**. Finally, a nucleophilic substitution reaction was performed with triphenylphosphine, in which the *p*-tosyloxy residue was chosen as the leaving group. Methylene groups in the ω-position of the alkyl side chain were split into a doublet of triplets by fluorine in NMR ($^{2}J_{HF}$: 47.2 Hz). We also confirmed 4-methylbenzenesulfonate as counterions by NMR.

For synthesis of the [^{18}F]-labeled compound, **1** was reacted with nca [^{18}F]fluoride in the presence of potassium carbonate (K_2CO_3) and the phase-transfer agent Kryptofix 2.2.2. Then, [^{18}F]**2** was reacted with triphenylphosphine to yield the target compound with no separation step. After purification of the [^{18}F]-labeled target compound by semiprep HPLC, [^{18}F]**3** was compared with the reference compound by analytical HPLC to determine the identity (Figure 2A and B). Figure 2B revealed a single peak, suggesting the formation of one product ([^{18}F]**3**) identical to the reference compound. Radiochemical yield ranged 15–20% in the labeled compound (EOS; corrected for decay). Radiochemical purity was >98% by analytical HPLC. The specific activity was >6.10–6.47 TBq/μmol.

When the radiotracer (0.37 MBq [^{18}F]**3**) was incubated in human serum at 37 °C for 4 h, the percentage of the remaining [^{18}F]**3** was >95%, indicating the relatively high in vitro stability of the radiotracer (Supporting Information).

A previous publication has reported the synthesis of the (3-[^{18}F]fluoropropyl)triphenylphosphonium cation, with 12% radiochemical yield.[12] In this previous study, the whole radiosynthesis was completed in 56 min, with an average specific radioactivity of 15.5 GBq/μmol. The radiochemical characteristics of [^{18}F]**3** and (3-[^{18}F]fluoropropyl)-triphenylphosphonium cation were quite similar, except that [^{18}F]**3** had a significantly higher specific activity. In the current study, we further used the fluoroalkylphosphonium cation derivative ([^{18}F]**3**) in biological studies, including a cellular uptake assay, biodistribution studies, and micro-PET imaging.

dx.doi.org/10.1021/bc2004439 | *Bioconjugate Chem.* 2012, 23, 431–437

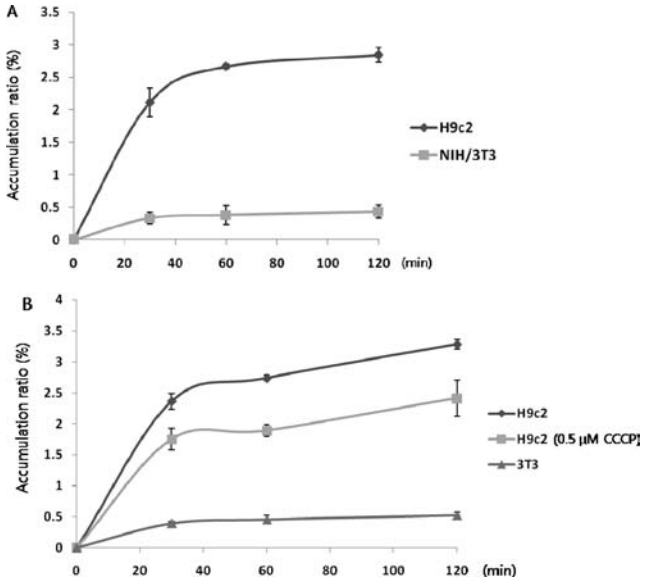


Figure 3. (A) Cell uptake of [^{3}H]-TPP in H9c2 and NIH/3T3 cells at 0.5, 1.0, or 2.0 h in a 37 °C incubator. Uptake by H9c2 cells was higher than uptake by NIH/3T3 cells for the entire time. This finding means that the mitochondria membrane potential of H9c2 cells was higher than that of NIH/3T3 cells. (B) Cell uptake of [^{18}F]**3** in H9c2 cells, H9c2 cells treated with 0.5 μM protonphore CCCP, and NIH/3T3 cells at 0.5, 1.0, or 2.0 h in a 37 °C incubator. Uptake by H9c2 cells was about 6-fold higher than uptake by NIH/3T3 cells. When incubated with 0.5 μM CCCP, the cellular uptake of [^{18}F]**3** was significantly inhibited ($P < 0.05$). All results are expressed as a percentage of applied radioactivity and are the means ± SD of three measurements.

Lipophilicity of Radiolabeled Compound. To assess the lipophilicity of [^{18}F]**3**, we measured the log P value of [^{18}F]**3**, which was 1.78 ± 0.05. Although there is little information available with regard to the optimal lipophilicity needed for the high myocardial selectivity of a radiotracer, a predictive model has been reported for the selective accumulation of phosphonium cations in myocardial cells.[16] For lipophilic cationic radiotracers (log P = 0.5−1.5) such as ^{99m}Tc-sestamibi

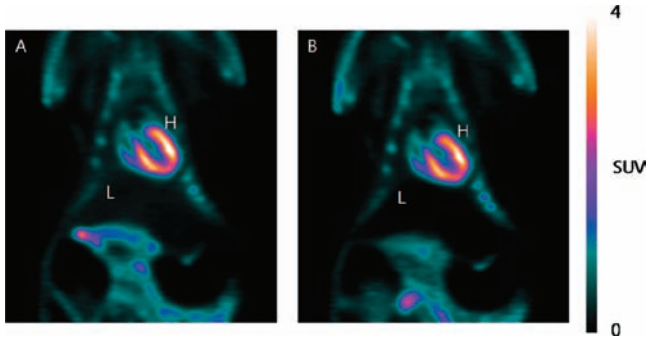


Figure 4. Micro-PET imaging (corona) of rats after i.v. injection of [^{18}F]**3**. Shown are images at 0.5 h (A) and 1.0 h (B) after injection of [^{18}F]**3**. H, heart; L, liver. The heart was visible with excellent heart-to-liver and heart-to-lung contrast at each time point after i.v. injection.

(log P = 1.1), their membrane diffusion kinetics are so fast they tend to localize in mitochondria-rich organs such as the heart.[16] Furthermore, because the alkyl group increases the hydrophobicity, the hydrophobic interaction between the triphenylphosphonium cation and the lipid core is attractive due to the hydrophobicity of the lipophilic phosphonium cation and increased entropy.[17−19]

In Vitro Cell-Uptake Assays. The mitochondrial membrane potential of H9c2 cells, which was assessed by a cellular [^{3}H]-TPP uptake assay, was significantly higher than that of NIH/3T3 cells (Figure 3A). Cell uptake values of [^{18}F]**3** in H9c2 and NIH/3T3 cells over incubation periods of 0.5, 1, and 2 h are shown in Figure 3B. The uptake increased from 2.37 ± 0.13% at 0.5 h to 3.28 ± 0.08% at 2 h. The uptake was about 6-fold higher than that of NIH/3T3 cells. When incubated with 0.5 μM of CCCP, cellular uptake of [^{18}F]**3** was significantly inhibited ($P < 0.05$) at all incubation time points (Figure 3B). These results clearly demonstrate that [^{18}F]**3** accumulates in the cells through the mitochondrial membrane potential.

Biodistribution Studies and Micro-PET Imaging. The in vivo biodistribution of [^{18}F]**3** was examined in BALB/c mice (Table 1). High levels of radioactivity accumulated in the heart. The myocardial uptake of [^{18}F]**3** was >20% ID/g at 10 min after radiotracer injection. The heart-to-blood ratio of [^{18}F]**3**

Table 1. Normal Biodistribution Studies in BALB/c Mice at 10, 30, 60, and 120 min after i.v. Injection of [^{18}F]3[a]

	10 min	30 min	60 min	120 min
Blood	0.72 ± 0.14	0.29 ± 0.02	0.19 ± 0.03	0.14 ± 0.01
Heart	21.84 ± 2.26	20.47 ± 4.35	23.20 ± 2.70	20.09 ± 3.12
Lung	6.57 ± 1.25	4.52 ± 0.57	3.70 ± 0.12	2.84 ± 0.17
Liver	5.13 ± 1.73	1.74 ± 0.11	1.30 ± 0.12	0.81 ± 0.20
Spleen	6.11 ± 2.22	3.29 ± 0.08	2.94 ± 0.19	2.37 ± 0.57
Stomach	6.48 ± 0.48	5.58 ± 1.11	5.58 ± 1.69	5.07 ± 2.13
Intestine	15.24 ± 2.90	11.06 ± 1.66	11.29 ± 2.10	3.47 ± 0.88
Kidney	56.63 ± 12.20	20.72 ± 1.20	12.68 ± 3.13	11.47 ± 1.84
Pancreas	12.32 ± 2.84	9.73 ± 0.32	10.09 ± 1.13	9.91 ± 1.68
Normal Muscle	4.24 ± 1.15	4.16 ± 0.49	4.53 ± 0.54	4.14 ± 0.28
Bone	5.22 ± 0.86	5.55 ± 1.15	7.30 ± 1.36	7.45 ± 1.86
Heart/blood	30.95 ± 4.80	71.87 ± 21.63	126.76 ± 22.51	138.61 ± 8.10
Heart/liver	4.58 ± 1.61	11.90 ± 3.37	17.83 ± 1.18	25.53 ± 5.88
Heart/lung	3.36 ± 0.30	4.50 ± 0.44	6.27 ± 0.65	7.07 ± 0.98
Heart/muscle	5.43 ± 1.76	4.91 ± 0.67	5.13 ± 0.35	4.83 ± 0.44

[a]Data are expressed as the percentage administered activity (injected dose) per gram of tissue (% ID/g, n = 12). The myocardial uptake of [^{18}F]**3** was >20% ID/g for the whole time after radiotracer injection. The heart-to-blood ratio of [^{18}F]**3** was >138, whereas the heart-to-lung, heart-to-liver, and heart-to-normal muscle ratios were >7, >25, and >4, respectively, at 120 min.

dx.doi.org/10.1021/bc2004439 | Bioconjugate Chem. 2012, 23, 431−437

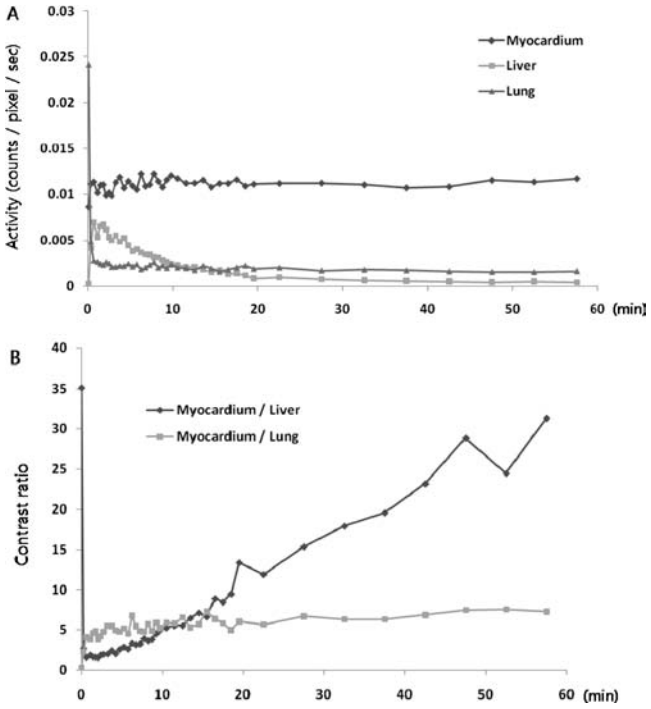


Figure 5. (A) Time−activity curves generated from dynamic PET images. [^{18}F]**3** accumulated specifically in the heart. The [^{18}F]**3** in liver was washed out rapidly but was retained in the myocardium for the whole time. (B) Contrast ratio of myocardium-to-liver and myocardium-to-lung for 1.0 h after i.v. injection of [^{18}F]**3**.

was >30 at 10 min, indicating rapid clearance of the compound from the blood. The heart-to-lung, heart-to-liver, and the heart-to-normal muscle ratios were >3, >4, and >5, respectively, at 10 min after radiotracer injection. Notably, the heart-to-blood and heart-to-liver ratios increased to >138 and >25 at 120 min after radiotracer injection, indicating that [^{18}F]**3** is optimal as a cardiac imaging agent.

Coronal micro-PET imaging was performed in rats at 0.5 h (Figure 4A) and 1 h (Figure 4B) after i.v. injection of [^{18}F]**3**. The results demonstrated good visualization of the heart, with excellent heart-to-background contrast at each time point. Time−activity curves for the myocardium, liver, and lung revealed rapid washout from the liver and lung after i.v. injection of [^{18}F]**3**. However, [^{18}F]**3** was retained at a constant level in the myocardium for up to 1.0 h after injection (Figure 5A). The myocardium-to-liver and myocardium-to-lung uptake ratios quickly reached 5.0 after [^{18}F]**3** injection (Figure 5B).

The rationale for preparing the 6-carbon spacer group was to decrease lipophilicity. Previous publications have reported that [^{18}F]-FBnTP is metabolically stable and demonstrates excellent characteristics as a cardiac imaging agent in healthy mice.[7] However, the myocardium-to-liver uptake ratio in the time-activity curve reached 1.0 at approximately 25 min after i.v. injection of [^{18}F]-FBnTP, indicating delayed washout from the liver. Clearance of the radiotracer from the liver would be dependent on the lipophilicity of the compound. Thus, in the current study, several kinds of radiolabeled phosphonium salts were synthesized to assess the appropriate lipophilicity by different carbon chain lengths; however, highly lipophilic structures (such as benzene rings) were not adopted for the radiolabeling of phosphonium salts. Compared to [^{18}F]**3**, the (3-[^{18}F]fluoropropyl)triphenylphosphonium cation[12] (a shorter-chain analog) showed lower myocardial uptake, whereas the (8-[^{18}F]fluorooctyl)triphenylphosphonium cation (a longer-chain analogue) showed higher liver uptake and delayed clearance (data not shown).

CONCLUSION

In the current study, we suggested the feasibility of a [^{18}F]-labeled phosphonium cation as a PET myocardial agent. Alkyltriphenylphosphonium cations are better candidates for the general delivery of compounds to mitochondria because they accumulate to a greater extent within the mitochondria in cells.[20] The [^{18}F]**3** compound was synthesized very easily from the reaction of triphenylphosphine with appropriate precursors, which have the proper cationic activity and lipophilicity to penetrate the mitochondrial membrane and accumulate inside. [^{18}F]**3** revealed good myocardial uptake, high myocardial selectivity and fast clearance from other organs. Future studies will be directed toward functional studies with diverse in vitro and small animal models.

ASSOCIATED CONTENT

Supporting Information

^{1}H and ^{13}C NMR spectra of all compounds. This material is available free of charge via the Internet at http://pubs.acs.org.

AUTHOR INFORMATION

Corresponding Author

*Jung-Joon Min, M.D., Ph.D., Department of Nuclear Medicine, Chonnam National University Medical School, 160 Ilsimri, Hwasun, Jeonnam 519-763, Republic of Korea; Phone 82-61-379-8476; Fax 82-61-379-8455; E-mail: jjmin@jnu.ac.kr. Kook-Hyun Yu, Ph.D., Department of Chemistry, Dongguk University-Seoul, 30 Pildong-ro 1-Gil, Jung-gu, Seoul, 100-715, Republic of Korea; Phone 82-2-2260-3709; Fax 82-2-2268-8204; E-mail: yukook@dongguk.edu.

Notes

The authors declare no competing financial interest.

ACKNOWLEDGMENTS

This research was supported by the National Research Foundation of Korea (NRF) (No. 2011-0029941), by the Brain Korea 21 Project funded by the Ministry of Education, Science, and Technology, and in part by the Nuclear R&D Program of the Korean Ministry of Education, Science and Technology.

REFERENCES

(1) Schwaiger, M., and Melin, J. (1999) Cardiological applications of nuclear medicine. *Lancet 354*, 661−6.

(2) Gibbons, R. J., Valeti, U. S., Araoz, P. A., and Jaffe, A. S. (2004) The quantification of infarct size. *J. Am. Coll. Cardiol. 44*, 1533−42.

(3) Knuuti, J., and Bengel, F. M. (2008) Positron emission tomography and molecular imaging. *Heart 94*, 360−7.

(4) Kim, D., Yu, K., Bom, H., and Min, J. (2007) Synthesis of (4-[^{18}F]Fluorophenyl)triphenylphosphonium as a Mitochondrial Voltage Sensor for PET. *Nucl. Med. Mol. Imaging 41*, 561−565.

(5) Madar, I., Ravert, H., Dipaula, A., Du, Y., Dannals, R. F., and Becker, L. (2007) Assessment of severity of coronary artery stenosis in a canine model using the PET agent ^{18}F-fluorobenzyl triphenyl phosphonium: comparison with ^{99m}Tc-tetrofosmin. *J. Nucl. Med. 48*, 1021−30.

(6) Min, J. J., Biswal, S., Deroose, C., and Gambhir, S. S. (2004) Tetraphenylphosphonium as a novel molecular probe for imaging tumors. *J. Nucl. Med. 45*, 636−43.

(7) Madar, I., Ravert, H., Nelkin, B., Abro, M., Pomper, M., Dannals, R., and Frost, J. J. (2007) Characterization of membrane potential-dependent uptake of the novel PET tracer ^{18}F-fluorobenzyl triphenylphosphonium cation. *Eur. J. Nucl. Med. Mol. Imaging 34*, 2057−65.
(8) Kroemer, G. (2003) Mitochondrial control of apoptosis: an introduction. *Biochem. Biophys. Res. Commun. 304*, 433−5.
(9) Cesselli, D., Jakoniuk, I., Barlucchi, L., Beltrami, A. P., Hintze, T. H., Nadal-Ginard, B., Kajstura, J., Leri, A., and Anversa, P. (2001) Oxidative stress-mediated cardiac cell death is a major determinant of ventricular dysfunction and failure in dog dilated cardiomyopathy. *Circ. Res. 89*, 279−86.
(10) Madar, I., Ravert, H. T., Du, Y., Hilton, J., Volokh, L., Dannals, R. F., Frost, J. J., and Hare, J. M. (2006) Characterization of uptake of the new PET imaging compound ^{18}F-fluorobenzyl triphenyl phosphonium in dog myocardium. *J. Nucl. Med. 47*, 1359−66.
(11) Yu, K. H., Kim, Y. S., Kim, S. W., Park, J. H., Yang, S. D., Herdering, W., and Knoechel, A. (2003) Synthesis of [^{18}F]-Fluoroclofilium as a potential cardiac imaging agent for PET studies. *J. Label. Compd. Radiopharm. 46*, 1151−1160.
(12) Ravert, H. T., Madar, I., and Dannals, R. F. (2004) Radiosynthesis of 3-[^{18}F]fluoropropyl and 4-[^{18}F]fluorobenzyl triarylphosphonium ions. *J. Label. Compd. Radiopharm. 47*, 469−476.
(13) Kim, Y. S., Yang, C. T., Wang, J., Wang, L., Li, Z. B., Chen, X., and Liu, S. (2008) Effects of targeting moiety, linker, bifunctional chelator, and molecular charge on biological properties of ^{64}Cu-labeled triphenylphosphonium cations. *J. Med. Chem. 51*, 2971−84.
(14) Steen, H., Maring, J. G., and Meijer, D. K. (1993) Differential effects of metabolic inhibitors on cellular and mitochondrial uptake of organic cations in rat liver. *Biochem. Pharmacol. 45*, 809−18.
(15) Cheng, Z., Winant, R. C., and Gambhir, S. S. (2005) A new strategy to screen molecular imaging probe uptake in cell culture without radiolabeling using matrix-assisted laser desorption/ionization time-of-flight mass spectrometry. *J. Nucl. Med. 46*, 878−86.
(16) Zhou, Y., and Liu, S. (2011) ^{64}Cu-Labeled Phosphonium Cations as PET Radiotracers for Tumor Imaging. *Bioconjugate Chem.*
(17) Demura, M., Kamo, N., and Kobatake, Y. (1987) Binding of lipophilic cations to the liposomal membrane: thermodynamic analysis. *Biochim. Biophys. Acta 820*, 303−308.
(18) Ono, A., Miyauchi, S., Demura, M., Asakura, T., and Kamo, N. (1994) Activation energy for permeation of phosphonium cations through phospholipid bilayer membrane. *Biochemistry 33*, 4312−8.
(19) Smith, R. A., Kelso, G. F., James, A. M., and Murphy, M. P. (2004) Targeting coenzyme Q derivatives to mitochondria. *Methods Enzymol. 382*, 45−67.
(20) Ross, M. F., Kelso, G. F., Blaikie, F. H., James, A. M., Cocheme, H. M., Filipovska, A., Da Ros, T., Hurd, T. R., Smith, R. A., and Murphy, M. P. (2005) Lipophilic triphenylphosphonium cations as tools in mitochondrial bioenergetics and free radical biology. *Biochemistry (Mosc.) 70*, 222−30.

Bioconjugate Chemistry

Article

pubs.acs.org/bc

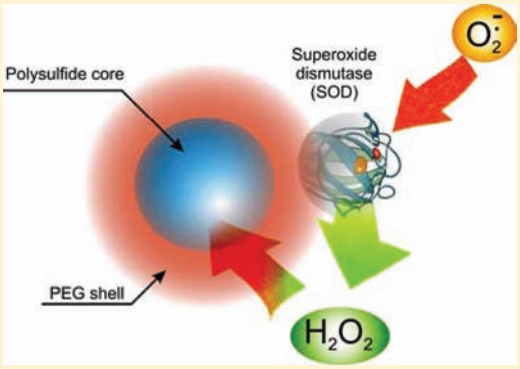
Scavenging ROS: Superoxide Dismutase/Catalase Mimetics by the Use of an Oxidation-Sensitive Nanocarrier/Enzyme Conjugate

Ping Hu[†] and Nicola Tirelli*[,‡,§]

[†]School of Pharmacy and Pharmaceutical Sciences, [‡]School of Materials, [§]School of Biomedicine, University of Manchester, Oxford Road, Manchester, M13 9PT, United Kingdom

Supporting Information

ABSTRACT: Reactive Oxygen Species (ROS) are quintessential inflammatory compounds with oxidizing behavior. We have successfully developed a micellar system with responsiveness at the same time to two of the most important ROS: superoxide and hydrogen peroxide. This allows for an effective and selective capture of the two compounds and, in perspective, for inflammation-responsive drug release. The system is composed of superoxide dismutase (SOD) conjugated to oxidation-sensitive amphiphilic polysulfide/PEG block copolymers; the conjugate combines the SOD reactivity toward superoxide with that of hydrophobic thioethers toward hydrogen peroxide. Specifically, here we have demonstrated how this hybrid system can efficiently convert superoxide into hydrogen peroxide, which is then "mopped-up" by the polysulfides: this *modus operandi* is functionally analogous to the SOD/catalase combination, with the advantages of (a) being based on a single and more stable system, and (b) a higher overall efficiency due the physical proximity of the two ROS-reactive centers (SOD and polysulfides).



INTRODUCTION

Reactive Oxygen Species (ROS), such as superoxide anion, hydroxyl radical, or hydrogen peroxide, are ubiquitous byproducts of cell metabolism with a double role of hazardous agents capable of extensive cellular damage but also signaling molecules;[1] ROS can stimulate a variety of phenomena, from mitosis to angiogenesis, and also tumorigenesis, but in particular they are closely associated with virtually all main inflammatory pathologies.[2−5]

A central target of our group is the development of oxidation-responsive (nano)materials, that can be used to develop advanced anti-inflammatory therapies. We have specifically focused on thioether-containing organic polymers (polysulfides) in the forms of micelles,[6] vesicles,[7] and nanoparticles,[8] which have shown promising results as *in vivo* carrier structures.[9] Their responsiveness is based on the morphological changes associated to the oxidation of hydrophobic thioethers to more hydrophilic sulfoxides and sulfones; this may lead to swelling or solubilization and, e.g., release of an encapsulated drug to an extent proportional to the concentration of oxidants. The synthetic strategies and the oxidation response of polysulfides are discussed in a recent review.[10]

In a previous study, we have demonstrated how polysulfide nanoparticles can also respond to oxidants that are generated enzymatically *in situ*:[11] by decorating the nanoparticle surface with glucose oxidase, hydrogen peroxide can be produced in close proximity to the polysulfide material in the presence of glucose; the resulting oxidation and swelling of the matrix permitted the release an encapsulated drug (doxorubicin). However, the responsiveness of polysulfides may depend on the nature of the oxidant: for example, the low solubility of very polar or ionic molecules may determine a slow or negligible response.

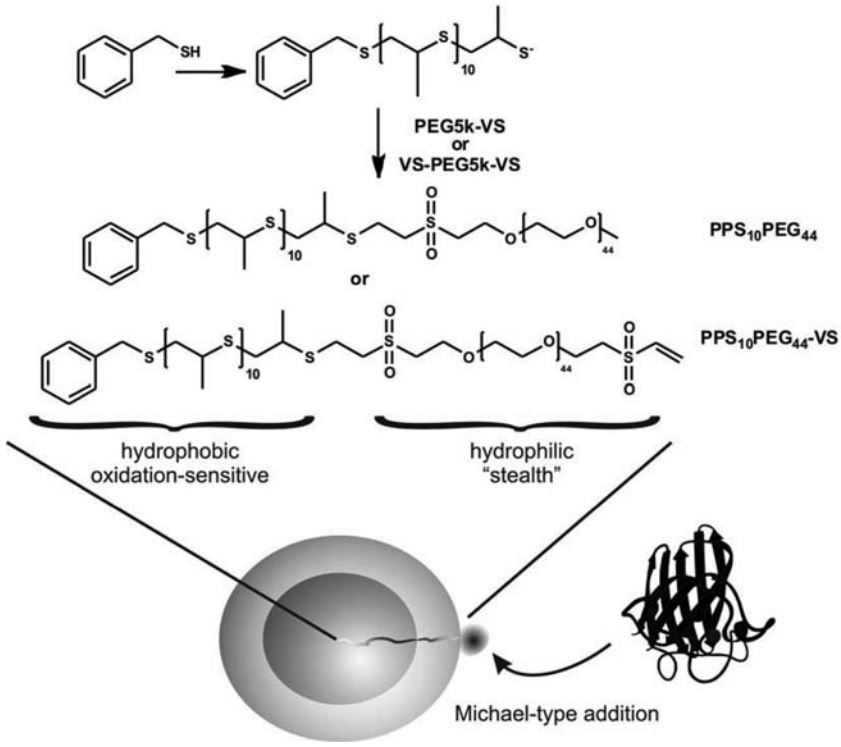
Superoxide is a ubiquitous ROS, most commonly produced by NAPDH oxidase in activated leukocytes,[2] although alternative sources exist, e.g., xanthine oxidase.[12] It is also one of the most dangerous ROS; besides its direct toxic action, it can produce a number of cytotoxic compounds, such as hydroxy radicals, peroxynitrite, or hydrogen peroxide. It has long been shown that superoxide can be scavenged by the combined action of superoxide dismutase (SOD) and catalase,[13−15] where the first enzyme converts it to hydrogen peroxide, which is then removed by the second one; however, this scavenging activity is rather short-lasting, due to the rather limited lifetime of the enzymes. Superoxide is anionic, thus poorly soluble in a hydrophobic matrix; it is also highly reactive and unselective, so scarce solubility in polysulfides is likely to result in negligible advantageous effects.

In the present research, we have focused on polysulfide-containing micelles (block copolymers of poly(propylene sulfide) (PPS) and PEG), studying their possible superoxide-scavenging activity and tackling the issue of improving it by conjugation with the most common naturally occurring, selective superoxide scavenger, i.e., superoxide dismutase.

Received: August 16, 2011
Revised: January 4, 2012
Published: January 31, 2012

ACS Publications © 2012 American Chemical Society

Scheme 1. Sequence of Preparative Steps Leading to PPSPEG Reactive Micelles That Allow the Incorporation of SOD through Michael-Type Addition of SOD Nucleophilic Groups onto Vinyl Sulfone Polymeric Termini



SOD is a general name for a class composed of four families of enzymes, i.e., Cu,Zn-, Fe-, Mn-, and Ni-SODs; as a common element, they all accelerate the transformation of the superoxide radical anion into H_2O_2 and molecular oxygen. This activity renders SOD one of the most ubiquitous enzymes for the defense of both prokaryotic and eukaryotic organisms from oxidative damage. A recent review of Bafana et al.[16] summarizes the state of the art about physiological and pathophysiological roles of SOD. SODs, and more specifically Cu,Zn-SOD, has been long researched as a possible means to treat a number of pathologies of inflammatory or tumoral nature.[17] In particular, a clear link has been established between forms of amyotropic lateral sclerosis and inactivation of SOD due to mutation,[18] but also other inflammatory pathologies with oxidative character, such as inflammatory bowel diseases,[19] have shown beneficial effects of SOD administration.[20]

Although SOD has shown efficacy in several inflammatory pathologies, it has not found widespread clinical application: its rapid renal clearance associated with a slow extravasation in peripheral tissues minimizes its beneficial effects on peripheral, inflamed tissues.[21]

A number of strategies have been attempted to overcome the poor pharmacokinetic behavior of SOD. A first approach focuses on the *in situ* sustained production of the enzyme through the use of genetically engineered cells[22] or bacteria;[23] although promising, this avenue is complicated by the generally low acceptance of therapies based on engineered cells. Another approach has tackled the development of SOD-mimetic compounds,[24,25] generally based on low molecular weight[26] or polymeric[27] Mn porphyrin but including also cerium oxide[28] or platinum[29] nanoparticles; although significant results have been reached, the rapid clearance of low molecular weight compounds and the regulatory approval of new active principles are significant hurdles.

A third, more proven way has seen the use of SOD conjugates. Poly(ethylene glycol) (PEG) is a "gold standard" to improve protein stability *in vivo*, reduce enzymatic degradability and immunogenicity, improve solubility, and reduce renal clearance. PEG has been conjugated to SOD using a variety of coupling reagents, e.g., cyanuric trichloride,[30] phenyl chloroformiate,[31] or carbonyl diimidazole.[32] There is ample evidence that PEGylation *per se* does not substantially alter SOD activity, as demonstrated in a number of *in vitro* and *in vivo*[33] models and also in clinical trials.[34] Other polymers have also been conjugated to SOD for the same purposes, e.g., PEG amphiphilic block copolymers, such as Pluronics,[35] or poly-(*N*-vinyl pirrolidone).[36] PEG has also been used as a spacer for the conjugation of SOD to a payload, such as hemoglobin,[37] to protect the latter from the action of free radicals.

In this study, we have prepared PPSPEG block copolymers through sequential ring-opening anionic polymerization of propylene sulfide initiated by benzyl mercaptane and end-capped by monovinyl sulfone terminated PEG (Scheme 1); the synthesis of these copolymers is described in a recent publication.[6] We have specifically focused on a low PPS length (PPS_{10}-PEG_{44}) to maximize the surface-to-volume ratio of the micelles and therefore maximize their response rate to waterborne oxidants. A vinyl sulfone-terminated block copolymer (PPS_{10}-PEG_{44}-VS) was prepared with an identical procedure and used to prepare mixed micelles that were then functionalized with SOD through Michael-type addition. We have then investigated the superoxide-scavenging ability of PPSPEG micelles with or without SOD.

EXPERIMENTAL PROCEDURES

Materials. Acetic acid, poly(ethylene glycol) monomethyl ether ($\overline{M_n}$ = 2000 and 5000 g/mol), sodium hydride, divinyl

dx.doi.org/10.1021/bc200449k | *Bioconjugate Chem.* 2012, 23, 438–449

sulfone, superoxide dismutase (Cu,Zn-SOD from bovine erythrocytes, lyophilized powder, 3780 U/mg protein, MW: 32.5 kDa), tris(2-carboxyethyl)phosphine hydrochloride solution (0.5 M), Sephadex G-100, glycerol, sodium dodecyl sulfate, β-mercaptoethanol, bromophenol blue, Coomassie brilliant blue R-250, barium chloride, iodine solution (0.05 M in water), 2,4,6-trinitrobenzenesulfonic acid solution (5% in water), BCA assay kit, SOD assay kit, Triton X-100, sodium hydroxide, Nile Red, hydrogen peroxide (30 wt % solution), xanthine, xanthine oxidase (from bovine milk, ammonium sulfate suspension, 1.0 U/mg protein, MW: 270 kDa), Catalase (from bovine liver, lyophilized powder, 4342 U/mg protein, MW: 250 kDa), and Celltiter 96 Aqueous Cell Proliferation assay kit (containing MTS and PES) were used as received from Sigma-Aldrich (Gillingham, United Kingdom). Macrophages J774.2 were obtained from the European Collection of Cell Cultures (Porton Down, UK). Phosphate buffered saline (PBS) was prepared from phosphate buffered saline (Dulbecco A) tablets (Oxoid limited, Basingstoke, UK). Water was purified through a Milli-Q system (Millipore, UK).

Physicochemical Characterization. *Molecular Characterization.* ^{1}H NMR spectra were recorded on 1 wt % polymer solutions in deuterated chloroform using a 300 MHz Bruker spectrometer. FT-IR spectra were recorded in ATR mode (Golden gate) on a Tensor 27 Bruker spectrometer. GPC was performed in THF on a Polymer Laboratories GPC 50 equipped with refractive index and viscosity detectors, using universal calibration with poly(styrene) standards. UV−vis and fluorescence readings were obtained on a BioTek Synergy 2 multiwell plate reader.

Dynamic Light Scattering (DLS). Size distributions were measured with the help of a Zetasizer Nano ZS Instrument (model ZEN2500, Malvern Instruments Ltd., UK). All the samples were analyzed at an angle of 114° and at a temperature of 25 °C.

Preparative Procedures. *Polymer Synthesis.* PEG2k-VS ($\overline{M_n}$ = 2100 g/mol, yield: 78 wt %), PEG5k-VS (5200 g/mol, yield: 81 wt %) were prepared via reaction of the corresponding monomethoxy PEG derivatives with an excess divinyl sulfone after deprotonation with catalytic amounts of NaH, as described in a previous publication.[6] PPS_{10}-PEG_{44} and PPS_{10}-PEG_{44}-VS were prepared through propylene sulfide anionic polymerization initiated by benzyl mercaptane and end-capped with PEG2k mono- or bis(vinyl sulfone) ($\overline{M_n} \sim$ 3000 g/mol, polymerization yield: 62 wt %, end-capping conversion: 94 mol % end-capping conversion 94 mol % calculated from the ratio of the ^{1}H NMR resonance of PEG terminal CH_3 at 3.4 ppm and that of the aromatic group of the initiator at 7.4 ppm[6]). Most SOD PEGylation experiments were conducted with PEG5k-VS, in order to have a hydrodynamic volume comparable to PPS_{10}-PEG_{44}-VS; PEG2k-VS was used only as a control for SDS-PAGE experiments.

Conjugation Experiments. Reaction with Native SOD. 2.5 mg of SOD were dissolved in 2 mL of 10 mM sodium phosphate buffer at pH 8.5. 8.8 mg of PEG5k-VS (1.6×10^{-3} mmol) were dissolved in 0.5 mL of the same buffer (corresponding to a 20:1 PEG-VS/SOD molar ratio) and were added to the SOD solution. The reaction mixture was allowed to react for 72 h at room temperature. A drop of NaOH (0.01 M) solution was then added to deactivate any unreacted vinyl sulfone groups, followed by a few drops of HCl solution (0.01 M) to restore neutrality.

Reaction with Reduced SOD. 2.5 mg of SOD were dissolved in 2 mL of 10 mM sodium phosphate buffer, pH 8.5; 47 μL of a 0.01 M TCEP (4.7×10^{-4} mmol) solution were then added and the solution was allowed to react for 2 h at room temperature. In control experiments, the solution was transferred into a dialysis tube (MWCO = 3000 g/mol), and dialyzed against 1 L 10 mM PBS buffer, pH 8.5, for 24 h to remove the reducing agent. The solution of reduced SOD with or without dialysis was then reacted with PEG-VS as previously described.

Conjugation of SOD to PPS_{10}-PEG_{44}-VS Micelles. 0.5 mL of a PPS_{10}-PEG_{44}-VS micelles dispersion (4.8 mg of a 9:1 PPS_{10}-PEG_{44}/PPS_{10}-PEG_{44}-VS molar ratio for a total 1.6×10^{-3} mmol of polymer chains) was employed in stead of a PEG-VS solution.

Purification through Size Exclusion Chromatography (SEC). The reaction mixtures (volume ~2.5 mL) were loaded on the top of a prewetted Sephadex G100 column (1.5 × 500 mm) and the system was eluted with the help of a pump (LDC Analytical, constaMetric 3200) operating at 1 mL/min, using 10 mM PBS buffer. The eluted profile of the sample was monitored using absorbance at 260 nm, collecting different fractions that were further characterized by SDS-PAGE.

Analytical Assays on PEGylated SOD. *SDS-PAGE.* SDS-PAGE analysis was performed on 4−12% polyacrylamide gels. First, the protein concentration of all samples was determined by the BCA assay using SOD as standard (see later). Then each sample was freeze−dried and redissolved in water to achieve the same concentration of protein (1 mg/mL). Each solution was mixed with the SDS-PAGE buffer (250 mM Tris pH 6.8, 25% glycerol, 2% SDS, 5% β-mercaptoethanol and 0.01% bromophenol blue) in a 1:1 volume ratio and heated at 95 °C for 5 min. The slab of gel was composed of 2 cm of stacking gel (4% acrylamide, 62.5 mM Tris pH6.8) and 6 cm of resolving gel (12% acrylamide, 375 mM Tris pH 8.8) with a thickness of 1.5 mm. The electrophoresis was performed at 120 V for 10 min, then increased to 200 V for the rest of the run. The gel was then incubated in a staining solution (0.025% Coomassie brilliant blue R-250 in 40% acetic acid, 20% methanol) for 1 h with gentle shaking, and washed with a destaining solution (40% acetic acid, 20% methanol) to remove excess stain.

Barium Iodide Assay. The concentration of PEG was determined by a modified barium iodide method:[38] 25 μL of barium chloride (5%, in 1 M HCl) was added to 100 μL of sample solution in a 96 well plate. The solution was mixed for 5 min at room temperature before 25 μL of iodine solution (0.1 M) was added to the well. The plate was allowed to stand for 15 min at room temperature to develop the color which was read at 535 nm by a plate reader (BioTek Synergy 2). The concentrations of PEG in PEG-SOD and PPSPEG-SOD samples were measured and calculated by comparing the readings with a PEG5k/PEG2k standard calibration curve. The influence of SOD to this method was investigated by measuring the absorbance of PEG standard solutions added with different amounts of (noncovalently bound) SOD.

BCA (Bicinchonic Acid) Assay. The concentration of total proteins was determined with a standard BCA assay: in a 96 well plate 100 μL of BCA assay reagent (Sigma-Aldrich) were added to 100 μL of SOD-containing solution/dispersion (e.g., PPSPEG-SOD micelles) previously purified through SEC. The plate was kept at room temperature for 16 h before the absorbance at 562 nm was read using a plate reader. The

concentration of SOD in the sample was calculated by comparing the reading with a standard SOD calibration curve.

The degree of PEGylation was calculated as the ratio molar concentration of PEG/molar concentration of SOD.

TNBS Assay. The number of PEG residues attached to SOD lysines was determined by measuring the primary amine content of SOD before and after conjugation through the colorimetric reaction with TNBS. Briefly, solutions at different concentrations of the native SOD and of PEGylated SOD were prepared in borate buffer (pH 9.3, 0.1 M). 50 μL of TNBS reagent (0.01 M) and 50 μL of 10% SDS were added to 50 μL of protein solution with 100 μL of borate buffer in a 96 well plate. The solution was allowed to react at 25 °C for 2 h. The absorbance at 420 nm of the sample was then measured and plotted versus the protein concentration: the number n of the reacted lysine residues on SOD is $n = 20 \times (1 - (slope_{PEG\text{-}SOD})/(slope_{SOD}))$ where 20 represents the number of the lysine residues present in SOD.

Evaluation of the Superoxide-Scavenging Activity. The superoxide-scavenging activity of SOD, PPS_{10}-PEG_{44}, and PPS_{10}-PEG_{44}-SOD was determined by the Sigma Aldrich (Dojindo) SOD assay kit, which is based on xanthine oxidase (XO) as the generator of superoxide and WST-1 as the chromophore's parent compound. Briefly, 20 μL of a solution of SOD, or of a dispersion of PPS_{10}-PEG_{44}-SOD at different concentrations and 20 μL of a solution of XO at variable concentration were added to 200 μL of a WST-1 standard solution in wells of a 96 well plate. The plate was incubated at 37 °C for 20 min and the absorbance was read at 450 nm using a plate reader. The activity of the superoxide scavenger was expressed as the inhibition percentage in relation to the absorbance of a blank sample.

Preparation and Characterization of PPS_{10}-PEG_{44}(-SOD) Micelles. PPS_{10}-PEG_{44} micellar dispersions were prepared through direct dispersion of the block polymers in PBS buffer (pH 7.4) at a concentration of 1 mg/mL and then possibly further diluted. PPS_{10}-PEG_{44}-SOD micelle dispersions in the same buffer were prepared and purified by size exclusion chromatography (SEC) on Sephadex G-100.

Cytotoxicity of PPS_{10}-PEG_{44} Micelles. Cytotoxicity of PPS_{10}-PEG_{44} micelles was assessed on a line of murine macrophages (J774.2) using a CellTiter 96 Aqueous Cell Proliferation Assay. Cells were seeded in a clear 96-well flat bottomed plate at a concentration of 2.5×10^4 cells per well and kept in 37 °C, 5% CO_2 incubator for 24 h to allow for cell adherence. On the next day, the cells were washed once with PBS, then PPS_{10}-PEG_{44} micelles in cell culture medium at concentrations of 1.9, 2.5, 3.8, 5, 7.5, 10, 15, and 20 mg/mL were added into each well and plain medium was used as a control. The plate was then incubated for 48 h at 37 °C, 5% CO_2 environment. After 48 h of incubation, the supernatant medium was removed, and the wells were rinsed twice with PBS (pH 7.4, 10 mM). Then 100 μL of culture medium without FBS and phenol red supplemented with 20 μL of MTS reagent was added into each well. After 3 h the absorbance of each well was read on a microplate reader (μQuant, Biotek) at 490 nm. Finally, in each well the cells were washed with PBS and were then exposed to a lytic solution of 0.5 wt % Triton X-100 in 0.2 N sodium hydroxide for 10 min at 37 °C, which was then employed to analyze the protein content through the QuantiPro BCA Assay Kit according to the manufacturer's recommendations. The relative cell viability (%) was calculated by $([A]_{test}/[\text{protein content}]_{test})/([A]_{control}/[\text{protein content}]_{control})$, where $[A]_{test}$ is the absorbance of the test sample and $[A]_{control}$ is the absorbance of a control sample (well containing cell culture medium without PPS_{10}-PEG_{44} micelles).

Nile Red Loading and Encapsulation Efficiency. 0.1 mL of dichloromethane solutions of Nile Red with variable concentrations (0.0625 to 2 mg/mL) were mixed with 1 mL of 1.0 mg/mL of pure PPS_{10}-PEG_{44} or of PPS_{10}-PEG44/PPS10-PEG_{44}-SOD 9:1 micellar dispersions, evaporating the organic solvent in a rotary evaporator (400 mbar for 5 min, followed by 80 mbar for 30 min, T = 25 °C). Any nonencapsulated payload was removed by centrifugation at 4500 rpm. To measure the amount of loaded Nile Red, 0.1 mL of *N*,*N*-dimethylformamide was added to 0.1 mL of drug-loaded micellar dispersion in order to solubilize the encapsulated compounds. The concentration of hydrophobe was then measured via its emission intensity at 620 nm (excitation in the window 540 ± 25 nm, emission in the window 620 ± 40 nm). The concentrations of samples were calculated by comparing the readings to a standard curve of Nile Red in 50% DMF. Drug loading (DL) and encapsulation efficiency (EE) were calculated as follows: DL (w/w) = (amount of loaded drug)/(amount of polymer), EE (wt %) = (actual amount of loaded drug)/(theoretical amount of loaded drug).

Oxidation Responsiveness of PPS_{10}-PEG_{44}(-SOD) Micelles. *Responsiveness to Hydrogen Peroxide. DLS.* One mL of a 1 mg/mL dispersion of PPS_{10}-PEG_{44} micelles prepared as previously described was added to 1 mL of a solution of hydrogen peroxide solution with variable concentration to yield a final H_2O_2 concentration of 0, 2, 5, and 10 wt %. The kinetics of oxidation was followed by recording the size distribution and the overall scattering intensity at room temperature as a function of time.

Nile Red Method. The experiments were prepared as above, diluting a 1 mg/mL micellar dispersion with a 15 μg/mL concentration of Nile Red with 1 mL of a solution of hydrogen peroxide solution. The fluorescence of Nile Red was measured at defined times (0, 0.1 h, 1 h, 2 h, 4 h, 5.5 h, 8 h, 12 h) using a plate reader with excitation filter at 540 ± 25 nm and emission filter at 620 ± 40 nm.

Responsiveness to Superoxide. Nile Red Assay. 0.5 mL of a 40 mM solution of xanthine and 0.1 mL of a 4×10^{-2} mM solution of xanthine oxidase were added to 2 mL of a Nile Red-loaded PPSPEG (3.3 mM of sulfides,15 μg/mL of Nile Red) or PPSPEG-SOD (3.3 mM of sulfides, 7.7×10^{-4} mM of conjugated SOD, 18 μg/mL of Nile Red) micellar dispersion. In different experiments 0.2 mL of a 6.1×10^{-3} mM solution of SOD and/or 0.2 mL of a 8×10^{-4} mM solution of catalase were added too. The molar concentrations of the enzymes are calculated by dividing their concentration in weight/volume by the molecular weight of the enzymes; this does not take into account the different purity of the preparations, and indeed these molar concentrations are just indicative values; it is important to note that the apparent molarity of SOD and catalase is much lower than that of XO, but the activity of their solutions is comparable.

Finally, variable amounts of PBS buffer (pH 7.4, 10 mM) was added to the dispersion which resulted in 4 mL of final mixture containing 1.7 mM of sulfides, 5 mM of xanthine, and 1×10^{-3} mM of xanthine oxidase without SOD (3.1×10^{-4} mM) and catalase (4×10^{-5} mM). The fluorescence intensity of the sample was then measured via its emission intensity at 620 nm (excitation in the window 540 ± 25 nm, emission in the window 620 ± 40 nm) at fixed times (0, 0.5, 1, 2, 3, 4, and 6 h).

dx.doi.org/10.1021/bc200449k | *Bioconjugate Chem.* 2012, 23, 438–449

The fluorescence intensity was presented as the percentage of the fluorescence intensity at 0 h.

Formazan (MTS) Assay. Superoxide was generated *in situ* through a xanthine–xanthine oxidase system and its presence was monitored via the reduction of MTS added to the system. Typical experiments were conducted in 96 well plates; in each well, 50 μL of PPS_{10}-PEG_{44} micellar dispersions (0, 0.033, 0.33, 3.3 mM of polymer) or 20 μL of SOD solution (0, 2×10^{-5}, 2×10^{-4}, 2×10^{-3} mM of enzyme) were added to 50 μL of 2 mM xanthine, 20 μL of xanthine oxidase (2×10^{-5}, 2×10^{-4}, 2×10^{-3} mM), 50 μL of 0.2 mM MTS, and variable amounts of PBS buffer (pH 7.4, 10 mM) to yield 200 μL of final solution which contains PPS_{10}-PEG_{44} micelles (0, 8.3×10^{-2}, 8.3×10^{-1}, 8.3 mM sulfides) or SOD (0, 2×10^{-6}, 2×10^{-5}, 2×10^{-4} mM), xanthine (0.5 mM), xanthine oxidase (2×10^{-6}, 2×10^{-5}, 2×10^{-4} mM) and MTS (0.05 mM). The enzymatic kinetics was monitored through the absorbance of MTS at 490 nm.

A purified PPS_{10}-PEG_{44}-SOD micelle dispersion (containing 0.33 mM polymer and 7.7×10^{-4} mM conjugated SOD) was also reacted with the superoxide-generating system. A final solution containing 8.3×10^{-1} mM sulfides and 1.9×10^{-4} mM conjugated SOD, 0.5 mM xanthine, 2×10^{-5} mM xanthine oxidase, and 0.05 mM MTS was employed for identical kinetics studies.

RESULTS AND DISCUSSIONS

Low Toxicity, Oxidation Responsiveness, but Poor Superoxide Scavenging Ability of PPS_{10}-PEG_{44}. PPS-based PEGylated materials (block copolymers in vesicular or micellar morphology, nanoparticles, etc.) are generally characterized by negligible cytotoxic effects on cells. For example, the exposure of a rather sensitive cell line, J774.2 murine macrophages, to PPS_{10}-PEG_{44} micelles caused no significant reduction in cell viability for PPSPEG concentrations up to 4 mg/mL; an IC_{50} was recorded in the region of 15 mg/mL (1.5 wt %).

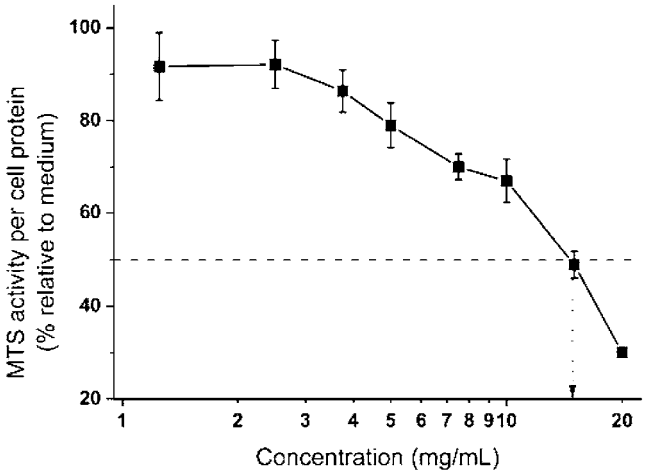


Figure 1. Viability of J774.2 macrophages as a function of the concentration of PPSPEG micelles after a 48 h exposure. The mitochondrial reductase activity (MTS assay) was normalized in relation to the protein content and reported as % of the control. The dashed line allows the identification of the IC_{50}.

The reaction of PPS with oxidants produces polar species, such as sulfoxides. As a result, when treated with a nonionic oxidant such as hydrogen peroxide, PPS_{10}-PEG_{44} micelles eventually solubilize in water (Figure 2). The micelles maintained their size substantially unchanged until complete solubilization, which occurred at a time increasingly longer for lower H_2O_2 concentrations (Figure 2A). On the other hand, their scattering gradually decreased in intensity, more rapidly with increasing H_2O_2 concentration (Figure 2B). Since the scattering intensity is proportional to the refractive index difference between micellar core and water, this result would indicate a gradual increase in the water content of PPS domains. This was confirmed by monitoring the fluorescence of Nile Red, whose fluorescence is quenched by the presence of water; this peculiarity is often used in studies of micellar aggregates.[39,40] Nile Red is encapsulated with high efficiency in PPS_{10}-PEG_{44} micelles (see later, Figure 8), its fluorescence decreased with time and H_2O_2 concentration (Figure 2C), with a kinetics very similar to that of the scattering intensity. The only noticeable difference was a certain retardation of Nile Red quenching (see Supporting Information, Figure 1SI); this lag is probably due to the need of a defined water concentration to achieve an appreciable quenching of NR emission in an apolar solvent.[6]

The PPS_{10}-PEG_{44} micelles appear therefore to undergo a gradual hydophobic-to-hydrophilic transition when exposed to a nonionic model oxidant, such as H_2O_2. However, the ionic nature of superoxide may limit its solubility in a polysulfide matrix, thus decreasing the possible response of PPS. Due to its instability, superoxide was generated *in situ* through the xanthine oxidase (XO)-mediated conversion of xanthine to uric acid; this method provides equimolar amounts of superoxide and H_2O_2 (Scheme 2, left), so we have examined the effects of XO on PPS_{10}-PEG_{44} micelles also in the presence of catalase, which selectively decomposes H_2O_2, and SOD, in order to separate the effects of the two oxidants.

The kinetics of oxidation was followed using Nile Red fluorescence (Figure 3); XO produced a significant and time-dependent hydrophilization, but no effect was recorded when XO was used in combination of catalase, with or without SOD; furthermore, the combination of XO and SOD, which increases the concentration of H_2O_2 and decreases that of superoxide, slightly accelerated the process of PPS hydrophilization (=lower NR fluorescence at all time points). These results indicated that XO could oxidize the PPS micellar core through the production of H_2O_2, while the presence of superoxide appeared to have no effect.

We have confirmed that the negligible effects of superoxide of PPS translated in a negligible superoxide-scavenging activity of PPS micelles, by monitoring their effect on the kinetics of a superoxide-mediated reaction: the oxidative conversion of MTS to MTS formazan (Scheme 2, right). SOD was used as a positive control and, as expected, it showed excellent superoxide scavenging activity (Figure 4, top): with [XO] and [SOD] = $2 \times 10^{-6} - 2 \times 10^{-4}$ mM, dose-dependent SOD effects were recorded for all combinations except when XO was present in large excess (XO 100 times more concentrated than SOD). On the other hand, the presence of PPS_{10}-PEG_{44} micelles did not produce any significant variation or delay in formazan production, even with concentrations up to 8.3 mM of sulfide groups (2.5 mg/mL) (Figure 4, bottom).

It could therefore be concluded that PPS_{10}-PEG_{44} micelles had a poor superoxide-scavenging capacity, due to the negligible reaction of the sulfide groups with superoxide.

Conjugation (PEGylation) of SOD. The SOD–PPSPEG conjugation chemistry should minimize the disruption to the protein secondary and tertiary structure, while also avoiding the

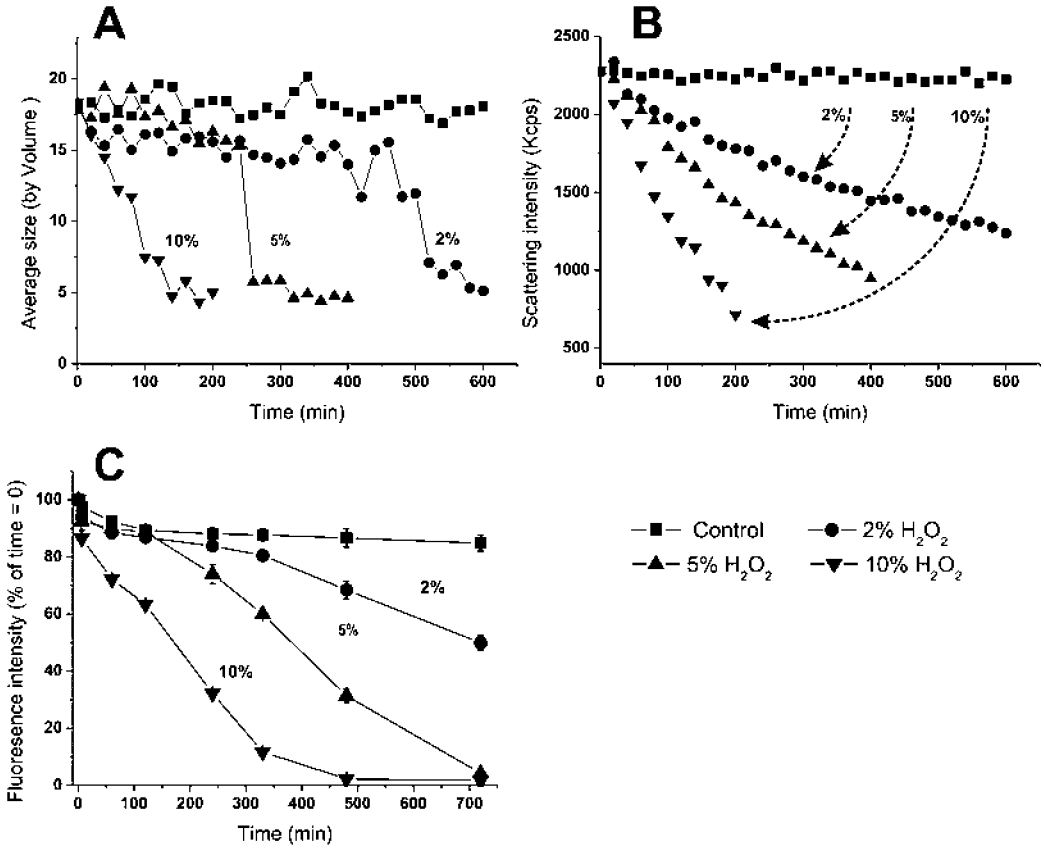
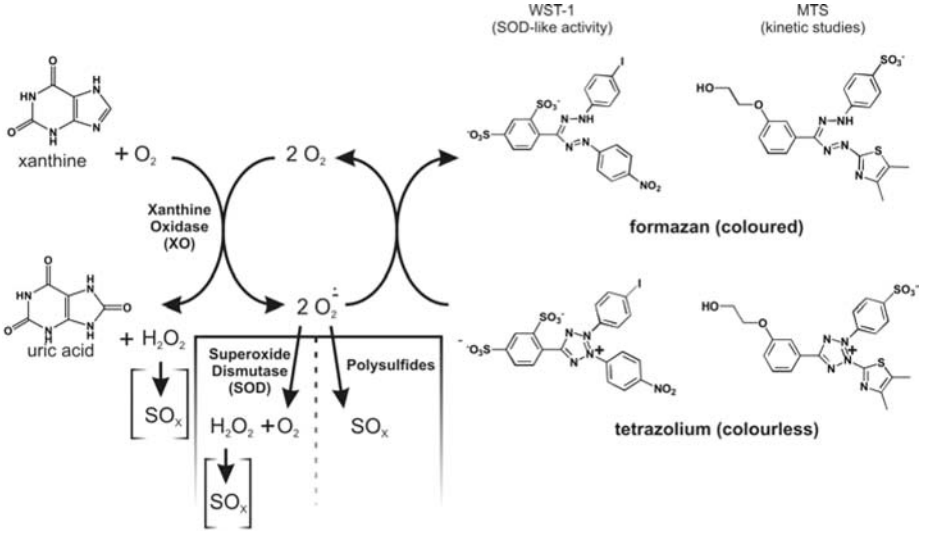


Figure 2. Influence of the concentration of hydrogen peroxide on volume-average micellar size (panel A, top left), on the scattering intensity of the suspension (panel B, top right), and on the fluorescence of encapsulated Nile Red (panel C, bottom left). PPS_{10}-PEG_{44} concentration: 0.5 mg/mL; Nile Red concentration: 7.5 μg/mL.

Scheme 2. Superoxide Generated *in Situ* through the Enzymatic Conversion of Xanthine to Uric Acid Can Be Detected Colorimetrically Using the Oxidation of Tetrazolium to Purple-Coloured Formazan[47] [a]



[a]Two water-soluble tetrazolium derivatives were used: MTS for most measurements and WST-1 for the assessment of SOD activity, which employed a commercially available, WST-1 based kit (Dojindo) The presence of other oxidizable compounds, such as polysulfides, or of superoxide dismutase (SOD) can reduce the conversion of tetrazolium at any given time point.

binding of multiple micelles to the same molecule of SOD that would lead to large-scale aggregation.

We have employed PEG or PPSPEG vinyl sulfones, whose preparation is described in a recent publication.[6] Vinyl sulfones are highly reactive Michael-type acceptors; differently from other Michael-type acceptors such as α,β-unsaturated esters and amides, their reaction products do not bear hydrolyzable groups and resist to an oxidizing environment. On the other hand, vinyl sulfones also react with water/hydroxyl anions (Scheme 3); this limits the efficiency of the bioconjugation

dx.doi.org/10.1021/bc200449k | *Bioconjugate Chem.* 2012, 23, 438–449

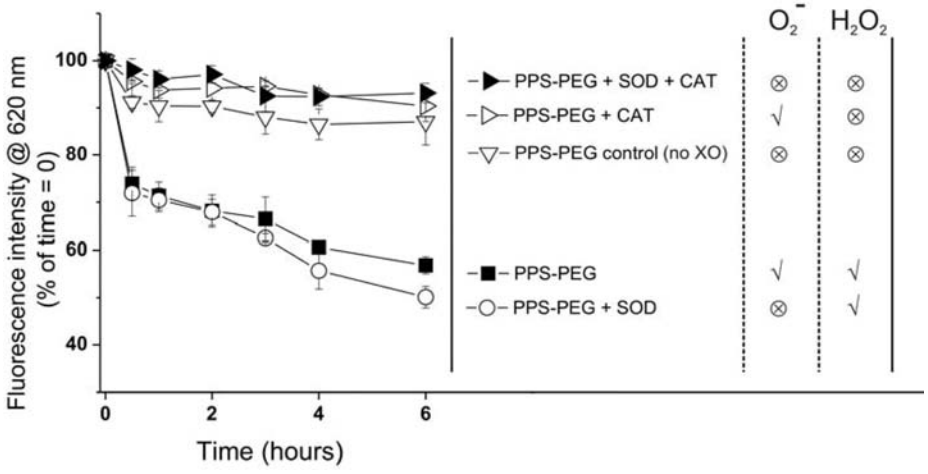


Figure 3. The fluorescence of Nile Red loaded in PPS_{10}-PEG_{44} micelles (15 μg NR per mg of PPSPEG) was examined as a function of time in the presence of XO as an oxidizing enzyme. In water buffers, XO is in a colloidal, rather opaque state, and this makes DLS measurements unreliable; on the other hand, Nile Red fluorescence was previously shown (Figure 2) to follow rather closely the phenomenon of PPS oxidation. Concentrations: PPS_{10}-PEG_{44}, 0.5 mg/mL (1.7 mM of sulfides); Nile Red, 15 μg/mL, 5 mM of xanthine, 1×10^{-3} mM of xanthine oxidase with/out SOD (3.1×10^{-4} mM) and catalase (4×10^{-5} mM)). The symbols on the right ($\surd$ or $\otimes$), respectively, indicate the presence or absence of the ROS, showing a response only when hydrogen peroxide was present.

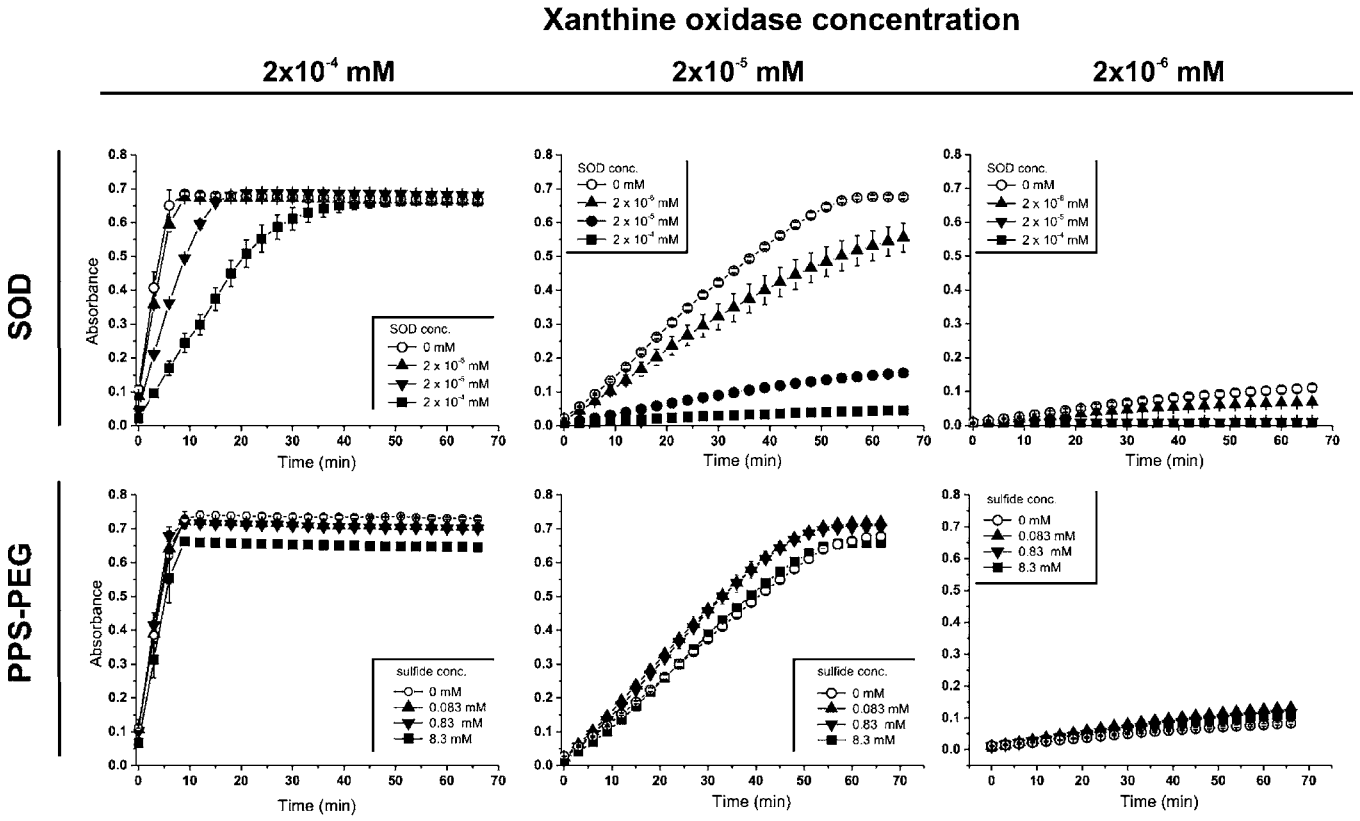


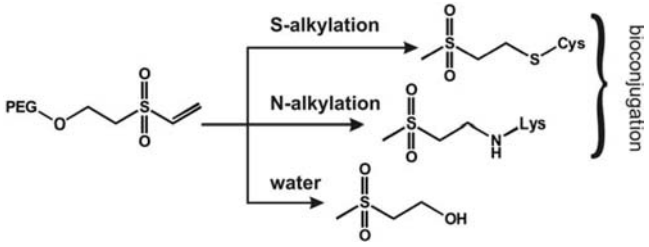
Figure 4. Formazan assay for assessing superoxide scavenging activity: the absorbance of oxidized MTS (at 490 nm) was recorded as a function of time and of the concentration of xanthine oxidase and of superoxide dismutase (SOD, upper half of the figure) or of PPSPEG (lower part of the figure). The presence of the latter did not influence the kinetics of the MTS conversion at any combination of XO and micelle concentrations. On the other hand, SOD showed a distinct dose-dependent retardation effect, which can be ascribed to the removal of superoxide.

reaction, which also allows minimizatio of the extent of multiple binding and therefore also the likelihood of micelle aggregation.

Due to the competitive reaction with water, a high yield of SOD PEGylation was obtained only by employing a large stoichiometric excess of vinyl sulfones, e.g., a 20-fold molar excess sulfone-terminated PEG (2 or 5 kDa) for a majority of SOD to be derivatized (see Supporting Information, Figure S2). Similar results were obtained on micelles containing 10 mol % of functional polymers (PPS_{10}-PEG_{44}-VS). The reaction products can be easily separated from unreacted SOD via SEC on Sephadex G100 (Figure 5). The purified products showed that roughly 2.5 mol % of vinyl sulfones reacted with SOD, corresponding to the presence one SOD every 420

dx.doi.org/10.1021/bc200449k | *Bioconjugate Chem.* 2012, 23, 438–449

Scheme 3. Possible Reactions of Vinyl Sulfone-Terminated PEG Constructs with Nucleophiles in a Protein-Containing Water Solution



polymer chains (from the weight ratio of PEG and protein measured through barium iodide and BCA assays, respectively). The aggregation numbers of PEG-based amphiphilic block copolymers with comparable molecular weight and similar micellar dimensions are often reported to be in the region of 50−100: 70 for high propylene oxide-content Pluronic P123,[41] 70−100 for hydrophobically modified PEGs,[42] 40−50 for PEG-PHB-PEG triblock copolymers.[43] We therefore assume to have about one conjugated SOD roughly every 5−10 micelles.

In terms of the regiochemistry, bovine Cu,Zn SOD is a 32.5 kDa dimeric structure, where each monomer presents 3 cysteine residues (C6 free, C55 and C146 involved in an intramolecular disulfide[44]) and 10 lysine ones, therefore allowing in principle for both N- and S-alkylation. The analysis of the purified PEG-SOD products showed a substantial identity between number of PEG chains per SOD and number of reacted lysine residues, even after reduction of the intramolecular disulfide with TCEP (Table 1; see also the SDS page analysis in Supporting Information, Figure S3), which demonstrates a conjugation through N-alkylation. It is worth pointing out that this may not apply to human Cu,Zn SOD, which bears a different number of cysteine residues (four, with C57 and C146 involved in the intramolecular disulfide[45]).

It is also noteworthy that the PEG vinyl sulfone/SOD molar ratio affected the ratio between tetra-PEGylated and native SOD, but not the number of PEG chains introduced: independently on the vinyl sulfone/SOD stoichiometric ratio,

Table 1. PEGylation Data for SOD (PEG5k-VS 20:1 Vinyl Sulfone/SOD Molar Ratio) after SEC Purification

	Native SOD	Reduced SOD
Average number of PEG chains per SOD[a]	3.74	3.59
Lysines modified by PEG[b]	4.15	3.93

[a]Calculated dividing the weight fractions of PEG (barium iodide assay) and SOD (BCA assay) by their respective molecular weights. [b]Difference in the number of free amines (TNBS assay) before and after the conjugation reaction.

SDS-PAGE showed no trace of di-, tri-, or penta-PEGylated derivatives. SOD has been shown to aggregate under mild conditions even in a mature and metalated form:[46] it is likely that, while aggregated SOD would be poorly reactive, the introduction of even only one PEG chain would solubilize it, thus allowing reaction of the vinyl sulfones with all readily available nucleophiles, i.e., four lysine residues per protein.

The introduction of SOD on micelles was not accompanied by any sound increase in size (Figure 6), thus confirming the

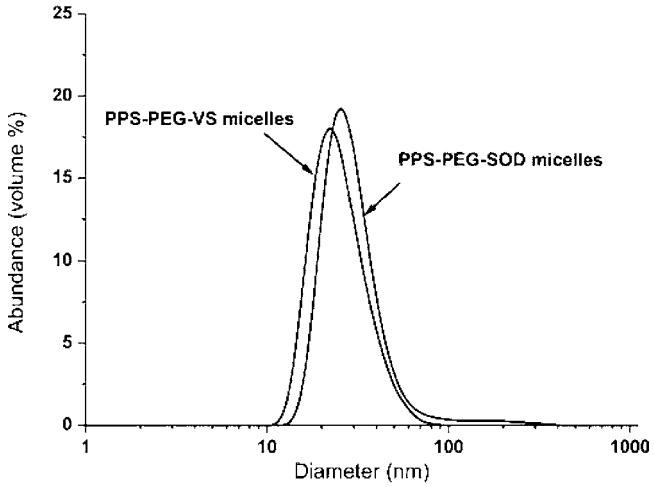


Figure 6. Size distribution of PPS_{10}-PEG_{44} micelles before and after functionalization with SOD. In the micelles, nonfunctional (methoxy-terminated) and functional (vinyl sulfone- or SOD-terminated) block copolymers were present in a 9:1 molar ratio.

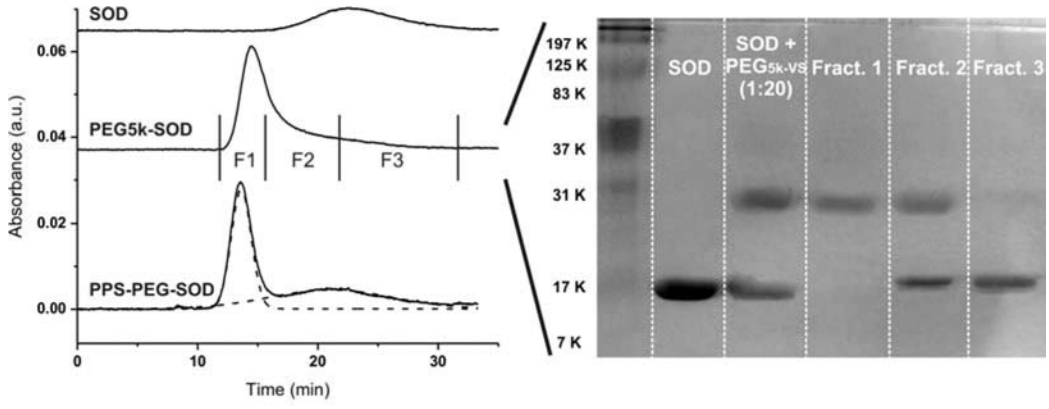


Figure 5. Left: Typical SEC elution curves of SOD before conjugation (top), after conjugation with PEG5k-VS (middle), and after conjugation with PPS_{10}-PEG_{44}-VS (bottom). Using appropriate SEC conditions (1 mL/min on Sephadex G100), the samples can be separated into three fractions, which are illustrated in the example of PEG-SOD. It is noteworthy that both the micelles and PEG5k-SOD are close to or beyond the exclusion limit of the column (hence their sharp peak), while the breadth of the SOD peak derives from the colloidal nature of the protein in water buffers (see also caption to Figure 3). Right: SDS-PAGE results for SOD (control), for the bioconjugation reaction product and the three different fractions obtained through SEC purification. Nonconjugated SOD is absent from fraction 1.

dx.doi.org/10.1021/bc200449k | *Bioconjugate Chem.* 2012, 23, 438−449

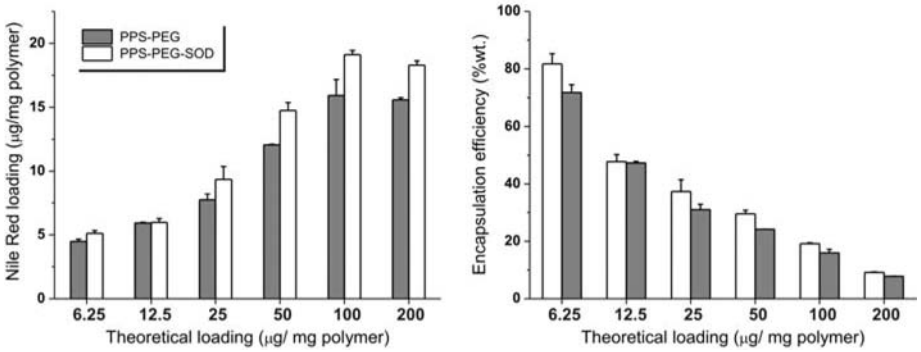


Figure 7. Loading (left) and encapsulation efficiency (right) of Nile Red in micelles of PPS_{10}-PEG_{44} or PPS_{10}-PEG_{44}-SOD was measured by adding DMF to a 1 mg/mL dispersions of loaded micelles and recording the emission of the resulting water/DMF 1:1 solutions. For weight ratios above 50 μg/mg polymer the micelles appear to reach saturation; however, the encapsulation efficiency was strongly reduced well before that point, which suggests the loading process not to be totally governed by a simple partition.

absence of multiple binding to SOD. Further, the presence of the enzyme had insignificant effects on the solubilization capacity of PPS_{10}-PEG_{44} micelles: using Nile Red as a model hydrophobic compound, nonfunctional and SOD-containing micelles exhibited a very similar maximum encapsulation capacity, i.e., 15 μg of dye per mg of block copolymer = 1.5 wt % (Figure 7, left), with an identical decrease of the encapsulation efficiency with increasing Nile Red concentration (Figure 7, right).

Superoxide- and Peroxide-Scavenging Behavior of PPSPEG-SOD. Differently from PPS-PEG, PPSPEG-SOD showed a clear capacity to inhibit the oxidative conversion of MTS, thus demonstrating a superoxide scavenging ability (Figure 8). In comparison to free SOD, the molar activity of the

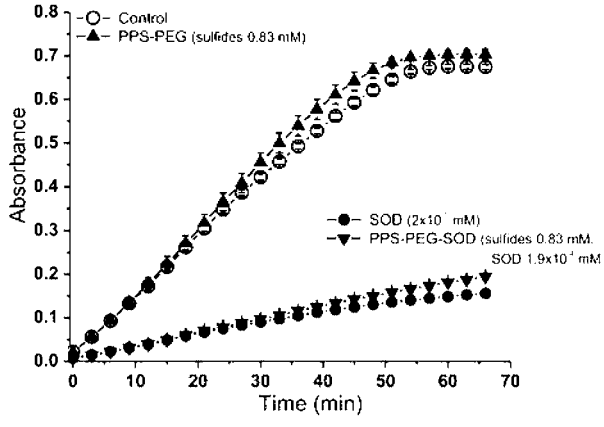


Figure 8. Results of the formazan assay (absorbance of MTS formazan as a result of superoxide production by XO and xanthine) for PPSPEG-SOD in comparison to SOD and PPSPEG alone. Concentration of XO: 2×10^{-5} mM.

conjugated enzyme significantly dropped, possibly because of increased steric hindrance and/or partial denaturation during conjugation. We have quantified this effect by measuring the decrease in the rate of WST-1 formazan production as a function of the molar concentration of free or conjugated SOD; expressing these results in terms of a percentage of inhibition (Figure 9, left), free SOD showed a half-maximal inhibitory concentration (IC_{50}) of 5.6×10^{-9} mM, which was reduced of about 1 order of magnitude by its conjugation either to PEG5k or to PPSPEG micelles.

Despite the significant drop in SOD activity, the enzyme-containing micelles were still able to significantly inhibit the superoxide-induced WST-1 oxidation at concentrations orders of magnitude lower than those affecting cell viability: for comparison, 0.03 mg/mL PPSPEG-SOD caused a 50% reduction in the WST-1 reaction rate, while a 50% reduction in L929 viability is obtained at a 500× larger concentration (15 mg/mL).

Additionally, the conjugation of SOD to PPSPEG appeared to provide remarkable stability to the enzyme. For example, PPSPEG-SOD showed a negligible IC_{50} increase after storage in PBS buffer (pH 7.4, 10 mM) for up to 3 months, whereas under the same conditions the activity of free SOD decreased by almost 3 orders of magnitude (see the increase in IC_{50} in Figure 9, right; compare black symbols to white ones). The encapsulation of organic hydrophobes in PPSPEG micelles makes use of an organic solvent (dichloromethane); neither this nor the presence of appreciable amounts of Nile Red (up to 1.5 wt % in relation to the polymers) appeared to affect the SOD activity (crossed symbols in Figure 10, right).

Due to the negligible effect of the Nile Red encapsulation, we have used the Nile Red assay to highlight any effect of the proximity of SOD on the H_2O_2 scavenging activity of PPSPEG. As previously discussed, xanthine oxidase generates also hydrogen peroxide, causing PPS oxidation also without SOD (see Figure 3). However, the activity of SOD increases the H_2O_2 concentration, supposedly accelerating the oxidation kinetics; a further acceleration may derive from the proximity between PPS and SOD, which would mean a higher local H_2O_2 concentration and therefore a higher efficiency in its uptake.

The experiments showed that free SOD already caused a slightly quicker PPS oxidation (= lower Nile Red fluorescence at any time point; compare white circles to black squares in Figure 10, left); however, the effect was much more noticeable for PPSPEG-SOD. This can be better seen in a plot of relative quenching efficiency (Figure 10, right), which more clearly depicts the higher efficiency of hydrogen peroxide capture following the chemical conjugation of SOD to PPSPEG chains. Therefore, the lower superoxide scavenging activity of the conjugates may be more than overcome by the higher efficiency in hydrogen peroxide scavenging, due to the physical proximity of PPS and SOD.

dx.doi.org/10.1021/bc200449k | *Bioconjugate Chem.* 2012, 23, 438–449

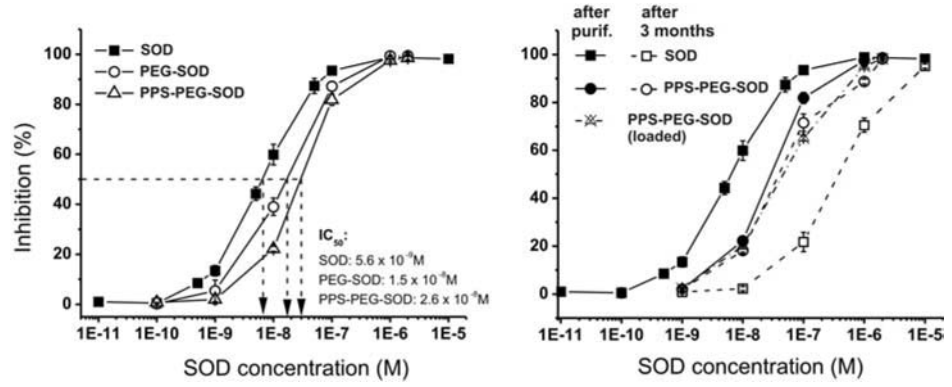


Figure 9. Inhibitory effect of free or conjugated SOD on the oxidation of WST-1 by superoxide. The percentage of inhibition was calculated from the slope of the absorbance at 450 nm vs time (see also Figure 4) considering the slope of the control sample (no SOD, no PPSPEG) to be the 0% inhibition. The IC_{50} is the SOD concentration necessary to achieve a 50% reduction in the slope. Left: comparison between free and conjugated (PEG5k or PPSPEG-SOD-containing micelles) SODs. Right: comparison between free SOD and PPSPEG-SOD after SEC purification and after a 3 month storage at 4 °C. The conjugated SOD showed no significant change in activity upon storage, and also upon loading with Nile Red.

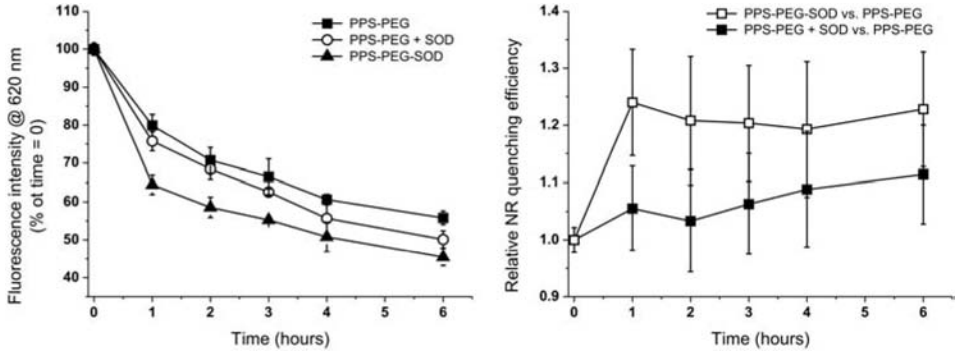


Figure 10. Left: Fluorescence of Nile Red as a function of time in the presence of XO, without SOD or with SOD free or conjugated to PPSPEG. Right: The data of the left graph are reported in a relative quenching scale, which is obtained dividing the fluorescence intensity of NR in PPSPEG micelles without SOD from that in the presence of free or conjugated enzyme. Concentrations: PPS_{10}-PEG_{44}, 0.5 mg/mL (1.5 mM of sulfides); Nile Red, 15 μg/mL, 5 mM of xanthine, 1×10^{-3} mM of xanthine oxidase without SOD (3.1×10^{-4} mM for both free and conjugated enzyme).

CONCLUSIONS

We have demonstrated that PPSPEG block copolymers are sensitive to hydrogen peroxide but not to superoxide; however, in combination with SOD they are capable of removing both ROS from a given environment. When the two components are covalently conjugated, the SOD-mediated removal of superoxide is considerably more efficient and the enzyme appears to be remarkably more stable. This result is clearly limited to *in vitro* measurements, and should be confirmed by studies *in vivo* or at least in plasma, where the presence of proteic components may affect both activity and stability of the enzymatic system.

The PPSPEG-SOD micellar conjugate shows therefore a functional similarity to the combination of SOD and catalase. A couple of points should be taken into account. (A) Safety: the final products of the scavenging cascade are sulfoxide-containing, water-soluble polymers. Their low molecular weight (max ~3000 g/mol) should ensure a relatively rapid renal clearance when in a nonaggregated (fully oxidized) form; on the other hand, their short-term toxicity is probably negligible: an ongoing study in our group (subject of a forthcoming publication) has shown very low cytotoxicity (IC_{50} > 20 mg/mL in L929 fibroblasts) independent of molecular weight. (B) Stability: PEGylation is known to reduce protein immunogenicity and proteolytic degradation, and we have shown that it has significantly increased the SOD stability against denaturation.

We therefore expect PPSPEG-SOD to have a significantly more sustained superoxide scavenging effect than SOD/catalase.

ASSOCIATED CONTENT

Supporting Information

Comparison of DLS and Nile Red quenching data for nonconjugate PPSPEG micelles, SDS pages for SOD PEGylation reaction products (different ratios SOD/PEG, reducing and nonreducing conditions). This material is available free of charge via the Internet at http://pubs.acs.org.

AUTHOR INFORMATION

Corresponding Author

*Tel.: +44 161 275 24 80. Fax: +44 161 275 23 96. E-mail: nicola.tirelli@manchester.ac.uk.

ACKNOWLEDGMENTS

P.H. thanks the University of Manchester for the award of an Overseas Research Studentship. The help of Ms. Jureerat Laliturai in cell culture is also gratefully acknowledged.

ABBREVIATIONS

DVS, Divinyl sulfone; PPS, Poly(propylene sulfide); PEG, Poly(ethylene glycol); SOD, Superoxide dismutase; TCEP, Tris(2-carboxyethyl)phosphine; SDS, Sodium dodecyl sulfate;

BCA, Bicinchoninic Acid; WST, Water-soluble tetrazolium; MTS, 3-(4,5-Dimethylthiazol-2-yl)-5-(3-carboxymethoxyphenyl)-2-(4-sulfophenyl)-2*H*-tetrazolium; PES, Phenazine ethosulfate

REFERENCES

(1) Droge, W. (2002) Free radicals in the physiological control of cell function. *Physiol. Rev. 82*, 47−95.

(2) Griendling, K. K., Sorescu, D., and Ushio-Fukai, M. (2000) Nad(p)h oxidase - role in cardiovascular biology and disease. *Circ. Res. 86*, 494−501.

(3) Halliwell, B. (2006) Oxidative stress and neurodegeneration: Where are we now? *J. Neurochem. 97*, 1634−1658.

(4) Madamanchi, N. R., Vendrov, A., and Runge, M. S. (2005) Oxidative stress and vascular disease. *Arterioscler. Thromb. Vasc. Biol. 25*, 29−38.

(5) Pavlick, K. P., Laroux, F. S., Fuseler, J., Wolf, R. E., Gray, L., Hoffman, J., and Grisham, M. B. (2002) Role of reactive metabolites of oxygen and nitrogen in inflammatory bowel disease. *Free Radic. Biol. Med. 33*, 311−322.

(6) Hu, P., and Tirelli, N. (2011) Inter-micellar dynamics in block copolymer micelles: Fret experiments of macroamphiphile and payload exchange. *React. Funct. Polym. 71*, 303−314.

(7) Napoli, A., Valentini, M., Tirelli, N., Muller, M., and Hubbell, J. A. (2004) Oxidation-responsive polymeric vesicles. *Nat. Mater. 3*, 183−189.

(8) Rehor, A., Hubbell, J. A., and Tirelli, N. (2005) Oxidation-sensitive polymeric nanoparticles. *Langmuir 21*, 411−417.

(9) Rehor, A., Schmoekel, H., Tirelli, N., and Hubbell, J. A. (2008) Functionalization of polysulfide nanoparticles and their performance as circulating carriers. *Biomaterials 29*, 1958−1966.

(10) Vo, C. D., Kilcher, G., and Tirelli, N. (2009) Polymers and sulfur: What are organic polysulfides good for? Preparative strategies and biological applications. *Macromol. Rapid Commun. 30*, 299−315.

(11) Rehor, A., Botterhuis, N. E., Hubbell, J. A., Sommerdijk, N., and Tirelli, N. (2005) Glucose sensitivity through oxidation responsiveness. An example of cascade-responsive nano-sensors. *J. Mater. Chem. 15*, 4006−4009.

(12) Borges, F., Fernandes, E., and Roleira, F. (2002) Progress towards the discovery of xanthine oxidase inhibitors. *Curr. Med. Chem. 9*, 195−217.

(13) Jolly, S. R., Kane, W. J., Bailie, M. B., Abrams, G. D., and Lucchesi, B. R. (1984) Canine myocardial reperfusion injury - its reduction by the combined administration of superoxide-dismutase and catalase. *Circ. Res. 54*, 277−285.

(14) Mates, J. M., Perez-Gomez, C., and De Castro, I. N. (1999) Antioxidant enzymes and human diseases. *Clin. Biochem. 32*, 595−603.

(15) Orr, W. C., and Sohal, R. S. (1994) Extension of life-span by overexpression of superoxide-dismutase and catalase in drosophila-melanogaster. *Science 263*, 1128−1130.

(16) Bafana, A., Dutt, S., Kumar, A., Kumar, S., and Ahuja, P. S. (2011) The basic and applied aspects of superoxide dismutase. *J. Mol. Catal. B-Enzym. 68*, 129−138.

(17) Fang, J., Seki, T., and Maeda, H. (2009) Therapeutic strategies by modulating oxygen stress in cancer and inflammation. *Adv. Drug Delivery Rev. 61*, 290−302.

(18) Kuzma-Kozakiewicz, M., and Kwiecinski, H. (2011) New therapeutic targets for amyotrophic lateral sclerosis. *Expert Opin. Ther. Targets 15*, 127−143.

(19) Kruidenier, L., Kulper, I., Lamers, C., and Verspaget, H. W. (2003) Intestinal oxidative damage in inflammatory bowel disease: Semi-quantification, localization, and association with mucosal antioxidants. *J. Pathol. 201*, 28−36.

(20) Segui, J., Gironella, M., Sans, M., Granell, S., Gil, F., Gimeno, M., Coronel, P., Pique, J. M., and Panes, J. (2004) Superoxide dismutase ameliorates tnbs-induced colitis by reducing oxidative stress, adhesion molecule expression, and leukocyte recruitment into the inflamed intestine. *J. Leukocyte Biol. 76*, 537−544.

(21) McCord, J. M., and Edeas, M. A. (2005) Sod, oxidative stress and human pathologies: A brief history and a future vision. *Biomed. Pharmacother. 59*, 139−142.

(22) Davis, A. S., Zhao, H., Sun, G. H., Sapolsky, R. M., and Steinberg, G. K. (2007) Gene therapy using sod1 protects striatal neurons from experimental stroke. *Neurosci. Lett. 411*, 32−36.

(23) Han, W., Mercenier, A., Ait-Belgnaoui, A., Pavan, S., Lamine, F., van Swam, I. I., Kleerebezem, M., Salvador-Cartier, C., Hisbergues, M., Bueno, L., Theodorou, V., and Fioramonti, J. (2006) Improvement of an experimental colitis in rats by lactic acid bacteria producing superoxide dismutase. *Inflamm. Bowel Dis. 12*, 1044−1052.

(24) Melov, S., Ravenscroft, J., Malik, S., Gill, M. S., Walker, D. W., Clayton, P. E., Wallace, D. C., Malfroy, B., Doctrow, S. R., and Lithgow, G. J. (2000) Extension of life-span with superoxide dismutase/catalase mimetics. *Science 289*, 1567−1569.

(25) Cuzzocrea, S., Riley, D. P., Caputi, A. P., and Salvemini, D. (2001) Antioxidant therapy: A new pharmacological approach in shock, inflammation, and ischemia/reperfusion injury. *Pharmacol. Rev. 53*, 135−159.

(26) Day, B. J., Shawen, S., Liochev, S. I., and Crapo, J. D. (1995) A metalloporphyrin superoxide dismutase mimetic protects against paraquat-induced endothelial cell injury, in vitro. *J. Pharmacol. Exp. Ther. 275*, 1227−1232.

(27) Yu, S. J., Yin, Y. Z., Zhu, J. Y., Huang, X., Luo, Q. A., Xu, J. Y., Shen, J. C., and Liu, J. Q. (2010) A modulatory bifunctional artificial enzyme with both sod and gpx activities based on a smart star-shaped pseudo-block copolymer. *Soft Matter 6*, 5342−5350.

(28) Heckert, E. G., Karakoti, A. S., Seal, S., and Self, W. T. (2008) The role of cerium redox state in the sod mimetic activity of nanoceria. *Biomaterials 29*, 2705−2709.

(29) Kajita, M., Hikosaka, K., Iitsuka, M., Kanayama, A., Toshima, N., and Miyamoto, Y. (2007) Platinum nanoparticle is a useful scavenger of superoxide anion and hydrogen peroxide. *Free Radical Res. 41*, 615−626.

(30) Beckman, J. S., Minor, R. L., White, C. W., Repine, J. E., Rosen, G. M., and Freeman, B. A. (1988) Superoxide-dismutase and catalase conjugated to polyethylene-glycol increases endothelial enzyme-activity and oxidant resistance. *J. Biol. Chem. 263*, 6884−6892.

(31) Veronese, F. M., Largajolli, R., Boccu, E., Benassi, C. A., and Schiavon, O. (1985) Surface modification of proteins - activation of monomethoxy-polyethylene glycols by phenylchloroformates and modification of ribonuclease and superoxide-dismutase. *Appl. Biochem. Biotechnol. 11*, 141−152.

(32) Beauchamp, C. O., Gonias, S. L., Menapace, D. P., and Pizzo, S. V. (1983) A new procedure for the synthesis of polyethylene glycol-protein adducts - effects on function, receptor recognition, and clearance of superoxide-dismutase, lactoferrin, and alpha-2-macroglobulin. *Anal. Biochem. 131*, 25−33.

(33) Mugge, A., Elwell, J. H., Peterson, T. E., Hofmeyer, T. G., Heistad, D. D., and Harrison, D. G. (1991) Chronic treatment with polyethylene-glycolated superoxide-dismutase partially restores endothelium-dependent vascular relaxations in cholesterol-fed rabbits. *Circ. Res. 69*, 1293−1300.

(34) Muizelaar, J. P., Marmarou, A., Young, H. F., Choi, S. C., Wolf, A., Schneider, R. L., and Kontos, H. A. (1993) Improving the outcome of severe head-injury with the oxygen radical scavenger polyethylene glycol-conjugated superoxide-dismutase - a phase-ii trial. *J. Neurosurg. 78*, 375−382.

(35) Yi, X. A., Zimmerman, M. C., Yang, R. F., Tong, J., Vinogradov, S., and Kabanov, A. V. (2010) Pluronic-modified superoxide dismutase 1 attenuates angiotensin ii-induced increase in intracellular superoxide in neurons. *Free Radical Biol. Med. 49*, 548−558.

(36) Caliceti, P., Schiavon, O., Morpurgo, M., Veronese, F. M., Sartore, L., Ranucci, E., and Ferruti, P. (1995) Physicochemical and biological properties of monofunctional hydroxy terminating poly(n-vinylpyrrolidone) conjugated superoxide-dismutase. *J. Bioact. Compat. Polym. 10*, 103−120.

(37) Nadithe, V., and Bae, Y. H. (2010) Synthesis and characterization of hemoglobin conjugates with antioxidant enzymes via

poly(ethylene glycol) cross-linker (hb-sod-cat) for protection from free radical stress. *Int. J. Biol. Macromol. 47*, 603−613.
(38) Sims, G. E. C., and Snape, T. J. (1980) A method for the estimation of polyethylene-glycol in plasma-protein fractions. *Anal. Biochem. 107*, 60−63.
(39) Bromberg, L. E., and Barr, D. P. (1999) Aggregation phenomena in aqueous solutions of hydrophobically modified polyelectrolytes. A probe solubilization study. *Macromolecules 32*, 3649−3657.
(40) Jiang, X., Lavender, C. A., Woodcock, J. W., and Zhao, B. (2008) Multiple micellization and dissociation transitions of thermo- and light-sensitive poly(ethylene oxide)-b-poly(ethoxytri(ethylene glycol) acrylate-co-o-nitrobenzyl acrylate) in water. *Macromolecules 41*, 2632−2643.
(41) Ganguly, R., Aswal, V. K., Hassan, P. A., Gopalakrishnan, I. K., and Kulshreshtha, S. K. (2006) Effect of sds on the self-assembly behavior of the peo-ppo-peo triblock copolymer (eo)(20)(po)(70)(eo)(20). *J. Phys. Chem. B 110*, 9843−9849.
(42) Vasilescu, M., Caragheorgheopol, A., and Caldararu, H. (2001) Aggregation numbers and microstructure characterization of self-assembled aggregates of poly(ethylene oxide) surfactants and related block-copolymers, studied by spectroscopic methods. *Adv. Colloid Interface Sci. 89*, 169−194.
(43) Li, X., Mya, K. Y., Ni, X. P., He, C. B., Leong, K. W., and Li, J. (2006) Dynamic and static light scattering studies on self-aggregation behavior of biodegradable amphiphilic poly(ethylene oxide)-poly(r)-3-hydroxybutyrate -poly(ethylene oxide) triblock copolymers in aqueous solution. *J. Phys. Chem. B 110*, 5920−5926.
(44) Aberneth, Jl, Steinman, H. M., and Hill, R. L. (1974) Bovine erythrocyte superoxide-dismutase - subunit structure and sequence location of intrasubunit disulfide bond. *J. Biol. Chem. 249*, 7339−7347.
(45) Kawamata, H., and Manfredi, G. (2008) Different regulation of wild-type and mutant cu,zn superoxide dismutase localization in mammalian mitochondria. *Hum. Mol. Genet. 17*, 3303−3317.
(46) Hwang, Y. M., Stathopulos, P. B., Dimmick, K., Yang, H., Badiei, H. R., Tong, M. S., Rumfeldt, J. A. O., Chen, P., Karanassios, V., and Meiering, E. M. (2010) Nonamyloid aggregates arising from mature copper/zinc superoxide dismutases resemble those observed in amyotrophic lateral sclerosis. *J. Biol. Chem. 285*, 41701−41711.
(47) Tan, A. S., and Berridge, M. V. (2000) Superoxide produced by activated neutrophils efficiently reduces the tetrazolium salt, wst-1 to produce a soluble formazan: A simple colorimetric assay for measuring respiratory burst activation and for screening anti-inflammatory agents. *J. Immunol. Methods 238*, 59−68.

Bioconjugate Chemistry

Article

pubs.acs.org/bc

Fluorinated Colloidal Gold Immunolabels for Imaging Select Proteins in Parallel with Lipids Using High-Resolution Secondary Ion Mass Spectrometry

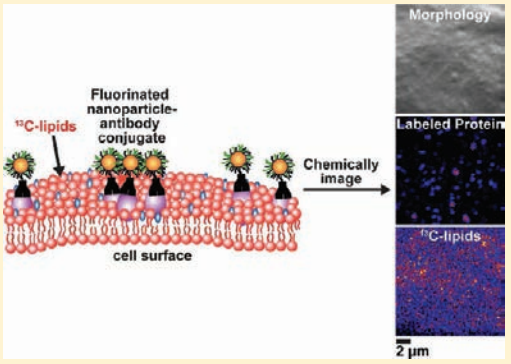
Robert L. Wilson,[†] Jessica F. Frisz,[†] William P. Hanafin,[‡] Kevin J. Carpenter,[§] Ian D. Hutcheon,[§] Peter K. Weber,[§] and Mary L. Kraft*[,‡,†]

[†]Department of Chemistry and [‡]Department of Chemical and Biomolecular Engineering, University of Illinois at Urbana−Champaign, Urbana, Illinois 61801, United States

[§]Glenn Seaborg Institute, Lawrence Livermore National Laboratory, Livermore, California 94551, United States

Supporting Information

ABSTRACT: The local abundance of specific lipid species near a membrane protein is hypothesized to influence the protein's activity. The ability to simultaneously image the distributions of specific protein and lipid species in the cell membrane would facilitate testing these hypotheses. Recent advances in imaging the distribution of cell membrane lipids with mass spectrometry have created the desire for membrane protein probes that can be simultaneously imaged with isotope labeled lipids. Such probes would enable conclusive tests to determine whether specific proteins colocalize with particular lipid species. Here, we describe the development of fluorine-functionalized colloidal gold immunolabels that facilitate the detection and imaging of specific proteins in parallel with lipids in the plasma membrane using high-resolution SIMS performed with a NanoSIMS. First, we developed a method to functionalize colloidal gold nanoparticles with a partially fluorinated mixed monolayer that permitted NanoSIMS detection and rendered the functionalized nanoparticles dispersible in aqueous buffer. Then, to allow for selective protein labeling, we attached the fluorinated colloidal gold nanoparticles to the nonbinding portion of antibodies. By combining these functionalized immunolabels with metabolic incorporation of stable isotopes, we demonstrate that influenza hemagglutinin and cellular lipids can be imaged in parallel using NanoSIMS. These labels enable a general approach to simultaneously imaging specific proteins and lipids with high sensitivity and lateral resolution, which may be used to evaluate predictions of protein colocalization with specific lipid species.



INTRODUCTION

To coordinate the numerous biological processes that occur at the cell's surface, the plasma membrane is compartmentalized into compositionally and functionally distinct domains.[1] Knowledge of component distribution in the plasma membrane facilitates identifying the mechanisms that underlie biological function. Given their key roles in biological processes, a number of labeling tools have been developed for detecting and imaging proteins. This includes genetically encoded fluorescent protein constructs and functionalized antibodies that can be detected with fluorescence or electron microscopy.[2−5] Use of these labels has revealed that certain membrane proteins cluster during cell signaling and virus budding, suggesting synergistic protein action may be a general mechanism that is common to membrane-mediated processes.[6−8]

Though important, protein clustering is only one aspect of the plasma membrane organization that influences biological processes. The local abundances of cholesterol and certain lipid species, such as sphingolipids and phosphatidylethanolamine, near membrane proteins are also reported to affect protein function.[6,8−11] To determine whether specific proteins are located within membrane domains that are enriched with particular lipid species, the protein and lipid species of interest must be visualized in parallel. However, imaging the lipid distribution in the plasma membrane is a significant challenge. The genetically encoded fluorescent tags and functionalized affinity labels that enable routine visualization of specific proteins with fluorescence or electron microscopy cannot be used to detect cholesterol or the majority of lipid species. Fluorescent lipid analogues can be visualized in parallel with membrane proteins labeled with genetically encoded fluorescent tags, but only a fraction of the lipids of interest will bear fluorophores, and these fluorophores may alter the localization of the labeled lipid.[12−14]

Secondary ion mass spectrometry (SIMS) is one of the few approaches for directly imaging the lipid organization in biological membranes without the use of fluorophores.[15−27] During SIMS analysis, a primary ion beam desorbs neutral and

Received: September 3, 2011
Revised: January 16, 2012
Published: January 30, 2012

ACS Publications © 2012 American Chemical Society

ionized molecules and molecular fragments from the sample's surface. The ionized species, which are called secondary ions, are analyzed by a mass spectrometer, and a mass spectrum of the molecules in the beam's focal area is generated. By scanning the analysis beam across the sample and collecting the resulting secondary ions, the intensities of the component-specific secondary ions detected at each position can be used to construct a map of the sample's surface composition. The distributions of lipids within cell membranes have been chemically imaged using time-of-flight SIMS (TOF-SIMS).[16−18] Because TOF-SIMS can detect intact and slightly fragmented molecular ions, this molecular imaging SIMS approach does not require labels to identify the parent molecule. However, TOF-SIMS imaging of distinct lipid microdomains in cell membranes has not yet been achieved, presumably due to limited sensitivity and spatial resolution.

A SIMS instrument capable of mapping the isotopic and elemental composition at the sample surface with a lateral resolution as good as 50 nm (Cameca NanoSIMS 50) has enabled detecting and imaging submicrometer-sized domains of isotopically labeled lipids in membranes.[21,23,28−30] Because this instrument detects monatomic and diatomic secondary ions, each species of interest must contain a distinct stable isotope so that the secondary ions generated during NanoSIMS analysis can be linked to the parent molecule.[21] The distinct stable isotopes that encode for component identity can be selectively incorporated into cholesterol and specific lipid species with established metabolic labeling techniques.[31−33] However, because proteins share the same amino acid building blocks, metabolic labeling cannot be used to selectively tag specific proteins with the orthogonal distinct isotopes or non-native elements that would permit them to be imaged in parallel to lipids with a NanoSIMS.

Existing approaches for selective protein labeling also have their limitations. Genetic methods for unnatural amino acid substitution[34] must be repeated for every protein of interest. Immunolabels have broader applicability, and commercially available colloidal gold-functionalized immunolabels produce distinctive $^{197}Au^-$ secondary ions that can be used to detect specific proteins with a NanoSIMS. Nevertheless, colloidal gold-functionalized immunolabels are not suitable for sensitive NanoSIMS detection in parallel with lipids. Specifically, the high magnetic field strength necessary to collect $^{197}Au^-$ secondary ions with the magnetic sector mass spectrometer on the NanoSIMS 50 precludes simultaneous detection of closely spaced masses, such as major and minor stable isotopes like $^{12}C^{14}N^-$ and $^{12}C^{15}N^-$, and even $^{12}C_2^-$ and $^{12}C^{14}N^-$. As a result, the ^{15}N- and ^{13}C-enrichment that is used to detect ^{15}N- and ^{13}C-labeled lipids, respectively, cannot be imaged in parallel with the $^{197}Au^-$ ions. Therefore, to image $^{197}Au^-$ and the lipid-related stable isotopic ratios, the magnetic field would have to be switched so that ions with different mass-to-charge ratios (m/z) could be consecutively collected on a detector. This approach reduces the measurement sensitivity because the colloidal gold-functionalized immunolabels and lipids are continuously sputtered from the sample, but only a subset of the characteristic ions are collected at any time. As a result, few counts of each species are collected for a given depth of analysis, which, in the case of the lipid membrane, is relatively shallow (<7 nm).

Antibodies functionalized with a distinctive and low molecular weight isotope or element could permit imaging specific proteins in parallel to lipids with a NanoSIMS. Fluorine is an attractive candidate elemental label due to its low abundance in biological materials and high secondary ion yields.[21,28] Methods to conjugate small fluorine-containing molecules to antibodies have been developed for positron-emission tomography applications.[35,36] However, we experimentally found that functionalizing antibodies with the high numbers of fluorinated molecules that enable sensitive detection with NanoSIMS compromised antibody binding.

Here, we report the development of a functionalized immunolabel for the detection of specific proteins in parallel with metabolically labeled lipids using NanoSIMS. The immunolabel consists of a colloidal gold nanoparticle that is functionalized with a partially fluorinated mixed monolayer and conjugated to a secondary antibody that permits selective protein labeling. The partially fluorinated mixed monolayer on the nanoparticle contains a large number of low mass, high yielding $^{19}F^-$ secondary ions, which permits highly sensitive NanoSIMS detection without compromising the simultaneous detection of lipid-specific secondary ions.[21,28] As a proof of concept, we have used this immunolabel to detect and image influenza hemagglutinin in parallel with isotope-labeled lipids in the plasma membranes of cells with a NanoSIMS. Hemagglutinin was selected as the protein of interest because its spatial organization in the membranes of transfected fibroblast cells is well-characterized.[37,38] In this report, we image all cellular lipid species due to the ease of isotopically labeling them, and they permit demonstrating that the fluorinated gold immunolabels can be detected in parallel to the minor and major stable isotopes that are used to visualize the lipid-specific isotope enrichment with a NanoSIMS.

MATERIALS AND METHODS

Materials. Uniformly carbon-13 labeled algal fatty acids (98 atom % carbon-13) were from Cambridge Isotope Laboratories. *N*-Hydroxysulfosuccinimide sodium salt (sulfo-NHS) was purchased from Prochem Inc. Hydrogen tetrachloroaurate(III) trihydrate ($HAuCl_4{\cdot}3H_2O$), Lipid-reduced fetal bovine serum (LR-FBS), and calf serum were from HyClone Laboratories. Poly(L-lysine) and chemical fixation reagents were from Electron Microscopy Sciences. Fatty acid-free bovine serum albumin (BSA), goat antimouse polyclonal antibody, $^{13}C_{18}$-steric acid (99 atom % carbon-13), and all other reagents were purchased from Sigma-Aldrich. Primary antibody (FC 125 antihemagglutinin developed in mouse) and the cell line that expresses influenza hemagglutinin (Clone 15 cell line) was the generous gift from Joshua Zimmerberg (Eunice Kennedy Shriver National Institute of Child Health and Human Development, National Institutes of Health, Bethesda, MD).

Synthesis of Gold Nanoparticles. 2.9 mL (6.4 mmol) of oleylamine was dissolved in 49 mL of toluene and brought to a slow reflux. $HAuCl_4{\cdot}3H_2O$ (24.3 mg, 0.062 mmol) was dissolved in 1.2 mL (3.7 mmol) of oleylamine and 1 mL of toluene. The gold solution was added to the refluxing toluene solution, refluxed for 2 h, and cooled to room temperature. Particles were purified by precipitation with 100 mL of methanol and centrifugation at 3000 rpm for 20 min. The particles were rinsed twice with methanol (50 mL) and dissolved in toluene (10 mL), producing a bright red colloidal solution.

Thiol Modification of Gold Nanoparticles. A solution of gold nanoparticles in toluene (3 mL) was added to 1*H*,1*H*,2*H*,2*H*-perfluorodecanethiol (8.5 μL, 0.029 mmol) in toluene (0.1 mL). After 2 min, 11-mercaptoundecanoic acid

dx.doi.org/10.1021/bc200482z | *Bioconjugate Chem.* 2012, 23, 450−460

(44.8 mg, 0.205 mmol) in toluene (0.4 mL) was added, resulting in a concentration of 8.3 mM 1*H*,1*H*,2*H*,2*H*-perfluorodecane thiol and 58.6 mM 11-mercaptoundecanoic acid. The reaction was stirred at room temperature for 18 h. Excess thiols were removed by pelleting the particles by centrifugation, decanting the supernatant, and resuspending the particles in 1.5 mL toluene. After repeating this process three times, the particles were resuspended in 1 mL of DMSO and stored at 4 °C. The particles were stable for at least one month under these conditions and did not exhibit irreversible flocculation.

XPS of Nanoparticles. XPS was performed on a Kratos Axis ULTRA with a monocromatic aluminum source, run at 150 w (15 kV) and spherical capacitor electron energy analyzer. The Kratos has a takeoff angle of 90° with respect to the sample plane with pass energies of 160 eV for surveys and 40 eV for high resolution. Spectra were calibrated using the carbon 1s peak at 285.0 eV. See SI for details of fitting XPS spectra for assessment of nanoparticle composition.

Qualitative Assessment of Nanoparticle Dispersibility in Aqueous Solution. To evaluate the dispersal of the nanoparticles in aqueous media, the particles were pelleted by centrifugation, the toluene was decanted, and phosphate buffered saline (PBS) was added. After brief sonication, particle dispersal was visually assessed. Solutions of well-dispersed particles were red in color. Poor dispersibility of the particles was evidenced by the solution's color changing from red to purple or blue, and the presence of particle precipitation.[39,40]

Lysine Modification of Gold Nanoparticles. Sulfo-NHS (44.0 mg, 0.205 mmol) and *N*,*N*′-dicyclohexylcarbodiimide (DCC) (59.3 mg, 0.287 mmol) were dissolved in 3 mL of DMSO and 0.68 mL of ethanol. Thiol-modified particles in DMSO (1 mL) were added to the sulfo-NHS and DCC solution and stirred for 3 h. Particles were pelleted by centrifugation, and resuspended in 1 mL of ethanol. Ethanol (4 mL) was added to lysine (1.68 g, 10.3 mmol) in 1.5 mL of water. One mL of particles modified with sulfo-NHS in ethanol was added to the lysine solution and stirred overnight. Excess lysine was removed by pelleting the particles with centrifugation, decanting the supernatant, and resuspending the particles in deionized water. After repeating this process four times, the particles were stored at room temperature in water until protein conjugation. Particles stored under these conditions for one year did not exhibit irreversible flocculation.

TOF-SIMS of Functionalized Nanoparticles. A PHI Trift-III TOF-SIMS (Physical Electronics Incorporated, Chanhassen, MN) instrument with a $^{197}Au^{+}$ liquid ion gun operated at 22 kV was used to collect positive-ion spectra in unbunched mode. The primary ion dose for each analysis was 3×10^{13} ions/cm^2. Twelve spectra were acquired from each set of thiol-functionalized nanoparticles. One of the twelve spectra of the nanoparticles modified with PFDT and MUDA (MUDA/PFDT-nanoparticles) was excluded from further analysis due to very low signal intensity. Each peak in a spectrum was normalized to the total intensity of all the peaks. Representative spectra were created by averaging the normalized intensities of the peaks in the 11 spectra of the MUDA/PFDT-nanoparticles and the 12 spectra of the nanoparticles that had lysine conjugated to the MUDA and PFDT monolayer (lysine/MUDA/PFDT-nanoparticles).

Ovalbumin and Antibody Oxidation and Reaction with Nanoparticles. Ovalbumin (5 mg) was dissolved in 5 mL of 0.1 M Na_2HPO_4 buffer at pH 7.5. 20 μL of 0.1 M $NaIO_4$ was added to 200 μL of ovalbumin solution, inverted several times, and the oxidation was allowed to proceed for 30 min in the dark. 60 μL of goat antimouse antibody solution (2.2 mg/mL) was desalted into 120 μL of 0.1 M Na_2HPO_4 buffer at pH 7.5 using Amicon Ultra-4 10K centrifuge filters, producing desalted antibody at a concentration of 1.1 mg/mL. 12 μL of 0.1 M $NaIO_4$ was added to the desalted antibody (120 μL), the reaction vial was inverted several times, and the oxidation was allowed to proceed for 30 min in the dark. A solution of oxidized goat antimouse polyclonal antibody (92.5 μL, 1.0 mg/mL) was added to 250 μL of lysine/MUDA/PFDT-nanoparticles in water and gently shaken. After 5 min, 111 μL of oxidized ovalbumin solution was added to the particles, gently shaken, and incubated overnight. To remove unconjugated protein, the functionalized particles were diluted in 700 μL of 0.1 M Na_2HPO_4 buffer (pH 7.5) containing 2% BSA, the solution was centrifuged at 5000 rpm for 20 min, the supernatant was removed, and fresh 2% BSA in buffer was added. This process was repeated a total of six times.

Evaluation of Aggregation of Antibody-Functionalized Particles with UV−vis. Absorbance measurements were performed on an Agilent 8453 UV−visible Spectrophotometer. Antibody-functionalized particles were diluted 1:1 with 0.1 M Na_2HPO_4 buffer (pH 7.5), and filtered through a 0.1 μm syringe filter prior to measurement. Additional buffer was added to the functionalized gold immunolabel solution to obtain surface plasmon resonance absorbance below unity.

ELISA Assay of Immunolabel Binding. Antibody binding affinity was assessed by ELISA using established protocols.[41] See also SI.

Cell Culture. Cells were grown in standard cell growth medium consisting of high glucose Dulbecco's modification of Eagle's medium (DMEM) supplemented with 10% calf serum, 10^4 U/mL penicillin G, and 10 mg/mL streptomycin. Silicon substrates were placed in a cell culture dish when the cells were passaged and incubated overnight to permit cell attachment to the substrates. To metabolically label the cellular lipids with carbon-13, Clone 15 cells were passaged into DMEM supplemented with 1% calf serum, 10% LR-FBS, 215 μM ^{13}C-fatty acids (4:1:28 mass ratio of UL-^{13}C-algal fatty acids/^{13}C-stearic acid/fatty acid-free BSA), 50 μM cholesterol, and 20 μM ethanolamine. The growth medium was supplemented with ^{13}C-fatty acid mixture and ethanolamine each day. On day 3, the cells were passaged. Cells (2×10^6 cells) were cultured in dishes containing fresh medium, supplements, and sterilized and poly(L-lysine)-coated 5×5 mm^2 silicon substrates for one day.

Analysis of ^{13}C-Fatty Acid Incorporation. Cells attached to the culture dish were used to assess the incorporation of ^{13}C-fatty acids into the cellular lipids. Cells were washed with PBS, detached from the dish, and collected via centrifugation. The lipids were extracted as reported,[42] and saponified with ethanolic KOH at 70 °C for 45 min. After acidification with HCl, the fatty acids were extracted into hexane and dried under N_2 (g). The residue was dissolved in MeOH:CH_2Cl_2 (1:2), and reacted with 2 M trimethylsilyldiazomethane for 60 min. The composition of the resulting fatty acid methyl esters (FAME) was assessed with a GC/MS system consisting of an Agilent 7890 gas chromatograph, an Agilent 5975 mass selective detector, and HP 7683B (Agilent Inc., Palo Alto, CA) autosampler. Gas chromatography was performed on a ZB-WAX (30 m × 0.25 mm I.D., 0.25 μm film thickness) capillary column (Phenomenex, Torrance, CA). Samples (1 μL) were

injected in split mode (5:1) to the GC/MS system. The mass spectrometer was operated in positive electron impact mode at 69.9 eV in the m/z 50−800 scan range, which was used to detect six FAMES: C16:0, C16:1, C18:0, C18:1, and C18:2. Spectra were evaluated using the HP Chemstation (Agilent) program. Identification was performed using mass spectra obtained from authentic standards and additionally confirmed with NIST08 and W8N08 libraries (John Wiley & Sons, Inc., USA).

Immunolabeling and Preservation. Substrates with adherent cells were rinsed twice each with PBS with calcium and magnesium and Hendry's phosphate buffer (HPB), and fixed for 10 min with 2% paraformaldehyde and 0.05% glutaraldehyde in 0.1 M HPB. Cells were rinsed twice with HPB, once with PBS without calcium and magnesium (PBS -M), blocked with immunowash buffer (PBS-M with 1% BSA), and incubated with 15 μL of 0.18 mg/mL primary antibody for 30 min. Excess primary antibody was removed by rinsing with immunowash buffer. The functionalized colloidal gold immunolabels were diluted 1:1 with 0.1 M Na_2HPO_4 buffer (pH 7.5) and filtered with a 0.1 μm syringe filter. Samples were incubated with 25 μL functionalized immunolabels for 30 min and rinsed twice with immunowash buffer and HPB. Cells were fixed with 4% glutaraldehyde in HPB for 30 min, washed twice with HPB and once with water, postfixed with 1% OsO_4 for 15 min, rinsed three times with water, and air-dried. Negative controls were prepared using immunowash buffer in place of the primary antibody.

SEM. Sample quality was assessed by imaging the cells at low magnification (500−1100×) using a Hitachi 4800 SEM with 1 kV accelerating voltage. The immunolabels on the cells were imaged on a JEOL 7000F with 15 kV accelerating voltage using a backscatter detector.

NanoSIMS Analysis. To prevent sample charging during SIMS analysis, the samples were coated with ~3 nm of iridium. While the depth of analysis employed in some of the following experiments did not exceed the thickness that the metal coating would be on an atomically flat surface, we empirically observed that the lipid-specific secondary ions in these experiments are detected at a more shallow sputtered depth than would be expected. We interpret this result to indicate that sample surface irregularity and discontinuities in the metal coating that are much smaller than the lateral resolution of these SIMS measurements (<100 nm) leaves the lipid more exposed than the apparent metal coating would indicate. High resolution SIMS was performed on a NanoSIMS 50 (Cameca, France) at Lawrence Livermore National Laboratory (Livermore, CA). Measurements were made with a 16 keV $^{133}Cs^+$ primary ion beam. Confirmation that the fluorine signal located the functionalized immunolabels was performed using a ~1.37 pA primary ion beam and simultaneously collecting the $^{19}F^-$ and $^{197}Au^-$ secondary ions and secondary electrons. Five replicate scans of 256 by 256 pixels with a dwell time of 1 ms/pixel were acquired for each 20 by 20 μm^2 analysis region, resulting in a pixel size of 78 by 78 nm^2 and a primary ion dose of 7.2×10^{14} ions/cm^2. The analysis depth was approximately 3 nm, calculated as reported using the sputtering rate of 2.5 nm·μm^2/pA·s that was determined on other biological samples.[43] For the simultaneous imaging of the hemagglutinin protein and cellular lipids, the $^{12}C^1H^-$, $^{13}C^1H^-$, and $^{19}F^-$ secondary ions and secondary electrons were simultaneously collected using a ~0.264 pA primary ion beam. A mass resolving power of ~6700 was used to separate isobaric interferences from the isotopes of interest. Four replicate scans of 256 by 256 pixels with a dwell time of 1 ms/pixel were acquired for each 15 by 15 μm^2 analysis region, resulting in a pixel size of 59 by 59 nm^2 and a primary ion dose of 1.9×10^{14} ions/cm^2. Each analysis overlapped with the preceding analysis region in order to facilitate stitching the resulting NanoSIMS images together in a mosaic. Images were cropped to show the region that did not overlap with a preceding analysis region. We calculated an analysis depth of approximately 0.8 nm using the sputtering rate of 2.5 nm·μm^2/pA·s for biological samples.[43]

NanoSIMS Image Analysis. A custom software package (L'IMAGE, L.R. Nittler, Carnegie Institution of Washington) run on the PV-Wave platform (Visual Numerics) was used to process the NanoSIMS data. $^{19}F^-$ images and ^{13}C-enrichment images that show the distributions of the fluorothiolate-functionalized colloidal gold immunolabels that locate the influenza hemagglutinin and the ^{13}C- lipids, respectively, were constructed using a 3 × 3-pixel boxcar smoothing algorithm, producing images with 176 nm lateral resolution. The ^{13}C-enrichment images were constructed by ratioing the $^{13}C^1H^-$ to the $^{12}C^1H^-$ secondary ion counts collected at every pixel, and then dividing that ratio by the natural abundance ratio (0.011237). Ratioing the $^{13}C^1H^-$ counts to the $^{12}C^1H^-$ counts minimizes signal variations induced by sample topography, producing a quantitative measure of the local enrichment in ^{13}C-labeled molecules compared to an unlabeled (natural abundance) cell.[44] The resulting ^{13}C-enrichment was color coded and mapped onto its corresponding pixel in the NanoSIMS image. See the SI for details of the statistical analysis of the NanoSIMS data.

RESULTS

Synthesis of the Fluorothiolate-Functionalized Colloidal Gold Immunolabel. Our strategy for immunolabel synthesis involved functionalizing the colloidal gold nanoparticle with a partially fluorinated mixed monolayer, and then conjugating the fluorinated nanoparticle to secondary antibodies (Figure 1). We selected a bioconjugation strategy in which

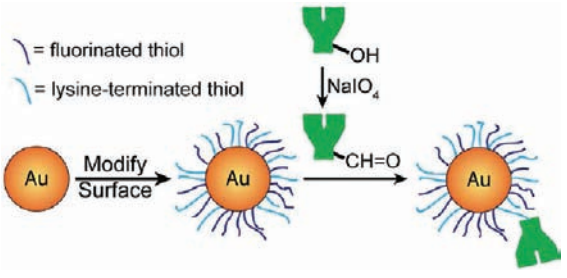


Figure 1. Synthesis of functionalized immunolabel consisting of an antibody attached to a gold nanoparticle (20-nm-diameter) functionalized with a partially fluorinated mixed monolayer. The gold nanoparticle is capped with a mixed monolayer composed of fluorinated and carboxylic acid-terminated thiols. The carboxylic acids are condensed with lysine, producing ionizable terminal amines. Aldehydes are generated on the glycosylated F_c region of the antibody and the glycosylated portions of the blocking protein, ovalbumin (not shown), by mild oxidation with sodium periodate. Reaction of the aldehydes on the antibody and ovalbumin with the amines on the fluorinated nanoparticles produces a stable linkage that does not interfere with antibody binding.

aldehydes are generated on the antibody's glycosylated, nonbinding, Fc region for covalent reaction with amines on

dx.doi.org/10.1021/bc200482z | Bioconjugate Chem. 2012, 23, 450−460

the nanoparticle, yielding a stable linkage that does not obstruct antibody binding.[40] To permit antibody attachment and to help render the particles dispersible in aqueous buffers, the thiols in the partially fluorinated mixed monolayer on the colloidal gold nanoparticle should have a chain length longer than seven methylene units and be capped with an ionizable amine moiety.[39,45,46] Because amine-terminated perfluoroalkanethiols of sufficient length were not commercially available, we created a mixed monolayer that consisted of a fluorinated alkane thiol (1*H*,1*H*,2*H*,2*H*-perfluorodecanethiol, PFDT) for NanoSIMS detection, and a carboxylic-acid-terminated thiol (11-mercaptoundecanoic acid, MUDA) that could be converted to an ionizable terminal amine by reaction with lysine.[47] We anticipated that the hydrophobic PFDT component might induce the resulting functionalized nanoparticles to flocculate in water, as nanoparticles modified with a PFDT monolayer are not dispersible in aqueous solvent mixtures.[48] However, the presence of an ionizable terminal moiety on the capping monolayer promotes nanoparticle dispersibility in water,[39,45,46] so we hypothesized that the ratio of MUDA to PFDT in the monolayer could be adjusted to produce water-dispersible and partially fluorinated nanoparticles.

Gold nanoparticles with an average diameter of 20 nm were synthesized using oleylamine to reduce Au^{3+} in toluene.[49] This nanoparticle size is a compromise between large particles that facilitate secondary characterization of cell labeling with SEM, and smaller particles that typically have higher immunolabeling efficiency.[50] To identify the reaction conditions that produced water-dispersible and fluorinated nanoparticles, we varied the molar ratio of MUDA to PFDT between 1:10 and 10:1, and assessed the particles' fluorine content and dispersibility in aqueous buffer. XPS measurements indicated that MUDA to PFDT ratios of 1:10 and 1:1 yielded fluorinated colloidal gold nanoparticles, but fluorine was not detected on the nanoparticles modified with a 10:1 ratio of MUDA to PFDT (Table 1). Nanoparticle dispersibility in aqueous buffer followed the opposite trend; only the nanoparticles modified with a 10:1 ratio of MUDA to PFDT exhibited adequate dispersion in PBS, signified by the solution's red color. The poor dispersibility of particles modified with 1:1 and 1:10 ratios of MUDA to PFDT was evident from the solution's color changing from red to purple or blue, and visible particle precipitation.[39,40] Subsequent investigations of MUDA to PFDT ratios between 1:1 and 10:1 indicated that a 7:1 ratio reproducibly produced water-dispersible and partially fluorinated nanoparticles when PFDT was allowed to react with the colloidal gold for 2 min prior to MUDA addition (Table 1). Finally, amine functionalities were generated on the surface of the nanoparticles that had been functionalized with a partially fluorinated mixed monolayer (MUDA/PFDT-nanoparticles) by condensing the terminal carboxylic acids on the monolayer with lysine.

Table 1. Fraction of PFDT in the Monolayers on Gold Nanoparticles That Were Modified with Various Ratios of MUDA:PFDT Measured with XPS

MUDA:PFDT ratio in reaction mixture	10:1	7:1 with delay[a]	1:1	1:10
Number of samples analyzed	4	6	6	4
Mean fraction of PFDT in monolayer ±1 s.d.	0 ± 0	0.16 ± 0.11	0.22 ± 0.07	0.54 ± 0.10

[a]MUDA was added 2 min after the addition of PFDT (see text for details).

The presence of lysine on the surface of the MUDA/PFDT-nanoparticles that had been reacted with lysine (lysine/MUDA/PFDT-nanoparticles) was verified with three methods. First, a fluorescamine-based colorimetric test confirmed the presence of primary amines that are characteristic of lysine on the lysine/MUDA/PFDT-nanoparticles, but not on the unmodified MUDA/PFDT-nanoparticles (SI Figure S1). Second, comparison of the XPS spectra of lysine/MUDA/PFDT-nanoparticles and MUDA/PFDT-nanoparticles demonstrated the presence of chemical bonds distinctive of lysine conjugation to the nanoparticles (Figure 2). Specifically, the nitrogen 1s peaks at 399.4 eV (C-NH_2) and 401.3 eV (N—C═O) that appeared in the XPS spectra of lysine/MUDA/PFDT-nanoparticles (Figure 2A and Figure S2) are indicative of the amines on the lysine residue and the formation of an amide bond with lysine, respectively. Additionally, the increase and shift in the carbonyl peak's maxima from 288.8 eV in the MUDA/PFDT-nanoparticle spectra to 288.3 eV in the lysine/MUDA/PFDT-nanoparticle spectra signified the presence of the carboxylic acid on lysine and amide bond formation (Figure

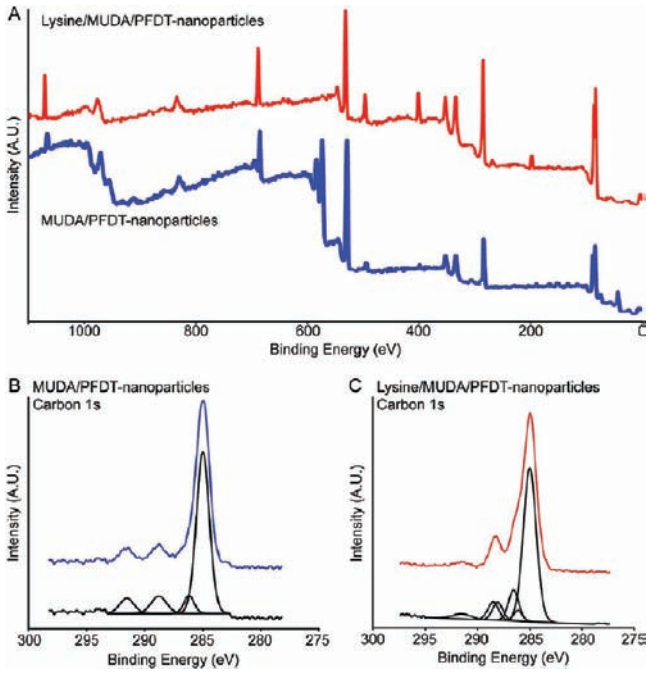


Figure 2. XPS spectra of lysine/MUDA/PFDT-nanoparticles and MUDA/PFDT-nanoparticles. (A) Survey scan lysine/MUDA/PFDT-nanoparticles (red) and MUDA/PFDT-nanoparticles (blue) shows that lysine modification induced the appearance of the nitrogen 1s peaks at ~400 eV due to the amine and amide bonds that are characteristic of lysine coupling. The high-resolution spectrum of the nitrogen 1s peak from lysine/MUDA/PFDT-nanoparticles is shown in Figure S2. (B) The photoelectron spectra (blue) of the carbon 1s scan acquired from the MUDA/PFDT-nanoparticles was fit with the following carbon peaks: CF_2 (291.5 eV), COOH (288.8 eV), C—S (286.1 eV), and CH_2 (285.0 eV). (C) The photoelectron spectra (red) of the carbon 1s scan acquired from the lysine/MUDA/PFDT-nanoparticles was fit with the following carbon peaks: CF_2 (291.5 eV), COOH (288.5 eV), CONH (288.1 eV), C—N (286.5 eV), C—S (286.1 eV), and CH_2 (285.0 eV).

dx.doi.org/10.1021/bc200482z | *Bioconjugate Chem.* 2012, 23, 450–460

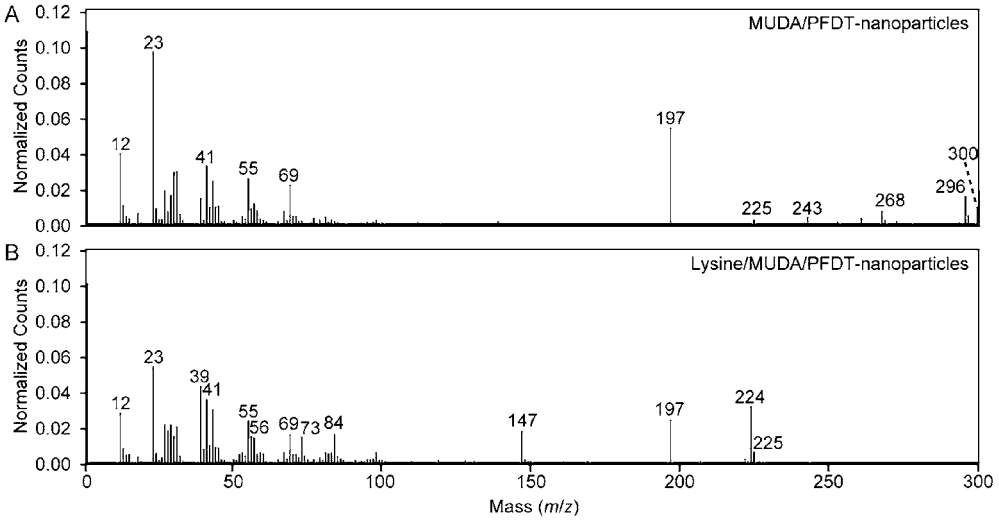


Figure 3. Representative positive ion TOF-SIMS spectra of (A) MUDA/PFDT-nanoparticles and (B) lysine/MUDA/PFDT-nanoparticles.

2B,C). Furthermore, the shoulder at 286.4 eV that appeared in the lysine/MUDA/PFDT-nanoparticle spectra is characteristic of the C−N single bonds in lysine (Figure 2C). Based on deconvolution of the carbonyl peak shown in Figure 2C into separate carboxylic acid and amide peaks, more than 90% of the MUDA carboxylic acids were covalently attached to lysine. Third, comparison of TOF-SIMS spectra of lysine/MUDA/PFDT-nanoparticles and MUDA/PFDT-nanoparticles demonstrated that lysine was covalently attached to the lysine/MUDA/PFDT-nanoparticles. Representative positive ion spectra of lysine/MUDA/PFDT-nanoparticles and MUDA/PFDT-nanoparticles are shown in Figure 3, where a range from m/z 1 to 300 is shown (ions with m/z > 300 have low detection efficiency with our TOF-SIMS instrumentation). Peaks that most likely correspond to gold (m/z 197), fluorinated PFDT fragment ions (m/z 69, 268, and 300 from CF_3^+, $C_5F_{11}^+$, and $C_6F_{12}^+$, respectively), and MUDA fragment ions (m/z 41, 55, 243, and 296 from $C_3H_5^+$, $C_4H_7^+$, CH_2SAu^+, and $C_5H_7SAu^+$, respectively) were visible in the spectra of the MUDA/PFDT-nanoparticles (Figure 3A). Additional peaks that likely correspond to lysine fragment ions (m/z 56, and 84 from $C_3H_6N^+$ and $C_5H_9N^+$, respectively)[51] and the sodium adduct of a lysine-amide fragment ion (m/z 224 from $C_9H_{17}N_2O_3Na^+$) were present in the spectra of the lysine/MUDA/PFDT-nanoparticles (Figure 3B). Although peak m/z 147 is often attributed to lysine,[51] its coappearance with peak m/z 73 in the lysine/MUDA/PFDT-nanoparticle spectra may instead indicate the presence of polydimethylsiloxane, a common surface contaminant.[52] Peaks with m/z between 200 and 300 that correspond to MUDA and PFDT fragment ions are not present in the lysine/MUDA/PFDT-nanoparticle spectra, possibly due to the suppression of these ions by the more basic lysine residues.[53] Altogether, these experiments confirm that lysine had been covalently attached to the MUDA/PFDT-nanoparticles.

Immunolabel synthesis was completed by attaching the fluorinated nanoparticles to secondary antibodies. We desired to limit the amount of antibody conjugated to each fluorinated colloidal gold nanoparticle in order to prevent cross-linking the antigens on the cell surface, but low protein coverage induces nanoparticle aggregation.[40] To obtain the high protein surface coverage that stabilizes the nanoparticles in buffered solution without increasing the antibody loading, we first reacted the nanoparticles with a small amount of oxidized antibody, and then blocked the nanoparticle surface with ovalbumin, a small, glycosylated protein. This was accomplished by mildly oxidizing the polyclonal goat antimouse antibodies and ovalbumin with sodium periodate, generating reactive aldehyde moieties on the glycosylated regions of the proteins.[40] These aldehydes were then reacted with the amines on the functionalized nanoparticles under nondenaturing conditions. The resulting fluorothiolate-functionalized colloidal gold immunolabels exhibited a UV−vis absorption maximum at ∼525 nm (SI Figure S3), indicating the absence of nanoparticle aggregation.[40] The affinity and selectivity of the immunolabels to their antigen, mouse antibody, was confirmed with ELISA.

Verification of Cell Labeling with Fluorothiolate-Functionalized Colloidal Gold Immunolabels. We evaluated the detection of the fluorothiolate-functionalized colloidal gold immunolabels that located specific proteins on cells with scanning electron microscopy (SEM) and high-resolution SIMS performed with a NanoSIMS 50. As stated in the Introduction, we focused on the detection of influenza hemagglutinin in the plasma membranes of transfected fibroblast cells (Clone 15 cell line) in these experiments because the spatial organization of this protein is well-characterized.[37,38] Influenza hemagglutinin in the plasma membranes of Clone 15 cells was selectively labeled with a mouse antihemagglutinin monoclonal primary antibody, followed by the fluorothiolate-functionalized colloidal gold immunolabels. The cells were chemically fixed and imaged with SEM (Figure 4) and NanoSIMS (Figure 5). As a negative control experiment, we also used SEM to image a Clone 15 cell that was not labeled with primary antibody prior to exposure to the fluorothiolate-functionalized colloidal gold immunolabels (negative control).

SEM imaging was performed using backscattered electron (BSE) mode to permit unambiguous detection of the colloidal gold nanoparticles, as elements with high atomic weight, such as gold, appear bright in BSE images. The fluorothiolate-functionalized colloidal gold immunolabels that located the influenza hemagglutinin were clearly visible on the surface of the immunolabeled cell (Figure 4A). Though individual gold nanoparticles were present, the majority of the immunolabels were clustered in two dimensions on the cell surface. This two-

dx.doi.org/10.1021/bc200482z | Bioconjugate Chem. 2012, 23, 450−460

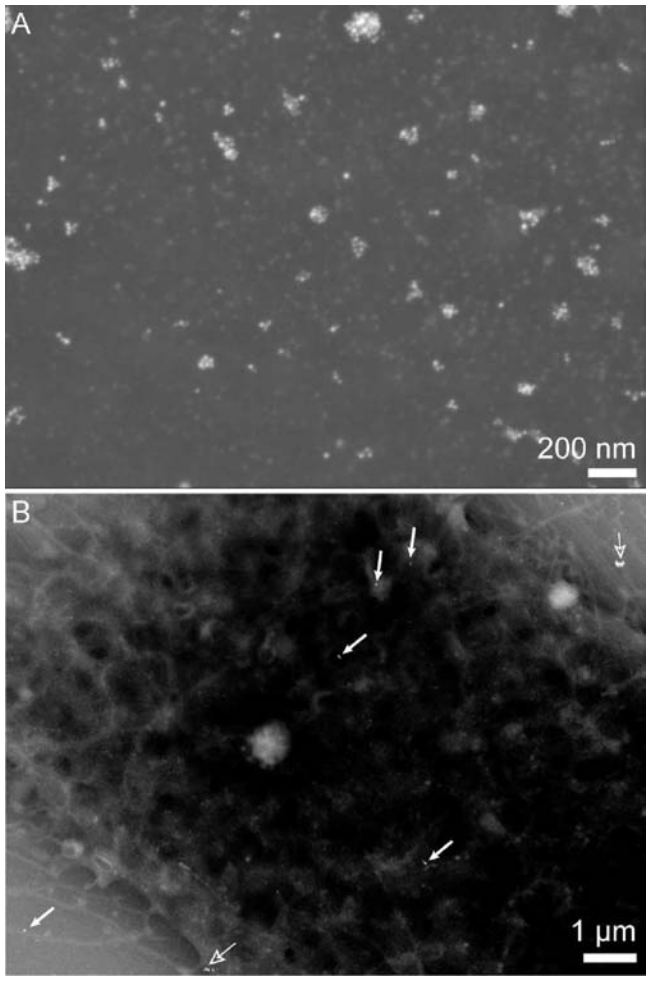


Figure 4. SEM images of immunolabeled cells taken in BSE mode. Elements with high atomic weight, such as gold, appear bright in BSE images, which allows unambiguous identification of the functionalized colloidal gold immunolabels. (A) The fluorinated colloidal gold immunolabels visible on the cell surface locate the influenza hemagglutinin protein. The immunolabels were often arranged in two-dimensional clusters on the cell surface that are similar to the previously reported clusters of colloidal gold immunolabels that locate hemagglutinin, and are indicative of hemagglutinin clustering within the plasma membrane.[37,38] (B) A larger region of the surface of the negative control cell was imaged to acquire an overview of the extent of nonspecific labeling. Few individual fluorinated gold immunolabels (closed arrows) and two very small immunolabel clusters (open-arrow) were detected on the Clone 15 cell that was not tagged with primary antibody prior to exposure to the fluorothiolate-functionalized colloidal gold immunolabels (negative control). The small amount of label present on the negative control sample indicated that little nonspecific binding occurred.

dimensional clustering of the colloidal gold immunolabels that locate hemagglutinin has been previously reported by others, and it is indicative of hemagglutinin accumulation within small domains in the plasma membrane.[37,38] In contrast, large immunolabel aggregates, such as those that occur when ovalbumin is not used to block the surfaces of the nanoparticles (SI Figure S4), are significantly larger and have a three-dimensional appearance. Thus, the two-dimensional clusters of fluorothiolate-functionalized colloidal gold immunolabels that we observed on the immunolabeled cell were indicative of hemagglutinin's native clustered distribution in the cell membrane, and not immunolabel aggregation. It is noteworthy that very few individual particles (Figure 4B, closed arrows) or immunolabel clusters (Figure 4B, open arrows) were visible on the negative control Clone 15 cell that was not labeled with primary antibody prior to treatment with the functionalized immunolabels. Thus, very little nonspecific binding occurred.

Four regions on an immunolabeled Clone 15 fibroblast cell were analyzed with NanoSIMS to confirm that the fluorine secondary ion signal could be used to detect the fluorothiolate-functionalized colloidal gold immunolabels. NanoSIMS analysis was performed on cells that had not been imaged with SEM in BSE mode because our earlier experiments indicated that electron impact at >5 kV during BSE imaging decomposed the fluorinated alkane thiols on the nanoparticles. As shown below, SEM imaging performed at low magnification with low voltage (≤5 kV), however, permitted both evaluation of cell preservation[26] and NanoSIMS detection of the fluorinated alkane thiols. A representative NanoSIMS secondary electron image that was acquired in parallel to the secondary ion images shows the morphology of the immunolabeled cell (Figure 5A). Individual nanoparticles are not visible in the secondary electron image because the nanoparticles were smaller than the lateral resolution of this NanoSIMS analysis (approximately 100 nm). The inability to detect nanoparticle aggregates in this image indicates that large (≥100 nm) aggregates of the functionalized immunolabels were not present. However, local elevations in the immunolabel-specific $^{197}Au^-$ and $^{19}F^-$ secondary ions are clearly visible in the NanoSIMS secondary ion images (Figure 5B and C, respectively). The local elevations in the $^{197}Au^-$ and $^{19}F^-$ secondary ions varied in intensity and often had multipixel dimensions, which suggests they represent the two-dimensional clusters of differing numbers of individual immunolabels that we observed with SEM. Statistical analysis of the ion signal intensities detected at 60 180 1-by-1-pixel subregions within the representative region that corresponded to the surface of the cell indicated that $^{19}F^-$ and $^{197}Au^-$ ion counts/pixel greater than 32 and 18, respectively, were statistically significant local elevations. As implied by the overlay of the $^{197}Au^-$ and $^{19}F^-$ ion images (SI Figure S5), this statistical analysis also confirmed that the $^{197}Au^-$ and $^{19}F^-$ ion signals were positively correlated (correlation coefficient = 0.87 at 95% confidence interval). The $^{197}Au^-$ and $^{19}F^-$ ion signals detected on the cell surface at the three other analysis regions were also positively correlated (correlation coefficients = 0.83, 0.67, and 0.86 for 42 262, 56 911, and 50 138 1-by-1-pixel regions, respectively, at 95% confidence interval), confirming that the $^{19}F^-$ signal was produced by the fluorothiolate-functionalized colloidal gold immunolabels. Altogether, these results demonstrate that the functionalized immunolabels could be detected with NanoSIMS via local elevations in the $^{19}F^-$ or $^{197}Au^-$ secondary ions.

Simultaneous Imaging of Influenza Hemagglutinin and All Cellular Lipid Species in the Cell Membrane. Next, we assessed the ability to image the fluorothiolate-functionalized colloidal gold immunolabels that locate hemagglutinin in the plasma membranes of Clone 15 cells in parallel with lipids using a NanoSIMS. Again, we chose to image all cellular lipid species due to the ease of incorporating commercially available uniformly ^{13}C-labeled fatty acids into cellular lipids, and the resulting ^{13}C-lipids permitted demonstrating that the $^{13}C^1H^-$ and $^{12}C^1H^-$ ions used to measure the lipid-specific ^{13}C-enrichment could be simultaneously detected with the fluorinated immunolabels. The Clone 15 cells we

dx.doi.org/10.1021/bc200482z | Bioconjugate Chem. 2012, 23, 450–460

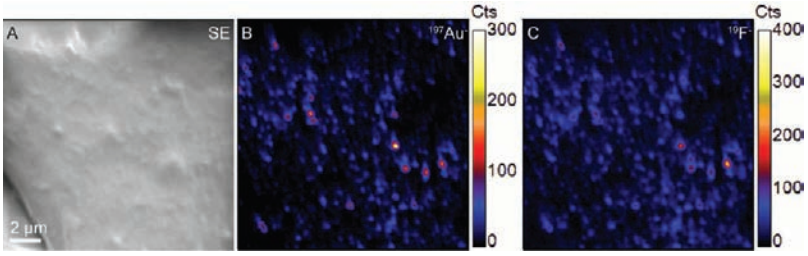


Figure 5. NanoSIMS images were acquired of a 15 by 15 μm^2 region on a Clone 15 cell that was labeled with fluorothiolate-functionalized colloidal gold immunolabels that bound to the primary antibodies against the influenza hemagglutinin within the plasma membrane. (A) The secondary electron (SE) image shows cell morphology. The fluorothiolate-functionalized colloidal gold immunolabels are not visible in the secondary electron image because they were smaller than the lateral resolution of the NanoSIMS analysis (~100 nm). The lack of nanoparticle aggregates visible in the SE image demonstrates the absence of large (≥100 nm) aggregates of immunolabels. (B) The $^{197}Au^-$ ion image shows the distribution of the fluorinated colloidal gold immunolabels on the cell surface. (C) The $^{19}F^-$ ion image also revealed the locations of the fluorinated colloidal gold immunolabels on the cell surface. As expected, the $^{197}Au^-$ and $^{19}F^-$ secondary ions were colocalized in the image, indicating that both secondary ion species located the influenza hemagglutinin on the cell surface.

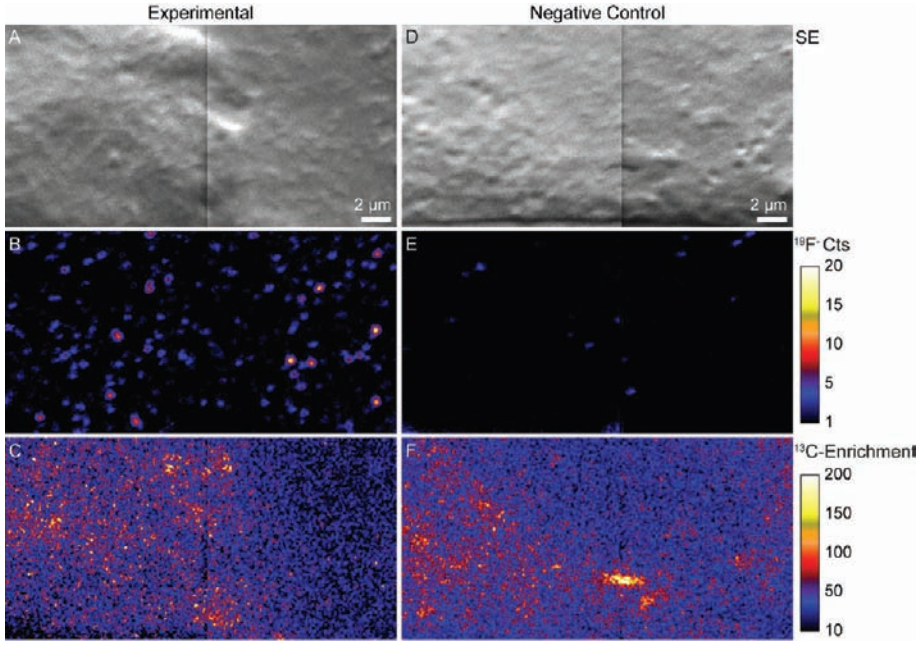


Figure 6. Mosaic of overlapping NanoSIMS images that were acquired on immunolabeled and unlabeled (negative control) Clone 15 cells that contained metabolically incorporated ^{13}C-lipids. (A) Secondary electron (SE) images show the morphology of the surface of the immunolabeled Clone 15 cell. (B) The $^{19}F^-$ NanoSIMS images acquired in parallel with the secondary electron (A) and ^{13}C-enrichment (C) images reveal the location of influenza hemagglutinin in the membrane of the immunolabeled cell. (C) The ^{13}C-enrichment images show the distribution of ^{13}C-lipids in the plasma membrane of the immunolabeled Clone 15 cell. (D) Secondary electron images of the surface of the negative control cell were acquired in parallel with $^{19}F^-$ and ^{13}C-enrichment images. (E) Few nonspecifically adsorbed immunolabels were present on the negative control Clone 15 cell. (F) The ^{13}C-enrichment images confirmed that ^{13}C-lipids were present in the plasma membrane of the negative control Clone 15 cell.

studied had been metabolically labeled such that approximately 55% and 90% of the fatty acids in the cellular glycolipids and sphingomyelin, respectively, were uniformly carbon-13 labeled prior to tagging the influenza hemagglutinin with the fluorinated immunolabels. As a negative control, we also analyzed metabolically labeled Clone 15 cells that were not exposed to primary antihemagglutinin antibody prior to the fluorothiolate-functionalized colloidal gold immunolabels. We imaged the fluorothiolate-functionalized colloidal gold immunolabels and ^{13}C-lipids in parallel by using NanoSIMS to simultaneously collect the $^{19}F^-$, $^{13}C^1H^-$, and $^{12}C^1H^-$ secondary ions. To minimize the fraction of secondary ions collected from the cytoplasm, NanoSIMS was performed with a lower primary ion dose than that used to evaluate immunolabel detection, resulting in a reduced secondary ion signal intensity compared to those obtained in Figure 5.

The secondary electron, $^{19}F^-$ ion, and ^{13}C-enrichment NanoSIMS images shown in Figure 6 are representative examples of the >50 other regions that we analyzed on five different cells (prepared on 2 separate days). Neither individual nanoparticles nor nanoparticle aggregates are visible in the NanoSIMS secondary electron images, confirming that large (≥100 nm) immunolabel aggregates were not present on the cells (Figure 6A and D). The locations of the hemagglutinin in the membrane are revealed by the regional elevations in the $^{19}F^-$ secondary ion counts that are visible in the representative NanoSIMS $^{19}F^-$ ion images of the immunolabeled cell (Figure 6B). Analysis of 79 596 1-by-1-pixel ROIs that corresponded to regions on the surface of the immunolabeled cell that did not

dx.doi.org/10.1021/bc200482z | Bioconjugate Chem. 2012, 23, 450–460

overlap with a preceding NanoSIMS measurement indicated that $^{19}F^-$ counts/pixel greater than 3 were statistically significant local elevations. In comparison, very little nonspecific labeling occurred on the negative control cell, as evidenced by the low number of pixels in which the $^{19}F^-$ secondary ion count exceeded unity (Figure 6E). The distribution of ^{13}C-lipids in the membrane of the immunolabeled and negative control cell are shown by the quantitative ^{13}C-enrichment images (Figure 6C and F) that were acquired in parallel to the $^{19}F^-$ ion images. The lateral variations in the ^{13}C-enrichment within the membrane suggest that the ^{13}C-lipids are unevenly distributed on the surface of both cells. Projection of the individual ion images onto the secondary electron image indicates that neither the immunolabels nor the ^{13}C-lipid distributions were correlated with cell topography (SI Figure S6A, S6B, S6D, and S6E). Similarly, the overlay of the $^{19}F^-$ ion and ^{13}C-enrichment NanoSIMS images (Figure S6C and S6F) indicates that the immunolabels on the experimental cell were not colocalized with lipid-enriched or lipid-depleted regions of the membrane. The lack of a correlation between the $^{19}F^-$ counts and the ^{13}C-enrichment on the experimental cell was confirmed by statistical analysis (correlation coefficient = −0.03 at the 95% confidence interval). The absence of a significant negative correlation between the immunolabel- and lipid-specific secondary ion signals indicates the immunolabels did not hinder the detection of the underlying membrane. Overall, these imaging data demonstrate the ability to directly visualize the distribution of a specific protein, influenza hemagglutinin, with respect to membrane lipids and cell surface morphology.

DISCUSSION AND CONCLUSION

In a previous study, we used NanoSIMS to image the lipid distribution within phase-separated model membranes with high lateral resolution.[23] Here, we extended NanoSIMS analysis to simultaneously imaging all cellular lipid species and influenza hemagglutinin within the plasma membranes of intact cells by developing new fluorine-functionalized antibodies that permit selective protein detection in parallel with lipid-specific isotopes. This demonstration provides a general framework for simultaneously imaging distinct proteins and lipid species within the plasma membranes of cells with high sensitivity and lateral resolution. Because secondary antibodies are used to create the immunolabels, any protein of interest can be detected and imaged simply by employing the corresponding primary antibody. Though we imaged all of the cellular lipid species here as a proof of concept, the distribution of a protein of interest with respect to more specific lipid species may be achieved by employing established methods to incorporate distinct stable isotopes into phosphatidylethanolamine,[54] cholesterol,[31] sphingolipids,[32] or gangliosides.[33] This approach may reveal whether the protein of interest is located within a membrane domain that is enriched with a particular lipid species when it is combined with cell preparation methods that do not induce reorganization of the lipid species.[26]

Our immunolabel synthesis strategy was optimized to permit sensitive NanoSIMS detection and broad applicability. A key feature of the immunolabel design is that the fluorinated moieties were not directly attached to the antibody. Conjugation of the antibodies to gold nanoparticles that were capped with a partially fluorinated mixed monolayer permitted functionalizing the antibody with a high number of fluorine atoms without loss of binding. The strategy for immunolabel synthesis can be easily modulated to further broaden immunolabel applicability. For example, immunolabels that permit additional proteins to be detected in parallel to those labeled with fluorinated colloidal gold immunolabels can be fabricated by functionalizing the colloidal gold with alkane thiols that contain other non-native elements (i.e., bromine) or stable isotopes (i.e., deuterium or nitrogen-15). Immunolabels with smaller gold nanoparticles may be desirable for reduction of the steric hindrance between probes that may occur during the labeling procedure.[55] Such immunolabels may be created by employing the Brust method for nanoparticle synthesis.[56] We expect that label-specific secondary ions produced by smaller immunolabels will also be detectable by NanoSIMS even though these gold nanoparticles will be too small to be resolved in the NanoSIMS secondary electron images.

Use of the fluorothiolate-functionalized colloidal gold immunolabels described herein with metabolic incorporation of distinct stable isotopes and NanoSIMS analysis will facilitate the testing of predictions that specific membrane proteins are located within distinct lipid environments. By combining this approach to imaging membrane components with complementary assays of protein function, the role of the local lipid composition on protein function might also be elucidated.

ASSOCIATED CONTENT

Supporting Information

Experimental protocols for the ELISA assay of immunolabel binding, peak fitting of XPS spectra for assessment of nanoparticle composition, and statistical analysis of NanoSIMS data. Images of colorimetric test for primary amines on lysine/MUDA/PFDT-nanoparticles, nitrogen 1s XPS spectrum of lysine/MUDA/PFDT-nanoparticles, UV−vis spectrum of antibody-functionalized nanoparticles, SEM and NanoSIMS images of aggregated immuonolabels, composite $^{19}F^-$, $^{197}Au^-$, and secondary electron image of cell, and composite $^{19}F^-$, ^{13}C-enrichment, and secondary electron images of cells. This material is available free of charge via the Internet at http://pubs.acs.org.

AUTHOR INFORMATION

Corresponding Author

*E-mail: mlkraft@illinois.edu. Tel: 217-333-2228.

Notes

The authors declare no competing financial interest.

ACKNOWLEDGMENTS

We thank Joshua Zimmerberg for providing the Clone 15 cell line and primary antibodies to the corresponding strain of influenza hemagglutinin, and we thank C. Ramon for technical assistance. M.L.K. holds a Career Award at the Scientific Interface from the Burroughs Wellcome Fund. Portions of this work were carried out in the Frederick Seitz Materials Research Laboratory Central Facilities, Univ. of Illinois, which is partially supported by the U.S. Department of Energy (DOE) under grants DEFG02- 07ER46453 and DE-FG02-07ER46471. Work at LLNL was supported by the Laboratory Directed Research and Development funding and performed under the auspices of the U.S. DOE under contract DE-AC52-07NA27344. This material is based upon work supported by the National Science Foundation under CHE − 1058809.

REFERENCES

(1) Radhakrishnan, K., Halasz, A., Vlachos, D., and Edwards, J. S. (2010) Quantitative understanding of cell signaling: the importance of membrane organization. *Curr. Opin. Biotechnol. 21*, 677−682.

(2) Metha, S., and Zhang, J. (2011) Reporting from the Field: Genetically Encoded Fluorescent Reporters Uncover Signaling Dynamics in Living Biological Systems. *Annu. Rev. Biochem. 80*, 375−401.

(3) Shu, X., Lev-Ram, V., Deerinck, T. J., Qi, Y., Ramko, E. B., Davidson, M. W., Jin, Y., WEllisman, M. H., and Tsien, R. Y. (2011) A Genetically Encoded Tag for Correlated Light and Electron Microscopy of Intact Cells, Tissues, and Organisms. *PLoS Biol. 9*, e1001041.

(4) Donaldson, J. G. (2002) Immunofluorescence Staining, in *Current Protocols in Immunology* pp 21.3.1−21.3.6, John Wiley & Sons, Inc.

(5) Schwartzbach, S. D. D., Osafune, T. (2010) in *Methods in Molecular Biology* (Walker, J. M., Ed.) Humana Press, New York.

(6) Takeda, M., Leser, G. P., Russell, C. J., and Lamb, R. A. (2003) Influenza virus hemagglutinin concentrates in lipid raft microdomains for efficient viral fusion. *Proc. Natl. Acad. Sci. U.S.A. 100*, 14610−14617.

(7) Wilson, B. S., Steinberg, S. L., Liederman, K., Pfeiffer, J. R., Surviladze, Z., Zhang, J., Samelson, L. E., Yang, L., Kotula, P. G., and Oliver, J. M. (2004) Markers for detergent-resistant lipid rafts occupy distinct and dynamic domains in native membranes. *Mol. Biol. Cell 15*, 2570−2592.

(8) Zheng, H., Chu, J., Qiu, Y., Loh, H. H., and Law, P. (2008) Agonist-selective signaling is determined by the receptor location within the domains. *Proc. Natl. Acad. Sci. U.S.A. 105*, 9421−9426.

(9) Paila, Y. D., Ganguly, S., and Chattopadhyay, A. (2010) Metabolic Depletion of Sphingolipids Impairs Ligand Binding and Signaling of Human Serotonin1A Receptors. *Biochemistry 49*, 2389−2397.

(10) Sjögren, B., and Svenningsson, P. (2007) Depletion of the lipid raft constituents, sphingomyelin and ganglioside, decreases serotonin binding at human 5-$HT_{7(a)}$ receptors in HeLa cells. *Acta Physiologica 190*, 47−53.

(11) Dowhan, W., and Bogdanov, M. (2011) Lipid-protein interactions as determinants of membrane protein structure and function. *Biochem. Soc. Trans. 39*, 767−774.

(12) Zhao, J., Wu, J., Shao, H., Kong, F., Jain, N., Hunt, G., and Feigenson, G. W. (2007) Phase studies of model biomembranes: Macroscopic coexistence of Lα + Lβ with light-induced co-existence of Lα + Lo phases. *Biochim. Biophys. Acta 1768*, 2777−2786.

(13) Devaux, P. F., Fellmann, P., and Herve, P. (2002) Investigation on lipid asymmetry using lipid probes: Comparison between spin-labeled lipids and fluorescent lipids. *Chem. Phys. Lipids 116*, 115−134.

(14) Maier, O., Oberle, V., and Hoekstra, D. (2002) Fluorescent lipid probes: some properties and applications (a review). *Chem. Phys. Lipids 116*, 3−18.

(15) Walker, A. V. (2008) Why is SIMS Underused in Chemical and Biological Analysis? Challenges and Opportunities. *Anal. Chem. 80*, 8864−8870.

(16) Ostrowski, S. G., Van Bell, C. T., Winograd, N., and Ewing, A. G. (2004) Mass spectrometric imaging of highly curved membranes during tetrahymena mating. *Science 305*, 71−73.

(17) Piehowski, P. D., Davey, A. M., Kurczy, M. E., Sheets, E. D., Winograd, N., Ewing, A. G., and Heien, M. L. (2009) Time-of-Flight Secondary Ion Mass Spectrometry Imaging of Subcellular Lipid Heterogeneity: Poisson Counting and Spatial Resolution. *Anal. Chem. 81*, 5593−5602.

(18) Kurczy, M. E., Piehowski, P. D., Van Bell, C. T., Heien, M. L., Winograd, N., and Ewing, A. G. (2010) Mass spectroscopy imaging of mating Tetrahymena show that changes in cell morphology relate to lipid domain formation. *Proc. Nat. Acad. Sci. U.S.A. 107*, 2751−2756.

(19) Lockyer, N. P., and Vickerman, J. C. (2004) Progress in cellular analysis using ToF-SIMS. *Appl. Surface Sci. 212−232*, 377−384.

(20) Guerquin-Kern, J.-L., Wu, T.-D., Quintana, C., and Croisy, A. (2005) Progress in analytical imaging of the cell by dynamic secondary ion mass spectrometry (SIMS microscopy). *Biochim. Biophys. Acta 1724*, 228−238.

(21) Boxer, S. G., Kraft, M. L., and Weber, P. K. (2009) Advances in Imaging Secondary Ion Mass Spectrometry for Biological Samples. *Annu. Rev. Biophys. 38*, 53−74.

(22) Anderton, C. R., Vaezian, B., Lou, K., Frisz, J. F., and Kraft, M. L. (2012) Identification of a Lipid-Related Peak Set to Enhance the Interpretation of TOF-SIMS Data from Model and Cellular Membranes. *Surf. Interface Anal. 44*, 322−333.

(23) Anderton, C. R., Weber, P. K., Lou, K., Hutcheon, I. D., and Kraft, M. L. (2011) Correlated AFM and NanoSIMS imaging to probe cholesterol-induced changes in phase behavior and non-ideal mixing in ternary lipid membranes. *Biochim. Biophys. Acta 1808*, 307−315.

(24) Vaezian, B., Anderton, C. R., and Kraft, M. L. (2010) Discriminating and Imaging Different Phosphatidylcholine Species within Phase-Separated Model Membranes by Principal Component Analysis of TOF-SIMS Images. *Anal. Chem. 82*, 10006−10014.

(25) Sjovall, P., Lausmaa, J., and Johansson, B. (2004) Mass Spectrometric Imaging of Lipids in Brain Tissue. *Anal. Chem. 76*, 4271−4278.

(26) Malm, J., Giannaras, D., Riehle, M. O., Gadegaard, N., and Sjovall, P. (2009) Fixation and Drying Protocols for the Preparation of Cell Samples for Time-of-Flight Secondary Ion Mass Spectrometry Analysis. *Anal. Chem. 81*, 7197−7205.

(27) Touboul, D., Halgand, F., Brunelle, A., Kersting, R., Tallarek, E., Hagenhoff, B., and Laprevote, O. (2004) Tissue Molecular Ion Imaging by Gold Cluster Ion Bombardment. *Anal. Chem. 76*, 1550−1559.

(28) Galli Marxer, C., Kraft, M. L., Weber, P. K., Hutcheon, I. D., and Boxer, S. G. (2005) Supported membrane composition analysis by secondary ion mass spectrometry with high lateral resolution. *Biophys. J. 88*, 2965−2975.

(29) Kraft, M. L., Weber, P. K., Longo, M. L., Hutcheon, I. D., and Boxer, S. G. (2006) Phase Separation of Lipid Membranes Analyzed with High-Resolution Secondary Ion Mass Spectrometry. *Science 313*, 1948−1951.

(30) Kraft, M. L., Fishel, S. F., Galli Marxer, C., Weber, P. K., Hutcheon, I. D., and Boxer, S. G. (2006) Quantitative analysis of supported membrane composition using the NanoSIMS. *Appl. Sur. Sci. 252*, 6950−6956.

(31) Campbell, S., Gaus, K., Bittman, R., Jessup, W., Crowe, S., and Mak, J. (2004) The raft-promoting property of virion-associated cholesterol, but not the presence of virion-associated Brij 98 rafts, is a determinant of human immunodeficiency virus type 1 infectivity. *J. Virol. 78*, 10556−10565.

(32) Chigorno, V., Riva, C., Valsecchi, M., Nicolini, M., Brocca, P., and Sonnino, S. (1997) Metabolic processing of gangliosides by human fibroblasts in culture. Formation and recycling of separate pools of ganglioside. *Eur. J. Biochem. 250*, 661−669.

(33) Schwarzmann, G., Hoffmann-Bleihauer, P., Schubert, J., Sandhoff, K., and Marsh, D. (1983) Incorporation of ganglioside analogues into fibroblast cell membranes. A spin-label study. *Biochemistry 22*, 5041−5048.

(34) Wang, L., and Schultz, P. G. (2005) Expanding the Genetic Code. *Angew. Chem., Int. Ed. 44*, 34−66.

(35) Garg, P. K., Garg, S., and Zalutsky, M. R. (1991) Fluorine-18 labeling of monoclonal antibodies and fragments with preservation of immunoreactivity. *Bioconjugate Chem. 2*, 44−49.

(36) Vaidyanathan, G., and Zalutsky, M. R. (1994) Improved synthesis of N-succinimidyl 4-[18F]fluorobenzoate and its application to the labeling of a monoclonal antibody fragment. *Bioconjugate Chem. 5*, 352−356.

(37) Hess, S. T., Kumar, M., Verma, A., Farrington, J., Kenworthy, A., and Zimmerberg, J. (2005) Quantitative electron microscopy and fluorescence spectroscopy of the membrane distribution of influenza hemagglutinin. *J. Cell Bio. 169*, 965−976.

(38) Hess, S. T., Gould, T. J., Gudheti, M. V., Maas, S. A., Mills, K. D., and Zimmerberg, J. (2007) Dynamic clustered distribution of hemagglutinin resolved at 40 nm in living cell membranes discriminates between raft theories. *Proc. Natl. Acad. Sci. U.S.A. 104*, 17370−17375.
(39) Weisbecker, C. S., Merritt, M. V., and Whitesides, G. M. (1996) Molecular Self-Assembly of Aliphatic Thiols on Gold Colloids. *Langmuir 12*, 3763−3772.
(40) Kumar, S., Aaron, J., and Sokolov, K. (2008) Directional conjugation of antibodies to nanoparticles for synthesis of multiplexed optical contrast agents with both delivery and targeting moieties. *Nat. Protocols 3*, 314−320.
(41) Gosling, J. P. (2005) in *A Practical Approach Series*, Oxford University Press, Inc., New York.
(42) Blight, E. G., and Dyer, W. J. (1959) A rapid method of total lipid extraction and purification. *Can. J. Biochem. Physiol. 37*, 911−917.
(43) Ghosal, S., Fallon, S. J., Leighton, T. J., Wheeler, K. E., Kristo, M. J., Hutcheon, I. D., and Weber, P. K. (2008) Imaging and 3D Elemental Characterization of Intact Bacterial Spores by High-Resolution Secondary Ion Mass Spectrometry. *Anal. Chem. 80*, 5986−5992.
(44) Lechene, C. P., Luyten, Y., McMahon, G., and Distel, D. L. (2007) Quantitative imaging of nitrogen fixation within animal cells. *Science 317*, 1563−1566.
(45) Johnson, S. R., Evans, S. D., and Brydson, R. (1998) Influence of a Terminal Functionality on the Physical Properties of Surfactant-Stabilized Gold Nanoparticles. *Langmuir 14*, 6639−6647.
(46) Selvakannan, P. R., Mandal, S., Phadtare, S., Pasricha, R., and Sastry, M. (2003) Capping of Gold Nanoparticles by the Amino Acid Lysine Renders Them Water-Dispersible. *Langmuir 19*, 3545−3549.
(47) Templeton, A. C., Hostetler, M. J., Warmoth, E. K., Chen, S., Hartshorn, C. M., Krishnamurthy, V. M., Forbes, M. D. E., and Murray, R. W. (1998) Gateway Reactions to Diverse, Polyfunctional Monolayer-Protected Gold Clusters. *J. Am. Chem. Soc. 120*, 4845−4849.
(48) Shah, P. S., Holmes, J. D., Doty, R. C., Johnston, K. P., and Korgel, B. A. (2000) Steric Stabilization of Nanocrystals in Supercritical CO_2 Using Fluorinated Ligands. *J. Am. Chem. Soc. 122*, 4245−4246.
(49) Hiramatsu, H., and Osterloh, F. E. (2004) A Simple Large-Scale Synthesis of Nearly Monodisperse Gold and Silver Nanoparticles with Adjustable Sizes and with Exchangeable Surfactants. *Chem. Mater. 16*, 2509−2511.
(50) Bergen en Henegouwen, P. M. P., and Leunissen, J. L. M. (1986) Controlled growth of colloidal gold particles and implications for labelling efficiency. *Histochem. Cell Biol. 85*, 81−87.
(51) Kulp, K. S., Berman, E. S. F., Kinze, M. G., Shattuck, D. L., Nelson, E. J., Wu, L., Montgomery, J. L., Felton, J. S., and Wu, K. J. (2006) Chemical and biological differentiation of three human breast cancer cell types using time-of-flight secondary ion mass spectrometry. *Anal. Chem. 78*, 3651−3658.
(52) Oran, U., Unveren, E., Wirth, T., and Unger, W. E. S. (2004) Poly-dimethyl-siloxame (PDMS) contamination of polystyrene (PS) oligomers samples: a comparison of time-of-flight static secondary ion mass spectrometry (TOF-SSIMS) and X-ray photoelectron spectroscopy (XPS) results. *Appl. Surf. Sci. 227*, 318−324.
(53) Jones, E. A., Lockyer, N. P., Kordys, J., and Vickerman, J. C. (2007) Suppression and Enhancement of Secondary Ion Formation Due to the Chemical Environment in Static-Secondary Ion Mass Spectrometry. *J. Am. Soc. Mass Spectrom. 18*, 1559−1567.
(54) Zhu, L., Johnson, C., and Bakovic, M. (2008) Stimulation of the human CTP: phosphatidylethanolamine cytidylyktransferase gene by early growth response protein 1. *J. Lipid Res. 49*, 2197−2211.
(55) Fujita, A., Cheng, J., and Fujimoto, T. (2009) Segregation of GM1 and GM3 clusters in the cell membrane depends on the intact actin cytoskeleton. *Biochim. Biophys. Acta 1791*, 388−396.
(56) Brust, M., Walker, M., Bethell, D., Schiffrin, D. J., and Whyman, R. (1994) Synthesis of Thiol-derivatised Gold Nanoparticles in a Two-phase Liquid-Liquid System. *Chem. Commun. 7*, 801−802.

Bioconjugate Chemistry

Article

pubs.acs.org/bc

Delivery of Floxuridine Derivatives to Cancer Cells by Water-Soluble Organometallic Cages

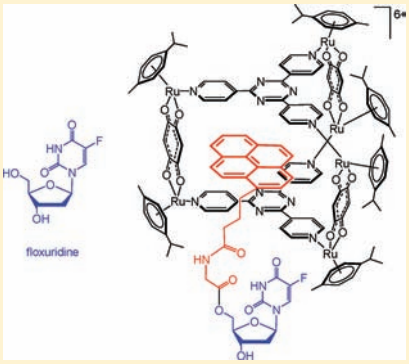
Jeong Wu Yi,[†] Nicolas P. E. Barry,[‡] Mona A. Furrer,[‡] Olivier Zava,[§] Paul J. Dyson,[§] Bruno Therrien,*[,‡] and Byeang Hyean Kim*[,†]

[†]Department of Chemistry, Division of IBB, Pohang University of Science and Technology, Pohang 790-784, Korea

[‡]Institut de Chimie, Université de Neuchâtel, 51 Ave de Bellevaux, 2000 Neuchâtel, Switzerland

[§]Institut des Sciences et Ingénierie Chimique, Ecole Polytechnique Fédérale de Lausanne (EPFL), 1015 Lausanne, Switzerland

ABSTRACT: The self-assembly of 2,4,6-tris(pyridin-4-yl)-1,3,5-triazine (tpt) triangular panels with *p*-cymene ($p\mathrm{Pr}^{i}\mathrm{C}_6\mathrm{H}_4\mathrm{Me}$) ruthenium building blocks and 2,5-dioxydo-1,4-benzoquinonato (dobq) or 5,8-dioxydo-1,4-naphthoquinonato (donq) bridges, in the presence of a pyrenyl-nucleoside derivatives (pyreneR), affords the triangular prismatic host–guest compounds $[(\text{pyrene-R})\subset\mathrm{Ru}_6(p\mathrm{Pr}^{i}\mathrm{C}_6\mathrm{H}_4\mathrm{Me})_6(\mathrm{tpt})_2(\mathrm{dobq})_3]^{6+}$ ($[(\text{pyrene-R})\subset\mathbf{1}]^{6+}$) and $[(\text{pyrene-R})\subset\mathrm{Ru}_6(p\mathrm{Pr}^{i}\mathrm{C}_6\mathrm{H}_4\mathrm{Me})_6(\mathrm{tpt})_2(\mathrm{donq})_3]^{6+}$ ($[(\text{pyrene-R})\subset\mathbf{2}]^{6+}$), respectively. The inclusion of six monosubstituted pyrenyl-nucleosides (pyrene-R1 = 5′-(1-pyrenyl butanoate)-2′-deoxyuridine, pyrene-R2 = 5-fluoro-5′-(1-pyrenyl butanoate)-2′-deoxyuridine, pyrene-R3 = 5′-{*N*-[1-oxo-4-(1-pyrenyl)-butyl]-glycyl}-2′-deoxyuridine, pyrene-R4 = 5-fluoro-5′-{*N*-[1-oxo-4-(1-pyrenyl)butyl]-glycyl}-2′-deoxyuridine, pyrene-R5 = 5-fluoro-5′-{*N*-[1-oxo-4-(1-pyrenyl)butyl]-phenylalanyl}-2′-deoxyvuridine, pyrene-R6 = 5-fluoro-5′-{*N*-[1-oxo-4-(1-pyrenyl)butyl]-phenylalanyl}-2′-deoxyuridine) has been accomplished. The carceplex nature of $[(\text{pyrene-R})\subset\mathbf{1}]^{6+}$ with the pyrenyl moiety firmly encapsulated in the hydrophobic cavity of the cage with the nucleoside groups pointing outward was confirmed by NMR spectroscopy and electrospray ionization mass spectrometry (ESI-MS), while the host–guest nature of $[(\text{pyrene-R})\subset\mathbf{2}]^{6+}$ was studied in solution by NMR techniques. In contrast to the floxuridine compounds used in the clinic, the host–guest complexes are highly water-soluble. Consequently, the cytotoxicities of these water-soluble compounds have been established using human ovarian A2780 and A2780cisR cancer cells. All the host–guest systems are more cytotoxic than the empty cages alone $[\mathbf{1}][\mathrm{CF_3SO_3}]_6$ ($\mathrm{IC_{50}}$ = 23 μM) and $[\mathbf{2}][\mathrm{CF_3SO_3}]_6$ ($\mathrm{IC_{50}}$ = 10 μM), the most active compound $[\text{pyrene-R4}\subset\mathbf{1}][\mathrm{CF_3SO_3}]_6$ being 2 orders of magnitude more cytotoxic ($\mathrm{IC_{50}}$ = 0.3 μM) on these human ovarian cancer cell lines (A2780 and A2780cisR).

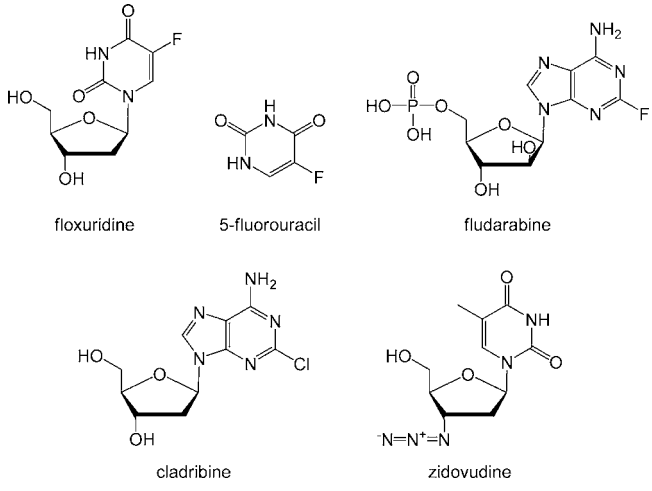


INTRODUCTION

Synthetic nucleoside derivatives are commonly employed as antiviral and anticancer drugs. They include floxuridine, 5-fluorouracil, fludarabine, cladribine, zidovudine, as well as others (Chart 1).[1] 5-Fluorouracil is a widely used antimetabolite for the treatment of human solid tumors including colorectal and breast cancers.[2] Similarly, 5-fluoro-2′-deoxyuridine (FdUrd, Floxuridine) is a 5-fluorouracil derivative known for its high antitumor activity against metastases of cancer.[3,4] Floxuridine has been utilized to treat human solid tumors; however, its therapeutic effect is limited by the efficiency of cellular uptake and bioavailability of the drug. In order to overcome these limitations, various synthetic approaches have been envisaged to enhance the cell permeability and cytotoxicity of floxuridine derivatives as potent anticancer drugs.[5−7]

Pyrenyl-functionalized nucleic acids are popular conjugate molecules in biological chemistry.[8] Indeed, the pyrenyl moiety fits perfectly between base pairs of DNA,[9] possesses interesting fluorescence properties,[10] and functionalization of pyrene is synthetically easy.[11] Therefore, several derivatives of pyrenyl-functionalized nucleic acids have been prepared in recent years.[12−17] However, despite such popularity and interest, low

Chart 1



Received: September 13, 2011
Revised: December 19, 2011
Published: January 22, 2012

ACS Publications © 2012 American Chemical Society

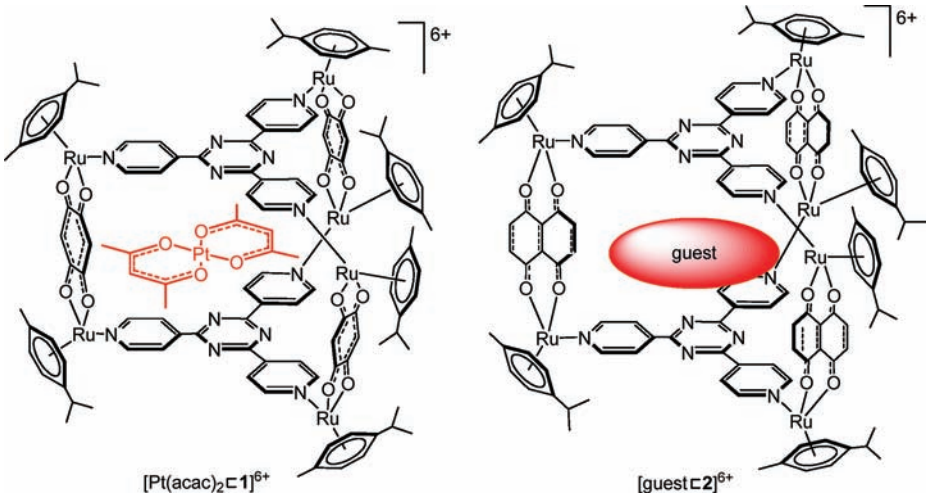


Figure 1. Metalla-prisms $[\{Pt(acac)_2\}\subset Ru_6(p\text{Pr}^iC_6H_4Me)_6(tpt)_2(dobq)_3]^{6+}$ ($[Pt(acac)_2\subset\mathbf{1}]^{6+}$)[15] and $[guest\subset Ru_6(p\text{Pr}^iC_6H_4Me)_6(tpt)_2(donq)_3]^{6+}$ ($[guest\subset\mathbf{2}]^{6+}$).[36]

cell internalization remains one of the limitations of pyrenyl-functionalized nucleic acids for biological applications.[18]

Ruthenium-based anticancer agents have attracted much interest in recent years,[19,20] and organometallic Ru(arene) compounds are the latest trend.[21−23] By modification of the ligand sphere and linking more than one metal center, the properties of the complexes can be altered to obtain desired biological characteristics.[24−26] Recently, new hybrid drug delivery systems built from arene ruthenium complexes have been developed.[27−30] These water-soluble organometallic metalla-cages are able to encapsulate guest molecules. For example, the hexacationic prism $[Ru_6(p\text{Pr}^iC_6H_4Me)_6(tpt)_2(dobq)_3]^{6+}$ ($[\mathbf{1}]^{6+}$) (tpt =2,4,6-tris-(pyridin-4-yl)-1,3,5-triazine; dobq = 2,5-dioxydo-1,4-benzoquinonato) was synthesized,[31] which was capable of encapsulating planar Pt and Pd acetylacetonate complexes (Figure 1) as well as planar aromatic compounds of various sizes.[32,33] Similarly, larger metalla-cages were synthesized such as $[Ru_6(p\text{Pr}^iC_6H_4Me)_6(tpt)_2(donq)_3]^{6+}$ ($[\mathbf{2}]^{6+}$) (tpt = 2,4,6-tris-(pyridin-4-yl)-1,3,5-triazine; donq = 5,8-dioxydo-1,4-naphthoquinonato) in which the guest molecule was free to escape from the cavity of the host in solution, thus providing host−guest systems (Figure 1).[34,35] In these complexes the encapsulated guest is stable, with the physical properties of the host being retained following encapsulation. The biological activity of these systems has been evaluated, and encouraging results were obtained. The metalla-prisms exhibit some activity which increases with the encapsulation of a guest, suggesting transport and leaching of the guest once inside the cell. Indeed, fluorescence experiments have been used to monitor the uptake of the fluorescent-labeled pyrenyl derivative 1-(4,6-dichloro-1,3,5-triazin-2-yl)pyrene (pyrene-X) to cancer cells demonstrating an uptake of the carceplex $[\text{pyrene-X}\subset Ru_6(p\text{Pr}^iC_6H_4Me)_6(tpt)_2(dobq)_3]^{6+}$ being 1 order of magnitude greater than that of pyrene-X alone.[36]

With a view to combine the drug delivery ability of the arene ruthenium metalla-prisms with the biological properties of pyrenyl-functionalized nucleic acids, a series of pyrenyl-nucleosides (pyrene-R) including derivatives analogous to floxuridine have been synthesized and encapsulated in the metalla-prisms $[\mathbf{1}]^{6+}$ and $[\mathbf{2}]^{6+}$. The *in vitro* anticancer activity of these water-soluble systems, $[\text{pyrene-R}\subset\mathbf{1}]^{6+}$ and $[\text{pyrene-R}\subset\mathbf{2}]^{6+}$, was evaluated against human ovarian A2780 and A2780cisR (acquired resistance to cisplatin) cancer cells. The implications of the nucleoside on the biological activity together with the ability of the metalla-prisms to deliver these hydrophobic molecules are discussed.

RESULTS AND DISCUSSION

The synthesis of the pyrenyl-nucleoside derivatives starts with conjugation of the butyryl pyrene derivatives, *N*-[1-oxo-4-(1-pyrenyl)butyl]-glycine ethyl ester and *N*-[1-oxo-4-(1-pyrenyl)butyl]-phenylalanine ethyl ester, with O-protected nucleosides. The butyryl pyrene derivatives conjugated with glycine and phenylalanine are obtained using typical peptidic coupling from 1-pyrene butyric acid. 3′-O-TBDMS-2′-deoxyuridine and 5-fluoro-3′-O-TBDMS-2′-deoxyuridine are prepared according to a published procedure[37] from the corresponding unprotected nucleoside in two steps (Scheme 1).

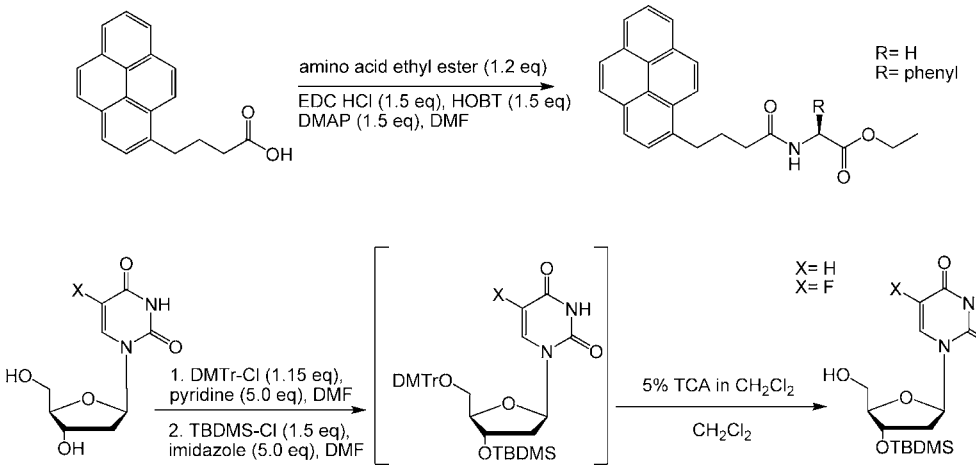
The pyrenyl modified nucleosides are synthesized through an esterification reaction between the butyl pyrenyl amino acids and deprotected silyl group via in situ reaction using tetrabutylammonium fluoride in THF (Scheme 2). These couplings give six pyrenyl-nucleoside derivatives which are characterized by ^1H and $^{13}C\{^1H\}$ NMR spectroscopy and mass spectrometry.

The encapsulation of the pyrenyl-nucleosides (pyrene-R1−6) in the metalla-prism $[\mathbf{1}]^{6+}$ is performed in a two-step process, in which the *p*-cymene ruthenium dobq (2,5-dioxydo-1,4-benzoquinonato) dinuclear complex is first reacted with silver triflate to produce a reactive intermediate, which is then combined with a 2:1 mixture of tpt (2,4,6-tris(pyridin-4-yl)-1,3,5-triazine) and the functionalized pyrenyl derivative (Scheme 3), affording the corresponding carceplex systems $[(\text{pyrene-R1−6})\subset\mathbf{1}][CF_3SO_3]_6$. These metalla-prisms are isolated in 69−73% yield and are characterized by ^1H and $^{13}C\{^1H\}$ NMR spectroscopy and electrospray ionization mass spectrometry.

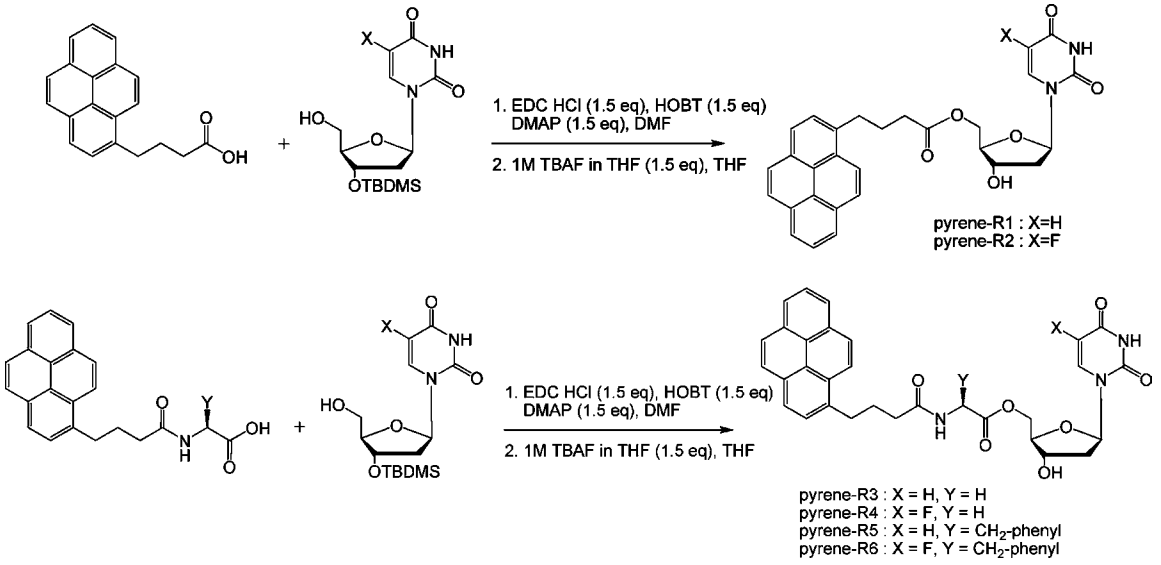
The encapsulation of the pyrenyl-nucleosides (pyrene-R1−6) in the larger metalla-prism $[\mathbf{2}]^{6+}$ is achieved following the same strategy as for $[(\text{pyrene-R1−6})\subset\mathbf{1}][CF_3SO_3]_6$ using the *p*-cymene ruthenium donq (5,8-dioxydo-1,4-naphthoquinonato) dinuclear complex (Scheme 4). The host−guest systems are isolated as their triflate salts $[(\text{pyrene-R1−6})\subset\mathbf{1}][CF_3SO_3]_6$ in good yield.

Under the electrospray ionization mass spectrometry (ESI-MS) conditions employed (see Experimental Section), all inclusion complexes are remarkably stable. The ESI mass spectra of all

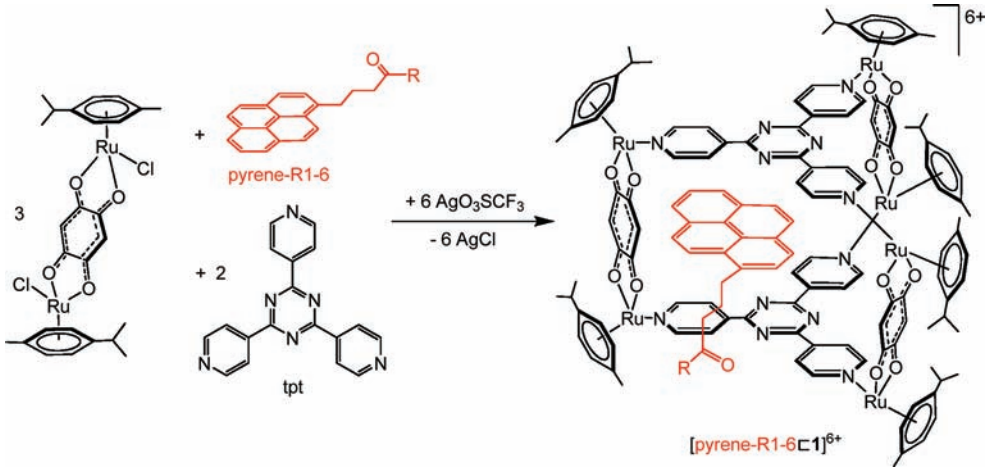
Scheme 1. Synthesis of Butyryl Pyrene Conjugated Amino Acids



Scheme 2. Synthesis of Modified Pyrenyl-Nucleoside Derivatives (Pyrene-R1-6)



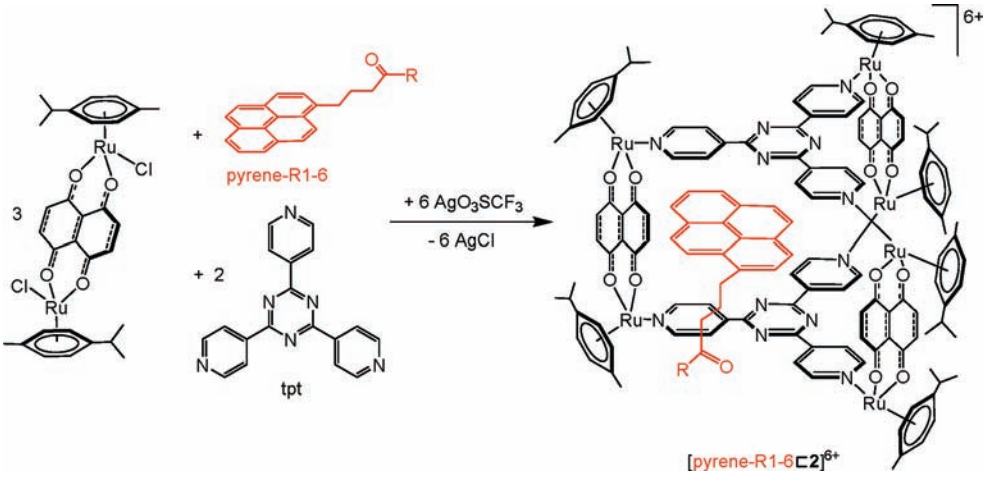
Scheme 3. Synthesis of the Carceplex Systems $[(\text{Pyrene-R1-6})\subset\mathbf{1}]^{6+}$



carceplex systems $[\text{pyrene-R}\subset\mathbf{1}][CF_3SO_3]_6$ show peaks corresponding to $[\text{pyrene-R} + \mathbf{1} + (CF_3SO_3)_3]^{3+}$ at m/z 1132.1 (R1), 1137.8 (R2), 1151.5 (R3), 1157.5 (R4), 1181.5 (R5), and 1186.8 (R6), respectively. Similarly, the ESI mass spectra of the host–guest systems $[\text{pyrene-R}\subset\mathbf{2}][CF_3SO_3]_6$ show peaks corresponding to $[\text{pyrene-R} + \mathbf{2} + (CF_3SO_3)_3]^{3+}$ at m/z 1182.8 (R1), 1188.1 (R2), 1201.5 (R3), 1207.5 R4), 1231.5 (R5), and 1236.5 (R6), respectively. These peaks are assigned unambiguously on the basis of

dx.doi.org/10.1021/bc200472n | Bioconjugate Chem. 2012, 23, 461–471

Scheme 4. Synthesis of the Host-Guest Systems $[(\text{Pyrene-R1-6})\subset\mathbf{2}]^{6+}$



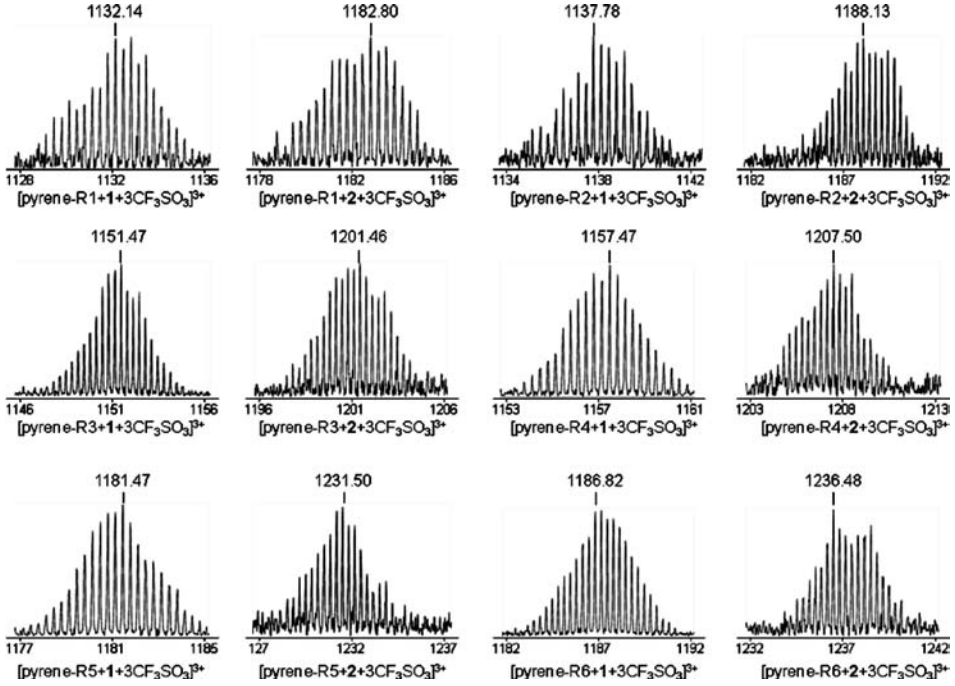


Figure 2. ESI mass of the peak envelopes corresponding to $[\text{pyrene-R} + \mathbf{1} + (CF_3SO_3)_3]^{3+}$ and $[\text{pyrene-R} + \mathbf{2} + (CF_3SO_3)_3]^{3+}$.

their characteristic Ru_6 isotope pattern (Figure 2). In addition to these parent peaks $[\text{pyrene-R} + \mathbf{1} + (CF_3SO_3)_3]^{3+}$ and $[\text{pyrene-R} + \mathbf{2} + (CF_3SO_3)_3]^{3+}$, a series of characteristic fragmentation peaks corresponding to the cages are observed. A typical spectrum is given in Figure 3, identifying the fragmentation peaks observed for $[\text{pyrene-R5}\subset\mathbf{1}][CF_3SO_3]_6$. This fragmentation pattern has been previously observed for related pyrene-R⊂cage systems.[32,33]

These systems are not only stable under ESI mass conditions, they are stable in solution at room and elevated temperature (45 °C) in D_2O, as well as in biological media (aqueous solution containing RPMI 1640 medium with 10% fetal calf serum (FCS) and antibiotics), showing no leaching of the guest molecules or breaking up of the cages. Consequently, the antiproliferative activity of the empty metalla-cages $[\mathbf{1}]^{6+}$, $[\mathbf{2}]^{6+}$ and all the inclusion systems $[\text{pyrene-R1}-6\subset\mathbf{1}]^{6+}$ and $[\text{pyrene-R1}-6\subset\mathbf{2}]^{6+}$ was evaluated against the human ovarian A2780 and A2780cisR (acquired resistance to cisplatin) cancer cell lines using the MTT assay, which measures mitochondrial dehydrogenase activity as an indication of cell viability. The IC_{50} values (IC_{50} is the drug concentration necessary for 50% inhibition of cell viability) are listed in Table 1 and are reported together with that of cisplatin for comparison purposes. It was not possible to obtain IC_{50} values for the pyrene-R compounds, i.e., in the absence of the metalla-cage, due to solubility problems in biological media.

All pyrene-R⊂cage complexes show higher cytotoxicity than their corresponding empty metalla-cages $[\mathbf{1}]^{6+}$ and $[\mathbf{2}]^{6+}$ on both A2780 and A2780cisR cancer cells. Moreover, they show activity comparable or superior to cisplatin with essentially the same level of activity on both nonresistant and cisplatin acquired resistance cell lines. In addition, as control experiments, the antiproliferative activity of the two butyryl pyrene derivatives *N*-[1-oxo-4-(1-pyrenyl)butyl]-glycine ethyl ester and *N*-[1-oxo-4-(1-pyrenyl)butyl]-phenylalanine ethyl ester was evaluated, and both show IC_{50} values >200 μM when tested alone, while the corresponding pyrenyl⊂cage systems possess IC_{50} values

dx.doi.org/10.1021/bc200472n | *Bioconjugate Chem.* 2012, 23, 461–471

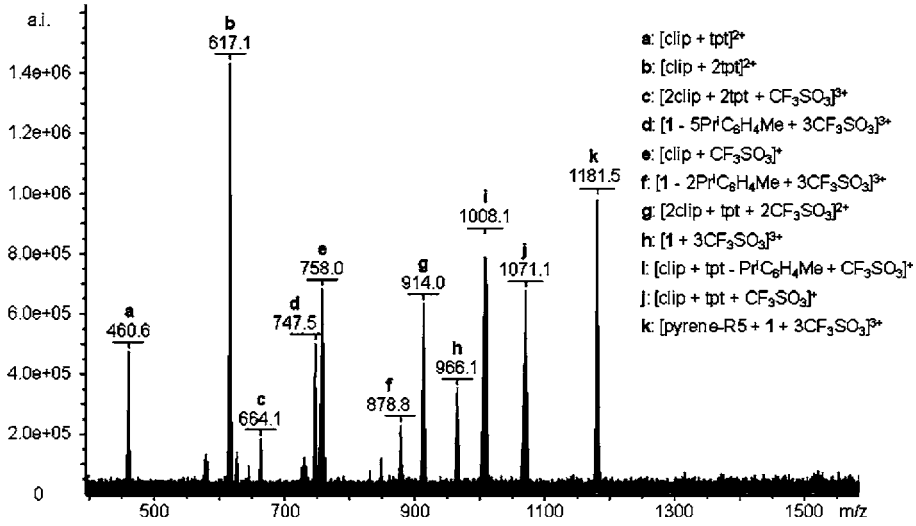


Figure 3. ESI mass spectrum of the $[\text{pyrene-R5}\subset\mathbf{1}][CF_3SO_3]_6$ system (clip = $\{Ru_2(p\text{Pr}^iC_6H_4Me)_2(\text{dobq})\}^{2+}$).

Table 1. IC_{50} Values for $[\mathbf{1}]^{6+}$, $[\mathbf{2}]^{6+}$, $[(\text{Pyrene-R1-6})\subset\mathbf{1}]^{6+}$, and $[(\text{Pyrene-R1-6})\subset\mathbf{2}]^{6+}$ Determined on Human Ovarian A2780 and A2780cisR Cancer Cell Lines

	$IC_{50}/\mu M$		
compound	A2780	A2780cisR	resistance factor (RF)
cisplatin	1.6 ± 0.3	8.6 ± 1.2	5.4
$[\mathbf{1}]^{6+}$	23 ± 2.1	25 ± 2.5	1.1
$[\mathbf{2}]^{6+}$	6.0 ± 1.2	5.2 ± 0.9	0.9
$[\text{pyrene-R1}\subset\mathbf{1}]^{6+}$	2.1 ± 0.14	2.2 ± 0.35	1.0
$[\text{pyrene-R1}\subset\mathbf{2}]^{6+}$	1.3 ± 0.05	1.2 ± 0.04	0.9
$[\text{pyrene-R2}\subset\mathbf{1}]^{6+}$	0.4 ± 0.03	1.3 ± 0.13	3.3
$[\text{pyrene-R2}\subset\mathbf{2}]^{6+}$	0.4 ± 0.10	0.4 ± 0.11	1.0
$[\text{pyrene-R3}\subset\mathbf{1}]^{6+}$	5.6 ± 0.9	6.1 ± 1.5	1.1
$[\text{pyrene-R3}\subset\mathbf{2}]^{6+}$	1.3 ± 0.3	1.4 ± 0.3	1.1
$[\text{pyrene-R4}\subset\mathbf{1}]^{6+}$	0.3 ± 0.03	0.3 ± 0.03	1.0
$[\text{pyrene-R4}\subset\mathbf{2}]^{6+}$	0.2 ± 0.02	0.4 ± 0.05	2.0
$[\text{pyrene-R5}\subset\mathbf{1}]^{6+}$	5.9 ± 0.3	5.7 ± 1.0	1.0
$[\text{pyrene-R5}\subset\mathbf{2}]^{6+}$	1.7 ± 0.06	1.4 ± 0.06	0.8
$[\text{pyrene-R6}\subset\mathbf{1}]^{6+}$	1.2 ± 0.03	1.0 ± 0.04	0.8
$[\text{pyrene-R6}\subset\mathbf{2}]^{6+}$	1.4 ± 0.18	1.7 ± 0.21	1.2

ranging from 2−5 μM. These observations are in agreement with results previously reported with other pyrenyl derivatives encapsulated in water-soluble arene ruthenium metalla-cages.[29−33,35,36] On closer inspection of the IC_{50} data, it is apparent that the fluorinated compounds (pyrene-R2, pyrene-R4, pyrene-R6) are more cytotoxic than their nonfluorinated counterparts (pyrene-R1, pyrene-R3, pyrene-R5). The high level of cytotoxicity of the pyrene-R4 derivatives of floxuridine, especially that involving the less cytotoxic metalla-cage, viz. $[\mathbf{1}]^{6+}$, are good candidates to improve the therapeutic efficiency of this clinically used compound.

CONCLUSION

In this study, water-soluble arene ruthenium metalla-cages were used to deliver pyrenyl-nucleosides to cancer cells. The different floxuridine-metalla-cage combinations exhibit excellent antiproliferative effects on both A2780 ovarian cancer cells and their cisplatin resistant strains. Hence these molecules could be a good therapeutic alternative to floxuridine which suffers from poor cellular uptake and bioavailability.

EXPERIMENTAL SECTION

General. $[Ru_2(p\text{Pr}^iC_6H_4Me)_2(\text{dobq})Cl_2]$,[31] $[Ru_2(p\text{Pr}^iC_6H_4Me)_2(\text{donq})Cl_2]$,[34] and 2,4,6-tris(4-pyridyl)-1,3,5-triazine[38,39] (tpt) were prepared according to published methods and all other reagents were commercially available (Sigma-Aldrich, S&T Pharma, TCI Europe) and used as received. The ^1H, $^{13}C\{^1H\}$ NMR spectra were recorded either on a Bruker AvanceII 400 MHz (University of Neuchatel) or a FT-300 MHz Bruker Apect 3000 (POSTECH, Korea) spectrometers by using the residual protonated solvent as internal standard. Infrared spectra were recorded as KBr pellets on a Bruker FT-IR PS55+ spectrometer. Mass spectra (FAB) were obtained using a Jeol JMS700 high-resolution mass spectrometer at the Korea Basic Science Center, Daegu, Korea. The melting range of the solids was determined with the melting point Gallenkamp apparatus. Electrospray ionization mass spectra were obtained in positive-ion mode on a Bruker FTMS 4.7T BioAPEX II mass spectrometer.

Synthesis of Butyryl Pyrene Conjugated Amino Acids. 1-Pyrene butyric acid (1.0 mmol), EDC·HCl (1.5 mmol), HOBT (1.5 mmol), and DMAP (1.5 mmol) in anhydrous DMF 10 mL were stirred at room temperature for 1 h. Amino acid ethyl ester (1.2 equiv) was added to the reaction mixture and stirred for an additional 2 h. The reaction mixture was concentrated *in vacuo*. The residue was diluted with dichloromethane (100 mL) and extracted with saturated $NaHCO_3$ aqueous solution, water, and brine sequentially. The organic layer was dried over anhydrous $MgSO_4$ and filtered. The filtrate was evaporated *in vacuo*, and the residue was recrystallized with EtOH to give pale-yellow solid.

Synthesis of *N*-[1-oxo-4-(1-pyrenyl)butyl]-glycine ethyl ester was prepared according to the general procedure as mentioned above from glycine ethyl ester hydrochloride (1.14 g, 8.17 mmol). Yield 2.24 g (73%); M.p.: 146−147 °C; ^1H NMR (300 MHz, $CDCl_3$): δ 8.25 (d, J = 9.0 Hz, 1H), 8.14−8.06 (m, 4H), 7.99−7.93 (m, 3H), 7.81 (d, J = 9.0 Hz, 1H), 5.94 (s, 1H, NH) 4.19 (q, J = 9.1 Hz, 2H, OCH_2CH_3), 4.00 (d, J = 6.0 Hz, 2H), 3.35 (t, J = 7.5 Hz, 2H, $PyCH_2CH_2CH_2-$), 2.33 (t, J = 7.5 Hz, 2H, $PyCH_2CH_2CH_2-$) 2.19 (m, 2H, $PyCH_2CH_2CH_2-$), 1.25 (t, J = 9.1 Hz, 3H, OCH_2CH_3); $^{13}C\{^1H\}$ NMR (75 MHz, $CDCl_3$): δ 172.1, 159.1, 156.8, 156.6, 144.0, 143.9, 141.5, 138.6, 132.7, 132.5, 128.0, 127.3, 125.3, 172.8, 170.1, 135.8, 131.4, 130.9, 130.0, 128.8, 127.5, 127.4,

dx.doi.org/10.1021/bc200472n | Bioconjugate Chem. 2012, 23, 461−471

126.7, 125.8, 125.1 125.0, 124.9, 124.8, 124.8, 123.4, 61.5, 41.4, 35.6, 32.7, 27.2, 14.1; IR (neat): 3310, 3037, 2937, 2867, 1739, 1651, 1537, 1198 cm^{-1}; HRMS-FAB (m/z): calcd for $C_{24}H_{24}NO_3^+$ $[M + H]^+$, 374.1756; found, 374.1751.

Synthesis of *N*-[1-oxo-4-(1-pyrenyl)butyl]-phenylalanine ethyl ester was prepared according to the general procedure as mentioned above from phenylalanine ethyl ester hydrochloride (1.27 g, 5.53 mmol). Yield 2.08 g (81%); M.p.: 157−158 °C; ^1H NMR (300 MHz, $CDCl_3$): δ 8.24 (d, J = 9.0 Hz, 1H), 8.13−8.03 (m, 4H), 7.98−7.94 (m, 3H), 7.78 (d, J = 9.0 Hz, 1H), 7.22−7.17 (m, 3H), 7.10 (m, 2H), 5.95 (d, J = 6.1 Hz, 1H), 4.90 (q, J = 6.1 Hz, 1H), 4.12 (q, J = 6.0 Hz, 2H), 3.29 (t, J = 9.1 Hz, 2H), 3.17−3.03 (m, 2H), 2.28−2.23 (m, 2H), 2.19−2.11 (m, 2H), 1.20 (t, J = 6.0 Hz, 3H); $^{13}C\{^1H\}$ NMR (75 MHz, $CDCl_3$): δ 172.2, 171.8, 136.0, 135.8, 131.4, 130.9, 130.0, 129.3, 128.8, 128.6, 127.5, 127.4, 127.3, 127.1, 126.7, 125.9, 125.1, 125.0, 124.9, 124.8, 123.42, 61.6, 53.1, 38.0, 35.8, 32.7, 27.2, 14.2; IR (neat): 3308, 3289, 3098, 2947, 2865, 1709, 1660, 1557, 1451, 1198 cm^{-1}; HRMS-FAB (m/z): calcd for $C_{31}H_{30}NO_3^+$ $[M + H]^+$, 464.2226; found, 464.2224.

Synthesis of 3′-O-Protected Nucleoside Derivatives. 3′-O-(*tert*-Butyldimethylsilyl)-2′-deoxynucleosides were prepared according to the published procedures.[37] A solution of 2′-deoxynucleoside (1.0 mmol), 4,4′-dimethoxytrityl chloride (DMTrCl) (1.15 mmol), and anhydrous pyridine (5.0 mmol) in anhydrous DMF (10 mL) was stirred at room temperature for 5 h. To the reaction mixture was then added methanol (1 mL) for quenching, and the mixture was stirred for 30 min. The reaction mixture was partitioned between dichloromethane (250 mL) and saturated $NaHCO_3$ aqueous solution (250 mL). The organic layer was washed with water two times and brine, dried over anhydrous Na_2SO_4, and filtered. The filtrate was concentrated and coevaporated with pyridine two times. The residue was dissolved in 10 mL of anhydrous DMF. To the solution was added imidazole (5.0 mmol) and the solution was stirred at room temperature for 30 min. After adding *tert*-butyldimethylsilyl chloride (1.5 mmol) the resulting reaction mixture was stirred overnight at room temperature. Then 100 mL of saturated $NaHCO_3$ aqueous solution was added, and the mixture was extracted with dichloromethane two times. The combined organic layer was washed with water three times then brine, dried with Na_2SO_4, and filtered. The filtrate was concentrated *in vacuo* and coevaporated with toluene three times. The residue was dried over 6 h *in vacuo* and used to the next step without further purification.

The concentrated residue was dissolved in 10 mL of anhydrous dichloromethane and stirred at 0−5 °C for 30 min. Then 10 mL of 5% trichloroacetic acid in dichloromethane was slowly added to the reaction mixture and the resulting reaction mixture was stirred at room temperature for 3 h. To the reaction mixture was then added 1 mL of methanol and 50 mL of saturated $NaHCO_3$ aqueous solution was added to the mixture. The organic layer was collected, dried over anhydrous Na_2SO_4, and filtered. The filtrate was evaporated *in vacuo*, and the residue was purified by column chromatography to give a white solid.

3′-*O*-(*tert*-Butyldimethylsilyl)-2′-deoxyuridine was prepared according to the general procedure as mentioned above from 2′-deoxyuridine (1.04 g, 4.56 mmol). Yield 1.23 g (79%); M.p.: 206−207 °C; ^1H NMR (300 MHz, $CDCl_3$): δ 9.10 (br s, 1H, exch D_2O, NH), 7.67 (d, 1H, J = 8.1 Hz, C6H), 6.18 (t, 1H, J = 6.6 Hz, C1′H), 5.75 (d, 1H, J = 8.1 Hz, C5H), 4.51−4.47 (m, 1H, C3′H), 3.95−3.91 (m, 2H, C4′H and C5′H), 3.78 (m, 1H, C5′H), 2.54 (br s, 1H, exch D_2O, OH), 2.31−2.27 (m, 2H, C2′H), 0.89 (s, 9H, $C(CH_3)_3$), 0.09 (s, 6H, $Si(CH_3)_2$); $^{13}C\{^1H\}$ NMR (75 MHz, $CDCl_3$): δ 163.2, 150.2, 141.1, 102.5, 87.6, 86.7, 71.4, 61.8, 40.9, 25.7, 18.0, −4.7, −4.9; IR (neat): 3447, 2963, 2930, 2857, 1699, 1559, 1472, 1274, 1082 cm^{-1}; HRMS-FAB (m/z): calcd for $C_{15}H_{27}N_2O_5Si^+$ $[M + H]^+$, 343.1689; found, 343.1687.

5-Fluoro-3′-*O*-(*tert*-butyldimethylsilyl)-2′-deoxyuridine was prepared according to the general procedure as mentioned above from 5-fluoro-2′-deoxyuridine (1.11 g, 4.51 mmol). Yield 1.24 g (76%); M.p.: 140.6−142 °C; ^1H NMR (300 MHz, $CDCl_3$): δ 8.84 (br s, 1H, exch D_2O, NH), 7.97 (d, 1H, J = 6.4 Hz, C6H), 6.23 (t, 1H, C1′H), 4.51 (m, 1H, C3′H), 4.00−3.95 (m, 2H, C4′H and C5′H), 3.83−3.78 (m, 1H, C5′H), 2.35−2.17 (2 m, 2H, C2′H), 0.90 (s, 9H, $C(CH_3)_3$), 0.09 (s, 6H, $Si(CH_3)_2$); $^{13}C\{^1H\}$ NMR (75 MHz, $CDCl_3$): δ 156.9, 148.7, 142.0, 138.9, 125.2, 124.8, 87.6, 86.3, 71.4, 61.8, 41.2, 25.7, 18.0, 4.7, −4.9; IR (neat): 3446, 3193, 2955, 2929, 2857, 1716, 1699, 1559, 1404, 1260, 1097 cm^{-1}; HRMS-FAB (m/z): calcd for $C_{15}H_{26}FN_2O_5Si^+$ $[M + H]^+$, 361.1595; found, 361.1597.

Synthesis of Modified Nucleosides Conjugated Pyrenyl Derivatives. Butyryl pyrene conjugated amino acids (1.0 mmol) and lithium hydroxide monohydrate (3.0 mmol) was stirred in THF/H_2O (4/1) at room temperature for 2−3 h. The resulting reaction mixture was neutralized with Dowex 50WX8−200 ion-exchange resin, filtered, and concentrated *in vacuo*. The residue was coevaporated with pyridine three times and dried *in vacuo*. Without further purification, the residue was dissolved with 20 mL of anhydrous DMF. To the solution were added EDC·HCl (1.5 mmol), HOBT (1.5 mmol), and DMAP (1.5 mmol) and stirred at room temperature for 1 h. 3′-*O*-TBDMS nucleosides (1.0 mmol) was added to the reaction mixture. The resulting reaction mixture was stirred at ambient temperature for 6 h. The reaction mixture was concentrated *in vacuo*. The residue was extracted between dichloromethane (150 mL) and 1 N HCl aqueous solution (10 mL). The organic layer was washed with water three times, dried over anhydrous $MgSO_4$, and filtered. The filtrate was evaporated *in vacuo*. The residue was dissolved with anhydrous THF and cooled at 0−5 °C. 1 M TBAF in THF (1.5 mL) was added slowly to the reaction mixture. The resulting reaction mixture was warmed up at room temperature and stirred for 6 h. Afterward, ethyl acetate was added to the mixture and the solution was washed with saturated $NaHCO_3$ aqueous solution, water, and brine sequentially. The organic layer was dried over anhydrous $MgSO_4$ and filtered. The filtrate was evaporated *in vacuo*, and the residue was purified by column chromatography to give a pale-yellow solid.

5′-(1-Pyrenyl butanoate)-2′-deoxyuridine (pyrene-R1) was prepared according to the general procedure as mentioned above from 3′-*O*-(*tert*-butyldimethylsilyl)-2′-deoxyuridine (212 mg, 0.62 mmol). Yield: 280 mg (91%); M.p.: 223−224 °C; ^1H NMR (300 MHz, acetone-d_6): δ 10.2 (s, 1H), 8.41(d, J = 9.6 Hz, 1H), 8.24−8.18 (m, 6H), 8.01 (m, 1H), 7.92 (m, 1H), 7.73 (d, J = 8.1 Hz, 1H, C6H), 6.34 (t, J = 6.6 Hz, 1H, C1′H), 5.67 (d, J = 8.1 Hz, 1H, C5H), 4.48 (m, 1H, C4′H), 4.42−4.18 (m, 2H, C5′H), 4.17−4.15 (m, 1H, C3′H), 3.40 (t, J = 7.5 Hz, 2H, Py$CH_2$$CH_2$$CH_2$), 2.56 (t, J = 7.2 Hz, 2H, PyCH$_2$CH$_2$$CH_2$), 2.41−2.32 (m, 2H, PyCH$_2$$CH_2CH_2$), 2.30−2.08 (m, 2H, C2′H); $^{13}C\{^1H\}$ NMR (75 MHz, acetone-d_6): δ 172.3, 162.5, 150.0, 139.6, 135.8, 131.1, 130.6, 129.6, 128.3, 127.1, 126.9, 126.2, 125.6, 124.6, 124.5, 124.4, 123.1, 101.6, 70.8, 63.5, 39.4, 32.9, 31.9, 26.5; IR (neat): 3421, 3044, 2947, 1698, 1653, 1460, 1383, 1272, 1248, 1089 cm^{-1}; HRMS-FAB

(m/z): calcd for $C_{29}H_{27}N_2O_6^+$ $[M + H]^+$, 499.1869; found, 499.1866.

5-Fluoro-5′-(1-pyrenyl butanoate)-2′-deoxyuridine (pyrene-R2) was prepared according to the general procedure as mentioned above from 5-fluoro-3′-*O*-(*tert*-butyldimethylsilyl)-2′-deoxyuridine (209 mg, 0.58 mmol). Yield: 267 mg (89%); M.p.: 216−218 °C; ^{1}H NMR (300 MHz, $CDCl_3$): δ 9.54 (s, 1H), 8.18 (d, 1H, J = 9.0 Hz), 8.08−7.95 (m, 7H), 7.75 (d, 1H), 7.51 (d, 1H, J = 5.7 Hz), 6.05 (t, 1H, C1′H), 4.30−4.26 (m, 1H, C4′H), 4.13−4.02 (m, 3H, C5′H and C3′H), 3.31 (m, 2H, PyCH_2CH$_2$CH$_2$), 2.43 (t, 2H, PyCH$_2$CH$_2$$CH_2$), 2.28−2.16 (m, 2H, PyCH$_2$$CH_2CH_2$), 1.88−1.83 (m, 2H, C2′H); ^{13}C{^{1}H} NMR (75 MHz, $CDCl_3$): δ 173.1, 156.9, 148.6, 142.0, 138.9, 135.1, 131.3, 130.1, 130.0, 128.7, 127.5, 127.3, 126.8, 125.9, 125.0, 124.9, 124.8, 123.9, 123.4, 123.1, 85.5, 84.3, 80.7, 63.3, 40.3, 33.5, 32.4, 26.4; IR (neat): 3447, 3198, 3043, 2949, 1734, 1717, 1473, 1418, 1264, 1086 cm^{-1}; HRMS-FAB (m/z): calcd for $C_{29}H_{26}FN_2O_6^+$ $[M + H]^+$, 517.1775; found, 517.1778.

5′-{*N*-[1-Oxo-4-(1-pyrenyl)butyl]-glycyl}-2′-deoxyuridine (pyrene-R3) was prepared according to the general procedure as mentioned above from 3′-*O*-(*tert*-butyldimethylsilyl)-2′-deoxyuridine (224 mg, 0.65 mmol). Yield: 316 mg (87%); M.p. M.p.: 231−233 °C; ^{1}H NMR (300 MHz, acetone-d_6): δ 10.1 (s, 1H), 8.45(d, 1H, J = 9.0 Hz), 8.24−8.15 (m, 5H), 8.08−7.93 (m, 3H), 7.75 (d, 1H, J = 8.1 Hz, C6H), 6.32 (t, 1H, J = 6.90 Hz, C1′H), 5.76 (d, 1H, J = 8.1 Hz, C5H), 4.72 (s, 1H), 4.50−4.48 (m, 1H, C4′H), 4.39−4.37 (m, 3H, C3′H and C5′H), 4.08 (d, 2H, J = 5.7 Hz, CαH), 3.42 (t, 2H, J = 7.5 Hz, PyCH_2CH$_2$CH$_2$), 2.45 (t, 2H, 7.2 Hz, PyCH$_2$CH$_2$$CH_2$), 2.34−2.28 (m, 2H, PyCH$_2$$CH_2CH_2$), 2.20−2.08 (m, 2H, C2′H); ^{13}C{^{1}H} NMR (75 MHz, acetone-d_6): δ 173.1, 169.9, 162.9, 150.4, 140.2, 136.7, 131.4, 131.0, 129.9, 128.7, 127.6, 127.3, 126.5, 125.9, 124.9, 124.8, 124.7, 123.7, 102.2, 84.9, 84.5, 71.1, 64.2, 41.1, 39.7, 34.9, 32.5, 27.6; IR (neat): 3333, 3046, 2940, 1753, 1696, 1540, 1460, 1271, 1191, 1088 cm^{-1}; HRMS-FAB (m/z): calcd for $C_{31}H_{30}N_3O_7^+$ $[M + H]^+$, 556.2084; found, 556.2086.

5-Fluoro-5′-{*N*-[1-oxo-4-(1-pyrenyl)butyl]-glycyl}-2′-deoxyuridine (pyrene-R4) was prepared according to the general procedure as mentioned above from 5-fluoro-3′-*O*-(*tert*-butyldimethylsilyl)-2′-deoxyuridine (204 mg, 0.57 mmol). Yield: 276 mg (85%); M.p.: 227−229 °C; ^{1}H NMR (300 MHz, DMSO-d_6): δ 8.39 (s, 1H), 8.36 (d, 1H, J = 9.3 Hz), 8.24−8.14 (m, 4H), 8.08 (s, 2H), 7.99 (t, 1H), 7.89 (t, 2H), 6.13 (t, 1H, J = 6.3 Hz, C1′H), 5.60 (br, 1H, NH), 4.30−4.25 (m, 3H, C4′H and C5′H), 3.96−3.89 (m, 3H, C3′H and CαH), 3.31 (t, 2H, J = 7.5 Hz, PyCH_2CH$_2$CH$_2$), 2.32 (t, 2H, J = 7.2 Hz, PyCH$_2$CH$_2$$CH_2$), 2.22−2.14 (m, 2H, PyCH$_2$$CH_2CH_2$), 2.04−1.99 (m, 2H, C2′H); ^{13}C{^{1}H} NMR (75 MHz, acetone-d_6): δ 173.6, 170.4, 157.8, 157.4, 149.5, 142.1, 139.0, 136.9, 131.3, 130.8, 129.7, 128.6, 128.0, 127.9, 127.7, 126.9, 126.6, 125.4, 125.3, 125.2, 125.0, 124.7, 124.6, 123.9, 85.1, 84.3, 79.4, 70.4, 64., 41.2, 3.1, 32.5, 27.9; IR (neat): 3429, 3027, 2941, 1696, 1664, 1559, 1194, 1027 cm^{-1}; HRMS-FAB (m/z): calcd for $C_{31}H_{29}FN_3O_7^+$ $[M + H]^+$, 574.1990; found, 574.1986.

5-Fluoro-5′-{*N*-[1-oxo-4-(1-pyrenyl)butyl]-phenylalanyl}-2′-deoxyuridine (pyrene-R5) was prepared according to the general procedure as mentioned above from 3′-*O*-(*tert*-butyldimethylsilyl)-2′-deoxyuridine (207 mg, 0.60 mmol). Yield: 316 mg (81%); M.p.: 238−239 °C; ^{1}H NMR (300 MHz, acetone-d_6): δ 10.2 (s, 1H), 8.42 (d, 1H), 8.26−8.00 (m, 7H), 7.90 (t, 1H), 7.71 (d, 1H, J = 8.1 Hz, C6H), 7.28−7.17 (m, 4H), 6.32 (t, 1H, J = 6.4 Hz, C1′H), 5.69 (d, 1H, J = 8.1 Hz, C5H), 4.78−4.72 (m, 1H, C4′H), 4.48−4.43 (m, 1H, CαH), 4.24−4.05 (m, 3H, C3′H and C5′H), 3.35−3.18 (m, 2H, PyCH_2CH$_2$CH$_2$), 3.11−3.09 (m, 2H, phenyl), 2.40−2.29 (m, 4H, PyCH$_2$$CH_2$$CH_2$), 2.14−2.12 (m, 2H, C2′H); ^{13}C{^{1}H} NMR (75 MHz, acetone-d_6): δ 172.7, 171.9, 162.8, 150.4, 140.3, 137.2, 136.7, 131.0, 129.9, 129.2, 128.7, 128.4, 127.6, 127.5, 127.3, 126.8, 126.5, 126.0, 124.9, 124.8, 123.7, 102.6, 84.9, 84.4, 71.5, 64.7, 54.5, 40.0, 37.3, 34.9, 32.4, 27.5; IR (neat): 3327, 3043, 2946, 1704, 1698, 1559, 1457, 1248, 1184, 1086 cm^{-1}; HRMS-FAB (m/z): calcd for $C_{38}H_{36}N_3O_7^+$ $[M + H]^+$, 646.2553; found, 646.2550.

5-Fluoro-5′-{*N*-[1-oxo-4-(1-pyrenyl)butyl]-phenylalanyl}-2′-deoxyuridine (pyrene-R6) was prepared according to the general procedure as mentioned above from 5-fluoro-3′-*O*-(*tert*-butyldimethylsilyl)-2′-deoxyuridine (224 mg, 0.62 mmol). Yield: 342 mg (83%); M.p.: 234−236 °C; ^{1}H NMR (300 MHz, acetone-d_6): δ 10.5 (s, 1H), 8.39 (d, 1H, J = 8.1 Hz), 8.24−8.13 (m, 6H), 8.04−7.99 (m, 3H), 7.67 (d, 1H, J = 7.5 Hz), 7.28−7.17 (m, 4H), 6.32 (t, 1H, J = 5.7 Hz, C1′H), 4.84−4.79 (m, 1H, C4′H), 4.55−4.51 (m, 1H, CαH), 4.37−4.13 (m, 3H, C3′H and C5′H), 3.33−3.22 (m, 2H, PyCH_2CH$_2$CH$_2$), 3.20−3.16 (m, 2H, phenyl), 2.38−2.11 (m, 4H, PyCH$_2$$CH_2$$CH_2$), 2.09−2.06 (m, 2H, C2′H); ^{13}C{^{1}H} NMR (75 MHz, acetone-d_6): δ 172.8, 171.7, 156.9, 149.0, 142.2, 139.1, 137.1, 136.6, 131.4, 130.0, 129.1, 128.7, 128.4, 127.5, 127.2, 126.7, 126.5, 126.0, 124.9, 124.8, 124.6, 124.5, 124.1, 123.7, 85.3, 84.7, 71.0, 64.5, 54.2, 39.6, 37.2, 34.9, 32.4, 27.5; IR (neat): 3402, 2964, 2929, 1717, 1700, 1653, 1540, 1473, 1361, 1264, 1079 cm^{-1}; HRMS-FAB (m/z): calcd for $C_{38}H_{35}FN_3O_7^+$ $[M + H]^+$, 664.2459; found, 664.2463.

Encapsulation of Modified Nucleosides Conjugated Pyrenyl Derivatives (Pyrene-R1−6) in Metalla-Cage [1]$^{6+}$. A mixture of $[Ru_2(p\text{Pr}^iC_6H_4Me)_2(dobq)Cl_2]$ (0.15 mmol), $AgCF_3SO_3$ (0.30 mmol), tpt (0.10 mmol), and pyrenyl derivatives (pyrene-R) (0.05 mmol) in MeOH (30 mL) was stirred at 60 °C for 15 h. The reaction mixture was kept in the dark. The resulting reaction mixture was filtered and concentrated *in vacuo*. The residue was dissolved in CH_2Cl_2 (2 mL), and diethyl ether (50 mL) was slowly added to precipitate the product, which was kept in the refrigerator for 2 h. The product was filtered and dried *in vacuo*.

[Pyrene-R1⊂1][CF$_3$SO$_3$]$_6$. This complex was synthesized according to the procedure described above using compound pyrene-R1 (27.1 mg, 0.05 mmol). Yield 136 mg (71%). ^{1}H NMR (300 MHz, acetone-d_6): δ 9.88 (s, 1H, N3H), 8.58 (s, 12H, H_α), 8.04 (br, 12H, H_β), 7.87 (d, 1H, J = 8.1 Hz, C6H), 7.05 (d, 1H, J = 9.0 Hz, H_{Py}), 6.89 (d, 1H, J = 15.6 Hz, H_{Py}), 6.84 (d, 1H, J = 15.6 Hz, H_{Py}), 6.57 (d, 1H, J = 9.3 Hz, H_{Py}), 6.42 (t, 1H, J = 6.3, C1′H), 6.38 (d, 1H, J = 3.9 Hz, H_{Py}), 6.24 (d, 12H, J = 6.0 Hz, H_{ar}), 6.19 (br, 8H, H_q and H_{Py}), 6.02 (d, 12H, J = 6.0 Hz, H_{ar}), 5.99 (m, 1H, H_{Py}) 5.85 (d, 1H, J = 7.5 Hz, H_{Py}), 5.60 (d, 1H, J = 8.1 Hz, C5H), 4.68−4.58 (m, 3H, C3′H and C5′H), 4.44−4.43 (m, 1H, C4′H), 2.99 (sept, 6H, J = 6.9 Hz, CH), 2.57−2.55 (m, 6H, PyCH_2CH$_2$$CH_2$ and C2′H), 2.23 (s, 18H, CH_3), 1.72−1.69 (m, 2H, PyCH$_2$$CH_2CH_2$), 1.42 (d, J = 6.90 Hz, 36H, CH_3); ^{13}C{^{1}H} NMR (75 MHz, acetone-d_6): δ 184.2, 172.8, 167.6, 162.7, 154.0, 150.5 143.6, 140.8, 135.5, 129.7, 129.1, 128.2, 127.5, 127.2, 126.9, 125.8, 124.9, 124.6, 124.4, 123.6, 122.8, 122.7, 122.2, 119.3, 104.1, 101.9, 99.2, 84.6, 83.8, 82.3, 71.1, 64.3, 38.7, 32.9, 31.8, 31.2, 26.4, 21.6, 17.2; IR (neat): 3446, 2964, 2927, 1717, 1521, 1376, 1258, 1030, 811 cm^{-1}; ESI-MS (m/z): 1132.14 [pyrene-R1 + **1** + $(CF_3SO_3)_3]^{3+}$.

[Pyrene-R2⊂1][CF$_3$SO$_3$]$_6$. This complex was synthesized according to the procedure described above using compound

dx.doi.org/10.1021/bc200472n | *Bioconjugate Chem.* 2012, 23, 461−471

pyrene-R2 (27.1 mg, 0.05 mmol). Yield 145 mg (72%). ^{1}H NMR (300 MHz, acetone-d_6): δ 10.4 (s, 1H, N3H), 8.57 (s, 12H, H_α), 8.04 (br, 12H, H_β), 8.02 (d, 1H, J = 6.9 Hz), 7.08 (d, 1H, J = 8.7 Hz, H_{Py}), 6.93 (d, 1H, J = 7.5 Hz, H_{Py}), 6.87(d, 1H, J = 8.4 Hz, H_{Py}), 6.58 (d, 1H, J = 9.3 Hz, H_{Py}), 6.40−6.34 (m, 2H, H_{Py} and C1′H), 6.21 (m, 19H, H_{ar}, H_q, and H_{Py}), 6.01 (m, 13H, H_{ar} and H_{Py}), 5.85 (d, 1H, J = 7.2 Hz, H_{Py}), 4.76−4.58 (m, 3H, C3′H and C5′H), 4.45−4.43 (m, 1H, C4′H), 2.98 (sept, 1H, J = 6.9 Hz, CH), 2.57−2.52 (m, 6H, Py$CH_2CH_2CH_2$ and C2′H), 2.22 (s, 18H, CH_3), 1.73−1.68 (m, 2H, PyCH$_2CH_2$CH$_2$), 1.42 (d, 36H, J = 6.9 Hz, CH_3); ^{13}C{^{1}H} NMR (75 MHz, acetone-d_6): δ 184.2, 172.8, 167.6, 153.8, 150.5 148.9, 143.6, 140.8, 135.4, 129.7, 129.1, 128.2, 127.9, 127.2, 127.0, 126.4, 125.8, 124.6, 124.2, 123.6, 122.9, 122.2, 119.3, 104.1, 101.9, 99.2, 85.2, 83.8, 82.3, 70.9, 66.7, 64.3, 38.7, 33.9, 31.2, 26.5, 21.6, 17.2; IR (neat): 3447, 2965, 2927, 1717, 1521, 1376, 1258, 1058, 1030, 811 cm^{-1}; ESI-MS (m/z): 1137.78 [pyrene-R2 + **1** + $(CF_3SO_3)_3$]$^{3+}$.

[Pyrene-R3⊂1][CF$_3$SO$_3$]$_6$. This complex was synthesized according to the procedure described above using compound pyrene-R3 (27.6 mg, 0.05 mmol). Yield 134 mg (69%). ^{1}H NMR (300 MHz, acetone-d_6): δ 10.02 (s, 1H, N3H), 8.57 (s, 12H, H_α), 7.96 (br, 12H, H_β), 7.81 (d, 1H, J = 8.1 Hz, C6H), 7.04 (d, 1H, J = 9.0 Hz, H_{Py}), 6.91 (d, 1H, J = 7.8 Hz, H_{Py}), 6.79 (d, 1H, J = 8.7 Hz, H_{Py}), 6.56 (d, 1H, J = 9.0 Hz, H_{Py}), 6.42 (t, 1H, J = 7.2 Hz, C1′H), 6.22 (m, 20H, H_{ar}, H_q, and H_{Py}), 6.00 (d, 12H, J = 6.3 Hz, H_{ar}), 5.80 (m, 2H, H_{Py}), 5.60 (d, 1H, J = 8.1 Hz, C5H), 4.60−4.52 (m, 3H, C3′H and C5′H), 4.26 (m, 3H, C4′H and CαH), 2.98 (sept, 6H, J = 6.9 Hz, CH), 2.56−2.55 (m, 2H, PyCH_2CH$_2$CH$_2$), 2.42 (m, 4H, PyCH$_2$CH$_2CH_2$ and C2′H), 2.22 (s, 18H, CH_3), 1.64 (m, 2H, PyCH$_2CH_2$CH$_2$), 1.40 (d, 36H, J = 6.9 Hz, CH_3); ^{13}C{^{1}H} NMR (75 MHz, acetone-d_6): δ 184.2, 173.0, 170.1, 162.9, 153.8, 150.4, 140.3, 136.7, 131.4, 131.0, 129.9, 128.7, 127.6, 127.3, 126.5, 125.9, 125.5, 124.9, 124.8, 124.7, 124.2, 123.7, 104.1, 102.0, 102.2, 99.3, 84.9, 84.5, 83.9, 82.2, 71.1, 64.2, 41.1, 39.7, 34.9, 32.5, 31.2, 27.6, 21.6, 17.2; IR (neat): 3447, 2965, 2927, 1684, 1540, 1375, 1259, 1058, 811 cm^{-1}; ESI-MS (m/z): 1151.47 [pyrene-R3 + **1** + $(CF_3SO_3)_3$]$^{3+}$.

[Pyrene-R4⊂1][CF$_3$SO$_3$]$_6$. This complex was synthesized according to the procedure described above using compound pyrene-R4 (28.7 mg, 0.05 mmol). Yield 143 mg (73%). ^{1}H NMR (300 MHz, acetone-d_6): δ 10.46 (s, 1H, N3H), 8.57 (s, 12H, H_α), 8.21−7.93 (br, d, 13H, H_β and C6H), 7.04 (d, 1H, J = 9.0 Hz, H_{Py}), 6.91 (d, 1H, J = 7.5 Hz, H_{Py}), 6.78 (d, 1H, J = 9.0 Hz, H_{Py}), 6.56 (d, 1H, J = 9.0 Hz, H_{Py}), 6.39 (t, 1H, J = 7.8 Hz, C1′H), 6.21 (d, m, 18H, J = 6.0 Hz, H_{ar} and H_q), 6.12−5.81 (m, 3H, H_{Py}), 6.00 (m, H_{ar} and H_{Py}), 5.81 (d, 1H, J = 7.8 Hz, H_{Py}) 4.65−4.48 (m, 3H, C3′H and C5′H), 4.28 (br, 3H, C4′H and CαH), 2.98 (sept, 6H, J = 6.9 Hz, CH), 2.58 (m, 2H, PyCH_2CH$_2$CH$_2$), 2.43 (m, 4H, PyCH$_2$CH$_2CH_2$ and C2′H), 2.22 (s, 18H, CH_3), 1.62 (m, 2H, PyCH$_2CH_2$CH$_2$), 1.40 (d, J = 6.90 Hz, 36H, CH_3); ^{13}C{^{1}H} NMR (75 MHz, acetone-d_6): δ 184.2, 173.5, 170.3, 167.6, 157.0, 153.8, 148.9, 143.3, 135.8, 129.7, 129.1, 128.1, 127.5, 127.2, 126.7, 126.2, 125.8, 125.4, 124.8, 124.5, 124.2, 123.5, 122.9, 122.7, 122.4, 119.3, 115.0, 104.1, 102.0, 99.2, 85.3, 84.8, 83.9, 82.2, 70.9, 64.5, 61.7, 41.1, 39.4, 35.1, 31.7, 31.2, 26.5, 21.6, 17.2; IR (neat): 3446, 2966, 2929, 1734, 1521, 1375, 1259, 1058, 811 cm^{-1}; ESI-MS (m/z): 1157.47 [pyrene-R4 + **1** + $(CF_3SO_3)_3$]$^{3+}$.

[Pyrene-R5⊂1][CF$_3$SO$_3$]$_6$. This complex was synthesized according to the procedure described above using compound pyrene-R5 (33.0 mg, 0.05 mmol). Yield 142 mg (70%). ^{1}H NMR (300 MHz, acetone-d_6): δ 10.15 (s, 1H, N3H), 8.57 (s, 12H, H_α), 8.30−7.91 (br, d, 13H, H_β and C6H), 7.53 (m, 5H, H_{ph}), 7.00 (d, 1H, J = 9.0 Hz, H_{py}), 6.87 (t, 1H, J = 8.1 Hz, H_{py}), 6.78 (m, 1H, H_{py}), 6.55 (m, 1H, H_{py}), 6.37−6.22 (m, 8H, C1′H, H_{Py} and H_q), 6.20 (d, 12H, J = 6.3 Hz, H_{ar}), 6.08−6.07 (m, 2H, H_{Py}), 6.00 (m, 13H, H_{ar} and H_{Py}), 5.94 (d, 1H, J = 8.1 Hz, H_{py}), 5.62 (d, 1H, J = 8.1 Hz, C5H), 4.89−4.77 (m, 1H, C4′H), 4.58−4.51 (m, 1H, CαH), 4.47−4.12 (m, 3H, C3′H and C5′H), 3.42−3.33 (m, 2H, PyCH_2CH$_2$CH$_2$), 3.00 (sept, 6H, J = 6.9 Hz, CH), 2.55−2.53 (m, 2H, PyCH$_2$CH$_2CH_2$), 2.41−2.38 (m, 2H, C2′H), 2.22 (s, 18H, CH_3), 1.62−1.60 (m, 2H, PyCH$_2CH_2$CH$_2$), 1.41 (d, 36H, J = 6.9 Hz, CH_3); ^{13}C{^{1}H} NMR (75 MHz, acetone-d_6): δ 184.2, 173.3, 172.1, 167.6, 163.1, 162.8, 153.8, 150.4, 143.3, 140.7, 140.5, 137.6, 135.7, 129.7, 129.1, 128.8, 128.1, 127.8, 127.1, 126.9, 126.2, 125.8, 125.3, 124.7, 124.2, 123.5, 122.8, 122.3, 119.3, 115.0, 104.1, 102.0, 99.2, 84.8, 83.8, 82.3, 71.6, 65.1, 55.6, 39.8, 37.5, 35.0, 31.7, 31.2, 26.3, 21.6, 17.2; IR (neat): 3447, 2965, 2927, 1717, 1521, 1376, 1259, 1058, 1031, 811 cm^{-1}; ESI-MS (m/z): 1181.47 [pyrene-R5 + **1** + $(CF_3SO_3)_3$]$^{3+}$.

[Pyrene-R6⊂1][CF$_3$SO$_3$]$_6$. This complex was synthesized according to the procedure described above using compound pyrene-R6 (33.1 mg, 0.05 mmol). Yield 142 mg (71%). ^{1}H NMR (300 MHz, acetone-d_6): δ 10.46 (s, 1H, N3H), 8.58 (s, 12H, H_α), 8.21−7.92 (br, d, 13H, H_β and C6H), 7.55−7.38 (m, 5H, H_{Ph}), 7.02 (m, 1H, H_{Py}), 6.95 (t, 1H, J = 6.3 Hz, H_{Py}), 6.80 (d, 1H, J = 8.4 Hz, H_{Py}), 6.77 (m, 1H, H_{Py}), 6.54−6.22 (m, 8H, C1′H, H_{Py} and H_q), 6.22 (d, 12H, J = 6.3 Hz, H_{ar}), 6.08−6.02 (m, 3H, H_{Py}), 6.01 (d, 12H, J = 6.0 Hz, H_{ar}), 5.99 (m, 1H, H_{Py}), 4.88−4.68 (m, 1H, C4′H), 4.54−4.42 (m, 1H, CαH), 4.28−4.24 (m, 3H, C3′H and C5′H), 3.38−3.36 (m, 2H, PyCH_2CH$_2$CH$_2$), 3.00 (sept, 6H, J = 6.9 Hz, CH), 2.55−2.53 (m, 2H, PyCH$_2$CH$_2CH_2$), 2.41−2.38 (m, 2H, C2′H), 2.24 (s, 18H, CH_3), 1.62−1.60 (m, 2H, PyCH$_2CH_2$CH$_2$), 1.41 (d, 36H, J = 6.9 Hz, CH_3); ^{13}C{^{1}H} NMR (75 MHz, acetone-d_6): δ 184.2, 173.2, 172.1, 167.7, 153.9, 148.9, 143.3, 137.4, 129.7, 129.4, 129.1, 128.6, 128.1, 127.8, 127.1, 126.9, 126.7, 126.2, 125.8, 125.2, 124.7, 124.5, 124.2, 123.5, 122.8, 122.7, 122.3, 119.3, 115.0, 104.1, 102.0, 85.3, 84.6, 83.8, 82.3, 71.2, 64.8, 55.4 39.5, 37.2, 35.0, 31.6, 31.2, 26.3, 21.6, 17.2; IR (neat): 3447, 2966, 2926, 1716, 1521, 1377, 1258, 1057, 1030, 811 cm^{-1}; ESI-MS (m/z): 1186.82 [pyrene-R6 + **1** + $(CF_3SO_3)_3$]$^{3+}$.

Encapsulation of Modified Nucleosides Conjugated Pyrenyl Derivatives (Pyrene-R1−6) in Metalla-Cage [2]$^{6+}$. A mixture of [Ru$_2$(pPr^{i}C$_6$H$_4$Me)$_2$(donq)Cl$_2$] (0.17 mmol), AgCF$_3$SO$_3$ (0.34 mmol), tpt (0.11 mmol), and pyrenyl derivatives (pyrene-R) (0.055 mmol) in MeOH (30 mL) was stirred at 60 °C for 15 h. The reaction mixture was kept in the dark. The resulting reaction mixture was filtrated and concentrated *in vacuo*. The residue was dissolved in CH_2Cl_2 (2 mL), and diethyl ether (50 mL) was slowly added to precipitate the product, which was kept in the refrigerator for 2 h. The product was filtered and dried *in vacuo*.

[Pyrene-R1⊂2][CF$_3$SO$_3$]$_6$. This complex was synthesized according to the procedure described above using compound pyrene-R1 (28 mg, 0.055 mmol). Yield: 164 mg (75%); ^{1}H NMR (300 MHz, acetone-d_6): δ 9.89 (s, 1H, N3H), 8.64 (s, 12H, H_α), 7.80 (m, 13H, H_β and C6H), 7.59 (s, 12H, H_q), 6.96 (m, 4H, H_{Py}), 6.44 (m, 4H, H_{Py}), 6.37 (m, 1H, C1′H), 6.01 (d, 12H, J = 5.7 Hz, H_{cym}), 5.78 (d, 12H, J = 5.7 Hz, H_{cym}), 5.50 (d, 1H, C5H), 5.12 (m, 1H, H_{Py}), 4.65−4.40 (m, 4H, C3′H and C5′H), 3.40 (t, 2H, PyCH_2CH$_2$CH$_2$), 2.94 (sept, 6H, J = 6.9, Hz,

dx.doi.org/10.1021/bc200472n | *Bioconjugate Chem.* 2012, 23, 461−471

$CH(CH_3)_2$), 2.38 (m, 6H, Py$CH_2CH_2CH_2$ and C2′H), 2.12 (s, 18H, CH_3), 1.35 (d, 36H, J = 6.9 Hz, CH(CH_3)$_2$); $^{13}C\{^1H\}$ NMR (75 MHz, acetone-d_6): δ 172.8, 171.1, 167.8, 162.6, 152.7, 150.4, 143.1, 141.0, 137.9, 135.0, 129.8, 128.9, 128.4, 127.9, 127.2, 126.1, 125.3, 125.1, 124,2, 123,7, 123.6, 122.9, 121.7, 119.3, 103.7, 102.3, 100.2, 71.2, 64.5, 38.6, 33.6, 31.6, 30.6, 26.5, 21.6, 16.4; IR (neat): 3447, 3066, 2967, 1734, 1535, 1460, 1275, 853 cm^{-1}; ESI-MS (m/z): 1182.80 [pyrene-R1 + **2** + $(CF_3SO_3)_3$]$^{3+}$.

[Pyrene-R2⊂2][CF_3SO_3]$_6$. This complex was synthesized according to the procedure described above using compound pyrene-R2 (29.0 mg, 0.06 mmol). Yield: 166 mg (74%); ^{1}H NMR (300 MHz, acetone-d_6): δ 9.89 (s, 1H, N3H), 8.64 (s, 12H, H_α), 7.99−7.74 (m, 13H, H_β and C6H), 7.59 (s, 12H, H_q), 6.98 (m, 4H, H_{Py}), 6.38 (m, 4H, H_{Py}), 6.29 (t, 1H, C1′H), 6.01 (d, 12H, J = 5.7 Hz, H_{cym}), 5.78 (d, 12H, J = 5.7 Hz, H_{cym}), 5.12 (m, 1H, H_{Py}), 4.68−4.43 (m, 4H, C3′H, C4′H and C5′H), 3.64 (t, 2H, Py$CH_2CH_2CH_2$), 2.96 (sept, 6H, J = 7.2 Hz, $CH(CH_3)_2$), 2.38 (m, 4H, Py$CH_2CH_2CH_2$ and C2′H), 2.11 (s, 18H, CH_3), 1.37 (d, 36H, J = 7.2 Hz, CH(CH_3)$_2$); $^{13}C\{^1H\}$ NMR (75 MHz, acetone-d_6): δ 172.8, 171.1, 167.8, 162.6, 156.7, 152.6, 150.3, 142.9, 141.0, 137.7, 135.1, 129.7, 128.9, 128.4, 127.9, 127.2, 126.1, 125.3, 125.0, 124,2, 123,7, 123.6, 123.0, 121.7, 119.4, 104.0, 100.2, 71.2, 64.4, 38.6, 33.5, 31.7, 30.6, 26.4, 21.5, 16.4; IR (neat): 3448, 3076, 2968, 1735, 1539, 1457, 1275, 1148, 853 cm^{-1}; ESI-MS (m/z): 1188.13 [pyrene-R2 + **2** + $(CF_3SO_3)_3$]$^{3+}$.

[Pyrene-R3⊂2][CF_3SO_3]$_6$. This complex was synthesized according to the procedure described above using compound pyrene-R3 (27.4 mg, 0.05 mmol). Yield: 141 mg (71%); ^{1}H NMR (300 MHz, acetone-d$_6$): δ 8.64 (s, 13H, H_α and C6H), 8.16−7.75 (m, 12H, H_β), 7.60 (s, 12H, H_q), 6.96 (m, 4H, H_{Py}), 6.53 (m, 2H, H_{Py}), 6.31 (m, 3H, H_{Py} and C1′H), 6.00 (d, 12H, J = 6.0 Hz, H_{cym}), 5.77 (m, 13H, H_{cym} and C5H), 5.22 (d, 1H, H_{Py}), 4.61−4.54(m, 4H, C3′H, C4′H and C5′H), 4.26 (m, 4H, Py$CH_2CH_2CH_2$ and $CH_{2\alpha}$), 2.96 (sept, 6H, J = 6.9 Hz, $CH(CH_3)_2$), 2.35−2.20 (m, 6H, Py$CH_2CH_2CH_2$ and C2′H), 2.12 (s, 18H, CH_3), 1.38 (d, 36H, J = 6.9 Hz, CH(CH_3)$_2$); $^{13}C\{^1H\}$ NMR (75 MHz, acetone-d$_6$): δ 173.5, 171.1, 170.3, 168.0, 162.9, 152.7, 150.4, 143.1, 140.5, 137.9, 135.0, 129.8, 128.8, 128.3, 127.9, 127.2, 126.7, 126.1, 124.9, 124.1, 123.7, 123.6, 123.0, 122.9, 121.5, 119.3, 115.1, 111.4, 103.7, 102.4, 100.2, 84.9, 83.0, 71.1, 64.6, 41.3, 39.5, 35.2, 31.6, 30.3, 26.6, 21.5, 16.4; IR (neat): 3447, 3067, 2967, 1734, 1536, 1457, 1275, 1030, 853 cm^{-1}; ESI-MS (m/z): 1201.46 [pyrene-R3 + **2** + $(CF_3SO_3)_3$]$^{3+}$.

[Pyrene-R4⊂2][CF_3SO_3]$_6$. This complex was synthesized according to the procedure described above using compound pyrene-R4 (27.3 mg, 0.05 mmol). Yield: 148 mg (76%); ^{1}H NMR (300 MHz, acetone-d$_6$): δ 8.64 (d, 13H, H_α and C6H), 8.16−7.75 (m, 12H, H_β), 7.60 (s, 12H, H_q), 6.95 (m, 4H, H_{Py}), 6.55 (m, 2H, H_{Py}), 6.33 (m, 3H, H_{Py} and C1′H), 6.00 (d, 12H, J = 6.3 Hz, H_{cym}), 5.77 (d, 12H, J = 6.0 Hz, H_{cym}), 5.24 (m, 1H, H_{Py}), 4.61−4.54(m, 4H, C3′H, C4′H, and C5′H), 4.08 (m, 4H, Py$CH_2CH_2CH_2$ and $CH_{2\alpha}$), 2.89 (sept, 6H, J = 6.9 Hz, $CH(CH_3)_2$), 2.38−2.20 (m, 6H, Py$CH_2CH_2CH_2$ and C2′H), 2.12 (s, 18H, CH_3), 1.32 (d, 36H, J = 6.9 Hz, CH(CH_3)$_2$); $^{13}C\{^1H\}$ NMR (75 MHz, acetone-d_6): δ 173.4, 171.1, 170.3, 168.0, 156.9, 156.3, 152.7, 148.9, 143.2, 142.1, 137.9, 129.8, 128.8, 127.8, 127.2, 126.7, 126.1, 124.8, 124.4, 123.7, 123.6, 123.0, 119.3, 115.0, 111.4, 103.7, 100.2, 85.2, 84.7, 83.0, 70.9, 64.5, 41.2, 39.3, 35.2, 31.7, 30.6, 26.6, 21.6, 16.4; IR (neat): 3447, 3066, 2967, 1735, 1539, 1457, 1275, 1057, 853 cm^{-1}; ESI-MS (m/z): 1207.50 [pyrene-R4 + **2** + $(CF_3SO_3)_3$]$^{3+}$.

[Pyrene-R5⊂2][CF_3SO_3]$_6$. This complex was synthesized according to the procedure described above using compound pyrene-R5 (31.0 mg, 0.048 mmol). Yield: 145 mg (73%); ^{1}H NMR (300 MHz, acetone-d_6): δ 10.04 (s, 1H, N3H), 8.62 (s, 13H, H_α and C6H) 8.25−7.73 (m, 14H, H_β and H_{Ph}), 7.57 (s, 12H, H_q), 7.31 (m, 3H, H_{Ph}), 6.92 (br, 4H, H_{Py}), 6.51 (m, 2H, H_{Py}), 6.23 (m, 3H, H_{Py} and C1′H), 5.99 (d, 12H, J = 6.0 Hz, H_{cym}), 5.79 (m, 1H, C5H), 5.76 (d, 12H, J = 6.0 Hz, H_{cym}), 5.57 (d, 1H, H_{Py}), 4.90 (m, 1H, C4′H), 4.54 (m, 1H, CH_α), 4.28−4.11 (m, 3H, C3′H and C5′H), 3.35 (m, 2H, Py$CH_2CH_2CH_2$), 2.95 (sept, 6H, J = 6.9 Hz, $CH(CH_3)_2$), 2.32 (m, 4H, Py$CH_2CH_2CH_2$ and C2′H), 2.11 (s, 18H, CH_3), 1.62 (m, 2H, Py$CH_2CH_2CH_2$), 1.37 (d, 36H, J = 6.9 Hz, CH(CH_3)$_2$); $^{13}C\{^1H\}$ NMR (75 MHz, acetone-d_6): δ 173.4, 172.7, 171.9, 167.9, 162.8, 152.7, 150.4, 143.2, 134.2, 137.8, 129.5, 129.4, 128.8, 128.6, 127.8, 126.9, 126.0, 125.0, 124.1, 123.7, 123.6, 119.3, 115.0, 111.4, 103.7, 102.4, 100.1, 84.9, 83.1, 71.2, 64.5, 39.9, 37.3, 35.2, 31.8, 30.5, 26.6, 21.6, 16.4; IR (neat): 3446, 2966, 2925, 1717, 1534, 1275, 1030, 852 cm^{-1}; ESI-MS (m/z): 1231.50 [pyrene-R5 + **2** + $(CF_3SO_3)_3$]$^{3+}$.

[Pyrene-R6⊂2][CF_3SO_3]$_6$. This complex was synthesized according to the procedure described above using compound pyrene-R6 (35.0 mg, 0.053 mmol). Yield: 162 mg (74%); ^{1}H NMR (300 MHz, acetone-d$_6$): δ 10.40 (s, 1H, N3H), 8.64 (s, 13H, H_α and C6H) 8.16−7.75 (m, 14H, H_β and H_{Ph}), 7.56 (s, 12H, H_q), 7.31 (m, 3H, H_{Ph}), 6.84 (br, 4H, H_{Py}), 6.47 (m, 2H, H_{Py}), 6.27 (m, 3H, H_{Py} and C1′H), 6.00 (d, 12H, J = 6.0 Hz, H_{cym}), 5.77 (d, 12H, J = 6.3 Hz, H_{cym}), 5.34 (d, 1H, H_{Py}), 4.86−4.79 (m, 1H, C4′H), 4.56 (m, 1H, CH_α), 4.30−4.22 (m, 3H, C3′H and C5′H), 3.38 (m, 2H, Py$CH_2CH_2CH_2$), 2.95 (sept, 6H, J = 6.9 Hz, $CH(CH_3)_2$), 2.32 (m, 4H, Py$CH_2CH_2CH_2$ and C2′H), 2.14 (s, 18H, CH_3), 1.42 (m, 2H, Py$CH_2CH_2CH_2$), 1.39 (d, 36H, J = 6.9 HZ, CH(CH_3)$_2$); $^{13}C\{^1H\}$ NMR (75 MHz, acetone-d_6): δ 173.1, 172.1, 171.0, 168.0, 156.9, 152.8, 148.8, 143.3, 137.9, 129.8, 129.5, 128.8, 128.7, 127.8, 127.1, 126.9, 126.1, 124.9, 124.1, 123.7, 123.6, 123.0, 121.6, 119.3, 115.1, 111.4, 103.7, 100.1, 85.3, 84.9, 83.1, 71.2, 64.8, 54.8, 39.4, 37.3, 35.1, 31.7, 26.6, 21.6, 16.4; IR (neat): 3447, 2966, 2925, 1734, 1559, 1273, 1147, 1030, 852 cm^{-1}; ESI-MS (m/z): 1236.48 [pyrene-R6 + **2** + $(CF_3SO_3)_3$]$^{3+}$.

Cell Culture and Inhibition of Cell Growth. Human A2780 ovarian carcinoma cells were obtained from the European Centre of Cell Cultures (ECACC, Salisbury, UK) and maintained in culture as described by the provider. The cells were routinely grown in RPMI 1640 medium containing 10% fetal calf serum (FCS) and antibiotics at 37 °C and 6% CO_2. For the evaluation of growth inhibition tests, the cells were seeded in 96-well plates and grown for 24 h in complete medium. Complexes were added to the required concentration and added to the cell culture for 72 h incubation. Solutions of the compounds were applied by diluting a freshly prepared stock solution of the corresponding compound in DMSO, with the final concentration of 0.05% in the medium. The MTT test was performed in the last 2 h without changing the culture medium. Following drug exposure, MTT (Sigma) was added to the cells at the final concentration of 0.2 mg/mL and incubated for 2 h, then the culture medium was aspirated and the violet formazan precipitate dissolved in DMSO. The optical density was quantified at 540 nm using a multiwell plate reader (iEMS Reader MF, Labsystems, US), and the percentage of surviving cells was calculated from the ratio of absorbance of treated to untreated cells. The IC_{50} values for the inhibition of cell growth were determined by fitting the plot of the percentage of surviving

dx.doi.org/10.1021/bc200472n | Bioconjugate Chem. 2012, 23, 461−471

cells against the drug concentration using a sigmoidal function (*Excel 2007*, Microsoft Corporation).

AUTHOR INFORMATION

Corresponding Author

*E-mails: bhkim@postech.ac.kr, bruno.therrien@unine.ch.

ACKNOWLEDGMENTS

Financial support of this work by the Strategic Korean-Swiss Cooperative program and a generous loan of ruthenium(III) chloride hydrate from Johnson Matthey Research Centre are gratefully acknowledged as well as the KNRRC program for modified nucleosides.

REFERENCES

(1) Galmarini, C. M., Mackey, J. R., and Dumontet, C. (2001) Nucleoside analogues: mechanisms of drug resistance and reversal strategies. *Leukemia 15*, 875−890.

(2) Longley, D. B., Harkin, D. P., and Johnston, P. G. (2003) 5-Fluorouracil: mechanisms of action and clinical strategies. *Nat. Rev. Cancer 3*, 330−338.

(3) Thomas, D. M., and Zalcberg, J. R. (1998) 5-Fluorouracil: a pharmacological paradigm in the use of cytotoxics. *Clin. Exp. Pharmacol. Physiol. 25*, 887−895.

(4) Nakagawa, H., Maeda, N., Tsuzuki, T., Suzuki, T., Hirayama, A., Miyahara, E., and Wada, K. (2001) Intracavitary chemotherapy with 5-fluoro-2′-deoxyuridine (FdUrd) in malignant brain tumor. *Jpn. J. Clin. Oncol. 31*, 251−258.

(5) Landowski, C. P., Song, X., Lorenzi, P. L., Hilfinger, J. M., and Amidon, G. L. (2005) Floxuridine amino acid ester prodrugs: enhancing Caco-2 permeability and resistance to glycosidic bond metabolism. *Pharm. Res. 22*, 1510−1518.

(6) Tsume, Y., Hilfinger, J. M., and Amidon, G. L. (2008) Enhanced cancer cell growth inhibition by dipeptide prodrugs of floxuridine: increased transporter affinity and metabolic stability. *Mol. Pharmaceutics 5*, 717−727.

(7) Senanayake, T. H., Warren, G., and Vinogradov, S. V. (2011) Novel anticancer polymeric conjugates of activated nucleoside analogues. *Bioconjugate Chem. 22*, 1983−1993.

(8) Østergaard, M. E., and Hrdlicka, P. J. (2011) Pyrene-functionalized oligonucleotides and locked nucleic acids (LNAs): tools for fundamental research, diagnostics, and nanotechnology. *Chem. Soc. Rev. 40*, 5771−5788.

(9) Guckian, K. M., Schweitzer, B. A., Ren, R. X.-F., Sheils, C. J., Tahmassebi, D. C., and Kool, E. T. (2000) Factors contributing to aromatic stacking in water: evaluation in the context of DNA. *J. Am. Chem. Soc. 122*, 2213−2222.

(10) Baba, M., Saitoh, M., Kowaka, Y., Taguma, K., Yoshida, K., Semba, Y., Kasahara, S., Yamanaka, T., Ohshima, Y., Hsu, Y.-C., and Lin, S. H. (2009) Vibrational and rotational structure and excited-state dynamics of pyrene. *J. Chem. Phys. 131*, 224318.

(11) Saito, I., Saito, Y., Hanawa, K., Hayashi, K., Motegi, K., Sekhar Bag, S., Dohno, C., Ichiba, T., Tainaka, K., and Okamoto, A. (2006) Highly selective fluorescent nucleobases for designing base-discriminating fluorescent probes. *Pure Appl. Chem. 78*, 2305−2312.

(12) Lee, I. J., Yi, J. W., and Kim, B. H. (2009) Probe for i-motif structure and G-rich strands using end-stacking ability. *Chem. Commun.*, 5383−5385.

(13) Seo, Y. J., Lee, I. J., and Kim, B. H. (2009) Homoadenine signaling system for SNP typing. *Mol. BioSyst. 5*, 235−237.

(14) Jeong, H. S., Kang, S., Lee, J. Y., and Kim, B. H. (2009) Probing specific RNA bulge conformations by modified fluorescent nucleosides. *Org. Biomol. Chem. 7*, 921−925.

(15) Seo, Y. J., Lee, I. J., Yi, J. W., and Kim, B. H. (2007) Probing the stable G-quadruplex transition using quencher-free and-stacking ethynyl pyrene-adenosine. *Chem. Commun.*, 2817−2819.

(16) Seo, Y. J., Rhee, H., Joo, T., and Kim, B. H. (2007) Self-duplex formation of an A^{py}-substituted oligodeoxyadenylate and its unique fluorescence. *J. Am. Chem. Soc. 129*, 5244−5247.

(17) Seo, Y. J., Jeong, H. S., Bang, E.-K., Hwang, G. T., Jung, J. H., Jang, S. K., and Kim, B. H. (2006) Cholesterol-linked fluorescent molecular beacons with enhanced cell permeability. *Bioconjugate Chem. 17*, 1151−1155.

(18) Kurreck, J. (2009) RNA interference: from basic research to therapeutic applications. *Angew. Chem., Int. Ed. 48*, 1378−1398.

(19) Hartinger, C. G., Zorbas-Seifried, S., Jakupec, M. A., Kynast, B., Zorbas, H., and Keppler, B. K. (2006) From bench to bedside − preclinical and early clinical development of the anticancer agent indazolium *trans*-[tetraclhorobis(1*H*-indazole)ruthenate(III) (KP1019 or FFC14A). *J. Inorg. Biochem. 100*, 891−904.

(20) Jakupec, M. A., Galanski, M., Arion, V. B., Hartinger, C. G., and Keppler, B. K. (2008) Antitumour metal compounds: more than theme and variations. *Dalton Trans.*, 183−194.

(21) Hartinger, C. G., and Dyson, P. J. (2009) Bioorganometallic chemistry − from teaching paradigms to medicinal applications. *Chem. Soc. Rev. 38*, 391−401.

(22) Süss-Fink, G. (2010) Arene ruthenium complexes as anticancer agents. *Dalton Trans. 39*, 1673−1688.

(23) Smith, G. S., and Therrien, B. (2011) Targeted and multifunctional arene ruthenium chemotherapeutics. *Dalton Trans. 40*, 10793−10800.

(24) Mendoza-Ferri, M.-G., Hartinger, C. G., Eichinger, R. E., Stolyarova, N., Severin, K., Jakupec, M. A., Nazarov, A. A., and Keppler, B. K. (2008) Influence of the spacer length on the *in vitro* anticancer activity of dinuclear ruthenium-arene compounds. *Organometallics 27*, 2405−2407.

(25) Mendoza-Ferri, M. G., Hartinger, C. G., Mendoza, M. A., Groessl, M., Egger, A. E., Eichinger, R. E., Mangrum, J. B., Farrell, N. P., Maruszak, M., Bednarski, P. J., Klein, F., Jakupec, M. A., Nazarov, A. A., Severin, K., and Keppler, B. K. (2009) Transferring the concept of multinuclearity to ruthenium complexes for improvement of anticancer activity. *J. Med. Chem. 52*, 916−925.

(26) Mendoza-Ferri, M. G., Hartinger, C. G., Nazarov, A. A., Eichinger, R. E., Jakupec, M. A., Severin, K., and Keppler, B. K. (2009) Influence of the arene ligand, the number and type of metal centers, and the leaving group on the *in vitro* antitumor activity of polynuclear organometallic compounds. *Organometallics 28*, 6260−6265.

(27) Therrien, B. (2009) Arene ruthenium cages: boxes full of surprises. *Eur. J. Inorg. Chem.*, 2445−2453.

(28) Vajpayee, V., Yang, Y. J., Kang, S. C., Kim, H., Kim, I. S., Wang, M., Stang, P. J., and Chi, K.-W. (2011) Hexanuclear self-assembled arene-ruthenium nano-prismatic cages: potential anticancer agents. *Chem. Commun. 47*, 5184−5186.

(29) Pitto-Barry, A., Barry, N. P. E., Zava, O., Deschenaux, R., Dyson, P. J., and Therrien, B. (2011) Double targeting of tumours with pyrenyl-modified dendrimers encapsulated in an arene-ruthenium metallaprism. *Chem.—Eur. J. 17*, 1966−1971.

(30) Pitto-Barry, A., Barry, N. P. E., Zava, O., Deschenaux, R., and Therrien, B. (2011) Encapsulation of pyrene-functionalized poly(benzyl ether) dendrons into a water-soluble organometallic cage. *Chem. Asian J. 6*, 1595−1603.

(31) Therrien, B., Süss-Fink, G., Govindaswamy, P., Renfrew, A. K., and Dyson, P. J. (2008) The "complex-in-a-complex" cations $[(acac)_2M\subset Ru_6(p\text{-}iPrC_6H_4Me)_6(tpt)_2(dhbq)_3]^{6+}$: a Trojan horse for cancer cells. *Angew. Chem., Int. Ed. 47*, 3773−3776.

(32) Mattsson, J., Govindaswamy, P., Furrer, J., Sei, Y., Yamaguchi, K., Süss-Fink, G., and Therrien, B. (2008) Encapsulation of aromatic molecules in hexanuclear arene ruthenium cages: a strategy to build up organometallic carceplex prisms with a dangling arm standing out. *Organometallics 27*, 4346−4356.

(33) Mattsson, J., Zava, O., Renfrew, A. K., Sei, Y., Yamaguchi, K., Dyson, P. J., and Therrien, B. (2010) Drug delivery of lipophilic pyrenyl derivatives by encapsulation in a water soluble metalla-cage. *Dalton Trans. 39*, 8248−8255.

(34) Barry, N. P. E., and Therrien, B. (2009) Host-guest chemistry in the hexanuclear (arene)ruthenium metalla-prismatic cage $[Ru_6(p\text{-cymene})_6(tpt)_2(dhnq)_3]^{6+}$. *Eur. J. Inorg. Chem.*, 4695−4700.
(35) Barry, N. P. E., Zava, O., Dyson, P. J., and Therrien, B. (2011) Excellent correlation between drug release and portal size in metalla-cage drug delivery systems. *Chem.—Eur. J. 17*, 9669−9677.
(36) Zava, O., Mattsson, J., Therrien, B., and Dyson, P. J. (2010) Evidence for drug release from a metalla-cage delivery vector following cellular internalization. *Chem.—Eur. J. 16*, 1428−1431.
(37) Sun, Y.-W., Chen, K.-M., and Kwon, C.-H. (2006) Sulfonyl-containing nucleoside phosphotriesters and phosphoramidates as novel anticancer prodrugs of 5-fluoro-2′-deoxyuridine 5′-monophosphate (FdUMP). *Mol. Pharmaceutics 3*, 161−173.
(38) Anderson, H. L., Anderson, S., and Sanders, J. K. M. (1995) Ligand binding by butadiyne-linked porphyrin dimers, trimers and tetramers. *J. Chem. Soc., Perkin Trans. 1*, 2231−2245.
(39) Therrien, B. (2011) Coordination chemistry of 2,4,6-tri(pyridyl)-1,3,5-triazine ligands. *J. Organomet. Chem. 696*, 637−651.

Bioconjugate Chemistry

Article

pubs.acs.org/bc

In Vitro Targeting of Avidin-Expressing Glioma Cells with Biotinylated Persistent Luminescence Nanoparticles

Thomas Maldiney,[†] Minna U. Kaikkonen,*[,‡] Johanne Seguin,[†] Quentin le Masne de Chermont,[†] Michel Bessodes,[†] Kari J. Airenne,[‡] Seppo Ylä-Herttuala,[‡,§,∥] Daniel Scherman,[†] and Cyrille Richard*[,†]

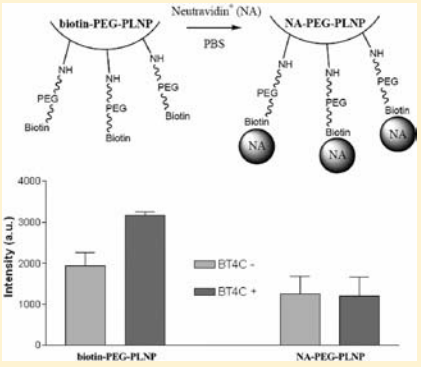
[†]Unité de Pharmacologie Chimique et Génétique et d'Imagerie, CNRS, UMR 8151, Inserm, U 1022, Université Paris Descartes, Sorbonne Paris Cité, Faculté des Sciences Pharmaceutiques et Biologiques, Paris, F-75270 Cedex, and ENSCP, Chimie Paristech, Paris, F-75231 Cedex, France

[‡]A.I. Virtanen Institute, Department of Biotechnology and Molecular Medicine, University of Eastern Finland, FIN-70211 Kuopio, Finland

[§]Gene Therapy Unit and [∥]Department of Medicine, Kuopio University Hospital, P.O. Box 1777, FI-70211 Kuopio, Finland

S *Supporting Information*

ABSTRACT: Far red emitting persistent luminescence nanoparticles (PLNP) were synthesized and functionalized with biotin to study their targeting ability toward biotin-binding proteins. First, the interaction of biotin-decorated PLNP with streptavidin, immobilized on a plate, was shown to be highly dependent on the presence of a PEG spacer between the surface of the nanoparticles and the biotin ligand. Second, interaction between biotin-PEG-PLNP and free neutravidin in solution was confirmed by fluorescence microscopy. Finally, in vitro binding study on BT4C cells expressing lodavin fusion protein, bearing the extracellular avidin moiety, showed that such biotin-covered PLNP could successfully be targeted to malignant glioma cells through a specific biotin−avidin interaction. The influence of nanoparticle core diameter, incubation time, and PLNP concentration on the efficiency of targeting is discussed.



INTRODUCTION

Optical imaging techniques have great potential to help us further understand biological processes at the molecular level and provide excellent tools for sensitive cancer diagnosis, particularly at the early stage of cancer development.[1] Biological optical imaging greatly relies upon the use of sensitive and stable optical labels. So far, organic dyes,[2,3] quantum dots,[4−6] and metal nanoparticles[7−9] are the most commonly used optical labels, but they also come with essential limitations. Organic dyes suffer from a short observation time, partly due to photobleaching, poor stability under physiological conditions, and limited Stokes shift. Although quantum dots display good photostability, size-dependent emissions, and high quantum yield, they still require constant excitation, which is responsible for undesirable autofluorescence and elevated background signal that reduce the sensibility of the assay.[10,11]

To overcome some of the inherent problems encountered with optical imaging probes,[12] we have recently reported the sol−gel synthesis of inorganic near-infrared persistent luminescence nanoparticles (PLNP), also referred to as nanophosphors, with the formula $Ca_{0.2}Zn_{0.9}Mg_{0.9}Si_2O_6$ doped with luminescent ions (0.5% Eu^{2+}, 1% Dy^{3+}, and 2.5% Mn^{2+}), which are suitable for in vivo imaging.[13] The key element of this technology resides in the ability to induce the optical excitation of the probe before systemic injection. The long lasting luminescence can last up to several hours and permits the avoidance of the background noise originating from in situ excitation. An in vivo study in healthy and tumor-bearing mice revealed that PLNP biodistribution was highly dependent on surface charge, PEGylation, and core diameter of the particle. Small and stealth PEGylated PLNP were shown to circulate much longer, postponing the uptake from the reticulo-endothelial system (RES) and showing promise for future application in cancer imaging.[14]

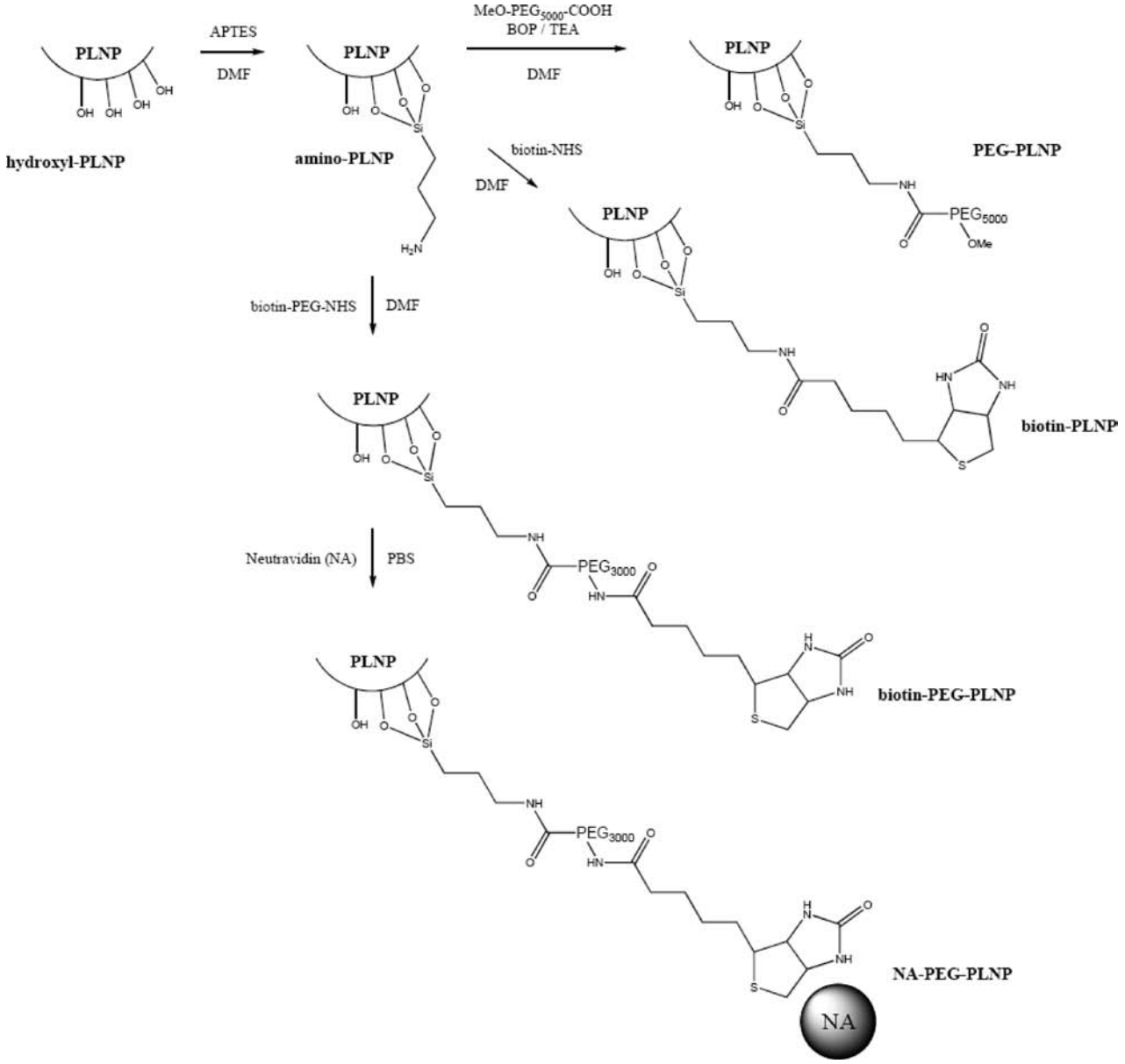
We have previously constructed a fusion protein, lodavin, which is composed of avidin and the endocytotic low-density lipoprotein (LDL) receptor to target biotinylated molecules to cells of a desired tissue.[15] Pursuing the idea that avidin−biotin technology holds great promise for targeted therapy and diagnosis,[16] we recently produced a lentiviral vector expressing lodavin, allowing the long-term expression of avidin on the surface of transduced glioma cells. Targeting of biotinylated nanoparticles loaded with paclitaxel to lodavin-expressing tumor cells was able to significantly decrease cell viability, demonstrating the therapeutic potential of this approach for targeted cancer therapy.[17]

In this article, we focus on the avidin−biotin technology as a versatile approach to target red-emitting nanophosphors into

Received: September 14, 2011
Revised: December 15, 2011
Published: January 17, 2012

 © 2012 American Chemical Society dx.doi.org/10.1021/bc200510z | *Bioconjugate Chem.* 2012, 23, 472−478

Scheme 1. Schematic Representation of PLNP Functionalization



tumor tissues or cells, taking advantage of the strongest noncovalent interaction found in nature (Ka ≅ 10^{15} M^{-1}).[18,19] We report the first use of biotinylated persistent luminescence nanoparticles to target avidin-expressing glioma cells, paving the way for new avenues of noninvasive optical imaging.

MATERIALS AND METHODS

Chemicals. BOP reagent (benzotriazole-1-yl-oxy-tris-pyrrolidino-phosphonium hexafluorophosphate) was purchased from Advanced ChemTech. (3-Aminopropyl)-triethoxysilane (99%), (+)-biotin *N*-hydroxysuccinimide ester (>98%), NeutrAvidin-Tetramethylrhodamine conjugate, and *O*-[2-(biotinyl-amino)-ethyl]-*O*′-[3-(*N*-succinimidyloxy)-3-oxopropyl]polyethylene glycol (3,000 Da) were obtained from Sigma-Aldrich. Triethylamine (>99.5%) and dimethylformamide (>99.9%) were purchased from SDS. Alpha-methoxy-omega-carboxylic acid poly(ethylene glycol) (3,000 Da) was purchased from Iris Biotech GmbH. Streptavidin coated plates were obtained from Nunc.

PLNP Synthesis and Populations Selection. Crude and crystallized material was synthesized according to a previously described protocol based on a sol−gel approach followed by heating at 1050 °C under reducing atmosphere.[20] Nanometer-sized particles were obtained by basic wet grinding of the solid (500 mg) for 15 min with a mortar and pestle in a minimum volume of 5 mM NaOH solution. Hydroxylation was then performed overnight by dispersing the ground powder in 50 mL of the same NaOH solution to get hydroxyl-PLNP.

The first population of nanoparticles, with a diameter of 180 nm, was selected from the whole polydisperse colloidal suspension by centrifugation on a SANYO MSE Mistral 1000 at 4500 rpm for 5 min. When the centrifugation time was lengthened to 30 min, a second population of 120 nm PLNP was obtained. They were located in the supernatant by dynamic light scattering. The supernatants were gathered and concentrated to a final 5 mg/mL suspension.

PLNP Functionalization. Amino-PLNP (Scheme 1) were obtained by the addition of 20 μL of 3-aminopropyl-

dx.doi.org/10.1021/bc200510z | *Bioconjugate Chem.* 2012, 23, 472−478

triethoxysilane (APTES 99%, Sigma-Aldrich) to a suspension of 5 mg of hydroxyl-PLNP in 2 mL of dimethylformamide (DMF). The final concentration of APTES, related to the added volume of DMF, was 1% v/v. The reaction mixture was sonicated the first 15 min using a Branson Ultrasonic Cleaner 1210 and kept under vigorous stirring for 5 h. Particles were washed from the unreacted APTES by three centrifugation and redispersion steps in DMF.

PEGylated PLNP were obtained by stirring 10 μmol of MeO-PEG-COOH (30 mg of MeO-PEG_{3000}-COOH), 5 mg of BOP reagent, 5 μL of triethylamine (TEA), and 5 mg amino-PLNP in 2 mL of DMF at room temperature for 12 h (Scheme 1). A similar washing procedure was used to remove the excess of PEG, BOP, and TEA. To ensure maximum PEG density, this functionalization step was performed overnight, under vigorous stirring, with a large excess of PEG and BOP reagent (20-fold molar excess compared to the free amino groups on the surface of amino-PLNP).

Biotin-PLNP (or biotin-PEG-PLNP) were obtained by stirring 10 μmol of biotin-NHS (or biotin-PEG-NHS) and 5 mg of amino-PLNP in 2 mL of DMF at room temperature for 15 h (Scheme 1). Finally, NA-PEG-PLNP were obtained by incubation of 2.5 mg of biotin-PEG-PLNP for 2 h with 100 μg of NeutrAvidin-Tetramethylrhodamine in PBS (Scheme 1). The resulting suspension was then centrifuged at 14 100 rpm for 5 min at room temperature to remove the excess of unbound proteins.

Each type of nanoparticle was characterized by using dynamic light scattering (DLS), trinitrobenzene sulfonate (TNBS qualitative test), to reveal free primary amines, and zeta potential measurements in 20 mM NaCl, performed on Zetasizer Nano ZS (Malvern Instruments, Southborough, MA) equipped with a 632.8 nm helium neon laser and 5 mW power, with a detection angle at 173° (noninvasive back scattering).

Thermogravimetric analysis (TGA) was performed using a Setaram Setsys evolution 1600 (Argon atmosphere, temperature range: from 20 to 780 °C, 10 °C/min) on 10 mg of the largest population of amino and biotin-PEG-covered PLNP (180 nm).

The interaction of NeutrAvidin-Tetramethylrhodamine conjugate (NA) with biotin-PEG-PLNP was assessed by fluorescence microscopy on an Axiophot fluorescence microscope (Carl Zeiss France, Le Pecq, France) using classical excitation and emission filters for rhodamine (545 nm excitation; 566 nm emission). Images were acquired with a retiga 2000 CCD camera (Q Imaging, Canada).

In Vitro Binding of Biotinylated Nanoparticles on Streptavidin-Coated Plates. After being washed three times with a 0.05% PBS/Tween 20 solution, increasing amounts of nanoparticles (PEG-PLNP, biotin-PLNP, biotin-PEG-PLNP) dispersed in PBS were deposited on a 96 well Nunc plate passively coated with streptavidin (Nunc A/S, Roskilde, Denmark), incubated for 1 h at room temperature, and washed three times to remove the unfixed nanoparticles. Red luminescence from PLNP after 320 nm excitation was used to follow their binding to streptavidin, using a Wallac Victor^2 Multilabel Counter from Perkin-Elmer (excitation filter, D355; emission filter, D615; counting delay, 1 ms; counting window, 5 ms; counting cycle, 6.1 ms).

Rat Glioma BT4C Cell Transduction. BT4C rat glioma cells (BT4C−) were transduced with 1:100 dilution of the Lodavin-viral stock. Three day post-transduction cells were stained with goat anti-avidinD (diluted 1:40; Vector Laboratories) followed by Alexa Fluor 647-conjugated donkey antigoat (1:200; Invitrogen) in 1% BSAand 10 mM HEPES in PBS. Positive cells (BT4C+) were separated by fluorescence-activated cell sorting and allowed to grow to confluency before freezing aliquots. The percentage of positive cells was monitored over several passages and was shown to remain constant (at least 55%).[17]

Cell Culture. BT4C cells were cultured in Dubecco's modified Eagle's medium (DMEM) supplemented with 10% fetal calf serum and antibiotics (100 μg/mL penicillin and 100 U/mL streptomycin). Cells were cultured at 37 °C in 5% CO_2 humidified atmosphere.

Immunofluorescence Cellular Assay. BT4C rat glioma cells were fixed (4% paraformaldehyde), permeabilized, and saturated with a 3% BSA solution containing 0.1% Triton X100. They were then processed for indirect immunofluorescence as follows: cells were incubated overnight at 4 °C with a monoclonal antiavidin antibody produced in mice (Sigma) at 1/2,000 dilution and further incubated with an antimouse fluorescein isothiocyanate (FITC) from Sigma at 1/400 dilution for 45 min in the dark at room temperature. The nuclei were stained with 4′,6-diamidino-2-phenylindole (DAPI) at 1/7000 dilution factor. Bright field and fluorescence photographs were taken on an Axiophot fluorescence microscope (Carl Zeiss France, Le Pecq, France) using classical excitation and emission filters for fluorescein (488 nm excitation; 530 nm emission). Images were acquired with a Retiga 2000 CCD camera (Q Imaging, Canada).

In Vitro Binding of Biotinylated PLNPs on BT4C Glioma Cells. The BT4C cells were seeded in flat bottom 96-well at a density of 10^4 cells/well and grown overnight in 100 μL of medium. For binding assay, each type of nanoparticle, with either 120 or 180 nm core diameters, was incubated at the concentrations of 150 μg/mL and 300 μg/mL for 15 or 30 min at 37 °C in complete DMEM culture medium. Cells were then washed three times with 10 mM PBS before the detection of photoluminescence from PLNPs using a Wallac Victor^2 spectrophotometer (355 nm excitation; 670 nm emission).

Statistical Analysis. All analyses were performed using GraphPad Prism software. In vitro experimentation results on BT4C cells were analyzed with classical unpaired t test using two-tailed P-values. Results with $p < 0.05$ were considered significant.

RESULTS AND DISCUSSION

PLNP Characterization. First, both hydroxyl-PLNP populations were characterized by dynamic light scattering (DLS) measurements to ensure the successful extraction of two different size distributions of nanoparticles. Results shown in Figure S1 (Supporting Information) reveal the selection of two narrow populations: one centered on 120 nm and the other around 180 nm, both displaying good polydispersity index (PDI), close to 0.1. Surface functionalization was followed by zeta potential measurement and TNBS test after each reaction step. Silanol groups on hydroxyl-PLNP are responsible for a negative surface potential at neutral pH (ζ = −20 mV). Conversion to amino-PLNP was assessed by positive TNBS test (PNLP turn orange) and a global positive surface charge (ζ = +30 mV) due to primary amines covering the probe. After further functionalization with either PEG, biotin, or biotin-PEG, the PLNP surface became neutral (ζ around 0 mV) and returned a negative TNBS test (no coloration of the particles). Such evolution of zeta potential values is in complete

dx.doi.org/10.1021/bc200510z | Bioconjugate Chem. 2012, 23, 472−478

agreement with our previous study on the circulation of intravenously injected PEGylated PLNP in mice.[14]

The precise estimation of the amount of biotin on biotin-PEG-PLNP was obtained from weight loss curves for 180 PLNP by thermogravimetric analysis (TGA). Results in Figure 1 reveal two main stages in surface decomposition of both amino-PLNP and biotin-PEG-PLNP. First, water trapped in the organic layer on the surface of PLNP evaporates before 375 °C.

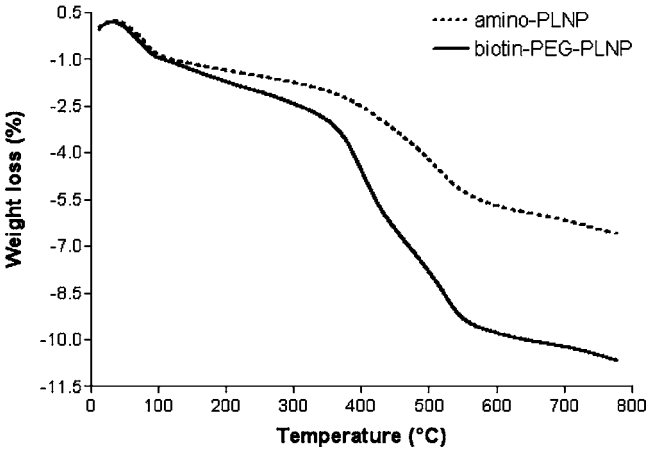


Figure 1. Weight loss curves for amino and biotin-PEG-functionalized 180 nm PLNP.

The second stage begins after 375 °C and corresponds to the decomposition of organic products, such as biotin, the APTES layer, and PEG coverage on the particles. We notice a clear stabilization in the decomposition dynamics after 550 °C. For this reason, by comparing mean weight loss percentages (average value in the 550−750 °C range) between amino-PLNP and biotin-PEG-PLNP, we could easily determine the amount of biotin-PEG grafted on the surface, therefore the approximate amount of biotin per unit mass of PLNP. Calculated values from weight loss percentages indicate that biotin concentration on biotin-PEG-PLNP reaches about 12.5 nmol/mg of PLNP. This value greatly corroborates our previous estimation of 5 kDa PEG concentration on similar PLNP: 15 nmol/mg.[14]

In Vitro Binding of Biotinylated Nanoparticles on Streptavidin-Coated Plates. To investigate the ability of the biotinylated PLNP to interact with streptavidin and study the influence of a PEG spacer on such interaction, we first focused on the binding of PLNP on passively coated streptavidin plates. Results from Figure 2A indicate that when using PEG-PLNP (circles) no nonspecific binding occurred since luminescence from particles was undetectable. Similarly, when biotin-PLNP were used (diamonds), no luminescence signal was detected indicating no binding of these nanoparticles on the streptavidin plate. It is possible that biotin, which is directly linked to the PLNP surface, cannot gain access to the streptavidin receptor. However, when the experiment was performed using biotin-PEG-PLNP (triangles), the luminescence was proportional to

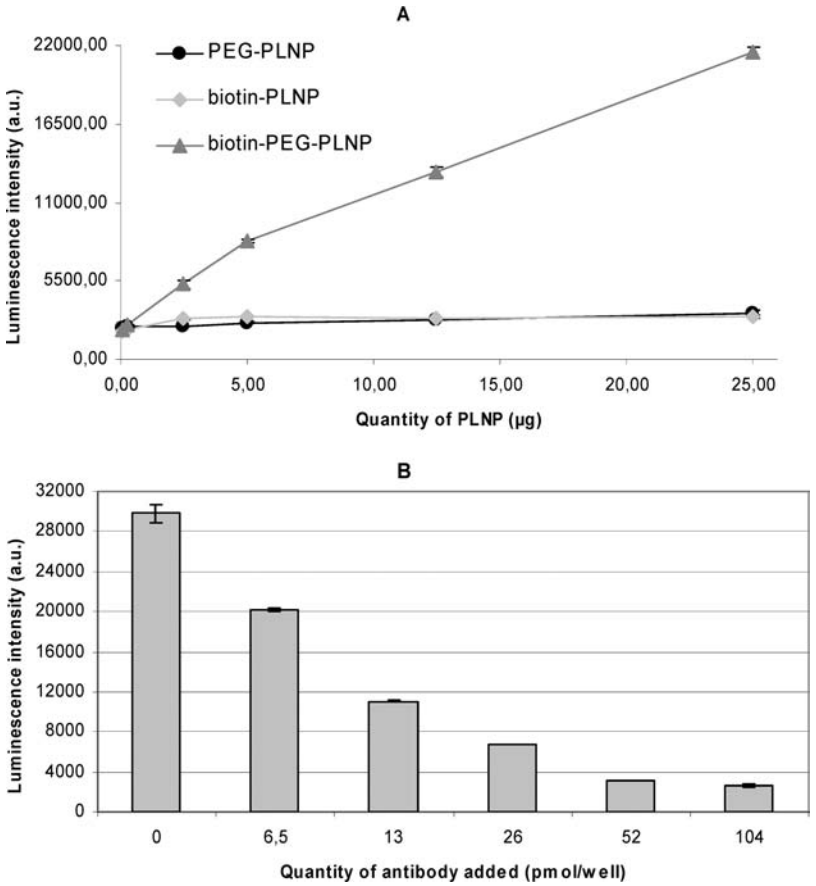


Figure 2. (A) Interaction of increasing amounts of PLNP with streptavidin coated on plates. (B) Effect of preincubation with a biotinylated antibody on the interaction of biotin-PEG-PLNP with streptavidin. In both cases, the signal corresponds to the detection of photoluminescence from PLNP using a Wallac Victor^2 spectrophotometer (355 nm excitation; 670 nm emission).

dx.doi.org/10.1021/bc200510z | *Bioconjugate Chem.* 2012, 23, 472−478

the quantity of nanoparticles deposited on the plate. Therefore, the PEG 3000 Da spacer appears to be essential for the interaction of biotin on plate-coated streptavidin. This result is in good agreement with several theoretical descriptions of the general ligand−receptor interaction in the presence of tethered polymer spacer.[21] More precisely, Szleifer's theoretical model applied to mimic the binding of biotin to streptavidin predicts that the spacer length is a critical parameter in the interaction and that longer PEG spacers would maximize biotin binding to its protein receptor.[22]

To confirm that the interaction of biotin-PEG-PLNP with the streptavidin plate was ligand/receptor dependent and specific to biotin, a second set of experiments was realized using a streptavidin coated plate in which the biotin receptors of the protein were partially saturated with a biotinylated antibody. As seen in Figure 2B, as the amount of biotinylated antibody increases, the intensity of the luminescence signal decreases. These results indicate that the binding of biotin-PEG-PLNP to streptavidin is ligand/receptor dependent and that the interaction is undoubtedly specific to biotin.

Immunofluorescence Cellular Assay. The expression of avidin fusion protein on transduced BT4C cells, referred to as BT4C+, was assessed by immunofluorescence microscopy using FITC staining of the monoclonal antibody antiavidin and nuclear staining with DAPI (Figure 3A and B). BT4C+

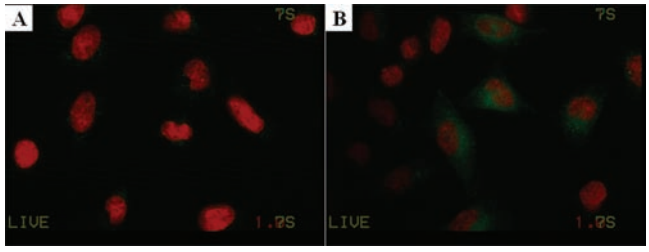


Figure 3. Immunofluorescence staining of wild-type BT4C (A) and transduced BT4C (B). Expression of lodavin appears in green in the photographs and DAPI staining of nuclei in red (field magnification: 400×).

cells displayed uniform FITC staining (green staining, Figure 3B) on the surface and in the cytoplasm of the cells, whereas in control BT4C cells, referred to as BT4C−, the green fluorescence was hardly detectable (Figure 3A). This result not only confirms the expression of lodavin on BT4C+ cells but also ensures the accessibility of avidin on their surface.

Fluorescence Microscopy of Neutravidin-Covered PLNP. The success of neutravidin interaction with biotin-PEG-PLNP was assessed by fluorescence microscopy. Results in Figure 4 show both biotin-PEG-PLNP (A,B) and NA-PEG-PLNP (C,D) under bright field (right) and after 545 nm of excitation (left). Before incubation with the protein, we can only distinguish PLNP under bright field observation (A), and the fluorescence signal does not reveal any particles (B). However, after neutravidin (NA) grafting, bright field (C) and fluorescence observations (D) reveal the exact same spots, corresponding to NA-PEG-PLNP. The interaction of neutravidin with nonbiotinylated PEG-PLNP did not lead to any fluorescence signal from rhodamine (data not shown).

Colloidal Stability in DMEM Culture Medium. Prior to any assay on glioma cells, PLNP colloidal stability in DMEM containing 10% FBS was studied for 25 min at different concentrations. Results in Figure 5 display the evolution of the

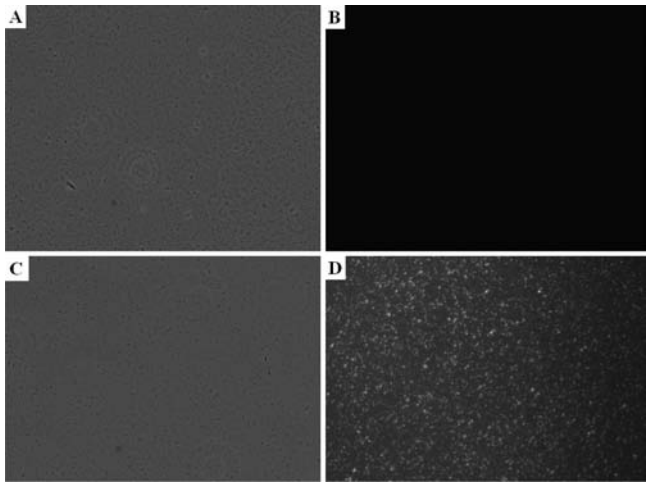


Figure 4. Bright field (A,C) and fluorescence micrographs (B,D) of biotin-PEG-PLNP (A,B) and NA-PEG-PLNP (C,D). We used classical excitation and emission filters for rhodamine (545 nm excitation; 566 nm emission). Images were acquired with a retiga 2000 CCD camera (Q Imaging, Canada).

hydrodynamic diameter of PLNPs at 150 and 300 μg/mL in culture medium for both populations (120 nm PLNPs in Figure 5A and 180 nm PLNPs in Figure 5B). First, we notice a clear stabilization of the hydrodynamic diameter in all conditions after approximately 10 min. Interestingly, neutravidin grafted on large particles (180 nm PLNP) does not seem to have any influence on the hydrodynamic diameter stabilization value of biotin-PEG-PLNP. Such behavior has already been witnessed on gelatin nanoparticles with similar size, on which neutravidin grafting did not seem to be responsible for any increase of hydrodynamic diameter, given the large nanoparticle core.[23] However, a different trend appears for smaller probes (120 nm PLNP) covered with neutravidin which stabilizes 50 nm above their initial value in the absence of protein coating, corresponding to a diameter 1.5 times larger than the initial one in the culture medium. This effect is very likely to be associated with the core diameter of the probe. Indeed, it is now well established that colloidal stability highly depends on the particle size and surface coverage.[24] Reimhult et al. observed the same trend when grafting neutravidin on small iron oxide nanoparticles and reported a 1.5 times increase of their hydrodynamic diameter value after the protein coverage in PBS.[25] Again, a noticeable increase in size upon addition of neutravidin has already been observed on 110 nm wide biotin-PEG-PLGA nanoparticles.[26] In the case of our PLNP, although the neutravidin protein is characterized by a high molecular weight as well as the relative large size of about 6 nm,[27] it is very unlikely to be the only cause to such an increase of the hydrodynamic diameter. As the measurements are realized in DMEM supplemented with 10% FBS, this size effect could be the result of a protein association between neutravidin and proteins from the serum.

In Vitro Binding of Biotinylated PLNPs on BT4C Glioma Cells. The in vitro binding of biotinylated PLNPs was studied on BT4C cells transduced with the avidin-fusion protein (BT4C+) as well as on control BT4C cells (BT4C−) at 37 °C in DMEM culture medium. As mentioned above, the interaction of biotin-PEG-PLNP with neutravidin was ensured by fluorescence microscopy (Figure 4). In order to unveil the best binding conditions and favor biotinylated-PLNP inter-

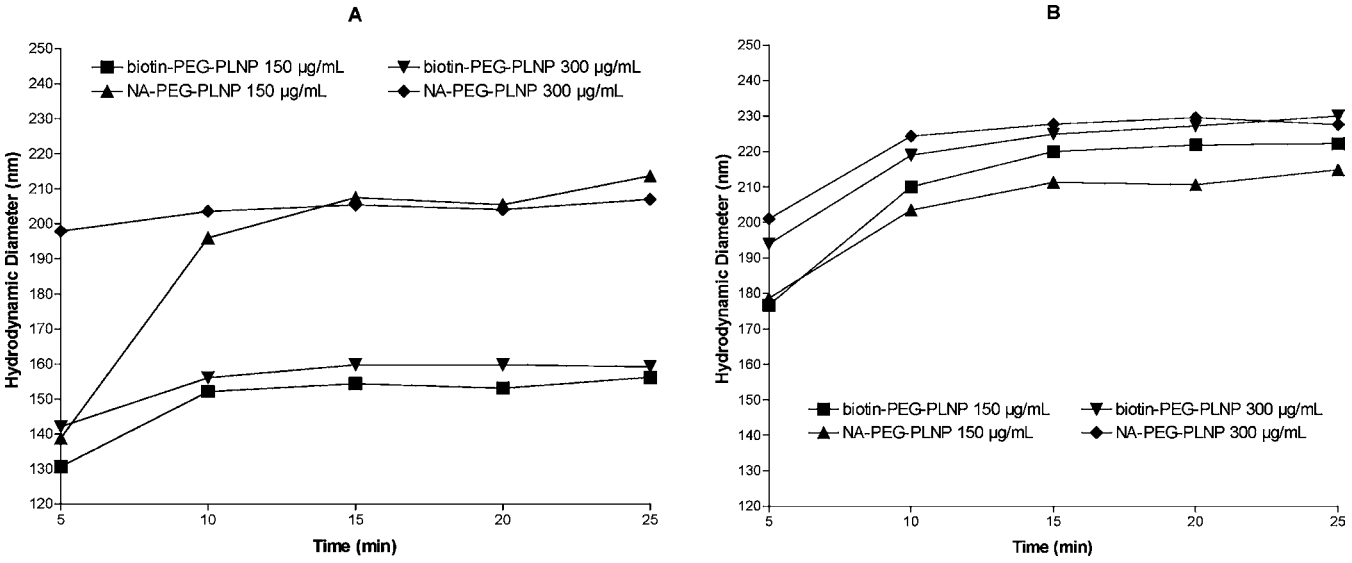


Figure 5. Colloidal stability obtained from DLS measurements of PLNP with either 120 nm core diameter (A) or 180 nm core diameter (B) in DMEM culture medium supplemented with 10% FBS.

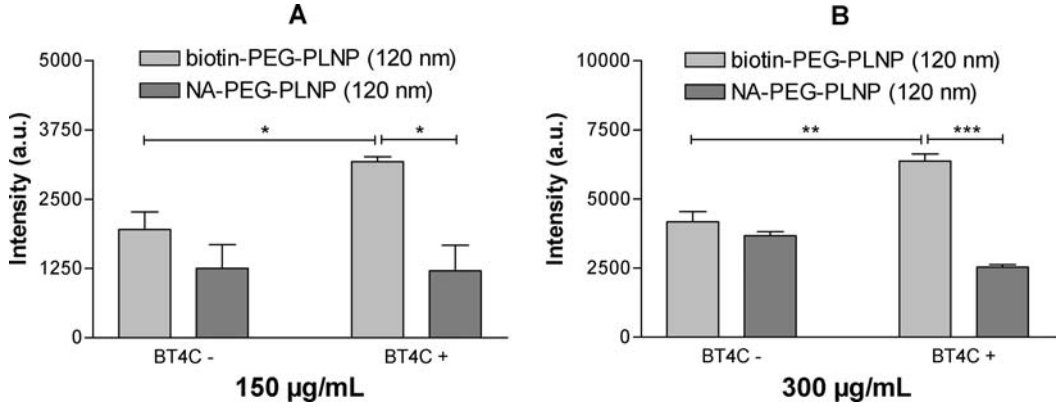


Figure 6. In vitro binding study on BT4C cells after 30 min of incubation at 37 °C with PLNP at 150 μg/mL (A) or 300 μg/mL (B). The signal corresponds to the detection of persistent luminescence from PLNP using a Wallac Victor^2 spectrophotometer (355 nm excitation; 670 nm emission).

action with cells, we studied the influence of particle concentration, hydrodynamic diameter, and binding time on the targeting of BT4C cells in vitro. Results in Figure 6 show the luminescence intensity from PLNP (120 nm core diameter) after 30 min of incubation time on both BT4C− and BT4C+ in DMEM. We noticed a similar trend for 150 μg/mL and 300 μg/mL concentrations. In both cases, biotinylated nanoparticles bound more efficiently to glioma cells expressing the avidin fusion protein (about 60% more signal than on control cells), indicating successful biotin-mediated targeting. However, in order to confirm the specific function of biotin in lodavin targeting and evaluate the proportion of binding related to endogenous biotin-binding proteins (other than lodavin), we achieved a similar assay with NA-PEG-PLNP, on which accessible biotins were saturated with neutravidins. We noticed a significant decrease in particle binding with both BT4C− and BT4C+ cells after biotin saturation with neutravidin (Figure 6). First, the results on BT4C− confirm the idea that part of the biotin-PEG-PLNP binding on BT4C cells is associated with endogenous biotin-binding proteins, unable to interact with NA-PEG-PLNP after biotin saturation. However, the comparison with the BT4C+ histogram ensures that the preferential binding of biotin-PEG-PLNP on BT4C cells expressing the fusion protein occurs through a specific interaction of biotin with the avidin moiety of lodavin. We observed the exact same trends following the binding of larger particles (180 nm core diameter) for 15 min (Figure S2, Supporting Information), yet accompanied with a significant decrease in biotin-PEG-PLNP selectivity toward lodavin-expressing cells.

CONCLUSIONS

In this study, we demonstrated successful functionalization of persistent luminescence nanoparticles with biotin and showed, in good agreement with several theoretical models, that the presence of a PEG spacer is critical to allow the efficient binding to streptavidin coated on a plate, by favoring the interaction between the protein and biotins grafted on the surface of the nanoparticle. Taking advantage of such streptavidin−biotin technology,[28] we reported the first use of biotinylated PLNP to target glioma cells expressing an avidin-fusion protein (lodavin), and we showed that the binding to lodavin-expressing cells is not only specific to biotin but also highly depends on the particle core diameter. This in vitro binding study, combined with the discovery of a novel efficient

dx.doi.org/10.1021/bc200510z | Bioconjugate Chem. 2012, 23, 472−478

composition with improved persistent luminescence,[29] thus provides interesting preliminary results for the future use of biotinylated red-emitting nanophosphors in vivo to specifically target the tumor microenvironment in glioma-bearing mice.

■ ASSOCIATED CONTENT

Supporting Information

Size distribution of each population (120 and 180 nm PLNP) obtained after DLS measurement as well as 15 min of *in vitro* binding of large biotinylated PLNPs (180 nm) on BT4C glioma cells. This material is available free of charge via the Internet at http://pubs.acs.org.

■ AUTHOR INFORMATION

Corresponding Author

*E-mail: minna.kaikkonen@uef.fi (M.U.K.); cyrille.richard@parisdescartes.fr (C.R.).

■ ACKNOWLEDGMENTS

This work was supported by European Community (Network of Excellence CLINIGENE LSHB-CT-2006-018933) and by French National Agency (ANR) in the frame of its program in Nanosciences and Nanotechnologies (NATLURIM project number ANR-08-NANO-025). M.U.K. was supported by Ark Therapeutics Oy and a grant from Academy of Finland.

■ REFERENCES

(1) Bruchez, M. J., Moronne, M., Gin, P., Weiss, S., and Alivisatos, A. P. (1998) Semiconductor nanocrystals as fluorescent biological labels. *Science 281*, 2013−2016.

(2) Banks, P. R., and Paquette, D. M. (1995) Comparison of three common amine reactive fluorescent probes used for conjugation to biomolecules by capillary zone electrophoresis. *Bioconjugate Chem. 6*, 447−458.

(3) Kogure, T., Karasawa, S., Araki, T., Saito, K., Kinjo, M., and Miyawaki, A. (2006) A fluorescent variant of a protein from the stony coral *Montipora* facilitates dual-color single-laser fluorescence cross-correlation spectroscopy. *Nat. Biotechnol. 24*, 577−581.

(4) Chan, W. C. W., and Nie, S. (1998) Quantum dot bioconjugates for ultrasensitive nonisotopic detection. *Science 281*, 2016−1018.

(5) Michalet, X., Pinaud, F. F., Bentolila, L. A., Tsay, J. M., Doose, S., Li, J. J., Sundaresan, G., Wu, A. M., Gambhir, S. S., and Weiss, S. (2005) Quantum dots for live cells, in vivo imaging, and diagnostics. *Science 307*, 538−544.

(6) Maysinger, D., Behrendt, M., Lalancette-Hebert, M., and Kriz, J. (2007) Real-time imaging of astrocyte response to quantum dots: in vivo screening model system for biocompatibility of nanoparticles. *Nano Lett. 7*, 2513−2520.

(7) Storhoff, J. J., Elghanian, R., Mucic, R. C., Mirkin, C. A., and Letsinger, R. L. (1998) One-pot colorimetric differentiation of polynucleotides with single base imperfections using gold nanoparticle probes. *J. Am. Chem. Soc. 120*, 1959−1964.

(8) Taton, T. A., Mirkin, C. A., and Letsinger, R. L. (2000) Scanometric DNA array detection with nanoparticle probes. *Science 289*, 1757−1760.

(9) He, H., Xie, C., and Ren, J. (2008) Nonbleaching fluorescence of gold nanoparticles and its applications in cancer cell imaging. *Anal. Chem. 80*, 5951−5957.

(10) Ntziachristos, V. (2006) Fluorescence molecular imaging. *Annu. Rev. Biomed. Eng. 8*, 1−33.

(11) Frangioni, J. V. (2003) In vivo near-infrared fluorescence imaging. *Curr. Opin. Chem. Biol. 7*, 626−634.

(12) Rice, B. W., Cable, M. D., and Nelson, M. B. (2001) *In vivo* Imaging of light-emitting probes. *J. Biomed. Opt. 6*, 432−440.

(13) le Masne de Chermont, Q., Chanéac, C., Seguin, J., Pellé, F., Maîtrejean, S., Jolivet, J. P., Gourier, D., Bessodes, M., and Scherman, D. (2007) Nanoprobes with near-infrared persistent luminescence for in vivo imaging. *Proc. Natl. Acad. Sci. U.S.A. 104*, 9266−9272.

(14) Maldiney, T., Richard, C., Seguin, J., Wattier, N., Bessodes, M., and Scherman, D. (2011) Effect of Core diameter, surface coating, and PEG chain length on the biodistribution of persistent luminescence nanoparticles in mice. *ACS Nano 5*, 854−862.

(15) Lehtolainen, P., Wirth, T., Taskinen, A. K., Lehenkari, P., Leppänen, O., Lappalainen, M., Pulkkanen, K., Marttila, A., Marjomäki, V., Airenne, K. J., Horton, M., Kulomaa, M. S., and Ylä-Herttuala, S. (2003) Targeting of biotinylated compounds to its target tissue using a low-density lipoprotein receptor-avidin fusion protein. *Gene Ther. 10*, 2090−2097.

(16) Lesch, H. P., Kaikkonen, M. U., Pikkarainen, J. T., and Ylä-Herttuala, S. (2000) Avidin-biotin technology in targeted therapy. *Expert Opin. Drug. Delivery 7*, 551−564.

(17) Lesch, H. P., Pikkarainen, J. T., Kaikkonen, M. U., Taavitsainen, M., Samaranayake, H., Lehtolainen-Dalkilic, P., Vuorio, T., Määttä, A. M., Wirth, T., Airenne, K. J., and Yla-Herttuala, S. (2009) Avidin fusion protein-expressing lentiviral vector for targeted drug delivery. *Hum. Gene Ther. 20*, 871−882.

(18) Chaiet, L., and Wolf, F. J. (1964) The properties of streptavidin, a biotin-binding protein produced by streptomycetes. *Arch. Biochem. Biophys. 106*, 1−5.

(19) Green, N. M. (1975) Avidin. *Adv. Protein Chem. 29*, 85−133.

(20) le Masne de Chermont, Q., Richard, C., Seguin, J., Chanéac, C., Bessodes, M., and Scherman, D. (2009) Silicates doped with luminescent ions: useful tools for optical imaging applications. *Proc. SPIE 7189*, 71890B/1−71890B/9.

(21) Longo, G., and Szleifer, I. (2005) Ligand-receptor interactions in tethered polymer layers. *Langmuir 21*, 11342−11351.

(22) Ren, C.-L., Carvajal, D., Shull, K. R., and Szleifer, I. (2009) Streptavidin-biotin binding in the presence of a polymer spacer. A theoretical description. *Langmuir 25*, 12283−12292.

(23) Tseng, C.-L., Wang, T.-W., Dong, G.-C., Wu, S. Y-H., Young, T.-H., Shieh, M.-J., Lou, P.-J., and Lin, F.-H. (2007) Development of gelatine nanoparticles with biotinylated EGF conjugation for lung cancer targeting. *Biomaterials 28*, 3996−4005.

(24) Zhang, G., Yang, Z., Lu, W., Zhang, R., Huang, Q., Tian, M., Li, L., Liang, D., and Li, C. (2009) Influence of anchoring ligands and particle size on the colloidal stability and *in vivo* biodistribution of polyethylene glycol-coated gold nanoparticles in tumor-xenografted mice. *Biomaterials 30*, 1928−1936.

(25) Amstad, E., Zurcher, S., Mashaghi, A., Wong, J. Y., Textor, M., and Reimhult, E. (2009) Surface Functionalization of single superparamagnetic iron oxide nanoparticles for targeted magnetic resonance imaging. *Small 5*, 1334−1342.

(26) Townsend, S. A., Evrony, G. D., Gu, F. X., Schulz, M. P., Brown, R. H. Jr., and Langer, R. (2007) Tetanus toxin C fragment-conjugated nanoparticles for targeted drug delivery to neurons. *Biomaterials 28*, 5176−5184.

(27) Berndt, M., Lorenz, M., Enderlein, J., and Diez, S. (2010) Axial nanometer distances measured by fluorescence lifetime imaging microscopy. *Nano Lett. 10*, 1497−1500.

(28) Maldiney, T., Byk, G., Wattier, N., Seguin, J., Kahndadash, R., Bessodes, M., Richard, C., and Scherman, D. (2012) Synthesis and functionalization of persistent luminescence nanoparticles with small molecules and evaluation of their targeting ability. *Int. J. Pharm. 423*, 102−107.

(29) Maldiney, T., Lecointre, A., Viana, B., Bessière, A., Bessodes, M., Gourier, D., Richard, C., and Scherman, D. (2011) Controlling electron trap depth to enhance optical properties of persistent luminescence nanoparticles for in vivo imaging. *J. Am. Chem. Soc. 133*, 11810−11815.

Bioconjugate Chemistry

Article

pubs.acs.org/bc

Assembly of Protein Building Blocks Using a Short Synthetic Peptide

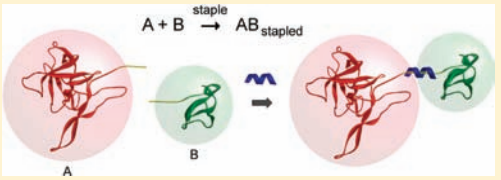
Enrico Ferrari,[†] Mikhail Soloviev,[‡] Dhevahi Niranjan,[†] Jason Arsenault,[†] Chunjing Gu,[†] Yvonne Vallis,[†] John O'Brien,[†] and Bazbek Davletov*[,†]

[†]MRC Laboratory of Molecular Biology, Hills Road, CB2 0QH Cambridge, United Kingdom

[‡]School of Biological Sciences, Royal Holloway University of London, Egham, TW20 0EX Surrey, United Kingdom

Supporting Information

ABSTRACT: Combining proteins or their defined domains offers new enhanced functions. Conventionally, two proteins are either fused into a single polypeptide chain by recombinant means or chemically cross-linked. However, these strategies can have drawbacks such as poor expression (recombinant fusions) or aggregation and inactivation (chemical cross-linking), especially in the case of large multifunctional proteins. We developed a new linking method which allows site-oriented, noncovalent, yet irreversible stapling of modified proteins at neutral pH and ambient temperature. This method is based on two distinct polypeptide linkers which self-assemble in the presence of a specific peptide staple allowing on-demand and irreversible combination of protein domains. Here we show that linkers can either be expressed or be chemically conjugated to proteins of interest, depending on the source of the proteins. We also show that the peptide staple can be shortened to 24 amino acids still permitting an irreversible combination of functional proteins. The versatility of this modular technique is demonstrated by stapling a variety of proteins either in solution or to surfaces.



INTRODUCTION

Combining proteins with different functions into a single entity can offer new opportunities to the field of protein engineering. Protein chimeras, made from protein building blocks that nature already optimized for a specific function by natural selection, could be especially attractive for multienzyme mediated catalysis,[1] nanobiotechnology,[2] and improved medicinal proteins.[3,4] Proteins carrying artificially combined domains are already widely used both in research and in medicine: recombinant proteins are often fused to affinity tags to facilitate their purification, fluorescent fusion proteins are used to track their localization in cells and throughout the body, biotin–protein conjugates are used for immobilization purposes, antibody conjugates are widely used for detection of antigens or for therapeutic use, and medicinal toxins can be targeted to new localities using various targeting domains.[3,4]

Despite the ever-growing interest in novel multimodular proteins, there are factors that limit development and production of such chimeras. A general versatile platform to develop multimodular functional proteins is still missing and successful production of protein chimeras still relies on an empirical approach. Recombinant DNA technology allows fusion of two or more modules in a single polypeptide chain; however, this strategy may not be convenient: for example, when production of the engineered chimera (i) leads to low expression levels or yields insoluble protein, (ii) results in orientation of fused parts not optimal for biological function, (iii) raises safety issues like in the case of modified botulinum neurotoxin,[5] or (iv) results in cytotoxicity.[6] Chemical cross-linking, on the other hand, utilizes physically separate proteins and relies on the reactivity of either natural (cysteine or lysine) or non-natural amino acids.[7] Site-specific chemical conjugation is, in practice, possible only in a limited number of cases, and chemical-cross-linking often leads to partially inactive chimeras or aggregated conjugates. Recently, several techniques utilized self-assembling linkers which can be fused to proteins prior to their assembly. 'Protein trans-splicing' technique utilized a split intein—mixing of two tagged proteins allowed binding, incision, and trans-thioesterification resulting in a covalent bondage of the two proteins.[8] In contrast, the 'expressed protein ligation' method[8] exploited the self-splicing capability of an intein, recombinantly fused to the C-terminal of a precursor protein, to trigger formation of α-thioester followed by trans-thioesterification to another protein carrying N-terminal cysteine. Both intein-based approaches require a number of critical steps and conditions to successfully orient and bind two precursor proteins and the conditions often cannot be practically fulfilled. Heterodimeric leucine zippers fused to proteins were proposed for protein linkage[9,10] but the affinity of natural leucine zippers is not strong enough to compete with recombinant fusion or chemical cross-linking. Another recently introduced platform, so-called dock-and-lock platform, relies on association of a sequence from Protein Kinase A (PKA) with A-Kinase Anchoring Protein (AKAP).[11] Recombinant fusion of two separate proteins of interest to the PKA and AKAP-derived peptides allows site-oriented protein assembly. However, the flexibility of this system is limited due to the obligatory

Received: September 20, 2011
Revised: January 25, 2012
Published: February 2, 2012

ACS Publications © 2012 American Chemical Society

dx.doi.org/10.1021/bc2005208 | *Bioconjugate Chem.* 2012, 23, 479–484

dimerizing nature of the PKA sequence and the necessity of introducing cysteines to stabilize the final assembled product.[11]

We recently described a new approach to assemble proteins in solution using a 52 aa synthetic peptide.[5] This approach relies on two polypeptide linkers which can be fused to proteins of interest and then 'stapled' together (Figure 1) resulting in an oriented, noncovalent, and yet irreversible complex. The linkers and the staple are derived from the uniquely stable SNARE coiled-coil complex.[12] Since each module can be developed and processed separately, we performed an optimization of this new, promising technique. Here we report that the staple can be shortened to 24 aa still allowing firm linking of proteins. In addition, we extend the technique to proteins which cannot be routinely obtained by bacterial expression.

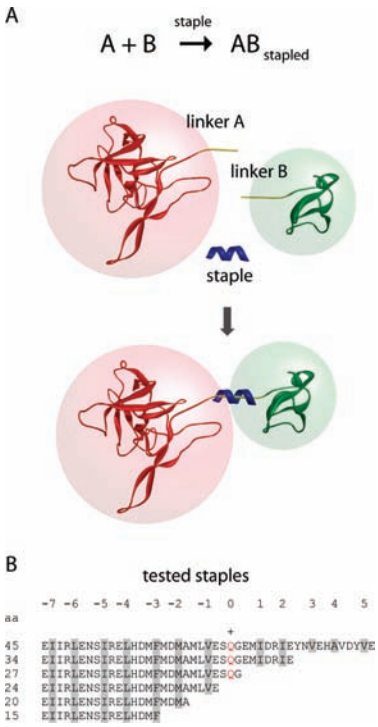


Figure 1. Schematic of protein stapling and design of staples. (A) Two protein modules are fused to separate linkers (yellow). In the presence of a peptide staple (blue), they assemble into an irreversible complex. (B) Tested staples range from 15 to 45 aa, encompassing 5 to 13 layers, characteristic of the coiled-coil SNARE complex structure.[12] Both the hydrophobic layers (boxed in gray) and so-called 'ionic' layer (glutamine in red) take part in the SNARE assembly.

EXPERIMENTAL PROCEDURES

Linkers/Staple Design and Synthesis. All recombinant proteins were expressed in BL21 strain of *E. coli* as glutathione-S-transferase (GST) C-terminal fusions cleavable by thrombin. The plasmid for expression was the pGEX-KG vector and the design, expression, and purification of all of them, except for the linker A-mCherry construct (see below), has been already reported.[13,14] Briefly, the linker A corresponds to the rat SNAP25 full-length sequence (GenBank: AAH87699.1), with all four cysteine residues mutated to alanine; the linker B corresponds to the rat synaptobrevin2 (NCBI Reference Sequence: NP_036795.1), amino acids 25 to 84. GST fusion constructs were purified by glutathione affinity chromatography and either cleaved using thrombin or eluted with excess of glutathione. The linker A-mCherry plasmid has been made by introducing the mCherry sequence from pmCherry-C1 vector (Clontech) into the *Eco*RI restriction site of pGEX-KG, following SNAP25 sequence (22−206 aa; four cysteines mutated to alanines). The botulinum neurotoxin serotype A (BoNT/A) light chain-translocation domain (LcTd) fusion to linker A and the linker B fusion to BoNT/A receptor binding domain (Rbd) have been previously described in detail.[13] The horseradish peroxidase (HRP)-linker B construct was made by cross-linking maleimide activated HRP (ThermoScientific) to a modified linker B peptide. The N-terminal acetylated and C-terminal amidated modified linker B peptide, with the sequence CGSGS RLQQT QAQVD EVVDI MRVNV DKVLE RDQKL SELDD RADAL QAGAS, was synthesized by Peptide Synthetics, UK, and stored in DMSO. See Supporting Information Table 1 for the list of all the recombinant proteins and the cross-linked conjugate used in this study.

Stapling peptides are based on rat syntaxin 1 (GenBank: EDM13396.1) and were synthesized by Peptide Synthetics, UK, and stored in DMSO. The native lysine was substituted with arginine to remove primary amines; individual sequences are shown in Figure 1B. All peptides have been modified with an acetyl group and FITC at the N-terminus and two additional lysine residues at the C-terminus were separated from the syntaxin motif by a flexible aminohexanoic acid linker. This design allows site-oriented attachment of the staples to bromocyanide (BrCN)-activated Sepharose 4B resin (Amersham Biosciences) via reactive lysines.[15] Both linkers and staples migrate as single bands on SDS-PAGE gels (NuPAGE 10% Bis-Tris Gel, Invitrogen) (Supporting Information Figure 1A). Among linkers A and B, only the linker A migrates sharply on native gels (12% Tris-HCL, Bio-Rad) (Supporting Information Figure 1B).

Proteins Stapling and Pull-Down Assays. The stapling reactions (Figures 2C, 4, and 5A) were performed in 20 mM Hepes, 100 mM NaCl, 0.8% *n*-octylglucoside (OG), pH 7.4 (buffer A). Linkers and protein modules fused to the linkers, were at 5 μM, and were incubated 1 h at 24 °C with a 1.5-fold excess of relevant staple. Electrophoresis in both the native gel in Figure 2C and the SDS-PAGE gel in Figure 5A was performed at 4 °C to avoid overheating of the protein assembly during the gel run. 300 μL samples of the 5 μM stapled proteins used in Figure 4 have been analyzed by size-exclusion chromatography to attest purity and integrity of the complexes using an AKTA purifier 10 system (GE Healthcare). The readouts at 280 and 490 nm have been acquired and 0.5 mL fractions have been collected and analyzed by Coomassie stained SDS-PAGE gels (Supporting Information Figure 2).

Pull-downs have been performed using BrCN-activated Sepharose beads after cross-linking of the staples as previously reported[15] (Figure 2A) or glutathione Sepharose beads after 1 h preincubation with 5 μM GST-linker fusion proteins (Figure 3). Incubations were performed in buffer A for 1 h at 24 °C with shaking, followed by extensive washes in buffer A to remove the unbound reagents. Fluorescence and absorbance readings in Figure 3 were performed using Saphire 2 plate reader (Tecan, Switzerland). Densitometry analysis of the Coomassie stained gels (Figure 2B) has been done using the software *Quantity One* v 4.5.1 (Bio-Rad). Stapled conjugates used in this work are listed in Supporting Information Table 1.

Biacore Assay. Analysis of binding and stapling was conducted using a Biacore 2000 system (Figures 2D, 5B, and SI Figure 4). CM5 chip (Biacore) was used to covalently

dx.doi.org/10.1021/bc2005208 | *Bioconjugate Chem.* 2012, 23, 479−484

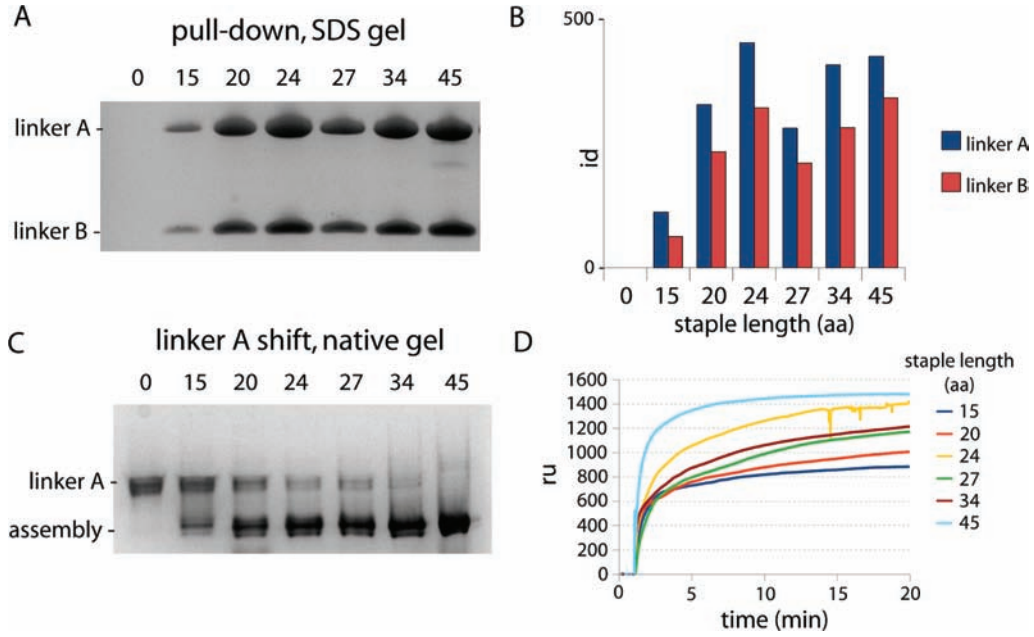


Figure 2. 24 aa and 45 aa staples exhibit the best linker binding properties. (A) Coomassie-stained SDS-PAGE gel showing the amounts of linkers A and B bound to staples immobilized on beads. The length of peptide staples is indicated above the gel. (B) Bar chart showing integrated density (id) values of Coomassie-stained protein bands in the SDS-PAGE gel from panel A. Note that the higher values for linker A compared to linker B are because larger proteins bind more Coomassie stain. (C) Coomassie-stained native gel showing a shift of linker A migration after 30 min incubation in the presence of linker B and indicated staples. (D) Biacore traces showing the stapling reaction on the chip surface carrying immobilized linker A. The traces were obtained following the injection of the linker B mixed at equimolar ratios with different staples. Values are in resonance units (ru) after subtraction of signals due to the loading buffer.

immobilize GST-linker A. For each staple, binding of linker B combined in equimolar ratio to the staple was recorded. All proteins/peptides were at 5 μM in buffer A and were applied to the chip at a rate of 5 μL/min for 20 min. For stability measurements (Figure 5B), the assembled complex was exposed to 1% SDS for 1 min.

Hippocampal Neurons Culture and Western Immunoblotting. Primary cultures of hippocampal neurons were prepared as previously described[5] and used after 7−10 days in culture. For imaging of the uptake of the reassembled toxins (Figure 4B), neurons were exposed to 10 nM of the indicated compound for 2 h, DAPI-stained, fixed with 4% PFA and the fluorescence was observed on a Radiance Confocal system (Zeiss/Bio-Rad) linked to a Nikon Eclipse fluorescence microscope equipped with an oil immersion objective (100×, 1.4 N.A.). The fluorescent staples alone have been used as a negative control (SI Figure 3). For the functionality assay (Figure 4C), neurons were incubated for 20 h with 10 nM of the indicated compound, lysed in 60 mM Tris (pH 6.8), 2 mM $MgCl_2$, 2% SDS, and benzonase (250 U/mL, Novagen). SNAP25 cleavage was then analyzed by immunobloting using an anti-SNAP25 antibody (clone SMI81, Covance) which recognizes both the cleaved and uncleaved proteins.

RESULTS

Optimization of the Staple. Syntaxin-derived SNARE motif used previously for stapling[5] is 52 aa in length, presenting a challenge for routine, mass-scale linking of proteins in solution or to surfaces. To determine the minimal length of staple (Figure 1B), we investigated the ability of chemically synthesized peptides, covalently attached to Sepharose beads, to pull-down linkers A and B (Figure 2A). The staples were immobilized on BrCN Sepharose beads via two lysines and then incubated with an excess of both linkers. As expected, binding of both linkers to the immobilized staples occurred in parallel and in equimolar ratio (Figure 2A). The Coomassie-stained SDS-PAGE gel and its densitometry quantitation (Figure 2B) show that efficient binding of linkers occurs only when the length of staples exceeds 20 aa with the 24 aa staple already reaching maximum. Interestingly, extending the staple to 27 aa compromises binding of the two linkers before the interaction recovers at the 45 aa length. Next, we exploited the ability of linker A and stapled assemblies to migrate in native gel electrophoresis as separate distinct bands (Figure 2C). We incubated the staples in the presence of the two linkers in solution for 60 min and then analyzed protein migration by Coomassie-staining of the nondenaturing gel. Figure 2C shows that staples as short as 20 aa can be effective in triggering linkers association. Indeed, linker A shifts into a faster migrating entity, most likely due to the addition of negative charges from linker B and the staples, and/or the tight structure of the resulting SNARE bundle.[12]

To further test the efficiency of the stapling reaction we employed the surface plasmon resonance (SPR) approach. Linker A was immobilized on the surface of the Biacore chip and an equimolar mixture of linker B and staple was injected into the microfluidic chamber. Figure 2D shows the traces acquired for each staple during the 20 min incubation. The end-point values show that larger staples yielded faster assembly; however, the 24 aa peptide clearly showed an increased binding compared to its neighbors. This confirms that the 24 aa peptide is uniquely effective in stapling reaction. Since dissociation of the linker A/linker B/staple complex was not observed with any of the staples used (see SI Figure 4), a dissociation constant K_D cannot be calculated. How different staples yield different

dx.doi.org/10.1021/bc2005208 | Bioconjugate Chem. 2012, 23, 479−484

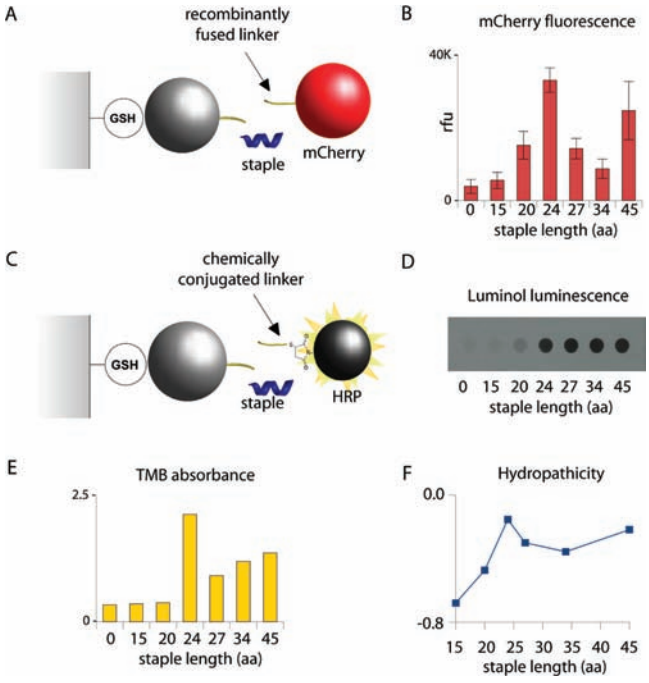


Figure 3. Peptide-dependent stapling of the mCherry fluorescent protein or horseradish peroxidase (HRP) to glutathione-S-transferase (GST). (A) Schematic showing GST-linker (gray) immobilized on glutathione beads which were used to pull-down mCherry (red). (B) Histogram showing relative fluorescence units (rfu) bound to GST-linker beads in presence of different staples. Error bars represent standard deviation (n = 3). (C) Schematic showing GST-linker (gray) immobilized on glutathione beads which were used to pull-down HRP. (D) X-ray film showing relative amount of HRP bound to beads in a 96-well plate in the presence of the different staples, revealed using a luminol reaction. (E) Histogram showing relative amount of HRP bound to GST-linker beads in the presence of the indicated staples as revealed by a TMB-based colorimetric reaction. (F) Plot showing grand average of hydropathicity (GRAVY) index of the stapling peptides as a function of their sequence and length.

resonance units in irreversible binding reactions after 20 min is currently unclear.

Stapling of Functional Proteins. Next we investigated the efficiency of stapling proteins with diverse functions. We fused one of the linkers to GST, functionality of which can be tested by binding to glutathione−Sepharose beads, whereas the other linker was fused to mCherry fluorescent protein. mCherry provides easy readout in pull-down experiments. Figure 3B shows that the amount of stapled mCherry has a similar trend to that in Figure 2, confirming that the 24 and 45 aa staples exhibit the strongest binding.

It was also important to assess the suitability of our stapling system to protein which cannot be routinely expressed, e.g., HRP. We designed a modified version of linker B specifically for the chemical cross-linking by adding a cysteine residue which can be reacted via maleimide reaction with proteins of interest. The modified linker B was conjugated to maleimide-activated HRP enzyme which can be easily detected via luminescent or colorimetric reactions. We then tested the ability of staples to attach the HRP enzyme to GST-linker A-containing beads in a 96-well plate. Following extensive washing of individual wells, the amount of HRP bound to Sepharose beads was estimated by the luminol reaction which emits light. Exposure of an X-ray film to the 96-well plate

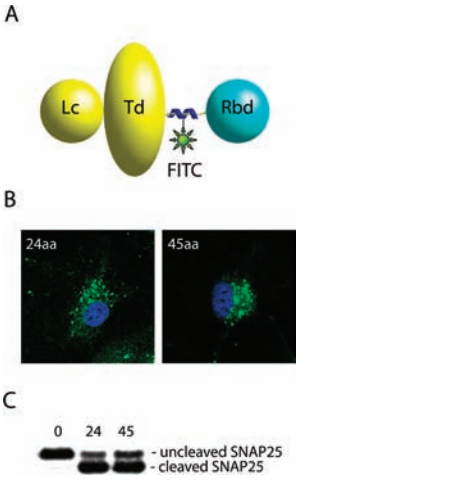


Figure 4. 24 aa peptide is sufficient for stapling functional parts of botulinum neurotoxin. (A) Schematic showing design of the botulinum construct: the Rbd part (light blue) is stapled to the enzymatic part (yellow), that consists of the light chain (Lc) and translocation domain (Td). LcTd-linker A is produced as a single protein. (B) Confocal fluorescence images showing the uptake by hippocampal neurons of the reassembled toxins stapled with the indicated length peptides labeled with FITC (green). Blue represents the DAPI-stained nucleus. (C) Western immunoblot showing the intact (upper bands) and cleaved (lower bands) endogenous SNAP25 upon incubation of hippocampal neurons with reassembled botulinum toxin stapled with the indicated length peptides.

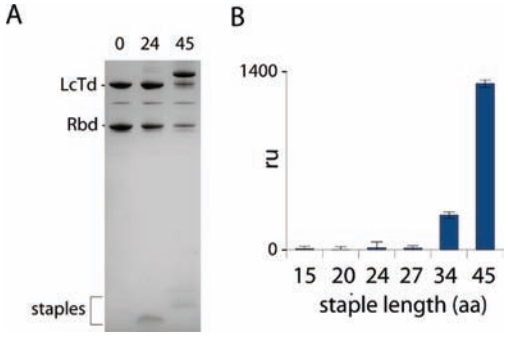


Figure 5. Resistance of stapled molecules to SDS. (A) A Coomassie stained SDS-PAGE gel showing the migration of BoNT/A LcTd-Rbd complexes stapled with the indicated length peptide. The individual components migrate as a 120 kDa (LcTd-linker A), a 55 kDa (linker B- Rbd) and less than 10 kDa bands (staples). Only when the staple is 45 aa long the assembly of the two modules is clearly visible in the gel as an increase in the molecular weight. (B) Stability of stapling by the indicated peptides under denaturing conditions. Bars indicate the amount in resonance units (ru) of linker B remaining on linker A-functionalized Biacore chip after incubation with 1% SDS. Error bars represent standard deviation (n = 4).

revealed that the HRP can be efficiently stapled to the GST-linker A beads and that the minimal staple must be at least 24 aa long (Figure 3D). A quantitative measurement of the bound HRP was obtained by the HRP-catalyzed colorimetric reaction in presence of the 3,3′,5,5′-tetramethylbenzidine (TMB), confirming the optimal length for the staple being 24 aa (Figure 3E).

To better understand the reason for the unique efficiency of the 24 aa staple, we analyzed the hydropathicity as a function of peptide length (analysis performed using ProtParam tool available at http://expasy.org/tools/protparam.html). The

dx.doi.org/10.1021/bc2005208 | Bioconjugate Chem. 2012, 23, 479−484

plot in Figure 3F revealed that the 24 aa staple is the most hydrophobic of all the stapling peptides, which may explain its enhanced ability to drive SNARE assembly which depends on N-to-C zippering of hydrophobic layers.[12] Extending the syntaxin peptides beyond 24 aa incorporates the ionic layer (see Figure 1B), bringing to the consequent drop in hydropathicity, likely explaining why 27 aa and 34 aa have a reduced ability to staple proteins. The hydropathicity increases again at 45 aa, with the incorporation of more hydrophobic layers, and the stapling efficacy increases accordingly.

Functional Testing of the 24 aa Staple. Next we tested whether the shortened peptides can allow a stable assembly as judged by a biologically relevant assay. We chose to staple two functional parts of botulinum neurotoxin type A (BoNT/A), widely known as BOTOX,[16,17] which needs to penetrate neuronal interior to proteolyze its molecular target, the SNAP25 protein. The two BoNT/A modules used in this work (see the Experimental Procedures section and Supporting Information Table 1) are the linker B - Rbd, which accomplish the function of binding to the specific neuronal receptors, and LcTd - linker A, whose functions are (i) translocation of the bound and endocytosed neurotoxin from the endocytic vesicles to the cytoplasm (Td part) and (ii) proteolysis of the target (Lc part) that eventually impairs the fusion of the synaptic vesicles and therefore the neurotransmitter release. Binding to neurons, entry into the cytosol, and cleavage of the molecular target occur only when the two modules are physically connected, and thus the BoNT/A offers a useful paradigm to study the functionality of the stapling method. We stapled the two neurotoxin parts using 24 aa and 45 aa peptides, both tagged with FITC, and applied the stapled fluorescent products to cultured mouse hippocampal neurons. Functionality of the stapled toxins was assessed by penetration of the fluorescently labeled toxin into neurons and proteolytic cleavage of intraneuronal SNAP25. Figure 4B shows that both stapled botulinum products efficiently entered the neuronal interior combining binding and translocation functions of the neurotoxin. Both the 24 and 45 aa stapled products triggered extensive cleavage of intraneuronal SNAP25 at 10 nM concentration, with no proteolytic cleavage detected in the absence of staples (Figure 4C). Clearly, the translocation module, LcTd, must be stapled to the binding part, Rbd, to be taken up by the endocytotic machinery. This proves that a staple as short as 24 aa is able to efficiently link the functional modules together allowing the neurotoxin to accomplish its sophisticated functions: binding to neuronal membranes, entry of the botulinum enzyme into cytosol, and a highly specific proteolysis of its intraneuronal target.

One feature of the stapling assembly is its resistance to SDS which could be useful in verifying the success of the stapling reaction simply by SDS-PAGE. We analyzed whether the two stapled botulinum products, which migrate identically in a size-exclusion chromatography (SI Figure 2), exhibit such SDS resistance. Figure 5A shows that, only in the presence of the 45 aa staple, the botulinum product becomes SDS-resistant, whereas SDS breaks the 24 aa stapled product into its constituent parts. To better understand the boundary where SDS resistance is acquired, we analyzed the resistance of linker/staple associations to 1% SDS solution using the surface plasmon resonance method. Figure 5B shows that only 45 aa staple was able to confer the SDS resistance to the stapling system, confirming possible utility of the longer linker in aiding visualization of stapled products in SDS-PAGE gels (Figure 5A).

DISCUSSION

Here we described optimization of the new protein stapling technique which allows linking of two modules using a synthetic peptide. We demonstrated that the staple as short as 24 amino acids in length can efficiently link proteins either in solution or to a surface. The shortening of the staple allows an easy and straightforward synthesis and also opens room for incorporation of other functionalities (for example, imaging reagents). We also demonstrated that the linkers can be chemically cross-linked to protein building blocks. The possibility to use the linking system for nonrecombinant proteins opens many possibilities for conjugation of widely used proteins such as naturally derived enzymes, lectins, growth factors, and so forth. When recombinantly fused, the linkers caused neither a reduction in the expression levels of proteins tested nor solubility issues. Conceivably, the unstructured nature of the SNARE-based linkers—prior to their assembly[12]—makes them easy to express with no deleterious effects on the function of the building blocks. In all cases, the obtained conjugates retained functions of individual modules.

Similarly to the intein-based protein trans-splicing technique and the dock-and-lock platform, protein stapling requires the expression of N-terminal and C-terminal linkers to bring together the two parts. However, there are important differences that can affect the choice of the ideal system for a specific use: SNARE-based protein stapling is robust in a very wide range of conditions while the intein mediated trans-esterification is highly affected by the chemical contest of the reaction or requires additional disulfide bridging in the case of the dock-and-lock platform. A sortase-driven protein conjugation, on the other hand, requires millimolar calcium and elevated pH and temperatures, limiting its utility.[18] SNARE-based protein stapling does not result in the formation of the peptide bond between the two parts, but allows parallel incorporation of chemical agents, e.g., fluorophores or other labeling compounds. Finally, while intein-based trans-splicing may allow reconstitution of a desired split-protein with fully preserved structure, the protein stapling evidently permits combinations of structurally unrelated proteins and thus could be suitable for production of multienzyme complexes, antibody−enzyme conjugates, heterofunctional targeting agents for binding two receptors, and so forth. The stapling mechanism between the two stapled domains can potentially give new beneficial features to the assembled product as was previously demonstrated for the stapled BoNT/A (preserved silencing of central neurons without muscle paralytic activity).[13]

In summary, we optimized the protein stapling method making it more attractive for protein engineering: (i) a functional peptide staple that is half the length of the previously reported, (ii) the possibility to cross-link a synthetic SNARE linker to a protein obtained by sources other than recombinant (e.g., HRP), and (iii) the possibility to immobilize a SNARE linker fusion protein to a surface through a staple (e.g., on a Biacore chip). Finally, we highlighted the possibility to follow supramolecular assembly by SDS-PAGE when using a 45 amino acid staple.

It is likely that future design and synthesis of supramolecular complexes and molecular machines made from heterologous protein domains[1,2,19,20] will be based on a modular approach. Clearly, production of individual building blocks carrying

SNARE linkers still relies on the recombinant fusion or on chemical cross-linking. However, once the expression of a SNARE linker-fusion protein is established, it will be straightforward to staple it to many protein or synthetic entities, fulfilling the step-by-step nature of the modular approach. On the contrary, the recombinant fusion of many different chimeras could be problematic in terms of time, different levels of expression, or even impossibility to synthesize the protein. Another specific advantage of the stapling method is the possibility to easily create protein−synthetic molecule conjugates. Pertinently, the fast SNARE-based assembly happens when the linkers and staple are at equimolar concentrations, while chemical cross-linking often requires a large excess of one of the reagents, leading to losses of valuable material and potential denaturation or aggregation. Moreover, the quick and robust self-assembling and the potential to visualize the assembled products in less than one hour together present a uniquely versatile platform for combinatorial assembly of multifunctional proteins.

■ ASSOCIATED CONTENT

Supporting Information

Table listing proteins and stapled assemblies used in this work; Coomassie stained SDS-PAGE and native gels showing purified linker A, linker B and staple; size-exclusion chromatography of the stapled BoNT/A LcTd-Rbd complexes used for the functional testing; confocal fluorescence images showing lack of uptake by hippocampal neurons of FITC-labeled staples in the absence of botulinum parts; Biacore traces showing the association of linker B on the chip surface carrying immobilized linker A in presence of different staples and indicating no complex dissociation for all individual staples. This material is available free of charge via the Internet at http://pubs.acs.org.

■ AUTHOR INFORMATION

Corresponding Author

*E-mail: bazbek@mrc-lmb.cam.ac.uk. Telephone: +44(0) 1223402009. Fax: +44(0)1223402310.

Notes

The authors declare no competing financial interest.

■ ABBREVIATIONS

BoNT/A, botulinum neurotoxin serotype A; DAPI, 4′,6-diamidino-2-phenylindole; FITC, fluorescein isothiocyanate; GST, glutathione S-transferase; HRP, horseradish peroxidase; OG, *n*-octyl-*β*-D-glucoside; SDS, sodium dodecyl sulfate; SNAP25, synaptosomal-associated protein 25; SNARE, soluble N-ethylmaleimide-sensitive factor attachment protein receptor; TMB, 3,3′,5,5′ tetramethylbenzidine

■ REFERENCES

(1) Niemeyer, C. M., Koehler, J., and Wuerdemann, C. (2002) DNA-Directed Assembly of Bienzymic Complexes from In Vivo Biotinylated NAD(P)H:FMN Oxidoreductase and Luciferase. *ChemBioChem 3*, 242−245.

(2) Heddle, J. G. (2008) Protein cages, rings and tubes: useful components of future nanodevices? *Nanotechnol. Sci. Appl. 1*, 67−78.

(3) Mantyh, P. W., Rogers, S. D., Honore, P., Allen, B. J., Ghilardi, J. R., Li, J., Daughters, R. S., Lappi, D. A., Wiley, R. G., and Simone, D. A. (1997) Inhibition of Hyperalgesia by Ablation of Lamina I Spinal Neurons Expressing the Substance P Receptor. *Science 278*, 275−279.

(4) Chaddock, J. A., Purkiss, J. R., Duggan, M. J., Quinn, C. P., Shone, C. C., and Foster, K. A. (2000) A conjugate composed of nerve growth factor coupled to a non-toxic derivative of *Clostridium botulinum* neurotoxin type A can inhibit neurotransmitter release in vitro. *Growth Factors 18*, 147−155.

(5) Darios, F., Niranjan, D., Ferrari, E., Zhang, F., Soloviev, M., Rummel, A., Bigalke, H., Suckling, J., Ushkaryov, Y., Naumenko, N., Shakirzyanova, A., Giniatullin, R., Maywood, E., Hastings, M., Binz, T., and Davletov, B. (2010) SNARE tagging allows stepwise assembly of a multimodular medicinal toxin. *Proc. Natl. Acad. Sci. U.S.A. 42*, 18197−18201.

(6) Wu, W., Wood, D. W., Belfort, G., Derbyshire, V., and Belfort, M. (2002) Intein-mediated purification of cytotoxic endonuclease I-TevI by insertional inactivation and pH-controllable splicing. *Nucl. Acid. Res. 30*, 4864−4871.

(7) Graaf, A. J., Kooijman, M., Hennink, W. E., and Mastrobattista, E. (2009) Nonnatural Amino Acids for Site-Specific Protein Conjugation. *Bioconjugate Chem. 20*, 1281−1295.

(8) Muralidharan, V., and Muir, T. W. (2006) Protein ligation: an enabling technology for the biophysical analysis of proteins. *Nat. Meth. 3*, 429−438.

(9) Kostelny, S. A., Cole, M. S., and Tso, Y. J. (1992) Formation of a bispecific antibody by the use of leucine zippers. *J. Immunol. 148*, 1547−1553.

(10) Chang, H. C., Bao, Z., Yao, Y., Tse, A. G., Goyarts, E. C., Madsen, M., Kawasaki, E., Brauer, P. P., Sacchettini, J. C., and Nathenson, S. G. (1994) A general method for facilitating heterodimeric pairing between two proteins: application to expression of alpha and beta T-cell receptor extracellular segments. *Proc. Natl. Acad. Sci. U.S.A. 91*, 11408−11412.

(11) Chang, C.-H., Rossi, E. A., and Goldenberg, D. M. (2007) The Dock and Lock Method: A Novel Platform Technology for Building Multivalent, Multifunctional Structures of Defined Composition with Retained Bioactivity. *Clin. Cancer Res. 13*, 5586s−5591s.

(12) Sutton, R. B., Fasshauer, D., Jahn, R., and Brunger, A. T. (1998) Crystal structure of a SNARE complex involved in synaptic exocytosis at 2.4 A resolution. *Nature 395*, 347−353.

(13) Ferrari, E., Maywood, E. S., Restani, L., Caleo, M., Pirazzini, M., Rossetto, O., Hastings, M. H., Niranjan, D., Schiavo, G., and Davletov, B. (2011) Re-Assembled Botulinum Neurotoxin Inhibits CNS Functions without Systemic Toxicity. *Toxins 3*, 345−355.

(14) Darios, F., Wasser, C., Shakirzyanova, A., Giniatullin, A., Goodman, K., Munoz-Bravo, J. L., Raingo, J., Jorgacevski, J., Kreft, M., Zorec, R., Rosa, J. M., Gandia, L., Gutierrez, M., Binz, T., Giniatullin, R., Kavalali, E. T., and Davletov, B. (2009) Sphingosine facilitates SNARE complex assembly and activates synaptic vesicle exocytosis. *Neuron 62*, 683−694.

(15) Ferrari, E., Darios, F., Zhang, F., Niranjan, D., Bailes, J., Soloviev, M., and Davletov, B. (2010) Binary polypeptide system for permanent and oriented protein immobilization. *J. Nanobiotechnol. 8*, 9.

(16) Montal, M. (2010) Botulinum Neurotoxin: A Marvel of Protein Design. *Annu. Rev. Biochem. 79*, 591−617.

(17) Davletov, B., Bajohrs, M., and Binz, T. (2005) Beyond BOTOX: advantages and limitations of individual botulinum neurotoxins. *Trends Neurosci. 28*, 446−452.

(18) Levary, D. A., Parthasarathy, R., Boder, E. T., and Ackerman, M. E. (2011) Protein-Protein Fusion Catalyzed by Sortase A. *PLOS One 6*, e18342.

(19) Stupp, S. I., LeBonheur, V., Walker, K., Li, L. S., Huggins, K. E., Keser, M., and Amstutz, A. (1997) Supramolecular Materials: Self-Organized Nanostructures. *Science 276*, 384−389.

(20) Yeates, T. O., and Padilla, J. E. (2002) Designing supramolecular protein assemblies. *Curr. Opin. Struct. Biol. 12*, 464−470.

Bioconjugate Chemistry

Article

pubs.acs.org/bc

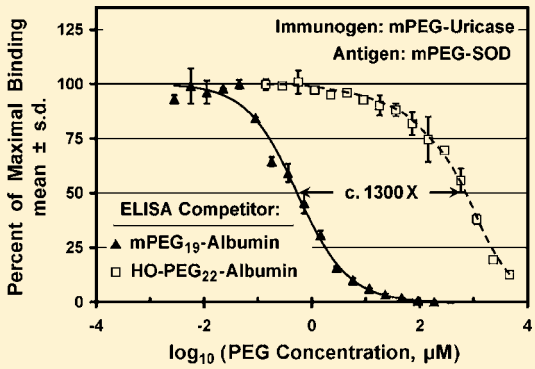
Role of the Methoxy Group in Immune Responses to mPEG-Protein Conjugates

Merry R. Sherman,* L. David Williams, Monika A. Sobczyk, Shawnya J. Michaels, and Mark G. P. Saifer

Mountain View Pharmaceuticals, Inc., 3475 Edison Way, Suite S, Menlo Park, California 94025-1821, United States

Supporting Information

ABSTRACT: Anti-PEG antibodies have been reported to mediate the accelerated clearance of PEG-conjugated proteins and liposomes, all of which contain methoxyPEG (mPEG). The goal of this research was to assess the role of the methoxy group in the immune responses to mPEG conjugates and the potential advantages of replacing mPEG with hydroxyPEG (HO-PEG). Rabbits were immunized with mPEG, HO-PEG, or *t*-butoxyPEG (*t*-BuO-PEG) conjugates of human serum albumin, human interferon-α, or porcine uricase as adjuvant emulsions. Assay plates for enzyme-linked immunosorbent assays (ELISAs) were coated with mPEG, HO-PEG, or *t*-BuO-PEG conjugates of the non-cross-reacting protein, porcine superoxide dismutase (SOD). In sera from rabbits immunized with HO-PEG conjugates of interferon-α or uricase, the ratio of titers of anti-PEG antibodies detected on mPEG-SOD over HO-PEG-SOD ("relative titer") had a median of 1.1 (range 0.9−1.5). In contrast, sera from rabbits immunized with mPEG conjugates of three proteins had relative titers with a median of 3.0 (range 1.1−20). Analyses of sera from rabbits immunized with *t*-BuO-PEG-albumin showed that *t*-butoxy groups are more immunogenic than methoxy groups. Adding Tween 20 or Tween 80 to buffers used to wash the assay plates, as is often done in ELISAs, greatly reduced the sensitivity of detection of anti-PEG antibodies. Competitive ELISAs revealed that the affinities of antibodies raised against mPEG-uricase were c. 70 times higher for 10 kDa mPEG than for 10 kDa PEG diol and that anti-PEG antibodies raised against mPEG conjugates of three proteins had >1000 times higher affinities for albumin conjugates with c. 20 mPEGs than for analogous HO-PEG-albumin conjugates. Overall, these results are consistent with the hypothesis that antibodies with high affinity for methoxy groups contribute to the loss of efficacy of mPEG conjugates, especially if multiply-PEGylated. Using monofunctionally activated HO-PEG instead of mPEG in preparing conjugates for clinical use might decrease this undesirable effect.



INTRODUCTION

Less than a decade after the first reports of the advantages of coupling proteins to the "non-immunogenic" polymer, poly(ethylene glycol) (PEG),[1−3] Richter and Åkerblom provided evidence for the induction of anti-PEG antibodies in rabbits exposed to methoxyPEG (mPEG) conjugates of proteins[4] and for the presence of anti-PEG antibodies in the sera of a small percentage of healthy blood donors.[5] Nevertheless, during more than three decades of research and the approval for clinical use of numerous PEGylated proteins and other PEGylated therapeutic agents, relatively few research groups have focused on the immunogenicity and antigenicity of the polymer component of PEGylated drugs (reviewed by Armstrong[6] and by Su et al.[7]). Since all of the approved PEGylated drugs, including proteins,[8−10] an aptamer,[11] and "stealth" liposomes,[12] contain mPEG, the role of the methoxy group of mPEG in the immune responses to PEGylated drugs and the potential advantages of using hydroxyPEG (HO-PEG), rather than mPEG, have been of particular interest in our research[13,14] (see Figure 1).

In a series of research reports and patents that have been published since 1999, Roffler, Cheng, and their colleagues described the development of a series of mouse monoclonal antibodies (mAbs) directed against the backbone of PEG.[7,15−21] They demonstrated the utility of such mAbs for the sensitive detection and quantitation of PEGylated drugs[7,18] and for the removal of potentially toxic PEGylated drugs from the circulation.[7,18−21] Several of these mAbs are available commercially from Abnova (Taipei City, Taiwan). Murine and rabbit anti-PEG mAbs and assay kits incorporating anti-PEG mAbs are now available from several other companies (e.g., ANP Technologies, Newark, DE; Epitomics, Burlingame, CA; Life Diagnostics, Inc., West Chester, PA; Meridian Life Science, Inc., Saco, ME; Silver Lake Research Corp., Monrovia, CA). The majority of these mAbs are directed against the PEG backbone, but at least one of them is directed against the methoxy group of mPEG (Epitomics, Clone PEG-B-47).

Other research groups have investigated the roles of polyclonal anti-PEG antibodies elicited in experimental animals and patients in altering the pharmacokinetics and pharmacodynamics of PEGylated agents that have been approved for

Received: October 11, 2011
Revised: February 1, 2012
Published: February 14, 2012

ACS Publications © 2012 American Chemical Society

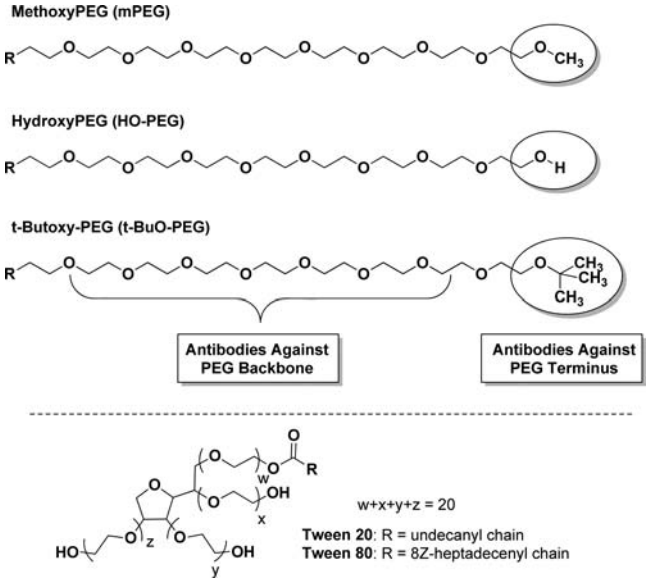
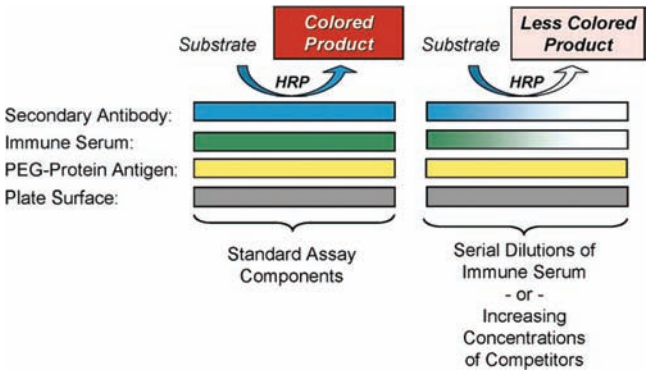


Figure 1. Partial structures of methoxyPEG, hydroxyPEG, and *t*-butoxyPEG and structures of Tween 20 and Tween 80. In the structures of the PEGs, R designates the rest of the polymer, including the proximal terminal group that reacts with the protein to form PEG conjugates; the domains that may serve as epitopes for the formation of anti-PEG antibodies, namely, the distal terminal groups (in shaded ovals) and the PEG backbone, are indicated. In the structures of Tween 20 and Tween 80, R designates the alkyl groups of the fatty acids that distinguish these two detergents from each other (lauric and oleic acids, respectively); 8Z designates the configuration around the double bond in the heptadecenyl chain.

clinical use or are in development. These include PEGylated red blood cells[22,23] and PEGylated liposomes,[24−29] as well as PEGylated proteins (reviewed by Armstrong[6]). Various techniques have been used to detect and characterize such antibodies, but the most widely used methods are enzyme-linked immunosorbent assays (ELISAs). These are used in various formats, including direct ELISAs and competitive ELISAs (see Scheme 1). In direct ELISAs, the independent variable is the dilution of immune serum. In competitive ELISAs, a single dilution of serum is tested in the presence of increasing concentrations of competitors, such as unconjugated PEGs or PEG-protein conjugates. In many publications and patents in which anti-PEG antibodies are measured by ELISAs, at least some of the washes of the assay plates contain Tween 20 or Tween 80 (polyoxyethylene sorbitan monolaurate or polyoxyethylene sorbitan monooleate, respectively).[7,19−21,30−32] Therefore, we investigated the effects of these PEG-containing detergents on the titers of anti-PEG antibodies detected by direct ELISAs (see Figures 1 and 5).

Since the terms antigenicity and immunogenicity are sometimes used imprecisely, it seems useful to specify that, in this report, immunogenicity refers to the ability of substances, e.g., protein conjugates of mPEG, HO-PEG, or *t*-butoxyPEG (*t*-BuO-PEG), to induce the production of antibodies in experimental animals or in humans. In contrast, antigenicity refers to the abilities of various substances, e.g., unconjugated PEGs or PEG-protein conjugates, to bind to anti-PEG antibodies to which they are exposed in vitro (see Scheme 1). In this research, the immunogens were conjugates of recombinant human interferon-α (IFN-α), porcine uricase, or human serum albumin (albumin), which contained between 1 and 17 molecules of PEG per protein

Scheme 1. Schematic of Enzyme-Linked Immunosorbent Assays (ELISAs) for Determining the Titer of Anti-PEG Antibodies by Direct ELISAs, Using Serial Dilutions of Serum from Immunized Rabbits, or for Determining the Relative Affinities of Binding to Various Competitors, Such as Free PEGs or PEG-Protein Conjugates, Using a Constant Dilution of Serum and Increasing Concentrations of the Competitors[a]



[a]Linkage of the secondary antibody (goat-anti-rabbit IgG) to horseradish peroxidase (HRP) enables colorimetric quantitation of the binding of the primary antibody to the assay plate.

molecule or subunit. The antigens used to coat the assay plates were conjugates of an unrelated protein, porcine Cu−Zn superoxide dismutase (SOD), to which the same small number of molecules of mPEG, HO-PEG, or *t*-BuO-PEG of the same size (10 kDa) were coupled using the same activation chemistry. In competitive ELISAs, the competitors were free mPEG, HO-PEG, or *t*-BuO-PEG or conjugates of albumin containing an average of c. 20 molecules of mPEG or HO-PEG per molecule of albumin.

Finally, since the results of the immunologic studies described herein are consistent with the hypothesis that PEG-protein conjugates synthesized with monofunctionally activated HO-PEG might be less antigenic and/or less immunogenic than the analogous mPEG conjugates, we performed experiments to compare the potencies in cell culture of analogous mPEG and HO-PEG conjugates of two recombinant human cytokines.

EXPERIMENTAL PROCEDURES

Reagents and Supplies. Reagents were from Sigma-Aldrich Chemical Co. (St. Louis, MO) unless otherwise noted. PEG molecular weight standards and 10 kDa mono-*t*-butoxyPEG were from Polymer Laboratories (Shropshire, UK, now part of Agilent Technologies, Santa Clara, CA). Other PEGs were from NOF Corporation (Tokyo, Japan), Shearwater Polymers (Huntsville, AL, now part of Nektar Therapeutics, San Francisco, CA) or SunBio (Anyang City, South Korea), as indicated. Human interferon-α-2b (IFN-α) was from Tianjin Hualida Bioengineering Co. (Tianjin, China). Erythropoietin BRP European Pharmacopoeia Reference Standard (35 280 IU/0.25 mg) and Mircera (100 μg/0.3 mL, Roche) were obtained from Bioassay GmbH (Heidelberg, Germany). Recombinant human erythropoietin-α (EPO, CYT-201) that was used for the synthesis of PEG conjugates was from ProSpec (Rehovot, Israel). Recombinant porcine uricase was from Bio-Technology General Ltd. (Rehovot, Israel, now part of Ferring S.A., Saint-Prex, Switzerland). Recombinant human granulocyte-macrophage colony-stimulating factor (GM-CSF) was obtained from Berlex

dx.doi.org/10.1021/bc200551b | *Bioconjugate Chem.* 2012, 23, 485−499

Biosciences (Richmond, CA). Plasbumin25 from Bayer Biological Products (Elkhart, IN) was used as human serum albumin. Daudi cells and TF-1 cells were from ATCC (Manassas, VA). Goat serum and most reagents used for cell culture were from GIBCO (now part of Invitrogen/Life Technologies, Carlsbad, CA). Alamar Blue, used for cell culture assays, Novex NuPAGE gels and Sypro Ruby were also from Invitrogen. Microplates used for fluorometric assays of cell growth were from Greiner Bio-One North America, Inc. (Monroe, NC). Immulon 2 HB microplates used for ELISAs were from Thermo Scientific (Rochester, NY). Trifluoroacetic acid (TFA) was from Supelco (Bellefonte, PA). Nonfat dry milk solids were from Western Family (Portland, OR). Spectra/Por 1 dialysis tubing was from Spectrum Laboratories (Rancho Dominguez, CA).

PEGylation Reagents and PEG-Protein Conjugates Used as Immunogens, Antigens, and Competitors in Immunologic Assays and in Cell Culture Assays. Table 1 summarizes the reagents used to immunize the rabbits and as antigens or competitors in the ELISAs. Details about the synthesis, purification, and physicochemical analyses of (1) the activated HO-PEGs and *t*-BuO-PEG; (2) the PEG-protein conjugates listed in Table 1, and (3) the HO-PEG conjugate of erythropoietin used in the cell culture assays are provided in the Supporting Information, which includes seven figures, numbered S1 through S7.

Table 1. Reagents Used as Immunogens and as Antigens and Competitors in ELISAs

Immunogens			
	polymer component		
protein component	end group	PEG M.W.	# of PEGs
human interferon-α	methoxy	20 kDa	1
		20 kDa	2
	hydroxy	20 kDa	1
		20 kDa	2
porcine uricase	methoxy	10 kDa	2.3[a]
	hydroxy	10 kDa	2.3[a]
human serum albumin	methoxy	10 kDa	17
	t-butoxy	10 kDa	17
Antigens			
	polymer component		
protein component	end group	PEG M.W.	# of PEGs
porcine superoxide dismutase (SOD)	methoxy	10 kDa	2.5[b]
	hydroxy	10 kDa	2.5[b]
	t-butoxy	10 kDa	2.5[b]
human interferon-α	(No PEG)		
Competitors			
free polymers	mPEG		10 kDa
			20 kDa
	PEG Diol		10 kDa
			20 kDa
	polymer component		
PEG-albumin conjugates	end group	PEG M.W.	# of PEGs
	methoxy	10 kDa	17–19
	hydroxy	10 kDa	17–22

[a]Number of PEGs per uricase subunit. [b]Number of PEGs per SOD subunit.

Determination of the Number of PEG Molecules Coupled per Protein Molecule. Size-exclusion chromatography (SEC) was performed on Superdex 200 or TSK G-5000PW$_{XL}$ columns from which the eluates were monitored by both UV absorbance and refractive index (RI). Peaks containing PEG-protein conjugates were analyzed by the method of Kunitani et al.[33] This method was used to characterize PEG conjugates of SOD, IFN-α, EPO, recombinant porcine uricase, and human serum albumin (albumin). These conjugates contained between 1 and 22 molecules of PEG per protein molecule or subunit. For conjugates of SOD, IFN-α, EPO, and uricase coupled to fewer than c. 5 molecules of PEG per protein subunit, the results for the PEG-to-protein ratio calculated from the SEC elution profiles were confirmed by polyacrylamide gel electrophoresis in the presence of sodium dodecyl sulfate (SDS-PAGE) on Novex NuPAGE gels. Replicate gels were stained for protein with Coomassie blue R-250 or Sypro Ruby and for PEG with a solution of KI and I_2 mixed with $BaCl_2$, by an adaptation of the method of Skoog.[34]

Animals and Immunizations. Eight groups of three rabbits were immunized with a PEG conjugate of one of the following proteins: IFN-α, porcine uricase, or human serum albumin. Specific pathogen-free New Zealand white rabbits were injected with PEGylated immunogens on days 0, 7, 14, 28, 56, and 84. The first immunization was in complete Freund's adjuvant. Subsequent immunizations were in incomplete Freund's adjuvant. Blood was collected prior to immunization (prebleed) and 6, 10, and 14 weeks after the first immunization (Bleeds 1, 2, and 3). Serum was prepared from each bleed by centrifugation and was kept frozen at −40 °C until use. All rabbit procedures were performed at Lampire Biological Laboratories (Pipersville, PA) by AAALAC-certified technicians in accordance with IACUC-approved protocols.

Direct Enzyme-Linked Immunosorbent Assays (Direct ELISAs). The PEGylated antigens used in direct ELISAs consisted of conjugates of SOD with 10 kDa mPEG, 10 kDa HO-PEG, or 10 kDa *t*-BuO-PEG that were synthesized, purified, and analyzed as described in the Supporting Information. The conjugates contained an average of c. 2−3 molecules of PEG per 16 kDa subunit of SOD. Concentrations of PEGylated antigens are expressed as protein concentrations (μg/mL). For most experiments, 100 μL of a solution of PEGylated SOD (10 μg/mL) prepared in 0.1 M sodium carbonate buffer, pH 10.3, was used to coat each well of the 96-well plates. When IFN-α was used as the antigen, 100 μL of a solution of 10 μg/mL of IFN-α in sodium carbonate buffer was placed in the wells, corresponding to 1 μg/well.

Immulon 2 HB 96-well microplates were coated with IFN-α or PEG-SOD by incubation overnight at 4 °C. Removal of unbound antigen and all washes of the plates were performed with a Denley Wellwash 4 plate washer (Needham Heights, MA). After removal of unbound antigen, the wells were washed three times with phosphate-buffered saline (PBS) and then incubated for 1 h at room temperature with 300 μL/well of Blocking Buffer (5% (w/v) nonfat dry milk solids in PBS). After removal of the Blocking Buffer, the plates were washed three times with PBS. Serial dilutions of rabbit sera in PBS containing 2% (v/v) goat serum (PBS-G) were added to the plates (100 μL/well), which were incubated for 1 h at 37 °C. The plates were then washed three times with PBS. No detergents such as Tween 20 or Tween 80 were included in the wash buffers except as indicated in Figure 5.

Goat anti-rabbit IgG (H & L chain specific) (1 mg/mL) conjugated to horseradish peroxidase (HRP) was used as the secondary antibody (Sigma) (see Scheme 1). For most assays,

dx.doi.org/10.1021/bc200551b | *Bioconjugate Chem.* 2012, 23, 485−499

the secondary antibody was diluted 1/10 000 in PBS-G, so that 100 μL/well contained 0.01 μg of antibody protein. If the peroxidase activity detected under the conditions described below was too high to obtain a linear increase in absorbance for at least 4 min, the secondary antibody was diluted 1/15 000 or 1/20 000 in PBS-G in subsequent experiments. After addition of the secondary antibody, the plates were incubated for 45 min at 37 °C. The plates were washed three times with PBS before the addition of 200 μL/well of peroxidase substrate, which was *o*-phenylenediamine dihydrochloride[35] (OPD), purchased as SIGMA*FAST* OPD. The substrate solution was prepared as close as possible to the time of use and stored briefly at room temperature, shielded from light. The substrate consists of two tablets (one OPD tablet and one urea hydrogen peroxide/buffer tablet), which were dissolved in 21 mL of water. This solution was filtered through a 0.2 μm syringe filter (Acrodisc 25 mm Syringe Filter, Pall Corporation, Ann Arbor, MI). The absorbance at 440 nm of the colored conjugate formed with peroxide was measured in a SpectraMax 250 microplate reader (Molecular Devices, Sunnyvale, CA) in kinetic mode for 6 min at 12 s intervals. The assay plate was shaken in the plate reader for 15 s before the first reading and for 3 s before each subsequent reading of the plate (see Scheme 1).

Competitive ELISAs. As in the direct ELISAs, Immulon 2 HB 96-well microplates were coated with mPEG-SOD, HO-PEG-SOD, or *t*-BuO-PEG-SOD by incubation overnight at 4 °C with 100 μL/well of antigens at 10 μg/mL in 0.1 M sodium carbonate buffer, pH 10.3. After removal of unbound antigen and three washes with PBS, the plates were blocked for 1 h at room temperature with 300 μL/well of Blocking Buffer. The plates were washed three times with PBS. Serial dilutions of the competitors in PBS-G (50 μL/well) were added to the wells, followed by 50 μL/well of diluted rabbit serum in PBS-G. Dilutions of sera used for competitive ELISAs were calculated to correspond to the highest dilution factor that provided maximal binding in direct ELISAs. Therefore, for competitive ELISAs, sera with higher titers were diluted more extensively than sera with lower titers. The dilution factors, which are indicated in the legends of Figures 6–8 and Figure 9B, ranged from 1/320 to 1/10 000. Samples were mixed by shaking the plate in the plate reader for 10 s before it was incubated for 1 h at 37 °C. After removal of unbound reactants, the plates were washed three times with PBS. The addition of secondary antibody, washing of plates, addition of HRP substrate, and monitoring of absorbance of the colored product were performed as described above for direct ELISAs.

Analysis of Data from ELISAs. The rates of increase in absorbance at 440 nm during the period of measurement were exported from the SpectraMax plate reader into Microsoft *Excel*. Usually, the increase in absorbance was linear during the first 4 min of measurements, with a correlation coefficient (R^2) greater than 0.98. For direct ELISAs, the rates (in milli-absorbance units/min) were graphed against the $\log_{10}$ of the serum dilution. For competitive ELISAs, the rates were graphed against the $\log_{10}$ of the final concentration of each competitor, in units of micromolar PEG.

Data in colorimetric assay units (mAU/min) were first analyzed as a function of the $\log_{10}$ of the serum dilution (direct ELISAs) or the $\log_{10}$ of the competitor concentration (competitive ELISAs) using *DPlot* software (HydeSoft Computing, LLC, Vicksburg, MS) to obtain the best fit to a sigmoid curve, using the equation

$$y = A + B/\left[1 + 10^{(C+Dx)}\right]$$

The results in colorimetric assay units were converted to percent of the maximal binding by subtracting A (the minimal value), dividing by B (the range of values), and multiplying by 100. The resultant values of the percent of the maximal binding in direct and competitive ELISAs were plotted against the $\log_{10}$ of serum dilution or the $\log_{10}$ of competitor concentration, respectively.

For direct ELISAs, the values of the parameters C and D from *DPlot* were used to calculate the dilution of serum corresponding to half-maximal binding of the antibodies to the assay plate (D_{50}), using the equation

$$D_{50} = 10^{(-C/D)}$$

The ratio of the values of D_{50} obtained when the same antiserum was tested against mPEG-SOD and against HO-PEG-SOD (at the same antigen concentration) was used as a measure of the relative titer against the two types of PEG (see Figures 2–4 and Table 2).

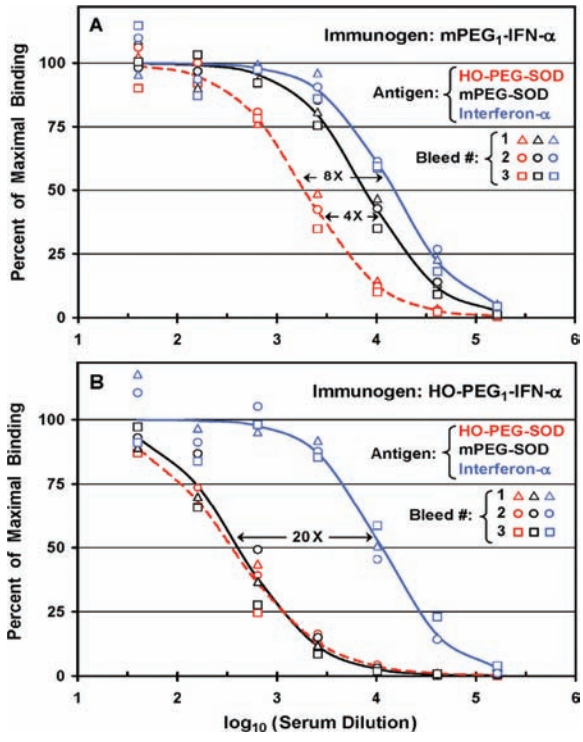


Figure 2. Titers of antibodies to HO-PEG, mPEG, and interferon-α were determined by direct ELISAs of sera prepared from each of three monthly bleeds of rabbits immunized with either $mPEG_1$-IFN-α (A) or $HO\text{-}PEG_1$-IFN-α (B). (A) Anti-PEG antibodies were measured on assay plates coated with 2 μg/well of superoxide dismutase (SOD) coupled to either 10 kDa HO-PEG (red symbols) or 10 kDa mPEG (black symbols). Anti-IFN-α antibodies were measured on assay plates coated with 1 μg/well of recombinant human IFN-α (blue symbols). Mean values in sera from Bleeds 1, 2, and 3 were calculated from results obtained with HO-PEG-SOD (red dashed line), mPEG-SOD (black solid line), or IFN-α (blue solid line) as the antigen. Black arrows indicate the ratios of titers detected against the various antigens. (B) Sera from Bleeds 1, 2, and 3 of a rabbit immunized with $HO\text{-}PEG_1$-IFN-α were analyzed in the same way as described for (A).

dx.doi.org/10.1021/bc200551b | *Bioconjugate Chem.* 2012, 23, 485–499

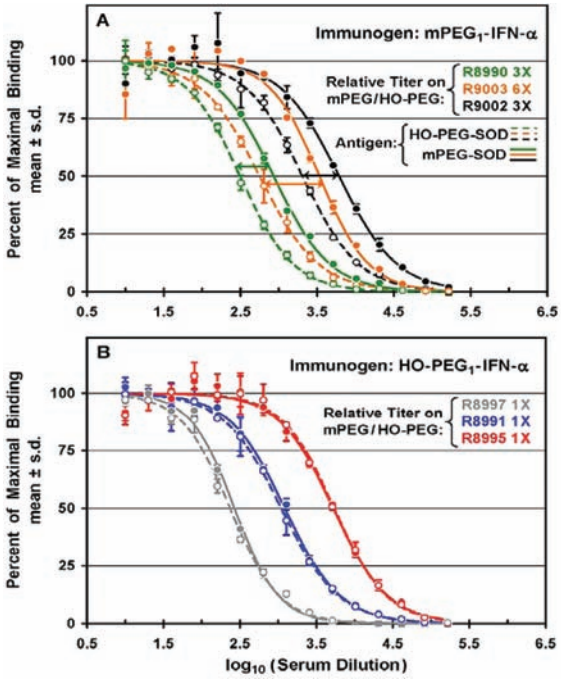


Figure 3. Titers of antibodies against mPEG and against HO-PEG were determined by direct ELISAs of sera from groups of three rabbits immunized with either $mPEG_1$-IFN-α (A) or HO-PEG_1-IFN-α (B). (A) Percentages of maximal binding to mPEG-SOD (filled symbols, solid curves) and to HO-PEG-SOD (open symbols, dashed curves) and the ratio of titers on mPEG/HO-PEG ("relative titers") are indicated for three rabbits immunized with $mPEG_1$-IFN-α. Data for each of rabbits R8990, R9002, and R9003 are shown in green, black, and orange, respectively. (B) Percentages of maximal binding to mPEG-SOD (filled symbols, solid curves) and to HO-PEG-SOD (open symbols, dashed curves) and the ratio of titers on mPEG/HO-PEG are indicated for three rabbits immunized with HO-PEG_1-IFN-α. Data for each of rabbits R8991, R8995, and R8997 are shown in blue, red, and gray, respectively.

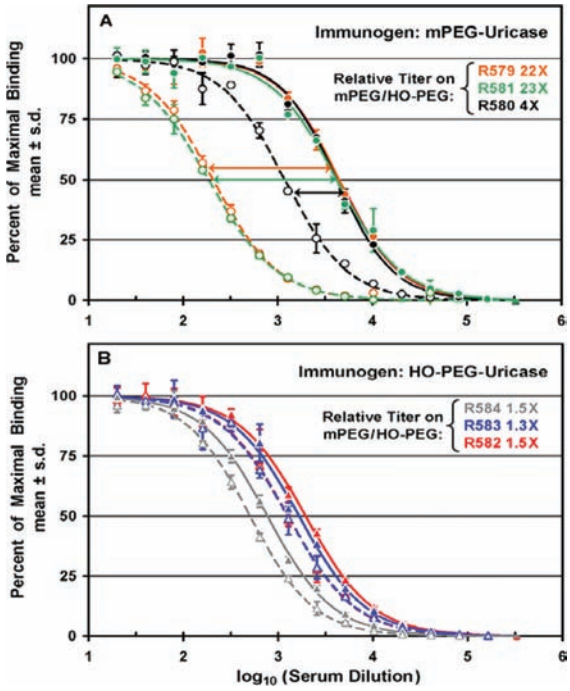


Figure 4. Titers of antibodies against mPEG and HO-PEG in sera from groups of three rabbits immunized with mPEG-uricase (A) or HO-PEG-uricase (B) were determined by direct ELISAs. PEG-uricase conjugates used as immunogens contained an average of 2.3 molecules of 10 kDa mPEG or HO-PEG per uricase subunit. (A) Percentages of maximal binding to mPEG-SOD (filled symbols, solid curves) and to HO-PEG-SOD (open symbols, dashed curves) and the relative titers on mPEG/HO-PEG are indicated for three rabbits immunized with mPEG-uricase. Data for each of rabbits R579, R580, and R581 are shown in orange, black, and green, respectively. (B) Percentages of maximal binding to mPEG-SOD (filled symbols, solid curves) and to HO-PEG-SOD (open symbols, dashed curves) and the relative titers on mPEG/HO-PEG are indicated for three rabbits immunized with HO-PEG-uricase. Data for each of rabbits R582, R583, and R584 are shown in red, blue, and gray, respectively.

For competitive ELISAs, the values of the parameters C and D from *DPlot* were used to calculate the competitor concentration that inhibited 50% of the binding of the antibodies to the antigen on the plate (IC_{50}), using the equation

$$IC_{50} = 10^{(-C/D)}$$

The ratio of the values of IC_{50} for two competitors assayed at the same dilution of a particular serum provides a measure of the relative affinities of the antibodies being tested for those competitors (see Figures 6–8 and 9B).

Cell Culture Assay of the Potencies of Interferon-α and PEG Conjugates. Interferon-α and four PEG-IFN-α conjugates were assayed for their abilities to inhibit the proliferation of Daudi cells, measured by a fluorometric assay with Alamar Blue as the indicator.[36,37] Daudi cells are human lymphoblastic B cells derived from a male patient with Burkitt's lymphoma.[38] The growth medium was RPMI 1640 with 2 mM L-glutamine containing 10% fetal bovine serum, 10 mM HEPES buffer, 1.5 g/L sodium bicarbonate, 1 mM sodium pyruvate, 1% (v/v) Pen/Strep. and 5.4 g/L D-(+)-glucose. All components of the medium were from GIBCO except for glucose, which was from Sigma-Aldrich. The cells were grown at 37 °C in humidified air containing 5% CO_2, with twice-weekly passages.

Cells in the log-phase of growth (150 μL of a suspension in growth medium of 250 000 cells/mL) were incubated for 4 h at 37 °C in humidified air containing 5% CO_2 in 96-well, flat, clear-bottom, black microplates. Serial dilutions in growth medium (50 μL) of IFN-α or mPEG-IFN-α or HO-PEG-IFN-α were added to the cells in the assay plates, which were incubated for 72 h under the same conditions as for growth. Alamar Blue (20 μL) was then added, and the incubation was continued for 4 h. The assay plates were shaken for 30 s on a JitterBug orbital shaker (Boekel Scientific, Feasterville, PA) both after the addition of the serial dilutions of IFN-α or the PEG conjugates and after the addition of Alamar Blue. The fluorescent signal was measured at excitation and emission wavelengths of 544 and 589 nm, respectively, in a fluorescence plate reader (Fluoroskan Ascent Model with *Ascent* software, Thermo Labsystems, Waltham, MA).

As in the analysis of data from ELISAs, data for cell growth in relative fluorescence units as a function of the concentration of IFN-α or PEG-IFN-α were analyzed using *DPlot* software to fit the equation

$$y = A + B/\left[1 + 10^{(C+Dx)}\right]$$

Using the minimal value (A) and the range of values (B) from the initial *DPlot*, the data were converted to Percent of Inhibitable Cell Growth, as shown in Figure 10A.

dx.doi.org/10.1021/bc200551b | *Bioconjugate Chem.* 2012, 23, 485–499

Table 2. Relative Titers of Antibodies Detected with mPEG-SOD/HO-PEG-SOD as the Antigen in Sera from Bleeds 2 and/or 3 of 23 Rabbits Immunized with Eight PEGylated Protein Immunogens

			relative titer					relative titer		
protein of immunogen	mPEG/protein (PEG M.W.)	rabbit #	mean	s.d.	*n*	HO-PEG/protein (PEG M.W.)	rabbit #	mean	s.d.	*n*
Human Interferon-α	1 (20 kDa)	R8990	3.0	0.8	4	1 (20 kDa)	R8991	1.1	0.1	2
		R9002	3.0	0.3	4		R8995	1.0	0.03	2
		R9003	4.8	0.9	5		R8997	0.9	0.2	4
Human Interferon-α	2 (20 kDa)	R8993	2.7	0.5	4	2 (20 kDa)	R8992	0.9	0.2	2
		R9001	5.5	1.0	4		R8994	1.1	0.2	2
		R9004[a]					R9000	0.9	0.1	2
Porcine Uricase	2.3/subunit (10 kDa)	R579	20	4.8	4	2.3/subunit (10 kDa)	R582	1.3	0.2	3
		R580	3.1	0.6	3		R583	1.1	0.2	3
		R581	18	4.8	5		R584	1.5	0.1	3
Human Serum Albumin	17 (10 kDa)	R12056	3.0	0.5	4					
		R12057	1.1	0.1	3					
		R12058	2.6	0.6	3					
		Median	*3.0*				*Median*	*1.1*		
		Range	*1.1–20*				*Range*	*0.9–1.5*		
	t-BuO-PEG/protein (PEG M.W.)									
Human Serum Albumin	17 (10 kDa)	R12059	1.8	0.5	2					
		R12060	1.2	0.2	2					
		R12061	1.7	0.3	2					

[a]Rabbit R9004 died before Bleed 2.

Cell Culture Assay of the Potencies of Erythropoietin and PEG Conjugates. The effects of EPO and of mPEG and HO-PEG conjugates of EPO on the proliferation of TF-1 cells were assessed using a fluorometric assay with Alamar Blue, as described above for the assay of IFN-α and its PEG conjugates using Daudi cells. TF-1 cells are factor-dependent erythroblastic cells derived from the bone marrow of a male patient with erythroleukemia.[39,40] Cells were cultured at 37 °C in humidified air containing 5% CO_2 in the same growth medium as used for Daudi cells, except that the growth medium for TF-1 cells was supplemented with 2.4 ng/mL GM-CSF.

TF-1 cells were collected in the log phase of growth and were centrifuged for 10 min at 1000 rpm at 4 °C. The supernatant was removed and the pellet was resuspended twice in 10 mL of assay medium, which is growth medium without added GM-CSF, to minimize the residual concentration of GM-CSF. Cells (100 μL of a suspension in assay medium of 100 000 cells/mL) were mixed with 100 μL of serial dilutions of growth factors (EPO or PEG-EPO conjugates) in assay medium in the wells of a 96-well, flat, clear-bottomed, black microplate. The cells were cultured for 72 h at 37 °C in humidified air containing 5% CO_2. Alamar Blue (25 μL) was then added and the incubation was continued for 6 h. The plates were shaken for 30 s on a JitterBug orbital shaker after the addition of the cell suspension to the growth factor dilutions and after the addition of Alamar Blue. The fluorescent signal was measured in a fluorescence plate reader, as described above for the Daudi cell assay. Data in relative fluorescence units were analyzed using *DPlot* software and the same equation shown above for the analysis of data from the Daudi cell assay. Using the minimal value (A) and range of values (B) from the initial *DPlot*, the data were converted to Percent of Maximal Cell Growth, as shown in Figure 10B.

RESULTS

Immune Responses to MonoPEG Conjugates of mPEG-Interferon-α and HO-PEG-Interferon-α Differ throughout Immunization. Direct ELISAs were performed on sera from three successive monthly bleeds of two rabbits immunized with either $mPEG_1$-IFN-α (Figure 2A) or $HO\text{-}PEG_1$-IFN-α (Figure 2B), using assay plates coated with mPEG-SOD, HO-PEG-SOD, or IFN-α (see Scheme 1). Chromatographic analyses of the PEG conjugates of SOD and IFN-α are provided in Figures S3 and S4 of the Supporting Information, respectively.

The titers of antibodies detected after immunization with IFN-α coupled to one molecule of 20 kDa mPEG ($mPEG_1$-IFN-α) were highest with IFN-α as the antigen, somewhat lower with mPEG-SOD, and lowest for HO-PEG-SOD as the antigen (Figure 2A). There were no significant differences among the results obtained with sera from Bleeds 1, 2, and 3 of this rabbit (represented by triangles, circles, and squares, respectively). Analogous data for sera from three bleeds of a rabbit immunized with IFN-α coupled to one molecule of 20 kDa HO-PEG ($HO\text{-}PEG_1$-IFN-α) are shown in Figure 2B. In this case, the titers of anti-PEG antibodies detected with mPEG-SOD and HO-PEG-SOD as the antigens were indistinguishable from each other and were about 20 times lower than the titer of antibodies detected against IFN-α. As in Figure 2A, there were no significant differences among the results obtained with sera prepared from Bleeds 1, 2, or 3 of this rabbit, which was immunized with $HO\text{-}PEG_1$-IFN-α.

In contrast with the results in Figure 2, for 1 of the 23 rabbits used in this research (R9003, which was immunized with $mPEG_1$-IFN-α), the titers of anti-PEG antibodies detected in serum from Bleed 1 were lower than those detected in sera from subsequent bleeds (data not shown). Therefore, all subsequent experiments were performed on sera from Bleed 2 and/or Bleed 3 of each rabbit, which gave similar results for all tested parameters.

Rabbits Immunized with $mPEG_1$-Interferon-α, but not with $HO\text{-}PEG_1$-Interferon-α, Have Higher Titers of Anti-PEG Antibodies Detected with mPEG-SOD than with HO-PEG-SOD. In the sera of three rabbits immunized with $mPEG_1$-IFN-α, a relatively narrow range of titers of antibodies was detected with mPEG-SOD as the antigen (solid curves in Figure 3A) and a slightly wider range of lower titers of

dx.doi.org/10.1021/bc200551b | *Bioconjugate Chem.* 2012, 23, 485–499

antibodies was detected with HO-PEG-SOD (dashed curves in Figure 3A). The highest titer of anti-PEG antibodies detected with mPEG-SOD (in serum from rabbit R9002) was c. 7 times higher than the lowest titer (in serum from rabbit R8990). For each serum sample, the ratio of the titers detected with mPEG-SOD to those detected with HO-PEG-SOD is referred to in this report as the "relative titer". Among the three rabbits in this experiment, the relative titers varied from 3 to 6 (indicated as 3× and 6×, respectively, in Figure 3A).

In sera from each of three rabbits immunized with HO-PEG_1-IFN-α, the titers of anti-PEG antibodies detected with mPEG-SOD as the antigen (solid curves in Figure 3B) and with HO-PEG-SOD as the antigen (dashed curves in Figure 3B) were indistinguishable from each other. This was true although the absolute titers of anti-PEG antibodies in the serum with the highest titer (from rabbit R8995) were c. 20 times those in the serum with the lowest titer (from rabbit R8997).

Rabbits Immunized with Multiply-PEGylated mPEG-Uricase, but not HO-PEG-Uricase, Have Higher Titers of Anti-PEG Antibodies Detected with mPEG-SOD than with HO-PEG-SOD. Direct ELISAs similar to those shown in Figure 3 were performed on sera from groups of three rabbits immunized with mPEG or HO-PEG conjugates of porcine uricase in which an average of 2.3 molecules of 10 kDa PEG were coupled per uricase subunit (see Figure S6). This extent of PEGylation corresponds to an average of about nine molecules of PEG per uricase tetramer, which is the active form of the enzyme.[14] The titers of anti-PEG antibodies for all three rabbits immunized with this mPEG-uricase conjugate were indistinguishable when tested on assay plates coated with mPEG-SOD (note the superposition of the three solid curves in Figure 4A). However, there were differences among the titers of antibodies detected in the same sera with HO-PEG-SOD as the antigen (dashed curves). The relative titers of antibodies against mPEG/HO-PEG varied from c. 4-fold for rabbit R580 to >20-fold for rabbits R579 and R581.

In sera from three rabbits immunized with HO-PEG-uricase, the titers of antibodies detected against either mPEG or HO-PEG were nearly indistinguishable (Figure 4B). The relative titers of antibodies against mPEG/HO-PEG varied only from about 1.3 to 1.5 in this experiment, in contrast with the much higher relative titers shown in Figure 4A.

Most Rabbits Immunized with mPEG Conjugates of Three Proteins Have Higher Titers of Anti-PEG Antibodies Detected with mPEG-SOD than with HO-PEG-SOD, Unlike Those Immunized with HO-PEG-Proteins. The results obtained in replicate analyses (between 2 and 5), similar to those shown in Figures 2–4, of sera from 23 of the 24 rabbits immunized for this study are summarized in Table 2. Since rabbit R9004 died before Bleed 2, no data for that rabbit are included in the table.

On the basis of the mean values of the relative titers for all 11 rabbits immunized with mPEG conjugates of three proteins, the median value of the relative titer was 3.0, with a range of 1.1–20. In contrast, each of nine rabbits immunized with HO-PEG conjugates of IFN-α or uricase had similar titers of anti-PEG antibodies detected on mPEG and HO-PEG antigens.

Sensitivity of Detection of Anti-PEG Antibodies Is Decreased by Tween 20 or Tween 80. Many procedures commonly used for the performance of direct or competitive ELISAs include the use of the detergents Tween 20[7,19–21,30,31] or Tween 80[32] in the solutions with which the assay plates are washed one or more times. The structures of these detergents are shown in Figure 1. Two of the experiments performed to assess the effects of Tween 20 or Tween 80 on the titers of anti-PEG antibodies detected by direct ELISAs are shown in Figure 5.

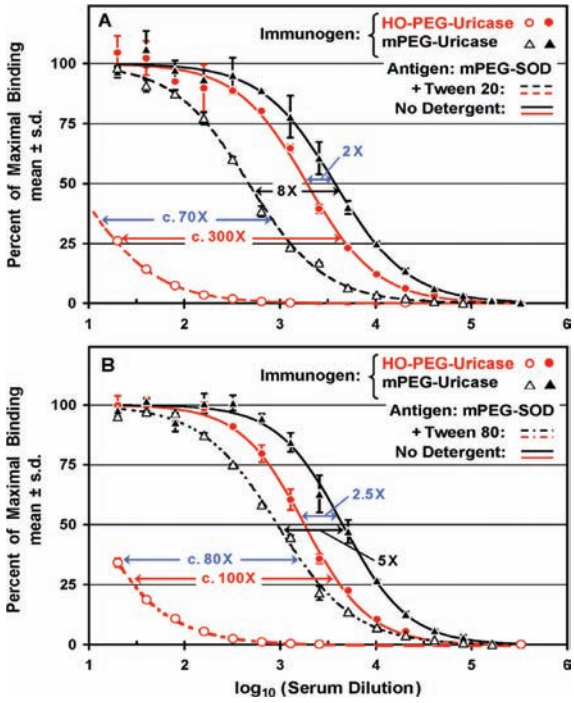


Figure 5. Washing the assay plate with Tween 20 or Tween 80, detergents that contain HO-PEG, decreased the titers detected by direct ELISAs of sera from rabbits immunized with HO-PEG-uricase (○, ●) or mPEG-uricase (Δ, ▲) and amplified the differences between the titers of anti-PEG antibodies detected in sera from these two rabbits. Direct ELISAs with mPEG-SOD as the antigen were performed as described in Experimental Procedures, except that the PBS used to wash one of the replicate assay plates before and after the addition of the enzyme-linked secondary antibody contained either 0.05% (v/v) Tween 20 (A) or 0.1% (v/v) Tween 80 (B). Higher titers were detected in the absence of detergent (filled symbols, solid curves) than in the presence of Tween (open symbols, dashed curves). The effects of each type of Tween on the results for the individual rabbits immunized with either HO-PEG-uricase or mPEG-uricase are shown by red arrows and black arrows, respectively. The ratios of titers detected in sera from these two rabbits in the presence or absence of Tween are shown by blue arrows.

Sera from two rabbits immunized with either mPEG-uricase or HO-PEG-uricase were tested in direct ELISAs on replicate assay plates coated with mPEG-SOD. In each experiment, one of the assay plates was washed without any detergent, as was done in all of the other ELISAs described in this report. The other assay plate was washed before and after the addition of the secondary antibody with PBS containing either 0.05% (v/v) Tween 20 (Figure 5A) or 0.1% (v/v) Tween 80 (Figure 5B).

When the assays were performed without the use of Tween in the washes (solid curves), the titer of anti-PEG antibodies detected in the serum of the rabbit immunized with mPEG-uricase was only 2–2.5 higher than that of the rabbit immunized with HO-PEG-uricase. In contrast, the titer of anti-PEG antibodies in serum from the same rabbit that was immunized with mPEG-uricase appeared to be higher by a factor of c. 70 or c. 80 when Tween 20 or Tween 80, respectively, was used in the washes before and after the addition of the secondary antibody (dashed curves). Figure 5 also shows that the apparent titers of

dx.doi.org/10.1021/bc200551b | Bioconjugate Chem. 2012, 23, 485–499

anti-PEG antibodies detected, on plates coated with mPEG-SOD, in the serum of a rabbit immunized with HO-PEG-uricase were decreased c. 300-fold or c. 100-fold (red arrows) when the plates were washed with buffers containing Tween 20 or Tween 80, respectively. In contrast, washing the assay plates with Tween 20 or Tween 80 decreased the apparent titers in serum from the rabbit immunized with mPEG-uricase only c. 8-fold or c. 5-fold, respectively (black arrows).

MethoxyPEG Binds More Tightly than PEG Diol to Antibodies Raised against mPEG-Interferon-α and mPEG-Uricase, but not to Antibodies Raised against HO-PEG-Uricase. The results of competitive ELISAs with 10 kDa mPEG (filled circles) and 10 kDa PEG diol (open circles) of three dilutions of serum from a rabbit immunized with $mPEG_2$-IFN-α are compared in Figure 6A. For all of the tested dilutions of serum (1/500, 1/1000, and 1/2000), the ratios of affinities for mPEG/PEG diol were between 30 and 40. On the other hand, the values of IC_{50} for each of the competitors varied in a nonlinear fashion with the dilution of the serum. Thus, a 4-fold decrease in the antibody concentration (from 1/500 to 1/2000) resulted in a 2-fold decrease in the values of IC_{50}.

In Figure 6B, the potency of 10 kDa mPEG (black symbols) is compared to that of 10 kDa PEG diol (red symbols) as competitors for the binding to mPEG-SOD of antibodies elicited by mPEG-uricase. The anti-PEG antibodies in the serum tested in Figure 6B exhibited c. 70-fold higher affinity for mPEG than for PEG diol of the same molecular weight. Similar results were obtained with sera from the other two rabbits immunized with mPEG-uricase (data not shown). In contrast, no significant difference was detected between the affinities of antibodies raised against HO-PEG-uricase for 10 kDa mPEG vs 10 kDa PEG diol, when tested on the same antigen (Figure 6C) or on HO-PEG-SOD as the antigen (data not shown). These results indicate that anti-PEG antibodies raised against mPEG conjugates have much higher affinities for mPEG than for PEG diol, while anti-PEG antibodies elicited by HO-PEG conjugates show no selectivity for the end-group of the polymer.

Although competitive ELISAs on a single dilution of a single serum sample provide information about the relative affinities of those antibodies for various competitors (e.g., 10 kDa mPEG vs 10 kDa PEG diol, as shown in Figure 6B), comparisons of the values of IC_{50} for different serum samples do not provide a valid comparison of affinities, because the values of IC_{50} do not vary linearly with the concentration of antibodies in each sample, as shown in Figure 6A.

Anti-PEG Antibodies against mPEG-Interferon-α or mPEG-Uricase Bind Cooperatively to Multiply-PEGylated mPEG-Albumin; Antibodies against HO-PEG-Uricase Bind Similarly to PEG Diol and to HO-PEG-Albumin. An albumin conjugate containing an average of 19 molecules of 10 kDa mPEG ($mPEG_{19}$-albumin) and free 10 kDa mPEG were tested as competitors for the binding to mPEG-SOD of antibodies raised against $mPEG_2$-IFN-α (Figure 7A). At the highest tested concentrations (c. 0.1−1 mM PEG), both competitors blocked the binding to the assay plate completely. In a range of lower concentrations, however, the multiply-PEGylated albumin conjugate was much more potent as a competitor than free mPEG. The molar concentration of free mPEG that inhibited 50% of the binding (IC_{50}) was c. 12 times higher than the concentration of mPEG in the albumin conjugate that was similarly inhibitory.

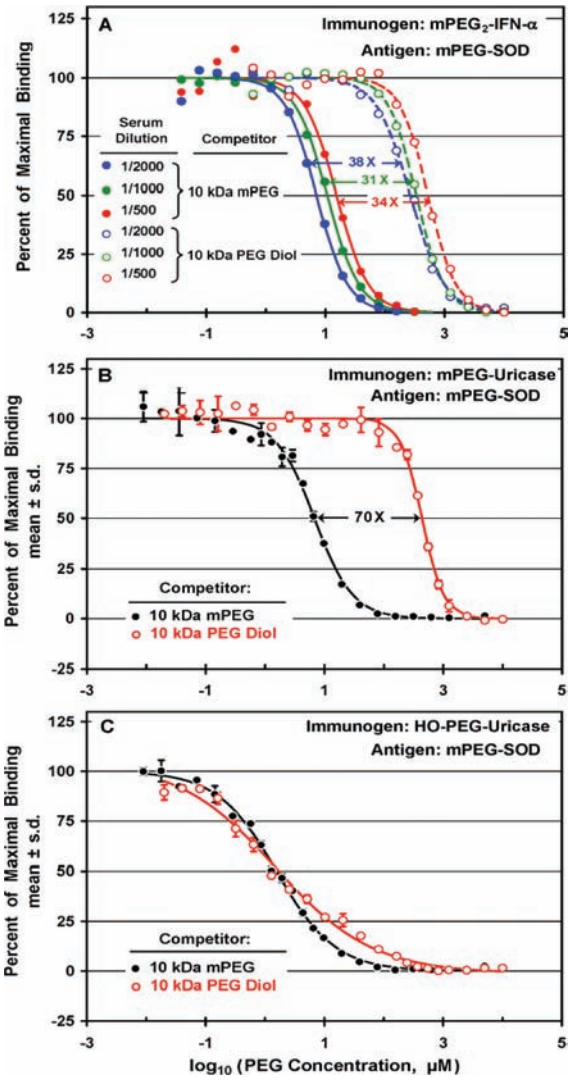


Figure 6. Competitive ELISAs were used to compare the inhibition by mPEG and by PEG diol (HO-PEG-OH) of the binding to mPEG-SOD of antibodies raised against $mPEG_2$-IFN-α (A), against mPEG-uricase (B), and against HO-PEG-uricase (C). Concentrations of competitors are expressed as micromolar PEG in the serum-containing assay mixtures. (A) Anti-PEG antibodies in serum from a rabbit immunized with $mPEG_2$-IFN-α bound 10 kDa mPEG (filled circles) 30-fold to 40-fold more tightly than 10 kDa PEG diol (open circles), regardless of the serum dilution in the range of 1/500 to 1/2000. (B) Anti-PEG antibodies in serum from a rabbit immunized with mPEG-uricase bound 10 kDa mPEG (●) c. 70 times more tightly than 10 kDa PEG diol (○). The serum was diluted 1/1000. (C) Competitive ELISAs of anti-PEG antibodies in serum from a rabbit immunized with HO-PEG-uricase revealed no preferential binding of 10 kDa mPEG (●) compared to 10 kDa PEG diol (○), although the slopes of the competition curves differed. The serum was diluted 1/500.

Experiments analogous to those in Figure 7A were performed on antiserum raised against mPEG-uricase containing an average of nine molecules of mPEG per uricase tetramer (Figure 7B). Again, the multiply-PEGylated albumin conjugate was more potent than free 10 kDa mPEG as an inhibitor of the binding of anti-PEG antibodies to mPEG-SOD. In this antiserum, the IC_{50} of free mPEG was c. 16 times higher than the IC_{50} of mPEG in the $mPEG_{19}$-albumin conjugate.

dx.doi.org/10.1021/bc200551b | Bioconjugate Chem. 2012, 23, 485−499

In contrast with the results for rabbits immunized with mPEG conjugates, the binding to HO-PEG-SOD of antibodies raised against HO-PEG-uricase is inhibited to a similar extent by 10 kDa PEG diol and by a HO-PEG conjugate of albumin (HO-PEG$_{17}$-albumin) at all tested competitor concentrations (Figure 7C).

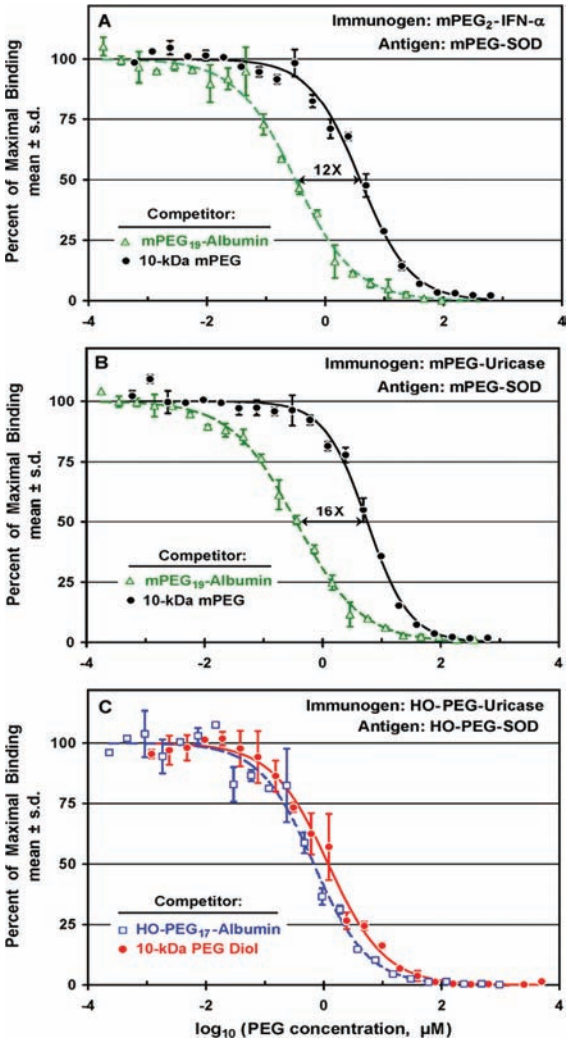


Figure 7. Competitive ELISAs with mPEG-SOD as the antigen were used to assess the cooperativity of binding by antibodies raised against either mPEG$_2$-IFN-α (A) or mPEG-uricase (B) to mPEG in conjugates with human serum albumin. Competitive ELISAs with HO-PEG-SOD as the antigen showed similar binding of antibodies raised against HO-PEG-uricase to free PEG diol and to HO-PEG in an albumin conjugate (C). Concentrations of all competitors are expressed as micromolar PEG in the serum-containing assay mixtures. (A) For anti-PEG antibodies raised against mPEG$_2$-IFN-α, the concentration of free 10 kDa mPEG (●) that inhibited 50% of the binding to mPEG-SOD (IC$_{50}$) was 12 times higher than the IC$_{50}$ for mPEG in an mPEG$_{19}$-albumin conjugate (△). The serum was diluted 1/1000. (B) For anti-PEG antibodies raised against mPEG-uricase, the IC$_{50}$ of free 10 kDa mPEG (●) was 16 times higher than the IC$_{50}$ of mPEG in an mPEG$_{19}$-albumin conjugate (△). The serum was diluted 1/1000. (C) Binding of antibodies raised against HO-PEG-uricase to HO-PEG-SOD was inhibited to a similar extent by free 10 kDa PEG diol (●) and by a conjugate of albumin with 17 molecules of 10 kDa HO-PEG (□). Because of the low titer of antibodies detected by direct ELISAs (see Figure 4B), this serum was diluted only 1/320.

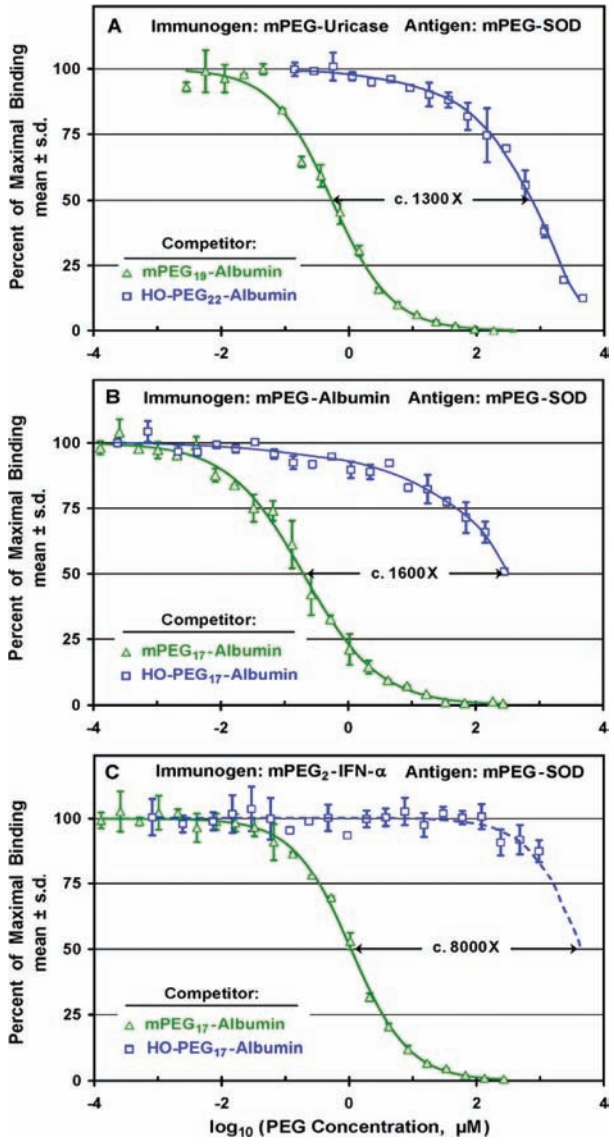


Figure 8. Affinities of antibodies in sera from rabbits immunized with multiply-PEGylated mPEG conjugates of porcine uricase (A), human serum albumin (B), or human interferon-α (C) for multiply-PEGylated conjugates of albumin with mPEG vs HO-PEG were compared in competitive ELISAs with mPEG-SOD as the antigen. Concentrations of all competitors are expressed as micromolar concentrations of PEG in the serum-containing assay mixtures. All of the sera used for these experiments were diluted 1/1000. (A) Increasing concentrations of conjugates of albumin containing c. 20 molecules of either 10 kDa mPEG (△) or 10 kDa HO-PEG (□) were used as competitors for anti-PEG antibodies raised against mPEG-uricase. The c. 1300-fold ratio of the values of IC$_{50}$ for the HO-PEG and mPEG conjugates of albumin is indicated. (B) Increasing concentrations of conjugates of human serum albumin with 17 molecules of either 10 kDa mPEG (△) or 10 kDa HO-PEG (□) were used as competitors for anti-PEG antibodies raised against mPEG$_{17}$-albumin. The c. 1600-fold ratio of the values of IC$_{50}$ for the HO-PEG and mPEG conjugates of albumin is indicated. (C) Increasing concentrations of mPEG$_{17}$-albumin gave a sigmoid competition curve (△) with an IC$_{50}$ of c. 1 μM mPEG and complete inhibition at <1 mM mPEG. Since the highest available concentration of HO-PEG$_{17}$-albumin (corresponding to c. 1 mM HO-PEG) inhibited only c. 13% of the binding (□), the data for HO-PEG$_{17}$-albumin were extrapolated (dashed curve) to provide an estimate of the relative affinities of the two competitors.

dx.doi.org/10.1021/bc200551b | *Bioconjugate Chem.* 2012, 23, 485–499

Antibodies Raised against mPEG Conjugates of Three Proteins Have Much Higher Affinities for Multiply-PEGylated mPEG-Albumin than for HO-PEG-Albumin of Similar Composition. As shown in Figure 8A, an mPEG conjugate of albumin was much more potent than HO-PEG-albumin as a competitor for the binding to mPEG-SOD of antibodies raised against mPEG-uricase. The potencies of these competitors, each of which contained an average of c. 20 molecules of PEG per albumin molecule, differed by a factor of c. 1300. Indeed, the affinity of the HO-PEG-albumin conjugate was so low that the binding of the anti-PEG antibodies to the assay plate was incompletely inhibited by the highest available concentration of this competitor. Figure 8B illustrates analogous results obtained in a comparison of the potencies of $mPEG_{17}$-albumin vs $HO\text{-}PEG_{17}$-albumin as competitors for the binding to mPEG-SOD of anti-PEG antibodies raised against $mPEG_{17}$-albumin. In this experiment, the highest available concentration of $HO\text{-}PEG_{17}$-albumin inhibited only c. 50% of the binding, and the affinity for $mPEG_{17}$-albumin was estimated to be *c.* 1600 times higher than the affinity for $HO\text{-}PEG_{17}$-albumin.

In analogous experiments performed with antiserum raised against $mPEG_2$-IFN-α, the affinity of the mPEG-albumin conjugate was estimated to be c. 8000 times that of the HO-PEG-albumin conjugate (Figure 8C). Since the highest available concentration of the HO-PEG-albumin conjugate inhibited only c. 13% of the binding, the data were extrapolated to obtain a rough estimate of IC_{50} of the HO-PEG-albumin conjugate (see dashed curve). Thus, anti-PEG antibodies elicited by conjugates of three proteins containing between 2 and 17 molecules of mPEG per protein molecule have affinities for multiply-PEGylated conjugates of albumin with mPEG that are at least 1000-fold higher than their affinities for HO-PEG albumin with a similar PEG-to-protein ratio.

Antibodies Raised against *t*-BuO-PEG-Albumin Have Higher Titers Detected on *t*-BuO-PEG than on mPEG or HO-PEG Antigens in Direct ELISAs and Higher Affinities for *t*-BuO-PEG than for mPEG or PEG Diol in Competitive ELISAs. Although the focus of this research is the role of the methoxy group of mPEG in the immune responses to mPEG-protein conjugates, a few experiments were performed to quantify and characterize the immune responses to a different alkoxy group at the distal terminus of an alkoxyPEG-protein conjugate. Three rabbits were immunized with a human serum albumin conjugate of 10 kDa *t*-BuO-PEG containing an average of 17 molecules of PEG per molecule of albumin (see Figures 1 and S7). The results of direct ELISAs of serum from one of these rabbits, in which the assay plates were coated with SOD conjugates of *t*-BuO-PEG, mPEG, or HO-PEG, are shown in Figure 9A. The anti-PEG antibodies generated against *t*-BuO-PEG_{17}-albumin show significant cross-reactivity with mPEG-SOD and slightly less cross-reactivity with HO-PEG-SOD. The mean titer of antibodies in the sera of these three rabbits detected with *t*-BuO-PEG-SOD as the antigen (39 000 ± 8000) was higher than the highest titers of anti-PEG antibodies detected with mPEG-SOD as the antigen for the groups of rabbits immunized with $mPEG_1$-IFN-α (see Figure 3A) or mPEG-uricase (see Figure 4A). As shown in Table 2, the antibodies raised against *t*-BuO-PEG_{17}-albumin have slightly higher titers detected in direct ELISAs with mPEG-SOD than with HO-PEG-SOD as the antigen, but the relative titers (detected on mPEG-SOD/HO-PEG-SOD) for all three rabbits immunized with *t*-BuO-PEG_{17}-albumin were lower than those of 10 of 11 rabbits immunized with mPEG-protein conjugates from which sera from Bleeds 2 and 3 were available.

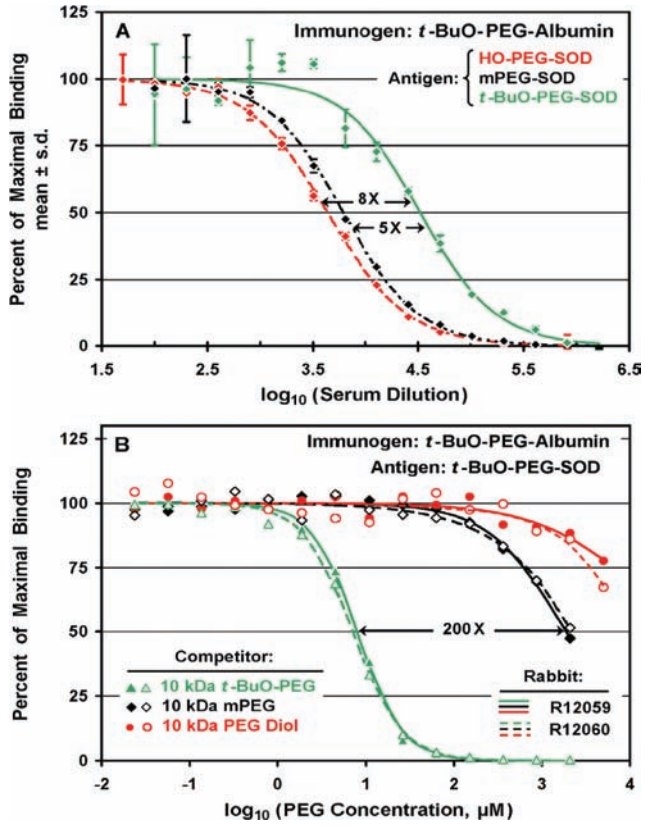


Figure 9. Selectivity of antibodies raised against a *t*-BuO-PEG conjugate of human serum albumin (*t*-BuO-PEG_{17}-albumin) was assessed by direct ELISAs (A) and by competitive ELISAs (B). (A) Direct ELISAs were performed on assay plates coated with SOD coupled to 10 kDa HO-PEG (red ◆), to 10 kDa mPEG (black ◆), or to 10 kDa *t*-BuO-PEG (green ◆) . In this serum, from rabbit R12059, higher titers were detected with *t*-BuO-PEG-SOD than with mPEG-SOD or with HO-PEG-SOD. (B) Competitive ELISAs were performed on a 1/10 000 dilution of the same serum for which direct ELISA data are shown in (A) (rabbit R12059; filled symbols, solid curves) and on the same dilution of serum from a similarly immunized rabbit (R12060; open symbols, dashed curves). The results revealed a high degree of selectivity of these antisera for 10 kDa *t*-BuO-PEG (△, ▲) compared to 10 kDa mPEG (◇, ◆) or to 10 kDa PEG diol (○, ●).

Figure 9B shows the results of competitive ELISAs of sera from two rabbits that were immunized with *t*-BuO-PEG_{17}-albumin, including the rabbit for which the results of direct ELISAs are shown in Figure 9A. About 40-fold higher selectivity of the antibodies raised against *t*-BuO-PEG_{17}-albumin for *t*-BuO-PEG compared to mPEG is revealed by the results of the competitive ELISAs for both rabbits (200× in Figure 9B) than by the direct ELISAs (5× in Figure 9A).

MethoxyPEG and HO-PEG Conjugates of Two Cytokines Have Equivalent Potencies in Cell Culture. To complement our studies of the immunologic properties of mPEG and HO-PEG conjugates of various proteins (see Figures 2−9), experiments were performed to determine whether the distal terminal group of the polymer affects the biological activities of PEG conjugates of two cytokines measured in vitro. Human IFN-α and human EPO were selected as examples of cytokines for which reliable cell culture assays of potency were available. MethoxyPEG and HO-PEG conjugates of IFN-α were tested on human Burkitt's lymphoma cells (Daudi cells), the proliferation of which is profoundly inhibited by IFN-α.[37,38] MethoxyPEG and HO-PEG conjugates of EPO were tested on human erythroleukemic cells

dx.doi.org/10.1021/bc200551b | *Bioconjugate Chem.* 2012, 23, 485−499

(TF-1 cells), the proliferation of which is stimulated by EPO and certain other cytokines.[39,40]

MonoPEGylated conjugates of IFN-α, synthesized by reductive alkylation with 20 kDa mPEG aldehyde or 20 kDa HO-PEG aldehyde (see Figures S1 and S4), were indistinguishable in their potencies as inhibitors of Daudi cell proliferation (Figure 10A). Both conjugates displayed c. 6% of the potency of unPEGylated IFN-α. Similarly, diPEGylated conjugates of IFN-α, synthesized using 20 kDa mPEG aldehyde or 20 kDa HO-PEG aldehyde, were indistinguishable in their potencies as inhibitors of the proliferation of Daudi cells, although both were c. 0.4% as potent as unPEGylated IFN-α and c. 7% as potent as the monoPEGylated conjugates.

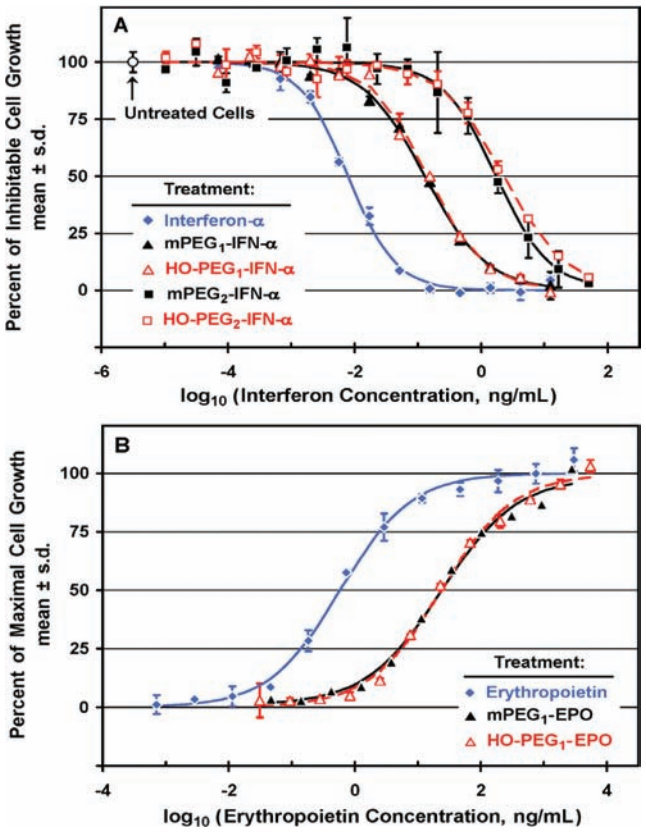


Figure 10. Cell culture assays responsive to human interferon-α (IFN-α; A) or human erythropoietin (EPO; B) were used to compare the potencies in vitro of analogous conjugates of these cytokines with HO-PEG and mPEG. A: Human lymphoma cells (Daudi cells) were treated for 3 days with serial dilutions of IFN-α (◆), with monoPEGylated conjugates of IFN-α made with 20 kDa mPEG (▲; $mPEG_1$-IFN-α) or 20 kDa HO-PEG (△; $HO\text{-}PEG_1$-IFN-α), or with diPEGylated conjugates of IFN-α made with 20 kDa mPEG (■) or with 20 kDa HO-PEG (□). After incubation of the cells with Alamar Blue, the fluorescent signal was measured to quantify cell growth, from which the percent of inhibitable cell growth was calculated. (B) Human erythroleukemic cells (TF-1 cells) were treated for 3 days with serial dilutions of EPO (◆), with a monoPEGylated conjugate with 30 kDa mPEG (▲; $mPEG_1$-EPO; Mircera), or with a monoPEGylated conjugate with 30 kDa HO-PEG (△; $HO\text{-}PEG_1$-EPO). After incubation of the cells with Alamar Blue, the fluorescent signal was measured to quantify cell growth, from which the percent of maximal cell growth was calculated.

The effects on TF-1 cell proliferation of a standard solution of EPO,[41] a monoPEGylated conjugate of EPO synthesized by reductive alkylation with 30 kDa HO-PEG aldehyde (see Figure S5), and a monoPEGylated conjugate of EPO containing 30 kDa mPEG, which is commercially available from Roche as Mircera,[42,43] were compared (Figure 10B). The potencies of the HO-PEG and mPEG conjugates of EPO were indistinguishable in this assay, although both conjugates were only c. 2% as potent as the EPO standard. Thus, for both IFN-α and EPO, conjugates with HO-PEG and mPEG had equivalent potencies in cell culture.

■ DISCUSSION

The goal of this research was to assess the role of the methoxy group of mPEG in the immunogenicity and antigenicity of mPEG-protein conjugates and the potential advantages of replacing mPEG with hydroxyPEG (HO-PEG) in the synthesis of PEG conjugates of proteins and other therapeutic agents. The results demonstrate that the methoxy groups of mPEG-protein conjugates contribute significantly to the titers of anti-PEG antibodies detected in the sera of rabbits immunized with mPEG conjugates of human interferon-α, human serum albumin, or porcine uricase (see Figures 2–4 and Table 2). Anti-PEG antibodies raised against mPEG conjugates of these proteins exhibit much higher affinities for multiply-PEGylated conjugates of albumin synthesized with mPEG than with HO-PEG (Figure 8). Additional results include the demonstration that (1) the use of the PEG-containing detergents Tween 20 and Tween 80 decreases the sensitivity of detection of anti-PEG antibodies by enzyme-linked immunosorbent assays (ELISAs) (Figure 5); (2) the titers of anti-PEG antibodies formed against *t*-BuO-PEG conjugates of albumin were higher than those elicited by mPEG-albumin conjugates, and (3) analogous HO-PEG and mPEG conjugates of two cytokines have indistinguishable biological activities in cell culture assays (Figure 10). While the immunologic data were obtained in experiments on groups of only three rabbits each immunized with an mPEG, a HO-PEG, or a *t*-BuO-PEG conjugate of one of three proteins, the results have intriguing implications for potential improvements in the pharmacokinetics and pharmacodynamics of a wide range of PEGylated drugs by avoiding the use of activated mPEG or other alkoxy PEGs in synthesizing the next generation of such drugs.

Development of Antibodies against PEGylated Therapeutic Enzymes Can Limit Their Efficacy. In 2000, Müller et al.[44] reported the accelerated clearance of an mPEG conjugate of asparaginase (Oncaspar) in a subset of pediatric leukemia patients who had no clinical evidence of an allergic reaction. Although there was no mention of anti-PEG antibodies in that report, subsequent analyses of stored sera from some of the patients in that study provided clear evidence of anti-PEG antibodies that were detected both by serological techniques and by flow cytometry.[45] Oncaspar is synthesized by coupling multiple strands of 5 kDa mPEG to L-asparaginase using the succinimidyl succinate derivative of mPEG.[9]

In 2006, Ganson et al.[30] reported that a subset of patients with refractory chronic gout who had received a single subcutaneous injection of an mPEG conjugate of a recombinant mammalian uricase cleared the conjugate exceptionally rapidly and that low titers of anti-PEG antibodies (IgG) were detected in the sera of some of these patients by about one week after the injection. In a subsequent Phase 1 trial in which the same mPEG-uricase was administered intravenously to subjects with refractory chronic gout, antibodies to PEG-uricase, described as "mostly IgG2 and specific for PEG", developed in 9 of 24 patients, in some of whom the enzyme was cleared rapidly without evidence of allergic reactions.[31] The results of a Phase 2

dx.doi.org/10.1021/bc200551b | *Bioconjugate Chem.* 2012, 23, 485–499

randomized study of this mPEG-uricase (now called pegloticase) were published in 2008,[46] and the results of two 6-month, randomized, controlled Phase 3 trials were published in 2011.[47] In the Phase 2 and Phase 3 trials, the absence of high titers of anti-pegloticase antibodies was correlated with persistent efficacy of the drug in lowering plasma uric acid concentrations. In the Phase 3 trials, a subset of the patients lost responsiveness within 3−4 months of treatment and this loss was associated with high titers of anti-pegloticase antibodies. However, the specificities of the antibodies for the enzyme vs the polymer component of the drug were not reported.[46,47] Pegloticase is synthesized by coupling an average of ten molecules of 10 kDa mPEG per subunit of recombinant mammalian uricase (resembling porcine uricase) using a *p*-nitrophenylcarbonate derivative of mPEG.[9,14]

These examples of the loss of responsiveness to mPEG conjugates of two therapeutic enzymes (asparaginase and uricase) that were synthesized using two different coupling chemistries suggest the possible clinical relevance of the present studies of the immunologic responses to mPEG-protein conjugates in experimental animals. The immunogenicity of the polymer component of two mPEG-protein conjugates suggests that patients who have been treated previously with one PEGylated drug may be at increased risk of adverse immunologic responses to a second PEGylated drug. Since the asparaginase sequence in Oncaspar is bacterial[44] and the uricase sequence in pegloticase is a mutein of porcine uricase,[14] we cannot extrapolate from the cited results with conjugates of foreign proteins in humans and rabbits to predict the relative immunogenicities in humans of mPEG vs HO-PEG conjugates of human proteins.

Anti-PEG Antibodies Formed against HO-PEG-Proteins Have the Same Titers on mPEG and HO-PEG Antigens and the Same Mean Affinities for mPEG and PEG Diol. In contrast with the results obtained for rabbits immunized with mPEG-proteins, direct ELISAs of sera from each of nine rabbits immunized with HO-PEG conjugates of IFN-α or uricase had indistinguishable titers of anti-PEG antibodies detected on mPEG-SOD and HO-PEG-SOD (see Table 2 and Figures 2B, 3B, and 4B). Similarly, competitive ELISAs show that anti-PEG antibodies elicited by HO-PEG-uricase do not bind preferentially to 10 kDa mPEG or 10 kDa PEG diol (see Figure 6C). These results imply that the anti-PEG antibodies elicited by HO-PEG-proteins are directed against the backbone of the polymer (see Figure 1) and that competition for their binding to a PEG-protein antigen is neither enhanced nor inhibited by the presence of a methoxy group in a competitor.

It should be noted that the titers of anti-PEG antibodies elicited by HO-PEG conjugates of uricase tended to be lower than the titers elicited by the corresponding mPEG conjugates (Figure 4). Therefore, sera from the rabbits immunized with HO-PEG-uricase were diluted less extensively than sera from rabbits immunized with mPEG-uricase for competitive ELISAs, e.g., the sera in Figure 6B and C were diluted 1/1000 and 1/500, respectively. Similarly, the sera in Figure 7B and C were diluted 1/1000 and 1/320, respectively. Under these conditions, the values of IC_{50} are not directly proportional to the affinities of the tested antibodies for the various competitors.

Anti-PEG Antibodies Formed against mPEG-Proteins Vary in Their Selectivities for the PEG Backbone and the Methoxy Group. In sera from 10 of 11 rabbits immunized with mPEG conjugates of three unrelated proteins (human IFN-α, porcine uricase and human serum albumin), the titers of anti-PEG antibodies detected by direct ELISAs on assay plates coated with mPEG conjugates of another unrelated protein, SOD, were higher than the titers detected in the same sera on assay plates coated with HO-PEG-SOD (see Table 2 and Figures 2A, 3A, and 4A]. The unusually high degree of selectivity for mPEG of the anti-PEG antibodies detected in sera from two of three rabbits immunized with mPEG-uricase suggests that the immunogenicity of this porcine enzyme to which the PEG is coupled may influence the impact of the terminal methoxy groups on the specificity of the antigen-binding sites of the anti-PEG antibodies (see Figure 1).

There were noteworthy differences within the two groups of rabbits immunized with mPEG conjugates of porcine uricase and human serum albumin, respectively. Among those immunized with mPEG-uricase, rabbit R580 had a mean relative titer of only 3.1 ± 0.6, while rabbits R579 and R581 had mean relative titers of 20 ± 4.8 and 18 ± 4.8, respectively. Within the group of rabbits immunized with $mPEG_{17}$-albumin, the mean relative titers of rabbits R12056 and R12058 were 3.0 ± 0.5 and 2.6 ± 0.6, respectively. Surprisingly, rabbit R12057 had indistinguishable titers on mPEG-SOD and HO-PEG-SOD in triplicate assays (mean relative titer = 1.1 ± 0.1). Rabbit R12057 was the only 1 of 11 rabbits immunized with mPEG conjugates of any of three different proteins in which the titer detected on mPEG-SOD was not at least twice that detected on HO-PEG-SOD. Competitive ELISAs of sera from that rabbit also showed no selectivity for mPEG vs PEG diol (data not shown). The results for this anomalous rabbit do not negate the overall conclusion about the importance of the methoxy group in the immune responses of *most* rabbits to mPEG-protein conjugates, but they signal the potential role of individual variation that might impact population studies in humans.

Antibodies against the Terminal Methoxy Group Dominate the Immune Responses to mPEG-Uricase. Figure 6B illustrates data from one rabbit immunized with mPEG-uricase in which the affinity for 10 kDa mPEG was 70 times higher than for 10 kDa PEG diol. Similar results were obtained when the same serum was tested with 20 kDa mPEG and 20 kDa PEG diol, as well as when sera from the other two rabbits immunized with mPEG-uricase were similarly tested (data not shown). The molecular weight of the methyl group that differentiates mPEG from HO-PEG is only 15 Da, which represents only 0.15% of the molecular weight of the 10 kDa competitors tested in these experiments. Therefore, it may seem surprising that the anti-PEG antibodies display so much higher affinities for the small group at the end of the polymer than for the large number of oxyethylene units (CH_2-CH_2-O) within the polymer backbone (c. 227 for 10 kDa PEGs). On the other hand, the ends of linear or branched polymers, especially the hydrophobic end containing a methoxy group (as in Figure 6A or B) or a *t*-butoxy group (as in Figure 9B), are more likely than the polymer backbone to be accessible to the antigen-binding sites of the antibodies (see Figure 1). The lack of absolute specificity of these antibodies for the terminal alkoxy groups is demonstrated by the observation that a sufficiently high concentration of PEG diol can completely inhibit the binding to mPEG-SOD of anti-PEG antibodies raised against mPEG-IFN-α or mPEG-uricase (see Figure 6A and B).

Multiple PEGylation Amplifies the Detectable Selectivity for mPEG vs HO-PEG of Anti-PEG Antibodies Formed against mPEG-Proteins. While several FDA-approved PEGylated therapeutic proteins in clinical use contain a single strand of mPEG (e.g., PegIntron,[9,48] Neulasta,[9,49] and Mircera[9,42,43]), several others contain derivatives of diPEG-lysine,

which have two methoxy groups (e.g., Pegasys,[9,48] Macugen,[11] and Cimzia[9,50,51]), and others contain multiple strands of "linear" mPEG (e.g., Adagen,[9,52] Oncaspar,[9,45] Somavert,[9,53] and KRYSTEXXA[9,14,46,47]). Our data suggest the potential clinical relevance of the present studies of the impact of multiple PEGylation on the antigenicity of mPEG-protein conjugates.

In contrast with the 12-fold and 16-fold differences between the affinities of anti-PEG antibodies elicited by two mPEG-protein conjugates for free 10 kDa mPEG vs an mPEG-albumin conjugate (see Figure 7A and B), no significant differences were detected between the affinities or the shapes of the competition curves obtained with free 10 kDa PEG diol and a HO-PEG-albumin conjugate as competitors for the binding to HO-PEG-SOD of antibodies raised against HO-PEG-uricase (see Figure 7C). A plausible interpretation is that anti-PEG antibodies directed against the backbone of the polymer can bind cooperatively to at least two sites within the backbone of a polymer as large as 10 kDa PEG diol. In that case, the presence of multiple strands of HO-PEG within the albumin conjugate would not further enhance the cooperativity of the binding. The absence of enhanced cooperativity in binding multiply-PEGylated protein conjugates distinguishes anti-PEG antibodies directed against the polymer backbone from those directed against the methoxy group(s) at the distal terminus or termini.

Anti-PEG Antibodies Raised against mPEG-Protein Conjugates Bind Multiply-PEGylated mPEG-Albumin Conjugates >1000-fold More Tightly than HO-PEG-Albumin Conjugates. In sera from rabbits immunized with mPEG conjugates of uricase, albumin or IFN-α, the affinities of anti-PEG antibodies for mPEG-albumin conjugates were about 3 orders of magnitude higher than for HO-PEG conjugates of albumin (Figure 8). Precise estimates of the relative affinities could not be obtained, since the highest available concentrations of the HO-PEG-albumin conjugates used as competitors inhibited only a fraction of the binding of the antibodies to mPEG-SOD on the assay plate. Su et al.[7] previously reported that anti-PEG antibodies bind best when PEG is linked to a protein or liposome or adsorbed on a surface. They also reported that the binding of their monoclonal antibodies to the PEG backbone was not influenced by the nature of the terminal groups of the PEG, which included HO-PEG and mPEG.

The Methoxy Group is Not Unique in Eliciting Anti-PEG Antibodies Directed against the Terminal Group of AlkoxyPEG-Protein Conjugates. In sera from three rabbits immunized with *t*-BuO-PEG$_{17}$-albumin (see Figure 9A), the mean titer detected with *t*-BuO-PEG-SOD as the antigen was about 7−10 times higher than the titers detected in sera of rabbits immunized with mPEG$_1$-IFN-α (see Figure 3A), mPEG-uricase (see Figure 4A), or mPEG-albumin (data not shown).

The immunogenicity of the *t*-butoxy group shown in Figure 9 is relevant to the potential use of this group as a removable blocking group in the synthesis of monofunctionally activated HO-PEG conjugates.[13] The use of *t*-BuO-PEG as an intermediate in the synthesis of the *p*-nitrophenylcarbonate derivative of HO-PEG (HO-PEG-NPC) is illustrated below:

$$t\text{−BuO−PEG−OH} + \text{pNP−COCl} \xrightarrow{[1]} t\text{−BuO−PEG−NPC} \xrightarrow{[2]} \text{HO−PEG−NPC}$$

The failure to remove even a small fraction of the *t*-butoxy groups in step [2] of the above reaction sequence would result in a preparation of HO-PEG-NPC in which traces of *t*-BuO-PEG-NPC could form highly immunogenic protein conjugates.

Buffers Containing Tween-Type Non-Ionic Detergents Interfere with Detection of Anti-PEG Antibodies by ELISAs. A few previous investigators have recognized the inhibitory effects of Tween on the detection and quantitation of anti-PEG antibodies[6,7] and a few companies that sell anti-PEG mAbs warn their customers to avoid the use of Tween (e.g., Silver Lake Research[54]). The dramatic effects of Tween 20 and Tween 80, illustrated in Figure 5, have clear implications for clinical studies that include attempts to quantify anti-PEG antibodies.[6,30,31,45] The data in Figure 5 and similar results on sera from other rabbits immunized with mPEG- or HO-PEG-uricase (results not shown) illustrate the distortion of the results of direct ELISAs of anti-PEG antibodies resulting from the use of the detergents Tween 20 and Tween 80, which contain short strands of PEG within their structures (see Figure 1).

Therapeutic Proteins Coupled to mPEG and HO-PEG Have Equivalent Potencies in Cell Culture. The in vitro biological activities of two PEGylated cytokines, one of which inhibits proliferation (interferon-α) and the other of which stimulates proliferation (erythropoietin) of the cells on which each was tested were unaffected by the substitution of HO-PEG for mPEG of the same molecular weight in their synthesis (see Figure 10). These results provide support for the proposal that conjugates synthesized with HO-PEG instead of mPEG will retain the desirable attributes of PEGylated therapeutic agents, even if they provoke fewer undesirable immune responses than those observed with mPEG conjugates.

Implications of These Results for Future Research and the Future Design and Development of PEGylated Proteins and Other Therapeutic Agents. Our demonstration that mPEG conjugates of three dissimilar proteins containing as few as 1 or as many as 17 molecules of mPEG elicit anti-PEG antibodies that are directed against the methoxy group has important implications for the clinical use of mPEG conjugates of enzymes, cytokines, and other therapeutic proteins. Armstrong et al.[45] recognized that anti-PEG antibodies were involved in the accelerated clearance of mPEG conjugates of asparaginase in a subset of patients treated with Oncaspar, and Ganson, Sundy, and their colleagues recognized that anti-PEG antibodies were correlated with the accelerated clearance of pegloticase in a subset of patients.[30,31] However, those reports did not evaluate the role of the methoxy groups of the mPEGs in the conjugates being studied.

The results presented above are consistent with the hypothesis that the accelerated clearance and the consequent loss of efficacy of mPEG conjugates of therapeutic agents might be decreased by synthesizing next-generation versions of these drugs with monofunctionally activated derivatives of hydroxy-PEG, instead of mPEG. The potential advantages of HO-PEG conjugates have been suggested in previous publications by several of the present authors.[13,14] Despite the convenience inherent in the use of mPEG for the synthesis of monofunctionally activated PEGylation reagents, the extra effort entailed in the use of monofunctionally activated HO-PEG may be justified by the decreased risk of treatment-limiting immune responses to the resultant HO-PEG conjugates (see Supporting Information).

The caveats on extrapolating from the present results to clinical situations include the facts that (1) all immunogens administered to rabbits in this study were emulsified in complete or incomplete Freund's adjuvant, (2) the clearance rates of the

various PEG conjugates could not be measured in these hyperimmune rabbits, and (3) antibody isotyping was not possible in this study because the secondary antibody used for all of the reported ELISAs was specific for the H and L chains of rabbit IgG, which can cross-react with the L chains of rabbit IgM. All of these factors are worthy subjects of future research. Finally, although all of the data in this report were obtained with PEG conjugates of proteins, the potential advantages of replacing activated mPEG with monofunctionally activated HO-PEG for synthesizing polymer conjugates of liposomes, viruses, red blood cells, aptamers, and other types of therapeutic agents also merit investigation.

■ ASSOCIATED CONTENT

Supporting Information

Descriptions of the synthesis, purification and physicochemical analyses of (1) the activated HO-PEGs and *t*-BuO-PEG; (2) the PEG-protein conjugates listed in Table 1, and (3) the HO-PEG conjugate of erythropoietin used in the cell culture assays. This material is available free of charge via the Internet at http://pubs.acs.org.

■ AUTHOR INFORMATION

Corresponding Author

*E-mail: sherman@mvpharm.com. Phone: 650-365-5515 x224. Fax: 650-365-5525.

Notes

The authors declare the following competing financial interest(s): All of the authors are employees of Mountain View Pharmaceuticals, Inc.

■ ACKNOWLEDGMENTS

This research was supported in part by a Qualifying Therapeutic Discovery Project grant from the U.S. government under the Patient Protection and Affordable Care Act (P.L. 111-148). We are grateful to John A. French for his contributions throughout this research, particularly with respect to the computer-assisted analysis of the data, and to Alexa L. Martinez for her participation in the early stages of this research. Dr. John A. Katzenellenbogen and Dr. Ralph W. Niven provided many insightful suggestions regarding the manuscript.

■ ABBREVIATIONS

AAALAC, Association for the Assessment and Accreditation of Laboratory Animal Care; ACN, acetonitrile; Albumin, human serum albumin; Blocking Buffer, 5% (w/v) nonfat dry milk solids in PBS; ELISA, enzyme-linked immunosorbent assay; EPO, recombinant human erythropoietin; GM-CSF, recombinant human granulocyte-macrophage colony-stimulating factor; HO-PEG, hydroxyPEG; HRP, horseradish peroxidase; IACUC, Institutional Animal Care and Use Committee; IFN-α, recombinant human interferon-α; mAU/min, milli-absorbance units/min; mAbs, monoclonal antibodies; mPEG, monomethoxypoly(ethylene glycol); NPC, *p*-nitrophenylcarbonate; OPD, *o*-phenylenediamine dihydrochloride; PBS-G, phosphate-buffered saline, pH 7.4, containing 2% (v/v) goat serum; PEG, poly(ethylene glycol); pNP-COCl, *p*-nitrophenylchloroformate; RI, refractive index; RP chromatography, reversed-phase chromatography; SEC, size-exclusion chromatography; SOD, porcine Cu−Zn superoxide dismutase; *t*-BuO-PEG, *t*-butoxyPEG; TFA, trifluoroacetic acid.

■ REFERENCES

(1) Abuchowski, A., van Es, T., Palczuk, N. C., and Davis, F. F. (1977) Alteration of immunological properties of bovine serum albumin by covalent attachment of polyethylene glycol. *J. Biol. Chem. 252*, 3578−3581.

(2) Abuchowski, A., McCoy, J. R., Palczuk, N. C., van Es, T., and Davis, F. F. (1977) Effect of covalent attachment of polyethylene glycol on immunogenicity and circulating life of bovine liver catalase. *J. Biol. Chem. 252*, 3582−3586.

(3) Lee, W. Y., and Sehon, A. H. (1978) Suppression of reaginic antibodies with modified allergens. I. Reduction in allergenicity of protein allergens by conjugation to polyethylene glycol. *Int. Arch. Allergy Appl. Immunol. 56*, 159−170.

(4) Richter, A. W., and Åkerblom, E. (1983) Antibodies against polyethylene glycol produced in animals by immunization with monomethoxy polyethylene glycol modified proteins. *Int. Arch. Allergy Appl. Immunol. 70*, 124−131.

(5) Richter, A. W., and Åkerblom, E. (1984) Polyethylene glycol reactive antibodies in man: Titer distribution in allergic patients treated with monomethoxy polyethylene glycol modified allergens or placebo, and in healthy blood donors. *Int. Arch. Allergy Appl. Immunol. 74*, 36−39.

(6) Armstrong, J. K. (2009) The occurrence, induction, specificity and potential effect of antibodies against poly(ethylene glycol). In *PEGylated Protein Drugs: Basic Science and Clinical Applications* (Veronese, F. M., Ed.) pp 147−168, Birkhäuser Verlag, Basel, Switzerland.

(7) Su, Y.-C., Chen, B.-M., Chuang, K.-H., Cheng, T.-L., and Roffler, S. R. (2010) Sensitive quantification of PEGylated compounds by second-generation anti-poly(ethylene glycol) monoclonal antibodies. *Bioconjugate Chem. 21*, 1264−1270.

(8) Fishburn, C. S. (2008) The pharmacology of PEGylation: Balancing PD with PK to generate novel therapeutics. *J. Pharm. Sci. 97*, 4167−4183.

(9) Alconcel, S. N. S., Baas, A. S., and Maynard, H. D. (2011) FDA-approved poly(ethylene glycol)-protein conjugate drugs. *Polym. Chem. 2*, 1442−1448.

(10) Duncan, R. (2011) Polymer therapeutics as nanomedicines: New perspectives. *Curr. Opin. Biotechnol. 22*, 492−501.

(11) Ng, E. W., and Adamis, A. P. (2006) Anti-VEGF aptamer (pegaptanib) therapy for ocular vascular diseases. *Ann. N.Y. Acad. Sci. 1082*, 151−171.

(12) Immordino, M. L., Dosio, F., and Cattel, L. (2006) Stealth liposomes: Review of the basic science, rationale, and clinical applications, existing and potential. *Int. J. Nanomedicine 1*, 297−315.

(13) Martinez, A. L., Sherman, M. R., Saifer, M. G. P., and Williams, L. D., Mountain View Pharmaceuticals, Inc. Polymer conjugates with decreased antigenicity, methods of preparation and uses thereof. U.S. Patent No. 8,129,330 B1, March 6, 2012.

(14) Sherman, M. R., Saifer, M. G. P., and Perez-Ruiz, F. (2008) PEG-uricase in the management of treatment-resistant gout and hyperuricemia. *Adv. Drug Delivery Rev. 60*, 59−68.

(15) Cheng, T.-L., Wu, P.-Y., Wu, M.-F., Chern, J.-W., and Roffler, S. R. (1999) Accelerated clearance of polyethylene glycol-modified proteins by anti-polyethylene glycol IgM. *Bioconjugate Chem. 10*, 520−528.

(16) Cheng, T.-L., Chen, B.-M., Chern, J.-W., Wu, M.-F., and Roffler, S. R. (2000) Efficient clearance of poly(ethylene glycol)-modified immunoenzyme with anti-PEG monoclonal antibody for prodrug cancer therapy. *Bioconjugate Chem. 11*, 258−266.

(17) Tsai, N., Cheng, T.-L., and Roffler, S. R. (2001) Sensitive measurement of polyethylene glycol-modified proteins. *BioTechniques 30*, 396−402.

(18) Cheng, T.-L., Cheng, C.-M., Chen, B.-M., Tsao, D.-A., Chuang, K.-H., Hsiao, S.-W., Lin, Y.-H., and Roffler, S. R. (2005) Monoclonal antibody-based quantitation of poly(ethylene glycol)-derivatized proteins, liposomes, and nanoparticles. *Bioconjugate Chem. 16*, 1225−1231.

(19) Roffler, S., Cheng, T.-L., and Wu, P.-Y., Academia Sinica, Monoclonal-antibody for analysis and clearance of polyethylene glycol

and polyethylene glycol-modified molecules. U.S. Patent No. 6,596,849 B1, Jul. 22, 2003.
(20) Roffler, S., Cheng, T.-L., and Wu, P.-Y., Academia Sinica, Monoclonal antibody for analysis and clearance of polyethylene glycol and polyethylene glycol-modified molecules. U.S. Patent No. 6,617,118 B2, Sept. 9, 2003.
(21) Roffler, S., Cheng, T.-L., and Wu, P.-Y., Academia Sinica, Monoclonal antibody for analysis and clearance of polyethylene glycol and polyethylene glycol-modified molecules. U.S. Patent No. 7,320,791 B2, Jan. 22, 2008.
(22) Armstrong, J. K., Wenby, R. B., Meiselman, H. J., and Fisher, T. C. (2003) *In vivo* survival of poly(ethylene glycol)-coated red blood cells in the rabbit. *Blood 102*, 94a.
(23) Garratty, G. (2008) Modulating the red cell membrane to produce universal/stealth donor red cells suitable for transfusion. *Vox Sang. 94*, 87−95.
(24) Dams, E. T. M., Laverman, P., Oyen, W. J. G., Storm, G., Scherphof, G. L., Van Der Meer, J. W. M., Corstens, F. H. M., and Boerman, O. C. (2000) Accelerated blood clearance and altered biodistribution of repeated injections of sterically stabilized liposomes. *J. Pharmacol. Exp. Ther. 292*, 1071−1079.
(25) Semple, S. C., Harasym, T. O., Clow, K. A., Ansell, S. M., Klimuk, S. K., and Hope, M. J. (2005) Immunogenicity and rapid blood clearance of liposomes containing polyethylene glycol-lipid conjugates and nucleic acid. *J. Pharmacol. Exp. Ther. 312*, 1020−1026.
(26) Środa, K., Rydlewski, J., Langner, M., Kozubek, A., Grzybek, M., and Sikorski, A. F. (2005) Repeated injections of PEG-PE liposomes generate anti-PEG antibodies. *Cell. Mol. Biol. Lett. 10*, 37−47.
(27) Judge, A., McClintock, K., Phelps, J. R., and MacLachlan, I. (2006) Hypersensitivity and loss of disease site targeting caused by antibody responses to PEGylated liposomes. *Mol. Ther. 13*, 328−337.
(28) Ishida, T., Wang, X. Y., Shimizu, T., Nawata, K., and Kiwada, H. (2007) PEGylated liposomes elicit an anti-PEG IgM response in a T cell-independent manner. *J. Controlled Release 122*, 349−355.
(29) Ishida, T., Kashima, S., and Kiwada, H. (2008) The contribution of phagocytic activity of liver macrophages to the accelerated blood clearance (ABC) phenomenon of PEGylated liposomes in rats. *J. Controlled Release 126*, 162−165.
(30) Ganson, N. J., Kelly, S. J., Scarlett, E., Sundy, J. S., and Hershfield, M. S. (2006) Control of hyperuricemia in subjects with refractory gout, and induction of antibody against poly(ethylene glycol) (PEG), in a phase I trial of subcutaneous PEGylated urate oxidase. *Arthritis Res. Ther. 8*, R12.
(31) Sundy, J. S., Ganson, N. J., Kelly, S. J., Scarlett, E. L., Rehrig, C. D., Huang, W., and Hershfield, M. S. (2007) Pharmacokinetics and pharmacodynamics of intravenous PEGylated recombinant mammalian urate oxidase in patients with refractory gout. *Arthritis Rheum. 56*, 1021−1028.
(32) Hatfield, R. M., Morris, B. A., and Henry, R. R. (1987) Development of an enzyme linked immunosorbent assay for the detection of humoral antibody to *Pasteurella anatipestifer*. *Avian Pathology 16*, 123−140.
(33) Kunitani, M., Dollinger, G., Johnson, D., and Kresin, L. (1991) On-line characterization of polyethylene glycol-modified proteins. *J. Chromatogr. 588*, 125−137.
(34) Skoog, B. (1979) Determination of polyethylene glycols 4000 and 6000 in plasma protein preparations. *Vox Sang. 37*, 345−349.
(35) Porstmann, B., Porstmann, T., and Nugel, E. (1981) Comparison of chromogens for the determination of horseradish peroxidase as a marker in enzyme immunoassay. *J. Clin. Chem. Clin. Biochem. 19*, 435−439.
(36) Ahmed, S. A., Gogal, R. M. Jr., and Walsh, J. E. (1994) A new rapid and simple non-radioactive assay to monitor and determine the proliferation of lymphocytes: An alternative to [^{3}H]thymidine incorporation assay. *J. Immunol. Methods 170*, 211−224.
(37) Evinger, M., Maeda, S., and Pestka, S. (1981) Recombinant human leukocyte interferon produced in bacteria has antiproliferative activity. *J. Biol. Chem. 256*, 2113−2114.
(38) Bekisz, J., Baron, S., Balinsky, C., Morrow, A., and Zoon, K. C. (2010) Antiproliferative properties of Type I and Type II interferon. *Pharmaceuticals (Basel) 3*, 994−1015.
(39) Kitamura, T., Tange, T., Terasawa, T., Chiba, S., Kuwaki, T., Miyagawa, K., Piao, Y.-F., Miyazono, K., Urabe, A., and Takaku, F. (1989) Establishment and characterization of a unique human cell line that proliferates dependently on GM-CSF, IL-3, or erythropoietin. *J. Cell. Physiol. 140*, 323−334.
(40) Kitamura, T., Takaku, F., and Miyajima, A. (1991) IL-1 up-regulates the expression of cytokine receptors on a factor-dependent human hemopoietic cell line, TF-1. *Int. Immunol. 3*, 571−577.
(41) Behr-Gross, M.-E., Daas, A., Burns, C., and Bristow, A. F. (2007) Collaborative study for the establishment of erythropoietin BRP batch 3. *Pharmeuropa Bio. 2007−1*, 49−66.
(42) Curran, M. P., and McCormack, P. L. (2008) Methoxy polyethylene glycol-epoetin beta: A review of its use in the management of anaemia associated with chronic kidney disease. *Drugs 68*, 1139−1156.
(43) Wedekin, M., Ehrich, J. H. H., and Pape, L. (2011) Effective treatment of anemia in pediatric kidney transplant recipients with methoxy polyethylene glycol-epoetin beta. *Pediatr. Transplant. 15*, 329−333.
(44) Müller, H.-J., Löning, L., Horn, A., Schwabe, D., Gunkel, M., Schrappe, M., von Schütz, V., Henze, G., Casimiro da Palma, J., Ritter, J., Pinheiro, J. P. V, Winkelhorst, M., and Boos, J. (2000) Pegylated asparaginase (Oncaspar^{TM}) in children with ALL: Drug monitoring in reinduction according to the ALL/NHL-BFM 95 protocols. *Br. J. Haematol. 110*, 379−384.
(45) Armstrong, J. K., Hempel, G., Koling, S., Chan, L. S., Fisher, T., Meiselman, H. J., and Garratty, G. (2007) Antibody against poly(ethylene glycol) adversely affects PEG-asparaginase therapy in acute lymphoblastic leukemia patients. *Cancer 110*, 103−111.
(46) Sundy, J. S., Becker, M. A., Baraf, H. S. B., Barkhuizen, A., Moreland, L. W., Huang, W., Waltrip, R. W. II, Maroli, A. N., and Horowitz, Z. (2008) Reduction of plasma urate levels following treatment with multiple doses of pegloticase (polyethylene glycol-conjugated uricase) in patients with treatment-failure gout. Results of a Phase II randomized study. *Arthritis Rheum. 58*, 2882−2891 for the Pegloticase Phase 2 Study Investigators.
(47) Sundy, J. S., Baraf, H. S. B., Yood, R. A., Edwards, N. L., Gutierrez-Urena, S. R., Treadwell, E. L., Vázquez-Mellado, J., White, W. B., Lipsky, P. E., Horowitz, Z., Huang, W., Maroli, A. N., Waltrip, R. W. II, Hamburger, S. A., and Becker, M. A. (2011) Efficacy and tolerability of pegloticase for the treatment of chronic gout in patients refractory to conventional treatment: Two randomized controlled trials. *JAMA 306*, 711−720.
(48) Foster, G. R. (2010) Pegylated interferons for the treatment of chronic hepatitis C: Pharmacological and clinical differences between peginterferon-α-2a and peginterferon-α-2b. *Drugs 70*, 147−165.
(49) Yang, B. B., and Kido, A. (2011) Pharmacokinetics and pharmacodynamics of pegfilgrastim. *Clin. Pharmacokinet. 50*, 295−306.
(50) Sandborn, W. J., Feagan, B. G., Stoinov, S., Honiball, P. J., Rutgeerts, P., Mason, D., Bloomfield, R., Schreiber, S., for the PRECISE 1 Study Investigators. (2007) Certolizumab pegol for the treatment of Crohn's disease. *N. Engl. J. Med. 357*, 228−238.
(51) Schreiber, S., Khaliq-Kareemi, M., Lawrance, I. C., Thomsen, O. Ø., Hanauer, S. B., McColm, J., Bloomfield, R., Sandborn, W. J., for the PRECISE 2 Study Investigators. (2007) Maintenance therapy with certolizumab pegol for Crohn's disease. *N. Engl. J. Med. 357*, 239−250.
(52) Booth, C., and Gaspar, H. B. (2009) Pegademase bovine (PEG-ADA) for the treatment of infants and children with severe combined immunodeficiency (SCID). *Biologics 3*, 349−358.
(53) Trainer, P. J., Ezzat, S., D'Souza, G. A., Layton, G., and Strasburger, C. J. (2009) A randomized, controlled multicentre trial comparing pegvisomant alone with combination therapy of pegvisomant and long-acting octreotide in patients with acromegaly. *Clin. Endocrinol. 71*, 549−557.
(54) Silver Lake Research. Reagent Specification Sheet Catalog #: CH2074, Anti-Polyethylene Glycol (PEG) Monoclonal Antibody.

Bioconjugate Chemistry

Article

pubs.acs.org/bc

Site-Selective Lysine Modification of Native Proteins and Peptides via Kinetically Controlled Labeling

Xi Chen,[†,‡] Kasturi Muthoosamy,[†] Anne Pfisterer,[§] Boris Neumann,[∥] and Tanja Weil*[,†,‡,§]

[†]Institute of Organic Chemistry III, University of Ulm, Albert-Einstein-Allee 11, 89081 Ulm, Germany

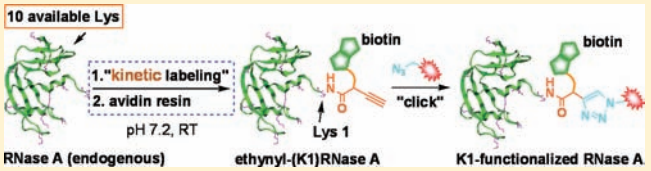
[‡]Department of Chemistry, National University of Singapore, 3 Science Drive 3, 117543 Singapore

[§]Max Planck Institute for Polymer Research, Ackermannweg 10, D-55128 Mainz, Germany

[∥]Proteome Factory AG, Magnusstr. 11, Haus 2, 1.OG, 12489 Berlin, Germany

Supporting Information

ABSTRACT: The site-selective modification of the proteins RNase A, lysozyme C, and the peptide hormone somatostatin is presented via a kinetically controlled labeling approach. A single lysine residue on the surface of these biomolecules reacts with an activated biotinylation reagent at mild conditions, physiological pH, and at RT in a high yield of over 90%. In addition, fast reaction speed, quick and easy purification, as well as low reaction temperatures are particularly attractive for labeling sensitive peptides and proteins. Furthermore, the multifunctional bioorthogonal bioconjugation reagent (**19**) has been achieved allowing the site-selective incorporation of a single ethynyl group. The introduced ethynyl group is accessible for, e.g., click chemistry as demonstrated by the reaction of RNase A with azidocoumarin. The approach reported herein is fast, less labor-intensive and minimizes the risk for protein misfolding. Kinetically controlled labeling offers a high potential for addressing a broad range of native proteins and peptides in a site-selective fashion and complements the portfolio of recombinant techniques or chemoenzymatic approaches.



INTRODUCTION

In recent years, there has been an emerging interest in the site-selective functionalization of proteins.[1] Major applications of modification approaches include the improvement of pharmacokinetic properties of therapeutic proteins by adding polymer chains,[2,3] glycoslation of proteins,[4] attachment of chromophores for studying protein dynamics[5] or protein folding,[6,7] fabrication of protein microarrays,[8,9] and tailoring novel biohybrid materials such as protein−polymer amphiphiles.[10] However, native protein labeling usually lacks site-selectivity since it is often challenging to address a single functional group only. In most cases, cysteine point mutations are introduced to allow site-specific attachment of functional groups.[11−13] Recently, the incorporation of noncanonical amino acids via either selective pressure incorporation[14,15] or nonsense coden suppression[16] allows introduction of functional groups that facilitate bioorthogonal reactions[17,18] such as click reactions,[19] Staudinger ligations,[20] or Sonogashira cross-coupling reactions[21] on proteins. Additionally, proteins have also been functionalized site-specifically via enzymatic post-translational modifications.[22] Most recently, the recombinant maltose binding protein has been modified site-specifically by applying a dirhodium metallopeptide catalyst utilizing a proximity-driven concept.[23]

Although biological approaches have been successful, the development of efficient and generally applicable chemical procedures toward site-specific modification of native proteins is still elusive. There have been few attempts such as targeting accessible disulfide bonds[24,25] or the N-terminus of a protein.[26] However, nonphysiological reaction conditions, lack of accessible disulfide bonds for intercalation, or N-termini not suitable for further chemical modifications often represent prevalent limitations. Frequently, protein mixtures of the native protein and the corresponding modified protein are obtained, as achieving either high conversions or facile purifications is often rather challenging.

Herein, lysine residues that are abundant in native proteins and peptides are targeted site-selectively under kinetically controlled modification conditions. Following this approach, the proteins ribonuclease A (RNase A) and lysozyme C as well as the peptide hormone somatostatin (SST-14) have been successfully decorated with a single substituent in a highly site-selective fashion. In addition, the multifunctional linker biotin-TEO-ethynyl-NHS (Figure 8a, **18**, TEO: tetraethylene oxide) has been designed that allows site-selective introduction of a bioorthogonal substituent at the protein surface. The kinetically controlled chemical labeling strategy reported herein benefits from a convenient reaction scheme and straightforward purification and it opens up various opportunities for precisely functionalizing proteins and peptides.

Received: October 14, 2011
Revised: February 3, 2012
Published: February 17, 2012

ACS Publications © 2012 American Chemical Society

dx.doi.org/10.1021/bc200556n | *Bioconjugate Chem.* 2012, 23, 500−508

EXPERIMENTAL PROCEDURES

Materials. D-biotin-amido-caproate-*N*-hydroxysuccinimidyl ester (Biotin-LC-NHS) (≥98%) for protein biotinylation was received from Sigma-Aldrich (Cat. No. B2643). Ribonuclease A (RNase A) and lysozyme from hen egg white (lysozyme C) were obtained from MP Biomedicals, LLC (Cat. No. 101076) and Fluka Biochemika (Cat. No. 62971), respectively. Somatostatin (SST-14) was supplied by GL Biochem (Shanghai). 10× Phosphate buffered saline, ultra pure grade, was purchased from First BASE (Cat. No. 2040). Pierce Monomeric Avidin Kit for affinity chromatography and Sephadex G-15 Gel for gel filtration were from Thermo Scientific (Cat. No. 20227) and Sigma-Aldrich (Cat. No. G15120), respectively. Bicinchoninic acid (BCA) assay kit for protein quantification was obtained from Novagen (Cat. No. 71285−3). UV analysis of protein fractions during gel filtrations and absorbance determinations for BCA assays were recorded on a BioTEK SYNERGY 4 Microplate Reader. All MALDI-ToF-MS spectra of the protein samples were recorded on an Autoflex MALDI-ToF (Bruker Daltonics) mass spectrometer or Applied Biosystems 4700 Proteomics Analyzer 88 using sinapinic acid solution as matrix. *nano*LC-MS^2 analysis of modified proteins were accomplished at Proteome Factory AG (Germany). NuPAGE Novex 4−12% Bis-Tris gel and its corresponding NuPAGE MES SDS running buffer for gel electrophoresis were purchased from Invitrogen. Baker's yeast ribonucleic acid (*S. cerensiae*) (yRNA) was purchased from Sigma-Aldrich (Cat. No. R6750). SYBR Safe DNA gel stain (10 000× concentrated) in DMSO was obtained from Invitrogen Molecular Probes (USA). Ultrapure grade Tris (Cat. No. 1400) and ultrapure grade EDTA (Cat. No. 1050) were purchased from First BASE. 384-well black microtiter plates for conducting the RNase A functional assay and sterile 96-well plate were received from Greiner Bio-One Ltd.. (UK) and Nunclon Surface (Denmark), respectively.

Site-Selective Biotinylation of RNase A (1) and Lysozyme C (4). Kinetically controlled site-selective biotinylation labeling includes six major steps and the procedure is briefly summarized in Scheme S1. Under minimized light exposure, 1 mL of freshly prepared protein solution (72.5 μM, 72.5 nmol) in PBS buffer (0.1 M, pH 7.2) was added into a 14 mL aluminum foil coated Epppendorf tube. Fresh biotin-LC-NHS solution (16.6 μg, 36.3 nmol) in dry DMSO (50 μL) was added by a 2.5 μL pipet with portions of 0.5 μL per addition per minute and immediately followed by an intensive vortex after capping. The addition was finished within 100 min and the reaction solution was allowed to shake at RT for an additional 1 h (Step I: the bioconjugation step). Subsequently, 33.2 μL of an ethanolamine solution (2.66 mg mol^{-1}, 1.45 μmol, 20 equiv relative to protein) were added into the reaction solution in PBS buffer (pH 7.2) in order to quench any traces of remaining unreacted biotin-LC-NHS (Step II: the quenching step). After overnight incubation, any biotin-containing small molecules were removed from the protein solution by gel filtration using Sephadex G-15 gel (1.5 kD cut off, Step III: the first biotin-removal step). The purified protein mixture solution was loaded onto a monomeric avidin resin column. Excess of native protein was first recovered by eluting the resin column with PBS buffer (pH 7.2), and then, the amount of recovered protein in the eluent was quantified by a BCA assay (Step IV: protein recovery step). Subsequently, biotinylated protein was obtained by eluting the resin column with PBS buffer (pH 7.2) containing additional 2 mM of biotin (Step V: affinity elution step). Gel filtration via Sephadex G-15 facilitated the separation of (+)-biotin as well as desalting of the monobiotinylated protein thus yielding the pure monobiotinylated protein in solution. The protein concentration was determined by the BCA assay (Step VI: the second biotin-removal step). The calculated labeling yield for biotin-LC-(K1)RNase A and biotin-LC-(K1)lysozyme C by considering the recovered native protein was determined as 92% (197 μg) and 94% (226 μg), respectively. Since biotin-LC-NHS is not readily water-soluble, minor amounts of DMSO (5% DMSO) were required. However, the functional assay of the recovered RNase A revealed that the enzymatic activity was retained completely.

Site-Selective Biotinylation of SST-14 (6) at K9. A solution of biotin-LC-NHS (64.6 μg, 0.142 μmol) in DMF (0.324 mL) was added via an autosyringe pump during 200 min into a solution of SST-14 (**6**, 0.775 mg, 0.473 μmol) in PBS buffer (0.1 M, pH 7.2, 10 mL) at 4 °C under stirring. The resultant solution was further stirred at 4 °C overnight. The reaction solution was analyzed by MALDI-ToF-MS spectroscopy using α-cyano-4-hydroxycinnamic acid (CHCA) as the matrix, revealing the monobiotinylation of SST-14. Herein, DMF was used instead of DMSO in order to avoid the solidification of DMSO at 4 °C.

Site-Selective Ethynylation of RNase A (1) Using Biotin-TEO-Ethynyl-NHS (18). The general procedure for the ethynylation of RNase A is similar to the biotinylation protocol. NHS ester (**18**) (6.8 mg, 5.85 μmol, 64% NHS ester content according to ^{1}H NMR,) was dissolved in 0.5 mL dry DMSO and this solution was added into 10 mL solution of RNase A in PBS buffer (1 mg mL^{-1}, 0.725 μmol) in 100 equal portions during 100 min. Then, the solution was stirred at RT for additional 1 h and 332 μL of an ethanolamine solution (2.66 mg mL^{-1}, 14.5 μmol) was added to quench any unreacted NHS ester. The resultant solution was shaken at RT overnight. Due to the loading capacity limit of the Monomeric Avidin Kit, 2.6 mL of protein solution was purified sequentially by gel filtration, affinity chromatography, and gel filtration, and lyophilized to afford 323 μg of monoethynylated RNase A. 1.82 mg of native RNase A was recovered and thus 777 μg of RNase A was consumed. Therefore, the labeling yield of monoethynylated RNase A was calculated as 40%.

It is noteworthy that 8 equiv of biotin-TEO-ethynyl-NHS (**18**) was used rather than 0.5 equiv since biotin-TEO-ethynyl-NHS (**18**) reacts more slowly than biotin-LC-NHS and, in addition, autohydrolysis takes place more rapidly most likely due to the enhanced water solubility of this reagent. This deactivation of **18** during the bioconjugation process reduces the effective amount of **18** in solution. Therefore, only a limited amount instead of an excess of **18** is available for reaction with RNase A. In order to minimize the autohydrolysis of **18**, minor amounts of DMSO were used to dissolve **18** instead of choosing pure water.

RESULTS AND DISCUSSION

RNase A Is Site-Selectively Modified at K1 under Kinetically Controlled Conditions and Preservation of Enzymatic Acitivity. Ribonuclease A (RNase A, **1**) is selected for site-specific modification since this enzyme is stable, well-characterized, and of therapeutic relevance as one of its close variants, onconase, is under clinical investigations as a potential cancer therapeutic.[27] RNase A carries ten lysine residues at its surface. In order to assess whether there is a preference for a

dx.doi.org/10.1021/bc200556n | *Bioconjugate Chem.* 2012, 23, 500−508

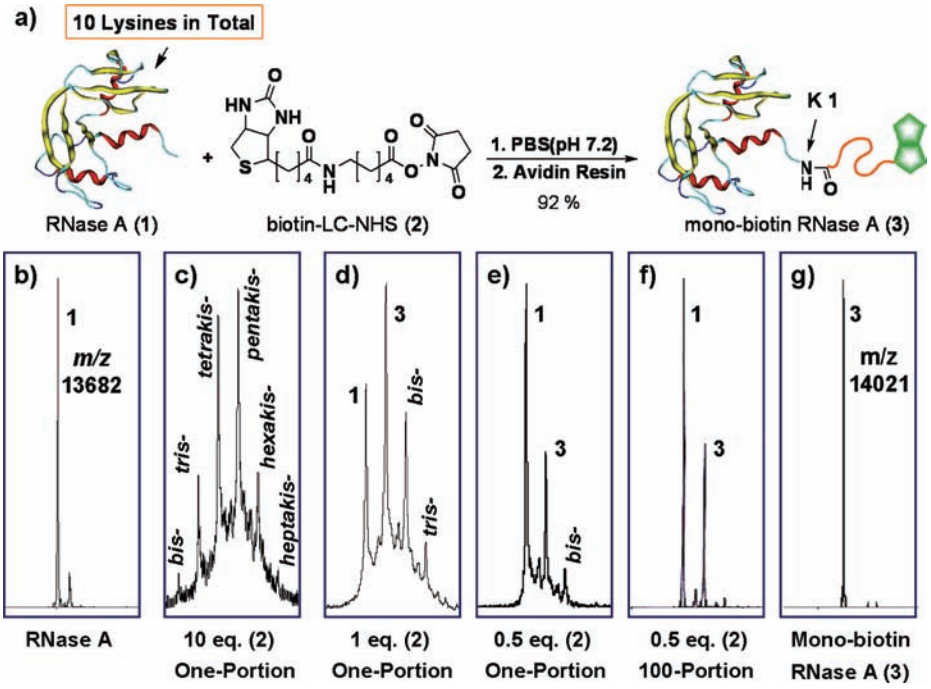


Figure 1. (a) Reaction scheme of the kinetically controlled labeling reaction of native RNase A (**1**) by applying biotin-LC-NHS (**2**); (b) the MS spectrum of native RNase A (**1**) (M.W. 13 681 g mol^{-1}); the MS spectra of biotinylated RNase A solution after one-portion addition of 10 equiv, 1 equiv, or 0.5 equiv of **2** for 2 h (c), (d), and (e), respectively; the MS spectrum of biotinylated RNase A solution by adding 0.5 equiv of **2** in 100 equal portions during 100 min and reacted for further 1 h; the MS spectrum of the affinity purified monobiotinylated RNase A (**3**, M.W. 14 020 g mol^{-1}).

single lysine residue, RNase A is reacted with the biotinylation reagent biotin-LC-NHS (**2**, Figure 1a) bearing an amine-reactive NHS group as well as a biotin tag for affinity purification. First, 10 equiv of biotin-LC-NHS (**2**) is added in a single portion to RNase A in PBS buffer (pH 7.2) at RT and the reaction is stirred for 2 h. The resulting MALDI-ToF-MS spectrum reveals a typical modification pattern as typically found in normal protein labeling reactions using NHS esters in excess (Figure 1c) and a mixture of bis-, tris-, tetrakis-, pentakis-, and heptakis- biotinylated RNase A has been obtained.

However, by decreasing the equiv of biotin-LC-NHS (**2**) relative to RNase A, a more selective labeling should be achieved since more reactive and accessible residues should react faster. Therefore, the amount of **2** is first decreased from 10 equiv to 1 equiv and is directly added into RNase A in one portion. After 2 h of reaction, aside from the unreacted native RNase A, mono-, bis-, and minor amounts of tris-biotinylated RNase A are found, suggesting an increase of selectivity (Figure 1d). Inspired by this result, the amount of biotin-LC-NHS (**2**) is further decreased from 1 equiv to 0.5 equiv and is added into RNase A PBS solution in one portion. Obviously, the selectivity is further increased, and apart from unreacted RNase A (**1**), monobiotinylated RNase A (**3**) is obtained as the major product, accompanied with minor amounts of bis-labeled product (Figure 1e).

In order to improve the selectivity of the labeling reaction, the ratio of biotin-LC-NHS (**2**) relative to RNase A could be further decreased. However, such an approach would substantially decrease the labeling yield, which is not favorable since proteins are usually expensive. Therefore, the total amount of **2** was kept to 0.5 equiv, but the mode of the addition of **2** was changed. 0.5 equiv of biotin-LC-NHS (**2**) has been divided into 100 equal portions and added stepwise during 100 min into the RNase A solution in PBS buffer. Under these conditions, only 0.01 equiv of **2** is added into protein solution at each time point, ensuring that RNase A always remains in excess compared to **2**. After completion of the addition of 0.5 equiv of **2**, the reaction solution is further incubated for 1 h followed by a MALDI-ToF-MS analysis. This time, only monobiotinylated RNase A is formed (Figure 1f). In case larger quantities of **2** are added in such a stepwise fashion, the formation of the bis-modified byproduct becomes evident, particularly if more than 0.7 equiv of **2** are added (data not shown). Therefore, 0.5 equiv of biotin-LC-NHS (**2**) relative to the amount of protein represents the best compromise of selectivity and protein yield.

Thereafter, the reaction solution is quenched by addition of ethanolamine solution and incubated overnight in order to deactivate any remaining traces of unreacted **2**. This is an essential step since it has been found that remaining unreacted NHS ester interacts with monobiotinylated RNase A after affinity purification, which again decreases the quality of monobiotinylated RNase A due to the formation of byproducts. Such deactivated biotin-containing small molecules are removed via gel-filtration and the protein solution which exclusively contains excess native RNase A and monobiotinylated RNase A is subjected to affinity purification. Monofunctionalized RNase A (**3**) is isolated from the native protein based on the highly specific interaction between biotin and the monomeric egg white protein avidin. Monomeric avidin based affinity chromatography is chosen since it allows elution of proteins under mild conditions at physiological pH, thus minimizing the risk for protein denaturation.[28] The isolated biotinylated RNase A exhibits a single peak with m/z 14021 $[M+H]^+$ (Figure 1g, Δ m/z 339.7 relative to RNase A), which

dx.doi.org/10.1021/bc200556n | *Bioconjugate Chem.* 2012, 23, 500–508

matches the calculated M.W. of 14020 g mol^{-1}. It is noteworthy that no traces of bis- or higher biotinylated RNase A proteins have been identified by applying high-resolution MALDI-ToF-MS.

Excessive amounts of RNase A could be easily recovered during the affinity chromatography step at physiological pH in order to avoid protein loss during modification. Briefly, after loading the native and biotinylated RNase A mixture onto the monomeric avidin resin column, the unreacted native RNase A is readily recovered by eluting the resin column with PBS buffer (0.1 M, pH 7.2) at RT. Subsequently, the biotinylated RNase A is obtained by eluting the resin column a second time with PBS buffer (0.1 M, pH 7.2) which contains additional 2 mM of (+)-biotin. According to BCA assay quantifications, out of 1 mg native RNase A, about 791 μg RNase A has been recovered and only 209 μg of RNase A (**1**) was consumed during the reaction. In this way, by considering the recovery of RNase A, a high yield of about 92% (197 μg) of monobiotinylated RNase A (**3**) has been obtained. Noteworthy, the recovered RNase A displays similar enzymatic activity, as the initial RNase A and no activity loss after recovery has been observed (Figure 4).

Thereafter, the lysine residue carrying the biotin substituent is determined by *nano*LC-tandem mass spectrometry in the high resolution mode to prove whether only the most reactive lysine residue has reacted site-selectively. After in-gel digestion of monobiotinylated RNase A (**3**) by chymotrypsin, peptide fragments are obtained and subjected to *nano*LC-MS^2 whereby each peptide fragment is fractionated by *nano*LC and identified by MS^2. The peptide fragment KETAAAKF (1−8) with m/z 1203.63 $[M+H]^+$ carries the biotin-LC moiety since it corresponds to the calculated M.W. of 1202.62 g mol^{-1}. Since this peptide contains two lysine residues, an additional MS^2 experiment has been recorded demonstrating that K1 rather than K7 is modified due to the presence of the fragments *b* 1 (Figure 2, modification at K1) and *y* 7 (Figure 2, no modification in ETAAAKF (2−8)) (Figure 2).

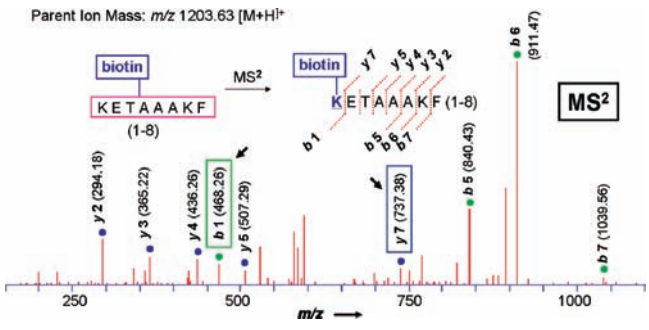


Figure 2. Full interpretation of the MS^2 spectrum of biotinylated peptide fragment KETAAAKF (1−8) demonstrating that the modification occurred at K1 rather than at K7.

It is noteworthy that peptide fragments bearing cysteine residues are not detected directly, since they are generally lost during in-gel digestion due to their Michael addition reactions with the polyacrylamide gel. In order to ensure that monobiotinylation has occurred only at K1 of KETAAKF (1−8), extracted ion chromatography (XIC) of both modified and unmodified KETAAKF (1−8) is performed (Figure 3a). The biotinylated KETAAAKF fragment exhibits a predominant peak in its XIC chromatograph at t_R 32.55 min (Figure 3a, top) and no unmodified KETAAAKF (1−8) is detected in its XIC chromatogram (Figure 3a, bottom), thus demonstrating that every K1 residue of KETAAAKF (1−8) has been modified. This observation together with the MALDI-ToF-MS spectrum revealing only monofunctionalized RNase A (Figure 3b) indicates that biotinylation occurs at K1 only. In this way, site-selectivity is demonstrated yielding biotin-LC-(K1)RNase A (**3**) under mild reaction conditions.

The catalytic activities of biotinylated RNase A as well as the recovered native RNase A are investigated in a functional RNase assay using Baker's yeast ribonucleic acid (yRNA) as substrate. yRNA forms a fluorescent complex in the presence of SYBR Safe DNA gel stain dye, and RNase A quickly degrades yRNA and destroys the fluorescent complex leading to fluorescence decay (Figure 4a). The initial speed of the fluorescence decay is proportional to the enzymatic activity and autohydrolysis of yRNA in the absence of RNase A is determined as control (green rhombic dots). According to Figure 4b, both native RNase A (brown triangular dots) and the recovered RNase A (orange rectangular dots) quickly hydrolyze yRNA at the same rate, suggesting no significant loss of enzymatic activity of the recovered RNase A. Bbiotin-LC-RNase A (**3**) also hydrolyzes yRNA leading to a decrease of the relative fluorescence unit (RFU) in the beginning but with a slightly reduced velocity (violet foursquare dots). According to the initial slopes of the blank control (k_1 −0.07), biotin-LC-RNase A (k_2 −0.56), and native RNase A (k_3 −0.63), the relative activity of biotin-LC-RNase A in relation to native RNase A is calculated to be $(k_2 - k_1)/(k_3 - k_1)$ = 88%. This indicates that modified RNase A still maintains significant catalytic activity, and minor activity loss might be attributed to steric hindrance due to the presence of the biotin-LC moiety.

Lysozyme C (4) Is Mono-Biotinylated at K1 under Kinetically Controlled Conditions. In order to demonstrate the general applicability of this kinetic chemical labeling scheme, the protein lysozyme from hen egg white (lysozyme C) (**4**) as well as the peptide hormone somatostatin (SST-14) (**6**) are biotinylated in a similar fashion. Lysozyme C reacts with peptidoglycans and hydrolyzes the glycosidic bond that connects *N*-acetylmuramic acid with the fourth carbon atom of *N*-acetylglucosamine. It has been applied successfully as a biopharmaceutical in many aspects, such as treating bactofugation, rendering modified lysozyme C products attractive for medicinal applications. Lysozyme C contains six lysine residues in total, and to the best of our knowledge, entirely chemical approaches toward site-selective modification of lysozyme C have not been achieved before. As described previously, lysozyme C (**4**) is treated with biotin-LC-NHS (**2**) under the same conditions used for RNase A (**1**) labeling (Figure 5a). The MALDI-ToF-MS spectrum (Figure 5b) confirms mono-biotinylation yielding biotin-LC-lysozyme C (**5**) with a corresponding molecular mass signal at m/z 14 644 $[M+H]^+$ (Figure 5b, right, calculated M.W. of **5** is 14 643 g mol^{-1} with a difference of 339.5 relative to native lysozyme C with m/z 14 305). According to *nano*LC-MS^2 together with XIC analysis (Figure 5c), K1 is identified as biotinylation site of lysozyme C. Starting from 1.04 mg of native lysozyme C (**4**), 764 μg of native lysozyme C have been recovered and 226 μg of biotin-LC-lysozyme C (**5**) have been isolated corresponding to a calculated yield of about 94% by considering the amount of recovered lysozyme C.

SST-14 Is Mono-Biotinylated at K9 under Kinetically Controlled Conditions. SST-14 represents a cyclic peptide hormone consisting of 14 residues, featuring a single disulfide

dx.doi.org/10.1021/bc200556n | *Bioconjugate Chem.* 2012, 23, 500−508

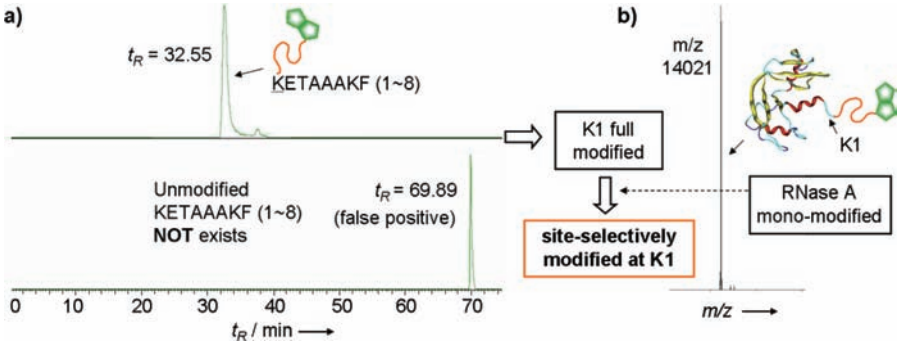


Figure 3. Demonstration of the site-selectivity. (a) The XIC chromatograph of the K1 biotinylated peptide fragment KETAAAKF (1−8) (up) and the XIC chromatograph of unmodified KETAAAKF (1−8) (down) indicate the formation of biotinylated KETAAAKF (1−8) and the absence of unmodified KETAAAKF fragments (1−8) suggesting that all K1 residues carry a single biotin group. Taking this information as well as monomodification of RNase A (Figure 3b) into account confirms the site-selectivity of the modification under kinetically controlled conditions.

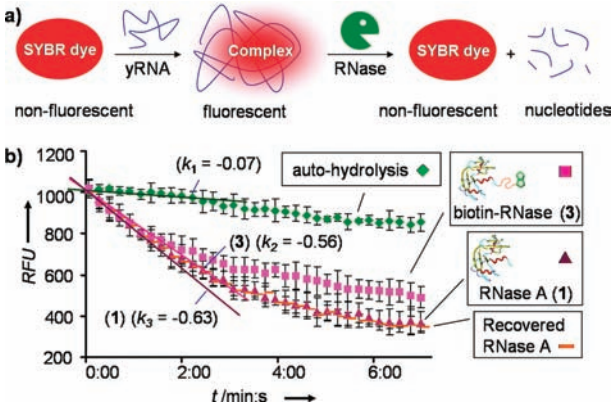


Figure 4. Functional RNase A assay. (a) General scheme of the functional assay: Nonfluorescent SYBR dye forms a fluorescent complex with yRNA which is subsequently decomposed by active RNase, yielding the nonfluorescent SYBR dye; (b) the functional assay diagram: The green rhombic dots represent autohydrolysis of yRNA; the violet foursquare dots suggest the enzymatic activity of biotin-LC-RNase A (**2**); the brown triangular dots and the orange rectangular dots reveal the activity of native RNase A and recovered RNase A, respectively.

bond (Csy3-Cys14), and contains three amino groups (Lys 4, Lys 9, and the N-terminus of Ala, Figure 6b). SST-14 plays an important role in many physiological processes, and its analogue, octreotide (Novartis Pharmaceuticals) with a higher stability, is in clinical use. Modification of this peptide hormone is of therapeutic interest to increase metabolic stability and it also offers the advantage of direct *nano*LC-MS^2-XIC analysis without the necessity for in-gel digestion. In this way, the entire modification pattern of SST-14 can be assessed. To contribute to the low stability of SST-14 and to improve site-selectivity, the labeling reaction is performed at 4 °C by adding a total amount of 0.3 equiv of biotin-LC-NHS (**2**) that is injected into the SST-14 solution during a time frame of 200 min (Figure 6a). Following this procedure, SST-14 has been monobiotinylated according to the MALDI-ToF-MS spectrum (Figure 6c). After reduction of the Cys3-Cys14 disulfide by TCEP (tris-(2-carboxyethyl)phosphine), the linearized peptide is directly analyzed by *nano*LC-MS^2-XIC. According to the XIC chromatograph, there is only a symmetric peak corresponding to monobiotinylated SST-14 (**7**, Figure S3). This suggests that the modification occurs at only one residue and the MS^2 spectrum confirms biotinylation at K9 only (Figure 6d). Direct evidence is obtained from the presence of the *b* 8 ion (proofing that A1 and K4 remain unmodified), the *b* 9 ion (indicating biotinylation at K9), and the *y* 5 ion (proof that TFTSC (10−14) remains unmodified). Thus, the site-selective modification of the small, native SST-14 peptide has been achieved at K9.

Solvent Accessibility as well as Interaction with Adjacent Amino Acids Might Contribute to the Observed Site-Selectivity of Kinetically Controlled Chemical Labeling. It has been demonstrated above that different lysine residues of proteins and peptides reveal significant alterations of their individual reactivities. In order to gain some additional insight into this phenomenon, we have carefully examined the crystal structure of RNase A and lysozyme C (Figure 7). First, the solvent accessibility[29] of all lysine residues of RNase A and lysozyme C is calculated by implementing 1RCA.pdb and 2ZYP.pdb into the software package *Molecular Operating Environment* (MOE, Chemical Computing Group). This analysis recognizes the steric hindrance in the surrounding of the respective lysine residues that might affect their relative reactivities. In the case of RNase A, the modified K1 residue is indeed the lysine residue showing the highest solvent accessibility (Figure 7a). Interestingly, the modified K1 residue of lysozyme C does not display the highest solvent accessibility, since according to the crystal structure of lysozyme C, K97 should be more accessible (Figure 7b, bottom). After close examination of the chemical environment of K1, a hydrogen bond interaction between the hydrogen atom of the ε-amino group of K1 and the oxygen of the adjacent carboxylic acid group of E7 is recognized (Figure 7b, top). Due to this interaction, the amino group of K1 might be less positively charged and thus more nucleophilic and reactive. However, these considerations are still very premature and higher-level calculations are required to elucidate the origin of the reactivity of different lysine residues. However, such studies assessing the reactivity of different amino acid residues on the surface of proteins might be of broad interest to allow a better understanding of post-translational modifications.

Kinetically Controlled Chemical Labeling Allows Introduction of an Ethynyl Group onto RNase A Facilitating Site-Specific Click Reaction. In the last step, the more sophisticated, multifunctional bioconjugation linker biotin-TEO-ethynyl-NHS (**18**, Figure 8a) is designed for integrating a single bioorthogonal ethynyl group onto K1 of RNase A. Biotin-TEO-ethynyl-NHS (**18**) bears a biotin tag for purification, an ethynyl group that allows click reactions, an amine-reactive NHS ester for protein functionalization, and a

dx.doi.org/10.1021/bc200556n | *Bioconjugate Chem.* 2012, 23, 500−508

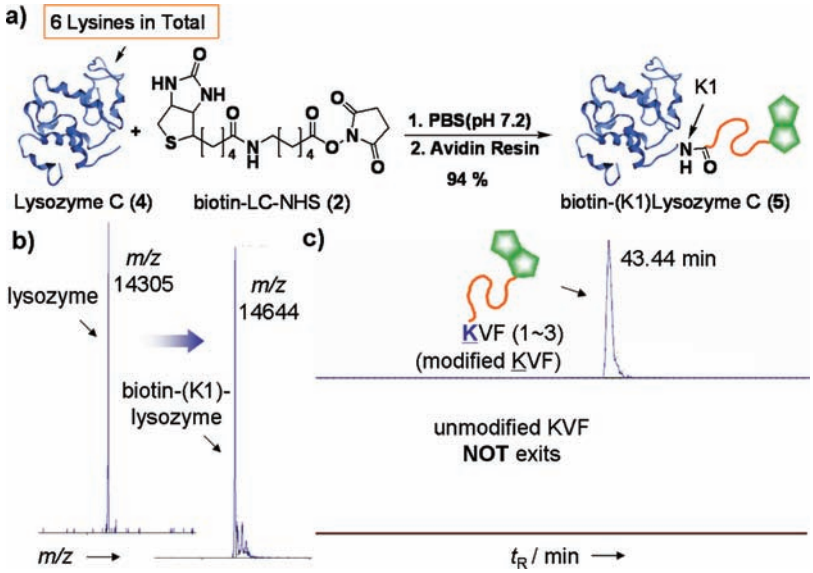


Figure 5. (a) Site-selective biotinylation scheme of lysozyme C (**4**) by applying biotin-LC-NHS (**2**); (b) MALDI-ToF-MS spectra of native lysozyme C (**4**, left) and biotinylated lysozyme C (**5**, right) demonstrating monomodification (the tiny peak with a slightly higher M.W. does not indicate bis-modification; see Supporting Information); (c) the XIC chromatographs of modified KVF (1−3) (above) and unmodified KVF (1−3) (bottom) suggest full modification of K1 of lysozyme C.

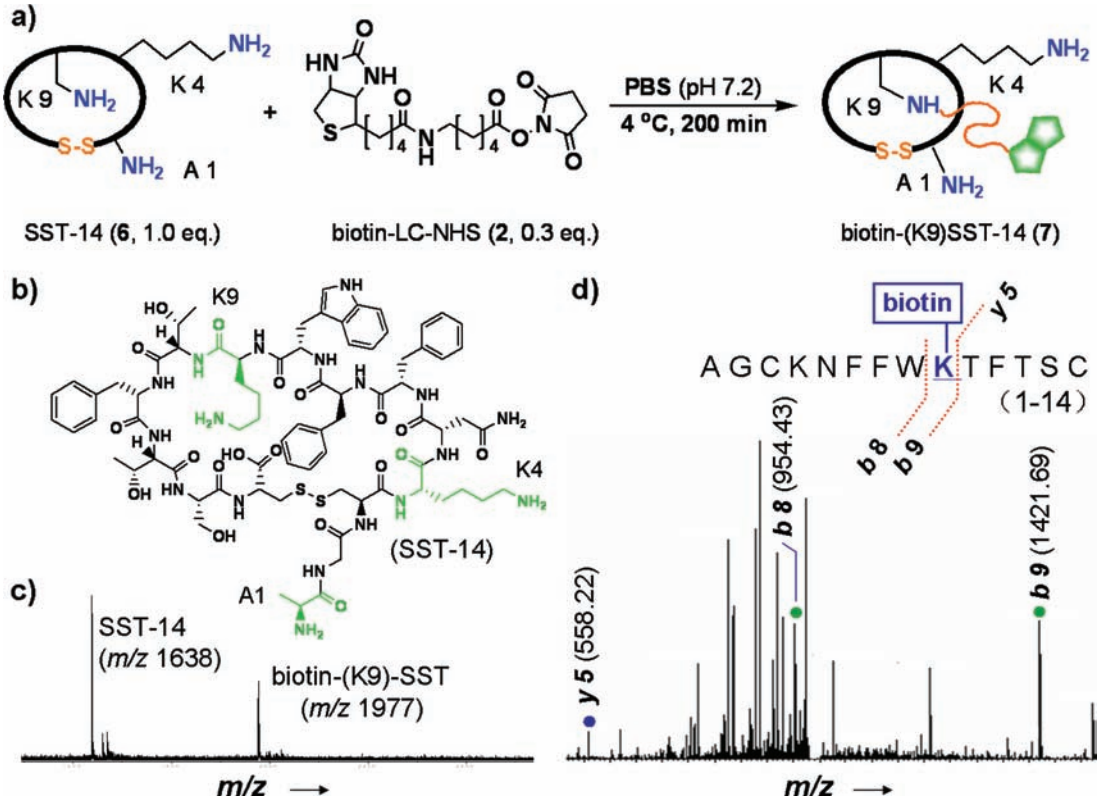


Figure 6. (a) Biotinylation scheme of SST-14 (**6**) by biotin-LC-NHS (**2**); (b) chemical structure of SST-14 (**6**) stressing all three amino groups of A1, K4 and K9, all highlighted in green; (c) MALDI-ToF-MS spectrum of the reaction mixture indicating monobiotinylation of SST-14 (**6**); (d) MS^2 spectrum of reduced monomodified SST-14 proves that biotinylation occurs at K9.

TEO spacer to impart water solubility. The synthesis of this bioorthogonal linker is accomplished in nine reaction steps, most of them proceeding with high yields (Figure 8b).

Briefly, 1 equiv of *tert*-butyl 2-bromoacetate (**8**) is treated with 2 equiv of *N*-propargylamine (**9**) under basic condition to afford *tert*-butyl 2-propargylaminoacetate (**10**), which is subsequently acylated by succinic anhydride to give **11**. In parallel, 4,7,10-trioxa-1,13-tridecanediamine (**12**) is protected to afford *N*-Boc-4,7,10-trioxa-1,13-tridecanediamine (**13**) and then coupled to biotin via EDC (1-ethyl-3-(3-dimethylaminopropyl)carbodiimide) condensation yielding biotin-TEO-NH(Boc) (**14**). Afterward, **14** is deprotected by

dx.doi.org/10.1021/bc200556n | *Bioconjugate Chem.* 2012, 23, 500−508

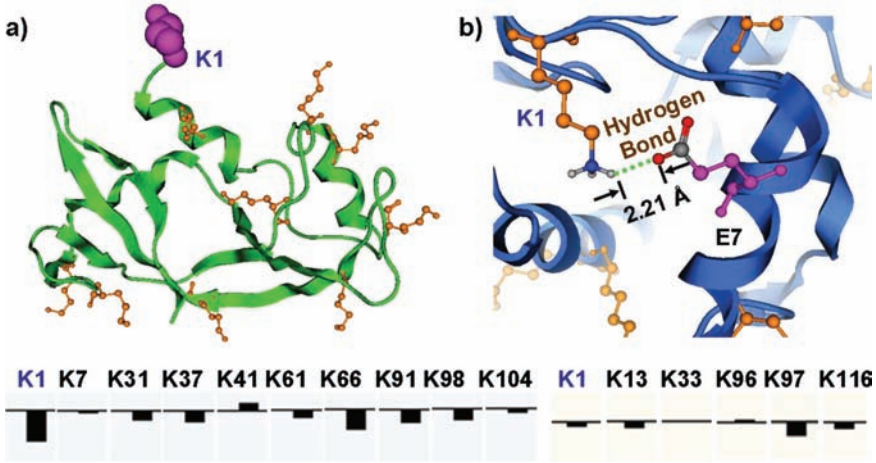


Figure 7. (a) Crystal structure of RNase A (PDB file: 1RCA.dpb) shows the presence of ten lysine residues of RNase A. K1 is highlighted in a violet ball-and-sphere model and exhibits the highest solvent accessibility. (b) Crystal structure of lysozyme C (PDB file: 2ZYP) reveals six lysine residues as well as a hydrogen bond interaction between K1 and E7 with a typical bond length of 2.21 Å. The relative solvent accessibility of each lysine residue of both RNase A and lysozyme C is given as column length (below) ("down" refers to accessible and "up" indicates buried inside).

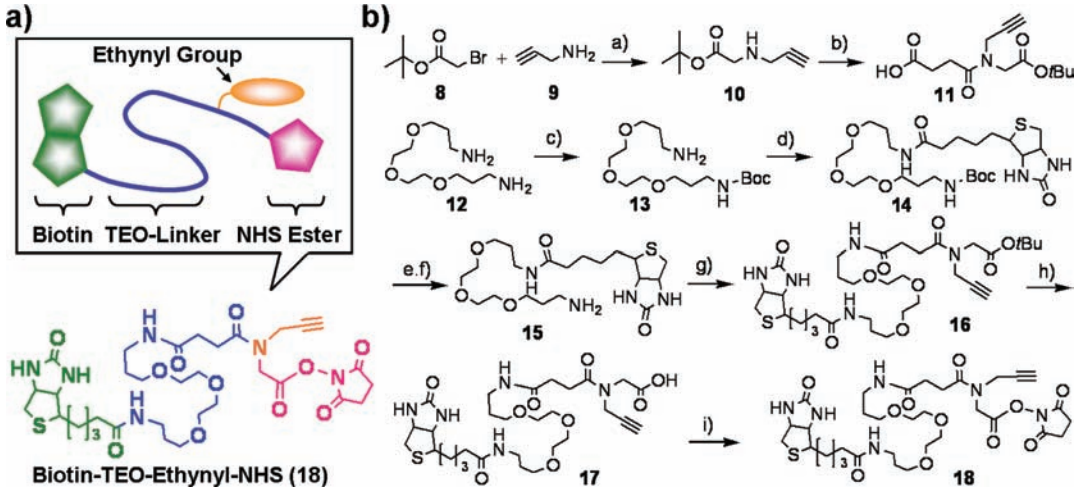


Figure 8. (a) Design of the ethynylation reagent (**18**), featuring a biotin tag, a water-soluble TEO linker, a bioorthogonal ethynyl group, and an amine-reactive NHS ester; (b) synthetic scheme toward biotin-TEO-ethynyl-NHS (**18**). (a) K_2CO_3/DMF, RT, 48 h, 66%; (b) succinic anhydride/DMF, RT, overnight, 79%; (c) $(Boc)_2O$, RT, overnight, 34%; (d) (+)-biotin, EDC/DMF, RT, 48 h, 73%; (e) TFA/DCM, RT, 12 min; (f) NH_3 (aq), quantitative yield from **14** to **15**; (g) **11**, HBTU, DIEA/DMF, RT, 48 h, 86%; (h) TFA/DCM, RT, 5 h, 70%; (i) NHS, EDC/DMF, RT, 25 h, 99%.

trifluoroacetic acid (TFA) to give biotin-TEO-NH_2 (**15**) and then coupled with **11** by HBTU (*O*-(benzotriazol-1-yl)-*N,N,N′,N′*-tetramethyluronium hexafluorophosphate) to yield **16**. Subsequently, **16** is deprotected by TFA to afford biotin-TEO-ethynyl-COOH (**17**). In the last step, **17** is activated with NHS yielding the target molecule biotin-TEO-ethynyl-NHS (**18**). Noteworthy, the synthesis of bioorthogonal linkers bearing alternative reactive groups could be achieved in principle by replacing *N*-propargylamine (**9**) by a corresponding primary amine, e.g., 2-azidoethylamine without the necessity to develop a novel synthetic scheme. All reaction steps and full characterizations are given in the Supporting Information.

As described above, small amounts of biotin-TEO-ethynyl-NHS (**18**) are added into a solution containing RNase A in 100 equal portions over a time period of 100 min (Figure 9a). Monoethynyl RNase A (**19**) is successfully isolated after purification and a predominant mass peak of *m/z* 14306 $[M+H]^+$ is found in the MALDI-ToF-MS spectrum matching its calculated M.W. of 14 305 g mol^{-1} (Figure 9b, left; M.W. of biotin-TEO-ethynyl: 623.8 g mol^{-1}). Thereafter, the modified protein (**19**) is in-gel digested by chymotrypsin and analyzed by *nano*LC-MS^2-XIC. The MS^2 spectrum of KETAAAKF (1−8) confirms the modification at K1 (Figure 9c), and the XIC chromatograph of both modified and unmodified KETAAAKF (1−8) indicates full labeling at K1 (Figure S2). Hence, ethynyl-(K1)RNase A has been achieved that allows further click labeling. According to BCA assay quantification, the yield of this ethynylation reaction is about 40% again considering the recovery of native RNase A. The relatively lower yield of this reaction is attributed to the monomeric avidin resin column supplied, as well as a lower reactivity of (**18**).

Finally, **19** is reacted with fluorogenic azidocoumarin (**20**) via Cu (I) catalyzed Huisgen 1,3-dipolar cycloaddition reaction to examine the accessibility of the integrated ethynyl group for further click labeling (Figure 9a, right). The application of azidocoumarin is of great advantage to prove that the click reaction has been successful since this chromophore only emits

dx.doi.org/10.1021/bc200556n | *Bioconjugate Chem.* 2012, 23, 500−508

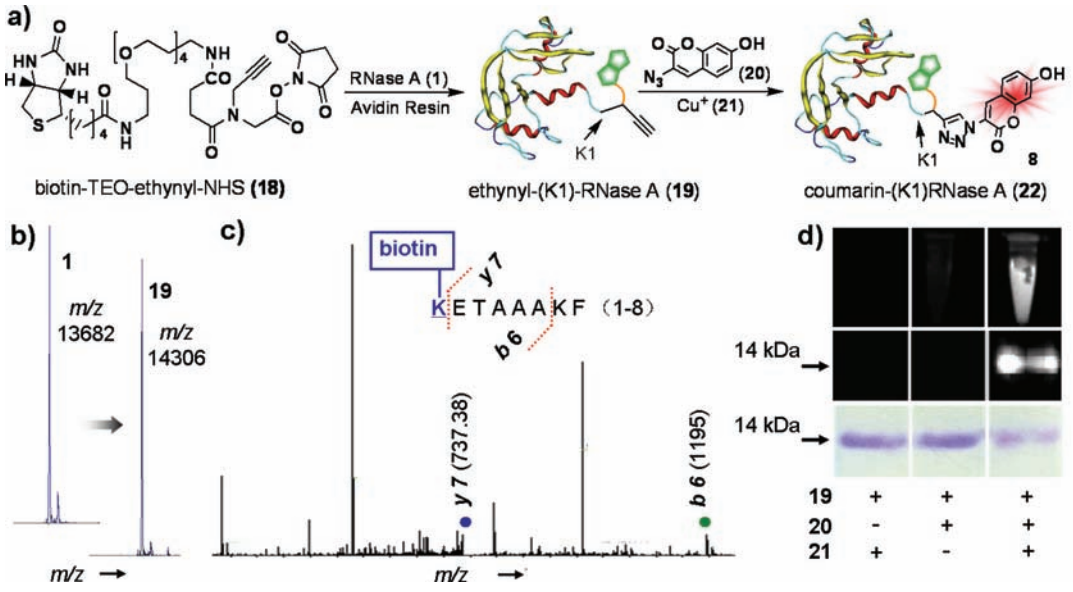


Figure 9. (a) Monoethynylation of RNase A using biotin-TEO-ethynyl-NHS (**18**) and subsequent labeling of ethynyl-(K1)RNase A (**19**) via Huisgen 1,3-dipolar cycloaddition reaction (click reaction) with azido-coumarin (**20**); (b) MALDI-ToF-MS spectrum of native RNase A (left) and ethynylated RNase A (right) indicating monomodification; (c) the MS^2 spectrum of modified KETAAAKF (1−8) proves modification at K1 rather than K7; (d) the fluorescence image of the reaction solution under UV irradiation (above), the fluorescence image of the gel (middle) and the Coomassie stain image of the gel (below) demonstrate the successful click reaction.

after the triazol ring has been formed. Under UV light excitation, the reaction solution reveals bright emission after about 24 h reaction time. In contrast, control solutions without azidocoumarin (Figure 9d, left) or Cu (I) catalyst (Figure 9d, middle) do not reveal any emission (Figure 9d, above). Gel electrophoresis analysis ascertains the formation of the click product coumarin-(K1)RNase A (**22**) due to the intensive fluorescent band at 14−15 kD corresponding to its M.W. of 14 508 g mol^{-1} (Figure 9d, right). This study successfully demonstrates the great potential of biotin-TEO-ethynyl-NHS (**18**) for the site-selective introduction of a single reactive ethynyl group into proteins. Ethynyl groups are of particular importance since they allow a broad range of site-selective post-translational modifications such as 1,3-dipolar Diels−Alder or Sonogashira reactions.

CONCLUSIONS

In summary, the synthesis of four monofunctionalized proteins/peptide, biotin-LC-(K1)RNase A (**3**), biotin-LC-(K1)lysozyme C (**5**), biotin-LC-(K9)SST-14 (**7**), as well as biotin-TEO-ethynyl-(K1)RNase A (**19**), has been presented. All biomolecules are decorated with a single substituent at a defined site based on the kinetically controlled reaction scheme. The reaction proceeds at mild conditions at physiological pH and RT as demonstrated by the retention of the catalytic activity of RNase A. In addition, fast reaction speed, quick and easy purification, as well as low reaction temperatures are particularly attractive for labeling sensitive peptides and proteins such as somatostatin or antibodies. Excess of unreacted proteins can be readily recovered without activity loss under physiological pH, contributing to the high labeling yield of over 90%. Furthermore, the bioorthogonal bioconjugation reagent, biotin-TEO-ethynyl-NHS (**18**), has been achieved allowing the site-selective incorporation of an ethynyl group for further site-selective labeling reactions. The introduced ethynyl group is accessible for, e.g., click chemistry as demonstrated by reacting ethynyl-(K1)RNase A with azidocoumarin.

The approach reported herein is fast (the entire process takes about 1−2 days), less labor-intensive, presumably of low cost, and it minimizes the risk of misfolding. Complementary to cysteine mutants, highly accessible and reactive lysine groups might also be introduced into the protein sequence via point mutations, thus opening up opportunities for dual-color labeling of proteins for single molecule experiments. Our results offer a high potential for addressing a broad range of native proteins and peptides in a site-selective fashion and complements the portfolio of recombinant techniques or chemoenzymatic approaches. Future studies will focus on the application of proteins as macromolecular building blocks for the formation of ordered supramolecular assemblies.

ASSOCIATED CONTENT

Supporting Information

Interpretation of XIC chromatographs, click labeling of ethynyl-(K1)RNase A (**19**), gel filtration and affinity chromatography procedures, BCA assay protocol, RNase A functional assay protocol, and the nine-step synthesis of biotin-TEO-ethynyl-NHS (**18**) including the full NMR spectra of all key intermediates. This material is available free of charge via the Internet at http://pubs.acs.org.

AUTHOR INFORMATION

Corresponding Author

*Fax: (+) 49-731-50-22883. Tel: + 49-731-5022870. E-mail: tanja.weil@uni-ulm.de.

Notes

The authors declare no competing financial interest.

ACKNOWLEDGMENTS

We thank J. Wilhelmi and A. Mishra for providing the functional RNase A assay protocol. This work was financially supported by the NUS start-up grant under the Grant No.

WBS-R-143-000-381-133 and the German Research Foundation (DFG) under grant P3246 029 and SFB 625.

REFERENCES

(1) Francis, M. B., and Carrico, I. S. (2010) New frontiers in protein bioconjugation. *Curr. Opin. Chem. Biol. 14*, 771−773.
(2) Harris, J. M., and Chess, R. B. (2003) Effect of PEGylation on pharmaceuticals. *Nat. Rev. Drug. Discovery 2*, 214−221.
(3) Bell, S. J., Fam, C. M., Chlipala, E. A., Carlson, S. J., Lee, J. I., Rosendahl, M. S., Doherty, D. H., and Cox, G. N. (2008) Enhanced circulating half-life and antitumor activity of a site-specific PEGylated interferon-α protein therapeutic. *Bioconjugate Chem. 19*, 299−305.
(4) Floyd, N., Vijayakrishnan, B., Koeppe, J. R., and Davis, B. G. (2009) Thiyl glycosylation of olefinic proteins: S-linked glycoconjugate synthesis. *Angew. Chem., Int. Ed. Engl. 48*, 7798−7802.
(5) Bagshaw, C. R., and Cherny, D. (2006) Blinking fluorophores: what do they tell us aboutprotein dynamics? *Biochem. Soc. Trans.*, 979−982.
(6) Michalet, X., Weiss, S., and Jäger, M. (2006) Single-molecule fluorescence studies of protein folding and conformational dynamics. *Chem. Rev. 106*, 1785−1813.
(7) Royer, C. A. (2006) Probing protein folding and conformational transitions with fluorescence. *Chem. Rev. 106*, 1769−1784.
(8) Hucknall, A., Kim, D. −H., Rangarajan, S., Hill, R. T., Reichert, W. M., and Chilkoti, A. (2009) Simple fabrication of antibody microarrays on nonfouling polymer brushes with femtomolar sensitivity for protein analytes in serum and blood. *Adv. Mater. 21*, 1968−1971.
(9) Chen, M. −L., Adak, A. −K., Yeh, N. −C., Yang, W. −B., Chuang, Y. −J., Wong, C. −H., Hwang, K. −C., Reuben, J. −R., Hwu, J. −R., Hsieh, S. −L., and Lin, C. −C. (2008) Fabrication of an oriented Fc-fused lectin microarray through boronate formation. *Angew. Chem., Int. Ed. Engl. 47*, 8627−8630.
(10) Löwik, D. W. P. M, Shklyarevskiy, I. O., Ruizendaal, L., Christianen, P. C. M., Maan, J. C., and van Hest, J. C. M. (2007) A highly ordered material from magnetically aligned peptide amphiphile nanofiber assemblies. *Adv. Mater. 19*, 1191−1195.
(11) Chalker, J. M., Bernardes, G. J. L., Lin, Y. A., and Davis, B. J. (2009) Chemical modification of proteins at cysteine: opportunities in chemistry and biology. *Chem. Asian J. 4*, 630−640.
(12) Smith, M. E. B., Schumacher, F. F., Ryan, C. P., Tedaldi, L. M., Papaioannou, D., Waksman, G., Caddick, S., and Baker, J. R. (2010) Protein modification, bioconjugation, and disulfide bridging using bromomaleimides. *J. Am. Chem. Soc. 132*, 1960−1965.
(13) Ryan, C. P., Smith, M. E. B., Schumacher, F. F., Grohmann, D., Papaioannou, D., Waksman, G., Werner, F., Baker, J. R., and Caddick, S. (2011) Tunable reagents for multi-functional bioconjugation: reversible or permanent chemical modification of proteins and peptides by control of maleimide hydrolysis. *Chem. Commun. 47*, 5452−5454.
(14) Tanrikulu, C., Schmitt, E., Mechulam, Y., Goddard, W. A. III, and Tirrell, D. A. (2009) Discovery of escherichia coli methionyl-tRNA synthetase mutants for efficient labeling of proteins with azidonorleucine in vivo. *Proc. Natl. Acad. Sci. U.S.A. 106*, 15285−15290.
(15) Kiick, K. L., van Hest, J. C., and Tirrell, D. A. (2000) Expanding the scope of protein biosynthesis by altering the methionyl-tRNA synthetase activity of a bacterial expression host. *Angew. Chem., Int. Ed. Engl. 39*, 2148−2152.
(16) Xie, J., and Schultz, P. G. (2006) A chemical toolkit for proteins—an expanded genetic code. *Nat. Rev. Mol. Cell. Biol. 7*, 775−782.
(17) Hackenberger, C. P. R, and Schwarzer, D. (2008) Chemoselective ligation and modification strategies for peptides and proteins. *Angew. Chem., Int. Ed. Engl. 47*, 10030−10074.
(18) Sletten, E. M., and Bertozzi, C. R. (2009) Bioorthogonal chemistry: Fishing for selectivity in a sea of functionality. *Angew. Chem., Int. Ed. Engl. 48*, 6974−6998.
(19) Lin, P. −C., Ueng, S. −H., Tseng, M. −C., Ko, J. −L., Huang, K. −T., Yu, S. −C., Adak, A. K., Chen, Y. −J., and Lin, C. −C. (2006) Site-specific protein modification through Cu^{I}-catalyzed 1,2,3-triazole formation and its implementation in protein microarray fabrication. *Angew. Chem., Int. Ed. Engl. 45*, 4286−4290.
(20) Saxon, E., and Bertozzi, C. R. (2000) Cell surface engineering by a modified Staudinger reaction. *Science 287*, 2007−2010.
(21) Pfeiffer, H., Rojas, A., Niesel, J., and Schatzschneider, U. (2009) Sonogashira and "click" reactions for the N-terminal and side-chain functionalization of peptides with $[Mn(CO)_3(tpm)]^+$-based CO releasing molecules (tpm = tris(pyrazolyl)methane). *Dalton Trans.*, 4292−4298.
(22) Sunbul, M., and Yin, J. (2009) Site specific protein labeling by enzymatic posttranslational modification. *Org. Biomol. Chem. 7*, 3361−3371.
(23) Chen, Z., Popp, B. V., Bovet., C. L., and Ball, Z. T. (2011) Site-specific protein modification with a dirhodium metallopeptide catalyst. *ACS Chem. Biol. 6*, 920−925.
(24) Shaunak, S., Godwin, A., Choi, J. −W., Balan, S., Pedone, E., Vijayarangam, D., Heidelberger, S., Teo, I., Zloh, M., and Brocchini, S. (2006) Site-specific PEGylation of native disulfide bonds in therapeutic proteins. *Nat. Chem. Biol. 2*, 312−313.
(25) Brocchini, S., Balan, S., Godwin, A., Choi, J. −W., Zloh, M., and Shaunak, S. (2006) PEGylation of native disulfide bonds in proteins. *Nat. Protoc. 1*, 2241−2252.
(26) Gilmore, J. M., Scheck, R. A., Esser-Kahn, A. P., Joshi, N. S., and Francis, M. B. (2006) N-Terminal protein modification through a biomimetic transamination reaction. *Angew. Chem., Int. Ed. Engl. 45*, 5307−5311.
(27) Ardelt, W., Shogen, K., and Darzynkiewicz, Z. (2008) Onconase and amphinase, the antitumor ribonucleases from rana pipiens oocytes. *Curr. Pharm. Biotechnol. 9*, 215−225.
(28) Henrikson, K. P., Allen, S. H. G., and Maloy, W. L. (1979) An avidin monomer affinity column for the purification of biotin-containing enzymes. *Anal. Biochem. 94*, 366−370.
(29) Thompson, M. J., and Goldstein, R. A. (1996) Predicting solvent accessibility: higher accuracy using Bayesian statistics and optimized residue substitution classes. *Proteins 25*, 38−47.

Bioconjugate Chemistry

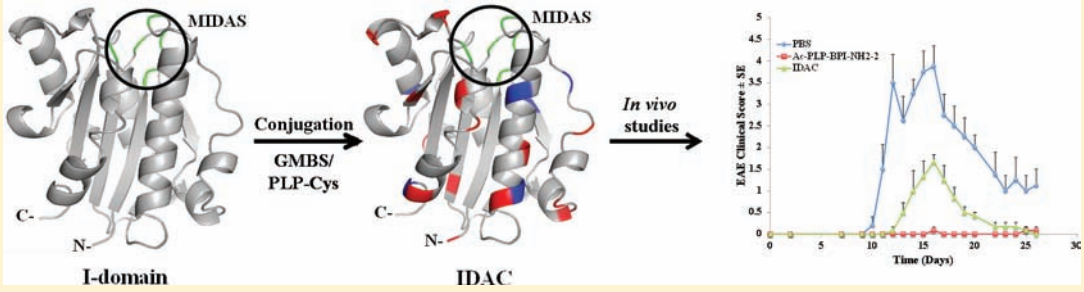
Article

pubs.acs.org/bc

I-Domain-Antigen Conjugate (IDAC) for Delivering Antigenic Peptides to APC: Synthesis, Characterization, and in Vivo EAE Suppression

Prakash Manikwar,[†] Barlas Büyüktimkin,[†] Paul Kiptoo,[†] Ahmed H. Badawi,[†] Nadezhda A. Galeva,[§] Todd D. Williams,[§] and Teruna J. Siahaan*[,†]

[†]Department of Pharmaceutical Chemistry, [§]Mass Spectrometry/Analytical Proteomics Laboratory, University of Kansas, Lawrence, Kansas 66047, United States



ABSTRACT: The objectives of this work are to characterize the identity of I-domain−antigen conjugate (IDAC) and to evaluate the in vivo efficacy of IDAC in suppressing experimental autoimmune encephalomyelitis (EAE) in mouse model. The hypothesis is that the I-domain delivers $PLP_{139-151}$ peptides to antigen-presenting cells (APC) and alters the immune system by simultaneously binding to ICAM-1 and MHC-II, blocking immunological synapse formation. IDAC was synthesized by derivatizing the lysine residues with maleimide groups followed by conjugation with PLP-Cys-OH peptide. Conjugation with PLP peptide does not alter the secondary structure of the protein as determined by CD. IDAC suppresses the progression of EAE, while I-domain and GMB-I-domain could only delay the onset of EAE. As a positive control, Ac-PLP-BPI-NH_2-2 can effectively suppress the progress of EAE. The number of conjugation sites and the sites of conjugations in IDAC were determined using tryptic digest followed by LC-MS analysis. In conclusion, conjugation of I-domain with an antigenic peptide (PLP) resulted in an active molecule to suppress EAE in vivo.

INTRODUCTION

Autoimmune diseases such as multiple sclerosis, rheumatoid arthritis, and type-1 diabetes are caused by the recognition and attack of self-tissues or organs by the host immune systems. In the case of multiple sclerosis (MS), the immune systems attack the myelin sheath of the neurons causing disruption of the signal translation in the central nervous system (CNS). One of the potential ways that T-cells recognize the myelin sheath is by activation of a subset of autoreactive T-cells, which recognize the self-myelin sheath. One possible mechanism of activation of a subpopulation T-cells is via formation of the "immunological synapse" at the interface between T-cells and antigen-presenting cells (APC). The immunological synapse is a "bull's eye"-like structure that is composed of a cluster of interactions between T-cell receptors (TCR) and major histocompatibility complex-peptide (MHC-p) at the center (Signal-1) and a cluster of interactions between costimulatory molecules (i.e., Signal-2: B7/CD28, ICAM-1/LFA-1) at the periphery of the bull's eye. The differentiation of naïve T-cells to a specific subset (i.e., Th1, Th2, Th17, T-reg) is strongly dependent on the type of costimulatory signal being delivered. Blocking Signal-2 during this process could lead to immune unresponsiveness of T cells called anergy.[1] Inhibition of ICAM-1/LFA-1 (Signal-2) interaction suppresses Th1-type immune response and could promote a noninflammatory suppressor and/or regulatory T cells.[2] Potential drugs such as monoclonal antibodies (mAb) or small molecules that block Signal-2 have been developed for treating autoimmune diseases; unfortunately, as a potential side effect, these drugs may suppress the general immune response and compromise the ability of the host to respond to pathogenic infections.

To overcome the general suppression of immune systems, our approach is to modulate the activation of a subpopulation of T-cells that recognizes a specific antigen using a bifunctional peptide inhibitor (BPI).[3] The BPI molecules are composed of an antigenic peptide for the specific disease conjugated to a cell adhesion peptide via a spacer.[4−8] GAD-BPI, PLP-BPI, and CII-BPI molecules have been shown to induce immunotolerance in nonobese diabetes (NOD),[6] experimental allergic encephalomyelitis (EAE),[3,4,7,8] and collagen-induced arthritis (CIA), respectively.

Received: October 28, 2011
Revised: February 24, 2012
Published: February 28, 2012

 © 2012 American Chemical Society dx.doi.org/10.1021/bc200580j | *Bioconjugate Chem.* 2012, 23, 509−517

The antigenic peptide is derived from epitope of the protein antigen responsible for the autoimmune disease, while the adhesion peptide is derived from the sequence of either LFA-1 (LABL) or ICAM-1 (cIBR1). The potential mechanism of action of BPI molecules is via simultaneous binding to MHC-II and ICAM-1 receptors on the surface of APC. The simultaneous binding to these two-target receptors prevents the translocation of Signal-1 and Signal-2 molecular complexes and inhibits the formation of the immunological synapse. As a result, the BPI molecules suppress the generation of inflammatory T-cells and possibly stimulate the formation of suppressor or regulatory T-cells.

Antigenic spreading has been shown to occur in the late stages of EAE and MS, where the antigenic determinant spreads to different epitopes within an antigenic protein (e.g., proteolipid protein (PLP)) or to epitopes of different antigenic proteins such as myelin basic protein (MBP) and myelin oligodendrocyte glycoprotein (MOG). Although BPI molecules have excellent efficacy to block the progress of EAE, BPI molecules are made from a single antigenic peptide conjugated to a single cell adhesion peptide. Therefore, BPI molecules may not be able to overcome antigenic spreading in EAE or MS. One way to overcome antigenic spreading is to deliver a mixture of BPI molecules with different antigenic peptides. Another way is to simultaneously deliver several different epitopes of antigenic proteins (e.g., PLP, MBP, or MOG) to APC by conjugating them to the I-domain protein to make an I-domain−antigen conjugate (IDAC).

As a proof-of-concept, several $PLP_{139-151}$ peptides were conjugated via maleimide spacers to several lysine residues on the IDAC molecule (Figure 1 and Table 1). The I-domain is the

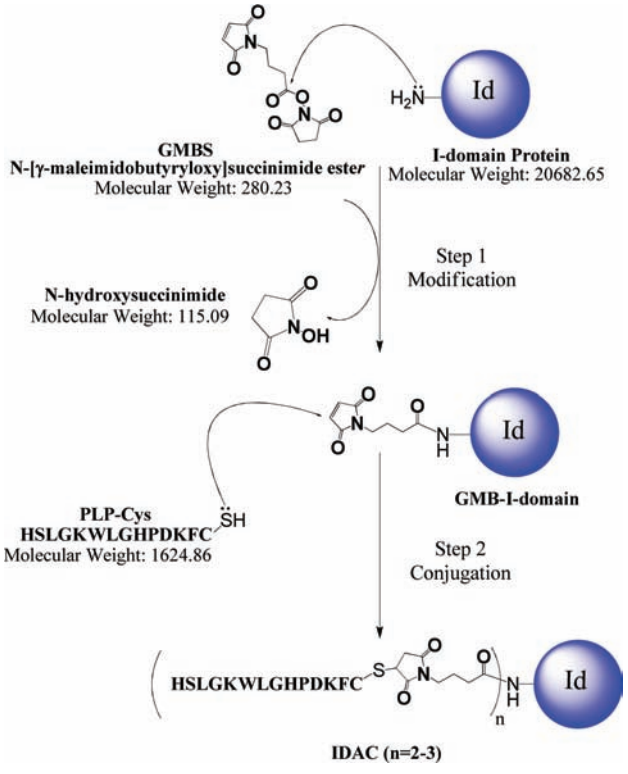


Figure 1. Schematic representation of a two-step conjugation reaction to prepare IDAC.

binding region of LFA-1 to ICAM-1, and it has been shown to interact with the D1 domain of ICAM-1.[9] Compared to the cell adhesion peptide LABL, the I-domain offers a unique divalent cation coordination site called metal ion-dependent adhesion site or MIDAS that interacts with the ICAM-1 D1 domain. Here, PLP-Cys-OH was conjugated to the GMB-I-domain to give IDAC, and the IDAC molecule was characterized by tryptic digest mass spectrometry.[10] The in vivo efficacy of IDAC was compared to those of negative control (PBS) and positive control (Ac-PLP-BPI-NH_2-2). The results showed that IDAC can delay the onset of EAE compared to PBS and IDAC strongly suppresses the progression of EAE.

EXPERIMENTAL PROCEDURES

Materials. The amino acids used for peptide synthesis were purchased from Peptide International (Louisville, KY). GMBS (*N*-[γ-maleimidobutyryloxy]succinimide ester) was from Pierce (Rockford, IL). Sequence-grade modified trypsin was from Promega (Madison, WI). All other chemicals or solvents were of analytical grade or better.

Mice. The in vivo studies were carried out using female inbred SJL/J ($H\text{-}2^S$) mice purchased from Charles River Laboratories, Inc. (Wilmington, MA). The animals were housed under specific pathogen-free conditions at an American Association for Accreditation of Laboratory Animal Care (AAALAC)-approved animal facility at The University of Kansas. The protocol for working with mice had been approved by the Institutional Animal Care and Use Committee (IACUC).

Peptide Synthesis. The sequences of peptides used in the present study are listed in Table 1. The standard Fmoc solid-phase peptide chemistry was used to synthesize all peptides on PEG-PS resin (Applied Biosystems, Foster City, CA) with the automated peptide synthesis system (Pioneer perspective Biosystems, Framingham, MA). Peptide synthesis and purification were conducted according to our previously published method.[4] All peptides were purified using semipreparative C_{18} reversed-phase HPLC, and the purity of each fraction from the preparative HPLC was determined by analytical HPLC. The pure fractions were pooled and lyophilized; the molecular weight of each peptide was confirmed by electrospray ionization mass spectrometry ($M+H^+$) (MW PLP-Cys-OH = 1624.86; Ac-PLP-BPI-NH_2-2 = 3416.95).

Preparation of I-Domain. The LFA-1 I-domain protein was overexpressed, refolded, and purified as previously described.[11] The protein purity, identity, and secondary structure were confirmed by SDS-PAGE, mass spectrometry, and far-UV circular dichroism (CD), respectively.

Synthesis of IDAC. As shown in Figure 1, two steps are required to prepare the IDAC. The first is to modify the amino groups of the N-terminal and side chain of lysine residues of I-domain by reacting them with *N*-[γ-maleimidobutyryloxy]-succinimide ester (GMBS). This step introduces maleimide groups on the I-domain to generate the GMB-I-domain. The second step is to conjugate the thiol group on the Cys residue of PLP-Cys-OH peptide to the maleimide groups on the I-domain to give IDAC.

Step 1. To a total of 20 mg of I-domain solution, a 10-fold molar excess of freshly prepared GMBS (2.71 mg) solution in DMSO (0.5 mL) was added dropwise followed by stirring of the mixture for 1 h at 24 °C. Then, the reaction mixture was subjected to purification through a Superdex 75 column to isolate the GMB-I-domain. The desired GMB-I-domain and the excess GMBS were eluted with PBS containing 10 mM $MgSO_4$. The fractions containing the GMB-I-domain were collected and concentrated by ultrafiltration. Modification on the I-domain

dx.doi.org/10.1021/bc200580j | *Bioconjugate Chem.* 2012, 23, 509−517

Table 1. List of Peptides and Proteins Used in the Present Study[a]

peptide/protein	sequence
Ac-PLP-BPI-NH_2-2	*Ac*-HSLGKWLGHPDKF-$(AcpGAcpGAcp)_2$-ITDGEATDSG-*NH_2*
IDAC	$(HSLGKWLGHPDKFC)_n$-linker-I-domain
GMB-I-domain	$[N$-(γ-maleimido)-1-oxybutyl$]_n$-I-domain
I-domain	MGNVDLVFLFDGSMSLQPDEFQKILDFMKDVMKKLSNTSYQFAAVQFSTSYKTEFDFSDYVKRKDP-DALLKHVKHMLLLTNTFGAINYVATEVFREELGARPDATKVLIIITDGEATDSGNIDAAKDIIRYIIGIGKHFQTKES-QETLHKFASKPASEFVKILDTFEKLKDLFTELQKKIY

[a]Ac = Acetyl and Acp = Aminocaproic acid.

using this method produced 3−10 maleimide groups per I-domain as determined by electrospray ionization mass spectrometry (ESI-MS).

Step 2. The conjugation reaction of the PLP-Cys-OH peptide to GMB-I-domain was carried out at pH 8.5 to give IDAC. To a solution containing 10 mg of GMB-I-domain, a 15 molar excess of PLP-Cys-OH dissolved in PBS was added dropwise. During addition of the peptide, the pH was constantly monitored and adjusted to 8.5. During the reaction, the final concentration of the protein was 2.0 mg/mL. The reaction was carried out for 1 h at 24 °C with constant stirring. After the reaction was completed, the solution pH was readjusted to pH 7.4. The resulting IDAC reaction mixture was purified using a Superdex 75 column. The fractions belonging to the IDAC were collected and concentrated by ultrafiltration. IDAC contained 1 to 5 peptide molecules per I-domain molecule as determined by ESI-MS. The purity of the IDAC was confirmed by SDS-PAGE gel and size-exclusion chromatography. The CD spectrum of the IDAC was compared with that of the parent I-domain protein.

LC-ESI-MS Analysis of Intact Protein. To obtain intact protein masses, pure protein samples obtained after SEC were analyzed by LC ESI-Q-TOF MS. HPLC separations were performed with a Water Acquity solvent delivery system using a binary gradient of solvent A composed of 98.92:1:0.08 H_2O/acetonitrile/formic acid (vol/vol/vol) and solvent B containing 98.92:1:0.08 acetonitrile/H_2O/formic acid (vol/vol/vol). Approximately 10 pmol of the sample was loaded onto a C_4 reversed-phase HPLC column (1 × 50 mm, 5 μm, 300 Å; Micro-Tech Scientific, Vista, CA) with a linear gradient from 20% to 60% B in 10 min with a flow rate of 20 μL/min followed by a wash and re-equilibration step. Furthermore, the HPLC system was coupled online to the electrospray source of a Q-TOF-2 mass spectrometer (Micromass UK Ltd., Manchester, U.K.). Mass spectra were acquired with instrument cone voltage 35 eV and collision energy 20 eV with Ar in the collision cell. The instrument was set up in positive reflector mode with a scan time of 5 s and in the mass range m/z 700−3000. The instrument was calibrated using NaI. The ion chromatograms were processed to obtain the molecular weights of the modified peptides using MaxEnt1 in the *MassLynx* v 4.1 software (Micromass UK Ltd.).

Gel Electrophoresis. The pure protein solution (i.e., 100 μg of IDAC or I-domain) obtained after SEC separation was mixed with a 4× Tris−glycine SDS sample buffer containing no reducing agent and loaded into 1.5-mm-thick 10-well NuPAGE Novex 4−12% Bis-Tris gradient gels. After running gel electrophoresis at 150 V for 70 min, the gels were stained with 0.25% Coomassie blue R250 solution (10% acetic acid/50% ethanol/40% water) for 30 min followed by destaining (10% acetic acid/25% ethanol/65% water) until the bands were visible and the background was clear.

In-Gel Trypsin Digestion. A standard in-gel protein digestion protocol was followed as described elsewhere.[12] Briefly, protein bands were excised from the gel and were digested with trypsin at an enzyme-to-substrate ratio of 1:25 (w/w) at 37 °C overnight. To stop the digestion, 2 μL of glacial acetic acid was added to each sample.

LC-MS/MS Analysis of Tryptic-Digest Products. The products of tryptic digest from I-domain and IDAC were introduced onto a capillary reversed-phase HPLC and CID spectra from peptides were obtained with a hybrid tandem hybrid ion trap/ion cyclotron resonance mass spectrometer (LTQFT ThermoFinnigan, Bremen, Germany) under conditions described previously.[13] The experimental raw data were processed using Bioworks software (*Thermo* v 2.0) to create an MS/MS peak list in a DTA format. Protein sequence mapping was performed using *Sequest*, *Mascot* (Matrix Science, v 2.2), and X!Tandem (www.thegpm.org) algorithms with a fragment ion mass tolerance of 0.20 Da and a parent ion tolerance of 1.2 Da. Amino groups of lysine residues and protein N-terminus were considered to be modified with maleimide linker moiety + dipeptide (Phe-Cys). The chemical composition of the modification for IDAC is $C_{20}H_{23}N_3O_6S$, delta monoisotopic mass 433.1308 and its maleimide hydrolysis product is $C_{20}H_{25}N_3O_7S$, delta monoisotopic mass 451.1413. Protein modification sites identified by tryptic digestion of the final construct are based on the assumption that trypsin cleaves at the carboxyl side of the lysine residue (^{12}K) of the peptide PLP-Cys-OH leaving a construct peptide of FC...linker...I domain tryptic peptide (see Figure 1 step 2). *Scaffold* software (Proteome Software Inc., v 2.06) was used to combine and validate MS/MS-based peptide identifications. Peptide identifications with greater than 50% probability as specified by the Peptide Prophet algorithm[14] were accepted for reporting protein coverage.

Induction and Suppression of EAE. *Disease Stimulation.* Female inbred SJL/J mice, 5−7 weeks old, were randomly divided into different groups. All mice were immunized with $PLP_{139-151}$ in Freund's complete adjuvant (CFA) to induce EAE, as reported previously.[3,4] The PLP/CFA emulsion (50 μL per site) was administered to four separate regions above the shoulder and on the flanks. In addition, 200 ng of pertussis toxin (List Biological Laboratories Inc., Campbell, CA) was injected intraperitoneally on days 0 and 2.

In Vivo Study. After disease stimulation, one group of mice received intravenous (i.v.) injections of 26 nmol/injection/day of the conjugate IDAC on days 4 and 7. The second and third groups of mice received i.v. injections of 100 nmol/injection/day of Ac-PLP-BPI-NH_2-2 and 100 μL of PBS, respectively, on days 4, 7, and 10. The animals were weighed and observed daily. Disease progression was evaluated by observation using a blinded method as reported previously.[3,4] The clinical scores were rated using the following scale: 0, no clinical signs of disease; 1, tail weakness or limp tail; 2, paraparesis (weakness or

dx.doi.org/10.1021/bc200580j | *Bioconjugate Chem.* 2012, 23, 509−517

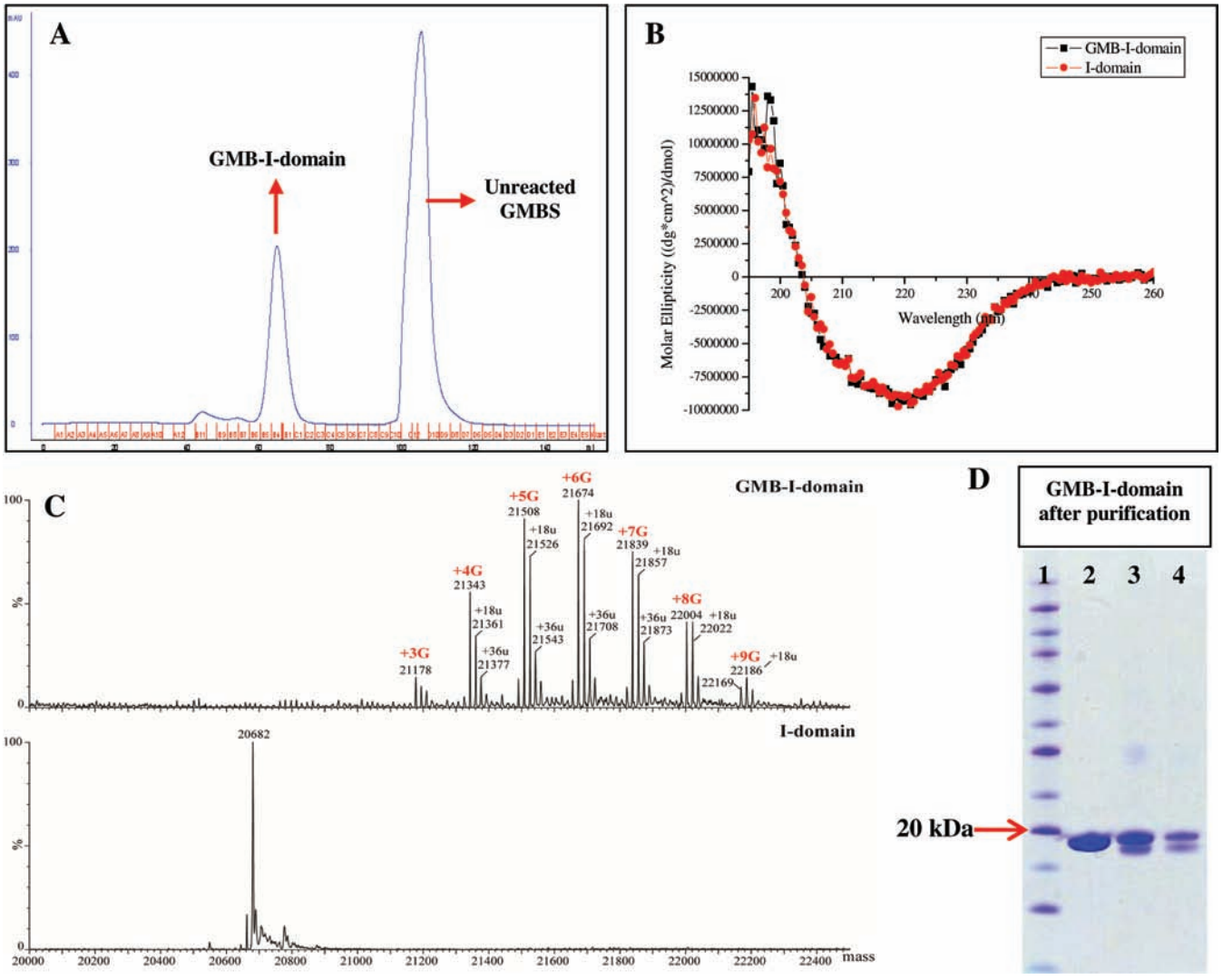


Figure 2. Purification and characterization of GMB-I-domain after the reaction of I-domain with GMBS. (A) SEC chromatogram showing the separation between GMB-I-domain and the remaining free GMBS. (B) CD spectra of the parent I-domain (red) and GMB-I-domain (black). (C) Deconvoluted mass spectra of LC ESI-MS analysis of the GMB-I-domain protein[8] and the unmodified I-domain protein (bottom). G, is the number of GMBS molecules conjugated. (D) SDS-PAGE analysis of pure GMB-I-domain protein after staining with Coomassie blue: molecular weight marker (lane 1), the I-domain protein (lane 2), the reaction mixture of I-domain protein and GMBS (lane 3), and GMB-I-domain protein (lane 4).

incomplete paralysis of one or two hind limbs); 3, paraplegia (complete paralysis of two hind limbs); 4, paraplegia with forelimb weakness or paralysis; and 5, moribund or dead. Mice were euthanized once they were found to be moribund.

Statistical Analysis. Statistical differences among the groups in clinical disease scores were determined by calculating the average score for each mouse from the day of disease onset to day 20 by One-way Analysis of Variance followed by Fisher's least significant difference using *StatView* (SAS Institute, Cary, NC). Statistical differences among the groups in body weight were also analyzed in the same way. The presence of significant difference is denoted with p-values of <0.05 or <0.001.

RESULTS

Synthesis and Characterization of IDAC. IDAC was prepared by conjugating the PLP-Cys-OH peptide to the N-terminus and side chain amino groups of the lysine residues in the I-domain (Figure 1). Thus, the amino groups in the I-domain were reacted with the active *N*-hydroxysuccinimide (NHS) ester of GMBS to produce GMB-I-domain protein via a stable amide bond (Step 1, Figure 1). The GMB-I-domain from the reaction mixture was purified from the excess GMBS using SEC (Figure 2A). Comparison of CD spectra of GMB-I-domain and I-domain shows that they have similar spectra (Figure 2B), indicating that adding GMB groups does not alter the secondary structure of the GMB-I-domain.

The composition of pure GMB-I-domain was analyzed by liquid chromatography coupled online with ESI-MS. The charge-deconvoluted MS spectrum shows three to nine γ-maleimidobutyryloxy (GMB) groups attached to the I-domain with the following masses: 21 178 Da, 21 343 Da, 21 508 Da, 21 674 Da, 21 839 Da, 22 004 Da, and 22 169 Da (top panel, Figure 2C). The differences in mass are 165 Da, which is consistent for a sequential addition of GMB group. The first peak at 21 178 Da corresponds to the I-domain molecular weight conjugated to three GMB groups; therefore, the remaining peaks correspond to the I-domain with four to nine covalently linked GMB groups, respectively. The parent I-domain has a MW of 20 682 (bottom panel, Figure 2C) and it was not found in the MS spectrum of GMB-I-domain (top panel, Figure 2C).

dx.doi.org/10.1021/bc200580j | *Bioconjugate Chem.* 2012, 23, 509–517

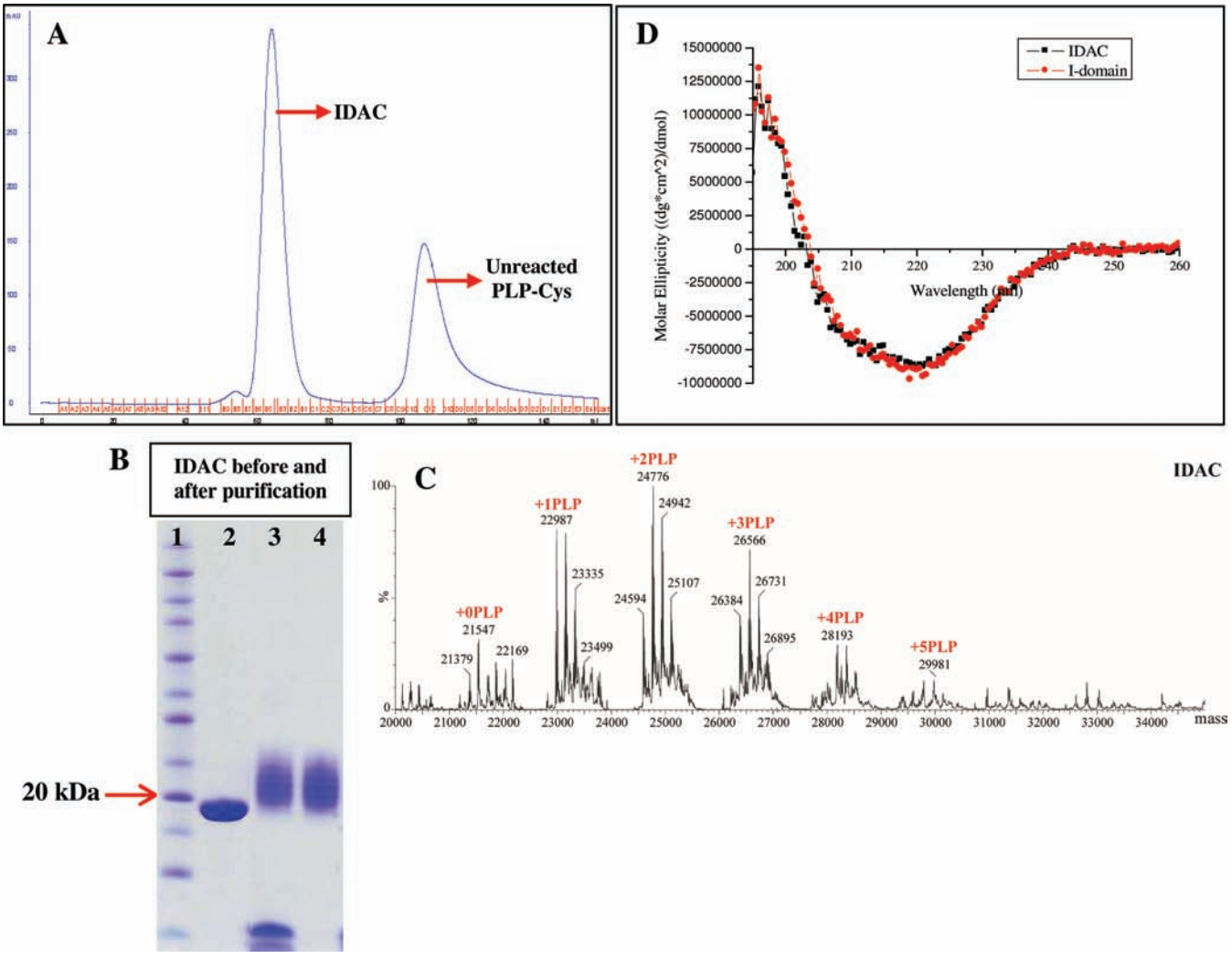


Figure 3. Purification and characterization of IDAC by SEC, SDS-PAGE, MS, and CD. (A) SEC chromatogram of IDAC, which is separated from the PLP-Cys peptide. (B) SDS-PAGE analysis of different proteins after staining with Coomassie blue: molecular weight marker (lane 1), the parent I-domain protein (lane 2), the reaction mixture at pH 8.5 to prepare IDAC (lane 3), and the purified IDAC (lane 4). (C) Charge deconvoluted mass spectra of the IDAC after LC desalting. PLP is the number of PLP molecules conjugated. (D) CD spectra of the parent I-domain (red) and IDAC (black).

Along with the desired GMB-I-domain peak, there are corresponding peaks with mass increases of 18 and 36 Da found in the MS spectra (top panel, Figure 2C). These peaks correspond to the hydrolysis of maleimide groups or maleic acid derivatives, which are attached to the I-domain.[15] The MS data correlate with the SDS-PAGE image of the isolated product of GMB-I-domain from SEC, which shows two bands on lane 4 in Figure 2D. These two bands are from the desired maleimide and maleic acid derivatives of I-domain with different electrophoretic mobility. Before purification, the reaction mixture (lane 3, Figure 2D) shows three bands, while the control I-domain (lane 2, Figure 2D) produces only one band. The formation of maleimide hydrolysis products is increased upon storage; thus, it is important that the GMB-I-domain be used within 48 h after SEC purification.

Conjugation of PLP-Cys-OH Peptide to GMB-I-Domain. PLP-Cys-OH is a peptide that contains $PLP_{139-151}$ sequence with an additional cysteine amino acid at the C-terminus with an open carboxylic acid (Cys-OH). PLP-Cys-OH was reacted with GMB-I-domain at pH 8.5 to prepare IDAC. In this case, the peptide conjugation is via nucleophilic attack of the maleimide groups on the GMB-I-domain by the thiol group of the Cys residue on the peptide (Step 2, Figure 1). Crude products were purified with SEC; the desired IDAC could be easily separated from PLP-Cys-OH (Figure 3A). The pure fractions of IDAC were pooled and concentrated. The crude and purified product was analyzed by SDS-PAGE gel against the parent I-domain (Figure 3B). As expected, the parent I-domain shows one single band with lower molecular weight than the conjugates (lane 2, Figure 3B). The gel of the crude product illustrates the presence of IDAC along with lower MW bands corresponding to PLP-Cys-OH (lane 3, Figure 3B). The gel of purified IDAC shows multiple bands, which have higher molecular weights than the parent I-domain and without the starting PLP-Cys-OH (lane 4, Figure 3B). The multiple bands on IDAC were due to various levels of peptide conjugates.

The charge deconvoluted LC-MS data indicated that 0−5 PLP peptides were attached to the IDAC with an average of 2.5 PLP peptides per I-domain (Figure 3C). Each subpopulation of peaks in the spectra of IDAC has various MW peaks due to the presence of different numbers of GMB groups, but the same number of PLP-Cys peptide attached to the I-domain.

dx.doi.org/10.1021/bc200580j | *Bioconjugate Chem.* 2012, 23, 509−517

The complexity in each of the subpopulations arises from the hydrolysis products of maleimide (Figure 4).[15] The CD spectrum

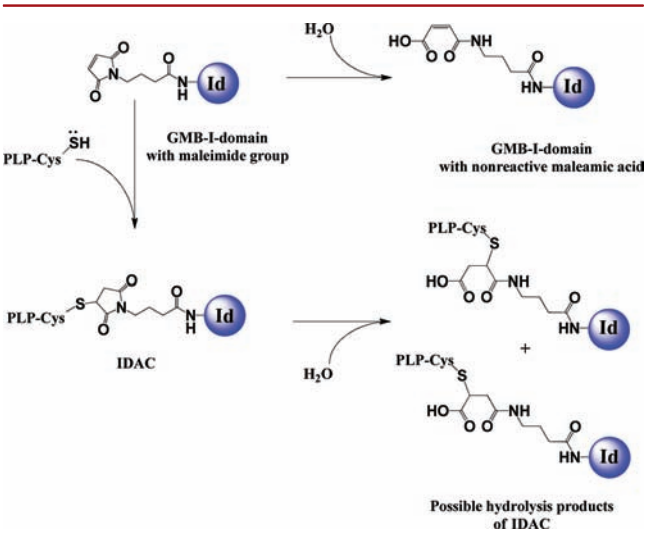


Figure 4. Schematic representation of possible hydrolysis products of GMB-I-domain and IDAC.

of each conjugate was similar to that of the parent I-domain protein (Figure 3D), indicating that conjugation of PLP-Cys peptide to the I-domain preserves the native secondary structure of the protein.

Structural Analysis of IDAC. To investigate the structure of IDAC, peptide mapping using tryptic digestion and mass spectrometry was used to determine the location of PLP peptides on the I-domain protein. The assumptions are that the modified lysine residues on the I-domain cannot be cleaved by trypsin, and the cleavage product of the lysine residue that is attached to the PLP peptide can be used to identify the modified lysine residue on the I-domain. The modified peptide fragments were identified using LC-MS/MS. The PLP peptide contains a Lys residue (Lys12), which also could be hydrolyzed by trypsin to produce a dipeptide, Phe-Cys-OH, which is attached to maleimidobutyryloxy. The attached dipeptide has a molecular weight of 433.1307 Da for Phe-Cys-OH. In addition, we observed Phe-Cys-OH conjugated to the peptide fragment via the hydrolysis product of maleimide, which has 18.0106 Da molecular weight added. The comparison of LC-MS/MS data from tryptic-digest fragments of the conjugates is summarized in Table 2. The LC-MS/MS sequence coverage for IDAC was 99%, and a total of 15 modified tryptic peptides were identified from IDAC. All of the conjugation sites were partially modified, and the number of unmodified peptides dominated the search profile. These modified peptides were unique and were found in the mapping profiles of the conjugates but not in the parent I-domain profile. The experimental and calculated mass values of the modified peptides were very close, with the average deviation being less than 0.1 Da.

Suppression of EAE by IDAC. The clinical scores indicate that two injections of IDAC have significant efficacy to suppress the progress of EAE compared to those treated with PBS ($p < 0.0001$, through days 12−17); however, three injections of Ac-PLP-BPI-NH_2-2 provide complete suppression of the disease ($p < 0.0001$, through days 12−17) (Figure 6A). The efficacy of IDAC is also reflected in the ability to prevent the changes of body weights of the mice significantly compared to PBS-treated mice (Figure 6B). The disease incidence was delayed in the

Table 2. Modification Sites in IDAC as Determined by Trypsin Digestion and LC-MS/MS

modified peptide	sequence	modified sites
T1	^{1}MGNVDLVFLFDGSMSLQPDEFQ^{23}K	M1
T2−3	^{24}ILDFMKDVM^{33}K	K29
T4−5	^{34}KLSNTSYQFAAVQFSTSY^{52}K	K34
T6−7	^{53}TEFDFSDYVK^{63}R	K62
T8−9	^{64}KDPDALL^{71}K	K64
T9−10	^{65}DPDALLKHV^{74}K	K71
T12−13	^{96}EELGARPDATKVLIIITDGEATDSGNIDAA^{126}K	K106
T13−14	^{107}VLIIITDGEATDSGNIDAAKDII^{130}R	K126
T15−16	^{131}YIIGIGKHFQT^{142}K	K137
T16−17	^{138}HFQTKESQETLH^{150}K	K142
T18	^{151}FASKPASEFV^{161}K	K154
T18−19	^{151}FASKPASEFVKILDTFE^{168}K	K161
T19−20	^{162}ILDTFEKL^{170}K	K168
T20−21	^{169}LKDLFTELQ^{178}K	K170
T21−22	^{171}DLFTELQK^{179}K	K178

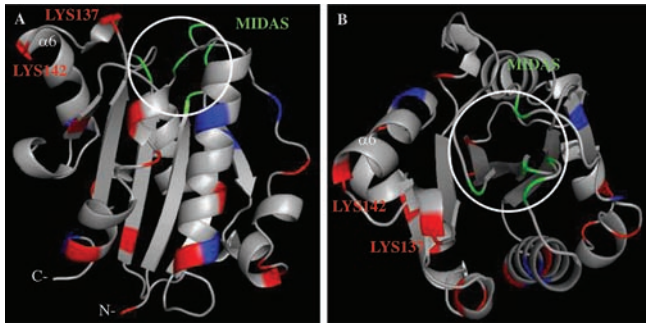


Figure 5. X-ray structure of I-domain (PDB code: 1ZON). The residues in red and blue are the respective modified and unmodified lysine sites in IDAC, and the residues in green are those located at the MIDAS region. The N- and C-termini are labeled as N- and C-, respectively. The protein images were created using the PyMOL molecular graphics system version 1.4.1. (A) Side view. (B) Top view.

IDAC-treated mice compared to PBS-treated mice ($p < 0.0001$, through days 12−24) and completely eliminated in Ac-PLP-BPI-NH_2-2-treated mice ($p < 0.0001$, through days 12−24) (Figure 6C).

DISCUSSION

Patients with autoimmune diseases such as multiple sclerosis, rheumatoid arthritis, and psoriasis are currently being treated with protein-derived drugs such as monoclonal antibodies and peptide polymers, which modulate the immune system. Current treatments for multiple sclerosis patients include Copaxone and Tysabri as well as anti-inflammatory agents (e.g., cortico-steroids, β-interferon-1a, mitoxantrone). Copaxone has side effects in patients, including hypersensitivity reaction, shortness of breath, diarrhea, back and neck pain, and fever. Tysabri, which binds to the α_4-subunit of $\alpha_4\beta_1$ and $\alpha_4\beta_7$ integrins to block leukocyte adhesion and infiltration into CNS, could cause progressive multifocal leuko-encephalopathy (PML) in patients, a life-threatening complication.[16] Similarly, PML was also observed in patients treated with other cell adhesion inhibitors such as Raptiva (Efalizumab, CD11a mAb) for psoriasis; thus, this drug was withdrawn from the market.[17,18] Because Tysabri and Raptiva bind to integrins, these antibodies presumably also

dx.doi.org/10.1021/bc200580j | Bioconjugate Chem. 2012, 23, 509−517

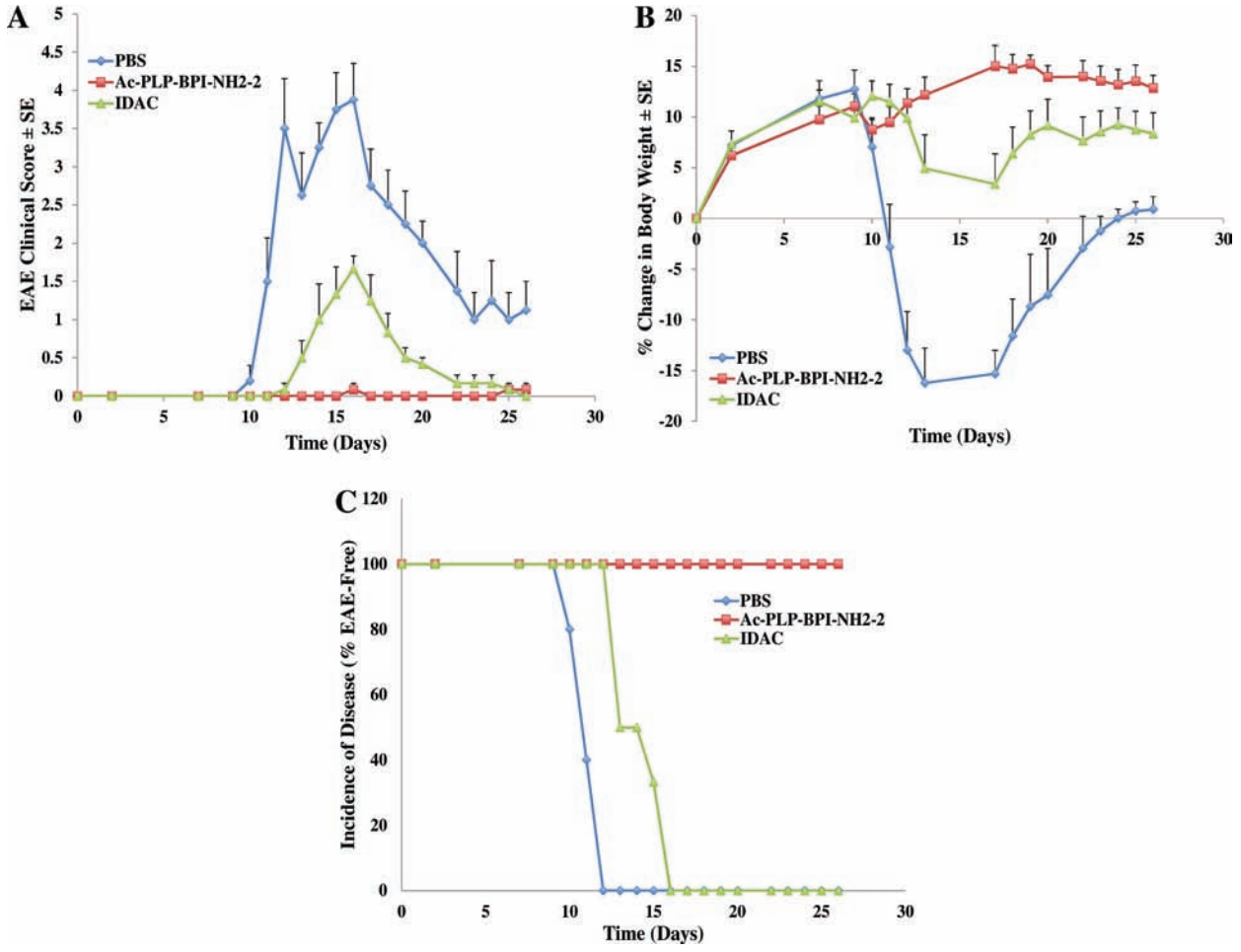


Figure 6. In vivo activity of IDAC, Ac-PLP-BPI-NH_2-2, and PBS in mouse EAE model. After immunization with PLP peptide in CFA, the mice received i.v. injections of 26 nmol/injection/day of the conjugate IDAC on days 4 and 7. For the Ac-PLP-BPI-NH_2-2 treatment group, the mice received i.v. injections of 100 nmol/injection/day of the peptide on days 4, 7, and 10. The control group was treated with PBS on days 4, 7, and 10. Disease progression was evaluated using (A) clinical disease scores, (B) change in body weight, and (C) incidence of disease. The results are expressed as the mean ± SE ($n \geq 6$).

suppress Signal-2 for T-cell activation in addition to blocking the cell adhesion. Blocking Signal-2 of the immunological synapse formation suppresses the general activation of T-cells that can respond to pathogens such as JC virus that causes PML. Therefore, there is a need to discover a new way to suppress T-cell activation in an antigen-specific manner without suppressing the general immune responses.

To address the issue of antigen-specific disease suppression while preserving the immune system's ability to fight to foreign pathogens, our group developed BPI molecules (GAD-BPI, PLP-BPI, and CII-BPI)[3,4,6−8] that were derived from antigenic peptides discovered by others.[19−24] In parallel to BPI molecules, we also developed IDAC molecule by conjugating several antigenic peptides to a single molecule of I-domain. Thus, the advantage of making IDAC is that the I-domain can be used to carry multiple copies of the antigenic peptides to improve the potency of the conjugate. In addition, the I-domain can also be utilized to carry multiple and different antigenic peptides to modulate different subpopulations of antigen-specific T-cells. We have shown that the fluorescence-labeled I-domain binds LFA-1 and is internalized by lymphocytes.[25] Similar to BPI molecules, IDAC conjugates are hypothesized to inhibit the immunological synapse formation during the process of T-cell activation by simultaneous binding of the PLP peptide and I-domain to MHC-II and ICAM-1, respectively, on APC. This simultaneous binding forms a bridge between the two receptors and eventually prevents the translocation and reorganization of Signal-1 and Signal-2.

In the present study, it was found that just two i.v. injections (26 nmol/injection) of IDAC inhibited the onset and progress of EAE more efficiently than PBS. The efficacy of IDAC is less than that of the BPI molecule. Increasing the dose to 50 nmol/injection or more by keeping the frequency of injections the same may further suppress the disease. It is also possible to increase the frequency of administration (3−4 i.v. injections) by keeping the dose constant. The structural analyses of IDAC indicated the molecule contains an average of 2.5 peptide molecules per I-domain molecule. To determine the conjugation sites, both the conjugate and the parent I-domain were subjected to tryptic digestion followed by LC-MS/MS analysis using our previous method.[10] IDAC has a total of 15 lysine residues that are modified by PLP-Cys-OH peptide (Table 2). Our previous studies showed that amidation and acetylation of the respective C- and N-termini of PLP peptide on BPI molecules enhanced the in vivo activity of BPI molecules. Recently, it was found that IDAC molecules with PLP peptides conjugated to the I-domain had better in vivo efficacy than IDAC with uncapped PLP peptides.

dx.doi.org/10.1021/bc200580j | *Bioconjugate Chem.* 2012, 23, 509−517

The locations of the modified (red) and unmodified (blue) lysine are indicated in the structure of I-domain (Figure 5). If the activity of IDAC is due to its simultaneous binding to ICAM-1 and MHC-II on the surface of APC, the most active conjugate should accommodate binding to these two receptors. It is known that the I-domain binds to ICAM-1 via its MIDAS region (green, Figure 5). From the model derived from the X-ray structure, it can be predicted that conjugation of PLP peptide at K137 and K142 would be the most probable sites to accommodate simultaneous binding of IDAC to MHC-II and ICAM-1. In the future, the most important site(s) for peptide conjugation will be determined using a single mutation of each Lys residue (i.e., K137 and K142) to a Cys residue followed by conjugation of PLP peptide. In this case, the peptide will be derivatized with a maleimide group. To illustrate, Lys142 can be mutated with Cys142 to give Cys142-I-domain. Then, Cys142-I-domain will be conjugated with PLP peptide to give PLP-Cys142-I-domain, and the in vivo activity of this new conjugate will be determined in the EAE mouse model. Using this method, we can pinpoint the conjugation site(s) that is important for the activity of the IDAC molecule. It is possible that multiple sites of peptide conjugation are necessary; in such a case, multiple Cys mutations can be carried out on a single I-domain protein. It has been found that double mutations of the I-domain (i.e., F265S and F292G) would increase the affinity of the mutant 2000-fold to ICAM-1.[26] Thus, IDAC molecules derived from the mutant I-domain could enhance their in vivo activity to suppress EAE.

In conclusion, we have shown the proof-of-concept that IDAC has efficacy in inhibiting the progress of EAE in the mouse model. In the future, there is a need to evaluate the mechanism of action of the IDAC molecule by evaluating the in vivo cytokine production to determine the balance between inflammatory (Th17 and Th1) T cells and regulatory T cells (T-reg). Furthermore, the side effects may be reduced or eliminated upon optimization of dose, schedule, route, and method of administration. As was recently shown for the BPI molecule, vaccine-like injection can reduce side effects; therefore, vaccine-like delivery of IDAC will also be explored.[27] To test the possibility of using IDAC molecules to suppress antigenic spreading, the I-domain will be conjugated to different antigenic peptides (PLP, MOG, and MBP) to produce multiantigen IDAC (MIDAC) and evaluated in EAE mice that are induced by different antigens (i.e., PLP, MOG, or MBP). The hope is that MIDAC molecules may offer a unique approach for the treatment of multiple sclerosis.

AUTHOR INFORMATION

Corresponding Author

*Tel.: (785) 864-7327. Fax: (785) 864-5736. E-mail: siahaan@ku.edu.

Notes

The authors declare no competing financial interest.

ACKNOWLEDGMENTS

This work has been funded by the National Institutes of Health (R01-AI-063002 and R56-AI-063002), and National Multiple Sclerosis Society. The Q-Tof2^{tm} was purchased with support from KSTAR, Kansas administered NSF EPSCoR and the University of Kansas. The Acquity UPLC was purchased with partial support from K-INBRE (www.kumc.edu/kinbre/). The CapXL HPLC and Protein Lynx Global Server software were obtained with supported by KCALSI (www.kclifesciences.org). We thank Dr. Francisco J. Blanco and Dr. Tahl Zimmerman for providing the LFA-1 I-domain plasmid. We also thank Nancy Harmony for proofreading the manuscript.

REFERENCES

(1) Schwartz, R. H. (2003) T cell anergy. *Annu. Rev. Immunol. 21*, 305−334.

(2) Salomon, B., and Bluestone, J. A. (1998) LFA-1 interaction with ICAM-1 and ICAM-2 regulates Th2 cytokine production. *J. Immunol. 161*, 5138−5142.

(3) Kobayashi, N., Kiptoo, P., Kobayashi, H., Ridwan, R., Brocke, S., and Siahaan, T. J. (2008) Prophylactic and therapeutic suppression of experimental autoimmune encephalomyelitis by a novel bifunctional peptide inhibitor. *Clin. Immunol. 129*, 69−79.

(4) Kobayashi, N., Kobayashi, H., Gu, L., Malefyt, T., and Siahaan, T. J. (2007) Antigen-specific suppression of experimental autoimmune encephalomyelitis by a novel bifunctional peptide inhibitor. *J. Pharmacol. Exp. Ther. 322*, 879−886.

(5) Manikwar, P., Kiptoo, P., Badawi, A. H., Buyuktimkin, B., and Siahaan, T. J. (2011) Antigen-specific blocking of CD4-specific immunological synapse formation using BPI and current therapies for autoimmune diseases. *Med. Res. Rev.* [Online early access] March 23.

(6) Murray, J. S., Oney, S., Page, J. E., Kratochvil-Stava, A., Hu, Y., Makagiansar, I. T., Brown, J. C., Kobayashi, N., and Siahaan, T. J. (2007) Suppression of type 1 diabetes in NOD mice by bifunctional peptide inhibitor: modulation of the immunological synapse formation. *Chem. Biol. Drug Des. 70*, 227−236.

(7) Ridwan, R., Kiptoo, P., Kobayashi, N., Weir, S., Hughes, M., Williams, T., Soegianto, R., and Siahaan, T. J. (2010) Antigen-specific suppression of experimental autoimmune encephalomyelitis by a novel bifunctional peptide inhibitor: structure optimization and pharmacokinetics. *J. Pharmacol. Exp. Ther. 332*, 1136−1145.

(8) Zhao, H., Kiptoo, P., Williams, T. D., Siahaan, T. J., and Topp, E. M. (2010) Immune response to controlled release of immunomodulating peptides in a murine experimental autoimmune encephalomyelitis (EAE) model. *J. Controlled Release 141*, 145−152.

(9) Shimaoka, M., Xiao, T., Liu, J. H., Yang, Y., Dong, Y., Jun, C. D., McCormack, A., Zhang, R., Joachimiak, A., Takagi, J., Wang, J. H., and Springer, T. A. (2003) Structures of the alpha L I domain and its complex with ICAM-1 reveal a shape-shifting pathway for integrin regulation. *Cell 112*, 99−111.

(10) Manikwar, P., Zimmerman, T., Blanco, F. J., Williams, T. D., and Siahaan, T. J. (2011) Rapid identification of fluorochrome modification sites in proteins by LC ESI-Q-TOF mass spectrometry. *Bioconjugate Chem. 22*, 1330−1336.

(11) Zimmerman, T., Oyarzabal, J., Sebastian, E. S., Majumdar, S., Tejo, B. A., Siahaan, T. J., and Blanco, F. J. (2007) ICAM-1 peptide inhibitors of T-cell adhesion bind to the allosteric site of LFA-1. An NMR characterization. *Chem. Biol. Drug Des. 70*, 347−353.

(12) Speicher, K., Kolbas, O., Harper, S., and Speicher, D. (2000) Systematic analysis of peptide recoveries from in-gel digestions for protein identifications in proteome studies. *J. Biomol. Technol. 11*, 74−86.

(13) Ikehata, K., Duzhak, T. G., Galeva, N. A., Ji, T., Koen, Y. M., and Hanzlik, R. P. (2008) Protein targets of reactive metabolites of thiobenzamide in rat liver in vivo. *Chem. Res. Toxicol. 21*, 1432−1442.

(14) Keller, A., Nesvizhskii, A. I., Kolker, E., and Aebersold, R. (2002) Empirical statistical model to estimate the accuracy of peptide identifications made by MS/MS and database search. *Anal. Chem. 74*, 5383−5392.

(15) Partis, M. D., Griffiths, D. G., Roberts, G. C., and Beechey, R. B. (1983) Cross-linking of protein by omega-maleimido alkanoyl N-hydroxysuccinimido esters. *J. Protein Chem. 2*, 263−277.

(16) Tan, C. S., and Koralnik, I. J. (2010) Progressive multifocal leukoencephalopathy and other disorders caused by JC virus: clinical features and pathogenesis. *Lancet Neurol. 9*, 425−437.

(17) Carson, K. R., Focosi, D., Major, E. O., Petrini, M., Richey, E. A., West, D. P., and Bennett, C. L. (2009) Monoclonal antibody-associated progressive multifocal leucoencephalopathy in patients treated with

rituximab, natalizumab, and efalizumab: a Review from the Research on Adverse Drug Events and Reports (RADAR) Project. *Lancet Oncol. 10*, 816−824.
(18) Pugashetti, R., and Koo, J. (2009) Efalizumab discontinuation: a practical strategy. *J. Dermatol. Treat. 20*, 132−136.
(19) Blanchfield, J. L., and Mannie, M. D. (2010) A GMCSF-neuroantigen fusion protein is a potent tolerogen in experimental autoimmune encephalomyelitis (EAE) that is associated with efficient targeting of neuroantigen to APC. *J. Leukoc. Biol. 87*, 509−521.
(20) Ni, J., Zhu, Y. N., Zhong, X. G., Ding, Y., Hou, L. F., Tong, X. K., Tang, W., Ono, S., Yang, Y. F., and Zuo, J. P. (2009) The chemokine receptor antagonist, TAK-779, decreased experimental autoimmune encephalomyelitis by reducing inflammatory cell migration into the central nervous system, without affecting T cell function. *Br. J. Pharmacol. 158*, 2046−2056.
(21) Wang, C., Gold, B. G., Kaler, L. J., Yu, X., Afentoulis, M. E., Burrows, G. G., Vandenbark, A. A., Bourdette, D. N., and Offner, H. (2006) Antigen-specific therapy promotes repair of myelin and axonal damage in established EAE. *J. Neurochem. 98*, 1817−1827.
(22) Falk, K., Rotzschke, O., Santambrogio, L., Dorf, M. E., Brosnan, C., and Strominger, J. L. (2000) Induction and suppression of an autoimmune disease by oligomerized T cell epitopes: enhanced in vivo potency of encephalitogenic peptides. *J. Exp. Med. 191*, 717−730.
(23) Luca, M. E., Kel, J. M., van Rijs, W., Wouter Drijfhout, J., Koning, F., and Nagelkerken, L. (2005) Mannosylated PLP(139−151) induces peptide-specific tolerance to experimental autoimmune encephalomyelitis. *J. Neuroimmunol. 160*, 178−187.
(24) Meiron, M., Zohar, Y., Anunu, R., Wildbaum, G., and Karin, N. (2008) CXCL12 (SDF-1alpha) suppresses ongoing experimental autoimmune encephalomyelitis by selecting antigen-specific regulatory T cells. *J. Exp. Med. 205*, 2643−2655.
(25) Manikwar, P., Tejo, B. A., Shinogle, H., Moore, D. S., Zimmerman, T., Blanco, F., and Siahaan, T. J. (2011) Utilization of I-domain of LFA-1 to Target Drug and Marker Molecules to Leukocytes. *Theranostics 1*, 277−289.
(26) Jin, M., Song, G., Carman, C. V., Kim, Y. S., Astrof, N. S., Shimaoka, M., Wittrup, D. K., and Springer, T. A. (2006) Directed evolution to probe protein allostery and integrin I domains of 200,000-fold higher affinity. *Proc. Natl. Acad. Sci. U.S.A. 103*, 5758−5763.
(27) Badawi, A. H., Kiptoo, P., Wang, W. T., Choi, I. Y., Lee, P., Vines, C. M., and Siahaan, T. J. (2011) Suppression of EAE and prevention of blood-brain barrier breakdown after vaccination with novel bifunctional peptide inhibitor. *Neuropharmacology 62*, 1874−1881.

Bioconjugate Chemistry

Article

pubs.acs.org/bc

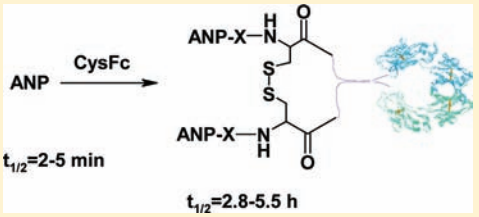
Atrial Natriuretic Peptide-Fc, ANP-Fc, Fusion Proteins: Semisynthesis, In Vitro Activity and Pharmacokinetics in Rats

Adam R. Mezo,*[,†] Kevin A. McDonnell,[‡] Susan C. Low,[‡] Jeff Song,[‡] Tom J. Reidy,[†] Qi Lu,[†] John V. Amari,[†] Todd Hoehn,[†] Robert T. Peters,[†] Jennifer Dumont,[†] and Alan J. Bitonti[†]

[†]Biogen Idec Hemophilia, 9 Fourth Avenue, Waltham, Massachusetts 02451, United States

Supporting Information

ABSTRACT: Atrial natriuretic peptide (ANP) may be a useful molecule for the treatment of cardiovascular diseases due to its potent natriuretic effects. In an effort to prolong the short *in vivo* half-life of ANP, fusions of the peptide to the Fc domain of IgG were generated using a semisynthetic methodology. Synthetic ANP peptides were synthesized with thioesters at either the N- or C-termini of the peptide and subsequently linked to the N-terminus of recombinantly expressed Fc using native chemical ligation. The linker length between the ANP and Fc moieties was varied among 2, 11, or 16 amino acids. In addition, either one ("monomeric") or two ("dimeric") ANP peptides were linked to Fc to study whether this modification had an effect on *in vitro* activity and/or *in vivo* half-life. The various constructs were studied for *in vitro* activity using a cell-based cGMP assay. The ANP-Fc fusion constructs were between 16- and ~375-fold weaker than unconjugated ANP in this assay, and a trend was observed where the most potent conjugates were those with longer linkers and in the dimeric configuration. The pharmacokinetics of several constructs were assessed in rats, and the half-life of the ANP-Fc's were found to be approximately 2 orders of magnitude longer than that of the unconjugated peptide. There was no significant difference in terminal half-life between the monomeric and dimeric constructs (2.8−5.5 h), but a trend was observed where the C_{max} of the monomeric constructs was approximately 3-fold higher than that of the dimeric constructs, although the origin of this effect is not understood. These novel ANP-Fc fusion constructs hold promise for future therapeutic application in the treatment of cardiovascular diseases.



INTRODUCTION

Atrial natriuretic peptide, ANP, was discovered in 1981 after it was observed that injection of heart atrial muscle extracts into rats resulted in natriuresis.[1] ANP was subsequently isolated in 1984 and characterized as a 28 amino acid peptide with a single cysteine disulfide loop.[2] ANP is released into circulation by the cardiac muscle when the heart undergoes increased atrial stretching. The peptide binds and activates the natriuretic peptide receptor A (NPR-A, also known as GC-A receptor), which is expressed in a variety of tissues, to release intracellular cGMP and trigger further signal transduction. The end result of ANP/NPRA/cGMP signaling is increased water and salt excretion, and thus lower blood volume and blood pressure.[3] Consequently, there has been intense research to develop ANP, and related natriuretic peptide factors, into viable cardio-protective drugs. One major challenge in the development of ANP-related drugs is the very short plasma half-life of ANP itself (2−5 min)[4−6] caused primarily by cleavage of the peptide by neutral endopeptidase NEP 24.11 and the clearance receptor natriuretic peptide receptor C (NPR-C).[7]

One approach to extending the half-life of peptide[8,9] and protein[10] therapeutics is fusion of the potential therapeutic moiety to the Fc domain of IgG for recycling via the neonatal Fc receptor, FcRn. FcRn is broadly expressed in a variety of tissues including endothelial cells and is thought to bind Fc in acidic endosomes, thereby diverting the protein from lysosomal degradation.[11] Subsequent shuttling and release of Fc at the cell surface serves to extend the *in vivo* half-life of Fc-linked moieties. The strategy of Fc fusions has been applied successfully to both peptides and proteins. An interesting adaptation of the Fc fusion approach is the generation of monovalent protein-Fc "monomers", whereby only a single effector moiety is linked to the dimeric Fc molecule.[12] This monomeric Fc fusion approach has resulted in enhanced biological activity and pharmacokinetic properties for several proteins when compared to those properties for the dimeric forms. Lastly, Fc fusion technology provides the possibility of efficient noninvasive delivery of Fc fusion proteins via FcRn.[13] For example, an erythropoietin-Fc fusion protein was absorbed through the lungs with high efficiency in cynomolgus monkeys using the FcRn pathway.[14]

We hypothesized that the Fc domain fusion to ANP would enhance the half-life of ANP via FcRn recycling, and also provide a degree of protection against protease cleavage and NPR-C clearance by steric hindrance. Herein, we describe the semisynthetic generation of ANP-Fc monomers and dimers using recombinant Fc and synthetic peptides. The ANP-Fc fusion proteins were characterized by several analytical

Received: November 6, 2011
Revised: January 16, 2012
Published: January 22, 2012

 © 2012 American Chemical Society

methods, as well as by an *in vitro* cGMP induction assay. Finally, the pharmacokinetics of the ANP-Fc fusions were assessed in rats for two monomeric and dimeric constructs.

MATERIALS AND METHODS

Cloning, Expression, and Purification of Cys-Fc. The human Cys-Fc sequence from IgG1 was obtained from a human leukocyte cDNA library with the mouse Igκ signal sequence using standard PCR techniques. The Cys-Fc sequence was then cloned into pEE12.4 (Lonza Group) to create pSYN-CysFc-004. See Supporting Information for protein sequence of CysFc. CHOK1SV suspension cells (Lonza) were transfected with pSYN-cysFc-004 by electroporation according to the manufacturer's instructions. Cells were selected with 25 μM MSX at 37 °C/5% CO_2 for three weeks. Transfected cells were expanded and adapted to serum-free suspension culture. CysFc expression levels were assessed using a protein A immunoprecipitation procedure followed by nonreducing SDS-PAGE analysis. Based on immunoprecipitation results, the cell line 9F4 was chosen for production. Cys-Fc was produced from 20 L of 9F4 cells. At the end of the production run, cells were removed by centrifugation and the conditioned medium concentrated 4-fold by tangential flow filtration. Cys-Fc was purified by protein A chromatography and eluted with 0.1 M sodium citrate containing 0.15 M sodium chloride, pH 3.4. The protein was then diafiltered into DPBS and stored at 4 °C until use.

Peptide Synthesis. Peptides were synthesized on an Advanced ChemTech 396Ω synthesizer using Fmoc-Gly-NovaSyn TGT resin (Novabiochem) and standard Fmoc-solid phase peptide synthesis using HBTU as the coupling agent, *N*,*N*-diisopropylethylamine (DIEA) as the base and *N*,*N*-dimethylformamide (DMF) as the solvent. Crude peptides were purified by reverse phase HPLC (Phenomenex Jupiter 5 μ C4 300 Å column, 250 × 21.20 mm) using gradients of acetonitirile in water with 0.1% TFA. Peptide purity was confirmed >90% by analytical RP-HPLC, and peptide identities were confirmed by electrospray MS.

Synthesis of C-Terminal ANP Thioesters. After automated synthesis, the N-terminus was protected by manually treating the resin with 10 equiv of di-*t*-butyl dicarbonate (Boc_2O) and 20 equiv of DIEA in DMF, and allowed to mix overnight at RT. The fully protected peptide was cleaved from the resin by mild acid cleavage in DCM with 30% 1,1,1,3,3,3-hexafluoro-2-propanol (HFIP) for two hours. The resin was filtered and the filtrate was concentrated in vacuo overnight, yielding the protected peptide with a free C-terminus. This material was treated with 1.5 equiv of glycine benzyl thioester hydrochloride salt (Gly(SBn)·HCl), 1.5 equiv of PyBOP (Novabiochem), and 4.5 equiv of DIEA in DMF and stirred for 18 h. The reaction mixture was concentrated in vacuo for 18 h. The protected peptide thioester was deprotected by treatment with 25 mL of cleavage cocktail (95% trifluoroacetic acid (TFA), 2.5% triisopropylsilane (TIS), and 2.5% ethanedithiol (EDT)) for two hours and 45 min, after which 2.5% (v/v) bromotrimethylsilane (TMSBr) was added and allowed to mix for 15 min. The reaction mixture was concentrated, and the crude peptide thioester was precipitated with cold diethyl ether (Et_2O). Peptide was centrifuged, supernatant decanted, and crude peptide was triturated two more times with cold Et_2O. The peptide was purified by HPLC, and fractions were analyzed by LC/MS for identity and purity. Fractions containing >90% peptide were pooled, flash frozen, and lyophilized.

Synthesis of N-Terminal ANP Thioesters. After automated synthesis, the *N*-terminus of the peptide thioesters was converted to a free carboxylic acid by manually treating the resin with succinic anhydride (10 equiv) and DIEA (10 equiv) in DMF for 2 h at RT. Reaction contents were removed via vacuum filtration, and the resin was washed with DMF and DCM, respectively. To generate the thioester, this material was treated with 5 equiv of Gly(SBn)·HCl, 5 equiv of PyBOP (Novabiochem), and 15 equiv of DIEA in DMF and stirred for 18 h at RT. The protected peptide thioester was cleaved from the resin and deprotected as described above. The peptide was isolated and purified as described above.

Conjugation of ANP Thioester Peptides to Cys-Fc. Cys-Fc (5 mg/mL in PBS, pH 7.4) was treated with 2-mercaptoethanesulfonic acid, sodium salt (MESNA, Sigma-Aldrich), such that the final concentration of MESNA was 20 mM. Peptide thioester was added to the reaction mixture (2−6 mol equiv depending on the peptide) and allowed to mix for 18 h at RT. The actual number of equivalents of peptide was selected based on pilot scale reactions such that an equal percentage of monomer (1 ANP peptide per Fc) and dimer (2 ANP peptides per Fc) conjugate was formed. The crude reaction mixture was diluted to 1 mg/mL in PBS and dialyzed against PBS (pH 7.4) (7 changes over 24 h). NuPage SDS-PAGE gels (Invitrogen) were used to determine the extent of reaction. Prior to protein purification, the conjugate was dialyzed into 50 mM Tris-HCl buffer pH 7.2.

Purification of the Semisynthetic ANP-Fc Conjugates. The dialyzed ANP-Fc conjugation reaction mixture was adjusted to a final concentration of 50 mM sodium acetate, pH 5.0, with 1 M sodium acetate, pH 5.0, then filtered through a 0.8/0.2 μm syringe filter. This clarified solution was loaded onto a 1 × 10 cm column packed with Fractoprep SO_3-650(M) cation exchange resin (CEX) equilibrated with 50 mM sodium acetate, pH 5.5. After loading the column was washed with 3 column volumes (CV) of equilibration buffer. The protein was eluted with a linear gradient from 0 to 0.5 M sodium chloride (in 50 mM sodium acetate pH 5.5) over 30 CV. Fractions were analyzed using NuPage SDS-PAGE gels and the fractions containing the majority of the monomer conjugate were pooled together, while separately the fractions containing the majority of the dimer conjugate were pooled together. The CEX pools were first adjusted to 0.1 M Tris pH 7.2 using a 1 M Tris pH 7.2 stock solution and were then adjusted to 1 M ammonium sulfate using a 3 M ammonium sulfate stock solution. After filtration with a 0.8/0.2 μM syringe filter, this clarified protein solution was loaded onto a 1 × 10 cm column packed with EMD Fractogel TA 650(S) thio-affinity column pre-equilibrated with 50 mM Tris, 1 M Ammonium Sulfate, pH 7.2. After washing the column with 3 CV of equilibration buffer, the protein was eluted with a decreasing linear gradient from 1.0 to 0.33 M ammonium sulfate over 20 CV. This was followed by a step gradient from 0.33 to 0 M Ammonium Sulfate. The peak fractions containing highly purified conjugate were identified using SDS-PAGE gels then pooled together. The final pool was dialyzed against 1× PBS. Protein concentration was determined using UV-280 nm analysis. If needed, the final protein was concentrated using Amicon Ultra-15 Centrifugal Concentration Unit(s) [Millipore]. The final protein was aseptically filtered through a 0.2 μm filter then aliquots were stored at −80 °C.

dx.doi.org/10.1021/bc200592c | *Bioconjugate Chem.* 2012, 23, 518−526

Size-Exclusion Chromatography of the Semisynthetic ANP-Fc Fusions. The aggregation content of the semisynthetic ANP-Fc fusion proteins was assessed using analytical size exclusion chromatography (SE-HPLC). A TSKgel Super SW2000 4.6 mm × 300 mm (Tosoh Biosciences) SE-HPLC column was run at a flow rate of 0.4 mL/min using PBS, pH 7.4, and 250 mM NaCl as the eluent. Samples of 5 μL of a 1.0 mg/mL solution were injected for each analysis. BioRad MW standards were injected prior to and after each set of injections to ensure the integrity of the column. Area under the curve integration was performed to determine the percent of each separated component peak.

Characterization of Free Peptide in the Semisynthetic ANP-Fc Fusions. The free unconjugated ANP peptide contaminant levels in the purified semisynthetic ANP-Fc fusions preps were analyzed using reversed-phase chromatography. A Protein C_4 reversed phase column (Grace Vydac) was injected with 100 μg of the purified semisynthetic Fc fusion protein. The two mobile phases were A) 0.1% TFA in water and B) 0.1% TFA in acetonitrile. The reversed phase chromatography was run using the following gradient profile over a total run time of 50 min (min): 0−0.5 min at 5% B, 5−35 min ramp up to 95%B, 35−40 min hold at 95%B, 40−42 min ramp down to 5%B, 42−50 min hold at 5%B. ANP fusions were analyzed neat and spiked with 0.1 μg of unconjugated free ANP peptide (0.1 μg spike is equivalent to 1.3 mol %) to visualize expected retention time and peak heights of potential contamination. The limit of quantitation of unconjugated free ANP using this method was 1.3% (mole/mole) (potential ANP contamination level). In addition, a 10 μg injection of the corresponding unconjugated peptide was injected to verify the retention time of the potential free peptide contamination.

Characterization of Peptide Disulfide Linkages in the Semisynthetic ANP-Fc Fusions. The disulfide linkages of the ANP-Fc fusion monomers and dimers were identified by combining trypsin digestion and nano-LC/MS/MS under reducing and nonreducing conditions (see Supporting Information). An Agilent 1100 HPLC binary system and a Thermo LCQ-Advantage ion trap mass spectrometer were used for the LC/MS/MS analysis. The unconjugated ANP peptide analogue (including GS linker region) of the ANP-Fc fusions was used as the positive control for the identification experiment. A 3 μg sample of peptide-Fc fusion (1 μg of free peptide in oxidized form) was diluted to a final volume of 30 μL with 100 mM ammonium acetate (pH 5.25). A 10 μL sample of a 0.01 μg/mL trypsin solution (trypsin gold, MS grade, Promega) was added to the protein/peptide solution and the digestion was carried out at 37 °C for 18 h. The digested sample was split into two aliquots of 20 μL. One aliquot of the digest (nonreduced condition) was frozen immediately and stored at −20 °C until analysis. The second aliquot was dried down *in vacuo* and redissolved with 20 μL of 50 mM Tris-HCl and 1 mM EDTA (pH 8.0). One microliter of DTT (0.2 M) was added and the solution was incubated at 56 °C for 30 min. Subsequently, 1 μL of 2-iodoacetamide (0.5 M) was added and the reaction proceeded for 30 min in the dark to generate the thiol-capped digestion sample. The unconjugated peptide digest was diluted 5-fold with water, and 0.5 μL of digested peptide-Fc fusion (or 1 μL of digested peptide) was loaded onto a self-packed C_{18} capillary LC column (YMC C_{18}, 5 μm, 10 cm long) for nano-LC/MS/MS analysis. The HPLC pump flow rate of 0.2 mL/min was split to obtain 1 μL/min for the capillary LC. The mobile phases used were 0.05 M acetic acid in water (A) and 0.05 M acetic acid in acetonitrile (B). The LC/MS data (nonreduced and reduced) were compared to theoretical masses corresponding to possible disulfide folding linkages for the digested fragments to determine whether or not the proper disulfides within the ANP peptide(s) had formed. The reduced peptide fragment sequence was confirmed by SEQUEST database searching of MS/MS data. The peptide digest data also confirmed the conjugation of the peptides to the N-termini of CysFc.

Characterization of the FcRn Binding Properties of the Semisynthetic ANP-Fc Fusions Using Surface Plasmon Resonance. All reagents for immobilization of FcRn to the Biacore chip were purchased from Biacore AB (Uppsala, Sweden). Soluble human FcRn (produced in CHO cells) was cross-linked to the dextran surface of a CM5 sensor chip by amine coupling using 1-ethyl-(3-dimethylaminopropyl)-carbodiimide hydrochloride (EDC) and N-hydroxysuccinimide (NHS) as recommended by Biacore. For immobilization, the FcRn was diluted to 10 μg/mL in 10 mM sodium acetate, pH 4.5. Residual sites on the dextran were blocked with 1 M ethanolamine hydrochloride pH 8.5. FcRn was immobilized to one flow cell on the sensor chip, while a control flow cell was blocked with ethanolamine for reference subtraction. Sufficient FcRn was bound to the chip to result in 400 to 600 response units (RU). Experiments were performed at pH 6 using 50 mM sodium phosphate, 100 mM sodium chloride, and 0.01% surfactant P20 (Biacore AB). Eleven 2-fold serial dilutions between 1 μM and 1 nM of the ANP-Fc or control proteins were injected over the FcRn-CM5 chip at 30 μL/min for 5 min. Bound protein was then dissociated from the chip for 2.5 min with running buffer. Any remaining protein was removed from the chip with a 27 s injection of pH 7.4 HBS-P buffer (0.01 M HEPES pH 7.4, 0.15 M NaCl, 0.005% v/v Surfactant P20) at 30 μL/min.

Sensorgrams were analyzed using *BiaEval* software version 3.1 (Biacore AB) and were baseline corrected using a buffer blank then baseline averaged. The Response Units at equilibrium (R_{eq}) values are plotted against concentration and the equilibrium affinity constants (K_D's) are then derived by fitting the data to a heterogeneous ligand model using *BiaEval* software. This model assumes that there are two classes of noninteracting binding sites of FcRn on the sensor chip. Thus, the K_D values are reported as two separate K_D's that contribute some fractional % to the theoretical maximal observed R_{eq} value (R_{max}).[15,16]

Generation of Stable Cell Lines for In Vitro NPRA Cell Assays. Full-length human NPRA, plasmids were purchased from OriGene Technologies, Inc., or sequence synthesized and subcloned into pcDNA3.1 mammalian expression vector (Invitrogen). The pcDNA3.1 NPR clones were transfected using Lipofectamine (Invitrogen) into HEK293 cells and stable cell lines were selected using G418. Clones were screened using the ANP-induced cGMP assay described below. High cGMP producing clones were expanded in DMEM containing, 100 μg/mL penicillin/streptomycin, L-glutamine, 400 μg/mL of G418, and 10% FBS (Hyclone, Logan, UT).

Natriuretic Peptide Induced cGMP Assay. HEK293 NPRA cells grown to 90% confluence were harvested with Versene (Invitrogen). Cells were washed and resuspended at 3.3×10^5 cells per mL in prewarmed Dulbecco's PBS, pH 7.4, 25 mM HEPES, 0.1% BSA, 1 mM 3-Isobutyl-1-methylxanthine (IBMX) [Assay Buffer]. 40 μL of cell suspension was added to 40 μL of ANP or ANP-Fc in Assay Buffer in triplicate and

dx.doi.org/10.1021/bc200592c | *Bioconjugate Chem.* 2012, 23, 518−526

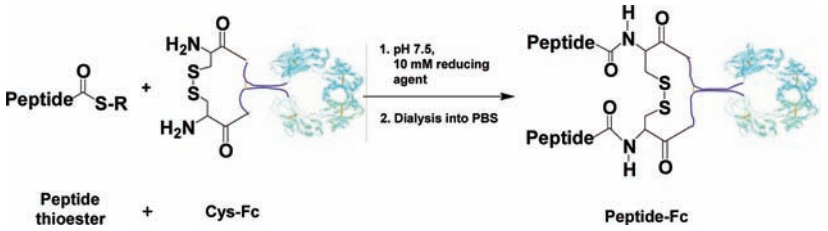


Figure 1. Schematic representation of the semisynthetic method used to generate the ANP-Fc fusion proteins.

incubated for 20 min at 37 °C. The cGMP concentration was measured using the HitHunter cGMP Assay Kit (DiscoveRx, Corporation Freemont, CA). cGMP production dose response curves were generated with a four parameter logistic equation fitted using the Levenberg−Marquardt algorithm in *XLfit4.2* data analysis software (ID Business Solutions, Ltd., Guildford, UK).

Pharmacokinetics of ANP-Fc 2m, 2d, 3m, and 3d. Female Wistar rats (~100 g; 4 rats/protein) were dosed IV with 0.5 mg/kg protein **2m**, **2d**, **3m**, and **3d** in PBS. Blood was collected from each rat by tail nick at 1, 2, 4, 8, 24, 48, and 72 h (protein **3d**) or 0.25, 1, 2, 4, 8, 24, 48, and 72 h (proteins **2m**, **3d**, and **3m**) after dosing. Blood (2 × 60 μL aliquots) was collected into microcapillary tubes (Fisher Scientific, catalog #22−362−574) containing one-tenth volume of 3.2% sodium citrate and plasma was generated by centrifugation. Plasma was stored at −20 °C until analysis by ANP-Fc/Fc ELISA and Fc/Fc ELISA. Pharmacokinetic parameters were assessed using WinNonlin pharmacokinetic software (*Pharsight* v 4.1 or 5.1)

All studies in animals were conducted using protocols that were approved by an Institutional Animal Care and Use Committee (IACUC), following the National Institutes of Health guidelines for the care and use of research animals.

ANP-Fc/Fc ELISA. 96-well plates (Costar, catalog #3369) were coated with 5 μg/mL (50 μL/well) mouse antihuman ANP (US Biologicals, catalog #A4150) in 50 mM of carbonate/bicarbonate buffer pH 9.6 at 4 °C overnight. Plates were blocked with 300 μL/well of PBS/5% BSA (Jackson ImmunoResearch, catalog #001−000−162) for 2 h at RT. Standards and samples (100 μL/well) were diluted in PBS/5% BSA and incubated for 2 h at RT. Standard curves ranged from 0.039 ng/mL to 10 ng/mL. Plates were washed three times with 300 μL/well of PBS containing 0.05% Tween-20 (PBST) in a Tecan plate washer. Plates were then incubated with 100 μL/well of goat antihuman (Fc specific) horseradish peroxidase (HRP) conjugated antibody (Pierce Biotechnology, catalog #31413) diluted 1:7500 in PBS/5%BSA for 3 h at RT. Plates were washed four times with 300 μL/well of PBST before development with 100 μL/well of TMB supersensitive substrate (BioFx Laboratories) at RT for approximately 6 min. Reactions were stopped by addition of 0.25 M of sulfuric acid (100 μL/well). Plates were read at 450 (−600) nm in a Spectromax plate reader.

Fc/Fc ELISA. 96-well plates (Costar, catalog #3369) were coated with 1 μg/mL (50 μL/well) goat antihuman IgG, Fc fragment (Pierce, catalogue #31123, stock = 1.8 mg/mL) in 0.1 M carbonate/bicarbonate buffer pH 9.2 and incubated at 37 °C for 1 h. Plates were blocked with 200 μL/well of PBS/2% BSA for 1 h at 37 °C. Standards and samples (100 μL/well) were diluted in PBS/2% BSA and incubated for 1 h at 37 °C. Plates were washed three times with 300 μL/well of PBST in a Tecan plate washer. Plates were then incubated with 100 μL/well of goat antihuman (Fc specific) horseradish peroxidase (HRP) conjugated antibody (Pierce Biotechnology, cat #31416) diluted 1:25 000 in PBS/2%BSA for 1 h at RT. Plates were washed three times with 300 μL/well of PBST before development with 100 μL/well of TMB solution (1:1 mix of TMB substrate and H_2O_2; Pierce) and until color developed. Reactions were stopped by addition of 2 M sulfuric acid (100 μL/well). Plates were read at 450 nm in a Spectromax plate reader.

RESULTS

Generation of Semisynthetic ANP-Fc Constructs. The ANP-Fc proteins were generated semisynthetically using native ligation chemistry.[17] This process involved the reaction of a recombinantly produced Fc fragment of IgG1 containing a N-terminal cysteine (CysFc) with various synthetically produced ANP thioesters to generate a native amide bond at the linkage site (Figure 1). ANP peptide was synthesized with the thioester at either the N-terminus or the C-terminus of ANP to study the effect of the different Fc fusion orientations on activity. To generate the CysFc protein, Fc from IgG1 was truncated at the first naturally occurring N-terminal hinge cysteine of Fc (NH_2−CPPCDKTH...; IgG1) such that no new cysteines were introduced into the sequence of Fc, yet retaining both hinge cysteines for hinge disulfide formation. The linker connecting ANP and Fc was composed of glycine and serine residues (GGS) to generate a flexible hydrophilic linker in the hopes of having minimal interference with the biological activity of ANP. Although additional non-natural linkers such as PEG would have been possible to incorporate into the model system, natural linker residues were selected in this study to model recombinant protein production. In addition, the linkers were designed to be stable and noncleavable for this initial study; however, future designs could also incorporate cleavable linker/prodrug technology in efforts to boost overall activity.[18,19] Lastly, the linker length was also varied from 2, 11, and 16 amino acids (Figure 2) to probe the effect of linker length on activity. The maximum length of a 16 amino acid linker was driven by peptide availability for this study; linkers of >16 amino acids would also be of interest to study in the future.

CysFc was cloned, expressed in CHO cells, and purified by protein A chromatography. Binding of CysFc to FcRn was confirmed using surface plasmon resonance (SPR) analysis (Table 2, *vide infra*). ANP thioesters were synthesized using standard Fmoc/tBu protocols with a few postsynthesis modifications. In the case of C-terminal thioesters, a mild acid-sensitive trityl-based polystyrene resin was used. After synthesis of the peptide on resin, treatment of the protected peptide with 1,1,1,3,3,3-hexafluoro-2-propanol in dicholoromethane cleaved the peptide from the resin, but left all of the remaining protecting groups intact. The free C-terminus of the peptide was coupled to glycine benzyl thioester (NH_2-Gly-SBn), then treated with TFA to cleave the remaining protecting

dx.doi.org/10.1021/bc200592c | *Bioconjugate Chem.* 2012, 23, 518−526

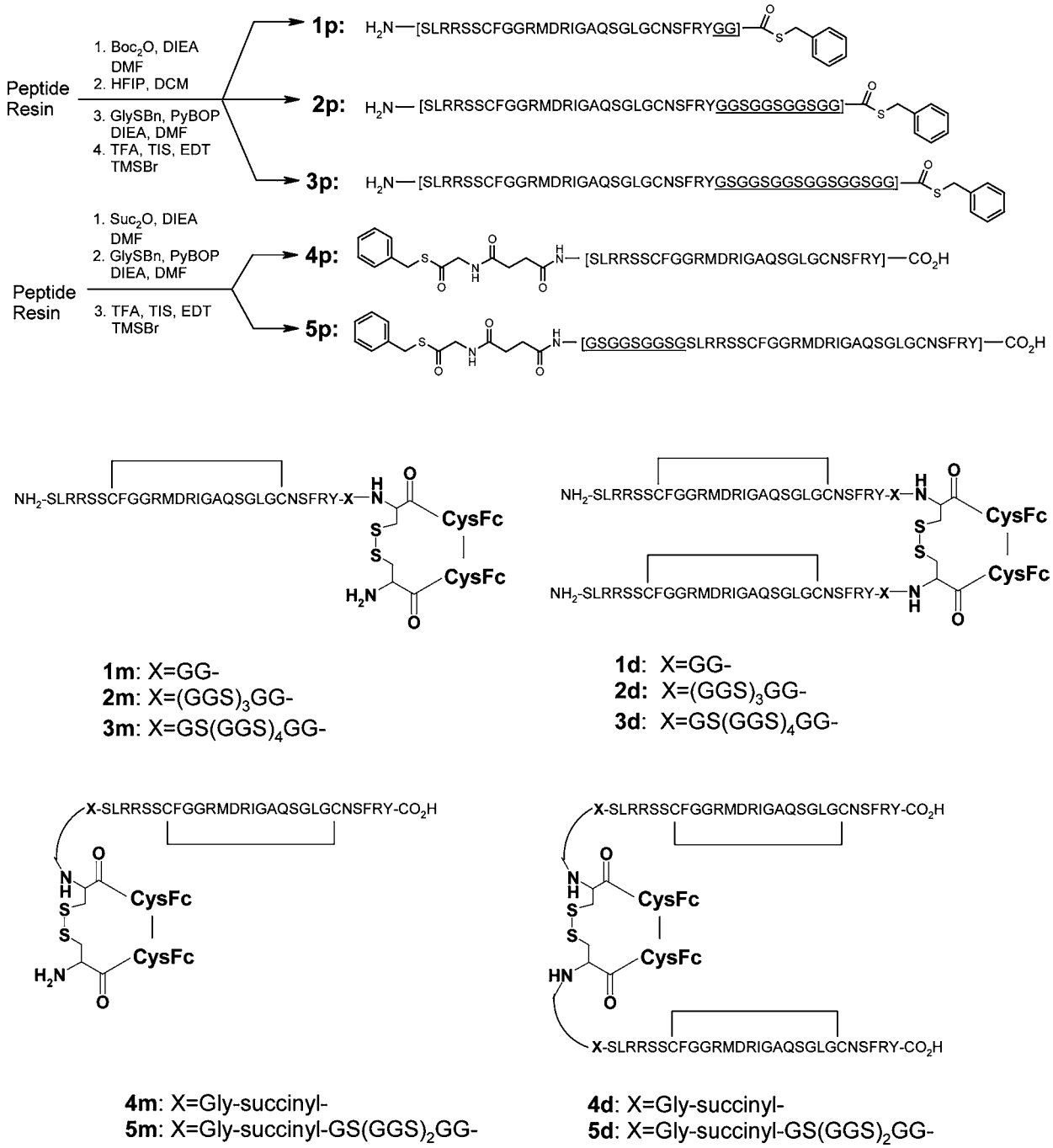


Figure 2. Schematic illustrating the synthesis and structures of various ANP peptides and the structures of various ANP-Fc protein constructs. Nomenclature: '**p**', peptide; '**m**', ANP-Fc monomer; '**d**', ANP-Fc dimer.

groups (Figure 2).[20] In the case of N-terminal thioesters, after peptide synthesis, the resin was treated with succinic anhydride to generate an N-terminal carboxylic acid which was subsequently coupled to NH_2-Gly-SBn to generate the N-terminal thioester. Subsequent purification by reversed phase HPLC provided peptides **1p**−**5p** (Figure 2).

Ligation of the ANP thioesters to CysFc was performed at neutral pH in the presence of a reducing agent and using a stoichiometrically limiting amount of peptide thioester, such that the reaction would generate a mixture of ANP-Fc "monomers" (single peptide linked to Fc), and ANP-Fc "dimers" (two peptides linked to Fc). The protein reaction mixtures were then extensively dialyzed into 50 mM Tris-HCl buffer at pH 7.2 to ensure that the hinge disulfide at the N-termini was regenerated as initially assessed by nonreducing SDS-PAGE. The proteins were purified using a two-step process: cation exchange chromatography followed by thiol-affinity chromatography. The cation exchange step separates the CysFc, the monomer and dimer ANP-Fc conjugates, while also removing the protein aggregates. The individual ANP-Fc conjugate cation exchange pools were independently put through a thiol-affinity chromatography purification step to remove the unconjugated free ANP peptide and to further purify the monomer and dimer conjugate species. It should be noted that the thiol-affinity method was developed and utilized as a result of its clean separation of the protein conjugates and the free peptide.

dx.doi.org/10.1021/bc200592c | *Bioconjugate Chem.* 2012, 23, 518−526

Therefore, unconjugated peptide is not expected to be present in the final purified proteins.

Analytical Characterization of Semisynthetic ANP-Fc Proteins. The purified ANP-Fc proteins were characterized by SDS-PAGE which was able to differentiate the proteins with zero, one, and two ANP peptides linked to Fc, with bands migrating consistent with their expected molecular weight (Figure 3). Densitometry was performed on the gels and it was

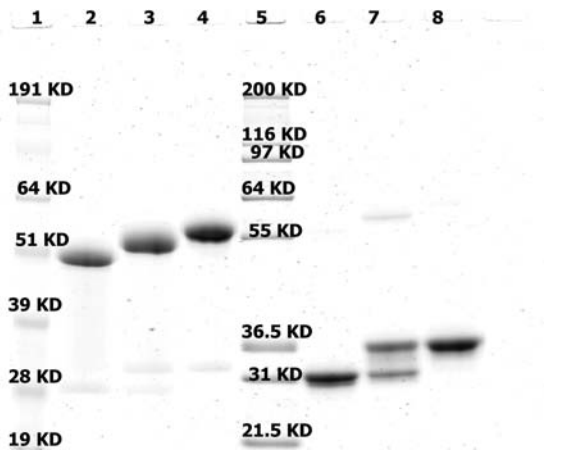


Figure 3. Representative SDS-PAGE analysis of ANP-Fc monomer **3m** and dimer **3d**. Lanes 1−4: nonreducing conditions; Lanes 5−8: reducing conditions. Lanes 1,5: molecular weight markers. Lanes 2,6: CysFc. Lanes 3,7: protein **3m**. Lanes **4,8**: protein **3d**.

estimated that each protein was >88% pure (Table 1). Analytical size-exclusion chromatography was used to monitor

Table 1. Summary of Analytical Characterization of ANP-Fc Fusion Proteins by SDS-PAGE, SEC-HPLC, and RP-HPLC[a]

protein name	reducing SDS-PAGE (% Purity)[b]	non-reducing SDS-PAGE (% Purity)	SE-HPLC % Expected Major Peak	RP-HPLC[c] % (mol/mol) unconjugated peptide
1m	48 + 40 = 88	93	97	<1.3
1d	99	92	99	<1.3
2m	53 + 44 = 97	97	99	<1.3
2d	99	95	99	<1.3
3m	59 + 37 = 96	96	>95	<1.3
3d	99	97	n/a	<1.3
4m	53 + 43 = 96	99	99	<1.3
4d	99	95	95	<1.3
5m	53 + 39 = 92	98	96	<1.3
5d	99	99	99	<1.3

[a]See Figure 1 legend for protein name nomenclature. [b]SDS-PAGE of monomeric constructs under reducing conditions is expected to result in two bands due to the dissociation of the Fc; the sum of their intensities would equal 100% for a pure protein. [c]The RP-HPLC assay was only applied to the semisynthetic constructs due to the known possibility of remaining unconjugated peptide.

possible aggregate formation, and each protein was determined to be >95% of the expected construct (Table 1 and Supporting Information). Although the protein purification methodology was developed to efficiently remove unconjugated peptide, there remains a theoretical risk that the final protein preparations contain unconjugated ANP peptide. A reversed-phase HPLC method was established to detect and quantify the levels of "free" unconjugated ANP peptide from the ligation reaction (Table 1 and Supporting Information). No ANP peptide was detected in any of the protein preparations where the limit of detection for this method was 1.3% (mol/mol) free ANP peptide. Finally, trypsin digestion/LC/MS/MS analysis was performed to ensure that the proper disulfide patterns within both ANP and Fc were present, and to confirm the site of conjugation to CysFc. The semisynthetic constructs possessed the expected ANP disulfide folding pattern, although a small fraction of disulfide misfolding was observed for some of the constructs. The percentage of misfolded disulfides was estimated to be 3−15% of the total (see Supporting Information), therefore the proteins were considered acceptable for further analysis. The trypsin digest also confirmed that site of peptide conjugation was at the N-terminal cysteine of CysFc as expected based on the selectivity of the native ligation methodology.

Affinity of Semisynthetic ANP-Fc Proteins to Human FcRn by SPR. The affinity of each ANP-Fc construct for human FcRn was assessed using surface plasmon resonance (SPR) to verify that the synthetic chemistry did not alter the FcRn-binding capabilities of the Fc domain. No significant changes in FcRn binding were observed as compared to the Cys-Fc control (Table 2 and Supporting Information).

Table 2. Summary of FcRn Surface Plasmon Resonance Data for Each of the Semisynthetic ANP-Fc Proteins[b]

protein name	K_{D1} (nM)	% R_{max}	K_{D2} (nM)	% R_{max}	total R_{max}	χ^2
CysFc	230	54	5.5	46	213	2.74
1m	186	52	2.5	48	261	4.75
1d	150	49	10.9	51	365	54.6[a]
2m	241	63	5.3	37	188	1.23
2d	256	60	3.9	40	240	9.99
3m	283	73	8.1	27	149	1.31
3d	204	63	3.9	37	210	8.7
4m	245	54	4.9	46	224	3.23
4d	204	50	3.7	50	258	5.99
5m	243	56	4.3	44	231	2.98
5d	213	55	4.0	45	230	4.35

[a]Value is higher than optimal range. Evaluation of raw sensorgram data above reveals that **1d** behaves comparably to CysFc (see Supporting Information). Binding reaches equilibrium quickly and dissociation is fast. The difference is that at the lower concentrations the signal for **1d** dimer is stronger than CysFc. [b]Since FcRn was immobilized, two K_D values are reported representing the low and high affinity population of binding sites, with their fractional occupancies reported as % R_{max}.[11,12]

Induction of cGMP in Cells Transfected with Human NPRA. The ability of the ANP-Fc constructs to activate NPRA and generate cGMP was assessed using HEK293 cells expressing human NPRA. All ANP-Fc fusions were found to be considerably weaker than the unconjugated ANP peptide (Table 3) in generating cGMP. Although the data were variable, in general, the ANP-Fc fusions with the longer linkers were more potent than those with shorter linkers (e.g., **3d** vs **1d**, $p < 0.01$). Fusion proteins with two ANP peptides linked to the Fc (dimers) were generally greater than or equal to 2-fold more potent than those proteins with only a single ANP linked to Fc (monomers) (e.g., **1m** vs **1d** × 2: $p = 0.1$), although one dimer (**4d**) was found to be statistically similar to its monomer (**4m**, $p > 0.2$). Lastly, there was no preference for either

dx.doi.org/10.1021/bc200592c | Bioconjugate Chem. 2012, 23, 518−526

Table 3. Induction of cGMP by ANP-Fc Fusions Using HEK293 Cells Transfected with Human NPRA

peptide/ protein	monomeric or dimeric ANP-Fc construct	linker composition	ANP termini linked to N-terminus of Fc	cGMP EC_{50} (nM)
hANP	n/a	n/a	n/a	0.87 ± 2.2 (n = 21)
CysFc	n/a	n/a	n/a	No activity at 1000 nM
1m	monomer	GG	C-terminus	329 (n = 2)
1d	dimer	GG	C-terminus	118 ± 55 (n = 4)
2m	monomer	$(GGS)_3GG$	C-terminus	327 (n = 2)
2d	dimer	$(GGS)_3GG$	C-terminus	68 (n = 2)
3m	monomer	$GS(GGS)_4GG$	C-terminus	83 ± 51 (n = 4)
3d	dimer	$GS(GGS)_4GG$	C-terminus	14 ± 1.3 (n = 4)
4m	monomer	Gly-succinyl	N-terminus	150 ± 49 (n = 4)
4d	dimer	Gly-succinyl	N-terminus	114 ± 40 (n = 3)
5m	monomer	Gly-succinyl-$GS(GGS)_2GG$	N-terminus	158 ± 101 (n = 4)
5d	dimer	Gly-succinyl $GS(GGS)_2GG$	N-terminus	66 ± 55 (n = 4)

orientation of ANP-Fc, since it was found that linking either the N- or C-terminus to Fc resulted in equivalent activity (e.g., **2d** and **5d**, p = 0.46). The most potent construct, **3d**, was approximately 16-fold weaker than unconjugated ANP.

Pharmacokinetics of ANP-Fc Proteins in Rats. The pharmacokinetics of ANP-Fc fusions **2m**, **2d**, **3m**, and **3d** were studied in rats to examine possible effects of linker length and configuration (monomeric vs dimeric) on pharmacokinetics. Two different methods were used to detect the protein: (1) an ANP-Fc/Fc ELISA to detect the intact ANP-Fc protein and (2) a Fc/Fc ELISA to detect only the Fc protein, thereby unaffected by potential ANP degradation.

It was found that, after intravenous administration, the half-life of the ANP-Fc constructs (3−6 h; Table 4) was greatly enhanced over that of the free peptide which has an estimated half-life of 2−5 min.[4−7] Interestingly, the monomeric ANP-Fc constructs (**2m**, **3m**) possessed a higher maximum plasma concentration (C_{max}) compared to that of the ANP-Fc dimers (**2d**, **3d**; p < 0.0001 and p < 0.0001, respectively), although the half-lives for the two types of constructs were similar (Figures 4−6). As a result, areas under the curve (AUC) for the monomers (**2m**, **3m**) were >5-fold greater than those of the corresponding dimers (**2d**, **3d**; Table 4). There was no significant effect of the two linker lengths on the pharmacokinetics, as may be expected given that the two linkers vary by only 5 amino acids. Lastly, it was found that the ANP-Fc/Fc and Fc/Fc detection methods provided significantly different results; the Fc/Fc ELISA data provided elevated serum concentrations and prolonged half-lives (Figure 4). These data suggest that the ANP peptide portion of the ANP-Fc fusion was partially degrading with time *in vivo*, although the extent of this degradation was not studied further.

Table 4. Summary of the Pharmacokinetic Parameters of Proteins 2m, 2d, 3m, and 3d after Intravenous Administration of 0.5 mg/kg Protein in Rats Using the ANP-Fc ELISA Detection Method to Detect Intact Protein

protein	C_{max} (ng/mL)	$T_{1/2}$ (h)	AUC (h·ng/mL)	C_{lp} (mL/h/kg)	V_{ss} (mL/kg)	MRT (h)
2m	4250	3.9	13947	36	202	3.8
2d	1280	2.8	2645	189	775	3.1
3m	3834	4.5	14590	34	220	4.4
3d	429[a]	5.5	2525	198	1583	5.5

[a] 1 h C_{max}; all other C_{max} values at 15 min.

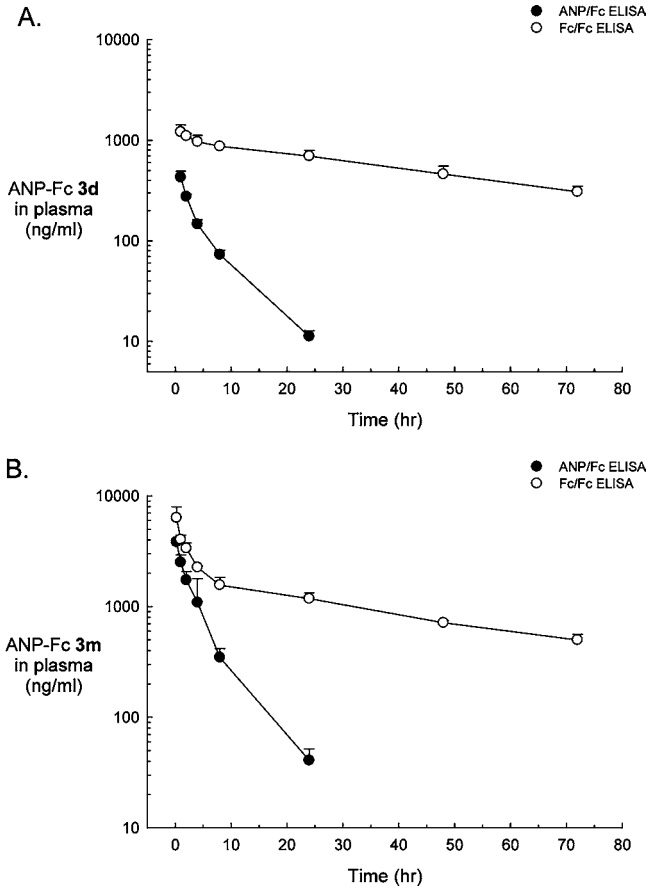


Figure 4. Pharmacokinetics of ANP-Fc dimer **3d** (A) and monomer **3m** (B) after a single IV dose of 0.5 mg/kg in Wistar rats. Detection of the protein was performed using an ANP-Fc specific ELISA and a Fc-Fc ELISA. The first time point for **3d** is 1 h, while the first time point for **3m** is at 15 min.

DISCUSSION

The generation of peptide-Fc fusion molecules is a powerful approach to extend the half-life of potential therapeutic peptides. This is made possible by FcRn whereby molecules fused to Fc can be taken up into cells by nonspecific pinocytosis

dx.doi.org/10.1021/bc200592c | *Bioconjugate Chem.* 2012, 23, 518−526

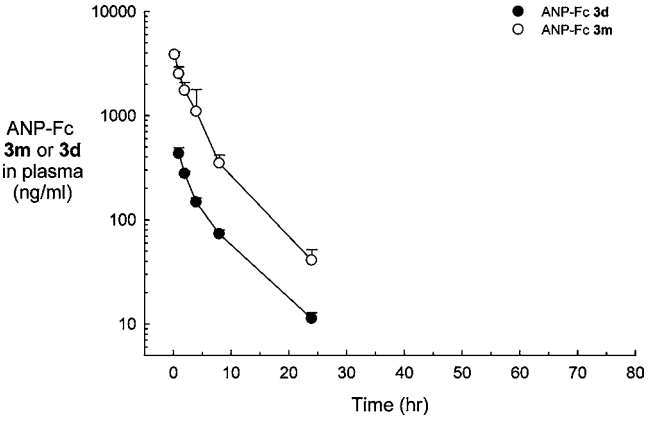


Figure 5. Comparison of the pharmacokinetics of ANP-Fc dimer **3d** and monomer **3m** after a single intravenous dose of 0.5 mg/kg in Wistar rats. An ANP-Fc ELISA was used to detect the intact proteins.

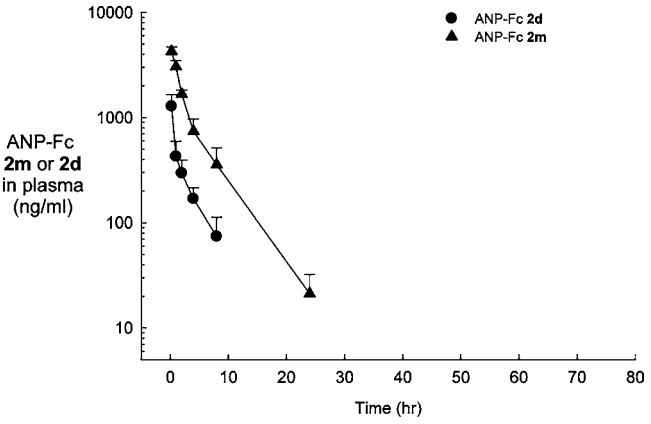


Figure 6. Comparison of the pharmacokinetics of ANP-Fc monomer **2m** and dimer **2d** after a single intravenous dose of 0.5 mg/kg in Wistar rats. An ANP-Fc ELISA was used to detect the proteins.

and subsequently shuttled back into circulation from within the cell by FcRn, thereby bypassing lysosomal degradation.[11] We describe here an approach to generate Fc fusions of ANP using a semisynthetic process. A recombinant Fc molecule possessing a N-terminal cysteine and an ANP thioester molecule can undergo a native ligation[17] reaction to yield a native peptide bond at the linkage site. Since the naturally occurring cysteine within hinge region of Fc was used for the ligation, via truncation of 5 residues at the N-terminus of the standard Fc sequence, no new non-native cysteines were incorporated into the final peptide−protein construct.

This semisynthetic approach allowed for the rapid screening of ANP-Fc linkers and orientations with the expectation that the molecules would be representative of the recombinant version. Data on construct **2d** indicate that this is the case since **2d** generated by both the semisynthetic method described herein, and by fully recombinant methods, had similar *in vitro* activities in the cGMP induction assay, as well as similar pharmacokinetic profiles (data not shown). Lastly, the semisynthetic approach allows for the incorporation of unnatural amino acids or other non-natural moieties into the peptide-Fc fusion, which may not be accessible using recombinant protein methods.

Various ANP-Fc constructs were studied to determine the most optimal fusion protein to advance further into development. It was found that the "dimeric" ANP-Fc construct **3d** with a 16 amino acid linker between ANP and Fc was the most active compound in the *in vitro* cGMP induction assay. This is likely due to decreased steric hindrance by Fc for the ANP-receptor interaction. It was also found that there were no significant differences in *in vitro* activity between the constructs where the N- or C-terminus of ANP was linked to Fc (e.g., **2d** vs **5d**). These data can be rationalized based on the fact that neither termini of ANP have been found to be critical for activity, in comparison to the core sequence within the cysteine loop which is known to be essential for activity.[21] Lastly, it was found that, in general, the dimeric Fc fusions were more active (mol:mol) *in vitro* than the monomeric analogues. This may be due to avidity effects of the two peptides attached to the single Fc. It should be noted that there exists a possibility that some of the *in vitro* data included herein may be confounded by contaminating free peptide still remaining in the protein preparation at levels below 1.3% (mol/mol). However, this risk may be theoretical, since a protein purification step was included to remove unconjugated free peptide. Future work should include a more sensitive method for detection of such unconjugated peptide species.

With the known enhanced pharmacokinetic properties of some monomeric-Fc fusion proteins over dimeric-Fc fusion proteins,[12] we were very interested in comparing the pharmacokinetics of these peptide-Fc fusions constructs. It was found that the monomeric constructs possessed increased C_{max} values as compared to the dimeric constructs, but with comparable half-lives in rats (**3m** vs **3d**). The origin of the increased C_{max} is not currently understood, but likely independent of FcRn since the terminal half-life of the monomeric and dimeric constructs remained similar. It is possible that the enhanced PK properties found with larger protein-Fc constructs is minimized due to the small size of the peptides linked to Fc.

Two ELISA methods were used to detect the ANP-Fc proteins in the PK experiments to study the possibility that the Fc would provide protection against cleavage of ANP by NEP 24.11. Indeed, the diverging curves in Figure 4 suggest that the half-life of ANP-Fc is much shorter than that of Fc alone, likely due to such protease degradation as previously reported.[4,7] However, the terminal half-life of 5−6 h for ANP-Fc is ∼100-fold longer than that of free ANP, which suggests that fusion of ANP to Fc provides a significant improvement in half-life despite the peptide cleavage. Future work could incorporate unnatural amino acids into the ANP sequence to stabilize the peptide and further prolong the half-life of the ANP-Fc fusions.

The most active construct **3d** is ∼16-fold weaker *in vitro* than free ANP in the generation of cGMP. However, this loss in activity may be more than compensated for by its ∼100-fold increase in terminal half-life. Future experiments *in vivo* will be needed to determine the overall efficacy of this new class of ANP molecules.

In conclusion, ANP-Fc fusions were generated by a semisynthetic method using a recombinantly derived Fc protein and synthetic peptides. The method allowed for the rapid generation of the ANP-Fc fusions in order to evaluate various linker lengths, orientations and configurations. It was found that the most active construct possessed two ANP peptides per Fc protein ("dimer") and a relatively long 16 amino acid linker between the ANP and Fc. The pharmacokinetics of the ANP-Fc fusions resulted in a ∼100-fold increase in terminal half-life of the ANP peptide which may compensate for the ∼16-fold loss

dx.doi.org/10.1021/bc200592c | *Bioconjugate Chem.* 2012, 23, 518−526

in activity *in vitro*. Future work will be aimed at assessing these constructs in cardiovascular disease models.

■ ASSOCIATED CONTENT

Supporting Information

Representative SPR sensorgrams, representative SEC and RP-HPLC chromatograms, LC/MS/MS peptide digestion results, sequence of CysFc. This material is available free of charge via the Internet at http://pubs.acs.org.

■ AUTHOR INFORMATION

Corresponding Author

*E-mail: adam.mezo@biogenidec.com; Tel: 781-522-4106; Fax: 781-547-6008.

Present Address

‡BIND Biosciences, 64 Sidney St., Cambridge, MA 02139, USA

Notes

The authors declare no competing financial interest.

■ ACKNOWLEDGMENTS

The authors would like to thank Kara Crowley and Alisa Kabcenell at Boehringer Ingelheim Pharmaceuticals Inc. (BIPI) for development and transfer of the cGMP assay, Keith Canada for work on the recombinant ANP-Fc fusions, and Uwe Schoenbeck, Christine Grygon and other BIPI colleagues for helpful discussions and support on this project. The authors also thank Biogen Idec Hemophilia and BIPI for financial support.

■ REFERENCES

(1) De Bold, A. J., Borenstein, H. B., Veress, A. T., and Sonnenberg, H. (1981) A rapid and potent natriuretic response to intravenous injection of atrial myocardial extract in rats. *Life Sci. 28*, 89−94.

(2) Kangawa, K., and Matsuo, H. (1984) Purification and complete amino acid sequence of alpha-human atrial natriuretic polypeptide (alpha-hANP). *Biochem. Biophys. Res. Commun. 118*, 131−139.

(3) Molkentin, J. D. (2003) A friend within the heart: natriuretic peptide receptor signaling. *J. Clin. Invest. 111*, 1275−1277.

(4) Murthy, K. K., Thibault, G., Garcia, R., Gutkowska, J., Genest, J., and Cantin, M. (1986) Degradation of the atrial natriuretic peptide factor in the rat. *Biochem. J. 240*, 461−469.

(5) Nakao, K., Sugawara, A., Morii, N., Sakamoto, M., Yamada, T., Itoh, H., Shiono, S., Saito, Y., Nishimura, K., Ban, T., Kangawa, K., Matsuo, H., and Imura, H. (1986) The pharmacokinetics of alpha-human atrial natriuretic polypeptide in healthy subjects. *Eur. J. Clin. Pharmacol. 31*, 101−103.

(6) Kimura, K., Yamaguchi, Y., Horii, M., Kawata, H., Yamamoto, H., Uemura, S., and Saito, Y. (2007) ANP is cleared much faster than BNP in patients with congestive heart failure. *Eur. J. Clin. Pharmacol. 63*, 699−702.

(7) Rademaker, M. T., Charles, C. J., Kosoglou, T., Protter, A. A., Espiner, E. A., Nicholls, M. G., and Richards, A. M. (1997) Clearance receptors and endopeptidase: equal role in natriuretic peptide metabolism in heart failure. *Am. J. Physiol. 273*, H2372−9.

(8) Glaesner, W., Vick, A. M., Millican, R., Ellis, B., Tschang, S.-H., Tian, Y., Bokvist, K., Brenner, M., Koester, A., Porksen, N., Etgen, G., and Bumol, T. (2010) Engineering and characterization of the long-acting glucagon-like peptide-1 analogue LY2189265, an Fc fusion protein. *Diabetes Metab. Res. Rev. 26*, 287−296.

(9) Molineaux, G., and Newland, A. (2010) Development of romiplostim for the treatment of patients with chronic immune thrombocytopenia: from bench to bedside. *Br. J. Heamatol. 150*, 9−20.

(10) Ashkenazi, A., Capon, D. J., and Ward, R. H. R. (1993) Immunoadhesins. *Int. Rev. Immunol. 10*, 219−227.

(11) Roopenian, D. C., and Akilesh, S. (2007) FcRn: the neonatal Fc receptor comes of age. *Nat. Rev. Immunol. 7*, 715−725.

(12) Dumont, J. A., Low, S. C., Peters, R. T., and Bitonti, A. J. (2006) Monomeric Fc fusions: impact on pharmacokinetic and biological activity of protein therapeutics. *BioDrugs 20*, 151−160.

(13) Bitonti, A. J., and Dumont, J. A. (2006) Pulmonary administration of therapeutic proteins using an immunoglobulin transport pathway. *Adv. Drug Delivery Rev. 58*, 1106−1118.

(14) Bitonti, A. J., Dumont, J. A., Low, S. C., Peters, R. T., Kropp, K. E., Palombella, V., Stattel, J. M., Lu, Y., Tan, C. A., Song, J. J., Garcia, A. M., Simister, N. E., Spiekermann, G. M., Lencer, W. I., and Blumberg, R. S. (2004) Pulmonary delivery of an erythropoietin Fc fusion protein in non-human primates through an immunoglobulin transport pathway. *Proc. Natl. Acad. Sci. U.S.A. 101*, 9763−9768.

(15) West, A. P., and Bjorkman, P. J. (2000) Crystal structure and immunoglobulin G binding properties of the human major histocompatibility complex-related Fc receptor. *Biochemistry 39*, 9698−9708.

(16) Vaugn, D. E., and Bjorkman, P. J. (1997) High-affinity binding of the neonatal Fc receptor to its IgG ligand requires receptor immobilization. *Biochemistry 36*, 9374−9380.

(17) Dawson, P. E., Muir, T. W., Clark-Lewis, I., and Kent, S. B. (1994) Synthesis of proteins by native chemical ligation. *Science 266*, 776−779.

(18) Kratz, F., Muller, I. A., Ryppa, C., and Warnecke, A. (2008) Prodrug Strategies in Anticancer chemotherapy. *ChemMedChem 3*, 20−53.

(19) Law, B., and Tung, C.-H. (2009) Proteolysis: A biological process adapted in drug delivery, therapy, and imaging. *Bioconjugate Chem. 20*, 1683−1695.

(20) Mezo, A. R., Cheng, R. P., and Imperiali, B. (2001) Oligomerization of uniquely folded mini-protein motifs: development of a homotrimeric *ββα* peptide. *J. Am. Chem. Soc. 123*, 3885−3891.

(21) Bovy, R. P. (1990) Structure activity in the atrial natriuretic peptide (ANP) family. *Med. Res. Rev. 10*, 115−142.

Bioconjugate Chemistry

Article

pubs.acs.org/bc

Development of Hypoxia Enhanced ^{111}In-Labeled Bombesin Conjugates: Design, Synthesis, and In Vitro Evaluation in PC-3 Human Prostate Cancer

Nilesh K. Wagh,[§] Zhengyuan Zhou,[§] Sunny M. Ogbomo,[§] Wen Shi,[§] Susan K. Brusnahan,[§] and Jered C. Garrison*[,§,†,‡,∥]

[§]Department of Pharmaceutical Sciences, College of Pharmacy,

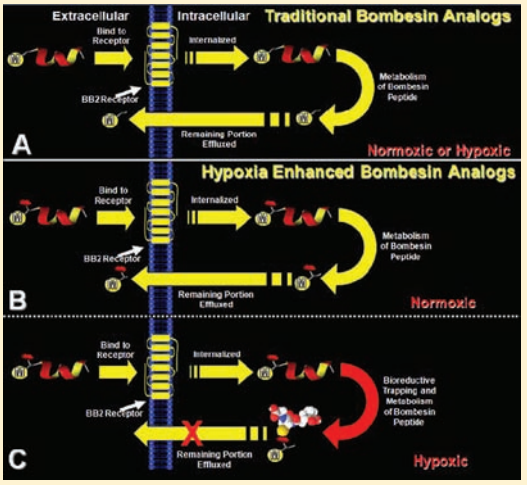
[†]Center for Drug Delivery and Nanomedicine,

[‡]Department of Biochemistry and Molecular Biology, College of Medicine,

[∥]Eppley Cancer Center. University of Nebraska Medical Center, 985830 Nebraska Medical Center, Omaha, Nebraska, United States

Supporting Information

ABSTRACT: The gastrin-releasing peptide receptor (BB2r) has shown great promise for tumor targeting due to the increase of the receptor expression in a variety of human cancers including prostate, breast, small-cell lung, and pancreatic cancer. From clinical investigations, prostate cancer has been shown to be among the most hypoxic of the cancers investigated. Many solid tumors contain regions of hypoxia due to poor organization and efficiency of the vasculature. However, hypoxia is typically not present in normal tissue. Nitroimidazoles, a thoroughly investigated class of hypoxia selective drugs, have been shown to be highly retained in hypoxic tissues. The purpose of this study is to determine if the incorporation of hypoxia trapping moieties into the structural paradigm of BB2r-targeted peptides will increase the retention time of the agents in prostate cancer tumors. The present work involves the design, syntheses, purification, and in vitro investigation of hypoxia enhanced ^{111}In-BB2r-targeted radioconjugates. A total of four BB2r-targeted conjugates (**1**−**4**) were synthesized and coupled with increasing numbers of 2-nitro-imidazoles, a hypoxia trapping moiety. Conjugates were radiolabeled with ^{111}In and purified by HPLC prior to in vitro studies. Receptor saturation assays under both normoxic and hypoxic conditions showed that the BB2r receptor expression on the PC-3 human prostate cancer cell line was not significantly affected by oxygen levels. Competitive binding assays revealed that incorporation of 2-nitroimidazoles had a detrimental effect to BB2r binding when adequate spacer groups, between the hypoxia trapping agent and the pharmacophore, were not employed. All of the 2-nitroimidazole containing BB2r-targeted agents exhibited significantly higher longitudinal retention in PC-3 cells under hypoxic conditions compared to the analogous normoxic studies. Protein association analysis revealed a 3-fold increase in binding of a 2-nitroimidazole containing BB2r-targeted agent under hypoxic relative to normoxic conditions. The positive nature of these results indicate that further exploration into the potential of hypoxia selective trapping agents for BB2r-targeted agents, as well as other targeted compounds, is warranted.



INTRODUCTION

Prostate cancer is among the most hypoxic of cancers found in the clinic.[1,2] This state of hypoxia is a result of the often chaotic and poor vascular organization in the tumor thereby inhibiting the ability of the microvasculature to efficiently deliver oxygen.[2] This chaotic vascular architecture often leads to a high degree of oxygenation heterogeneity, with the tumor containing anoxic, hypoxic, and normoxic regions, depending on the distance of the tissue from the nearest vascular vessel. Hypoxia has been and continues to be a major obstacle in the treatment of numerous cancers, including prostate cancer, due to the increased chemotherapy and radiotherapy resistance of hypoxic tissue.[2,3] While the average fraction of hypoxic tissue in prostate cancer tumors is not well-known, it is expected that the fraction of hypoxic cells would be significant.[4,5] Since hypoxia is a property that is not exhibited in most normal human tissues, several classes of bioreductive prodrugs (i.e., nitroimidazoles, aromatic N-oxides, and quinones) are under development to exploit the hypoxic nature of tumors for diagnostic and therapeutic applications. One class of bioreductive hypoxia

Received: November 8, 2011
Revised: January 16, 2012
Published: February 2, 2012

 © 2012 American Chemical Society dx.doi.org/10.1021/bc200600w | *Bioconjugate Chem.* 2012, 23, 527−537

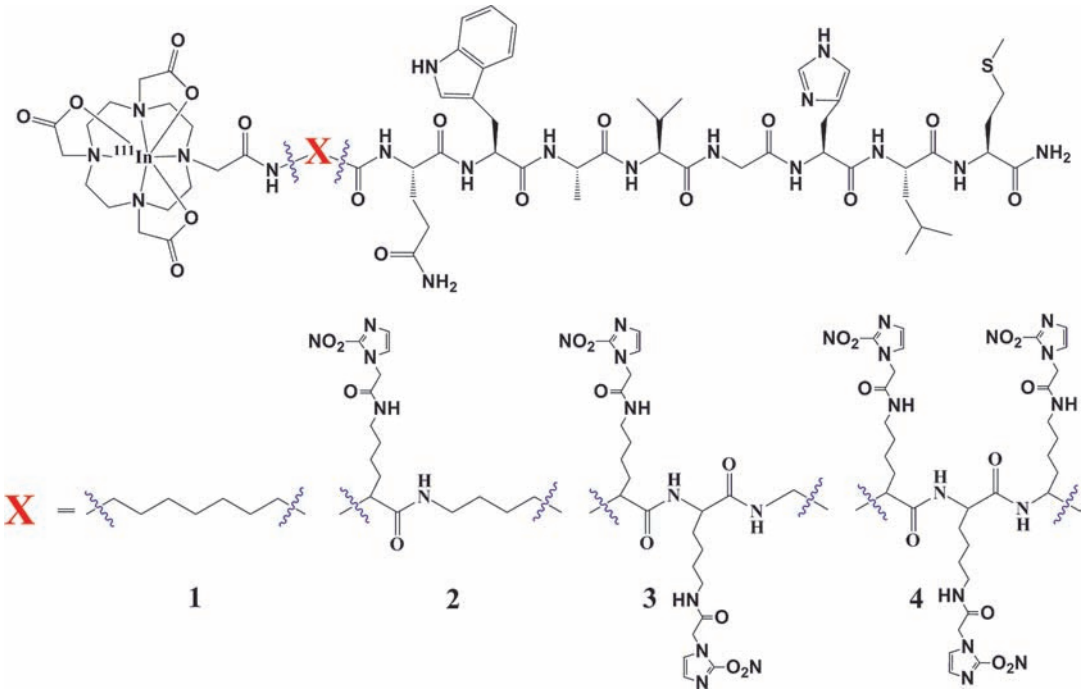


Figure 1. Hypoxia enhanced ^{111}In-BB2r-targeted conjugates.

targeting agents that has undergone extensive basic and clinical investigation is nitroimidazoles.[6−8] In hypoxic environments, this class of agent is selectively reduced ("triggered") thereby generating a reactive electrophile that becomes trapped in the hypoxic cell. In particular, 2-nitroimidazole derivatives have been actively investigated for the development of hypoxia targeted agents capable of quantitating the hypoxic burden present in tumors using standard nuclear medicine imaging modalities.[9−13]

The BB2 receptor (BB2r), also known as the Gastrin-Releasing Peptide (GRP) receptor, is a subtype of the Bombesin receptor family.[14] The BB2r has been thoroughly investigated for the role the receptor plays in neoplastic tissue transformation and growth.[15−17] From these studies and subsequent work, it was demonstrated that the BB2r is expressed in significantly higher densities on a number of human tumors and cancer cell lines, including prostate cancer tissues, relative to normal tissues.[15,16,18,19] These studies have provided the impetus for the development of BB2r-targeted agents for both diagnostic imaging and therapeutic applications. To date, most of these agents have revolved around synthetic analogues of Bombesin (BBN)—a fourteen amino acid, amphibian peptide that shares a C-terminal binding region sequence homology (Trp-Ala-Val-Gly-His-Leu-Met-NH_2, BBN(8−14)NH_2) with GRP (the native ligand for the BB2r).[20] Analogues utilizing the BBN(8−14)NH_2 sequence are able to agonistically bind to the BB2r with high (typically nanomolar) affinity and facilitate endocytosis of the agent into the cell.

For BB2r-targeted drugs, as well as most small molecule based targeted ligands, the targeted conjugates typically demonstrate maximum tumor accumulation shortly after administration (∼15−60 min).[20−22] Unfortunately, one of the major challenges faced by many targeted peptides is the significant clearance of the drug relatively quickly (∼1−4 h p.i.), after peak accumulation in the tumor, thereby reducing the diagnostic or therapeutic efficacy of the BB2r-targeted agent. In an attempt to increase the effectiveness of BB2r-targeted drugs, we and others have begun to evaluate various means of increasing the retention of the radiolabeled drug in prostate cancer tumors.[23] Herein, we report the evaluation of BB2r-targeted agents that include the use of 2-nitroimidazoles as hypoxia trapping moieties to increase the retention of the drug in hypoxic tumor cells. Specifically, we synthesized four BB2r-targeted agents, that include (0−3) 2-nitroimidazole moieties, and evaluated the in vitro binding affinity and retention efficacy of the radioconjugates in normoxic and hypoxic PC-3 human prostate cancer cells. The structures of synthesized agents are depicted in Figure 1.

EXPERIMENTAL SECTION

Unless otherwise noted all solvents were used without further purification. Deionized water was purified by a Millipore (U.S.) Mili-Q-Biocel. Ethylbromoacetate was purchased from Acros Organics (U.S.). Silica and TLC plates were purchased from Sorbent Technologies (U.S.). Acetonitrile, formic acid, *N,N*-diisopropylethylamine (DIEA), *N,N*-dimethylformamide (DMF), dichloromethane (DCM), *N,N′*-dicyclohexylcarbodiimide (DCC), *N*-methylpyrrolidone (NMP), thioanisol, L-ascorbic acid, 4-(2-hydroxyethyl)-1-piperazineethanesulfonic acid (HEPES), bovine serum albumin (BSA), and sodium dodecyl sulfate (SDS) were purchased from Fisher Scientific (U.S.). 2-Nitroimidazole was purchased from Amfinecom (U.S.). *O*-Benzotriazole-*N,N,N′,N′*-tetramethyl-uronium-hexa-fluoro-phosphate (HBTU), Fmoc-protected natural amino acids, and the appropriate Rink Amide resins were purchased from Nova Biochem (U.S.). Fmoc-5-AOC and Fmoc-5-Ava were purchased from CreoSalus (U.S). Phosphate buffered saline (PBS) and Mammalian Protein Extraction Reagent (M-PER) were purchased from Thermo Scientific (U.S.). Indium-111 chloride ($^{111}InCl_3$) was purchased from MDS Nordion (Canada). Naturally abundant indium chloride ($^{nat}InCl_3$), triisopropyl silane, and 3,6-dioxa-1,8-octanedithiol were purchased from Sigma-Aldrich (U.S.). The [^{125}I-Tyr$_4$]-Bombesin

dx.doi.org/10.1021/bc200600w | *Bioconjugate Chem.* 2012, 23, 527−537

was purchased from Perkin-Elmer (U.S.). Cation exchange resin was purchased from Bio Rad (USA). Prostate cancer (PC-3) cell lines were obtained from American Type Culture Collection (U.S.) and cultured under vendor recommended conditions. Roswell Park Memorial Institute (RPMI) 1640 media and TrypLE Express were purchased from Invitrogen/GIBCO (U.S.). Hypoxyprobe-1 Plus Kit was purchased from Hypoxyprobe, Inc. (U.S). Flow Cytometry Staining Buffer and Foxp3 Permeabilization Buffer were purchased from eBioscience (U.S.). The peptides were synthesized on a Liberty microwave peptide synthesizer from CEM (U.S.). Nuclear magnetic resonance spectra were recorded on Varian (U.S.) 500 MHz INOVA spectrometer. ^{1}H NMR chemical shifts are expressed as δ values (parts per million) and peaks are described as s for singlet and d for doublet. ^{13}C NMR chemical shifts are expressed as δ values using acetone as an internal reference. HPLC/MS analyses were performed on a Waters (U.S.) e2695 system equipped with a Waters 2489 absorption detector and a Waters Qtof Micro electrospray ionization mass spectrometer. Evaluation and purification of radiolabeled conjugates was performed on a Waters 1515 binary pump equipped with a Waters 2489 absorption detector and a Bioscan (U.S.) Flow Count radiometric detector system. A Phenomenex (U.S.) Jupiter 10 μ Proteo 250 × 10 mm semiprep column was used for the purification of bulk amounts of peptides. For the purification of conjugates, ^{nat}In-conjugates, and ^{111}In-radioconjugates a Phenomenex Jupiter 10 μ Proteo 250 × 4.60 mm analytical column was employed. Solid-phase extraction was performed using Empore (U.S.) C_{18} 10 mm high performance extraction disks. The separation of macromolecules and small molecules was performed using Amicon Ultra (Ireland) Ultracel-30kDa centrifugal filters in protein association analysis. Gamma decay detection of ^{111}In and ^{125}I for the *in vitro* binding, receptor saturation, efflux studies, and protein binding fractionation studies were accomplished using a LTI (U.S.) Multi-Wiper nuclear medicine gamma counter. Flow cytometry studies were performed on BD FACSAria cell sorter (U.S.).

Synthesis of 2-Nitroimidazole Acetic Acid (2-NIAA). The synthesis of 2-NIAA was carried out as reported in the literature by Gariépy and co-workers.[24] A brief description of the two-step procedure is reported below.

Synthesis of 2-Nitroimidazole Ethyl Acetate (2-NIEA). 2-Bromoethyl acetate (1.2 mL, 7.18 mmol) was added to a solution of 2-nitroimidazole (1 g, 8.84 mmol) and potassium carbonate (2.0 g, 14.5 mmol) in dry acetonitrile (15 mL). The mixture was stirred for 24 h at room temperature, and the resulting precipitate was filtered and washed with acetone. Evaporation of the filtrate yielded a yellow oil (1.7 g). The pure product was isolated from the crude oil using flash chromatography (silica gel) eluted with CH_2Cl_2/MeOH/NH_3 (50:7:1) as yellowish oil: 0.9 g (52.9% yield); Analyses for 2-nitroimidazole ethyl acetate: ^{1}H NMR ($CDCl_3$): 7.260 (d, J = 3.7 Hz, 1H, H-imidazole ring), 7.089 (d, J = 1.5 Hz, 1H, H-imidazole ring), 5.10 (s,2H, NCH_2COO), 4.29 (q, 2H, OCH_2CH_3), 1.30 (t, 3H,OCH_2CH_3); ^{13}C NMR ($CDCl_3$): 166.0 (C═O), 128.5 (CH-imidazole ring), 126.5 (CH-imidazole ring), 62.6 (NCH_2COO), 50.9 (OCH_2CH_3), 14.0 (OCH_2CH_3).

Preparation of 2-Nitroimidazole Acetic Acid (2-NIAA). The purified oil of 2-NIEA (0.9 g) was mixed into a solution of NaOH (4 N, 2.5 mL), water (10 mL), and MeOH (10 mL). The resulting solution was stirred at room temperature until no ester derivative was evident by TLC (30 min), at which point a cation-exchange resin (H^+, Bio-Rad, 4 g), which had been protonated by washing with H_2SO_4 (1 N; 30 mL; pH 2.5) and drying of the filtrate yielded a yellow paste (1.09 g). Chromatography of crude product on silica gel [mobile phase, CH_2Cl_2/CH_3CN/HCOOH (30:10:1)] yielded a white crystalline solid: 0.25 g. Analyses for 2-nitroimidazole acetic acid: ^{1}H NMR ^{1}H (D_2O) δ H 7.28 (1H, s, H-imidazole ring), 7.06 (1H, s, H-imidazole ring), 4.93 (2H, s, NCH_2COO), 3.80 (1H, broad, COOH); ^{13}C NMR(D_2O) 172.20 (C═O), 128.03 (CH-imidazaole ring), 127.27 (CH-imidazole ring), 52.10 (NCH_2COOH).

X-ray Crystallographic Analysis. With respect to X-ray crystallography studies, single crystals were obtained by slow evaporation of a methanolic solution of 2-NIAA. Crystal data for 2-NIAA: $C_5H_5N_3O_4$, MW = 171.12 g/mol, monoclinic, space group $P2_1/n$, a = 7.3412(8) Å, b = 8.2046(9) Å, c = 11.5678(13) Å, $\alpha = \gamma = 90°$, β = 103.796(2)°, V = 676.65(13) Å^3, Z = 4, D_{calc} = 1.639 Mg/m^3, μ = 0.147 mm^{-1}, T = 100(2) K, Data was collected on a Bruker SMART 1K CCD. Refinement of data with $I > 2\sigma(I)$(1630 independent reflections, R_{int} = 0.0217) gave a $R_1(F)$ = 0.0349 and a $wR_2(F^2)$ = 0.0946 for all data with a GOF = 1.055. Crystallographic data for the structural analysis has been deposited with the Cambridge Crystallographic Data Center (CCDC 838909). Copies of this information may be obtained free of charge from the CCDC (www: http://www.ccdc.cam.ac.uk) or from e-mail jcgarrison@unmc.edu.

Solid-Phase Peptide Synthesis (SPPS). Peptide synthesis was performed using an automated solid-phase peptide synthesizer employing traditional Fmoc chemistry and using a Rink Amide resin. Briefly, the resin (100 μmol of the resin substituted peptide anchors) was deprotected using piperidine, resulting in the formation of a primary amine from which the C-terminus of the growing peptide was anchored. The Fmoc protected amino acids (300 μmol) with appropriate orthogonal protection were activated with HBTU and sequentially added to the resin. The resulting peptide was orthogonally deprotected and cleaved from the resin using a cocktail consisting of triisopropylsilane (0.1 mL), water (0.1 mL), 3,6-dioxa-1,8-octanedithiol (0.1 mL), trifluoroacetic acid (4.625 mL), and thioanisole (0.075 mL), respectively. The cleaved peptide was subsequently precipitated and washed using cold (0 °C) methyl-*tert*-butyl ether (10 mL × 3). The crude conjugate was dried by a centrivap concentrator and weighed. The purity of the crude **1**, **2***, **3***, and **4*** conjugates ranged from 58% to 71% by RP-HPLC. Isolated yields were 17.5%, 11.9%, 14.7%, and 21.0% for **1**, **2***, **3**,* and **4***, respectively. ES-MS was used to determine the molecular mass of the prepared peptides. All conjugates were peak purified to ≥95% purity and quantified by RP-HPLC prior to in vitro investigations.

Coupling of 2-NIAA to Bombesin Conjugates. After purification of the conjugates, the 2-nitroimidazole acetic acid was manually coupled to ϵ-amino group of the lysine residue for each peptides **2***, **3***, and **4*** (15 mg each) using standard amidation chemistry. Briefly, the 2-NIAA (4.95, 9.40, 14.85 mg, respectively) was dissolved in M HBTU/DMF (0.45, 171 μL) solution followed by addition of DIEA/NMP solution (2.0 M, 96 μL). This solution was allowed to stand for 15 min before addition of the conjugate in DMF (200 μL). The reaction mixture was stirred for 3 h at room temperature and subsequently evaporated to dryness. The residue was redissolved in water/acetonitrile (8:2), peak purified by RP-

HPLC and characterized by mass spectrometry. Isolated conjugation yields were 34.2%, 38.7%, and 43.4% for **2**, **3**, and **4**, respectively.

Labeling with $^{nat}InCl_3$. For the convenient characterization of the ^{111}In-Bombesin conjugates, naturally abundant ^{nat}In was used to substitute for ^{111}In in the ES-MS and in vitro binding studies. A sample of conjugates (0.75 mg) was dissolved in ammonium acetate buffer (0.5 M, 200 μL, pH 5.5) and mixed with a solution of $^{nat}InCl_3$ (1.1 mg, 10 μmol). The solution was heated for 60 min at 90 °C. After cooling to room temperature, ^{nat}In-conjugates were then peak purified by RP-HPLC. Isolated yields were 36.7%, 29.6%, 33.5%, and 41.9% for **^{nat}In-1**, **^{nat}In-2**, **^{nat}In-3**, and **^{nat}In-4**, respectively. All ^{nat}In-conjugates were ≥95% purity before mass spectrometric characterization and in vitro binding studies were performed.

Radiolabeling with $^{111}InCl_3$. A 250 μg sample of the conjugate was dissolved in ammonium acetate buffer (0.5 M, 250 μL, pH 5.5). $^{111}InCl_3$ (1 mCi) was added to the vial containing the conjugate, and the solution was heated for 60 min at 90 °C and allowed to cool to room temperature. The resulting radioconjugates were peak purified using RP-HPLC (≥95%) and concentrated using C18 extraction disk. Elution of the extraction disk with ethanol/sterile saline solution (6:4, 600 μL) delivered the radioconjugate in high purity. L-Ascorbic acid (~20 mg) was added to all radioconjugates to reduce radiolysis. Radiolabeling yields for **^{111}In-1**, **^{111}In-2**, **^{111}In-3**, and **^{111}In-4** were 32.3%, 23.6%, 26.9%, and 36.1%, correspondingly.

HPLC Purification and Analysis Methodology. When necessary, bulk sample purification was performed using a semipreparative Proteo column with a flow rate of 5.0 mL/min. Sample purification for in vitro studies was performed on analytical Proteo column with a flow rate 1.5 mL/min. HPLC solvents consisted of H_2O containing 0.1% formic acid (solvent A) and acetonitrile containing 0.1% formic acid (solvent B). For unlabeled and $^{111/nat}$In-conjugates of **1**−**3**, an initial gradient of 85% A: 15% B linearly decreased to 75% A:25% B over a 15 min time period. For unlabeled and $^{111/nat}$In-conjugates of **4**, an initial gradient of 80% A:20% B linearly decreased to 70% A:30% B over a 15 min time period. At the end of the run time for all HPLC experiments, the column was flushed with the gradient 5% A:95% B and re-equilibrated to the starting gradient.

In Vitro Competitive Cell-Binding Studies. For in vitro binding studies, the inhibitory concentration (IC_{50}) for all conjugates and ^{nat}In-conjugates were determined using the PC-3 human prostate cancer cell line. ^{nat}In-conjugates were used as substitutes for the corresponding ^{111}In- radioconjugates. Briefly, the PC-3 cells (~3×10^4) were suspended in RPMI 1640 media (pH 7.4, 4.8 mg/mL HEPES, and 2 mg/mL BSA) and incubated at 4 °C for 40 min in the presence of radiolabeled [^{125}I-Tyr$_4$]-Bombesin and various concentrations of the ^{nat}In-conjugate. At the end of the incubation period, the cells were centrifuged, aspirated, and washed with media a total of four times. The cell associated activity was measured using a gamma counter and the IC_{50} values determined by nonlinear regression using the one-binding site model of Graphpad *PRISM* 5 (U.S.).

Flow Cytometric Analysis of Hypoxic Cell Induction. The PC-3 cells were plated at a concentration of 1×10^6 cells/well in 6 well plates, and incubated overnight in normoxic (95% air, 5% CO_2) and hypoxic (94.9% N_2, 0.1% O_2, 5% CO_2) environments. The cells were washed twice with PBS and incubated with 10 μM Pimonidazole in 1 mL fresh medium (control well media did not contain Pimonidazole) for 2 h. Cells were again washed twice with PBS and detached from the well surface using TrypLE for 15 min at 37 °C. As per manufacturer's protocols, 10^6 cells were treated with Foxp3 permeabilization solution at 4 °C for 30 min, washed with buffer and resuspended. The PC-3 cells were subsequently incubated with the FITC-labeled Hypoxyprobe-1 monoclonal antibody (mAb1) (1:100 dilution in 0.5% BSA in PBS) in the dark at room temperature for 30 min. The stained cells were washed once, fixed in paraformaldehyde, and subject to flow cytometric analysis. Cells were analyzed using a FACSAria instrument and *FloJo* software.

Receptor Saturation Binding Assays. Receptor saturation studies were performed on PC-3 cells under normoxic (95% air, 5% CO_2) and hypoxic (94.9% N_2, 0.1% O_2, 5% CO_2) conditions. PC-3 cells (3×10^4/well) were incubated overnight in 24-well plates at 37 °C in RPMI 1640 media (pH 7.4, 4.8 mg/mL HEPES, and 2 mg/mL BSA) in hypoxic conditions. On the day of the experiment, the cells were seeded with fresh culture medium and incubated for 4 h under normoxic or hypoxic conditions. Upon completion of the incubation, PC-3 cells were incubated with (30 000 cpm) [^{125}I-Tyr$_4$]-Bombesin and a series of [Tyr$_4$]-Bombesin concentrations ranging from 0.469 nM to 120 nM for 1 h at 4 °C. Nonspecific binding was determined using 3 μM of the [Tyr$_4$]-Bombesin in the presence of the radioligand. At the end of the incubation time, cells were aspirated and washed thrice with cold media and the remaining radioactivity was measured by solubilizing the cells with 10% SDS. Nonlinear regression analysis was then performed using Graphpad *PRISM* 5 (U.S.) to determine the B_{max} and K_d values for each experiment.

Efflux Studies. Efflux studies were performed using PC-3 cells under normoxic (95% air, 5% CO_2) and hypoxic (94.9% N_2, 0.1% O_2, 5% CO_2) conditions. PC-3 cells were incubated in six-well plates (0.5×10^6/well) under hypoxic conditions overnight in RPMI 1640 media (pH 7.4, 4.8 mg/mL HEPES, and 2 mg/mL BSA). On the day of the experiment, the medium was removed, and the cells were washed with cold medium and incubated for 4 h under normoxic and hypoxic condition. Cells were incubated for an additional 2 h at 37 °C in the presence of 100 000 cpm of each ^{111}In-radioconjugate. Upon completion of the incubation at time points 0, 30, 60, 90, and 120 min, cells were washed thrice with media to discard the unbound peptide. Surface bound radioactivity was removed by washing the cells twice with an acid wash (50 mM glycine-HCl/0.1 M NaCl buffer, pH 2.8). The cells were then lysed at 37 °C using a 10% aqueous SDS solution. The radioactivity of the effluxed, surface bound and internalized fractions for each radioconjugate was determined using a gamma counter. Statistical analyses were performed by two-way analysis of variance (ANOVA) using Graphpad *PRISM* 5 (U.S.).

Cellular Protein Analysis. For the cellular fractionation studies, the procedure for the preparation of normoxic and hypoxic PC-3 was carried out as outlined in the efflux studies above. On the day of the experiment, the medium was removed, and the cells were washed with warm medium and incubated for 4 h under normoxic and hypoxic conditions. PC-3 cells were incubated for an additional 2 h at 37 °C in the presence of 30,000 cpm of each ^{111}In-radioconjugate. At the end of this time, the cells were washed thrice with warm medium to remove the unbound, extracellular radioconjugates and allowed to incubate for an additional hour at 37 °C. Subsequently, PC-3 cells were washed thrice with PBS and lysed using 1 mL of M-PER at 37 °C. The cellular debris was

centrifuged down and the supernatant was then transferred to an Amicon Ultracel 30kDa filter device with an extra PBS (1 mL). The samples were centrifuged at 4000 × *g* for 10 min and washed with PBS (1 mL × 2) per wash. The radioactivity associated with the molecular weight fractions was determined using a gamma counter.

RESULTS

Synthesis of 2-Nitroimidazole Acetic Acid (2-NIAA). In order to couple the 2-nitroimidazole to the BB2r-targeted peptide conjugates, the acetic acid derivative was synthesized as outlined in literature procedures.[24] Initially, the 2-nitroimidazole ethyl acetate was synthesized by formation of the potassium 2-nitroimidazole salt and subsequent reaction with 2-bromoethyl acetate. Conversion of the 2-nitroimidazole ethyl acetate to the acetic acid derivative was achieved using a cation exchange column pretreated with dilute H_2SO_4 prior to elution. The chemical constitution of 2-NIAA was confirmed by NMR and single crystal X-ray crystallography. All ^1H and ^{13}C NMR data agreed with literature values. The molecular structure of 2-NIAA is depicted in Figure 2.

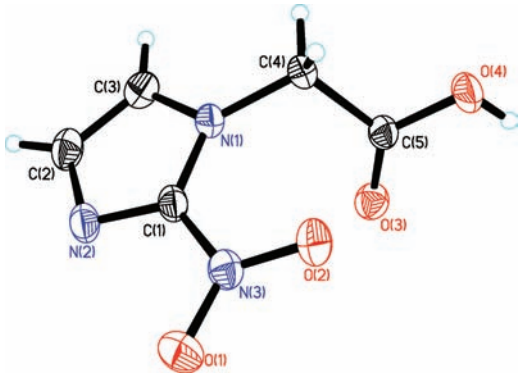


Figure 2. ORTEP representation of the 2-NIAA with thermal ellipsoids drawn at 50% probability. Selected bond lengths (Å) and angles (deg): O(1)−N(3) = 1.2223 (15), O(2)−N(3) = 1.2309 (14), N(3)−C(1) = 1.4387 (17), N(1)−C(1) = 1.3572 (16), N(2)−C(1) = 1.3161 (16), C(2)−C(3) = 1.372 (2), O(3)−C(5) = 1.2012 (16), O(4)−C(5) = 1.3206 (16), C(4)−C(5) = 1.5144 (17), O(1)−N(3)−O(2) = 125.13 (12), O(1)−N(3)−C(1) = 117.15 (11), O(2)−N(3)−C(1) = 117.71 (11), O(3)−C(5)−O(4) = 126.24 (12), O(3)−C(5)−C(4) = 124.77 (12), O(4)−C(5)−C(4) = 108.98(11).

Conjugate Synthesis and Radiolabeling. The conjugates were synthesized using standard solid-phase peptide synthesis. Specifically, four radioconjugates were synthesized using the DOTA-**X**-BBN(8−14)NH_2 paradigm (Figure 1). The conjugates were purified by RP-HPLC and isolated with yields of 17.5%, 11.9%, 14.7%, and 21.0% for conjugates **1**, **2***, **3***, and **4***, correspondingly. RP-HPLC retention times and mass spectrometric identification of the conjugates are listed in Table 1. Subsequently, 2-NIAA was coupled to the ε-amino group of lysine residue(s) of the conjugates using HBTU, DIEA, and NMP in DMF. Analysis by RP-HPLC revealed that the coupling reactions were completed within 3 h. The products obtained were consequently purified by RP-HPLC and characterized by ES-MS (Table 1). The yields of conjugates **2**, **3**, and **4** were 34.2%, 38.7%, and 43.3%, respectively.

Labeling and purification of the conjugates with ^{nat}In and ^{111}In were carried out under nearly identical conditions. In brief, $^{111/nat}InCl_3$ was incubated with the desired conjugate in ammonium acetate buffer (0.1 M, pH 5.5) at 90 °C for 1 h. Radiolabeling yields for ^{111}In-1, ^{111}In-2, ^{111}In-3, and ^{111}In-4 were 32.3%, 23.6%, 26.9%, and 36.1%, correspondingly. Purification of the $^{111/nat}$In-conjugates was accomplished by RP-HPLC. Concentration of RP-HPLC eluent was achieved by solid phase extraction on C_{18} column with typically ≥90% recovery. Prior to in vitro analysis, ^{111}In-1−4 were found to have 99.0%, 99.3%, 97.7%, and 95.3% radiochemical purity, correspondingly, as determined by RP-HPLC. Retention times and mass spectrometric characterization of the ^{nat}In-conjugates are given in Table 1.

In Vitro Competitive Cell-Binding Studies. The BB2r binding affinity of the unlabeled and ^{nat}In Bombesin conjugates was assessed by competitive binding assays performed at 4 °C using the BB2r-positive human prostate cancer PC-3 cell line. All conjugates and ^{nat}In-conjugates were able to displace [^{125}I-Tyr$_4$]-Bombesin from BB2r binding sites on the PC-3 cell membranes in a dose-dependent manner as shown by the displacement curves (Supporting Information). For ^{nat}In-labeled conjugates, conjugates **1** and **2** demonstrated the highest affinity binding (23.5 ± 15.9, 5.70 ± 1.31 nM) to the BB2r. Conjugates **3** and **4** exhibited substantially poorer binding affinity, relative to **1** and **2**, with affinities of 93.0 ± 37.3 nM and 342 ± 99 nM, correspondingly. Some differences in binding affinity were observed between unlabeled and ^{nat}In-

Table 1. Mass Spectrometric and RP-HPLC Characterization of Conjugates

	analogue	molecular formula	MS calculated	MS observed[a]	RP-HPLC retention time[b]	IC_{50}[c]/nM
1	DOTA-8 AOC−BBN(8−14) NH_2	$C_{67}H_{106}N_{18}O_{17}S$	1467.7	1468.0	14.99	10.2 ± 3.5
2*	DOTA [(D)K-5-AVA]−BBN(8−14) NH_2	$C_{70}H_{112}N_{20}O_{18}S$	1553.8	1553.4	11.10	-
3*	DOTA [(D)K-(D)K-G]−BBN(8−14) NH_2	$C_{73}H_{118}N_{22}O_{19}S$	1639.8	1639. 5	6.50	-
4*	DOTA [(D)K-(D)K-(D)K]−BBN(8−14) NH_2	$C_{77}H_{127}N_{23}O_{19}S$	1710.9	1711.3	9.0	-
2	DOTA [(D)K(2-NIAA)-5-AVA]−BBN(8−14) NH_2	$C_{75}H_{115}N_{23}O_{21}S$	1706.8	1707.1	12.05	10.8 ± 2.8
3	DOTA [(D)K(2-NIAA)-(D)K(2-NIAA)-G]−BBN(8−14) NH_2	$C_{83}H_{124}N_{28}O_{25}S$	1945.9	1946.1	14.01	48.5 ± 27.1
4	DOTA [(D)K(2-NIAA)-(D)K(2-NIAA)-(D)K(2-NIAA)]−BBN(8−14) NH_2	$C_{92}H_{136}N_{32}O_{28}S$	2170.0	2170.4	14.76	1110 ± 205.0
In-1	In-DOTA-8AOC−BBN(8−14) NH_2	$C_{67}H_{103}N_{18}O_{17}SIn$	1580.5	1580.2	15.94	23.5 ± 15.9
In-2	In-DOTA [(D)K(2-NIAA)-5-AVA]−BBN(8−14) NH_2	$C_{75}H_{112}N_{23}O_{21}SIn$	1819.7	1819.5	12.67	5.70 ± 1.31
In-3	In-DOTA [(D)K(2-NIAA)-(D)K(2-NIAA)-G]−BBN(8−14) NH_2	$C_{83}H_{121}N_{28}O_{25}SIn$	2058.9	2058.6	14.19	93.0 ± 37.3
In-4	In-DOTA [(D)K(2-NIAA)-(D)K(2-NIAA)-(D)K(2-NIAA)-G]−BBN(8−14) NH_2	$C_{92}H_{133}N_{32}O_{28}SIn$	2283.1	2283.2	15.04	342 ± 99.0

[a]For convenient mass spectra analysis ^{111}In was replaced by ^{nat}In. [b]RP-HPLC methods described in Methods section. [c]Values represent mean ± SEM (n = 6).

dx.doi.org/10.1021/bc200600w | *Bioconjugate Chem.* 2012, 23, 527−537

labeled conjugates, but analysis of the data revealed no overall trend.

Hypoxia Staining and Fluorescence Analysis. Before beginning hypoxia experiments, the conditions used for the generation of hypoxic cells were validated by hypoxia staining. PC-3 cells were placed under hypoxic or normoxic conditions overnight and were subsequently exposed to Pimonidazole for 2 h. Pimonidazole, a 2-nitroimidazole based agent, has been widely used for the detection and quantification of hypoxia.[25−27] After exposure to Pimonidazole, the cells were permeabilized and incubated with a FITC-conjugated primary antibody against Pimonidazole adducts. The fluorescence analysis of the stained PC-3 cells by flow cytometry is depicted in Figure 3. Mean fluorescence of the normoxic PC-3 cells

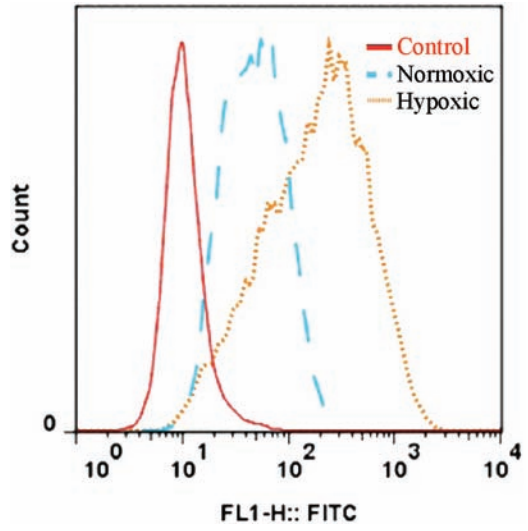


Figure 3. Flow cytometric analysis of Pimonidazole binding under control (no Pimonidazole), normoxic (95% air, 5% CO_2) and hypoxic (94.9% N_2, 0.1% O_2, 5% CO_2) conditions in PC-3 cells.

treated with Pimonidazole was 56.8. Treatment of hypoxic PC-3 with the hypoxia staining agent yielded a significant increase in antibody binding with a mean fluorescence of 286. The increase in antibody binding for the hypoxic cells corresponds, as expected, with an increase in hypoxia staining due to a drop in the O_2 concentration. Based on previous literature reports, the values from this study are consistent with hypoxia being generated in the PC-3 cells and therefore subsequent in vitro studies were carried out employing the hypoxia generating conditions of this experiment.[25]

Receptor Saturation Binding Assays. In order to determine if and to what extent the receptor expression changes under hypoxic conditions, receptor saturation studies were performed to quantify the receptor expression in PC-3 cells under normoxic and hypoxic conditions. The receptor saturation assays revealed that under normoxic and hypoxic conditions there were 0.35 ± 0.08 million and 0.30 ± 0.06 million binding sites, respectively, per PC-3 cell. The dissociation constant (K_d) values were found to be 1.0 ± 0.05 nM and 0.9 ± 0.08 nM, correspondingly, for normoxic and hypoxic PC-3 cells. Under the conditions of our experiments, these receptor saturation studies indicate that the BB2r expression at the cell surface does not significantly change with oxygen levels.

Efflux Studies. To evaluate the ability of the 2-nitroimidazole hypoxia trapping moieties to enhance the retention of the BB2r-targeted drugs, efflux studies were performed under normoxic and hypoxic environments to determine the rate at which the ^{111}In-labeled radioconjugates **1**−**4** were effluxed from the PC-3 cells. In these studies, **^{111}In-1**, which does not have a 2-nitroimidazole incorporated into the structure of the radioconjugate, is the control and will be used to compare the relative effectiveness of the hypoxia trapping conjugates (**^{111}In-2**−**4**) in both hypoxic and normoxic conditions.

The radioconjugates were incubated in the presence of the PC-3 cells for 2 h prior to the start of the efflux studies. During this incubation time period, **^{111}In-1** and **^{111}In-2** demonstrated significant accumulation of the radioactivity with 22.6% and 20.5%, respectively, of the added radioconjugates internalized under normoxic conditions (Supporting Information). The same radioconjugates demonstrated a marked decline in overall uptake under hypoxic conditions with 17.8% and 15.0% internalized, respectively, in the same time span. In comparison, **^{111}In-3** and **^{111}In-4** demonstrated internalization of only 1.4% and 0.8%, correspondingly, of the added radioactivity under normoxic conditions. Under hypoxic conditions, the **^{111}In-3** and **^{111}In-4** radioconjugates exhibited uptakes of 1.3% and 1.2%, respectively, during the incubation period. Comparison of the internalization of the radioconjugates revealed that internalization corresponded well with the binding affinities observed in the competitive binding assays. Also, internalization under hypoxic conditions yielded significantly lower uptake for **^{111}In-1** and **^{111}In-2** relative to **^{111}In-3** and **^{111}In-4**.

The efflux of the radioconjugates over time viewed as a percentage of the initial internalized activity is depicted in Figure 4. At all time points investigated, the radioconjugates

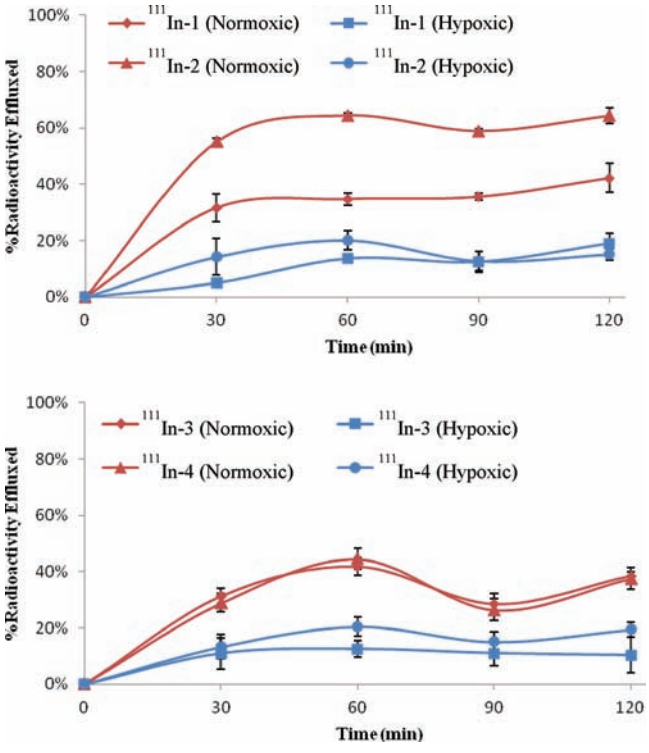


Figure 4. Efflux assays depicted as percentage of initial internalized activity for the ^{111}In-radioconjugates in PC-3 cells. Values are mean ± SEM (n = 3).

dx.doi.org/10.1021/bc200600w | *Bioconjugate Chem.* 2012, 23, 527−537

demonstrated significantly higher retention of the radioconjugates under hypoxic conditions relative to normoxic. In the normoxic studies, the ^{111}In radioconjugates **1**−**4** demonstrated substantial efflux with 32%, 55%, 31%, and 29%, respectively, of the radioactivity material being externalized within the first 30 min of the experiment. Under hypoxic conditions, radioconjugates **1**−**4** exhibited significantly lower clearance of the radioactivity with 5%, 14%, 11%, and 13% of the intracellular radioactivity being externalized from the cell. After the initial 30 min time point, the rate of clearance of the radioactivity substantially declined under both normoxic and hypoxic conditions. With the exception of ^{111}**In-2**, the radioconjugates demonstrated an increased retention of 20−30% of the initial internalized activity under hypoxic relative to normoxic conditions. Interestingly, ^{111}**In-2** exhibited a 50% increase in retention under hypoxic conditions which is significantly higher than the other radioconjugates.

An alternative way to view the effect hypoxia has upon the clearance of the radioconjugates is by directly comparing the internalized activity of the radioconjugate for each time point under normoxic and hypoxic conditions. The hypoxia enhancement factor (HEF) is the ratio of the internalized activity of the radioconjugate under hypoxic conditions over the internalized activity observed under a normoxic environment. The HEF ratios for each radioconjugate at each time point are depicted in Figure 5. With the exception of ^{111}**In-4**, all of the radio-

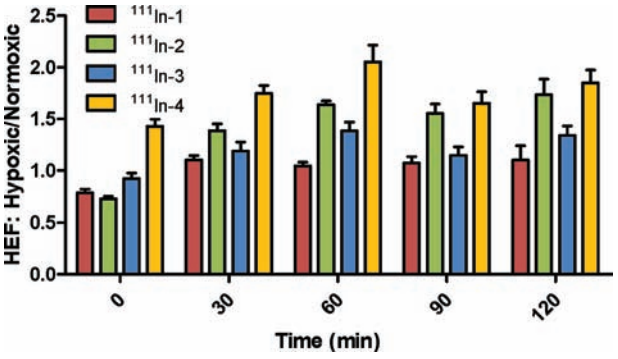


Figure 5. HEF ratios for the efflux studies of ^{111}In-BB2r-targeted radioconjugates under normoxic (95% air, 5% CO_2) and hypoxic conditions (94.9% N_2, 0.1% O_2, 5% CO_2). Values are mean ± SEM (n = 3).

conjugates at the initial time point demonstrated favored retention of the radioconjugates in normoxic conditions, although by the 30 min time point, all of the radioconjugates displayed significantly higher retention in hypoxic relative to normoxic cells (i.e., HEF > 1). This observation corresponds with the substantially higher clearance of the radioconjugates under normoxic relative to hypoxic conditions noted during the first 30 min of the efflux experiment. From 30 to 120 min, the ^{111}In-labeled radioconjugates **1**−**4** demonstrated an average HEF ratio of 1.08 ± 0.03, 1.58 ± 0.15, 1.27 ± 0.12 and 1.83 ± 0.17, respectively. The radioconjugates ^{111}**In-2**−**4** exhibited significantly (p < 0.001−0.05) higher average HEF ratios compared to control (i.e., ^{111}**In-1**). However, the HEF ratios of ^{111}**In-3** were substantially lower than that of either ^{111}**In-2** or ^{111}**In-4**. For ^{111}**In-1**, the control for this experiment, the radioconjugate exhibited no higher than a 10% increase in retention under hypoxic conditions from time points 30 to 120 min.

Cellular Protein Analysis. In a hypoxic environment, 2-nitroimdazoles undergo reduction and eventual irreversible conjugation with intracellular nucleophiles. It has been estimated that approximately 20% of such adduct formations are with nucleophilic groups (e.g., thiols) on proteins.[28,29] In order to better evaluate the protein binding capabilities of the 2-nitroimidazole containing BB2r-targeted agents, the protein association properties of ^{111}**In-2** were evaluated against the controls, ^{111}**In-1** and [^{125}I-Tyr$_4$]BBN, under hypoxic and normoxic environments. The radioconjugates ^{111}**In-3** and ^{111}**In-4** were not evaluated because of the poor internalization of these analogues. After 2 h of incubation with the radioconjugates under hypoxic or normoxic conditions, the PC-3 cells were lysed using a protein extraction reagent, centrifuged, and the supernatant filtered using a 30kDa centrifugal filter. Analysis of the protein associated radioactivity as a percentage of total intracellular activity is depicted in Figure 6. The radioconjugates ^{111}**In-1** and [^{125}I-Tyr$_4$]BBN both

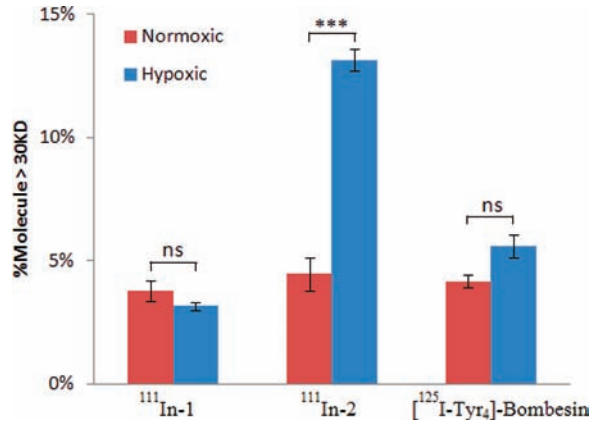


Figure 6. Protein association studies for ^{111}**In-1**, ^{111}**In-2**, and [^{125}I-**Tyr$_4$**]-BBN under normoxic (95% air, 5% CO_2) and hypoxic (94.9% N_2, 0.1% O_2, 5% CO_2) conditions in PC-3 cells. Values are mean ± SEM (n = 3).

demonstrated similar levels, approximately 3.15−5.60%, of protein association during the timespan of the experiment. Statistical analysis of the ^{111}**In-1** and [^{125}I-Tyr$_4$]BBN data revealed no significant impact on protein association under hypoxic or normoxic conditions. For the ^{111}**In-2** radioconjugate, the protein association under normoxic conditions was statistically the same as those found in controls. However, ^{111}**In-2** demonstrated a protein association under hypoxic conditions of approximately 13% which was 3-fold higher than that observed under a normoxic environment. These findings strongly imply that the mechanism of protein retention of ^{111}**In-2** is associated with the 2-nitroimidazole moiety and is oxygen dependent.

■ DISCUSSION AND CONCLUSION

In the area of cancer diagnostics and therapeutics, targeted, low molecular weight agents, such as those based on small peptides, sugars and steroids, generally offer the advantage of rapid tumor targeting and swift clearance from nontarget tissues relative to the analogous large molecular weight counterparts (e.g., antibodies, nanoparticles, etc.).[30−33] However, one significant challenge with low molecular weight, targeted agents has been obtaining optimal retention in the target tissue due to significant clearance of the radiotracer from the tumor. Since

dx.doi.org/10.1021/bc200600w | Bioconjugate Chem. 2012, 23, 527−537

most of the targeted agents develop maximal accumulation in the target site within a short time (i.e., 15 min to 1 h) after administration, it would be advantageous to develop techniques to selectively increase retention in the tumor thereby increasing the diagnostic and therapeutic efficacy of the agents.

Tumor hypoxia is the result of the inefficiency of the vascular architecture to adequately deliver nutrients, such as oxygen, to areas within the tumor. Since it has been demonstrated that human cancers, including prostate cancer, have significant levels of hypoxia, the development of hypoxia targeted drugs for both diagnostic and therapeutic applications in cancer has been an active area of research.[2,13,34−38] In particular, 2-nitroimidazole derivatives, which selectively reduce and become trapped within hypoxic cells, have been among the most thoroughly investigated class of hypoxia selective agents. This study seeks to design BB2r-targeted agents that incorporate the hypoxia selective trapping agent 2-nitroimidazole into the linking group of the radioconjugate. It is estimated that upon reduction and activation of the 2-nitroimidazole approximately 20% of the hypoxia selective agent become irreversibly conjugated to proteins within the cell.[29] In order to determine if one or more 2-nitroimidazoles would increase the retention of the radioconjugate in hypoxic cells, **^{111}In-2−4** were synthesized with one, two, or three 2-nitroimidazoles, respectively, incorporated into the linking group of the radioconjugate. Radioconjugate **^{111}In-1** is a thoroughly investigated BB2r-targeted peptide that does not contain 2-nitroimidazole moieties and thus was used as the control in our experiments.[22]

Synthesis of the ^{111}In-labeled radioconjugates **1−4** began with the synthesis of the 2-NIAA according to literature procedures.[24] The 2-NIAA was thoroughly characterized by NMR and the structural constitution of the moiety confirmed by X-ray crystallography. Conjugates **1** and **2−4*** were synthesized and purified by RP-HPLC in fairly low yields (12−22%). Coupling of the 2-NIAA to the conjugates **2*−4*** was accomplished using standard amidation chemistry. Further purification of **2−4** by RP-HPLC provided the conjugates in modest yields (34−44%). Radiolabeling of conjugates **1−4** proceeded easily and with high purity (≥95%) using standard radiolabeling conditions.[22]

In vitro competitive BB2r binding assays of **^{111}In-1−4** were performed using PC-3 cells with [^{125}I-Tyr$_4$]-Bombesin as the competitive radioligand. For the natural indium labeled conjugates, these studies demonstrated the following trend: **^{111}In-2** > **^{111}In-1** > **^{111}In-3** > **^{111}In-4**. By analyzing the structure−activity relationship with respect to binding affinity, it was determined that inclusion of more than one 2-nitroimidazole in the linking group had an unfavorable effect on the binding affinity of the radioconjugate. This strongly indicates that the 2-nitroimidazoles are interfering, through charge or sterics, with the ability of the pharmacophore (i.e., BBN(8−14)NH$_2$) to bind strongly to the BB2r. Since the pK_a of 1-substituted-2-nitroimidazoles, such as misonidazole, are generally significantly below physiological pH, the 2-nitroimidazoles are likely not charged.[39,40] Given this, it is probable that the loss in binding affinity in **^{111}In-3** and **^{111}In-4** are primarily a result of steric interference of the 2-nitroimidazole trapping moieties with the BB2r-targeting vector. Based on the **^{111}In-2** radioconjugate, the inclusion of a linker between the 2-nitroimidazole-amino acid residue and the pharmacophore of at least five carbon lengths is needed to achieve more optimal binding. This need for adequate spacers will be considered when designing future 2-nitroimidazole containing radioconjugates.

In order to examine the effect hypoxia has on the uptake and retention of the designed ^{111}In labeled radioconjugates, the conditions for the generation of hypoxic PC-3 cells was first validated. For this purpose Pimonidazole, a well-known and commonly used agent for the assessment of cellular hypoxia, was used for the confirmation of hypoxia generation in PC-3 cells.[25−27] The targeting mechanism of the Pimonidazole utilizes the same 2-nitroimidazole moiety employed in the design of the **^{111}In-2−4** radioconjugates. Exposure of PC-3 cells incubated under the hypoxic conditions of our studies revealed a 5-fold increase in Pimonidazole binding compared to PC-3 cells incubated under normoxic conditions as determined by flow cytometry. These results are consistent with similar hypoxia analysis utilizing Pimonidazole.[25] Since Pimonidazole utilizes the same 2-nitroimidazole moiety for hypoxia targeting as the ^{111}In labeled radioconjugates in our study, the cellular hypoxia generated utilizing our conditions were determined to be sufficient for the evaluation of the BB2r expression and the efficacy of the radioconjugates in PC-3 cells.

The design of targeted agents that are selectively enhanced toward hypoxic cells requires an understanding of the expression of the target under normoxic as well as hypoxic conditions. Since these agents gain entry into the cell through receptor-mediated endocytosis, if expression of the receptor target is significantly down-regulated under hypoxic conditions, any enhancement in hypoxic retention is likely to be substantially inhibited. Conversely, if under hypoxic conditions the target increases in expression; both the targeting and hypoxia enhancement of the drug would be expected to be improved. With this in mind, receptor saturation studies were undertaken to evaluate the expression of the BB2r on the surface of the PC-3 cells under hypoxic and normoxic conditions. From these studies, it was determined that the BB2r expression was 0.35 ± 0.08 and 0.30 ± 0.06 million receptors per PC-3 cell under normoxic and hypoxic conditions, correspondingly. During this study, oxygen levels, at least throughout the course of our investigation, did not play a significant role in the surface receptor expression of the BB2r. These findings are in accordance with a report from Martínez and colleagues of the BB2r expression in the H209 human lung cancer cell line under normoxic and hypoxic conditions.[41] With respect to overall BB2r expression of the PC-3 cells, the values obtained agree well with other reports.[42]

Efflux studies were performed under normoxic and hypoxic conditions to evaluate the efficacy of the hypoxia trapping moieties to enhance retention in hypoxic cells. The initial 2 h incubation of the radioconjugates with the PC-3 cells yielded a bimodal uptake pattern. **^{111}In-1**, the control for our experiment, and **^{111}In-2** demonstrate significant (22.6% and 20.5% of the dose, respectively) uptake, while **^{111}In-3** and **^{111}In-4** exhibited significantly lower internalization (1.4% and 0.8%, respectively). Based on the in vitro binding data, the significant decline in internalization with respect to **^{111}In-3** and **^{111}In-4** is likely due to the poor receptor affinity of these radioconjugates relative to **^{111}In-1** and **^{111}In-2**. Interestingly, for some of the radioconjugates, oxygen levels seemed to have a significant effect on the initial uptake values of the radioconjugates. This is particularly true for **^{111}In-1** and **^{111}In-2** in which a significant reduction of 25% was observed under hypoxic conditions for both radioconjugates. The cause for this decline is unknown; however, it was interesting to note that, within the first 30 min

of the efflux study at normoxia, all radioconjugates undergo substantial decline (29−55%) to levels that are significantly below that of the hypoxic levels. Contrarily, for the hypoxic studies, the amount of internalized activity declined relatively little (5−15%) during the same time period. Further investigations are needed to elucidate the exact cause for these contrasting observations. After the initial 30 min time point, there was relatively little decline in internalized activity among the radioconjugates.

As stated earlier, normoxic levels of internalized activity initially were greater, except for ^{111}**In-4**, in normoxic rather than the hypoxic studies, although by 30 min, the situation had reversed itself with all radioconjugates demonstrating hypoxic/normoxic ratios greater than 1. The radioconjugate ^{111}**In-4** demonstrated the highest average hypoxia enhancement (1.83 ± 0.17) followed closely by ^{111}**In-2** (1.58 ± 0.15). Interestingly, ^{111}**In-3** has a fairly low average enhancement of 1.27 ± 0.12 compared to ^{111}**In-2**. Given that ^{111}**In-3** has two 2-nitroimidazole moieties in comparison to one incorporated into ^{111}**In-2**, the lower hypoxia enhancement is unexpected. The reason for this circumstance is not clear. Remarkably, even the control in our experiment, ^{111}**In-1**, demonstrated a small (≤10%) increase in retention under hypoxic conditions. Speculatively, the retention in the control under hypoxic conditions may be attributed to slower metabolism kinetics or other hypoxia-impaired cellular functions needed to efflux the radioconjugates. Ultimately, more studies, which are in progress, are needed to obtain a clearer understanding of this process. Nevertheless, all of the experimental radioconjugates (i.e., ^{111}**In-2−4**) demonstrated significantly higher hypoxia enhancement than observed in the control, strongly suggesting that 2-nitroimidazoles are at least partially responsible for this enhancement.

It is well-known that 2-nitroimidazole derivatives based on small molecules bind irreversibly to proteins under hypoxic conditions.[25,26,29] In order to elucidate whether or not BB2r-targeted agents employing 2-ntiroimidazoles can conjugate to proteins, the cellular protein of the PC-3 cells were isolated after incubation with ^{111}**In-1**, ^{111}**In-2**, and [^{125}I-Tyr$_4$]BBN under hypoxic and normoxic conditions. The controls, ^{111}**In-1** and [^{125}I-Tyr$_4$]BBN, demonstrated 3.15−5.60% association with the proteins under both normoxic and hypoxic conditions. Statistical analysis of the difference between the hypoxic and normoxic protein association for the controls revealed no statistically significant difference ($p > 0.05$). Since the controls do not contain reactive moieties that would be expected to irreversibly bind to macromolecules, the protein association for the controls are most likely due to reversible, nonspecific binding. Under normoxic conditions the ^{111}**In-2** radioconjugate demonstrated similar protein association as controls. However, under hypoxic conditions the ^{111}**In-2** radioconjugate demonstrated a 3-fold increase in protein association ($p < 0.001$). These results indicate that the increase in protein association of ^{111}**In-2** is oxygen dependent and is consistent with the trapping mechanism of the 2-nitroimidazole. While the exact binding mode of the ^{111}**In-2** with proteins is not known beyond doubt, the findings from a superfluity of 2-nitroimidazole literature and the results of this study lead us to the conclusion that the increased protein association of the ^{111}**In-2** radioconjugate is likely irreversibly bound to the proteins. Assuming the ^{111}**In-2** protein association under normoxic conditions is reversible nonspecific binding, the increased protein association of the radioconjugate under hypoxic conditions signifies that ∼10% of the internalized cellular activity is likely irreversibly bound to cellular proteins.

In conclusion, we have synthesized and evaluated three BB2r-targeted radioconjugates that have 2-nitroimidazole hypoxia trapping moieties conjugated to the linking group of the peptide for the purpose of enhancing retention in hypoxic cancers. Our studies indicate that placement of the 2-nitroimidazole moieties close to the pharmacophore has a detrimental effect on the ability of the radioconjugate to adequately bind to the BB2r. The BB2r-targeted agents that include 2-nitroimidazole moieties demonstrated improved longitudinal retention in hypoxic relative to normoxic PC-3 cells. Additionally, we found that the inclusion of 2-nitroimidazole moieties in the BB2r-targeted agent design significantly increases protein association, by a likely irreversible conjugation reaction, under hypoxic conditions. Also, evaluation of the PC-3 human prostate cancer cell line reveals that the BB2r expression is not dependent on oxygen levels and suggests that the BB2r would therefore still be a valid target on the hypoxic fraction of BB2r-postive prostate cancer cells. While further work is still needed, this work suggests a potential new avenue to significantly increase the cellular retention of many targeted agents in hypoxic cancers. Our future work will focus on elucidating the mechanisms of retention of the hypoxia enhanced BB2r-targeted agents and evaluating the efficacy of these agents in in vivo cancer models.

■ ASSOCIATED CONTENT

Supporting Information

Crystallographic details, selected ES-MS spectra, *In Vitro* Competitive Cell-Binding displacement curves, and Receptor Saturation curves. This material is available free of charge via the Internet at http://pubs.acs.org.

■ AUTHOR INFORMATION

Corresponding Author

*Phone: 001-402-559-3453. Fax: 001-402-559-9365. E-mail: jcgarrison@unmc.edu.

Notes

The authors declare no competing financial interest.

■ ACKNOWLEDGMENTS

The authors would like to gratefully acknowledge the National Cancer Institute (4 R00 CA137147) and the National Center for Research Resources (5 P20 RR021937) for the funding and support of this research. The author J.C.G. would like to thank Dr. Charles L. Barnes in the Department of Chemistry at the University of Missouri-Columbia for the use of his X-ray diffractometer. Also, J.C.G. would like to acknowledge Dr. Timothy Hoffman and the Harry S. Truman Veterans' Hospital for the use of laboratory space and equipment during the initial phases of this work. N.K.W. would like to acknowledge Dr. V. M. Kulkarni for encouragement.

■ ABBREVIATIONS:

BB2r, Gastrin-Releasing Peptide Receptor; BBN, Bombesin; DIEA, *N*,*N*-diisopropylethylamine; DMF, *N*,*N*-dimethylformamide; DCM, dichloromethane; DCC, *N*,*N*′-dicyclohexylcarbodiimide; NMP, *N*-methylpyrrolidone; ^{111}In, ^{111}Indium; ^{nat}In, ^{natural}Indium; HEPES, 4-(2-hydroxyethyl)-1-piperazineethanesulfonic acid; BSA, bovine serum albumin; SDS, sodium

dodecyl sulfate; HBTU, *O*-benzotriazole-*N*,*N*,*N*′,*N*′-tetramethyl-uronium-hexafluoro-phosphate; PBS, phosphate buffered saline; 2-NIAA, 2-nitroimidazole acetic acid; 2-NIEA, 2-nitroimidazole ethyl acetate; B_{max}, total receptor number; K_d, dissociation constant; HEF, hypoxia enhancement factor

REFERENCES

(1) Anastasiadis, A. G., Stisser, B. C., Ghafar, M. A., Burchardt, M., and Buttyan, R. (2002) Tumor hypoxia and the progression of prostate cancer. *Current Urology Reports 3*, 222−228.

(2) Brown, J. M., and William, W. R. (2004) Exploiting tumour hypoxia in cancer treatment. *Nat. Rev. Cancer 4*, 437−447.

(3) Höckel, M., and Vaupel, P. (2001) Tumor hypoxia: Definitions and current clinical, biologic, and molecular aspects. *J. Natl. Cancer Inst. 93*, 266−276.

(4) Movsas, B., Chapman, J. D., Greenberg, R. E., Hanlon, A. L., Horwitz, E. M., Pinover, W. H., Stobbe, C., and Hanks, G. E. (2000) Increasing levels of hypoxia in prostate carcinoma correlate significantly with increasing clinical stage and patient age - An Eppendorf pO(2) study. *Cancer 89*, 2018−2024.

(5) Movsas, B., Chapman, J. D., Hanlon, A. L., Horwitz, E. M., Pinover, W. H., Greenberg, R. E., Stobbe, C., and Hanks, G. E. (2001) Hypoxia in human prostate carcinoma - An Eppendorf Po-2 study. *American Journal of Clinical Oncology - Cancer Clinical Trials 24*, 458−461.

(6) Weinmann, M., Welz, S., and Bamberg, M. (2003) Hypoxic radiosensitizers and hypoxic cytotoxins in radiation oncology. *Curr. Med. Chem.: Anti-Cancer Agents 3*, 364−374.

(7) Nunn, A., Linder, K., and Strauss, H. W. (1995) Nitroimidazoles and Imaging Hypoxia. *Eur. J. Nucl. Med. 22*, 265−280.

(8) Krohn, K. A., Link, J. M., and Mason, R. P. (2008) Molecular imaging of hypoxia. *J. Nucl. Med. 49* (Suppl 2), 129S−148S.

(9) Chapman, J. D., Engelhardt, E. L., Stobbe, C. C., Schneider, R. F., and Gerald, G. E. (1998) Measuring hypoxia and predicting tumor radioresistance with nuclear medicine assays. *Radiother. Oncol. 46*, 229−237.

(10) Engelhardt, E. L., Schneider, R. F., Seeholzer, S. H., Stobbe, C. C., and Chapman, J. D. (2002) The synthesis and radiolabeling of 2-nitroimidazole derivatives of cyclam and their preclinical evaluation as positive markers of tumor hypoxia. *J. Nucl. Med. 43*, 837−850.

(11) Evans, S. M., Kachur, A. V., Shiue, C.-Y., Hustinx, R., Jenkins, W. T., Shive, G. G., Karp, J. S., Alavi, A., Lord, E. M., Dolbier, W. R. Jr., and Koch, C. J. (2000) Noninvasive detection of tumor hypoxia using the 2-nitroimidazole [F-18]EF1. *J. Nucl. Med. 41*, 327−336.

(12) Yamamoto, F., Oka, H., Antoku, S., Ichiya, Y., Masuda, K., and Maeda, M. (1999) Synthesis and characterization of lipophilic 1-[F-18]fluoroalkyl-2-nitroimidazoles for imaging hypoxia. *Biol. Pharm. Bull. 22*, 590−597.

(13) Yang, D. J., Ilgan, S., Higuchi, T., Zareneyrizi, F., Oh, C.-S., Liu, C.-W., Kim, E. E., and Podoloff, D. A. (1999) Noninvasive assessment of tumor hypoxia with Tc-99m labeled metronidazole. *Pharm. Res. 16*, 743−750.

(14) Jensen, R. T., Battey, J. F., Spindel, E. R., and Benya, R. V. (2008) International union of pharmacology. LXVIII. Mammalian bombesin receptors: Nomenclature, distribution, pharmacology, signaling, and functions in normal and disease states. *Pharmacol. Rev. 60*, 1−42.

(15) Markwalder, R., and Reubi, J. C. (1999) Gastrin-releasing peptide receptors in the human prostate: Relation to neoplastic transformation. *Cancer Res. 59*, 1152−1159.

(16) Gugger, M., and Reubi, J. C. (1999) Gastrin-releasing peptide receptors in non-neoplastic and neoplastic human breast. *Am. J. Pathol. 155*, 2067−2076.

(17) Fleischmann, A., Laderach, U., Friess, H., Buechler, M. W., and Reubi, J. C. (2000) Bombesin receptors in distinct tissue compartments of human pancreatic diseases. *Lab. Invest. 80*, 1807−1817.

(18) Cornelio, D. B., Roesler, R., and Schwartsmann, G. (2007) Gastrin-releasing peptide receptor as a molecular target in experimental anticancer therapy. *Ann. Oncol. 18*, 1457−1466.

(19) Reubi, J. C., Wenger, S., Schmuckli-Maurer, J., Schaer, J.-C., and Gugger, M. (2002) Bombesin receptor subtypes in human cancers: Detection with the universal radioligand ^{125}I-[D-TYR^{6}, β-ALA^{11}, PHE^{13}, NLE^{14}] bombesin(6−14). *Clin. Cancer Res. 8*, 1139−1146.

(20) Ananias, H. J., de Jong, I. J., Dierckx, R. A., van de Wiele, C., Helfrich, W., and Elsinga, P. H. (2008) Nuclear imaging of prostate cancer with gastrin-releasing-peptide-receptor targeted radiopharmaceuticals. *Curr. Pharm. Des. 14*, 3033−3047.

(21) Garrison, J. C., Rold, T. L., Sieckman, G. L., Figueroa, S. D., Volkert, W. A., Jurisson, S. S., and Hoffman, T. J. (2007) In vivo evaluation and small-animal PET/CT of a prostate cancer mouse model using ^{64}Cu bombesin analogs: Side-by-side comparison of the CB-TE2A and DOTA chelation systems. *J. Nucl. Med. 48*, 1327−1337.

(22) Garrison, J. C., Rold, T. L., Sieckman, G. L., Naz, F., Sublett, S. V., Figueroa, S. D., Volkert, W. A., and Hoffman, T. J. (2008) Evaluation of the pharmacokinetic effects of various linking group using the 111In-DOTA-X-BBN(7−14)NH2 structural paradigm in a prostate cancer model. *Bioconjugate Chem. 19*, 1803−1812.

(23) Hueting, R., Christlieb, M., Dilworth, J. R., Garcia Garayoa, E., Gouverneur, V., Jones, M. W., Maes, V., Schibli, R., Sun, X., and Tourwe, D. A. (2010) Bis(thiosemicarbazones) as bifunctional chelators for the room temperature 64-copper labeling of peptides. *Dalton Trans 39*, 3620−32.

(24) Gariépy, J., Rémy, S., Zhang, X. G., Ballinger, J. R., Bolewska-Pedyczak, E., Rauth, M., and Bisland, S. K. (2002) A simple two-step approach for introducing a protected diaminedithiol chelator during solid-phase assembly of peptides. *Bioconjugate Chem. 13*, 679−684.

(25) Koch, C. J. (2008) Importance of antibody concentration in the assessment of cellular hypoxia by flow cytometry: EF5(1) and Pimonidazole. *Radiat. Res. 169*, 677−688.

(26) Ljungkvist, A. S., Bussink, J., Kaanders, J. H., and van der Kogel, A. J. (2007) Dynamics of tumor hypoxia measured with bioreductive hypoxic cell markers. *Radiat. Res. 167*, 127−45.

(27) Carnell, D. M., Smith, R. E., Daley, F. M., Saunders, M. I., Bentzen, S. M., and Hoskin, P. J. (2006) An immunohistochemical assessment of hypoxia in prostate carcinoma using Pimonidazole: Implications for radioresistance. *International Journal of Radiation Oncology Biology Physics 65*, 91−99.

(28) Yaromina, A., Zips, D., Thames, H. D., Eicheler, W., Krause, M., Rosner, A., Haase, M., Petersen, C., Raleigh, J. A., Quennet, V., Walenta, S., Mueller-Klieser, W., and Baumann, M. (2006) Pimonidazole labelling and response to fractionated irradiation of five human squamous cell carcinoma (hSCC) lines in nude mice: the need for a multivariate approach in biomarker studies. *Radiother. Oncol. 81*, 122−9.

(29) Raleigh, J. A., and Koch, C. J. (1990) Importance of thiols in the reductive binding of 2-nitroimidazoles to macromolecules. *Biochem. Pharmacol. 40*, 2457−2464.

(30) Fischman, A. J., Babich, J. W., and Strauss, H. W. (1993) A ticket to ride: peptide radiopharmaceuticals. *J. Nucl. Med. 34*, 2253−2263.

(31) Rudin, M., and Weissleder, R. (2003) Molecular imaging in drug discovery and development. *Nat. Rev. Drug Discovery 2*, 123−131.

(32) Kaltsas, G., Rockall, A., Papadogias, D., Reznek, R., and Grossman, A. B. (2004) Recent advances in radiological and radionuclide imaging and therapy of neuroendocrine tumours. *Eur. J. Endocrinol. 151*, 15−27.

(33) Willmann, J. K., van Bruggen, N., Dinkelborg, L. M., and Gambhir, S. S. (2008) Molecular imaging in drug development. *Nat. Rev. Drug Discovery 7*, 591−607.

(34) Brown, J. M. (2000) Exploiting the hypoxic cancer cell: mechanisms and therapeutic strategies. *Mol. Med. Today 6*, 157−162.

(35) Piert, M., Machulla, H. J., Picchio, M., Reischl, G., Ziegler, S., Kumar, P., Wester, H. J., Beck, R., McEwan, A. J. B., Wiebe, L. I., and Schwaiger, M. (2005) Hypoxia-specific tumor imaging with F-18-fluoroazomycin arabinoside. *J. Nucl. Med. 46*, 106−113.

(36) Reischl, G., Dorow, D. S., Cullinane, C., Katsifis, A., Roselt, P., Binns, D., and Hicks, R. J. (2007) Imaging of tumor hypoxia with [I-124] IAZA in comparison with [F-18] FMISO and [F-18]FAZA - first small animal PET results. *J. Pharm. Pharm. Sci. 10*, 203−211.
(37) Eschmann, S. M., Paulsen, F., Bedeshem, C., Machulla, H. J., Hehr, T., Bamberg, M., and Bares, R. (2007) Hypoxia-imaging with F-18-misonidazole and PET: Changes of kinetics during radiotherapy of head-and-neck cancer. *Radiother. Oncol. 83*, 406−410.
(38) Hoigebazar, L., Jeong, J. M., Choi, S. Y., Choi, J. Y., Shetty, D., Lee, Y. S., Lee, D. S., Chung, J.-K., Lee, M. C., and Chung, Y. K. (2010) Synthesis and characterization of nitroimidazole derivatives for ^{68}Ga-labeling and testing in tumor xenografted mice. *J. Med. Chem. 53*, 6378−6385.
(39) Dennis, M. F., Stratford, M. R., Wardman, P., and Watts, M. E. (1985) Cellular uptake of misonidazole and analogues with acidic or basic functions. *International Journal of Radiation Biology and Related Studies in Physics, Chemistry and Medicine 47*, 629−643.
(40) Gerweck, L. E. (1998) Tumor pH: implications for treatment and novel drug design. *Semin. Radiat. Oncol. 8*, 176−182.
(41) Martínez, A., Zudaire, E., Julián, M., Moody, T. W., and Cuttitta, F. (2005) Gastrin-releasing peptide (GRP) induces angiogenesis and the specific GRP blocker 77427 inhibits tumor growth in vitro and in vivo. *Oncogene 24*, 4106−4113.
(42) Lantry, L. E., Cappelletti, E., Maddalena, M. E., Fox, J. S., Feng, W., Chen, J., Thomas, R., Eaton, S. M., Bogdan, N. J., Arunachalam, T., Reubi, J. C., Raju, N., Metcalfe, E. C., Lattuada, L., Linder, K. E., Swenson, R. E., Tweedle, M. F., and Nunn, A. D. (2006) ^{177}Lu-AMBA: synthesis and characterization of a selective ^{177}Lu-labeled GRP-R agonist for systemic radiotherapy of prostate cancer. *J. Nucl. Med. 47*, 1144−1152.

Bioconjugate Chemistry

Article

pubs.acs.org/bc

New Lyophilized Kit for Rapid Radiofluorination of Peptides

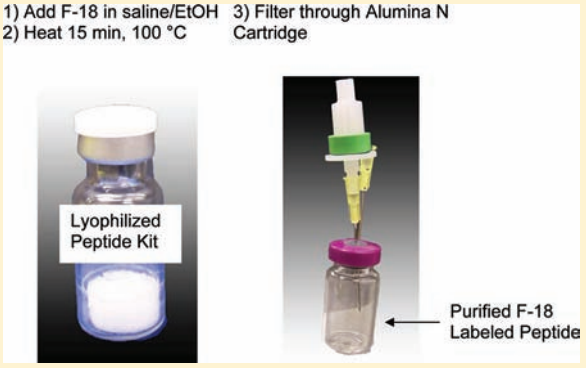
William J. McBride,*[,†] Christopher A. D'Souza,[†] Habibe Karacay,[‡] Robert M. Sharkey,[‡] and David M. Goldenberg*[,‡]

[†]Immunomedics, Inc., Morris Plains, New Jersey

[‡]Center for Molecular Medicine and Immunology and the Garden State Cancer Center, Morris Plains, New Jersey

Supporting Information

ABSTRACT: Radiolabeling compounds with positron-emitting radionuclides often involves a time-consuming, customized process. Herein, we report a simple lyophilized kit formulation for labeling peptides with ^{18}F, based on the aluminum-fluoride procedure. The prototype kit contains IMP485, a NODA (1,4,7-triazacyclononane-1,4-diacetate)-MPAA (methyl phenylacetic acid)-di-HSG (histamine-succinyl-glycine) hapten-peptide, [NODA-MPAA-D-Lys(HSG)-D-Tyr-D-Lys(HSG)-NH_2], used for pretargeting, but we also examined a similar kit formulation for a somatostatin-binding peptide [IMP466, NOTA-D-Phe-Cys-Phe-D-Trp-Lys-Thr-Cys-Throl] bearing a NOTA ligand to determine if the benefits of using a kit can be extended to other AlF-binding peptides. The NODA-MPAA ligand forms a single stable complex with $(AlF)^{2+}$ in high yields. In order to establish suitable conditions for a facile kit, the formulation was optimized for pH, peptide to Al^{3+} ratio, bulking agent, radioprotectant, and the buffer. For optimal labeling, the kit was reconstituted with an aqueous solution of $^{18}F^-$ and ethanol (1:1), heated at 100−110 °C for 15 min, and then simply and rapidly purified using one of two equally effective solid-phase extraction (SPE) methods. $Al^{18}F$-IMP485 was isolated as a single isomer complex, in high yield (45−97%) and high specific activity (up to 223 GBq/μmol), within 20 min. The labeled product was stable in human serum at 37 °C for 4 h and *in vivo*, urine samples showed the intact product was eliminated. Tumor targeting of the $Al^{18}F$-IMP485 in nude mice bearing human colon cancer xenografts pretargeted with an anti-CEACAM5 bispecific antibody showed very low uptake (0.06% ± 0.02 ID/g) in bone, further illustrating its stability. At 1 h, pretargeted animals had high $Al^{18}F$-IMP485 tumor uptake (28.1% ± 4.5 ID/g), with ratios of 9 ± 4, 123 ± 38, 110 ± 43, and 120 ± 108 for kidney, liver, blood and bone, respectively. Tumor uptake remained high at 3 h postinjection, with increased tumor/nontumor ratios. The NOTA-somatostatin-binding peptide also was fluorinated with good yield and high specific activity in the same kit formulation. However, yields were somewhat lower than those achieved with IMP485 containing the NODA-MPAA ligand, likely reflecting this ligand's superior binding properties over the simple NOTA. These studies indicate that ^{18}F-labeled peptides can be reproducibly prepared as stable Al−F complexes with good radiochemical yield and high specific activity using a simple, one-step, lyophilized kit followed by a rapid purification by SPE that provides the ^{18}F-peptide ready for patient injection within 30 min.



INTRODUCTION

^{18}F is the most commonly used isotope for positron-emission tomography (PET) due to its nearly ideal imaging properties (β+ 0.635 MeV 97%, $T_{1/2}$ 110 min). The increasing demand for ^{18}F, primarily used to prepare 2-[^{18}F]fluoro-deoxyglucose (FDG), has led to greater availability and lower costs. Its ∼2-h half-life also is matched well for compounds like peptides that clear rapidly from the blood, and thus there are considerable efforts underway to develop other ^{18}F-labeled peptide-imaging agents. Ordinarily, ^{18}F is attached to peptides by binding it to a carbon atom,[1−4] but attachments to silicon[5−8] and boron[9] also have been reported. Binding to carbon usually involves multistep syntheses, sometimes taking several hours to complete, which can be problematic for an isotope with a 110-min half-life. However, recent advances have reduced synthesis to a single step,[10,11] but this method does not work well with peptides containing a tyrosine group, and the peptides must be purified by HPLC to increase their specific activity.

Peptides are labeled routinely with radiometals, usually in 15 min and in quantitative yields.[12,13] For PET imaging, copper-64 and gallium-68 have been bound to peptides via a chelate with good yields, specific activity, stability, and imaging properties.[14] Since fluoride binds to most metals,[15] we sought to determine if an ^{18}F-metal complex could be bound to a chelate on a targeting molecule. We focused on the binding of an $(Al^{18}F)^{2+}$ complex since the aluminum−fluoride bond is one of the strongest fluoride−metal bonds and the $(AlF)^{2+}$ complex is known to bind to ligands.[16] Initial feasibility studies using an

Received: November 11, 2011
Revised: December 22, 2011
Published: January 25, 2012

 © 2012 American Chemical Society

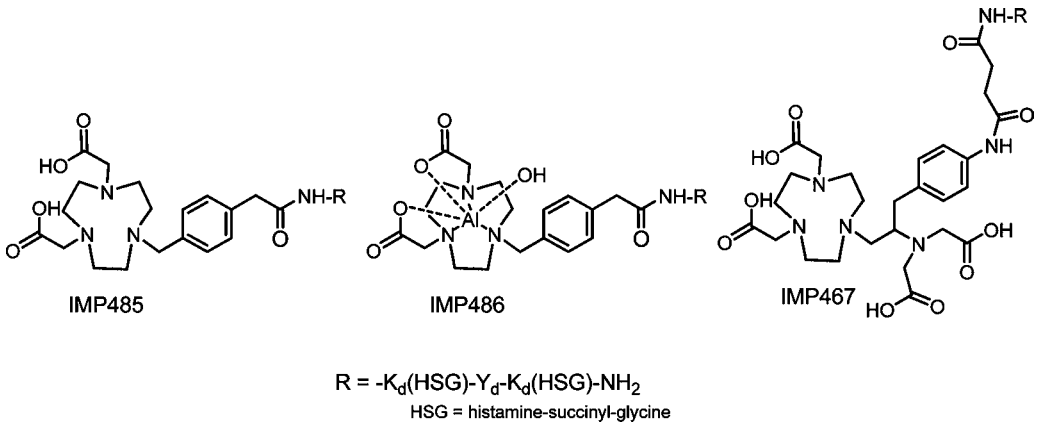


Figure 1. Structures of IMP485 and IMP486 as compared to the hapten-peptide ligand reported previously IMP467.

^{18}F-labeled peptide for *in vivo* targeting of cancer with a bispecific antibody (bsMAb) pretargeting system were reported.[17] The pretargeting procedure was shown to be highly sensitive and specific for localizing cancer, even more than ^{18}F-FDG.[18−23]

In the initial study, we found an $(Al^{18}F)^{2+}$ complex could bind stably to a 1,4,7-triazacyclononane-1,4,7-triacetic acid (NOTA) ligand in aqueous solution, but the yields were low, and the labeled peptide had to be purified by HPLC to obtain the specific activity needed for imaging. We then compared the labeling of four different NOTA ligands with $(Al^{18}F)^{2+}$, and found that while all these ligands formed stable complexes, the isolated yields varied from 5.8% to 87%, depending on the ligand used.[24] The peptide with the highest yield, IMP467 (Figure 1), contained the *C-NETA* ligand, which has enhanced binding kinetics for some metals.[25] An important additional finding was that IMP467 could be labeled with $^{18}F^-$ in saline, which is a commercially available source of purified $^{18}F^-$ typically used for bone imaging.

The investigations with the NOTA compounds provided us with important leads in determining ways to optimize a chelate for binding AlF. We subsequently developed a new ligand that contains 1,4,7-triazacyclononane-1,4-diacetate (NODA) attached to a methyl phenylacetic acid (MPAA) group for IMP485.[26] This ligand is synthesized more easily than *C-NETA* and has the added advantage of forming a single stable complex with $(AlF)^{2+}$. Since our original report of NOTA-based chelating agents, the AlF-radiolabeling method has been investigated by several other groups. For example, together with a group of our collaborators, a NOTA-octreotide peptide, IMP466, was fluorinated in good yields with excellent stability and targeting *in vivo*.[27−29] Others have confirmed the AlF fluorination potential using RGD peptides and some simple derivatives of NODA.[30−32]

In our earlier reports, we showed that the labeling procedure could be performed simply in solution using a one-pot method.[24,26] This success suggested that a lyophilized kit could be prepared similar in concept to those used with ^{99m}Tc.[33,34] A validated lyophilized kit that enables rapid and reproducible labeling of a peptide by the simple addition of USP $^{18}F^-$ in saline, a brief heating step, followed by a rapid and simple purification process, as described here, should make the ^{18}F-labeling of molecules more compatible with the already established good manufacturing practices (GMP) applied to the labeling of ^{99m}Tc-agents. Such kits also could expand the use of ^{18}F-labeled agents for monitoring the biodistribution and localization of various compounds. While we suspect different agents will have different requirements for kit formulation and optimal labeling, the process we describe here to develop the kits for IMP485 and the somatostatin-binding peptide, IMP466, should provide important insights for preparing agents for use with the AlF-labeling procedure.

MATERIALS AND METHODS

All commercial chemicals were of analytical grade and used without further purification. L-(+)-ascorbic acid, $AlCl_3{\cdot}6H_2O$, 4-morpholineethanesulfonic acid (MES), and sodium hydroxide, 99.99%, were purchased from Sigma-Aldrich (Milwaukee, WI). N-2 hydroxyethylpiperazine-*N*′-2-ethane-sulfonic acid (HEPES) was obtained from Calbiochem (La Jolla, CA). Sodium acetate, *α*,*α*-trehalose, potassium biphthalate (KHP), and acetic acid were from J. T. Baker (Phillipsburg, NJ). The analytical and preparative reverse-phase HPLC (RP-HPLC) columns were purchased from Phenomenex (Torrance, CA) and Waters Corp. (Milford, MA). No-carrier-added [^{18}F]-fluoride was purchased from IBA Molecular (Somerset, NJ) and used for initial serum stability and biodistribution studies. $^{18}F^-$ in saline (for human use) was obtained from PETNET Solutions (Hackensack, NJ) and used for the kit optimization experiments. Solid-phase extraction (SPE) cartridges (Sep-Pak light QMA, Sep-Pak light Alumina N, Sep-Pak Accell plus CM, and Oasis HLB) were acquired from Waters (Milford, MA). Female nude mice (NCr nu-m), 23.1 ± 2.3 g, were procured from Taconic Farms (Germantown, NY).

The recombinant, humanized, tri-Fab bispecific monoclonal antibody (bsMAb), TF2, was provided by IBC Pharmaceuticals, Inc. (Morris Plains, NJ). TF2 binds divalently to carcinoembryonic antigen (CEACAM5 or CD66e) and monovalently to the synthetic hapten, HSG (histamine-succinyl-glycine).[35]

IMP485, IMP486, and IMP466. IMP485 [NODA-MPAA-D-Lys(HSG)-D-Tyr-D-Lys(HSG)-NH_2] and IMP486 [AlOH-NODA-MPAA-D-Lys(HSG)-D-Tyr-D-Lys(HSG)-NH_2, i.e., IMP485 preloaded with aluminum] were synthesized as described previously.[26] IMP466, which contains the NOTA ligand, was synthesized as described elsewhere.[27]

IMP485 Initial Kit Formulation. Stock solutions of IMP485 and $AlCl_3{\cdot}6H_2O$ were dissolved in 2 mM sodium acetate buffer and adjusted to ∼pH 4. Ascorbic acid and *α*,*α*-trehalose solutions were prepared in DI water.

Prior experience with IMP485 radiolabeling performed in solution phase provided important insights regarding the basic starting conditions that might be compatible with lyophilized

dx.doi.org/10.1021/bc200608e | *Bioconjugate Chem.* 2012, 23, 538−547

kit formulation.[26] Many of these initial studies were performed using 3-mL vials containing 40 nmol of IMP485, with the kits formulated in a variety of ways to examine how these changes might affect the radiolabeling yields. Additional information concerning the specific formulation/conditions under evaluation is provided in Results. Briefly, kits were made with varying volumes of the α,α-trehalose stock solution, such that the α,α-trehalose concentration by weight would be ~2.5, 5, 10, 20, and 50%, respectively, when reconstituted in 0.2 mL of saline. In addition to testing trehalose, other bulking agents (sorbitol, glycine, mannitol, and sucrose) were examined. Additional 40-nmol IMP485 kits were formulated with varying amounts of $AlCl_3$ (40, 36, 32, 28, 24, and 20 nmol) included to examine different peptides to $AlCl_3$ ratios (1:1, 1:0.9, 1:0.8, 1:0.7, 1:0.6, and 1:0.5, respectively). Kits containing IMP486 were prepared without the addition of the $AlCl_3$ solution because the ligand was prefilled 100% with Al^{3+} according to previously published methods.[26]

In order to evaluate the effect of pH on radiolabeling yields, 40-nmol kits of IMP485 and IMP486 were adjusted to the pH ranges of 3.3 to 5.1 and 3.4 to 4.98, respectively. A second set of 20-nmol kits of IMP486 was made and adjusted to the pH range 3.61 to 4.4. Kits were also formulated in various buffers, such as HEPES/HOAc, MES/HOAc, citrate, ascorbate, and KHP, with and without 0.1 mg ascorbate.

Typically, the filled vials were frozen and lyophilized. However, in one set of studies, the vials containing 40-nmol IMP485, 24 nmol of Al^{3+}, 10 mg of trehalose, and 0.1 mg ascorbic acid, all adjusted to ~1 mL, were stored under nitrogen at 2−8 °C until lyophilization (no delay or a 1-, 2-, or 3-day delay).

Final Formulation and Lyophilization of 20-nmol IMP485 Kits. The final formulation consisted of dissolving the peptide (IMP485) in DI water to obtain a 2-mM solution. The $AlCl_3{\cdot}6H_2O$ was dissolved in 2 mM KHP and adjusted to pH 4. Ascorbic acid was dissolved in DI H_2O at 5 mg/mL. The KHP was dissolved in DI H_2O to obtain a 0.06 M solution at pH 3.99, and α,α-trehalose dihydrate was dissolved in DI H_2O to obtain a 5% solution.

The bulk solution used to fill vials was prepared by mixing the 2 mM IMP485 solution with the 2 mM Al^{3+}/KHP solution, the ascorbic acid solution, the 0.06 M KHP buffer, and the α,α-trehalose, and then DI H_2O was added to obtain the bulk solution. The solution was adjusted to pH 4.0 with a few microliters of 1 M KOH and then dispensed in 1-mL aliquots into the vials for lyophilization. The filled vials were frozen and then transferred to the shelf of the Virtis Advantage lyophilizer (Gardiner, NY) cooled to −16 °C. When the vacuum went below 100 mTorr, the shelf temperature was increased to 0 °C. After 16 h, the shelf temperature was increased to 20 °C for 4 h. The vials were then sealed under vacuum and removed from the lyophilizer.

Kits were made with 10, 20, 40, 100, and 200 nmol of peptide (using increasing amounts of the stock 2-mM IMP485 solution). For those kits, the amount of Al^{3+} added was adjusted to keep the ratio of nmol of peptide to nmol of Al^{3+} constant at 1 nmol of peptide to 0.6 nmol of Al^{3+}. All of the other kit ingredients were unchanged from the kit formulation described above, regardless of the amount of peptide used.

Formulation of IMP466 Kits. IMP466 kits were formulated in the same way as IMP485 kits, except the final pH of the kit solution was adjusted to pH 4.1.[27,28]

Radiolabeling and Purification. The lyophilized peptides were radiolabeled by adding $^{18}F^-$ in 100 to 200 μL saline to the crimp-sealed vial and then heating to 90−110 °C for 15 min. In some cases, an equal volume of ethanol was added with $^{18}F^-$. The peptides were purified by one of two methods. HLB purification was performed by first adding DI water to the vial in fractions (5 mL total volume), which were transferred to a dilution vial, and the entire contents of the dilution vial were applied to a Waters HLB column Oasis HLB 1-mL (30 mg) flangeless cartridge. The HLB cartridge was placed on a crimp-sealed vial, drawing the waste liquid containing the unbound ^{18}F into the vial under vacuum. The reaction vial then was washed with aliquots of DI water. The column was eluted directly into a vial containing buffered, lyophilized ascorbic acid (~pH 5.5, 15 mg), using three, 200-μL portions of 1:1 EtOH/DI water.

The percent isolated yield in the product vial was determined by measuring and adding the activity found in the HLB cartridge, the reaction vial, the water wash, and the product vial to account for the total activity. When the isolated yield calculation was compared to the decay-corrected method, the yields were found to be essentially identical, indicating that all of the ^{18}F-activity was accounted for.

The second method utilized an Alumina N cartridge as described by others.[32] At the end of the reaction time, saline was added to the reaction vial, which was drawn into a syringe and passed through the Alumina N cartridge. The vial was washed with more saline, which was also pushed through the Alumina N cartridge into the product vial.

Serum Stability. The purified radiolabeled IMP485 in 50 μL 1:1 EtOH/H_2O was mixed with 150 μL of human serum and placed in the HPLC autosampler heated to 37 °C and analyzed by RP-HPLC, using an in-line radiation detector.

***In Vivo* Studies.** All animal studies were approved by CMMI's institutional animal safety committee. Nude mice bearing subcutaneous LS174T human colon cancer xenografts were injected with 106 μg (~1 nmol) of TF2 anti-CEACAM5 × anti-HSG bsMAb followed 16 h later with $Al^{18}F$-IMP485 (1.04 MBq, 5.2 × 10^{-11} mol, 100 μL, iv) that was prepared using a 40-nmol IMP486 kit to an effective specific activity of 20.4 GBq/μmol after HLB purification. The animals were necropsied at 1 and 3 h post injection. Other animals were given the $Al^{18}F$-IMP485 alone and necropsied at the same times.

RESULTS

Kit Formulation. *Bulking Agents.* A lyophilized kit containing such small amounts of product requires a bulking agent. Thus, starting with 40 nmol IMP485 kits (containing 20 nmol Al^{3+}, ascorbate/acetate buffer, pH 4.0), we examined five different bulking agents to assess which would produce an acceptable cake with minimal impact on the radiolabeling reaction. Kits were formulated with 10 mg of each bulking agent with identical amounts of the other formulation reagents, adjusted to approximately the same pH. After lyophilization, the kits were labeled by adding ~74 MBq $^{18}F^-$ in 200 μL saline (no ethanol added) and heated to ~105 °C for 15 min and then purified by the HLB method. The isolated yields were 83%, 42%, 82%, 66%, and 81% for sorbitol, glycine, mannitol, sucrose, and α,α-trehalose, respectively. The sorbitol formulation collapsed to a gum on lyophilization, while both the mannitol and α,α-trehalose formulations formed acceptable cakes and were labeled in high yield. Changing the final

concentration of α,α-trehalose in the kit (40 nmol IMP485, 200 μL $^{18}F^-$ in saline, 105 °C) from 2.5 to 50% (5 mg to 100 mg/kit) by weight had no effect on radiolabeling yields, with an average of 83.3 ± 0.65% (n = 5) for all concentrations of α,α-trehalose tested.

IMP485 kits could be stored at 2−8 °C under nitrogen for up to three days before lyophilization without impacting radiolabeling yields.

Effect of pH. We found previously that radiolabeling is pH-sensitive and needs to be adjusted to the ligand and possibly even to the peptide and the ligand.[24] Whereas the optimal pH for IMP461, IMP466, and IMP467 was reported to be 4.1, 4.1, and 4.5, respectively,[24,27] the optimal pH for both IMP485 and IMP486 kits was 4.0 ± 0.2. In both cases, the yields fell rapidly outside the ideal pH zone. For example, using 20-nmol kits of IMP486 (containing 10 mg of trehalose, 0.1 g of ascobate, 20 nmol of Al^{3+}, in acetate buffer) labeled with 200 μL of 1.8−2.4 GBq $^{18}F^-$ in saline (no ethanol added), the yields were 50%, 63%, 66%, 55%, and 50% at pH 3.6, 3.8, 4.0, 4.2, and 4.4, respectively. It is important to note that the lower yields in this study reflected the use of 20-nmol kits rather than 40-nmol kits used in the previous section.

Effect of Buffer. In this series, 40-nmol kits containing 20 nmol Al^{3+} and 10 mg trehalose were formulated using MES, HEPES, KHP, citrate, ascorbate, and acetate buffers, all adjusted to pH 4 before lyophilization. We noted that when reconstituted with saline, the pH of some of the kits changed after they were lyophilized. The kits initially formulated with acetate buffers without ascorbic acid had the largest pH change after lyophilization, probably due to the loss of acetic acid during freeze-drying. The radiolabeling yields of those kits were lower (45−71%). The KHP-buffered kit had the best yield in the ascorbate-free batch (71% yield). The pH was more consistent between formulation and lyophilization with most of the buffers tested when 0.1 mg of ascorbic acid was present in the vials. The yields derived from kits formulated with HEPES, MES, NaOAc, and KHP in the presence of 0.1 mg of ascorbic acid were similar (83−86% isolated yield). Thus, ascorbic acid appears to serve as a significant nonvolatile buffer that stabilizes the pH similarly before and after lyophilization, allowing better control of pH, which, in turn, ensures optimal labeling efficiency.

To determine the effect of KHP on the labeling efficiency, kits with 0.1, 1.22, 8, 16, and 32 μmol of KHP were tested. Kits having 1.22 μmol of KHP maintained the pH at the desired level (4.0 ± 0.2) and gave a better labeling yield than 0.1 μmol KHP kits. The kits with ≥8 μmol of KHP had progressively lower yields. We suspect that KHP and ascorbate might be acting both as buffers and as transfer ligands to increase the labeling yields with those excipients. Citric acid is not a good buffer for AlF labeling, giving low yields even when only 50 μL of 2 mM citrate were used in the presence 0.1 mg of ascorbate.

Radioprotectants. Ascorbic or gentisic acid often are added to radiopharmaceuticals during preparation to minimize radiolysis. Ascorbic acid was included routinely in vials used to isolate the HLB-purified product, but we also examined the importance of having ascorbic acid added during the labeling procedure. When IMP485 (20 nmol, containing 10 mg of trehalose and 10 nmol Al^{3+}) was formulated with 0.1, 0.5, and 1.0 mg of ascorbic acid/acetate buffers at pH 4.1−4.2 and labeled with $^{18}F^-$ in 200 μL of saline, final yields were 51, 31, and 13%, respectively, suggesting that 0.1 mg of ascorbic acid was the maximum amount that could be included in the formulation without reducing yields. Formulations containing gentisic acid/acetate did not label as well as the ascorbic acid kits.

Peptide to Aluminum Ratio. The optimal IMP485 to Al^{3+} mole ratio was 1:0.6, but good yields were obtained with ratios from 1:0.5 to 1:1.

Recommended Kit Formulation Buffer. The culmination of the above testing led us to conclude that the optimal formulation buffer for the IMP485 kits contained the peptide with Al^{3+} in a 1:0.6 ratio, along with 0.1 mg of ascorbic acid, 1.22 μmol of KHP, and 10 mg of α,α-trehalose dihydrate adjusted to pH 4.0 ± 0.2.

Optimizing Radiolabeling Yields. We reported previously that adding ethanol can enhance the ^{18}F-radiolabeling yields.[26] Therefore, various ratios of saline to ethanol were tested with 20-nmol IMP485 kits in 400 μL total volume and 60 MBq of $^{18}F^-$ that were heated at 107 °C for 15 min. The vials tested contained 100%, 75%, 50%, and 25% saline mixed with ethanol, affording $Al^{18}F$-IMP485 in isolated yields of 48.8, 67.1, 86.2, and 84.4%, respectively. The data indicate that yields are best when the mixture contains between 50 and 75% ethanol. Comparable radiolabeling yields of 83% and 81% were obtained when 20-nmol kits of IMP485 and IMP486 were labeled with ∼1.5 GBq of $^{18}F^-$ in 100 μL of saline and 100 μL of EtOH, respectively.

Using the recommended formulation buffer, we next prepared IMP485 kits with 10, 20, 40, 100, and 200 nmol of peptide and then test-labeled with $^{18}F^-$ (∼37 MBq) in 400 μL of 1:1 saline/ethanol (peptide concentration during radiolabeling ranged from 25 to 500 μM) for 15 min at 50, 70, 90, 100, and 110 °C. At this point, we also changed our SPE-purification procedure, favoring an Alumina N cartridge reported by others.[32] The Alumina N method reduces the time required to isolate the purified product since it flows through the cartridge rather than binding to the resin and requiring elution, as in the HLB purification procedure. RP-HPLC analysis of IMP485 and IMP466 purified by HLB and Alumina N showed <1% to undetectable amounts of ^{18}F. The results clearly indicate that the reaction must be heated to 100 to 110 °C to obtain the maximum yield (Figure 2), and nearly

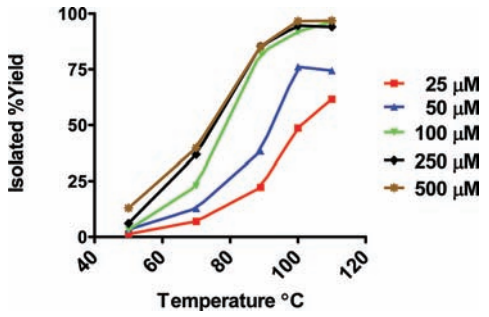


Figure 2. Isolated % yield vs reaction temperature at different IMP485 concentrations. The labeling reactions were performed in 400 μL of 1:1 ethanol/saline for 15 min at the temperatures indicated.

quantitative radiolabeling yields can be obtained with peptide concentrations of 100 μM (40 nmol of peptide in 400 μL 1:1 saline/ethanol) or higher.

The optimum reaction time was studied next with 20-nmol IMP485 kits labeled with ∼37 MBq $^{18}F^-$ in 400 μL of 1:1 ethanol/saline at 108 °C for 5 to 60 min. Maximum yields were obtained after 15 min of heating, with a specific activity of ∼1

dx.doi.org/10.1021/bc200608e | Bioconjugate Chem. 2012, 23, 538−547

GBq/μmol (Table 1). Indeed extending the incubation period to 30 min did not improve the yield appreciably, with any gain

Table 1. Radiolabeling Yields as a Function of Time and $^{18}F^-$-Activity[a]

	30 MBq	2.5 GBq	
reaction time (min)	% yield	% yield	specific activity GBq/μmol
5	51.1	ND	
10	77.1	ND	
15	86.4	74.3	76.5
20	ND	77.3	78.5
30	91.4	79.2	74.0
60	83.1	ND	

[a] ^{18}F in 200 μL of saline was added to a 20-nmol IMP485 kit with 200 μL of ethanol and heated to 108−110 °C for the times indicated. Purification by Alumina N.

made in yield being offset by the ^{18}F decay occurring over this additional time. These same kits showed optimal labeling yields again within 15 min using ∼2.5 GBq of $^{18}F^-$ in 400 μL 1:1 ethanol saline at 110 °C, and while the isolated yields decreased somewhat with this higher level of activity, the specific activity increased to ∼75 GBq/μmol. Kits prepared with $^{18}F^-$ received on 4 separate days, with ∼1.68 to 2.57 GBq of $^{18}F^-$, had yields ranging from 70 to 84% and specific activities from 48 to 85 GBq/μmol (Supporting Information, Table 1).

To assess the labeling yields with even higher amounts of ^{18}F, we performed one additional procedure using a 20-nmol IMP485 kit and 10.8 GBq of $^{18}F^-$ in 400 μL 1:1 ethanol saline at 108 °C for 15 min. After purification through an Alumina N cartridge and in a total reaction and purification time of just ∼20 min, 4.46 GBq (45.6% yield) of Al^{18}F-IMP485 was obtained with a specific activity of 222.8 GBq/μmol (assumes no loss in IMP485).

When Al^{18}F-IMP485 was mixed with at least a 20-fold molar excess of TF2 and then analyzed by SE-HPLC, the peptide shifted from a retention time of ∼17 to 9 min, the retention time of TF2, indicating the labeled peptide retained HSG-binding and antibody-binding (Supporting Information, Figure 1, traces A and B).

In order to determine if the same kit formulation could be applied to another peptide, IMP466, a somatostatin-binding peptide described previously was examined.[27,28] Kits were made with the same ingredients as IMP485, but the pH was adjusted to 4.1 prior to lyophilization. Initial labeling was performed in concert with IMP485 using ∼2.5 GBq of $^{18}F^-$ (refer to Table 1), examining reaction times between 15 and 30 min. As shown in Table 2, maximum yields were obtained within 15 min at 110

Table 2. Comparison of High-Dose $^{18}F^-$ Labeling in Kits Containing 20 nmol of IMP466[a]

reaction time (min)	starting activity (GBq)	isolated activity (GBq)	specific activity (GBq/μmol)	isolated % yield
15	2.51	1.21	60.5	54.6
20	2.51	1.17	58.5	55.7
30	2.39	1.08	54.0	58.1

[a] Each 20-nmol kit received ∼2.5 GBq of $^{18}F^-$ in 200 μL of saline plus 200 μL of ethanol. After incubation at 110 °C for the times indicated, the products were purified on an Alumina N cartridge.

°C. The lower yields for IMP466 compared to IMP485 suggested that the NODA-MPAA ligand affords higher yields as compared to those of the simple NOTA ligand. Another study compared $^{18}F^-$ labeling of IMP466 to IMP485 with increasing amounts of each peptide (10, 20, 40, 100, and 200 nmol) using ∼14 to 20 MBq of $^{18}F^-$ in 400 μL 1:1 ethanol saline at 110 °C for 15 min (Supporting Information, Table 2). The data demonstrate that each peptide could be radiolabeled to near quantitative levels, but the simple NOTA required 5-times more moles of peptide than the NODA-MPAA containing IMP485. To illustrate this point further, we prepared an octreotide analogue containing the NODA-MPAA (IMP490; Supporting Information) and formulated in acetate buffered kits in the same manner as IMP485. The ^{18}F-radiolabeling yield in the acetate-buffered kits for IMP490 and IMP485 was similar, supporting our position that the NODA-MPAA ligand improves yields as compared to the simple NOTA.

Stability and Biodistribution of Al^{18}F-IMP485. RP-HPLC of Al^{18}F-IMP485 (1.9 MBq/μmol) incubated in fresh human serum at 37 °C for 4 h showed no evidence of destabilization (Supporting Information, Figure 2), being identical to the original labeled peptide HPLC trace (data not shown). The labeled product was also injected into tumor-bearing mice. Al^{18}F-IMP485 had low uptake in all normal tissues (Figure 3C), e.g., 0.18 ± 0.03% and 0.17 ± 0.06% injected dose/gram (ID/g) at 1 h for liver and blood, respectively, with higher uptake in the kidneys (3.33 ± 0.56% ID/g and 2.27 ± 0.29% ID/g at 1 and 3 h, respectively), which is expected because the peptide is eliminated in the urine. Bone uptake was also low, averaging 0.11 ± 0.02% ID/g at 1 h, decreasing to 0.08 ± 0.03% ID/g at 3 h, indicating that the Al^{18}F complex was stably bound to the peptide. Tumor uptake of Al^{18}F-IMP485 alone was 0.31 ± 0.11% and 0.09 ± 0.02% at 1 and 3 h, respectively. However, in animals pretargeted with TF2, tumor uptake was 28.1 ± 4.5% ID/g and 26.5 ± 6.0% ID/g at 1 and 3 h, respectively, illustrating that the peptide retained HSG binding antibody (Figure 3A). High tumor uptake in the TF2-pretargeted animals resulted in high T/NT ratios, e.g., 123 ± 38, 9 ± 4, and 110 ± 43 at 1 h, and 189 ± 43, 12 ± 3, and 1240 ± 490 at 3 h postinjection of the peptide in liver, kidney, and blood, respectively (Figure 3B).

RP-HPLC traces of urine taken from a mouse 50 min after Al^{18}F-IMP485 injection were identical to the injected product, again indicating the stability of the Al^{18}F binding to the ligand (Figure 4). Samples of urine from the mice given the peptide alone examined by SE-HPLC also showed that the radiolabeled peptide shifted to a shorter retention time after TF2 addition, indicating that all of the activity was attached to the peptide and that the peptide affinity for TF2 was unchanged, even after injection and excretion in urine (Supporting Information, Figure 1, traces C and D).

■ DISCUSSION

We reported previously a simple one-pot method for preparing ^{18}F-labeled peptides using the AlF method in solution.[26] Our primary goal here was to simplify the method even further by examining whether peptides coupled with AlF-binding ligands could be formulated and lyophilized so that upon reconstitution with $^{18}F^-$ in saline, the final product could be isolated quickly and easily.

Most ^{18}F-peptide radiolabeling processes are complicated, take several reaction steps, and require specialized and costly equipment, as well as highly trained personnel, but recently,

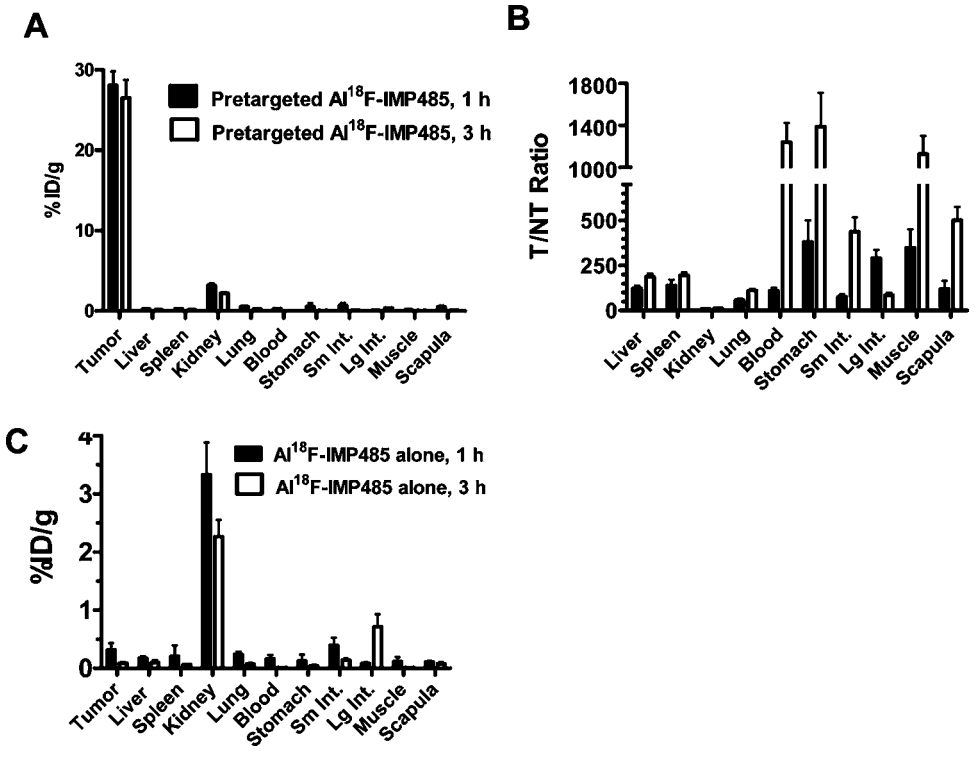


Figure 3. Biodistribution at 1 h (black bars) and 3 h (white bars) postinjection of $Al^{18}F$-IMP485 in nude mice bearing sc LS174T human colon cancer xenografts. (A and B) $Al^{18}F$-IMP485 (n = 7) percent uptake and T/NT ratios, respectively, at 1 and 3 h in mice pretargeted with TF2 anti-CEACAM5 bsMAb 16 h prior to injection of the peptide. (C) Percent uptake of $Al^{18}F$-IMP485 (n = 6) alone at 1 and 3 h.

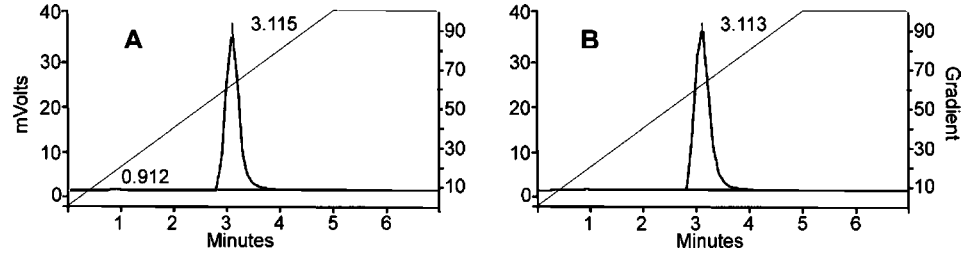


Figure 4. RP-HPLC of $Al^{18}F$-IMP485 after purification (A) and activity recovered from mouse urine at 50 min PI (B).

there has been some progress in simplifying labeling procedures. For example, one method involves binding ^{18}F to silicon using isotopic exchange to displace ^{19}F with ^{18}F either as a two-step prosthetic labeling method[5] or as a direct labeling of peptides and proteins.[6−8] The exchange is performed at room temperature in a DMSO solution over 5 min, producing the directly ^{18}F-labeled peptide in 38% yield and with a specific activity of up to 56 GBq/μmol.[6] One drawback of this method is that the silicon-binding substrate is lipophilic, which can lead to high liver uptake for ^{18}F-labeled peptides. However, hydrophilic groups can be added to the peptide to compensate for the lipophilicity of the silicon acceptor.[6]

A one-step carbon-fluoride ^{18}F-labeling method for peptides also has been explored.[10,11] In that procedure, the peptide contains a trimethylammonium-leaving group attached to an aromatic ring containing an electron-withdrawing group. The $^{18}F^-$ is dried down (10 min) with K222/K_2CO_3 or Cs_2CO_3, and heated (90 °C) with the peptide for 10 min to substitute the ^{18}F for the trimethylammonium group. The reaction mixture is then purified by HPLC to produce the high specific activity ^{18}F-labeled peptide (170 GBq/μmol) in 15% decay-corrected isolated yield. The radiolabeled peptide showed good tumor targeting with minimal hepatobiliary clearance, probably due to the addition of two hydrophilic cysteic acid groups on the peptide.

Taking the lead from simple methods to label chelate-conjugated antibodies and peptides quantitatively with radiometals, we examined a similar approach for ^{18}F. Knowing that ^{18}F binds avidly to aluminum, we showed the feasibility of binding $(AlF)^{2+}$ to a NOTA chelate attached to peptide used in our bsMAb pretargeting system;[17] however, because of low and variable yields, other related NOTA-based ligands were explored that gave more consistent and higher yields and specific activity.[24] More recently, a new NODA-MPAA ligand was evaluated for peptide labeling that forms a single, stable, octahedral complex with $(AlF)^{2+}$ with the fluorine in an axial position,[26] whereas the earlier ligand−peptides (IMP449, IMP461, and IMP467) formed two complexes. Having a single complex would be important for some receptor-targeting agents if there were differences in affinity when multiple complexes occur. Another notable difference with the new ligand is that the same labeling yields are obtained with the preformed aluminum complex (IMP486) and the peptide formulated with Al^{3+} in the kit. Labeling yields with the other Al-NOTA-peptide

dx.doi.org/10.1021/bc200608e | Bioconjugate Chem. 2012, 23, 538−547

complexes were consistently lower than those obtained by mixing the NOTA-peptide with Al^{3+} and then heating with $^{18}F^-$ in saline. All of these advances led to the current effort to develop a simple one-step kit that would provide a useful platform for commercial development. Indeed, the AlF technology perfectly lends itself to a simple kit.

In addition to exploring suitable $Al^{18}F$-binding ligands, another one of the early hurdles in this work was the source of $^{18}F^-$. Unfortunately, there is no single consistent source and specification for $^{18}F^-$, and in our early studies, we found $^{18}F^-$ contained variable amounts of metals and even other trace radionuclides, making it necessary to purify $^{18}F^-$ before use.[36] However, $^{18}F^-$ in saline used for bone imaging gave more consistent labeling results. Starting with an already approved radiopharmaceutical is an important first step toward the development of a commercial kit.

On the basis of our prior experience in developing a simple lyophilized kit for ^{99m}Tc-labeling of an antibody Fab' fragment,[34] we knew the most important aspect of developing a kit was the formulation buffer. Working with our prototype peptide, IMP485, that is being used for pretargeted imaging studies, we examined a number of issues related to consistent labeling and proper lyophilization. Important to the lyophilization process was the use of a suitable bulking agent. While a few candidates appeared to be suitable, we elected to use α,α-trehalose since it yielded an acceptable cake upon lyophilization without affecting labeling yields at varying concentrations. Another issue was the buffer composition. Here again, several buffers were examined, but we selected KHP because it gave the best yields in the absence of ascorbate. This result suggests it might have a role as a transfer ligand, albeit the possibility for this would need further investigation. We examined a range of KHP concentrations, finding ~1 μmol to give better pH stabilization without reducing yields. It should be noted that while there has been some concern over phthalate esters used in plastics, the material safety data sheet for KHP indicates a LD_{50} > 3200 mg/kg when administered orally to rats. Although KHP performed well in the absence of ascorbate, we included ascorbate in the formulation buffer as a radioprotectant to minimize the chance for radiolytic processes that might occur during the labeling procedure, even if the kit were used with high amounts of ^{18}F (e.g., 10.8 GBq was used herein) at high temperatures. Finally, we reaffirmed previous studies performed in solution labeling that verified the optimal pH range for IMP485 and that the formulation buffer would maintain this pH after lyophilization, as well as affirming improvements in labeling yields with the addition of 1:1 EtOH/saline.

Using kits prepared with the optimal formulation buffer, additional studies were conducted to assess the necessary temperature and timing for the labeling procedure, and how the concentration of the peptide would affect labeling yields. These studies showed that labeling yields improved as the temperature increased, with maximum yields peaking at ≥90 °C. Heating for 15 min provided high yields, with longer times possibly enhancing the yields slightly, but not sufficiently enough to warrant the loss in isotopic decay that would otherwise occur.

Naturally, the concentration of the peptide also affected yields. For example, in our initial testing of formulation conditions, we simply added $^{18}F^-$ in 200 μL of saline without EtOH, even though our prior experience in solution labeling with IMP485 showed higher yields.[26] Nevertheless, with kits containing 40 nmol of IMP485 (hence IMP485 concentration was 200 μM), yields between 75 and 85% were common with ~37 MBq of ^{18}F. However, to increase the specific activity, the amount of IMP485 in the kit was reduced to 20 nmol, where in the absence of EtOH, yields of only 50% were achieved, but with 1:1 EtOH, yields improved to ~80−85%, even though the peptide's molar concentration is reduced. Thus, the specific activity of a 40-nmol kit using 37 MBq of ^{18}F in only saline (0.2 mL) would be ~0.74 MBq/μmol, a 20-nmol kit under the same conditions even with reduced yields would increase to ~0.925 MBq/μmol, but the specific activity of a 20-nmol kit labeled with 37 MBq in saline (0.2 mL) and EtOH (0.2 mL) would be ~1.48 MBq/μmol. Currently, the minimum volume of the $^{18}F^-$ in saline from our commercial source is 0.2 mL, but if reaction volumes could be decreased, the amount of peptide in the kit could also be decreased, and the specific activity would likely increase. It is important to note that higher levels of $^{18}F^-$ activity can be delivered in 0.2 mL, and thus the specific activity can be improved. A specific activity of 223 GBq/μmol (6015 Ci/mmol) was achieved with a 20-nmol kit, and while the yields decreased to ~45%, it is likely that even higher specific activities could be achieved if more $^{18}F^-$ activity were added. For high-dose labeling, further kit optimization may improve the yields. However, depending on the desired specific activity, one could even achieve near quantitative yields with higher amounts of the peptide.

In this instance, the specific activity of $Al^{18}F$-IMP485 used in the pretargeting study was 20.4 GBq/μmol (550 Ci/mmol), which was sufficient to obtain excellent tumor targeting in our pretargeting model. In general, 37 GBq/μmol (1000 Ci/mmol) is considered suitable for most receptor targeting agents. We have shown that we can obtain a specific activity as high as 223 GBq/μmol, which would allow over three half-lives (~6 h) to deliver the $Al^{18}F$-IMP485 for injection into the patient and still have a usable specific activity. In the method described here, we do not separate IMP485 and the unlabeled Al-IMP485 (IMP486) from the $Al^{18}F$-IMP485. This is analogous to the many Tc-99m or In-111 kits available where only a portion of the targeting agent actually contains the radioisotope but the specific activity is still high enough to achieve targeting. In many cases, HPLC purification can be used to separate the unreacted peptide and the Al-peptide from the $Al^{18}F$-peptide if desired. We have developed HPLC purification methods for both $Al^{18}F$-IMP485[26] and $Al^{18}F$-IMP466.[27,28] We believe that HPLC purification will not be necessary as long as the specific activity of the labeled peptide relative to the sum of the unlabeled targeting components is greater than 37 GBq/μmol.

Because the number of receptor sites is usually limited, most often it is desirable to have a high specific activity peptide to avoid blocking target receptors with the excess unlabeled peptide. While the minimal specific activity required for receptor targeting will likely depend on the target, in some cases excess peptide is present during the labeling procedure to improve yields, and then very often, the final labeled peptide is isolated from the unlabeled peptide by HPLC. At least in one case, a radiolabeled peptide was generated with a high specific activity and an excellent yield (79%) without the need for HPLC purification.[37] With the AlF procedure, a SPE-purification is all that is necessary to remove unbound ^{18}F. We previously used HLB purification, which first binds the peptide to the resin in the cartridge, and after washing to remove unbound materials, the desired product is eluted in 50% EtOH. Shetty et al.[32] recently reported excellent separation of unbound ^{18}F from the $(Al^{18}F)^{2+}$-complex using an Alumina N cartridge. We confirmed that with this

procedure, the unwanted products are bound to the Alumina N resin, and thus the purification is simplified to a single step, further reducing the overall labeling/purification time.

These studies confirmed the excellent labeling yields with the new NODA-MPAA ligand over the NOTA derivatives we had described previously.[26] While adding the NODA-MPAA ligand to a receptor-targeting peptide could alter the affinity of the peptide for the receptor, it is usually possible to modify the receptor-targeting peptide to compensate for the effect of an added metal-binding ligand. In order to assess the robustness of our formulation conditions, we examined a second peptide, IMP466. This somatostatin-binding peptide was prepared with the simple NOTA ligand, and even though we suspected labeling yields would be lower than that found with the NODA-MPAA ligand, our goal was simply to show the value of formulating chelate-conjugated peptides in a lyophilized kit form. With just a minor adjustment to the final pH, the IMP466 kits were shown to label reproducibly and with just a simple filtration step for purification. High specific activity (60 GBq/μmol) Al^{18}F-NOTA-IMP466 could be obtained in about 20 min, including the labeling and purification steps. Indeed, no HPLC-purification was required to obtain the high specific activity peptide. Our previous work showed that the tumor targeting and biodistribution of the Al^{18}F complex was similar to the ^{68}Ga complex with the same NOTA-octreotide analogue.[27]

Many ^{18}F-labeling processes are being adapted for use by remotely operated automated machines, which reduce radiation exposure to workers and are highly amenable for developing a reproducible, GMP process. The introduction of a preformulated AlF kit will serve only to further improve the simplicity and reproducibility of preparing fluorinated peptides. We have experienced that the AlF-labeling method is reliable, giving similar labeling yields from day to day, and after over 100-kit labels, we have not encountered a single failure. The formulation of peptides into kits can remove uncertainties of obtaining a successful labeled product, and because of its simplicity, additional studies can be easily performed in a single day. For example, for the studies reported in Figure 2, 25 kits were labeled and purified in about 4 h. Given the successes that are starting to be reported in the literature from others who have evaluated the AlF procedure,[29−32] we believe many other peptides can be formulated and labeled in a similar way and without the need for expensive equipment. We note that some of these early reports by others have not utilized some of the enhancements that we have developed, and thus, their yields have been lower. However, in all these reports, the labeled products were prepared simply, quickly and often at higher specific activity than with other methods. Undoubtedly, some peptides will be challenged by the insertion of a metal-binding ligand in their structure, but often the peptide's structure can be modified without seriously affecting its receptor binding. For those peptides or other compounds that might be affected by the high temperatures required for (Al^{18}F)$^{2+}$ insertion in the ligand, we recently presented an alternative 2-step procedure that allows for rapid fluorination of an antibody Fab′ fragment.[38] Thus, we are confident that the AlF procedure can be adapted for use with many different agents and thus expand the introduction of more ^{18}F-labeled compounds for molecular imaging.

CONCLUSIONS

The NODA-MPAA-containing peptide, IMP485, can be formulated conveniently into a lyophilized kit and radiolabeled with ^{18}F$^-$ in saline in high yield and specific activity, using only an inexpensive, disposable, Alumina N or a reverse-phase SPE cartridge (HLB) for purification. Importantly, the ligand used in IMP485 forms a single complex with (Al^{18}F)$^{2+}$. The Al^{18}F-IMP485 peptide is stable *in vivo* and *in vitro* and has excellent tumor targeting in a pretargeting human colorectal cancer xenograft model. The same ligand and kit formulation can be applied to receptor-targeting peptides, such as somatostatin, which can tolerate heating to 100 °C. We believe that the development of these single-vial freeze-dried kits, which can be radiolabeled with a high degree of reproducibility, simplifies the ^{18}F-labeling methodology, thereby making it amenable for use in a clinical setting.

ASSOCIATED CONTENT

Supporting Information

Description of HPLC methods and HPLC chromatograms. This material is available free of charge via the Internet at http://pubs.acs.org.

AUTHOR INFORMATION

Corresponding Author

*(W.J.M.) Immunomedics, Inc., 300 The American Road, Morris Plains, NJ 07950. Tel: 973-605-8200 ext. 233. Fax: 973-605-1340. E-mail: bmcbride@immunomedics.com. (D.M.G.) Center for Molecular Medicine and Immunology, 300 The American Road, Morris Plains, NJ 07950. E-mail: dmg.gscancer@att.net.

Notes

W.J.M., C.A.D., and D.M.G. are employed or have financial interest in Immunomedics, Inc., or IBC Pharmaceuticals, Inc. R.M.S. and H.K. have no financial interests to declare.

ACKNOWLEDGMENTS

We thank Lenka Muskova and Jayson Jebsen for their technical assistance. This project was supported in part by the National Center for Research Resources and the National Institute of Biomedical Imaging and Bioengineering of the National Institutes of Health through Grant Number 5R44RR028018-03 to W.J.M.

REFERENCES

(1) Miller, P. W., Long, N. J., Vilar, R., and Gee, A. D. (2008) Synthesis of ^{11}C, ^{18}F, ^{15}O, and ^{13}N radiolabels for positron emission tomography. *Angew. Chem., Int. Ed. 47*, 8998−9033.

(2) Olberg, D. E., and Hjelstuen, O. K. (2010) Labeling strategies of peptides with ^{18}F for positron emission tomography. *Curr. Top. Med. Chem. 10*, 1669−1679.

(3) Cai, L., Lu, S., and Pike, V. W. (2008) Chemistry with [^{18}F]fluoride ion. *Eur. J. Org. Chem.*, 2853−2873.

(4) Mamat, C., Ramenda, T., and Weust, F. R. (2009) Recent applications of click chemistry for the synthesis of radiotracers for molecular imaging. *Mini-Rev. Org. Chem. 6*, 21−34.

(5) Schirrmacher, E., Wängler, B., Cypryk, M., Bradtmöller, G., Schäfer, M., Eisenhut, M., Jurkschat, K., and Schirrmacher, R. (2007) Synthesis of *p*-(di-*tert*-butyl[^{18}F]fluorosilyl)benzaldehyde ([^{18}F] SiFA-A) with high specific activity by isotopic exchange: a convenient labeling synthon for the ^{18}F-labeling of N-amino-oxy derivatized peptides. *Bioconjugate Chem. 18*, 2085−2089.

(6) Wängler, C., Waser, B., Alke, A., Iovkova, L., Buchholz, H.-G., Niedermoser, S., Jurkschat, K., Fottner, C., Schirrmacher, R., Reubi, J.-C., Wester, H.-J., and Wängler, B. (2010) One-step ^{18}F labeling of carbohydrate-conjugated octreotate-derivatives containing a silicon-fluoride-acceptor (SiFA): in vitro and in vivo evaluation as tumor imaging agents for positron emission tomography (PET). *Bioconjugate Chem. 21*, 2289−2296.

(7) Wängler, B., Quandt, G., Iovkova, L., Schirrmacher, E., Wängler, C., Boening, G., Hacker, M., Schmoeckel, M., Jurkschat, K., Bartenstein, P., and Schirrmacher, R. (2009) Kit-like ^{18}F-labeling of proteins: synthesis of 4-(Di-*tert*-butyl[^{18}F]fluorosilyl)benzenethiol (Si[^{18}F]FA-SH) labeled rat serum albumin for blood pool imaging with PET. *Bioconjugate Chem. 20*, 317−321.

(8) Iovkova, L., Wängler, B., Schirrmacher, E., Schirrmacher, R., Quandt, G., Boening, G., Schürmann, M., and Jurkschat, K. (2009) *Para*-Functionalized aryl-di-*tert*-butylfluorosilanes as potential labeling synthons for ^{18}F radiopharmaceuticals. *Chem.—Eur. J. 15*, 2140−2147.

(9) Ting, R., Harwig, C., Keller, U. A. D., McCormick, S., Austin, P., Overall, C. M., Adam, M. J., Ruth, T. J., and Perrin, D. M. (2008) Toward [^{18}F]-labeled aryltrifluoroborate radiotracers: in vivo positron emission tomography imaging of stable aryltrifluoroborate clearance in mice. *J. Am. Chem. Soc. 130*, 12045−12055.

(10) Honer, M., Mu, L., Stellfeld, T., Graham, K., Martic, M., Fischer, C. R., Lehmann, L., Schubiger, P. A., Ametamey, S. M., Dinkelborg, L., Srinivasan, A., and Borkowski, S. (2011) ^{18}F-labeled bombesin analog for specific and effective targeting of prostate tumors expressing gastrin-releasing peptide receptors. *J. Nucl. Med. 52*, 270−278.

(11) Becaud, J., Mu, L., Schubiger, P. A., Ametamey, S. M., Graham, K., Stellfeld, T., Lehmann, L., Borkowski, S., Berndorf, D., Dinkelborg, L., Srinivasan, A., Smits, R., and Koksch, B. (2009) Direct one-step ^{18}F-Labeling of peptides via nucleophilic aromatic substitution. *Bioconjugate Chem. 20*, 2254−2261.

(12) Meares, C. F., and Wensel, T. G. (1984) Metal chelates as probes of biological systems. *Acc. Chem. Res. 17*, 202−209.

(13) Scheinberg, D. A., Strand, M., and Gansow, O. A. (1982) Tumor imaging with radioactive metal chelates conjugated to monoclonal antibodies. *Science 215*, 1511−1513.

(14) Fani, M., Pozzo, L. D., Abiraj, K., Mansi, R., Tamma, M. L., Cescato, R., Waser, B., Weber, W. A., Reubi, J. C., and Maecke, H. R. (2011) PET of receptor-positive tumors using ^{64}Cu- and ^{68}Ga-somatostatin antagonists: the chelate makes the difference. *J. Nucl. Med. 52*, 1110−1118.

(15) Tewson, T. J. (1989) Procedures, pitfalls and solutions in the production of [^{18}F]2-deoxy-2-fluoro-D-glucose: a paradigm in the routine synthesis of fluorine-18 radiopharmaceuticals. *Nucl. Med. Biol. 16*, 533−551.

(16) Martin, R. B. (1996) Ternary complexes of Al^{3+} and F^- with a third ligand. *Coord. Chem. Rev. 141*, 23−32.

(17) McBride, W. J., Sharkey, R. M., Karacay, H., D'Souza, C. A., Rossi, E. A., Laverman, P., Chang, C.-H., Boerman, O. C., and Goldenberg, D. M. (2009) A novel method of ^{18}F radiolabeling for PET. *J. Nucl. Med. 50*, 991−998.

(18) Gold, D. V., Goldenberg, D. M., Karacay, H., Rossi, E. A., Chang, C.-H., Cardillo, T. M., McBride, W. J., and Sharkey, R. M. (2008) A novel bispecific, trivalent antibody construct for targeting pancreatic carcinoma. *Cancer Res. 68*, 4819−4826.

(19) Sharkey, R. M., Cardillo, T. M., Rossi, E. A., Chang, C.-H., Karacay, H., McBride, W. J., Hansen, H. J., Horak, I. D., and Goldenberg, D. M. (2005) Signal amplification in molecular imaging by pretargeting a multivalent, bispecific antibody. *Nature Med. 11*, 1250−1255.

(20) McBride, W. J., Zanzonico, P., Sharkey, R. M., Norén, C., Karacay, H., Rossi, E. A., Losman, M. J., Brard, P. -Y., Chang, C.-H., Larson, S. M., and Goldenberg, D. M. (2006) Bispecific antibody pretargeting PET (immunoPET) with an ^{124}I-labeled hapten-peptide. *J. Nucl. Med. 47*, 1678−1688.

(21) Sharkey, R. M., Karacay, H., Vallabhajosula, S., McBride, W. J., Rossi, E. A., Chang, C.-H., Goldsmith, S. J., and Goldenberg, D. M. (2008) Metastatic human colonic carcinoma: molecular imaging with pretargeted SPECT and PET in a mouse model. *Radiology 246*, 497−507.

(22) Schoffelen, R., Sharkey, R. M., Goldenberg, D. M., Franssen, G., McBride, W. J., Rossi, E. A., Chang, C.-H., Laverman, P., Disselhorst, J. A., Eek, A., van der Graaf, W. T. A., Oyen, W. J. G., and Boerman, O. C. (2010) Pretargeted immunoPET imaging of CEA-expressing tumors with a bispecific antibody and a ^{68}Ga and ^{18}F-labeled hapten-peptide in mice with human tumor xenografts. *Mol. Cancer Ther. 9*, 1019−1027.

(23) Rossi, E. A., Goldenberg, D. M., Cardillo, T. M., McBride, W. J., Sharkey, R. M., and Chang, C.-H. (2006) Stably tethered multifunctional structures of defined composition made by the dock and lock method for use in cancer targeting. *Proc. Natl. Acad. Sci. U.S.A. 103*, 6841−6846.

(24) McBride, W. J., D'Souza, C. A., Sharkey, R. M., Sharkey, R. M., Karacay, H., Rossi, E. A., Chang, C.-H., and Goldenberg, D. M. (2010) Improved ^{18}F labeling of peptides with a fluoride-aluminum-chelate complex. *Bioconjugate Chem. 21*, 1331−1340.

(25) Chong, H.-S., Garmestani, K., Ma, D., Milenic, D. E., Overstreet, T., and Brechbiel, M. W. (2002) Synthesis and biological evaluation of novel macrocyclic ligands with pendent donor groups as potential yttrium chelators for radioimmunotherapy with improved complex formation kinetics. *J. Med. Chem. 45*, 3458−3464.

(26) D'Souza, C., McBride, W. J., Sharkey, R. M., Todaro, L., and Goldenberg, D. M. (2011) High-yielding aqueous ^{18}F-labeling of peptides via Al^{18}F chelation. *Bioconjugate Chem. 22*, 1793−1803.

(27) Laverman, P., McBride, W. J., Sharkey, R. M., Eek, A., Joosten, L., Oyen, W. J. G., Goldenberg, D. M., and Boerman, O. C. (2010) A novel facile method of labeling octreotide with ^{18}F-fluorine. *J. Nucl. Med. 51*, 454−461.

(28) Laverman, P., D'Souza, C. A., Eek, A., McBride, W. J., Sharkey, R. M., Oyen, W. J. G., Goldenberg, D. M., and Boerman, O. C. (2011) Optimized labeling of NOTA-conjugated octreotide with F-18. *Tumor Biol.*, DOI: 10.1007/s13277-011-0250-x.

(29) Leyton, J., Iddon, L., Perumal, M., Indrevall, B., Glaser, M., Robins, E., George, A. J. T., Cuthbertson, A., Luthra, S. K., and Aboagye, E. O. (2011) Targeting somatostatin receptors: preclinical evaluation of novel ^{18}F-fluoroethyltriazole-tyr^3-octreotate analogs for PET. *J. Nucl. Med. 52*, 1441−1448.

(30) Liu, S., Liu, H., Jiang, H., Xu, Y., Zhang, H., and Cheng, Z. (2011) One-step radiosynthesis of ^{18}F-AlF-NOTA-RGD$_2$ for tumor angiogenisis PET imaging. *Eur. J. Nucl. Med. Mol. Imaging 38*, 1732−1741.

(31) Lang, L., Li, W, Guo, N., Ma, Y., Zhu, L., Kiesewetter, D., Shen, B., Niu, G., and Chen, X. (2011) Comparison study of [18F]FAl-NOTA-PRGD2 for PET imaging of U87MG tumors in mice. *Bioconjugate Chem 22*, 2415−2422.

(32) Shetty, D., Choi, S. Y., Jeong, J. M., Lee, J. Y., Hoigebazar, L., Lee, Y.-S., Lee, D. S., Chung, J.-K., Lee, M. C., and Chung, Y. K. (2011) Stable aluminum fluoride chelates with triazacyclononane derivatives proved by X-ray crystallography and ^{18}F-labeling study. *Chem. Commun. 47* (34), 9732−9734.

(33) Technical reports series no. 466. (2008) Technetium-99m Radiopharmaceuticals: Manufacture of Kits, International Atomic Energy Agency, Vienna, Austria.

(34) Griffiths, G. L., Goldenberg, D. M., Jones, A. L., and Hansen, H. J. (1992) Radiolabeling of monoclonal antibodies and fragments with technetium and rhenium. *Bioconjugate Chem. 3*, 91−99.

(35) Rossi, E. A., Goldenberg, D. M., Cardillo, T. M., McBride, W. J., Sharkey, R. M., and Chang, C.-H. (2006) Stably tethered multifunctional structures of defined composition made by the dock and lock method for use in cancer targeting. *Proc. Natl. Acad. Sci. U.S.A. 103*, 6841−6846.

(36) Ferguson, D., Orr, P., Gillanders, J., Corrigan, G., and Marshall, C. (2011) Measurement of long lived radioactive impurities retained in the disposable cassettes on the tracerlab MX system during the production of [^{18}F]FDG. *Appl. Radiat. Isot. 69*, 1479−1485.

(37) Marik, J., and Sutcliffe, J. L. (2006) Click for PET: rapid preparation of [^{18}F]fluoropeptides using Cu^{I} catalyzed 1,3-dipolar cycloaddition. *Tetrahedron Lett. 27*, 6681−6684.
(38) McBride, W. J., D'Souza, C. A., Sharkey, R. M., and Goldenberg, D. M. (2012) The radiolabeling of proteins by the [^{18}F]AlF method. *Appl. Radiat. Isot. 70*, 200−204.

Bioconjugate Chemistry

Article

pubs.acs.org/bc

Fibrin Specific Peptides Derived by Phage Display: Characterization of Peptides and Conjugates for Imaging

Andrew F. Kolodziej,[†] Shrikumar A. Nair,[†] Philip Graham,[†] Thomas J. McMurry,[†] Robert C. Ladner,[‡] Charles Wescott,[‡] Daniel J. Sexton,[‡] and Peter Caravan*[,§,∥]

[†]EPIX Pharmaceuticals, Inc., Cambridge, Massachusetts, United States

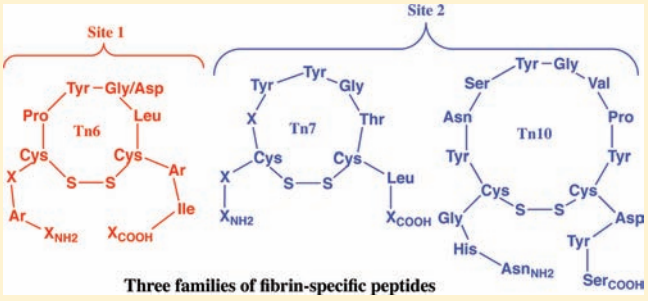
[‡]Dyax Corp., Cambridge, Massachusetts, United States

[§]Athinoula A. Martinos Center for Biomedical Imaging, Department of Radiology, Massachusetts General Hospital, Charlestown, Massachusetts, United States

[∥]Department of Radiology, Harvard Medical School, Boston, Massachusetts, United States

Supporting Information

ABSTRACT: Peptides that bind to fibrin but not to fibrinogen or serum albumin were selected from phage display libraries as targeting moieties for thrombus molecular imaging probes. Three classes of cyclic peptides (cyclized via disulfide bond between two Cys) were identified with consensus sequences XArXCPY(G/D)LCArIX (Ar = aromatic, Tn6), X_2CXYYGTCLX (Tn7), and NHGCYNSYGVPYCDYS (Tn10). These peptides bound to fibrin at ∼2 sites with K_d = 4.1 μM, 4.0 μM, and 8.7 μM, respectively, whereas binding to fibrinogen was at least 100-fold weaker. The peptides also bind to the fibrin degradation product DD(E) with similar affinity to that measured for fibrin. The Tn7 and Tn10 peptides bind to the same site on fibrin, while the Tn6 peptides bind to a unique site. Alanine scanning identified the N- and C-terminal ends of the Tn6 and Tn7 peptides as most tolerant to modification. Peptide conjugates with either fluorescein or diethylenetriaminepentaaceto gadolinium(III) (GdDTPA) at the N-terminus were prepared for potential imaging applications, and these retained fibrin binding affinity and specificity in plasma. Relaxivity and binding studies on the GdDTPA derivatives revealed that an N-terminal glycyl linker had a modest effect on fibrin affinity but resulted in lower fibrin-bound relaxivity.



Three families of fibrin-specific peptides

INTRODUCTION

Thrombotic diseases, including atherothrombosis and stroke, are the leading cause of death in the Western world, and consequently, there is considerable need for new diagnostic agents and therapies. Aberrant fibrin clot formation is associated with thrombotic disease and is initiated by the proteolysis of fibrinogen by thrombin and subsequent fibrin polymerization. Fibrin is well suited as a marker for diagnostic imaging and a depot for targeted therapy as it is inexorably linked to thrombosis and is abundant in thrombi (20−200 μM). Several groups have explored fibrin specific antibodies coupled to radionuclides, nanoparticles, or incorporated into echogenic liposomes as potential contrast agents for nuclear, optical or ultrasound imaging.[1] With respect to thrombolytic agents, antifibrin antibody conjugation has been investigated as a mechanism to enhance the specificity and reactivity of plasminogen activators.[2] Additionally, conjugation of the thrombin inhibitor hirudin[3] or the Factor Xa inhibitor tick anticoagulant peptide[4] to antifibrin antibodies has improved the specificity and efficacy of these inhibitors, suggesting that a fibrin targeting strategy may also yield more potent antithrombotic agents.

In addition to monoclonal antibodies and the protein tissue plasminogen activator (t-PA), fibrin targeting has also been achieved through small peptides. MR contrast agents were reported that contain fibrin-specific peptide(s) conjugated to multiple gadolinium complexes. Such agents, like EP-2104R, have demonstrated efficacy in thrombus detection in a number of preclinical models of thrombosis,[5−11] and recent data in human subjects has also proved promising.[12] However, there has been little reported on the fibrin specific peptides themselves: their identification, specificity, cross-reactivity for different fibrin binding sites, the effects of chelate conjugation, and sensitivity to amino acid substitution.

In this article, we describe the strategy used to identify fibrin binding peptides with high specificity for fibrin over fibrinogen and other serum proteins. Three families of peptides were identified, and the interaction of these peptides with fibrin, the soluble fibrin fragment DD(E), and fibrinogen is probed with four techniques: plate-based depletion assay, fluorescence

Received: November 14, 2011
Revised: January 2, 2012
Published: January 22, 2012

ACS Publications © 2012 American Chemical Society

Table 1. Peptides and Peptide Conjugates Discussed in This Work[a]

compd	sequence	K_d (N_{bd}) fibrin[b]	K_d (N_{bd}) DD(E)[c]	K_i DD(E)[d]
Tn6-1	WFHCPYDLCHIL	4.1 ± 0.4 (2.3 ± 0.1)	n.d.	3.1 ± 0.4
Tn6-2a	WECPYGLCWIQ	2.9 ± 0.2 (2.4 ± 0.4)	0.85 ± 0.03 (2.0 ± 0.1)	0.9 ± 0.2
Tn6-2b	QWECPYGLCWIQ	n.d.	n.d.	2.3 ± 0.5
Tn6-2b-Fl	Fluor-Aca-QWECPYGLCWIQ	n.d.	0.057 ± 0.006	n.d.
Tn6-1-Gd	GdDTPA-GG-WFHCPYDLCHIL	3.1 ± 0.3 (2.3 ± 0.1)	n.d.	2.2 ± 0.2
Tn7-3	LPCDYYGTCLD	4.0 ± 0.3 (2.1 ± 0.05)	2.2 ± 0.06 (1.9 ± 0.1)	2.8 ± 0.7
Tn7-3-Fl	Fluor-Aca-LPCDYYGTCLD	n.d.	1.3 ± 0.4	n.d.
Tn7-3a-Gd	GdDTPA-LPCDYYGTCLD	6.9 ± 0.8 (3.0 ± 0.1)	n.d.	2.9 ± 0.2
Tn7-3b-Gd	GdDTPA-GLPCDYYGTCLD	8.4 ± 0.5 (1.8 ± 0.1)	n.d.	3.9 ± 0.3
Tn10-4	Ac-NHGCYNSYGVPYCDYS	8.7 ± 1.5 (2.3 ± 0.1)	3.0 ± 0.1 (1.6 ± 0.1)	3.5 ± 0.3
Tn10-4-Fl	Fluor-AEGTGSNHGCYNSYGVPYCDYSAPG	n.d.	2.7 ± 0.6	n.d

[a]Equilibrium dissociation (K_d) and inhibition (K_i) constants are given in micromolar (μM). Values in parentheses represent the number of equivalent binding sites, N_{bd}, obtained from the fit to the data. [b]Direct binding to the fibrin coated plate. [c]Direct binding to DD(E) measured by fluorescence anisotropy for Tn6-2b-Fl, Tn7-3-Fl, and Tn10-4-Fl and by isothermal calorimetry for the other compounds. [d]Determined by inhibition of binding of the corresponding fluorescent probe, e.g., Tn6-1, inhibiting the binding of Tn6-2b-Fl.

Table 2. Structural Requirements for Tn6, Tn7, and Tn10 Peptides, As Determined by Alanine Scanning and DD(E) Binding[a]

Tn6-1	K_i (μM)	Tn6-2b	K_i (μM)	Tn7-3	K_i (μM)	Tn10-4	K_i (μM)
WFHCPYDLCHIL	3.1	QWECPYGLCWIQ	2.3	LPCDYYGTCLD	2.8	NHGCYNSYGVPYCDYS	3.5
AFHCPYDLCHIL	8.0	**A**WECPYGLCWIQ	--	**A**LCDYYGTCLD	3.1	NHGCYDSYGVPYCDYS	>100
W**A**HCPYDLCHIL	3.9	Q**A**ECPYGLCWIQ	4.3	L**A**CDYYGTCLD	2.9	NHGCYNYYGVPYCDYS	5.9
WF**A**CPYDLCHIL	3.3	QW**A**CPYGLCWIQ	6.2	LPC**A**YYGTCLD	5.9	NHGCYNYYGTPYCDYS	>500
WFHC**A**YDLCHIL	62	QWEC**A**YGLCWIQ	32	LPCD**A**YGTCLD	4.5	NHGCYDYYGTPYCDYS	>500
WFHCP**A**DLCHIL	16	QWECP**A**GLCWIQ	42	LPCDY**A**GTCLD	>100		
WFHCPY**A**LCHIL	16	QWECPY**A**LCWIQ	7.7	LPCDYY**A**TCLD	12		
WFHCPYD**A**CHIL	97	QWECPYG**A**CWIQ	93	LPCDYYG**A**CLD	>100		
WFHCPYDLC**A**IL	28	QWECPYGLC**A**IQ	4.3	LPCDYYGTC**A**D	15		
WFHCPYDLCH**A**L	19	QWECPYGLCW**A**Q	17	LPCDYYGTCL**A**	7.3		
WFHCPYDLCHI**A**	2.6	QWECPYGLCWI**A**	--	LPCDYYG**V**CLD	28		

[a]Binding of Tn7−Tn10 hybrid peptides are also presented. Data obtained by FP probe displacement assay using **Tn6-2b-Fl** (Tn6) and **Tn7-3-Fl** (Tn7 and Tn10). Standard errors were ≤10%.

polarization of fluorescent probes and competitive binding, isothermal calorimetry, and proton relaxation rate enhancement. The cross-reactivity of these peptides for specific fibrin binding sites is also examined. The critical residues required for binding are probed using alanine and other amino acid substitutions, providing data on the critical binding motif while pointing to conjugation strategies compatible with maintaining binding affinity. The effect of fluorescein or GdDTPA conjugation on protein binding, relaxivity, and specificity is also explored. While aspects of the *in vivo* efficacy of some of these peptides as conjugates to GdDTPA have been reported, the discovery, identity, and properties of these sequences have not been previously described in detail.

EXPERIMENTAL PROCEDURES

Protein Preparation. Human fibrinogen was purchased from American Diagnostica. Human citrated plasma was obtained from the American Red Cross and used without further processing. The soluble fibrin fragment DD(E) was prepared as previously described.[13] DD(E) used in this study contained subunits of 61 kD and 72 kD, assigned to fragments E_1 and E_2 and present in a roughly 1:1 ratio, and 180 kD (fragment DD).

Phage Display. Tn6, Tn7, and Tn10 libraries were constructed as gene III coat protein fusions by Dyax Corporation and are described elsewhere.[14] Phage selection was conducted through four rounds. Before each round, libraries were depleted of fibrinogen binders by incubating the phage with biotinylated fibrinogen bound to bead immobilized streptavidin. Fibrin binding phage were selected by contacting these nonbinding phages with either fibrin (polymerized in a microtiter plate well) or biotinylated DD(E), bound to bead immobilized streptavidin, and eluting the bound phage. Fibrin specific clones from round four were identified by phage ELISA assays as having high response against fibrin and DD(E), but low response against fibrinogen, and human serum albumin. Fibrin plates were prepared with fibrinogen (50 μL, 0.075 mg/mL) in 50 mM Tris, pH 7.4, 150 mM NaCl, and 5 mM sodium

citrate polymerized in the wells of a 96 well plate (Immulon-II) by the addition of $CaCl_2$ (7 mM) and thrombin (1 U/mL) and dried overnight at 37 °C).

Peptide Synthesis. Peptides were synthesized by standard Fmoc solid phase protocols using rink amide or NovasynTGR-amide resin from EMD Biosciences, and prepared as C-terminal amides. Masses of all compounds were verified by electrospray mass spectrometry, and purities were >90% as assessed by HPLC. All peptides were prepared as cyclic cysteine disulfides, except where noted. Compounds are denoted by the phage library from which they were derived followed by a number to denote the sequence and then "Fl" or "Gd" if derivatized with fluorescein or GdDTPA, e.g., Tn7-3-Fl denotes a peptide derived from the Tn7 library, sequence 3, and derivatized with fluorescein. Specific sequences are listed in Tables 1 and 2. Conjugate **Tn7-3b-Gd** was reported previously[15] and in that publication is referred to as EP-782.

Fibrin Binding. The fibrin binding assay has been described previously.[16] For peptide binding experiments, fibrin plates were prepared as for the phage display but at higher fibrin concentration (100 μL; 2.5 mg/mL). Peptide or conjugate (1−100 μM; 100 μL/well), dissolved in water, was incubated in duplicate fibrin plate wells for 2 h at 37 °C. Peptide concentrations of the peptide solution added to the wells, $[Peptide]_{total}$, and in the well supernatant at equilibrium, $[Peptide]_{free}$, were quantified by RP-HPLC (C4 column) interfaced to a mass spectrometer or fluorescence detector. Bound peptide concentration was calculated as the difference $[Peptide]_{total} - [Peptide]_{free}$. The dissociation constant, K_d, and number of binding sites, N_{bd}, were determined from a nonlinear least-squares fit of the data, N_{bd} vs $[Peptide]_{free}$, to a single class of sites binding model where N_{bd} is the number of molecules bound per mol fibrin (fbn), and [fbn] is the fibrin concentration (eq 1).

$$\frac{[\text{Peptide}]_{\text{bound}}}{[\text{fbn}]_{\text{total}}} = \frac{N_{bd} \times [\text{Peptide}]_{\text{free}}}{([\text{Peptide}]_{\text{free}} + K_d)} \quad (1)$$

Fluorescence Polarization. Peptide and peptide conjugate binding to DD(E) was measured by a fluorescence polarization (FP) assay. The anisotropy (r_{obs}) of the fluorescein labeled peptides (Fluor·pep) binding to DD(E) (0−20 μM) or fibrinogen (0−40 μM) was measured in TBS·Ca at fixed **Tn6-2b-Fl** (0.05 μM), **Tn7-3-Fl** (0.1 μM), or **Tn10-4-Fl** (0.1 μM) concentrations, and the data were fit to a single site model[17] to obtain the dissociation constant for the DD-(E)·(fluorescent peptide, "Fl") complex, K_d, and reference values for r_{bd}, the anisotropy of "Fl" when fully bound to DD(E), and r_{fr}, the anisotropy in solution.

$$r_{obs} = r_{fr} + \frac{r_{bd} - r_{fr}}{[Fl]_T} \times \frac{([DD(E)]_t + [Fl]_t + K_d) - \sqrt{([DD(E)]_t + [Fl]_t + K_d)^2 - 4[Fl]_t[DD(E)]_t}}{2} \quad (2)$$

Nonfluorescent peptide binding to DD(E) was measured by fluorescent peptide displacement. Tn6 binding: DD(E) (150 nM), **Tn6-2b-Fl** (50 nM) and peptide (0.1−40 μM) were mixed in TBS·Ca containing 0.01% Triton X100. Tn7 binding: DD(E) (1.5 μM) and **Tn7-3-Fl** (1 μM) and competing peptide (0.1−50 μM) were mixed in TBS·Ca. Sample r_{obs} (100 μL, n = 3 wells) was measured in a 96-well microplate (Costar Cat. No. 3915), using a Tecan Polarian 96-well FP microplate reader (ex = 485 nm; em = 535 nm). In the presence of an inhibitor, an apparent dissociation constant for the fluorescent probe, K_d^{app}, is determined, eq 3. The inhibition constant, K_i, is related to K_d^{app} by eq 4 where K_d is the true dissociation constant of the fluorescent probe measured in the absence of inhibitor. K_i values were obtained by least-squares fitting of the data as described elsewhere.[18]

$$r_{obs} = r_{fr} + \frac{r_{bd} - r_{fr}}{[Fl]_T} \times \frac{([DD(E)]_t + [Fl]_t + K_d^{app}) - \sqrt{([DD(E)]_t + [Fl]_t + K_d^{app})^2 - 4[Fl]_t[DD(E)]_t}}{2} \quad (3)$$

$$K_d^{app} = K_d\left(1 + \frac{[\text{Inhibitor}]_{\text{free}}}{K_i}\right) \quad (4)$$

Isothermal Calorimetry. Peptide binding to fibrinogen or DD(E) was measured by isothermal calorimetry (ITC) carried out at MicroCal, LLC Northampton, MA. Heat changes were measured for titration of peptides **Tn6-2a** (721 μM), **Tn7-3** (1.097 mM), or **Tn10-4** (551 μM) into DD(E) (16 μM in TBS·Ca) or fibrinogen (18 μM in TBS containing 10 mM citrate). Integrated heats of binding data determined from the DD(E) titrations were fit to a single class of sites, non-cooperative binding model.[19]

Relaxation Rate Measurements. Solvent water ^1H relaxation rates ($1/T_1$) were measured using a Bruker NMS 120 minispec operating at 0.47 T and 37 °C. Solutions (200 μL) containing 0−250 μM GdDTPA or **Tn7-3a-Gd** were prepared in pH 7.4 TBS with or without 30 μM fibrinogen. The fibrinogen solutions were converted to fibrin gels by the addition of by addition of 4 μL of 2 M $CaCl_2$ and 2 μL of 100 U/mL thrombin solution, followed by rapid mixing and then equilibration for at least 30 min. Relaxivity of the fibrin-bound complex, r_1^{bd}, and the unbound complex, r_1^{free}, were determined by a nonlinear least-squares fit of eqs 5 and 6 where f^{bd} and f^{free} are the mol fraction of the bound and unbound species, respectively, and $1/T_1^0$ is the relaxation rate in the absence of Gd. In the absence of fibrin, $f^{bd} = 0$, and r_1^{free} is determined from a linear fit of $1/T_1$ vs [Gd].

$$\frac{1}{T_1} = \frac{1}{T_1^0} + (f^{\text{free}} r_1^{\text{free}} + f^{bd} r_1^{bd}) \times [Gd]; \quad f^{\text{free}} + f^{bd} = 1 \quad (5)$$

$$f^{bd} = \frac{([Gd] + N_{bd}[fbn] + K_d) - \sqrt{([Gd] + N_{bd}[fbn] + K_d)^2 - 4[Gd]N_{bd}[fbn]}}{2[Gd]} \quad (6)$$

RESULTS

Phage Display. Our strategy for isolating fibrin specific peptides by phage display relied upon three key elements: alternative target presentations, negative selection to remove fibrinogen binders, and selection from multiple phage libraries. The target fibrin was presented in two different forms, as polymerized, gelled fibrin and as the plasmin degradation product DD(E). DD(E) is a useful soluble model of the insoluble fibrin polymer and has been shown to retain many epitopes unique to fibrin, including the D-D and D-E domain interfaces, factor XIIIa cross-links on the γ-chain, and a fibrin specific t-PA binding site.[20] Fibrin was presented as a thin dried film, a format that minimized nonspecific phage retention, while maintaining fibril structures similar to those of wet clots.[21] The fibrin clots were stable to the phage selection procedures with negligible loss of protein from the plate upon repeated washing, and bound fibronectin (IC_{50} = 4.9 ± 1.9 nM, ELISA data not shown) with affinity similar to previously reported values.[22] The high degree of structural similarity between fibrin and fibrinogen necessitated a negative screen to remove the fibrinogen-binding phage, which was repeated before each round of panning to promote removal of fibrinogen binders potentially carried over and amplified from the previous round.

Fibrin specific phage were obtained from three phage libraries, all containing cysteine disulfide cross-linked sequences: $X_3CX_4CX_3$ (Tn6 library), $X_3CX_5CX_3$ (Tn7), and $X_3CX_8CX_3$ (Tn10) where X was variagated. These selectants were identified after four rounds of selection by phage ELISA, as yielding high responses on the immobilized DD(E) and fibrin but low background signals with immobilized fibrinogen and HSA. Sequencing of these clones (>20/library) yielded a single consensus sequence for each library. The two unique sequences obtained from the Tn6 library, QWECPYGLCWIQ and WFHCPYDLCHIL, together conformed to a XArXCPY-(G/D)LCArIX (Ar = aromatic) consensus. The 10 unique Tn7 sequences aligned with a X_2CXYYGTCLX sequence where the YYGT sequence was strictly conserved along with a preference for polar amino acids (H, D, S, and N) at the lone variable position within the disulfide loop. A single sequence was obtained from the Tn10 selection, NHGCYNSYGVPYCDYS, which contained a 'SYGV' motif that appeared to be functionally homologous to the 'YYGT' motif of the Tn7 sequence. Sequences for the Tn6, Tn7 and Tn10 peptides were compared against the protein sequence database, but no proteins having a functional role related to fibrin(ogen) recognition or hemostasis were found. The Tn7 consensus sequence YYGT is similar to a surface exposed loop on the fibrin(ogen) gamma chain YYQGGT, γ(348−353), and to the sequence SYGT, α(257−261), but no functional role has been ascribed to these sequences.

Analysis of Peptide Binding to Fibrin, DD(E), and Fibrinogen. *Fibrin Binding Measurements.* Peptides corresponding to representative selected sequences from the Tn6, Tn7, and Tn10 libraries were synthesized, and binding to fibrin films was measured in a microtiter plate equilibrium binding assay. This method allowed for rapid diffusion of the peptide into the fibrin gel, and equilibrium was reached within 45 min, as assessed by time courses of peptide uptake into fibrin. Peptides derived from the two Tn6 sequences, **Tn6−1** and **Tn6-2a** (truncation of the N-terminal glutamine from the phage derived sequence **Tn6-2b** increased affinity 2-fold and improved peptide solubility), bound to fibrin with similar affinities (Table 1 and Figure 1) . A representative Tn7 peptide, **Tn7-3**, and the Tn10 peptide **Tn10-4** also bound with affinities in the low micromolar range (Table 1). Notably, all peptides bound to approximately two binding sites per fibrin monomer, consistent with the dimeric structure of this protein. Peptide affinities, however, were considerably lower than expected based on phage ELISA where very tight binding was observed. This affinity difference was probably due to avidity effects arising from polyvalent peptide display (up to five peptides per phage), although some additional affinity due to the native phage protein cannot be ruled out. No fibrin binding was observed for a modified Tn7 peptide (sequence LPCDYY-GACLD), where the single threonine residue was replaced with alanine. This observation highlighted the importance of this consensus residue in fibrin binding and also indicated that binding measurements were not complicated by peptide entrapment.

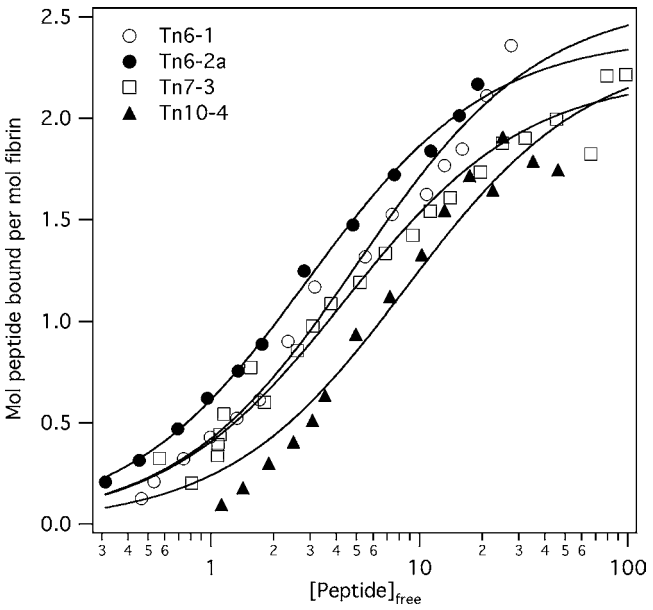


Figure 1. Fibrin binding data for the **Tn6-1**, **Tn6-2a**, **Tn7-3**, and **Tn10-4** peptides, and fits to single class-of-sites binding model demonstrating low micromolar affinity and binding to two sites on fibrin. Standard errors for individual points were <15% of the ordinate value.

Fluorescence Polarization. Selectivity and affinity of the Tn6, Tn7, and Tn10 peptides to DD(E) and fibrinogen was measured by a fluorescence polarization assay using N-terminal fluorescein conjugates of these peptides. Affinity of the fluorescein derivatives of the Tn7 and Tn10 peptides to

DD(E) was low micromolar, similar to that of the parent peptides to fibrin or DD(E) (Table 1 and Figure 2). However,

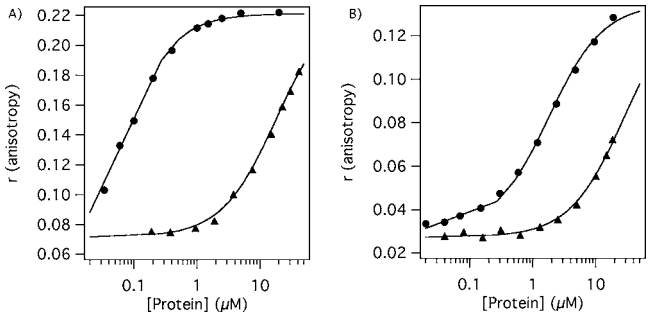


Figure 2. Binding of fluorescein labeled peptides **Tn6-2b-Fl** (0.050 μM, panel A) and **Tn7-3-Fl** (0.100 μM, panel B) to DD(E) (●) and to fibrinogen (▲) demonstrating high selectivity for DD(E) over fibrinogen.

affinity of **Tn6-2b-Fl** for DD(E) was higher with K_d = 0.057 μM (Figure 2). Binding was saturable for all 3 fluorescent probes.

Binding of unlabeled Tn6 and Tn7 peptides to DD(E) was measured by a competition assay (Figure 3) and compared to

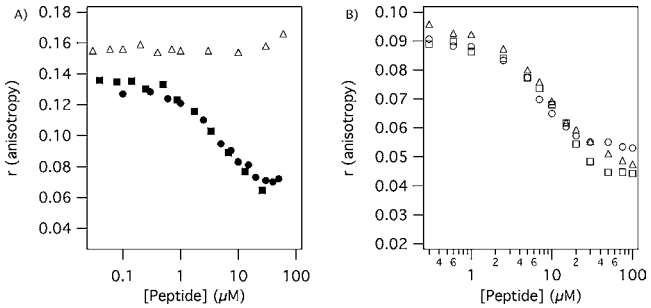


Figure 3. DD(E) (1.5 μM) binding measured by the displacement of fluorescent probes. (A) **Tn6-2b-Fl** (0.050 μM) is displaced by Tn6 compounds **Tn6-1** (●) and **Tn6-1-Gd** (■) but not by Tn10 peptide **Tn10-4** (△). (B) **Tn7-3-Fl** (1.0 μM) is displaced by Tn7 compounds **Tn7-3** (○) and **Tn7-3b-Gd** (□) and by the Tn10 peptide **Tn10-4** (△) indicating that the Tn7 and Tn10 binding site is the same.

the fluorescein labeled analogues. **Tn7-3** displaced **Tn7-3-Fl** with K_i = 2.8 μM, an affinity similar to the fluorescein labeled probe. However, **Tn6-2a** displaced **Tn6-2b-Fl** with K_i = 0.9 μM, a 16-fold reduction in binding affinity compared to the fluorescent probe, indicating that the aromatic fluorescein moiety enhanced the affinity of this peptide (Figure 3). Likewise, **Tn6-1**, the other Tn6 sequence type, displaced **Tn6-2b-Fl** with K_i = 3.1 μM. The DD(E) competition assay also established that the Tn6 and Tn7 peptides bind to separate sites on DD(E), since **Tn6-1** and **Tn6-2a** failed to reduce **Tn7-3-Fl** anisotropy, nor did the Tn7 peptide **Tn7-3** displace **Tn6-2b-Fl**. However, **Tn10-4** did displace **Tn7-3-Fl** (K_i = 3.5 ± 0.3 μM) with affinity similar to that of **Tn7-3** indicating that peptide **Tn10-4** also binds to the Tn7 site. The Tn10 peptide could not displace the Tn6 probe at concentrations up to 100 μM.

Despite some functional sequence homology, in that the DYYGT sequence in Tn7 has similarity to the NSYGV sequence in Tn10, the DYYGT sequence cannot functionally substitute for the associated residues in the Tn10 sequence. Four hybrid peptides of the Tn10 peptide were prepared, focusing on the N^6, S^7, and V^{10} positions. Replacement of S^7 with tyrosine had little effect, while substitution of N^6 with aspartate, V^{10} with threonine, or all three residues together sharply reduced binding (Table 2). Conversely, replacement of T^8 in **Tn7-3** with its β-branched analogue valine reduced binding to DD(E) 10-fold. Despite binding to the same site, the residue preference and orientation is exquisitely sensitive to constraints of the disulfide architecture.

The fluorescein labeled peptides exhibited strong selectivity for DD(E) over fibrinogen when anisotropy changes were examined. The data for **Tn6-2b-Fl** (Figure 2a) fit to a K_d = 22 μM, 400-fold weaker than to DD(E). The fibrinogen affinity of the unlabeled peptide was much weaker since the fluorescein moiety enhanced fibrinogen binding, as observed with DD(E). The Tn6 data were shifted only slightly in the presence of a 100-fold excess of the unlabeled **Tn6-1**; see Supporting Information. When binding of **Tn6-1** (0−50 μM) to fibrinogen was assessed at a fixed concentration of fibrinogen (7 μM) and **Tn6-2b-Fl** (0.1 μM), displacement was partial and did not change for **Tn6-1** concentrations >20 μM. Overall, the data indicated that **Tn6-1** competed poorly with **Tn6-2b-Fl**, and a K_d > 200 μM was estimated. For **Tn7-3-Fl**, the anisotropy increased in the presence of fibrinogen, but the change was small and nearly linear with increasing fibrinogen concentration, suggesting that the anisotropy effects were due largely to increasing viscosity at high fibrinogen concentrations (Figure 2b). Consistent with a nonspecific effect, the anisotropy increase was not reversed by competition, as anisotropy data obtained in the presence of a 100-fold (100 μM) excess of unlabeled Tn7 peptide (**Tn7-3**) were nearly identical; see Supporting Information. In summary, both the Tn6 and Tn7 sequences have a ∼100-fold selectivity for DD(E) over fibrinogen, as measured by this method.

Isothermal Calorimetry. Isothermal calorimetry (ITC) data for binding of the Tn6, Tn7, and Tn10 peptides to DD(E) and fibrinogen confirmed the affinity and specificity measurements obtained by fluorescence polarization (Figure 4). Data for these peptides titrated into a DD(E) solution displayed exothermic binding heats, and it appeared at the end of the titrations that nearly all DD(E) binding sites had been occupied by ligand. Binding constants for all three peptides were very close to the values obtained from the fluorescence polarization assay (Table 1). In addition, the data fit to stoichiometries of 2 binding events per DD(E), indicating that, like fibrin, the peptides bind independently to two binding sites on DD(E).

Data for **Tn6-2a** titrated with fibrinogen displayed very small, constant heat effects that were comparable to the control, indicating that any binding interaction between the Tn6 peptide and fibrinogen is weak with K_d > 50 μM. The data for **Tn7-3** and **Tn10-4** titrated with fibrinogen were more complex. Addition of these peptides to concentrated fibrinogen solutions resulted in fibrinogen aggregation, and formation of a watery gel. However, the heat released with each **Tn7-3** addition to fibrinogen was very small compared to those observed with DD(E) and probably arose from fibrinogen aggregation. In a separate experiment (see Supporting Information), **Tn7-3** was added to a fibrinogen solution (5 mg/mL), and the scattered light intensity, measured by absorbance at 350 nm, increased in 10 min from 0.04 to 0.32 in a sigmoidal transition, confirming that peptide addition induced the aggregation of the fibrinogen. This phenomenon did not occur in citrated human plasma, presumably due to lower fibrinogen concentration and an

dx.doi.org/10.1021/bc200613e | *Bioconjugate Chem.* 2012, 23, 548−556

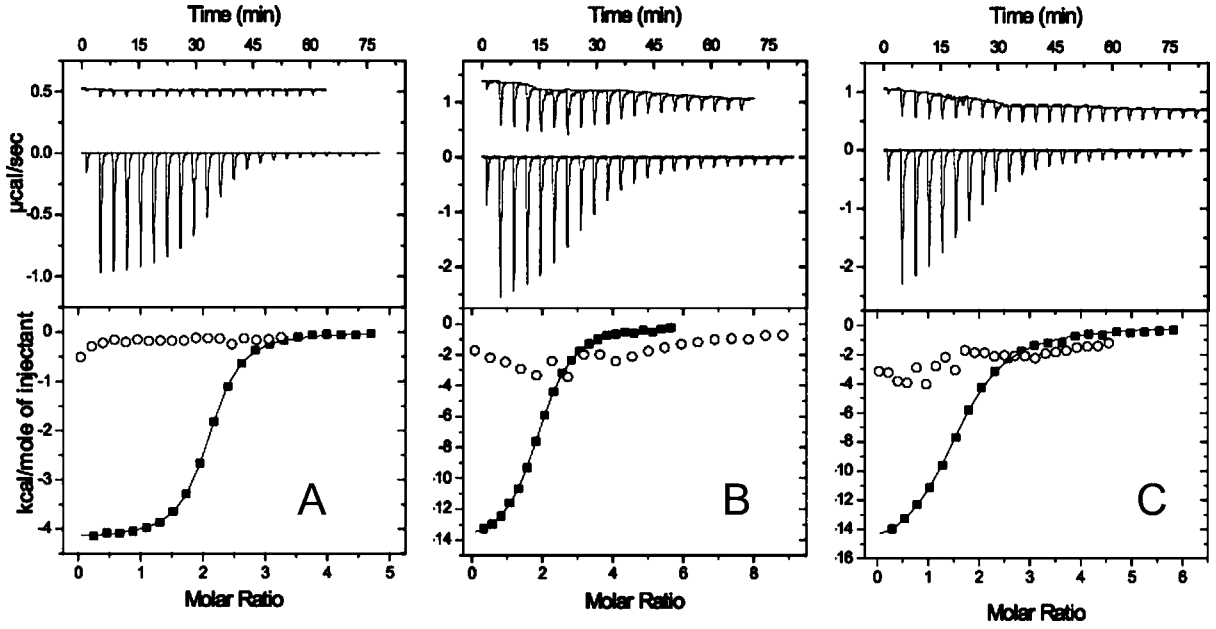


Figure 4. Calorimetry data for peptide binding to fibrinogen and DD(E). Upper panels: raw heat data measured over a series of injections (fibrinogen, top curves; DD(E), lower curves). Lower panels: integrated heat per mol injected peptide plotted against the molar ratio of added peptide to protein (fibrinogen binding, ○, no fit; DD(E) binding, ■, with fit). Conditions for titrations and data were as follows. Figure 4a: **Tn6-2a** (721 μM) into 28.5 μM fibrinogen, 10 μL/inj. and 24.7 μM DD(E), 5 μL/inj. B: 1.099 mM **Tn7-3** into 17.5 μM fibrinogen, 10 μL/inj. and 16 μM DD(E) 10 μL/inj. C: 462 μM **Tn10-4** into 17.5 μM fibrinogen, 10 μL/inj. and 551 μM **Tn10-4** into 16 μM DD(E), 10 μL/inj.

overall high protein concentration that would disfavor fibrinogen self-association. The titration calorimetry data did not fit to a standard binding model, but it can be inferred that **Tn7-3** affinity to fibrinogen is very weak, with $K_d \gg 20$ μM. Very similar results were obtained for **Tn10-4**, consistent with the prior observation that it binds to the same site on fibrin as **Tn7-3**.

Peptide Binding Determinants. To identify residues in the Tn6 and Tn7 sequences required for fibrin binding, each position (except the cysteines) was systematically changed to alanine (Table 2) and tested for binding to DD(E) in the fluorescence polarization assay. The two Tn6 peptides bind in a similar fashion with residues P^5, Y^6, and L^8 within the PY(G/D)L consensus sequence exhibiting particular sensitivity to substitution and conferring most of the binding affinity. In addition, alanine substitutions at the residues flanking the C-terminal cysteine, especially the aromatic W^{10}/H^{10} and hydrophobic I^{11} sites, led to much weaker binding than similar substitutions at the N-terminal flanking region, indicating that the C-terminus contributes more to the peptide−fibrin interaction. For the Tn7 sequence, a substantial reduction in binding was observed for changes at Y^6 and T^8, highlighting the critical role of these conserved residues for fibrin binding. Reduction of hydrophobicity at L^{10} also lowered binding affinity, indicating a secondary contribution from this residue. Substitution of the other exocyclic residues or at the D^4 position had little effect on binding, consistent with the greater variability observed at these sites in the sequences obtained by phage display.

The conformation as maintained by the cyclic disulfide was also critical for high affinity binding. Reduction of the disulfide in **Tn6-1** and **Tn7-3** with excess tris(2-carboxyethyl)phosphine (TCEP) or substitution of the cysteines with serine in **Tn7-3** abrogated binding to DD(E) and fibrin completely. Even modulation of the disulfide conformation reduced binding considerably. For example, in **Tn6-1** either L-cysteine replaced with D-cysteine or in **Tn7-3** substitution of C^3 with penicillamine (β, β'-dimethylcysteine) resulted in nonbinding peptides.

Gd-DTPA Derivatives. Prototype fibrin targeted MRI contrast agents were synthesized by conjugating the paramagnetic gadolinium chelate Gd(DTPA) to the N-terminus of **Tn6-1** and **Tn7-3** via 0−2 glycyl linkers. Despite the addition of the large Gd(DTPA) moiety, the conjugates **Tn6-1-Gd** and **Tn7-3b-Gd** bound to DD(E) and to fibrin in TBS buffer with affinity similar to that of the parent peptides (Table 1). When binding to fibrin was measured in human citrated plasma, the fibrin affinity was only decreased 2−3-fold: **Tn6-1-Gd** bound to fibrin with K_d = 3.1 ± 0.3 μM and 2.3 ± 0.1 sites per fibrin monomer, while **Tn7-3b-Gd** bound with K_d = 8.4 ± 0.5 μM and 1.8 ± 0.1 sites/fibrin. For the Tn7 peptide, both peptide derivatization and plasma binding contributed roughly equally to the observed lower binding affinity, as the K_d values in buffer (Table 1) were intermediate between those measured for the peptide in TBS and for the conjugate in plasma. No measurable fibrin binding was observed for a scrambled version of **Tn7-3b-Gd** (sequence DTPA-GYLCGDYTLCPD-NH_2).[15]

The presence of the paramagnetic Gd(III) moiety allows estimation of fibrin affinity using the proton relaxation enhancement (PRE) effect. The longitudinal relaxation rate ($1/T_1$) of solvent water increases if the peptide conjugate binds to protein. Solutions containing varying concentrations of **Tn7-3a-Gd** were prepared either in TBS or in TBS containing 30 μM fibrinogen. The fibrinogen solutions were converted to fibrin gels by the addition of $CaCl_2$ and thrombin. Figure 5 shows that $1/T_1$ is higher for **Tn7-3a-Gd** in the presence of fibrin compared to buffer only. The $1/T_1$ data is nonlinear for the data in fibrin indicative of a saturable binding event. A control study showed no enhancement of $1/T_1$ for GdDTPA in fibrin gel compared to GdDTPA in buffer demonstrating a specific interaction between **Tn7-3a-Gd** and fibrin.

dx.doi.org/10.1021/bc200613e | *Bioconjugate Chem.* 2012, 23, 548−556

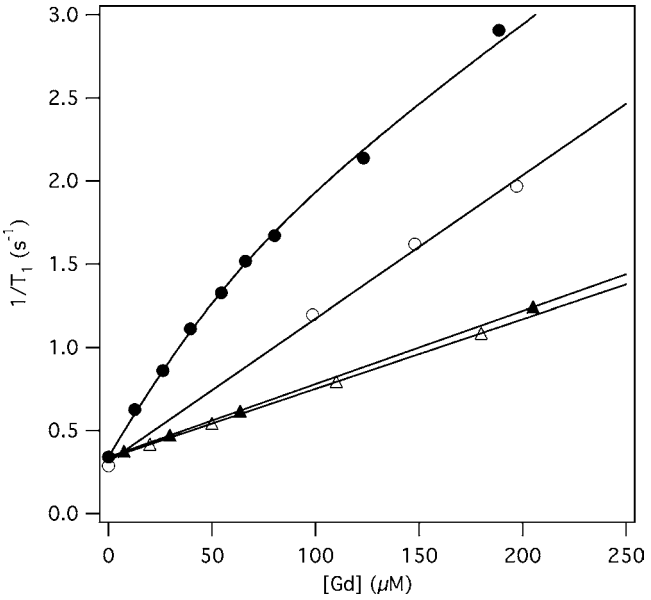


Figure 5. Relaxation rate data for **Tn7-3a-Gd** (circles) and GdDTPA (triangles) in the presence (filled symbols) and absence (open symbols) of 30 μM fibrin. Solid lines are fits to the data as described in the text.

The relaxivity of **Tn7-3a-Gd** bound to fibrin was 25.5 ± 0.7 $mM^{-1}s^{-1}$ at 37 °C, 0.47 T, which is significantly higher than that for **Tn7-3b-Gd** under the same conditions (14.9 $mM^{-1}s^{-1}$), whereas the relaxivity in the absence of fibrin was similar for the two compounds: 8.6 ± 0.3 and 10.1 $mM^{-1}s^{-1}$ for **Tn7-3a-Gd** and **Tn7-3b-Gd**, respectively.[15] The increased fibrin-bound relaxivity of **Tn7-3a-Gd** can be attributed to the lack of the glycyl linker. The GdDTPA moiety is coupled directly to the leucine N-terminus resulting in restricted rotational motion when the compound binds fibrin. While placing the large GdDTPA group close to the conserved portion of the binding sequence could be expected to reduce affinity, in this case affinity was similar regardless of the spacer, while there was a clear advantage to minimizing the spacer length to obtain optimal relaxivity properties.

DISCUSSION

We describe three families of small peptides that discriminate in their binding between two distinct conformational states of fibrinogen, the soluble protein central to hemostasis, and fibrin, the polymerized form that provides the structural network of thrombi. These cyclic peptide classes were obtained by phage display from three disulfide constrained libraries that exhibited high binding affinity to fibrin, in the low micromolar range, and >100-fold selectivity for fibrin over fibrinogen. Fibrin and DD(E) binding was assessed by four independent methods: plate-based depletion, fluorescence polarization and probe displacement, isothermal calorimetry, and proton relaxation enhancement assays. No evidence was observed for specific fibrinogen binding in these assays. Peptide binding to DD(E) was comparable to fibrin, which is evidence that DD(E) is a good structural model for fibrin since the neo-epitopes recognized by these peptides are structurally maintained and accessible in both proteins. It is remarkable that this degree of specificity is conferred by such short peptides, especially given that much of the overall conformation is expected to be similar between fibrin and fibrinogen.[23] A few residues on each peptide were responsible for fibrin recognition, and these hot spots corresponded to conserved residues highlighted in the phage display results. A peptide architecture rigidified by disulfide bonds also proved crucial to holding the peptides in a high affinity conformation.

All peptides bound to two sites per fibrin monomer, consistent with the dimeric structure of fibrin. These peptides potentially recognize new surfaces formed by interdomain contacts present in fibrin but absent in fibrinogen, or they bind to surfaces exposed by domain movements induced by fibrin polymerization. Identification of the binding site location may help elucidate conformational differences between fibrin and fibrinogen and is ongoing. The fibrin N-termini, well-known epitopes recognized by fibrin-specific antibodies[24] but absent in DD(E), as well as the "a" and "b" holes, fully or partially occupied in fibrin, can be ruled out. The Tn7/Tn10 binding site is of particular interest as it may be involved in fibrin polymerization, as suggested by these peptides' ability to induce fibrinogen self-association and gelation. By binding at an interface, such as between the D-E or D-D domains, it may stabilize a complex of three fibrinogen monomers oriented to form a DD(E)-like structure that has similar surface interactions between the monomers but is of course absent in any covalent cross-links or "a" and "b" site occupation. Such peptide−fibrinogen complexes, even if present at low concentration, evidently speed the rate of protofibril nucleation, the rate determining step in (thrombin independent) fibrin gel assembly,[25] seeding further aggregation.

The N-terminus of all three classes of peptide can be modified with either a fluorophore or a GdDTPA moiety without significant loss of affinity, provided a spacer (e.g., glycine) is introduced at the N-terminus. The GdDTPA conjugates of the Tn6 and Tn7 peptides both retained excellent *in vitro* selectivity and high fibrin binding affinity in plasma, despite the presence of fibrinogen at a concentration equimolar to fibrin and 660 μM HSA. The low micromolar binding constants are within the range required for fibrin targeting *in vivo* since the high concentration of fibrin in human thrombi (25−200 μM) should promote binding of these compounds under physiological conditions. For the conjugates here, we conservatively expect a percent bound of >80% resulting in a fibrin/plasma ratio of >4:1. Moreover, the two peptide binding sites per fibrin molecule doubles the effective capacity, providing an added enhancement in imaging sensitivity.

The feasibility of this approach was recently demonstrated with imaging agents based on the Tn6 peptide termed EP-1873 and EP-2104R,[16,26] and on the Tn7 peptide.[15,27,28] These compounds contain a modified form of the parent Tn6 (or Tn7) peptide and have four Gd chelates attached. The Gd-modified peptides, both Tn6 and Tn7, maintain >100-fold specificity for fibrin over fibrinogen and >1000-fold specificity for fibrin over serum albumin.[16,27] These agents were used in swine models of coronary thrombosis,[5,7] pulmonary embolism,[7,8,10] atrial thrombus,[8] and cerebral venous sinus thrombosis,[11] rabbit models of ruptured atherosclerotic plaque[26] and carotid thrombosis,[29] and rat models of ischemic stroke.[30,31] Recent clinical trial data with a fibrin-targeted gadolinium-based probe, EP-2104R, indicated that this probe can identify thrombi in the heart chambers, carotid arteries, or aortic arch.[32] The positive image contrast persists for hours,[12] indicating a slow off-rate of the peptide from the clot due to the high concentration of fibrin binding sites.

These peptides could also find applications in other modalities. Fluorescence imaging of fibrin is readily achieved with the fluorescein derivatives described herein, and such probes may find use in optical imaging applications such as intravital microscopy.[33] Alternatively, these peptides could be coupled to plasminogen activators to enhance the clot specificity of fibrinolytic treatments or be conjugated to antithrombotic compounds to inhibit active clotting factors associated with pathological thrombi while minimizing systemic side effects. These small peptides are easily synthesized and may be readily conjugated without loss of function, thus providing a new and more flexible approach to fibrin targeting than any previous strategies.

CONCLUSIONS

Phage display, with a preselection to remove fibrinogen and serum protein binders, is a powerful tool to identify fibrin specific peptides. Three classes of disulfide bridged cyclic peptides were identified that bind to two unique sites on fibrin and DD(E). The peptides show only weak nonspecific affinity to fibrinogen or plasma proteins. Alanine and other point substitutions identify the amino acids critical to fibrin binding within these short peptides. The peptides are readily modified at the N-terminus without affinity loss and represent useful building blocks to create conjugates for fibrin-targeted imaging or therapy.

ASSOCIATED CONTENT

Supporting Information

Additional details of the phage display study, protein preparations, binding assays, and peptide and conjugate syntheses. This material is available free of charge via the Internet at http://pubs.acs.org.

AUTHOR INFORMATION

Corresponding Author

*A.A. Martinos Center for Biomedical Imaging, Department of Radiology, Massachusetts General Hospital, Suite 2301, 149 Thirteenth Street, Charlestown, MA 02129. Tel: +1 617 643 0193. E-mail: caravan@nmr.mgh.harvard.edu.

ACKNOWLEDGMENTS

This work was supported in part by Award Number R21NS075627 from the National Institute of Neurological Disorders and Stroke to P.C.

REFERENCES

(1) Morawski, A. M., Lanza, G. A., and Wickline, S. A. (2005) Targeted contrast agents for magnetic resonance imaging and ultrasound. *Curr. Opin. Biotechnol. 16*, 89−92.

(2) Runge, M. S., Harker, L. A., Bode, C., Ruef, J., Kelly, A. B., Marzec, U. M., Allen, E., Caban, R., Shaw, S. Y., Haber, E., and Hanson, S. R. (1996) Enhanced thrombolytic and antithrombotic potency of a fibrin-targeted plasminogen activator in baboons. *Circulation 94*, 1412−1422.

(3) Peter, K., Graeber, J., Kipriyanov, S., Zewe-Welschof, M., Runge, M. S., Kubler, W., Little, M., and Bode, C. (2000) Construction and functional evaluation of a single-chain antibody fusion protein with fibrin targeting and thrombin inhibition after activation by factor Xa. *Circulation 101*, 1158−1164.

(4) Hagemeyer, C. E., Tomic, I., Jaminet, P., Weirich, U., Bassler, N., Schwarz, M., Runge, M. S., Bode, C., and Peter, K. (2004) Fibrin-targeted direct factor Xa inhibition: construction and characterization of a recombinant factor Xa inhibitor composed of an anti-fibrin single-chain antibody and tick anticoagulant peptide. *Thromb. Haemost. 92*, 47−53.

(5) Botnar, R. M., Buecker, A., Wiethoff, A. J., Parsons, E. C., Katoh, M., Katsimaglis, G., Weisskoff, R. M., Lauffer, R. B., Graham, P. B., Gunther, R. W., Manning, W. J., and Spuentrup, E. (2004) In vivo magnetic resonance imaging of coronary thrombosis using a fibrin-binding molecular magnetic resonance contrast agent. *Circulation 110*, 1463−1436.

(6) Sirol, M., Fuster, V., Badimon, J. J., Fallon, J. T., Moreno, P. R., Toussaint, J. F., and Fayad, Z. A. (2005) Chronic thrombus detection with in vivo magnetic resonance imaging and a fibrin-targeted contrast agent. *Circulation 112*, 1594−1600.

(7) Spuentrup, E., Buecker, A., Katoh, M., Wiethoff, A. J., Parsons, E. C., Botnar, R. M., Weisskoff, R. M., Graham, P. B., Manning, W. J., and Gunther, R. W. (2005) Molecular magnetic resonance imaging of coronary thrombosis and pulmonary emboli with a novel fibrin-targeted contrast agent. *Circulation 111*, 1377−1382.

(8) Spuentrup, E., Fausten, B., Kinzel, S., Wiethoff, A. J., Botnar, R. M., Graham, P. B., Haller, S., Katoh, M., Parsons, E. C., Manning, W. J., Busch, T., Gunther, R. W., and Buecker, A. (2005) Molecular magnetic resonance imaging of atrial clots in a swine model. *Circulation 112*, 396−399.

(9) Spuentrup, E., Katoh, M., Wiethoff, A. J., Parsons, E. C., Botnar, R. M., Mahnken, A. H., Gunther, R. W., and Buecker, A. (2005) Molecular magnetic resonance imaging of pulmonary emboli with a fibrin-specific contrast agent. *Am. J. Resp. Crit. Care Med. 172*, 494−500.

(10) Spuentrup, E., Katoh, M., Buecker, A., Fausten, B., Wiethoff, A. J., Wildberger, J. E., Haage, P., Edward, C. P., Botnar, R. M., Graham, P. B., Vettelsehoss, M., and Gunther, R. W. (2007) Molecular MR imaging of human thrombi in a swine model of pulmonary embolism using a fibrin-specific contrast agent. *Invest. Radiol. 42*, 586−595.

(11) Stracke, C. P., Katoh, M., Wiethoff, A. J., Parsons, E. C., Spangenberg, P., and Spuntrup, E. (2007) Molecular MRI of cerebral venous sinus thrombosis using a new fibrin-specific MR contrast agent. *Stroke 38*, 1476−1481.

(12) Spuentrup, E., Botnar, R. M., Wiethoff, A. J., Ibrahim, T., Kelle, S., Katoh, M., Oezgun, M., Nagel, E., Vymazal, J., Graham, P. B., Gunther, R. W., and Maintz, D. (2008) MR imaging of thrombi using EP-2104R, a fibrin-specific contrast agent: initial results in patients. *Eur. Radiol. 18*, 1995−2005.

(13) Moskowitz, K. A., and Budzynski, A. Z. (1994) The (DD)E complex is maintained by a composite fibrin polymerization site. *Biochemistry 33*, 12937−12944.

(14) Sato, A. K., Sexton, D. J., Morganelli, L. A., Cohen, E. H., Wu, Q. L., Conley, G. P., Streltsova, Z., Lee, S. W., Devlin, M., DeOliveira, D. B., Enright, J., Kent, R. B., Wescott, C. R., Ransohoff, T. C., Ley, A. C., and Ladner, R. C. (2002) Development of mammalian serum albumin affinity purification media by peptide phage display. *Biotechnol. Prog. 18*, 182−192.

(15) Nair, S., Kolodziej, A. F., Bhole, G., Greenfield, M. T., McMurry, T. J., and Caravan, P. (2008) Monovalent and Bivalent Fibrin-specific MRI Contrast Agents for Detection of Thrombus. *Angew. Chem., Int. Ed. 47*, 4918−4921.

(16) Overoye-Chan, K., Koerner, S., Looby, R. J., Kolodziej, A. F., Zech, S. G., Deng, Q., Chasse, J. M., McMurry, T. J., and Caravan, P. (2008) EP-2104R: a fibrin-specific gadolinium-based MRI contrast agent for detection of thrombus. *J. Am. Chem. Soc. 130*, 6025−6039.

(17) Burke, T., Bolger, R., Checovich, W., and Lowery, R. (1996) Measurement of Peptide Binding Affinities Using Fluorescence Polarization, in *Phage Display of Peptides and Proteins: A Laboratory Manual* (Kay, B. K., Winter, J., and McCafferty, J., Eds.) pp 305−326, Academic Press, San Diego, CA.

(18) Feng, S., Kasahara, C., Rickles, R. J., and Schreiber, S. L. (1995) Specific interactions outside the proline-rich core of two classes of Src homology 3 ligands. *Proc. Natl. Acad. Sci. U.S.A. 92*, 12408−12415.

(19) Indyk, L., and Fisher, H. F. (1998) Theoretical aspects of isothermal titration calorimetry. *Methods Enzymol. 295*, 350−64.

(20) Yakovlev, S., Makogonenko, E., Kurochkina, N., Nieuwenhuizen, W., Ingham, K., and Medved, L. (2000) Conversion of fibrinogen to fibrin: mechanism of exposure of tPA- and plasminogen-binding sites. *Biochemistry 39*, 15730−15741.
(21) Tymkewycz, P. M., Creighton-Kempsford, L. J., Hockley, D., and Gaffney, P. J. (1992) Screening for fibrin specific monoclonal antibodies: the development of a new procedure. *Thromb. Haemost. 68*, 48−53.
(22) Makogonenko, E., Tsurupa, G., Ingham, K., and Medved, L. (2002) Interaction of fibrin(ogen) with fibronectin: further characterization and localization of the fibronectin-binding site. *Biochemistry 41*, 7907−7913.
(23) Doolittle, R. F. (2003) Structural basis of the fibrinogen-fibrin transformation: contributions from X-ray crystallography. *Blood Rev. 17*, 33−41.
(24) Hui, K. Y., Haber, E., and Matsueda, G. R. (1983) Monoclonal antibodies to a synthetic fibrin-like peptide bind to human fibrin but not fibrinogen. *Science 222*, 1129−1132.
(25) Hantgan, R., McDonagh, J., and Hermans, J. (1983) Fibrin assembly. *Ann. N.Y. Acad. Sci. 408*, 344−366.
(26) Botnar, R. M., Perez, A. S., Witte, S., Wiethoff, A. J., Laredo, J., Hamilton, J., Quist, W., Parsons, E. C., Vaidya, A., Kolodziej, A., Barrett, J. A., Graham, P. B., Weisskoff, R. M., Manning, W. J., and Johnstone, M. T. (2004) In vivo molecular imaging of acute and subacute thrombosis using a fibrin-binding magnetic resonance imaging contrast agent. *Circulation 109*, 2023−2029.
(27) Zhang, Z., Kolodziej, A. F., Greenfield, M. T., and Caravan, P. (2011) Heteroditopic binding of magnetic resonance contrast agents for increased relaxivity. *Angew. Chem., Int. Ed. 50*, 2621−2624.
(28) Zhang, Z., Kolodziej, A. F., Qi, J., Nair, S. A., Wang, X., Case, A. W., Greenfield, M. T., Graham, P. B., McMurry, T. J., and Caravan, P. (2010) Effect of peptide-chelate architecture on metabolic stability of peptide-based MRI contrast agents. *New J. Chem.*, 611−616.
(29) Sirol, M., Aguinaldo, J. G., Graham, P. B., Weisskoff, R., Lauffer, R., Mizsei, G., Chereshnev, I., Fallon, J. T., Reis, E., Fuster, V., Toussaint, J. F., and Fayad, Z. A. (2005) Fibrin-targeted contrast agent for improvement of in vivo acute thrombus detection with magnetic resonance imaging. *Atherosclerosis 182*, 79−85.
(30) Uppal, R., Catana, C., Ay, I., Benner, T., Sorensen, A. G., and Caravan, P. (2011) Bimodal thrombus imaging: simultaneous PET/MR Imaging with a fibrin-targeted dual PET/MR probe: feasibility study in rat model. *Radiology 258*, 812−820.
(31) Uppal, R., Ay, I., Dai, G., Kim, Y. R., Sorensen, A. G., and Caravan, P. (2010) Molecular MRI of intracranial thrombus in a rat ischemic stroke model. *Stroke 41*, 1271−1277.
(32) Vymazal, J., Spuentrup, E., Cardenas-Molina, G., Wiethoff, A. J., Hartmann, M. G., Caravan, P., and Parsons, E. C. Jr. (2009) Thrombus imaging with fibrin-specific gadolinium-based MR contrast agent EP-2104R: results of a phase II clinical study of feasibility. *Invest. Radiol. 44*, 697−704.
(33) Falati, S., Gross, P., Merrill-Skoloff, G., Furie, B. C., and Furie, B. (2002) Real-time in vivo imaging of platelets, tissue factor and fibrin during arterial thrombus formation in the mouse. *Nat. Med 8*, 1175−1181.

Bioconjugate Chemistry

Article

pubs.acs.org/bc

New Substrates and Enzyme Assays for the Detection of Mucopolysaccharidosis III (Sanfilippo Syndrome) Types A, B, C, and D by Tandem Mass Spectrometry

Brian J. Wolfe,[†] Farideh Ghomashchi,[†] Tim Kim,[†] Cynthia A. Abam,[†] Martin Sadilek,[†] Rhona Jack,[‡] Jerry N. Thompson,[§] C. Ronald Scott,[∥] Michael H. Gelb,*[,†,⊥] and Frantisek Turecek*[,†]

[†]Department of Chemistry, Bagley Hall, University of Washington, Box 351700, Seattle, Washington 98195-1700, United States

[‡]Seattle Children's Hospital, 4800 Sand Point Way NE, Seattle, Washington 98105, United States

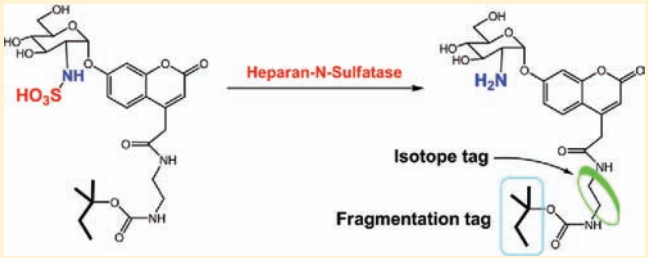
[§]Department of Genetics, University of Alabama, Birmingham, Alabama 35294, United States

[∥]Department of Pediatrics, RR 310 Health Science Building, University of Washington, Box 356320, Seattle, Washington 98195-6320, United States

[⊥]Department of Biochemistry, University of Washington, Box 357350, Seattle, Washington 98195-7350, United States

Supporting Information

ABSTRACT: The clinical phenotype of Sanfilippo Syndrome is caused by one of four enzyme deficiencies that are associated with a defect in mucopolysaccharide metabolism. The four subtypes (A, B, C, and D) are each caused by an enzyme deficiency involved in the degradation of heparan sulfate. We have developed a highly efficient synthesis of the substrates and internal standards required for the enzymatic assay of each of the four enzymes. The synthesis of the substrates involves chemical modification of a common intermediate. The substrates and internal standards allow the measurement of the enzymes relevant to heparan *N*-sulfatase (type A); *N*-acetyl-α-glucosaminidase (type B); acetyl-CoA:α-glucosamide *N*-acetyltransferase (type C); and *N*-acetylglucosamine 6-sulfatase (type D). The internal standards are similar to the substrates and allow for the accurate quantification of the enzyme assays using tandem mass spectrometry. The synthetic substrates incorporate a coumarin moiety and can also be used in fluorometric enzyme assays. We confirm that all four substrates can detect the appropriate Sanfilippo Syndrome in fibroblast lysates, and the measured enzyme activities are distinctly lower by a factor of 10 when compared to fibroblast lysates from unaffected persons.



INTRODUCTION

Mucopolysaccharidosis III types A, B, C, and D (Sanfilippo syndrome, MPS III type A, B, C, and D) are a group or autosomal recessive lysosomal storage disorders (LSD) caused by a deficiency of any of four distinct enzymes which degrade the glycosaminoglycan (GAG) heparan sulfate. The enzymes are located in lysosomes and, when deficient, are unable to degrade heparan sulfate. This allows the accumulation of heparan in cells leading to somatic changes and intellectual deficits.[1] Each MPS III is caused by a deficiency of a specific enzyme: heparan *N*-sulfatase (sulfamidase, EC 3.10.1.1), α-*N*-acetyl-glucosaminidase (EC 3.2.1.50), acetyl-CoA:α-glucosaminide acetyltransferase (EC 2.3.1.78), and *N*-acetylglucosamine 6-sulfatase (EC 3.1.6.14) for types A, B, C, and D, respectively.[2] Although the enzyme deficiencies are biochemically distinct, the clinical phenotype is similar. MPS III is characterized by slowly progressive degeneration of the central nervous system, whereas somatic changes are mild and often diagnostically nonspecific. Diagnosis of MPS III is often delayed beyond four years of age due to mild somatic effects and unreliable tests for urinary GAGs.[1]

The most reliable methods of detection of the forms of MPS III rely on specific enzyme assays. Radiolabel,[3−7] spectrophotometric,[8,9] and fluorescence-based assays[10−14] have been developed to monitor MPS III enzyme activities; substrates for fluorescence-based assays are available commercially from Moscerdam (http://moscerdam.com). These assays for MPS IIIA, C, and D do not form fluorescent products and require addition of a coupling hydrolytic enzyme to generate the fluorescent 4-methylumbelliferone product.

We have developed tandem mass spectrometric assays[15] for the detection of several LSDs caused by deficiencies of enzymes in glycosaminoglycan degradation pathways. These included assays for α-L-iduronidase (MPS I),[16] iduronate-2-sulfatase (MPS II),[17] *N*-acetylgalactosamine-6-sulfate sulfatase (MPS

Received: November 15, 2011
Revised: February 28, 2012
Published: February 28, 2012

ACS Publications © 2012 American Chemical Society

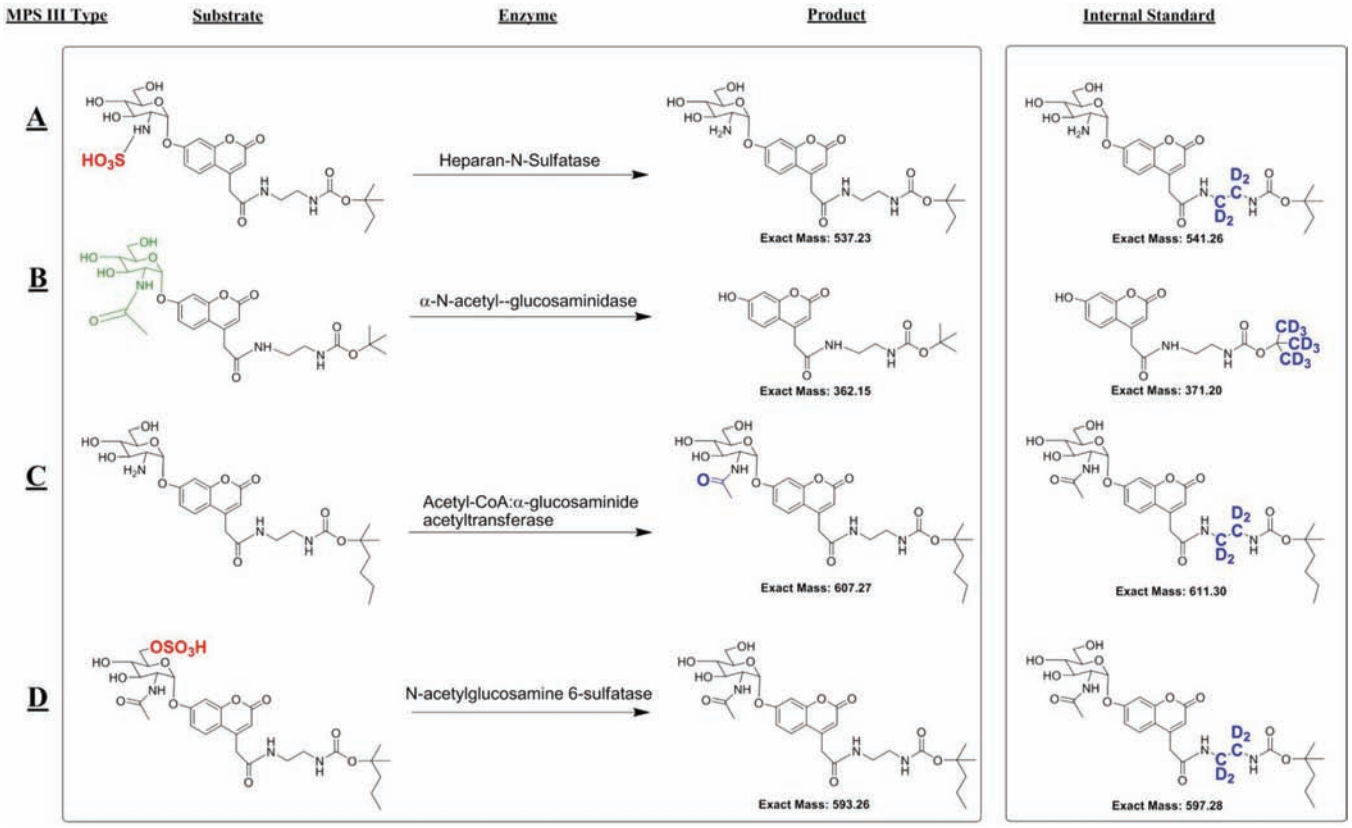


Figure 1. Substrates, enzymatic products, and internal standards used to diagnose MPS III types A–D.

IV),[18] and *N*-acetylgalactosamine-4-sulfate sulfatase (MPS VI).[19,20] The assays require incubation with a synthetic substrate and a 2 or 3 mm punch of a dried blood spot from a newborn report card, followed by a single-step extraction,[21] or HPLC workup,[22] and quantitation of the enzyme product by tandem mass spectrometry. This approach is dictated by the need for early detection of those inborn errors for which there exists efficient treatment. MPS III is different in that there is currently no marketed treatment. However, a treatment for MPS IIIA is in development,[23] and thus, it is useful to explore the possibility of early detection of this LSD using an enzyme assay.

We previously developed a set of assays to measure enzyme activities in cultured fibroblasts for MPS III patients by using affinity capture–release purification of biotin-tagged products and internal standards followed by electrospray MS.[24,25] Although this assay set was robust and straightforward, the synthesis of biotinylated substrate-conjugates was tedious and unsuitable for scaled-up production. In addition, sample dilution upon affinity capture–release made the affinity-based method unsuitable to extend to dried blood spots. Because of the superior selectivity and sensitivity of tandem mass spectrometry, the affinity chromatography step can now be avoided and the assays performed with simpler substrates. Here, we report the development of a highly efficient synthesis of a simplified set of substrates, which are prepared from a common intermediate. We also prepared a set of internal standards that allow for the quantitation of MPS III enzyme activities by tandem MS. The chemical structures of the new compounds are shown in Figure 1. Also reported are new fragmentation mass tags for the detection of MPS III enzyme products and internal standards, which are completely orthogonal by ion masses within this group of enzymes, and also across the entire portfolio of 15 tandem mass spectrometric LSD assays developed by our lab.

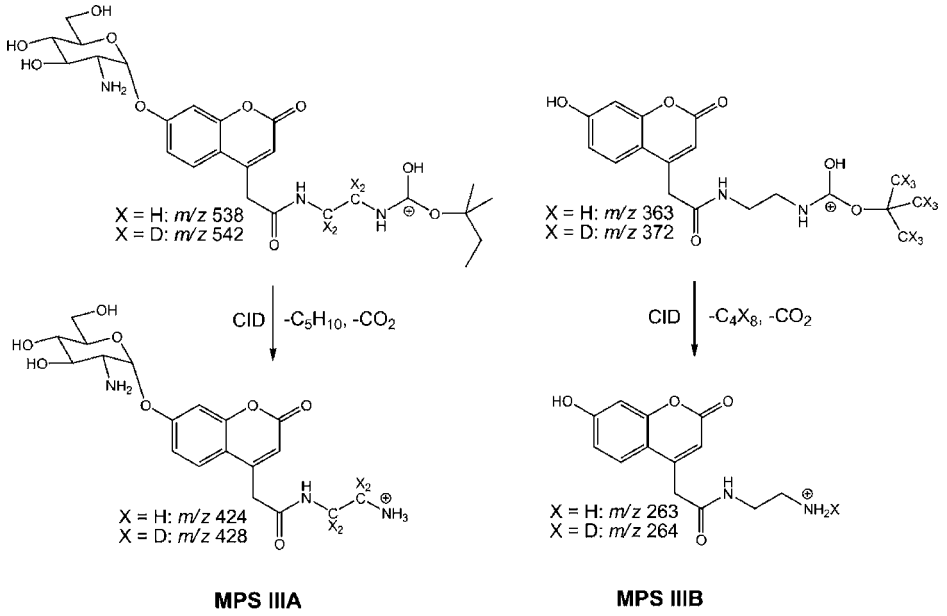
EXPERIMENTAL PROCEDURES

Materials. All chemicals were reagent grade and were used as received. (1,1,2,2-d_4)-Ethylenediamine and *tert*-butyl-d_9-alcohol were purchased from CDN Isotopes. Acetyl-CoA and synthetic chemicals were purchased from Sigma Aldrich. Cell culture media and buffer solutions were purchased from Invitrogen. T-25 and T75 flasks were purchased from Corning Inc. All experiments with human cell lines were conducted in compliance with Institutional Review Board guidelines. All MPS-III affected patients had been diagnosed previously with established clinical and biochemical procedures. Patient fibroblast cells were obtained from the Coriell Institute for Medical Research and were grown using their standard protocols (http://ccr.coriell.org/Sections/Support/Global/Fibroblast.aspx?PgId=214). The specific cell lines used were catalog number GM00312 (Type A), GM02931 (Type B), GM05157 (Type C), and GM05093 (Type D). Details of the syntheses of the substrates and internal standards are provided in the Supporting Information.

Standard Assay Procedure. Cells were harvested from T75 flasks by quickly removing the fibroblast growth medium, then incubating the cells in 8–9 mL 0.53 mM ethylenediaminetetraacetic acid (EDTA) in Hank's balanced salt solution (HBSS) for a couple of minutes. The cells were monitored under the microscope, and as soon as the cells began to constrict or round at the edges, the EDTA solution was removed. Next, 4–5 mL of 0.05% trypsin EDTA solution was added. The cells were monitored under the microscope for a

dx.doi.org/10.1021/bc200609x | *Bioconjugate Chem.* 2012, 23, 557–564

Scheme 1. Mass Spectrometric Fragmentations of Product and Internal Standard Ions for MPS IIIA and MPS IIIB Assays



few minutes until the cells detached. If necessary, the flask was tapped to help to dislodge the cells. When the cells were almost all dislodged, 5−7 mL of media was added, and the suspension was mixed a few times by gentle aspiration using the pipettor to give a uniform suspension. The solution was then placed in a 15 mL falcon tube and centrifuged at 100 *g* for 10 min to give a pellet. The solution was then removed without disturbing the pellet. The pellet was gently washed quickly with 2 × 100 μL of deionized water with care taken not to disturb the pellet. The cells were then diluted in less than 100 μL of deionized water and the sample was sonicated on ice using a microtip probe for 3 × 1 s bursts until the sample became homogeneous. The protein concentration was then measured using the standard Bradford assay[26] and the samples were stored at −80 °C until they were analyzed.

For the MPS III Type B and C assays, 10 μL of 100 mM sodium citrate buffer, pH 4.5, containing 0.75 mM MPS III type B and C substrates was combined in a 1.5 mL Eppendorf tube with 5 μL of 9.6 mM acetyl-CoA solution in the same buffer solution. The cell lysate containing 30 μg of fibroblast protein was added followed by water to give the solution a total volume of 30 μL. The final composition of the solution is 50 mM citrate buffer pH 4.5 with 0.25 mM substrate, 1.6 mM acetyl-CoA, and 30 μg of protein. Stock solutions of substrates were prepared in methanol and stored at −20 °C. An appropriate volume of each substrate was transferred to Eppendorf tube, methanol was removed in a vacuum centrifuge (Speed-Vac), and assay buffer was added to prepare the assay cocktail. We have not yet evaluated the long-term stability of the substrates in the assay cocktail.

The MPS III type A and D assays were carried out in a separate Eppendorf tube with 10 μL 100 mM sodium acetate buffer pH 5.5 which contained 75 mM lead(II) acetate and 2.5 mM of each substrate. To each assay, 60 μg of fibroblast protein was added followed by deionized water to give a total volume of 20 μL. The final composition is 50 mM acetate buffer pH 5.5 with 37.5 mM lead(II) acetate, 1.25 mM substrate, and 60 μg of protein. MPS III type A and D substrates were stored as stock solutions and assay cocktail prepared as for the other substrates. Stock solutions of acetyl-CoA were prepared in assay buffer and stored at −20 °C.

All assays were allowed to incubate for 16 h at 37 °C in a thermostatted air shaker at 225 rpm. The assays were then quenched with 0.5 mL of water containing 1 nmol of the internal standards. Internal standard stock solutions were made in methanol (stored at −20 °C), and these were directly added to the assay mixture (typically 10 μL).

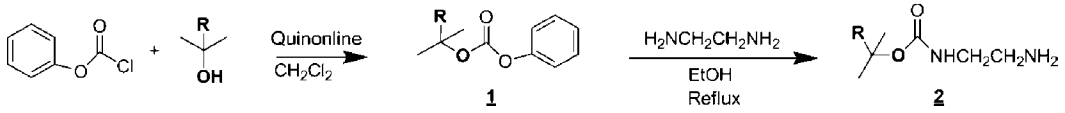
To the MPS III type A and D assay was added a suspension of DEAE in water (150 μL, containing ∼100 μL of settled beads). The samples were mixed on a vortexer for ∼1−2 s to ensure uniform mixing. The addition of DEAE removed the unreacted sulfated substrate from the samples in order to prevent nonenzymatic dissociation of the sulfate group in electrospray and ion transport, which can cause a high background. The Eppendorf tube was then centrifuged and the top 0.5 mL was removed and submitted to C-18 solid-phase extraction using a vacuum manifold (Millipore Inc., MAVM0960R) system connected to an aspirator.

The next step was to pass the sample through a reverse-phase solid-phase cartridge to remove buffer salts. C-18 resin (Aldrich, octadecyl-functionalized silica gel #377635) slurry in methanol (100 μL containing ∼70 μL of resin) was pipetted into a 1 mL pipettor tip plugged with cotton. The top region of the tip was sprayed with methanol using a squirt bottle to push remaining solid-phase particles to the bottom of the tip. The column was washed with ∼0.5 mL water with suction to remove residual methanol. The 0.5 mL assay samples were loaded onto the solid-phase bed, and suction was applied to draw the sample into the bed over 20−30 s. The products and internal standards were eluted into a 1.5 mL Eppendorf tube by adding 100 μL of 80/20 acetonitrile/water with 0.2% formic acid and applying suction over ∼10 s. Ten microliters of the elution solvent was then injected into the mass spectrometer for analysis. If desired, it is possible to store these samples at −20 °C for several days prior to mass spectrometry.

Mass Spectrometry. Mass spectrometry was performed on a Waters Quattro Micro tandem quadrupole instrument using positive ion mode selected reaction monitoring (SRM) and

dx.doi.org/10.1021/bc200609x | *Bioconjugate Chem.* 2012, 23, 557−564

Scheme 2. Synthesis of the Linkers



sample flow injection at 0.1 mL/min in 80/20 acetonitrile/water with 0.2% formic acid and electrospray ionization. Using manual injection, a 10 μL aliquot of the 100 μL sample volume was injected for each analysis. Collision induced ion dissociations occurred in the *t*-alkoxycarbamoyl groups that were designed to give mutually exclusive ion m/z ratios to allow multiplexing not only within the group of MPS III enzymes, but also across the entire portfolio of LSD assays. The ion structures relevant for the MPS IIIA and MPS IIIB dissociations are shown in Scheme 1; those for the MPS IIIC and MPS IIID ion dissociations involve ions which have *t*-alkoxycarbamoyl groups homologous to that in MPS IIIA. The relevant mass transitions used for SRM analysis of the MPS III type A assay were m/z 538.2 → m/z 424.5 and m/z 542.2 → m/z 428.5 for MPS III-A-P and MPS III-A-IS, respectively, using a cone voltage of 25 V and a collision energy of 15 eV. The mass transitions used for SRM analysis of the MPS III type B assay were m/z 363.1 → m/z 263.5 and m/z 372.1 → m/z 264.4 for MPSIII-B-P and MPSIII-B-IS, respectively, with a cone voltage of 25 V and a collision energy of 10 eV. The mass transitions used for SRM analysis of the MPS III type C assay were m/z 630.2 → m/z 488.5 and m/z 634.2 → m/z 492.5 for MPS III-C-P and MPS III-C-IS, respectively, with a cone voltage of 35 V and a collision energy of 30 eV. The mass transitions used for SRM analysis of the MPS III type D assay were m/z 616.3 → m/z 488.5 and m/z 620.3 → m/z 492.5 for MPS III-D-P and MPS III-D-IS, respectively, with a cone voltage of 45 V and a collision energy of 30 eV.

The product concentration was then determined from the SRM ion intensity ratio of the product to internal standard, the known internal standard concentration, and the products/internal standard response ratio (R), which was obtained by calibration over a 0.0−2.0 range of molar ratios, The calibration curves to determine the relative response factors for products to internal standards are given in Figures S1−S4 (Supporting Information). The enzyme activity was calculated as nmol/(h mg protein) from the amount of product formed, the incubation time, and the amount of protein added to the assay. Other mass spectrometry settings were as follows: capillary voltage, 3.75 kV; extractor, 1 V; RF Lens, 0 V; source temperature, 80 °C; desolvation temperature, 350 °C; cone gas flow, 50 L/h; desolvation gas flow, 650 L/h; LM 1 resolution, 15; HM resolution, 15; ion energy 1, 0.2 eV; entrance, 15 V; exit, 15 V; LM 2 resolution, 15; HM 2 resolution, 15; ion energy 2, 2.0 eV; multiplier, 650 V; gas cell Pirani pressure, 2.23 × 10^{-3} mbar; dwell time, 100 ms with 20 ms delay.

RESULTS AND DISCUSSION

Substrate, Product, and Internal Standard Synthesis. The substrates all have an umbelliferyl-α-glucosamine scaffold, which is unmodified (type B), modified by N-sulfation (type A), modified by N-acetylation (type C), or the N-acetylated glucosamine is 6-O sulfated (type D). Importantly, the common scaffold allows for an efficient synthetic design involving a single pivot intermediate. The umbelliferyl group bears a hydrophobic linker with a terminal carbamylated amine. The hydrophobic linker assures good retention of the products and internal standards on the reverse-phase cartridges used to remove buffer salts prior to ESI mass spectrometry. The carbamylated amines provide a site that readily undergoes collision-induced dissociation in the mass spectrometry. Fragmentation along a single pathway improves assay sensitivity. We decided to add mass variation to the alkoxy portion of the carbamate rather than using various length methylenediamine linkers. The latter would inevitably result in mass redundancies with some of the other lysosomal enzyme products and internal standards we have developed previously.[15−22] By avoiding these overlaps, we anticipate being able to incorporate the MPS III assays together with assays of other LSDs in the future. We thus used a common ethylenediamine linker, which is commercially available in tetra-deuterated form, and a series of different *t*-alkoxycarbamido (*t*-AOC) groups. For the type B substrate, we used a standard *t*-butoxy group (*t*-BOC). The *t*-AOC groups for the type A, C, and D substrates and internal standards were modified with one, three, or two extra carbons, respectively (Figure 1). The internal standards were deuterium labeled in the ethylenediamine linker for the type A, C, and D internal standards and on the *t*-BOC group for the type B assay.

The *t*-AOC derivatives were synthesized using the appropriate alcohols and phenylchloroformate (Scheme 2) to form a carbonate (**1**) which was then refluxed in ethanol with ethylenediamine to give the desired compound (**2**). The internal standards contained either a heavy d_4-ethylenediamine chain or a d_9-*t*-BOC group (Figure 2) made from either ethylene-d_4-diamine or *tert*-butyl-d_9-alcohol, both commercially available from CDN Isotopes.

The starting compound of the carbohydrate synthesis was 2-azido-2-deoxy-D-glucopyranosyl fluoride 3,4,6-triacetate (**3**, Scheme 3), which was synthesized from commercially available

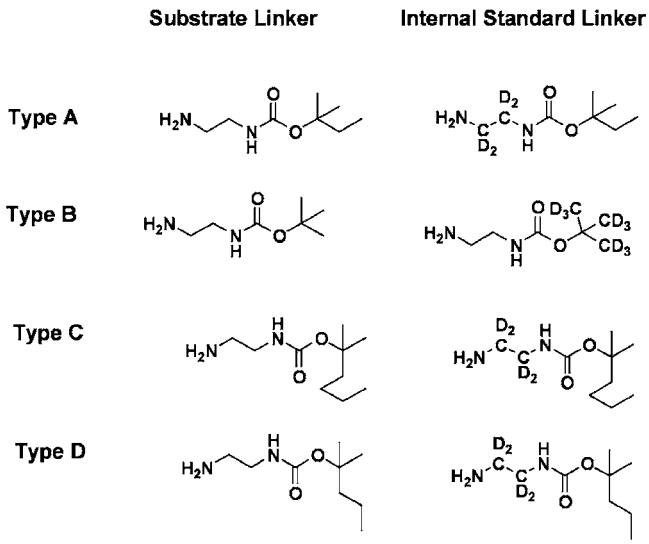
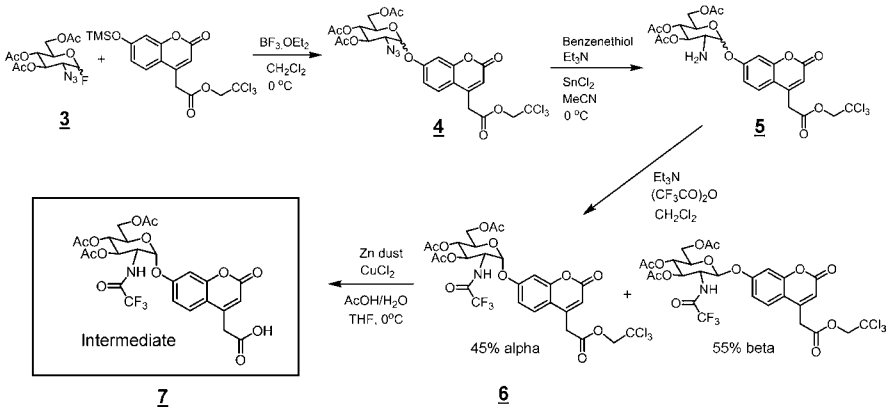


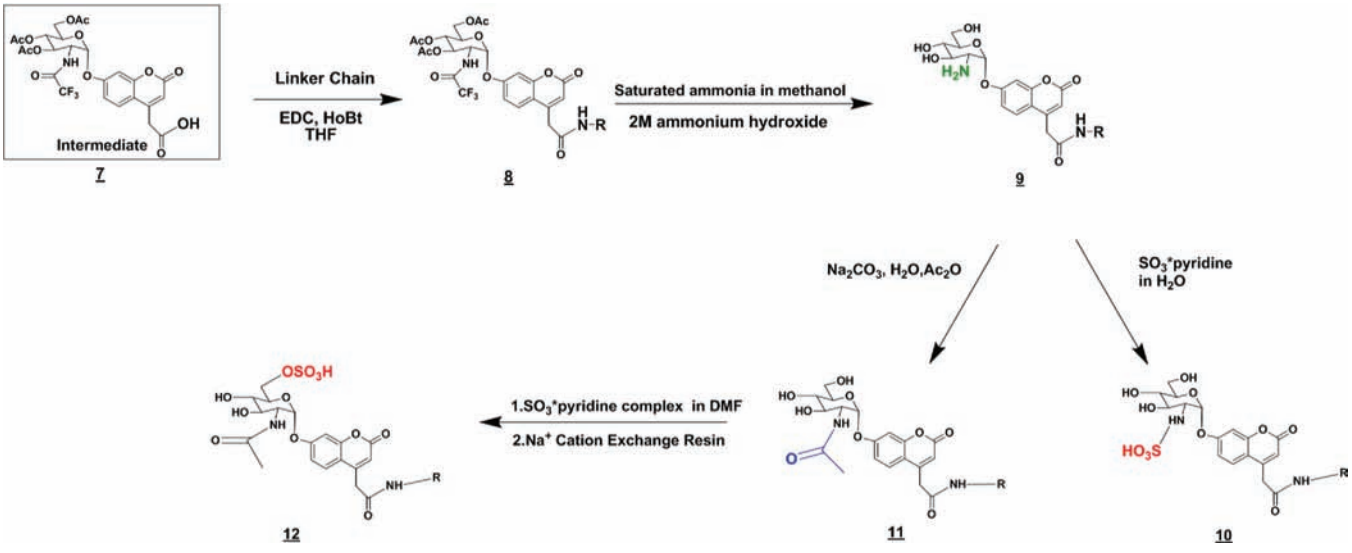
Figure 2. The different linkers that are used for the substrates, and internal standards for each assay type.

dx.doi.org/10.1021/bc200609x | *Bioconjugate Chem.* 2012, 23, 557−564

Scheme 3. Synthesis of the Intermediate (7)



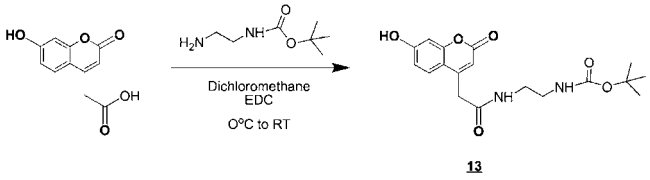
Scheme 4. Synthesis of the Substrates and Internal Standards from Intermediate 7



D-glucal using previously described techniques.[27,28] The coumarin aglycone was made as described previously.[17] Coupling of the coumarin and **3** gave a mixture of 40% α and 60% β enantiomers (**4**). The α-anomer is generally more difficult to obtain than the β-anomer, and we consider the 40/60 α/β ratio to be acceptable. These two anomers were not readily separated on silica gel; however, we found that they do separate well after the next two synthetic steps, reduction of the azide to give amine (**5**) and N-trifluoroacetylation to give (**6**). Diastereoisomers ***6α*** and ***6β*** were readily separated on silica (R_f = 0.4 for α and 0.3 for β in $CHCl_3$/MeOH 3%). The trichloroethyl ester in the α-linked glycoside (**6**) was removed using Zn to form the free carboxyl group in the common intermediate (**7**) from which all substrates, enzymatic products, and internal standards could be synthesized in four steps or less. Using this intermediate the desired linker can be attached via standard 1-ethyl-3-(3-dimethylaminopropyl) carbodiimide (EDC) peptide coupling (Scheme 4) (**8**). The carbohydrate was then fully deprotected (**9**) and either N-sulfated (**10**), N-acetylated (**11**), or N-acetylated and then sulfated at O-6 (**12**) to give all substrates and internal standards.

The type B product and internal standard (**13**) were made by coupling the desired diamine chain to 7-hydroxycoumarin-4-acetic acid using a standard EDC coupling procedure in dichloromethane (Scheme 5).

Scheme 5. Synthesis of the Product and Internal Standard for the MPS III Type B Assay



Mass Spectrometric Analysis. Electrospray ionization tandem mass spectrometry of the products and internal standards showed linear responses (R^2 = 0.98–0.998) over a range of product/internal standard ratios (Figures S1–S4, Supporting Information). The slopes of the calibration curves varied, giving different response factors for the A–D types. The largest difference was found for type A where the response factor was 0.42 disfavoring the product against the internal standard. The other response factors were 0.66, 0.53, and 1.6 for the B, C, and D types, respectively. Note that the internal standards are isotopologues of the enzyme products and their respective response factors are usually expected to be close to 1.0. The reasons for the observed variations were not clear. The response factors were used in the calculations of product formation in the assays.

dx.doi.org/10.1021/bc200609x | *Bioconjugate Chem.* 2012, 23, 557–564

The MPS III A, B, and D assays showed an approximately linear increase in product formation versus incubation time up to 24 h (SI Figures S5 and S6). The type C enzyme activity leveled off after ~6 h of incubation time (SI Figure S6). Despite this time course of type C assay, all the assays were still incubated for 16 h so that they could be processed at the same time. The amount of substrate enzymatically converted to product increased in an approximately linear fashion with increasing amounts of fibroblast protein for all assays (SI Figures S7 and S8).

Enzyme activities were measured in cultured cells from patients who had been previously diagnosed with MPS III A–D syndromes, and the measured activities were compared among the cell lines and with blanks (Figure 3). Three blanks which

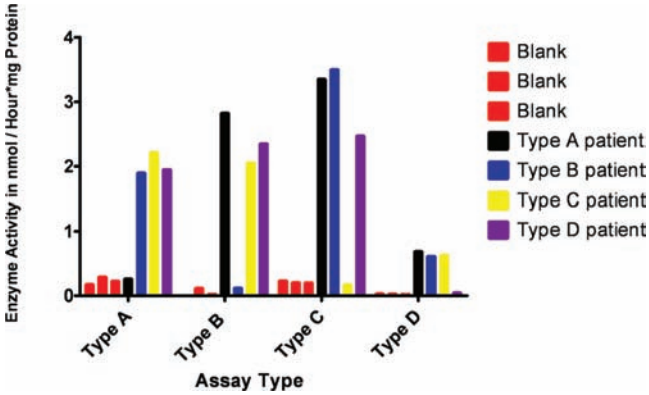


Figure 3. Enzyme activities in cultured fibroblasts from MPS III type A, B, C, and D patients.

contained water instead of cellular protein had heparan-*N*-sulfatase (type A) activities of 0.17, 0.29, and 0.22 nmol/(h mg protein). The patients' type A enzyme activities were measured as 0.25, 1.9, 2.2, and 1.9 nmol/(h mg protein) for MPS III type A, B, C, and D patients. The MPS III type A patient showed enzyme activity close to the blanks, while the MPS III type B–D samples had heparan-*N*-sulfatase activities at least 6.5 times higher than the background signal. The MPS III type B blanks showed α-*N*-acetyl-glucosamidase activity of 0.00, 0.11, and 0.01 nmol/(h mg protein). The patient α-*N*-acetyl-glucosamidase activities were 2.8, 0.11, 2.0, and 2.3 for the type A–D patients, respectively. This showed that the MPS III type B patient had a measured α-*N*-acetyl-glucosamidase activity close to the blanks, while the other patients' activities were at least 18 times higher than background. The MPS III type C assay blanks had acetyl-CoA:α-glucosaminide acetyltransferase activities of 0.22, 0.20, and 0.19 nmol/(h mg protein). The patients had acetyl-CoA:α-glucosaminide acetyltransferase activities of 3.3, 3.5, 0.16, and 2.5 nmol/(h mg protein) for type A–D, respectively. Thus, the MPS III type C patient activity was close to the blank while the other patients' activities were at least 11 times higher than background. Finally, the *N*-acetylglucosamine-6-sulfatase (MPS III type D) activities of the blanks were 0.02, 0.02, and 0.01 nmol/(h mg protein). The patients activities were 0.68, 0.60, 0.62, and 0.04 nmol/(h mg protein), with the MPS III type D patient activity being at least 15 times lower than the others. The activity data are compiled in Table 1.

We did not use fibroblasts from healthy individuals in the current study. The previous assays using biotinylated substrates and healthy individual fibroblasts showed normal activity ranges

Table 1. Enzyme Activities (nmol/(h mg protein) for the MPS III Type A–D Patients

	enzyme activity[a,b]						
assay type	blank	blank	blank	type A patient	type B patient	type C patient	type D patient
MPS IIIA	0.17	0.29	0.22	**0.25**	1.9	2.2	1.9
MPS IIIB	0.00	0.11	0.01	2.8	**0.11**	2.0	2.3
MPS IIIC	0.22	0.20	0.19	3.3	3.5	**0.16**	2.5
MPS IIID	0.02	0.02	0.01	0.68	0.60	0.62	**0.04**

[a]In units of nmol/(h mg protein). [b]From triplicate injections with coefficients of variation <10%.

in fibroblasts 0.30–0.64, 1.4–2.7, 1.5–5.4, and 0.067–0.092 nmol/(h mg protein) for the MPS III type A, B, C, and D assays, respectively.[24,25] The results with the new substrates are comparable for the B and C types. The MPS III type A and D activities achieved with the new substrates were 3- and 10-fold higher, respectively, than those previously reported.[25]

CONCLUSIONS

The main purpose of this study was to develop structurally simpler MPS III type A–D substrates and internal standards that are prepared from a common, late-stage synthetic intermediate that is converted to final reagents in 4 or fewer steps. The MPS III type A–D substrates are among the most structurally complex in the set of reagents needed for biochemical assay of LSD in general, and the synthetic achievement in this study should allow for production of reagents in amounts needed for expanded scope MPS III A–D assays. This would be implemented, should newborn screening of these disorders become desirable, especially for MPS IIIA since a treatment option is in clinical trials. Substrates were designed to avoid mass overlaps between these reagents and the full set of other substrates that we have developed for mass spectrometry assays of other lysosomal storage diseases.[15–22] In addition, the generated products contain a labile carbamate unit that directs fragmentation in tandem mass spectrometry (to improve assay sensitivity) and a hydrophobic component that allows for buffer removal prior to mass spectrometry. We show that these substrates readily detect the enzymes in fibroblasts relevant to MPS III A–D and are specific for each enzyme since the activities are close to background in the appropriate fibroblasts from MPS III A–D patients.

As will be reported shortly, we have developed a simplified assay of 9 different enzymes relevant to 9 LSDs that makes use of only 2 blood spot punches incubated in 2 buffers (6-plex +3-plex) and that uses rapid liquid chromatography in-line with tandem mass spectrometry. The latter allows almost all of the premass spectrometry sample preparation steps to be eliminated (i.e., DEAE capture, solid-phase extraction).[17,29] Work is underway in our laboratories to explore the use of these new MPS III A–D reagents for assays using dried blood spot punches, with a minimal number of assay buffers, and employing the liquid chromatography step to replace premass spectrometry sample processing.

Finally, since all of the reagents reported in this study contain the umbelliferone unit, they are anticipated to also work using fluorometric procedures to assay the MPS III A–D enzymes.[11–14] Thus, the reagents offer the choice of two

dx.doi.org/10.1021/bc200609x | *Bioconjugate Chem.* 2012, 23, 557–564

different assay platforms. However, the advantage of tandem mass spectrometry is that it allows for many LSD enzymes to be assayed using a single and rapid readout.

■ ASSOCIATED CONTENT

Supporting Information

Detailed synthetic procedures, spectroscopic data, Schemes S1−S4, and Figures S1−S8. This material is available free of charge via the Internet at http://pubs.acs.org.

■ AUTHOR INFORMATION

Corresponding Author

*F.T.: Phone 206-685-2041, Fax 206-685-8665, e-mail: turecek@chem.washington.edu. M. H. G.: Phone 206-543-7142, Fax 206-685-8665, e-mail: gelb@chem.washington.edu.

Notes

The authors declare no competing financial interest.

■ ACKNOWLEDGMENTS

Support of this research by the NIH-National Institute of Diabetes, Digestive and Kidney Diseases (Grant R01 DK067859) is gratefully acknowledged.

■ REFERENCES

(1) Neufeld, E., and Muenze, J. (2011) The Online Metabolic and Molecular Bases of Inherited Diseases (Valle D., Beaudet, A. L., Vogelstein, B., Kinzler K. W., Antonarakis, S. E., and Ballabio, A., Eds.) pp. 1−73, Chapter 136, Part 16: Lysosomal Disorders.

(2) Valstar, M. J., Ruijter, G. J. G., van Diggelen, O. P., Poorthuis, B. J., and Wijburg, F. A. (2008) Sanfilippo syndrome: A mini-review. *J. Inherit. Metabol. Dis 31*, 240−252.

(3) Hopwood, J. J., and Elliott, H. (1981) The diagnosis of the Sanfilippo C syndrome, using monosaccharide and oligosaccharide substrates to assay acetyl-CoA: 2-amino-2-deoxy-α-glucoside N-acetyltransferase activity. *Clin. Chim. Acta 112*, 67−75.

(4) Hopwood, J. J., and Elliott, H. (1981) Selective depolymerization of heparin to produce radiolabeled substrates for sulfamidase, 2-acetamido-2-deoxy-α-D-glucosidase, acetyl-CoA: 2-amino-2-deoxy-α-D-glucoside N-acetyltransferase, and 2-acetamido-2-deoxy-D-glucose 6-sulfate sulfatase. *Carbohydr. Res. 91*, 165−190.

(5) Hopwood, J. J., and Elliott, H. (1982) Detection of the Sanfilippo type B syndrome using radiolabelled oligosaccharides as substrates for the estimation of α-N-acetylglucosaminidase. *Clin. Chim. Acta 120*, 77−86.

(6) Reynertson, R., Campbell, P., Ford, J. D., Jacobsson, I., Rodén, L., and Thompson, J. N. (1983) New oligosaccharides from heparin and heparan sulfate and their use as substrates for heparin-degrading enzymes. *J. Biol. Chem. 258*, 7449−7459.

(7) Thompson, J. N., Rodén, L., and Reynertson, R. (1986) Oligosaccharide substrates for heparin sulfamidase. *Anal. Biochem. 152*, 412−422.

(8) Nowakowski, R. W., Thompson, J. N., and Taylor, K. B. (1989) Sanfilippo syndrome, type D: a spectrophotometric assay with prenatal diagnostic potential. *Pediatr. Res. 26*, 462−466.

(9) Thompson, J. N., Huffman, P. S., McConkie-Rosell, A., and Hessling, J. (1993) Prenatal diagnosis of Sanfilippo syndrome type A by early amniocentesis. *Biochem. Mol. Biol. Int. 29*, 793−797.

(10) Marsh, J., and Fensom, A. H. (1985) 4-Methylumbelliferyl α-N-acetylglucosaminidase activity for diagnosis of Sanfilippo B disease. *Clin. Genetics 27*, 258−262.

(11) Voznyi, Y. V., Karpova, E. A., Dudukina, T. V., Tsvetkova, I. V., Boer, A. M., Janse, H. C., and van Diggelen, O. P. (1993) A fluorometric enzyme assay for the diagnosis of Sanfilippo disease C (MPS III C). *J. Inherit. Metabol. Dis. 16*, 465−472.

(12) He, W., Voznyi, Y. V., Boer, A. M., Kleijer, W. J. J., and van Diggelen, O. P. (1993) A fluorometric enzyme assay for the diagnosis of Sanfilippo disease type D (MPS IIID). *J. Inherit. Metabol. Dis. 16*, 935−941.

(13) He, W., Voznyi, Ya, V., Huijmans, J. G., Geilen, G. C., Karpova, E. A., Dudukina, T. V., Zaremba, J., Van Diggelen, O. P., and Kleijer, W. J. (1994) Prenatal diagnosis of Sanfilippo disease type C using a simple fluorometric enzyme assay. *Prenat. Diagn. 14*, 17−22.

(14) Karpova, E. A., Voznyi, Y. V., Keulemans, J. L. M., Hoogeveen, A. T., Winchester, B., Tsvetkova, I. V., and van Diggelen, O. P. (1996) A fluorometric enzyme assay for the diagnosis of Sanfilippo disease type A (MPS IIIA). *J. Inherit. Metabol. Dis. 19*, 278−285.

(15) Li, Y., Scott, C. R., Chamoles, N. A., Ghavami, A., Pinto, B. M., Tureček, F., and Gelb., M. H. (2004) Direct multiplex assay of lysosomal enzymes in dried blood spots for newborn screening. *Clin. Chem. 50*, 1785−1796.

(16) Blanchard, S., Sadilek, M., Scott, C. R., Turecek, F., and Gelb, M. H. (2008) Tandem mass spectrometry for the direct assay of lysosomal enzymes in dried blood spots: application to screening newborns for mucopolysaccharidosis I (Hurler-Scheie syndrome). *Clin. Chem. 54*, 2067−2070.

(17) Wolfe, B. J., Blanchard, S., Sadilek, M., Scott, C. R., Turecek, F., and Gelb, M. H. (2011) Tandem mass spectrometry for the direct assay of lysosomal enzymes in dried blood spots: application to screening newborns for mucopolysaccharidosis II (Hunter syndrome). *Anal. Chem. 83*, 1152−1156.

(18) Khaliq, T., Sadilek, M., Scott, C. R., Turecek, F., and Gelb, M. H. (2011) Tandem mass spectrometry for the direct assay of lysosomal enzymes in dried blood spots: application to screening newborns for mucopolysaccharidosis IVA (Morquio A). *Clin. Chem. 57*, 128−131.

(19) Duffey, T. A., Khaliq, T., Scott, C. R., Turecek, F., and Gelb, M. H. (2010) Design and synthesis of substrates for newborn screening of Maroteaux-Lamy and Morquio A syndromes. *Bioorg. Med. Chem. Lett. 20*, 5994−5996.

(20) Duffey, T. A., Sadilek, M., Scott, C. R., Turecek, F., and Gelb, M. H. (2010) Tandem mass spectrometry for the direct assay of lysosomal enzymes in dried blood spots: application to screening newborns for mucopolysaccharidosis VI (Maroteaux-Lamy syndrome). *Anal. Chem. 82*, 9587−9591.

(21) Duffey, T. A., Bellamy, G., Elliott, S., Fox, A. C., Glass, M., Turecek, F., Gelb, M. H., and Scott, C. R. (2010) Triplex tandem mass spectrometry for newborn screening of Fabry, Pompe and mucopolysaccharidosis I (Hurler syndrome): results of a pilot study. *Clin. Chem. 56*, 1854−1861.

(22) Spacil, Z., Elliott, S., Reeber, S. L., Gelb, M. H., Scott, C. R., and Turecek, F. (2011) Comparative fast liquid chromatography: application to newborn screening of Pompe, Fabry,and Hurler diseases. *Anal. Chem. 83*, 4822−4828.

(23) Ruijter, J., Valstar, M. J., and Wijburg, F. A. (2011) Mucopolysaccharidosis type III (Sanfilippo syndrome): emerging treatment strategies. *Curr. Pharm. Biotechnol. 12*, 923−930.

(24) Gerber, S. A., Turecek, F., and Gelb, M. H. (2001) Design and synthesis of substrate and internal standard conjugates for profiling enzyme activities in the Sanfilippo syndrome by affinity chromatography/electrospray ionization mass spectrometry. *Bioconjugate Chem. 12*, 603−615.

(25) Gerber, S. A., Scott, C. R., Turecek, F., and Gelb, M. H. (2001) Direct profiling of multiple enzyme activities in human cell lysates by affinity chromatography/electrospray ionization mass spectrometry. *Anal. Chem. 73*, 1651−1657.

(26) Bradford, M. M. (1976) A rapid and sensitive method for the quantitation of microgram quantities of protein utilizing the principle of protein-dye binding. *Anal. Biochem. 72*, 248−254.

(27) Tailler, D., Jacquinet, J. C., Noiret, A. M., and Beau, J. M. (1992) An expeditious and stereocontrolled preparation of 2-azido-2-deoxy-β-D-glucopyranose derivatives from D-glucal. *J. Chem. Soc., Perkin Trans. 1*, 3163−3164.

(28) Dasgupta, F., and Masada, R. I. (2002) Synthesis of 7-O-(2-deoxy-2-sulfamido-α-D-glucopyranosyl)-4-methylcoumarin sodium salt: a fluorogenic substrate for sulfamidase. *Carbohydr. Res. 337*, 1055−1058.

(29) Metz, T. F., Mechtler, T. P., Orsini, J. J., Martin, M., Shushan, B., Herman, J. L., Ratschmann, R., Item, C. B., Streubel, B., Herkner, K. R., and Kasper, D. C. (2011) Simplified newborn screening protocol for lysosomal storage disorders. *Clin. Chem. 57*, 1286−1294.

Bioconjugate Chemistry

Article

pubs.acs.org/bc

Directed, Strong, and Reversible Immobilization of Proteins Tagged with a β-Trefoil Lectin Domain: A Simple Method to Immobilize Biomolecules on Plain Agarose Matrixes

Fernando López-Gallego,[†] Ivan Acebrón,[‡] Jose Miguel Mancheño,[‡] Sebastian Raja,[§] M. Pilar Lillo,[§] and Jose Manuel Guisán Seijas*[,†]

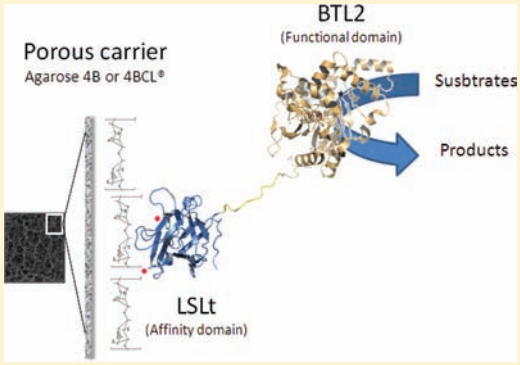
[†]Departamento de Biocatálisis, Instituto de Catálisis, CSIC, Campus UAM, Cantoblanco 28049, Madrid, Spain

[‡]Grupo de Cristalografía y Biología Estructural, Instituto Rocasolano, CSIC, Serrano 119, 28006 Madrid, Spain

[§]Grupo de Biofísica Molecular, Instituto Rocasolano, CSIC, Serrano 119, 28006 Madrid, Spain

Supporting Information

ABSTRACT: A highly stable lipase from *Geobacillus thermocatenolatus* (BTL2) and the enhanced green fluorescent protein from *Aquorea victoria* (EGFP) were recombinantly produced N-terminally tagged to the lectin domain of the hemolytic pore-forming toxin LSLa from the mushroom *Laetiporus sulphureus*. Such a domain (LSL_{150}), recently described as a novel fusion tag, is based on a β-trefoil scaffold with two operative binding sites for galactose or galactose-containing derivatives. The fusion proteins herein analyzed have enabled us to characterize the binding mode of LSL_{150} to polymeric and solid substrates such as agarose beads. The lectin-fusion proteins are able to be quantitatively bound to both cross-linked and non-cross-linked agarose matrixes in a very rapid manner, resulting in a surprisingly dynamic protein distribution inside the porous beads that evolves from heterogeneous to homogeneous along the postimmobilization time. Such dynamic distribution can be related to the reversible nature of the LSL_{150}−agarose interaction. Furthermore, this latter interaction is temperature dependent since it is 4-fold stronger when the immobilization takes place at 25 °C than when it does at 4 °C. The strongest lectin−agarose interaction is also quite stable under a survey of different conditions such as high temperatures (up to 60 °C) or high organic solvent concentrations (up to 60% of acetonitrile). Notably, the use of cross-linked agarose would endow the system with more robustness due to its better mechanical properties compared to the noncross-linked one. The stability of the LSL_{150}−agarose interaction would prevent protein leaching during the operation process unless high pH media are used. In summary, we believe that the LSL_{150} lectin domain exhibits interesting structural features as an immobilization domain that makes it suitable to reversibly immobilize industrially relevant enzymes in very simple carriers as agarose.



INTRODUCTION

Enzyme immobilization has facilitated the process development of many biotransformations,[1,2] mainly because of the heterogeneous nature of the resulting biocatalysts. Such carrier-bound enzymes are easily and readily separated from the reaction mixture, enabling continuous operation.[3,4] There are many immobilization strategies that comprise reversible to irreversible attachments,[5−10] random to site-directed bindings,[11−13] and one-pot to several-pot methodologies.[8,14−16] Among all those immobilization technologies, specific immobilization of tagged proteins has been broadly used for many biotechnological applications.[17−19] Those tags may be either a small peptide of few aminoacids, such as the famous 6xHis-tag, or a larger and folded binding protein such as the glutathione *S*-transferase (26 kDa).[17] In general, all these systems reversibly and specifically immobilize the fusion protein readily expressed to be purified in one-pot.[20,21] In addition to the simplicity provided by these tags to the purification/immobilization protocols, it should be noted that many such affinity tags, overall those larger and folded ones, act as solubility enhancers increasing the production yield of soluble recombinant fusion protein.[22]

Lectin domains have been broadly applied in biosensor and microarray technologies, overall in the field of the glycobiotechnology.[23,24] Concanavalin A is one of the most used lectins to specifically immobilize glycoproteins; however, such a protein is normally attached to the solid surface rather than tagged to the target recombinant protein.[25,26] In this regard, we have recently described that the β-trefoil lectin domain of the pore-forming toxin LSLa from the mushroom *Laetiporus sulphureus* (LSL_{150})[27] exhibits properties typical of fusion tags which have permitted one to set up a novel protocol for the production and purification of recombinant proteins N-terminally tagged with such a domain.[28,29] This new protocol

Received: November 17, 2011
Revised: February 28, 2012
Published: February 28, 2012

 © 2012 American Chemical Society dx.doi.org/10.1021/bc2006237 | *Bioconjugate Chem.* 2012, 23, 565−573

involves a simple, selective, and effective interaction between LSL_{150} and the chemical structure of polymerized agarose.[28,29] In this sense, the high resolution crystal structures of both unliganded LSL_{150} and LSL_{150} complexed with lactose permitted the detailed characterization of the sugar-binding mode of this lectin, revealing two lactose binding sites of the lectin as well as notable solvent rearrangements occurring upon lactose binding.[29] Therefore, it seems that the binding of LSL_{150} to agarose polymers must rely on those two functional sugar-binding sites.

Despite the large number of affinity tags currently described in the literature,[17,19] the vast majority of them have been applied in the recombinant protein production/purification process as chromatographic-based systems. Only a handful of them have been used as reversible immobilization platforms to make heterogeneous biocatalysts with industrial perspectives.[30−32] The immobilization via affinity tags enables the oriented immobilization of the fusion protein, with the linker between the N-terminal tag and the C-terminal companion acting as the spacer arm between the support surface and the catalytic domain, preserving the activity of the C-terminal enzyme within the immobilized composite.[30,33,34] Moreover, this methodology allows the one-pot purification/immobilization process because of the high selective interaction between the affinity tag and the carrier. One of the most representative examples for affinity immobilization is the 6x-His-tag system,[20,35] although few new methods have been developed in the past decade.[14,21,30] Nevertheless, many of these methodologies require functionalized carriers, for example, with metal chelates, alkyl-sulfates groups, glutathione, etc., increasing the cost and the complexity of the process.[18] On the contrary, in the system described in this work, the galactose-specific LSL_{150} domain is bound to nonactivated agarose matrixes which are more than 50 times less expensive than, for example, the manose−agarose matrixes needed for purifying recombinant MBP-tagged proteins.[28,36]

In this work, we make use of nonactivated commercial agarose (agarose 4B or agarose 4BCL) as carriers to specifically and reversibly immobilize two biotechnologically relevant proteins that have been produced as fusion proteins with LSL_{150} as the N-terminal tag: the cysteine-less mutant of the lipase from *Geobacillus thermocatenolatus*[37] (BTL2) and the enhanced green fluorescent protein from *Aquorea victoria* (EGFP). Optimal immobilization was achieved by contacting the carrier and the fusion proteins at 25 °C for at least 18 h. The interaction between LSL_{150} and the carrier was highly stable under drastic conditions such as 60% of organic solvent or 60 °C since the fusion protein remained bound to the carrier under those harsh conditions.

EXPERIMENTAL PROCEDURES

Materials. Agarose 4B and 4BCL were purchased from Agarose Bead Technologies (Madrid, Spain). Lactose was purchased from Sigma Chem. Co (St. Louis, USA). Restriction endonucleases and DNA polymerase were purchased from Fermentas International Co. and Biotools (Madrid, Spain), respectively. Other reagents were of analytical grade.

Cloning and Fusion Protein Production. The expression vector pKLSLt[29] was used as a template for the preparation of the plasmids pKLSLt-BTL2 and pKLSLt-EGFP coding for LSLt-BTL2 and LSLt-EGFP, respectively. As previously reported,[29] in pKLSLt the 3′-end of the LSL_{150} coding sequence is followed by an in-frame sequence coding for a flexible linker sequence (amino acids ASSS), the tobacco etch virus (TEV) endoprotease cleavage site (amino acids ENLYFQG), and a stop codon. That is, LSLt is LSL150 plus a four-residue linker and the TEV recognition sequence. Preparation of pKLSLt-BTL2 involved the amplification of the gene encoding for the lipase from *Geobacillus thermocatenolatus* (BTL2) by PCR with the PrimeSTAR HS DNA polymerase (Takara) using appropriate primers (forward, 5′-TGAAAACCTGTATTTCCAGGGCATGGCATCCC-CACGCGCCAA TG-3′; reverse, 5′-TCAGCTTCC-TTTCGGGCTTTGTTATTAAGGCCGCAAACTCGCCA AC-3′). The purified PCR product was then inserted into the pKLSLt vector by using the restriction-free and ligation-free cloning strategy previously described.[38] *Escherichia coli* DH5α cells were transformed, and recombinant plasmids and their sequences confirmed by DNA sequence analysis. Preparation of the pKLSLt-EGFP expression vector and production and purification of the fusion proteins were as indicated previously.[29] Briefly, the respective plasmids were used to transform *E. coli* BL21 (DE3) cells (Novagen, Germany). Transformed cells were grown at 37 °C in LB media containing 50 μg/mL kanamycin until the culture turbidity (OD_{600}) reached 0.6−0.8, when they were induced with 0.3 mM isopropyl-β-D-thiogalactoside (IPTG). After induction, the cultures were grown at 16 °C for 20 h before harvesting the cells by centrifugation at 4000*g* for 15 min. Cell pellets were suspended in 25 mL of 20 mM Tris-HCl, pH 8.0, and 100 mM NaCl and flash frozen at −80 °C until further use.

Purification of LSLt-BTL2 and LSLt-EGFP. The purification of LSLt-BTL2 and LSLt-EGFP was accomplished by affinity chromatography on Sepharose 4B at 4 °C using a BioLogic LP chromatography system (BioRad) and an Econo Gradient Pump (BioRad). Columns were prepared in-house using glass Econo-Column columns (2.5 × 10 cm; BioRad). Prior to sample loading, the resin was exhaustively washed with binding buffer (20 mM Tris-HCl, pH 8.0, 100 mM NaCl, and 0.04% (w/v) sodium azide). Cleared cell extracts were directly loaded onto the column at 2.5 mL/min, which was then washed with binding buffer overnight at 4 °C. Fusion proteins were then eluted with elution buffer (20 mM Tris-HCl, pH 8.0, 100 mM NaCl, 0.04% sodium azide (w/v), and 0.2 M lactose) at 3 mL/min. Fractions containing the eluted fusion proteins were pooled and dialyzed overnight at 4 °C against binding buffer to remove bound lactose. Finally, polishing size-exclusion chromatography on 16/60 HiLoad Superdex 75 (GE Healthcare) was carried out to resolve the fusion proteins from potential soluble aggregates. Fractions were pooled and concentrated by ultrafiltration with YM-10 membranes (Amicon). Protein materials were stored at −80 °C. Protein purity was checked by SDS−PAGE. Regeneration of the Sepharose 4B column was done by washing with five volumes of elution buffer and then with five additional volumes of binding buffer.

Immobilization of LSLt-Tagged Proteins on Agarose-Type Carriers. Ten milliliters of 3 U/mL or 40 U/mL LSLt-BTL2 solution or 10 mL of 1 mg/mL LSLt-EGFP solution were incubated with 1 wet gram of either agarose 4B or 4BCL at different temperatures (4 or 25 °C) for different times. Supernatant and suspension samples were withdrawn at different times, and lipase activity of LSLt-BTL2 or protein concentration of LSLt-EGFP was determined according to the assay described by Fernández-Lorente et al.[39] and Bradford,[40] respectively.

Elution of Different LSLt-BTL2 Derivatives under Lactose Gradients. Different LSLt-BTL2 derivatives (0.1 g) were incubated for 30 min at pH 7 and 25 °C with 1 mL of lactose solution at different concentrations (0−400 mM). Activity of both supernatant and suspension was measured as described by Fernández-Lorente.[39]

Stability Studies of the LSLt Domain. LSLt-BTL2 derivatives immobilized on agarose 4BCL at 25 °C for 18 h were incubated at different postimmobilization conditions. Then, 0.1 g of such a derivative was incubated for 1 h with 1 mL of different buffer solutions at different pH values (50 mM sodium acetate, pH 5; 50 mM sodium phosphate, pH 7; 50 mM sodium carbonate, pH 10), at different temperatures (25, 45, and 60 °C), at different acetonitrile concentrations (20, 40, and 60%) and in the presence of 0.2% Triton X-100 at pH 7. Activity of both supernatant and suspension was measured as described by Fernández-Lorente.[39]

Confocal Laser Scanning Microscopy. Derivatives of LSLt-EGFP rapidly immobilized at 4 °C on either agarose 4B or 4BCL were resuspended in a ratio of 1/10 (w/v) (solid derivative/buffer). Postimmobilization fluorescence of such derivatives was monitored using an inverted Leica TCS SP5 laser confocal microscope with a 10× plan-apochromatic objective. Sequential scanning mode was used to avoid cross-talk between channels. All images shown correspond to a single confocal section. Images were processed with the LAS AF Leica application suite and Adobe Photoshop CS2 (Adobe Systems Inc.).

RESULTS AND DISCUSSION

Production and Characterization of LSLt-BTL2 and LSLt-EGFP. The cysteine-less mutant of the thermophilic lipase from *Geobacillus thermocatenolatus*[37] (BTL2) together with the enhanced green fluorescent protein from *Aquorea victoria* (EGFP) have been recombinantly produced N-terminally tagged with the fusion tag LSLt (see Experimental Procedures), resulting in the constructions LSLt-BTL2 and LSLt-EGFP, respectively. As we have recently described,[29] this novel fusion tag, based on the β-trefoil lectin domain of the pore-forming toxin LSLa from the mushroom *L. sulphureus*,[12] exhibits properties typical of both solubility enhancers and affinity tags, playing a passive role in the folding of its C-terminal partners. In this regard, LSLt-tagged EGFP showed the same spectroscopic behavior of untagged EGFP in solution, with a predominant fluorescence lifetime of 2.85 ns (see Table S1, Supporting Information);[41] moreover, the fluorescence decay of LSLt-tagged EGFP revealed the same lifetime components as those previously reported for free EGFP.[41] However, and as expected for the higher molecular weight of the fusion protein (45 kDa) relative to EGFP (27 kDa), the fluorescence anisotropy of LSLt-EGFP decayed more slowly than the free EGFP (Figure S1, Supporting Information). As a whole, these results show that LSLt does not affect the intrinsic spectroscopic behavior of EGFP, which agrees well with this tag playing no role in the folding of its C-terminal counterpart.

Likewise, the characterization of the hydrolytic activity of LSLt-BTL2 revealed that the genetic fusion of LSLt to the N-terminal end of the lipase did not affect its catalytic properties indicating both a proper folding of BTL2 and the lack of steric restraints imposed by the presence of the tag affecting the catalytic activity (Table 1). Moreover, LSLt-BTL2 was as stable as BTL2 (Figure S2, Supporting Information) when both soluble proteins were incubated at 45 °C. Moreover, the fusion of LSLt to reporter proteins has provided us for the first time with the opportunity to analyze the immobilization and elution behavior of such a lectin domain on agarose-type carriers even under drastic conditions. In the case of LSLt-BTL2, the highly stable enzymatic activity incorporated into the carrier could be spectrophotometrically monitored in an easy manner. In the same way, the microscopic distribution of the lectin domain within the pores of the carrier was also possible by monitoring LSLt-EGFP green fluorescence by a confocal scanning laser microscope (CLMS).

Table 1. Steady-State Kinetics Parameters of BTL2 Cysteine-Less Variant and the Same Variant Fused to a LSLt Domain

enzyme	V_{max} (U/mg)	K_m (mM)	K_{cat} (s^{-1})	K_{cat}/K_m ($s^{-1}\cdot M^{-1}\cdot 10^4$)
BTL2[a]	95.9 ± 0.2	1.46 ± 0.51	69.5 ± 0.2	4.7
LSLt-BTL2[b]	78 ± 3	1.2 ± 0.1	56.8 ± 2.2	4.8
Ag4BCL[c] (LSLt-BTL2)	75 ± 4	2.3 ± 0.1	54 ± 3	2.3

[a]This is the BTL2 variant where the two native cysteines were changed by two serines. [b]LSLt-BTL2. It is the cysteine-less BTL2 mutant N-terminally fused to LSLt. [c]Ag4BCL(LSLt-BTL2). It is the cysteine-less BTL2 mutant N-terminally fused to LSLt immobilized on plain agarose 4BCL.

Immobilization of Recombinant Proteins Fused to LSLt on Agarose Beads. LSLt-BTL2 and LSLt-EGFP were immobilized on two different types of agarose beads: agarose 4B and agarose 4BCL. The former is only polymerized agarose, whereas in the latter, the polymerized agarose has been cross-linked with epychloridrine in order to stabilize the agarose beads under harsh conditions. Noteworthy, both BTL2 and EGFP lacking the LSLt tag did not bind to either agarose 4B or 4BCL; therefore, immobilization specifically took place through interaction between the lectin domain and the agarose surface. Figure 1 shows the immobilization parameters (immobilization yield and expressed activity) of low loads of LSLt-BTL2 (30 $U\cdot g_{carrier}^{-1}$) on both agarose-based carriers. In both cases, the fusion protein was quantitatively bound to the matrixes apparently with similar immobilization rates (Figure 1A). Much higher loads of protein could be immobilized on plain-agarose beads; in fact, the maximum loading capacity of these matrixes was 43 mg of LSLt-BTL2 per g of wet matrix. Nevertheless, when immobilization conditions were forced (400 $U\cdot g_{carrier}^{-1}$), the immobilization rate was slightly higher for agarose 4B (Figure 1B). The different immobilization kinetics observed might rely on the particular chemical structures of the two agarose-type resins. Whereas agarose 4B keeps intact the polymeric structure of the agarose, the cross-linking treatment of agarose 4BCL alters the chemical structure of the β-1,3-D-galactose and α-1,3,4,6-anhydro-L-galactose monomers found in the agarose polymer, and consequently, the lectin-agarose 4BCL interaction might be affected.

Surprisingly, the expressed activity of the immobilized lipase decreased as a result of the immobilization process. The final expressed activities were 60 and 50% of the LSLt-BTL2 activity in solution, when the protein was immobilized on agarose 4B and 4BCL, respectively (Figure 1A). Typically, reduced values of enzymatic activities upon enzyme immobilization can be explained in terms of protein inactivation promoted by the immobilization protocol or to the existence of a rate-limiting diffusion of the substrate into the porous carrier. We believe that, in our case, the first possibility can be discarded because, *a*

dx.doi.org/10.1021/bc2006237 | *Bioconjugate Chem.* 2012, 23, 565−573

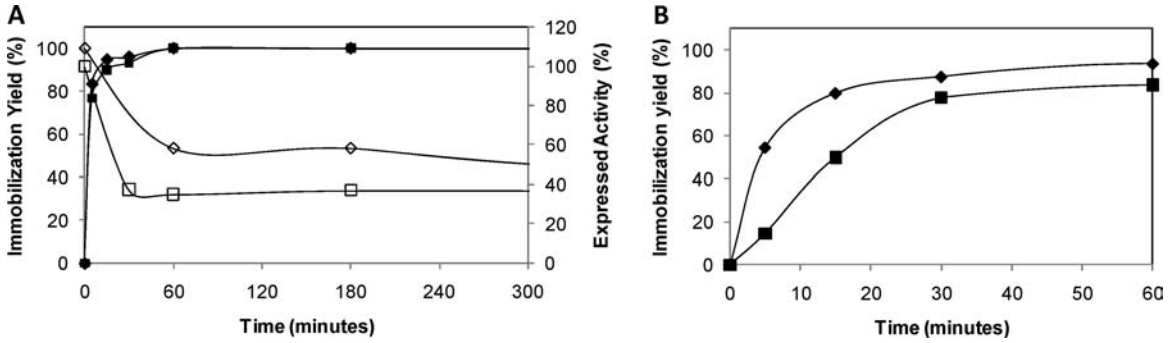


Figure 1. Immobilization of LSLt-BTL2 on different agarose type matrixes. LSLt-BTL2 was immobilized on agarose 4B (rhombus) and on agarose 4BCL (squares). Immobilization yield (closed symbols) and expressed activity (open symbols) were calculated for each immobilization experiment. (A) The immobilization was carried out by incubating 30 U of LSLt-BTL2 activity per gram of support in an immobilization ratio of 0,25 m^2 of support per mL of immobilization mixture. (B) Immobilization was carried out incubating 400 U of LSLt-BTL2 activity per gram of support in an immobilization ratio of 2.5 m^2 of support per mL of immobilization mixture. In both cases, immobilization occurred at pH 7 and 25 °C. Immobilization patterns were quite similar between both types of agarose matrixes, and only when immobilization conditions were forced to immobilize high amounts of enzyme, a slight faster immobilization could be observed with agarose 4B. Data corresponded to the mean value of three independent experiments where error was never higher than 5%.

priori, the LSLt-BTL2 orientation on the support surface (the N-terminal end of the lipase, and therefore the LSLt tag, is located on the opposite site of the active center of the enzyme) is favorable to avoid a direct interaction between the lipase active center and the support surface that might affect the binding pocket conformation (Figure 2). Hence, it seems

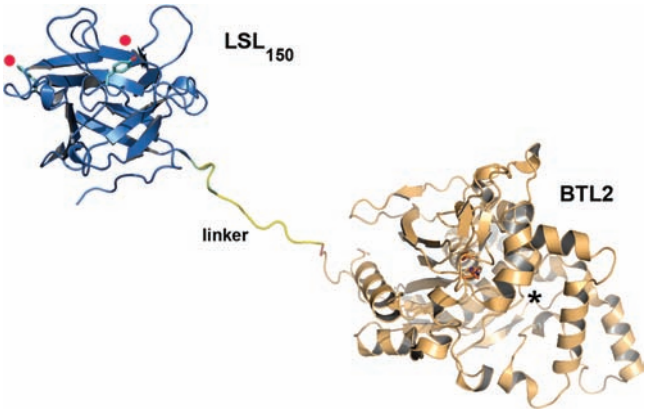


Figure 2. Putative atomic model of LSLt-BTL2. This tentative model has been built considering the crystal structures of both LSL_{150} (PDB code: 2Y9F) and BTL2 (PDB code: 2W22), with an extended linker containing 11 amino acid residues to provide a flexible region between the N-terminal lectin module that directly interacts with the matrixes and the accompanying C-terminal lipase. The two red circles indicate the β and γ sugar-binding sites (Tyr-91 from the β site and Phe-139 from the γ site, shown as sticks), and the asterisk indicates the entrance to the active site (the residues that make up the catalytic triad are also shown as sticks).

plausible to think that reduction of the expressed activity was due to rate-limiting substrate diffusion into the carrier since the activity measurements were carried out under nonsaturating substrate (500 μM pNPB) conditions because it was quite insoluble in aqueous media. In fact, the eluted activity per gram of support of the LSLt-BTL2 derivatives incubated for 24 h with 400 mM of lactose was roughly double the expressed activity of the immobilized protein per gram and almost the same as the immobilized activity per gram (Table S2, Supporting Information). Moreover, the apparent K_m value of the immobilized protein was increased by a factor of 2 (Table 1). These facts support the idea that LSLt-BTL2 in its immobilized form was subjected to higher mass transfer restrictions than its soluble one. One of the main reasons that would explain the diffusional limitations observed for well-oriented and nondeactivated enzymes immobilized on porous carriers would be their distribution throughout the porous surface.[42,43] It has been reported that heterogeneous enzyme distribution leads to a much better catalytic effectiveness under conditions of mass transfer limitations than those enzymes homogeneously distributed across the porous surface.[43] Hence, in the heterogeneous systems, the higher effectiveness would rely on the easier diffusivity of the reactants to the enzyme catalytic centers. In our case, the protein distribution is essentially driven by the interaction between the lectin module of the fusion protein and the agarose surface. In order to study the protein distribution within the carrier, LSLt-EGFP was immobilized on both agarose 4B and 4BCL, and the resulting derivatives were analyzed by CLMS. Surprisingly, a homogeneous distribution of LSLt-EGFP was found in both agarose 4B and 4BCL, which *a priori* does not agree with the fact that proteins rapidly immobilized show heterogeneous distributions, being mainly located at the bead outline.[44] To shed light on this apparent discrepancy, we dynamically studied the post-immobilization localization of LSLt-EGFP. First, LSLt-EGFP was rapidly immobilized on both agarose 4B and 4BCL at 4 °C, and after 1 min, the immobilization suspension was filtered and washed to remove unbound protein. Finally, beads containing immobilized LSLt-EGFP were diluted in aqueous media, and their fluorescence was recorded at various time intervals. Interestingly, it could be observed how proteins migrated inside the porous surface during postimmobilization incubation (Figure 3A). At short postimmobilization times, LSLt-EGFP was mainly heterogeneously distributed colonizing only the outer surface of the beads, while at longer postimmobilization times, LSLt-EGFP colonized the whole porous surface revealing a homogeneous protein distribution, which was stable in the time scale herein consider (videos S1 and S2, Supporting Information). This dynamic behavior of the LSLt-EGFP distribution presumably reveals an underlying LSLt-agarose binding mode based on the rapid and reversible association/dissociation process inside the pores. Although this system is

dx.doi.org/10.1021/bc2006237 | *Bioconjugate Chem.* 2012, 23, 565–573

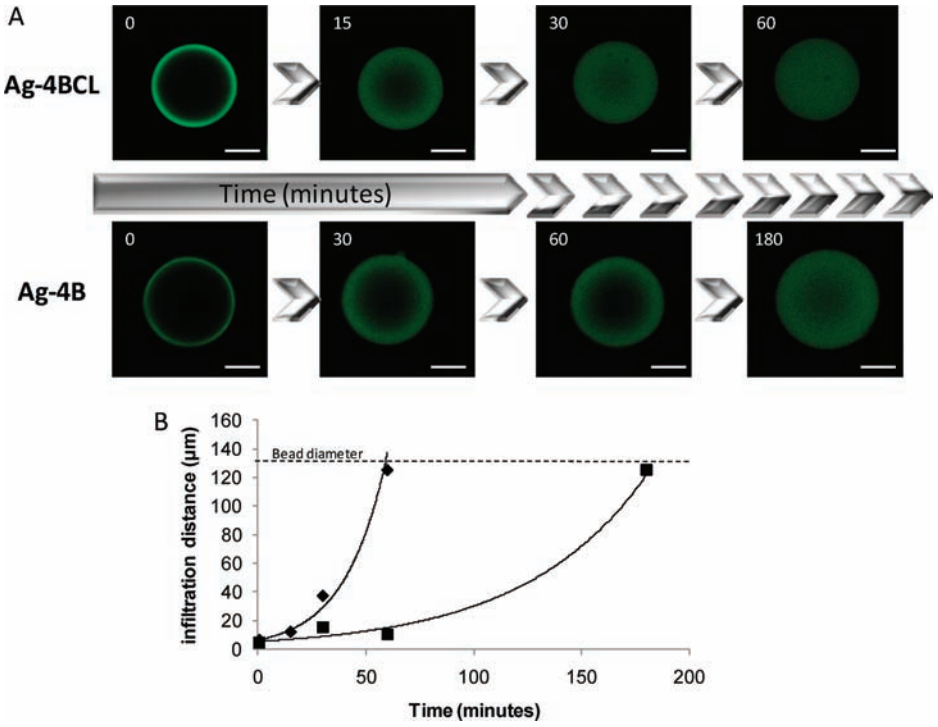


Figure 3. Time-dependence of the spatial distribution of LSLt-EGFP inside different agarose type matrixes. The immobilizations were carried out by incubation of 1 mg of LSLt-EGFP per gram of each support. When LSLt-EGFP was quantitative bound, the derivatives were vacuum filtered and resuspended in 25 mM sodium phosphate buffer, pH 7, and subsequently analyzed by CLMS. (A) CLMS images recorded at different time intervals. (B) The infiltration distance of LSLt-EGFP was calculated at different times by measuring the size of the radius occupied by 90% of the total fluorescence given by such a protein on agarose 4B (rhombus) and on agarose 4BCL (squares). The experimental data were fitted to the mathematical equation $D_i = A \cdot e^{\sqrt{Vd \cdot t}}$ in order to determine the distribution velocity (V_d). It can be observed how in both agaroses the LSLt-EGFP was infiltrated deeper and deeper through the porous surface along time. The full homogeneous distribution took longer when the immobilization carrier was agarose 4B. The size of the agarose beads represented in this figure is roughly 125 μm, and the white scale bar is 50 μm.

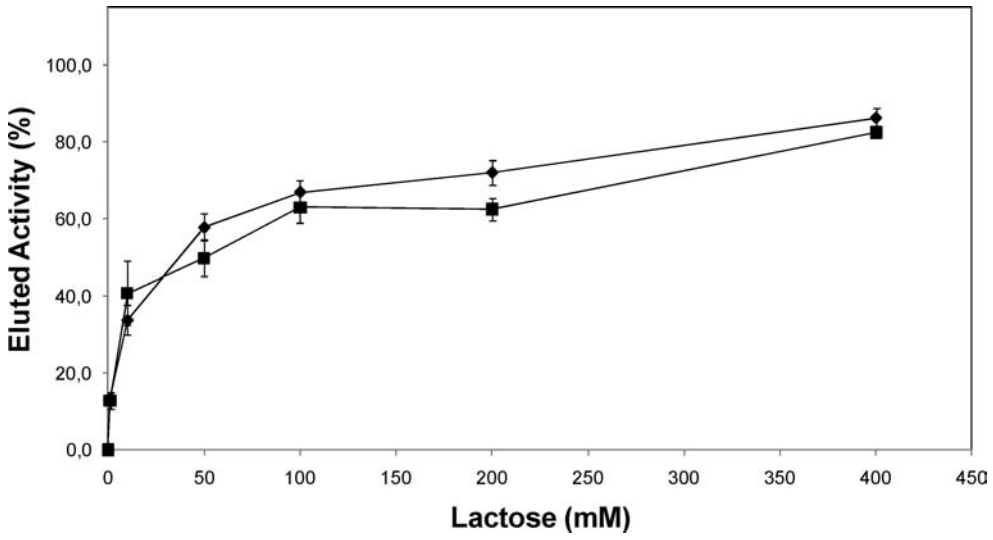


Figure 4. Binding strength of the interaction between the LSLt domain and different types of agarose matrixes. LSLt-BTL2 immobilized on agarose matrixes at 4 °C for 15 min (100% of immobilization) was eluted with different concentrations of lactose (0–400 mM). This experiment allows us to evaluate the apparent affinity of the LSLt domain to the galactose units forming the agarose structure. The two studied matrixes were agarose 4B (rhombus) and agarose 4BCL (squares). The data shown are the means of three independent experiments with SD (±) represented as error bars.

shifted to the associated state, which allows quantitative immobilization, the reversible nature of the interaction would enable the observed protein migration from a heterogeneous distribution to a homogeneous one. This migration from crowded regions to less busy ones would be possible because of the higher availability of galactose-type affinity groups in the noncolonized areas. In this context, the proteins dissociated within the agarose particles would tend to interact with noncolonized areas inside the porous structure where the density of the galactose-type groups is higher, and therefore, the association would be favored. Noteworthy, the rate of LSLt-EGFP distribution throughout the porous surface was almost 3-

dx.doi.org/10.1021/bc2006237 | *Bioconjugate Chem.* 2012, 23, 565–573

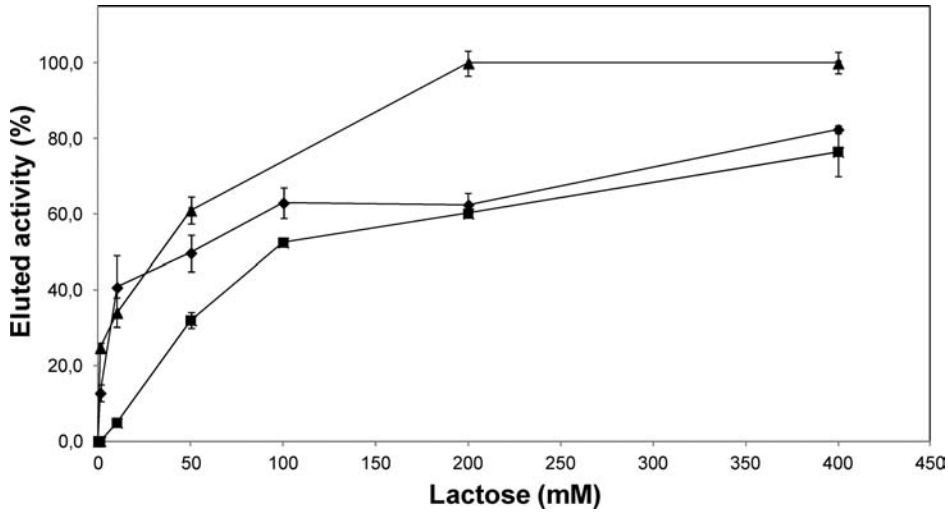


Figure 5. Effect of temperature and time of immobilization on the binding strength of the LSLt domain to agarose 4BCL. Different immobilized derivatives of LSLt-BTL2 on agarose 4BCL were eluted under different concentrations of lactose (0–400 mM). This experiment allows us to evaluate how strong the LSLt domain is bound to the galactose units forming the agarose 4BCL structure. The immobilizations were prepared at two different temperatures, 25 °C (squares) and 4 °C (triangles), for 18 h, observing a higher binding strength when the immobilization was carried out at higher temperature. LSLt-BTL2 was also immobilized at 25 °C for 15 min (rhombus) observing that the first elution fraction was weakly bound for short immobilization times than for longer ones. Data correspond to the mean value of three independent experiments with SD (±) represented as error bars.

fold faster when the fusion protein was immobilized on agarose 4BCL than when it was on agarose 4B (Figure 3B and Table S3, Supporting Information). In this regard, the different chemical structure of both agarose matrixes might be affecting to the association/dissociation equilibrium of the lectin-agarose binding. Hence, at least at short postimmobilization times, the lectin domain seemed to be more easily dissociated from agarose 4BCL than from 4B since LSLt-EGFP distribution evolved faster in the former agarose (video S1, Supporting Information) than in the latter (video S2, Supporting Information) (Figure S3 and Table S3, Supporting Information).

Therefore, it can be concluded that the immobilization of LSLt-tagged proteins on agarose-based matrixes is highly rapid, yielding homogeneous protein distributions. As far as we know, this is the first time where homogeneous protein distributions throughout porous surfaces has been achieved by immobilizing low loads of one protein. It was possible because of the postimmobilization migration experienced by the immobilized proteins (Figure S3, Supporting Information). This particular feature has many potential applications such as new lab-on-a-chip devices to detect important analytes in medical or environmental chemistry[45] or in the ordered assembly of biomolecular platforms inside porous materials in combination with other immobilization chemistries that promote heterogeneous protein distribution.[46,47]

Reversibility of the LSLt–Agarose Interaction: Effect of Different Variables on the Strength of the Lectin–Agarose Interaction. As shown above, the interaction between LSLt and different agarose matrixes occurs through a reversible interaction; in fact, fusion proteins can be eluted by incubation at high lactose concentrations during the purification protocol.[28,29] Now, we have further analyzed this dissociation process by studying its dependence on lactose concentration, which in turn allows us to evaluate the apparent affinity of LSLt toward the agarose beads system. Figure 4 shows that LSLt-BTL2 was similarly eluted from both agarose 4B and 4BCL, suggesting that LSLt binds to both matrixes with the same strength, at least at the macroscopic level. Since cross-linked carriers provide better mechanical properties, allowing biocatalysts to work under more drastic operational conditions, we believe that this result may open up applications of LSLt in applied biocatalysis as a generic, immobilizing domain of proteins on agarose-based carriers.

In addition, we have also analyzed the effect of temperature and time of immobilization on the binding strength of LSLt. With this aim, LSLt-BTL2 was immobilized on agarose 4BCL for different times (15 min and 18 h) at different temperatures (4 and 25 °C), and the immobilized derivatives were then incubated with different lactose concentrations. Temperature was revealed as the most important parameter affecting the strength of the lectin–agarose bead interaction (Figure 5). For instance, the 60% of the LSLt-BTL2 immobilized at 4 °C for 18 h was eluted with 50 mM lactose, whereas at least 200 mM lactose was needed to elute the same activity percentage of LSLt-BTL2 immobilized at 25 °C for the same time (Figure 5); it would mean a 4-fold harder elution by carrying out the immobilization at 25 °C. The same effect was observed for derivatives immobilized only for 15 min but at different temperatures. Although the incubation time did not affect as much as the temperature to the binding strength, it is interesting to highlight how for the derivatives immobilized for 15 min at 25 °C, the earlier eluted fractions needed lower lactose concentration than the same fraction from derivatives immobilized for longer times at the same temperature (Figure 5).

The temperature-based versatility of the binding strength of the lectin–agarose interaction would make this system suitable only for either protein purification or one-pot protein purification/immobilization. In this way, for purification purposes strong binding would not be desired because the protein must be eluted later, whereas for applied purification/immobilization protocols, strong binding would be preferred in order to avoid the protein leaching during the operation

dx.doi.org/10.1021/bc2006237 | *Bioconjugate Chem.* 2012, 23, 565–573

process. Hence, by switching the immobilization conditions from low temperatures and short immobilization times to medium temperatures and longer incubation times, the purification methodology would become useful for immobilizing proteins.

Stability of LSLt Domain under Different Conditions. The immobilization of LSLt-fusion proteins on agarose matrixes relies on its sugar-binding properties, which in turn depends on its β-trefoil structure, in particular, on the native state of its two operative sugar-binding sites.[48] Hence, full or partial unfolding of the LSLt domain would promote the release of the fusion protein from the solid composite. In applied biocatalysis, the reaction conditions may be quite drastic and denaturing for protein structures. In order to evaluate the stability of the LSLt domain tertiary structure, the optimal derivative of LSLt-BTL2 immobilized on agarose 4BCL was incubated under different conditions of pH, temperature, and the presence of organic solvents. It is important to note that since soluble LSLt-BTL2 retained 100% of its initial activity under all studied conditions due to its intrinsic high stability, the obtained results depended exclusively on the stability of the LSLt domain. Table 2 shows that the LSLt domain was highly stable against temperature and tolerated relatively high concentrations of acetonitrile (more than 90% of immobilized enzyme remained on the carrier after incubation at up to 60 °C or up to 60% of acetonitrile). Nevertheless, LSLt–agarose bead binding was seriously affected by alkaline conditions because the fusion protein was totally released from the carrier. Nonionic surfactans such as Triton X-100 also disrupted the interaction between LSLt and the agarose beads. Therefore, alkaline conditions and detergents seemed to promote the β-trefoil structural distortions that lead to the dissociation of the lectin domain from the agarose matrix. However, in spite of the low stability of the LSLt domain in these latter conditions, this methodology is quite robust for a large variety of reaction conditions. Immobilization based on the use of LSLt may be used in fine chemistry reactions where substrates often present solubility issues, and organic solvents are required in the reaction media. Furthermore, enzyme derivatives immobilized via lectin might be also used in reaction environments where medium-high temperatures (40–60 °C) are needed, as, for example, in food chemistry for lactose-free processes where elevated temperatures are used to avoid microbial contaminations. Therefore, the robustness of LSLt–agarose bead interaction, the simplicity of the one-pot purification/immobilization protocol, and the relative low cost of the nonactivated agarose carriers present this methodology as a new opportunity to prepare cost-effective immobilized biocatalysts with attractive industrial perspectives.

Table 2. Elution of LSLt-BTL from Agarose 4BCL under Different Conditions

elution conditions[a]	eluted BTL2 activity (%)[b]
buffer sodium phosphate, pH 7, 25 °C	**0**
buffer sodium phosphate, pH 7, 45 °C	**7**
buffer sodium phosphate, pH 7, 60 °C	**3**
buffer sodium acetate, pH 5, 25 °C	**20**
buffer sodium carbonate, pH 10, 25 °C	**100**
buffer sodium phosphate, pH 7, 25 °C, Triton X-100 0,2%	**60**
acetonitrile 20%, pH 7, 25 °C	**10**
acetonitrile 40%, pH 7, 25 °C	**0**
acetonitrile 60%, pH 7, 25 °C	**5**

[a]Under all elution conditions, the soluble LSLt-BTL2 kept 100% of its initial activity. [b]Eluted BTL2 activity is defined as the lipase activity measured with *p*NPB (see methods) in the supernatant regarding the immobilized activity before the immobilized enzyme was incubated at different conditions. The eluted activities are the mean of three independent experiments, and the error was never higher to 10%.

CONCLUSIONS

The LSLt domain was genetically fused to the N-terminal end of two different proteins: cysteine-less mutant of BTL2, a thermostable lipase, and EGFP, an excellent reporter protein. The resulting fusion proteins were immobilized onto different agarose-type carriers via affinity interaction between such lectin domains and the galactose units present in the structure of the agarose beads. The fusion of catalytic and reporter proteins to the LSLt domain allowed the study of the immobilization kinetics of this system revealing a novel mechanism involving a rapid immobilization step on both noncross-linked and cross-linked agarose matrixes followed by a dynamic distribution of the proteins throughout the porous surface. Slight differences were observed in the binding of LSLt to either agarose 4B or 4BCL, indicating that binding was slightly more favorable for the former one. Furthermore, the interaction between the lectin and agarose was temperature-dependent since the binding was 4-fold stronger when the immobilization took place at 25 °C than when it did at 4 °C. The strongest interaction, lectin–agarose, was also quite stable under a survey of different conditions such as high temperatures (up to 60 °C) or high organic solvent concentrations (up to 60% of acetonitrile). Hence, this lectin domain seems to be suitable to reversibly immobilize enzymes industrially relevant in very simple carriers as agarose. Although immobilization was a little more efficient on noncross-liked agaroses, the use of cross-linked ones is more interesting because of their better mechanical properties. This immobilization also enables the one-pot purification and immobilization thanks to the highly specific and strong interaction between the lectin domain and the agarose surface.

ASSOCIATED CONTENT

Supporting Information

Experimental procedures II; spectroscopic behavior of both EGFP and LSLt-EGFP; effect of the LSLt tag on the final stability of the soluble fusion protein; determination of diffusion restriction observed during the immobilization process of LSLt-BTL2 on agarose matrixes; and dynamic distribution of LStL-GFP throughout agarose porous surface. This material is available free of charge via the Internet at http://pubs.acs.org.

AUTHOR INFORMATION

Corresponding Author

*Phone: +34915854809. Fax: +34 915854760. E-mail: jmguisan@icp.csic.

Notes

The authors declare no competing financial interest.

ACKNOWLEDGMENTS

This work has been sponsored by the Spanish Ministry of Science and Innovation (BFU2010-17929). CTQ2010-16457

(to S.R. and M.P.L.). We gratefully acknowledge CSIC for the grant JAE-doc 108.

REFERENCES

(1) Sheldon, R. A. (2007) Enzyme immobilization: the quest for optimum performance. *Adv. Synth. Catal. 349*, 1289−1307.
(2) Mateo, C., Palomo, J. M., Fernandez-Lorente, G., Guisan, J. M., and Fernandez-Lafuente, R. (2007) Improvement of enzyme activity, stability and selectivity via immobilization techniques. *Enzyme Microb. Technol. 40*, 1451−1463.
(3) Berne, C., Betancor, L., Luckarift, H. R., and Spain, J. C. (2006) Application of a microfluidic reactor for screening cancer prodrug activation using silica-immobilized nitrobenzene nitroreductase. *Biomacromolecules 7*, 2631−2636.
(4) Betancor, L., Berne, C., Luckarift, H. R., and Spain, J. C. (2006) Coimmobilization of a redox enzyme and a cofactor regeneration system. *Chem. Commun. (Cambridge)*, 3640−3642.
(5) Wang, F., Guo, C., Liu, H. Z., and Liu, C. Z. (2007) Reversible immobilization of glucoamylase by metal affinity adsorption on magnetic chelator particles. *J. Mol. Catal. B: Enzym. 48*, 1−7.
(6) Mateo, C., Abian, O., Fernandez-Lafuente, R., and Guisan, J. M. (2000) Reversible enzyme immobilization via a very strong and nondistorting ionic adsorption on support−polyethylenimine composites. *Biotechnol. Bioeng. 68*, 98−105.
(7) Wang, P. Y., Tsai, S. W., and Chen, T. L. (2008) Improvement of enantioselectivity and stability of Klebsiella oxytoca hydrolase immobilized on Eupergit C 250L. *J. Chem. Technol. Biotechnol. 83*, 1518−1525.
(8) Wang, L., Ran, Q., Tian, Y., Xu, J., Xian, Y., Peng, R., and Jin, L. (2010) Covalent immobilization of redox protein via click chemistry and carbodiimide reaction: Direct electron transfer and biocatalysis. *J. Colloid Interface Sci. 350*, 544−550.
(9) Mateo, C., Grazú, V., Pessela, B. C. C., Montes, T., Palomo, J. M., Torres, R., López-Gallego, F., Fernández-Lafuente, R., and Guisán, J. M. (2007) Advances in the design of new epoxy supports for enzyme immobilization-stabilization. *Biochem. Soc. Trans. 35*, 1593−1601.
(10) Guisán, J. M. (1988) Aldehyde-agarose gels as activated supports for immobilization-stabilization of enzymes. *Enzyme Microb. Technol. 10*, 375−382.
(11) Puertas, S., Batalla, P., Moros, M., Polo, E., Del Pino, P., Guisan, J. M., Grazu, V., and de la Fuente, J. M. (2011) Taking advantage of unspecific interactions to produce highly active magnetic nanoparticle-antibody conjugates. *ACS Nano 5*, 4521−4528.
(12) Godoy, C. A., de las Rivas, B., Grazu, V., Montes, T., Guisán, J. M., and López-Gallego, F. (2011) Glyoxyl-disulfide agarose: a tailor-made support for site-directed rigidification of proteins. *Biomacromolecules 12*, 1800−1809.
(13) Mansfeld, J., and Ulbrich-Hofmann, R. (2000) Site-specific and random immobilization of thermolysin-like proteases reflected in the thermal inactivation kinetics. *Biotechnol. Appl. Biochem. 32*, 189−195.
(14) Cuetos, A., Valenzuela, M. L., Lavandera, I., Gotor, V., and Carriedo, G. A. (2010) Polyphosphazenes as tunable and recyclable supports to immobilize alcohol dehydrogenases and lipases: Synthesis, catalytic activity, and recycling efficiency. *Biomacromolecules 11*, 1291−1297.
(15) Fuentes, M., Pessela, B. C. C., Maquiese, J. V., Ortiz, C., Segura, R. L., Palomo, J. M., Abian, O., Torres, R., Mateo, C., Fernández-Lafuente, R., and Guisán, J. M. (2004) Reversible and strong immobilization of proteins by ionic exchange on supports coated with sulfate-dextran. *Biotechnol. Prog. 20*, 1134−1139.
(16) Mateo, C., Bolivar, J. M., Godoy, C. A., Rocha-Martin, J., Pessela, B. C., Curiel, J. A., Muñoz, R., Guisan, J. M., and Fernandez-Lorente, G. (2010) Improvement of enzyme properties with a two-step immobilizaton process on novel heterofunctional supports. *Biomacromolecules 11*, 3112−3117.
(17) Hedhammar, M., Gräslund, T., and Hober, S. (2005) Protein engineering strategies for selective protein purification. *Chem. Eng. Technol. 28*, 1315−1325.
(18) Saleemuddin, M. (1999) Bioaffinity based immobilization of enzymes. *Adv. Biochem. Eng. Biotechnol. 64*, 203−226.
(19) Terpe, K. (2003) Overview of tag protein fusions: from molecular and biochemical fundamentals to commercial systems. *Appl. Microbiol. Biotechnol. 60*, 523−533.
(20) Ueda, E. K. M., Gout, P. W., and Morganti, L. (2003) Current and prospective applications of metal ion-protein binding. *J. Chromatogr., A. 988*, 1−23.
(21) Luke, J. M., Carnes, A. E., Sun, P., Hodgson, C. P., Waugh, D. S., and Williams, J. A. (2011) Thermostable tag (TST) protein expression system: Engineering thermotolerant recombinant proteins and vaccines. *J. Biotechnol. 151*, 242−250.
(22) Esposito, D., and Chatterjee, D. K. (2006) Enhancement of soluble protein expression through the use of fusion tags. *Curr. Opin. Biotechnol. 17*, 353−358.
(23) Hu, S., and Wong, D. T. (2009) Lectin microarray. *Proteom. Clin. Appl. 3*, 148−154.
(24) Tetala, K. K. R., and Van Beek, T. A. (2010) Bioaffinity chromatography on monolithic supports. *J. Sep. Sci. 33*, 422−438.
(25) Mao, X., Luo, Y., Dai, Z., Wang, K., Du, Y., and Lin, B. (2004) Integrated lectin affinity microfluidic chip for glycoform separation. *Anal. Chem. 76*, 6941−6947.
(26) Tang, J., Liu, Y., Yin, P., Yao, G., Yan, G., Deng, C., and Zhang, X. (2010) Concanavalin A-immobilized magnetic nanoparticles for selective enrichment of glycoproteins and application to glycoproteomics in hepatocelluar carcinoma cell line. *Proteomics 10*, 2000−2014.
(27) Mancheño, J. M., Tateno, H., Goldstein, I. J., Martinez-Ripoll, M., and Hermoso, J. A. (2005) Structural analysis of the Laetiporus sulphureus hemolytic pore-forming lectin in complex with sugars. *J. Biol. Chem. 280*, 17251−17259.
(28) Mancheño, J. M., and Angulo, I. (2009) Fusion Proteins Having a Beta-Trefoil-Type Domain: Method for Obtaining Same and Use Thereof, WO121994.
(29) Angulo, I., Acebron, I., de Las Rivas, B., Munoz, R., Rodriguez-Crespo, I., Menendez, M., Garcia, P., Tateno, H., Goldstein, I. J., Perez-Agote, B., and Mancheno, J. M. (2011) High-resolution structural insights on the sugar-recognition and fusion tag properties of a versatile b-trefoil lectin domain from the mushroom *Laetiporus sulphureus*. *Glycobiology 21*, 1349−1361.
(30) Wiesbauer, J., Bolivar, J. M., Mueller, M., Schiller, M., and Nidetzky, B. (2011) Oriented immobilization of enzymes made fit for applied biocatalysis: non-covalent attachment to anionic supports using Zbasic2Module. *ChemCatChem 3*, 1299−1303.
(31) Johnson, C. P., Jensen, I. E., Prakasam, A., Vijayendran, R., and Leckband, D. (2003) Engineered protein a for the orientational control of immobilized proteins. *Bioconjugate Chem. 14*, 974−978.
(32) Nordon, R. E., Craig, S. J., and Foong, F. C. (2009) Molecular engineering of the cellulosome complex for affinity and bioenergy applications. *Biotechnol. Lett. 31*, 465−476.
(33) Cassimjee, K. E., Kourist, R., Lindberg, D., Wittrup Larsen, M., Thanh, N. H., Widersten, M., Bornscheuer, U. T., and Berglund, P. (2011) One-step enzyme extraction and immobilization for biocatalysis applications. *Biotechnol. J. 6*, 463−469.
(34) Holland-Nell, K., and Beck-Sickinger, A. G. (2007) Specifically immobilised aldo/keto reductase AKR1A1 shows a dramatic increase in activity relative to the randomly immobilised enzyme. *ChemBioChem 8*, 1071−1076.
(35) Kim, M. I., Kwon, S. J., and Dordick, J. S. (2009) In vitro precursor-directed synthesis of polyketide analogues with coenzyme a regeneration for the development of antiangiogenic agents. *Org. Lett. 11*, 3806−3809.
(36) Tielker, D., Rosenau, F., Bartels, K. M., Rosenbaum, T., and Jaeger, K. E. (2006) Lectin-based affinity tag for one-step protein purification. *Biotechniques 41*, 327−332.
(37) Godoy, C. A., de las Rivas, B., Bezbradica, D., Bolivar, J. M., López-Gallego, F., Fernandez-Lorente, G., and Guisan, J. M. (2011) Reactivation of a thermostable lipase by solid phase unfolding/refolding. Effect of cysteine residues on refolding efficiency. *Enzyme Microb. Technol. 49*, 388−394.

(38) Geiser, M., Cebe, R., Drewello, D., and Schmitz, R. (2001) Integration of PCR fragments at any specific site within cloning vectors without the use of restriction enzymes and DNA ligase. *Biotechniques 31* (88−90), 92.
(39) Fernandez-Lorente, G., Godoy, C. A., Mendes, A., Lopez-Gallego, F., Grazu, V., de las Rivas, B., Palomo, J., Hermoso, J., Fernandez-Lafuente, R., and Guisan, J. (2008) Solid-phase chemical amination of a lipase from bacillus thermocatenulatus to improve its stabilization via covalent immobilization on highly activated glyoxyl-agarose. *Biomacromolecules 9* (9), 2553−2561.
(40) Bradford, M. M. (1976) A rapid and sensitive method for the quantitation of microgram quantities of protein utilizing the principle of protein dye binding. *Anal. Biochem. 72*, 248−254.
(41) Uskova, M. A., Borst, J. W., Hink, M. A., van Hoek, A., Schots, A., Klyachko, N. L., and Visser, A. J. (2000) Fluorescence dynamics of green fluorescent protein in AOT reversed micelles. *Biophys. Chem. 87*, 73−84.
(42) Ladero, M., Santos, A., and Garca-Ochoa, F. (2001) Diffusion and chemical reaction rates with nonuniform enzyme distribution: An experimental approach. *Biotechnol. Bioeng. 72*, 458−467.
(43) Borchert, A., and Buchholz, K. (1984) Improved biocatalyst effectiveness by controlled immobilization of enzymes. *Biotechnol. Bioeng. 26*, 727−736.
(44) Bolivar, J. M., Hidalgo, A., Sanchez-Ruiloba, L., Berenguer, J., Guisan, J. M., and Lopez-Gallego, F. (2011) Modulation of the distribution of small proteins within porous matrixes by smart-control of the immobilization rate. *J. Biotechnol. 155*, 412−420.
(45) Jokerst, J. V., Chou, J., Camp, J. P., Wong, J., Lennart, A., Pollard, A. A., Floriano, P. N., Christodoulides, N., Simmons, G. W., Zhou, Y., Ali, M. F., and McDevitt, J. T. (2011) Location of biomarkers and reagents within agarose beads of a programmable bio-nano-chip. *Small 7*, 613−624.
(46) Logan, T. C., Clark, D. S., Stachowiak, T. B., Svec, F., and Fréchet, J. M. J. (2007) Photopatterning enzymes on polymer monoliths in microfluidic devices for steady-state kinetic analysis and spatially separated multi-enzyme reactions. *Anal. Chem. 79*, 6592−6598.
(47) Teeuwen, R. L. M., Zuilhof, H., De Wolf, F. A., and Van Hest, J. C. M. (2009) Temperature-controlled positioning of fusion proteins in microreactors. *Soft Matter. 5*, 2261−2268.
(48) Medin, A. (1995) *Studies on Structures and Properties of Agarose*, Uppsala University, Uppsala, Sweden.

Bioconjugate Chemistry

Article

pubs.acs.org/bc

Dual Peptide Nucleic Acid- and Peptide-Functionalized Shell Cross-Linked Nanoparticles Designed to Target mRNA toward the Diagnosis and Treatment of Acute Lung Injury

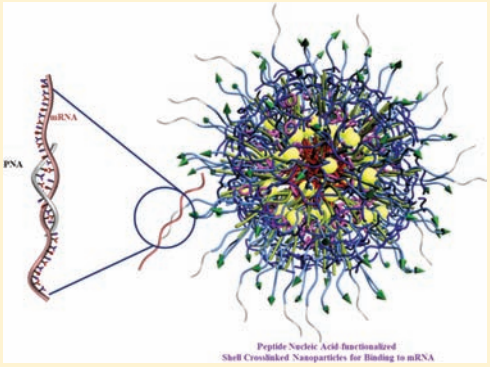
Ritu Shrestha,[†] Yuefei Shen,[‡] Kevin A. Pollack,[†] John-Stephen A. Taylor,*[,‡] and Karen L. Wooley*[,†]

[†]Departments of Chemistry and Chemical Engineering, Texas A&M University, P.O. Box 30012, College Station, Texas 77842-3012, United States

[‡]Department of Chemistry, Washington University in Saint Louis, Saint Louis, Missouri 63130, United States

Supporting Information

ABSTRACT: In this work, multifunctional biosynthetic hybrid nanostructures were prepared and studied for their potential utility in the recognition and inhibition of mRNA sequences for inducible nitric oxide synthase (iNOS), which are overexpressed at sites of inflammation, such as in cases of acute lung injury. Shell cross-linked knedel-like polymer nanoparticles (SCKs) that present peptide nucleic acids, for binding to complementary mRNAs, and cell penetrating peptides (CPPs), to gain cell entry, along with fluorescent labels and sites for radiolabeling, were prepared by a series of robust, efficient, and versatile synthetic steps that proceeded from monomers to polymers to functional nanoparticles. Amphiphilic block graft copolymers having combinations of methoxy- and thioacetyl-terminated poly(ethylene glycol) (PEG) and DOTA-lysine units grafted from the backbone of poly(acrylic acid) (PAA) and extending with a backbone segment of poly(octadecyl acrylate-*co*-decyl acrylate) (P(ODA-*co*-DA)) were prepared by a combination of reversible addition−fragmentation chain transfer (RAFT) polymerization and chemical modification reactions, which were then used as the building blocks for the formation of well-defined SCKs decorated with reactive thiols accessible to the surface. Fluorescent labeling with Alexa Fluor 633 hydrazide was then accomplished by amidation with residual acrylic acid residues within the SCK shells. Finally, the PNAs and CPP units were covalently conjugated to the SCKs via Michael addition of thiols on the SCKs to maleimide units on the termini of PNAs and CPPs. Confirmation of the ability of the PNAs to bind selectively to the target iNOS mRNAs when tethered to the SCK nanoparticles was determined by *in vitro* competition experiments. When attached to the SCKs having a hydrodynamic diameter of 60 ± 16 nm, the K_d values of the PNAs were ca. an order of magnitude greater than the free PNAs, while the mismatched PNA showed no significant binding.



INTRODUCTION

The mortality associated with acute lung injury (ALI) and acute respiratory distress syndrome (ARDS) remains high in the U.S. and around the world,[1] establishing the need for improved treatment and prevention strategies. ALI is an inflammatory process in the airspaces and lung parenchyma that is characterized by fluid accumulation (pulmonary edema) and it can progress to an acute stage that presents necrosis of the lung tissue.[2] One of the major indications of ALI is the overexpression of inducible nitric oxide synthase (iNOS), an enzyme that is found predominantly in the cells of epithelial origin. The production of iNOS is caused by the activation of proinflammatory cytokines such as interleukin-lβ (IL-lβ) and tumor necrosis factor-α (TNF-α), which are signaling molecules that are released as a part of the immune response due to the presence of bacterial products (e.g., lipopolysaccharides (LPS)).[3] The upregulation of iNOS results in the production of nitric oxide (NO), which when present in regulated amount can act as a mediator of vital biological functions in the lung.[4] However, the overexpression of this enzyme leads to the production of high concentrations of NO in an unregulated fashion, causing harm to cells and resulting in cell death.[5] Studies have shown that the inhibition of iNOS prevents the accumulation of NO and improves the symptoms of ALI.[6,7]

Because inducible nitric oxide synthase is both a biomarker and an exacerbating agent for ALI, there is great interest in the development of diagnostic agents and inhibitors for iNOS. Most of the work in this area has focused on imaging agents[8−10] and inhibitors for the iNOS protein[11] as well as imaging agents for detecting the formation of the nitric oxide that iNOS catalyzes.[12−14] An alternative strategy would be to target the mRNA encoding the iNOS protein with antisense agents that could have a dual function of both detecting iNOS

Received: November 18, 2011
Revised: January 24, 2012
Published: February 28, 2012

ACS Publications © 2012 American Chemical Society

dx.doi.org/10.1021/bc200629f | *Bioconjugate Chem.* 2012, 23, 574−585

mRNA expression level and inhibiting translation of the mRNA to the protein. One ideal class of antisense agents for this purpose is peptide nucleic acids (PNAs), which are synthetic analogues of DNA, in which the sugar phosphate backbone is replaced with an uncharged pseudopeptide backbone composed of *N*-(2-amino-ethyl)glycine units to which the nucleobases are linked through methylene carbonyl linkers.[15,16] Their attractiveness stems from their stability to degradation *in vivo*, high affinity for mRNA, and ability to block translation.[17−19] Additionally, PNAs are able to invade regions of secondary structure in the target mRNA, and the resulting PNA·RNA complexes are resistant to the action of RNase H which would otherwise degrade the mRNA and result in a loss of signal. While there are several reports on the use of PNAs to both inhibit[19] and image gene expression,[20−24] application of PNAs as regulators and imaging agents of gene expression *in vivo* has been hampered by their poor cellular uptake and rapid clearance.[15,25,26] To overcome the permeability problems, PNAs have been conjugated to a variety of cell penetrating peptides and other ligands, which have been shown to improve their uptake in cell culture through endocytosis though they often remain trapped in endosomes.[27,28] In addition, simple cell penetrating PNA conjugates suffer from rapid clearance *in vivo* due to their small size. One way to circumvent these problems is to conjoin PNAs with nanoparticles having optimal cell penetrating, endosomal escape, pharmacokinetic, and biodistribution properties.

In our group, we have had long-standing interest in developing novel polymeric systems and chemistries for the preparation of shell cross-linked knedel-like (SCK) nanoparticles[29−33] and fine-tuning of existing nanostructures[34−39] for a diverse set of applications in biomedical research.[40−48] SCKs are composed of block copolymers with hydrophilic and hydrophobic segments, making them amphiphilic and prone to self-assembly in selective solvents. Due to cross-linking between adjacent groups present in the shell, SCKs possess structural stability. Moreover, their tunable size, shape, and ability to perform chemical modifications within selective subparticle regions[49,50] allows for the conjugation of biologically active ligands,[41,43,51,52] such as PNAs,[53] to their surfaces, making them a versatile agent for gene delivery and transfection.[52,54−57] In the past, we have employed PNAs conjugated to SCKs to direct their assembly into higher-order structures via selective and tunable binding interactions,[53] and for intracellular delivery of PNA through a bioreductively cleavable linker.[54] The versatility of SCKs also allows for fine-tuning of the core properties, resulting in shape-adaptable nanoparticles[58−61] that might enhance multivalent binding recognition events. Herein, we report the design and synthesis of hierarchically assembled, multifunctional SCKs that are conjugated with PNAs specific for iNOS mRNA to promote recognition and inhibit iNOS expression. These SCKs were also conjugated to the protein transduction domain of human immunodeficiency virus type 1 TAT protein to facilitate cellular entry, and to a fluorescent probe or DOTA for labeling with the PET imaging radionuclide ^{64}Cu for imaging purposes. The PNA-SCK conjugates were shown to sequence-specifically bind to iNOS mRNA with high affinity by comparing the binding of matched and mismatched PNA−SCK conjugates.

EXPERIMENTAL SECTION

Materials and Methods. Polymerizations were performed on a double manifold with glassware and syringes that were dried in an oven (100 °C) for at least 1 h, and with syringes that were washed with N_2 (3×), prior to use. *tert*-Butyl acrylate (*t*-BA, 99%) was received from Sigma-Aldrich Company (St. Louis, MO), distilled over calcium hydride, and stored under N_2 prior to use. Octadecyl acrylate, decyl alcohol, trifluoroacetic acid (TFA, 95%; Aldrich), 2,2′-(ethylenedioxy)-bis(ethylamine) (97%, Aldrich), 1-(3′-dimethylaminopropyl)-3-ethylcarbodiimide methiodide (EDCI, 98%, Aldrich), hydroxybenzotriazole (HOBT, Aldrich), 2-(1*H*-benzotriazol-1-yl)-1,1,3,3-tetramethyluronium hexafluorophosphate (HBTU, Aldrich), Boc-NH-PEG$_{3\ kDa}$-NH$_2$ (Rapp Polymere, Tübingen, Germany), MeO-PEG$_{2\ kDa}$-NH$_2$ (Rapp Polymere, Tübingen, Germany), hydroxyl amine hydrochloride (98%, Aldrich), Sephadex G50 (Medium, GE Healthcare, Piscataway, NJ), *N*-succinimidyl-*S*-acetylthiopropionate (SATP) (Pierce, Rockford, IL), and 4-maleimido butyric acid (Aldrich), *N*,*N*-diisopropylethylamine (DIPEA) (Aldrich), diethyl ether (anhydrous) (Aldrich), Alexa Fluor 633 hydrazide (Invitrogen), and *O*-(7-azabenzo-triazol-1-yl)-1,1,3,3-tetramethyluronium hexafluorophosphate (HATU) were used as received. Fmoc-XAL PEG-PS resin was purchased from PerSeptive Biosystems (Ramsey, MN). GGYGRKKRRQRRR-maleimide was purchased from Chengdu Kaijie Biopharmaceuticals Co., Ltd. (Chengdu, China). PNA monomers (Fmoc-A-(Bhoc)-OH, Fmoc-C-(Bhoc)-OH, Fmoc-G-(Bhoc)-OH, and Fmoc-T-OH) were obtained from Panagene (Daejeon, Korea). *S*-1-Dodecyl-*S*′-(*α*,*α*′-dimethyl-*α*″-acetic acid)trithiocarbonate) (DDMAT) and Boc-protected DOTA-lysine (a lysine derivative of 1,4,7,10-tetraazocyclododecane-*N*,*N*′,*N*″,*N*‴-tetraacetic acid (DOTA)) were synthesized as reported previously.[44−46,62] All other reagents were obtained from Sigma-Aldrich and used as received. Ellman's reagent kit (Pierce) was used for Ellman's assay, with the calibration curve constructed using cysteine monohydrate in aqueous buffer (100 mM PBS, 0.1 M NaCl, 10 mM EDTA, pH 7.4) at 412 nm. Spectra/Por membrane tubes were purchased from Spectrum Medical Industries, Inc., and were used for dialysis. Nanopure water (18 MΩ·cm) was acquired by means of a Barnstead Nanopure ultrapure water purification system (Thermo Scientific, Asheville, NC).

^{1}H NMR and ^{13}C NMR spectra were recorded on an Inova 300 or Mercury 300 spectrometer interfaced to a UNIX computer using *VnmrJ* software. Samples were prepared as solutions in $CDCl_3$, CD_2Cl_2, or DMF-d_7 and solvent protons were used as internal standard. IR spectra were recorded on an IR Prestige 21 system (Shimadzu Corp., Japan). A small amount of sample was placed to cover the ATR crystal for IR measurements. Data were analyzed using *IRsolution* software. UV−vis absorption measurements were made using a UV-2550 system (Shimadzu Corp., Japan) using PMMA cuvettes. Spectra were analyzed with *UV-Probe* v 2.33 software.

Gel permeation chromatography was conducted on a system equipped with a Waters Chromatography, Inc. (Milford, MA) model 1515 isocratic pump and a model 2414 differential refractometer with a three-column set of Polymer Laboratories, Inc. (Amherst, MA) Styragel columns (PL$_{gel}$ 5 μm Mixed C, 500 Å, and 10^4 Å, 300 × 7.5 mm columns) and a guard column (PL$_{gel}$ 5 μm, 50 × 7.5 mm). The system was equilibrated at 40 °C in tetrahydrofuran (THF), which served as the polymer solvent and eluent (flow rate set to 1.00 mL/min). The differential refractometer was calibrated with Polymer Laboratories, Inc., polystyrene standards (300 to 467 000 Da). Polymer solutions were prepared at a concentration of ca. 3 mg/mL with 0.05% vol toluene as flow rate marker and an

dx.doi.org/10.1021/bc200629f | *Bioconjugate Chem.* 2012, 23, 574−585

injection volume of 200 μL was used. Data were analyzed using *Empower Pro* software from Waters Chromatography Inc.

Differential scanning calorimetry studies were performed on a Mettler Toledo DSC822 calibrated according to the standard procedures using indium. The heating rates were 10 °C min^{-1} and cooling rates were 5 °C min^{-1} with a temperature range of −120−150 °C. The crystalline melting point (T_m) and crystallization temperature (T_c) were determined during the second heating or cooling cycles, respectively. Thermogravimetric analysis was performed under Ar atmosphere using a Mettler Toledo model TGA/DSC1 with a heating rate of 10 °C/min. Measurements were analyzed using Mettler Toledo *STARe* software v 10.00.

Samples for TEM were prepared by depositing 5 μL of sample to glow discharged carbon coated copper grids. Excess sample was wicked off using filter paper and the grids were allowed to dry in air for 1 min. The grids were then stained with 5 μL of 2% uranyl acetate and excess stain was wicked off using filter paper. Specimens were observed on a JEOL 1200EX transmission electron microscope operating at 100 kV and micrographs were recorded at calibrated magnifications using an SIA-15C CCD camera. The final pixel size was 0.42 nm/pixel. The number-average particle diameters (D_{av}) and standard deviations were generated from the analysis of particles from at least two different micrographs.

Dynamic light scattering (DLS) measurements were conducted using Delsa Nano C from Beckman Coulter, Inc. (Fullerton, CA) equipped with a laser diode operating at 658 nm. Size measurements were made in water (n = 1.3329, η = 0.890 cP at 25 ± 1 °C; n = 1.3293, η = 0.547 cP at 50 ± 1 °C; n = 1.3255, η = 0.404 cP at 70 ± 1 °C). Scattered light was detected at 165° angle and analyzed using a log correlator over 70 accumulations for a 0.5 mL of sample in a glass sizing cell (0.9 mL capacity). The photomultiplier aperture and the attenuator were automatically adjusted to obtain a photon counting rate of ca. 10 kcps. The calculations of the particle size distribution and distribution averages were performed using CONTIN particle size distribution analysis routines. Prior to analysis, the samples were filtered through a 0.45 μm Whatman nylon membrane filter (Whatman, Inc.). The samples in the glass sizing cell were equilibrated at the desired temperature for 5 min before measurements were made. The peak average of histograms from intensity, volume, or number distributions out of 70 accumulations was reported as the average diameter of the particles.

PNA synthesis was carried out on an automated ABI 8909 synthesizer (Applied Biosystems, Carlsbad, CA) with a PNA option. High-pressure liquid chromatography (HPLC) of PNAs was carried out on Beckman Coulter System Gold 126 HPLC system. Matrix-assisted laser desorption ionization (MALDI) mass spectra of PNA conjugates were measured on a PerSeptive Voyager RP MALDI-time-of-flight (TOF) mass spectrometer using CHCA as a matrix and calibrated versus insulin (average [M + H] = 5734.5) which was present as an internal standard.

DNA was 5′-labeled by [γ-^{32}P]-ATP with T4 polynucleotide kinase. DNA, T4 polynucleotide kinase buffer, H_2O, [γ-^{32}P]-ATP, and T4 polynucleotide kinase were mixed together and incubated for 1 h at 37 °C, followed by boiling for 20 min to inactivate the kinase. Radiolabeled DNA bands with corrected sizes were purified from polyacrylamide gel and taken forward for further experiments.

*Synthesis of Poly(tert-butyl acrylate) ($PtBA_{140}$) (**1**).* To a 100 mL Schlenk flask equipped with a stir bar, DDMAT (284 mg, 0.779 mmol) was added as a chain transfer agent followed by AIBN (6.40 mg, 39.0 μmol) and 2-butanone (11.2 g, 156 mmol). Monomer *t*BA (20.0 g, 156 mmol) was added and the Schlenk flask was then sealed with a rubber septum. The reaction mixture was allowed to stir at room temperature to ensure homogeneity. After performing four freeze−pump−thaw cycles, the reaction mixture was allowed to equilibrate to room temperature before being inserted into a preheated oil bath at 60 °C. The kinetics of polymerization were monitored by analyzing aliquots at predetermined times via ^{1}H NMR spectroscopy. After 2 h, the desired conversion was achieved and the reaction was quenched by immersing the Schlenk flask into liquid N_2. A minimum amount of THF was used to dissolve the reaction mixture which was precipitated three times into a mixture of methanol and ice to afford the homopolymer of P*t*BA. The polymer was dissolved in dichloromethane and dried over magnesium sulfate. Finally, the solvent was removed under vacuum to yield (13.0 g, 68% yield, based upon 80% conversion) of poly(*tert*-butyl acrylate) as a bright yellow powder. $(M_n)_{NMR}$ = 18.3 kDa. $(M_n)_{GPC}$ = 23.6 kDa. $(M_w)_{GPC}$ = 26.4 kDa. PDI = 1.12. IR: 2920, 2830, 1716, 1443, 1364, 1285, 1125, 813, 745 cm^{-1}. ^{1}H NMR (CD_2Cl_2) δ: 0.85 (t, J = 7.0 Hz, C***H***$_3$CH$_2$−), 1.20−1.85 (br, −CHC***H***$_2$− of the polymer backbone, alkyl chain initiator and HOOCC(C***H***$_3$)$_2$−), 2.20 (br, −C***H***CH$_2$− of the polymer backbone), 3.20 (t, J = 7.0 Hz, -SCSC***H***$_2$-), 4.6−4.7 (br, −CH$_2$C***H***S−) ppm. ^{13}C NMR (CD_2Cl_2) δ: 12.5, 22.7, 27.9, 29.5, 36.1, 37.3, 41.9−42.4, 80.2, 173.9−174.1 ppm. DSC: (T_g) = 48 °C. TGA: T_{onset} = 186 °C, $T_{decomposition}$: (186−228 °C) 37.5% mass loss; (228−307 °C) 7.5% mass loss; (307−472 °C) 27% mass loss; 28% mass remaining.

*Synthesis of Poly(tert-butyl acrylate)$_{140}$-b-poly(octadecyl acrylate$_{16}$-codecyl acrylate$_{43}$) ($PtBA_{140}$-b-P(ODA_{16}-co-DA_{43})) (**2**).* To a 50 mL flame-dried Schlenk flask equipped with a stir bar, ODA (1.67 g, 5.14 mmol) was added followed by DA (2.95 g, 13.9 mmol), P*t*BA (3.50 g, 0.190 mmol), and a stock solution of AIBN (1.56 mg, 9.50 μmol) prepared in toluene. The monomers and macrochain transfer agent were allowed to dissolve in toluene (3.50 g, 38.0 mmol). The reaction mixture was degassed by three freeze−pump−thaw cycles and allowed to warm to room temperature. Polymerization was facilitated by immersing the Schlenk flask into a preheated oil bath at 70 °C. Progress of polymerization was monitored by ^{1}H NMR spectroscopy of aliquots at predetermined times. Upon attaining the desired degree of polymerization, after 1.5 h, the reaction was quenched by immersing the reaction flask into liquid N_2. The reaction mixture was dissolved in a minimum amount of THF (6.00 mL) and three consecutive precipitations were performed in methanol in an ice bath. After the final precipitation, a yellow powder (3.35 g, 70% yield, based on 60% conversion) was obtained after removal of solvent and subsequent drying in vacuo. $(M_n)_{NMR}$ = 32.6 kDa. $(M_n)_{GPC}$ = 26.8 kDa. $(M_w)_{GPC}$ = 29.7 kDa. PDI = 1.10. IR: 2920, 2830, 1716, 1443, 1364, 1285, 1125, 813, 745 cm^{-1}. ^{1}H NMR (CD_2Cl_2) δ: 0.88 (t, J = 6.9 Hz, −C***H***$_3$CH$_2$− of ODA, DA and chain transfer agent), 1.35−1.76 and 1.70−1.98 (br, −C***H***$_2$CH− backbone of PODA, PDA, CTA, and HOOCC-(C***H***$_3$)$_2$-), (2.05−2.40 (br, −CH$_2$C***H***−), 4.00 (br, −OC***H***$_2$CH$_2$−, PODA, PDA) ppm. ^{13}C NMR (CD_2Cl_2) δ: 13.8, 22.7, 25.9, 27.7−27.8, 28.7, 29.4, 29.6, 31.9, 34.5−37.5, 41.4−41.9, 64.6, 80.2, 173.8−174.1 ppm. DSC: (T_g) = 41 °C.

dx.doi.org/10.1021/bc200629f | *Bioconjugate Chem.* 2012, 23, 574−585

(T_m) = −2.2 and 9.1 °C. (T_c) = −6.8 and 3.4 °C. TGA: T_{onset} = 209 °C, $T_{decomposition}$: (209−250 °C) 11% mass loss; (250−485 °C) 70% mass loss; 20% mass remaining.

*Synthesis of Poly(acrylic acid)$_{140}$-b-poly(octadecyl acrylate$_{16}$-codecyl acrylate$_{43}$) (PAA$_{140}$-b-P(ODA$_{16}$-co-DA$_{43}$)) (**3**).* A round-bottom flask equipped with stir bar was charged with **2** (1.00 g, 30.7 μmol). Dichloromethane (10 mL) was added followed by dropwise addition of TFA (10 mL) and the reaction mixture was allowed to stir for 24 h at RT. The solvent was removed under vacuum and the polymer was allowed to dissolve in a minimum amount of THF. Upon extensive dialysis against nanopure water and lyophilization, a pale white fluffy solid of PAA$_{140}$-*b*-P(ODA$_{16}$-*co*-DA$_{43}$) (**3**) (0.74 g, 98%) was obtained. $(M_n)_{NMR}$ = 24.7 kDa. IR: 3600−2350, 1716, 1443, 1250, 1159, 830, 750 cm^{-1}. ^{1}H NMR (DMF-d_7) δ: 0.86 (t, J = 6.6 Hz, −C***H***$_3$CH$_2$− of ODA, DA and chain transfer agent), 1.15−1.4 (br, -C***H***$_2$- alkyl chain of PODA, PDA, CTA, and HOOCC(C***H***$_3$)$_2$-), 1.95−2.1 (br, -C***H***$_2$CH- backbone of PODA, PDA, and CTA), 2.05−2.20 (br, -CH$_2$C***H***- backbone of PODA, PDA, and CTA), 4.00 (br, -OC***H***$_2$CH$_2$-, PODA, PDA) ppm. ^{13}C NMR (DMF-d_7) δ: 14.5, 23.5, 27.0, 29.5, 30.5, 31.0, 33.0, 35.1−37.5, 41.5−43.0, 65.0, 174.1−175.1, 175.9 ppm. DSC: (T_g) = 129.5 °C. (T_m) = 6.3 °C, (T_c) = 3.1 °C. TGA: T_{onset} = 190 °C, $T_{decomposition}$: (190−294 °C) 18% mass loss; (294−495 °C) 68% mass loss; 14% mass remaining.

*Synthesis of Poly(acrylic acid$_{137}$)-g-DOTA$_3$-b-poly(octadecyl acrylate$_{16}$-codecyl acrylate$_{43}$) (PAA$_{137}$-g-(CONH-lysine-DOTA-Boc)$_3$-b-P(ODA$_{16}$-co-DA$_{43}$)) (**4**). General Procedure for Amidation, Involving the Attachment of DOTA.* A 50 mL flame-dried RB flask equipped with a stir bar was charged with **3** (350 mg, 14.1 μmol) and DMF (5.00 g). Stock solutions of HOBT, HBTU, and CONH-lysine-DOTA-Boc were prepared in dry DMF. After the polymer was allowed to dissolve completely, HBTU (56.1 mg, 0.148 mmol), HOBt (19.9 mg, 0.148 mmol), and DIPEA (6.19 mg, 0.148 mmol) were added at intervals of 30 min. DOTA-lysine (51.7 mg, 73.8 μmol) was added and the solution was stirred for 24 h at RT. The reaction mixture was then transferred to dialysis tubing (MWCO ca. 6000−8000 Da) presoaked in nanopure water. Extensive dialysis against nanopure water followed by lyophilization afforded a white powder of **3** (235 mg, 89.0%, 3 DOTA-lysine per chain, 60% coupling efficiency). M_n = 26.7 kDa. IR: 3400−2570, 1715, 1580, 1477, 1250, 1160, 978, 830, 750 cm^{-1}. ^{1}H NMR (DMF-d_7) δ: 0.86 (t, J = 6.6 Hz, -C***H***$_3$CH$_2$- of ODA, DA, and chain transfer agent, C***H***$_3$-*tert*-butyl groups of DOTA), 1.15−1.4 (br, -C***H***$_2$-alkyl chain of PODA, PDA, CTA, and HOOCC(C***H***$_3$)$_2$-), 1.95−2.1 (br, -C***H***$_2$CH- backbone of PODA, PDA, and CTA) 2.05−2.20 (br, -CH$_2$C***H***- backbone of PODA, PDA, and CTA), 2.3−2.4 (br, DOTA), 2.95−3.10 (br, DOTA), 4.00 (br, -OC***H***$_2$CH$_2$-, PODA, PDA) ppm. ^{13}C NMR (DMF-d_7) δ: 14.5, 23.5, 27.0, 29.5, 30.5, 31.0, 33.0, 35.1−37.5, 41.5−43.0, 53.0, 56.0, 65.0, 82.0, 174.1−175.1, 177.6 ppm. DSC: (T_g) = 131.8 °C. (T_m) = 1.0 °C, (T_c) = −3.0 °C. TGA: T_{onset} = 112 °C, $T_{decomposition}$: (112−190 °C) 9% mass loss; (190−247 °C) 7% mass loss; (264−278 °C) 7% mass loss; (278−395 °C) 38% mass loss; (395−500 °C) 19% mass loss; 20% mass remaining.

*Synthesis of Poly(acrylic acid)$_{131}$-g-(PEG$_{3\ kDa}$-Boc)$_3$-g-(mPEG$_{2\ kDa}$)$_3$-g-(CONH-lysine-DOTA-Boc)$_3$-b-poly(octadecyl acrylate$_{16}$-codecyl acrylate$_{43}$) (PAA$_{131}$-g-(PEG$_{3\ kDa}$-Boc)$_3$-g-(mPEG$_{2\ kDa}$)$_3$-g-(CONH-lysine-DOTA-Boc)$_3$-b-P(ODA$_{16}$-co-DA$_{43}$)) (**5**).* A reaction mixture of **4** (97.0 mg, 3.63 μmol), HBTU (19.4 mg, 51.1 μmol), HOBt (12.1 mg, 51.1 μmol), DIPEA (6.58 mg, 51.1 μmol), 2 kDa mPEG-NH$_2$ (25.8 mg, 12.8 μmol), and 3 kDa Boc-NH-PEG-NH$_2$ (82.3 mg, 12.8 μmol) in DMF was allowed to undergo reaction under the general procedure outlined for amidation above to yield an amorphous white solid of **5**, PAA$_{131}$-*g*-(PEG$_{3\ kDa}$-Boc)$_3$-*g*-(mPEG$_{2\ kDa}$)$_3$-*g*-(CONH-lysine-DOTA-Boc)$_3$-*b*-P(ODA$_{16}$-*co*-DA$_{43}$) (133 mg, 88%), having ca. 3 of each type of PEG per chain, 75% coupling efficiency. $(M_n)_{NMR}$ = 41.6 kDa. IR: 3600−2580, 1715, 1543, 1455, 1250, 1160, 1114, 966, 807, 760 cm^{-1}. ^{1}H NMR (DMF-d_7) δ: 0.86 (t, J = 6.6 Hz, -C***H***$_3$CH$_2$- of ODA, DA, and chain transfer agent, C***H***$_3$-*tert*-butyl groups of DOTA), 1.15−1.4 (br, C***H***$_2$-alkyl chain of PODA, PDA, CTA, and HOOCC(C***H***$_3$)$_2$-), 1.95−2.10 (br, -C***H***$_2$CH- backbone of PODA, PDA, and CTA) 2.05−2.20 (br, 3 H, -CH$_2$C***H***- backbone of PODA, PDA, and CTA), 2.30−2.4 (br, DOTA), 2.95−3.10 (br, DOTA), 3.20 (s, -OC***H***$_3$, PEG), 3.50 (-C***H***$_2$-,br, PEG), 4.00 (br, -OC***H***$_2$CH$_2$-, PODA, PDA) ppm. ^{13}C NMR (DMF-d_7) δ: 14.5, 23.5, 27.0, 29.5, 30.5, 31.0, 33.0, 35.1−37.5, 41.5−43.0, 52.0, 56.0, 58.6, 65.0, 70.8, 82.0, 174.6, 176.8 ppm. DSC: (T_m) = −43.8 °C, (T_m) $_{(ODA\text{-}co\text{-}DA)}$ = 8.2 °C, (T_m) $_{(PEO)}$ = 33.6 °C, (T_c) = −44.3 and 3.8 °C. TGA: T_{onset} = 150 °C, $T_{decomposition}$: (150−438 °C) 68% mass loss; (438−500 °C) 6% mass loss; 26% mass remaining.

*Synthesis of Poly(acrylic acid)$_{131}$-g-(PEG$_{3\ kDa}$-NH$_2$)$_3$-g-(mPEG$_{2\ kDa}$)$_3$-g-(CONH-lysine-DOTA-COOH)$_3$-b-poly(octadecyl acrylate$_{16}$-codecyl acrylate$_{43}$) (PAA$_{131}$-g-(PEG$_{3\ kDa}$-NH$_2$)$_3$-g-(mPEG$_{2\ kDa}$)$_3$-g-(CONH-lysine-DOTA-COOH)$_3$-b-P(ODA$_{16}$-co-DA$_{43}$)) (**6**).* In a round-bottom flask was placed **5** (90.0 mg, 2.16 μmol), and TFA (6.00 mL) was added dropwise. The reaction mixture was allowed to stir for 24 h at RT. The TFA was then removed under a flow of N_2, the polymer was dissolved in THF, the solution was then dialyzed against nanopure water, and the polymer was isolated by lyophilization to obtain **6** as a fluffy white powder (55 mg, 65%). $(M_n)_{NMR}$ = 41.0 kDa. IR: 3600−2600, 1715, 1590, 1430, 1250, 1135, 945, 820, 760 cm^{-1}. ^{1}H NMR (DMF-d_7) δ: 0.86 (t, J = 6.6 Hz, -C***H***$_3$CH$_2$- of ODA, DA, and chain transfer agent), 1.15−1.4 (br, C***H***$_2$- alkyl chain of PODA, PDA, CTA, and HOOCC(C***H***$_3$)$_2$-), 1.95−2.1 (br, -C***H***$_2$CH- backbone of PODA, PDA, and CTA), 2.05−2.20 (br, -CH$_2$C***H***- backbone of PODA, PDA, and CTA), 2.3−2.4 (br, DOTA), 2.95−3.10 (br, DOTA), 3.20 (s, -OC***H***$_3$, PEG), 3.50 (-C***H***$_2$-, br, PEG), 4.00 (br, 4 H, -OC***H***$_2$CH$_2$-, PODA, PDA) ppm. ^{13}C NMR (DMF-d_7) δ: 14.5, 23.5, 27.0, 29.5, 30.5, 31.0, 33.0, 35.1−37.5, 41.5−43.0, 52.0, 58.0, 58.6, 65.0, 70.5, 174.1−175.1, 176.8 ppm. DSC: (T_m) = −43.5 °C, (T_m)$_{(ODA\text{-}co\text{-}DA)}$ = 10.8 °C, (T_m)$_{(PEO)}$ = 29.8 °C, (T_c) = −35.2 and 3.9 °C. TGA: T_{onset} = 150 °C, $T_{decomposition}$: (150−438 °C) 68% mass loss; (438−500 °C) 6% mass loss; 26% mass remaining.

*Synthesis of Poly(acrylic acid)$_{131}$-g-(PEG$_{3\ kDa}$- NHCO-C$_2$H$_4$-SCOCH$_3$)$_3$-g-(mPEG$_{2\ kDa}$)$_3$-g-(CONH-lysine-DOTA-COOH)$_3$-b-poly(octadecyl acrylate$_{16}$-codecyl acrylate$_{46}$) (PAA$_{131}$-g-(PEG$_{3\ kDa}$-NHCO-C$_2$H$_4$-SCOCH$_3$)$_3$-g-(mPEG$_{2\ kDa}$)$_3$-(CONH-lysine-DOTA-COOH)$_3$-b-P(ODA$_{16}$-co-DA$_{43}$)) (**7**).* In a round-bottom flask, **6** (30 mg, 0.68 μmol) was dissolved in dry DMF (4.00 mL), SATP (4.74 mg, 20.5 μmol), DIPEA (20 μL, 0.1 μmol) was added and the reaction mixture was stirred at RT. The reaction mixture was then transferred into presoaked dialysis tubing (MWCO *ca.* 6000−8000 Da) to remove small molecule impurities. After extensive dialysis and lyophilization **7** was obtained (25 mg, 82%). $(M_n)_{NMR}$ = 41.7 kDa. IR: 3600−2600, 1715, 1590, 1415, 1250, 1120, 920, 820, 730 cm^{-1}. ^{1}H NMR (DMF-d_7) δ: 0.86 (t, J = 6.6 Hz, −C***H***$_3$CH$_2$ of ODA,

dx.doi.org/10.1021/bc200629f | *Bioconjugate Chem.* 2012, 23, 574−585

DA, and chain transfer agent), 1.15−1.40 (br, CH_2- alkyl chain of PODA, PDA, CTA, and HOOCC(CH_3)$_2$), 1.95−2.10 (br, -CH_2CH- backbone of PODA, PDA, and CTA), 2.05−2.20 (br, -CH$_2$CH- backbone of PODA, PDA, and CTA), 2.30−2.40 (br, DOTA), 2.71−2.75 (br, -CH_2S-), 2.95−3.10 (br, DOTA), 3.50 (-OCH_2-CH_2O-,br, PEG) 4.00 (br, -OCH_2CH$_2$-, PODA, PDA) ppm. ^{13}C NMR (DMF-d_7) δ: 14.5, 23.5, 27.0, 29.5, 30.5−31.5, 33.0, 35.1−37.5, 41.5−43.0, 55.8, 57.5, 65.0, 70.5, 174.1−175.1, 176.5 ppm. DSC: (T_m) = −44.3 °C, $(T_m)_{(ODA\text{-}co\text{-}DA)}$ = 11.3 °C, $(T_m)_{(PEO)}$ = 27.8 °C, (T_c) = −36.4 and 6.1 °C. TGA: T_{onset} = 170 °C, $T_{decomposition}$: (170−283 °C) 4% mass loss; (283−460 °C) 87.3% mass loss; 8.7% mass remaining.

*Procedure for the Preparation of Micelles (**8**).* To **7** in DMF (8.0 mg, 1.0 mgmL^{-1}) was added an equal volume of nanopure water dropwise via a syringe pump over the course of 3 h. The mixture was allowed to stir for 16 h at RT and was then transferred to presoaked dialysis tubing (MWCO ca. 6000−8000 Da) and dialyzed against nanopure water for ca. 4 d to remove the organic solvent and give a final polymer concentration of 0.32 mgmL^{-1}. $(D_h)_n$ (DLS) = 43 ± 8 nm; $(D_h)_{vol}$ (DLS) = 63 ± 6 nm; $(D_h)_{int}$ (DLS) = 124 ± 20 nm; D_{av} (TEM) = 36 ± 4 nm.

*Procedure for the Preparation of SCKs (**9**).* To a solution of micelles (**8**) (15 mL, 0.32 mg mL^{-1}) was added 2,2′-(ethylenedioxy)bis(ethylamine) (0.63 mg, 4.3 μmol, to achieve nominal cross-linking through 20% of the COOH groups) from a stock solution via a syringe pump over 30 min. The reaction mixture was allowed to stir at RT for 30 min and EDCI (1.17 mg, 3.93 μmol) was added as a solution in water via syringe pump over 15 min. The reaction mixture was allowed to stir at RT for 24 h and was then transferred to presoaked dialysis tubing (MWCO ca. 6000−8000 Da) and dialyzed for ca. 4 d to afford the SCK solution with a final concentration of 0.29 mg mL^{-1}. $(D_h)_n$ (DLS) = 48 ± 7 nm; $(D_h)_{vol}$ (DLS) = 79 ± 10 nm; $(D_h)_{int}$ (DLS) = 123 ± 9 nm; D_{av} (TEM) = 41 ± 4 nm.

*Conjugation of Alexa Fluor 633 Hydrazide to SCKs (**10**).* To a SCK solution (8.0 mL, 0.29 mg mL^{-1}) at 0 °C was added a stock aqueous solution of EDCI (2.41 mg, 8.10 μmol) over a period of 3 min, and the mixture was allowed to stir for 20 min. Sulfo-NHS (1.78 mg, 8.10 μmol) was added from a stock solution prepared in nanopure water and the reaction was stirred for 2 h. The pH of the solution was adjusted to 7.2 using PBS buffer (pH 8.86, 0.2 M) and Alexa Fluor 633 hydrazide (72.0 μg, 0.064 μmol) was added to the reaction mixture from a stock solution in DMSO. The reaction mixture was allowed to stir for 24 h in the dark and was then transferred to presoaked dialysis tubing (MWCO ca. 6000−8000 Da) and dialyzed against NP water for 5 d in an Al-foil-wrapped beaker. The concentration of dye was found to be 12.0 μM from UV−vis spectroscopy. $(D_h)_n$ (DLS) = 60 ± 16 nm; $(D_h)_{vol}$ (DLS) = 79 ± 30 nm; $(D_h)_{int}$ (DLS) = 125 ± 53 nm; D_{av} (TEM) = 40 ± 4 nm.

*Deprotection of Masked Thiols of Alexa Fluor 633 Hydrazide Labeled SCKs (**11**).* Hydroxyl amine hydrochloride (75.0 μL, 0.5 M) in aqueous buffer (100 mM, 150 mM NaCl) was added to a stirred solution of SCK **10** (5.0 mL) suspended in buffer (100 mM, 150 mM NaCl) and the reaction mixture was allowed to stir for 3 h at RT. The solution was assayed by Ellman's assay and the thiol content was determined to be 33 ± 4 μM. The solution was immediately used for conjugation with maleimide-functionalized PNAs and CPPs.

*Synthesis of Maleimide−PNA Conjugates (**12**).* PNAs were synthesized continuously on universal support XAL-PEG-PS resin at a 2 μmol scale with standard solid phase Fmoc chemistry on an Expedite 8909 Synthesizer. After completion of automated synthesis, PNAs were cleaved from the solid support and the bases were deprotected using trifluoroacetic acid: *m*-cresol (4:1, v/v) for 3 h and then precipitated with diethyl ether. The crude products were purified by HPLC and characterized by MALDI-TOF. PNAs were then dissolved in NMP: dimethylsulfoxide (DMSO) (7:3, v/v) with 15 min vigorous stirring. Maleimide dissolved in NMP was added to the PNA solution followed by addition of DIEA (16 μL) and the reaction mixture was maintained at room temperature for 2.5 h with gentle shaking. Excess cold diethyl ether (anhydrous) was added to precipitate the PNA−maleimide conjugates. The PNA−maleimide conjugates were dried under nitrogen and characterized by MALDI-TOF mass spectrometry.

*General Procedure for Conjugation of SCKs with iNOS PNAs with and without TAT (**13**).* To a SCK solution (750 μL, 0.29 mg mL^{-1}) suspended in buffer (100 mM PBS, 150 mM NaCl, pH 7.2), citric acid buffer (pH 5.12) was used to adjust the pH to 6.5. A concentrated solution of iNOS PNA (Maleimide-TTTCCTTTTCCTCTTTCA or Maleimide-TGTCCTCCTTTTCTTTCA) (5.0 nmol in DMF) in (100 mM PBS, 150 mM NaCl, pH 7.4) was added to the SCK solution to prepare SCKs with mismatch or match PNAs. Additionally, TAT (Maleimide-GGYGRKKRRQRRR) (6.7 nmol from a stock solution in DMF) was added to the reaction mixture of SCKs with either match or mismatch PNA sequences to prepare PNA-SCK-TAT conjugates. The reaction mixture was stirred at room temperature for 6 h and remaining thiols were capped by addition of 4-maleimido-butyric acid (1 mg suspended in 100 mM PBS, 150 mM NaCl, pH 7.4). The reaction was stirred for 16 h before being purified by SephadexG-50 gel column. D_{av} (TEM) = 28 ± 5 nm.

*Preparation of Biotinylated iNOS mRNA (**14**).* Image CloneID 4978648 containing the iNOS mRNA sequence (Gene Bank BC062378, ATCC cloning no. 10470196) was obtained from ATCC. The plasmid DNA was purified and linearized at the unique XbaI site before transcription. Transcription reactions were carried out using the Promega RiboMAX large scale RNA production system utilizing the SP6 promoter (Promega). Transcription proceeded with SP6 RNA polymerase, NTPs, and Bio-UTP (Roche) for 4 h at 37 °C, and followed by DNase I treatment, phenol:chloroform:isoamylalcohol (25:24:1) extraction, and ethanol precipitation. The final purified iNOS RNA was quite homogeneous and corresponded in size to the expected 4 Kb transcript.

Binding Affinity of ODNs to iNOS mRNA by a Dynabead-Based Binding Assay. The radiolabeled ODN (100 pM) was incubated with biotinylated mRNA (0.01, 0.1, 1, 10, 100 nM) and 1 μL of RNase inhibitor for 4 h at 37 °C in a total volume of 100 μL. Streptavidin coated Dynabeads were added and mixed for 30 min. The beads were then separated by a magnet, washed twice, and resuspended in 100 μL of hybridization buffer (5 m M Tris-HCl, pH 7.0, 1 mM EDTA, 0.1 M NaCl). Solutions were then counted by liquid scintillation to give bound fractions directly.

The dissociation constants were determined by nonlinear fitting of the fraction bound versus RNA concentration data to

the analytical expression shown below for a two state binding equilibrium using the *Kaleidagraph* program.

$$F_B = \mathrm{NSB} + \left\{\mathrm{SB} \times \left[([L] + K_d + [\mathrm{RNA}]) - \sqrt{([L] + K_d + [\mathrm{RNA}]^2 - 4 \times [\mathrm{RNA}])}\right]\right\} / \left(2 \times [L]\right) \quad (1)$$

where F_B is the experimentally determined fraction of bound ODN, NSB is the fraction of ODN that is nonspecifically bound, SB is the fraction of ODN that can be specifically bound and was set equal to (1-NSB), [L] is total ODN concentration, K_d is dissociation constant of the ODN, and [RNA] is total RNA concentration.

Binding Affinity of iNOS PNA-SCK-TAT for iNOS mRNA by a Competition Assay. Biotinylated mRNA (10 pM) was incubated with 1000 pM radiolabeled ODN and 1 μL of RNase inhibitor for 4 h at 37 °C, to which unlabeled competitor PNAs (0, 0.001, 0.01, 0.1, 1, 10 nM) or iNOS PNA-SCK-TAT (0, 0.01, 0.1, 1, 10, 100, and 1000 nM, concentration calculated based on PNA concentration) were added. The streptavidin coated Dynabeads were added and mixed for another 30 min at 37 °C. Following incubation, the reaction mixture was separated by a magnetic field, washed twice, and resuspended in hybridization buffer (5 mM Tris-HCl, pH 7.0, 1 mM EDTA, 0.1 M NaCl). The solution containing bound ODNs was counted by liquid scintillation. Additionally, SCK-TAT alone served as a control group.

The fraction of antisense ODN bound to the RNA (B) was then plotted against the competitor PNA concentration ([PNA]), and an IC_{50} value is determined (the concentration of competitor PNA that reduces binding of the ODN by 50%) by fitting the data according to a standard equation. Once the IC_{50} values are obtained, the K_ds for the PNAs can be determined using a simple relationship involving the IC_{50} and the K_d for the antisense ODN.

$$B = B_{\min} + \frac{B_{\max} - B_{\min}}{1 + 10^{\log[\mathrm{PNA}] - \log(IC_{50})}} \quad (2)$$

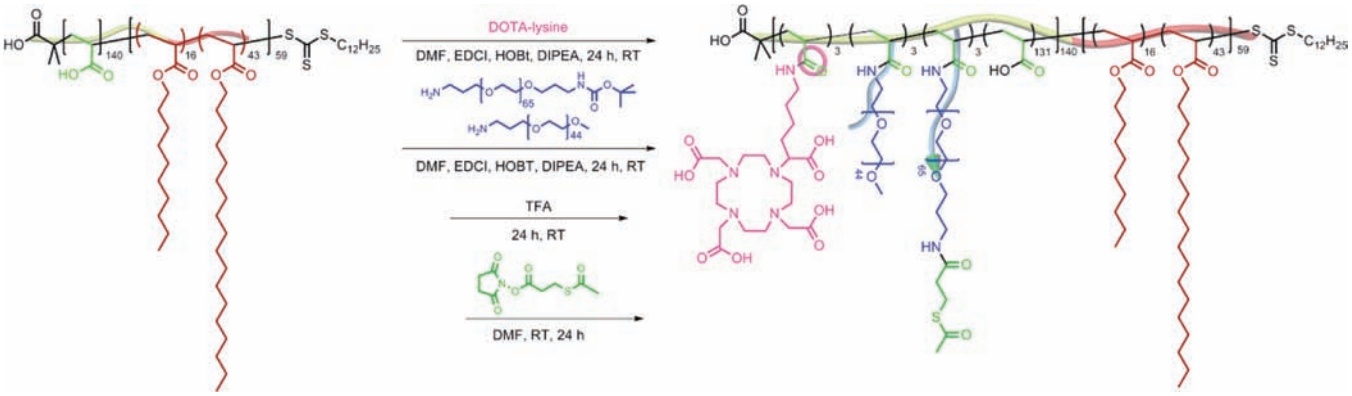
$$K_d(\mathrm{PNA}) = \frac{IC_{50}}{1 + \frac{[\mathrm{ODN}]}{K_d(\mathrm{ODN})}} \quad (3)$$

RESULTS AND DISCUSSION

Design of the PNA Nanoparticles. The PNA nanoparticles were designed to meet a number of criteria for future applications as imaging and knockdown agents for iNOS expression. The first was that the nanoparticle be able to enter cells efficiently so as to be able to engage the iNOS mRNA in the cytoplasm. The second was that the attached PNAs would be able to freely interact with the mRNA. The third was that the nanoparticle would be capable of being detected by both fluorescent and PET imaging modalities. The fourth was that the nanoparticles avoid detection by the mononuclear phagocytic system (MPS), also referred to as the reticuloendothelial system (RES), which would otherwise result in their rapid clearance from the blood. To meet these criteria, a PEGylated shell cross-linked nanoparticle was chosen in which the PNAs and the TAT peptide would be attached to the ends of the PEG chains, while the imaging agents would be conjugated to the polyacrylate shell. PEGylation has been previously shown to impart stealth character to SCKs and prolong their retention in the blood,[44,46] presumably by shielding the polyacrylate core from components of the MPS. The TAT peptide was chosen to facilitate endocytosis of the SCKs,[63,64] and to enable TAT to interact with the cell surface, it was attached to the ends of the PEG chains, using a thiol coupling strategy.[49] Likewise, the PNAs were designed to also be attached to the ends of the PEG chains to enable them to interact with the mRNA in the cytoplasm. The imaging agents were designed to be attached to the polyacrylate shell to minimize their exposure to the MPS. The polyacrylate shell was also expected to serve additional functions to serve as a robust network for maintaining the nanoparticle structure and to, potentially, facilitate rupture of the endosome upon lowering of the pH during endosomal acidification.[65]

Synthesis of the SCK Nanoparticles. The block copolymer precursor used in this study was prepared by a two-step reversible addition−fragmentation chain transfer (RAFT) polymerization process, followed by deprotection (Scheme 1), as described in previous work by our group.[58] *S*-1-Dodecyl-*S*′-(α,α′-dimethyl-α″-acetic acid) trithiocarbonate (DDMAT) was used as a chain transfer agent to synthesize an initial P*t*BA$_{140}$ **1** homopolymer, which served as a macrochain transfer agent. This macrochain transfer agent was then employed during the copolymerization of octadecyl acrylate and decyl acrylate to afford P*t*BA$_{140}$-*b*-P(ODA$_{16}$-*co*-DA$_{43}$), **2**, having a narrow molecular weight distribution (PDI < 1.10) (Figure 1). The *tert*-butyl protecting groups were removed via acidolysis with TFA in CH_2Cl_2 to yield the amphiphilic block copolymer of PAA$_{140}$-*b*-P(ODA$_{16}$-*co*-DA$_{43}$), **3**. The PAA$_{140}$-*b*-P(ODA$_{16}$-*co*-DA$_{43}$) polymer

Scheme 1. Synthesis of Amphiphilic Functional Block Graft Copolymer 7



dx.doi.org/10.1021/bc200629f | *Bioconjugate Chem.* 2012, 23, 574−585

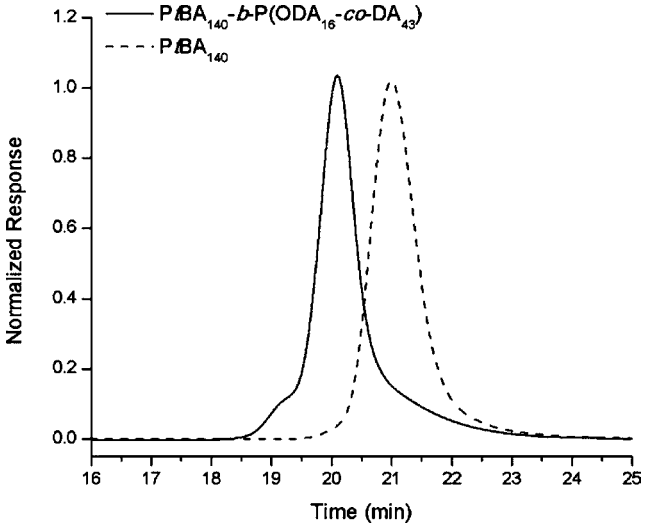


Figure 1. GPC traces for P*t*BA **1** and P*t*BA-*b*-P(ODA-*co*-DA) **2**.

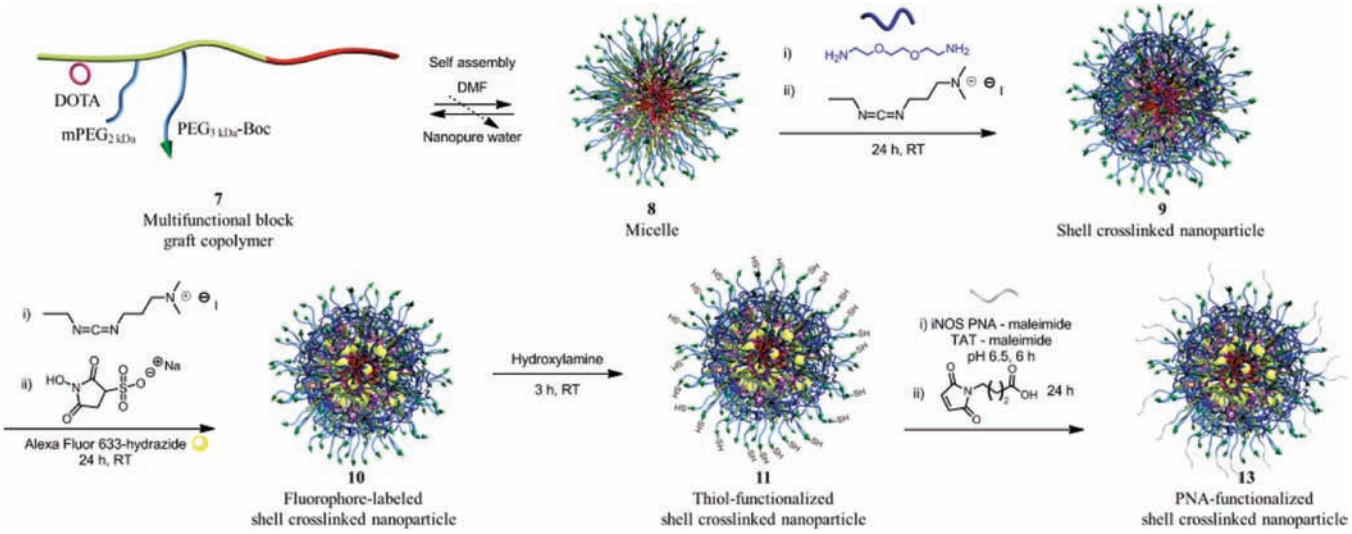
was further functionalized with chelators and PEO grafts to provide for terminal coupling sites for attachment of the biologically active ligands (PNA and TAT) and to allow for direct, future translation to *in vivo* studies. The block copolymer was first functionalized with Boc-protected DOTA-lysine via amidation of acrylic acid repeat units of the polymer to afford **4** with ca. 3 DOTA-lysines per polymer backbone. DOTA serves as a chelator for ^{64}Cu which will allow the resulting nanoparticles to be used for PET imaging *in vivo*.[44−46,66] Furthermore, different lengths of PEO grafts (2 kDa and 3 kDa) were appended to the polymer backbone to obtain **5**, using similar amidation chemistry to yield ca. 3 of each type of PEO per polymer chain. The 2 kDa PEO grafts provide stealth properties for the nanoparticles, while the 3 kDa PEO chains, after chain terminus deprotection and modification, additionally, provide reactive sites. The Boc-protecting groups from DOTA and 3 kDa PEOs were removed using TFA in a global deprotection step revealing amines at their termini. In the last step, methyl ester protected sulfohydryl groups were introduced at the NH_2-termini of the 3 kDa PEOs by reaction with SATP to yield functional block graft copolymers, **7** (Table 1). After each chemical transformation of the amphiphilic block copolymers, purification was performed via extensive dialysis against nanopure water and the polymers were isolated by lyophilization.

Preparation of Functionalized and Labeled Nanoparticles. SCKs were prepared by the solution-state assembly of the amphiphilic block graft copolymers in water followed by crosslinking reactions selectively throughout the hydrophilic shell layer (Scheme 2). After dissolving **7** in DMF at a concentration

Table 1. Summary of Polymers Prepared

	polymer	DOTA	PEG	$SCOCH_3$	M_n [Da] ^1H NMR	M_n [Da] GPC	M_w [Da] GPC	PDI GPC
1	P*t*BA$_{140}$	-	-	-	18 300	12 000	13 200	1.1
2	P*t*BA$_{140}$-*b*-P(ODA$_{16}$-*co*-DA$_{43}$)	-	-	-	32 600	20 800	25 500	1.2
3	PAA$_{140}$-*b*-P(ODA$_{16}$-*co*-DA$_{43}$)	-	-	-	24 700	-	-	-
4	PAA$_{137}$-*g*-(CONH-lysine-DOTA-Boc)$_3$-*b*-P(ODA$_{16}$-*co*-DA$_{43}$)	3	-	-	26 700	-	-	-
5	PAA$_{131}$-*g*-(PEG$_{3\ kDa}$-Boc)$_3$-*g*-(mPEG$_{2\ kDa}$)$_3$-*g*-(CONH-lysine-DOTA-Boc)$_3$-*b*-P(ODA$_{16}$-*co*-DA$_{43}$)	3	3	-	41 600	-	-	-
6	PAA$_{131}$-*g*-(PEG$_{3\ kDa}$-NH_2)$_3$-*g*-(mPEG$_{2\ kDa}$)$_3$-*g*-(CONH-lysine-DOTA-COOH)$_3$-*b*-P(ODA$_{16}$-*co*-DA$_{43}$)	3	3	-	41 000	-	-	-
7	PAA$_{131}$-*g*-(PEG$_{3\ kDa}$-NHCO-C_2H_4-$SCOCH_3$)$_3$-*g*-(mPEG$_{2\ kDa}$)$_3$-(CONH-lysine-DOTA-COOH)$_3$-*b*-P(ODA$_{16}$-*co*-DA$_{43}$)	3	3	3	41 700	-	-	-

Scheme 2. Self-Assembly of the Multifunctional Block Graft Copolymer 7 into Micelle 8, Crosslinking into SCK 9, Conjugation of Alexa Fluor 633 Hydrazide 10, and Functionalization with PNAs and TAT to Give the Final Bios ynthetic Hybrid Nanostructure 13



dx.doi.org/10.1021/bc200629f | *Bioconjugate Chem.* 2012, 23, 574−585

of 1 mg·mL^{-1}, self-assembly was induced by gradual addition of an equal amount of water over a period of 3 h. The aqueous micelle solution was allowed to stir overnight and was then transferred to dialysis tubing (MWCO 6–8 kDa) and dialyzed against nanopure water for 4 d to remove organic solvent. The SCKs were obtained by cross-linking approximately 20% of the acrylic acid segments by amidation with the amine groups of the cross-linker (2,2′-ethylenedioxy)bis(ethylamine), in the presence of EDCI, followed by extensive dialysis to remove unreacted small molecule starting materials and reaction by products.

Alexa Fluor 633 hydrazide was attached to the SCKs, to serve as a fluorescent probe, by performing postassembly conjugation of the hydrazide group of the dye to EDCI-activated acrylic acids in the shell of the SCKs at 0 °C. The reaction was carried out for 24 h in the dark and the fluorescently labeled SCKs were purified by extensive dialysis for 5 d against nanopure water to remove unconjugated dye molecules.

Bioconjugation of TAT and PNAs to the SCK Nanoparticles. By introducing a masked thiol on to the end of the 3 kDa PEO terminus, a surface functional nanoparticle was designed and prepared that could undergo conjugation with biomacromolecules, e.g., proteins,[49] peptides, and nucleic acid sequences, through efficient reactions, such as thiol-maleimide, thiol-haloacetyl, or disulfide couplings. The acetyl protecting groups of the masked thiols were removed by reaction with the addition of a 0.1 M hydroxylamine solution for 4 h (Scheme 2). The thiol content of the nanoparticles was then evaluated using Ellman's assay and was determined to be 33 ± 4 μM. Ellman's assay of SCKs before reacting with hydroxylamine showed undetectable concentration of −SH. The resulting reactive −SH sites were expected to be presented on the surface of the SCK nanostructures, allowing for surface availability of biologically active ligands and were, therefore, utilized for conjugation of the PNAs as mRNA recognition elements and TAT CPPs for cell entry. These SCKs were subjected to reaction, coincidentally, with PNAs and TAT that were functionalized with maleimide, at pH 6.5 for 6 h at 0 °C. Two anti-iNOS PNAs, PNA240 and PNA480, and mismatch controls were selected for conjugation to the SCKs (Table 2),

Table 2. ODN and PNA Sequences Used

sequence ID	sequence (5′-3′ or amino-carboxy)
240	5′-TGT CCT TTT CCT CTT TCA-3′
240 (mm)	5′-TGT CCT CCT TTT CTT TCA-3′
480	5′-TGA AAT CCG ATG TGG CCT-3′
480 (mm)	5′-TAG AAT CCA GTG GTG CCT-3′

from a set of PNAs previously shown to have similar affinity for iNOS mRNA, but differing abilities to inhibit iNOS expression.[67] In each case, the unreacted thiols were capped using 4-maleimido butyric acid. The nanoparticle conjugates were purified with Sephadex G-50 columns and the amounts of PNAs incorporated into the SCK samples were calculated by UV–vis spectroscopy (Figure 2A and B) using the inherent wavelength of 260 nm for PNAs.

Characterization of Nanoparticles. The size and shape of the SCKs were determined using DLS and TEM. DLS analysis showed that the hydrodynamic diameters of the SCKs were slightly larger than were the diameter values determined by TEM, due to the hydration of the hydrophilic shell in aqueous conditions. The micelles and SCKs were 48 ± 7 nm by DLS and 41 ± 4 nm by TEM (Figure 3). The average core diameters

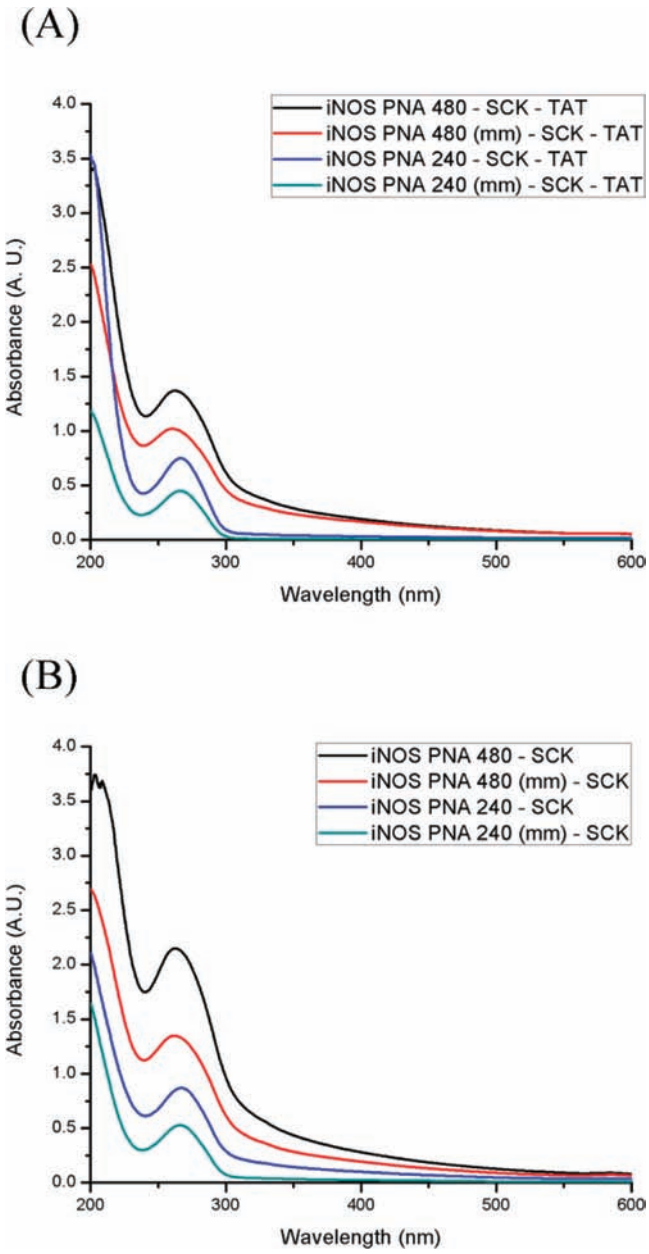


Figure 2. (A) UV–vis spectra of iNOS PNA–SCK conjugates, (B).UV–vis spectroscopy of iNOS PNA-SCK-TAT conjugates.

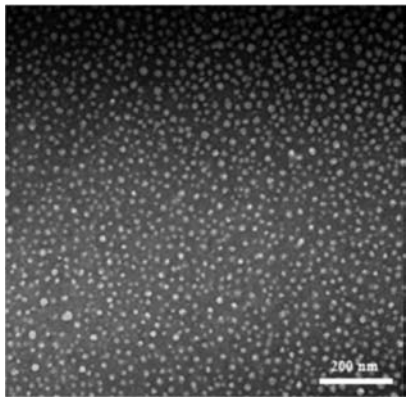


Figure 3. TEM image of SCKs **9**.

dx.doi.org/10.1021/bc200629f | *Bioconjugate Chem.* 2012, 23, 574–585

of the nanoparticles after conjugation with PNAs and TAT were determined using TEM (Supporting Information Figure 1) and were found to be ca. 28 ± 5 nm.

Binding Affinity of the PNA and PNA–SCK Conjugates for iNOS mRNA. The binding affinities of the PNA and PNA–SCK conjugates were determined by a competition assay against radiolabeled ODNs targeting the same site on the mRNA. To carry out this assay, we first determined the binding affinity of the ODNs targeting the same site as the PNA using a Dynabead assay that we had previously developed for this purpose.[68] The target mRNA was produced by transcription from an iNOS cDNA clone *in vitro* with Bio-dUTP to incorporate biotin groups into the RNA to enable it to be retrieved with streptavidin coated magnetic beads. The 5′-radiolabeled antisense ODNs were then incubated with the iNOS RNA and allowed to equilibrate for 4 h, after which the Dynabeads were added to bind to the mRNA, which could then be immobilized with a magnetic field. The solution containing the free ODNs was removed from the reaction tube, and both the free and bound fractions were quantified by liquid scintillation counting. The ratio of bound to free ODN vs concentration was then fit to a standard equation (eq 1), from which the dissociation constant (K_d) could be determined. As can be seen in Table 3, ODNs

Table 3. Binding Affinities of ODNs, PNAs, PNA-SCK, and iNOS PNA-SCK-TAT Conjugates

sequence ID	ODN (nM)	PNA (nM)	PNA-SCK (nM)	PNA-SCK-TAT (nM)
240	7.3 ± 1.2	0.10 ± 0.052	3.2 ± 2.0	1.4 ± 0.5
240 mm	-	>10000	>1000	>1000
480	5.2 ± 2.5	0.086 ± 0.026	1.1 ± 0.3	1.7 ± 1.0
480 mm	-	>10000	>1000	>1000
No PNA	-	-	>1000	>1000

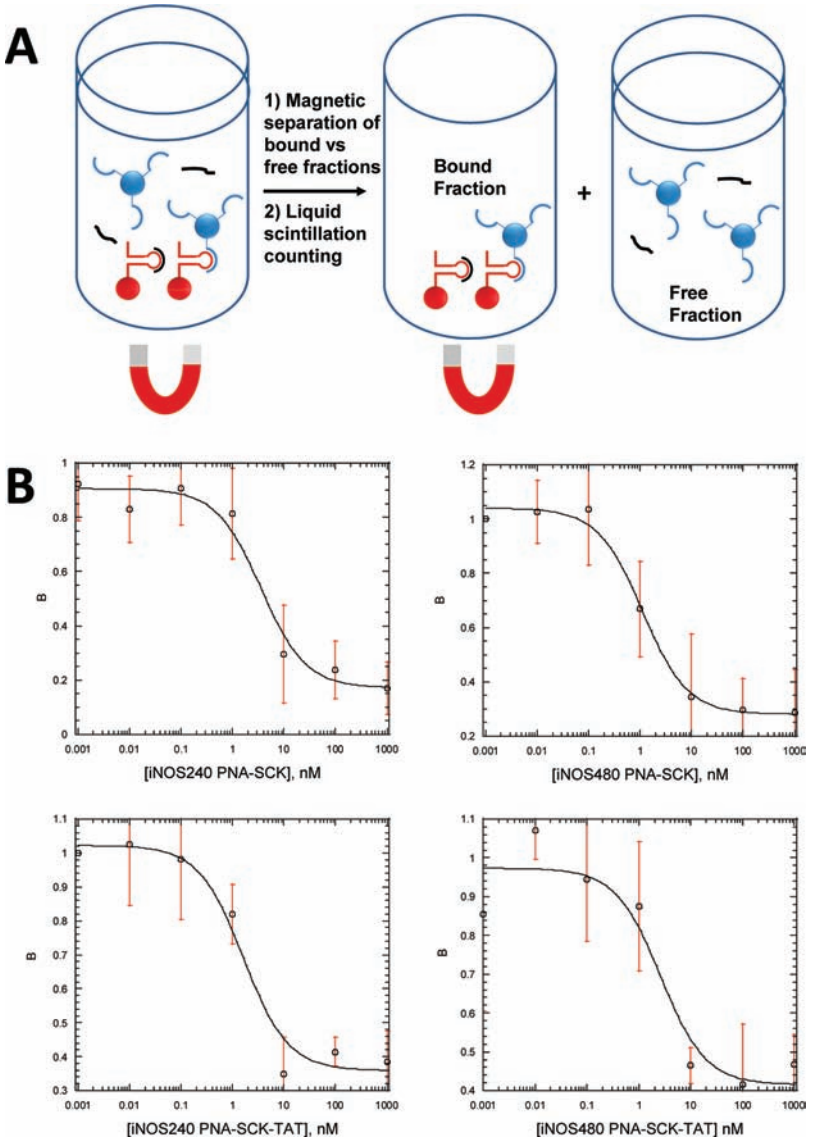


Figure 4. Dynabead competition assay to determine iNOS mRNA binding affinity of SCK-PNA conjugates. (A) Biotinylated iNOS mRNA (10 pM) bound to streptavidin coated Dynabeads were incubated with 1 nM 5′-radiolabeled 240 or 480 antisense ODN and increasing concentrations of the corresponding SCK-PNA conjugate. After incubation for 4 h, the bound versus free fractions were separated by a magnet and the radioactivity in each fraction was quantified by liquid scintillation counting. (B) Plots of the average fraction of mRNA bound by radioactively labeled ODN vs the SCK-PNA conjugates from three experiments fit to the analytical expression (2) described in the Experimental Section from which the IC_{50} was extracted. The data in Table 3 were obtained from averaging fits to each independent experiment (see Supporting Information).

dx.doi.org/10.1021/bc200629f | *Bioconjugate Chem.* 2012, 23, 574–585

designed on the basis of binding sites identified by the RT-ROL mapping assay (iNOS240, iNOS480)[67] showed very high affinity with dissociation constants (K_d's) of 7.3 ± 1.2 and 5.2 ± 2.5 nM (Table 3).

Once the binding affinity of the ODNs was established, the binding affinity of PNAs and PNA-SCK conjugates to iNOS mRNA could be determined by a competition assay in which the concentration of ODN was held constant and the concentration of the PNA or PNA-SCK was varied (Figure 4). The K_d could then be calculated from the IC_{50}. As can be seen in Table 3, the two PNAs, PNA-240, and PNA-480 showed similar K_d's of 101 ± 52 and 86 ± 26 pM, while the mismatched PNAs had K_d's of >10 nM. When conjugated to the SCKs, the binding affinity of the PNAs appeared to decrease about 30- to 10-fold, respectively, to 3.2 ± 2.0 and 1.1 ± 0.3 nM, while the mismatched PNAs showed no significant affinity. The decrease in affinity of the PNAs upon conjugation could be due to a number of factors, such as electrostatic repulsion between the SCK and the RNA, or steric interference by a bound RNA molecule. The binding affinity of the iNOS PNA-SCK-TAT conjugates, which could have been expected to be higher due to the positive charge of the TAT peptide, was not significantly different from the conjugates lacking the TAT peptide.

CONCLUSIONS

SCKs covalently conjugated with iNOS PNAs and CPPs have been prepared and their binding affinities with complementary mRNAs postconjugation were evaluated. Specific effort was made to have these biologically active units presented from the outermost surface of the SCKs, by employing well-defined multistep polymerization and polymer modification reactions that involved combinations of stealthy PEG chain grafts. The binding affinity measurements demonstrated that the PNAs retain molecular recognition selectivity even after undergoing coupling onto the nanoscopic SCK objects. The shapes and sizes of SCKs remained almost the same in the resulting nanoconjugates. By partitioning various optical and radiolabeling sites and reactive functionalities for conjugation of biological ligands within a size-, shape-, and flexibility-controlled nanoscopic framework, these biosynthetic hybrid materials provide preliminary steps toward the development of hierarchical nanostructures that hold great promise as antisense imaging agents and therapeutics. The availability of particles with tunable compositions and properties will allow us to fine-tune the PNA–RNA molecular recognition events, while balancing the electrostatic binding and repulsion.[55,56] With the high levels of sophistication that are possible via simple iterations of controlled polymer chemistries, there are several functions whose biological performances are yet to be evaluated. Extended *in vitro* and *in vivo* studies are underway.

ASSOCIATED CONTENT

Supporting Information

Additional TEM images and binding affinity data. This material is available free of charge via the Internet at http://pubs.acs.org.

AUTHOR INFORMATION

Corresponding Author

*Karen L. Wooley, E-mail: wooley@chem.tamu.edu. John-Stephen A. Taylor, E-mail: taylor@wuchem.wustl.edu.

Notes

The authors declare no competing financial interest.

ACKNOWLEDGMENTS

This material is based upon work supported by the National Heart Lung and Blood Institute of the National Institutes of Health as a Program of Excellence in Nanotechnology (HHSN268201000046C) and by the Office of Naval Research (N00014-10-1-0527). The Welch Foundation is gratefully acknowledged for support through the W. T. Doherty-Welch Chair in Chemistry, Grant No. A-0001.

REFERENCES

(1) Rubenfeld, G. D., Caldwell, E., Peabody, E., Weaver, J., Martin, D. P., Neff, M., Stern, E. J., and Hudson, L. D. (2005) Incidence and Outcomes of Acute Lung Injury. *New Engl. J. Med. 353*, 1685–1693.

(2) Goodman, R. B., Pugin, J., Lee, J. S., and Matthay, M. A. (2003) Cytokine-mediated inflammation in acute lung injury. *Cytokine Growth Factor Rev. 14*, 523–535.

(3) Hemmrich, K., Kröncke, K.-D., Suschek, C. V., and Kolb-Bachofen, V. (2005) What sense lies in antisense inhibition of inducible nitric oxide synthase expression? *Nitric Oxide 12*, 183–199.

(4) Guo, F. H., Deraeve, H. R., Rice, T. W., Stuehr, D. J., Thunnissen, F. B. J. M., and Erzurum, S. C. (1995) Continuous Nitric-Oxide Synthesis by Inducible Nitric-Oxide Synthase in Normal Human Airway Epithelium in-Vivo. *Proc. Natl. Acad. Sci. U.S.A. 92*, 7809–7813.

(5) Sittipunt, C., Steinberg, K. P., Ruzinski, J. T., Myles, C., Zhu, S., Goodman, R. B., Hudson, L. D., Matalon, S., and Martin, T. R. (2001) Nitric oxide and nitrotyrosine in the lungs of patients with acute respiratory distress syndrome. *Am. J. Respir. Crit. Care Med. 163*, 503–10.

(6) Hosogi, S., Iwasaki, Y., Yamada, T., Komatani-Tamiya, N., Hiramatsu, A., Kohno, Y., Ueda, M., Arimoto, T., and Marunaka, Y. (2008) Effect of inducible nitric oxide synthase on apoptosis in Candida-induced acute lung injury. *Biomed. Res.-Tokyo 29*, 257–266.

(7) Mehta, S. (2005) The effects of nitric oxide in acute lung injury. *Vasc. Pharmacol. 43*, 390–403.

(8) Zhang, J., McCarthy, T. J., Moore, W. M., Currie, M. G., and Welch, M. J. (1996) Synthesis and evaluation of two positron-labeled nitric oxide synthase inhibitors, S-[11C]methylisothiourea and S-(2-[18F]fluoroethyl)isothiourea, as potential positron emission tomography tracers. *J. Med. Chem. 39*, 5110–8.

(9) Panda, K., Chawla-Sarkar, M., Santos, C., Koeck, T., Erzurum, S. C., Parkinson, J. F., and Stuehr, D. J. (2005) Visualizing inducible nitric-oxide synthase in living cells with a heme-binding fluorescent inhibitor. *Proc. Natl. Acad. Sci. U.S.A. 102*, 10117–10122.

(10) Towner, R. A., Smith, N., Doblas, S., Garteiser, P., Watanabe, Y., He, T., Saunders, D., Herlea, O., Silasi-Mansat, R., and Lupu, F. (2010) In vivo detection of inducible nitric oxide synthase in rodent gliomas. *Free Radical Biol. Med. 48*, 691–703.

(11) Hesslinger, C., Strub, A., Boer, R., Ulrich, W. R., Lehner, M. D., and Braun, C. (2009) Inhibition of inducible nitric oxide synthase in respiratory diseases. *Biochem. Soc. Trans. 37*, 886–91.

(12) Lim, M. H., Xu, D., and Lippard, S. J. (2006) Visualization of nitric oxide in living cells by a copper-based fluorescent probe. *Nat. Chem. Biol. 2*, 375–380.

(13) Ouyang, J., Hong, H., Zhao, Y., Shen, H., Shen, C., Zhang, C., and Zhang, J. (2008) Bioimaging nitric oxide in activated macrophages in vitro and hepatic inflammation in vivo based on a copper–naphthoimidazol coordination compound. *Nitric Oxide 19*, 42–49.

(14) Zhou, D., Lee, H., Rothfuss, J. M., Chen, D. L., Ponde, D. E., Welch, M. J., and Mach, R. H. (2009) Design and synthesis of 2-amino-4-methylpyridine analogues as inhibitors for inducible nitric oxide synthase and in vivo evaluation of [18F]6-(2-fluoropropyl)-4-methyl-pyridin-2-amine as a potential PET tracer for inducible nitric oxide synthase. *J. Med. Chem. 52*, 2443–53.

(15) Koppelhus, U., and Nielsen, P. E. (2003) Cellular delivery of peptide nucleic acid (PNA). *Adv. Drug Delivery Rev. 55*, 267–280.

(16) Nielsen, P. E., Egholm, M., Berg, R. H., and Buchardt, O. (1991) Sequence-selective recognition of DNA by strand displacement with a thymine-substituted polyamide. *Science 254*, 1497–1500.

(17) Nielsen, P. E. (2004) PNA Technology. *Mol. Biotechnol. 26*, 233−48.
(18) Lundin, K. E., Good, L., Stromberg, R., Graslund, A., and Smith, C. I. (2006) Biological activity and biotechnological aspects of peptide nucleic acid. *Adv. Genet. 56*, 1−51.
(19) Nielsen, P. E. (2010) Gene targeting and expression modulation by peptide nucleic acids (PNA). *Curr. Pharm. Des. 16*, 3118−23.
(20) Shi, N., Boado, R. J., and Pardridge, W. M. (2000) Antisense imaging of gene expression in the brain in vivo. *Proc. Natl. Acad. Sci. U.S.A. 97*, 14709−14.
(21) Rao, P. S., Tian, X., Qin, W., Aruva, M. R., Sauter, E. R., Thakur, M. L., and Wickstrom, E. (2003) 99mTc-peptide-peptide nucleic acid probes for imaging oncogene mRNAs in tumours. *Nucl. Med. Commun. 24*, 857−63.
(22) Sun, X., Fang, H., Li, X., Rossin, R., Welch, M. J., and Taylor, J. S. (2005) MicroPET imaging of MCF-7 tumors in mice via unr mRNA-targeted peptide nucleic acids. *Bioconjugate Chem. 16*, 294−305.
(23) Santangelo, P., Nitin, N., and Bao, G. (2006) Nanostructured probes for RNA detection in living cells. *Ann. Biomed. Eng. 34*, 39−50.
(24) Jia, F., Figueroa, S. D., Gallazzi, F., Balaji, B. S., Hannink, M., Lever, S. Z., Hoffman, T. J., and Lewis, M. R. (2008) Molecular imaging of bcl-2 expression in small lymphocytic lymphoma using 111In-labeled PNA-peptide conjugates. *J. Nucl. Med. 49*, 430−8.
(25) Lendvai, G., Estrada, S., and Bergstrom, M. (2009) Radiolabelled oligonucleotides for imaging of gene expression with PET. *Curr. Med. Chem. 16*, 4445−61.
(26) Iyer, A. K., and He, J. (2011) Radiolabeled oligonucleotides for antisense imaging. *Curr. Org. Synthesis 8*, 604−614.
(27) Zhilina, Z. V., Ziemba, A. J., and Ebbinghaus, S. W. (2005) Peptide nucleic acid conjugates: synthesis, properties and applications. *Curr. Top. Med. Chem. 5*, 1119−31.
(28) Abes, R., Arzumanov, A. A., Moulton, H. M., Abes, S., Ivanova, G. D., Iversen, P. L., Gait, M. J., and Lebleu, B. (2007) Cell-penetrating-peptide-based delivery of oligonucleotides: an overview. *Biochem. Soc. Trans. 35*, 775−9.
(29) Thurmond, K. B., Kowalewski, T., and Wooley, K. L. (1997) Shell cross-linked knedels: A synthetic study of the factors affecting the dimensions and properties of amphiphilic core-shell nanospheres. *J. Am. Chem. Soc. 119*, 6656−6665.
(30) Thurmond, K. B., Huang, H. Y., Clark, C. G., Kowalewski, T., and Wooley, K. L. (1999) Shell cross-linked polymer micelles: stabilized assemblies with great versatility and potential. *Colloids Surf., B: Biointerfaces 16*, 45−54.
(31) Remsen, E. E., Thurmond, K. B., and Wooley, K. L. (1999) Solution and surface charge properties of shell cross-linked knedel nanoparticles. *Macromolecules 32*, 3685−3689.
(32) Thurmond, K. B., Kowalewski, T., and Wooley, K. L. (1996) Water-soluble knedel-like structures: The preparation of shell-cross-linked small particles. *J. Am. Chem. Soc. 118*, 7239−7240.
(33) Samarajeewa, S., Shrestha, R., Li, Y., and Wooley, K. L. (2012) Degradability of Poly(Lactic Acid)-Containing Nanoparticles: Enzymatic Access through a Cross-Linked Shell Barrier. *J. Am. Chem. Soc. 134*, 1235−42.
(34) Pochan, D. J., Chen, Z. Y., Cui, H. G., Hales, K., Qi, K., and Wooley, K. L. (2004) Toroidal triblock copolymer assemblies. *Science 306*, 94−97.
(35) Pochan, D. J., Cui, H. G., Chen, Z. Y., and Wooley, K. L. (2009) Origins of toroidal micelle formation through charged triblock copolymer self-assembly. *Soft Matter 5*, 1269−1278.
(36) Pochan, D. J., Zhong, S., Cui, H. G., Chen, Z. Y., and Wooley, K. L. (2008) Helix self-assembly through the coiling of cylindrical micelles. *Soft Matter 4*, 90−93.
(37) Pochan, D. J., Zhu, J. H., Zhang, K., Wooley, K. L., Miesch, C., and Emrick, T. (2011) Multicompartment and multigeometry nanoparticle assembly. *Soft Matter 7*, 2500−2506.
(38) Cui, H. G., Chen, Z. Y., Zhong, S., Wooley, K. L., and Pochan, D. J. (2007) Block copolymer assembly via kinetic control. *Science 317*, 647−650.
(39) Sorrells, J. L., Shrestha, R., Neumann, W. L., and Wooley, K. L. (2011) Porphyrin-crosslinked block copolymer assemblies as photophysically-active nanoscopic devices. *J. Mater. Chem. 21*, 8983−8986.
(40) Becker, M. L., Bailey, L. O., and Wooley, K. L. (2004) Peptide-derivatized shell-cross-linked nanoparticles. 2. Biocompatibility evaluation. *Bioconjugate Chem. 15*, 710−717.
(41) Becker, M. L., Remsen, E. E., Pan, D., and Wooley, K. L. (2004) Peptide-derivatized shell-cross-linked nanoparticles. 1. Synthesis and characterization. *Bioconjugate Chem. 15*, 699−709.
(42) Joralemon, M. J., Murthy, K. S., Remsen, E. E., Becker, M. L., and Wooley, K. L. (2004) Synthesis, characterization, and bioavailability of mannosylated shell cross-linked nanoparticles. *Biomacromolecules 5*, 903−913.
(43) Joralemon, M. J., Smith, N. L., Holowka, D., Baird, B., and Wooley, K. L. (2005) Antigen-decorated shell cross-linked nanoparticles: Synthesis, characterization, and antibody interactions. *Bioconjugate Chem. 16*, 1246−1256.
(44) Sun, X. K., Rossin, R., Turner, J. L., Becker, M. L., Joralemon, M. J., Welch, M. J., and Wooley, K. L. (2005) An assessment of the effects of shell cross-linked nanoparticle size, core composition, and surface PEGylation on in vivo biodistribution. *Biomacromolecules 6*, 2541−2554.
(45) Welch, M. J., Sun, G., Xu, J., Hagooly, A., Rossin, R., Li, Z., Moore, D. A., Hawker, C. J., and Wooley, K. L. (2007) Strategies for optimized radiolabeling of nanoparticles for in vivo PET Imaging. *Adv. Mater. 19*, 3157−+.
(46) Sun, G., Hagooly, A., Xu, J., Nystrom, A. M., Li, Z. C., Rossin, R., Moore, D. A., Welch, M. J., and Wooley, K. L. (2008) Facile, efficient approach to accomplish tunable chemistries and variable biodistributions for shell cross-linked nanoparticles. *Biomacromolecules 9*, 1997−2006.
(47) Lin, L. Y., Lee, N. S., Zhu, J., Nystrom, A. M., Pochan, D. J., Dorshow, R. B., and Wooley, K. L. (2011) Tuning core vs. shell dimensions to adjust the performance of nanoscopic containers for the loading and release of doxorubicin. *J. Controlled Release 152*, 37−48.
(48) Nystrom, A. M., Xu, Z. Q., Xu, J. Q., Taylor, S., Nittis, T., Stewart, S. A., Leonard, J., and Wooley, K. L. (2008) SCKs as nanoparticle carriers of doxorubicin: investigation of core composition on the loading, release and cytotoxicity profiles. *Chem. Commun.*, 3579−3581.
(49) Nystrom, A. M., and Wooley, K. L. (2008) Thiol-functionalized shell crosslinked knedel-like (SCK) nanoparticles: A versatile entry for their conjugation with biomacromolecules. *Tetrahedron 64*, 8543−8552.
(50) Zhang, S., Li, Z., Samarajeewa, S., Sun, G., Yang, C., and Wooley, K. L. (2011) Orthogonally Dual-Clickable Janus Nanoparticles via a Cyclic Templating Strategy. *J. Am. Chem. Soc. 133*, 11046−9.
(51) Pan, D., Turner, J. L., and Wooley, K. L. (2003) Folic acid-conjugated nanostructured materials designed for cancer cell targeting. *Chem. Commun.*, 2400−2401.
(52) Zhang, K., Fang, H. F., Chen, Z. Y., Taylor, J. S. A., and Wooley, K. L. (2008) Shape effects of nanoparticles conjugated with cell-penetrating peptides (HIV Tat PTD) on CHO cell uptake. *Bioconjugate Chem. 19*, 1880−1887.
(53) Turner, J. L., Becker, M. L., Li, X. X., Taylor, J. S. A., and Wooley, K. L. (2005) PNA-directed solution- and surface-assembly of shell crosslinked (SCK) nanoparticle conjugates. *Soft Matter 1*, 69−78.
(54) Fang, H., Zhang, K., Shen, G., Wooley, K. L., and Taylor, J. S. (2009) Cationic shell-cross-linked knedel-like (cSCK) nanoparticles for highly efficient PNA delivery. *Mol. Pharm. 6*, 615−26.
(55) Zhang, K., Fang, H. F., Wang, Z. H., Li, Z., Taylor, J. S. A., and Wooley, K. L. (2010) Structure-activity relationships of cationic shell-crosslinked knedel-like nanoparticles: Shell composition and transfection efficiency/cytotoxicity. *Biomaterials 31*, 1805−1813.
(56) Zhang, K., Fang, H., Wang, Z., Li, Z., Taylor, J. S., and Wooley, K. L. (2010) Structure-activity relationships of cationic shell-crosslinked knedel-like nanoparticles: shell composition and transfection efficiency/cytotoxicity. *Biomaterials 31*, 1805−13.

(57) Zhang, K., Fang, H., Wang, Z., Taylor, J. S., and Wooley, K. L. (2009) Cationic shell-crosslinked knedel-like nanoparticles for highly efficient gene and oligonucleotide transfection of mammalian cells. *Biomaterials 30*, 968−77.
(58) Nystrom, A. M., and Wooley, K. L. (2008) Construction of thermoresponsive SCKs through tuning the crystalline melting point of the core domain. *Soft Matter 4*, 849−858.
(59) O'Connor, R. D., Zhang, Q., Wooley, K. L., and Schaefer, J. (2002) Crystallization of poly(epsilon-caprolactone) under nanoparticle confinement. *Helv. Chim. Acta 85*, 3219−3224.
(60) Zhang, Q., Clark, C. G., Wang, M., Remsen, E. E., and Wooley, K. L. (2002) Thermally-induced (re)shaping of core-shell nanocrystalline particles. *Nano Lett. 2*, 1051−1054.
(61) Zhang, Q., Wang, M., and Wooley, K. L. (2005) Nanoscopic confinement of semi-crystalline polymers. *Curr. Org. Chem. 9*, 1053−1066.
(62) Lai, J. T., Filla, D., and Shea, R. (2002) Functional polymers from novel carboxyl-terminated trithiocarbonates as highly efficient RAFT agents. *Macromolecules 35*, 6754−6756.
(63) Liu, J., Zhang, Q., Remsen, E. E., and Wooley, K. L. (2001) Nanostructured materials designed for cell binding and transduction. *Biomacromolecules 2*, 362−8.
(64) Zhang, K., Fang, H., Chen, Z., Taylor, J.-S. A., and Wooley, K. L. (2008) Shape Effects of Nanoparticles Conjugated with Cell-Penetrating Peptides (HIV Tat PTD) on CHO Cell Uptake. *Bioconjugate Chem. 19*, 1880−1887.
(65) Pack, D. W., Hoffman, A. S., Pun, S., and Stayton, P. S. (2005) Design and development of polymers for gene delivery. *Nat. Rev. Drug Discovery 4*, 581−593.
(66) Rossin, R., Pan, D. P. J, Qi, K., Turner, J. L., Sun, X. K., Wooley, K. L., and Welch, M. J. (2005) Cu-64-labeled folate-conjugated shell cross-linked nanoparticles for tumor imaging and radiotherapy: Synthesis, radiolabeling, and biologic evaluation. *J. Nucl. Med. 46*, 1210−1218.
(67) Fang, H., Shen, Y., and Taylor, J. S. (2010) Native mRNA antisense-accessible sites library for the selection of antisense oligonucleotides, PNAs, and siRNAs. *RNA 16*, 1429−35.
(68) Fang, H., Yue, X., Li, X., and Taylor, J. S. (2005) Identification and characterization of high affinity antisense PNAs for the human unr (upstream of N-ras) mRNA which is uniquely overexpressed in MCF-7 breast cancer cells. *Nucleic Acids Res. 33*, 6700−11.

Bioconjugate Chemistry

Article

pubs.acs.org/bc

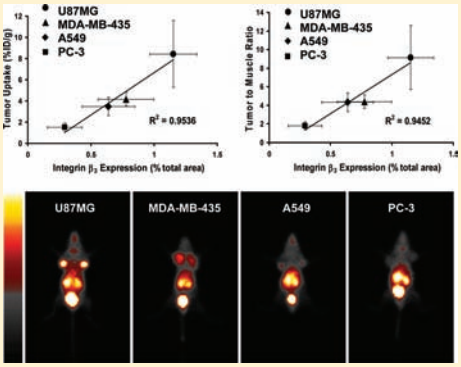
Evaluation of ^{99m}Tc-Labeled Cyclic RGD Dimers: Impact of Cyclic RGD Peptides and ^{99m}Tc Chelates on Biological Properties

Yang Zhou, Young-Seung Kim, Xin Lu, and Shuang Liu*

School of Health Sciences, Purdue University, West Lafayette, Indiana, United States

Supporting Information

ABSTRACT: The main objective of this study is to explore the impact of cyclic RGD peptides and ^{99m}Tc chelates on biological properties of ^{99m}Tc radiotracers. Cyclic RGD peptide conjugates, HYNIC-K(NIC)-RGD_2 (HYNIC = 6-hydrazinonicotinyl; RGD_2 = E[c(RGDfK)]$_2$ and NIC = nicotinyl), HYNIC-K(NIC)-3G-RGD_2 (3G-RGD_2 = Gly-Gly-Gly-E[Gly-Gly-Gly-c(RGDfK)]$_2$), and HYNIC-K(NIC)-3P-RGD_2 (3P-RGD_2 = PEG_4-E[PEG_4-c(RGDfK)]$_2$), were prepared. Macrocyclic ^{99m}Tc complexes [^{99m}Tc(HYNIC-K(NIC)-RGD_2)-(tricine)] (**1**), [^{99m}Tc(HYNIC-K(NIC)-3G-RGD_2)(tricine)] (**2**), and [^{99m}Tc-(HYNIC-K(NIC)-3P-RGD_2)(tricine)] (**3**) were evaluated for their biodistribution and tumor-targeting capability in athymic nude mice bearing MDA-MB-435 human breast tumor xenografts. It was found that **1**, **2**, and **3** could be prepared with high specific activity (~111 GBq/μmol). All three ^{99m}Tc radiotracers have two major isomers, which show almost identical uptake in tumors and normal organs. Replacing the bulky and highly charged [^{99m}Tc(HYNIC)(tricine)(TPPTS)] (TPPTS = trisodium triphenylphosphine-3,3′,3″-trisulfonate) with a smaller [^{99m}Tc(HYNIC-K(NIC))(tricine)] resulted in less uptake in the kidneys and lungs for **3**. Surprisingly, all three ^{99m}Tc radiotracers shared a similar tumor uptake (**1**, 5.73 ± 0.40%ID/g; **2**, 5.24 ± 1.09%ID/g; and **3**, 4.94 ± 1.71%ID/g) at 60 min p.i. The metabolic stability of ^{99m}Tc radiotracers depends on cyclic RGD peptides (3P-RGD_2 > 3G-RGD_2 ~ RGD_2) and ^{99m}Tc chelates ([^{99m}Tc(HYNIC)(tricine)(TPPTS)] > [^{99m}Tc(HYNIC-K(NIC))(tricine)]). Immunohistochemical studies revealed a linear relationship between the $\alpha_v\beta_3$ expression levels and tumor uptake or tumor/muscle ratios of **3**, suggesting that **3** is useful for monitoring the tumor $\alpha_v\beta_3$ expression. Complex **3** is a very attractive radiotracer for detection of integrin $\alpha_v\beta_3$-positive tumors.



INTRODUCTION

Over the past several years, we have been using a ternary ligand system (HYNIC, tricine and TPPTS) (Figure 1A: HYNIC = 6-hydrazinonicotinyl; TPPTS = trisodium triphenylphosphine-3,3′,3″-trisulfonate) for ^{99m}Tc-labeling of small biomolecules (BMs), which include chemotactic peptides and LTB_4 receptor antagonists for imaging infection and inflammation,[1,2] integrin $\alpha_v\beta_3$ receptor antagonists for tumor imaging,[3−7] and GPIIb/IIIa receptor antagonists for imaging thrombus.[8−10] This ternary ligand system forms complexes [^{99m}Tc(HYNIC-BM)(tricine)-(TPPTS)] (Figure 1A: BM = peptide and nonpeptide receptor ligand) with extremely high specific activity.[8,10] These ternary ligand ^{99m}Tc complexes are stable for >6 h, and are often formed as equal mixtures of two diastereomers if the biomolecule has a chiral center. The composition of ternary ligand ^{99m}Tc complexes has been determined to be 1:1:1:1 for Tc/HYNIC-BM/tricine/TPPTS through a series of mixed ligand experiments, and further confirmed by LC-MS at both the tracer (^{99m}Tc) and macroscopic (^{99}Tc) levels.[11,12] The utility of HYNIC for the ^{99m}Tc-labeling of small biomolecules has been reviewed extensively.[13,14]

In our previous communications,[15,16] we reported several phosphine and pyridine-containing HYNIC chelators and their corresponding macrocyclic ^{99m}Tc complexes. We found that the attachment site of the lysine (K) linker is critical for the formation of macrocyclic ^{99m}Tc complexes. For example, if the linker is attached to the 3-position of the pyridine ring, HYNIC derivatives form complexes [^{99m}Tc(HYNIC-K(NIC)-BM)-(tricine)] (Figure 1B: NIC = nicotinyl) in high yield (>95%). The HPLC data suggest that these complexes exist in solution as four isomers: two diastereomers and two conformational isomers, which interconvert rapidly at room temperature.[15,16] While conformational isomers are formed because of the rigidity of macrocycle, diastereomers are formed due to a combination of the chirality of the lysine linker and of the Tc chelate.[15,16]

To demonstrate the utility of HYNIC-K(NIC) as a bifunctional coupling agent (BFC), we prepared three new cyclic RGD peptide conjugates, HYNIC-K(NIC)-RGD_2 (RGD_2 = E[c(RGDfK)]$_2$), HYNIC-K(NIC)-3G-RGD_2 (3G-RGD_2 = Gly-Gly-Gly-E[Gly-Gly-Gly-c(RGDfK)]$_2$), and HYNIC-K(NIC)-3P-RGD_2 (3P-RGD_2 = PEG_4-E[PEG_4-c-(RGDfK)]$_2$). We also prepared their macrocyclic complexes [^{99m}Tc(HYNIC-K(NIC)-RGD_2)(tricine)] (**1**), [^{99m}Tc-

Received: November 21, 2011
Revised: February 19, 2012
Published: February 27, 2012

ACS Publications © 2012 American Chemical Society

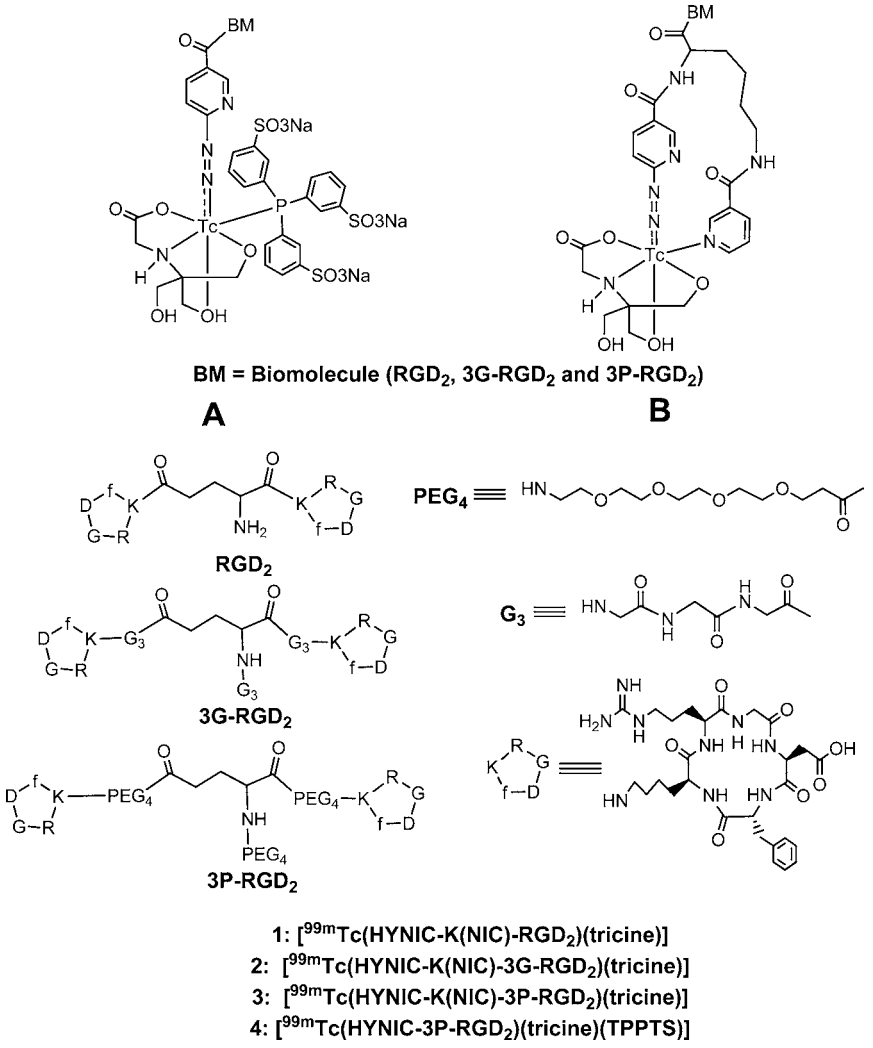


Figure 1. Structure of cyclic RGD peptide dimers and their ^{99m}Tc complexes. Structure A represents the ternary ligand system, in which tricine and TPPTS are used as coligands to stabilize the ^{99m}Tc-HYNIC core. Structure B represents the chelating HYNIC system with tricine as the only coligand to complete the octahedral coordination sphere of technetium. In this way, the bulky and highly charged TPPTS is eliminated. The small letter "f" represents D-phenylalanine.

(HYNIC-K(NIC)-3G-RGD$_2$)(tricine)] (**2**), and [^{99m}Tc-(HYNIC-K(NIC)-3P-RGD$_2$)(tricine)] (**3**), and evaluated them in athymic nude mice bearing MDA-MB-435 human breast tumor xenografts for their tumor-targeting capability and biodistribution. For comparison purposes, we also evaluated [^{99m}Tc(HYNIC-3P-RGD$_2$)(tricine)(TPPTS)] (Figure 1: **4**) in the same tumor-bearing animal model. The main objective of this study is to explore the impact of RGD peptides (RGD$_2$, 3G-RGD$_2$ and 3P-RGD$_2$) and ^{99m}Tc chelates ([^{99m}Tc-(HYNIC)(tricine)(TPPTS)] versus [^{99m}Tc(HYNIC-K(NIC))-(tricine)]) on biological properties of ^{99m}Tc radiotracers.

EXPERIMENTAL SECTION

Materials and Instruments. Chemicals were purchased from Sigma Aldrich (St. Louis, MO), and were used without purification. BOC-Lys(nicotinoyl)-OH was purchased from Bachem Biosciences Inc. (Prussia, PA). Cyclic RGD peptides G$_3$-E[G$_3$-c(RGDfK)]$_2$ (3G-RGD$_2$) and PEG$_4$-E[PEG$_4$-c-(RGDfK)]$_2$ (3P-RGD$_2$) were custom-made by Peptides International, Inc. (Louisville, KY). Sodium succinimidyl 6-(2-(2-sulfonatobenzaldehyde)hydrazono)nicotinate (HYNIC-OSu) was prepared according to the literature method.[17] [^{99m}Tc(HYNIC-3P-RGD$_2$)(tricine)(TPPTS)] (**4**) was prepared using the procedure described in our previous reports.[18] NMR spectra were recorded on a 300 MHz Bruker ARX FT NMR spectrometer and reported as ppm relative to TMS. The ESI (electrospray ionization) mass spectral data were collected on a Finnigan LCQ classic mass spectrometer, School of Pharmacy, Purdue University. Na^{99m}TcO$_4$ was obtained from a commercial ^{99}Mo/^{99m}Tc Technelite generator (North Billerica, MA).

HPLC Methods. The semiprep HPLC method (Method 1) used a LabAlliance HPLC system equipped with a UV/vis detector (λ = 254 nm) and Zorbax C$_{18}$ semiprep column (9.4 nm × 250 mm, 100 Å pore size; Agilent Technologies, Santa Clara, CA). The flow rate was 2.5 mL/min and the mobile phase was isocratic with 70% A (0.1% TFA in water) and 30% B (0.1% TFA in methanol) at 0−5 min, followed by a gradient mobile phase going from 30% B at 5 min to 70% B at 20 min. HPLC Method 2 used the LabAlliance HPLC system equipped with a β-ram IN/US detector (Tampa, FL) and Zorbax C$_{18}$ column (4.6 mm × 250 mm, 300 Å pore size; Agilent Technologies, Santa Clara, CA). The flow rate was 1 mL/min. The gradient mobile phase started with 90% A (25 mM

dx.doi.org/10.1021/bc200631g | Bioconjugate Chem. 2012, 23, 586−595

NH_4OAc, pH = 6.8) and 10% B (acetonitrile) to 85% A and 15% B at 5 min, followed by a gradient mobile phase going from 15% B at 5 min to 20% B at 20 min and to 60% B at 25 min. HPLC Method 3 started with 90% A (25 mM NH_4OAc, pH = 6.8) and 10% B (acetonitrile) to 85% A and 15% B at 5 min, followed by a gradient mobile phase going from 15% B at 5 min to 40% B at 20 min and to 60% B at 25 min.

BOC-Lys(nicotinoyl)-OSu (BOC-K(NIC)-OSu). Dicyclohexylcarbodiimide (DCC: 61.9 mg, 300 μmol) was added to a solution containing BOC-Lys(nicotinoyl) (101 mg, 290 μmol) and *N*-hydroxysuccinimide (NHS: 34.5 mg, 300 μmol) in 3 mL of anhydrous DMF. The reaction mixture was stirred at room temperature for 5 h. The white precipitate was filtered and discarded. The filtrate was evaporated to dryness under reduced pressure. The residue was dissolved in dichloromethane (3 mL). After filtration, the filtrate was concentrated to 1 mL. The solution was added dropwise into diethyl ether (20 mL) to give white precipitate. The solid was filtered, washed with diethyl ether (3 × 5 mL), and dried under vacuum to give the crude product BOC-K(NIC)-OSu. The yield was 75.8 mg (~60%). ^1H NMR ($CDCl_3$): 1.60 (s, 9H, $(CH_3)_3CO$), 1.75 (m, 2H, CH_2), 1.88 (m, 2H, CH_2), 2.12 (m, 2H, CH_2), 3.01 (s, 4H, $COCH_2CH_2CO$), 3.66 (t, 2H, CH_2CH_2NH), 5.10 (dd, H, NHCHCO), 7.54 (t, H, aromatic), 8.36 (d, H, aromatic), 8.88 (d, H, aromatic), and 9.15 (s, H, aromatic).

BOC-Lys(nicotinoyl)-E[c(RGDfK)]$_2$ (BOC-K(NIC)-RGD$_2$). BOC-K(NIC)-OSu (8.9 mg, 20 μmol) and E[c(RGDfK)]$_2$ (4.8 mg, 4 μmol) were dissolved in anhydrous DMF (2 mL). Upon addition of 3 drops of diisopropylethylamine (DIEA), the resulting solution was stirred at room temperature overnight. After addition of water (2 mL), the pH in the mixture was adjusted to 6.0−7.0. The product was separated from the reaction mixture by HPLC (Method 1). Lyophilization of collected fractions at 20.7 min afforded the expected product BOC-K(NIC)-RGD$_2$. The yield was 3.1 mg (47%). ESI-MS: m/z = 1651.5 for $[M + H]^+$ (M = 1650.8 calcd. for $[C_{76}H_{110}N_{22}O_{20}]^+$).

Lys(nicotinoyl)-E[c(RGDfK)]$_2$ (K(NIC)-RGD$_2$). Boc-K(NIC)-RGD$_2$ was dissolved in neat TFA (2.0 mL). After stirring at room temperature for 15 min, TFA was removed. The residue was dissolved in 2 mL of 0.1 M NH_4OAc buffer (100 mM, pH = 7.0). The product was separated from the mixture by HPLC (Method 1). Lyophilization of collected fractions at 16.5 min afforded K(NIC)-RGD$_2$. The yield was 2.5 mg (~86%). ESI-MS: m/z = 1552 for $[M + H]^+$ (M = 1550.8 calcd. for $[C_{71}H_{102}N_{22}O_{18}]^+$).

HYNIC-Lys(nicotinoyl)-E[c(RGDfK)]$_2$ (HYNIC-K(NIC)-RGD$_2$). HYNIC-OSu (3.5 mg, 8 μmol) and K(NIC)-RGD$_2$ (2.5 mg, 1.6 μmol) were dissolved in DMF (2 mL). After addition of DIEA (3 drops), the reaction mixture was stirred at room temperature for 24 h. Upon addition of 2 mL NH_4OAc buffer (100 mM, pH = 7.0), the product was separated from the mixture by HPLC (Method 1). Lyophilization of collected fraction at 18.7 min afforded HYNIC-K(NIC)-RGD$_2$. The yield was 1.1 mg (38%). ESI-MS: m/z = 1854.3 for $[M + H]^+$ (M = 1553.8 calcd. for $[C_{84}H_{111}N_{25}O_{22}S]^+$).

BOC-Lys(nicotinoyl)-Gly$_3$-E[Gly$_3$-c(RGDfK)]$_2$ (BOC-K(NIC)-3G-RGD$_2$). BOC-K(NIC)-OSu (6.3 mg, 14 μmol) and Gly$_3$-E[Gly$_3$-c(RGDfK)]$_2$ (5.1 mg, 2.8 μmol) were dissolved in DMF (2 mL). To the mixture was added 3 drops of DIEA. The solution was stirred at room temperature overnight. After addition of water (2 mL), the pH was adjusted to 6.0−7.0. The product was separated from the reaction mixture by HPLC (method 1). Lyophilization of collected fractions at 19.3 min afforded BOC-K(NIC)-3G$_3$-RGD$_2$. The yield was 3.0 mg (50%). ESI-MS: m/z = 2163.9 for $[M + H]^+$ (M = 2164 calcd. for $[C_{94}H_{137}N_{31}O_{29}]^+$).

Lys(nicotinoyl)-Gly$_3$-E[Gly$_3$-c(RGDfK)]$_2$ (K(NIC)-3G-RGD$_2$). Boc-K(NIC)-3G-RGD$_2$ was dissolved in 2.0 mL of anhydrous TFA. After stirring at room temperature for 15 min, excess TFA was removed. The residue was dissolved in 2 mL of 0.1 M NH_4OAc buffer (100 mM, pH = 7.0), and the resulting solution was subjected to HPLC purification (Method 1). The fractions at 16.7 min were collected. Lyophilization of collected fractions afforded K(NIC)-3G-RGD$_2$. The yield was 2.9 mg (~90%). ESI-MS: m/z = 2064.4 for $[M + H]^+$ (M = 2063.9 calcd. for $[C_{89}H_{129}N_{31}O_{27}]^+$).

HYNIC-Lys(nicotinoyl)-Gly$_3$-E[Gly$_3$-c(RGDfK)]$_2$ (HYNIC-K(NIC)-3G-RGD$_2$). HYNIC-OSu (3.1 mg, 7 μmol) and K(NIC)-3G-RGD$_2$ (2.9 mg, 1.4 μmol) were dissolved in DMF (2 mL). After addition of DIEA (3 drops), the mixture was stirred at room temperature for 2 days. Upon addition of 2 mL NH_4OAc buffer (100 mM, pH = 7.0), the product was separated by HPLC (Method 1). Lyophilization of collected fraction at 15.5 min afforded HYNIC-K(NIC)-3G-RGD$_2$. The yield was 0.5 mg (15%). ESI-MS: m/z = 2366.9 for $[M + H]^+$ (M = 2367 calcd. for $[C_{102}H_{138}N_{34}O_{31}S]^+$).

BOC-Lys(nicotinoyl)-PEG$_4$-E[PEG$_4$-c(RGDfK)]$_2$ (BOC-K(NIC)-3P-RGD$_2$). BOC-K(NIC)-OSu (5.4 mg, 12 μmol) and PEG$_4$-E[PEG$_4$-c(RGDfK)]$_2$ (5.0 mg, 2.4 μmol) were dissolved in DMF (2 mL). To the mixture was added DIEA (3 drops). The solution was stirred at room temperature overnight. After addition of water (2 mL), the pH was adjusted to 6.0−7.0. The product was separated from the reaction mixture by HPLC (method 1). Lyophilization of collected fractions at 21.5 min afforded the intermediate BOC-K(NIC)-3P-RGD$_2$. The yield was 3.4 mg (60%). ESI-MS: m/z = 2392.4 for $[M + H]^+$ (M = 2392.2 calcd. for $[C_{109}H_{173}N_{25}O_{35}]^+$).

Lys(nicotinoyl)-PEG$_4$-E[PEG$_4$-c(RGDfK)]$_2$ (K(NIC)-3P-RGD$_2$). Boc-K(NIC)-3P-RGD$_2$ was dissolved in 2.0 mL of TFA. After stirring the solution at room temperature for 15 min, TFA was removed, and the residue was dissolved in 2 mL of 0.1 M NH_4OAc buffer (100 mM, pH = 7.0). The product was separated from the mixture by HPLC (Method 1). Lyophilization of collected fractions at 14.2 min afforded the expected product K(NIC)-3P-RGD$_2$. The yield was 3.0 mg (~90%). ESI-MS: m/z = 2294 for $[M + H]^+$ (M = 2292.2 calcd. for $[C_{104}H_{165}N_{25}O_{33}]^+$).

HYNIC-Lys(nicotinoyl)-PEG$_4$-E[PEG$_4$-c(RGDfK)]$_2$ (HYNIC-K(NIC)-3P-RGD$_2$). HYNIC-OSu (2.9 mg, 6.5 μmol) and K(NIC)-3P-RGD$_2$ (3.0 mg, 1.3 μmol) were dissolved in DMF (2 mL). After addition of DIEA (3 drops), the mixture was stirred at room temperature for 3 days. The product was separated from the reaction mixture by HPLC (Method 1). Lyophilization of collected fraction at 18 min afforded the expected product HYNIC-K(NIC)-3P-RGD$_2$. The yield was 1.0 mg (30%). ESI-MS: m/z = 2595.3 for $[M + H]^+$ (M = 2595.2 calcd. for $[C_{117}H_{174}N_{28}O_{37}S]^+$).

^{99m}Tc-Labeling and Dose Preparation. To a 5 cc vial were added the HYNIC-peptide conjugate (25 μg), 0.4 mL of 0.25 M succinate buffer (pH = 4.8), and 0.4 mL of tricine solution (25 mg/mL in 0.25 M succinate buffer). After addition of 0.5 mL of $^{99m}TcO_4^-$ (370−740 MBq in saline) and 25 μL of $SnCl_2$ (1.0 mg/mL in 0.1 N HCl), the vial was heated at 100 °C for 20 min in a water bath. The vial was then allowed to stand at room temperature for ~5 min. A sample of the

resulting solution was analyzed by radio-HPLC (Method 2). Log *P* values were determined according to the literature procedure.[18] For biodistribution studies, ^{99m}Tc radiotracers were purified by HPLC. Volatiles in the mobile phase were removed under vacuum. Doses were prepared by dissolving the radiotracer in saline to ~1110 kBq/mL. For imaging studies, doses were prepared by dissolving the radiotracer in saline to ~37 MBq/mL. In the blocking experiment, RGD_2 was dissolved in the dose solution to a concentration of 3.5 mg/mL. The resulting solution was filtered with a 0.20 μm Millex-LG filter before being injected into animals. Each animal was injected with ~0.1 mL of the dose solution.

Interconversion of Isomers. Complex **2** was prepared according to the procedure above. Peak A and Peak C were collected into two separate round-bottom flasks. After complete removal of the HPLC mobile phases, the residue in each flask was redissolved in saline (1 mL). The resulting solution was analyzed by radio-HPLC (Method 2) at t = 0, 1, 2, 3, and 5 h postpurification for Peak A and t = 0.5, 1.5, 2.5, 3.5, and 5.5 h postpurification for Peak C.

Animal Model. Biodistribution and imaging studies were performed in compliance with the NIH animal experimentation guidelines (*Principles of Laboratory Animal Care*, NIH Publication No. 86−23, revised 1985). The protocol was approved by the Purdue University Animal Care and Use Committee (PACUC). All human tumor cell lines (U87MG, MDA-MB-435, A549, and PC-3) were obtained from ATCC (Manassas, VA). U87MG glioma cells were cultured in the Minimum Essential Medium, Eagle with Earle's Balanced Salt Solution (nonessential amino acids sodium pyruvate). PC-3 and A549 cancer cells were cultured in the F-12 medium (GIBCO, Grand Island, NY). MDA-MB-435 breast cancer cells were grown in the RPMI Medium 1640 with L-glutamine (GIBCO, Grand Island, NY). All tumor cell lines were supplemented with 10% fetal bovine serum and 1% penicillin and streptomycin solution, and grown at 37 °C in a humidified atmosphere of 5% CO_2 in air. Cells were grown as monolayers and were harvested or split when they reached 90% confluence to maintain exponential growth. Female athymic *nu/nu* mice were purchased from Harlan at 4−5 weeks of age, and were implanted with 5×10^6 tumor cells in 0.1 mL of saline into the shoulder flanks. All procedures were performed in a laminar flow cabinet using aseptic techniques. Four to six weeks after inoculation, the tumor size was 0.1−0.5 g, and animals were used for biodistribution and imaging studies.

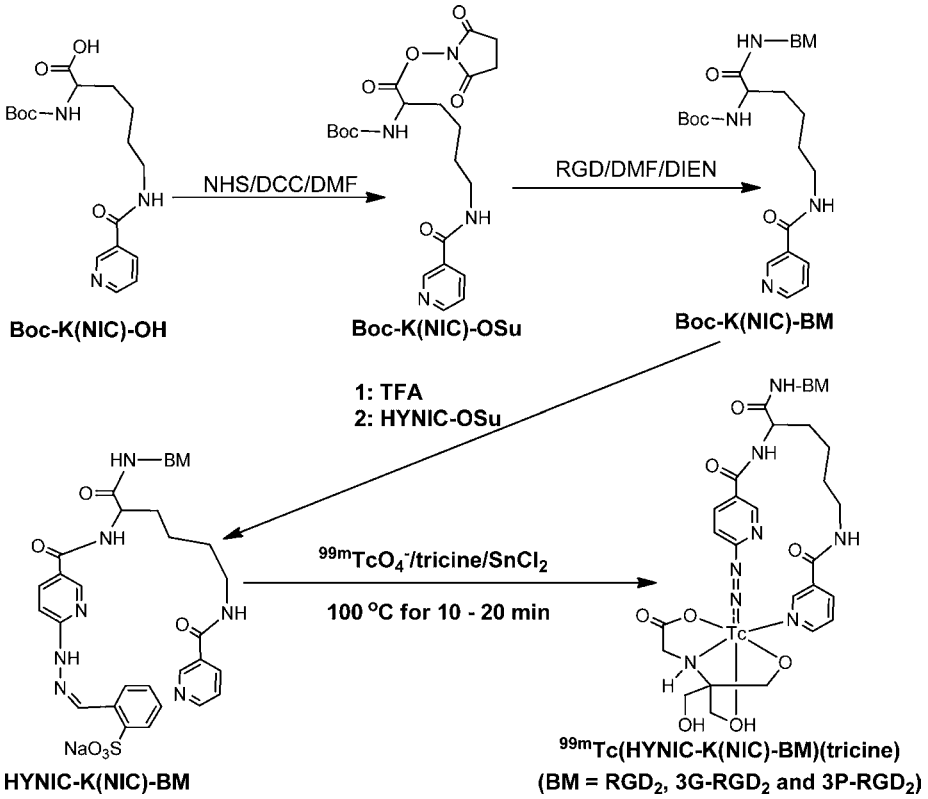
Biodistribution Protocol. Four tumor-bearing mice (20−25 g) were randomly selected, and each animal was administered with ~111 kBq of the ^{99m}Tc radiotracer by tail vein injection. The animals were sacrificed by sodium pentobarbital overdose (~200 mg/kg) at 60 min postinjection (p.i.). Blood was withdrawn from the heart of tumor-bearing mice. Tumors and normal organs (brain, eyes, heart, spleen, lungs, liver, kidneys, muscle, and intestine) were harvested, washed with saline, dried with absorbent tissue, weighed, and counted on a Perkin-Elmer Wizard 1480 γ-counter (Shelton, CT). The organ uptake was calculated as the percentage of injected dose per gram of organ mass (%ID/g). For **3**, the biodistribution data were collected at 30, 60, and 120 min p.i., and four animals were used at each time point. For the blocking experiment, four tumor-bearing athymic nude mice were used, and each animal was administered with ~111 kBq of **3** along with ~350 μg (~14 mg/kg) of RGD_2. Biodistribution data (% ID/g) and tumor-to-background (T/B) ratios are reported as an average plus the standard deviation on the basis of the results from four tumor-bearing mice (8 tumors). Comparison between two radiotracers or between two different tumor types was made using the one-way ANOVA test (*GraphPad Prism* 5.0, San Diego, CA). The level of significance was set at $p < 0.05$.

Planar Imaging. Planar imaging was performed by using athymic nude mice (n = 3) bearing U87MG, MDA-MB-435, A549, or PC-3 tumor xenografts. Each animal was administered with ~10 MBq of ^{99m}Tc radiotracer in 0.1 mL saline via tail vein injection. Animals were then anesthetized with intraperitoneal injection of ketamine (80 mg/kg) and xylazine (12 mg/kg), and were then placed supine on a custom-made single-head mini γ-camera (Diagnostic Services Inc., NJ) equipped with a parallel-hole, low-energy, and high-resolution collimator. Anterior images were acquired at 15, 30, 60, and 120 min p.i. and stored digitally in a 128 × 128 matrix. The acquisition count limits were set at 300 K. After completion of imaging, animals were sacrificed by sodium pentobarbital overdose (~200 mg/kg). The whole-body planar images were selected and reported without filtration.

Metabolism. Normal athymic nude mice (n = 3) were used for metabolism studies. Each mouse was administered with ~3.7 MBq of **1**, **2**, or **3** via tail vein. The urine samples were collected at 30 and 120 min p.i. by manual void, and were mixed with equal volume of 50% acetonitrile aqueous solution. The mixture was centrifuged at 8000 rpm. The supernatant was collected and filtered. The filtrate was analyzed by HPLC. Feces samples were collected at 120 min p.i. and suspended in 20% acetonitrile aqueous solution after homogenization. The resulting mixture was vortexed for ~5 min. After centrifuging at 8000 rpm, the supernatant was collected and filtered. The filtrate was analyzed by HPLC. The percentage radioactivity recovery was determined by γ-counting for urine and feces samples.

Immunohistochemistry. Tumor tissues were harvested, snap-frozen immediately in the OCT (optimal cutting temperature compound) solution, and cut into slices (5 μm). After drying thoroughly, the slides were fixed with ice-cold acetone for 10 min and dried in air for 20 min. Sections were blocked with 10% goat serum for 30 min, and then were incubated with the hamster anti-integrin β_3 antibody (1:100, BD Biosciences, San Jose, CA) and rat anti-CD31 antibody (1:100, BD Biosciences, San Jose, CA) for 1 h at room temperature. After incubating with Cy3-conjugated goat anti-hamster and FITC-conjugated goat anti-rat secondary antibodies (1:100, Jackson ImmunoResearch Inc., West Grove, PA) and washing with PBS, the fluorescence was visualized with an Olympic BX51 microscope (Olympus America Inc., Center Valley, PA). All pictures were taken under 200× magnification using the same exposure time. The average area of positively stained CD31 or β_3 on cryostat sections from at least 15 randomly selected fields in each group was calculated to assess the relative expression in tumor tissues by the NIH *ImageJ* software. The fluorescent density data were expressed as a percentage of the total area, presented as the mean ± S.D., and plotted against the %ID/g tumor uptake (radioactivity density) and T/B ratios of complex **3**. Experiments were performed three times. Statistical analysis was performed by Newman-Keuls multiple comparison. The level of significance was set at $p < 0.05$.

Chart 1. Representative Synthetic Scheme for Preparation of HYNIC-Conjugated Cyclic RGD Peptides and Their Corresponding Macrocyclic ^{99m}Tc Complexes



RESULTS

HYNIC-Conjugate Synthesis. As illustrated in Chart 1, HYNIC-K(NIC)-RGD$_2$, HYNIC-K(NIC)-3G-RGD$_2$, and HYNIC-K(NIC)-3P-RGD$_2$ were prepared by reacting K(NIC)-RGD$_2$, K(NIC)-3G-RGD$_2$, and K(NIC)-3P-RGD$_2$, respectively, with excess HYNIC-OSu in DMF in the presence of DIEA. All new cyclic RGD peptide conjugates were purified by semiprep HPLC and characterized by ESI-MS. Their HPLC purities were >95% before being used for ^{99m}Tc-labeling.

Radiochemistry. ^{99m}Tc complexes **1**−**3** were prepared according to Chart 1 from the reaction of the HYNIC conjugate with $^{99m}TcO_4^-$ in the presence of excess tricine and stannous chloride. ^{99m}Tc-Labeling was completed by heating the reaction mixture at 100 °C for 20−30 min. The [^{99m}Tc]-colloid formation was minimal (<0.5%) if more than 10 mg tricine was used in each vial. Complexes **1**, **2**, and **3** could be prepared with high radiochemical purity (RCP >90%) and very high specific activity (~111 GBq/μmol). Their partition coefficients were determined in an equal volume mixture of 1-octanol and 25 mM phosphate buffer (pH = 7.4). The calculated log *P* values of complexes **1**−**3** along with their HPLC retention times are summarized in Table 1.

Isomerism. Figure 2 illustrates representative radio-HPLC chromatograms of macrocyclic ^{99m}Tc complexes **1**−**3**. As expected, there were two pairs of peaks (designated as **A**−**D**) for **1** and **2**. We isolated **A** and **C** for complex **2**, and studied their relationship with **B** and **D**. It was found that **A** was able to convert to **D** while **C** was converted to **B** even at room temperature (Figure SI1). There was no interconversion between **A** and **B** or **C** and **D**, suggesting that **A** and **D** (or **C** and **B**) are conformational isomers due to restricted rotations of the macrocycle (Figure 1B). Similar results were also obtained in our previous studies.[15,16] However, we were not able to separate the four isomers of **3** despite many attempts to change chromatographic conditions by using different HPLC columns, flow rates, and ionic strength of the mobile phase. It is possible that the lipophilicity of the four isomers in **3** is so close that it always shows one single radiometric peak in its radio-HPLC chromatogram.

Table 1. Radiochemical Purity (RCP), HPLC Retention Time and Log *P* Values for ^{99m}Tc-Labeled Cyclic RGD Peptides

		retention time (min)		
radiotracer	RCP (%)	A	C	log *P* value
1	>90	14.2	16.1	−3.39 ± 0.06
2	>95	10.9	13.4	−3.25 ± 0.08
3	>95	13.7		−2.25 ± 0.07
4	>95	12.9		−4.35 ± 0.10

Biodistribution. Table 2 lists biodistribution data of **3** in athymic nude mice bearing MDA-MB-435 human breast tumor xenografts at 30, 60, and 120 min p.i. We also obtained 60 min biodistribution data (Table SI1) of **1**, **2**, and **4**. The 60 min data were used because the blood radioactivity accumulation was relatively low at this time point (Figure 3A). The tumor uptake values of **3** were 3.90, 4.94, and 4.85%ID/g at 30, 60, and 120 min p.i., respectively (Table 2). Its liver uptake values were 2.45, 1.77, and 2.05%ID/g with tumor/liver ratios of 1.64, 2.88, and 2.38 at 30, 60, and 120 min p.i., respectively. Replacing [^{99m}Tc(HYNIC)(tricine)(TPPTS)] with [^{99m}Tc(HYNIC-K(NIC))(tricine)] resulted in lower uptake in the kidneys and lungs for **3** (Figure 3A: $p < 0.05$). Complex **1** also had high tumor uptake (5.73 ± 0.40%ID/g), which was comparable to

dx.doi.org/10.1021/bc200631g | *Bioconjugate Chem.* 2012, 23, 586−595

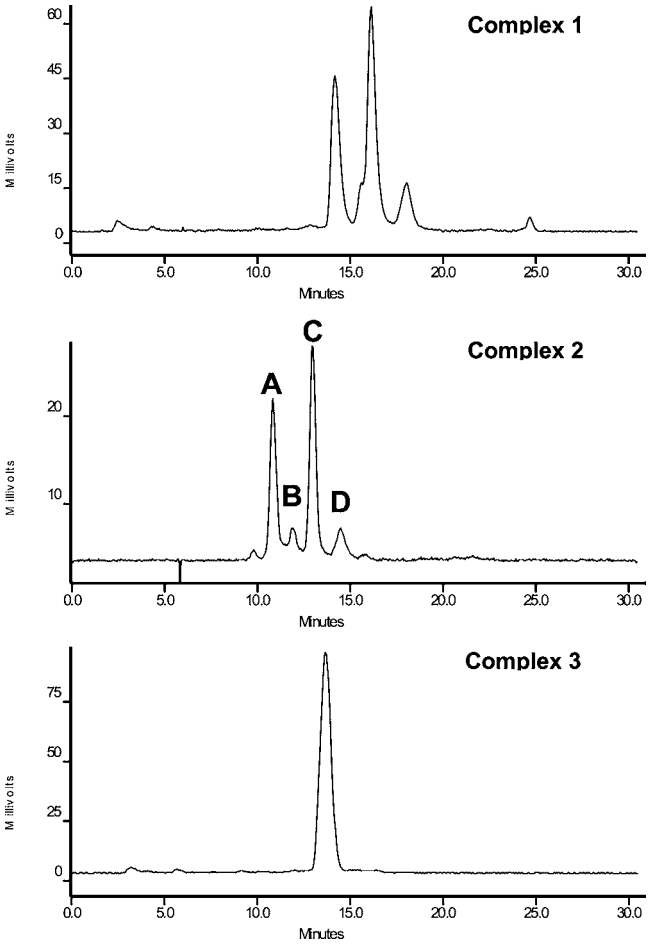


Figure 2. Representative radio-HPLC chromatograms of **1** (top), **2** (middle), and **3** (bottom). The two pairs of radiometric peaks were designated as **A**–**D** for complexes **1** and **2**.

that of **3** (4.94 ± 1.71%ID/g) within the experimental error. Complex **2** had the best tumor/liver ratio (Figure 3B: 4.1 ± 0.97).

Bioequivalence of Isomers. We compared the 60 min organ uptake of purified Peak **A** and Peak **C** of complex **2** in athymic nude mice bearing MDA-MB-435 breast cancer xenografts, and found that these two isomers had almost identical biodistribution patterns (Table S1). For example, the tumor uptake was 5.24 ± 1.09%ID/g for Peak **A** and 4.55 ± 1.44%ID/g for Peak **C**. The blood radioactivity was 0.60 ± 0.15%ID/g for Peak **A** and 0.56 ± 0.20%ID/g for Peak **C**. Their uptake values in normal organs were also comparable within the experimental error except that in the intestine (Table S1). Since there was an interconversion between isomer **A** and **D** or **C** and **B**, we believe that different isomers in macrocyclic complexes **1** and **3** will also have equivalent tumor uptake.

Table 2. Biodistribution Data of 3 in Athymic Nude Mice (n = 4) Bearing MDA-MB-435 Human Breast Tumor Xenografts

organ	30 min	60 min	120 min
blood	0.99 ± 0.07	0.84 ± 0.09	0.49 ± 0.15
brain	0.18 ± 0.05	0.14 ± 0.03	0.10 ± 0.05
eyes	0.98 ± 0.28	1.64 ± 0.38	0.85 ± 0.30
heart	1.21 ± 0.43	0.93 ± 0.37	0.83 ± 0.27
intestine	6.22 ± 1.00	5.56 ± 2.73	7.26 ± 4.55
kidneys	11.32 ± 2.87	6.41 ± 2.78	7.04 ± 3.30
liver	2.45 ± 0.62	1.77 ± 0.70	2.05 ± 0.68
lungs	3.34 ± 0.54	2.19 ± 0.94	2.05 ± 0.58
muscle	1.07 ± 0.43	0.74 ± 0.32	0.53 ± 0.09
spleen	1.84 ± 0.43	1.09 ± 0.44	1.37 ± 0.41
MDA-MB-435	3.90 ± 0.54	4.94 ± 1.71	4.85 ± 1.73
tumor/blood	3.19 ± 0.98	5.84 ± 1.75	9.64 ± 1.21
tumor/liver	1.64 ± 0.32	2.88 ± 0.83	2.38 ± 0.76
tumor/lung	1.17 ± 0.14	2.36 ± 0.66	2.31 ± 0.46
tumor/muscle	3.93 ± 1.01	7.07 ± 2.72	9.48 ± 4.15

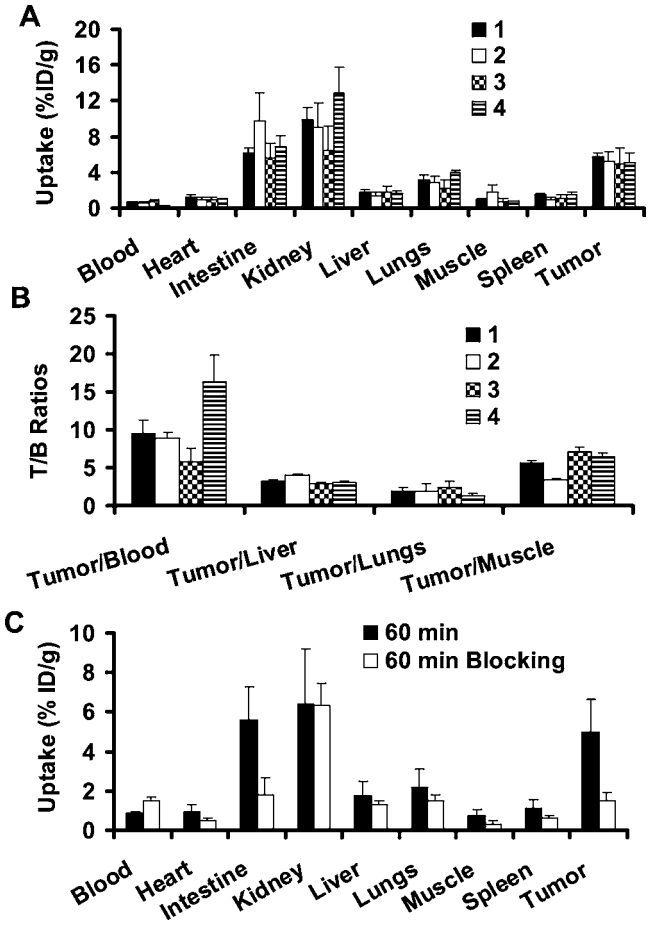


Figure 3. Comparison of biodistribution data (A) and the selected T/B ratios (B) of **1**, **2**, **3**, and **4** at 60 min p.i. in athymic nude mice (n = 4) bearing MDA-MB-435 breast tumor xenografts. (C) Comparison of biodistribution data **3** in the absence/presence of excess RGD_2 (350 μg/mouse) at 60 min p.i. in the athymic nude mice (n = 4) bearing MDA-MB-435 breast tumor xenografts.

Integrin $\alpha_v\beta_3$ Specificity. Figure 3C compares the organ uptake of **3** in the absence/presence of RGD_2 at 60 min p.i. Co-injection of excess RGD_2 significantly blocked its tumor uptake (1.48 ± 0.42%ID/g with RGD_2 vs 4.94 ± 1.71%ID/g without RGD_2). The normal organ uptake was also blocked by RGD_2. For example, the uptake values of **3** in the intestine, lungs, and spleen were 5.56 ± 1.73, 2.19 ± 0.94, and 1.09 ± 0.44%ID/g, respectively, without RGD_2, while its uptake values in the same organs were 1.82 ± 0.86, 1.52 ± 0.27, and 0.65 ± 0.07%ID/g, respectively, in the presence of RGD_2.

Metabolism. We examined the metabolic stability of complexes **1**–**3** using normal athymic nude mice. It was found that the radioactivity recovery from the urine and feces

dx.doi.org/10.1021/bc200631g | Bioconjugate Chem. 2012, 23, 586–595

samples was >95% for all three radiotracers. There were metabolites detected in both urine and feces samples over the 2 h study period for **1** (Figure SI2). Peak **A** was completely metabolized while Peak **C** still remained intact. There was also significant metabolism of **2** during its excretion via both renal and hepatobiliary routes (Figure SI2). However, very little metabolite was detected in urine samples for **3** over the 2 h period and ~65% of **3** remained intact in the feces sample.

Comparison of Tumor Uptake in Different Animal Models. We compared the uptake of **3** in the xenografted U87MG, MDA-MB-435, A549, and PC-3 tumors (Table SI2). As illustrated in Figure 4A, U87MG gliomas had the highest uptake, and the uptake of PC-3 tumor was the lowest. Its uptake in MDA-MB-435 and A549 tumors was comparable within experimental error. The tumor uptake of **3** followed a general trend: U87MG (8.43 ± 3.14%ID/g) > MDA-MB-435 (4.94 ± 1.71%ID/g) ≈ A549 (3.47 ± 0.88%ID/g) ≫ PC-3 (1.52 ± 0.42%ID/g). To further illustrate this trend, we obtained whole-body images (Figure 4B) of athymic nude mice bearing U87MG, MDA-MB-435, A549, and PC-3 tumor xenografts. Once again, the U87MG glioma had the highest uptake with the best contrast. PC-3 tumors were not clearly visualized. The T/B contrast in the planar images for MDA-MB-435 and A549 tumors was not as good as that of U87MG gliomas, but it was much better than that of the PC-3 tumors.

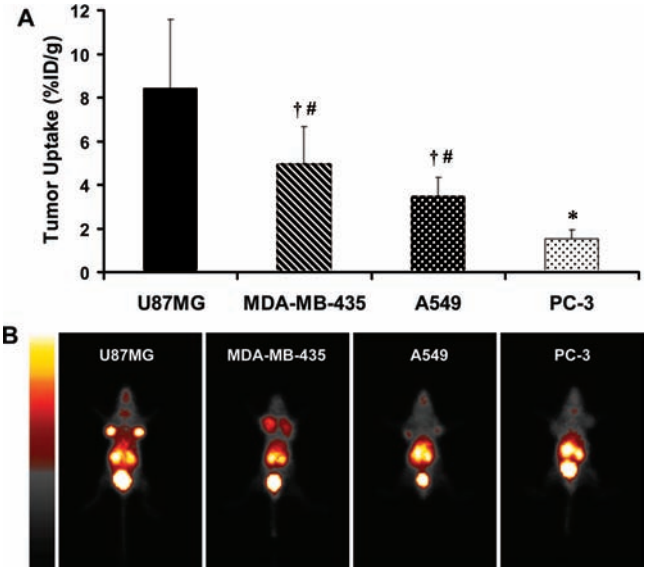


Figure 4. (A) Comparison of the %ID/g tumor uptake of **3** in the athymic nude mice bearing U87MG, MDA-MB-435, A549, and PC-3 tumor xenografts at 60 min p.i. The tumor uptake data are expressed as %ID/g ± SD (* $p < 0.05$, significantly different from all other groups; † $p < 0.05$, significantly different from U87MG group; # $p < 0.05$, significantly different from PC-3 group). (B) Planar images of the athymic nude mice bearing U87MG, MDA-MB-435, A549, and PC-3 tumor xenografts at 60 min p.i.

Comparison of Tumor $\alpha_v\beta_3$ Expression Levels. Immunohistochemistry was performed to determine the $\alpha_v\beta_3$ levels in tumor tissues according to the literature method.[28] Figure SI3 illustrates microscopic fluorescence images of the xenografted tumor tissues (U87MG, MDA-MB-435, A549, and PC-3) labeled with anti-integrin β_3 (red) and anti-CD31 (green) antibodies. In the overlay images, the green color indicates the presence of blood vessels, red color indicates the presence of β_3, and yellow color indicates the β_3 expressed on the tumor vasculature. Figure 5 shows the quantitative analysis of β_3 (A) and CD31 (B) for U87MG, MDA-MB-435, A549, and PC-3 tumor tissues. The β_3 expression level (fluorescence density) was defined by the percentage of red-colored area over the total area in each slice of tumor tissue. Since $\alpha_{IIB}\beta_3$ is expressed almost exclusively on activated platelets, the relative fluorescent intensity in tumor tissue is predominantly from the contribution of $\alpha_v\beta_3$. Blood vessel density (CD31 expression level) was quantified by measuring the percentage of green-colored area over the total area in each slice of tumor tissue. We found that the $\alpha_v\beta_3$ expression level was the highest in U87MG glioma and the lowest in PC-3 prostate tumor tissues. It followed the trend U87MG > MDA-MB-435 ≈ A549 > PC-3 (Figure 5A), which is completely consistent with the tumor uptake data (Figure 4). The CD31 expression levels (blood vessel density) followed the same order U87MG > MDA-MB-435 ≈ A549 > PC-3 (Figure 5B). Similar results were also obtained for **4** in our previous studies.[19]

Relationship between $\alpha_v\beta_3$ Expression and Tumor Uptake or Tumor/Muscle Ratios. Figure 5C shows plot of the %ID/g tumor uptake (radioactivity density) of **3** and $\alpha_v\beta_3$ levels (fluorescence density) in U87MG, MDA-MB-435, A549, and PC-3 tumor tissues. Apparently, there is a linear relationship between the %ID/g tumor uptake of **3** and $\alpha_v\beta_3$ levels with R^2 being 0.9536. The same linear relationship was also seen between the T/M ratios of **3** and $\alpha_v\beta_3$ levels with R^2 being 0.9452 (Figure 5D).

DISCUSSION

In this study, we evaluated the impact of cyclic RGD peptides and ^{99m}Tc chelates on biodistribution properties and metabolic stabilities of ^{99m}Tc radiotracers. We found that **1**, **2**, and **3** all have two major isomers (Figure 2), which have almost identical tumor uptake and biodistribution properties (Table SI2). Replacing [^{99m}Tc(HYNIC)(tricine)(TPPTS)] with a smaller [^{99m}Tc(HYNIC-K(NIC))(tricine)] resulted in less uptake in kidneys and lungs for **3** (Figure 3A: $p < 0.05$). The blocking experiment (Figure 3C) showed that their tumor uptake is $\alpha_v\beta_3$-specific. This conclusion is completely consistent with our previous findings.[18]

In principle, HYNIC can be used for ^{99m}Tc-labeling of any small biomolecule.[13,14] However, problems may arise when biomolecules contain one or more disulfide linkages, which are often vital to retaining the rigid cyclic conformation and maintaining their high receptor binding affinity. The use of a large amount of TPPTS in combination with high-temperature heating may destroy the S−S disulfide bonds and cause adverse effect on the biological properties of ^{99m}Tc-labeled small biomolecules. When HYNIC-K(NIC) is used as the BFC, $SnCl_2$ is the reducing agent and tricine is used to stabilize the ^{99m}Tc-HYNIC core.[16] There is no need for TPPTS either as reducing agent for $^{99m}TcO_4^-$ or co-ligand to stabilize the ^{99m}Tc-HYNIC core. In this respect, HYNIC-K(NIC) offers significant advantages over HYNIC as the BFC for ^{99m}Tc-labeling of small biomolecules with one or more disulfide linkages.

Recently, we found that 3P-RGD$_2$ and 3G-RGD$_2$ (Figure 1) have a significant advantage over RGD$_2$ with respect to their $\alpha_v\beta_3$ binding affinity and the tumor uptake of their radiotracers in the xenografted U87MG human glioma.[20−26] However, this advantage disappeared in the xenografted MDA-MB-435 breast tumor model, because all three ^{99m}Tc radiotracers share a similar tumor uptake (**1**, 5.73 ± 0.40%ID/g; **2**, 5.24 ± 1.09%

dx.doi.org/10.1021/bc200631g | Bioconjugate Chem. 2012, 23, 586−595

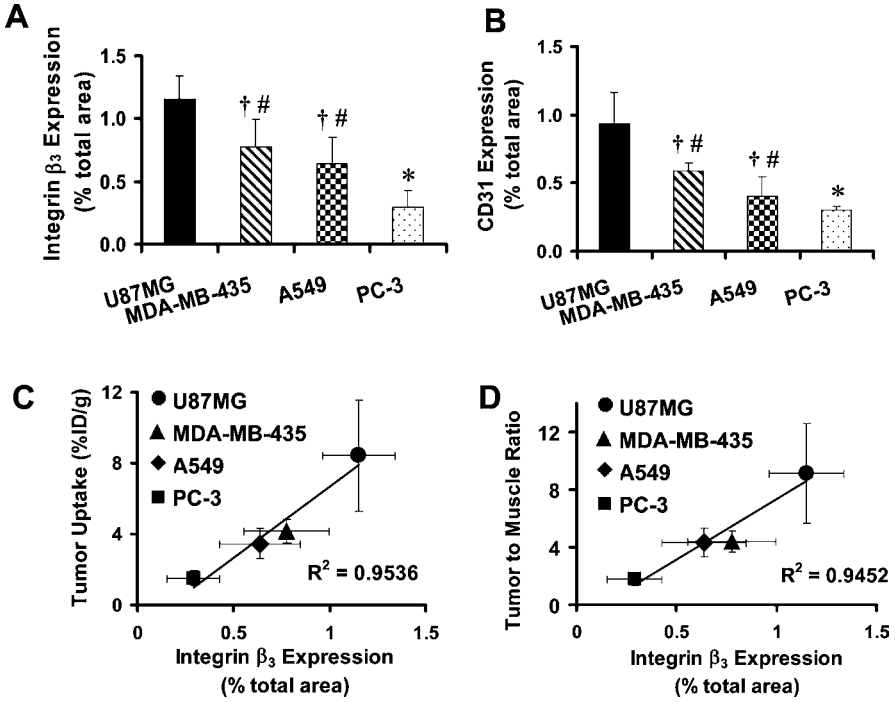


Figure 5. Top: Quantitative analysis of β_3 (A) and CD31 (B) immunostaining from the xenografted tumor tissues (U87MG, MDA-MB-435, A549, and PC-3). The CD31 expression was represented by the percentage of green area over the total area in each slice of tissue. The total integrin β_3 expression (tumor cells and neovasculature) was represented by the percentage of red area over the total area in each slice of tumor tissue. Each data point was derived from at least 15 different areas of the same tissue (100× magnification). Experiments were repeated three times independently with similar results. Values are means ± SD (* $p < 0.05$, significantly different from all the other groups; † $p < 0.05$, significantly different from the U87MG group; # $p < 0.05$, significantly different from the PC-3 group). Bottom: Relationship between the relative β_3 expression (fluorescence density) obtained from tissue staining and the %ID/g tumor uptake (C: radioactivity density) or tumor/muscle ratios (D) of **3** in four different xenografted tumors (U87MG, MDA-MB-435, A549, and PC-3).

ID/g; and **3**, 4.94 ± 1.71%ID/g) at 60 min p.i. A possible explanation is the fact that the $\alpha_v\beta_3$ level in xenografted MDA-MB-435 breast tumors is significantly lower than that in the U87MG glioma xenografts.[19,26] If the $\alpha_v\beta_3$ density is high, the distance between two neighboring $\alpha_v\beta_3$ sites will be short, which makes it easier for a multimeric RGD peptide to achieve bivalency. If the $\alpha_v\beta_3$ density is low, the distance between two neighboring $\alpha_v\beta_3$ sites will be long, and it might be more difficult for the same multimeric cyclic RGD peptide to achieve simultaneous $\alpha_v\beta_3$ binding.

Among the ^{99m}Tc radiotracers evaluated in this study, **3** has the highest metabolic stability, but it was not as good as that of **4**.[18] To determine if the metabolic instability of **3** affects the linear relationship between its %ID/g tumor uptake and the $\alpha_v\beta_3$ expression levels, we performed biodistribution studies to quantify the tumor uptake of **3** and immunohisochemical staining studies to quantify the $\alpha_v\beta_3$ and CD31 expression levels in the xenografted U87MG, MDA-MB-435, A549, and PC-3 tumors. We found that **3** had the highest uptake in U87MG glioma and lowest uptake in PC-3 tumors, and its tumor uptake followed the trend of U87MG > MDA-MB-435 ≈ A549 > PC-3 (Figure 4A), which was further confirmed by planar imaging studies (Figure 4B). The $\alpha_v\beta_3$ levels follow the order U87MG > MDA-MB-435 ≈ A549 > PC-3 (Figure 5A). The linear relationship between the $\alpha_v\beta_3$ expression levels and its tumor uptake (Figure 5C) or tumor/muscle ratios (Figure 5D) suggests that **3** is useful for monitoring the tumor $\alpha_v\beta_3$ expression, and its metabolic instability did not affect the linear relationship between its tumor uptake and the $\alpha_v\beta_3$ levels.

The ability to noninvasively estimate the $\alpha_v\beta_3$ level is important for the selection of the appropriate cancer patients who will benefit most from the anti-$\alpha_v\beta_3$ and anti-angiogenesis therapy.[27−32] For example, if the cancer patient has high tumor uptake of **3**, he/she would be most likely responsive to the anti-$\alpha_v\beta_3$ treatment. Conversely, if the cancer patient shows little tumor uptake of **3**, the anti-$\alpha_v\beta_3$ therapy would not be effective regardless of the amount of anti-$\alpha_v\beta_3$ drug administered to the cancer patient. It is important to realize that the $\alpha_v\beta_3$ levels obtained from imaging studies are used only in relative terms (high, medium, and low). In clinical settings, it is possible to compare the $\alpha_v\beta_3$ levels obtained from two control levels: one from highly aggressive glioma with very high $\alpha_v\beta_3$ expression, and the other obtained from much less aggressive tumors with low $\alpha_v\beta_3$ expression to determine more precisely whether the tested level is high, low, or intermediate.

■ CONCLUSION

In conclusion, we found that HYNIC-K(NIC) is a useful BFC for routine ^{99m}Tc-labeling of small biomolecules. Replacing the highly charged [^{99m}Tc(HYNIC)(tricine)(TPPTS)] with a much smaller [^{99m}Tc(HYNIC-K(NIC))(tricine)] resulted in less uptake in the kidneys and lungs. The metabolic stability of ^{99m}Tc radiotracers depends on both RGD peptides (3P-RGD$_2$ > 3G-RGD$_2$ ≈ RGD$_2$) and ^{99m}Tc chelates ([^{99m}Tc(HYNIC)-(tricine)(TPPTS)] > [^{99m}Tc(HYNIC-K(NIC))(tricine)]). However, the metabolic instability of **3** has little effect on its tumor-targeting capability, and the linear relationship between the tumor $\alpha_v\beta_3$ expression levels and its tumor uptake or tumor/muscle ratios. We believe that **3** is a very attractive

dx.doi.org/10.1021/bc200631g | Bioconjugate Chem. 2012, 23, 586−595

radiotracer for early cancer detection and noninvasive monitoring of the tumor $\alpha_v\beta_3$ expression before and after anti-$\alpha_v\beta_3$ therapy.

■ ASSOCIATED CONTENT

Supporting Information

Biodistribution data of **1**, **2**, **3**, and **4** (Table SI1) in the athymic nude mice (n = 4 with 8 tumors) bearing MDA-MB-435 tumor xenografts at 1 h p.i., biodistribution data (Table SI2) of **3** in the athymic nude mice (n = 4 with 8 tumors) bearing four different human tumor xenografts at 1 h p.i., the radio-HPLC chromatograms of **2** (Figure SI1) to show the interconversion from **A** to **D** (top) and **C** to **B** (bottom) at room temperature, radio-HPLC chromatograms of **1**, **2**, and **3** (Figure SI2) in the saline (A) before injection, in the urine at 30 min p.i. (B) and 120 min p.i. (C), and in the feces (D) at 120 min p.i., and representative microscopic fluorescence images (Figure SI3) of the xenografted tumor tissues (U87MG, MDA-MB-435, A549, and PC-3). This material is available free of charge via the Internet at http://pubs.acs.org.

■ AUTHOR INFORMATION

Corresponding Author

*Phone: 765-494-0236. Fax: 765-496-1377. E-mail: liu100@purdue.edu.

Notes

The authors declare no competing financial interest.

■ ACKNOWLEDGMENTS

This work was supported by Purdue University, and research grants: R01 CA115883 (S.L.) from the National Cancer Institute (NCI) and KG111333 (Y. Z. and S. L.) from the Susan G. Komen Breast Cancer Foundation.

■ REFERENCES

(1) Edwards, D. S., Liu, S., Ziegler, M. C., Harris, A. R., Crocker, A. C., Heminway, S. J., Barrett, J. A., Bridger, G. J., Abrams, M. J., and Higgins, J. D. (1999) RP463: A stabilized technetium-99m complex of a hydrazino nicotinamide conjugated chemotactic peptide for infection imaging. *Bioconjugate Chem. 10*, 884−891.

(2) Brouwers, A. H., Laverman, P., Boerman, O. C., Oyen, W. J. G., Barrett, J. A., Harris, T. D., Edwards, D. S., and Corstens, F. H. M. (2000) A ^{99m}Tc-labeled leukotriene B4 receptor antagonist for scintigraphic detection of infection in rabbits. *Nucl. Med. Commun. 21*, 1043−1051.

(3) Liu, S., Edwards, D. S., Ziegler, M. C., Harris, A. R., Hemingway, S. J., and Barrett, J. A. (2001) ^{99m}Tc-Labeling of a hydrazinonictotinamide-conjugated vitronectin receptor antagonist. *Bioconjugate Chem. 12*, 624−629.

(4) Liu, S., Hsieh, W. Y., Kim, Y. S., and Mohammed, S. I. (2005) Effect of coligands on biodistribution characteristics of ternary ligand ^{99m}Tc complexes of a HYNIC-conjugated cyclic RGDfK dimer. *Bioconjugate Chem. 16*, 1580−1588.

(5) Jia, B., Shi, J., Yang, Z., Xu, B., Liu, Z., Zhao, H., Liu, S., and Wang, F. (2006) ^{99m}Tc-labeled cyclic RGDfK dimer: initial evaluation for SPECT imaging of glioma integrin $\alpha_v\beta_3$ expression. *Bioconjugate Chem. 17*, 1069−1076.

(6) Liu, S., Hsieh, W. Y., Jiang, Y., Kim, Y. S., Sreerama, S. G., Chen, X., Jia, B., and Wang, F. (2007) Evaluation of a ^{99m}Tc-labeled cyclic RGD tetramer for noninvasive imaging integrin $\alpha_v\beta_3$-positive breast cancer. *Bioconjugate Chem. 18*, 438−446.

(7) Liu, S., Kim, Y. S., Hsieh, W. Y., and Sreerama, S. G. (2008) Coligand effects on solution stability, biodistribution and metabolism of ^{99m}Tc-labeled cyclic RGDfK tetramer. *Nucl. Med. Biol. 35*, 111−121.

(8) Edwards, D. S., Liu, S., Barrett, J. A., Harris, A. R., Looby, R. J., Ziegler, M. C., Heminway, S. J., and Carroll, T. R. (1997) A new and versatile ternary ligand system for technetium radiopharmaceuticals: water soluble phosphines and tricine as coligands in labeling a hydrazino nicotinamide-modified cyclic glycoprotein IIb/IIIa receptor antagonist with ^{99m}Tc. *Bioconjugate Chem. 8*, 146−154.

(9) Edwards, D. S., Liu, S., Harris, A. R., Poirier, M. J., and Ewels, B. A. (1999) ^{99m}Tc-labeling hydrazones of a hydrazinonicotinamide conjugated cyclic peptide. *Bioconjugate Chem. 10*, 803−807.

(10) Liu, S., Edwards, D. S., Harris, A. R., Ziegler, M. C., Poirier, M. J., Ewels, B. A., DiLuzio, W. R., and Hui, P. (2001) Towards developing a non-$SnCl_2$ formulation for DMP444: a new radiopharmaceutical for thrombus imaging. *J. Pharm. Sci. 90*, 114−123.

(11) Liu, S., Edwards, D. S., Harris, A. R., Heminway, S. J., and Barrett, J. A. (1999) Technetium complexes of a hydrazinonicotinamide-conjugated cyclic peptide and 2-hydrazinopyridine: Synthesis and characterization. *Inorg. Chem. 38*, 1326−1335.

(12) Liu, S., Ziegler, M. C., and Edwards, D. S. (2000) Radio-LC-MS for the characterization of ^{99m}Tc-labeled bioconjugates. *Bioconjugate Chem. 11*, 113−117.

(13) Liu, S., and Edwards, D. S. (1999) ^{99m}Tc-labeled small peptides as diagnostic radiopharmaceuticals. *Chem. Rev. 99*, 2235−2268.

(14) Liu, S. (2005) 6-Hydrazinonicotinamide derivatives as bifunctional coupling agents for ^{99m}Tc-labeling of small biomolecules. *Top. Curr. Chem. 252*, 117−153.

(15) Purohit, A., Liu, S., Casebier, D., and Edwards, D. S. (2003) Phosphine-containing HYNIC derivatives as potential bifunctional chelators for ^{99m}Tc-labeling of small biomolecules. *Bioconjugate Chem. 14*, 720−727.

(16) Purohit, A., Liu, S., Casebier, D., Haber, S. B., and Edwards, D. S. (2004) Pyridine-containing HYNIC-derivatives as potential bifunctional chelators for ^{99m}Tc-labeling of small biomolecules. *Bioconjugate Chem. 15*, 728−737.

(17) Harris, T. D., Sworin, M., Willianms, N., Rajopadhye, M., Damphousse, P. R., Glowacka, D., Poirier, M. J., and Yu, K. (1998) Synthesis of stable hydrazones of a hydrazinonicotinyl-modified peptide for the preparation of ^{99m}Tc-labeled radiopharmaceuticals. *Bioconjugate Chem. 10*, 808−814.

(18) Wang, L., Kim, Y. S., Shi, J., Zhai, S., Jia, B., Liu, Z., Zhao, H., Wang, F., Chen, X., and Liu, S. (2009) Improving tumor targeting capability and pharmacokinetics of ^{99m}Tc-labeled cyclic RGD dimers with PEG4 linkers. *Mol. Pharmaceutics 6*, 231−245.

(19) Zhou, Y., Kim, Y. S., Chakraborty, S., Shi, J., Gao, H., and Liu, S. (2011) ^{99m}Tc-labeled cyclic RGD peptides for noninvasive monitoring of tumor integrin $\alpha_v\beta_3$ expression. *Mol. Imaging 10*, 386−397.

(20) Shi, J., Wang, L., Kim, Y. S., Zhai, S., Liu, Z., Chen, X., and Liu, S. (2008) Improving tumor uptake and excretion kinetics of ^{99m}Tc-labeled cyclic Arginine-Glycine-Aspartic (RGD) dimers with triglycine linkers. *J. Med. Chem. 51*, 7980−7990.

(21) Shi, J., Wang, L., Kim, Y. S., Jia, B., Zhao, H., Wang, F., and Liu, S. (2009) ^{99m}TcO(MAG2−3G3-dimer): A new integrin $\alpha_v\beta_3$-targeted radiotracer with high tumor uptake and favorable pharmacokinetics. *Eur. J. Nucl. Med. Mol. Imaging 36*, 1874−1884.

(22) Shi, J., Wang, L., Kim, Y. S., Zhai, S., Liu, Z., Chen, X., and Liu, S. (2009) Improving tumor uptake and pharmacokinetics of ^{64}Cu-labeled cyclic RGD dimers with triglycine and PEG_4 Linkers. *Bioconjugate Chem. 20*, 750−759.

(23) Shi, J., Wang, L., Kim, Y. S., Chakraborty, S., Jia, B., Wang, F., and Liu, S. (2009) 2-Mercaptoacetylglycylglycyl (MAG_2) as a bifunctional chelator for ^{99m}Tc-labeling of cyclic RGD dimers: effects of technetium chelate on tumor uptake and pharmacokinetics. *Bioconjugate Chem. 20*, 1559−1568.

(24) Liu, Z., Niu, G., Shi, J., Liu, S. L., Wang, F., Liu, S., and Chen, X. (2009) ^{68}Ga-labeled cyclic RGD dimers with Gly_3 and PEG_4 linkers: promising agents for tumor integrin $\alpha_v\beta_3$ PET imaging. *Eur. J. Nucl. Med. Mol. Imaging 36*, 947−957.

(25) Liu, Z., Liu, S., Wang, F., Liu, S., and Chen, X. (2009) Noninvasive imaging of tumor integrin expression using ^{18}F-labeled

RGD dimer peptide with PEG_4 linkers. *Eur. J. Nucl. Med. Mol. Imaging 36*, 1296−1307.
(26) Liu, S. (2009) Radiolabeled cyclic RGD peptides as integrin $\alpha_v\beta_3$-targeted radiotracers: maximizing binding affinity via bivalency. *Bioconjugate Chem. 20*, 2199−2213.
(27) Miller, J. C., Pien, H. H., Sahani, D., Sorensen, A. G., and Thrall, J. H. (2005) Imaging angiogenesis: applications and potential for drug development. *J. Natl. Cancer Inst. 97*, 172−187.
(28) Cai, W., Rao, J., Gambhir, S. S., and Chen, X. (2006) How molecular imaging is speeding up antiangiogenic drug development? *Mol. Cancer Ther. 5*, 2624−2633.
(29) Niu, G., and Chen, X. (2008) Has molecular and cellular imaging enhanced drug discovery and drug development? *Drugs R D 9*, 351−368.
(30) Michalski, M. H., and Chen, X. (2011) Molecular imaging in cancer treatment. *Eur. J. Nucl. Med. Mol. Imaging 38*, 358−377.
(31) Grégoire, V., and Chiti, A. (2011) Molecular imaging in radiotherapy planning for head and neck tumors. *J. Nucl. Med. 52*, 331−334.
(32) Beer, A. J., and Schwaiger, M. (2011) PET of $\alpha_v\beta_3$-integrin and $\alpha_v\beta_5$-integrin expression with ^{18}F-fluciclatide for assessment of response to targeted therapy: ready for prime time? *J. Nucl. Med. 52*, 335−337.

Bioconjugate Chemistry

Article

pubs.acs.org/bc

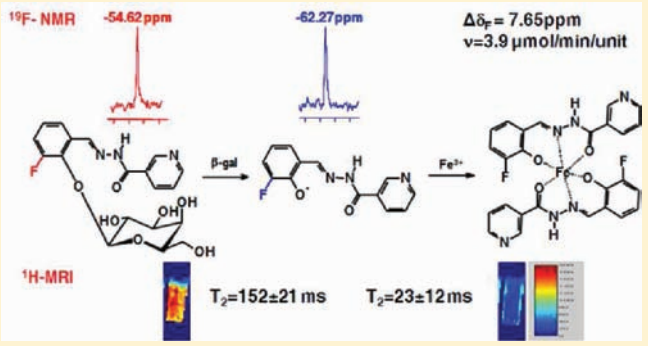
Dual $^{19}F/^{1}H$ MR Gene Reporter Molecules for *in Vivo* Detection of β-Galactosidase

Jian-Xin Yu, Vikram D. Kodibagkar,† Rami R. Hallac, Li Liu, and Ralph P. Mason*

Department of Radiology, The University of Texas Southwestern Medical Center, Dallas, Texas, United States

Supporting Information

ABSTRACT: Increased emphasis on personalized medicine and novel therapies requires the development of noninvasive strategies for assessing biochemistry *in vivo*. The detection of enzyme activity and gene expression *in vivo* is potentially important for the characterization of diseases and gene therapy. Magnetic resonance imaging (MRI) is a particularly promising tool, since it is noninvasive and has no associated radioactivity, yet penetrates deep tissue. We now demonstrate a novel class of dual $^{1}H/^{19}F$ nuclear magnetic resonance (NMR) *lacZ* gene reporter molecule to specifically reveal enzyme activity in human tumor xenografts growing in mice. We report the design, synthesis, and characterization of six novel molecules and evaluation of the most effective reporter in mice *in vivo*. Substrates show a single ^{19}F NMR signal and exposure to β-galactosidase induces a large ^{19}F NMR chemical shift response. In the presence of ferric ions, the liberated aglycone generates intense proton MRI T_2 contrast. The dual modality approach allows both the detection of substrate and the imaging of product enhancing the confidence in enzyme detection.



INTRODUCTION

Several reporter proteins have been used in gene expression and regulation studies including β-galactosidase (β-gal), firefly luciferase (luc), β-glucuronidase, fluorescent proteins (such as green fluorescent protein, GFP), transferrin and ferritin, the enzymes creatine and arginine kinase, tyrosinase, and polycations such as poly lysine.[1,2] Historically, the *lacZ* gene encoding β-gal has been widely used with applications ranging from molecular biology to small animal investigations and clinical trials including assays of clonal insertion, transcriptional activation, protein expression, and protein interaction.[3,4] Recently, various innovative approaches to assessing β-gal activity *in vivo* have been presented exploiting gadolinium contrast enhanced ^{1}H magnetic resonance imaging (MRI) or ^{19}F NMR,[5−12] optical,[13−18] and radionuclide imaging.[19−21] Traditional ^{19}F NMR spectroscopy approaches have the advantage of detecting both the substrate and the product simultaneously,[7−9] but while imaging is feasible,[22,23] the achievable signal-to-noise has so far been insufficient for imaging in animals. By comparison, ^{1}H MRI contrast can be far more sensitive, but the presence of substrate and the formation of product may not be readily identifiable due to tissue heterogeneity. We have demonstrated an Fe(III)-based ^{1}H MRI approach using the commercially available black histological stain sodium 3,4-cyclohexenoesculetin-β-D-galactopyranoside (S-Gal sodium salt) to detect β-gal activity in stably transfected *lacZ* expressing cancer cells *in vitro* and *in vivo* and this approach was also used to label and track stem cell localization.[24,25] It occurred to us that the approaches could be combined, whereby ^{19}F NMR spectroscopy would define substrate accumulation and conversion, while iron based ^{1}H MRI contrast reveals regional enzyme activity.

Escherichia coli (*lacZ*) β-gal catalyzes the hydrolysis of β-D-galactopyranosides by cleavage of the C−O bond with β-configuration between D-galactose and the aglycone. Considering the multiple requirements for an enzyme responsive $^{19}F/^{1}H$ MRI indicator, we chose salicylaldehyde nicotinoyl hydrazone, salicylaldehyde isonicotinoyl hydrazone, and salicylaldehyde benzoyl hydrazone as aroylhydrazone chelators based on reported characteristics.[26−28] A fluorine atom introduced at the *ortho* or *para* position to the $C_{1(gal)}$-O bond in the salicylaldehyde fragment was expected to display a large ^{19}F NMR chemical shift in response to cleavage by β-gal.[29]

We now report proof of principle using a fluorosalicylaldehyde aroylhydrazone β-D-galactopyranoside, which provides a ^{19}F NMR signal sensitive to β-gal enzyme cleavage and the liberated aglycone spontaneously traps ferric ions generating ^{1}H MRI contrast on T_2-weighted images (Figure 1). We currently add ferric ammonium citrate, but contrast could, in principle, develop from entrapment of endogenous Fe^{3+}.

EXPERIMENTAL PROCEDURES

Detailed molecular characterization results based on chemical shift assignment and chemical analyses are provided in

Received: November 30, 2011
Revised: February 17, 2012
Published: February 18, 2012

 © 2012 American Chemical Society

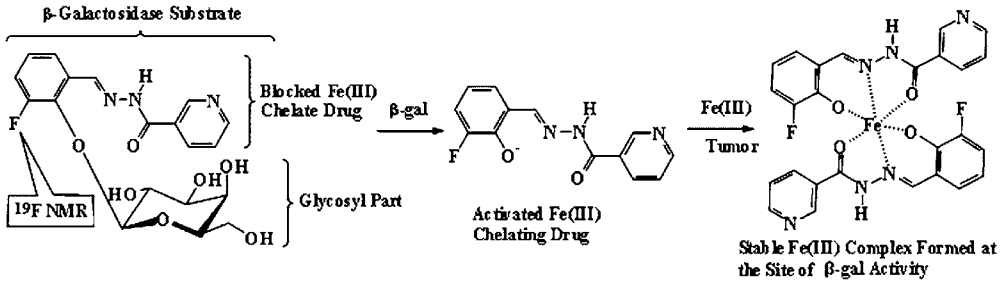


Figure 1. Proposed mode of action: β-galactosidase activity is detected by ^{19}F NMR chemical shift accompanying release of aglycone and ^{1}H MRI contrast induced by ferric ion complex.

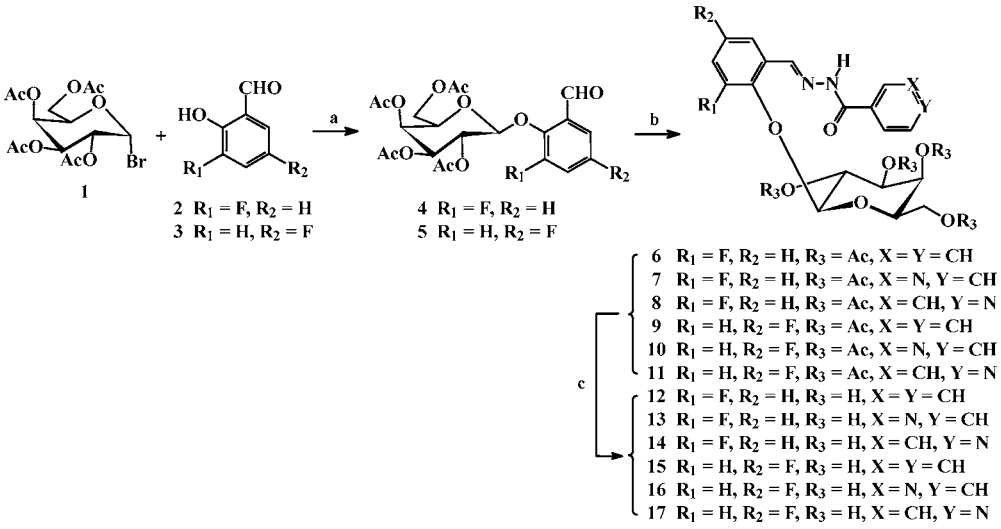


Figure 2. Reactions and the structures of **1**−**17**. Reaction conditions: (a) CH_2Cl_2−H_2O, pH 8−9, 50 °C, TBAB, N_2, 5−6 h, 92% (→**4**) or 86% (→**5**), respectively; (b) EtOH, AcOH (20 μL), benzoic hydrazide, nicotinic hydrazide or isoniazide (1.1 equiv), 80 °C, N_2, 4−5 h, 100% (→**6**), 90% (→**7**), 95% (→**8**), 95% (→**9**), 100% (→**10**), and 93% (→**11**) respectively; (c) 0.5 M NH_3-MeOH, 0 °C→r.t., 24 h, quantitative yields.

Supporting Information. All *in vivo* studies were performed with approval from the Institutional Animal Care and Use Committee.

The synthetic route and structures of **1**−**17** are shown in Figure 2. Reaction of 2,3,4,6-tetra-*O*-acetyl-α-D-galactopyranosyl bromide **1** (Sigma Chemical Company, St Louis, MO) with 3- or 5-fluorosalicylaldehydes **2** or **3** at 50 °C catalyzed by tetrabutylammonium bromide (TBAB) in an aqueous dichloromethane biphasic system (pH 8−9) under N_2 afforded 2-[(2′,3′,4′,6′-tetra-*O*-acetyl-β-D-galactopyranosyl)oxy]-3 or 5-fluorobenzaldehydes **4** or **5** in high yields (82−92%). Treatment of **4** or **5**, respectively, with 1.1 equiv of benzoic hydrazide, nicotinic hydrazide, or isoniazid in acidic medium at 80 °C produced the corresponding 2-[(2′,3′,4′,6′-tetra-*O*-acetyl-β-D-galactopyranosyl)-oxy]-3 or 5-fluorobenzaldehyde aroylhydrazones **6**−**11** in 90−100% yields, which were deacetylated with NH_3/MeOH from 0 °C to room temperature giving their free galactopyranosides **12**−**17** in quantitative yields.

Detailed Syntheses. *2-[(2′,3′,4′,6′-Tetra-O-acetyl-β-D-galactopyranosyl)oxy]-3 or 5-Fluoro-benzaldehydes **4**−**5**. General Procedure.* A solution of 2,3,4,6-tetra-*O*-acetyl-α-D-galactopyranosyl bromide **1** (615 mg, 1.5 mmol) in CH_2Cl_2 (10 mL) was added dropwise to a vigorously stirred biphasic mixture (pH 8−9) of 3- or 5-fluorosalicylaldehyde (**2**−**3**) (252 mg, 1.8 mmol) and tetrabutylammonium bromide (TBAB) (160 mg, 0.5 mmol) in CH_2Cl_2−H_2O (20 mL, 1:1 v/v) over a period of 1 h at 50 °C under N_2, and the stirring continued for 4−5 h until TLC showed complete reaction. The products were extracted with CH_2Cl_2 (4 × 25 mL), washed, dried (Na_2SO_4), evaporated under reduced pressure to give a syrup, which was purified by column chromatography on silica gel to give 2-[(2′,3′,4′,6′-tetra-*O*-acetyl-β-D-galactopyranosyl)oxy]-3 or 5-fluorobenzaldehydes **4**−**5**, as white crystals in >85% yield.

*2-[(2′,3′,4′,6′-Tetra-O-acetyl-β-D-galactopyranosyl)oxy]-3 or 5-Fluorobenzaldehyde Aroylhydrazones **6**−**11**. General Procedure.* A solution of 2-[(2′,3′,4′,6′-tetra-*O*-acetyl-β-D-galactopyranosyl)oxy]-3 or 5-fluorobenzaldehyde **4** or **5** (200 mg, 0.44 mmol) in anhydrous EtOH (15 mL) containing AcOH (20 μL) was stirred vigorously respectively with benzoic hydrazide, nicotinic hydrazide, or isoniazid (0.48 mmol, 1.1 equiv) at 80 °C under N_2 until TLC showed that the reaction was complete, then coevaporated with toluene to dryness *in vacuo*. Crystallization from EtOH-H_2O or chromatography of the crude syrup on silica gel with appropriate eluents yielded the corresponding 2-[(2′,3′,4′,6′-tetra-*O*-acetyl-β-D-galactopyranosyl)oxy]-3 or 5-fluorobenzaldehyde aroylhydrazones **6**−**11** in 90−100% yields.

*2-[(β-D-Galactopyranosyl)oxy]-3 or 5-Fluorobenzaldehyde Aroylhydrazones **12**−**17**. General Procedure.* A solution of 2-[(2,3,4,6-tetra-*O*-acetyl-β-D-galactopyranosyl)oxy]-3 or 5-fluorobenzaldehyde aroylhydrazones **6**−**11** (200 mg) in anhydrous MeOH (20 mL) containing 0.5 M NH_3 was vigorously stirred from 0 °C to room temperature overnight until TLC showed complete reaction, then evaporated to dryness *in vacuo*. Chromatography of the crude syrup on silica gel with EtOAc-MeOH afforded

dx.doi.org/10.1021/bc200647q | *Bioconjugate Chem.* 2012, 23, 596−603

the corresponding free β-D-galactopyranosides **12**−**17** in quantitative yields.

3-Fluorosalicylaldehyde Nicotinoyl Hydrazone (3-FBNH)-Hydrolysis Product of ***13***. A solution of 3-fluorosalicylaldehyde (330 mg, 2.36 mmol) in anhydrous EtOH (15 mL) containing AcOH (20 μL) was stirred vigorously with nicotinic hydrazide (323 mg, 2.36 mmol) at 80 °C under N_2 until TLC showed that the reaction was complete, then coevaporated with toluene to dryness *in vacuo*. Crystallization from EtOH-H_2O yielded **3-FBNH** (526 mg) as white needles.

***Fe:3-FBNH** Complex*. To a solution of 3-FBNH (500 mg, 1.93 mmol) and Et_3N (195 mg, 1.93 mmol) in anhydrous MeOH (100 mL) was added dropwise a solution of $Fe(ClO_4)_3{\cdot}6H_2O$ (446 mg, 0.97 mmol) in anhydrous MeOH (50 mL) with stirring and gentle reflux under N_2 for 30 min. Upon cooling, a fine black precipitate was obtained, which was filtered, washed with EtOH then Et_2O, and dried *in vacuo* yielding **Fe-3-FBNH** Complex $[Fe(3\text{-FBNH-H})_2](ClO_4){\cdot}3H_2O$ (576 mg) as black powder. Anal. Calcd. for $C_{26}H_{24}ClFeN_6O_{11}F_2$ (%): C, 43.03, H, 3.34, N, 11.59; Found: C, 42.95, H, 3.41, N, 11.48.

Detection of β-Galactosidase by ^{19}F NMR in Solution. 2-[(β-D-galactopyranosyl)oxy]-3-fluorobenzaldehyde nicotinoyl hydrazone **13**, 2-[(β-D-galactopyranosyl)oxy]-3-fluorobenzaldehyde isonicotinoyl hydrazone **14** (2.11 mg, 5.0 μmol), or 2-[(β-D-galactopyranosyl)oxy]-5-fluorobenzaldehyde benzoylhydrazone **15** (2.10 mg, 5.0 μmol) were dissolved in PBS (595 μL) and a solution of β-gal (5 μL, 1 unit/μL; E801A, Aldrich) was added. ^{19}F NMR time course spectra were acquired immediately at 376 MHz in 102 s each and continued at 37 °C over 4 h to assess relative rates of activity. **13** was also examined by ^{19}F MRI. In this case, **13** (7 mg) was dissolved in PBS/DMSO (250 μL 1:1 mixture) at 37 °C and β-galactosidase (E801A 20 units) added. ^{19}F MR images were acquired at 376 MHz with 930 μm in plane resolution across a 30 mm × 30 mm field of view and 10 mm slice thickness in 4 min 16 s each using 8 averages at each phase encode and TR = 1000 ms, TE = 1.6 ms, and 90° flip angle.

^{1}H MRI T_2 Maps of Phantoms of ***13*** *and S-Gal in Agar*. Mixtures of agar and 3,4-cyclohexenoesculetin-β-D-galactopyranoside sodium (S-Gal sodium salt, Sigma-Aldrich Inc., St. Louis, MO) (5 mM, 40 μL) + ferric ammonium citrate (FAC 2.5 mM, 40 μL) or **13** (5 mM, 40 μL) + FAC (2.5 mM, 40 μL) with or without β-gal (E801A, 5 units) were prepared in sections of 384 well plates cut to fit in a 1 turn, 2 cm volume solenoid coil. T_2 maps were acquired at 4.7 T using a spin echo sequence with variable echo times. MRI parameters were: FOV = 40 mm × 40 mm, matrix 128 × 128, slice thickness = 1 mm, TR = 6 s, TE = 10, 20, 30, 50, 80, 100, 150, and 200 ms.

Detection of β-Galactosidase by ^{19}F NMR in Cells. Human MCF7 breast and PC3 prostate cancer cells were transfected to stably express the *E. coli lacZ* gene constitutively, as described previously.[8,9] Wild-type and *-lacZ* cells were grown in culture dishes under standard conditions and harvested for NMR tests. ^{19}F NMR spectra were acquired at 9.4 T up to 40 h after addition of **13** (2.11 mg, 5.0 μmol) to MCF7 cells (5.0×10^6) in 600 μL PBS, and in some cases, Fe^{3+} (FAC 2.5 μmol) was added. In addition to evaluating intact cells, additional tests were conducted with lysed cells. For comparison, equal numbers of cells were prepared for evaluation intact or following lysis. Cell lysis was achieved by a freeze/thaw method: equal numbers of MCF7-*lacZ* or PC3-*lacZ* cells were suspended in PBS and then frozen at −80 °C for 10 min before thawing at room temperature over 3 cycles.

In Vivo MR Studies. PC3 cells (wild type or transfected to stably express *lacZ*[8]) were implanted subcutaneously in thighs of SCID mice (n = 3). NMR studies were performed at 4.7 T using a Varian Unity INOVA horizontal bore scanner (200.1 MHz for ^{1}H, 188.2 MHz ^{19}F). When the tumors reached ∼0.8 cm in diameter, mice were anesthetized (isoflurane/air) and placed on a platform with the tumor-bearing leg inserted into a 2-cm-diameter home-built volume coil (tunable from 200.1 MHz for ^{1}H to 188.2 MHz for ^{19}F). The animal temperature was maintained at 37 °C by a warm pad with circulating water. The mouse bed was inserted into the bore of the MR scanner and shimming was performed on the tissue water proton signal. T_1 and T_2 maps of the tumor were measured using a spin echo sequence with varying repetition and echo times (acquisition parameters: field of view (FOV) 50 mm × 50 mm, matrix 128 × 128, slice thickness 1 mm, 15 slices). The mouse-bearing platform was removed from the magnet and a solution of **13** (50 μL 50 mM, DMSO/PBS 1:1 v/v) was injected directly into the tumor in a "fan" pattern. The platform was replaced in the magnet and ^{19}F NMR spectra were obtained immediately after retuning the coil to the ^{19}F resonance frequency. Each spectrum was acquired in 166 s (acquisition parameters: pulse width 45 μs, 128 acquisitions, spectral width 100 ppm, 60 Hz exponential line broadening). The mouse-bearing platform was again removed from the magnet and a solution of FAC (50 μL 50 mM, PBS) was now injected directly into the tumor in a similar pattern to **13**. ^{19}F NMR spectra were obtained and the coil was retuned to the ^{1}H frequency, and new T_1 and T_2 maps were acquired. For analysis, regions with injected contrast agent were identified based on the T_2- and T_1-weighted images (to delineate tumor boundary and locate the injected Fe^{3+} ions, respectively). For one animal, no injection site could be identified inside the tumor and hence the data for this tumor were not used. To confirm β-gal activity in tumors, tissues were embedded in Tissue-Tek OCT (Miles Laboratory, Elkhart, IN, USA), and frozen in liquid nitrogen. Cryostat sections (8 μm) were collected on gelatin-coated glass slides and stained with X-gal and eosin (Sigma) for β-gal activity.

Testing Product Aglycone Visibility in Vivo. A mixture of sodium trifluoroacetate (50 mM) and aglycone (**3-FBNH** (3 or 6 mg in total volume 50 μL or 100 μL of a 3:1 mixture of DMSO:PBS) was injected into muscle of three adult 129S-Gt(ROSA)26Sor/J mice (2 live and 2 post mortem). ^{19}F NMR spectra were acquired immediately at 4.7 T and every 2 min. NaTFA served as a chemical shift reference at 0 ppm.

RESULTS

Each of the target reporter molecules was achieved in high yield and structures were confirmed by NMR and chemical analyses (see Supporting Information). The anomeric β-D-configuration of compounds **4**−**17** in the $^4C_1$ chair conformation was confirmed by the observed ^{1}H NMR chemical shifts (δ_H 4.79−5.12 ppm) of the anomeric protons and the $J_{1,2}$ (J ∼8 Hz) and $J_{2,3}$ (J ∼10 Hz) coupling constants.[29] The anomeric carbon resonances appeared at $\delta_{C\text{-}1'}$ 100.05−105.23 ppm in accord with the β-D-configuration. ^{19}F NMR chemical shifts were measured with respect to sodium trifluoroacetate (NaTFA, δ = 0 ppm) in a capillary as an external standard. **12**−**17** each gave a single narrow ^{19}F NMR signal between δ_F −44.0 and −55.0 ppm (Table 1) essentially invariant ($\Delta\delta_F \leq 0.05$ ppm) with pH in the range 3−12 and temperatures from 25 to 37 °C in 0.9% saline or rabbit whole blood.

Table 1. ^{19}F NMR Chemical Shifts (ppm) of 12−17 and Hydrolytic Rates (μmol/min/unit) of 13−15 with β-gal[a]

No.	12	13	14	15	16	17
$\delta_{F\ (substrate)}$	−54.84	−54.62	−54.60	−44.38	−45.02	−45.03
$\delta_{F\ (aglycone)}$	---	−62.27	−62.03	−49.61	---	---
$\Delta\delta_F$	---	7.65	7.43	5.23	---	---
$\nu_{(\mu mol/min/unit)}$	---	3.91	1.67	0.55	---	---

[a] β-gal (E801A) at 37 °C in PBS (0.1 M, pH = 7.4).

When β-gal (E801A) was added to **12**−**17** in phosphate buffered saline (PBS) at 37 °C, only **13**−**15** were hydrolyzed releasing the 3- or 5-fluorobenzaldehyde aroylhydrazones appearing also as single narrow ^{19}F signals shifted upfield between $\Delta\delta_F$ = 5.23−7.65 ppm (δ_F −49.0 to −63.0 ppm) (Figures 3 and S1; Table 1), which is comparable to shifts reported previously for ^{19}F NMR gene reporter molecules.[7−9,29,30] The hydrolysis of **13**−**15** proceeded smoothly indicating that the liberated aglycones 3- or 5-fluorobenzaldehyde aroylhydrazones had no inhibitory effects on β-gal, and the shapes of the kinetic curves suggest straightforward zero-order kinetics. The rate of reaction of **13** ($\nu_{(E801A)}$ = 3.91 μmol/min/unit) was comparable to that reported previously for 3-*O*-(β-D-galactopyranosyl)-6-fluoropyridoxol (GFPOL)[30] and much faster than the other molecules here, so it was chosen for further studies. Enzyme induced hydrolysis was also observable by ^{19}F MRI (Figure 3). Titration of product 3-fluorobenzaldehyde nicotinoyl hydrazone (3-FBNH) showed a small chemical shift (~0.5 ppm) in the pH range 6.5−7.7 (Figure S2).

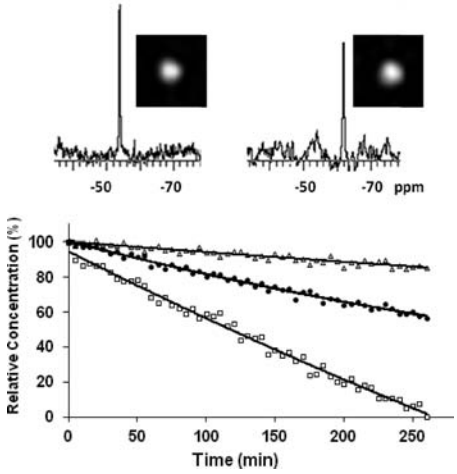


Figure 3. Substrate response to β-galactosidase. Graph shows the loss of each of the three agents **13**−**15** (5.0 μmol; □, **13**; ●, **14**; Δ, **15**) when incubated with β-galactosidase (E801A, 5 units) in PBS (0.1 M, 600 μL) at 37 °C, as detected by ^{19}F NMR spectroscopy revealing that **13** reacts fastest. When β-galactosidase (20 units) was added to a solution of **13** (7 mg 16.5 μmol) in 250 μL PBS/DMSO 1:1 at 37 °C, conversion was detectable by ^{19}F NMR spectroscopy and imaging at 9.4 T (376 MHz: baseline at left and after 2.5 h at right) showing product 3-fluorobenzaldehyde nicotinoyl hydrazone (**3-FBNH**).

Proton MRI of agar phantoms of **13** or commercial S-Gal (3,4-cyclohexenoesculetin β-D-galactopyranoside) with ferric ions showed very similar T_2 (152 ± 21 ms vs 156 ± 25 ms; Figure 4). Incorporation of β-gal in the agar yielded much reduced T_2 values and the difference was much greater for **13** than S-Gal (23 ± 12 ms vs 78 ± 11 ms: alternately, ΔR_2 36.9 s^{-1} vs 6.4 s^{-1}). By analogy with S-Gal,[24] we attribute the relaxation

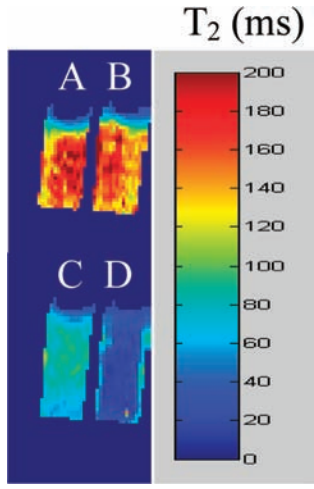


Figure 4. ^{1}H MRI T_2 maps of phantoms of 13 and S-Gal in agar. Comparison of T_2 shortening due to addition of β-gal enzyme to commercial substrate S-Gal or **13**. (A) S-Gal (5 mM) + Fe^{3+} (2.5 mM); (B) **13** (5 mM) + Fe^{3+} (2.5 mM); (C) as (A) + β-gal (E801A, 5 units); (D) as (B) + β-gal (E801A, 5 units).

enhancement to formation of complex between 3-FBNH and Fe^{3+}. Chemical analysis indicated a 1:2 Fe^{3+}:**3-FBNH** complex.

When **13** was incubated with MCF7 human breast tumor cells for 5 h in PBS at 37 °C under 5% CO_2 in air, no changes were observed in the ^{19}F NMR spectrum. Addition of **13** to stably transfected MCF7-*lacZ* cells led to cleavage in a smooth monotonic manner with a rate of 0.25 μmol/min per million cells, and appearance of a new ^{19}F signal of the released aglycone 3-fluorobenzaldehyde nicotinoyl hydrazone (**3-FBNH**) around −62.27 ppm (Figure 5). When ferric ammonium citrate (FAC) was added after 28 h, the product aglycone ^{19}F signal immediately disappeared, which we attribute to a paramagnetic relaxation enhancement in the Fe^{3+}:**3-FBNH** complex.

Given that conversion of substrate appeared much slower in cells than with enzyme *in vitro*, tests were conducted to compare intact and lysed cells. Incubation of **13** with equal numbers of intact or lysed MCF7-*lacZ* cells showed 25% conversion after overnight incubation (14 h), whereas lysed cells showed 75%. Similarly, PC3-*lacZ* cells showed only 15% conversion, while lysed PC3-*lacZ* cells showed 85%.

As an initial proof of principle, **13** and FAC were injected into wild type (WT) and *lacZ*-transfected PC3 human prostate tumor xenografts growing in mice (Figure 6). Spin−lattice relaxation time (T_1)-weighted images showed a local hyperintensity associated with the ferric ions, and a corresponding drop in the T_1 values was observed. For groups of tumors, there was no significant difference between mean baseline T_1 (2.4 ± 0.4 s; n = 2 WT vs 2.4 ± 0.3 s; n = 3 *lacZ*; $p > 0.8$). Following injection of contrast agent (i.e., **13** plus FAC), T_1 decreased in WT tumors (T_1 = 1.5 ± 0.4, $p < 0.2$), but the change was significant in *lacZ* tumors (T_1 = 1.1 ± 0.4; $p < 0.01$). For the

dx.doi.org/10.1021/bc200647q | *Bioconjugate Chem.* 2012, 23, 596−603

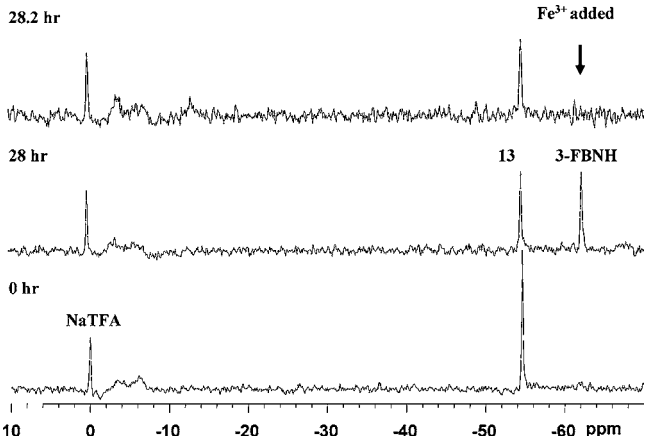


Figure 5. Detection of β-gal activity in cultured cells. 376 MHz ^{19}F NMR spectra of **13** (2.11 mg, 5.0 μmol) after addition to stably transfected MCF7-*lacZ* cells (5.0×10^6). Fe^{3+} (2.5 μmol) was added after 28 h. Each spectrum was acquired in 205 s, and enhanced with an exponential line broadening 40 Hz.

same regions of the tumors, a large signal decrease was observed in spin−spin (T_2)-weighted ^{1}H images in PC3-*lacZ* tumors only at the injection site. T_2 was similar before injection of contrast agent (T_2 = 55 ± 5 ms (*lacZ*) vs T_2 = 52 ± 16 ms (WT)). Following administration of contrast agent, T_2 changed significantly in *lacZ* tumors (T_2 = 39 ± 5 ms; $p < 0.05$), but not in WT tumors (T_2 = 53 ± 15 ms; $p > 0.9$). ^{19}F spectroscopy showed the presence of substrate **13** in the WT tumors, which decreased slowly (Figure 7), but no aglycone product. In corresponding PC3-*lacZ* tumors, no substrate or product signal was observed by ^{19}F NMR. Enzyme activity was confirmed postmortem based on X-gal staining of slices of PC3-*lacZ* tumors, which turned intense blue, whereas wild-type tumors showed no blue color (Figure 6).

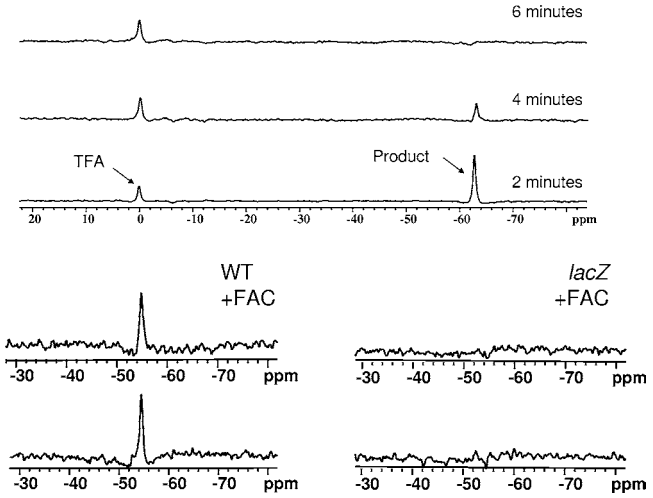


Figure 7. Detection of β-gal activity *in vivo* by ^{19}F NMR. Left: Following injection of **13** (1 mg) into a PC3-WT tumor, ^{19}F NMR spectroscopy showed substrate at −54.6 ppm with respect to sodium trifluoroacetate reference (lower spectrum). Following injection of 0.6 mg FAC, the substrate remained visible (upper left). Spectra were acquired in about 2½ min and enhanced with 60 Hz exponential line broadening prior to Fourier transformation giving a SNR of 35. Right: Similar injection into PC3-*lacZ* tumor showed minimal ^{19}F NMR signal and there was minimal change after addition of FAC (upper). Upper spectra: A mixture of sodium trifluoroacetate and aglycone (**3-FBNH**; 3 mg) in total volume of 50 μL was injected into muscle of a dead adult 129S-Gt(ROSA)26Sor/J mouse. ^{19}F NMR spectra were acquired immediately and every 2 min. NaTFA served as a chemical shift reference at 0 ppm and remained quite constant. Meanwhile aglycone was initially seen with SNR = 194 at −62.8 ppm, but signal decreased and was no longer observed after 6 min.

Lack of detectable ^{19}F NMR could have been caused by clearance of the product from *lacZ* tumors *in vivo* or potentially precipitation of the product by association with ferric ions,

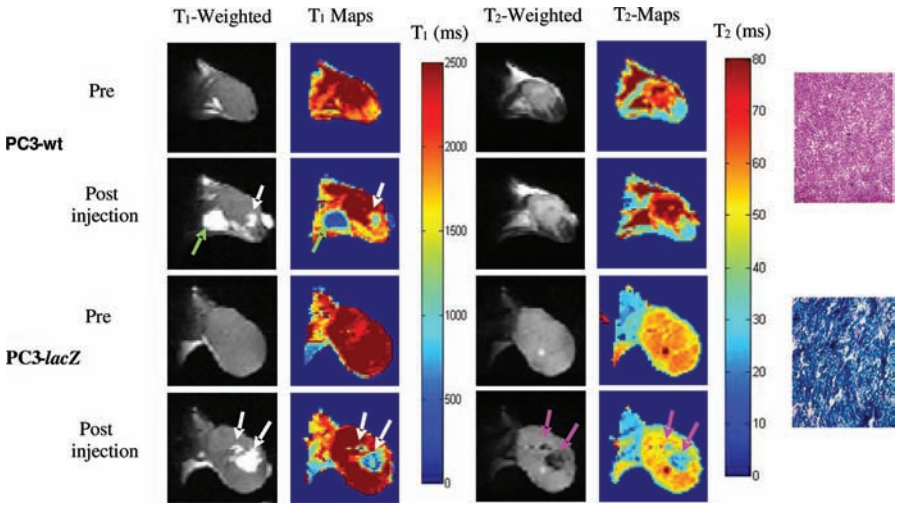


Figure 6. Imaging β-gal activity *in vivo*. *In vivo* study showing *lacZ* gene-reporter activity detected by ^{1}H MRI in representative PC3 tumor xenografts in SCID mice after intratumoral injection (100 μL total volume) of ferric ammonium citrate (FAC) and **13**. The presence of FAC + **13** is seen in T_1-weighted images (TR/TE = 300/12 ms) and T_1 maps (white arrows) in both wild-type tumors (columns 1 and 2, row 2) and *lacZ* tumors (columns 1 and 2, row 4). Baseline tumor T_1 = 2.8 ± 0.1 s for *lacZ* and 2.6 ± 0.2 s for WT, versus 1.1 ± 0.6 s for *lacZ* and 1.8 ± 0.5 s for WT following injection of **13** + FAC. Significant change in T_2-weighted images (TR/TE = 6000/50 ms, column 3, row 4) and T_2 values (column 4, row 4) was seen only in the *lacZ*-transfected tumors post-injection of FAC and **13** (pink arrows). Baseline T_2 = 56 ± 4 ms for *lacZ* and T_2 = 63 ± 7 ms for WT became T_2 = 34 ± 10 ms for *lacZ* and T_2 = 63 ± 18 ms for WT. Green arrow indicates anomalous injection outside tumor, and this region was excluded from analysis. Histological sections at right (original magnification × 100) confirm intense β-gal expression in *lacZ* tumor based on X-gal and H&E staining (blue, lower slide) with essentially no activity in WT tumor (pink, upper slide).

dx.doi.org/10.1021/bc200647q | *Bioconjugate Chem.* 2012, 23, 596−603

rendering it NMR invisible. To gain further insight into the lack of ^{19}F signal, product aglycone was injected into muscle of ROSA26 mice, which express *lacZ* throughout their bodies. Internal NaTFA standard and aglycone were immediately detectable, but over a few minutes, the aglycone signal at −61.5 ppm disappeared in both live and dead mice, while TFA remained visible in the dead animal (Figure 7).

DISCUSSION

We have demonstrated a novel dual $^{19}F/^{1}H$ MR *lacZ* gene detection approach by introducing a fluorine atom into iron-chelating aroylhydrazone aglycones of β-D-galactopyranosides. When activated by β-gal, the released fluoroaroylhydrazones display a distinct chemical shift with respect to the substrate and can be spontaneously trapped by Fe^{3+} at the site of enzyme activity forming highly relaxing complexes *in situ*. The complexes cause strong T_2 relaxation, providing ^{1}H MRI contrast to reveal *lacZ* expression.

We believe the T_1 contrast following injection is attributable to free ferric ions from FAC and this was observed in both WT and *lacZ* tumors (Figure 6). However, β-gal activity was clearly revealed by the colocalized hypointensity in T_2-weighted images and corresponding significant shortening in T_2, whereas no T_2 contrast was observed for WT tumors.

The utility of a reporter molecule is predicated on a reasonable rate of activity. The conversion rates *in vitro* were very slow (Figure 3). Aglycone was released much more rapidly by lysed MCF7-*lacZ* or PC3-*lacZ* cells indicating that cell permeation is a strong barrier to activity. However, contrast was observed almost immediately in *lacZ* tumors upon direct intratumoral injection. Such differential rates of activity have also been reported for ^{19}F reporters.[8,9] The ultimate goal is development of reporter molecules which may be administered systemically. At this stage, the method requires direct intratumoral injection, but we note that this limitation has also been encountered by most other reports regarding reporter molecules for β-gal using NMR, radionuclides, or photoacoustic tomography.[8,9,12,16,21,24] To date, systemic administration has generally been restricted to optical imaging approaches[14,18,31] and a single report regarding a Gd-based contrast agent.[6]

Ideally, ^{19}F NMR would show both substrate and product, and this was observed in cells (Figure 5). However, the liberated product signal was absent in the presence of ferric ions and *in vivo*. This could be attributed to clearance of the product from *lacZ* tumors and ROSA26 muscle *in vivo*, but the postmortem test in the ROSA26 mouse also indicated signal disappearance over a period of 6 min consistent with precipitation of the product (possibly in association with endogenous ferric ions), which renders it NMR invisible. ^{19}F signal for TFA remained visible over this time. The ^{19}F NMR is able to locate substrate, but not product, and we are seeking alternate molecules, which can reveal both substrate and product.

In the present studies, we added exogenous ferric ions, but we note that cancer cells often exhibit elevated iron levels and a number of Fe-chelators have been proposed for cancer therapy.[32] Indeed, aroyl hydrazones are in clinical use as ferric ion scavenging agents[33] suggesting a potential for clinical theranostic application. There is an extensive literature on aroyl hydrazones regarding thermodynamic characteristics of ferric ion complexes,[26,28] and we assume that ^{19}F analogues presented here behave similarly. We were not able to obtain a crystal structure of the complex, but chemical analysis confirmed a 2:1 structure.

^{19}F NMR is gaining popularity as a reporter for diverse enzyme reactions based on various strategies. The simplest is change in chemical shift that we and others have exploited extensively.[8,9,34,35] More recently, differential relaxation rates have been exploited based on paramagnetic relaxation enhancement (PRE)[10,36] or differential restricted mobility[37,38] to reveal enzyme activity based on changes in line broadening. In addition, several recent reports have presented bimodal reporter strategies revealing enzyme activity based on ^{19}F NMR and fluorescence.[38,39]

Ultimately, we hope to develop this approach for systemic delivery of reporter molecules, but direct injection into the tissues of interest already demonstrates selective detection of *lacZ* expression versus WT. The multimodality approach represents a new paradigm exploiting ^{19}F NMR together with both T_1 and T_2 ^{1}H MRI contrast to reveal the presence or absence of enzyme activity. The observations are in accord with renewed excitement and innovations in ^{19}F NMR notably for detecting enzyme activity.[37,39−42]

ASSOCIATED CONTENT

Supporting Information

Experimental details and molecular characterization. This material is available free of charge via the Internet at http://pubs.acs.org.

AUTHOR INFORMATION

Corresponding Author

*Phone: (214)-648-8926. Fax: (214)-648-4538. E-mail: Ralph.Mason@UTSouthwestern.edu.

Present Address

†Currently at the School of Biological and Health Systems Engineering, Arizona State University, Tempe, AZ

Notes

The authors declare no competing financial interest.

ACKNOWLEDGMENTS

Supported in part by NCI R21 CA120774, DOD Breast Cancer Initiative IDEA award DAMD17-03-1-0343, and the Small Animal Imaging Research Program, which is supported in part by NCI U24 CA126608 and P30 CA142543. NMR experiments were conducted at the Advanced Imaging Research Center, an NIH BTRP facility (P41-RR02584). We are grateful to Praveen K. Gulaka, Jennifer Magnusson, Jennifer McAnally, and Ya Ren for expert technical assistance.

REFERENCES

(1) Gilad, A. A., Winnard, P. T., van Zijl, P. C. M., and Bulte, J. W. M. (2007) Developing MR reporter genes: promises and pitfalls. *NMR Biomed. 20*, 275−290.

(2) Razgulin, A., Ma, N., and Rao, J. H. (2011) Strategies for in vivo imaging of enzyme activity: an overview and recent advances. *Chem. Soc. Rev. 40*, 4186−4216.

(3) Kruger, A., Schirrmacher, V., and Khokha, R. (1998) The bacterial lacZ gene: An important tool for metastasis research and evaluation of new cancer therapies. *Cancer Metast. Rev. 17*, 285−94.

(4) de Almeida, R. A., Burgess, D., Shema, R., Motlekar, N., Napper, A. D., Diamond, S. L., and Pavitt, G. D. (2008) A Saccharomyces cerevisiae cell-based quantitative beta-galactosidase handling and assay compatible with robotic high-throughput screening. *Yeast 25*, 71−76.

(5) Louie, A. Y., Huber, M. M., Ahrens, E. T., Rothbacher, U., Moats, R., Jacobs, R. E., Fraser, S. E., and Meade, T. J. (2000) In vivo

visualization of gene expression using magnetic resonance imaging. *Nat. Biotechnol. 18*, 321−325.
(6) Chang, Y. T., Cheng, C. M., Su, Y. Z., Lee, W. T., Hsu, J. S., Liu, G. C., Cheng, T. L., and Wang, Y. M. (2007) Synthesis and characterization of a new bioactivated paramagnetic gadolinium(111) complex [Gd(DOTA-FPG)(H2O)] for tracing gene expression. *Bioconjugate Chem. 18*, 1716−1727.
(7) Cui, W., Otten, P., Li, Y., Koeneman, K., Yu, J., and Mason, R. P. (2004) A novel NMR approach to assessing gene transfection: 4-fluoro-2-nitrophenyl-β-D-galactopyranoside as a prototype reporter molecule for β-galactosidase. *Magn. Reson. Med. 51*, 616−20.
(8) Liu, L., Kodibagkar, V. D., Yu, J.-X., and Mason, R. P. (2007) ^{19}F-NMR detection of lacZ gene expression via the enzymic hydrolysis of 2-fluoro-4-nitrophenyl β-D-galactopyranoside *in vivo* in PC3 prostate tumor xenografts in the mouse. *FASEB J. 21*, 2014−2019.
(9) Yu, J. X., Kodibagkar, V. D., Liu, L., and Mason, R. P. (2008) A ^{19}F NMR Approach using Reporter Molecule Pairs to Assess β-Galactosidase in Human Xenograft Tumors in Vivo. *NMR Biomed. 21*, 704−12.
(10) Mizukami, S., Matsushita, H., Takikawa, R., Sugihara, F., Shirakawa, M., and Kikuchi, K. (2011) ^{19}F MRI detection of β-galactosidase activity for imaging of gene expression. *Chem. Sci. 2*, 1151−1155.
(11) Hanaoka, K., Kikuchi, K., Terai, T., Komatsu, T., and Nagano, T. (2008) A Gd^{3+}-based magnetic resonance imaging contrast agent sensitive to beta-galactosidase activity utilizing a receptor-induced magnetization enhancement (RIME) phenomenon. *Chem.—Eur. J. 14*, 987−995.
(12) Arena, F., Singh, J. B., Gianolio, E., Stefania, R., and Aime, S. (2011) beta-Gal Gene Expression MRI Reporter in Melanoma Tumor Cells. Design, Synthesis, and in Vitro and in Vivo Testing of a Gd(III) Containing Probe Forming a High Relaxivity, Melanin-Like Structure upon beta-Gal Enzymatic Activation. *Bioconjugate Chem. 22*, 2625−2635.
(13) Kamiya, M., Kobayashi, H., Hama, Y., Koyama, Y., Bernardo, M., Nagano, T., Choyke, P. L., and Urano, Y. (2007) An enzymatically activated fluorescence probe for targeted tumor imaging. *J. Am. Chem. Soc. 129*, 3918−3929.
(14) Tung, C. H., Zeng, Q., Shah, K., Kim, D. E., Schellingerhout, D., and Weissleder, R. (2004) In vivo imaging of beta-galactosidase activity using far red fluorescent switch. *Cancer Res. 64*, 1579−83.
(15) Josserand, V., Texier-Nogues, I., Huber, P., Favrot, M. C., and Coll, J. L. (2007) Non-invasive in vivo optical imaging of the lacZ and luc gene expression in mice. *Gene Ther. 14*, 1587−1593.
(16) Li, L., Zemp, R. J., Lungu, G., Stoica, G., and Wang, L. H. V. (2007) Photoacoustic imaging of lacZ gene expression in vivo. *J. Biomed. Optics 12*, 020504.
(17) Kamiya, M., Asanuma, D., Kuranaga, E., Takeishi, A., Sakabe, M., Miura, M., Nagano, T., and Urano, Y. (2011) beta-Galactosidase Fluorescence Probe with Improved Cellular Accumulation Based on a Spirocyclized Rhodol Scaffold. *J. Am. Chem. Soc. 133*, 12960−12963.
(18) Liu, L., and Mason, R. P. (2010) Imaging beta-Galactosidase Activity in Human Tumor Xenografts and Transgenic Mice Using a Chemiluminescent Substrate. *PLOS One 5*, e12024.
(19) Lee, K. H., Byun, S. S., Choi, J. H., Paik, J. Y., Choe, Y. S., and Kim, B. T. (2004) Targeting of lacZ reporter gene expression with radioiodine-labelled phenylethyl-beta-d-thiogalactopyranoside. *Eur. J. Nucl. Med. Mol. Imaging 31*, 433−8.
(20) Celen, S., Deroose, C., de Groot, T., Chitneni, S. K., Gijsbers, R., Debyser, Z., Mortelmans, L., Verbruggen, A., and Bormans, G. (2008) Synthesis and evaluation of F-18- and C-11-labeled phenyl-galactopyranosides as potential probes for in vivo visualization of LacZ gene expression using positron emission tomography. *Bioconjugate Chem. 19*, 441−449.
(21) Van Dort, M. E., Lee, K. C., Hamilton, C. A., Rehemtulla, A., and Ross, B. D. (2008) Radiosynthesis and Evaluation of 5-[I-125]-Iodoindol-3-yl-beta-D-Galactopyranoside as a beta-Galactosidase Imaging Radioligand. *Mol. Imaging 7*, 187−197.
(22) Kodibagkar, V. D., Yu, J., Liu, L., Hetherington, H. P., and Mason, R. P. (2006) Imaging β-galactosidase activity using ^{19}F chemical shift imaging of LacZ gene-reporter molecule 2-fluoro-4-nitrophenol-β-D-galactopyranoside. *Magn. Reson. Imaging 24*, 959−962.
(23) Yu, J. X., Liu, L., Kodibagkar, V. D., Cui, W., and Mason, R. P. (2006) Synthesis and Evaluation of Novel Enhanced Gene Reporter Molecules: Detection of b-Galactosidase Activity Using ^{19}F NMR of Trifluoromethylated Aryl β-D-Galactopyranosides. *Bioorg. Med. Chem. 14*, 326−33.
(24) Cui, W., Liu, L., Kodibagkar, V. D., and Mason, R. P. (2010) S-Gal®, A novel ^{1}H MRI reporter for β-galactosidase. *Magn. Reson. Med. 64*, 65−71.
(25) Bengtsson, N. E., Brown, G., Scott, E. W., and Walter, G. A. (2010) lacZ as a Genetic Reporter for Real-Time MRI. *Magn. Reson. Med. 63*, 745−753.
(26) Dubois, J. E., Fakhrayan, H., Doucet, J. P., and Chahine, J. M. E. (1992) Kinetic and Thermodynamic Study of Complex-Formation between Iron(Ii) and Pyridoxal Isonicotinoylhydrazone and Other Synthetic Chelating-Agents. *Inorg. Chem. 31*, 853−859.
(27) Kalinowski, D. S., and Richardson, D. R. (2005) The Evolution of Iron Chelators for the Treatment of Iron Overload Disease and Cancer. *Pharmacol. Rev. 57*, 547−583.
(28) Yu, Y., Kalinowski, D. S., Kovacevic, Z., Siafakas, A. R., Jansson, P. J., Stefani, C., Lovejoy, D. B., Sharpe, P. C., Bernhardt, P. V., and Richardson, D. R. (2009) Thiosemicarbazones from the Old to New: Iron Chelators That Are More Than Just Ribonucleotide Reductase Inhibitors. *J. Med. Chem. 52*, 5271−5294.
(29) Yu, J. X., Otten, P., Ma, Z., Cui, W., Liu, L., and Mason, R. P. (2004) A Novel NMR Platform for Detecting Gene Transfection: Synthesis and Evaluation of Fluorinated Phenyl β-D-Galactosides with Potential Application for Assessing LacZ Gene Expression. *Bioconjugate Chem. 15*, 1334−1341.
(30) Yu, J. X., Ma, Z., Li, Y., Koeneman, K. S., Liu, L., and Mason, R. P. (2005) Synthesis and Evaluation of a Novel Gene Reporter Molecule: Detection of β-galactosidase activity Using ^{19}F NMR of a Fluorinated Vitamin B6 conjugate. *Med. Chem. 1*, 255−262.
(31) Wehrman, T. S., von Degenfeld, G., Krutzik, P., Nolan, G. P., and Blau, H. M. (2006) Luminescent imaging of beta-galactosidase activity in living subjects using sequential reporter-enzyme luminescence. *Nat. Methods 3*, 295−301.
(32) Whitnall, M., Howard, J., Ponka, P., and Richardson, D. R. (2006) A class of iron chelators with a wide spectrum of potent antitumor activity that overcomes resistance to chemotherapeutics. *Proc. Natl. Acad. Sci. U.S.A. 103*, 14901−14906.
(33) Richardson, D. R., Kalinowski, D. S., Lau, S., Jansson, P. J., and Lovejoy, D. B. (2009) Cancer cell iron metabolism and the development of potent iron chelators as anti-tumour agents. *Biochim. Biophys. Acta 1790*, 702−717.
(34) Yu, J. X., Kodibagkar, V., Cui, W., and Mason, R. P. (2005) ^{19}F: a versatile reporter for non-invasive physiology and pharmacology using magnetic resonance. *Curr. Med. Chem. 12*, 818−848.
(35) Dresselaers, T., Theys, J., Nuyts, S., Wouters, B., de Bruijn, E., Anne, J., Lambin, P., Van Hecke, P., and Landuyt, W. (2003) Non-invasive F-19 MR spectroscopy of 5-fluorocytosine to 5-fluorouracil conversion by recombinant Salmonella in tumours. *Br. J. Cancer 89*, 1796−1801.
(36) Senanayake, P. K., Kenwright, A. M., Parker, D., and van der Hoorn, S. K. (2007) Responsive fluorinated lanthanide probes for F-19 magnetic resonance spectroscopy. *Chem. Commun.*, 2923−2925.
(37) Takaoka, Y., Kiminami, K., Mizusawa, K., Matsuo, K., Narazaki, M., Matsuda, T., and Hamachi, I. (2011) Systematic Study of Protein Detection Mechanism of Self-Assembling (19)F NMR/MRI Nanoprobes toward Rational Design and Improved Sensitivity. *J. Am. Chem. Soc. 133*, 11725−11731.
(38) Tanaka, K., Kitamura, N., and Chujo, Y. (2011) Bimodal Quantitative Monitoring for Enzymatic Activity with Simultaneous Signal Increases in (19)F NMR and Fluorescence Using Silica

Nanoparticle-Based Molecular Probes. *Bioconjugate Chem. 22*, 1484−1490.
(39) Mizukami, S., Takikawa, R., Sugihara, F., Shirakawa, M., and Kikuchi, K. (2009) Dual-Function Probe to Detect Protease Activity for Fluorescence Measurement and F-19 MRI. *Angew. Chem., Int. Ed. 48*, 3641−3643.
(40) Mizukami, S., Takikawa, R., Sugihara, F., Hori, Y., Tochio, H., Walchli, M., Shirakawa, M., and Kikuchi, K. (2008) Paramagnetic relaxation-based F-19 MRI probe to detect protease activity. *J. Am. Chem. Soc. 130*, 794−5.
(41) Higuchi, M., Iwata, N., Matsuba, Y., Sato, K., Sasamoto, K., and Saido, T. C. (2005) F-19 and H-1 MRI detection of amyloid beta plaques in vivo. *Nat. Neurosci. 8*, 527−533.
(42) Tanabe, K., Harada, H., Narazaki, M., Tanaka, K., Inafuku, K., Komatsu, H., Ito, T., Yamada, H., Chujo, Y., Matsuda, T., Hiraoka, M., and Nishimoto, S. (2009) Monitoring of Biological One-Electron Reduction by F-19 NMR Using Hypoxia Selective Activation of an F-19-Labeled Indolequinone Derivative. *J. Am. Chem. Soc. 131*, 15982−3.

Bioconjugate Chemistry

Article

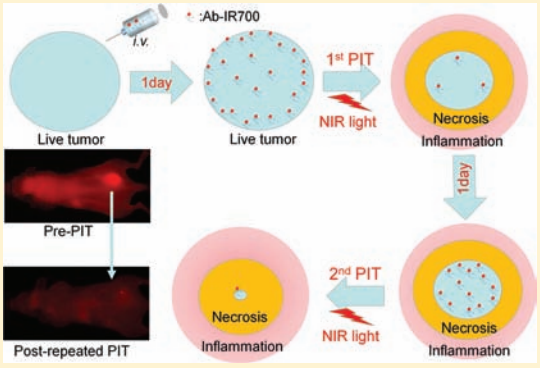
pubs.acs.org/bc

Near-infrared Theranostic Photoimmunotherapy (PIT): Repeated Exposure of Light Enhances the Effect of Immunoconjugate

Makoto Mitsunaga, Takahito Nakajima, Kohei Sano, Peter L. Choyke, and Hisataka Kobayashi*

Molecular Imaging Program, Center for Cancer Research, National Cancer Institute, National Institutes of Health, Bethesda, Maryland 20892-1088, United States

ABSTRACT: Armed antibody-based targeted molecular therapies offer the possibility of effective tumor control with a minimum of side effects. Photoimmunotherapy (PIT) employs a monoclonal antibody–phototoxic phthalocyanine dye, IR700 conjugate, that is activated by focal near-infrared (NIR) light irradiation after antibody binding to the targeted tumor cell surface leading to rapid necrotic cell death. Therapy by single NIR light irradiation was effective without significant side effects; however, recurrences were seen in most treated mice probably because of inhomogeneous distribution of panitumumab–IR700 immunoconjugate in the tumor, leading to ineffective PIT. We describe here an optimized regimen of effective PIT method for the same HER1-overexpressing tumor model (A431) with fractionated administration of panitumumab–IR700 conjugate followed by systematic repeated NIR light irradiation to the tumor based on timing of antibody redistribution into the remnant tumor under the guidance of IR700 fluorescence signal. Eighty percent of the A431 tumors were eradicated with repeated PIT without apparent side effects and survived tumor-free for more than 120 days even after stopping therapy at day 30. Therapeutic effects were monitored using IR700 fluorescent signal. PIT is a promising highly selective and clinically feasible theranostic method for treatment of mAb-binding tumors with minimal off-target effects.



INTRODUCTION

Targeted cancer therapies offer the promise of more effective tumor control with fewer side effects than conventional cancer therapies. The class of molecular therapies based on monoclonal antibodies (mAb) is highly selective for tumors expressing particular antigens; however, with few exceptions, patient outcomes have been only modestly improved when the naked mAb is used as monotherapy or in combination with other therapies.[1−3] The primary mechanisms of action of mAb therapy are thought to be antibody-dependent cellular cytotoxicity (ADCC), complement-dependent cytotoxicity (CDC), and/or receptor signaling blockade.[4,5] Another way in which mAbs can be used in therapy is as vectors for the delivery of other therapies, such as toxins or radioisotopes;[6,7] however, the toxicity of such immunotoxins or radioimmunotherapeutics are often dose-limiting due to off-target effects to normal organs.

We recently reported a new form of mAb-based immunotherapy termed "photoimmunotherapy" (PIT) that utilizes an mAb conjugated with a near-infrared (NIR) phthalocyanine dye, IRDye700DX (IR700). IR700 was originally designed as a fluorescent agent and its therapeutic properties were only recently discovered. As a consequence, IR700 is not only phototoxic, but also fluorescent, and thus can be used as an imaging agent. Additionally, when exposed to more intense levels of NIR light, the conjugate becomes lethal, but only to those cells to which the conjugate is bound.[8] NIR light exposure leads to rapid, target-selective necrotic cell death in vitro. In addition, effective tumor shrinkage was obtained even with a single administration of mAb–IR700 followed by a single exposure to NIR light in vivo. Although single administration of the therapy (agent + NIR light) was highly effective, recurrences were seen in treated mice, because inhomogeneous mAb–IR700 distribution in the targeted tumor could lead to not killing a small fraction of cancer cells, to which mAb–IR700 did not bind with NIR light. Unlike nontargeting small molecule photosensitizers, mAb–IR700 conjugate stays longer in the blood circulation, which allows unbound mAb–IR700 to redistribute into the remnant target tumor after the first NIR light irradiation. This suggested that repeated administrations of the therapy (agent + NIR light) could theoretically lead to even better tumor control. In this study, we investigated the optimization of treatment regimens by fractionated dosing of mAb–IR700 conjugate and NIR light irradiation in order to enhance the effectiveness and safety of PIT employing an anti-human epidermal growth factor receptor type 1 (HER1) mAb, panitumumab–IR700 (Pan–IR700) conjugate in a xenograft tumor model.

Received: December 1, 2011
Revised: January 20, 2012
Published: February 27, 2012

ACS Publications

This article not subject to U.S. Copyright. Published 2012 by the American Chemical Society

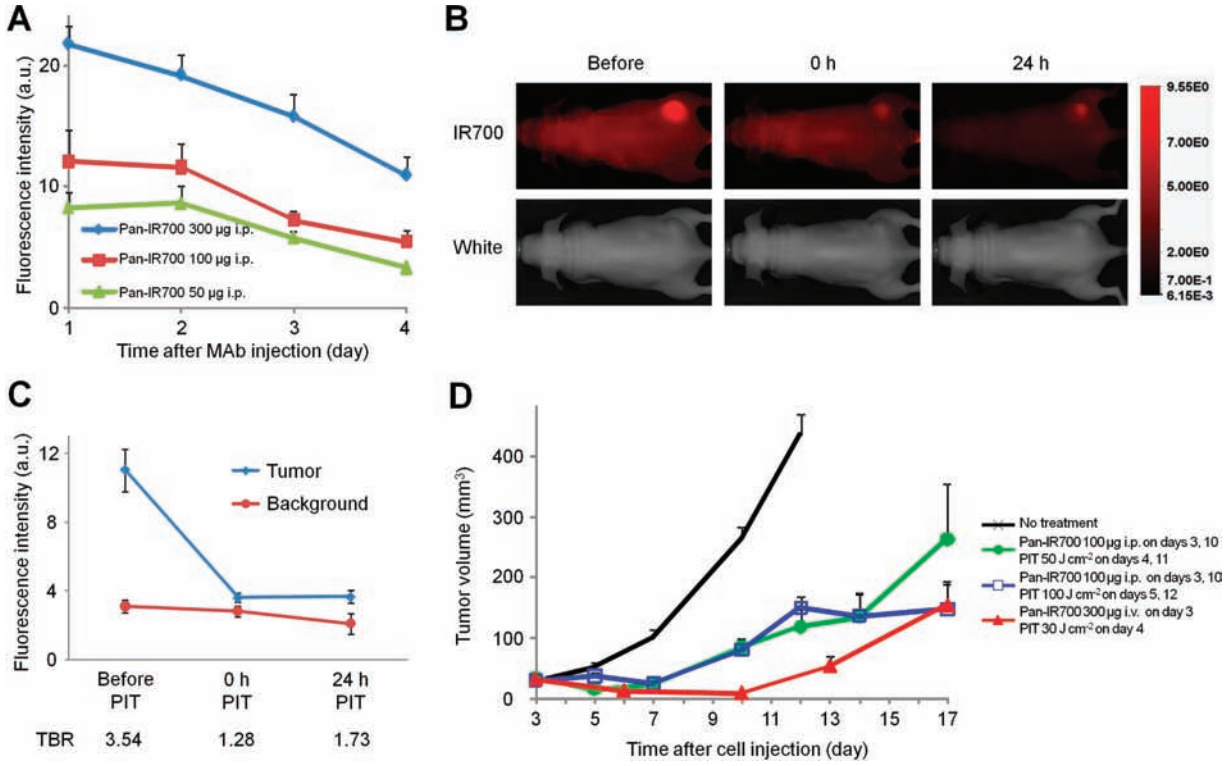


Figure 1. Effectiveness of fractionated Pan−IR700 with multiple NIR light exposures as detected by IR700 fluoresence. Pan−IR700 was administered to A431 tumor-bearing mice which were then exposed to NIR light and imaged with a fluorescent camera. (A) IR700 fluorescence of A431 tumors over time (n = 3 mice in each group). (B) Images of A431 tumor bearing mice before (left), immediately after (center), and 24 h after (right) PIT with 50 J cm^{-2} NIR light irradiation. IR700 fluorescence signal in the tumor decreased to background level immediately after PIT (center). Signal within the tumor increased 24 h after PIT indicating reaccumulation of Pan−IR700 due to circulating Pan−IR700 (right). (C) IR700 fluorescence of A431 tumor before and after NIR light irradiation. Data are mean ± s.e.m. (n = 4 mice). (D) Tumor volume reduction in response to Pan−IR700 PIT in A431 xenograft tumor ($n \geq 10$ mice in each treatment group).

EXPERIMENTAL PROCEDURES

Reagents. A water-soluble, silicon−phthalocyanine derivative, IRDye 700DX NHS ester (IR700; $C_{74}H_{96}N_{12}Na_4O_{27}S_6Si_3$, molecular weight 1954.22), was obtained from LI-COR Bioscience (Lincoln, NE). Panitumumab, a fully humanized IgG_2 mAb directed against the HER1, was purchased from Amgen (Thousand Oaks, CA). All other chemicals used were of reagent grade.

Synthesis of IR700-Conjugated Panitumumab. Panitumumab (1 mg, 6.8 nmol) was incubated with IR700 (66.8 μg, 34.2 nmol, 5 mmol L^{-1} in DMSO) in 0.1 mol L^{-1} Na_2HPO_4 (pH 8.5) at room temperature for 2 h. The mixture was purified with a Sephadex G50 column (PD-10; GE Healthcare, Waukesha, WI). The protein concentration was determined with Coomassie Plus protein assay kit (Thermo Fisher Scientific Inc., Rockford, IL) by measuring the absorption at 595 nm with spectroscopy (8453 Value System; Agilent Technologies, Santa Clara, CA). The concentration of IR700 was measured by absorption with spectroscopy to confirm the number of fluorophore molecules conjugated to each mAb molecule.

Cells. HER1-expressing A431 cells were grown in RPMI 1640 supplemented with 10% fetal bovine serum and 1% penicillin/streptomycin in tissue culture flasks in a humidified incubator at 37 °C in an atmosphere of 95% air and 5% carbon dioxide.

In Vivo Photoimmunotherapy for A431 Tumors with Pan-IR700. All in vivo procedures were conducted in compliance with the Guide for the Care and Use of Laboratory Animal Resources (1996), U.S. National Research Council, and approved by the local Animal Care and Use Committee. Six- to eight-week-old female homozygous athymic nude mice were purchased from Charles River (NCI-Frederick). During the procedure, mice were anesthetized with isoflurane. One million A431 cells were injected subcutaneously in the right dorsum of the mice. In order to determine tumor volume, the greatest longitudinal diameter (length) and the greatest transverse diameter (width) were determined with an external caliper. Tumor volume based on caliper measurements was calculated by the following formula; tumor volume = length × width^2 × 0.5.[9] Tumors reaching approximately 40 mm^3 in volume were selected for the study. Selected mice were randomized into 7 groups of at least 10 animals per group for the following treatments: (1) no treatment; (2) 100 μg of panitumumab i.p. every week, no NIR light exposure; (3) 100 μg of Pan-IR700 i.p. every week, no NIR light exposure; (4) PBS i.p. every week, NIR light was administered at 50 J cm^{-2} on day 1 after injection and 100 J cm^{-2} on day 2 after injection; (5) 100 μg of Pan-IR700 i.p. every week, NIR light was administered at 50 J cm^{-2} on day 1 after injection; (6) 100 μg of Pan-IR700 i.p. every week, NIR light was administered at 100 J cm^{-2} on day 2 after injection ; (7) 100 μg of Pan-IR700 i.p. every week, NIR light was administered at 50 J cm^{-2} on day 1 after injection and 100 J cm^{-2} on day 2 after injection. These therapies were performed every week for up to 4 weeks until mice had to be euthanized due to tumor growth of >500 mm^3. Mice were monitored daily, and tumor volume was measured three times a week until the

dx.doi.org/10.1021/bc200648m | Bioconjugate Chem. 2012, 23, 604−609

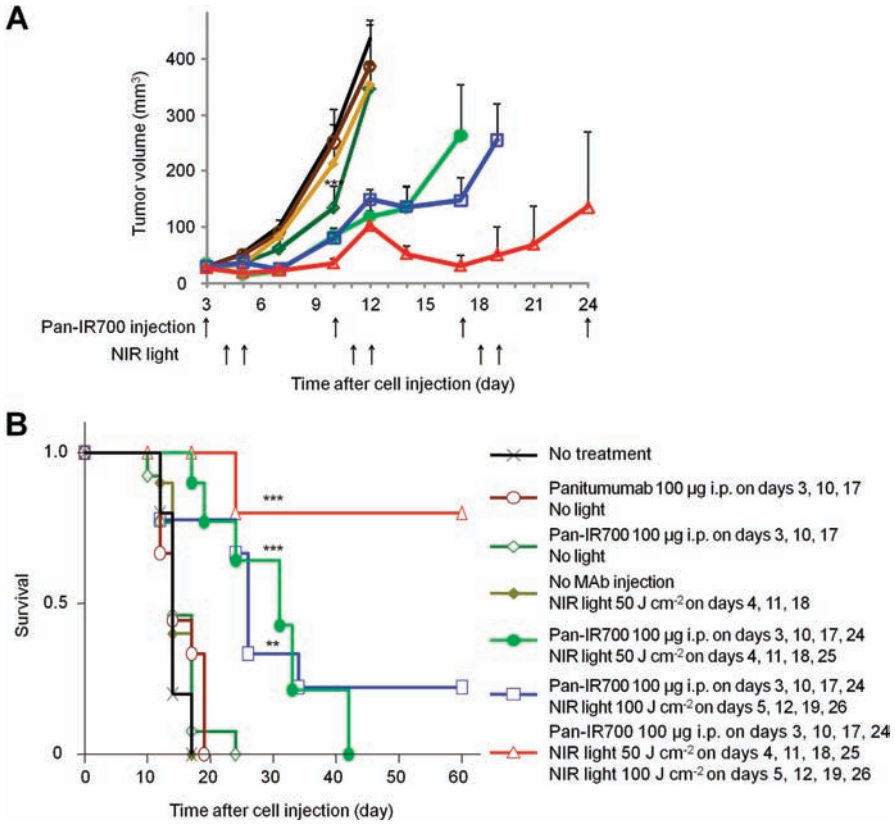


Figure 2. Optimized regimen of PIT resulted in complete pathologic response in mice with A431 xenograft tumors. (A) Repeated Pan−IR700 mediated PIT leads to more effective tumor volume reduction (n = 10 mice in each treatment group; *** $P < 0.001$ vs nontreatment control mice). Note that data were analyzed and shown only when each group of tumors did not exceed 500 mm^3. (B) Repeated Pan−IR700 mediated PIT led to prolonged survival (n = 10 mice in each treatment group; *** $P < 0.001$, ** $P < 0.01$ vs nontreatment control mice).

tumor volume reached 500 mm^3, at which time mice were euthanized with carbon dioxide. An LED light source (L690−66−60, Marubeni America Co., Santa Clara, CA) was used for NIR irradiation of PIT at 670 to 710 nm (peak at 690 nm). Fluorescence images, as well as white light images, were obtained using a Pearl Imager (LI-COR Biosciences) with a 700 nm fluorescence channel with a 685 nm laser excitation. For analyzing fluorescence intensities, tumors of the same size were compared and regions of interest (ROI) were placed over the entire tumor. Average fluorescence intensity of each ROI was calculated.

Histological Analysis. To evaluate serial histological changes after PIT and microdistribution of Pan-IR700, a light and fluorescence microscopy study was performed (BX51, Olympus America). A431 tumors were harvested in 10% formalin 1 h and 1 d after 50 J/cm^2 of PIT. Serial 10 μm slice sections were fixed on 2 slide glasses without staining or with H-E staining. The filter set to detect IR700 fluorescence consisted of a 590−650 nm excitation filter and a 665−740 nm band-pass emission filter.

Statistical Analysis. Data are expressed as mean ± s.e.m. Statistical analyses were carried out using a statistics program (*GraphPad Prism*; GraphPad Software Inc., La Jolla, CA). The Student's t test was used to compare the treatment effects with controls. The cumulative probability of survival (based on the failure of the tumor to reach 500 mm^3) was estimated in each group with the use of the Kaplan−Meier survival curve analysis, and the results were compared with use of the log-rank test with Bonferroni's correction for multiple comparisons. $P < 0.05$ was used to determine statistical significance.

RESULTS

Repeated Irradiation of NIR Light Can Minimize Dose of Pan−IR700 Conjugate without Compromising Therapeutic Effect of PIT. In prior studies, we have used 300 μg as the dose of Pan−IR700. We examined the effect of the lower dose (100 μg) of Pan−IR700 used in this study. As expected, highest IR700 signals were obtained at 1 day after injection in each group and the tumor-based fluorescence was lower with the decreased dose of Pan−IR700 (Figure 1A). Interestingly, the target-to-background ratio (TBR) of IR700 fluorescence intensity in A431 tumor decreased to background level just after NIR light irradiation that ensured sufficient therapeutic effects to all cancer cells to which Pan−IR700 bound (Figure 1B,C). Circulating Pan−IR700 reaccumulated in the remnant tumor mass within a day, leading to an increase in TBR on fluorescence imaging (Figure 1B,C). This indicated that Pan−IR700 was still accumulating in the surviving cancer cells even after initial treatment with NIR light, and therefore, the second dose of NIR light irradiation at 100 J cm^{-2} was effective in treating the tumors (2 days after Pan−IR700 administration). Therefore, the reduced dose of Pan−IR700 (100 μg) did not compromise PIT efficacy and still enabled visualization with IR700 fluorescence (Figure 1D).

HER1-Specific Tumor Shrinkage in Response to Pan−IR700 Mediated Repeated PIT. The efficacy of repeated NIR irradiation regimen was studied in 7 groups of A431 tumor

dx.doi.org/10.1021/bc200648m | *Bioconjugate Chem.* 2012, 23, 604−609

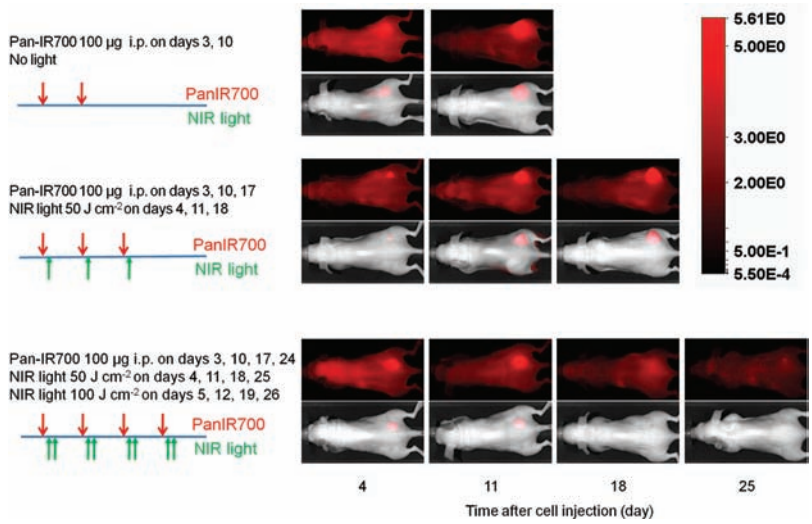


Figure 3. Monitoring accumulation of Pan−IR700 into tumors using NIR fluorescence imaging. Monitoring PIT with Pan−IR700 fluorescence. Images were obtained 1 day after Pan−IR700 injection just before NIR light irradiation. Tumor growth or regression in response to Pan−IR700 mediated PIT was observable with IR700 fluorescence.

bearing mice (n = 10 mice in each group). All treated tumors were less than 500 mm^3 in accordance with our institution's animal care and use guidelines. After 100 μg of Pan−IR700 injection, which was administered every week for up to 4 weeks, A431 tumors were treated with or without NIR light on day 1 (50 J cm^{-2}), day 2 (100 J cm^{-2}), or both days. Tumor volume was significantly reduced in A431 tumors treated with Pan−IR700 and NIR light compared with untreated control mice. Mice injected with panitumumab but not exposed to NIR light showed no significant treatment effect (each PIT group; P < 0.001 vs untreated control mice analyzed at 9 days after first Pan−IR700 injection). Similarly, mice exposed to NIR light alone had no treatment effect. However, multiple NIR light irradiations following Pan−IR700 led to more effective tumor reduction (Figure 2A). In survival analysis, multiple Pan−IR700 injection followed by multiple NIR light irradiation contributed to prolonged survival in the PIT treatment groups. Notably, 80% of A431 tumors were eradicated, and the mice survived for 120 days in the mice treated with Pan−IR700 injection followed by NIR light irradiation on day 1 (50 J cm^{-2}) and day 2 (100 J cm^{-2}) (Figure 2B) vs control mice that required euthanasia by 24 days.

Detection and Monitoring in Response to PIT with NIR Fluorescence. We have shown previously that IR700 fluorescence can be used to monitor Pan−IR700 in tumors. One day after Pan−IR700 injection, intratumoral fluorescence was detectable. Mice receiving 100 μg of Pan−IR700 but no NIR light served as controls in this case. In the group not receiving NIR light, increased IR700 fluorescence was observed; however, reductions in fluorescence were observed in tumors receiving Pan−IR700 and NIR light. When injected Pan−IR700 for the next PIT and IR700 fluorescence was down to the background level at the tumor site, no tumor recurrence was observed; however, when IR700 fluorescence was higher than the background level, regrowth was observed within 8 days (Figure 3).

Histological Changes and Microdistribution of Pan−IR700. Few fluorescent cells in diffuse necrotic cells with microhemorrhage are shown 1 h after PIT (Figure 4, right upper images). Scattered fluorescent microclusters of surviving tumor cells are shown 1 d after PIT (Figure 4, left lower images). All cancer cells in clusters are fluoresced that indicate Pan−IR700 homogeneously distributed in surviving and proliferating cancer cells. This result supports the effective PIT at the second exposure of NIR light.

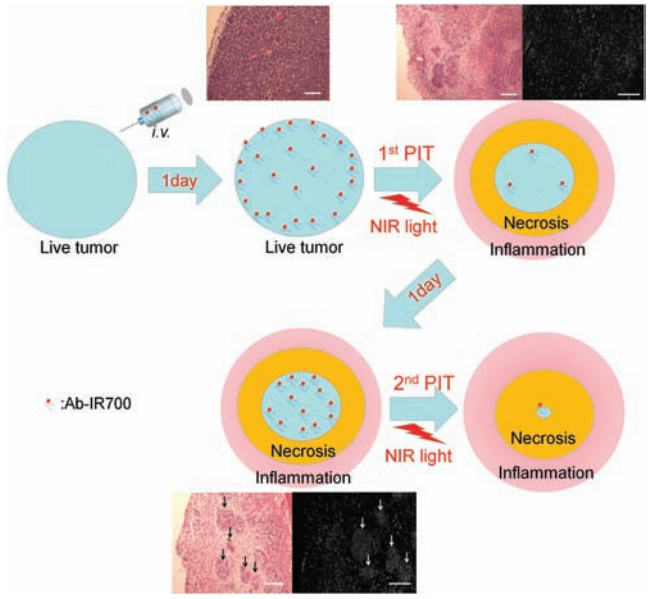


Figure 4. Serial histology pictures and microdistribution of IR700 fluorescence in the tumor 1 h and 1 d after first PIT are shown together with a schema for explaining the effectiveness of repeated PIT. Few fluorescent cells in diffuse necrotic cells with micro-hemorrhages are shown 1 h after PIT (right upper images). Scattered fluorescent microclusters of surviving tumor cells are shown 1 d after PIT (left lower images). All cancer cells in clusters (black arrows) have fluoresced (white arrows) indicating Pan−IR700 homogeneously distributed in surviving and proliferating cancer cells.

DISCUSSION

We have recently reported that HER1 target-specific cell killing was achieved in response to a single dose of Pan−IR700 and NIR light both in vitro and in vivo.[8] Pan−IR700 localized specifically in HER1-positive A431 tumors in vivo, and tumor

dx.doi.org/10.1021/bc200648m | Bioconjugate Chem. 2012, 23, 604−609

shrinkage was confirmed after only one dose of Pan−IR700 (300 μg) followed by one exposure to NIR light irradiation (30 J cm^{-2}). However, in that study, tumor regrowth was eventually seen. In the current study, we demonstrate that repeated doses of smaller amounts of Pan−IR700 and repeated exposures of NIR light resulted in complete responses in A431 tumors. This was in marked contrast to controls that received Pan−IR700 but no light or light exposure without Pan−IR700. Thus, this study suggests that complete pathologic responses in solid tumors are possible with PIT by using fractionated doses of the mAb−IR700 conjugate and repeated light exposures of NIR.

Preferable distribution of therapeutic mAb in the tumor is required for the effective target-specific tumor cell killing; however, generally mAb distribution is inhomogeneous in most tumors, especially in peripheral localization where xenografted tumors receive good blood supply, leading to require multiple high-dose mAb administration.[8,10−12] Similar to unlabeled mAb, efficacy of mAb−IR700 mediated PIT is partly determined with mAb−IR700 microdistribution in the targeted tumor.

We used a similar cumulative dose of Pan−IR700 but fractionated into four doses to cover four weeks to safely perform PIT with more effective results (Figure 2A,B).[8] Since the maximum concentration of IR700 in A431 tumors became lower using repeated 100 μg doses vs a single dose of 300 μg (Figure 1A), prudent increasing NIR light exposure from 30 J cm^{-2} to 50 J cm^{-2} should be considered. Additionally, lowering the dose leads to distributing the mAb−IR700 conjugate peripherally within the xenografted tumor. Therefore, PIT with 100 μg of Pan−IR700 showed reduced cell killing in the center of the tumor as shown in this study.[8,13] To overcome this problem, the Pan−IR700 conjugate was allowed to reaccumulate in the treated tumor 1 day after immediate killing of most peripheral cancer cells near tumor vasculatures with the first NIR light irradiation, because massive crashing of cells near the tumor vessels facilitated delivery of mAb−IR700 conjugate far away from the tumor vessel into the center part of tumor. Since NIR light irradiation does not have a dose limitation, a repeated NIR light exposure at a day after the first therapy successfully facilitated killing in the central part of the tumor (Figure 1B). Therefore, additional NIR irradiation 1 day after the first therapy (2 days after Pan−IR700 administration) greatly enhanced the therapeutic effect of PIT (Figure 4). With this therapeutic regimen, by fractionating the Pan−IR700 injections followed by multiple NIR irradiation, complete tumor eradication was observed in more than half the treated mice, while most of the mice treated with a one-shot irradiation regimen of PIT died due to tumor regrowth (Figure 1D).

The Pan−IR700 conjugate can also be used to monitor the effects of PIT due to the fluorescence emitted by the IR700 (Figure 3). However, the fluorescence of IR700 is relatively weak and is best for shallow targets, whereas the PIT effects can extend several centimeters beneath the skin surface. Nevertheless, for endoscopic or surgical uses of PIT the fluorescent features of mAb−IR700 can be considered an advantage. The next step of this study is to compare this method with recently developed approaches of the photodynamic therapy[14,15] by using orthotopic tumor models, which will be superior models for human cancer,[16] employing fluorescence protein as an internal tumor marker.[17]

In conclusion, by fractionating the administration of Pan−IR700 and applying repeated NIR light irradiation, highly effective tumor treatments based on the effective tumor redistribution of Pan−IR700, including complete pathologic responses, were achieved, with no apparent side effects in a majority of A431 bearing mice. Thus, PIT using mAb−IR700 conjugates is a promising theranostic method for highly selective cancer treatment and monitoring.

AUTHOR INFORMATION

Corresponding Author

*Phone: 301-451-4220; Fax: 301-402-3191; E-mail: kobayash@mail.nih.gov.

Grant Support

This research was supported by the Intramural Research Program of the National Institutes of Health, National Cancer Institute, Center for Cancer Research.

Notes

The authors declare no competing financial interest.

REFERENCES

(1) Weiner, L. M., Surana, R., and Wang, S. (2010) Monoclonal antibodies: versatile platforms for cancer immunotherapy. *Nat. Rev. Immunol. 10*, 317−327.

(2) Waldmann, T. A. (2003) Immunotherapy: past, present and future. *Nat Med 9*, 269−277.

(3) Reichert, J. M., Rosensweig, C. J., Faden, L. B., and Dewitz, M. C. (2005) Monoclonal antibody successes in the clinic. *Nat. Biotechnol. 23*, 1073−1078.

(4) Clynes, R. A., Towers, T. L., Presta, L. G., and Ravetch, J. V. (2000) Inhibitory Fc receptors modulate in vivo cytotoxicity against tumor targets. *Nat. Med. 6*, 443−446.

(5) Reff, M. E., Carner, K., Chambers, K. S., Chinn, P. C., Leonard, J. E., Raab, R., Newman, R. A., Hanna, N., and Anderson, D. R. (1994) Depletion of B cells in vivo by a chimeric mouse human monoclonal antibody to CD20. *Blood 83*, 435−445.

(6) Pastan, I., Hassan, R., Fitzgerald, D. J., and Kreitman, R. J. (2006) Immunotoxin therapy of cancer. *Nat. Rev. Cancer 6*, 559−565.

(7) Goldenberg, D. M., Sharkey, R. M., Paganelli, G., Barbet, J., and Chatal, J. F. (2006) Antibody pretargeting advances cancer radioimmunodetection and radioimmunotherapy. *J. Clin. Oncol. 24*, 823−834.

(8) Mitsunaga, M., Ogawa, M., Kosaka, N., Rosenblum, L. T., Choyke, P. L., and Kobayashi, H. (2011) Cancer cell-selective in vivo near infrared photoimmunotherapy targeting specific membrane molecules. *Nat. Med. 17*, 1685−1691.

(9) Euhus, D. M., Hudd, C., LaRegina, M. C., and Johnson, F. E. (1986) Tumor measurement in the nude mouse. *J. Surg. Oncol. 31*, 229−234.

(10) Kosaka, N., Ogawa, M., Paik, D. S., Paik, C. H., Choyke, P. L., and Kobayashi, H. (2010) Microdistribution of fluorescently-labeled monoclonal antibody in a peritoneal dissemination model of ovarian cancer. *Proc. SPIE 7576*, 7576041−7576049.

(11) von Mehren, M., Adams, G. P., and Weiner, L. M. (2003) Monoclonal antibody therapy for cancer. *Annu. Rev. Med. 54*, 343−369.

(12) Jain, R. K., and Baxter, L. T. (1988) Mechanisms of heterogeneous distribution of monoclonal antibodies and other macromolecules in tumors: significance of elevated interstitial pressure. *Cancer Res. 48*, 7022−7032.

(13) Kosaka, N., Ogawa, M., Paik, D. S., Paik, C. H., Choyke, P. L., and Kobayashi, H. (2010) Semiquantitative assessment of the microdistribution of fluorescence-labeled monoclonal antibody in small peritoneal disseminations of ovarian cancer. *Cancer Sci. 101*, 820−825.

(14) Kimura, H., Lee, C., Hayashi, K., Yamauchi, K., Yamamoto, N., Tsuchiya, H., Tomita, K., Bouvet, M., and Hoffman, R. M. (2010) UV light killing efficacy of fluorescent protein-expressing cancer cells in vitro and in vivo. *J. Cell Biochem. 110*, 1439−1446.

(15) Tsai, M. H., Aki, R., Amoh, Y., Hoffman, R. M., Katsuoka, K., Kimura, H., Lee, C., and Chang, C. H. (2010) GFP-fluorescence-guided UVC irradiation inhibits melanoma growth and angiogenesis in nude mice. *Anticancer Res. 30*, 3291−3294.
(16) Hoffman, R. M. (1999) Orthotopic metastatic mouse models for anticancer drug discovery and evaluation: a bridge to the clinic. *Invest. New Drugs 17*, 343−359.
(17) Hoffman, R. M. (2005) The multiple uses of fluorescent proteins to visualize cancer in vivo. *Nat. Rev. Cancer 5*, 796−806.

■ NOTE ADDED AFTER ASAP PUBLICATION

This paper was published on the Web on February 27, 2012, with an error in an author name. The corrected version was reposted on March 21, 2012.

Bioconjugate Chemistry

Article

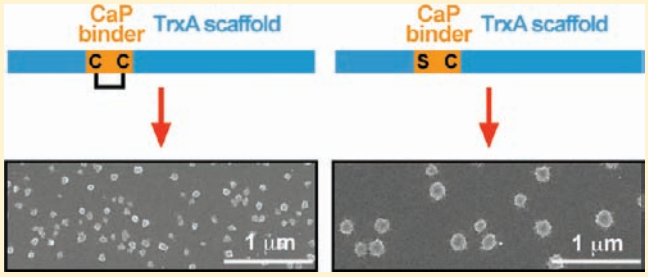
pubs.acs.org/bc

Biomineralization and Size Control of Stable Calcium Phosphate Core−Protein Shell Nanoparticles: Potential for Vaccine Applications

David Chiu,[†] Weibin Zhou,[†] Sathana Kitayaporn,[†] Daniel T. Schwartz,[†] Kaja Murali-Krishna,[‡,∥] Terrance J. Kavanagh,[§] and François Baneyx*[,†]

[†]Department of Chemical Engineering, [‡]Department of Immunology, and [§]Department of Environmental and Occupational Health Sciences, University of Washington, Seattle, Washington 98195, United States

ABSTRACT: Calcium phosphate (CaP) polymorphs are nontoxic, biocompatible and hold promise in applications ranging from hard tissue regeneration to drug delivery and vaccine design. Yet, simple and robust routes for the synthesis of protein-coated CaP nanoparticles in the sub-100 nm size range remain elusive. Here, we used cell surface display to identify disulfide-constrained CaP binding peptides that, when inserted within the active site loop of *Escherichia coli* thioredoxin 1 (TrxA), readily and reproducibly drive the production of nanoparticles that are 50−70 nm in hydrodynamic diameter and consist of an approximately 25 nm amorphous calcium phosphate (ACP) core stabilized by the protein shell. Like bone and enamel proteins implicated in biological apatite formation, peptides supporting nanoparticle production were acidic. They also required presentation in a loop for high-affinity ACP binding as elimination of the disulfide bridge caused a nearly 3-fold increase in hydrodynamic diameters. When compared to a commercial aluminum phosphate adjuvant, the small core−shell assemblies led to a 3-fold increase in mice anti-TrxA titers 3 weeks postinjection, suggesting that they might be useful vehicles for adjuvanted antigen delivery to dendritic cells.



INTRODUCTION

Because they are highly biocompatible and nontoxic, calcium phosphate (CaP) nanoparticles have been explored in applications ranging from hard tissue regeneration to the delivery of small molecules, oligonucleotides, and proteins.[1,2] CaP also holds promise as a vaccine adjuvant[3−5] where nanoscale formulations have been shown to be more effective than micrometer-sized particles at targeting lymph node dendritic cells (DCs) for enhancing immunity.[6,7] Unfortunately, unstabilized CaP colloids have a strong tendency to aggregate, and their controlled synthesis is challenging because even small variations in pH, temperature, calcium:phosphate ratio, or precipitation technique can significantly affect particle stoichiometry, crystallinity, morphology, and size.[8−10] A wide variety of CaP synthesis schemes have been developed, ranging from microemulsion technologies[11−13] to the use of citrate,[14] surfactants,[15] porphyrin,[16] and oligonucleotides[17] as capping agents. However, reproducible production of stable CaP colloids in the sub-100 nm range remains difficult, and their controlled conjugation with peptides or proteins by any mechanism other than adsorption requires multiple chemical derivatization and purification steps.

In vertebrate bones, CaP is present in the form of hydroxyapatite [HA; $Ca_{10}(PO_4)_6(OH)_2$] nanocrystals that are 30−50 nm long, 20−25 nm wide, and 1.5−4 nm thick.[18] These nanoplates are embedded in a composite of collagen fibrils and noncollagenous proteins that exhibit Ca^{2+} and hydroxyapatite binding properties by virtue of being phosphorylated and rich in negatively charged (acidic) residues.[19] Several noncollagenous phosphoproteins have been shown to promote HA nucleation and to control the kinetics of crystal growth,[19,20] suggesting that they may be good candidates for the biomimetic mineralization of CaP nanoparticles. However, the same proteins can also inhibit mineralization, and the mechanisms that are at play for either process remain unclear and controversial.[19,20]

Solid binding peptides (SBPs) isolated by phage or cell surface display[21] present an alternative to naturally occurring proteins for the biomineralization of technologically valuable materials.[22] In this molecular biomimetic approach to material synthesis, SBPs are used either in isolation or as part of a larger protein or organism to nucleate, organize, and assemble inorganic structures with nanoscale control of composition and architecture.[23,24] The approach is powerful. For example, we have shown that "designer proteins" incorporating SBPs can be used to nucleate and cap Cu_2O nanoparticles under thermodynamically unfavorable conditions,[25] organize these nanoparticles onto DNA guides,[25] control the size and shape of silver crystals,[26] and mineralize multicolored ZnS quantum dots whose protein shell is active for antibody binding.[27,28]

Here, we describe disulfide-constrained CaP binding peptides that, when inserted within the active site loop of *Escherichia coli*

Received: December 2, 2011
Revised: January 19, 2012
Published: January 22, 2012

 © 2012 American Chemical Society

Table 1. Physicochemical Characteristics of CaP Binding Peptides Isolated by Cell Surface Display and Tested for Mineralization Ability (top) and Comparison to Hydroxyapatite Binding Peptides Identified by Phage Display (bottom)

Name	Sequence[a]	M_r (Da)	pI	Hydropathy[b]	Reference
PN21	*CGP*LGMRSESAIGKE*GPC*	1277.4	6.14	-0.483	This work
PN38	*CGP*EDIDAVSVGEVQ*GPC*	1260.3	3.43	0.017	This work
PN52	*CGP*PAQAHPWPHRYG*GPC*	1416.5	9.18	-1.517	This work
PA01[c]	*CGP*VRRLMGGSWKRV*GPC*	1444.7	12.3	-0.483	This work
PA44	*CGP*KDVVVGVPGGQD*GPC*	1169.3	4.21	-0.033	This work
PA93	*CGP*GHLSPRFRGGRG*GPC*	1296.4	12.3	-1.175	This work
HABP1	*C*MLPHHGA*C*	761.9	6.69	-0.129	45
CLP12	NPYHPTIPQSVH	1389.5	6.92	-1.025	46
HA-1	SVSVGMKPSPRP	1214.4	11.0	-0.475	51
S	STLPIPHEFSRE	1412.5	5.38	-0.758	52
V	VTKHLNQISQSY	1417.5	8.57	-0.725	52

[a]Amino acids are color-coded as follows: hydrophobic, gray; acidic, red; basic, cyan; hydroxyl side chain, olive; amide side chain, teal. Invariant tripeptides flanking the dodecamers are italicized. [b]Positive hydropathy scores denote hydrophobic sequences, while negative scores denote hydrophilic ones. The higher and lower the score, the more hydrophobic and hydrophilic, respectively, the sequence is. [c]The PA01 sequence was isolated more than 50 times on both annealed and nonannealed samples.

thioredoxin 1 (TrxA), reproducibly mineralize nanoparticles that are 50−70 nm in hydrodynamic diameter and consist of an ≈25 nm amorphous calcium phosphate (ACP) core stabilized by a protein shell. We further show that disruption of the disulfide bond causes an increase of ∼3-fold in the diameter of mineralized particles, indicating that the conformation of an SBP can have a profound influence on the mineralization process. Finally, we provide preliminary evidence that the small CaP core−protein shell nanoparticles might be effective vehicles for delivery of adjuvanted antigen to DCs.

EXPERIMENTAL PROCEDURES

Electrodeposition of Calcium Phosphate on Titanium. CaP chips were synthesized using a modification of published protocols.[29,30] Briefly, calcium phosphate was electrodeposited with a constant current of −2.5 mA/cm^2 for 20 min at 60 °C on a 0.127 mm thick titanium foil [>99.9% (Sigma-Aldrich)] from an electrolyte consisting of 100 mM $Ca(NO_3)_2$ and 50 mM $NH_4H_2PO_4$. All experiments were conducted in a quiescent 150 mL cell using a platinum wire for a counter-electrode. Half of the samples were annealed by being heated for 8 h at 450 °C in an oven while the rest were dried with N_2.

Selection of CaP Binding Peptides. The FliTrx cell surface display system (Invitrogen) was used to select disulfide-constrained CaP binding dodecapeptides through five rounds of biopanning as previously described.[28,31] Independent selections were conducted on ∼1 cm^2 annealed and non-annealed substrates. Randomly selected colonies (78 for annealed samples and 66 for nonannealed samples) were sequenced using the Big Dye Terminator sequencing kit (Applied Biosystems) using either 5′-ATTCACCTGACTGAC-GAC-3′ as a forward primer or 5′-CCCTGATATTCGT-CAGCG-3′ as a reverse primer. Six clones lacking internal cysteine residues and exhibiting a broad range of hydrophobicities and isoelectric points (Table 1) were selected for further studies.

Construction, Expression, and Purification of CaP Binding Proteins. Derivatives of *E. coli* thioredoxin 1 (TrxA) displaying disulfide-constrained CaP binding peptides in place of the Cys-Gly-Pro-Cys active site sequence of native TrxA were constructed as previously described.[28] Briefly, pFliTrx derivatives encoding the target dodecapeptides were digested with *Apa*LI and *Rsr*II, and the purified 220 bp fragment was ligated with the backbone of pT-Trx[32] that had been digested with the same enzymes. The resulting plasmids were named pTrxA-PA*x* or pTrxA-PN*x*, where PA and PN refer to sequences selected on annealed (PA) and nonannealed (PN) CaP chips, respectively, and *x* denotes the numerical identifier of the CaP binding peptide. The Cys[32] residue of TrxA::PA44 and TrxA::PN21 was converted to a serine by site-directed mutagenesis of the corresponding plasmids using the QuikChange (Stratagene) kit and primers 5′-CTGGGCA-GAGTGGTCCGGTCCGAAAGATG-3′ and 5′-CATCTTTCGGACCGGACCACTCTGCCCAG-3′. The integrity of all constructs was verified by DNA sequencing.

BL21(DE3) cells harboring the plasmids described above were grown to midexponential phase (A_{600} ≈ 0.5) in 500 mL of LB medium supplemented with 34 μg/mL chloramphenicol. Protein synthesis was initiated by addition of 0.4 mM isopropyl thiogalactopyranoside (IPTG), and cultures were immediately transferred to a water bath held at 25 °C. After being incubated at this temperature for 4 h, cells were sedimented by centrifugation at 3000*g* for 15 min, resuspended in 20 mM Tris-HCl (pH 7.5), 2.5 mM EDTA, and 1 mM PMSF to a concentration of 100 A_{600} units/mL, and disrupted by three cycles of homogenization on a French pressure cell operated at 10000 psi. Insoluble material was removed by centrifugation at 14000*g* for 15 min. Aliquots of clarified extracts (≈15 mL) were transferred to 30 mL Corex tubes and held in an 80 °C water bath for 10 min to precipitate the majority of host proteins. Aggregated fractions were removed by centrifugation at 14000*g* for 10 min. Supernatants were diluted with 60 mL of buffer A [20 mM Tris-HCl (pH 7.5)] and loaded onto a DE52 (Whatman) anion exchange column (7.0 cm length and 1.0 cm diameter) equilibrated in buffer A. The column was developed in the same buffer at a rate of 1 mL/min for 60 min to wash out contaminants, and purified designer proteins were recovered in the 25−100 mM NaCl fractions of a 60 min gradient elution (0 to 500 mM NaCl in buffer A). Proteins were dialyzed against ddH_2O overnight and stored at −80 °C. Purity was determined on overloaded gels using a modified sodium dodecyl sulfate−polyacrylamide gel electrophoresis protocol.[33]

Biomineralization of CaP Nanoparticles. For biomineralization experiments, a 1.8 mL solution containing 5 μM

dx.doi.org/10.1021/bc200654v | *Bioconjugate Chem.* 2012, 23, 610−617

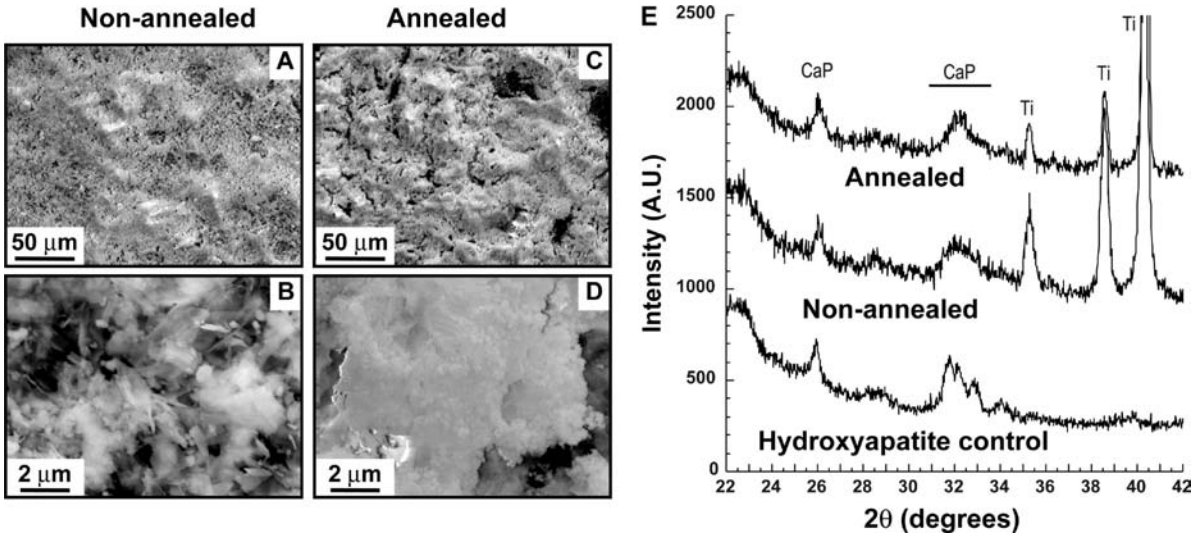


Figure 1. Characterization of CaP chips. Nonannelaed (A and B) and annealed (C and D) samples were imaged by SEM at two different magnifications. Panel E shows XRD spectra for both samples. Hydroxyapatite powder was used as a control. Reflections corresponding to CaP phases and the underlying Ti substrate are labeled.

protein in a 1 mM $(NH_4)_2HPO_4/NH_4H_2PO_4$ mixture (pH 7.5) was placed in a 15 mL, round-bottom, disposable borosilicate tube (VWR) that had been cleaned with ddH_2O, acetic acid, acetone, and ultrapure ddH_2O, in sequence, and fitted with a 1 cm diameter stir bar. The mixture was held at 4 °C for 30 min at a stirring rate of 6 (Corning PC-310), after which 200 μL of a 16.7 mM solution of $Ca(NO_3)_2$ was fed in 8 μL increments ~5 s apart using a 25G delivery needle or Pipetman (Eppendorf P20). The mixture was allowed to age for 2 h at 4 °C and held at room temperature for 12−24 h before being characterized.

Analytical Techniques. Hydrodynamic diameters were measured by dynamic light scattering (DLS) on a Nano-ZS Zetasizer (Malvern). For transmission electron microscopy (TEM) imaging, 5 μL of the solution was deposited on a carbon-coated copper TEM grid and allowed to air-dry. Low- and high-resolution TEM images and selected area electron diffraction (SAED) patterns with an aperture size of 40 μm were collected on a FEI Tecnai G2 F20 S/TEM instrument operated at an accelerating voltage of 200 kV. For scanning electron microscopy (SEM) imaging, samples (≈100 μL) were allowed to contact clean, ≈1 cm^2 silicon wafers for 30 min, and excess fluid was removed by wicking with a laboratory tissue. The substrate was rinsed with ddH_2O to remove salts, air-dried, and coated with a 7−10 nm Au/Pd film. Micrographs were taken with a FEI Sirion scanning electron microscope at an acceleration voltage of 10 keV. Energy dispersive X-ray spectroscopy (EDS) was used to find the average ratio of calcium, phosphorus, and oxygen in the substrate. X-ray diffraction (XRD) measurements were taken on a Bruker D8 Focus instrument using Cu Kα radiation. Data were collected for 2θ values ranging from 22° to 42° with 0.02° steps.

Animal Studies. The adjuvancy effect of biofabricated CaP nanoparticles was compared to that of AdjuPhos (Brenntag Biosector), a commercial aluminum phosphate adjuvant consisting of 0.49% (w/w) aluminum and 1.52% phosphate. CaP nanoparticles were synthesized using TrxA::PA44 as described in Biomineralization of CaP Nanoparticles except that all solutions were made in endotoxin-free water (MD Bio) and all glassware was passivated by being rinsed in tap water, acetic acid, ddH_2O, acetone, and ultrapure ddH_2O before being autoclaved at 120 °C for 30 min. Pyrogens were inactivated by baking the glassware at 250 °C for 30 min. After being aged at 4 °C for 2 h, samples were filtered through a 0.22 μm cellulose acetate filter and split into two halves, one of which was used for DLS characterization and protein assays and the other for immunization in mice. The final protein concentration was found to be 3.2 μM by a Bradford assay because of losses incurred during filtration. However, the size of the particles remained in the 70 nm range. As a control, a preparation of 3.2 μM TrxA::PA44 in a 1 mM $(NH_4)_2HPO_4/NH_4H_2PO_4$ mixture (pH 7.5) was filtered through a 0.22 μm membrane and supplemented with 1.65 mM AdjuPhos (an aluminum concentration identical to that of the calcium in the nanoparticles). Groups of five C57BL/6 mice (6−10 weeks old and weighing 20−30 g) were injected subcutaneously with 4 × 50 μL of the preparations described above into the four foot pads for a total antigen load of 8 μg. No inflammation was observed at injection sites, and animals were bled at 9 and 21 days. Anti-TrxA IgG titers were measured in serum with an enzyme-linked immunosorbent assay (ELISA) essentially as described previously[34] using plates coated with wild-type TrxA and validated for linearity with mouse anti-TrxA rabbit monoclonal antibodies (Invitrogen, clone C63C6).

RESULTS

Selection of Calcium Phosphate Binding Peptides. Among the various inorganic compounds that hold promise for DC maturation, we selected calcium phosphate (CaP) because it is cheap, biocompatible, biodegradable, and likely to be safe. CaP adjuvants are typically synthesized by uncontrolled precipitation schemes, yielding a broad distribution of agglomerates that range in size from 300 nm to 4 μm and have calcium:phosphate (Ca:P) molar ratios ranging from 1.35 to 1.83.[35] In one of the most detailed analyses to date, Jiang and co-workers[36] reported that a commercial adjuvant manufactured by the former Reheis Inc. consisted of calcium-deficient hydroxyapatite with a Ca:P ratio of 1.39 and contained needlelike particles and irregularly shaped plates. However, others[37] have found commercial adjuvants to have a Ca:P ratio

dx.doi.org/10.1021/bc200654v | Bioconjugate Chem. 2012, 23, 610−617

of 1.5, a molecular composition closer to that of tricalcium phosphate [$Ca_3(PO_4)_2$].

Our first task was to generate CaP "chips" that were chemically and morphologically representative of commercial CaP adjuvants and compatible with the FliTrx cell surface display system that we have previously used to identify SBPs.[28,31] To this end, we electrodeposited ≈10 μm thick calcium phosphate films on titanium foil from a $Ca(NO_3)_2$/$NH_4H_2PO_4$ electrolyte (Electrodeposition of Calcium Phosphate on Titanium). Because high temperatures drive off coordinated water from inorganic materials, half of the samples were annealed by heating at 450 °C for 8 h, while the rest were dried under a nitrogen stream and characterized as deposited.

SEM imaging revealed that the annealed samples (Figure 1C,D) consisted primarily of spherical nodules, while nonannealed chips also contained crystalline platelets and needles (Figure 1A,B). The Ca:P ratio was found to be 1.44 for annealed samples and 1.32 for nonannealed samples by energy dispersive X-ray spectroscopy (EDS) analysis in the scanning electron microscope. In addition, reflections characteristic of calcium phosphate-containing phases were identified in the 26° and 31−34° 2θ regions of both samples by X-ray diffraction [XRD (Figure 1E)]. Thus, our electrodeposited CaP chips are compositionally and morphologically similar to typical calcium phosphate adjuvants.[35−37]

In the *E. coli* FliTrx cell surface display system,[38] random dodecapeptides are displayed as disulfide-constrained loops within the active site of *E. coli* thioredoxin 1 (TrxA), which is itself inserted within the major flagellar protein FliC. We used FliTrx biopanning to isolate CaP binding peptides on both annealed and nonannealed substrates. Because there are multiple solutions to the problem of inorganic binding,[21] sequences obtained after biopanning did not converge toward a consensus. We arbitrarily chose a subset of six peptides exhibiting a broad range of pIs and hydrophilicities for further work with the expectation that some would function as efficient CaP mineralizers. Three of these (PN series) were isolated using nonannealed chips, while the others (PA series) were selected on annealed substrates (Table 1).

Protein-Aided Mineralization of CaP Nanoparticles. An accurate comparison of the mineralizing ability of these CaP binding peptides would ideally require that they exhibit the same solubility (which is generally not true of short hydrophobic peptides such as those listed in Table 1) and that they be displayed within the same structural context. To address this issue, we constructed a series of *E. coli* TrxA derivatives in which the authentic cysteine-glycine-proline-cysteine (CGPC) active site sequence was replaced with one of the CaP binding dodecamers in Table 1 flanked by invariant Cys-Gly-Pro (CGP) and Gly-Pro-Cys (GPC) tripeptides. The resulting proteins, which are monomeric and range in molecular mass from 12.87 to 13.14 kDa, were expressed at ~35% of the level of the total cellular protein and in a mostly soluble form using T7-driven transcription (Figure 2, lanes 1−3). Because TrxA exhibits high thermostability,[39] it was possible to achieve 80% purification by heating crude cell extracts at 80 °C for 10 min and removing aggregated host proteins by centrifugation (Figure 2, lanes 4 and 5). High-purity material (≈99%) could then be recovered in a single ion exchange chromatography step (Figure 2, lane 6).

Because calcium phosphate does not exhibit useful optical absorption or emission properties, we screened CaP binding TrxA derivatives for their ability to mediate nanoparticle

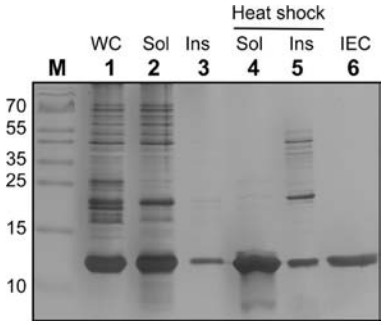


Figure 2. Purification of TrxA::PA44 by heat shock and ion exchange chromatography (IEC): lane M, markers; lane WC, whole cells; lanes Sol and Ins, soluble and insoluble fractions, respectively, before and after incubation at 80 °C for 10 min; lane IEC, ion exchange chromatography purification of heat-shocked soluble fractions. The positions of the molecular mass markers (lane M) are indicated in kilodaltons on the left of the gel, which was stained with silver to reveal purified protein and contaminants.

formation using dynamic light scattering (DLS), a technique that provides information about the hydrodynamic diameter of colloids in suspension. We dedicated significant effort to optimizing the synthesis step and tested different calcium and phosphate salts, pH values, protein concentrations, mixing regimes, temperatures, and aging times, eventually settling on the protocol described in Biomineralization of CaP Nanoparticles. Experiments conducted in the absence of protein or with wild-type TrxA gave rise to the precipitation of large polydisperse species (Figure 4A,B). However, among the six proteins tested, three (TrxA::PN21, TrxA::PN38, and TrxA::PA44) proved suitable for the reproducible production of sub-100 nm CaP particles. Of note, TrxA::PA01 was ineffective in mediating nanoparticle formation in spite of the fact that the PA01 sequence was isolated multiple times on both annealed and nonannealed chips. Thus, there is no correlation between promiscuous binding and nanoparticle synthesis ability.

Hydrodynamic diameters determined by DLS were 70 ± 20 nm in the case of TrxA::PN21 and TrxA::PN38 and 60 ± 20 nm in the case of TrxA::PA44. The colloids were clear and stable for at least 3 weeks when stored at 4 °C, indicating the presence of a capping protein shell. TEM imaging of TrxA::PA44-mineralized samples (Figure 3A,B) confirmed the presence of roughly spherical species that had an average diameter of 25 ± 5 nm (n = 110). The discrepancy with diameters obtained by DLS is likely due to the difficulty in obtaining good contrast when imaging CaP by TEM and to the fact that hydrated particles are bounded by a protein shell that adds to their size. Based on the lack of observable particle faceting and the fact that selected area electron diffraction (SAED) patterns were diffuse and lacked rings or spots (Figure 3C), it is likely that the templated material is amorphous calcium phosphate [ACP; $Ca_9(PO_4)_6$], a noncrystalline phase of calcium phosphate that is the initial solid precipitating from supersaturated solutions.[40]

Controlling Particle Size: Influence of the Disulfide Bond. CaP binding sequences are displayed within a disulfide-bonded loop both during the initial FliTrx screen and following transfer to the soluble TrxA scaffold. This conformational context has been shown to influence the adhesion of certain solid binding peptides to their cognate inorganics,[41−44] but how it impacts materialization remains unclear. To explore this issue,

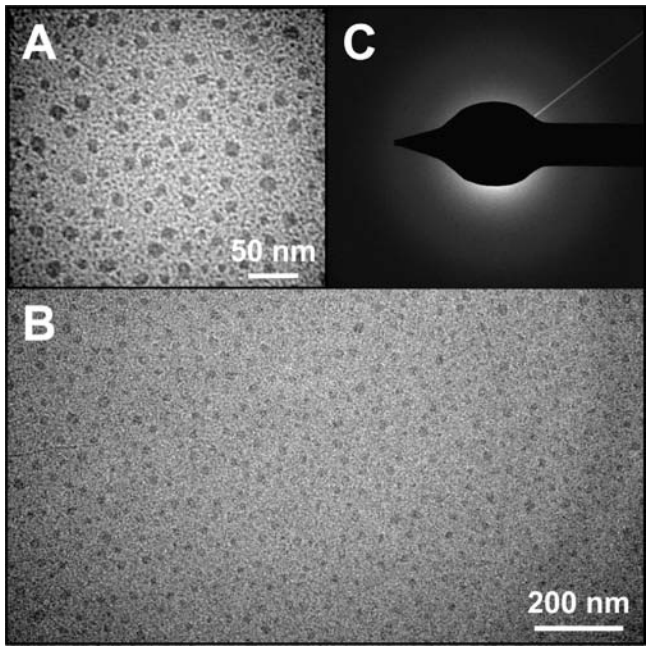


Figure 3. TEM analysis of nanoparticles produced in the presence of TrxA::PA44. High-resolution (A) and low-resolution (B) TEM images show the characteristic size and polydispersity of CaP nanoparticles obtained under our experimental conditions. (C) Selected area electron diffraction (SAED) patterns were diffuse with no distinguishable spots or rings, suggesting that the mineral is amorphous calcium phosphate (ACP).

we use site-directed mutagenesis to convert the first cysteine residue of TrxA::PA44 to serine and conducted side by side mineralization experiments with no protein, wild-type TrxA, TrxA::PA44, and the TrxA::PA44-C32S mutant. Samples were transferred to silicon oxide substrates, coated with a 7−10 nm layer of gold−palladium, and imaged by SEM.

In agreement with DLS data and consistent with the low-solubility product of calcium phosphate, precipitation in the absence of additive gave rise to heterogeneous populations enriched in micrometer size particles (Figure 4A) while mineralization in the presence of wild-type TrxA led to the formation of aggregates consisting of interconnected nodules extending over large dimensions (Figure 4B). As expected from TEM imaging (Figure 3), and in sharp contrast with the results described above, samples prepared in the presence of TrxA::PA44 were populated by discrete and mostly spherical particles whose mean size (70 ± 15 nm; n = 44) was within the expected range when taking into account the thickness of the Au/Pd coating. Remarkably, altering the conformation of the PA44 peptide by elimination of the disulfide bond led to a net reduction in the number of particles and a concomitant 3-fold increase in average diameter as determined by analysis of SEM images (170 ± 30 nm; n = 55) and confirmed by DLS measurements (210 ± 50 nm). Similar results were obtained when the same cysteine to serine substitution was introduced into TrxA::PN21. We conclude that the conformational context plays an important role in determining the affinity and/or capping ability of several of our binders, a feature that can be exploited for manufacturing core−shell particles of different sizes.

Immunogenicity. Conjugates between nanoparticles and antigenic molecules hold potential for effective vaccination because of the fact that particles with diameters inferior to 100 nm drain to the lymph nodes where the probability of encountering immature DCs increases.[6,7] We therefore used TrxA::PA44 to synthesize CaP nanoparticles as described above, except that depyrogenated glassware and endotoxin-free water were used in all steps and that the solution was filtered through a sterile 0.2 μm membrane to eliminate large particulate contaminants. Groups of five C57BL/6 mice were vaccinated subcutaneously with the nanoparticle formulation (8 μg of total protein load) or with the same amount of soluble TrxA::PA44 supplemented with enough of the commercial adjuvant AdjuPhos so that the Al^{3+} concentration would equal that of Ca^{2+} in the nanoparticulate formulation. After 9 days, anti-TrxA titers were slightly higher in the serum of nanoparticle-treated animals than in control mice (Figure 5). However, whereas antibody levels remained constant over time in the control group, they were more than 3 times higher in mice vaccinated with the nanoparticle formulation 21 days postchallenge.

DISCUSSION

We have isolated disulfide-constrained dodecapeptides suitable for the synthesis of stable sub-100 nm nanoparticles consisting of an ACP core capped by a protein shell. The three sequences supporting nanoparticle formation [PA44, PN21, and PN38 (Table 1)] contained at least two and up to four negatively charged aspartates (D) and/or glutamates (E). Overrepresentation of these acidic amino acids was not unexpected because they have high affinity for Ca^{2+} ions and are found in high proportions and local densities in proteins involved in biological apatite formation.[18,19] In contrast, the three CaP binders that failed to yield stable nanoparticles (PN52, PA01, and PA93) all contained three or more basic residues and carried a net positive charge under our synthesis conditions (pH 7.5). Remarkably, hydroxyapatite binders identified by others through bacteriophage display (Table 1) were also enriched with histidines (H), arginines (R), and lysines (K). Two of these peptides were previously tested for CaP mineralization, albeit under different conditions than used in the present study. In a synthetic form, peptide HABP1 caused the formation of octacalcium phosphate [OCP; $Ca_8H_2(PO_4)_6{\cdot}5H_2O$] crystals that projected from a central core and were 400−800 nm in width and several micrometers in length.[45] On the other hand, synthetic CLP12 promoted the mineralization of micrometer-sized hydroxyapatite plates consisting of randomly oriented ≈20 nm nanocrystals.[46] It is therefore clear that acidic amino acids are not absolutely required for a peptide to either bind CaP or template the mineralization of thermodynamically stable calcium phosphate polymorphs (e.g., HA and OCP). However, our results suggest that aspartic acid and glutamic acid are important for capping and stabilizing nanoscale clusters of ACP, which should be the first CaP phase to precipitate out of solution.[40] Considering that ACP can convert to more energetically favorable phases such as OCP and biological apatites,[47] it is tempting to hypothesize that transient sequestration of ACP nanoparticles could be one of the mechanisms by which acidic bone and enamel-associated proteins regulate biomineralization. This process would be a useful complement to face-specific adsorption mechanisms[20] in preventing runaway crystal growth.

The phage and cell surface display libraries that are typically used to pan for solid binding peptides (SBPs) can yield linear or disulfide-bonded sequences.[21] In traditional applications (e.g., epitope mapping and identification of protein interaction

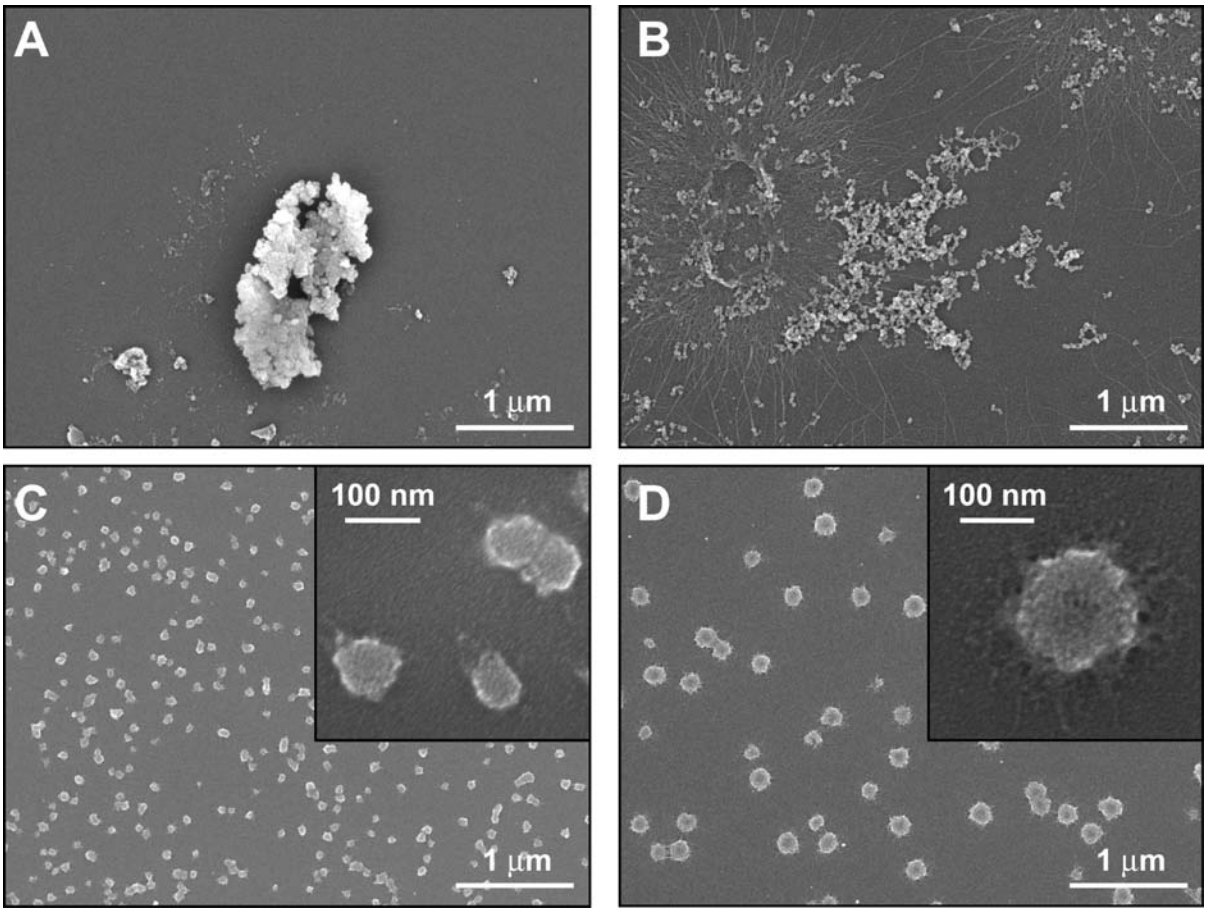


Figure 4. SEM imaging of CaP structures mineralized in the absence of protein (A) or in the presence of wild-type TrxA (B), TrxA::PA44 (C), and TrxA::PA44-C32S (D). The insets of panels C and D show higher-resolution images.

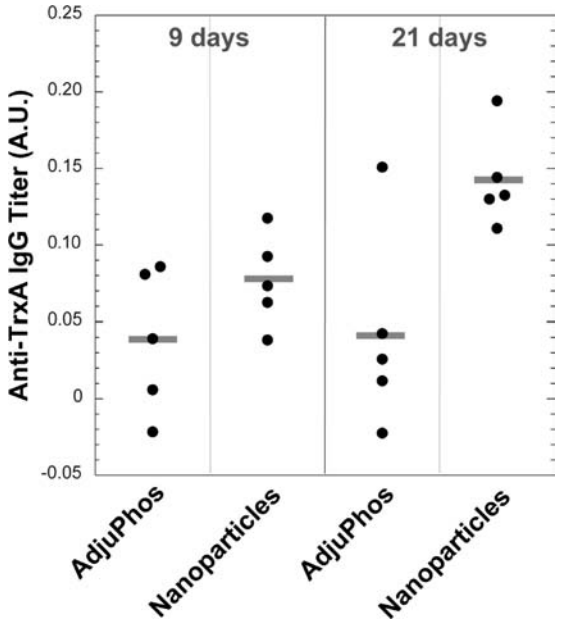


Figure 5. Anti-TrxA IgG titers in the serum of C57BL/6 mice measured by an ELISA 9 and 21 days postchallenge with TrxA::PA44 and alum or TrxA::PA44-stabilized nanoparticles. Titers for individual animals and cohort means (horizontal bars) are shown. Data are corrected for preimmune backgrounds. Confidence levels are 84.6% for 9 day data and 98.5% for 21 day data.

domains), disulfide-bonded peptides are generally more efficient binders because they exhibit a low degree of conformational freedom and make stable contacts with protein targets. In solid binding, however, the impact of conformational flexibility is less clear. For instance, we previously reported that presentation in a disulfide-constrained loop is critical for a cuprous oxide binding peptide to adhere to this material.[42] Similarly, a disulfide-bonded conformation increased the affinity of both a platinum- and gold-binding peptide for Pt and Au surfaces, respectively, relative to the corresponding linear conformations.[43,44] By contrast, presentation in a loop had no effect on the adsorption behavior of a different gold binder[43] and decreased the affinity of a TiO_2/SiO_2 binding peptide for these oxides.[41] PA44 and PN21 likely belong to the former category of solid binders because a lower affinity of TrxA::PA44-C32S (and TrxA::PN21-C32S) for CaP, paired with the rapid kinetics of ACP formation,[47] would manifest itself by the growth of larger particles before protein capping occurs. From a practical standpoint, the ability to manipulate particle size via a single mutation in the CaP binding sequence should prove useful for tethering different loads of protein/antigen on the nanoparticle surface.

The observation that nanoparticles <100 nm in diameter preferentially accumulate in the lymph nodes where they encounter a high concentration of immature DCs has been exploited in the design of synthetic nanovaccines that are more efficient at triggering adaptive immunity.[6,48−50] The TrxA::-PA44-mineralized particles described herein are in the proper

dx.doi.org/10.1021/bc200654v | *Bioconjugate Chem.* 2012, 23, 610−617

size range for effective diffusion into the lymphatic system and comprise a CaP core that may serve as a "danger signal" to activate DC maturation. As a preliminary test of our design, we vaccinated mice with TrxA::PA44 that was in a nanoparticle-bound formulation or supplemented with the commercial adjuvant AdjuPhos. We found that although anti-TrxA levels were comparable in the two cohorts 9 days postinjection, there was 3 times more anti-TrxA in the serum of animals vaccinated with nanoparticles than in the control group ($p < 0.05$) after 3 weeks. We are aware that absolute antibody titers were low, which is likely due to the fact that *E. coli* TrxA is 30% identical to mouse TrxA and a poor immunogen. Nevertheless, our results suggest that direct mineralization of antigen shell−CaP core nanoparticles might be a simple and cost-effective route for nanovaccine manufacturing. We are currently exploring this concept further using TrxA::PA44−ovalbumin fusion proteins.

CONCLUSIONS

We have identified CaP binding dodecapeptides that are acidic and suitable for the synthesis of calcium phosphate core−protein shell nanoparticles. The hydrodynamic diameter of these hybrid structures can be varied from ∼60 to ∼200 nm by eliminating the disulfide bond holding the CaP binding sequence in a constrained loop. Considering that the nanoparticle formulation enhances TrxA immunogenicity and because TrxA fusions are easy to construct and purify, such inorganic core−protein shell architectures might prove useful for delivering adjuvanted antigens to DCs.

AUTHOR INFORMATION

Corresponding Author

*Telephone: (206) 685-7659. Fax: (206) 685-3451. E-mail: baneyx@uw.edu.

Present Address

[‖]Department of Pediatrics, Emory University School of Medicine, Atlanta, GA 30322.

Author Contributions

D.C. and W.Z. contributed equally to this work.

Notes

The authors declare no competing financial interest.

ACKNOWLEDGMENTS

We are grateful to Zahra Afsharinejad for performing the ELISAs and to Shobana Vaidyanathan for help with animal studies. This work was supported by a Grand Challenge Exploration grant from the Bill and Melinda Gates Foundation, a National Science Foundation-Nanotechnology and Interdisciplinary Research Team award on Protein-Aided Nanomanufacturing (CMMI-0709131), the National Science Foundation (NSF) Genetically Engineered Materials Science and Engineering Center (DMR-0520657), and National Institutes of Health Grants P30ES007033 and U19ES019545. Part of the work was conducted at the University of Washington Nanotech User Facility, a member of the NSF National Nanotechnology Infrastructure Network.

ABBREVIATIONS

ACP, amorphous carbon phosphate; CaP, calcium phosphate; TrxA, *E. coli* thioredoxin 1; ACP, amorphous calcium phosphate; DC, dendritic cell; HA, hydroxyapatite; SBP, solid binding peptides; OCP, octacalcium phosphate.

REFERENCES

(1) Bose, S., and Tarafder, S. (2011) Calcium phosphate ceramic systems in growth factor and drug delivery for bone tissue engineering: A review. *Acta Biomater.*, DOI: DOI: 10.1016/j.actbio.2011.11.017.

(2) Uskoković, V., and Uskoković, D. P. (2011) Nanosized hydroxyapatite and other calcium phosphates: Chemistry of formation and application as drug and gene delivery agents. *J. Biomed. Mater. Res., Part B 96*, 152−191.

(3) Aggerbeck, H., Fenger, C., and Heron, I. (1995) Booster vaccination against diphtheria and tetanus in man: Comparison of calcium-phosphate and aluminum hydroxide as adjuvants. *Vaccine 13*, 1366−1374.

(4) He, Q., Mitchell, A., Morcol, T., and Bell, S. J. D. (2002) Calcium phosphate nanoparticles induce mucosal immunity and protection against herpes simplex virus type 2. *Clin. Diagn. Lab. Immunol. 9*, 1021−1024.

(5) He, Q., Mitchell, A. R., Johnson, S. L., Wagner-Bartak, C., Morcol, T., and Bell, S. J. D. (2000) Calcium phosphate nanoparticle adjuvant. *Clin. Diagn. Lab. Immunol. 7*, 899−903.

(6) Manalova, V., Flace, A., Bauer, M., Schwarz, K., Saudan, P., and Bachman, M. F. (2008) Nanoparticles target distinct dendritic cell populations according to their size. *Eur. J. Immunol. 38*, 1404−1413.

(7) Reddy, S. T., Rehor, A., Schmoekel, H. G., Hubbell, J. A., and Swartz, M. A. (2006) In vivo targeting of dendritic cells in lymph nodes with poly(propylene sulfide) nanoparticles. *J. Controlled Release 112*, 26−34.

(8) Al-Qasas, N. S., and Rohani, S. (2005) Synthesis of pure hydroxyapatite and the effect of synthesis conditions on its yield, crystallinity, morphology and mean particle size. *Sep. Sci. Technol. 40*, 3187−3224.

(9) Ferraz, M. P., Monteiro, F. J., and Manuel, C. M. (2004) Hydroxyapatite nanoparticles: A review of preparation methodologies. *J. Appl. Biomater. Biomech. 2*, 74−80.

(10) Rodriguez-Lorenzo, L. M., and Vallet-Regi, M. (2000) Controlled crystallization of calcium phosphate apatites. *Chem. Mater. 12*, 2460−2465.

(11) Bose, S., and Saha, S. K. (2003) Synthesis and characterization of hydroxyapatite nanopowders by emulsion technique. *Chem. Mater. 15*, 4464−4469.

(12) Morgan, T. T., Muddana, H. S., Altinoglu, E. I., Rouse, S. M., Tabaković, A., Tabouillot, T., Russin, T. J., Shanmugavelandy, S. S., Butler, P. J., Eklund, P. C., Yun, J. K., Kester, M., and Adair, J. H. (2008) Encapsulation of organic molecules in calcium phosphate nanocomposite particles for intracellular imaging and drug delivery. *Nano Lett. 8*, 4108−4115.

(13) Roy, I., Mitra, S., Maitra, A., and Mozumdar, S. (2003) Calcium phosphate nanoparticles as novel non-viral vectors for targeted gene delivery. *Int. J. Pharm. 250*, 25−33.

(14) Martins, M. A., Santos, C., Almeida, M. M., and Costa, M. E. (2008) Hydroxyapatite micro- and nanoparticles: Nucleation and growth mechanisms in the presence of citrate species. *J. Colloid Interface Sci. 318*, 210−216.

(15) Cai, Y. R., Liu, Y. K., Yan, W. Q., Hu, Q. H., Tao, J. H., Zhang, M., Shi, Z. L., and Tang, R. K. (2007) Role of hydroxyapatite nanoparticle size in bone cell proliferation. *J. Mater. Chem. 17*, 3780−3787.

(16) Ganesan, K., Kovtun, A., Neumann, S., Heumann, R., and Epple, M. (2008) Calcium phosphate nanoparticles: Colloidally stabilized and made fluorescent by a phosphate-functionalized porphyrin. *J. Mater. Chem. 18*, 3655−3661.

(17) Welzel, T., Meyer-Zaika, W., and Epple, M. (2004) Continuous preparation of functionalised calcium phosphate nanoparticles with adjustable crystallinity. *Chem. Commun. 21*, 1204−1205.

(18) Palmer, L. C., Newcomb, C. J., Kaltz, S. R., Spoerke, E. D., and Stupp, S. I. (2008) Biomimetic systems for hydroxyapatite mineralization inspired by bone and enamel. *Chem. Rev. 108*, 4754−4783.

(19) George, A., and Veis, A. (2008) Phosphorylated proteins and control over apatite nucleation, crystal growth and inhibition. *Chem. Rev. 108*, 4670−4693.
(20) Hunter, G. K., O'Young, J., Grohe, B., Karttunen, M., and Golberg, H. A. (2010) The flexible polyelectrolyte hypothesis of protein-biomineral interaction. *Langmuir 26*, 18639−18646.
(21) Baneyx, F., and Schwartz, D. T. (2007) Selection and analysis of solid-binding peptides. *Curr. Opin. Biotechnol. 18*, 312−317.
(22) Dickerson, M. B., Sandhage, K. H., and Naik, R. R. (2008) Protein- and peptide directed synthesis of inorganic materials. *Chem. Rev. 108*, 4935−4978.
(23) Sarikaya, M., Tamerler, C., Jen, A. K., Schulten, K., and Baneyx, F. (2003) Molecular biomimetics: Nanotechnology through biology. *Nat. Mater. 2*, 577−585.
(24) Sarikaya, M., Tamerler, C., Schwartz, D. T., and Baneyx, F. (2004) Materials assembly and formation using engineered polypeptides. *Annu. Rev. Mater. Res. 34*, 373−408.
(25) Dai, H., Choe, W. S., Thai, C. K., Sarikaya, M., Traxler, B. A., Baneyx, F., and Schwartz, D. T. (2005) Nonequilibrium synthesis and assembly of hybrid inorganic-protein nanostructures using an engineered DNA binding protein. *J. Am. Chem. Soc. 127*, 15637−15643.
(26) Grosh, C., Schwartz, D. T., and Baneyx, F. (2009) Protein-based control of silver growth habit using electrochemical deposition. *Cryst. Growth. Des. 9*, 4401−4406.
(27) Zhou, W., and Baneyx, F. (2011) Aqueous, protein-driven synthesis of transition metal-doped ZnS immuno-quantum dots. *ACS Nano 5*, 8013−8018.
(28) Zhou, W., Schwartz, D. T., and Baneyx, F. (2010) Single pot biofabrication of zinc sulfide immuno-quantum dots. *J. Am. Chem. Soc. 132*, 4731−4738.
(29) Balamurugan, A., Benhayoune, H., Dumelie, N., Laquerriere, P., and Ferreira, J. M. F. (2008) Electrodeposition of fluorine-doped calcium phosphate coatings onto Ti6Al4V alloy: Chemical and structural characterization. *J. Am. Ceram. Soc. 91*, 2797−2801.
(30) Dumelie, N., Benhayoune, H., Richard, D., Laurent-Maquin, D., and Balossier, G. (2008) In vitro precipitation of electrodeposited calcium-deficient hydroxyapatite coatings on Ti6Al4V substrate. *Mater. Charact. 59*, 129−133.
(31) Thai, C. K., Dai, H., Sastry, M. S., Sarikaya, M., Schwartz, D. T., and Baneyx, F. (2004) Identification and characterization of Cu_2O- and ZnO-binding polypeptides by *Escherichia coli* cell surface display: Toward an understanding of metal oxide binding. *Biotechnol. Bioeng. 87*, 129−137.
(32) Yasukawa, T., Kanei-Ishii, C., Maekawa, T., Fujimoto, J., Yamamoto, T., and Ishii, S. (1995) Increase of solubility of foreign proteins in *Escherichia coli* by coproduction of the bacterial thioredoxin. *J. Biol. Chem. 270*, 25328−25331.
(33) Okajima, T., Tanabe, T., and Yasuda, T. (1993) Nonurea sodium dodecyl sulfate-polyacrylamide gel electrophoresis with high-molarity buffers for the separation of proteins and peptides. *Anal. Biochem. 211*, 293−300.
(34) Zhang, W., Zhang, W., Tang, Y., Zhang, J., and Liu, J. N. (2006) Characterization of an anti-thioredoxin monoclonal antibody. *Biotechnol. Lett. 28*, 183−188.
(35) Gupta, R. K., Rost, B. E., Relyved, E., and Siber, G. R. (1995) Vaccine design. In *Vaccine design* (Powell, M. F., and Newman, M. J., Eds.) pp 239−241, Plenum Press, New York.
(36) Jiang, D., Premachandra, G. S., Johnston, C., and Hem, S. L. (2004) Structure and adsorption properties of commercial calcium phosphate adjuvant. *Vaccine 23*, 693−698.
(37) Relyved, E. H. (1986) Preparation and use of calcium phosphate adsorbed vaccines. *Dev. Biol. Stand. 65*, 131−136.
(38) Lu, Z., Murray, K. S., Van Cleave, V., LaVallie, E. R., Stahl, M. L., and McCoy, J. M. (1995) Expression of thioredoxin random peptide libraries on the *Escherichia coli* cell surface as functional fusions to flagellin: A system designed for exploring protein-protein interactions. *Nat. Biotechnol. 13*, 366−372.
(39) LaVallie, E. R., DiBlasio, E. A., Kovacic, S., Grant, K. L., Schendel, P. F., and McCoy, J. M. (1993) A thioredoxin gene fusion expression system that circumvents inclusion body formation in the *E. coli* cytoplasm. *Nat. Biotechnol. 11*, 187−193.
(40) Zhao, J., Liu, Y. J., Sun, W.-B., and Zhang, H. (2011) Amorphous calcium phosphate and its applications in dentistry. *Chem. Cent. J. 5*, 40.
(41) Chen, H. B., Su, X. D., Neoh, K.-G., and Choe, W. S. (2009) Context-dependent adsorption behavior of cyclic and linear peptides on metal oxide. *Langmuir 25*, 1588−1593.
(42) Choe, W. S., Sastry, M. S. R., Thai, C. K., Dai, H., Schwartz, D. T., and Baneyx, F. (2007) Conformational control of inorganic adhesion in a designer protein engineered for cuprous oxide binding. *Langmuir 23*, 11347−11350.
(43) Hnilova, M., Oren, E. E., Seker, U. O. S., Wilson, B. R., Collino, S., Evans, J. S., Tamerler, C., and Sarikaya, M. (2008) Effect of molecular conformations on the adsorption behavior of gold-binding peptides. *Langmuir 24*, 12440−12445.
(44) Seker, U. O. S., Wilson, B., Dincer, S., Kim, I. W., Oren, E. E., Evans, J. S., Tamerler, C., and Sarikaya, M. (2007) Adsorption behavior of linear and cyclic genetically engineered platinum binding peptides. *Langmuir 23*, 7895−7900.
(45) Gungormus, M., Fong, H., Kim, I. L., Evans, J. S., Tamerler, C., and Sarikaya, M. (2008) Regulation of in vitro calcium phosphate mineralization by combinatorially selected hydroxyapatite-binding peptides. *Biomacromolecules 9*, 966−973.
(46) Chung, W. J., Kwon, K. Y., Song, J., and Lee, S. W. (2011) Evolutionary screening of collagen-like peptides that nucleate hydroxyapatite crystals. *Langmuir 27*, 7620−7628.
(47) Rabadjeva, D., Gergulova, R., Titorenkova, R., Tepavitcharova, S., Dyulgerova, E., Balarew, C., and Petrov, O. (2010) Biomimetic transformations of amorphous calcium phosphate: Kinetic and thermodynamic studies. *J. Mater. Sci.: Mater. Med. 21*, 2501−2509.
(48) Fifis, T., Gamvrellis, A., Crimeen-Irwin, B., Pietersz, G. A., Li, J., Mottram, P. L., McKenzie, I. F. C., and Plebanski, M. (2004) Size-dependent immunogenicity: Therapeutic and protective properties of nano-vaccines against tumors. *J. Immunol. 173*, 3148−3154.
(49) Reddy, S. T., Swartz, M. A., and Hubbell, J. A. (2006) Targeting dendritic cells with biomaterials: Developing the next generation of vaccines. *Trends Immunol. 27*, 573−579.
(50) Reddy, S. T., van der Vlies, A. J., Simeoni, E., Angeli, V., Randolph, G. J., O'Neil, C. P., Lee, K. L., Swartz, M. A., and Hubbell, J. A. (2007) Exploiting lymphatic transport and complement activation in nanoparticle vaccines. *Nat. Biotechnol. 25*, 1159−1164.
(51) Weiger, M. C., Park, J. J., Roy, M. D., Stafford, C. M., Karim, A., and Becker, M. L. (2010) Quantification of the binding affinity of a specific hydroxyapatite binding peptide. *Biomaterials 31*, 2955−2963.
(52) Segvich, S. J., Smith, H. C., and Kohn, D. H. (2009) The adsorption of preferential binding peptides to apatite-based materials. *Biomaterials 30*, 1287−1298.

Bioconjugate Chemistry

Article

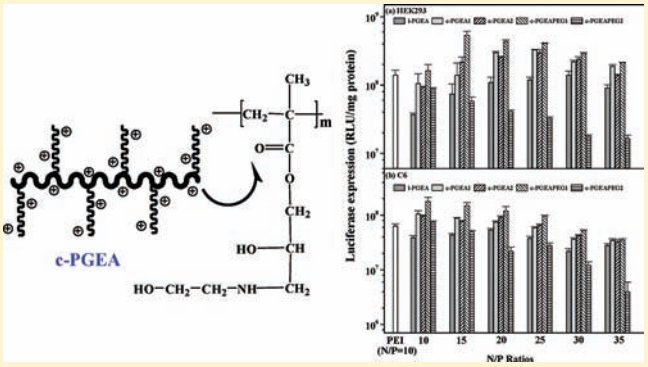
pubs.acs.org/bc

Facilitation of Gene Transfection with Well-Defined Degradable Comb-Shaped Poly(glycidyl methacrylate) Derivative Vectors

X. C. Yang,† M. Y. Chai,† Y. Zhu, W. T. Yang, and F. J. Xu*

State Key Laboratory of Chemical Resource Engineering, Key Laboratory of Carbon Fiber and Functional Polymers, Ministry of Education College of Materials Science & Engineering, Beijing University of Chemical Technology, Beijing, China 100029

ABSTRACT: Recently, we reported that ethanolamine (EA)-functionalized poly(glycidyl methacrylate) (PGMA) vectors (PGEAs) can produce good transfection efficiency, while exhibiting very low toxicity. Further improvement in degradability and transfection efficiency of the PGEA vectors will facilitate their application in gene therapy. Comb-shaped cationic copolymers have been of interest and importance as nonviral gene carriers. Herein, the degradable high-molecular-weight comb-shaped PGEA vectors (c-PGEAs) composed of the low-molecular-weight PGEA backbone and side chains were prepared by a combination of atom transfer radical polymerization (ATRP) and ring-opening reactions. The PGEA side chains were linked with the PGEA backbones via hydrolyzable ester bonds. Such comb-shaped c-PGEA vectors possessed the degradability, good pDNA condensation ability, low cytotoxicity, and good buffering capacity. More importantly, the comb-shaped c-PGEA vectors could enhance the gene expression levels. Moreover, the PGEA side chains of c-PGEA could also be copolymerized with some poly(poly(ethylene glycol)ethyl ether methacrylate) species to further improve the gene delivery system.



INTRODUCTION

Successful gene therapy depends on the design of gene delivery vectors with low cytotoxicity and high transfection efficiency. In comparison with viral vectors and cationic lipids, cationic polymers have been receiving considerable attention, because of their low host immunogenicity, high flexibility, and easy preparation.[1,2] Under physiological conditions, polycations can spontaneously condense negatively charged DNA into compact nanocomplexes, reduce the electrostatic repulsion between DNA and cell surfaces, protect plasmid DNA from enzymatic degradation by nucleases, and facilitate cellular transfection. Many kinds of polycations, including polyethylenimine (PEI),[3,4] poly(tertiaryamine methacrylate),[4] poly(L-lysine),[5] and polyamidoamine,[6] have been reported to be capable of gene delivery. High transfection efficiency is generally associated with a devastating toxicity.

We recently reported that ethanolamine (EA)-functionalized poly(glycidyl methacrylate) (PGMA) or PGEA with plentiful flanking secondary amine and hydroxyl groups can produce good transfection efficiency in different cell lines, while exhibiting low toxicity.[7,8] It was noted that such a PGEA vector was nondegradable and its good transfection efficiency was dependent on the high molecular weight. A water-soluble polymer with high molecular weight is not suitable for filtration through human kidney membrane due to the large hydrodynamic radius.[9,10] Further improvement in degradability and transfection efficiency of the PGMA derivative vectors will benefit constructing better gene-delivery systems.

Comb-shaped cationic copolymers have been of interest and importance as nonviral gene carriers.[4,11−13] A comb-shaped copolymer is a special type of branched polymer composed of one main polymer backbone and some polymer side chains. The side chains could be structurally distinct and extend from the main backbone. The comb-shaped architectures probably could enhance the interaction of the cationic species with pDNA or cellular membranes. It was reported that, in comparison with high-molecular-weight cationic homopolymers, the comb cationic copolymers containing low-molecular-weight polycation side chains exhibited much higher gene transfection efficiency and lower cytotoxicity.[12,13] The reactive epoxy groups of PGMA could be converted into initiation sites for forming side chains to produce the comb-like copolymers. In this work, the degradable high-molecular-weight comb-shaped PGMA derivative vectors (c-PGEA), where the low-molecular-weight PGEA side chains were linked with the PGEA backbones via the ester bonds, were proposed via facile atom transfer radical polymerization (ATRP)[4,14] (Figure 1). Such degradable comb-shaped c-PGEA vectors could facilitate the resultant gene delivery and benefit the final removal of the PGEA vectors from the body. Moreover, the PGEA side chains of c-PGEA could also be copolymerized with poly(poly(ethylene glycol)ethyl ether methacrylate) (PPEGEEMA) to further improve the gene transfection efficiency. The proposed degradable comb-shaped c-PGEA vectors would become promising candidates as safe and efficient vectors for future gene therapies.

Received: December 6, 2011
Revised: January 16, 2012
Published: February 14, 2012

ACS Publications © 2012 American Chemical Society

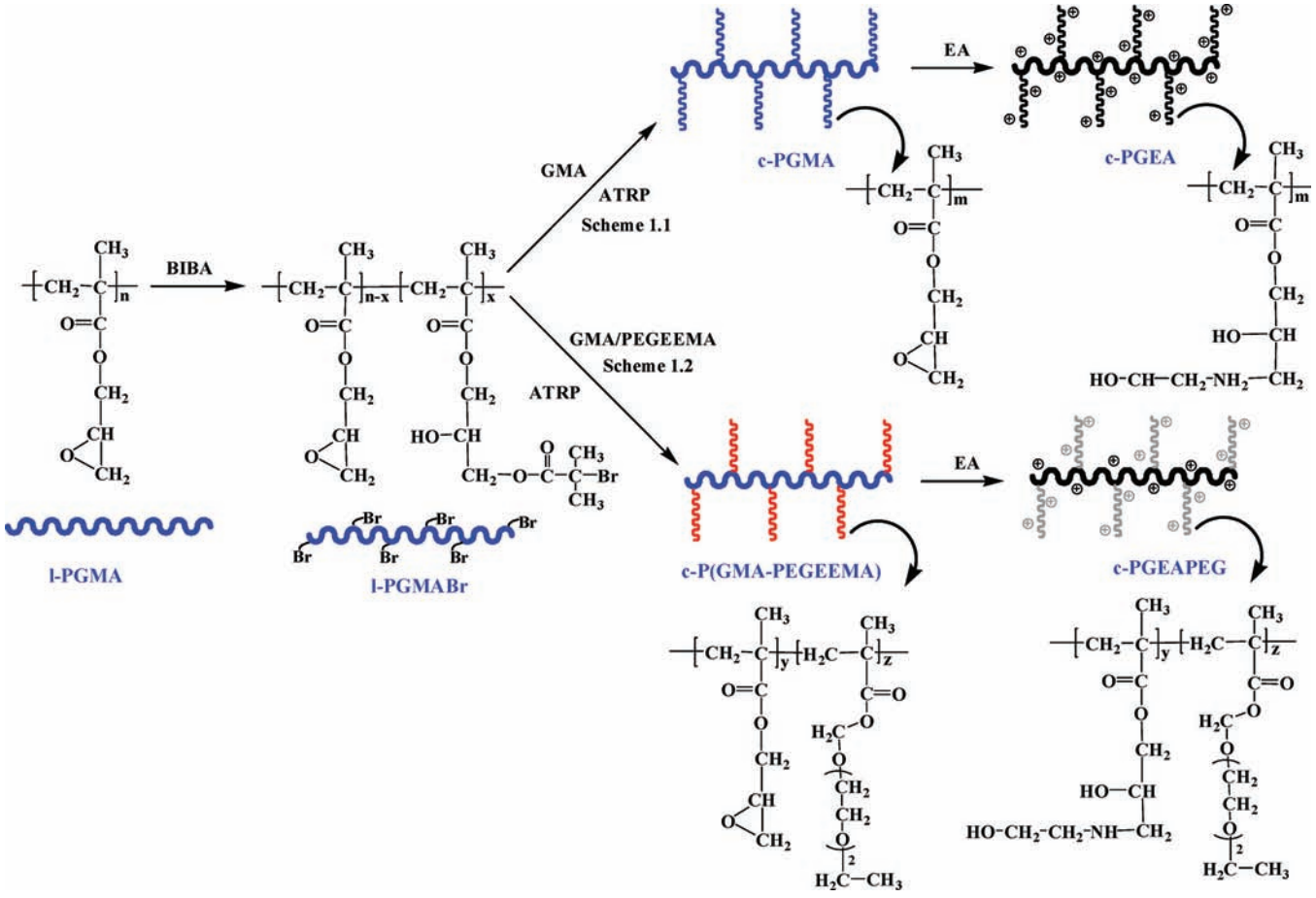


Figure 1. Preparation processes of different comb-shaped poly(glycidyl methacrylate) (PGMA) derivative vectors.

EXPERIMENTAL PROCEDURES

Materials. Branched polyethylenimine (PEI, M_w ~25 000 Da), glycidyl methacrylate (GMA, 98%), poly(ethylene glycol)-ethyl ether methacrylate) (PEGEEMA, M_n ~ 246), ethanolamine (EA, 98%), 1,1,4,7,10,10-hexamethyltriethyenetetramine (HMTETA, 99%), α-bromoisobutyric acid (BIBA, 98%), ethyl bromoisobutyrate (99%), and copper(I) bromide (CuBr, 99%) were obtained from Sigma-Aldrich Chemical Co., St. Louis, MO. GMA and PEGEEMA were used after removal of the inhibitors in a ready-to-use disposable inhibitor-removal column (Sigma-Aldrich). 3-(4,5-Dimethylthiazol-2-yl)-2,5-diphenyl tetrazolium bromide (MTT), penicillin, and streptomycin were also purchased from Sigma-Aldrich Chemical Co., St. Louis, MO. C6 and HEK293 cell lines were purchased from the American Type Culture Collection (ATCC, Rockville, MD).

Introduction of ATRP Initiation Sites onto PGMA Backbones. The linear PGMA (l-PGMA) backbones were first synthesized using a molar feed ratio [GMA (12 mL)]:[ethyl bromoisobutyrate]:[CuBr]:[HMTETA] of 140:1:1:1.5 at 50 °C in 24 mL of GMA/THF (1/1, v/v). The reaction was performed in a 50 mL flask equipped with a magnetic stirrer and under the typical conditions of ATRP. GMA, THF, ethyl bromoisobutyrate, and HMTETA were introduced into the 50 mL flask equipped with a magnetic stirrer. The reaction mixture was degassed by bubbling argon for 20 min. Then, CuBr was added into the mixture and the flask was then sealed with a rubber stopper under an argon atmosphere. The polymerization was allowed under continuous stirring at 50 °C to produce l-PGMA from 2 h of ATRP (M_n = 9.5 × 10^3 g/mol, PDI = 1.32). The reaction was stopped by exposing to air. The l-PGMA was precipitated in excess methanol to remove the catalyst complex. The crude polymer was purified by reprecipitation cycles into methanol to remove the reactant residues, prior to being dried under reduced pressure.

As shown in Figure 1, the introduction of the ATRP initiation sites onto l-PGMA was performed via the direct ring-opening reactions of the epoxy groups of l-PGMA with α-bromoisobutyric acid (BIBA) to produce the bromoisobutylryl-terminated l-PGMA (l-PGMA-Br) for the subsequent ATRP. The two l-PGMA-Br macroinitiators with the different distribution of initiation sites were prepared by adjusting the BIBA/l-PGMA feed ratio. With the predetermined molar feed ratio (1/5 or 1/8) of the BIBA/epoxy units, the BIBA (2.11 or 1.32 mmol) in 2 mL of THF was added dropwise at ambient temperature into the flask containing l-PGMA (10.56 mmol) in 10 mL of THF. The reaction was allowed to proceed at 40 °C for 24 h to produce the l-PGMA-Br. The final reaction mixture was precipitated and washed with excess diethyl ether, prior to being dried under reduced pressure.

Synthesis of Comb-Shaped Cationic PGMA Derivatives. For the preparation of comb-like PGMA (c-PGMA) polymers via ATRP, the molar feed ratio [GMA (4 mL)]:[CuBr]:[HMTETA] of 100:1:1.5 was used at 50 °C in 8 mL of GMA/THF (1/1, v/v) containing 0.3 g of l-PGMABr. The reaction was conducted in a 25 mL flask equipped with a magnetic stirrer and under the typical conditions for ATRP. GMA, l-PGMABr, and HMTETA were introduced into the flask containing 8 mL of GMA/THF (1/1, v/v), and the

dx.doi.org/10.1021/bc200658r | Bioconjugate Chem. 2012, 23, 618–626

reaction mixture was degassed by bubbling argon for 20 min. Then, CuBr was added into the mixture under an argon atmosphere. The flask was then sealed with a rubber stopper under an argon atmosphere. The polymerization was allowed to proceed under continuous stirring at 50 °C for 4 h to produce c-PGMA. The final reaction mixture was precipitated and washed with excess methanol, prior to being dried under reduced pressure. For the preparation of comb-like P(GMA-PEGEEMA) (c-P(GMA-PEGEEMA)) polymers via ATRP, the molar feed ratio [GMA (3.4 or 3.7 mL) + PEGEEMA (0.6 or 0.3 mL))]:[CuBr]:[HMTETA] of 100:1:1.5 was used at 50 °C in 8 mL of GMA/THF (1/1, v/v) containing 0.3 g of l-PGMABr. The polymerization was allowed to proceed for 4 h to produce c-P(GMA-PEGEEMA). The ATRP reaction and product purification were performed using the same procedures as those described above.

Different EA-functionalized PGMA derivatives were prepared by reacting l-PGMA, c-PGMA, or c-P(GMA-PEGEEMA) with ethanolamine (EA). 0.4 g of l-PGMA, c-PGMA, or c-P(GMA-PEGEEMA) was dissolved in 7 mL of DMF. Four mL of EA and 2 mL of triethyleneamine were then added. The reaction mixture was stirred at 50 °C for 72 h to produce l-PGEA, c-PGEA, or c-PGEAPEG (Figure 1). The final reaction mixture was precipitated with excess diethyl ether. The crude produce was purified by 24 h dialysis against DDW using a dialysis membrane (MWCO 3500) prior to lyophilization.

Polymer Characterization. The molecular weights of polymers were determined by gel permeation chromatography (GPC), chemical structure by nuclear magnetic resonance (NMR) spectroscopy, and chemical composition by X-ray photoelectron spectroscopy (XPS). GPC measurements were performed on a Waters GPC system equipped with Waters Styragel columns, a Waters-2487 dual wavelength (λ) UV detector, and a Waters-2414 refractive index detector. Monodispersed poly(ethylene glycol) standards were used to obtain a calibration curve. ^{1}H NMR spectra were measured by accumulation of 1000 scans at a relaxation time of 2 s on a Bruker ARX 300 MHz spectrometer, using $CDCl_3$ (for PGMA) or D_2O (for PGEA) as the solvent. XPS measurements were performed on a Kratos AXIS HSi spectrometer using a monochromatized Al K_α X-ray source (1486.6 eV photons) and procedures similar to those described earlier.[7]

Degradation Study. The degradation of c-PGEA was analyzed using GPC. c-PGEA was dissolved in PBS solution (pH 7.4), which was constantly shaken in a 37 °C incubator at 100 rpm. The PHPD solution was withdrawn at different time points for GPC analysis to determine the relative molecular mass of degraded products.

Characterization of Polymer/pDNA Complexes. The plasmid (encoding *Renilla* luciferase) used in this work was pRL-CMV (Promega Co., Cergy Pontoise, France), which was cloned originally from the marine organism *Renilla reniformis*. The plasmid DNA (pDNA) was amplified in *Escherichia coli* and purified according to the supplier's protocol (Qiagen GmbH, Hilden, Germany). The purified pDNA was resuspended in Tris-EDTA (TE) buffer, pH 7.4, and kept in aliquots of 0.5 mg/mL in concentration. All polymer stock solutions were prepared at a nitrogen concentration of 10 mM in distilled water. Solutions were filtered via sterile membranes of 0.2 μm average pore size and stored at 4 °C. Polymers to DNA ratios are expressed as molar ratios of nitrogen (N) in PGEAs to phosphate (P) in DNA (or as N/P ratios). The average mass weight of 325 per phosphate group of DNA was assumed. All polymer/pDNA complexes were formed by mixing equal volumes of polymer and pDNA solutions to achieve the desired N/P ratio. Each mixture was vortexed and incubated for 30 min at room temperature. Each cationic polymer was examined for its ability to bind pDNA through agarose gel electrophoresis using the similar procedures as those described earlier.[12] The particle sizes and zeta potentials of the polymer/pDNA complexes were measured in triplicate using a Zetasizer Nano ZS (Malvern Instruments, Southborough, MA) and procedures similar to those described earlier.[12]

Cell Viability. The cytotoxicity of the polymer vectors was evaluated using the 3-(4,5-dimethylthiazol-2-yl)-2,5-diphenyl tetrazolium bromide (MTT) assay in HEK293 and C6 cell lines. They were cultured in Dulbecco's modified eagle medium (DMEM), supplemented with 10% heat-inactivated fetal bovine serum (FBS), 100 units/mL of penicillin, and 100 μg/mL of streptomycin at 37 °C, under 5% CO_2 and 95% relative humidity atmosphere. The cells were seeded in a 96-well microtiter plate at a density of 10^4 cells/well and incubated in 100 μL of DMEM/well for 24 h. The culture media were replaced with fresh culture media containing serial dilutions of polymers or 10 μL polymer/pDNA complex solution (containing 0.5 μg of pDNA) at various N/P ratios, and the cells were incubated for 24 h. Then, 10 μL of sterile-filtered MTT stock solution in PBS (5 mg/mL) was added to each well, reaching a final MTT concentration of 0.5 mg/mL. After 5 h, the unreacted dye was removed by aspiration. The produced formazan crystals were dissolved in DMSO (100 μL/well). The absorbance was measured using a microplate reader (Spectra Plus, Tecan, Zurich, Switzerland) at a wavelength of 570 nm. The cell viability (%) relative to control cells cultured in media without polymers was calculated from $[A]_{test}/[A]_{control} \times 100\%$, where $[A]_{test}$ and $[A]_{control}$ are the absorbance values of the wells (with the polymers) and control wells (without the polymers), respectively. For each sample, the final absorbance was the average of those measured from six wells in parallel.

***In Vitro* Transfection Assay.** Transfection assays were performed using plasmid pRL-CMV as the reporter gene in HEK293 and C6 cell lines. In brief, the cells were seeded in 24-well plates at a density of 5×10^4 cells in 500 μL of medium/well and incubated for 24 h. The polymer/pDNA complexes of N/P ratios from 10 to 35 were prepared a priori by adding the polymer into the DNA solutions, followed by vortexing and incubation for 30 min at room temperature. At the time of transfection, the medium in each well was replaced with 300 μL of fresh normal serum medium (supplemented with 10% FBS). The polymer/pDNA complexes were added (20 μL/well containing 1.0 μg of pDNA) into the transfection medium and incubated with the cells for 4 h under the standard incubation conditions. Then, the medium was replaced with 500 μL of the fresh normal medium (supplemented with 10% FBS). The cells were further incubated for an additional 20 h under the same conditions, giving rise to a total transfection time of 24 h.[12] The cultured cells were washed with PBS twice and lysed in 100 μL of the cell culture lysis reagent (Promega Co., Cergy Pontoise, France). Luciferase gene expression was quantified using a commercial kit (Promega Co., Cergy Pontoise, France) and a luminometer (Berthold Lumat LB 9507, Berthold Technologies GmbH. KG, Bad Wildbad, Germany). Protein concentration in the cell samples was analyzed using a bicinchoninic acid assay (Biorad Lab, Hercules, CA). Gene expression results were expressed as relative light units (RLUs) per milligram of cell protein lysate (RLU/mg protein). All experiments were

repeated at least three times. The data were collected in triplicate and expressed as mean ± standard deviations.

Determination of Buffering Capacity. The buffering capacity of cationic polymers in the pH range 2−10 was determined by acid−base titration.[7,12] Polymers were dissolved into 20 mL of saline (0.9% NaCl solution) with a 10 mM amino group concentration. The solutions were titrated with a 0.1 N HCl solution with various volume increments. The pH of all the solutions was measured using a TOLEDO 320 pH meter (METTLER).

RESULTS AND DISCUSSION

Preparation of the PGMA Backbones with ATRP Initiation Sites. As shown in Figure 1, the degradable comb-shaped PGMA derivative vectors composed of the PGEA backbones and PGEA-based side chains were prepared by a combination of the ATRP and ring-opening reactions. The starting linear PGMA (l-PGMA) with about 67 GMA units (number average molecular weight (M_n) = 9.5 × 10^3 g/mol, polydispersity index (PDI) = 1.32, Table 1) was first synthesized via ATRP. The introduction of the ATRP initiation sites onto l-PGMA was performed via the direct ring-opening reactions of some epoxy groups of l-PGMA with α-bromoisobutyric acid (BIBA) to produce the bromoisobutylryl-terminated l-PGMA (l-PGMABr).

Table 1. Characterization of the Comb-Shaped PGMA-Based Polymers

sample	reaction time (h)	M_n (g/mol)[b]	PDI[b]	monomer repeat units per main chain (and side chain) GMA	PEGEEMA
l-PGMA[a]	2	9.5 × 10^3	1.32	67[b]	
c-PGMA1[c]	4	5.5 × 10^4	1.41	67 (25)[b]	
c-PGMA2[d]	4	5.2 × 10^4	1.52	67 (38)[b]	
c-P(GMA-PEGEEMA)1[e]	4	4.9 × 10^4	1.49	67 (20)[f]	1.4[f]
c-P(GMA-PEGEEMA)2[g]	4	6.4 × 10^4	1.87	67 (25)[f]	3.5[f]

[a]Synthesized using a molar feed ratio [GMA (12 mL)]:[ethyl bromoisobutyrate]:[CuBr]: [1,4,7,10,10,-hexamethyl triethylenetetramine, HMTETA] of 140:1:1:1.5 at 50 °C in 24 mL of GMA/THF (1/1, v/v). [b]Determined from GPC results. PDI = weight average molecular weight/number average molecular weight, or M_w/M_n. [c]Synthesized using a molar feed ratio [GMA (4 mL)]:[CuBr]:[HMTETA] of 100:1:1.5 at 50 °C in 8 mL of GMA/THF (1/1, v/v) containing 0.3 g of l-PGMABr1, where every 5.2 repeat units contains about one initiation site. [d]Synthesized using a molar feed ratio [GMA (4 mL)]:[CuBr]:[HMTETA] of 100:1:1.5 at 50 °C in 8 mL of GMA/THF (1/1, v/v) containing 0.3 g of l-PGMABr2, where every 8.5 repeat units contains about one initiation site. [e]Synthesized using a molar feed ratio [GMA (3.7 mL)+PEGEEMA (0.3 mL)]:[CuBr]:[HMTETA] of 100:1:1.5 at 50 °C in 8 mL of GMA/THF (1/1, v/v) containing 0.3 g of l-PGMABr1. [f]Determined from M_n and ^{1}H NMR data. [g]Synthesized using a molar feed ratio [GMA (3.4 mL)+PEGEEMA (0.6 mL)]:[CuBr]:[HMTETA] of 100:1:1.5 at 50 °C in 8 mL of GMA/THF (1/1, v/v) containing 0.3 g of l-PGMABr1.

The representative structures of l-PGMA and l-PGMABr were first characterized by ^{1}H NMR spectra as shown in Figure 2a,b, respectively. For l-PGMA, the signals at δ = 3.8 and 4.3 ppm corresponded to the methylene protons adjacent to the oxygen moieties of the ester linkages (***a***, $\underline{CH_2}$−O−C═O). The peaks at δ = 3.2 ppm (***b***) and δ = 2.63 and 2.84 ppm (***c***) could be assigned to the protons of the epoxide ring. The ratio of peak areas of ***a***, ***b***, and ***c*** is about 2:1:2, indicating that the epoxy groups of the PGMA remained intact throughout ATRP. After the ring-opening reactions of some epoxy groups with BIBA, the new peaks of l-PGMABr at δ = 1.85, δ = 3.5, and δ = 4.15 ppm were mainly attributable to the methyl protons (***f***, C(Br)−$\underline{CH_3}$) of the 2-bromoisobutyryl groups, the $\underline{CH}$−OH methylidyne protons (***e***), and the methylene protons (***d***, $\underline{CH_2}$−O−C═O) from the ring-opening reactions, respectively. When ATRP is carried out from a multifunctional backbone with a high local concentration of initiation sites, the radical−radical coupling of the propagating chains will occur and result in a gel. In order to avoid potential gelation and introduce some flexibility onto the comb-like cationic copolymers, the l-PGMABr with moderate initiation sites is desired for subsequent comb-shaped copolymers. In this work, the concentration of initiation sites can be controlled by adjusting the feed ratio of the BIBA/epoxy units. With the predetermined molar feed ratio (1/5 or 1/8) of the BIBA/epoxy units, based on the area ratio of peak ***d*** and peak ***a***, the l-PGMABr1 (where every 5.2 repeat units contains about one initiation site) and l-PGMABr2 (where every 8.5 repeat units contains about one initiation site) were prepared in this work (Table 1). Such prepared l-PGMA-Br with moderate initiation sites could avoid potential gelation during ATRP.

In addition, l-PGMA and l-PGMABr were also characterized by X-ray photoelectron spectroscopy (XPS). Their representative C 1s spectra were shown in Figure 3a,b, respectively. The C 1s core-level spectrum of PGMA could be curve-fitted into three peak components with binding energies (BE's) at about 284.6, 286.2, and 288.4 eV, attributable to the $\underline{C}$−H, $\underline{C}$−O, and O═$\underline{C}$−O species, respectively, in an approximate ratio of 3:3:1, consistent with the chemical structure of PGMA. After the ring-opening reactions, the C 1s spectral line shape of l-PGMABr with the increased compositional ratio of the $\underline{C}$−H species was obviously different from that of the original l-PGMA. The corresponding Br 3d core-level spectrum (with BE at about 69 eV) of l-PGMABr was shown in Figure 3b′. The above XPS results also clearly confirmed the successful preparation of l-PGMABr.

Synthesis of Comb-Shaped Cationic PGMA Derivatives. Well-defined comb-shaped PGMA (c-PGMA) polymers were subsequently synthesized via ATRP of GMA from l-PGMABr (Figure 1 and Table 1). After 4 h of ATRP, the c-PGMA1 (M_n = 5.5 × 10^4 g/mol) and c-PGMA2 (M_n = 5.2 × 10^4 g/mol) were prepared uisng the l-PGMABr1 and l-PGMABr2 macroinitiators, respectively. Based on the assumption of one initiation site out of every 5.2 repeat units for l-PGMABr1 or every 8.5 repeat units for l-PGMABr2, the total numbers of GMA repeat units per side chain were 25 for c-PGMA1 and 38 for c-PGMA2, respectively (Table 1). The typical ^{1}H NMR and C 1s XPS spectra of c-PGMA were shown in Figures 2c and 3c, respectively. As expected, their spectra were very similar to those of l-PGMA (Figure 2a and Figure 3a). In addition, the polydispersity indexes (PDIs) of c-PGMA1 and c-PGMA2 are comparable to that of l-PGMA (Table 1), indicating that ATRP from the starting l-PGMA-Br macroinitiator is well-controlled.

It was reported that the introduction of poly(poly(ethylene glycol)ethyl ether methacrylate) (PPEGEEMA) into the cationic gene vectors could probably enhance the gene transfection efficiency.[15] In this work, PPEGEEMA was also

dx.doi.org/10.1021/bc200658r | Bioconjugate Chem. 2012, 23, 618−626

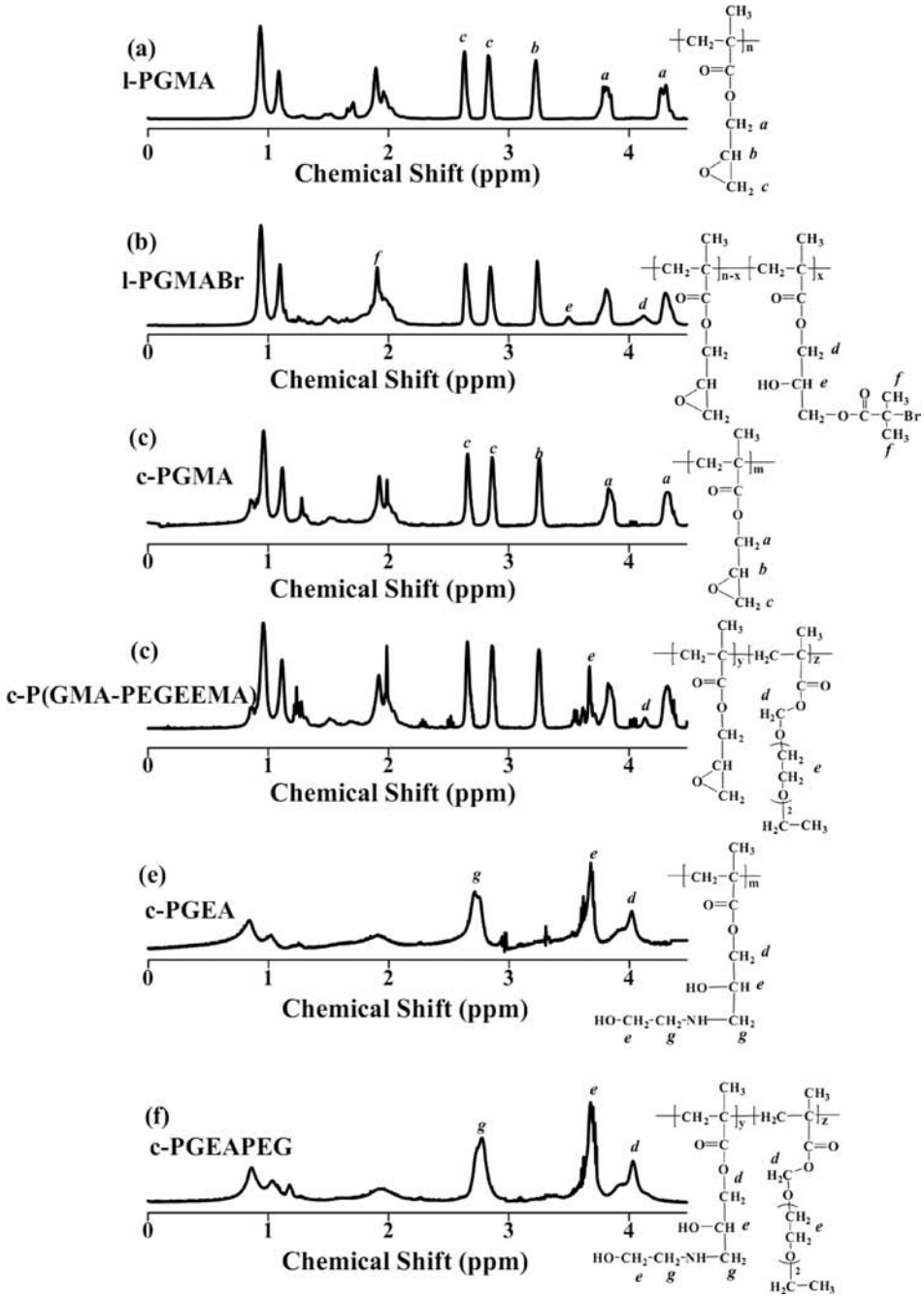


Figure 2. 300 MHz ^{1}H NMR spectra of (a) l-PGMA, (b) l-PGMABr, (c) c-PGMA, (d) c-P(GMA-PEGEEMA), (e) c-PGEA, and (f) c-PGEAPEG.

copolymerized into PGMA side chains to produce the comb-like P(GMA-PEGEEMA) (c-P(GMA-PEGEEMA)) polymers (Figure 1). The c-P(GMA-PEGEEMA)1 (M_n = 4.9 × 10^4 g/mol) and c-P(GMA-PEGEEMA)1 (M_n = 6.4 × 10^4 g/mol) polymers were prepared via 4 h of ATRP using different molar feed ratio of GMA and PEGEEMA monomers from the l-PGMABr1 macroinitiators (Table 1). The typical ^{1}H NMR spectrum of c-P(GMA-PEGEEMA) was shown in Figure 2d. In comparison with the spectrum of c-PGMA (Figure 2c), the new peaks of c-P(GMA-PEGEEMA) at δ = 3.7 and δ = 4.15 ppm were mainly attributable to the methylene protons (***e***, O−$\underline{CH_2}$ and ***d***, $\underline{CH_2}$−O−C═O) of the P(PEGEEMA) species. Based on the area ratio of peak ***d*** and peak ***a*** of c-P(GMA-PEGEEMA), the total numbers of GMA (and PEGEEMA) repeat units per side chain were 20 (and 1.4) for c-P(GMA-PEGEEMA)1 and 25 (and 3.5) for c-P(GMA-PEGEEMA)2, respectively (Table 1).

The ethanolamine (EA)-functionalized PGMA derivatives were prepared by reacting l-PGMA, c-PGMA1, c-PGMA2, c-P(GMA-PEGEEMA)1, or c-P(GMA-PEGEEMA)2 with EA to produce the corresponding l-PGEA, c-PGEA1, c-PGEA2, c-PGEAPEG1, or c-PGEAPEG2 vectors (Figure 1). The typical ^{1}H NMR spectra of c-PGEA and c-PGEAPEG were shown in Figure 2e and f, respectively. After the ring-opening reactions of PGMA species with EA, the peaks (***b***,***c***) associated with the epoxide ring had disappeared completely. The peaks (***a***, $\underline{CH_2}$−O−C═O) at δ = 3.8 and 4.3 ppm shifted to one new position (***d***) at δ = 4.05 ppm. The new peak at δ = 2.7 ppm was mainly attributable to the methylene protons (***g***, NH−$\underline{CH_2}$). The strong peak at δ = 3.7 ppm was associated with the $\underline{CH}$−OH

dx.doi.org/10.1021/bc200658r | *Bioconjugate Chem.* 2012, 23, 618−626

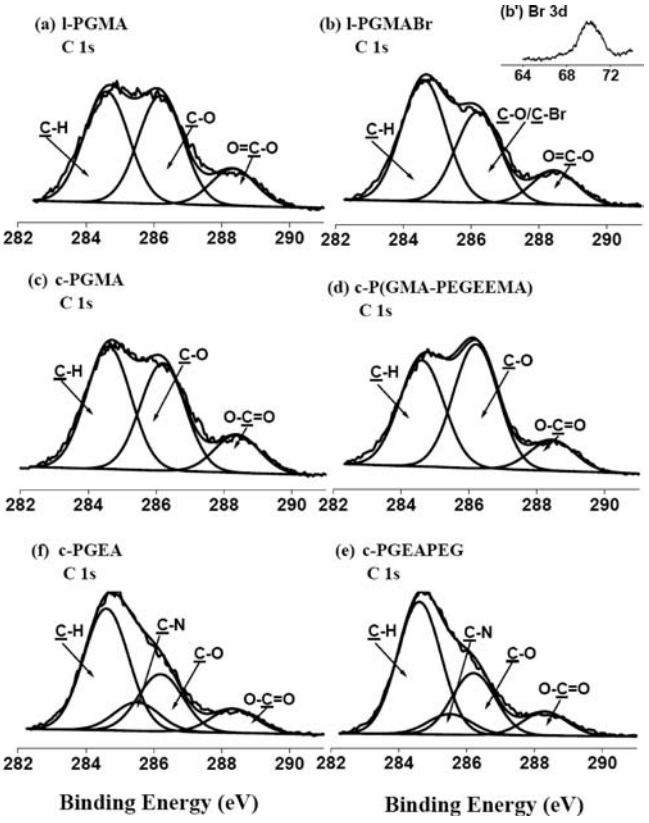


Figure 3. XPS C 1s spectra of (a) l-PGMA, (b) l-PGMABr, (c) c-PGMA, (d) c-P(GMA-PEGEEMA), (e) c-PGEA, and (f) c-PGEAPEG, and (b′) Br 3d core-level spectrum of l-PGMABr.

methylidyne and $\underline{CH_2}$−OH or O−$\underline{CH_2}$ methylene protons (*e*). The representative XPS C 1s spectra of c-PGEA and c-PGEAPEG were shown in Figure 3e and f, respectively. They could be curve-fitted into four peak components with BE's at about 284.6, 285.5, 286.2, and 288.4 eV, attributable to the $\underline{C}$−H, $\underline{C}$−N, $\underline{C}$−O, and O=$\underline{C}$−O species, respectively. After the ring-opening reactions, the C 1s spectral line shapes of c-PGEA and c-PGEAPEG were significantly different from their corresponding counterparts (Figure 3c,d). The above results indicated that the oxirane rings of PGMA were opened by EA under the present reaction conditions.

Degradation Study. l-PGEA backbone was homopolymer and is nondegradable due its C−C linkages. For the above comb-shaped cationic PGMA derivatives, the low-molecular-weight PGEA or PGEAPEG side chains were linked with the PGEA backbones via hydrolyzable ester linkages, which would make the PGEA side chains cleavable from the l-PGEA backbone. Thus, the molecular weight of c-PGEA could be slowly degraded with degradation time as shown in Figure 4, arising from the hydrolysis of ester linkages. Such degradation could benefit the final removal of vectors from the body.

Biophysical Characterization of Cationic Vector/pDNA Complexes. A successful gene delivery system requires that plasmid DNA (pDNA) has to be condensed by polycation into nanoparticles small enough to facilitate cellular uptake. The ability to condense DNA is a prerequisite for polymeric gene vectors. In this work, the ability of the PGMA derivative vectors to condense pDNA was confirmed by agarose gel electrophoresis, and particle size and zeta potential measurements. The formation of the polymer/pDNA complexes was first analyzed by their electrophoretic mobility on an agarose gel at

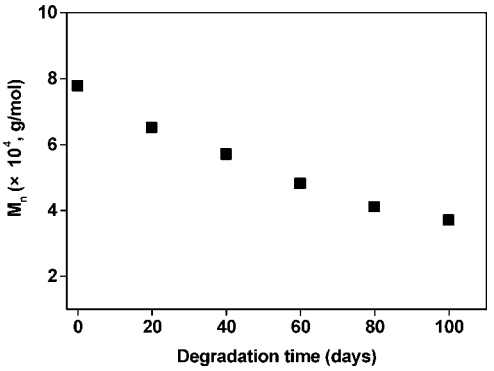


Figure 4. Change of molecular weight of c-PGEA1 with degradation time in PBS (pH 7.4) at 37 °C.

various N/P ratios. Figure 5 shows the gel retardation results of various cationic PGMA derivative/DNA complexes with in-

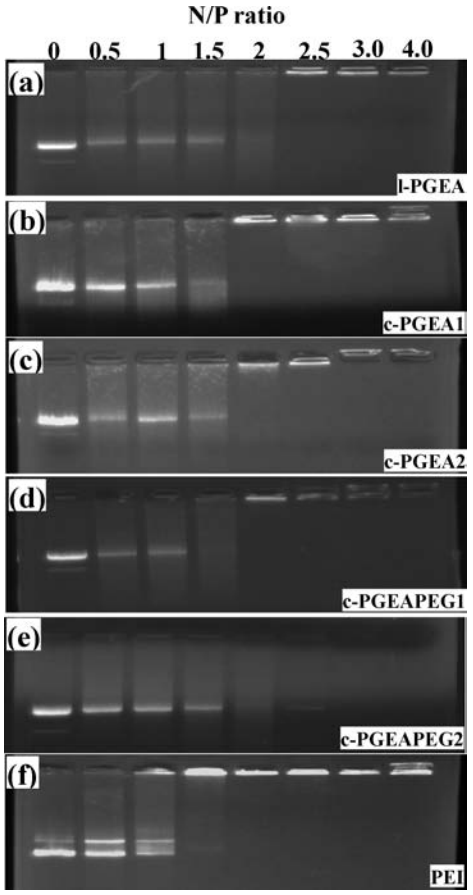


Figure 5. Electrophoretic mobility of plasmid DNA (pDNA) in the complexes of the cationic polymers ((a) l-PGEA, (b) c-PGEA1, (c) c-PGEA2, (d) c-PGEAPEG1, (e) c-PGEAPEG2, and (f) PEI) at various N/P ratios.

creasing nitrogen/phosphate (N/P) ratios in comparison with that of PEI (25 kDa). l-PGEA compacted pDNA completely at the N/P ratios of above 2.5. c-PGEAs exhibited slightly higher condensation capability than l-PGEA and inhibited the migration of pDNA at the N/P ratios of above 2.0, similar to that of the control PEI. The above indicated that the high-molecular-weight c-PGEAs benefited the interaction with pDNA. The c-PGEAPEG1 and c-PGEAPEG2 samples could

dx.doi.org/10.1021/bc200658r | *Bioconjugate Chem.* 2012, 23, 618−626

completely inhibit the migration of pDNA at the N/P ratios of 2.0 and 3.0, respectively, indicating that excess neutral P(PEGEEMA) species in the c-PGEAPEG vectors would decrease the pDNA condensation capability.

The particle size and surface charge of complexes are important factors in modulating their cellular uptake. All the cationic vectors could efficiently compact pDNA into small nanoparticles, as shown in Figure 6a. Generally, the hydrodynamic size

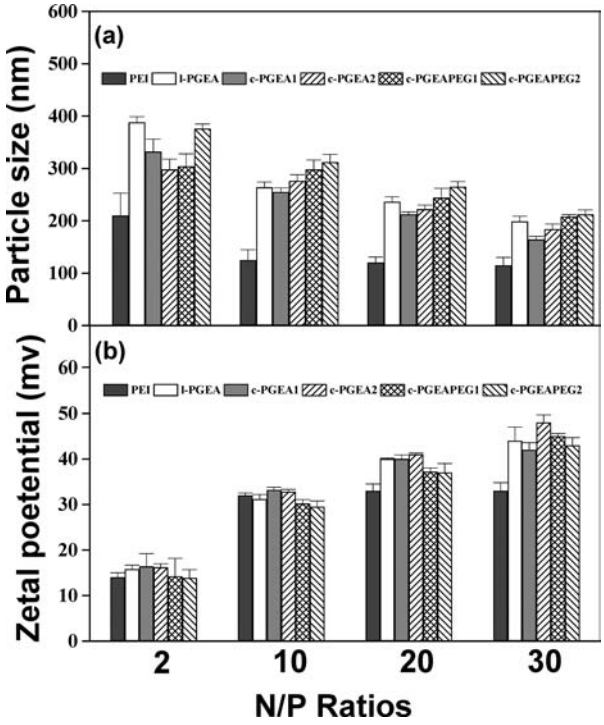


Figure 6. Particle size (a) and zeta potential (b) of the complexes between the cationic polymers (l-PGEA, c-PGEA1, c-PGEA2, c-PGEAPEG1, c-PGEAPEG2, and PEI) and pDNA at various N/P ratios.

of the complex decreased with increasing N/P ratio. At the N/P ratio of 2.0, loose large aggregates were formed, due to the lower amount of cationic polymers. At the N/P ratios of above 10, all PGEAs and PGEAPEGs could condense pDNA into nanoparticles of 200 to 300 nm in diameters. The complex sizes of l-PGEA/pDNA were lower than those of c-PGEA/pDNA at most N/P ratios, which was consistent with the relative low condensation ability of l-PGEA/pDNA (Figure 5). Zeta potential is an indicator of surface charges on the polymer/pDNA nanoparticles. As indicated in Figure 6b, the complex surfaces were positive. A positively charged surface allows electrostatic interaction with anionic cell surfaces and facilitates cellular uptake.

Cell Viability Assay. Cytotoxicity is another important factor to be considered in selecting polymeric gene carriers. A successful delivery system should have high transfection efficiency and minimal toxicity. Figure 7 shows the *in vitro* MTT assay results of cytotoxicity of l-PGEA, c-PGEAs, and c-PGEAPEGs, and PEI in HEK293 and C6 cell lines. All of the cationic polymers exhibit a dose-dependent cytotoxicity effect. l-PGEA and c-PGEAs exhibited substantially lower toxicity than PEI. The slopes of the dose-dependent cytotoxicity curves for PEI were sharply steeper. A high concentration of amino groups is always considered an important factor leading to high

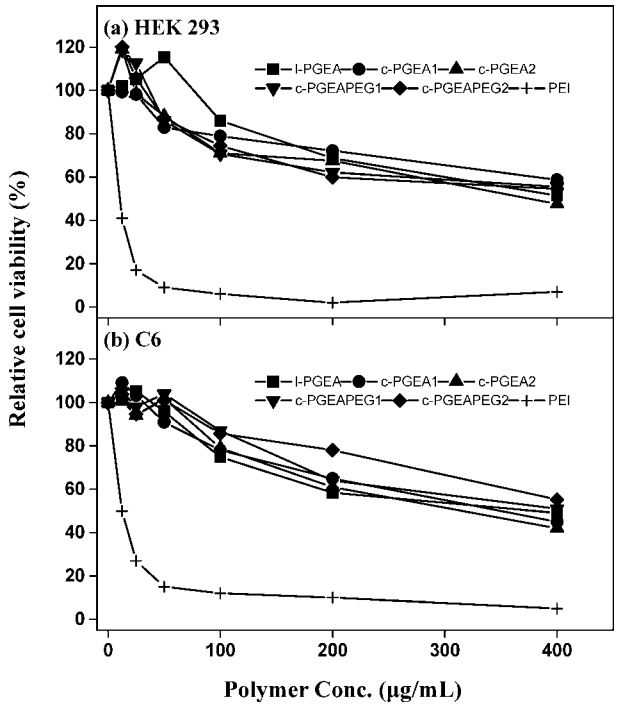


Figure 7. Cell viability assay in (a) HEK293 and (b) C6 cells with various concentrations of l-PGEA, c-PGEA1, c-PGEA2, c-PGEAPEG1, c-PGEAPEG2, and PEI (25 kDa). Cell viability was determined by the MTT assay and expressed as a percentage of the control cell culture.

cytotoxicity. PEI is mainly composed of secondary amine groups. The uniform nonionic hydrophilic hydroxyl groups in PGEAs not only resulted in a lower relative concentration of amino groups, but probably also shielded the harmful charges of the cationic carriers. The above results were consistent with those reported earlier.[7,8] It was well-known that the cytotoxicity of polycations increases with the molecular weight.[16] However, no obvious difference in cytotoxicity was observed between the l-PGEA and high-molecular-weight c-PGEA vectors, indicating that the introduction of the low-molecular-weight cationic PGEA side chains did not affect substantially the cytotoxicity.

The cell viability of the polymer/pDNA complexes as a function of the N/P ratio was also evaluated by using MTT assay (Figure 8). The N/P ratio had a profound impact on the cytotoxicity of complexes. The cell viability of all polymer/pDNA complexes was observed to decrease with increasing N/P ratios. For the cytotoxicity assay at the given N/P ratio, the cells were incubated in 100 μL of DMEM/well containing 0.5 μg of pDNA. Based on the average mass weights of 325 per phosphate group of DNA and of 203 per nitrogen group of PGEA, the cationic polymer concentrations at the test N/P ratios of 10, 20, and 35 were about 31, 62, and 109 μg/mL, respectively. At higher N/P ratios, the transfection formulation also contains free polymer, besides the compact and positively charged polymer/pDNA complexes. The increased free cationic polymers produced the increasing cytotoxicity. The results of Figure 8 were consistent with those of Figure 7. At the same N/P ratio, no obvious difference was observed among the l-PGEA, c-PGEA, and c-PGEAPEG-mediated complexes, where the control PEI/pDNA complexes exhibited much higher cytotoxicity.

***In Vitro* Transfection Assay.** The *in vitro* gene transfection efficiency of the cationic vector/pDNA complexes was assessed using luciferase as a gene reporter in HEK293 and C6 cell lines in the complete serum media. Figure 9 shows the gene

dx.doi.org/10.1021/bc200658r | *Bioconjugate Chem.* 2012, 23, 618–626

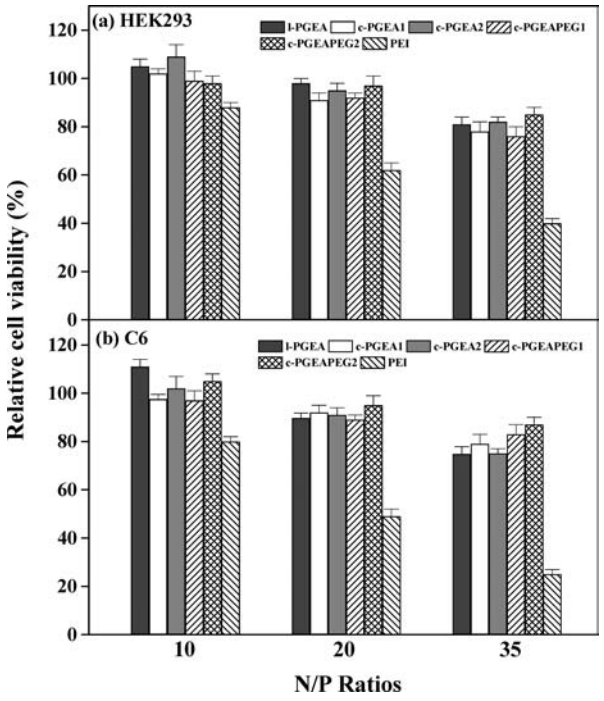


Figure 8. Cell viability of polymer/pDNA complexes at different N/P ratios in (a) HEK293 and (b) C 6 cell line.

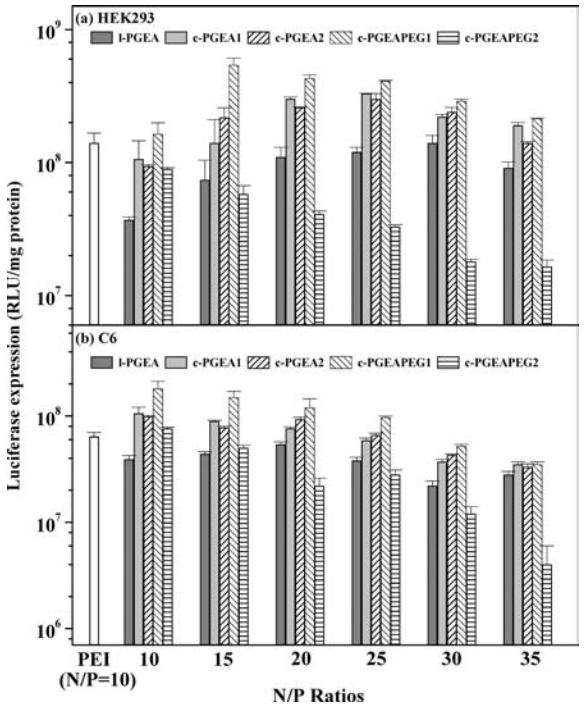


Figure 9. *In vitro* gene transfection efficiency of the cationic polymers (l-PGEA, c-PGEA1, c-PGEA2, c-PGEAPEG1, and c-PGEAPEG2)/pDNA complexes at various N/P ratios in comparison with that of PEI (25 kDa) at the optimal N/P ratio of 10 in (a) HEK293 and (b) C 6 cells.

transfection efficiency of l-PGEA, c-PGEAs, and c-PGEAPEGs at various N/P ratios in comparison with that of PEI at a N/P ratio of 10, at which branched PEI (25 kDa) usually exhibits the highest transfection efficiency.[7,8,12−15] The transfection efficiency generally first increases at lower N/P ratios and then decreases slightly with the increase in N/P ratios. At lower N/P ratios, pDNA cannot be condensed efficiently by the polymers, and the resultant loose polymer/pDNA complex cannot enter the cell easily. In general, after reaching the optimal N/P ratio, the transfection efficiency decreases as the N/P ratios further increase. At higher N/P ratios, the transfection formulation also contains free cationic polymers causing cytotoxicity (Figure 8), besides the compact and positively charged polymer/pDNA complexes. The increasing cytotoxicity may result in a reduction in the transfection efficiency. In both cell lines, the c-PGEA vectors exhibited much higher gene transfection efficiency that mediated by l-PGEA at most N/P ratios. The transfection efficiency of PGEA is dependent on the molecular weights.[7] The high-molecular-weight c-PGEA vectors could increase the binding ability and complex stability, probably leading to a much higher transfection efficiency. No obvious difference was observed in the transfection efficiencies mediated by c-PGEA1 (derived from c-PGMA1) and c-PGEA2 (derived from c-PGMA2), probably due to their similar molecular weights, although they possessed different distributions of the ATRP initiation sites (Table 1).

As shown in Figure 9, c-PGEAPEG1 (derived from c-P(GMA-co-PEGEEMA)1) exhibited significantly higher transfection efficiencies than those mediated by c-PGEA1 (derived from c-PGMA1) at most N/P ratios in both cell lines, although they possessed the similar molecular weights (Table 1). The above results suggested that the introduced suitable amount of P(PEGEEMA) species can further enhance the gene transfection efficiency, which was consistent with the earlier report.[15] The good biocompatibility of the P(PEGEEMA), as well as its shielding effect, probably contributed to the enhanced transfection efficiency. However, c-PGEAPEG2 (derived from c-P(GMA-co-PEGEEMA)2) exhibited significantly lower transfection efficiencies than those mediated by c-PGEA1 at most N/P ratios in both cell lines. c-PGEAPEG2 contained a higher amount of P(PEGEEMA) species. The excess P(PEGEEMA) parts would decrease the pDNA condensation capability (Figure 5), which probably led the lower gene expression levels.

Buffering Capacity. After cellular entry via endocytosis, the polymer/plasmid complexes were transported into the lysosome. Efficient escape from endosomes is one of the most important factors to be considered for the design of gene delivery vehicles. This event is associated with the buffering capacity of gene vectors, in which vectors undergo change from extracellular environment to endosomal acid environment.[17] By disrupting the endosomal membrane, polycations with high buffering capacity can mediate efficient escape from endosome to cytosol triggered by the acidic environment of endosome. The buffering capacity of the cationic polymers is very useful for the endosomal release of pDNA to the cytoplasm. In this study, acid−base titration under the given 10 mM amino group concentration was performed to evaluate the proton-buffering effects of l-PGEA, c-PGEAs, and c-PGEAPEGs (Figure 10). l-PGEA showed significantly higher buffering capacity than PEI (25 kDa), a well-known transfection agent for its strong proton-sponge effect.[18] This is consistent with our earlier report.[7] The local environment of the nonionic hydrophilic hydroxyl groups of PGEA as well as its ester species may benefit the improvement the buffering capacity. No obvious difference was observed in the buffering capacities of the l-PGEA, c-PGEA1, c-PGEA2, and c-PGEAPEG1 vectors in the entire test pH range. However, in comparison with c-PGEAPEG1 and PGEA, c-PGEAPEG2 demonstrated a much higher buffering capacity, probably due to its higher amount of P(PEGEEMA) species (Table 1). Unfortunately, as

dx.doi.org/10.1021/bc200658r | *Bioconjugate Chem.* 2012, 23, 618−626

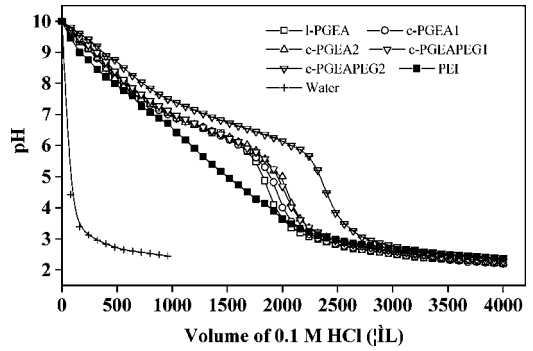


Figure 10. Determination of the buffer capacity of l-PGEA, c-PGEA1, c-PGEA2, c-PGEAPEG1, c-PGEAPEG2, PEI, and water by acid–base titration. The cationic polymer solutions with 10 mM amino group concentration were titrated with 0.1 M HCl solution.

shown in Figure 9, c-PGEAPEG2 exhibited much lower gene expression levels, which was probably caused by the decreased pDNA condensation capability of c-PGEAPEG2 (Figure 5). The above results indicated that, in addition to buffering capacity, an efficient gene delivery system still requires other beneficial factors such as good pDNA condensation capability.

■ CONCLUSIONS

The ATRP initiation sites had been successfully introduced onto PGMA backbones. The degradable high-molecular-weight comb-shaped PGMA derivative (c-PGEA) vectors composed of the low-molecular-weight PGEA backbone and side chains were subsequently prepared by the combination of ATRP and ring-opening reactions. Such comb-shaped c-PGEA vectors could possess the good pDNA condensation ability, low cytotoxicity, and good buffering capacity. More importantly, the c-PGEA vectors could improve the gene expression levels and their degradability would benefit the final removal of PGEA from the body. In addition, the PGEA side chains of c-PGEA could also be copolymerized with some PEGEEMA species to further enhance the gene transfection efficiency. Thus, the improvement in degradability and transfection efficiency of PGMA derivative vectors would facilitate the development of effective gene carrier systems.

■ AUTHOR INFORMATION

Corresponding Author

*E-mail: xufj@mail.buct.edu.cn.

Author Contributions

†X. C. Yang and M. Y. Chai contributed equally to this work.

Notes

The authors declare no competing financial interest.

■ ACKNOWLEDGMENTS

This work was supported by National Natural Science Foundation of China (grant numbers 21074007 and 51173014), Research Fund for the Doctoral Program of Higher Education of China (project no. 20090010120007), Program for New Century Excellent Talents in University (NCET-10-0203), SRF for ROCS, SEM and National High Technology Development Program of China (863 Program 2011AA030102).

■ REFERENCES

(1) Hunt, K. K., and Vorburger, S. A. (2002) Gene therapy: hurdles and hopes for cancer treatment. *Science 297*, 415–416.

(2) Niidome, T., and Huang, L. (2002) Gene therapy progress and prospects: nonviral vectors. *Gene Ther. 9*, 1647–1652.

(3) Bisht, H. S., Manickam, D. S., You, Y., and Oupicky, D. (2006) Temperature-controlled properties of DNA complexes with poly(ethylenimine)-*graft*-poly(*N*-isopropylacrylamide). *Biomacromolecules 7*, 1169–1178.

(4) Xu, F. J., and Yang, W. T. (2011) Polymer vectors via controlled/living radical polymerization for gene delivery. *Prog. Polym. Sci. 36*, 1099–1131.

(5) Wagner, E., Ogris, M., and Zauner, W. (1998) Polylysine-based transfection systems utilizing receptor-mediated delivery. *Adv. Drug Delivery Rev. 30*, 97–113.

(6) Kukowska-Latallo, J. F., Bielinska, A. U., Johnson, J., Spindler, R., Tomalia, D. A., and Baker-Jr, J. R. (1996) Efficient transfer of genetic material into mammalian cells using starburst polyamidoamine dendrimers. *Proc. Natl. Acad. Sci. U.S.A. 93*, 4897–4902.

(7) Xu, F. J., Chai, M. Y., Li, W. B., Ping, Y., Tang, G. P., Yang, W. T., Ma, J., and Liu, F. S. (2010) Well-Defined poly(2-hydroxyl-3-(2-hydroxyethlamino)propyl methacylate) vectors with low cytotoxicity and high gene transfection efficiency. *Biomacromolecules 11*, 1437–1442.

(8) Xu, F. J., Zhu, Y., Chai, M. Y., and Liu, F. S. (2011) Comparison of ethanolamine/ethylenediamine-functionalized poly(glycidyl methacrylate) for efficient gene delivery. *Acta Biomater. 7*, 3131–3140.

(9) Jeong, B., Bae, Y. H., Lee, D. S., and Kim, S. W. (1997) Biodegradable block copolymers as injectable drug-delivery systems. *Nature 388*, 860–862.

(10) Li, J., Li, X., Ni, X., Wang, X., Li, H., and Leong, K. W. (2006) Self-assembled supramolecular hydrogels formed by biodegradable PEO–PHB–PEO triblock copolymers and α-cyclodextrin for controlled drug delivery. *Biomaterials 27*, 4132–4140.

(11) Asayama, S., Maruyama, A., Cho, C. S., and Akaike, T. (2007) Design of comb-type polyamine copolymers for a novel pH-sensitive DNA carrier. *Bioconjugate Chem. 8*, 833–838.

(12) Ping, Y., Liu, C. D., Tang, G. P., Li, J. S., Li, J., Yang, W. T., and Xu, F. J. (2010) Functionalization of chitosan via atom transfer radical polymerization for gene delivery. *Adv. Funct. Mater. 20*, 3106–3116.

(13) Wang, Z. H., Li, W. B., Ma, J., Tang, G. P., Yang, W. T., and Xu, F. J. (2011) Functionalized nonionic dextran backbones by atom transfer radical polymerization for efficient gene delivery. *Macromolecules 44*, 230–239.

(14) Siegwart, D. J., Oh, J. K., and Matyjaszewski, K. (2011) ATRP in the design of functional materials for biomedical applications. *Prog. Polym. Sci. 37*, 18–37.

(15) Xu, F. J., Zhang, Z. X., Ping, Y., Li, J., Kang, E. T., and Neoh, K. G. (2009) Star-shaped cationic polymers by atom transfer radical polymerization from β-cyclodextrin cores for non-viral gene delivery. *Biomacromolecules 10*, 285–293.

(16) Wetering, P. V. D., Moret, E. E., Nieuwenbroek, N. M. E., Steenbergen, M. J. V., and Hennink, W. E. (1999) Structure-activity relationship of water-soluble cationic methacrylate/methacrylmide polymers for nonviral gene delivery. *Bioconjugate Chem. 10*, 589–597.

(17) Boussif, O., Lezoualc'h, F., Zanta, M. A., Mergny, M. D., Scherman, D., Demeneix, B., and Behr, J. P. (1995) A versatile vector for gene and oligonucleotide transfer into cells in culture and in vivo: polyethylenimine. *Proc. Natl. Acad. Sci. U.S.A. 92*, 7297–7301.

(18) Wang, D. A., Narang, A. S., Kotb, M., Gaber, A. O., Miller, D. D., Kim, S. W., and Mahato, R. I. (2002) Novel branched poly(ethylenimine)-cholesterol water-soluble lipopolymers for gene delivery. *Biomacromolecules 3*, 1197–1207.

Bioconjugate Chemistry

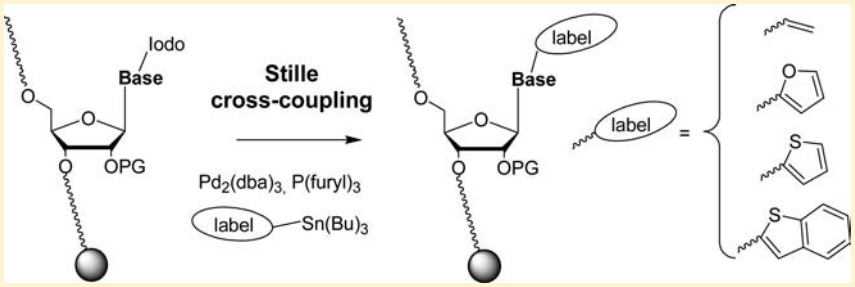
Article

pubs.acs.org/bc

Postsynthetic on Column RNA Labeling via Stille Coupling

Lena Wicke and Joachim W. Engels*

Institute for Organic Chemistry and Chemical Biology, Johann Wolfgang Goethe University, Max-von-Laue Strasse 7, 60438 Frankfurt am Main, Germany



ABSTRACT: Stille Coupling is a versatile C−C bond forming reaction with high functional group tolerance under mild conditions. Our on column synthesis concept for RNA modification is based on the incorporation of iodo substituted nucleotide precursors to RNA during automated standard solid phase synthesis via TBDMS-, TC-, and ACE- protecting group strategies. Subsequently, the RNA, still bound on solid support, is ready for orthogonal postsynthetic functionalization via Stille cross-couplings utilizing the advantages of solid phase synthesis. Several monomer test reactions were employed with 2-iodo adenosine and 5-iodo uridine and organostannanes as coupling partners under different conditions, changing the catalyst/ligand system, temperature, and reaction time as well as conventional heating and microwave irradiation. Finally, Stille cross-couplings under optimized conditions were transferred to fully protected 5-mer and 12-mer RNA oligonucleotides on-column. Deprotection and cleavage from solid support resulted in site-specifically labeled oligonucleotides. Derivatizations via Stille cross-couplings were performed initially with vinyltributylstannane as well as later with 2-furanyl-, 2-thiophene-, and benzothiophene-2-tributylstannanes yielding fluorescently functionalized RNA.

INTRODUCTION

Over the past decades, synthetic oligonucleotides gained increased importance in the interdisciplinary field of natural sciences and medicine. Particularly RNA, which plays various key roles in cellular processes where it functions in catalysis and regulation, has become of great interest.[1−4] In addition to applications of chemically modified RNA in therapy,[5] such as the antisense strategy[6] and RNA-interference,[7] labeled oligonucleotides are crucial tools for analysis of structure and dynamics,[8] particularly, to investigate its function, folding and mechanisms by spectroscopic techniques such as fluorescence spectroscopy (e.g., FRET),[9] EPR, or NMR spectroscopy.[10,11]

Several chemical modifications are described for DNA as well as for RNA. For an improved cellular uptake and increased nuclease resistance, they are primarily found at the sugar phosphate backbone (e.g., thiophosphates etc.), on the termini (e.g., cholesterol or bile acid), and in the 2′-position of ribose (e.g., cationic or lipophilic groups or as locked nucleic acids).[12,13] Dyes or radicals (e.g., fluorescent or spin labels) for spectroscopic purposes and photolabile groups in caged oligonucleotides can be conjugated to the sugar−phosphate backbone or in the 2′-position but are mainly attached to the base moiety.[8,14−16]

Generally, in addition to the possibility of synthesizing functionalized oligonucleotides via enzymatic incorporation, chemical derivatization mainly consists of the synthesis of modified phosphoramidites. They can be directly incorporated to oligonucleotides or by postsynthetic approaches in which stable precursor nucleotides are inserted and subsequently modified with a range of functional groups.[17] The former mentioned strategy is straightforward in assembling during solid-phase synthesis and subsequent purification but is not convergent and suffers from the time-consuming and sometimes complicated preparation of differently modified phosphoramidites. They are potentially sensitive to the conditions of automated oligonucleotide synthesis and also might limit the overall yield after insertion. The second procedure turns out to follow a more sophisticated strategy providing greater flexibility and synthetic ease, but the challenge is to find suitable and selective methods qualified for postsynthetic applications.[18−21]

One of the first postsynthetic approaches reported in literature for oligonucleotides is the substitution reaction of convertible nucleotides[18,22−34] bearing leaving groups such as fluorine, triazole, or substituted phenyls at the base with, e.g., amine-, thio-, or alkoxy nucleophiles. It has been recently applied to introduce rigid nitroxide radicals to RNA for EPR spectroscopy.[35] Other substitution reactions are related to electrophilic alkylbromides[36,37] conjugated to the sugar, and

Received: December 7, 2011
Revised: January 19, 2012
Published: February 9, 2012

ACS Publications © 2012 American Chemical Society

dx.doi.org/10.1021/bc200659j | *Bioconjugate Chem.* 2012, 23, 627−642

also, postsynthetic reactions on thio-substituted nucleosides involved in transfer-RNA or playing a role in cross-linking reactions of DNA[29,34,38,39] are reported. Furthermore, thiols or amines and lately seleno nucleophiles[40] were converted postsynthetically with reactive electrophiles such as activated esters, thiocyanates, or acid chlorides.[17] Labeling biomolecules by new bio-orthogonal methods[17] comprises, e.g., the Diels–Alder reaction, Staudinger ligation, and the so-called Click reaction (Huisgen-Sharpless [3 + 2] cycloaddition). The latter one is intensely used for postsynthetic modification primarily for DNA[41−44] but also for RNA.[45] Further prominent alternatives for postsynthetic conjugation of labels to oligonucleotides are palladium or copper catalyzed coupling reactions. Most notable is the Sonogashira cross-coupling, first reported by Khan and Grinstaff et al.[46] for modifying DNA on solid support, followed by Wagenknecht et al.[47] who attached 1-ethinylpyrene to DNA and our work applying a slightly modified procedure to generate EPR probes by introducing spin labels to DNA[48−50] and also to RNA[50−52] (using the TBDMS as well as the ACE protecting group strategy) as well as performing the synthesis of fluorescent RNA oligonucleotides.[53] While all early publications describe the cross-coupling during oligonucleotide synthesis in a semiautomated manner at the 5′-end and subsequent continuation of synthesis to fully assembled oligonucleotides, the postsynthetic Sonogashira in recent years could be employed by us[54] and other groups[55] after the complete synthesis without interruption. This "total post-synthetic" strategy avoids lower coupling yields after functionalization during automated synthesis and also permits one to introduce labels that are sensitive to synthesizer reagents such as acid or oxidants. A further postsynthetic, metal-mediated reaction has been presented by Matsuda et al.[20] who attached functional molecules to DNA via copper-catalyzed oxidative acetylenic coupling on column. Recently, palladium cross-couplings were extended to the Suzuki–Miyaura cross-coupling, used in arylation of guanine.[56] Contrary to the afore cited Sonogashira cross-couplings and the oxidative acetylenic homocoupling, this method is performed on deprotected DNA, already cleaved from solid support.

These studies demonstrate the progress achieved in convenient synthesis of modified oligonucleotides, and further elaboration is encouraged; nevertheless, there is a growing demand[40] in developing advanced approaches, in particular for RNA on a postsynthetic level that is described less extensively than for DNA.

We are interested in the synthetic aspect concerning the conjugation of labels to RNA at the nucleobases with the objective to obtain site-specifically functionalized oligonucleotides. For this aim, we would like to profit from a combination of both concepts, the efficiency of the postsynthetic approach and the advantage of on column synthesis.[20,46] This provides a fast and economical strategy in which only very small absolute amounts of reagents (coupling partner and catalyst/ligand) are necessary. Furthermore, it benefits from the high-yield coupling as well as ease of separation and purification of the desired product on solid support.

The success of postsynthetic derivatization depends on the chemoselectivity and yield of the reaction.[21] Thus, a convenient, orthogonal, and mild chemical method that lacks side reactions and is compatible with RNA in regard to stability and solid support conditions is required. For our purposes, most promising candidates are palladium-catalyzed cross-couplings starting from halogenated base residues as phosphoramidite precursors that are commercially available or can be prepared without large synthetic effort. For reasons of versatility, we chose the Stille cross-coupling[57] that fulfils the qualifications for the postsynthetic reaction of RNA on solid-phase. This method tolerates a wide range of functionalities, proceeds under mild conditions without the need of a base, and utilizes reagents stable against air and moisture.[58,59] The Stille cross-coupling uses vinylic or aromatic alkylstannanes as coupling partners, which might be the only drawback in terms of the toxicity of organotin compounds. This handicap is diminished to some extent in our approach on solid-phase as only very small amounts of tin reagents are used and can be easily separated from the product on bead by simple washing.

In this article, we present the palladium mediated Stille cross-coupling on monomeric model compounds and demonstrate, for the first time, the feasibility of the Stille cross-coupling for the convenient synthesis of postsynthetically modified RNAs on column. To show the generality and applicability of our new approach, we synthesized a set of 5-mer and 12-mer RNAs via TBDMS, TC (thiomorpholine-carbothioate)- and ACE [bis-(acetoxyethyloxy)-methyl] protecting group strategies. There we attached different coupling partners to iodinated uridine and adenosine resulting in modified RNA that is ready for further modification or can be used for fluorescence spectroscopy.

EXPERIMENTAL PROCEDURES

General. All reagents were of the highest commercially available quality and were used as received. It must be noted that the organo(tributyl)tin reagents are toxic and can harm health via inhalation, skin contact, and ingestion.

NMR spectra were recorded on Bruker AM, DPX, and AV instruments at 250, 300, and 400 MHz and 300 K. Chemical shifts (δ) are reported in ppm relative to the solvent signal. The fine structure of proton signals was specified with s (singlet), d (doublet), t (triplet), q (quartet), m (multiplet), dd (doublet of doublet), dt (doublet of triplet), and bs (broad singlet). Assignments were made by DEPT, COSY, HSQC, and HMBC experiments.

Thin layer chromatograms (TLC) were recorded on 60 F_{254} plates from Merck (thickness of layer 0.2 mm). Column chromatography was carried out on silica gel 60 (40–63 μm, Merck).

Reversed phase (RP) HPLC was performed on a Jasco LC-2000Plus HPLC system equipped with a Jasco UV 2075Plus detector (detection at 254 nm) and a preparative Phenomenex Jupiter Proteo C12 column (250 × 15 mm) or an analytical Jupiter Proteo C12 column (250 × 4.6 mm). Anion-exchange (AE) HPLC was carried out on a Jasco LC-900 HPLC system equipped with a Jasco UV-970 detector (detection at 254 nm) and a Dionex BioLC DNAPac PA-100 (250 × 9 mm) column.

ESI-Mass spectrometry for monomers was performed on a Fisons instrument equipped with a VG platform II with a quadrupol analyzer or on a Nano-ESI Mariner Biospectrometry Workstation from PerSeptive Biosystems.

High resolution mass spectrometry (HRMS) was provided by a MALDI Orbitrap LTQ XL instrument (Thermo Fisher) equipped with a 337 nm nitrogen laser. 4-Hydroxy alpha cyanocinnamic acid was applied as the matrix, and the matrix peaks were used as lock masses for internal calibration.

Oligonucleotides were analyzed via ESI mass spectrometry using a LCMS instrument with microTOF-Q II analyzer (Bruker). An Agilent 1200 Series HPLC using the eluent

dx.doi.org/10.1021/bc200659j | Bioconjugate Chem. 2012, 23, 627–642

methanol/0.005 M TEAA buffer (gradient 0−60%) was applied as the LC system.

UV spectroscopy was carried out on a Jasco V650 spectrophotometer using 1.0 cm cuvettes typically in 10 μM concentration. Fluorescence spectroscopy was performed on a Hitachi F4500 fluorescence spectrometer using 0.3 cm cuvettes in 10 μM concentration.

The numbering of atoms in the nucleoside parts is according to IUPAC (the common numbering convention of nucleosides).

Stille Cross-Coupling on Monomers. Synthesis of modified nucleosides via Stille cross-coupling is based on procedures already reported. While we used the Stille cross-coupling on monomers as a model reaction to establish a setting qualified for transfer to RNA, we modified the conditions with respect to solvent, temperature, catalyst/ligand loading, and reaction time. In general, we applied two main procedures (method A following Nair et al[60−62] and method B following Farina et al[63]). Particular changes in the mentioned parameters are presented in the Results and Discussion section. To screen suitable conditions, optimized experiments were mostly controlled by RP-HPLC [analytical Phenomenex Jupiter Proteo C12 column (250 × 4.6 mm) using the gradient 8−17% C within 20 min, 10% A constantly (eluent A, 1 M TEAA buffer, pH 6.5; eluent B, Millipore water; eluent C, acetonitrile; 1 mL/min flow)] to monitor conversion rates. Experiments under defined setups were also accomplished to isolate, purify, and characterize the modified nucleosides after synthesis. For that purpose, we followed the procedures described below. The analytical data found for the known compounds **2**, **4**, **5**, **6**, **8**, **9**, and **10** are fully consistent with the data already reported. Compound **7** has not been described yet and is completely characterized here.

General Procedures. Method A 1 (Procedure According to Nair et al.[60−62]). In a dry 2-neck flask under argon, typically 100 mg of nucleoside was dissolved in 2 mL of DMF, and consecutively 4.4 mol % $Pd(MeCN)_2Cl_2$ and 1.1 equiv tributyl organostannane were added. The yellow reaction mixture was heated at 90 °C for 3 h and changed color over orange and brown to black. After cooling to ambient temperature, the catalyst was filtered off and washed with ethyl acetate. The yellow filtrate was concentrated under reduced pressure and the crude product purified by silica gel column chromatography using the gradient 9:1 DCM/MeOH. The product as an off-white solid was usually obtained in 90−99%.

Method A 2 (Procedure According to Nair et al.[60−62]). This procedure is identical to method A 1 with the difference that an increased amount of 5.4 mol % $Pd(MeCN)_2Cl_2$ and additionally 12 mol % ligand P(*o*-tol)$_3$ was applied.

Method B 1 (Based on the Procedure of Farina et al.[63]). In a dry 2-neck flask under argon, typically 100 mg of nucleoside was dissolved in 2 mL of DMF, 5 mol % $Pd_2(dba)_3$ was added, and the black-colored reaction mixture was stirred for 5 min. Subsequently, 1.1 equiv tributyl organostannane was dropped on the suspension over 5 min resulting in brightening up, and the green−yellow reaction mixture was stirred for typically 3 h at 60 °C. After filtration through Celite, the solvent was removed under reduced pressure, and the crude product was purified by column chromatography using the gradient 9:1 DCM/MeOH. The product as an off-white solid was usually obtained in a yield of 90−99%.

Method B 2 (Based on the Procedure of Farina et al.[63]). This procedure is identical to method B 1 with the difference that 5.4 mol % $Pd_2(dba)_3$ was used, and 12 mol % ligand P(fur)$_3$ was added at the same time.

2-Vinyladenosine[64,65] (2). Compound **2** was prepared, isolated, and purified following method A 1 (99% yield), method A 2 (99% yield), and method B 1 (95% yield).

R_F = 0.17 (CH_2Cl_2/MeOH = 9:1). ^{1}H NMR (400 MHz, DMSO-d_6,): δ = 3.53−3.59 (1H, m, 5′-C*H*), 3.65−3.70 (1H, m, 5′-C*H*), 3.94−3.98 (1H, m, 4′-C*H*), 4.16 (1H, bs, 3′-C*H*), 4.65 (1H, q, J = 5.2 Hz, 2′-C*H*), 5.20 (1H, d, J = 3.0 Hz, 3′-O*H*), 5.39 (1H, dd, J = 6.8 and 4.6 Hz, 5′-O*H*), 5.44 (1H, d, J = 5.6 Hz, 2′-O*H*), 5.55 (1H, dd, J_{cis} = 10.4 and J_{gem} = 2.2 Hz, vinyl-C*H2*$_a$″), 5.88 (1H, d, J = 6.4 Hz, 1′-C*H*), 6.37 (1H, dd, J_{trans} = 17.3 and J_{gem} = 2.2 Hz, vinyl-C*H2*$_b$″), 6.60 (1H, dd, J_{trans} = 17.3 and J_{cis} = 10.4 Hz, vinyl-C*H1*″), 7.29 (2H, bs, N*H*$_2$), 8.32 (1H, s, 8-C*H*) ppm.

^{13}C NMR (100 MHz, DMSO-d_6, 300 K): δ = 62.75 (5′-CH_2), 70.74 (3′-CH_2), 73.22 (2′-CH), 85.88 (4′-CH), 87.64 (1′-CH), 118.28 (5-*C*), 121.10 (HC=CH_2), 136.88 (HC=CH_2), 140.30 (8-CH), 149.58 (4-*C*), 155.65 (6-CNH_2), 157.69 (2-*C*-vinyl) ppm.

ESI(+)-MS (m/z) calcd, 293.11 [$C_{12}H_{15}N_5O_4$]; found, 294.1 [M + H]$^+$. HRMS (M + H): calcd, 294.11968 and 295.12304; found, 294.11969 and 295.12219.

5-Vinyluridine[63,66] (4). Compound **4** was prepared, isolated, and purified following method B 2 with a reaction time of only 2 h (control via RP-HPLC) in a yield of 90%.

R_F = 0.14 (CH_2Cl_2/MeOH = 9:1). ^{1}H NMR (250 MHz, DMSO-d_6): δ = 3.54−3.62 (1H, m, 5′-C*H*), 3.66−3.74 (1H, m, 5′-C*H*), 3.84−3.88 (1H, m, 4′-C*H*), 3.98−4.09 (2H, m, 2′-C*H* and 3′-C*H*), 5.06 (1H, d, J = 5.2 Hz, 3′-O*H*), 5.12 (1H, dd, J_{cis} = 11.5 and J_{gem} = 2.0 Hz, vinyl-C*H2*$_a$″), 5.23 (1H, t, J = 4.8 Hz, 5′-O*H*), 5.40 (1H, d, J = 5.3 Hz, 2′-O*H*), 5.78 (1H, d, J = 4.5 Hz, 1′-C*H*), 5.92 (1H, dd, J_{trans} = 17.7 and J_{gem} = 2.0 Hz, vinyl-C*H2*$_b$″), 6.37 (1H, dd, J_{trans} = 17.7 and J_{cis} = 11.5 Hz, vinyl-C*H1*″), 8.20 (1H, s, 6-C*H*); 11.42 (1H, bs, N*H*) ppm.

^{13}C NMR (75 MHz, DMSO-d_6): δ = 61.50 (5′-CH_2), 69.12 (3′-CH), 73.56 (2′-CH), 84.37 (4′-CH), 87.71 (1′-CH), 111.11 (5-*C*-vinyl), 114.16 (HC=CH_2), 128.89 (HC=CH_2), 138.03 (6-*C*H), 150.22 (2-*C*O), 162.41 (4-*C*O) ppm.

ESI(−)-MS (m/z) calcd, 270.09 [$C_{11}H_{14}N_2O_6$]; found, 269.1 [M − H]$^-$.

2-Fur(2-yl)adenosine[67] (5). Compound **5** was prepared, isolated, and purified following method B 1 (99% yield) as well as method B 2 (99% yield) in a reaction time of 4 h (control via TLC, eluent 9:1 DCM/MeOH) for both procedures.

R_F = 0.18 (CH_2Cl_2/MeOH = 9:1). ^{1}H NMR (250 MHz, DMSO-d_6,): δ = 3.53−3.62 (1H, m, 5′-C*H*), 3.66−3.74 (1H, m, 5′-C*H*), 3.95−3.99 (1H, m, 4′-C*H*), 4.16−4.21 (1H, m, 3′-C*H*), 4.67 (1H, dt, J = 5.9 and 5.4 Hz, 2′-C*H*), 5.11 (1H, dd, J = 6.3 and 5.1 Hz, 5′-O*H*), 5.20 (1H, d, J = 4.5 Hz, 3′-O*H*), 5.44 (1H, d, J = 6.1 Hz, 2′-O*H*), 5.92 (1H, d, J = 6.3 Hz, 1′-C*H*), 6.62 (1H, dd, J = 3.2 and 1.7 Hz, Furyl-*H4*″), 7.12 (1H, d, J = 3.2 Hz, Furyl-*H3*″),7.40 (2H, bs, N*H*$_2$), 7.79 (1H, bs, Furyl-*H5*″), 8.35 (1H, s, 8-C*H*) ppm.

^{13}C NMR (100 MHz, DMSO-d_6): δ = 61.46 (5′-CH_2), 70.46 (3′-CH), 73.01 (2′-CH), 85.54 (4′-CH), 87.11 (1′-CH), 110.87 (furyl-*C3*″), 111.56 (furyl-*C4*″), 117.83 (5-*C*), 139.75 (8-CH), 144.11 (furyl-*C5*″), 149.67 (4-*C*), 151.14 (2-*C*-furyl), 152.37 (furyl-*C2*″), 155.68 (6-CNH_2) ppm.

ESI(+)-MS (m/z) calcd, 333.11 [$C_{14}H_{15}N_5O_5$]; found, 334.3 [M + H]$^+$, 356.4 [M + Na]$^+$.

HRMS (M + H): calcd, 334.11460 and 335.11795; found, 334.11488 and 335.11821.

dx.doi.org/10.1021/bc200659j | *Bioconjugate Chem.* 2012, 23, 627−642

2-Thien(2-yl)adenosine[67] (6). Compound **6** was prepared, isolated, and purified following method B 2 (98% yield) in a reaction time of 6 h (control via TLC, eluent 9:1 DCM/MeOH).

R_F = 0.20 (CH_2Cl_2/MeOH = 9:1). ^{1}H NMR (250 MHz, DMSO-d_6): δ = 3.53−3.62 (1H, m, 5′-C*H*), 3.67−3.75 (1H, m, 5′-C*H*), 3.94−3.99 (1H, m, 4′-C*H*), 4.20−4.56 (1H, m, 3′-C*H*), 4.72 (1H, dt, *J* = 5.8 and 5.4 Hz, 2′-C*H*), 5.05 (1H, t, *J* = 5.7 Hz, 5′-O*H*), 5.22 (1H, d, *J* = 4.6 Hz, 3′-O*H*), 5.46 (1H, d, *J* = 6.1 Hz, 2′-O*H*), 5.91 (1H, d, *J* = 6.1 Hz, 1′-C*H*), 7.14 (1H, dd, *J* = 3.6 and 4.8 Hz, thienyl-*H4*″), 7.37 (2H, bs, NH_2), 7.62 (1H, d, *J* = 4.7 Hz, thienyl-*H5*″), 7.82 (1H, d, *J* = 3.3 Hz, thienyl-*H3*″), 8.33 (1H, s, 8-C*H*) ppm.

^{13}C NMR (62.9 MHz, DMSO-d_6): δ = 61.65 (5′-CH_2), 70.71 (3′-*C*H), 73.06 (2′-*C*H), 85.54 (4′-*C*H), 87.41 (1′-*C*H), 118.07 (5-*C*), 127.04 (thienyl-*C3*″), 127.79 (thienyl-*C5*″), 128.74 (thienyl-*C4*″), 140.13 (8-*C*H), 144.20 (thienyl-*C2*″), 149.80 (4-*C*), 154.78 (2-*C*-thienyl), 155.61 (6-*C*NH_2) ppm.

ESI(+)-MS (*m*/*z*) calcd, 349.08 [$C_{14}H_{15}N_5O_4S$]; found, 350.3 [M + H]$^+$, 372.5 [M + Na]$^+$.

HRMS (M + H): calcd, 350.09175, 351.09511 and 352.08755; found, 350.09203, 351.09465 and 352.08778.

2-Benzo[*b*]thienyladenosine (7). Compound **7** was prepared, isolated, and purified following method B 2 (90% yield after several purification steps) in a reaction time of 6 h (control via TLC, eluent 9:1 DCM/MeOH). In this experiment, the crude product was treated with numerous washes by hexane to remove the remaining tributyltin iodide. To accomplish sufficient purity, an analytical amount of product was furthermore purified via RP-HPLC [preparative Phenomenex Jupiter Proteo C12 column (250 × 15 mm) using the gradient 3−60% C within 45 min, 10% A constantly (eluent A, 1 M TEAA buffer, pH 6.5; eluent B, Millipore water; eluent C, acetonitrile; 6 mL/min flow)], and a pure product of high quality in 90% could be recovered.

R_F = 0.22 (CH_2Cl_2/MeOH = 9:1). ^{1}H NMR (250 MHz, DMSO-d_6): δ = 3.55−3.64 (1H, m, 5′-C*H*), 3.69−3.77 (1H, m, 5′-C*H*), 3.95−3.99 (1H, m, 4′-C*H*), 4.21−4.26 (1H, m, 3′-C*H*), 4.73 (1H, q, *J* = 5.8 Hz, 2′-C*H*), 5.04 (1H, t, *J* = 5.7 Hz, 5′-O*H*), 5.24 (1H, d, *J* = 4.7 Hz, 3′-O*H*), 5.49 (1H, d, *J* = 6.1 Hz, 2′-O*H*), 5.96 (1H, d, *J* = 6.0 Hz, 1′-C*H*), 7.39 (2H, dd, *J* = 3.1 and 6.0 Hz, benzothienyl-*H6*″ *and H7*″), 7.47 (2H, bs, NH_2), 7.91−7.98 (2H, m, benzothienyl-*H5*″ *and H8*″), 8.15 (1H, s, benzothienyl-*H3*″), 8.40 (1H, s, 8-C*H*) ppm.

^{13}C NMR (100 MHz, DMSO-d_6): δ = 61.61 (5′-CH_2), 70.58 (3′-*C*H), 73.18 (2′-*C*H), 85.48 (4′-*C*H), 87.24 (1′-*C*H), 118.39 (5-*C*), 122.45 (benzothienyl-*C8*″), 123.57 (benzothienyl-*C3*″), 124.46 (benzothienyl-*C5*″ *and C6*″), 125.22 (benzothienyl-*C7*″), 139.76 (benzothienyl-*C9*″), 140.32 (benzothienyl-*C4*″), 140.42 (8-*C*H), 144.33 (benzothienyl-*C2*″), 149.87 (4-*C*), 154.67 (2-*C*-benzothienyl), 155.65 (6-*C*NH_2) ppm.

ESI(−)-MS (*m*/*z*) calcd, 399.10 [$C_{18}H_{17}N_5O_4S$]; found, 398.4 [M − H]$^-$.

HRMS (M + H): calcd, 400.10740, 401.11076, and 402.10320; found, 400.10708, 401.10931 and 402.10313

5-Fur(2-yl)uridine[68] (8). Compound **8** was prepared, isolated, and purified following method B 2 in a reaction time of 4 h (control via TLC, eluent 9:1 DCM/MeOH). The product could be obtained in 99% yield as an off-white solid but is light-sensitive (color turns to orange if the compound is disposed to light).

R_F = 0.21 (CH_2Cl_2/MeOH = 9:1). ^{1}H NMR (300 MHz, DMSO-d_6): δ = 3.57−3.70 (2H, m, 5′-CH_2), 3.88−3.91 (1H, m, 4′-C*H*), 4.01 (1H, pt, *J* = 4.6 Hz, 3′-C*H*), 4.11 (1H, pt, *J* = 5.0 Hz, 2′-C*H*), 5.10 (1H, bs, 3′-O*H*), 5.18 (1H, bs, 5′-O*H*), 5.42 (1H, bs, 2′-O*H*), 5.86 (1H, d, *J* = 5.1 Hz, 1′-C*H*), 6.52 (1H, dd, *J* = 1.8 and 3.3 Hz, furyl-*H4*″), 6.85 (1H, d, *J* = 3.1 Hz, furyl-*H3*″), 7.60 (1H, d, *J* = 1.7 Hz, furyl-*H5*″), 8.41 (1H, s, 6-C*H*); 11.65 (1H, bs, N*H*) ppm.

^{13}C NMR (100 MHz, DMSO-d_6): δ = 61.50 (5′-CH_2), 70.56 (3′-*C*H), 74.45 (2′-*C*H), 85.66 (4′-*C*H), 89.11 (1′-*C*H),105.57 (5-*C*-furyl), 107.86 (furyl-*C3*″), 111.46 (furyl-*C4*″), 134.83 (6-*C*H), 141.47 (furyl-*C5*″), 146.29 (furyl-*C2*″), 149.60 (2-*C*O), 160.02 (4-*C*O) ppm.

ESI(−)-MS (*m*/*z*) calcd, 310.08 [$C_{13}H_{14}N_2O_7$]; found, 309.3 [M − H]$^-$.

HRMS (M + Na): calcd, 333.06932 and 334.07268; found, 333.06950 and 334.07116.

5-Thien(2-yl)uridine[69] (9). Compound **9** was prepared, isolated, and purified following method B 2 (99% yield) in a reaction time of 3 h (control via TLC, eluent 9:1 DCM/MeOH).

R_F = 0.27 (CH_2Cl_2/MeOH = 9:1). ^{1}H NMR (250 MHz, DMSO-d_6): δ = 3.59−3.67 (1H, m, 5′-C*H*), 3.71−3.79 (1H, m, 5′-C*H*), 3.90−3.92 (1H, m, 4′-C*H*), 4.03−4.15 (2H, m, 2′- and 3′-C*H*), 5.07 (1H, d, *J* = 5.4 Hz, 3′-O*H*), 5.41 (1H, t, *J* = 4.6 Hz, 5′-O*H*), 5.45 (1H, d, *J* = 5.2 Hz, 2′-O*H*), 5.83 (1H, d, *J* = 4.1 Hz, 1′-C*H*), 7.04 (1H, dd, *J* = 3.7 and 5.1 Hz, thienyl-*H4*″), 7.40 (1H, dd, *J* = 3.7 and 1.0 Hz, thienyl-*H3*″), 7.45 (1H, dd, *J* = 5.1 and 1.0 Hz, thienyl-*H5*″), 8.64 (1H, s, 6-C*H*); 11.68 (1H, bs, N*H*) ppm.

^{13}C NMR (62.9 MHz, DMSO-d_6): δ = 60.07 (5′-CH_2), 69.25 (3′-*C*H), 74.16 (2′-*C*H), 84.54 (4′-*C*H), 88.58 (1′-*C*H), 108.16 (5-*C*-thienyl), 122.42 (thienyl-*C3*″), 125.54 (thienyl-*C5*″), 126.25 (thienyl-*C4*″), 133.79 (thienyl-*C2*″), 135.59 (6-*C*H), 149.43 (2-*C*O), 161.15 (4-*C*O) ppm.

ESI(−)-MS (*m*/*z*) calcd, 326.06 [$C_{13}H_{14}N_2O_6S$]; found, 325.2 [M − H]$^-$.

HRMS (M + Na): calcd, 349.04648, 350.04983 and 351.04227; found, 349.04693, 350.05079, and 351.06179.

5-Benzo[*b*]thienyluridine[70] (10). Compound **10** was prepared, isolated, and purified following method B 2 (95% yield) in a reaction time of 3 h (control via TLC, eluent 9:1 DCM/MeOH). In this experiment, the crude product was additionally extracted between aqueous potassium fluoride solution and ethyl acetate to remove the remaining tributyltin iodide.

R_F = 0.34 (CH_2Cl_2/MeOH = 9:1). ^{1}H NMR (250 MHz, DMSO-d_6): δ = 3.65−3.72 (1H, m, 5′-C*H*), 3.78−3.86 (1H, m, 5′-C*H*), 3.94−3.97 (1H, m, 4′-C*H*), 4.07−4.19 (2H, m, 2′- and 3′-C*H*), 5.12 (1H, d, *J* = 5.3 Hz, 3′-O*H*), 5.49−5.54 (2H, m, 2′-O*H* and 5′-O*H*), 5.85 (1H, d, *J* = 3.7 Hz, 1′-C*H*), 7.26−7.38 (2H, m, benzothienyl-*H6*″ *and H7*″), 7.78 (1H, s, benzothienyl-*H3*″), 7.79 (1H, m, benzothienyl-*H5*″), 7.90 (1H, d, *J* = 7.1 Hz, benzothienyl-*H8*″), 8.83 (1H, s, 6-C*H*); 11.78 (1H, bs, N*H*) ppm.

^{13}C NMR (63 MHz, DMSO-d_6): δ = 59.91 (5′-CH_2), 69.08 (3′-*C*H), 74.28 (2′-*C*H), 84.44 (4′-*C*H), 88.82 (1′-*C*H), 107.73 (5-*C*-benzothienyl), 119.01(benzothienyl-*C3*″), 121.77 (benzothienyl-*C8*″), 122.94 (benzothienyl-*C5*″), 123.87 (benzothienyl-*C6*″), 124.21 (benzothienyl-*C7*″), 135.01 (benzothienyl-*C2*″), 137.46 (6-*C*H), 138.73 (benzothienyl-*C4*″), 138.94 (benzothienyl-*C9*″) 149.42 (2-*C*O), 161.22 (4-*C*O) ppm.

ESI(−)-MS (*m*/*z*) calcd, 376.07 [$C_{17}H_{16}N_2O_6S$]; found, 375.3 [M − H]$^-$, 411.3 [M + Cl]$^-$.

dx.doi.org/10.1021/bc200659j | *Bioconjugate Chem.* 2012, 23, 627−642

HRMS (M + Na): calcd, 399.06213, 400.06548, and 401.05792; found, 399.06232, 400.06669, and 401.07729.

Preparation of TC Protected 5-Iodo Uridine Phosphoramidite. Synthesis of 5-iodo uridine phosphoramidite via TC protection was performed according to the procedure reported by Caruthers et al.[71] for natural nucleosides. Marckiewicz protected 5-iodo uridine **11** was synthesized via standard methods (see, e.g., Matsuda et al.[72]).

2′-*O*-(Thiocarbonylimidazolyl)-3′,5′-*O*-(tetraisopropyldisiloxane-1,3-diyl)-5-iodo Uridine (12). Silyl protected 5-iodo uridine **11** (1.32 g, 2.15 mmol) was dissolved in 13.2 mL of dry MeCN under argon. Subsequently, 0.58 g (3.23 mmol) of 1,1′-thiocarbonyldiimidazole and 15.9 mg (0.13 mmol) of DMAP were added, and the reaction was stirred for 6 h at 30 °C. After cooling for 2 h at −20 °C, the product had crystallized to a white solid and was isolated by filtration. Dried under vacuum, 1.17 g (1.62 mmol, 75%) of the 2′-thiocarbonylimidazole product **12** was obtained.

^{1}H NMR (250 MHz, DMSO-d_6): δ = 0.80−1.09 (28 H, m, 2 × Si(C*H*(CH_3)$_2$)$_2$); 3.94−4.02 (1H, m, 4′-C*H*), 4.10−4.13 (2H, m, 5′-CH_2), 4.77−4.83 (1H, m, 3′-C*H*), 5.91−5.93 (1H, d, *J* = 1.4 Hz 1′-C*H*), 6.35 (1H, dd, *J* = 5.7 Hz, *J* = 1.4 Hz, 2′-C*H*), 7.11−7.13 (1H, m, imidazolyl), 7.86−7.88 (1H, m, imidazolyl), 8.05 (1H, s, imidazolyl), 8.55 (1H, s, 6-C*H*); 11.82 (1H, bs, N*H*) ppm.

^{13}C NMR (75 MHz, DMSO-d_6): δ = 11.97, 12.03, 12.26, 12.55, 16.43, 16.80, 16.87, 17.02, 17.20, 17.30, 60.34, 69.34, 69.55, 81.26, 82.72, 88.94, 118.55, 130.88, 136.94, 145.84, 149.72, 160.52, 183.07 ppm.

ESI(+)-MS (*m*/*z*) calcd, 722,11 [$C_{25}H_{39}IN_4O_7SSi_2$]; found, 724.2 [M + H]$^+$.

2′-*O*-(1,1-Dioxo-1λ^6-thiomorpholine-4-carbothioate)-3′,5′-*O*-(tetraisopropyldisiloxane-1,3-diyl)-5-iodo Uridine (13). Compound **12** (1.75 g (2.42 mmol)) was dissolved in 20 mL of dry MeCN under argon by heating with a heatgun. While the reaction mixture was still hot, 0.36 g (2.66 mmol) of thiomorpholine-1,1-dioxide was added and the reaction stirred for 6.5 h at 30 °C. The reaction was controlled via TLC (95:5 DCM/isopropanol), and after completion, the solvent was removed. The crude product was subsequently purified by column chromatography (gradient 99:1 DCM/isopropanol) and dried under vacuum yielding in 1.72 g (2.18 mmol, 90%) of product **13**.

R_F = 0.54 (DCM/isopropanol = 95:5). ^{1}H NMR (400 MHz, DMSO-d_6): δ = 0.97−1.08 (28 H, m, 2 × Si(C*H*(CH_3)$_2$)$_2$); 3.09−3.16 (2H, m, thiomorpholine); 3.31−3.39 (2H, m, thiomorpholine); 3.89−4.48 (7H, m, 4′-C*H*, 5′-CH_2, thiomorpholine), 4.70−4.74 (1H, m, 3′-C*H*), 5.73 (1H, d, *J* = 1.7 Hz, 1′-C*H*), 6.11 (1H, dd, *J* = 5.9 Hz, *J* = 5.9 Hz, 2′-C*H*), 8.07 (1H, s, 6-C*H*); 11.82 (1H, bs, N*H*) ppm.

^{13}C NMR (75 MHz, DMSO-d_6): δ = 11.83, 12.05, 12.31, 12.57 (2 × Si(CH(CH_3)$_2$)$_2$); 16.64, 16.73, 16.80, 16.82, 17.03, 17.20, 17.22, 17.30 (2 × Si(CH(CH_3)$_2$)$_2$); 43.47, 48.05, 50.52, 50.97 (thiomorpholine); 60.42 (5′-CH_2); 68.91 (3′-CH), 69.62 (6-*C*-I), 80.66 (2′-CH), 81.38 (4′-CH), 90.01 (1′-CH), 146.30 (6-CH), 149.72 (2-CO), 160.52 (4-CO), 183.07 (C═S) ppm.

HRMS (M + Na): calcd, 812.09944, 813.10279, 814.09523, and 815.09859; found, 812.10108, 813.10375, 814.09516, and 815.10020.

2′-*O*-(1,1-Dioxo-1λ^6-thiomorpholine-4-carbothioate)-5-iodo Uridine (15). Compound **13** (1.98 g (2.51 mmol)) was dissolved in 20 mL of 2-MeTHF under argon, and 1.22 mL (15.06 mmol) pyridine was added. The reaction mixture was then cooled to 0 °C, and 0.78 mL of 70% HF in pyridine was added dropwise with stirring. After addition, the reaction was stirred for 22 h at room temperature. Reaction control was performed via TLC (95:5 DCM/isopropanol). The reaction mixture was extracted with water twice, the combined aqueous layers were re-extracted with 2-MeTHF, and the combined organic layers were dried over anhydrous sodium sulfate. Sodium sulfate was removed by filtration and the solvent evaporated under vacuum (keeping the water bath temperature less than 40 °C). For further purification, column chromatography with DCM and 5−10% isopropanol was carried out, and after drying under high vacuum, product **15** was obtained in 85% (1.17 g, 2.13 mmol) yield.

R_F = 0.12 (DCM/isopropanol = 95:5). ^{1}H NMR (300 MHz, DMSO-d_6): δ = 3.20−3.31 (4H, m, thiomorpholine); 3.62−3.68 (2H, m, 5′-CH_2), 4.01−4.50 (6H, m, 4′-C*H*, 3′-C*H*, thiomorpholine), 5.34 (1H, t, *J* = 4.5 Hz, 5′-O*H*), 5.62 (1H, d, *J* = 5.2 Hz, 3′-O*H*), 5.66 (1H, dd, *J* = 5.4 Hz, *J* = 6.4 Hz, 2′-C*H*), 6.06 (1H, d, *J* = 6.5 Hz, 1′-C*H*), 8.41 (1H, s, 6-C*H*); 11.72 (1H, bs, N*H*) ppm.

^{13}C NMR (75 MHz, DMSO-d_6): δ = 43.47, 48.12, 50.39, 50.63 (thiomorpholine); 60.98 (5′-CH_2); 69.27 (3′-CH), 70.16 (6-*C*-I), 81.59 (2′-CH), 85.68 (1′-CH), 86.51 (4′-CH), 144.48 (6-CH), 150.68 (2-CO), 160.35 (4-CO), 186.34 (*C*═S) ppm.

HRMS (M + Na): calcd, 547.96528, 548.96863 and 549.96107; found, 547.96419, 548.96757 549.95986.

2′-*O*-(1,1-Dioxo-1λ^6-thiomorpholine-4-carbothioate)-5′-*O*-(4,4′-dimethoxytrityl)-5-iodo Uridine (16). Compound **15** (1.77 g (2.51 mmol)) was dissolved in 40 mL of dry DCM under argon and cooled to 0 °C. In the first instance, 0.65 equiv (0.18 mL, 1.63 mmol) of NMM and 0.6 equiv (0.51 g, 1.51 mmol) of DmTrCl were added to the reaction mixture with stirring at 0 °C. More NMM (0.65 equiv) and DmTrCl (0.6 equiv) were added in portions while the reaction was controlled by TLC (95:5 DCM/isopropanol). The conversion was complete after 4 h, and the reaction mixture was quenched with MeOH, extracted with saturated $NaHCO_3$ and DCM, and the combined organic fractions dried over sodium sulfate. After evaporation of the solvent, the crude product was purified by column chromatography (gradient: DCM with 1−5% isopropanol) yielding in 70% (1.49 g, 1.76 mmol) product **16**.

R_F = 0.49 (DCM/isopropanol = 95:5). ^{1}H NMR (300 MHz, DMSO-d_6): δ = 3.16−3.31 (6H, m, thiomorpholine,, 5′-CH_2); 3.74 (6H, s, 2 × OCH_3) 4.11−4.51 (6H, m, 4′-C*H*, 3′-C*H*, thiomorpholine), 5.70 (1H, d, *J* = 5.4 Hz, 3′-O*H*), 5.91 (1H, t, *J* = 6.2 Hz, 2′-C*H*), 6.09 (1H, d, *J* = 6.4 Hz, 1′-C*H*), 6.88−6.91 (4H, m, DmTr); 7.21−7.36 (7H, m, DmTr); 7.45−7.47 (2H, m, DmTr); 8.10 (1H, s, 6-C*H*); 11.81 (1H, bs, N*H*) ppm.

^{13}C NMR (75 MHz, DMSO-d_6): δ = 43.49, 48.19, 50.39, 50.61 (thiomorpholine); 54.97 (2 × OCH_3); 63.41 (5′-CH_2); 68.99 (3′-CH), 70.59 (6-*C*-I), 81.04 (2′-CH), 84.22 (4′-CH), 85.88 (1′-CH), 86.13 (OC-triphenyl); 113.22, 126.69, 127.60, 127.88, 129.73, 135.00, 135.18 (DmTr); 144.42 (6-CH), 150.11 (2-CO), 158.06 (DmTr); 160.32 (4-CO), 186.36 (*C*═S) ppm.

ESI(+)-MS (*m*/*z*) calcd, 872,08 [$C_{35}H_{36}IN_3O_{10}S_2Na$]; found, 872.26 [M + Na]$^+$.

2′-*O*-(1,1-Dioxo-1λ^6-thiomorpholine-4-carbothioate)-5′-*O*-(4,4′-dimethoxytrityl)-5-iodo uridine-3′-*O*-(β-cyanoethyl)-*N*,*N*-diisopropyl-phosphoramidite (14). Nucleoside **16** (1.51 g (1.78 mmol)) was dissolved in 40 mL of dry DCM under argon and 0.29 mL (2.67 mmol) of NMM and 0.48 mL (2.14 mmol) of 2-cyanoethyl-*N*,*N*-diisopropylchloro-

dx.doi.org/10.1021/bc200659j | *Bioconjugate Chem.* 2012, 23, 627−642

phosphoramidite were added. After 1 h, a precipitate formed and was dissolved by the addition of 10 mL of DCM with stirring. The reaction was controlled via TLC (95:5 DCM/isopropanol); after 2 h, the conversion was still incomplete, and thus, another 0.08 mL (0.71 mmol) of NMM and 0.12 mL (0.53 mmol) of 2-cyanoethyl-*N*,*N*-diisopropylchlorophosphoramidite were added. The reaction showed to be complete after 3.5 h and was stopped by the addition of DCM and saturated $NaHCO_3$. After separation, the organic phase was extracted with saturated NaCl and subsequently dried over anhydrous sodium sulfate. Finally, the DCM layer was filtered and evaporated. The resulting oil was dissolved in DCM and purified by chromatography on a column pre-equilibrated with 10% acetone and 1% TEA in hexanes. After neutralization of the silica gel, the excess TEA was removed by flushing the column with a volume of 35% acetone in hexanes. Separation was performed using the gradient 35−40% acetone in hexane, and product **14** was obtained as colorless foam in 75% (1.4 g, 1.34 mmol) yield. To remove the remaining phosphitylation reagent, the phosphoramidite was precipitated from DCM/hexane giving a white solid.

R_F = 0.25 (hexane/acetone = 6:4). ^{1}H NMR (400 MHz, DMSO-d_6): 0.95−1.20 (12H, m, 2 × CH(CH_3)$_2$); 2.76 and 2.89 (2H, 2 × t, J = 5.9 Hz, OCH_2CH_2CN); 3.13−3.59 (8H, m, thiomorpholine, 2 × $CH(CH_3)_2$, 5′-CH_2); 3.65−3.71 (1H, m, OCH_2CH_2CN); 3.73 and 3.74 (6H, 2 × s, 2 × OCH_3); 3.84−3.94 (1H, m, OCH_2CH_2CN); 3.98−4.10 (2H, m, thiomorpholine); 4.24−4.31 (1H, m, 4′-C*H*); 4.47−4.50 (1H, m, thiomorpholine); 4.68−4.82 (2H, m, 3′-C*H*, thiomorpholine), 5.88 and 5.94 (1H, 2 × t, J = 5.9 Hz, 2′-C*H*); 6.06−6.08 (1H, m, 1′-C*H*), 6.86−6.90 (4H, m, DmTr); 7.23−7.36 (7H, m, DmTr); 7.45−7.47 (2H, m, DmTr); 8.09 and 8.11 (1H, 2 × s, 6-C*H*); 11.83 (1H, bs, N*H*) ppm.

^{31}P NMR (400 MHz, DMSO-d_6): δ = 149.11 and 149.80 (diasteromers, relation 6:4) ppm.

ESI(+)-MS (m/z) calcd, 1072,19 [$C_{44}H_{53}IN_5O_{11}PS_2Na$]; found, 1072.32 [M + Na]$^+$.

Synthesis, Postsynthetic Stille Cross-Coupling, Purification, and Characterization of Oligonucleotides. Oligonucleotide synthesis via TBDMS- or TC[71]-chemistry was accomplished using an Expedite Nucleic Acid Synthesis System from PerSeptive Biosystems in 1 μmol scale using standard protocols. Nucleotide building blocks and cpg-solid support were purchased from SAFC-Proligo (Sigma-Aldrich) for TBDMS strategy or Link technology for TC protected building blocks. Oligonucleotide synthesis via ACE chemistry[73] in 0.2 or 1 μmol scale was performed on a rebuilt ABI 392 synthesizer (Applied Biosystems) with phosphoramidites and polystyrene solid support purchased from Thermo Fisher (Dharmacon). Besides the unmodified nucleotide building blocks, also 5-iodo uridine phosphoramidites for TBDMS and ACE strategy were commercially available, and TC-protected 5-iodo uridine phosphoramidite was prepared as described in the previous section according to the procedure for unmodified building blocks reported by Caruthers et al.[71] 2-Iodo adenosine phosphoramidite via ACE strategy was synthesized as described before.[52,53] Every RNA synthesis was carried out in DMTr-off modus.

General Procedure for the Pd(0) Catalyzed Stille Cross-Coupling of Iodo Modified Oligonucleotides with Tributyl Organo Stannanes Following Method B 2. After completion of automated RNA synthesis on solid support, the columns with fully assembled RNA were dried under vacuum, flushed with argon, and a solution of 14 mg (15 equiv) of $Pd_2(dba)_3$ and 7 mg (30 equiv) of P(furyl)$_3$ in 150 μL of absolute DMF was added and dispersed under exclusion of air via syringes placed on both ends of the column and allowed to sit for 5 min. Meanwhile, a solution of 60 equiv tributyl organostannane in 100 μL of absolute DMF was prepared, subsequently added to the column−syringe system, thoroughly mixed, and reacted in the oven at 60 °C for 2−18 h with occasional moving of the syringes back and forth.

When the reaction had proceeded, the reaction solution was removed, and the RNA on column was washed consecutively with DMF, DCM, hexane, DCM, MeCN, 0.1 M aqueous EDTA, Millipore water, and MeCN. After drying the solid support, the RNA was cleaved, deprotected, and purified as usually performed for unmodified RNA.

General Procedure for Deprotection and Cleavage of TBDMS Protected RNA from cpg Following a Standard Procedure. For deprotection and cleavage of base-labile groups, the resin loaded with modified RNA was removed from the column, suspended in 1 mL of a 3:1 mixture of 37% aq ammonia/ethanol and incubated at 35 °C for 18−24 h. Afterward, the supernatant was separated, the cpg material was washed for 3 times with DEPC water, and the combined fractions were evaporated to dryness. For removing the 2′-TBDMS group, the oligonucleotide was dissolved in 0.3 mL of a 6:3:4 mixture of 1-methyl-2-pyrrolidon/triethylamine/triethylamine trihydrogenfluoride complex, vortexed, and incubated for 90 min at 60 °C. Subsequently, 1.2 mL *n*-butanol was added to the clear solution, mixed, and left for 1 h at −75 °C. To isolate the precipitated RNA, the mixture was centrifuged at 0 °C and 12500 rpm for 30 min, and after decanting supernatant, the residue presented the completely deprotected RNA pellet ready for purification.

General Procedure for Deprotection and Cleavage of TC Protected RNA from cpg, Based on the Procedure Described by Caruthers[71] and Following the Recommendations of Link Technology. The cpg material was left in the synthesizer column, dried under vacuum, and flushed with argon. The resin was washed for 3 min with 20% diethylamine in dry acetonitrile, washed with acetonitrile, and dried. Afterward, the cpg material was treated with 0.5 mL 1:1 ethylene diamine/dry toluene for 2 h. After washing with abs. acetonitrile and drying the resin still in column, the RNA was eluted by the addition of 2 mL 0.1 M TEAA buffer (sterile). When the solution was concentrated, the residue exhibited the deprotected crude RNA pellet.

General Procedure for Deprotection and Cleavage of ACE Protected RNA from Polystyrene Following the Reported Procedure.[74] First, the phosphate protecting groups were cleaved on solid support by treatment with 2 mL of a 0.4 M solution of disodium-2-carbamoyl-2-cyanoethylene-1,1-dithiolate-trihydrate (S_2Na_2) in DMF/H_2O = 98:2 within 20 min. Deprotection of the exocyclic protection groups and cleavage of acetate of the 2′-ACE group as well as cleavage of the oligonucleotides from solid support was effected by treatment with a 40% aqueous solution of methylamine for 10 min at 55 °C. The final cleavage of the 2′-ACE protecting group was performed under sterile conditions with a TEMED/acetic acid buffer adjusted to pH 3.8 for 30 min at 60 °C.

General Procedure for Separation and Purification of Oligonucleotides. The crude RNA was purified by AE-HPLC (A, sterile DEPC water; B, 1 M LiCl sterile; gradient for 12-mers, 0−80% B within 40 min; gradient for 5-mers, 0−50% B

dx.doi.org/10.1021/bc200659j | *Bioconjugate Chem.* 2012, 23, 627−642

within 40 min) with a semipreparative Dionex DNAPac PA-100 column (9 × 250 mm) and 5 mL/min flow. Further purification as well as concurrent desalting was accomplished by RP-HPLC using a preparative (250 × 15 mm) Phenomenex C12 column with the following gradient (eluent A, 1 M TEAA buffer sterile, pH 6.5; eluent B, DEPC water; eluent C, acetonitrile; constant 10% A, 0−3 min, 0% C; and 3−26.5 min, 0−45% C, 6 mL/min flow). For small quantities, an analytical (250 × 4.6 mm) Phenomenex C12 column was used (gradient: A, 1 M TEAA buffer sterile, pH 6.5; B, DEPC water; C, acetonitrile; constant 10% A, 0−2 min, 0% C; and 2−25 min, 0−30% C, 1 mL/min flow).

Concentrated RNA fractions were analyzed via ESI mass spectrometry on a LCMS system.

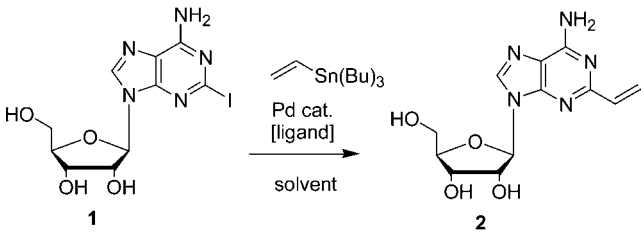
The masses for the synthesized RNAs **ON 1−ON 18** are presented in Tables 6 and 7 in the Results and Discussion section and were found to be in agreement with calculated values.

RESULTS AND DISCUSSION

Test Reactions on Monomer Model Compounds. Stille cross-coupling is a completely new approach in combination with nucleic acids on solid support; thus, model studies on the monomer level prior to transfer to oligonucleotides were required. To find proper conditions, stability and reactivity screenings were investigated with respect to the commonly reported reflux temperature preferred for Stille cross-couplings. This should be alleviated in a still reasonable reaction time to obtain a suitable method compatible with RNA on column. Some examples of Stille cross-couplings on monomeric purines and pyrimidines are described, and first studies of palladium-catalyzed cross-couplings involving nucleosides are presented by Nair et al.[60−62,64] They reported the reaction of inosine, nebularine, and adenosine derivatives toward alkylation in the rarely explored 2-position. In a general procedure for Stille cross-coupling, they used vinyl(tributyl)stannane at 90 °C in toluene for ribose-protected and DMF for the unprotected nucleoside with $Pd(MeCN)_2Cl_2$ as catalyst and optionally the ligand P(*o*-tol)$_3$.

According to this, our first experimental series included test reactions with unprotected 2-iodo adenosine **1** and commercially available vinyl(tributyl)stannane (Scheme 1). We

Scheme 1. Stille Cross-Coupling on Model Compound 2-Iodo Adenosine with Vinyl(tributyl)stannane as the Test Reaction



followed the mentioned procedure with $Pd(MeCN)_2Cl_2$ to estimate the feasibility for reactions on RNA (Table 1). After accomplishing excellent results under the reported conditions ($Pd(MeCN)_2Cl_2$, 90 °C, 3 h) with and without using the ligand P(*o*-tol)$_3$ (exp. nos. 1 and 2), we further explored prolonged reaction times at room temperature intending a setting that might be more suitable for the RNA oligonucleotide. As shown

Table 1. First Experiments on Stille Cross-Couplings for the Reaction of 2-Iodo Adenosine 1 to 2-Vinyl Adenosine 2 Using a Catalyst/Ligand System Based on the Procedure Described by Nair et al.[60−62]

exp. no.	cat.	lig.	temp.	time	conversion
1[a]	$Pd(MeCN)_2Cl_2$	P(tol)$_3$	90 °C	3 h	99%
2[a]	$Pd(MeCN)_2Cl_2$	no	90 °C	3 h	99%
3[a]	$Pd(MeCN)_2Cl_2$	no	r.t.	72 h	75%
4[a]	$Pd(MeCN)_2Cl_2$	P(tol)$_3$	r.t.	72 h	34%
5[a]	$Pd(MeCN)_2Cl_2$	no	r.t.	18 h	75%
6[b]	$Pd(MeCN)_2Cl_2$	no	r.t.	18 h	72%
				350 h	78%
7[b]	$Pd(MeCN)_2Cl_2$	no	60 °C	2.5 h	66%
				72 h	85%
				350 h	95%
8[b,c]	$Pd(MeCN)_2Cl_2$	no	60 °C, MW	6 h	99%
9[b,d]	$Pd(MeCN)_2Cl_2$	no	60 °C, MW	2 min	99%

[a]Product **2** was isolated and purified, and the conversion was determined via the integration of proton NMR spectra. [b]The reaction mixture was not worked up, but conversion rates were monitored by the integration of HPLC chromatograms. [c]Microwave induced reaction was performed in an open reflux system with 100 W. [d]Microwave induced reaction was performed in a sealed tube with 70 W, 99% conversion considering that no compound **1** could be detected anymore but that traces of a side-product was formed.

in Table 1, we could only isolate the product 2-vinyl adenosine **2** in 75% yield (exp. nos. 3 and 5) and were not able to observe conversion higher than 78% via RP-HPLC control even after several days (exp. no. 6). The use of ligand P(*o*-tol)$_3$ (exp. no. 4) seemed not to have any accelerating but rather a negative effect on the conversion rate and was therefore omitted for further tests. Obviously, there was no benefit in intensely prolonged reaction times because a sort of steady state arose after one day. This phenomenon could be due to decomposition of the catalyst $Pd(MeCN)_2Cl_2$, which would be in analogy to what Farina et al.[63] suggested in their studies on Stille cross-couplings on 5-iodo uracil with this particular catalyst. Although tests with slightly increased temperatures of 50−60 °C (Table 1, exp no. 7) turned out to be an improvement, there was a need for better conversion rates in a reasonable time period at least for the monomer model. Therefore, we exposed our reaction mixture to microwave irradiation (Table 1, exp. nos. 8 and 9) resulting in accelerated conversion either in an open system under reflux conditions (60 °C, 100 W, complete conversion after 6 h) or in a sealed tube (100% conversion after 2 min at 60 °C and 70 W, but a side product apart of the desired product **2** occurred as a shoulder in HPLC control). As we could neither separate nor characterize the side product under these rather harsh and thus not necessarily suitable conditions, we did not follow this method anymore. According to Aucagne et al.,[59] who reported the need for double-coupling for nearly complete conversion when working with Stille-cross-couplings on monomeric uridines on solid support, and also according to our experience with Sonogashira cross-couplings on oligonucleotides,[51] we tested here the benefit of double-couplings for the Stille reaction on the monomer level but could not determine a significant acceleration.

In summary, the particular conditions for Stille cross-coupling with $Pd_2(MeCN)_2Cl_2$ did not succeed at room temperature or slightly increased temperature in an adequate

dx.doi.org/10.1021/bc200659j | Bioconjugate Chem. 2012, 23, 627−642

time range but showed promising results either at 90 °C in 3 h or at 60 °C and 100 W for 6 h under microwave irradiation in an open flask.

We did not deepen tests under the described procedure but switched to another catalyst system permitting milder conditions. For that purpose, we followed the less commonly used method described by Farina et al.[63] who applied Stille cross-couplings resulting in 5-substituted uracil and uridine derivatives with $Pd_2(dba)_3$ and the ligand $P(furyl)_3$. The priority of Farina's work was to investigate approaches for substituted uracils; thus, they used for reasons of solubility *N*-methyl-pyrrolidone and focused on exploring the palladium ligand. They found $Pd(MeCN)_2Cl_2$ and $Pd(PPh_3)_4$ [tetrakis-(triphenylphosphine)] to be unsatisfactory for their systems. But conversion of 5-iodoridine to 5-vinyluridine in 16 h at room temperature with the aforementioned $(Pd)_2(dba)_3$/$P(furyl)_3$ in 89% yield turned out to be successful. They could extend these results to the ribose-protected uridine derivative only by a longer reaction time of 40 h, increasing temperature to 50 °C and use of THF. On the basis of this, our next experimental series (Table 2) first comprised reactions of

Table 2. Further Experiments on Stille Cross-Couplings for Reaction of 2-Iodo Adenosine 1 to 2-Vinyl Adenosine 2 Using a Catalyst/Ligand System Based on the Procedure Described by Farina et al.[63] as well as Additional Catalyst Tests

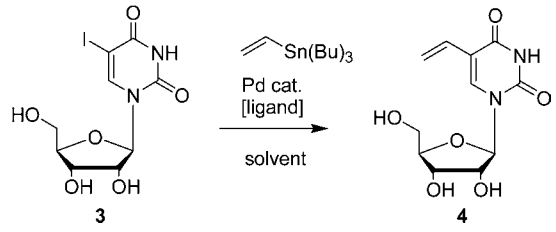
exp. no.	cat.	lig.	temp.	time	conver sion
10[a]	$Pd_2(dba)_3$	$P(fur)_3$	r.t.	168 h	5%
11[b]	$Pd_2(dba)_3$	$P(fur)_3$	r.t.	18 h	10%
				120 h	30%
12[c]	$Pd_2(dba)_3$	$P(fur)_3$	r.t.	18 h	10%
				120 h	27%
13[b,d]	$Pd_2(dba)_3$	$P(fur)_3$	r.t.	18 h	25%
				72 h	50%
14[c,d]	$Pd_2(dba)_3$	$P(fur)_3$	r.t.	18 h	20%
				72 h	60%
15[c]	$Pd(PPh_3)_2Cl_2$	no	r.t.	23 h	27%
				48 h	45%
16[c]	$Pd(PPh_3)_4$	no	r.t.	27 h	22%
17[c,d]	$Pd_2(dba)_3$	no	r.t.	23 h	88%
				350 h	90%
18[c,d]	$Pd_2(dba)_3$	no	60 °C	3 h	99%
19[c,d]	$Pd_2(dba)_3$	$P(fur)_3$	60 °C	3 h	99%
20[c,d,e]	$Pd_2(dba)_3$	no	50 °C	3 h	>95%

[a]The reaction was carried out in THF as the solvent. [b]The reaction was carried out in NMP as the solvent. [c]The reaction was carried out in DMF as the solvent. [d]Compared to the original procedure (2 mol % cat. and 4 mol % ligand), we increased the loading of catalyst (5.4 mol %) and ligand (12 mol %). [e]Complete conversion was only reproducible if Stille coupling was performed twice.

our model 2-iodo adenosine **1** to 2-vinyl adenosine **2** (Scheme 1) under the originally presented conditions of Farina et al.[63] with $Pd_2(dba)_3$/$P(furyl)_3$ at room temperature. To also cover solvent effects for this particular catalyst/ligand system, we did not only use DMF but also NMP and THF. Not unexpectedly since the solubility of **1** is poor in THF, this test afforded almost no conversion (exp. no. 10). However, the coupling reaction in NMP and DMF proceeded but turned out to be very slow (Table 2, exp. nos. 11 and 12). In contrast to the results of Farina, the conversion here was in both cases only 10% after 18 h representing an immensely differing behavior of the purine nucleoside **1**. Higher loading of catalyst and ligand showed slightly better reactivity (3 days: 60% conversion in DMF, 50% in NMP, Table 2, exp. nos. 13 and 14) but were not sufficient for our purposes. Considering the strong dependence and sensibility of altered conditions and types of nucleobases, other Pd catalysts such as $Pd(PPh_3)_2Cl_2$ [bis-(triphenylphosphine) palladiumdichloride], were applied for the reaction of 2-iodo adenosine **1** with vinyl(tributyl)stannane. $Pd(PPh_3)_2Cl_2$ was also introduced more recently for Stille cross-couplings of, e.g., furane to purines by Persson et al.[67] and to uridine by Tor et al.[68] under reflux conditions in THF or dioxane. In our case, the reaction was carried out in DMF at room temperature yielding in 27% product **2** after 23 h and 45% **2** after 48 h (Table 2, exp. no. 15), which could not be increased while prolonging the time. Also the alternative of using $Pd(PPh_3)_4$ at room temperature showed only a conversion of 22% after 27 h (Table 2, exp. no. 16) and therefore did not meet our requirements. On the basis of the observation that the kind of ligand and also the fact of whether it is added at all play an eminent role (discussed by Farina et al.[63] and also noted by us in our first model reactions with $Pd(MeCN)_2Cl_2$), the next investigations were performed with $Pd_2(dba)_3$ without utilizing $P(furyl)_3$ as ligand. Surprisingly, the relationship of converted product **2** to starting material **1** was almost reciprocal in comparison to the earlier test reactions: after 23 h, already 88% of product **2** had formed (Table 2, exp. no. 17). Unfortunately, again a kind of steady state seemed to appear when conversion came up to 90%; no complete conversion could be accomplished even after two weeks. Nevertheless, these conditions were almost optimal and were extended to slightly increased temperatures. These experiments presented the breakthrough as full conversion could be detected after 3 h at 60 °C (exp. no. 18). Interestingly, higher temperature also allowed the addition of ligand showing the same result of completion after 3 h (exp. no. 19). Furthermore, we expanded that discovery to test the same setup at only 50 °C (exp. no. 20). The findings were in principle consistent with the ones at 60 °C but were only reproducible when double coupling was performed.

After establishing successful conditions suitable for RNA on solid support for 2-iodo adenosine **1**, the next step was to extend the studies to 5-iodo uridine **3** (Scheme 2 and Table 3).

Scheme 2. Stille Cross-Coupling on Model Compound 5-Iodo Uridine with Vinyl(tributyl)stannane as the Test Reaction



We performed a similar test series applying HPLC control, beginning with Stille cross-couplings of unprotected 5-iodo uridine **3** and vinyl(tributyl)stannane under the now optimized conditions using the catalyst $Pd_2(dba)_3$ at 60 °C. When we employed $P(furyl)_3$ as ligand, complete conversion could be observed after 3 h (Table 3, exp. no. 21) in analogy to the

dx.doi.org/10.1021/bc200659j | *Bioconjugate Chem.* 2012, 23, 627–642

Table 3. Stille Cross-Couplings on 5-Iodo Uridine 3 to 5-Vinyl Uridine 4 Using the Setup That Was Optimized for the Adenosine Derivative (compare Table 2, Exp. No. 18−20) and Comparison with Another Catalyst System

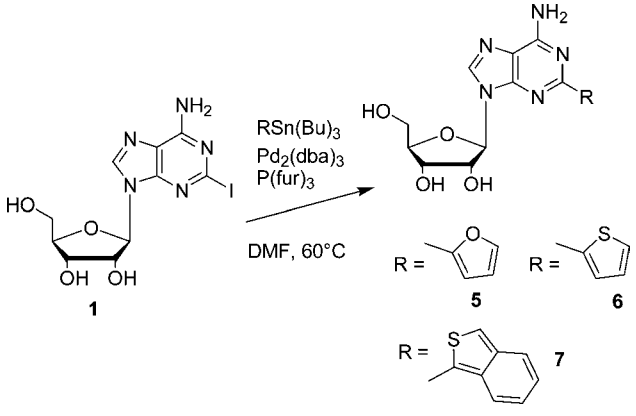
exp. no.	cat.	lig.	temp.	time	conver sion
21	$Pd_2(dba)_3$	$P(fur)_3$	60 °C	3 h	99%
22	$Pd_2(dba)_3$	no	60 °C	3 h	41%
				72 h	79%
23	$Pd_2(dba)_3$	$P(fur)_3$	50 °C	3 h	99%
24	$Pd(MeCN)_2Cl_2$	no	90 °C	3 h	<30%

adenosine derivative. Amazingly, this was not possible without utilizing the ligand, and in 3 h at 60 °C, only 41% 5-vinyluridine **4** formed and could be only increased to 79% product **4** after 3 days of reaction time (Table 3, exp. no. 22). This means, that contrary to adenosine **1** that reacted with and without ligand, the presence of $P(furyl)_3$ is obligatory for Stille cross-coupling of 5-iodo uridine **3**. However, further tests on 5-iodo uridine **3** utilizing the ligand at 50 °C and only 2 h of reaction time lead to complete conversion (Table 3, exp. no. 23). This indicates that uridine **3** is even more reactive than 2-iodo adenosine **1** if optimized conditions are applied. These results agree with those of Agrofoglio et al.[58] and Farina et al.[63] who emphasized the importance of the kind of ligand in Stille cross-couplings with uracil/uridine derivatives and basically found similar trends. Our reactions with higher catalyst loading and the use of unprotected 5-iodo uridine **3** in DMF showed even better conversion rates.

Overall, it was a challenging task to find a general setup (e.g., the mentioned influence of applying ligand and excellent results for adenosine in Table 1, exp. nos. 1 and 2 compared to Table 3, exp. no. 24 showing the incompatibility with uridine under identical conditions), but in the end, we successfully developed conditions available for both nucleosides.

Nevertheless, it was our intention to enlarge the scope of feasible Stille cross-coupling partners for our methodology. Therefore, we investigated the coupling with 2-furyl-thienyl- and benzothienyl organostannanes resulting in potentially fluorescent adenosine and uridine derivatives (compounds **5**−**10**) with our established procedure using $Pd_2(dba)_3/P(furyl)_3$ in DMF at 60 °C (Schemes 3 and 4 and Table 4). The

Scheme 3. Synthesis of Heteroaryl Modified Adenosine Derivatives via Stille Cross-Coupling under Optimized Conditions



conversion could be monitored via TLC, and the reaction in case of furane was complete after 3 h for 2-iodo adenosine **1**

Scheme 4. Synthesis of Heteroaryl Modified Uridine Derivatives via Stille Cross-Coupling under Optimized Conditions

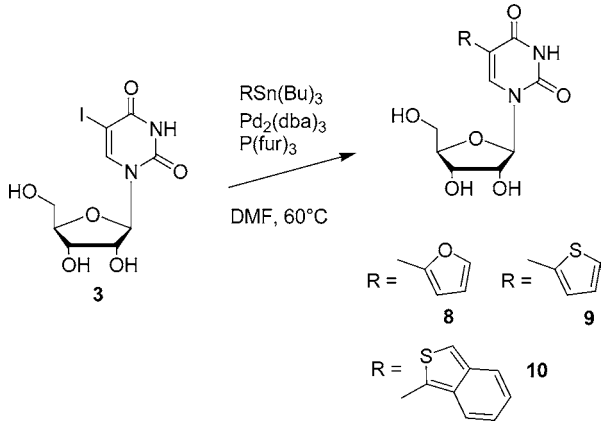


Table 4. Stille Cross-Couplings with Heterocyclic Aryl Compounds on 2-Iodo Adenosine 1 and 5-Iodo Uridine 3 Following the Established Procedure

exp. no.	starting material	coupling partner	time	product
25	**1**	2-furyl-(tributyl)stannane	3 h	**5**
26	**1**	2-thienyl-(tributyl)stannane	6 h	**6**
27	**1**	2-benzothienyl-(tributyl) stannane	8 h	**7**
28	**3**	2-furyl-(tributyl)stannane	3 h	**8**
29	**3**	2-thienyl-(tributyl)stannane	3 h	**9**
30	**3**	2-benzothienyl-(tributyl) stannane	3 h	**10**

and 5-iodo uridine **3** as well (Table 4, exp. nos. 25 and 28). However, this was a convenient result concerning the application to RNA as this was comparable to the tests with vinyl organostannane. Furthermore, we obtained under mild conditions the same excellent yields of over 95% after purification similar to that of Persson et al.[67] in refluxing THF after 72 h with respect to the protected adenosine derivative and such as Tor et al.[68] who treated 5-iodo uridine for only 2 h but at 90 °C. For the coupling on iodo uridine **3**, we found the same fast conversion yielding 5-thienyl and 5-benzothienyl uridine **9** and **10** after 3 h (Table 4, exp. nos. 29 and 30). Again, the already published procedures[69,70] reported longer reaction times or higher temperatures as well as decreased yields of only 66% in the case of attaching benzothiophene. The adenosine derivative **1** required in our hands a slightly prolonged reaction time of 6 h for thiophene (opposite to the published method[67] of 50 h refluxing in THF) and 8 h for Stille cross-coupling with the benzo[*b*]thienyl stannane presenting the new compound **7** (Table 4, exp. nos. 29 and 30). Although the reactivity seemed to be reduced in comparison to experiments with vinyl- and furyl stannane, the reaction time should still qualify also for applications on RNA. Prolonged coupling times for 2-iodo purine derivatives have also been reported in two diploma theses[75,76] performed in our working group that evaluated Suzuki cross-couplings on protected or unprotected 2-iodo inosines with 3-furyl, -thienyl, and -benzothioenyl at 100 °C in 93 h. In agreement with our finding of lower reactivity for the Stille cross-coupling with benzothiophene (Table 4, exp. no. 27), defined conditions in the case of Suzuki cross-coupling[75] had to be applied for

dx.doi.org/10.1021/bc200659j | *Bioconjugate Chem.* 2012, 23, 627−642

conversion, and the resulting yield was worse compared to that of 3-furane and 3-thiophene. This might be due to higher sterical hindrance and additionally to an electronically more complex structure. Although the reactivity trends show similar behavior for both cross-coupling types, it must be pointed out that the Stille cross-coupling following our optimized method proceeded under much milder conditions in a still reasonable time (60 °C in 8 h instead of 100 °C in 93 h). In conclusions, we were able to establish reaction conditions permitting Stille cross-coupling on 2-iodo adenosine **1** and 5-iodo uridine **3** with different coupling partners that should be compatible with RNA on solid support.

Furthermore, the heterocyclic-modified nucleosides (**5**−**10**) that had been synthesized were subsequently characterized with respect to their photophysical properties (Table 5). The

Table 5. Photophysical Properties in Water of Furyl, Thienyl, and Benzothienyl Modified Adenosine and Uridine Derivatives 5−10[a]

compd	absorption λ_{max} [nm]	emission λ_{max} [nm]
2-(fur-2-yl) adenosine **5**	301	385
2-(thien-2-yl) adenosine **6**	310	410
2-(benzothien-2-yl) adenosine **7**	319	423
5-(fur-2-yl) uridine **8**	317	444
5-(thien-2-yl) uridine **9**	315	446
5-(benzothien-2-yl) uridine **10**	319	459

[a]The nucleoside compounds were measured at room temperature in water containing 0.1% DMSO as solvent maintaining a concentration of 10 μM.

maxima of absorption and emission were determined in water because enhanced emission can be observed in an aqueous environment[68−70] and due to the option of comparing the data with the later described RNA also measured in water. The spectra show equivalent results in the case of the uridine set (**8**−**10**) that was already examined by Tor et al.[68−70]. To the best of our knowledge, no fluorescent studies about the adenosine derivatives (**5**−**7**) exist so far; they are only described in the literature as potential antiviral agents.[67] This might be due to the low fluorescent intensity (especially compared to the uridine derivatives), even if the emission can be found in the visible range.

Stille Cross-Coupling on RNA. The now optimized conditions for the monomers were transferred to RNA with the difference that higher excesses of reagents and catalyst loading were used. The reasons for this were, on the one hand, of practical origin as handling of catalytic amounts with respect to a scale of 1 μmol or less oligonucleotide is difficult. Also, the overload should compensate for the fact that the RNA is bound on solid-phase, and the reaction, therefore, is heterogeneous. Furthermore, employing high excess in reactions on solid support is in general widely used and particularly applied for the derivatization of oligonucleotides.[20,46,51]

Our first experiments on oligonucleotides are presented under conditions we investigated on monomers at the beginning (compare Scheme 1 and Table 1, entries 7 and 8). Thus, we performed Stille cross-couplings on RNA with $Pd(MeCN)_2Cl_2$ as catalyst at 90 °C in 3 h and at 60 °C under microwave irradiation for 6 h, respectively. That setup intended to check the stability of RNA under this rather harsh setting and to confirm the need for further monomer test reactions to find milder conditions. Not unexpectedly, these trials on mixed 12-mer RNAs with incorporated 2-iodo adenosine did not result in the desired product, but besides traces of breakdown products, unreacted 12-mer, and unidentified compound with a higher mass than the starting material or the product, the main material could not be isolated anymore.

For that reason, we switched to our alternative method proceeding under milder conditions ($Pd_2(dba)_3$/$P(fur)_3$ at 60 °C, presented in Table 2, exp. no. 19). The first studies following this approach consisted of Stille couplings of mixed sequences containing 2-iodo adenosine and 5-iodo uridine with vinyl(tributyl)stannane. The results were promising as traces of product could be observed in mass spectroscopy, but still the isolation of the product in good yield had not been accomplished. To simplify the setup and subsequent purification as well as characterization, we decided to use less complex sequences and carried out Stille cross-coupling with poly uridine 5- and 12-mers (Figure 1). For that, we

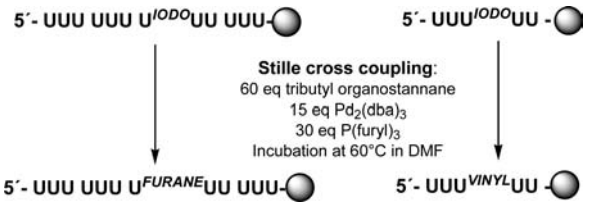


Figure 1. Stille cross-couplings on poly uridine model RNAs with vinyl- and furyl(tributyl)stannane under defined conditions.

incorporated commercially available 5-iodo uridine phosphoramidite and synthesized 2-iodo adenosine phosphoramidite[52,53] in the center of the RNA strand as well as at the 5′-end. We performed the coupling reaction with 60 equiv of vinyl- or furyl(tributyl)-stannane under optimized conditions: 15 equiv of $Pd_2(dba)_3$ as a catalyst, 30 equiv of P(furyl) as a ligand for 12−18 h in DMF at 60 °C. Additionally, we carried out double coupling under identical conditions for 6−10 h with washing-off of the reagents in between to ensure complete conversion. This proceedure turned out to be successful, and the desired site-specifically labeled oligonucleotides could be isolated after deprotection, cleavage from solid support, separation on anion exchange HPLC, and desalting. Coupling yields of separated RNAs were found to be comparable to those of unmodified reference oligonucleotides in automated standard synthesis. All modified RNAs were characterized via mass spectrometry (Table 6, **ON 1**−**ON 7**).

Conversion was found to be complete, and no starting material containing iodo modified RNA was isolated. This represents a remarkable result, in particular regarding the fact that postsynthetic Stille cross-couplings at intrastrand positions succeeded in the same degree as those on 5′-terminal nucleotides. The efficiency of that totally postsynthetic strategy highlights our method compared to other postsynthetic reactions such as the above-noted Sonogashira cross-couplings described by Khan et al.[46] and Wagenknecht et al.,[47] which were limited by the fact that conversion only proceeded on the free 5′-end requiring interruption of automated oligonucleotide synthesis.

Since we explored not only the commonly used TBDMS but also the ACE strategy[73] to take the same advantages such as the use of mild reagents and excellent yields evaluated by us for Sonogashira cross-couplings,[52] we discovered that applying

dx.doi.org/10.1021/bc200659j | Bioconjugate Chem. 2012, 23, 627−642

Table 6. Synthesis of Modified RNA via Stille Cross-Couplings under Conditions Presented in Figure 1 with Double-Coupling: Results of Mass Spectrometry[a]

name	sequence	modification	exact mass calculated	mass found [Da]
ON 1[b]	5′- U*UU UU	vinyl	1494.19	1494.2
ON 2[b]	5′- UUU* UU	vinyl	1494.19	1494.2
ON 3[b]	5′- UUA* UU	vinyl	1517.22	1517.2
ON 4[b]	5′- UUU UUU U*UU UUU	furyl	3676.37	3676.4
ON 5[c]	5′- UUU* UU	vinyl	1494.19	1494.2
ON 6[c]	5′- UUU* UU	furyl	1534.19	1534.1
ON 7[c]	5′- UUU UUU U*UU UUU	furyl	3676.37	3676.5
ON 8[c]	5′- UUU* UU	thienyl	1550.16	1550.2
ON 9[c]	5′- UUU* UU	benzothienyl	1600.17	1600.2
ON 10[c]	5′- UUU UUU U*UU UUU	thienyl	3692.34	3692.4
ON 11[c]	5′- UUU UUU U*UU UUU	benzothienyl	3742.37	3742.4

[a]In the experimental series presented in this table, also fractions containing the mass of reduced deiodinated RNA could be isolated, but no starting material was found. [b]Synthesis was performed via ACE protecting group strategy; besides, the desired modified RNA single and multiple methylated product (+14) could be also found. [c]Synthesis was performed via the TBDMS protecting group strategy.

Stille cross-coupling on ACE protected RNA containing uridine yields in methylated side products besides the desired product (Table 6, **ON 1**−**ON 4**). This will be discussed in detail elsewhere (manuscript in preparation).

Because of finding the ACE strategy not completely satisfactory, further expanding the scope of Stille cross-coupling with more coupling partners was only performed with TBDMS protected RNA. This was achieved by attaching thiophene and benzothiophene to 5- and 12-mer poly uridines (Table 6, **ON 8**−**ON 11**) providing not just the furyl-modified (**ON 6** and **ON 4**/**7**) but a complete set of aryl-substituted poly uridine oligonucleotides possibly exhibiting fluorescent properties.

Actually, in the case of RNA synthesis via the TBDMS strategy and subsequent Stille cross-coupling (**ON 8**−**ON 11**), the only isolated fraction not identical with the product (20−30%, determined via integration of RP-HPLC peaks, conform to the relationship of isolated amounts of side product and desired derivatized RNA) had been characterized as reduced, deiodinated species in full length. This electrophilic reduction during the catalytic cycle is in general known for palladium-catalyzed cross-couplings, and most notably Stille couplings using $Pd_2(dba)_3$ were reported to show particular side products.[63,77] The origin of the side reaction is uncertain; an alkyl transfer with β-elimination might induce the reductive elimination, but a radical mechanism could also be involved.[77] While Farina et al.[63] described uracil as the side product in Stille cross-couplings of 5-iodo uracil with vinyl(tributyl)-stannane in the presence of $Pd_2(dba)_3$, we have never observed this under our conditions in 3 h at 60 °C on a nucleoside level. It could be interpreted as a kind of "overloading" for treating the oligonucleotide with respect to a high excess of catalyst, long reaction time, and double-coupling. In fact, if exposure of RNA to conditions of Stille cross-coupling had been diminished, deiodination resulting from reduction could be prevented. This we proved by employing Stille cross-coupling with furyl(tributyl)stannane on TBDMS protected poly uridine 11-mer for only 10 h in a single instead of double coupling leading to full conversion without any side product (Table 7, **ON 12**, and Figure 2).

Table 7. Further Synthesis of Modified RNA via Stille Cross-Couplings under Conditions Presented in Figure 1 in a Single Coupling and Decreased Reaction Time: Results of Mass Spectrometry[a]

name	sequence	modification	reaction time	exact mass calculated	mass found [Da]
ON 12[b]	5′- UUU UUU*UU UUU	furyl	10 h	3370.34	3370.4
ON 13[c]	5′- UUU UUU U*UU UUU	furyl	13 h	3676.37	3676.4
ON 14[d]	5′- AAA AAA* AAA AAA	thienyl	7 h	3968.66	3968.9
ON 15[d]	5′- AAA AAA* AAA AAA	benzothienyl	7 h	4018.67	4018.9
ON 16[d]	5′- AAA AAA* AAA AAA	furyl	2 h	3952.69	3952.9
ON 17[d]	5′- CUU UUC A*UU CUU	furyl	2 h	3696.44	3696.7
ON 18[b]	5′- CGA CU*A UAG UCG	furyl	7 h	3859.56	3859.7

[a]In the experimental series presented in this table, no starting material and only traces under 5% of reduced deiodinated RNA could be isolated. [b]Synthesis was performed via the TBDMS protecting group strategy. [c]Synthesis was performed via the TC protecting group strategy. [d]Synthesis was performed via the ACE protecting group strategy; for **ON 14**−**ON 16**, only desired modified RNA was obtained, and for **ON 17** containing U, traces of single and multiple methylated product (+14) were also found but could be separated via RP-HPLC.

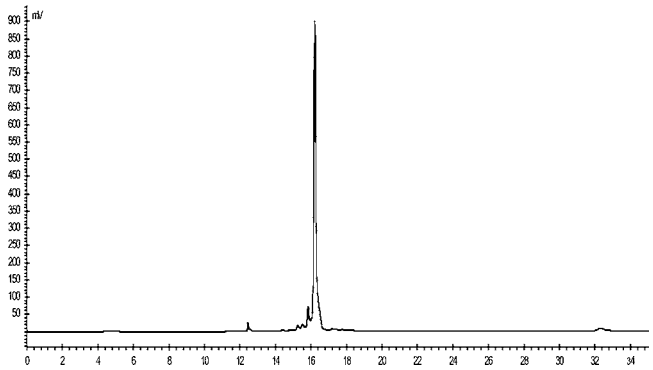
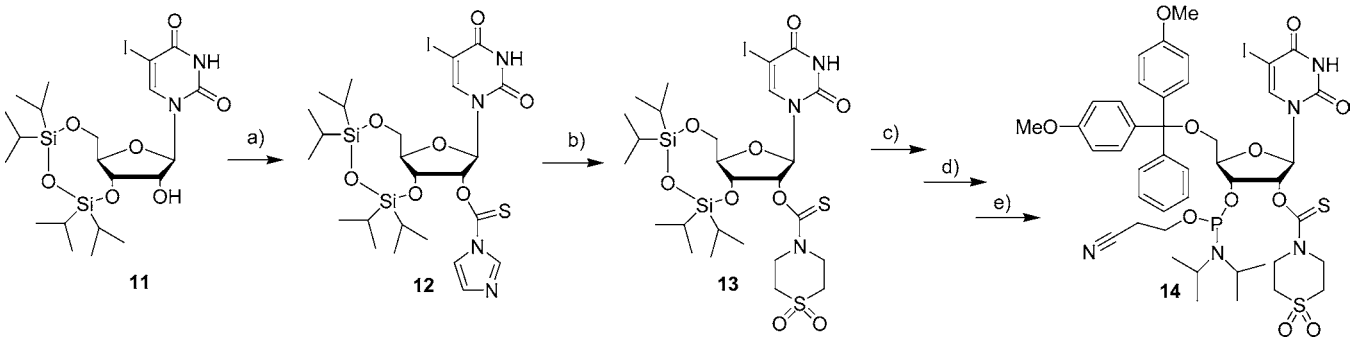


Figure 2. Reversed phase HPLC chromatogram of furyl-modified 11mer **ON 12**. The TBDMS protected RNA was synthesized as described in the text and Table 7. After automated solid phase synthesis, derivatization by Stille cross-coupling under optimized conditions (decreased reaction time and single coupling) was performed. Separation of the 11-mer from natural breakdown sequences via ion exchange HPLC showed a similar pattern compared to unmodified samples, and subsequent desalting and purification on preparative RP HPLC (shown here) result in one main peak (retention time 16.2 min) identified as pure furyl-coupled RNA. The small signal at 15.8 min retention time (<5% of all material) presents traces of deiodinated, reduced side-product and can be separated from the main fraction.

The same result with excellent conversion rate and very good overall yield of site-specifically furyl-labeled RNA (Table 7, **ON 13**) could be found when we expanded our protecting group

dx.doi.org/10.1021/bc200659j | Bioconjugate Chem. 2012, 23, 627−642

Scheme 5. Synthesis of TC Protected 5-Iodo Uridine Phosphoramidite 14[a]



[a](a) 1,1′-Thiocarbonylimidazole, DMAP, MeCN, r.t., 6 h; (b) thiomorpholine-1,1′-dioxide, MeCN, r.t., 6 h; (c) HF/pyridine, 2-MeTHF, 0 °C-r.t., 22 h; (d) DmTrCl, NMM, DCM, 0 °C, 4 h; (e) 2-cyanoethyl-*N*,*N*-diisopropylchloro-phosphoramidite, NMM, DCM, r.t., 3.5 h.

strategies to the TC chemistry recently described by Caruthers et al.[71] In order to investigate this experiment, we prepared the TC protected 5-iodo uridine phosphoramidite **14** (Scheme 5) following the procedure reported by Caruthers et al.[71] on natural nucleosides for subsequent incorporation to RNA. Applying the TC strategy turned out to be fully compatible with our Stille cross-coupling approach in a single reaction overnight.

Hence, additional derivatizations by Stille cross-coupling to further elaborate the universality of our method were performed under decreased reaction times. These experiments showed the versatility for adenosine rich sequences that were reported to effect complications[56] and moreover to complete the analogue set with furyl-, thienyl-, and benzothienyl-modified adenosine building blocks (Table 7, **ON 14**−**ON 16**). In order to prove further applicability for our approach, we also applied Stille cross-coupling to more complex mixed RNA sequences on iodo uridine as well as on iodo adenosine with furane (Table 7, **ON 17** and **ON 18**). All modified RNAs could be successfully synthesized and isolated, and the selected conditions and also reduced reaction time was even satisfactory for the self-complementary sequence being sterically more hindered as well as for the less reactive iodo adenosine. At least coupling with furyl(tributyl)stannane on 2-iodo adenosine afforded fully modified **ON 16** and **ON 17** in only 2 h. In particular, noteworthy is the ease of attaching benzothiophene to iodo adenosine in RNA in excellent yield in 7 h despite the necessity for prolonged reaction times for the nucleoside monomers. Thus, it could be shown that this approach for the Stille cross-coupling seems general for different coupling partners. It provides therefore another benefit compared to Suzuki cross-coupling studies on DNA by Manderville et al.[56] who observed a significant amount of unreacted starting material in the coupling of 8-bromo desoxyadenosine with benzothienyl boronic acid.

Besides the fact that modifications on the 2-position of adenosine inserted into RNA have been in general only rarely explored, our particular 2-aryl purine modifications in RNA (**ON 3**; **ON 14**−**ON 17**) present new compounds. To the best of our knowledge, 2-functionalized riboadenosines reported so far are only established for pyrene and radical spin label modifications used by us in an A-form RNA double helix in the minor groove.[50−54] Since the linkage to the label had been acetylenic resulting from Sonogashira cross-coupling on RNA so far, we expanded here the substitution pattern to aryls via Stille cross-coupling.

The convenience of our method is clearly demonstrated by the fact that we are able to generate a set of differently labeled RNAs deriving from just one precursor. That way, both series of modified uridine (**ON 7**, **ON 10**, and **ON 11**) and adenosine (**ON 14**−**ON 16**) 12-mer oligonucleotides could be easily synthesized from iodo substituted RNAs that were prepared in good yield during automated solid-phase synthesis. Afterward, the solid support was divided and Stille cross-coupling was performed in parallel synthesis with furyl, thienyl, and benzothienyl for each RNA. The common way of inserting modified phosphoramidites such as, e.g., a 3-furyl inosine derivative that was incorporated into model RNA in our working group,[76] resulted in the corresponding modified oligonucleotide but turned out to be much more time-consuming and less efficient in preparation and yield when compared to the divergent postsynthetic strategy described herein.

Tor et al.[68−70,78,79] presented one more alternative to synthesize modified RNA via enzymatic incorporation of a particular modified triphosphate. This technique was used for 5-uridine functionalization by furyl, thienyl, and benzothienyl to build up RNA containing the so-called responsive fluorescent nucleoside analogues that are sensitive to changes in the microenvironment. This basically represents the same class of target RNA we synthesized to show the versatility of our approach. According to Tor et al.,[68] the transcription process using modified nucleoside triphosphates accepted by T7 RNA polymerase is prior to the complicated synthesis up to modified phosphoramidites because of only two synthesis steps and more effective incorporation. However, while Tor et al. synthesized defined RNA strands (e.g., HIV-1 TAR construct[78]) with particularly emissive pyrimidine nucleosides to monitor RNA−ligand interactions by fluorescence measurements, we primarily focused on developing a new, reliable method allowing efficient attachment of a variety of labels to easily access iodo modified RNA, also avoiding the synthesis of complexly modified phosphoramidites. As result, a universal strategy to site-specifically modified oligonucleotides that can be applied independent of sequence, position of modification, kind of nucleobase, and sort of conjugate is provided.

In analogy to earlier examined monomers (compare Table 5), we attained the same typical absorption and emission maxima for 5-fur(2-yl), thien(2-yl) and benzothien(2-yl) uridine 5-mer and 12-mer RNA in water (Table 8, **ON 6**−**ON 11**). The almost identical emission bands of the modified single-stranded RNA compared to the free nucleoside suggest

dx.doi.org/10.1021/bc200659j | *Bioconjugate Chem.* 2012, 23, 627−642

Table 8. Photophysical Properties of a Set of 2-Furyl, Thienyl, and Benzothienyl Modified 5-mer and 12-mer RNA[a]

name	sequence	modification	absorption λ_{max} [nm]	emission λ_{max} [nm]
ON 6	5′- UUU* UU	furyl	320	444
ON 8	5′- UUU* UU	thienyl	317	449
ON 9	5′- UUU* UU	benzothienyl	322	470
ON 7	5′- UUU UUU U*UU UUU	furyl	320	444
ON 10	5′- UUU UUU U*UU UUU	thienyl	319	450
ON 11	5′- UUU UUU U*UU UUU	benzothienyl	322	470
ON 14	5′- AAA AAA* AAA AAA	furyl	310	405
ON 15	5′- AAA AAA* AAA AAA	thienyl	312	405
ON 16	5′- AAA AAA* AAA AAA	benzothienyl	325	407
ON 17	5′- CUU UUC A*UU CUU	furyl	312	406
ON 18	5′- CGA CU*A UAG UCG	furyl	322	435

[a]The oligonucleotides were measured at room temperature in sterile water as solvent maintaining a concentration of 10 μM.

that the modified nucleosides remain also in the oligomer in a polar environment, which is in full agreement with results of Tor et al.[68] Significant in the first instance is the very high intensity and bathochromic shift of benzothienyl modified RNA (**ON 8** and **ON 11**) that helps in investigating nucleic acid dynamics and recognition processes.[70]

Also, the aryl-modified adenosine sequences were characterized with respect to their fluorescence properties. Contrary to the uridine series, there is no significant bathochromic shift from the furyl- over thienyl- up to benzothienyl-modified RNA (Table 8, **ON 14**−**ON 16**). As expected from the results of the nucleoside monomers, the fluorescence intensity of adenosine modifications is decreased compared to the uridine ones. For mixed sequences, the same trend in a hyperchromic effect for furyl modified uridine (**ON 18**) and an emission in the visible range but with low intensity for furyl modified adenosine (**ON 17**) could be observed. In addition, the self-complementary RNA **ON 18** shows a slightly hypochromic emission (435 nm) compared to the free nucleoside **8** (444 nm) suggesting that the secondary structure can change the polar environment to some extent.

CONCLUSIONS

In conclusion, we have demonstrated the proof of principle for the palladium-mediated Stille cross-coupling as a convenient strategy for postsynthetic modification of RNA on column. Our concept of postsynthetic derivatization combines the advantages of solid support approaches with respect to high conversion and excellent yields while using only economical amounts of reagents. An additional benefit is easy access to diversely modified RNAs arising from just one oligonucleotide precursor.

To the best of our knowledge, this is the first time that Stille cross-coupling on oligonucleotides has been described. Hence, our studies broadened the range of available metal-catalyzed methods (that facilitate the use of well accessible halogenated nucleotide precursors) such as Sonogashira cross-coupling,[46,47,51,53] copper-catalyzed oxidative acetylenic coupling,[20] and Suzuki−Miyaura cross-coupling[56] that were reported so far for modifying oligonucleotides postsynthetically. Particularly, with regard to the wide range of studies requiring labeled RNA, which is less stable and therefore synthetically more challenging than DNA, our Stille cross-coupling presents a reliable and mild approach. Hence, the scope and linker pattern of the Sonogashira coupling as the only existing technique qualified for RNA so far is extended.

The Stille cross-coupling was found to show large differences in reactivity at decreased temperatures with respect to the catalyst/ligand system for purine or pyrimidine nucleosides even on a monomer level. Nevertheless, we could successfully transfer the on nucleoside optimized reaction conditions now to Stille cross-coupling on RNA. We confirmed the eligibility and universality of the established setup for intrastrand or at terminal position inserted 5-iodo uridine as well as 2-iodo adenosine with various coupling partners using different sequences.

Moreover, we were able to show that Stille cross-coupling can be in principle applied for RNA synthesized via different protecting group strategies (TBDMS, TC, and ACE). Whereas the applicability of our method concerning ACE-protected RNA containing uridine is limited due to the formation of methylated side-products, the compatibility with TBDMS as well as with TC chemistry independently of the sequence is shown to be excellent.

As Nair et al.[60] indicated for monomers, it is noteworthy to mention that the vinyl-coupled RNAs are key precursors for further functionalization. By dihydroxylation and periodate cleavage, an aldehyde function is created. These aldehydes can be used as precursors for building up benzimidazoles known as important pharmacophores. Recently, an efficient microwave-assisted synthesis of 5-benzimidazolyl-2′-desoxyuridines resulting in high fluorescent activity was developed in our group.[80] Both aspects of Stille cross-coupling directly resulting in functionally modified RNA or affording a precursor qualified for further derivatization open the opportunity for convenient synthesis of modified RNA.

AUTHOR INFORMATION

Corresponding Author

*Phone: +49-69-79829150. Fax: +49-69-79829148. E-mail: joachim.engels@chemie.uni-frankfurt.de.

Notes

The authors declare no competing financial interest.

ACKNOWLEDGMENTS

We thank Aljoscha Joppe, Jolanta Brzezinska, and Maximilian Buff for help in phosphoramidite preparation as well as Stefan Bernhardt and Martin Held for technical support in oligonucleotide synthesis, HPLC purification, and LCMS mass spectrometry.

ABBREVIATIONS

cpg, controlled pore glass; DCM, dichloromethane; DEPC, diethylpyrocarbonate; DMAP, 4-(dimethylamino)pyridine; DMF, *N*,*N*-dimethyl formamide; DmTrCl, 4,4′-dimethoxytriphenylmethyl chloride; EDTA, ethylenediaminetetraacetate; MeCN, acetonitrile; NMM, *N*-methylmorpholine; $Pd_2(dba)_3$, tris(dibenzylideneacetone)dipalladium(0); $Pd(MeCN)_2Cl_2$, palladium(II) chloride diacetonitrile complex; $P(fur)_3$, tri-2-

furylphosphine; P(*o*-tol)$_3$, tri(*o*-toluyl)phosphine; TEA, triethylamine; TEAA, triethylammoniumacetate; TEMED, tetramethylethylenediamine; THF, tetrahydrofuran

REFERENCES

(1) Goodchild, J. (1990) Conjugates of oligonucleotides and modified oligonucleotides: a review of their synthesis and properties. *Bioconjugate Chem. 1*, 165−187.

(2) Tor, Y. (1999) RNA and the small molecule world. *Angew. Chem., Int. Ed. 38*, 1579−1582.

(3) Petersen, C. P., Doench, J. G., Grishok, A., and Sharp, P. A. (2006) RNA Continues to Triumph over DNA: The Biology of Short RNAs, *The RNA World*, 3rd ed. (Gesteland, R. F., Cech, T. R., and Atkins, J. F., Eds.) pp 535−567, Chapter 19, Cold Spring Harbor Laboratory Press, New York.

(4) Storz, G., and Gottesman, S. (2006) RNA Continues to Triumph over DNA: Versatile Roles of Small Regulators in Bacteria, *The RNA World*, 3rd ed. (Gesteland, R. F., Cech, T. R., and Atkins, J. F., Eds.) pp 567−595, Chapter 20, Cold Spring Harbor Laboratory Press, New York.

(5) Melnikova, I. (2007) RNA-based therapies. *Nature Rev. Drug Discovery 6*, 863−864.

(6) Uhlmann, E., and Peyman, A. (1990) Antisense oligonucleotides: a new therapeutic principle. *Chem. Rev. 90*, 543−584.

(7) Kurreck, J. (2009) RNA interference: from basic research to therapeutic applications. *Angew. Chem., Int. Ed. 48*, 1378−1398.

(8) Hobartner, C., and Wachowius, F. (2010) Chemical RNA modifications for studies of RNA structure and dynamics. *ChemBioChem 11*, 469−480.

(9) Mollova, E. T. (2002) Single-molecule fluorescence of nucleic acids. *Curr. Opin. Chem. Biol. 6*, 823−828.

(10) Quin, P. Z. (2004) Application of EPR and NMR methods to the study of RNA. *Curr. Opin. Struct. Biol. 14*, 350−359.

(11) Nielsen, G., Stadler, M., Jonker, H., Betz, M., and Schwalbe, H. (2009) NMR: Applications in Chemical Biology, *Wiley Encyclopedia of Chemical Biology*, Vol. 3, pp 350−374, Wiley Interscience, New York.

(12) Lehmann, T. J., Serwe, M., Caselmann, W. H., and Engels, J. W. (2001) Design and properties of hepatitis C virus antisense oligonucleotides for liver specific drug targeting. *Nucleosides, Nucleotides Nucleic Acids 20*, 1343−1346.

(13) Manoharan, M. (2004) RNA interference and chemically modified small interfering RNAs. *Curr. Opin. Chem. Biol. 8*, 570−579.

(14) Wojczewski, C., Stolze, K., and Engels, J. W. (1999) Fluorescent oligonucleotides: versatile tools as probes and primers for DNA and RNA analysis. *Synlett 10*, 1667−1678.

(15) Sigurdsson, S. T. (2011) Nitroxides and nucleic acids: Chemistry and electron paramagnetic resonance (EPR) spectroscopy. *Pure Appl. Chem. 83*, 677−686.

(16) Mayer, G., and Heckel, A. (2006) Biologically active molecules with a "light switch". *Angew. Chem., Int. Ed. 45*, 4900−4921.

(17) Marx, A., and Weisbrod, S. H. (2008) Novel strategies for the site-specific covalent labelling of nucleic acids. *Chem. Commun.*, 5675−5685.

(18) Macmillan, A. M., and Verdine, G. L. (1990) Synthesis of functionally tethered oligodeoxynucleotides by the convertible nucleoside approach. *J. Org. Chem. 55*, 5931−5933.

(19) Kahl, J. D., and Greenberg, M. M. (1999) Introducing structural diversity in oligonucleotides via photolabile, convertible C5-substituted nucleotides. *J. Am. Chem. Soc. 121*, 597−604.

(20) Minakawa, N., Ono, Y., and Matsuda, A. (2003) A versatile modification of on-column oligodeoxynucleotides using a copper-catalyzed oxidative acetylenic coupling reaction. *J. Am. Chem. Soc. 125*, 11545−11552.

(21) Kierzek, E., Kierzek, R. (2004) Synthesis of oligoribonucleotides containing N-6-alkyladenosines and 2-methylthio-N-6-alkyladenosines. *Curr. Protoc. Nucleic Acid Chem.* Chapter 4, unit 4.23.21−24.23.21.

(22) Harris, C. M., Zhou, L., Strand, E. A., and Harris, T. M. (1991) New strategy for the synthesis of oligodeoxynucleotides bearing adducts at exocyclic amino sites of purine nucleosides. *J. Am. Chem. Soc. 113*, 4328−4329.

(23) Kim, S. J., Stone, M. P., Harris, C. M., and Harris, T. M. (1992) A postoligomerization synthesis of oligodeoxynucleotides containing polycyclic aromatic hydrocarbon adducts at the N(6) position of deoxyadenosine. *J. Am. Chem. Soc. 114*, 5480−5481.

(24) Johnson, F., Habus, I., Gentles, R. G., Shibutani, S., Lee, H. C., Iden, C. R., and Rieger, R. (1992) Site-specific adduct formation in oligomeric DNA using a new protecting group. *J. Am. Chem. Soc. 114*, 4923−4924.

(25) Macmillan, A. M., and Verdine, G. L. (1991) Engineering tethered DNA-molecules by the convertible nucleoside approach. *Tetrahedron 47*, 2603−2616.

(26) Allerson, C. R., Chen, S. L., and Verdine, G. L. (1997) A chemical method for site-specific modification of RNA: The convertible nucleoside approach. *J. Am. Chem. Soc. 119*, 7423−7433.

(27) Xu, Y. Z., Zheng, Q., and Swann, P. F. (1992) Synthesis by post-synthetic substitution of oligomers containing guanine modified at the 6-position with S-derivatives, N-derivatives, O-derivatives. *Tetrahedron 48*, 1729−1740.

(28) Xu, Y. Z., Zheng, Q. G., and Swann, P. F. (1992) Synthesis of DNA containing modified bases by postsynthetic substitution: Synthesis of oligomers containing 4-substituted thymine-O4-alkylthymine, 5-methylcytosine, N4-(dimethylamino)-5-methylcytosine, and 4-thiothymine. *J. Org. Chem. 57*, 3839−3845.

(29) Xu, Y. Z., Zheng, Q. G., Urwin, G., and Swann, P. F. (1997) Site-specific introduction of functional groups onto bases in synthetic oligonucleotides for biological applications. *Nucleosides, Nucleotides Nucleic Acids 16*, 1559−1562.

(30) Gao, H., Fathi, R., Gaffney, B. L., Goswami, B., Kung, P. P., Rhee, Y., Jin, R., and Jones, R. A. (1992) 6-O-(Pentafluorophenyl)-2′-deoxyguanosine: a versatile synthon for nucleoside and oligonucleotide synthesis. *J. Org. Chem. 57*, 6954−6959.

(31) Miles, R. W., Samano, V., and Robins, M. J. (1995) Nucleic-acid related-compounds 0.86. Nucleophilic functionalization of adenine, adenosine, tubercidin, and formycin derivatives via elaboration of the heterocyclic amino group into a readily displaced 1,2,4-triazol-4-yl substituent. *J. Am. Chem. Soc. 117*, 5951−5957.

(32) Haginoya, N., Ono, A., Nomura, Y., Ueno, Y., and Matsuda, A. (1997) Nucleosides and nucleotides 0.160. Synthesis of oligodeoxyribonucleotides containing 5-(N-aminoalkyl)carbamoyl-2′-deoxyuridin by a new postsynthetic modification method and their thermal stability and nuclease-resistance properties. *Bioconjugate Chem. 8*, 271−280.

(33) Komatsu, Y., Kumagai, I., and Ohtsuka, E. (1999) Investigation of the recognition of an important uridine in an internal loop of a hairpin ribozyme prepared using post synthetically modified oligonucleotides. *Nucleic Acids Res. 27*, 4314−4323.

(34) Avino, A., Garcia, R. G., and Eritja, R. (2004) Synthesis of oligoribonucleotides containing 4-thiouridine using the convertible nucleoside approach and the 1-(2-fluorophenyl)-4-methoxypiperidin-4-yl group. *Nucleosides, Nucleotides Nucleic Acids 23*, 1767−1777.

(35) Bennati, M., Sicoli, G., Wachowius, F., and Hobartner, C. (2010) Probing secondary structures of spin-labeled RNA by pulsed EPR spectroscopy. *Angew. Chem., Int. Ed. 49*, 6443−6447.

(36) Wu, X. L., and Pitsch, S. (1999) Functionalization of the sugar moiety of oligoribonucleotides on solid support. *Bioconjugate Chem. 10*, 921−924.

(37) Wu, X. L., and Pitsch, S. (2000) Synthesis of 5 ′-C- and 2′-O-(bromoalkyl)-substituted ribonucleoside phosphoramidites for the post-synthetic functionalization of oligonucleotides on solid support. *Helv. Chim. Acta 83*, 1127−1144.

(38) Kierzek, E., and Kierzek, R. (2003) The synthesis of oligoribonucleotides containing N-6-alkyladenosines and 2-methylthio-N-6-alkyladenosines via post-synthetic modification of precursor oligomers. *Nucleic Acids Res. 31*, 4461−4471.

(39) Coleman, R. S., and Kesicki, E. A. (1994) Synthesis and postsynthetic modification of oligodeoxynucleotides containing 4-thio-2′-deoxyuridine (D(S4)U). *J. Am. Chem. Soc. 116*, 11636−11642.

(40) Huang, Z., and Zhang, W. (2011) Synthesis of the 5′-Se-thymidine phosphoramidite and convenient labeling of DNA oligonucleotide. *Org. Lett. 13*, 2000−2003.
(41) Carell, T., Gierlich, J., Burley, G. A., Gramlich, P. M. E., and Hammond, D. M. (2006) Click chemistry as a reliable method for the high-density postsynthetic functionalization of alkyne-modified DNA. *Org. Lett. 8*, 3639−3642.
(42) Seela, F., and Sirivolu, V. R. (2006) DNA containing side chains with terminal triple bonds: Base-pair stability and functionalization of alkynylated pyrimidines and 7-deazapurines. *Chem. Biodiversity 3*, 509−514.
(43) Seela, F., and Sirivolu, V. R. (2007) Nucleosides and oligonucleotides with diynyl side chains: Base pairing and functionalization of 2′-deoxyuridine derivatives by the copper(I)-catalyzed alkyne-azide 'click' cycloaddition. *Helv. Chim. Acta 90*, 535−552.
(44) Vogel, S., Jakobsen, U., Shelke, S. A., and Sigurdsson, S. T. (2010) Site-directed spin-labeling of nucleic acids by click chemistry: detection of abasic sites in duplex DNA by EPR spectroscopy. *J. Am. Chem. Soc. 132*, 10424−10428.
(45) Beal, P. A., Peacock, H., and Maydanovych, O. (2010) N(2)-Modified 2-aminopurine ribonucleosides as minor-groove-modulating adenosine replacements in duplex RNA. *Org. Lett. 12*, 1044−1047.
(46) Grinstaff, M. W., and Khan, S. I. (1999) Palladium(0)-catalyzed modification of oligonucleotides during automated solid-phase synthesis. *J. Am. Chem. Soc. 121*, 4704−4705.
(47) Rist, M., Amann, N., and Wagenknecht, H. A. (2003) Preparation of 1-ethynylpyrene-modified DNA via Sonogashira-type solid-phase couplings and characterization of the fluorescence properties for electron-transfer studies. *Eur. J. Org. Chem.*, 2498−2504.
(48) Strube, T., Schiemann, O., MacMillan, F., Prisner, T., and Engels, J. W. (2001) A new facile method for spin-labeling of oligonucleotides. *Nucleosides, Nucleotides Nucleic Acids 20*, 1271−1274.
(49) Schiemann, O., Piton, N., Mu, Y. G., Stock, G., Engels, J. W., and Prisner, T. F. (2004) A PELDOR-based nanometer distance ruler for oligonucleotides. *J. Am. Chem. Soc. 126*, 5722−5729.
(50) Schiemann, O., Piton, N., Plackmeyer, J., Bode, B. E., Prisner, T. F., and Engels, J. W. (2007) Spin labeling of oligonucleotides with the nitroxide TPA and use of PELDOR, a pulse EPR method, to measure intramolecular distances. *Nat Protoc. 2*, 904−923.
(51) Piton, N., Schiemann, O., Mu, Y. G., Stock, G., Prisner, T., and Engels, J. W. (2005) Synthesis of spin-labeled RNAs for long range distance measurements by PELDOR. *Nucleosides, Nucleotides Nucleic Acids 24*, 771−775.
(52) Piton, N., Mu, Y. G., Stock, G., Prisner, T. F., Schiemann, O., and Engels, J. W. (2007) Base-specific spin-labeling of RNA for structure determination. *Nucleic Acids Res. 35*, 3128−3143.
(53) Grünewald, C., Kwon, T., Piton, N., Forster, U., Wachtveitl, J., and Engels, J. W. (2008) RNA as scaffold for pyrene excited complexes. *Bioorg. Med. Chem. 16*, 19−26.
(54) Romainczyk, O., Endeward, B., Prisner, T. F., and Engels, J. W. (2011) The RNA-DNA hybrid structure determined by EPR, CD and RNase H1. *Mol. Biosyst. 7*, 1050−1052.
(55) Richert, C., Kottysch, T., Ahlborn, C., and Brotzel, F. (2004) Stabilizing or destabilizing oligodeoxynucleotide duplexes containing single 2′-deoxyuridine residues with 5-alkynyl substituents. *Chem.—Eur. J. 10*, 4017−4028.
(56) Manderville, R. A., Omumi, A., Beach, D. G., Baker, M., and Gabryelski, W. (2011) Postsynthetic guanine arylation of DNA by Suzuki-Miyaura cross-coupling. *J. Am. Chem. Soc. 133*, 42−50.
(57) Stille, J. K. (1986) The palladium-catalyzed cross-coupling reactions of organotin reagents with organic electrophiles. *Angew. Chem., Int. Ed. 25*, 508−523.
(58) Agrofoglio, L. A., Gillaizeau, I., and Saito, Y. (2003) Palladium-assisted routes to nucleosides. *Chem. Rev. 103*, 1875−1916.
(59) Aucagne, V., Berteina-Raboin, S., Guenot, P., and Agrofoglio, L. A. (2004) Palladium-catalyzed synthesis of uridines on polystyrene-based solid supports. *J. Comb. Chem. 6*, 717−723.
(60) Nair, V., Turner, G. A., and Chamberlain, S. D. (1987) Novel approaches to functionalized nucleosides via palladium-catalyzed cross coupling with organostannanes. *J. Am. Chem. Soc. 109*, 7223−7224.
(61) Nair, V., Turner, G. A., Buenger, G. S., and Chamberlain, S. D. (1988) New methodologies for the synthesis of C-2 functionalized hypoxanthine nucleosides. *J. Org. Chem. 53*, 3051−3057.
(62) Nair, V., and Buenger, G. S. (1988) Rare purine nucleosides: congeners of the antibiotic, nebularine. *Synthesis*, 848−850.
(63) Farina, V., and Hauck, S. I. (1991) Palladium-catalyzed approach to 5-substituted uracil and uridine derivatives. *Synlett*, 157−159.
(64) Nair, V., Purdy, D. F., and Sells, T. B. (1989) Synthesis of congeners of adenosine resistant to deamination by adenosine-deaminase. *J. Chem. Soc. Chem. Commun.*, 878−879.
(65) Vanaerschot, A. A., Mamos, P., Weyns, N. J., Ikeda, S., Declercq, E., and Herdewijn, P. A. (1993) Antiviral activity of C-alkylated purine nucleosides obtained by cross-coupling with tetraalkyltin reagents. *J. Med. Chem. 36*, 2938−2942.
(66) Evans, C. H., Jones, A. S., and Walker, R. T. (1973) Incorporation of 5-substituted uracil derivatives into nucleic-acids-I. Synthesis of some 5-substituted uracils. *Tetrahedron 29*, 1611−1614.
(67) Persson, T., Gronowitz, S., Hornfeldt, A. B., and Johansson, N. G. (1995) Synthesis and antiviral effects of 2-heteroaryl substituted adenosine and 8-heteroaryl substituted guanosine derivatives. *Bioorg. Med. Chem. 3*, 1377−1382.
(68) Srivatsan, S. G., and Tor, Y. (2007) Fluorescent pyrimidine ribonucleotide: Synthesis, enzymatic incorporation, and utilization. *J. Am. Chem. Soc. 129*, 2044−2053.
(69) Srivatsan, S. G., and Tor, Y. (2009) Enzymatic Incorporation of emissive pyrimidine ribonucleotides. *Chem. Asian J. 4*, 419−427.
(70) Pawar, M. G., and Srivatsan, S. G. (2011) Synthesis, photophysical characterization, and enzymatic incorporation of a microenvironment-sensitive fluorescent uridine analog. *Org. Lett. 13*, 1114−1117.
(71) Dellinger, D. J., Timar, Z., Myerson, J., Sierzchala, A. B., Turner, J., Ferreira, F., Kupihar, Z., Dellinger, G., Hill, K. W., Powell, J. A., Sampson, J. R., and Caruthers, M. H. (2011) Streamlined process for the chemical synthesis of RNA using 2′-O-thionocarbamate-protected nucleoside phosphoramidites in the solid phase. *J. Am. Chem. Soc. 133*, 11540−11556.
(72) Matsuda, A., Takenuki, K., Tanaka, M., Sasaki, T., and Ueda, T. (1991) Nucleosides and nucleotides. 97. Synthesis of new broad spectrum antineoplastic nucleosides, 2′-deoxy-2′-methylidenecytidine (DMDC) and its derivatives. *J. Med. Chem. 34*, 812−819.
(73) Scaringe, S. A., Wincott, F. E., and Caruthers, M. H. (1998) Novel RNA synthesis method using 5′-O-silyl-2′-O-orthoester protecting groups. *J. Am. Chem. Soc. 120*, 11820−11821.
(74) Scaringe, S. A., Kitchen, D., Kaiser, R., and Marshall, W. S. (2004) Preparation of 5′-silyl-2′-orthoester ribonucleosides for use in oligoribonucleotide synthesis. *Curr. Protoc. Nucleic Acids Chem.* Chapter 2, unit 2.10.11−12.10.15.
(75) Seven, I. (2010) Suzuki-Kreuzkupplungen an 2-halogen-substituierten Purinnucleosiden, Diploma Thesis, Institute for Organic Chemistry and Chemical Biology, Goethe University Frankfurt, Germany.
(76) Paetzold, M. (2010) Synthese fluoreszierender Inosinderivate als Bausteine für die RNA-Synthese, Diploma thesis, Institute for Organic Chemistry and Chemical Biology, Goethe University Frankfurt, Germany.
(77) Farina, V., Krishnamurthy, V., and Scott, W. J. (1998) *The Stille Reaction, Side Reactions: Electophile Reduction*, published in association with Organic Reactions, Inc.; John Wiley & Sons, New York.
(78) Srivatsan, S. G., and Tor, Y. (2007) Using an emissive uridine analogue for assembling fluorescent HIV-1 TAR constructs. *Tetrahedron 63*, 3601−3607.
(79) Srivatsan, S. G., and Tor, Y. (2007) Synthesis and enzymatic incorporation of a fluorescent pyrimidine ribonucleotide. *Nat. Protoc. 2*, 1547−1555.

(80) Krim, J., Grünewald, C., Taourirte, M., and Engels, J. W. (2012) Efficient microwave-assisted synthesis, antibacterial activity and high fluorescence of 5 benzimidazolyl-2′-deoxyuridines. *Bioorg. Med. Chem. 20*, 480−486.

Bioconjugate Chemistry

Article

pubs.acs.org/bc

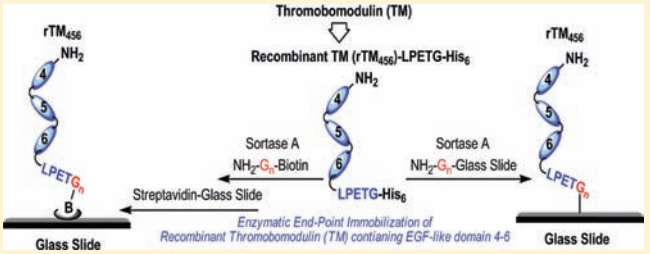
End-Point Immobilization of Recombinant Thrombomodulin via Sortase-Mediated Ligation

Rui Jiang, Jacob Weingart, Hailong Zhang, Yong Ma, and Xue-Long Sun*

Department of Chemistry, Cleveland State University, Cleveland, Ohio 44115, United States

Supporting Information

ABSTRACT: We report an enzymatic end-point modification and immobilization of recombinant human thrombomodulin (TM), a cofactor for activation of anticoagulant protein C pathway via thrombin. First, a truncated TM mutant consisting of epidermal growth factor-like domains 4−6 (TM_{456}) with a conserved pentapeptide LPETG motif at its *C*-terminal was expressed and purified in *E. coli*. Next, the truncated TM_{456} derivative was site-specifically modified with *N*-terminal diglycine containing molecules such as biotin and the fluorescent probe dansyl via sortase A (SrtA) mediated ligation (SML). The successful ligations were confirmed by SDS−PAGE and fluorescence imaging. Finally, the truncated TM_{456} was immobilized onto an *N*-terminal diglycine-functionalized glass slide surface via SML directly. Alternatively, the truncated TM_{456} was biotinylated via SML and then immobilized onto a streptavidin-functionalized glass slide surface indirectly. The successful immobilizations were confirmed by fluorescence imaging. The bioactivity of the immobilized truncated TM_{456} was further confirmed by protein C activation assay, in which enhanced activation of protein C by immobilized recombinant TM was observed. The sortase A-catalyzed surface ligation took place under mild conditions and occurs rapidly in a single step without prior chemical modification of the target protein. This site-specific covalent modification leads to molecules being arranged in a definitively ordered fashion and facilitating the preservation of the protein's biological activity.



INTRODUCTION

Immobilization of protein onto solid surfaces is widely used in the preparation of functional protein microarrays, in the development of protein-based bioassays, biosensors, and for medical device surface functionalization, and various other applications.[1] The success of all these technologies relies on the immobilization technique employed to attach a functional protein to the corresponding surface. Nonspecific physical adsorption or chemical cross-linking with appropriate surfaces results in the immobilization of the protein in random orientations and with reduced activity. Thrombomodulin (TM) is an endothelial integral membrane protein and acts as a major cofactor in the protein C anticoagulant pathway.[2] When bound to TM on the endothelial surface, thrombin is unable to activate fibrin generation or activate platelets. Instead, it becomes a potent activator of protein C. Subsequently, the activated form of protein C (APC), an anticoagulant protease, selectively inactivates coagulation factors Va and VIIIa, providing an essential feedback mechanism in preventing excessive coagulation. Therefore, TM serves as an excellent target for the engineering of antithrombogenic surfaces for cardiovascular biomaterials by immobilizing TM.[3] In the past decade, several groups have covalently immobilized TM onto polymeric surfaces for generating antithrombogenic materials. Kishida et al. conjugated recombinant human thrombomodulin to both aminated and carboxylated surfaces, including poly(vinyl amine) and poly(acrylic acid) surface-grafted polyethylene, and a surface-hydrolyzed poly(ether urethaneurea).[4−6] Similarly, Vasilets et al. immobilized TM onto poly(acrylic acid) surface-grafted PTFE.[7] Alternatively, Cutler et al. physically adsorbed and cross-linked soluble human TM onto small-caliber ePTFE grafts and reported promising short-term antithrombotic results *in vivo*.[8] Other investigators, such as Sperling et al. and Han et al. have tethered TM to surfaces by using polyethylene glycol spacers.[9,10] However, many of these methods may negatively impact activity of the TM due to harsh conjugation conditions possibly leading to protein denaturation and random-site conjugation leaving limited accessibility to the active region of the protein, both potentially hampering the desired bioactivity. The latter issue resulting from common conjugation techniques has been reported in studies where the cofactor activity of human TM for protein C activation decreases upon immobilization due to the potential conformation variation caused by the random covalent immobilization.[10]

In order to generate the stable, functional, homogeneous, and oriented protein immobilization, attention has focused on methods that enable the efficient and site-specific covalent immobilization of recombinant proteins. Recently, a short TM construct containing epidermal growth factor (EGF)-like

Received: December 12, 2011
Revised: February 28, 2012
Published: February 28, 2012

ACS Publications © 2012 American Chemical Society

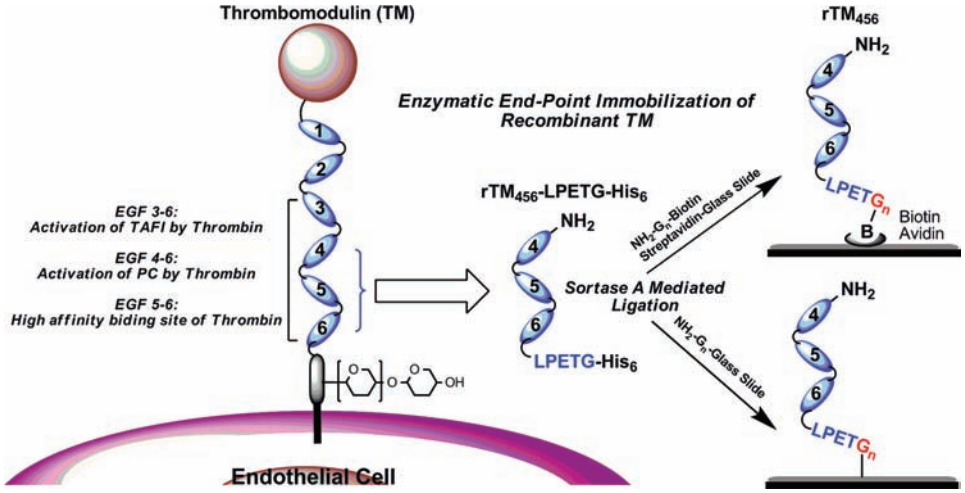


Figure 1. Illustration of endothelial thrombomodulin (TM) and site-specific end-point immobilization of LPETG-tagged recombinant thrombomodulin (rTM_{456}) through sortase A-mediated ligation (SML). EGF: epidermal growth factor-like domain.

domains 4−6 with an azide-functionalized methionine analogue as a *C*-terminal linker was synthesized in *E. coli* for site-specific immobilization of the recombinant TM derivative at the *C*-terminus through click chemistry[11] and Staudinger ligation.[12] Incorporation of azide-functionalized amino acids into proteins *in vivo* provides opportunities for protein modification under native conditions and selective labeling of proteins in the intracellular environment. However, the expression yield for recombinant protein with non-natural amino acid incorporation is generally too low for protein modification and practical applications. Also, the incorporation of non-natural amino acids involves complicated and time-consuming molecular biology procedures.

Enzymatic post-translational modifications have recently provided robust tools for covalent protein conjugations. For example, sortase A (SrtA) has been studied extensively for protein ligation applications.[13] Sortase A, a transpeptidase from *S. aureus*, is present on the plasma membrane and catalyzes a cell wall sorting reaction that attaches surface proteins to the cell wall envelope.[14] SrtA recognizes substrates containing a pentapeptide LPXTG motif (X being any amino acid) and cleaves the amide bond between the Thr and Gly residues with an active site cysteine to generate a covalent acyl-enzyme intermediate. The carboxyl group of Thr of the thioester intermediate is then attacked by the amino terminus of an oligoglycine nucleophile, resulting in the formation of a native covalent peptide bond.[15−18] The advantage of sortase-mediated ligation (SML) is that the reaction takes place in a site-specific manner under mild conditions and occurs rapidly in a single step without prior chemical modification of the target protein. Employing such a strategy, we report an enzymatic end-point modification and immobilization of recombinant TM via SML. Briefly, a truncated TM mutant consisting of epidermal growth factor-like domains 4−6 (rTM_{456}) with a conserved pentapeptide LPETG motif at its *C*-terminal was expressed and purified in *E. coli*, which is for SML with *N*-terminal oligoglycine-containing molecules. It has been shown that LPETG is the optimal isoform of the LPXTG motif.[19] Two strategies for site-directed immobilization of recombinant TM via their *C*-terminus to different solid supports were demonstrated (Figure 1). First, the rTM_{456} was biotinylated via SML and then immobilized onto streptavidin-functionalized glass slide surfaces. Second, the rTM_{456} was immobilized onto *N*-terminal diglycine-functionalized glass slide surfaces via SML directly. The bioactivity of immobilized rTM_{456} was further confirmed by protein C activation assay, which showed enhanced protein C activation. Overall, sortase A-catalyzed surface ligation is mild, rapid, and occurs in a single step without prior chemical modification of the target protein. Site-specific covalent attachment leads to molecules being arranged in a definite, orderly fashion and allows the use of spacers and linkers to help minimize steric hindrances between the protein and the surface, thus facilitating the protein's stability and biological activity. Since TM is a transmembrane glycoprotein of the endothelium of blood and lymphatic vessels and the basis of a major natural anticoagulant system, the reported strategies should provide an ideal approach for the engineering of antithrombogenic surfaces for cardiovascular biomaterials, minimizing incompatibility and thrombosis.

■ MATERIALS AND METHODS

Materials. All solvents and reagents were purchased from commercial sources and were used unless otherwise noted. Human protein C, human thrombin, and human antithrombin III were obtained from Haematologic Technologies Inc., Chromogenic thrombin substrate BIOPHEN-CS01 was obtained from Aniara, and the DNA fragments encoding the TM derivative and sortase A were synthesized by Genscript Inc..

Synthesis of DiGly-Biotin and DiGly-Dansyl. A solution of Biotin ethylenediamine (36 mg, 0.129 mmol, Sigma) in 1 mL of dry DMF was treated with triethylamine (0.1 mL, 0.71 mmol) and allowed to stir at room temperature for 30 min. The solution was then added to a solution of *Z*-Gly-Gly-*p*-nitrophenyl ester (100 mg, 0.258 mmol, Sigma) in dry DMF (4 mL) via syringe. The reaction mixture was stirred for 24 h at room temperature under $Ar_{(g)}$ and then concentrated under vacuum to give a residue, which was then dissolved in MeOH (10 mL) to which 50 mg of Pd/C (10% wt.) was added. The reaction solution was degassed under vacuum and then backfilled with hydrogen gas via a hydrogen gas balloon and stirred for 6 h at room temperature. Finally, the reaction solution was filtered to remove the Pd/C (10% wt.) catalyst, and the filtrate was concentrated to give a residue, which was purified by silica gel column using chloroform/methanol (5:1)

dx.doi.org/10.1021/bc200661w | *Bioconjugate Chem.* 2012, 23, 643−649

as elutent to afford diGly-biotin (36 mg, 70%). ^{1}H NMR (D_2O) δ: 4.39 (m, 1 H, C*H*-1-Biotin), 4.19 (m, 1 H, C*H*-4-Biotin), 3.87 (s, 2H, CH_2-Gly), 3.73 (s, 2H, CH_2-Gly), 3.39 (t, 2H, CH_2CH_2), 3.13 (t, 2H, CH_2CH_2), 3.60 (dd, 1 H, CH-Biotin), 2.91 (m, 1H, CH-Biotin), 2.79 (dd, 1 H, CH-Biotin), 2.60 (m 1 H, CH-Biotin), 2.06 (t, 1 H, CH2CO-Biotin), 1.53, 1.43, 1.22 (m, 6 H, (CH_2)3-Biotin). Under similar reaction conditions, diGly-Dansyl was synthesized from *Z*-Gly-Gly-*p*-nitrophenyl ester (100 mg, 0.258 mmol, Sigma) and Dansyl ethylenediamine (38 mg, 0.129 mmol, Sigma) in 73% (40 mg). ^{1}H NMR (D_2O) δ: 8.34 (d, 1H, aromatic), 8.09 (m. 2H, aromatic), 7.55 (m, 2H, aromatic), 7.26 (m, 1H, aromatic), 3.58 (s, 2H, CH_2-Gly), 3.37 (s, 2H, CH_2-Gly), 3.02 (t, 2H, CH_2CH_2), 2.91 (t, 2H, CH_2CH_2), 2.71 (s, 6H, CH_3x2).

Synthesis of Gly-Gly-Modified Glass Slides. Several precut pieces of the amine-coated glass slide were placed in a small recystallization dish. To the dish was added 10 mL of an incubation solution of ~20 mM *Z*-GG-*p*-nitrophenyl ester in dry DMF, and then 5 drops of triethylamine (Et_3N) were added. The dish was then immediately covered and placed on a mechanical shaker to shake gently overnight at room temperature. After 24 h, the slides were removed from the incubation solution and sequentially rinsed with EtOH, doubly distilled H_2O, EtOH again, and then blown dry with argon gas.

To deprotect the *Z*-group at the *N*-terminus of the diglycine residues, the newly functionalized glass slides were gently placed into a 100 mL round-bottom flask turned on its side. To the flask was added 8 mL of a 3:1 methanol/H_2O solution and ~5 mg of Pd/C (10 wt %). A 3-way stopcock with a hydrogen balloon was then attached to the flask. Prior to introducing H_2 gas into the vessel, the air was slowly evacuated while slowly flushing with argon gas over a period of ~5 min. After the air was removed, H_2 gas was introduced into the systemm and the flask was set on a mechanical shaker to shake gently for 5 h at room temperature performing hydrogenolysis of the benzyl carbamate-protecting group. Then, the vessel was flushed with argon to remove the excess H_2, and the slides were then removed and rinsed with a 1:1 methanol/H_2O solution. The slides were then blown dry with argon gas and set into a plastic container to be stored in a 4−8 °C refrigerator until further use.

Expression and Purification of TM_{456} Fusion Protein. The gene encoding the EGF domain 4−6 of human thrombomodulin (corresponding to residues 345−473) with a *C*-terminal LPETG motif and an *N*-terminal human Factor Xa cleavage site (IEGRS) was designed and synthesized (Genscript Inc.). In order to prevent oxidation and reduce proteolytic susceptibility, three residues of TM were mutated (M388L, R456G, and H457Q) as described before[20] (see Supporting Information for protein sequence). The gene fragment was then inserted into the NcoI-*Bam*HI sites of the pET39b vector to get the new expression plasmid, pET39b-TM_{456}. This new construct was transformed in *E.coli* BL21 (DE3) and grown at 37 °C to an OD (600 nM) of 0.8. Protein expression was induced by the addition of IPTG to a final concentration of 1 mM, and the *E. coli* culture was incubated overnight at 25 °C. The bacteria were then centrifuged at 6,000*g* for 10 min, and the pellet was then resuspended in 40 mL of lysis buffer (20 mM Tris and 150 mM NaCl, pH 8.0), and following lysis by sonication, the extract was then loaded onto a 5 mL HiTrap Chelating column (GE Healthcare) charged with Ni^{2+} ions and eluted with 20 mM Tris, 0.5 M NaCl, and 250 mM imidazole, pH 8.0. The chromatographic fractions were analyzed by 12% gradient SDS−PAGE gel electrophoresis and visualized by Western blot analysis using mouse monoclonal antibody toward human TM. The nitrocellulose membrane was developed using the ECL plus Western blotting detection kit (Amersham Biosciences, U.K.). Pooled fractions containing recombinant TM were collected and then dialyzed against 20 mM Tris and 150 mM NaCl, pH 8.0, and lyophilized to afford DsbA/LPETG-tagged TM_{456} fusion protein (dlTM_{456}F). FXa cleavage removed the fusion DsbA tag and generated the target LPETG-tagged TM_{456} fusion protein (lTM456F).

Expression and Purification of Soluble SrtA. Soluble SrtA with a C-terminal His6-tag was expressed and purified from *E. coli* BL21, and briefly, the gene encoding *S. aureus* COL SrtA-ΔN59 (residues 60−206) was inserted into NcoI-XhoI sites of the pET28b vector. The plasmid pET28b-SrtA was transformed into *E. coli* BL21 (DE3). The cells were grown in LB medium to an OD (600 nm) of 0.8 at 37 °C, and protein expression was induced by the addition of IPTG to a final concentration of 0.5 mM. After growth for an additional 4 h at 37 °C, the cells were harvested by centrifugation and resuspended in 40 mL of lysis buffer containing 20 mM Tris and 250 mM NaCl, pH 8.0, and lysed by sonication. The extract was centrifuged at 20,000*g* for 20 min, and the supernatant was applied onto a 5 mL HiTrap Chelating column (GE Healthcare) charged with Ni^{2+} ions and eluted with 20 mM Tris, 0.5 M NaCl, and 250 mM imidazole, pH 8.0. The pooled fractions containing rSrtA were collected and then dialyzed against 20 mM Tris and 150 mM NaCl, pH 8.0, and stored at −80 °C until use.

***C*-Terminal Covalent Modification of TM_{456} Fusion Protein via SML.** dlTM_{456}F (10 μM) was mixed with SrtA (5 μM) and biotin/dansyl modified diglycine nucleophiles (100 μM) in reaction buffer (20 mM Tris, 150 mM NaCl, and 5 mM $CaCl_2$, pH 8.0), and the reaction mixture was then incubated at 37 °C for 6 h. For further immobilization reactions, unreacted diglycine nucleophiles were removed by dialysis against 20 mM Tris and 150 mM NaCl, pH 8.0. In order to detect the TM_{456} conjugates, the reaction mixtures were loaded on SDS−PAGE and analyzed by fluorescence imaging or under UV light.

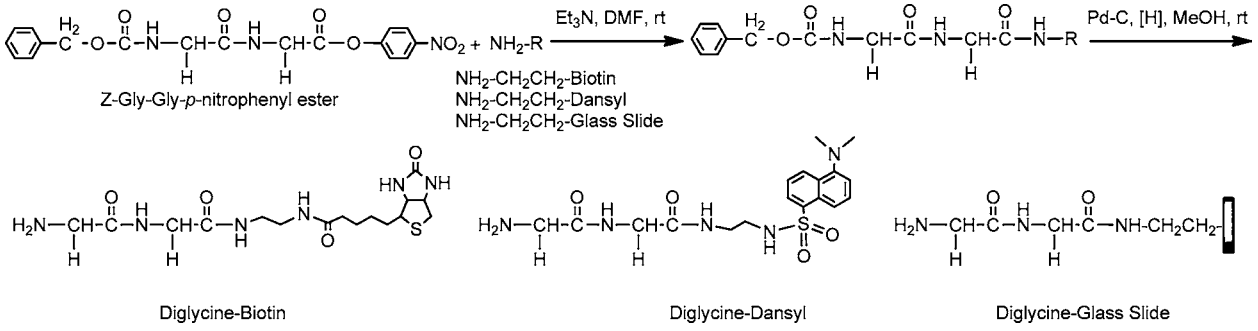
OG488 Labeling of TM_{456} Fusion Protein. dlTM_{456}F was labeled with Oregon Green 488 (OG488) succinimidyl ester (Molecular Probes, Inc.). Briefly, to a solution of 150 μL of carbonate−bicarbonate buffer (pH 9.0), 50 μL of OG488 solution (10 mg/mL in DMSO) was added, followed by 150 μL aqueous dlTM_{456}F solution (2 mg/mL). The mixture was gently vortexed at room temperature in the dark for 2 h. After the coupling reaction, the unreacted OG488 was removed by dialysis using centrifuge filter devices with a cutoff molecular weight of 10,000 Da to afford OG488-labeled dlTM_{456}F.

End-Point Immobilization of TM_{456} Fusion Protein onto Solid Supports. For immobilization of biotinylated dlTM_{456}F, the mixture containing biotinylated OG488-dlTM_{456}F from above was incubated with Streptavidin coated glass slides (1 × 2 cm, Xenopore, Hawthorne, NJ) at 37 °C for 1 h, and the glass slides were then rinsed with PBS (pH 7.4) for 1 h to remove any unbounded proteins. Surface-bound OG488-labeled dlTM_{456}F was further detected by fluorescence image at EX/EM = 480/520.

For direct immobilization of dlTM_{456}F via SML, OG488-labeled dlTM_{456}F (2 μM) was coincubated with SrtA (1 μM) and diglycine-coated glass slides (1 × 2 cm) in reaction buffer (20 mM Tris, 150 mM NaCl, and 5 mM $CaCl_2$, pH 8.0) for 16 h at room temperature. Then the glass slides were removed from reaction buffer and were washed with the PBS (pH 7.4)

dx.doi.org/10.1021/bc200661w | *Bioconjugate Chem.* 2012, 23, 643−649

Scheme 1. Synthesis of Diglycine Containing Biotin, Dansyl, and Glass Slide Conjugates



for 1 h to remove unreacted dlTM$_{456}$F prior to measuring TM activity. The successful immobilization was confirmed upon examining the fluorescence image of OG488-labeled dlTM$_{456}$F (EX/EM = 480/520 nm).

Protein C Activation Activity Assay of Immobilized TM$_{456}$ Fusion Protein. The cofactor activity of immobilized dlTM$_{456}$F was assessed by protein C activation assay as previously described with some modification.[10] The dlTM$_{456}$F-immobilized glass slide (1 × 2 cm) was placed in a 6-well plate and immersed in 3 mL of assay buffer (20 mM Tris, 150 mM NaCl, and 5 mM $CaCl_2$, pH 8.0) containing 300 nM of human protein C, and the reaction was initiated with the addition of human α-thrombin to a final concentration of 10 nM. After incubation for 2 h at 37 °C with shaking, protein C activation was terminated by addition of 30 μL of human antithrombin III (1 mg/mL) and 2 μL of heparin (10 U/mL) and further incubated for 5 min at 37 °C. The enzymatic activity of activated protein C was measured by the addition of chromogenic substrate H-D-Phe-Pip-Arg-*p*Na, 2HCl (0.5 mM), and after 20 min incubation, the change in absorbance at 405 nm was measured.

RESULTS AND DISCUSSION

Expression of TM$_{456}$ Fusion Protein and Recombinant SrtA. TM is a membrane protein and is composed of five distinct domains: an NH_2-terminal domain, a domain containing six epidermal growth factor (EGF)-like structures, an O-glycosylation site-rich domain, a transmembrane domain, and a cytoplasmic domain. It has been reported that the region including the fourth, fifth, and sixth EGF-like structures (EGF 4−6) is the minimum domain required for protein C-activating cofactor activity and the protein's subsequent anticoagulant activity.[21,22] In this study, a fragment containing the last three consecutive EGF-like domains 4−6 of human TM (TM$_{456}$) was chosen as the target protein to test the enzyme-mediated ligation using various substrates, such as biotinylation, fluorophore labeling, and immobilization. To closely mimic the TM structure as it appears at the cell surface and consequently preserve its antithrombotic bioactivity, we investigated the site-specific immobilization of the recombinant TM at the *C*-terminus via SML (Scheme 1). In order to reduce steric effects and increase the flexibility of *C*-terminal LPETG motif, eight hydrophilic amino acids at the *C*-terminal of EGF4−6 of the native TM (KVDGGDSG, corresponding residue 465−472) were retained (Figure 2A). Also, a LPETG-His6 tag was genetically fused to the *C*-terminal of TM$_{456}$. The gene construct was synthesized and inserted into expression vector pET39b. Vector pET39b-TM$_{456}$ was constructed for expression of an *N*-terminal DsbA/LPETG-tagged TM$_{456}$

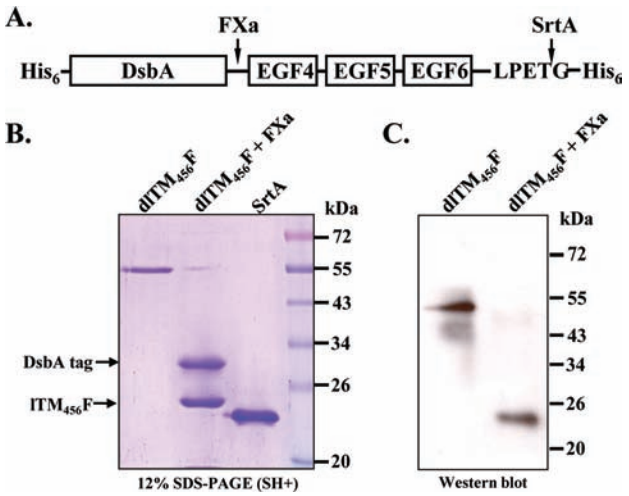


Figure 2. Structure of DsbA/LPETG-tagged TM$_{456}$ fusion protein (dlTM$_{456}$F) (A) and its SDS−PAGE characterization (B): lane 1, purified dlTM$_{456}$F; lane 2, dlTM$_{456}$F incubated with human Factor Xa; lane 3, purified SrtA-ΔN59; lane 4, molecular makers. Western blot analysis (C): lane 1, purified dlTM$_{456}$F; lane 2, dlTM$_{456}$F incubated with human Factor Xa.

derivative with two His6 tags at both termini (dlTM$_{456}$F) (Figure 2A). Protein expression was conducted in the *E. coli* culture overnight at 25 °C. Purified dlTM$_{456}$F (~55 kDa) was analyzed by SDS−PAGE (Figure 2B), and further confirmed by Western blot (Figure 2C) and protein C activation assay (Figures 4B and 5B). Treatment with Factor Xa removed the DsbA fusion tag (~33 kDa) and generated the target lTM$_{456}$F (~22 kDa, Figure 2B and C). Since the *SrtA* reaction is highly specific, the reaction can take place even in the presence of impure protein, with the exception of impure protein containing *N*-terminal oligoglycine; thus, the use of the impure target TM$_{456}$ after fusion tag removal was acceptable. In this study, dlTM$_{456}$F was used for the reason that there are 21 lysine residues in DsbA-tagged TM$_{456}$, which can be more efficiently labeled by OG488 succinimidyl ester compared with only one lysine residue in lTM$_{456}$.

Wild type SrtA is a polypeptide of 206 amino acids with an *N*-terminal membrane-spanning region; therefore, the full-length *SrtA* is difficult to purify in sufficient amounts. However, truncated SrtA protein with 59 *N*-terminal amino acids deleted (SrtA-ΔN59), which encode the outer-membrane region of wild type SrtA, was readily expressed and purified as a soluble protein. SrtA-ΔN59 has been expressed and used in previous studies since it retains the same transpeptidation activity as the full-length SrtA enzyme.[15,17] Expression vector pET28b-SrtA

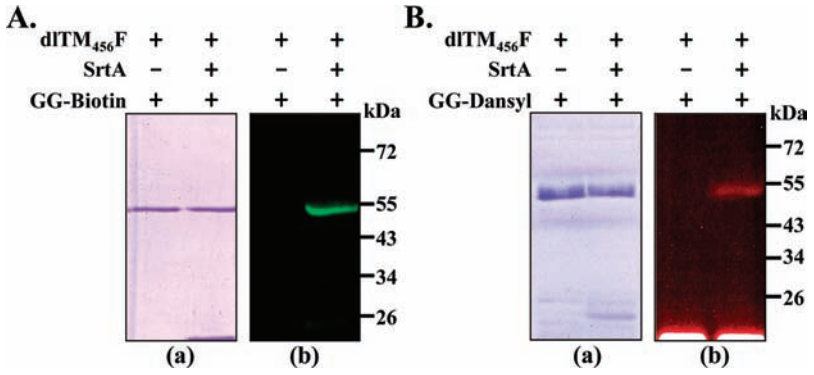


Figure 3. SrtA mediated site-specific biotinylation and dansylation of dlTM$_{456}$F. (A) Reactions between dlTM$_{456}$F (10 μM) and GG-Biotin (100 μM) in the presence or absence of SrtA (5 μM) analyzed by SDS−PAGE (a) and fluorescence scanning imaging of biotinylated dlTM$_{456}$F confirmed by incubation of SDS−PAGE gel with Streptavidin-Bodipy (EX/EM = 480/520) (b). (B) Reactions between dlTM$_{456}$F and GG-Dansyl in the presence or absence of SrtA. Reaction mixtures were analyzed by SDS−PAGE (a) and its photo image for Dansyl-labeled dlTM$_{456}$F taken under UV light (b).

was constructed for expression of soluble SrtA with a His6 tag at its *C*-terminal. The proteins were expressed in *E. coli* cells and in one step, purified in large amounts. The transpeptidation activity of SrtA was verified by penta-glycine and sortase substrate Abz-Leu-Pro-Glu-Thr-Gly-Lys(Dnp)-NH_2 (Anaspec) (Supporting Information).

Site-Specific Modification of TM$_{456}$ Fusion Protein with DiGly-Biotin and DiGly-Dansyl via SML. With dlTM$_{456}$F and SrtA in hand, site-specific modification of dlTM$_{456}$F with *N*-terminal oligoglycine-containing molecules via SML was investigated. Although single glycine at the *N*-terminus of nucleophile is sufficient for sortase-catalyzed transpeptidation, it has been reported that maximum reaction efficiency is generally obtained with substrates in which two or more glycines are incorporated, the addition of any more glycines having no significant effect on the reaction rate[15] Therefore, diglycine was chosen as the nucleophile in our study. Two kinds of diglycine-containing molecules, diGly-Biotin and diGly-Dansyl, were prepared for site-specific modification of dlTM$_{456}$F via SML (Figure 3). DiGly-Biotin and diGly-Dansyl were synthesized in two steps, first amidation of Biotin-ethylenediamine and Dansylethylenediamine with commercially available Z-Gly-Gly-*p*-nitrophenyl ester (Sigma), followed by removal of the *Z*-protection group under hydrogenation conditions (Scheme 1). The resulting compounds were characterized by ^{1}H NMR and FTIR spectroscopy. In the same reaction process, diglycine-functionalized glass slides were also prepared from amine-functionalized glass slides (Xenopore, Hawthorne, NJ) for dlTM$_{456}$F immobilization via SML as depicted below (Scheme 1).

To investigate whether the LPETG moiety in the dlTM$_{456}$F was reactive toward diglycine, dlTM$_{456}$F was mixed with SrtA and diGly-Biotin in the presence of Ca^{2+} following the conditions mentioned in Materials and Methods. The products were analyzed by SDS−PAGE. Within the gel, it was very difficult to observe the band migration of the biotinylated product due to the minute change in molecular weight of the dlTM$_{456}$F conjugate (less than 1 kDa). Therefore, the gel was incubated with a Bodipy-labeled streptavidin (Sigma) solution, allowing the biotinylated dlTM$_{456}$F to be visualized by fluorescence scanning imaging, whereas no unbiotinylated dlTM$_{456}$F was observed in the absence of SrtA in the control reaction (Figure 3Ab). Furthermore, dansylation of the dlTM$_{456}$F via SML was conducted successfully under the same conditions as those in biotinylation. The protein sample was separated by electrophoresis, and dansyl labeling was verified by visualizing the fluorescent bioconjugate under UV light (Figure 3Bb). Overall, these results indicated that the LPETG moiety at the *C*-terminal of dlTM$_{456}$F can be site-specifically modified with diglycine-containing molecules via SML.

End-Point Immobilization of TM$_{456}$ Fusion Protein via SML. Streptavidin/biotin-based protein immobilization has been widely used for functional surface fabrication.[23] In this study, immobilization of biotinylated TM456 onto a streptavidin-covered glass slide surfaces was investigated first. dlTM$_{456}$F was prelabeled with Oregon green 488 (OG488) before biotinylation. The reaction mixture containing biotinylated dlTM$_{456}$F from above was incubated with streptavidin-coated glass slides (Xenopore, Hawthorne, NJ) in PBS (pH 7.4) buffer for 1 h at room temperature. Then the glass slides were removed from the reaction solution and washed with PBS buffer for 1 h to remove unreacted dlTM$_{456}$F prior to measuring TM activity. The successful immobilization was confirmed by the fluorescence image of OG488 labeled dlTM$_{456}$F (Figure 4Ab), while no fluorescence image was observed with dlTM$_{456}$F without biotinylation (Figure 4Aa). Next, the biological activity of the immobilized dlTM$_{456}$F was accessed via the activation of human protein C. Figure 4B shows the absorbance variation of the chromogenic substrate at 405 nm for different glass slides. In order to compare the relative activity of immobilized dlTM$_{456}$F with free dlTM$_{456}$F, activities of various concentrations of free dlTM$_{456}$F were measured under the same conditions. As a result, the dlTM$_{456}$F-immobilized glass slides exhibited a protein C activation-promoting capability comparable to that of 2−3 μg of free dlTM$_{456}$F in this analysis with the surface areas of the covered glass substrates being ~2 cm^2. By contrast, the precursor streptavidin-glass slide, which was preincubated with a mixture of dlTM$_{456}$F without biotinylation, did not enhance the protein C activation to any degree above that of 1 μg of free dlTM$_{456}$F. These results indicated that biotinylated dlTM$_{456}$F from a mixture of proteins can be efficiently and selectively immobilized onto streptavidin- or avidin-coated solid supports. The biotin-mediated immobilization strategy has its advantages and disadvantages. For example, the protein biotinylation reaction is more effective than the direct protein−surface reaction due to the small molecule weight of diGly-biotin with

dx.doi.org/10.1021/bc200661w | *Bioconjugate Chem.* 2012, 23, 643−649

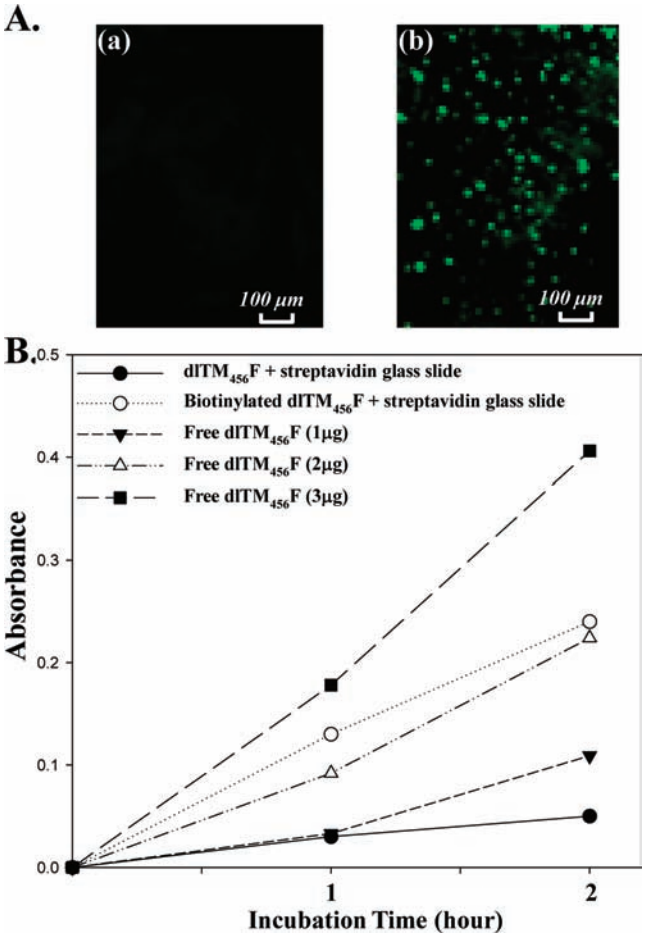


Figure 4. (A) Fluorescence images of streptavidin-coated glass slides incubated with (a) OG488-labeled $dlTM_{456}F$ and (b) biotinylated OG488-labeled $dlTM_{456}F$ (Ex/Em = 480/520). (B) Protein C activation assay for (●) the streptavidin-glass slide pretreated with $dlTM_{456}F$ in the presence of SrtA; (○) streptavidin-glass slide pretreated with biotinylated $dlTM_{456}F$ in the presence of SrtA; (▼) 1 μg of free $dlTM_{456}F$; (Δ) 2 μg of free $dlTM_{456}F$; and (■) 3 μg of free $dlTM_{456}F$ measured in the same assay condition for immobilized dlTM456F.

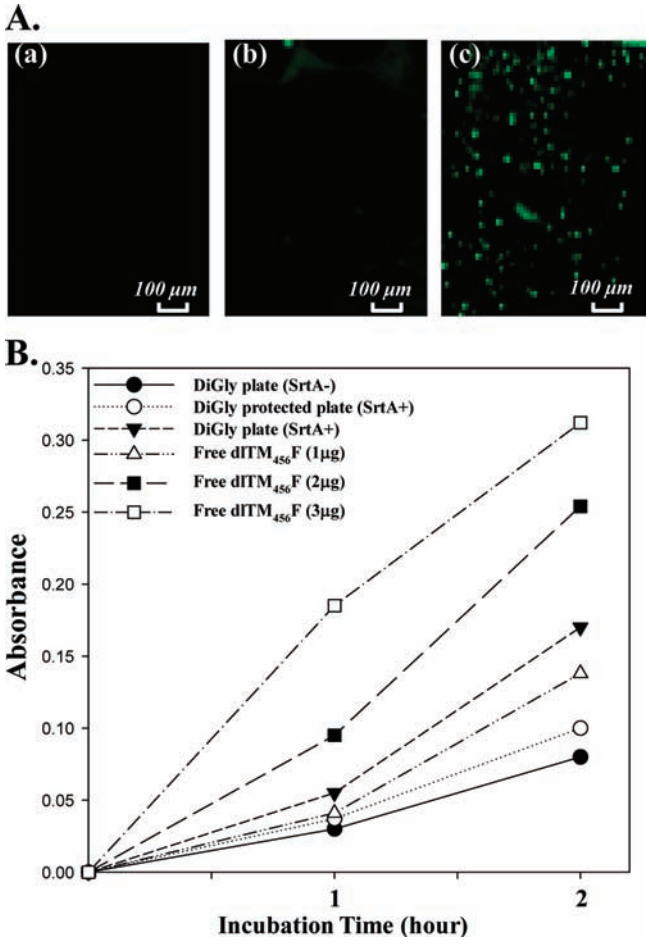


Figure 5. (A) Direct immobilization of $dlTM_{456}F$ via SML. OG488-labeled $dlTM_{456}F$ in 20 mM Tris, 150 mM NaCl, and 5 mM Ca^{2+}, pH 8.0, was incubated with (a) the diglycine plate without *SrtA*; (b) Z-group protected diglycine plate and SrtA; and (c) diglycine plate and SrtA, respectively. OG488 was detected by fluorescence image (EX/EM = 480/520). (B) Protein C activation assay of (●) the diglycine plate pretreated with dlTM456F without SrtA; (○) Z-group protected diglycine plate pretreated with dlTM456F and SrtA; (▼) diglycine plate pretreated with $dlTM_{456}F$ and SrtA; (Δ) 1 μg of free dlTM456F; (■) 2 μg of free $dlTM_{456}F$; and (□) 3 μg of free $dlTM_{456}F$ measured in the same assay condition for immobilized $dlTM_{456}F$.

lower steric hindrance. However, streptavidin−biotinylated protein interaction might be hindered due to protein size. Also, streptavidin immobilization is costly and thus is not ideal for practical applications in the future.

Finally, direct site-specific immobilization of $dlTM_{456}F$ onto diglycine-derivatized glass slides via SML was investigated. The diglycine-functionalized glass slides obtained above were used for the SML. In this experiment, *Z*-group protected diglycine-glass slides (Figure 5Ab) were used as the control. The successful immobilization was confirmed by fluorescence imaging (Figure 5Ac). The protein C activation activity of immobilized $dlTM_{456}F$ was then further evaluated. The absorbance variation of the cleaved chromogenic substrate at 405 nm is shown in Figure 5B. $dlTM_{456}F$-immobilized glass slides generated a tremendous amount of APC, compared to the control diGly slides treated without SrtA and *Z*-protected diglycine glass slides (Figure 5B). The relative activity of $dlTM_{456}F$-immobilized glass slides was approximately that of 1−2 μg of free $dlTM_{456}F$ as determined under the same conditions as those described above. The results confirmed that in the presence of SrtA, $dlTM_{456}F$ can be site-specifically immobilized onto oligoglycine-derivatized glass slides directly and exhibit protein C activation-promoting capabilities approximately that of 1−2 μg of free $dlTM_{456}F$. Overall, the SrtA-mediated surface ligation was capable of being performed under mild conditions, occurring rapidly in a single step without any prior chemical modification of the target protein. Importantly, the site-specific covalent attachment leads to molecules being arranged in a definitively ordered fashion and thus facilitates protein's biological activity.

■ CONCLUSIONS

We have designed and expressed a truncated TM mutant consisting of epidermal growth factor-like domains 4−6 (EGF 4−6) with a conserved pentapeptide LPETG motif at its *C*-terminal for end-point immobilization via SML. The SML provides a convenient and mild approach to the covalent linkage of LEPTG-tagged TM to small molecules or solid supports. The TM_{456} was successfully immobilized onto a diglycine modified glass slide surface by a single-step reaction

dx.doi.org/10.1021/bc200661w | *Bioconjugate Chem.* 2012, 23, 643−649

scheme via SML, and biotinylated TM_{456} was successfully immobilized via the streptavidin−biotin interaction. The sortase-mediated immobilization method presented here has several advantages over traditional methods. First, chemo-and bio-orthogonal immobilization provides a simple and convenient route to uniform protein immobilization in short times creating dense surface coverages. Second, mild immobilization conditions and even low temperatures minimize chances of protein denaturation. Finally, direct immobilization of recombinant proteins from crude cell lysates makes it feasible to fabricate protein arrays in high throughput fashion by eliminating time-consuming and costly purification steps. As TM is a transmembrane protein of the endothelium of blood and lymphatic vessels and the basis of a major natural anticoagulant system, the reported strategies provide an ideal mimetic approach for the engineering of antithrombogenic surfaces for cardiovascular biomaterials minimizing incompatibility and thrombosis.

■ ASSOCIATED CONTENT

Ⓢ Supporting Information

^{1}H NMR and IR spectra of diGly-biotin and diGly-dansyl, full amino acid sequence of TM_{456} fusion protein, and enzymatic activity assay of recombinant SrtA. This material is available free of charge via the Internet at http://pubs.acs.org.

■ AUTHOR INFORMATION

Corresponding Author

*2121 Euclid Avenue SI 313, Cleveland, OH 44115. Phone: (216) 687-3919. Fax: (216) 687-9298. E-mail: x.sun55@csuohio.edu.

Notes

The authors declare no competing financial interest.

■ ACKNOWLEDGMENTS

This work was supported by National Institutes of Health grant 1R01HL102604-2 and Ohio Research Scholar Program and National Science Foundation MRI Grant (CHE-1126384). We thank Dr. Dale Ray at Case NMR Center for the NMR study.

■ REFERENCES

(1) Wong, L. S., Khan, F., and Micklefield, J. (2009) Selective covalent protein immobilization: strategies and applications. *Chem. Rev. 109*, 4025−4053.

(2) Esmon, C. T. (1995) Thrombomodulin as a model of molecular mechanisms that modulate protease specificity and function at the vessel surface. *FASEB J. 9*, 946−955.

(3) Tseng, P., Jordan, S. W., Sun, X. -L., and Chaikof, E. L. (2006) Catalytic efficiency of a thrombomodulin-functionalized membrane-mimetic film in a flow model. *Biomaterials 27*, 2768−2775.

(4) Kishida, A., Ueno, Y., Fukudome, N., Yashima, E., Maruyama, I., and Akashi, M. (1994) Immobilization of human thrombomodulin onto poly(ether urethane urea) for developing antithrombogenic blood-contacting materials. *Biomaterials 15*, 848−852.

(5) Kishida, A., Ueno, Y., Maruyama, I., and Akashi, M. (1994) Immobilization of human thrombomodulin on biomaterials: evaluation of the activity of immobilized human thrombomodulin. *Biomaterials 15*, 1170−1174.

(6) Kishida, A., Ueno, Y., Maruyama, I., and Akashi, M. (1994) Immobilization of human thrombomodulin onto biomaterials. Comparison of immobilization methods and evaluation of antithrombogenicity. *ASAIO J. 40*, 840−845.

(7) Vasilets, V. N., Hermel, G., König, U., Werner, C., Müller, M., Simon, F., Grundke, K., Ikada, Y., and Jacobasch, H. J. (1997) Microwave CO_2 plasma-initiated vapour phase graft polymerization of acrylic acid onto polytetrafluoroethylene for immobilization of human thrombomodulin. *Biomaterials 18*, 1139−1145.

(8) Li, J. M., Singh, M. J., Nelson, P. R., Hendricks, G. M., Itani, M., Rohrer, M. J., and Cutler, B. S. (2002) Immobilization of human thrombomodulin to expanded polytetrafluoroethylene. *J. Surg. Res. 105*, 200−208.

(9) Sperling, C., Salchert, K., Streller, U., and Werner, C. (2004) Covalently immobilized thrombomodulin inhibits coagulation and complement activation of artificial surfaces *in vitro*. *Biomaterials 25*, 5101−5113.

(10) Han, H. S., Yang, S. L., Yeh, H. Y., Lin, J. C., Wu, H. L., and Shi, G. Y. (2001) Studies of a novel human thrombomodulin immobilized substrate: surface characterization and anticoagulation activity evaluation. *J. Biomater. Sci. Polym. Ed. 12*, 1075−1089.

(11) Sun, X. -L., Stabler, C. L., Cazalis, C. S., and Chaikof, E. L. (2006) Carbohydrate and protein immobilization onto solid surfaces by sequential Diels-Alder and azide-alkyne cycloadditions. *Bioconjugate Chem. 17*, 52−57.

(12) Stabler, C., Sun, X. -L., Cui, W., Wilson, J., Haller, C., and Chaikof, E. L. (2007) Surface re-engineering of pancreatic islets. *Bioconjugate Chem. 18*, 1713−1715.

(13) Proft, T. (2010) Sortase-mediated protein ligation: an emerging biotechnology tool for protein modification and immobilisation. *Biotechnol. Lett. 32*, 1−10.

(14) Perry, A. M., Ton-That, H., Mazmanian, S. K., and Schneewind, O. (2002) Anchoring of surface proteins to the cell wall of *Staphylococcus aureus*. III. Lipid II is an in vivo peptidoglycan substrate for sortase-catalyzed surface protein anchoring. *J. Biol. Chem. 277*, 16241−16248.

(15) Tsukiji, S., and Nagamune, T. (2009) Sortase-mediated ligation: a gift from Gram-positive bacteria to protein engineering. *ChemBioChem. 10*, 787−798.

(16) Ton-That, H., Liu, G., Mazmanian, S. K., Faull, K. F., and Schneewind, O. (1999) Purification and characterization of sortase, the transpeptidase that cleaves surface proteins of *Staphylococcus aureus* at the LPXTG motif. *Proc. Natl. Acad. Sci. U.S.A. 96*, 12424−12429.

(17) Lu, C., Zhu, J., Wang, Y., Umeda, A., Cowmeadow, R. B., Lai, E., Moreno, G. N., Person, M. D., and Zhang, Z. (2007) *Staphylococcus aureus* sortase A exists as a dimeric protein in vitro. *Biochemistry 46*, 9346−9354.

(18) Ilangovan, U., Ton-That, H., Iwahara, J., Schneewind, O., and Clubb, R. T. (2001) Structure of sortase, the transpeptidase that anchors proteins to the cell wall of *Staphylococcus aureus*. *Proc. Natl. Acad. Sci. U.S.A. 98*, 6056−6061.

(19) Kruger, R. G., Otvos, B., Frankel, B. A., Bentley, M., Dostal, P., and McCafferty, D. G. (2004) Analysis of the substrate specificity of the *Staphylococcus aureus* sortase transpeptidase SrtA. *Biochemistry 43*, 1541−1551.

(20) Li, W., Adams, T. E., Nangalia, J., Esmon, C. T., and Huntington, J. A. (2008) Molecular basis of thrombin recognition by protein C inhibitor revealed by the 1.6-A structure of the heparin-bridged complex. *Proc. Natl. Acad. Sci. U.S.A. 105*, 4661−4666.

(21) Zushi, M., Gomi, K., Yamamoto, S., Maruyama, I., Hayashi, T., and Suzuki, K. (1989) The last three consecutive epidermal growth factor-like structures of human thrombomodulin comprise the minimum functional domain for protein C-activating cofactor activity and anticoagulant activity. *J. Biol. Chem. 264*, 10351−10353.

(22) Fuentes-Prior, P., Iwanaga, Y., Huber, R., Pagila, R., Rumennik, G., Seto, M., Morser, J., Light, D. R., and Bode, W. (2000) Structural basis for the anticoagulant activity of the thrombin-thrombomodulin complex. *Nature 404*, 518−525.

(23) Rusmini, F., Zhong, Z., and Feijen, J. (2007) Protein immobilization strategies for protein biochips. *Biomacromolecules 8*, 1775−1789.

Bioconjugate Chemistry

Article

pubs.acs.org/bc

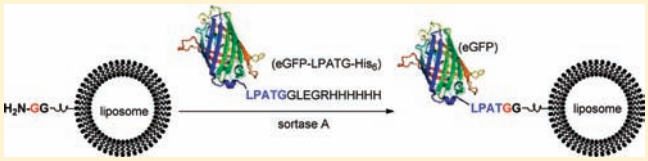
New Method for Site-Specific Modification of Liposomes with Proteins Using Sortase A-Mediated Transpeptidation

Xueqing Guo,† Zhimeng Wu,† and Zhongwu Guo*

Department of Chemistry, Wayne State University, 5101, Cass Avenue, Detroit, Michigan 48202, United States

Supporting Information

ABSTRACT: A new method was developed for site-specific modifications of liposomes by proteins via sortase A (SrtA)-mediated transpeptidation reactions. In this regard, the enhanced green fluorescent protein (eGFP) was biologically engineered to carry at its polypeptide *C*-terminus the LPATG motif recognized by SrtA and used as the protein donor for linking to liposomes that were decorated with phospholipids carrying a diglycine motif as the other SrtA substrate and the eGFP acceptor. Under the influence of SrtA, eGFP was efficiently attached to liposomes, as proved by analyzing the enzymatic reaction products and the resultant fluorescent liposomes. It was observed that increasing the concentration and the distance of the diglycine motif on and from the liposome surface could significantly improve the efficiency of liposome modification by proteins. It is anticipated that this strategy can be widely useful for the modification of liposomes by other proteins.



INTRODUCTION

Liposomes have been widely used as simple models of cells or cell membranes in biological studies, as vehicles for targeted drug delivery, and so on, due to their structural versatility in terms of size, composition, and surface property.[1,2] In this context, numerous methods have been developed for liposome modification and functionalization.[3] For example, bioactive molecules and other molecular tags were attached to the liposome surface by amine-carboxylic acid condensation reactions,[4] disulfide[5] or hydrazine[6] formation reactions, thiol addition to maleimide,[7−10] and amine−amine cross-linking.[11] However, an important issue about these coupling methods is that they are not regiospecific, especially when macrobiomolecules such as proteins are involved, thus resulting in heterogeneous products and nonspecific liposome modification. Moreover, biological and chemical compatibility is another potential concern. For instance, the presence of one protein on the liposome surface may affect the attachment of another protein by these coupling methods. To address these issues, several biologically compatible and chemically selective coupling methods, such as those based on "click" reaction,[12] the Staudinger ligation,[13,14] and native chemical ligation (NCL),[15−17] have been developed. Although these coupling methods have been proved useful, their application to large proteins has been hindered by the difficult access to proper substrates and reactive intermediates. Consequently, more flexible and site-specific coupling methods are desirable for protein attachment to liposomes. For this purpose, we developed here a novel strategy based on sortase-catalyzed transpeptidation.

Sortases are a family of transpeptidases found in gram-positive bacteria[18] and responsible for anchoring surface proteins to the bacterial cell wall via the so-called "sorting reaction".[19] Sortase A (SrtA) of *Staphylococcus aureus* origin is a typical member of the sortase family, which recognizes a unique pentapeptide LPXTG, where X is variable, at the upstream of the *C*-terminal domain of target proteins, cleaves the amide bond between T and G to form a reactive thioester linkage with T, and finally transfers the carboxylic group of T to substrate peptidoglycans carrying an *N*-terminal glycine to give the transpeptidation products (Scheme 1A).[20] It has been demonstrated that SrtA is rather substrate promiscuous and has been used to mediate the coupling of proteins to a variety of amino nucleophiles.[21−24] Accordingly, we envisioned that SrtA may be utilized to site-specifically attach proteins to liposomes, which are equipped with glycine residues, in the presence of other proteins or biomolecules, as outlined in Scheme 1B. As such, proteins to be attached to liposomes need to carry the LPXTG motif near their *C*-termini, which can be very easily achieved via gene engineering and recombinant protein techniques. In this work, we have demonstrated the feasibility of the new strategy for liposome functionalization by preparing modified liposomes bearing glycine residues, expressing proteins carrying the *C*-terminal LPXTG motif, and attaching the recombinant proteins to the modified liposomes by SrtA.

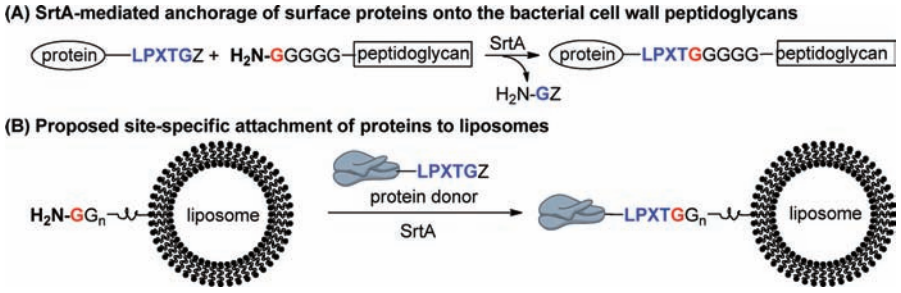
EXPERIMENTAL PROCEDURES

General Methods. NMR spectra were recorded on a 400 MHz spectrometer with chemical shifts reported in ppm (δ) in reference to $SiMe_4$ if not specified otherwise. Coupling constants (J) are reported in hertz (Hz). High-resolution (HR) ESI MS was performed on a Micromass Autospec Ultima magnetic sector mass spectrometer or on Waters GCT time-of-

Received: December 29, 2011
Revised: February 28, 2012
Published: February 28, 2012

 © 2012 American Chemical Society

Scheme 1



flight mass spectrometers. MALDI-TOF MS was obtained on a Bruker Ultraflex mass spectrometer. Thin layer chromatography (TLC) was performed on silica gel GF254 plates detected by charring with phosphomolybdic acid in EtOH solution. Commercial anhydrous solvents and other reagents were used without further purification. 1,2-Distearoyl-*sn*-glycero-3-phosphoethanolamine-*N*-[amino(poly(ethylene glycol))2000] (NH_2-PEG-DSPE), 1,2-distearoyl-*sn*-glycero-3-phosphocholine (DSPC), and cholesterol were purchased from Avanti Polar Lipids, Inc., USA.

***N*-[*tert*-Butyloxycarbonyl-L-glycinyl-L-glycinyl] 1,2-Distearoyl-*sn*-glycero-3-phosphoethanolamine (5).** After 2-(*N*-*tert*-butyloxycarbonyl-L-glycinyl-L-glycinylamino ethyl) phosphonate **4** (200 mg, 0.426 mmol) and 1,2-distearoyl-*sn*-glycerol **3** (293 mg, 0.469 mmol) were coevaporated with dry pyridine three times and dried at high vacuum for 2 h, the mixture was dissolved in dry pyridine (3 mL). A solution of pivaloyl chloride (54 μL, 0.426 mmol) in pyridine (2 mL) was added to the solution at rt under N_2. The reaction was monitored by TLC until it was finished (5 h). The reaction mixture was cooled to 0 °C, and a solution of I_2 (108.2 mg, 0.426 mmol) in 1.1 mL of pyridine and water (10:1) was added. The reaction was completed in 3 h and quenched by the addition of saturated aqueous $Na_2S_2O_3$ solution. The mixture was extracted with chloroform three times, and the organic phase was combined, dried, and concentrated. The residue was purified by a silica gel column to give **5** (254 mg, 62%). ^{1}H NMR ($CDCl_3/CD_3OD$ 3:1, 400 MHz): δ 4.99 (s, 1H), 4.17 (m, 1H), 3.92 (m, 1H), 3.73 (s, 5H), 3.63 (s, 2H), 3.23 (s, 2H), 3.13 (m, 1H), 2.96 (q, CH_2 of Et_3N, 1.35 H), 2.08 (m, 4H), 1.38 (s, 4H), 1.24 (s, 9H), 1.16 (t, CH_3 of Et_3N, 3.5H), 1.10 (m, 60H), 0.66 (t, J = 6.4 Hz, 6H). ^{13}C NMR ($CDCl_3/CD_3OD$ 3:1, 100 MHz): δ 173.7, 173.3, 79.9, 70.2, 62.4, 45.7, 34.0, 33.9, 31.7, 29.5–28.9(m), 28.0, 24.7, 24.6, 22.5, 13.8, 8.2. ^{31}P NMR ($CDCl_3/CD_3OD$ 3:1, 161 Hz): δ −3.42. HRMS (negetive mode): calcd for $C_{50}H_{95}N_3O_{12}P$, 960.6653; found, 960.6653.

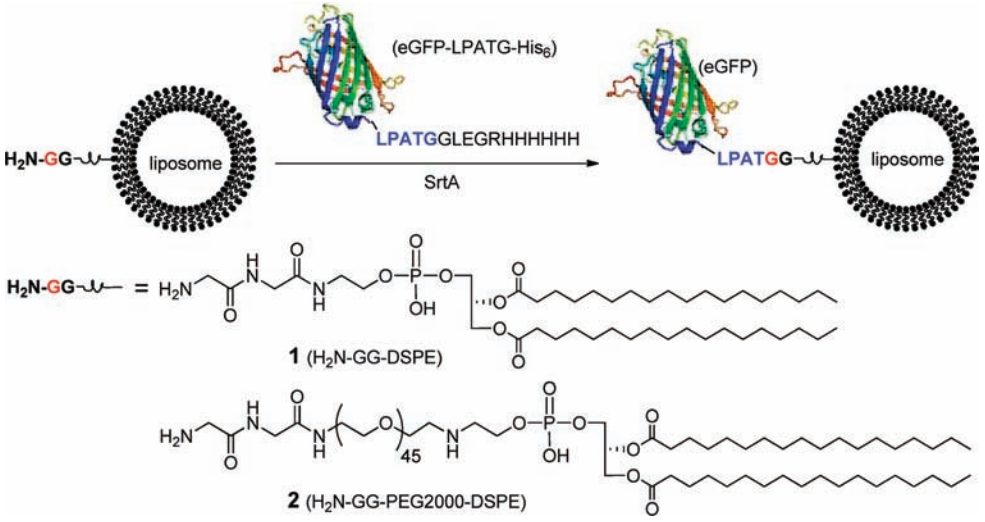
***N*-[L-Glycinyl-L-glycinyl] 1,2-Distearoyl-*sn*-glycero-3-phosphoethanolamine (NH_2-Gly-Gly-DSPE) (1).** Compound **5** (50 mg, 0.052 mmol) was dissolved in a mixture of TFA and DCM (1:1, 2 mL) containing 20 μL of triethylsilane. The reaction mixture was stirred at rt for 2 h. Then, solvents were removed under reduced pressure, and the crude product was washed with diethyl ether to afford **1** (40.3 mg, 90%). ^{1}H NMR ($CDCl_3/CD_3OD$ 3:1, 400 MHz): δ 5.02 (s, 1H), 3.96 (m, 1H), 3.76–3.70 (broad, 5H), 3.54 (broad s, 2H), 3.22 (broad s, 2H), 3.16 (s, 1H), 2.98 (q, CH_2 of Et_3N, 1.22 H), 2.11 (m, 4H), 1.40 (s, 4H), 1.13–1.01 (m, 60H), 0.68 (t, J = 6.4 Hz, 6H). ^{13}C NMR ($CDCl_3/CD_3OD$ 3:1, 100 MHz): δ 173.8, 173.4, 70.1, 63.5, 62.7, 62.3, 46.0, 41.2, 40.5, 34.0, 33.8, 31.7, 29.5–28.9(m), 24.7, 24.6, 22.4, 13.7, 8.2. ^{31}P NMR ($CDCl_3/CD_3OD$ 3:1, 161 Hz): δ 0.733; MALDI-TOF MS: calcd for $C_{45}H_{88}N_3O_{10}P$, 861.6; found, 862.4 (M + H^+). HR MS (negetive mode): calcd for $C_{45}H_{87}N_3O_{10}P$, 860.6129; found, 860.6130.

***N*-[L-Glycinyl-L-glycinyl-amino(poly(ethylene glycol)) 2000] 1,2-Distearoyl-*sn*-glycero-3-phosphoethanolamine (NH_2-Gly-Gly-PEG2000-DSPE) (2).** After NH_2-PEG2000-DSPE (**7**) (100 mg, 35.8 μmol) was dissolved in DCM (5 mL) under an atmosphere of argon, BocNH-Gly-Gly-OSu (**6**, 24 mg, 71.67 μmol) and triethylamine (10 μL, 71 μmol) were added to the solution. The reaction was stirred at rt overnight. The solution was concentrated under reduced pressure, and the crude product was purified by silica gel column chromatography to give **8** (106 mg, ~100%). Compound **8** (106 mg, 35.1 μmol) was dissolved in a mixture of TFA and DCM (2 mL, 1:1) containing 20 μL of triethylsilane, and the reaction mixture was stirred at rt for 2 h. Then, solvents were removed, and the crude product was washed with diethyl ether to afford **2** (86 mg) as a mixture with a molecular weight range of 2,665–3,369 (see Supporting Information).

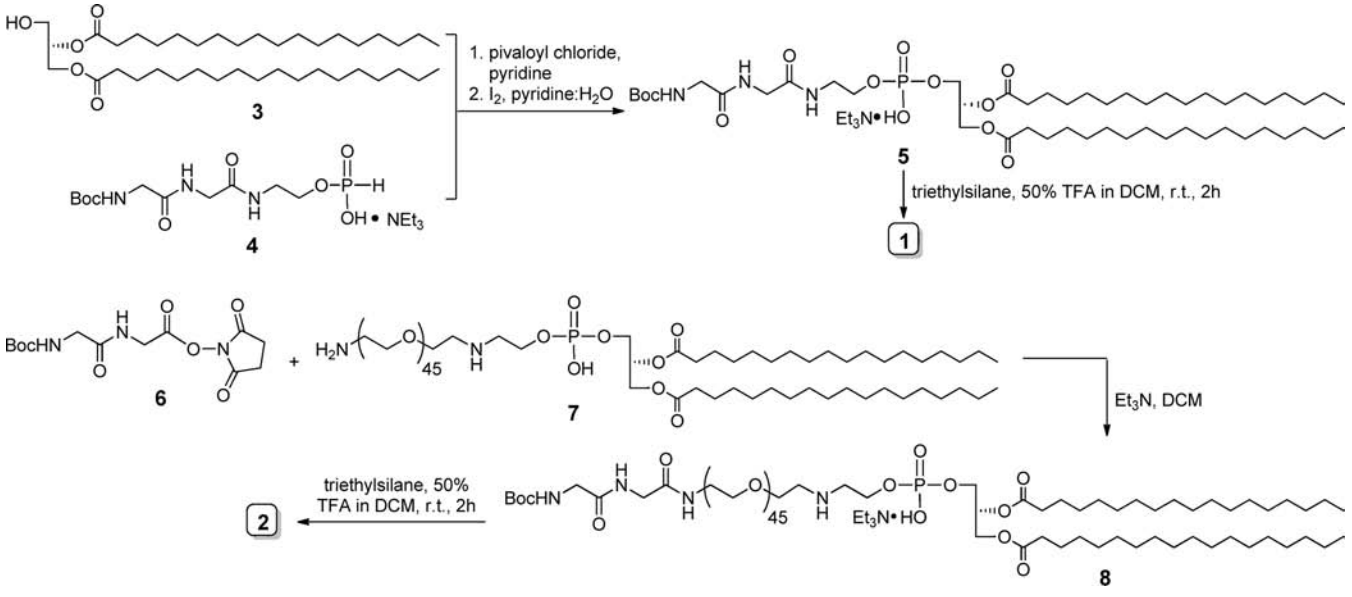
Protein Expression and Purification. Fluorescent protein vector pcDNA3-EmGFP was purchased from Invitrogen Company. Primer pairs FF-NdeI (5′-GATATTCCATATGGTGAGCAAGGGCGA-3′) and RF-XhoI (5′-CTCGAGGCCACCGGTCGCCGGCAGCTTGTACAGCTCGTCCAT-3) were used to PCR amplify EmGFP from the pcDNA3-EmGFP. RF-XhoI primer contains the SrtA-recognized sorting signal sequence LPATG. Both the PCR product and pET23a were excised with NdeI and XhoI. After purification with 1% agarose gel purification kit (Invitrogene), the products were ligated together with T4 DNA ligase overnight at 4 °C and then transformed into the DH5α host strain and selected on LB–ampicillin agar plates. DNAs were sequenced to prove their identity. The positive clone was double cleaved by EcoRI and XhoI, and then blunted and religated with T4 DNA Blunting and Ligation kit for protein expression. EmGFP with SrtA-signal was expressed in BL21-DE3 *E. coli* (Invitrogen). *E. coli* cultures were allowed to reach an OD600 of 0.7 before the induction of expression by the addition of 1 mM of isopropyl thioglucoside (IPTG, Fisher). After further incubation at 37 °C for 3 h, the cultures were pelleted by centrifugation. B-per solution (Pierce) was added to the thawed pellet to solubilize the cells, and the manufacturer's protocol was followed closely to isolate soluble protein. Protein purification using the His_6 affinity tag and a Ni-NTA resin column followed the procedure outlined by Qiagen. Protein-enriched fractions were combined and dialyzed against Tris buffer (50 mM, pH 8) containing 150 mM of NaCl, using a Slide-A-Lyzer dialysis cassette (Pierce) with a MWCO of 10 kDa for 48–60 h with buffer changed at

dx.doi.org/10.1021/bc200694t | *Bioconjugate Chem.* 2012, 23, 650–655

Scheme 2



Scheme 3



least three times. The calculated MW of enhanced green fluorescent protein (eGFP) is 28.760 kDa, which was observed with MALDI-TOF MS.

Liposome Preparation. A mixture of DSPC (15 mg, 20.4 μmol), cholesterol (4 mg, 10.2 μmol), and **1** (0.35 mg, 0.408 μmol) or **2** (1.19 mg, 0.408 μmol) (2% of total lipids) were dissolved in 3.0 mL of chloroform and methanol (1:1). Solvents were removed on an evaporator under reduced pressure to form a thin lipid film on the flask wall, which was kept in a high vacuum overnight. The lipid film was swelled in 2.0 mL of Tris buffer (50 mM, pH 7.4) to form a multilamellar vesicle suspension that was immersed in a 65 °C water bath for 1 h. The lipid suspension thus formed was extruded through a polycarbonate membrane (pore size 100 nm) to afford small unilamellar vesicles (SUVs), which were concentrated 4 times to give liposomes for ligation reactions. SUVs containing 5% of **1** (0.88 mg, 1.02 μmol) or **2** (2.98 mg, 1.02 μmol) were prepared by the same protocol.

Ligation of eGFP to Functionalized Liposomes. Liposomes (42 μL) prepared above were mixed with 15 μL of 2 M Tris-HCl buffer (pH 7.5) containing 10 μL of NaCl (1.5 M), 1 μL of 0.5 M $CaCl_2$, 2 μL of 0.1 M mercaptoethanol, and 10 μL of 1 mM eGFP. Then, 20 μL of SrtA (100 μM) was added. The solution was incubated at 37 °C overnight, followed by ultracentrifugation at 300,000*g* and 15 °C for 1 h. The supernatant was removed, and the pellet containing liposomes was suspended in 100 μL of Tris-HCl buffer. This process was repeated twice. The pellet was then diluted to 100 μL with Tris-HCl buffer and finally analyzed with SDS−PAGE and a fluorometer. The fluororesence intensity of eGFP-modified liposomes was measured using an exciting wavelength of 360 nm.

RESULTS AND DISSCUSSION

In this study, enhanced green fluorescent protein (eGFP) was employed as a model to probe the new liposome functionalization strategy outlined in Scheme 1B. eGFP as a protein donor was designed to contain a LPATG motif near its *C*-terminus. Furthermore, a histidine affinity tag (His_6), which is commonly used to facilitate the purification of recombinant proteins by a

dx.doi.org/10.1021/bc200694t | *Bioconjugate Chem.* 2012, 23, 650−655

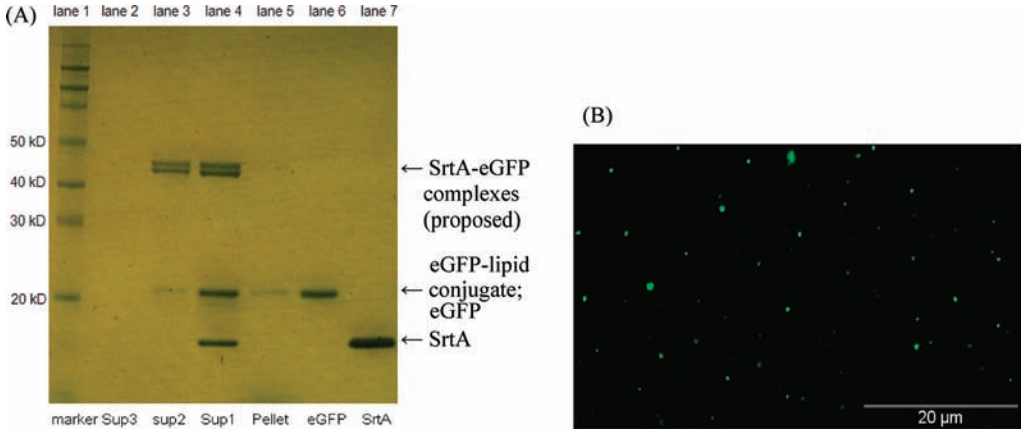


Figure 1. SDS−PAGE and fluorescence imaging analyses of liposomes decorated with 2% of **1** upon reacting with eGFP-LPATG-His_6 and SrtA. (A) SDS−PAGE results: lane 1, molecular weight markers; lanes 2 and 3, PBS solution obtained from the second and first washing of liposomes, respectively; lane 4, supernatant of the reaction mixture; lane 5, liposome pellet after 2 times of washing with PBS; lane 6, standard eGFP substrate (eGFP-LPATG-His_6); lane 7, SrtA. (B) Fluorescence imaging result of the eGFP-decorated SULs.

Ni^{2+} column, was linked to the LPATG motif. This design would ensure the removal of the His_6 tag upon enzymatic coupling reactions (Scheme 2). eGFP-LPATG-His_6 was prepared by the conventional recombinant protein technique using *Escherichia coli* (*E. coli*), as described in detail in the Experimental Procedures section.

We designed two lipid molecules as nucleophilic substrates of SrtA, which were incorporated in the liposome for SrtA-mediated site-specific transpeptidation reactions. One has a diglycine motif directly linked to the amino group of 1,2-distearoyl-*sn*-glycero-3-phosphoethanolamine (DSPE) (**1**, Scheme 2), and the other has the diglycine motif attached to polyethylene glycol (PEG)-modified DSPE (**2**). Compounds **1** and **2** differ in that **2** has a spacer inserted between diglycine and DSPE thus their diglycine motifs have different distances from the liposome surface. The comparison of their reactions would disclose how the bulky liposome might affect SrtA-mediated transpeptidation. We selected to incorporate a diglycine in these nucleophiles because previous studies showed that a single glycine is sufficient for the enzymatic reaction though a diglycine motif and may be a slightly better substrate for SrtA.[25,26]

The synthesis of compounds **1** and **2** is outlined in Scheme 3. Phosphorylation of lipid **3** by freshly prepared **4** was achieved in a two-step one-pot manner to afford phospholipid **5** in a moderate yield (62%), which was finally deprotected with 50% trifluoroacetic acid (TFA) in dichlorometane (DCM) to give the desired product **1** in an excellent yield (90%). Compound **2** was easily prepared from commercially available PEG2000-modified DSPE 7 in two separate steps, including the coupling reaction with the activated ester of diglycine **6** in the presence of triethylamine and deprotection with 50% TFA in DCM. Both **1** and **2** were characterized by NMR and MS.

Compounds **1** and **2** were used to prepare small unilamellar liposomes (SULs) by the extrusion method.[27] In brief, after DSPC and cholesterol (2:1 molar ratio) were mixed with **1** or **2** in a specific concentration (2% or 5% molar ratio of total lipids) in chloroform and methanol (1:1), the solvents were removed under reduced pressure to form a thin lipid film on the flask wall. The lipid film was then swelled in Tris buffer in a 65 °C water bath to result in a suspension containing multilamellar vesicles that were extruded through a polycarbonate membrane (pore size: 100 nm) to form SULs. Dynamic light scattering analysis of the SULs revealed that they had an average diameter of about 110−130 nm with a rather narrow dispersion range (see Supporting Information).

The SULs obtained above were then employed to explore liposome modification by proteins via SrtA-mediated ligation reactions. In this context, SULs were mixed with eGFP-LPATG-His_6 in buffer followed by addition of SrtA, and the reaction mixture was incubated at 37 °C overnight. To verify the ligation reaction and assess the reaction efficiency, SULs were separated from SrtA and unreacted eGFP-LPATG-His_6 via ultracentrifugation, followed by washing with phosphate buffered saline (PBS), as described by Mulder and co-workers.[15] The eGFP-modified liposomes, as well as the ligation product, were subjected to sodium dodecyl sulfate−polyacrylamide gel electrophoresis (SDS−PAGE) and fluorescence imaging analyses.

Shown in Figure 1 are the results of ligation reactions between eGFP-LPATG-His_6 and SULs containing 2% of **1**. SDS−PAGE analysis revealed that, after washed with PBS once, the SUL pellet was essentially free of soluble proteins (Figure 1A, lane 2). Nonetheless, PBS washing was repeated two to three times to ensure that SrtA and unreacted eGFP substrate were completely removed. The resultant SULs still showed a fluorescent protein band (Figure 1A, lane 5) with molecular weight consistent with that of the desired ligation product. However, the difference of the molecular weights of the substrate protein and the conjugate product is only 566 Da; thus, they are difficult to distinguish by SDS−PAGE. Additional experimental proofs for the formation of the desired product are as follows: (1) the band shown in lane 5 (Figure 1A) was not observed in the control experiment, where SrtA was absent (data not shown), suggesting that the substrate protein did not adhere to SULs and was completely removed by washing and that the observed protein must have been covalently attached to SULs; and (2) the results of lipid **2** (as discussed in detail later) clearly showed that after washing SULs as described herein no substrate protein remained in the SUL pellet. Moreover, we observed that the isolated SULs showed strong fluorescence under a microscope (Figure 1B). All of the results supported the idea that eGFP was indeed attached to liposomes via SrtA-mediated ligation.

The ligation reactions between eGFP-LPATG-His_6 and liposomes containing 2% of **2** under the same conditions

dx.doi.org/10.1021/bc200694t | *Bioconjugate Chem.* 2012, 23, 650−655

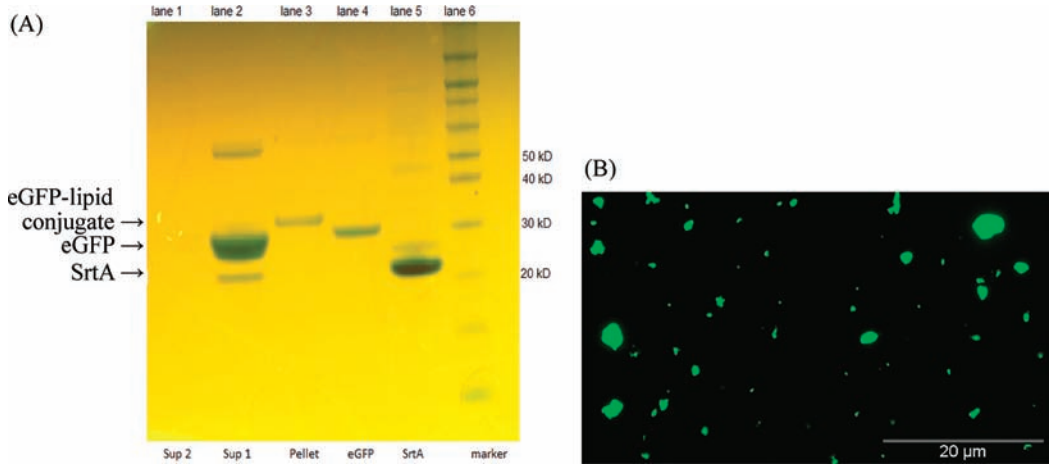


Figure 2. SDS–PAGE and fluorescence imaging analyses of liposomes decorated with 2% of **2** upon reacting with eGFP-LPATG-His_6 and SrtA. (A) SDS–PAGE results: lane 1, PBS solution obtained from the first washing of liposomes; lane 2, supernatant of the reaction mixture; lane 3, liposome pellet after 2 times of washing with PBS; lane 4, standard eGFP substrate (eGFP-LPATG-His_6); lane 5, SrtA; lane 6: molecular weight markers. (B) Fluorescence imaging result of the eGFP-decorated SULs.

gave results (Figure 2) similar to that of **1**. Again, after washing with PBS once, the SUL pellet was basically free of soluble proteins (Figure 2A, lane 1). The washed SUL pellet showed a fluorescent protein band (Figure 2A, lane 3) that had the molecular weight in agreement with that of the desired ligation product (~30,217 Da) and significantly larger than that of SrtA (17,865 Da, lane 5) and eGFP-LPATG-His_6 (28,760 Da, lane 4). The molecular weight difference (~1,457 Da) between the ligation product of **2**, that is, eGFP-LPATGG-PEG2000-DSPE, and substrate protein eGFP-LPATG-His_6 was much larger than the difference (566 Da) between the ligation product of **1**, eGFP-LPATGG-DSPE, and the substrate protein; thus, the product band was well separated from the substrate band in Figure 2A. Clearly, no substrate protein was detected in the SUL pellet (lane 3), proving that all soluble proteins were washed away and that the substrate protein itself did adhere to SULs. The isolated SULs were also observed to exhibit strong fluorescence under a microscope (Figure 2B). These results have unambiguously proved that eGFP was indeed covalently attached to **2** on liposomes in the presence of SrtA.

After having established the validity of the new strategy for liposome modification, we then assessed the efficiency of the ligation reaction based on the unique property of eGFP, namely, that it emits fluorescence at 535 nm with an excitation wavelength of 360 nm. As shown in Table 1, for liposomes containing 2% of the diglycine–lipid conjugates **1** and **2**, the fluorescent intensity of eGFP-modified liposomes of **2** was about 33% stronger than that of eGFP-modified liposomes of **1**, suggesting higher modification efficiency of **2** than that of **1** on the liposome surface under the given conditions.

Table 1. Fluorescence Intensities of eGFP-Modified Liposomes Containing 2% and 5% of 1 and 2

UMLs Carrying Different Concentrations of **1** or **2**	Fluorescence Intensities of eGFP-Modified Liposomes[a]
UML with 2% of **1**	7007
UML with 2% of **2**	9325
UML with 5% of **1**	10464
UML with 5% of **2**	46681

[a]Fluorescence intensity was the average of triplicate experiments.

We also compared the reactivity of liposomes containing different concentrations of **1** and **2**, and the results are outlined in Table 1. Clearly, eGFP-modified liposomes carrying 5% of **1** and **2** had significantly stronger fluorescent intensities than eGFP-modified liposomes carrying 2% of **1** and **2**, indicating that the former had more eGFP molecules attached to their surface. For example, the fluorescent intensity of eGFP-modified liposomes carrying 5% of **1** was ca. 50% higher than that of liposomes carrying 2% of **1**, whereas the fluorescent intensity of eGFP-modified liposomes carrying 5% of **2** was ca. 400% higher than that of liposomes carrying 2% of **2**.

These results suggest that both the concentration and the structure of the functionalized lipids used to decorate liposomes had a significant influence on their modification efficiencies. As expected, liposomes containing a higher concentration (5%) of substrate lipids **1** and **2** were more effectively modified with eGFP than liposomes containing a lower concentration (2%) of **1** and **2**. It was also observed that under the same conditions liposomes of **2** were much more effectively modified than liposomes of **1**. The latter observation may be the result of steric effect. The presence of a flexible PEG fragment in **2** may have extended the distance of the lipid diglycine motif from the liposomal surface so as to significantly reduce its stric hindrance, increase its accessibility, and improve the SrtA-mediated reactions, when compared to **1** that has the diglycine residue directly anchored onto the liposome surface.

In summary, we have demonstrated that SrtA can be utilized to efficiently modify liposomes via site-specific reactions between an eGFP substrate carrying the sorting signal LPXTG and liposomes carrying functionalized lipid substrates with a diglycine motif. To the best of our knowledge, this is the first report of using SrtA to site-specifically modify liposomes. This approach should be a useful alternative to other strategies for the preparation of functionalized liposomes and is expected to be widely applicable to the attachment of other proteins to liposomes.

■ ASSOCIATED CONTENT

Ⓢ Supporting Information

Data of the dynamic light scattering analysis of liposomes and NMR and MS spectra of all synthetic intermediates and target

molecules. This material is available free of charge via the Internet at http://pubs.acs.org.

AUTHOR INFORMATION

Corresponding Author

*Tel: 1-313-577-2557. E-mail: zwguo@chem.wayne.edu.

Author Contributions

†These authors contributed equally to this work.

Notes

The authors declare no competing financial interest.

ACKNOWLEDGMENTS

This work was supported by National Science Foundation (CHE-1053848) and National Institutes of Health (R01 GM090270) of USA and the Mizutani Glycoscience Foundation of Japan.

REFERENCES

(1) Allen, T. M., and Cullis, P. R. (2004) Drug delivery systems: Entering the mainstream. *Science 303*, 1818−1822.

(2) Torchilin, V. P. (2005) Recent advances with liposomes as pharmaceutical carriers. *Nat. Rev. Drug Discovery 4*, 145−160.

(3) Gurny, R., Nobs, L., Buchegger, F., and Allemann, E. (2004) Current methods for attaching targeting ligands to liposomes and nanoparticles. *J. Pharm. Sci. 93*, 1980−1992.

(4) Maruyama, K., Ishida, O., Tanahashi, H., Iwatsuru, M., Sasaki, K., Eriguchi, M., and Yanagie, H. (2001) Liposomes bearing polyethyleneglycol-coupled transferrin with intracellular targeting property to the solid tumors in vivo. *Pharm. Res. 18*, 1042−1048.

(5) Martin, F. J., Hubbell, W. L., and Papahadjopoulos, D. (1981) Immunospecific targeting of liposomes to cells: a novel and efficient method for covalent attachment of Fab' fragments via disulfide bonds. *Biochemistry 20*, 4229−4238.

(6) Hansen, C. B., Kao, G. Y., Moase, E. H., Zalipsky, S., and Allen, T. M. (1995) Attachment of antibodies to sterically stabilized liposomes: evaluation, comparison and optimization of coupling procedures. *Biochim. Biophys. Acta 1239*, 133−144.

(7) Crosasso, P., Brusa, P., Dosio, F., Arpicco, S., Pacchioni, D., Schuber, F., and Cattel, L. (1997) Antitumoral activity of liposomes and immunoliposomes containing 5-fluorouridine prodrugs. *J. Pharm. Sci. 86*, 832−839.

(8) Ansell, S. M., Tardi, P. G., and Buchkowsky, S. S. (1996) 3-(2-Pyridyldithio)propionic acid hydrazide as a cross-linker in the formation of liposome-antibody conjugates. *Bioconjugate Chem. 7*, 490−496.

(9) Fleiner, M., Benzinger, P., Fichert, T., and Massing, U. (2001) Studies on protein-liposome coupling using novel thiol-reactive coupling lipids: Influence of spacer length and polarity. *Bioconjugate Chem. 12*, 470−475.

(10) Takasaki, J., and Ansell, S. M. (2006) Micelles as intermediates in the preparation of protein-liposome conjugates. *Bioconjugate Chem. 17*, 438−450.

(11) Torchilin, V. P., Khaw, B. A., Smirnov, V. N., and Haber, E. (1979) Preservation of antimyosin antibody-activity after covalent coupling to liposomes. *Biochem. Bioph. Res. Commun. 89*, 1114−1119.

(12) Hassane, F. S., Frisch, B., and Schuber, F. (2006) Targeted liposomes: Convenient coupling of ligands to preformed vesicles using "click chemistry". *Bioconjugate Chem. 17*, 849−854.

(13) Sun, X. L., Zhang, H. L., and Ma, Y. (2009) Chemically-selective surface glyco-functionalization of liposomes through Staudinger ligation. *Chem. Commun.*, 3032−3034.

(14) Sun, X. L., Ma, Y., and Zhang, H. L. (2010) Surface-bound cytomimetic assembly based on chemoselective and biocompatible immobilization and further modification of intact liposome. *Bioconjugate Chem. 21*, 1994−1999.

(15) Reulen, S. W. A., Brusselaars, W. W. T., Langereis, S., Mulder, W. J. M., Breurken, M., and Merkx, M. (2007) Protein-liposome conjugates using cysteine-lipids and native chemical ligation. *Bioconjugate Chem. 18*, 590−596.

(16) Reulen, S. W. A., and Merkx, M. (2010) Exchange kinetics of protein-functionalized micelles and liposomes studied by forster resonance energy transfer. *Bioconjugate Chem. 21*, 860−866.

(17) Chu, N. K., Olschewski, D., Seidel, R., Winklhofer, K. F., Tatzelt, J., Engelhard, M., and Becker, C. F. W. (2010) Protein immobilization on liposomes and lipid-coated nanoparticles by protein trans-splicing. *J. Pept. Sci. 16*, 582−588.

(18) Mazmanian, S. K., Liu, G., Ton-That, H., and Schneewind, O. (1999) *Staphylococcus aureus* sortase, an enzyme that anchors surface proteins to the cell wall. *Science 285*, 760−763.

(19) Mazmanian, S. K., Ton-That, H., and Schneewind, O. (2001) Sortase-catalysed anchoring of surface proteins to the cell wall of *Staphylococcus aureus*. *Mol. Microbiol. 40*, 1049−1057.

(20) Ilangovan, U., Ton-That, H., Iwahara, J., Schneewind, O., and Clubb, R. T. (2001) Structure of sortase, the transpeptidase that anchors proteins to the cell wall of *Staphylococcus aureus*. *Proc Natl Acad Sci U S A 98*, 6056−6061.

(21) Popp, M. W.-L., and Ploegh, H. L. (2011) Making and breaking peptide bonds: protein engineering using sortase. *Angew. Chem., Int. Ed. 50*, 5024−5032.

(22) Proft, T. (2010) Sortase-mediated protein ligation: an emerging biotechnology tool for protein modification and immobilisation. *Biotechnol. Lett. 32*, 1−10.

(23) Tsukiji, S., and Nagamune, T. (2009) Sortase-mediated ligation: a gift from Gram-positive bacteria to protein engineering. *ChemBioChem 10*, 787−798.

(24) Wu, Z., and Guo, Z. (2012) Sortase-mediated transpeptidation for site-specific modification of peptides, glycopeptides, and proteins. *J. Carbohydr. Chem. 31*, 48−66.

(25) Wu, Z., Guo, X., Wang, Q., Swarts, B. M., and Guo, Z. (2010) Sortase A-catalyzed transpeptidation of glycosylphosphatidylinositol derivatives for chemoenzymatic synthesis of GPI-anchored proteins. *J. Am. Chem. Soc. 132*, 1567−1571.

(26) Guo, X., Wang, Q., Swarts, B. M., and Guo, Z. (2009) Sortase-catalyzed peptide-glycosylphosphatidylinositol analog ligation. *J. Am. Chem. Soc. 131*, 9878−9879.

(27) Strijkers, G. J., Mulder, W. J., van Heeswijk, R. B., Frederik, P. M., Bomans, P., Magusin, P. C., and Nicolay, K. (2005) Relaxivity of liposomal paramagnetic MRI contrast agents. *Magma 18*, 186−192.

Bioconjugate Chemistry

Article

pubs.acs.org/bc

Detection of MMP-2 and MMP-9 Activity *in Vivo* with a Triple-Helical Peptide Optical Probe

Walter J. Akers,[†] Baogang Xu,[†] Hyeran Lee,[†] Gail P. Sudlow,[†] Gregg B. Fields,[‡] Samuel Achilefu,[†] and W. Barry Edwards*[,§]

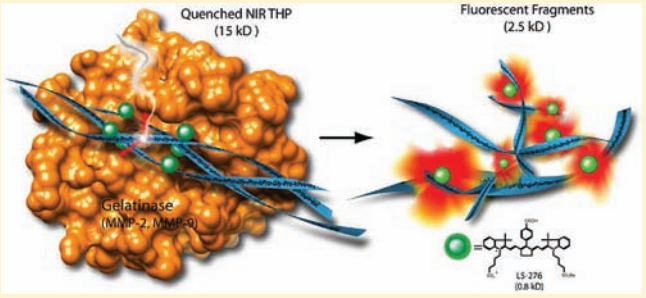
[†]Mallinckrodt Institute of Radiology, Washington University, School of Medicine, St. Louis, Missouri 63110, United States

[‡]Torrey Pines Institute for Molecular Studies, 11350 SW Village Parkway, Port St. Lucie, Florida 34987, United States

[§]Department of Radiology, University of Pittsburgh, Pittsburgh, Pennsylvania, 15219, United States

Supporting Information

ABSTRACT: We report a novel activatable NIR fluorescent probe for *in vivo* detection of cancer-related matrix metalloproteinase (MMP) activity. The probe is based on a triple-helical peptide substrate (THP) with high specificity for MMP-2 and MMP-9 relative to other members of the MMP family. MMP-2 and MMP-9 (also known as gelatinases) are specifically associated with cancer cell invasion and cancer-related angiogenesis. At the center of each 5 kDa peptide strand is a gelatinase sensitive sequence flanked by 2 Lys residues conjugated with NIR fluorescent dyes. Upon self-assembly of the triple-helical structure, the 3 peptide chains intertwine, bringing the fluorophores into close proximity and reducing fluorescence via quenching. Upon enzymatic cleavage of the triple-helical peptide, 6 labeled peptide chains are released, resulting in an amplified fluorescent signal. The fluorescence yield of the probe increases 3.8-fold upon activation. Kinetic analysis showed a rate of LS276-THP hydrolysis by MMP-2 (k_{cat}/K_M = 30,000 s^{-1} M^{-1}) similar to that of MMP-2 catalysis of an analogous fluorogenic THP. Administration of LS276-THP to mice bearing a human fibrosarcoma xenografted tumor resulted in a tumor fluorescence signal more than 5-fold greater than that of muscle. This signal enhancement was reduced by treatment with the MMP inhibitor Ilomostat, indicating that the observed tumor fluorescence was indeed enzyme mediated. These results are the first to demonstrate that triple-helical peptides are suitable for highly specific *in vivo* detection of tumor-related MMP-2 and MMP-9 activity.



INTRODUCTION

MMPs are a family of zinc dependent proteases capable of degrading extracellular matrix (ECM) components and other extracellular proteins. MMPs are synthesized as inactive zymogens (proMMPs) and are either secreted into the extracellular space or anchored to the cell membrane. Activation requires removal of the propeptide domain by proteolysis to expose the active site within the catalytic domain.[1]

A number of MMPs are overexpressed in various human cancers. Among these are MMP-2 (gelatinase A, 72 kDa gelatinase, or 72 kDa type IV collagenase) and MMP-9 (gelatinase B, 92 kDa gelatinase, or 92 kDa type IV collagenase), both referred to collectively as gelatinases. MMP-2 and MMP-9 are secreted as zymogens usually by stromal cells such as fibroblasts.[2,3] Cancer types that have shown increased expression of MMP-2 and MMP-9 include breast,[4,5] colorectal,[6,7] prostate,[8,9] and gastric cancer.[10,11] MMP-2 overexpression is strongly linked to melanoma progression, whereas relatively little MMP-2 expression is observed in normal tissues of the skin.[12] These tissues are highlighted because they are accessible to the penetration depth of NIR light or are accessible with endoscopes fitted with NIR reflectance imaging sensors.[13]

Gelatinases are important imaging targets due to their possible prognostic capability. For example, increased MMP-2 expression predicts decreased disease free survival in human prostate cancer.[14] Additionally, MMP-2 in breast carcinoma correlated with shortened recurrence-free survival and relative overall survival.[15] Therefore, the development of specific gelatinase imaging probes would be of great interest in unraveling their role in tumor biology in animal models or diagnosing, directing, or monitoring therapy in humans. Imaging probes have been reported for detecting MMPs with nuclear imaging (either PET or SPECT), optical imaging, and magnetic resonance imaging (reviewed in ref 16). At present, peptide substrates for gelatinase activity, while efficiently hydrolyzed by MMP-2, are relatively promiscuous and are subject to hydrolysis by other members of the MMP family.[17−19] An understanding of molecular events, such as enzyme activity, requires high specificity of the quenched probe

Received: January 18, 2012
Published: February 6, 2012

ACS Publications © 2012 American Chemical Society

dx.doi.org/10.1021/bc300027y | *Bioconjugate Chem.* 2012, 23, 656−663

for the substrate. The current lack of specificity of peptide-based substrates is hindering imaging of gelatinase activity *in vivo* and is thus limiting an understanding of how gelatinases could serve as markers for cancer progression or for monitoring the severity of other diseases.[20,21]

For this reason, a triple-helical peptide (THP) that is highly specific for MMP-2 and MMP-9 has been chosen for NIRF imaging. The self-assembling THP incorporates a native collagen sequence (residues 437−447) from the α1 chain of type V collagen.[22,23] This natural collagen sequence, modified to contain a pair of Lys residues flanking the hydrolysis site, contains at both the *N*- and *C*-termini repeating Gly-Pro-4-hydroxy-L-proline (GPO) triplets that result in self-assembly of three single-stranded peptides into one triple-helical peptide. The support for triple-helicity is evident in the strong molar ellipticity at λ = 225 nm which diminishes upon thermal denaturation of the helix. The type V collagen sequence GPPG~VVGEKGEQ (the scissile bond lies between G and V), as a single-stranded peptide (i.e., without the GPO triplets), was hydrolyzed extremely slowly by either MMP-2 or MMP-9.[24] Therefore, it is the triple-helical structural feature, along with the sequence, that imparts the substrate specificity among the various MMPs.[24] We hypothesized that the THP backbone would serve as the core of a quenched fluorescent probe for detection of MMP activity in cancer and other diseases. We have constructed an activatable molecular probe by covalently conjugating NIR fluorescent dyes (LS276) to ε-amino groups of Lys that flank the hydrolysis site (Figure 1A). LS276 is a

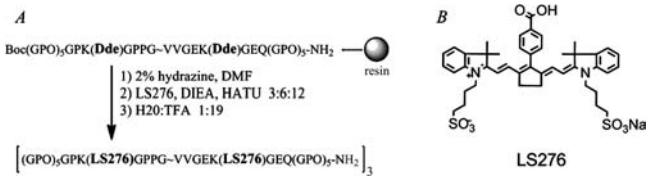


Figure 1. (A) Solid-phase synthesis of LS276-THP ("O" represents 4-hydroxy-L-proline). (B) Chemical structure of LS276.

highly fluorescent, monofunctional, water-soluble heptamethine cyanine dye (Figure 1B).[25] The close proximity of dyes renders them relatively nonfluorescent. The single-stranded peptides were synthesized entirely on the solid phase, and LS276 was incorporated, while the peptide was resin-bound. After cleavage from the resin, the resulting triple-helical peptide, LS276-THP, was evaluated *in vitro* to determine whether the addition of the fluorophores impeded the formation of the triple-helix resulting in detrimental increases of the K_M value to MMP-2. Additionally, LS276-THP was tested *in vivo* for its ability to visualize gelatinase activity in a tumor bearing animal model.

EXPERIMENTAL PROCEDURES

Materials. Ilomastat was purchased from Calbiochem (La Jolla, CA). Dimethyl sulfoxide (DMSO) was purchased from Sigma Aldrich (St. Louis, MO). MMPSense 680 was purchased from VisEn Medical (Bedford, MA) and prepared according to the manufacturer's instructions.

Synthesis. The THP was synthesized as previously described (Figure 1).[22] After removal of the 1-(4,4-dimethyl-2,6-dioxocyclohexylidene)ethyl (Dde) protecting groups (2% hydrazine and DMF), rinsing (3 × 5 mL DMF, 10% aqueous DMF, CH_2Cl_2, and CH_3OH), and drying (*in vacuo*), LS276 was conjugated to the ε-amino groups of Lys (25 mg resin, resin/LS276/DIEA/HATU 1:6:24:12) in DMF. After reaction (3.5 h), the mixture was filtered and rinsed (3 × 5 mL DMF, CH_2Cl_2, CH_3OH). The Kaiser test was negative indicating complete coupling of LS276. The peptide was cleaved from the resin (water/TFA 1:19, 3 h), diluted with water, and lyophilized. The crude mixture was redissolved (0.0001% ammonia, pH 8) and purified by size exclusion gel chromatography (G-25). Substitution levels were determined by absorption (λ = 780 nm, ε = 220,000 cm^{-1} M^{-1}) and the ninhydrin method utilizing bovine insulin as a standard.[25,26] The molecular weight was confirmed by ESI-TOF-MS (Figure S1, Supporting Information).

Quenching. To determine the amount of quenching, the fluorescence of unhydrolyzed LS276-THP (f_{intact}) was compared with the fluorescence of completely hydrolyzed LS276-THP ($f_{hydrolyzed}$), utilizing $[(f_{hydrolyzed} - f_{intact})/f_{hydrolyzed}] \times 100$ = % quenched. Three concentrations of LS276-THP (0.25, 0.5, and 1.0 μM, n = 3 per concentration) were digested with MMP-2 (20 nM) until fluorescence reached a plateau with no further increases (3.75 h).

Enzyme Assays. The proenzyme of MMP-2 was activated using 4-aminophenylmercuric acetate (APMA). APMA (10 mM, 3.5 mg/mL) in assay buffer (50 mM tricine at pH 7.4, 50 mM NaCl, 10 mM $CaCl_2$, and 0.05% Brij-35) was diluted to 2 mM prior to addition to the proenzyme solution. ProMMP-2 was activated by adding APMA (2 mM) to a proMMP-2 solution in equal parts by volume for a final solution of 1 mM (1 h, 37 °C) of each component. Enzyme kinetics were carried out using activated MMP-2 at nominal concentrations of 5 nM at 37 °C. The rates of hydrolysis were determined by liberated fluorescence units in a microtiter plate reader ($\lambda_{excitation}$ = 780 nm; $\lambda_{emission}$ = 810 nm). The relative fluorescent units were converted to molar units utilizing LS276 as an external standard.[25] The error values are standard error of the mean. The amount of active enzyme (E_T) was taken from published values of the % active enzyme generated under identical conditions (70%, MMP-2).[27,28] K_M values were determined by nonlinear regression utilizing $V_o = V_{MAX}[S]/(K_M + [S])$ (GraphPad Prism version 5.04 for Windows, GraphPad Software, San Diego, CA), and k_{cat} was determined from E_T and V_{MAX}.

Immunohistochemistry. Ten micrometer thick sections were cut from tumor tissue snap-frozen in OCT media for routine staining with hematoxylin and eosin (H&E) and IHC staining with MMP-9 and MMP-2. The polyclonal antibodies used were Antimouse MMP-9 (5 μg/mL) and Antimouse/rat MMP-2 (5 μg/mL) from R&D Systems, Inc. (Minneapolis, MN). Immunohistochemical analysis staining was done with the Vectastain Elite ABC Kit (Vector Laboratories, Burlingame, CA). The reaction products were visualized using diaminobenzidine (DAB) (Vector Laboratories, Burlingame, CA) as a chromogen. The sections were counterstained with hematoxylin. As negative controls, primary antibody was replaced with 1× PBS.

***In Vivo* Imaging.** For imaging studies, human fibrosarcoma xenografts were grown by subcutaneous injection of 200,000 HT1080 cells (ATCC) in the flanks of 6-week old male NCR nude mice (Taconic Farms, Hudson, NY). Tumor-bearing mice received 1 mg/kg LS276-THP probe i.p. (20 nmol in 250 μL PBS) (n = 4). A second group (n = 3) was treated with Ilomastat (1 mg/kg in DMSO i.p.) 2 h before LS276-THP injection and again 4 and 20 h after injection. A third group (n = 3) received 2 nmol MMPSense 680 i.v. Mice in the LS276-

THP groups were imaged using the Kodak IS4000MM multimodal imaging system (Carestream Health, New Haven, CT) immediately and at 1, 4, and 24 h after LS276-THP injection, followed by *ex vivo* fluorescence biodistribution imaging of organ tissues. Fluorescence images were acquired using $\lambda_{excitation}$ = 755 ± 35 nm and $\lambda_{emission}$ = 830 ± 75 nm detection, 60 s exposure with 2 × 2 binning. Mice in the MMPSense 680 group were imaged with the Pearl NIR fluorescence imaging system (LiCor Biosciences, Lincoln, NE) with $\lambda_{excitation}$ = 685 nm and $\lambda_{emission}$ = 720 nm collection. Region of interest (ROI) analysis was performed using ImageJ software (LS276-THP groups) or Pearl Cam Software (MMPSense 680). Mean fluorescence intensity values for tumor and contralateral flank ROIs were plotted versus time to analyze biodistribution and activation kinetics. Fluorescence values for *ex vivo* tissues were normalized to equalize blood fluorescence levels due to differences in absolute values between imaging systems and detection wavelengths. Statistical significance was calculated with a one-tailed, unpaired *t*-test (GraphPad Prism, version 5.04 for Windows, GraphPad Software, San Diego, CA). Outlying data were analyzed with the Grubb's test. All animal studies were conducted by protocols approved by the Animal Studies Committee at Washington University School of Medicine.

RESULTS AND DISCUSSION

Probe Development and Characterization. Near infrared fluorescent THP probes were synthesized for specific detection of MMP-2 and MMP-9 activity *in vivo*. We hypothesized that full substitution of the two Lys ε-amino groups per peptide strand would result in high efficiency quenching of fluorescence upon self-assembly of the triple-stranded peptide structure. Fluorescence would then be regenerated by gelatinase catalyzed hydrolysis, reporting MMP-2/-9 activity in aggressive tumors.

Currently, carbocyanine analogues, especially indocyanine green (ICG), are widely used as optical reporters for *in vivo* imaging of tumors because of their established safety profile in humans and known photophysical properties.[29,30] The carbocyanine dyes absorb and emit light in the NIR and therefore are suitable for imaging superficial or even deep-tissue disease states. Because our ultimate goal is to develop enzyme activatable probes for preclinical drug testing and diagnostic use in humans, we have utilized the NIR dye LS276. LS276 is compatible with relatively harsh basic conditions of solid-phase peptide synthesis and incorporates a single carboxylic acid group for conjugation to amino groups of resin-bound peptides.[25] Mass spectrometric analysis of the purified LS276-THP indicated a disubstituted single-stranded peptide: calculated $(M + H)^+$ = 5666; observed $(M + H)^+$ = 5667 (Figure S1, Supporting Information), which was corroborated by ninhydrin analysis that showed a substitution level of 6 LS276:1 THP indicating complete conjugation of LS276 to the ε-amino groups of Lys while the peptide was resin-bound. The emission spectrum of LS276-THP shifted slightly to the red by ~6 nm relative to unconjugated LS276, but otherwise, the spectral properties of LS276-THP were unchanged indicating stability during peptide synthesis (Figure 2).

By comparing the fluorescence of a fully proteolyzed sample of LS276-THP with an undigested sample, an average value of quenching of 73.5% ± 0.5% (standard deviation) of LS276 fluorescence was observed in the THP. By comparison, more flexible single-stranded peptides, such as the MMP-7 substrate

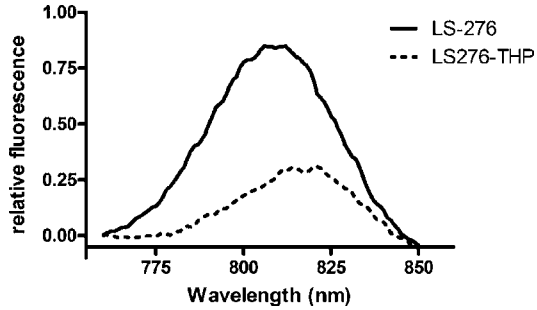


Figure 2. Fluorescence spectra of LS276 (solid) and LS276-THP (dashed), where $\lambda_{excitation}$ = 780 nm and $\lambda_{emission}$ = 760–850 nm.

GVPLSLTMGC bearing a heterologous donor and acceptor pair of near-infrared dyes on the *N*- and *C*-termini, yielded a level of 85% quenching with an approximate 7-fold increase after digestion with MMP-7.[31] In flexible peptides, a mechanism of quenching has been attributed to the formation of intramolecular dimers between the donor and quencher fluorophores.[32] Examination of the absorption profile of LS276-THP under conditions too dilute for intermolecular aggregation (33 nM) provided evidence of H-aggregation by the absorption at λ = 715 nm relative to the absorption of the nonaggregated dye (λ = 815 nm) (Figure 3A).[33,34] Furthermore, as the triple-helix started to unwind during melting, the absorption band due to H-aggregation decreased while that of the nonaggregated dye increased (Figure 3B). This indicated that quenching, at least in part, was due to sandwich-style stacking of the fluorophores. The triple-helical backbone is somewhat rigid, limiting the possibility of intramolecular collisional quenching. The level of quenching determined for the LS276-THP is lower than that reported for other NIR fluorogenic probes that have been used *in vivo*;[26,35,36] however, these molecular probes were based on short peptide sequences that have lower selectivity for MMP-2/-9. Moreover, achieving visualization of protease activity *in vivo* relies on a complex interplay of factors including extravasation of the probe into the tumor, enzyme-mediated proteolysis, and retention of the proteolyzed fragments within the tumor.

Plotting the change in absorbance of the LS276-THP at λ = 815 nm as a function of temperature yielded a sigmoidal plot with a midpoint transition temperature of 41 °C (T_M = 41 °C) (Figure 3B). While determining the melting temperature in this fashion does not take into account the conformational state of the triple-helical backbone, this value compares well with that previously determined for the fluorogenic THP [$(GPO)_5$GPK-((7-methoxycoumarin-4-yl)acetyl)GPPG~VVGEK(2,4-dinitrophenyl)GEQ$(GPO)_5]_3$ (T_M = 45 °C),[24] showing that there was no destabilization of the triple-helix upon incorporation of LS276.

Kinetics of Proteolysis. To determine whether the addition of the fluorophores perturbed the triple-helix and altered substrate avidity for the gelatinases, enzyme kinetic parameters were determined (Figure 4). LS276-THP was efficiently hydrolyzed by MMP-2 (K_M = 2.2 ± 0.24 μM, k_{cat} = 0.066 s^{-1}, and k_{cat}/K_M = 30,000 s^{-1} M^{-1}). The kinetic constants and catalytic rate were of similar magnitude to those observed for MMP-2 hydrolysis of a fluorogenic THP with the sequence of [$(GPO)_5$GPK((7-methoxycoumarin-4-yl)acetyl)-GPPG~VVGEK(2,4-dinitrophenyl)GEQ$(GPO)_5]_3$ (K_M = 4.4 μM, k_{cat} = 0.062 s^{-1}, and k_{cat}/K_M = 14,000 s^{-1} M^{-1}).[24] The

dx.doi.org/10.1021/bc300027y | *Bioconjugate Chem.* 2012, 23, 656–663

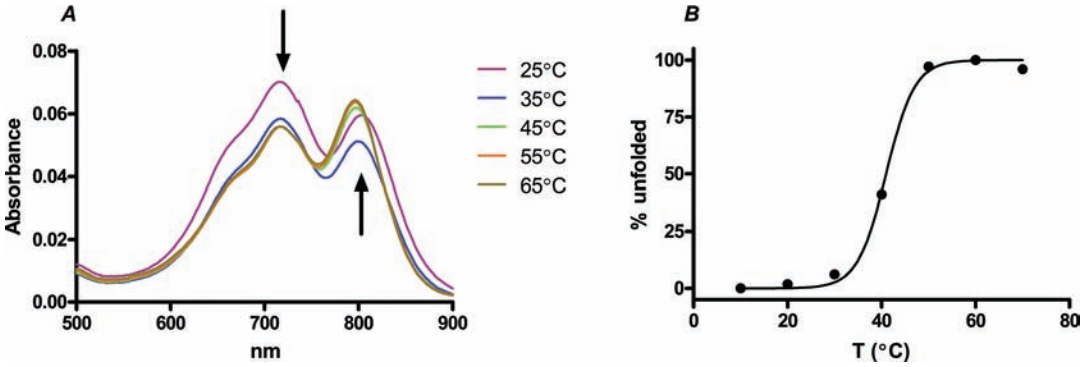


Figure 3. (A) Absorbance of LS276-THP with varying temperature. (B) Thermal transition curve for LS276-THP.

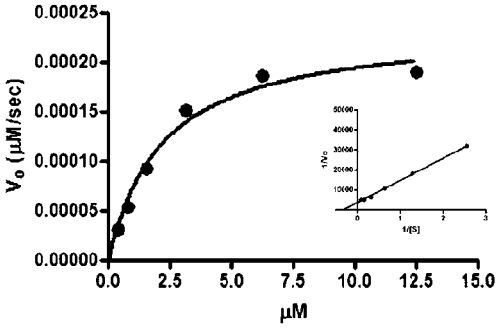


Figure 4. Proteolysis of increasing concentrations of LS276-THP by MMP-2. Lineweaver–Burk analysis is provided in the inset. Error bars indicating standard deviation are too narrow to be visualized on this plot.

comparable kinetic constants indicate that LS276 incorporation was not detrimental to efficient MMP-2 hydrolysis.[37] This result suggests that the THP could accommodate a variety of near-infrared dyes with differing sizes and chemical properties (such as varying hydrophobicity or ionizable functional groups). A prior study examining MMP-2 hydrolysis of fluorogenic THPs possessing methoxycoumarin analogues reached a similar conclusion.[38]

The k_{cat}/K_M value provides an important criterion in the evaluation of a substrate with quenched fluorophores for molecular imaging. Those substrates with the highest k_{cat}/K_M values would be expected to be the most rapidly hydrolyzed before wash-out from the target site, resulting in greater signal-to-noise. *In vivo* protease imaging is in a nascent stage, but the feasibility of these studies in small animals has been reported. For example, MMP-2 activity in mouse models was visualized with a poly lysine-PEG copolymer, of relatively high molecular weight (450 kDa), when conjugated to a peptide with a sequence of -Pro-Leu-Gly~Val-Arg-Gly-.[35,39] This peptide itself was a substrate for MMP-2 (k_{cat} = 4.1 s^{-1} and K_M = 290 μM; $k_{cat}/K_M = 1.4 \times 10^4$ $M^{-1}s^{-1}$).[19] Presumably, conjugation to the polymer did not change these kinetic parameters. In another

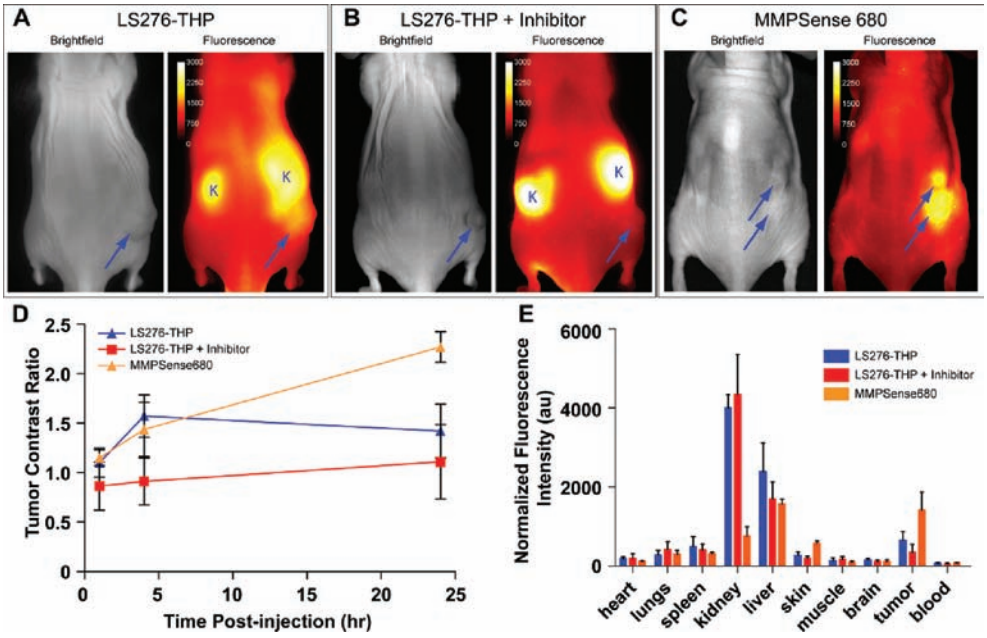


Figure 5. Representative *in vivo* whole-body images of mice bearing HT1080 tumor xenografts 24 h after an injection of (A) LS276-THP, n = 4; (B) LS276-THP and inhibitor, n = 3; or (C) MMPSense 680, n = 3. Tumors (arrows) and kidney (K) regions are marked. (D) The ratio of tumor and contralateral thigh ROI fluorescence with respect to time show the time dependent activation of the molecular probes. (E) *Ex vivo* fluorescence biodistribution confirmed the high fluorescence in the noninhibited tumors and the high retention of LS276-THP in the mouse kidneys relative to the larger MMPSense 680. Error bars represent standard deviation; au = arbitrary units.

dx.doi.org/10.1021/bc300027y | *Bioconjugate Chem.* 2012, 23, 656–663

study, a fluorescein-linear peptide bearing a MMP-7 hydrolysis site and tetramethylrhodamine (TMR) were conjugated to a polyamido-amino dendrimeric polymer (14 kDa).[26] Fluorescein was the FRET donor and TMR the acceptor. The dendrimeric peptide was efficiently (k_{cat}/K_M = 1.9 × 10^5 M^{-1} s^{-1}) and selectively (MMP-2 k_{cat}/K_M = 3.4 × 10^3 M^{-1} s^{-1}, MMP-3 k_{cat}/K_M = 1.5 × 10^4 M^{-1} s^{-1}) cleaved by the target, MMP-7. While the endogenous fluorescence was competing with fluorescein fluorescence, a subcutaneous tumor (MMP-7 positive) was visualized relative to a control (MMP-7 negative). An additional example was *in vivo* tumor imaging with a polymeric quenched-fluorescent probe activated by cathepsin D.[40] The peptide substrate bearing the Cy5.5 quenched probes had a relatively high efficiency for cathepsin D mediated hydrolysis (k_{cat}/K_M = 7 × 10^6 M^{-1} s^{-1}). Together, these examples suggest that there is a range of k_{cat}/K_M values of ∼1 × 10^4 to 7 × 10^6 M^{-1} s^{-1} for substrates that successfully imaged *in vivo* proteolytic activity.[35,39,40] The k_{cat}/K_M value for LS276-THP hydrolysis by MMP-2 falls inside this range, and due to its kinetic parameters, it is suitable for *in vivo* imaging of gelatinase activity.

***In Vivo* Imaging of MMP Activity with LS276-THP and MMPSense 680.** Planar fluorescence imaging was performed in mice bearing HT1080 subcutaneous xenografts after contrast agent injection. The HT1080 human fibrosarcoma is well known for its high expression of gelatinases.[18,41,42] Intravenous administration of LS276-THP resulted in rapid clearance of the conjugate with no observable visualization of gelatinase activity in the tumor (data not shown). Unlike large molecular weight polymers, such as MMPSenseTM 680, LS276-THP is below the renal filtration threshold leading to fast clearance via the kidneys. Intravenous administration resulted in low tumor-specific contrast, likely due to rapid washout of the relatively small probe (∼15 kDa, data not shown). To slow the uptake and clearance of LS276-THP and maintain a steady concentration of the gelatinase sensing probe in blood, it was administered intraperitoneally.

Planar fluorescence imaging after injection of the LS276-THP probe demonstrated low initial fluorescence intensity followed by high peak fluorescence at 4 h postinjection and cleared from most tissues after 24 h (Figure 5). While tumor fluorescence was partially obscured by an overwhelming signal from the ipsilateral kidney, the fluorescence intensity from the tumor region was higher than that of the contralateral flank at 4 and 24 h. This rapid increase in fluorescence intensity was not observed in mice treated with Ilomastat, a pan MMP inhibitor. Ilomastat is a potent inhibitor of gelatinase activity (K_i = 0.5 nM, MMP-2; K_i = 0.2 nM, MMP-9).[43] Instead, a steady increase in fluorescence intensity occurred, indicating incomplete inhibition of tumor-associated MMP-2/MMP-9 activity. The fluorescence intensities in the tumor region relative to the contralateral thigh shows that LS276-THP had maximum contrast at 4 h relative to mice receiving LS276-THP and inhibitor (Figure 5A and B). Normalized fluorescence biodistribution measured from *ex vivo* tissues confirmed higher tumor accumulation for LS276-THP relative to LS276-THP in Ilomastat-treated controls (Figure 5E). The *ex vivo* tumor-to-muscle ratio of fluorescence was 5.36 ± 2.32 for LS276-THP versus 1.99 ± 0.42 for LS276-THP + inhibitor ($P < 0.05$).

Because planar imaging is surface weighted, the relatively high fluorescence from the skin obscured the fluorescence signal from the tumor. To obtain a better understanding of whether the observed tumoral fluorescence was mediated by enzyme hydrolysis, an *ex vivo* fluorescence imaging biodistribution was performed. High fluorescence intensity was observed from the liver and kidneys, indicating a mixed clearance pathway for the probe and possibly for the hydrolyzed fragments (Figure 5). Fluorescence was also observed in nontarget tissues including lungs, spleen, and skin that was not reduced with the inhibitor ($P > 0.05$). However, the tumor mediated accumulation was reduced by the inhibitor Ilomastat ($P < 0.05$). While Ilomastat is a pan-MMP inhibitor, the THP sequence used in this work has already been shown to be impervious to the proteolysis of other tumor specific MMPs such as MMP-1, MMP-13, and MMP-14. Other tumor MMPs that are activated in cancer such as MMP-7 need not have been investigated because they do not proteolyze collagen in the α1(V)436−447 region.[24] Additionally, examination of the dissected HT1080 tumors by immunohistochemistry and fluorescence imaging showed strong expression at the tumor periphery, consistent with previous observations of gelatinase expression (Figure 6).[44,45]

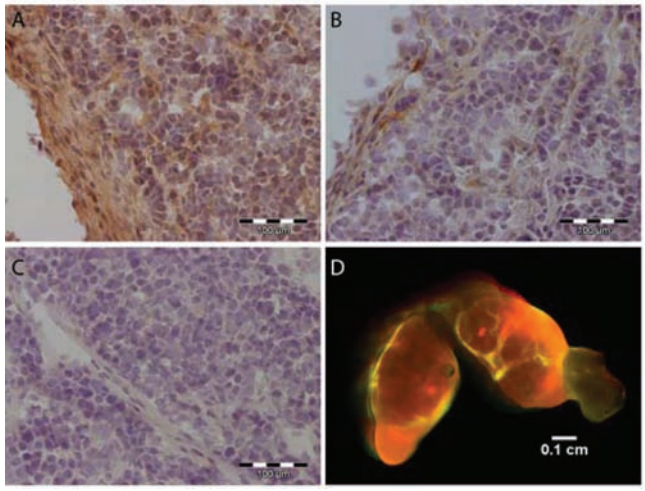


Figure 6. Immunohistochemistry for MMP-2 (A), MMP-9 (B), and secondary antibody control (C) with hematoxylin counterstain in HT1080 xenograft cryosections. (D) Fluorescence imaging of HT1080 tumor xenograft 24 h after an injection of the LS276-THP probe.

The correlation of intense fluorescence and as well as intense staining at the tumor periphery colocalizes gelatinase expression with NIR fluorescence and supports the conclusion of gelatinase mediated proteolysis of LS276-THP. Taken together, these results strongly support MMP-2 mediated activation of LS276-THP.

To place these results in perspective, the tumor associated fluorescence of MMPSense 680 was investigated in the same tumor model. This is a commercially available pan-matrix metalloproteinase imaging agent that has been utilized in a variety of animal models to investigate MMP activity as a function of disease.[20,21] MMPSense 680 has a molecular weight of 450 kDa and consists of relatively short peptides bearing fluorophores conjugated to a polymer backbone. Within the peptide is an MMP sensitive sequence. The close proximity of the fluorophores results in quenching of the fluorescence. Fluorescence dequenching is observed after enzyme mediated hydrolysis as the peptide fragments bearing the fluorophores are liberated from the polymer. The molecular weight of MMPSense 680 is relatively large; therefore, it was adminis-

dx.doi.org/10.1021/bc300027y | *Bioconjugate Chem.* 2012, 23, 656−663

tered intravenously rather than impose the additional barrier of peritoneal absorption with i.p. administration.

The tumor-specific fluorescence contrast with MMPSense 680 increased over time for 24 h, indicating that the higher molecular weight resulted in greater residence time in the tumor tissue and therefore greater activation. By 24 h postinjection, the tumor contrast for MMPSense 680 was about 2-fold higher than the contralateral thigh, while the contrast ratio for LS276-THP remained at about 1.5, unchanged from the 4 h time point. Another factor that could have contributed to the higher tumoral activation of MMPSense 680 was the lack of MMP selectivity. The peptide bearing the quenched fluorophores that is conjugated to the polymeric backbone of MMPSense 680 contains the sequence -PLGVR-, which is subject to proteolysis by members of the MMP family that include, in addition to the gelatinases, MMP-1, MMP-3, and MMP-7.[35,46,47] These MMPS are included in those that have been shown to be expressed by the human fibrosarcoma cell line HT1080[48] but are not always associated with tumor invasiveness or aggressive phenotypes.[11,14,15,49,50] In fact, the correlation of MMP-2/-9 activity with tumor aggressiveness is a driving force in the development of new inhibitors.[51−53] These contrasting results indicate that both increased tumor residence time and increased quenching efficiency are needed to improve the contrast enhancement due to MMP-2 activation in triple-helical peptides. While the tumor-specific fluorescence enhancement is slightly higher with MMPSense 680 relative to that of LS276-THP in this study, the utilization of triple-helical peptides represents a leap forward in selectively visualizing gelatinase activity by replication of the natural enzyme substrate.

CONCLUSIONS

Overall, we have presented the synthesis and characterization of a THP bearing NIR dyes with a relatively high degree of quenching. This probe, LS276-THP, retained the kinetic parameters of the previously described fluorogenic THP and was efficiently hydrolyzed by MMP-2. LS276-THP enabled the visualization of MMP-2 activity in mice bearing human tumors, which was diminished with a known inhibitor. This work represents the first report of the use of a THP for *in vivo* imaging of proteolytic activity. Work is in progress to increase the quenching levels and serum half-life to affect greater *in vivo* contrast enhancement for sensing tumor-related MMP-2 activity.

ASSOCIATED CONTENT

Supporting Information

ES-MS of LS276-THP. This material is available free of charge via the Internet at http://pubs.acs.org.

AUTHOR INFORMATION

Corresponding Author

*100 Technology Drive, Suite 452, University of Pittsburgh, Pittsburgh, PA 15219. Phone: (412) 624-6873. Fax: (412)-624-2598. E-mail: edwardsw@upmc.edu.

Notes

The authors declare no competing financial interest.

ACKNOWLEDGMENTS

This work was supported in part by NIH grants R21 CA CA131660-02 and 3R21CA131660-02S1 (to W.B.E.), R01CA098799 (to G.B.F.) from the National Cancer Institute and K01RR026095 (to W.J.A.) from the National Center for Research Resources. Mass spectrometry was provided by the Washington University Mass Spectrometry Resource, an NIH Research Resource (P41RR0954).

REFERENCES

(1) Sternlicht, M. D., and Werb, Z. (2001) How matrix metalloproteinases regulate cell behavior. *Annu. Rev. Cell Dev. Biol. 17*, 463−516.

(2) Egeblad, M., and Werb, Z. (2002) New functions for the matrix metalloproteinases in cancer progression. *Nat. Rev. Cancer 2*, 161−174.

(3) Kalluri, R., and Zeisberg, M. (2006) Fibroblasts in cancer. *Nat. Rev. Cancer 6*, 392−401.

(4) Pacheco, M. M., Mourao, M., Mantovani, E. B., Nishimoto, I. N., and Brentani, M. M. (1998) Expression of gelatinases A and B, stromelysin-3 and matrilysin genes in breast carcinomas: clinicopathological correlations. *Clin. Exp. Metastasis 16*, 577−585.

(5) Remacle, A. G., Noel, A., Duggan, C., McDermott, E., O'Higgins, N., Foidart, J. M., and Duffy, M. J. (1998) Assay of matrix metalloproteinases types 1, 2, 3 and 9 in breast cancer. *Br. J. Cancer 77*, 926−931.

(6) Baker, E. A., Bergin, F. G., and Leaper, D. J. (2000) Matrix metalloproteinases, their tissue inhibitors and colorectal cancer staging. *Br. J. Surg. 87*, 1215−1221.

(7) Baker, E. A., and Leaper, D. J. (2002) Measuring gelatinase activity in colorectal cancer. *Eur. J. Surg. Oncol. 28*, 24−29.

(8) Kuniyasu, H., Troncoso, P., Johnston, D., Bucana, C. D., Tahara, E., Fidler, I. J., and Pettaway, C. A. (2000) Relative expression of type IV collagenase, E-cadherin, and vascular endothelial growth factor/vascular permeability factor in prostatectomy specimens distinguishes organ-confined from pathologically advanced prostate cancers. *Clin. Cancer Res. 6*, 2295−2308.

(9) Upadhyay, J., Shekarriz, B., Nemeth, J. A., Dong, Z., Cummings, G. D., Fridman, R., Sakr, W., Grignon, D. J., and Cher, M. L. (1999) Membrane type 1-matrix metalloproteinase (MT1-MMP) and MMP-2 immunolocalization in human prostate: change in cellular localization associated with high-grade prostatic intraepithelial neoplasia. *Clin. Cancer Res. 5*, 4105−4110.

(10) Nomura, H., Fujimoto, N., Seiki, M., Mai, M., and Okada, Y. (1996) Enhanced production of matrix metalloproteinases and activation of matrix metalloproteinase 2 (gelatinase A) in human gastric carcinomas. *Int. J. Cancer 69*, 9−16.

(11) Sier, C. F., Kubben, F. J., Ganesh, S., Heerding, M. M., Griffioen, G., Hanemaaijer, R., van Krieken, J. H., Lamers, C. B., and Verspaget, H. W. (1996) Tissue levels of matrix metalloproteinases MMP-2 and MMP-9 are related to the overall survival of patients with gastric carcinoma. *Br. J. Cancer 74*, 413−417.

(12) Hofmann, U. B., Westphal, J. R., Zendman, A. J., Becker, J. C., Ruiter, D. J., and van Muijen, G. N. (2000) Expression and activation of matrix metalloproteinase-2 (MMP-2) and its co-localization with membrane-type 1 matrix metalloproteinase (MT1-MMP) correlate with melanoma progression. *J. Pathol. 191*, 245−256.

(13) Piao, D., Xie, H., Zhang, W., Krasinski, J. S., Zhang, G., Dehghani, H., and Pogue, B. W. (2006) Endoscopic, rapid near-infrared optical tomography. *Opt. Lett. 31*, 2876−2878.

(14) Trudel, D., Fradet, Y., Meyer, F., Harel, F., and Tetu, B. (2003) Significance of MMP-2 expression in prostate cancer: an immunohistochemical study. *Cancer Res. 63*, 8511−8515.

(15) Talvensaari-Mattila, A., Paakko, P., and Turpeenniemi-Hujanen, T. (2003) Matrix metalloproteinase-2 (MMP-2) is associated with survival in breast carcinoma. *Br. J. Cancer 89*, 1270−1275.

(16) Scherer, R. L., McIntyre, J. O., and Matrisian, L. M. (2008) Imaging matrix metalloproteinases in cancer. *Cancer Metastasis Rev. 27*, 679−690.

(17) Aguilera, T. A., Olson, E. S., Timmers, M. M., Jiang, T., and Tsien, R. Y. (2009) Systemic in vivo distribution of activatable cell

penetrating peptides is superior to that of cell penetrating peptides. *Integr. Biol.: Quant. Biosci. Nano Macro 1*, 371−381.
(18) Bremer, C., Tung, C. H., and Weissleder, R. (2002) Molecular imaging of MMP expression and therapeutic MMP inhibition. *Acad. Radiol. 9* (Suppl 2), S314−S315.
(19) Seltzer, J. L., Akers, K. T., Weingarten, H., Grant, G. A., McCourt, D. W., and Eisen, A. Z. (1990) Cleavage specificity of human skin type IV collagenase (gelatinase). Identification of cleavage sites in type I gelatin, with confirmation using synthetic peptides. *J. Biol. Chem. 265*, 20409−20413.
(20) Kaijzel, E. L., van Heijningen, P. M., Wielopolski, P. A., Vermeij, M., Koning, G. A., van Cappellen, W. A., Que, I., Chan, A., Dijkstra, J., Ramnath, N. W., Hawinkels, L. J., Bernsen, M. R., Lowik, C. W., and Essers, J. (2010) Multimodality imaging reveals a gradual increase in matrix metalloproteinase activity at aneurysmal lesions in live fibulin-4 mice. *Circulation Cardiovasc. Imaging 3*, 567−577.
(21) Littlepage, L. E., Sternlicht, M. D., Rougier, N., Phillips, J., Gallo, E., Yu, Y., Williams, K., Brenot, A., Gordon, J. I., and Werb, Z. (2010) Matrix metalloproteinases contribute distinct roles in neuroendocrine prostate carcinogenesis, metastasis, and angiogenesis progression. *Cancer Res. 70*, 2224−2234.
(22) Yu, Y., Berndt, P., Tirrell, M., and Fields, G. B. (1996) Self assembling amphiphiles for construction of protein molecular architecture. *J. Am. Chem. Soc. 118*, 12515−12520.
(23) Fields, C. G., Lovdahl, C. M., Miles, A. J., Hagen, V. L., and Fields, G. B. (1993) Solid-phase synthesis and stability of triple-helical peptides incorporating native collagen sequences. *Biopolymers 33*, 1695−1707.
(24) Lauer-Fields, J. L., Sritharan, T., Stack, M. S., Nagase, H., and Fields, G. B. (2003) Selective hydrolysis of triple-helical substrates by matrix metalloproteinase-2 and -9. *J. Biol. Chem. 278*, 18140−18145.
(25) Lee, H., Mason, J. C., and Achilefu, S. (2006) Heptamethine cyanine dyes with a robust C-C bond at the central position of the chromophore. *J. Org. Chem. 71*, 7862−7865.
(26) McIntyre, J. O., Fingleton, B., Wells, K. S., Piston, D. W., Lynch, C. C., Gautam, S., and Matrisian, L. M. (2004) Development of a novel fluorogenic proteolytic beacon for in vivo detection and imaging of tumour-associated matrix metalloproteinase-7 activity. *Biochem. J. 377*, 617−628.
(27) Okada, Y., Morodomi, T., Enghild, J. J., Suzuki, K., Yasui, A., Nakanishi, I., Salvesen, G., and Nagase, H. (1990) Matrix metalloproteinase 2 from human rheumatoid synovial fibroblasts. Purification and activation of the precursor and enzymic properties. *Eur. J. Biochem. 194*, 721−730.
(28) Vempati, P., Karagiannis, E. D., and Popel, A. S. (2007) A biochemical model of matrix metalloproteinase 9 activation and inhibition. *J. Biol. Chem. 282*, 37585−37596.
(29) Hawrysz, D. J., and Sevick-Muraca, E. M. (2000) Developments toward diagnostic breast cancer imaging using near-infrared optical measurements and fluorescent contrast agents. *Neoplasia 2*, 388−417.
(30) Tsilou, E., Csaky, K., Rubin, B. I., Gahl, W., and Kaiser-Kupfer, M. (2002) Retinal visualization in an eye with corneal crystals using indocyanine green videoangiography. *Am. J. Ophthalmol. 134*, 123−125.
(31) Pham, W., Choi, Y., Weissleder, R., and Tung, C. H. (2004) Developing a peptide-based near-infrared molecular probe for protease sensing. *Bioconjugate Chem. 15*, 1403−1407.
(32) Packard, B. Z., Toptygin, D. D., Komoriya, A., and Brand, L. (1996) Profluorescent protease substrates: intramolecular dimers described by the exciton model. *Proc. Natl. Acad. Sci. U.S.A. 93*, 11640−11645.
(33) Almutairi, A., Akers, W. J., Berezin, M. Y., Achilefu, S., and Frechet, J. M. (2008) Monitoring the biodegradation of dendritic near-infrared nanoprobes by in vivo fluorescence imaging. *Mol. Pharmaceutics 5*, 1103−1110.
(34) Philip, R., Penzkofer, A., Baumler, W., Szeimies, R. M., and Abels, C. (1996) Absorption and fluorescence spectroscopic investigation of indocyanine green. *J. Photochem. Photobiol., A 96*, 137−148.
(35) Bremer, C., Tung, C. H., and Weissleder, R. (2001) In vivo molecular target assessment of matrix metalloproteinase inhibition. *Nat. Med. 7*, 743−748.
(36) Weissleder, R., Tung, C. H., Mahmood, U., and Bogdanov, A. Jr. (1999) In vivo imaging of tumors with protease-activated near-infrared fluorescent probes. *Nat. Biotechnol. 17*, 375−378.
(37) Lauer-Fields, J. L., Nagase, H., and Fields, G. B. (2000) Use of Edman degradation sequence analysis and matrix-assisted laser desorption/ionization mass spectrometry in designing substrates for matrix metalloproteinases. *J. Chromatogr., A 890*, 117−125.
(38) Lauer-Fields, J. L., Kele, P., Sui, G., Nagase, H., Leblanc, R. M., and Fields, G. B. (2003) Analysis of matrix metalloproteinase triple-helical peptidase activity with substrates incorporating fluorogenic L- or D-amino acids. *Anal. Biochem. 321*, 105−115.
(39) Mahmood, U., and Weissleder, R. (2003) Near-infrared optical imaging of proteases in cancer. *Mol. Cancer Ther. 2*, 489−496.
(40) Tung, C. H., Mahmood, U., Bredow, S., and Weissleder, R. (2000) In vivo imaging of proteolytic enzyme activity using a novel molecular reporter. *Cancer Res. 60*, 4953−4958.
(41) Faust, A., Waschkau, B., Waldeck, J., Holtke, C., Breyholz, H. J., Wagner, S., Kopka, K., Heindel, W., Schafers, M., and Bremer, C. (2008) Synthesis and evaluation of a novel fluorescent photoprobe for imaging matrix metalloproteinases. *Bioconjugate Chem. 19*, 1001−1008.
(42) van Duijnhoven, S. M., Robillard, M. S., Nicolay, K., and Grull, H. (2011) Tumor targeting of MMP-2/9 activatable cell-penetrating imaging probes is caused by tumor-independent activation. *J. Nucl. Med. 52*, 279−286.
(43) Galardy, R. E., Cassabonne, M. E., Giese, C., Gilbert, J. H., Lapierre, F., Lopez, H., Schaefer, M. E., Stack, R., Sullivan, M., Summers, B., et al. (1994) Low molecular weight inhibitors in corneal ulceration. *Ann. N.Y. Acad. Sci. 732*, 315−323.
(44) Jones, J. L., Glynn, P., and Walker, R. A. (1999) Expression of MMP-2 and MMP-9, their inhibitors, and the activator MT1-MMP in primary breast carcinomas. *J. Pathol. 189*, 161−168.
(45) Singer, C. F., Kronsteiner, N., Marton, E., Kubista, M., Cullen, K. J., Hirtenlehner, K., Seifert, M., and Kubista, E. (2002) MMP-2 and MMP-9 expression in breast cancer-derived human fibroblasts is differentially regulated by stromal-epithelial interactions. *Breast Cancer Res. Treat. 72*, 69−77.
(46) Jones, E. F., Schooler, J., Miller, D. C., Drake, C. R., Wahnishe, H., Siddiqui, S., Li, X., and Majumdar, S. (2012) Characterization of human osteoarthritic cartilage using optical and magnetic resonance imaging. *Mol. Imaging Biol. 14*, 32−39.
(47) Zhu, L., Xie, J., Swierczewska, M., Zhang, F., Quan, Q., Ma, Y., Fang, X., Kim, K., Lee, S., and Chen, X. (2011) Real-time video imaging of protease expression in vivo. *Theranostics 1*, 18−27.
(48) Giambernardi, T. A., Grant, A. M., Taylor, G. P., Hay, R. J., Maher, V. M., McCormick, J., and Klebe, R. J. (1998) Overview of matrix metalloproteinase expression in cultured human cells. *Matrix Biol. 16*, 483−496.
(49) Hofmann, U. B., Westphal, J. R., Van Muijen, G. N., and Ruiter, D. J. (2000) Matrix metalloproteinases in human melanoma. *J. Invest. Dermatol. 115*, 337−344.
(50) Hofmann, U. B., Westphal, J. R., Waas, E. T., Becker, J. C., Ruiter, D. J., and van Muijen, G. N. (2000) Coexpression of integrin alpha(v)beta3 and matrix metalloproteinase-2 (MMP-2) coincides with MMP-2 activation: correlation with melanoma progression. *J. Invest. Dermatol. 115*, 625−632.
(51) Nuti, E., Casalini, F., Santamaria, S., Gabelloni, P., Bendinelli, S., Da Pozzo, E., Costa, B., Marinelli, L., La Pietra, V., Novellino, E., Margarida Bernardo, M., Fridman, R., Da Settimo, F., Martini, C., and Rossello, A. (2011) Synthesis and biological evaluation in U87MG glioma cells of (ethynylthiophene)sulfonamido-based hydroxamates as matrix metalloproteinase inhibitors. *Eur. J. Med. Chem. 46*, 2617−2629.
(52) Testero, S. A., Lee, M., Staran, R. T., Espahbodi, M., Llarrull, L. I., Toth, M., Mobashery, S., and Chang, M. (2010) Sulfonate-containing thiiranes as selective gelatinase inhibitors. *ACS Med. Chem. Lett. 2*, 177−181.

(53) Wang, J., Medina, C., Radomski, M. W., and Gilmer, J. F. (2011) N-Substituted homopiperazine barbiturates as gelatinase inhibitors. *Bioorg. Med. Chem. 19*, 4985−4999.

Bioconjugate Chemistry

Technical Note

pubs.acs.org/bc

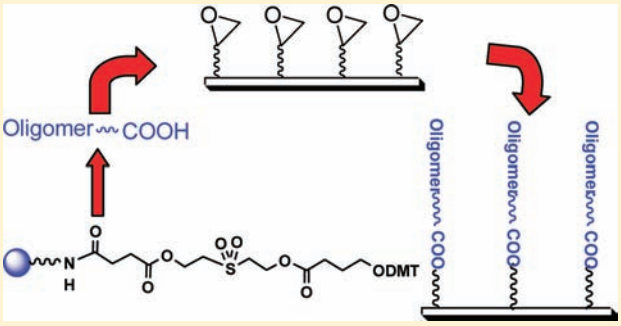
Engineered Polymer-Supported Synthesis of 3′-Carboxyalkyl-Modified Oligonucleotides and Their Applications in the Construction of Biochips for Diagnosis of the Diseases

Satyakam Patnaik,[†] Sandip K. Dash,[†] Dalip Sethi,[†] Ashok Kumar,[†] K. C. Gupta,*[,†,‡] and Pradeep Kumar*[,†]

[†]CSIR-Institute of Genomics and Integrative Biology, Delhi University Campus, Mall Road, Delhi −110 007, India

[‡]CSIR-Indian Institute of Toxicology Research, M. G. Marg, Lucknow-226001 U. P., India

ABSTRACT: An engineered polymer support **5** has been prepared for the solid-phase assembly of 3′-carboxyalkyl-modified oligonucleotides using commonly available reagents. A two-step deprotection procedure resulted in the quantitative cleavage of oligonucleotides from the support and removal of the protecting groups from phosphodiesters and exocyclic amino groups of the nucleic bases. The fully deprotected oligomers, obtained in high yield, were desalted and analyzed on RP-HPLC. After characterization by MALDI-TOF, these carboxyalkylated oligonucleotides were immobilized onto the epoxy-functionalized glass microslides to prepare biochips. The performance of these biochips was evaluated under different sets of conditions and then successfully validated by the detection of base mismatches and human infectious disease, bacterial meningitis, caused by *N. meningitidis*.



INTRODUCTION

In the past two decades, solid-phase oligonucleotide synthesis has played a key role in the rapid development of molecular diagnostics.[1−3] A wide range of protocols have been designed and developed to introduce reactive functionalities at their termini for the synthesis of oligonucleotide conjugates.[4−6] Since 5′-modifications require preparation of phosphoramidite reagents of the linkers/modified nucleosides under strictly anhydrous conditions and preclude labeling of oligonucleotides, 3′-modified oligonucleotides have become increasingly useful. Moreover, these modifications can easily be incorporated by employing engineered polymer supports.[7] Therefore, 3′-modified oligonucleotides bearing reactive functionalities such as aminoalkyl, carboxyl, mercaptoalkyl, aminooxyalkyl, and phosphoryl are finding important biomedical applications.[8]

Recently, microarrays have extensively been used for various applications such as the detection of nucleic acid sequences, gene expression analysis, mutation detection, and so forth.[9,10] The technology is based on hybridization of targets with the immobilized probes, either single- or double-stranded nucleic acids, followed by detection through a scanning process. Many different microarray formats and platforms have been developed; however, the deposition method (or postsynthesis immobilization method) has remained a preferred choice for fabrication of oligonucleotide microarrays (biochips) for routine biological applications, as it offers flexibility in terms of ligands and surfaces used as well as different chemistries for the attachment of probes on a surface of choice.[11−13] Among various surfaces, glass has been the most preferred surface owing to its low intrinsic fluorescence and superior optical properties. A plethora of reports have been published on covalent and physical attachment of oligonucleotides on glass surface.[13−21] Physically adsorbed oligonucleotides usually result in poor hybridization efficiency, while the covalently linked probes require active functional groups on the surface as well as on the probe sequences, which result into immobilization of the oligonucleotide probes onto the surface either in the presence of a coupling reagent or in its absence. Among various modified oligonucleotides, the most commonly used are aminoalkyl-, aminooxyalkyl-, mercaptoalkyl-, carboxyalkyl-, and phosphate-modified oligonucleotides, which are immobilized on the functionalized glass surfaces.[22−27] As mentioned in the literature, covalently linked probes offer advantages of higher stability and hybridization efficiency compared to noncovalently attached; some of the commonly used attachment chemistries are epoxide−amine, epoxide−thiol, epoxide−aminooxyalkyl, aldehyde−amine, and semicarbazide−aldehyde. Among various functionalized surfaces, epoxide-based surfaces are the most commonly used, as epoxides are known to be reactive toward electrophilic as well as nucleophilic groups. Recently, in a published report from our group, *S*-4,4′-dimethoxytrityl-3-mercaptopropionic acid has been employed as a reagent for the spectrophotometric estimation of solid supported epoxy functions,[28] where it was observed that carboxyalkyl reagent reacted efficiently with epoxy functions.

Received: November 12, 2011
Revised: January 12, 2012
Published: February 27, 2012

ACS Publications © 2012 American Chemical Society

dx.doi.org/10.1021/bc200610u | *Bioconjugate Chem.* 2012, 23, 664−670

Taking a cue from this study, we decided to explore this reaction to immobilize carboxyalkyl-modified oligonucleotides onto epoxy-functionalized glass surfaces to fabricate biochips for diagnostic purposes. To synthesize 3′- or 5′-carboxyalkyl-modified oligonucleotides, there are several protocols reported in the literature; however, they all suffer from drawbacks. They are either quite time-consuming and tedious or require methanolic sodium hydroxide during the final deprotection step, which poses a serious drawback in the case of base-labile modified oligonucleotides.

Meningitis is a serious life-threatening disease that causes inflammation of the meninges (outer covering membrane) in the brain and spinal cord of the patients.[29] Meningitis can be caused by viruses, fungi, or bacteria. Viral and fungal meningitis are mild and get cured within a week or two without any medication. Bacterial meningitis is the most dangerous and may prove to be lethal if it is not treated in time. Various methods have been reported for diagnosis of bacterial meningitis, but these are either time-consuming or expensive and suffer from limitations.[30−36] Therefore, a rapid, simple, and sensitive method is required for early diagnosis of meningitis, which can save lives of several people during outbreaks of the disease.

Here, we report preparation of an engineered polymer support for the synthesis of 3′-carboxyalkyl-modified oligonucleotides using commercially available reagents and chemicals. The support-bound oligonucleotides were fully deprotected in a two-step procedure, viz., (i) treatment with 0.5 M DBU in dry THF for 2 h and (ii) aqueous ammonia (30%) treatment for 16 h at 60 °C. The deprotected oligomers, after characterization, were analyzed on RP-HPLC and used for the construction of microarrays on the epoxy-functionalized glass microslides for the detection of mismatches as well as human infectious diseases. The modified oligonucleotides were immobilized with high immobilization efficiency and signal-to-noise ratio (∼98). The constructed microarrays efficiently discriminated base mismatch and further used for the detection of human bacterial meningitis, caused by infection of *N. meningitidis*.

■ EXPERIMENTAL PROCEDURES

General. Reagents and chemicals used in the present investigation were purified prior to their use. The reactions requiring anhydrous conditions were carried out under a blanket of dry argon gas. 4-Dimethylaminopyridine (DMAP), 1,8-diazabicycloundec-7-ene (DBU), 4-hydroxybutyric acid, CPG-500 support, and unmodified glass microslides were procured from Sigma-Aldrich Chemical Co., St. Louis, MO. Tetrachlorofluoresceinyl-phosphoramidite (TET-phosphoramidite) was purchased from Applied Biosystems Inc., Foster City, CA. Other ancillary reagents and chemicals were locally sourced. ^{1}H NMR spectra were recorded on a Bruker Avance 300 spectrometer operating at 300 MHz and the chemical shifts (δ) reported in ppm. Matrix assisted laser desorption ionization−time-of-flight (MALDI-TOF) mass spectrometry was carried out on a Bruker (Billerica, MA) using 3-hydroxypicolinic acid−picolinic acid doped with ammonium tartarate and 3,5-dihydroxybenzoic acid as matrices for oligonucleotides and small molecules, respectively. Reversed-phase HPLC was performed on a Agilent 1100 series system fitted with a variable DAD detector set at 254 ± 8 nm and a fluorescence detector with excitation at 515 nm and emission at 560 nm, using Hypersil Gold C-18 column from Thermo Electron Inc., USA. Elutions were carried out with increasing gradient of MeCN in an ammonium acetate buffer, pH 7.0.

Preparation of Polymer Support for the Synthesis of 3′-Carboxyalkyl-Modified Oligonucleotides. *O-(4,4′-Dimethoxytrityl)-2,2′-sulfonyldiethanol-O-succinate.* 2,2′-Sulfonyl-diethanol (10 mmol) **1** was dried by coevaporation with pyridine (2 × 25 mL) and finally taken up in dry pyridine (15 mL), and 4,4′-dimethoxytrityl chloride (DMTrCl) (11 mmol) and 4-dimethylaminopyridine (1 mmol) were added. The reaction mixture was stirred at room temperature for 3 h, and after completion of reaction (as monitored on TLC), the solvent was removed and the resulting residue was dissolved in ethyl acetate (50 mL). The organic phase was washed with water (2 × 25 mL), collected, dried over anhydrous sodium sulfate, filtered, and concentrated in vacuo to obtain *O*-(4,4′-dimethoxytrityl)-2,2′-sulfonyldiethanol in ∼82% yield, which was characterized by its ^{1}H NMR and mass spectroscopy. ^{1}H NMR ($CDCl_3$), δ: 3.16 (m, 4H), 3.9−4.2 (m, 4H), 6.7−7.5 (m, 13H); MS (m/z): 456 (calcd.), 480 ($M+H^+$+Na^+) (found).

In the subsequent step, *O*-(4,4′-dimethoxytrityl)-2,2′-sulfonyldiethanol (2 mmol), 4-dimethylaminopyridine (1 mmol), succinic anhydride (4 mmol), and triethylamine (TEA) (2.5 mmol) were taken up in 1,2-dichloroethane (EDC) (5 mL) and the reaction mixture was kept at 45 °C for 20 min. The reaction mixture was then diluted with 1,2-dichloroethane (25 mL) and washed with cold 5% aqueous citric acid (2 × 10 mL) and saturated sodium chloride solution (2 × 10 mL), respectively. The organic phase was collected, dried over anhydrous sodium sulfate, filtered, and solvent removed on a rotary evaporator to obtain *O*-(4,4′-dimethoxytrityl)-2,2′-sulfonyldiethanol-*O*-hemisuccinate **2** in quantitative yield, which was then characterized by its ^{1}H NMR. ^{1}H NMR ($CDCl_3$) δ: 2.35−2.55 (m, 4H), 3.21 (m, 4H), 4.1−4.3 (m, 4H), 6.8−7.7 (m, 13H).

*Attachment of **2** to 3-Aminopropylated CPG.* *O*-(4,4′-Dimethoxytrityl)-2,2′-sulfonyldiethanol-*O*-hemisuccinate (56 mg, 100 μmol), bromotrichloromethane (BTCM) (10 μL, 100 μmol), and DMAP (24.4 mg, 200 μmol) were dissolved in acetonitrile (MeCN) (1.0 mL). To the above reaction mixture, triphenylphosphine (TPP) (13.1 mg, 50 μmol), dissolved in acetonitrile (0.5 mL), was added and the mixture was swirled for 30 s followed by addition of 3-aminopropylated CPG (500 mg). After stirring the suspension for 30 min at room temperature, the support was recovered on a sintered disk glass funnel, washed with acetonitrile (5 × 20 mL) and diethyl ether (2 × 10 mL), respectively, and dried under vacuum. The residual amino groups on the support were capped with a solution of Ac_2O/TEA/*N*-methylimidazole/dichloroethane (1:1:0.4:6, v/v/v/v) for 30 min at room temperature. After washings with dichloroethane (4 × 5 mL), the functionalized polymer support **3** was dried in vacuo and subjected to treatment with 3% trichloroacetic acid (TCA) in dichloroethane to remove dimethoxytrityl protecting groups from the hydroxyl functions. After 10 min, the support **4** was again washed with dichloroethane (5 × 5 mL) followed by diethyl ether (2 × 5 mL) and dried in vacuo.

In the final step, *O*-4-(4,4′-dimethoxytrityl)-hydroxybutyric acid (610 mg, 1.6 mmol)[37] and 2-(1*H*-benzotriazol-1-yl)-1,1,3,3-tetramethyluronium hexafluorophosphate (HBTU) (608 mg, 1.6 mmol) were dissolved in anhydrous *N*,*N*-dimethylformamide (DMF) (3 mL) containing dry pyridine (50 μL). After swirling the reaction mixture for 2−3 min, hydroxylated polymer support **4** (300 mg) was added and the contents were left over a shaker for 30 min at room temperature. The support was then filtered, washed thoroughly with DMF (4 × 10 mL), MeCN (4 × 10 mL), and diethyl ether (2 × 10 mL), and dried in vacuo. Subsequently, the capping followed by washing steps, as mentioned above, was

dx.doi.org/10.1021/bc200610u | *Bioconjugate Chem.* 2012, 23, 664−670

repeated to block residual hydroxyl groups. The fully functionalized support **5** was dried and stored at 4 °C.

Synthesis, Purification, and Characterization of Oligonucleotide Sequences. A number of oligonucleotide sequences were synthesized on the engineered support **5** as well as the standard polymer supports. Labeled oligomers were synthesized by performing the last coupling with the label-phosphoramidite in an analogous manner the normal nucleoside−phosphoramidites were coupled. Synthesis was carried out at 0.2 μmol on Pharmacia Gene Assembler Plus following the standard protocol supplied by the manufacturer.[38] After synthesis, oligomers assembled on unmodified supports were fully deprotected using 30% ammonium hydroxide at 60 °C for 16 h, while the oligomers synthesized on support **5** were deprotected in a two-step protocol. The first step comprises treatment of support bound oligonucleotide with a solution of 1,8-diazabicycloundec-7-ene (0.5 M in THF, 0.5 mL) for 2 h at room temperature followed by concentration in vacuo. In the second step, the residue was dissolved in aqueous ammonia (30%, 1 mL) and kept at 60 °C for 16 h. Subsequently, the ammoniacal solutions were concentrated in vacuo. The residue, in each case, was dissolved in dd water (200 μL) and applied onto a reverse-phase silica gel column. After thorough washings with dd water, elution was effected by 30% acetonitrile and the fractions containing the oligomer sequence were concentrated in a speed vac. Further, these oligomers were characterized by MALDI-TOF. Purity of the oligonucleotide sequences was assessed on Agilent 1100 series HPLC system.

Buffers Used in the Study. The following buffers were used: (1) Reaction buffer: 100 mM phosphate buffer, pH 8.0. (2) Washing buffer: 100 mM phosphate-buffer-saline (PBS), pH 7.0. (3) Hybridization buffer: 100 mM phosphate buffer containing 750 mM sodium chloride, pH 7.0. (4) Capping buffer: 0.5 M 2-Mercaptoethanol in 100 mM PBS, pH 8.0.

Epoxy-Functionalized Glass Microslides. Unmodified glass microslides were functionalized following the standard procedure from our laboratory.[27]

Determination of Threshold pH Required for Immobilization of Carboxyalkyl-Modified Oligonucleotides. In order to determine the optimal pH to immobilize 3′-carboxyalkyl-modified oligonucleotides onto epoxy-glass microslide, a 20mer-oligomer, TET-d(GTC AAG ATT CAG TTC TTC AT)-OPO_3-$(CH_2)_3$COOH, was dissolved in buffers of different pH (5−12) and spotted (0.5 μL) manually onto epoxy-microslide at 5 μM concentration. The slide was kept in a humidified chamber at 55 °C for 2 h followed by sequential washings with the washing buffer (4 × 20 mL) and water (2 × 20 mL). After drying the slide under vacuum, it was subjected to visualization under a microarray laser scanner.

Determination of Threshold Concentration of Oligonucleotides Required for Visualization of Fluorescent Spots on Epoxy-Functionalized Microslide. A serially diluted oligomer sequence, TET-d(GTC AAG ATT CAG TTC TTC AT)-OPO_3-$(CH_2)_3$COOH, dissolved in the reaction buffer (40, 20, 10, 5, 2.5 μM), was spotted onto epoxy-functionalized glass microslide and the slide incubated at 55 °C for 2 h in a humidified environment. Subsequently, the slide was washed with the washing buffer (3 × 20 mL), followed by water (2 × 20 mL), and after drying, the spots were visualized under a laser scanner.

Determination of Threshold Time and Temperature Required for Efficient Immobilization of 3′-Carboxyalkyl-Modified Oligonucleotides onto Epoxy-Glass Microslide. Oligomer sequence, TET-d(GTC AAG ATT CAG TTC TTC AT)-OPO_3-$(CH_2)_3$COOH, was dissolved in the reaction buffer and spotted at 5 μM concentration in duplicates onto epoxy-functionalized glass microslides. The microslides were kept in a humidified environment at 35 °C for different time intervals (60, 120, 180, 240, 300, 360, 420, 480, 540, and 960 min). After the stipulated time, slides were subjected to processing as described above. Similarly, time kinetics were also carried out at 45, 55, and 65 °C.

Detection of Base Mismatches through Hybridization Assay. The specificity of the projected system was shown by hybridizing the immobilized carboxyalkyl-modified oligonucleotides (with zero and single mismatch and noncomplementary to target) with a TET-labeled complementary target oligonucleotide sequence (complementary to zero mismatched probe). Three oligonucleotide sequences, viz., d(TTG CCA GGT AAC ACG CGT GT)-OPO_3-$(CH_2)_3$COOH, d(TTG CCA GGT TAC ACG CGT GT)-OPO_3-$(CH_2)_3$COOH, and d(CTG AAC CTG TCA GCG GGT AT)-OPO_3-$(CH_2)_3$COOH, were immobilized following the protocol described above. After the usual processing, the residual epoxy groups were blocked by the treatment of the capping buffer at 55 °C for 30 min. Subsequently, the slide was washed with the washing buffer (3 × 20 mL) and subjected to hybridization with a labeled complementary target sequence, TET-d(ACA CGC GTG TTA CCT GGC AA), dissolved in the hybridization buffer (30 μM, 50 μL), following the reported procedure.[24] After washings with the hybridization buffer (3 × 20 mL), the slide was scanned under a laser scanner and the fluorescence intensity of the spots quantified.

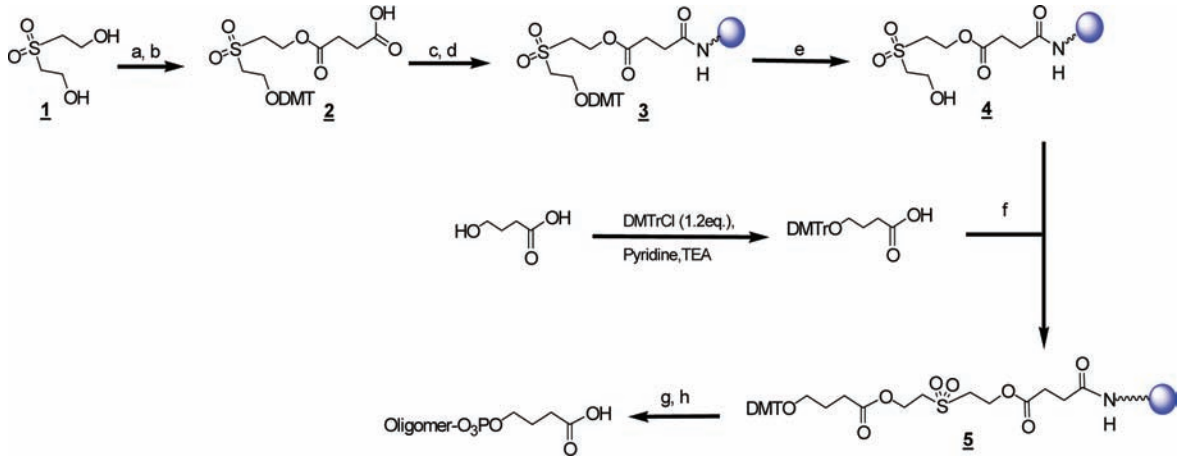
Detection of Human Bacterial Meningitis. *PCR Amplification.* PCR was carried out in 25 μL PCR tube containing 0.25 mM dNTPs, forward primer [TET-d(CAC AAA GCT GCC AAA CAC AT)], reverse primer [TET-d(GAA GCG TAT GCT TGG TGG TT)], genomic DNA (50 ng/reaction), *taq* polymerase (0.75 units), and Milli-Q water. Reactions were carried out on Bio-Rad (M.J.) Thermal Cycler using the following profile: (i) 5 min at 95 °C, initial denaturation step; (ii) 35 cycles of 1 min at 95 °C, denaturation step; 40 s at 61.6 °C, annealing step; 2 min at 72 °C, extension step; (iii) 7 min at 72 °C, final extension step; hold temperature, 4 °C. The labeled PCR amplicon, 304 bp fragment of *opc* gene, was analyzed on agarose gel electrophoresis and detected by ethidium bromide (10 μg/mL) in the standard TAE buffer, pH 8.

Hybridization with PCR Amplicons. Two probe sequences, viz., d(CAC AAA GCT GCC AAA CAC AT)-OPO_3-$(CH_2)_3$COOH (complementary) and d(GAT TAC GCC GCT CAA ACC AC)-OPO_3-$(CH_2)_3$COOH (control, noncomplementary), were tethered onto epoxy-functionalized glass microslide, as described above. After the capping step, the spots on the microslide were exposed to denatured amplicons for hybridization following the standard procedure.[27] After the usual processing, the spots were visualized under a laser scanner.

Instrumentation and Signal Quantification. Microslides were scanned on a ScanArray Gx Plus microarray scanner (Perkin) fitted with Cy3 optical filter at 20 μm resolution. PMT gain and laser power were set at 80% and 90%, respectively. Fluorescence intensity of the spots was quantified and graphs were plotted in MS *Excel*. Each experiment was repeated at least three times and the data represent the averages of these repetitions.

dx.doi.org/10.1021/bc200610u | *Bioconjugate Chem.* 2012, 23, 664−670

Scheme 1. Preparation of Engineered Polymer Support 5 for the Synthesis of 3′-Carboxyalkyl-Modified Oligonucleotides[a]



[a]Reagents and chemicals: (a) DMTrCl/Pyridine; (b) Succinic anhydride, DMAP, TEA, EDC; (c) BTCM, DMAP, TPP; (d) 3-Aminopropyl-CPG; (e) 3% TCA in EDC; (f) HBTU, DMF/Pyridine; (g) Oligonucleotide synthesis; (h) Deprotection.

RESULTS AND DISCUSSION

The projected strategy was designed with the following points in mind: preparation of the engineered polymer support should be simple; it should not involve expensive reagents and chemicals; synthesis and deprotection should not deviate too much from the conventional steps; the immobilization procedure should be efficient and devoid of any condensing or coupling reagent; immobilization and hybridization efficiency should be high enough to visualize the spots at minimal concentration. Thus, the preparation of the engineered polymer support begins with the synthesis of monotritylated sulfonyldiethanol ($DMTrOCH_2$-$CH_2SO_2CH_2CH_2OH$) in ~82% yield from 2,2′-sulfonyldiethanol **1** and 4,4′-dimethoxytrityl chloride in pyridine under anhydrous conditions. The monotritylated compound was then reacted with succinic anhydride to generate hemisuccinate **2** in near-quantitative yield, which was coupled, in the next reaction, to 3-aminopropyl-controlled pore glass (3-AP-CPG) to generate polymer support **3**. After blocking the residual amino groups on the polymer support, 4,4′-dimethoxytrityl groups were removed from the support and the hydroxyl groups so generated on the support **4** were coupled with *O*-4,4′-dimethoxytrityl-4-hydroxybutyric acid using HBTU, as a condensing reagent, followed by capping of residual hydroxyl groups to obtain a fully functionalized polymer support **5** (Scheme 1) for solid-phase synthesis of 3′-carboxyalkyl-modified oligonucleotides.

Utility of the projected polymer support **5** was demonstrated by synthesizing a number of oligonucleotide sequences bearing 3′-carboxyalkyl groups. Syntheses were carried out at 0.2 μmol using the standard protocol on a Pharmacia Gene Assembler Plus. Fully deprotected oligonucleotides were obtained in a two-step process. In a typical experiment, support-bound oligomer sequence, d(TTT TTT TTT TTT TTT TTT TT), was treated with a solution of 1,8-diazabicycloundec-7-ene (DBU, 0.5 M in THF, 0.5 mL) for 2 h at room temperature. This resulted in the cleavage of 3′-carboxyalkyl-modified oligonucleotide from the polymer support as well as removal of β-cyanoethyl from internucleotide phosphates. The solution was concentrated and treated with ammonium hydroxide (30%) for 16 h at 60 °C, which removed the protecting groups from nucleic bases. The ammoniacal solution was collected, concentrated, and the residue dissolved in water, neutralized with acetic acid, and applied onto a reverse-phase silica gel column. The oligomer was eluted with 30% acetonitrile and concentrated in a speed vac. The desalted oligomer was analyzed on RP-HPLC. Figure 1a shows the elution profile of d(TTT TTT TTT TTT TTT TTT TT)-OPO_3-$(CH_2)_3COOH$, which was further characterized by MALDI-TOF (m/z: 6212.3, M+Na^+). Similarly, other oligonucleotide sequences, used in the present study, including labeled oligomers were synthesized on modified and unmodified polymer supports, deprotected, and lyophilized. A typical RP-HPLC profile of labeled oligomer, TET-d(GTC AAG ATT CAG TTC TTC AT)-OPO_3-$(CH_2)_3COOH$, is depicted in Figure 1b.

In the subsequent step, to explore the immobilization of the oligonucleotides with 3′-carboxyl group onto epoxy-activated glass microslides to fabricate oligonucleotide microarrays useful for disease diagnosis, various parameters were investigated in detail. Epoxy functions on the cleaned glass microslides were generated by the treatment of a 2% solution of 3-glycidyloxypropyltriethoxysilane (GOPTS) in toluene following the standard procedure.[27] The uniformity of epoxy-functionalization of the microslides was assessed by spotting TET-d(GTC AAG ATT CAG TTC TTC AT)-OPO_3-$(CH_2)_3COOH$, dissolved in the reaction buffer, randomly all over the surface using a 2.0 μL pipet. The average fluorescence intensity of the spots, after extensive washings with the washing buffer, was found to be in the range of ~65−69 A.U., which confirmed the uniformity of the functionalization of the microslides.

In order to arrive at the optimal pH required to tether 3′-carboxyalkylated oligomer sequence, TET-d(GTC AAG ATT CAG TTC TTC AT)-OPO_3-$(CH_2)_3COOH$, onto the epoxy-glass microslide, immobilization reaction was carried out in buffers of different pHs 5, 7, 8, 10, and 12. After usual washing and drying steps, the microslide was subjected to visualization under a microarray laser scanner. The spots corresponding to pH 8 displayed the highest fluorescence intensity (Figure 2). This could be attributed to the carboxylate-catalyzed opening of the epoxide ring, which resulted in the efficient immobilization of oligomer sequence. Lower attachment density at pH < 8 might be due to inefficient reaction of carboxyalkyl−oligonucleotides with epoxy-functionalized glass substrate. Therefore, the rest of the experiments were carried out at pH 8. Likewise, the vulnerability of epoxide ring at higher pH might be the reason for lower immobilization of carboxyalkylated

dx.doi.org/10.1021/bc200610u | *Bioconjugate Chem.* 2012, 23, 664−670

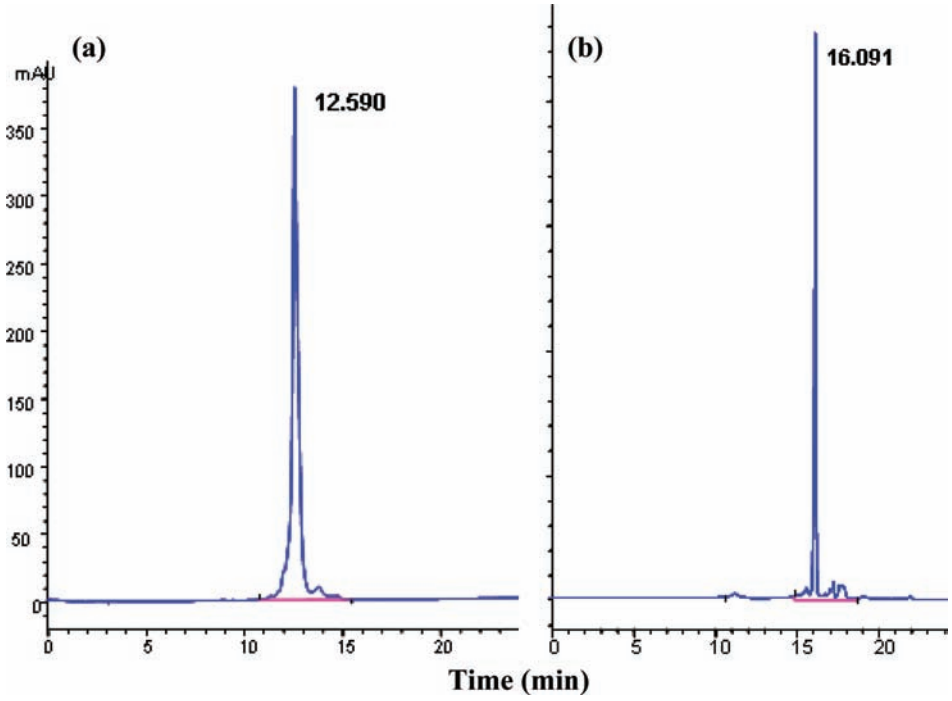


Figure 1. RP-HPLC elution profiles of (a) crude d(TTT TTT TTT TTT TTT TTT TT)-OPO_3-$(CH_2)_3$COOH and (b) crude TET-d(GTC AAG ATT CAG TTC TTC AT)-OPO_3-$(CH_2)_3$ COOH.

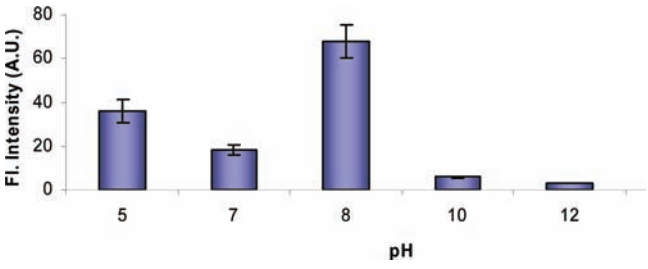


Figure 2. Immobilization of TET-d(GTC AAG ATT CAG TTC TTC AT)-OPO_3-$(CH_2)_3$ COOH onto epoxy-functionalized glass microslide under different pH conditions.

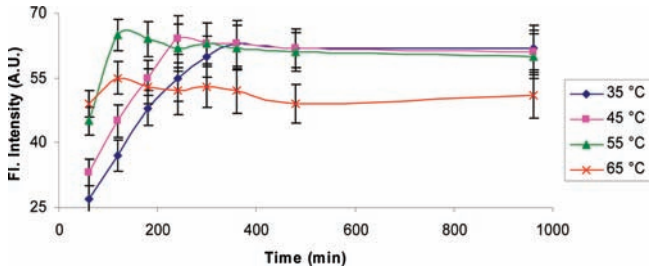


Figure 3. Time kinetics to determine threshold time required for immobilization of TET-d(GTC AAG ATT CAG TTC TTC AT)-OPO_3-$(CH_2)_3$ COOH onto epoxy-functionalized glass microslides at different temperatures (35, 45, 55, and 65 °C).

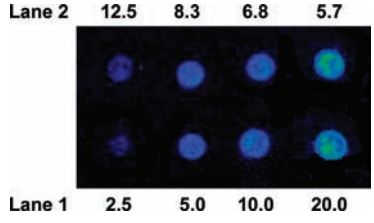


Figure 4. Optimal concentration of TET-d(GTC AAG ATT CAG TTC TTC AT)-OPO_3-$(CH_2)_3$ COOH required to visualize fluorescent spots under microarray laser scanner. Lane 1: Concentration of probe sequence (μM); Lane 2: Immobilization efficiency (%).

oligonucleotides that resulted in the poor fluorescence of the spots.

To determine the threshold time, temperature, and concentration required for immobilization and visualization of the immobilized oligomers, kinetic studies were undertaken. Oligomer sequence TET-d(GTC AAG ATT CAG TTC TTC AT)-OPO_3-$(CH_2)_3$COOH was spotted in duplicate onto epoxy-functionalized microslides at 5 μM concentration and the slides kept in a humidified chamber inside an incubator at 35 °C. Slides, withdrawn at regular time intervals (120, 180, 240, 300, 360, 480, and 960 min), were washed, dried, and scanned under a microarray scanner. Similarly, microslides were spotted with the oligomer, kept at different temperatures (45, 55, and 65 °C), withdrawn at the same time intervals, processed as described in the Experimental Procedures, and scanned under a scanner. Scanning followed by quantification results showed that reaction between epoxy function and 3′-carboxyalkylated oligomer completes in 360 min at 35 °C, 240 min at 45 °C, and 120 min at 55 and 65 °C (Figure 3). However, at 65 °C, the fluorescence intensity of the spots decreased considerably, which might be due to partial deactivation of epoxy groups on the microslides at this temperature. Therefore, immobilization reactions were performed at 55 °C for 2 h in the rest of the experiments. In a similar fashion, threshold concentration required for visualization of spots was determined by spotting serially diluted (20, 10, 5, 2.5, and 1.25 μM) oligomer sequence on the epoxy-functionalized microslide for 2 h at 55 °C. After washings and drying, the microslide was subjected to laser scanning, and the spots, visualized under a laser scanner, showed a pattern of

dx.doi.org/10.1021/bc200610u | *Bioconjugate Chem.* 2012, 23, 664–670

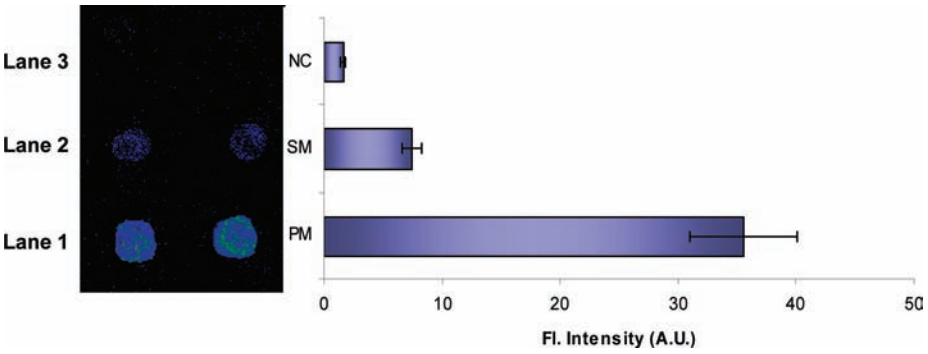


Figure 5. Detection of base mismatch with quantitative data analysis. Probe sequences, viz., d(TTG CCA GGT AAC ACG CGT GT)-OPO_3-$(CH_2)_3$COOH (Lane 1), d(TTG CCA GGT TAC ACG CGT GT)-OPO_3-$(CH_2)_3$COOH (Lane 2), and d(CTG AAC CTG TCA GCG GGT AT)-OPO_3-$(CH_2)_3$COOH (Lane 3), were immobilized onto epoxy-functionalized glass microslide and hybridized with TET-d(ACA CGC GTG TTA CCT GGC AA) followed by image capturing under microarray laser scanner.

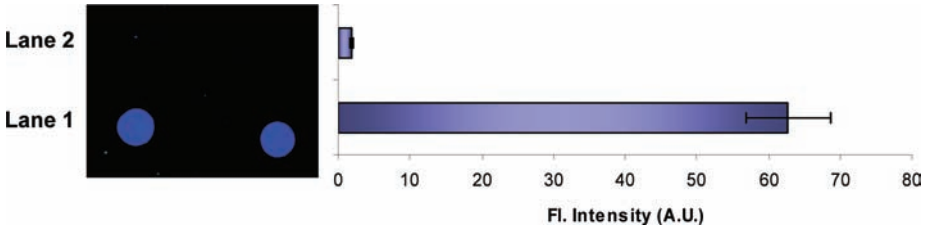


Figure 6. Detection of human bacterial meningitis. Lane 1: Probe sequence, d(CAC AAA GCT GCC AAA CAC AT)-OPO_3-$(CH_2)_3$COOH [*m/z* 6236.5 ($M+Na^+$)]. Lane 2: Control probe, d(GAT TAC GCC GCT CAA ACC AC)-OPO_3-$(CH_2)_3$COOH [6217.7 ($M+Na^+$)].

increasing fluorescence upon increasing the concentration of immobilized probe. However, spots pertaining to concentration 5 μM were sufficiently visible (Figure 4); therefore, the same concentration was used for all the studies.

In order to demonstrate the specificity of the strategy, a base mismatch study was performed by immobilizing three 3′-carboxyalkyl-modified probes (containing zero and single mismatch and a noncomplementary) onto epoxy-functionalized glass microslides. After usual processing, the microslide was subjected to hybridization with a labeled complementary target (complementary to zero mismatch probe). After washings and drying, the microslide was scanned and the results revealed that spots corresponding to perfectly matched duplex displayed the highest fluorescence, while single mismatched-duplex exhibited significantly low fluorescence and the spots corresponding to noncomplementary probe did not show any significant fluorescent signals (Figure 5).

Further, to validate the projected strategy, a microarray was fabricated using a unique probe sequence of the meningitis gene (*opc*) and a noncomplementary probe as a control. Hybridization of immobilized spots with labeled PCR amplicons, followed by washings and scanning under a microarray laser scanner, resulted in the image shown in Figure 6. Spots corresponding to *opc* gene of bacterial meningitis showed fluorescence, while no such signals were obtained in the spots corresponding to control probe signifying the specificity of the system to prepare biochips for the detection of human bacterial meningitis and other diseases.

CONCLUSIONS

In conclusion, we have demonstrated the utility of the engineered polymer support for the solid-phase synthesis of 3′-carboxyalkyl-modified oligonucleotides. These modified oligonucleotides were then used to construct microarrays for base mismatch study and detection of human infectious disease, meningitis. The projected strategy can be used not only for preparation of microarrays (biochips), but also for making conjugates for various biological applications.

AUTHOR INFORMATION

Corresponding Author

*Dr. P. Kumar: Tel. +91 11 27662491; Fax +91 11 27667471; E-mail: pkumar@igib.res.in. Dr. K. C. Gupta: Tel. +91 522 2621856; Fax +91 522 2628227; E-mail: kcgupta@igib.res.in; kcgupta@iitr.res.in.

Notes

The authors declare no competing financial interest.

ACKNOWLEDGMENTS

Authors thank Dr. Shashi Khare, National Centre for Disease Control (NCDC), Delhi, India, for providing bacterial meningitis samples and facilities. One of the authors, S.K.D., gratefully acknowledges UGC, New Delhi, for the award of Junior Research Fellowship.

REFERENCES

(1) Sanghvi, Y. S. (2001) A status update of modified oligonucleotides for chemotherapeutics applications. In *Current Protocols in Nucleic Acid Chemistry*, Chapter 4, Unit 4.1; J. Wiley: New Jersey.

(2) Hughes, R. A., Miklos, A. E., and Ellington, A. D. (2011) Gene synthesis: Methods and applications. *Methods Enzymol. 498*, 277−309.

(3) Kuwahara, M., and Sugimoto, N. (2010) Molecular evolution of functional nucleic acids with chemical modifications. *Molecules 9*, 5423−5444.

(4) Singh, Y., Murat, P., and Defranque, E. (2010) Recent developments in oligonucleotides conjugation. *Chem. Soc. Rev. 39*, 2054−2070.

(5) Zatsepin, T. S., and Oretskaya, T. S. (2004) Synthesis and applications of oligonucleotides-carbohydrate conjugates. *Chem. Biodivers. 1*, 1401−1417.
(6) Beaucage, S. L. (2008) Solid-phase synthesis of siRNA oligonucleotides. *Curr. Opin. Drug Discover. Dev. 11*, 203−216.
(7) Pon, R. T. (2001) Solid-phase supports for oligonucleotide synthesis. In *Current Protocols in Nucleic Acid Chemistry*, Chapter 3, Unit 3.1; J. Wiley: New Jersey.
(8) Vaijayanthi, B., Kumar, P., Ghosh, P. K., and Gupta, K. C. (2003) Recent advances in oligonucleotide synthesis and their applications. *Ind. J. Biochem. Biophys. 40*, 377−391.
(9) Marshall, A., and Hodgson, J. (1998) DNA chips: An array of possibilities. *Nat. Biotechnol. 16*, 27−31.
(10) Ramsay, G. (1998) DNA chips: State-of-the art. *Nat. Biotechnol. 16*, 40−44.
(11) Pirrung, M. C. (2002) How to make a DNA chip. *Angew. Chem. Int. Engl. 41*, 1276−1289.
(12) Beaucage, S. L. (2001) Strategies in the preparation of DNA oligonucleotide arrays for diagnostic applications. *Curr. Med. Chem. 8*, 1213−1244.
(13) Sethi, D., Gandhi, R. P., Kumar, P., and Gupta, K. C. (2009) Chemical strategies for immobilization of oligonucleotides. *Biotech. J. 4*, 1513−1529.
(14) Broude, N. E., Woodward, K., Cavallo, R., Cantor, C. R., and Englert, D. (2001) DNA microarrays with stem-loop DNA probes: Preparation and applications. *Nucleic Acids Res. 29*, e92.
(15) Mahajan, S., Kumar, P., and Gupta, K. C. (2006) Oligonucleotide microarrays: Immobilization of phosphorylated oligonucleotides on epoxylated surface. *Bioconjugate Chem. 17*, 1184−1189.
(16) Mahajan, S., Kumar, P., and Gupta, K. C. (2006) An efficient and versatile approach for the construction of oligonucleotide microarrays. *BioMed. Chem. Lett. 16*, 5654−5658.
(17) Sethi, D., Kumar, A., Gupta, K. C., and Kumar, P. (2008) A facile method for the construction of oligonucleotides microarrays. *Bioconjugate Chem. 19*, 2136−2143.
(18) Sethi, D., Kumar, A., Gandhi, R. P., Kumar, P., and Gupta, K. C. (2010) New protocol for oligonucleotide microarray fabrication using SU-8 coated glass microslides. *Bioconjugate Chem. 21*, 1703−1708.
(19) Kumar, A., Larsson, O., Parodi, D., and Liang, Z. (2000) Silanized nucleic acids: A general platform for DNA immobilization. *Nucleic Acids Res. 28*, e71.
(20) Kamisetty, N. K., Pack, S. P., Nonogawa, M., Yamada, K., Yoshido, Y., Kodaki, T., and Makino, K. (2009) Stabilization of the immobilized linkers and DNA probes for DNA microarray fabrication by end-capping of the remaining unreacted silanol on the glass. *J. Biotechnol. 140*, 242−245.
(21) Preininger, C., Sauer, U., Dayteg, J., and Pichler, R. (2005) Optimizing processing parameters for signal enhancement of oligonucleotide and protein arrays on ARChip epoxy. *Bioelectrochemistry 67*, 155−162.
(22) Pack, S. P., Kamisetty, N. K., Nonogawa, M., Devarayapalli, K. C., Ohtani, K., Yamada, K., Yoshida, Y., Kodaki, T., and Makino, K. (2007) Direct immobilization of DNA oligomers onto the amine-functionalized glass surface for DNA microarray fabrication through the activation-free reaction of oxanine. *Nucleic Acids Res. 35*, e110.
(23) Lockett, M. R., Phillips, M. F., Jarecki, J. L., Peelen, D., and Smith, L. M. (2008) A tetrafluorophenyl activated ester self-assembled monolayer for immobilization of amine-modified oligonucleotides. *Langmuir 24*, 69−75.
(24) Rogers, Y.-H., Jiang-Baucom, P., Huang, Z.-J., Bogdanov, V., Anderson, S., and Boyce-Jacino, M. T. (1999) Immobilization of oligonucleotides onto a glass support via disulfide bonds: A method for preparation of DNA microarrays. *Anal. Biochem. 266*, 23−30.
(25) Nonglaton, G., Benitez, I. O., Guisle, I., Pipelier, M., Léger, J., Dubreuil, D., Tellier, C., Talham, D. R., and Bujoli, B. (2004) New approach to oligonucleotide microarrays using zirconium phosphonate-modified surfaces. *J. Am. Chem. Soc. 126*, 1497−1502.
(26) Mahajan, S., Sethi, D., Seth, S., Kumar, A., Kumar, P., and Gupta, K. C. (2009) Construction of oligonucleotides microarrays (biochips) via thioether linkage for the detection of bacterial meningitis. *Bioconjugate Chem. 20*, 1703−1710.
(27) Sethi, D., Patnaik, S., Kumar, A., Gandhi, R. P., Gupta, K. C., and Kumar, P. (2009) Polymer supported synthesis of aminooxyalkylated oligonucleotides, and some applications in the fabrication of microarrays. *Bioorg. Med. Chem. 17*, 5442−5450.
(28) Mahajan, S., Kumar, P., and Gupta, K. C. (2006) S-(4,4′-Dimethoxytrityl)-3-mercaptopropionic acid, an efficient reagent for estimation of epoxy functionalities on microslides used for biochips. *Anal. Biochem. 353*, 299−301.
(29) Hart, C. A., and Rogers, T. R. F. (1993) Meningococcal disease. *J. Med. Microbiol. 39*, 3−25.
(30) Gray, L. D., and Fedorko, D. P. (1992) Laboratory diagnosis of bacterial meningitis. *Clin. Microbiol. Rev. 5*, 130−145.
(31) Jarvinen, A., Laakso, S., Piiparinen, P., Aittakorpi, A., Lindfors, M., Huopaniemi, L., Piiparinen, H., and Mäki, M. (2009) Rapid identification of bacterial pathogens using a PCR and microarray-based assay. *BMC Microbiol. 9*, 1−16.
(32) Patel, M. K., Solanki, P. R., Seth, S., Gupta, S., Khare, S., Malhotra, B. D., and Kumar, A. (2009) *ctrA* gene based electrochemical DNA sensor for detection of meningitis. *Electrochem. Commun. 11*, 969−973.
(33) Patel, M. K., Solanki, P. R., Khare, S., Gupta, S., Malhotra, B. D., and Kumar, A. (2010) Electrochemical DNA sensor for *Neisseria meningitidis* detection. *Biosens. Bioelectron. 25*, 2586−2591.
(34) Filippis, I., Nascimento, C. R. S., Clementino, M. B. M., Sereno, A. B., Rebelo, C., Souza, N. N. F., and Riley, L. W. (2005) Rapid detection of *Neisseria meningitidis* in cerebro-spinal fluid by one-step polymerase chain reaction of the *nspA* gene. *Diagn. Microbiol. Infect. Dis. 51*, 85−90.
(35) Fraiser, C., Stor, R., Tenebray, B., Sanson, Y., and Nicolas, P. (2009) Use of a new single multiplex PCR based assay for direct simultaneous characterization of six *N. meningitidis* serogroups. *J. Clin. Microbiol. 47*, 2662−2666.
(36) Kumar, A., Asha, D., Singh, S., and Khare, S. (2011) *opc* gene as a specific genetic marker for human bacterial meningitis. *J. Biosci. Medicine 1*, 1−4.
(37) Yoo, D. J., and Greenberg, M. M. (1995) Synthesis of oligonucleotides containing 3′-alkyl carboxylic acids using universal, photolabile solid phase synthesis supports. *J. Org. Chem. 60*, 3358−3364.
(38) *LKB Gene Assembler Plus Manual*(1988) Pharmacia, Uppsala, Sweden.